GEOTECHNICAL SPECIAL PUBLICATION NO. 181

GEOTECHNICAL EARTHQUAKE ENGINEERING AND SOIL DYNAMICS IV

PROCEEDINGS OF THE CONFERENCE

May 18–22, 2008
Sacramento, California

SPONSORED BY
The Geo-Institute of the American Society of Civil Engineers

EDITED BY
David Zeng
Majid T. Manzari
Dennis R. Hiltunen

Published by the American Society of Civil Engineers

GEOTECHNICAL SPECIAL PUBLICATION NO. 181

GEOTECHNICAL EARTHQUAKE ENGINEERING AND SOIL DYNAMICS IV

PROCEEDINGS OF THE CONFERENCE

May 18–22, 2008
Sacramento, California

SPONSORED BY
The Geo-Institute of the American Society of Civil Engineers

EDITED BY
David Zeng
Majid T. Manzari
Dennis R. Hiltunen

Published by the American Society of Civil Engineers

Copyright and Disclaimer

ISBN: 978-0-7844-0975-6

Any statements expressed in these materials are those of the individual authors and do not necessarily represent the views of ASCE, which takes no responsibility for any statement made herein. No reference made in this publication to any specific method, product, process or service constitutes or implies an endorsement, recommendation, or warranty thereof by ASCE. The materials are for general information only and do not represent a standard of ASCE, nor are they intended as a reference in purchase specifications, contracts, regulations, statutes, or any other legal document.

ASCE makes no representation or warranty of any kind, whether express or implied, concerning the accuracy, completeness, suitability, or utility of any information, apparatus, product, or process discussed in this publication, and assumes no liability therefore. This information should not be used without first securing competent advice with respect to its suitability for any general or specific application. Anyone utilizing this information assumes all liability arising from such use, including but not limited to infringement of any patent or patents.

Copyright © 2008 by the American Society of Civil Engineers.
All Rights Reserved.

ASCE and American Society of Civil Engineers—Registered in U.S. Patent and Trademark Office.

Photocopies and reprints.
You can obtain instant permission to photocopy ASCE publications by using ASCE's online permission service (www.pubs.asce.org/authors/RightslinkWelcomePage.html). Requests for 100 copies or more should be submitted to the Reprints Department, Publications Division, ASCE, (address above); email: permissions@asce.org. A reprint order form can be found at www.pubs.asce.org/authors/reprints.html.

American Society of Civil Engineers
ASCE International Headquarters
1801 Alexander Bell Drive
Reston, VA 20191-4400 USA

Call Toll-Free in the U.S.: 1-800-548-2723 (ASCE)
Call from anywhere in the world: 1-703-295-6300
Internet: http://www.pubs.asce.org

Preface

The papers contained in this publication were prepared for presentation in GEESD IV, the 4th decennial Geotechnical Earthquake Engineering and Soil Dynamics Conference organized by the EESD Committee of the ASCE Geo-Institute. GEESD IV follows the highly successful GEESD conferences in Seattle, Washington (1998); Park City, Utah (1988); and Pasadena, California (1978). The conference covers a broad field of topics in soil dynamics and geotechnical earthquake engineering, including engineering seismology, dynamic material properties, geophysical methods, SASW benchmarking, site response, liquefaction, ground improvement, embankment dams, tailings dams, landfills, levees, lifelines and networks, mapping and zoning, NEESR research, numerical modeling, piers and wharves, retaining structures, foundation dynamics, soil-structure interaction, stability of natural slopes, and surface fault rupture.

The organizing committee invited nine outstanding keynote speakers and ten theme lecturers to present papers on developments in important areas of geotechnical earthquake engineering. The committee reviewed over 400 abstracts and 260 papers. The papers received undergo a peer review before being accepted. The standards for the peer review followed those required for ASCE Geotechnical Special Publications. Each paper must receive two positive reviews to be accepted and must be revised to conform to the mandatory revisions of the reviewers. Due to a tight schedule, there was not enough time for more than one cycle of review and revision. In the end, 234 papers were accepted for publication. All the papers are eligible for discussion in the ASCE Journal of Geotechnical and Geoenvironmental Engineering and for ASCE awards.

The paper review would have been impossible without the help of a group of lead reviewers, who, on behalf of the Proceedings and Publications Committee, organized and in some cases conducted the review of a group of papers. The editors would like to acknowledge the invaluable contribution of the following lead reviewers:

Pedro Arduino
Scott Brandenberg
William Frasier
Laureano Hoyos
Amir Kaynia
Xiang-Song Li
Gopal Madabhushi
George Mylonakis
Adrian Rodriguez-Marek
Brent Rosenblad
Usama. El Shamy
Joseph Wartman
Liping Yan
E. Zhai
Dominic Assimaki
Mandar Dewoolkar
Russell Green
Tom Holzer
Mike Kalinski
Jeen-Sheng Lin
N. Matasovic
Soheil Nazarian
Ellen Rathje
Raj Siddharthan
Mingjian Tao
Yu-Hsing Wang
Bill Yu
Ariyaputhirar Balakrishnan
Ali Eliadorani
Yousef Hashash
Boris Jeremic
James N. Lee
Hoe I. Ling
Jorge Meneses
Ronald Pak
Kyle Rollins
Mike Sharp
Thusyanthan
Jerry Wu
Mourad Zeghal

The lead reviewers were helped by the following highly qualified reviewers in the review process:

F. Abedzadeh
Carlos Amante
Ralph Archuleta
Rajendram Arulnathan
George Athanasopoulos
Ariya Balakrishnan
James Bay
Jon Bischoff
David M. Boore
Scott J. Brandenberg
Billy Camp
Kemal Önder Çetin
Qimin Chen
Daniel B. Chu
Brady Cox
Craig A. Davis
Jeffrey S. Dingrando
Allison Faris
Keyvan Fotoohi
M. Ghannad
Robert Goughnour
Brian Greene
Kate Gunberg
Tarik Hadj-Hamou
Youssef Hashash
Bruce Hilton
Laureano Hoyos
Mahadevan Ilankatharan
Hsein Juang
Thangalingam Kanagalingam
Stephanie A. King
Ramachandran Kulasingam
Christian Ledezma
X.S. Li
Nina Liu
Barbara Luke
Nicolas Malasavage
Neven Matasovic
Claudia Medina
H.Y. Ming
Kanthasamy K. Muraleetharan
Erfan Nezami
Ronald Pak
Achilleas Papadimitriou
Bashar Alramahi
Donald Anderson
Pedro Arduino
Dominic Assimaki
Laurie Baise
Paola Bandini
Michael Beaty
Antonio Bobet
Ross Boulanger
Andrew Brennan
Antonio Carraro
C. Yoga Chandran
Xin Chen
Ulas Cilingir
Karina Dahl
Anirban De
Jiwei Duan
Americo Fernandez
Mahmoud El Gamal
James Gingery
Vladimir Grazier
Nenad Gucunski
Marte Gutierrez
Stuart Haigh
Chunmei He
Sahadat Hossain
Roman Hryciw
Allen Jones
Michael Kalinski
Pirooz Kashighandi
Tadahiro Kishida
Dominik Lang
Jong-Sub Lee
Chi-Tseng Ted Liu
Yan Liu
Alan J. Lutenegger
Erik Malvick
John McCartney
Jorge Meneses
Robb E. Moss
George Mylonakis
Guney Olgun
Aasha Pancha
Aris Papadopoulos
Jorge Alva
Scott Anderson
Richie Armstrong
Adda Athanasopoulos
Jack Baker
Steven F. Bartlett
Victoria Bennet
Fabian Bonilla
Aaron Bradshaw
Peter M. Byrne
Gonzalo Castro
Nien Chang
Deepankar Choudhury
Ryan Cole
Panos Dakoulas
Christopher M. Dietel
Cedric Fairbanks
Jon B. P. Fletcher
Louis Ge
Eric Gottheld
Russell Green
Simon Gudina
B.B. Guzina
Curt Haselton
Greg Hempen
Jeffery Howard
Jianping Hu
Shawn O. Jones
Ronnie Kamai
Dong-Soo Kim
Alexander Kozak
Hubert Law
Anne Lemnitzer
Gang Liu
Thomas Lok
B.K. Maheshwari
Geoffrey R. Martin
Nason McCullough
Paul Michaels
Charles S. Mueller
Erik J. Newman
Rolando Orense
Miguel Pando
Duhee Park

Richard Pearce
Arben Pitarka
Anand Puppala
N. (Ravi) Ravichandran
Adrian Rodriguez-Marek
Dario Rosidi
Rodolfo B. Sancio
Hassan Sedarat
Anastasios Sextos
Lisheng Shao
Francisco Silva-Tulla
Shin-Tai Song
William J Stephenson
Luis Suez
Mahdi Taiebat
Salih Tileylioglu
Andrew Tolleson
Chi-Chin Tsai
Roberto Vasallo
Jui-pin Wang
Lei Wei
Dharma Wijewickreme
Ching-Liu Wu
J. Yang
Xinbao Yu
Dimitris Zekkos
Feng Zhang
Michael Pender
Dimitrios Pitilakis
Tong Qiu
Michael Reichle
Stefan Romanoschi
David Saftner
Marika Santagata
Hope A. Seligman
Anoosh Shamsabadi
Thevachandran Shenthan
Siva Sivathayalan
Alan Stadler
Patrick Strenk
Erwin Supranata
Payman Kahili Tehrani
John C. Tinsley, III
Aurel Trandafir
Wen Tseng
Christos Vrettos
Yu-Hsing Wang
Daniel Whang
Robert A Williams
Min-hao Wu
Zhaohui Yang
Xiong (Bill) Yu
Aspa Zerva
Jian Zhang
Zhigang Peng
Carmine Polito
Alan Rauch
Glenn Rix
Brent Rosenblad
Pijush Samui
Sireesh Saride
Kallol Sett
Usama El Shamy
Parisa Shokouhi
Darin Sjoblom
Konstantin Stamatopoulos
D. Su
Ertugrul Taciroglu
Eric Thompson
Binod Tiwari
Thaleia Travasarou
Javier Ubilla
Judith Wang
Joseph Wartman
David White
Chris J. Wills
Horng-Jyh Yang
Sungmin Yoon
Zia Zafir
Jinxing Zha
Jie Zhang

The editors would like to thank the conference chairman, Ross Boulanger, for his tireless efforts and invaluable contribution. Also, we would like to acknowledge the significant assistance by Ms. Sheana Singletary, Program Administrator of ASCE Conference and Meetings Services.

Finally, we would like to express our sincere appreciation to all the authors for their significant contributions to the success of the conference.

Xiangwu (David) Zeng
Case Western Reserve University

Majid Manzari
George Washington University

Dennis Hiltunen
University of Florida

Geotechnical Special Publications

1 *Terzaghi Lectures*
2 *Geotechnical Aspects of Stiff and Hard Clays*
3 *Landslide Dams: Processes, Risk, and Mitigation*
7 *Timber Bulkheads*
9 *Foundations & Excavations in Decomposed Rock of the Piedmont Province*
11 *Dynamic Response of Pile Foundations¥ Experiment, Analysis and Observation*
14 *Geotechnical Aspects of Karst Terrains*
15 *Measured Performance Shallow Foundations*
16 *Special Topics in Foundations*
17 *Soil Properties Evaluation from Centrifugal Models*
18 *Geosynthetics for Soil Improvement*
19 *Mine Induced Subsidence: Effects on Engineered Structures*
21 *Hydraulic Fill Structures*
22 *Foundation Engineering*
23 *Predicted and Observed Axial Behavior of Piles*
24 *Resilient Moduli of Soils: Laboratory Conditions*
25 *Design and Performance of Earth Retaining Structures*
27 *Geotechnical Engineering Congress*
28 *Detection of and Construction at the Soil/Rock Interface*
29 *Recent Advances in Instrumentation, Data Acquisition and Testing in Soil Dynamics*
32 *Embankment of Dams¥James L. Sherard Contributions*
33 *Excavation and Support for the Urban Infrastructure*
34 *Piles Under Dynamic Loads*
35 *Geotechnical Practice in Dam Rehabilitation*
37 *Advances in Site Characterization: Data Acquisition, Data Management and Data Interpretation*
39 *Unsaturated Soils*
40 *Vertical and Horizontal Deformations of Foundations and Embankments*
41 *Predicted and Measured Behavior of Five Spread Footings on Sand*
42 *Serviceability of Earth Retaining Structures*
43 *Fracture Mechanics Applied to Geotechnical Engineering*
44 *Ground Failures Under Seismic Conditions*
45 *In Situ Deep Soil Improvement*
46 *Geoenvironment 2000*
47 *Geo-Environmental Issues Facing the Americas*
48 *Soil Suction Applications in Geotechnical Engineering*
49 *Soil Improvement for Earthquake Hazard Mitigation*
50 *Foundation Upgrading and Repair for Infrastructure Improvement*
51 *Performance of Deep Foundations under Seismic Loading*
52 *Landslides under Static and Dynamic Conditions¥Analysis, Monitoring, and Mitigation*
53 *Landfill Closures¥Environmental Protection and Land Recovery*
54 *Earthquake Design and Performance of Solid Waste Landfills*
55 *Earthquake-Induced Movements and Seismic Remediation of Existing Foundations and Abutments*
56 *Static and Dynamic Properties of Gravelly Soils*
57 *Verification of Geotechnical Grouting*
58 *Uncertainty in the Geologic Environment*
59 *Engineered Contaminated Soils and Interaction of Soil Geomembranes*
60 *Analysis and Design of Retaining Structures Against Earthquakes*
61 *Measuring and Modeling Time Dependent Soil Behavior*
62 *Case Histories of Geophysics Applied to Civil Engineering and Public Policy*
63 *Design with Residual Materials: Geotechnical and Construction Considerations*
64 *Observation and Modeling in Numerical Analysis and Model Tests in Dynamic Soil-Structure Interaction Problems*
65 *Dredging and Management of Dredged Material*
66 *Grouting: Compaction, Remediation and Testing*
67 *Spatial Analysis in Soil Dynamics and Earthquake Engineering*
68 *Unsaturated Soil Engineering Practice*
69 *Ground Improvement, Ground Reinforcement, Ground Treatment: Developments 1987-1997*
70 *Seismic Analysis and Design for Soil-Pile-Structure Interactions*
71 *In Situ Remediation of the Geoenvironment*
72 *Degradation of Natural Building Stone*
73 *Innovative Design and Construction for Foundations and Substructures Subject to Freezing and Frost*

74 *Guidelines of Engineering Practice for Braced and Tied-Back Excavations*
75 *Geotechnical Earthquake Engineering and Soil Dynamics III*
76 *Geosynthetics in Foundation Reinforcement and Erosion Control Systems*
77 *Stability of Natural Slopes in the Coastal Plain*
78 *Filtration and Drainage in Geotechnical/Geoenvironmental Engineering*
79 *Recycled Materials in Geotechnical Applications*
80 *Grouts and Grouting: A Potpourri of Projects*
81 *Soil Improvement for Big Digs*
82 *Risk-Based Corrective Action and Brownfields Restorations*
83 *Design and Construction of Earth Retaining Systems*
84 *Effects of Construction on Structures*
85 *Application of Geotechnical Principles in Pavement Engineering*
86 *Big Digs Around the World*
87 *Jacked Tunnel Design and Construction*
88 *Analysis, Design, Construction, and Testing of Deep Foundations*
89 *Recent Advances in the Characterization of Transportation Geo-Materials*
90 *Geo-Engineering for Underground Facilities*
91 *Special Geotechnical Testing: Central Artery/Tunnel Project in Boston, Massachusetts*
94 *Performance Confirmation of Constructed Geotechnical Facilities*
95 *Soil-Cement and Other Construction Practices in Geotechnical Engineering*
96 *Numerical Methods in Geotechnical Engineering: Recent Developments*
97 *Innovations and Applications in Geotechnical Site Characterization*
98 *Pavement Subgrade, Unbound Materials, and Nondestructive Testing*
99 *Advances in Unsaturated Geotechnics*
100 *New Technological and Design Developments in Deep Foundations*
101 *Slope Stability 2000*
102 *Trends in Rock Mechanics*
103 *Advances in Transportation and Geoenvironmental Systems Using Geosynthetics*
104 *Advances in Grouting and Ground Modification*
105 *Environmental Geotechnics*
106 *Geotechnical Measurements: Lab & Field*
107 *Soil Dynamics and Liquefaction 2000*
108 *Use of Geophysical Methods in Construction*
109 *Educational Issues in Geotechnical Engineering*
110 *Computer Simulation of Earthquake Effects*
111 *Judgment and Innovation: The Heritage and Future of the Geotechnical Engineering Profession*
112 *Soft Ground Technology*
114 *Soils Magic*
115 *Expansive Clay Soils and Vegetative Influence on Shallow Foundations*
116 *Deep Foundations 2002: An International Perspective on Theory, Design, Construction, and Performance*
117 *Discrete Element Methods: Numerical Modeling of Discontinua*
118 *A History of Progress: Selected U.S. Papers in Geotechnical Engineering*
119 *Soil Behavior and Soft Ground Construction*
120 *Grouting and Ground Treatment*
121 *Probabilistic Site Characterization at the National Geotechnical Experimentation Sites*
122 *Sinkholes and the Engineering and Environmental Impacts of Karst*
123 *Recent Advances in Materials Characterization and Modeling of Pavement Systems*
124 *GeoSupport 2004: Drilled Shafts, Micropiling, Deep Mixing, Remedial and Specialty Foundation Systems*
125 *Current Practices and Future Trends in Deep Foundations*
126 *Geotechnical Engineering for Transportation Projects*
127 *Recycled Materials in Geotechnics*
128 *Soil Constitutive Models: Evaluation, Selection, and Calibration*
129 *Advances in Designing and Testing Deep Foundations*
130 *Advances in Pavement Engineering*
131 *Contemporary Issues in Foundation Engineering*
132 *Advances in Deep Foundations: In Memory of Michael W. O'Neill*
133 *Earthquake Engineering and Soil Dynamics*
134 *Soil Dynamics Symposium in Honor of Professor Richard D. Woods*
135 *Erosion of Soils and Scour of Foundations*
136 *Innovations in Grouting and Soil Improvement*

137 ***Legal and Liability Issues in Geotechnical Engineering***
138 ***Site Characterization and Modeling***
139 ***Calibration of Constitutive Models***
140 ***Slopes and Retaining Structures under Seismic and Static Conditions***
141 ***International Perspectives on Soil Reinforcement Applications***
142 ***Waste Containment and Remediation***
143 ***Geomechanics: Testing, Modeling, and Simulation***
144 ***Sinkholes and the Engineering and Environmental Impacts of Karst***
145 ***Seismic Performance and Simulation of Pile Foundations in Liquefied and Laterally Spreading Ground***
146 ***Asphalt Concrete: Simulation, Modeling and Experimental Characterization***
147 ***Unsaturated Soils 2006***
148 ***Advances in Unsaturated Soil, Seepage, and Environmental Geotechnics***
149 ***Site and Geomaterial Characterization***
150 ***Soil and Rock Behavior and Modeling***
151 ***Advances in Earth Structures: Research to Practice***
152 ***Ground Modification and Seismic Mitigation***
153 ***Foundation Analysis and Design: Innovative Methods***
154 ***Pavement Mechanics and Performance***
155 ***Underground Construction and Ground Movement***
156 ***Geomechanics II: Testing, Modeling, and Simulation***
157 ***Computer Applications in Geotechnical Engineering***
158 ***Contemporary Issues in Deep Foundations***
159 ***Case Studies in Earth Retaining Structures***
160 ***Dynamic Response and Soil Properties***
161 ***Embankments, Dams, and Slopes: Lessons from the New Orleans Levee Failures and Other Issues***
162 ***Problematic Soils and Rocks and In Situ Characterization***
163 ***Geoenvironmental Engineering***
164 ***Innovative Applications of Geophysics in Civil Engineering***
165 ***Geosynthetics in Reinforcement and Hydraulic Applications***
166 ***Educational Activities in Geotechnical Engineering***
167 ***Geotechnics of Soil Erosion***
168 ***Grouting for Ground Improvement: Innovative Concepts and Applications***
169 ***Soil and Material Inputs for Mechanistic-Empirical Pavement Design***
170 ***Probabilistic Applications in Geotechnical Engineering***
171 ***Advances in Shallow Foundations***
172 ***Soil Improvement***
173 ***Advances in Measurement and Modeling of Soil Behavior***
174 ***Designing Our Underground Space***
175 ***Field Measurements in Geomechanics 2007***
176 ***Analysis of Asphalt Pavement Materials and Systems: Emerging Methods***
177 ***GeoCongress 2008: Geotechnics of Waste Management and Remediation***
178 ***GeoCongress 2008: Geosustainability and Geohazard Mitigation***
179 ***GeoCongress 2008: Characterization, Monitoring, and Modeling of GeoSystems***
180 ***From Research to Practice in Geotechnical Engineering***

Ground Motions

Keynote—Nonlinear Seismic Ground Response Analysis: Code Usage Protocols and Verification against Vertical Array Data
Jonathan P. Stewart and Annie O. L. Kwok

Assessment of Ground Motion Selection and Modification (GMSM) Methods for Non-Linear Dynamic Analyses of Structures
Christine A. Goulet, Jennie Watson-Lamprey, Jack Baker, Curt Haselton, and Nico Luco

Identification of Near-Fault Velocity Pulses and Prediction of Resulting Response Spectra
Jack W. Baker

Preliminary Estimation of Seismically Induced Ground Strains from Spatially Variable Ground Motions
Timothy D. Ancheta, Jonathan P. Stewart, Norman A. Abrahamson, and Robert L. Nigbor

Probabilistic Use of Arias Intensity in Geotechnical Earthquake Engineering
J. K. Howard, W. A. Fraser, and M. G. Schultz

Seismic Design Criteria Ground Motions
Joe Litehiser and James E. Marrone

Seismic Hazard Analysis and Probabilistic Ground Motions in the Upper Mississippi Embayment
J. Alfredo Fernandez and Glenn J. Rix

Site Response

A Simplified Constitutive Model to Simultaneously Match Modulus Reduction and Damping Soil Curves for Nonlinear Site Response Analysis
Camilo Phillips and Youssef M. A. Hashash

Basin Effects in the Upper Mississippi Embayment
J. Alfredo Fernandez and Glenn J. Rix

Comparing Weak- and Strong-Motion Spectral Ratios at the Turkey Flat Site Effects Test Area, Parkfield, California: Possible Nonlinear Soil Behavior
Chris H. Cramer

Consequences of Solution Non-Uniqueness in Surface Wave Tests for Seismic Response Studies
Sebastiano Foti, Cesare Comina, Deniele Boiero, and Laura Valentina Socco

Developing Site-Specific Design Response Spectra for a Type F Site Due to Liquefaction
Endi Zhai

Dynamic Response of Unsaturated Non-Collapsible and Collapsible Deposits
Claudia Medina and Mourad Zeghal

Evaluation of Site Response for Deepwater Field
Fabrizio Ardoino, Chiara M. Traverso, and Eric J. Parker

Hysteretic Damping Correction and Its Effect on Non-Linear Site Response Analyses

Zhi-Liang Wang, C. Y. Chang, and C. C. Chin

Influence of Rate Dependent Soil Behavior on Propagated Ground Motion
Dong-Yup Kwak, Jae-Kwang Ahn, Duhee Park, and Youssef M. A. Hashash

Modeling Nonlinear Site Response Uncertainty in the Los Angeles Basin
Dominic Assimaki, Wei Li, Jamison M. Steidl, and Jan Schmedes

Nonlinear Shear Wave Propagation in Strain Stiffening and Strain Softening Soil
Jui-Ching Chou and Bruce Kutter

Parametric Analysis of the Seismic Response of Irregular Topographic Features
Arash Razmkhah, Mohsen Kamalian, and Roham Golrokh

Seismic Response of the San Francisco International Airport Airfield during the 1989 Loma Prieta Earthquake
Lelio H. Mejia, Jiaer Wu, Zhaohui Yang, and Jim Chiu

Site Response Analysis for Tito Scalo Area (PZ) in the Basilicata Region, Italy
Antonio Cavallaro, Salvatore Grasso, and Michele Maugeri

Site Response to Vertical Earthquake Motion
J. Yang and X. R. Yan

Spatial Analysis of Damage Distribution in the 2001 Southern Peru Earthquake
Nicholas E. Malasavage and Joseph Wartman

Strain-Dependent Soil Properties Estimated from Downhole Array Recordings at Kashiwazaki-Kariwa Nuclear Power Plant during the 2007 Niigata-Ken Chuetsu-Oki Earthquake
Kohji Tokimatsu and Ryosuke Sugimoto

The Turkey Flat Blind Prediction Experiment for the September 28, 2004 Parkfield Earthquake: Comparison with Other Turkey Flat Recordings
Hamid R. Haddadi, Anthony F. Shakal, and Charles R. Real

The Turkey Flat Blind Prediction Experiment for the September 28, 2004 Parkfield Earthquake: General Overview and Models Tested
Charles R. Real, Anthony F. Shakal, and Brian E. Tucker

Two Dimensional Evaluation of Site Effect in Rectangular Valleys
Nima Tafazzoli, Mohammad Hassan Baziar, and Habib Shahnazari

Mapping and Faulting

Theme Paper—Probabilistic Liquefaction Hazard Mapping
Thomas L. Holzer

A Deformation-Based Approach for Mapping Earthquake-Induced Liquefaction Hazard
Charles R. Real, Keith L. Knudsen, and Marvin O. Woods

A New Site Classification System Based on Strong Motion Analysis in Iran
M. R. Ghayamghamian and A. R. Nojavan

An Evaluation of Site Classification for National Strong-Motion Recording Stations in Turkey
M. A. Sandkkaya, M. T. Ylmaz, B. S. Bakr, and S. Akkar

Earthquake Loss Estimation Tool for Urban Areas
Atilla Ansal, Asli Kurtulus, and Gökce Tönük

Geological and Microtremor Survey, Damage Distribution, and Reconstruction of Muzaffarabad and Surroundings after the 2005 Kashmir Earthquake
Kazuo Konagai, Jorgen Johansson, Atsunori Numata, Shigeki Takatsu, and Takaaki Ikeda

Incorporating the Effects of Site Geology in CEUS Hazard Maps
Chris H. Cramer

Seismic Microzonation of Shiraz City, Southwest of Iran
A. Ghalandarzadeh, S. Sahraeian, A. Kavand, and B. Kamrani Moghaddam

The Effect of Shallow Foundation Position on Their Interaction with Reverse Faults
Waqas Ahmed, Fraser Bransby, and Shuichi Nagaoka

Dynamic Properties of Soils

Cyclic Shear Tests of Municipal Waste in Large Triaxial Device for Identification of Its Dynamic Properties
Ikuo Towhata and Masaaki Uno

Density Effects on the Aging Behavior of Sands and the Anisotropy of Aging-Induced Stiffness Increases
Yu-Hsing Wang and King-Yuen Tsui

Development of a P-Wave Measurement System for Laboratory Specimens
Sajjad Maqbool and Junchi Koseki

Development of Buried Sensors for Stiffness Measurements of Soft Clays Using Bender Elements
Jae Woo Jung, Chul Soo Park, and Young Jin Mok

Development of Methods to Predict the Dynamic Behavior of Fine Coal Refuse: Preliminary Results from Two Sites in Appalachia
Michael E. Kalinski and Joshua L. Phillips

Dynamic Performance of Toyoura Sand Reinforced with Randomly Distributed Carpet Waste Strips
H. Ghiassian, R. Jamshidi, and A. R. Tabarsa

Dynamic Properties of Coal Waste Refuse in a Tailings Dam
Xiangwu Zeng, James A. Goble, and Lei Fu

Dynamic Properties of Saturated Compacted Soils
Chia-Pin Wu, Jin-Hung Hwang, and Tsai-Kuey Chien

Dynamic Response of Unsaturated Soils Using Resonant Column and Bender Element Testing Techniques
L. R. Hoyos, P. Takkabutr, A. J. Puppala, and Md. S. Hossain

Effective Soil Density for Small Strain Shear Wave Propagation
Tong Qiu and Patrick J. Fox

Effects of Cyclic Rotation of Principal Stress Axes and Intermediate Principal Stress Parameter on the Deformation Behavior of Sands
Jian-Min Zhang, Zhao-Xia Tong, and Yi-Lin Yu

Evaluation of Dynamic Properties of a Calcite Cemented Gravely Sand
S. Mohsen Haeri, Mohammad Reza Shakeri, and S. Ali Shahcheraghi

Pore Fluid Induced Damping of Saturated Soil in Resonant Column Tests
Tong Qiu

Sand Aging Field Study
R. A. Green, R. D. Hryciw, D. A. Saftner, C. D. P. Baxter, Y. Jung, and T. Jirathanathaworn

Stress Integration Approach for Soil Damping Measurements in Torsional Testing
Inthuorn Sasanakul, James A. Bay, and Yoon-Shin Bae

Water, Inertial Damping, and the Complex Shear Modulus
Paul Michaels

Dynamic Properties of Naturally-Cemented Silts
Ravi Murthy, Soheil Nazarian, and Miguel Picornell

Geophysical Measurement Techniques

A Comparison of Shear Wave Velocity Profiles from SASW, MASW, and ReMi Techniques
Khiem T. Tran and Dennis R. Hiltunen

Deep Shear Wave Velocity Profiling of Poorly Characterized Soils Using the NEES Low-Frequency Vibrator
Brent L. Rosenblad, Kenneth H. Stokoe II, Jianhua Li, Brad Wilder, and Farn-Yuh Menq

Development and Applications of In-Hole Seismic Method to Measure Shear Wave Velocity of Subsurface Materials
Chul Soo Park, Jae Woo Jung, and Young Jin Mok

Use of Shear Wave Velocity to Estimate Settlement Potential in Mine Spoils
Michael E. Kalinski

Inversion Algorithm to Evaluate Velocity Profiles from Downhole Seismic Tests
J. Alfredo Fernandez, Glenn J. Rix, and Savannah Gowdy

Liquefaction

General

Characterizing the Liquefaction Resistance of Aged Soils
Hossein Hayati, Ronald D. Andrus, Sarah L. Gassman, Michael Hasek, William M. Camp, and Pradeep Talwani

Comparison of Recently Developed Liquefaction Analysis Methods at Two Fluvial Sand Sites
Tianfei Liao, John R. Davie, Hazem A. Sarhan, and Emre Biringen

Cyclic Response of a Sand with Thixotropic Pore Fluid
C. S. El Mohtar, J. Clarke, A. Bobet, M. Santagata, V. Drnevich, and C. Johnston

Effect of High Confining Stresses on Static and Cyclic Strengths of Mine Tailing Materials

Michael Riemer, Yoshi Moriwaki, and James Obermeyer

Effects of Mica Content on Cyclic Resistance of Poorly-Graded Sand
Kimberly Schmidt

Effects of Stress Reduction Factors on Liquefaction Analysis
Gökce Tönük and Atilla Ansal

Influence of Aging on Liquefaction Potential: Preliminary Results
Robb Eric S. Moss, David M. Thornhill, Ashley I. Nelson, and Darcie A. Levulett

Investigating the Critical State Using Laboratory Ring Shear Tests
Abouzar Sadrekarimi and Scott M. Olson

Liquefaction Resistance Recovered From "On-the-Fly" CPTu-Measured Pore Pressures
Michael Fitzgerald and Derek Elsworth

Numerical and Physical Modeling of Liquefaction Mechanisms in Layered Sands
Pelin Tohumcu zener, Kutay zaydn, and Mehmet Berilgen

Observations on Sand Boils from Simple Model Tests
Andrew Brennan

Pore Structure Variation of Porous Media under Vibrations
Ming Xiao and Lakshmi N. Reddi

The Effect of the Hammer Energy Efficiency Ratio on SPT-Based Liquefaction Evaluation
Troy Hull, Jason Butler-Brown, and Travis Willis

The Rigidity Recovery of Post Liquefied Soils
Seiji Kano, Hiroshi Kidera, Yasushi Sasaki, Takashi Ikeoka, and Koichi Ichii

The Seismic Dilatometer Marchetti Test (SDMT) for Evaluating Liquefaction Potential under Cyclic Loading
S. Grasso and M. Maugeri

Using Decision-Tree Learning to Assess Liquefaction Potential from CPT and V_s
Gary Livingston, Michael Piantedosi, Pradeep Kurup, and T. G. Sitharam

Effects on Structures and Foundations

An Experimental Study of the Effect of Seepage Force on Liquefaction of Soil in Embankments
Gang Liu, Xiangwu Zeng, and Xiangsong Li

Assessment of Structure-Induced Liquefaction Triggering
Berna Unutmaz and K. Onder Cetin

Centrifuge Experimentation of Building Performance on Liquefied Ground
Shideh Dashti, Jonathan Bray, Michael Riemer, and Dan Wilson

Components of Dynamic Subgrade Reaction on Pile in Saturated Sand
Hideki Funahara

Effect of Soil Liquefaction on Flexural Behavior of Axially and Laterally Loaded Piles
R. S. Meera and P. K. Basudhar

FD Solutions for Static and Dynamic Winkler Models with Lateral Spread Induced Earth Pressures on Piles
D. W. Chang, B. S. Lin, C. H. Yeh, and S. H. Cheng

Mechanism of Pile Group Settlement in Liquefiable Soils
Jonathan Knappett and Gopal Madabhushi

Performance-Based Seismic Response of Pile Foundations
Brendon A. Bradley, Misko Cubrinovski, and Rajesh P. Dhakal

Plastic Hinge Formation in Pile Foundations Due to Liquefaction-Induced Loads
S. R. Rajaparthy, Z. Zhang, T. C. Hutchinson, and F. Lang

The Role of Soil Compressibility in Centrifuge Model Tests of Piles Foundation Undergoing Lateral Spreading of Liquefied Soil
Marcelo Gonzles, Javier Ubilla, Tarek Abdoun, and Ricardo Dobry

Liquefaction of Silty Soils

Cyclic Failure of Fine-Grained Soils during the 1999 Kocaeli Earthquake
Volkan Okur, Selim Altun, and Atilla Ansal

Cyclic Shear Response of Undisturbed and Reconstituted Low-Plastic Fraser River Silt
Dharma Wijewickreme and Maria V. Sann

Effect of Fines on Sand Residual Strength after Liquefaction
Pedro de Alba and Thomas P. Ballestero

Effect of Sand Gradation and Fines Type on Liquefaction Behaviour of Sand-Fines Mixture
Md. Mizanur Rahman and Sik-Cheung Robert Lo

Effects of Fines on Undrained Behaviour of Sands
Misko Cubrinovski and Sean Rees

Effects of Permeability on Liquefaction Resistance and Cone Resistance
S. Thevanayagam and N. Ecemis

Liquefaction Behavior of Mississippi River Silts
Ali M. Izadi, Ronaldo Luna, and Richard W. Stephenson

Liquefaction Resistance of Sands Containing Varying Amounts of Fines
G. A. Athanasopoulos and V. C. Xenaki

Post-Liquefaction Shear Behavior of Bonneville Silty-Sand
Zahra A. Amini and Aurelian C. Trandafir

Probabilistic Assessment of Cyclic Soil Straining in Fine-Grained Soils
H. Tolga Bilge and K. Onder Cetin

Shaking Table Test on a Large Specimen of Mailiao Silty Sand
Tzou-Shin Ueng, Chia-Han Chen, Cheng-Fu Tsou, and Yi-Cheng Chen

Ground Improvement

Keynote—Recent Developments in Ground Improvement for Mitigation of Seismic Risk to Existing Embankment Dams

James K. Mitchell

Application of Deep Dynamic Compaction to U.S. Route 44 Relocation Project
Yong Tan

Centrifuge Testing of Prefabricated Vertical Drains for Liquefaction Remediation
Antonio Marinucci, Ellen Rathje, Seiji Kano, Ronnie Kamai, Carolyn Conlee, Rachelle Howell, Ross Boulanger, and Patricia Gallagher

Colloidal Silica Gel and Sand Mixture Dynamic Properties
Laura Spencer, Glenn J. Rix, and Patricia Gallagher

Compaction Grouting to Mitigate Liquefaction for a New Medical Retail Building
Mark Russell, Jeff Geraci, and David Murray

Cone Penetration Resistance Variation with Time after Blast Liquefaction Testing
Kyle M. Rollins and Joshua K. S. Anderson

Cone Penetration Testing before, during, and after Blast-Induced Liquefaction
William M. Camp III, Paul W. Mayne, and Kyle M. Rollins

Dynamic Response of an Embankment during Stone-Column Piling
Dario Rosidi, Areq Gharabegian, and Deh-Jeng Jang

Evaluation of a Geogrid-Reinforced Soil Mat to Mitigate Post-Liquefaction SettlementsA Case Study
James R. Gingery and Scott M. Merry

First Applications of the SAVE Compozer Method (Non-Vibratory Stone Columns) for Soil Densification in the U.S.
Jun Mukai, Masaru Sakakibara, Juan I. Baez, Sean G. Callan, and Hideo Tsuboi

Imaging a Grouted Column in a Centrifuge Model Using Shear Wave Velocity Tomography
Scott J. Brandenberg

Increase in Cyclic Liquefaction Resistance of Sandy Soil Due to Installation of Drilled Displacement Piles
Timothy C. Siegel, Willie M. NeSmith, and W. Morgan NeSmith

Liquefaction Potential Mitigation Using Rapid Impact Compaction
Lori A. Simpson, Serena T. Jang, Cary E. Ronan, and Lisa M. Splitter

Monitoring for Successful Site Improvement
Brian D. Bauldry, Lisheng Shao, and Francis B. Gularte

Numerical Modeling of the Seismic Response of Columnar Reinforced Ground
C. Guney Olgun and James R. Martin II

Relations between Penetration Resistance and Cyclic Strength to Liquefaction as Affected by K_C-Conditions
Kenji Harada, Kenji Ishihara, Rolando P. Orense, and Jun Mukai

Seismic Response Evaluation of an Onshore Building Site Improved by Deep Mixed Foundation System
Raj V. Siddharthan and Ali Porbaha

Shear Stress Redistribution as a Mechanism to Mitigate the Risk of Liquefaction
Russell A. Green, C. Guney Olgun, and Kord J. Wissmann

Study on Uplift Behaviour of Plate Anchor in Geogrid Reinforced Sand Bed
K. Ilamparuthi, P. T. Ravichandran, and M. Mohammed Toufeeq

Uplift Testing of Rammed Aggregate Pier Systems
Tom Farrell, Brendan FitzPatrick, and William Kenney

Numerical Modeling

DEM Simulation of the Seismic Response of Shallow Foundation on Liquefiable Soil
U. El Shamay

Efficient Numerical Modeling of Liquefaction-Induced Deformations of Soil Structures
Achilleas Papadimitriou, Konstantinos Andrianopoulos, and George Bouckovalas

Numerical Simulation of Seismic Ground Motion Isolation Using Fully Coupled Nonlinear Response in Saturated Sands
Mahdi Taiebat, Boris Jeremi, Zhao Cheng, and Yannis Dafalias

Transient Boundary Integral Equation of Dynamic Unsaturated Poroelastic Media
Iman Ashayeri, Mohsen Kamalian, and Mohammad Kazem Jafari

Soil-Structure Interaction (SSI)

General

Determination of Soil-Structure Interaction Effects for a Model Test Structure Using Parametric System Identification Procedures
Salih Tileylioglu, Robert L. Nigbor, and Jonathan P. Stewart

Dimensional Analysis of Soil-Foundation-Structure System Subjected to Near Fault Ground Motions
Jian Zhang and Yuchuan Tang

Dimensional Response Analysis of Inelastic Structures
Nicos Makris and Theodoros Psychogios

Dynamic Effects of Impact Machine Foundations
Mark R. Svinkin

Physical and Numerical Modeling of Dynamic Soil-Structure Interaction
Mohammad H. T. Rayhani and Hesham El Naggar

Response Sensitivity Analysis of Soil-Structure Interaction (SSI) Systems
Quan Gu and Joel P. Conte

Seasonally Frozen Soil Effects on the Nonlinear Behavior of a Parking Garage
Feng Xiong, Zhaohui (Joey) Yang, Feifei Bai, and He Liu

Sliding Blocks under Near-Fault Pulses: Closed-Form Solutions
Elia Voyagaki, George Mylonakis, and Ioannis N. Psycharis

SSI and Shallow Foundations

Advanced 3-D Seismic Soil-Structure Interaction Analysis of a Cellular-Raft Foundation in Soft Clay
Juan M. Mayoral, Miguel P. Romo, and Sergio Martinez

Dynamic Soil-Structure Interaction for SDOF Structures on Footings and Piles
Andreas Maravas, George Mylonakis, and Dimitris L. Karabalis

Effect of Critical Contact Area Ratio on Moment Capacity of Rocking Shallow Footings
Sivapalan Gajan and Bruce L. Kutter

Material Model Parameters for Shallow Foundation Numerical Analysis
Prishati Raychowdhury and Tara Hutchinson

Numerical Simulation of a Soil Model-Model Container-Centrifuge Shaking Table System
Mahadevan Ilankatharan and Bruce Kutter

Numerical Simulation of Displacement Functions of Strip Footings
Abir Jendoubi, Frdric Legeron, and Mourad Karray

Wave Propagation under Vertically Excited Surface Foundation
Jaehun Ahn, Giovanna Biscontin, and Jose M. Rosset

SSI and Pile Foundations

Analysis of Statnamic Behavior of Full-Scale Pile Group in Soft Clays and Silts
Tetsuo Tobita, Gi Cheon Kang, Susumu Iai, and Kyle M. Rollins

Cyclic P-Y Curves for a Pile in Cohesive Soil
Travis M. Gerber and Kyle M. Rollins

E-Defense Facility: A Frontier in Geotechnical Physical Modeling
Ramin Motamed, Ikuo Towhata, and Tsuyoshi Honda

Nonlinear Behavior of Single Piles Vibrating Vertically
Jin-xing Zha and George Gazetas

Non-Linear Dynamic Response of Deepwater Suction Pile Foundation
Fabrizio Ardoino, Chiara M. Traverso, and Eric J. Parker

Piles under Earthquake Loads
Shamsher Prakash and Vijay K. Puri

Response of Clay-Pile System under Earthquake Loading
Subhadeep Banerjeer, Siang Huat Goh, and Fook Hou Lee

Static and Dynamic Lateral Load Tests on a Pile Cap with Partial Gravel Backfill
Kyle M. Rollins, Ku Hyun Kwon, and Travis M. Gerber

Undrained Tip Response of Drilled Shaft in Cohesionless Soils
Sherif Elfass and Gary Norris

SSI and Retaining Structures

Analysis of the Seismic Behaviour of Propped Retaining Structures
Luigi Callisto, Fabio M. Soccodato, and Riccardo Conti

Distribution of Seismic Earth Pressures on Gravity Walls by Wave-Based Stress Limit Analysis
Panos Kloukinas, George Mylonakis, and Costas Papantonopoulos

Dynamic Centrifuge Study of Seismically Induced Lateral Earth Pressures on Retaining Structures
Nicholas Sitar and Linda Al Atik

Excitation and Flexibility Effects on Dynamic Response of Cantilever Retaining Walls
zgr L. Erturul, Selman Salam, and M. Yener zkan

Extended Veletsos-Younan Model for Geofoam Compressible Inclusions behind Rigid, Non-Yielding Earth-Retaining Structures
John S. Horvath

Lateral Seismic Soil Pressures on Soldier Pile Walls
Jin-xing Zha

Permanent Seismic Deformation of MSE Walls with Uneven Reinforcement
Raj V. Siddharthan and Gopalan Vishnan

Seismic Earth Pressures behind Retaining Walls: Effects of Rigid-Body Motions
Chulmin Jung and Antonio Bobet

Seismic Lateral Earth Pressure Reduction on Earth-Retaining Structures Using Geofoams
John S. Horvath

Seismic Modeling of a 135-Foot-Tall MSE Wall
D. D. Lindquist

The Effect of Amplification on the Seismic Stability of Reinforced Soil Slopes Using Horizontal Slice Method
Hamid Reza Nouri and Ali Fakher

Bridges

Centrifuge Modeling of Pile Pinning Effects
R. J. Armstrong, R. W. Boulanger, U. Gulerce, B. L. Kutter, and D. W. Wilson

Closed-Form Force-Displacement Backbone Curves for Bridge Abutment-Backfill Systems
Anoosh Shamsabadi and Liping Yan

Development of Innovative Foundation Systems to Optimize Seismic Behavior of Bridge Structures
Lijun Deng, Emrah Erduran, Jose Ugalde, Sivapalan Gajan, Sashi Kunnath, and Bruce Kutter

Factors that Affect the Performance of Bridge Foundations Undergoing Liquefaction-Induced Lateral Spreading
Christian Ledezma and Jonathan D. Bray

Proposed Changes to AASHTO LRFD Bridge Design Specifications for the Seismic Design of Retaining Walls
Donald G. Anderson, Geoffrey R. Martin, I. P. Lam, and J. N. Wang

Seismic Soil-Foundation Investigation of the Brooklyn Bridge

M. K. Yegian, S. Arzoumanidis, K. Kishore, J. Patel, S. K. Jain, B. P. Strohman, and N. Edwards

Seismic Response of a Typical Highway Bridge in Liquefiable Soil
HyungSuk Shin, Pedro Arduino, Steven L. Kramer, and Kevin Mackie

Sensitivity Study of an Older-Vintage Bridge Subjected to Lateral Spreading
Scott J. Brandenberg, Pirooz Kashighandi, Jian Zhang, Yili Huo, and Minxing Zhao

Soil-Structure Interaction Analysis of Bridge Columns Supported on CISS Piles
Pedro F. Silva and Majid T. Manzari

Geoscience and Geotechnical Aspects of Recent Earthquakes
Robert C. Lo and Yumei Wang

Effect of Backfill Soil Type on Stiffness and Ultimate Capacity of Bridge Abutments
A. Bozorgzadeh, S. A. Ashford, and J. I. Restrepo

Seismic Behavior of 2D Topographic Features Subjected to Vertically Propagating Incident SV at High Frequencies
Arash Razmkhah, Mohsen Kamalian, and Hamid Alielahi

Dams and Levees

Characterizing the Earthquake Ground Shaking Hazard in the Sacramento-San Joaquin Delta, California
Ivan Wong, Patricia Thomas, Jeffrey Unruh, Kathryn Hanson, and Robert Youngs

Damage Assessment and Seismic Modeling of Dams in Connection with the 2006 Hawaii Earthquakes
Horst G. Brandes, Peter G. Nicholson, and Ian N. Robertson

Deformation Analysis for Seismic Retrofit of an Embankment Dam
Vlad Perlea, David Serafini, Ethan Dawson, and Michael Beaty

Dynamic Behavior for Lightweight Spillway with Geosynthetics on Small Earth Dam
Toshinori Kawabata, Kazunori Uchida, Tomohiro Kitano, Koji Watanabe, and Yoshiyuki Mohri

Earthquake-Induced Deformations of Partially Saturated Embankments
Rolando P. Orense, Masayuki Hyodo, Norimasa Yoshimoto, and Junya Ohashi

Effect of Heterogeneous Soil Strength on the Seismic Residual Displacement of Embankments
Yoshiya Hata, Koji Ichii, Takashi Tsuchida, Seiji Kano, and Norihiko Yamashita

Geotechnical Investigations and Site Characterization of the Success Dam Seismic Remediation Project
David C. Serafini and Mathew G. Allen

Motion Characteristics of Compacted Earth Dams under Small Earthquake Excitations in Taiwan
Jin-Hung Hwang, Chia-Pin Wu, and Jui-Te Chou

Nonlinear Dynamic SSI Analyses of a Concrete Water Reservoir
Wolfgang Roth, Bei Su, Ethan Dawson, Allan Porush, Meang Hassel, Lynn Shutt, and Mohsen Beikae

Seismic Characterization and Its Limited Implication for San Pablo Dam

Yoshi Moriwaki, Andrew Dinsick, John Barneich, Guilaine Roussel, Atta Yiadom, Fred Starr, and Phalkun Tan

Seismic Deformation Analyses of the New Coquitlam Dam
Li Yan, Alex Sy, and T. Thavaraj

Seismic Rehabilitations of Miyun Reservoir
Lei Fu

Seismic Vulnerability of the Sacramento-San Joaquin Delta Levees
Said Salah-Mars, Arulnathan Rajendram, Ram Kulkarni, Martin W. McCann, Jr., Segaran Logeswaran, Kanagalingam Thangalingam, Ralph Svetich, and Sean Bagheban

Using ShakeMap and ShakeCast to Prioritize Post-Earthquake Dam Inspections
William A. Fraser, David J. Wald, and Kuo-Wan Lin

Walnut Canyon Dam Seismic Performance Evaluation
John Barneich, Yoojoong Choi, David Shen, Yoshi Moriwaki, and Phalkun Tan

Wavelet Signal Processing Technique in Analyzing Earthquake Records of Masjed Soleyman Embankment Dam
M. Davoodi and M. Amel Sakhi

Embankments and Slopes

Centrifuge Modeling of Earthquake-Induced Failure Process of Soil Slopes
Ga Zhang, Jiyun Qian, and Jian-Min Zhang

Constructing Hillside Ozone Facilities in a High Seismic Zone
M. Hassel, A. Woo, and M. Beikae

Displacement-Based Seismic Stability Analyses of Reinforced and Unreinforced Slopes Using Planar Failure Surfaces
Deepankar Choudhury and Deepa Modi

Energy-Based Evaluation of Earthquake-Induced Slope Failure and Its Application
Takaji Kokusho and Tomohiro Ishizawa

Failure Mechanisms of Landfills under Dynamic Loading
Varvara Zania, Yiannis Tsompanakis, Prodromos Psarropoulos, and Achilleas Papadimitriou

Validation of Generic Municipal Solid Waste Material Properties for Seismic Design of Landfills
Adda Athanasopoulos-Zekkos, Dimitrios Zekkos, and Neven Matasovic

Pipelines

Assessing Geotechnical Hazards for Water Pipes with Uniform Confidence Level
Craig A. Davis

Characteristics of Uplifting Velocity of a Buried Pipe in Liquefied Ground
Koji Ichii, Nobuyasu Seto, and Hiroshi Kidera

Shake-Table Testing and FLAC Modeling of Liquefaction-Induced Slope Failure and Damage to Buried Pipelines
Lei Qiao, Chang Yuan, Masakatsu Miyajima, and Endi Zhai

Soil-Pipeline Interaction Behavior under Strike-Slip Faulting
Da Ha, Tarek H. Abdoun, and Michael J. ORourke

Ports

Theme Paper—Seismic Performance and Design of Port Structures
Susumu Iai, Tetsuo Tobita, and Yukio Tamari

Comparison of Panama Wharf Performance Using Numerical Analysis and Limit Equilibrium Methods
King H. Chin, Daniel W. Mageau, and Scott T. Peterson

Full-Scale Lateral Pile Load Test in Rock Fill
Yohsuke Kawamata, Scott A. Ashford, and Nontapat Nimityongskul

Geotechnical Considerations and Soil-Structure Interaction: Proposed ASCE Standards for Seismic Design of Piers and Wharves
Arul K. Arulmoli, Gayle S. Johnson, Peter Yin, Omar A. Jaradat, and Timothy W. Mays

Integrating Soil-Structure Interaction Analyses of Pile-Supported Wharfs in Seismic Risk Management of Port Systems
Varun and Dominic Assimaki

Seismic Retrofit and Improvement of Alpha-Bravo Wharves in Guam
(Raj) S. Varatharaj, Arul K. Arulmoli, Dick Chan, Kijun Ahn, and Ukrit Siriprusanan

Tunnels and Other Underground Structures

Keynote—Centrifuge Testing of the Seismic Performance of a Submerged Cut-and-Cover Tunnel in Liquefiable Soil
Bruce L. Kutter, Jui-Ching Chou, and Thaleia Travasarou

Theme Paper—Earthquake Engineering for Tunnels and Large Underground Structures: A Case History
Ignacio Arango

Cut-and-Cover Structures: Seismic Response and Design
Ching L. Wu, Farhang Ostadan, Wen S. Tseng, and James Chai

Damage of New Sanyi Railway Tunnel during the 1999 Chi-Chi Earthquake
Chih-Chieh Lu and Jin-Hung Hwang

Seismic Analyses for the Fourth Bore of Caldecott Tunnel
Chien-Tai Yang, Hubert Law, and Anoosh Shamsabadi

Seismic Analyses of the Bay Tunnel
Yiming Sun, Steve Klein, John Caulfield, Victor Romero, and Johanna Wong

Seismic Response Analyses for the Silicon Valley Rapid Transit Project
Peter Chiu, Daniel E. Pradel, Annie On-Lei Kwok, and Jonathan P. Stewart

Development and Verification of a Pseudo-Static Solution for Evaluation of Seismic-Induced Deformations of Rectangular Tunnels
Hongbin Huo

Other Topics in Geotechnical Earthquake Engineering and Soil Dynamics

Keynote—Performance-Based Earthquake Engineering: Opportunities and Implications for Geotechnical Engineering Practice
Steven L. Kramer

Full-Scale Laboratory Tests Using a Shape-Acceleration Array System
T. Abdoun, V. Bennett, R. Dobry, S. Thevanayagam, and L. Danisch

Recent Improvements in MOC for Earthquake Response
Richard P. Ray

Some Characteristics of Ground Vibration as Induced by High-Speed Trains
Yit-Jin Chen, Yi-Jiun Shen, Kuo-Yen Chen, and Shih-Ming Chang

Nonlinear Seismic Ground Response Analysis: Code Usage Protocols and Verification against Vertical Array Data

Jonathan P. Stewart[1], M. ASCE and Annie O.L. Kwok[2], M. ASCE

[1]Professor and Vice Chair, Dept. of Civil & Environmental Engr., Univ. of Calif., Los Angeles, 5731 Boelter Hall, Los Angeles, CA 90095; jstewart@seas.ucla.edu
[2] Project Engineer, Praad Geotechnical, Inc., 5465 S. Centinela Avenue, Los Angeles, CA 90066; AnnieOLKwok@engineering.ucla.edu

ABSTRACT: One-dimensional seismic ground response analyses are often performed using equivalent-linear procedures, which require few, generally well-known parameters. Nonlinear analyses have the potential to more accurately simulate soil behavior, but their implementation in practice has been limited because of poorly documented and unclear parameter selection and code usage protocols as well as inadequate documentation of the benefits of nonlinear modeling relative to equivalent linear modeling. Regarding code usage/parameter selection protocols, the following are described: (1) when input motions are from ground surface recordings, we show that the full outcropping motion should be used without converting to a "within" condition; (2) Rayleigh damping should be specified using at least two matching frequencies with a target level equal to the small strain soil damping; (3) the "target" soil backbone curves used in analysis can be parameterized to capture either the soil's dynamic shear strength when large-strain soil response is expected (strains approaching 1%), relatively small-strain response (i.e., $\gamma < 0.3\%$) as inferred from cyclic laboratory tests, or a hybrid of the two; (4) models used in nonlinear codes inevitably represent a compromise between the optimal fitting of the shapes of backbone and hysteretic damping curves, and we present two alternatives for model parameterization. The parameter selection and code usage protocols are tested by comparing predictions to data from vertical arrays. We find site amplification to be generally underpredicted at high frequencies and overpredicted at the elastic site period, where a strong local resonance occurs that is not seen in the data. We speculate that this bias results from over-damping.

INTRODUCTION

Nonlinear ground response analysis is seldom used in practice by non-expert users because parameter selection and code usage protocols are poorly documented and understood, the effect of parametric variability on the analysis results is generally unknown, and the benefits of nonlinear analysis relative to the widely-used equivalent-linear analysis are generally unquantified and unclear. We report results of a

benchmarking project for nonlinear ground response analysis codes organized through the Pacific Earthquake Engineering Research (PEER) center Lifelines program (Stewart et al. 2007). The objective of the project was to "de-mystify" nonlinear ground response analysis routines for practicing engineers by providing clear and well documented code usage protocols, to verify the codes as implemented with the usage protocols against vertical array data, and to investigate the differences between predictions provided by nonlinear and equivalent-linear analyses.

This paper provides an overview of the principal results of benchmarking project. The topics covered include the following:

1. Suppose that ground response analyses are to be performed using a given control motion accelerogram. We address whether that motion should be used as-recorded of if it should be modified to a "within" condition.
2. Most nonlinear codes utilize Rayleigh damping so that a finite level of damping is present regardless of the backbone curve. We address the manner by which Rayleigh damping should be specified.
3. Material behavior is described by a nonlinear backbone curve along with rules for constructing unloading and reloading rules (e.g. Masing's rules). We review the parameters describing the backbone curve and provide guidelines for evaluating those parameters given the information typically available from geotechnical site investigations. Issues related to the simultaneous matching of modulus reduction and damping curves are also discussed.
4. Using available vertical array data, nonlinear codes are applied using recorded downhole motions along with the code usage protocols from (1)-(3). We evaluate residuals between recorded and calculated ground surface motions to assess the codes' performance.
5. The results from (4), along with additional simulations run at stronger levels of shaking, are compared to similar results from equivalent-linear analysis to investigate differences between results provided by the two methods of analysis.

Issues (1)-(2) are presented in detail by Kwok et al. (2007) and hence are discussed here only briefly.

NONLINEAR TIME DOMAIN METHODS OF ANALYSIS

Equivalent-linear methods of analysis, which operate in the frequency domain, use for each layer of the site time-invariant soil properties (shear modulus G and soil hysteretic damping β). Time-domain analysis methods allow soil properties within a given layer to change with time as the strains in that layer change. Modified frequency-domain methods have also been developed (Kausel and Assimaki, 2002; Assimaki and Kausel, 2002) in which soil properties in individual layers are adjusted on a frequency-to-frequency basis to account for the strong variation of shear strain amplitude with frequency. Since the frequencies present in a ground motion record vary with time, this can provide a reasonable approximation of the results that would be obtained from a truly nonlinear, time-stepping procedure. Nonetheless, the present focus is on true, time-stepping procedures.

The method of analysis employed in time-stepping procedures can in some respects be compared to the analysis of a structural response to input ground motion (Clough and Penzien, 1993; Chopra, 2000). As shown in Figure 1, the layered soil column is idealized either as a multiple degree of freedom lumped mass system or a continuum discretized into finite elements with distributed mass. Whereas frequency-domain methods are derived from the solution of the wave equation with specified boundary conditions, time domain methods solve a system of coupled equations that are assembled from the equation of motion. Table 1 summarizes the manner in which mass is distributed and nonlinear behavior is simulated for the five nonlinear codes considered here.

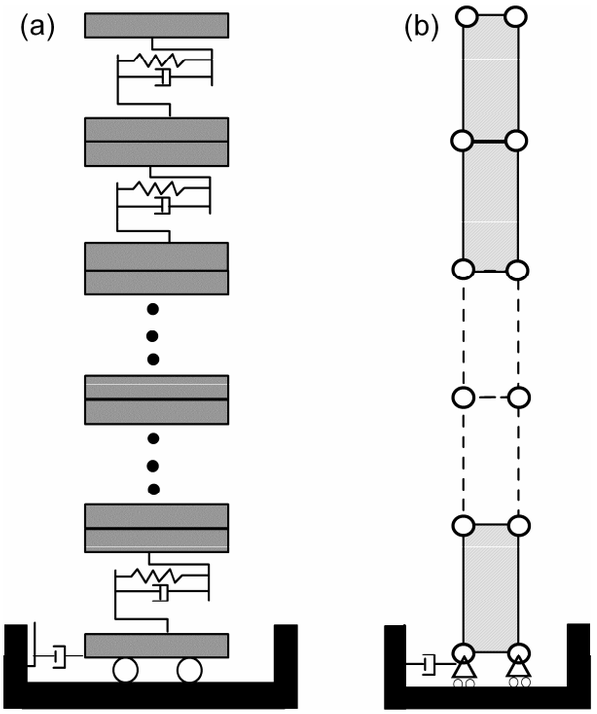


FIG. 1. (a) lumped mass system; (b) distributed mass system

The system of coupled equations is discretized temporally and a time-stepping scheme such as the Newmark β method is employed to solve the system of equations and to obtain the response at each time step. TESS utilizes an explicit finite difference solution of the wave propagation problem that is the same as the solution scheme used in FLAC developed by HCItasca. Unlike in frequency-domain analysis where the control motion could be specified anywhere within the soil column, in time domain analysis the control motion must be specified at the bottom of the system of lumped masses or finite elements.

Table 1. Mass representation and constitutive models used in nonlinear codes

Nonlinear Code	Mass Representation	Constitutive Model
D-MOD_2	Lumped Mass	MKZ (Matasovic and Vucetic , 1993)
DEEPSOIL	Lumped Mass	Extended MKZ (Hashash and Park, 2001)
OpenSees	Distributed Mass	Multi-yield surface plasticity (Ragheb, 1994; Parra, 1996; Yang, 2000)
SUMDES	Distributed Mass	Bounding surface plasticity (Wang, 1990) and other models
TESS	Distributed Mass	HDCP (EPRI, 1993)

NONLINEAR CODE USAGE AND PARAMETER SELECTION PROTOCOLS

Specification of Input Motion

Input motions are specified at the bottom of the 1D site profile in nonlinear analyses. There has been confusion regarding whether the motions specified at the base of the profile should represent an outcropping condition (i.e., equivalent free-surface motions that are twice the amplitude of the incident wave due to full reflection) or a within condition (i.e., the sum of the incident waves and downward propagating waves reflected from overlying layer interfaces). A closely related question is whether the base condition (representing the material below the site column) should be elastic or rigid. For some of the codes used in this research, past practice had been to calculate within motions at the profile base using equivalent-linear analyses, and specify those motions as the input for nonlinear analysis along with an elastic base. For other codes, full outcropping motions were used with an elastic base.

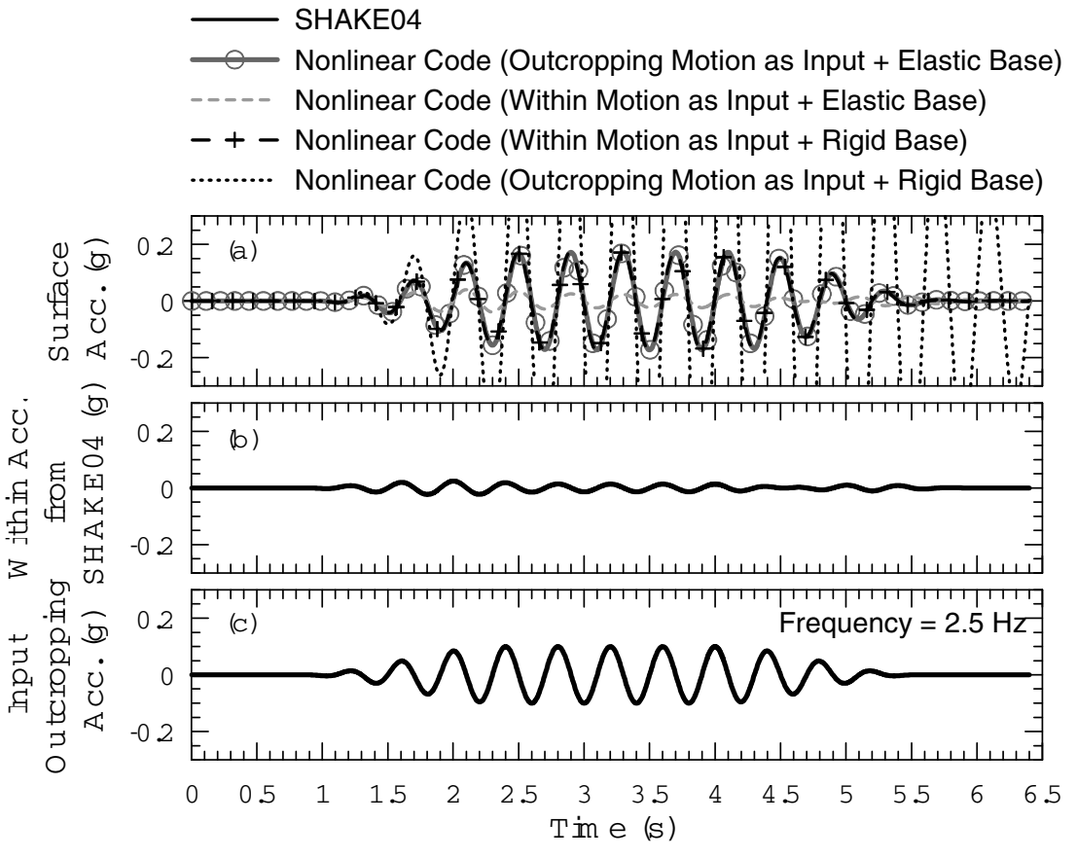


FIG. 2. Acceleration histories for the one-layer problem (Kwok et al. 2007)

To clarify this issue, we exercised nonlinear codes for cases with known elastic solutions. An illustrative example of those calculations is a single soil layer (thickness = 30 m; V_s = 300 m/s) overlying an elastic half-space with V_s = 600 m/s. All soil properties were taken as elastic, and viscous damping was set to zero (i.e., the nonlinear codes

were used with linear backbone curves). A sinusoidal acceleration history matching the site frequency of 2.5 Hz was specified at the top of the halfspace for time domain analyses. The same motion was specified as outcropping for linear frequency domain analyses (SHAKE04, Youngs, 2004).

Figure 2 (bottom frame) shows the input acceleration history, while the middle frame shows the resulting within motion at the layer interface from frequency-domain analyses. Since the 2.5 Hz motion has a node (i.e., zero amplitude at all times) at the interface depth, the within motion decays to null upon achieving a steady state condition. As shown in Figure 2 (top frame), surface acceleration histories obtained from both frequency and time domain analyses match well. These and other similar results suggest that input motions should be specified for an outcropping condition in time domain analyses, and used with an elastic base. Other work has similarly shown that within motions can be used with a rigid base, which would be appropriate practice for applying recorded downhole motions in time domain analyses (Kwok et al., 2007).

Specification of Viscous Damping

In most nonlinear codes, some form of viscous damping is used to provide for damping in the analysis at very small strains where the hysteretic damping from the non-linear soil models is nearly zero (an exception is TESS, which does not require viscous damping). There are a number of options for modeling viscous damping. As illustrated in Figure 3, there are three principal issues: (1) the form of the damping formulation (simplified versus full or extended Rayleigh damping; Park and Hashash, 2004); (2) the target viscous damping ratio (labeled ζ_{tar} in Figure 3) that is matched at specified target frequencies; and (3) the matching frequencies (one, two, and four for simplified, full, and extended Rayleigh damping, respectively). The current versions of all the aforementioned codes except TESS allow use of simplified and full Rayleigh damping. Extended Rayleigh damping is available in DEEPSOIL. TESS does not use Rayleigh damping, instead utilizing unload-reload rules that provide hysteretic damping even at small strains.

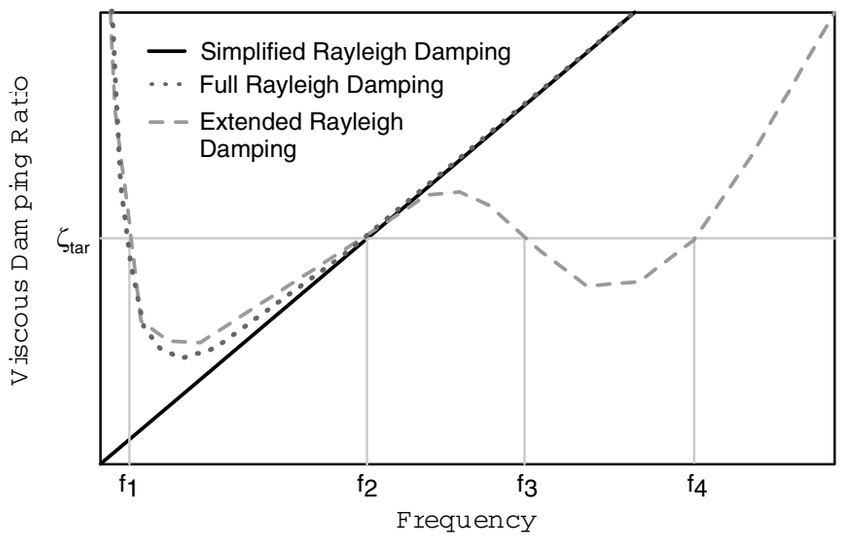


FIG. 3. Illustration of viscous damping models (after Park and Hashash, 2004)

Few protocols are available for guiding users in the selection of the model-type and parameters described above. One set of guidelines has been presented by Park and Hashash (2004) in which the model parameters are selected through an iterative process in which frequency and time domain elastic solutions are matched over a frequency range of interest (because frequency domain analyses using equivalent viscous damping provide a "correct" response against which the viscous damping formulation for the time domain can be calibrated). The procedure is implemented through a user interface.

Kwok et al. (2007) compared results of linear time domain analyses for three site profiles to solutions from linear frequency domain analyses with a specified amount of equivalent viscous damping (fixed at 5%). The three selected sites represent a broad range of site conditions: shallow stiff soil over rock, soft clay overlying stiffer sediments and rock, and very deep soils typical of the Los Angeles basin. A representative example of these results is shown in Figure 4 for a deep soil site (La Cienega). In Figure 4, the red spectrum (equivalent linear) represents the "correct" result to which the time domain results are compared. Equivalent-linear analyses are exact in this case because the analyses are linear visco-elastic.

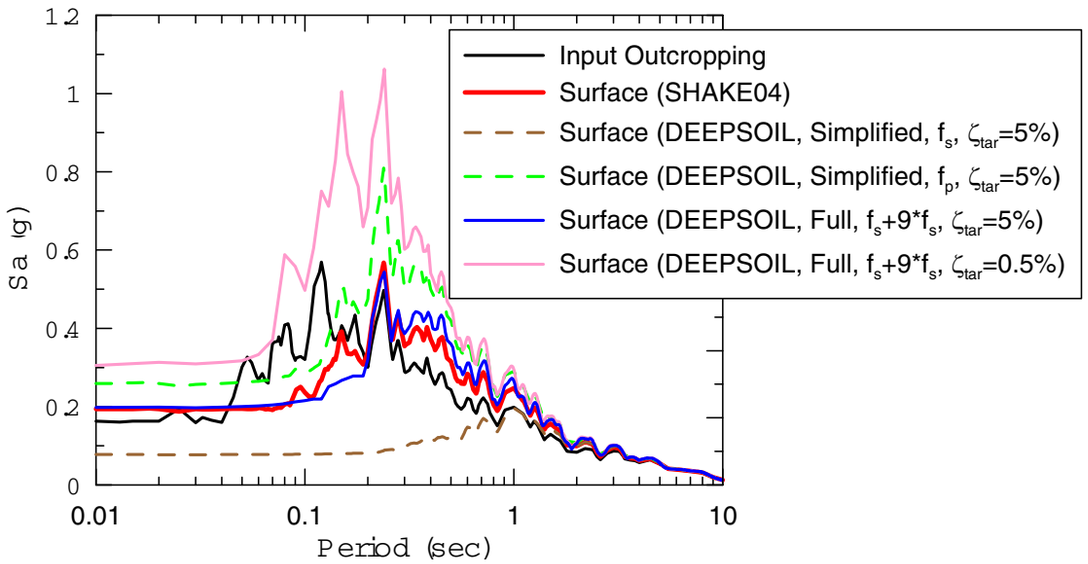


FIG. 4. Comparison of response spectra for La Cienega. Results are shown for DEEPSOIL, but similar results were obtained for D-MOD_2 and OPENSEES.

The principal results of these simulations, most of which are illustrated in Figure 4, are as follows:

- Full Rayleigh damping is preferred to simplified. Figure 4 shows examples of significant misfit in the simplified Rayleigh damping results – a low matching frequency (f_s=site frequency) produces overdamping while a high matching frequency (f_p=predominant frequency of input motion) produces underdamping. The point is that a good match over a wide frequency range is generally not possible with a simplified Rayleigh damping model. The full Rayleigh damping result in Figure 4 (blue line) is based on matching frequencies iterated on to

optimize the fit per the Park and Hashash (2004) procedure; it is seen that the second matching frequency is able to significantly improve the fit.

- The target damping level should match the small-strain soil damping (5% in Figure 4). The use of a much smaller damping value has been advocated by some users. As shown in Figure 4 (result for 0.5%, pink spectrum) produces underdamping.
- For applications where a non-iterative procedure is desired for specification of full Rayleigh damping target frequencies, the site frequency and five times the site frequency will usually suffice (not illustrated in Figure 4).

Parameterization of Nonlinear Material Behavior

Backbone Curve

Figure 5 shows a typical nonlinear backbone curve for a soil element, which has a hyperbolic shape defined by initial small strain secant shear modulus (G_{max}) and shear strength (τ_{ff}). The classical definition of reference strain is the ratio $\gamma_{ref} = \tau_{ff} / G_{max}$ (Hardin and Drnevich, 1972). The parametric description of the nonlinear backbone curve in the past has generally required the specification of this reference strain along with a number of curve fitting parameters. A practical problem with this approach is that the shear strength at rapid strain rate, needed to define reference strain, is often not available. Another problem is that the shape of the backbone curve at small strains may be inconsistent with laboratory test data.

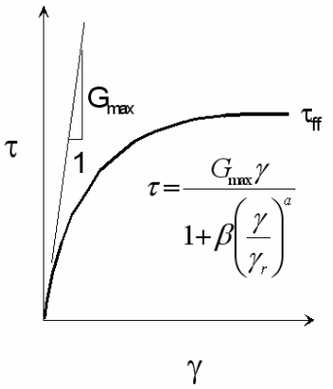


FIG. 5. Schematic illustration of backbone curve used for nonlinear ground response

At least for problems involving low to moderate strain levels, a "pseudo-reference strain" (γ_r) can be used in lieu of the strength-based reference strain. The term pseudo-reference strain is used to avoid confusion with reference strain as defined by Hardin and Drnevich (1972). Pseudo reference strain is defined from a laboratory modulus reduction curve as the shear strain at which $G/G_{max} = 0.5$. This definition arises from hyperbolic fits of G/G_{max} curves according to

$$G / G_{\max} = \frac{1}{1 + \beta\left(\gamma / \gamma_r\right)^a} \tag{1}$$

where β and a are fitting parameters generally taken as 1 and 0.92, respectively (Darendeli, 2001). The advantages of using pseudo reference strain are that (1) γ_r can be readily evaluated from material-specific modulus reduction curves evaluated from laboratory testing and (2) lacking material-specific testing, empirical relationships exist to predict γ_r as a function of basic parameters such as PI, overburden stress, and overconsolidation ratio (Darendeli, 2001; Zhang et al., 2005).

Because pseudo reference strains are determined from modulus reduction curves that are typically defined for strains less than 1%, a backbone curve described by a hyperbolic curve fit using γ_r would not necessarily be expected to accurately represent soil behavior at large strain, including the shear strength. We investigate this problem by examining the degree to which the shear strength implied by the use of Eq. 1 (approximately $G_{max} \times \gamma_r$) is realistic. This is done using ratios of G_{max} to shear strength, for which empirical relationships are available from Weiler (1988). The ratios from Weiler are for soils with OCR=1-5, confining pressures σ= 100-500 kPa and PI=15-45. Weiler's undrained shear strengths (S_u) are based on direct simple shear testing. Weiler's G_{max} / S_u ratio is compared to the inverse of Darendeli's (2001) estimate of γ_r (which is approximately the ratio of G_{max} to the large-strain asymptote of the hyperbolic curve, taken as shear strength).

As observed from Figure 6, the G_{max}/effective-strength ratios implied by pseudo reference strain γ_r are significantly higher than those from Weiler for an overburden stress of σ =100 kPa. This bias implies that the shear strength implied by γ_r is underestimated by Darendeli's relationships at σ=100 kPa. This bias disappears at larger overburden pressures (σ=500 kPa). Accordingly, at relatively shallow depths, the use of backbone curves derived from the pseudo reference strain parameter may overestimate the soil nonlinearity at large strains.

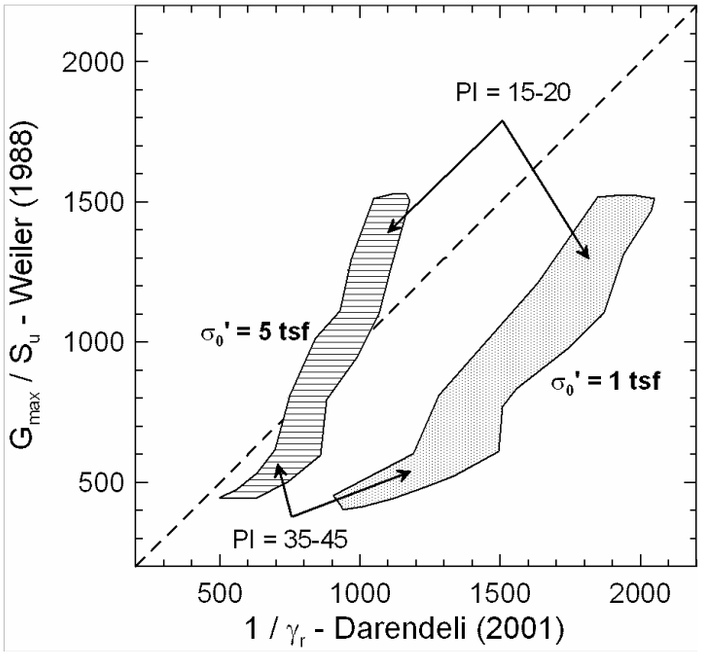


FIG. 6. Comparison of G_{max}/S_u ratio from Weiler (1988) to inverse of pseudo reference strain ($1/\gamma_r$) from Darendeli (2001). Quantity $1/\gamma_r$ is approximately the ratio of G_{max} to the shear strength implied by the use of pseudo reference strain for fitting nonlinear backbone curves.

Recommendations for the evaluation of backbone curve parameters are given in a subsequent section following a discussion of material damping.

Material Damping

Masing's rules (Masing, 1926) and extended Masing rules (Vucetic, 1990; Pyke, 1979) are employed in nonlinear analysis in conjunction with the backbone curve to describe unloading, reloading and cyclic degradation behavior of soil. Material damping is directly proportional to the area contained within a cyclic stress-strain loop, and hence is sensitive to the shape of the backbone curve and unload/reload rules. The damping at large strain that results from the use of Masing or extended Masing rules tends to be over-estimated relative to laboratory measurements.

There are three schools of thought on managing the over-estimation of damping. One approach is to select model parameters for the backbone curve (and hence modulus reduction curves) that optimally fit the target data and accept the resulting overestimation of damping using Masing's rules. A second approach is to select model parameters that optimize the fitting of modulus reduction and damping curves simultaneously (across the strain range of interest).

The third approach is to introduce an additional parameter that changes the shape of the unload/reload curves so that both modulus reduction and damping curves can be fit simultaneously. Lo Presti et al. (2006) allows unloading and reloading curves to have a shape scaled from that of the backbone curve by a factor of n (for the original Masing criteria, $n = 2$). Lo Presti et al. provide recommendations for estimating n as a function of soil type, strain level and number of cycles for the motion. Wang et al. (1980) suggest an approach in which a damping correction factor is applied to the Masing rule damping. These unload/reload rules are not yet implemented in the nonlinear codes listed in Table 1, and hence this approach is not discussed further.

Parameter Selection for Backbone Curves and Damping

There are two basic elements to the specification of parameters describing the nonlinear backbone curve and damping. The first element is to select the target shape of the backbone curve (equivalently, the modulus reduction curve) and the damping curve. The second element is to select model parameters that describe the target relationships within a reasonable degree of approximation for the problem at hand.

Element (1) – Target Curves: The ideal characterization would involve material-specific cyclic testing across the strain range of interest. This testing would include characterization of the material's dynamic shear strength for large-strain problems. However, material specific testing is usually not available, requiring the nonlinear behavior to be described using published correlations relating soil index properties, stress state, and stress history to parameters describing modulus reduction and damping curves (e.g., Darendeli, 2001; Zhang et al., 2005). Those relationships are usually well defined to shear strains of approximately 0.3-0.7%. This is illustrated in Figure 7, which shows the modulus reduction-strain values in the database used by Darendeli (2001). As described previously, those relationships do not typically provide an adequate representation of the shear strength. Guidelines for undrained shear strength evaluation and estimation are given in Ladd (1991); those estimates should be adjusted in consideration of rate effects, as described for example by Sheahan et al. (1996).

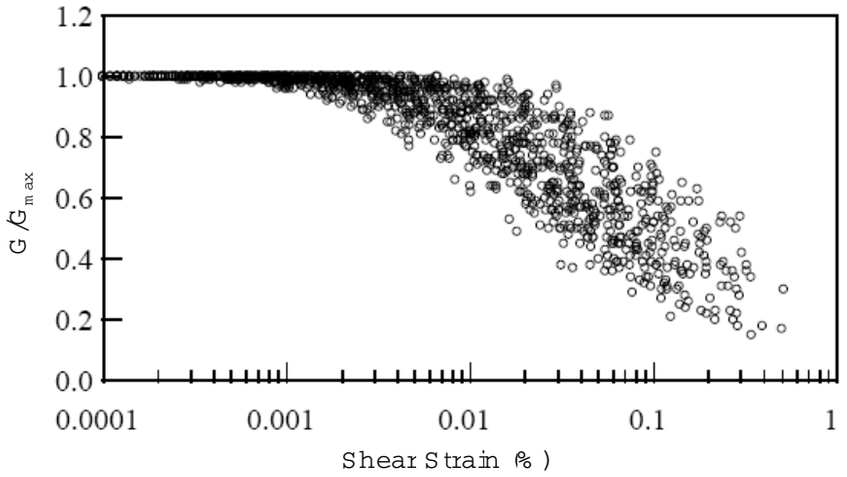


FIG. 7. Modulus-reduction-strain values in the database used by Darendeli (2001)

For problems involving large strain soil response, traditional practice has been to use a hyperbolic stress-strain curve (Eq. 1) with the strength-based reference strain. However, as shown in Figure 8, because of the misfit of reference strain and pseudo reference strain, this approach provides a poor match to small-strain modulus reduction behavior from laboratory tests. Accordingly, we recommend an alternative approach illustrated in Figure 8 and explained in the following: (1) use cyclic test results or correlation relationships to define the shape of the backbone curve to strain level γ_1 (typically taken as 0.1-0.3%); (2) estimate the material shear strength (τ_{ff}) for simple shear conditions with appropriate adjustment for rate effects; (3) estimate modulus reduction ordinates between strain γ_1 and the shear strength with the following hyperbolic relationship:

$$G/G_{\gamma_1} = \frac{1}{1+G_{\gamma_1}(\gamma-\gamma_1)/\tau_{ff}} \text{ (applies for } \gamma > \gamma_1 \text{ only)} \quad (2)$$

where $G_{\gamma 1}$=secant shear modulus from Step (1) at $\gamma=\gamma_1$. An example application of this procedure is given by Chiu et al. (2008). At present, only OpenSees allows the input of the G/G_{max} curve ordinates so that this formulation could be directly applied.

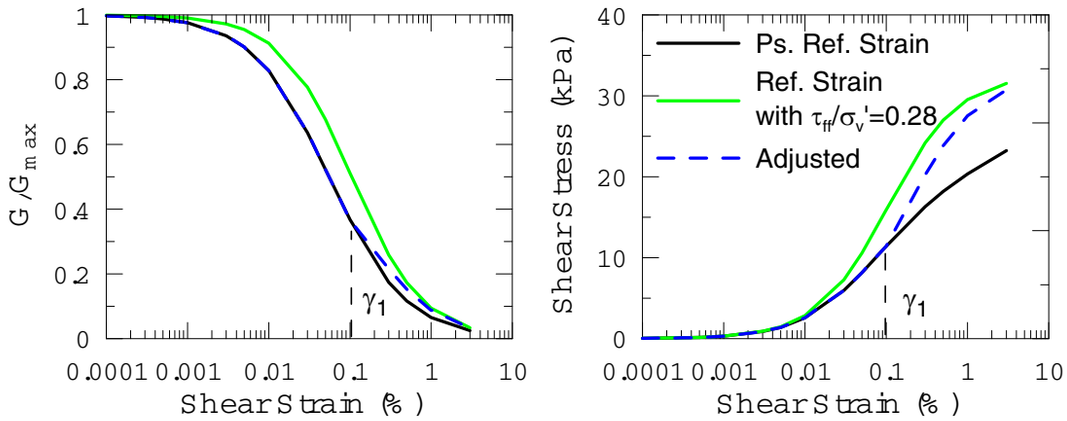


FIG. 8. Modulus reduction and stress-strain curves implied by pseudo reference strain from Darendeli (2001), reference strain model, and proposed procedure (*PI*=20, *OCR*=1, σ_v'= 100 kPa, V_s=135 m/s)

Element (2) – Approximation of Target Curves: As noted above, an exact match of target curves is not possible when Masing rules or extended Masing rules are used to describe the unload-reload relationship. Until nonlinear codes implement the capability to simultaneously match both modulus reduction and damping curves, mis-match of one or both of these curves is unavoidable. As mentioned previously, one approach is to match the target modulus reduction curve as accurately as possible and accept the misfit of damping. Another is to optimize the fit of both simultaneously.

We have worked with Hashash and Phillips (pers. comm., 2006) to devise a scheme to search for model parameters to achieve the aforementioned fitting approaches (in addition, the scheme allows optimization of the fitting of the damping curve only, although this approach is usually not considered). The scheme requires the specification of target material curves at (user-) predetermined strain levels. The fitting error is considered up to a maximum strain level (usually between 0.1 and 1%). The best combination of model parameters would be the one that gives the least error between the target curves and model curves. This error is quantified as:

$$\varepsilon = \sqrt{(w_{G/G_{\max}} \times \bar{\varepsilon}_{G/G_{\max}})^2 + (w_\beta \times \bar{\varepsilon}_\beta)^2} \tag{3}$$

where $\bar{\varepsilon}_{G/G_{\max}}$ and $\bar{\varepsilon}_\beta$ represent the mean error for the fitting of modulus reduction and damping curves respectively. Error term $\bar{\varepsilon}_{G/G_{\max}}$ is calculated as:

$$\bar{\varepsilon}_{G/G_{\max}} = \frac{\sqrt{\sum \left(\varepsilon_{G/G_{\max}}(\gamma_i)\right)^2}}{N} \tag{4}$$

The numerator in Eq. 4 is the summation of fitting error from the lowest specified strain level to the maximum strain level. N is the number of strain levels included in the summation. Error term $\bar{\varepsilon}_\beta$ is calculated in a similar way as for $\bar{\varepsilon}_{G/G_{\max}}$. Terms $w_{G/G_{\max}}$ and w_β in Eq. 3 are weight factors whose values depend on the choice of fitting approach. Table 2 summarizes the values of weight factors under different fitting approaches. Figure 9 shows the difference in the fitted modulus reduction and damping curves (relative to target data) when different fitting approaches are employed.

Table 2. Weight criterion for different fitting approaches

Fitting Approach	**Weight Criterion**
MR	$w_{G/G_{\max}} = 1;\ w_\beta = 0$
MRD	$(w_{G/G_{\max}})^2 + (w_\beta)^2 = 1$ $\frac{w_{G/G_{\max}}}{w_\beta} = \begin{cases} 1, & \beta_{\max} > 25\% \\ 1 + \frac{0.25 - \beta_{\max}}{0.15}, & 10\% < \beta_{\max} < 25\% \\ 2, & \beta_{\max} < 10\% \end{cases}$
D	$w_{G/G_{\max}} = 0;\ w_\beta = 1$

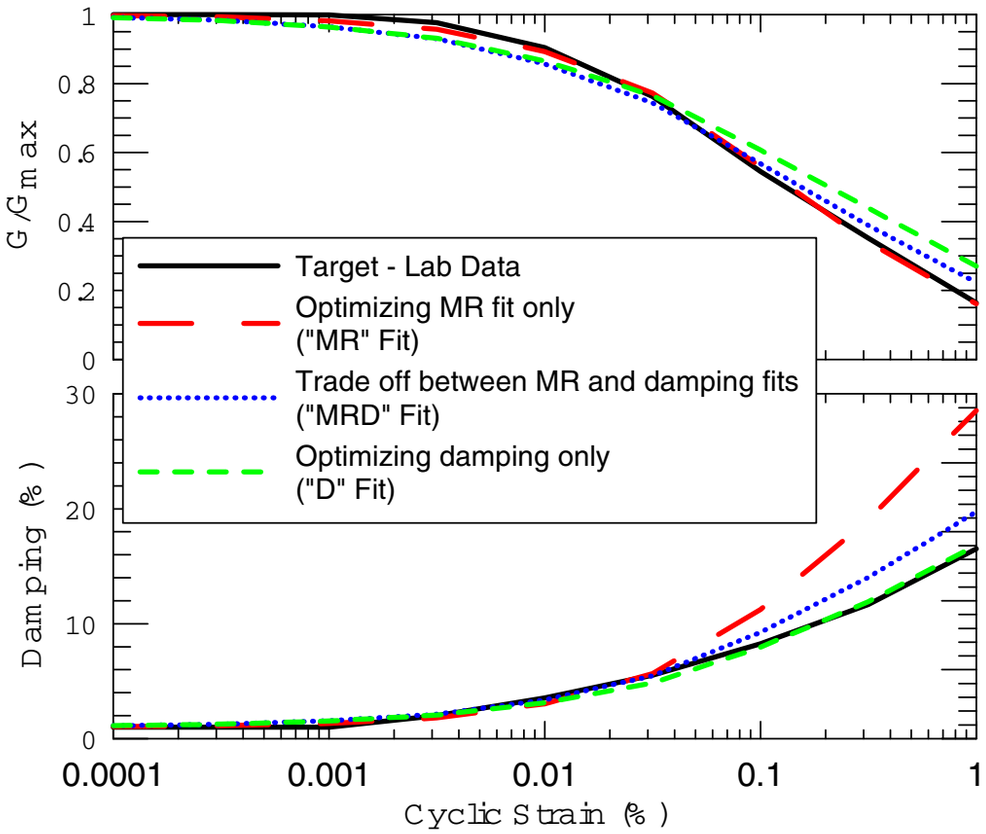


FIG. 9. Different approaches in fitting modulus reduction and damping curves in nonlinear analysis

To illustrate how different fitting approaches may influence ground motion predictions, nonlinear ground response analyses are performed for two strong motion sites with different fitting of target curves. The two sites are Apeel 2 in Redwood City, which is a soft clay site consisting of Bay Mud, and Sepulveda VA hospital in Los Angeles, which is a relatively stiff soil site. The calculations were performed using the DEEPSOIL code. The target nonlinear modulus reduction and damping curves were taken as Seed and Idriss (1970) upper bound for modulus reduction and lower bound for damping in shallow sand layers, EPRI (1993) deep curves (251-500 ft) for deep sand (depth > 60 m), Sun et al. (1988) for Bay Mud at Apeel 2, and Vucetic and Dobry (1991) for other clayey soils. Scaled versions of an outcropping broadband synthetic motion (Silva, pers. comm., 2004) are used as input. Figure 10 shows predicted ground surface motions for Apeel 2 and Sepulveda, respectively. It is observed that when the input motion is relatively low-amplitude (about 0.2 g), predictions for all three fitting approaches are similar. When the shaking is relatively strong (about 0.7 g), predictions for the “MR” fitting approach are smaller than those from the other approaches, which is due to the larger high-strain damping ratio associated with the “MR” fitting approach. Another observation is that the soft site is more sensitive to the different fitting approaches than the stiff site. This occurs because the softer site has larger strains for a given input motion amplitude.

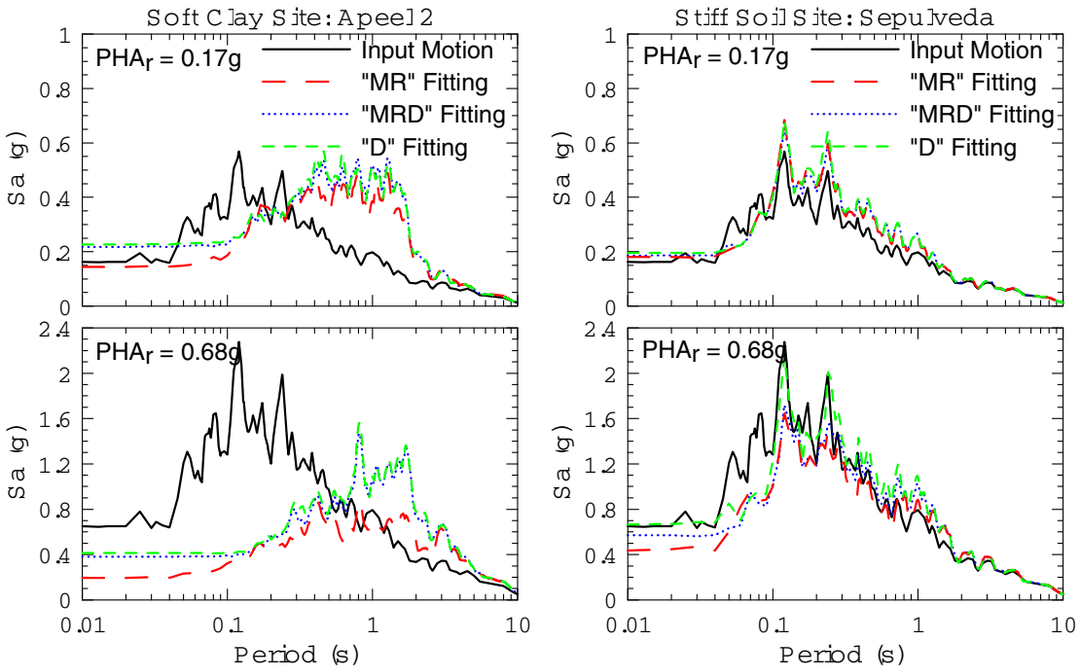


FIG. 10. Prediction results for soft clay site (Apeel 2) and stiff soil site (Sepulveda) with model curves obtained from different approaches to fitting modulus reduction and damping curves in nonlinear analysis

VALIDATION OF CODE PREDICTIONS AGAINST VERTICAL ARRAY DATA

Having developed the parameter selection protocols, it is necessary to test the effectiveness of those protocols by comparing code predictions to data. It is also important to study the uncertainties in predictions due to various sources of variability (material properties and modeling schemes). We utilize data from vertical array sites for this purpose. Four vertical array sites have been considered to date: Turkey Flat, California; La Cienega, California; KGWH02, Japan (Kiknet site); and Lotung, Taiwan. Analyses are preformed using an equivalent-linear procedure (SHAKE04) and the nonlinear codes listed in Table 1.

We describe the results for the La Cienega site in some detail. Brief overviews of the principal findings from the other sites are then provided.

La Cienega Site

Site Model and Strong Motion Data

We define “baseline” dynamic properties for the site along with a representation of material property variability. The baseline shear wave velocity (V_s) profile was developed from site-specific SASW and suspension logging data. Baseline modulus reduction and damping curves are derived from material-specific testing for 13 depth intervals. Log-normal, depth-dependent standard deviations on V_s are taken from an

empirical model (Toro, 1997). Log-normal standard deviations on modulus reduction and damping curves are taken as the standard deviations of the Darendeli (2001) model residuals. Additional details on the selected soil properties are given in Stewart et al. (2007). Strong motion data are taken from a M_w=4.2 event that occurred 2.7 km from the site on 09/09/2001.

Comparison of Model Predictions to Data

Figure 11 shows 5% damped acceleration response spectra of the horizontal recorded surface motions and prediction results obtained using the baseline geotechnical model while Figure 12 compares the predicted acceleration histories with the recordings (DEEPSOIL predictions only). Residuals are calculated as:

$$R(T) = \ln\left(S_a(T)\right)_{data} - \ln\left(S_a(T)\right)_{pre} \quad (5)$$

where $\ln\left(S_a(T)\right)_{data}$ is the natural log of the recording's spectral acceleration at period T and $\ln\left(S_a(T)\right)_{pre}$ is the natural log of the predicted spectral acceleration.

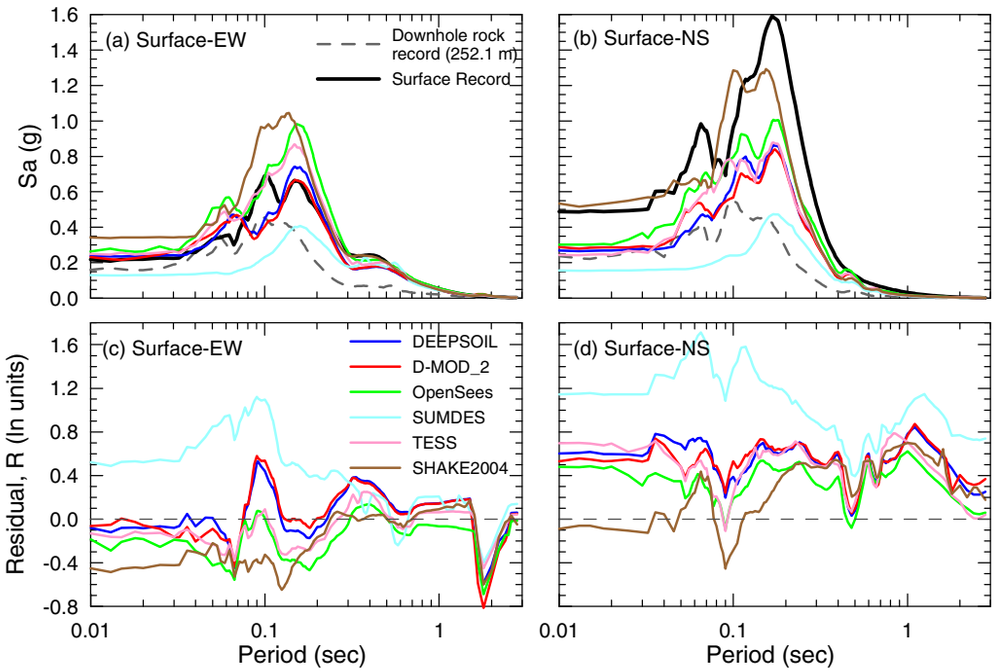


FIG. 11. Acceleration response spectra for data and simulation results compared through direct spectral ordinates and prediction residuals for ground surface. Results shown for two horizontal directions. Results shown to a maximum period of 1/(1.25*f_{HP}), where f_{HP} = high pass corner frequency.

As shown in Figure 12, the general comparison of the acceleration histories to data is quite favorable, although there is some bias towards over-prediction of the largest pulses in the record in the EW direction and under-prediction in the NS direction. The error appears to be related to the shape of the pulses near their tips.

Those errors in the acceleration histories translate into errors in spectra as well. For the

EW component at the ground surface, predictions from codes DEEPSOIL and D-MOD_2 are similar to each other and are generally close to the data, although they are underpredicting at periods between 0.07 and 0.12 sec. Predictions from codes OpenSees and TESS have similar trends and are also close to the data, except for overprediction near the period of 0.15 sec. SUMDES is underpredicting at periods below 0.5 sec which is probably due to the use of a simplified Rayleigh damping formulation in the version of this code that was used. Close examination of the spectra and residuals reveals that predictions from all codes have bumps near T=2 sec, which corresponds to the elastic period of the site from the base recording to the ground surface. For the NS component at the ground surface, all nonlinear codes are underpredicting at periods below 0.5 sec. Although not shown here for brevity, similar misfits of predictions relative to data occur at depths of 18.3 m and 100.6 m.

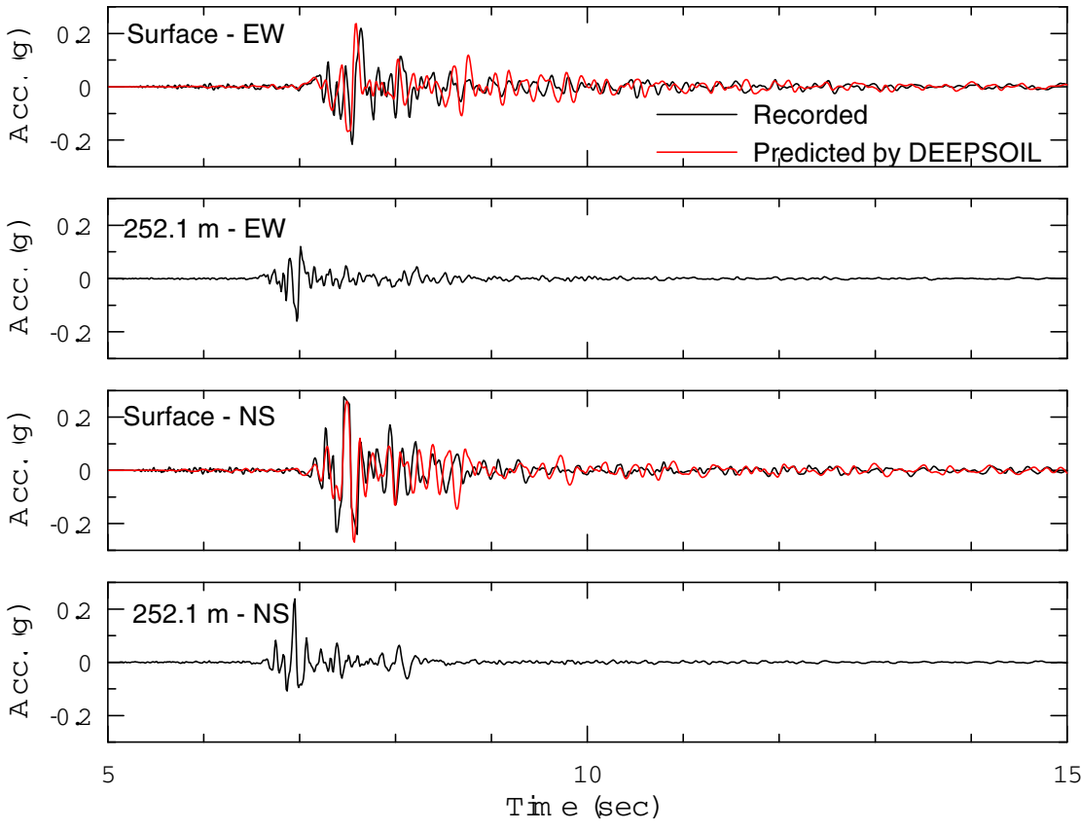


FIG. 12. Acceleration histories for data and simulation results from DEEPSOIL for ground surface

Contributions to the uncertainty in simulation results from model-to-model variability and material variability are considered. To evaluate model-to-model variability, we first take the median estimate $\ln\left(\overline{S}_a(T)\right)$ from the five nonlinear model predictions using baseline properties. Model variability, σ_m, is then calculated from the variance as follows:

$$\sigma_m^2(T) = Var\left(S_a(T)\right)_{pre} = \frac{\sum_i \left[\ln\left(S_a(T)\right)_{pre,i} - \ln\left(\bar{S}_a(T)\right)\right]^2}{N-1} \quad (6)$$

where N = number of predictions (five) and $\ln\left(S_a(T)\right)_{pre,i}$ = natural log of predicted spectral acceleration from code i. Figure 13 shows the variation of σ_m with period.

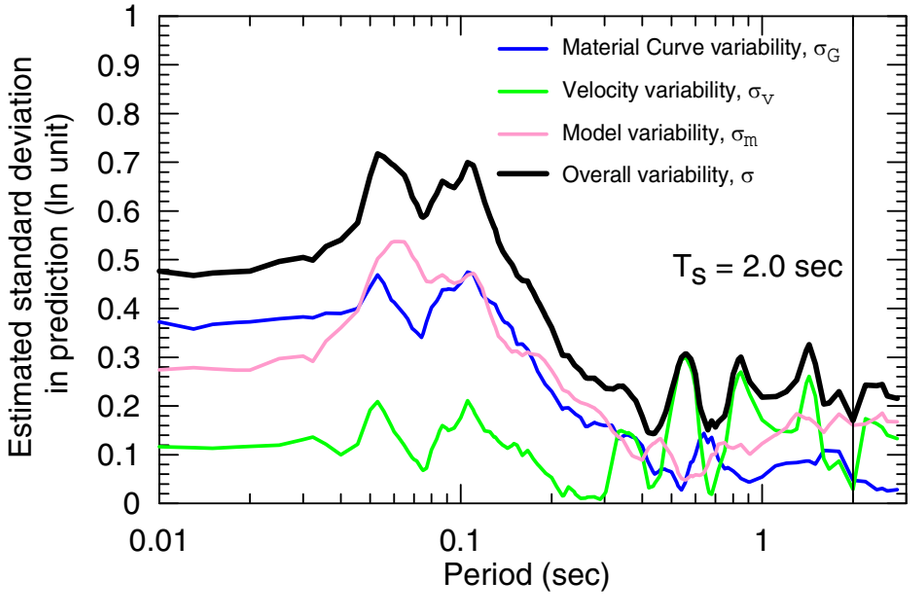


FIG. 13. Standard deviation terms associated with geometric mean acceleration response spectral ordinates for ground surface. T_s = elastic site period.

Variability in predictions from uncertain shear wave velocity and uncertain modulus reduction and damping curves is considered using only the DEEPSOIL code. To calculate the standard deviation due to velocity variability, ground motions are predicted based on two non-baseline velocity profiles (mean ± $\sqrt{3}$ standard deviation velocities). The standard deviation of the ground motions due to the variability in velocity (denoted σ_v) is estimated according to the first-order second moment (FOSM) method (Baker and Cornell, 2003; Melchers, 1999) as follows:

$$\sigma_v = \sum_{i=1}^{3} w_i (\ln(S_a(T)_i - \overline{\ln(S_a(T))})^2 \quad (7)$$

where

$$
\begin{aligned}
&S_a(T)_1 = S_a(T)_{V_s:\mu} \\
&S_a(T)_2 = S_a(T)_{V_s:\mu+\sqrt{3}\sigma_{V_s}} \\
&S_a(T)_3 = S_a(T)_{V_s:\mu-\sqrt{3}\sigma_{V_s}} \\
&\overline{\ln(S_a(T))} = \sum_{i=1}^{3} w_i \ln(S_a(T)_i) \\
&w_1 = 2/3;\ \mathrm{w}_2 = \mathrm{w}_3 = 1/6
\end{aligned}
\tag{8}
$$

The standard deviation due to the variability in material curves (denoted σ_G) is estimated similarly to σ_v. Figure 13 shows the estimated standard deviation in prediction due to different sources of variability. For $T < 0.4$ sec, the model and material curve variability dominate while for $T > 0.4$ sec velocity variability is strongest.

To study site response at different levels of input motion, site amplification factors are compiled from ground motions recorded at La Cienega from 1999-2005. Predicted amplification factors of geometric mean response spectral accelerations are derived at specified periods using the baseline geotechnical model for all codes. To estimate amplification factors for different amplitudes of input motions, the recording shown in Figure 12 is scaled down to various degrees. Figure 14 shows that the predicted amplification factors demonstrate a similar trend with respect to base motion peak acceleration (PGA^r) as those observed from data. This suggests that nonlinearity is modeled well by nonlinear codes over this range of input motions. The level of predicted amplification is biased at multiple periods. For example, at the elastic site period (2 sec), the predicted amplification is larger than suggested by data.

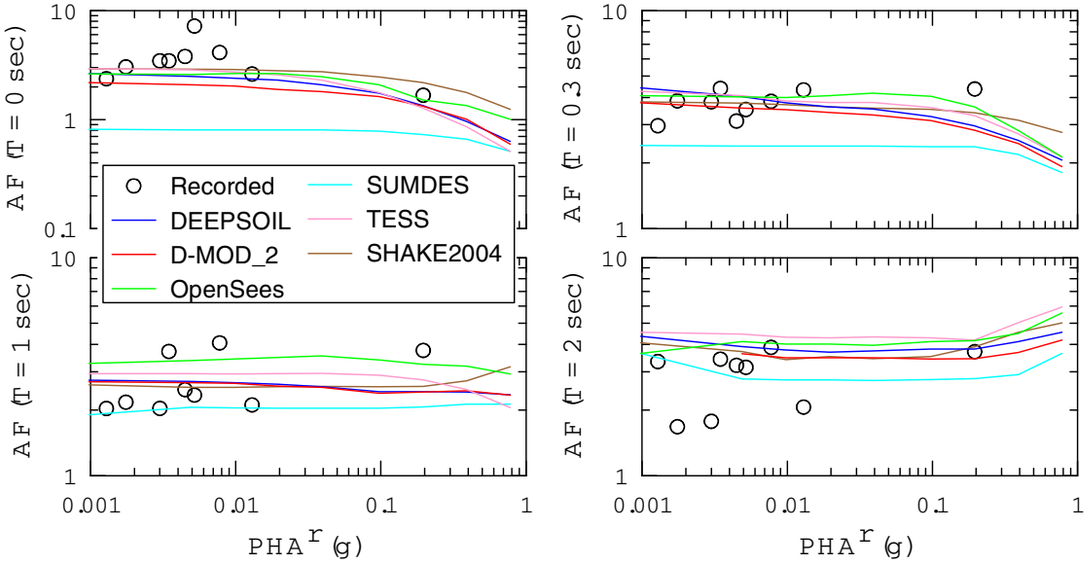


FIG. 14. Theoretical and observed amplification factors at the La Cienega site.

Other Sites

Three other vertical array sites were analyzed in a manner similar to La Cienega – Turkey Flat, KGWH02 (Kiknet), and Lotung. Results for all sites are given in Stewart et al. (2007). Results for the Turkey Flat site, which were originally provided as part of a blind prediction exercise, are also given in Kwok et al. (2008 – in press).

For all sites except Turkey Flat, residuals for very low periods (reflecting PGA) are positive, indicating that the models are underpredicting high frequency components of ground motion. Near the elastic site period (T_s), the models produce a local "bump" in the spectrum that results in overprediction. At periods significantly greater than T_s, residuals disappear due to the lack of a significant site effect.

The above misfits can have many sources. In general, there are two possible sources of misfit – error in the input data (velocity profiles or nonlinear curves) or error in the models and their parameter selection protocols. Errors in velocity profile were checked by comparing observed (small amplitude) shear wave travel time to the time implied the model. With the exception of the Kiknet site, these checks confirm the velocity profile used in the analysis. For Kiknet, observed travel times are less than model travel time, which may be due to waves entering from the side of the relatively narrow basin in which the site is located. Apart from velocity, other possible sources of error include incorrect modeling of material curves (modulus reduction and damping) or the presence of site response physics that cannot be captured by a 1D model. Because modulus reduction effects are likely relatively modest given the low strain levels excited by the subject earthquakes, error in the modeling in modulus reduction is not likely the source of the misfit.

Given that site amplification is under-predicted for all three sites considered across a broad frequency range, a likely source of bias is overdamping in the models. This overdamping could reflect bias in the material damping curves or excessive Rayleigh damping. Further research is needed to resolve these possible sources of bias.

We next discuss trends in the period-dependence of the standard deviation terms. In Figure 15, uncertainties in predictions due to different sources of variability are plotted as a function of period (left frame) and period ratio (right frame; period ratio = T/T_s, where T_s = elastic site period). Variability of predictions due to material curve uncertainty seems to be most pronounced at periods less than 0.5 sec and has no clear association with the site period. Moreover, material curve uncertainty only produces significant response variability for relatively thick site profiles – it is not a significant issue for Turkey Flat, which is a shallow soil site.

The effect of velocity variability can have a strong influence on the predictions near the elastic site period. However, this strong influence is only observed for sites with large impedance contrast (Turkey Flat and KGWH02), which dominates the site response in those cases. This is shown in Figure 15 by a peak in the σ_v term near T/T_s = 1.0. Such a peak does not occur for the Lotung or La Cienega sites, which have a gradual variation of velocity with depth and no pronounced impedance contrast.

Model-to-model variability is most pronounced at low periods, where the differences result principally from different damping formulations. Given the modest ground motions at the investigated sites, it is expected that variations in the viscous damping

formulations are principally driving this variability. As noted previously, predictions from SUMDES, which had only the simplified Rayleigh damping formulation at the time these predictions were made, are much lower than the predictions from codes with full Rayleigh damping formulation. This is a major contributor to the model-to-model variability at low periods.

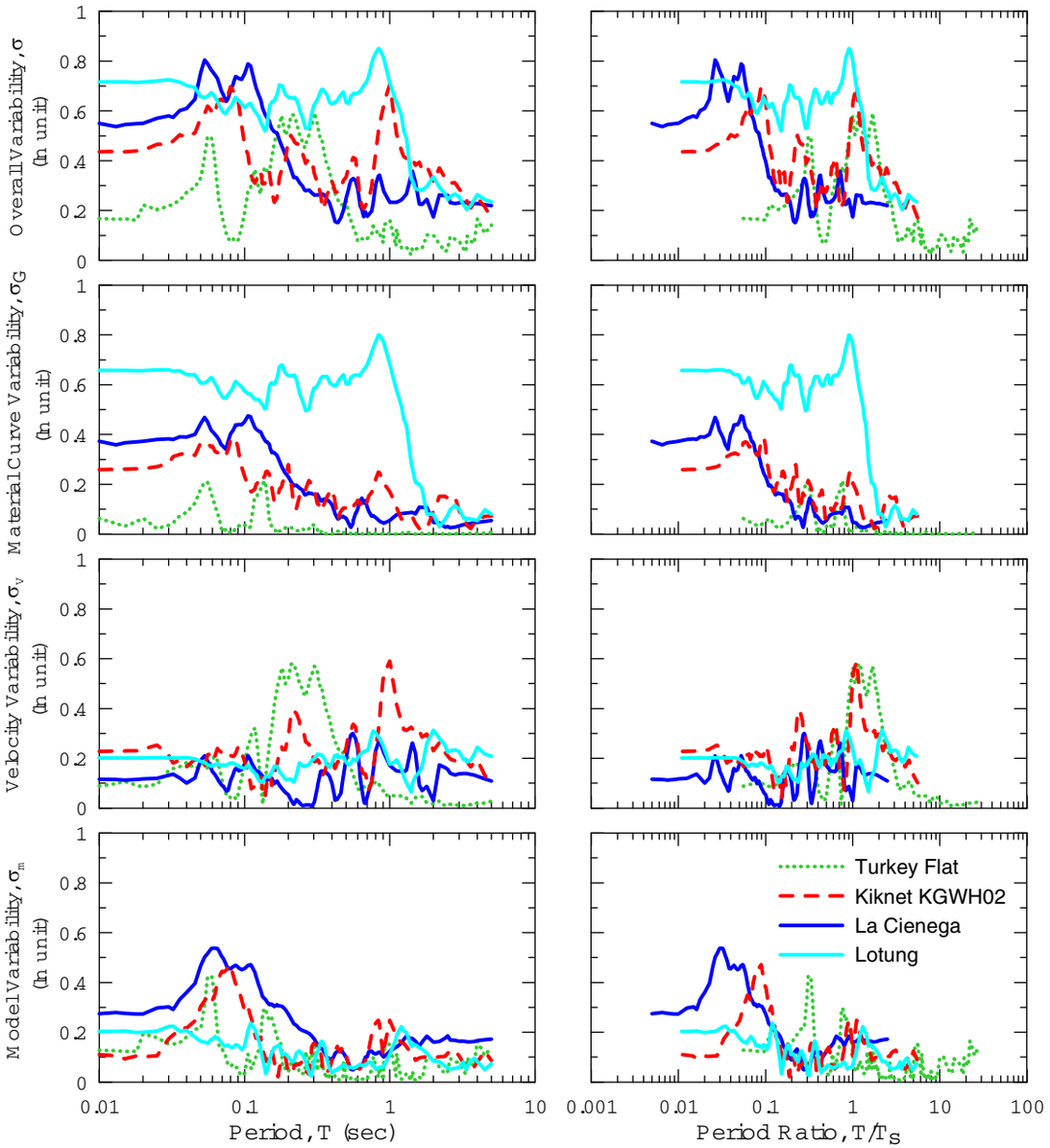


FIG. 15. Comparison of variabilities across four vertical array sites

COMPARISON OF EQUIVALENT LINEAR AND NONLINEAR RESULTS

The predictions of ground motions at vertical array sites described in the previous section were made using both equivalent-linear and nonlinear codes. The aforementioned comparisons of model predictions to data showed similar trends for

both methods of analysis, although the positive residuals at short periods were generally smaller for equivalent-linear.

More meaningful insight into the differences between equivalent-linear and nonlinear ground motion predictions can be made when the codes are exercised at relatively strong shaking levels that induce large strains. Representative results are shown in Figure 16, which shows for the La Cienega site geometric mean horizontal component predicted spectra, amplification factors (=surface/input outcropping spectral accelerations), and spectral shapes (S_a/PGA) for a low-strain condition (left side, which corresponds to observed motions during 2001 event) and a large-strain condition produced through the use of a large amplitude synthetic input motion (right side). The results shown in Figure 16 apply for the baseline geotechnical model described previously. Also shown for reference purposes are predictions of empirical models for amplification (middle frames; Choi and Stewart, 2005) and spectral shape (bottom frames; Campbell and Bozorgnia, 2007). The empirical amplification model is exercised for the site's V_{s30} (260 m/s) and corresponding input *PGA*. The empirical spectrum from which spectral shape is evaluated is calculated using M_w=7.5, site-source distance=10 km, and strike-slip focal mechanism (for synthetic).

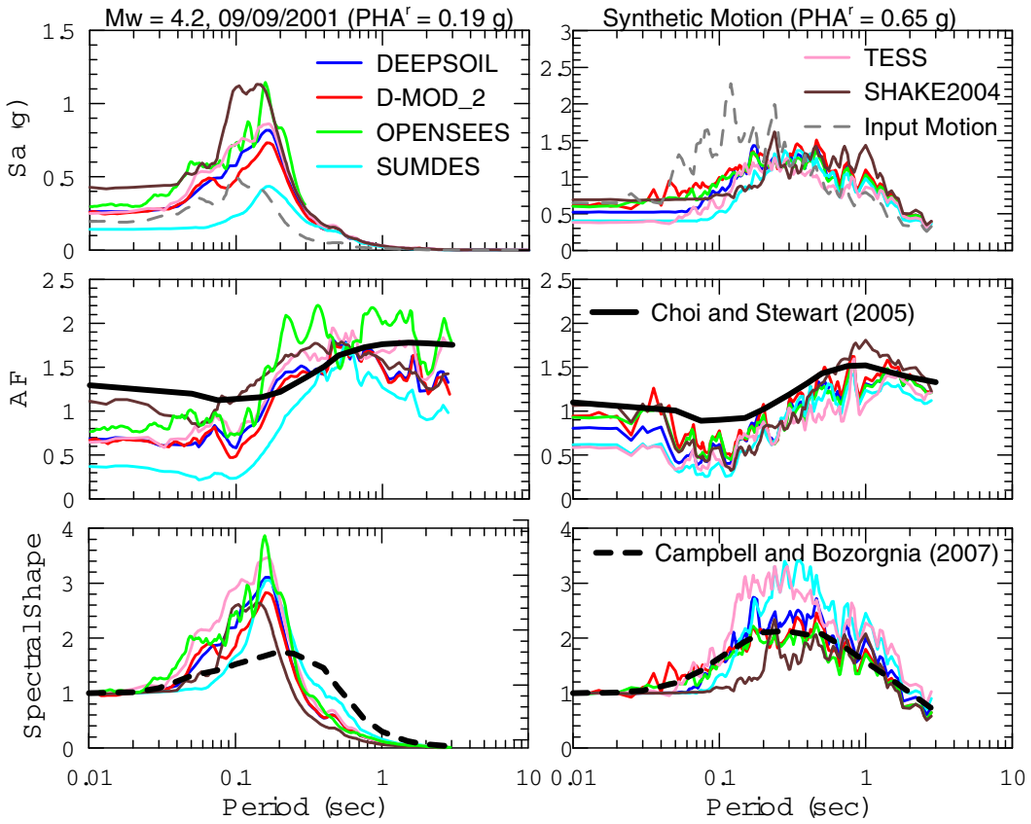


FIG. 16. Comparison of computed spectra, amplification factors, and spectral shapes of predicted motions at La Cienga site

As shown in the bottom frames of Figure 16, the spectral shapes from equivalent-linear and nonlinear models are similar to each other for the 2001 input motion that induces relatively low strain but are significantly different for the large amplitude synthetic

motion. For the large-strain simulation, the spectral shapes at low periods (< ~0.2 sec) from equivalent linear analyses are flatter and have less period-to-period fluctuations than those from nonlinear analyses or empirical models. This aspect of equivalent-linear results is believed to be non-physical and can be overcome with nonlinear analysis. As shown in the middle frames, the flatness of the equivalent linear spectrum is associated with a dip in the amplification factors between periods of approximately 0.03 and 0.3 sec. That dip is less pronounced in the nonlinear codes, which produce amplification factor shapes more compatible with the empirical model.

RECOMMENDATIONS AND CONCLUSIONS

In this article, we present the principal findings of a large, multi-investigatory project directed towards establishing consensus guidelines for the use of nonlinear ground response analyses in engineering practice. Our intent is to make nonlinear analyses more accessible to engineering practitioners and enhance their usage for situations where it is justified. We recognize that the nonlinear codes considered here are one-dimensional, which has its own set of limitations for situations where the site response may be influenced by relatively complex basin geometry or topography.

Nonlinear analyses may provide an improved estimate of ground motion relative to equivalent-linear when ground strains become "large." This can be judged for a given application by examining response spectra and amplification factors from equivalent-linear analysis – caution should be exercised if they exhibit a flat spectrum or a "hole" in the amplification factors at short periods. We speculate that this is caused by overdamping of high-frequency components of ground motion, which occurs principally early in the record (p-waves) when the amplitude of shaking (and material damping) are low. This certainly occurs when shear strains approach 1%, although in deep soil sites it has been observed to occur for peak strains as low as 0.2-0.3%.

When nonlinear analyses are performed, the following guidelines are recommended for code usage and parameter selection:

1. Input motions should be used as-recorded (without modification). Outcropping recorded motions should be applied at the base of a site model with an elastic base. Downhole recorded motions should be applied with a rigid base.
2. For codes that require it, viscous damping should be specified using a full Rayleigh damping formulation with the target damping level ζ_{tar}=small strain soil hysteretic damping. The first matching frequency should be the site frequency. The second frequency should be selected so as to optimize the match of elastic frequency- and time-domain analysis for the site. A reasonable approximation for many applications is to take the second frequency as approximately five times the site frequency.
3. The target backbone curve for a site is best determined through material specific cyclic testing along with dynamic strength testing. If this is not available, the shape of the backbone curve at small- to modest-strains (up to approximately 0.1-0.3%) can be estimated using empirical relationships that take index properties, confining pressure, and stress history as input. Procedures to estimate undrained shear strength through stress

normalization are well established (Ladd, 1991), but require modification for rate effects (e.g., Sheahan et al., 1996).

4. For problems involving small-strain response, target backbone curves can be defined using modulus reduction relationships without consideration of shear strength. For problems involving moderate to large strain response, a hybrid representation that accounts for the shape of the modulus reduction curve at small strains and shear strength at large strain is recommended (see Eq. 2 and Figure 8).
5. Ultimately it is hoped that procedures for simultaneously matching target modulus reduction and material damping curves will be implemented in nonlinear codes, but this is not currently available. At present, users can choose to match the modulus reduction curve only (MR fitting) or modulus reduction and damping curves simultaneously (MRD fitting). We recommend the use of both approaches for large strain problems to bound the solution.

When applied to vertical array sites, these protocols generally produce reasonable results, although there is some indication of possible overdamping at high frequencies and overestimation of site amplification at the resonant frequency of the site model. Additional work to validate and further refine these procedures is ongoing by the project team.

ACKNOWLEDGMENTS

Financial support for the benchmarking of nonlinear ground response analysis procedures was provided by PEER Lifelines project 2G02, which is sponsored by the Pacific Earthquake Engineering Research Center's Program of Applied Earthquake Engineering Research of Lifeline Systems. The PEER Lifelines program, in turn, is supposed by the State Energy Resources Conservation and Development Commission and the Pacific Gas and Electric Company. This work made use of Earthquake Engineering Research Centers Shared Facilities supported by the National Science Foundation under Award #EEC-9701568. In addition, the support of the California Department of Transportation's PEARL program is acknowledged. This work would not have been possible without close collaboration with a number of code developers including Youssef Hashash, Neven Matasovic, Robert Pyke, Zhiliang Wang, and Zhaohio Yang. Their insights and spirit of collaboration are truly appreciated. This project has also benefited from the helpful suggestions of an advisory panel consisting of Drs. Yousef Bozorgnia, Susan Chang, Brian Chiou, Ramin Golesorkhi, I.M. Idriss, Erol Kalkan, Robert Kayen, Steven Kramer, Faiz Makdisi, Geoff Martin, Lelio Mejia, Tom Shantz, Walter Silva, and Joseph Sun. Christine Goulet is thanked for her review of this manuscript.

REFERENCES

Assimaki, D. and E. Kausel (2002). "An equivalent linear algorithm with frequency- and pressure-dependent moduli and damping for the seismic analysis of deep sites," *Soil Dynamics and Earthquake Engrg.*, 22(3), 959-965

Baker, J.W. and C.A. Cornell (2003). "Uncertainty specification and propagation for loss estimation using FOSM methods," *Proceedings, 9th Int. Conf. on Applications of Statistics and Probability in Civil Engineering (ICASP9)*, San Francisco, California: Millpress. 8p.

Chiu, P., D.E. Pradel, A.O.L. Kwok, and J.P. Stewart (2008). "Seismic response analyses for the Silicon Valley Rapid Transit Project," *Proc. 4th Decennial Geotechnical Earthquake Engineering and Soil Dynamics Conference*, ASCE, Sacramento, CA

Chopra, A.K. (2000). *Dynamics of Structures*, 2nd Ed., Prentice Hall

Clough, G.W., and J. Penzien (1993). *Dynamics of Structures*, 2nd Ed., McGraw-Hill, New York.

Darendeli, M. (2001). "Development of a new family of normalized modulus reduction and material damping curves." *Ph.D. Dissertation*, Dept. of Civil Eng., Univ. of Texas, Austin.

Electrical Power Research Institute, EPRI (1993). "Guidelines for determining design basis ground motions," *Rpt. No. EPRI TR-102293*, Palo Alto, CA.

Hardin, B.O. and V.P. Drnevich (1972). "Shear modulus and damping in soils: design equations and curves," J. of the Soil Mechanics and Foundations Div., ASCE, 98 (SM7), 667-692

Hashash, Y.M.A. and D. Park (2001). "Non-linear one-dimensional seismic ground motion propagation in the Mississippi embayment," *Eng. Geology*, 62(1-3), 185-206.

Kausel, E. and D. Assimaki (2002). "Seismic simulation inelastic soils via frequency-dependent moduli and damping." *J. of Engrg. Mech.*, ASCE, 128(1), 34-47.

Kwok, O.A., J.P. Stewart, and, Y.M.A. Hashash (2008) "Nonlinear ground response analysis of Turkey Flat shallow stiff soil site to strong ground motion," *Bull. Seism. Soc. Am.*, 98 (1), in press.

Kwok, O.A., J.P. Stewart, Y.M.A. Hashash, N. Matasovic, R. Pyke, Z. Wang, and Z. Yang (2007). "Use of exact solutions of wave propagation problems to guide implementation of nonlinear seismic ground response analysis procedures," *J. Geotech. & Geoenvir. Engr.,* ASCE, 133 (11), 1385-1398.

Ladd, C.C. (1991). "Stability evaluation during staged construction: 22nd Terzaghi Lecture." *J. Geotech. Engr.*, ASCE, 117(4), 537-615.

Lo Presti, D.C.F., C.G. Lai, and I. Puci (2006). "ONDA: Computer code for nonlinear seismic response analyses of soil deposits." *J. of Geotech. and Geoenvir. Eng.*, ASCE, 132(2), 223-236

Masing, G. (1926). "Eigenspannungen and verfertigung beim messing." *Proc. 2nd Int. Congress on Applied Mech.*, Zurich.

Matasovic, N. and M. Vucetic (1993). "Cyclic Characterization of Liquefiable Sands," *J. of Geotech. Eng.*, ASCE, 119(11), 1805-1822

Melchers, R.E. (1999). *Structural Reliability Analysis and Prediction*. John Wiley and Sons, Chichester.

Park, D. and Y.M.A. Hashash (2004). "Soil damping formulation in nonlinear time domain site response analysis," *J. of Earthquake Eng.,* 8(2), 249-274.

Parra, E. (1996). "Numerical modeling of liquefaction and lateral ground deformation including cyclic mobility and dilation response in soil systemsm" *PhD Dissertation*,

Dept. of Civil Engrg., Rensselaer Polytechnic Institute, Troy, NY.

Pyke, R.M. (1979). "Nonlinear soil models for irregular cyclic loadings," *J. Geotech. Eng.*, ASCE, 105(GT6), 715-726.

Ragheb, A. M. (1994)."Numerical analysis of seismically induced deformations in saturated granular soil strata," *PhD Dissertation*, Dept. of Civil Eng., Rensselaer Polytechnic Institute, Troy, NY.

Seed, H.B. and I.M. Idriss (1970). "Soil moduli and damping factors for dynamic response analyses," *Report EERC 70-10*, Earthquake Engineering Research Center, University of California, Berkeley.

Sheahan, T.C., C.C. Ladd, and J.T. Germaine (1996). "Rate-dependent undrained shear behavior of saturated clay." *Journal of Geotechnical Engineering*, ASCE, 122(2), 99-108

Stewart, J.P., A.O.L. Kwok, Y.M.A. Hashash, N. Matasovic, R. Pyke, Z. Wang, Z. Yang (2007) "Benchmarking of nonlinear grotechnical ground response analysis procedures." *Rpt. No. PEER-2007/XX*, Pacific Earthquake Engineering Research Center, Univ. of California, Berkeley (in press).

Sun, J.I., R. Golesorkhi, and H.B. Seed (1988). "Dynamic moduli and damping ratios for cohesive soils," *Rpt. No. UCB/EERC-88/15*, Earthquake Engineering Research Center, Univ. of California, Berkeley.

Toro, G. R. (1997). ''Probabilistic models of shear-wave velocity profiles at the Savannah River site, South Carolina.'' *Rep. to Pacific Engineering and Analysis*, El Cerrito, Calif.

Vucetic, M. (1990). "Normalized behavior of clay under irregular cyclic loading." *Canadian Geotech. J.*, 27, 29-46.

Vucetic, M. and R. Dobry (1991). "Effect of soil plasticity on cyclic response," *J. Geotech. Engrg.*, ASCE, 117(1), 89-107.

Wang, Z.L. (1990). "Bounding surface hypoplasticity model for granular soils and its applications." *PhD. Dissertation*, Univ. of Calif., Davis

Wang, Z.L., Q.Y. Han, and G.S. Zhou (1980). "Wave propagation method of site seismic response by visco-elastoplastic model," *Proc. of Seventh World Conf.e on Earthquake Eng.*, V2, 379-386

Weiler, W.A. (1988). "Small strain shear modulus of clay," *Proc. of ASCE Conference on Earthquake Engineering and Soil Dynamics II: Recent Advances in Ground Motion Evaluation*, Geotechnical Special Publication 20, ASCE, New York, 331-345.

Yang, Z. (2000). "Numerical modeling of earthquake site response including dilation and liquefaction," *PhD Dissertation*, Dept. of Civil Eng. and Eng. Mech., Columbia University, NY, New York

Youngs, R.R. (2004). *Software validation report for SHAKE04*, Geomatrix Consultants

Zhang, J., R.D. Andrus and C.H. Juang (2005) "Normalized shear modulus and material damping ratio relationships," *J. Geotech. and Geoenvir. Eng.*, ASCE, 131(4), 453-464.

Assessment of Ground Motion Selection and Modification (GMSM) methods for non-linear dynamic analyses of structures

Christine A. Goulet[1], UCLA, Jennie Watson-Lamprey[2], Watson-Lamprey Consulting, Jack Baker[3], Stanford University, Curt Haselton[4], CSU Chico, Nico Luco[5], USGS.

[1] PhD Candidate, Department of Civil and Environmental Engineering, University of California, Los Angeles, CA, 90095 goulet@ucla.edu
[2] President, Watson-Lamprey Consulting, 1212 32nd St., Oakland, CA 94608, Jennie.WatsonLamprey@gmail.com
[3] Assistant Professor, Stanford University, Stanford, CA, 94305, bakerjw@stanford.edu
[4] Assistant Professor, Department of Civil Engineering, California State University Chico, Chico, CA, 95929-0930, chaselton@csuchico.edu
[5] Research Structural Engineer, United States Geological Survey, PO Box 25046, MS 966, Denver, CO 80225, nluco@usgs.gov

ABSTRACT

As non-linear response history analyses are becoming more prevalent in practice, there is a need to better understand how the selection and modification (e.g., amplitude scaling or spectrum matching) of records will influence the resulting structural response predictions. There are currently many methods of ground motion selection and modification available, but little guidance is available to engineers on which methods are appropriate for their specific application. The Ground Motion Selection and Modification Program was formed within the Pacific Earthquake Engineering Research (PEER) Center to address this issue. This paper presents the current methodology developed by the Program as well as sample results from the first pilot study completed in 2006. Preliminary results show that for a first-mode-dominated structure, one can improve the prediction of its response by taking into account record properties that are important to the non-linear response of the building when selecting and scaling ground motion records.

INTRODUCTION

There are currently many methods of ground motion selection and modification (GMSM) available for use in dynamic analyses. Unfortunately, there is no consensus as to the accuracy and precision of these methods in predicting the structural

response, thus the choice of which method to use remains largely subjective. This has a significant impact on the engineering community since non-linear response is sensitive to the selection and modification of input ground motions.

The Ground Motion Selection and Modification (GMSM) Program was formed to confront these issues (http://peer.berkeley.edu/gmsm/). One of the main objectives of the GMSM Program is to systematically review different GMSM procedures, and evaluate their respective accuracy and precision in predicting nonlinear dynamic structural responses. As a central part of this effort, the GMSM Program is currently collaborating with over 20 researchers and practitioners in the fields of Earthquake Engineering and Seismology. The list of collaborators includes several who are contributing to the development of new performance-based design criteria as part of the PEER Tall Buildings Initiative (http://peer.berkeley.edu/tbi/). The program intends for its results to become an important resource for engineers using non-linear dynamic analyses in their projects.

GMSM METHODS

The first task of the GMSM Program was to compile a list of existing GMSM methods. To date a list of over 40 different methods and variants has been developed.

In order to compare the methods in a consistent manner, they were first grouped according to their objective. Some methods aim to estimate the average (or median) structural response for a given earthquake scenario, whereas others also attempt to estimate the corresponding variability in structural response. For some methods, the earthquake scenario is defined by only its magnitude and distance to the location of the structure (as well as other characteristics of the rupture and site in some cases), whereas for others the ground motion amplitude (e.g., spectral acceleration at the fundamental period of the structure) at the location is additionally specified. Each of these cases are being considered in this overall effort, but this paper focuses on methods for which the objective is prediction of the median structural response for a given earthquake magnitude, source-to-site distance and a ground motion amplitude parameter.

In order to organize the comparison of results, these methods have also been grouped into the following general categories:

- Methods based on scaling to a Uniform Hazard Spectrum (UHS) associated with the target spectral acceleration of the first-mode of the structure, $Sa(T_1)$. These methods include the approach prevalent in current building codes (e.g., ASCE Standard 7-05, 2005).

- Methods that take into account the record properties that tangibly affect the non-linear response of the structure. These methods include those based on spectral shape, and those that account for the non-linear response through record properties other than spectral acceleration.

To date, the only GMSM methods studied in detail are those that directly scale existing records. Spectrum-compatible motions and synthetic motions will be addressed in later studies.

METHODOLOGY OVERVIEW

The GMSM Program is working toward systematically assessing many different GMSM methods for multiple earthquake scenarios and a large variety of non-linear structures, including buildings, bridges, earth dams, nuclear power-plants, etc. To this end, the GMSM Program is currently working on a set of pilot studies, each with the same basic methodology. This section explains the assessment methodology used in the Program, as applied to the first pilot study, which was initiated in 2006. In this study, the non-linear response of a code-conforming four-story reinforced concrete frame building was analyzed for a deterministic seismic event. The structural model used in the initial analysis was developed at Stanford University for the collaborative "PEER Benchmark Project" with researchers at the University of California at Los Angeles and the California Institute of Technology (Goulet et al. 2007). For the second phase of studies, initiated in 2007, three additional structural models were introduced and the methodology was applied in the same manner. The goal of these studies is to determine which GMSM methods produce unbiased estimates of structural response parameters with low standard error, and to understand what elements of these methods contribute to a better prediction. Once this is determined, predicting the full distribution of response will then be addressed by the Program.

Earthquake Scenarios

The choice of earthquake scenarios was dictated by an interest in the practical relevance of the findings of this study. The first event considered is a strike-slip fault rupture, magnitude 7 earthquake, 10 km from a site with a V_{s30} of 400 m/s (average shear wave velocity of the upper 30 meters of the soil column). A second similar scenario event of magnitude 7.5 was also defined for the same site conditions and style of faulting. In California, a magnitude 7 or 7.5 event within 20 km is often a hazard-controlling source and the site condition represents an average stiffness for alluvial deposits in urban areas. In an effort to push the structural response well into the non-linear range, the target ground motion level for the M7 event has been defined as the 98^{th} percentile prediction, which is equivalent to the median plus two standard deviations, or an epsilon (ε) value of 2. Another reason to use $\varepsilon = 2$ is that the relatively large epsilon leads to a more significant difference between those methods that take epsilon (or another indicator of spectral shape) into account and those that do not. Epsilon values around 2 are also not uncommon for seismic hazard in California at or beyond the 2% in 50 year exceedance code requirement. For the second M7.5 scenario, the 84^{th} percentile is used (equivalent to $\varepsilon = 1$), which is consistent with the deterministic ground motions currently used for design near many major faults. Results for both scenarios (M=7, $\varepsilon = 2$ and M=7.5, $\varepsilon = 1$) will be compared for a selected structure in an effort to generalize the results.

Structural Models

Table A shows the structural models developed for these systematic studies. The four building models considered so far are all reinforced-concrete structures. Buildings A, B and C are modeled in OpenSees (OpenSees, 2007) and building D is modeled in Drain-2DX (Prakash et. al. 1993). Additional information regarding the models can be found in Haselton (2006) and Zareian (2006). While selecting structures, there was a desire to cover a range of height and number of stories (and first-mode period (T_1)), and varying expected levels of non-linearity in the structure. All the structures were analyzed for the M7, ε =2 scenario. Structure C was also analyzed for the M7.5, ε =1 scenario. The shear-wall structure (D) was chosen to be 12 stories tall for comparison with the 12-story frame (B). Although there are differences in the modeling details between the OpenSees and the Drain models, it is interesting to compare the two general structural types. For reasons of brevity, this paper shows only the results for building A with the M7, ε =2 scenario.

Table A. Summary of structural models

Building	*Stories*	*Type*	*Compliance*	T_1^* *(s)*
A	4	Modern special moment frame	2003 IBC, ASCE7-02, ACI 318-02	0.97
B	12	Modern special moment frame	2003 IBC, ASCE7-02, ACI 318-02	2.01
C	20	Modern special moment frame	2003 IBC, ASCE7-02, ACI 318-02	2.63
D	12	Modern (ductile) planar shear wall	None specifically, but consistent with modern planar wall design	1.20

* First-mode natural period.

GMSM Suite Solicitation

Ground motion records were solicited from GMSM method developers and users. The contributors were asked to provide suites of seven ground motions selected and scaled to predict median structural response given the magnitude 7 earthquake at a distance of 10 km from the site defined earlier and 98th percentile spectral acceleration at the fundamental period of the structure. The initial choice of requesting seven records was based on building code requirements (ASCE 2005). For the first round (building A), 112 time series, comprising 16 suites of ground motion records were submitted.

For the second study, the request was for four independent sets of seven time series for each structure and earthquake scenario. Each set of seven records is used to predict the median structural response, and the difference in prediction between sets is noted. In addition, the combined set of 28 records will be used to estimate both the median and standard deviation of response conditioned on the given event. This will

allow the group to address the question of the minimum number of ground motions that should be used to efficiently and sufficiently predict the response.

The Point of Comparison

A point of comparison for the median structural response conditioned on 98th percentile ground motion (spectral acceleration) at the fundamental period of the structure for the specified earthquake is calculated using a large suite of earthquake records corresponding to the desired earthquake scenario. An extensive set of structural simulations is performed for this suite of records consistent with the specified earthquake scaled by factors of 1, 2, 4 and 8. A regression is then performed, which takes into account spectral shape and removes the effects of scaling bias. This regression is used to obtain a probability distribution for the Engineering Demand Parameter (EDP) of interest. The point of comparison analysis takes into account differences in spectral shape, magnitude, distance and other record properties. Additional information regarding this procedure can be found in Watson-Lamprey (2007). Figure 1 shows the predicted probability density function for the maximum inter-story drift ratio (MIDR) of Building A. The MIDR is the EDP of interest in this paper, and the median prediction below is used as a point of comparison for the predictions of all the GMSM methods being considered.

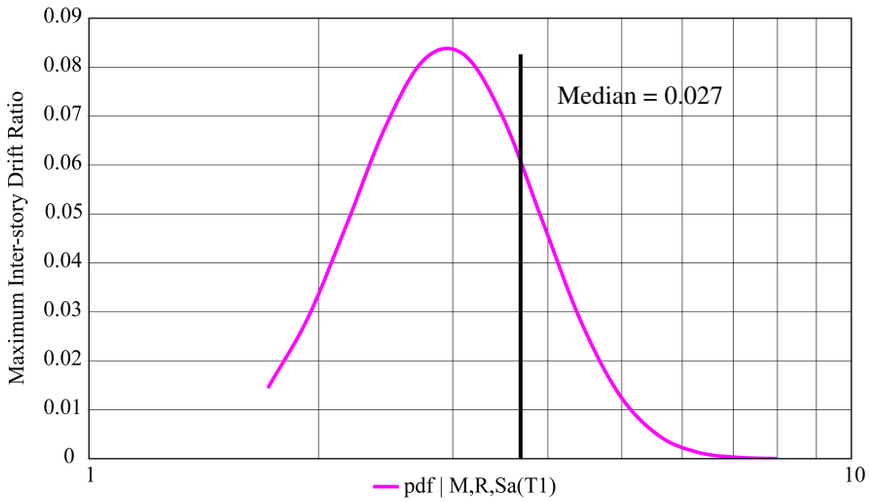


FIG. 1. Probability density function for maximum inter-story drift ratio of building A for the M7 deterministic earthquake scenario.

SAMPLE RESULTS

The following results are for building A for the M=7, ε =2 scenario. The maximum inter-story drift ratios (MIDR) for each of the ground motion records submitted for building A are shown on Figure 2. The median of the seven MIDR values is shown as a long dash for each method, while the red line represents the point of comparison value of 0.027. There is large scatter in the MIDR values predicted for each ground motion of a single ground motion suite, and there is also large variability in the median predicted values from each suite.

Methods 1 through 10 all fall in the first group of methods: those based on scaling to a UHS, such as in code-based methods. The results from suites 1 through 10 exhibit a large scatter. They also tend to overestimate the median response. All these suites matched, on average, the 98th-percentile random horizontal ground motion elastic response spectrum, but recall that the median MIDR of interest is conditioned on only the spectral value at the first mode.

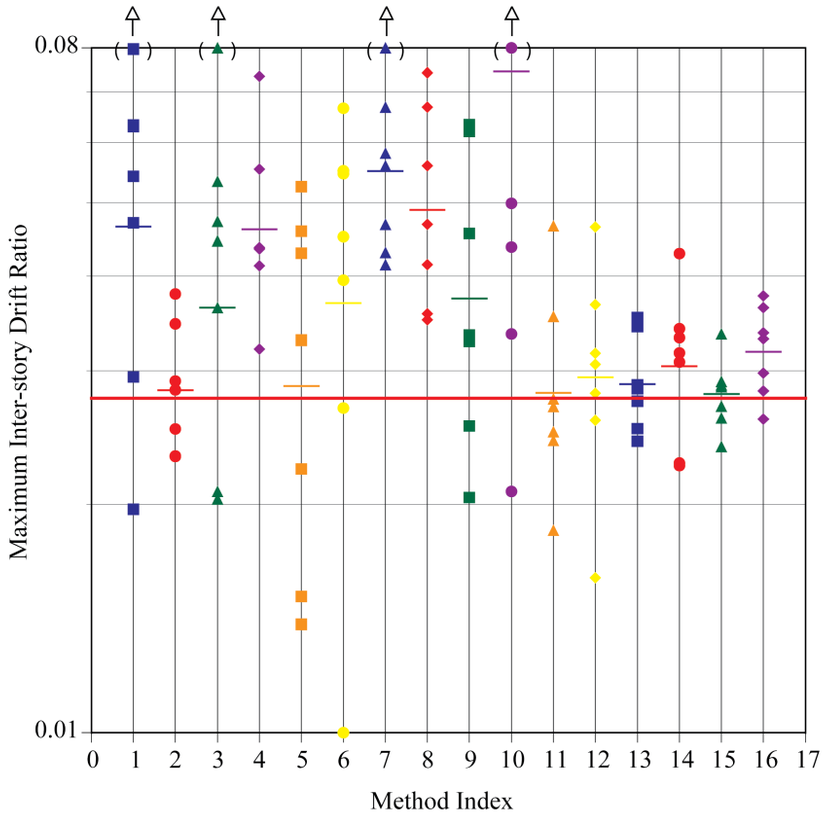


FIG. 2. Summary of results for ground motions submitted, building A. The horizontal red line represents the point of comparison.

Since the structure is non-linear, the *effective* first mode period increases as it yields. The spectral shape beyond the original fundamental period is therefore important when predicting MIDR. The expected response spectrum for a given set of magnitude, distance and ε or *Sa(T)* values is called the conditional mean spectrum (CMS). Computation of the condition mean spectrum requires knowledge of a mean and standard deviation of logarithmic spectral acceleration at all periods, as given by a ground motion prediction (attenuation) model, and a target magnitude, distance and "ε" value from either a target scenario or a probabilistic seismic hazard analysis disaggregation. In addition, the knowledge of correlations between *Sa* values at two periods is required, which is available in the form of an analytical predictive equation obtained from empirical studies (Baker and Cornell 2006). The CMS for structure A is shown on Figure 3. The spectral shape beyond the fundamental period conditioned

on the 98th percentile values is lower than the 98th percentile spectrum, as indicated by the CMS. In effect, these suites (1 through 10) were attempting to predict the response from a more extreme realization of earthquake ground motions. The CMS was identified as an important part of many GMSM methods and was thus included in the second-phase solicitation sent out in 2007.

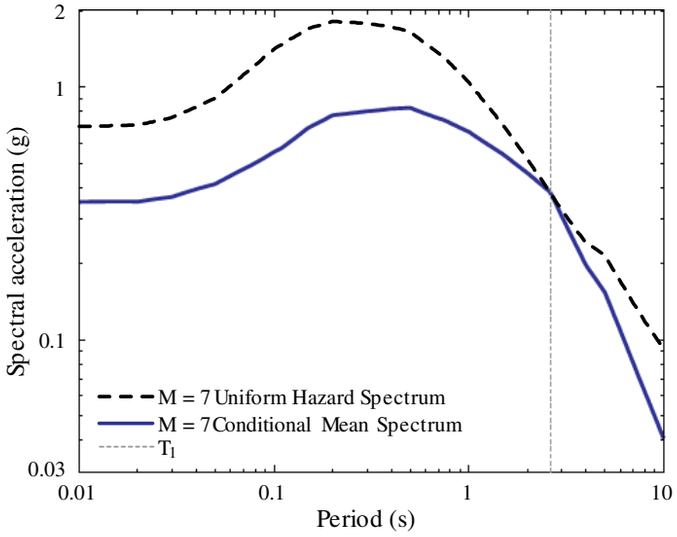


FIG. 3. Conditional mean and uniform hazard spectra for M7, ε =2 scenario, building A.

Methods 11 through 16, on the other hand, incorporate record properties that tangibly affect the non-linear response of the structure. Some by either tracking the expected spectral shape or selecting/scaling based on the expected values of other record properties that are important for non-linear response. These suites exhibit much smaller dispersion and appear to provide estimates of the median maximum inter-story drift ratio with a greater degree of accuracy.

Examples of Spectra Obtained from Two Methods

The different scaled spectra for method 9 are shown in Figure 4 as a representative example of the first group of methods. This method over-predicted the MIDR by about 30% relative to the point of comparison. There is a large scatter in the spectra, but they match on average the target 98th-percentile ground motion from short periods up to a period of approximately three seconds.

Figure 5 shows the scaled spectra for method 15. This suite predicted the median maximum inter-story drift ratio within 1% of the point of comparison. The spectra for method 15 only match the 98th-percentile predicted ground motion at the fundamental period. There is a smaller scatter in the spectra beyond the fundamental period compared to method 9 (Figure 4) and, on average, the spectra fall lower on the graph.

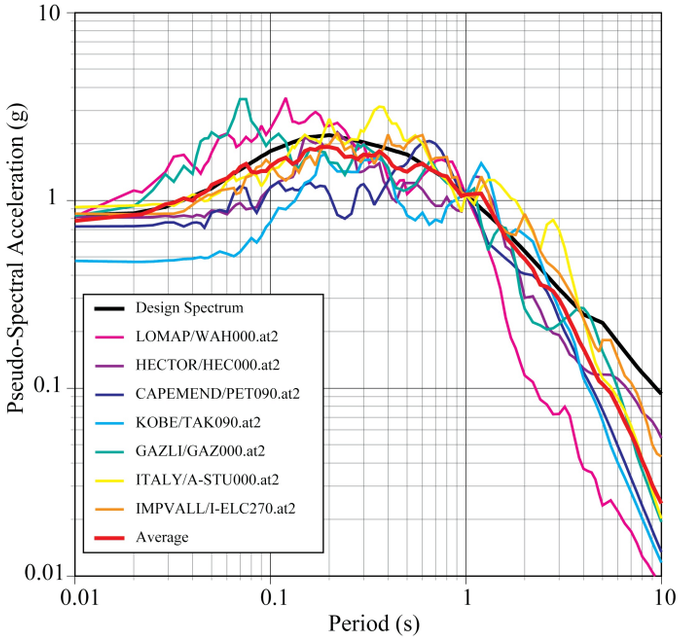


FIG. 4. Example of scaled spectra for method 9.

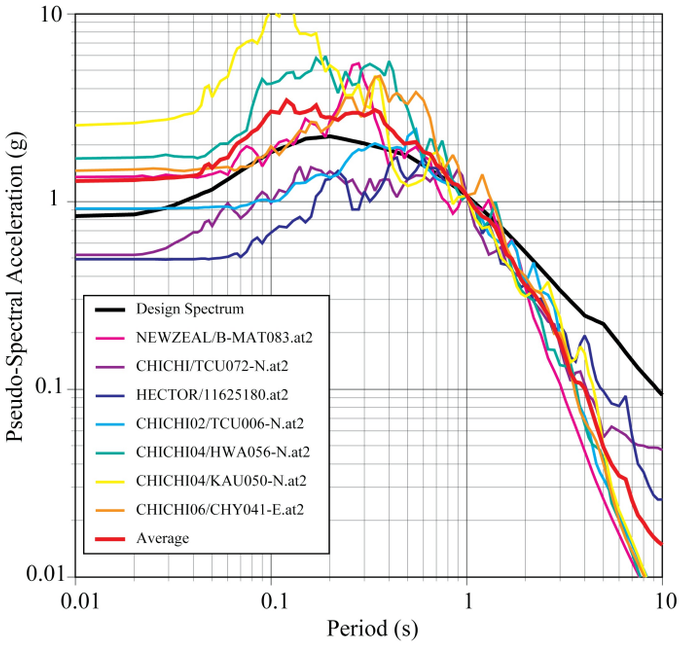


FIG. 5. Example of scaled spectra for method 15.

It is interesting to note that although these differences in spectral shape might be considered rather small, they do have an important consequence on the median MIDR predictions (overestimation by 30% in one case and within 1% in the other).

CONCLUSIONS AND FUTURE EFFORTS

The paper presented an overview of the current GMSM Program methodology for evaluating ground motion selection and modification methods for non-linear structural dynamic analyses. Sample results from the first pilot study have also been presented. These preliminary results show that GMSM methods that consider ground motion properties that tangibly affect the non-linear response of the structure tend to offer a better prediction of the maximum inter-story drift ratio. These methods provide a better median prediction, relative to the point of comparison, with a smaller dispersion.

Evaluating predictions of median structural response parameters for buildings is an important first step towards identifying appropriate ground motion record selection and modification methods, but MIDR is not the only response quantity of interest, nor are buildings the only application for non-linear dynamic analysis. The GMSM Program plans to generalize these findings and provide the engineering community with GMSM recommendations. This will involve future work in performing similar evaluations for prediction of variability in structural response, looking at additional response quantities such as peak floor accelerations and peak base shear, and performing comparisons for other types of systems for which non-linear dynamic analysis is performed (e.g. bridges, dams, nuclear power-plants, etc.).

The GMSM Program is currently evaluating GMSM methods for the three newly-added structures (buildings B, C and D). The results from this wider range of structural types will expand and generalize the findings of this paper, and ensure that the conclusions drawn from the overall study will be valid under more general conditions. Future efforts will continue widening the range of structures analyzed, and extend the methodology for study of spectrum-matched and simulated ground motions.

ACKNOWLEDGMENTS

This paper is dedicated to the memory of Professor Allin Cornell. He was an active player in the GMSM Program, a pioneer to our field and a mentor for many...

This work was supported primarily by the Earthquake Engineering Research Centers Program of the National Science Foundation, under award number EERC-9701568 through the Pacific Earthquake Engineering Research Center (PEER). Any opinions, findings, and conclusions or recommendations expressed in this material are those of the authors and do not necessarily reflect those of the National Science Foundation. Supplementary funding was also provided to Christine Goulet from the National Sciences and Engineering Research Council of Canada, and to Curt Haselton from the Pacific Gas and Electric Company. The authors would like to thank the other GMSM Program leaders: Norm Abrahamson, Erol Kalkan, Tom Shantz, Nilesh Shome, Polsak Tothong, and Farzin Zareian. The GMSM Program would also like to thank the contributing researchers and practitioners for their time and effort in providing

ground motion record suites and ideas. Without their help and collaboration, this work could not have been achieved. These contributors are: Arzhang Alimoradi, Paolo Bazzurro, Jamshid Ghaboussi, Charles Kircher, Stephen Mahin, Frank McKenna, Coleen McQuoid, Praveen Malhotra, Jack Moehle, Farzad Naeim, Maury Power, Ellen Rathje, Brian Skyers, Jonathan Stewart, Gang Wang, Andrew Whittaker, Tony Yang and Bob Youngs. A special thank you goes to Yousef Bozorgnia who has led and guided the Program for its first two years.

REFERENCES

American Concrete Institute (2002). Building Code Requirements for Structural Concrete (ACI 318-02), Farmington Hills, MI.

American Society of Civil Engineers (2005). ASCE7-05: Minimum Design Loads for Buildings and Other Structures, Reston, VA.

American Society of Civil Engineers (2002). ASCE7-02: Minimum Design Loads for Buildings and Other Structures, Reston, VA.

Baker, J. W., and Cornell, C. A. (2006). "Correlation of response spectral values for multi-component ground motions." *Bulletin of the Seismological Society of America*, Vol. 96(1): 215-227.

Goulet, C.A., Haselton, C.B., Mitrani-Reiser, Beck, J.L., Deierlein, G., Porter, K.A., Stewart, J.P. (2007). "Evaluation of the Seismic Performance of a Code-Conforming Reinforced-Concrete Frame Building - From Seismic Hazard to Collapse Safety and Economic Losses." *Earthquake Engineering and Structural Dynamics,* Vol. 36(13): 1973-1997.

Haselton, C.B. (2006). Assessing Seismic Collapse Safety of Modern Reinforced Concrete Moment Frame Buildings, Ph.D. Dissertation, Department of Civil and Environmental Engineering, Stanford University.

International Code Council (2003). 2003 International Building Code, Falls Church, VA.

Pacific Earthquake Engineering Research Center (2006). PEER NGA Strong Motion Database, University of California, Berkeley, http://peer.berkeley.edu/nga/

Prakash, V., Powell, G. H., Campbell, S. (1993). DRAIN-2DX: basic program description and user guide. *Report No. UCB/SEMM-93/17*. University of California at Berkeley, Berkeley, California.

Open System for Earthquake Engineering Simulation (2007). OpenSees user's manual. Pacific Earthquake Engineering Research Center, University of California, Berkeley, http://opensees.berkeley.edu/

Watson-Lamprey, J. A. (2007). "Selection and Scaling of Ground Motion Time Series", Ph.D. Dissertation, Department of Civil and Environmental Engineering, University of California, Berkeley

Zareian, F. (2006). "Simplified Performance-Based Earthquake Engineering". Ph.D. Dissertation, Department of Civil and Env. Engineering, Stanford University.

Identification of near-fault velocity pulses and prediction of resulting response spectra

Jack W. Baker[1], M. ASCE

[1]Assistant Professor, Dept. of Civil and Environmental Eng.; Terman Engineering Center #240, Stanford University, Stanford, CA 94304; bakerjw@stanford.edu

ABSTRACT: Pulse-like near-fault ground motions resulting from directivity effects are a special class of ground motions that are challenging to characterize for seismic performance assessment. These motions contain a pulse in the velocity time history of the motion, often occurring in the direction perpendicular to the fault rupture at locations near the fault where the earthquake rupture has propagated towards the site. A recently proposed wavelet-based signal processing approach is used on a large ground motion library to empirically identify these pulses in ground motions. Example results are presented to demonstrate that the identified motions are often observed at sites where directivity effects are expected (although no claim is made that all observed pulses are due to directivity). The response spectra of these records are then studied using this approach, and it is seen that their spectra can be described using an existing ground motion prediction (attenuation) model coupled with a narrow-band amplification function in the region of the pulse period. The modified prediction can be incorporated in probabilistic seismic hazard analysis, providing a direct and transparent method of accounting for directivity effects.

INTRODUCTION

Pulse-like near-fault ground motions resulting from directivity effects are a special class of ground motions that are particularly challenging to characterize for seismic performance assessment. These motions contain a 'pulse' in the velocity time history of the motion, ideally in the direction perpendicular to the fault rupture, and generally occurring at locations near the fault where the earthquake rupture has propagated towards the site (see examples in Figure 1). Despite our growing understanding of these ground motions, it is still difficult to identify this effect and account for it in ground motion prediction (attenuation) models.

The author recently proposed a ground motion processing that allows for automated detection of directivity pulses (Baker 2007). That detection scheme is here used on a large ground motion library to empirically identify those records containing pulses.

Those records are then analyzed to determine the effect of the pulses on resulting response spectra. This analysis is needed to for so-called narrow-band predictions of response spectra from near-fault ground motions, which can then be incorporated into a generalization of probabilistic seismic hazard analysis that accounts for directivity effects (Tothong et al. 2007). Taken with other parallel developments, this work helps point the way towards a comprehensive framework to understand and account for directivity effects in engineering design. The benefits of such an approach are improved understanding of the impact that directivity has on seismic hazard, a more transparent method of accounting for these effects, and a potential reduction in conservatism associated with using "worst case" directivity scenarios for design.

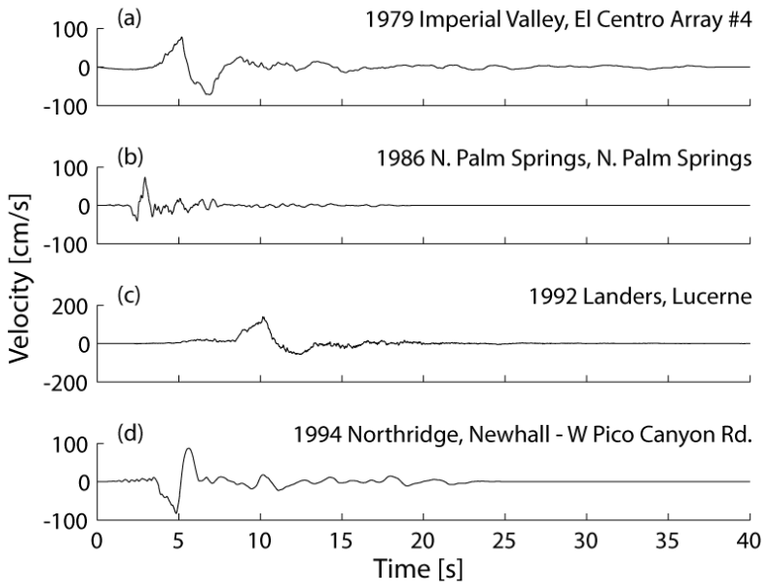


Figure 1: Four example pulse-like near-fault ground motions.

PULSE IDENTIFICATION AND EXTRACTION

The pulse extraction procedure used here relies on wavelet analysis to identify large pulses in the velocity time history of a ground motion (e.g., Mallat 1999). The wavelet transform is analogous to a Fourier transform, except that non-stationary functions are used for the decomposition instead of continuous sine functions in the case of the Fourier transform. A variety of "mother wavelets" can be used for the analysis; this mother wavelet is scaled (dilated) and translated to represent various components of the signal. A wavelet basis function is thus defined as

$$\Phi_{s,l}(t) = \frac{1}{\sqrt{s}}\Phi\left(\frac{t-l}{s}\right) \tag{1}$$

where $\Phi(\cdot)$ is the mother wavelet function, s is the scale parameter that dilates the wavelet, and l is the location parameter that that translates the wavelet in time. The ground motion of interest is then transformed into coefficients for these wavelet

functions with varying scale and location. There are two types of wavelet transforms available to analysts. Loosely speaking, the *discrete wavelet transform* computes only coefficients for the minimum number of wavelet basis functions needed to reconstruct a signal, while the *continuous wavelet transform* computes coefficients for every possible scale and location. Here the continuous transform is used, as it will precisely identify the scale and location of large velocity pulses of interest.

The utility of this signal processing procedure is that if the wavelet basis function is similar in shape to velocity pulses caused by directivity, then the velocity pulse will show up in the wavelet transform as a large coefficient for the wavelet having a scale and location associated with the pulse. That wavelet coefficient can be used to both detect the presence of a pulse, as well as to extract the pulse from the ground motion.

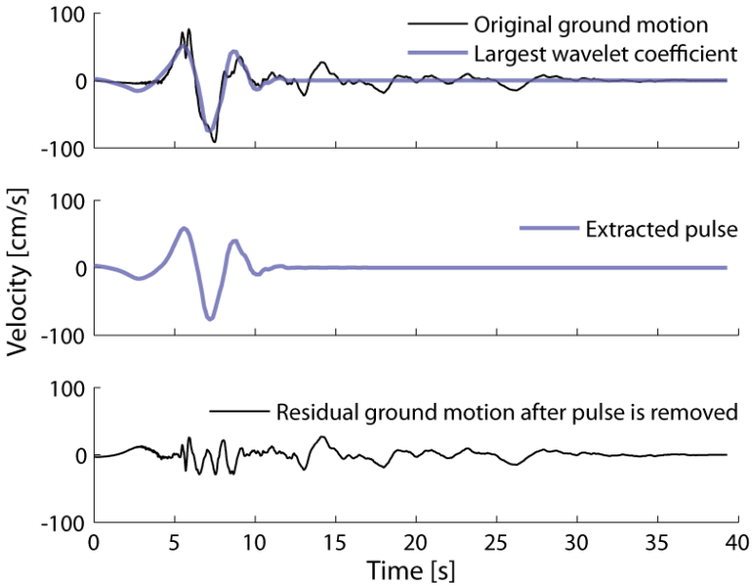


Figure 2: Illustration of the decomposition procedure used to extract the pulse portion of the 1979 Imperial Valley El Centro Array #5 recording.

Results from this algorithm are shown in Figure 2. The continuous wavelet transform is performed on the original ground motion, and the largest wavelet coefficient is identified. That wavelet, which represents the largest velocity pulse in the signal, is then refined by adding up to nine additional wavelets having the same dominant frequency and located in the region of the original wavelet. The refined pulse is then subtracted from the original ground motion, leaving a residual ground motion that contains all information not included in the pulse. Pulses are identified by comparing the peak ground velocity and energy of the residual ground motion relative to the original ground motion. This wavelet-based extraction procedure is the most important part of the pulse-identification approach, but two additional criteria were proposed as potentially useful supplemental tests. First, ground motions with a peak ground velocity of less than 30 cm/s were excluded from consideration, as the low peak velocity would suggest that even if a pulse-like feature is present in a given ground motion, the low ground motion amplitude suggests that the feature may not be

caused by directivity. Second, a criterion was applied to ensure that the velocity pulse appears early in the strong ground shaking, where a directivity pulse is expected to occur. Complete details of this algorithm, which has been described only schematically here, are given by Baker (2007).

OBSERVATIONS FROM PAST EARTHQUAKES

One benefit of this analysis procedure is that large numbers of ground motions can be processed. The algorithm requires only a few seconds on a desktop computer to analyze a typical ground motion (consisting of several thousand discrete velocity values), so the approximately 3500 fault-normal ground motions from the Next Generation Attenuation (NGA) project were analyzed, and 91 pulse-like ground motions were detected. It should be noted that not all of these pulses are necessarily caused by directivity effects, although individual study of the records suggests that at least a majority are. (In particular, long-period record processing can make a static displacement due to fling effects look like a directivity pulse.) Because this procedure is at present the only way to automatically classify large numbers of ground motions, it has been implemented in the Pacific Earthquake Engineering Research (PEER) center's Design Ground Motion Library (DGML).

Having this large set of classified ground motions allows for several new ways to study pulses. Figure 3 shows maps of locations with ground motion recordings in past earthquakes, with the style of the points indicating the classification of that particular recording. It can be seen that pulses are generally observed at locations close to the fault where the rupture propagated towards the site. It is also interesting to note that at some sites very close to the faults, no pulse is observed, indicating that even at locations where directivity effects are likely, they are not certain to occur. Iervolino and Cornell (2007) have used regression analysis on this dataset to develop predicted probabilities of occurrence of pulses, as a function of several predictor variables relating to source/site geometry.

The period of an extracted velocity pulse can be defined as the period for which the Fourier spectrum of the pulse's wavelet is maximized. Many authors have noted a dependence of pulse period on the magnitude of the causal earthquake, and that trend was also confirmed using this dataset (e.g., Bray and Rodríguez-Marek 2004; Mavroeidis and Papageorgiou 2003; Somerville 2003). Baker (2007) obtained the following predictive relationship for pulse period

$$E\left[\ln T_p\right] = -5.78 + 1.02M \tag{2}$$

where T_p is the period of the pulse (as determined using wavelet analysis), $E[\ ]$ denotes an expected (mean) value, and M is the earthquake's moment magnitude. The standard deviation of observed $\ln T_p$ values about this mean prediction is 0.55.

RESPONSE SPECTRA OF PULSE-LIKE MOTIONS

The effect of near-fault directivity on observed response spectra was first studied

systematically by Somerville et al. (1997), who predicted a broad-band modification to amplify all spectral values monotonically as a function of source/site geometry parameters that suggest directivity effects might be present. But a more accurate model would amplify spectral accelerations only in a narrow band around the pulse period. (Alavi and Krawinkler 2001; Fu and Menun 2004; Somerville 2003; Tothong and Cornell 2007).

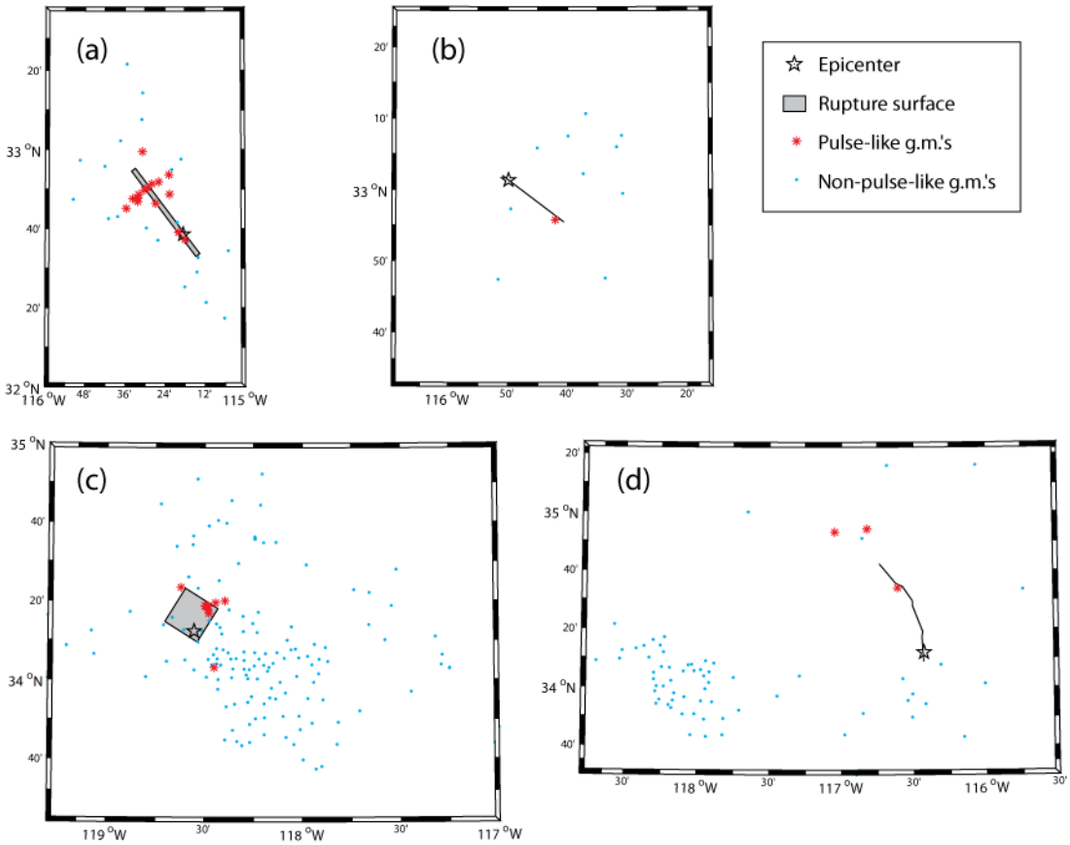


Figure 3: Maps of rupture projection and observed ground motions from four example earthquakes: (a) 1979 Imperial Valley, (b) 1987 Superstition Hills, (c) 1994 Northridge, (d) 1992 Landers.

The wavelet decomposition described above greatly facilitates quantification of the effect of the pulse on the response spectrum. In Figure 4, (pseudo) acceleration spectra of four pulse-like motions are shown, along with spectra of the motions after the pulses have been extracted. Median predicted spectra (Boore and Atkinson 2007) are also shown, as well as marks indicating the motions' pulse periods. It is apparent that the pulses cause amplification of the records' spectra, in the region of the pulse period. These amplification regions are shaded in Figure 4 for emphasis.

To more systematically quantify this amplification effect, the response spectra of all 91 pulse-like motions were studied. Two normalizations were performed to facilitate comparison of the records. Rather than study the response spectra directly, deviations from predicted spectra were computed. These deviations are quantified by

the parameter ε, which measures the number of standard deviations by which an observed spectral acceleration (Sa) differs from a its predicted Sa at the given period

$$\varepsilon(T) = \frac{\ln Sa(T) - \mu_{\ln Sa(T)}}{\sigma_{\ln Sa(T)}} \tag{3}$$

where $\mu_{\ln Sa(T)}$ and $\sigma_{\ln Sa(T)}$ are the mean and standard deviation of a ground motion's log Sa value from a ground motion prediction model (e.g., Boore and Atkinson 2007), and $Sa(T)$ is the observed spectral acceleration value. The observation in Figure 4 that Sa's are higher than predicted in the region of the pulse period means that we expect positive ε's near T_p.

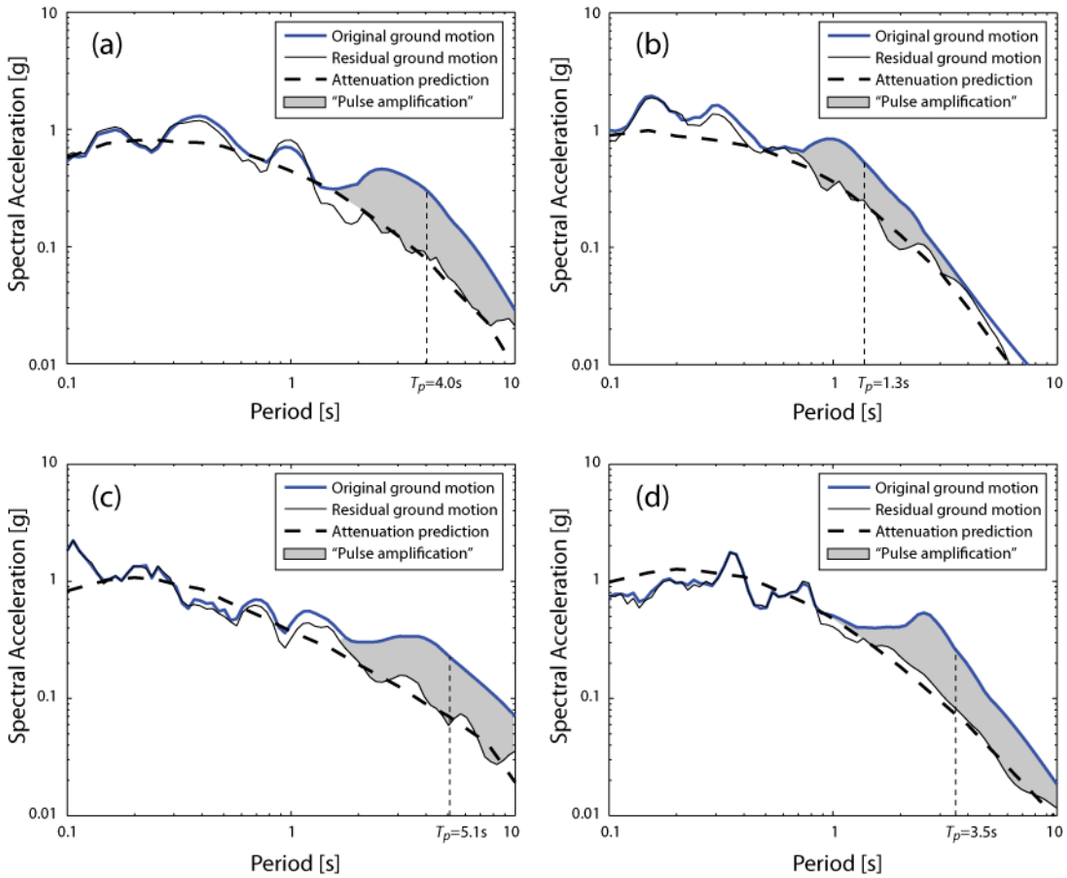


Figure 4: Response spectra of pulse-like ground motions before and after pulse extraction, and the Boore and Atkinson (2007) median prediction for each ground motion. (a) Imperial Valley, El Centro Array #5. (b) N. Palm Springs, N. Palm Springs. (c) Landers, Lucerne. (d) Northridge, Jensen Filter Plant Generator.

To allow comparison of records having differing pulse periods, we plot these ε's versus T/T_p (where T_p is the period of the pulse), as shown in Figure 5a. It is clear from this figure that the response spectrum is systematically higher than predicted at T

= T_p, with 90 of the 91 records having positive ε values, and the remaining record being only slightly negative. Next, in Figure 5b, we see the ε values of the residual ground motions (i.e., the ground motions with the pulses removed). The mean ε values of these ground motions are very close to zero at all periods. This suggests that the residual ground motions have spectra that are on average equal to the predictive model, indicating that removal of the pulse did not overcompensate and make the residual records weaker than ground motion models would predict.

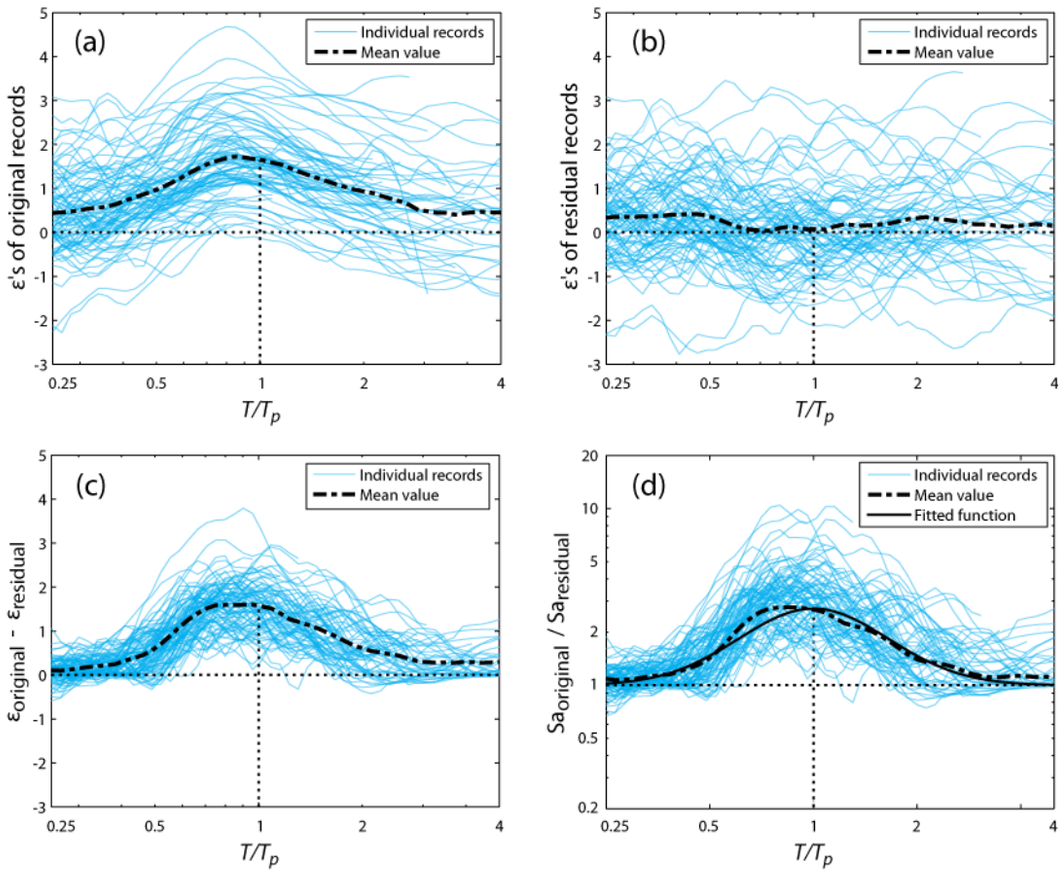


Figure 5: Epsilons and response spectra from pulse-like ground motions. (a) Epsilons from original ground motions. (b) Epsilons from residual ground motions. (c) Difference in ε between the original and residual ground motions. (d) Ratio of original spectral accelerations to residual spectral accelerations.

These results indicate that a practical approach to predict spectral accelerations of these records is to predict the spectra of the residual ground motions using existing ground motion models for "ordinary" motions, and then add an amplification factor around the pulse period to account for the contribution of the pulse. In Figure 5c, the difference in ε values between the original and residual ground motions is plotted. To make this result more conveniently usable in the form of a ground motion model, we return to spectral acceleration values in Figure 5d, where the ratios of the original record's spectral acceleration value to the residual record's spectral acceleration values are plotted. It is seen that addition of the pulse multiplies the spectral

acceleration by an average of 2.7 at T_p, and 1.5 when $T/T_p = 2$ or 0.5. The mean value of this ratio is approximated by the following Gaussian (bell-curve) function around T_p

$$\ln\left[Sa_{original}(T) / Sa_{residual}(T) \right] = e^{-2\ln(T/Tp)} \quad (4)$$

This appears to closely fit the trend seen in Figure 5d, but future work will derive response spectra of the wavelet function used for pulse extraction, and may result in a more theoretically justified amplification function. This simple model, in which the amplification is only a function of pulse period, may also be refined after further study. It should be noted that Tothong (personal communication 2005, Tothong et al. 2007) was the first to develop and use a plot like Figure 5a, and the only new development here is to use wavelet processing to decouple *Sa*'s from the pulse and residual, so that they can be studied separately.

Given that the mean ln*Sa* of the residual ground motions is well-predicted by standard ground motion models (as seen in Figure 5b), and that the mean of the pulse amplification is well-predicted by equation (4), a simple ground motion model for pulse-like motions is given by:

$$\mu_{\ln Sa_{original}}(T, T_p) = \mu_{\ln Sa_{residual}}(T) + e^{-2\ln(T/Tp)} \quad (5)$$

where $\mu_{\ln Sa_{residual}}(T)$ is the mean logarithmic spectral acceleration value predicted by a standard ground motion model, and $\mu_{\ln Sa_{original}}(T, T_p)$ is the new prediction of the pulse-like ground motion. The standard deviation of normalized residuals from this prediction is approximately one, which indicates that the standard deviation of the original ground motion model need not be modified. Note that this prediction assumes the existence of a pulse, and also assumes knowledge of T_p (because the amplification function is dependent upon T_p). Because this model amplifies a narrow region around T_p rather than amplifying the response spectra in a more general way, it is classified as a "narrow-band" directivity model (Somerville 2003; Tothong et al. 2007).

IMPLICATIONS FOR SEISMIC HAZARD ANALYSIS

This model of the previous section can easily produce predicted response spectra for pulse-like motions with a given period, but not all near-fault records contain pulses, and pulses will also have varying periods. Probabilistic seismic hazard analysis accounts for unknown future magnitudes and distances when computing seismic hazard, and can be generalized to also account for unknown directivity effects in future ground motions. Tothong has described how these generalizations can be implemented, and presented the needed mathematics (Tothong et al. 2007). In addition to the response spectrum prediction presented here, and the prediction of pulse periods from equation (2), that procedure also requires a prediction of the probability that a pulse will occur at a given site susceptible to directivity; one such prediction is available from Iervolino and Cornell (2007). Calculations of this type, which explicitly account for directivity, can accurately amplify seismic hazard curves to account for pulses, and hazard deaggregation can also be used to identify the probability that a

given ground motion intensity level is caused by a pulse-like ground motion. Further work is planned to more completely describe the orientation of velocity pulses, and that concept could also be adopted into a PSHA framework.

The focus of this work is on the impact of directivity pulses on response spectra, but the resulting structural responses may or may not be fully accounted for by the increased *Sa* values predicted here. Several researchers have concluded that *Sa* at the first-mode period of the structure is not sufficient to predict the effect of directivity pulses on nonlinear multi-degree-of-freedom structures (e.g., Alavi and Krawinkler 2001; Luco and Cornell 2007; Tothong and Cornell 2007 are recent examples among others). The *Sa* predictions presented here could also be incorporated into vector-valued PSHA, which Baker and Cornell found may account for directivity effects by measuring response spectra at multiple periods (2007). Further work is needed on this topic.

CONCLUSIONS

An algorithm for identifying strong velocity pulses in recorded ground motions has been briefly summarized and applied to a set of approximately 3500 fault-normal ground motions. The calculations identified 91 pulse-like ground motions and computed their associated pulse periods. Maps of these pulses suggest that many of them occured at source-to-site geometries likely to have experienced directivity effects. The acceleration spectra of these 91 motions were then studied in more detail.

It was observed that the spectra of these records are systematically larger than predicted at periods near the velocity-pulse period. When the pulses were extracted from these records, the residual ground motions were well-described by existing ground motion prediction models, indicating that a simple narrow-band amplification could be applied around the pulse period to substantially account for the additional effect of the pulse. The 91 ground motions were used to estimate this amplification factor. The resulting prediction requires knowledge of the period of the pulse, which will not be known *a priori* for future ground motions. This can be addressed within probabilistic seismic hazard analysis, however, using the same approach by which uncertain future magnitudes and distances are currently addressed (Tothong et al. 2007). The resulting ground motion hazard curves should provide a more rigorous and justifiable accounting for the effects of directivity, and may provide tools to calibrate the near-fault design factors specified by building codes.

The large quantity of data used here is not easily reported in a written publication. A dedicated website has been created at *http://stanford.edu/~bakerjw/pulse-classification.html*, as a repository for algorithms, as well as a collection of figures showing time histories, response spectra and maps of this data. The website more completely documents the approach used here, and should be a useful resource for others interested in performing this type of analysis.

ACKNOWLEDGMENTS

Thanks to Polsak Tothong and Allin Cornell for discussions that motivated some of

these calculations. This material is based upon work supported by the National Science Foundation under Award Number CMMI-0726684. Any opinions, findings, and conclusions or recommendations expressed in this publication are those of the author and do not necessarily reflect the views of the National Science Foundation.

REFERENCES

Alavi, B., and Krawinkler, H. (2001). "Effects of near-fault ground motions on frame structures." *Blume Center Report #138*, Stanford, California, 301 p.

Baker, J. W. (2007). "Quantitative Classification of Near-Fault Ground Motions Using Wavelet Analysis." *Bulletin of the Seismological Society of America*, 97(5), 1486-1501.

Baker, J. W., and Cornell, C. A. (2007). "Vector-valued intensity measures for pulse-like near-fault ground motions." *Engineering structures*, (in press).

Boore, D. M., and Atkinson, G. M. (2007). "Boore-Atkinson NGA Ground Motion Relations for Peak and Spectral Ground Motion Parameters." *PEER 2007/01*, Pacific Earthquake Engineering Research Center, Berkeley, California, 234 p.

Bray, J. D., and Rodríguez-Marek, A. (2004). "Characterization of forward-directivity ground motions in the near-fault region." *Soil Dynamics and Earthquake Engineering*, 24(11), 815-828.

Fu, Q., and Menun, C. (2004). "Seismic-environment-based simulation of near-fault ground motions." *Proceedings, 13th World Conference on Earthquake Engineering*, Vancouver, Canada, 15.

Iervolino, I., and Cornell, C. A. (2007). "Prediction of the occurence of velocity pulses in near-fault ground motions." *Bulletin of the Seismological Society of America*(in review).

Luco, N., and Cornell, C. A. (2007). "Structure-Specific Scalar Intensity Measures for Near-Source and Ordinary Earthquake Ground Motions." *Earthquake Spectra*, 23(2), 357-392.

Mallat, S. G. (1999). *A wavelet tour of signal processing*, Academic Press, San Diego.

Mavroeidis, G. P., and Papageorgiou, A. S. (2003). "A Mathematical Representation of Near-Fault Ground Motions." *Bulletin of the Seismological Society of America*, 93(3), 1099-1131.

Somerville, P. G. (2003). "Magnitude scaling of the near fault rupture directivity pulse." *Physics of the Earth and Planetary Interiors*, 137(1), 12.

Somerville, P. G., Smith, N. F., Graves, R. W., and Abrahamson, N. A. (1997). "Modification of Empirical Strong Ground Motion Attenuation Relations to Include the Amplitude and Duration Effects of Rupture Directivity." *Seismological Research Letters*, 68(1), 199-222.

Tothong, P., and Cornell, C. A. (2007). "Probabilistic Seismic Demand Analysis Using Advanced Ground Motion Intensity Measures, Attenuation Relationships, and Near-Fault Effects." *PEER 2006-10*, Pacific Earthquake Engineering Research Center, University of California at Berkeley, Berkeley, California, 205 p.

Tothong, P., Cornell, C. A., and Baker, J. W. (2007). "Explicit-Directivity-Pulse Inclusion in Probabilistic Seismic Hazard Analysis." *Earthquake Spectra*, 23(4), 867-891

PRELIMINARY ESTIMATION OF SEISMICALLY INDUCED GROUND STRAINS FROM SPATIALLY VARIABLE GROUND MOTIONS

Timothy D. Ancheta[1], Jonathan P. Stewart[2], Norman A. Abrahamson[3], and Robert L. Nigbor[4]

[1]Graduate student researcher, Dept. of Civil & Environmental Engineering, Univ. of Calif. Los Angeles, 5371 Boelter Hall, Los Angeles, CA 90095; tancheta@ucla.edu
[2]Professor and Vice Chair, Dept. of Civil & Environmental Engineering, Univ. of Calif. Los Angeles, 5371 Boelter Hall, Los Angeles, CA 90095; jstewart@seasnet.ucla.edu
[3]Seismologist, PG&E, PO Box 770000, San Francisco, CA 94177; NAA2@pge.com
[4]Researcher, Dept. of Civil & Environmental Engineering, Univ. of Calif. Los Angeles, 5371 Boelter Hall, Los Angeles, CA 90095; nigbor@ucla.edu

ABSTRACT: A model for horizontal peak ground strain (*PGS*) is developed in consideration of three fundamental contributions to spatially variable ground motion (SVGM): (1) spatial incoherence effects, which contribute to phase variability in a stochastic sense; (2) wave passage effects, which contribute to phase variability in a deterministic sense; and (3) amplitude variability. Previous models for each of these effects are reviewed and compared to array data from Borrego Valley, California. Published empirical models for coherency and amplitude variability are found to represent reasonably well the Borrego data. We extend previous work by considering correlations of amplitude and phase variability (generally found to be small) and characterizing the coherency-dependent probabilistic distribution of phase variability. Using the aforementioned amplitude and phase variability models, a procedure is developed to generate simulated acceleration records from a seed record. The procedure is applied to a suite of Northridge earthquake recordings to predict ground strains, which are found to be strongly dependent on the peak ground velocity (*PGV*) of the seed motion and the separation distance between the seed and simulated motions. The dependence of *PGS* on *PGV* saturates for large *PGV* (> 50 cm/sec).

INTRODUCTION

A number of approaches have been described in the literature for characterizing ground strain from strong ground motion. One prevailing approach examines strains along a particular alignment (e.g., a pipeline or tunnel) due to wave passage (e.g., Newmark, 1967). In this approach, peak ground strain (*PGS*) is represented as some fraction of the ratio of peak ground velocity (*PGV*) to shear wave velocity (V_s). The main drawback for this approach is that it does not capture additional sources of spatially variable ground motions (SVGM) including incoherent waves and spatially variable site response. Accordingly, it is often preferred for strains to be inferred from recordings of dense field arrays, in which many SVGM effects are implicitly included. There are two general categories of approaches for doing this. The first approach uses a geodetic technique to infer strains directly from differences in ground displacement histories at adjacent stations O'Rourke et al. (1984), Bodin et al. (1997), Paolucci and

Smerzini (2007), Paolucci and Pitilakis (2007). The second approach, used by this study, uses SVGM models of Fourier amplitude and phase variation in a forward modeling sense to generate a simulated motion from a seed recording. Similar approaches have been used previously by Zerva and Zervas (2002) and Abrahamson (1992b). The simulation of SVGM through analysis of amplitude and phase variability recognizes three fundamental sources of ground motion spatial variability:

1. Variability of phase from wave passage.
2. Random (or stochastic) variability of phase, which is often expressed mathematically by a coherency function.
3. Variability of amplitude, which can be expressed by a standard deviation term.

This paper describes the development of a model to predict *PGS* in consideration of the above sources of SVGM. We evaluate phase and amplitude variability relative to existing models using previously unanalyzed array data from Borrego Valley, California. We then describe the development of new procedures for evaluating simulated ground motions from a seed record. Those procedures are then used to estimate ground strains, and predictive equations for *PGS* are developed and compared to previous work. This paper is a brief synopsis of this work, which is described in more detail by Stewart et al. (2007).

DATA SUMMARY

The Borrego Valley Differential Array (BVDA) is located in the San Jacinto Mountains, 40 km west of the Salton Sea in southern California (Kato et al, 1998). It is situated in the northern portion of the Borrego Valley which is an alluvial flood plain which widens to the south. The BVDA consists of multiple surface and downhole arrays, however only the main linear array recordings are used. The array configuration is shown on Figure 1.

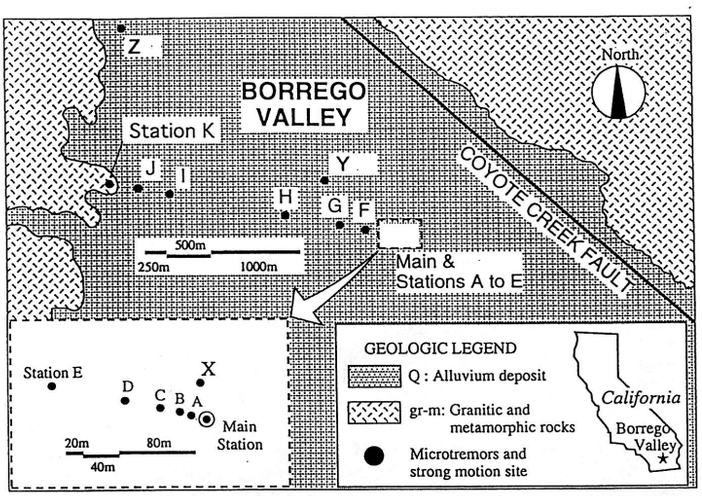


FIG. 1. Plan view of Borrego Valley showing location of BVDA (Kato et al. 1998).

The data was selected from stations 0 (main) and A through E, which are located 10, 20, 40, 60, 80, 160 meters from the main station. The underlying soils consist of medium to very dense coarse to medium grained sands with S-wave velocities of 400 to 600 m/s. The soil overlies a granitic basement located approximately 230 m below the surface with S-wave velocity of greater than 2500 m/s (Kato et al, 1998). From the nearly 200 events recorded, 16 were selected based on a high signal to noise ratio

and minimum 1 sec window length for shear waves to optimize bandwidth. These criteria limit the selected earthquakes to events with M > 2.5, typically with epicentral distances < 80 km.

The array data was pre-processed before application to estimate the coherency and amplitude variability. The S-wave window was identified and used in the analyses. This was done because prior work has shown shear waves to produce larger strains than p-waves or surface waves (e.g., Gupta, 2004). To model the deterministic and stochastic variation separately, the S-wave windows were aligned in time with reference station 0 to remove wave passage effects. After extraction the aligned S-wave signals were tapered in the time domain to minimize errors/bias in subsequent frequency domain analysis.

COHERENCY

Coherency is used to quantify phase variation between two signals. To quantify the random phase variation, we use lagged coherency defined as follows (Abrahamson 1992a):

$$\left|\gamma_{jk}(\omega)\right| = \left| \frac{S_{jk}(\omega)}{\left[S_{jj}(\omega) S_{kk}(\omega)\right]^{1/2}} \right| \tag{1}$$

where S_{jj} and S_{kk} are the power spectral density functions of stations j and k, S_{jk} is the cross power spectral density function, and ω is the circular frequency (radians/sec). The statistical distribution of lagged coherency data is approximately normal when transformed using a $\tanh^{-1}$ function (Abrahamson 1992a).

Values of lagged coherency are sensitive to the smoothing method that is used (e.g., lagged coherency of unsmoothed records is unity). We smooth the data using an 11-point (M=5) Hamming lag window (Brillinger, 1981; Abrahamson, 1992a), which is a frequency-domain smoothing procedure applied to power spectra. The application of smoothing produces a trade-off between resolution and data scatter – as the level of smoothing increases the scatter of the coherency decreases but the mean value also decreases. Additional justification for the smoothing procedure adopted here is given by Abrahamson (1992a) and Stewart et al. (2007).

Abrahamson (1992a) developed an empirical model for lagged coherency using recordings from the LSST (Large Scale Seismic Test) array in Taiwan. The model takes as input frequency (f) and separation distance (ξ). For large frequencies, the model converges asymptotically to a value of $|\gamma|$=0.35, which corresponds to the lagged coherency of white noise for the selected level of smoothing.

The lagged coherency of the BVDA data is plotted against the Abrahamson (1992a) model in Figure 2. The model generally fits the BVDA data well, although there is bias for frequencies below 10 Hz (under-prediction for ξ=10 m; over-prediction for ξ>10 m).

BVDA data were also used to investigate the distribution of the random phase variation and the correlation between random phase components. This information is

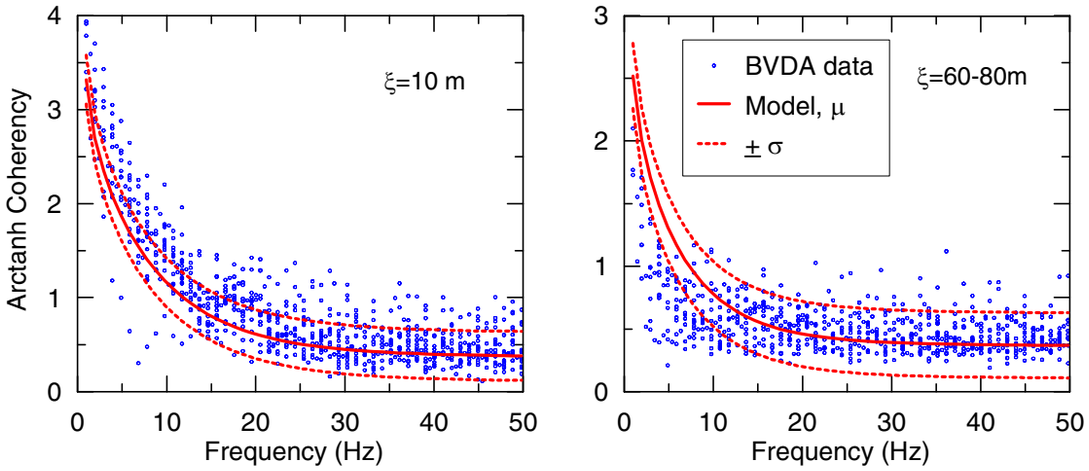


FIG. 2. Transformed lagged coherency data from BVDA plotted again model of Abrahamson (1992a). μ=median; σ=standard deviation.

important for the generation of simulated motions, as described subsequently. Histograms of wrapped phase differences between station pairs are plotted for various frequency bins in Figure 3. The standard deviation terms, $\sigma_{\phi,wr}$, reported in Figure 3 are those of the data with their shown distribution, which appears to be a hybrid of a normal distribution and a uniform distribution (the latter dominating at higher frequencies). However, Stewart et al. (2007) showed that the distributions in Figure 3 are for all practical purposes normal distributions (standard deviation = σ_ϕ) of unwrapped phase differences – in other words, the warping of the tails of the distribution occurs because of wrapping. Because of the effects of wrapping, $\sigma_\phi \geq \sigma_{\phi,wr}$).

As described further in Stewart et al. (2007), correlation coefficients of phase variations from frequency-to-frequency average approximately zero, indicating that variability of wrapped phase angle is essentially random.

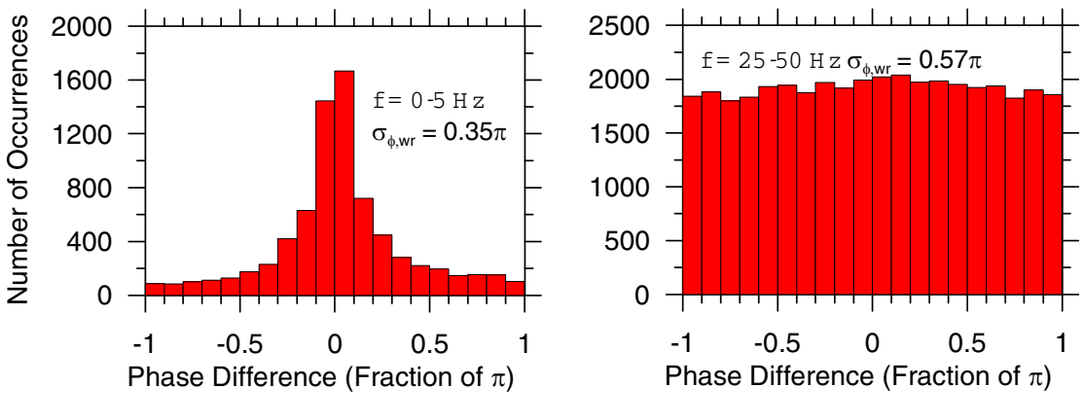


FIG. 3. Histogram of wrapped differences between Fourier Phases from all BVDA station pairs for separate frequency bins as noted.

AMPLITUDE VARIATION

The amplitude variation between two stations is taken as the difference of the natural logs of the Fourier amplitudes and is denoted $\Delta A(f,\xi)$. If a series of values of ΔA are collected, the distribution should have zero mean. The standard deviation of the distribution is denoted $\sigma_{\Delta A}(f,\xi)$. Standard deviation term $\sigma_{\Delta A}$ is calculated using unsmoothed Fourier amplitude spectra so as to be compatible with the procedure for generating simulated ground motions described below.

An empirical function for $\sigma_{\Delta A}(f,\xi)$ has been developed by Abrahamson (2007, personal communication) as follows:

$$\sigma_{\Delta A}(f,\xi) = A\left(1-e^{Bf+C\xi}\right) \tag{2}$$

where A-C are regression parameters with values A=0.93, B=–0.163, and C=–0.0019. This regression was performed using the maximum likelihood method by selecting the best fit line for many different arrays from soil sites (Chiba, Hollister, Imperial Valley Differential Array, LSST).

The model represented by Eq. 2 was compared to BVDA data. Figure 4 shows the model for $\sigma_{\Delta A}$ plotted against data for all of the BVDA selected events. Each blue dot in Figure 4 represents a standard deviation ($\sigma_{\Delta A}$) calculated on all data within the specified separation distance range for a fixed frequency. The results show that amplitude variability is more strongly dependent on frequency than on separation distance and that $\sigma_{\Delta A}$ reaches a limiting value of 0.929 at high frequencies (regardless of separation distance). The fit to the data is generally satisfactory.

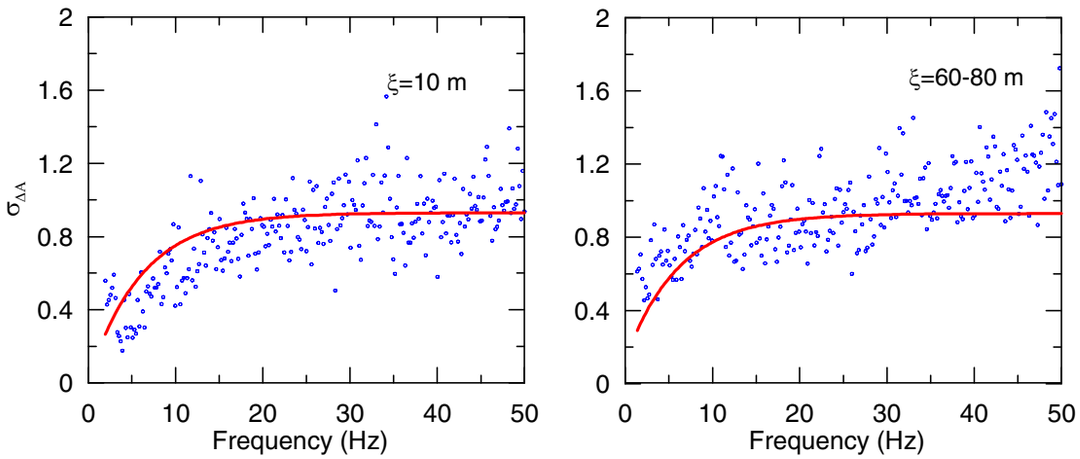


FIG. 4. Plot of $\sigma_{\Delta A}$ from BVDA data compared to model

As described further in Stewart et al. (2007), correlation coefficients of amplitude variability from frequency-to-frequency range from about 0.3 for frequency steps of approximately 0.2 Hz to nearly zero for frequency steps approaching 10 Hz. Correlations between differences of natural logarithms of amplitude and unmodified phase differences at a common frequency were also investigated and found to be nearly zero. Based on these result, we assume amplitude residuals to be uncorrelated with each other and with phase.

GENERATION OF SPATIALLY VARIABLE GROUND MOTIONS

In this section, we describe the process adopted for the generation of a pair of spatially variable ground motions (SVGM). One of the motions is referred to as the "seed" motion and consists simply of an individual recording. The second motion is different from the first as a result of a modification of the phase and amplitude; that motion is referred to as the "simulated" motion. For the development of the strain model herein we assume the new location is oriented in the direction of the wave ray path as we use the full apparent wave velocity with a slowness of S=0.4 sec/km.

Consider a seed motion with phase ϕ_k. The phase of the simulated motion ϕ_j is evaluated by adding a stochastic component ε_{jk} along with the phase shift from wave passage:

$$\phi_j(f) = \phi_k(f,\xi) + \varepsilon_{jk}(f) + 2\pi f \xi S \tag{3}$$

A separate random number ε_{jk} is used for each frequency except the zero frequency component (f=0) because of the lack of correlation of random phase variations across frequencies. Each random number is generated according to a normal distribution with μ=0 and standard deviation=σ_ϕ (i.e., standard deviation of unwrapped phase angles). Term σ_ϕ is related to lagged coherency -- as $|\gamma|$ drops σ_ϕ increases. Stewart et al. (2007) derive the relationship between $|\gamma|$ and σ_ϕ, which is found to follow the relationship shown in Figure 5. The minimum value of 0.33 corresponds to the limiting value of lagged coherency obtained from BVDA data for the selected method of smoothing. After generating a realization of ε_{jk} and adding the phase shift from wave passage per Eq. 3, the modified phase is then wrapped to be within the limits of [-π, π].

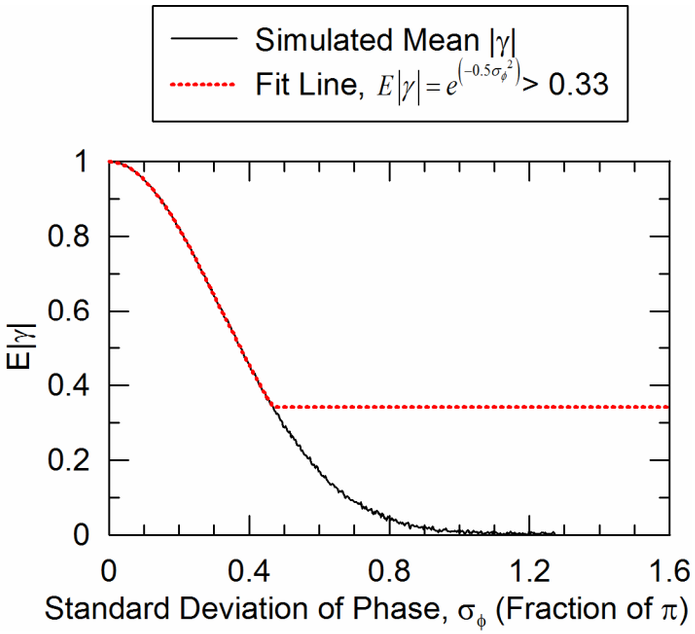


FIG. 5. Relationship between sigma and lagged coherency

As with the phase variation, the Fourier amplitude of the seed motion is modified by adding a stochastic component ε_{jk} as shown below:

$$A_j(f) = \exp\left\{\ln\left[A_k(f)\right] - \varepsilon_{jk}(f)\cdot\frac{1}{\sqrt{2}}\sigma_{\Delta A}(f)\right\} \tag{4}$$

The random numbers for amplitude are generated according to a normal distribution with μ=0 and standard deviation= $\sigma_{\Delta A}$, where $\sigma_{\Delta A}$ is in turn calculated using Eq. 2. Independent random numbers are used for each frequency except the DC-component, which is not modified. The random numbers used for amplitude are independent of those used for phase due to the lack of correlation.

PREDICTION MODEL FOR STRAINS

In this section we develop a predictive model for *P*eak *G*round *S*train (*PGS*). A suite of N_s seed motions is selected from Northridge earthquake recordings with a range of amplitudes. For seed motion *i*, a simulated motion is generated using the procedure given in the above section for a given separation distance ξ. The seed and simulated acceleration are integrated twice to displacement histories. A strain history is calculated as the difference between the seed and simulated displacement histories normalized by ξ. The peak value of strain from the strain history is taken as *PGS*. The simulation procedure is repeated approximately 30 times to generate a suite of *PGS* values for seed motion *i* and separation distance ξ. This is repeated for all N_s seed motions and for a suite of separation distances. Using those results, a prediction equation was developed to estimate *PGS* as a function of separation distance ξ and peak ground velocity (*PGV*).

The seed motions utilized in this work are from stations with NEHERP C and D site categories. One component of motion was arbitrarily selected for each site. All data was taken from the PEER database (http://peer.berkeley.edu/nga/). The selected stations are listed by Stewart et al. (2007).

A baseline correction procedure was developed to minimize the effect of long period noise on *PGS* estimates. The full baseline correction procedure is given by Stewart et al. (2007), but the most important aspect of the procedure is that baseline correction was applied to the differential displacement between the seed and simulated displacements. This avoids the potential for errors associated with inconsistent baseline correction of the two records. We used a baseline correction consisting of a high-order polynomial without constant or slope terms fit to the acceleration-time data. A 10^{th} order polynomial was used; however it was found that the order of the polynomial used was relatively inconsequential to the *PGS* estimates.

Individual estimates of PGS from the Northridge accelerograms are given in Figure 6. Each "column" of points corresponds to the 30 *PGS* estimates for a given record. For a given separation distance (ξ), *PGS* is seen to increase with *PGV* initially, but then to saturate for large *PGV*. This behavior can be captured with a hyperbolic function, as shown by the fit curves in Figure 6. A preliminary model for PGS conditional on PGV and ξ is given by the following expression:

$$PGS = \frac{PGV}{\left(a_1\xi - a_2\xi^2\right) + \left(b_1\xi - b_2\xi^2\right)\cdot PGV \cdot R} \tag{5}$$

where a_1-a_2 and b_1-b_2 represent regression coefficients given in Figure 6. The log-normal standard deviation of the residuals σ_{PGS}=0.72.

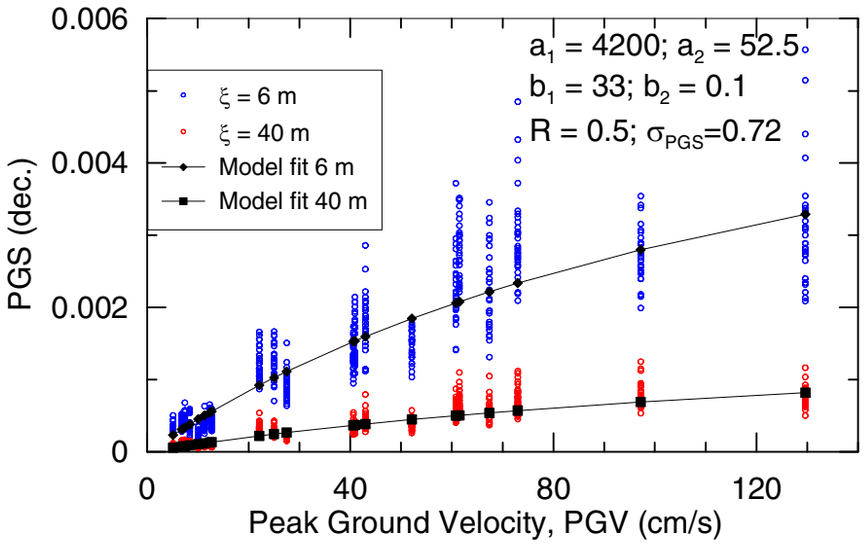


FIG. 6. Plot of model fit to *PGS* data for ξ = 6 m and 40 m

Figure 7 compares strain estimates developed in this study to those from Abrahamson (2003) and Paolucci and Smerzini (2007). Those previous studies parameterized *PGS* in terms of peak displacement (*PGD)*. To facilitate a side-by-side comparison, regression analyses were performed as described above using *PGD* as the intensity measure in lieu of *PGV*. Note that the effect of separation distance was not considered in the previous work. For low *PGD*, the published models pass near the lower bound of our curves, generally being consistent with ξ=24-40 m.

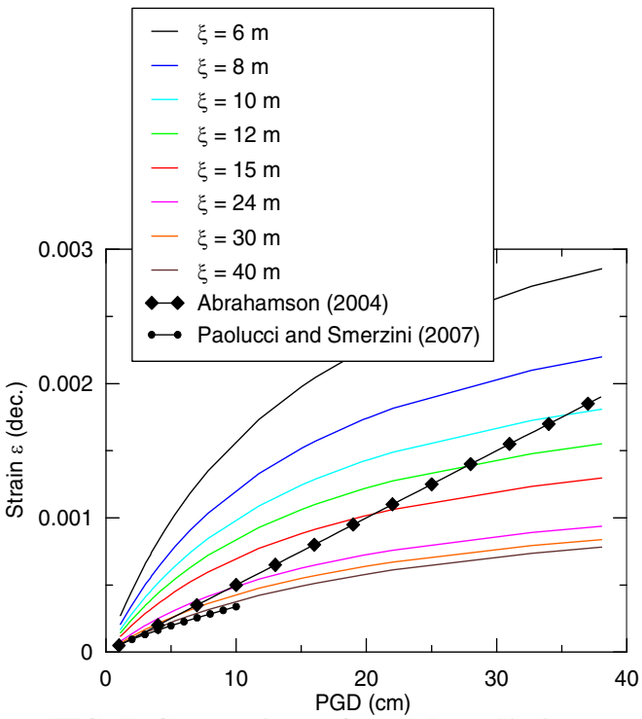


FIG. 7. Comparison of model predictions from present study (colored lines) to

To provide insight that assists in interpreting the trends in the *PGV-PGS* relationship, we identify the frequency range that controls strains. This is done for the Northridge records by exercising the simulated motion generation routine by modifying the coherency and amplitude over a frequency range of zero to a cutoff frequency f_c. Limiting frequency f_c was taken as 0.2%, 1.0%, 2.0%, 10%, 20%, 40%, 60%, 80%, and 100% of the Nyquist frequency (f_{Nyq}). The original procedure takes $f_c = f_{Nyq}$. By successively dropping f_c below f_{Nyq}, we investigate the influence of the different

frequency ranges on ground strains. The results are shown in Figure 8 and indicate that the randomization of frequencies beyond ~4-5 Hz does not appreciably affect strain estimates. Peak strains drop as f_c is dropped across the range of ~0.3 to 4 Hz. These results indicate that components of ground motion in that approximate frequency range control ground strains.

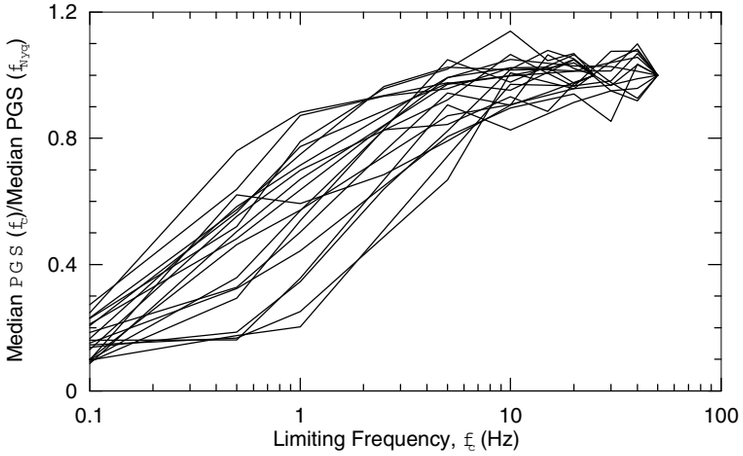


FIG. 8. Variation of PGS with frequency *f* implied by PGS model in Eq. 5.

SUMMARY AND LIMITATIONS

We develop a preliminary model relating peak transient ground strain to peak velocity and separation distance. The model accounts for known sources of spatially variable ground motion including wave passage, incoherent waves, and differential site response, at least to the extent that those effects are captured in the underlying models for coherency and amplitude variability. Those underlying models were developed from relatively weak motion data (PGV < 30 m/s) and an inherent assumption associated with the procedure used here is that the coherency and amplitude variability models apply for larger shaking amplitudes as well. Validation of the computed strains against strains directly inferred from array data is being completed at present.

Our preliminary model is considered applicable to stiff soils sites, separation distances of ξ=6-85 m, and $PGV \leq 120$ cm/sec. The *PGS* model is developed using ground motion recordings from only one event, hence possible effects of magnitude have not yet been investigated. Major new features of this model relative to previous work are the saturation of strain at high PGV and the dependence on ξ.

ACKNOWLEDGEMENTS

This work was supported by Subcontract No. 14 between UCLA and the Consortium of Universities for Research in Earthquake Engineering. This support is gratefully acknowledged. The helpful suggestions of Drs. Brian McDonald and John Osteraas of Exponent and Professor Jonathan Bray of UC Berkeley are appreciated.

REFERENCES

Abrahamson, N.A. (1992a). "Spatial variation of earthquake ground motion for application to soil-structure interaction," *Rpt. No. EPRI TR-100463*, Electrical Power Research Institute, Palo Alto, CA, March.

Abrahamson, N.A. (1992b). "Generation of spatially incoherent strong motion time histories," *Proc. 10th World Conf. Earthquake Engineering*, Vol. II, 845-850.

Abrahamson, N.A. (2003). "Model for strains from transient ground motions," in *CUREE Publication No. EDA-04*, Consortium of Universities for Research in Earthquake Engineering, Richmond, CA, pp 43-79.

Bodin, P., Gomberg, J., Singh, S.K., and Santoyo, M.A. (1997). "Dynamic deformations of shallow sediments in the Valley of Mexico: Part I: Three dimensional strains and rotations recorded on a seismic array," *Bull. Seism. Soc. Am.*, 87, 528-539.

Brillinger, D.R. (1981). *Time series data analysis and theory*, Expanded Edition, Holden Day, San Francisco, CA.

Gupta, A., editor (2004). *Workshop Proceedings: Effects of Earthquake-Induced Transient Ground Surface Deformations on At-Grade Improvements*, CUREE Publication No. EDA-04, Richmond, CA.

Kato, K., Takemura, M., Konno, T., Uchiyama, S., Iizuka, S. and Nigbor, R.L. (1998). "Borrego Valley downhole array in southern California: Instrumentation and preliminary site effect study," *Proc. 2nd Int'l Symposium on the Effects of Surface Geology on Seismic Motion*, Yokohama, Japan.

Newmark, N.M. (1968). "Problems in wave propagation in soil and rock," *Proceedings of the International Symposium on Wave Propagation and Dynamic Properties of Earth Materials*, Albuquerque, NM.

O'Rourke, M.J. Castro, G., and Hossain, I. (1984). "Horizontal soil strain due to seismic waves," *J. Geotech. Engrg.*, ASCE, 110 (9), 1173-1187.

Paolucci, R. and Pitilakis, K. (2007). *Chapter 18: Seismic Risk Assessment of Underground Structures Under Transient Ground Deformation*, Earthquake Geotechnical Engineering, 4th International Conference on Earthquake Geotechnical Engineering – Invited Lectures, K. Pitilakis (editor), 433-459.

Paolucci, R. and Smerzini, C. (2007). "Earthquake induced transient ground strains from dense seismic networks," *Earthquake Spectra*. In review.

Stewart, J.P., Ancheta, T.D., Nigbor, R.L., Bray, J.D., Mason, H.B., Bernardini, J.A., Abrahamson, N.A., and McDonald, B. (2007). "Ground strains from strong ground motion: preliminary empirical characterization and effect on shallow foundations," Report to CUREE. September.

Zerva, A. and Zervas, V. (2002). "Spatial variation of seismic ground motions: an overview," *App. Mech. Rev.*, 55 (3), 271-297.

Probabilistic Use of Arias Intensity in Geotechnical Earthquake Engineering

J.K. Howard[1], P.G., E.G., W.A. Fraser[2], P.G., E.G., and M.G. Schultz[3], P.E.

[1]Senior Engineering Geologist, California Division of Safety of Dams, 2200 X St. Suite 200, Sacramento, CA, 95818; jhoward@water.ca.gov
[2]Chief, Geology Branch, California Division of Safety of Dams; billf@water.ca.gov
[3]Supervising Engineer, California Division of Safety of Dams; schultz@water.ca.gov

ABSTRACT: When earthquake engineering is concerned with both the amplitude and durational aspects of ground motion, it commonly uses seismic loading in the form of a time history. The translation of traditional probabilistic seismic hazard analysis (PSHA), i.e., based on peak acceleration/response, into a time history can be complicated by deaggregation sensitivity to choice of motion parameter. The complication is exacerbated when peak motion only partially addresses damage potential. Energy-based parameters, such as Arias Intensity, address both amplitude and durational aspects of seismic shaking. To the extent that energy content correlates with damage potential, PSHA using AI (or some other energy measure) yields hazard curves that facilitate the translation of probabilistic load into a time series and, through deaggregation, facilitates the development of design earthquake scenarios and time histories. Potential applications range from assessing the conservatism of a time history's loading, to developing a suite of time histories with specific probabilistic loads for damage sensitivity analysis. Examples of AI-based and peak acceleration-based PSHA for exceedance return periods suggested for dams (thousands of years) show that AI-based deaggregation focuses on larger earthquakes where peak acceleration-based deaggregation indicates competing scenarios.

INTRODUCTION

Physics distinguishes between the concepts of *force*, *energy*, and *work*. Where force represents the potential to move an object, work represents the object's displacement as force is applied. Work is done by transferring energy, the capacity to do work, to an object or material.

A measure of the energy of earthquake shaking can be an important predictor of both structural performance and geotechnical behavior. Dynamic geotechnical analyses are commonly concerned with the potential work (strain, deformation, sliding displacement, etc) that an earthquake is capable of doing, so it follows that their results depend on the energy content represented by the applied seismic load. Ground motion energy content is controlled by both its amplitude and durational aspects, which include the number of significant strong motion cycles present.

Simplified analyses for embankment deformation (Makdisi and Seed 1978) and liquefaction (e.g., Seed et al. 1983) use seismic loading in the form of peak acceleration and a proxy for durational aspects, such as earthquake magnitude. Rigorous analyses commonly use design earthquake motion in the form of a time series (time history).

A design earthquake time history is typically developed from a "seed" record that is adjusted to meet frequency and amplitude characteristics defined by a target acceleration response spectrum. Because a time history represents motion generated by a unique earthquake scenario, the target usually represents a specific magnitude, source-to-site geometry, and site condition. The seed record selection can be critical because the target spectrum does not constrain durational aspects of shaking, and should be consistent with the design earthquake scenario. Factors controlling durational aspects include magnitude, site condition, source-site geometry, and rupture direction (directivity). Arias Intensity (AI), a measure closely related to the energy content of strong motion, accounts for amplitude and durational aspects of strong motion. For that reason, the California Division of Safety of Dams (DSOD) is considering AI targets to help develop and/or assess the conservatism of design earthquakes. Deterministic AI targets are yielded by recent empirical attenuation formulas for AI (Travasarou et al. 2003; Watson-Lamprey and Abrahamson 2006), which also can be used in probabilistic seismic hazard analysis (PSHA).

DSOD presently uses maximum earthquake scenarios to evaluate more than 1200 dams under its jurisdiction. Though deterministic, the resulting seismic hazard analyses have probabilistic considerations. The target motion's fractile level (50^{th} to 84^{th} percentile) is guided by a Consequence-Hazard matrix that considers the consequence of dam failure and the likelihood of the event, and the analysis includes a probabilistic assessment of the conservatism of the resulting peak acceleration (Fraser and Howard 2002). Fraser and Burns (2004) reviewed the probabilities attained by peak accelerations used by DSOD for dam analysis. Potentially, probabilistic use of an energy based parameter such as AI represents a more rigorous and practical measure of the conservatism of design ground motions.

Integrating traditional probabilistic seismic hazard analysis (PSHA) with analyses using a time series introduces complexities. Traditional PSHA uses a probability function for peak motion, typically peak ground acceleration (PGA) and/or spectral acceleration (SA) response, given the occurrence of some earthquake magnitude, M, at a distance, R, from the site. The aggregate probability of exceeding various levels of PGA or SA at some response period is computed for all possible M-R scenarios on each source around the site, yielding a hazard curve that shows amplitude of peak motion vs. annual exceedance probability (or its inverse, return period). One can select PGA and SA values for an exceedance probability of interest, and construct an entire response spectrum with uniform probability, i.e., a *uniform hazard spectrum* (UHS). Regardless, such PSHA output does not represent motion from a unique earthquake scenario, which complicates its translation into a time history. PSHA has seen widespread use in structural engineering in part because seismic loading has been commonly used in the form of response spectra (e.g., Chopra 2005), thus allowing UHS to be used directly. With knowledge of a structure's vibration modes, the engineer would use a response spectrum to assess peak earthquake stresses and whether design limits are exceeded.

PSHA *deaggregation* can be used to develop a design earthquake that represents a probabilistic load. Deaggregation shows the earthquake scenario(s) contributing most to the PSHA. Typically, modal deaggregation (giving most-likely combinations of M-R-ε [1]) is done because it indicates realistic earthquake scenarios. Such results can be sensitive to response period, probability level, and computational details of the analysis, and there are important considerations regarding how deaggregation scenario motions should be scaled to probabilistic levels (Abrahamson 2006). If a structure is sensitive to a range of vibration periods, multiple deaggregations addressing that SA range are needed, and any (modal) deaggregation may indicate several scenarios with comparable (or significant) likelihood, which can result in a number of design earthquake scenarios for engineering consideration. The engineer may omit some based on perceived damage potential, but when the analysis is non-linear or otherwise sensitive to durational aspects, it may be difficult or even inappropriate to relate damage potential to any given peak motion parameter. These uncertainties and complexities are multiplied to the extent that other probabilistic loading levels are of interest, e.g., for assessing sensitivity of performance.

USE AND PREDICTION OF ARIAS INTENSITY

Arias (1970) developed an intensity measure of seismic shaking obtained by integrating the square of the acceleration over the duration of a time history:

$$I_a = \frac{\pi}{2g}\int_0^{\infty}[a(t)]^2 dt \qquad (1)$$

where a(t) is in units of g and I_a has units of velocity (m/sec). Arias related this measure to the cumulative energy per unit weight absorbed by a continuous spectrum of undamped simple oscillators responding to the time series.

An advantage of AI is that it accounts for durational aspects of shaking. Studies have correlated AI (or similar measures of strong motion energy content) with liquefaction triggering potential (Kayen and Mitchell 1997; Kramer and Mitchell 2006), landslide triggering (Wilson and Keefer 1985; Harp and Wilson 1995); and Newmark displacement (Travasarou et al. 2003) as seen in Figure 1. Yule et al. (2004) concluded that AI represents damage potential to embankment dams on liquefiable foundations better than peak acceleration or peak velocity.

Engineering use of a strong motion parameter also requires a reliable predictive relation for it. Early empirical relations for AI by Wilson and Keefer (1985) and Wilson (1993) were poorly constrained. Recently, Travasarou et al. (2003) and Watson-Lamprey and Abrahamson (2006) used records representative of California's shallow crustal tectonics to develop empirical attenuation relations for average AI of the horizontal motion components based on magnitude, distance, site condition, and other factors controlling strong motion character (explicitly or implicitly). The Travasarou relation is readily used in PSHA because its functional form parallels those of existing peak motion relations. Indeed, Kramer and Mitchell (2006, p.430)

[1] Epsilon (ε) represents the number of standard deviations needed in an attenuation formula using M and R to reproduce the probabilistic value.

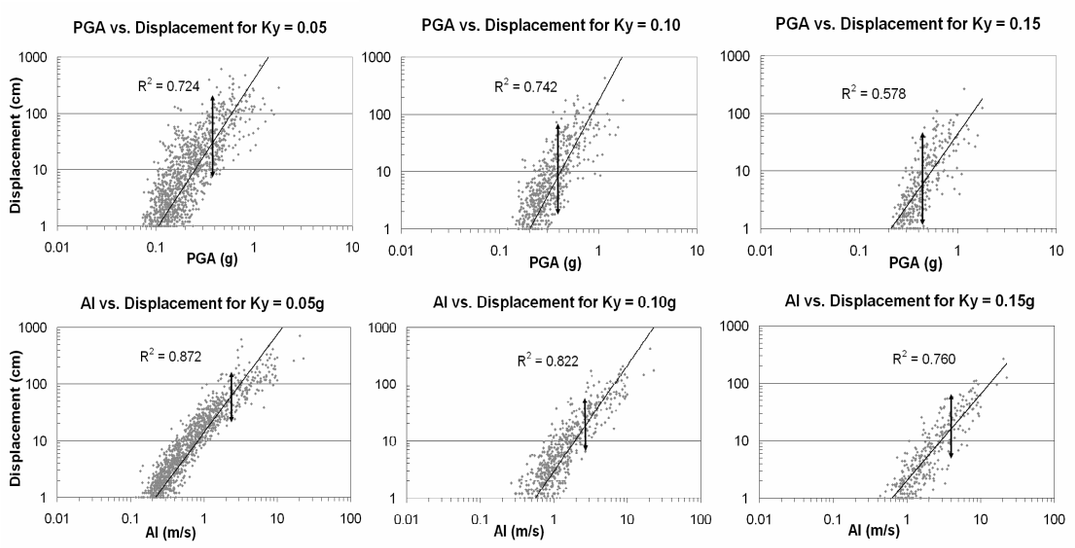


FIG. 1. Newmark displacement for K_y = 0.05, 0.10, and 0.15 vs. PGA (top) and AI (bottom) for 2137 records from events ≥ M6 (after Jibson and Jibson, 2003). Note displacement ranges for comparable motion intensities.

give an example of probabilistic use of this relation. The Watson-Lamprey and Abrahamson's (2006) relation is based partly on ground motion estimates (PGA, $SA_{T=1s}$), which complicates its use probabilistically, and it was not used in our study.

PSHA: ARIAS INTENSITY VS. PEAK MOTION

A custom version of EZ-FRISK that incorporates AI attenuation was developed by RISK Engineering at the authors' request. Presented below are comparisons of PSHA using AI (PSHA/AI) and PSHA using PGA (PSHA/PGA) for four California sites. The relation of Travasarou et al. (2003) was used for AI, and three "NGA" attenuation formulas were used for PGA: Boore and Atkinson (2007), Chiou and Youngs (2006), and Campbell and Bozorgnia (2007). All the analyses used USGS (2002) fault and background source models. Site condition was represented by V_{s30} for NGA relations and "BRM" site class (Rodriguez-Marek et al. 2001) for the Travasarou et al. relation. Probabilistic comparisons were made for exceedance return periods (ERP) of thousands of years, in keeping with 3,000 to 10,000-yr criteria suggested for large dams (USCOLD 1999). Directivity was not included.

Figure 2 shows PSHA hazard curves and modal magnitude-distance deaggregation at 2500-yr ERP for a decomposed granite site in the San Bernardino Mountains, which was modeled with V_{s30} = 500 m/s for PSHA/PGA and BRM class C for PSHA/AI. The site is close to the Cleghorn and North Frontal faults and within 8 km of the San Andreas fault. PGA deaggregation indicates the most likely scenario is a M6.5 @ 2.5 km (Cleghorn), but AI deaggregation focuses on a M7.7 event on the San Andreas fault. The AI hazard curve indicates 50th and 84th percentile predictions (3.0 and 8.5 m/s) for that scenario have ERPs of 200 and 850 years, respectively. Likewise, the 2500-yr AI (15 m/s) represents a 95th percentile estimate for a M7.7.

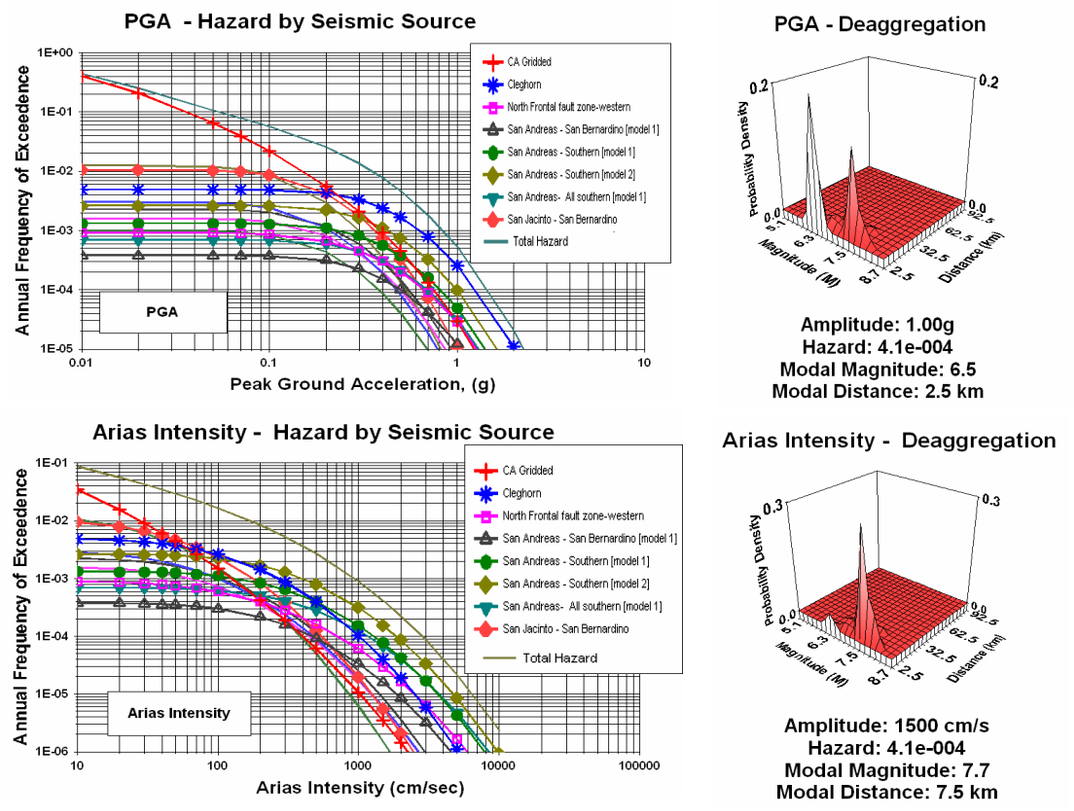


FIG. 2. PSHA hazard curves and magnitude-distance deaggregation for PGA and AI for a weathered rock site in the San Bernardino Mountains.

Figure 3 gives results for a deep soil site southeast of Bakersfield about 20 km from the White Wolf fault, the source of the 1952 M7.3 Kern County earthquake, but closer to several M5+ aftershocks. Other active faults nearby include the Plieto Thrust, San Andreas, and Garlock faults. The site condition was modeled using V_{s30} = 300 m/s and BRM class D. Significantly different most-likely scenarios are indicated by magnitude-distance deaggregation based on PGA (M6.1 at 7.5km) and AI (M7.3 at 22.5 km) for 3000-yr ERP motions. The AI hazard curves show the White Wolf fault overshadowing background seismicity at longer return periods, and the total hazard yields ERPs of ~700 and 3500 years for 50th and 84th percentile AI predictions (1.3 and 3.2 m/s) for the M7.3 scenario.

Figure 4 represents a soft rock site (V_{s30} = 500 m/s, BRM class C) in western Santa Clara Valley, 8.5 km from the San Andreas fault. PGA hazard is influenced by several sources, and becomes controlled by events on the Monte Vista-Shannon fault, 2.5 km away, at ERP above 5000 years. AI hazard is dominated by events on the San Andreas for ERPs above 200 years. At 5000-yr levels, PGA deaggregation shows modes at both M6.7 at 2.5 km and M7.9 at 8.5 km, whereas AI deaggregation focuses only on the latter scenario. The AI hazard curve shows that 50th and 84th percentile AI estimates for a M7.9 at 8.5 km (2.9 and 8.2 m/s) have 350- and 1700-yr ERPs.

Figure 5 shows results at ERPs of about 10,000-yrs for a rock site (V_{s30} = 800 m/s, BRM class B) east of Sacramento in an area of low seismic activity. Modal magnitude-distances are M6.1 at 7.5 km (background seismicity) for PGA deaggrega-

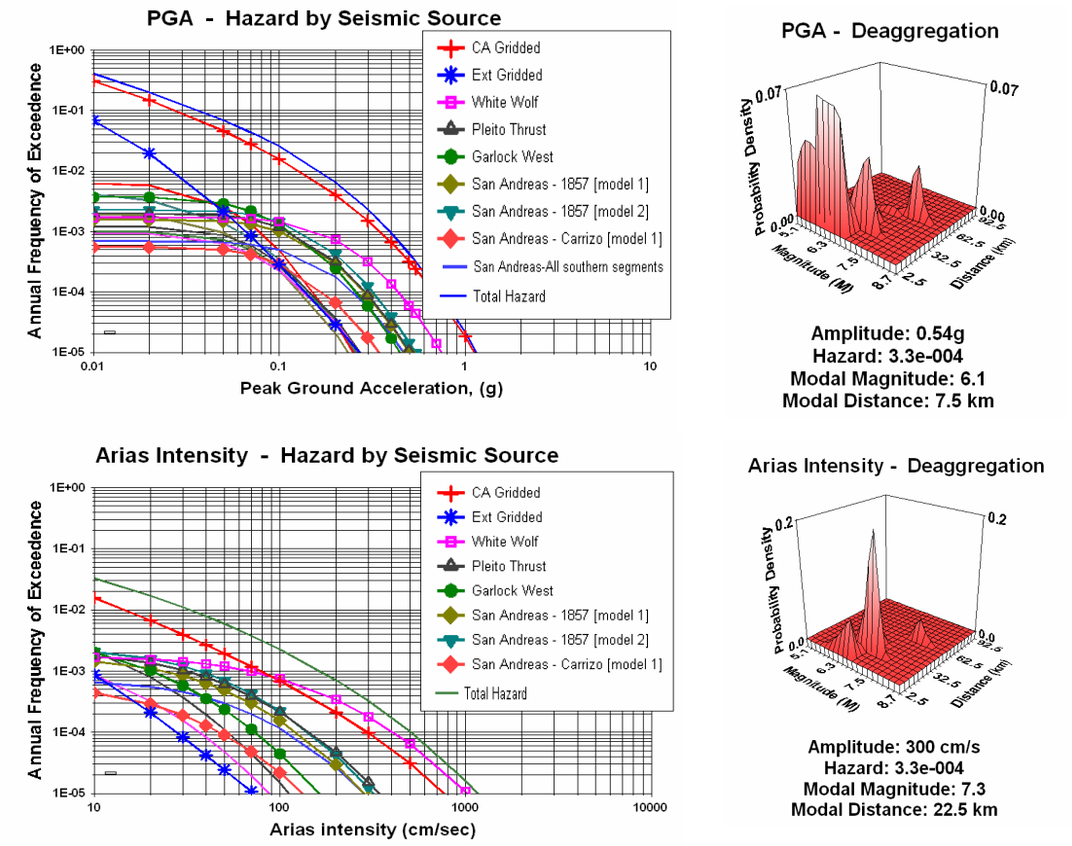


FIG. 3. PSHA hazard curves and magnitude-distance deaggregation using PGA (top) and AI (bottom) for a soil site southeast of Bakersfield, California.

tion, M7.9 at 160 km (San Andreas event) for $SA_{T=1s}$, and M6.5 at 78 km (western Great Valley blind thrust event) for AI. The ERP of 84th percentile AI estimates for these scenarios ranges from less than 500 years to 5000 years (for M6.1 @ 7.5 km).

DISCUSSION

As discussed in Abrahamson (2006), traditional PSHA can be sensitive to the lower-bound magnitude (LBM) used in source modeling. The LBM, which represents the minimum event size expected to cause damage, is used because small earthquakes can produce large peak motions. Thus, the LBM is a concession to the limitations of peak motion to indicate damage potential. Inasmuch as AI scales strongly with magnitude, LBM selection loses significance with PSHA based on AI.

The examples presented mainly compare probabilistic AI and PGA. Baker (2007) found that AI correlates well with PGA and short-period SA through T = 1 s, which supports Travasarou et al. (2003) findings that AI may be more suited to analysis of relatively stiff structures. These conclusions also suggest that deaggregation results for PSHA/AI and PSHA/PGA would be similar, yet this was not demonstrated in our study. That the correlation does not maintain through the PSHA apparently owes to AI's stronger dependence on earthquake magnitude.

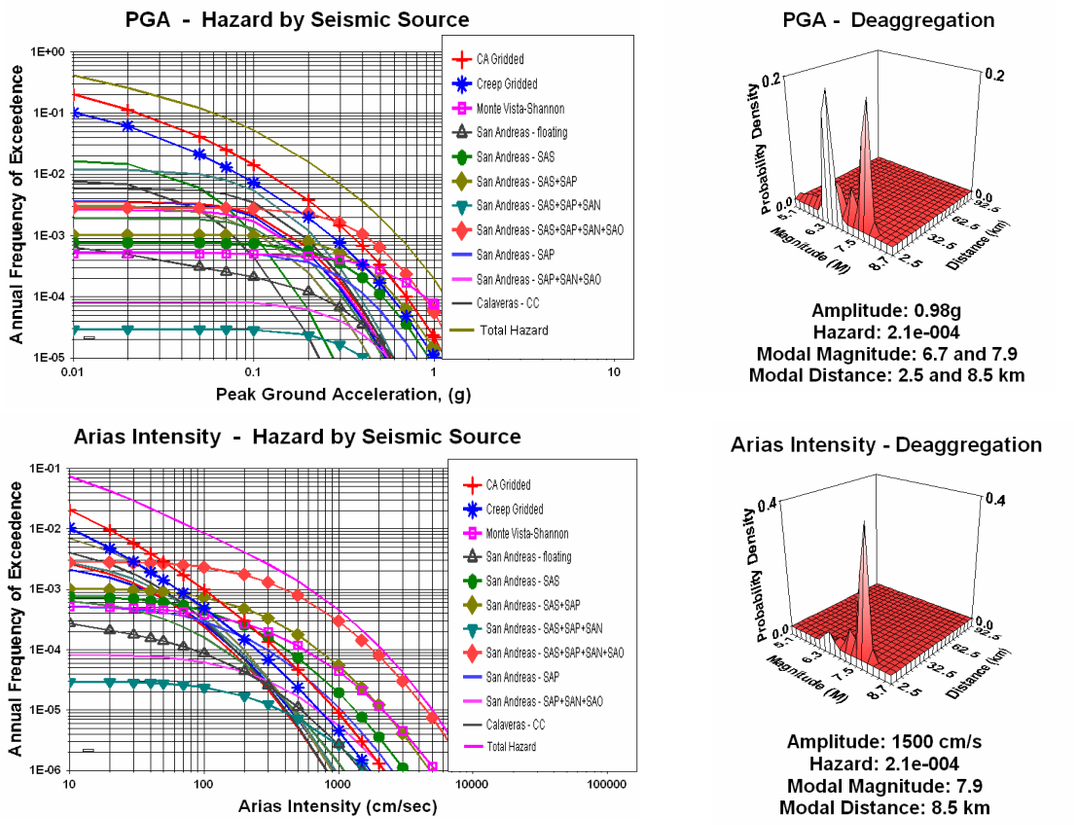


FIG. 4. PSHA hazard curves and magnitude-distance deaggregation using PGA (top) and AI (bottom) for a soft rock site west of Santa Clara Valley, California.

Other examples show that AI deaggregation results can converge with those based on peak motion at sites dominated by a single source, which can occur close to major active faults. However, differences still can arise when the source's seismic activity is characterized by a range of magnitudes and recurrence rates.

Conceptually, PSHA based on the energy content of ground motion is intriguing. We chose AI for our study because it has precedent for use in geotechnical analysis, and robust AI predictive relations exist with functional forms that facilitate probabilistic application. Regardless, AI may not be the ideal parameter for predicting engineering performance; its suitability depends on its correlation with engineering damage potential. Although AI may correlate better than peak motion parameters in geotechnical applications, Kramer and Mitchell (2006) found that a similar energy-based parameter employing an intensity threshold (CAV_5) was superior to AI for liquefaction triggering analysis. Their predictive relation for CAV_5, which is similar to the Travasarou formula for AI, can also be incorporated in PSHA readily, and its use merits further study for other geotechnical applications.

Lastly, probabilistic use of AI does not necessarily suggest fewer seed records should be considered for any given design earthquake scenario. Figure 1 shows performance variations do occur with records of equal AI.

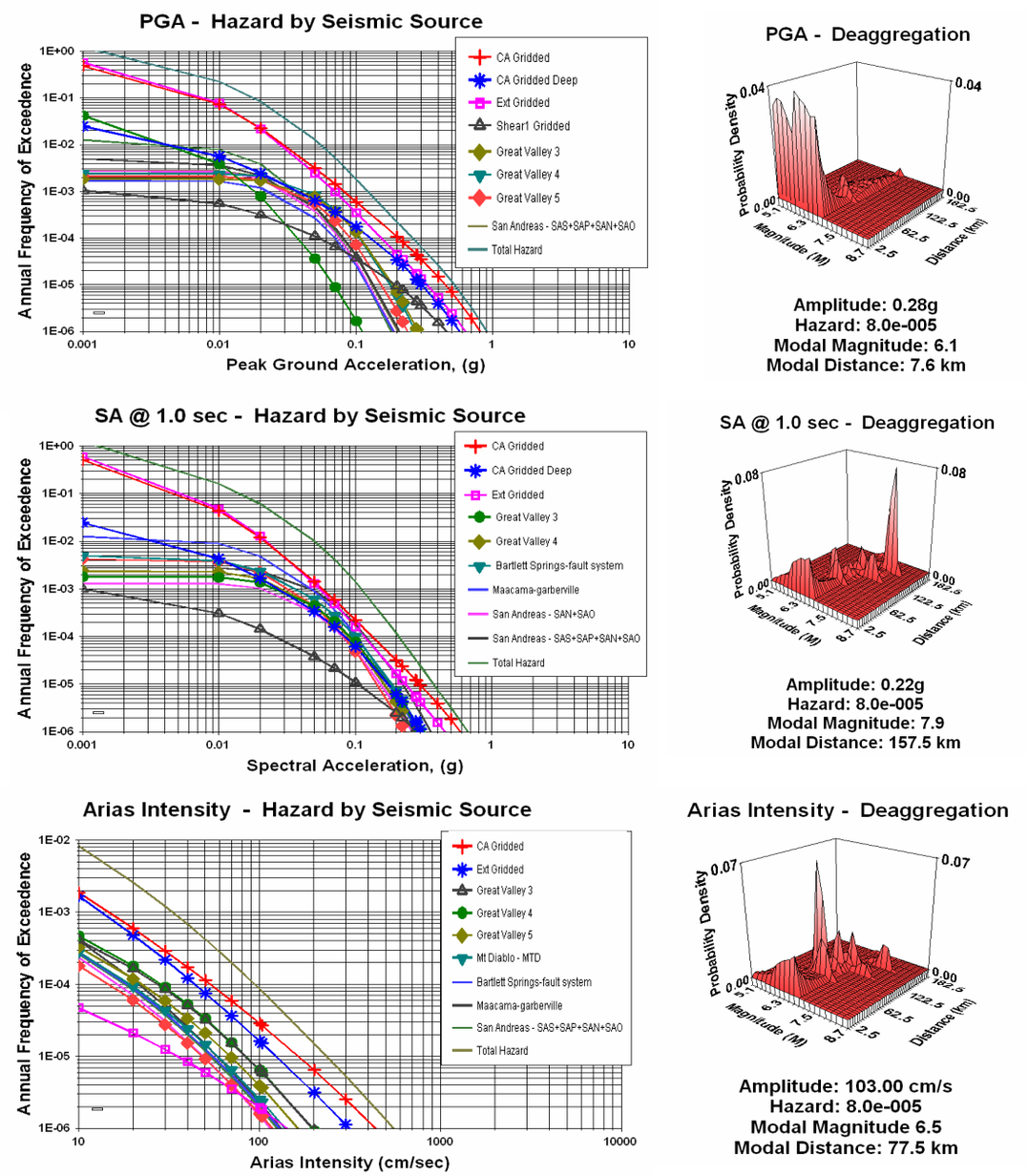


FIG. 5. PSHA hazard curves and magnitude-distance deaggregation using (top to bottom) PGA, $SA_{T=1.0s}$, and AI for a rock site east of Sacramento.

CONCLUSIONS

An energy-based probabilistically-derived ground motion parameter represents an attractive concept for earthquake engineering. Probabilistic use of AI, which is closely related to the energy content of strong motion, should be considered for analyses that use seismic loading in the form of a time history. Such analyses commonly address structures and situations sensitive to both the amplitude and durational aspects of seismic shaking. The empirical predictive relationship for AI developed by Travasarou et al (2003) is readily usable for this purpose.

Probabilistic use of ground motion energy content potentially facilitates and/or improves the application of PSHA to geotechnical analysis requiring earthquake loading in the form of a time history. To the extent that energy content correlates with geotechnical performance, an AI hazard curve suggests a more direct means for relating exceedance probability to the loading represented in a time history, and together with deaggregation of PSHA/AI, can directly guide the development of design earthquake scenarios. Examples show that PSHA based on AI vs. PGA or $SA_{T = 1s}$ can focus on significantly different modal deaggregation scenarios. Our results indicate that, relative to PGA, deaggregation of probabilistic AI generally focuses on larger magnitude scenarios that generally have more energy content.

While no single ground motion measure may fully capture all aspects important to engineering performance, probabilistic use of energy measures such as Arias Intensity potentially fills a gap and enhances existing practice. Probabilistic AI could be used to efficiently develop suites of time histories representing various probabilities for engineering fragility/sensitivity analyses, or simply to judge the conservatism of a proposed design earthquake motion.

ACKNOWLEDGMENTS

The views expressed are those of the authors and not necessarily those of the California Department of Water Resources' Division of Safety of Dams. We thank Rich Dobbs and Robin McGuire of RISK Engineering for software and technical support that made this study possible. We also are grateful for the insight, advice, and assistance of Mike Beaty, Ariya Balakrishnan, and two anonymous reviewers.

REFERENCES

Arias, A. (1970). "A measure of earthquake intensity". In *Seismic Design for Nuclear Power Plants*, Hansen, R.J., (ed.). MIT Press, Cambridge, Mass., 438-483.

Abrahamson, N.A. (2006). "Seismic hazard assessment: problems with current practice and future developments." *First European Conference on Earthquake Engineering and Seismology*, Geneva, Switzerland, 3-8 September, 2006, 17pp.

Baker, J.W. (2007), "Correlation of ground motion intensity parameters used for predicting structural and geotechnical performance". In *Applications of Statistics and Probability in Civil Engineering*, Kanda, Takada, and Furuta (eds.), Taylor and Francis Group, London, 1-7.

Boore, D.M., and Atkinson, G.A. (2007). "Boore-Atkinson NGA ground motion relations for the geometric mean horizontal component of peak and spectral ground motion parameters". PEER report 2007/ 01, 234pp.

Campbell, K.W., Bozorgnia, Y. (2006). "Campbell-Bozorgnia NGA Ground Motion Relations for the Mean Horizontal Component of Peak and Spectral Ground Motion Parameters". PEER report 2007/02, 234pp.

Chiou, B S.-J.; Youngs, R.R (2007). "Chiou and Youngs PEER-NGA Empirical Ground Motion Model for the Average Horizontal Component of Peak Acceleration and Pseudo-Spectral Acceleration for Spectral Periods of 0.01 to 10 Seconds - Interim Report for USGS Review". June 14, 2006 (Revised Editorially July 10, 2006), 219pp.

Chopra, A.K. (2005). "Earthquake Dynamics of Structures, A Primer" Second edition. Earthquake Engineering Research Institute Monograph MNO-11, 129p.

Fraser, W.A., and Burns, R.B. (2004). "Evaluating the conservatism of deterministic ground motion estimates using PSHA for California dams". *Program with Abstracts, 2004 Annal. Mtg. Assoc. Engrg. Geologists. AEG News* (47): 43.

Fraser, W.A., and Howard, J.K. (2002). "Guidelines for use of the Consequence-Hazard Matrix and selection of ground motion parameters". DSOD Technical Reference, http://www.damsafety.water.ca.gov/docs/CHM.pdf

Harp, E.L., and Wilson, R.C. (1995). "Shaking intensity thresholds for rock falls and slides: Evidence from the 1987 Whittier Narrows and Superstition Hills earthquake strong motion records". *Bulletin of the Seismological Society of America*, Vol. 85 (6): 1739-1757.

Jibson, R.W. and Jibson, M.W. (2003). "Java programs for using Newmark's method and simplified decoupled analysis to model slope performance during earthquakes". U. S. Geological Survey, Open File report 03-005.

Kayen, R. E. and Mitchell, J. K. (1997). "Assessment of liquefaction potential during earthquakes by Arias intensity". *J Geotech. Geoenviron. Eng*., Vol. 123 (12): 1162-1174.

Kramer, S.L. and Mitchell, R.A. (2006), "Ground motion intensity measures for liquefaction hazard evaluation" *Earthquake Spectra*, Vol. 22: 413-438.

Makdisi, F.I., and Seed, H.B. (1978) "Simplified procedure for estimating dam and embankment earthquake-induced deformations". *J. Geotech. Eng. Division*, ASCE v.104 (GT7): 849-867.

Rodriguez-Marek, A., Bray, J.D., and Abrahamson, N.A. (2001). "An empirical geotechnical site response procedure". *Earthquake Spectra*, Vol. 17: 65-87.

Seed, H.B., Idriss, I.M., and Arango, I. (1983) "Evaluation of liquefaction potential using field performance data". *J. Geotech. Engineering,* ASCE Vol.109 (3): 458-482.

Travasarou, T., Bray, J. and Abrahamson, N. (2003). "Empirical attenuation relationship for Arias Intensity". *Earthquake Engineering and Structural Dynamics,* Vol. 23: 1133-1155.

USCOLD (1999)."Updated guidelines for selecting seismic parameters for dam projects," prepared by Committee on Earthquakes, April, 63 pp.

Watson-Lamprey, J., and Abrahamson, N. (2006). "Selection of ground motion time series and limits on scaling". *Soil Dynamics and Earthquake Engineering*, Vol..26: 477-482.

Wilson, R.C. (1993). "Relation of Arias Intensity to Magnitude and Distance in California". U.S. Geological Survey, Open File Report 93-556, 42pp.

Wilson, R.C. and Keefer, D.K. (1985). "Predicting aerial limits of earthquake-induced landsliding". In, J.I. Ziony (ed.), *Evaluating earthquake hazards in the Los Angeles region - An Earth-Science perspective*. U.S. Geological Survey, Professional Paper 1360, 316-345.

Yule, D.E., Matheu, E.E., and Beaty, M.H. (2004). "Duration parameters for the selection of ground motion time histories for non linear analysis of embankment dams". *Technical Report, 36th Joint Meeting U.S.-Japan Panel on Wind and Seismic Effects*, National Institute of Standards and Technology, Gaithersburg, Maryland, 17-22 May 2004.

SEISMIC DESIGN CRITERIA GROUND MOTIONS

Joe Litehiser[1] and James E. Marrone[2]

[1]Chief Seismologist, Bechtel Corporation, PO Box 193965, San Francisco, CA 94119. E-mail: jjlitehi@bechtel.com
[2]Senior Scientist, Bechtel Corporation, PO Box 193965, San Francisco, CA 94119. E-mail: jmarrone@bechtel.com

ABSTRACT: Ground motions are derived for application to Project-specific design criteria. Both probabilistic and deterministic seismic design ground motions are developed satisfying design requirements, and using seismic source and ground motion attenuation models similar to those employed for earlier extensions to the BART system. Specifically, the Silicon Valley Rapid Transit Project (SVRT) alignment seismic design criteria for permanent structures require determination of the greater of ground motions from a site-specific 10% in 50 years [approximately, 500-year return period] probabilistic analysis or the median deterministic ground motions from the maximum magnitude events on the major active faults in the immediate vicinity: the San Andreas, Hayward, and Calaveras faults. For convenience, the continuum of design ground motion response spectra within this range were segregated into smooth enveloping horizontal and vertical surface outcrop spectra over the frequency range of 100 to 0.1 Hz and for National Earthquake Hazards Reduction Program (NEHRP) Site Class D for "North," "Central," and "South" reaches of the alignment. Based on these analyses this report defines seismic design ground motion response spectra for permanent and temporary structures for these three reaches.

INTRODUCTION

All design development for SVRT is performed to comply with BART Facilities Standards except as specifically modified or supplemented for the SVRT, as well as to meet federal, state and local requirements [see Litehiser et al. 2003, SVRT 2005].

Although the BART criteria considered a deterministic contribution only from the San Andreas fault, for the SVRT alignment the seismic design team considered the San Andreas, Hayward-Rodgers Creek and Calaveras faults. These three are the most significant faults near the SVRT project. As discussed below the probabilistic ground motions generally dominate the criteria ground motions, except for some long period deterministic ground motions from the Hayward-Rodgers Creek fault toward the north end of the alignment.

In addition, with advice from the seismic design team and Seismic Advisory Board, and based on the regional subsurface conditions, SVRT established that reference ground motions of the seismic design criteria are to consider soil conditions consistent with NEHRP Site Class D. Finally, design ground motions of 10% probability in 10 years with a minimum of 0.2g are also proposed for temporary excavation support structures, based on Caltrans criteria for temporary bridges and modification in consideration of Bay Area seismicity.

SEISMIC DESIGN CRITERIA

The proposed seismic design criteria from the SVRT-adapted BART Facility Standards that are the basis for this ground motions study are, in most relevant part:

5.1 Design Ground Motions

The higher ground motions from a site-specific 10% in 50-year probabilistic analysis ground motion or the median deterministic ground motions from the San Andreas, Hayward and Calaveras faults maximum magnitude events shall be used in the design of bridges and revenue structures.

The maximum magnitude events shall be as follows:

San Andreas - magnitude 8.0
Hayward - magnitude 7.25
Calaveras - magnitude 7.0

Revenue structures are structures whose structural integrity is necessary for continued operation of trains, and include aerial guideways, passenger stations, tunnels, cut-and-cover subway structures, ventilation structures, and earth retaining structures along the track alignments. For the Tunnel Segment of the SVRT project, the revenue structures include the bored tunnels, tunnel portals, crossover structure, and ventilation structures.

Two horizontal (fault normal and fault parallel) and vertical response spectra shall be developed.. . . .

Assuming NEHRP soil type D based on regional subsurface conditions for SVRT project-wide use, baseline probabilistic and deterministic ground motion estimates shall be made for the free-field ground surface. Modifications of this baseline estimate may be made as appropriate either to account for detailed knowledge of site-specific foundation conditions indicating departure from NEHRP soil-type D conditions at the ground surface or to account for differences between surface motions and the depth of subsurface facilities.

The design of the temporary excavation support structures of the SVRT Tunnel Segment, erected for the construction of permanent structures, shall use a reduced design ground motion level based on the 10% in 10 year probabilistic ground motion with peak horizontal ground acceleration not less than 0.2g.

SEISMIC DESIGN GROUND MOTION APPROACH

The general approach for determining the seismic design ground motions is similar to that followed in the BART Seismic Retrofit program (Litehiser et al., 2003). Basically, analyses are performed at a number of points along the alignment to determine two ground motion components of the criteria: 1) ground motions corresponding to a 500-year return period, or 10% probability of exceedance in 50 years; and 2) the median ground motion from the maximum magnitude events on the San Andreas, Hayward, or Calaveras faults. For both the probabilistic and deterministic components the same ground motion attenuation relations are used to

calculate multiple (11) spectral ordinates: PGA and for periods of 0.075, 0.1, 0.2, 0.3, 0.5, 1.0, 1.5, 2.0, 3.0, and 4.0 seconds. At each analysis point and for each spectral ordinate the greater of the probabilistic and deterministic ground motions is taken, defining the "design spectrum" at that point and for that measure of ground motion. It was intended to evaluate the ground motion spectra from the various analysis sites in expectation that two or three representative spectra could be used to define the reference ground motion for the entire SVRT alignment.

While the basic ground motion spectra – as represented by response spectra for 5% critical damping – are intended to be for average horizontal ground motions corresponding to the required reference Site Class D, additional characteristics of observed earthquake ground motions were considered, including:

- Directivity effects
- Vertical earthquake motions
- Basin and deep soil effects

The effects determined to be significant are implemented as appropriate scaling factors to the basic horizontal ground motion spectra resulting in design spectra.

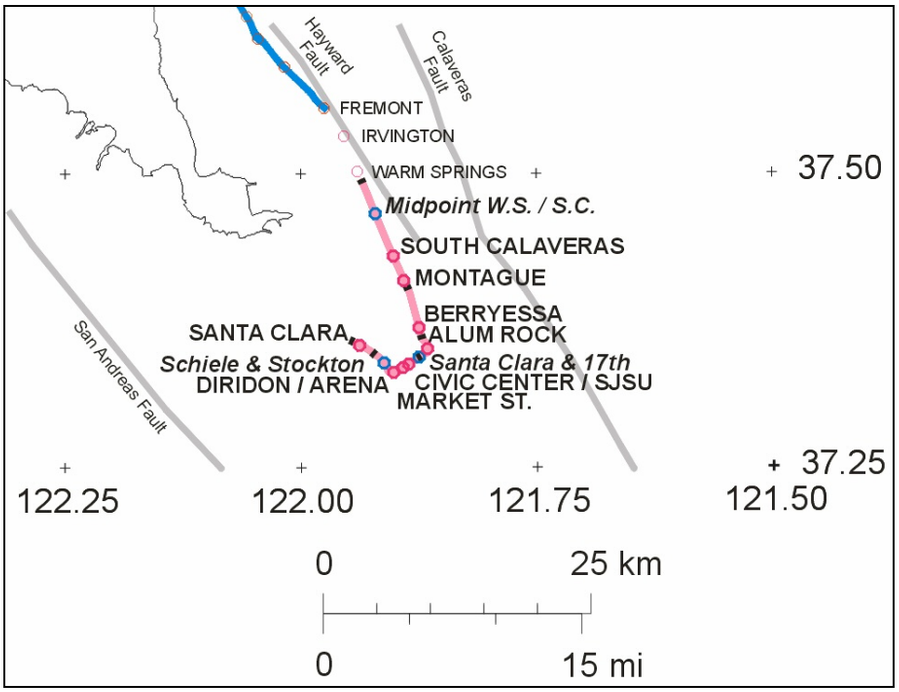


Figure 1. Map of the proposed SVRT alignment (light red line) and 17 sites considered for the seismic ground motion analysis: Blue line indicates the existing BART alignment, currently ending at Fremont.

Figure 1 indicates the 17 sites at which seismic ground motion analysis was performed. Up to eight BART station locations were proposed – from the South Calaveras station at the northern end of the alignment to the Santa Clara station at the southwest end. Additional points for seismic analysis were identified near the intersection of Santa Clara and 17th and the intersection of Schiele and Stockton Streets. Because the South Calaveras station is some distance south of the actual

northern end of SVRT alignment, an additional analysis site was selected midway between South Calaveras and the proposed Warm Springs station, which is part of a separate BART extension project from Fremont to Warm Springs. Originally, the SVRT alignment was divided into five segments. The six joint locations delineating the beginning and ending of the five segments were also used as analysis sites. At the time of the study segments 1 and 2 are referred to as the Line Segment, segments 3 and 4 are referred to as the Tunnel Segment, and segment 5 refers to the Yard and Shops part of the alignment.

SEISMIC SOURCE MODEL

The seismic source model developed for the ground motion hazard analysis for the SVRT project includes characterization for all seismogenic sources that could cause strong ground shaking at SVRT project facilities. The seismic source model, based on the fault model of the Working Group on California Earthquake Probabilities [WGCEP] in 2003 [referred to as WG02]) is used in its entirety for the probabilistic elements of the design criteria. However, only the San Andreas, Hayward, and Calaveras faults are considered for the deterministic element of the design criteria. The source model includes characterization of known fault sources as well as possibly unknown fault sources. The known fault sources include major strike-slip faults such as the San Gregorio, San Andreas, Hayward, Calaveras, Rodgers Creek, Concord-Green Valley, and Greenville faults, as well as other reverse and strike-slip faults that lie between the major strike-slip faults. The model also incorporates possibility for earthquakes to occur on un-mapped faults, by incorporating areal zones bounded by the major strike-slip faults. Each seismogenic source is characterized by a geometry, maximum magnitude distribution, and rate of earthquake occurrence. For the probabilistic seismic hazard analysis, the range of possible source parameters (alternative values and alternative models) is incorporated in the analysis through the use of logic trees. For the deterministic analysis of the San Andreas, Hayward, and Calaveras faults, the expected maximum magnitude is assessed.

A detailed description of this seismic source model is beyond the scope of this paper, but may be found in Silicon Valley Rapid Transit Project (2005).

GROUND MOTION ATTENUATION

Four equally weighted empirical relations were used in both probabilistic and deterministic horizontal ground motion analyses to represent the epistemic uncertainty in ground motion for this study: Abrahamson and Silva (1997), Boore et al. (1997), Sadigh et al. (1997), and Campbell and Bozorgnia (2003). The site category flag or shear-wave velocity was set to be consistent with the midrange for NEHRP soil type "D."

Two of the four the relations also modeled vertical ground motions and were used to develop ratios of vertical-to-horizontal ground motions [V/H].

In 2002 the Next Generation Attenuation Project of the Pacific Earthquake Engineering Research [PEER] Lifelines Program [http://peer.berkeley.edu/products/nga_project.html] was begun to develop updated attenuation relationships

for shallow crustal earthquakes in the western United States. The NGA ground motion models were not available until the latter part of 2007.

An analysis of ground motion residuals (i.e., observed ground motions *minus* ground motions predicted by the above four attenuation relationships) was performed using both the limited strong ground motion data recordings in the area from the 1989 Loma Prieta earthquake and more global strong ground motion data recorded on deep soil sites. It was concluded that the use of these four attenuation models did not introduce a significant bias in the ground motion study.

PROBABILISTIC GROUND MOTIONS

The procedure for performing a Probabilistic Seismic Hazard Analysis (PSHA) was described first by Cornell (1968) and has undergone substantial development since that time. The PSHA methodology is now used by the United States Geological Survey (USGS) to map ground shaking hazard in the United States. The current procedures for PSHAs are described in several publications (National Research Council, 1988; Earthquake Engineering Research Institute, 1989; Coppersmith, 1991; and U.S. Army Corps of Engineers [USACE], 1998). Site-specific ground motions using PSHA for the SVRT sites were developed using the procedures described in these publications.

For the purpose of design of permanent structures, 500-year (approximately the same as the 10% probability of exceedance in 50-yr, or the 475-yr) horizontal equal hazard spectra, 5% critical damping, were calculated for each of the 17 analysis sites. Similarly, for the purpose of design of temporary structures, 100-year (approximately the same as the 10% probability of exceedance in 10 years, or the 95-yr) horizontal equal hazard spectra, 5% critical damping, were also calculated for each of the 17 analysis sites. These analyses showed that probabilistic spectra decrease in high frequency amplitude from the north end of the alignment to the south and southwest end of the alignment. Similar, though less pronounced trend is apparent in the long periods, as well. Further, these spectra indicated a gap between the Montague and Berryessa spectra, which is likely due to the increased distance from the south end of the Hayward fault.

DETERMINISTIC GROUND MOTIONS

For the purpose of developing seismic design ground motion spectra for the permanent structures, the log-average median horizontal soil response spectra, 5% critical damping, were calculated using the same set of four attenuation relations used in the probabilistic analysis for each of the 17 analysis sites and considering each of the San Andreas, Hayward, and Calaveras faults. The maximum magnitude used for each fault is 8.0, 7.25, and 7.0, respectively. The magnitude 7.25 for the Hayward fault is based on the assumption of co-rupture of the Hayward and Rodgers Creek fault as considered by WG02. In this context this fault is referred to as the Hayward-Rodgers Creek fault. These maximum magnitudes were taken as values near the high end of the magnitude distributions presented by the 2002 Working Group (WGCEP, 2003).

As was the case for the probabilistic spectra, the deterministic spectra decrease in high frequency amplitude from the north end of the alignment to the south and southwest end of the alignment. For the long periods, the amplitudes also tend to decrease from the north end of the alignment southward, as distance from the Hayward-Rodgers Creek increases. This trend reverses at about Segment Joint 2/3 or the Alum Rock station, where the distance to the San Andreas fault is decreasing along the alignment from north to south and southwest, resulting in the San Andreas-derived long period spectral values overtaking the amplitudes from the closer, smaller magnitude Hayward-Rodgers Creek fault, resulting in increasing response spectral values in the long periods from Alum Rock to the southwest end of the alignment.

Similar to what was observed for the probabilistic spectra, though more prominently, there is a notable gap between the Montague and Berryessa deterministic response spectra, which is due to the increased distance to the south end of the Hayward-Rodgers Creek fault, or about 4 and 8 km, respectively.

DEVELOPMENT OF HORIZONTAL GROUND MOTION RESPONSE SPECTRA FOR PERMANENT AND TEMPORARY STRUCTURES

Table 1 indicates the greater of the probabilistic (500-year) and deterministic (median) response spectra, for each location and period.

Table 1. Dominant Source for Horizontal Ground Motion Response Spectra for Permanent Structures

RESPONSE SPECTRA: 5% CRITICAL DAMPING											
LOCATIONS	Frequency (Hz)										
	33	13.3	10	5	3.33	2	1	0.667	0.5	0.33	0.25
	Period (s)										
	0.03	0.075	0.1	0.2	0.3	0.5	1	1.5	2	3	4
Sgmt Joint 0/1	P	P	P	P	P	P	D:HR	D:HR	P	D:HR	D:HR
[Midpoint W.S./S.C.]	P	P	P	P	P	P	D:HR	D:HR	D:HR	D:HR	D:HR
So Calaveras	P	P	P	P	P	P	D:HR	D:HR	D:HR	D:HR	D:HR
Montague	P	P	P	P	P	P	P	D:HR	P	P	P
Sgmt Joint 1/2	P	P	P	P	P	P	P	P	P	P	P
	⋮	⋮	⋮	⋮	⋮	⋮	⋮	⋮	⋮	⋮	⋮
Sgmt Joint 5/-	P	P	P	P	P	P	P	P	P	P	P

Notes: **D:HR**: Deterministic, Hayward-Rodgers Creek **P**: Probabilistic
Probabilistic motions are dominant for all frequencies for all locations from Segment Joint 1/2 [near Montague] to Segment Joint 5/- at the end of the alignment [near Santa Clara station (see Figure 1).

No directivity is included in these results. Examination of specific spectral acceleration values for the 17 sites analyzed suggests that design ground motion response spectra for the SVRT alignment can be satisfied by three representative ground motion spectra denoted the “North ,” “Central,” and “South” Ground Motion Response Spectra. These spectra are based, respectively, on the Segment Joint 0/1 analysis site, the Montague station analysis site, and the envelope of response spectral values from all analysis sites from the south end of the alignment to the Berryessa station, inclusive.

For the temporary structures only the 100-year probabilistic ground motions are considered. The suite of 100-year spectra may be grouped into North, Central, and South spectra, facilitating the same distinction of three representative response spectra.

DIRECTIVITY EFFECTS

Most ground motion attenuation relations, including those used here, average out the theoretical effects that have begun to be observed that relate to specific fault rupture direction – e.g., toward or away from a given site location – and the horizontal orientation of site ground motion relative to the causative fault – e.g., fault normal or fault parallel. The combined effects of rupture directivity and fault-orientation ("fault-normal" or "fault-parallel") are generally referred to as "directivity effects". The amplification (or de-amplification) effects of rupture directivity and fault-relative orientation have been modeled by Somerville et al. (1997) and modified for PSHA application by Abrahamson (2000). Average directivity scaling factors were determined from the PSHA and applied to the horizontal design spectra discussed above. For the SVRT alignment these effects range from about 0% to 33% increase in spectral accelerations for periods between 1 and 4 or greater seconds for the fault-normal component and up to a 9% decrease in fault-parallel motions.

SMOOTHED HORIZONTAL DESIGN GROUND MOTION RESPONSE SPECTRA

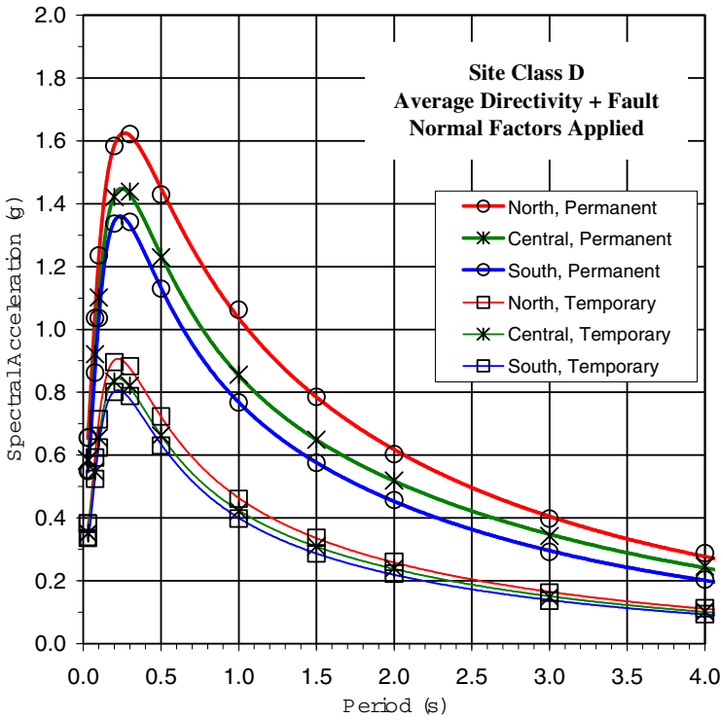


Figure 2. Discrete spectral acceleration points and smoothed horizontal design ground motion response spectra including average plus fault-normal directivity.

Figure 2 shows the horizontal design response spectra, for both permanent and temporary structures, developed for the more conservative fault-normal case.

DEVELOPMENT OF VERTICAL DESIGN GROUND MOTION RESPONSE SPECTRA FOR PERMANENT AND TEMPORARY STRUCTURES

Average ratios of vertical-to-horizontal spectral response (V/H) were developed using both probabilistic and deterministic results for all 17 analysis sites. Values of this ratio for permanent structures ranged from 1.6 for high frequencies for the North and Central alignment segments to 0.3 for lower frequencies for all three segments. For temporary structures the range was 1.4 to 0.3 over the same locations and frequencies. The V/H ratios were applied to the horizontal spectra to obtain North, Central, and South vertical response spectra for both permanent and temporary seismic design criteria.

BASIN AND DEEP SOIL EFFECTS

The SVRT alignment extends from just south of the Warm Springs terminus of the BART system into the northeastern Santa Clara Valley. Based on inversion of gravity data (Brocher et. al., 1997) the Santa Clara Valley is underlain by two sedimentary basins embedded between the San Andreas and Hayward and Calaveras faults, which form its west and east boundaries, respectively. The two basins occur on the eastern and western sides of the Valley with a saddle between them. The southern part of the Line Segment and the eastern part of the Tunnel Segment lie just within the Evergreen Basin on the eastern side of the Santa Clara Valley. The balance of the Tunnel Segment and the Yard and Shops Segment are over the saddle between the basins.

Preliminary investigations of basin and deep soil effects were examined and it was concluded that the soil ground motion attenuation relations used already to develop the design ground motions encompass, possibly conservatively, amplification that may be expected from basin and/or deep soil given the project alignment location geologic setting. The SVRT Project seismic design ground motions response spectra do not incorporate these effects explicitly but do adequately incorporate them implicitly by the use of generic attenuation relationships that represent both the empirical data and its scatter.

CONCLUSIONS

Application of criteria developed for the BART extensions and modified for the SVRT project to incorporate additional faults in the deterministic component of the analysis lead to seismic design ground motions broadly applicable to three separate segments of the SVRT alignment (North, Central, and South) and two levels of design (for permanent and temporary structures). The criteria incorporate recent seismic source parameters for the Bay Area, theoretical advances describing strong ground motion near an active fault, and are robust and self-consistent. These criteria provide a sound basis for seismic design of SVRT structures.

ACKNOWLEDGMENTS

Seismic source model details were developed by Donald Wells. Robert Youngs performed all probabilistic analyses, including those leading to probabilistic V/H ratios and directivity effects. Nick Gregor performed an evaluation showing that there was no need to incorporate a basin effect beyond that implied by the empirical attenuation relations used for the analysis.

REFERENCES

Abrahamson, N. A. and Silva, W.J. (1997). "Empirical Response Spectral Attenuation Relations for Shallow Crustal Earthquakes," *Seismological Research Letters*, 68: 94-127.

Abrahamson, N.A. (2000). "Effects of rupture directivity on probabilistic seismic hazard analysis," *Proceedings of the 6th International Conference on Seismic Zonation,* Palm Springs, CA.

Bechtel Infrastructure Corporation & the Bechtel/HNTB Team (2002). "Development of BART Seismic Retrofit Design Ground Motion Criteria, BART Seismic Retrofit Program." submitted to San Francisco Bay Area Rapid Transit District, dated May 9, 2002.

Boore, D. M., Joyner, W.B., and Fumal, T.E. (1997). "Equations for estimating horizontal response spectra and peak acceleration from western North American earthquakes: a summary of recent work," *Seismological Research Letters*, 68: 128-153.

Brocher, T.M., Brabb, E., Catchings, R., Fuis, G., Fumal, T., Jachens, R., Jayko, A. S., Kayen, R., McLaughlin, R., Parsons, T., Rymer, M., Stanley, R., and Wentworth, C. (1997). "A crustal scale 3-D seismic velocity model for the San Francisco Bay Area, California," *EOS Transactions, American Geophysical Union,* 78 (47): F435

Campbell, K.W. and Bozorgnia, Y. (2003). "Updated near-source ground-motion (attenuation) relations for the horizontal and vertical components of peak ground acceleration and acceleration response spectra," *Bull. Seism. Soc. Am.*, 93: 314-331.

Coppersmith, K.J. (1991). "Seismic Source Characterization for Engineering Seismic Hazard Analysis," *Proceedings of the Fourth International Seismic Zonation Conference*, 1: 1-60.

Cornell, C.A. (1968). "Engineering Seismic Risk Analysis," *Bulletin of the Seismological Society of America*, 58: 1583-1606.

Earthquake Engineering Research Institute (1989). "The Basics of Seismic Risk Analysis," *Earthquake Spectra*, 5 (4): 675-702.

Litehiser, J., Gregor, N., Marrone, J. Ostadan, F. and Youngs, R. (2003). "BART Seismic Retrofit Project: Characterization of Design Ground Motion", *Proceedings of the Sixth U.S. Conference and Workshop on Lifeline Earthquake Engineering*.

National Research Council (1988). "Probabilistic Seismic Hazard Analysis," National Academy Press, Washington, D.C., 97 p.

Sadigh, K., Chang, C.-Y., Egan, J.A., Makdisi, F., and Youngs, R.R. (1997). "Attenuation relationships for shallow crustal earthquakes based on California strong motion data," *Seismological Research Letters*, 68: 180-189.

Silicon Valley Rapid Transit Project (2005). "Report on Seismic Ground Motions." SVRT Report P0503-D300-RPT-DE-012, San Jose, California.

Somerville, P. G., Smith, N.F., Graves, R.W., and Abrahamson, N.A. (1997). "Modification of Empirical Strong Ground Motion Attenuation Relations to Include the Amplitude and Duration Effects of Rupture Directivity," *Seismological Research Letters*, 68: 199-222.

USACE (1998). "Seismic Design for Buildings," Appendices, TI 809-04: Report Prepared by URS Greiner, Inc.

Working Group on California Earthquake Probabilities (WG02) (2003). "Earthquake Probabilities in the San Francisco Bay Region: 2002–2031," *U.S. Geological Survey Open-File Report 03-214*.

Seismic Hazard Analysis and Probabilistic Ground Motions in the Upper Mississippi Embayment

J. Alfredo Fernandez[1] and Glenn J. Rix[2]

[1] Graduate Research Assistant, Georgia Institute of Technology, School of Civil and Environmental Engineering, 790 Atlantic Dr. Atlanta, GA 30332; jafernandez@gatech.edu
[2] Professor, Georgia Institute of Technology, School of Civil and Environmental Engineering, 790 Atlantic Dr. Atlanta, GA 30332; glenn.rix@ce.gatech.edu

ABSTRACT

The evaluation of the seismic hazard for a particular site involves the estimation of ground motions associated with potentially damaging earthquakes. Typically the seismic hazard is first computed at the bedrock level. To obtain the seismic hazard at the soil surface, the mean rock hazard is usually multiplied either by a mean amplification function or by a set of average site amplification factors. In this type of approach the variability in the site response is often lost or is not coupled appropriately with the variability associated with the rock hazard. Recent studies have proposed methods to account for the site response in probabilistic seismic hazard analyses using a probabilistic approach. Although these more refined procedures take into account the uncertainty in the entire earthquake process, the most accurate approach to develop site-specific ground motions is the use of site-specific soil attenuation relationships in the probabilistic seismic hazard calculations. Ground motion attenuation relationships were developed for soil sites in the Upper Mississippi Embayment that incorporate uncertainties in the earthquake source, path, and site processes. These attenuation relationships have been used for deterministic and probabilistic seismic hazard analyses for the region. Suites of probabilistic ground motions have been generated for selected cities within the Upper Mississippi Embayment.

INTRODUCTION

The evaluation of the seismic hazard for a particular site involves the estimation of ground motions associated with potentially damaging earthquakes. The seismic hazard may be evaluated by deterministic and probabilistic procedures. In a deterministic analysis a particular earthquake scenario is assumed by specifying an earthquake size and location. A probabilistic analysis explicitly considers the uncertainties in earthquake size, location, and time of occurrence, and along with the

use of attenuation relationships it provides estimates of the likelihood of earthquake ground motion at a given site. Typically the seismic hazard is first computed at the bedrock level either by performing a site-specific seismic hazard analysis or by using regional seismic hazard maps (e.g., Frankel et al., 2002).

To obtain the seismic hazard at the soil surface, the mean rock hazard at the bedrock level is usually multiplied either by a mean amplification function or by a set of average site amplification factors. In the first approach the amplification function is determined by driving through the soil column a suite of acceleration time histories compatible with the rock hazard level using an equivalent linear or fully nonlinear site response analysis. An average of the response spectral ratios of ground surface to rock motions is used to obtain the soil response spectrum. Typically, the local site conditions are characterized by using the best estimates of the dynamic soil properties and shear-wave velocity profile. In the second approach average site coefficients are used to adjust the rock hazard to account for site effects. These methodologies produce soil ground motion levels with unknown exceedance rates when combined with probabilistic seismic hazard analysis (PSHA) at the rock level (Bazzurro and Cornell, 2004; Goulet et al., 2007). Moreover the characterization of variability in dynamic soil properties is often lost in this type of approach.

Recent studies have proposed methods to account for site response in probabilistic seismic hazard analyses using a probabilistic approach (Baturay and Stewart, 2003; Bazzurro and Cornell, 2004; Cramer, 2003; Goulet et al., 2007). Although these more refined procedures take into account the variability in the entire earthquake process, the most accurate approach to develop site-specific ground motions is by using site-specific soil attenuation relationships in the probabilistic seismic hazard calculations, assuming that appropriate epistemic and aleatory uncertainties are incorporated in the development of the attenuation relationship (Bazzurro and Cornell, 2004; Goulet and Stewart, 2007; Goulet et al., 2007; Silva and Costantino, 2002). Soil attenuation relationships already account for correlations among the processes of earthquake generation, and therefore avoid the process of coupling the variability in rock motions and in site response. Thus, the attenuation relationships developed by Fernandez and Rix (2006) for soil sites in the Upper Mississippi Embayment have been used for deterministic and probabilistic seismic hazard analyses for the region. The seismic hazard estimation incorporates the epistemic variability accommodated in the attenuation relationships with the use of three source models and three stress drop values. Typical geological units of the region, Embayment depth, and non-linear soil behavior have been considered by the use of site-specific soil attenuation relationships.

SEISMIC HAZARD ANALYSES

Deterministic and probabilistic seismic hazard analyses were performed for seven selected cities within the Upper Mississippi Embayment including Memphis, TN; Jonesboro, AR; Jackson, TN; Blytheville, AR; Paducah, KY; Cape Girardeau, MO; and Little Rock, AR. Figure 1 shows a map of the Embayment along with the

location of the selected cities. Both Lowlands and Uplands soil profiles were considered for the city of Memphis, TN, because portions of the city are in each soil type. The probabilistic hazard analyses were performed using EZ-FRISK™, a computer program for earthquake ground motion estimation developed by Risk Engineering, Inc.

The characterization of seismic sources implemented in the PSHA is the same characterization that the U.S. Geological Survey used to develop the Seismic Hazard Maps 2002 for the CEUS region (Frankel et al., 2002) including the New Madrid and Charleston, SC seismic sources and background seismicity of the CEUS. Figure 2 shows the geographical location of the seismic sources considered in the analyses excluding background seismicity along with the extent of the Upper Mississippi Embayment.

Attenuation relationships and their inherent uncertainty must be specified to estimate ground motions at the site as a function of earthquake magnitude and distance to the seismic source. The soil attenuation relationships developed by Fernandez and Rix (2006) for the Upper Mississippi Embayment were selected to perform the seismic hazard analyses. The attenuation relationships incorporate the effects of the entire earthquake process generation including source, path, and site effects, and the non-linear behavior of the deep soil profile in the Embayment. The soil attenuation relationships were developed for the two typical soil profiles in the Embayment – Lowlands and Uplands – and seven Embayment depth bins ranging from 6 m to 1220 m. The attenuation relationships used in the PSHA for each city

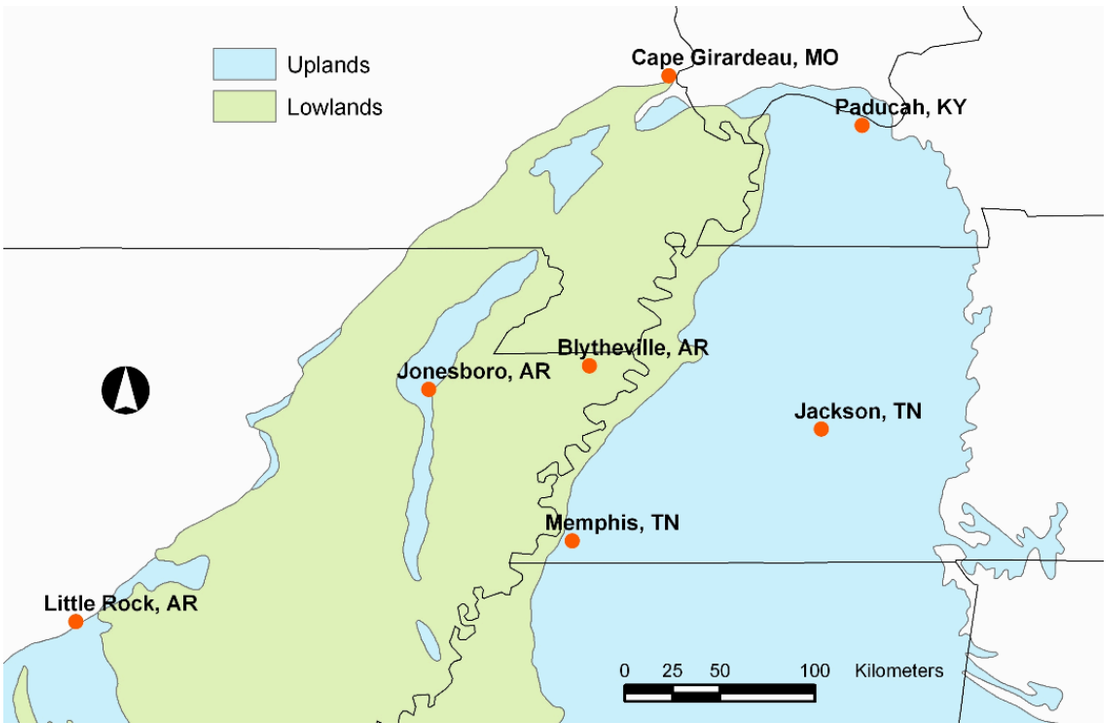


FIG. 1. Upper Mississippi Embayment and selected cities.

were selected based upon the type of soil profile and depth to the bedrock in each city.

The epistemic variability on attenuation relationship is incorporated by using three source models – Atkinson and Boore (1995), Frankel et al. (1996), and Silva et al. (2003), and three values of the stress drop parameter, $\Delta\sigma$ – median case, 100% higher (high case), and 50% lower (low case). The Atkinson and Boore (1995) source model is insensitive to the stress drop and therefore only one case is implemented for this model. The weights assigned to each hypothesis in the analyses are 2/3, 1/6, and 1/6 for the median, high and low stress drop values as suggested by Silva et al. (2003), and 1/3, 1/3, and 1/3 for the three source models because the lack of evidence that a particular model fits observed data better than the other two models. It is important to note that the selection of weights has an impact on the results; however the end-user can select other weights to combine the seven hypotheses if desired.

The combination of source models and stress drop values results in seven independent hazard curves for each city. Figure 3 compares the seven different soil hazard curves for PGA in Memphis, TN. The figure shows the scatter due to the epistemic variability in source model and stress drop value. The seven hazard curves for a particular city were combined into a single mean hazard curve (McGuire, 2004; McGuire et al., 2005; Musson, 2005). The mean hazard curve is computed as the weighted average of the seven individual hazard curves using the weights defined above. Hazard curves were obtained for 50 spectral periods distributed between 0.01 and 5 seconds.

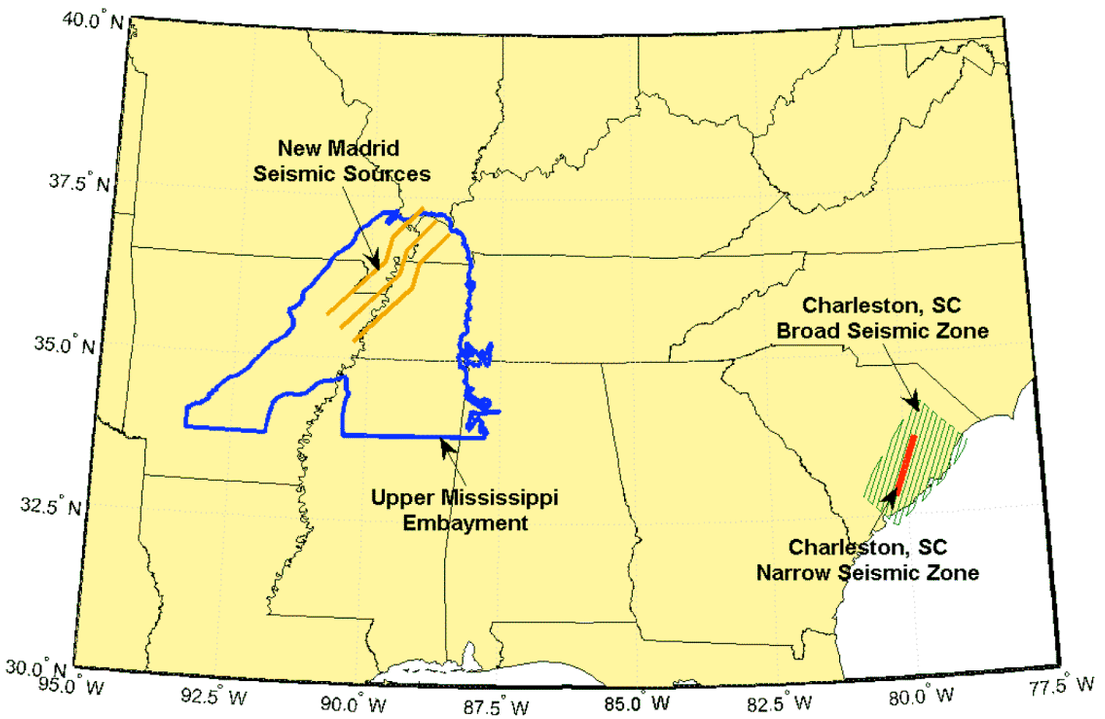


FIG. 2. Upper Mississippi Embayment and geographical location of seismic sources.

The hazard deaggregation was performed for each individual attenuation equation and then the probability density functions were combined using the same weights assigned to each attenuation equation to calculate the hazard deaggregation of the mean hazard curve. Figure 4 shows the mean hazard deaggregation for PGA and return period of 2475 years in Memphis, TN. In this study the width of the magnitude, distance, and epsilon bins was 0.1, 2.5, and 0.2 respectively. The New Madrid seismic zone with ground motions associated with the mean + 1 standard deviation and M 7.7 dominate the seismic hazard in the Upper Mississippi Embayment. The Charleston, SC seismic sources do not contribute to the seismic hazard in the region.

Hazard curves were used to calculate response spectra of constant probability or uniform hazard spectra (UHS). If multiple hypotheses are considered in the seismic hazard analysis, a PSHA results in multiple hazard curves and uniform hazard spectra. The weighted mean UHS is calculated as the weighted average of the hazard curves (G. Toro, personal communication). The mean hazard curves were used to calculate soil uniform hazard spectra for three return periods — 475, 975 and 2475 years — corresponding to a 10%, 5%, and 2% of probability of exceedance in 50 years, respectively. Figure 5 shows the mean UHS and its associated variability for a return period of 2475 years in Memphis, TN. The resonant peaks of the UHS reflect

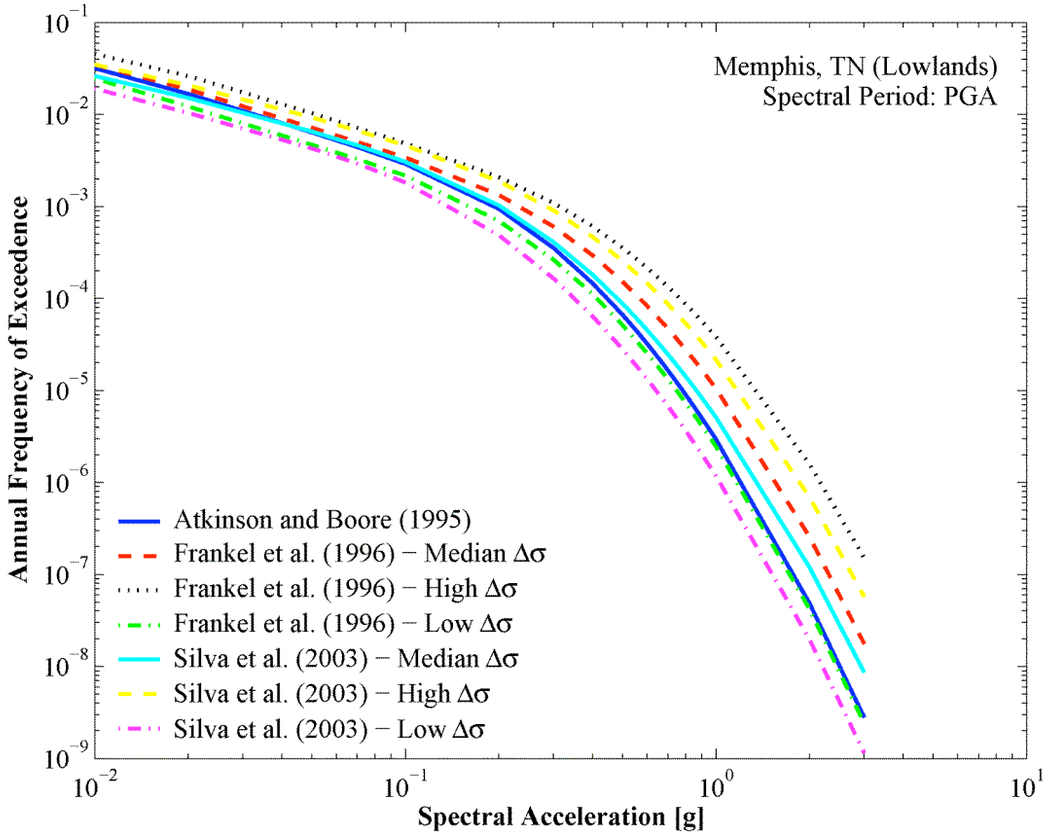


FIG. 3. PGA hazard curves for Memphis, TN.

the Embayment depth at this city. The standard deviation represents the scatter observed in the hazard curves due to the different attenuation models and not in the individual UHS.

REGIONAL SEISMIC HAZARD MAPS

The soil attenuation relationships were also used to perform probabilistic seismic hazard analyses for the entire region. The seismic sources characterization used in the PSHA for the selected cities was also implemented in the regional seismic hazard analyses.

The soil attenuation relationships were developed for two soil profiles – Lowlands and Uplands – and seven Embayment depth bins. Thus, to perform the regional seismic hazard analyses the entire Upper Mississippi Embayment was subdivided in 14 areas. Appropriate soil attenuation relationships were selected for the PSHA calculations in each area.

The regional probabilistic seismic hazard analyses were computed on a 0.1-degree square grid. Epistemic variability was incorporated in the analyses by using seven attenuation relationships corresponding to the source models and stress drop values described above. The seismic hazard analyses incorporate the non-linear soil behavior implemented in the soil attenuation relationships.

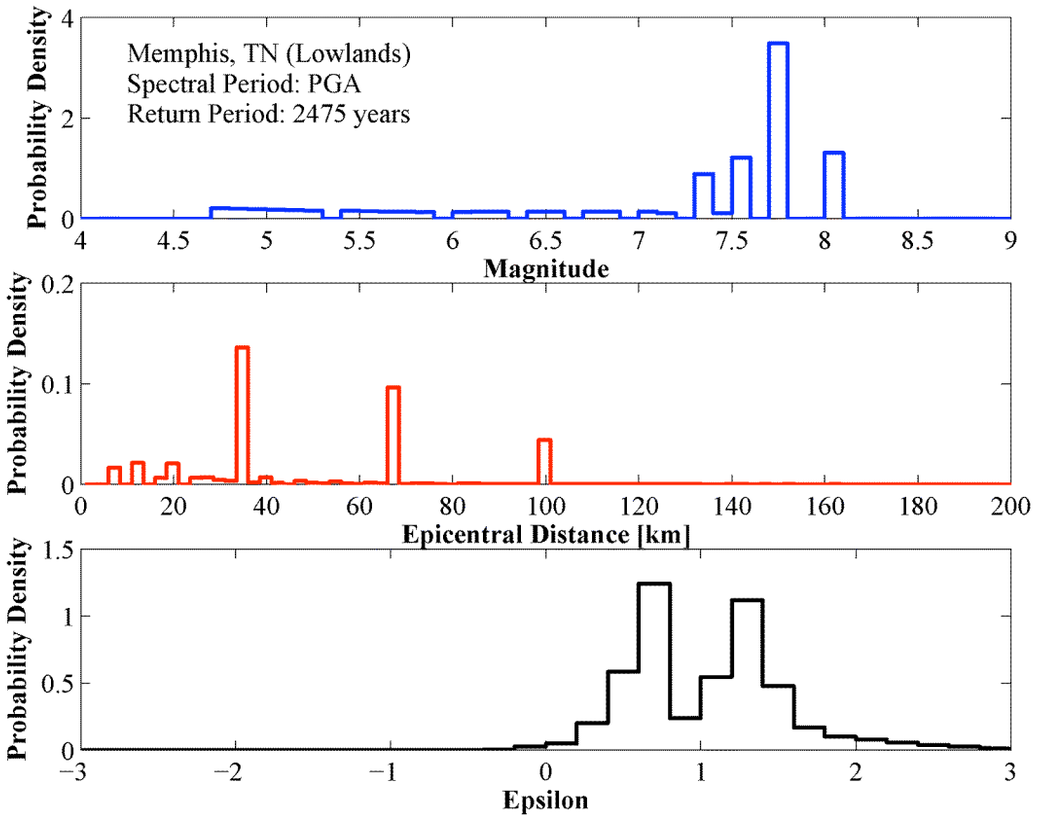


FIG. 4. Mean hazard deaggregation for Memphis, TN.

The regional analyses were used to generate seismic hazard maps for the Upper Mississippi Embayment. The seven hazard values obtained on each grid point were combined using the same weights defined above to generate seismic hazard maps for three ground motion amplitudes, mean and +/- 1 standard deviation. Following the same procedure used in analysis of the selected cities, the hazard values from the different models were combined in the frequency of exceedence space and then transformed into uniform hazard spectra. The seismic hazard maps were generated for three return periods – 475, 975 and 2475 years, and for 50 spectral periods distributed between 0.01 and 5 seconds. Figure 6 shows a sample of the hazard maps generated.

PROBABILISTIC GROUND MOTIONS

The soil UHS calculated in this study were used to generate suites of spectrum-compatible ground motions for each selected city. The time histories are probabilistic ground motions compatible with three hazard levels corresponding to return periods of 475, 975, and 2475 years.

In order to provide time histories with similar characteristics of observed records, the smooth UHS was modified by adding spectral ordinates variations in such a way

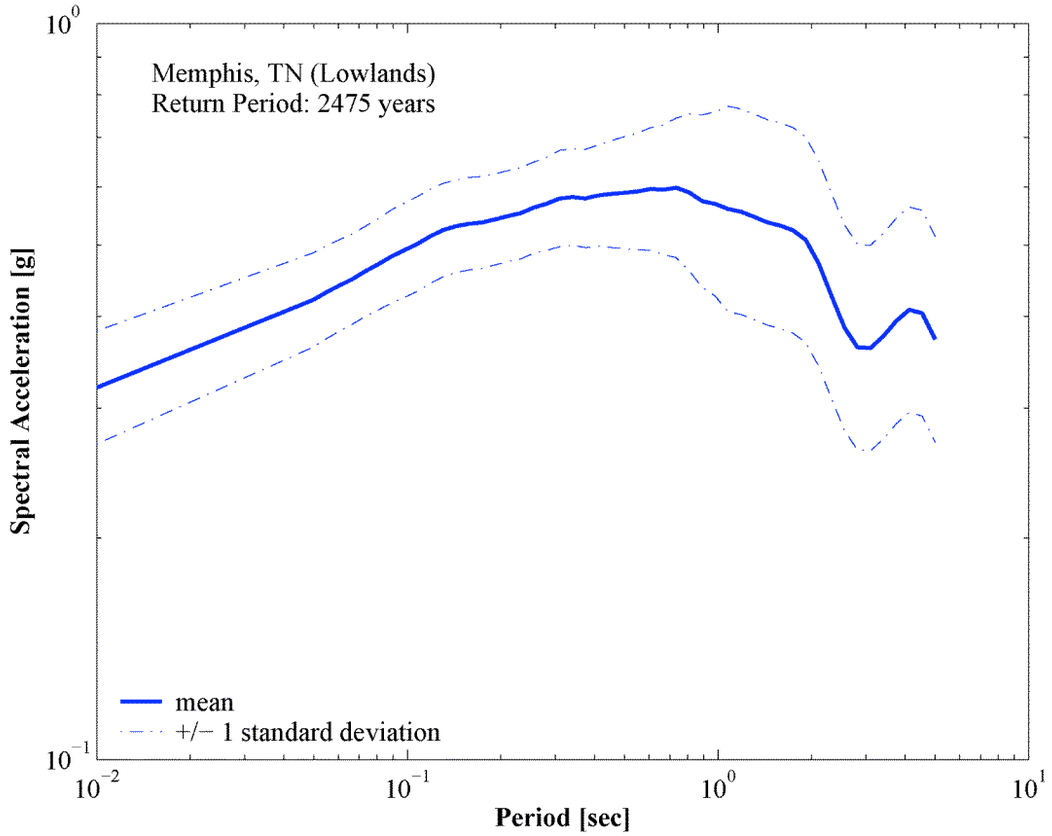


FIG. 5. Soil UHS for Memphis, TN (Lowlands).

that the general spectral shape was preserved but it resembled more a real earthquake response spectrum. Spectral variations were introduced by adding the frequency-to-frequency variability observed in real earthquakes to the mean UHS. This variability was derived from the correlation function developed by Baker and Cornell (2006).

The unconditional LU method (Davis, 1987) was used to simulate 10 response spectra for each hazard level to obtain time histories compatible with the UHS via spectral matching. The spectral matching process was performed in EZFRISK^{TM} using a time domain approach based on the RSMP99 code of the computer program SpectralMatch developed by Norman Abrahamson (Risk Engineering Inc., 2005). The initial ground motions were selected from the time history database developed by McGuire et al. (2001). The selection of the initial time histories was performed using records having similar magnitudes, epicentral distances, and site conditions to the earthquakes that dominate the hazard in each city as given by the hazard deaggregation. Baseline correction was applied to the acceleration time histories resulting from the spectral matching process. Velocity and displacement time histories were computed by numerical integration of the corrected acceleration time history.

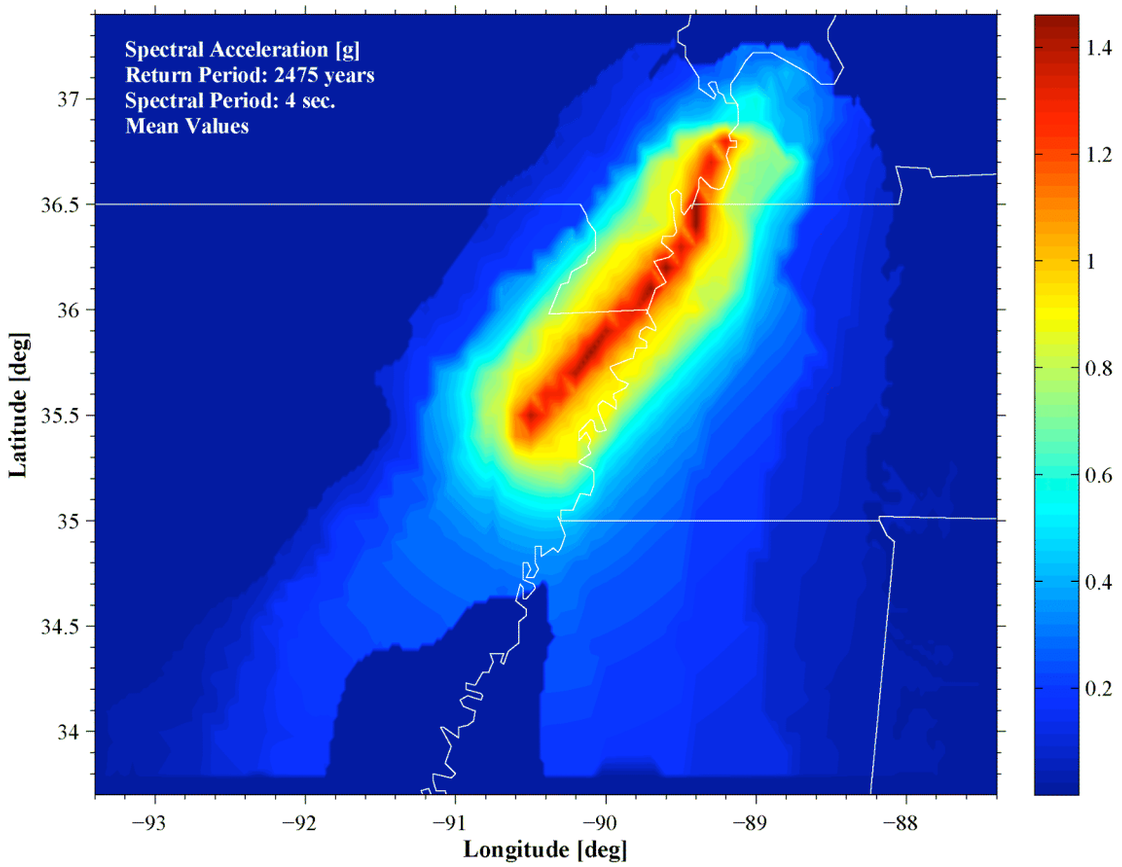


FIG. 6. Example of seismic hazard map.

Ten acceleration, velocity, and displacement time histories were generated for each hazard level, for a total of 30 ground motions for each city. The suites of ground motions are intended to represent the epistemic and aleatory variability characterized in the soil attenuation relationships developed for the region. The ground motions account for site-specific conditions and non-linear soil behavior, and provide a set of time histories for direct use in engineering design applications in the region. The ground motions are available at http://geosystems.ce.gatech.edu/soil_dynamics.

CONCLUSIONS

Seismic hazard analyses have been performed in the Upper Mississippi Embayment using soil attenuation relationships developed for the region. The hazard curves and uniform hazard spectra generated herein incorporates the epistemic variability accommodated in the attenuation relationships by the use of three source models and three stress drop values. Typical geological units of the region, Embayment depth, and non-linear soil behavior have been considered by the use of site-specific soil attenuation relationships. A major advantage of using soil attenuation equations in PSHA is that no coupling is necessary between probabilistic hazard analyses for rock conditions and site response. These soil attenuation relationships already account for correlation among all the processes of the earthquake generation and propagation and therefore provide a direct approach for developing hazard consistent soil motions.

The seismic hazard analyses performed in this study have been incorporated into MAEviz (http://mae.ce.uiuc.edu/software_and_tools/maeviz.html) to estimate ground motions in the Upper Mississippi Embayment. MAEviz is a seismic risk assessment software developed by the Mid-America Earthquake (MAE) Center and the National Center for Supercomputing Applications (NCSA).

ACKNOWLEDGMENTS

This work was funded by the Mid-America Earthquake Center under a grant from the Earthquake Engineering Research Center's program of the National Science Foundation under Award No. EEC-9701785.

REFERENCES

Atkinson, G. M., and Boore, D. M. (1995). "Ground Motion Relations for Eastern North America." *Bulletin of the Seismological Society of America*, 85(1), 17 - 30.

Baker, J., and Cornell, C. A. (2006). "Correlation of Response Spectral Values for Multicomponent Ground Motions." *Bulletin of the Seismological Society of America*, 96(1), 215 - 227.

Baturay, M. B., and Stewart, J. P. (2003). "Uncertainty and Bias in Ground-Motion Estimates from Ground Response Analyses." *Bulletin of the Seismological Society of America*, 93(5), 2025-2042.

Bazzurro, P., and Cornell, C. A. (2004). "Nonlinear Soil-Site Effects in Probabilistic Seismic-Hazard Analysis." *Bulletin of the Seismological Society of America*, 94(6), 2110 - 2123.

Cramer, C. H. (2003). "Site-Specific Seismic-Hazard Analysis that is Completely Probabilistic." *Bulletin of the Seismological Society of America*, 93(4), 1841-1846.

Davis, M. W. (1987). "Production of Conditional Simulations via the LU Triangular Decomposition of the Covariance Matrix." *Mathematical Geology*, 19(2), 91 - 98.

Fernandez, J. A., and Rix, G. J. (2006). "Soil Attenuation Relationships and Seismic Hazard Analyses in the Upper Mississippi Embayment." *Eighth U.S. National Conference on Earthquake Engineering 8NCEE*, San Francisco, CA.

Frankel, A., Mueller, C., Barnhard, T., Perkins, D., Leyendecker, E. V., Dickman, N., Hanson, S., and Hopper, M. (1996). "National Seismic Hazard Maps: Documentation." *OFR 96-532*, U.S. Geological Survey.

Frankel, A., Petersen, M., Mueller, C., Haller, K., Wheeler, R., Leyendecker, E. V., Wesson, R., Harmsen, S., Cramer, C., Perkins, D., and Rukstales, K. (2002). "Documentation for the 2002 Update of the National Seismic Hazard Maps." *U.S. Geological Survey OFR 02-420*.

Goulet, C. A., and Stewart, J. P. (2007). "Probabilistic versus Deterministic Implementation of Nonlinear Site Factors in Seismic Hazard Analysis." *2007 Asian-Pacific Network of Centers for Earthquake Engineering Research (ANCER) Meeting*, Hong Kong, China.

Goulet, C. A., Stewart, J. P., Bazzurro, P., and Field, E. H. (2007). "Integration of Site-Specific Ground Response Analysis Results into Probabilistic Seismic Hazard Analyses." *4th International Conference on Earthquake Geotechnical Engineering*, Thessaloniki, Greece, Paper No. 1486.

McGuire, R. K. (2004). *Seismic Hazard and Risk Analysis*, Earthquake Engineering Research Institute, Oakland, CA.

McGuire, R. K., Cornell, C. A., and Toro, G. R. (2005). "The Case for Using Mean Seismic Hazard." *Earthquake Spectra*, 21(3), 879-886.

McGuire, R. K., Silva, W. J., and Costantino, C. J. (2001). "Technical Basis for Revision of Regulatory Guidance on Design Ground Motions: Hazard- and Risk-Consistent Ground Motion Spectra Guidelines." *NUREG/CR-6728*, U.S. Nuclear Regulatory Commission, Washington, DC.

Musson, R. M. W. (2005). "Against Fractiles." *Earthquake Spectra*, 21(3), 887-891.

Risk Engineering Inc. (2005). "EZ-FRISK Version 7.14, User's Manual." Risk Engineering Inc., Software for Earthquake Ground Motion Estimation.

Silva, W., and Costantino, C. (2002). "Development of Site-Specific Design Ground Motions in Western and Eastern North America." *Soil Dynamics and Earthquake Engineering*, 22, 755-764.

Silva, W., Gregor, N., and Darragh, R. (2003). "Development of Regional Hard Rock Attenuation Relations for Central and Eastern North America, Mid-Continent and Gulf Coast Areas." Pacific Engineering and Analysis, El Cerrito, CA.

A simplified constitutive model to simultaneously match modulus reduction and damping soil curves for nonlinear site response analysis

Camilo Phillips[1] and Youssef M. A. Hashash[2]

ABSTRACT: A persistent problem with the more widely used non-linear soil models employed in site response analysis is their inability to match measured modulus reduction and damping curves simultaneously. One possible approach for selecting a model's material properties is to match the modulus reduction curve obtained from soil tests while disregarding the mismatch with the damping curve. Although, this approach might work well when the soil is subjected to small strains, for large strains the damping is generally overestimated. Alternatively model parameters can be selected to approximately match both modulus reduction and damping curves over a desired strain range.

Various authors proposed possible solutions to this mismatch. One approach uses a reduction factor for the hysteretic damping to better match the damping ratio at larger strains. Other approaches use advanced material constitutive models.

This paper presents a new damping reduction factor, which modifies the hysteresis loops from the extended Masing rules, and a fitting procedure for both modulus reduction and damping curves. The damping reduction factor is implemented in conjunction with the hyperbolic model in the site response analysis program DEEPSOIL. Two examples of 1-D site response analyses are presented to illustrate the performance of the new formulation.

INTRODUCTION

Numerous seismic events, such as the 1985 Michoacan earthquake, the 1989 Loma Prieta earthquake, the 1994 Northridge earthquake, the 1995 Kobe earthquake, and the 1999 Armenia Earthquake have demonstrated the relevance of local geologic and geomorphologic conditions on the seismic ground response. The changes in the intensity and the frequency content of the motion due to the propagation of the seismic waves on soil deposits and the presence of topographic features, commonly referred to as site effects, have a direct impact on the response of the structures located at the site during an earthquake event. One dimensional site response analysis methods are widely used to

[1] Graduate Research Assistant, Department of Civil and Environmental Engineering, University of Illinois at Urbana – Champaign. 205 N. Mathews Avenue, Urbana, Illinois, 61801. email: cphilli3@uiuc.edu
[2] Associate Professor, Department of Civil and Environmental Engineering, University of Illinois at Urbana – Champaign. 205 N. Mathews Avenue, Urbana, Illinois, 61801. email: hashash@uiuc.edu

quantify the effect of soil deposits on propagated ground motion. These methods can be divided in two main categories: (1) frequency domain analyses, including the *equivalent linear analysis* and (2) time domain analyses including nonlinear analysis.

Frequency domain methods are the most widely used to estimate site effects due to their simplicity, flexibility and low computational requirements,. However, there are some cases (e.g. high seismic intensities at rock base and/or high strain levels in the soil layers) in which an equivalent soil stiffness and damping for each layer cannot represent the behavior of the soil column over the entire duration of a seismic event. In these cases, a non-linear time domain solution is used to represent the variation of the shear modulus (G) and the damping ratio (ξ) during shaking. In nonlinear models ξ is primarily represented in the form of hysteretic damping resulting from unload-reload stress-strain loops. Additional velocity proportional viscous damping is added to represent damping at small strains (Park and Hashash, 2004 and Kwok et. al, 2007). The discussion in this paper focuses on hysteretic damping. Even though the non-linear model implemented in site response analysis should be able to match both G & ξ variation with cyclic shear strain, the most widely used non-linear stress-strain relationships (e.g. DESRA, DMOD, DEEPSOIL) which employ the extended Masing unloading-reloading rules (Masing, 1926 and Kramer, 1996) are not able to provide the required match (Stokoe et al., 2004 and Kwok et. al, 2007)

One common solution to the problem is to match only the modulus reduction curve (G/G_0) obtained from soil tests. This solution provides a good match for the damping at small strains; however, for larger shear strains ($\gamma > 10^{-3}$) the resulting damping is usually greater than the measured value. This difference usually leads to an underestimation of shear strains and/or surface intensities at the ground surface. In theory, better model performance would be expected if the parameters of the non-linear model are calibrated using both curves at the same time, however, for simple non-linear models such as the hyperbolic model this approach introduces differences in stiffness of the modeled behavior compared with the target curves for low to medium strains. Approaches that provide a better match for both curves (modulus reduction and damping) simultaneously were proposed by Stokoe et al. (2004) and Gerolymos and Gazetas (2005).

Using nearly 200 dynamic test results, Stokoe et al. (2004) developed an empirically based modified hyperbolic model to predict the linear and nonlinear dynamic response of different soil types. The developed model implemented a reduction factor shown in Eqs. (1) and (2) which effectively alters the extended Masing rules. The model reduces the hysteretic damping by 40% for small strains ($\gamma < 10^{-5}$) and by 70% for large strains ($\gamma > 10^{-2}$), obtaining damping values close to the ones measured in laboratory test. However, this results in a decrease in damping for strains greater than 10^{-2} which is in contrast to curves obtained from laboratory tests:

$$\zeta_{hysteretic} = F(\gamma_m) \cdot \zeta_{Masing} \tag{1}$$

$$F(\gamma_m) = b\left(\frac{G}{G_0}\right)^c \tag{2}$$

Gerolymos and Gazetas (2005) developed a phenomenological constitutive model for the non-linear 1-D ground response analysis of layered sites. The proposed model, a

special form of Bouc-Wen viscoplastic model, is able to reproduce nonlinear hysteretic behavior for different types of soils and has the ability to generate simultaneously realistic modulus and damping curves. The model requires information on anisotropic behavior of the soil and shape of the unload-reload loop. This information is not available for most soils, thus it is difficult to quantify required model constants.

A modified hyperbolic model is developed in this paper and implemented in 1-D wave propagation software DEEPSOIL (Hashash et al. 2005) to perform non-linear site response analyses. The model includes a reduction factor that modifies the Masing unloading-reloading rules and provides a better agreement with the damping curves for larger shear strains, but preserves the simplicity of the solution proposed by Stokoe et al. (2004).

As indicated earlier, soil damping in nonlinear analysis is the result of the addition of a viscous damping (also referred as small strain damping) and hysteretic damping. This paper provides a solution to properly represent the hysteretic damping. Issues related to viscous damping (e.g. overestimation for high frequencies Park and Hashash, 2004) are out of the scope of this paper, though the authors are currently working on this topic.

MODIFIED HYPERBOLIC MODEL

The backbone curve for the hyperbolic model can be expressed as:

$$\frac{G}{G_0} = \frac{1}{1 + \beta \cdot \left(\frac{\gamma}{\gamma_r} \right)^s} \tag{3}$$

whereby, γ: given shear strain, γ_r: reference shear strain, β: dimensionless factor and, s: dimensionless exponent. Hashash and Park (2001), in order to represent the dependence of modulus on confining pressure, propose the following expression for γ_r:

$$\gamma_r = a \left(\sigma' / \sigma_{ref} \right)^b \tag{4}$$

Figure 1a shows a hysteretic loop at a maximum shear strain of 1% using Masing unload-reload rules, the corresponding secant and the maximum shear moduli. Figure 1b plots the corresponding G/G_0 curve as a function of maximum shear strain levels also known as the modulus reduction curve.

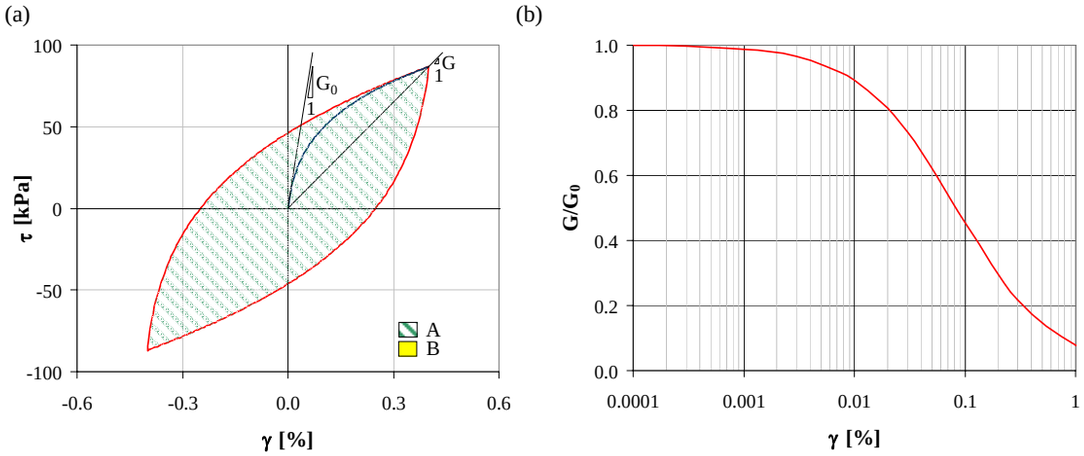


Figure 1 a) Secant shear modulus (G). b) G/G_0 modulus reduction curve

The soil damping ratio (ξ) is composed of two terms; small strain damping ($\xi_{small\ strain}$) and hysteretic damping ($\xi_{hysteretic}$). Equation 3 shows the expression used to calculate $\xi_{hysteretic}$, in which $\xi_{hysteretic}$ is proportional to the ratio of the area enclosed by the hysteretic loop and the triangular area corresponding to the work develop by an equivalent linear material (Figure 1a).

$$\zeta_{hysteretic} = \frac{A}{4\pi \cdot B} \tag{5}$$

A and B correspond to enclosed area by the hysteretic loop and triangular area presented in Figure 1a respectively.

Several authors (e.g Seed et al., 1986 or Stokoe et al., 2004) reported that $\xi_{hysteretic}$ calculated based on Masing rules (ξ_{Masing}) yields greater damping values for medium to large strains compared to the damping values obtained in dynamic tests as illustrated in Figure 2.

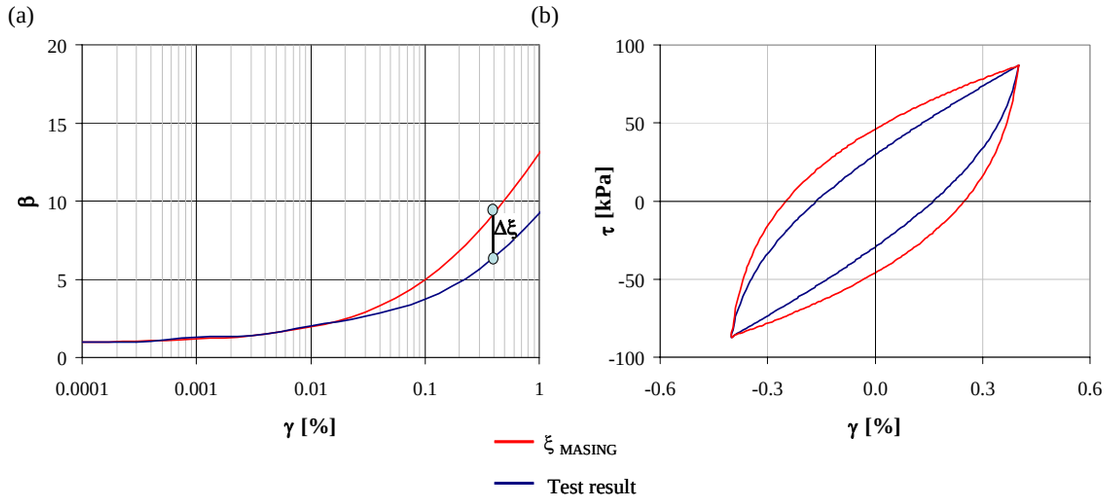


Figure 2 Overestimation of hysteretic damping using Masing rules. a) Damping curve. b) Hysteretic loop.

Stokoe et al. (2004) suggested the reduction factor $F(\gamma_m)$ as shown in Eq. (1). Since it is very difficult to implement the reduction factor as the ratio between each empirical damping value and the corresponding Masing damping ratio (calculated by fitting the modulus reduction curve and following the Masing rules), Stokoe et al. (2004) proposed the expression in Eq. (2). However, the equation results in a decrease in damping for larger strains. The authors, following a similar approach, propose the use of Eq. (6) that relates the reduction factor to the maximum shear strain level (γ_m).

$$F(\gamma_m) = p_1 - p_2 \left(1 - \frac{G_{\gamma_m}}{G_0}\right)^{p_3} \tag{6}$$

Whereby, p_1, p_2 and p_3 are non-dimensional parameters determined by obtaining the best possible fit with the target damping curve. $G_{\gamma m}$ is the secant modulus corresponding to the maximum shear strain level.

The expression for $F(\gamma_m)$ is based on evaluation of more than 40 modulus reduction and damping curves obtained from laboratory tests and calculated from hyperbolic model with Masing rules. In the most widely used laboratory procedures to determine the

modulus reduction and the damping curve (e.g. Resonant Column, Cyclic Triaxial, etc.) the level of shear strain increases during the test, therefore, γ_m is equal to the reported cyclic shear strain at a given loading stage. The modulus reducing and damping curves fitting procedures consist of the following three steps:

1) Determine the best backbone curve parameters of the modified hyperbolic model to fit the modulus reduction curve
2) Calculate the corresponding damping curve using the back-bone curve (determined in the previous step) and Masing rules.
3) Estimate the reduction factor parameters (p_1, p_2 and p_3) that provide the best fit for the damping curve.

A comparison between three available procedures to fit a hyperbolic model to modulus reduction and damping curves are presented: (a) modulus reduction and damping fitting using the reduction factor (MRDF), (b) modulus reduction and damping curve matching with the unmodified hyperbolic model –without the use of any reduction factor that modifies the Masing rule- (MRD), and (c) modulus reduction matching method (MR) with the unmodified hyperbolic model.

Figure 3 presents the results obtained using the three fitting procedures (MRDF, MRD, and MR) for the curves proposed by Vucetic and Dobry (1991) for PI equal to 100%. For the three procedures the strain range to fit the curve was between $\gamma = \{10^{-6}$ and $10^{-2}\}$. A very good agreement with empirical curves (modulus reduction and damping curve) is obtained using the proposed model (MRDF).

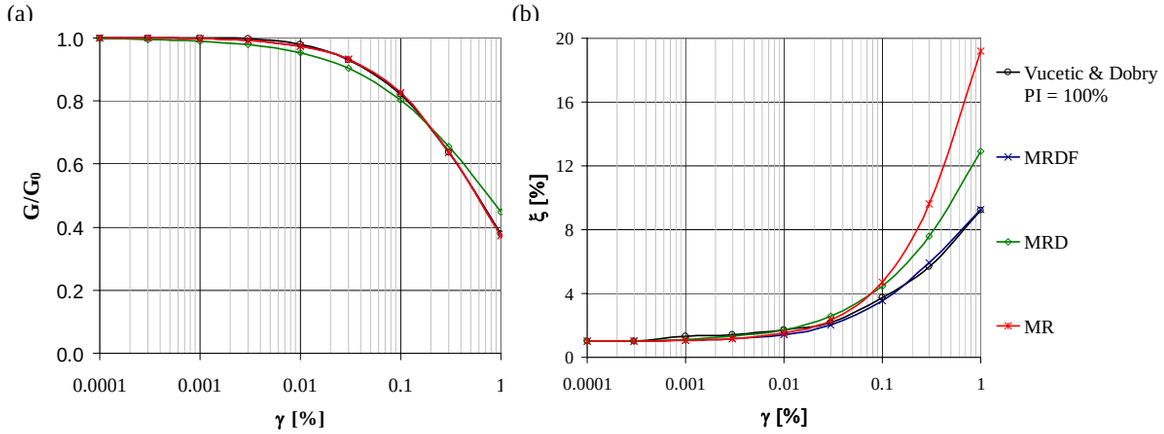


Figure 3 Comparison between the a) modulus reduction curves and b) damping curves for different fitting procedures. Target Model Vucetic and Dobry (1991) PI = 100

IMPLEMENTATION OF THE PROPOSED MODEL IN DEEPSOIL SITE RESPONSE ANALYSIS

The proposed model is implemented in the 1-D site response analysis DEEPSOIL by including the reduction factor to modify the unloading-reloading equations. The stress-strain model implemented by Hashash and Park in DEEPSOIL is an extension of the model developed by Clough and Duncan (1971) that has been used extensively in static and dynamic analyses of geotechnical structures. Eq. (7) and Eq. (8) are used to represent

the loading and the unloading or reloading conditions respectively to calculate the stress corresponding to a given strain.

$$\tau = \frac{G_0 \cdot \gamma}{1 - \beta \cdot \left(\frac{\gamma}{\gamma_r} \right)^s} \tag{7}$$

$$\tau = F(\gamma_m) \cdot \left[\frac{G_0 \cdot \left(\frac{\gamma - \gamma_{rev}}{2} \right)}{1 - \beta \cdot \left(\frac{\gamma - \gamma_{rev}}{2 \cdot \gamma_r} \right)^s} - \frac{G_0 (\gamma - \gamma_{rev})}{1 - \beta \cdot \left(\frac{\gamma_m}{\gamma_r} \right)^s} \right] + \frac{G_0 (\gamma - \gamma_{rev})}{1 - \beta \cdot \left(\frac{\gamma_m}{\gamma_r} \right)^s} + \tau_{rev} \tag{8}$$

Whereby, γ: given shear strain, γ_r: reference shear strain, β: dimensionless factor, s: dimensionless exponent, γ_{rev}: reversal shear strain, τ_{rev}: reversal stress, γ_m: maximum shear strain, $F(\gamma_m)$: reduction factor and G_0: initial shear modulus. The following two examples illustrate the performance of the proposed model in time domain non-linear analyses. The corresponding predictions using the frequency domain equivalent-linear procedure are also included.

Example 1

In this example a 30 m thick high plasticity cohesive deposit is subjected to a sinusoidal excitation at the base (a_{max} = 0.04 g and f = 1 Hz). The deposit has a constant shear wave velocity (Vs = 150 m/s), uniform unit weight (17 kN/m^3) and the modulus reduction and damping curves as recommended by Vucetic and Dobry (1991) (Figure 4).

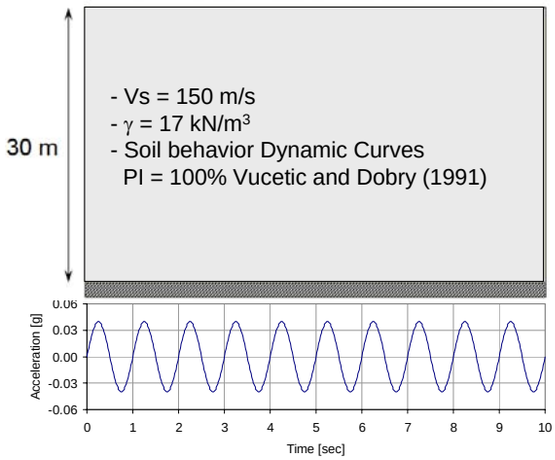


Figure 4 General characteristic of the soil profile modeled in example No 1

The resulting surface ground motions, the maximum strain profile and surface response spectra are presented in Figure 5 and Figure 6 respectively. These figures include results using MRDF, MRD, and MR fitting procedures for time domain non-linear analyses and the corresponding frequency domain (FD) analysis developed using the equivalent-linear analysis procedure implemented in DEEPSOIL by Hashash et al. (2005).

The results show that the decrease of damping generated by the use of the damping reduction factor (MRDF) produces an increase in computed maximum shear strain values and spectral accelerations (more than 35% of difference between MRDF and MR results for a structural period of 1.0 sec) for periods close to the deposit's fundamental period. For the present example frequency domain equivalent-linear analysis (FD) provides results very similar to the ones obtained using the MRDF procedure when response spectra are compared, however, the maximum shear strain profiles are quite different.

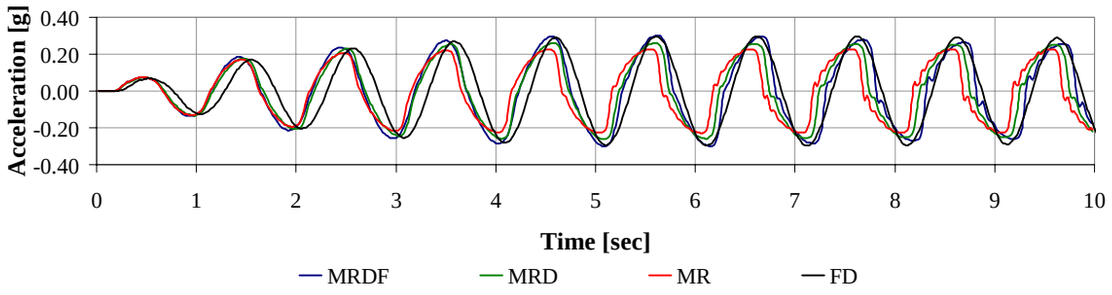


Figure 5 Example 1 Computed acceleration time histories at ground surface.

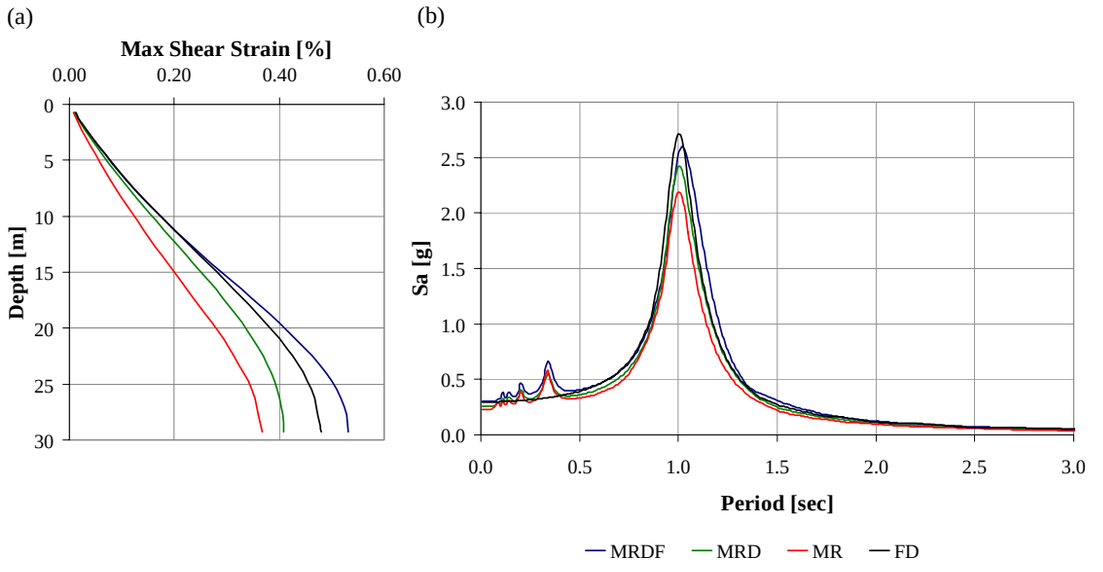


Figure 6 Example 1 computed a) Maximum shear strain profile and b) 5% damped surface response spectra comparison

Example 2

This example models the Treasure Island soil profile (Figure 7). The input motion corresponds to the 1971 San Fernando earthquake motion recorded at Pasadena Seismo Laboratory station (obtained from PEER 2000). The input motion has a_{max} = 0.2 g.

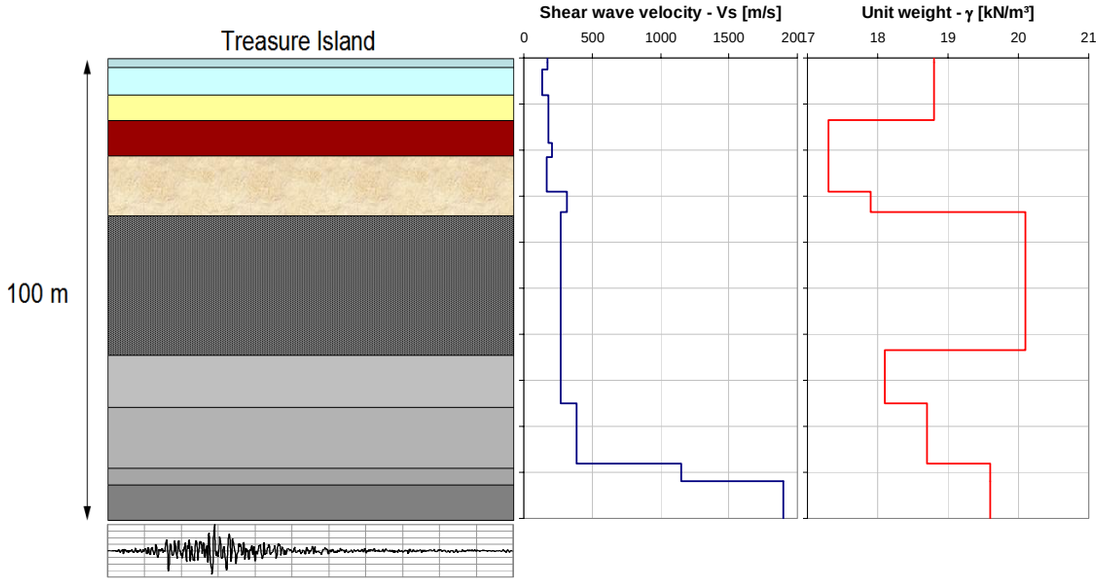


Figure 7 Soil profile modeled in Example 2

The analysis results are presented in Figure 8 and Figure 9. The results show trends similar to those obtained in Example 1; differences greater than 35% for periods close to the soil column fundamental period. However, in this example due to the complex relationship between strain, stress and propagated acceleration a decrease in spectral accelerations (when MRDF and MR results are compared) for periods lower than 0.4 sec is observed. Lower spectral values for low periods when MRDF model is employed are the result of the softening of the upper layers of the soils profile induced by greater shear strains (when MRDF and MR results are compared). When the stiffness of the soil profile decreases the soil column behaves as a high frequency filter reducing the high frequency content of the motion at surface. The use of equivalent-linear method (FD) results in underestimation of the ground motion at short periods and overestimation of the ground motion intensities for periods close to the fundamental period of the soil column.

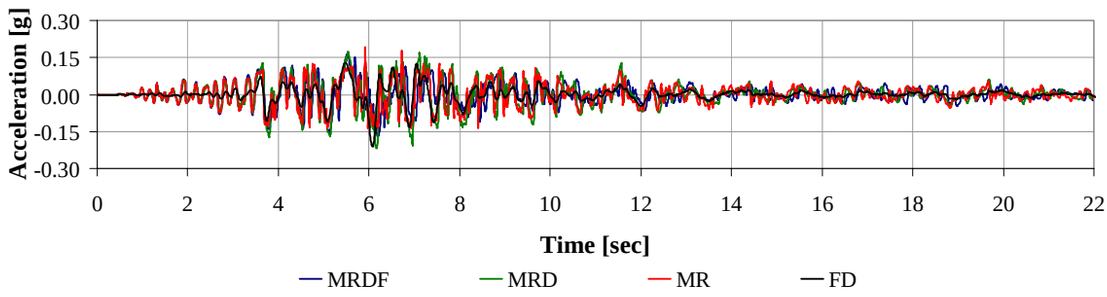


Figure 8 Computed ground surface acceleration time histories

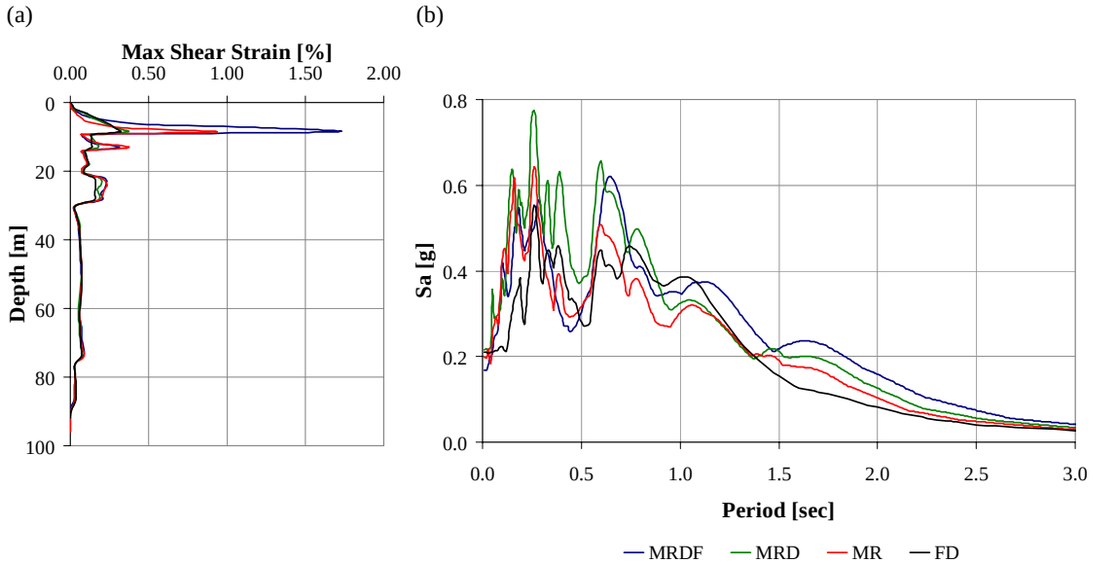


Figure 9 Treasure Island Soil profile a) Maximum shear strain profile and b) surface response spectra comparison

DISCUSSION AND CONCLUSIONS

A simplified constitutive model to simultaneously match modulus reduction and damping soil curves for nonlinear site response analysis is introduced. The proposed model uses the widely used modified hyperbolic model to represent the modulus reduction backbone curve. A damping reduction factor, that modifies the Masing rule, is introduced such that hysteretic damping matches more closely measured strain dependent damping

The model is implemented in DEEPSOIL to assess the model's impact on site response analysis results. Two idealized site response analyses show important amplification in spectral accelerations for periods close to the fundamental period of the soil columns; this conclusion is in good agreement with the results obtained by Gerolymos and Gazetas (2005) in the seismic response analysis of Port Island.

The use of more realistic hysteretic damping values in site response analysis, as expected, results in a decrease in the dissipated energy compared to conventional models, and therefore, an increase in computed stresses and strains inside the soil profile. The increase in shear strains induces softening of the soil profile that alters the response of the soil column and the amplitude and frequency content of the motion at surface.

The parameters for the proposed model can be readily determined from widely available modulus reduction and damping curves and can be used in engineering practice. The work presented in this paper is part of an ongoing effort by the authors which includes additional developments related to small strain damping and comparisons with measurements from vertical arrays.

REFERENCES

Clough, G. W., and Duncan, J. M. (1971). ‘‘Finite element analyses of retaining wall behavior.’’ J. Soil Mech. Found. Div., Am. Soc. Civ. Eng., pp. 97-12!, 1657–1673.

Gerolymos, N., and Gazetas, G. (2005). "Constitutive Model for 1-D Cyclic Soil Behavior Applied to Seismic Analysis of Layered Deposits." *Soils and Foundations*, 45(3), 147-159.

Kramer, S. L. (1996). "Geotechnical earthquake engineering", Prentice-Hall, Englewood Cliffs, N.J.

Kwok, A. O.L, Stewart, J. P, Hashash, Y. M.A, Matasovic, N., Pyke, R. Wang, Z. and Yang, Z. (2007). "Use of exact solutions of wave propagation problems to guide implementation of nonlinear seismic ground response analysis procedures." *Journal of Geotechnical and Geoenvironmental Engineering*, Vol 133, No 11. pp. 1395-1388. November, 2007

Hashash, Y. M. A., and Park, D. (2001). "Non-linear one-dimensional seismic ground motion propagation in the Mississippi embayment." Engineering Geology, 62(1-3), 185-206

Hashash, Y. M. A., Tsai, C.C., and Park, D. (2005). "DEEPSOIL V.2.6 1-D wave propagation Analysis Program for Geotechnical Site Response Analysis of Deep Soil Deposits." Board of Trustees of University of Illinois at Urbana-Champaign and Youssef Hashash, Urbana. http://cee-zzvy.cee.uiuc.edu/Website/Deepsoil/.

Masing, G. (1926) "Eigenspannungen und Verfestigung beim Messing." *2nd International Congress of Applied Mechanics*.

Park, D., and Hashash, Y. M. A (2004). "Soil damping formulation in nonlinear time domain response analysis." *Soil Dynamics and Earthquake Engineering*, 22 (7), pp. 611-624.

PEER. (2000). "PEER Strong Motion Database." PEER.

Seed, H. B., Wong, R. T., Idriss, I. M., and Tokimatsu, K. (1986). "Moduli and Damping Factors for Dynamic Analyses of Cohesionless Soils." *Journal of the Soil Mechanics and Foundations Division, ASCE*, 112(SM11).

Stokoe, K. H., Darendeli, R. B., Gilbert, R. B., Menq, F. Y., and Choi, W. K. (2004). "Development of a new family of normalized modulus reduction and material damping curves." University of Texas at Austin, Austin.

Vucetic, M., and Dobry, R. (1991). "Effect of Soil Plasticity on Cyclic Response." *Journal of the Soil Mechanics and Foundations Division, ASCE*, 117(1), 89-107.

Basin Effects in the Upper Mississippi Embayment

J. Alfredo Fernandez[1] and Glenn J. Rix[2]

[1] Graduate Research Assistant, Georgia Institute of Technology, School of Civil and Environmental Engineering, 790 Atlantic Dr. Atlanta, GA 30332; jafernandez@gatech.edu
[2] Professor, Georgia Institute of Technology, School of Civil and Environmental Engineering, 790 Atlantic Dr. Atlanta, GA 30332; glenn.rix@ce.gatech.edu

ABSTRACT

Site effects play a very important role in characterizing earthquake ground surface motions. At the edges of sedimentary basins, the large velocity contrast between soil and rock generates basin-induced surface waves that propagate in the horizontal direction inside the basin resulting in ground motions with long duration and high low-frequency energy. The 2-D non-linear seismic response of the Upper Mississippi Embayment has been computed to evaluate these basin effects in the region. The analyses have been performed using an indirect boundary integral – discrete wave number method. The non-linear soil behavior has been incorporated by using an equivalent linear approach. For the range of periods implemented in the analyses, 2 to 10 seconds, no significant difference was observed between the soil amplification of 1-D and 2-D models of the Upper Mississippi Embayment, except for sites located in a narrow region along the basin edge and periods longer than 4 seconds, where higher ground amplification was observed due to basin-edge effects. Possible differences in ground motion duration due to basin effects are not included in these analyses and must be accounted for separately if necessary.

INTRODUCTION

Many earthquakes have provided evidence of the important influence of local site conditions on earthquake ground motions. Several wave propagation methods have been developed to quantify site effects and determine the characteristics of surface ground motions. Usually the influence of soil conditions on strong ground motions is evaluated by using a 1-D wave propagation formulation where the site geometry is modeled by horizontal layers over a half-space. In general this simple model is capable of representing the basic characteristics of the site amplification. However there are ground response problems where more complex analyses are required. Examples of these cases are locations where the soil layers are confined by the surrounding rock to form sedimentary basins. The assumptions of the 1-D model are

not valid for this type of geometry and a 2-D or 3-D model is needed to evaluate the seismic response of these structures. At the edges of the basin, strong diffraction takes place due to the large velocity contrast between soil and rock. Such diffraction creates basin-induced surface waves that propagate in the horizontal direction inside the basin. These basin effects result in ground motions with longer duration and more low-frequency energy than predicted by the 1-D model (Kawase, 2003).

Extensive evidence of these basin-induced long period waves in real earthquakes can be found in the literature. Hanks (1975) found that surface waves contributed significantly to the long-period motions in the 1971 San Fernando, California, earthquake. Boore (1999) showed that a sea-floor recording of the 1990 Upland, California, earthquake was dominated by long-period, late-arriving surface waves generated at the edge of the Los Angeles basin. Graves and Wald (2004) demonstrated that the longer duration and amplification of motion observed in the San Bernardino, California, area during the 1999 Hector Mine earthquake were caused by the generation of surface waves in the San Bernardino basin.

The Mississippi Embayment is a wedge-shaped syncline structure that extends from southern Illinois to the Gulf of Mexico and is centered along the Mississippi River. The Upper Mississippi Embayment consists of soft sediments with thickness varying from a few meters to a maximum of about 1200 meters south of Memphis, TN. Figure 1 shows sediment thickness contours of the Upper Mississippi Embayment. The geometry of the Embayment may potentially generate basin-induced surface waves that might affect earthquake ground motions in the region. During the 1991 **M** 4.6 Risco, MO, earthquake, Dorman and Smalley (1994) observed long duration

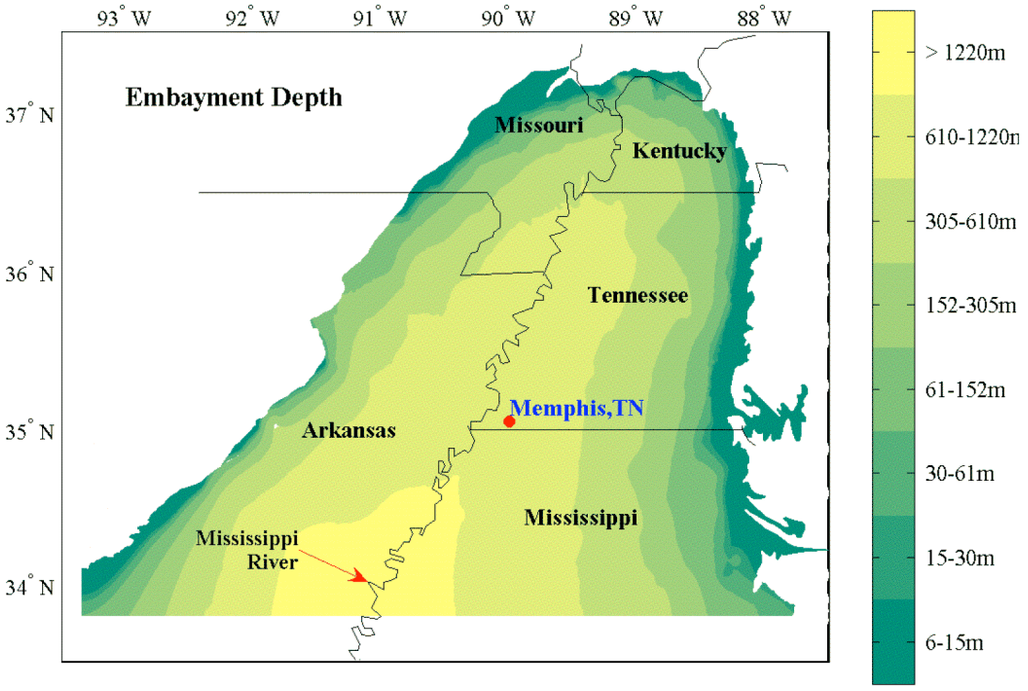


FIG. 1. Sediment thickness contours of the Upper Mississippi Embayment.

(approx. 3 minutes) ground motions with Love waves having periods of 3 to 5 seconds in seismograms recorded in Memphis, TN. Dorman and Smalley (1994) noted that the direct path carried most of the energy and multi-path arrivals and reflection and refraction of surface waves were not important. Bodin and Horton (1999) and Bodin et al. (2001) used microtremor observations to evaluate resonant periods of the Mississippi Embayment using the horizontal-to-vertical (H/V) spectral ratios. They found that the resonant periods correlate well with the depth of the Embayment, and estimated a resonant period 4.6 seconds for Memphis, TN.

Previous studies have also accounted for basin effects in numerical simulations of ground motions in the Embayment. Atkinson and Beresnev (2002) simulated ground motions for the city of Memphis, TN using the finite-fault stochastic method and incorporated the possible basin effects by modifying the simulated response spectra with the empirical amplification factors developed by Joyner (2000) from earthquakes recorded in the Los Angeles basin. More recently Saikia et al. (2006) evaluated the effects of the Mississippi Embayment on the amplification of seismic waves by using 2-D and 3-D finite-differences simulations. Saikia et al. (2006) concluded that a 1-D model estimates ground motions adequate for engineering purposes at sites located in the central part of the Embayment for earthquakes generated in the New Madrid seismic zone. However due to the large size of the Embayment, the analyses implemented a minimum grid spacing of 500 m and a single layer with a minimum shear wave velocity of 600 m/sec was used to represent the sediments. A more detailed model is needed to assess Embayment effects at sites located near the edges of the basin where the potential of basin edge effects is high (Saikia et al., 2006).

Numerical analyses using a 3-D model of the entire Upper Mississippi Embayment along with a detailed profile of the sediments incorporating non-linear soil behavior are needed to evaluate basin effects in the region and thus confirm the conclusions of Saikia et al. (2006). However this would require significant computational resources due to the vast size of the Embayment. Due to this limitation, a 2-D model has been selected to evaluate the non-linear seismic response of the Upper Mississippi Embayment. Numerical analyses via domain approaches (i.e. finite-differences or finite-elements) would still require large computational resources because a detailed profile of the soil layers is needed to incorporate their non-linear behavior. The boundary element method is considered more suitable for the analysis of the Embayment because it requires only the discretization of the boundaries of the domains. In this study a combination of the boundary element methods proposed by Bravo et al. (1988) and Zheng and Dravinski (1998) to evaluate the linear response of sedimentary basins under incident SH plane waves is implemented to evaluate the 2-D seismic response of the Embayment.

DESCRIPTION OF THE METHOD

The Bravo et al. (1988) procedure combines the indirect boundary element method (IBEM) to analyze the seismic wave field in the half-space with the discrete wavenumber representation of propagator matrices to study the seismic wave field in

the sediments inside the basin. Zheng and Dravinski (1998) proposed a similar method to investigate the scattering of SH waves by a sedimentary basin of arbitrary shape using the IBEM to treat both the half-space and the basin. In this study the formulation of Zheng and Dravinski (1998) is used to solve the wave field in the half-space because it is more computationally efficient, and the discrete wavenumber representation of propagator matrices proposed by Bravo et al. (1988) is used to solve the wave field inside the basin. In this way only the discretization of the boundary between the basin and the half-space is needed, and the propagator matrices provide a high resolution characterization of the sediments profile to incorporate the non-linear soil behavior. A detailed description of the methods can be found in the literature (Bravo et al., 1988; Gil-Zepeda et al., 2003; Zheng and Dravinski, 1998).

The non-linear soil behavior is implemented in the analysis by using an equivalent linear approach based on random vibration theory, RVT (Silva et al., 1991). RVT is used to estimate peak time domain values of shear strains based on the shear strain power spectrum. The procedure is similar to the estimation of peak shear strains values in the time domain used by the program SHAKE (Schnabel et al., 1972). However the frequency domain approach eliminates the need of a suite of time domain control motions to obtain a statistically stable estimate of site response (Silva et al., 1991).

The effective shear strain in each layer used in the equivalent linear approach is determined as the 65% of the peak shear strain. Due to the 2-D nature of the problem, the value of the shear strain in a given layer varies horizontally across the layer. To calculate the effective shear strain in each layer, the representative peak shear strain is estimated as the maximum of the peak shear strains computed at different points horizontally distributed along the layer. This homogenization of shear strains across each soil layer is an approximation of the real 2-D response, and it was incorporated in the analysis to be consistent with the propagator matrices approach. Future analyses are required to evaluate the significance of this assumption on the results calculated by proposed method.

ASSESSMENT OF THE METHOD

The performance of the method has been evaluated by comparing the linear response of a homogeneous semi-circular basin (Fig. 2) to an incident plane SH wave

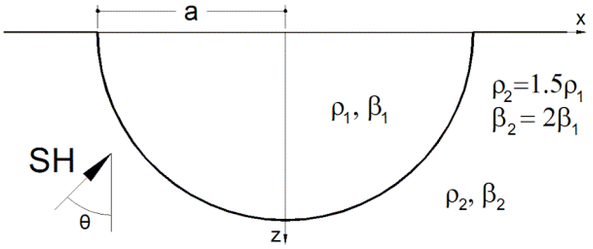


FIG. 2. Model of semi-circular basin.

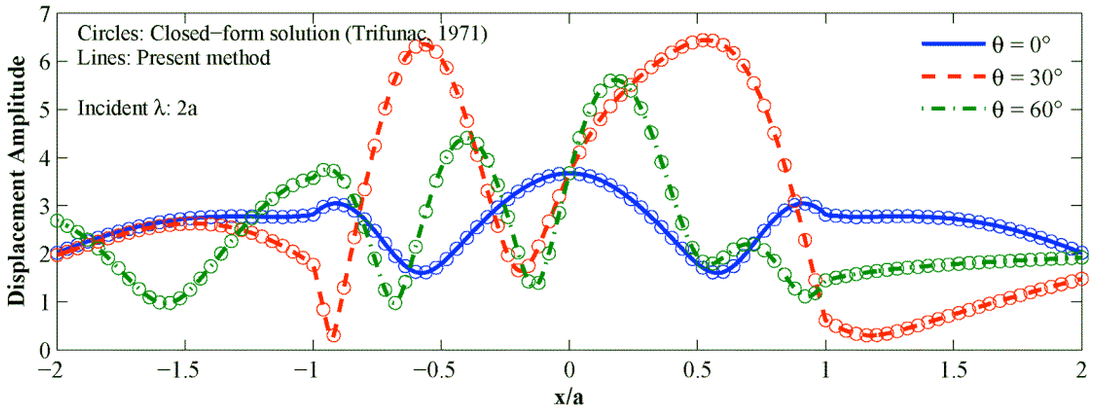


FIG. 3. Surface displacement response of a semi-circular basin.

calculated by the presented method with the closed-form solution provided by Trifunac (1971). Figure 3 compares the surface displacement amplitudes for different angles of incidence due to an incident wave of unit amplitude and wavelength equal to the diameter of the basin. In order to evaluate the performance of the propagator matrices, the sediments inside the basin were subdivided in three layers with the same material properties. The agreement of the surface basin response calculated by both methods is excellent. It is important to note the dependence of the basin response on the incident angle.

UPPER MISSISSIPPI EMBAYMENT

The 2-D non-linear seismic response of the Upper Mississippi Embayment has been evaluated at an East-West cross-section passing through Memphis, TN as shown in Figure 4. Generic modulus reduction and damping ratio curves developed by EPRI (1993) were used to characterize the dynamic soil properties. The sediments of the Upper Mississippi Embayment can be classified in two different categories: the Lowlands profile representing Holocene deposits typically found on the alluvial plains in the Mississippi River flood plain, and the Uplands profile consisting of Pleistocene deposits located on terraces overlooking the Mississippi River. Figure 5 shows the soil shear-wave velocity profiles for the Lowlands and Uplands used by Fernandez and Rix (2006) to develop soil attenuation relationships for the region. Fernandez (2007) showed that both soil profiles induce similar one-dimensional ground motion amplification in the low-frequency range, which is where basin effects are expected to occur. For these reason, only the Lowlands shear-wave velocity

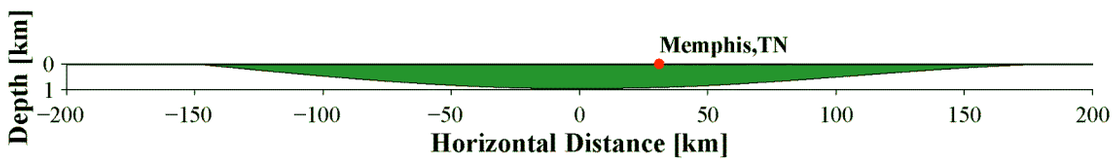


FIG. 4. East-West cross-section of the Upper Mississippi Embayment passing through Memphis, TN (vertical-to-horizontal scale ratio = 10:1).

profile was implemented in the analysis. The shear-wave velocity of the half-space corresponds to the value at a depth of 1 km of the crustal velocity model developed by Catchings (1999) for the city of Memphis, TN. This shear-wave velocity value is 3520 m/sec. The mass density profile was taken from Romero (2001). The initial value of small-strain damping ratio profile is based on the damping curves developed by EPRI (1993).

The soil amplification factors developed for the region by Toro and Silva (2001) using a 1-D analysis were used to compare the results of the 2-D response computed herein. To evaluate the effects of the non-linear soil behavior in site response, Toro and Silva (2001) used seven rock input motions corresponding to PGA's ranging from 0.05g to 0.75g. The rock ground motion corresponding to a PGA of 0.40g was used as the input motion in this study; however similar results were obtained for other values of PGA. The analysis was performed for five angles of incidence including 0°, 30°, -30°, 60°, and -60°, and for periods longer than 2 seconds due to computational resources limitation. However basin effects are expected to occur in the long-period range.

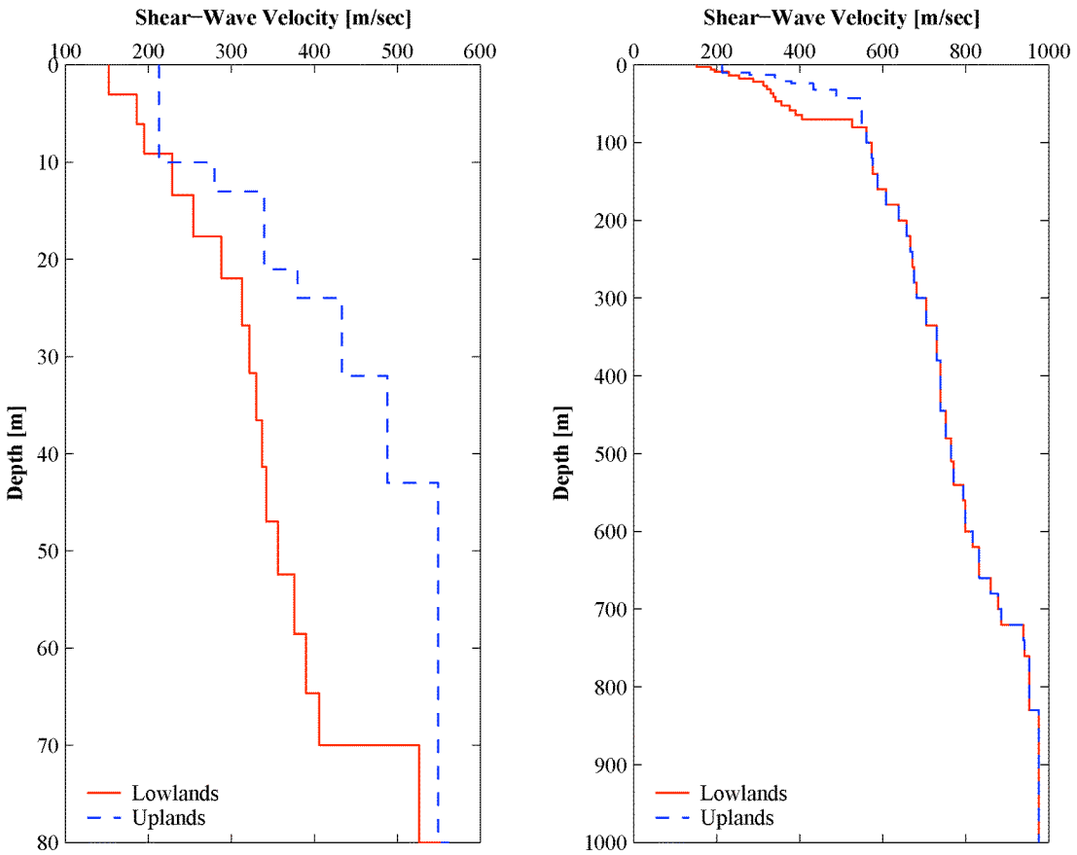


FIG. 3. Near-surface shear-wave velocity profiles.

Figure 6 compares the 1-D and 2-D soil amplification relative to the bedrock ground motion amplitude for the seven Embayment depth categories used in Toro and Silva (2001). The 2-D amplification corresponds to the average of the response due to the five incident angles. For the central part of the Embayment (i.e. sediments depth from 30 to 1220 m) no difference is observed between the 1-D and 2-D models. However, for Embayment depths less than 30 m (i.e. the edges of the basin) and periods longer than 4 seconds, there is a significant difference between the 1-D and 2-D response. In these cases, the 2-D model predicts higher amplification and displays the characteristics of basin edge effects as defined by Kawase (1996; 2003), where constructive interference occurs between basin-induced surface waves and direct body waves propagating from the bottom of the basin. This observation is consistent with the results of Saikia et al. (2006), where basin effects were observed only in a narrow area along the basin edge. Saikia et al. (2006) attributed these effects to the very strong velocity contrast between the rock and the upper sediments.

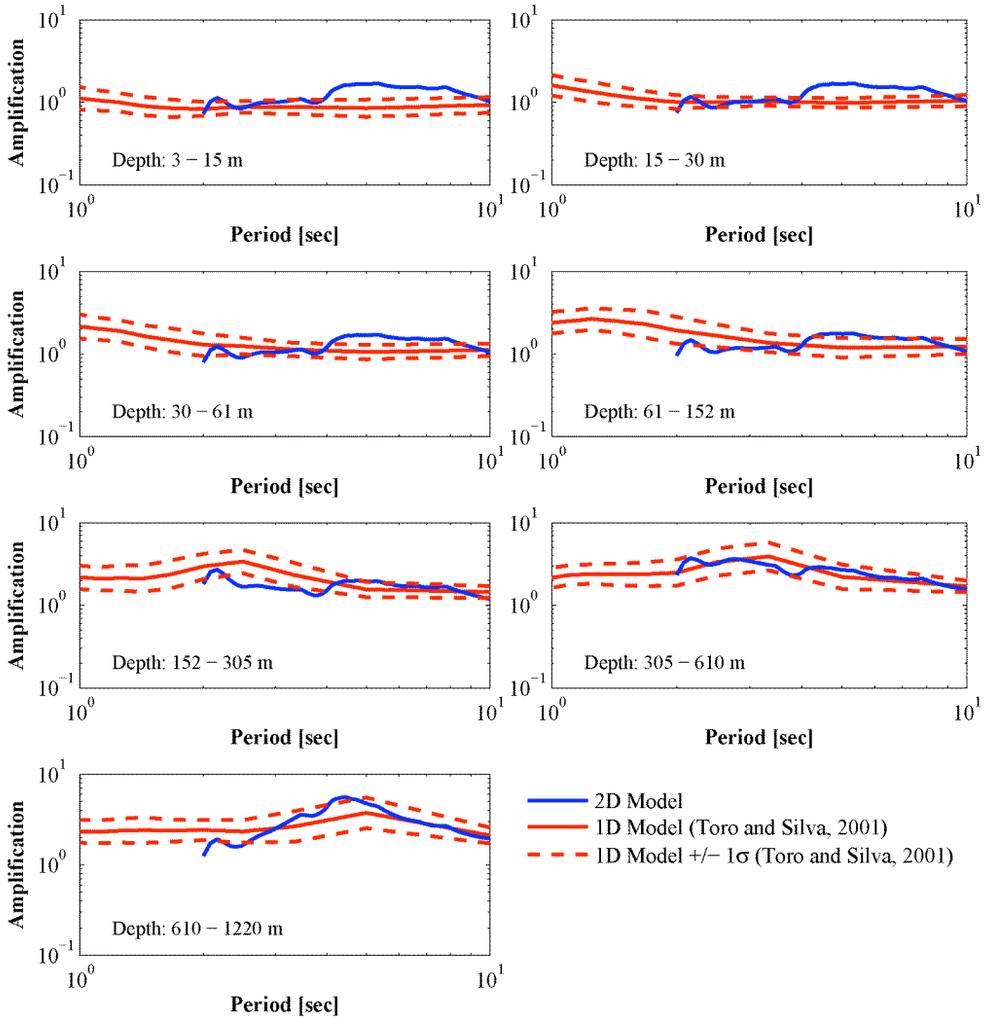


FIG. 4. Comparison of 1D and 2D soil amplification.

The good agreement between the seismic response of the 1-D and 2-D models, particularly in the central part of the basin, is due to the geometry of the Embayment. The longest spectral period considered in the analyses is 10 seconds, which corresponds to an incident wavelength of 35.2 km. This wavelength is approximately 10% of the total width of the model of the basin (~325 km) as shown in Figure 4. The longest wavelength is small compared to the dimension of the irregularity, and therefore the incident motion is not affected by the 2-D geometry of the basin. Longer wavelengths ($T > 10$ sec.) comparable to the dimensions of the Embayment are needed to excite the 2-D response of the basin; however these wavelengths (or periods) are not important for engineering purposes.

Kawase (2003) stated that for sedimentary basins with large width to depth ratios (i.e. shape ratio), as in the case of the Upper Mississippi Embayment with a shape ratio of approximately 300, body waves vertically propagating from the bottom of the structure arrive earlier to a surface station located on the central part of the basin than surface waves generated at the edges, and therefore no 2-D effects are observed. The long resonant periods of 4 to 5 seconds observed in Memphis, TN, as shown in Figure 6 for depths 610-1220 m, can be predicted by a 1-D wave propagation model, as has been demonstrated by Fernandez and Rix (2006) and Fernandez (2007), and supports the conclusions by Bodin and Horton (1999), Bodin et al. (2001), and Fernandez (2007) that Embayment depth is one of the most important factors that controls ground motion amplitude in the region.

It is important to note that comparisons between 1-D and 2-D models described above pertain only to the amplitude of the ground motions. Basin effects may also cause significant changes to the duration of the ground motion as observed by Dorman and Smalley (1994). Evaluating these effects requires analyses in the time domain, which is beyond the scope of the present study.

CONCLUSIONS

The 2-D non-linear seismic response of the Upper Mississippi Embayment has been evaluated by using a procedure that combines the indirect boundary element method and the discrete wavenumber representation of propagator matrices. Non-linear soil behavior was incorporated in the analysis by using an equivalent linear approach based on random vibration theory. For the range of periods implemented in the analysis, no significant difference was observed between the soil amplification of the 1-D and 2-D models of the Upper Mississippi Embayment, except for sites located in a narrow region along the basin edge and periods longer than 4 seconds, where higher ground motion amplification was observed due to basin-edge effects. Thus, basin effects are important for long-period structures located near the edges of the Embayment. If desired, the soil attenuation relationship developed by Fernandez and Rix (2006) can be corrected to account for higher amplification in the long-period range ($T \geq 4$ sec.) at shallow depths (≤ 30 m). Possible differences in the duration of ground motion due to basin effects must be accounted for separately.

ACKNOWLEDGMENTS

This work was funded by the Mid-America Earthquake Center under a grant from the Earthquake Engineering Research Center's program of the National Science Foundation under Award No. EEC-9701785.

REFERENCES

Atkinson, G. M., and Beresnev, I. A. (2002). "Ground Motions at Memphis and St. Louis from M 7.5–8.0 Earthquakes in the New Madrid Seismic Zone." *Bulletin of the Seismological Society of America*, 92(3), 1015 - 1024.

Bodin, P., and Horton, S. (1999). "Broadband Microtremor Observation of Basin Resonance in the Mississippi Embayment, Central US." *Geophysical Research Letters*, 26(7), 903-906.

Bodin, P., Smith, K., Horton, S., and Hwang, H. (2001). "Microtremor Observations of Deep Sediment Resonance in Metropolitan Memphis, Tennessee." *Engineering Geology*, 62(1-3), 159-168.

Boore, D. M. (1999). "Basin Waves on a Seafloor Recording of the 1990 Upland, California, Earthquake: Implications for Ground Motions from a Larger Earthquake." *Bulletin of the Seismological Society of America*, 89(1), 317-324.

Bravo, M. A., Sanchez-Sesma, J., and Chavez-Garcia, F. J. (1988). "Ground Motion on Stratified Alluvial Deposits for Incident SH Waves." *Bulletin of the Seismological Society of America*, 78(2), 436-450.

Catchings, R. D. (1999). "Regional V_p, V_s, V_p/V_s, and Poisson's Ratios across Earthquake Source Zones from Memphis, Tennessee, to St. Louis Missouri." *Bulletin of the Seismological Society of America*, 89(6), 1591 - 1605.

Dorman, J., and Smalley, R. (1994). "Low-Frequency Seismic Surface Waves in the Upper Mississippi Embayment." *Seismological Research Letters*, 65(2), 137-148.

Electric Power Research Institute. (1993). "Guidelines for Determining Design Basis Ground Motions." *EPRI TR-102293*, Electric Power Research Institute, Palo Alto California.

Fernandez, J. A. (2007). "Numerical Simulation of Earthquake Ground Motions in the Upper Mississippi Embayment," Ph.D. Dissertation, Georgia Institute of Technology, Atlanta, GA.

Fernandez, J. A., and Rix, G. J. (2006). "Soil Attenuation Relationships and Seismic Hazard Analyses in the Upper Mississippi Embayment." *Eighth U.S. National Conference on Earthquake Engineering 8NCEE*, San Francisco, CA.

Gil-Zepeda, S. A., Montalvo-Arrieta, J. C., Vai, R., and Sanchez-Sesma, F. J. (2003). "A Hybrid Indirect Boundary Element - Discrete Wave Number Method Applied to Simulate the Seismic Response of Stratified Alluvial Valleys." *Soil Dynamics and Earthquake Engineering*, 23(1), 77-86.

Graves, R. W., and Wald, D. J. (2004). "Observed and Simulated Ground Motions in the San Bernardino Basin Region for the Hector Mine, California, Earthquake." *Bulletin of the Seismological Society of America*, 94(1), 131-146.

Hanks, T. C. (1975). "Strong Ground Motion of the San Fernando, California, Earthquake: Ground Displacements." *Bulletin of the Seismological Society of America*, 65(1), 193-225.

Joyner, W. B. (2000). "Strong Motion from Surface Waves in Deep Sedimentary Basins." *Bulletin of the Seismological Society of America*, 90(6 PT B), 95-112.

Kawase, H. (1996). "The Cause of the Damage Belt in Kobe: "The Basin-Edge Effect", Constructive Interference of the Direct S-Wave with the Basin-Induced Diffracted/Rayleigh Waves." *Seismological Research Letters*, 67(5), 25-34.

Kawase, H. (2003). "Site Effects on Strong Ground Motions." International Handbook of Earthquake and Engineering Seismology, Part B, W. H. Lee, H. Kanamori, P. C. Jennings, and C. Kisslinger, eds., Academic Press, 1013-1030.

Romero, S. M. (2001). "Ground Motion Amplification of Soils in the Upper Mississippi Embayment," Ph.D. Dissertation, Georgia Institute of Technology, Atlanta, GA.

Saikia, C. K., Pitarka, A., and Ichinose, G. A. (2006). "Effects of Irregular Structure of the Mississippi Embayment on Ground-Motion Amplification." *Bulletin of the Seismological Society of America*, 96(4), 1448-1473.

Schnabel, P. B., Lysmer, J., and Seed, H. B. (1972). "SHAKE: A Computer Program for Earthquakes Response Analysis of Horizontally Layered Sites." *UCB/EERC-72/12*, Earthquake Engineering Research Center, University of California, Berkeley, California.

Silva, W. J., Wong, I. G., and Darragh, R. B. (1991). "Engineering Characterization of Earthquakes Strong Ground Motions with Applications to the Pacific Northwest." *Open-File Report 91-441-H*, U.S. Geological Survey.

Toro, G. R., and Silva, W. (2001). "Scenario Earthquakes for Saint Louis, MO, and Memphis, TN, and Seismic Hazard Maps for the Central United States Region Including the Effect of Site Conditions." *Technical Report, USGS Grant 1434-HQ-97-GR-02981*, Risk Engineering, Inc., Boulder, CO.

Trifunac, M. D. (1971). "Surface Motion of a Semi-Cylindrical Alluvial Valley for Incident Plane SH Waves." *Bulletin of the Seismological Society of America*, 61(6), 1755-1770.

Zheng, T., and Dravinski, M. (1998). "Amplification of SH Waves by an Orthotropic Basin." *Earthquake Engineering and Structural Dynamics*, 27(3), 243-257.

Comparing Weak- and Strong-Motion Spectral Ratios at the Turkey Flat Site Effects Test Area, Parkfield, California: Possible Nonlinear Soil Behavior

Chris H. Cramer, RG/RGP

Research Associate Professor, Center for Earthquake Research and Information, University of Memphis, 3890 Central Ave., Memphis, TN 38152-3050, cramer@ceri.memphis.edu

ABSTRACT: The prediction of soil response at a site is an important aspect of estimating ground motion from future earthquakes. The soil response at the Turkey Flat Site Effects Test Area from the 2004 Parkfield M6.0 earthquake (0.3g) is compared via spectral ratios to the response from the 1995 weak-motion based predictions of Cramer (1995) and from 0.1g and less strong-motion recordings from seven M3-5 Parkfield and the M6.5 San Simeon earthquakes. At Turkey Flat four recording sites are spaced across the two-kilometer wide, shallow, stiff-soil valley: Rock South, Valley Center, Valley North, and Rock North. Rock South is located 5 km from the San Andreas Fault and the 2004 Parkfield rupture. Near-field and azimuthal effects in the 0-5 Hz frequency band are present in the 2004 Rock South records, but not in the records at the other sites 6-7 km from the San Andreas Fault. Thus the 2004 Rock North mainshock record provides better predictions of the 2004 strong ground motions at both valley sites. Comparisons of the mainshock spectral ratios to both sets of weaker-motion mean spectral ratios suggests nonlinear soil behavior in the shallow soils at the Valley Center site and linear soil behavior elsewhere.

INTRODUCTION

On September 28, 2004, a M6.0 earthquake occurred in Parkfield, California, generating up to one third g ground motions at the Turkey Flat Site Effects Test Area (Figure 1) five kilometers from the rupture. The test area was established in 1987 (Real et al., 2006) and is the site of an international site effects experiment endorsed by the International Associations of Physics of the Earth's Interior (IASPEI) and Earthquake Engineers (IAEE). Turkey Flat is a shallow (25 m) stiff-soil valley over soft California rock. The axis of the two-kilometer wide valley trends NW-SE and is roughly parallel to the San Andreas Fault, the source of the 2004 event. Strong ground motion predictions (with uncertainties) based on spectral ratios derived from weak-motion recordings were published by Cramer (1995). These predictions are for

site effects only and not source or path effects, which are important in the 2004 Parkfield earthquake data.

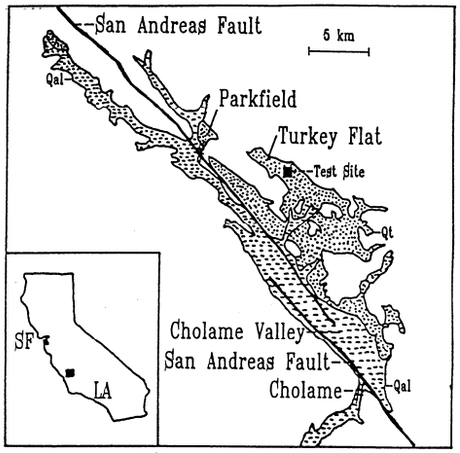


FIG. 1. Location map for Turkey Flat Site Effects Test Area. Inset shows the location of the test area in central California and relative to San Francisco (SF) and Los Angeles (LA). The main map shows the location relative to Parkfield and the San Andreas Fault. Qal (dashed stippling) represent Quaternary alluvial deposits and Qt (dotted stippling) represents Quaternary terrace deposits.

A Turkey Flat strong ground-motion blind prediction test was completed in February 2006 (Real et al., 2006). The complete set of 2004 strong motion recordings at Turkey Flat were not released until September, 2006 after the completion of the blind prediction test, except for a valley-edge rock record in the first phase of the test (March through September 2005) and a sub-valley bedrock record in the second phase of the test (October 2005 through February 2006). Additionally, seven sets (for all Turkey Flat sites) of less than 0.1 g recordings of M3-5 Parkfield and the M6.5 San Simeon earthquakes (Table 1) became available in August 2007. These form a second group of weaker-motion recordings available for analysis and comparison to the 2004 M6.0 Parkfield mainshock strong-motion records, which was not included in this second group of recordings.

Table 1. Earthquakes providing Turkey Flat Strong-Motion Sensor Recordings

Earthquake	Mag.	Location	Comment
1993/04/03 21:21	4.2	35.942N, 120.493W	Parkfield
2003/12/22 11:15	6.5	35.710N, 121.100W	San Simeon
2004/09/28 10:15	6.0	35.810N, 120.370W	Mainshock
2004/09/28 10:19	4.2,3?	35.844N, 120.402W	2 Aftershocks, 17s apart
2004/09/28 10:24	4.7	35.810N, 120.350W	Aftershock
2004/09/28 10:33	3.7	35.815N, 120.363W	Aftershock
2004/09/28 12:31	4.0	35.840N, 120.390W	Aftershock
2004/09/29 10:10	5.0	35.954N, 120.502W	Aftershock

In this paper I compare both sets of weaker-motion spectral ratios with the 2004 strong-motion observations at four sites (Figure 2): two rock sites (South and North) on each side of the valley and two valley sites (Center and North). The Rock South and Valley Center sites have downhole sensors in bedrock 24 m below the surface. Additionally, the Valley Center site has a sensor 10 m below the surface within the valley sediments. All four sites have surface sensors. All sensors have three components that are recorded.

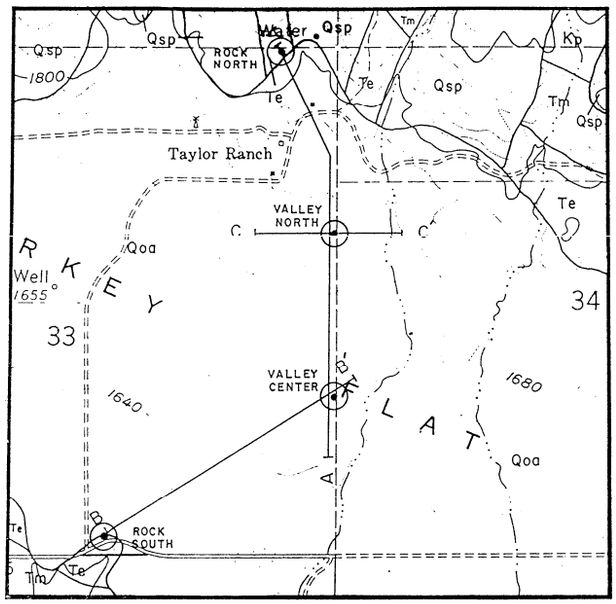


FIG. 2. A map of the Turkey Flat Site Effects Test Area showing locations of the four ground-motion recording sites, and three lines of profiles corresponding to geophysical surveys.

METHOD

The spectral ratio method is used in the analysis of both the weak- and strong-motion recordings at Turkey Flat. Fourier spectral ratios are used, as soil response analysis is based on the physics of vertical wave propagation. Equivalent linear methods, such as SHAKE, involve a frequency-domain approach of applying transfer functions to Fourier spectra (Idriss and Sun, 1992; Kramer, 1996). One of the goals of the Cramer (1995) study was to use Fourier spectral ratios as transfer functions to predict strong ground motions at each site given a record at the reference site. Also, Fourier spectral ratios are used in this study for comparison with the spectral ratios in Cramer (1995).

Most simply, a Fourier spectral ratio R between two sites as a function of frequency is the ratio of the amplitude portion of the Fourier transform of the waveform at each site. That is, $R(f) = S_1(f)/S_2(f)$, where S_1 is the Fourier amplitude spectrum at site 1

and S_2 is the Fourier amplitude spectrum at site 2. At a given site the spectrum S is composed of a combination of earthquake source (E), propagation path (P), and site effects (K) [$S = E(f)*P(f,R)*K(f)$, where R is distance from the source to the site]. Usually, a site on rock (without soil) is used as the second or reference site so as to isolate soil response to site 1 and simplify interpretation. For close station spacing such as at Turkey Flat ($\leq$ 2 km), spectral ratios remove the effects of earthquake source and propagation path to the site, leaving the effects of geologic conditions at the sites [$R = S_1/S_2 = (E*P_1*K_1)/(E*P_2*K_2) = K_1/K_2$, when P_1 and P_2 are nearly identical]. At close distances to the rupture, such as in 2004, the canceling out of source and path effects via spectral ratios is less effective, allowing rupture (near-field) and possibly path effects to appear in the spectral ratios.

Prior to forming spectral ratios, all Fourier spectra were smoothed using a 1 Hz running mean filter. For the 1988 very weak motion data recorded on weak-motion sensors, mean spectral ratios and their standard deviations were calculated from 33 earthquakes to the north and northeast ranging in distance from 15 to 254 km from Turkey Flat. Full details of the application of the spectral ratio method to the weak-motion data are provided in Cramer (1995). For the second set of 8 weaker-motion records (0.001-0.1 g) recorded on the strong-motion sensors, earthquake to site distances ranged from 5-16 km for the Parkfield events and 69-71 km for the San Simeon earthquake, all to the south, west, and northwest of Turkey Flat.

The modeling of observed spectral ratios in this paper is the same as the transfer function modeling approach used in Cramer (1995). Transfer functions (spectral ratios) are modeled using the available geotechnical data (see Cramer, 1995). Modeling of site response is a non-unique process, so assumptions must be made to simplify the modeling task and to model the form of the site response observed. The modeling has been simplified by assuming that S waves are vertically propagating and that the site response to S waves is one-dimensional (1D), linear, and viscoelastic. The medium is also assumed to be isotropic and plane layered. Further, because spectral ratios are relative site response observations, it is assumed that they can be modeled by the relative site amplification function in the computer program SHAKE (1975 version) (Schnabel et al., 1972), which does not use modulus and damping curves.

Model fitting to observed spectral ratios is accomplished by adjusting shear-wave velocities (Vs) and damping ratios for each layer to match frequency peaks and amplitudes of the spectral ratios, respectively. Uncertainty in the fits to the observed ratios are within 5% and 0.02 for Vs and damping ratio, respectively (Cramer, 1995).

RESULTS

Spectral Ratios

The availability of two sets of weaker-motion spectral ratios at Turkey Flat, one from the 1988 (Cramer, 1995) and one from 1993-2004 (excluding the 2004

mainshock), provides a unique opportunity to evaluate the stability of the spectral ratio approach over time. Figure 3 shows the Rock South downhole versus surface mean and plus/minus one standard deviation spectral ratios for both weaker-motion datasets along with the mainshock north component spectral ratio (only horizontal component available on the Rock South downhole sensor for the mainshock). For the 2004 recordings, the west horizontal downhole component at Rock South was not recording. So the mean spectral ratios involving the Rock South downhole sensor are for north component only. The remaining weaker-motion spectral ratios are for the geometric mean of both horizontal components. In Figure 3 we see the general agreement and stability among the two weaker-motion datasets and the mainshock spectral ratio, which is expected for a rock site.

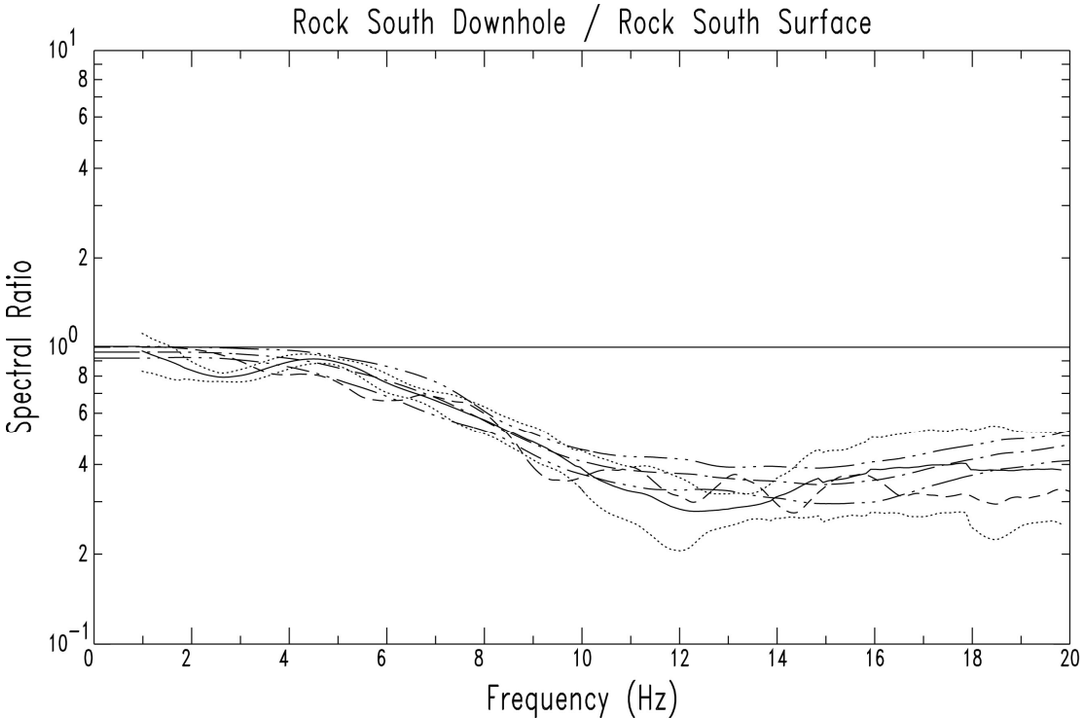


FIG. 3. Strong- and weak-motion spectral ratios for Rock South downhole vs. surface recordings. Two sets of mean and plus/minus one standard deviation (sd) spectral ratios are shown [solid (mean) and dotted (sd) set from Cramer, 1995; dot-dashed (mean) and double-dot-dashed (sd) set from strong-motion sensors 1993-2004 excluding the 2004 mainshock]. The 2004 mainshock north component spectral ratio is also shown (dashed line). The solid horizontal line indicates a spectral ratio of 1.

The Rock South mainshock records (surface and downhole) have near-field effects (Shakal et al., 2006a) that are not present in the other mainshock recordings at Turkey Flat. This makes the Rock South records poor predictors (over predictors) of mainshock ground motions at other sites (Shakal et al., 2006b). Thus Rock North has been used as the reference site for most of the spectral ratios presented in this paper. The exception is the bottom-hole vs. surface spectral ratios for Rock South (Figure 3).

Figure 4 presents spectral ratios from both sets of weaker-motion recordings [1988 from Cramer (1995) and 1993-2004] along with 2004 mainshock spectral ratios for the north, west, and geometric mean horizontal components. In the 0-5 Hz band on the Rock South surface and downhole spectral ratios with respect to Rock North (Figure 4a-b), the 2004 mainshock ratios are much higher than the 1988 spectral ratios (at the 95% confidence level) suggesting that this difference could be due to the near-field effects on the Rock South records cited above. However, the mainshock ratios show much less of a difference (at only the 70% confidence level or less) with the 1993-2004 weaker-motion ratios. This difference between the 1988 and the 1993-2004 spectral ratios in the 0-5 Hz band at Rock South may arise from an azimuthal dependence (northeast vs. southwest) in the site response at Rock South. Thus, because the mainshock rupture is to the south and west of Turkey Flat, an azimuthal-dependent site-response as well as near-field effects may have contributed to differences in response between Rock South and other Turkey Flat sites during the 2004 Parkfield mainshock.

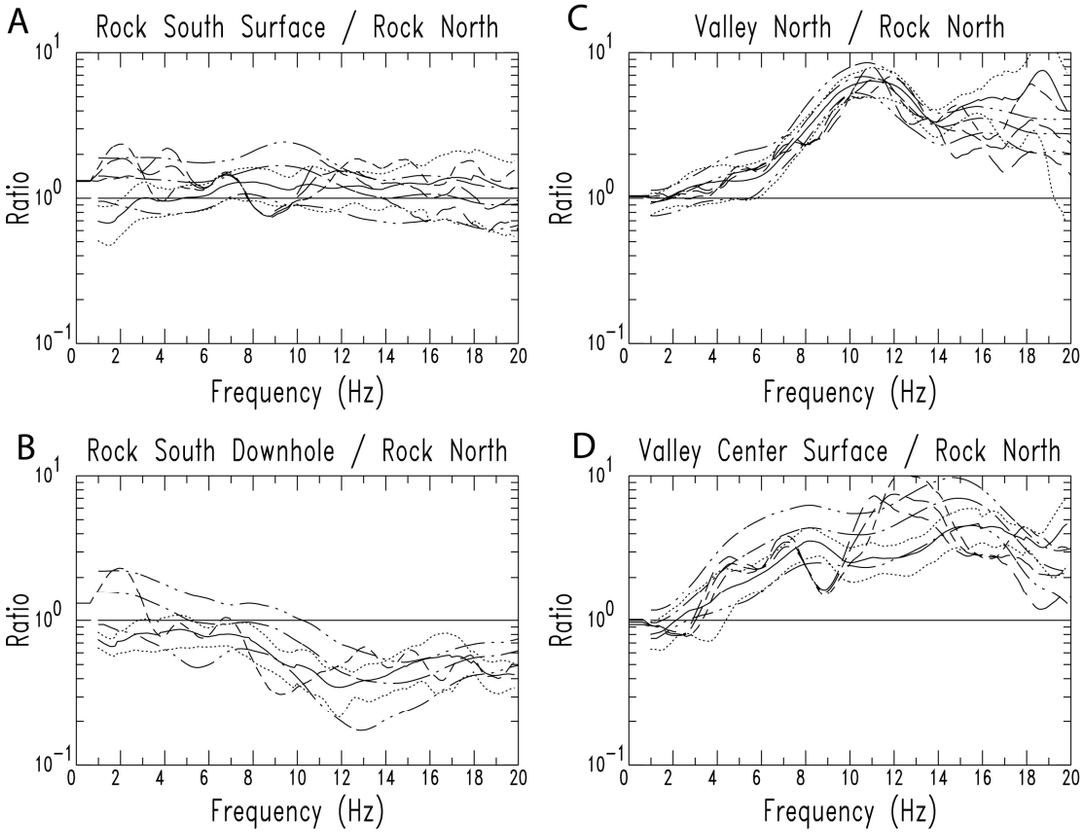


FIG. 4. Spectral ratios with respect to Rock North for the 2004 Parkfield strong-motion recordings (two short and a long dashed line – geometric mean, short dashed line – north component, long dashed line – west component) compared with 1988 and 1993-2004 weak-motion mean spectral ratios and their standard deviations (sd): a) Rock South surface, b) Rock South downhole, c) Valley North, and d) Valley Center surface. Weak-motion means and sd are represented using

the same line types as in Figure 3. The solid horizontal line indicates a spectral ratio of 1.

Rock North is not a perfect candidate for the reference site. For the 2004 mainshock, there is a resonance peak between 8 and 10 Hz at Rock North as seen in Figure 4 as a valley (decreased ratio) in that frequency band, particularly on the Valley Center and Rock South 2004 mainshock ratios and less so on the Valley North 2004 mainshock ratios. However, the 1988 and 1993-2004 weak-motion mean spectral ratios generally agree with each other at the 95% confidence level of the estimate of the mean (roughly represented by the sample plus/minus one standard deviations shown), although not always as already pointed out for the 0-5 Hz band at Rock South.

Linear behavior for the 2004 mainshock at the rock sites and Valley North is confirmed by the mainshock spectral ratio comparisons in Figures 3 and 4. At Valley North the agreement among datasets is very good (Figure 4c), although the uncertainty (scatter) increases above 14 Hz. Hence, linear soil behavior up to 0.25 g is indicated at the Valley North site. Any changes confined to a thin soil layer less than 1 m in thickness at Valley North cannot be resolved due to the increased uncertainty above 14 Hz.

The spectral ratios for the Valley Center surface 2004 mainshock relative to Rock North show possible nonlinear soil behavior during the 2004 mainshock (Figure 4d). There is a shift to lower frequencies in the 2004 mainshock spectral ratios with respect to both sets of weaker-motion ratios. This shift is mainly for the highest peak, which moves from 14-16 Hz for the weaker-motion ratios to 12-13 Hz for the mainshock ratios.

Figure 5 presents the horizontal-geometric-mean spectral ratios for each of the 1993-2004 earthquakes at the Valley Center surface site relative to the Rock North site, including the 2004 mainshock. The 1993-2004 earthquakes were all recorded using the strong-motion sensors. The mainshock ratio (solid line without symbols) is distinct from the aftershock ratios (dotted lines), San Simeon earthquake ratio (long dashed line), and the 1993 Parkfield M4.2 earthquake ratio (short dashed line). [Solid lines with symbols are the results of modeling spectral ratios for the mainshock (octogon) and other 2004 earthquakes (triangle), which are discussed below.] The shifting of the main spectral ratio peak from 14-16 Hz to 12-13 Hz is a phenomenon only associated with the mainshock that does not affect the San Simeon ratio or any aftershock ratios, which are from four minutes to a day after the mainshock. This strongly suggests nonlinear soil behavior at Valley Center during the 2004 Parkfield mainshock. [The 1993 Parkfield spectral ratio, along with the 1988 weak-motion spectral ratios, shows a downward shift with time of the main peak frequency from 16-17 Hz to 14-15 Hz, which is likely due to long-term soil property changes at Valley Center due to seasonal changes (climate) and aging after site-disturbance during installation.]

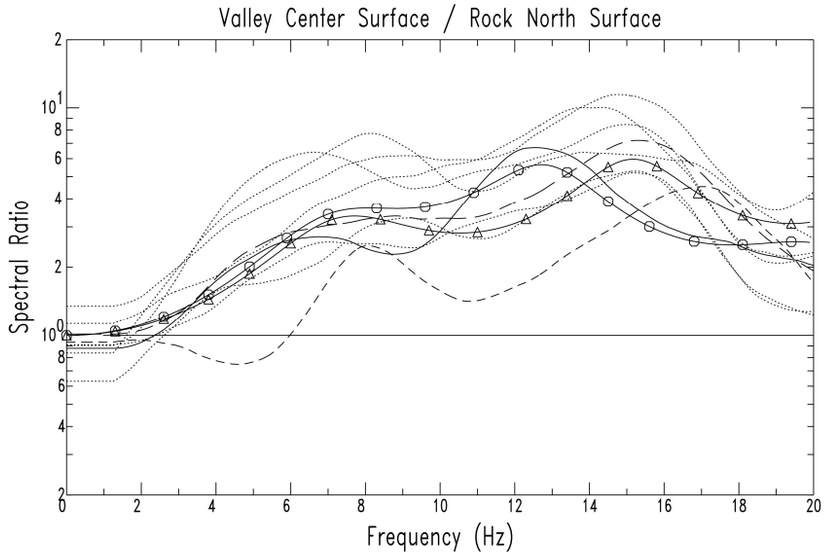


Figure 5. Horizontal mean spectral ratios at Valley Center surface with respect to Rock North for 1993-2004 earthquakes (Table 1). Solid line no symbols - 2004 mainshock ratio. Dotted lines - 2004 aftershock ratios. Long dashed line - San Simeon earthquake ratio. Short dashed line - 1993 Parkfield M4.2 earthquake ratio. Solid line with triangles - 2004 weak-motion modeling ratio. Solid line with octagons - 2004 mainshock (strong-motion) modeling ratio.

Transfer function modeling using SHAKE (symbols on solid lines in Figure 5) indicates that the lowering of Vs is 5% to 25% in the upper 7 m of the soil column (Table 2). Modeling uncertainties are $\pm$0.02 in damping ratio and $\pm$ 5% in velocity (Cramer, 1995). The 2004 weak-motion model in Table 2 is based on the Valley Center in situ measurements of Cramer (1995, Table 2) with damping ratio adjusted to 0.03 to better match 2004 weak-motion spectral ratio amplitudes (triangle solid line vs. dotted and long dashed lines in Figure 5). The 2004 strong-motion model shows the adjustments to better match the mainshock spectral ratio amplitudes and the change in frequency of the largest peak (octagon solid line vs. solid line without symbols). While the modeling is not perfect, it does show significant changes (decrease of 25%) in Vs in the top layer during the mainshock for a surface PGA of 0.3 g. Changes in damping ratio are harder to resolve given the uncertainty.

TABLE 2. Weak- and Strong-Motion Modeling Results at Valley Center

Layer No.	Thickness (m)	2004 Weak-Motion		2004 Strong-Motion	
		Damping Ratio	Vs (m/s)	Damping Ratio	Vs (m/s)
1	1.8	0.03	130	0.05	97
2	4.9	0.03	354	0.07	336
3	14.	0.03	622	0.07	622
4	--	0.01	1317	0.01	1317

2005 Strong Motion Predictions

I participated in the 2005 Turkey Flat strong-motion blind prediction tests first using the Rock South surface R1 record to predict all other mainshock recordings and then using the Valley Center bottom-hole D3 record to predict the mid-hole (D2) and surface (V1) mainshock recordings at Valley Center. Two prediction methods were used, the 1988 weak-motion spectral ratios of Cramer (1995) and SHAKE91 (Idriss and Sun, 1992) using the preferred geotechnical models of Cramer (1995) with a 10% randomization in parameters. Similar results were obtained using SHAKE91 without geotechnical parameter randomization. Standard modulus and damping curves for Turkey Flat were used in the SHAKE91 calculations.

As indicated above, near-field and possibly azimuthal effects in the Rock South mainshock recording caused overestimates in the mainshock ground motion predictions at Rock North, Valley North, and Valley Center using the R1 record. But the predictions of the Rock South downhole D1 record (only N-S horizontal component recorded the mainshock) are very good. Peak ground acceleration (PGA) predictions for the N-component were 0.15 g using 1988 spectral ratios and 0.16 g using SHAKE91, while the actual mainshock D1 recording had a PGA of 0.16 g.

2005 strong-motion predictions at Valley Center D2 and V1 sensor locations based on the D3 record where mixed in their effectiveness due to potential nonlinear soil effects represented in the velocity model differences presented in Table 2. For the D2 predictions, the 1988 weak-motion spectral ratios gave N and W component PGAs of 0.10 and 0.12 g, while SHAKE91 gave PGAs of 0.09 and 0.12 g respectively. The actual mainshock PGAs are 0.12 and 0.13 g, so the predictions were close but slight underestimates. For the V1 predictions, the 1988 spectral ratio approach gave N and W component PGAs of 0.16 and 0.14 g and SHAKE91 gave values of 0.25 g for both horizontal components. The 10% velocity randomization used in the SHAKE91 predictions tended to increase ground motion estimates at stronger levels of ground shaking as seen in the V1 predictions. Actual PGAs recorded at V1 are 0.29 g on both horizontal components. Confirmed changes in shallow soil Vs during the 2004 mainshock (possible nonlinear soil effect) can explain the under prediction of ground motions and the poorer performance of strong-motion predictions at the Valley Center site, especially at V1.

SUMMARY

A comparison between strong-motion spectral ratios from recordings at the Turkey Flat Site Effects Test Area for the 2004 M6.0 Parkfield earthquake and two sets of weak-motion spectral ratios (1988 and 1993-2004) confirm a ~25% decrease in shear-wave velocity (Vs) in the shallow soils at the Valley Center recording site during the M6.0 mainshock. This suggests possible nonlinear soil behavior at the Valley Center Site due to strong ground motion with a peak ground acceleration (PGA) of 0.3 g at

the surface. Linear soil and rock response is suggested for the remaining three sites at PGAs up to 0.25 g.

ACKNOWLEDGEMENTS

The author gratefully acknowledges support from the Center for Earthquake Research and Information and from the California Geological Survey, Strong Motion Instrumentation Program for conducting this comparison study. I am also grateful to the U.S. Geological Survey for supporting my participation in the 2005 Turkey Flat blind prediction test as their employee. I wish to thank two anonymous reviewers for their suggestions for improving this manuscript. This paper is Center for Earthquake Research and Information contribution #521.

REFERENCES

Cramer, C.H. (1995). "Weak-motion observations and modeling for the Turkey Flat, U.S., site-effects test area near Parkfield, California." *Bull. Seismo. Soc. Am.*, Vol. 85 (2): 440-451.

Idriss, I.M., and Sun, J.I. (1992). *User's Manual for SHAKE91*, Center for Geotechnical Modeling, Dept. of Civil and Environmental Engineering, University of California, Davis, California.

Kramer, S.L. (1996). *Geotechnical Earthquake Engineering*, Prentice Hall, Upper Saddle River, New Jersey.

Real, C.R., Shakal, A.F., and Tucker, B.E. (2006). "Overview of the Turkey Flat ground motion prediction experiment." *Proceedings of SMIP06 Seminar on Utilization of Strong-Motion Data, September 28, 2006, Oakland, California*, 117-136.

Shakal, A., Haddadi, H., Grazier, V., Lin, K., and Huang, M. (2006a). "Some key features of the strong motion data from the M6.0 Parkfield, California, earthquake of 28 September 2004." *Bull. Seismo. Soc. Am.*, Vol. 96 (4B): S90-S118.

Shakal, A., Haddadi, H., and Real, C. (2006b). "Recorded data and preliminary review of predictions in the Turkey Flat blind prediction experiment for the September 28, 2004 Parkfield earthquake." *Proceedings of SMIP06 Seminar on Utilization of Strong-Motion Data, September 28, 2006, Oakland, California*, 137-152.

Schnabel, P.B., Lysmer, J., and Seed, H.B. (1972). *SHAKE, a computer program for earthquake response analysis of horizontally layered sites*, Earthquake Engineering Research Center, University of California, Rept. No. EERC 72-12.

Consequences of solution non-uniqueness in surface wave tests for seismic response studies

Sebastiano Foti [1], Cesare Comina[2], Daniele Boiero [3] and Laura Valentina Socco[4]

[1] Assistant Professor, Dept. of Structural and Geotechnical Engineering, Politecnico di Torino, Italy
[2] Research Associate, Dept. of Structural and Geotechnical Engineering, Politecnico di Torino, Italy
[3] PhD Student, Dept. of Land, Environment and Geotechnologies, Politecnico di Torino, Italy
[4] Assistant Professor, Dept. of Land, Environment and Geotechnologies, Politecnico di Torino, Italy

ABSTRACT: Surface wave tests are based on the solution of an inverse problem for soil profile identification from the experimentally measured dispersion curve. Most criticism for this testing methodology arises from the non-uniqueness of the solution, i.e. several sets of model parameters can give very similar dispersion curves. In this paper some implications of solution non-uniqueness in seismic response studies are investigated using both synthetic numerical simulations and experimental data. Adopting a Monte Carlo approach for the inverse problem, possible solutions of the inversion process are selected such that they can be considered equally good with respect to the experimental data. This set of soil profiles is subsequently used to evaluate the seismic response of the site. It is shown that equivalent profiles with respect to surface wave testing are equivalent also with respect to site amplification and $V_{S,30}$ determination.

INTRODUCTION

The small strain shear modulus, which is a fundamental parameter for seismic site response analysis, is strongly affected by disturbance induced by sampling and reconsolidation in laboratory.

It is therefore necessary to use in situ seismic methods to obtain a reasonable estimate of this parameter (Stokoe and Santamarina, 2000). Non invasive seismic testing techniques have become more and more popular in this respect because they are cost and time effective options for testing large areas and provide global information of the behavior of the soil deposit. Among them, surface wave tests are widely used, also because they do not suffer from theoretical and practical limitations that affect body wave techniques (e.g. SH refraction surveys).

Since surface wave tests are based on the solution of an inverse problem, the major criticism in their respect is related to the non-uniqueness of the solution and to the equivalence problem. Indeed several different profiles can be associated to numerical dispersion curves of Rayleigh waves showing an equally good agreement with the

experimental one. It is possible therefore to identify equivalent solutions, i.e. their associated misfit is small if compared to the uncertainty in the measurement and estimation of the experimental dispersion curve. This causes a certain level of uncertainty in the final profile adopted for the soil.

Nevertheless it is worthwhile to consider that since the dispersion curve is associated to the global dynamic behavior of the site and a soil model similar to the one adopted for the interpretation of surface wave data (a stack of homogeneous isotropic layers) is used for several engineering applications, the equivalence problem is likely to have no severe consequences. If several soil profiles are equivalent in terms of surface wave propagation they are likely to be equivalent also in terms of the seismic site response if it is evaluated using a 1D model.

This aspect is systematically explored in the present work by the use of a Monte Carlo approach for the inversion process. The inversion problem is solved exploring the space of the model parameters and selecting a set of profiles which, in statistical terms, are equivalent with respect to the experimental dispersion curve and its uncertainty. Equivalent profiles are subsequently used for numerical simulations of seismic site response to assess the influence of uncertainty and non-uniqueness of the inversion solution. A synthetic example and a real case history are reported.

SURFACE WAVE TESTS

Surface wave tests are based on the property of geometrical dispersion which makes the velocity of propagation of Rayleigh waves frequency dependent in vertically heterogeneous media. The experimental dispersion curve can be evaluated using a variety of processing techniques (e.g. Foti, 2005; Socco and Strobbia, 2004) and it is then used for the solution of the inverse problem aimed at the identification of the parameters of the soil model. In particular the soil deposit is usually modeled as a stack of homogeneous linear elastic layers and the parameters to be identified are the layer thicknesses and shear wave velocities. Poisson ratios and density variations are usually neglected because of the small sensitivity of the Rayleigh wave dispersion curve to these parameters (Nazarian, 1984).

In general it is possible to distinguish between active surface wave tests, in which the waves are on-purpose generated using a seismic source, and passive surface wave tests, which are based on the analysis of microtremors. The main difference in terms of results between active and passive surface wave tests is related to the different frequency range in which the information can be retrieved. Indeed while in active tests is usually very easy to generate and detect high frequency components, microtremors are typically rich of energy in the low frequency band. Combined use of passive and active methods has been suggested to improve both resolution and depth of investigation (Tokimatsu, 1995; Rix et al., 2002; Foti et al., 2007).

Once the experimental dispersion curve has been estimated several strategies can be adopted to identify model parameters. However the resulting inverse problem is ill-posed from the mathematical point of view and it is not possible to demonstrate the uniqueness of its solution (Tarantola, 2005). This aspect becomes particularly critical when a deterministic approach (local search method) is adopted for the inversion, since the final result become very sensitive to the initial model and the inversion process can easily be biased by wrong choices in term of model parameterization that lead the solution into local minima.

MONTE CARLO INVERSION

In the present study a global search method based on a Monte Carlo (MC) procedure (Boiero et al., 2006) has been used for the inversion, to obtain a number of profiles which can be considered statistically equivalent with respect to the experimental data. A population of 10^5 synthetic models has been randomly generated after defining the number of layers and the starting upper and lower boundary for each model parameter. For each model, the fundamental mode curve is computed using the Transfer Matrix approach (Thomson, 1950; Haskell, 1953). The algorithm has been designed to be particularly efficient thanks to the introduction of scale properties of the dispersion curve (Socco and Strobbia, 2004).

The misfit function between experimental and numerical dispersion curve is then evaluated for each random profile, accounting for the data uncertainty and the statistical number of degrees of freedom. The misfit function considered in the present study is:

$$\chi^2 = \frac{\sum_{1}^{m} \left(V_t - V_e\right)^2 \cdot \sigma_e^{-2}}{m - \left(2 \cdot n + 1\right) - 1} \qquad (1)$$

where V_t and V_e are respectively the theoretical and experimental phase velocities, σ_e contains the data uncertainties, m is the number of points in the dispersion curve and n is the number of layers above the half-space in the model.

The misfit is evaluated for each profile and it is then normalized with respect to the lowest misfit for the whole population. A Fisher test (Sachs, 1984) on the χ^2 ratio is eventually used to select a set of models which can be considered statistically equivalent for a fixed level of confidence. The result of the inversion is therefore a group of profiles having a misfit on the dispersion curve lower than a certain variable threshold.

SYNTHETIC CASE

A synthetic dataset has been generated to assess the consequences of non-uniqueness comparing the results of MC inversion with the "true" solution of the inverse problem. The numerical dispersion curve has been generated for a given "real" soil profile; it has been then perturbed with Gaussian (4 to 7 %) noise to simulate a synthetic "experimental" curve to be used in the inversion process with the aforementioned MC algorithm. The result of the inversion is a set of 6 shear wave velocity profiles (Figure 1-a), whose correspondent numerical dispersion curves show a similar fitting with respect to the synthetic "experimental" one (Figure 1-b). It is noteworthy that the differences between the resulting profiles are significant especially in the position of the second interface and in the value of V_S for the halfspace, whereas the differences in the top portion of the models are reduced. This result is consistent with the higher resolution of surface wave test close to the ground surface.

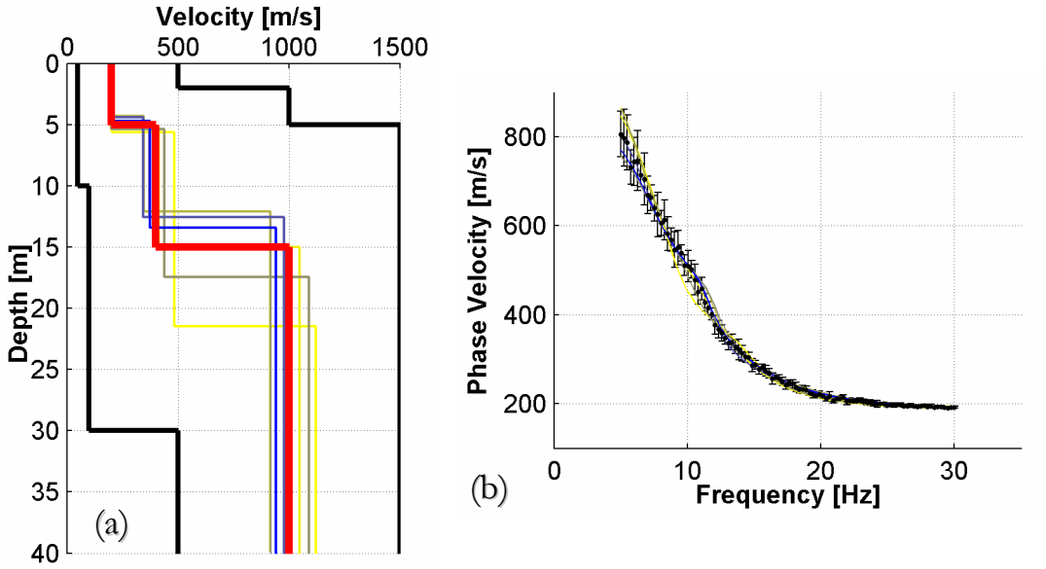


FIG. 1. Synthetic case: a) Shear wave velocity profiles from the MC inversion compared to "real" profile (thick red line); the outer profiles in black are the boundaries for the random generation of the population of profiles; b) dispersion curves associated to the solutions of the MC inversion compared to synthetic experimental dispersion curve (black points);

In Figure 1 a relative misfit representation is adopted, for both soil profiles and corresponding dispersion curves, on the basis of the absolute difference between each profile misfit and the lowest misfit, so that the darkest color corresponds to the profile having the lowest misfit and better approximation to the "experimental" dispersion curve. The same representation will be used consistently in the remaining part of the paper by associating the results of the simulations from a given soil profile with its relative misfit value.

The best fitting profile is very close to the "real" profile; nevertheless also the other solutions are associated to dispersion curves sufficiently close to the "experimental" one, so that each of them could be selected by the inversion process as equivalently good. In particular a deterministic inversion, on the same data, with a local search algorithm could give any of the selected profile as final result.

In order to investigate the consequences of this uncertainty in shear wave velocity profile, the seismic site response has been then assessed using the code Shake91 (Idriss and Sun, 1992). The shear wave velocity profiles obtained from the MC inversion have been used for independent runs of the numerical analysis.

Initially a linear elastic analysis has been performed in order to assess the problem of non-uniqueness avoiding the interference on the results derived from the choice of stress-strain relationships and seismic input. In Figure 2-a the amplification functions of the equivalent profiles are presented in comparison to the one obtained from the "real" profile while in Figure 2-b a similar comparison is reported in terms of response spectra for a real accelerogram (a record from the Umbria Earthquake of 1997).

These results clearly show that equivalent profiles in terms of surface wave inversion are equivalent also in terms of seismic site response. In particular the first resonance peak of the amplification function is very well identified by all the equivalent profiles,

both in terms of frequency and amplification value. The amplification functions are practically coincident for the frequency band below 10 Hz, which is relevant for most earthquakes. Indeed the difference in terms of response spectra (Figure 2-b) are negligible, so that it is possible to state that any one of the profiles obtained with surface wave inversion is equally good from the point of view of site response.

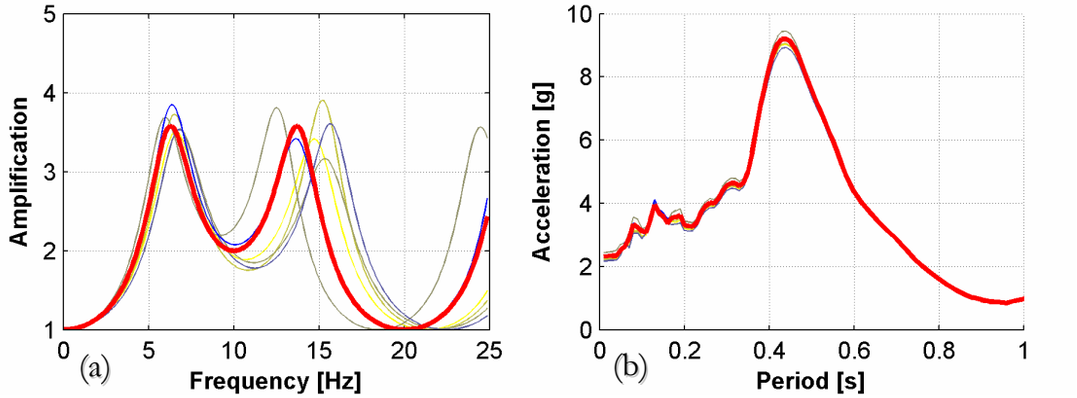


FIG. 2. Synthetic study – Elastic Analysis: comparison of results obtained with the equivalent profiles and the "real" profile (thick red line): a) Amplification functions; b) Response Spectra (record from the 1997 Umbria Earthquake).

In order to confirm the above findings with more realistic analysis, the evaluation of site response has been repeated with a linear equivalent approach. The stiffness and damping ratio decaying curves have been selected from available standard curves from the literature. In particular the two top layers have been assigned decaying curves for sands (Seed et al., 1986), whereas typical decaying curves for rocks have been selected for the halfspace below.

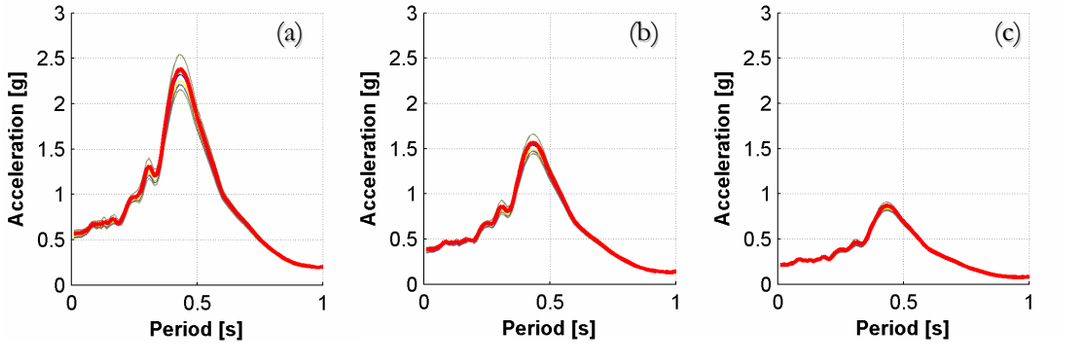


FIG. 3. Synthetic study – Equivalent Linear Viscoelastic Analysis: comparison of response spectra from the equivalent profiles and the "real" one (thick red line) for the Umbria 1997 Earthquake record scaled for different values of outcrop PGA: a) Zone 1: 0.35g b) Zone 2: 0.25g c) Zone 3: 0.15g.

Since in this case the final result is strongly dependent on the input motion assigned at the outcrop, the analyses have been performed by scaling the same record from the Umbria 1997 Earthquake for peak ground acceleration on rock outcrop equal to 0.15g, 0.25g and 0.35g, which are the design values for the seismic Zones in Italy. The

response spectra on the ground surface for the different profiles are reported in Figure 3 and confirm the conclusions drawn from the linear elastic analysis, i.e. the shear wave velocity profiles from surface wave inversion produce a final result of the site response analysis equivalent to the one obtained using the "true" profile.

The scaling of the same accelerogram for different values of PGA is however not fully realistic because the frequency content and many other motion parameters are quite different for strong and weak ground motions. Hence it has been decided to complement the study on the synthetic example, repeating the site response analysis with a more consistent set of input motions. In particular two different sets of real earthquake records have been selected as the input motion (Dall'Ara et al., 2006). Each set is composed of 7 accelerograms which are compatible with the design spectrum of Eurocode 8 (CEN, 2004), meaning that the average of their response spectra is close to the design response spectrum, according to the criteria described in Eurocode 8. The two set of accelerograms selected are associated to a PGA on rock outcrop equal respectively to 0.35g and 0.25g, which are the values adopted for the Zone 1 and 2 of the Italian seismic zonation. For each profile, the response spectra for the spectrum-compatible accelerograms have been evaluated and then averaged. Figure 4 reports the comparison between the average spectrum for each of the profiles from surface wave inversion compared to the results obtained for the "true" profile. Again the results show only minor differences, whereas the shape and absolute values of the response spectra are very similar.

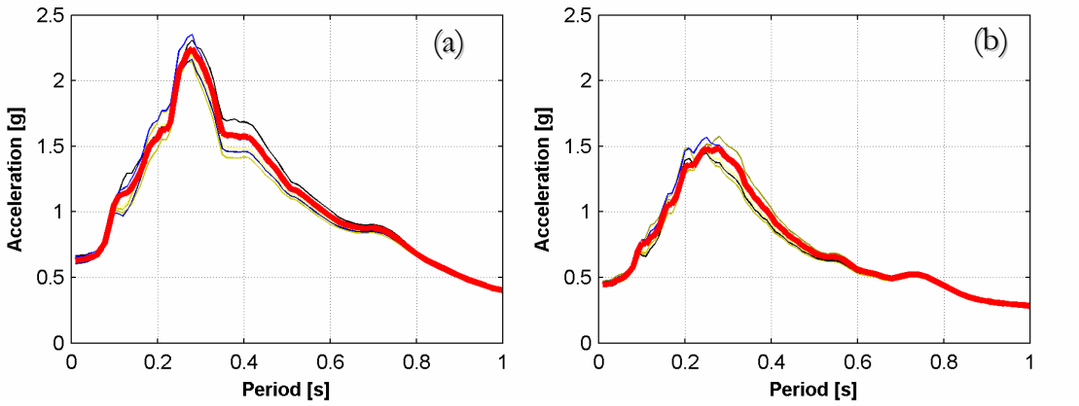


FIG. 4. Synthetic study – Mean Response Spectra of the two sets of spectrum-compatible accelerograms from the equivalent profiles compared to the synthetic one (thick red line) for: a) Zone 1 b) Zone 2.

CASE HISTORY

The case history herein presented is related to a site located in La Salle (Valle d'Aosta) on a wide fluvial fan, mainly composed by gravels and sands with some silt content. A borehole logged up to 50 m from the ground surface for the execution of a Down-Hole test reports layers of gravelly sands and silty sands with gravel. Undisturbed sampling was not feasible at this site because of the nature of the sediments; the decaying curves which will be used for site response analysis have hence been taken from the literature (Seed et al., 1986).

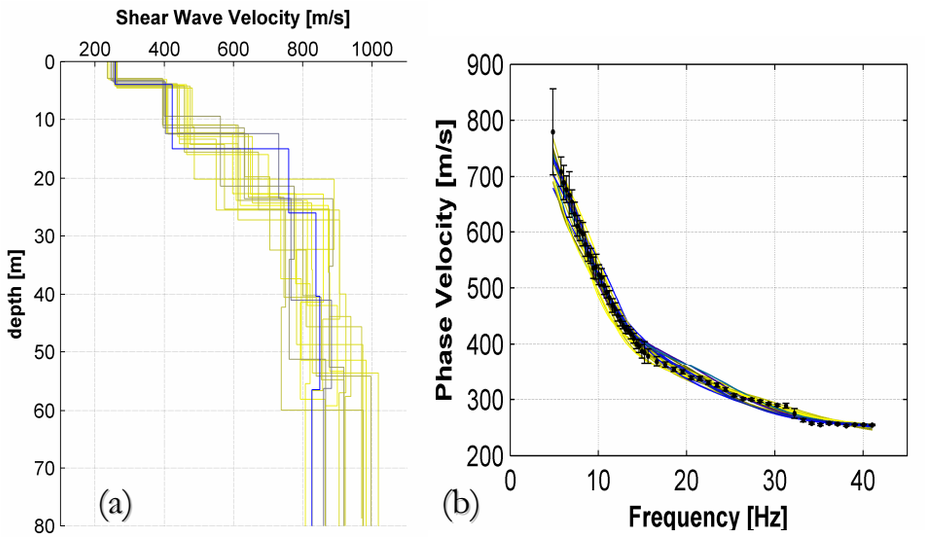


FIG. 5. Active and Passive Surface Wave test results: a) Shear wave velocity profiles from the MC inversion; b) dispersion curves associated to the solutions of the MC inversion compared to the experimental dispersion curve (black points).

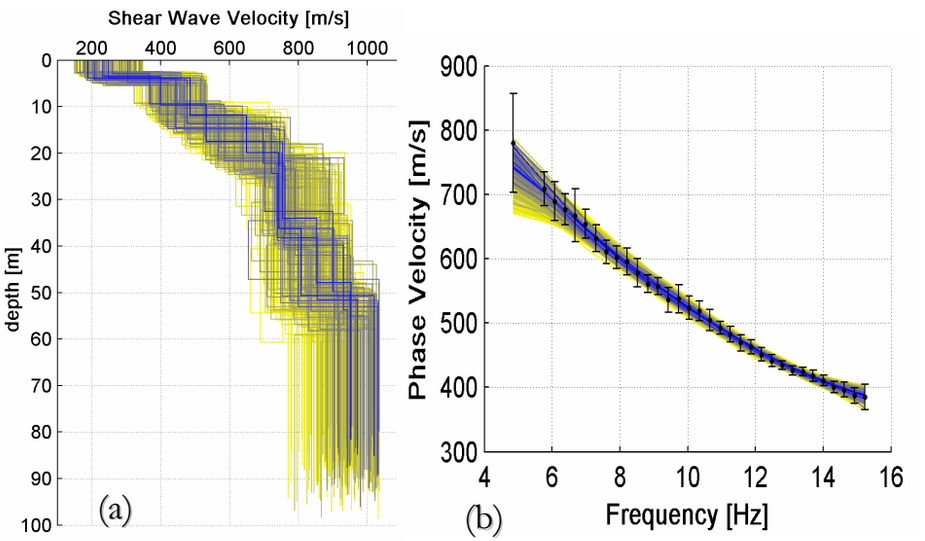


FIG. 6. Passive Surface Wave test results: a) Shear wave velocity profiles from the MC inversion; b) dispersion curves associated to the solutions of the MC inversion compared to the experimental dispersion curve (black points).

Surface wave tests have been performed at this site using both active and passive methods (Foti et al., 2007). The active data have been collected using a multistation setup with 48, 4.5 Hz geophones aligned along a straight line starting from the source with a 1.5 m spacing. The acquisition of microtremors has been carried out using a 75 m circular array with 12, 2 Hz geophones along the circumference. The following procedure has been adopted to obtain the best estimate of experimental dispersion curve and its uncertainty: separate dispersion curves have been evaluated for each active shot or passive acquisition; they have been subsequently used to get average values and standard deviations at the different sampling frequencies (Foti et al., 2007).

The experimental data have been analysed twice: once combining the information of active and passive tests and a second time using only the result derived by microtremors. This double analysis has the scope of assessing the consequences of lack of information in the high frequency range, which is the case when only passive data are collected, on the final results.

Figures 5 and 6 report the result of the MC inversion process for the two datasets. Clearly the combination of active and passive experimental data leads to a much higher resolution for shallow layers, thanks to the availability of high frequency data. Moreover the number of selected profiles for the same level of confidence is much lower than for the case in which only passive data are used. This is partly due to the fact that the misfit function is influenced also by the standard deviation of the experimental data and this is much lower for active tests (see Figure 5-b). In general it is possible to state that the experimental test in which only passive data are used leads to a much higher uncertainty. In any case for both analyses the range of variation of each model parameter is quite high. In order to assess the consequences of such uncertainty, seismic response studies using a linear equivalent approach have been performed for each of the selected profiles.

The reference ground motion has been selected on the basis of probabilistic seismic hazard studies (Naso et al., 2005) and to the simplified de-aggregation procedure proposed by Bommer et al. (2000). From the above procedure, the reference earthquake for La Salle site is given by a Magnitude 5.5 event at epicentral distance 18 km, associated to a normal fault rupture. Using this parameters, real accelerograms recorded on rock sites have been selected from the European Strong Motion Database (Ambraseys et al., 2002). These records have been scaled to the PGA for the site, which is equal to 0.11 g for a return period of 475 years.

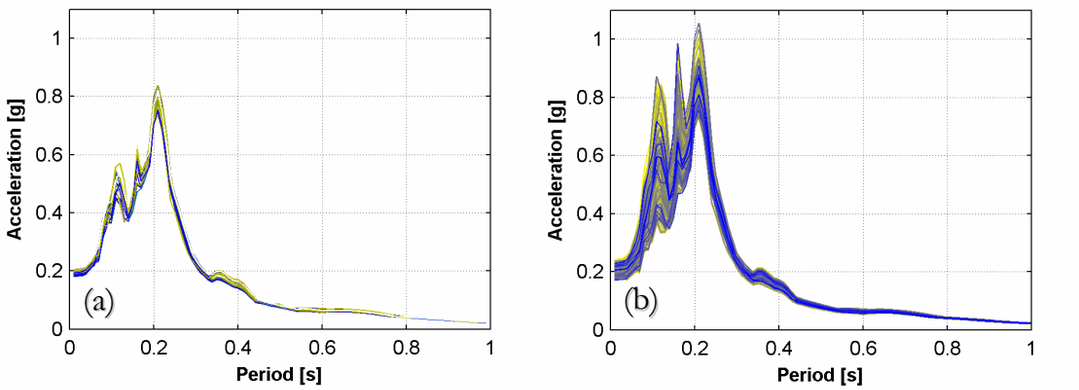


FIG. 7. Response Spectra of equivalent profiles: a) Combined Active and Passive tests; b) Passive tests.

The results obtained in terms of response spectra for the same reference ground motion are presented in Figure 7 for the two testing conditions considered. It can be noticed how for both datasets the shape of the response spectra is quite consistent for the different profiles, nevertheless the range of variability of the response spectra associated to the analysis of passive data alone is quite high whereas the results for the combined active-passive data are very satisfactory.

SOME COMMENTS ON $V_{S,30}$

The weighted average of shear wave velocities in the shallowest 30m is often used as a parameter to discriminate soil classes with respect to seismic design (e.g. Eurocode 8, CEN, 2004)). In Figure 8 the results in terms of $V_{S,30}$ for the set of profiles of Figure 5-a and 6-a respectively are reported. Clearly surface wave tests can be considered a reliable and consistent method for the determination of this parameter. Indeed both the distributions have a mean value around 490 m/s with maximum deviations of the order of 5% in the case of purely passive tests (Figure 8-b) and of 3% for combined active and passive tests (Figure 8-a). Moreover it can be noticed how for seismic classification the use of only passive tests does not imply relevant consequences on the determination of $V_{S,30}$.

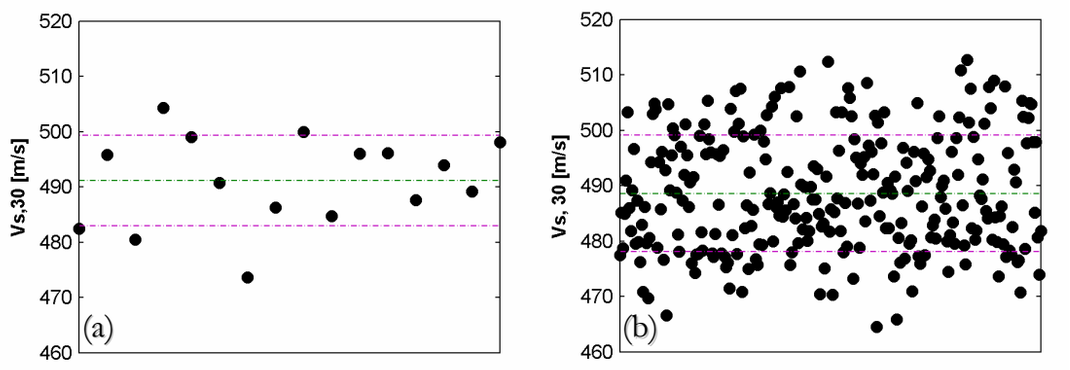


FIG. 8. $V_{S,30}$ determined from surface wave equivalent profiles: a) Combined Active and Passive tests (Fig. 5a); b) Passive tests (Fig. 6a).

CONCLUSIONS

Non-uniqueness of the solution and the associated uncertainty, are often considered the great pitfall of surface wave tests. This study on synthetic and real experimental data shows how the consequences of such uncertainties are very limited for seismic site response studies, at least where a 1D approach is deemed to be reasonable. Indeed shear wave velocity profiles which can be considered equivalent with respect to Rayleigh wave dispersion are also equivalent with respect to site response. This feature, which can be considered somewhat expected a priori on the basis of the similitude of the underlying soil models, confirms the effectiveness of surface wave tests in site characterization for seismic response studies.

ACKNOWLEDGMENTS

The authors wish to thank Mr. Marco Arnolfo for his contribution in performing numerical simulations and Giampiero Bianchi for his help in data acquisition. For the case history, the experimental tests have been sponsored by the *Natural Risk Management and Observational Seismology Department* of Valle d'Aosta region, in the framework of the SISMOVALP Project financed by the European Union.

REFERENCES

Ambraseys, N., Smit, P., Sigbjornsson, R., Suhadolc, P. and Margaris, B. "Internet-Site for European Strong-Motion Data", European Commission, Research-Directorate General, Environment and Climate Programme, 2002.

Boiero D., Wisén R. and Socco L.V. "Scale property Monte Carlo driven inversion of surface wave data", Proc. of Meeting Near Surface Geophysics Section of EAGE, Helsinki, CD-Rom, 2006.

Bommer J., Scott, S. & Sarma S. "Hazard-consistent earthquake scenarios", Soil Dynamics and Earthquake Engineering, 19, 219-231, 2000.

Dall'Ara A., Lai C.G., Strobbia C. "Selection of spectrum-compatible real accelerograms for seismic response analyses of soil deposits. Proc. of the First European Conference on Earthquake Engineering an Seismology, Geneve, CD-Rom, 2006

CEN. "EN 1998-1 Eurocode 8: Design of structures for earthquake resistance", Brussels, 2004

Foti S. "Surface Wave Testing for Geotechnical Characterization", in Surface Waves in Geomechanics: Direct and Inverse Modelling for Soils and Rocks, CISM Series, Number 481, Lai C.G. and Wilmanski K. eds, Springer, Wien, 47-71, 2005.

Foti S., Comina C., Boiero D. "Reliability of combined active and passive surface wave methods", RIG (Italian Geotechnical Journal), AGI, 41 (2), 39-47, 2007.

Haskell N.A. "The dispersion of surface waves on multilayered media", Bullettin of the Seismological Society of America, vol. 43 (1), pp. 17-34, 1953.

Idriss I.M. and Sun J.I. "Shake91 User's Manual", University of California at Davis, 1992.

Naso G., Petitta M. & Scarascia Mugnozza G. (Eds) "La Microzonazione Sismica. Metodi, esperienze e normativa". Dipartimento della Protezione Civile - Servizio Sismico Nazionale. CD-Rom, 2005 (in Italian).

Nazarian S. "In situ determination of elastic moduli of soil deposits and pavement systems by Spectral-Analysis-of-Surface waves method", PhD Diss., Un. of Texas at Austin. 1984

Rix G.J., Hebeler G.L. and Orozco, M.C. "Near surface vs profiling in the New Madrid Seismic Zone using surface wave methods", Seismological Research Letters, 73(3), 380-392, 2002.

Sachs L. "Applied Statistics: A Handbook of Techniques", Springer-Verlag. Wien, 1984.

Seed H.B., Wong R.T., Idriss I.M., Tokimatsu K. "Moduli and damping factors for dynamic analyses of cohesionless soils", J. Geotechn. Eng., ASCE, 112, 11, 1016-1032 , 1986.

Socco L.V., Strobbia C. "Surface Wave Methods for near-surface characterisation: a tutorial", Near Surface Geophysics, 2,4 165-185, 2004.

Stokoe K.H., Santamarina J.C. "Seismic-wave-based testing in geotechnical engineering", Proc. of GeoEng 2000, Melbourne, CD-Rom, 2000.

Tarantola, A. "Inverse problem theory and methods for model parameter estimation", SIAM, Philadelphia, USA, 2005.

Thomson W.T. " Transmission of elastic waves through a stratified solid medium", J. Applied Physics, vol. 21 (1), pp. 89-93, 1950.

Tokimatsu, K. "Geotechnical Site Characterization using Surface Waves" Proceedings, First International Conference on Earthquake Geotechnical Engineering, IS-Tokyo '95, Tokyo, Balkema, Rotterdam, 1333-1368, 1995.

Developing Site-Specific Design Response Spectra for a Type F Site due to Liquefaction

Endi Zhai[1], Ph.D., P.E., G.E. M. ASCE

[1]Principal Geotechnical Engineer, Kleinfelder West, Inc., 8 Pasteur, Suit 190, Irvine, CA 92618; ezhai@kleinfelder.com

ABSTRACT: This paper presents a practical approach to develop a site-specific design acceleration response spectral (ARS) curve for a soil profile Type F site due to liquefaction. A site development consisted of four main structures up to 12-stories high over a two- to three-level parking structure in Marina Del Ray, California. Based on the 2001 California Building Code (CBC) Table 16-J, the site was classified as Type F, requiring a site-specific evaluation. A site-specific probabilistic seismic hazard analysis (PSHA) was performed to develop the target uniform hazard spectra (UHS). An equivalent-linear one-dimensional seismic response analysis using the computer program SHAKE91 (Idriss and Sun, 1992) was performed and compared with the nonlinear effective-stress seismic response analyses using the computer code FLAC (Itasca, 2006) and D-MOD2000 (GeoMotions, LLC, 2007). Differences and deficiencies of the response spectra between using the equivalent-linear and nonlinear effective-stress seismic response analyses are discussed and the recommendations for structures having a different fundamental period of vibration are made.

INTRODUCTION

A marine site development consists of approximately four main structures up to 12-stories high over a two- to three-level parking structure, which will encompass approximately 6.5-acre area bounded by two channels in Marina Del Ray, California. The site location map is presented in Figure 1. The subsurface soils encountered during our field exploration consisted of 10 to 15 feet of fill underlain by 15 to 25 feet of very soft to medium stiff clay. Below the clay layer was about 20 to 30 feet of loose to medium dense silty sand to sand susceptible to liquefaction subjected to the Design Basis Earthquake (DBE) having 10% probability of exceedance in 50 years. Dense to very dense sand to gravelly sand layer was present below the liquefiable sand layer. Design groundwater level was 10 feet below grade. Based on the 2001 CBC Table 16-J, the site was classified as Type F, requiring a site-specific evaluation.

Present adjacent to the site are several active faults including the Santa Monica fault, Newport-Inglewood (L.A. Basin) fault, Palos Verdes fault, Malibu Coast fault and



Figure 1 Site Location Map

Hollywood fault which are within 15 km to the site. We performed a PSHA for the DBE. This resulted in a peak ground acceleration (PGA) of about 0.5g associated with a moment magnitude of 6.7. Since to depth of the bedrock was unknown and anticipated to be too deep for a site response model, we developed the target UHS corresponding to a firm-ground condition. To provide the site-specific response spectra for the design, we developed three sets of ground motions which are compatible with the target UHS which considered the near source rupture directivity effects (Somerville et al, 1997 and Abrahamson, 2000). Three sets of time histories were selected from the COSMOS/PEER database based on the closest similarity of the seismological and geological features, and then spectrally-matched to the target UHS.

The free-field, site-specific horizontal ARS curves for the fault-normal (FN) and the fault-parallel (FP) directions were developed using the equivalent-linear one-dimensional seismic response software SHAKE91 (Idriss and Sun, 1992). Strain-compatible material curves for the liquefiable sand layer was represented by the curves for clay based on an undrained shear strength equal to the residual strength (Seed and Harder, 1990). The equivalent-linear analysis used the averaged linear-elastic properties (i.e. secant modulus) and assumed the post-liquefaction softened properties for the liquefiable sand from the beginning of shaking. A nonlinear effective-stress analysis was performed using the commonly-used linear elastic/plastic (Mohr-Coulomb) model armed with a practical-oriented excess pore-pressure model (Dawson et al., 2001) programmed in FLAC, and the results compared with those obtained with the equivalent-linear analysis. The differences and deficiencies of the results from both the equivalent-linear and the simplified linear elastic/plastic models are discussed and the recommendations made.

PRABABILISTIC SEISMIC HAZARD ANALYSIS

The DBE for the project was based on the 2001 CBC, corresponding to a 10% probability of exceedance in 50 years. Our probabilistic seismic source model is based on the seismic source model used in developing the 2002 Probabilistic Seismic Hazard Maps by California Geological Survey (CGS) for the State of California (Cao et al., 2003) which were included in the commercial computer program EZ-FRISK V7.2 (Risk Engineering, Inc., 2006) that was used for this analysis. The attenuation

relationships selected in our analysis were the same as used by CGS for the 2002 Southern California Hazard Map. Since the site is situated in a region likely affected by near-source ground motions, we have included the rupture directivity and near-source effects using Somerville et al. (1997) and Abrahamson (2000). The results were obtained by taking an average of the hazard results from these attenuations relationships.

The peak ground horizontal acceleration (in units of gravity) for the firm ground condition was computed to be 0.42g. The results of our deaggregation analysis to estimate the controlling earthquake magnitude and distance associated with the DBE event are Mw 6.7 and 8.5 km, respectively.

Due to an unknown depth to bedrock, a seismic response model including the bedrock was not considered feasible. Therefore, a UHS for a firm-ground condition was developed which is corresponding to the dense to very dense sand to gravelly sand presented approximately 80 to 100 feet below grade. UHS values for two orthogonal horizontal directions, FN and FP were computed for a damping ratio of 5 percent of critical. Figure 2 presents the target UHS for and the spectral matching results which will be described in the following section.

EQUIVALENT-LINEAR SEISMIC RESPONSE ANALYSIS USING SHAKE

Input Motions

Three times histories were selected from the COSMOS/PEER database and used as references based on the closest similarity of seismological and geological features. The first reference time history was the record from Capitola Fire Station (Record No. CPT-000) from the 1989 Loma Prieta earthquake. The second one was recorded at EL Centro Array #9 (Record No. EC9-180) from the 1940 EL Centro earthquake. The third one was recorded at Sherman Oaks Station (Record No. SOK-000) during the 1994 Northridge earthquake.

The above selected motions were spectrally matched to the target UHS for the firm-ground condition. The spectral matching procedure began with the reference acceleration time-history whose characteristics reasonably represent the firm ground motions expected for the site. This reference time-history has individual spectral peaks and valleys that deviate from the smooth uniform hazard spectra. The matching procedure

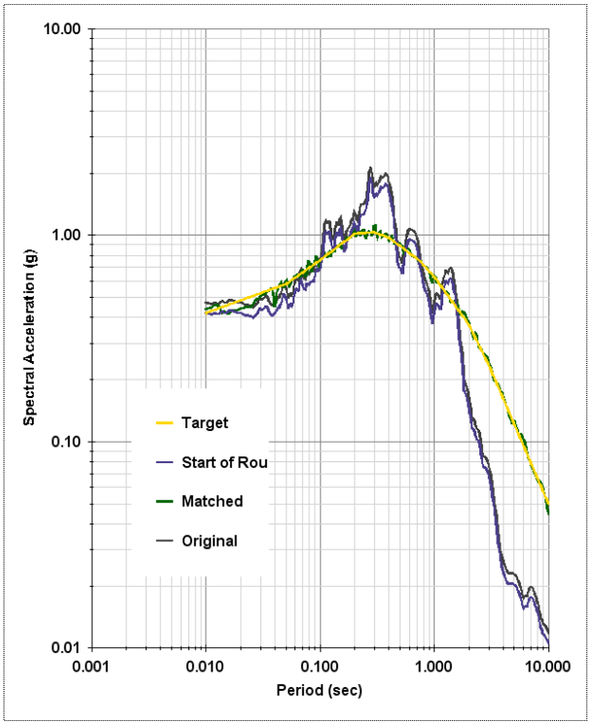


Figure 2 Target UHS and Spectral Matching

Table 1. Soil Properties

No. of Soil Layer	Depth (ft)		USCS Soil Type	Total Unit Weight (pcf)	Shear Strength[1)]		Shear Wave Velocity (ft/s)	Shear Modulus (psf)	Strain-Dependent Shear Modulus / Damping Curve
	From	To			Cohension (psf)	Angle of Friction (deg)			
1	0	10	Fill	120	100	30	550	1.13E+06	FML 0 to 10 m
2	10	30	Clay	120	500	0	400	5.97E+05	FMH 0 to 10 m
3	30	50	Liq' sand	120	200	30	600	1.34E+06	FMH 10 to 20 m
4	50	70	Silt	120	300	32	700	1.83E+06	FML 10 to 20 m
5	70	85	Sand	120	100	35	1000	3.73E+06	PCA 20 to 40 m
6	85	100	Silt	120	500	28	850	2.70E+06	FML 20 to 40 m
7	Below 100		Sand	130	100	38	1000	4.04E+06	Base

Notes: 1) Used only in FLAC analysis
2) Roblee and Chiou (2004); PCA 10 to 20 m was used for Layer 3 in FLAC & D-MOD
3) FLAC Hyst. damping and D-MOD2000 Parameters were curve-fitted based on the above curves

reduced these deviations in the period range important to the structure while preserving the non-stationary characteristics. We used the computer code RSPMATCH (Abrahamson, 1992) to perform the spectral matching. The spectrally matched results for CPT-000 in FN direction are presented in Figure 2 and the results of the times histories are presented in Figure 3.

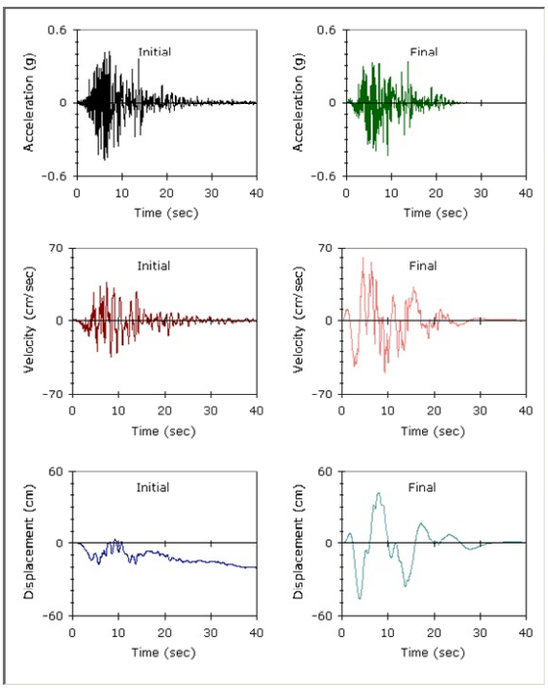


Figure 3 Spectrally Matched Input Firm-Ground Motions

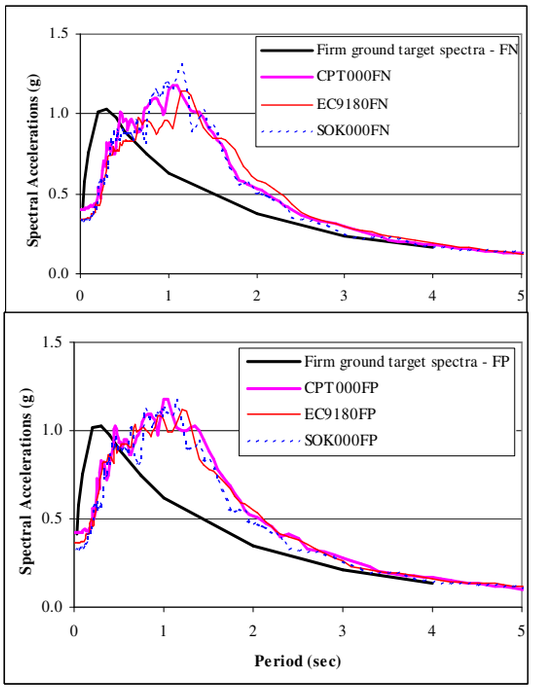


Figure 4 Computed ARS Curves using SHAKE

Site Seismic Response Analysis

The site-specific soil profile based on our field and laboratory investigations are summarized in Table 1. A liquefaction analysis was performed prior to the site seismic response analysis. The strain-compatible shear modulus and damping ratio curves for the liquefiable sand layers were represented by the curves for clay corresponding to an undrained shear strength equal to the residual strength (Seed and Harder, 1990). The outcropping accelerations time histories as shown in Figure 3 were used as input motions at the base. The computed surface ARS curves for FN and FP are plotted in Figure 4.

The results indicate that the computed ARS curves are much lower in the periods smaller than approximately 0.5 second, and much higher in the periods greater than approximately 1.0 second than the target UHS.

NONLINEAR EFFECTIVE-STRESS SEISMIC RESPONSE ANALYSES

Analysis Approach and Model Makeup for FLAC Analyses

We used the commonly-used Mohr-Coulomb (linear elastic/perfectly plastic) soil model coupled with a practice-oriented pore-pressure generation model which was programmed into the commercial computer code FLAC using programming language FISH that is embedded within FLAC. Pore-pressures are generated in response to shear stress cycles, which follow the industrial standard cyclic-stress approach developed by Seed and coworkers (Seed et al., 1976; Seed et al., 1979). However, unlike the equivalent-linear approach where liquefaction potential is assessed as a post-processing step, pore-pressure generation in FLAC is incremental and fully integrated with the nonlinear dynamic analysis. The simultaneous coupling of pore-pressure generation with nonlinear, plasticity based, stress analysis is believed to produce a more realistic dynamic response than can be achieved with equivalent-linear method.

The soil column profile presented in Table 1 was modeled as a single column in FLAC. Additional soil parameters needed include shear strength, cyclic-strength curve-a relation between the cyclic-stress ratio and the number of cycles required to reach liquefaction, and soil damping ratios. The shear strength parameters include friction angle and cohesion which were determined based on the in-situ and laboratory testing results. The cyclic strength curve was derived from the equivalent SPT blow counts $(N_1)_{60cs}$ for clean sand using empirical relationship by Youd et al. (2001). The cyclic resistance ratio (CRR) corresponding to an Mw 7½ was 0.21 based on the $(N_1)_{60cs}$ value of 19. The magnitude scaling factor (Youd et al., 2001) was used to convert the CRR values corresponding to the deaggregated controlling magnitude of Mw 6.7. Hysteretic damping for each layer was obtained by curve-fitting the strain-compatible shear modulus/damping curves as listed in Table 1 using the Hardin/Drnevich model (Itasca, 2006).

In the initial static analysis to compute the in-situ stresses, the base boundary was fixed both horizontally and vertically and the side boundaries were only fixed horizontally. For dynamic analyses, the based boundary was set as the compliant base

allowing a transmitting boundary condition and side boundaries were replaced with free-field boundaries to provide a compatible 1-dimensional model similar to the SHAKE model. The outcropping velocity time histories as shown in Figure 3 were converted into stress waves using a firm-ground shear wave velocity of 1,000 ft/sec (see Table 1) and the upward propagating motion was used as input motions at the base.

Analysis Approach and Model Parameters for D-MOD2000 Analyses

D-MOD2000 uses the MKZ constitutive model (Matasovic and Vucetic 1993, 1995) to define the initial backbone curve. The dynamic equation of motion is solved in the time domain using the dynamic response scheme developed by Lee and Finn (1978). The soil behavior is modeled by a nonlinear backbone curve with the MKZ model parameters β and s being curve-fitted to match shear modulus reduction curve as listed in Table 1. The stiffness and damping of soil are represented with nonlinear hysteretic springs connected to lumped masses. Additional viscous damping is included through the use of viscous dashpots. The input full Rayleigh damping parameters α_R and β_R were estimated using a target damping ratio of 0.5%, a site frequency of about 0.59 second (based on average shear wave velocity) and n=5. Other input parameters used were selected based on recommendations provided in D-MOD2000 user's manual (GeoMotions, LLC, 2007). Viscous base boundary was used based on the firm-ground base properties as listed in Table 1. The outcropping accelerations time histories as shown in Figure 3 were used as input motions at the base.

Analysis Results

The ARS computed with FLAC and D-MOD2000 utilizing the nonlinear, effective-stress approaches described above, are plotted in Figure 5. Only the results from the CPT000FN input motion were plotted. The results from the other input motions are similar. It can be seen that the computed surface response spectra from FLAC and D-MOD2000 are in good agreement. It is interesting to note that the time histories of excess pore pressure ratios from FLAC and D-MOD2000 are very similar.

In contrast to the ARS from the equivalent-linear runs, the nonlinear, effective-stress runs generated PGA values (corresponding to zero period) of approximately 0.2g, which is about one-half of that generated from the SHAKE analyses. In view that the input motions were the same, the difference in PGA values from the equivalent-linear and nonlinear effective-stress analyses are significant. The less PGA values from the effective-stress analyses were due to liquefaction at Layer 3 which started pore pressure buildup at about 3 seconds and reached about 100 percent of excess pore pressure ratio at about 13 seconds, as shown in Figure 6. Because the equivalent-linear analysis uses the averaged linear-elastic properties (i.e. secant modulus) and assumed post-shaking softened properties for the liquefiable layer at the beginning of shaking, the computed dynamic response tends to be too low in the beginning and too high towards the end of shaking. The difference between these two approaches is much more significant between 0.5 and 1.5 seconds. The ARS values between 0.5 and 1.5 seconds computed with the nonlinear, effective-stress analysis are much lower than

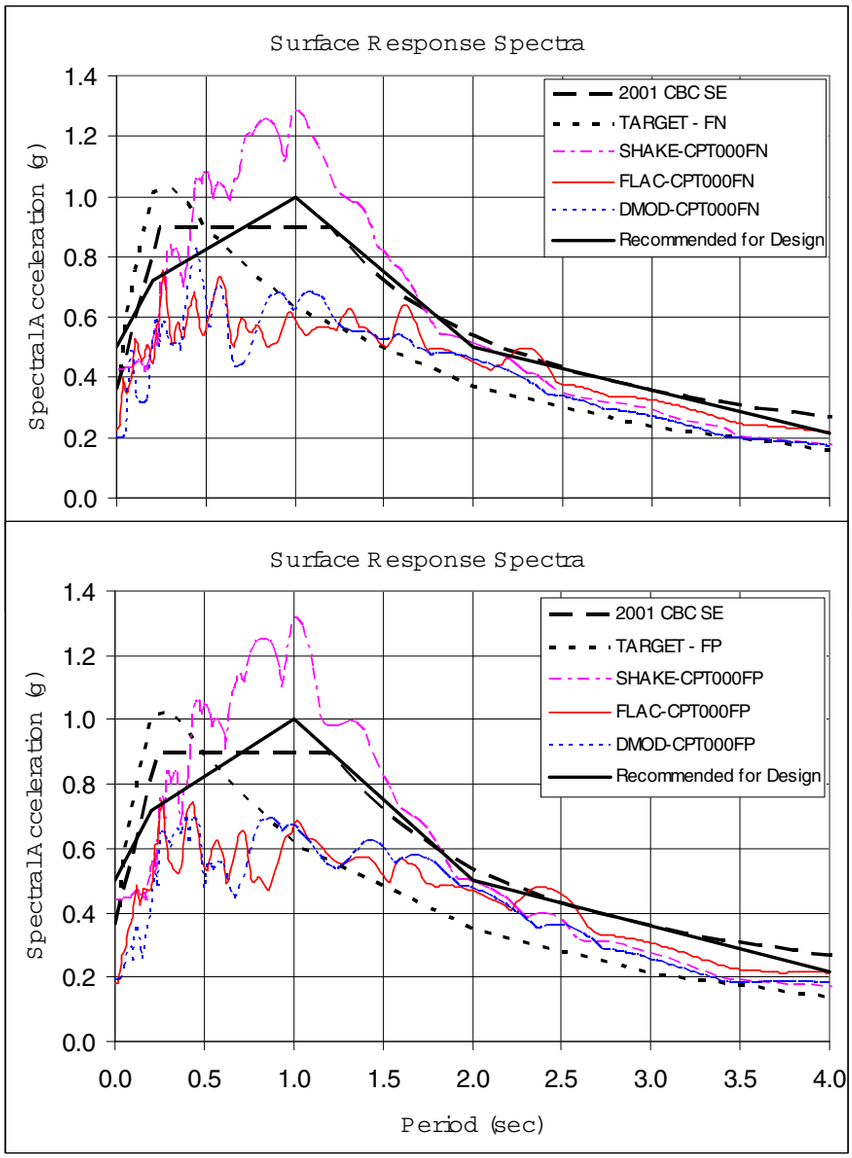


Figure 5 Surface Response Spectra

those obtained with the equivalent-linear analysis. On the other hand, the ARS values at the longer periods (after 1.5 seconds) are similar. It needs to be noted that the maximum shear strain in Layer 3 when liquefaction is reached is more than 1% in FLAC and D-MOD2000. On the contrary, it only reached 0.2% in the last iteration of SHAKE runs. This less cyclic degradation in stiffness tends to significantly over-predict the response.

Response spectrum based on the 2001 California Building Code assuming liquefaction does not occur (corresponding to a soil profile Type E due to 20 feet of soft clay above the liquefiable sand layer) was plotted in Figure 5. Also plotted in Figure 5 is the recommended design response spectrum which will be discussed in the following section.

CONCLUSIONS AND RECOMMENDATIONS

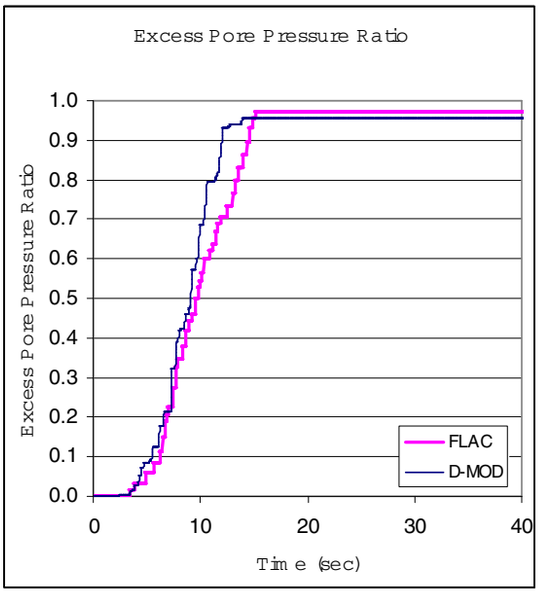


Figure 6 Excess Pore Pressure Ratio Buildup

Site-specific seismic response analyses were performed and presented in this paper for a Type F marine site due to liquefaction. Three sets of acceleration time histories were selected from the COSMOS/PEER database based on the closest similarity of seismological and geological features, and then spectrally-matched to the target UHS. There is a significant difference between the equivalent-linear total-stress and nonlinear effective-stress analyses. Since Layer-3 liquefies subject to the DBE, it would behave as a base isolator. The equivalent-linear analysis resulted in much lower shear strain in the liquefiable layer and much higher PGA values and spectral accelerations between approximately 0.5 and 1.5 seconds. Due to large shear strain caused by liquefaction in Layer 3, the equivalent-linear approach analysis is deemed not appropriate to model the site response. The nonlinear effective-stress analyses from both FLAC and D-MOD2000 provided similar results and validated each other. It is believed the FLAC and D-MOD2000 results are more reasonable for the site because the FLAC and D-MOD2000 models can simulate liquefaction effect (see Figure 6). The slight difference between the FLAC and D-MOD2000 results are expected as they use different pore pressure generation models. However, from a design standpoint, these results should be used with the following recommended modifications due to uncertainties in earthquake shaking level (a shorter return-period earthquake may generate high response due to less liquefaction potential, i.e., less base-isolation effect), and structural foundation effect (usually stiffen the site), etc.

A recommended design response spectrum has to meet the code minimum requirements even though a site-specific response analysis is performed. Based on ASCE 7-05 (2006), it is recommended that the design spectral acceleration value at any period shall not be less than 80 percent of the spectral acceleration value determined for soil profile Type E. The design spectral acceleration value at a period of 0.2 second should be taken from the site-specific (nonlinear effective-stress) response spectrum at a period of 0.2 second, except that it should not be taken less than 90 percent of the peak spectral acceleration value at any period larger than 0.2 second. The design spectral acceleration value at a period of 1 second should be taken as the greater of the site-specific (nonlinear effective-stress) response spectrum at a period of 1 second or 2 times the spectral acceleration value at a period of 2 seconds. Furthermore, the project site Local Coastal Plan requires that new development over three stories in height shall be designed with a PGA value no less than 0.5g. The

project consisted of four main structures up to 12-stories high over a two- to three-level parking structure, therefore, a PGA value of 0.5g is recommended. The recommended design spectral curve is plotted in Figure 5.

ACKNOWLEDGMENTS

Mr. Brian Crystal and other Kleinfelder staff are highly appreciated for their contributions to the field and laboratory investigations to come up with the soil properties used in the analyses.

REFERENCES

2001 California Building Code, ICBO.

Abrahamson, N.A., (1992). "Non-stationary spectral matching program RspMatch."

Abrahamson, N.A. (2000). "Effects of rupture directivity on probabilistic seismic hazard analysis", *Proceedings of the 6th International Conference on Seismic Zonation*, Palm Springs, California, November 12-15.

ASCE 7-05, (2006). "Minimum Design Loads for Buildings and Other Structures."

Cao, T., Bryant, W.A., Rowshandel, B., Branum, D., and Wills, C.J. (2003). "The revised 2002 California probabilistic seismic hazard maps, California Geological Survey, June.

Dawson, E. M., W. H. Roth, S. Nesarajah, G. Bureau and C. A. Davis, 2001. A practice oriented pore-pressure generation model, *Proceedings of the 2nd International FLAC Conference*, Lyon, France, 47-54.

GeoMotions, LLC, (2007). "D-MOD2000 User's Manual.".

Itasca Consulting Group, Inc., (2006). "FLAC – Fast Lagrangian analysis of continua, user's manual."

Idriss I.M. and J.I. Sun. (1992). "A computer program for conducting equivalent linear seismic response analyses of horizontally layered soil deposits."

Matasovic, N. and M. Vucetic (1993). "Cyclic characterization of liquefiable sands." J. of Geotech. Engrg., ASCE, 119(11), 1805-1822.

Matasovic, N. and M. Vucetic (1995). "Generalized cyclic degradation-pore pressure generation model for clays, J. Geotech. Engrg., ASCE, 121(1), 33-42.

Risk Engineering, (2006). EZ-FRISK, Version 7.12

Roblee C. and B. Chiou, (2004). "A proposed geoindex model for design selection of non-linear properties for site response analyses", Proceedings of the Int'l Workshop on Uncertainties in Nonlinear Soil Properties and their Impact on Modeling Dynamic Soil Response, UC Berkeley, March 18-19.

Seed, H.B., P.P. Martin, and J. Lysmer, (1976). "Pore-water pressure changes during soil liquefaction." *Journal of the Geotechnical Engineering Division*, ASCE, 102(GT4), 323-346.

Seed, H.B., (1979). "Soil liquefaction and cyclic mobility evaluation for level ground during earthquakes." *Journal of the Geotechnical Engineering Division*, ASCE, 105(GT2), 201-255.

Seed R.B. and L.F. Harder, (1990). "SPT-based analysis of cyclic pore-pressure generation and undrained residual strength." *Proceedings, H.B. Seed Memorial*

Symposium, UC Berkeley, Vol. 2, 351-376.

Somerville, P.G., Smith, N.F., and Graves, R.W. (1997). "Modification of empirical strong ground motion attenuation relationships to include the amplitude and duration effects of rupture directivity." *Seismological Research Letters*, Vol. 68, No. 1, January/February.

Youd, T. L., et al., (2001). "Liquefaction resistance of soils: summary report from the 1996 NCEER and 1998 NCEER/NSF workshops on evaluation of liquefaction resistance of soils." *Journal of Geotechnical and Geoenvironmental Engineering*, 127(10), 297-313.

Dynamic Response of Unsaturated Non-Collapsible and Collapsible Deposits

Claudia Medina[1], A.M. ASCE, and Mourad Zeghal[2], M. ASCE.

[1] Postdoctoral Research Associate, Department of Civil and Environmental Engineering, School of Engineering, Rensselaer Polytechnic Institute,110 8th St., Troy, NY 12180-3590; PH (518) 276-8771; FAX (518) 276-4833; e-mail: medinc@alum.rpi.edu
[2] Associate Professor, Department of Civil and Environmental Engineering, School of Engineering, Rensselaer Polytechnic Institute,110 8th St., Troy, NY 12180-3590; PH (518) 276-2836; FAX (518) 276-4833; e-mail: zhegal@rpi.edu

ABSTRACT: This paper presents a micro-mechanical study of the response of unsaturated non-collapsible and collapsible soil deposits when subjected to a dynamic base excitation. The discrete element method was employed to idealize the soil skeleton. The effects of interparticle water bridges in a pendular state were modeled using suction forces. Periodic boundaries in the two lateral directions (El Shamy, 2004) and a high gravitational field were used to reduce the number of particles, required to achieve a realistic simulation of a soil deposit, to a computationally manageable value. Numerical simulations were conducted to assess the impact of moisture content on the dynamically induced settlements of unsaturated non-collapsible and collapsible soil deposits. The outcome of these simulations provided a valuable insight on the associated response mechanisms.

INTRODUCTION

The dynamic response of cohesionless soil deposits during earthquakes and other dynamic excitations is frequently associated with settlements of the ground surface. Such settlements often lead to differential movements and damage to foundations, embankments and other civil systems, as observed during major earthquakes such as San Fernando 1971; Northridge 1994; Kobe, 1995 (Slosson, 1975; Stewart et al., 2004). At the micro level, these settlements are linked to a denser packing of the soil particles. The presence of water bridges at particle interfaces of an unsaturated granular soil deposit leads to intricate response patterns associated with the densification process.

Unsaturated soils are three-phase mixtures consisting of a skeleton of mineral particles, pore liquid (generally water), and pore gas (generally air). The response of these soils is strongly affected by the solid-particle and pore-water interaction.

Depending on the moisture content, this water may exist in pendular, funicular or capillary state (Newitt & Conway-Jones, 1958). At low levels, moisture consists only of isolated pendular water bridges. These isolated bridges are stable and generate suction forces that hold neighboring soil particles together, increasing shear strength and stiffening soil response. These forces are associated with surface tension of water and difference between the pore-water and pore-air hydrostatic pressures across the water bridge. These suction forces enable the development of loose collapsible arrangements of particles. The water bridges break when these deposits are subjected to large seismically induced shear deformations. The increase in soil strength mentioned above is lost leading to a large non-reversible volumetric collapse of the soil structure along with significant densification and settlements.

Analysis and modeling of the response of unsaturated soils have been addressed using the mixture-theory within a context of continuum formulations (e.g., Li & Zienkiewicz, 1992; Schrefler & Zhan, 1993). Constitutive models based on a critical state framework that involve two independent stress state variables (e.g., Alonso et al., 1990; Wheeler & Sivakumar, 1995), as well as on the fundamental principles of thermodynamics (e.g., Hutter et al., 1999; Borja, 2004) were used to describe the response of these soils. However, there is still a current need for a better understanding of the response of unsaturated soils, especially from a micro-scale perspective. In this regard, the discrete element method has recently been used to investigate the micromechanical response of these soils (e.g., Gili & Alonso 2002; Liu & Sun 2002).

A realistic modeling of pendular state unsaturated granular soils was achieved in this study by using a discrete formulation. The discrete element method (DEM) was used to idealize soil particles and interparticle suction and viscous forces were employed to model the effect of pendular water bridges. Numerical simulations were conducted to asses the impact of moisture content on the dynamic response and settlement of level-sites of non-collapsible and collapsible unsaturated soil deposits when subjected to a dynamic excitation.

DISCRETE MODEL FOR UNSATURATED PENDULAR GRANULAR SOILS

A discrete idealization is used to study the dynamic response of unsaturated granular soils in a pendular state (Medina, 2007). As mentioned above, the discrete element method (Cundall & Strack, 1979) is used to simulate these soils as an assemblage of interacting spherical particles. For unsaturated soils in a pendular state, the particles are subjected to gravity forces and interparticle (repulsion) contact forces, along with (attraction) forces exerted by pendular water bridges. A complete description of the motion of the soil is provided by solving the equations of linear and angular momentum for each particle (i.e., Newton's second law). For a particle p these equations are given by:

$$m_p \dot{\mathbf{v}}_p = m_p \mathbf{g} + \sum_c \mathbf{f}_c + \sum_b \mathbf{f}_b \tag{1}$$

$$I_p \dot{\boldsymbol{\omega}}_p = \sum_c \mathbf{r}_c \times \mathbf{f}_c \tag{2}$$

where $\mathbf{v}_p$ and $\boldsymbol{\omega}_p$ are translational and rotational velocity vectors (a superposed dot indicates a time derivative), m_p and I_p are particle mass and moment of inertia, $\mathbf{g}$ is gravity vector, $\mathbf{f}_c$ refers to the interparticle contact force at contact c (c = 1, 2,...), $\mathbf{r}_c$ is vector connecting the center of particle p to the location of contact c, and $\mathbf{f}_b$ is force exerted by the pendular water bridge b (b = 1, 2,...). The bridge force includes suction and viscous components $\mathbf{f}_s$ and $\mathbf{f}_v$ (i.e., $\mathbf{f}_b = \mathbf{f}_s + \mathbf{f}_v$). The suction component corresponds to an attractive force that arises from the water surface tension and the reduced hydrostatic pressure (difference between the pore-water and pore-air hydrostatic pressure). The viscous component arises from the flow of water within the bridge. The bridge force is assumed to be radial and does not generate a moment. When two particles become in contact, the interparticle contact force $\mathbf{f}_c$ and the bridge force $\mathbf{f}_b$ (due to the generation of a water bridge) are taken into account. Only the bridge force, $\mathbf{f}_b$ intervenes when two particles, formerly in contact, are moving away from each other, until the critical rupture distance of the pendular water bridge is reached (Lian et al., 1993).

A contact law provided the interparticle forces as a function of the relative movement of the particles. The normal interparticle contact forces were modeled using a nonlinear Hertz spring (Mindlin & Deresiewicz, 1953) in parallel with a dashpot. The shear interparticle contact forces were idealized using a Kelvin model (elastic spring in parallel with a dashpot) in series with a frictional slider. The shear and normal interparticle contact forces are related by a slip Coulomb relationship (Itasca, 2003).

The suction component $\mathbf{f}_s$ develops when a pendular water bridge forms between two particles. For a pendular state and small particles (diameters less than about 1mm), the effects of gravity are negligible and this component accounts for the reduced hydrostatic pressure, ΔP within the water bridge and the force caused by the water surface tension, T_s at the water-air-particle interface. The suction component is then given by (Hotta et al., 1974):

$$\mathbf{f}_s = \left(\pi R_2^2 \Delta P + 2\pi T_s R_2\right)\mathbf{n} \tag{3}$$

where $\mathbf{n}$ is the outward unit vector at the location of the water bridge b, and ΔP is the reduced hydrostatic pressure given by the Laplace-Young equation (Fisher, 1926):

$$\Delta P = T_s\left(\frac{1}{R_1} - \frac{1}{R_2}\right) \tag{4}$$

in which R_1 and R_2 are radii of the principal curvature of the pendular bridge. Assuming a toroidal approximation of the liquid bridge (Fisher, 1926), R_1 and R_2 may be related geometrically to the volume of the bridge (Figure 1). This procedure gives an implicit relationship between the suction force and the water bridge geometrical parameters. An alternative explicit relationship (somewhat similar to those published by others, e.g., Weigert & Ripperger, 1999; Soulié, et al., 2006) was developed (Medina, 2007) using regression and optimization techniques. This explicit relationship is appropriate for discrete element implementations. Figure 1 shows the

suction force obtained using the developed explicit relationship along with that provided by the implicit equations described above. This force is presented in a normalized form $\mathbf{f}_s^* = \mathbf{f}_s/(2\pi T_s R_{p1})$ as a function of normalized interparticle separation distance $\delta = d/R_{p1}$ (Fig. 1) for monosize particles, different size particles and a particle and a wall. Details of the computation of $\mathbf{f}_s$ as a function of water content and particle separation distance are given by Medina (2007).

In a dynamic problem, the bridge force includes a viscous component that arises when the involved two particles move with respect to each other leading to a water flow in the bridge. This component is significant when the pore liquid viscosity is high or particles are approaching each other at high relative velocities (Adams & Perchard, 1985). The viscous force also results from the dynamic formation and breakage of liquid bridges. Based on the lubrication theory, the normal component of this force may be expressed by the following equation (Adams & Perchard, 1985) for the case of significantly stiff particles:

$$\mathbf{f}_v^{\,n} = 6\pi\,\mu\,R^*\,\mathrm{v}_n\,\frac{R^*}{d} \tag{5}$$

where μ is viscosity of the bridge fluid, v_n is relative normal velocity between the two involved particles, d is interparticle separation distance and R^* is reduced particle radius expressed in terms of the radii of the two spherical particles, $1/R^*=1/R_{p1}+1/R_{p2}$, where R_{p1} and R_{p2} are radii of particles 1 and 2. There is no rigorous analytical solution for the component of the viscous force in the tangential direction (Goldman et al., 1967). Nevertheless, published computational research (e.g., Lian & Thornton, 1993; Lian et al., 1998) strongly suggests that the effect of this component is negligible for granular materials.

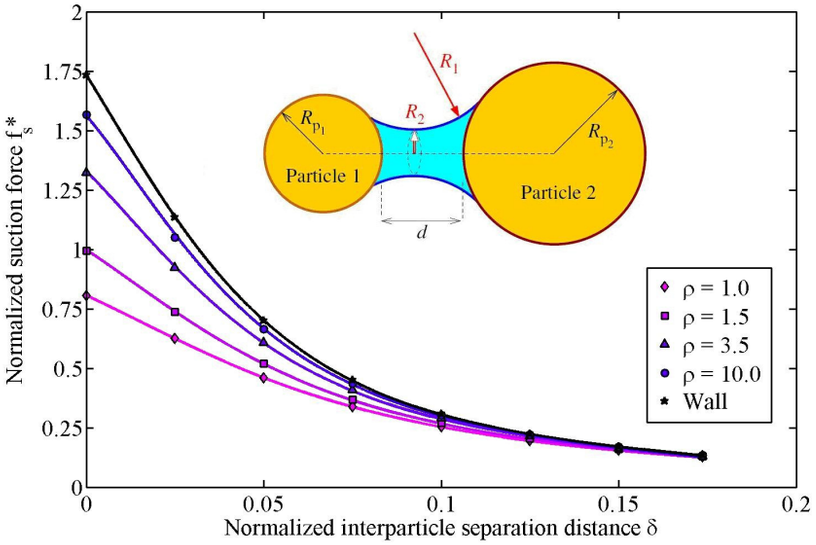


FIG. 1. Explicit (solid lines) and implicit (discrete points) functions of the variation of the normalized suction force component $\mathbf{f}_s^* = \mathbf{f}_s/(2\pi T_s R_{p1})$ as function of the normalized interparticle separation distance $\delta = d/R_{p1}$ (for equal size particle, $\rho = R_{p2}/R_{p1} = 1$, different size particle, $\rho > 1$, and the limiting case of a particle and a wall, $\rho \sim \infty$).

NUMERICAL SIMULATIONS

Numerical simulations were conducted to analyze the effect of moisture content on the dynamic response and settlement of level-sites of non-collapsible and collapsible unsaturated soil deposits when subjected to a dynamic excitation (Fig. 2). These simulations employed the PFC3D software (Itasca 2003) along with the water bridge model described above. The developed explicit model for the bridge suction and viscous forces was coded and linked to PFC3D computing environment (Medina 2007). Soil particles where pluviated within a parallelepiped domain having periodic boundaries in the lateral directions to simulate a semi-infinite deposit (Figure 2a). The periodic deposit was subjected to a high gravity (g) field in order to achieve a realistic deposit height. Specifically, the employed model consisted of a 614 mm high deposit that was subjected to a 50 g gravitational field (Fig. 2a). The employed high g-level mimics the conditions of centrifuge testing of small-scale geotechnical models. Thus, the employed model represented a 3.05 m high prototype deposit (Taylor, 1995). In this regard, the surface tension of the pore water was scaled up to account for the employed high gravitational field (Table 1). The deposit grains were idealized using spherical particles with a uniform size distribution (with diameters ranging from 0.55 mm to 0.85 mm, Table 1). Three level-site deposits were generated by sedimenting particles in: (1) dry condition, (2) dry condition and then wetting them, and (3) wet condition. The employed moisture content was about 2%. From a macro-scale point of view, the water was distributed uniformly among all locations. At the microlevel, water was spread among the pendular water bridges proportionally to the average number of water bridges per particle and the volume of involved particles, as suggested by the experimental investigations conducted by Kohonen et al. (2004).

The two deposits sedimented in dry conditions (one dry and the other dry and then wetted) were marked by a significantly dense configuration and stable condition (hereafter referred to as non-collapsible deposits), as expected (Figure 2b, this figure exhibits only the particles that intersect the central vertical plane of the deposit). The associated dry-unit-weight (average value of about 15 kN/m^3) was basically uniform with depth. The associated relative density was about 50%. Adding water (in the form of pendular bridges at particle contacts) had only negligible impact on the deposit configuration. In contrast, sedimentation of moist particles led to a deposit that exhibited a significantly loose and collapsible configuration (referred to as collapsible deposit), as shown in Figure 2b. The collapsible deposit was associated with large pore volumes and a negative relative density enabled by the suction forces provided by the pendular water bridges. This was especially the case near the free surface where the deposit had a noticeable bulking effect (Fig. 2b).

Average values of the deposit parameters and variables were monitored during the course of the simulation using spherical control volumes along the vertical central axis of the deposit. These parameters and variables are presented in this paper in prototype units (Taylor, 1995) exclusively. The deposits were subjected to a dynamic base excitation consisting mostly of a sinusoidal acceleration of 2 Hz with maximum amplitude of 0.4 g.

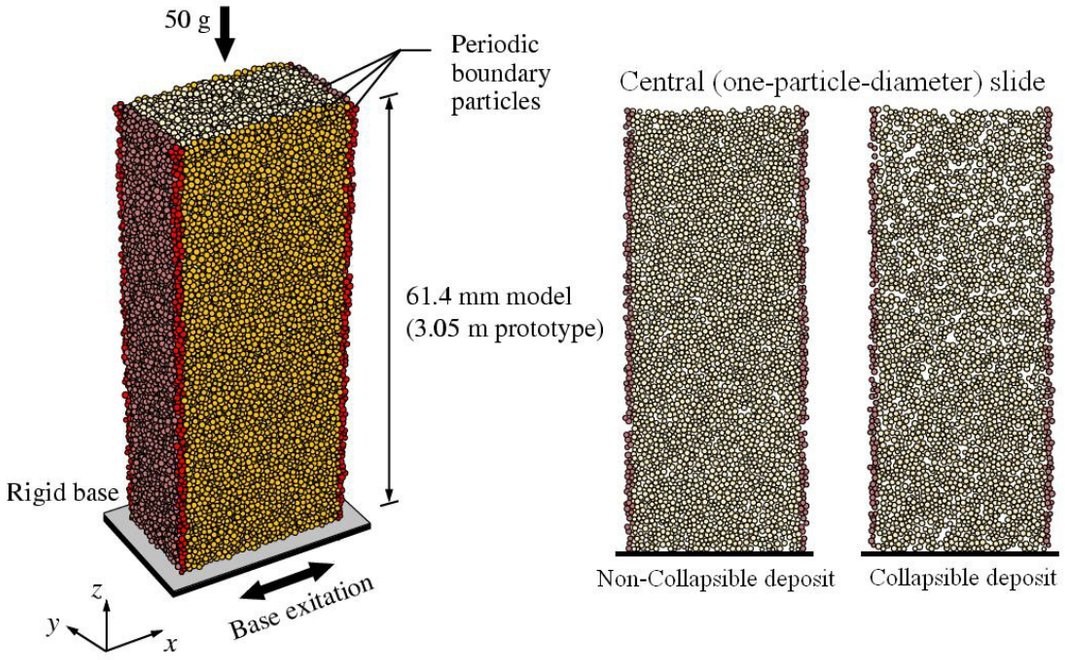


FIG. 2. Analyzed non-collapsible and collapsible soil deposit. (a) Three-dimensional view of the periodic granular deposit, and (b) Particle configuration along the non-collapsible and collapsible unsaturated deposits central vertical plane before dynamic excitation.

Table 1. Granular deposit simulation data (model unit).

Particles	
Diameter	0.55 mm to 0.85 mm
Shear modulus	3.0×10^{8} N/m^2
Poisson's ratio	0.22
Friction coefficient	0.5
Mass density	2,500 kg/m^3
Initial height of deposit	61 mm
Fluid	
Water content	0 % and 2 %
Surface tension	50 × 0.072 N/m
Computation parameters	
g-level	50
Input acceleration	0.4 g
Time step for DEM	1.0×10^{-7} s
Approx. number of particles	70,000

The analyzed three level-site unsaturated deposits (non-collapsible-dry, non-collapsible-with moisture content of 2%, and collapsible-with moisture content of 2%) exhibited accelerations that were remarkably similar at all levels, in spite of the

difference in porosity, particle arrangement and moist content between the deposits (Figure 3). The associated velocities of shear wave propagation were slightly higher for the non-collapsible deposit with a water content of 2%, due to a higher shear stiffness provided by the suction forces developed at the pendular water bridges. A minor deamplification in the last 3 cycles may be appreciated for the case the collapsible deposit with water content of 2%.

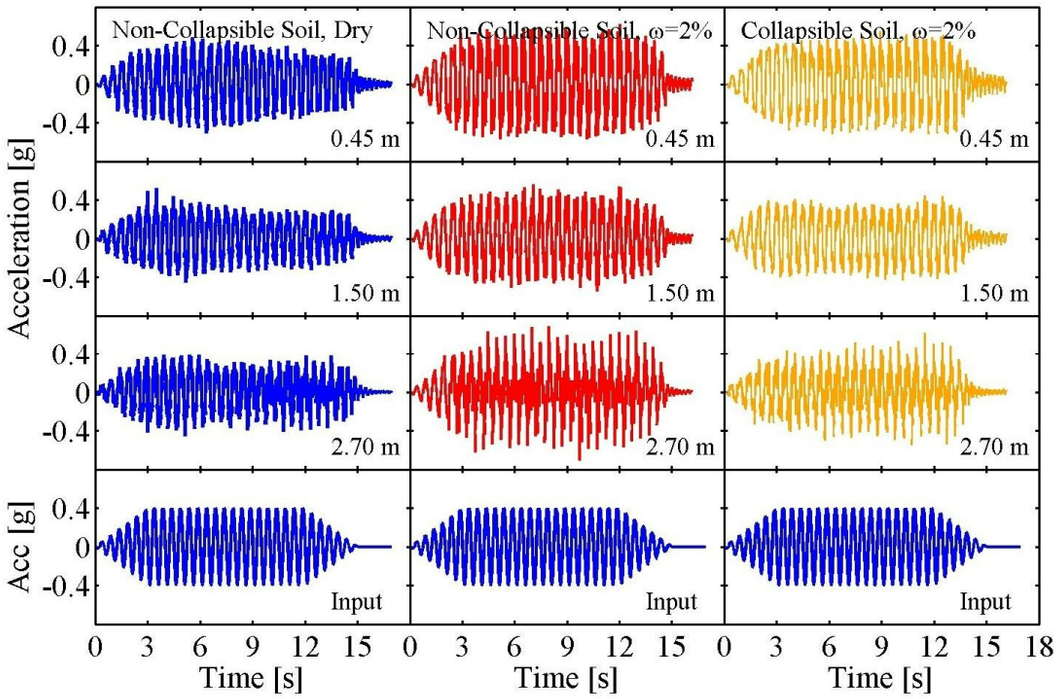


FIG. 3. Acceleration time histories of analyzed non-collapsible and collapsible unsaturated deposits at selected depth locations.

The shear stress-strain histories of the analyzed non-collapsible and collapsible unsaturated deposits are shown in Fig. 4. The response of the non-collapsible dry deposit was characterized by large shear strains, especially near the free surface (as large as 4.0% at 0.5 m depth and 1% at 2.7 m depth). These large strains were associated with significant hysteretic energy dissipation as indicated by the large areas of the stress strain cycles. As the shaking progressed, the non-collapsible dry deposit densified and experienced a decrease in shear strain amplitudes as well as level of hysteretic energy dissipation. In contrast, the stress-strain history of the non-collapsible deposit with a water content of 2% was characterized by significantly smaller shear strains than the dry one (Fig. 4). These small strains were associated with considerably low hysteretic energy dissipation reflecting a more elastic and stable deposit enabled by the suction forces developed at the pendular water bridges. Alternatively, the collapsible deposit with a water content of 2% showed larger shear strain than the non-collapsible deposit with 2% of water content and comparable to the dry non-collapsible deposit at medium and deep locations. At shallow depth, shear strain amplitudes were considerably smaller, in spite of the high porosity and loose particle arrangement.

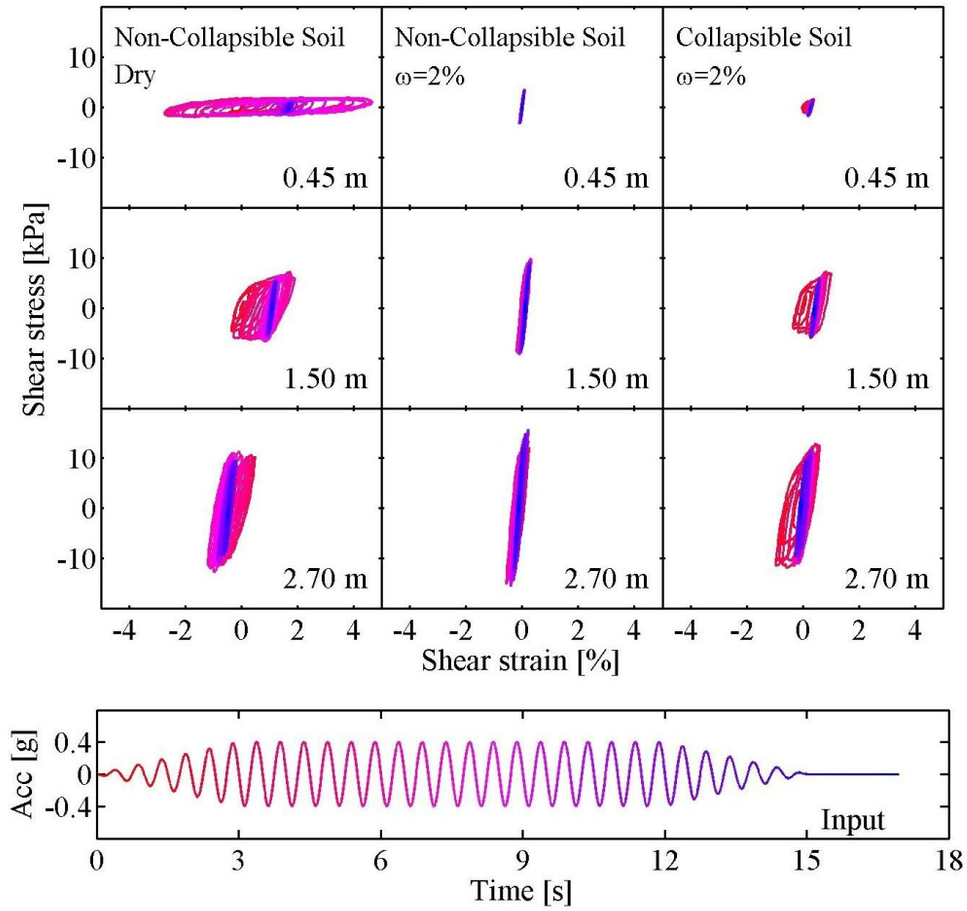


FIG. 4. Shear stress-strain time histories of analyzed non-collapsible and collapsible unsaturated deposits at selected locations.

The densification processes induced by the dynamic excitation led to a surface settlement of the dry non-collapsible deposit of about 20 cm, which is comparable to the collapsible deposit, settlement of about 17 cm (Fig. 5). On the contrary, the non-collapsible deposit with 2% of water content had a surface settlement of about 2 cm. Figure 5 shows that the densification of the studied deposits decreased somewhat exponentially with the number of shaking cycles. The first few cycles were associated with the largest densification rate in the three cases.

CONCLUSIONS

A discrete element model was used to study the dynamic response of unsaturated non-collapsible and collapsible soil deposits. The effects associated with pendular water bridges were considered using suction forces. The dynamic response of level-sites of unsaturated soils was found to be strongly affected by the solid-particle and pore-water interaction. Suction forces of the water bridges increased shear strength and stiffened soil response. The employed model provided a tool to shed light on the dynamic response mechanisms of unsaturated soils in a pendular state.

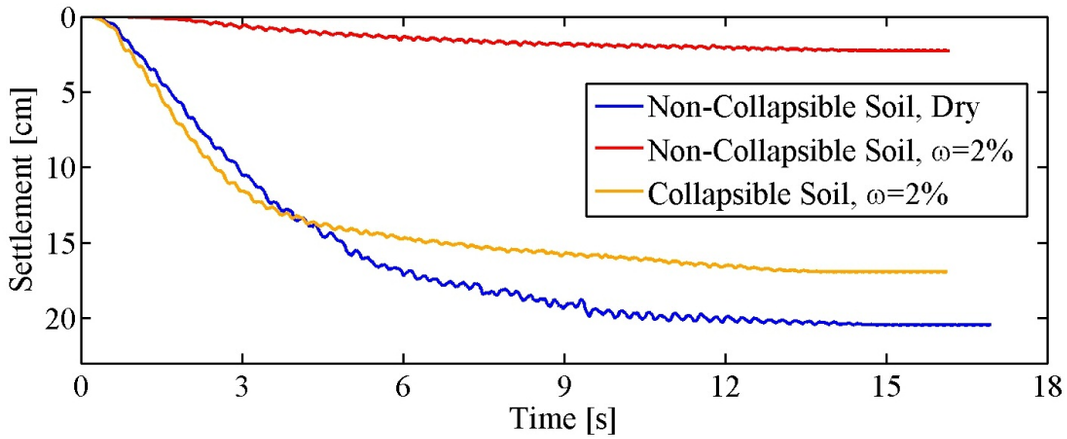


FIG. 5. Surface settlement time histories of analyzed non-collapsible and collapsible unsaturated deposits (prototype units).

ACKNOWLEDGEMENTS

The code for periodic boundaries of the DEM analyses was the outcome of a collaboration of Dr. U. El Shamy of Southern Methodist University and Dr. M. Zeghal.

REFERENCES

Adams, M.J., and Perchard, A. (1985) "The cohesive forces between particles with interstitial liquid," In Proc. *IChemE Symposium Series*, No. 91, 147–160.

Alonso, E.E., Josa, A. and Gens, A. (1990) "A constitutive model for partially saturated soils," *Géotechnique*, 40(3), 405–430.

Borja, R.I. (2004) "Cam-Clay plasticity. Part V: A mathematical framework for three phase deformation and strain localization analyses of partially saturated porous media," *Computer Methods in Applied Mechanics and Engineering*, 193, 5301–5338.

Cundall, P.A. and Strack, O.D.L. (1979) "A discrete numerical model for granular assemblies," *Géotechnique*, 29(1), 47–65.

El Shamy, U. (2004) "A coupled continuum-discrete fluid–particle hydromechanical model for granular soil liquefaction," Ph.D. Thesis, Rensselaer Polytechnic Institute, Troy, NY.

Fisher, R.A. (1926) "On the capillary forces in an ideal soil; corrections of formulae given by W. B. Haines," *Journal of Agricultural Science*, 16, 492–505.

Gili, J.A. and Alonso, E.E. (2002) "Microstructural deformation mechanisms of unsaturated granular soils," *International Journal for Numerical and Analytical Methods in Geomechanics*, 26, 433–468.

Goldman, A.J., Cox, R.G. and Brenner, H. (1967) “Slow viscous motion of a sphere parallel to a plane wall - i. Motion through a quiescent fluid.” *Chemical Engineering Science*, 22, 637–651.

Hotta, K., Takeda, K. and Iinoya, K. (1974) "The capillary binding force of a liquid bridge," *Powder Technology*, 10, 231–242.

Hutter, K., Laloui, L. and Vulliet, L. (1999) "Thermodynamically based mixture models of saturated and unsaturated soils," *Mechanics of Cohesive-frictional Materials*, 4(4), 295–338.

Itasca (2003) Particle Flow Code, PFC3D, release 3.0. Itasca Consulting Group, Inc., Minneapolis, Minnesota.

Li, X and Zienkiewicz, O.C. (1992) "Multiphase flow in deforming porous media and finite element solutions," *Computer and Structures*, 45(2), 211–227.

Lian, G., Adams, M.J. and Thornton, C. (1998) "Discrete particle simulation of agglomerate impact coalescence." *Chemical Engineering Science*, 53, 3381–3391.

Lian, G. and Thornton, C. (1993) "Effect of liquid bridge forces on agglomerate collisions." In *Powders and Grains* 93. Rotterdam, Netherlands. Balkema Publishers. Pages 59–64.

Lian, G., Thornton, C. and Adams, M.J. (1993) "A theoretical study of the liquid bridge force between two rigid spherical bodies," *Journal of Colloid and Interface Science*, 161, 138–147.

Liu, S.H. and Sun, D.A. (2002) "Simulating the collapse of unsaturated soil by DEM," *International Journal for Numerical and Analytical Methods in Geomechanics*, 26, 633–646.

Medina, C. (2007) "A micro-mechanical study of the response of unsaturated pendular state granular soils," Ph.D. Thesis, Rensselaer Polytechnic Institute, Troy, NY.

Mindlin, R. and Deresiewicz, H. (1953) "Elastic spheres in contact under varying oblique forces," *Journal of Applied Mechanics*, ASME, 20, 327–344.

Newitt, D.M. and Conway-Jones, J.M. (1958) "A contribution to the theory and practice of granulation," *Transactions of the Institution of Chemical Engineers*, 36, 422–442.

Schrefler, B.A. and Zhan, X. (1993) "A fully coupled model for water flow and airflow in deformable porous media," *Water Resources Research*, 29, 155–167.

Soulie, F., Cherblanc, F., El Youssoufi, M.S. and Saix C. (2006) "Influence of liquid bridges on the mechanical behaviour of polydisperse granular materials," *International Journal for Numerical and Analytical Methods in Geomechanics*, 30, 213–228.

Stewart, J.P., Smith, P.M., Whang, D.H. and Bray, J.D. (2004) "Seismic compression of two compacted earth fills shaken by the 1994 Northridge earthquake," *Journal of Geotechnical and Geoenvironmental Engineering*, 130(5), 461–476.

Slosson, J.E. (1975) "Effects of the earthquake on residential areas. San Fernando, California, earthquake of 9 february, 1971," Technical Report Bulletin No. 196, Chapter 19, California Division of Mines and Geology, Sacramento, California.

Taylor, R.N. (ed.) (1995). Geotechnical Centrifuge Technology. Chapman and Hall, London, UK.

Weigert ,T. and Ripperge,r S. (1999) "Calculation of the liquid bridge volume and bulk saturation from the half-filling angle," *Particle and Particle Systems Characterization*, 16, 238–242.

Wheeler, S.J. and Sivakumar, V. (1995) "An elasto-plastic critical state framework for unsaturated soils," *Géotechnique*, 45(1), 35–53.

Evaluation of Site Response For Deepwater Field

Fabrizio Ardoino[1], Chiara M. Traverso[2] and Eric J. Parker[3], M. ASCE, P.E.

[1]Geotechnical Engineer, D'Appolonia S.p.A., Via San Nazaro 19, 16145 Genoa, Italy; fabrizio.ardoino@dappolonia.it
[2]Geohazard Unit Manager, D'Appolonia S.p.A., Via San Nazaro 19, 16145 Genoa, Italy; chiara.traverso@dappolonia.it
[3]Offshore Division Manager, D'Appolonia S.p.A., Via San Nazaro 19, 16145 Genoa, Italy; eric.parker@dappolonia.it

ABSTRACT: The move of the offshore industry into ever greater water depths presents significant challenges for geotechnical and seismic engineering. Soil conditions at deepwater sites are well outside the range of typical onshore experience. Given the very low strength soils, earthquake loads often control foundation design. In these conditions the evaluation of seismic design criteria is critical to project success. This paper discusses the site response analysis for a field in 650 m water depth offshore the Nile Delta. Soil amplification predicted using the SHAKE type equivalent linear analyses is compared to a non-linear approach. The equivalent linear approach is seen to predict significantly larger spectral acceleration than the non-linear analysis for these soil conditions. Implications for seismic design criteria are discussed.

INTRODUCTION

Deepwater sites present a number of challenges for the geotechnical earthquake engineer. The seabed soils are typically very soft, normally consolidated clays, with shear strengths much lower than those encountered onshore. In these low strength soils earthquake conditions can control foundation design. For many large projects the design earthquake ground motion is based on a site specific probabilistic seismic hazard assessment (PSHA). As attenuation laws are not available for very soft soil conditions, the ground motion is computed for "stiff soil" or "rock" site conditions. A site response analysis is then used to transfer the PSHA results to the mudline. This paper presents an example amplification analysis for a deepwater site, and discusses some of the pitfalls of

conventional site response analysis in deepwater soil conditions.

SITE CONDITIONS

The site in question is located in 650 m water depth offshore the North African coast. Soil conditions are representative of many deepwater sites both in the Mediterranean and other areas. The soils comprise a thick sequence of high plasticity normally consolidated clays. Figure 1 summarizes the Atterberg limits, water contents and total unit weight of soil samples collected in the offshore block. The soils are high plasticity clays generally classified as CH in the USCS system. The horizontal lines on the left graph show the plastic and liquid limit measured on samples from piston cores and deep boreholes at the site. The PI is variable and scattered in the upper 10 m of the profile, ranging from about 55 to 100. Below this depth, the PI is of the order of 40 or 50. For design, a constant PI of 50 was considered.

The total unit weight also increases with depth, and the design profile was taken as 13.1 kN/m^3 at the mudline increasing to 16.9 kN/m^3 at 100 m penetration. The liquidity index and measured shear strength of the soils suggests light overconsolidation in the first few meters, followed by an essentially normally consolidated profile.

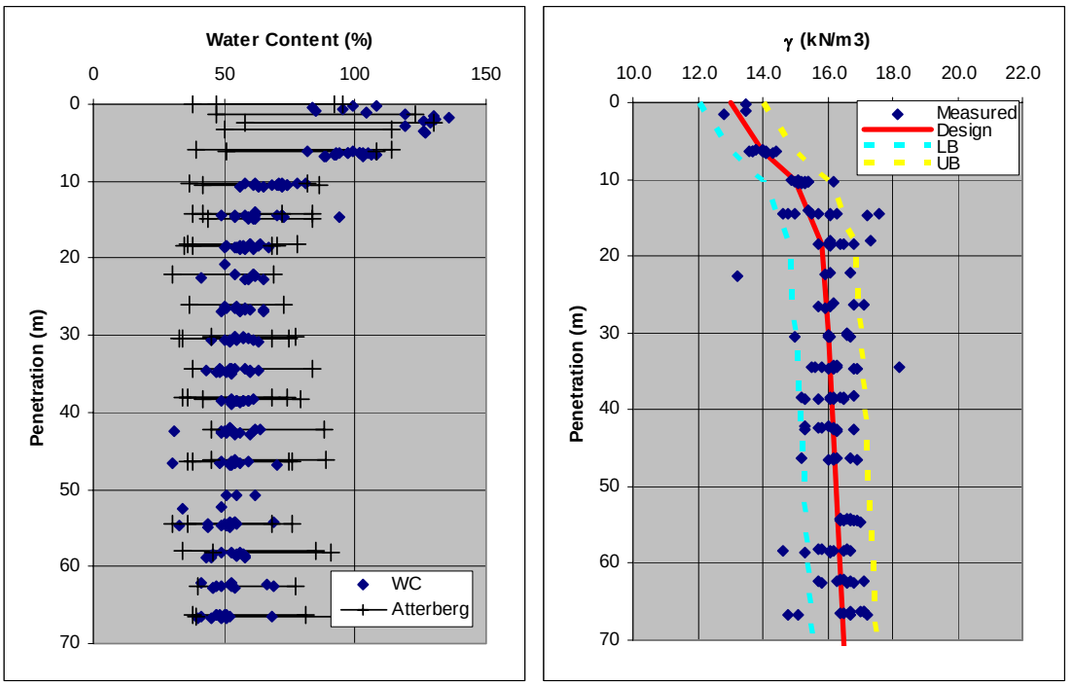


FIG. 1. Index Soil Properties.

The geophysical surveys indicated a significant unconformity in the offshore block at depth between 80 and 120 m. While the nature of the unconformity was not confirmed by boreholes, this horizon represents a change in soil density and/or stiffness. For the amplification study this contact was taken as stiff soil level, using a design value of 100 m. This choice is supported by the numerical work of Ni et al. (1997) who found that amplification response of soil deposits deeper than about 100 m are very similar.

The shear wave velocity (Vs) was measured in-situ using the seismic CPT. The Vs measurements were performed down to 70 m penetration. Figure 2 shows the measured values of shear wave velocity from the geotechnical investigation. The measured data are compared to predictions using the Hardin (1978) correlation. A design profile for this analysis was chosen to give a best match to the field data and theoretical predictions.

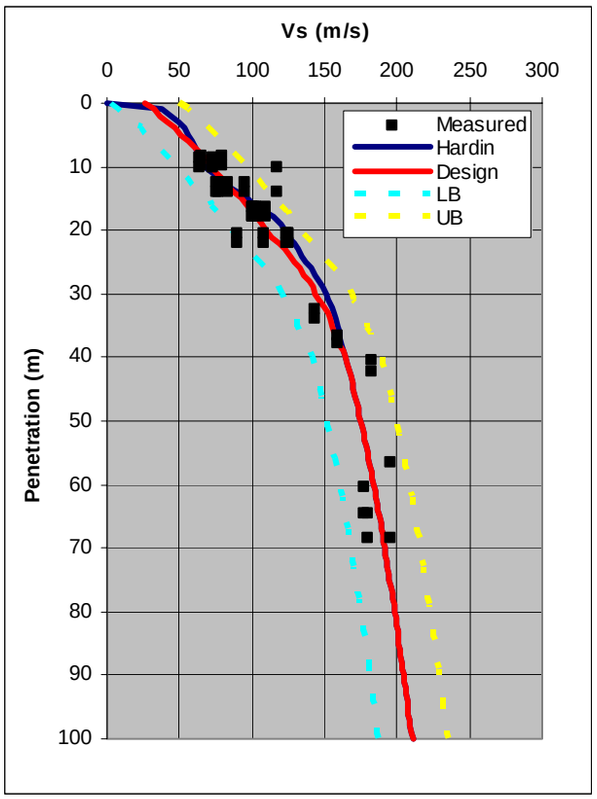


FIG. 2. Shear Wave Velocity Profile.

Non-linear soil behavior under cyclic loading is simulated considering the reduction of shear modulus with increasing strain level. As no site specific test data were available, the degradation curves were based on the Vucetic and Dobry (1991) correlations with

soil plasticity index. Figure 3 shows the assumed curves of shear modulus reduction and increase of damping ratio with shear strain for the soils at the site. The calculated damping ratio shown in the figure refers to hysteretic damping evaluated with the Iwan and Mróz non-linear soil model discussed later.

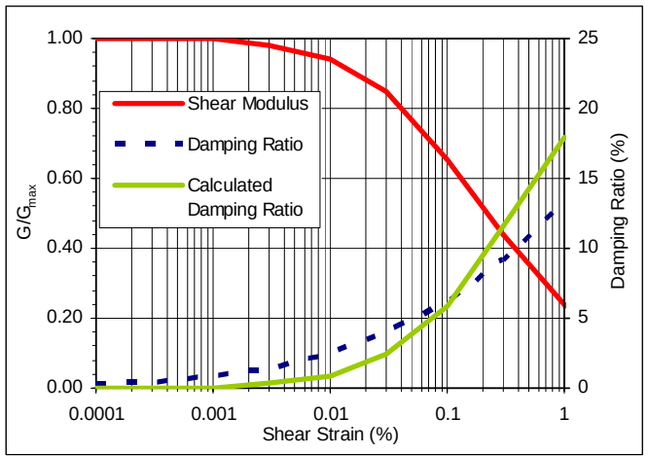


FIG. 3. G/Gmax and Soil Damping.

TIME HISTORIES

The seismic input for considered are the stiff soil hazard curves and a set of 18 selected earthquake time histories considered representative of the seismic ground motion expected at the site. Competent stiff soil was defined as having shear wave velocity of 360 to 750 m/s.

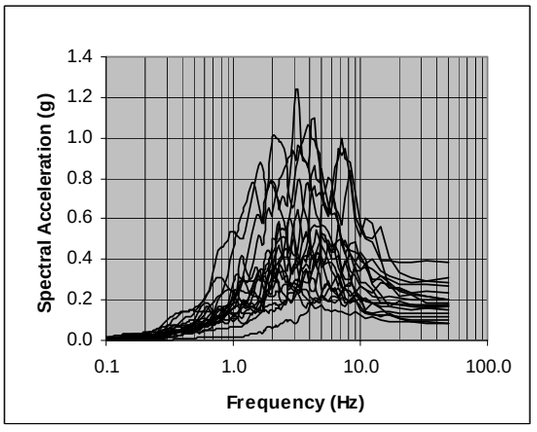


FIG. 4. Recorded Stiff Soil Earthquake Time Histories.

A suite of 18 earthquake strong motion time histories was selected for the site response analysis. The earthquake records were chosen to match the dominant magnitude and distance from the PSHA hazard deaggregation. In general in this area hazard is controlled by a small frequent earthquake occurring near the location. For PGA the bivariate mode was an earthquake with magnitude 5.1 and distance 13 km. To capture the majority of the hazard contribution, and to provide a better record set, the range of M, R considered was magnitude 5.1 to 7.4, distance 2 to 46 km. All of the time histories were recorded on stiff soil sites. One horizontal component was randomly chosen from each earthquake of the selected set for the response analysis. Figure 4 shows the 5% damped response spectra for the selected time histories.

METHODOLOGY FOR SITE RESPONSE ANALYSIS

Two approaches were considered to evaluate site response, an equivalent linear analysis and a non-linear model. The equivalent linear analysis was performed using the EERA software (Bardet et al., 2000). The program utilizes the same algorithm as the well-known SHAKE software (Schnabel et al., 1972; Idriss and Sun, 1991). The ground response analysis is performed in the frequency domain. The soil profile is represented as a series of infinite horizontal layers overlying elastic bedrock. Standard wave mechanics is applied to develop transfer functions relating displacement, velocity and acceleration of the individual layers. The input ground motion is assumed to be composed entirely of vertically propagating horizontal shear waves. An iterative technique is used to select Gs and γ as a function of computed ground strain.

The non-linear analysis used the NERA software (Bardet and Tobita, 2001). This approach considers the site response in the time domain, and allows for soil yielding under high strain levels. The soil model is based on Iwan (1967) and Mróz (1967). The model generates piecewise a stress strain relationship to match the G/Gmax backbone curve. Damping is considered as the work performed during a single loop of the load-unload cycle. NERA performs the site response analysis in the time domain. The soil profile is represented by a series of uniform, infinite horizontal layers overlying elastic bedrock. Propagation of bedrock motion through the soil profile is computed using a finite difference scheme based on the Newmark central difference algorithm.

COMPARISION OF EQUIVALENT LINEAR AND NON-LINEAR RESULTS

The scope of this paper is to compare the linear equivalent model to results of a non-linear analysis. The analysis consisted in propagating the 18 earthquake time histories shown in Figure 4 through a 100 m soil column and computing the resulting Spectral Amplification Ratio (SAR). SAR is defined as the frequency dependent ratio of computed spectral acceleration at the mudline to stiff soil outcrop spectral acceleration. The earthquake records were scaled to PGA of 0.05 g, 0.10 g, 0.15 g, 0.20 g and 0.25 g

to evaluate the effects of different levels of ground shaking. This range was intended to be representative of the expected ground motion at the site. The main findings of the comparison between equivalent linear and non-linear analysis are discussed in the following.

Comparison of Computed Strain Profiles

Figure 5 shows profiles of effective shear strain in the soil profile for input PGA of 0.001 and 0.20 g. The lower value of input motion is intended to capture the elastic soil response, while the higher level is typical of a design earthquake. For low seismic input the equivalent linear and non-linear analyses give similar results. For the 0.20 g PGA the equivalent linear model predicts a strong strain discontinuity at about 8 m. This is seen as nearly a soil failure in the model. The non-linear analysis gives a gradually increasing strain from about 25 m depth, which is considered a more reasonable response for a uniform soft clay profile.

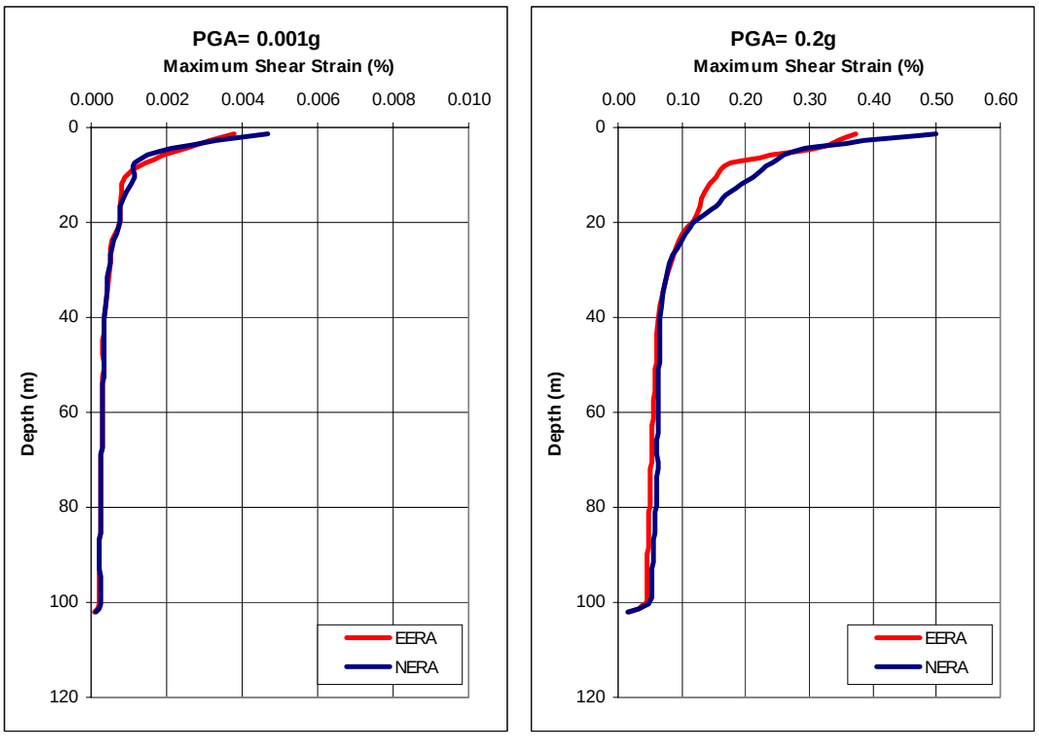


FIG. 5. Effective Shear Strain Profiles.

Effects of Input PGA on Amplification

Figure 6 shows SAR as a function of peak ground acceleration on stiff soil for frequencies of 33 Hz (PGA) and 2 Hz. The figures show SAR computed using the equivalent linear EERA and non-linear NERA analyses. The points on the graph represent the computed spectral amplification for specific earthquake time histories. The following general observations may be made regarding the results:

- The mean SAR computed from both EERA and NERA analyses show a monotonic decreasing trend. For increasing input PGA there is comparatively less amplification. The decrease in amplification is stronger for the non-linear analysis;
- The EERA analysis predicts amplification of PGA for all levels of input motion. The non-linear analysis suggests that there is deamplification of PGA above about 0.1g;
- Both EERA and NERA predict amplification at 2 Hz over the full range of input motion. The equivalent linear analysis, however, predicts greater amplification at high input acceleration;
- The SAR calculated by NERA are lower than the corresponding values from EERA for each individual case study. For stiff soil PGA greater than 0.10 g the non-linear analysis shows deamplification of PGA at mudline. There is no deamplification for 2 Hz.

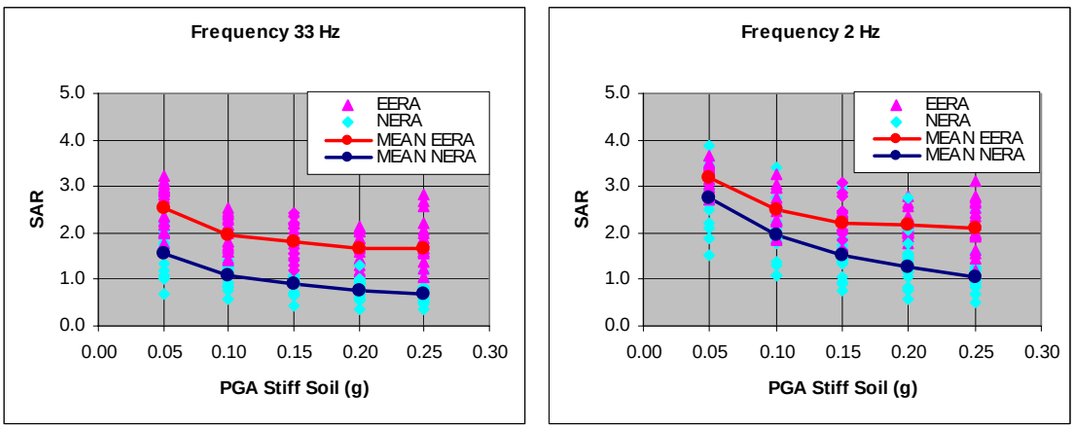


FIG. 6. Spectral Amplification Ratio as function of PGA.

Effects of Frequency on Amplification

Figure 7 shows spectral amplification as a function of frequency. The time histories were scaled to a specified PGA and SAR was computed as a function of frequency. The

figure shows the mean and mean ± one standard deviation (σ) SAR considering input of PGA 0.001 g and 0.2 g. The overall shapes of the SAR curves are reasonable. For the elastic response (0.001 g) the amplification factor is between 2 and 4. For the 0.20 g input PGA the amplification is less than 3 for low frequencies, and reduces or deamplifies above 1 Hz. For the elastic response the ± σ bands for the two approaches overlap, subjecting that the results are not statistically significant at 68% level. For the stronger ground motion input, however, the confidence bands do not overlap above 1 Hz.

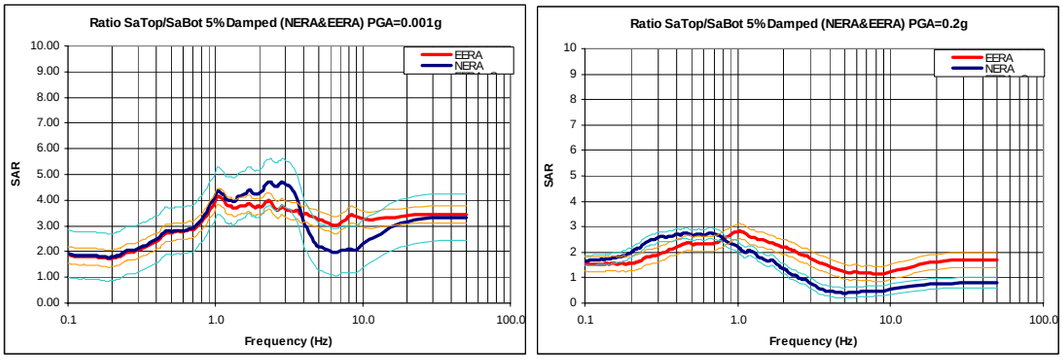


FIG. 7. Spectral Amplification Ratio as function of frequency.

As expected, there are differences in the predictions of the equivalent linear and non-linear analyses for the strong input. At high frequencies the amplification predicted by NERA is about 50 to 60% of that computed using the equivalent linear model. Note that this is consistent with similar analyses presented by Biscontin and Pestana (2006) for submarine slopes in soft clay. For frequencies below about 1 Hz the results of the two analyses are similar. NERA shows a tendency for the amplification peak to shift to lower frequencies for stronger ground shaking, and in fact for some frequencies predicts higher amplification than NERA. The peak shift reflects the softening of the soil column and lowering of the fundamental frequency.

Saturation of PGA

A critical issue for design is the amplification or deamplification of PGA for long return period events. Specifically, the question is if there is a tendency for PGA to reach a limiting "saturated" value for high levels of input shaking. To investigate the saturation issue a series of additional analysis of PGA at grade were performed using the NERA software. The input records were scaled to PGA values from 0.05 to 0.35 g. Figure 8 shows the results of the analysis. Each point on the graph represents the computed PGA for a single time history, while the line represents the average surface PGA.

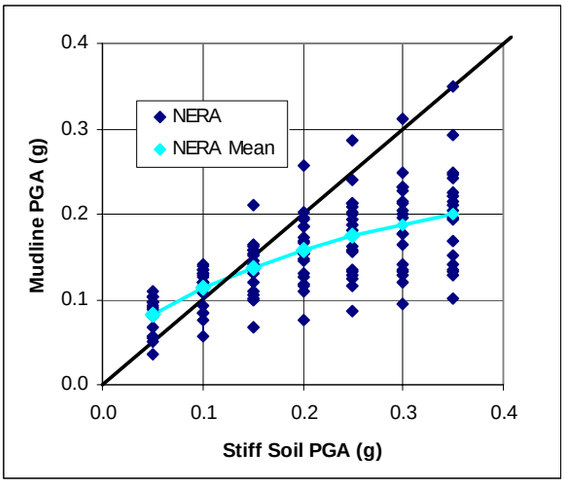


FIG. 8. Saturation of PGA in Non-linear analysis.

The site behavior is clearly non-linear, with slight amplification of surface PGA for input of less than about 0.1 g, and deamplification above about 0.12 g. The mean response does show saturation, although the PGA of the individual time histories shows more scatter. For input PGA of 0.20 g (not an unusual value for design in the area) the average NERA response is 0.14 g, and the surface PGA only exceeds 0.20 g for one time history.

CONCLUSIONS

The conclusions of the study are that special attention is needed for site response analysis for deepwater locations. The soil profiles at deepwater sites are usually very soft, normally consolidated clays. There is little direct engineering experience with the behavior of these materials under earthquake loading, and standard engineering practice may not be adequate. Several observations can be made from this study:

- Site response of deepwater sites is expected to be strongly non-linear. The equivalent linear approach in amplification studies may not reflect this behavior;
- While non-linear behavior can reduce amplification of PGA at the mudline, it may also lead to greater amplification at lower frequencies. This concept is important for long period structures;
- There is considerable variability in the amplification predicted between different earthquake time histories. The significance of this variability should be considered, particularly in terms of probabilistic design.

REFERENCES

Bardet, J.P. and Tobita, T. (2001). *NERA, A Computer Program for Nonlinear Earthquake Site Response Analyses of Layered Soil Deposits*, University of Southern California, Department of Civil Engineering, April.

Bardet, J.P., Ichii, K. and Lin, C.H. (2000). *EERA, A Computer Program for Equivalent-linear Earthquake Site Response Analyses of Layered Soil Deposits*, University of Southern California, Department of Civil Engineering, August.

Biscontin, G. and. Pestana, J.M. (2006). "Factors affecting seismic response of submarine slopes." *Natural Hazards and Earth System Sciences*, Vol. 6: 97-107.

Hardin, B.O. (1978). "The Nature of Stress-Strain Behavior of Soils," *Proceedings, Earthquake Engineering and Soil Dynamics*, ASCE, Pasadena, California, Vol. 1: 3-89.

Idriss, I.M. and Sun, J.I. (1992). *User's Manual for SHAKE91*, Center for Geotechnical Modeling, Department of Civil Engineering, University of California, Davis.

Iwan, W.D. (1967). "On a Class of Models for the Yielding Behavior of Continuous and Composite Systems," *Journal of Applied Mechanics*, ASME, Vol. 34: 612-617.

Mróz, Z. (1967). "On the Description of Anisotropic Work Hardening", *Journal of Mechanics and Physics of Solids*, Vol. 15: 163-175.

Ni, S-D, Siddharthan, R.V. and Anderson, J.G. (1997). "Characteristics of Nonlinear Response of Deep Saturated Soil Deposits", *Bulletin of the Seismological Society of America*, Vol. 87 (2): 342-355.

Schnabel, P.B., Lysmer, J. Seed, H.B.(1972). *SHAKE: A Computer Program for Earthquake Response Analysis of Horizontally Layered Sites*, Report No. UCB/EERC-72/12, Earthquake Engineering Research Center, University of California, Berkeley, December, 102p.

Vucetic, M. and Dobry, R. (1991). "Effect of Soil Plasticity on Cyclic Response", *Journal of Geotechnical Engineering*, ASCE, Vol. 117 (1): 89-107.

Hysteretic Damping Correction and its Effect on Non-linear Site Response Analyses

Zhi-Liang Wang[1], M. ASCE, C.Y. Chang[1], M. ASCE, and C.C. Chin[2], M. ASCE

[1]Geomatrix Consultants, Inc. 2101 Webster Street, 12 Floor, Oakland, CA 94612, USA; zlwang@geomatrix.com
[1]Geomatrix Consultants, Inc. 2101 Webster Street, 12 Floor, Oakland, CA 94612, USA; cychang@geomatrix.com
[2]Hatch Mott McDonald. Pleasanton, California, USA; chih-cheng.chin@hatchmott.com

ABSTRACT: Both of equivalent linear and non-linear site response analyses utilize soil dynamic properties expressed by strain amplitude dependent modulus reduction and damping ratio relations. Most of the non-linear site response methods use Masing rule to define the unloading and re-loading paths that results in overestimated hysteretic damping at large shear strain amplitude. In this paper, site response analyses of a soft clay site under very strong input motions at the rock base are performed using the equivalent linear approach (SHAKE analysis) and a non-linear approach (i.e. program FLAC with a user-defined soil model). A 'generalized Masing rule' was implemented in the user defined soil model to correct the hysteretic damping for the unloading and re-loading stress-strain loops to be consistent with the experimental damping. The non-linear site response analyses, we performed, indicate that, with the hysteretic damping correction, the computed surface acceleration and peak shear stress along the depth do not change significantly compared with those without hysteretic damping correction. But the induced peak shear strains in the soft layers are noticeably different between the case with hysteretic damping correction through the generalized Masing rule and that using the original Masing rule.

INTRODUCTION

Site response analyses are a significant component in the seismic safety design of critical structures. Equivalent linear approach is still the main analytical tool, while the non-linear analysis techniques are being rapidly developed. Both methods require soil dynamic properties, i.e. strain amplitude dependent modulus reduction and damping ratio curves, and both methods are facing the same challenge of modeling site responses of very strong input motions in very soft soil deposits. In a recent publication (Stewart et al, 2006), selected non-linear site response programs were reviewed. It is pointed out that non-linear models often use Masing (1926) rule as shown in Eq. (1)

$$\frac{\tau - \tau_r}{n} = f\left(\frac{\gamma - \gamma_r}{n}\right) \quad (1)$$

i.e., the Masing rule requires scaling the skeleton curve by a factor of n = 2 to define the unloading and reloading stress-strain loops. At large strain levels, the hysteretic damping resulted from the Masing rule is overestimated compared with laboratory test results. Although this problem was noticed decades ago, but the influence of the high hysteretic damping on the computed site response is still unclear to-date.

It has been realized that Masing rule should be revised in order to closely simulate soil behavior under cyclic and irregular loadings. There are a number of propositions to modify the Masing rule in the literature. Cundall-Pyke hypothesis (Pyke, 1979) assumes that the scale factor, n in Eq. (1), for the skeleton curve, varies with stress level and is less than 2. But, such modified Masing rule still generates high hysteretic damping at large strain levels (Stewart et al, 2006). A 'generalized' Masing curve (Wang et el., 1980) was proposed that adjusts the area of stress-strain loops, at different reversal stress levels, to fit a given soil damping curve. This approach does not need any analytical function form for the backbone (skeleton) curve, and the selected modulus reduction and damping ratio curves are directly input to a site response analysis program. The correction factors are calculated by the program to fit the damping ratio curve. Ishihara et al. (1985) used a 'fictitious' skeleton curve for the unloading and re-loading so that the damping curve can be approximated at different strain levels. From a number of site response analyses, they found out that the computed peak acceleration and maximum shear stresses were similar between the cases with and without damping fit. They explained that 'the acceleration at the surface is much affected by the shear strength of the layer which will experience large strains. Hence, it is important to model the skeleton curve of the weakest layer with care.'

Later on, a modified second Masing criterion (Tatsuoka et al., 1993) was developed that allows the scale factor, n, to assume virtually any value. Presti et al. (2006) adopted this method for site response analyses at Borgo (Fabriano, Italy), it was found that using n = 5, the damping curve is closer to the given soil damping ratio curve than that using n = 2 (i.e., original Masing rule) and the peak accelerations are higher using n = 5 than using n = 2. However, the computed shear strains were all less than 0.1%, i.e. not in the high damping range. Another generalized Masing rule using variable scale factor n was formulated by Archuleta et al. (1999) and used in site response analyses. At the time of this paper preparation, research work to investigate the influence of hysteretic damping on computed seismic response is ongoing (Bonilla et al. 2003).

In the present paper, the equivalent linear technique implemented in the computer program SHAKE and the non-linear approach using the bounding surface hypo-plasticity model (Wang, 1990, Wang et al., 1990) implemented in the computer program FLAC, were used to compute the response of a soft clay site subjected to strong input motions. Non-linear analyses were performed for two approaches to treating unloading and re-loading stress-strain paths (i.e., hysteretic damping) using (1) the Masing rule and (2) the generalized Mashing rule to compare the results of the site response analyses. The model parameters of the soil model for the nonlinear approaches were calibrated against the shear modulus reduction curves used in

SHAKE analyses.

MODEL SIMULATIONS FOR MODULUS REDUCTION AND DAMPING CURVES

A skeleton curve of the stress-strain relationship can be derived from the incremental equations of the model (based on Wang, 1990), i.e.

$$\gamma G_{\max} = \tau - \frac{2\tau_f}{h_r}[\frac{\tau}{\tau_f} + \ln(1 - \frac{\tau}{\tau_f})] \quad (2)$$

in which τ is shear stress, γ is shear strain, τ_f is shear stress at failure, G_{max} is initial shear modulus and h_r is a model parameter selected to fit a given modulus reduction curve described as follows:

$$G / G_{\max} = \tau / \gamma / G_{\max} \quad (3)$$

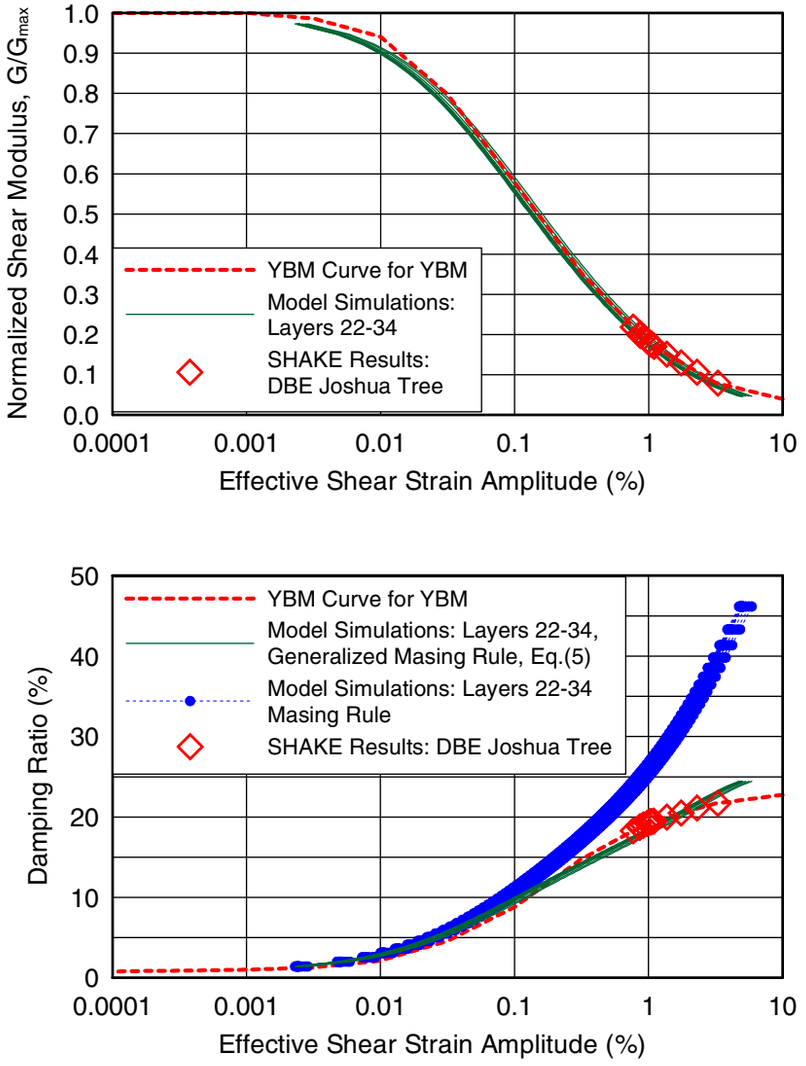


Fig. 1. Model Simulation for Young Bay Mud (YBM)

As an example, the model simulation for soft clay layers of the selected soil profile is presented on Figures 1 using the calibrated model parameter, h_r. As shown on Figure 1, the soil model simulations are in a good agreement with the modulus reduction curves. The model hysteretic damping curves derived from the Masing rule governing the unloading-reloading are also shown on Figure 1. However the data show that the Masing damping is higher than the prescribed curves especially at strains higher than 0.5 %.

HYSTERETIC DAMPING CORRECTION IN NON-LINEAR ANALYSES

In non-linear analyses, for a skeleton or backbone curve with shear strength as an upper limit (or an asymptotic line), the model damping based on the Masing rule, for simulating unloading and re-loading, approaches $2/\pi$ (or 63%) as a limit when soil approaches to failure at very large strains. That means it is impossible to fit the given damping ratio that normally is about 25 to 30 percent at high strain levels. There are two possible ways to fit the damping curve. The first way is to define a backbone curve that does not use the strength limit (e.g., the Martin-Davidenkov model implemented in a modified DESRA program- MARDES (Chang et al., 1990). In such a model, three parameters are used to reasonably fit both shear modulus reduction and damping curves. But, the drawback is that there is no strength limit, such that for high acceleration input motions or in weak soil layers, it may compute shear stresses much higher than the soil strength, as often encountered in equivalent linear models (e.g., SHAKE).

The favorable way is to modify the Masing rule that is used to simulate the stress-strain curve during unloading and re-loading phase. The Masing rule is simply a doubled backbone (or skeleton) curve for unloading (i.e., in Eq. (1), n=2). A generalized Masing rule was proposed by Wang et al. (1980). That model fits both modulus reduction and damping curves by adjusting the area in a stress-strain cycle, as shown on Figure 2. The generalized Masing rule is described as follows:

Skeleton (or backbone) curve: $$\tau = f(\gamma) \tag{4}$$

Generalized Masing curve with damping correction:

$$\tau - \tau_r = k(\gamma_r)[2f(\frac{\gamma - \gamma_r}{2}) - G(\gamma_r)(\gamma - \gamma_r)] + G(\gamma_r)(\gamma - \gamma_r) \tag{5}$$

in which $k(\gamma_r)$ is the damping correction factor that is the ratio of the damping prescribed by the desired damping curve based on laboratory data and the model damping computed from the given modulus reduction curve, $f(\gamma)/\gamma/G_{max}$, using the original Masing curve at reversal stress level τ_r.

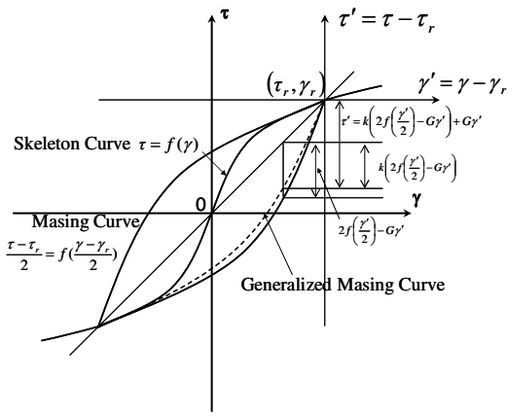


Fig. 2. Generalized Masing Curve

IMPLEMENTATION OF DAMPING CORRECTION PROCEDURE

The bounding surface plasticity model (Wang, 1990) was incorporated with program FLAC and applied to a number of seismic deformation projects (Wang et al., 2006). Recently, we have implemented the above generalized Masing rule into the FISH code of the soil model for the FLAC program so that the revised model is capable to fit a given damping curve for stress-strain loops in the cyclic unloading-reloading phase. The basic content of the implementation is as follows:

(1) Differentiate Eq. (5) to obtain the tangential shear modulus of the generalized Masing curve and apply it to the plastic tangential modulus in the unloading and re-loading phase of the original model (Wang, 1990).

(2) A hypothesis is made that assumes the damping correction factor $k(\gamma_r)$ only depends on the current reversal stress level and is independent of prior loading history.

(3) As used in the original model, a maximum prior-stress bounding surface is used to distinguish a virgin loading phase (where the skeleton curve is applicable) and a reverse loading phase (where the generalized Masing rule is acting). If the stress level exceeds the maximum prior-stress level, the virgin loading phase resumes.

(4) For simplicity, the damping correction factor $k(\gamma_r)$ is assumed to relate to the modulus reduction curve as follows:

$$k(\gamma_r) = \left(G(\gamma_r)/G_{\max}\right)^{\beta} \tag{6}$$

Note that, from Eqs. (2) and (3), the $k(\gamma_r)$ in Eq.(6) is a function of reversal stress τ_r. The new model parameter β can be determined by comparing the model damping based on the Masing rule with the prescribed damping at a desirable shear strain level (say, at 1% strain level) such that the desired damping can be obtained by the value of the damping correction factor, $k(\gamma_r)$ calculated in accordance with Eq. (6), multiplied by the value of the damping based on the Masing rule of Eq. (1) (n=2).

To illustrate the performance of the modified model code using the generalized

Masing rule, the corrected hysteretic damping curves are also presented on Figure 1. Figure 1 shows that the damping curves between the prescribed curves (short dashed curves) and those derived based on the Masing rule and the generalized Masing rule. The shear modulus reduction curve is derived from the backbone curve for virgin loading phase. The model damping curves are derived from either the Masing rule or the generalized Masing rule which is the product of the damping from Masing rule and damping correction factors based on Eq. (6), for each stress reversal on unloading/re-loading paths. The Masing rule gives substantially high damping at shear strains greater than 0.5 %. The generalized Masing rule results in a reasonably good fit to the damping curve at shear strains higher than 0.5 %.

Figure 3a shows stress-strain loops for four cycles with increasing stress amplitude using the Masing rule (no damping correction) and the generalized Masing rule (with damping correction). Note that the skeleton curve is derived based on a given modulus reduction curve, i.e., Eq. (2). It can be seen that the loops derived using the generalized Masing rule for an unloading and reloading phase are narrower than those using the Masing rule for higher reversal stress levels. Figure 3b shows the four cycles with decreasing stress amplitude following the first four cycles of increasing stress amplitudes. As the reversal stress level decreases, the differences in the stress-strain loops based on the Masing rule and the generalized Masing rule become smaller, and it is not affected by the prior loading histories as expected from the hypothesis we made. This is a significant hypothesis that affects the computed results.

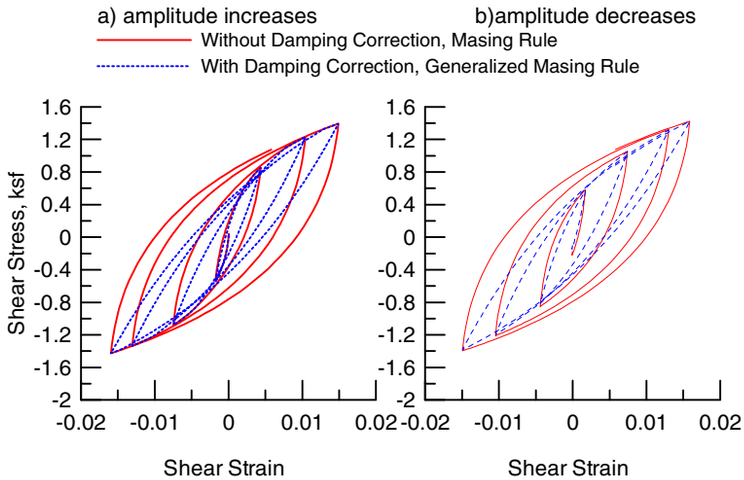


Fig. 3. Stress Strain Loops with and without Hysteretic Damping Fitting

EQUIVALENT AND NONLINEAR SITE RESPONSE EXAMPLES

For a soft clay site in Bay Area, California, the dynamic soil properties of Young Bay Mud (YBM) and Old Bay clay are based on recently obtained test data. Geophysical measurement of wave velocities was performed at nearby boring locations. Soil strength data were also evaluated from in-situ vane shear tests and laboratory triaxial tests. Site response analyses were first performed using the computer program SHAKE to compute the mud line motions at this soft clay site due to strong input motions. The bounding surface hypo-plasticity model (Wang, 1990,

Wang et al., 1990) and the computer program FLAC, were used for the non-linear analyses with the generalized Masing rule and the commonly used Masing rule. The model parameters, h_r (in Eq. (1)) and β (in Eq. (6)), used to simulate the given modulus and damping curves for each of the soil layers in the soil profile and to perform the non-linear analysis, are presented in Table 1. Note that for the non-linear analysis without hysteretic damping correction, parameter $\beta = 0$ (i.e. $k(\gamma_r)$=1.0) was used.

Computed surface accelerations from the FLAC and SHAKE analyses are compared on Figure 4. These comparisons indicate that the non-linear FLAC analysis produced reasonable motions when compared with those of SHAKE. Note that in the YBM layers, the SHAKE computed shear strains exceeding 1% as shown on Figure 1 by diamond symbols. In the SHAKE analysis, the high frequency contents of the input motion are filtered out. The Masing damping simulated in the non-linear FLAC analysis is higher than the specified damping ratio (at high strains), but did not filtered out the high frequency content of the input motion as shown on Figure 4.

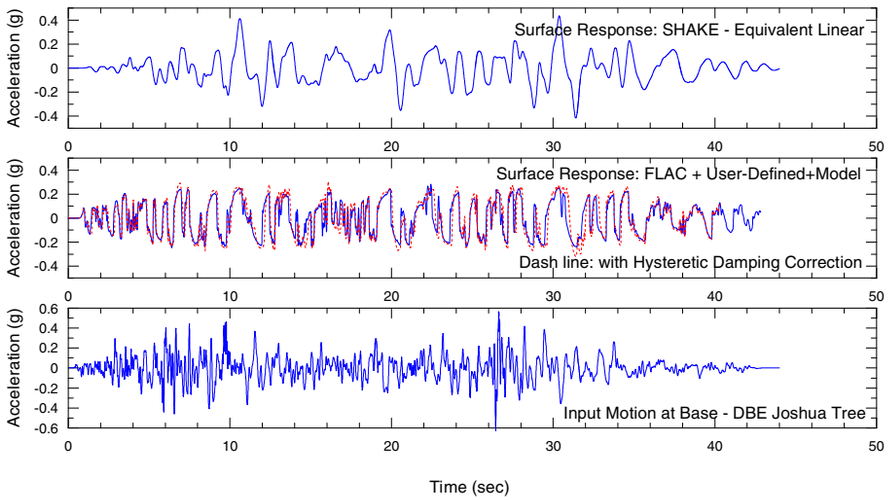


Fig. 4. Comparison of Computed Surface Acceleration Time Histories

Table 1 Model Parameters Used to Simulate Modulus and Damping Curves

Soil Type	Layer Number	h_r in Eq. (1)	β in Eq. (6)	Curves used in equivalent Linear Analysis (SHAKE)
Fill	35 to 43	0.34	0.21	YBM Site-Specific Curves
YBM	22 to 34	0.36	0.21	YBM Site-Specific Curves
Silty Fine Sand	19 to 21	0.20	0.09	Mid-range Sand, Seed & Idriss, 1970
Dense Silty Sand	16 to 18	0.60	0.32	Upper G/Gmax, Seed & Idriss, 1970; Damping, Idriss, 1990
OBC	8 to 15	0.80	0.40	OBC Site-Specific Curves
Fine Sand	6 to 7	0.28	0.20	Upper G/Gmax, Seed & Idriss, 1970; Damping, Idriss, 1990
Gravel	3 to 5	0.34	0.20	Upper G/Gmax, Seed & Idriss, 1970; Damping, Idriss, 1990

For the FLAC analyses, Figure 4 shows that differences in the computed ground surface motions, using the Masing rule versus using the generalized Masing rule, are small. The computed peak values of shear stress level, shear strain, and acceleration with depth are compared on Figure 5. It is noticed that the computed peak strains in the soft YMB layers are different between the cases with and without hysteretic damping corrections. But the computed failure ratios (i.e. peak shear stresses divided by the shear strength) are close for the two cases, because the shear stresses in the weak soil layers approach to the same shear strength while the developed shear strains are different. The computed peak accelerations are also similar in the two cases (with and without hysteretic damping corrections), except in the soft YBM layers. The above observations are consistent with the site response results (with and without damping corrections) presented by Ishihara et al. (1985).

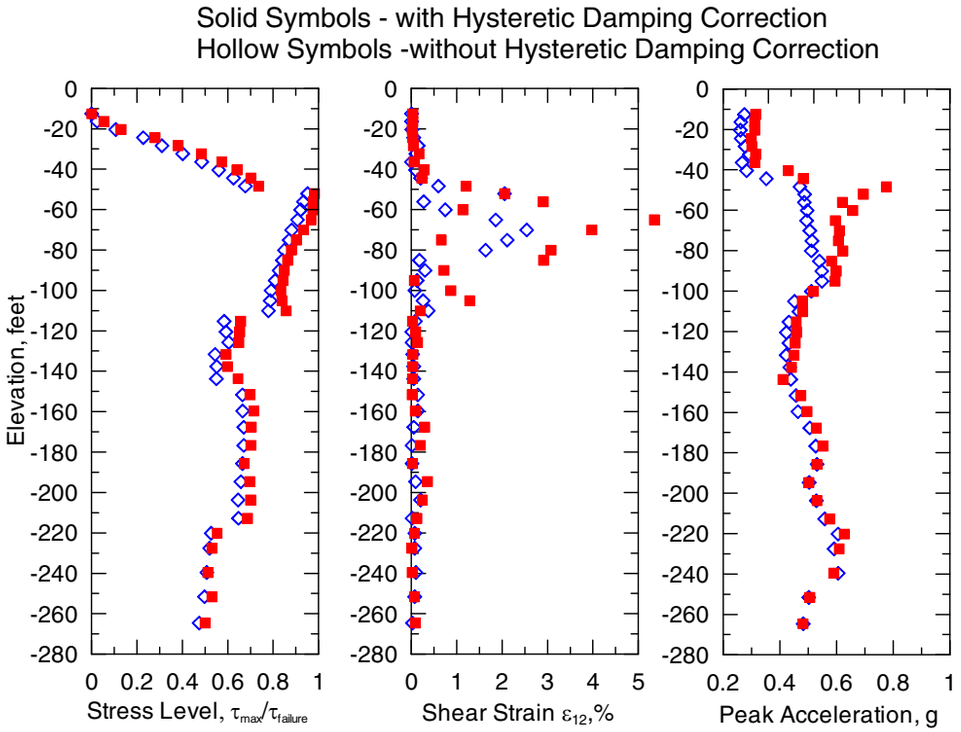


Fig.5. Computed Site Response, with and without Damping Corrections

In order to verify the above observations, another input motion (Kobe), developed to match the same design spectrum as the first motion (Joshua Tree), was also used to repeat the non-linear analyses at the same soft clay site. Again, the computed surface motions are not significantly affected by the hysteretic damping correction. The computed spectral accelerations from the two input motions, with and without hysteretic damping corrections, are presented on Figure 6. It is shown that the two input motions generate somewhat different spectral accelerations of the surface motions. However, the differences between cases with or without hysteretic damping corrections, for the same input motion, are relatively small.

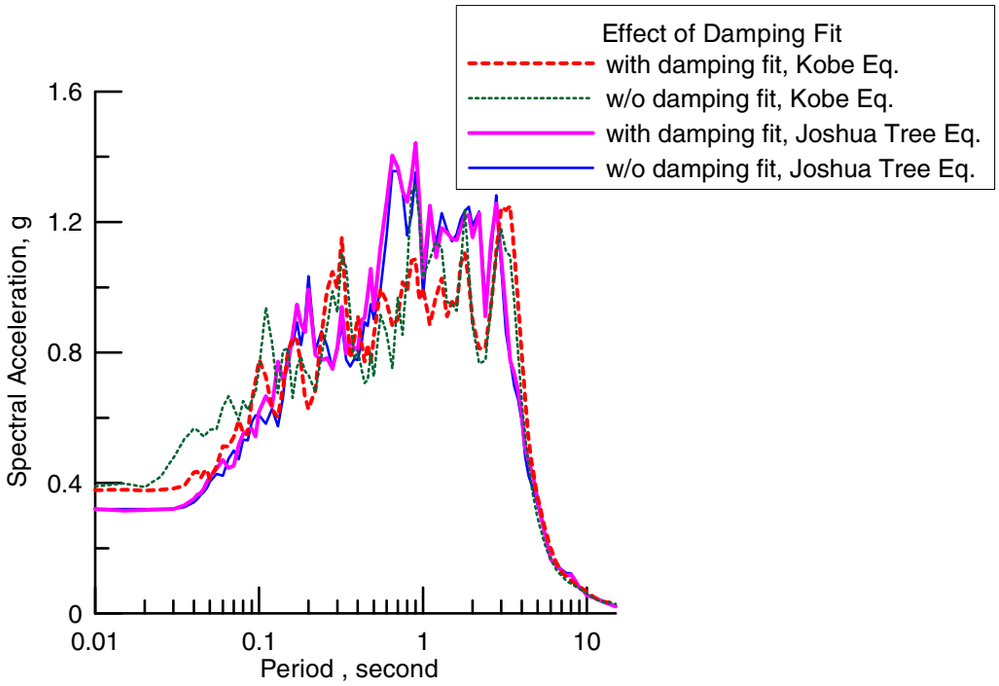


Fig.6. Computed Spectral Accelerations at Mud Line based on Two Input Motions, at a Soft Clay Site

CONCLUSION

In site response analyses using non-linear models, damping fitting is an issue existing for decades. This is because most of the non-linear model used the Masing rule for unloading and re-loading stress-strain loops. The equivalent hysteretic damping from stress-strain loops at high strains are generally higher than that of normally used damping ratio curves for equivalent linear analyses. The effect of damping misfit in non-linear site response analyses is not clear. Little research works on this topic were reported in the literature. The study reported here uses a generalized Masing rule for the unloading and reloading stress-strain loops, and the damping ratio curves can be fit reasonably well. The approach was implemented in a non-linear soil model to perform the site response analyses.

The effect of hysteretic damping correction on the surface response under strong earthquake input motion is examined for a soft soil site. The limited results show that only minor differences are computed between the surface responses from analyses with (using the generalized Masing rule) and without (using the Masing rule) damping correction, except the noticeable differences in the computed peak shear strains and peak accelerations in the soft soil layers for which the induced shear stress approaches failure. This is not a general conclusion for different soil sites, and the analyses we performed are total stress analyses without considering the effect from excess pore water pressure. Our opinion is that more research efforts are warranted to

clarify the effect of overestimated hysteretic damping.

ACKNOWLEDGMENTS

The authors appreciate Dr. Bonilla for the references and research information he provided.

REFERENCES

Archuleta, R.J., L.F. Bonilla, and D. Lavallee (2000). "Nonlinearity in Observed and Computed Accelerograms" *Proceedings of the 12th World Conference on Earthquake Engineering*, published by Aston Koedyk Ltd. Paper Reference Number 0338.

Bonilla, L.F. Tsuda, K. and Archuleta, R.J. (2003). "Influence of the Hysteretic Damping Ratio on the Computation of Nonlinear Site Response (Abstract)." European Geophysical Union Meeting, Nice, France.

Chang, C.-Y., Mok, C.M., Power, M.S., Tang, Y.K., Tang, H.T. and Stepp, J.C. (1990). " Equivalent Linear Versus Nonlinear Ground Response Analyses at Lotoung Seismic Experiment Site," *Proceedings ofthe4th U.S. National Conference on Earthquake Engineering*, May 20-24, Palm Aprings, CA, V.1:327-333.

Ishihara, K., Yoshida, S. and Tsujino S. (1985). "Modeling of Stress-strain Relation of Soils," *Proceedings of the 5th International Conference on Numerical Methods in Geomechanics*, Nagoya:373-380.

Idriss, I.M. (1990). "Response of Soft Soil Sites during Earthquakes." *Proceedings: H. Bolton Seed Memorial Symposium*, v. 2: 273-289.

Lo. Presti, D.C.F., Lai, C.G. and Puci I. (2006). "ONDA: Computer code for nonlinear seismic response analyses of soil deposits." *Journal of Geotechnical and Geoenvironmental Engineering*, ASCE, 132(2): 223-236

Masing, G.(1926). "Eigenspannungen und verfestigung bein messing (self stretching and hardening for brass)." *Proceedingsof the 2nd Int. Congress for Applied Mechanics*, Zurich, Switzerland:332-335.

Pyke, R.M.(1979). "Non-linear Soil Models for Irregular Loadings." *Journal of Geotechnical Engineering,* ASCE, 105(6):715-726.

Stewart, J.P., O.L.A. Kwok, Y.M.A. Hashash, N. Matasovic, R. Pyke, Z.L. Wang, and Z. Yang (2006). "Overcoming hurdles that limit the application of nonlinear seismic ground response analysis in engineering practice," *Proceedings of the 5th National Seismic Conference on Bridges and Highways*, San Francisco, CA

Tatsuoka, F. Siddique, M.S.A, Park, C.-S., Sakamoto, M, and Abe, F. (1993). "Modeling Stress-strain Relations of Sand." *Soils Found.*, 33(2):60-81.

Wang, Z.L., H. Qing-Yu, and Z. Gen-Shou. (1980). "Wave Propagation Method of Site Seismic Response by a Visco-Elastoplastic Model," *Proceedings of the 7th World Conference on Earthquake Engineering*, v. 2: 279-386.

Wang, Z.L. (1990). "Bounding Surface Hypoplasticity Model for Granular Soils and its Applications," Ph.D. Thesis, University of California at Davis. (*Dissertation Information Service*, Order No. 9110679, Ann Arbor, MI 48106.)

Wang, Z.L, Y.F. Dafalias, and C.K. Shen (1990). "Bounding Surface Hypoplasticity Model for Sand," *Journal of Engineering Mechanics*, ASCE, vol. 116, no. 5: 983-1001.

Wang, Z.L, Makdisi, F.I. & Egan (2006). "Practical Applications of a Non-linear Approach to Analysis of Earthquake-Induced Liquefaction and Deformation of Earth Structures," *Journal of Soil Dynamics & Earthquake Engineering,* v. 26, no. 2-4:231-252.

Influence of rate dependent soil behavior on propagated ground motion

Dong-Yup Kwak[1], Jae-Kwang Ahn[2], Duhee Park[3], Youssef M.A. Hashash[4]

[1]Graduate student, Department of Civil Engineering, Hanyang University, Haengdang-dong, Sungdong-gu, Seoul, Korea; duckkwak@hanyang.ac.kr

[2]Graduate student, Department of Civil Engineering, Hanyang University, Haengdang-dong, Sungdong-gu, Seoul, Korea; jjang909@hanyang.ac.kr

[3]Assistant Professor, Department of Civil Engineering Hanyang University, Haengdang-dong, Sungdong-gu, Seoul, Korea; dpark@hanyang.ac.kr,

[4]Associate Professor, Department of Civil and Environmental Engineering University of Illinois at Urbana-Champaign, 205 N. Mathews Avenue, Urbana, Illinois, U.S.A., hashash@uiuc.edu

ABSTRACT

Laboratory test results indicate that cyclic cohesive soil behavior is influenced by the rate of loading. However, such behavior is most often ignored in the site response analysis. This paper develops three models of rate-dependent dynamic soil behavior based on available laboratory data and implemented in a one-dimensional equivalent linear site response analysis program. The site response analysis results show that rate-dependent shear modulus and damping can have a pronounced influence on propagated weak ground motion, but a secondary influence on propagated strong motion. Rate-dependence of damping ratio has a greater impact on the computed response than rate-dependence of the shear modulus.

1. INTRODUCTION

One-dimensional site response analysis is widely performed to characterize the seismic site effects during a seismic event (Idriss 1990; Kramer 1996; Hashash and Park 2001). Analysis techniques include equivalent linear frequency domain approach (Schnabel 1972), and nonlinear time domain approach (Borja et al. 2002; Hashash and Park 2002; Matasovic 1993).

Most of these approaches assume that dynamic soil behavior is rate-independent, even though laboratory tests show that the shear modulus and soil damping of cohesive soil are influenced by the rate of loading (Richardson and Whitman 1963; Rix and Meng 2005; Whitman 1957). Meng (2006) uses a linear visco-elastic model to represent the response of a single soil layer subjected to shaking to study rate-dependent soil behavior influence on site response amplification. The study is limited by the simplifying assumptions employed about the soil profile and linear soil response and is only applicable to weak ground motions.

This paper develops and implements a set of rate dependent shear modulus and damping models in a modified equivalent linear analysis site response analysis procedure to approximate the rate-dependent soil behavior. The proposed models account for the frequencies at which the shear wave velocity profile and the dynamic soil curves (modulus reduction and damping curves) are obtained.

The models are used to conduct a study that investigates the influence of a) rate dependence of the maximum shear modulus and modulus reduction curves, and b) rate dependence of damping.

2. RATE-DEPENDENT MODELS FOR DYNAMIC SOIL BEHAVIOR

The standard normalized shear modulus reduction and damping curves are only dependent on shear strain amplitude and additional functions are needed to characterize the rate-dependency of shear modulus and damping ratio. This paper develops two separate models for rate dependent shear modulus and damping. Both models can estimate the dynamic property for a given rate of loading. Another important issue that is accounted for in the proposed models is the frequency at which the dynamic properties are measured at. The rate of loading effect is already embedded in the standard shear modulus reduction curves, damping curves, and shear wave velocity measured from a geophysical test. In the following, it is demonstrated how such embedded effect is accounted for in the proposed models. Note that the models are developed based on the undrained laboratory test results. Since the generated pore water pressure data are not available, it is not possible to determine whether the amount of excess pore pressure development is influenced by the rate of loading and the resulting rate dependency of the soil behavior is due to water, or whether it is an intrinsic attribute of cohesive soils. More study is needed to clarify the relationship between soil-water vs. rate of loading. This study uses the laboratory test results directly in developing the models.

2.1 Rate-Dependent Shear Modulus

The shear modulus is determined by multiplying the maximum shear modulus at very small strains to the normalized shear modulus reduction curve. The maximum shear modulus is commonly calculated from the shear wave velocity profile obtained from a geophysical test, while the shear modulus reduction curve is developed from a laboratory test. The shear wave velocity and the shear modulus reduction curve are often obtained at different loading frequencies.

The rate-dependency of the shear modulus is determined in three steps, as illustrated in Fig. 1.

(1) Determining the maximum shear modulus at the reference frequency, $G_{max,\ Ref.\ freq.}$, from the shear modulus back-calculated from the measured shear wave velocity, $G_{max,\ f(Vs)}$. f(Vs) is the frequency at which the shear wave velocity is measured.

For step 1, a function that relates the loading frequency with the shear modulus is needed. This paper uses the laboratory test results by Kim et al. (1991), developed at strain amplitudes between 0.001 and 0.01%, as shown in Fig. 1a. The function relates the shear modulus to the rate of loading (expressed as the loading frequency). Note that the function is normalized to the shear modulus obtained at a loading frequency of 0.5 Hz and is termed “G/G(0.5 Hz)” in the following.

Fig. 1a shows that normalized shear modulus increases with increase in the loading frequency. Since the effect of the shear strain amplitude on the rate-

dependency of the shear modulus is not yet clearly defined, it is assumed that the normalized relationship is not only applicable between shear strain amplitudes between 0.001 and 0.01%, but to all strain levels. Using Fig. 1a, $G_{max,\ Ref.\ freq.}$ can be calculated as follows:

$$G_{max,Ref.freq.} = \frac{\left[G/G(0.5Hz)\right]_{Ref.freq.}}{\left[G/G(0.5Hz)\right]_{f(Vs)}} G_{max,f(Vs)} \tag{1}$$

where $\left[G/G(0.5Hz)\right]_{Ref.freq.}$ and $\left[G/G(0.5Hz)\right]_{f(Vs)}$ are normalized shear moduli at frequencies Ref. freq. and f(Vs), respectively.

(2) Calculate the shear modulus reduction curve at a given loading frequency based on the reference curve obtained at the reference frequency. The reference shear modulus reduction curve represents the ratio of G_f obtained at the reference frequency ($G_{Ref.\ freq.}$) to the G_{max} also measured at the reference frequency ($G_{max,\ Ref.\ freq.}$). By using the normalized rate-dependent function (Fig. 1a), the shear modulus (G_f) at a given loading frequency (*f*) can be calculated from the $G_{Ref.\ freq.}$ using the following equation:

$$\frac{G_f(\gamma)}{G_{max,\ Ref.freq.}} = \frac{\left[G/G(0.5Hz)\right]_f}{\left[G/G(0.5Hz)\right]_{Ref.freq.}} \frac{G_{Ref.freq.}(\gamma)}{G_{max,\ Ref.freq.}} \tag{2}$$

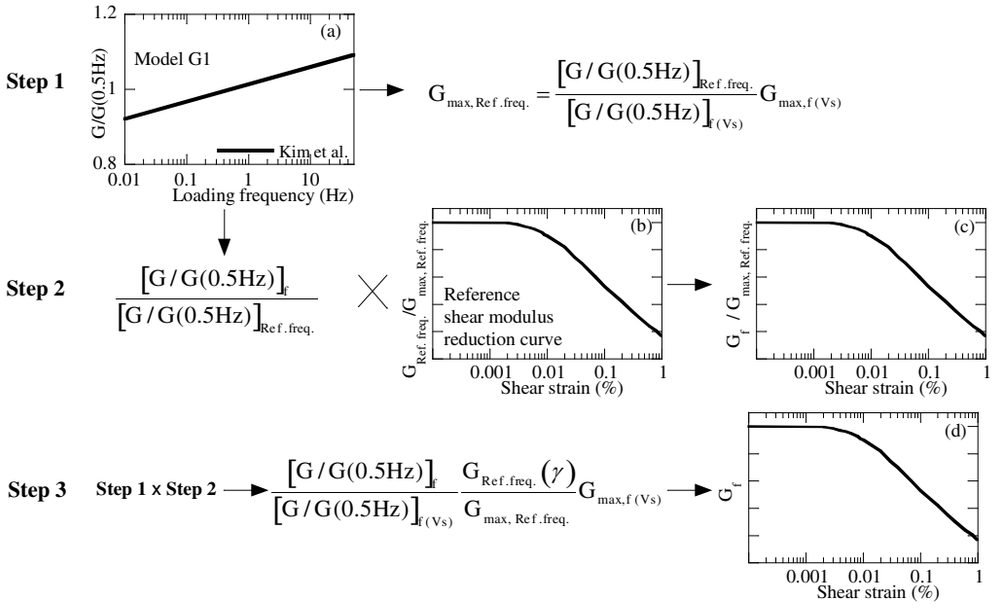


FIG. 1. Schematic drawing showing the proposed rate-dependent shear modulus.

Note that $G_{Ref.\ freq.}(\gamma)/G_{max,\ Ref.\ freq.}$ is the shear strain dependent reference shear modulus reduction curve (Fig. 1b).

The resulting shear modulus reduction curve at loading frequency *f* normalized to the maximum shear modulus obtained at reference frequency is shown in Fig. 1c.

(3) Multiply $G_{max,\ Ref.\ freq.}$ calculated in step 1 by the normalized shear modulus reduction curve obtained in step 2, resulting in the following equation:

$$G_f(\gamma) = \frac{\left[G/G(0.5\text{Hz})\right]_f}{\left[G/G(0.5\text{Hz})\right]_{f(Vs)}} \frac{G_{Ref.freq.}(\gamma)}{G_{max,\ Ref.freq.}} G_{max,f(Vs)} \tag{3}$$

Eq. (3) shows that the rate-dependent shear modulus is not influenced by the reference frequency. Its effect cancels out when multiplying Eq. (1) and (2) because the frequency dependent relationship in Fig. 1a is independent of the amplitude of the shear strain. The rate-dependent shear modulus is only influenced by the frequency at which the shear wave velocity is obtained, f(Vs), and the loading frequency of the input ground motion.

2.2 Rate-Dependent Damping

The damping ratio curve is composed of small strain damping defined at strain level below linear threshold and hysteretic damping induced by nonlinear hysteretic behavior. Due to the limited test results on rate dependency of the small strain damping at high strains, only the small strain damping is assumed to be rate dependent.

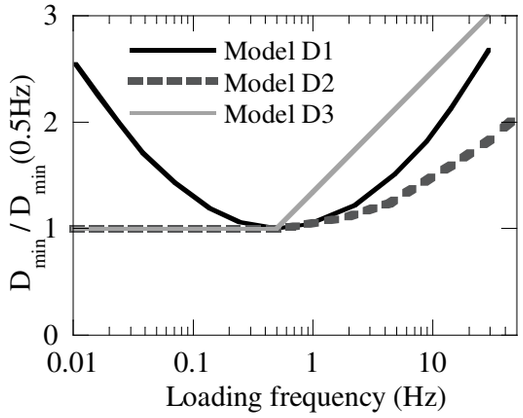


FIG. 2. The proposed rate-dependency of the small strain damping ratio model.

The rate-dependency of the small strain damping is defined using a normalized function that relates the loading frequency to the small strain damping ratio. The rate-dependent damping ratio is calculated by adding the rate-dependent small strain damping to the rate-independent hysteretic damping.

Three types of normalized functions are used to represent the range of laboratory test results, as shown in Fig. 2. Note that the small strain damping is normalized to the small strain damping obtained at a loading frequency of 0.5 Hz.

Model D1 is based on the data of Rix and Meng (2005). Model D2 is based on Kim et al. (1991), using only the curve defined at the shear strain of 0.001%. Model D3 is based on the data of Darendeli (2001). A cutoff is used such that the normalized damping does not decrease below the value at 0.5 Hz to be consistent with the observed behavior. For all models, the small strain damping increases with increase in loading frequency at frequencies higher than 0.5 Hz.

3. RATE-DEPENDENT BEHAVIOR IN EQUIVALENT LINEAR ANALYSIS

A simplified equivalent linear analysis procedure that approximates the rate-dependent soil behavior is developed. The new procedure is built upon the currently available one-dimensional site response code DEEPSOIL (www.uiuc.edu/~deepsoil) (Hashash and Park 2001; Hashash and Park 2002; Park and Hashash 2004). DEEPSOIL can be used to perform both non-linear and equivalent linear site response analysis. The equivalent linear analysis feature is similar to SHAKE 91 (Schnabel et al. 1972), with no limitation on the number of layers and material properties. In addition, various types of complex shear moduli can be selected (Park 2004).

In a frequency domain solution, applying the boundary condition results in the following recursive formula between the motions of two subsequent layers *m* and *m+1* as follows:

$$A_{m+1} = \frac{1}{2}A_m(1+\alpha^*_m)e^{ik^*_m h_m} + \frac{1}{2}B_m(1-\alpha^*_m)e^{-ik^*_m h_m}$$
$$B_{m+1} = \frac{1}{2}A_m(1-\alpha^*_m)e^{ik^*_m h_m} + \frac{1}{2}B_m(1+\alpha^*_m)e^{-ik^*_m h_m} \quad (4)$$

$A_{m+1}(w)$, $B_{m+1}(w)$ = upward downward components of the ground motion of layer $m+1$, $\alpha^*_m = \dfrac{\rho_m\left[\sqrt{G_m/\rho_m}\right]_m\left[1+i\xi_m\right]}{\rho_{m+1}\left[\sqrt{G_m/\rho_m}\right]_{m+1}\left[1+i\xi_{m+1}\right]}$, and $k^*_m = \dfrac{\omega}{\left[\sqrt{G_m/\rho_m}\right]_m\left[1+i\xi_m\right]}$, ρ = density, ξ = damping ratio.

The proposed procedure uses simulates the rate dependent shear modulus and damping by redefining α_m and k^*_m of Eq. (4) as follows:

$$\alpha^*_m(\omega) = \frac{\rho_m\left[\sqrt{G_m(\omega)/\rho_m}\right]_m\left[1+i\xi_m(\omega)\right]}{\rho_{m+1}\left[\sqrt{G_{m+1}(\omega)/\rho_m}\right]_{m+1}\left[1+i\xi_{m+1}(\omega)\right]} \quad (5)$$

$$k^*_m(\omega) = \frac{\omega}{\left[\sqrt{G_m(\omega)/\rho_m}\right]_m \left[1 + i\xi_m(\omega)\right]} \tag{6}$$

$G(\omega)$ and $\xi(\omega)$ are selected from the rate-dependent shear modulus and damping models described in the previous section, which are capable of accounting for the frequency at which the soil curves and the shear wave profile is obtained.

4. INFLUENCE OF RATE-DEPENDENT SOIL BEHAVIOR ON SITE RESPONSE ANALYSIS

A series of equivalent linear analyses are performed to evaluate the effect of the rate-dependent soil behavior on propagated ground motion. The profile used in the analyses is the 32 m thick profile in Pusan, located in the southern coast of Korea. The shear wave velocity of the bedrock is 760 m/sec. The profile is composed of thick, uniform soft clay called Pusan Clay. The profile will be termed "Profile 1" in the following.

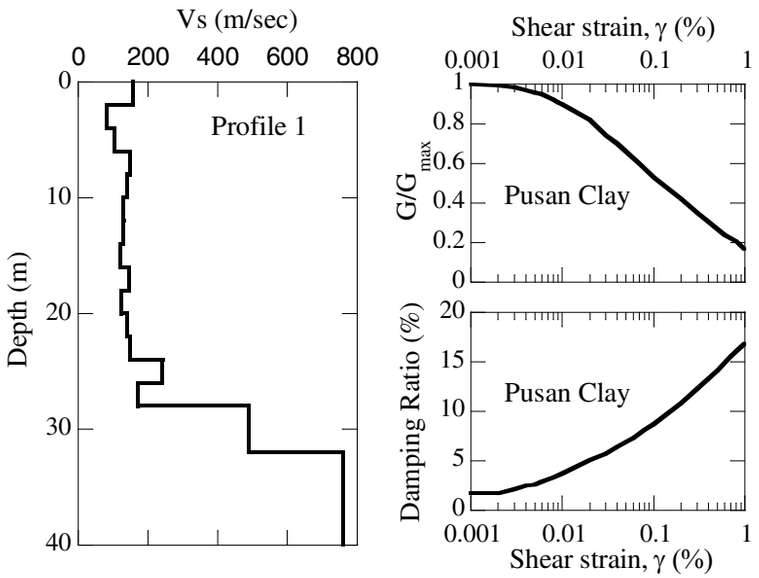


FIG. 3. Soil profiles and dynamic properties used in the study.

Two ground motions are used:

a. The recorded motion at Big Tujunga station during Hector Mine earthquake (a_{max} = 0.007g, M=7.0, U.S.A., 1999).
b. The recorded at Ofunato during Miyagi-Oki earthquake (a_{max} = 0.226g, M=7.4, Japan, 1978).

The number of iterations used in the analyses is ten to ensure convergence. The ratio of the effective to the maximum shear strain is 0.65.

In the following, two reference frequencies are used, which are 0.5 and 25 Hz. The 0.5 Hz is representative of the loading frequency of a TS device and shear wave velocity measurement, while the 25 Hz is representative of a RC test. The analyses will demonstrate how the frequency at which the dynamic curves will influence the calculated response relative to the standard rate independent analyses.

4.1 Effect of Rate-Dependent Shear Modulus

In the following analyses, the small strain damping is assumed to be rate-independent to only investigate the influence of the rate dependent shear modulus.

As shown in Eq. (3), the shear modulus is not dependent on the reference frequency, but only on the frequency at which the shear wave velocity is measured. Two f(Vs) are used, which are 1 and 10 Hz, to cover the range of frequencies encountered in geophysical tests (Bang 2006).

The computed 5% damped surface response spectra are shown in Fig. 4. The results show that the reference frequency at which the shear wave velocity profiles are obtained has a minor influence on the computed response because the difference in the shear modulus between 1 and 10 Hz is not pronounced. In the following analyses, it is assumed at the shear wave velocity profile is obtained at a frequency of 1 Hz.

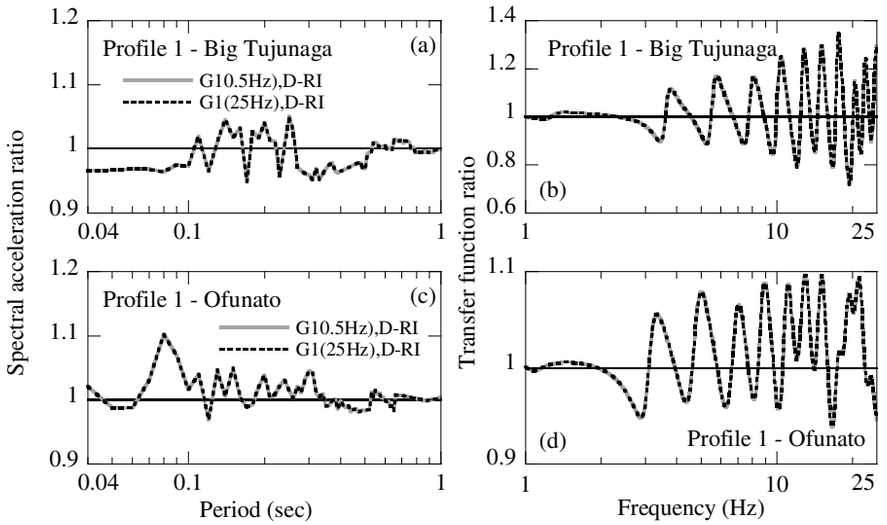


FIG. 4. Effect of rate-dependency of the shear modulus.

4.2 Effect of Rate-Dependent Damping

Identical set of analyses are performed to evaluate the influence of rate-dependent small strain damping and the computed response spectra and transfer functions are shown in Fig. 5. Three small strain damping models, D1 to D3,

described in the previous section and shown in Fig. 2, are used. The shear modulus in the analysis is assumed to be rate-independent.

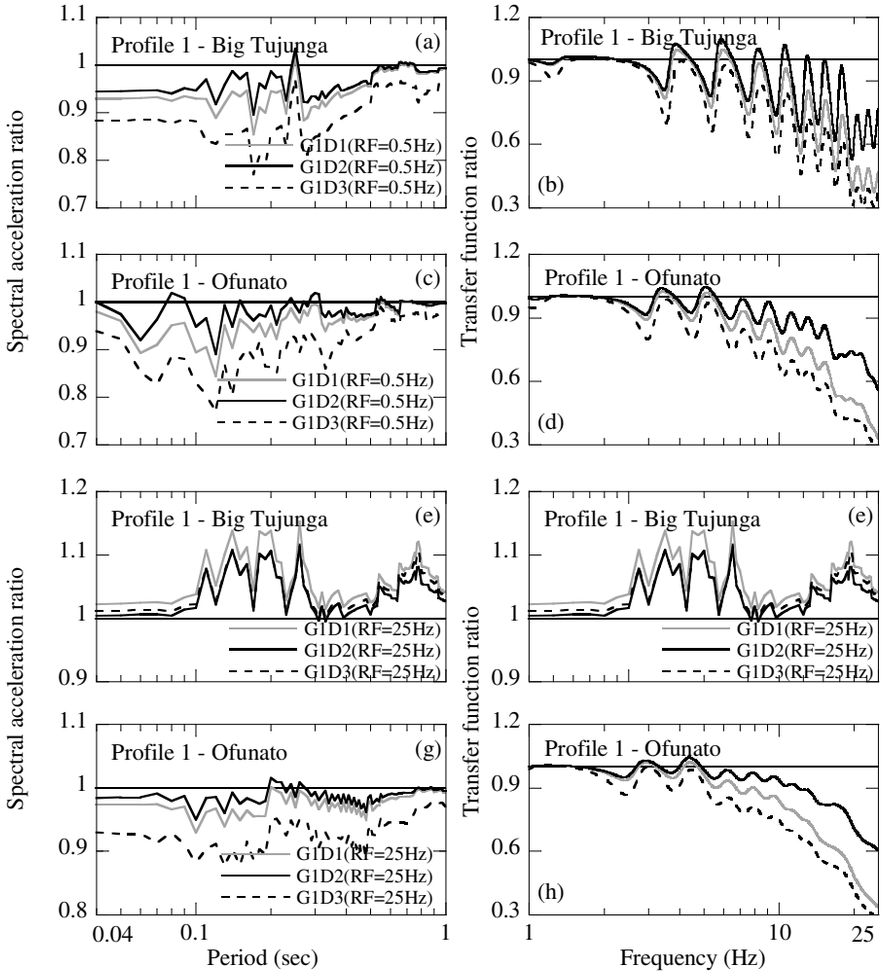


FIG. 5. Effect of the rate-dependency of the small strain damping.

The rate-dependent small strain damping does not result in shifting of the transfer function, but either elevates or lowers the function, as shown in Fig. 5b, d, e, f. When assuming that the reference frequency is 0.5 Hz, the rate-dependent small strain damping becomes larger than the rate-independent model. Therefore, the computed response spectrum and transfer function are lower, as shown in Fig. 5a - d. If the reference frequency is 25 Hz, the estimated small strain damping is smaller than the rate-independent model. For such case, the computed response spectrum and transfer function are larger than the rate-independent analysis, as shown in Fig. 5e - f. The rate-dependency of the small strain damping models has a more pronounced influence on the propagated ground motion compared to the shear modulus, as can be inferred by comparing Fig. 4 and Fig. 5. Among three small strain damping models,

D3 results in the strongest influence on the ground motion when the reference frequency is 0.5 Hz. The reason can be easily explained by Fig. 2, which shows that the rate-dependency of model D3 is the highest. The results of D1 and D2 are very similar, both resulting in lower influence compared to model D3. The difference between the models is very small when the reference frequency = 25 Hz.

5. LIMITATIONS OF THE PROPOSED MODEL

It should be noted that the proposed procedure is an approximate solution and all the limitations of the equivalent linear procedure are applicable to the model. Most importantly, the rate dependence of the shear modulus and damping is defined at a representative strain. In reality, the rate dependence of the shear modulus and damping depend not only on the loading frequency, but also on the strain level.

The proposed model will therefore underestimate the rate-dependency for high frequency components of the ground motions, for which small shear strains are expected, and overestimate this dependency at strains higher than the effective shear strain. A new nonlinear model or a modified equivalent linear model needs to be developed to improve the solution accuracy.

6. CONCLUSIONS

Laboratory tests show that the rate of loading alters the behavior of cohesive soils, both shear modulus and damping ratio increasing with increase in rate of loading. A series of modified equivalent linear analyses are performed to characterize the effect of the rate- dependent soil behavior on site response analysis. Results indicate that while the rate- dependent nature of the shear modulus has limited influence on propagation of the seismic waves, the rate-dependent damping ratio has a more pronounced influence, filtering out high frequency components due to the higher damping ratio at high rate of loading. The effect becomes relevant when propagating a motion rich in high frequency content and low in amplitude. The influence is also influenced by the frequency at which the dynamic soil curves are obtained.

ACKNOWLEDGEMENT

This work was supported by the Korea Research Foundation Grant funded by the Korean Government (MOEHRD, Basic Research Promotion Fund) (KRF-2006-003-D00579). The authors gratefully acknowledge this support.

REFERENCES

Bang, E.S. (2006). *Personal communications.*

Borja, R. D., Duvernay, B. G., and Lin, C. H. (2002). "Ground response in Lotung: total stress analyses and parametric studies." *J. of Geotechnical and Geoenvironmental Engrg.*, 128 (1): 54-63.

Darendeli, M. B. (2001). Development of a new family of normalized modulus reduction and material damping curves. Ph.D. Thesis, *University of Texas at Austin*, Austin.

Hashash, Y. M. A., and Park, D. (2001). "Non-linear one-dimensional seismic ground motion propagation in the Mississippi embayment." *Engrg. Geology*, 62 (1-3): 185-206.

Hashash, Y. M. A., and Park, D. (2002). "Viscous damping formulation and high frequency motion propagation in non-linear site response analysis." *Soil Dynamics and Earthquake Engrg.*, 22 (7): 611-624.

Idriss, I. M. (1990). "Response of soft soil sites during earthquakes." *Proc. Symposium to Honor H.B. Seed.* Berkeley, CA. BiTech Publishers, Vol.2, 273-289.

Kim, D. S., Stokoe, K. H., and Hudson, W. R. (1991). "Deformational characteristics of soils at small to intermediate strains from cyclic tests." *Report Research Report 1177-3*, University of Texas at Austin, Austin, TX.

Kramer, S. L. (1996). *Geotechnical Earthquake Engrg*., Prentice Hall, Upper Saddle River, N.J.

Matasovic, N. (1993). "Seismic response of composite horizontally-layered soil deposits." *Ph.D. Thesis*, University of California, Los Angeles.

Meng, J. (2006). "Earthquake ground motion simulation with frequency-dependent soil properties." *Soil Dynamics and Earthquake Engrg.*, **27**(3): 234-241.

Park, D. (2004). "Estimation of non-linear seismic site effects for deep deposits of the Mississippi Embayment." *Mid America Earthquake Center CD Release 04-06*, Urbana.

Park, D., and Hashash, Y. M. A. (2004). "Soil damping formulation in nonlinear time domain site response analysis." *J. of Earthquake Enrg.*, 8 (2): 249-274.

Richardson, A. M., and Whitman, R. V. (1963). "Effect of strain-rate upon undrained shear resistance of a saturated remoulded fat clay." *Geotechinique*, **13**(4): 310-324.

Rix, G. J., and Meng, J. W. (2005). "A non-resonance method for measuring dynamic soil properties." *Geotechnical Testing Journal*, 28 (1): 1-8.

Roesset, J. M. (1977). "Soil amplification of earthquakes." *Numerical Methods in Geotechnical Engrg*. John Wiley, New York: 649-682.

Schnabel, P. B., Lysmer, J. L., and Seed, H. B. (1972). "SHAKE: A computer program for earthquake response analysis of horizontally layered sites." *Report EERC-72/12, Earthquake Engrg. Research Center*, Berkeley, CA.

Vucetic, M., and Dobry, R. (1991). "Effect of soil plasticity on cyclic response." *J. of Geotechnical Engrg.*, 117 (1), 87-107.

Whitman, R. V. (1957). "The behaviour of soils under transient loadings." *Proc. 4th Int. Conf. on Soil Mechanics and Foundation Engrg.* London. Butterworths Scientific Publications, Vol.1, 207-210.

Modeling nonlinear site response uncertainty in the Los Angeles Basin

Dominic Assimaki[1], M. ASCE, Wei Li[2], Jamison M. Steidl[3], and Jan Schmedes[4]

[1]Assistant Professor, School of Civil and Environmental Engineering, Georgia Institute of Technology, 790 Atlantic Drive, NW, Atlanta, GA30332-0355; dominic@gatech.edu
[2]Graduate Research Assistant, School of Civil and Environmental Engineering, Georgia Institute of Technology, 790 Atlantic Drive, NW, Atlanta, GA30332-0355; wli3@mail.gatech.edu
[3]Associate Research Seismologist, Institute for Crustal Studies, University of California, Santa Barbara, 1140 Girvetz Hall, Santa Barbara, CA93106; steidl@crustal.ucsb.edu
[4] Graduate Research Assistant, Institute for Crustal Studies, University of California, Santa Barbara, 1140 Girvetz Hall, Santa Barbara, CA93106; jasch@crustal.ucsb.edu

ABSTRACT: We investigate the variability in ground motion predictions that results from the methodology selected for the realization of strong motion site response analyses of typical soil profiles in the Los Angeles (LA) Basin. For this purpose, site-specific regional velocity and attenuation structures are compiled using geotechnical data at three downhole arrays, low-strain velocity and attenuation profiles obtained via waveform inversion of weak motion records, and crustal velocity structures as described by the Southern California Earthquake Centre Community Velocity Model (SCEC CVM IV). Successively, broadband ground motions are simulated by means of a finite source model for rupture scenaria of weak, medium and large magnitude events (M=3.5-7.5) at stations located on a regular 2D grid within distances 5-75km from the fault. Observed estimates of site response at the stations of interest are first compared to simulated small magnitude rupture scenaria. Parametric studies are next conducted for each fixed magnitude (fault geometry) scenario by varying the source-to-site distance and source parameters for the ensemble of site conditions. Elastic, equivalent linear and nonlinear simulations are implemented for the base-model velocity and attenuation structures and nonlinear soil properties, to examine the variability in ground motion predictions as a function of ground motion amplitude and frequency content, and nonlinear site response methodology. Results of this study are currently being used to develop supplementary criteria for the NEHRP site classification system to describe the nonlinearity susceptibility of soft sediments, and thus establish a cost-effective and computationally-efficient framework for site parameterization and response simulation defined as a function of source-path-site-effects and design sophistication level. The reflection of nonlinear site response modeling uncertainty is finally depicted in the estimation of synthetic ground motion amplification factors, which are compared to the currently employed NEHRP factors.

INTRODUCTION

There exists nowadays general agreement between the earthquake engineering and seismological community that nonlinear site effects should be accounted for in strong ground motion predictions. Nonetheless, there still exists large degree of uncertainty concerning: (i) the site classification scheme that should be used to quantify the susceptibility of soil profiles to nonlinearity, (ii) the methodology to be employed for the efficient prediction of nonlinear effects, and (iii) the associated cost-effective site investigation program. Towards reducing these uncertainties, seismic observations of site response -and downhole instrumentation in particular- can provide critical constraints on interpretation methods for surface observations, as well as information on the real material behavior under the in-situ state of stress subjected to a wide range of loading conditions. Focusing on the regional site characteristics of Southern California, we here investigate the modeling uncertainty introduced in broadband ground motion simulations by the nonlinear site response methodology selection at three downhole arrays in the Los Angeles Basin. For this purpose, site-specific regional velocity and attenuation structures are initially compiled, and broadband ground motions are simulated for rupture scenaria of weak, medium and large magnitude events (M=3.5-7.5). Parametric studies are next conducted for each fixed magnitude (fault geometry) scenario by varying the source-to-site distance and source parameters for the ensemble of site conditions. Elastic, equivalent linear and nonlinear simulations are initially validated for a limited number of observations, and successively implemented in conjunction with the broadband synthetics to examine the variability in ground motion predictions as a function of ground motion amplitude and frequency content and site response methodology. The modeling uncertainty thus introduced in broadband ground motion predictions is assessed by means of the coefficient of variance of the alternative models. A frequency index is developed to describe the frequency content of incident ground motion, which, in conjunction with the rock-outcrop acceleration level, is used to identify the site and ground motion conditions where incremental nonlinear analyses should be employed in lieu of approximate methodologies. Finally, site amplification factors based on synthetic ground motions are computed and compared to currently employed factors in engineering practice.

SITE CONDITIONS AT THREE DOWNHOLE ARRAYS IN THE LA BASIN

The soil profiles at three instrumented geotechnical downhole arrays in Southern California (La Cienega, Meloland and Obregon Park) are investigated in this study. Their coordinates in the basin may be found at http://www.cosmos-eq.org/index.html. Geotechnical data available at these stations comprise downhole and suspension logging shear wave velocity profiles (V_s), as well as scarce laboratory resonant column modulus degradation and damping curves. Weak motion seismic waveform inversion (Assimaki et al, 2006) was employed for the estimation of the local attenuation and density profiles. The idealized 1D shear wave velocity (V_s), attenuation (Q) and density profiles are illustrated in Fig. 1a, along with the available on-site geotechnical investigation data of velocity distribution at the corresponding sites. Note that V_s profiles were also evaluated by means of the inversion, and were shown to compare very

well with the suspension logging data. The attenuation (Q) profiles estimated via inversion of multiple seismograms in the near-surface, however, show a relatively wide statistical distribution due to the simplified approximation of the soil profile in the forward model operator. In particular, the inversion algorithm assumes a horizontally stratified medium with homogeneous layers subjected to vertically propagating anti-plane shear waves, which cannot account for the strong scattering of high frequency components due to the small-scale heterogeneities in the near-surface soil layers.

Crustal compressional velocity (V_p), shear velocity (V_s) and density models (ρ) were also extracted at the locations of the three arrays from the Southern California Community Velocity Model IV (SCEC CVM IV: http://www.data.scec.org/3Dvelocity/). These one-dimensional crustal models were refined in the near surface by incorporating the local geotechnical information from suspension logging tests and downhole array seismogram inversion results, and were successively used in simulations of broadband ground motion synthetics.

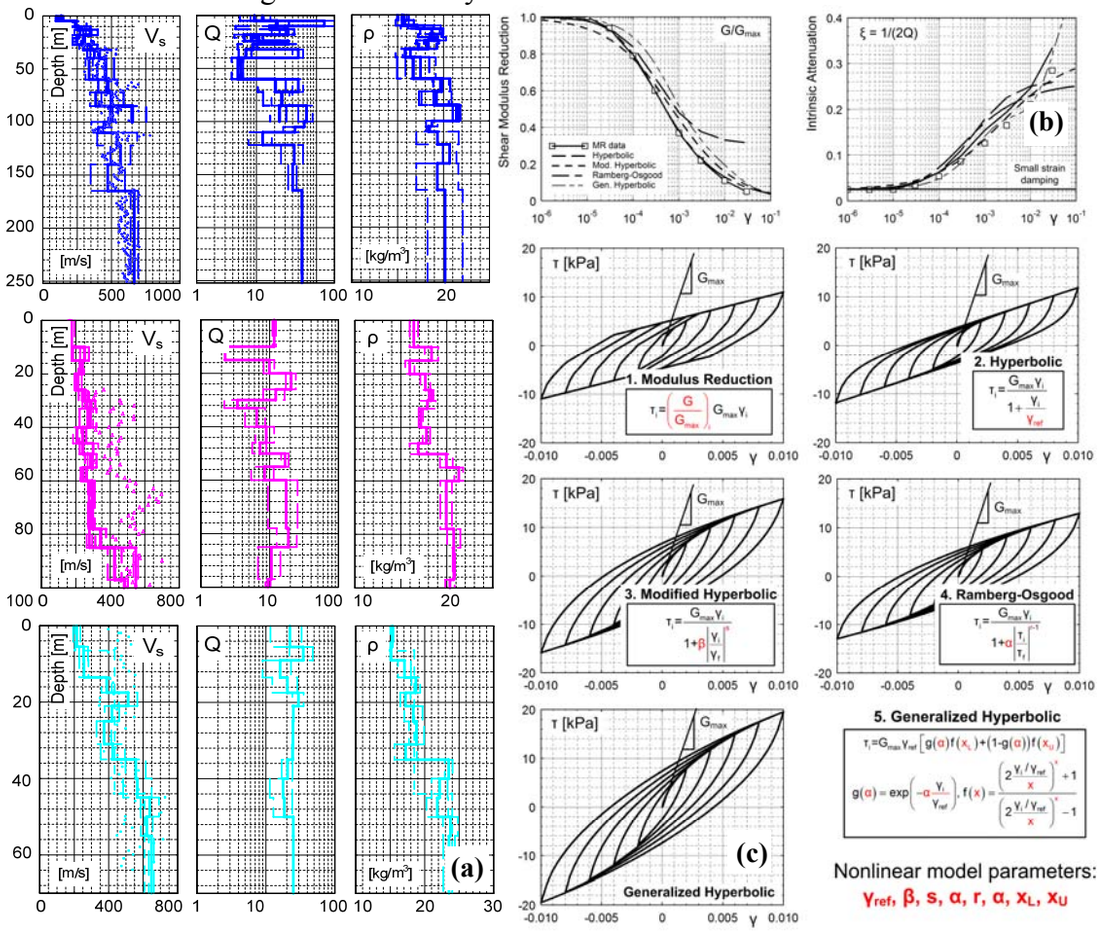


FIG. 1. (a) V_s, Q and ρ profiles evaluated by seismogram inversion at the three stations: (top) La Cienega, (middle) Meloland and (bottom) Obregon Park; (b) Fitted dynamic soil properties to laboratory data from samples at 7.5m depth at La Cienega for the nonlinear models investigated; and (c) Predicted stress-strain hysteresis loops for the material in (b) with initial shear modulus $G_{max}=10^4$ kPa, subjected to a series of cyclic strain time histories with increasing amplitude.

BROADBAND GROUND MOTION SIMULATIONS

Due to the scarcity of recordings at the three stations, strong ground motion synthetics were computed for multiple rupture scenaria over a wide range of epicentral distances, to develop a statistically significant number of observations justifying the soundness of the target uncertainty analysis. Broadband ground motion time-histories were here simulated for multiple strike-slip fault rupture scenaria over a 100x100km^2 square grid. The calculation of broadband time histories of ground motion was evaluated by means of the hybrid low- /high-frequency approach with correlated source parameters (Liu et al, 2007). In this approach, low frequency synthetics (<1 Hz) are computed in a 3D velocity structure using a finite-difference method, while broadband synthetics are computed in a 1D velocity model using a frequency-wavenumber method. Successively, the broadband ground motion synthetics were corrected for local site and nonlinear soil effects by the alternative strong motion site response methodologies investigated in this study by deconvolution of the linear elastic synthetics to the incident waveforms at the base of the profiles and successive equivalent linear and nonlinear wave propagation. The statistics of strong motion site response uncertainty were successively based on the ensemble of synthetic ground motion scenaria. For more information, the reader is referred to Assimaki et al (2007).

STRONG MOTION SITE RESPONSE NUMERICAL SIMULATIONS

In current engineering practice, site response calculations accommodate the strain dependencies of dynamic soil properties via two alternative approaches referred to as equivalent-linear and nonlinear analyses, and briefly described in the ensuing. This study attempts to quantify the relative advantages of increased accuracy of the complex formulations compared to the computationally efficient, approximate results of simplified models.

The equivalent-linear approach (Seed and Idriss, 1970) is an iterative linear viscoelastic site response algorithm, in which soil nonlinearity is represented by linear, strain-compatible soil properties estimated for characteristic strain levels. These strain levels are estimated as a fraction of the peak strain computed at the center of each soil layer of the profile, strain-compatible soil parameters are selected using moduli degradation and damping curves, the linear response calculation is repeated, and iterations are performed until convergence. This stepwise analysis procedure has been formalized into a 1D site response analysis code termed SHAKE (Schnabel et al., 1972), which currently is the most widely used analysis package for this category of problems in practice. The linear stress-strain material behavior and total stress approach associated with equivalent linear models, however, entirely prohibits their use for problems that involve large levels of strain and soft/very soft sedimentary sites. On the other hand, in the nonlinear formulations of soil behavior, the wave equation is directly integrated in the time-domain and the material properties are adjusted to the instantaneous levels of strain and loading path. Nonlinear constitutive models can simulate soil behavioral features such as updated stress-strain relationships and/or cyclic modulus degradation, which are critical for the prediction of large strain problems at soft sedimentary sites.

The alternative nonlinear constitutive models investigated are listed below with increasing degree of complexity in terms of the input parameters required; they include the multi-linear, the hyperbolic (Ishihara, 1996), the Ramberg-Osgood (R-O) (Faccioli et al, 1973), the modified hyperbolic (Matasovic & Vucetic, 1995) and the generalized hyperbolic (Hayashi et al, 1992) idealized monotonic stress-strain relationships. An example of the fitted modulus reduction and damping vs. shear strain curves for the ensemble of idealized nonlinear stress-strain behaviors investigated in this study is shown in Fig. 1b, along with the predicted stress-strain hysteresis loops for a material with the illustrated nonlinear response and initial shear modulus $G_{max}=10^4$ kPa, subjected to a series of cyclic strain time histories with increasing amplitude (Fig. 1c). The modulus degradation and damping curves illustrated correspond to the nonlinear material properties at the La Cienega SMGA, as estimated from laboratory experiments conducted on samples extracted at depth 7.5m (http://geoinfo.usc.edu/rosrine/). Nonlinear dynamic soil properties for all three SMGA that are available at this database were implemented for the simulations conducted in this study. For more information, the reader is referred to Assimaki et al (2007).

The low-strain material damping was incorporated into the time-domain simulations by the memory-variable technique originally described by Day and Minster (1984), by means of which this frequency independent soil property may be accurately modeled over a wide frequency range via a linear combination of multiple relaxation mechanisms. This approach is described in detail by Liu and Archuleta (2006). Hysteresis behavior was implemented by means of the original Masing (Masing, 1926) and extended Masing formulation (Pyke, 1979). Note that the extended Masing rules are consistent with a series of mechanical models described by Iwan (1967), according to which the shear strain may be easily decomposed into elastic and plastic components as required by the formulation of incremental elasto-plasticity. This model was here implemented for the incremental solution of the wave equation in nonlinear media, and comprises a group of elastic-perfectly plastic elements in parallel (i.e. a linear elastic spring and a rigid slip element connected in series).

STRONG MOTION SITE RESPONSE PREDICTIONS VS OBSERVATIONS

The approximate and incremental nonlinear models described above were initially validated for weak seismic motion recorded at the three stations. Successively, the effectiveness of nonlinear predictions was investigated for the limited number of strong motion recordings. A typical example of a medium intensity event (M4.2, PGA= 0.22g) recorded at the La Cienega SMGA is shown in Fig. 2, where the predictions by the ensemble of models are compared against the response spectrum of the recorded motion on ground surface. While the intensity of ground motion is not adequate to illustrate the advantages of implementation of an elaborate nonlinear model in lieu of the approximate equivalent linear method, the average spectrum predicted by the incremental nonlinear analyses is shown to be in better agreement with the observed response and was used in the ensuing as proxy for the *true strong motion site response* (Fig. 2). Similar results were obtained for the ensemble of ground motion recordings at all three SMGA in the LA Basin. Fig. 2 also shows the variation of the averaged error between predicted and observed ground motions as a function of the observed PGA on

ground surface. Assuming that the latter may describe the ground motion intensity, it can be readily seen that the error estimated from the average response of nonlinear predictions is e_{SA}<20% for the entire spectrum of ground motion intensities, while, as expected, the error of the response predicted by means of the linear elastic operator is shown to be proportional to the amplitude of PGA. The ensemble of weak and strong motion recordings used for benchmarking and error estimation purposes were obtained from the Engineering Strong Motion Data Center of the California Integrated Seismic Network (http://www.cisn.org/).

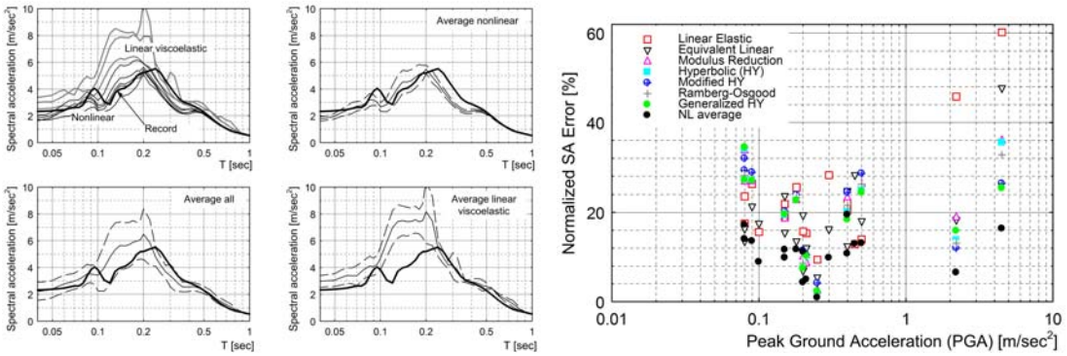


FIG. 2. Comparison between observations and predictions of strong ground motion, using the ensemble of approximate and nonlinear site response models: (left) La Cienega SMGA (09/09/2001 M4.2 event) and (right) cumulative error.

MODELING UNCERTAINTY IN NONLINEAR SITE RESPONSE ANALYSES

The ensemble of site response models are successively used to for the assessment of the relative modeling uncertainty of site response predictions in strong ground motion broadband simulations. The site response modeling uncertainty was first evaluated by means of the coefficient of variance (COV) in predictions of site-to-rock outcrop spectral amplification as a function of the station distance from the ground surface projection of the fault (R) and the magnitude (M) of the simulated rupture scenario. Results indicated that the M-R description of ground motion may not be used effectively as a proxy to describe the nonlinearity susceptibility of a given soil profile. Note that the nonlinearity susceptibility of a site is a function both of the site conditions and the incident ground motion intensity and frequency content, and while the former describes the strength of the material, the latter represents the amplitude of wavelengths of the same order of magnitude as the soft layers of the profile that may potentially be driven to the nonlinear range. Therefore, a description based on the M-R of the station and the site conditions is not adequate to describe the ground motion frequency content, which in turn defines the susceptibility of the site to nonlinear effects.

Based on this interpretation, an alternative index was developed to describe the variability in predicted ground motion intensity measures (IM's) introduced by the site response model implemented in broadband ground motion simulations. Referred to as the normalized central ground motion frequency (f_N), this index corresponds to the ratio of the central frequency of the linear elastic transfer function of the profile under investigation (f_{c_S}), to the central rock-outcrop ground motion frequency (f_{c_RO}) (here evaluated as the linear elastic response of a B-C boundary site). The central frequency

is defined as the ratio of the second to the first order spectral moments of the corresponding amplitude spectrum. Fig. 3a depicts the variation of the COV averaged across the ground surface response spectrum (SA) for the period range T=0–1.0s as a function of f_N and PGA_{RO}, the latter used as a proxy for the intensity of incident ground motion. It should be noted herein that by describing the nonlinearity susceptibility as a function of the normalized frequency content of seismic motion and the PGA_{RO}, both components (fault-normal and -parallel) of the horizontal ground motion may be simultaneously accounted. Used in conjunction with PGA_{RO} that describes the intensity of incident ground motion in absence of the soil column nonlinear effects, the normalized frequency index is a measure of the frequency content similarity between incident ground motion and soil transfer function, and thus indicates the amplification potential of the site conditions under investigation for the seismic event of interest.

As can be readily seen in Fig. 3, the COV in predicted ground surface spectral acceleration of the alternative approximate and elaborate nonlinear site response methodologies increases with increasing ground motion intensity (here represented by the increasing PGA_{RO}) and is shown to attain maximum values for normalized central frequencies f_N on the order of [0.4-0.6]. The latter is attributed to the fact that as the motion intensity increases, the nonlinear soil response in the near-surface becomes more pronounced, which is manifesting through reduction of the shear wave velocity. In turn, this instantaneous (strain-compatible) softening of the material results in reduction of the central frequency of the surface-to-rock outcrop transfer function at the site of interest, namely the numerator of the normalized central frequency index (f_N). The intensity-frequency content regions that correspond to large values of COV imply large incompatibilities among the alternative site response methodologies in estimating the ground surface spectral acceleration, and the sensitivity of the predicted ground motion to the selected model indicates that incremental nonlinear analyses should be conducted to ensure credibility of the predictions. For more information, the reader is referred to Assimaki et al (2007).

SITE AMPLIFICATION FACTORS IN ATTENUATION RELATIONS

In this section, we investigate the effects of nonlinear site response modeling uncertainty in the development of amplification factors for implementation in synthetic attenuation relations, by computing the spectral amplification at different periods for the nonlinear site response predictions averaged across the ensemble of models. The site-specific amplification factors for the three sites under investigation are compared in Fig. 3b to the values suggested by the NEHRP (BSSC 2001), and to recently published amplification factors (Choi & Stewart, 2005) for the corresponding site conditions.

As can be readily seen for Class C (Obregon Park) site conditions, currently employed amplification factors are in excellent agreement with the synthetic database of site response analyses developed in this study. Similar results are observed for the Class D soil profile (La Cienega), with the exception of the divergence depicted between published relationships and synthetic amplification factors in the low-amplitude PGA_{RO} region of the mid-period (T=1.0s) components. On the other hand, strong deviation of the synthetic from the currently employed amplification factors is observed for the Class E site (i.e. Meloland), especially in the mid-period range (T=1.0s). Both

the NEHRP and Choi & Stewart (2005) site amplification factors are shown to overestimate the amplification anticipated (or underestimate the extent of nonlinearity exerted by the soil profile) by a factor on the order of 1.5, while the effect is more pronounced in the mid-period range of the spectrum (T=1.0s). This indicates that currently employed amplification factors may be implemented to predict the level of amplification for Class C and D site conditions, while site-specific simulations should be employed for strong ground motion analyses at Class E sites, and for this case in particular, incremental nonlinear analyses for levels of $PGA_{RO} > 0.2g$.

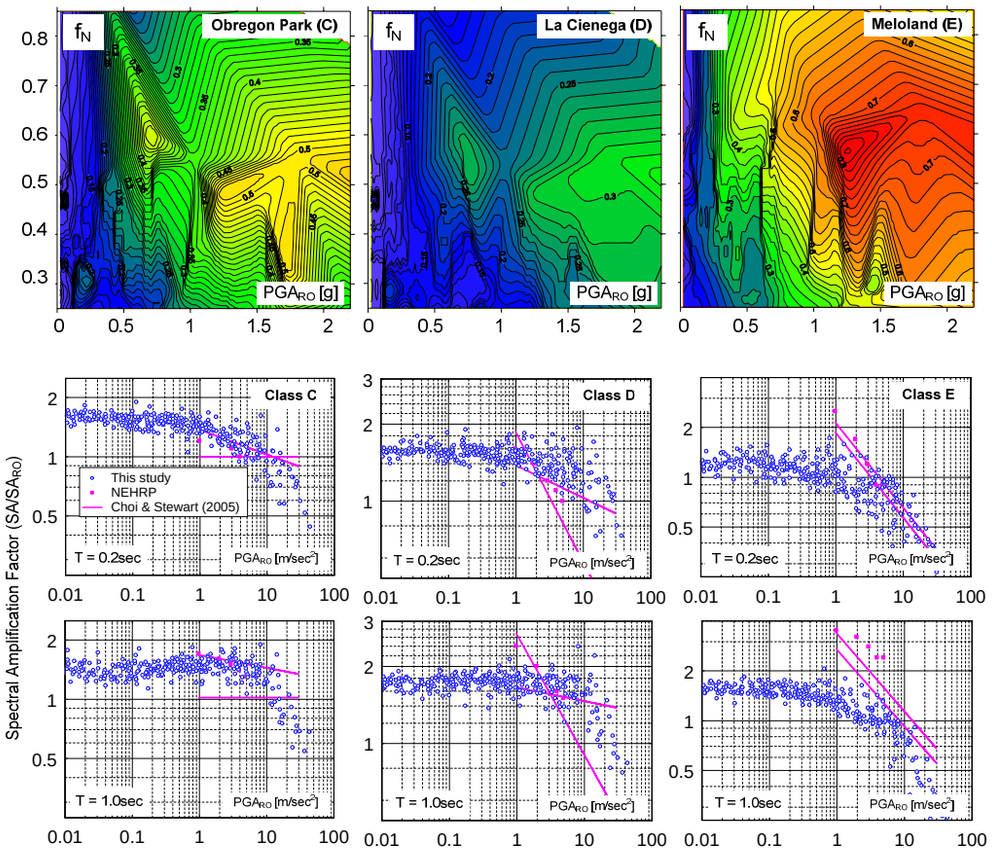


FIG. 3. (top) Contour maps of the average COV of predicted SA for the nonlinear models as a function of the PGA_{RO} and the frequency index (f_N) at three sites representative of Classes C, D and E; (bottom) Comparison of amplification factors averaged over the ensemble of nonlinear models to currently employed factors for the site conditions at three SMGA in the Los Angeles Basin.

CONCLUSIONS

In this paper, downhole observations were combined with broadband ground motion synthetics for characteristic profiles in the LA Basin, to investigate the variability in ground motion estimation that is introduced by methodology selected for the assessment of site response. The modeling nonlinear site response uncertainty introduced in the broadband ground motion predictions was reported by means of the COV of site amplification, defined as the averaged ratio of predicted spectral acceleration (SA) to

the corresponding intensity measure on the ground surface of a typical NEHRP BC boundary profile (V_{s30}=760m/s). A frequency index was developed and implemented to describe the variability in predicted ground motion intensity measures (IM's) introduced by the site response model. Referred to as the normalized central ground motion frequency (f_N), this index corresponds to the ratio of the central frequency of the profile linear elastic transfer function under investigation (f_{c_S}) to the central rock-outcrop (BC boundary) ground motion frequency (f_{c_RO}). Used in conjunction with the intensity of incident ground motion in absence of ground surface effects (PGA_{RO}), the normalized frequency index is a measure of the frequency content similarity between incident ground motion and soil transfer function, and thus indicates the amplification potential of the site conditions under investigation for the seismic event of interest.

The COV in predicted ground surface spectral acceleration was shown to increase with increasing ground motion intensity, and to attain maximum values for normalized central frequencies f_N on the order of 0.5. The intensity-frequency content regions corresponding to large values of COV were coined to large incompatibilities among the alternative site response methodologies in estimating the ground surface spectral acceleration, and the ground motion prediction sensitivity to the selected model was shown to indicate that incremental nonlinear analyses should be conducted to ensure credibility of the strong motion site response. Finally, currently employed low- and mid-period site amplification factors for Class C, D and E site conditions were compared to the best estimates of nonlinear ground surface site response in this study. For Class C site conditions, currently employed amplification factors were found to be in excellent agreement with the synthetic factors developed in this study. Similar results were observed for the Class D soil profile, with the exception of the divergence between published relationships and synthetic amplification factors in the low-amplitude PGA_{RO} region of the mid-period (T=1.0s) components. Strong deviation of the synthetic from the currently employed amplification factors was observed for the Class E site, especially in the mid-period range (T=1.0s).

Selection of the appropriate methodology for prediction of soil nonlinearity in strong ground motion is based on the anticipated strain amplitude, and while EQL formulations have been shown to produce reasonable results for low strain amplitudes, nonlinear methods are necessary to capture large, irreversible deformations. The accuracy of nonlinear site-response analyses, however, depends on the constitutive model used, and elaborate constitutive models require numerous parameters which must be determined through lab tests and/or field tests; in turn, this additional effort involved to develop the required parameters, often limits their frequency of use. We have briefly described a comprehensive modeling uncertainty analysis of strong motion site response at three downhole array sites in the Los Angeles Basin, and introduced a set of criteria for the identification of combinations of site conditions and ground motion characteristics where different degree of complexity models should be employed for the evaluation of credible predictions. Extension of this study to a large sample of site conditions and regional hazard-consistent ground motion scenaria would lead to the establishment of guidelines for the assessment of credible, cost-effective and efficient strong motion site effects in engineering practice and in seismology.

ACKNOWLEDGMENTS

This research was supported by the Southern California Earthquake Center. SCEC is funded by NSF Cooperative Agreement EAR-0106924 and USGS Cooperative Agreement 02HQAG0008. The SCEC contribution number for this paper is 1122.

REFERENCES

Assimaki, D., J.H. Steidl and P.C. Liu (2006). Attenuation and velocity structure for site response analyses via downhole seismogram inversion, PAGEOPH, Vol. 163, No. 1, 81-118

Assimaki D., Li W., Steidl J.H. & Schmedes J. (2007). Modeling nonlinear site response uncertainty in broadband ground motion simulations for the Los Angeles basin, Bulletin of the Seismological Society of America (in press)

Building Seismic Safety Council (BSSC), 2001. NEHRP Provisions, Federal Emergency Management Agency, FEMA-368 and FEMA-369, Washington D.C., February

Choi, Y. and Stewart, J.P. (2005). Nonlinear site amplification as function of 30 m shear wave velocity, Earthquake Spectra, 21 (1), 1-30

Day, S. M., and J. R. Minster (1984). Numerical simulation of attenuated wavefields using a Pade approximant method, Geophys. J. R. Astr. Soc. 78, 105–118

Faccioli, E.E., V. Santayo and J.L. Leone (1973). Microzonation criteria and seismic response studies for the city of Managua, Proc. of Earthquake Engineering, Res. Dist. Conf. Managua, Nicaragua, Earthquake of December 23, 1972, 1:271-291

Hayashi, H., M. Honda, and Yamada T. (1992). Modeling of nonlinear stress strain relations of sands for dynamic response analysis, In Proc. World Conf. on Earthquake Engineering, Vol. 11, pp. 6819-6825, Madrid, Spain, Balkema, Rotterdam

Ishihara, K. (1996). Soil Behavior in Earthquake Geotechnics, Oxford Press, 350 pp

Iwan, W.D. (1967), On a Class of Models for the Yielding Behavior of Continuous and Composite Systems. J. Appl. Mech., ASME, Vol. 34, pp. 612-617

Liu P.-C. and Archuleta R.J. (2006). Efficient Modeling of Q for 3D Numerical Simulation of Wave Propagation, Bulletin of the Seismological Society of America, Vol. 96, No. 4A, pp. 1352–1358

Liu P.-C., Archuleta R.J. and Hartzell S.H. (2007). Prediction of Broadband Ground-Motion Time Histories: Hybrid Low/High-Frequency Method with Correlated Random Source Parameters, BSSA, 96, 2118-2130

Masing, G., (1926). Eigenspannungen und Verfertigung beim Messing, Proceedings 2nd International Congress on Applied Mechanics, Zurich

Matasovic M. & Vucetic M. (1995). Generalized Cyclic-Degradation-Pore-Pressure Generation Model for Clays, J. Geotech. Engrg., Volume 121, Issue 1, pp. 33-42

Schnabel, P.B., Lysmer, J., and Seed, H.B. (1972). SHAKE: A computer program for earthquake response analyses of horizontally layered sites. Report No. EERC 72-12, Univ. of California, Berkeley

Seed, H. B. and I.M. Idriss (1970). Soil moduli and damping factors for dynamic response analyses. Earthquake Engin. Res. Center, Univ. of Calif. at Berkeley, UCB/EERC-70/10

Nonlinear Shear Wave Propagation in Strain Stiffening and Strain Softening Soil

Jui-Ching Chou[1] and Bruce Kutter[2]

[1]Ph.D. candidate, Department of Civil and Environmental Engineering
University of California, Davis, CA, USA
[2]Professor, Department of Civil and Environmental Engineering
University of California, Davis, CA, USA

ABSTRACT: Linear or equivalent linear wave propagation models, such as SHAKE, assume that the shear wave velocity is constant, hence the wave form is not distorted during propagation. If the tangent shear modulus is not constant, then perturbations in stress travel at different speed depending on the tangent modulus at that point and time. In cyclic loading, the shear stress-strain curve can be concave down, which we call strain-softening (near failure, for example) or concave up, which we call strain-stiffening (if there are negative pore pressures being generated due to dilatancy). In strain stiffening soil, the peak of a stress wave travels faster than the front, the wave front sharpens, and there is a possibility to form a shock wave. If the soil is strain softening, the peak travels slower than the front and the wave front elongates to form a dispersed wave.
In this study, we describe evidence of nonlinear wave propagation including formation of shock waves that has been observed using a vertical array of accelerometers in centrifuge model tests and in real earthquake data. Implications of non-linear wave propagation in strain-stiffening and strain-softening soil are discussed. We also look at the reflection phenomena of nonlinear waves at rigid and free boundaries. One result is that for a soil that is undergoing cyclic mobility (negative pore pressure development during loading, and positive pore pressure development during unloading), the wave sharpens as it approaches the ground surface and the reflected wave is almost negligible.

INTRODUCTION

Commonly, linear or equivalent linear wave propagation models, such as SHAKE, are used to predict the wave propagation during earthquakes. These models assume that the tangent shear modulus is constant. Therefore, the frequency of a wave pulse is constant and is not distorted during propagation.

Field observations at numerous sites during numerous earthquakes indicate that large amplitude spikes in the ground surface acceleration have been observed at sites where liquefaction effects are indicated (e.g., Youd and Holzer 1994, Frankel et al.

2002, Bonilla et al. 2005); this runs contrary to a common belief that liquefaction isolates the ground surface from large accelerations. Many researchers have determined that the spikes are caused by a sudden stiffening of the soil associated with pulses of negative pore pressure. Negative pore pressure pulses are a feature that is commonly observed during undrained cyclic loading of dilatant soil.

In cyclic loading, the shear stress-strain curve can be concave down, which we call strain-softening (near failure, for example) or concave up, which we call strain-stiffening (associated with increases in effective stress caused by negative pore pressures). Either in strain-softening or strain-stiffening material, the tangent shear modulus is not a constant. If the tangent shear modulus is not constant, then perturbations in stress travel at different speed depending on the tangent modulus at that point and time.

In strain stiffening soil, the peak of a stress wave travels faster than the front, the wave front sharpens, and there is a possibility to form a shock wave. If the soil is strain softening, the peak travels slower than the front and the wave front elongates to form a dispersed wave.

NONLINEARITY OF SOIL BEHAVIOR

In cyclic loading of soil, it is useful to distinguish two common classes of nonlinearities which have significant effect on wave propagation phenomena (Kutter 2006).

(1) Strain-softening nonlinearity: tangent shear modulus degrades as strain increases (e.g., hyperbolic stress-strain law).
(2) Strain-stiffening nonlinearity: tangent shear modulus increases as strain increases (e.g., effect of dilatancy on saturated sand).

Strain-Softening Nonlinearity

The effects of this type of nonlinear soil behavior on ground motions has been understood since Seed and Idriss (1970) published their report “Soil moduli and damping factors for dynamic response analysis”. They presented modulus degradation curves (Figure 1) for site response analysis that indicate that shear modulus monotonically decreases as the magnitude of shear strain increases. Hyperbolic stress-strain relations also presume “strain-softening nonlinearity”: the initial shear modulus is the maximum shear modulus, and the modulus degrades as strain increases. The effects of strain-softening nonlinearity on site response have been the subject of

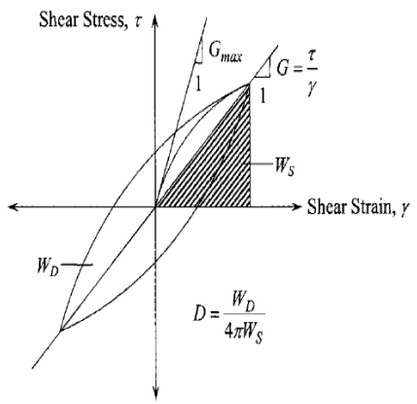


FIG.1 Hysteresis loop for one cycle showing G, G_{max}, and Damping, D for a strain-softening soil.

investigations by many researchers. Beresnev and Wen (1996), Kausel and Assimaki (2002), Ni et al. (1997) are just a few relatively recent examples. Strain-softening nonlinearity tends to result in attenuation of large accelerations, especially those that mobilize shear stresses that approach the shear strength of the soil. The prevalence of site response analyses that assume strain-softening nonlinearity may be partly responsible for the widely held belief that nonlinearity will tend to limit the peak ground accelerations. The belief turns out to be correct for softening soil, but it is not generally correct for strain-stiffening soils.

Strain-Stiffening Nonlinearity

It is well known that stress-strain relationships for soils can show both strain softening and strain-stiffening. The torsional shear test data from Ishihara (1985) in Figure 2 show this very clearly. The amplitude of cyclic shear-strain increases and the average shear modulus of the soil decreases with the number of cycles – a strain-softening phenomenon. But, if you consider one individual cycle, the mean effective normal stress oscillates and we clearly see a strain-stiffening behavior.

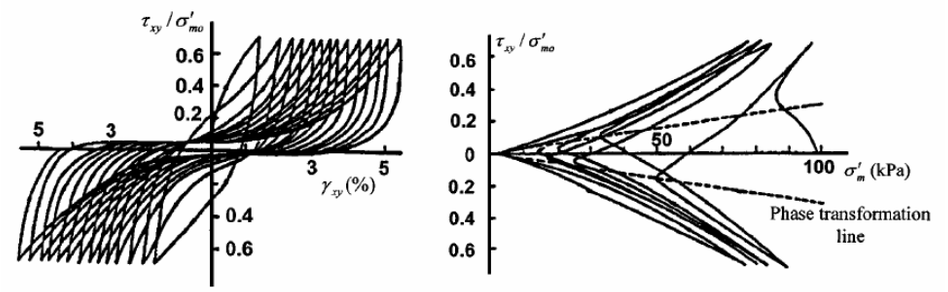


FIG.2 Undrained torsional shear behavior of Fuji River Sand at a relative density of 75% (Ishihara 1985).

Shock Wave and Dispersed Wave

In strain stiffening soil, the peak of a stress wave locates at the end of the concave up curve. The tangent shear modulus at the peak of a stress wave is higher than at the front of a stress wave. Therefore, the shear wave velocity at the peak is faster than at the front. When the peak travels faster, the wave front sharpens, and there is a possibility to form a shock wave. If the soil is strain softening, the peak of a stress wave locates at the end of the concave down curve. Therefore, the peak travels slower than the front and the wave front elongates to form a dispersed wave.

FIELD OBSERVATIONS

Recent observations from ground motion instrumentation indicate that although liquefaction results in a general softening of the soil and an increase in the predominant period of the motion, but at the same time, high frequency spikes or cusps of

acceleration have been observed. The magnitude of these spikes can be quite large (Figures 3-5).

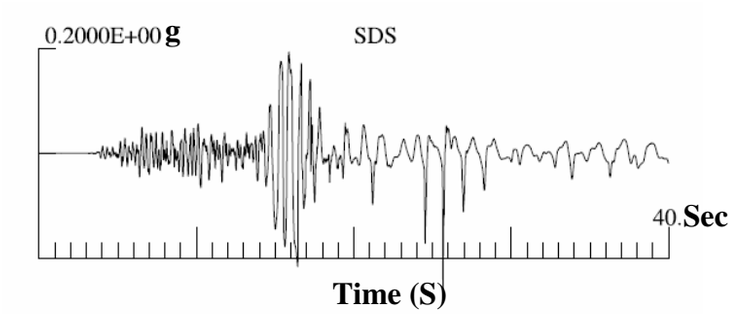


FIG.3 Ground surface accelerations at a site a few kilometers south of downtown Settle in the M 6.8 Nisqually, Washington earthquake. Note the large one-sided spikes between t = 24 - 29 s. (Data from Frankel et al. 2002)

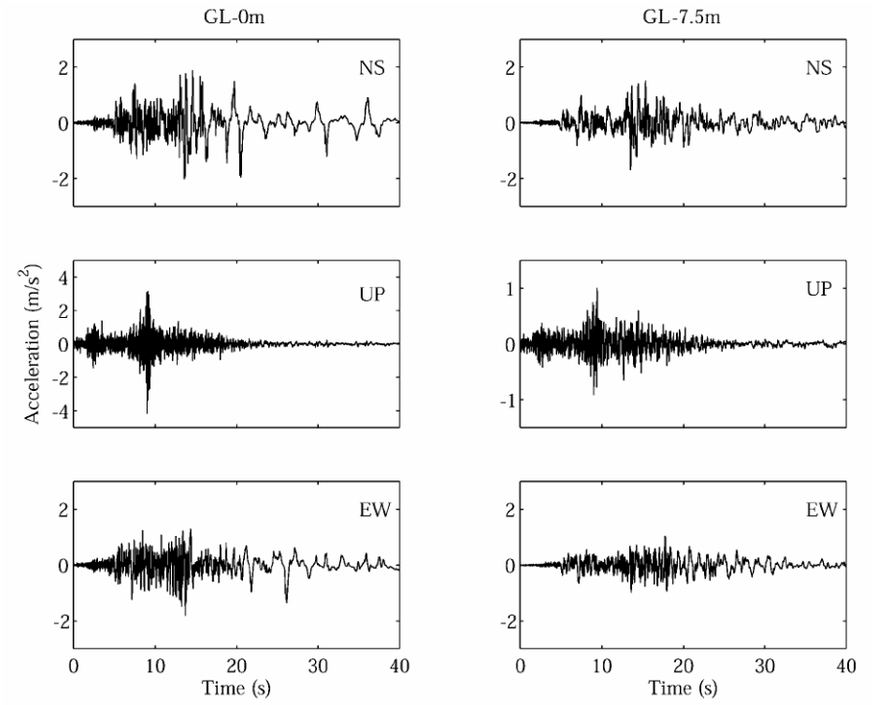


FIG.4 Spiky horizontal ground accelerations observed at the Wildlife Refuge during Superstition Hills Earthquake. Spikes are apparent at the surface (GL-0m) but not at depth (GL-7.5m) (Figure from Bonilla et al. 2005).

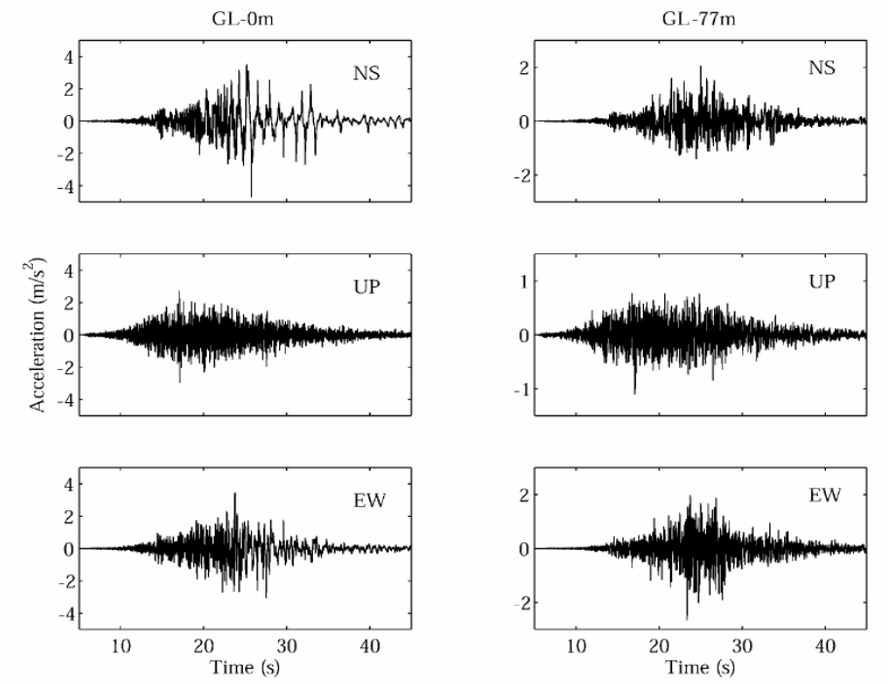


FIG.5 Surface (GL-0 m) and borehole (GL-77 m) acceleration time histories for a dense sand deposit during the 1993 Kushiro-oki earthquake. One spike approaches 0.5 g in amplitude and spikes continue well after accelerations subside. (Figure from Bonilla et al. 2005.)

Youd and Holzer (1994) after analyzing the pore pressure and acceleration data from the Wildlife Site (accelerations are shown in Figure 4) explained that as the ground oscillated back and forth, displacement was arrested by dilatancy that caused a sudden drop of pore pressure accompanied by a sudden deceleration. They explained that the concurrent dips in acceleration and pore-pressure records indicate that the liquefied soil was in a state of cyclic mobility. Youd and Holzer (1994) explained that the spikes in surface acceleration occurred later in the record because ground oscillation actually increased in amplitude for about 20 s after the primary train of acceleration pulses had passed through the site. More recently, Holzer and Youd (2007) explained that Love waves were responsible for the long period motions. The spiky accelerations that occurred as a result of long period excitation may be approximated as shock waves.

Zeghal et al. (1994), Zeghal and Elgamal (1996), Youd and Holzer (1994), Bonilla et al. (2005), and Holzer and Youd (2007) analyzed acceleration and pore pressure data from the Wildlife Site obtained during the Superstition Hills Earthquake and found that pulses of negative pore water pressure coincided with large shear strains. They also observed stiffening of the soil at the site associated with the reduction in pore water pressure and the increase in effective stress. They were able to back-calculate stress-strain and stress path relationships for the soil at the Wildlife Site and observed that the patterns (Figure 6) were similar to those observed in laboratory tests (Figure 2).

Frankel et al. (2002), based on observations in the M 6.8 Nisqually earthquake, observed cusped, one-sided, acceleration time series at three sites for which nearby liquefaction was observed, and presented a strong case demonstrating that nonlinearity can have significant effects on the character of the ground surface motions, and supported the explanation that the spikes are associated with the stiffening of the soil due to the negative pore pressures that develop due to soil dilatancy. Bonilla et al. (2005) presented similar evidence of cusps in the 1993 Kushiro-Oki, Japan, and the 1979 Imperial Valley, California, 1994 Northridge, and 1995 Kobe earthquakes. They point out that the large peak accelerations (as large as 0.8 g) in surface motions of liquefiable soils are inconsistent with the common expectation that amplification factors will reduce due to soil nonlinearity.

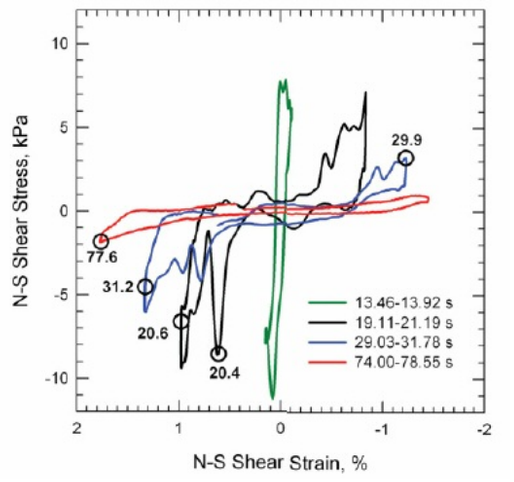


FIG.6 The stress-strain curve (from Holzer and Youd 2007) was obtained by processing accelerometer data at the Wildlife Site according to the procedures developed by Zeghal and Elgamal (1994).

Recently, a large earthquake occurred on July 16, 2007 in Chuetsu region, Niigata, Japan. From the report, liquefaction occurred in this area and horizontal acceleration spikes were observed in the acceleration time histories (Figure 7). Also, from the

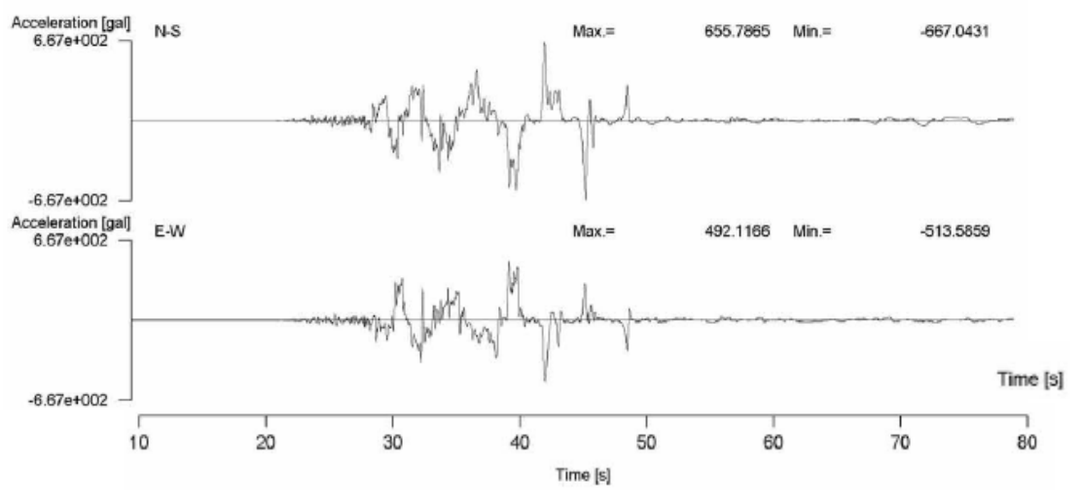


FIG.7 Ground surface acceleration time histories for the 2007 Niigata, Japan earthquake. (Figure from Preliminary report of the July 16, 2007 Niigata Earthquake.)

acceleration time histories, the horizontal peak accelerations are observed in these spikes between 25 and 30 seconds.

CENTRIFUGE DATA

Kutter and Wilson (1999) recognized that many aspects of the propagation of acceleration spikes in centrifuge model tests could be explained as Shock waves. Shock waves are characterized by an abrupt change (a discontinuity) in the wave moving through the medium; for the problem at hand, the spikes in acceleration correspond to discontinuities in shear stress, ground velocity, and pore water pressure. Shock waves are theoretically possible in material that displays Strain-Stiffening Nonlinearity.

Figure 8 shows data from Kutter et al. (2004) obtained from a dense vertical array in a layered soil profile. The left side of Figure 8 shows a schematic of the soil layering, and the accelerometer locations are indicated by arrows. The base layer (with H2 = 9 m) consisted of sand with relative density of 80%, the layer with H1 = 4.5 m consisted of sand with relative density of 50%, and the top layer is an approximately 2 m thick sloping clay layer. The entire box is sloping to the left so that lateral spreading could be studied. From these data it was clear to see that pulses travel at a variety of speeds, some of them disappear, and some of them focus into spikes. The spikes are unsymmetrical due to the existence of a static shear stress in the direction of the sloping ground. Some pulses were observed to travel as slow as 11 m/s. Also, wave velocities are obviously not constant, some small waves coalesce into sharper waves, sometimes forming a sharp spike and then the spike waves sometimes grow and sometimes die as they propagate through the soil.

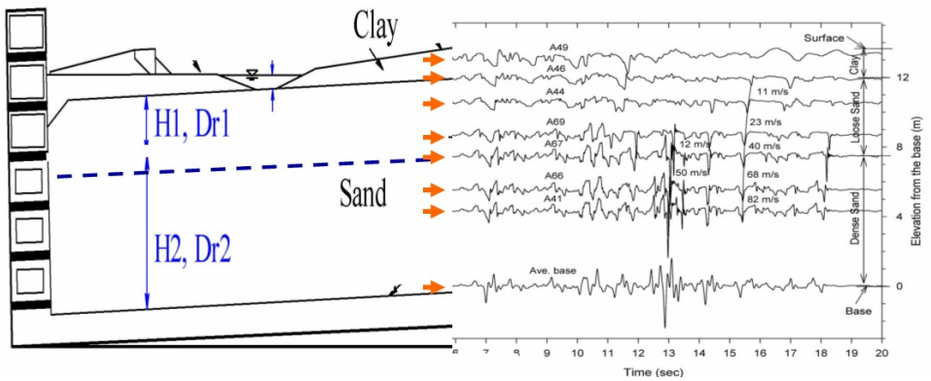


FIG.8 Data from Kutter et al. (2004) showing location of sensors in a centrifuge model container, and the acceleration records in a large shaking event. Time and depth have been scaled by a factor of 30 to prototype scale.

Taboada and Dobry (1998) studied effects of frequency, peak acceleration, and ground slope on the development of spiky accelerations, when sinusoidal accelerations were input to the base of a centrifuge model container. The spikes tended to arrest the lateral spreading deformations, and hence tended to be unsymmetrical for sloping ground. Figure 9 shows an example plot from their paper also illustrating the dependence of the spikes on the frequency of the ground motion. This result is consistent with the findings of Youd and Holzer that the spikes are more likely to be triggered by long period motions.

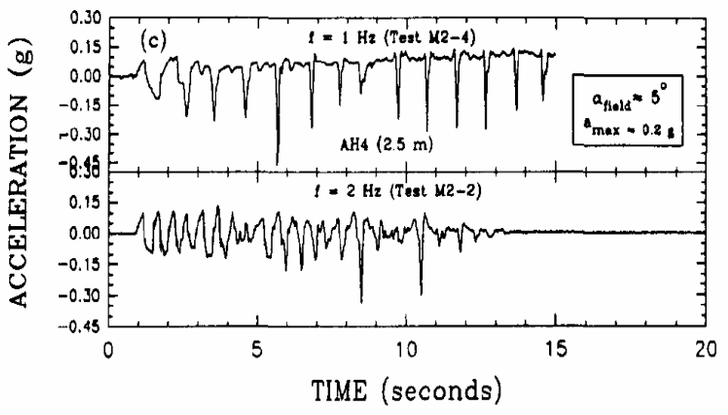


FIG.9 Taboada and Dobry (1998) observed from centrifuge model tests the effects of ground slope and shaking frequency on spikes in the motion at the ground surface. Example results here show the effect of frequency for a slope of 5°

THEORY OF NONLINEAR WAVE PROPAGATION AND NUMERICAL MODELING

Kutter and Wilson (1999) hypothesize that the formation of the spikes may be described using nonlinear wave propagation theory, including shock wave theory. According to basic theory of shock waves, the shock waves will propagate at a speed corresponding to the secant stiffness between the wave front and the peak (Bedford and Drumheller 1994). Figure 10 defines the peak and initial shear modulus and the secant

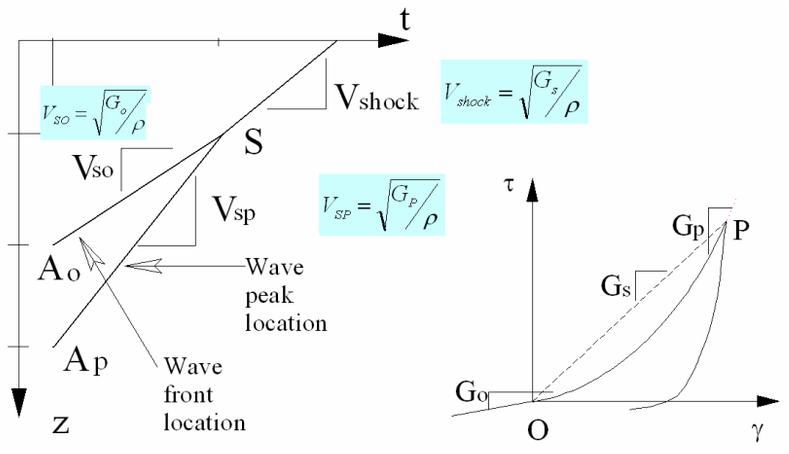


FIG.10 Characteristics showing the propagation of the front of a wave, traveling at V_{so} meeting the peak of a wave, traveling at V_{sp}, meeting to form a shock wave at the point labeled "S". The stress strain curve on the right defines the initial, peak and secant shear moduli that correspond to V_{so}, V_{sp}, and V_{shock}. (Adapted from Kutter and Wilson 1999)

shear modulus in a strain-stiffening soil, and shows a characteristic diagram for an upward propagating wave with the peak catching the front at point S, where a discontinuous wave is formed. According to the secant shear modulus, the shock wave may travel at quite a low velocity.

CONCLUSIONS

When sand is subjected to undrained cyclic loading, two types of soil nonlinearities will occur, strain-softening and strain-stiffening nonlinearities. These two nonlinearities cause the nonlinearity of the tangent shear modulus which results in the nonlinear wave propagation phenomenon. Therefore, assuming a constant tangent shear modulus during the wave propagation at particular shear strain point is inappropriate. In strain-softening nonlinearity, the shear modulus degrades as strain increases (e.g., hyperbolic stress-strain law) and there is a possibility to form a dispersed wave. In Strain-stiffening nonlinearity, shear modulus increases as strain increases (e.g., effect of dilatancy on saturated sand) and a shock wave may be formed.

Based on the nonlinear wave propagation theory, shock waves should be expected to occur in strain-stiffening material. Based on laboratory tests, it is well known that undrained dilantant soil that is approaching liquefaction prominently displays strain-stiffening behavior .The shock wave velocity depends on the secant shear modulus between the wave front and the shock front. Therefore, the shock wave will travel at a quite low velocity.

Formal training of geotechnical earthquake engineers tends to emphasize linear wave propagation theory, making it difficult to understand basic concepts of wave propagation in nonlinear media. Understanding wave propagation in “liquefied” soil requires understanding of nonlinear wave propagation theory.

Ongoing studies are directed to quantify the factors that control the maximum size of the acceleration spikes (e.g., pulse width and peak acceleration). Relative density, permeability, grain size effects, and amplitude of ground oscillation are expected to play a role in the size of the acceleration spikes. Finally, the occurrence of large acceleration spikes may be alarming since peak acceleration is a common parameter upon which designs are based. The short duration of the spikes is a mitigating factor, which might limit the importance of the large spikes. Quantification of the importance of the amplitude and width of the spikes requires additional study.

ACKNOWLEDGMENTS

Daniel Wilson contributed to the development of the concepts of using shock waves to describe acceleration spikes. Centrifuge model tests were supported by the National Science Foundation, under award number EEC-9701568 through the Pacific Earthquake Engineering Research Center (PEER).

REFERENCES

Bedford, A. and Drumheller, D.S. (1994). "Introduction to elastic wave propagation," Wiley, Chichester.

Beresnev, I. A., and K. L. Wen (1996). "Nonlinear site response—a reality?" *Bull. Seism. Soc.*

Am., 86, pp. 1964-1978.

Bonilla, L. F., Archuleta, R. J. and Lavallee, D. (2005). "Hysteretic and Dilatant Behavior of Cohesionless Soils and Their Effects on Nonlinear Site Response: Field Data Observations and Modeling." *Bull. Seism. Soc. Am.*, 95, pp. 2373-2395.

Drumheller, D.S. (1998), "Introduction to Wave Propagation in Nonlinear Fluids and Solids." Cambridge University, 536 pages.

Frankel, A. D., D. L. Carver, and R. A. Williams (2002). "Nonlinear and linear site response and basin effects in Seattle for the M 6.8 Nisqually, Washington earthquake." *Bull. Seism. Soc. Am.*, 92, pp. 2090–2109.

Holzer, T,L., and T.L. Youd (2007). "Liquefaction. Ground Oscillation, and Soil Deformation at the Wildlife Array, California." *Bull. Seism. Soc. Am.*, In Press.

Ishihara, K. (1985). "Stability of natural deposits during earth-quakes." Proc.*, 11th Int. Conf. on Soil Mechanics and Foundation Engineering,* Vol. 2, San Francisco, pp. 321–376.

Jiao, Y.Y., Fan, S.C.; Zhao, (2005). "Numerical investigation of joint effect on shock wave propagation in jointed rock masses." *Journal of Testing and Evaluation*, v 33, n 3. pp. 197-203

Kausel, E., and D. Assimaki (2002). "Seismic simulation of inelastic soils via frequency-dependent moduli and damping." *J. Eng. Mech.*, 128, pp. 34–45.

Kutter, B. L. (2006). "Phenomena associated with undrained and partly drained dilatant soil." *International Conference on Physical Modeling in Geotechnics,* ISSMGE, Hong Kong, pp. 165-170.

Kutter B.L & Wilson D.W. (1999). "De-liquefaction shock waves." Proceedings *7th U.S Japan Workshop on earthquake resistant design of life line facilities and countermeasures against liquefaction*, pp. 295-310.

Kutter B.L., Gajan, S.M., Manda, K.K. and Balakrishnan, A., (2004). "Effects of layer thickness and density on settlement and lateral spreading." *Journal of Geotechnical and Geo-environmental Engineering*, ASCE, Vol. 130, No.6, pp. 603-614.

Ni, S. H., Siddharthan, R. V. and Anderson, J. G. (1997). "Characteristics of nonlinear soil response of deep saturated soil deposits." *Bull. Seism. Soc. Am.*, 87, pp. 342–355.

Seed, H. B., and Idriss, I. M. (1970). "Soil moduli and damping factors for dynamic response analysis." *Report EERC 70-10*, University of California, Earthquake Engineering Research Center, Berkeley, CA.

Taboada, V.M. and Dobry, R. (1998). "Centrifuge modeling of earthquake-induced lateral spreading." *J. Geotech. and Geoenvir. Engrg.*, 124, pp. 1195

Tobita, T., Ghayamghamian, M. R., Kang, G., Iai, S., (2007). "Preliminary report of the July 16, 2007 Niigata prefecture Chuetsu Off shore (Niigata-ken Chuetsu-Oki), Japan, Earthquake"

Youd, T. L., and T. L. Holzer (1994). "Piezometer performance at the wildlife liquefaction site." *California, J. Geotech. Eng.*, 120, no. 6, pp. 975–995.

Zeghal, M., and A. W. Elgamal (1994). "Analyses of site liquefaction using earthquake records." *J. Geotech. Eng.*, 120, no. 6, pp. 996-1017.

Zeghal, M., A. W. Elgamal, and E. Parra (1996). "Analyses of site liquefaction using downhole array seismic records." *11th World Conference on Earthquake Engineering*, paper 371, pp. 23–28 June 1996, Acapulco, Mexico.

Parametric Analysis of the Seismic Response of Irregular Topographic Features

Arash Razmkhah[1], Mohsen Kamalian [2], Roham Golrokh[3]

[1] Assistant Professor, Faculty of Engineering, Islamic Azad University, South Tehran Branch, Tehran, IRAN, Email: ar.razm@iiees.ac.ir
[2] Assistant Professor, Geotechnical Engineering Research Centre, IIEES, Tehran, IRAN, Email: kamalian@iiees.ac.ir
[3] M.Sc Geotechnical Engineer, Zamiran Consulting Engineers, Tehran, IRAN, Email: roham.golrokh@gmail.com

ABSTRACT: Since the 2D modeling of topographic features, through numerical analysis, has been done up to now, all by symmetrical geometries, there is a problem that, whether the seismic response of asymmetrical models are so different or not. As the natural features are not symmetric, it is so important for engineers to know whether they can analyze them based on symmetrical models and how much is their risk. Therefore, in this paper we have evaluated the 2D site response based on parametric study of several asymmetric geometry models of hill (asymmetric semi-sine, triangular and trapezoidal shapes) and have compared them with the response of their corresponded symmetrical models. The studies have been done in time domain and soil material is considered linear elastic. Also, the assumed input motion was a Ricker type wavelet which was considered as SV and P plane wave and applied vertically. All calculations are executed in time-domain using the direct boundary element method. Clear perspectives of the amplification patterns of the hill are presented by investigation of the frequency-domain responses. In general the results shown that the increase of asymmetry rate between two side of features model haven't has a considerable effect on their seismic response and the response are mainly affected by geometric properties of the part of models which includes larger surface of model plane. Also the opposite component of incident motion wave response at the crest has been more amplified due to asymmetry affects.

INTRODUCTION

In the recent past there have been numerous cases of recorded motion and observed earthquake damage pointing toward topographic amplification as an important effect. Very high acceleration recorded at Pacoima Dam (1.25g) during the 1971 San-Fernando earthquake [26,5] and Tarzana hill (1.78g) during the 1994 Northridge earthquake [25] have been at least partly attributed to topographic effects.

Observations from the 1983 Coalinga earthquake [10], the 1985 Chile earthquake [9], the 1987 Superstition Hills earthquake [10] as well as observations from recent earthquakes in Greece [2,8] are only some examples of catastrophic events, during which severe structural damage has been reported on high elevated regions.

Although nowadays it is well established that the seismic ground response of surface topographies could be different compared to those of the free field motion during earthquakes, but there are only few structural codes which have considered this issue (Eurocode8) [11]. This is due to complex nature of the seismic wave scattering by topographical structures which can only be solved accurately, economically and under realistic conditions, by advanced numerical methods. A recent compilation of works on the numerical modeling of seismic wave propagation has been presented by Bard [3], Beskos [4] and Sanchez-Sesma et al. [24].

Bouchon [7] was the first who attempted to evaluate the effect of semi-sine shaped hills on the surface motion. He used a frequency domain method which had been developed by Aki and Larner [1] and studied incident SH, P and SV waves. However, as Bouchon [7] mentioned, this method resulted in unreliable amplification factors for incident P and SV waves due to complicated calculations especially in high frequencies.

Later Geli et al. [14] studied by use of the Aki and Larner method, the seismic behavior of 2D semi-sine shaped hills affected by non homogeneity of the media and existence of adjacent similar hills. But their study too, was restricted to a specific shape ratio of 0.5 and to the special case of the incident SH wave.

Sanchez-Sesma [23] was the first who assessed the seismic behavior of sharp corner-type hills but he has considered only triangular hills, SH incident wave and one specified Poisson's ratio. Then, Moczo et al. [22] evaluated the seismic behavior of trapezoidal hills. Their studies were consisted of SV incident wave and only one shape ratio, crest angel and Poisson ratio.

Kamalian and his colleagues were the first group who implemented wide range parametric study on the seismic behavior of semi-sine [20], semi-elliptical [18], trapezoidal [17] and triangular [21] Hills subjected to vertical in plane P and SV incident waves for different Poisson ratios. These studies have been done in time domain and soil material is considered linear elastic.

However, as it has been mentioned, all studies carried out on symmetric models, and the asymmetric geometry affect on seismic response of features still is an unconsidered problem. Therefore this paper presents the results of a wide range numerical parametric study on amplification pattern of 2D homogenous asymmetric semi-sine, triangular and trapezoidal shaped hills subjected to vertically propagating incident SV and P waves, using time-domain boundary element (BE) method.

PARAMETRIC STUDY METODOLOGY

The properties of the 2D homogenous asymmetric semi-sine, triangular and trapezoidal shaped hill models (Figure 1) investigated in this parametric study defined as Table 1. The chosen parameters are based on previous studies on corresponding symmetrical models [17, 20, 21]. In this paper and due to keeping

abbreviation, only the results of SV waves and one of the poisson's ratios (0.33) will be presented and discussed.

Table 1. Formulas and Properties Used for Modeling in the Study

Feature Shape	Boundary Formula (ξ)	Shape Ratio (h/b_i)		Slope Angle (degree)	
		Left Side	Right Side	Left Side	Right Side
Semi-Sine	$\|x\| \le b_i : \xi_i(x) = 0.5h(1+\cos(\pi x/b_i))$ $\|x\| \ge b_i : \xi_i(x) = 0$ i=1,2 (See Figure 1)	0.2	0.1	-	-
		0.4	0.3	-	-
		0.6	0.5	-	-
		0.8	0.7	-	-
		0.5	0.3	-	-
		0.7	0.5	-	-
		0.5	0.1	-	-
		0.7	0.3	-	-
		0.7	0.1	-	-
		0.8	0.2	-	-
		0.8	0.1	-	-
Triangular	$\xi_i(x) = x(h/b_i)$ i=1,2 (See Figure 1)	0.2	0.1	-	-
		0.4	0.3	-	-
		0.6	0.5	-	-
		0.8	0.7	-	-
		0.5	0.3	-	-
		0.7	0.5	-	-
		0.5	0.1	-	-
		0.7	0.3	-	-
		0.7	0.1	-	-
		0.8	0.2	-	-
		0.8	0.1	-	-
Trapezoidal	---	0.1	0.1	15	30
		0.1	0.1	15	45
		0.1	0.1	30	45
		0.3	0.3	30	45
		0.5	0.5	30	45

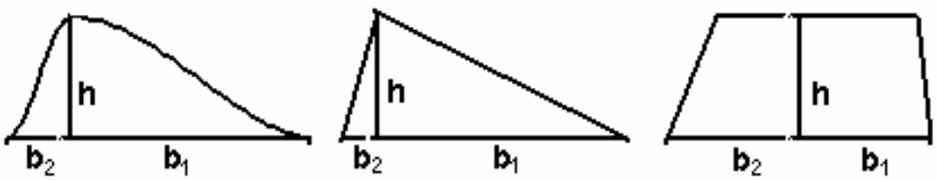


Figure 1. Geometry of the studied 2D homogenous asymmetric semi-sine, triangular and trapezoidal shaped hills

Where $\mathbf{b_i}$ and **h** denote the half of width and height of the hill, respectively.

In order to find out the pattern of asymmetric hill response, models were subjected to the vertically propagating Ricker type SV and P wave (Figures 2-a, 2-b), formulated as follow:

$$f(t) = [1-2(\pi.f_p.(t-t_0))^2]e^{-(\pi.f_p.(t-t_0))^2}$$

Where f_p and t_0, denote the predominant frequency and an appropriate time shift parameter, respectively. The applied incident Ricker-typed wavelet in all models here has had same parameters such as: f_P= 3(Hz), t_0= 0.45(s).

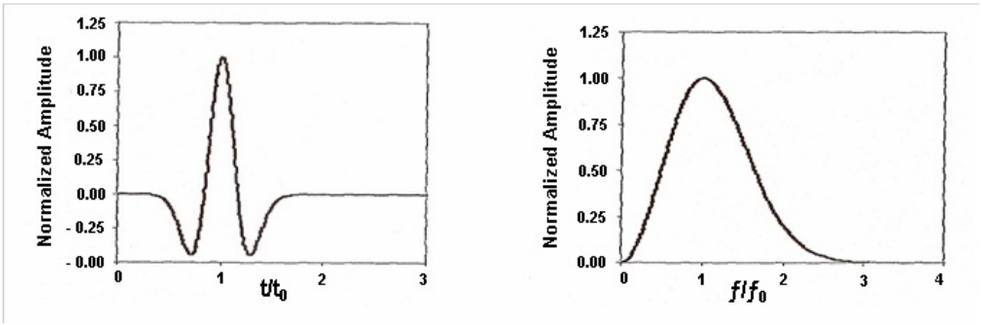


Figure 2-a. Normalized input motion of the Riker wavelet in time domain

Figure 2-b. Normalized input motion of the Riker wavelet in frequency domain

The BE formulation was implemented in a general purpose two-dimensional nonlinear two-phase BEM/FEM code named as HYBRID [12, 13, 15]. Several examples were solved in order to show the accuracy and efficiency of this implemented BE algorithm in carrying out site response analysis of topographic structures [16 to 21].

All results have been presented in dimensionless forms, using the dimensionless frequency Ω (or its inverse: the dimensionless period) definition. The dimensionless period physically means as the ratio of the incident's wave length to the width of the hill (Ω= Bf/V, where B, f and V are feature width, frequency and velocity of shear incident wave, respectively).

Based on engineering interests, a dimensionless period interval of 0.25 to 8.33 was considered, which corresponds to incident waves with wave lengths of 0.25 to 8.33 times the hill's width. This broad period interval was divided into the following five subintervals: 0.25 to 0.50 (P1), 0.50 to 1.00 (P2), 1.00 to 2.00 (P3), 2.00 to 4.17 (P4) and 4.17 to 8.33 (P5), corresponding to incident waves with very short, short, medium, large and very large wave lengths, respectively. For the reason of simplicity and following the well known concept of average horizontal spectral amplification (AHSA) defined by Borcherdt et al. [6] as spectral ratios representing averages over short, intermediate, mid and long period bands, five distinct amplification factors were computed for every point along the hill, by averaging the corresponding amplification curve over each of the above mentioned five period subintervals P1 to

P5. Whereas the results will be used for engineering purposes and microzonation study of areas the mean deamplification of features considered as unit.

RESULTS OF PARAMETRIC ANALYSIS

This section presents the results of the implemented parametric study, which demonstrates the sensitivity of 2D shaped hill's amplification patterns on various asymmetry geometry conditions. As already was mentioned, in this paper only the seismic response of features subjected to incident SV will be presented. So the results illustrated in this paper have been limited to SV wave responses. But, In general the final conclusions include both P and SV wave patterns.

Amplification Pattern at the Crest of Hills

Figure 3 shows the crest amplification patterns of 2D symmetric and asymmetric semi-sine shaped hills with a various combinations of sides shape ratio which subjected to incident SV and P waves. The amplifications about incident SV wave major component (horizontal component) at features crest are indicated in the figure.

As indicated, increasing the shape ratio increases the characteristic period of the hill and its corresponding amplification factor. Also the amplification patterns show that if the motion period of incident wave be higher than characteristic period of feature, the shape ratio changing and geometry irregularity affect on amplification could be negligible, but in fewer motion period condition or equal with, the amplification will be affected considerably, especially in the case of larger shape ratios. In condition that a side of feature has small shape ratio (e.g. shape ratio=0.1) or large angle, the shape ratio (or angle) changes of other side don't have noticeable effect on crest amplification. Because generally, the amplification of feature response are affected by part of feature includes larger area, so the smaller shape ratios (or larger angle) which resulting larger area have main rule in this cases. As example, the amplification of asymmetric feature included 0.8 and 0.1 oppositely shape ratios is not noticeable different with the symmetric feature included 0.1 and 0.1 oppositely shape ratios. But the amplification of a feature included two big shape ratios (e.g. 0.7 and 0.8 oppositely) will be considerable.

The amplification pattern and characteristic period changing of features subjected to incident P wave are similar to ones subjected to SV wave. Although the range of crest amplifications due to incident P wave are less than SV wave ones.

Also the results show that the irregularity of features has a considerable effect on seismic responses for opposite component of incident wave. As can be seen in Figure 4 the amplification of symmetric features motion subjected to opposite component of incident wave is naught, but in the case of asymmetric features it will be considerable.

Mean Amplification of Hills

Figure 5 shows the mean amplification factor of 2D triangular shaped hills with a various combinations of side shape ratios which subjected to incident SV waves in

the classified dimensionless period limits and serious differential shape ratios. The range of mean amplifications related to incident SV wave major component on the asymmetric shaped hills with 0.1 differential shape ratios for sides (feature left shape ratio minus right shape ratio) are shown in the figure. The curves patterns addition to confirming the results of Figure 3 in previous paragraph shows that irrespective of the shape ratio, the dimensionless period of incident wave motion which illustrates wave length plays a key rule in determining the amplification range of the hill. Regarding the P and SV major component, if the incident waves posses a long or very long wave length (medium or short dimensionless period limits), the hill would experience greater amplification, which increases with the shape ratio.

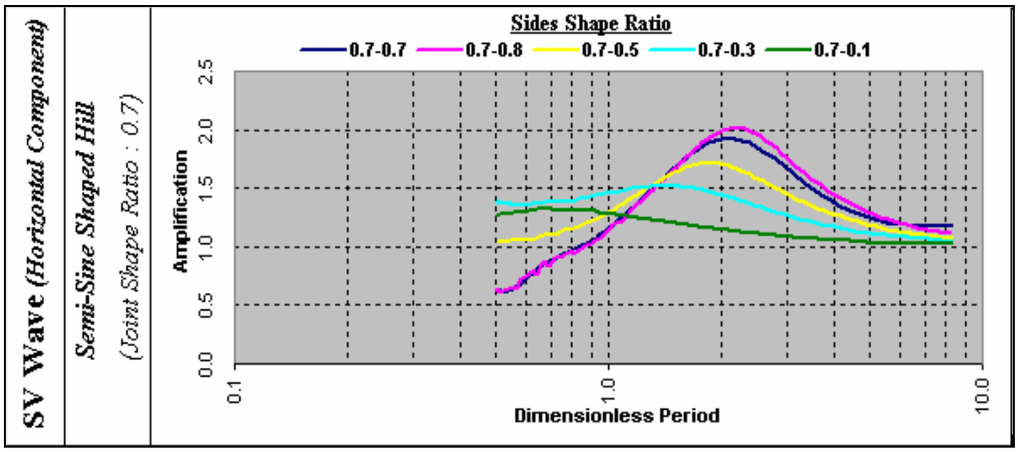


Figure 3. Comparative curves of features crest amplification Vs. dimensionless period for major component of incident SV wave, with various combinations of side shape ratios, for asymmetric semi-sine shaped hill.

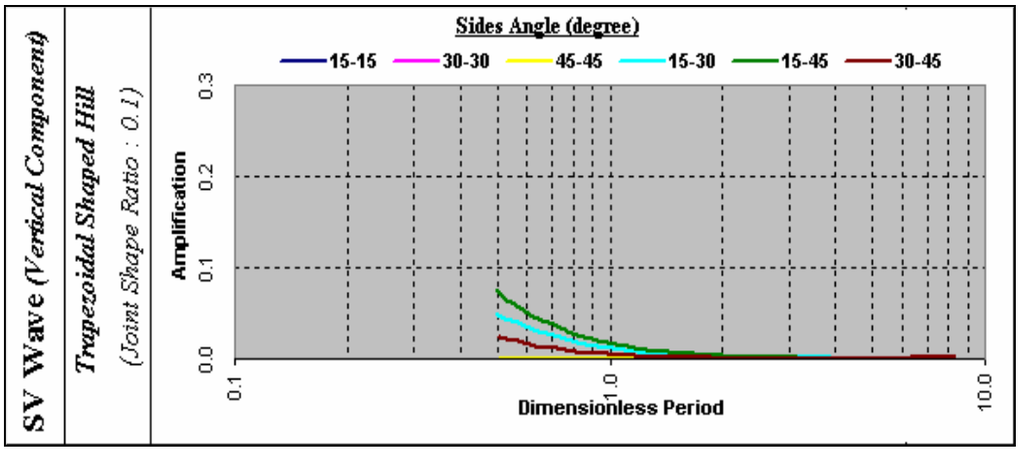


Figure 4. Comparative curves of features crest amplification Vs. dimensionless period for opposite component of SV wave, for various combinations of side angles, for symmetric and asymmetric trapezoidal shaped hill.

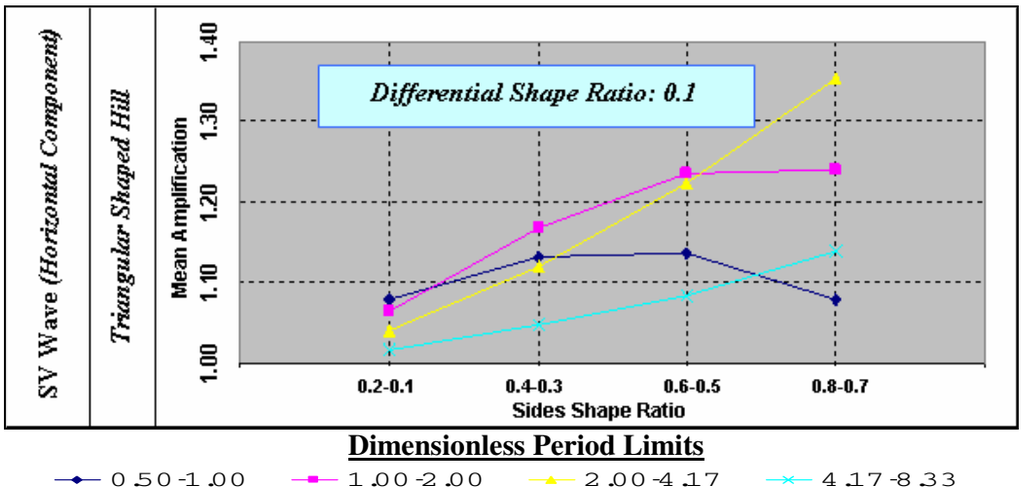


Figure 5. Comparative curves of mean amplification factor for major component of incident SV wave, based on differential shape ratio ($S.R_{left}$ – $S.R_{right}$), for various combinations of symmetric and asymmetric triangular shaped side shape ratios, in considerable dimensionless period limits.

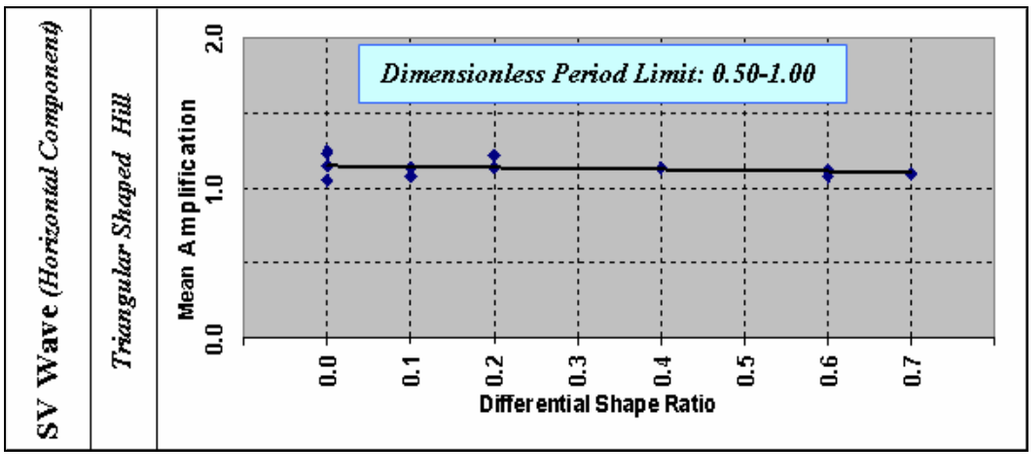


Figure 6. Comparative curves of mean amplification factor for major component of incident SV wave, based on differential shape ratio, for triangular shaped hill, in (0.50-1.00) dimensionless period limit, short wave lengths limits.

Figure 6 shows the best fit lines for mean amplification factor of 2D asymmetric triangular shaped hills versus differential shape ratios between feature sides subjected to incident SV wave. The results indicated here for short dimensionless period limits. As it seen, the differential shape ratio (or angle for trapezoidal shaped features) dose not have considerable effect on mean amplification and can not illustrate the changes of mean amplification, solely. So the related best fit lines are nearly straight.

General conclusion illustrates that the seismic response of asymmetric hills are controlled by the part of feature which have smaller shape ratio (or larger angle for trapezoidal shaped) causes larger area of the feature that we named it "basic shape ratio" here. Therefore, as a result of this parametric analysis some linear formula presented here which make a relation between "basic shape ratio" and irregularity of triangular and semi-sine shaped hill, to estimate the amplification of seismic response for symmetric and asymmetric ones. The formula are shown for a semi-sine shaped hill with "basic ratio=0.3" which subjected to a horizontal component of incident SV wave in Figure 7 and others listed in Table 2.

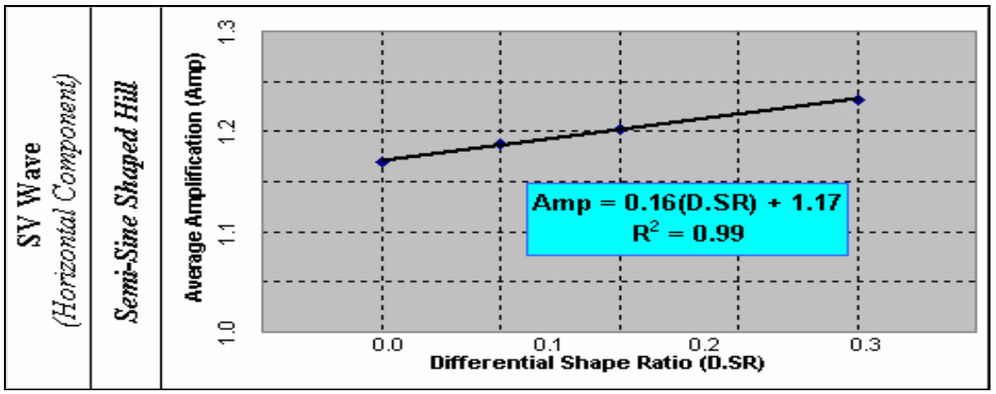


Figure 7. Linear formula for a semi-sine shaped hill with "basic ratio=0.3", subjected to horizontal component of incident SV wave.

Table 2. Linear formulas for estimating the amplification of symmetric and asymmetric triangular and semi-sine shaped hills

Basic Shape Ratio	*Semi-Sine Shaped Hill*		*Triangular Shaped Hill*	
	P Wave (Vertical Component)	**SV Wave** (Horizontal Component)	**P Wave** (Vertical Component)	**SV Wave** (Horizontal Component)
0.1	Amp=0.03(D.SR)+1.02	Amp=0.05(D.SR)+1.07	Amp=0.04(D.SR)+1.02	Amp=0.05(D.SR)+1.06
0.3	Amp=0.10(D.SR)+1.06	Amp=0.16(D.SR)+1.17	Amp=0.11(D.SR)+1.04	Amp=0.15(D.SR)+1.15
0.5	Amp=0.09(D.SR)+1.12	Amp=0.18(D.SR)+1.25	Amp=0.14(D.SR)+1.09	Amp=0.22(D.SR)+1.22
0.7	Amp=0.02(D.SR)+1.16	Amp=0.34(D.SR)+1.40	Amp=0.10(D.SR)+1.15	Amp=0.21(D.SR)+1.33

CONCLUSION

This study includes a comparative analysis for determination of amplification patterns of 2D homogenous asymmetric semi-sine, triangular and trapezoidal shaped hills and symmetrical ones subjected to vertically propagating SV and P waves, by

numerically investigation of the hill's response using the time domain boundary element method. It has been shown that:

• The amplification potential of the symmetric and asymmetric shaped hill is strongly influenced by the length of the incident wave, by the shape ratio and in a less order of importance by the wave type.

• In the case of incident waves with lengths of longer than the width of the hill, where the predominant periods are usually equal to or greater than its characteristic period, the amplification curve finds it's maximum at the crest. And in the case of incident waves with smaller lengths the amplification could be negligible.

• Differential shape ratios or angles between feature sides don't have a considerable effect on seismic mean amplification, so can not illustrate the changes of mean amplification. The major effect of feature geometry corresponds with the shape ratio or angle of feature part which has smaller shape ratio (or larger angle) causes larger area, named here "basic shape ratio or angle".

REFERENCES

1- Aki K and Larner K. "Surface motion of a layered medium having an irregular interface due to incident plane SH waves" Journal of Geophysical Research , 75, 933-954, 1970.

2- Athanasopoulos GA, Pelekis PC and Leonidou EA. "Effects of Surface Topography on Seismic Ground Response in the Egion (Greece) 15-6-1995 Earthquake" Soil Dynamics and Earthquake Engineering, 18, 135-149, 1999.

3- Bard PY."Effects of surface geology on ground motion: recent result and remaining issues."Proc.10th European Conf. on Earth, Eng.Vienna, 305-323, 1994.

4- Beskos DE. Boundary element methods in dynamic analysis: Pt. II (1986-1996), Appl Mech Rev, 50,149-197, 1997.

5- Boore DM. "The effect of simple topography on seismic waves: implications for the accelerations recorded at Pacoima Dam, San Fernando Valley, California" Bull Seismol Soc Am, 63, 16031609,1973.

6- Borcherdt, RD. "Estimates of site-dependent response spectra for design (Methodology and Justification)" Earthquake Spectra, 10, 617-653, 1994.

7- Bouchon M. "Effect of Topography on Surface Motion" Bull Seismol Soc Am, 63, 615-632, 1973.

8- Bouckovalas GD and Kouretzis G. " Review of Soil and Topography Effects in the September 7, 1999 Athens (Greece) Earthquake," Proceedings of the Fourth International Conference on Recent Advances in Geotechnical Earthquake Engineering and Soil Dynamics And Symposium in Honor of Professor WD Liam Finn, San Diego, California, 2001.

9- Celebi M. "Topographical and geological amplifications determined from strong-motion and aftershock records of the 3 March 1985 Chile earthquake," Bull Seismol Soc Am, 77, 1147-1167,1987.

10- Celebi M. "Topographic and geological amplification: Case studies and engineering implications," Structural Safety, 10, 199-217, 1991.

11- Eurocode8 (EC8),Design provisions for earthquake resistance of structures, 1998.

12- Gatmiri B., Kamalian M. "Time Domain Two-Dimensional HYbrid FEM / BEM Dynamic Analysis Of Non-Linear Saturated Porous Media," Proc. 2nd Canadian Specialty Conference On Computing In Geotechnique, 2002a.
13- Gatmiri B and Kamalian M. "Combination of boundary element and finite element methods for evaluation of dynamic response of saturated porous media" Proc. 5th European Conference on Numerical Methods in Geotechnical Engineering, 2002b.
14- Geli L, Bard PV, Julien B. "The effect of topography on earthquake ground motion: a review and new results," Bull Seismol Soc Am, 78, 42-63, 1988.
15- Kamalian, M. "Time domain two-dimensional hybrid FEM/BEM dynamic analysis of non-linear saturated porous media" Ph.D. Dissertation, Tehran University, 2001 (In Persian).
16- Kamalian M, Gatmiri B, Sohrabi-Bidar A. "On Time-Domain Two-Dimensional Site Response Analysis of Topographic Structures by BEM" JSEE, 5, 35-45, 2003.
17- Kamalian, M., Jafari MK, Sohrabi-Bidar A and Razmkhah A. "Amplification Pattern of 2D Trapezoidal Shaped Hills Subjected To Vertically Propagating Incident Waves", published in Tarbiat Modares Engineering Journal, 2004. (In Persian)
18- Kamalian, M., M.K. Jafari, A. Razmkhah and A. Sohrabi-Bidar, "Amplification Pattern of 2D Semi-Elliptical Shaped Hills Subjected To Vertically Propagating Incident Waves,"published in AmirKabir Engineering Journal, 2004. (In Persian)
19- Kamalian, M., Jafari, MK., Sohrabi-bidar, A., Razmkhah, A., Gatmiri, B., "Time-domain twodimensional site response analysis of non-homogeneous topographic structures by a hybrid BE/FE method," Soil Dyn Earthquake Eng., 26:753-765, 2006.
20- Kamalian, M., Jafari M.K, Sohrabi-Bidar A and Razmkhah A. "Amplification Pattern of 2D Semi-Sine Shaped Hills Subjected To Vertically Propagating Incident Waves" Accepted to published in Earthquake Spectra Journal, 2007.
21- Khosravi H, Razmkhah A, Kamalian M."Parametric Analysis of The seismic Response of Triangular Shaped Topographic Features in Time Domain." M.Sc. Thesis,Islamic Azad University , Arak branch,Iran, 2006.(In Persian).
22- Moczo P, Bystricky E, Kristek J, Carcione J.M. and Bouchon M, "Hybrid modeling of P-SV seismic motion at in homogenous viscoelastic topographic structures," Bull. Seism. Soc. Am., Vol. 87, pp. 1305-1323, 1997.
23- Sanchez–Sesma FJ and M. Campillo. "Diffraction of P, SV and Rayleigh Waves by topographical features: a boundary integral formulation," Bull. Seism. Soc. Am., 81, 1991.
24- Sanchez-Sesma FJ, Palencia VJ and Luzon F. "Estimation of local site effects during earthquakes: an overview," ISET Journal of Earthquake Technology, 39, 167-193, 2002.
25- Spudich P, Hellweg M and Lee WHK."Directional topographic site response at Tarzana observed in aftershocks of the 1994 Northridge, California, Earthquake: Implications for main shock motions" Bull Seismol SocAm, 86, S139-S208, 1996.
26- Trifunac MD. and Hudson DE. "Analysis of the Pacoima Dam accelerograms – San Fernando earthquake of 1971," Bull Seismol Soc Am, 61, 1393-1411, 1971

Seismic Response of the San Francisco International Airport Airfield during the 1989 Loma Prieta Earthquake

Lelio H. Mejia[1], M. ASCE, P.E., Jiaer Wu[2], M. ASCE, P.E., Zhaohui Yang[3], P.E., Jim Chiu[4], P.E.

[1]Principal, URS Corporation, 1333 Broadway, Oakland, CA 94612; lelio_mejia@urscorp.com
[2]Engineer, URS Corporation, 1333 Broadway, Oakland, CA 94612; jerry_wu@urscorp.com
[3]Engineer, URS Corporation, 1333 Broadway, Oakland, CA 94612; zhaohui_yang@urscorp.com
[4]Civil Engineer, San Francisco Airport Commission, Facilities Operations and Maintenance, P.O. Box 8097, San Francisco, CA 94128; Jim.Chiu@flysfo.com

ABSTRACT: Whereas seismic response analyses are commonly performed to evaluate the effects of deep soil sites on earthquake ground motions, relatively limited experience is available with the response of sites underlain by deep deposits of geologically young clays under strong earthquake shaking. This paper illustrates the use of nonlinear and equivalent-linear analysis techniques for evaluation of the seismic response of the San Francisco International Airport airfield, which is underlain by Young San Francisco Bay Mud and fill deposits. Site response analyses for rock motions representative of the 1989 Loma Prieta earthquake were able to simulate the recorded surface motions at the airport during the earthquake, and indicate that peak accelerations on the airfield were lower than at the recording station.

INTRODUCTION

The earliest developments of the San Francisco International Airport (SFIA) were built onto low-lying pastures and farm fields that had been reclaimed from San Francisco Bay about 25 km south of San Francisco, California. Subsequent expansion of the airport involved successive episodes of fill placement within San Francisco Bay from the 1920's through the 1970's. In general, the fill was constructed by placing materials in shallow water, using bulldozers to push the fill onto the bay bottom, and by compacting the materials above the water table. Rock breakwaters were constructed to protect the exposed fill perimeter.

The soils and rock underlying the airfield include bedrock of the Franciscan Formation, alluvial sediments and older marine clay deposits locally known as Old Bay Mud (OBM), young marine clay and silt deposits locally known as Young Bay Mud (YBM), and fill. The fill consists primarily of silty and clayey sands and silts

and clays with an average thickness of about 10 to 20 feet. The water table is generally between 5 to 10 feet beneath the fill surface.

The airport is located within the seismically active region between the Pacific and North American tectonic plates. The San Andreas fault, the source of the magnitude **M** 7.9 1906 San Francisco earthquake is about 6 km to the west of the site and the Hayward fault, the source of a **M** 6.8 earthquake in 1868, lies about 24 km to the east. Other sources of potential future large earthquakes in the region include the Calaveras, San Gregorio, Greenville, and Concord-Green Valley faults.

The approach to seismic analysis of the airfield consisted of evaluating the site response to the earthquake motions, assessing the potential for ground failure, and assessing the consequences of ground failure. The analyses of site response were performed using one-dimensional equivalent-linear and nonlinear procedures. The site response analyses were used to estimate the motions at the ground surface throughout the airfield and the seismic stresses, strains, and deformations in the subsurface soils.

ONE-DIMENSIONAL SITE RESPONSE ANALYSES

One-dimensional (1D) site response analyses were performed to evaluate the seismic response of the airfield during the 1989 Loma Prieta earthquake. An accelerograph at the airport (see Figure 1) recorded the ground motions from the earthquake. Analyses were first performed for the site of the airport recording station using equivalent-linear techniques with the computer program SHAKE (Schnabel et al, 1972).

Analytical models were developed for the accelerograph site using borehole and shear wave velocity data obtained at that location (Figure 2). Three models were developed to consider uncertainties in the stratigraphy of the station site and in the dynamic properties of the site soils. The best estimate model was based on the Vs profile measured by the USGS (1992), while the other two models were developed to perform parametric analyses and evaluate the suitability of the site characterization and response analysis procedures.

The rock motions recorded at the Sierra Point recording station, about 8 km north of the airport (see Figure 1), were used as a proxy for the rock motions at the airport recording site. Figure 3 shows the 360^o component of the ground motion time histories recorded at the Sierra Point station and at the airport station during the Loma Prieta earthquake (Shakal et al. 1989). SHAKE analyses were performed for the 90^o and 360^o components of motion. Analyses were also performed for the 45^o component because plots of horizontal particle motion suggest that the intensity of ground motions in that direction was slightly higher than in other directions.

The results of the analyses using the best estimate model are shown in Figures 3 and 4. It can be seen that the calculated surface motions for the 360^o direction are in reasonable agreement with the recorded motions. The degree of agreement for the 90^o direction (and the 45^o direction) is lesser. The response calculated with alternative parametric models is generally lower in intensity and thus is in lesser agreement with the recorded response.

Nonlinear analyses were also performed with the finite difference program FLAC (Itasca, 2000) using the airport recording station motions. The FLAC analyses used a Masing-type hysteretic model to simulate the nonlinear stress-strain behavior of the site soils. That model is typically defined by a stress-strain backbone curve. The backbone curves for the various site soils were developed to match the modulus reduction curves used in SHAKE. To simulate damping at small strains in the analysis, a small amount of Rayleigh damping was included in the model. The basic material properties and soil layering in the FLAC model are identical to those used in the SHAKE analyses. The calculated surface motions are compared with the recorded motions in Figure 5. It may be seen that the calculated motions are slightly lower than the SHAKE calculated motions, but still in reasonable agreement with the recorded motions.

Analyses were also performed using five site response models representative of the subsurface conditions throughout the airfield. Those analyses were performed to estimate the surface ground motions that occurred in the airfield area for comparison with the known performance of the airfield during the earthquake. The modulus reduction and damping curves of the main stratigraphic units were the same as those of the best estimate model for the airport recording station. In view of the differences between the calculated and recorded motions at the airport station, and to account for uncertainties in the intensity of the input rock motions, the site response analyses of the airfield were performed using the unscaled recorded rock motions as well as scaled rock motions. For the latter analyses, the input rock motions were scaled by factors of 1.4 and 1.1 for the 90º and 360º components, respectively. An example of the calculated acceleration and shear stress-strain profiles beneath the airfield for one of the five models used in the analyses is shown in Figure 6. It may be seen that the largest shear strains develop in the near-surface layers that have relatively low shear wave velocities.

Figure 7 shows a plot of the calculated surface peak ground accelerations (PGAs) against the input rock motion PGAs together with the observed data and relationship presented by Idriss (1990) for soft soil sites. It may be seen that the calculated PGAs in the airfield are within the range of other observations during the 1989 Loma Prieta earthquake, and are generally lower than the PGA's calculated for the airport recording station.

TWO-DIMENSIONAL ANALYSES

Two-dimensional (2D) analyses were performed using a cross section of the airfield dikes and the computer program FLAC to estimate the potential for seismically-induced displacements near the edge of the fill and shoreline. The cross section was selected to be generally representative of the conditions along a significant portion of the shoreline. The mesh of the FLAC model is shown in Figure 8. The analyses were performed using the hysteretic model described above. Additional parametric analyses were performed using the Mohr-Coulomb model.

Free-field boundaries were used on the two sides of the mesh for the dynamic analysis. The input motions were applied to the base of the 2D model assuming a rigid-base condition. To develop the input motion, a 1D model was first developed

for the soil profile beneath the airfield at the location of the 2D analysis section. The 1D model was analyzed using SHAKE for the rock outcrop motions, and the "within" motion calculated at the elevation of the base of the 2D model was used as the input motion for the 2D analyses.

The 2D model was subjected to the Loma Prieta earthquake motion using the 45^{o} component of the Sierra Point record. Using the hysteretic model, the calculated surface PGA was about 0.2g near the crest edge of the fill and the calculated permanent lateral displacement was negligible. Similar results were obtained using the Mohr-Coulomb model. Thus, the calculated deformations agree with the lack of damage of the airfield perimeter observed after the Loma Prieta earthquake.

LIQUEFACTION ANALYSIS

The fills encountered in the airfield area consist of a relatively broad range of soils. Therefore, the susceptibility to and potential for liquefaction of the fill can vary significantly within short distances. Whereas fine-grained soils of moderate to high plasticity are generally considered not susceptible to liquefaction, cohesionless soils and fine-grained soils of low plasticity, such as ML silts, are considered potentially liquefiable. To evaluate the liquefaction susceptibility of fine-grained soils within the airfield fill (and which make up a major portion of the fill), the procedures proposed by Seed et al. (2003) and by Idriss and Boulanger (2004) were used. Fill samples with measured Atterberg Limits were "screened" with those procedures, and the fraction of samples deemed "susceptible to liquefaction" was calculated. Based on the results of the screening, 20 percent of the "ML" silts and 100 percent of the cohesionless soils in the fill, including clean and silty sands and gravels, were judged to be susceptible to liquefaction. On that basis, it was estimated that approximately 30 to 40 percent of the airfield fill materials are susceptible to liquefaction.

A large number of Standard Penetration Test (SPT) blow counts in the fill were analyzed using the Seed et al. and Idriss and Boulanger procedures to determine the liquefaction potential of the soils identified as susceptible to liquefaction. A number of SPT blow counts were found to correspond to samples having insufficient information to determine their liquefaction susceptibility. Of those samples, 30 to 40 percent were assumed to be susceptible to liquefaction. The results of the SPT-based evaluation of liquefaction potential indicate that between 8 to 18 percent of the fill materials below the water table might have liquefied during the Loma Prieta earthquake.

In addition to the SPT data, 98 Cone Penetration Test (CPT) soundings were utilized to evaluate the liquefaction potential of the fill materials. Those CPT soundings are distributed throughout the airfield and represent a relatively unbiased sampling of the overall fill beneath the airfield.

Because the CPT does not yield soil samples for testing or classification, the reliability of existing empirical soil behavior classification procedures was examined. Seven pairs of CPTs and borings were made in close proximity to each other to check the CPT classification procedures of Robertson (1990). The fill samples taken from the soil borings were compared with the soil behavior type assigned in the nearby CPT soundings at the same depths. Generally, the comparison results were not

satisfactory indicating that the CPT data alone are insufficient to consistently and correctly identify the soil classification or liquefaction susceptibility of the airfield fill materials.

Nevertheless, CPT-based liquefaction potential analyses were performed using the Moss et al. (2005) procedure. The calculated liquefaction potential was compared with the calculated SPT-based liquefaction potential in a total of thirteen pairs of CPT soundings and soil borings and the overall agreement between the SPT- and CPT-based analysis results was found to be satisfactory provided the estimated percentage of liquefaction-susceptible soils in the fill was considered. Idriss and Boulanger (2004) also provided a CPT-based liquefaction analysis procedure, but that procedure is applicable to relatively clean sands, and thus, was not used in the study.

Based on the good agreement between the SPT- and CPT-based analyses, the liquefaction potential throughout the airfield fill was evaluated using all CPT soundings. The thickness of fill zones estimated to have liquefied during the Loma Prieta earthquake on the basis of the CPT soundings was found to be 2 feet or less beneath a major portion of the airfield, although zones up to 5 feet thick were found in some areas. Those results are in reasonable agreement with the observed performance of the airfield during the earthquake considering the fact that roughly the upper 5 to 10 feet of the fill is above the water table.

No ground failure or evidence of liquefaction was observed in the airfield during the 1989 Loma Prieta earthquake, except for one localized observation of sand boils along the shoreline, near the north end of the NE-SW runways. On the other hand, extensive evidence of ground failure in the form of liquefaction sand boils and significant ground deformations was observed in the area south of Market Street in San Francisco. Because ground motion recordings indicate that rock motions in that area and at the airport were similar, the large difference in performance between the two sites would have to be ascribed to differences in the soil conditions, and most probably the character of the fills.

CONCLUSIONS

Comprehensive seismic response analyses were performed as part of a broad study to assess the likely seismic performance of the airfield at the SFIA during future earthquakes. The site response analyses were used primarily to estimate the intensity of earthquake motions at the ground surface throughout the airfield and the associated stresses, strains, and deformations in the subsurface soils. The following conclusions may be drawn based on the analyses for the 1989 Loma Prieta earthquake:

1. The selected 1D models and analysis procedures yield calculated ground motions that are in reasonable agreement with the ground motions recorded at the airport strong motion station during the 1989 Loma Prieta earthquake.
2. The peak ground surface accelerations experienced on the airfield during the earthquake are likely to have been smaller than those recorded at the airport strong motion station.
3. Permanent displacements of the airfield and perimeter dikes calculated using the selected 1D and 2D models and analysis procedures are in good agreement with the observed airfield performance during the earthquake.

4. An estimated 30 to 40 percent of the fill materials beneath the airfield are likely to be susceptible to liquefaction. The remainder of the fill soils are not likely susceptible to liquefaction due to their clayey nature. The extent of liquefaction within the fill was evaluated using SPT- and CPT-based analysis procedures, and was found to be in reasonable agreement with the observed performance of the airfield during the earthquake.

ACKNOWLEDGMENTS

The authors wish to thank the San Francisco Airport Commission for granting the permission to publish this technical paper. The authors also like to acknowledge Professors I.M. Idriss and Raymond B. Seed of the University of California who provided guidance throughout the study and reviewed the results.

REFERENCES

Idriss, I.M. (1990). “Response of soft soils during earthquakes,” H.Bolton Seed Memorial Symposium Proceedings, Bitech, Vancouver, B.C.

Idriss, I.M. and Boulanger, R.W. (2004). “Semi-empirical procedures for evaluating liquefaction potential during earthquakes,” Proceedings, 11th ICSDEE and 3rd ICEGE, Berkeley, California.

Itasca, (2000). “FLAC, fast lagrangian analysis of continua, version 4.0, user’s guide,” Itasca Consulting Group, Inc., Minneapolis, Minnesota.

McKenna, F. and Fenves, G.L (2001). “The OpenSees command language manual, version 1.2.” Pacific Earthquake Engrg. Research Center, Univ. of Calif., Berkeley.

Moss, R.E.S., Seed, R.B., Kayen, R.E., Stewart, J.P. and Tokimatsu, K. (2005). “Probabilistic Liquefaction Triggering based on the Cone Penetration Test,” ASCE Geotechnical Special Publications 130-142 & GRI-18.

Redpath Geophysics, (1991). “Seismic velocity logging in the San Francisco Bay Area,” Report prepared for Electric Power Research Institute, August.

Robertson, P.K., (1990) “Soil classification using CPT,” *Canadian Geotechnical Journal*, Vol. 27, No. 1, pp. 151-158.

Schnabel, P.B., Lysmer, J. and Seed, H.B. (1972). “SHAKE: A computer program for earthquake response analysis of horizontally layered sites,” Report No. UC/EERC-72/12, University of California, Berkeley, December.

Seed, R.B., Cetin, K.O., Moss, R.E.S., Kammerer, A., Wu, J., Pestana, J., Riemer, M., Sancio, R.B., Bray, J.D., Kayen, R.E. and Faris, A. (2003). "Recent advances in soil liquefaction engineering: a unified and consistent framework," Report No. EERC 2003-06, University of California, Berkeley, June.

Shakal, A.F., M. Huang, M. Reichle, C. Ventura, T. Cao, R. Sherburne, M. Savage, R. Darragh, and C. Petersen. (1989). “CSMIP Strong-Motion Records from the Santa Cruz Mountains (Loma Prieta), California Earthquake of 17 October 1989, California Division of Mines and Geology, Report No. OSMS 89-06.

USGS (1992). “Seismic velocities and geologic logs from borehole measurements at seven strong-motions stations that recorded the 1989 Loma Prieta earthquake,” U.S. Geological Survey Open-file Report 92-287, Menlo Park, California.

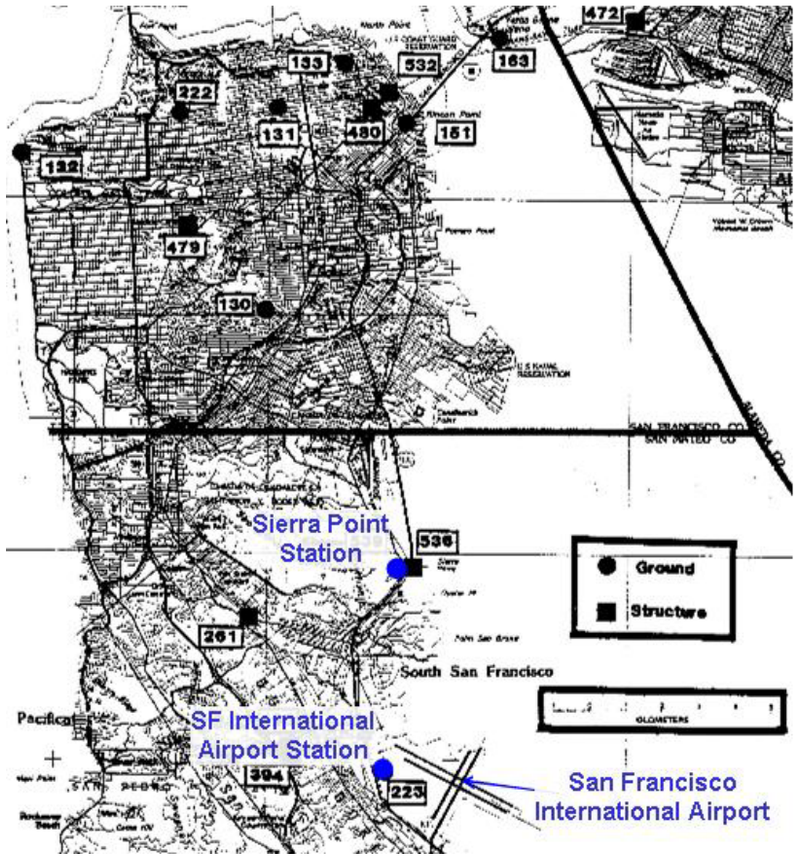
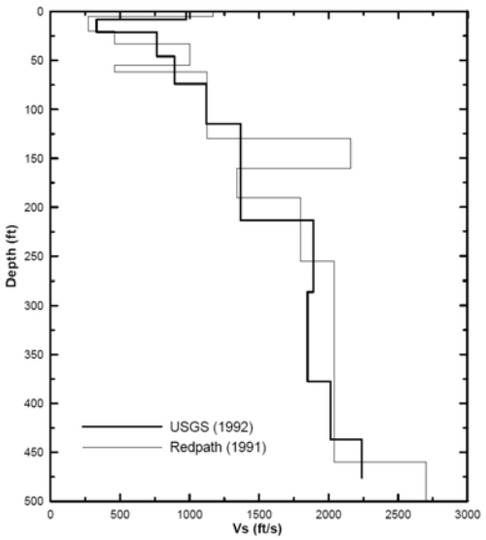


Fig. 1. Locations of San Francisco International Airport and Nearby Strong Motion Recording Stations (Modified after Shakal et al. 1989)

Layer	Depth to Top of Layer (ft)	Stratum/Soil type		Best Estimate Model	
				S Velocity (ft/s)	Total unit weight (pcf)
1	0	Fill	SM	980	122
2	8	YBM	CH	330	98
3	21	ULS	SM	770	125
4	46	OBM	CH	890	110
5	56	Colma formation	SM	890	120
6	74		SM	1120	125
7	95		SM/SP	1120	125
8	115		SP	1370	125
9	142		ML	1370	125
10	173	Colma formation	SP	1370	125
11	213		ML	1890	130
12	286		SP	1850	130
13	377		SP	2020	130
14	437	Merced formation	Mudstone	2240	140
15	491	Franciscan formation	Sandstone	4000	140

(a) Model Characteristics



(b) V_S Measurements

Fig. 2. Site Response Model for Airport Recording Station

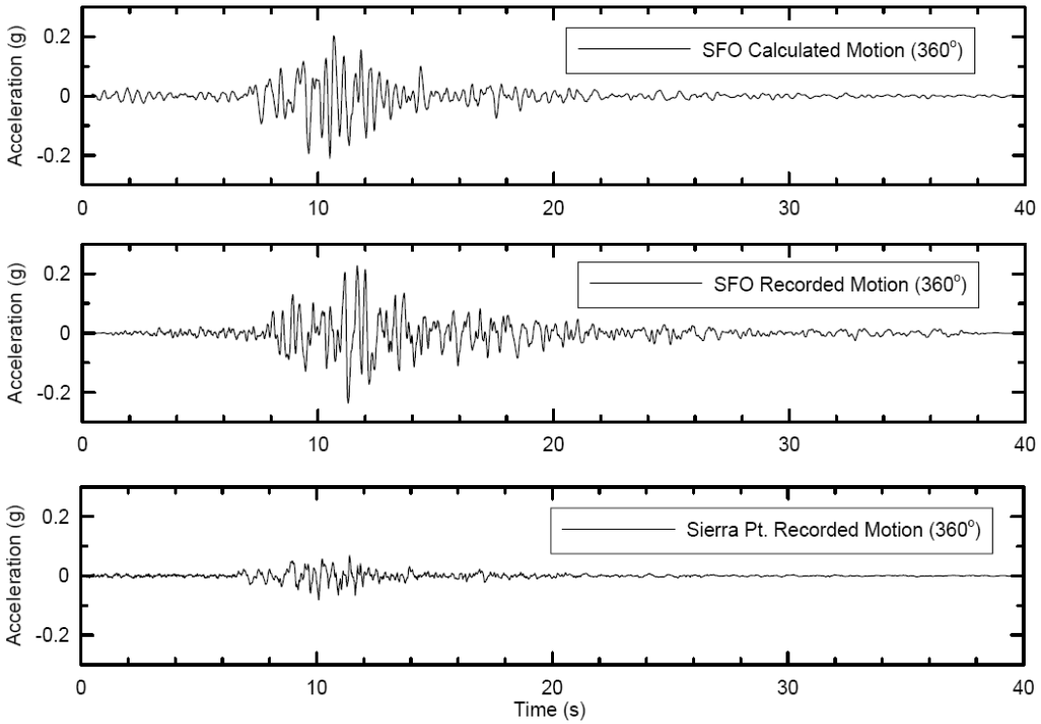


Fig. 3. Recorded and Calculated Acceleration Time Histories from SHAKE Analysis, Airport Recording Station

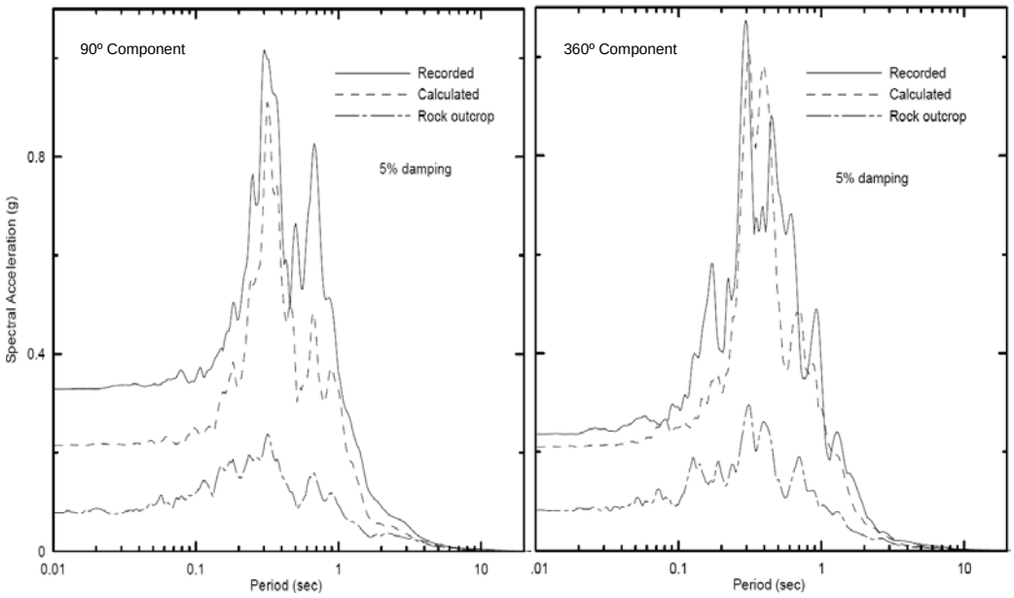


Fig. 4. Recorded and Calculated Acceleration Response Spectra from SHAKE Analysis, Airport Recording Station

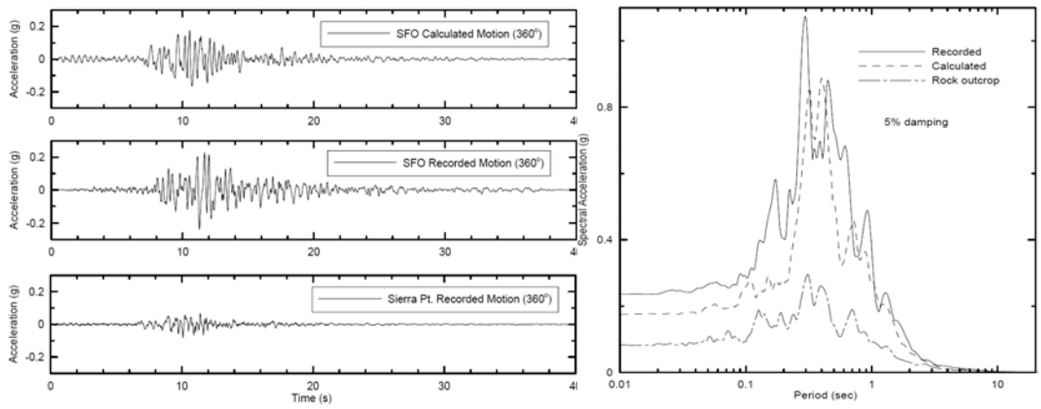


Fig. 5. Recorded and Calculated 360º-Component Motions from 1D FLAC Analysis, Airport Recording Station

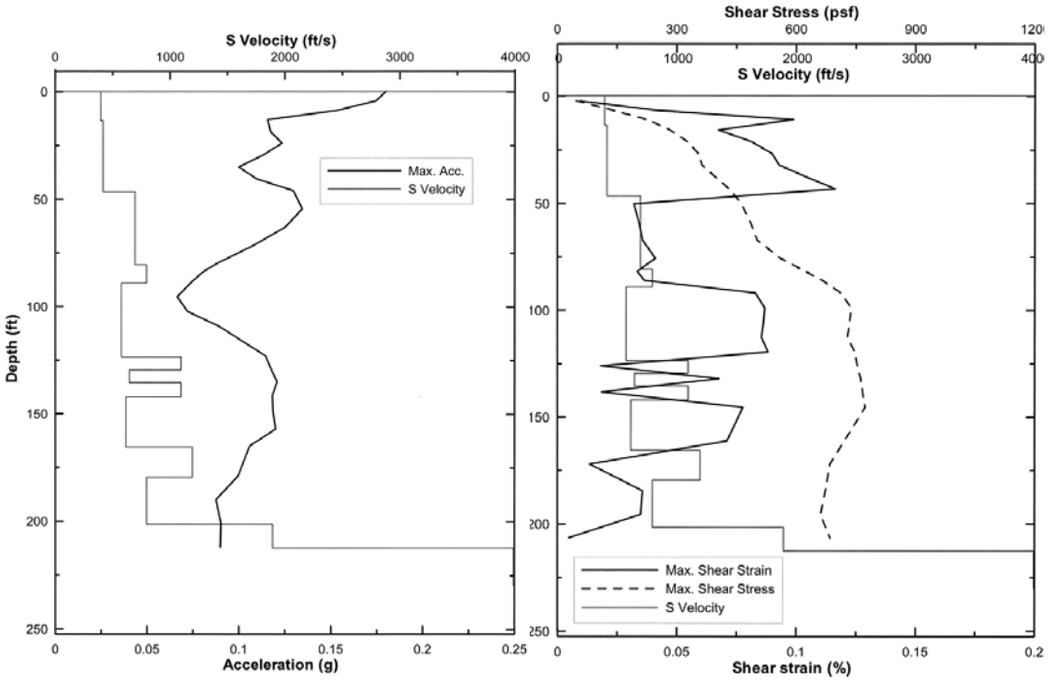


Fig. 6. Results of SHAKE Analysis for Selected Airfield Site Model

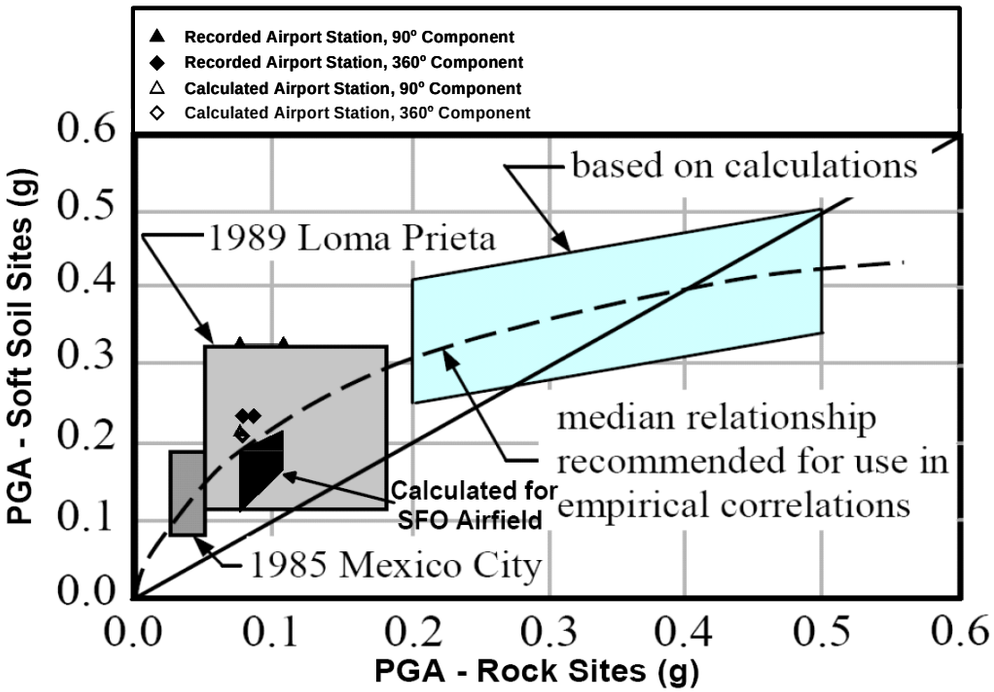


Fig. 7. Comparison of Calculated PGAs at the Airport with Data and Relationship presented by Idriss (1990)

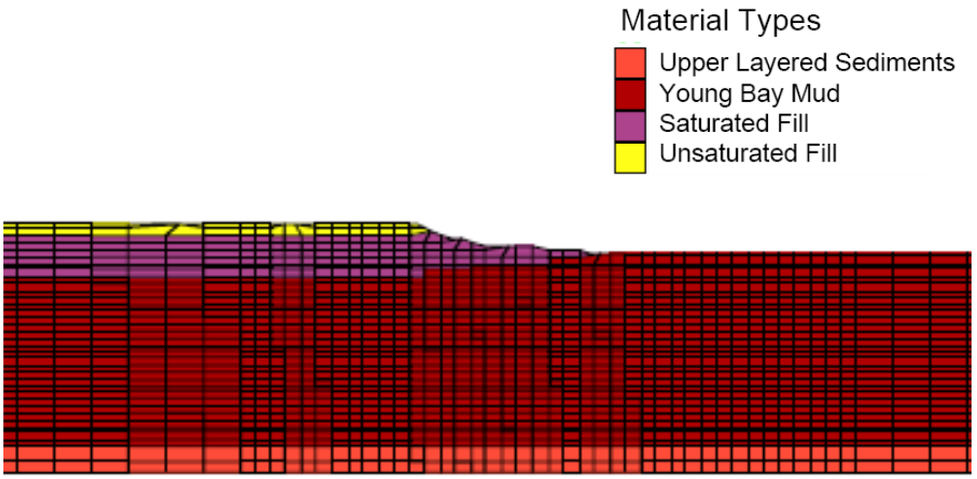


Fig. 8. Portion of FLAC Mesh for Airfield Perimeter Dike Cross Section

Site Response Analysis for Tito Scalo Area (PZ) in the Basilicata Region, Italy

Antonio Cavallaro[1], Salvatore Grasso[2] and Michele Maugeri[3]

[1]Researcher, Ph. Doctor in Geotechnical Engineering, CNR-IBAM, Via A. di Sangiuliano n. 162, 95124 Catania, Italy; acava@dica.unict.it
[2]Ph. Doctor in Geotechnical Engineering, University of Catania, Department of Civil and Environmental Engineering, Viale A. Doria 6, 95125 Catania, Italy; sgrasso@dica.unict.it
[3]Full Professor, Ph. Doctor in Geotechnical Engineering, University of Catania, Department of Civil and Environmental Engineering, Viale A. Doria 6, 95125 Catania, Italy; mmaugeri@dica.unict.it

ABSTRACT: The Tito Scalo site, located near the city of Potenza in the Basilicata region in Southern Italy, is a high seismic risk area. Borings and dynamic in situ tests have been performed. Among them Down Hole (D-H), Noise Analysis Surface Waves (NASW) and Seismic Dilatometer Marchetti Tests (SDMT) have been carried out, with the aim to evaluate the of shear-wave velocity (V_s) profile of the soil. The results show a very detailed and stable shear-wave profile. After evaluating the synthetic accelerograms at the bedrock, the ground response analysis at the surface, in terms of time histories and response spectra, has been obtained by two non-linear models GEODIN (Frenna and Maugeri, 1995) and EERA (Bardet et al., 2000).

INTRODUCTION

The site under consideration is located in the Basilicata region, which is a seismically active area of Italy. Since 1561, the Tito Scalo area has been struck by fifteen earthquakes with an MKS intensity from III to X.

In order to study the possible amplification phenomena of the Tito Scalo site, a comprehensive laboratory and in situ investigation has been carried out to obtain a soil profile with special attention being paid to the variation of the shear-wave Velocity (V_s) with depth. Deep site investigation have been undertaken for site characterization of the soil. Borings and dynamic in situ tests have been performed. Among them Down Hole (D-H) (Huang et al., 2004; Nunziata et al., 2004), Noise Analysis Surface Waves (NASW) (Louie J. N., 2001; Mucciarelli et al. 2003) and Seismic Dilatometer Marchetti Tests (SDMT) (Martin an Mayne, 1997, 1998). The Down Hole and Seismic Dilatometer Marchetti Tests were performed down to a depth of 40 meters while NASW was performed down to a depth of 60 meters. This paper tries to summarize this information in a comprehensive way in order to provide a case record of site characterization for seismic response analysis. Finally, synthetic seismograms have been obtained for the site long a set of six receivers placed at different depths,

starting from the surface down to almost 40 m. After evaluating the synthetic accelerograms at the bedrock, the ground response analysis at the surface, in terms of time histories and response spectra, has been obtained by two 1-D non-linear models. In particular the study regarded the evaluation of site effects in correspondence of the sites, to which corresponds a different value of the Seismic Geotechnical Hazard.

GEOLOGY AND BASIC SOIL PROPERTIES

The deposit under consideration lies in the S. Loja plane. The area is confined on the North by the Li Foj mount, on the West by the Arioso mount and Pierfaone mount, on the South by the Passo della Sellata Relief, and on the North-West by the South-West border of Potenza Basin. The S. Loja basin deposit placed on the axial zone of Lucano Apennine consists of soils derived from paleogeographic Mesozoic of Lagonegro basin.

Two boreholes (20 m and 40 m) were performed to characterize the investigated area. The water level is located at few meter below the ground level. The deposit is characterized by clayey soils with insertion of silty lenses and sand. The detritus component increase with the depth. Four undisturbed samples were retrieved at the depths of 7 m (grey-green clay with high plasticity), 9.50 m (brown plastic clay), 20.50 m (grey clay) and 27.50 m (overconsolidated grey-brown clay). The general characteristics and index properties of the Tito Scalo soil are shown, as a function of depth, in Table A.

Table A. General characteristics and index properties of the Tito Scalo soil.

Depths [m]	γ *[kN/m^3]*	γ_s *[kN/m^3]*	γ_D *[kN/m^3]*	W_n *[%]*	*LL [%]*	*PL [%]*	*PI [%]*
7	19.7	27.1	15.8	25	55.9	23.6	32.3
9.50	17.8		12.4	43	67.5	31.6	35.9
20.50	19.6		15.4	27			
27.50	18.7		14.0	34			

Where: γ: Unit Weight Total; γ_s: Unit Weight Solids; γ_D: Unit Weight Dry; W_n: Water Content; LL: Liquid Limit; PL: Plasticity Limit; PI: Plasticity Index.

3. SHEAR MODULUS

3.1 Shear-Wave Velocity V_s: In Situ Measurements

The small strain ($\gamma \leq 0.001$ %) shear modulus, G_o, was determined from SDMT, NASW and a Down Hole (D-H) test. Moreover it was attempted to assess G_o by means of empirical correlations, based either on penetration test results or on laboratory test results (Jamiolkowski et al., 1995).

The Seismic Dilatometer Marchetti (SDMT) is an instrument resulting from the combination of the DMT blade with a modulus measuring the shear wave velocity. The seismic modulus is an instrumented tube, located above the blade (see Figure 1), housing two receivers at a distance of 0.50 m. The test configuration "two

receivers"/"true interval" avoids the problem connected with the possible inaccurate determination of the "first arrival" time sometimes met with the "pseudo interval" configuration (just one receiver). Also the pair of sismograms at the two receivers corresponds to the same blow, rather than at two successive blows - not necessarily identical. The adoption of the "true interval" configuration considerably enhances the repeatability in the V_s measurement.

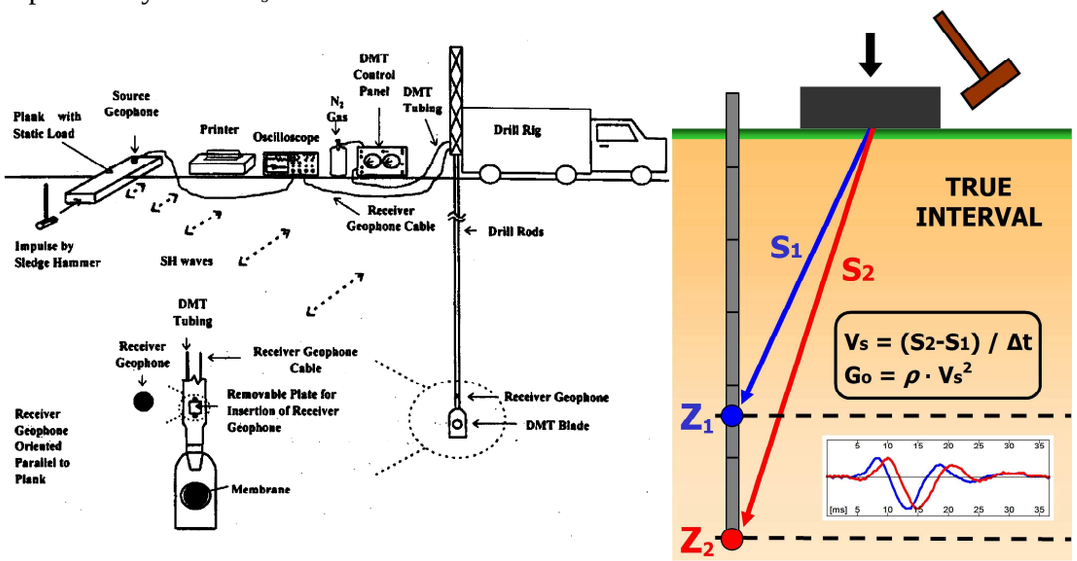


FIG. 1. SDMT setup and scheme for the measure of V_s.

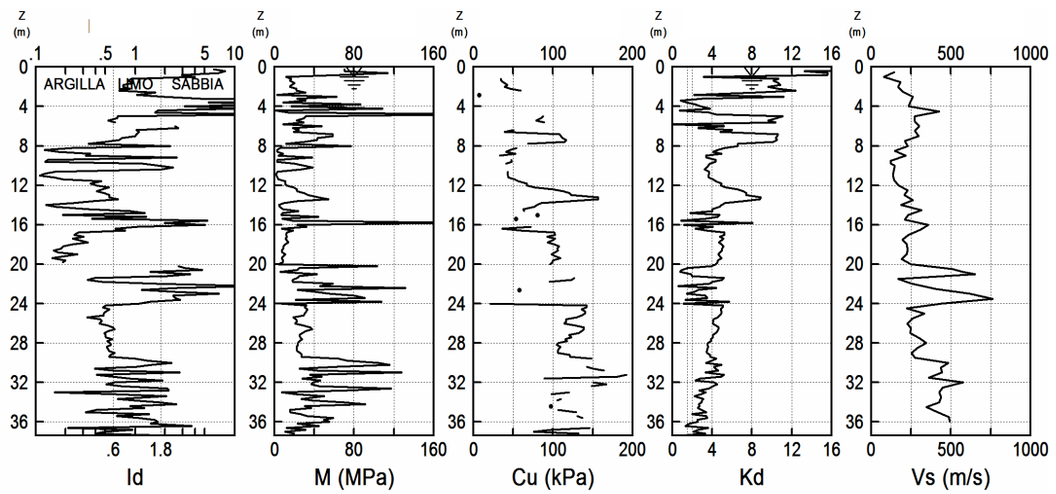


FIG. 2. Summary of SDMT's in Tito Scalo area.

The SDMT provides a simple means for determining the initial elastic stiffness at very small strains and in situ shear strength parameters at high strains in natural soil deposits.

Source waves are generated by striking a horizontal plank at the surface that is oriented parallel to the axis of a geophone connected to a co-axial cable with an

oscilloscope (Martin and Mayne, 1997, 1998). The measured arrival times at successive depths provide pseudo interval V_s profiles for horizontally polarized vertically propagating shear waves (Figure 1). V_s may be converted into the initial shear modulus G_o. The combined knowledge of G_o and of the one dimensional modulus M (from DMT) may be helpful in the construction of the G-Gamma modulus degradation curves (Cavallaro et al.,2006). The V_s determinations are executed at 0.50 m depth intervals.

A summary of SDMT parameters are shown in Figure 2 where:
I_d: Material Index; gives information on soil type (sand, silt, clay); M: Vertical Drained Constrained Modulus; C_u: Undrained Shear Strength; K_d: Horizontal Stress Index; V_s: Shear Waves Velocity. The profile of K_d is similar in shape to the profile of the overconsolidation ratio OCR. K_d = 2 indicates in clays OCR = 1, K_d > 2 indicates overconsolidation. A first glance at the K_d profile is helpful to "understand" the deposit.

The Noise Analysis Surface Waves (NASW) is based on two fundamental ideas. The first is that common seismic-refraction recording equipment, set out in a way almost identical to shallow P-wave refraction surveys, can effectively record surface waves at frequencies as low as 2 Hz. The second idea is that a simple, two-dimensional slowness-frequency (p-f) transform of a microtremor record can separate Rayleigh waves from other seismic arrivals, and allow recognition of true phase velocity against apparent velocities. Figure 3 shows the values of V_s obtained in situ from a D-H test, NASW test and SDMT. In the superficial strata V_s by SDMT is about 250 m/s. In the deeper strata V_s values are about 450 m/s. At the depths of 20 and 24 m V_s is about 700 m/s in correspondence of sandy strata. These high V_s values by SDMT show the effect of soil disturbance during the test. The V_s values, experimentally determined during D-H and NASW tests, did not show any important variation in the transition zone at depths 20 and 24 m, where thin layers of sand exist.

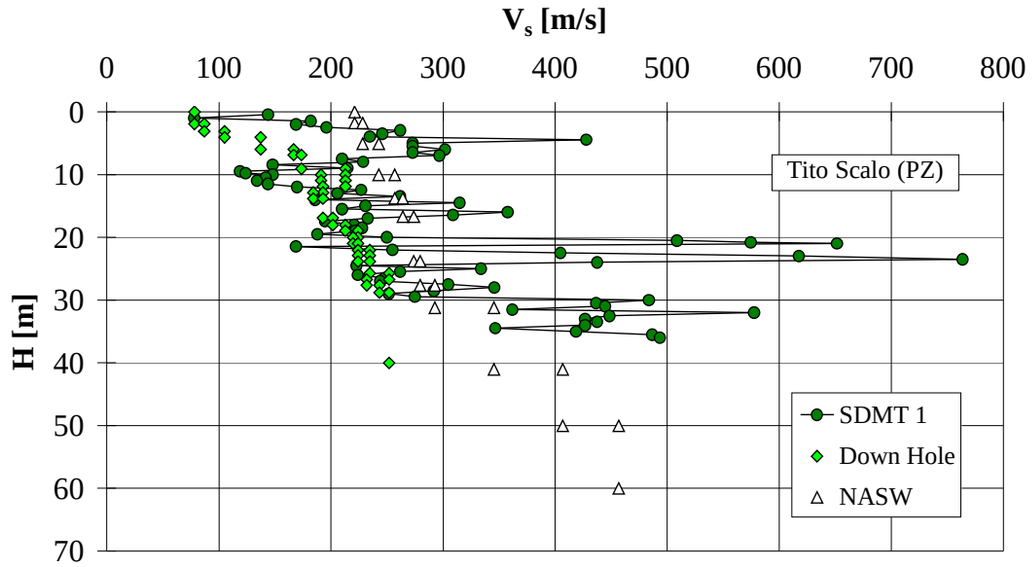


FIG. 3. V_s from different in situ tests.

3.2 Evaluation of G_o from Empirical Correlations

Because it is not always possible to perform dynamic in situ tests it was also attempted to evaluate the small strain shear modulus by means of the following empirical correlations based on in situ test results or laboratory results available in literature.

a) Hryciw (1990):

$$G_o = \frac{530}{(\sigma'_v/p_a)^{0.25}} \frac{\gamma_D/\gamma_w - 1}{2.7 - \gamma_D/\gamma_w} K_o^{0.25} \cdot (\sigma'_v \cdot p_a)^{0.5} \quad (1)$$

where: G_o, σ'_v and p_a are expressed in the same unit; p_a = 1 bar is a reference pressure; γ_D and K_o are respectively the unit weight and the coefficient of earth pressure at rest, as inferred from SDMT results according to Marchetti (1980);

b) Jamiolkowski et. al. (1995):

$$G_o = \frac{600 \cdot \sigma'^{0.5}_m p_a^{0.5}}{e^{1.3}} \quad (2)$$

where: $\sigma'_m = (\sigma'_v + 2 \cdot \sigma'_h)/3$; p_a = 1 bar is a reference pressure, "e" is the void ratio by laboratory tests; G_o, σ'_m and p_a are expressed in the same unit. The values for parameters which appear in equation (2) are equal to the average values that result from laboratory tests performed on quaternary Italian clays and reconstituted sands. A similar equation was proposed by Shibuya and Tanaka (1996) for Holocene clay deposits. Equation (2) incorporates a term which expresses the void ratio; the coefficient of earth pressure at rest only appears in equation (1). However only equation (1) tries to obtain all the input data from the SDMT results.

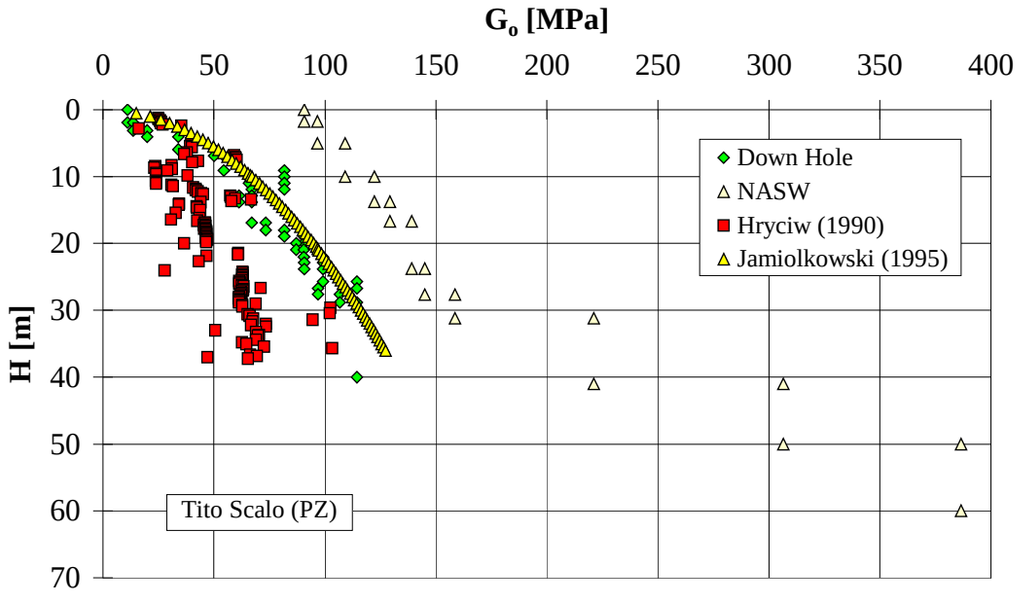


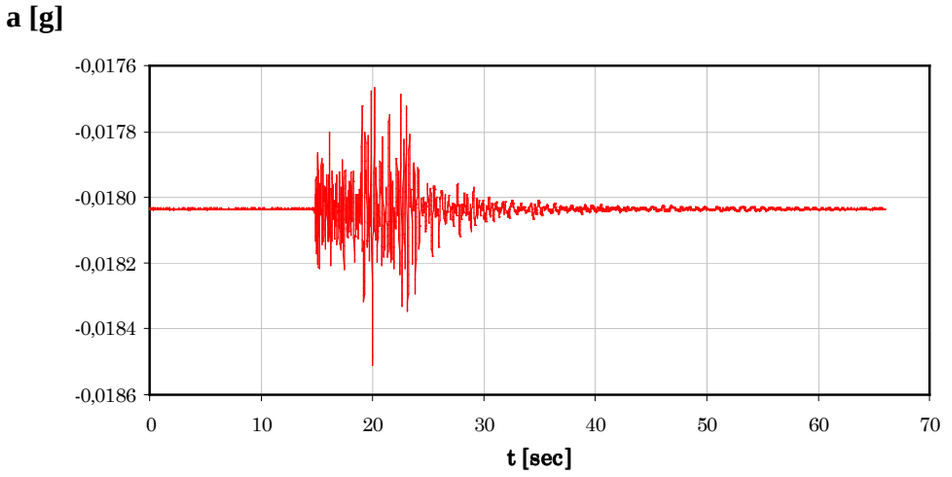
FIG. 4. G_o from different empirical correlations.

The G_o values obtained with the methods above indicated are plotted against depth in Figure 4. The method by Jamiolkowski et al. (1995) was applied considering a given profile of void ratio. The coefficient of earth pressure at rest was inferred from SDMT.

All the considered methods show different G_o values of the soil for depths between 15 and 30 m. On the whole, equation (1) seems to provide the most accurate trend of G_o with depth, as can be seen in Figure 4. A good agreement exists between empirical correlations and D-H test. The SDMT material index indicated the presence of sandy layers at depth of about 20 and 24 m and at the same depths the dilatometer modulus increased. However the method by Hryciw (1990) was not capable of detecting these sandy strata as can be seen in Figure 4. It is worthwhile to point out that equation (1) underestimated G_o for depths between 20 and 30 m.

GROUND RESPONSE ANALYSIS AT THE SOIL SURFACE USING DIFFERENT V_S PROFILES

The site response was made by the 1-D non-linear computer code GEODIN. The code implements a one-dimensional simplified, hysteretic model for the non-linear soil response (Frenna and Maugeri, 1995). The S-wave propagation obtained by DH, NASW and SDMT occurs on a 1-D column having shear behavior. The column is subdivided in several, horizontal, homogeneous and isotropic layers characterized by a non-linear spring stiffness $G(\gamma)$, a dashpot damping $D(\gamma)$ and a soil mass density ρ. Moreover, to take into account the soil non-linearity, models of shear modulus and damping ratio against strain have been inserted in the code. The 1-D columns have a height of 20 m and of 40 m and are excited at the base by accelerograms obtained from the recording of a local earthquake at 35 m depth (see Figure 5). The analysis provides the time-history response in terms of displacements, velocity and acceleration at the surface. Using this time history, response spectra concerning the investigated site have been deduced. The soil response at the surface was also modeled using the linear equivalent computer code EERA (Bardet et al., 2000) for calculating amplitude ratios and spectral acceleration.



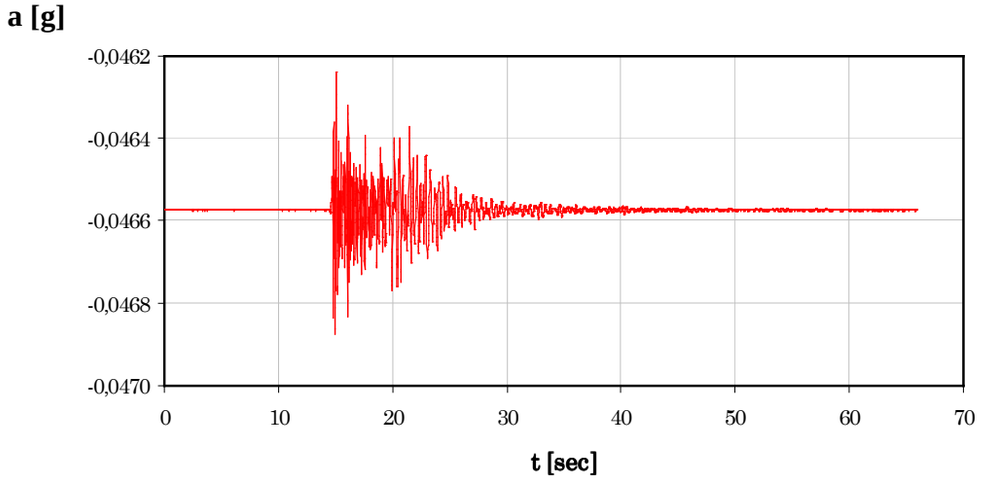
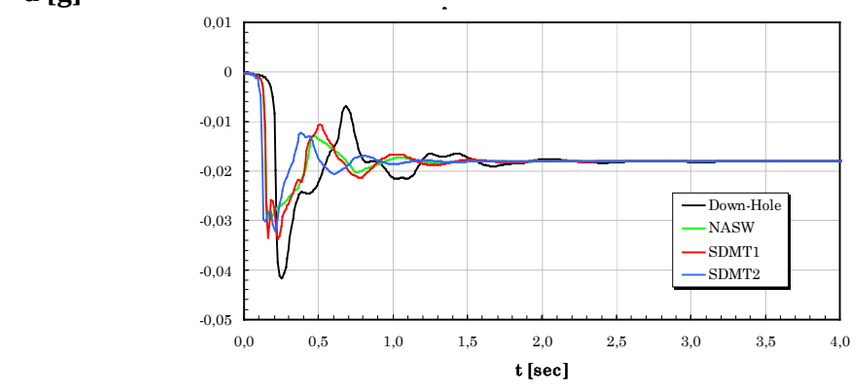
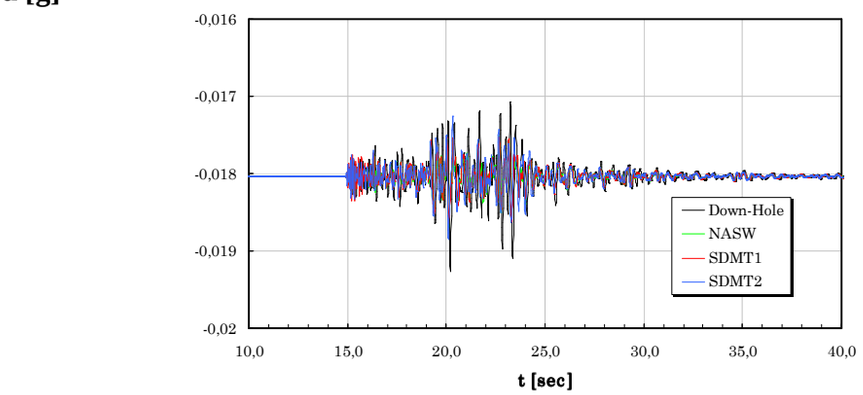


FIG. 5. Acceleration (g) of the N-S (top) and E-W (bottom) components of the recorded local earthquake used for analyses of local seismic response.

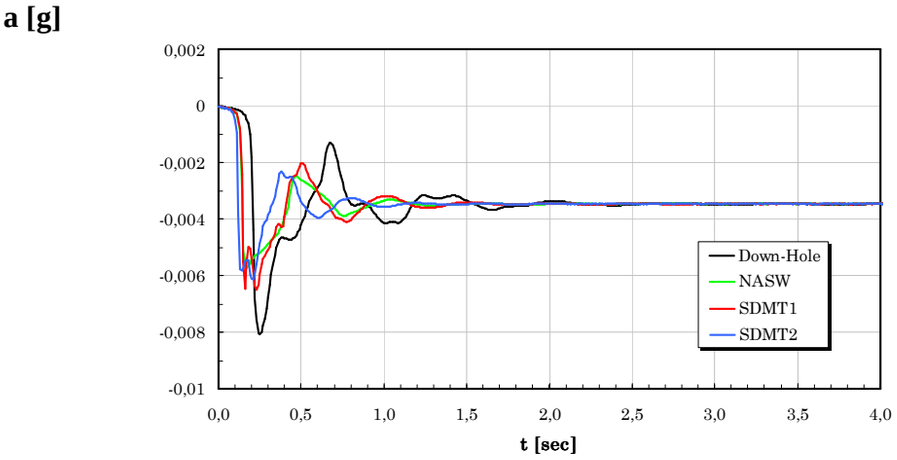
In Figure 6 is reported the time history of accelerations at the soil surface, while Figg. 7 and 8 show respectively amplitude ratios and response spectra obtained using GEODIN and EERA.



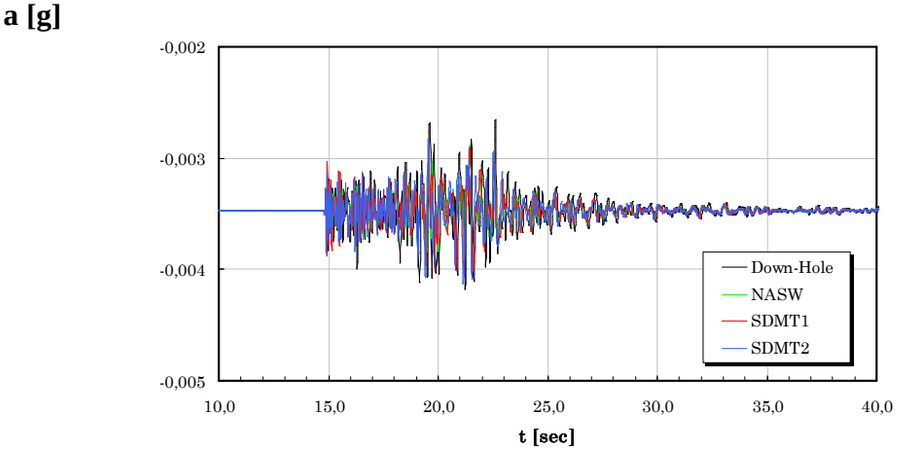
(a)



(b)



(c)



(d)

FIG. 6. Time histories at the soil surface (g) of the recorded local earthquake: a) N-S component [0÷4] sec; b) N-S component [10÷40] sec; c) E-W component [0÷4] sec; d) E-W component [10÷40] sec.

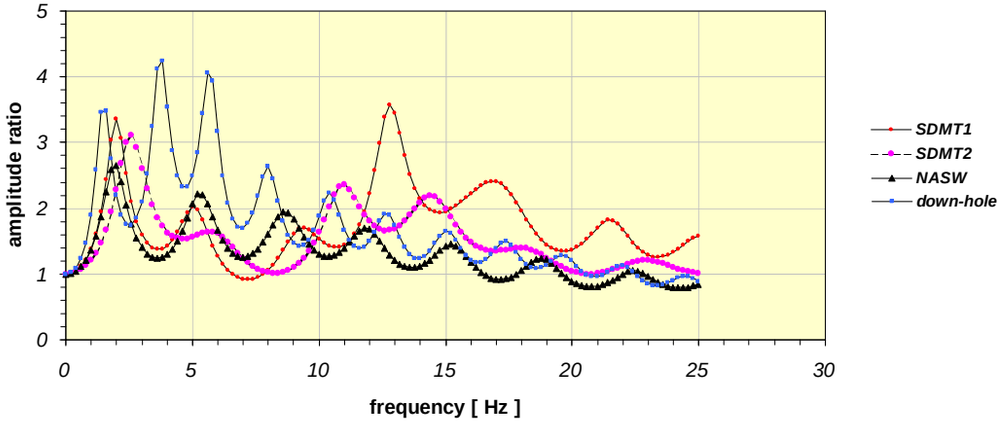


FIG. 7. Transfer functions obtained from analyses using different Vs profiles.

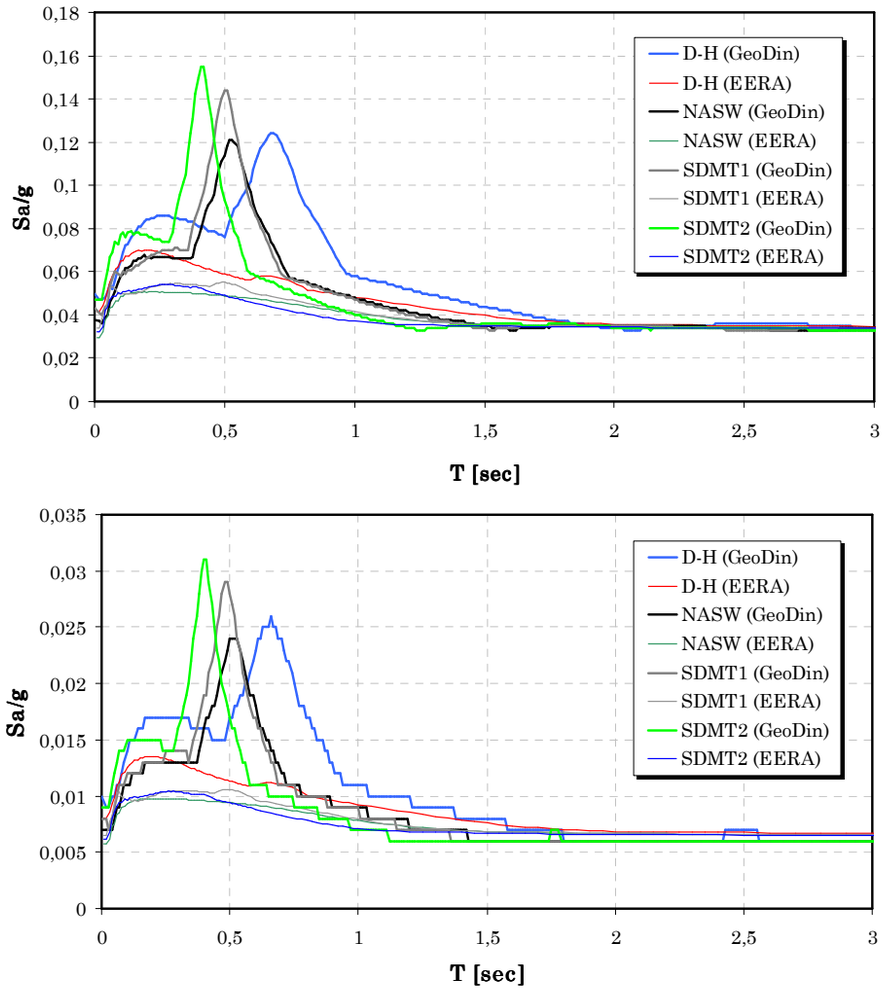


FIG. 8. Response spectra at the soil surface obtained from GEODIN and EERA using different Vs profiles for the N-S (top) and E-W (bottom) components of the recorded local earthquake.

CONCLUSIONS

A site characterization for seismic response analysis of Tito Scalo area has been presented in this paper. On the basis of the data shown it is possible to draw the following conclusions:

- SDMT were performed up to a depth of 40 meters. The results show a very detailed and shear wave profile;
- D-H and NASW tests did not investigate the transition zone where thin layers of sand exist;
- empirical correlations were used to infer G_o from SDMT and in situ tests. The values of G_o were compared to those measured with SDMT, D-H and NASW tests. This comparison indicates that some agreement exists between empirical correlations and D-H test;

- SDMT, because of three independent measurements of p_o (the lateral stress required to cause lift-off of a steel membrane located at the centre of one side the blade), p_1 (the stress required to cause movement at the membrane centre of 1.1mm) and V_s, gives shear modulus at small strain and large strain for detecting soil non linearity;
- a comparison between models obtained using D-H, NASW and SDMT investigations to calculate V_s profiles has been made; the comparison indicates that all the models show comparable results in the estimation of the fundamental frequency.

ACKNOWLEDGMENTS

The authors wish to thank the geotechnical engineer Emanuele Carpenzano for his contribution to the work.

REFERENCES

Cavallaro A., Grasso S. and Maugeri M., (2006). "Clay Soil Characterisation by the New Seismic Dilatometer Marchetti Test (SDMT)"; *Proceedings of the 2nd International Conference on the Flat Dilatometer*, Washington, 2 - 5 April 2006, p. 261-268.

Bardet, J. P., K. Ichii, and C. H. Lin, (2000). "EERA: A Computer Program for Equivalent-Linear Earthquake Site Response Analyses of Layered Soil Deposits. User Manual", *University of Southern California*, 40 pp.

Frenna, S. M. and Maugeri, M. (1995). "GEODIN: A Computer Code for Seismic Soil Response." *Proceeding of the. 9th Italian Conference of Computational Mechanics*, Catania, Italy, 20-22 June 1995, (in Italian): 145 - 148.

Hryciw, R.D. (1990). "Small Strain Shear Modulus of Soil by Dilatometer." *Journal of the Geotechnical Engineering Division, ASCE*, Vo. 116, N°. 11: 1700-1715.

Huey-Chu Huang, Shin-Wei Huang, and Hung-Chie Chiu (2004). "Observed Evolution of Linear and Nonlinear Effects at the Dahan Downhole Array, Taiwan: Analysis of the September 21, 1999 M 7.3 Chi-Chi Earthquake Sequence." *Pure and Applied Geophysics* **162**(1): 1-20.

Jamiolkowski, M., Lo Presti, D.C.F. and Pallara, O. (1995). "Role of In-Situ Testing in Geotechnical Earthquake Engineering." *Proceedings of* the *3rd International Conference on Recent Advances in Geotechnical Earthquake Engineering and Soil Dynamic*, State of the Art 7, St. Louis, Missouri, April 2-7, 1995, vol. II: 1523-1546.

Louie J. N. (2001). "Faster, Better: Shear-Wave Velocity to 100 Meters Depth from Refraction Microtremor Arrays." *Bulletin of the Seismological Society of America*, 2001, vol. 91, no. 2 (April), p. 347-364.

Marchetti, S. (1980). "In Situ Tests by Flat Dilatometer." *Journal of the Geotechnical Engineering Division*, ASCE, Vol. 106, N°. GT3, March, 1980: 299-321.

Martin, G.K. and Mayne, P.W. (1997). "Seismic Flat Dilatometers Tests in Connecticut Valley Vaeved Clay." *ASTM Geotechnical Testing Journal*, 20 (3): 357-361.

Martin, G.K. and Mayne, P.W. (1998). "Seismic Flat Dilatometers Tests in Piedmont Residual Soils." *Geotecnical Site Characterization*, Vol. 2, Balkema, Rotterdam:

837-843.
Mucciarelli M., Gallipoli M. R., and Arcieri M. (2003). "The Stability of the Horizontal-to-Vertical Spectral Ratio of Triggered Noise and Earthquake Recordings." *Bulletin of the Seismological Society of America*, Vol. 93, No. 3, pp. 1407–1412, June 2003.
Nunziata, C., Natale, M., and Panza, G.F. (2004). "Seismic Characterization of Neapolitan Soils." *Pure and Applied Geophysics* 161(5-6): 1285-1300
Shibuya, S. and Tanaka, H. (1996). "Estimate of Elastic Shear Modulus in Holocene Soil Deposits." *Soils and Foundations*, Vol. 36, N°. 4, p. 45-55.

This page intentionally left blank

Site Response to Vertical Earthquake Motion

J. Yang[1], M. ASCE and X.R. Yan[2]

[1]Assistant Professor, Department of Civil Engineering, The University of Hong Kong, Hong Kong, China; junyang@hku.hk
[2]Graduate student, Department of Civil Engineering, The University of Hong Kong, Hong Kong, China

ABSTRACT: Evaluation of ground response is one of the fundamental problems in earthquake geotechnical engineering. Current practice has tended to focus on horizontal earthquake motion and ignore the effect of vertical motion. Because of strong vertical ground motions recorded in recent earthquakes, great concern has arisen over the behavior of vertical motion and its effect on engineering structures. This paper presents a practical procedure for the analysis of site response to vertical earthquake motion. The procedure involves the use of dynamic stiffness matrix method and is built in the modern MATLAB environment to take full advantages of the matrix operations in MATLAB. The nonlinear soil behavior is accounted for through the well-accepted equivalent linear approach. Comparisons of the predictions from the procedure against downhole array records show reasonably good agreement.

INTRODUCTION

Earthquake ground motions at a given location comprise both horizontal and vertical components. That means, during earthquakes an engineering site is subjected not only to horizontal shaking, but also to vertical excitation. Site response to vertical earthquake motion, compared with that to the horizontal shaking, appears to have received much less attention in the past three decades. Current practice has tended to focus on the effect of horizontal motion and simply disregard the vertical component. This practice is due mainly to the consideration that engineering structures have adequate resistance to dynamic forces induced by the vertical ground motion, which is generally smaller in magnitude and richer in high frequencies than its horizontal counterpart.

In recent earthquakes, strong vertical ground motions have been repeatedly recorded. For example, the peak vertical accelerations recorded during the Northridge earthquake of 1994 (NCEER 1997) were up to 1.18g (g is the gravitational acceleration). During the 1995 Kobe earthquake, the downhole arrays installed at a reclaimed site recorded the peak vertical acceleration of being twice as high as the

peak horizontal acceleration (Yang and Sato 2000). Having these observations in mind, great concern has arisen over the behavior of vertical motion as well as its potential effect on engineering structures. In this paper, a simple procedure for vertical site response is presented for the purpose of practical applications. The procedure involves the use of dynamic stiffness matrix method and the well-accepted equivalent linear approach for nonlinear soil behavior. The applicability of the procedure is evaluated by using ground motion records from a downhole array.

FORMULATION

As an acceptable simplification, the problem of vertical site response can be regarded as the problem of one-dimensional propagation of compressional waves involving vertical displacement w:

$$\rho \frac{\partial^2 w}{\partial t^2} = E_c \frac{\partial^2 w}{\partial z^2} + \tilde{\eta} \frac{\partial^3 w}{\partial z^2 \partial t} \tag{1}$$

where E_c is the constrained modulus of soil and $\tilde{\eta}$ is viscosity coefficient. They are defined respectively as

$$E_c = \frac{1-\upsilon}{(1+\upsilon)(1-2\upsilon)} E \qquad \tilde{\eta} = 2E_c \tilde{\zeta} / \omega \tag{2}$$

in which E is Young's modulus, υ is Poisson's ratio, and $\tilde{\zeta}$ is the damping ratio for vertical motion. It is convenient to express the complex shear modulus in terms of the damping ratio as $E_c^* = E_c\left(1+2i\tilde{\zeta}\right)$.

The solution of Eq. (1) takes the following form:

$$w(z,t) = \left(Ce^{i\tilde{k}z} + De^{-i\tilde{k}z}\right)e^{i\omega t} = W(z,\omega)e^{i\omega t} \tag{3}$$

where the first term $Ce^{i\tilde{k}z}$ represents the incident wave traveling in the negative z-direction and the second term $De^{-i\tilde{k}z}$ represents the reflected wave traveling in the positive z-direction (Fig. 1). The parameter $\tilde{k}$ is the wave number given by $\tilde{k} = \sqrt{\rho\omega^2 / E_c^*}$.

Now, consider a multi-layered soil-rock system shown in Fig. 1. In the framework of the dynamic stiffness method (Kausel and Roesset 1981; Wolf 1994), the tractions at the top and bottom of the layer *m*, N_m and N_{m+1}, can be given by

$$N_m = -E^* W_{m,z}(z=0) \quad N_{m+1} = E^* W_{m,z}(z=h_m) \tag{4}$$

The dynamic force-displacement relationship can then be established for layer *m* as

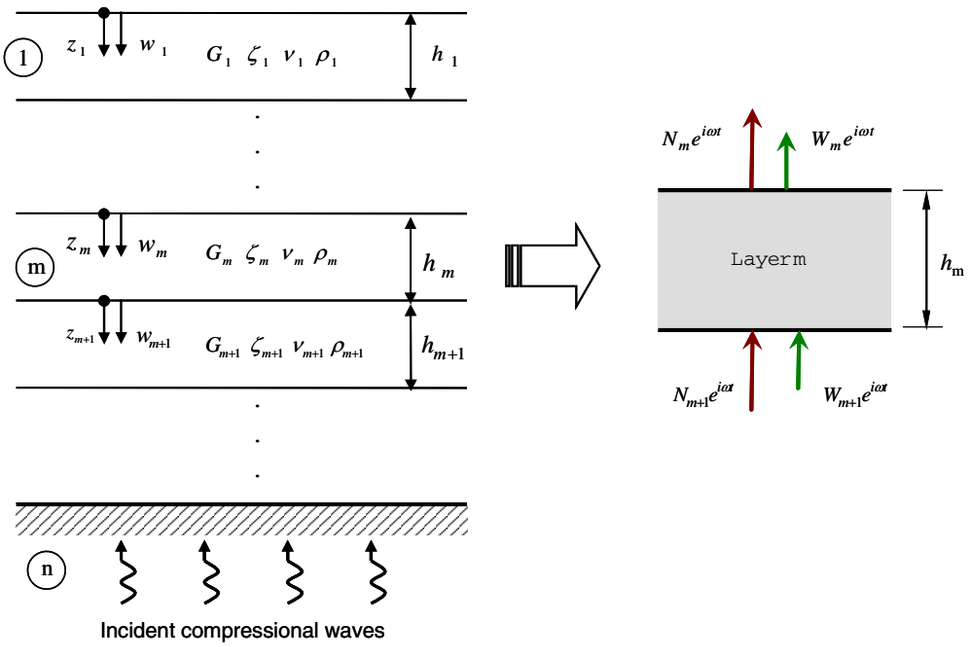


FIG. 1 Multi-layered soil-bedrock system.

$$\begin{Bmatrix} N_m(\omega) \\ N_{m+1}(\omega) \end{Bmatrix} = \begin{bmatrix} \tilde{A}_m & \tilde{B}_m \\ \tilde{B}_m & \tilde{A}_m \end{bmatrix} \begin{Bmatrix} W_m(\omega) \\ W_{m+1}(\omega) \end{Bmatrix} \tag{5}$$

where

$$\tilde{A}_m = \frac{\sqrt{\rho_m E_{cm}^*}\,\omega}{\sin\left(\tilde{k}_m h_m\right)}\cos\left(\tilde{k}_m h_m\right) \qquad \tilde{B}_m = -\frac{\sqrt{\rho_m E_{cm}^*}\,\omega}{\sin\left(\tilde{k}_m h_m\right)} \tag{6}$$

By assembling the stiffness matrix of each layer, the total force-displacement relationship for the layered system is given by

$$\begin{bmatrix} \tilde{A}_1 & \tilde{B}_1 & & & & & & \\ \tilde{B}_1 & \tilde{A}_1+\tilde{A}_2 & \tilde{B}_2 & & & & & \\ & \tilde{B}_2 & \tilde{A}_2+\tilde{A}_3 & \tilde{B}_3 & & & & \\ & & \tilde{B}_3 & \tilde{A}_3+\tilde{A}_4 & & & & \\ & & & & \tilde{B}_{n-3} & \tilde{A}_{n-3}+\tilde{A}_{n-2} & \tilde{B}_{n-2} & \\ & & & & & \tilde{B}_{n-2} & \tilde{A}_{n-2}+\tilde{A}_{n-1} & \tilde{B}_{n-1} \end{bmatrix} \begin{Bmatrix} W_1 \\ W_2 \\ W_3 \\ W_4 \\ W_{n-1} \\ W_n \end{Bmatrix} = \begin{Bmatrix} 0 \\ 0 \\ 0 \\ 0 \\ 0 \\ 0 \end{Bmatrix} \tag{7}$$

Note that there are (*n-1*) equations with *n* unknowns in Eq. (7). Given the bedrock motion at the top of the layer *n*, the motions in all upper layers can be computed conveniently. If rock outcropping motion is given, a radiation dashpot with the damping coefficient of $\rho_{rock} v_{prock}$ is introduced to radiate the energy transmitted from the soil to the bedrock, where ρ_{rock} and v_{prock} are the mass density and compressional wave velocity of the rock.

NONLINEAR SOIL BEHAVIOR

The nonlinear and inelastic behavior of soil under cyclic loading has long been established in geotechnical engineering (e.g., Seed and Idriss 1970). To approximate the actual nonlinear response of a soil, shear modulus reduction curves and damping ratio curves are often established and an equivalent linear approach is utilized in the analysis of horizontal site response (Idriss and Sun 1992; Bardet et al. 2000). For vertical motion, however, reliable test results for the constrained modulus degradation and strain-dependent damping ratio are scarce. Here, an assumption is introduced that the Poisson's ratio is a constant such that the reduced shear modulus and shear wave velocity, produced from the horizontal site response analysis, can be transformed to the constrained modulus and compressional wave velocity. With regard to the soil damping, it is assumed, for the first instance, that the damping ratio for vertical motion ($\tilde{\zeta}$) has the same value as that for horizontal motion (ζ).

VERIFICATION

Based on the formulation described above, a computer program named PASS has been developed in the modern MATLAB environment to analyze both vertical and horizontal site response. The accuracy and efficiency of PASS in the horizontal site response analysis has been evaluated by comparisons with SHAKE (Yang and Yan 2007). Here, a hypothesized site is used to examine the transfer function of vertical motion predicted by PASS. The site comprises a homogeneous single layer of 30m overlying a rock half-space (Fig. 2). The shear wave velocity of the soil layer, V_s, is assumed to be 200 m/s, and the compressional wave velocity, V_p, is 1000 m/s. The site may be classified as stiff soil site based on the shear wave velocity. In the computation, the damping ratio of the soil is assumed to be 0, 5%, and 10% respectively. As shown in Fig. 2, PASS predicts the predominant frequency of 8.32 Hz, which is very close to the analytical prediction. Infinite amplification takes place in the case where the soil has no damping (i.e. elastic response). When the damping ratio of the soil varies from 5% to 10%, the peak amplification is reduced by 50%.

Next, consider a real site in Parkfield, California in which a downhole array has been installed. The soil profile is shown in Fig. 3, along with the profiles of V_s and V_p (Real 1988) The thickness of the clay layer is about 2.4 m and the underlying silty clay is approximately 5.2 m thick. The mass densities of the clay and the silty clay are 1500 and 1900 kg/m^3, respectively. The site was subjected to an earthquake on September

28, 2004 and the time histories of accelerations were successfully recorded at the surface and depths. In this study, the accelerations in the east-west and up-down directions recorded by the accelerometer at the depth of 11m are used as the bedrock input motions (see Fig. 4). The attenuation property of the soils measured using field seismic methods (Real 1988) showed a significant scatter, but basically showed high values. For the first instance, the shear modulus reduction curve and the damping ratio

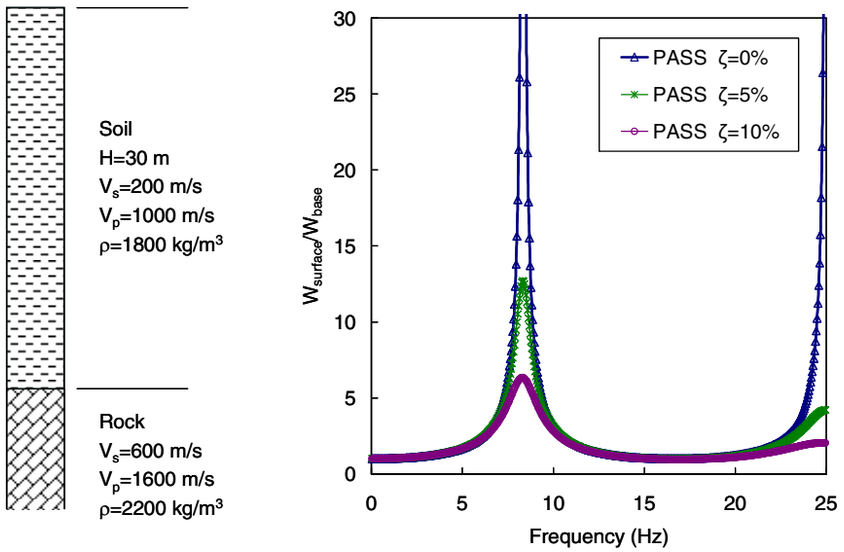


FIG. 2. Transfer function of vertical motion at the hypothesized site.

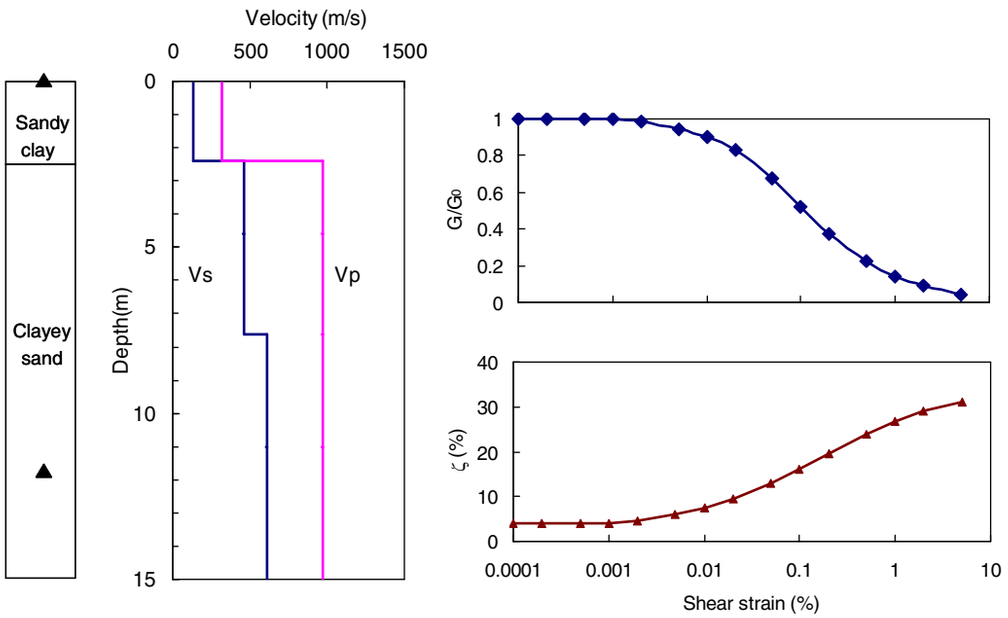


FIG. 3. Simplified soil profile of the downhole array site.

curve proposed by Sun et al. (1988) for clay soil are assumed to approximately represent the nonlinear behavior of the soils at the site (Fig. 3). In Fig. 5, the surface horizontal acceleration computed by PASS is compared with the recorded one, while the predicted and recorded vertical accelerations at the surface are compared in Fig. 6. It is clear that a fairly good agreement is obtained for both vertical and horizontal components of ground motions. This good agreement is also observed in the response spectra shown in Fig. 7.

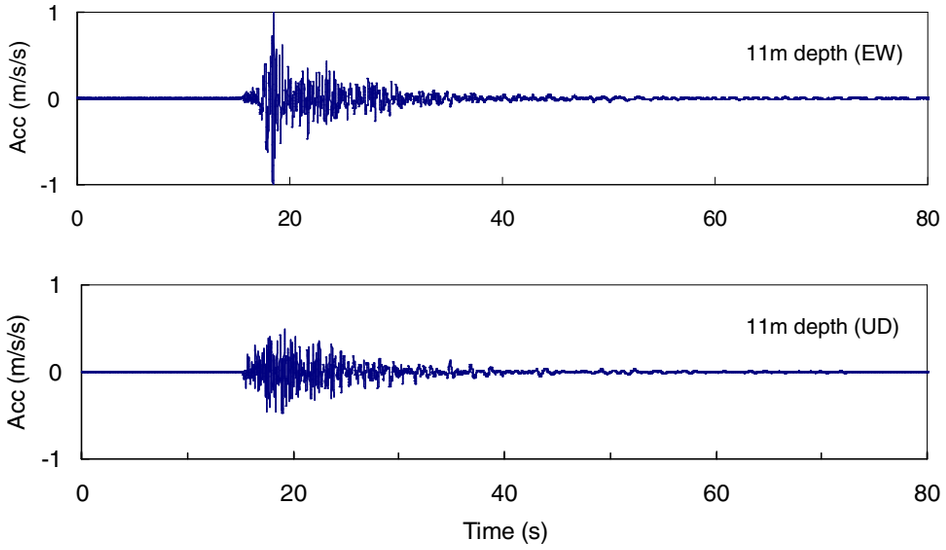


FIG. 4. Recorded accelerations at depth of 11m.

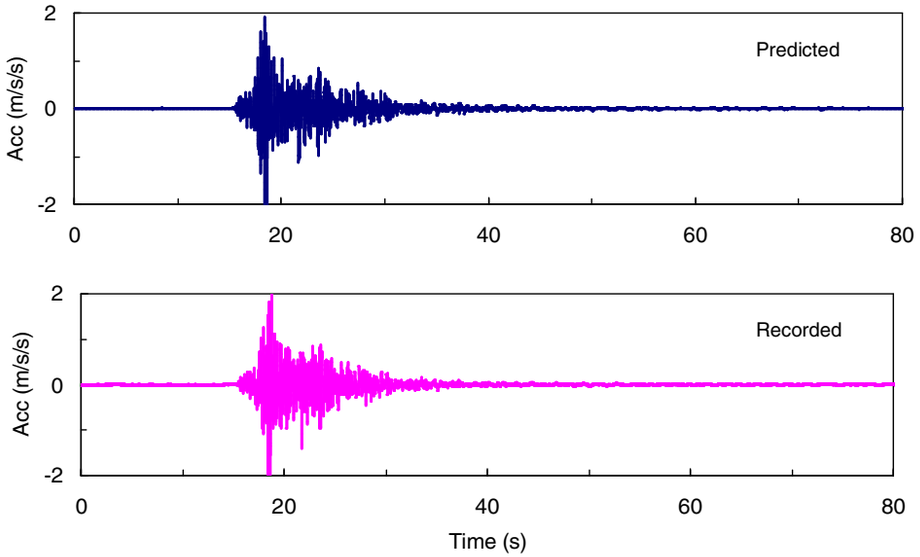


FIG. 5. Predicted and recorded horizontal accelerations at surface.

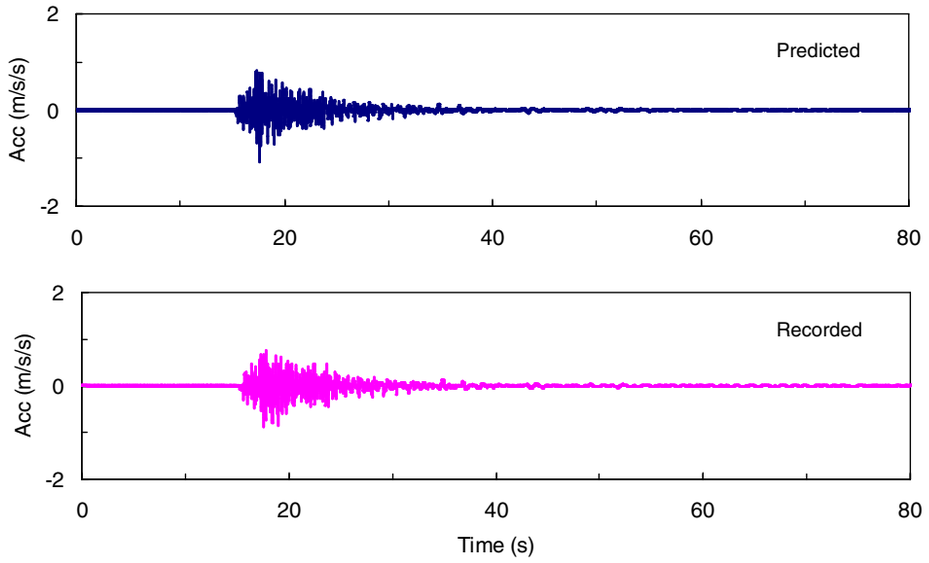
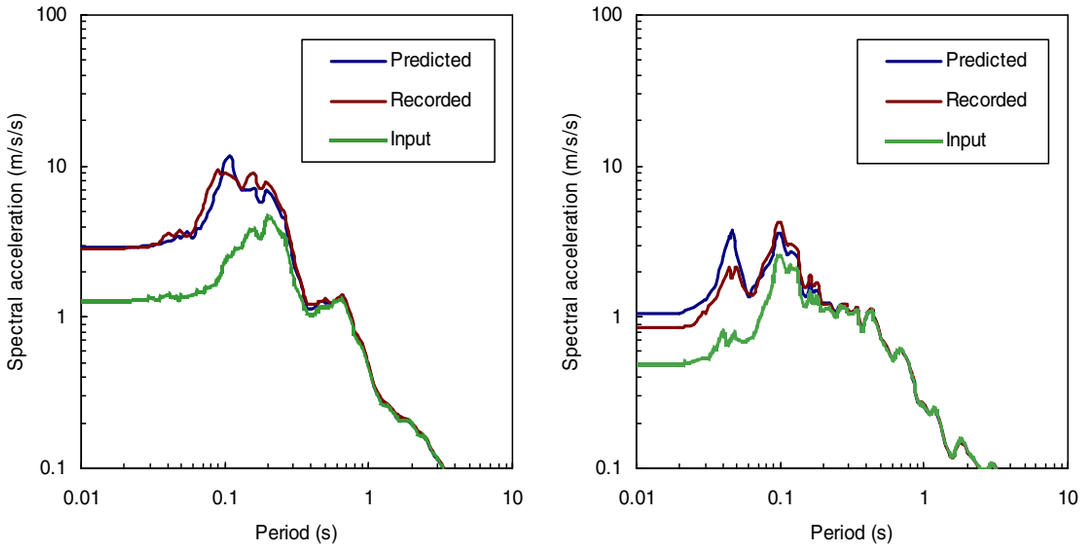


FIG. 6. Predicted and recorded vertical accelerations at surface.



(a) (b)

FIG. 7. Predicted and recorded response spectra: (a) horizontal; (b) vertical.

CONCLUSIONS

Earthquake ground response in vertical direction has not been extensively studied in the past. In this paper, a practical procedure has been presented for the analysis of site response to vertical earthquake motion. The procedure involves the use of dynamic

stiffness matrix method and is built in the modern MATLAB environment to take full advantages of the matrix operations in MATLAB. The nonlinear soil behavior is accounted for through the equivalent linear approach and the assumption of constant Poisson's ratio. The comparisons between the downhole array records and the predictions by the proposed procedure have shown reasonably good agreement and the applicability of the procedure. Due to limited space, more detailed investigation into the behavior of vertical site response using the procedure will be presented in separate papers.

ACKNOWLEDGMENTS

The work was supported by the Research Grants Council of Hong Kong under grant No. HKU7127/04E. This support is gratefully acknowledged. The authors would also like to thank the California Geological Survey for making available the downhole array records.

REFERENCES

Bardet, J.P., Ichii, K., and Lin, C.H. (2000). EERA: a computer program for equivalent-linear earthquake site response analyses of layered soil deposits. *Report*, Dept. of Civil Engrg., University of Southern California.

Idriss, I.M., and Sun, J.I. (1992). User's manual for SHAKE91. *Report*, Dept. of Civil and Environ. Engrg., University of California, Davis.

Kausel, E., and Roesset, J.M. (1981). "Stiffness matrices for layered soils." *Bulletin Seism. Soc. Ame.* 71(6), 1743-1761.

NCEER (1997). FHWA/NCEER workshop on national representation of seismic ground motion for new and existing highway facilities. *Tech. Report*, NCEER-97-0010, National Center for Earthquake Engrg. Research, Buffalo, New York.

Real, C. R. (1988). Turkey Flat, USA site effects test area: site characterization (Report 2). *Tech. Report* No. 88-2, California Dept. of Conservation Division of Mines and Geology, California.

Seed, H.B., and Idriss, I.M. (1970). Soil moduli and damping factors for dynamic response analyses. *Report*, EERC 70-10, Earthquake Engrg. Research Center, University of California, Berkeley.

Sun, J.I., Golesorkhi, R., and Seed, H.B. (1988). Dynamic moduli and damping ratios for cohesive soils. *Report*, UCB/EERC 88/15, Earthquake Engrg. Research Center, University of California, Berkeley.

Wolf, J.P. (1994). Foundation vibration analysis using simple physical models. Prentice Hall.

Yang, J., and Sato, T. (2000). "Interpretation of seismic vertical amplification observed at an array site." *Bulletin Seism. Soc. Ame.* 90(2), 275-285.

Yang, J., and Yan, X.R. (2007). "Ground response analysis using a matrix formulation." *Proc., 4th Int. Conf. Earthquake Geotech. Engrg.* (CD-ROM), Thessaloniki, Greece, Paper No. 1624.

Spatial Analysis of Damage Distribution in the 2001 Southern Peru Earthquake

Nicholas E. Malasavage[1] and Joseph Wartman[2], M. ASCE

[1] Graduate Student Researcher and [2]Associate Professor, Civil, Arch. & Env. Engineering, Drexel University, 3141 Chestnut Street, Philadelphia, PA 19104.

ABSTRACT: Damage distribution surveys have long been used as a means for estimating relative ground shaking intensity. In the absence of dense instrumental arrays, these surveys can be used to identify and delineate geotechnical earthquake hazard zones. The traditional means of analyzing spatially distributed damage survey data is qualitative or semi-quantitative in nature. While this may be a satisfactory approach in situations where there is a marked contrast in building performance, its effectiveness is limited when damage contrasts are subtle, and spatial patterns are less obvious. In this paper we present a quantitative approach [Getis-Ord (Gi*) statistic] for interpreting and analyzing earthquake damage surveys. By implementing neighborhood-scale spatial analysis within a Geographical Information Systems (GIS) framework, statistically significant concentrations of elevated (and/or low) damage concentrations can be identified and quantified. An example application of this method is applied to a damage survey from the 2001 Southern Peru Earthquake (M_w8.4). In contrast to preliminary studies that suggested damage concentrations were a consequence of topographic amplification, the spatial analyses demonstrated that hotspots of damage are generally correlated with flatter ground in the study area

INTRODUCTION

Damage distribution surveys have long been used as a means for estimating relative ground shaking intensity. In the absence of dense instrumental arrays, these surveys can be used to identify and delineate geotechnical earthquake hazard zones (e.g. Harbi et al., 2007, Trifunac & Todorovska, 2004, Azzaro et al., 2004). Conventional methods of analyzing damage survey data are qualitative or semi-quantitative in nature (e.g. visual identification of clusters of severely damaged, "red-tagged" structures, normalizing number of damaged structures by area, etc.). While this approach may be satisfactory in situations where there is a marked contrast in building performance, its effectiveness is limited when damage contrasts are subtle and spatial patterns are less obvious. Moreover, qualitative techniques for identifying damage clusters often fail to account for important factors such as building type and/or quality of construction.

In this paper we present a quantitative approach for interpreting and analyzing earthquake damage surveys. By implementing a neighborhood-scale (~1 km^2) spatial analysis within a Geographical Information Systems (GIS) framework, statistically significant concentrations of elevated (and/or low) damage levels can be identified and quantified. We accomplish this by applying the Getis-Ord (Gi*) statistic within a moving window neighborhood analysis. This analysis efficiently produces a single value output for each input that dually describes the existence of "clustered" damage as well as its statistical significance (Getis & Ord 1992). This approach has been successfully used to investigate other spatially dependant phenomena such as high crime areas, (e.g. Ratcliffe & McCullagh 1999), disease outbreaks (e.g. Ord & Getis, 1995) and international conflicts (e.g. Anselin 1995).

Advantages of this approach over qualitative techniques include its (i) ability to identify subtle, but nevertheless statistically significant patterns and trends, (ii) scalability [i.e., applicability over a wide range of spatial scales], and (iii) capability of generating highly effective and easily communicated graphical displays of large quantities of geographically distributed data. In the following sections we describe the use of the Getis-Ord (Gi*) statistic to identify damage patterns in the town of Moquegua, Peru, which was struck by a large earthquake in 2001. This work is part of a larger research effort to statistically correlate structural damage to underlying geophysical and earthquake characteristics such as topography, subsurface conditions, and earthquake ground motion.

Damage in San Francisco, Moquegua in the 2001 Southern Peru Earthquake

The June 23, 2001 M_w 8.4 Southern Peru earthquake affected a widespread area that included several important population centers in southern Peru and northern Chile (Rodriguez-Marek et al. 2003, Wartman et al 2003). The earthquake occurred along the subduction boundary of the Nazca and the South American plates. Adobe buildings and older structures were most susceptible to damage, though a significant number of modern engineered structures were also impacted by the earthquake. The absence of ground failure (e.g. liquefaction, landslides) in the immediate area suggests that damage was primarily a result of inertial effects. Coincidentally, the only strong motion station in the Peruvian network to record the event was located near the study area in the city of Moquegua. This instrument recorded a peak horizontal ground horizontal acceleration of 0.30 g.

In this research we utilized high quality structural damage survey data (PREDES 2003) for the 1 km^2 hillside neighborhood of San Francisco, located in the city of Moquegua. The city is situated in an alluvial basin adjacent to the Moquegua River and experienced especially high concentrations of damage in San Francisco (Figure 1). While much of Moquegua is relatively flat, the San Francisco section of the city is distinguished by its variation in topography.

The neighborhood is situated on a geologic outcrop that includes three ridges rising roughly 100 m above the central portion of the city (topography on Figure 2). The outcrop, which daylights in the upper half of each ridge, consists of stiff

conglomerate classified locally as the Moquegua Formation. This outcrop is also the primary source of alluvium/colluvium that forms a soil mantle that generally thickens with decreasing elevation. Soil thickness ranges from 0 m on the hillside, to 6 m in valley and flatland areas. Near surface groundwater is not present in the neighborhood.



FIG 1: Damage to structures in the hillside neighborhood of San Francisco.

Several preliminary reconnaissance reports hypothesized that the high levels of damage to structures in San Francisco was due to strong ground shaking exasperated by topographic amplification (e.g. Rodriguez-Marek et al. 2001, Kosaka-Masuno et al. 2001, Kusunoki 2002). While this is a plausible explanation, data published later including the cited damage surveys and a post-earthquake building material loan inventory (Banco Municipal, 2003) did not demonstrate conclusively that damage concentrations were solely focused near the crests of neighborhood slopes. To test the topographic amplification hypothesis, a series of analyses were performed to identify locations of statistically significant concentrations of damage. The results of these damage cluster analyses indicate that the performance of both modified adobe and stronger confined masonry dwellings was better on hillside locales than flatland areas.

DAMAGE DISTRIBUTION

Several damage surveys of the area have been published, including a detailed account produced by Peru's Center for the Study and Prevention of Disasters (PREDES 2003), which rated the performance of each dwelling in the neighborhood as either good, moderate or poor, corresponding to buildings that exhibited no

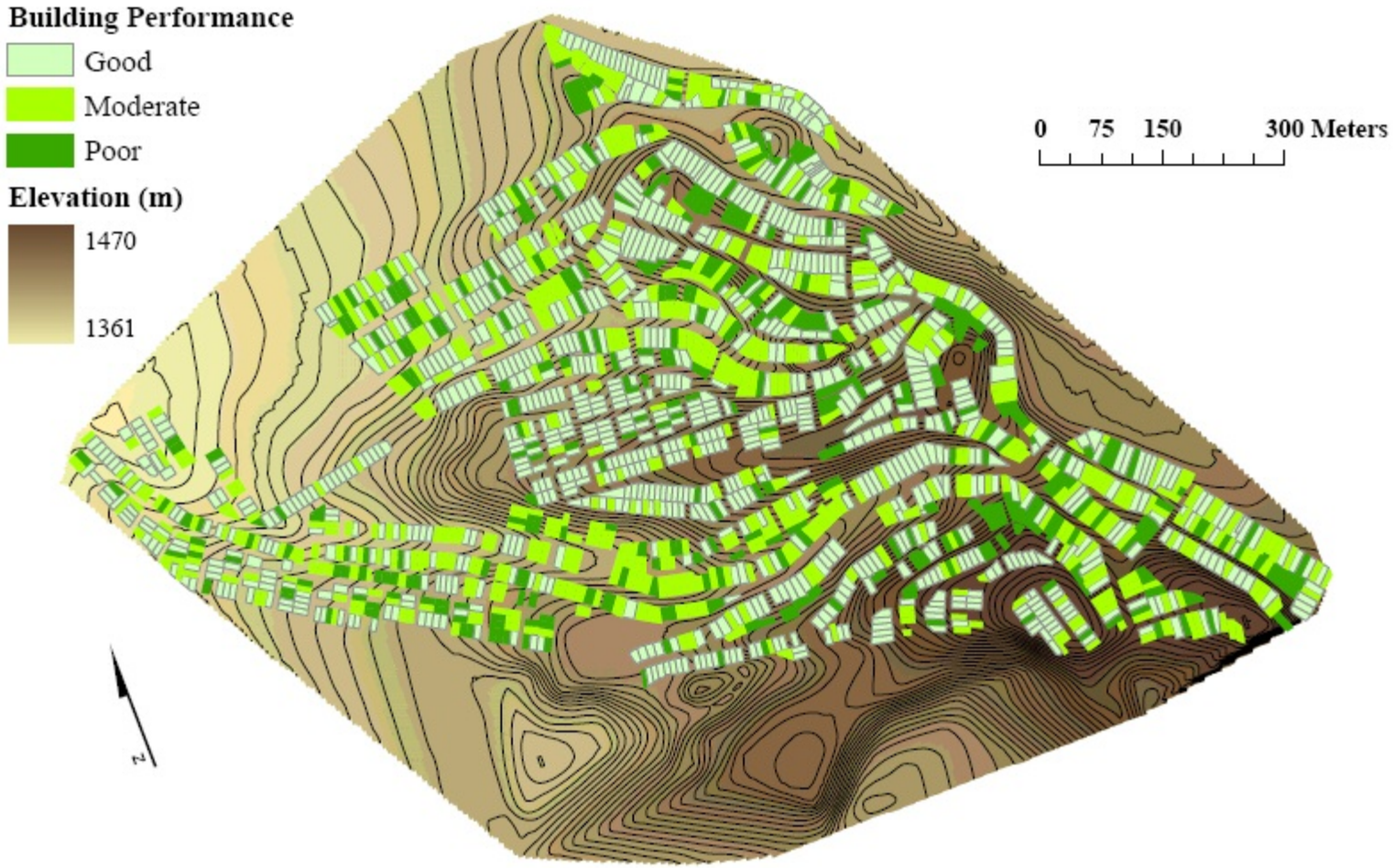
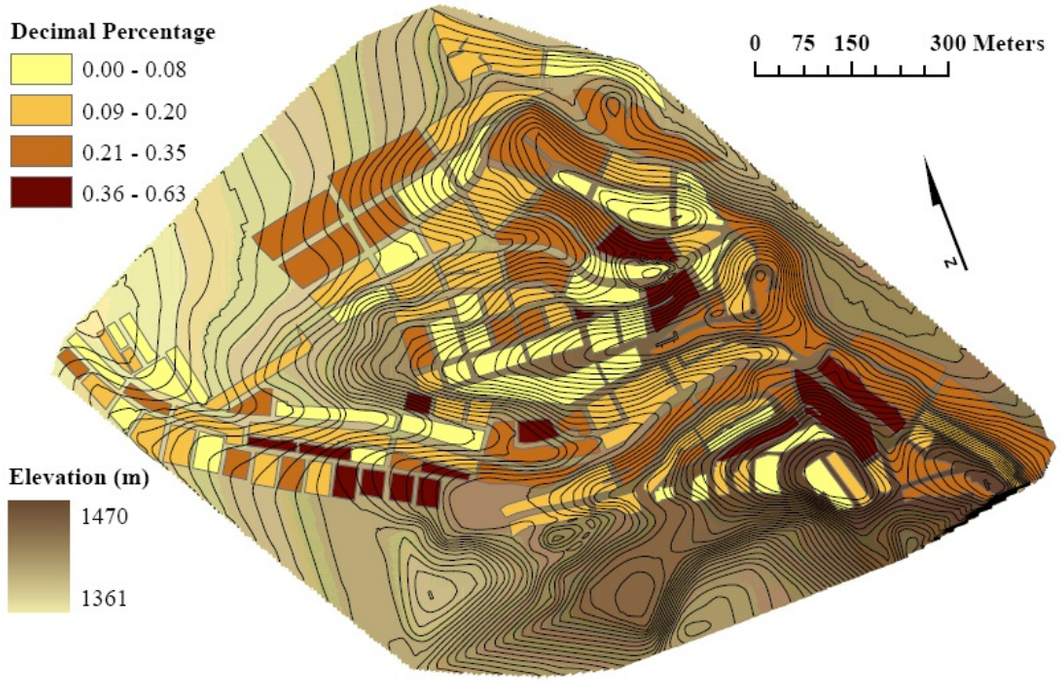
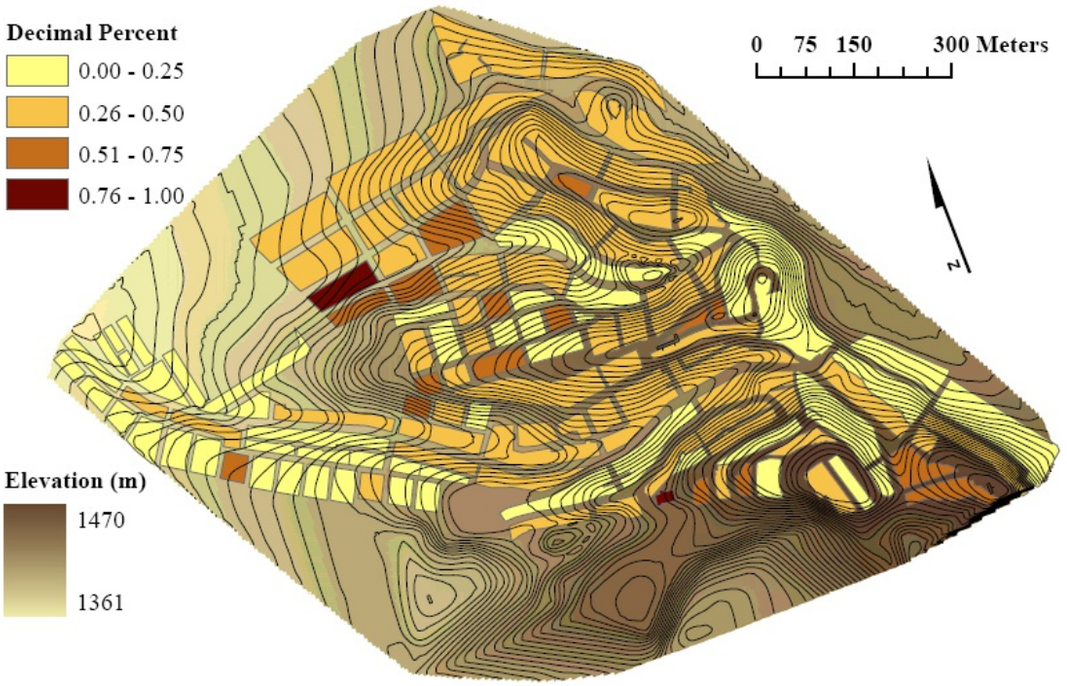


FIG 2: Damage distribution of all structures and topography in San Francisco.



(a)



(b)

FIG 3: Damage as interpreted as (a) percent area per block with poor building performance and (b) percent area awarded building material loans.

significant damage, significant cracks to loading bearing members, and collapse, respectively. The performance of all buildings surveyed in this study is shown in Figure 2. Note the absence of any clear patterns of damage. Traditional qualitative or semi-quantitative methods were used in an attempt to illustrate patterns in damage distribution. These included determining the percent area of severely damaged lots for each block (Figure 3a) and the percent area which received building material loans following the event (Figure 3b). However, none of these methods, or combinations thereof, produced conclusive results.

SPATIAL CLUSTER ANALYSIS

Spatial clustering analysis was conducted to identify statistically significant spatial concentrations of damage. The analysis was performed using the Getis-Ord (G_i^*) statistic, implemented with the commercially available GIS software ArcView (ESRI, 2007). The Gi* statistic works within the framework of a neighborhood analysis, where a given characteristic of a specific point within the study area is assumed to be influenced by other adjacent known data points up to a selected (i.e., user-defined) threshold distance (Lo and Yeung, 2002). The statistic is expressed as:

$$G_i^*(d) = \frac{\sum_j w_d^*(i,j) z(j)}{\sum_j z(j)};$$

where $w_d^*(i,j)$ is a matrix describing the influence of adjacent points surrounding $z(j)$, the point of interest (within the threshold distance), and $\sum_j z(j)$ is the summation of attribute values for known points within the threshold distance .

While several methods for analyzing point patterns within a neighborhood framework exist, the G_i^* statistic was selected for several reasons:

1. The statistic has been validated in other research with datasets similar to that of this study (e.g. Ratcliffe & McCullagh 1999, Ord & Getis 1995, Anselin 1995).
2. Application of the statistic is straightforward, and in contrast with other approaches, requires nether advanced calibration nor significant pre-processing
3. The statistic describes both the statistical significance (if there is a cluster) and the type of clustering (i.e., high or low values).

The value of the G_i^* statistic is a "Z-score," which is also the standard deviation of the data point with respect to the normal distribution of its surrounding neighbors (Ebdon, 1985). Therefore, highly negative or highly positive Z-score values indicate statistically significant clusters of respectively high ("hotspots") or low ("coldspots") values (Getis & Ord, 1992).

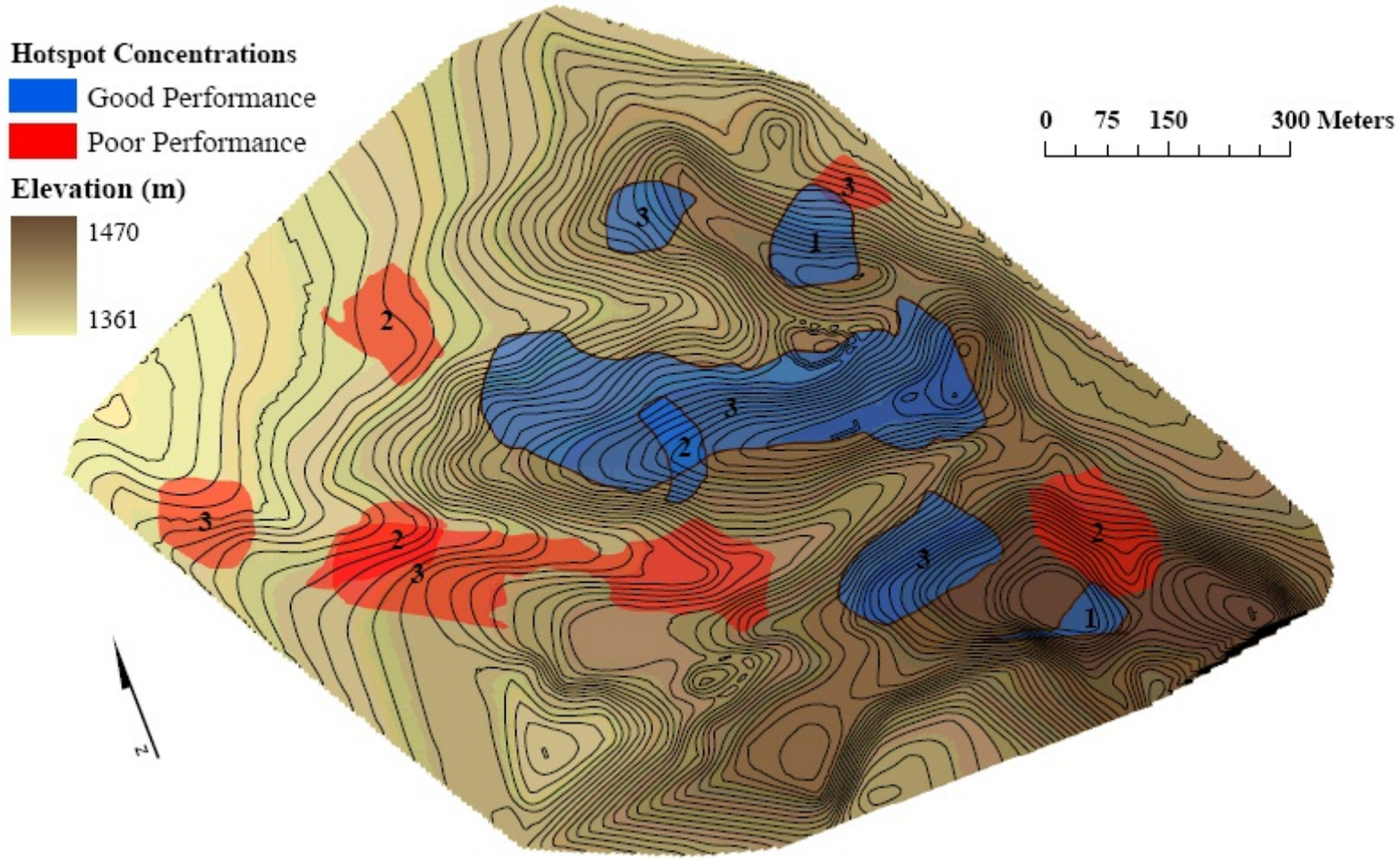


FIG 4: Overlaid results of the 95% confidence interval for "coldspot" (low damage) and "hotspot" (high damage") identified in the analyses of damage distribution for (1) adobe, (2) masonry and (3) modified adobe building types.

Analyses were conducted in a manner that minimized the effects of building type and optimized the performance of the statistic, as we are aware of no reliable correlation for cross referencing damage between different building types. For example, equivalent shaking may cause moderate damage in masonry structures, while collapsing adobe dwellings. Therefore, three separate analyses (one for each respective construction material) were conducted. An appropriate threshold distance for each neighborhood analysis was estimated to be between 40 and 100 m, corresponding to the varying ridge-to-ridge distance within the neighborhood. This choice facilitates the comparison of flatland to adjacent hillsides and vice versa, while minimizing biases induced by global comparisons. Distances were then refined in a trial-and-error fashion by applying different window radii within this range. Through this process we determined the window size that corresponded to the highest degree of statistical confidence for clustering for each respective building type (50 to 80 m in the final analyses). These unique window sizes are a function of both the spatial distribution and diversity of each dataset. Through this procedure the effects of "diluting" patterns, which occurred with large windows, or alternatively, not capturing surrounding data when too small a window was specified (i.e., "tunnel-vision effect") were minimized.

As the G_i^* statistic is a standard deviation, it expresses how different from the average (standard deviation equal to zero) each data point is. Therefore, greater non-zero values represent an increasing likelihood of clustering. For this study, output values less than -1.96 and greater than 1.96 (i.e., 95% confidence interval), were used as a threshold to delineate the extent of each hot- or coldspot of damage (Figure 4) in the GIS. These values correspond to a statistical significance of 5%, implying the mapped clusters have only a 5% likelihood of being a result of random chance.

DISCUSSION AND CONCLUSIONS

In contrast to preliminary studies that suggested damage concentrations were a consequence of topographic amplification, the spatial analyses results shown in Figure 4 indicate that hotspots of damage are generally correlated with flatter ground in the study area. Moreover, damage coldspots generally overlie areas of topographic relief. Since the marked areas represent a 95% confidence interval, it is unlikely that the observed clustering is a result of random chance. Although this by itself does not disqualify the hypothesis that topographic amplification played a role in damage distribution, it does suggest, at a minimum, that these effects were less significant than originally thought. Our ongoing research is examining the possible contribution of other factors such as site amplification in the observed damage distribution in San Francisco.

In this paper we presented a new approach for analyzing patterns in earthquake damage distribution. This method provides a reliable statistical basis for identifying and delineating patterns of favorable or poor seismic performance. This approach is particularly valuable in studies, such as that presented here, where spatial patterns are subtle, but nevertheless significant. In these situations, the effectiveness of traditional qualitative or semi-quantitative methods to distinguish patterns in raw or processed

data by visual interpretation alone is often limited. The current study suggests that when employed over a large regional scale with high quality damage inventories, spatial analysis methods can be valuable for hazard zonation studies. Moreover, the combination of continuing computational advances and development of commercial software has made it significantly easier to perform such analyses.

ACKNOWLEDGEMENTS

Financial support for this research was provided by the National Science Foundation under Grants CMS-0134370 and CMS-0201468. Any opinions, findings, and conclusions or recommendations expressed in this material are those of the writers and do not necessarily reflect the views of the National Science Foundation..

REFERENCES

Anselin, L. (1995). "Local indicators of spatial association – LISA." *Geographical Analysis*, 27(2):93-115.

Azzaro, R., Barbano, M.S., Camassi, R., D'Amico, S., Mostaccio, A., Piangiamore, G., and Scarfi, L. (2004). "The earthquake of 6 September 2002 and the seismic history of Palermo (Northern Sicily, Italy): Implications for the seismic hazard assessment of the city." *J. of Seismology*, 8: 525-543.

Ebdon, D. (1985). Statistics in Geography: 2nd Edition. *Blackwell Publishing Ltd*, Malden, MA, U.S.A, 240p.

ESRI (2007). ArcGIS Desktop, Version 9.2, 380 New York Street, Redlands, CA 92373-8100.

Getis, A., & Ord, J.K. (1992). "The analysis of spatial association by use of distance statistics." *Geographical Analysis*, 24(3):189-206.

Harbi, A., Maouche, S., Ousadou, F, Rouchiche, Y., Yelles-Chaouche, A., Merahi, M., Heddar, A., Nouar, O., Kherroubi, A., Beldjoudi, H., Avadi, A., Benouar, D. (2007). "Macroseismic study of the Zemmouri Earthquake of 21 May 2003 (Mw6.8, Algeria)." *Earthquake Spectra*, 23(2):315-332.

Lo, C.P. and Yeung, A.K.W. (2002). Concepts and Techniques of Geographic Information Systems. *Prentice Hall Inc.*, Upper Saddle River, NJ, U.S.A., 492p.

Kosaka-Masuno, M., Gonzales-Zenteno, E., Arias-Barahona, H., Minaya-Lizarraga, A., Faran-Bazan, E., Ticona-Paucara, J. (2001). "Seismic Hazard Evaluation in the city of Moquegua." *Convenio UNSA-INDECI. Proyect PER 98/018 PNUDINDECI*, San Agustin de Arequipa National University, Arequipa, Peru.

Kusunoki, K. (2002), "Report on the damage investigation of the 2001 Atico Earthquake in Peru." *Building Research Institute of Japan*. 27 p.

Ord, J.K. and Getis, A. (1995). "Local spatial autocorrelation statistics: distributional issues and an application." *Geographical Analysis*, 27(4):286-306.

Center for the Study and Prevention of Disasters (PREDES). (2003), "Study of the physical environment, social economics and evaluation of the risk in the neighborhood of San Francisco with reference to the District of Moquegua and Mariscal Nieto Province." *Center for the Study and Prevention of Disasters*, 261p.

Ratcliffe, J.H. and McCullagh (1999). "Hotbeds of crime and the search for spatial accuracy." *J. of Geographical Systems*, 1:385-398.

Rodriguez-Marek, A., Williams, J.L., Wartman, J., Repetto, P.C. (2003), "Ground motion and site response." Chapter 2 of the Southern Peru Earthquake of June 21, 2001 Reconnaissance Report, *Earthquake Spectra*, 19(S1):11-34.

Trifunac, M.D. and Todorovska, M.I. (2004). "1971 San Fernando and 1994 Northridge, California, earthquakes: did the zones with severely damaged buildings reoccur?" *Soil Dynamics and Earthquake Engineering*, 24:225-239.

Wartman, J., Rodriguez-Marek, A, Repetto, P. and Keefer, D. (2003). "Ground Failure," Chapter 3 of the Southern Peru Earthquake of June 21, 2001 Reconnaissance Report, *Earthquake Spectra*, 19(S1):35-56.

STRAIN-DEPENDENT SOIL PROPERTIES ESTIMATED FROM DOWNHOLE ARRAY RECORDINDS AT KASHIWAZAKI-KARIWA NUCLEAR POWER PLANT DURING THE 2007 NIIGATA-KEN CHUETSU-OKI EARTHQUAKE

Kohji Tokimatsu[1], M. ASCE and Ryosuke Sugimoto[2]

[1]Professor, Tokyo Institute of Technology, 2-12-1 O-okayama, Meguro-ku, Tokyo 152-8552, Japan, Kohji@o.cc.titech.ac.jp
[2]Graduate Student, Tokyo Institute of Technology, 2-12-1 O-okayama, Meguro-ku, Tokyo 152-8552, Japan, rsugi5@mail.arch.titech.ac.jp

ABSTRACT: Strain-dependent shear moduli and damping ratios are estimated for the deposit of the Service Hall at the Kashiwazaki-Kariwa nuclear power plant based on shear stress-strain time histories that can be directly determined from its downhole array recordings during the 2007 Niigata-ken Chuetsu-oki earthquake. The Holocene dune sand with V_s = 310-350 m/s at depths less than about 70 m shows strong nonlinearity with a shear modulus ratio of about 0.3 and a damping ratio of about 30 % at a maximum shear strain of about $3x10^{-1}$%. The reduction in shear modulus ratio is consistent with previous laboratory test results for sand consolidated under similar confining pressures but the corresponding damping ratio seems to be slightly higher than that of the previous studies. The mudstone with V_s =500 m/s located at depths greater than about 100 m does not show any strong nonlinearity with a shear modulus ratio of about 0.6 and a damping ratio of about 10 % at a maximum shear strain of about $1.5x10^{-1}$%. The strong nonlinearity of the Holocene dune sand during the main shock might have lowered the amplitude ratios between the near-surface layer and the bedrock in the short period range significantly compared with those of other smaller events.

INTRODUCTION

The Niigata-ken Chuetsu-oki earthquake (M_j=6.8) occurred at 10:13 a.m. on July 16, 2007, with an epicenter off the Niigata Prefecture and with a focal depth of about 15 km. The quake affected the coastal areas of the southwestern Niigata prefecture including Kashiwazaki city and Kariwa village as well as the Kashiwazaki-Kariwa nuclear power plant of Tokyo Electric Power Company (TEPCO). The earthquake claimed a death toll of eleven, with almost two thousand injuries. More than thirty-five thousand residential houses either totally collapsed or were partially damaged. The strong ground motions recorded by K-NET (National Research

Institute for Earth Science and Disaster Prevention, 2007) near Kashiwazaki municipal building had a spiky peak acceleration of 0.67g, suggesting cyclic mobility behavior of the ground.

Both ground shaking and ground failure problems affected residential houses in the area. Most of the houses affected by ground shaking were very old, built with traditional Japanese construction technique and with large opening along the street, and thus constituted a soft first story prone to deformation parallel to the street during strong shaking. Many of them collapsed in parallel to the weak axis of the building or to the strong axis of the ground motion (NW-SE) in the area. Many houses on reclaimed alluvial sandy deposits and slopes of sand dunes suffered from ground failure problems involving soil liquefaction. Ground failure problems also affected many infrastructures such as railways, highways, roads, bridges, embankments and lifelines (Kayen et al, 2007).

A matter of utmost concern is the performance of the Kashiwazaki-Kariwa nuclear power plant during and after the earthquake. A fire broke out around a house electric transformer and many less critical structures as well as incidental components such as pipes and ducts were damaged; however, three reactors in full operation as well as one in a start-up state were automatically shutdown and all the critical structures including reactor and turbine buildings seemed to be in good conditions.

A total of 97 accelerometers of old and new systems were installed at the site (TEPCO, 2007a). The old system includes 36 stations in the reactor and turbine buildings, 2 for the main exhaust stacks, and 29 on and in the ground, while the new system includes 28 in the reactor and turbine buildings, and 2 on the ground surface at Units 1 and 5. The strong motions at 33 locations were recorded for the main shock, but unfortunately, the recordings obtained at the other 63 locations from the old system as well as one from the new system, including three free-field downhole arrays close to the reactor buildings, were lost, with the exception of the peak values of the old system. The recovered 33 recordings included all of the new system except one in the Unit 3 turbine building, and one 4-depth free-field downhole array at the Service Hall of the old system (TEPCO, 2007a, 2007b).

The downhole array recordings at the Service Hall seemed particularly important not only to determine the input base rock motions for analytically reviewing dynamic behavior of the critical buildings but also to estimate nonlinear dynamic soil properties at the site under high confining pressures that are difficult to observe in the conventional laboratory test but definitely required for the analysis. The objective of this paper is to estimate strain-dependent shear moduli and damping ratios for the site based on shear stress-strain time histories that can be directly determined from its downhole array recordings during the 2007 Niigata-ken Chuetsu-oki earthquake.

SITE CONDITIONS AND OBSERVED RECORDINGS

The Kashiwazaki-Kariwa nuclear power plant is located along the coast on the north

of Kashiwazaki city, about 16 km from the epicenter. Figure 1 shows an aerial photograph from the Japanese Geographical Survey Institute (GSI, 2007) taken after the main shock. The plant is not only one of the largest nuclear power plants in the world, having seven generators (Units 1 through 7) with a total output capacity of 8.2 GW within an area of 4.2 km^2, but also the first one that experienced strong ground shaking. The Service Hall downhole array and its observation station are located on the east of the main gate, as indicted in Fig. 1.

Figure 2 shows the geological and geophysical logs along with the location of the downhole accelerometers. The elevation of the site is 67.5 m, which is 62.2 m or 55.2 m higher than those (5.3m or 12.3 m) of Units 1-4 or 5-7. The surface layers of the Holocene and Pleistocene sand dune deposits overlie the Pleistocene Yasuda Formation that in turns overlies the Pliocene Nishiyama Formation. The shear wave velocities of the Holocene sand dune (New sand dune), Pleistocene sand dune (Banjin Formation), Yasuda Formation, and Nishiyama Formation are 310, 310-350, 350, and 500-640 m/s, respectively. Their mass densities are estimated to be 1.65, 1.65-1.80, 1.80, and 1.65-1.75 Mg/m^3, respectively.

The Service Hall downhole array includes four three-component accelerometers installed at depths of 2.4 m, 50.8 m, 99.4m, and 250 m. The NS and EW directions of the accelerometers were set to the two principal axes of the plant buildings and thus were rotated clockwise 18.9 degrees from the true ones. The ground water table was located at a depth of about 35 m. The 2007 Niigata-ken Chuetsu-oki earthquake caused a ground settlement of about 15 cm around the observation station at the Service Hall. No apparent sign of soil liquefaction was identified nearby.

Downhole array recordings for the main shock as well as six aftershocks are available (TEPCO, 2007a-2007c). Figure 3 shows the acceleration and displacement time histories of downhole array recordings during the main shock. Figure 4 shows

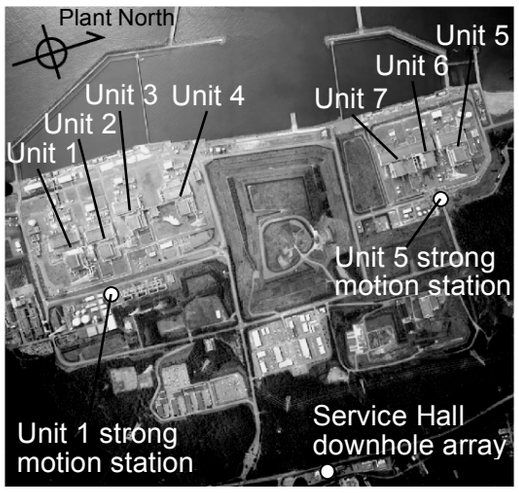


FIG.1. Aerial photograph at TEPCO's Kashiwazaki-Kariwa nuclear power plant

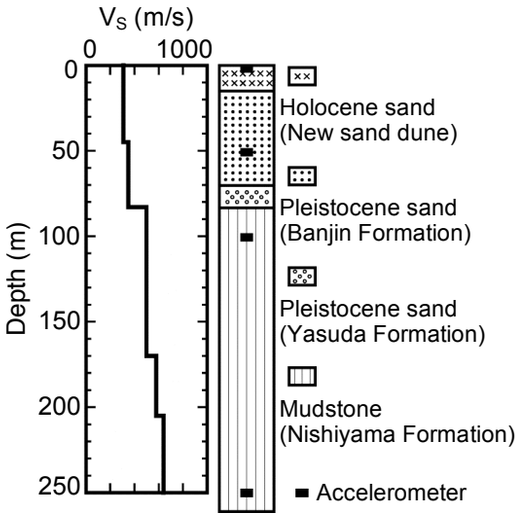


FIG. 2. Geological and geophysical logs with accelerometer locations at Service Hall

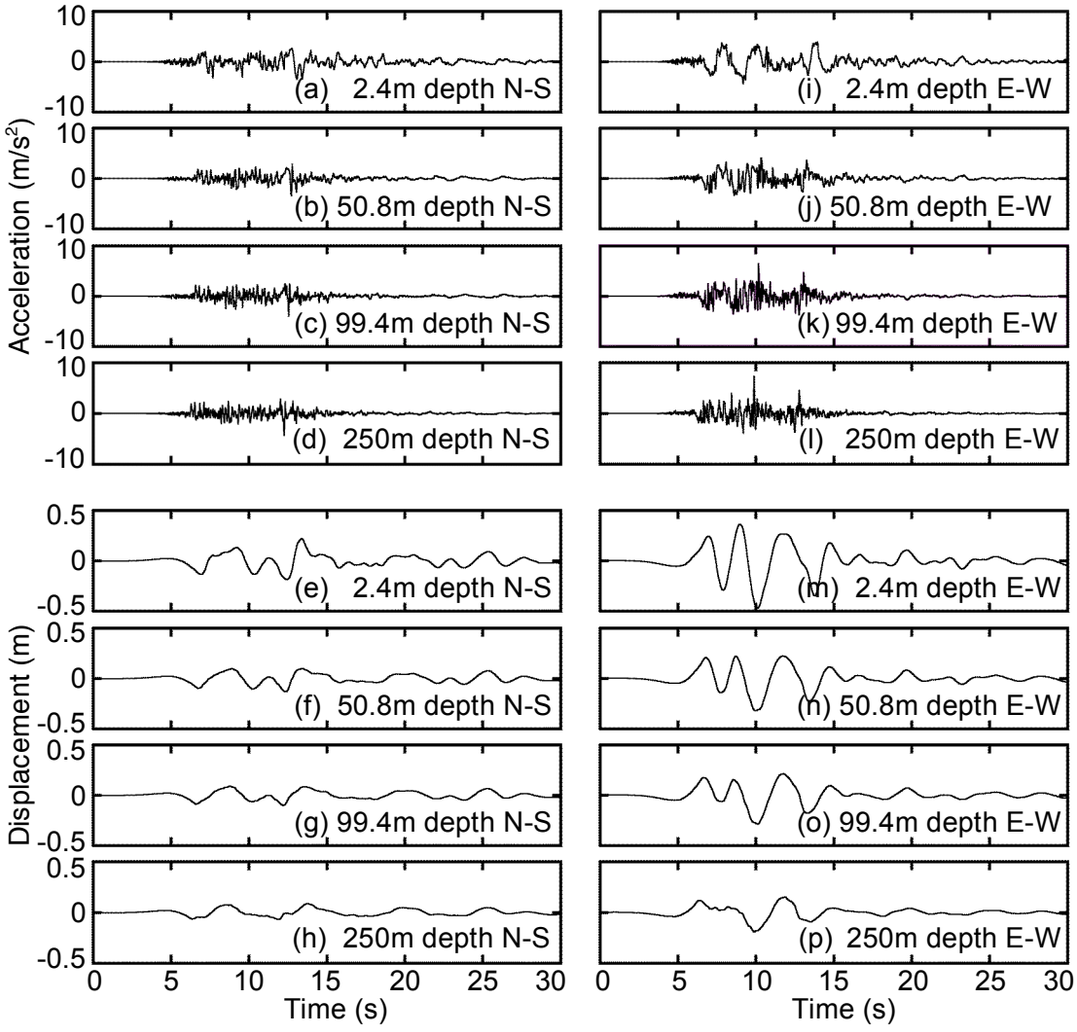


FIG. 3. Acceleration and displacement time histories of downhole array recordings during main shock

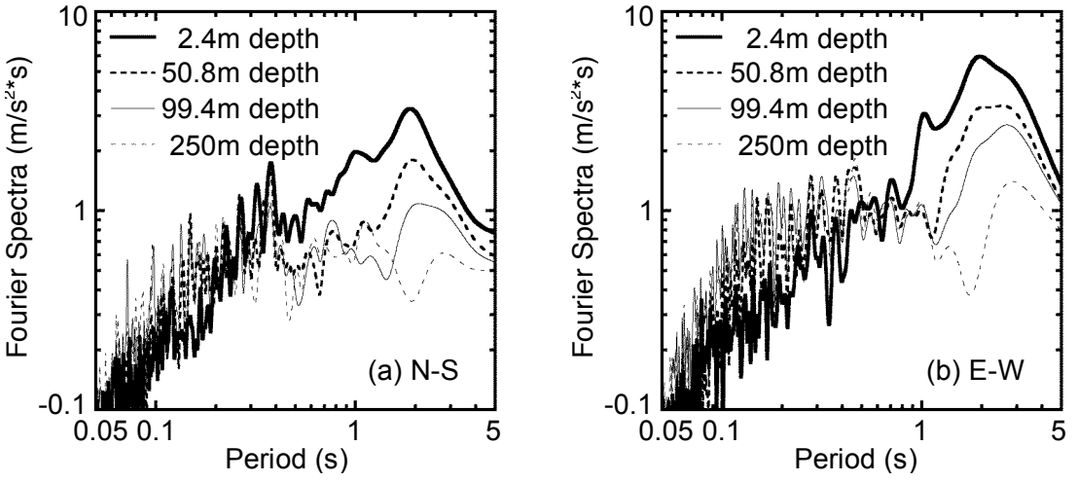


FIG. 4. Fourier spectra at four depths during main shock

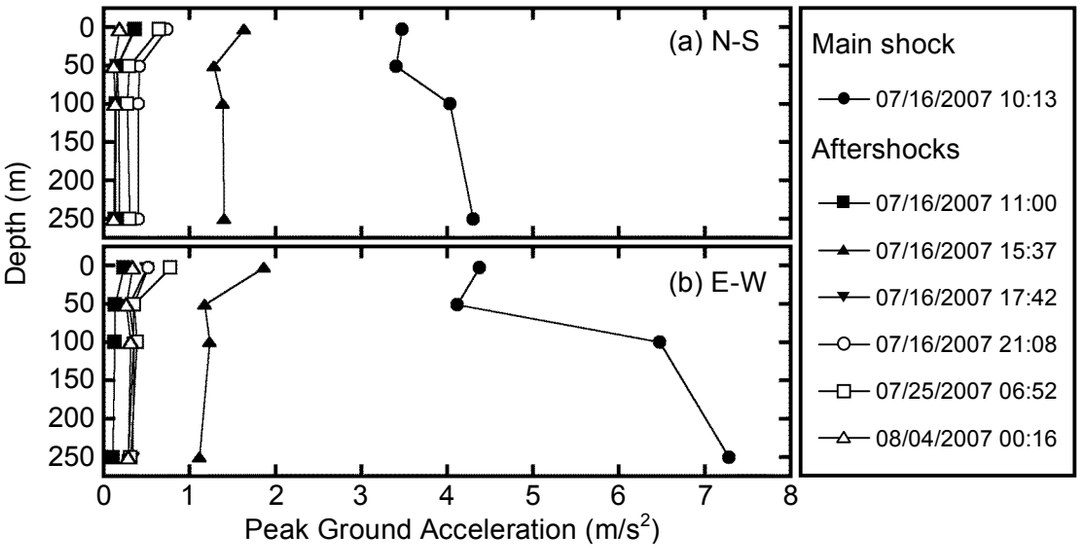


FIG. 5. Distributions of peak horizontal ground acceleration with depth for main shock and aftershocks

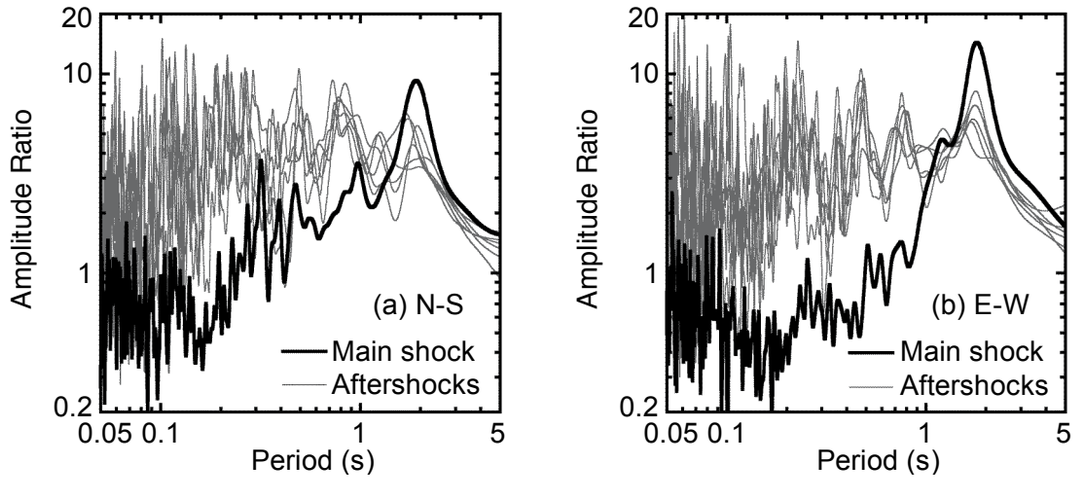


FIG. 6. Transfer functions between 2.4 and 250 m depths for main shock and aftershocks

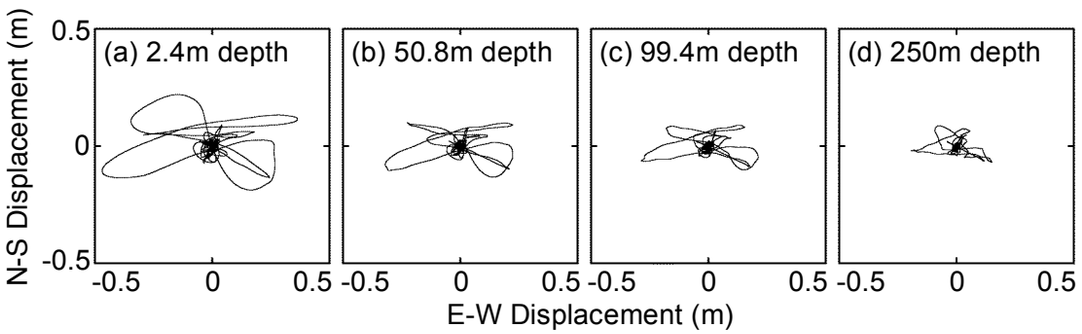


FIG. 7. Two-dimensional displacement orbits on the horizontal plane at four depths

their Fourier spectra and Figure 5 shows the distributions of peak horizontal ground acceleration with depth for the main shock together with those for the aftershocks. The horizontal peak ground accelerations were de-amplified towards the ground surface only for the main event, losing their short period component.

Figure 6 compares the amplitude ratios between 2.4 m and 250 m depths for the main shock and aftershocks. The amplitude ratios at periods less than 1 s are significantly lower in the main shock than in any of the six aftershocks. These findings suggest that degradation of stiffness and/or increase in damping of near-surface soil might have occurred during the main shock and lowered the amplitude ratios in the short period range during main shock significantly compared with those of the aftershocks. Figure 7 shows two-dimensional displacement orbits on the horizontal plane at the four depths. The ground motions dominate in the E-W direction, which is nearly perpendicular to the coastline.

METHOD FOR ESTIMATING SHEAR STRESS-STRAIN TIME HISTORIES

Zeghal et al (1995) presented a method to estimate shear stress-strain time histories from an analysis of downhole array recordings, based on the theory of vertically propagating shear waves through the horizontally stratified deposit as shown in Figure 8. It is assumed that the deposit consists of N layers including the bottom half-space and that downhole array recordings are obtained at the top of each layer.

Using linear interpolation between downhole accelerations, the shear stress τ_i at the top of i-th layer may be approximated by (Zeghal et al, 1995):

$$\tau_i(t) = \sum_{k=1}^{i-1} \rho_k \frac{\ddot{u}_k + \ddot{u}_{k+1}}{2} \Delta z_k \qquad (1)$$

where t = time; ρ_k and Δz_k = mass density and thickness of k-th layer; and $\ddot{u}_k$ = absolute acceleration of k-th sensor.

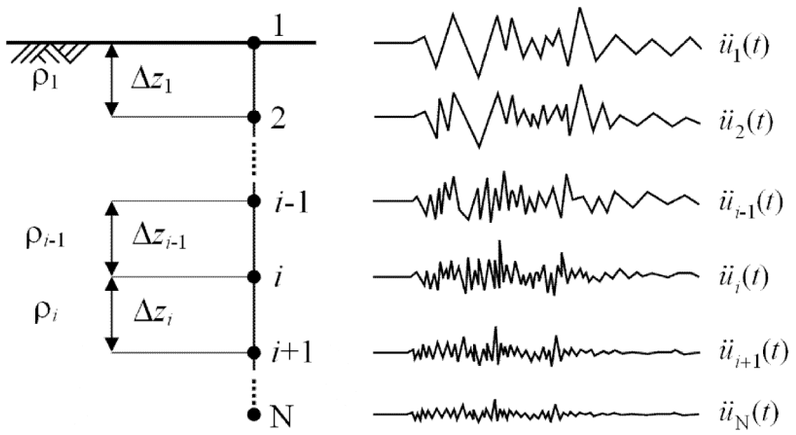


FIG. 8. Analytical model of downhole array

Similarly, the corresponding shear strain at the top of i-th layer may be approximated by (Zeghal et al, 1995):

$$\gamma_i(t) = \frac{1}{\Delta z_{i-1} + \Delta z_i}\left[\frac{u_{i+1} - u_i}{\Delta z_i}\Delta z_{i-1} + \frac{u_i - u_{i-1}}{\Delta z_{i-1}}\Delta z_i\right] \quad (2)$$

where u_i = absolute displacement of i-th sensor, which may be obtained through double integration of the corresponding acceleration with time.

To apply the abovementioned method to the Service Hall downhole array recordings, the ground surface motions that did not exist were numerically estimated based on a computer program similar to SHAKE (Schnabel et al, 1972) with the recorded motions at 2.4 m depth, assuming that the surface soil is linear elastic. Resulting errors in estimated shear stress and strain associated with this assumption for i > 2 are either negligibly small or zero.

The accuracy of shear stress and strain estimated from Eqs. (1) and (2) also depends on the downhole sensor spacing and wavelength ($\lambda = V_s/f$, where f = frequency) of the recorded accelerations (Zeghal et al, 1995) as well as on the resulting ground displacements. As most energy of the downhole array recordings is within the frequency range of 0.3-1.0 Hz, the recorded accelerations were low-pass filtered with a cutoff frequency of 2 Hz, and the displacement were determined by double integration of acceleration with time after eliminating frequency components less than 0.15 Hz. The shear stress-strain time histories at two seismometer depths, i. e. 50.8 m, 99.4m, were then estimated.

EVALUATION OF STRAIN-DEPENDENT PROPERTIES

Figures 9 and 10 are shear stress and strain time histories in the E-W direction at the two depths. Figures 11(a) and 11(b) show the shear stress strain relations at the two depths. The stress-strain loops of the Holocene dune sand at a depth of 50 m are thick elliptical, showing strong nonlinearity with shear strains up to $3x10^{-1}$%.

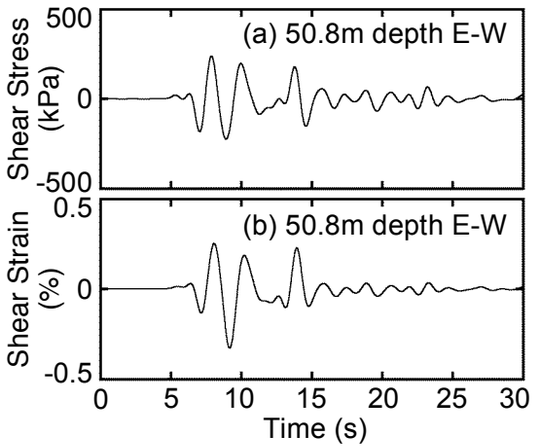


FIG. 9. Shear stress strain time histories in the E-W direction at 50.8 m depth

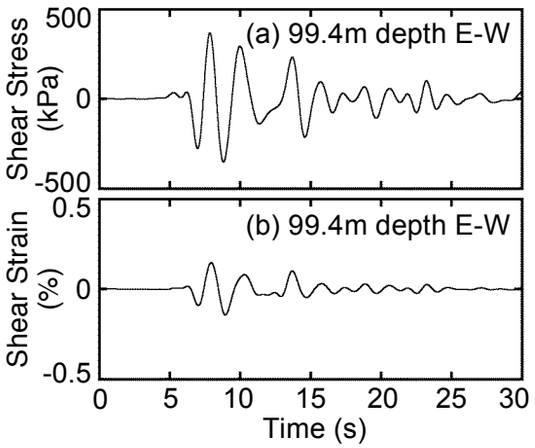


FIG. 10. Shear stress strain time histories in the E-W direction at 99.4 m depth

In contrast, those of the mudstone at a depth of 100 m are flat elliptical, showing lesser nonlinearity with shear strains up to $1.5x10^{-1}$%.

Figures 12 (a)-(d) show relations of shear moduli and damping ratios with shear strain at the two depths, determined from the stress-strain loops such as shown in Fig. 11. The shear modulus at each depth has been normalized with respect to its elastic shear modulus ($G_o = \rho V_s^2$ and V_s = shear wave velocity of the corresponding layer).

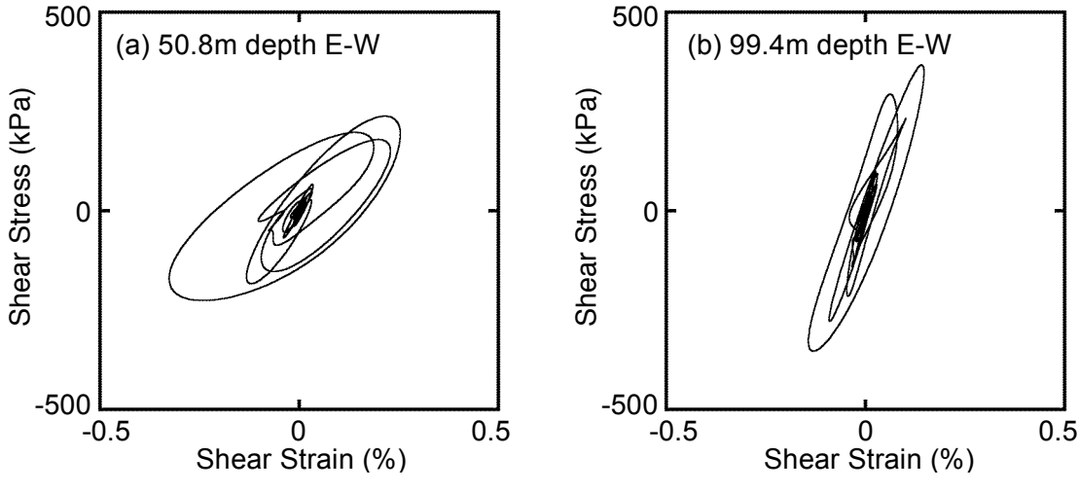


FIG. 11. Shear stress strain relations at two depths

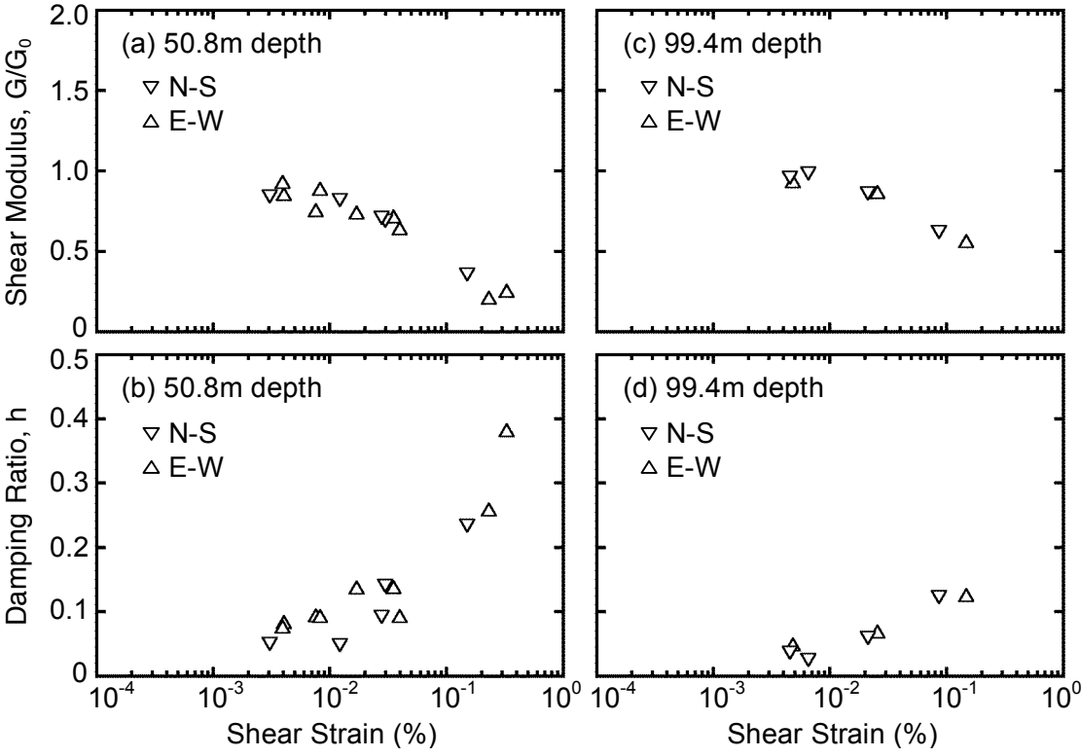


FIG. 12. Relations of shear modulus and damping ratios with shear strain at two depths

The shear modulus ratios at both depths are close to unity at small strains less than 10^{-2}%, suggesting that the estimated values are reasonably reliable. The Holocene dune sand at 50 m depth does exhibit strain dependent behavior in which shear modulus ratio decreases with increasing shear strain and reaches about 0.3 at a shear strain of $3x10^{-1}$%. The trend is consistent with the laboratory test result for sand consolidated under similar confining pressures (Kokusho, 1980). Its damping ratio increases with increasing shear strain, reaching about 30% at a shear strain of $3x10^{-1}$%. The estimated damping seems to be slightly higher than that of the laboratory test result at the same strain level (Kokusho, 1980). The mudstone at 100 m depth does also show but lesser nonlinear behavior in which the shear modulus ratio decreases to 0.6 at a shear strain of $1.5x10^{-1}$%, with a damping ratio of about 10 %. Thus, the degradation of stiffness and increase in damping of the Holocene dune sand during the main shock might have lowered the amplitude ratios between the near-surface layer and the bedrock in the short period range compared with those of the aftershocks.

CONCLUSIONS

Strain-dependent shear moduli and damping ratios have been estimated for the deposit of the Service Hall at the Kashiwazaki-Kariwa nuclear power plant based on shear stress-strain time histories that were directly determined from its downhole array recordings during the 2007 Niigata-ken Chuetsu-oki earthquake. The following conclusions may tentatively be made:

(1) The Holocene dune sand with V_s = 310-350 m/s at depths less than about 70 m showed strong nonlinearity with a shear modulus ratio of about 0.3 and a damping ratio of about 30 % at shear stains up to about $3x10^{-1}$%. The reduction in shear modulus ratio is consistent with the laboratory test results for sand consolidated under similar confining pressures but the corresponding damping ratio seems to be slightly higher than that of the previous studies.
(2) The mudstone with V_s =500 m/s located at depths greater than about 100 m did not show any strong nonlinearity with a shear modulus ratio of about 0.6 and a damping ratio of about 10 % at shear strains of about $1.5x10^{-1}$%.
(3) The strong nonlinearity of the Holocene dune sand during the main shock might have lowered the amplitude ratios between the near-surface layer and the bedrock in the short period range significantly compared with those of the aftershocks.

ACKNOWLEDGEMENTS

The strong motion array records and geological and geophysical logs at the Service Hall of the Kashiwazaki-Kariwa nuclear power plant, used in this study, were provided by Tokyo Electric Power Company (TEPCO, 2007a and 2007b). The field investigation at the site was made possible through the courtesy of TEPCO.

REFERENCES

GSI (2007): Release of aerial photographs of area affected by the 2007

Niigata-Chuetsu Oki Earthquake, Geographical Survey Institute, available at http://www.gi.go.jp

Kayen, R. et al (2007): Preliminary observations on the Niigata-Chuetsu Oki, Japan, Earthquake of July 16, 2007, EERI-GEER Web Report 2007-1 v.6.

K-NET (2007): Kyoshin Network, National Research Institute for Earth Science and Disaster Prevention, available from: http://www.kyoshin.bosai.go.jp/k-net/

Kokusho, T. (1980): cyclic triaxial test of dynamic soil properties for wide strain range, Soils and Foundations, Vol. 20, No. 2, 45-60.

Schnabel, P. B., Lysmer, J. and Seed, H. B. (1972), "SHAKE-A Computer Program for Earthquake Response Analysis of Horizontally Layered Sites," EERC Report, No.72-12.

TEPCO (2007a). Report on analysis of observed records at Kashiwazaki-Kariwa Nuclear Power Plant during the Niigata-Chuetsu-Oki earthquake 2007.

TEPCO (2007b). Acceleration time histories at Kashiwazaki-Kariwa nuclear power plant during the 2007 Niigata-ken Chuetsu-oki earthquakes, Main shock at 10:13 a.m. on July 16, 2007, CD-ROM.

TEPCO (2007c). Acceleration time histories at Kashiwazaki-Kariwa nuclear power plant during the 2007 Niigata-ken Chuetsu-oki earthquakes, 6 aftershocks, CD-ROM.

Zeghal, M., Elgamal, A.W., Tang, H.T., and Stepp, J.C. (1995): Loutung downhole array II: Evaluation of soil nonlinear properties, Journal of Geotechnical Engineering, Vol. 121, No. 4, 363-378, 1995.

The Turkey Flat Blind Prediction Experiment for the September 28, 2004 Parkfield Earthquake: Comparison with other Turkey Flat Recordings

Hamid R. Haddadi[1], Anthony F. Shakal[2], and Charles R. Real[3]

[1] Senior Seismologist, California Geological Survey, 801 K Street, Sacramento, CA, hhaddadi@conservation.ca.gov

[2] Supervising Engineering Geologist, California Geological Survey, 801 K Street, Sacramento, CA, tshakal@conservation.ca.gov

[3] Supervising Engineering Geologist, California Geological Survey, 801 K Street, Sacramento, CA, creal@conservation.ca.gov

ABSTRACT: A blind prediction experiment was conducted for the Turkey Flat test area data after the September 28, 2004 Parkfield earthquake. The results of the test were reviewed at the Turkey Flat Blind Prediction workshop in 2006. The predicted ground motions at the center of the valley significantly exceeded the observed ground motions. In this study, records of Parkfield aftershocks and two other events, including the 2003 San Simeon earthquake, are analyzed and compared with the 2004 Parkfield mainshock records.

Comparison of the observed ground motions at the surface and at depth at the rock outcrop station shows little amplification from a depth of 24 m to the surface. This observation may be expected as the instruments at both the surface and at depth are located in the same rock formation.

Average rock motions beneath the valley center site are considerably weaker than those recorded 800 m away at a similar depth below the rock outcrop. This observation implies that the recorded motion at depth under the rock outcrop should not be applied directly as the input motion at depth under the sedimentary valley for the purpose of predicting ground motion at the surface.

The peak ground accelerations at the surface at the center of the valley are largest for nearly all events. The ratio of the peak acceleration from the surface to depth varies from about 1.5 to more than 6. The smallest amplification is for the distant M6.5 San Simeon earthquake of 2003, which has a lower dominant frequency content than the frequencies amplified at the valley center site.

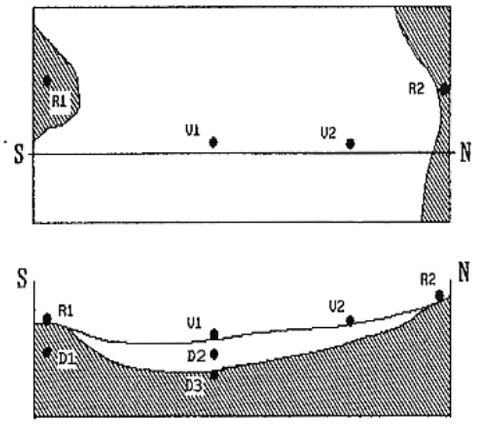


FIG. 1. Schematic illustration of the Turkey Flat strong-motion array stations (after Tucker and Real, 1986).

INTRODUCTION

The California Geological Survey established a test area across a small sedimentary valley, called Turkey Flat, east of Parkfield in central California to study site effects in the late 1980s (Tucker and Real, 1986). The site was selected near Parkfield because it is a seismically active area and the occurrence of a moderate earthquake was anticipated. A goal was to select a simple site that would not require the use of complex models for ground motion prediction. The geophysical properties of the site were characterized in a cooperative effort by CGS, geotechnical firms, and the IASPEI/IAEE Joint Working Group on Effects of Surface Geology on Seismic Motion. The test site was instrumented by CSMIP, the California Strong Motion Instrumentation Program of CGS, with a strong motion array with a total of 21 accelerometers at the surface and at depth (7 triaxial packages). The Turkey Flat array was then maintained for nearly two decades. A M6.0 earthquake occurred in 2004 and was well recorded throughout the array, providing the records necessary to conduct the long awaited blind prediction test (Shakal et al., 2006a). A companion paper in the proceedings describes the general overview of the Turkey Flat blind prediction test.

TURKEY FLAT BLIND PREDICTION ARRAY

Turkey Flat is a site with thin, stiff alluvium over rock. Basement rocks outcrop along the southern and northern edges of the valley. The site is about 5 km from the San Andreas Fault. The geophysical measurements and other background of the Turkey Flat experiment are described in greater detail in Real et al., 2006 and 2008.

The Turkey Flat strong-motion array extends across a sedimentary valley as indicated in Figure 1. At a rock outcrop at the southern edge of the valley (station

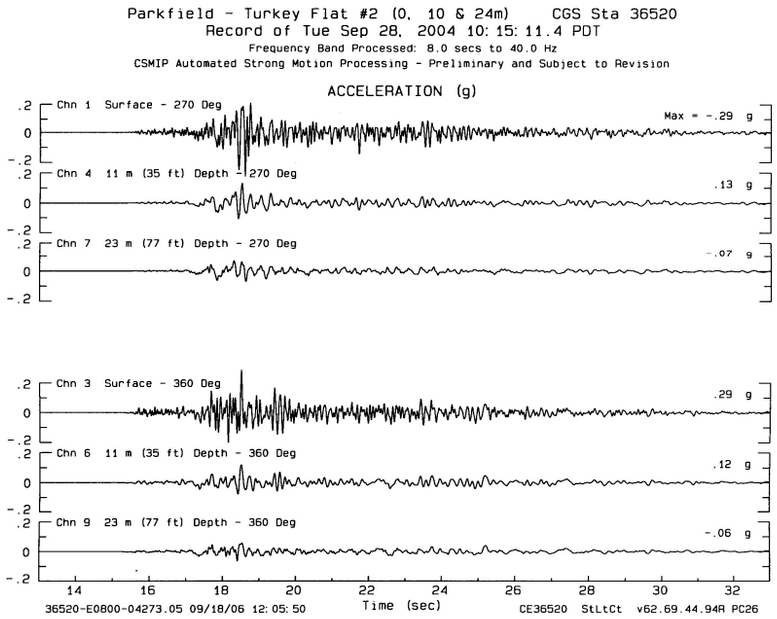


FIG. 2. Horizontal components of the acceleration for the Parkfield mainshock at the valley-center station TF#2 at the surface, 11 m depth (D2) and 23 m depth (D3).

TF#1) there is a surface-sensor site (R1) and downhole sensors at about 24 m (D1). At a station at the center of the valley (TF#2) there is a surface site (V1), downhole sensors at mid-height in the sediments (D2, at about 11 m), and downhole sensors (D3) in the rock beneath the sediments at about the same depth as the downhole at the southern edge of the valley (D1). There is a second valley site about three-fourths across the valley (TF#3), and a rock outcrop site on the northern side of the valley (TF#4), both with surface-only accelerometers (V2 and R2, respectively).

Each location has a triaxial set of force-balance accelerometers that are recorded by a 12-bit digital solid-state recorder. For reference, the distance from V1 to V2 is about 500 m, and from V1 to R1 about 800 m.

Data of the 2004 Parkfield Earthquake

The M6.0 Parkfield earthquake occurred on September 28, 2004 and the origin was at an epicentral distance of about 7 km from the station TF#1. The earthquake was recorded throughout the Parkfield array and the Turkey Flat array and provided a unique set of near-field strong motion records (Shakal et al., 2006a, b, and c). The Parkfield earthquake record at the valley center station TF#2 is shown in Figure 2. A significant difference was observed between the records from 24 m depth at the rock outcrop site and the valley center site (i.e., at D1 and D3 respectively). The peak

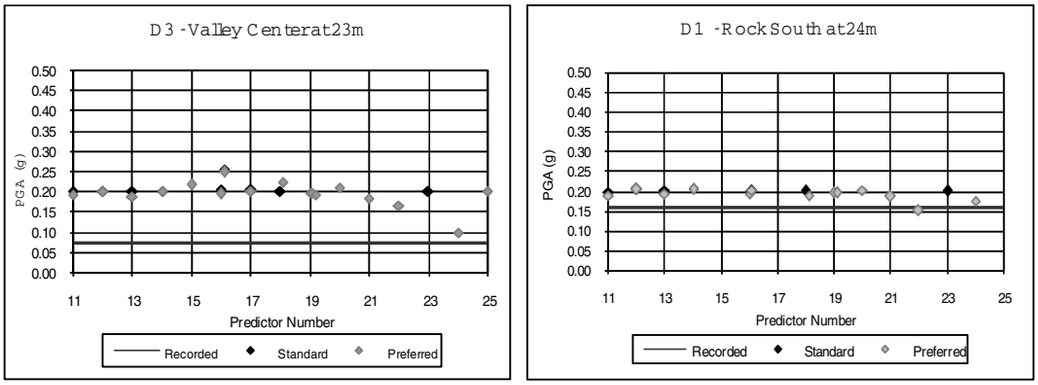


FIG. 3. Peak accelerations (EW) predicted by the predictor teams for D3 (left) and D1 (right) given the record at R1, compared to the observed values (line), for predictions using the Standard soil model (black symbols) and using Preferred models (gray symbols), after Shakal et al., 2006.

ground acceleration at D1 was 0.16g while it was only 0.07g at D3. D1 and D3 are located in the same rock formation at similar depths, about 800 m apart.

Blind Prediction Results

In the first phase of the prediction experiment, acceleration time histories recorded on the rock outcrop near the valley edge (R1) were provided to participants, along with a "Standard" model of the subsurface geotechnical properties based on geotechnical measurements made in the 1980s (e.g., Real et al., 2006). Participants were asked to make predictions of the ground motions at the valley center surface site (V1) and the other recording locations for which, as part of a long-term plan, records were withheld by CGS. A workshop at which predictions were compared to each other and the recorded motions was held on September 21, 2006 in San Francisco (Real et al., 2006; Shakal et al., 2006a).

Phase 1 predictions, based on the rock outcrop record at the valley edge (R1), over predict peak accelerations at D3 by 50% and peak response spectral values by as much as 3 - 5 times. The various predictions are quite similar to one another, but not as similar to the recorded motions. The predictions also indicate that the use of nonlinear versus equivalent-linear computational methods did not significantly improve the results. The level of ground motion might not have been strong enough to induce nonlinear response of the dry, stiff sediments at Turkey Flat. Figure 3 compares the predictions of PGA at D3 with the observed.

In Phase 2 of the experiment, the rock record at the base of the valley sediments (D3) was released and the other sites were to be predicted based on that. The Phase 2 predictions, using the actual recorded motions at the base of the valley sediments, are much closer to the observations. The spectra at periods beyond about 0.4 second

Table 1. The data set of recordings at the Turkey Flat array stations

Event No.	Date/ Time	Mag	Epicenter Lat	Lon	Distance (km) to: TF#1	TF#2	TF#3	TF#4	PGA (g) at Surface TF#1	TF#2	TF#3	TF#4
1	4/3/1993 21:21:24 PST	4.2	35.942	120.493	14.1	14.5	14.3	13.9	0.03	0.03	0.08	0.05
2	12/22/2003 11:15:56 PST	6.5	35.710	121.100	69.6	70.4	70.6	70.6	0.04	0.04	0.03	0.02
3	9/28/2004 10:15:24 PDT	6.0	35.810	120.370	7.6	8.2	8.6	9.2	0.25	0.30	0.26	0.11
4	9/28/2004 10:19:24 PDT	4.2	35.844	120.402	5.5	6.3	6.6	7.0	0.05	0.17	0.07	0.03
5	9/28/2004 10:24:15 PDT	4.7	35.810	120.350	7.6	8.0	8.4	9.1	0.05	0.07	0.05	0.01
6	9/28/2004 10:33:56 PDT	3.7	35.815	120.363	7.0	7.5	8.0	8.6	0.02	0.03	0.03	0.01
7	9/28/2004 12:31:27 PDT	4.0	35.840	120.390	5.1	5.9	6.3	6.7	0.01	0.05	0.02	0.01
8	9/29/2004 10:10:04 PDT	5.0	35.954	120.502	15.5	15.9	15.7	15.2	0.02	0.04	0.04	0.03

(frequencies below 2.5 Hz) cluster around each other and the observed spectra. Details of the comparison are given in Shakal et al., 2006a.

The 2006 Turkey Flat workshop recommended that more conclusive evidence of the similarity or dissimilarity of geotechnical properties at locations D1 and D3 be obtained in order to understand the difference in ground motion recordings at the two sites. The workshop also recommended that records obtained at the Turkey Flat array

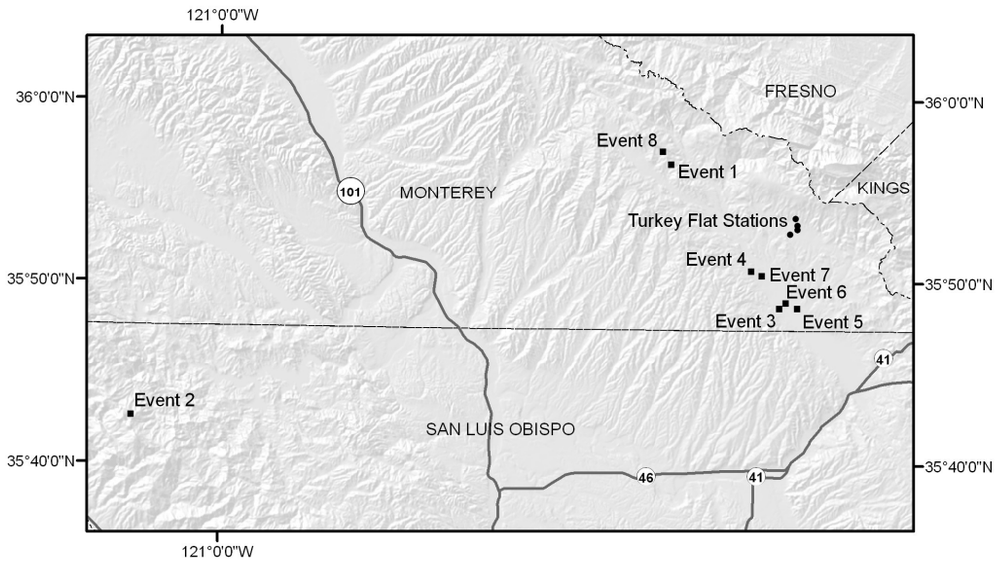


FIG. 4. Map showing the location of the Turkey Flat array in central California and the location of the earthquakes listed in Table 1.

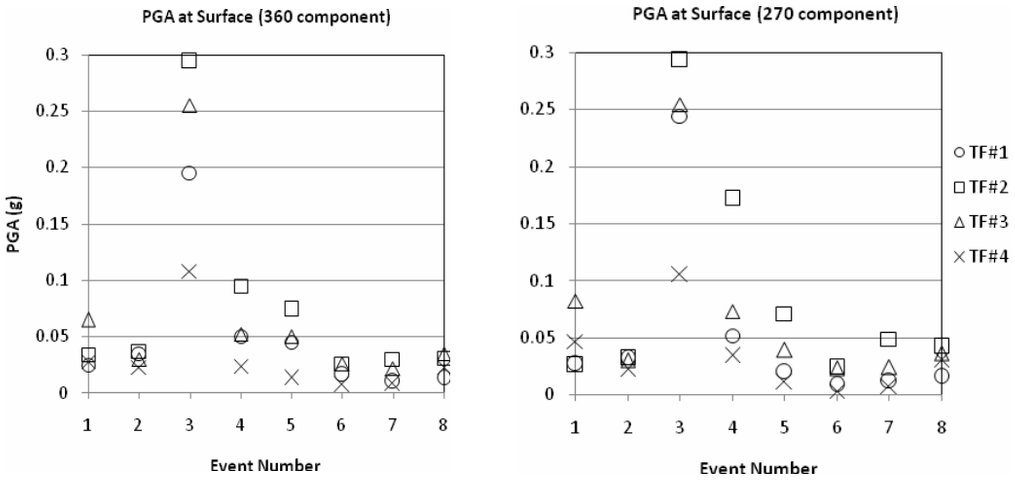


FIG. 5. Comparison of the surface-motion PGA values recorded during the 8 events at the Turkey Flat array stations.

from other earthquakes be analyzed to see if the same results would be obtained regarding the ground motion variations at the surface and at depth. In this paper a data set including 8 events that occurred from 1993 through 2004 recorded at the Turkey Flat stations are analyzed and implications for the variability of Turkey Flat site response is discussed. The complete data set is available for download by interested researchers at ftp://ftp.consrv.ca.gov/pub/dmg/csmip/TurkeyFlatData.

DATA SET RECORDED AT TURKEY FLAT STATIONS

The data set consists of all 8 events recorded with ground motions over about 1% g at the Turkey Flat array since it was installed. In addition to the M6.0 Parkfield mainshock of 2004, the data set includes records from a M4.2 event in 1993, the M6.5 San Simeon earthquake of 2003, and five aftershocks of the Parkfield earthquake. Summary information for the events and records are given in Table 1.

The map in Figure 4 shows the locations of the events listed in Table 1 and the location of the array stations. All the events are within 15 km of the array stations except for the San Simeon earthquake of 2003 (event 2) which is located about 70 km WSW of the array.

Peak Ground Accelerations

The PGA values recorded on the ground surface at the Turkey Flat stations are shown in Figure 5 for the events of Table 1. The comparison shows that the ground motion acceleration at station TF#2, at valley center, is consistently greater than the motion at the other Turkey Flat stations for almost all of the events. This site also has the greatest thickness of valley sediments in the array.

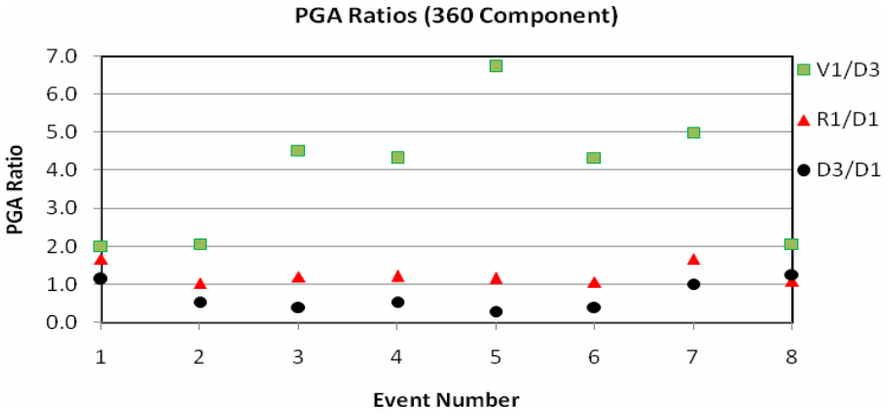


FIG. 6. PGA ratios, surface-to-depth at rock south, TF#1 (R1/D1, triangles), depth at TF#2 to depth at TF#1 (D3/D1, circles), and surface-to-depth at valley center, TF#2 (V1/D3, squares).

During the Parkfield earthquake of 2004, at station TF#1 a PGA of 0.19g was recorded at the surface (R1) and the PGA was 0.16g at 24 m depth (D1). Both R1 and D1 are located in the same rock formation, and not much amplification was observed. Expanding this comparison to the other events, the PGA ratio of R1/D1 for each of the events of Table 1 is shown in Figure 6. The ratio is about 1 for all events, without much variation.

Further analysis shows that the level of ground motion at depth below the valley (D3) is significantly lower than at the same depth below the rock outcrop (D1) in the Parkfield earthquake recordings. Besides being at approximately the same depth (24

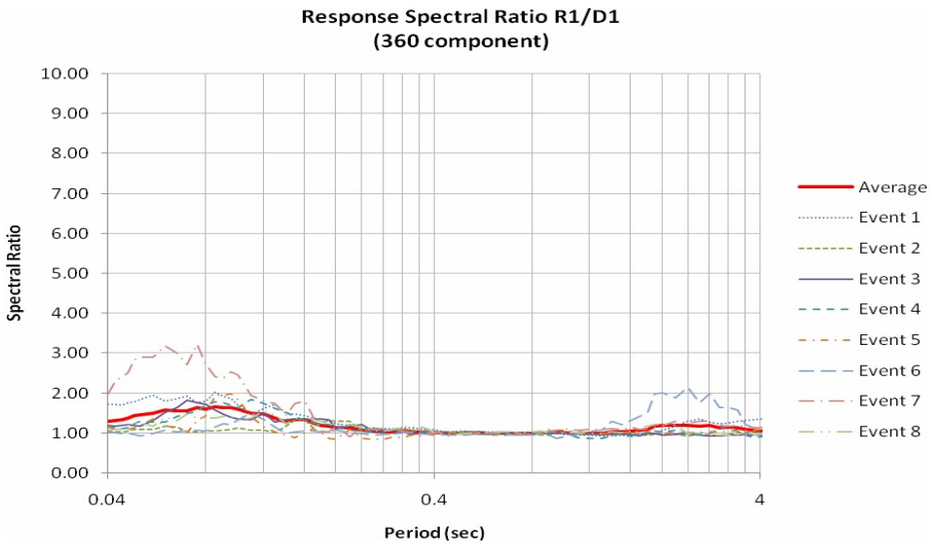


FIG. 7. Response spectral acceleration ratio R1/D1 for the event set.

m), D1 and D3 are in the same rock formation and separated by only 800 m. As concluded at the 2006 Turkey Flat workshop, this is an important observation warranting investigation. Most of the events in the data set show the same pattern as the Parkfield event, with peak acceleration at D3 lower than at D1. The PGA ratio, D3/D1, is shown in Figure 6 for the full data set. The ratio is low (0.5 or less) for events 2 through 6 with the smallest ratio of 0.28 for event 5. Event 2 is the San-Simeon teleseism; event 7 has the smallest motions in the data set.

As shown in Fig. 2, the Parkfield event showed depth-to-surface amplification at valley center station TF#2. The PGA was amplified from 0.06g at 24 m (D3) to 0.29g at the surface (V1). A similar amplification was observed for the other events. The V1/D3 ratios are shown in Fig. 6 and indicate that the PGA is amplified by a factor ranging from 2 to over 6 with many near 4, like the mainshock.

Response Spectral Acceleration

The ratio R1/D1of the response spectral acceleration at the ground surface to that at depth at the rock south site, TF#1 is shown in Figure 7. It shows that over the period range 0.04-4.0 seconds (2.5 to 25 Hz) there is little or no amplification from depth to the surface. Note that both R1 and D1 are located in the same rock formation.

In Phase 2 of the Turkey Flat Experiment the predictors were given the ground motion at depth at the valley-center station (D3) and asked to predict the motion at the surface (V1). Most of these Phase 2 predictions were close to the recorded motion for the 2004 Parkfield earthquake. The response spectral acceleration ratio V1/D3 for the event set and its average are shown in Figure 8. The average V1/D3 ratio shows the most significant amplification at periods less than about 0.2 sec (frequencies above 5 Hz).

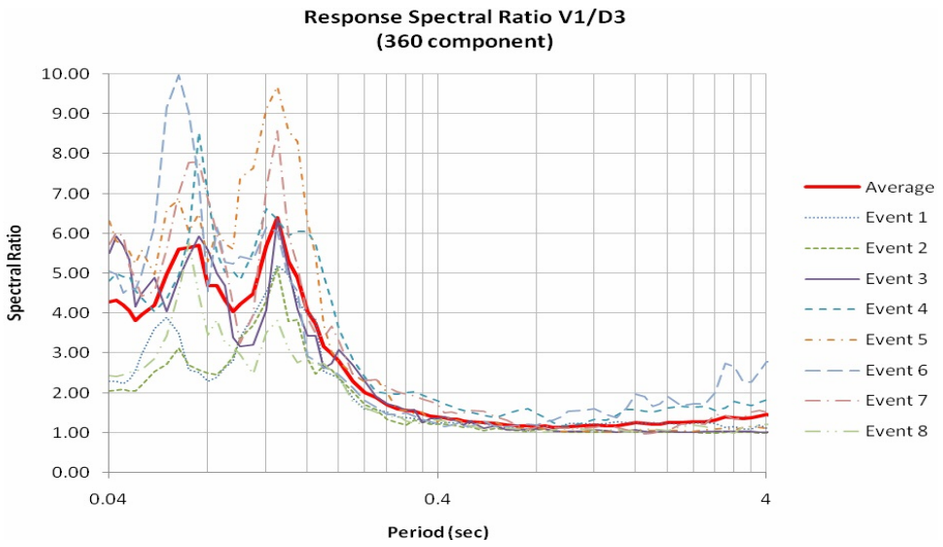


FIG. 8. Response spectral acceleration ratio of V1/D3 for the event set data

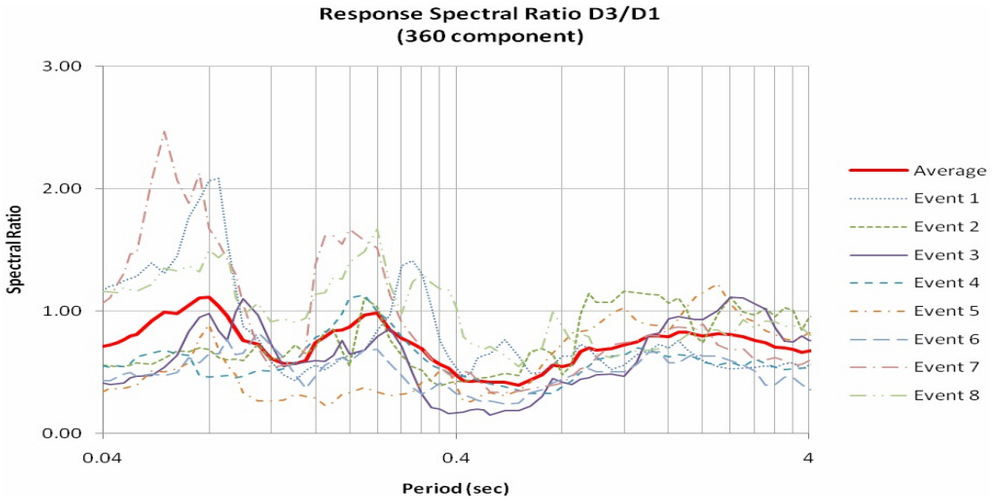


FIG. 9. Response spectral acceleration ratio of the motion at the two downhole sites, D3 and D1.

The response spectral acceleration ratio for the two downhole sites, D3 and D1, for the data set and the average are shown in Figure 9. Even though both D1 and D3 are located in the same formation and at similar depths, the average ground motion at D3 is lower than that at D1 for almost all periods in the 0.04 – 4 sec range. The average is near 1 at about .08 sec (12 Hz) and again near 0.5 sec (4 Hz). At all other periods the motion is lower at D3, under the valley. This difference was noted at the Turkey Flat workshop for 2004 Parkfield and this study shows it also occurs for ground motions from other earthquakes recorded by the array. This result suggests that the lower motion at D3 is not related to the earthquake, but may be due to three-dimensional effects or differences in geologic properties at greater depth not recognized during the 1980s site characterization. Further site characterization studies using current state-of-practice methods may be very important to understanding the reason for low ground motions at D3.

SUMMARY

The Turkey Flat Blind predictions of the ground motion at the valley center based on the ground motion recorded at the rock outcrop (R1) agreed with one other, but exceed the observed ground motions significantly.

The analysis of peak ground accelerations and response spectral values for the events in this study show that there is not much ground motion amplification from depth to the surface at the rock outcrop TF#1 site (D1 to R1). At the valley center

site (TF#2) an average spectral ground motion amplification of 4 to 6 times is observed from depth to the surface (D3 to V1) in the 0.04 – 0.16 second range.

Although the instruments at a depth of about 24 m under the rock outcrop at TF#1 (D1) and under the valley center at TF#2 (D3) are in the same rock formation, and separated by only 800 m, the ground motion under the valley center (D3) is consistently smaller than the motion at D1at most periods in the 0.04 to 4.0 sec range. This helps to explain why all the predictions based on R1 over-predicted the surface ground motions at the valley center site. Since this data set consists of events that occurred at different distances and magnitudes, the lower motions observed at D3 are most likely not due to source or path effects. It is possible that the Turkey Flat site might not be as simple a site as assumed, in terms of the effects of the conditions at depth, or the effects of three-dimensional valley geometry. Thus, a principal conclusion is that surface motions at a valley edge may not always be reliable input motion for predicting site response of valley sediments. Furthermore, greater emphasis should be placed on thorough site characterization before making the assumption that surface rock motions at a nearby site can be used to make good estimates of rock motions beneath valley sediments.

REFERENCES

Real, C., Shakal, A., and Tucker, B. (2006). "Overview of the Turkey Flat ground motion prediction experiment." *Proc. SMIP06 Seminar on Utilization of Strong-Motion Data*, p. 117-136, Oakland, California.

Real, C., Shakal, A., and Tucker, B. (2008). "The Turkey Flat Blind Prediction Experiment for the September 28, 2004 Earthquake: General Overview and Models Tested." (this volume).

Shakal, A., Haddadi, H., and Real, C. (2006a). "Recorded Data and Preliminary Review of Predictions in the Turkey Flat Blind Prediction Experiment for the Sep 28, 2004 Parkfield Earthquake." *Proc. SMIP06 Seminar on Utilization of Strong-Motion Data*, p. 137-152, Oakland, California.

Shakal, A., Haddadi, H., Graizer, V., Lin, K., and Huang, M. (2006b). "Some key features of the strong-motion data from the M6.0 Parkfield, California earthquake of 28 September 2004." *Bulletin of the Seismological Society of America* Vol. 96, no. 4B, S90-S118.

Shakal, A., Haddadi, H., and Huang, M. (2006c). "Note on the very high-acceleration Fault Zone 16 record from the 2004 Parkfield earthquake." *Bulletin of the Seismological Society of America,* Vol. 96, no. 4B, S119-S142.

Tucker, B. and Real, C. (1986). Turkey Flat, USA Site Effects Test Area – Report 1: Needs, Goals and Objectives, TR 86-1, California Department of Conservation, Division of Mines and Geology.

The Turkey Flat Blind Prediction Experiment for the September 28, 2004 Parkfield Earthquake: General Overview and Models Tested

Charles R. Real[1], Anthony F. Shakal[2], and Brian E. Tucker[3]

[1] Supervising Engineering Geologist, California Geological Survey, 801 K Street, Sacramento, CA; creal@conservation.ca.gov

[2] Supervising Engineering Geologist, California Geological Survey, 801 K Street, Sacramento, CA; tshakal@conservation.ca.gov

[3] President, GeoHazards International, Palo Alto, CA; tucker@geohaz.org

ABSTRACT: A blind test has been conducted for site response of the Turkey Flat Site Effects Test Area, near Parkfield, California to the September 28, 2004 M6.0 Parkfield Earthquake. Acceleration time histories recorded on bedrock near one valley edge were provided along with detailed geotechnical properties at all recording sites to interested participants. Participants were asked to make predictions of the ground motions at the five other recording locations (3 surface and 2 downhole), while records were withheld by CSMIP until all predictions were received and officially logged. A second series of predictions were made based on ground motions recorded in bedrock beneath the valley floor. In all there were 15 participating teams from 4 countries that submitted a total of 92 sets of blind predictions, 45 for Part 1 and 47 for Part 2 of the test. Of the 92 sets of predictions, 18 are from industry, 54 from academia, and 20 from government sectors. Site response models tested fall into three categories, with 55 prediction sets based on equivalent linear methods, 33 based on non-linear, and 4 based on other approaches. Predictions generally overestimate valley response, with little improvement using independently interpreted verses standard geotechnical models. Results indicate a marked improvement for site-response predictions based on input of actual rock motions recorded immediately beneath the valley sediments. The strong-motion test demonstrates that surface motions at a valley edge may not always be reliable input motion for estimating site response of valley sediments. This paper provides an overview of the Turkey Flat strong-motion blind test, and summarizes the various soil models and computational models submitted for the test. A companion paper in these proceedings discusses quantitative results of the blind test and comparison with other data (Haddadi, et al., 2008).

INTRODUCTION

The Turkey Flat test area was established 20 years ago to help determine the *state-of practice* in estimating the effects of surface geology on earthquake ground motion. The California Geological Survey (CGS) joined the IASPEI/IAEE working group on the Effects of Surface Geology on ground motion to promote installation of strong-motion arrays specifically designed to study the site-effects phenomena (Kudo, 2003). CGS's Strong-Motion Instrumentation Program (CSMIP) established the Turkey Flat test area in 1987 near the town of Parkfield in the central California Coast Ranges (Figure 1). An earlier "blind" test of weak motion was conducted in 1990 to predict the test area's low-strain seismic response, with most results falling within the expected range of uncertainty considering the large scatter in measured geotechnical properties. Those test results focused on the need to reduce uncertainties in the geotechnical parameters that drive site response codes (Field and Jacobs, 1993; Cramer and Real, 1992).

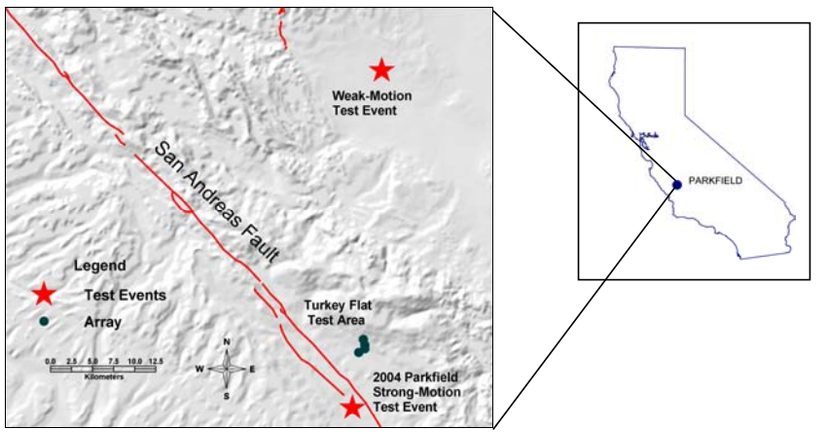


FIG. 1. Turkey Flat Site Effects Test Area

On September 28, 2004 the Turkey Flat test area array recorded the M6.0 Parkfield Earthquake, providing the necessary data to conduct the long-awaited strong-motion blind test. That event triggered a complete review of the Turkey Flat Experiment (Real et al., 2006), followed by a workshop and preliminary reviews of the strong-motion test and comparison of predictions (Shakal et al., 2006).

SITE CHARACTERIZATION

Beginning late 1987 and continuing through 1988, a comprehensive program of site characterization was carried out that included multiple investigation teams, both domestic and abroad, that conducted a broad range of field and laboratory geophysical and geotechnical tests (Real and Tucker, 1988).

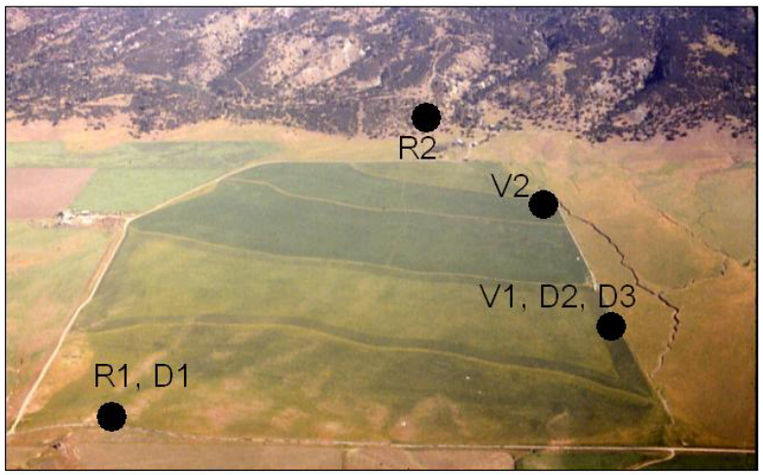


FIG. 2. Oblique aerial view of Turkey Flat strong-motion array.

The site-characterization program categorized the Turkey Flat test area as a shallow 25m deep stiff-soil site with a depth to half-width ratio of 1:40, consisting of unsaturated clayey sand and sandy clays derived from the mountain slopes along the eastern edge of the valley (Figure 2). Repeated measurements during the wet and dry seasons show the water table generally remains below the sediment bedrock interface. The interface slopes from the edges toward the valley center with little intervening relief, and is marked by a shear-wave impedance contrast of about 3. Although simple, the site is one where surface geology has a measurable site response, and where 1-D equivalent-linear ground motion models would be expected to perform well. Details of the site-characterization program are reported by Real (1988).

The Turkey Flat test area instrument array is composed of four recording sites: Rock South (R1), Valley Center (V1), Valley North (V2), and Rock North (R2), with downhole sensors at Rock South (D1) at 24m depth, and Valley Center at 10m depth in sediments (D2) and at 24m depth in bedrock (D3) (Figures 2-3). Each sensor location consists of 3-component forced-balance accelerometers. The strong-motion array was carefully maintained for 17 years by CSMIP. In 2001, 3 years prior to the occurrence of the 2004 Parkfield Earthquake, instrumentation was upgraded to12-bit solid-state digital recorders, which resulted in high-quality records of the 2004 Parkfield event.

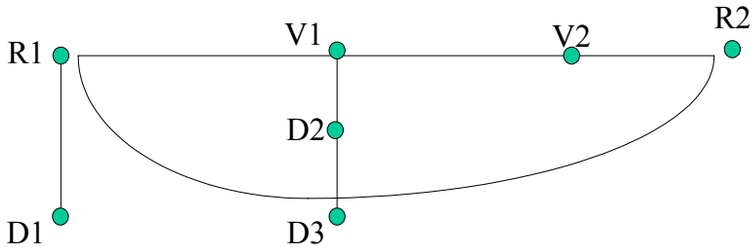


FIG. 3. Vertical schematic profile of the Turkey Flat strong-motion array.

STRONG-MOTION BLIND TEST

The M6.0 Parkfield earthquake occurred on September 28, 2004, rupturing the ground surface for a distance of 25 km along the San Andreas Fault (Shakal et al., 2005). The fault rupture is within about 4 km southwest of the Rock South recording site (Figures 4-5). The main shock was well recorded by the dense Parkfield array, revealing a complex pattern of highly variable ground motions (Figure 5).

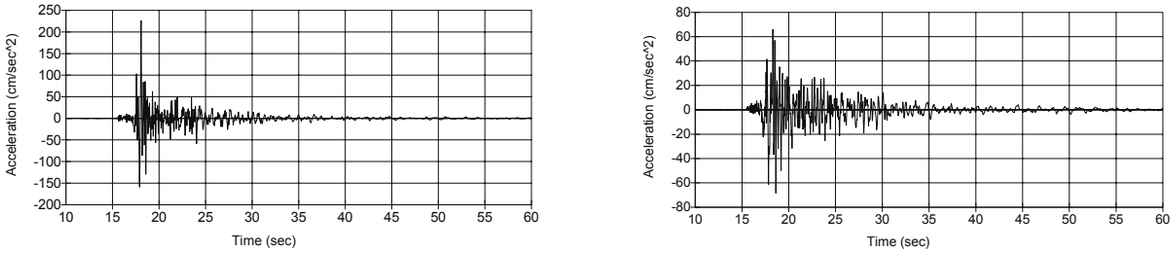


FIG. 4. 2004 Parkfield mainshock recorded at R1 - surface rock at valley edge (left), and at D3 - rock beneath Valley Center (right) of the Turkey Flat array.

Near-fault peak accelerations range from .13g to over 2.0g, while accelerations stations separated by only 2-3 km differed by nearly an order of magnitude (Shakal et al., 2005). Possibly due to source and/or site effects, the high degree of ground shaking variability over short distance is under investigation. No significant directivity is evident from the dense near-field Parkfield Strong-Motion Array data, which may be due to bilateral rupture along the San Andreas Fault during the 2004 event (Shakal et al., 2005).

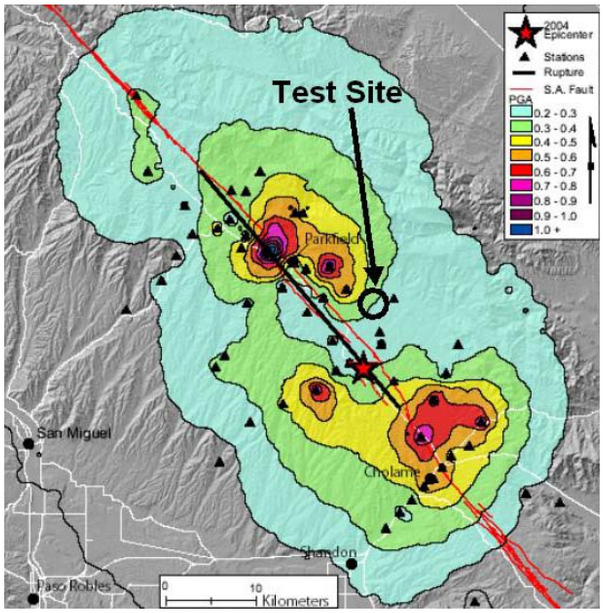


FIG 5. Near-field peak acceleration map of M6.0 2004 Parkfield Earthquake (Shakal et al., 2005).

Turkey Flat lies between the two high acceleration lobes at each end of the fault rupture as shown in Figure 5. The main shock produced a peak rock acceleration of 0.245g at station Rock South (surface), and 0.07g at station D3 (rock beneath valley) of the Turkey Flat array (Figure 4). The Rock South records were processed and distributed March 2005 for the beginning of the strong-motion blind test (Real and Shakal, 2005), and the D3 records were distributed 7 months later.

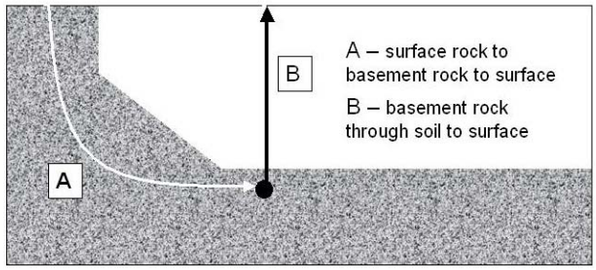


FIG. 6. Diagram of two-part test scheme to assess basement and valley-sediment response.

The Turkey Flat strong-motion blind test was carried out in two parts (Figure 6), beginning in March 2005 and concluding in September 2006. Acceleration time histories recorded on bedrock near one valley edge were provided along with detailed geotechnical properties at all recording sites to interested participants. Participants were asked to make predictions of the ground motions at the five other recording locations (3 surface and 2 downhole), while records were withheld by CSMIP until all predictions were received and officially logged (Part A). A second series of predictions were made based on ground motions recorded in bedrock beneath the valley floor (Part B). The 2-step approach allows separating how much uncertainty in predicted response at the ground surface is due to uncertainty in estimating the basement response from how much is due to modeling of the soil column.

Computational Models

There are 15 participating teams from 4 countries that submitted a total of 92 sets of blind predictions, 45 for Part 1 and 47 for Part 2 of the test. Of the 92 sets of predictions, 18 are from industry, 54 are from academia, and 20 are from government sectors (Table 1). Each *prediction set* corresponds to various sensor locations depending on the level of participation, and varies for Part 1 and Part 2.

Table 1. Number of site response prediction sets for Turkey Flat blind test.

Sector	Part 1		Part 2		Total
	Preferred	Standard	Preferred	Standard	
Industry	5	4	5	4	18
Academia	15	11	17	11	54
Government	5	5	5	5	20

Table 2 identifies the various computer codes and model categories being tested. All prediction sets are 1-D analyses except 3 that are 2-D. Also indicated for each code/model being tested are the numbers of prediction sets that have been submitted for the array, and the number of site response predictions tallied by individual sensor locations (horizontal component pairs) for Part A and Part B, all subtotaled by model category.

Table 2. Site response codes tested and number of predictions.

Category	Method/Code	No. Sets	Analysis Performed	No. Predictions[2]	
				Part A	Part B
Equivalent Linear	SHAKE04	2	1-D	0	4
	SHAKE96B	4	1-D	12	4
	SHAKE91	18	1-D	29	16
	SHAKE72	4	1-D	12	10
	TremorKA	2	1-D	6	2
	TremorN2	2	1-D	6	2
	DeepSoil	6	1-D	12	6
	FDM	4	1-D	12	6
	BESOIL	2	1-D	6	2
	RASCAL	4	1-D	12	4
	SuperFLUSH[1]	2	2-D	6	2
	DYNEQ	5	1-D	15	4
	Subtotal	(55)	Subtotal	(128)	(62)
Nonlinear	DMOD-2[1]	6	1-D	4	10
	DeepSoil	6	1-D	12	6
	TESS	4	1-D	7	4
	FLAC[1]	4	1-D	4	4
	FLAC[1]	1	2-D	0	2
	OpenSees[1]	4	1-D	5	4
	SUMDES[1]	4	1-D	4	4
	NOAHW[1]	2	1-D	6	2
	Subtotal	(31)	Subtotal	(42)	(36)
Other	SSR	2	Empirical transfer function	6	5
	PEXT	2	1-D Source, path, site	6	6
	Subtotal	(4)	Subtotal	(12)	(11)
	Total	90[3]	Total	182	109

[1] Also capable of 2- and/or 3-D analyses. [2] Count is for horizontal component pairs. [3]Two additional sets were submitted that averaged the results from several different codes.

The grand total of individual predictions, most provided in the 4 basic forms described previously, exceeds 250 (or more than 500 for individual horizontal components). Thus, the level of participation is believed to be sufficient to draw meaningful conclusions regarding the state-of-practice in site response analysis, and a preliminary comparison of prediction results has been made (Shakal et al., 2006).

Preferred Soil Models

The weak- and strong-motion tests differ in that the latter required submittal of predictions based on a user-preferred soil model. While only 6 predictions based on a

user-preferred model were submitted for the weak-motion test, 22 were submitted for the strong-motion test.

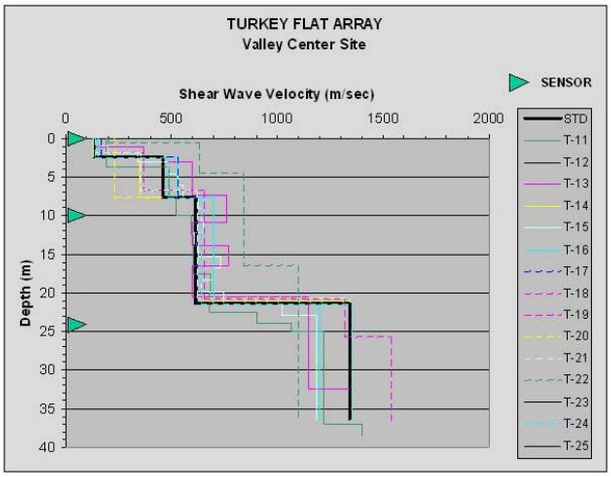


FIG. 7. Preferred velocity models used by various prediction teams.

Figures 7 and 8 show preferred velocity and slowness profiles (inverse of velocity) derived by the participants from the site characterization field measurements, and indicate substantial variability in judgment among predictors. Slowness is linearly related to the time seismic waves spend traveling through each layer. The importance of the near-surface layers is clearly indicated by their increased wave travel times. It has been shown that site response of Turkey Flat is sensitive to velocity of the upper few meters (Field and Jacob, 1993).

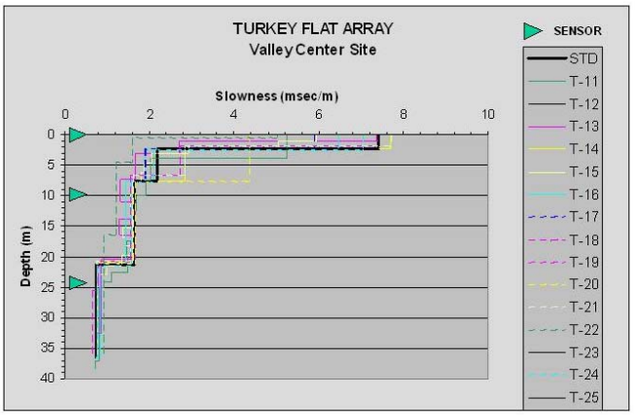


FIG. 8. Velocity slowness from models used by various prediction teams.

Variability of the preferred modulus reduction and damping curves used by predictors is shown in Figures 9 and 10 respectively. In addition to these parameters,

nonlinear computational models include other parameters used to define the hysteretic behavior of soils under cyclic loading, which are code specific and vary.

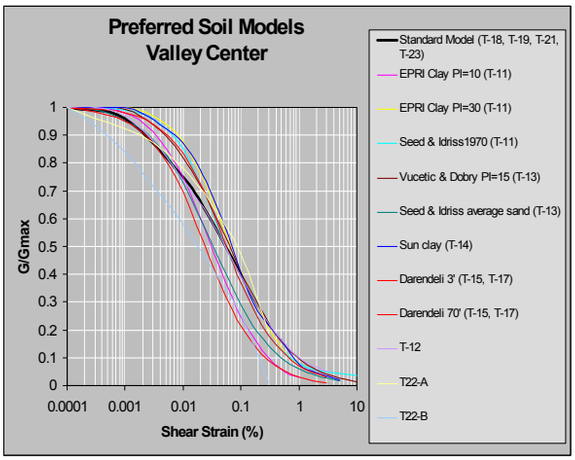


FIG. 9. Modulus-reduction curves used by the various prediction teams.

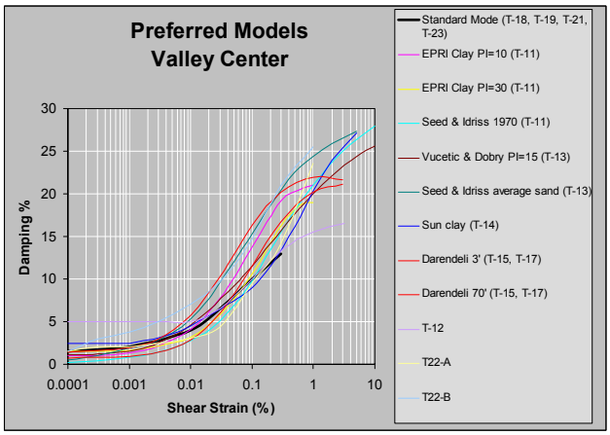


FIG. 10. Preferred damping curves used by the various prediction teams.

In general, results of the strong-motion test reveal that regardless of variability of preferred soil properties, and use of linear and non-linear codes, predictions are more similar to each other than to observations (Shakal et al., 2006). Part A predictions over estimate site response at the surface and in rock beneath the valley sediments. Comparison of Part A and Part B results indicate that predictions of valley sediment response improve when actual input rock motions recorded immediately beneath the valley sediments are substituted for estimates based on surface rock records.

DISCUSSION

Two points to consider when evaluating the accuracy of the predictions are: 1) potential variability of ground motion caused by effects of the source and/or path on

ground motions recorded across the array due to the close proximity to the test event surface fault rupture, and 2) improvements in the state-of-practice of site characterization since establishment of the Turkey Flat test site. Analysis of other events recorded at Turkey Flat suggests that potential near-source effects from the blind test event do not appear significant, and that over-predictions of valley site response in Part A predominantly result from over-estimates of base-input rock motions beneath the valley that may result from insufficient characterization of a more complicated geologic structure (Haddadi et al., 2008).

Uncertainty of site response parameters and geologic structure derived from measurements made in the late 1980's may be greater than what would result from the current state-of-practice because of interim improvements in field and laboratory testing. This questions the validity of combining circa 1990 practice in site characterization with 2005 practice in site response modeling in order to draw conclusions about the overall reliability of current practice in site response analysis. A site characterization program at Turkey Flat that is representative of current practice might better explain the observed pattern of ground motions and improve our understanding of current site-response estimation capability.

CONCLUSIONS

A blind test of seismic site response prediction at the Turkey Flat Site Effects Test Area has been successfully conducted for the 2004 M 6.0 Parkfield Earthquake. Estimates of site response tend to cluster and generally exceed the observed response of the valley sediments and bedrock beneath them regardless of geotechnical model and computational method. Significant differences in observed rock motions at depth, and the inability to accurately predict them leads to the conclusion that input ground motions at the valley edge may not always permit reliable estimates of valley sediment response, underscoring the need for thorough site characterization. Observed ground motions and blind test results at Turkey Flat are discussed in greater detail in a companion paper (Haddadi et al., 2008).

A website has been established to provide updates and disseminate information regarding the Turkey Flat Site Effects Test Area and the blind site response tests:
http://www.quake.ca.gov/turkeyflat.htm.

ACKNOWLEDGMENTS

We thank the following companies for their voluntary contributions: LeRoy Crandall Associates (now MACTEC, Inc.), Dames & Moore (now URS Corporation), Geomatrix Consultants, Harding Lawson Associates, Lawrence Livermore National Laboratory, OYO Corporation, Kajima Corporation, Pitcher Drilling company, and Qest Consultants. We also wish to thank the California Department of Transportation for their assistance in field operations.

We especially wish to thank all participants in both the weak-motion and strong-motion blind tests and members of the Turkey Flat Steering Committee. Most of all

we are grateful for the generosity and kindness of the landowners, who understood the value of this project and who made their land available for the Turkey Flat, USA Site Effects Test Area.

REFERENCES

Cramer, C.H., and C.R. Real (1992). "A statistical analysis of submitted site-effects predictions for the weak-motion blind prediction test conducted at the Turkey Flat, USA, site effects test area near Parkfield, California." *Proceedings of the International Symposium on the Effects of Surface Geology on Seismic Motion, March, 1992, Odawara, Japan vol. 2*. Association for Earthquake Disaster Prevention, Tokyo, Japan, 15-20.

Field, E.H. and K.H. Jacob (1993). "Monte-Carlo Simulation of the Theoretical Site Response Variability at Turkey Flat, California, Given the Uncertainty in the Geotechnically Derived Input Parameters." *Earthquake Spectra 9* (4): 669-702.

Haddadi, H., Shakal, A.F., and Real, C.R. (2008). "The Turkey Flat Blind Prediction Experiment for the September 28, 2004 Parkfield Earthquake: Comparison with Other Turkey Flat Recordings." (this volume).

Kudo, K. (2003). "IASPEI/IAEE Joint Working Group on the Effects of Surface Geology on Seismic Motion." *International Handbook of Earthquake Engineering and Engineering Seismology 81.7* (CD-ROM #2).

Real, C.R., Shakal, A.F., and Tucker, B.E. (2006). "Turkey Flat, U.S.A., Site Effects Test Area: Anatomy of a Blind Ground-Motion Prediction Test." *Proceedings of the Third International Symposium on the Effects of Surface Geology on Seismic Motion, Aug 30 – Sept 1, 2006, Grenoble, France*, Vol. 1, 47-66.

Real, C.R., Shakal, A.F., and V. Graizer (2005). "Blind prediction test of the response of Turkey Flat Site Effects Test Area to the September 28, 2004 Parkfield Earthquake." *Proceedings of the IASPEI General Assembly, October 2-8, 2005, Santiago, Chile*.

Real, C.R. and A.F. Shakal (2005). "Turkey Flat, USA Site Effects Test Area – Report 7: Strong-Motion Test: Prediction Criteria and Input Rock Motions." *California Geological Survey*, OSMS 05-1, 33 p.

Real, C.R. (1988). "Turkey Flat, USA Site Effects Test Area – Report 2: Site Characterization." *California Division of Mines and Geology*, TR 88-2.

Real, C.R. and B.E. Tucker (1988). "Ground Motion Site Effects Test Area Near Parkfield, California." *Proceedings Ninth World Conference on Earthquake Engineering, Tokyo, Japan VIII*, 187-191.

Shakal, A.F., Haddadi, H., and Real, C.R. (2006). "Recorded Data and Preliminary Review of Predictions in the Turkey Flat Blind Prediction Experiment for the September 28, 2004 Parkfield Earthquake." *Proceedings of the SMIP06 Seminar on Utilization of Strong-Motion Data, Oakland, CA*, 137-152.

Shakal, A., Graizer, V., Huang, M., Borcherdt, R., Haddadi, H., Lin, K., Stephens, C., and P. Roffers (2005). "Preliminary Analysis of Strong-motion Recordings form the 28 September 2004 Parkfield, California Earthquake." *Seismological Research Letters 76* (1), 27-39.

Two Dimensional Evaluation of Site Effect in Rectangular Valleys

Nima Tafazzoli[1] , Mohammad Hassan Baziar[2] , Habib Shahnazari[3]

[1]MS Engineer, College of Civil Engineering, Iran University of Science and Technology, nimatafazzoli@yahoo.com
[2]Professor, College of Civil Engineering, Iran University of Science and Technology, Baziar@iust.ac.ir
[3]Assistant Professor, College of Civil Engineering, Iran University of Science and Technology, hshahnazari@iust.ac.ir

ABSTRACT: Ground response analysis in two dimensional modeling is one of the problems considered in geotechnical earthquake engineering. In many cases, a site might be located on an alluvial valley and two dimensional analysis should be performed instead of one dimensional analysis in order to obtain reliable surface accelerations. In this research rectangular valleys with different ratios of width to thickness are modeled in two dimensions and the acceleration response of soil on the middle point of surface is evaluated. Results indicate that the amplification of the motions in two dimensional models with different width to thickness ratios of the valley differs from those calculated by one dimensional technique. The ratio of the width to thickness for which the results of one and two dimensional analysis are similar, is also determined.

INTRODUCTION

Earthquakes are one of the most devastating natural hazards in the world which cause great loss of lives and properties every year. The countries in earthquake prone areas are frequently suffering lots of damages due to occurrence of strong earthquakes. The effect of the earthquakes, however, is dependent upon many factors including geotechnical properties of the site at the proximity of the event as well as the topography and geometry of the site, source characteristics and path of the waves initiated from the earthquake.

Ground response analysis is one of the most important problems considered in the geotechnical earthquake engineering field. Macmurdo (1824) noted that buildings situated on rock were not by any means so much affected as those, whose foundations did not reach to the bottom of the soil in the 1819 earthquake in cutch, India. In the report on the 1857 neapolitan earthquake, Mallet (1862) noted the effect

of local geology conditions on the damage. Wood (1908) and Reid (1910) showed that the intensity of ground shaking in the 1906 San Francisco earthquake was related to soil and geologic conditions.

Often, the site effect response of a valley filled with alluvium is obtained using one dimensional equivalent linear method (Schnabel et al, 1972) or nonlinear model (Lee and Finn, 1978). However, one dimensional analysis can be used only for nearly flat regions. In other words, in many cases, a site might be located on a narrow alluvial valley and two dimensional analysis should be performed to obtain reliable results.

Local site conditions can influence important earthquake characteristics such as amplitude, frequency content and duration of the motion. The extent of the soil influence depends on the geometry and material properties of the soil layers, site topography, and the characteristics of the input motion.

The alluvium basement interface generates surface waves and the alluvium may trap body and surface waves (Finn and Nichols, 1988, Silva, 1989). These waves amplify the motion and increase the duration over that predicted by one dimensional analysis. These effects were very pronounced in the lake-bed motions in Mexico City during the 1985 earthquake. A number of cases which show the engineering implications of valley effects have been presented by Faccioli (1991), Bard and Gariel (1986).

Assimaki and Gazetas (2004) performed a parametric study on the eastern bank of the Kifisos river canyon to evaluate the significance of topographic and soil effects on the seismic response of slopes. Athanasopoulos et al. (1999) studied the non-uniform distribution of damage in terms of surface topography effects by conducting seismic response analyses of a simplified two dimensional profile of the Egion town. Makra et al. (2005) studied a two dimensional model which has been constructed and validated for Euroseistest valley in northern Greece and compared the results with the obtained ones from one dimensional models. Tafazzoli and Baziar (2005) investigated the site effect problem in the city of Bam in Iran and showed the importance of the knowledge of the soil characteristics and the bedrock. The two dimensional analysis of the city of the Bam was also studied and results obtained from one and two dimensional modeling were compared (Baziar et al., 2006).

More research were done by McPhee et al. (2007), Ge and Chen (2007), Furumura and Hayakawa (2007), Ferretti et al. (2007), Nisii et al. (2007), Hartzell et al. (2006), and Di Giulio et al. (2006) related to topographic amplification in sedimentary valleys.

In this research rectangular valleys with different ratios of width to thickness are modeled using two dimensional modeling and Ricker wavelet as input motion with different amplitudes and periods, applied to the bedrock.

SOIL MODELING AND INPUT MOTION

In this research a number of models of valleys with rectangular shape and different alluvium shear wave velocities (constant in depth), strength parameters, and thickness of alluviums are considered and the amplifications of one dimensional and two dimensional analyses are compared. The typical shape of these valleys is shown in Figure 1. Thickness of the alluviums in these models is 30m and 50m. More

details of these models are summarized in Table 1.

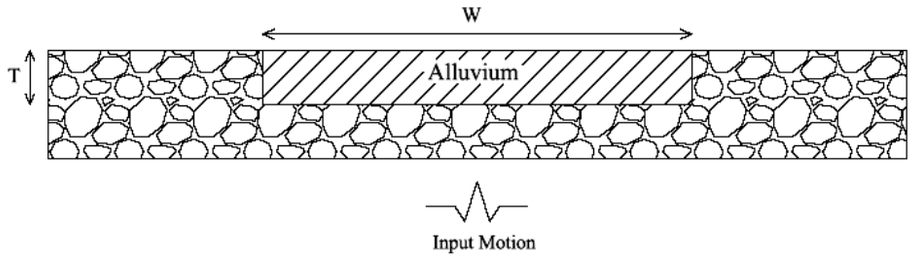


Figure 1. Rectangular valley filled with alluviums

Table 1. Different models for dynamic analyses

Soil Parameters	Case No.	φ (°)	C (kPa)	a_{max} (g)
Vs= 800 m/s	1	35	0	0.1
Unit Weight=23 (kN/m3)	2	35	0	0.3
	3	30	0	0.1
Vs= 500 m/s	4	25	0	0.1
Unit Weight =19 (kN/m3)	5	30	0	0.3
	6	25	0	0.3
	7	23	0	0.1
Vs= 270 m/s	8	20	0	0.1
Unit Weight =18 (kN/m3)	9	23	0	0.3
	10	20	0	0.3
	11	20	8	0.1
Vs= 120 m/s	12	17	10	0.1
Unit Weight =17 (kN/m3)	13	20	8	0.3
	14	17	10	0.3

For one dimensional analysis, SHAKE program was employed (Schnabel et al., 1972). In one dimensional analysis, the nonlinear behavior of soils can be considered by equivalent linear method. The equivalent linear method has been used for many years to calculate the wave propagation and response of the acceleration in soil and rock layers. This method doesn't capture directly nonlinear effects because it assumes linearity during the solution process. In this method strain dependent modulus and damping curves are only taken into account in an average sense, in order to approximate some effects of nonlinearity. The equivalent linear shear modulus is generally taken as a secant shear modulus and the equivalent linear damping ratio as the damping ratio that produces the same energy loss in a single cycle as the actual hysteresis loop. Since the linear approach requires that G and ξ be constant for each soil layer, determining the G and ξ values, consistent with the level of strain induced in each layer, are required. To solve this problem, an objective definition of strain level is needed. The modulus reduction and damping ratio curves, obtained from laboratory tests, and simple harmonic loading are used to characterize the strain level by the peak shear strain amplitude. In this research the model

presented by Vucetic and Dobry (1991) was applied.

Finite Difference method was used for two dimensional response analyses by using the FLAC program (Itasca, 2005). The Mohr-Coulomb model was used for nonlinear behavior of the soil. As it can be seen in table (1) different friction angle and cohesion were used for different soil groups. Also Rayleigh damping was used with minimum damping of 5%. The maximum acceleration on the surface of the models was considered as representatives of ground motion characteristics. The distribution of these quantities on the ground surface was studied considering the effects of geometric irregularities. Furthermore, two dimensional acceleration responses were compared with one dimensional response for horizontally stratified layers. In the bedrock shear wave velocity of 1500 m/s, cohesion of 45MPa, and friction angle of 40 degrees were used.

For the input motion of the dynamic analysis, beta type of Ricker wavelets with different frequencies as defined in Equation 1, were applied to the interface of the rock and alluvium and the acceleration responses in different points of the soil were evaluated for different models.

$$U(t) = \left[1 - 2b(t - t_0)^2\right]\exp\left[-b(t - t_0)^2\right] \quad (1)$$

Where $b=(\pi f_0)^2$, with f_0 as the characteristic frequency, and t_0 is time of max amplitude of the wave. A Ricker wave with amplitude of 0.3g, characteristic frequency of 4.5 Hz and time of max acceleration of 0.5 sec is shown in Figure 2.

The size of mesh, used in finite difference solutions, was selected to be less than one-tenth of the wavelength associated with the frequency component of the input wave. It was changed for each model due to frequency of the input motion. The input motion was applied to the bedrock while the vertical boundaries of the sides have been placed far enough from the topographical irregularity, where free field motion could be assumed. The lateral boundaries of the main grid were coupled to the free field grid by viscous dashpots to simulate a quiet (non-reflective) boundary as mentioned in the FLAC manual.

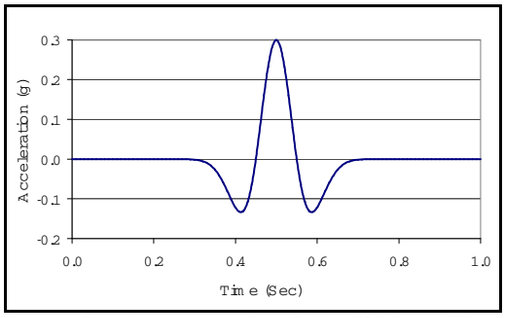


Figure 2: An example of the Ricker Wave

COMPARISON OF ONE AND TWO DIMENSIONAL ANALYSES

The results of our analyses indicate that the amplification of the motion in two dimensional models of the valleys with different width to depth ratios differs from the amplification of the motions obtained in one dimensional ones. The response of the valley for different width to depth ratios in two dimensional analysis is determined using different soil parameters. The effects of surface topography and alluvium-filled valleys on site response have been previously evaluated by Silva (1989). He showed that with the ratio of width to depth greater than four in locations away from the edges, one dimensional analysis results are reliable within a factor of two. Here it seems that for width to depth ratio greater than around eight the response of two dimensional analysis is similar to one dimensional analysis in the central region of the valley. In most of the cases decreasing trend of acceleration is seen from the beginning of the curve to the end of that with difference in their amplitude. This means that when the ratio of the width to thickness increases, the effect of the irregularity of the valley in the central region decreases. Results of analyses for all of models are shown in Figures 3 to 10. In all of the models, input motions with frequency content in the 1 to 10Hz range was applied.

In some cases disorderedly is seen in the curves such as ascending of the amplitude which mostly occurs in the low ratios of the width to thickness. This shows that due to the reflection of the waves from the boundaries, the waves can be amplified when the ratio of the width to thickness increases.

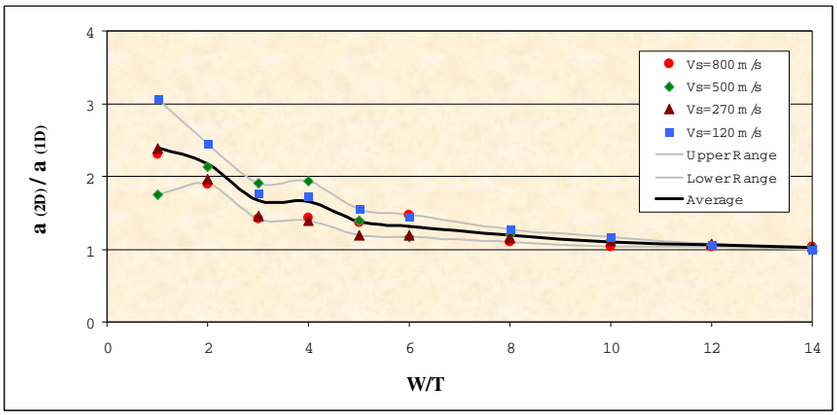


Figure 3: Normalized acceleration for different ratios of width to thickness (Case Numbers: 1 , 3 , 7 , 11) (T=30m , Amplitude of input motion=0.1g)

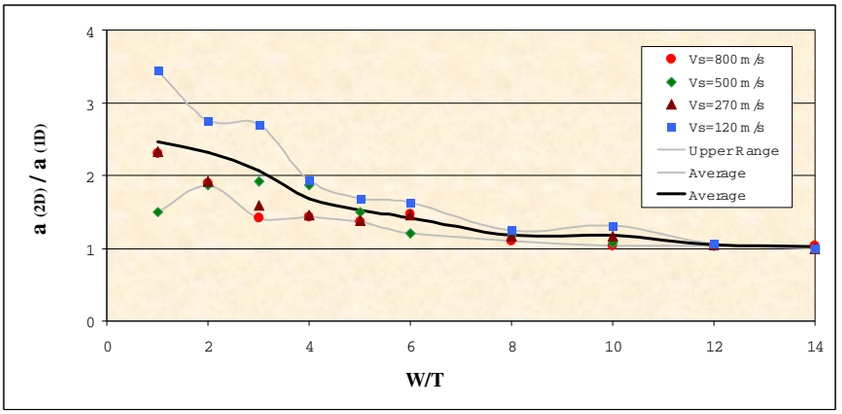


Figure 4: Normalized acceleration for different ratios of width to thickness (Case Numbers: 1 , 4 , 8 , 12) (T=30m , Amplitude of input motion=0.1g)

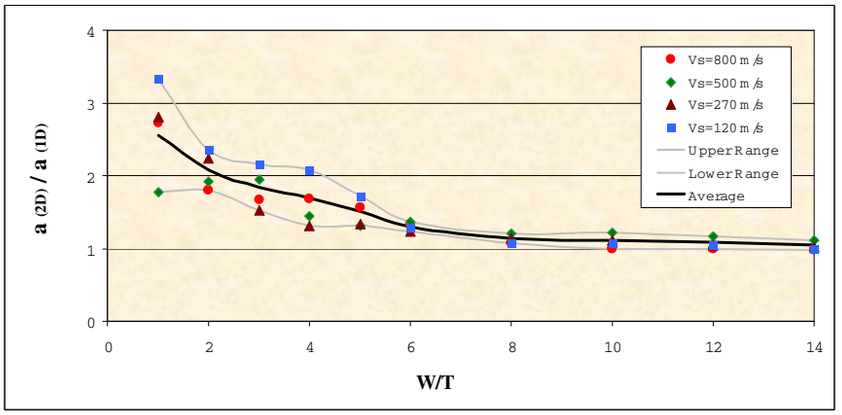


Figure 5: Normalized acceleration for different ratios of width to thickness (Case Numbers: 2 , 5 , 9 , 13) (T=30m , Amplitude of input motion=0.3g)

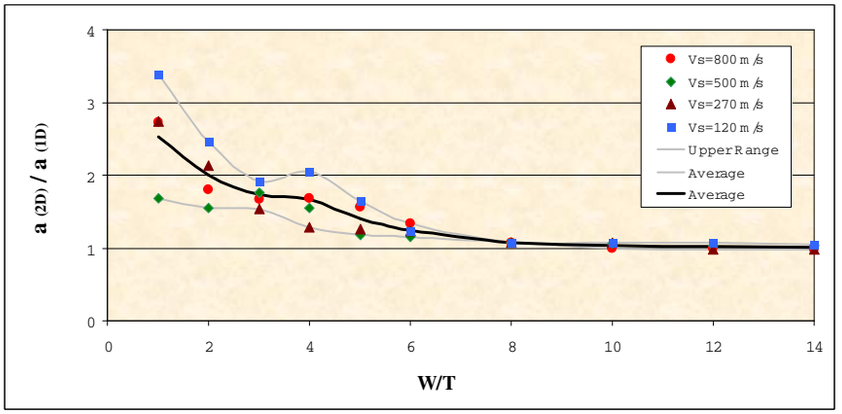


Figure 6: Normalized acceleration for different ratios of width to thickness (Case Numbers: 2 , 6 , 10 , 14) (T=30m , Amplitude of input motion=0.3g)

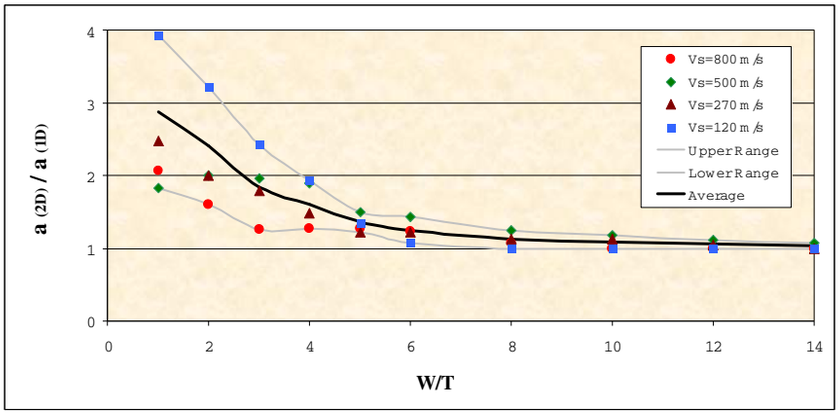


Figure 7: Normalized acceleration for different ratios of width to thickness (Case Numbers: 1 , 3 , 7 , 11) (T=50m , Amplitude of input motion=0.1g)

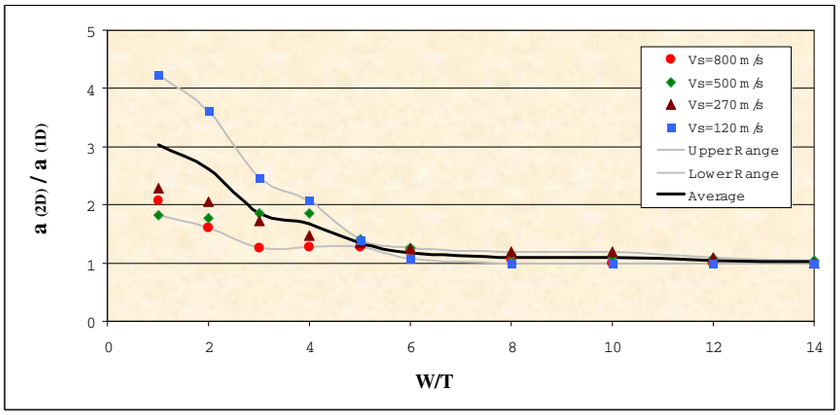


Figure 8: Normalized acceleration for different ratios of width to thickness (Case Numbers: 1 , 4 , 8 , 12) (T=50m , Amplitude of input motion=0.1g)

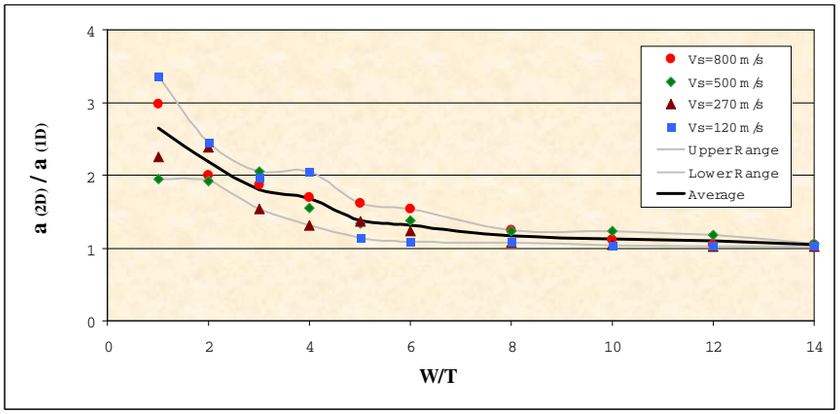


Figure 9: Normalized acceleration for different ratios of width to thickness (Case Numbers: 2 , 5 , 9 , 13) (T=50m , Amplitude of input motion=0.3g)

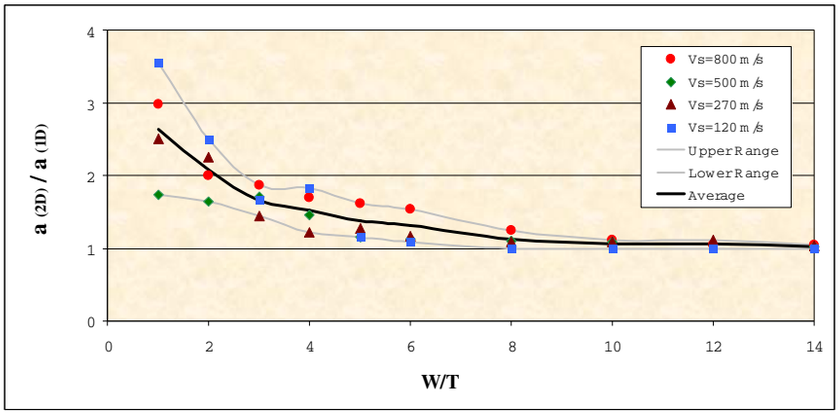


Figure 10: Normalized acceleration for different ratios of width to thickness (Case Numbers: 2 , 6 , 10 , 14) (T=50m , Amplitude of input motion=0.3g)

The dependency of the natural period of the valley can also be obtained from our analyses. As it was mentioned before, the analyses were performed using the ricker waves with different periods. Based on accelerations corresponding to frequencies of input motion, it can be concluded that the natural period of the valley increases with increasing the width to thickness ratio and in large ratios it is the same as one dimensional one. The natural one dimensional period of the soil can be calculated from the Equation 2:

$$T = \frac{4H}{V_s} \tag{2}$$

From this equation, the natural one dimensional period of the soil is depended on the height and the shear wave velocity of the soil layer. Our two dimensional analyses results show that the natural period also depends on the width of the valley. This is shown in Figures 11 and 12.

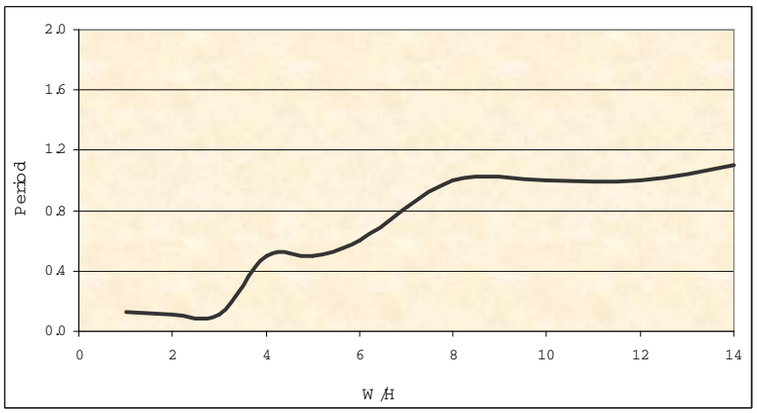


Figure 11: Natural 2D period of the valley for different ratios of width to thickness (Case Number: 11)

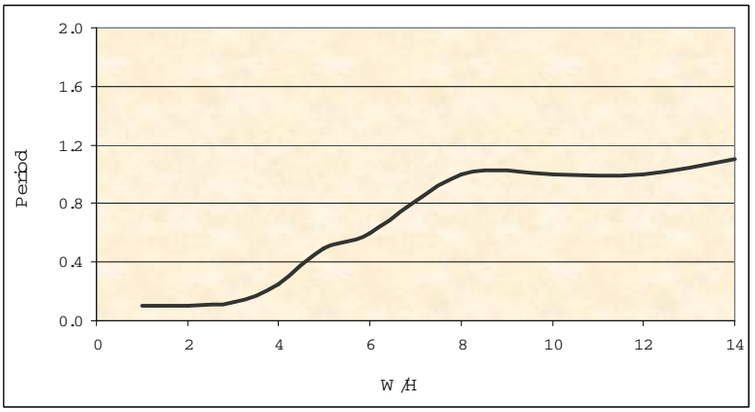


Figure 12: Natural 2D period of the valley for different ratios of width to thickness (Case Number: 12)

CONCLUSIONS

In this study rectangular valleys with different width to depth ratios were modeled using one and two dimensional nonlinear technique. The thickness of the alluviums in these models was 30m and 50m.

Our results indicate that the amplification of the ground motions in two dimensional models with different width to depth ratios of the valley differs from that of one dimensional models. For width to depth ratio of around eight, results of two and one dimensional analysis are similar. These results could be considered for locations far away enough from the edge of the valley.

As a consequence of the two dimensional analysis, when the width to thickness ratio of the valley increases, the effect of the irregularity decreases in the central region. In some cases due to the reflection of the waves from the boundaries, the waves can be amplified when the ratio of the width to thickness increases.

We also investigated the natural period of the valley in two dimensional modeling. We found that the natural period of the valley also depends on the width besides the thickness and shear wave velocity of the alluvium deposits. Based on our analyses, it can be concluded that the natural period of the valley increases with increasing the width to thickness ratio and it will be the same as one dimensional one in the great ratios.

Further research are needed to realize the effect of the sedimentary deposits, effect of real ground motion with different frequency content, edge effect of the valley, etc.

REFERENCES

Assimaki, D., and Gazetas, G. (2004) “Soil and Topographic Amplification on Canyon Banks and the 1999 Athens Earthquake.” *Journal of Earthquake Engineering*, Vol 8, No. 1, 1-43.

Athanasopoulos, G.A., Pelekis, P.C., and Leonidou E.A. (1999). “Effect of surface topography on seismic ground response in the Egion (Greece) 15 June 1995 earthquake.” Journal of Soil Dynamics and Earthquake Engineering, 18(2), 135-

149.
Bard, P.Y., and Gariel, J.C. (1986). “The seismic response of two dimensional sedimentary deposits with large vertical velocity gradients.” Bulletin of Seismological Society of America, No. 76, 343-346.
Baziar, M.H., Tafazzoli, N., and Fatemi Aghda, M. (2006). “2D evaluation of site effect in the city of Bam.” Proceedings of the 1st European conference on earthquake engineering and seismology, No. 188, Geneva, Switzerland.
Di Giulio, G., Cornou, C., Ohrnberger, M., Wathelet, M., and Rovelli, A., (2006) “Deriving Wavefield Characteristics and Shear-Velocity Profiles from Two-Dimensional Small-Aperture Arrays Analysis of Ambient Vibrations in a Small-Size Alluvial Basin, Colfiorito, Italy.” Bulletin of the Seismological Society of America, 96: 1915-1933.
Faccioli, E. (1991) “Seismic amplification in the presence of geological and topographic irregularities.” Proceedings of 2nd International Conference on Recent Advances in Geotechnical Earthquake Engineering and Soil Dynamics, st. Louis, Missouri, Vol. 2, pp. 1779-1797.
Ferretti, G., Massa, M., Isella, L., and Eva C. (2007) “Site-Amplification Effects Based on Teleseismic Wave Analysis: The Case of the Pellice Valley, Piedmont, Italy.” Bulletin of the Seismological Society of America, 97: 605-613.
Finn, W.D. Liam, and Nichols, A.M. (1988). “Seismic response of long period sites: Lessons from the September 19, 1985 Mexican earthquake.” Canadian Geotechnical Journal, 128-137.
Furumura, T., and Hayakawa, T., (2007) “Anomalous Propagation of Long-Period Ground Motions Recorded in Tokyo during the 23 October 2004 Mw 6.6 Niigata-ken Chuetsu, Japan, Earthquake.” Bulletin of the Seismological Society of America, 97: 863-880.
Ge Zengxi, and Chne Xiaofei (2007) “Wave Propagation in Irregularly Layered Elastic Models: A Boundary Element Approach with a Global Reflection/Transmission Matrix Propagator.” Bulletin of the Seismological Society of America, 97: 1025-1031.
Hartzell, S., Harmsen, S., Williams, R.A., Carver, D., Frankel, A., Choy, G., Liu, P., Jachens, R.C., Brocher, T.M., and Wentworth, C.M. (2006) “Modeling and Validation of a 3D Velocity Structure for the Santa Clara Valley, California, for Seismic-Wave Simulations.” Bulletin of the Seismological Society of America, 96: 1851-1881.
Itasca (2005), FLAC Manual
Kramer, S.L. (1996). Geotechnical Earthquake engineering, Prentice Hall, Upper Saddle River, New Jersey.
Lee, M.K.W. and Finn, W.D.L. (1978). DESRA-2 ,Dynamic Effective stress response analysis of soil deposits with energy transmitting boundary including assessment of liquefaction potential, Soil Mechanics Series No. 38, Dept. of Civil Engineering, University of British Columbia, Vancouver, B.C..
MacMurdo, J. (1824). “Papers relating to the earthquake which occurred in India in 1819.” Philosophical Magazine, Vol. 63, 105-177.
Mallet, R. (1862). Great Neapolitan Earthquake of 1857, London, 2 vols.

Makra, K., Chavez-Garcia, F.J., Raptakis, D., and Pitilakis, K. (2005). "Parametric analysis of the seismic response of a 2D sedimentary valley: implications for code implementations of complex site effects." Journal of Soil Dynamics and Earthquake Engineering, 25(4), 303-315.

McPhee, D.K., Langenheim, V.E., Hartzell, S., McLaughlin, R.J., Aagaard, B.T., Jachens, R.C., and McCabe, C. (2007) "Basin Structure beneath the Santa Rosa Plain, Northern California: Implications for Damage Caused by the 1969 Santa Rosa and 1906 San Francisco Earthquakes." Bulletin of the Seismological Society of America, 97: 1449-1457.

Nisii, V., Saccorotti, G., and Nielsen S., (2007) "Detailed Analysis of Wave Propagation beneath the Campi Flegrei Caldera, Italy" Bulletin of the Seismological Society of America, 97: 440-456.

Reid, H.F. (1910). The California Earthquake of April 18, 1906, Publication 87, Vol. 21, Carnegie Institute of Washington, Washington, D.C..

Schnabel, P.B., Lysmer, J., and Seed, H.B. (1972) "SHAKE: a computer program for earthquake response analysis of horizontally layered sites," Report EERC 72-12, Earthquake Engineering Research Center, University of California, Berkeley.

Silva, W.J. (1988). "Soil response to earthquake ground motion." EPRI report NP-5747, Electric Power Research Institute, Palo Alto, California.

Tafazzoli N., and Baziar M.H. (2005). "Evaluation of the Site Effect in the City of Bam." Conference on Bam Earthquake, Reconstruction and Future of it, published in ASAS journal Vol.18, Bam, Iran, May 18-19.

Vucetic, M., and Dobry, R. (1991). "Effect of soil plasticity on cyclic response." Journal of Geotechnical Engineering, ASCE, Vol. 117, No. 1, pp. 89-107.

Wood, H.O. (1908). "Distribution of apparent intensity in San Francisco, in the California earthquake of April 18, 1906." Report of the State Earthquake Investigation Commission, Carnegie Institute of Washington, Washington, D.C., 1, 220-245.

This page intentionally left blank

Probabilistic Liquefaction Hazard Mapping

Thomas L. Holzer[1]

[1]Engineering Geologist, U.S. Geological Survey, 345 Middlefield Road, Menlo Park, CA 94025; tholzer@usgs.gov

ABSTRACT: Many investigators have applied the liquefaction potential index (LPI) to map regional liquefaction hazard. LPI, which integrates the liquefaction potential of susceptible soil elements at a specific location into a single value, has been used to assess both (1) spatial variability of liquefaction potential, and (2) liquefaction potential of surficial geologic units. A promising application to mapping has been the establishment of a median threshold LPI value at which liquefaction effects occur. This threshold when applied to complementary cumulative frequency distributions of LPI for spatially homogeneous surficial geologic units yield liquefaction probability curves for surficial geologic units that can be used for hazard mapping. Both probabilistic liquefaction scenario maps and PSHA-based liquefaction hazard maps have been produced with this approach. The scenario maps compare favorably with historical liquefaction in the mapped areas.

INTRODUCTION

Regional mapping of liquefaction hazard has evolved during the last few decades from research to regulatory endeavors (Power and Holzer, 1996). Despite this evolution, most liquefaction hazard mapping is primarily descriptive and qualitative in nature. This descriptive state-of-the-art of liquefaction hazard mapping stands in contrast with the quantitative state-of-the-art of mapping earthquake shaking hazard. Probabilistic mapping of shaking, which was originally proposed by Cornell (1968), is now firmly established and widely used in engineering practice (McGuire, 2004). In fact, confidence in the methodology has progressed to where it is now the basis in many building codes for estimating shaking hazard (BSSC, 2001; Frankel et al., 2002). The methodology is known as probabilistic seismic hazard analysis (PSHA). A comparable probabilistic framework, here referred to as probabilistic liquefaction hazard analysis (PLHA), is an important need for future liquefaction hazard mapping.

A major obstacle to the implementation of PLHA has been the absence of a widely accepted engineering demand parameter, i.e., a liquefaction intensity parameter that measures the severity of liquefaction at a site. Recently, several investigators have produced probabilistic liquefaction hazard maps for earthquake scenarios that use a parameter known as the liquefaction potential index (LPI) as an intensity parameter.

Although LPI has been widely used for seismic microzonation, the application to probabilistic mapping is new. This paper describes LPI and evaluates its potential application to probabilistic liquefaction hazard mapping.

Characterization of regional liquefaction hazard in a probabilistic framework has two important applications in addition to the informational aspect of indicating locations of significant hazard. First, as the practice of earthquake engineering transitions to performance-based design (Porter et al., 2007), characterization of hazard in a manner suitable for estimating risk is desirable. This requires that the hazard causing the risk be cast in a probabilistic framework. And second, the rapidly developing field of loss and damage estimation requires annual probabilities of hazard to compute annualized loss and damage.

LIQUEFACTION PREDICTION

Resistance of a soil to liquefaction is determined by a combination of multiple soil properties and environmental factors (Seed and Idriss, 1982). All of these properties and factors should be taken into account in an ideal evaluation of the liquefaction resistance of a soil. Because a comprehensive evaluation of soil properties and environment is neither feasible nor practical, simplified approaches have been developed. These approaches are divided here into two categories, geotechnical and geological. Although treated separately here, the approaches often are combined for regional liquefaction hazard mapping.

The most widely-used geotechnical approach is the simplified procedure (Seed and Idriss, 1971). In this procedure, two parameters are used to predict liquefaction potential: (1) a seismic demand parameter that measures the strength of the earthquake loading, and (2) a capacity parameter that measures the resistance of the soil to liquefaction. The former parameter is based on peak ground acceleration (PGA). The latter parameter is usually based on the field penetration resistance at a specific depth. For an updated and comprehensive description of the procedure, the reader is referred to Youd et al. (2001).

The simplified procedure relies on field case histories where penetration resistance was measured in soils that were inferred either to have or not to have liquefied in historical earthquakes. These penetration resistance values are compared to seismic demand at each site, and a boundary curve is drawn between the liquefied and nonliquefied case histories. The original boundary curve was deterministic and hand drawn. Statistical analyses of the case history data, however, permit points to be associated with a probability of liquefaction (Cetin et al., 2004; Juang et al., 2003; Liao et al., 1988; Moss et al., 2006; Toprak et al., 1999; Youd and Noble, 1997).

The challenge in applying the simplified procedure to regional mapping is that penetration values measure liquefaction resistance at only a specific depth in the soil layer. Values do not predict the overall liquefaction hazard at a site, i.e., the response of the entire soil column. Thus, the geotechnical approach, which is useful for engineering analysis at specific sites, must be supplemented with other parameters or considerations if it is to predict liquefaction hazard on a regional basis. Examples where this has been done include regional mapping of lateral spread hazard by Olsen et al. (2007), who relied on soil parameters identified by Youd et al. (2002), and by Mabey et al. (1993), who relied on thickness of the liquefiable layer.

The geological approach is based on observed variations in response of different geologic deposits to earthquake shaking. This variability is caused by differences in liquefaction susceptibility. These differences are attributable to both the sedimentary process responsible for deposition of each type of geologic unit and its geologic history. The geological approach was introduced by Youd and Hoose (1977), who proposed a generic classification of the liquefaction susceptibility of different deposits on the basis of their geology and age. For example, river channel deposits less than 500 years old have a very high susceptibility, whereas channel deposits of Pleistocene age (>12,000 years old) have a very low susceptibility. For application to specific areas, the geological approach is often augmented with the geotechnical approach by using penetration tests in the geologic units to develop a susceptibility ranking of the geologic units (e.g., Tinsley et al., 1985). Baise et al. (2006) recently proposed a formal process to perform this ranking if the number of penetration tests in the different geologic units is sufficient. Similarly, if locations of liquefaction during historical earthquakes in the study area are known, the liquefaction performance of a geologic unit may be included as a factor in its susceptibility ranking (e.g., Witter et al., 2006).

The geological approach is appealing for regional mapping of liquefaction hazard because of the practicality of mapping the surficial geology of large regions. This vastly increases the efficiency of the production of hazard maps. It also can improve the accuracy with which boundaries of hazard zones can be delineated because they commonly coincide with boundaries between geologic units. Thus, the challenge for regional mapping of liquefaction hazard is how to combine geotechnical assessments of liquefaction susceptibility with geology in such a manner that it permits probabilistic assessments of liquefaction hazard on a spatial basis.

LIQUEFACTION POTENTIAL INDEX

LPI has been used for several decades to map the spatial variability of liquefaction hazard. Recently several investigators have used the index to characterize the variability of the liquefaction potential of geologic deposits. For hazard mapping, the advantage of LPI over the simplified procedure is that it predicts the liquefaction potential of the entire soil column at a specific location. The simplified procedure only predicts liquefaction potential of a soil element. By combining all of the factors of safety from a boring or sounding into a single value, LPI provides a spatially distributed parameter if multiple borings or soundings are conducted in a deposit.

The liquefaction potential index was originally proposed by Iwasaki et al. (1978) to estimate the potential for liquefaction to cause foundation damage. As a historical footnote, Iwasaki et al. (1978) used the symbol I_L for LPI, but subsequently changed it to P_L (Iwasaki et al., 1982). Because of the potential for confusion with commonly used symbols for the Atterberg liquid limit (I_L) and the probability of liquefaction of a soil element (P_L), the author prefers use of LPI (Note: Yegian and Whitman (1978) also proposed a Liquefaction Potential Index that they defined as the ratio of the shear stress caused by the earthquake to the resistance of the sand to shaking. Their index did not receive widespread acceptance, and the ratio is now known as the liquefaction factor of safety.).

LPI as originally defined by Iwasaki et al. (1978) weighs factors of safety and thickness of potentially liquefiable layers according to depth. It assumes that the severity of liquefaction is proportional to:

1. cumulative thickness of the liquefied layers;
2. proximity of liquefied layers to the surface; and
3. amount by which the factor safety (*FS*) is less than 1.0, where *FS* is the ratio of soil capacity to resist liquefaction to seismic demand imposed by the earthquake.

Iwasaki et al. (1978) defined LPI as:

$$LPI = \int_0^{20m} F\, w(z)\, dz \tag{1}$$

where

$$F = 1 - FS \quad \text{for } FS \le 1 \tag{2a}$$

$$F = 0 \quad \text{for } FS > 1 \tag{2b}$$

$$w(z) = 10 - 0.5\, z, \text{ where } z \text{ is the depth in meters.} \tag{2c}$$

The weighting factor, $w(z)$, proposed by Iwasaki et al. (1978) ranges from one at the surface to zero at 20 m. F=0 above the water table.

Iwasaki et al. (1982) and Toprak and Holzer (2003) have evaluated the significance of LPI values. Both compiled case histories that compared LPI with liquefaction observations.

The evaluation by Iwasaki et al. (1982) was based on 6 historical earthquakes in Japan where liquefaction had been reported. They concluded that "severe liquefaction is likely" at sites with LPI>15 and that "severe liquefaction is not likely" at sites with LPI<5. Their categories were based on the general likelihood of liquefaction occurrence rather than the nature of the ground deformation. From Iwasaki et al. (1982, Fig. 5), one can infer that LPI>15 at 50% of the liquefaction sites and LPI<5 at more than 75% of the sites without liquefaction effects. Their evaluation relied on standard penetration tests (SPT) blow counts to compute LPI values.

Iwasaki et al. (1982) computed factors of safety with an alternative to the Seed-Idriss simplified procedure, which they referred to as "a simple analysis." Their boundary curve is determined by median grain size (d_{50}). There is no fines correction as in the Seed-Idriss simplified procedure. Their boundary curve differs from that of the simplified procedure, generally producing lower factors of safety for clean sand as d_{50} decreases (Fig. 1). For the comparison, Japanese blow counts for $(N_1)_{60}$<20 were reduced by 10% for consistency with U.S. practice (Seed et al., 1985, p. 1433).

Toprak and Holzer (2003) evaluated LPI in two contexts, frequency and nature of ground deformation. They estimated both the probability of surface manifestations of liquefaction as a function of LPI and correlated LPI with the actual nature of the surface effects. The evaluations relied on LPI values from cone penetration test (CPT) soundings at sites with surface manifestations of liquefaction during the 1989 Loma Prieta, California, earthquake. Factors of safety were computed with Robertson and Wride (1998), the CPT-based procedure recommended by Youd et al. (2001).

To evaluate frequency, Toprak and Holzer (2003) placed LPI values into bins of one LPI unit. Each LPI value was classified as to whether or not liquefaction effects

were observed near the sounding. For each bin, frequency or probability of liquefaction was computed by dividing the number of soundings where liquefaction effects were observed nearby by the total number in the bin. They concluded that "the probability of surface manifestations of liquefaction is 58 and 93%, respectively, when LPI equals or exceeds 5 and 15." Toprak and Holzer (2003) recognized a potential for sampling bias in probability estimates if subsurface exploration is conducted primarily in areas of liquefaction. To reduce the impact of sampling bias, their recommended probabilities were computed only from field studies where CPT tests had been conducted both in and out of the liquefaction areas. They described but excluded probability estimates from other case histories where exploration was conducted principally in the area affected by liquefaction.

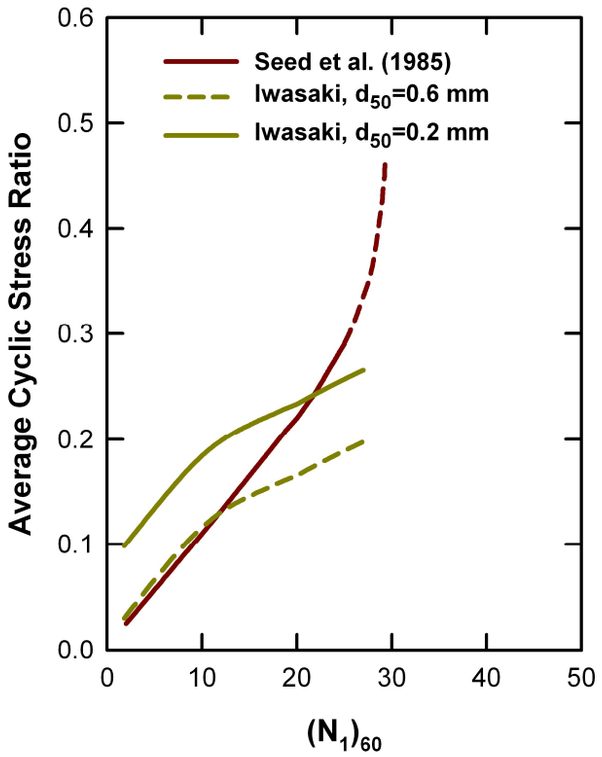


FIG. 1. Comparison of SPT boundary curves from the simplified procedure for clean sand (Seed et al., 1985) and the "simple analysis" by Iwasaki et al. (1982).

To evaluate the correlation of LPI with the severity of the surface manifestations of liquefaction, Toprak and Holzer (2003) grouped soundings into four categories based on surface effects that were observed near soundings: none, only sand boils, inchoate patterns of ground cracks, and lateral spreading. They observed that the median values of LPI were 5 and 12, respectively, in areas with sand boils and lateral spreads. Lower and upper quartiles were 3 and 10 for sand boils and 5 and 17 for lateral spreads. In addition, the threshold of LPI≥5 is supported by a field investigation of liquefaction at Oceano, California in 2003. Liquefaction caused by the M6.6 San Simeon earthquake generally occurred at locations where LPI ≥ 5 (Holzer et al., 2005a).

A few investigators have proposed modifying the severity term, *F*, in LPI (Eq. 2a). Sonmez (2003) expressed concern with the capability of LPI to identify "marginally" liquefiable soils, by which he meant soils with *FS* near one. Accordingly, Sonmez (2003) modified *F* so that it was nonzero for $0.95 \leq FS < 1.2$. This introduction of conservatism is consistent with recommendations by Seed and Idriss (1982) to adopt a *FS* between 1.25 and 1.5 to identify potentially problematic soils for engineering design. The primary impact of the modification is that it produces nonzero, but low, LPI values for soils that may warrant more detailed investigation of their liquefaction potential. This modification allowed Sonmez (2003) to subdivide the category LPI<5 by adding a hazard boundary at LPI=2.

Lee et al. (2003) proposed that *F* be replaced with the conditional probability of liquefaction derived by Juang et al. (2003). The conditional probability, $P_L = 1/[1 + (FS/0.96)^{4.5}]$, estimates the probability of liquefaction for a given soil element given a factor of safety. Lee et al. (2003) also recommended usage of the simplified procedure for the CPT as implemented by Juang et al. (2003). Lee et al. (2003) compared values computed with the redefined LPI to the occurrence of liquefaction caused by the 1999 Chi Chi earthquake and discovered it produced significantly higher values than the calibration of Iwasaki et al. (1982). This prompted them to rename their parameter the liquefaction risk index. Sonmez and Gokceoglu (2005) adopted the revision of LPI by Lee et al. (2003), but renamed it the liquefaction severity index. They also proposed a 5-category severity scale. Their parameter is not to be confused with the liquefaction severity index of Youd and Perkins (1987) that predicts ground displacement caused by lateral spreading.

To make the hazard scale of the liquefaction risk index more consistent with the LPI scale of Iwasaki et al. (1982), Li et al. (2006b) conducted a series of sensitivity tests and redefined $F = P_L - 0.35$ if $P_L \geq 0.35$ and $F = 0$ if $P_L < 0.35$. Based on this definition of *F* and the simplified procedure proposed by Idriss and Boulanger (2006), Li et al. (2006) computed revised LPI values for the 1999 Chi Chi, Taiwan, earthquake and all of the case histories reported by Toprak and Holzer (2003). They correlated these values with field-based estimates of the "probability of ground failure" and proposed a new set of liquefaction hazard categories based on these probabilities. The upper boundaries to their "risk of ground failure" categories "extremely low to none, low, medium, high, and very high" respectively, correspond to revised LPI values (and *probability of ground failure*) of 3.5 (*0.1*), 5.4 (*0.3*), 7.8 (*0.7*), 9.7 (*0.9*), and 14.1 (*1.0*). They did not recognize LPI=5, which corresponds to a probability of ground failure of 0.24, as a boundary. Their analysis of the probability of ground failure did not consider potential sampling bias. It included case histories that were excluded by Toprak and Holzer (2003) because of concerns with sampling bias. The high probabilities at intermediate LPI values might also be explained by the observation that the Youd et al. (2001) CPT-based curve is associated with a 50% probability of liquefaction (Juang et al., 2002; Toprak et al., 1999). This would yield lower LPI values when used in the traditional way as a deterministic curve.

Juang et al. (2005), following the correlation by Toprak and Holzer (2003) of LPI with type of ground deformation, proposed a damage state parameter, the damage severity index, to predict actual liquefaction-induced foundation damage. The parameter was correlated with both the revised LPI and the "probability of ground

failure" computed by Li et al. (2006b). Juang et al. (2005) advised caution in its application until the correlation could be evaluated with more case histories.

PROBABILISTIC HAZARD MAPS FOR SCENARIO EARTHQUAKES

Applications of LPI to Liquefaction Hazard Mapping

LPI has been used by many investigators to map liquefaction hazard at regional scales (Table 1). Most of the maps relied on the scale proposed by Iwasaki et al. (1982) to indicate hazard (see entries labeled "Iwasaki scale" in Table 1). With this scale, hazard boundaries are defined at LPI values of 5 and 15. Recently, three investigators have produced maps that rely on LPI to estimate the probability of liquefaction (see entries labeled "Probability" in Table 1). All of the maps in Table 1 are based on scenario earthquakes, except those by Cramer et al. (2008), which are probabilistic liquefaction hazard maps.

Table 1. Published liquefaction hazard maps based on LPI

Date	*Authors*	*Location*	*Country*	*Evaluation of LPI*
1982	Iwasaki et al.	Shizuoka Pref.	Japan	Iwasaki scale
1994	Kayabili and West	Evansville, IN	U.S.	Iwasaki scale
1998	Divakarla et al.	w. Puerto Rico	U.S.	Iwasaki scale
1998	Hosseini	Busehr	Iran	Iwasaki scale
1998	Luna and Frost	Treasure Island, CA	U.S.	Iwasaki scale
1999	Cresellani et al.	Romagna Coast	Italy	Iwasaki scale
2002	Holzer et al.	Oakland, CA	U.S.	Probability
2003	Sonmez	Inegol	Turkey	Iwasaki scale
2004	Uluzay and Kuru	Ceyhan	Turkey	Iwasaki scale
2005	Papthanassiou et al.	Lefkada	Greece	Iwasaki scale
2007	Rix and Romero-Hudock	Memphis, TN	U.S.	Probability
2007	Hayati and Andrus	Charleston, SC	U.S.	Iwasaki scale
2007	Juang and Li	Charleston, SC	U.S.	Probability*
2007	Lenz and Baise	Oakland, CA	U.S.	None
2008	Cramer et al.	Memphis, TN	U.S.	Probability

*Significant modification of definition of LPI.

Iwasaki et al. (1982) were the first to map liquefaction hazard with the "Iwasaki scale." Using their scale, they mapped areas of "no, possible and likely liquefaction" in Shizuoka Prefecture, Japan. They also relied on different types of surficial geology–"topographic zones"–to assign hazard ratings to areas. Since then, many other maps based on the "Iwasaki scale" have been published. Kayabali and West (1994) produced the first map in the United States, publishing maps of Evansville, Indiana, for two earthquake scenarios. Frost et al. (1997) were the first to implement LPI in a geographic information system and mapped liquefaction hazard on an island underlain by sandy artificial fill in San Francisco Bay, California (Luna and Frost,

1998). Maps based on the "Iwasaki scale" or modifications of it have been published for Busehr, Iran (Hosseini, 1998), western Puerto Rico (Divakarla et al., 1998),the Romagna coast, Italy (Crespanelli et al., 1999), Inegol, Turkey (Sonmez, 2003), Ceyhan Turkey (Ulusay and Kuru, 2004), Lefkada, Greece (Papathanassiou et al., 2005), and Charleston, South Carolina (Hayati and Andrus, 2007). In addition to the map by Iwasaki et al. (1982), Kayabali and West (1994), Hayati and Andrus (2007), and Lenz and Baise (2007) explicitly considered surficial geology. The other maps were based strictly on the spatial pattern of LPI. Not included here is the map by Li et al. (2006a), who mapped liquefaction probabilities in Yuanlin, Taiwan, for the 1999 Chi Chi earthquake. Their approach was partially calibrated with 1999 liquefaction effects in Yuanlin.

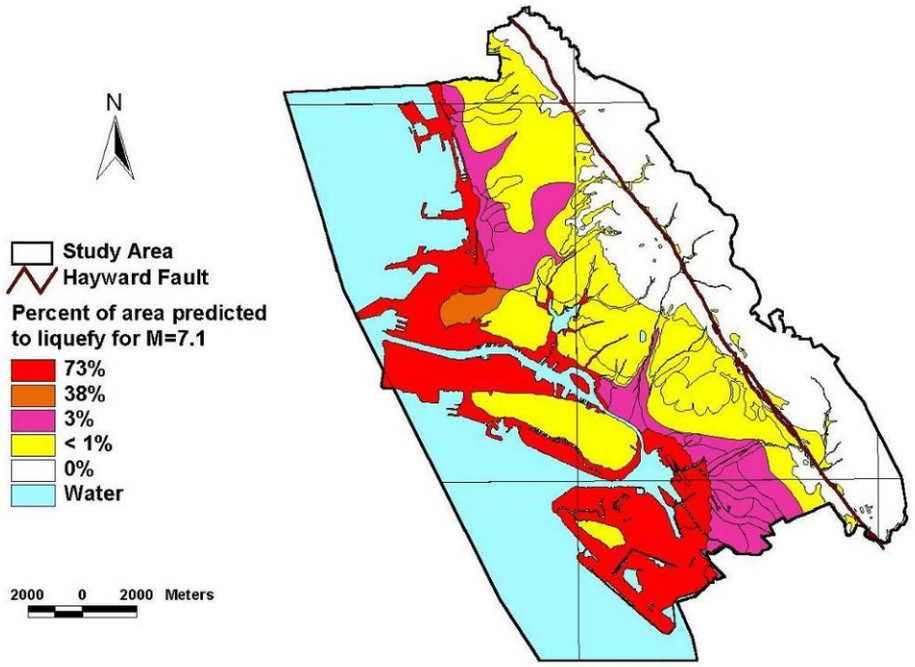


FIG. 2. Map of the greater Oakland area, California, showing percent of area expected to exhibit liquefaction during a M7.1 Hayward Fault earthquake (Holzer et al., 2002).

Mapping Liquefaction Probability

Two approaches that rely on LPI have been developed for probabilistic mapping of liquefaction. One approach relies on the LPI values of surficial geologic units (Holzer et al., 2002; 2006a). They used complementary cumulative frequency distributions of LPI of surficial geologic units to estimate probabilities of surface manifestations of liquefaction. The other approach relies directly on LPI values to estimate the spatial pattern of probabilities (Juang and Li, 2007). Both approaches use versions of the Seed-Idriss simplified procedure to compute LPI.

The liquefaction hazard map of the greater Oakland, California, area (Fig. 2) illustrates the approach proposed by Holzer et al. (2002; 2006a). It was the first regional portrayal of the probability of liquefaction based on LPI. Rix and Romero-

Hudock (2007) subsequently adopted the approach to map liquefaction hazard in Memphis, Tennessee. The greater Oakland map was based on existing surficial geologic maps and multiple seismic CPT soundings conducted in each of the surficial geologic units (Fig. 3). LPI values were computed for each sounding for scenario earthquakes on the nearby (<6 km) Hayward Fault. LPI values for each scenario were grouped by surficial geologic unit and complementary cumulative frequency distributions of the LPI values were plotted. Based on the threshold value recommended by Toprak and Holzer (2003), the frequency at LPI≥5 was used to estimate the percent area underlain by the surficial geologic unit that would exhibit surface manifestations of liquefaction. Complementary cumulative frequency values for the M7.1 (PGA=0.4 g) scenario are shown in Fig. 4. The distributions shown in Fig. 4 are called complementary cumulative frequency distributions because the frequency starts at 100% and decreases to zero with increasing LPI. Complementary cumulative frequency also is known as the frequency of exceedance.

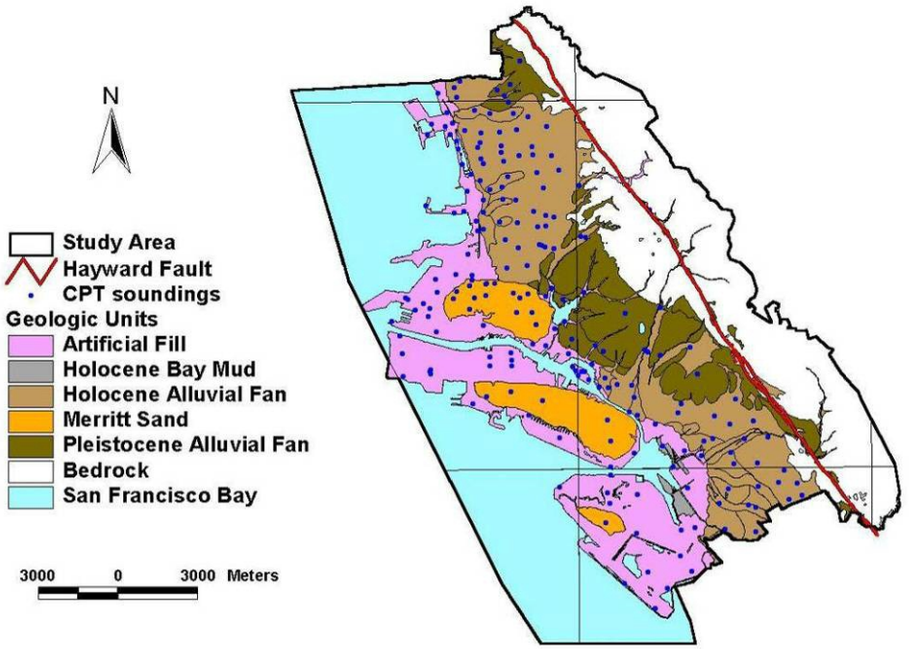


FIG. 3. Map of surficial geology of greater Oakland area, California, with CPT soundings. (Geology simplified from Helley and Graymer, 1997)

Although the complementary cumulative frequency at LPI≥5 was interpreted by Holzer (2002) to be the percent area with surface manifestations of liquefaction, it also can be interpreted as the conditional probability of liquefaction at a randomly selected location within the geologic unit given an earthquake magnitude and PGA (Holzer et al., 2006a). This assumes the unit is spatially homogeneous. The choice of interpretation of the complementary cumulative frequency is determined by the intended audience for the maps. For public officials and the general public, percent area generally may be more understandable. For engineering applications, conditional probability may be preferred.

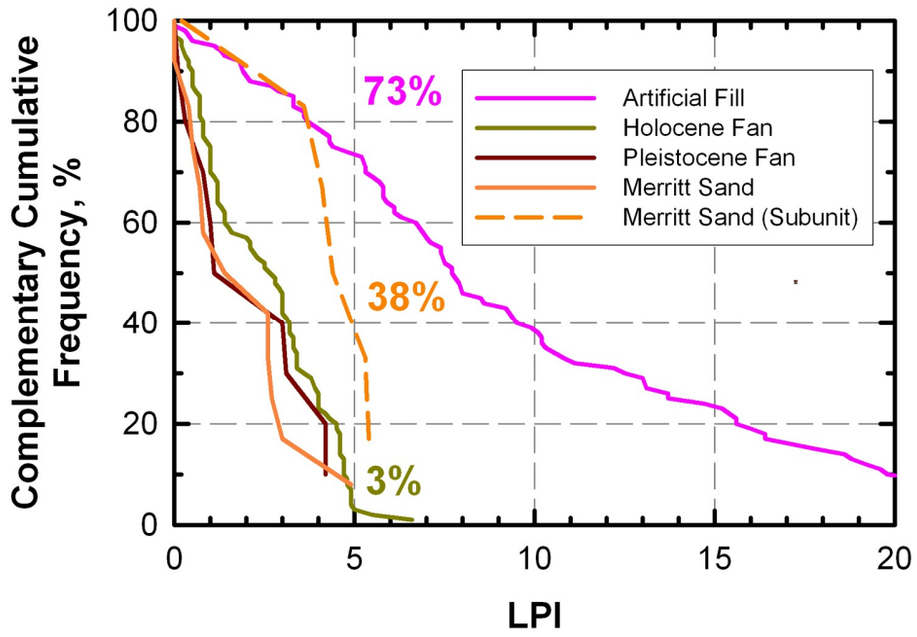


FIG. 4. Complementary cumulative frequency distributions of LPI for surficial geologic units in the greater Oakland area that were used to produce the map in Fig. 2. Earthquake scenario was a M7.1 earthquake with PGA=0.4 g. (Holzer et al., 2006a)

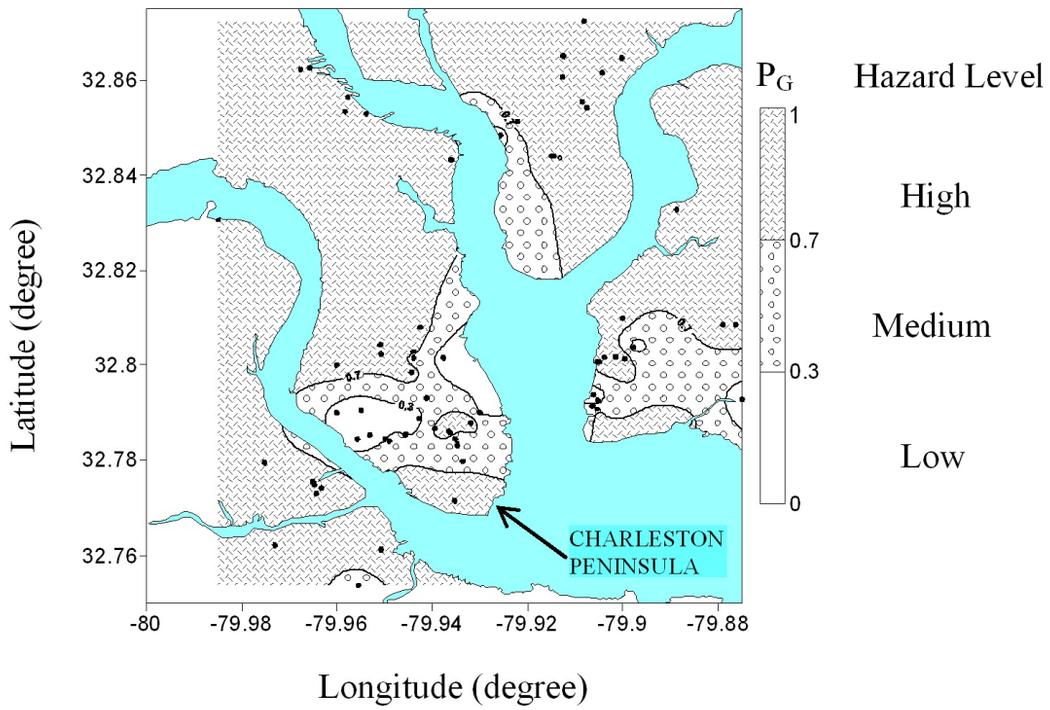


FIG. 5. Probability of liquefaction on the Charleston, South Carolina, peninsula (Juang and Li, 2007, Fig. 8)

In the approach by Juang and Li (2007), site specific LPI values are computed and used to estimate the probability of ground failure at the location of each sounding. Individual probability values are then contoured or grouped to identify areas of different liquefaction potential (Fig. 5). Surficial geologic units are only modestly considered in their approach. For their mapping of the Charleston, South Carolina, peninsula, only two geological aspects were considered. Oligocene sediment in the Cooper Group, popularly known as the Cooper marl in the Charleston area, was assumed to be nonliquefiable. If a CPT sounding was less than 20 m deep but penetrated marl, they assumed that severity term, *F*, equaled zero within the marl. They also used surficial geology as a basis for estimating site amplification factors for PGA.

Effect of Spatially Variable Ground Motion

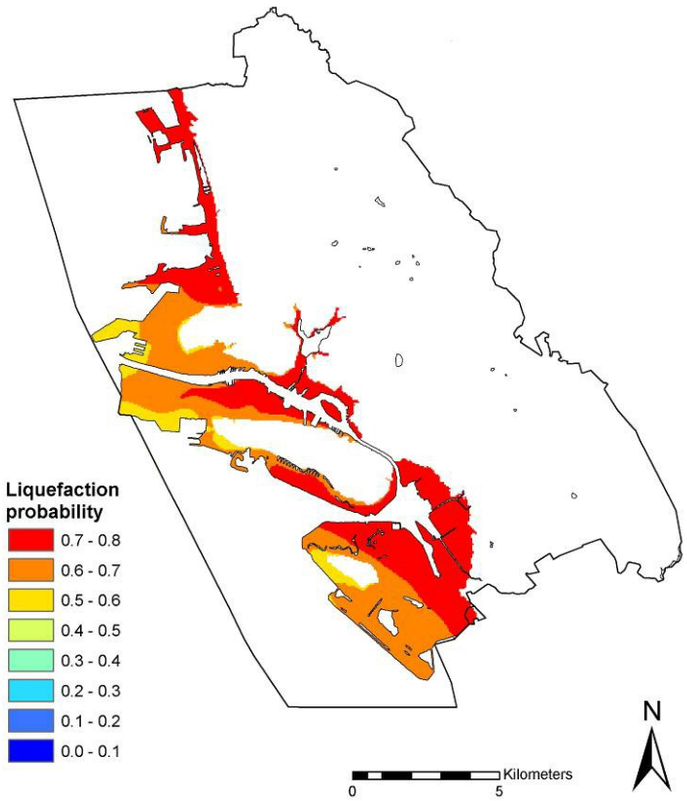


FIG. 6. Liquefaction probabilities of sandy artificial fills in the greater Oakland area based on spatially variable ground motion for M6.9 Hayward Fault earthquake. Same study area as Fig. 2. (Holzer et al., 2006b, Fig. 4)

Most of the earthquake scenarios that were used to create the maps compiled in Table 1 assume a constant PGA. This assumption can significantly oversimplify

ground shaking in areas that are prone to liquefaction. Liquefiable sediments generally occur in settings such as valleys, basins, and as fills along shorelines where thickness of underlying sediment changes laterally. These settings can cause local variations of shaking, i.e., nonuniform site response. The impact of locally variable site response on liquefaction probability is illustrated for the sandy artificial fill in the Oakland area by comparing Figs. 2 and 6. The map in Fig. 2 was based on a spatially constant PGA=0.4 g. The map in Fig. 6 is based on estimates of PGA that considered both the local 30-m, time-averaged velocity (Holzer et al., 2005b) and distance from the fault. Although the probability of liquefaction is high in both scenarios, consideration of site response introduces significant spatial variability into the liquefaction probability.

Table 2. Probabilities of surface manifestations of liquefaction for different seismic loadings of sandy artificial fills along the eastern shore of San Francisco Bay near Oakland, California (Holzer et al., 2006b).

PGA, g	*M8*	*M7.5*	*M7*	*M6.5*	*M6*	*M5.5*	*M5*
0	0	0	0	0	0	0	0
0.10	0	0	0	0	0	0	0
0.15	0.18	0.08	0.03	0	0	0	0
0.20	0.42	0.26	0.17	0.04	0	0	0
0.25	0.57	0.47	0.30	0.18	0.05	0	0
0.30	0.67	0.58	0.48	0.28	0.17	0.04	0
0.40	0.76	0.69	0.64	0.53	0.38	0.20	0.05
0.50	0.78	0.76	0.72	0.66	0.54	0.40	0.18
0.60	0.79	0.78	0.77	0.71	0.65	0.54	0.30

Predicting the probability of surface manifestations of liquefaction with spatially variable ground motions can be computationally simplified by curve fitting the relation between probability and PGA. Fig. 7b shows the relation for the Oakland artificial fills for a M6.9 earthquake, where the probability was inferred from the complementary cumulative frequency distributions of LPI (Fig. 7a). Holzer et al. (2006c) fit these data with a 3-parameter logistic equation (Fig. 7b). Rix and Romero-Hudock (2007) generalized the relation to other earthquake magnitudes by scaling the seismic demand (PGA) by the magnitude scaling factor (MSF) from the simplified procedure (Fig. 7c). For the simplified procedure as described in Youd et al. (2001), $MSF = 10^{2.24}/M^{2.56}$, where M is moment magnitude. Data points in Fig. 7c are based on the LPI≥5 threshold from complementary cumulative frequency distributions for the combinations of earthquake magnitudes and PGA compiled in Table 2. Herein for a specific surficial geologic unit, the relation between probability of surface manifestations of liquefaction and PGA scaled for magnitude will be referred to as the "liquefaction probability curve."

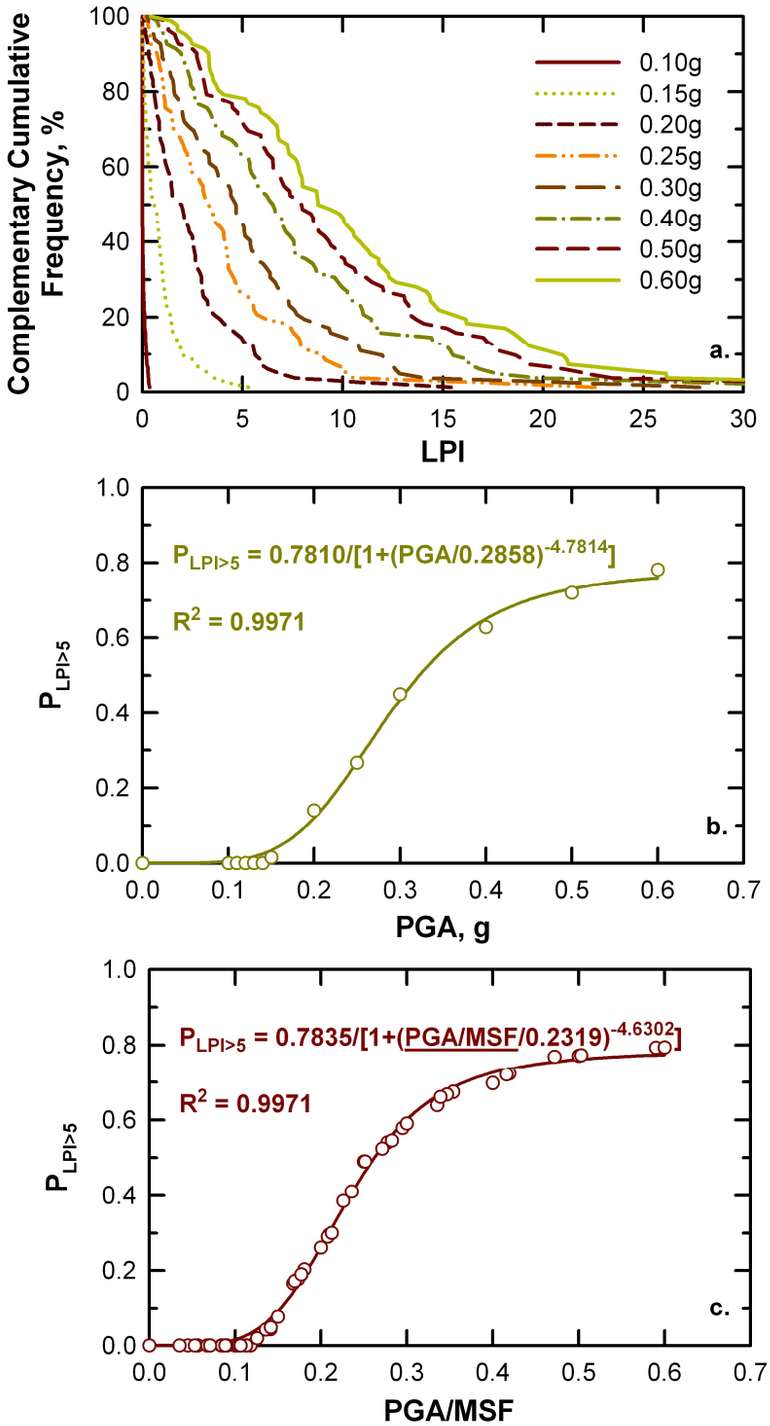


FIG. 7. Statistical properties of sandy artificial fills along shoreline of San Francisco Bay in the greater Oakland area, California. a. Complementary cumulative frequency distributions of LPI for different PGAs and M6.9 earthquake. b. Liquefaction probabilities for M6.9 earthquake. c. Liquefaction probability curve for a magnitude-scaled PGA.

Effect of Depth to Water Table

Depth to the ground water table is an important consideration for hazard mapping. It can significantly affect LPI values. Depth to the water table for the hazard maps of greater Oakland was incorporated directly into the complementary cumulative frequency distributions of LPI. Ground water in the Oakland area is not developed and the water table is stable except for a seasonal fluctuation. LPI values for each sounding were computed with the water-table depth at the location of the sounding. These values were then used to compute the complementary cumulative frequency distributions. In general, this approach requires that the water-table surface be carefully mapped. During the CPT field exploration, depth to the water table was measured if possible at each sounding after the cone was withdrawn. These measurements were then combined with water tables measured in commercial borings to generate a map with hydrologically reasonable gradients.

Where water tables undergo large secular or seasonal fluctuations, selection of the water table for a scenario requires careful consideration. Options for scenario hazard maps include using the extreme (maximum and minimum) depths, historical shallowest depth, and mean depth to water table. The historical shallowest water table may be appropriate for basins where water levels have been lowered by pumping, but may return to natural levels. Figs. 8 and 9 illustrate the impact of water-table depth on LPI and liquefaction hazard. Fig. 8 shows the variation of LPI with depth for different types of surficial geology. Fig. 9 compares the resulting hazard for two water-table scenarios for the northern Santa Clara Valley, California.

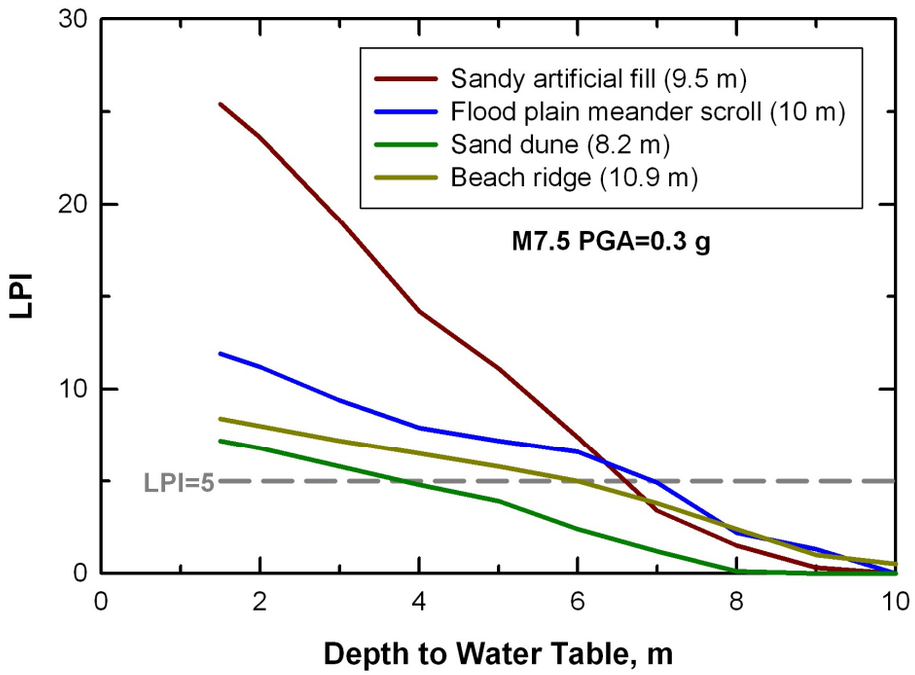


FIG. 8. LPI as a function of depth to water table for four CPT soundings completed in different Holocene geologic units. Values are based on a M7.5 earthquake and PGA=0.3 g. Unit thickness is shown in parentheses in legend.

Fig. 8 illustrates the effect on LPI of depth to the water table for individual CPT soundings completed in four different surficial geologic units: sandy artificial fill, flood plain meander scroll deposit, sand dune, and beach ridge. The unit penetrated by each sounding was approximately 10 m thick, mostly susceptible to liquefaction, and Holocene in age. Values were computed for each sounding for a M7.5 earthquake with PGA=0.3 g. LPI decreases with increasing depth to the water table for all four units, decreasing to less than five at depths ranging from 4 m for the sand dune deposit to 7 m for the meander scroll deposit. In a deposit with approximately constant *FS*, the slope of the curve of LPI versus water table is a function of *FS*, being higher for units with lower *FS*. The thickness of liquefiable sediment only affects the absolute value of LPI.

Fig. 9 illustrates the accommodation of a temporally variable water table into liquefaction hazard mapping of the northern Santa Clara Valley, California for a M7.8 earthquake on the nearby San Andreas Fault. The fault extends far outside of the study area. Two alternative water-table scenarios were considered. Ground-water levels, particularly in the confined aquifer beneath the valley, are subject to large fluctuations because ground water is managed and heavily pumped. The water table in the shallow unconfined aquifer also undergoes water-level fluctuations because of the Mediterranean climate and anthropogenic modifications of the hydrogeologic regime. Two different water-table depth scenarios–1.5 m and 5 m–were assumed in order to capture the approximate temporal extremes of the hazard in the central part of the valley where the hazard is greatest. The 1.5-m depth corresponds approximately to the historical high water level reported in the central part of the study area. These levels still recur during years of high rainfall. The 5-m depth corresponds approximately to the seasonal low in the central part of the area. Probabilities were estimated for both water-table depths. Hazard in the area with the 1.5-m-deep water table (see Fig. 9a) significantly decreases if the water table is at 5 m (see Fig. 9b).

Spatial Homogeneity of Surficial Geologic Units

Groupings of soundings to compute complementary cumulative frequency distributions are an important consideration in the approach by Holzer et al. (2002; 2006a). Grouping by surficial geologic unit assumes that each unit is approximately spatially homogeneous from a liquefaction hazard perspective. Common practice when mapping surficial geologic units is to use criteria based on geomorphologic expression and agricultural soil type, and not based on geotechnical properties. Groupings can be evaluated by comparing liquefaction probability curves for different surficial geologic units (Fig. 10). Comparison of the data in Fig. 10 for Holocene alluvial fan deposits in the northern Santa Clara Valley (Fig. 11) indicates that Qhly (young Holocene levee deposits) has a significantly higher hazard than do the other units, Qhf/Qhfy, Qhff, and Qhl. In fact, the other fan deposits are indistinguishable from a liquefaction hazard perspective and can be fit adequately with a single curve. The comparison suggests that all of the facies in the Holocene

alluvial fan deposits except for Qhly can be treated as a single unit from a liquefaction hazard perspective.

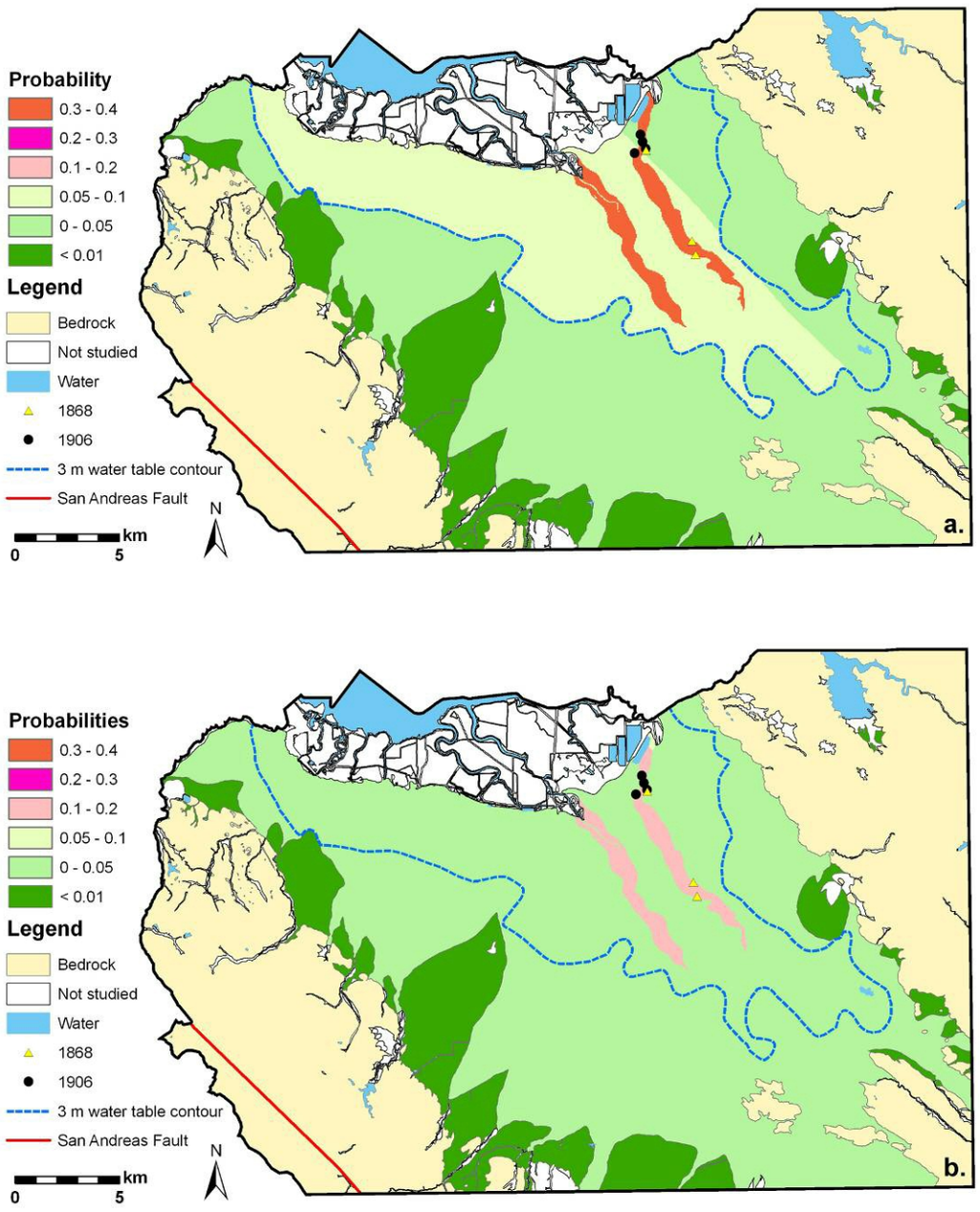


FIG. 9. Probability of liquefaction in the northern Santa Clara Valley, California, for a M7.8 earthquake on the San Andreas Fault. The area is at the south end of San Francisco Bay. a. Assumed water-table depth is 1.5 m in the central part of the valley (outlined in blue). Water-table depth is 5 m elsewhere. b. Assumed water-table depth is 5 m.

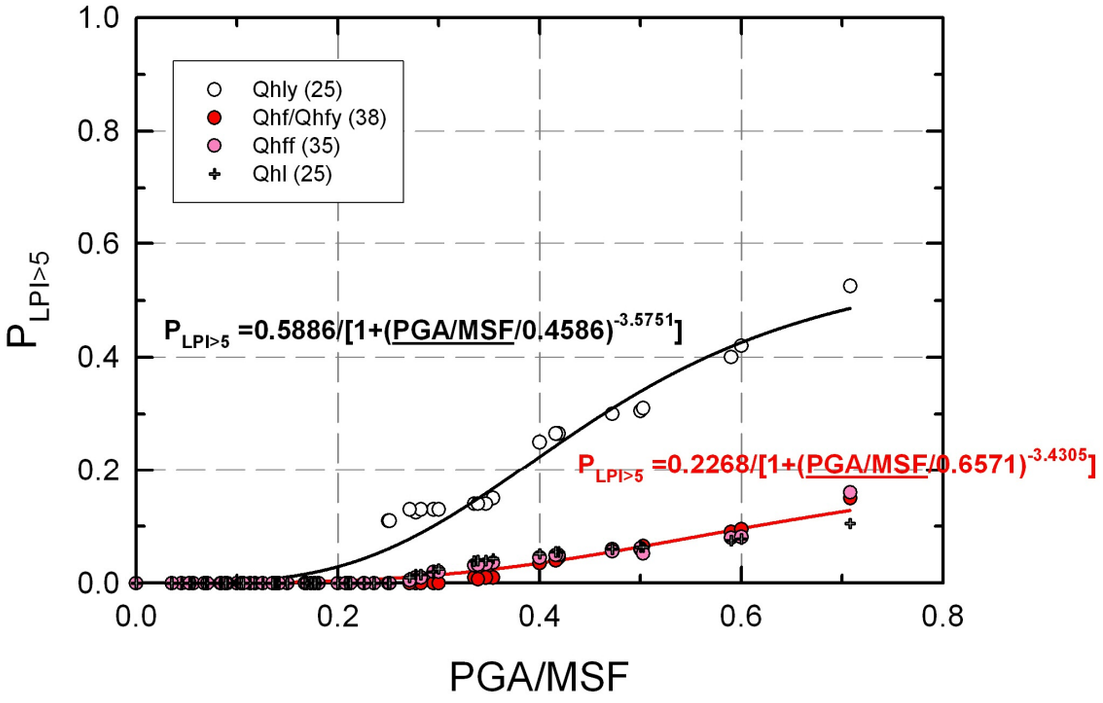


FIG. 10 Liquefaction probability curves for Holocene alluvial fan deposits in the northern Santa Clara Valley, California. Number of soundings in each deposit is shown in parentheses. Water table depth is 5 m.

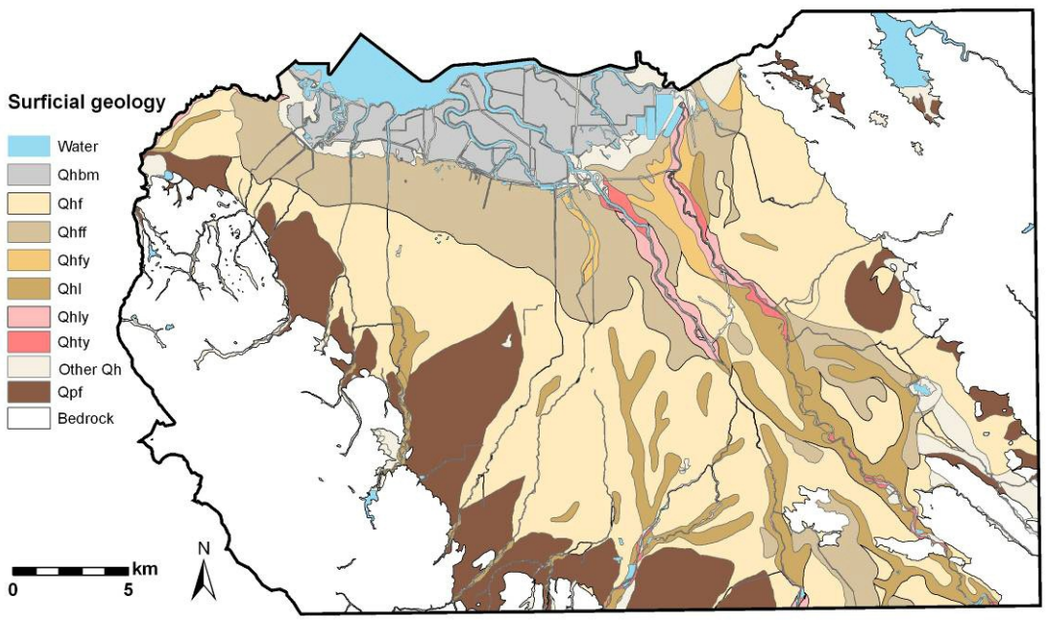


FIG. 11. Map of surficial geology of northern Santa Clara Valley, California (Simplified from Witter et al., 2006). Qh and Qp, respectively, are Holocene and Pleistocene units.

Geologic considerations also may provide useful insight for groupings. In the greater Oakland area, mapped Holocene alluvial fan facies could not be distinguished at depth with CPT soundings, which is consistent with the depositional framework of the alluvial-fan environment. The Holocene alluvial fan was an active depositional surface until urbanization and channelization of streams began late in the 19th century. Such fans aggrade as streams migrate laterally across the surface of the fan. Thus, the modern patterns of sedimentary deposition, which are what is being geologically mapped, should not be expected to extend to depth, particularly along the transverse axes of the fans. Because Holocene fan facies could not be distinguished from a geotechnical perspective, they were grouped together to produce a single complementary cumulative frequency distribution of LPI.

Conversely, a mapped surficial unit may be spatially inhomogeneous from a geotechnical perspective despite being mapped as a single surficial unit by geologists. For example, subsurface exploration by CPT of the Merritt Sand revealed that the formation had significantly higher liquefaction potential in the western part of its outcrop area in Oakland than elsewhere. Holzer et al. (2006a) inferred that that the western part had a different geologic stratigraphy and history and they recognized it as a separate geotechnical unit based on its liquefaction potential.

Finally, thickness of a mapped unit can be important when using surficial geologic maps to delineate liquefaction hazard. Where a unit (or part of it) is thin and above the water table, the liquefaction hazard derives from underlying units that are below the water table and not from the mapped surficial unit. With the Oakland map for example, the area where Holocene alluvial fan deposits were above the water table was delineated using the water-table map, and the liquefaction hazard determined for the underlying Pleistocene alluvial fan deposits was assigned to this area (Holzer et al., 2006a).

Mapping Severity of Liquefaction

Most LPI-based liquefaction hazard maps predict areas of potential liquefaction, not the severity of the ground deformation. Toprak and Holzer (2003) proposed that the intensity of ground deformation generally increases with LPI, and that a threshold LPI≥12 corresponds to the onset of lateral spreading. Fig. 12 is a map of the Santa Clara Valley that uses this threshold to estimate the probability of lateral spreading. The map was prepared with the same procedure as that used to produce the map in Fig. 9, but by using the higher LPI threshold, the probability applies to lateral spreading. The reliability of lateral spread hazard maps based solely on LPI remains to be demonstrated. Although some correlation between ground deformation and LPI is to be expected, lateral spreading also is influenced by factors not included in LPI, such as local static shear stress, continuity of liquefiable layers, and whether or not the soil is contractive.

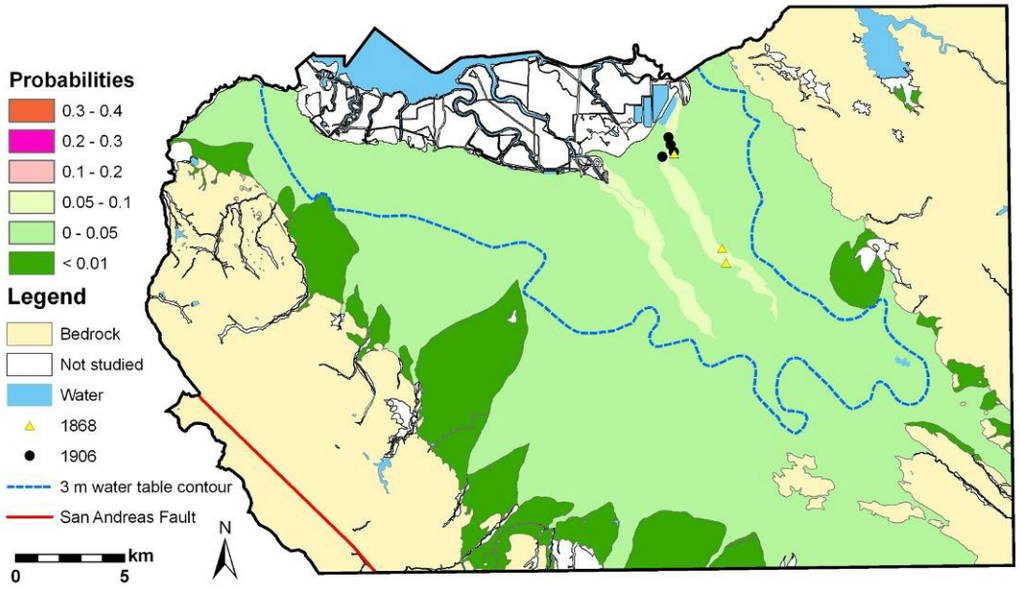


FIG. 12. Probability of liquefaction-induced lateral spreading in the northern Santa Clara Valley, California, for a M7.8 earthquake on the San Andreas Fault. Water table conditions are same as those used to produce liquefaction map in Fig. 8a.

Evaluations of Probabilistic Scenario Maps

The ultimate test of a mapping methodology is the accuracy of its predictions. At this early phase of the development of probabilistic liquefaction hazard maps, probabilistic scenario maps are particularly useful because predictions can be evaluated either with historical events or after future earthquakes that approximate the proposed scenario.

The percent area that is predicted to show evidence of liquefaction in the greater Oakland area is consistent with experience in recent earthquakes where similar geologic deposits have been subjected to near-field ground motion. For example, the ~73% of the area underlain by artificial fill that is predicted to liquefy is consistent with the extensive liquefaction of loose fills during the 1995 earthquake in Kobe, Japan (Hamada et al., 1995). Similarly, the ~3% of the area underlain by Holocene alluvial fan deposits that is predicted to liquefy is consistent with field observations following the 1994 Northridge, California, M6.7 earthquake, where a small area underlain by the alluvial fan deposits liquefied in the epicentral area in the San Fernando Valley (Holzer et al., 1999). One, albeit modest, test of the predictive capability of the methodology used for the Oakland map is the liquefaction performance of sandy artificial fill during the 1989 Loma Prieta (M6.9) earthquake. Based on maps of liquefaction caused by the earthquake (Tinsley et al., 1998), approximately 14% of the area underlain by artificial fill liquefied. Complementary cumulative frequency distributions of LPI for a Loma Prieta earthquake scenario predict that 13% of the fill should have liquefied (Holzer et al., 2006c). Fig. 13

compares locations of liquefaction caused by the 1989 Loma Prieta earthquake with predicted liquefaction probabilities. Liquefaction in general occurred in areas of higher probability (>0.1).

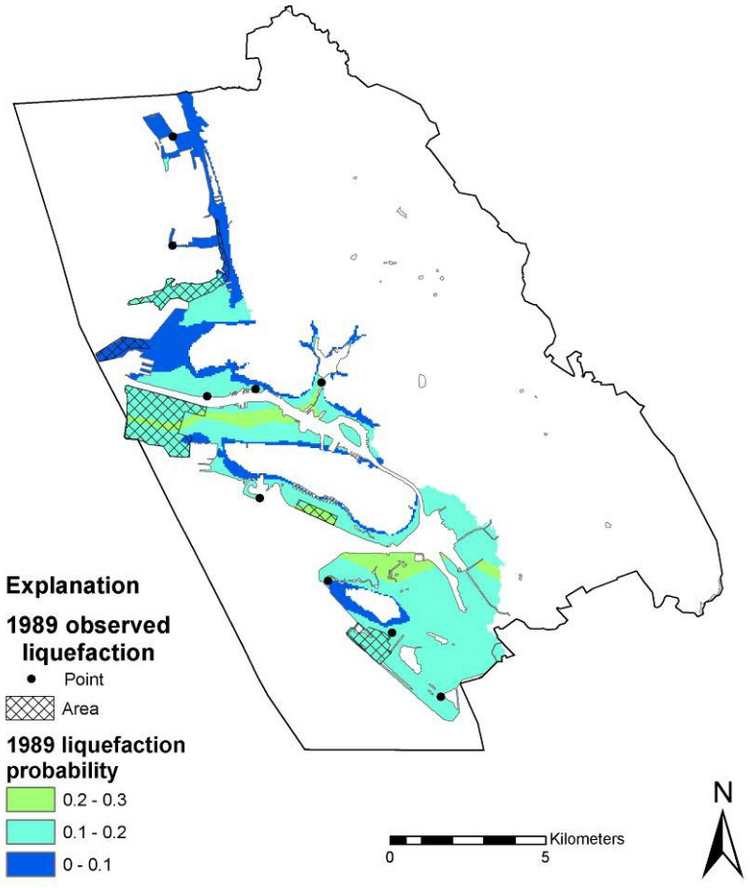


FIG. 13. Comparison of predicted liquefaction probabilities for the 1989 M6.9 Loma Prieta earthquake and locations of observed liquefaction in sandy artificial fills along eastern margin of San Francisco Bay, near Oakland, California. (Holzer et al., 2006c, Fig. 10).

Liquefaction predicted by the hazard map for northern Santa Clara Valley can be evaluated to a limited extent with observations from large historical earthquakes. The valley was strongly shaken by the 1868 M~6.7 Hayward Fault and 1906 M7.8 San Andreas Fault earthquakes. Lawson (1908) and Youd and Hoose (1978) described multiple occurrences of liquefaction during these earthquakes. Reports of liquefaction were limited to the flood plain of Coyote Creek, the easternmost of the two high (probability>0.3) hazard areas (Fig. 9a). Many of the descriptions suggested lateral spreading. However, a systematic exploration for these effects was not conducted following each earthquake.

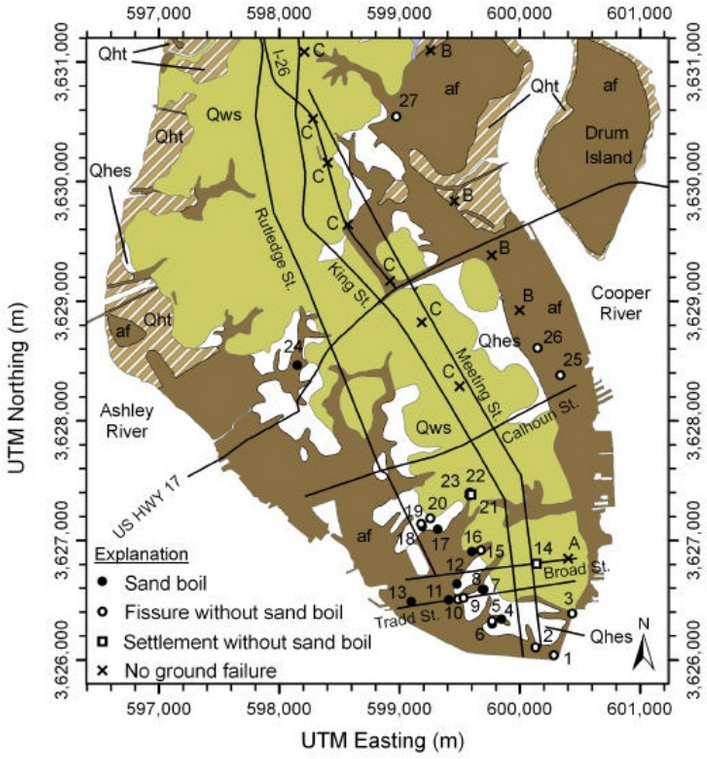


FIG. 14. Geologic map of Charleston peninsula, South Carolina, by Weems and Lemon, 1993), with locations of 1886 liquefaction and ground deformation (Hayati and Andrus, 2007, Fig. 2). [af is artificial fill; Qht are Holocene tidal marsh deposits; Qhes are Pleistocene barrier island deposits; and Qws are barrier sand facies of the Pleistocene Wando Formation.]

The liquefaction hazard map of the Charleston peninsula (Fig. 5) by Juang and Li (2007) can be evaluated with locations of liquefaction in 1886 (Fig. 14). Although liquefaction was extensive at the southern tip of the Charleston peninsula in their area of high hazard, it is not extensive in their high hazard area in the northern part of the peninsula. The high hazard zone at the tip of the peninsula is based on a single CPT sounding. Locations of historical liquefaction in Charleston appear to be better predicted by the hazard map prepared by Hayati and Andrus (2007) (Fig. 15). They computed median LPI values for surficial geologic units and applied the Iwasaki scale to classify hazard areas.

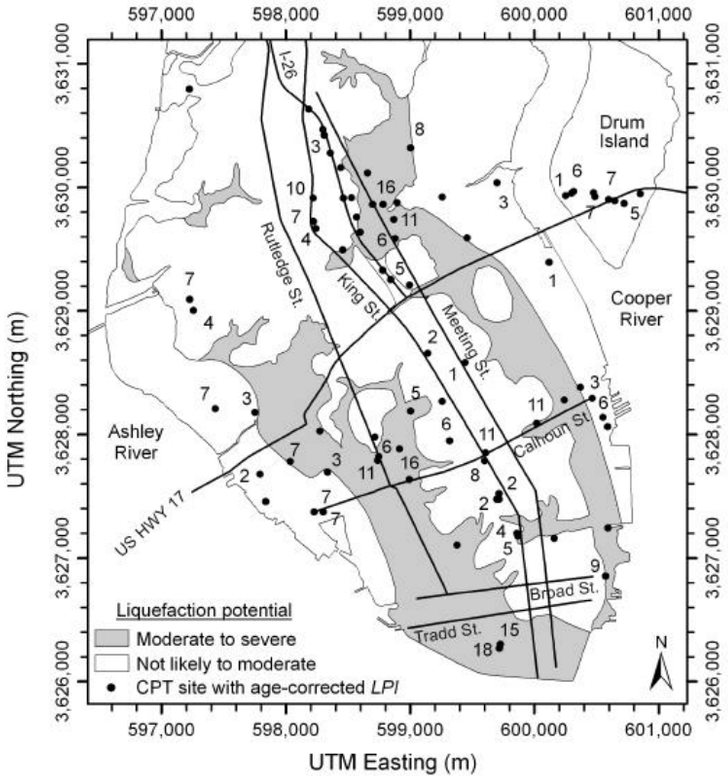


FIG. 15. Liquefaction hazard map of the Charleston peninsula, South Carolina, by Hayati and Andrus (2007, Fig. 7).

PROBABILISTIC LIQUEFACTION HAZARD EVALUATIONS AND MAPPING

Probabilistic liquefaction hazard analysis is just an extension of the PSHA methodology that was developed by Cornell (1968). In fact, to paraphrase McGuire (2004), a PLHA map should simply be viewed as a process by which probabilistic results are computed and documented. A reasonable goal of regional mapping of probabilistic liquefaction hazard is to predict the spatial distribution of the probability of liquefaction for a given return period.

In recent years the trend in engineering practice to apply probabilistic criteria to seismic design has prompted several efforts to characterize liquefaction hazard at specific sites in a probabilistic framework. Typically these efforts have predicted annual probabilities of liquefaction based on blow counts in critical susceptible layers. These efforts have sought neither to predict probabilities of the consequences of the liquefaction of a layer nor to map liquefaction hazard on a regional basis. Their focus has been on site specific investigations. These efforts might be more appropriately called probabilistic hazard liquefaction evaluations.

The first probabilistic hazard liquefaction evaluation of which the author is aware was by Yegian and Whitman (1978). They predicted the annual probability of liquefaction for a specific site condition based on a theoretical relation between

earthquake magnitude and maximum distance to liquefaction. Atkinson et al. (1984) combined a deterministic version of the Seed-Idriss simplified procedure (Seed and Idriss, 1982) and Cornell's (1968) PSHA to predict annual probability of liquefaction as a function of SPT blow count. Marrone et al. (2003) were the first to incorporate probabilistic versions of the simplified procedure into a PSHA-type liquefaction analysis. They estimated annual probabilities of liquefaction at specific sites of engineering interest. Kramer and Mayfield (2007) performed a similar analysis and applied the probabilistic update by Cetin et al. (2004) to the simplified procedure to predict the return period of liquefaction for generic site conditions.

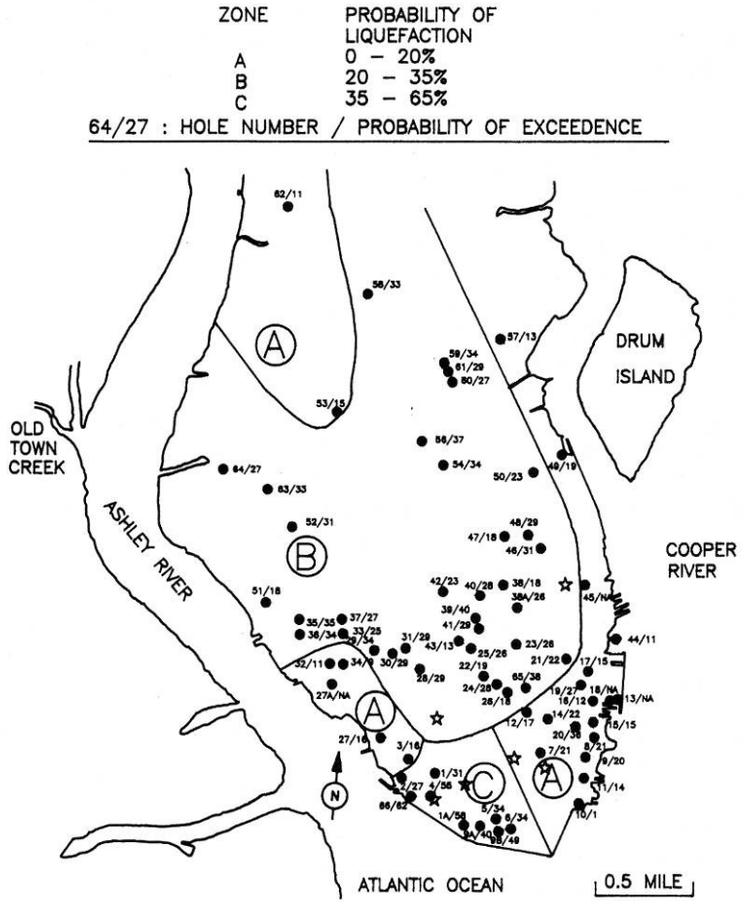


FIG. 16. Liquefaction probability of exceedance in 50 years for the Charleston peninsula, South Carolina. Stars show locations of liquefaction in 1886. (Elton and Hadj-Hamou (1990, Fig. 6).

Youd and Perkins (1978) were the first to apply PSHA concepts to regional mapping of liquefaction hazard. They outlined a procedure that combined a map of "ground failure susceptibility" of geologic units with a map of "ground failure opportunity" to produce a map of "ground failure potential." Ground failure opportunity was based on an empirical relation between earthquake magnitude and the maximum distance to liquefaction. Combining the magnitude-distance relation

with a Poisson earthquake source model, they circumscribed areas with different return periods within which local liquefaction could be expected. A formal procedure to combine the maps was stymied, however, by the absence of a quantitative characterization of liquefaction susceptibility. Thus, the map of "ground failure potential" consisted of two overlaid maps: (1) a ground failure susceptibility map that showed relative liquefaction susceptibility of deposits, and (2) a ground failure opportunity map that delineated areas of potential liquefaction with different return periods (Youd and Perkins, 1978, Fig. 7).

Elton and Hadj-Hamou (1990) used SPT penetration resistance to estimate ground failure potential on the Charleston peninsula, South Carolina. They identified and characterized the susceptibility of liquefiable layers with SPT blow counts in more than 200 soil borings. The layers were portrayed in 71 composite borings, and the variability of the blow counts was used to estimate the uncertainty of the liquefaction susceptibility of the layer. The liquefaction probability at each composite boring was determined by the layer with the highest probability. The liquefaction probability was defined as the probability of exceedance in 50 years of the critical PGA, which is the PGA required to cause $FS<1$ in the layer. They subdivided the peninsula into three zones on the basis of their range of probabilities (Fig. 16). Adequate surficial geologic maps were not available at the time of the mapping to help delineate the boundaries of the zones, but the zones loosely corresponded to the surficial geology as subsequently mapped by Weems and Lemon (1993) shown in Fig. 14. The map implies only the most susceptible layer liquefied. It does not predict the consequences of the liquefaction of the layer.

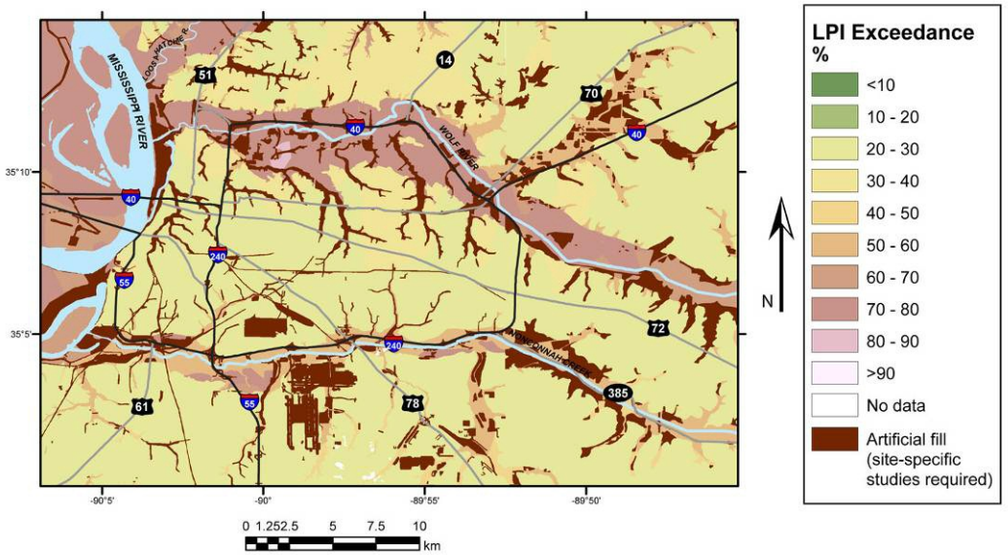


FIG. 17. Probabilistic liquefaction hazard map of Memphis, Tennessee showing 5% probability of exceedance in 50 years of LPI>5. (Cramer et al., 2008, Fig. 6b)

Cramer et al. (2008) were the first to use LPI in a formal PLHA to produce probabilistic liquefaction hazard maps. Their maps of Memphis, Tennessee, predicted probabilities of exceeding LPI values of 5 and 15. These are the thresholds, respectively at which severe liquefaction is unlikely and likely with the Iwasaki scale.

They produced maps for 10%, 5%, and 2% probabilities of exceedance in 50 years, i.e., return periods of 495, 975, 2475 years, respectively. The maps were developed from probabilistic ground motions and earthquake magnitudes from the USGS national seismic hazard model (Frankel et al., 2002). Liquefaction potential was estimated with liquefaction probability curves developed by Rix and Romero-Hudock (2007) for surficial geologic units in Memphis. Cramer et al. (2008) included the effect of site response on ground motion. Their liquefaction hazard map with a 5% probability of exceedance in 50 years of LPI>5 (Fig. 17) predicts a hazard that is comparable to the hazard in the probabilistic liquefaction scenario map by Rix and Romero-Hudock (2007) for a M7.7 earthquake in the southern New Madrid seismic zone. Ground motions for the M7.7 earthquake and the probabilistic PGA map with a 5% probability of exceedance in 50 years are similar.

DISCUSSION

LPI has become a popular parameter for regional mapping of both liquefaction potential and probability of liquefaction. Its advantage for mapping over the simplified procedure is that it predicts the liquefaction performance of the entire soil column, not just a soil element or layer. This is a significant advantage because, as a spatial parameter, LPI can be used to predict the spatial pattern of liquefaction, not just the liquefaction of layers. LPI also can enable usage of surficial geologic maps to expedite regional liquefaction hazard mapping.

Two approaches that rely on LPI have been developed for probabilistic mapping of liquefaction. The approach by Holzer et al. (2002; 2006a) uses complementary cumulative frequency distributions of LPI to estimate liquefaction probabilities of spatially homogeneous surficial geologic units. By applying threshold values at which either liquefaction or lateral spreading is expected, the conditional probability of liquefaction (or lateral spreading) given an earthquake magnitude and PGA can be estimated. Both probabilistic liquefaction scenario maps and PSHA-based liquefaction hazard maps have been produced with this approach. The approach by Juang and Li (2007) relies directly on the spatial pattern of LPI values to estimate liquefaction probabilities. Both approaches rely on versions of the Seed-Idriss simplified procedure to compute LPI.

The ultimate test of these approaches is how well maps based on them predict actual liquefaction performance. The predicted performance of deposits in the greater Oakland area and the northern Santa Clara Valley, California, are consistent with both their historical performance and the performance of similar geologic deposits in other earthquakes. The tests are modest, however. Comparison of predictions with observations from 1886 for the Charleston peninsula by Juang and Li (2007) is less clear, but predicted probabilities appear to be high.

The dependency of LPI on the simplified procedure raises several issues. On the one hand the dependency is an advantage in that LPI relies on a well established geotechnical methodology to analyze liquefaction potential. On the other hand it is a disadvantage in that the simplified procedure continues to evolve. Probabilistic versions of the simplified procedure introduce another complication. While these probabilistic versions reflect the growing demand in engineering design for probabilistic evaluations of risk, they require a modification of the original definition

of LPI, which is based on factor of safety. Lee et al. (2003) attempted such a redefinition of LPI, but found it produced an LPI scale that differed significantly than those by Iwasaki et al. (1982) and Toprak and Holzer (2003). As was discussed, this prompted them to rename their index parameter. Nevertheless, probabilistic versions of the simplified procedure have the advantage of reconciling fundamental differences in the statistical significance of factors of safety determined by CPT and SPT-based deterministic boundary curves. For example, Toprak et al. (1999) associated the SPT- and CPT-based deterministic boundary curves recommended by Youd et al. (2001) with probabilities of liquefaction triggering of 20% (for blow counts less than 10) and 50%, respectively.

There is a need for caution when different versions of the simplified procedure are used to calibrate LPI than are used to map with LPI. Although some investigators have been consistent in using the same version of the simplified procedure for both calibration and mapping, others have not. Maps that rely on the calibration by Iwasaki et al. (1982) but rely on another version for mapping are challenging to evaluate. As indicated by Fig. 1, the factor of safety computed by the "simple analysis" of Iwasaki et al. (1982) may differ substantially from that by the Seed-Idriss simplified procedure. Some investigators have addressed the impact of different versions of the Seed-Idriss simplified procedure by comparing predictions with different versions. Sensitivity tests by Kayabili and West (1994), Cresellani et al. (1999), and Lee et al. (2003) indicated the impact of different versions on mapping was minor.

The reliability of the simplified procedure for evaluation of the liquefaction potential of pre-Holocene geologic deposits is particularly important for liquefaction hazard mapping. Older Holocene and Pleistocene surficial geologic deposits typically must be evaluated in regional mapping efforts. The simplified procedure is based on case histories that include only Holocene deposits. It is not known how well the procedure evaluates the liquefaction potential of Pleistocene deposits, which typically have undergone more diagenesis and earthquake shaking than Holocene deposits. Some investigators (e.g., Leon et al., 2006) have proposed age corrections when applying the simplified procedure to these older deposits.

LPI also has some inherent shortcomings when it is applied to regional mapping. The reliance on complementary cumulative frequency distributions of LPI requires a large number of soundings or borings in geologic deposits with low liquefaction potential. For example, a deposit with a liquefaction probability of 10% can be characterized with a small number (<30) of borings or soundings. As the probability decreases, the number of exploratory soundings or borings required to document the liquefaction potential of the surficial unit increases. LPI is not an efficient tool for mapping in these types of deposits if the purpose is to distinguish differences between deposits with low liquefaction potential. LPI also is not a reliable predictor of the performance of soils in which the liquefaction hazard derives from thin but continuous liquefiable layers. Such soils will have low LPI, which suggest a low hazard, but the continuity of the layers may provide conditions conducive to lateral spreading. The Balboa Boulevard lateral spread, which failed during the 1994 Northridge, California, earthquake in a thin liquefied interval, is an example of this condition (Holzer et al., 1999).

Although probabilistic mapping of liquefaction hazard may meet the demand by engineers for performance-based design, it can obscure nonprobabilistic insights from surficial geologic mapping that can further resolve liquefaction hazard. For example, Holzer and Bennett (2007) documented how specific geologic conditions determined the boundaries of many lateral spreads. These boundaries are where ground strains are largest. Locations of lateral spreads and their boundaries may be more deterministic than a probabilistic map might imply.

ACKNOWLEDGMENTS

The author thanks Chris H. Cramer and T. Leslie Youd for constructive reviews of the manuscript. Thomas E. Noce drafted Figs. 9, 11, and 12. The author also thanks Ronald D. Andrus and John C. Tinsley, III, for comments on parts of the manuscript. The author is indebted to Michael J. Bennett, Thomas E. Noce, and Selcuk Toprak for their collaborative exploration of LPI. The PG&E-USGS CRADA and Nuclear Regulatory Commission supported parts of this research.

REFERENCES

Atkinson, G.M., Finn, W.D.L., and Charlwood, R.G. (1984). "Simple computation of liquefaction probability for seismic hazard applications." *Earthquake Spectra* 1(1): 107-123.

Baise, L.G., Higgins, R.B., and Brankman, C.M. (2006). "Liquefaction hazard mapping-Statistical and spatial characterization of susceptible units." *J. Geotechnical and Geoenvironmental Engrg.* 132(6): 705-715.

BSSC (2001). "2000 Edition NEHRP recommended provisions for seismic regulations for new buildings and other structures," FEMA 368, Part 1 (provisions), Federal Emergency Management Agency, Washington, D.C.

Cetin, K.O., Seed, R.B., Kiureghian, A.D., Tokimatsu, K., Harder, L.F., Kayen, R.E., and Moss, R.E.S. (2004). "Standard penetration test-based probabilistic and deterministic assessment of seismic soil liquefaction potential." *J. Geotechnical and Geoenvironmental Engrg.* 130(12): 1314-1340.

Cornell, C.A. (1968). "Engineering seismic risk analysis." *Seismological Society of America Bull.* 58(5): 1583-1606.

Cramer, C.H., Rix, G.J., and Tucker, K. (2008). "Probabilistic liquefaction hazard maps for Memphis, Tennessee." *Seismological Research Letters* 78 (in press).

Crespanelli, T., Madiai, C., and Vannucchi, G. (1999). "Zoning for liquefaction risk in an Italian coastal town using CPT." *Earthquake Geotech. Engrg.*, A.A. Balkema, Rotterdam: 561-566.

Divakarla, P.K., Hoyos, L.R., Jr., and Macari, E.J. (1998). "Assessment of liquefaction potential of western Puerto Rico." *Proc. 3rd Geotechnical Earthquake Engrg. and Soil Dynamics Conference*. ASCE/Reston: 530-541.

Elton, D.J., and Hadj-Hamou, T. (1990). "Liquefaction potential map for Charleston, South Carolina." *J. Geotechnical Engrg.* 116(2): 244-265.

Frankel, A., Petersen, M., Mueller, C., Haller, K., Wheeler, R., Leyendecker, E., Wesson, R., Harmsen, S., Cramer, C., Perkins, D., and Rukstales, K. (2002).

"Documentation for the 2002 update of the national seismic hazard maps." *Open-file Report 02-420*, U.S. Geological Survey, Denver, CO.

Frost, J.D., Carroll, D.P., and Rockaway, T.D. (1997). "Spatial liquefaction analysis." *Spatial Analysis in Soil Dynamics and Earthquake Engrg*., GSP No. 67, ASCE, New York/NY: 70-86.

Hamada, M., Isoyama, R., and Wakamatsu, K. (1995). "The 1995 Hyogoken-Nanbu (Kobe) earthquake-Liquefaction, ground displacement, and soil condition in the Hanshin area." The School of Science and Engrg., Waseda University, Tokyo: 194 p.

Hayati, H., and Andrus, R. (2007). "Liquefaction potential map of Charleston, South Carolina, based on the 1886 earthquake." Final report to the U.S. Geological Survey (06HQGR0058).

Helley, E.J., and Graymer, R.W. (1997). "Quaternary geology of Alameda County, and parts of Contra Costa, Santa Clara, San Mateo, San Francisco, Stanislaus, and San Joaquin Counties, California: A digital database." *Open-file Report 97-97*, U.S. Geological Survey, Menlo Park, CA.

Holzer, T.L., and Bennett, M.J. (2007). "Geologic and hydrogeologic controls of boundaries of lateral spreads: Lessons from USGS case histories." *First North American Landslide Conference*, SP No. 23, AEG: 502-522.

Holzer, T.L., Bennett, M.J., Noce, T.E., Padovani, A.C., and Tinsley, J.C., III (2002). "Liquefaction hazard and shaking amplification maps of Alameda, Berkeley, Emeryville, Oakland, and Piedmont: A digital database." *Open-file Report 02-296*, U.S. Geological Survey, Menlo Park, CA.

Holzer, T.L., Bennett, M.J., Noce, T.E., Padovani, A.C., and Tinsley, J.C., III (2006a). "Liquefaction hazard mapping with LPI in the greater Oakland, California, area." *Earthquake Spectra* 22(3): 693-708.

Holzer, T.L., Bennett, M.J., Ponti, D.J., and Tinsley, J.C., III (1999). "Liquefaction and soil failure during the 1994 Northridge earthquake." *J. Geotechnical and Geoenvironmental Engrg.* 125(6): 438-452.

Holzer, T.L., Blair, J.L., Noce, T.E., and Bennett, M.J. (2006b). "LiqueMap: A real-time post earthquake map of liquefaction probability." *Proc. 8th U.S. National Conference on Earthquake Engrg.* (CD-ROM), EERI, Oakland, CA.

Holzer, T.L., Blair, J.L., Noce, T.E., and Bennett, M.J. (2006c). "Predicted liquefaction of East Bay fills during a repeat of the 1906 San Francisco earthquake." *Earthquake Spectra* 22(S2): S261-S278.

Holzer, T.L., Noce, T.E., Bennett, M.J., Tinsley, J.C., III and Rosenberg., L.I. (2005a). "Liquefaction at Oceano, California, during the 2003 San Simeon earthquake." *Seismological Society of America Bull.* 95(6): 2396-2411.

Holzer, T.L., Padovani, A.C., Bennett, M.J., Noce, T.E., and Tinsley, J.C., III (2005b). "Mapping NEHRP V_{S30} site classes." *Earthquake Spectra* 21(2): 353-370.

Hosseini, S.M.M.M. (1998). "Microzonation for liquefaction in Busehr, Iran." *Proc. 11th European Conference on Earthquake Engrg.* (CD-ROM), A.A. Balkema, Rotterdam.

Idriss, I.M., and Boulanger, R.W. (2006). "Semi-empirical procedures for evaluating liquefaction potential during earthquakes." *Soil Dynamics and Earthquake Engrg.* 26(2-4): 115-130.

Iwasaki, T., Tatsuoka, F., Tokida, K.-i., and Yasuda, S. (1978). "A practical method for assessing soil liquefaction potential based on case studies at various sites in Japan." *Proc. 2nd International Conference on Microzonation*: 885-896.

Iwasaki, T., Tokida, K., Tatsuoka, F., Watanabe, S., Yasuda, S., and Sato, H. (1982). "Microzonation for soil liquefaction potential using simplified methods." *Proc. 3rd International Earthquake Microzonation Conference*: 1319-1330.

Juang, C.H., Jiang, T., and Andrus, R.D. (2002). "Assessing probability-based methods for liquefaction potential evaluation." *J. Geotechnical and Geoenvironmental Engrg.* 128(7): 580-589.

Juang, C.H., and Li, D.K. (2007). "Assessment of liquefaction hazards in Charleston quadrangle, South Carolina." *Engrg. Geology* 92(1-2): 59-72.

Juang, C.H., Yuan, H., Lee, D.-H., and Lin, P.-S. (2003). "Simplified cone penetration test-based method for evaluating liquefaction resistance of soils." *J. Geotechnical and Geoenvironmental Engrg.* 129(1): 66-80.

Juang, C.H., Yuan, H., Li, D.K., Yang, S.H., and Christopher, R.A. (2005). "Estimating severity of liquefaction-induced damage near foundation." *Soil Dynamics and Earthquake Engrg*. 25(5): 403-411.

Kayabali, K., and West, T.R. (1994). "Liquefaction susceptibility evaluation for the City of Evansville, Indiana." *Bull. Association Engrg. Geologists* 31(2): 231-253.

Kramer, S.L., and Mayfield, R.T. (2007). "Return period of soil liquefaction." *J. Geotechnical and Geoenvironmental Engrg.* 133(7): 802-813.

Lawson, A.C. (Editor) (1908). "The California Earthquake of April 18, 1906." *Report of the State Earthquake Investigation Commission*. Carnegie Institution of Washington Publication No. 87: 192 p.

Lee, D.-H., Ku, C.-S., and Yuan, H. (2003). "A study of the liquefaction risk potential at Yuanlin, Taiwan." *Engrg. Geology* 71(1-2): 97-117.

Lenz, J.A., and Baise, L.G. (2007). "Spatial variability of liquefaction potential in regional mapping using CPT and SPT data." *Soil Dynamics and Earthquake Engrg.* 27(7): 690-702.

Leon, E., Gassman, S.L., and Talwani, P. (2006). "Accounting for soil aging when assessing liquefaction potential." *J. Geotechnical and Geoenvironmental Engrg.* 132(3): 363-377.

Li, D.K., Juang, C.H., and Andrus, R.D. (2006a). "Estimation of liquefaction effect by means of liquefaction potential index." GSP No. 152. ASCE, Reston/VA: 359-364.

Li, D.K., Juang, C.H., and Andrus, R.D. (2006b). "Liquefaction potential index: a critical assessment using probability concept." *Taiwan Geotechnical Society J. GeoEngrg.* 1(1): 11-24.

Liao, S.S.C., Veneziano, D., and Whitman, R.V. (1988). "Regression models for evaluating liquefaction probability." *J. Geotechnical Engrg.* 114(4): 389-411.

Luna, R., and Frost, D.J. (1998). "Spatial liquefaction analysis system." *J. Computing in Civil Engrg.* 12(1): 48-56.

Mabey, M.A., Madin, I.P., Youd, T.L., and Jones, C.F. (1993). "Earthquake hazards of the Portland quadrangle, Multnomah and Washington Counties, Oregon, and Clark County, Washington." *Geological Map Series GMS-79*, Oregon Department of Geology and Mineral Industries, Portland, OR.

Marrone, J., Ostadan, F., Youngs, R., and Litehiser, J. (2003). "Probabilistic liquefaction hazard evaluation: Method and application." *Proc. 17th International Conference on Structural Mechanics in Reactor Technology* (CD-ROM).

McGuire, R.K. (2004). "Seismic hazard and risk analysis." *Monograph 10*, EERI, Oakland, CA: 221 p.

Moss, R.E.S., Seed, R.B., Kayen, R.E., Stewart, J.P., Kiureghian, A.D., and Cetin, K. (2006). "CPT-based probabilistic and deterministic assessment of in situ seismic soil liquefaction potential." *J. Geotechnical and Geoenvironmental Engrg.* 132(8): 1032-1051.

Olsen, M.J., Bartlett, S.F., and Solomon, B.J. (2007). "Lateral spread hazard mapping of the Northern Salt Lake Valley, Utah, for a M7.0 earthquake." *Earthquake Spectra* 23(1): 95-114.

Papathanassiou, G., Pavlides, S., and Ganas, A. (2005). "The 2003 Lefkada earthquake: Field observations and preliminary microzonation map based on liquefaction potential index for the town of Lefkada." *Engrg. Geology* 82(1): 12-31.

Porter, K., Kennedy, R., and Bachmann, R. (2007). "Creating fragility functions for performance-based earthquake engineering." *Earthquake Spectra* 23(2): 471-489.

Power, M.S., and Holzer, T.L. (1996). "Liquefaction maps." *TechBrief 1*, Applied Technology Council, Redwood City, CA: 12 p.

Rix, G.J., and Romero-Hudock, S. (2007). Liquefaction potential mapping in Memphis and Shelby County, Tennessee. Report to U.S. Geological Survey, http:/earthquake.usgs.gov/ regional/ceus/products/download/Memphis_LPI.pdf: 27 p.

Robertson, P.K., and Wride (Fear), C.E. (1998). "Evaluating cyclic liquefaction potential using the cone penetration test." *Canadian Geotech. J.* 35(3): 442-459.

Seed, H.B., and Idriss, I.M. (1971). "Simplified procedure for evaluating soil liquefaction potential." *J. Soil Mechanics and Foundation Engrg.* 97(9): 1249-1273.

Seed, H.B., and Idriss, I.M. (1982). "Ground motions and soil liquefaction during earthquakes." *Monograph 5*. EERI, Oakland, CA: 134 p.

Seed, H.B., Tokimatsu, K., Harder, L.F., and Chung, R.M. (1985). "Influence of SPT procedures in soil liquefaction resistance evaluations." *J. Geotechnical Engrg.* 111(12): 1425-1445.

Sonmez, H. (2003). "Modification of the liquefaction potential index and liquefaction susceptibility mapping for a liquefaction-prone area (Inegol, Turkey)." *Environmental Geology* 44(7): 862-871.

Sonmez, H., and Gokceoglu, C. (2005). "A liquefaction severity index suggested for engineering practice." *Environmental Geology* 48(1): 81-91.

Tinsley, J.C., III, Egan, J.A., Kayen, R.E., Bennett, M.J., Kropp, A., and Holzer, T.L. (1998). "Appendix: Maps and descriptions of liquefaction and associated effects." *The Loma Prieta, California, earthquake of October 17, 1989-Liquefaction.* Professional Paper 1551-B, U.S. Geological Survey, Menlo Park, CA: B287-B314.

Tinsley, J.C., Youd, T.L., Perkins, D.M., and Chen, A.T.F. (1985). "Evaluating liquefaction potential." *Evaluating earthquake hazards in the Los Angeles region-an earth science perspective*. Professional Paper 1360, U.S. Geological Survey, Menlo Park, CA: 263-315.

Toprak, S., and Holzer, T.L. (2003). "Liquefaction potential index: Field assessment." *J. Geotechnical and Geoenvironmental Engrg.* 129(4): 315-322.

Toprak, S., Holzer, T.L., Bennett, M.J., and Tinsley, J.C., III (1999). "CPT- and SPT-based probabilistic assessments of liquefaction potential." *Proc. 7th U.S.-Japan Workshop on Earthquake Resistant Design of Lifeline Facilities and Countermeasures Against Liquefaction*. Multidisciplinary Center for Earthquake Engrg. Technical Report MCEER-99-0019: 69-86.

Ulusay, R., and Kuru, T. (2004). "1998 Adana-Ceyhan (Turkey) earthquake and a preliminary microzonation based on liquefaction potential for Ceyhan Town." *Natural Hazards* 32(1): 59-88.

Weems, R.E., and Lemon, E.M., Jr. (1993). "Geology of the Cainhoy, Charleston, Fort Moultrie, and North Charleston Quadrangles, Charleston and Berkeley Counties, South Carolina." *Miscellaneous Investigation Series I-1935*, U.S. Geological Survey, Reston, VA.

Witter, R.C., Knudsen, K.L., Sowers, J.M., Wentworth, C.M., Koehler, R.D., and Randolph, C.E. (2006). "Maps of Quaternary deposits and liquefaction susceptibility in the central San Francisco Bay region, California." *Open-file Report 06-1037*, U.S. Geological Survey, Menlo Park, CA.

Yegian, M.K., and Whitman, R.V. (1978). "Risk analysis for ground failure by liquefaction." *J. Geotechnical Engrg.* 104(GT7): 921-938.

Youd, T.L., Hansen, C.M., and Bartlett, S.F. (2002). "Revised MLR equations for prediction of lateral spread displacement." *J. Geotechnical and Geoenvironmental Engrg.* 128(12): 1007-1017.

Youd, T.L., and Hoose, S.N. (1977). "Liquefaction susceptibility and geologic setting, World Conference on Earthquake Engineering." *Proc. 6th World Conference on Earthquake Engrg.*: 2189-2194.

Youd, T.L., and Hoose, S.N. (1978). "Historic ground failures in Northern California triggered by earthquakes." *Professional Paper 993*, U.S. Geological Survey, Menlo Park, CA, 177 p.

Youd, T.L. , Idriss, I.M., Andrus, R.D., Arango, I., Castro, G., Christian, J.T., Dobry, R., Finn, W.D.L., Harder, L.F., Jr., Hynes, M.E., Ishihara, K., Koester, J.P., Liao, S.S.C., Marcuson, W.F., III, Martin, G.R., Mitchell, J.K., Moriwaki, Y., Power, M.S., Robertson, P.K., Seed, R.B., and Stokoe, K.H., II (2001). "Liquefaction resistance of soils: Summary report from the 1996 NCEER and 1998 NCEER/NSF workshops on evaluation of liquefaction resistance of soils." *J. Geotechnical and Geoenvironmental Engrg*. 127(10): 817-833.

Youd, T.L., and Noble, S.K. (1997). "Liquefaction criteria based on statistical and probabilistic analyses." *Evaluation of liquefaction resistance of soils.* National Center for Earthquake Engrg. Research Technical Report NCEER-97-0022: 201-205.

Youd, T.L., and Perkins, D.M. (1978). "Mapping liquefaction-induced ground failure potential." *J. Geotechnical Engrg.* 104(4): 433-446.

Youd, T.L., and Perkins, D.M. (1987). "Mapping of liquefaction severity index." *J. Geotechnical Engrg.* 113(11): 1374-1392.

A Deformation-Based Approach for Mapping Earthquake-Induced Liquefaction Hazard

Charles R. Real[1], Keith L. Knudsen[2], and Marvin O. Woods[3]

1 Supervising Engineering Geologist, California Geological Survey, 801 K Street, Sacramento, CA, creal@conservation.ca.gov

2 Senior Engineering Geologist, California Geological Survey, 345 Middlefield Rd., Menlo Park, CA

kknudsen@conservation.ca.gov

3 Engineering Geologist, California Geological Survey, 801 K Street, Sacramento, CA

mowoods@conservation.ca.gov

ABSTRACT: A deformation-based approach for mapping earthquake-induced liquefaction hazard has been developed that utilizes recently generated predictive relationships for shear-strain potential. These new relationships are used to calculate "Displacement Potential Index" given induced cyclic stress ratio and normalized fines-corrected standard penetration resistance (Faris, 2004). Conventional liquefaction hazard mapping is based on qualitative assessments of surface deposits, their geomorphology, environment and recency of deposition, and past performance from post-earthquake investigations. This new method is a more quantitative, deformation-based approach that emphasizes the severity of ground failure rather than mere likelihood of liquefaction. These new methods are being investigated for use in improving delineation of California's regulatory liquefaction hazard zones.

Over 650 boring logs have been analyzed for 18 Quaternary geologic map units in a pilot study covering a portion of the southern San Francisco Bay Area in Santa Clara County. A sufficient number of boring logs were available for nine of the Quaternary units to permit reclassification into four liquefaction susceptibility units, for which parametric modeling was performed and ground deformation hazard mapped over the test area. Pilot study results show good agreement with historical occurrences of liquefaction.

INTRODUCTION

Early methods of mapping liquefaction hazard over large areas have mostly relied upon geological and geomorphological criteria that relate to the depositional

environment and age of deposits and field performance during past earthquakes (Youd and Perkins, 1978). Once the potential for liquefaction failure of geologically youthful deposits has been categorized, their mapped distributions are then used to extrapolate hazard potential over the area of interest. Recent efforts have improved that approach by facilitating the ranking of hazard potential by using more field measurements such as standard penetration and cone penetrometer tests and liquefaction potential index (Witter et al., 2006; Holzer et al., 2006). Such assessments primarily reflect the potential for onset of liquefaction, with little beyond an ordinal ranking for how severe the surface ground deformation and attendant damage potential might be.

Although these methods have formed the basis for delineating regulatory liquefaction hazard zones in California (Real, 2002), they are highly conservative and potential ground deformation may be a better indicator of potential damage. We first describe a deformation-based method of mapping liquefaction hazard potential that is applicable to areas where geotechnical borings are plentiful, followed by a brief overview of its application to a study area located in the southern San Francisco Bay area.

METHODOLOGY

Previous methods of estimating liquefaction deformation have followed three approaches: 1) empirically-derived relationships for predicting lateral spread displacement, 2) physics-based site-specific approaches using nonlinear, strain-history finite element and finite difference methods, and 3) hybrid methods. The first consists of analyzing a soil column by identifying which sediment layers in a borehole liquefy under a given seismic demand and estimating the amount of strain based on empirical relations derived from measurements in the field and laboratory. The updated simplified procedure for liquefaction potential (Cetin et al., 2004) is used to identify which layers liquefy, while the resulting fines-corrected penetration resistance ($N_{1,60,cs}$) and seismic demand are used to estimate the induced strain for each layer (Wu, 2002). The strain is then multiplied by the liquefied layer thickness and summed layer by layer to yield the amount of displacement expected at the site. Recent work has extended this approach to estimating displacement potential due to both volumetric and shear strain, and for large as well as small displacements (Faris, 2004; Seed et al., 2003; Wu , 2002). Unlike liquefaction potential index the displacement potential has provided a basis for mapping potential deformation in quantitative units that make physical sense (Knudsen et al., 2004a, 2004b; Rosinski et al., 2004). We further develop this approach to characterize and reclassify surface geology in terms of liquefaction response using the concepts of strain and displacement potential.

Like previous approaches, we use geologic maps to help extrapolate hazard throughout the geographic area, but calibrate it in a quantitative way that reflects the sediment body's capacity for permanent surface deformation as a function of thickness of liquefiable material (considering penetration resistance, fines content, soil type, etc.), depth to sediment saturation, and level of shaking. A key feature of

our approach is that by isolating these three independent variables and mapping them separately it allows more of the spatial variability of liquefaction to be accounted for. Areal grids of these three parameters are prepared and integrated to yield shear-strain and displacement grids for the mapping area. The method requires abundant geotechnical boring logs that are well distributed spatially and detailed Quaternary geologic maps that delineate sediments with respect to the age and environment of sediment deposition. Mapped Quaternary geology units are reclassified into susceptibility units based on their liquefaction response. Although primarily a 2-D approach, variability of surface unit response at depth is modeled parametrically, the results of which becomes a multi-dimensional lookup table to yield strain and displacement indices at a point on the ground surface.

The proposed liquefaction mapping method consists of five basic steps as illustrated in Figure 1: 1) Analysis of boring logs to yield depth of basement, depth to saturation, and required geotechnical parameters (soil indices, penetration resistance, unit weights, etc.), 2) Assessment of liquefaction opportunity (magnitude-weighted peak ground acceleration on alluvium), 3) Analysis of boring log sediment susceptibility to liquefaction and geologic unit reclassification, 4) Analysis of liquefaction potential to develop a hazard potential matrix, and 5) Calculation of shear-strain and displacement potential grids that represent hazard over the map area.

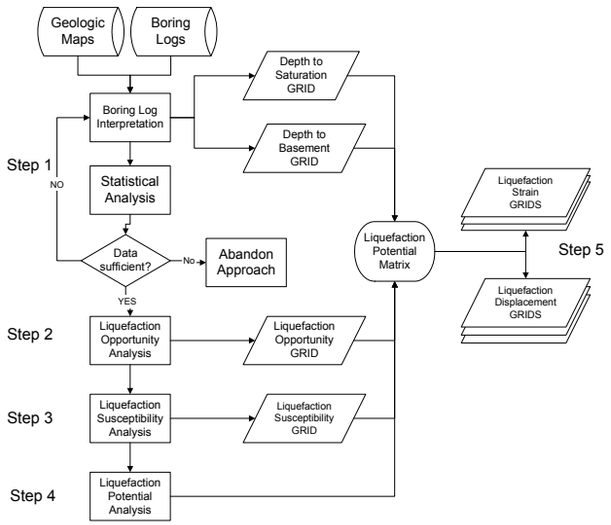


FIG. 1. Proposed liquefaction deformation mapping procedure.

Step 1

The first step is to collect and interpret boring logs to estimate depth to sediment saturation and depth to liquefaction basement. Basement is defined as bedrock or a prescribed depth beyond which liquefaction is not expected to occur. The results are used to prepare *depth-to-liquefaction basement* and *depth-to-saturation grids* over the region by interpolating a continuous surface between boreholes. Geostatistical analysis of borehole spatial distribution can be used to determine adequacy and

character of sampling so sufficient data and appropriate methods of interpolation can be identified. This type of analysis is common practice in the exploration of mineral and petroleum resources and for groundwater resource and environmental studies, and provides a mapping of subsurface parameters over a study area. The first step also includes statistical analysis of measured geotechnical parameters and their derivatives, such as $N_{1,60,cs}$ and response parameters such as strain potential index (SPI) and displacement potential index (DPI) (Faris, 2004; Seed et al., 2003; Wu, 2002), which are used to reclassify and calibrate liquefaction response of surficial geology units.

A principal component of the proposed mapping methodology involves parametric modeling of the liquefaction response of the soil column represented by each boring log in terms of SPI. SPI requires calculation of liquefaction potential according to the simplified method to yield induced cyclic stress ratio (CSR) and $N_{1,60,cs}$ for each liquefied layer identified in the boring log. These parameters are then used to estimate SPI from the limiting shear-strain potential curves shown in Figure 2 for each layer that liquefies.

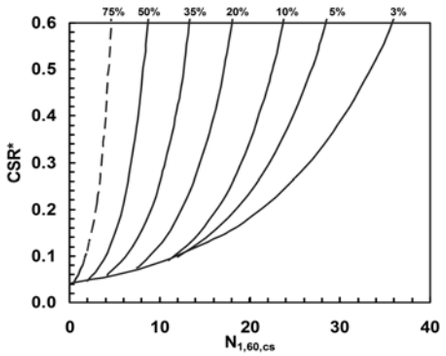


FIG. 2. Limiting shear-strain potential (SPI) curves (Faris, 2004; Wu, 2002).

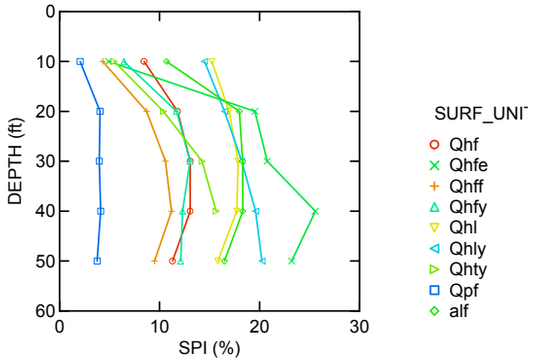


FIG. 3. Liquefaction response curves of susceptibility.

Multiplying SPI by the layer thickness yields displacement potential of each liquefied layer. Summing displacement of each liquefied layer from the ground surface to a prescribed depth and dividing by that depth yields shear-strain potential for that portion of the soil column according to the following equation:

$$\varepsilon(z) = 1/z \{\sum H_i * \text{SSTRAIN}(\text{CSR}, N_{1,60,cs})_i\} \quad \text{for } i = 1, \text{ to number of liquefied layers to depth } z \tag{1}$$

Where, H is thickness of liquefied layer, CSR is induced cyclic stress ratio, $N_{1,60,cs}$ is normalized fines-corrected blowcount, and SSTRAIN is a lookup-table function for shear-strain potential.

Modeling is accomplished by progressively incrementing the level of shaking and depth-to-saturation over a prescribed range in the calculation of liquefaction potential, and computing shear-strain potential repeatedly for prescribed depth ranges

and for all combinations of independent variable values using equation 1. For clarity, we note that the term "depth range" means depth measured from the ground surface to a prescribed point below the ground surface. This yields a 3-D liquefaction boring response matrix of shear-strain potential for prescribed intervals of ground shaking, depth-to-saturation, and thickness of soil column for each boring log. These data are key derivative parameters for estimating liquefaction hazard susceptibility and hazard potential. Step 1 is completed when a sufficient number of boring logs having the necessary geotechnical parameters and suitable spatial sampling are acquired that will allow statistically significant correlation with surficial geology units. Without a sufficient number of borings (>20 for each depth range of each geologic unit) the method may not reliable, and other approaches to mapping liquefaction hazard should be considered.

Step 2

Ground shaking over the study area is characterized in Step 2. Areal distribution of ground shaking is represented by a *liquefaction opportunity grid*, consisting of magnitude-weighted peak ground acceleration for alluvial site condition computed from a modified probabilistic seismic hazard analysis (PSHA). In the PSHA integration process, ground shaking hazard estimates are multiplied by the reciprocal of the duration weighting factor used in the updated simplified procedure for estimating liquefaction potential (Cetin et al., 2004). This approach probabilistically accounts for the effects of earthquake duration on liquefaction potential, and produces results that can be used directly in the simplified procedure for calculating liquefaction factor of safety without additional scaling (Real et al., 2000). The resulting parameter is a magnitude-weighted peak ground acceleration, which we define as liquefaction opportunity.

Step 3

Step three generates a *liquefaction susceptibility grid* by reclassifying the surficial geology units based on a statistical analysis of geotechnical parameters and the computed liquefaction response strain-potential matrix that results from the borehole log analysis of step 1. To rank a geologic unit's susceptibility to liquefaction, we determine how samples of its soil column would respond to strong shaking when fully saturated. Holding depth-to-saturation and level of ground shaking constant while computing liquefaction potential of each geologic unit allows comparisons to be made among soil column responses that reflect properties of the sediment only; that is, their propensity to liquefy. For comparison purposes we arbitrarily define liquefaction-deformation susceptibility to be the shear-strain potential for 100% saturation of the soil column subjected to a liquefaction opportunity of 0.4g. That condition represents but one set of parameter combinations produced by the modeling process of step 1. The complete set of modeled responses from a boring log collectively defines the liquefaction potential of the represented soil column.

The first step in reclassification is to generate a median response for each geologic map unit by grouping the borehole data by the units they penetrate at the surface, and calculating a median shear-strain potential for each map unit. The process is

optimized by calculating shear-strain potential as described in step 1, only calculating median depth-interval displacements using *all* borings that penetrate completely through a given depth interval. Here the term "depth interval" means that portion of the soil column between two prescribed depths in the soil column (we use 10 ft increments). The procedure first takes shear-strain potential from the boring response matrix, and multiplies it by its corresponding depth range to yield displacement potential for each depth range, and then systematically differences them to yield displacement potential for each depth interval for each boring in the group. The median displacement over each depth interval is then calculated, using all borings for a given group that penetrate completely through the prescribed interval. Summing each median depth-interval displacement from the ground surface to the prescribed depth range and dividing by that depth yields median shear-strain potential. This process is repeated for all prescribed depth ranges for each mapped alluvial unit.

Strain-depth curves (*liquefaction response curves*) of susceptibility shown in Figure 3 allow visual comparisons to be made among individual borehole logs and geologic map units that reflect only the sediment's capacity to liquefy and deform, independent of variations of depth to saturation or level of shaking. Geologic units are grouped (reclassified) into "susceptibility units" having similar propensity for deformation by comparing the liquefaction response curves and statistical distributions of soil properties. Classical statistical methods of multivariate analysis can be applied to grouped parameters assuming their distributions are normal. Most liquefaction-related parameter distributions show lognormal behavior that can be converted to normal by power-law transformation.

Step 3 is an interactive process that can result in splitting and lumping of surface geology map units based on similarity, supplemented by review of topography, air photos, and other remote sensing data commonly used for geologic mapping. The process constitutes a remapping of surface geology based on a sediment deposit's propensity to liquefy, and is most efficient when working with geologic maps that have already carefully differentiated Quaternary deposits based on their depositional environment and age. The result of step 3 is a fourth grid over the region of interest that we define as liquefaction susceptibility grid that, when combined with the liquefaction opportunity, depth-to-saturation, and depth-to-liquefaction basement grids, is used to map hazard.

Step 4

Step four creates a *hazard potential matrix* (HPM) that is used to integrate the above four spatial grids to produce derivative grids of spatially variable ground deformation potential and uncertainty (first and third quartiles). The HPM is made by repeating the process of step 3, only grouping by all borings falling within the newly-defined liquefaction susceptibility units. The result is a hazard potential matrix for each newly defined susceptibility unit in terms of median shear-strain potential and associated quartiles. The HPM is the key component of the proposed mapping process that allows the spatial variability of the independent variables to be accounted for and mapped independently using familiar surface and subsurface mapping methods. This is an improvement over approaches to liquefaction mapping

that rely only on ranking surface geology, and using contact boundaries to define areas of hazard.

Step 5

The final step in mapping liquefaction hazard is to combine the spatial grids using the hazard potential matrix to produce a grid of shear-strain potential over the area of interest. This can be accomplished on a raster GIS platform with grid analysis capability. Values in each cell of the four grids (liquefaction susceptibility, ground shaking, depth-to-liquefaction basement, depth-to-saturation) can be re-coded to indices that correspond to the parameter ranges used to model the HPM. They then become an index to the HPM array in a lookup-table sense. For a particular cell location, the indices for each parameter are read from the four grids and used to extract the value of shear-strain potential from the hazard potential matrix to produce the strain-potential grid. Additional grids can be produced in the same manner only extracting quartile values instead of the median to provide some uncertainty bounds on the mapping.

The final set of hazard grids is produced by a transformation from shear-strain potential to displacement potential and uncertainty. This is easily done by selecting the shear-strain potential grids and multiplying them by the depth-to-liquefaction basement grid to yield grids of DPI median displacement and quartiles.

SANTA CLARA VALLEY PILOT STUDY

We tested the proposed procedure in Santa Clara Valley, located at the southern end of the San Francisco Bay, California, where Quaternary deposits have been carefully subdivided and mapped at 1:24,000 scale and regulatory liquefaction zones have been delineated. That work made available digital maps of historical-high groundwater, ground shaking liquefaction opportunity, and numerous borehole logs. More than 650 geotechnical borings were interpreted and analyzed as described above, shear-strain potential calculated for each, and a depth-to-liquefaction basement map prepared. Borehole data collected were sufficient to reclassify only 9 of 18 mapped Quaternary units in the study area, as sampling was inadequate for the other 9 (Table 1). The preliminary result is a liquefaction potential map depicted in this paper by shaded areas that correspond to deformation potential (Figure 4). Gray scale ranges from dark to light, corresponding from low to high deformation potential respectively. The proposed method shows promise as indicated by the good correlation of bright, high-hazard areas with historical occurrences of liquefaction shown in Figure 4. The black crosses mark locations of observed surface effects over the entire map area from liquefaction during past earthquakes, and are generally located within or near areas of higher hazard. Note that Coyote Creek is the sinuous dark line crossing diagonally northwest to southeast, where extensive liquefaction occurred in 1906. The black straight line extending diagonally northeast from the map center is a pipeline right-of-way that was carefully examined but showed no signs of ground failure following the 1989 Loma Prieta earthquake.

Nearly 50 Quaternary geologic units have been mapped in the San Francisco Bay region (Witter et al., 2006). Of these, only 18 occurred in the pilot study area, and of these only the 9 units above had a sufficient number of geotechnical boring logs to be statistically meaningful in the reclassification process. The 9 geologic units were reclassified into 4 liquefaction susceptibility units based on each unit's liquefaction response curve (Figure 2). Of the remaining 9 units, 5 had no boring log samples and occurred in only a few places of limited areal extent, and the other 5 were sampled by only a few boring logs and were lumped together as a fifth unit of questionable reliability in the analysis. Those units with insufficient borehole data can be assigned to susceptibility units based on geologic/geomorphic understanding of their expected similarities with other geologic map units.

Table 1. Reclassified Quaternary geologic map units.

Quaternary Geologic Map Unit	Description	Liquefaction Susceptibility Unit
Qhl	Holocene alluvial fan levee deposits	Unit A
alf	Artificial fill – levee deposits	
Qhly	Latest Holocene alluvial fan-levee deposits	
Qhf	Holocene alluvial fan deposits	Unit B
Qhff	Holocene alluvial fan fine facies deposits	
Qhfy	Latest Holocene alluvial fan deposits	
Qhty	Latest Holocene stream terrace deposits	
Qpf	Latest Pleistocene alluvial fan deposits	Unit C
Qhfe	Holocene fine grained alluvial fan-esturine complex deposits	Unit D

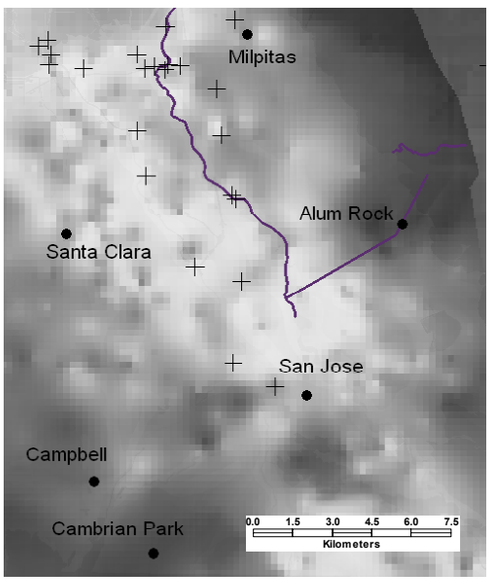


FIG. 4. Liquefaction potential map of the Santa Clara Valley region, South San Francisco Bay, California. Black crosses are locations of historical liquefaction.

DISCUSSION

SPI and DPI are indices only, and should not be taken as actual strain or displacement. The proposed method does not consider static driving stresses, proximity to free-faces or sloping ground; however, we are investigating use of the alpha parameter for sloping terrain (Faris, 2004). Consequently, we presently show mapping results in a qualitative manner in Figure 4. Nonetheless, the results demonstrate that using the concept of shear-strain potential in the proposed methodology allows a higher resolution in mapping relative liquefaction deformation hazard, which focuses attention on areas where the hazard is high and the associated damage potential is more likely to require mitigation.

CONCLUSIONS

A method of mapping liquefaction hazard based on ground deformation potential is proposed that utilizes the concepts of strain and displacement potentials. The method can be applied in areas where Quaternary deposits have been well differentiated based on age and depositional environment, and where abundant, spatially distributed geotechnical borings are available. Maps resulting from the proposed method indicate the potential for liquefaction-induced deformation, and include supplemental maps that provide some indication of uncertainty in the assessment. These maps can help to infer damage potential, and have great promise in forming a new, more effective basis for delineating regulatory hazard zones for construction by focusing attention where liquefaction deformation is most likely to occur.

ACKNOWLEDGMENTS

This study was supported in part by grant award SA-3266TB from the Pacific Earthquake Engineering Research Center, Richmond, California. The authors wish to thank Drs. Jiaer Wu and Allison Faris, and Professor Raymond Seed for valuable discussion regarding this work. We also wish to than Tianqinq Cao of the California Geological Survey for developing the probabilistic liquefaction opportunity grid used in the pilot study, and Anne Rosinski of the California Geological Survey, who performed much of the analysis of boring logs in the pilot study.

REFERENCES

Cetin, K.O., Seed, R.B., Der Kiureghian, A., Tokimatsu, K., Harder, L.F., Kayen, R.E., and Moss, R.E.S. (2004). “Standard Penetration Test-based probabilistic

and deterministic assessment of seismic soil liquefaction potential." *Journal of the Geotechnical and Geoenvironmental Engineering*, 130(12):1314–1340.

Faris, A. (2004). Probabilistic Models for Engineering Assessment of Liquefaction-Induced Lateral Spreading Displacements. *PhD. Thesis*, University of California, Berkeley, California,184 p.

Holzer, T.L., Bennett, M.J., Noce, T.E., Padovani, A.C., and Tinsley, J.C., III (2006). "Liquefaction hazard mapping with LPI in the greater Oakland, California, area." *Earthquake Spectra*, 22(3): 693-708.

Knudsen, K.L., Rosinski, A., and Seed, R.B. (2004a). "Production of Regional Liquefaction-Induced Deformation Maps." *Proceedings, 11th International Conference on Soil Dynamics and Earthquake Engineering and the 3rd International Conference on Earthquake Geotechnical Engineering* (a jointly convened conference pairing), University of California at Berkeley, January 2004.

Knudsen, K.L., Rosinski, A., Wiegers, M.O., Real, C.R., Wu, J., and Seed, R.B (2004b). "Investigation of Methods to Produce Regional Maps of Liquefaction-Induced Deformation." *Pacific Earthquake Engineering Research Center*, Final Report 3G01-FR[1]: 61 p.

Real, C.R. (2002). "California's Seismic Hazards Mapping Act: Geoscience and Public Policy." in, Bobrowsky, P.T., ed., *Geoenvironmental Mapping: Methods Theory and Practice*, A.A. Balkema, Exton, PA: 93-120.

Real, C.R., Petersen, M.D., McCrink, T.P. and Cramer, C.H. (2000). "Seismic Hazard Deaggregation in zoning earthquake-induced ground failures in southern California." *Proceedings of the Sixth International Conference on Seismic Zonation, November 12-15, Palm Springs, California*, (CD-ROM), EERI, Oakland, CA.

Rosinski, A., Knudsen, K.L., Wu, J., Seed, R.B., and Real, C.R. (2004). "Development of Regional Liquefaction-Induced Deformation Hazard Maps." in, Yegian, M.K. and Kavazanjian, E., eds., *Geotechnical Engineering for Transportation Projects*, ASCE Geotechnical Special Publication No. 126: 797-806.

Seed, R.B., Cetin, K.O, Moss, R.E.S., Kammerer, A.M., Wu, J., Pestana, J.M., Riemer, M.F., Sancio, R.B., Bray, J.D., Kayen, R.E., and Faris, A. (2003). "Recent Advances in Soil Liquefaction Engineering: A Unified and Consistent Framework." *26th annual ASCE Los Angeles Geotechnical Spring Seminar Keynote Presentation, H.M.S. Queen Mary, Long Beach California, April 30, 2003*, 71 p.

Witter, R.C., Knudsen, K.L, Sowers, J.M., Wentworth, C.M., Koehler, R.D., Randolph, C.E., Brooks, S.K., and Gans, K.D. (2006). "Maps of Quaternary deposits and liquefaction susceptibility in the central San Francisco Bay region, California." *U.S. Geological Survey Open-File Report 2006-1037.*

Wu, J. (2002). Liquefaction Triggering and Post Liquefaction Deformations of Monterey 0/30 Sand Under Uni-Directional Cyclic Simple Shear Loading. *PhD. Thesis*, University of California, Berkeley, CA.

Youd, T.L. and Perkins (1978). "Mapping of Liquefaction Induced Ground Failure Potential." *Journal of Geotechnical Engineering Division*, ASCE, 104(4): 433-446.

A New Site Classification System Based on Strong Motion Analysis in Iran

Ghayamghamian M.R[1], Nojavan A.R[2]

[1]Associate Professor, International Institute of Earthquake Engineering and Seismology (IIEES), P.O. Box 19395-3913, Tehran, Iran. Tel: +98 21 22831116-19, Fax: +98 21 22299479, e-mail: mrgh@iiees.ac.ir
[2]Master of Earthquake Engineering, International Institute of Earthquake Engineering and Seismology (IIEES), P.O. Box 19395-3913, Tehran, Iran. e-mail: alireza_eq@yahoo.com

ABSTRACT: The recent five earthquakes in Iran offered many good quality strong motion data at 242 Iranian free-field strong motion stations. These data provide a unique opportunity for site effect analysis and the study of a practical site classification system. The horizontal to vertical spectral ratio (HVSR) of S-wave was used to estimate the soil amplification characteristics at the sites. The strong motion station sites were classified using identified site dominant period and geological data according to Japanese code and 2003 IBC provision. Furthermore, the response spectral shape (RSS) method was also employed in site classification mostly for checking purpose. A choice of site class for each strong motion station was made by comparison among different classifications. The station sites were classified into I, II, III and IV categories (from hard to soft), which are comparable to B, C, D, and E in the 2003 IBC provision. A successful comparison between HVSR and RSS results gives a good support to the classification results. Furthermore, the mean of HVSR for all the records from the earthquakes were calculated according to the site classes, and compared with those of pervious studies in Taiwan and Japan. A good conformity among different outcomes used to validate the classification results. Finally, a new classification system for the site categorization in Iran is introduced, and compared with the one proposed in Iranian building code.

INTRODUCTION

Ground shaking characteristics can be strongly affected by the local site effects. It is well known that the distribution of damage during strong earthquakes is largely controlled by the site conditions. The seismic waves radiated from the source are modified by the physical properties of upper soil layers as they reach to the surface. Different site conditions can induce amplifications of different period ranges in the response spectra (Seed et al., 1976). A building may be more severely damaged if the natural periods of the structure happen to be close to the amplified periods of the ground (Lee et al., 2001). An earthquake response spectrum compatible with local site condition, anchoring to appropriate peak ground acceleration (PGA), is a common input for a seismic design of buildings and dynamic analysis of structures.

The effective earthquake protection requires the efficient construction codes and seismic design, which, in turn, are based on study of the regional strong motion data. Therefore, it is important to modify the site classification scheme in design codes based on recent high quality strong motion data.

Recently, the seismic network in Iran is well developed and recorded large numbers of waveforms. However, no geophysical or geotechnical information are available in most of the stations. Zare et al. (1999) made an attempt to evaluate site effects for some of Iranian strong motion stations using HVSR of strong ground motions. The majority of their data consists of accelerograms recorded by analog instruments. The analog records generally show low signal-to-noise ratio (SNR) and large base line drifts due to digitization problems. Even the accelerograms recorded by digital instruments in that time revealed very small SNR ratio in the frequency lower than 1.5 Hz. The application of the records with high SNR in narrow frequency band may place some limitations on the accuracy of site effect estimation. Recently, the ISMN stations are mostly equipped with digital instruments (SSA-2) and well maintenance by building and housing research center (BHRC), which is a responsible organization for ISMN. This improved a lot the quality of recorded accelerograms that result in large SNR over wide frequency range. Since then, many large earthquakes (M_w>6.0) occurred in Iran within 2002-2006. These data are invaluable for strong motion studies and site effect analyses, as well as for the study of a practical site classification system.

In this study, we analyzed 730 accelerogram recordings obtained at 242 stations of the Iranian strong motion network. These are mostly selected from the data of five recent earthquakes in Iran, which are Changureh-Avaj (2002), Bam (2003), Firozabad-Kojour (2004), Dahooye-Zarand (2005) and Qeshm (2005) earthquakes. The site response on earthquake ground motion is empirically evaluated using horizontal to vertical spectral ratio. Furthermore, the existing geological and geomorphologic data are analyzed. If available, geotechnical information and subsurface shear-wave velocity from geophysical investigations are also utilized (Komak Panah et al., 2002; Jafari et al., 2005; Kaviani and Ghayamghamian, 1999). Based on these information and the identified dominant period of the sites from HVSR, the station sites are classified into four categories, namely I (rock), II (hard soil), III (stiff soil), and IV (soft soil), comparable to B, C , D and E in the 2003 IBC provision, using Japanese code (1980) and IBC (2003) provision. Furthermore, to reduce the limitation on the accuracy of the results, the classification based on response spectral shape is also performed mostly for purpose of comparison and checking (Seed et al. 1976). The results are compared among different classifications, and then an evaluation of the site class is made for each strong motion station. The mean of HVSRs are also presented for the four site classes and compared with those of previous studies in Taiwan and Japan. Finally, a simple classification scheme for site categorization in Iran is presented.

GEOMORPHOLOGIC AND GEOLOGICAL DATA

Geological and geomorphologic maps together with available geotechnical and geophysical information are employed in this study. The small scale geological map

(1/50,000) for the stations in studied areas are seldom available. Thus, the 1/100,000 scale maps are used, when 1/50,000 maps are not available. Based on geological map and some field investigations, the studied areas mainly covered by sedimentary Tertiary rock (limestone, sand stone, shale and marl) with limited outcrops of the igneous and metamorphic rocks (Class B or Class C in IBC 2003). Late Quaternary deposits, such as sand, silt, clay and gravel deposits, are considered as engineering soils (class D or class E in IBC 2003). There was no hard rock (Class A in 2003 IBC) or very soft soil (Class F in 2003 IBC) in the sites under study. The vast fan deposits, sand dunes, and rugged mountains are the main morphological features in the areas. The thickness of deposits is different from a few meters in the slopes up to more than few hundred meters at the alluvial plains.

Geophysical and geotechnical borehole data are limited and mostly available in the urban areas and some highway projects. The BHRC also conducted a few seismic investigations for shear-wave velocity estimation in some ISMN station sites. Komak Panah et al. (2002) gathered the available shear-wave velocities and geotechnical information at the 50 station sites in east-central of Iran. They investigated on the relation between shear-wave velocities (V_s) and SPT-N values (N) for the upper-most 30 meters for fine (silt and clay) and course (sand and gravel) materials as $Vs= 106\ N^{0.41}$ and $Vs= 75\ N^{0.50}$, respectively. These relations are used to estimate the shear-wave velocity of the sites at which only geotechnical information are available. Due to scarce amount of geotechnical and geophysical data, the classification of free-field strong motion stations are mainly depend on the empirical analysis of the recorded strong ground motions at the sites that will be explained later on.

EARTHQUAKE DATA AND PROCESSING

Most procedures for estimation the site response from earthquake data are based on spectral ratio analysis in the frequency domain (i.e. non-parametric method). It is well-known that the site effect estimation using spectral ratio analysis is very sensitive to the amount of the noise and its frequency distribution in the records (Safak, 1991; Ghayamghamian, 2005). The application of the records with large level of the noise and/or narrow reliable frequency range may place some limitation on the accuracy of site effect estimation and may introduce some errors into the classification scheme. We carefully selected records from five large shallow earthquakes, which recently occurred in north north-west, south-east and south of Iran, triggering 242 ISMN stations during their occurrences (see Fig. 2 for the location of earthquake epicenters). To reduce the uncertainty, the records that could reveal significant source or basin effects, such as Bam station record in Bam earthquake, are not used in the analysis. Description of these earthquakes and number of stations triggered by each earthquake are listed in Table 1. It is interesting to note that all the earthquakes are in the same range of magnitude and depth.

A total of 730 strong motion records from 242 stations are used for the present study. The noise level is estimated by taking motions prior to the first arriving energy of the accelerogram (pre-event noise). SNR for different events were calculated by taking the root-mean-square (rms) of noise-to-signal Fourier spectral ratio. The spectral amplitudes, for which the SNR ratio exceeded 2, were further processed.

Table 1. Earthquake specifications and strong motion records used in this study

No.	Name	Date	Lat. (^{0} N)	Long. (^{0} E)	Depth (km)	Mag. (M_W)	Number of Stations
1	Changureh -Avaj	2002/06/22	35.67	48.93	10	6.5	63
2	Bam	2003/12/26	29.01	58.26	8	6.5	25
3	Firozabad-Kojour	2004/05/28	36.37	51.68	12-14	6.2	116
4	Dahoyee-Zarand	2005/02/22	30.76	56.74	12	6.4	27
5	Qeshm	2005/11/27	26.78	55.90	10-12	6.0	11

Variations of noise levels against frequency for the accelerograms were also studied. The results showed that the noise level is considerable mainly in the frequencies lower than 0.25 Hz. Considering the combined effect of noise and truncation (time windowing of the record), the lowest frequency in our study varied from 0.25 to 0.5 Hz. As a result, the number of analyzed spectral amplitudes in the low-frequency range was a bit smaller than that at the higher frequency. The data are corrected for the base line drift and filtered mostly from 0.25 to 20 Hz using Butterworth (FIR type) filter.

SITE EFFECT ANALYSIS

The HVSR, which originally proposed for microtremor measurements, extrapolated to the S-wave by Lermo and Chavez-Garcia in 1993. Their study revealed very good matching between earthquake motion-based HVSR estimates and those supplied by the reference site method. The comparison between HVSR for the shear-wave of earthquake motion and ideally uphole to downhole spectral ratio using downhole array data also verified a good correlation (Tsubio et al., 2001; Ghayamghamian, 2005). Furthermore, the HVSR is commonly more stable among different earthquakes because it is more independent of the earthquake source and wave propagation path (Aki, 1988; Atkinson 1993; Yamazaki & Ansary, 1997). Thus, although the physical concept of the HVSR for shear waves of earthquake motion is not yet clear, the HVSR seems to reasonably estimate the site dominant period and provide a powerful tool for site effect estimation and classification based on the surface accelerograms.

Komak Panah et al. (2002) performed theoretical 1D equivalent linear analysis using SHAKE91 program at 21 ISMN station sites in east of Iran, where they conducted the geophysical and geotechnical investigations at the sites. They found a good agreement between the identified site dominant period from HVSR and those of theoretical ones obtained by SHAKE91. These results provide more confirmation to the accuracy of the identified site dominant period from the HVSR and its

application in site effect estimation and classification of Iranian strong motion station sites.

The HVSR was applied to estimate soil amplification characteristics at all the strong motion station sites. To this end, the Fourier amplitude spectra for horizontal and vertical components were generally calculated for 10 s time window after S-wave arrival and were smoothed using a rectangular moving average window of bandwidth 0.4 Hz. Next, the HVSR was calculated as an average of N/V and E/V spectral ratios for two horizontal components at each station. Furthermore, different time window lengths and spectral methods (e.x. cross-spectrum) were analyzed in the calculation of spectral ratio to assure the accuracy and stability of the results. The calculated HVSR are averaged for different events at a station and determined as a representative of site amplification function for that station. Finally, the dominant period of identified site amplification functions was determined and utilized in site classification of the strong motion stations. In addition, the reference site method is also applied using the same procedure of spectral ratio analysis for the sites where the suitable reference site can be found (Ghayamghamian, 2004, Ghayamghamian and Rahimzadeh, 2005; Jafari et. al. 2006).

CLASSIFICATION METHODOLOGY

Extensive site effect studies have been undertaken over the past decades and many site classification schemes, such as Japanese code (1980), UBC (1997), NEHRP (1997), and IBC (2003) have been proposed. The site classification systems also include the dominant period of the site as a key parameter, which can be reliably estimated from empirical methods (Rodriguez-Marek et al., 2001; Lee et al., 2001; Japan Road Association, 1980).

In this study, we first classified the ISMN station using Japanese code (1980) based on identified dominant periods from HVSR. According to Japanese code, the dominant period (T_G) for rock and hard soil sites is less than 0.2 seconds (Type I), for hard soil T_G=0.2-0.4s (Type II), for medium soil T_G =0.4-0.6s (Type III), and for soft soil T_G>0.6s (Type IV). We determine the site classes according to identified dominant period, which fall within the above-mentioned period bands. In the second step, the sites are classified using IBC (2003) provision by employing geologic, geomorphologic, and if available geophysical and geotechnical information. When the detail geophysical or geotechnical information were not available at the sites, the type and thickness of soil deposits were evaluated from geologic and geomorphologic maps and/or by visual inspection of existing hand made boreholes in the area during field investigations. Figure 1 shows the HVSR results for all the records from the earthquakes, according to the site classes together with their mean and mean plus one standard deviation.

Earthquake response spectra alone are also useful for site classification, when geologic data are not sufficient. Seed et al. (1976) used the normalized shape characteristics of strong motion response spectra at a 5% damping ratio to explore site conditions. However, the strong motion from different sources and paths may also affect the spectral shapes and should be used carefully (Atkinson, 1993; Theodulidis et al. 1996). Then, in the third step, we also performed classifications by

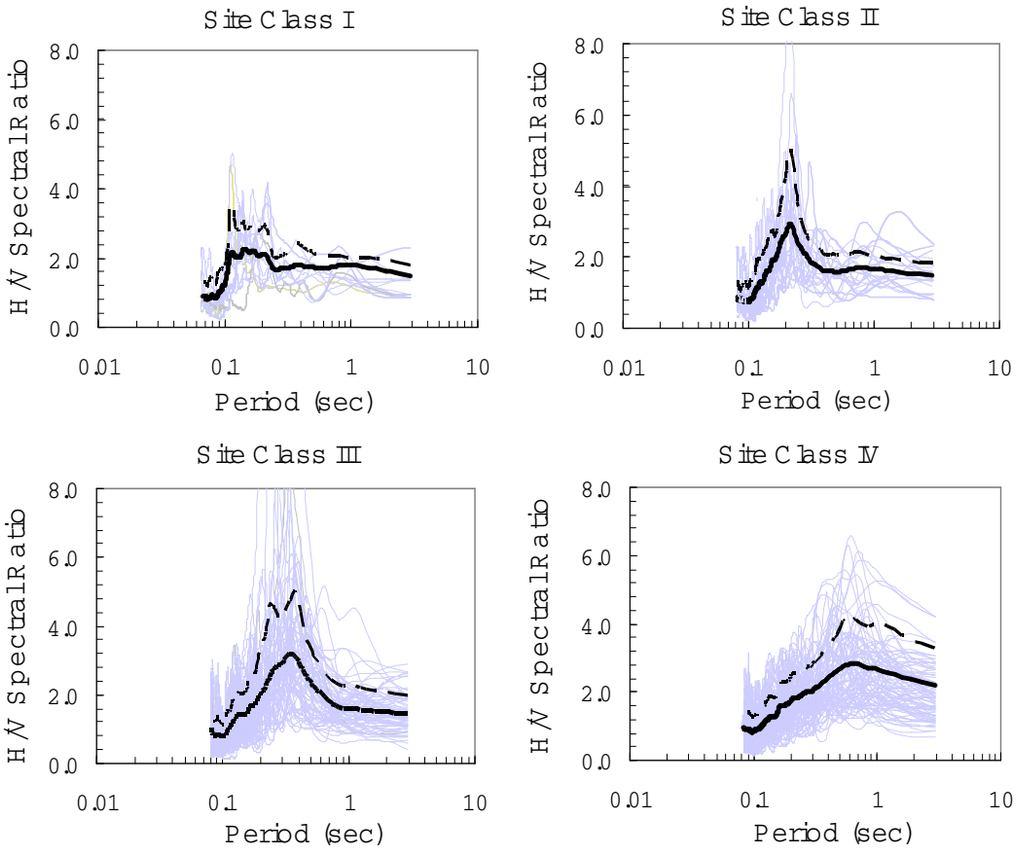


FIG.1. The HVSR of strong motion data together with the mean (bold continuous line) and 84 percentile (bold dashed line) of spectral ratios for different site classes of ISMN stations.

using the mean response spectral shape utilizing four site conditions (Type 1 through Type 4) proposed by Seed et al. (1976). A final evaluation of the site class is made by comparison among the results of different classifications. If there is no geological information can be found for classification by different methods, the site marked as questionable and omitted from the lists. Finally, 213 ISMN station sites are classified here. It should be mentioned that the problematic sites were screened out from the Figure 1. The distribution of the sites based on final site classification is shown in Figure 2.

COMPARISON OF SITE CLASSIFICATIONS AND DISCUSSION

Figure 3 summarizes the mean of HVSR and RSS curves for the four site classes. The ISMN strong motion stations were categorized into four classes, namely classes I, II, III, IV. From Figure 3, it is clear that site class I (class B) and site class IV (class E) have completely different spectral shapes and spectral ratios. However, site class II (class C) and class III (class D) are not so different. The site classes in

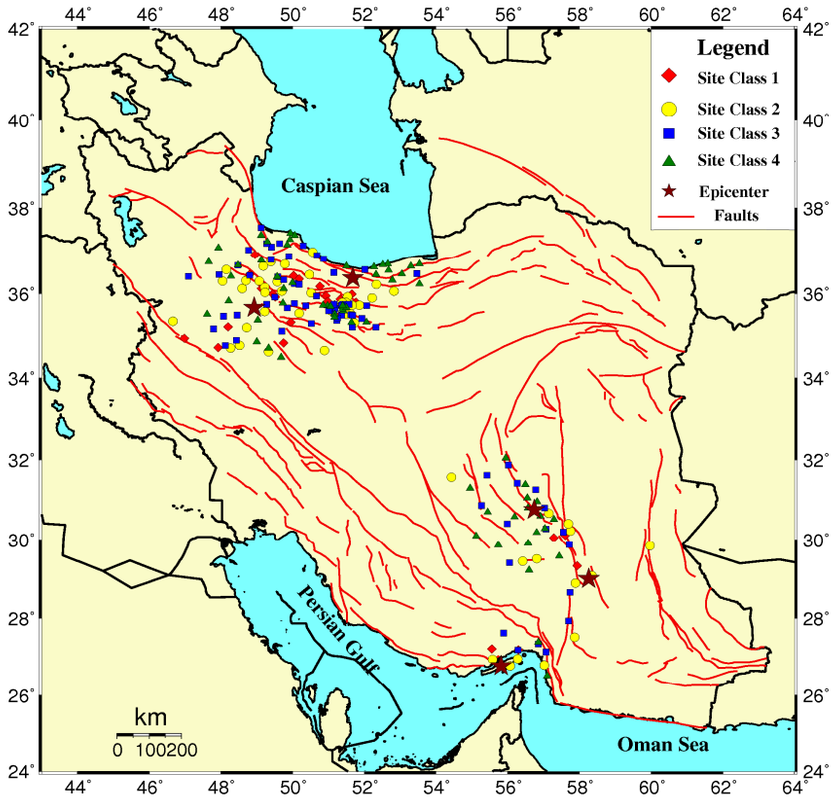
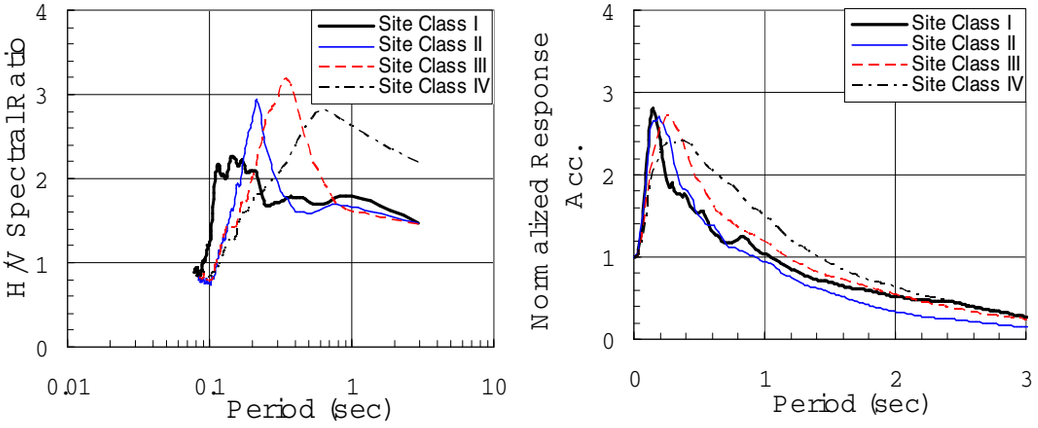


FIG.2. The location of earthquake epicenters and 213 ISMN stations classified in this study with their assigned site class.



(a) **(b)**

FIG.3. Comparison among the four site classes of mean HVSRs and RSSs for strong motion data. (a) Mean HVSR for the four site classes. (b) Mean response spectral shapes for four site classes.

HVSRs can easily be identified since the amplification period ranges are obvious (Figure 3a). The different site classes can be also differentiated in RSSs. However, the period ranges of site classes are rather close, especially for the site classes I and II (Figure 3b). The clear frequency range for different site classes in Figure 3a might be attributed to the effective cancellation of the source and path effects using HVSR method. In Figure 3, class I (rock) emphasize at about 0.17 seconds shows nearly uniform shape on the HVSR. Class IV (soft soil) can be easily recognized, because of its peak at long periods (>0.5 sec). The dominant period for site class II (hard soil) and class III (stiff soil) is in the range of 0.17-0.3 s and 0.3-0.5 s, respectively.
Zhao (reported in Lee et al., 2001) also applied HVSR for the site classification of K-NET strong motion stations in Japan. Furthermore, Lee et al. (2001) classified Taiwan strong motion stations employing both HVSR and RSS methods. In Tables 2 to 4, sites classified based on Proposed Site Classification method (P.S.C), Japanese Code, R.S.S, and IBC2003 methods have been compared. Furthermore, In Figure 4, the HVSRs used in site classification scheme of K-NET and Taiwan strong motion stations are compared by those of determined in this study. From this figure, site class I (class B) has a dominant period at 0.17 s in Iran and Japan, which is lower

Table 2: Comparison of classified sites based on P.S.C. and Japanese Code methods

P.S.C / J. Code	I	II	III	IV	Total
I	26	2	0	0	28
II	0	51	13	0	64
III	0	1	55	2	58
IV	0	0	2	61	63
Total	26	54	70	63	213

Table 3: Comparison of classified sites based on P.S.C. and R.S.S methods

P.S.C / R.S.S	I	II	III	IV	Total
I	24	0	0	0	24
II	2	35	0	0	37
III	0	19	51	0	70
IV	0	0	19	63	82
Total	26	54	70	63	213

Table 4: Comparison of classified sites based on P.S.C. and IBC 2003 methods

P.S.C / IBC 2003	I	II	III	IV	Total
B	26	11	0	0	37
C	0	40	12	2	54
D	0	3	58	7	68
E	0	0	0	54	54
Total	26	54	70	63	213

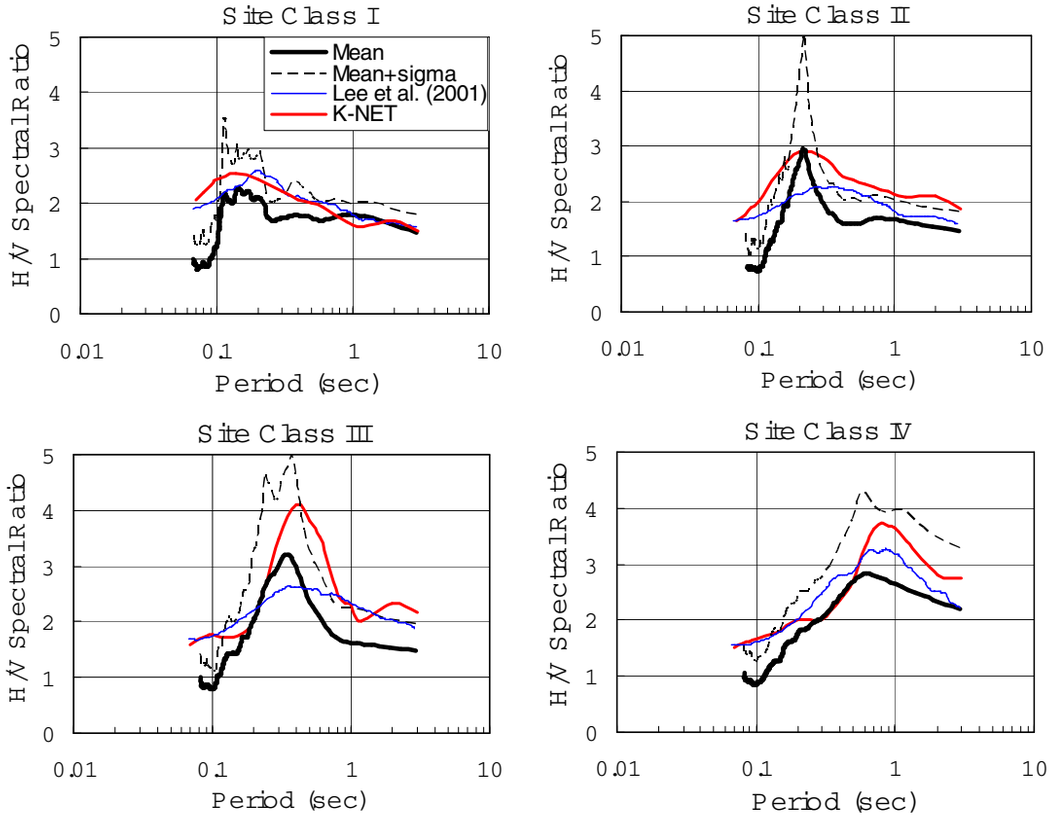


FIG.4. The comparison of the mean HVSRs of Iranian strong motion data used in this study with those of proposed for four site classes by Zhao for K-Net stations in Japan and Lee et al. for Taiwan strong motion stations.

than the one observed in Taiwan (~0.2 s). This may indicate that the rock conditions in Taiwan are not as strong as the ones in Japan and Iran. The site class II in Iran and Japan reveals the same period and smaller than the one observed in Taiwan. The periods of soil classes III and IV in Iran show smaller values than those of observed in Taiwan and Japan. In general, the results show that the HVSRs for the site classes are fairly consistent with those of four site classes in Japan and Taiwan. Furthermore, the results of site classification between HVSR and RSS methods are found to be in good agreement that implies our classification results are acceptable. Based on geological data and the identified amplification period ranges observed in HVSRs and RSSs for different site classes, it is possible to define a new classification system for Iranian sites as described in Table 5. The shear wave velocity for the upper 30 meters is also calculated ($T=4H/V$, where H is thickness of surface soil （assumed to be 30 m), V is shear wave velocity and T is the site dominant period). In addition, the shear wave velocity for different site classes in Iranian design code (standard 2800) is compared with those of obtained here as shown in Table 5.

Table 5. The proposed site classification system and the comparison between V_s^{30} from this study and those of given in Iranian building code

Site Class	Descri-ption	Site Dominant Period (sec)	V_s^{30} of this study (m/s)	V_s^{30} of Iranian building code (m/s)	Geological Condition
I	Rock	>0.17	>700	>750	Igneous and metamorphic rocks, limestone, Sandstone.
II	hard soil	0.17-0.3	400-700	375-750	Shallow to intermediate stiff soil, compact soil with well to medium cementation, old alluvium terraces or colluviums.
III	stiff soil	0.3-0.5	400-240	375-175	Deep stiff soil, soils with inter-bed of fine and coarse material, alluvial terraces with weak cementation.
IV	Soft soil	<0.5	<240	<175	Deep to medium thickness of soft clay, silty or sandy clay mostly alluvial plain.

CONCLUSIONS

In this study, we analyzed 730 accelerogram recordings obtained at 242 stations of the Iranian strong motion network. The horizontal to vertical spectral ratio was basically used to estimate the site amplification characteristics at the stations. Based on dominant period of the sites from HVSR and existing geological data, the station sites were classified according to the classification schemes given by 1980 Japanese code and 2003 IBC. Furthermore, the station sites were also classified using response spectral shape method for checking purpose and providing more confirmation to the accuracy of the results. The choice of site class for each strong motion station was made by comparison among different classifications. If there is no consistency between the results from different classification methods or the reliable geological or geomorphologic information can not be found, the site marked as problematic site and excluded from the results. Finally, we assigned a site class for 213 ISMN stations. The station sites were classified into four site classes namely I (rock), II (hard soil), III (stiff soil), and IV (soft soil). The mean values of HVSR and RSS for different categories reveal a clear variation of amplification period ranges, especially for HVSRs. This may use to indicate the accuracy of our classification results. The HVSRs for different site classes were further examined by comparison with those of found for K-NET stations in Japan and Taiwan strong motion stations. The amplification characteristics for different site classes in Iran, Japan and Taiwan are generally found to be in agreement that used to validate our classification results.

Based on the outcome, a new practical classification system for site categorization in Iran is proposed (Table 5).

ACKNOWLEDGMENTS

The authors are grateful to the Building and Housing Research Center (BHRC) for providing ground motion data.

REFERENCES

Atkinson, G. M. (1993). "Notes on ground motion parameters for Eastern North America: duration and H/V ratio." *Bull. Seis. Soc. Am*. 83: 587-596.

Ghayamghamian M.R. (2004)."Site Effects Estimation in Bam City." In: Faridi (ed) Proceedings of the International Conference on earthquake, Kerman, Iran, 2004.

Ghayamghamian M.R. and Rahimzadeh S. (2005). "Site effect estimation and classification for BHRC station in Tehran using reference site method." *Bulletin of IIEES* 8:14-30.

Ghayamghamian M.R., (2005). "Segmental cross-spectrum as a new technique in site response estimation using spectral ratio analysis." *Journal of Earthquake Engineering* 9: 247-264.

International Conference of Building Officials (ICBO) (2003). *International Building Code*, Whittier, California.

International Conference of Building Officials (ICBO) (1997). *Uniform Building Code*, Whittier, California.

Jafari M.K., Ghayamghamian M.R., Davoodi M., Kamalian M., Sohrabi M. (2006). "Site effects of the 2003 Bam, Iran, earthquake." *Earthquake Spectra* 21: S125-S136.

Japan Road Association (1980). "Specification for highway bridges." Part V, Earthquake Resistant Design, Tokyo.

Komak Panah A., Hafezi Moghddas N., Ghayamghamian M. R., Motosaka M., Jafari M. K. and Uromieh A. (2002). "Site effect classification in East-Central of Iran." *Journal of Seismology and Earthquake Engineering* 4: 37-46.

Lermo, J. and Chavez-Garcia F. (1993). "Site effect evaluation using spectral ratios with only one station.", *Bull. Seis. Soc. Am.* 83: 1574-1594.

Lee C. T., Cheng C. T., Liao C .W. and Tsai Y .B. (2001). "Site classification of Taiwan free- field strong motion stations." *Bull. Seis. Soc. Am.* 91: 1283-1297.

Nakamura Y. (1989). "A method for dynamic characteristics estimation of subsurface using microtremor on the ground surface." QR RTRI 30: 25-33.

Rodriguez-Marek A., Bray J. D. and Abrahamson N. (2001). "An empirically based geotechnical seismic site response procedure." *Earthquake Spectra* 17: 65- 88.

Seed, H. B., Ugas C. and Lysmer J. (1976). "Site-dependent spectra for earthquake-resistant design." *Bull. Seis. Soc. Am*. 66: 221-243.

Theodulidis N., Bard P.Y., Archuleta R. and Bouchon M. (1996) Horizontal-to-vertical spectral ratio and geological conditions: The case of Garner Valley downhole array in southern California. Bull. Seis. Soc. Am. 86: 306-319.

Tsuboi S., Saito M. and Ishihara Y. (2001). "Verification of Horizontal-to-Vertical spectral ratio technique for estimation of site response using borehole seismographes." *Bull. Seis. Soc. Am.* 1: 499-510.

Zare, M., Bard P.Y. and Ghafory-Ashtiany M. (1999). "Site characterizations for the Iranian strong motion network." *Soil Dyn. and Earthq. Eng.* 18: 101-123.

An Evaluation of Site Classification for National Strong-Motion Recording Stations in Turkey

Sandıkkaya M.A.[1], Yılmaz M.T.[2], Bakır B.S.[3] and Akkar S.[3]

[1] Research Assistant, Department of Civil Engineering, Middle East Technical University , 06531 Ankara, Turkey; askaya@metu.edu.tr

[2]Assistant Professor, Department of Engineering Sciences, Middle East Technical University, 06531 Ankara, Turkey

[3]Associate Professor, Department of Civil Engineering, Middle East Technical University, 06531 Ankara, Turkey

ABSTRACT

Since 1976, the General Directorate of Disaster Affairs of Turkey has deployed several strong-motion accelerographs at selected sites, particularly along the North Anatolian Fault zone. Within the framework of the project entitled Compilation of National Strong Ground Motion Database in Accordance with International Standards, initiated in 2006, site conditions at a total of 153 strong-motion sites were investigated within the upper 30 m depth through boreholes including Standard Penetration Testing (SPT) and surface seismics. A preliminary assessment of the site characterization was held by making use of the mean shear-wave velocity of the uppermost 30 m depth with reference to the NEHRP provisions. The recorded accelerograms and corresponding catalogue information were compiled for these strong-motion sites using the available information from national and international databases. The 5% damped normalized elastic acceleration spectra of the accelerograms recorded for events with $M_w \geq 4.0$ were computed and categorized according to the site class and M_w. Mean normalized spectra computed for different M_w and site class bins were compared in order to investigate the significance of site class on the spectral response. NEHRP site classification is evaluated within the limitations of available data and findings.

Keywords: Strong ground motion, site classification, response spectrum, site response, seismic hazard.

INTRODUCTION

Turkish national strong-motion network maintained by the General Directorate of Disaster Affairs of Turkey contains voluminous records of accelerograms from various strong-motion events recorded at different sites. Within the framework of the project entitled Compilation of National Strong Ground Motion Database in Accordance with International Standards, these records were recompiled from the national and international databases to improve the event catalogue of Turkish strong-motion database. A total of 153 strong-motion sites were investigated within this scope. Soil column lithology was described for the upper 30m soil profile through boreholes. The site surveys included Standard Penetration Testing (SPT) and Multi-channel Analysis of Surface Waves (MASW). These investigations also consisted of sampling and laboratory testing for soil classification wherever applicable.

In this study, the dependency of spectrum shape on the site class and moment magnitude is investigated by employing the normalized response spectra of the selected records. The site classes are determined in accordance with the mean shear-wave velocity ($\overline{v}_s$) and mean SPT blow-counts for the uppermost 30 m soil profile, in accordance with the NEHRP provisions (BSSC, 2003). Based on the available data and the results obtained, the magnitude effect on the NEHRP site classes C and D is discussed.

SITE CLASSIFICATION

The shear-wave velocity profiles obtained from the MASW measurements are used to compute the mean shear-wave velocity ($\overline{v}_s$) for each site according to equation 3.5-1 of the NEHRP provisions. Among 153 strong-motion sites, the 65 are classified as class C ($360<\overline{v}_s\leq760$), 85 are classified as class D ($180\leq\overline{v}_s\leq360$) and the remaining 3 are classified as class B ($760<\overline{v}_s\leq1500$). Neither class A ($\overline{v}_s>1500$) nor class E ($\overline{v}_s<180$) sites are available in the dataset. In order to investigate the consistency between the SPT and shear-wave velocity based site classification criterion in the NEHRP provisions, the strong-motion sites are also classified according to the mean standard penetration resistance, $\overline{N}$, of the uppermost 30m soil profile by applying equation 3.5-2 of the NEHRP provisions. Donut type hammer was used for SPT, in accordance with the ASTM 1586 D. The number of sites classified according to the $\overline{N}$ based criterion are 71, 74 and 8 for class C ($\overline{N}>50$), class D ($15\leq\overline{N}\leq50$) and class E ($\overline{N}<15$), respectively. This additional study classified a total of 8 strong-motion sites as class E. The number of class C sites was increased to 71 whereas the number of the class D sites was reduced to 74. Hence, class D sites dominated the database by either criterion.

In SPT testing, when 50 blows are reached for any 15 cm increment the test is halted and the "refusal" is indicated on the bore-log. Accordingly, the ultimate standard penetration resistance of 100 blows is taken in all cases where the refusal is attained. Through comparisons of the SPT results and the shear-wave velocity profiles of the investigated sites, it is observed that the refusal is generally met whenever the shear-wave velocity of a layer exceeded 400 m/s.

The site classes with respect to $\overline{N}$ and $\overline{v}_s$ based criteria are shown in Figure 1. Accordingly, 40 out of 153 strong-motion sites have inconsistent site classifications. The investigation of the possible causes of these inconsistencies is currently underway. However, a preliminary study of these sites reveals that the total thickness of layers with SPT refusal plays a significant role on the observed inconsistencies between the two classification criteria at most sites. In view of that, site classification based on $\overline{v}_s$ criterion is used in the assessment of the site class to investigate the influence of M_w on the spectral shapes, which is presented in the next section.

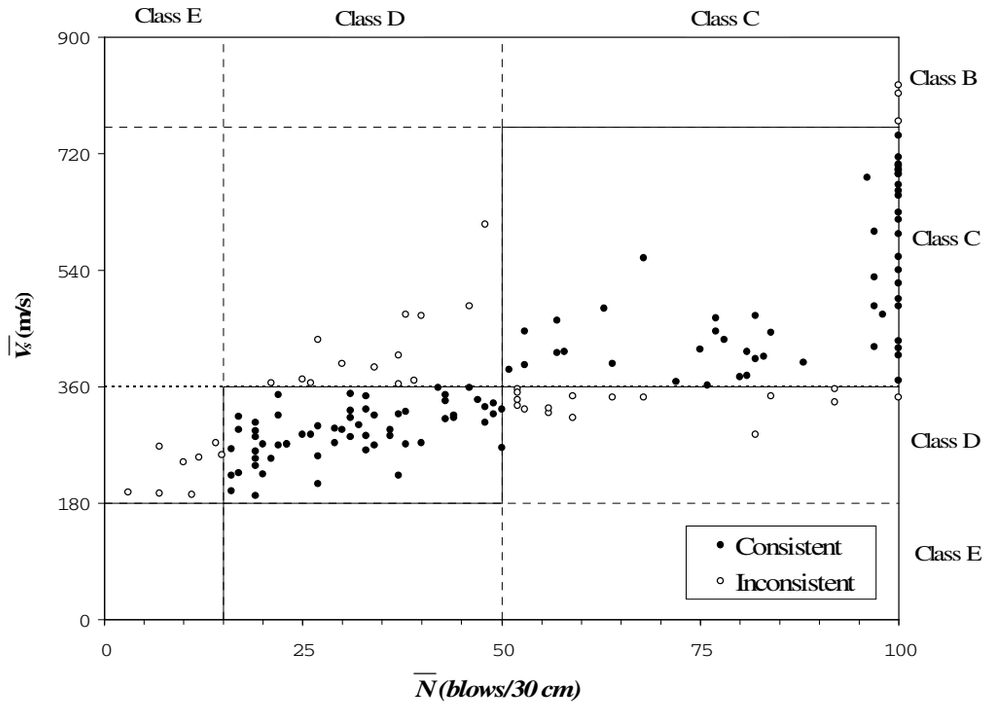


Figure 1. Comparison of site classes according to $\overline{N}$ and $\overline{v}_s$ based site classification criteria.

INVESTIGATION OF SPECTRUM SHAPES

Horizontal components of the recorded accelerograms that meet the criteria listed below are included in the study investigating the influence of M_w on the spectral shapes

1. Site class information is available,
2. Record taken between the years 1976 and 2006,
3. Moment magnitude, M_w, of the event is greater than 4.0,
4. Peak horizontal acceleration, PHA, is greater than 0.0075g,
5. Record is free of non-standard errors described by Douglas (2003).

Figure 2 presents the scatter of these records as a function of $\bar{v}_s$ and M_w for two PHA levels: PHA≤0.05g and PHA>0.05g. There are 129 and 146 records from class D and class C sites, respectively. Of the 281 records, only 6 conform to class B sites. PHA of 68 records is greater than 0.05g. Since the number of records from class B sites is limited, the spectral comparisons were considered only for the records from class C and class D sites.

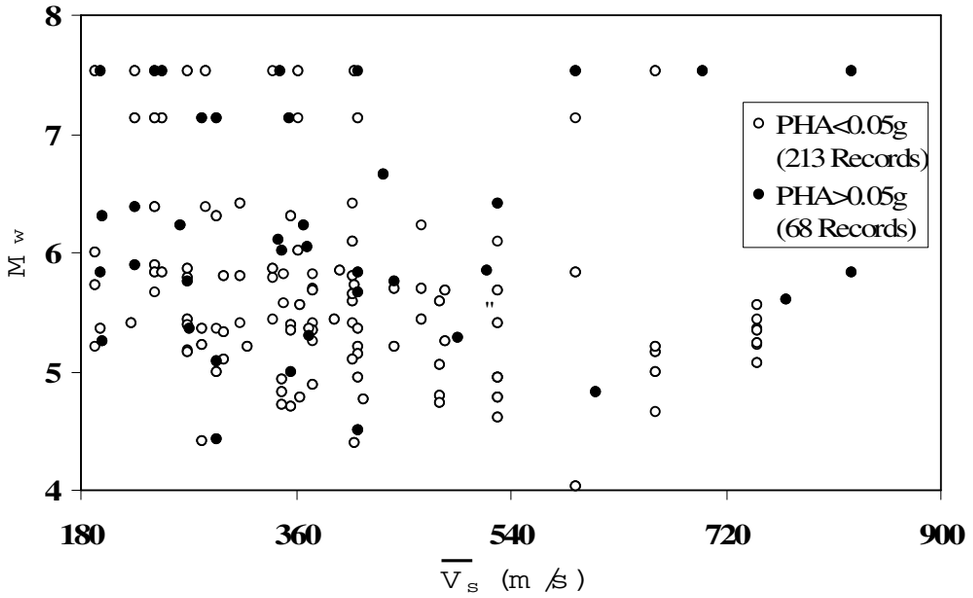


Figure 2. The scatter diagram of 281 records employed in the spectral analyses.

A total of 275 records from 49 strong-motion sites were processed by a two-pass Butterworth 4-pole band-pass filter. The choices of low-cut and high-cut frequencies as well as the details of filtering are presented by Yenier et. al (2006). The choice of low-cut and high-cut filter frequencies delimit the periods with reliable information on the response spectrum. Akkar and Bommer (2006) proposed long period filter cut-off period (T_c) criteria bounding the useable period ranges of elastic spectral quantities. Accordingly, for analogue instruments, the useable period for rock, stiff and soft sites is bounded by $0.65T_c$, $0.65T_c$ and $0.70T_c$, respectively; whereas for digital instruments and respective sites the useable period is bounded by $0.80T_c$, $0.90T_c$ and $0.97T_c$. Hence, considering the existing instrument types and different site classes, it is concluded that the upper period limit of 2.5 s is appropriate for spectral calculations.

The elastic response spectrum (SA) of each filtered record was computed for 5% damping. Each spectrum was normalized by the corresponding effective peak acceleration (EPA) that is defined as the average spectral acceleration over the period range of 0.1 to 0.5 s divided by 2.5 (Kramer, 1996). Then, the normalized spectra were grouped according to $\bar{v}_s$ and M_w to evaluate the effects of these parameters on the spectral shape. The mean normalized spectra for each subgroup are presented in Figure 3. The upper row plots correspond to the normalized spectra for class C recordings divided into 3 different magnitude bins. The lower row plots present similar information for class D records.

Comparisons of the mean spectra reveal the effect of moment magnitude and site class on the spectrum shape. The corner period that separates the constant spectral plateau from the descending branch shifts to longer periods with increasing Mw. For both site classes, the mean spectrum has a very narrow constant plateau for $4.0 \leq M_w < 5.0$. In this magnitude range, the spectral period that corresponds to the peak normalized SA ranges between 0.1 and 0.2 s for both site classes. The normalized SA values at long periods tend to increase and decay in a slower manner with increasing M_w. For the largest magnitude bin and class D, the constant spectral plateau is significantly wider and spectrum decreases very slowly when compared to the other subgroups.

In Figure 4, the mean normalized spectra of class C and class D records are compared for the three magnitude ranges. The upper, middle and lower panels present the site class based comparisons for $4.0 \leq M_w < 5.0$, $5.0 \leq M_w < 6.0$ and $6.0 \leq M_w < 7.5$, respectively. The smoothed design spectra recommended by the NEHRP provisions are also superimposed to these plots. A good agreement between the mean normalized spectra and the smoothed design spectrum is observed except for the magnitude range $4.0 \leq M_w < 5.0$ and class C sites (Figure 4.a). The records satisfactorily reflect the effect of site conditions on the spectrum shapes; a more detailed investigation of this issue through employing the distance to source information is left as a future study.

Considering the variability of normalized spectra within each group, the statistical significance of the foregoing conclusions is investigated. For that purpose, the ratio of the mean SA on intermediate period band (0.5 s to 1.5 s) to mean SA on the short period band (0.1 s to 0.5s) is calculated for each spectrum. The short and intermediate period band definitions are consistent with those of Borcherdt (1994). The calculated ratio is referred to as the spectrum shape factor (SSF).

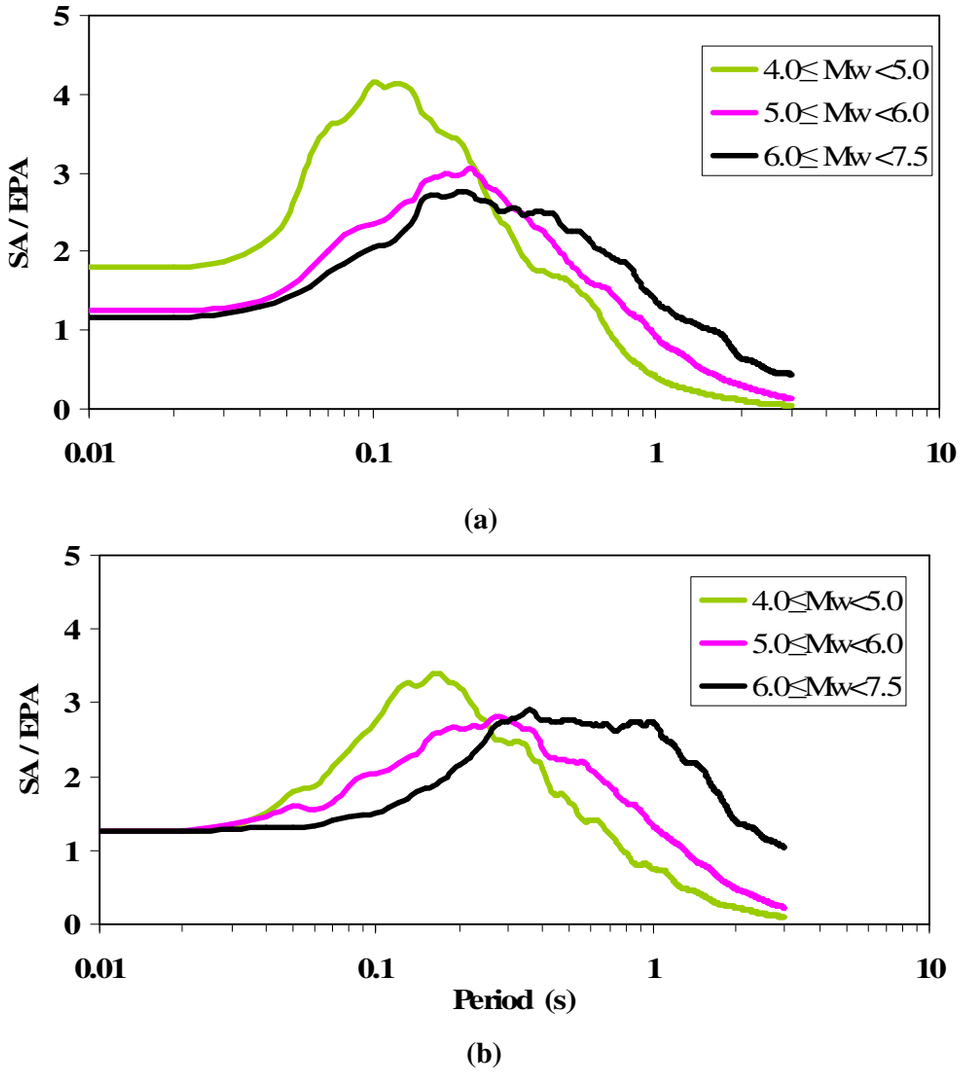


Figure 3. Mean normalized response spectra for different magnitude ranges of earthquakes, for (a) class C sites, and (b) class D sites.

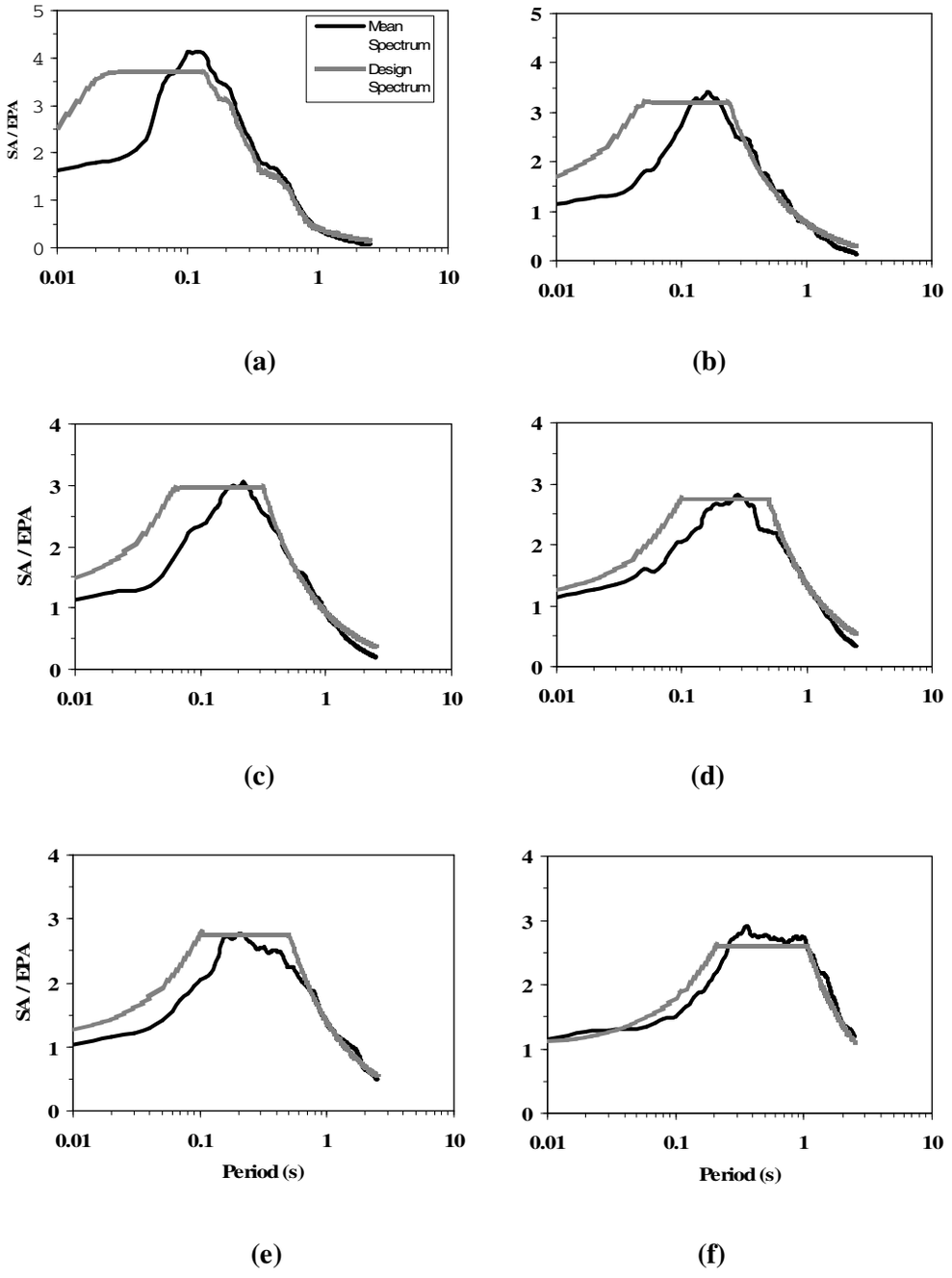


Figure 4. Comparison of mean normalized elastic response spectra and smooth design spectra defined in the NEHRP provisions for (a) Class C sites with 4.0≤ M_w<5.0, (b) Class D sites with 4.0≤ M_w<5.0, (c) Class C sites with 5.0≤ M_w<6.0 (d) Class C sites with 5.0≤ M_w<6.0, (e) Class C sites with 6.0≤ M_w<7.5 and (f) Class D sites with 6.0≤ M_w<7.5.

The value of SSF is expected to increase by increasing M_w and by decreasing $\overline{v}_s$, displaying a tendency towards a flatter spectrum shape. Hence, the sample space of SSF values for each site class and magnitude range was formed through the computation of SSF for each selected record. Assuming that SSF is a log-normally distributed variable, the one tailed Student's t-Test for unequal sample variance is utilized in order to test the hypotheses:

H_0: $\mu_I=\mu_{II}$

H_a: $\mu_{II}>\mu_I$

where, μ_I and μ_{II} are the mean of the logarithms of SSF of the first and second group under consideration, respectively, and group II is chosen as the one with larger magnitude values or the one with softer site conditions (i.e., class D). The calculated P-values are presented in Table 1. Considering the range of P-values, the largest of which is 1.9%, H_0 is rejected with a reasonable significance level for each test. Therefore, the foregoing conclusions related to the comparisons of mean normalized spectra appear to be statistically significant.

Table1. P-values obtained through Student's t-Test

Group I		Group II		P-value
Site Class	**M_w**	**Site Class**	**M_w**	
C	4.0-5.0	D	4.0-5.0	0.019
C	5.0-6.0	D	5.0-6.0	0.000
C	6.0-7.5	D	6.0-7.5	0.001
C	4.0-5.0	C	5.0-6.0	0.000
C	5.0-6.0	C	6.0-7.5	0.000
D	4.0-5.0	D	5.0-6.0	0.007
D	5.0-6.0	D	6.0-7.5	0.000

CONCLUSIONS

Utilizing the recently compiled Turkish strong-motion database, the variability of normalized elastic acceleration response spectra due to site and magnitude effects is investigated. Site classes of Turkish national strong-motion recording stations are identified by the two criteria based on the mean shear-wave velocity and the mean standard penetration resistance defined in the NEHRP provisions. However, it is found that 26% of the encountered sites provide inconsistent site classification regarding $\overline{N}$ and $\overline{v}_s$ based criteria. A great majority of the strong-motion sites can be classified as class C or class D sites.

The maximum moment magnitude and peak horizontal acceleration of the records is 7.4 and 0.82g respectively. A preliminary study on the selected 281 horizontal records captured at these sites reveals that the data offer a sample set that is suitable for investigation of the relationship between the moment magnitude and the shape of response spectrum. Besides, the records satisfactorily reprove the site effect on the response spectra.

ACKNOWLEDGEMENTS

This study is funded by the Scientific and Technological Research Council of Turkey under Award No. 105G016. The authors express their sincere gratitude for this financial support. Emrah Yenier and Özgür Erdoğan provided most of the processed data.

REFERENCES

Akkar, S. and Bommer, J.J. (2006). "Influence of long-period filter cut-off on elastic spectral displacements" *Earthquake Engineering and Structural Dynamics*, 35: 1145-1165.

Borcherdt, R.D. (1994). "Estimates of Site Dependent Response spectra for Design (Methodology and Justification)" *Earthquake Spectra*, 10(4): 617-653

Building Seismic Safety Council, BSSC (2003). "NEHRP Recommended Provisions for Seismic Regulations for New Buildings and Other Structures, Part 1 - Provisions and Part 2 - Commentary", Federal Emergency Management Agency, Washington D.C.

Douglas, J. (2003). "What is a poor quality strong-motion record?" *Bulletin of Earthquake Engineering,* 1:141-156

General Directorate of Disaster Affairs, Earthquake Research Department Database, (2006). General Directorate of Disaster Affairs web-site: http://angora.deprem.gov.tr

Kramer, S.L. (1996). Geotechnical Earthquake Engineering, Prentice-Hall Inc. NJ.

Yenier, E., Denizlioglu, A.Z., Colakoglu, Z. and Akkar, S. (2006). "A comparative evaluation of data processing schemes using Turkish strong-motion data" *First European Conference on Earthquake Engineering and Seismology, Geneva, September 3-8*, Paper number: 793.

This page intentionally left blank

Earthquake Loss Estimation Tool for Urban Areas

Atilla Ansal[1], M. ASCE, Asli Kurtulus[2], M. ASCE and Gökce Tönük[3]

[1]Professor, Bogazici University, Kandilli Observatory and Earthquake Research Institute, Istanbul, Turkey; ansal@boun.edu.tr
[2]Research Associate, Bogazici University, Kandilli Observatory and Earthquake Research Institute, Istanbul, Turkey; asli.kurtulus@boun.edu.tr
[3]Research Assistant, Bogazici University, Kandilli Observatory and Earthquake Research Institute, Istanbul, Turkey; gokce.tonuk@boun.edu.tr

ABSTRACT: A software package, KoeriLoss2, is developed to perform earthquake damage estimation for urban areas based on detailed analyses of local site effects. The first stage of the approach involves generation of microzonation maps with respect to ground motion parameters for the investigated area using separately calculated regional seismic hazard input data. The effects of local geological and geotechnical site conditions are taken into account using representative soil profiles with shear wave velocities extending down to the engineering bedrock ($V_s \geq 750$m/s). 1D site response analyses are conducted using Shake91 to calculate an average site specific PGA and elastic acceleration response spectrum on the ground surface. In the second stage of the approach, vulnerability of the building and pipeline inventories are estimated using ground shaking parameters and empirical relationships. A pilot study is conducted for Zeytinburnu and Bakirkoy districts in Istanbul, Turkey to demonstrate the applicability of KoeriLoss2.

INTRODUCTION

Earthquake loss estimation scenarios are necessary for assigning the priorities in the implementation of the risk reduction, hazard mitigation measures, and for disaster preparedness. The process of loss estimation due to earthquakes involves compilation of building inventories, analysis of seismic hazard on the ground surface and estimation of vulnerability of the building inventories due the computed earthquake ground motion characteristics. Several methodologies were developed over the past years that focus on various aspects of loss estimation process. Advances in computer technology enabled rapid performance of different components of the methodologies and useful display of end results. Software packages, where different analyses were carried out simultaneously, have been developed to provide practical tools for the implementation of the loss estimation methodologies (e.g. Zonno et al., 2003; Sousa et al., 2004; Molina-Palacios and Lindholm, 2006). None of the loss estimation methodologies adopted in these software packages involves detailed

analysis of local site effects when predicting ground motion characteristics. The software package presented in this study provides an alternative loss estimation methodology, where local site effects are taken into account by performing 1D site-specific site response analyses using Shake91 (Idriss and Sun, 1992).

KOERILOSS2 SEISMIC LOSS ESTIMATION TOOL

KoeriLoss2 computes the earthquake damage to buildings and pipelines in an urban area for a given scenario earthquake. The methodology used in the loss estimation is composed of two main stages. The first stage involves generation of microzonation maps with respect to earthquake ground motion parameters due to the selected regional earthquake hazard scenario. The area under investigation is divided into cells (typically 250m×250m) by a grid system. Earthquake hazard parameters in terms of peak ground acceleration (PGA) and spectral accelerations at the engineering bedrock along with soil profiles representing local site conditions with shear wave velocity profiles extending down to the engineering bedrock (Vs $\geq$ 750m/s) are assigned for each cell. Earthquake characteristics on the ground surface for each cell are calculated using one-dimensional site response analyses, Shake91 (Idriss and Sun, 1992). The variations of PGA, peak ground velocity (PGV) and spectral accelerations at T=0.2s and 1s on the ground surface are calculated and displayed as GIS maps.

The second stage of the methodology involves vulnerability analyses for building and pipeline inventories. Site-specific spectral accelerations (at T=0.2s and T=1s) are used to assess the vulnerability of the building stock. The displacement-based approach of Hazus (1999) is adopted in the evaluation of building damages. The damage in the buildings is classified according to five descriptive damage states: none, slight, moderate, extensive and complete. Site-specific PGV values are used to assess the vulnerability of pipeline inventory with respect to wave propagation. Empirical correlations (ALA, 2001) which relate damage rate to PGV are used to predict damage in pipeline systems in terms of repair rate and number of pipe repairs. Damage distributions in buildings and pipelines are displayed as GIS maps.

The methodology is automated into a Visual Basic application which utilizes Excel and Fortran codes for calculations and uses GIS based software, MapInfo, to display loss estimation results. The flow chart for KoeriLoss2 is schematically illustrated in Figure 1.

The information that should be provided by the user for operation of KoeriLoss2 involves the following data files:

1. A text file containing PGA, spectral accelerations at T=0.2s and T=1s for each cell at the engineering bedrock as determined from earthquake hazard analyses.
2. Text files for the selected acceleration time histories compatible with the regional seismic hazard.
3. An excel spreadsheet that requires user to enter information about geotechnical site conditions at each cell in the grid system. The information that should be provided by the user includes soil type, soil layer thickness, ground water level and shear wave velocity profile down to the engineering bedrock ($V_s \geq$ 750m/s) for each cell.

4. A text file that includes dynamic soil properties (shear modulus reduction and material damping ratio curves) for all soil types.
5. An excel spreadsheet that requires user to enter information about building inventory in terms of a so-called 'Bijk building matrix'. The "i" in the Bijk matrix shows the construction type as: (1) Reinforced concrete frame building, (2) Masonry building, (3) Reinforced concrete shear wall building, (4) Precast building. The number of stories ("j" dimension of the matrix) is defined as: (1) Low rise (1-4 stories, including basement), (2) Mid rise (5-8 stories, including basement), (3) High-rise (more than 8 stories, including basement). The construction date ("k" dimension of the matrix) is defined as: (1) Construction year: Pre-1979 (included) and (2) Construction year: Post-1980.
6. An excel spreadsheet that requires user to enter information about pipeline inventory in terms of length, material and diameter of pipelines.

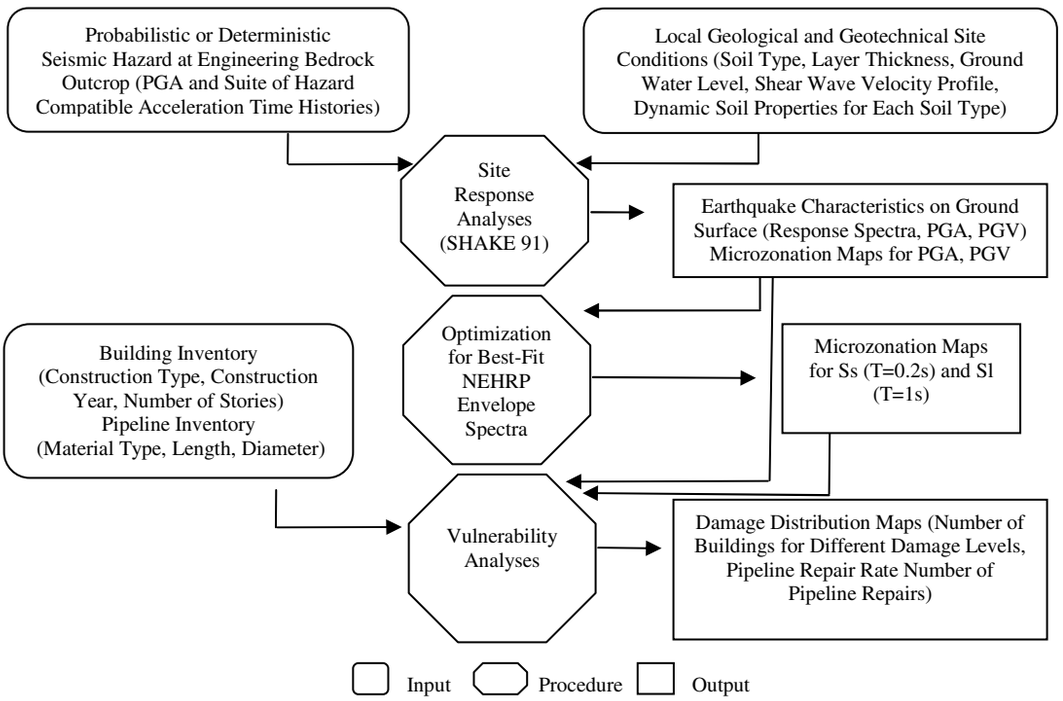


FIG. 1. Schematic illustration of KoeriLoss2 software procedures for loss estimation in urban areas.

KoeriLoss2 operates as a single executable file within Excel using Visual Basic (VBA) environment. Given the data files described above, KoeriLoss2 calculates ground motion parameters on the ground surface and estimates damage in the inventories. Microzonation maps with respect to PGA, PGV and spectral accelerations at T=0.2s and 1s and damage distribution maps in terms of number of buildings for each building damage state for each building type, repair rate and number of repairs for pipelines are produced as outputs of the software procedure.

PILOT STUDY FOR ZEYTINBURNU AND BAKIRKOY IN ISTANBUL

KoeriLoss2 was used to perform the damage scenario for Zeytinburnu and Bakirkoy district in Istanbul, Turkey as a part of a EU FP6 Project – LessLoss (Spence, 2007). The area is approximately 40 km^2 with mostly low to mid-rise residential buildings. The natural gas pipeline inventory consists of steel transportation pipes with diameters changing between 4" and 30".

Seismic Hazard and Site Response Analyses

In the first step of damage scenario a grid system composed of cells of 250m×250m was defined for the study area. Probabilistic seismic hazard analysis was carried out to evaluate PGA and spectral accelerations at T=0.2s and T=1s for each cell on the engineering bedrock (Erdik et al., 2005). A regional time dependent Poisson model for the return period of 475 years corresponding to 10% probability of exceedance in 50 years was adopted in the analysis (Erdik et al., 2004). Earthquake records compatible with the estimated seismic hazard were compiled and used for site response analyses by scaling the acceleration time histories with respect to PGA estimated from the seismic hazard analysis for each cell (Durukal et al., 2006). The scaled acceleration time histories were used as outcrop motions in site response analyses. In order to evaluate the spectrum compatibility, the acceleration response spectra of the PGA-scaled acceleration time histories were also compared with the lowest and highest NEHRP (2003) spectra determined for the region-specific earthquake hazard study.

The local site conditions were characterized based on available soil borings, in-hole PS-Logging and surface seismic wave measurements conducted in the area (Kilic et al., 2006; Iyisan, 1996). One representative soil profile with shear wave velocities extending down to the engineering bedrock (Vs $\geq$ 750m/s) was determined for each cell. Typical soil profiles from the study area are shown in Figure 2. Empirical relationships available locally and internationally were used to define the variation of dynamic shear modulus and damping with shear strain.

Shake91 (Idriss and Sun, 1992) was utilized to perform site response analyses using three input motions and a representative soil profile for each cell. Shake 91 (Idriss and Sun, 1992) computes acceleration-time history (therefore, PGA) and the elastic response spectrum on the ground surface for a given input motion and a soil profile. PGV values were obtained through integration of acceleration-time histories on the ground surface.

The averages of three values of PGA, PGV and ground response spectra for each cell were determined to define the variation of ground shaking parameters due to the probabilistic seismic hazard scenario. The average acceleration response spectrum for each cell was used to determine spectral accelerations at short and long periods. An optimization algorithm was used to determine the NEHRP (2003) envelope spectrum which is the best fit for the average acceleration response spectrum (Ansal et al., 2006). Microzonation maps showing the variations of PGA, PGV and spectral accelerations in Bakirkoy and Zeytinburnu districts were generated using MapInfo and illustrated in Figures 3 through 5.

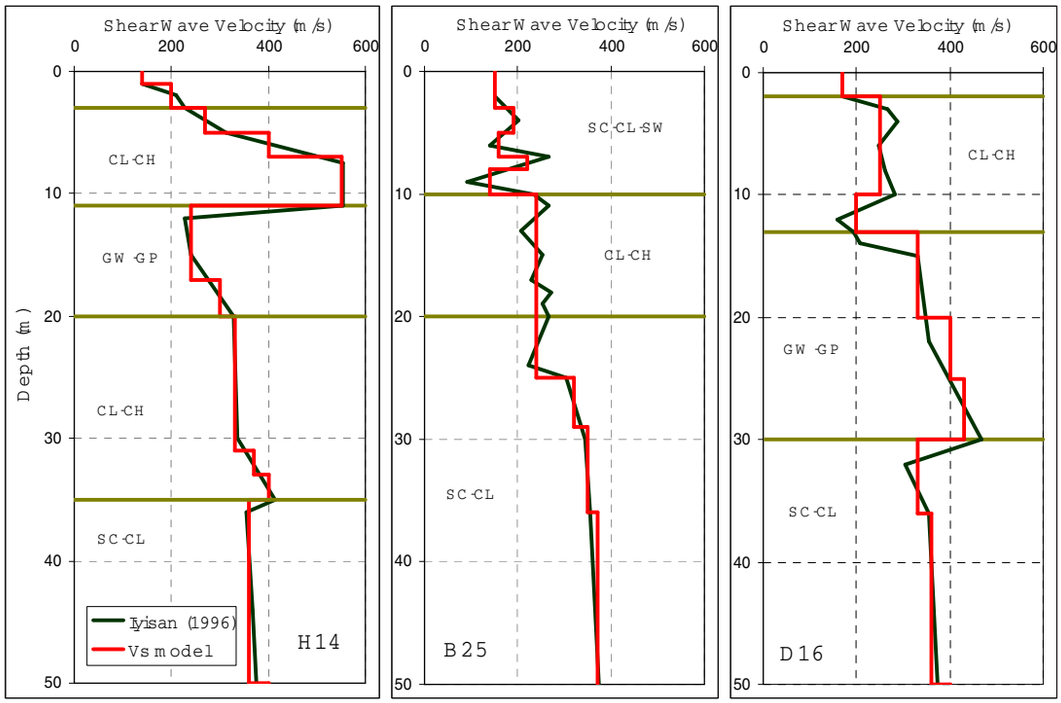


FIG. 2. Typical soil and shear wave velocity profiles for the top 50m in the study area.

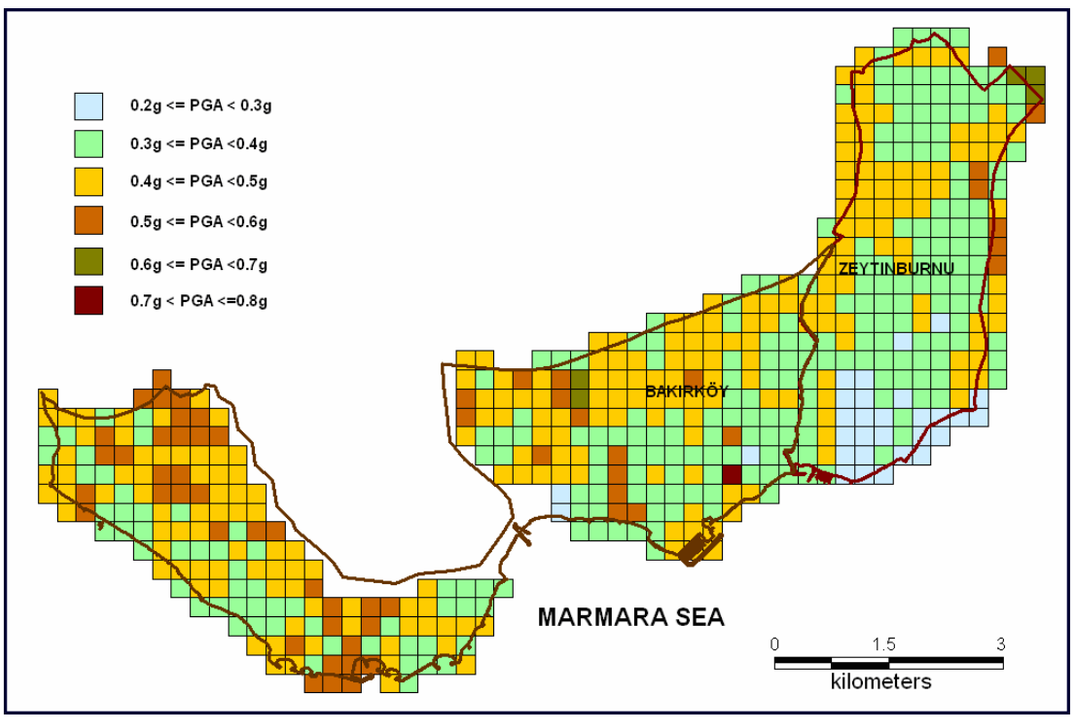


FIG. 3. Microzonation map with respect to PGA for the study area.

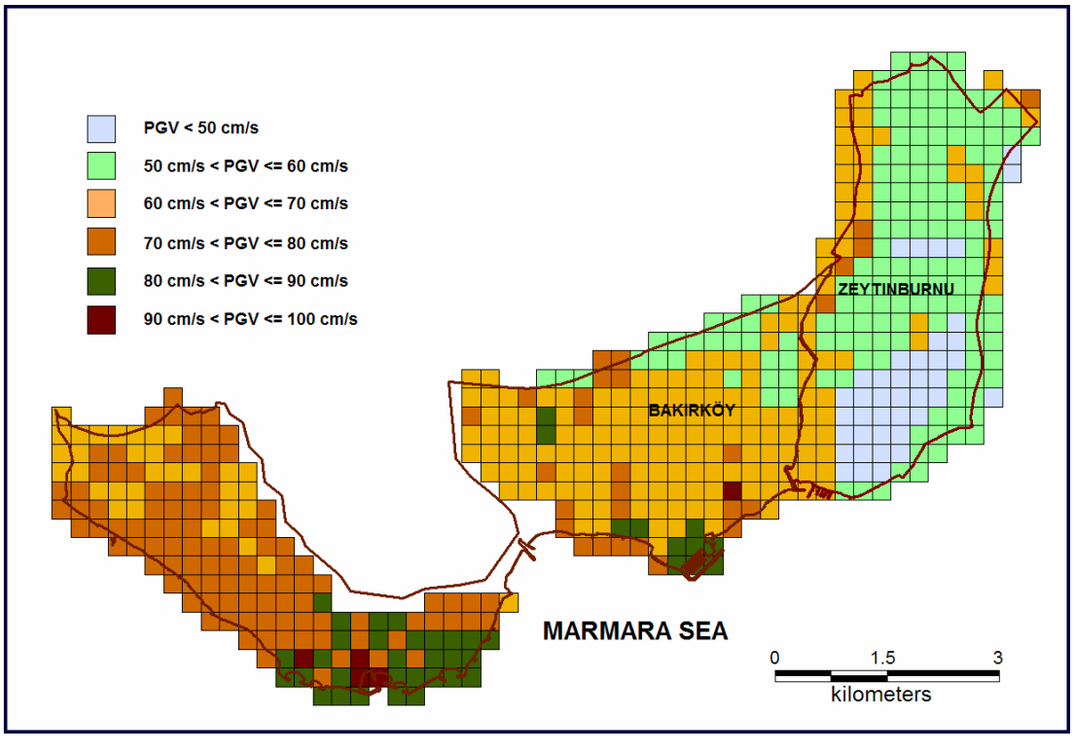


FIG. 4. Microzonation map with respect to PGV for the study area.

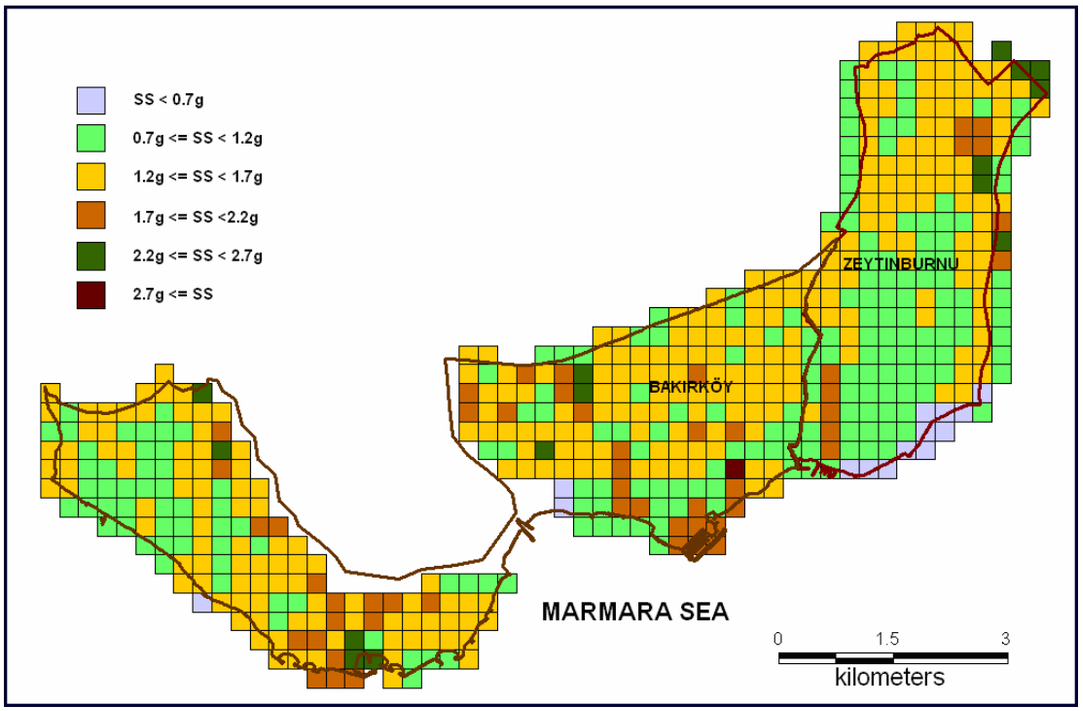


FIG. 5. Microzonation maps with respect to short period (T=0.2s) spectral acceleration for the study area.

Vulnerability Analyses and Loss Estimations

The building inventory indicates that almost all of the buildings in Zeytinburnu are reinforced concrete frame buildings and most of the buildings fall into the mid rise building group (Aydınoglu and Polat, 2004). Region-specific vulnerability relationships (Erdik et al., 2002) for each type of building that relate spectral displacements to building damage for each damage state were used to evaluate damage ratios for different building types in the study area. Figure 6 illustrates examples of the vulnerability relationships that were used to evaluate damage in reinforced concrete frame buildings.

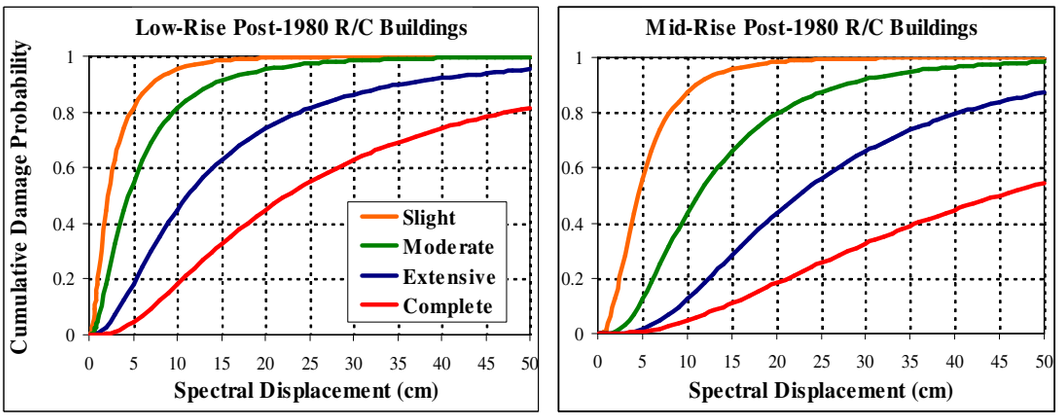


FIG. 6. Vulnerability relationships for reinforced concrete frame buildings: (a) low-rise buildings (for 1-4 stories) and (b) mid-rise buildings (for 5-8 stories).

The distribution of number of buildings at each damage state for all building types in the area were computed and displayed in maps showing number of buildings at each cell for all building types and damage states. In Figure 7 total numbers of reinforced concrete frame buildings at complete damage state are shown for each cell. A summary of the estimated damage in Zeytinburnu is presented in Table 1.

The natural gas pipeline inventory in Zeytinburnu and Bakirkoy were compiled based on information provided by Istanbul Gas Distribution Industry and Trade Co. Inc. The information consisted of length, diameter and material properties of the main steel pipeline system. An empirical correlation between peak ground acceleration PGV and pipeline damage proposed by ALA (2001):

$$RR(\text{repair/km}) = 0.002415 * K * PGV \quad (1)$$

was used to determine expected repair rate and number of repairs in the pipeline system due to wave propagation where PGV (cm/s) is the peak velocity on the ground surface and K is a coefficient depending on material type (K = 1.45 for welded steel pipes). ALA (2001) relationship was selected for this study since it has the largest database (data from 18 earthquakes and all types of pipe materials). Numbers of expected repairs at each cell were calculated as the product of repair rate and total

pipeline length. Damage distribution maps that show the variation of repair rate and number of pipe damages are presented in Figures 8 and 9, respectively.

TABLE 1 Damage scenario for buildings in Zeytinburnu.

Building Type	Total Number of Buildings	Number of Buildings				
		None	Slight	Moderate	Extensive	Complete
112	3402	425	741	1262	651	323
122	10339	1521	4549	3028	777	464
132	144	22	67	27	18	10
212	1831	184	404	512	383	349
222	22	1	6	8	4	3
ALL	15738	2153	5766	4837	1833	1149

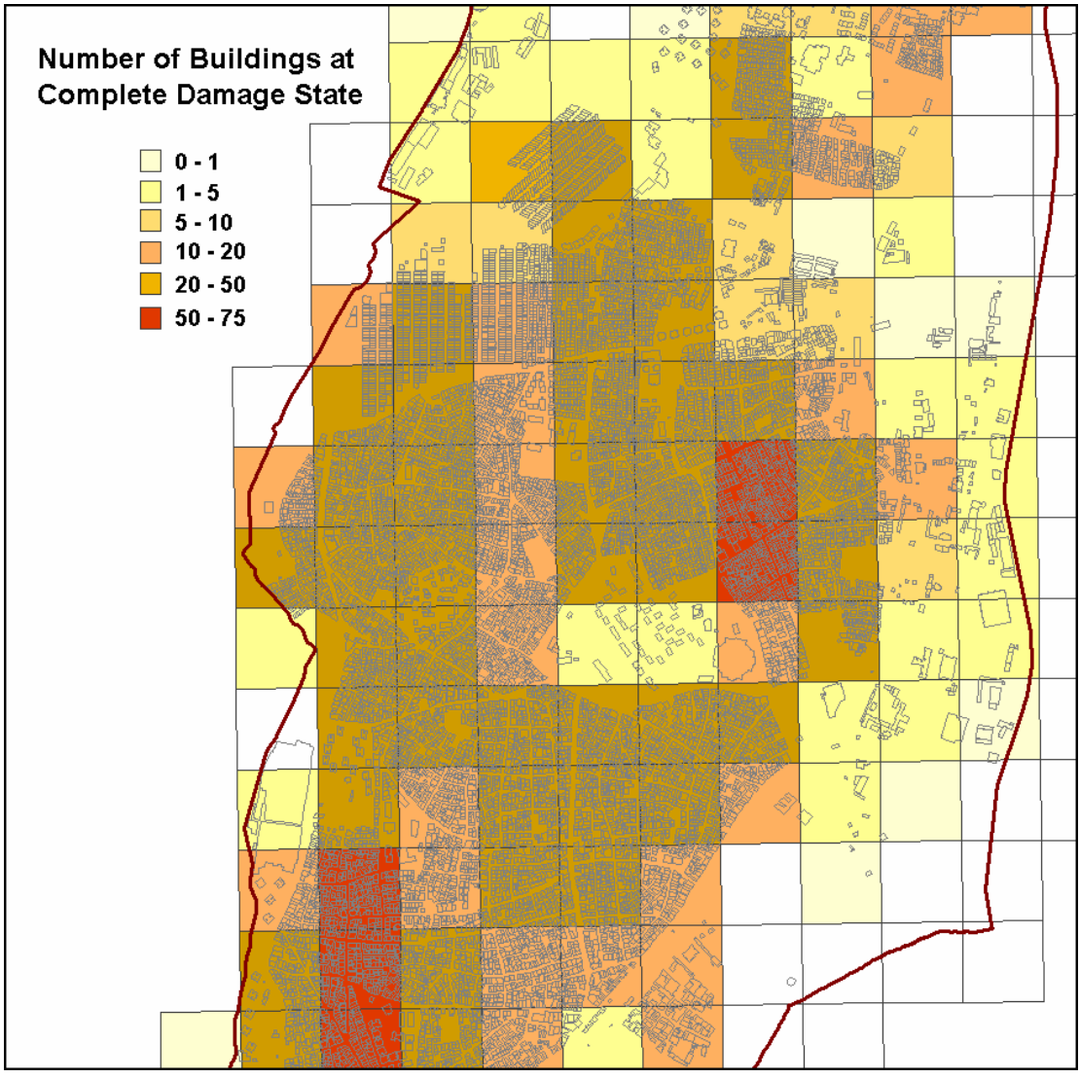


FIG. 7. Distribution of number all types of reinforced concrete frame buildings at complete damage state in Zeytinburnu district.

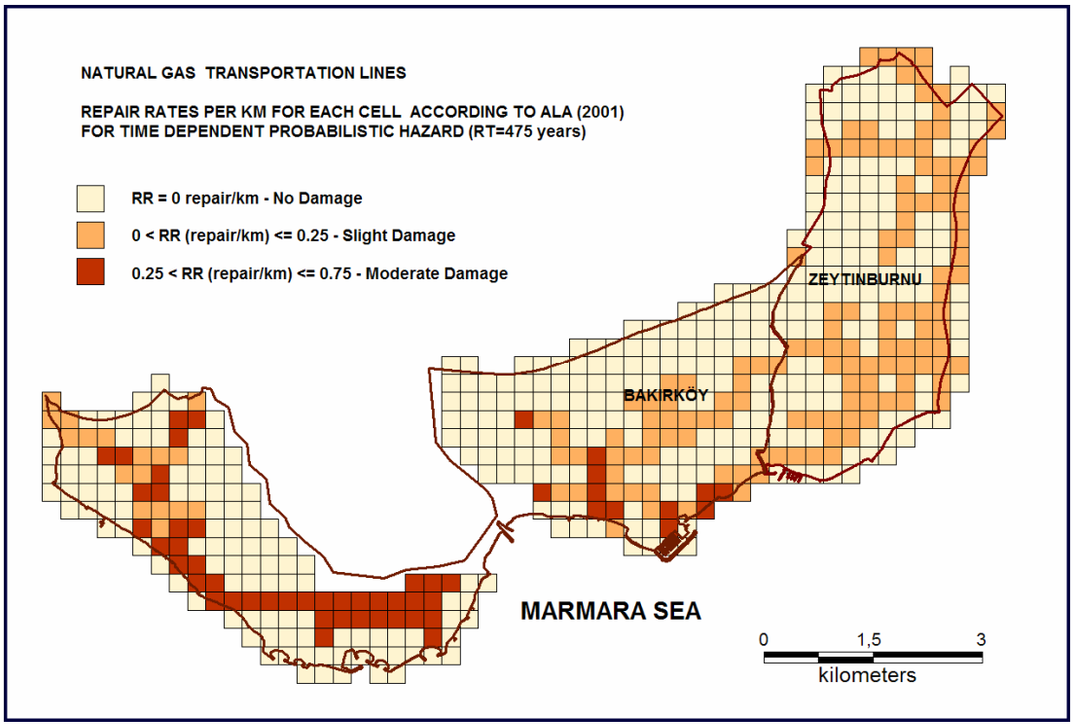


FIG. 8. Distribution of repair rate due to wave propagation in natural gas pipeline system in Bakirkoy and Zeytinburnu.

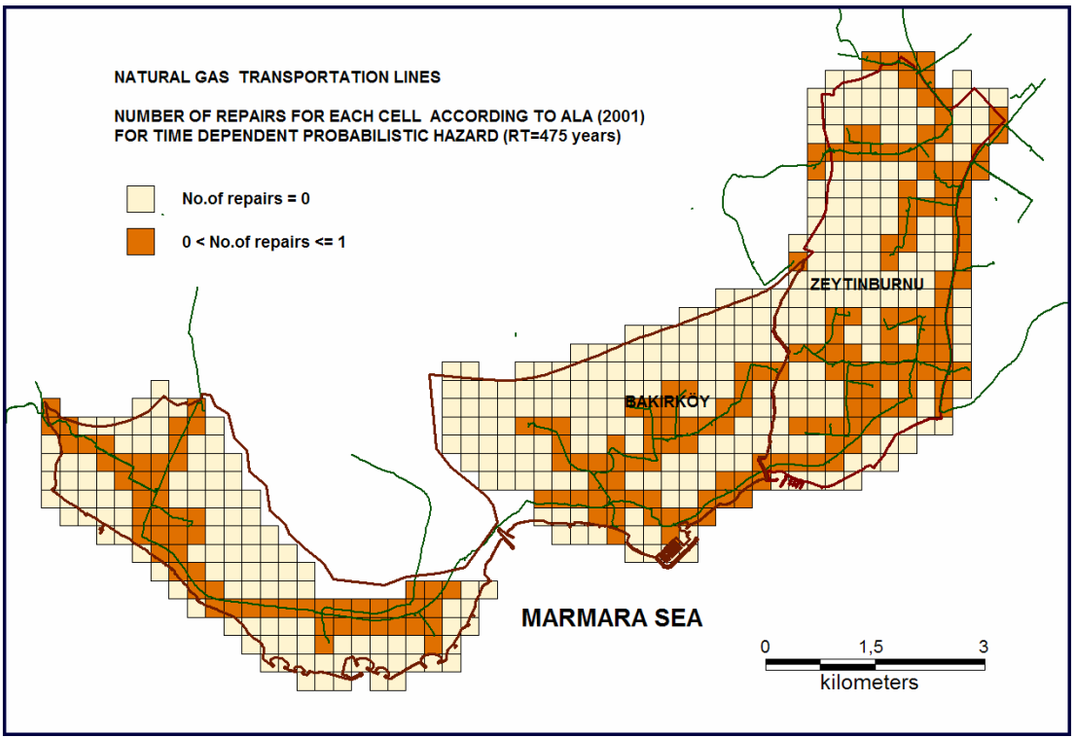


FIG. 9. Distribution of number of pipe repairs due to wave propagation in natural gas pipeline system in Bakirkoy and Zeytinburnu.

CONCLUSIONS

A software tool, KoeriLoss2, was developed to estimate earthquake damage in urban areas. The software package utilizes earthquake hazard parameters and local soil profiles with shear wave velocities extending down to engineering bedrock (Vs ≥ 750m/s) as inputs for 1D site response analyses (Shake91). Earthquake ground motion parameters on the ground surface are computed from site response analyses are employed in empirical relationships to evaluate vulnerability of building and pipeline inventories. A pilot study performed for two districts in Istanbul, Turkey was used to demonstrate the applicability of KoeriLoss2.

ACKNOWLEDGMENTS

The earthquake damage scenario software (KoeriLoss2) is developed as a part of the EU FP6 Project on "LessLoss - Risk Mitigation for Earthquakes and Landslides". The Authors would like to acknowledge the support and contributions of all their colleagues in the Earthquake Engineering Department of Kandilli Observatory and Earthquake Research Institute and specially of Prof.M.Erdik, Prof.N.Aydinoglu, Asc.Prof.E.Durukal, M.Demircioglu, K.Sesetyan, and U.Hancilar.

REFERENCES

ALA (American Lifelines Alliance) (2001) Seismic Fragility Formulations for Water Systems, Part 1-Guideline, http://www.americanlifelinesalliance.org

Ansal, A., Tönük, G., Demircioglu, M., Bayraklı,Y., Sesetyan,K., Erdik,M (2006) "Ground Motion Parameters for Vulnerability Assessment", *Proceedings of the First European Conference on Earthquake Engineering and Seismology*, Geneva, Paper Number: 1790

Aydinoglu, N and Polat, Z. (2004) First level evaluation and assessment of building earthquake performance, Report for the Istanbul Master Plan Zeytinburnu Pilot Project, Metropolitan Municipality of Istanbul, Planning and Construction Directorate (in Turkish)

Durukal,E., Ansal,A., and Tönük,G. (2006) "Effect of Ground Motion Scaling and Uncertainties in Site Characterization on Site Response Analyses", *Proceedings of the 100th Anniversary Earthquake Conference Commemorating the 1906 San Francisco Earthquake*, San Francisco, USA, 2006.

Erdik, M., Demircioglu, M., and Sesetyan, and Durukal, E. (2005), Assessment of earthquake hazard for Bakirköy, Gemlik, Bandırma, Tekirdağ and Körfez, WB MEER Project -A3 Component, Microzonation and Hazard Vulnerability Studies For Disaster Mitigation in Pilot Municipalities, Bogazici University, Kandilli Observatory and Earthquake Engineering Research Institute.

Erdik, M., Demircioglu, M., Sesetyan, K., Durukal, E., and Siyahi, B. (2004) "Earthquake Hazard in Marmara Region", *Soil Dynamics and Earthquake Engineering*, 24: 605-631

Erdik,M., M,N.Aydınoğlu, A.Barka, Ö.Yüzügüllü, B.Siyahi, E.Durukal, Y.Fahjan, H.Akman, G.Birgören, Y.Biro, M.Demircioğlu, C.Özbey and K.Şeşetyan, (2002) BU-ARC, Earthquake Risk Assessment for Istanbul Metropolitan Area, Project Report, Bogazici University Publication.

HAZUS (1999) Earthquake Loss Estimation Methodology, Technical Manual, RMS, NIBS and FEMA.

Idriss, I. M. Sun, J. I. (1992) Shake91, A Computer Program for Conducting Equivalent Linear Seismic Response Analysis of Horizontally Layered Soil Deposits Modified based

on the original SHAKE program Published in 1972 by Schnabel, Lysmer and Seed.

Iyisan, R. (1996) "Correlations between Shear Wave Velocity and In-situ Penetration Test Results", *Technical Journal of Turkish Chamber of Civil Engineers*, 7(2):1187-1199 (in Turkish).

Kilic, H., Özener, P.T., Ansal, A., Yıldırım, M. Özaydın, K., Adatepe, S. (2006) "Microzonation of Zeytinburnu Region with respect to Soil Amplification: A Case Study", *Journal of Engineering Geology*, 86:238-255.

Molina-Palacios, S and Lindholm, C.D. (2006) SELENA V1.0 User and Technical Manual, NORSAR, Norway http://www.norsar.no/seismology/selena.html

NEHRP (2003) Recommended Provisions For New Buildings and other Structures, FEMA-450, prepared by the Building Seismic Safety Council for the Federal Emergency Management Agency, Washington, DC.

Sousa, M. L., Campos, A. C., Carvalho, A., and Coelho, E. (2004) "An Automatic Seismic Scenario Loss Methodology Integrated on a Geographic Information System", *Proc. 13th World Conference on Earthquake Engineering*, Vancouver, Paper No. 2526.

Spence,R ed. (2007) Earthquake Disaster Scenario Prediction and Loss Modelling for Urban Areas, *EU FP6 Project on Risk Mitigation for Earthquakes and Landslides*, Report No.7,

Zonno, G., Garcia-Fernandez,M., Jimenez, M.J., Menoni, S., Meroni1, F., and Petrini,V. (2003) "The SERGISAI procedure for seismic risk assessment", *Journal of Seismology*, 7: 259–277.

This page intentionally left blank

Geological and microtremor survey, damage distribution, and reconstruction of Muzaffarabad and surroundings after the 2005 Kashmir earthquake

Kazuo Konagai[1], Jorgen Johansson[2], Atsunori Numata[3], Shigeki Takatsu[4], and Takaaki Ikeda[5]

[1]Professor, IIS, The University of Tokyo, Komaba 4-6-1, Meguro, Tokyo 153-8505, konagai@iis.u-tokyo.ac.jp
[2]Lecturer, IIS, The University of Tokyo, Komaba 4-6-1, Meguro, Tokyo 153-8505, jorgen@iis.u-tokyo.ac.jp
[3]Senior Researcher, Research Institute of Technology, TOBISHIMA Corporation, 5472, Kimagase, Noda-City, Chiba 270-0222, Atsunori_numata@tobishima.co.jp
[4]Researcher, CTI Engineering Co., LTD., takatsu@iis.u-tokyo.ac.jp
[5]Senior Researcher, Research Institute of Technology, TOBISHIMA Corporation, 5472, Kimagase, Noda-City, Chiba 270-0222, Takaaki_Ikeda@tobishima.co.jp

ABSTRACT: Heavy damage was observed in Muzaffarabad, Pakistan due to the 2005 Kashmir earthquake, especially on terraces with thick well compacted gravel deposits and along the terrace rims. We evaluated the damage distribution visually from Ikonos satellite images. In an effort to contribute to the restoration of Muzaffarabad city and its future urban and infrastructure development, we investigated the area's geomorphology and measured microtremors at some 20 locations. The four terraces in the city consist of well compacted gravel deposits and our microtremor results indicate slightly higher amplification values and lower fundamental frequencies on the thicker deposits in the South-East of the city, where damage was very severe. We hope our study will be a good complement to JICA's (Japan International Cooperation Agency) Master plan for the city's reconstruction.

INTRODUCTION

A large earthquake of M 7.6 occurred in the North Eastern Frontier Area of Pakistan (Epicenter: 34.493°N, 73.629E), about 90 km NNE of Islamabad at 8:28 local time, Oct. 8, 2005. This earthquake resulted in wide-spread devastation. At least 73,236 people died, making this devastation the worst that this country had ever experienced since 1900.

The Japan Society of Civil Engineers (JSCE) together with the Architectural Institution of Japan (AIJ) and "Engineers without Borders" (EWBJ) has been exchanging expertise and opinions among Japanese and Pakistani organizations for better rehabilitation since they dispatched the first advance body for a quick reconnaissance. Reflecting these discussions, JSCE decided to dispatch the fifth team to the affected area with the following objectives: 1) Estimating permeability of a huge landslide dam at Hattian for a better stabilization of the soil mass, and 2) measuring microtremors in Muzaffarabad for estimating soil properties to understand damage distributions and thus to reflect the findings in the ongoing rehabilitation projects.

Here we present the findings of the microtremor measurements obtained during the quick four-day survey of the fifth team, and proposals to mitigate

earthquake-inflicted losses. Providing both Japan and Pakistan experts and persons in charge with a rough-and-ready overview will be important for taking measures for better rehabilitations and precautions against possible secondary and future disasters.

ESTIMATION OF GEOLOGICAL STRUCTURE IN MUZAFFARABAD

The tectonic setting around Muzaffarabad is complicated and the same fault is known under different names (see e.g. Dunning et. al., 2007). Even though the Tanda fault does not pass directly beneath Muzaffarabad, but on its eastern border, heavy damage was observed. Damage was especially severe on terraces with thick deposits and along the terrace rims, as compared to the damage of buildings located on shallow deposits or directly on bedrock.

In an effort to contribute to the restoration of Muzaffarabad city (see map in FIG. 1) and its future urban and infrastructure development, the geologist in our team has quickly surveyed the area's geomorphology (see FIG. 2.) To further quantify these observations, we have also performed microtremor measurements at selected locations shown in FIG. 3a. Here follows a brief description and analysis of the results which we hope will be a good complement to the Japan International Cooperation Agency Master Plan (JICA, 2006) herein after referred to as "JICA MP".

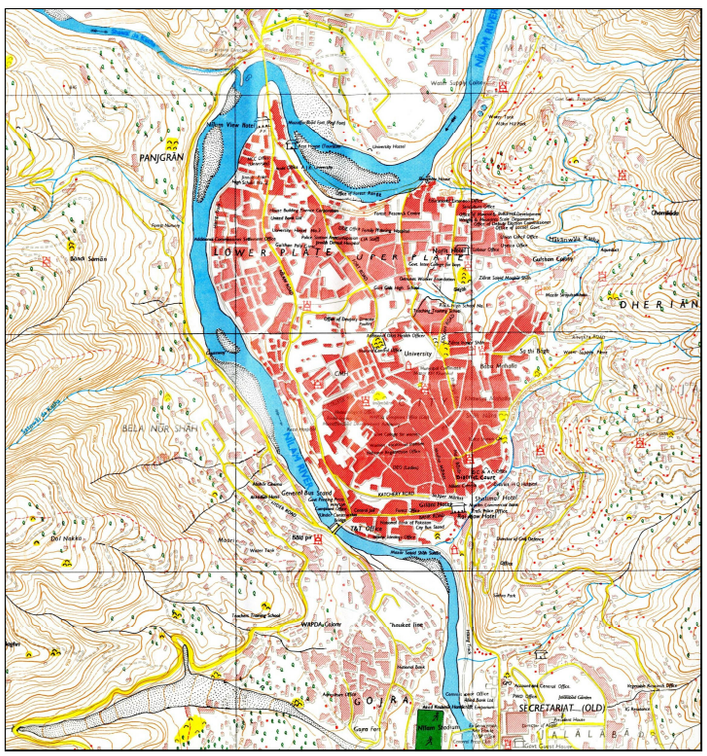


FIG. 1. Map of Muzaffarabad city and surroundings

Description of Terraces in Muzaffarabad

There are four confirmed diluvial terraces in the city and its vicinity (see FIG. 2). Terrace 1 follows the eastern mountain side and its border with terrace 2 is a fairly straight line in the north-south direction. The university is located in this area. Both the soccer stadium and the market place are situated on terrace 2. Terrace 3 covers a wider area in the northern part of the city and in its central part the Fort road runs in a NNW-SSE direction through a large housing zone. Finally, terrace 4 is located closest to the Neelum river. The border between the 3rd and 4th terrace is delineated by the Neelum road.

In general the terrace deposits consist of a well compacted weakly cemented gravel layers with inclusion of conglomerates. We estimated maximum thickness to 40m on terrace 1, based on the height of very steep slopes located at point EW0201 shown in FIG. 3. Bedrock outcrops were confirmed at a location at the southern part of the border between terrace 3 and 4, close to the rim, on the border between terrace 2 and 3, and also along the Neelum river (spelled “Nilam” in Urdur on the map in FIG. 1).

Cross sections of the terraces, based on lines in FIG. 3(a), are given in FIG. 4-FIG. 6. The East-West cross sections (FIG. 5 (a) and FIG. 6(a)) show that the difference in elevation of each terrace is about 10 to 20 meters as we go from the east to the west in the southern part of the city. However, in the northern part the height differences between the terraces are smaller.

MICROTREMOR INVESTIGATION AND DAMAGE DISTRIBUTION

Microtremors were measured along three lines, one N-S trending line (green) and two E-W trending lines (yellow and blue), as shown in FIG. 3. The damage level was first estimated visually from an Ikonos satellite image, as shown in FIG. 3b (orange dots show severely damaged dwellings). The damage level was also observed at each microtremor point during the field measurement, and classified into three categories marked with colored lines at the bottom of the cross sections in FIG. 4(a) - FIG. 6(a).

We used a microtremor equipment SPC35 and SPC51 produced by Tokyo Sokushin (http://www.to-soku.co.jp/monitoring%20spc-51%20(e).htm) and data was processed with the software Geopsy (www.geopsy.org) to obtain H/V ratios, according to the so called Nakamura’s technique (see e.g. Bard et. al. 2004).

At many locations we could not identify clear peaks in the H/V spectra and we interpret this as that there is no clear impedance contrast between bedrock and the overlaying stiff terrace material, whose shear wave velocity, Vs is about 500-600 m/s. The velocity was estimated from SPAC measurements in August 2007 (Konagai et. al.) We indicate the locations where we could not identify a peak, with a 0 frequency in plots FIG. 4(b), FIG. 5(b), and FIG. 6(b). We are now reevaluating some of the results, and therefore, below, we give a preliminary description of our findings so far.

Starting with the North-South trending line (green), FIG. 4(a) (NS cross section) shows how the elevation changes from 690 m at point NS03 to 720 m at point NS04-NS06, reaches a maximum elevation of 740 m at point NS07- NS09 and then decreases to 710 m at point NS10.

Rock outcrops were confirmed at the boundary between terrace 2 and 3, at points NS06 and NS10. The high level of damage (see color legend for damage level scale) observed at points NS04 and NS05, and between points NS06 and NS07 coincides with a higher level of microtremor amplification at NS05 and NS06 as shown in FIG. 4(c).

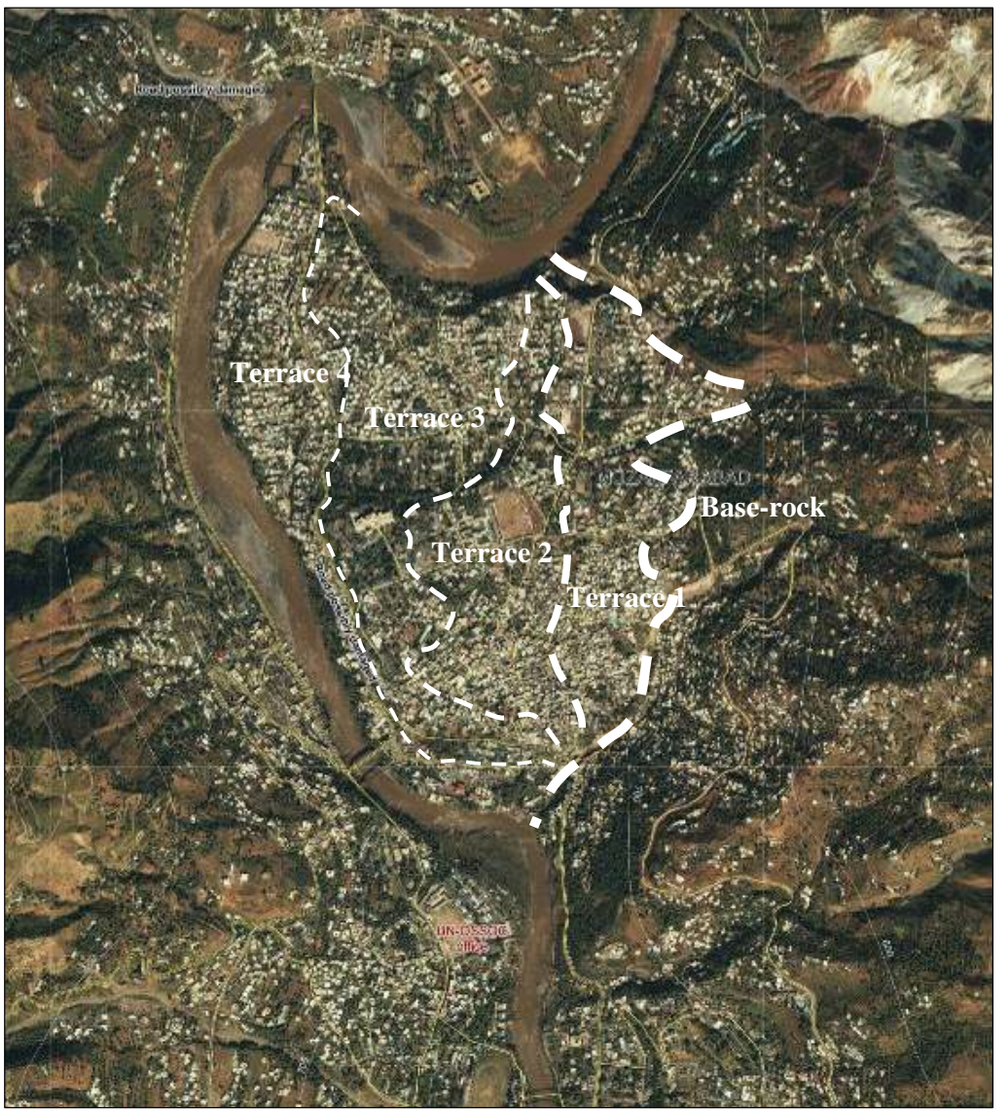


FIG. 2. Aerial photo of Muzaffarabad city with inferred geological terraces.

Continuing with the East-West 01 line (yellow in FIG. 3), as we move from EW0101to EW0103, we see that the fundamental frequency decreases from 10 to 7 Hz (see FIG. 5), indicating a possible increase in soil thickness and/or softer soils and at point EW0103 the amplification is about 6. As we move further west to points EW0104- EW0105, the gravel layer is probably thinning as indicated by increasing

fundamental frequency and also by outcrops along the river. At EW0106 we could not identify a clear peak.

At point EW0201 and EW0202 of the East-West 02 trending line (blue), the damage level is very high as seen in FIG. 3b) and FIG. 6. The fundamental frequency is relatively low (3.5 to 6 Hz) at points EW0201 and EW0202 which seems plausible because sediments of about 40 m thickness were observed at these points. Based on the formula $f=4H/V_s$, where H is the deposit thickness, a frequency, f ,of 3.5 Hz would correspond to an average shear wave velocity, V_s, of 560 m/s, which coincides with estimates obtained with so called SPAC array measurements of surface waves performed in August 2007 (Konagai et. al.) Going west, down to the points EW0203 and EW0204, the fundamental frequency increases to 8 and 12Hz, respectively. At points EW0205 and EW0206, there was no clear peak (below 25 Hz) in the H/V ratio most likely indicating very shallow soil layers; we observed bedrock at point EW0206.

In general we observe higher level of amplification (above 4, see FIG. 6(c)) and lower fundamental frequency (as estimated with the H/V ratio) in the area of the high damage in the southern part of Terrace 1 as shown in FIG. 3b.

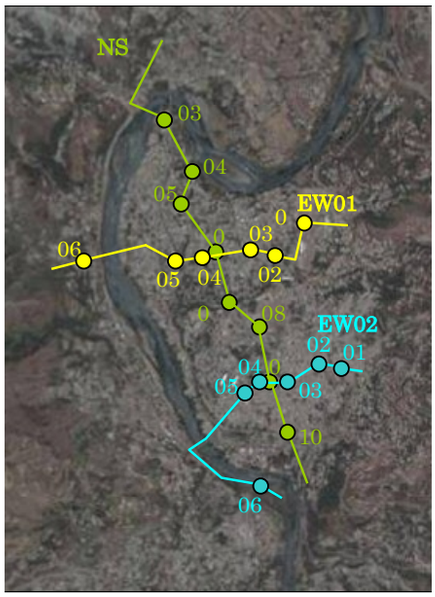


FIG. 3a. (Above.) Microtremor observation lines.

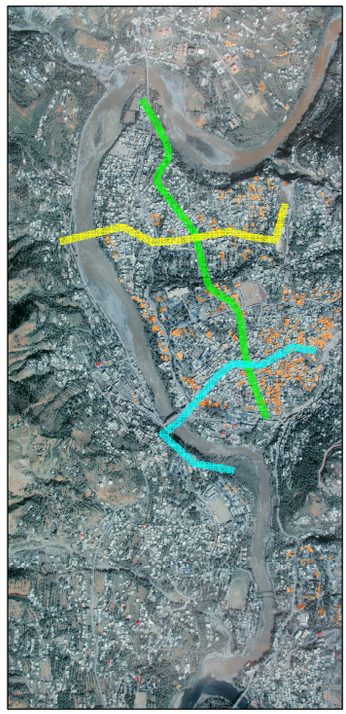


FIG. 3b. (Above right.) More damage is indicated as orange dots in the southern part around point 1 and 2 of the EW02 line, where there is a thicker gravel layer. Orange dots are the houses with thinner and vaguer edges as detected in Ikonos images before and after the earthquake.

DISCUSSION AND RECOMMENDATIONS

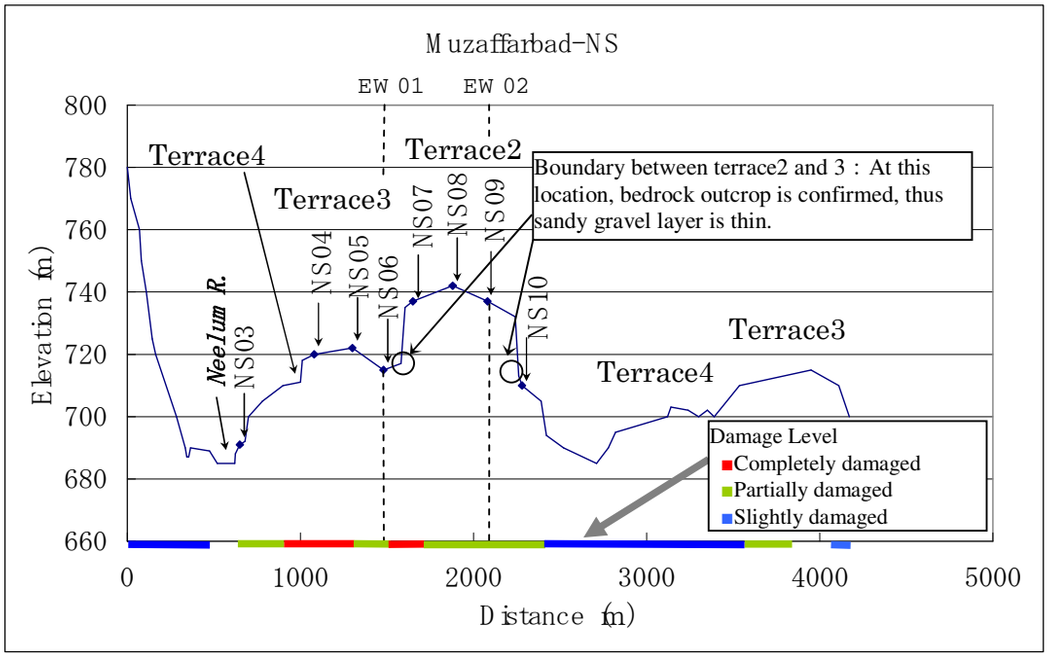
A geological and geotechnical investigation in Muzaffarabad for rehabilitation and restoration of the city and surroundings has been performed. Ikonos satellite imagery of Muzaffarabad area shows cluster-wise distribution of damage in urbanized zones of the city. This distribution seems to be related to the thickness of the sediments. As the thickness increases, damage seems to be more severe, like in the areas to east of the market (such as Zones #13, #14 in the JICA MP for rehabilitating the city) in the southern part of Terrace 1, which is also indicated by lower fundamental frequencies in our microtremor investigation.

As described in the JICA MP, locating open spaces and expanding the road network will make the area more robust against possible future disasters, allowing easy and quick access to the area, and thus providing refugees with space for shelter, necessary goods, and emergency services.

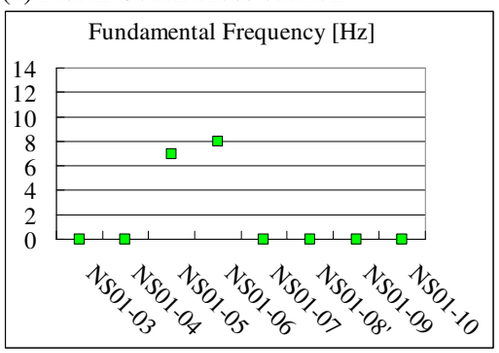
Among options for rehabilitating Muzaffarabad, one feasible idea is to create satellite towns outside the municipal boundary as described in the JICA MP. Construction on terraces would be appropriate for developing satellite towns, while avoiding their unstable rims. Slope failures at these rims occurred in the 2005 earthquake e.g. in the south-east at point EW0201. For houses and buildings on or near the terrace rim it is necessary to take measures of strengthening not only the main structure, but also the foundations. Possible measures include strong slab foundations, and/or pile foundations.

One difficulty in geohazard mitigation will be the maintenance of roads, which will have to cross deep gorges, in the mountains created by seismic faults (such as Tanda and Muzaffarabad faults). During the earthquake slope failures created debris deposits (sources) beneath the mountains and during heavy rains further debris flows can occur (see FIG. 7 for an example.) These flows will most likely follow the gorges, namely branches of the Jhelum and Neelum rivers crossing roads and suspending traffic. Clearing debris remaining on the roads would be just a stopgap. We suggest point-wise connections of existing roads by constructing new bridges etc. and the construction of cost-effective bypasses that would allow for bi-directional traffic.

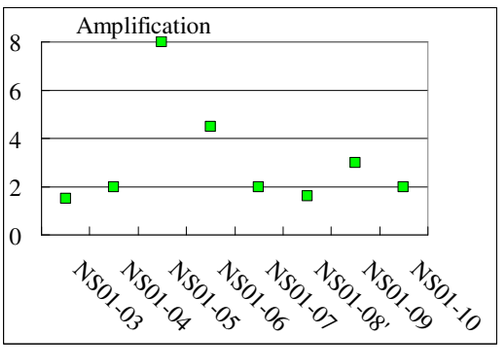
The terrace deposits themselves are well compacted, but strong shakes, especially in combination with erosion by rain increases the collapse risk. Where deemed necessary, the terrace rims should be reinforced and/or or covered with rock-fall prevention net.



(a) North-South cross section

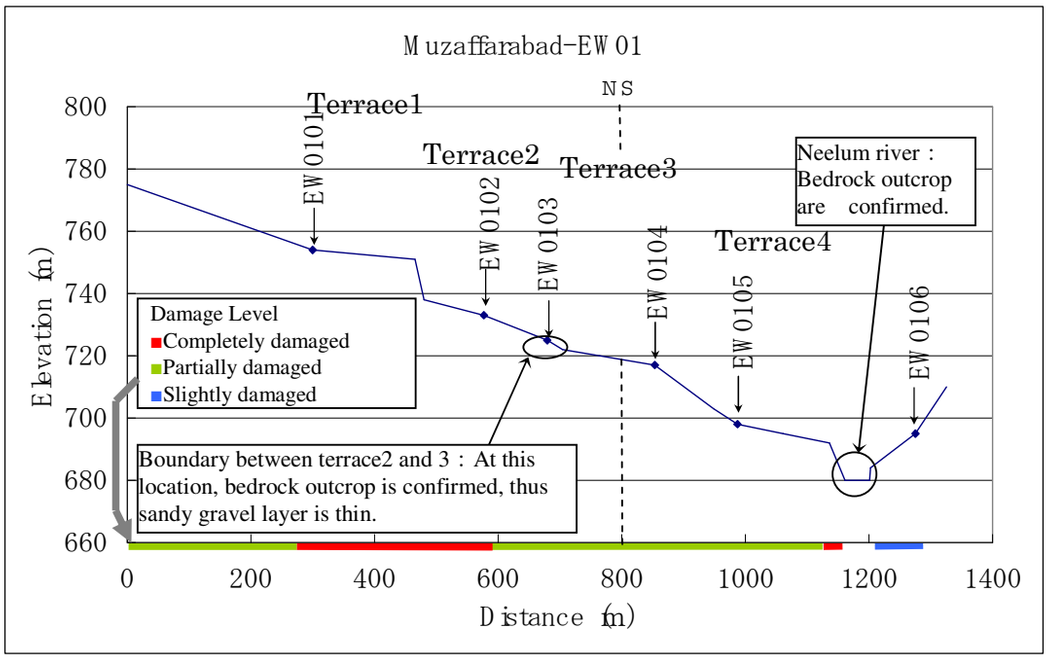


(b) fundamental frequencies

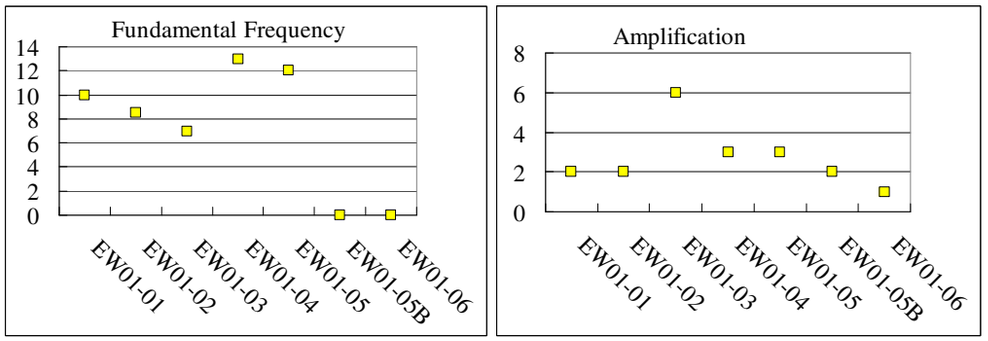


(c) amplification

FIG. 4. North-South trending line (green in FIG. 3 and FIG. 3b) cross-section in (a). (b) shows fundamental period/frequency of vibration and (c) possible amplification of ground motions, both estimated from H/Vspectral ratio

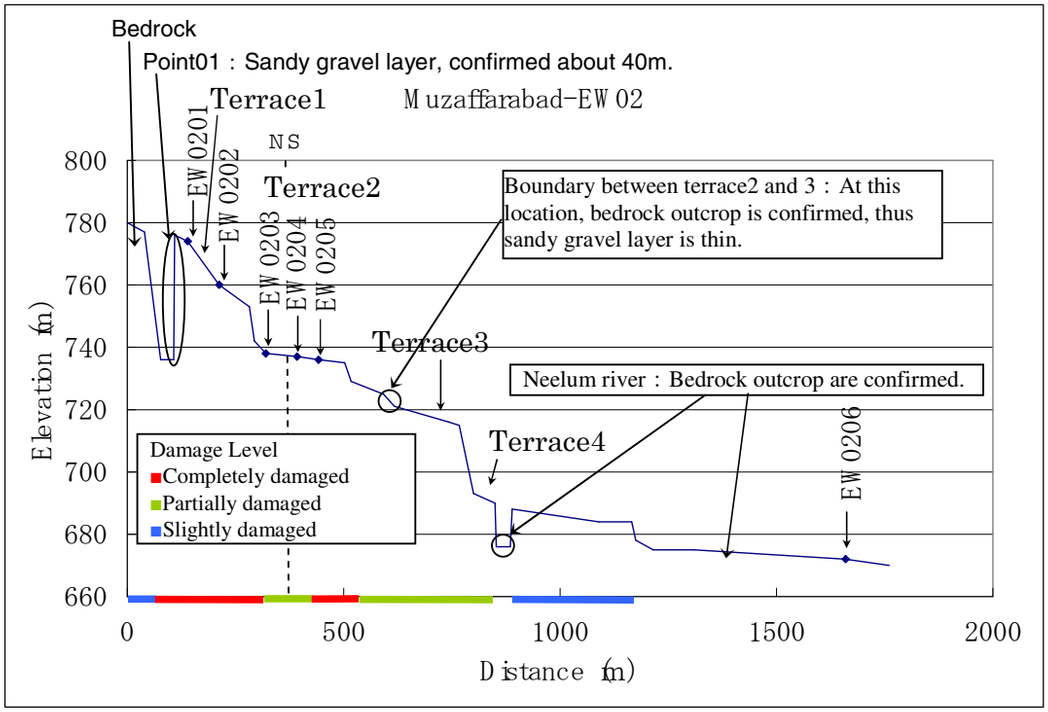


(a) East West cross section 1.

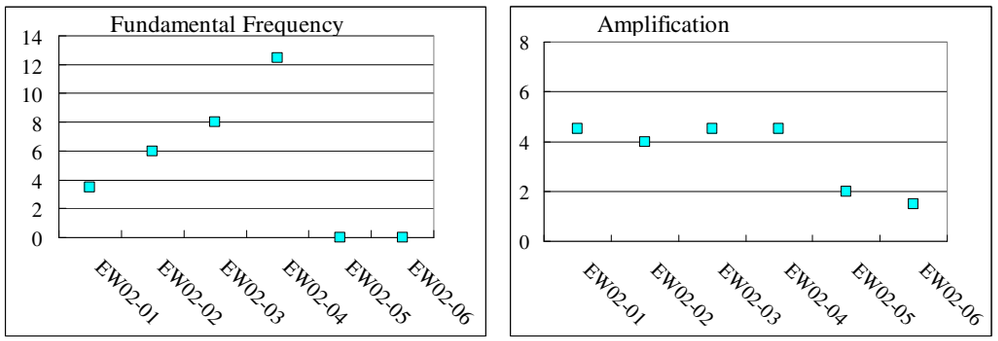


(b) fundamental frequencies (c) amplification

FIG. 5. East-West trending line #1 (yellow in FIG. 3 and FIG. 3b).



(a) East West cross section 2.



(b) fundamental frequencies (c) amplification

FIG. 6. East-West trending line #1 (blue in FIG. 3 and FIG. 3b).



FIG. 7. A several meters thick debris flow deposits accumulated during the monsoon period after the earthquake.

CONCLUSIONS

We have performed a geohazard study to complement current studies in for the planning of land use and reconstruction of Muzaffarabad and surroundings.

Our findings indicate that microtremor measurements in combination with interpretation of local geology allow us to roughly explain the damage distribution due to the 2005 Kashmir earthquake.

JICA has suggested creating satellite towns on terraces. To reduce the impact of future and secondary disasters we suggest that these towns should be connected with bridges passing over the deep gorges where debris flows are likely to occur.

Several detailed recommendations, such as avoiding construction nearby terrace rims and the importance of proper foundations and slope protection, were also outlined.

An important point is that secondary disasters can last for many decades and should be taken into account in land use plans etc.

ACKNOWLEDGMENTS

We are much indebted and thankful to Mr. Tahir Sharif, Director, Earthquake Reconstruction and Rehabilitation Authority,(ERRA), Government of Pakistan; Mr. Arshid Mehmood Abbasi and Mr. Zahid Amin, Chief Officer and Administrator of Municipal Corporation Muzaffarabad, Azad Kashmir, Pakistan; and local experts from Tobishima Co, who took care of the logistics in Pakistan. The members are also grateful to many experts from Japan International Cooperation Agency (JICA), and National Highway Authority, Pakistan (NHA), for their valuable suggestions and numerous discussions during the survey. We wish to further collaborate with Pakistan experts for possible countermeasures, e.g., reconstruction of damaged structures, retrofitting of existing structures and reducing risk related to geohazards.

REFERENCES

Dunning, S.; Mitchell, W.; Rosser, N. and Petley, D. (2007). “The Hattian Bala rock avalanche and associated landslides triggered by the Kashmir Earthquake of 8 October 2005.” *Engineering Geology*,, 93, 130-144

Geopsy software. (2007). http://www.geopsy.org/

Pierre-Yves BARD et. al. (2004). “Guidelines For The Implementation Of The H/V Spectral Ratio Technique On Ambient Vibrations.” *SESAME European research project*, http://sesame-fp5.obs.ujf-grenoble.fr/index.htm

Japan International Cooperation Agency (JICA). (2006). ”The Urgent Development Study on Rehabilitation and Reconstruction in Muzaffarabad City in the Islamic Republic of Pakistan”, *Interim Report*, Vol 1 and 2. Herein called JICA Master Plan or JICA MP.

Kazuo Konagai, Takaaki Ikeda, Atsunori Numata and Shigeki Takatsu, (2007), Personal communication

Incorporating the Effects of Site Geology in CEUS Hazard Maps

Chris H. Cramer, RG/RGP

Research Associate Professor, Center for Earthquake Research and Information, University of Memphis, 3890 Central Ave., Memphis, TN 38152-3050, cramer@ceri.memphis.edu

ABSTRACT: The effects of local geology, including uncertainty, have been incorporated into several central and eastern U.S. seismic hazard products. The approach is to generate site amplification distributions on a grid for a given period using three dimensional geological/geophysical/geotechnical models (urban hazard maps) or reference profiles keyed to surface geology and depth-to-bedrock (regional hazard maps) (Cramer, 2006). A derived shear-wave velocity profile for a grid point is randomized along with dynamic soil properties and the choice of input ground motion to represent model uncertainties. A Monte Carlo approach is used to estimate the lognormal mean and standard deviation of the site amplification distribution. Probabilistic seismic hazard maps use the full site amplification distribution and scenario (deterministic) maps use the appropriate fractile site amplification (median or 84th percentile). Computational efficiency and soil response program calibration are important aspects of this procedure.

INTRODUCTION

Seismic hazard maps that include the effects of local geology are key to making such maps more realistic and hence more usable to the seismic hazard community. The U.S. Geological Survey (USGS) has an urban seismic-hazard mapping program that has developed hazard maps with the effects of local geology for Memphis, TN, Oakland, CA, and Seattle, WA. These maps use site amplification distributions developed from three dimensional geological/geophysical/geotechnical models of local geology to incorporate the effects of local geology. For more regional applications where detailed three-dimensional models are not yet available, an alternative approach has been developed using regional reference shear-wave velocity (Vs) profiles keyed to available surface geology and depth-to-bedrock information. For the central and eastern U.S. (CEUS), Cramer et al. (2004, 2006) developed the urban seismic hazard mapping approach. Cramer (2006) extended this approach to regional hazard mapping for the Mississippi embayment.

The focus of this paper is to briefly review the methodology of incorporating the effects of local geology into seismic hazard maps, discuss the computational efficiency

limitations of representative soil response computer programs, and present the calibration approach taken concerning site amplification calculations, particularly at high ground motions (> 0.3 g). Figure 1 shows the location of both the Memphis urban hazard mapping study area and the upper Mississippi embayment regional study area that will be used in examples provided in this paper.

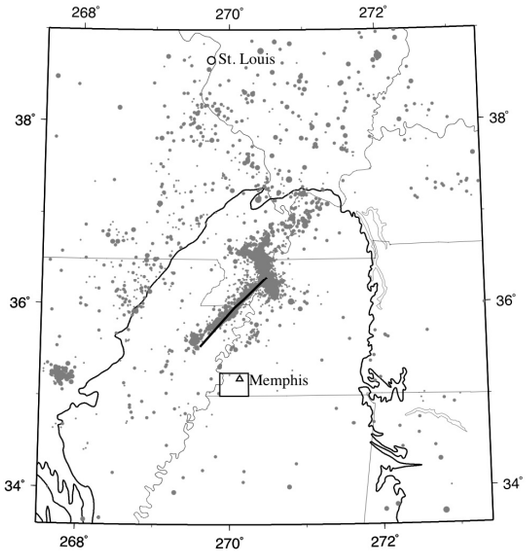


FIG. 1. Map showing the location of the Memphis study area (box near Memphis) and the upper Mississippi embayment study area (entire map) for examples used in this paper. The outline of the embayment is shown as a heavy line. Grey dots show earthquake epicenters. The black line is the fault rupture used in one of the New Madrid M7.7 scenarios. The triangle in the Memphis study area is the location of the MLGW water well referenced in Figure 4.

METHODS

Common current practice is to estimate NEHRP soil class (FEMA, 1998) for a site and apply soil-amplification factors based on Borcherdt (1994). A true site-specific amplification estimate is developed from geological, geophysical, and geotechnical subsurface information. A soil profile above bedrock is developed to represent soil type, boundaries, shear-wave velocity (Vs), bulk density, intrinsic shear-wave damping or attenuation (Qs), and dynamic soil properties (usually described by the dependence of modulus and damping curves on strain). This soil-profile information is commonly input into a soil-response program (often SHAKE) and a single 1D site-amplification factor calculated relative to hard rock. For the CEUS, hard rock is taken as rock with a Vs of 2.8 km/s to match the hard-rock Vs of CEUS ground motion prediction (attenuation) equations used in seismic hazard analysis. This soil profile and its dynamic soil properties are randomized over the uncertainty ranges in soil properties, and a distribution of possible site amplifications developed. The state of practice, in this case, is to apply the median site amplification to hard-rock probabilistic seismic hazard estimates to obtain probabilistic estimates of ground motion at a site. However, at large ground motions (>0.3 g) this approach can lead to the underestimation of probabilistic hazard by more than 10%. More accurate results are obtained by using a fully

probabilistic approach in which bedrock ground-motion prediction relations are made site specific by using the site-amplification distribution in the probabilistic seismic hazard calculations (Cramer, 2003, 2005). Basically, because possible rock ground motions and site amplifications for a given site are distributions, there are several combinations of rock ground motion and site amplification that give the same soil ground motion. The probability of a given soil ground motion is then the sum of the product of the probabilities of rock ground motion and site amplification for each combination that yields that soil ground motion. The probability of exceeding a given level of soil ground motion (soil hazard curve) is easily derived from this probability distribution of having a given soil ground motion. Additionally, soil amplification is a nonlinear process at strong levels of ground motion (> 0.1 g) that precludes the simple multiplying of means (and summing of variances) that can be done with linear distributions. Figure 2 provides an example of this nonlinear behavior where a hard-rock hazard curve is increased at low levels of motion due to soil amplification but decreased at high levels of motion due to nonlinear soil deamplification.

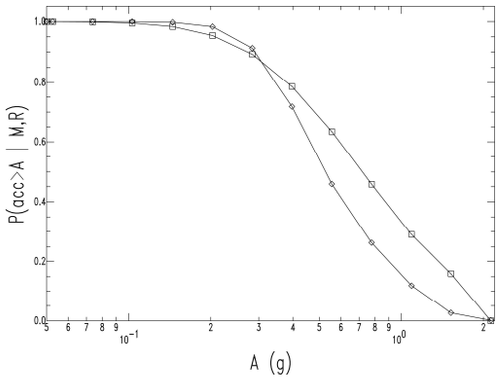


FIG. 2. Converting a hard-rock (squares) ground-motion hazard curve to a site-specific soil-response (diamonds) ground-motion hazard curve for a specific magnitude (M), distance (R), and ground-motion prediction relationship by using the procedure of Cramer (2003). This conversion occurs before summing hazard curves within the hazard integral of probabilistic seismic hazard analysis.

For the Memphis urban hazard maps, databases of geological, geophysical, and geotechnical information from water well logs, boring logs, and shallow Vs measurements have been gathered (Gomberg et al., 2003). A 3D model of the lithology and its uncertainties was then generated from this information (Figure 3). Seismic-hazard calculations were done on a grid (Cramer et al., 2004). For a given grid point, a Vs profile and its uncertainties are estimated from the 3D model of stratigraphy. Next, site-amplification distributions are generated using an equivalent-linear code (SHAKE91) calibrated to newer soil-response codes and randomizing the Vs profile and dynamic soil properties (see following section for details of validation and calibration tests of SHAKE91 at high ground motions and thick soil columns). To generate a site amplification distribution the soil profile, dynamic soil properties, and input time history (from a suite of 16 time histories recorded or simulated at rock sites within 50 km of the rupture) are randomized and the median and logarithmic standard deviation determined from 100 Monte Carlo realizations. Finally, completely probabilistic seismic hazard at

the grid point is calculated from the resulting site-amplification distributions using the approach of Cramer (2003, 2005). As shown in Figure 2, this is done by modifying the bedrock ground motion prediction relations used in the USGS national seismic-hazard map calculations (Frankel et al., 2002) to site-specific relations prior to calculating the seismic hazard.

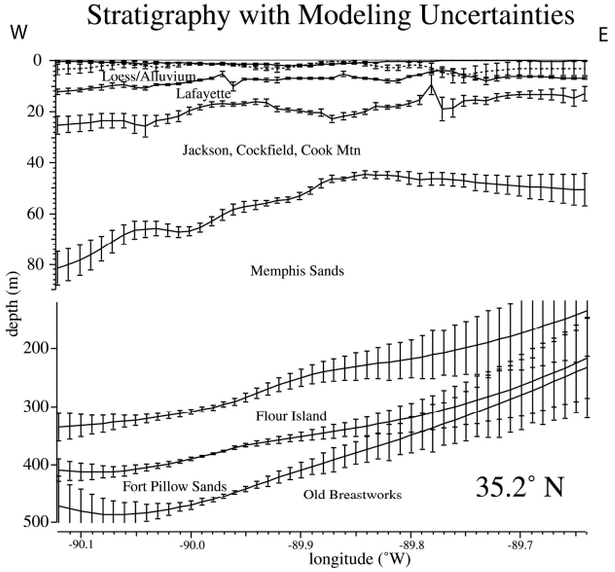


FIG. 3. E-W geologic cross-section through downtown Memphis generated from a 3D well information database. Error bars indicate uncertainty in layer boundaries. Note change in depth scale at 90 m. Modified from Gomberg et al., 2003.

For the entire upper Mississippi embayment (regional approach), there is not enough detailed geological information to use the approach used in the Memphis hazard maps. For such a regional approach, the procedure used for Memphis has been modified to follow the approach used by Toro and Silva (2001). Instead of a 3D lithologic model, Quaternary (lowlands) and Tertiary (uplands) reference profiles are used based on the work of Romero and Rix (2001). Each reference profile is subdivided into seven depth-to-bedrock ranges based on available sediment thickness categorizations, and site-amplification distributions are estimated for each depth-to-bedrock range by the same profile randomization procedure used to generate the Memphis hazard maps. Separate hazard maps (probabilistic and deterministic) for each reference profile and basement depth range have been generated. For a probabilistic map, the fully probabilistic approach of Cramer (2003, 2005) is again used. The final hazard maps are assembled by using the mapped surface geology and depth-to-basement to select the appropriate hazard curve at each grid point from the generated suite of hazard maps.

In estimating site-amplification distributions at each period of interest, 100 Monte Carlo simulations from the randomized soil profile are used. For these kinds of studies, the periods of interest are typically peak ground acceleration (PGA), and 0.2 s and 1.0 s spectral acceleration (Sa). To describe the distribution estimates of median and one logarithmic standard deviation variation (68% confidence limits) in the site amplification are made at each of ten input ground-motion levels ranging form 0.01 to 1.0 g at the

surface. The period-specific surface rock-ground-motion levels used are 0.01, 0.05, 0.1, 0.2, 0.3, 0.4, 0.5, 0.6, 0.8, and 1.0 g. Because ground-motion prediction relations are for surface ground motions, the free surface effect (a doubling of the amplitude) needs to be properly accounted for. Ground motions recorded at the surface but used as input ground motions to the bedrock-soil interface must be reduced by a factor of 2 (change from outcrop to within rock motion). Once the soil response has been calculated, it may be necessary to multiply by a factor of two depending on the program used (change back to outcrop from within soil motion). A key criterion in selecting a program to compute soil-amplification distributions is how quickly the needed 3000 calculations per grid point can be made.

CALCULATION AND CALIBRATION

The computational efficiency of the soil response calculations as well as their accuracy are important in completing hazard maps that include the effects of site geology. The approach of this paper uses SHAKE91 (Idriss and Sun, 1992) because of its computational speed (fraction of a second per run) to perform the 1000 soil response iterations per ground motion period used to develop that period's site amplification distribution at each grid point. Besides SHAKE91, other newer but computationally more intensive soil-response programs were also evaluated for use in the above procedure. The other programs evaluated were NOAH (Bonilla, 2001; Bonilla et al., 2004), DEEPSOIL (Hashash and Park, 2001, 2002), and TREMORKA (Bonilla, written communication, 27 October 2003; Hartzell et al., 2004). NOAH is a finite-difference nonlinear site response code, which can include pore-pressure effects. DEEPSOIL is a finite-element nonlinear PC-based code with a user interface. TREMORKA is an equivalent-linear implementation using the frequency-dependent damping approach of Kausal and Assimaki (2002). The two fully nonlinear codes take several minutes per run to estimate soil response for a thick soil profile (> 100 m). TREMORKA runs faster, taking a half to one minute per run. This is still slower than SHAKE91 at a fraction of a second per run.

There are two concerns about the accuracy of SHAKE programs that need to be addressed before relying on SHAKE91 in the above automated-procedure. The first is the accuracy of response calculations at strong levels of shaking (> 0.3 g). The version of SHAKE91 used is from the NISEE Software Library, distributed by the University of California, Berkeley (www.eerc.berkeley.edu). I modified SHAKE91 for increased precision and stability at strong levels of ground motion according to the suggestions of Stephen Hartzell (doubling variable precision, written communication, 2002). Additionally, older versions of SHAKE such as SHAKE91 have a problem with odd numbers of soil layers above the half-space, although even numbers of layers work well (Bill Joyner, written communication, 1998). I modified SHAKE91 to detect and avoid an odd number of layers above the half-space by splitting the thickest layer in half when an odd number of soil layers are detected.

To validate the accuracy of SHAKE91 at strong levels of ground motion, a validation test among SHAKE91, TREMORKA, and DEEPSOIL was performed with a 0.5 g record

as input. Table 1 shows the 50-m profile and dynamic soil properties used in the test. This soil profile and set of dynamic properties was chosen to eliminate all other variations affecting soil response except the method of soil response calculation. Figure 4 shows the 5%-damped elastic response spectra results for the validation test. The outcrop (surface record) procedure outlined earlier was used in all test runs. For clarity in showing the variability over all periods and not just at periods of highest amplitude, a logarithmic amplitude axis was chosen in Figure 4. The differences among the response spectra at high frequency (greater than 1 Hz) are about 30%. TREMORKA tends to provide a soil response higher than SHAKE91, as one would expect from TREMORKA's frequency-dependent damping versus SHAKE91's frequency-independent damping. The results from SHAKE91 compare quite favorably (within about 15% in spectral amplitude) with those from DEEPSOIL at these high levels of ground motion.

TABLE 1. Fifty-meter soil profile and properties used in the validation test[a].

Layer	Depth to Top (m)	Thickness (m)	Damping Ratio	Density (g/cc)	Vs (m/s)
1	0	4	0.05	2.0	177
2	4	8	0.05	2.0	228
3	12	16	0.02	2.0	280
4	28	22	0.02	2.0	520
5	50	---	0.001	2.8	2800

[a] Modulus and damping curves for all soil layers (1-4) are the Vucetic and Dobry (1991) curve for a plasticity index of 30.

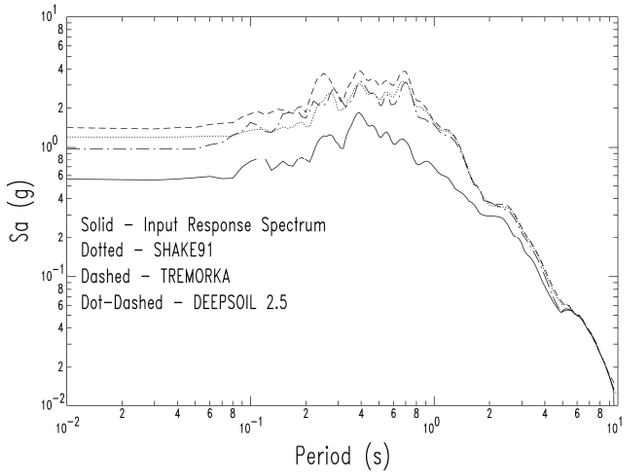


FIG. 4. Results from a validation test showing 5%-damped elastic spectra from SHAKE91 (dotted), TREMORKA (dashed), and DEEPSOIL (dot-dashed) for a 50-m soil profile and common dynamic soil properties (see Table 1) and input ground-motion record (solid).

Equivalent-linear soil response codes with frequency-independent damping, such as SHAKE91, are known to over damp high frequency response when computing soil responses of thick soil profiles (> 100 m) (Toro and Silva, 2002; Hashash and Park, 2001,

2002; Hartzel et al., 2004). This can be overcome by limiting nonlinear soil behavior to layers above a fixed depth when using SHAKE-like codes for soil amplification calculations. Thus a calibration test is needed to determine the appropriate limiting depth for nonlinear behavior when using SHAKE91 for soil response calculations in the CEUS.

Figure 5 shows the calibration test results using a soil profile from MLGW well site 236 (Figure 1). In Figure 5 the comparison of soil responses (5% damped elastic response spectra) for 0.5 g PGA input surface ground motions is derived using SHAKE91, DEEPSOIL, TREMORKA, and SHAKE91 limited to linear soil response below 80, 300, and 400 m. A common surface ground motion record was used as input by appropriately converting from outcrop to within rock motion. While a 0.1g input surface time series leads to output differences among the various programs of less than 50%, differences are much greater for a 0.5 g input surface time series shown in Figure 5. DEEPSOIL has a lower high-frequency response than TREMORKA except at 0.2-0.5 s (5 to 2 Hz). By visual comparison, SHAKE91 limited to linear soil response below 300 m seems to match the output of the newer soil-response codes better than the other two depth limitations shown, although it seems to consistently underestimate the amplitude response between 0.2 and 0.5 s (5 to 2 Hz) in the example shown.

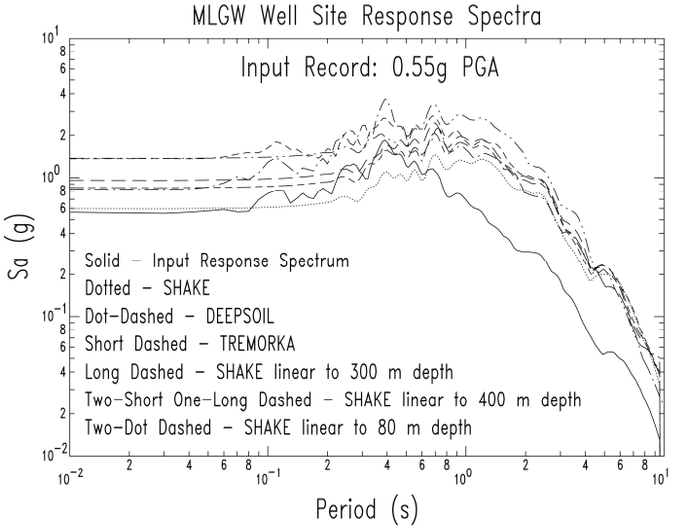


FIG. 5. Output 5%-damped elastic response spectra comparison among soil-response computer programs for the MLGW water well site shown in Figure 1. Solid response spectrum is for the input surface ground motion for the bedrock-soil input record.

RESULTS

Examples of PGA probabilistic seismic hazard maps with the effects of local geology are shown in Figures 6-7 for Memphis, TN (urban) and the upper Mississippi embayment (regional). Figure 6 is a comparison between an urban and regional hazard map maps, which both include the effects of local geology. Nonlinear soil response smoothes out and flattens the PGA hazard gradient across the Memphis urban study area.

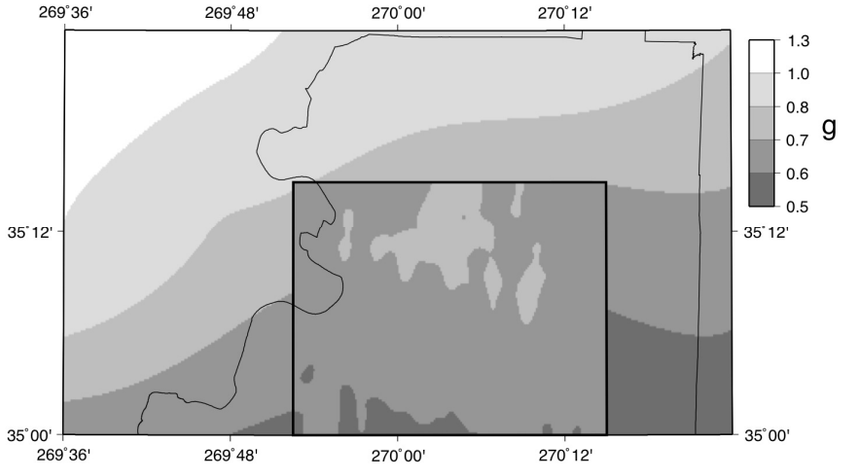


FIG. 6. Probabilistic seismic hazard map showing PGA hazard for the Memphis area with a 2%-in-50-year probability of exceedance. The smaller Memphis urban hazard map is inset into the corresponding regional seismic hazard map, both of which include the effect of site geology.

Figure 7 shows a PGA probabilistic seismic hazard map for the upper Mississippi embayment. Short periods, including PGA, tend to be deamplified (by up to 30%) by the thick sediments of the embayment, which reduces short period ground motion hazard relative to the national maps (Cramer, 2006). Unfortunately, long periods (1 s and greater) tend to be significantly amplified (doubled) by the embayment sediments without significant reductions due to nonlinear soil behavior (Cramer, 2006).

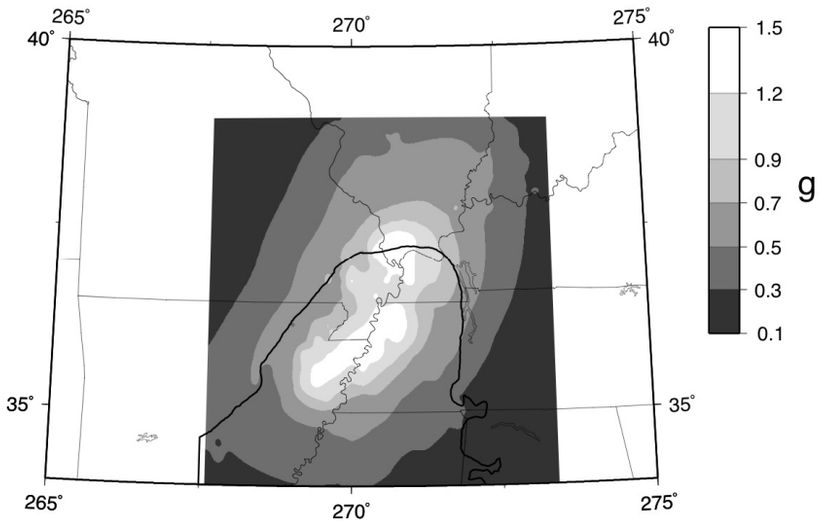


FIG. 7. Embayment regional hazard map for PGA that include the effect of site geology. The map is for a 2%-in-50-year probability of exceedance. The thick irregular black line shows the Mississippi embayment boundary.

Besides probabilistic hazard maps, scenario (deterministic) hazard maps for ground motion and liquefaction hazards have been produced for the Memphis study area.

Regional scenario maps using modified Mercalli intensity (MMI) have also been produced using the 1.0 s to MMI conversion of Kaka and Atkinson (2005): MMI = 4.14 + 1.81*$\log_{10}$(1.0 s Sa). Scenarios generated so far are for the New Madrid and Wabash Valley seismic zones. Additionally, input files for HAZUS are available for these M6 and M7 scenarios. They include maps of PGA, PGV, 0.3 s, and 1.0 s, where PGV was derived from 1.0 s spectral acceleration (Sa) using the HAZUS conversion formula: PGV = 37.27*(1.0 s Sa). These scenario maps can be used in emergency planning and response exercises and are available at http://earthquake.usgs.gov/regional/ceus/.

ACKNOWLEDGEMENTS

The author gratefully acknowledges the support for this study provided by the U.S. Nuclear Regulatory Commission and the U.S. Geological Survey. The author also wishes to thank two anonymous reviewers for their suggested improvements to the manuscript. This paper is Center for Earthquake Research and Information contribution #520.

REFERENCES

Bonilla, L.F. (2001). *NOAH: user's manual*, Institute for Crustal Studies, University of California, Santa Barbara, 38 pp.

Bonilla, L.F., Archeleta, R.J., and Lavellee, D. (2004). "Hysteretic and dilatant behavior of cohesionless soils and their effects on nonlinear site response: field data observations and modeling." *Bull. Seismo. Soc. Am.*, Vol. 95 (6), 2373-2395.

Borcherdt, R.D. (1994). "Estimates of site-dependent response spectra for design (methodology and justification)." *Earthquake Spectra*, Vol. 10 (4), 617-653.

Cramer, C.H. (2003). "Site-specific seismic hazard analysis that is completely probabilistic." *Bull. Seismo. Soc. Am.*, Vol. 93 (4), 1841-1846.

Cramer, C.H. (2005). "Erratum: Site-Specific Seismic Hazard Analysis that is completely probabilistic." *Bull. Seismo. Soc. Am.*, Vol. 95 (5), 2026.

Cramer, C.H. (2006). "Quantifying the uncertainty in site amplification modeling and its effects on site-specific seismic-hazard estimation in the upper Mississippi embayment and adjacent areas." *Bull. Seismo. Soc. Am.*, Vol. 96 (6), 2008-2020.

Cramer, C.H., Gomberg, J.S., Schweig, E.S., Waldron, B.A., and Tucker, K. (2004). *Memphis, Shelby County, Tennessee, seismic hazard maps*, U.S. Geological Survey, Open-File Report 04-1294, 41pp.

Cramer, C.H., Gomberg, J.S., Schweig, E.S., Waldron, B.A., and Tucker, K. (2006). "First USGS urban seismic hazard maps show effects of soils." *Seismo. Res. Lett.*, Vol. 77 (1), 23-29.

FEMA (1998). *NEHRP recommended provisions for seismic regulations for new buildings and other structures: Part 1 – Provisions* (1997 Edition), Federal Emergency Management Agency, FEMA 302 / February 1998, p. 35.

Frankel, A.D., Petersen, M.D., Mueller, C.S., Haller, K.M., Wheeler, R.L., Leyendecker, E.V., Wesson, R.L., Harmsen, S.C., Cramer, C.H., Perkins, D.M., and Rukstales, K.S. (2002). *Documentation for the 2002 update of the national seismic hazard maps*, U.S. Geological Survey, Open-File Report 02-420.

Gomberg, J., Waldron, B., Schweig, E., Hwang, H., Webbers, A., Van Arsdale, R., Tucker, K., Williams, R., Street, R., Mayne, P., Stephenson, W., Odum, J., Cramer, C., Updike, R., Hutson, S., Bradley, M. (2003). "Lithology and shear velocity in Memphis, Tennessee." *Bull. Seismo. Soc. Am.*, Vol. 93 (3), 986-997.

Hartzell, S., Bonilla, L.F., and Williams, R.A. (2004). "Prediction of nonlinear soil effects." *Bull. Seismo. Soc. Am.*, Vol. 94 (5), 1609-1629.

Hashash, Y.M.A, and Park, D. (2001). "Non-linear one-dimensional seismic ground motion propagation in the Mississippi embayment." *Eng. Geol.*, Vol. 62, 185-206.

Hashash, Y.M.A., and Park, D. (2002). "Viscous Damping formulation and High Frequency Motion Propogation in Non-Linear Site Response Analysis." *Soil Dynamics and Earthquake Engineering*, Vol. 22, 611-624.

Idriss, I.M., and Sun, J.I. (1992). *User's manual for SHAKE91*, Center for Geotechnical Modeling, Department of Civil and Environmental Engineering, University of California, Davis, California.

Kaka, S.I., and Atkinson, G.M. (2005). "Empirical ground-motion relations for ShakeMap applications in southeastern Canada and the northeastern United States." *Seismo. Res. Lett.*, Vol. 76 (2), 274-282.

Kausel, E., and Assimaki, D. (2002). "Seismic simulation of inelastic soils via frequency-dependent moduli and damping." *J. Eng. Mech.*, Vol. 128, 34-47.

Romero, S., and Rix, G.J. (2001). "Regional variations in near surface shear wave velocity in the Greater Memphis area." *Eng. Geol.*, Vol. 62, 137-158.

Toro, G.R. and Silva, W.J. (2001). *Scenario Earthquakes for Saint Louis, MO, and Memphis, TN, and Seismic Hazard Maps for the Central United States Region Including the Effect of Site Conditions*, Risk Engineering, Inc., Final Tech. Report.

Vucetic, M, and Dobry, R. (1991). "Effect of soil plasticity on cyclic response." *J. Geothech. Eng. ASCE*, Vol. 117, 89-107.

SEISMIC MICROZONATION OF SHIRAZ CITY, SOUTHWEST OF IRAN

A.Ghalandarzadeh[1], S.Sahraeian[2], A.Kavand[3], B.Kamrani Moghaddam[4]

[1] Assistant Professor, Department of Civil engineering, University of Tehran, Tehran, Iran, aghaland@ut.ac.ir

[2] M.S Student, Department of Civil engineering, University of Tehran, Tehran, Iran, sadegh_sahraeian@yahoo.com

[3] Ph.D Student, Department of Civil engineering, Sharif University of Technology, Tehran, Iran, ali_kavand@yahoo.com

[4] M.S Student, Department of Civil engineering, University of Tehran, Tehran, Iran, babakkamrani@yahoo.com

ABSTRACT: This paper aims to study the soil dynamics characteristics of central part of Shiraz city near the monument of Persepolis, southwest of Iran. The parameter investigated is natural period of soil sediment. The technique used to obtain this parameter is microtremor measurements. Microtremor measurements were obtained at 120 stations in the city. The data was recorded for two periods of fifteen minutes. Segmental Cross Spectra were applied to calculate spectra. Nakamura's method (H/V) was used for analyzing the measured data. At each site, natural period values were obtained. Because of low accuracy of amplification factors that achieved by microtremor measurements, this factor is neglected in this study. Iso-period map of this part of the city was prepared. The calculated natural periods were compared to those obtained through one dimensional analysis for some existing geotechnical borehole information. It showed that the predicted fundamental period by microtremor method compares well comparable to that obtained by one dimensional analysis.

INTRODUCTION

The ground is always vibrating at minute amplitudes. Microtremors are ambient vibrations of the ground caused by natural or artificial disturbances such as wind, sea waves, traffic and industrial machinery. The vibration amplitude of the microtremor is typically less than several microns. Seismometers of high sensitivity are used for microtremor measurements (**TC4** 1993). The application of microtremors to determine dynamic characteristics (natural period and amplification factor) of soil layers was pioneered by Kanai and Tanaka (Kanai, K. and Tanaka, T. 1954), (Kanai, K. and Tanaka, T. 1961). Nowadays microtremor measurements are popular in site characterization due to their simplicity, low cost and minimal disturbance to other activities.

Methods for analyzing microtremors are generally divided into two main categories: non-reference site (H/V) and reference site (Hs/Hr) techniques. In (Hs/Hr) method, Hs is horizontal spectrum of the measured microtremor on

sediment and Hr is horizontal spectrum of the record on reference site. In this method at nearby sites, source and path effects are assumed to be identical and reference site is free of any site effect. Therefore, motion recorded at the reference station is representative of the excitation arriving at the interface sediments under the soft soil site and spectral ratio, (Hs/Hr), constitute a reliable estimate of site response. In other words, by dividing Hs to Hr, transfer function of soil can be obtained. This technique, introduced first by Borcherdt (Borcherdt, R. D. 1970), is still widely used and is very popular for the analysis of weak or strong motion records. It has been applied to microtremors by Kagami et al. (Kagami, H., Okada, S., shiono, K., Oner, M., Dravinski, M. and Mal, A. k. 1986) and has yielded good results. A technique using horizontal to vertical spectral ratios (H/V) of the microtremors, which was first applied by Nogoshi and Igarashi (Nogoshi, M. and Igarashi, T. 1970), (Nogoshi, M. and Igarashi, T. 1971) and popularized by Nakamura (Nakamura, Y. 1989), has been widely used to estimate the site effects. Several recent applications of this technique have proved to be effective in estimating natural periods (Field, E. H. and Jacob, K. H. 1993), (Ohmachi, T., Konno, K., Endoh, T. and Toshinawa, T. 1994) as well as relative amplification factors (Lermo, J. and Chavez-Garcia, F. J. 1994), (Konno, K. and Ohmachi, T. 1995). In this method the average spectrum of N-S and E-W component of microtremors is divided by the spectrum of Z component which is named H/V spectral ratio. Peak of the H/V curve shows the natural period and amplification factor of the sediment.

Several methods have been proposed for spectral characterization of ground motions including microtremors. Fourier spectrum is the most convenient one that is used widely. Some investigations showed that different methods give similar results (Dimitriu, P. P., Papaioannou, Ch. and Theodulidis, N. P. 1998). However some researchers declare that a suitable spectral method gives more reliable results. For instance Ghaemmaghamian and Kawakami investigated the aspects of spectral analysis of microtremors (Ghayamghamian, M. R. and Kawakami, H. 1997). They introduced segmental cross-spectrum (SCS) method, as an effective tool for counteracting unknown effects like source effects and noise in input and output measurements. They evaluated the performance of SCS method in contrast with the conventional methods, i.e. Fourier or power spectra through the mathematical modeling and numerical simulations. Results of their studies indicated that SCS gives more reliable results for both amplification factor and natural resonance frequency of the site than conventional methods (Ghayamghamian, M. R. and Kawakami, H. 1997). This method makes use of two-sided cross-spectral functions of two different segments of the microtremor signal.

SURFACE GEOLOGY OF SHIRAZ CITY

Shiraz city is located in region with a non-uniform topography. The north and northwest of the city is hillside that takes higher altitudes. The city is coming to the south and southeast parts extended on sediments with lower altitude. Accordingly soil deposits thicken from northwest to southeast. The water level is located shallower in the southeast and southeastern parts. The minimum underground water table is at even 3-4 meters below the ground surface in these areas. A river crossing the city from northwest to southeast sense to have influenced the characteristics of the sediments. Based on the field study that has been done during the current research on the existing open trenches, the type of soil sediments is mostly gravely

soil in upstream areas whereas it becomes more or less finer soils such as clay or clay-mixed silt and sand at downstream areas.

MICROTREMOR MEASUREMENT

Microtremor measurement was recorded at 120 sites in central part of Shiraz city in December 2006. To assess accuracy of the microtremor measurement and influence of time of measurements on results, microtremor measurements repeated in 104 stations in June 2007. Figure 1 shows the distribution of these sites throughout Shiraz city.

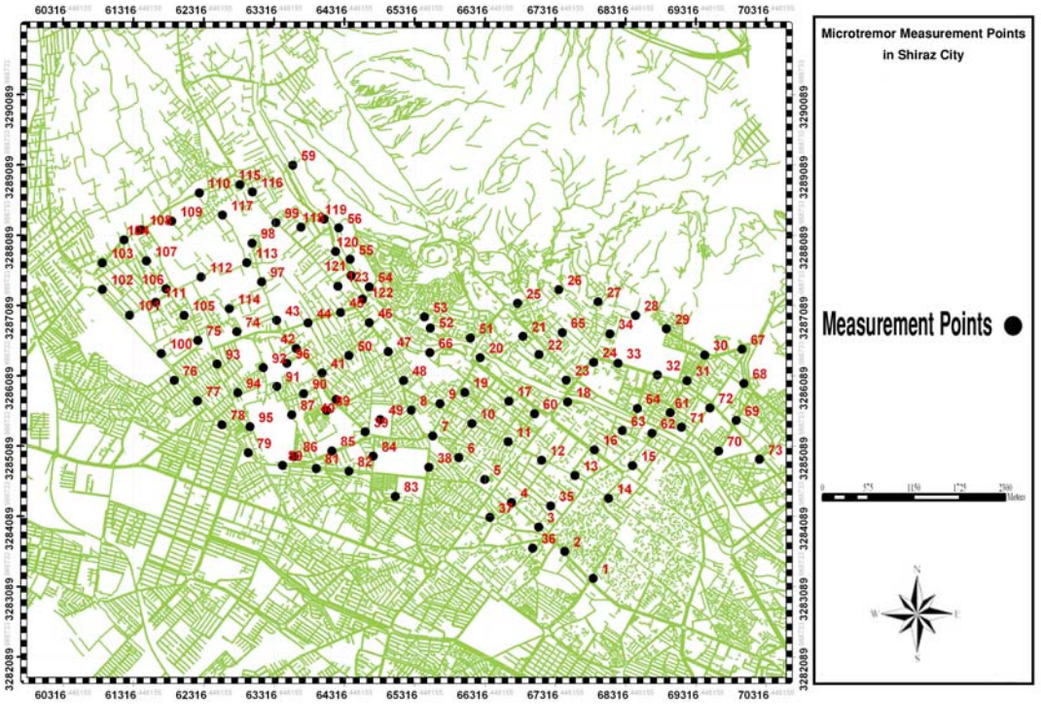


Fig. 1 - Microtremor measurement points throughout Shiraz city

The equipment used to record the microtremors was a seismometer with 0.5 Hz natural frequency by Sedisfore, Germany (Fig.2).



Fig. 2 - Microtremor measurement in Shiraz city

Seismometers comprise three components, which can record the two horizontal motions (in longitudinal and latitudinal directions) and the vertical motion. Sampling frequency is 500Hz and the length of each record is 15 min. Measurements were recorded twice times at each observation point. In measurements, special emphasis was given to minimizing artificial noises due to traffic and human activities. Figure 3 shows a typical record at site 11.

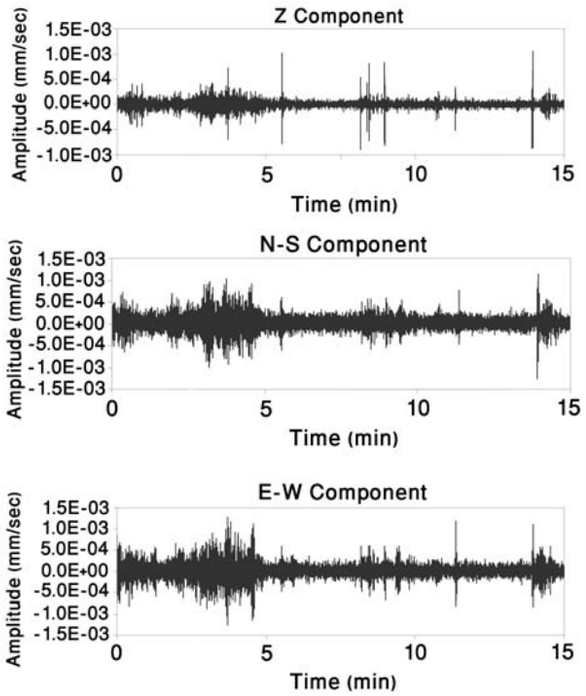


Fig. 3 - Microtremor recorded at site 11

To process microtremor data, a computer program was developed in MATLAB, using the Signal Processing Toolbox. In order to find the best processing method, a special emphasis was given to the processing procedure of microtremors. A time window length of 20 seconds with an overlapping value of 10% and a Hamming window type were distinguished to be the best choices in the processing of microtremor data.

SEISMIC MICROZONATION MAPS

At each station, data were analyzed using H/V technique. Segmental cross spectrum was used for spectral calculation. In Figure 4, for example, an H/V spectral ratio curve is shown.

Natural period values at each site were determined and based on the obtained results iso-period map of central part of Shiraz city was prepared. This microzonation map is presented in Figure 5. Because of low accuracy of amplification factors that achieved by microtremor measurements, this factor is neglected in this study.

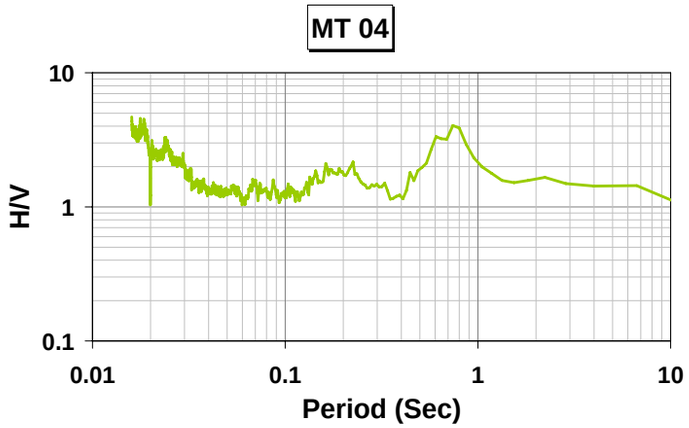


Fig. 4 - H/V spectral ratio curve

Iso-period map shown in figure 5 shows a zone from northwest to southeast having higher natural period. From geological point of view a river that crosses the city from northwest to southeast could create such high period zone. Moreover the natural period increases inside this zone from northwest to southeast. It seems thicker and probably finer deposits are formed in downstream side of the river that flows from northwest to southeast. Parallel to this zone a low period zone could be recognized in northern part. It is noteworthy to note that this area is a hillside with clear rock outcropping.

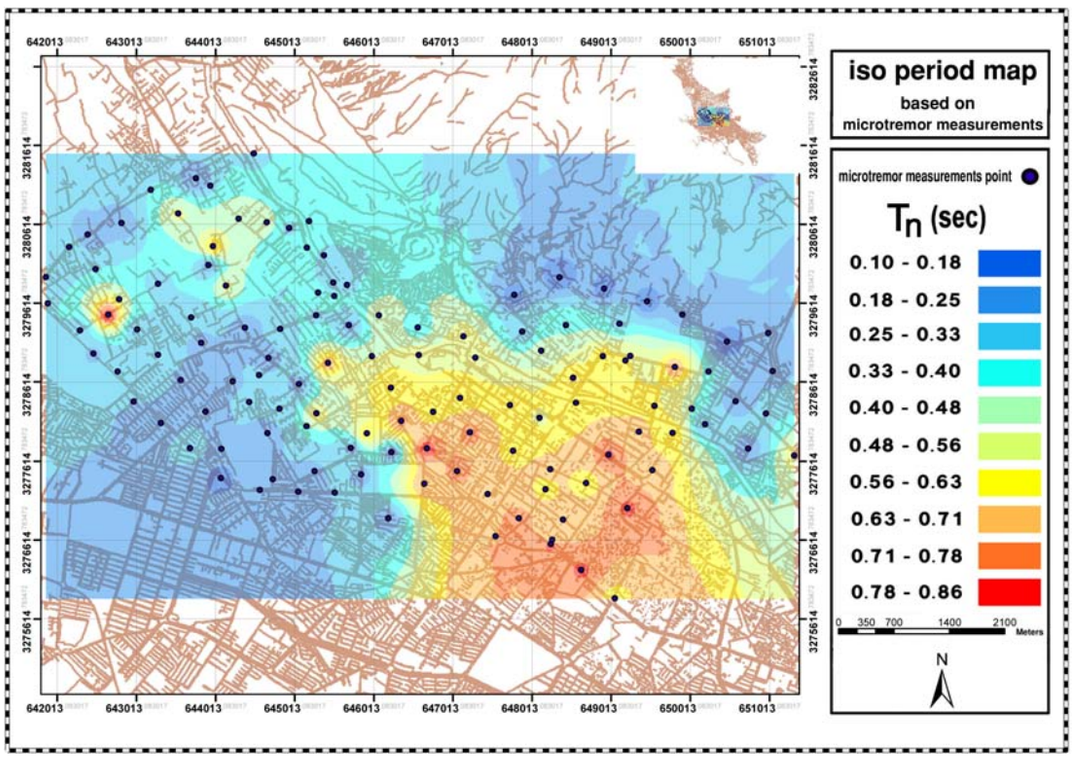


Fig. 5 – Iso period map based on microtremor measurements

COMPARISON OF TWO SERIES OF MEASURMENTS

It is of interest to examine that whether the obtained predominant period of each site remains the same, if different records are used. In other words the H/V curves should be stationary. Therefore, as noted before, measurements were repeated in 104 sites and after analyzing the records the results showed that time did not influence the spectral ratio (H/V) of the microtremors. In figure 6 the spectral ratio (H/V) of the microtremors in two sites where second series of recording were obtained, are compared. Figure 6 depicts that the results are similar and peaks of (H/V) diagrams did not change with time of recording.

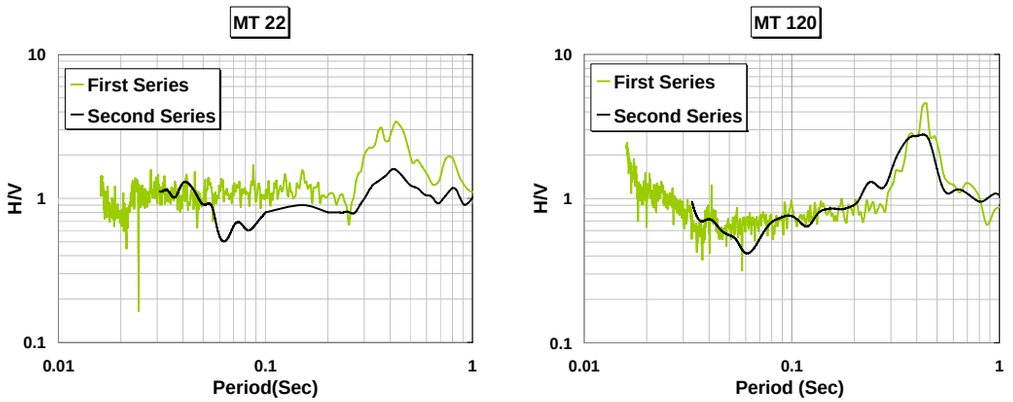


Fig. 6 – Comparison of two series of records

Although the two spectra yield similar value of T_n, the shapes are different. Probably different traffic or ambient vibration at the time of second measurement causes difference in shapes.

COMPARISON OF RESULTS OF MICROTREMOR MEASURMENT AND INFORMATION OF EXISTING GEOTECHNICAL BOREHOLES

In order to assess accuracy of calculated ground natural periods, the results compared to those obtained through analysis of some existing geotechnical borehole information. Only those boreholes are used that the bedrock is achieved in them or SPT blow count were above 50 at the depths more than 20 meters. Geotechnical information such as soil type, depth and SPT blow count (N_{spt}) were obtained from borehole reports for 27 sites. One sample borehole log for site 8 is presented in Table 1.

Based on the existing empirical relations between shear wave velocity (V_s) and N_{spt}, shear wave velocity (V_s) was estimated for different layers at each borehole and one dimensional equivalent linear analysis was performed for each site. The experimental relations used in this part are (**TC4** 1993):

1. $V_S = 84N^{0.31}$ (Ohba & Trauma)
2. $V_S = 69N^{0.17}D^{0.2}EF$ (Ohta & Goto 1978)

3. $V_S = 61N^{0.5}$ (Seed & Idriss 1981)

where N, D, F and E are SPT blow count, the soil depth, grain size coefficient and soil type coefficient respectively.

Table 1. Soil Profile in Borehole 8

Depth (m)		Unified Class	Soil Description	Depth	SPT Blow Count			
From	To			(m)	15	15	15	SUM
0	3	GC-GM	Silty clayey GRAVEL with sand	3	31	35	40	75
3	4	GM	Silty GRAVEL with sand - medium	4	8	11	12	23
4	7	GC	Clayey GRAVEL with sand - medium	6	9	8	9	17
7	8	SM	Silty SAND with gravel - medium	8	6	6	6	12
8	11	GC-GM	Silty clayey GRAVEL with sand - dense	10	6	13	18	31
10.5	13	GM	Silty GRAVEL with sand - medium	12	9	10	11	21
12.5	14	GC-GM	Silty clayey GRAVEL with sand	14	10	11	12	23
14	16	GM	Silty GRAVEL with sand medium	16	11	12	13	25
16	18	GC	Clayey GRAVEL with sand - medium	18	50	-	-	-
18	29	-	Boulder and weathered rock	29	-	-	-	-

The average value of shear wave velocity from these relations is used for one dimensional analysis. The earthquake records used in the present study are summarized in Table 2. All acceleration time histories have been recorded on the rock or stiff soil (V_s>750m/s).

Table 2. Earthquake Records

Earthquake	Epicentral Distance (km)	Peak Acceleration (g)	Station Name
Tabas	37	0.3	Dayhook
Manjil	43	0.50	Abbar
Northridge	36.1	0.23	MT

All the time histories are scaled down to 0.2g and then applied to the considered soil layers. Two typical transfer functions which were produced by one dimensional analysis are presented for two boreholes in figure 7.

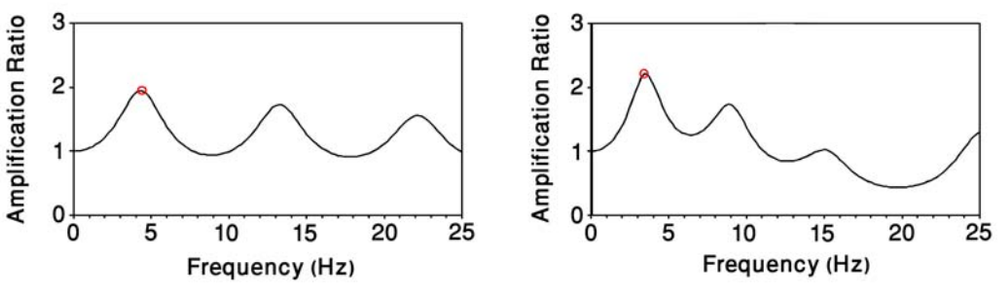


Fig.7 – Transfer function of boreholes No.7 and No.8 respectively

As it is shown in figure 8, the values of natural periods by means of one dimensional analysis are plotted versus natural periods which obtained by microtremor measurements for all 27 sites. As shown in the figure the results of one dimensional analysis of boreholes are more or less compatible to those obtained from microtremor measurements. Nevertheless, the natural periods that were obtained from one dimensional analysis are somehow smaller than those obtained from microtremors. This could be due to poor estimation of V_s based on the empirical equations.

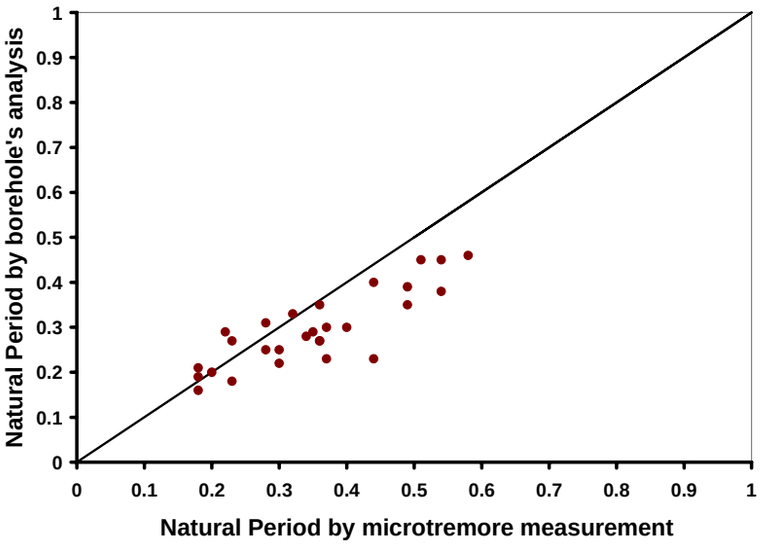


Fig. 8 – Comparison of natural periods that obtained by two methods

CONCLUSION

Seismic microzonation iso-period map for central part of Shiraz city were prepared by means of microtremor measurements. The natural periods that were obtained from microtremor measurements are in a good agreement with that of one dimensional analysis. According to the presented iso-period map it can be concluded that:

1. Natural period of sediments in central part of the studied area are larger than periods in western and eastern marginal parts. It may show that the depth of sediments in central part is larger or central part is softer in general.
2. The eastern part being hillside may suggest that the smaller values of natural period estimated by microtremors make sense.
3. Because of existence of a river crossing the city from northwest to southeast and possibility of thick and soft sediments in this area the higher period zone observed in the same location on the map looks reasonable.
4. Natural periods of sediments increase from northwest to southeast. The reason can be thicker and probably finer deposits that are formed

in downstream side of the river that flows from northwest to southeast.

5. Because of poor estimation of V_s based on the empirical equations, the natural periods that obtained by one dimensional analysis of boreholes are somehow smaller than those obtained from microtremor measurements. However the results of two methods are compatible.

ACKNOWLEDGMENTS

The authors appreciate the support of the Housing & Urban Development Organization of Fars State, Building & Housing Research Center of Iran, Dr Tabatabae, Mr Aghae, Mr Salamat and Mr Salimi.

REFERENCES

Technical Committee for Earthquake Geotechnical Engineering, **TC4** (1993):"Manual for zonation on seismic geotechnical hazards", *International Society for Soil Mechanics and Foundation Engineering*.

Kanai, K. and Tanaka, T. (1954): "Measurement of the microtremor", *Bulletin of Earthquake Research Institute, Tokyo University*, 32, 199-209.

Kanai, K. and Tanaka, T. (1961): "On microtremors". VIII, *Bulletin of Earthquake Research Institute, Tokyo University*, 39, 97-114.

Borcherdt, R. D. (1970): "Effects of local geology on ground motion near San Francisco Bay", *Bulletin of seismological society of America*, 60, 29-61.

Kagami, H., Okada, S., shiono, K., Oner, M., Dravinski, M. and Mal, A. k. (1986): "Observation of 1 to 5 second microtremors and their application to earthquake engineering. Part III. A two-dimensional study of site effects in S. Fernando valley", *Bulletin of seismological society of America*, 76, 1801-1812.

Nogoshi, M. and Igarashi, T. (1970): "On the propagation characteristics of microtremors", *J. Seism. Soc. Japan*, 23, 264-280 (in Japanese with English abstract).

Nogoshi, M. and Igarashi, T. (1971): "On the Amplitude characteristics of microtremors", *J. Seism. Soc. Japan*, 24, 24-40 (in Japanese with English abstract).

Nakamura, Y. (1989): "A method for dynamic characteristics estimation of subsurface using microtremor on the ground surface", *QR of RTRI 30*, no. 1, February, 25-33.

Field, E. H. and Jacob, K. H. (1993): "The theoretical response of sedimentary layers to ambient seismic noise", *Geophysical Research Letters*, 20-24, 2925-2928.

Ohmachi, T., Konno, K., Endoh, T. and Toshinawa, T. (1994): "Refinement and application of an estimation procedure for site natural periods using microtremor", *Journal of Japan Society of Civil Engineers*, 489, I-27, 251-261 (in Japanese with English abstract).

Lermo, J. and Chavez-Garcia, F. J. (1994): "Are microtremors useful in site response evaluation?", *Bulletin of seismological society of America*, 84, 1350-1364.

Konno, K. and Ohmachi, T. (1995): "A smoothing function suitable for estimation of amplification factor of the surface ground from microtremor and its application", *Journal of Japan Society of Civil Engineers*, 525, I-33, 247-259 (in Japanese with English abstract).

Dimitriu, P. P., Papaioannou, Ch. and Theodulidis, N. P. (1998): "EURO-SEISTEST strong motion array near Thessaloniki, Northern Greece: a case study of site effects", *Bulletin of seismological society of America*, 88, No. 3, 862-873.

Ghayamghamian, M. R. and Kawakami, H. (1997): "Segmental cross-spectrum in microtremor spectral ratio analysis", *7th International Conference on Structural Safety and Reliability, Kyoto, November 24-28*, 1487-1494.

The effect of shallow foundation position on their interaction with reverse faults

Waqas Ahmed[1], Fraser Bransby[2] and Shuichi Nagaoka[3]

[1]Research student, Civil Engineering, University of Dundee, Dundee DD1 4HN, UK; w.ahmed@dundee.ac.uk
[2]Senior Lecturer, Civil Engineering, University of Dundee, Dundee DD1 4HN, UK; m.f.bransby@dundee.ac.uk
[3]Research student, Civil Engineering, University of Dundee, Dundee DD1 4HN, UK; s.z.nagaoka@dundee.ac.uk

ABSTRACT: The paper reports a series of centrifuge model tests designed to study the effect of foundation position on the interaction of reverse, dip-slip faults with shallow foundations. All tests are conducted with a 15 m deep, dry sand layer and a reverse fault with dip angle 60^o. Results of a 'free-field' test are first presented which allows the fault rupture propagation through the soil to be investigated when no foundation is present. Additional tests are then reported in which shallow foundations are placed at different positions relative to the fault. It is seen that interaction between the foundation and the fault often causes deviation of the fault from the free-field condition, and this may protect the foundation from damage. This has also been observed in recent case histories. In addition, the response of the foundation as characterized by its rotation is very sensitive to the exact position of the foundation - the interaction between the foundation and the fault is subtle. Design should consider carefully the position of the fault emergence with respect to shallow foundations.

INTRODUCTION

During earthquakes, faults may emerge at the ground surface. When infrastructure is present the fault emergence may destroy or cause significant damage to infrastructure close to the fault. The amount of damage will depend on the proximity of the fault and the magnitude of displacement, the type of infrastructure and the soil conditions. Recent observations after the large earthquakes in 1999 (Chi-Chi and Turkey) revealed large fault expressions and subtle interaction with surface infrastructure, especially for shallow foundations (e.g. Youd et al., 2000; Ulusay et al., 2002; Pamuk et al., 2005). It was revealed in some cases that deviation of fault rupture was caused by the presence of heavily loaded shallow foundations (e.g. Anastasopoulos and Gazetas, 2007; El Nahas et al., 2006) suggesting that appropriate foundation design could protect buildings from significant damage.

This paper investigates the behavior of shallow foundations subject to reverse faulting by carrying out a series of centrifuge model tests. A typical problem geometry is shown in Figure 1. A shallow foundation of breadth, B rests on the soil surface (subject to bearing pressure, q) before a reverse fault propagates upwards through the soil from the bedrock discontinuity. The fault may emerge at the ground surface directly beneath the foundation or on either side depending on the position of the foundation and/or any interaction between the fault location and the foundation.

This paper examines specifically the effect of the foundation position on the fault-foundation interaction. This is important for foundation design as the exact position of the fault emergence is often difficult to know before the earthquake event. Hence, it may be necessary to know what extremes of foundation behavior may be expected. In the model tests, experiments are repeated with similar soil and fault conditions, but with a change in foundation position in each test. This allows the effect of foundation position to be studied directly.

In this paper, the test conditions are explained, the results are then presented and conclusions are finally given.

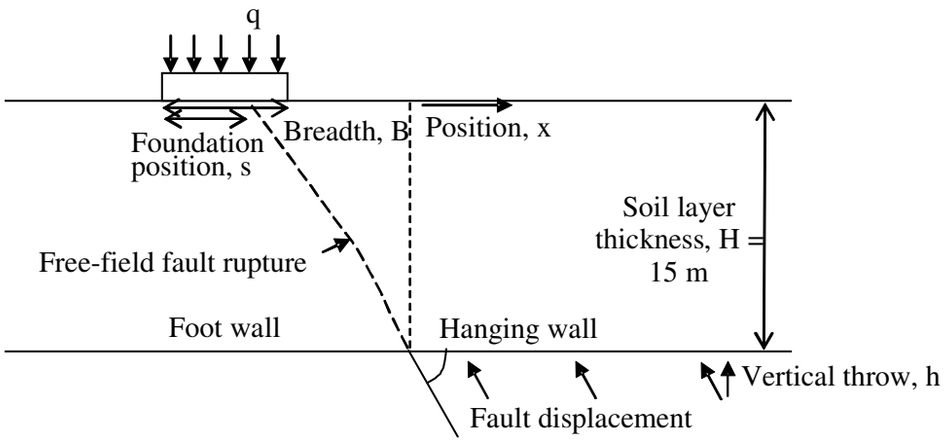


FIG. 1. The geometry of the problem studied.

EXPERIMENTAL METHOD

Experiments were conducted in the Dundee geotechnical centrifuge. All linear dimensions were reduced by a factor of 115 compared to a full scale prototype and the geotechnical centrifuge was spun to generate a radial acceleration of 115 times Earth's gravity. Scaling laws (e.g. Schofield, 1980) mean that the reduced scale model will behave as a prototype 115 times larger.

Experiments were conducted using a split box specially designed to allow fault rupture events to be modeled (Figure 2). More details of the apparatus are given by El Nahas et al. (2006) and Anastasopoulos et al. (2007). The split box allows reverse or normal faults of dip angle 60^o to be generated through the soil during centrifuge flight. In addition, two Perspex sides to the box perpendicular to the fault strike allow digital photography of a vertical plane in the soil.

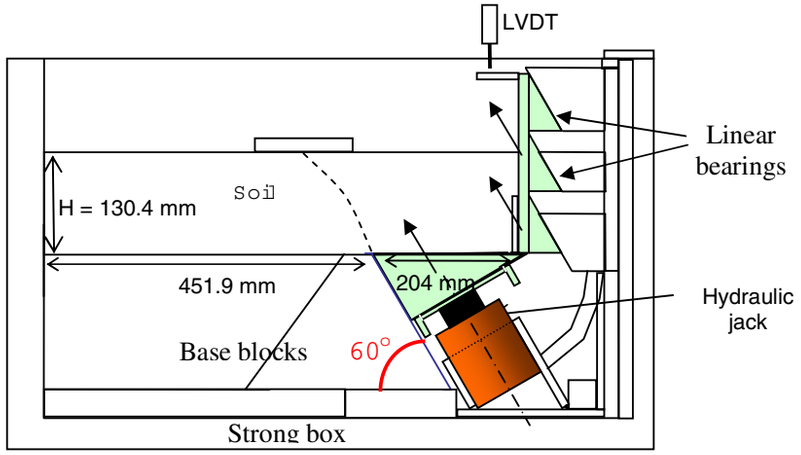


FIG 2. Schematic of the centrifuge modeling apparatus.

A Fontainebleau sand sample 656 mm wide by 130.4 mm high (and 500 mm broad) was pluviated dry into the split box (Fig. 2). The sand has d_{50} = 0.3 mm, is uniformly graded, and was prepared at a relative density of approximately 65%. An aluminum block 88 mm broad by 10 mm high and 498 mm long was placed on the top surface of the soil in the appropriate position to represent the foundation. The centrifuge was then spun to give 115g at which acceleration the soil will represent a prototype soil sample 75.9 m wide, 15 m deep and 50 m broad. The self weight of the block then exerted a bearing pressure, q = 37 kPa and gave a prototype foundation breadth, B = 10 m.

The fault was initiated by pumping oil into a hydraulic jack positioned on one side of the split box (Fig. 2). This caused the jack to extend, raising the shaded side of the split box as shown in Figure 2. Tests were carried out statically with digital photography of the soil conducted at approximately 50 displacement increments up to a maximum fault throw of 4.52 m (39.30 mm at model scale).

Four centrifuge tests are reported in this paper (see Table 1). An initial test (WA01) was conducted without a foundation present to find the location of the fault in the 'free-field' conditions. Next, three foundation tests were conducted with the foundation placed at different positions with respect to the free-field fault rupture emergence (Table 1) to see how changing foundation position affected the amount of damage caused to the foundation.

Table 1. Model test conditions

Test Identifier	Position of Foundation Centre, x (m)*	Foundation Position (s/B)	Relative density of sand (%)
WA01	--	--	73.0
WA13	-12.54	0.443	63.6
WA09	-6.93	-0.118	65.8
WA10	-14.46	0.635	62.1

* Position relative to free-field fault position.

RESULTS

Free-field condition

The experiment investigating the propagation of a reverse fault through soil without a foundation present ('free-field' test) was conducted first. This was required to find where the free-field fault would emerge at the ground surface, so that foundations in later tests could be placed appropriately and any modification of the fault rupture position due to the foundation could be examined.

An example image captured 'in flight' at the end of the free-field fault is shown in Figure 3. When the image was captured the vertical component of fault displacement, 'throw', h = 2.48 m. At this stage of displacement, the hydraulic jack is extended and can be seen on the bottom right of the image.

Figure 3 reveals a strong displacement discontinuity propagating upwards from the base 'bedrock' discontinuity to the soil surface. The fault dip angle (sketched on Fig. 3) reduces as the soil surface is approached and the fault emerges on the soil surface. Soil to the left of the fault (on the foot wall side of the fault) appears relatively undisturbed, whereas the soil on the right of the fault (on the hanging wall side of the fault) has been distorted by propagation of the fault. This distorted zone has a breadth approximately equal to the soil depth. Soil to the right of the distorted zone appears to have lifted rigidly in the direction of the fault dip and the soil surface remains horizontal. The above simple observation suggests that if no interaction were present, foundations situated entirely on the undisturbed soil zones (i.e. to the left of the free-field fault rupture (s/B > 1), or positioned more than approximately one soil depth to the right (s/B < -H/B)) may remain undamaged. However, foundations in the distorted zone are liable to be rotated and/or damaged significantly.

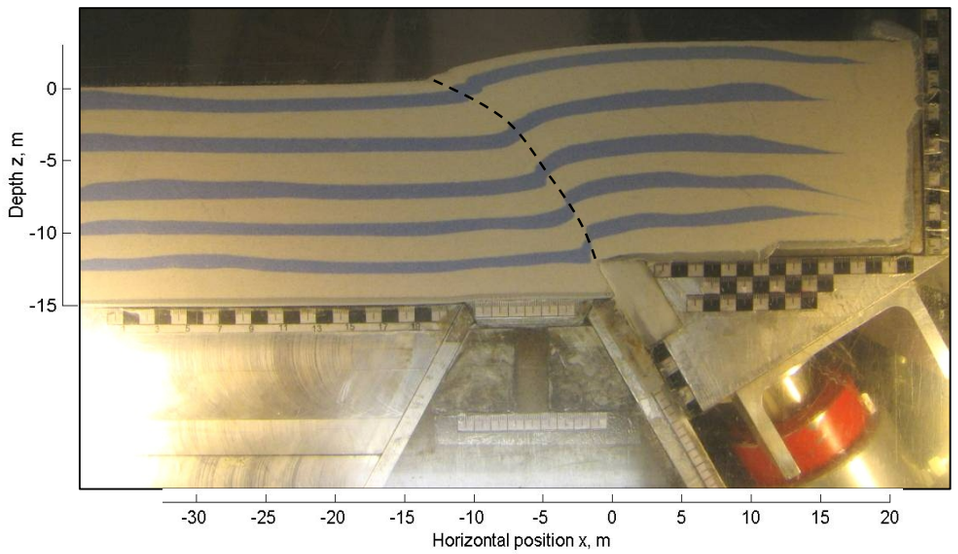


FIG. 3. Image captured for free-field fault test (WA01) at a fault throw, h = 2.48 m.

Examination of the sequence of digital images captured during the simulated faulting event revealed that the fault propagation was progressive as reported previously (e.g. Roth et al., 1981; Cole & Lade, 1984; Bray, 1990; Bray et al., 1994). Small fault displacements produced only general distortion of the soil, before larger displacements generated a shear localization at the base of the soil layer near the bedrock. Further fault throw was required to propagate the fault to the soil surface (which occurred when h = 1.71 m). The changing pattern of soil distortion with magnitude of fault throw will lead to different types of interaction with overlying shallow foundations.

Foundation positioned with s/B = 0.44

All foundation tests were conducted in the same soil conditions as for the free-field test (H = 15 m; D_r = 60%) but with the addition of a foundation of breadth, B = 10 m and bearing pressure, q = 37 kPa. In the first foundation test (WA13), the foundation was position so that the free-field fault would have emerged near the center of the foundation (i.e. s/B = 0.443). The full test conditions are shown in Figure 4.

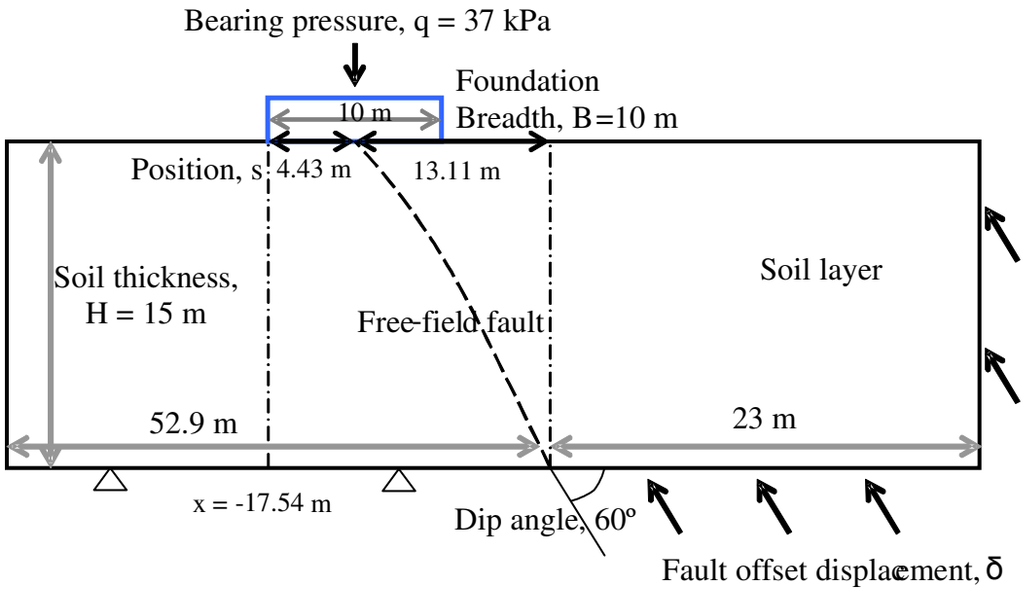


FIG. 4. The geometry of test WA13.

An example image captured at a fault throw, h = 4.38 m is shown in Figure 5. There is evidence of significant foundation rotation and of the development of two strong localizations. This main strong localization ('L1' in Fig. 5) was first mobilized at a fault throw, h = 2.63 m and the dip angle of this fault reduces significantly as it approaches the soil surface. This fault rupture emerges beneath the left hand (foot wall) side of the foundation about 1 m from the far edge. Thus, the fault has deviated approximately 6 m to the foot wall side due to the presence of the foundation. The 2nd localization ('L2' in Fig. 5) was generated only for very large throws.

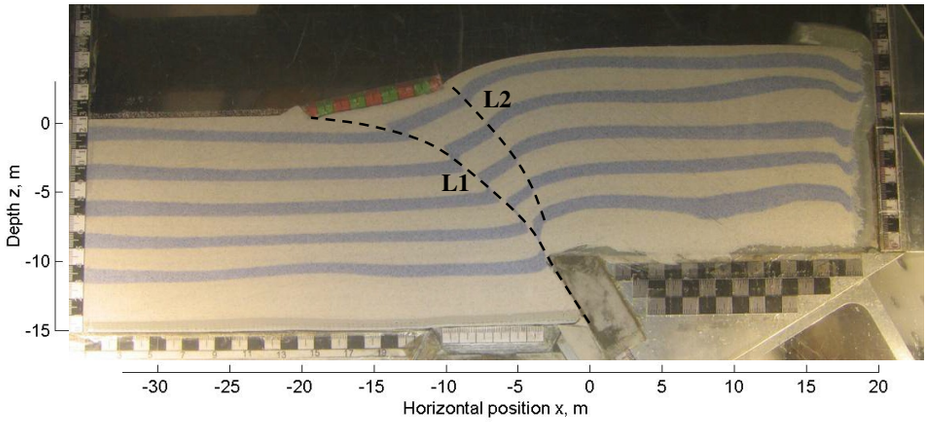


FIG. 5. Image taken during text WA13 (s/B = 0.44) with fault throw, h = 4.38 m.

Despite the deviation of the main fault, it still emerges beneath the foundation and causes large foundation rotation (approximately 11^{o} in Fig. 5). In addition, the foundation has been pushed sideways by the fault and the far side of the foundation has dug into the soil, pushing out a 'wave' of soil in front of it. Both aspects of behavior are likely to damage a real foundation significantly.

The foundation rotations were measured using the Geo-PIV program of White et al. (2003) where the displacement of selected patches on the foundation were calculated by comparing the digital images taken at different fault displacements. The rotation of the foundation against fault throw is shown in Figure 6 and reveals that the rotations are not linear with respect to fault throw. Only small rotations are generated when h < 0.5 m, after which foundation rotation increase rapidly with respect to fault throw, before increasing more slowly when h > 2.5 m.

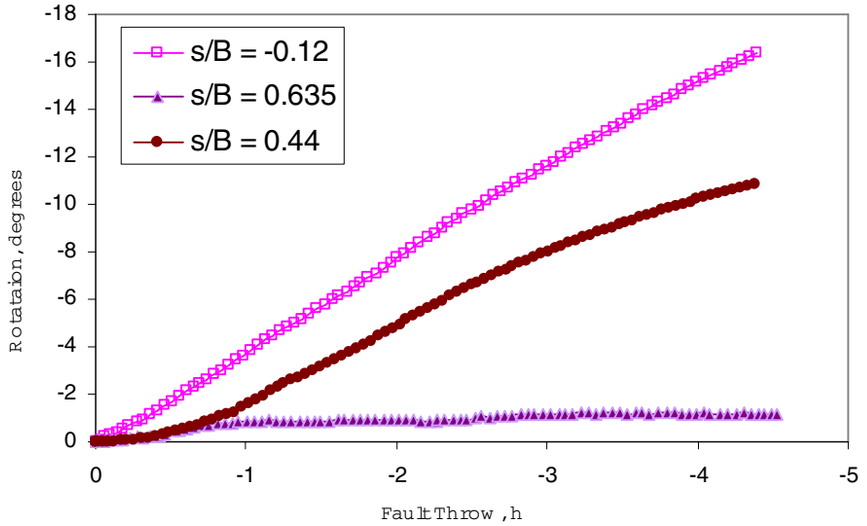


FIG. 6. Foundation rotation against fault throw (all foundation tests)

Foundation positioned with s/B = -0.12

Test WA09 was conducted with the foundation positioned so that the free-field fault would just miss the foot wall edge of the foundation (s/B = -0.118). An image captured at a fault throw, h = 4.39 m is shown as Figure 7. The main fault (L1 in Fig. 7) emerges in approximately the same position as the free-field fault, missing the foundation to the left. Despite this, the foundation has rotated even more than in the previous test (rotation = 16.4^o) due to the deforming soil on the hanging wall side of the fault. The calculated foundation rotations are shown on Figure 6. Larger rotation was generated than in the previous test and this time the rotation appeared to increase almost linearly with respect to increase in fault throw (approximately 3.75^o/m). Clearly, the change in foundation position has affected the response of the foundation.

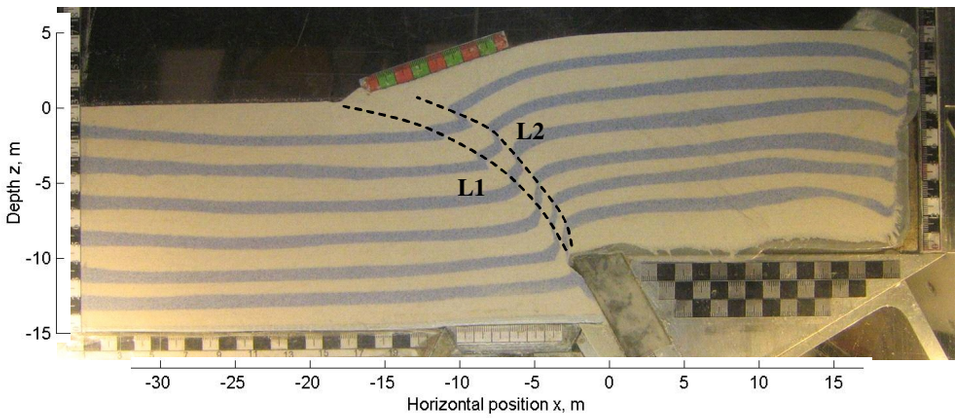


FIG. 7. Digital image captured during test WA09 (s/B = -0.118) at h = 4.39 m.

Foundation positioned with s/B = 0.635

The final foundation test (WA10) had the foundation positioned so that a free-field fault would emerge approximately B/3 from the right of the foundation (i.e. s/B = 0.635) to examine a fault emerging near the opposite edge of the foundation compared to the previous test (WA09).

Figure 8 shows the final image captured 'in flight' for a fault throw, h = 3.26 m. Very different response is seen compared to the previous tests. The main fault (L2 in Fig. 8) emerges on the hanging wall side of the foundation and there is almost no foundation rotation (rotation = 1.2^o for Fig. 8). For this foundation position, the fault rupture has emerged approximately 4 m nearer the fault (i.e. to the hanging wall side) compared to the free-field condition. Note that this is the opposite direction of deviation compared to the test with s/B = 0.44 (test WA13).

Foundation rotation is plotted against fault throw on Figure 6. When h < 0.5 m, the foundation rotations are very similar to those in test WA13 (s/B = 0.44), but larger fault throws cause no further increase in foundation rotation. This may be because once the final mechanism forms with a localization to the right of the foundation, the

foundation rests on the foot wall side of the fault where there is no further soil deformation. The foundation is clearly protected from significant damage even for large fault throws. Again, this shows that the position of the foundation is critical to its interaction with the fault.

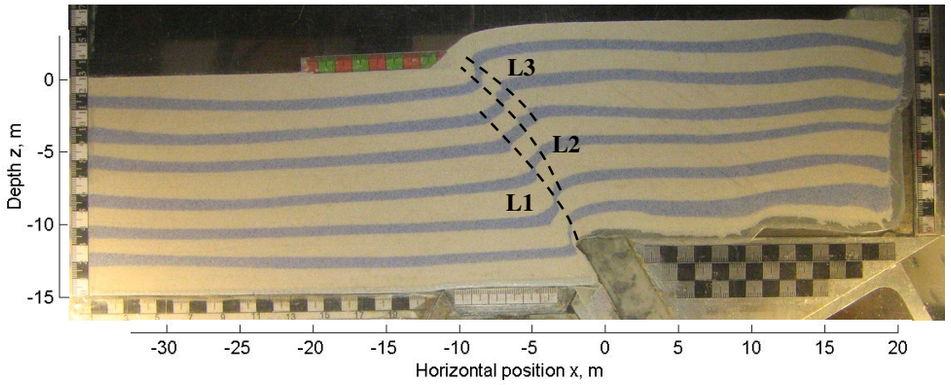


FIG. 8. Digital image captured during test WA10 (s/B = 0.64) at h = 3.26 m

CONCLUSIONS

A series of centrifuge model tests has been conducted to investigate how the position of a shallow foundation affects the amount of foundation damage in close proximity to reverse faulting. The main findings were as follows:

- A free-field test revealed a progressive failure and an overall dip angle in the soil layer lower than in the bedrock as seen by previous researchers.
- The position of a foundation was critical to its performance. For a fault throw of 4 m, rotations varied between 1.1^{o} and 15.1^{o} in the tests for foundations which were otherwise identical except for their position.
- The foundations were able to deviate the fault from the free-field position due to fault-footing interaction. However, this did not prevent foundation rotation unless the foundation was then fully on the foot wall side of the fault rupture.
- When designing a foundation where the position of the fault rupture emergence is not known, a range of possible positions should be considered to capture the worst case. This is not necessarily when the free-field fault would strike the foundation in the centre.

ACKNOWLEDGMENTS

The first author is supported by a scholarship from National Centre of Excellence in Geology, University of Peshawar, Pakistan. This is gratefully acknowledged.

REFERENCES

Anastasopoulos I., and Gazetas G., (2007) "Foundation-Structure Systems over a Rupturing Normal Fault : I. Observations after the Kocaeli 1999 Earthquake", *Bulletin of Earthquake Engineering*. Vol. 5(3): 253-275.

Anastasopoulos, I., Gazetas, G., Bransby, M.F., Davies, M.C.R and El Nahas, A. (2007): "Fault Rupture Propagation through Sand : Finite Element Analysis and Validation through Centrifuge Experiments." *ASCE Journal of Geotechnical and Geoenvironmental Engineering*, Vol.133 (8): 943-958.

Bray, J.D. (1990), "*The effects of tectonic movements on stresses and deformations in earth embankments"*, Ph.D. Dissertation*,* University of California, Berkeley.

Bray, J.D., Seed, R.B., Cluff, L.S., and Seed, H.B. (1994), "Earthquake Fault Rupture Propagation through Soil", *Journal of Geotechnical Engineering,* ASCE, Vol. 120 (3): 543-561.

Cole, D. A., Jr. and Lade, P. V. (1984): "Influence zones in alluvium over dip-slip faults". ASCE Journal of Geotechnical Engineering, Vol. 110: 599-615.

El Nahas, A., Bransby, M.F. and Davies, M.C.R. (2006): "Centrifuge modelling of the interaction between normal fault rupture and rigid, strong raft foundations." *Proc. International Conference on Physical Modelling in Geotechnics*, Hong Kong, August 2006. pp. 337-342.

Pamuk, A., Kalkanb, E., Linga, H.I. (2005), "Structural and geotechnical impacts of surface rupture on highway structures during recent earthquakes in Turkey", *Soil Dynamics and Earthquake Engineering*, Vol. 25: 581-589.

Roth, W.H, Scott, R.F, and Austin, I. (1981), "Centrifuge modelling of fault propagation through alluvial soils", *Geophysical Research Letters*, Vol. 8 (6): 561–564.

Schofield, A.N. (1980): "Cambridge University Geotechnical Centrifuge Operations." Rankine lecture, *Geotechnique,* Vol. 30 (3): 227-268.

Ulusay, R., Aydan, O., Hamada, M. (2002), "The behaviour of structures built on active fault zones: Examples from the recent earthquakes of Turkey", *Structural Engineering & Earthquake Engineering, JSCE*, Vol. 19 (2): 149–167.

White, D. J., Take, W. A. and Bolton, M.D. (2003): "Soil deformation measurement using particle image velocimetry (PIV) and photogrammetry". *Géotechnique*, Vol. 53 (7): 619-631

Youd, T. L., Bardet, J-P, and Bray, J.D. (2000), "Kocaeli, Turkey, Earthquake of August 17, 1999 Reconnaissance Report", *Earthquake Spectra*, Suppl. A to Vol. 16, 456.

This page intentionally left blank

Cyclic shear tests of municipal waste in large triaxial device for identification of its dynamic properties

Ikuo Towhata [1] and Masaaki Uno[2]

[1] Professor, Department of Civil Engineering, The University of Tokyo, 7-3-1, Hongo, Bukyo-ku, Tokyo 113-8656, Japan. towhata@geot.t.u-tokyo.ac.jp
[2] Fudo Tetra Corporations

ABSTRACT: The present study aims to develop urban area on an existing landfill. To achieve this goal, it is important to understand the mechanical properties of municipal solid waste. Since particle size of waste is large, a large triaxial shear device was employed for mechanical waste tests. Among results, this paper addresses triaxial compression, cyclic behavior, and mitigation of creep by means of preloading. The second topic concerns modulus and damping ratio changing with strain amplitude

INTRODUCTION

Landfill in this paper stands for a facility where municipal solid waste is disposed. In the recent times there are such landfills which are located close to mega cities where space for more urban development is strongly desired. This is particularly the case in Japanese mega cities where urban planning in practice did not reserve sufficient open space for future development. What is interesting in an engineering sense is that many mega cities in Japan are situated in coastal regions and that their municipal waste is disposed in landfill in artificial islands. Accordingly, there are huge waste islands existing near mega cities which may be an alternative choice for missing open space for future development. Although this idea is interesting, there are problems as well which have to be solved by geotechnical engineering.

One of those problems is the long-lasting subsidence of waste deposits. Fig. 1 illustrates an example in which the rate of subsidence in many landfills in Tokyo Bay area is plotted against age. The age stands for the years which were elapsed after the end of waste disposal. It is therein seen that subsidence continues for more than 25 years although the rate of subsidence decays with time. As a consequence, surface structures suffer from significant ground subsidence (Fig. 2). Note that the waste deposit in this place is located above the ground water level and most probably the subsidence was generated not by consolidation and drainage of pore water but creep deformation. It is interesting, however, that one of the former waste landfills in Tokyo, which is more than 50 years old, looks stable and now is utilized as an urban area (Fig. 3). It is therefore

reasonable to state that subsidence of municipal waste is stabilized after 50 years. The present study attempts to shorten this time period in order to facilitate the urban development.

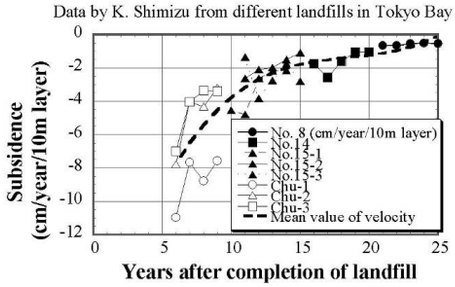


FIG.1. Rate of subsidence of municipal waste deposits in Tokyo (after Shimizu et al., 1989).



FIG.2. Consequence of ground subsidence



FIG.3. Shiomi area of Tokyo which used to be municipal waste landfill



FIG.4. In-door ski hall resting upon municipal waste landfill.

The use of former landfill for human activities is not a very new idea. For example, Fig. 4 illustrates an in-door ski hall in Neuss of Germany. This refined structure is supported by concrete footings embedded in the surface cover soil and is equipped with elaborate measures against possible ground subsidence. It seems difficult, however, to apply this technology directly to Japanese cities where earthquake effects are significantly more serious. In this regard, the second problem which was investigated in the present study is the behavior of municipal waste undergoing cyclic load such as what occurs during earthquakes.

Mechanical properties of municipal solid waste have been investigated at several institutions. For example, Kölsch (1996) conducted tension tests in a large scale to show the important role of fibrous inclusions in generation of tensile resistance of waste mass. In line with this, Towhata et al (2004) conducted triaxial shear tests to show that fibers develop significant shear resistance, making the stress-strain behavior nearly linear. Similar finding was made by Zekkos et al. (2007) as well. As for cyclic behavior, Matasovic and Kavazanjian (1998) carried out cyclic shear tests on large reconstituted specimens to investigate the variation of shear rigidity and damping ratio with strain amplitude. When they worked in the strain amplitude only greater than 0.1 %, the observed behavior of waste was similar to that of soils. The damping ratio at 0.1 %

strain, for example, was between 15 and 23 %. Augello et al. (1998) attempted to evaluate the shear modulus and damping ratio by using earthquake motions recorded on the same landfill as shear tests by Matasovic and Kavazanjian (1998) concerned. It is interesting that the obtained damping ratio at, for example, 0.1 % strain was 5 - 8 %, being less than shear tests revealed. The reason for this is unknown.

TESTED MATERIAL AND TRIAXIAL DEVICE

The present study was performed on real municipal waste which was collected from municipal waste landfill in Tokyo. While there are two kinds of municipal waste there, the softer waste which is composed mainly of plastics was employed, while the other waste, which is incinerated ash, has very stable mechanical nature. This contrast is illustrated in Fig. 5 in which Swedish weight sounding data is plotted against depth for both plastic and ash sites. Note that penetration stopped in the ash site within 0.5 m from the surface. Thus, the following study concerns only plastic municipal waste whose composition is as shown in Fig. 6. The specific gravity of this material, which was determined by a conventional soil-mechanic method, was as low as $G_s = 1.324$ g/cm^3. Since the plastic waste contained pieces of 3 to 5 cm in size, the reasonable sample size for mechanical tests is not less than 30 cm. Hence, a large triaxial shear device was employed in which a tested specimen measured 30 cm in diameter and 60 cm in height. The confining pressure was produced by negative pore pressure, while the axial load by an air cylinder. The axial deformation was measured by two LVDTs attached to the top cap. Since the cap was connected with the loading ram in a rigid manner, no rotation or rocking occurred to the cap (see Fig. 7). Moreover, the specimen was encased in a water-filled cylinder, and the lateral strain was obtained by measuring the level of water surface. Fig. 8 demonstrates a specimen prior to axial shear. This specimen was prepared by 6-layer tamping of air-dry waste, with 100-times tamping of the surface per each layer. The employed hammer was of 5.2 kg in weight and the height of fall was approximately 20-30 cm.

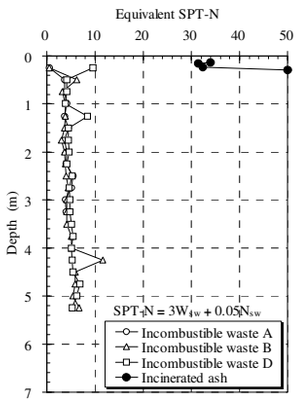


FIG. 5. Swedish weight sounding data converted to equivalent SPT-*N* at municipal waste sites.

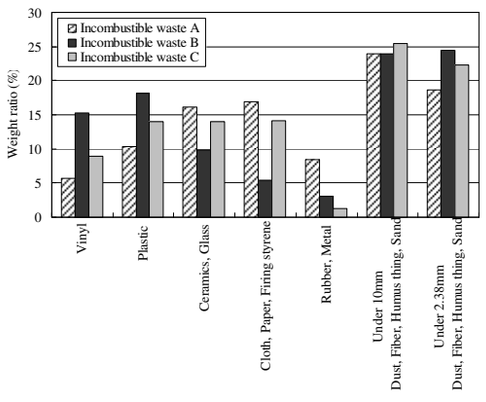


FIG. 6. Composition of plastic waste.

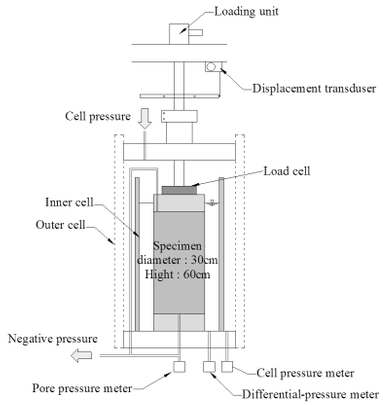


FIG. 7. Structure of large triaxial device.



FIG. 8. Tested specimen in large triaxial device.

TEST RESULTS ON CREEP BEHAVIOR OF PLASTIC WASTE

Firstly, the creep was investigated by consolidating air-dry specimen under 15 kPa of isotropic confining pressure and applying thereinafter deviatoric stress (q) of either 45 or 60 kPa for four hours. Then the deviator stress was unloaded to 30 kPa and was kept constant for another four hours. In soft-soil engineering, this time variation of stress is called preloading and has been well-established for acceleration of the consolidation settlement. The time history of the axial strain during this loading is illustrated in Fig. 9. It is therein seen that the creep deformation continued to increase linearly with the logarithm of time, implying the development of ground subsidence for a long time. In contrast, the strain was stabilized after unloading. Thus, it is likely that preloading for longer times mitigates more significantly the problem of creep-induced subsidence.

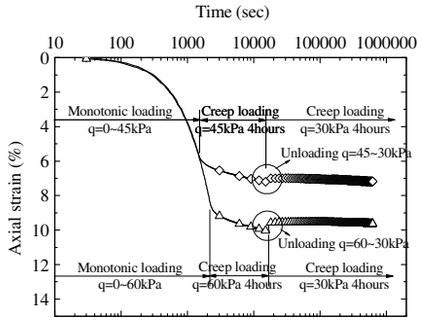


FIG. 9. Creep axial strain during loading and unloading of deviatoric stress.

TEST RESULTS ON SHEAR DEFORMATION

Triaxial compression tests were conducted on air-dry plastic waste which had the dry density of 0.65～0.75 g/cm^3. Specimens were isotropically consolidated under σ'_c=

15, 30, or 45 kPa, followed by drained axial compression. The test results in Fig. 10 indicate that the stress-strain behavior of the waste is very soft but nearly linear; no clear yielding is detected therein. This is found particularly noteworthy when the data is compared with the yielding stress-strain behavior of Toyoura sand in the same figure. It is also detected in the figure that the rigidity of waste increases when its density increases and when the confining stress level is raised. The latter nature is consistent with the behavior of soils in general, suggesting that municipal waste is a target of soil mechanics.

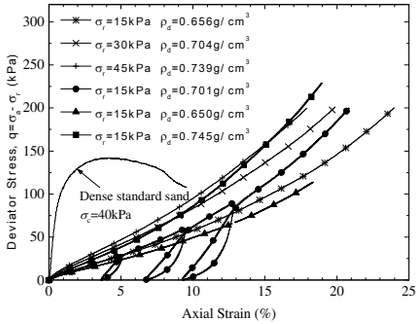


FIG. 10. Triaxial compression tests on plastic waste.

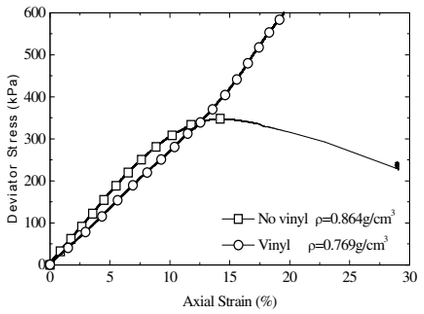


FIG. 11. Triaxial compression tests on bio-treated waste.

To further confirm the soft and linear behavior of waste, raw and bio-treated waste was tested. This material was obtained from the Jever landfill near Wilhelmshafen in Germany. Fig. 11 similarly exhibits linear behavior when the tested waste contained pieces of vinyl. Noteworthy is that yielding occurred when those vinyl pieces were eliminated. It is hence inferred that vinyl and other fibrous sheets, which are aligned upon tamping in the horizontal direction, are subjected to tension upon triaxial compression to a large strain level, and reinforce the stress-strain behavior of the specimen. This nature is similar to that of reinforced soil in which steel or plastic grids and sheets are embedded in the horizontal direction and increase the overall strength due to their tensile strength. To further confirm this point, Fig. 12 may be referred to. A vertical cliff in this figure has been stable for years due to many fibrous materials and even paper in the waste.



FIG. 12. Stable vertical cliff in Göttingen landfill in Germany.

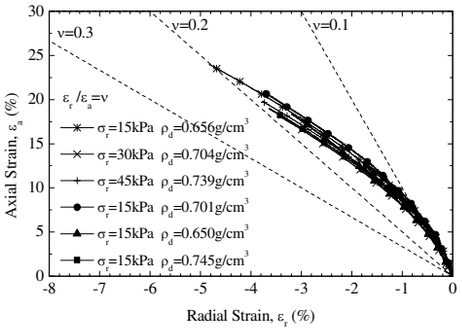


Fig. 13. Relationship between axial strain and lateral strain of plastic waste undergoing triaxial compression.

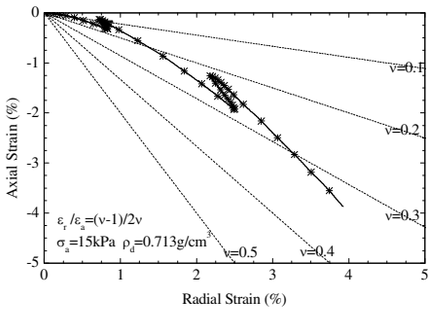


Fig. 14. Relationship between axial strain and lateral strain of plastic waste undergoing triaxial extension.

Fig. 13 demonstrates the variation of radial and axial strains of plastic waste specimens during triaxial compression. The ratio of these two strain components gives the values of Poisson ratio. Being around 0.1 when strain is small, and increasing towards 0.2 as the strain gets greater, Poisson ratio (ν) of plastic waste is nearly independent of the sample density and confining stress level. By assuming linear and isotropic elasticity, the earth pressure coefficient at rest, $Ko = \nu/(1-\nu)$, was calculated to be 0.11 to 0.25. This range of *Ko* appears to be smaller than that of soils in general. It seems, therefore, that the lateral expansion of waste is reduced by the tensile strength of fibrous inclusions.

To further investigate the anisotropic nature of Poisson ratio, triaxial extension tests were conducted by increasing the lateral stress, while maintaining the axial stress constant. Since a specimen contracts in the radial direction during this kind of loading, reinforcement by expansion of fibers does not occur. The obtained relationship between the radial strain and the axial strain is presented in Fig. 14. From this figure, the Poisson ratio at a strain level of 2% is found to be 0.2 to 0.3. Being greater than the aforementioned range of 0.1 to 0.2 during triaxial compression, this greater value of Poisson ratio in the course of triaxial extension suggests the lack of reinforcement in the axial direction.

CYCLIC TRIAXIAL TESTS

Since the seismic loading is significantly important in civil engineering of Japan, cyclic triaxial tests were carried out on plastic waste specimens in order to understand the seismic behavior of waste. Attention therein was paid mainly to shear modulus and damping ratio of the waste, while shear failure was out of scope. This is because of the significant shear strength of the plastic waste with fibrous inclusions (Figs. 10 and 12). For cyclic tests, specimens were isotropically consolidated under 15, 30, or 45 kPa. An example of the recorded cyclic stress-strain relationships are demonstrated in Fig. 15. Accordingly, variations of secant modulus and damping ratio with the strain amplitude

are plotted in Figs. 16 and 17, respectively. Similar to existing knowledge on soils, the modulus decreases, while the damping ratio increases, with the increasing strain amplitude. Note, however, that modulus is very small as illustrated in Fig. 10. Since the modulus increases with the effective stress (Fig. 16), it is reasonable to state that the dynamic behavior of plastic waste is governed by soil-mechanic principles. In contrast, the effect of confining stress on damping ratio is not clear.

Figs. 16 and 17 indicate significant variation of modulus and damping ratio in the strain range less than 0.01 %. This problem is so far considered to be related with the large size of waste components (grains and fibers) that makes small deformation of a specimen uncertain. Under greater strain, in contrast, the monitored behavior of specimens was more stable. The damping ratio at, for example, 0.1 % strain was approximately 6 %, which is consistent with back calculation made by Augello et al. (1998). The maximum value of 20 % in damping ratio is compatible with that of soil.

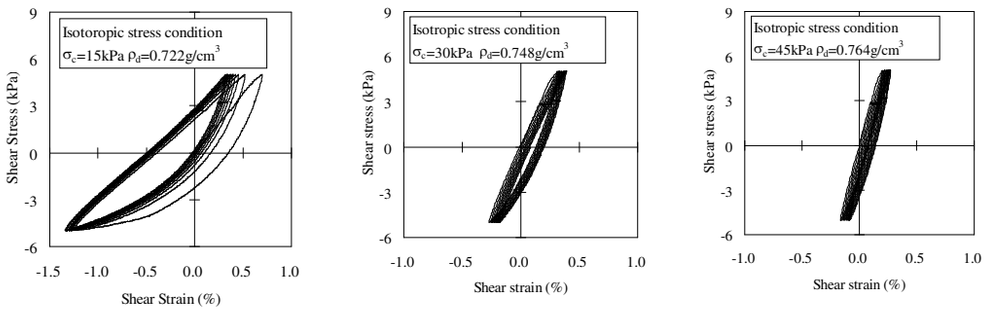


Fig. 15. Cyclic stress-strain relationship of plastic waste in triaxial apparatus.

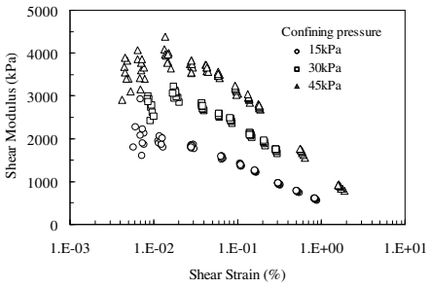


FIG. 16. Relationship between shear modulus and strain amplitude during cyclic triaxial tests.

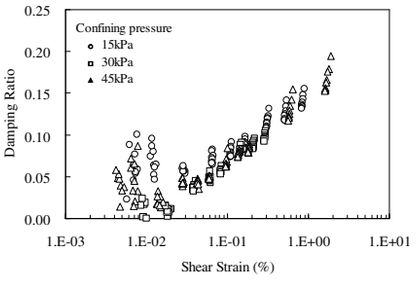


FIG. 17. Relationship between damping ratio and strain amplitude during cyclic triaxial tests.

CYCLIC TRIAXIAL SHEAR ON ANISOTROPICALLY CONSOLIDATED SPECIMENS

One of the problems in seismic effects on geotechnical structures is the residual deformation. This deformation is induced by accumulation of strain in the direction of the initial static shear. With this in mind, cyclic triaxial shear was conducted on anisotropically consolidated specimens. In the case of Fig. 18, air-dry specimens were consolidated under the lateral stress of σ_r' =15 kPa and the deviatoric stress of 45, 90, and 135 kPa. The amplitude of the superimposed cyclic stress was 5 kPa with the number of cycles of 10. The stress-strain behavior during cyclic loading is demonstrated in Fig. 19. It is seen there that the development of strain was reduced as the deviatoric stress increased. This increase in sample rigidity is a consequence of the increase in the effective mean principal stress. Consequently, the extent of residual deformation is not significant. By comparing Fig. 19 with the stress-strain behavior of isotropically consolidated specimen (Fig. 15), it is found that the behavior in Fig. 19 is more linear and that the modulus in Fig. 19 is greater. This is because the anisotropic state of stress induced axial compression and lateral extension in the tested specimen, which in turn induced tension in horizontally layered plastics and reinforcement.

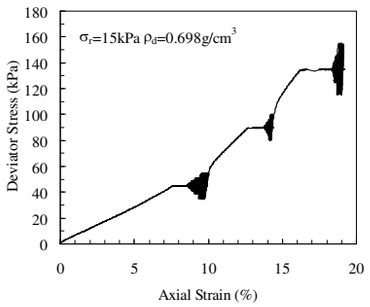


FIG. 18. Cyclic triaxial shear at anisotropic stress states.

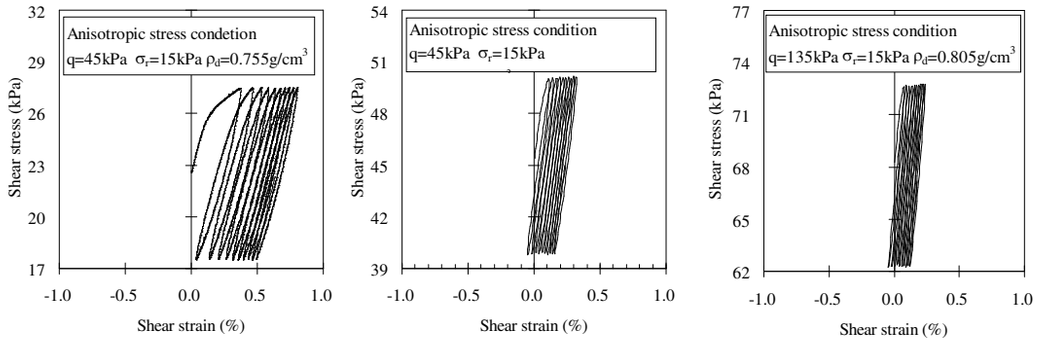


FIG. 19. Accumulation of strain during superposition of cyclic stress on static shear stress.

The modulus and damping ratio are illustrated in Figs. 20 and 21. Although there is uncertainty, as shown in Figs. 16 and 17, in the measured modulus when the strain is less than 0.01 %, Fig. 20 reveals that modulus increases as the mean effective stress (σ_r'+q/3) increases. Moreover, the degradation of modulus is evident when strain amplitude increases. In contrast, the damping ratio in Fig. 21 is greater under lower level of effective mean stress. This behavior is consistent with the behavior of soils.

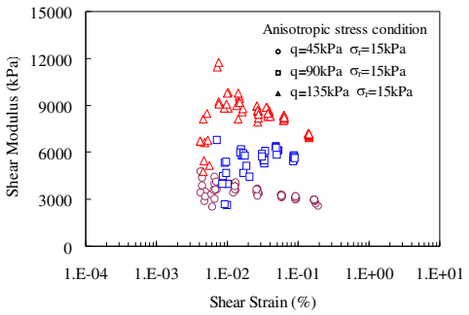


FIG. 20. Variation of modulus with strain amplitude under anisotropic stress state.

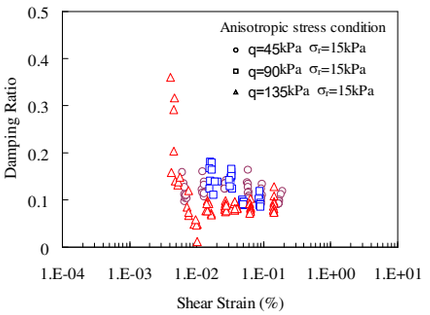


FIG. 21. Variation of damping ratio with strain amplitude under anisotropic stress state.

ON USE OF FORMER LANDFILL FOR URBAN DEVELOPMENT

The present study intends to develop geotechnology which can turn existing landfill islands into urban areas. Although there are examples of an urban area which used to be a landfill, the stabilization of the ground, which means completion of long-term creep, takes as long as 50 years. To shorten this time, preloading is an effective way (Fig. 9).
There are many discussions on recycling of municipal waste. For example, incinerated ash is converted to pavement materials and plastics are turned to fibers and then working uniforms. The major problem lying in those ideas is the shortage of demands as compared with the amount of waste generation. Furthermore, it is often argued that recycling needs to separate useful materials out of others, clean them, and purify. This procedure requires human efforts and fuels, making the total cost higher than what is needed for producing similar materials from raw natural resources.
The present study, in contrast, intends to convert the vast space of existing landfill islands (Fig. 22) to a future urban area. This idea could be called recycling of space. Since preloading is an established geotechnical engineering, it is very possible to terminate the long-term subsidence of waste deposits. By producing inexpensive vast land near a mega city, planning of future city development will be made easier and more flexible.

CONCLUDING REMARKS

Laboratory tests were conducted on plastic components of municipal solid waste by

using a large triaxial device. Creep tests revealed that preloading, in which stress is increased and then decreased to a working level, can terminate the long-term ground settlement. Triaxial compression tests showed that plastic waste is reinforced by fibers which are aligned in the horizontal direction. Finally, cyclic loading showed the variation of modulus and damping ratio changing with strain amplitude. The ranges of modulus degradation and damping ratio are similar to those of soils which have been safely treated by existing geotechnology. Thus, from the geotechnical view points, the recycling of landfill space to an urban development space is very promising.



FIG. 22. Municipal waste landfill in Tokyo Bay.

ACKNOWLEDGMENT

The authors express their sincere gratitude to the environmental authority of Tokyo Metropolitan Government who supplied testing materials to the present study. Special thanks are extended also to Dr. F. Kölsch who supported the author's study in Germany.

REFERENCE

1- Augello, A. J., Bray, J. D., Abrahamson, N. A. and Seed, R. B. (1998) Dynamic properties of solid waste based on back-analysis of OII landfill, J. Geotech. Geoenviron. Eng., ASCE, Vol. 124, No. 3, pp. 211-222.

2- Kölsch, F. (1996) Der Einfluss der Faserbestandteile auf die Scherfestigkeit von Siedlungsabfall, Doctoral Thesis, Leichtweiss-Institut für Wasserbau,. Technische Universität Braunschweig.

3- Matasovic, N. and Kavazanjian Jr., E. (1998) Cyclic characterization of OII landfill solid waste, J. Geotech. Geoenviron. Eng., ASCE E, 124(3), 197-210.

4- Shimizu, K., Ebina, S., Saito, S. and Mizukoshi, K. (1989) Geotechnical study of refuse landfill in Tokyo Port (10)- Subsidence of refuse landfill -, Proc. 24th Japan National Conf. Soil Mechanics and Foundation Engineering, Tokyo, Vol.1, 149-150.

5- Towhata, I., Kawano, Y., Yonai, Y., and Kölsch, F. (2004) Laboratory tests on dynamic properties of municipal waste, Proc. 11th Int. Conf Soil Dynam. Earthq. Eng. and 3rd Int. Conf. Earthq. Geotech. Eng., Berkeley, Vol. 1, pp. 688-693.

6- Zekkos, D., Bray, J. D., Athanasopoulos, G. A., Riemer, M. F., Kavazanjian Jr., E., Founta, P. A. and Grizi, A. F. (2007) Compositional and loading rate effects on the shear strength of municipal solid waste, Proc. 4th Int. Conf. Earthq. Geotech. Eng., Thessaloniki, Paper No. 1525.

Density Effects on the Aging Behavior of Sands and the Anisotropy of Aging-induced Stiffness Increases

Yu-Hsing Wang[1], M. ASCE and King-Yuen Tsui[2]

[1]Associate Professor, Department of Civil Engineering, The Hong Kong University of Science and Technology, Clear Water Bay, Kowloon, Hong Kong; ceyhwang@ust.hk
[2]Research student, Department of Civil Engineering, The Hong Kong University of Science and Technology, Clear Water Bay, Kowloon, Hong Kong; ceronny@ust.hk

ABSTRACT: This study investigates the density effect on the aging behavior of sands and explore whether the aging-induced stiffness gain is isotropic by nature. The results of resonant column tests on Ottawa sand samples reveal that the medium-dense sample had the highest aging rate, as determined by its shear-modulus increase, followed by the dense and loose sand samples. This result might be attributed to two competing processes, the tendency toward force-chain homogenization and the susceptibility to local structure collapse. This attribution does not apply to Toyoura sand samples, which suggests that the effect of packing density on the aging behavior of sand indeed varies with the type of sand. Bender element tests in the true triaxial apparatus demonstrate that aging behavior is not isotropic by nature because the increase of shear wave velocities in different polarization planes varies under isotropic stress states. Increasing the stress in one direction leads to more significant increases in the velocities that are either polarized or propagating in that direction.

INTRODUCTION

In the geotechnical context, aging is a general term that describes the time-dependent variations of soil properties under constant external conditions such as the same stress state. There are well-documented aging phenomena, including increases in the cone penetration resistance (Mitchell and Solymar 1984; Solymar 1984; Charlie et al. 1992; Joshi et al. 1995), in the shear strength (Daramola 1980), and in the shear modulus (Afifi and Woods 1971; Afifi and Richart 1973; Anderson and Stokoe 1978). In the case of dry, clean sands, the process of mechanical aging proposed by Mesri et al. (1990) and Schmertmann (1991) is often used to account for the measured time-dependent property changes in sands. This process suggests that the continuous particle rearrangement is the underlying mechanism leading to aging. In elaborating on the process of mechanical aging, Wang et al. (2008) used numerical simulations by the discrete element method (DEM) to demonstrate that contact creep leads to the homogenization of contact forces, which stabilizes the soil structure and therefore enhance the mechanical properties of

soils.

The relative density is one of the factors that influence aging behavior in soils. Li and Yang (1998), Baxter and Mitchell (2004), and Wang and Tsui (2008) reported that denser materials exhibit higher increases in shear stiffness (measured by percentage). However, the associated underlying mechanisms of aging remain undescribed. Bowman and Soga (2003) suggested that a less pronounced aging effect in a loose sample might be attributed to the occurrence of local structure collapse, but experimental evidence is yet to be offered. In this context, the first objective of this paper is to reexamine the effect of relative density on the aging rate using resonant column tests and to offer appropriate explanations for the experimental findings. The issue of whether the aging-induced stiffness gain is isotropic has not yet been investigated. The second objective here is to investigate this issue using bender element tests in the true triaxial apparatus.

EXPERIMENTAL DETAILS

Toyoura sand and Ottawa sand (20-30) were used in the experiments of this study. The maximum and minimum void ratios were 0.987 and 0.589, respectively, for Toyoura sand, and 0.749 and 0.459, respectively, for Ottawa sand.

Resonant Column Tests

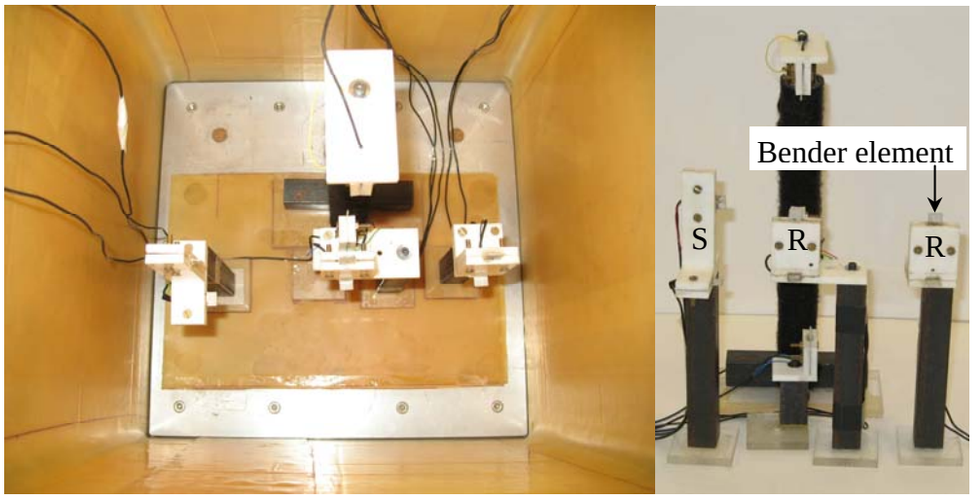
Resonant column tests were used to study the aging behaviors of sands with different relative densities. Samples of around 35 mm in diameter and 76 mm in height were prepared with different relative densities, D_r, i.e., dense, medium-dense, loose. Dry sand was used in preparing the dense and medium-dense samples. In preparing the loose sample, moist sand with a water content of about 1% was used. The loose sample was first compacted to the desired density followed by passing dry air through the sample for 18 hours using a vacuum pressure of about 5 kPa to reattain the air-dried condition. The dry air was generated by pumping air through a column filled with hydrous $CaSO_4$. During the assembly process of the resonant column system, a vacuum pressure of 25 kPa was applied to hold the sand sample. The relative density of the sample was determined after this assembly process was completed. An LVDT was also installed such that the axial displacements during the loading as well as the aging process could be recorded. All soil samples were loaded to an isotropic confining pressure of 100 kPa with a subsequent two days of aging. Small-strain shear moduli and damping ratios of the samples were measured at various time intervals over the aging period, by shearing at small strains and the values taken at the strain of about 5×10^{-4}% were used to evaluate the aging effect.

Bender Element Tests in the True Triaxial Apparatus

To investigate whether aging effects on the stiffness gain are isotropic in nature, a bender-element set was installed in a 300 mm × 300 mm × 300 mm true triaxial apparatus as shown in Fig. 1. The details of the true triaxial apparatus are described by Wang et al. (2006). The bender-element set contained nine bender elements, which were able to measure different shear wave velocities, i.e., V_{HH}, V_{HV}, and V_{VH}, where the first subscript represents the direction of the wave propagation and the second subscript

represents the polarization direction, and H and V stand for the horizontal and vertical directions, respectively. In each velocity measurement, one bender element served as the source (S) and another two were used as receivers (R). In such an arrangement, the arrival time of the S-wave can be determined by the cross-correlation peak of the two receiver signals. Toyoura sand was loaded into the device by the air pluviation method with six-layer compaction. The relative density, D_r, was about 75%. Loading was applied individually in the three principal stress directions. In the first test, an isotropic confining pressure of 100 kPa was applied for seven days of aging. The sample in the second test was aged also for seven days but under anisotropic stress conditions. Under the anisotropic stress conditions, the mean stress was still equivalent to 100 kPa but the ratio between the horizontal and vertical stresses was 0.5, i.e., σ_V = 150 kPa and σ_{H1} = σ_{H2} = 75 kPa where H_1 and H_2 represent the two horizontal directions. In both tests, the changes in the three shear wave velocities, i.e., V_{HH}, V_{HV}, and V_{VH}, over the aging period were compared to find out whether they were isotropic to aging effects.

(a)



(b)

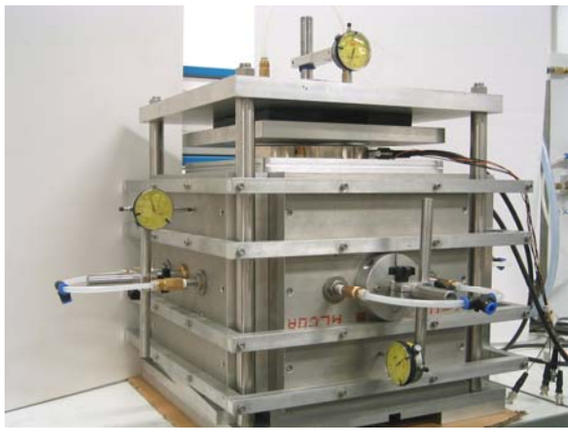


FIG. 1. The experimental setup: (a) the bender element set; (b) the true triaxial apparatus (after Wang et al. 2006; Wang and Mok 2008).

EXPERIMENTAL RESULTS AND DISCUSSION

Aging in Soils with Different Relative Densities

Fig. 2 presents the contact-force distribution of samples with different densities from DEM simulations where the line thickness is proportional to the magnitude of the contact force. The simulation details can be found in Wang et al. (2008). The contact-force distribution is more uniform when the sample becomes denser. Therefore, as the dense sample originally has a relatively homogeneous force-chain network, the development of contact-force homogenization induced by contact creep during aging is expected to be less pronounced than in the loose sample. Thus, the aging-induced stiffness increase is also expected to be smaller in the dense sand compared with the loose sand. However, if local structure collapse occurs in the loose sand, as suggested by Bowman and Soga (2003), the associated stiffness increase can be smaller than that in the dense sand where the chance for local structure collapse is relatively less. Also, the measured axial strain, ε_a, during the aging period should be higher in the loose sand than in the dense sand. Following this logic, the medium-dense sand should have the highest aging rate as measured by the stiffness gain. This is because, on the one hand, the medium-dense sand has less homogenous contact-forces when compared with dense sand, which increases the tendency of contact-force homogenization during aging and therefore the corresponding stiffness gain. On the other hand, medium-dense sand has higher resistance to local structure collapse when compared with loose sand, which therefore minimizes the chance of stiffness reduction. The results shown in Fig. 3 and summarized in Table 1 for Ottawa sand samples confirm the above suggestions. In this figure and table, the ratio of $\Delta G/G_{in}$ is used to present the rate of aging where ΔG is the change of the shear modulus with respect to its initial value, G_{in}, at a time equal to 1 minute. As summarized in Table 1, at the end of two days of aging, the loose sample had the highest axial strain and the lowest aging rate; the medium-dense sample had the highest aging rate; the dense sample had the lowest axial strain. Nevertheless, as shown in Fig. 4 and Table 2, although the dense and medium-dense Toyoura sand samples had a higher stiffness increase than the loose sample, the same conclusions cannot be drawn. For instance, the loose Toyoura sand had the lowest axial strain and the dense Toyoura sand had the highest one. This is completely opposite to the results from the Ottawa sand samples.

The above findings suggest that the effect of packing density on the aging behavior of sand indeed varies with the type of sand. Any universal underlying mechanism is still elusive. In Tables 1 and 2, the changes in the damping ratios of the samples are also shown but a definite trend in response to the density effect cannot be identified.

The Anisotropy of Aging

Figs. 5 and 6, based on the results of the bender element tests in the true triaxial apparatus, demonstrate the evolution of the S-wave velocities along the three principal stress directions during a seven-day aging period. The ratio of $\Delta V/V_{in}$ is used here to quantify the rate of aging, where ΔV is the change in the velocity with respect to its initial value, V_{in}, at a time equal to 1 minute.

As shown in Fig. 5, even if the loading is isotropic, the aging behavior in terms of the stiffness increase is not. The V_{HV} produces the highest increasing rate followed by

V_{HH} and V_{VH}. When the loading condition is changed to an anisotropic state, the vertical stress becomes the major principal stress and the anisotropy of aging in the stiffness gain is more prominent. The V_{VH} and V_{HV} display a greater aging rate when compared with V_{HH}, which might be explained as follows. The contact forces tend to align with the major principal stress (Oda et al. 1982; Rothenburg and Bathurst 1989). Creep is a time-dependent deformation in response to loading and the evolution in contact forces during aging may continue the same tendency to become more parallel to the major principal stress direction, i.e., in the vertical direction of the test. This tendency in turn increases the S-wave velocities in the polarization plane involving the stress from the vertical direction, i.e., V_{VH} and V_{HV}. Note that V_{VH} jumps from the lowest aging rate under isotropic loading conditions to the highest at anisotropic stress conditions. This observation implies that the major principal stress induces more significant aging effects on the S-wave velocity that propagates in the same direction. In short, the above discussions clearly reveal the anisotropy of aging in the stiffness gain; however, the underlying mechanisms still require further study.

Table 1. Summary of the changes in the axial strain and the small-strain shear modulus and damping ratio in the Ottawa sand samples after two days of aging.

Density State	$\varepsilon_{a\text{-}2d}$[a] (%)	G_{in}[b] (MPa)	$\Delta G_{2d}/G_{in}$[c] (%)	D_{in}[b] (MPa)	$\Delta D_{2d}/D_{in}$[c] (%)
Dense (D_r = 82%)	2.7×10^{-3}	121.3	4.9	0.264	-35.3
Medium-dense (D_r = 50%)	5.3×10^{-3}	92.7	6.0	0.248	-31.0
Loose (D_r = 29%)	5.3×10^{-3}	82.0	4.1	0.243	-30.8

[a] $\varepsilon_{a\text{-}2d}$: axial strain after two days of aging.
[b] G_{in}, D_{in}: small-strain shear modulus and damping ratio at the initial state, i.e., at aging time = 1min.
[c] $\Delta G_{2d}/G_{in}$, $\Delta D_{2d}/D_{in}$: ratios after two days of aging.

Table 2. Summary of the changes in the axial strain and the small-strain shear modulus and damping ratio in the Toyoura sand samples after two days of aging.

Density State	$\varepsilon_{a\text{-}2d}$ (%)	G_{in} (MPa)	$\Delta G_{2d}/G_{in}$ (%)	D_{in} (MPa)	$\Delta D_{2d}/D_{in}$ (%)
Dense (D_r = 77%)	6.6×10^{-3}	103.0	5.4	0.281	-39.7
Medium-dense (D_r = 62%)	6.6×10^{-3}	83.0	5.3	0.503	-49.4
Loose (D_r = 27%)	3.9×10^{-3}	72.3	4.6	0.354	-26.3

CONCLUSIONS

The results of resonant column tests on Ottawa sand demonstrate that the medium-dense sample has the highest aging rate, as determined by the shear-modulus increase, followed by the dense and loose samples. In addition, the loose sample has the highest axial strain. This observation might be attributed to two competing processes, i.e., the tendency toward force-chain homogenization and the susceptibility to local structure collapse. The tendency of force-chain homogenization, which is expected to be more pronounced when the packing is looser, can increase the shear modulus of soils during aging. The susceptibility to local structure collapse, which, however, leads to a decrease in the shear modulus and an increase in the axial strain during aging, is expected to be higher when the packing is looser. This explanation does not apply to Toyoura sand samples, which suggests that the effect of packing density on the aging behavior of sands indeed varies with the type of sands. In these two sand samples, although the damping ratio continuously decreases during aging, there is also no definite trend that can be identified for the density effect.

Bender element tests in the true triaxial apparatus demonstrate that the increase in V_{HH}, V_{VH}, and V_{HV} are different under an isotropic stress state, which suggests aging behavior in the stiffness gain is not isotropic by nature. Increasing the stress in one direction produces more significant increase in the S-wave velocities that are either polarized or propagating in that direction.

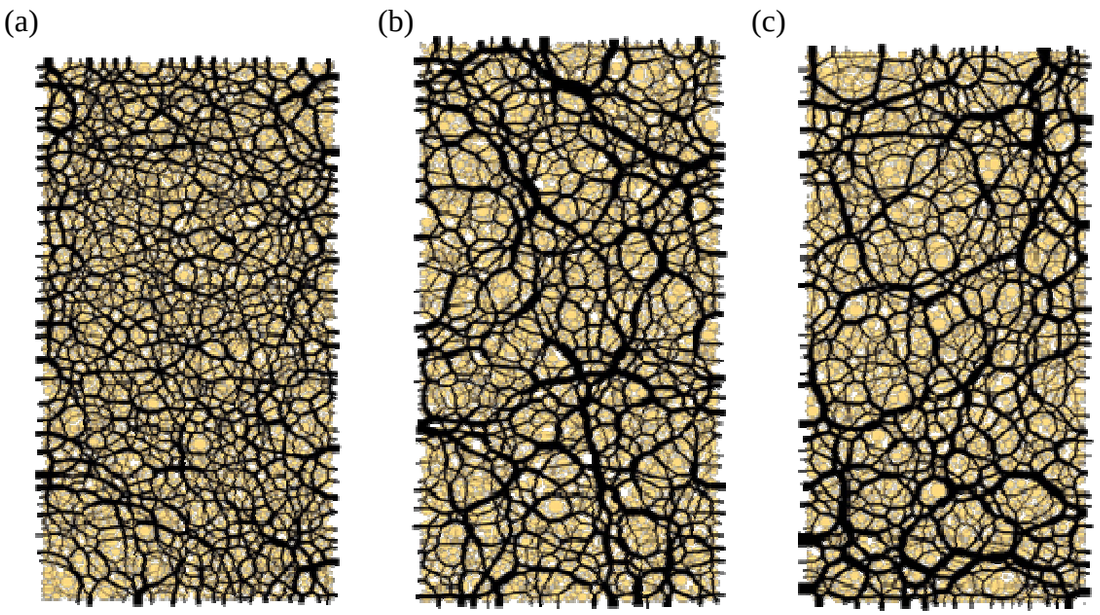


FIG. 2. The contact-force distributions obtained from the DEM simulations on (a) a dense sample (porosity n = 0.1558), (b) a medium dense sample (n = 0.1816), and (c) a loose sample (n = 0.2122) under a confining pressure of 400 kPa.

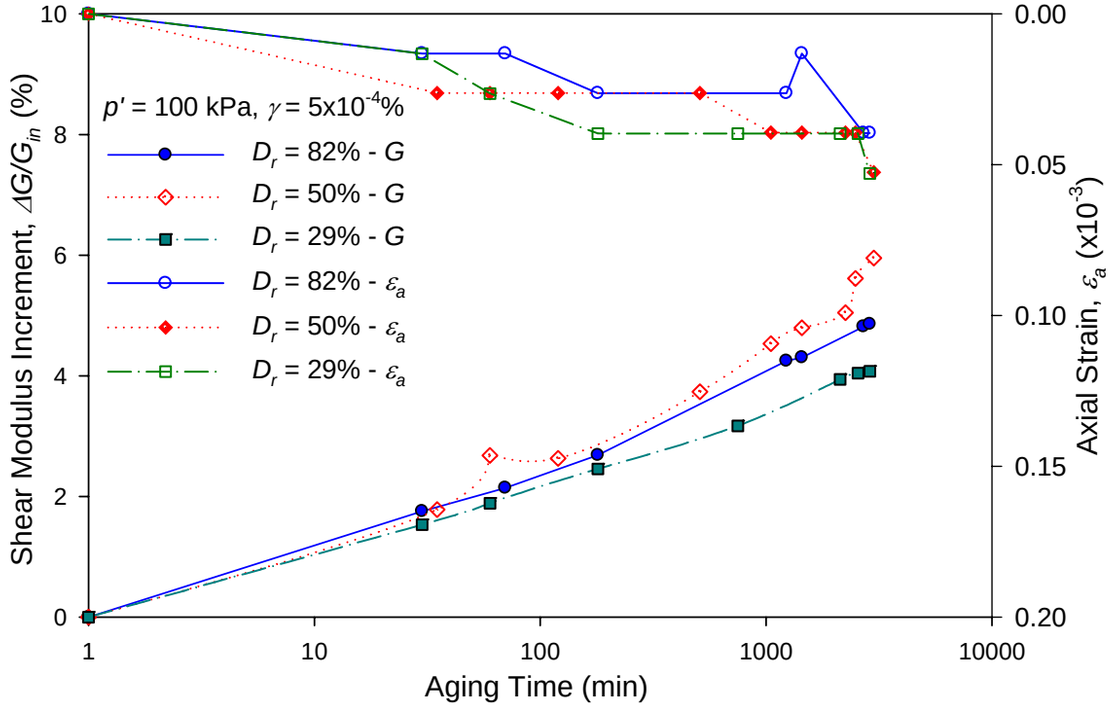


FIG. 3. Variations in the small-strain shear-modulus increment, $\Delta G/G_{in}$, and the axial strain in Ottawa sand samples with different relative densities.

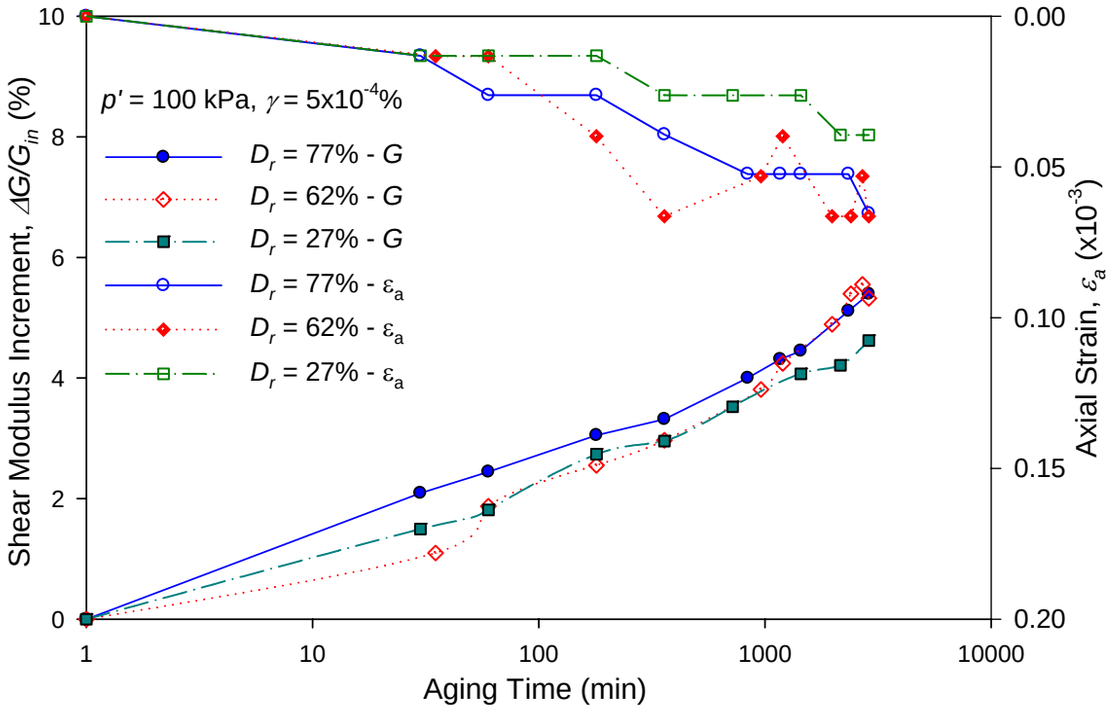


Fig. 4. Variations inthe small-strain shear-modulus increment, $\Delta G/G_{in}$, and the axial strain in Toyoura sand samples with different relative densities.

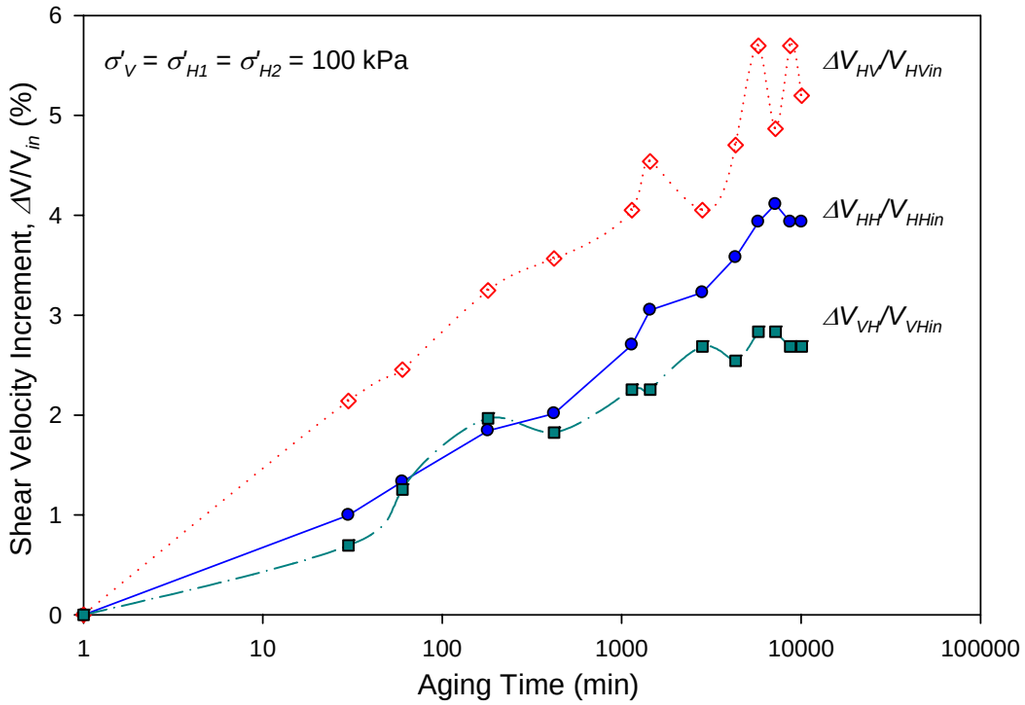


Fig. 5. Shear wave velocity increments in V_{HH}, V_{HV} and V_{VH} of the Toyoura sand sample under an isotropic stress state.

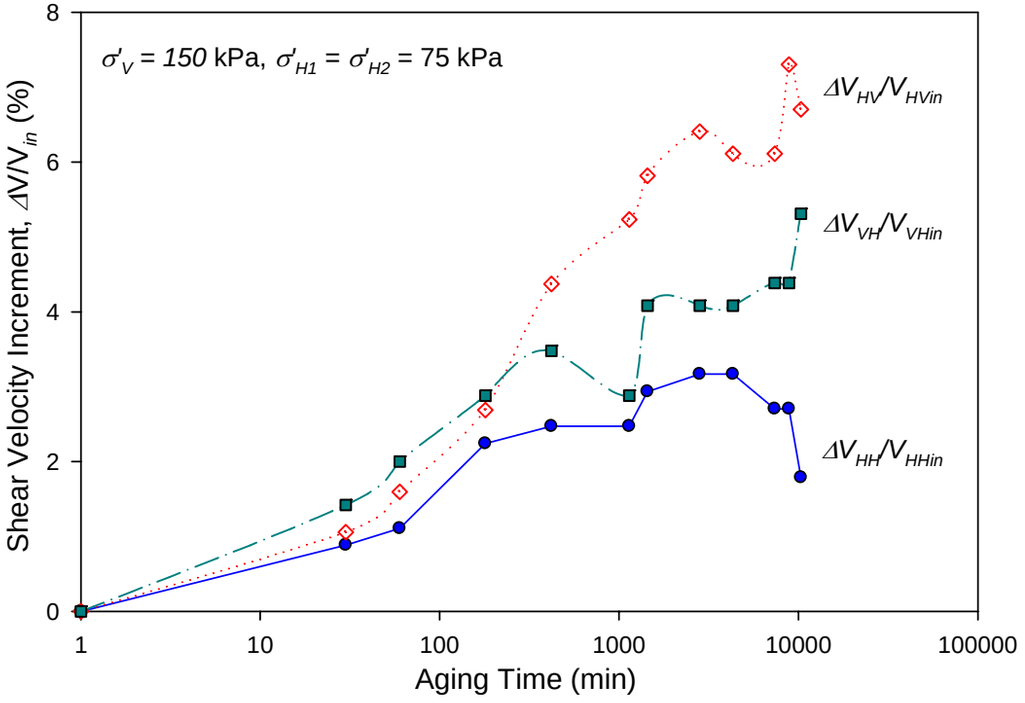


Fig. 6. Shear wave velocity increments in V_{HH}, V_{HV} and V_{VH} of the Toyoura sand sample under an anisotropic stress state.

ACKNOWLEDGMENTS

This research was supported by the Hong Kong Research Grants Council and the Hong Kong University of Science and Technology.

REFERENCES

Afifi, S.S., and Richart, F.E. (1973). "Stress-history effects on shear modulus of soils." *Soils and Foundations*, Vol. 13 (1): 77-95.

Afifi, S.S., and Woods, R.D. (1971). "Long-term pressure effects on shear modulus of soils." J. Soil Mech. Found. Div., ASCE, Vol. 97(SM10): 1445-1460.

Anderson, D.G., and Stokoe II, K.H. (1978). "Shear modulus, a time-dependent soil property." *Dynamic Geotechnical Testing*, ASTM STP 654, ASTM, Philadelphia: 66-90.

Baxter, D.D.P., and Mitchell, J.K. (2004). "Experimental study on the aging of sands." *J. Geotech. and Geoenvir. Engrg., ASCE*, Vol. 130(10): 1051-1062.

Bowman, E.T., Soga, K. (2003). "Creep, ageing and microstructural change in dense granular materials." *Soils and Foundations*, Vol. 43(4): 107-118.

Charlie, W.A., Rwebyogo, M.F.J., and Doehring, D.O. (1992). "Time-dependent cone penetration resistance due to blasting." *J. Geotech. Engrg., ASCE*, Vol. 118(8): 1200-1215.

Daramola, O. (1980). "Effect of consolidation age on stiffness of sand." *Géotechnique*, Vol. 30(2): 213-216.

Joshi, R.C., Achari, G., Kaniraj, S.R., and Wijiweera, H. (1995). "Effect of aging on the penetration resistance of sands." *Can. Geotech. J.*, Vol. 32(5): 767-782.

Li, X.S., and Yang, W.L. (1998). "Effects of vibration history on modulus and damping of dry sand." *J. Geotech. and Geoenvir. Engrg.*, Vol. 124(11): 1071-1081.

Mesri, G., Feng, T.W., and Benark, J.M. (1990). "Postdensification penetration resistance of clean sands." *J. Geotech. Engrg., ASCE*, Vol. 116(7): 1095-1115.

Mitchell, J.K., and Solymar, Z.V. (1984). "Time-dependent strength gain in freshly deposited or densified sand." *J. Geotech. Engrg., ASCE*, Vol. 110(11): 1559-1576.

Oda, M., Konishi, J. and Nemat-Nasser, S. (1982). "Experimental micromechanical evaluation of strength of granular materials: effect of particle rolling." *Mech. Mater.*, Vol. 1, 267-283.

Rothenburg, L. and Bathurst, R.J. (1989). "Analytical study of induced anisotropy in idealized granular materials." *Géotechique*, Vol. 49: 601-614.

Schmertmann, J.H. (1991). "The mechanical aging of soils." *J. Geotech. Engrg.*, Vol. 117(9): 1286-1330.

Solymar, Z.V. (1984). "Compaction of alluvial sands by deep blasting." *Can. Geotech. J.*, Vol. 21(2): 305-321.

Wang, Y.H. and Mok, C.M.B. (2008). "Mechanisms of small-strain stiffness anisotropy in sands." submitted to *J. of Geotech. and Geoenvir. Engrg., ASCE.*

Wang, Y.H., and Tsui, K.Y. (2008). "Experimental characterization of the dynamic property changes in aged sands." submitted to *J. Geotech. and Geoenvir. Engrg., ASCE*.

Wang, Y.H., Xu, D., and Tsui, K.Y. (2008). "Discrete element modeling of contact

creep and aging in sand." *J. Geotech. and Geoenvir. Engrg., ASCE*. [accepted for publication]

Wang, Y.H., Yan, W.M., and Lo, K.F. (2006). "Damping ratio measurements by the spectral ratio method." *Can. Geotech. J.*, Vol. 43(11): 1180-1194.

Development of a P- wave measurement system for laboratory specimens

Sajjad Maqbool[1], Junichi Koseki[2]

ABSTRACT

A new system, capable of generating and receiving P-waves in the laboratory specimens, is developed. P-waves were generated using a multi-layered piezoelectric actuator made of ceramics placed above the top cap and were received at two different levels at the side of specimen using two piezoelectric accelerometers. Triggering to generate P-waves was made by employing single pulse, single sinusoidal or continuous sinusoidal waves. Dynamic vertical Young's moduli (E_d) were computed from the travel time of the waves between two accelerometers and the corresponding travel distance between them. E_d obtained from this system were compared with the statically measured vertical Young's moduli (E_s) evaluated by conducting small unloading/reloading cycles on the same specimens. The stress level was kept constant to make both measurements just one after the other.

For this study, four tests were conducted using medium and large scale triaxial apparatuses. The testing material included Toyoura sand (Uniformly-graded sand from Japan) and Chiba gravel (Well-graded sandy gravel from Japan).

As a result of this study single pulse or single sinusoidal triggering was found better than continuous sinusoidal triggering. Moreover, no significant effect of specimen size was observed in E_s and E_d for Toyoura sand specimens. Next, E_d obtained was larger than E_s in both types of materials. Lastly, the difference between E_s and E_d increased with the increase in particle size of specimens. Such difference was about 15-25% in Toyoura sand specimens and it was about 100% in loose Chiba gravel specimens.

Key words: *P-wave, gravel, sand, accelerometers, Young's modulus.*

INTRODUCTION

Adequate information on dynamic behavior of soil is of great importance in solving many engineering problems, such as the design of foundations for machines or the propagation of shock waves generated by earthquakes. The tests to measure such

[1] Associate Professor, Department of Transportation Engineering and Management, University of Engineering and Technology, Lahore, Pakistan. E.mail. sajjadmaqbool@hotmail.com.
Ph. +0092-(0)300-461-8959.
[2] Professor, Institute of Industrial Science, The University of Tokyo, Japan.

dynamic behavior provide expeditious means of measuring the small-strain deformation characteristics of soils. Accurate assessment of stiffness is very important to develop several relationships (Lo Presti et al. 2006).

In-situ wave measurements, based on the cross-hole and down-hole methods, have been used for a long time in real construction sites (Stokoe & Hoar, 1978). Recently measurement of wave velocities in the laboratory has also become popular, and researchers have recognized that "static" and "dynamic" properties are no more different from each other (Woods, 1991). Precise static small strain measurements in the laboratory tests have bridged the gap of strain levels between "static" and "dynamic" behavior (Tatsuoka and Shibuya, 1992).

In this study, very small unloading/reloading cycles were applied at some stress levels, and strains were measured locally using local deformation transducers within a very small strain range (< 0.001%) at the specimen sides. This method is herein called as "static". For "dynamic" measurement, P-wave system was developed to obtain small strain stiffness of sand and gravel in laboratory. This system enabled us to apply single pulse, single sinusoidal and continuous sinusoidal waves. To obtain clear wave signals, stacking technique was used.

The first part of this paper identifies the apparatus, measurement techniques, testing material and testing program employed in this laboratory study. The second part discusses the procedures of developing P-wave system. Lastly we discuss the effect of specimen size, particle size and density on small strain stiffness obtained by the static and the dynamic methods. The conclusion summarizes the results of the study.

TESTING MATERIAL, EQUIPMENT AND TEST PROCEDURES

In this study, the first two specimens labeled Sand-1 and TC-7 were prepared from Toyoura sand (D_{max}=0.35 mm, D_{50}=0.21 mm and U_c=1.7) employing air-pluviation technique. Other two specimens labeled TC-13 and TC-15 were prepared from Chiba gravel (D_{max} = 38 mm, D_{50} = 6 mm and U_c = 33) employing compaction in layers at a moisture content of 5.5%. The gradation curves of both the materials are shown in Fig.1. In the first specimen sand-1, the specimen was cylindrical in shape with the dimensions of 10 cm in diameter and 20 cm in height (Fig.2). All other specimens were 23.5 cm x 23.5 cm in cross-section and 50 cm high (Fig.3).

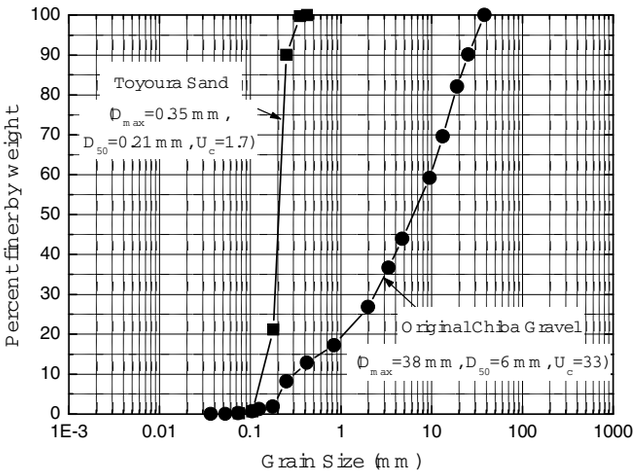


Fig.1. Gradation chart for the testing materials

To measure the vertical stress, σ_1, a load cell is located just above the top cap inside the triaxial cell in order to eliminate the effects of piston friction (Tatsuoka, 1988). The vertical strain ε_1 was measured not only with the external displacement transducer but also with a pair of vertical local deformation transducers (V-LDTs) (Goto et al, 1991), located each on opposite side surfaces of the specimen. The horizontal stress σ_3 was applied through the water in the cell, which was measured with a high capacity differential pressure transducer (HCDPT). In large specimens, horizontal strain ε_3 was measured with three pairs of horizontal local deformation transducers (H-LDTs).

In the testing program, Sand-1 was first subjected to isotropic consolidation from a stress state of 30 kPa up to 80 kPa. It was then subjected to isotropic unloading from a stress state of 80 kPa down to 50 kPa. Similarly TC-7, TC-13 and TC-15 were subjected to isotropic consolidation from a stress state of 50 kPa up

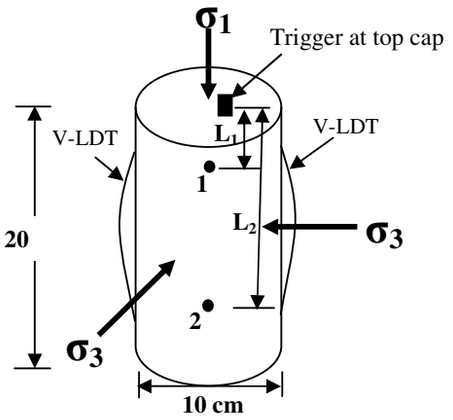


Fig. 2. Medium size triaxial specimen.

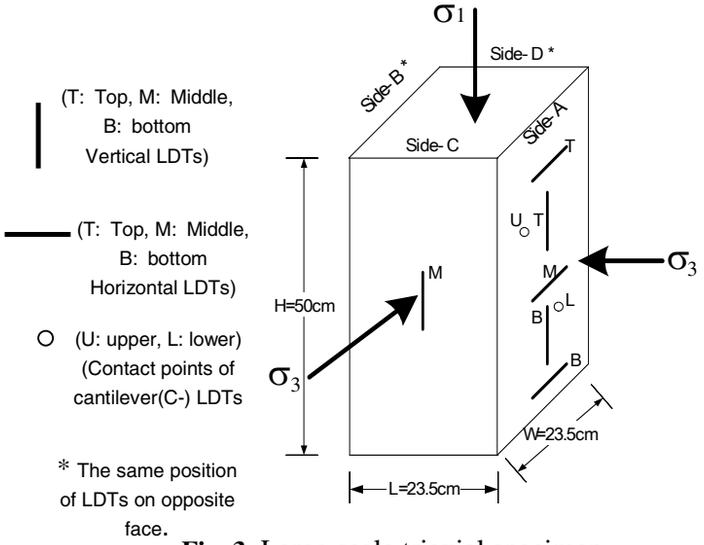


Fig. 3. Large scale triaxial specimen.

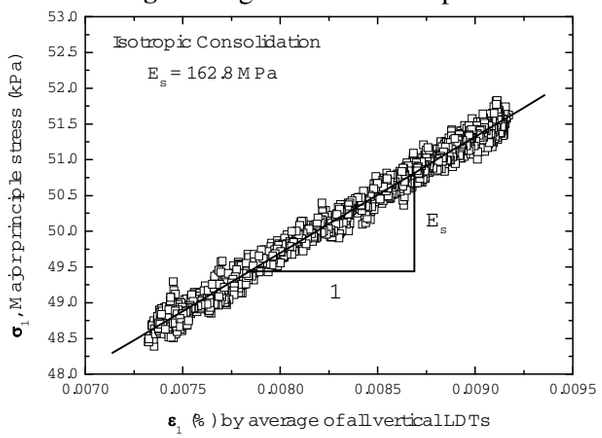


Fig.4. Typical small cyclic loading.

to 100 kPa and were then subjected to isotropic unloading from a tress state of 100 kPa down to 50 kPa. The unloading stress path was included in order to confirm the stress-state dependency of quasi-elastic properties already measured during the initial loading stress path 1. During isotropic consolidation, in addition to dynamic measurement, small amplitude unload/reload cycles were applied at various stress states to evaluate the values of dynamic and static small strain stiffness. Typical stress-strain relationship during a small vertical loading cycle is shown in Fig. 4. Throughout the tests, the backpressure was set equal to the atmospheric pressure.

P-wave measurement system

This system included two major components; wave generating system and wave receiving system. To generate P-waves, a special type of wave source (denoted as trigger), as shown in Fig. 5, was employed. It is a multi-layered piezoelectric actuator made of ceramics (dimensions of 10 mm x 10 mm x 20 mm, mass of 35 gram and natural frequency of 69 kHz, the commercial name is AE 1010D16 of TOKIN company) and a thick steel bar that was bent in a U shape. The actuator was driven by inputting an electric signal of +25 volt in a form of pulse. The mass of each steel bar is 60 grams, and such a large mass was required to provide the reaction force against the dynamic excitation by the piezoelectric actuator. The actuator was put inside the U-shaped steel bar, and they were covered by another steel plate. To generate the vertical compression wave that transmits from the top to the bottom of the specimen, the trigger was glued above the top cap close to the center in the case of the medium scale triaxial apparatus (Fig. 2). In the case of the large-scale true triaxial apparatus, as shown in Fig.6, the trigger was glued inside the top cap.

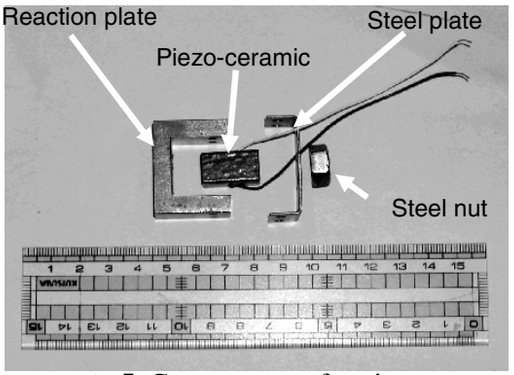
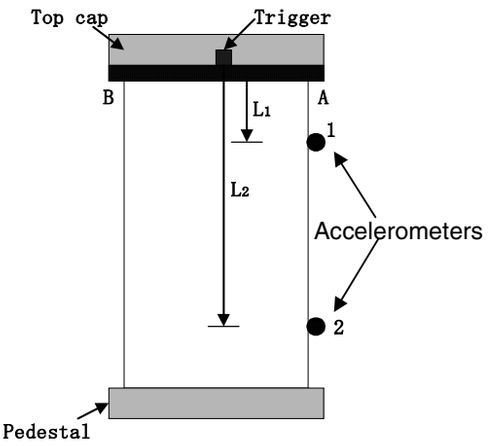


Fig.5. Components of a trigger.



1: output-1 accelerometer
2: output-2 accelerometer
L_1:distance between trigger and output-1 accelerometer
L_2:distance between trigger and output-2 accelerometer

Fig.6. Positioning of trigger and accelerometers on large scale triaxial specimen.

To receive P- waves, two types of piezoelectric accelerometers were employed as shown in Fig. 7. Type-1 accelerometers were cylindrical in shape with diameter of 3.6 mm, height of 3 mm, mass of 0.16 gram and natural frequency of 60 kHz. The output voltage of these accelerometers was sometimes significantly low, therefore while testing on large-size specimens; type-2 accelerometers were introduced. These were box-shaped with sizes of 4 mm x 4 mm x 13 mm, mass of 1.3 gram and natural frequency of 4 kHz and the output voltage was always high enough. For each test, the testing conditions are given in Table 1.

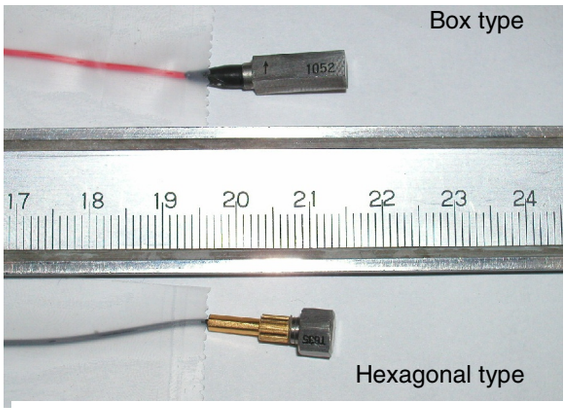


Fig.7. Types of accelerometers.

Table 1: Specifications of Toyoura sand and Chiba gravel specimens;

S.No.	Label	Specimen Size	Material	Dry density (g/cm^3)	Trigger & Accelerometers
1	Sand-1	10 D x 20 H (Medium size)	Toyoura Sand	1.61	P_{out} (Box type)
2	TC-7	23.5x23.5x50	Toyoura Sand	1.62	P_{in} (Hexagonal type)
3	TC-13	23.5x23.5x50	Chiba Gravel	1.92	P_{in} (Hexagonal type)
4	TC-15	23.5x23.5x50	Chiba Gravel	2.01	P_{in} (Box type)

Small strain stiffness by dynamic method

P-wave velocity V_p is directly related to the small-strain vertical Young's modulus, E_d, of the material by the dynamic measurement as:

$$E_d = \rho\, Vp^2 \qquad (1)$$

Where ρ is the mass density of the specimen, and the compression wave velocity V_p was calculated by

$$V_p = L/t \quad (2)$$

Here t is the travel time of the wave to cover the distance L. The distance L was computed by using the following equations considering the trigger as a point source to generate the compression waves as shown in Figs. 2 & 6.

$$L = L_2 - L_1 \quad (3)$$

Where L_2 and L_1 are the planar distances measured on the side of specimen as shown in Figs. 2 & 6. Such assumption was made after detailed study made by Maqbool (2005).

All the above parameters could be calculated or measured easily except for the travel time "t". A number of methods to obtain "correct" travel time have been employed by several researchers. For example, AnhDan et al. (2002) used the peak-to-peak travel time, while Jovicic et al. (1996) have recommended using the first arrival of the wave. Other researchers have suggested estimation of the travel time from several characteristic points, such as the first rising points, first peaks and first zero-crossing points in the input and output signals. There are also some researchers who have suggested to conduct analysis in the frequency domain to determine the

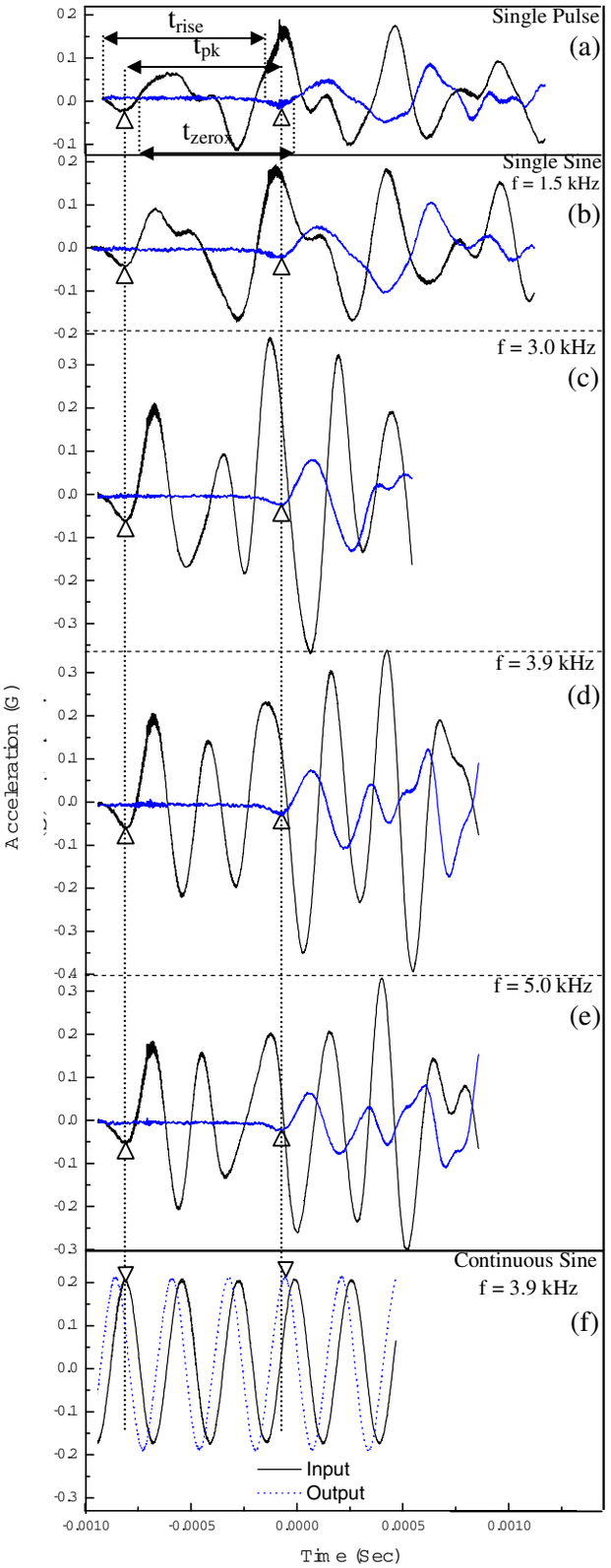


Fig.8. Recorded wave signals

phase angle either indirectly (e.g. Viggiani & Atkinson, 1995) or directly using phase-sensitive detection techniques (e.g. Blewett et al., 1999).

Travel time computation

In this study the wave signals were recorded at two different levels over the specimen using output-1 and output-2 accelerometers labeled as "1" and "2" respectively (Figs. 2 & 6). Different techniques were employed to compute the travel time and compared.

In the first technique as shown in Fig. 8, "t" was determined using the first peaks of output-1 and output-2 waves. It will be called "peak to peak" travel time technique denoted as "t_{pk}". In this technique, the observer has to decide the correct peak point. In case of noise-free signal records, the error on decision of "correct peak" is lesser than in case of noisy signal records. The authors recommend using this technique for the determination of correct travel time when the data is almost noise free.

In the second technique, as shown in Fig. 8, "t" was computed from the first rising point of the first output-1 wave to the first rising point of the first output-2 wave. It will be called as "first rise to first rise" technique denoted as "t_{rise}". In this method, a problem lies with the decision of first rising point in both signal records. It may depend on observer's judgment to decide the correct rising point. After comparing a number of wave signal records obtained in the second series of tests, it was found that t_{rise} was in general 5% larger than t_{pk}.

Based on the above comparison, it was found that, if the signal record is noise free, "t_{pk}" is easily employed. In the following test results, "t_{pk}" was used to compute the travel time. To obtain clear signals of the output-2 waves, stacking technique has been recommended in the literature. Maqbool et al. (2004) found that wave signals became clear when stacking was made for 128 times.

TEST RESULTS AND DISCUSSION

To compute wave velocity, single pulse, single sinusoidal and continuous sinusoidal wave triggering was made as shown in Fig. 8. Wave velocity obtained by single sinusoidal wave triggering made at the frequency of 1.5-5 kHz was found similar to that obtained by single pulse triggering. Such range of frequency was obtained by applying Fast Fourier Transform (FFT) at the first half cycle of output-1 wave in single pulse triggering. On the other hand, while computing wave velocity by continuous sinusoidal triggering, it was difficult to decide the output-2 wave corresponding to its output-1 wave. The wave velocity obtained by this method was mostly different from that obtained by single pulse triggering. As shown in Fig.9, the wave velocity obtained by considering third peak of the continuous sinusoidal wave received as output-2 is found largely dependent on triggering frequency. The difference between wave velocities obtained by different techniques was negligible at triggering frequency of 3.90 kHz. This value of triggering frequency was obtained after employing FFT at the first half cycle of the single pulse wave. As a result of

these measurements, single pulse wave triggering was decided to be the most reliable to be employed to compute E_d in this study.

Vertical Young's moduli of "Sand-1", evaluated by the static and dynamic measurements are compared in Fig. 10. Dynamic vertical Young's moduli (E_d) were 15-25% larger than static vertical Young's moduli (E_s) in this test. Such difference could not be expected due to the difference in strain level because in both measurements, the strain level was within the elastic range. In order to confirm this behavior, TC-7 was conducted using large size specimens. In this test, E_s and E_d were found repeatable and E_d was found 15-25% larger than E_s. Such results proved no effect of specimen size on E_s and E_d.

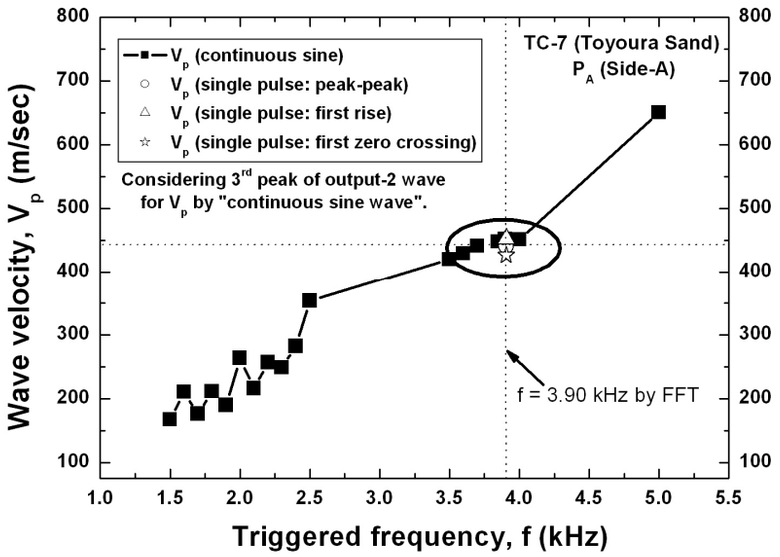


Fig.9. Effects of triggering frequency on compression wave velocity.

In last two tests TC-13 and TC-15, E_d was found larger than E_s though the difference between E_d and E_s depended on dry density of the specimens as shown in Fig.11. The difference was about 100% in loose Chiba gravel specimen (TC-13). The possible reason for such behavior is that

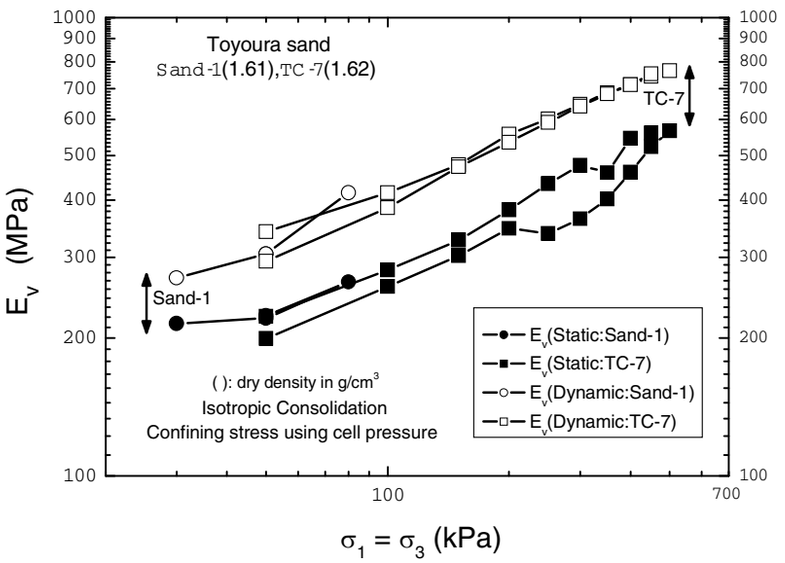


Fig.10. Vertical Young's moduli of Toyoura sand.

the wave does not reflect the overall cross-sectional property of the specimen rather it travels through the shortest path made by interlocking of bigger particles, resulting into larger Young's moduli as compared to those by the static measurement. On the other hand, static measurement represents the overall behavior of the specimen. Similar results have been also reported in the literature by Tanaka et al. (2000). The difference in the Young's moduli would increase with the decrease in the dry density, since looser specimens would have larger structural or microscopic heterogeneity than denser ones.

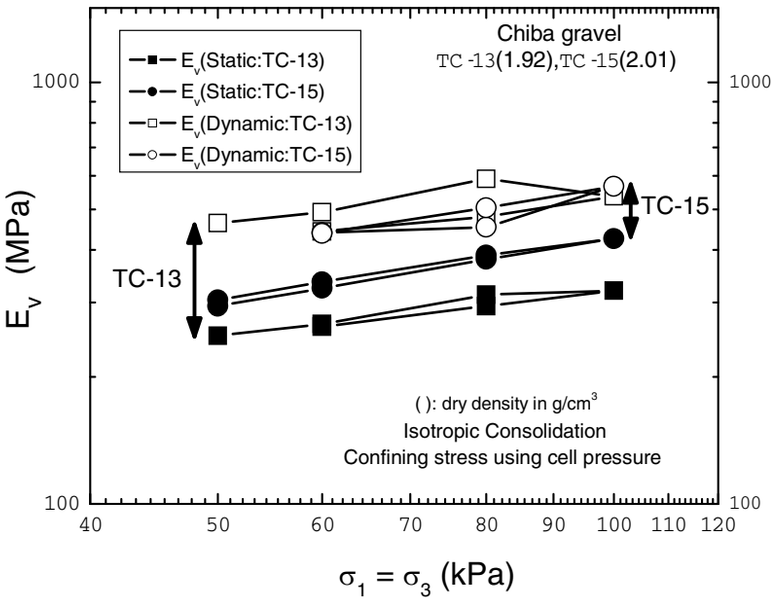


Fig.11. Vertical Young's moduli of Chiba gravel.

CONCLUSIONS

The following conclusions can be drawn from the test results presented in this paper:

1- Single pulse or single sinusoidal triggering was found better than continuous sinusoidal triggering.
2- No significant effect of specimen size was observed in measurement of E_s or E_d for Toyoura sand specimens.
3- E_d obtained was larger than E_s in both types of materials.
4- The difference between E_s and E_d increased with the increase in particle size. Such difference was about 15-25% in Toyoura sand specimens and it was about 100% in loose Chiba gravel specimens.

ACKNOWLEDGEMENT

The authors would like to thank Mr. Takeshi Sato, Research Support Promotion Member, Institute of Industrial Science, The University of Tokyo, for providing technical support in conducting experiments at IIS. Thanks also go to the Ministry of Science, Culture and Education of Japan for its financial support to the first author to study as PhD student at The University of Tokyo, Japan.

REFERENCES

AnhDan, L.Q., Koseki, J. and Sato, T. (2002). "Comparison of Young's moduli of dense sand and gravel measured by dynamic and static methods." Geotechnical Testing Journal, Vol.25, No.4, pp.349-368.

Blewett, J., Blewett, I.J. and Woodward, P.K. (1999). "Measurement of shear-wave velocity using phase-sensitive detection techniques." Canadian Geotechnical Journal, No.36, pp.934-939.

Goto, S., Tatsuoka, F., Shibuya, S., Kim, Y.S. and Sato, T. (1991). "A simple gauge for local small strain measurements in the Laboratory." Soils and Foundations, No.1, Vol.31, pp.169-180.

Jovicic, V., Coop, M.R., and Simic, M. (1996). "Objective criteria for determining G_{max} from bender element tests." Geotechnique, Vol.46, No.2, pp.357-362.

Lo Presti, D., Pallara, O. and Mensi, E. (2006). "Characterization of soil deposits for seismic response analysis." Soil Stress-Strain Behavior: Measurement, Modeling and Analysis published by Springer, The Netherlands, on Geotechnical Symposium in Roma, Italy. pp. 109-157.

Maqbool, S. (2005). "Effects of compaction on strength and deformation properties of gravel in triaxial and plane strain compression tests." PhD thesis, The University of Tokyo, Japan.

Maqbool, S., Sato, T. and Koseki, J. (2004). "Measurement of Young's moduli of Toyoura sand by static and dynamic methods using large scale prismatic specimen." Proceedings of the Sixth International Summer Symposium, JSCE, Saitama, Japan; 233-236.

Stokoe, K.H., II and Hoar, R. J. (1978). "Field measurement of shear wave velocity by crosshole and downhole seismic methods." Proceedings of the Conference on Dynamic Methods in Soil and Rock Mechanics, Karlsruhe, Germany, Vol.III, pp.115-137.

Tanaka, Y., Kudo, K., Nishi, K., Okamoto, T., Kataoka, T. and Ueshima, T. (2000). "Small strain characteristics of soils in Hualien, Taiwan." Soils and Foundations, Vol.40, No.3, pp.111-125.

Tatsuoka, F. and Shibuya, S. (1992). "Deformation characteristics of soils and rocks from field and laboratory tests." Proc. of 9th Asian Regional Conference of SMFE, Bangkok, Vol. 2, pp.101-170.

Viggiani, G. and Atkinson, J.H. (1995). "Interpretation of bender element tests." Geotechnique, Vol.45, No.1, pp.149-154.

Woods, R.D. (1991). "Field and laboratory determination of soil properties at low and high strains." Proc. of 2nd International Conference on Recent Advances in Geotechnical Earthquake Engineering and Soil Dynamics, pp.1727-1741.

Development of Buried Sensors for Stiffness Measurements of Soft Clays Using Bender Elements

Jae Woo Jung[1] , Chul Soo Park[1] and Young Jin Mok[2] , P.E.

[1]Research Assistant, Dept. of Civil Eng., Kyunghee University, Korea; jujawo@khu.ac.kr
[2]Professor, Dept. of Civil Eng., Kyunghee University, Korea; yjmok@khu.ac.kr, corresponding author

ABSTRACT : The use of vertical drains, along with pre-loading, is the most popular method of soil improvement in coastal areas to meet growing demand for diverse uses of limited land space. Piezometers are the key instrument for continuous monitoring throughout the consolidation period. Basically, piezometers have several disadvantages such as incapability of providing any mechanical properties, meticulous installation procedures, misleading results caused by unexpected hydrogeologic boundary condition, and relatively high damage rate. As an alternative instrument for monitoring soil improvement, a piezo-electric sensor was elected to measure stiffness changes during consolidation. The piezo-electric sensor is composed of two bender elements mounted on a frame. Bender elements, composed of piezo-materials and metal shims, have favorable features suitable to field instrumentation such as simple principle of energy conversion, excellent control capability and small physical size. The prototype sensors have been developed through extensive in-house program to optimize in terms of data quality and installation convenience. The first prototype sensor was implemented in coastal mud using SPT(standard penetration test) rods pushed with a routine boring machine and excellent shear wave signals were measured. The sensor is on the further collective refining process.

INTRODUCTION

The use of vertical drains, along with pre-loading, is the most popular method of soil improvement in coastal areas to meet growing demand for diverse uses of limited land space. Monitoring and performance assessment of soil improvement are performed using various instruments including piezometer and settlement gauge, and in-situ testing techniques, such as cone penetration and field vane shear tests (Bo et al. 2003). Piezometers are the key instrument (if extremely say, the only accessible tool) for continuous monitoring throughout the consolidation period. Basically, piezometers are installed to monitor the dissipation of excess pore pressure in the soil and the degree of consolidation is, in turn, used as a measure of improvement. However, the instrumentation can not provide any mechanical properties improved after the completion of consolidation. Very meticulous care is

necessary in installation procedures including calibration, drilling, packing sand filter around the probe, sealing with bentonite, and backfilling the borehole. Also excess pore pressure can be misinterpreted due to the deviation of pore pressure profile from static condition caused by hydrogeologic boundary condition (Schiffman et al. 1994). Problems of damage can be often encountered especially on the pneumatic piezometers installed in highly compressible soft clay (Bo et al. 2003). As an alternative of the piezometer, a piezo-electric sensor has been developed to monitor stiffness changes during consolidation. This sensor can be easily installed by pushing into the ground with SPT(standard penetration test) rods.

The piezo-electric sensor is composed of two bender elements mounted on a frame. Bender elements, composed of piezo-materials and metal shims, have favorable features suitable to field instrumentation such as simple principle of energy conversion, excellent control capability and small physical size. At the preliminary stage of its development, the basic configuration of the sensor was contrived. Extensive in-house research of optimizing bender elements for the best performance and installation method has been carried out in a barrel of kaolinite slurry (Mok et al. 2007; Jung 2005b; Jung et al. 2005). The first prototype sensor was installed into coastal mud using SPT rods pushed with a routine boring machine and excellent shear waves were measured in field implementation.

BENDER ELEMENTS

A bender element consists of two piezoceramic sheets sandwiching a central metal shim as it is shown in FIG. 1. Bender elements can be made into various shape, size, and arrangement of piezoceramic sheets and metal shims. They can be optimized with proper shape, thickness and material stiffness depending upon usage purposes. FIG. 2 shows the process of manufacturing a bender element by cutting a piezoceramic sheet into proper size, bonding components, connecting electrodes and coating.

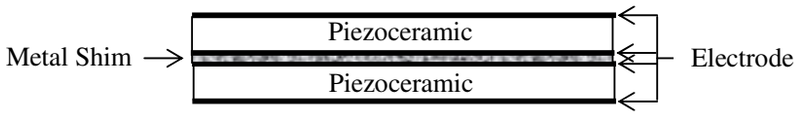


FIG. 1. Structure of a bender element

The bender element can bend as piezoceramic sheet on one side expands while the other side contracts with an applied voltage. Expanding and contracting of the sheets are reversed as the direction of the voltage is changed. Thus, application of an AC voltage enables the element vibrate and be used as an actuator. On the other hand, if the element is deformed by outside force, it generates voltage and can be used as a receiver.

There are two types of bender elements: series-connected and parallel-connected. With the same voltage applied, the parallel-connected bender element generates twice the tip displacement as the series-connected bender element. On the other hand, series-connected bender elements can generate twice the voltage as parallel

bender elements under the same deformation. Thus, parallel-connected bender elements are used as actuators (source) while series-connected bender elements are better suited as receivers (Jung 2005a).

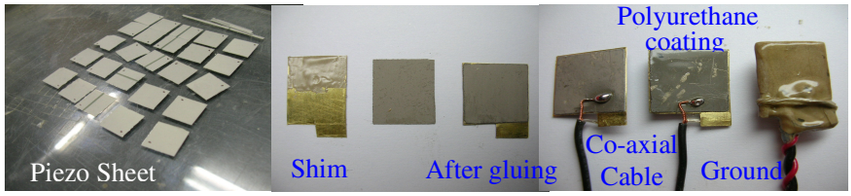


FIG. 2. Manufacturing process of a bender element

BASIC CONFIGURATION OF THE SENSOR

Cross-rod Configuration

Cross-rod configuration was adopted in the initiation of the research, because excellent shear wave signals were surely expected. The cross-rod configuration is almost identical to crosshole seismic test as shown in FIG. 3. One rod was mounted with source benders and the other rod with receiver benders, respectively. Each pair of source and receiver benders was used to generate one cycle of harmonic perturbation and to monitor the shear wave motion at each location. As a preliminary stage of their field applications, cross-rod arrangement has been carried out in a barrel of kaolinite slurry and excellent shear wave signals were obtained (Mok et al. 2006; Jung et al. 2005).

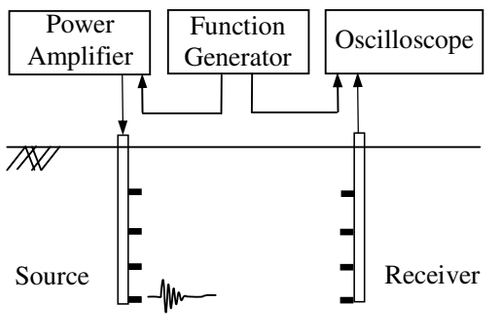


FIG. 3. Cross-rod configuration

Bender elements of 1.5cm long and 1.5cm wide were mounted at every 0.5 meter on source and receiver rods as shown in FIG. 4. A small metal plate(same size as bender elements) was also mounted right below each element to protect the element during penetration. The source and receiver rods were pushed 2 meters deep into coastal mud near PyungTaek-city with bare hands. The distance between source and receiver rods was 20cm. Excellent shear wave signals were recorded at the depth of 0.5, 1.0, 1.5 and 2.0 meters and travel times were “picked” as shown in FIG. 4. The

arrows in the figure indicate the first arrivals of shear wave energy. Shear wave velocities were calculated by dividing travel distance (here, 20 cm) by travel time at each depth and plotted in FIG. 4. This scheme would be surely applicable to field if two instrumented rods can be pushed down with maintaining equal distance. Otherwise, extra efforts of installing and measuring dual-axis inclinometers are required to track down the accurate travel distance. Implementation of this configuration to field was considered somewhat complicated and research effort was redirected to single-rod arrangement as below.

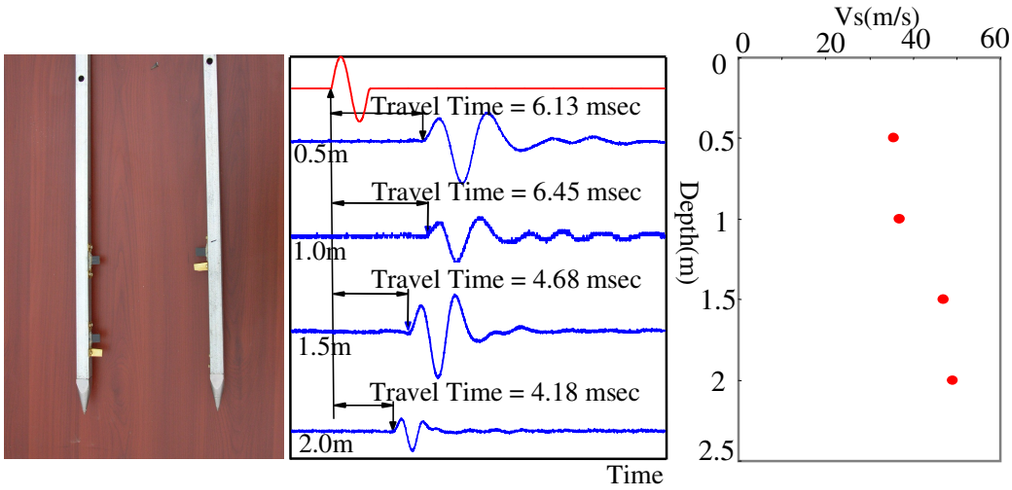


FIG. 4. Field cross-rod test

Single-rod Configuration

A pair of source and receiver benders was mounted on one rod. It has advantages over cross-rod such as the use of one rod only and the fixed distance between source and receiver. However, the noise through the rod is a formidable price paid for using one rod only and should be eliminated. Several mounting schemes of bender elements were attempted in the laboratory and the final version was adopted for field testing. The first scheme was the direct mounting of the bender elements on the rod as shown in FIG. 5. Net distance between two benders was fixed as 10 cm. The noise, which looked like the same as input, was predominated and any discernible shear wave energy could not be identified. Two arms were attached to the rod and source and receiver benders were mounted at the end of each arm, facing each other. Surprisingly the noise through the rod almost disappeared and “signature wavelet” of shear wave energy propagated through soil, was dominated and became discernible.

Plat-shape of arm ensured intimate contact with surrounding soil and was very effective in the dissipation of the noise into the ambient ground. But the mounting arms are not amiable in pushing the rod into the ground. The arms were folded during penetration and unfolded in place by pulling cables attached to the arms for measurements. FIG. 6 shows swing-arm scheme with the arms unfolded and the shear wave signal recorded in the coastal mud. The noise, with high frequency and small amplitude, arrived before the major signature wavelet of shear wave energy

through soil. The noise interference was not decisive for "picking" the first arrival time of the shear wave.

The conclusive finding is that the plate-shape arm could radiate the noise through, if intimately contacted with, the surrounding soil and save the formidable effort to devise any complicated damping mechanism. The frame consists of a stem and two arms, at whose end the source and receiver bend elements were mounted. Optimizing process has been conducted with this basic arrangement as below.

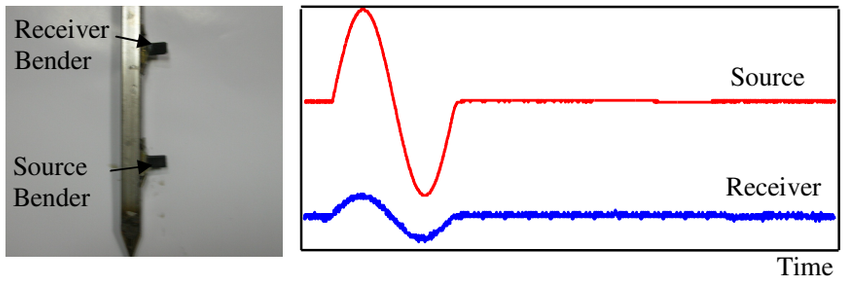


FIG. 5. Direct mounting scheme and measured signal

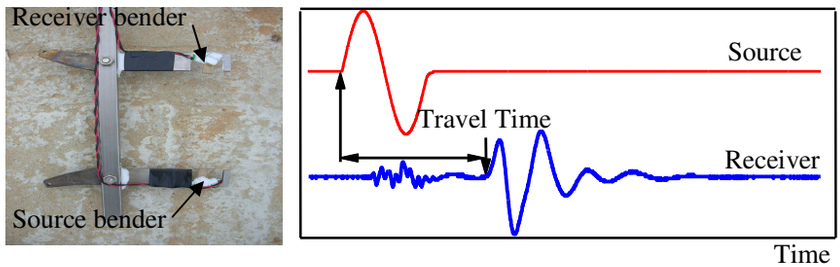


FIG. 6. Plate-shape arm mounting and measured shear wave signal

EVOLUTING PROTOTYPE SENSORS

Optimizing Sensor

The basic frame of the sensor consists of a stem and two arms. The contact area with soil is the key parameter for the reduction of the noise. The amount of noise reduction should be proportional to the contact area. Optimal sizes of the frame and arms were determined with the quality of the shear wave measured with changing the dimension of the frame (Mok et al. 2007). The finalized prototype sensor consists of a stem of T-type section, (whose flange, web and thickness are 30mm, 30mm and 5mm, respectively) and two arms of plate-type (which are 50mm long and 30mm wide) as shown FIG. 7. The arms were connected with pins rather than bolting or welding to reduce the noise further. The sensor was tested with changing frequency of driving voltage to the source bender in the barrel of kaolinite slurry as shown FIG. 8. The best shear wave signals were measure with the driving frequency in the range of 800 to 1200 Hz. The prototype sensor was installed by pushing with SPT(standard penetration test) rods at the depth of 6 meters in a costal site as shown

FIG. 9 and 10. The measure shear wave signals are shown in FIG. 8. The signals are not as excellent as those measured in the laboratory, but still are decent enough to pick the first arrival time. The one cycle of low frequency noise came from the cross-talk caused by high driving voltage of source bender element. The noise through the frame is shown as high frequency wavelets overriding the cross-talk of low frequency. In the field, the grounding of long cables was not as good as in the laboratory to eliminate the cross-talk. Also, the contact between the sensor and the surrounding soil did not seem to be intimate because of the wobbling of SPT rod during installation.

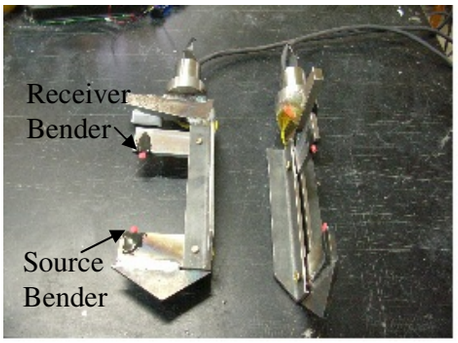
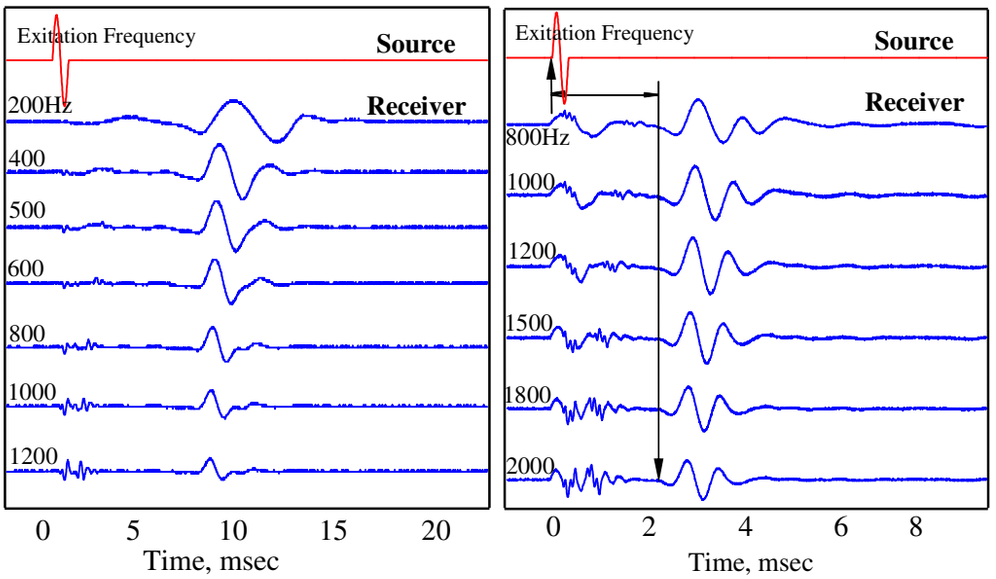


FIG. 7. 1st Prototype sensor



a) in Laboratory b) at Field

FIG. 8. Shear wave signals measure with the 1st prototype sensor.



FIG. 9. Boring machine and SPT rods



FIG. 10. The sensor connected to SPT rod.

Lattice-Type Arm

The length of arm was reduced and the contact area was compensated with the wings attached to the arm plate as shown FIG. 11. The basic idea is the same as the radiator grill. The lattice structure maintains the same contact area, through which the noise is radiated to the surrounding soil, as the 1st prototype and enables the sensor to be more compact. The measured shear waves in the laboratory were as good as those recorded with 1st prototype as shown FIG. 6 (Mok et al. 2007).

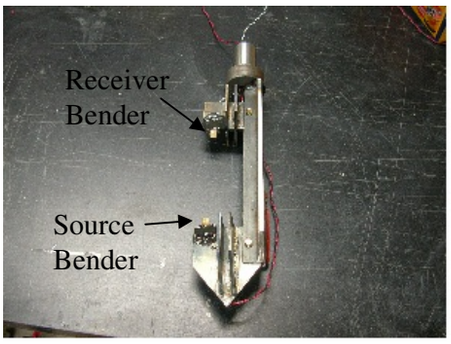


FIG. 11. Lattice type arms of the 2nd prototype sensor.

Other Considerations

The sensors are installed into coastal mud and bender elements should be well protected against corrosion by salty water. Bender elements coated with various coating compounds have been immersed under the salt water and tested regularly over a year. Urethane and Teflon(TFE) compounds turn out to work well.

The cable is at least more than 10 meters in the field and expected to pick up electric noise. A shielded coaxial cable, with a ground line and outer woven shield under jacket, was determined to use after collective testing of various cable types. Also two separate cables were connected to source and receiver bender elements, respectively, to avoid cross-talk problem caused by high driving voltage of source bender.

FIELD APPLICATION

The sensors were installed at a PBD(plastic board drain) site near Incheon, Korea to monitor stiffness change of the clay after preloading. The spacing of vertical drains was 2.4m in both lateral directions. Four sensors were installed at the depth of 3, 5 and 8 meters separately (square symbols in FIG. 12) before applying preloading. Three sensors were connected with rods and installed at the depth of 3, 5 and 8 meters in a row (cross symbol). Because of heavy rain, shear wave measurements were not done right after installation, but delayed 12 days. The first measurement shear wave signals are shown in Figs. 13 and 14. One out of the seven sensors did not work. The noise transmitted through the sensor frame, was eliminated quite well. The cross-talk was still present in the signals of three sensors as shown in the right signals of FIG. 14, it does not interfere with the signature wavelet of shear wave energy though. The other three signals are very quiet before the arrival of shear waves. The performance of the sensors is very satisfactory. The shear wave profile is shown in FIG. 15. Subsequent measurements will add stiffened profiles as consolidation takes place after preloading. The profile reflects the stiffness of disturbed state caused during penetration of the sensors. A new type of the sensor, whose basic shape looks like a fork composed of two thin blades, was invented to reduce the disturbance effect on stiffness during field installation (Jung et al. 2008).

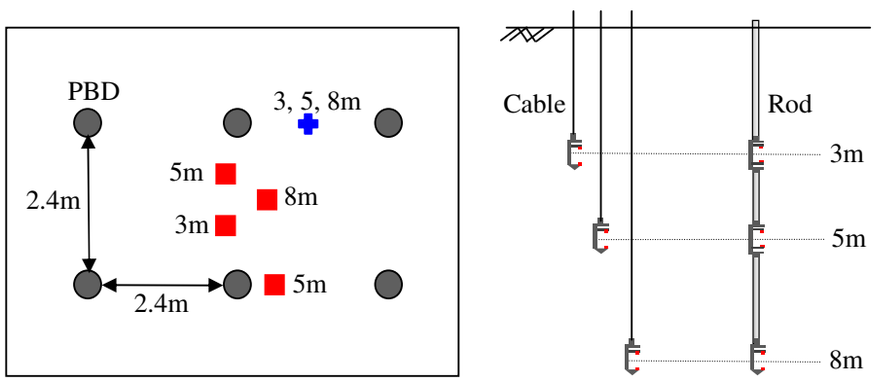


FIG. 13. Field arrangement of sensor installation.

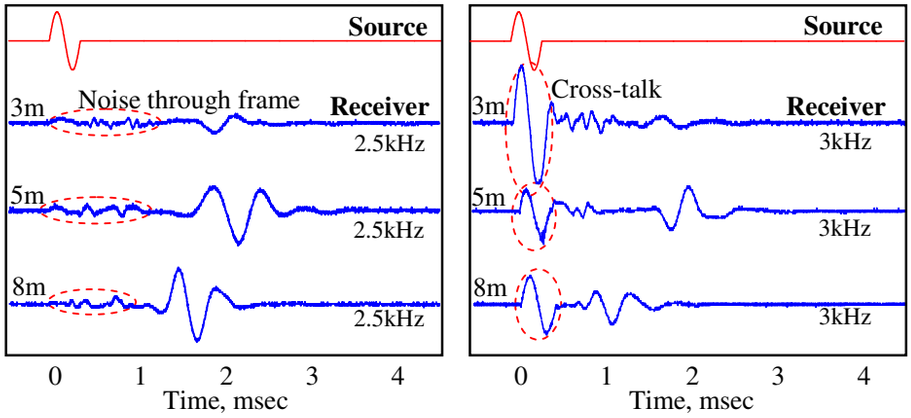


FIG. 14. Shear wave signals measured before preloading.

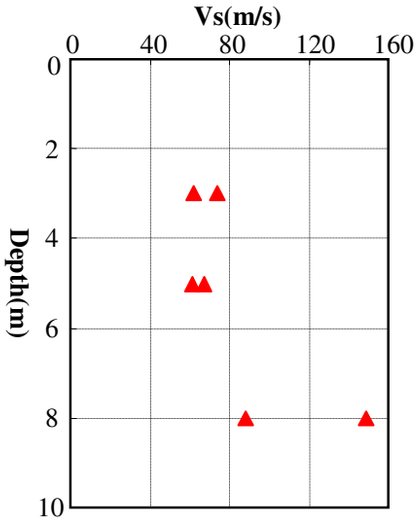


FIG. 15. Shear wave profile before preloading.

CONCLUSIONS

As an alternative instrument for monitoring soil improvement, a piezo-electric sensor was considered to use for monitoring stiffness changes during consolidation. The piezo-electric sensor is composed of two bender elements mounted on a frame. Bender elements, composed of piezo-materials and metal shims, have favorable features suitable to field instrumentation such as simple principle of energy conversion, excellent control capability and small physical size.

The prototype sensors have been developed through extensive in-house program to optimize in terms of data quality and installation convenience. The first prototype sensor was implemented in coastal mud using SPT rods pushed with a routine boring

machine and excellent shear wave signals were measured. The sensor is on the further collective refining process to be an excellent field instrument for soil improvement. The field implementation is planed at several vertical drain and vacuum consolidation sites in near future.

ACKNOWLEDGEMENTS

The research was supported by a grant(Code No.; C105A1000013-06A030001220) funded by Ministry of Construction & Transportation of Korean government. The authors also would like to thank Dr. K.H. Stokoe, II and Mr. M.J. Jung at the University of Texas at Austin for their help to initiate the research.

REFERENCES

Jung, J.W., Mok, Y.J. and Jang, I.S. (2005), "A Pilot Study of Implementing Bender Elements to In-situ Civil Engineering Measurements," *Journal of the Korean Geotechnical Society(written in Korean)*, Vol. 21(5): 215-223.

Jung, M.J. (2005a), "Shear Wave Velocity Measurements of Normally Consolidated Kaolinite Using Bender Elements." *Master Thesis*, University of Texas at Austin.

Jung, J.W. (2005b), "A Pilot Study of Bender Elements in Stiffness Measurements of Civil Engineering Materials," *Master Thesis(written in Korean)*, Kyung Hee University, Korea.

Jung, J.W., Park, C.S. and Mok, Y.J. (2008), "Development of Penetration-type Bender Element Probe for Stiffness Measurements of Soft Soils" *Journal of Geotechnical and Geoenvironmental Engineering (submitted).*

Mok, Y.J. et al. (2007), "Implementation of Piezoelectronics to Sustained Evaluation of Mechanical Characteristics of Soft Clay," 2nd *Annual Report(written in Korean)*, KICTTEP.

Mok, Y.J., Jung, J.W., and Han, M.J.(2006), "Implementation of Bender Elements to In-situ Measurements of Stiffness of Soft Soil," *Journal of the Korean Geotechnical Society(written in Korean)*, Vol. 22(11): 37-45.

M.W.Bo, J.Chu, B.K.Low and V.Choa(2003), *Soil Improvement ; Prefabricated Vertical Drain Techniques*, Thomson

Schiffman, R. L., McArthur, J. M. and Gibson, R. E. (1994), "Consolidation of clay layer: hydrogeologic boundary condition," *Journal of Geotechnical Engineering*, Vol. 120(6): 1089-1095

Development of Methods to Predict the Dynamic Behavior of Fine Coal Refuse: Preliminary Results from Two Sites in Appalachia

Michael E. Kalinski, Ph.D., P. E.[1]
Joshua L. Phillips, E.I.T.[2]

ABSTRACT

Over the past 40 years, approximately 15 mine tailings dams have failed worldwide as a result of earthquake shaking. Methods to analyze the dynamic response and liquefaction resistance exist for soil, but fine coal refuse, including slurry that is hydraulically placed behind the dike, is inherently different than soil. Therefore, a research study is underway to understand and predict the dynamic behavior of fine coal refuse. To date, field testing has been performed at two coal refuse impoundments in eastern Kentucky. Laboratory resonant column testing was used to measure modulus reduction curves (i.e. the relationship between shear modulus, material damping, and shear strain) of undisturbed specimens. Field standard penetration testing, seismic cone penetrometer testing, and geophysical surface wave testing was performed to measure blow count (N_{60}), cone tip resistance (q_c), and shear wave velocity (v_s). Field vane shear data were acquired to correlate peak and residual undrained shear strength to q_c. Preliminary results of this study include development of modulus reduction curves for fine refuse and development of methods to estimate peak and undrained shear strength based on in situ CPT testing. Future results will include correlation of overburden-corrected field data to cyclic resistance ratio (CRR) to predict liquefaction resistance.

INTRODUCTION

Coal refuse dams are constructed to contain waste materials produced as a result of mining activities. Coal refuse dams consist of a dike of coarse refuse (i.e. well-graded sand and gravel), with fine refuse hydraulically placed behind the dike from a discharge point near the crest. The three basic construction methods include upstream, centerline, and downstream construction. As the pool of fine refuse fills behind the dam, the dike is expanded upward, and coal refuse dams can reach hundreds of feet in height. Of the three construction types, the upstream construction method (Fig. 1) is most critical with respect to slope stability, because more of the critical failure surface passes through the weaker fine refuse.

[1] University of Kentucky, Department of Civil Engineering, 161 Raymond Bldg., Lexington, KY 40506-0281; PH (859) 257-6117, FAX (859) 257-4404; email: kalinski@engr.uky.edu
[2] University of Kentucky, Department of Civil Engineering, 161 Raymond Bldg., Lexington, KY 40506-0281; PH (859) 257-6117, FAX (859) 257-4404; email: jlphil0@engr.uky.edu

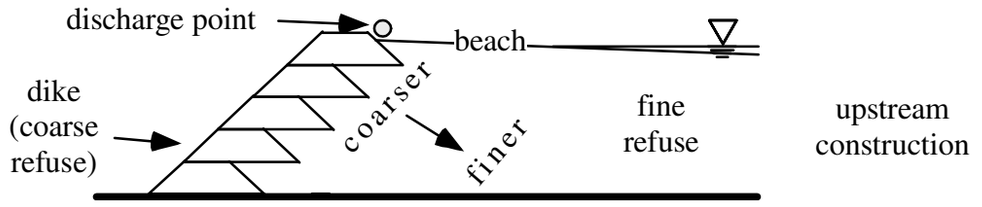


Fig. 1. Configurations of a mine tailings dam built using upstream construction.

There are approximately 1,555 tailings impoundments in the United States, with coal refuse dams concentrated in Appalachia, and metal tailings dams concentrated in the west (NSF, 2003). According to the National Inventory of Dams, approximately one-third of the 1,555 tailings structures in the United States are determined to be high-hazard potential, in which failure would likely result in loss of human life. Tailings dams are also common throughout the world. Over the past 40 years, approximately 80 tailings dams have failed worldwide with a resulting uncontrolled release. Fifteen of these failures were the result of liquefaction due to earthquake shaking. Noteworthy examples include the 1965 El Cobre Dam system failure in Chile, where over 200 people were killed with an associated release of roughly 2 million tons of material (Dobry and Alvarez, 1967), and the 1978 Mochikoshi tailings dams in Japan, where one dam failed during the earthquake and a second dam failed 24 hours later due to the gradual increase in pore pressures from liquefaction of material behind the dam (Ishihara, 1993). These failures had associated with them liquefaction of fine-grained materials that are often considered to be liquefaction resistant. To date, there have been no earthquake-induced tailings dam failures in the United States.

Methods to analyze liquefaction resistance in soil deposits, such as those summarized by the National Center for Earthquake Engineering Research (NCEER) as described by Youd et al. (2001), may be useful to delineate liquefiable zones within slurry dams if appropriate modifications are made. This approach consists of estimating the cyclic resistance ratio (CRR) based on laboratory methods (cyclic triaxial or cyclic simple shear) or in situ methods (standard penetration test (SPT), cone penetration test (CPT), or shear wave velocity (v_s) measurement). The factor of safety against liquefaction for horizontally layered sites is calculated by dividing the CRR by the cyclic stress ratio (CSR), which is a measure of cyclic earthquake loading.

However, fine refuse is inherently different than fine-grained soil. Fine refuse is silty and normally consolidated with a high in situ water content, and are more akin to rock flour than naturally occurring soil. Fine refuse may also be underconsolidated with excess pore water pressures due to rapid loading and low in situ hydraulic conductivity. This reduces static and seismic stability by reducing the initial effective stress. The particle shape, angularity, specific gravity of soil solids, and mineralogical composition of fine refuse is significantly different than typical fine-grained soil that is considered to be liquefaction-resistant. As a result, fine refuse slurry is not necessarily resistant to liquefaction just because it is fine-grained.

Relatively little available data exist for fine coal refuse because of the difficulties involved with obtaining high-quality samples. Fine refuse can be very soft and should be sampled using specialized methods such as fixed piston sampling or freezing (Poulos et al, 1985), but access to the refuse may be impeded by the fact that large equipment cannot be operated directly on the soft "beach" portion of an impoundment structure. Thus, it would be advantageous to develop in situ methods as an alternative to laboratory-based methods to minimize the need for recovery of specimens for estimating CRR.

In addition to the dynamic behavior of fine coal refuse, undrained shear strength, including peak strength (S_p) and residual strength (S_r), are important parameters in assessing the stability of tailings dams where liquefaction has occurred. For fine refuse, the material collapses and flows (liquefies) at high strains, so S_r can be taken as the post-liquefaction strength. When only part of the structure has liquefied, S_p and S_r are both important for assessing the overall stability of the structure. Sampling and laboratory strength testing of fine refuse is difficult due to its soft nature, so estimation of strength using in situ methods is a practical alternative. Castro and Troncoso (1989) estimated residual strength ratios for very loose fine refuse in Chilean tailings dams using vane shear tests, and demonstrated the usefulness of an in situ strength measurement method to estimate the residual strength ratio for prediction of post-liquefaction strength. However, the strength of fine coal refuse is site-specific, and more data are needed so that the peak and residual strength of fine coal refuse possessing a wide range of attributes (void ratio, age, water content, etc.) can be reliably estimated.

Some efforts have been made towards understanding and predicting the cyclic behavior and liquefaction resistance of fine refuse (e.g. Ishihara et al. 1981; Peters and Verdugo, 2003; Vidich et al., 1998), and assessing the post-earthquake stability of tailings dams using peak and residual strengths (e.g. Castro, 2003). However, a comprehensive understanding and unified approach towards the assessment of the dynamic behavior of mine refuse is lacking. These concerns were reiterated at the 2003 International Workshop on Seismic Stability of Tailings Dams held at Case Western Reserve University. The workshop was jointly sponsored by the National Science Foundation (NSF) and the Mine Safety and Health Administration (MSHA), and was attended by numerous experts from industry, academia, and government (NSF, 2003).

OVERVIEW OF THE STUDY

In light of this discussion, a study is underway to understand and predict the dynamic behavior of mine tailings dam materials. Laboratory resonant column testing is being performed to measure modulus reduction behavior in terms of shear modulus and material damping. Laboratory cyclic triaxial testing will be used to determine liquefaction resistance in terms of CRR. The effect of parameters such as void ratio, fines content, age, water content, and confining stress on the dynamic behavior of the materials is being investigated. Special measures have been taken to recover specimens for laboratory testing, including fixed piston sampling, and construction of surface pads in the beach areas of the impoundments to reduce surface pressures of field equipment. Field SPT, CPT, and seismic testing have been performed, and methods are being developed to use

SPT blow count (N_{60}), cone tip resistance (q_c), and shear wave velocity (v_s), to assess in situ liquefaction resistance in terms of CRR. In situ vane shear data are also being used to develop a CPT-based method to estimate peak and residual undrained shear strength of fine refuse.

Two representative tailings dams were selected for sampling and evaluation. The two dams include the Abner Fork impoundment in Harlan County, Kentucky, and the Big Branch impoundment in Knott County, Kentucky. The Abner Fork impoundment has a total permitted capacity of approximately 70 million cubic feet, with an elevation difference from crest to toe of approximately 760 ft, and is one of the largest tailings impoundments in the United States. The Abner Fork impoundment was constructed by mostly upstream construction, and has been continually active since the early 1980s. The Big Branch impoundment was originally constructed in the 1980s, but sat dormant for much of the past 20 years. However, activity at Big Branch has recently resumed, and it is currently an active facility. It has a total design capacity of 2.2 million cubic feet, and an elevation difference from crest to toe of approximately 360 ft. In general, fine refuse at Abner Fork are much stiffer than those at Big Branch due to the extensive usage of wick drains in the refuse at Abner Fork (Thacker et al., 1988). These two structures were selected with the guidance of Dr. Kelvin Wu, formerly of MSHA, because they are both representative of typical upstream construction, and they are both relatively well-documented.

RESULTS

Abner Fork

Field testing was performed at the Abner Fork impoundment in August 2006. Field testing included SPT sampling, fixed piston sampling, sCPTu measurements, downhole seismic, SASW, and in situ vane shear testing. Laboratory testing has included resonant column testing. Testing was performed at locations on the crest and upstream toe as shown in Fig. 2. Testing at the upstream toe was performed by pushing a pad of coarse refuse out into the pool. Depth to fine refuse was about 50% greater than expected at both locations due to the effects of coarse refuse displacing the fine refuse out into the pool during upstream construction.



Fig. 2. Photograph showing testing at Abner Fork

Measured parameters, including N_{60}, q_c, v_s, and vane shear strength, are summarized in Fig. 3. Pore pressure measurements taken during CPT testing indicated that the material was normally consolidated, and excess pore pressures did not exist within the fine refuse. These results indicate that, as expected, the fine refuse at Abner fork were relatively stiff and competent, presumably due to use of wick drains within the refuse. Total unit weights of the specimens were typically around 90 pcf, and moisture contents of the fine refuse ranged between 25 and 29%. When comparing Figs. 3a and 3b, it is apparent that the material beneath the upstream toe is softer than the material beneath the crest, presumably because it has not been subjected to as much overburden stress.

Due to the stiff nature of the specimens, large strains could not be generated during resonant column testing, and measurements were limited to the small-strain range. Atterberg limit testing on the fine refuse indicated that it had liquid limits ranging from 22% to 35%, and plasticity indices ranging from 3% to 10%, which classifies it as a low-plasticity silt (ML) according to the Unified Soil Classification System. Vucetic and Dobry curves (1991) may therefore be applicable to estimate modulus reduction curves for the refuse based on plasticity index by treating the fine refuse as a low-plasticity soil. Within the small-strain range, shear wave velocities measured from resonant column testing ranged from 1,500 – 2,000 ft/s, with corresponding shear moduli ranging from 45-92 ksi, and material damping ranging from 0.6 – 2.0%.

Vane shear test data were correlated to CPT tip resistance to develop a method to correlate CPT to shear strength using the generic relationship (Robertson and Campanella, 1983):

$$S = \frac{q_c - \sigma_v}{N_k}, \tag{1}$$

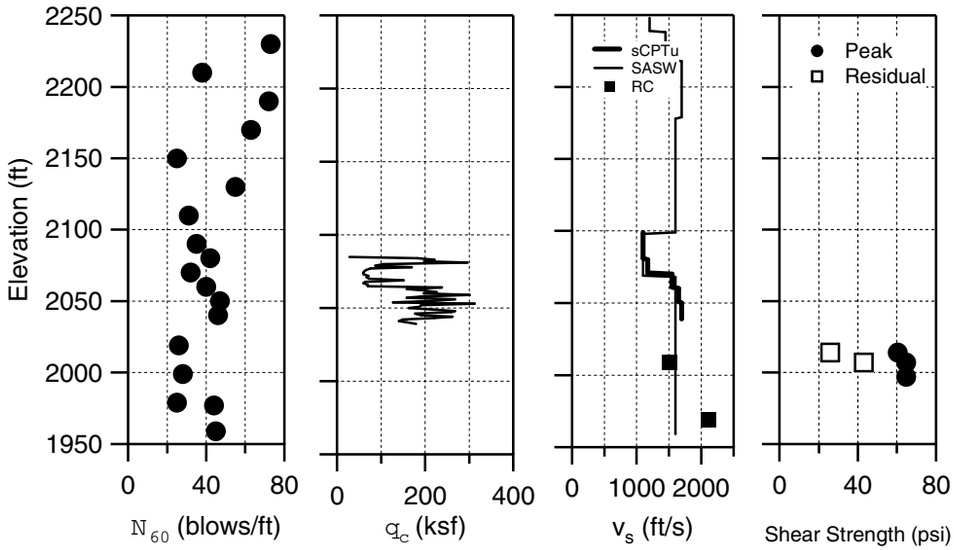
where S is undrained shear strength, σ_v is vertical total stress, and N_k is a fitting parameter. The fitting parameter N_k varied within the refuse, but correlated reasonably well with overburden-corrected CPT tip resistance (q_{c1}) as shown in Fig. 4a. Therefore, peak and residual shear strength can be reasonably predicted using CPT tip resistance.

Big Branch

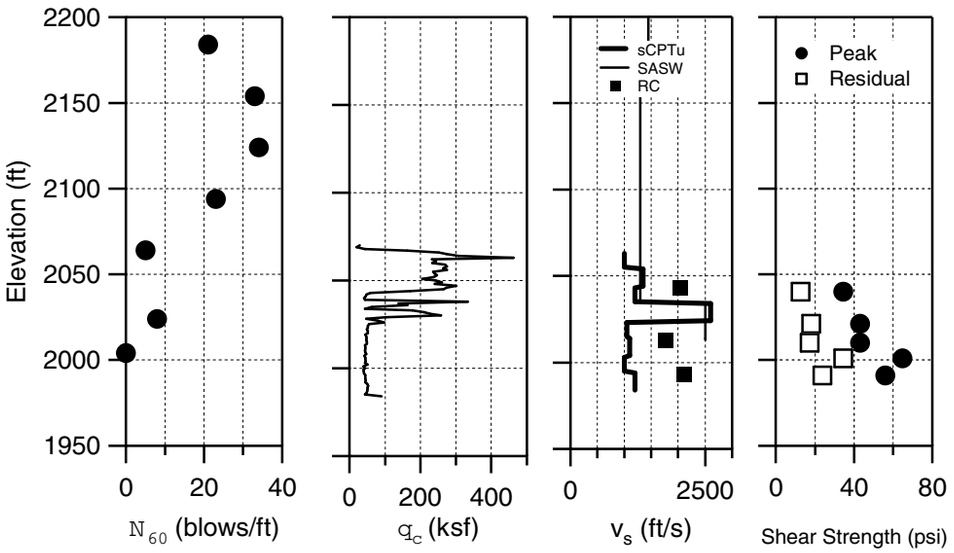
Field testing occurred at the Big Branch impoundment in August 2007, and included SPT, CPTu, fixed piston sampling, and in situ vane shear testing. Testing occurred at two locations near the upstream toe as shown in Fig. 5, and construction of an upstream construction pad was not needed. Unlike Abner Fork, the material at Big Branch was very soft, so attempts to perform downhole seismic testing and seismic CPT testing were unsuccessful. The field data, summarized in Fig. 6, reveal the soft nature of the material. Pore pressure measurements taken during CPT testing indicated that the material was normally consolidated, and excess pore pressures did not exist within the fine refuse. In situ moisture contents ranged from 33% to 40%, which is higher than the refuse encountered at Abner Fork. Atterberg limit testing on the fine refuse indicated that it had liquid limits ranging from 38% to 54%, and plasticity indices ranging from 12% to 20%,

which classifies it as a borderline low-plasticity silt (ML) to low-plasticity clay (CL) according to the Unified Soil Classification System.

When comparing Figs. 3 and 6, it is apparent that the material at Big Branch was much softer. This was attributed to two reasons: 1) the presence of a system of horizontal wick drains at Abner Fork, and 2) the fact that the coarse refuse upon which testing was performed at Big Branch (Fig. 5) had only been placed about a month before field testing.

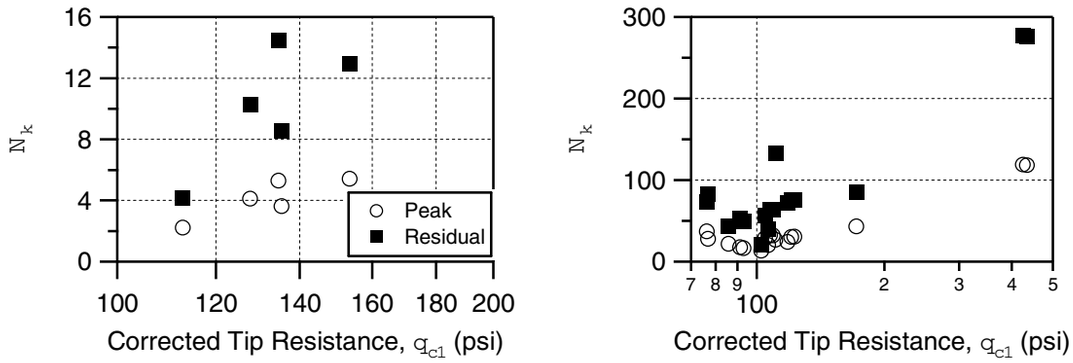


a. from crest of dam (fine refuse from 1956-2030 ft)



b. from upstream toe of dam (fine refuse from 1984-2064 ft)

Fig. 3. Summary of data acquired at Abner Fork



a) Abner Fork *b) Big Branch*

Fig. 4. Correlation between N_k and q_{c1} for Abner Fork.



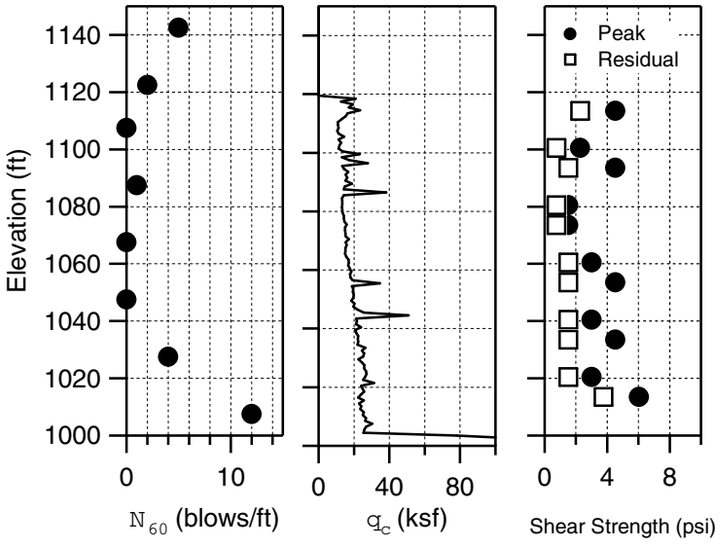
Fig. 5. Photograph illustrating testing at Big Branch.

Vane shear test data from Big Branch were correlated to CPT tip resistance to develop a method to correlate CPT to shear strength in a manner similar to Abner Fork. The fitting parameter N_k varied within the refuse, but correlated reasonably well with q_{c1} as shown in Fig. 4b. Therefore, peak and residual shear strength can be estimated using CPT tip resistance. However, these results are significantly different than the results shown in Fig. 4a, which indicates the site-specific nature of using such an approach.

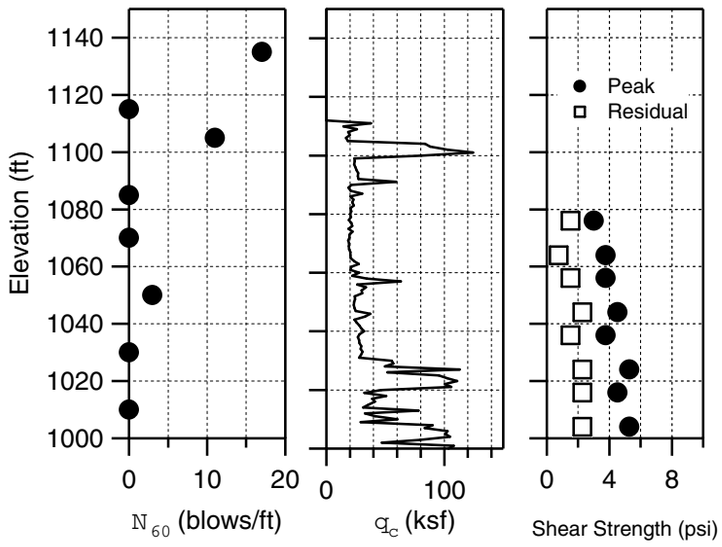
CONCLUSIONS

This short paper presents a preliminary set of results from two tailings impoundments in eastern Kentucky. The ultimate goal of this study is to develop a universal approach to predicting the seismic behavior of dams. This is an ongoing study, so future efforts will include testing more sites, incorporating existing data from other studies, and correlation of field data to cyclic triaxial data to develop field-based

approaches to predicting cyclic resistance. However, some useful conclusions can be drawn from the preliminary results presented herein:



a. from toe of dam (fine refuse from1000-1110 ft)



b. from bench near upstream toe (fine refuse from 1000-1085 ft)

Fig. 6. Summary of field results from Big Branch.

- The thickness of coarse refuse overlying fine refuse in impoundments constructed using the upstream construction method can be up to 50% thicker in reality than as indicated on design cross-sections due to the effect of coarse refuse displacing the fine refuse out into the pool. This means that model cross-sections based on design drawings may

underestimate the actual amount of coarse refuse in the cross-section, which would generally lead to an overly conservative analyses.

- The total unit weight of fine refuse can be relatively low, and can average around 90 pcf. Stability analyses performed using typical soil unit weights of around 120 pcf may therefore be in error.

- Fine refuse possess low to moderate plasticity, and can be classified as lean clays (CL) or low-plasticity silts (ML). This is useful in selecting appropriate modulus reduction curves for calculating the structural response of impoundments to earthquake shaking.

- Small-strain material damping of fine refuse is typically on the order of 0.6-2.0%.

- CPT tip resistance can be used to estimate peak and residual shear strength of fine refuse based on correlations with in situ vane shear test results. However, these results seem to be site-specific, and more investigation is needed to develop a universal approach to estimate fine refuse strength based on CPT data.

ACKNOWLEDGMENTS

The authors would like to thank the National Science Foundation for sponsoring this project under Award #0448717. We would also like to thank Barry Thacker of GeoEnvironmental Associates, Inc., Kelvin Wu of MSHA (retired), Harlan Cumberland Coal Company, and International Coal Group.

REFERENCES

Castro, G., 2003 "Evaluation of Seismic Stability of Tailings Dams," *Proceedings of the 12th PanAmerican Conference on Soil Mechanics and Geotechnical Engineering*, June 22-26, 2003, Cambridge, Massachusetts, pp. 2229-2234.

Castro, G., and Troncoso, J., 1989, "Effects of 1989 Chilean Earthquake on three Tailings Dams," *Proceedings of the Fifth Chilean Conference on Seismology and Earthquake Engineering*, Santiago, Chile.

Dobry, R., and Alavarez, L., 1967, "Seismic Failures of Chilean Tailings Dams," *Journal of the Soil Mechanics and Foundations Division, Proceedings of the ASCE*, Vol. 93, No. SM6, pp. 237-260.

Ishihara, K., Yasuda, S., and Yokota, K., 1981, "Cyclic Strength of Undisturbed Mine Tailings," *Proceedings of the International Conference on Recent Advances in Geotechnical Earthquake Engineering and Soil Dynamics*, April 26-May 3, 1981, Saint Louis, Missouri.

Ishihara, K., 1993, "Post-Earthquake Failure of a Tailings Dam Due to Liquefaction of the Pond Deposit" *Proceedings of the Third International Conference on*

Case Histories in Geotechnical Engineering, July 1-4, 1993, Saint Louis, Missouri, pp. 1129-1143.

NSF, 2003, *Proceedings of the International Workshop on Seismic Stability of Tailings Dams,* http://ecivwww.cwru.edu/civil/xxz16/Tailings%20Dam/.

Peters, G., and Verdugo, R., 2003, "Seismic Considerations on Tailings Dams Design," *Proceedings of the 12th PanAmerican Conference on Soil Mechanics and Geotechnical Engineering*, June 22-26, 2003, Cambridge, Massachusetts, pp. 2241-2246.

Poulos, S. J., Castro, G., and France, J. W. 1985, "Liquefaction Evaluation Procedure," *Journal of Geotechnical Engineering,* Vol. 111, No. 6, pp. 772-792.

Robertson, P. K., and Campanella, R. G., 1983, "Interpretation of Cone Penetration Tests, Part II: Clays" *Canadian Geotechnical Journal*, Vol. 20, No. 4, pp. 734-754.

Thacker, B. K., Ullrich, C. R., Athanasakes, J. G., and Smith, G., 1988, "Evaluation of Coal Refuse Impoundment Built by the Upstream Method," *Geotechnical Special Publication No. 21,* American Society of Civil Engineers, pp. 730-749.

Vidich, S. D., Beckwith, G. H., and Keaton, J. R., 1998, "Liquefaction Assessment of Mine Tailings Dams," *Geotechnical Site Characterization*, P. Robertson and P. Mayne, Eds., Balkema, pp. 543-548.

Vucetic, M., and Dobry, R., 1991, "Effect of Soil Plasticity on Cyclic Response," *Journal of Geotechnical Engineering,* Vol. 117, No. 1, pp. 89-107.

Youd, T. L., Idriss, I. M., Andrus, R. D., Arango, I., Castro, G., Christian, J. T., Dobry, R., Finn, W. D. L., Harder, L. F., Hynes, M. E., Ishihara, K., Koester, J. P., Liao, S. C., Marcuson, W. F., Martin, G. R., Mitchell, J. K., Moriwaki, Y., Power, M. S., Robertson, P. K., Seed, R. B., and Stokoe, K. H., 2001, "Liquefaction Resistance of Soils: Summary Report from the 1996 NCEER and 1998 NCEER/NSF Workshops on Evaluation of Liquefaction Resistance of Soils, " *Journal of Geotechnical and Geoenvironmental Engineering*, American Society of Civil Engineers, Vol. 127, No. 10, pp. 817-833.

DYNAMIC PERFORMANCE OF TOYOURA SAND REINFORCED WITH RANDOMLY DISTRIBUTED CARPET WASTE STRIPS

H. Ghiassian [1], R. Jamshidi [2] and A.R. Tabarsa [3]

[1] Assoc. Prof., Dept. of Civ. Engrg., Iran University of Science and Technology, Narmak, Tehran, Iran
[2] PhD candidate, Dept. of Civ. Engrg., Iran University of Science and Technology, Narmak, Tehran, Iran
[3] PhD candidate, Dept. of Civ. Engrg., Iran University of Science and Technology, Narmak, Tehran, Iran

ABSTRACT: A fiber reinforced soil behaves as a composite material in which fibers of relatively high tensile strength are embedded in a matrix of relatively plastic soil. Shear stresses in the soil mobilize tensile resistance in the fibers, which in turn imparts greater strength to the soil. In this paper a study on the influence of synthetic fibrous materials in improving the dynamic strength characteristics of a fine sandy soil is reported. The project is aimed at converting fibrous carpet waste into a value-added product for soil reinforcement.

A series of strain controlled large cyclic triaxial tests were carried out on Toyoura sand specimens reinforced with randomly distributed carpet strips. The dynamic strength characteristics of the reinforced sand are defined in terms of deformation modulus and damping ratio. The effects of parameters such as fiber content and fiber aspect ratio, have been studied. The results clearly indicate the effectiveness of the reinforcement in improving the dynamic properties of fine sand.

INTRODUCTION

Earthquake geotechnical engineering in Iran has received tremendous boost after the Bam earthquake of 2003. Earthquakes are not uncommon, but the damage suffered during earthquakes is on the rise because of the population growth, overcrowding of civil engineering facilities in urban areas and improper understanding of ground behavior among many. Developments in earthquake geotechnical engineering which include understanding ground behavior during shaking, effects of earthquake on geotechnical facilities, site amplification studies, etc. have also shown tremendous progress.

Unfortunately in Iran, though some analytical works are carried out in the field of earthquake geotechnical engineering, very little work is reported on element tests, model tests and analysis of field data. Lack of facilities for laboratory studies and unavailability of instrumentation in the field can be attributed as the main reasons.

At the other hand, as the world population grows, so do the amount and type of waste being generated. Many of the wastes produced today will remain in the environment for many years. The creation of non-decaying waste materials, combined with a growing consumer population, has resulted in a waste disposal crisis. One solution to this crisis lies in recycling waste into useful products. A great amount of fibrous textile waste is discarded into landfills each year all over the world. About half of this waste is from carpet, with the main constituents being plastic and polymeric fibers, which decays at a very slow rate and is difficult to handle in landfills. In the U.S., the annual cost of landfilling this waste is estimated at $200 million, costing the industry over $5 million (Wang, 1993). In Iran the above mentioned costs and expenses are remarkable because using carpet and moquette is very popular between all urban and rural families although there is no official report. One promising reuse of these wastes will be to convert them into value-added products for soil reinforcement. Soil reinforcement technique with randomly distributed fibers is used in a variety of applications like, retaining structures, embankments, subgrade stabilization etc. Random fiber reinforcement is a variant of admixture stabilization in which, discrete fibers are added and mixed with the soil in the same manner as cement, lime or other. Various types of randomly distributed elements, such as polymeric mesh elements, metallic fibers, synthetic fibers and discontinuous multioriented polypropylene elements had been used to reinforce soils. Many studies have been conducted relating to the behavior of soil reinforced with randomly distributed fibers under static loading conditions. However, the studies on behavior of soils reinforced with randomly distributed elements under cyclic loading are very limited in the literature.

The capability of synthetic fiber reinforcement for improving the behavior of sand has been demonstrated by Al-Refeai (1991), Wang (1993), and Ghiassian et al. (2004) using triaxial tests, Guido et al. (1995) and Take et al. (1997) using CBR tests, Noorany and Uzdavines (1989) using cyclic triaxial tests, and Maher and Woods (1990) using resonant-column and torsional shear tests.

Many laboratory tests have been tried to simulate the field condition during earthquakes. Cyclic torsional shear tests, triaxial compression tests, simple shear tests and ring shear tests are among a few popular laboratory methods to study the behavior of ground during dynamic loading. However, in spite of their high quality and accuracy, they fail to present the field behavior precisely or some times may not be confirmed whether they are really representing field conditions. For the purpose of ascertaining these aspects, instrumentation and recordings in the field have been made in some cases. Even then the available data are rather few. As a compromise between the two, laboratory large scale element tests can be adopted. These tests offer an opportunity to obtain more practical data as it will be possible to use longer fibers as reinforcement while it is hindered while small models are considered. However, these tests cannot be performed for many times, due to the difficulties embedded in sample preparation and the expenses. Even though laboratory experiments and practice show the beneficial contribution of randomly distributed fibers as sand reinforcement under static or dynamic loading, to the authors' knowledge, there is no information in the literature on the large element test modeling of sand reinforced with recycled carpet waste strips under dynamic loads. In this paper, large cyclic triaxial machine was utilized to study on effectiveness of randomly distributed geotextile fibers in

improving dynamic properties of fine sand is reported. The geotextile fibers were chosen for their similarity to the fibers used in carpets and moquettes which are mainly polypropylene, polyethylene and polyester.

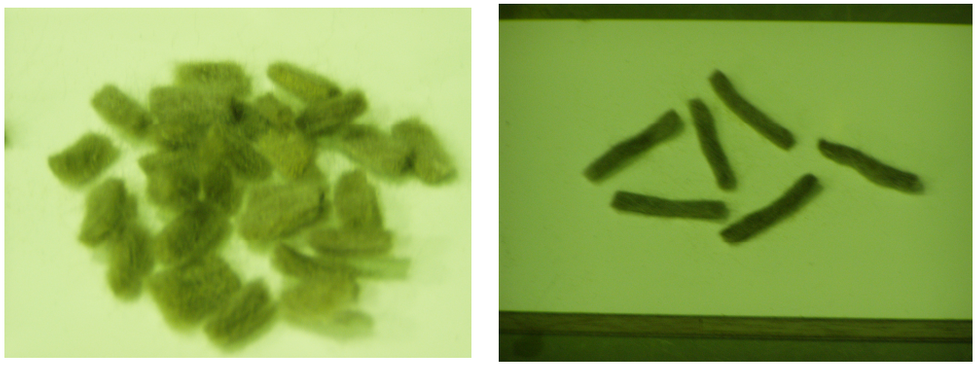
MATERIAL USED FOR TESTING

Tests were performed using Japanese Standard Toyoura Sand, physical properties of which are given in Table 1. The reinforcing fibers were prepared by cutting geotextile fabric to short strips with 5×5 mm2 square cross section and lengths of 15 and 45 mm corresponding to the aspect ratios (A_R, length/width) of 3 and 9 respectively. Specific gravity of solids (G_s) is about 1.0. Various amount of fibers were added to the soil; fiber content (W_f, defined as weight of fiber/weight of sand×100) of 0%, 0.25%, 0.5%, 0.75% and 1% were used. A typical view of fiber elements used in the present study is shown in Fig. 1.

Table 1. Physical properties of Toyoura sand

Maximum Grain Diameter (mm)	Dmax = 0.42
Mean Grain Diameter (mm)	D50 = 0.19
Fines Content (less than 0.075mm)	F.C. = 0%
Specific Gravity	Gs = 2.653
Plasticity Index	P.I. = 0
Maximum Void Ratio	emax = 0.977
Minimum Void Ratio	emin = 0.597

Physical properties of Toyoura sand were obtained from Towhata (1982)



Fiber aspect ratio: 3 **Fiber aspect ratio: 9**

FIG. 1. Details of reinforcement used

EXPERIMENTAL SET UP

Strain controlled cyclic triaxial compression tests were performed to determine the effect of fiber reinforcement on dynamic properties of Toyoura sand using the large

cyclic triaxial testing apparatus, which is shown in Fig. 2. This testing unit has a built-in loading frame which accommodates the triaxial cell. The triaxial cell was fitted with a load cell to measure the applied cyclic axial load.

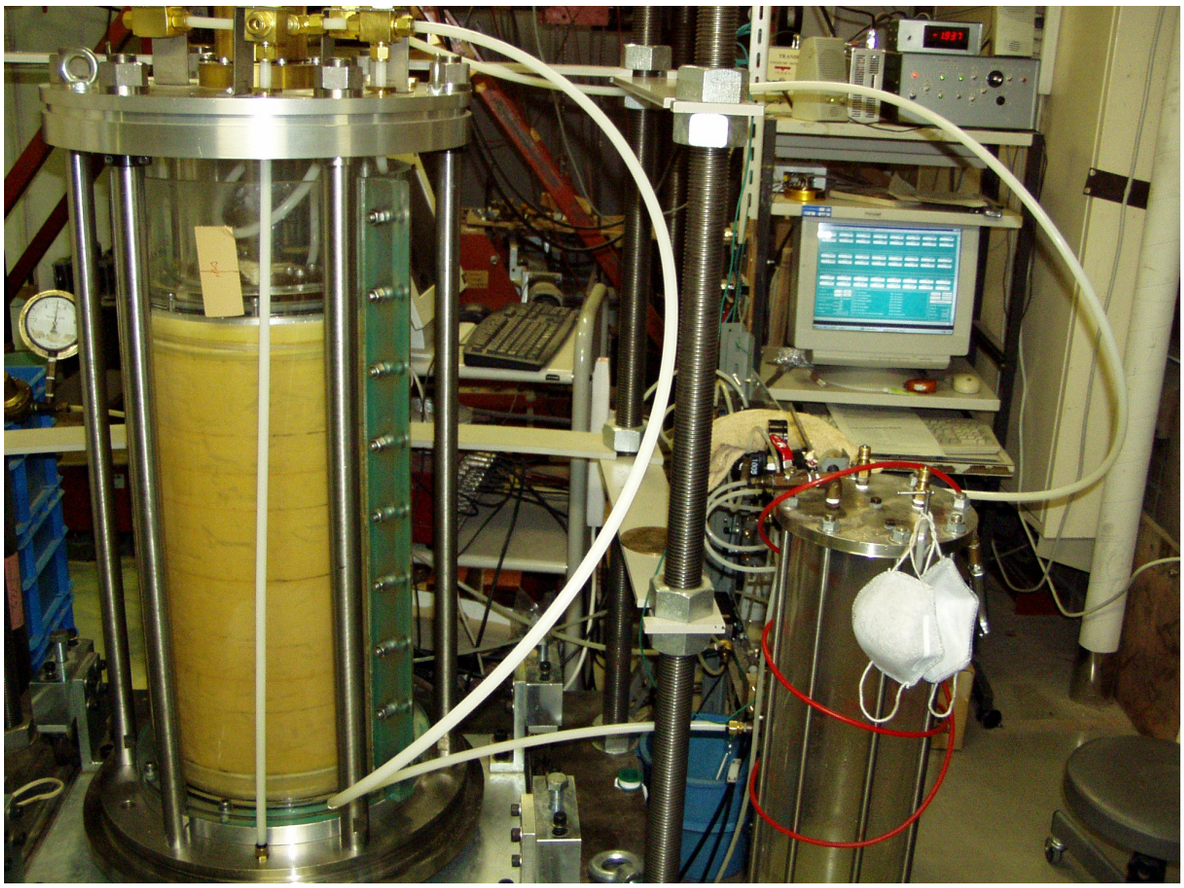


FIG. 2. Cyclic triaxial setup

The loading system is an automated gear-clutch loading (GCL) system driven by an AC-servo motor shown in Fig. 3 (Santucci de Magistris et al., 1999, Tatsuoka et al., 2000). This loading system is strain-controlled and the typical strain rates applied range from 0.001%/min to 0.1%/min. It was observed that the cyclic stress applied by this machine has approximately a saw-tooth profile. At a loading period of around 1s (1Hz), however, the feedback and control mechanism of this loading system becomes utterly unreliable.

A linear variable displacement transducer (LVDT) was used for the measurement of axial displacement. Cell pressure was supplied through applying a vacuum inside the specimen. A diaphragm type pressure transducer was used for the vacuum measurement inside the specimen. A differential pressure transducer was also used to measure the volume change of the specimen. All these transducers were connected to data acquisition system through multi-channel carrier frequency amplifier.

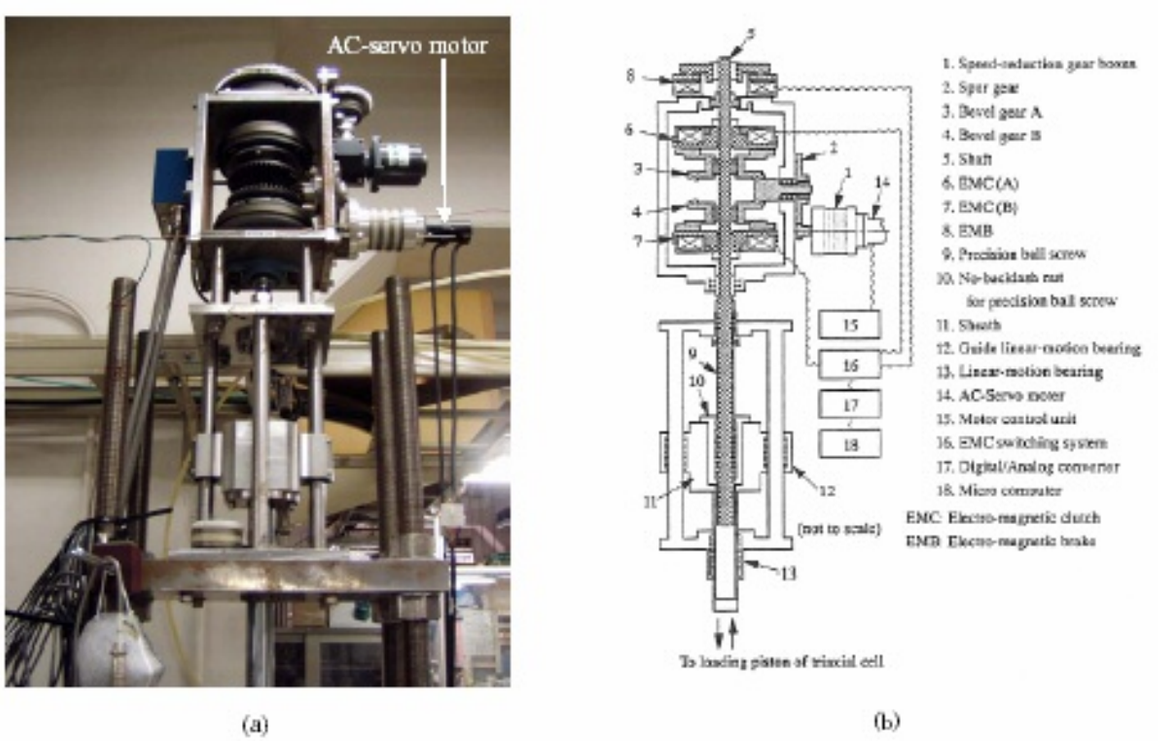


FIG. 3. A 5-ton automated AC-servo motor-driven, gear-clutch loading system at the Geotechnical Engineering Laboratory, University of Tokyo: (a) photograph, (b) schematic diagram (Santucci de Magistris et al., 1999, Tatsuoka et al., 2000)

EXPERIMENTAL PROCEDURE

Preparation of Samples

A cylindrical specimen with 300 mm diameter and 600 mm height was employed in this experiment. Dry tamping was adopted as the sample preparation technique. Outer rim of the bottom platen was coated with silicon grease. A latex rubber membrane was attached to the bottom platen with rubber bands and then O-Rings were placed. Specimen split mold was placed to the pedestal with the latex rubber membrane extending up through it and then the split mold was fixed by screws. The latex rubber membrane was stretched tightly over the interior surface of the split mold and the top portion of the membrane was folded down equally over the mold, taking care that the membrane not to be twisted or pinched (Fig. 4). A vacuum was supplied to the split mold to pull the membrane against the side of the mold and hold it tightly during the compaction operation. Fiber reinforced sample was divided into six portions and the weight of each part was predetermined depending on the desired relative density and fiber content. Each of the six portions of the sample was poured one by one inside the mould. Each part was then compacted and top of each compacted layer was scarified and cleared off slightly before placing the next layer to promote proper bonding and

reduce stratification. According to the desired level of relative density for sandy part (50% in this research) and the fiber content, the total weight of sand and fiber was determined, mixed and poured into the space for each layer. Then the surface was leveled by a small shovel. Soil was tamped to achieve the desired compaction by means of a wooden weight. Tamping was continued until the desired marked level was reached. The outer rim of the top platen was cleaned; the top platen was placed onto the sand by bringing the cap close up to the top of specimen and the loading rod was released using the Allen wrench. The cover plate was lowered to seat on the tie rods and then the loading rod was fixed using Allen wrench. The outer rim of the top platen was coated with silicone grease to make a good, leak proof seal at the top. The membrane was rolled off the mold and onto the top platen and sealed to the platen with rubber band. The vacuum was released to the mold; with the drainage line to the lower platen closed, the line from the top platen to the vacuum was attached and a vacuum of equal to the desired confining pressure (50 kPa in this work) was applied. The specimen mold was then removed and the membrane was observed for holes and obvious leaks. The Lucite cylinder was placed on the cell base, rotated and brought to the right position. The balance of tie rods were placed and fixed using spacers and then nuts.



FIG. 4. Membrane and mold for large triaxial setup

The chamber was placed in the compression machine and fixed in position then the loading rod was connected to the loading shaft. The water was poured in the cell, sensors were connected, loading rod was released and the test was started.

Test Procedure

Triaxial tests were carried out on Toyoura sand samples reinforced with geotextile fibers at wide range of cyclic stress level. Relative density and confining pressure was kept constant for different tests. The relative density of Toyoura sand adopted for testing is 50%. Since the confining stress applied to the specimen was supplied through vacuum inside the sample, the tests were carried out at relatively low confining stress levels of 50 kPa. The cyclic loading in triaxial compression test is characterized by the term cyclic stress ratio (CSR=$\Delta\sigma d/2\sigma'0$), i.e. the ratio of the maximum cyclic shear stress ($\tau_{cyc}= \Delta\sigma_{dcyc}/2$) to the initial effective confining pressure $\sigma'0$: In the present study, cyclic tests were carried with CSR of 0.05, 0.1, and 0.2 to 1. In order to avoid extension loading on specimen and also to model the static shear stress during earthquake loading, 100 kPa deviatoric stress was applied to the specimen before starting the cyclic loading stage.

The behavior of Toyoura sand reinforced with randomly distributed geosynthetic fiber elements was ascertained by carrying out tests on reinforced sand samples with 50% relative density at confining stress levels of 50 kPa. The fiber content varied from 0 to 1% (as a percentage weight of dry sand) and A_R (length to diameter ratio for fibers) varied between 3 and 9. In all tests the specimen was loaded under the dry condition during each loading cycle. The cyclic axial load was applied to isotropically confined specimens by a gear-clutch loading system to make the cyclic strain-control test. Although the loading frequency was 0.05 Hz to 0.01 Hz which is much lower than that for usual dynamic tests, it may be justified by the previous researches finding virtually no significant effect of loading rate on the dynamic properties of sands (Hardin, 1965).

STRESS-STRAIN ANALYSIS

For the experiments on this study, tests were conducted in a completely dry condition. It is readily understood that for the triaxial stress condition the modulus of deformation, E can be derived from equation 1 in terms of the axial stress amplitude, $\Delta\sigma$, the axial strain amplitude, $\Delta\varepsilon$.

$$E = \Delta\sigma / \Delta\varepsilon \quad (1)$$

The electric signals of the axial deformation and the axial load, after having been passed through a wave filter circuit to cut off high frequency noise, were introduced to an X-Y recorder to draw a stress-strain loop as schematically illustrated in Fig. 5 for each cycle. From the loop the equivalent modulus called the secant modulus was determined by the slope of the straight line connecting the two extremes of the loop. The equivalent damping ratio, h, was calculated in terms of the ratio of the area $\Delta A_{\Delta abc}$ enclosed by the loop and the triangular area A_L shown in Fig. 5 by the following equation.

$$h = \Delta A_L / (\pi A_{\Delta abc}) \quad (2)$$

The MATLAB (copyright The MathWorks Inc.) was utilized to run all calculations.

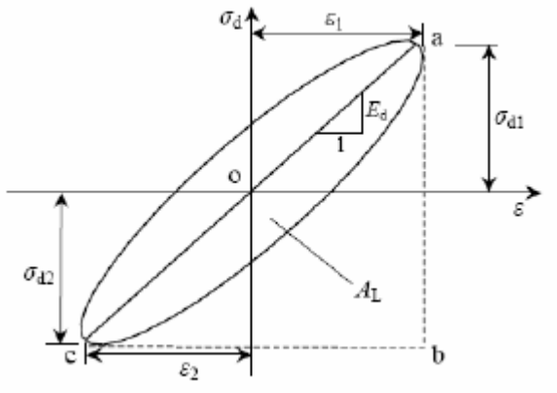


FIG. 5. Schematic stress-strain loop

RESULTS AND DISCUSSIONS

Figs. 6 and 7 contain curves of the deformation modulus versus axial strain relationships on the semi-logarithmic graph obtained from different tests of the medium dense sand (R.D =50%) for the fiber content ranging from 0 to 1%. Confining stress is 50 kPa and was kept constant for all tests. Two different aspect ratios were employed in this series of test to study the reinforcing effect of fiber length. Taking it for granted from other research works that a rational G~logγ curve should decrease when γ increases, each curve shows the continuous decrease of the modulus as the axial strain increases for the order of 10^{-4} to 10^{-2}. It is apparent that the average curve corresponding to each fiber content shifts consistently to the top along E-axis as the fiber content becomes higher.

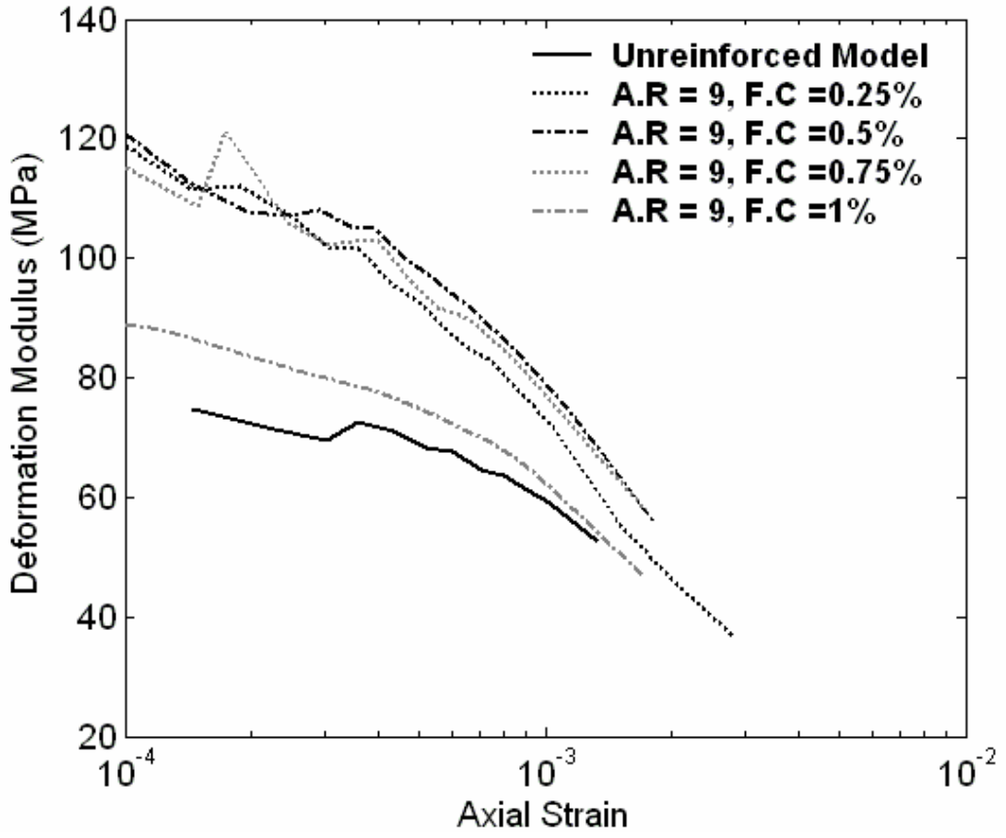


FIG. 6. Effect of fiber content on deformation characteristics of reinforced Toyoura sand (σ_3 = 50 kN/m^2, A_R = 9)

Fig. 6 provides the results for experiments carried out on Toyoura sand reinforced with long fibers (A_R=9). It reveals that higher deformation modulus is attained when fiber contents increases to 0.5%. At higher fiber contents, the deformation modulus starts decreasing and drops as the stiffness of the system declines due to fiber inclusion. Fiber inclusion as such, introduces soft spots within the reinforced sand and imparts shear resistance to sand by mobilizing friction between sand grains and fibers which itself mobilizes the tensile strength of fibers. As the fiber content increases excessively, the homogeneity of the sample will not be the same because of the segregation between sand particles and reinforcement. As a result, there will be local deformations within fibrous zones and, failure will happen due to excessive axial strain leading to less deformation modulus. Fig. 6 compares the behavior of Toyoura sand samples both unreinforced and reinforced with long fibers (A_R=9) with different fiber contents. From the figure, it is observed that an optimum fiber content of 0.5% exists for Toyoura sand reinforced with geotextile fibers with A_R of 9. The optimum condition corresponds to the highest deformation modulus.

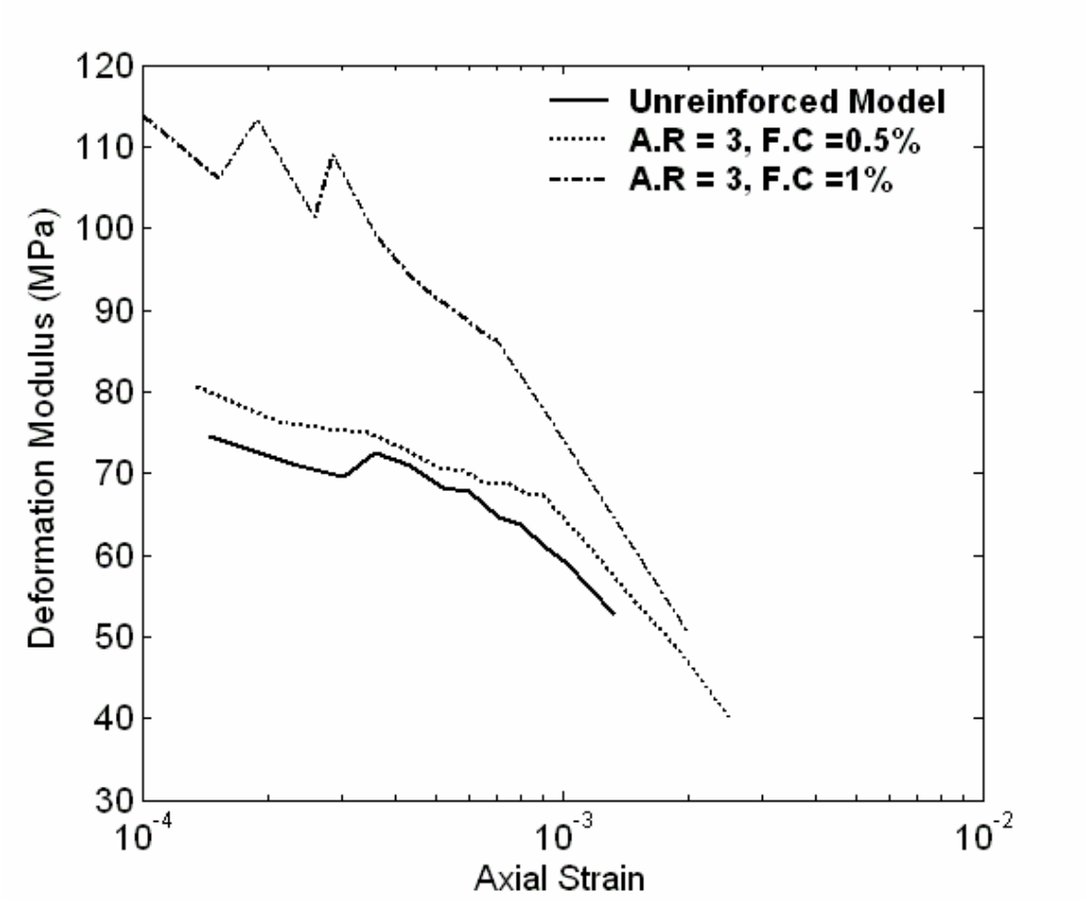


FIG. 7. Effect of fiber content on deformation characteristics of reinforced Toyoura sand (σ_3 = 50 kN/m^2, A_R = 3)

Curves in Fig. 7 present the results for experiments carried out on Toyoura sand reinforced with short fibers (A_R=3). It is observed that the deformation modulus

increases as the fiber content increases and there is no optimum condition like observed for long fibers (A_R=9). The comparison of dynamic behavior of fiber reinforced Toyoura sand at fiber content of 0.5% for both short and long fibers is shown in Fig. 8. In this case, the A_R of 9 presents more effectiveness in comparison to the model reinforced with shorter fibers, A_R of 3. Fig. 8 indicates the superiority of long fibers over short fibers for improving deformation modulus in 0.5% fiber content. It is due to the fact that the longer fibers provide better interlocking property of Toyoura sand material.

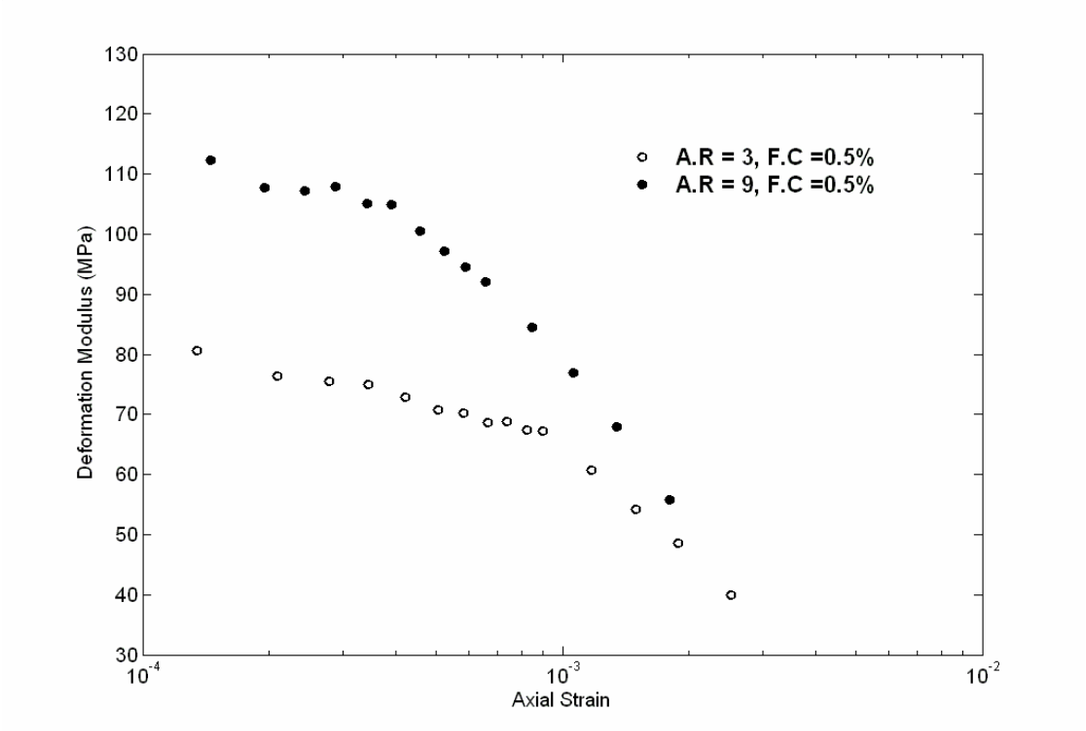


FIG. 8. Effect of fiber length on deformation characteristics of reinforced Toyoura sand (σ_3 = 50 kN/m^2, W_f = 0.5%)

CONCLUSION

The inclusion of fibers has an influence on the dynamic response of dry fine sand, namely, shear modulus, G, and damping ratio, D. This influence is primarily a function of certain parameters (i.e., cyclic shearing strain amplitude and confining stress) and fiber properties (i.e., content, orientation, aspect ratio and modulus). In this research study, only the strain amplitude, fiber content and fiber aspect ratio were considered. From the experimental study carried out on randomly distributed fiber-reinforced Toyoura sand the following conclusions are drawn.

1. For long fibers (A_R=9) deformation modulus increases with an increasing amount of fiber to about 0.5%, then to start decreasing at more fiber content by weight. Optimum percentage of fiber content is found to be 0.5% against

deformation characteristics.

2. The gain in dynamic resistance of Toyoura sand due to fiber reinforcements is more pronounced at longer fiber length. Longer fibers improve the deformation characteristics by providing better interlocking property of Toyoura sand material.
3. Reinforcing fine sand with carpet fibers is an advisable choice among available ground improvement techniques to improve dynamic properties of fine sand.

ACKNOWLEDGMENT

Large cyclic triaxial tests were carried out with the excellent assistance of technical staff at the geotechnical laboratory, University of Tokyo, which is acknowledged with thanks.

REFERENCES

Al-Refeai, T.O., 1991, "Behavior of Granular Soils Reinforced with Discrete Randomly Oriented Inclusions", Geotextile and Geomembranes,Vol. 10, No. 3, pp. 319-333.

Ghiassian, H., Poorebrahim, G. R., and Gray D. H. 2004. Soil reinforcement with recycled carpet wastes. Journal of Waste Management & Research (WMR), International Solid Waste Association (ISWA), 22(2), 108-114.

Guido, V.A., Aprile, J.J. and Sabalis, P.A., 1995, "The Effect of Randomly Dispersed Reinforcement on the California Bearing Ratio of Soils", Proceedings of Geosynthetics '95, IFAI, Vol. 1, Nashville, Tennessee, USA, February 1995, pp. 147-152.

Hardin, B.O. (1965): "The nature of damping in sands," Proc. of ASCE, Vol. 91, SM1, pp. 63-97.

Kokusho, T., 1980, "Cyclic triaxial test of dynamic soil properties for wide strain range." Soils Found., 20_2_, 45–60.

Maher, M.H. and Woods, R.D., 1990, "Dynamic Response of Sand Reinforced with Randomly Distributed Fibers", Journal of Geotechnical Engineering, Vol. 116, No. 7, pp. 1116-1131.

Noorany, I. and Uzdavines, M., 1989, "Dynamic Behavior of Saturated Sand Reinforced with Geosynthetic Fibers", Proceedings of Geosynthetics '89, IFAI, Vol. 2, San Diego, California, USA, February 1989, pp. 385-396.

Santucci de Magistris, F., Koseki, J., Amaya, M., Hamaya, Sato, T. and Tatsuoka, F. (1999): A triaxial testing system to evaluate stress-strain behavior of soils for wide range of strain and strain rate, Geotech. Testing J., 22 (1), 44-60.

Take,W.A, Irving, J., Bischoff, P.H. and Valsangkar, A.J., 1997, "Synthetic Fiber Reinforcement of Clayey Sand and Silt Subgrade and Sand Sub-base", Proceedings of the International Conference on Ground Improvement Techniques, Subrahmanyam, M.S., Editor, May 1997, University of Macau, Macau, pp. 547-552

Tatsuoka, F., Santucci de Magistris, F., Hayano, K., Momoya, Y., and Koseki, J. (2000): Some new aspects of time effects on the stress-strain behavior of stiff

geomaterials, The Geotechnics of Hard Soils-Soft Rocks (Evangelista and Picarelli eds.), Balkema, 1285- 1372.

Towhata, I., 1982, “The effect of principal stress axis rotation on the cyclic shear deformation characteristics of sand.”, Doctoral thesis, The University of Tokyo.

Wang, Y., Cho B. S., and. Zureick A. H., 1993, "Fiber Reinforced Concrete Using Recycled Carpet Industrial Waste and Its Potential Use in Highway Construction", Proceedings of the Symposium on Recovery & Effective Reuse of Discarded Materials & By-Products for Construction of Highway Facilities, Denver, CO, 4.111-4.117.

This page intentionally left blank

Dynamic Properties of Coal Waste Refuse in a Tailings Dam

Xiangwu Zeng[1], M. ASCE, James A. Goble [2], M. ASCE, and Lei Fu[3]

[1]Professor, Department of Civil Engineering, Case Western Reserve University, 10900 Euclid Avenue, Cleveland, OH 44106-7201; xxz16@cwru.edu
[2] Senior Engineer, Bowser-Morner Associates, 2416 Over Drive, Lexington, KY 40511; jgoble@bowser-morner.com
[3] Senior Geotechnical Engineer, URS Corporation, 200 Orchard Ridge Drive, Gaithersburg, MD 20878; lxf28@yahoo.com

ABSTRACT: Failure of tailings dams due to earthquakes occurred several times in the past, causing significant loss of properties and human lives as well as severe environmental problems. In the US, government regulatory agencies such as the Office of Surface Mining (OSM) and the Mine Safety and Health Administration (MSHA) require comprehensive seismic analyses in the design of tailings dams. This paper presents the results of an extensive laboratory testing program on coarse and fine coal waste refuses. Representative samples were taken from a tailings dam in the Appalachian coalfield. Shear modulus and damping ratio versus shear strain curves for the two types of refuse are established. In addition, the response of fine refuse to cyclic loading including the generation of excess pore pressure was investigated using cyclic triaxial tests. Implications for design are discussed.

INTRODUCTION

Sulfur dioxide and ash emitted when coal is burned in power plants are one of the major sources of air pollution and solid waste in the world. In order to comply with the government air quality regulations in the US, coal is often processed to remove some impurities before it is transported to power plants. Each year, millions of tons of refuse are produced and need to be stored in coal producing regions. Coal processing waste dams used to store coal slurry have many characteristics in common with a broader class of structures known as tailings dams, which are made by hydraulically placed fills held in place by an embankment.

Fine refuse from coal processing is in general too wet to be placed in fills and is disposed as slurry in an impoundment. The consolidation of the fine refuse, which has a typical particle size similar to that of fine sand, silt, or clay, may take months or even years to finish. To support the slurry, an embankment of coarse refuse is constructed using the downstream, centerline, or upstream methods of construction as shown in Fig. 1. A major design consideration is a slope stability analysis which evaluates the

possibility of sliding of a segment of the embankment together with the fine refuse in the impoundment.

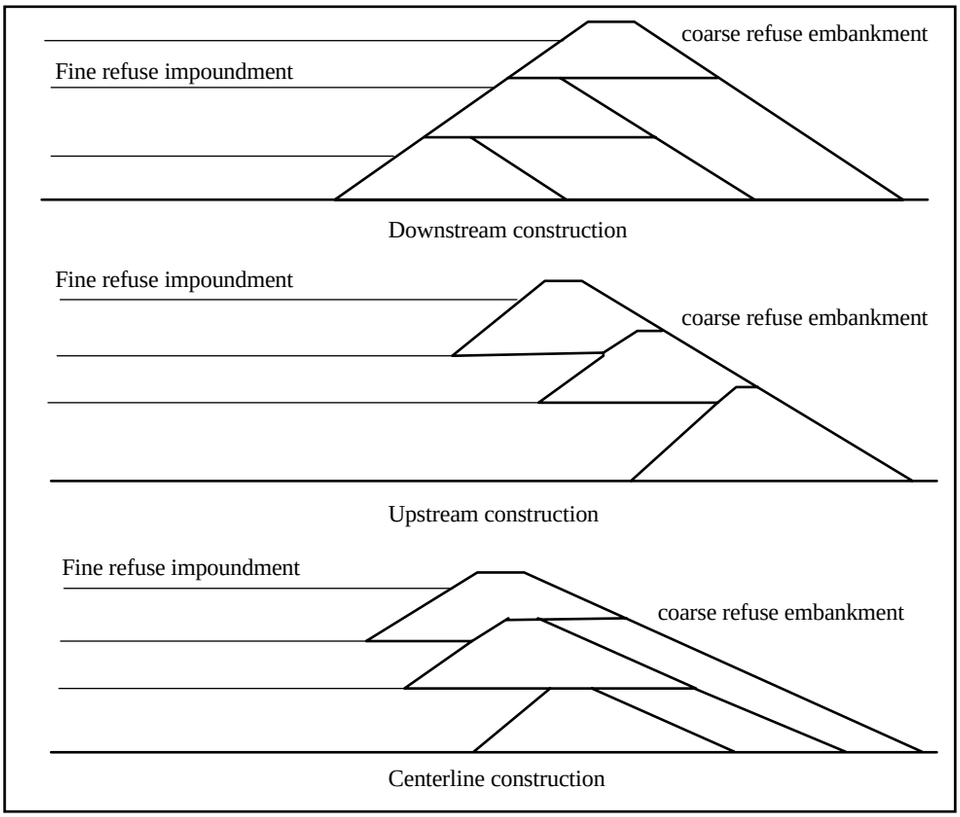


FIG. 1. Three construction methods for tailings dam.

It is reported by Gardner and Wu (2002) of MSHA that the seismic stability of coal waste impoundments is of great national interest. According to the National Inventory of Dams, there are 711 coal waste tailings dams in the United States and 241 of them are classified as having high hazard potential by the FEMA hazard rating system. One of the critical issues in seismic stability analysis is the possibility of liquefaction of fine refuse. For natural soils, this task is often carried out using the empirical approach, “Simplified Procedure for Evaluating Soil Liquefaction Potential” by Seed and Idriss (1971). However, the structure, fabric, angularity, specific gravity, and composition of fine refuse are quite different from natural soil. Moreover, according to experimental data on fine refuse at a number of sites in the field (Huang and Li, 1987), the non-plastic fine particles make up more than 50% of the fine refuse. Therefore, the data fall beyond the extreme of the empirical plot for liquefaction potential.

Stability analysis of tailings dams under earthquake loading is quite complex because: (1) there is limited information on the dynamic properties of coal-waste refuse; (2) there are generally excess pore pressures present within the fine refuse due to the permeability of the refuse being low and the fact that refuse consolidation is a continuing process since material placement is almost daily for the life of the facility;

and (3) the void ratio of fine refuse is still high even for conditions of 90% consolidation. In the event of an earthquake, excess pore pressure in the material can quickly build-up and cause a severe reduction in the drained strength of the material.

The problem of dynamic instability of mining waste was first realized by Casagrande (1950). He concluded that "chemical and mining wastes consisting of flour-sized material, are usually deposited hydraulically in very loose condition. Although they may appear stable behind some of the flimsiest dikes and in some cases supported only by a thin wall of the same material which has dried along the slopes, they are extremely sensitive to disturbance and constitute treacherous conditions which in some instances have caused disastrous flow slides with much loss of life and property."

Failure of tailings dams during earthquakes has been reported in seismically active countries such as Chile and Japan. Dobry and Alvarez (1967) reported widespread tailings dam failures during earthquakes in Chile. For instance, the El Cobre dams were almost completely destroyed during the 1965 earthquake. More than 2 million tons of tailings flowed into the valley, traveled 12 km in a few minutes, destroyed part of the town of El Cobre, and killed more than 200 people. The major cause of the failures was believed to be the overall slope stability failure as a result of soil liquefaction as shown by the existence of silt boiling. Failures with similar patterns were also reported in Japan during earthquakes (Ishihara, 1992). Such failure can cause not only property damage but also environmental problems as the waste material can be hazardous. For example, during the Near Izu Oshima earthquake of January 14, 1978 in Japan, a tailings dam failure released 76,000 m^3 of tailings waste contaminated with sodium cyanide which caused a major environmental problem (Marcuson *et al.*, 1979).

The seismic stability of coal-waste tailings dams has been a major concern for federal agencies such as the Office of Surface Mining (OSM) and the Mine Safety and Health Administration (MSHA), as well as the coal industries. The Committee on Earthquake Engineering of the National Research Council (1985) conducted a state-of-the-art review on liquefaction, and tailings dams were identified as one type of high-risk structures vulnerable to flow failure due to liquefaction of tailing materials. Since the 1990s, OSM and MSHA require comprehensive seismic analyses in the design of new tailings dams before approval of a construction permit. There is also an on-going effort to analyze the seismic stability of existing tailings dams. However, only a few studies on the seismic stability of tailings dams have been reported. Thacker et al. (1988) conducted an experimental study on the mechanical properties of coal refuse, and the results were used to analyze the seismic stability of a tailings dam using a pseudo-static type of analysis. Data from a cyclic triaxial test showed that excess pore pressure built up in the fine refuse under cyclic shear stress. Zeng et al. (1998a, 1998b, 1998c) conducted in-situ SPT tests and laboratory tests on fine refuse from a tailings dam in eastern Kentucky. It was found that the fine refuse was a silt-like powder with low plasticity. The specific gravity of the refuse was about 2, much lower than a typical soil. A group of centrifuge tests was conducted on models constructed by the upstream method and the downstream method. Excess pore pressure was recorded in the fine refuse, but no liquefaction was observed. Large deformation occurred when an earthquake with moderate intensity was applied,

especially for the model constructed by the upstream method with poorly consolidated fine refuse. Castro (2003) reviewed the current practice in seismic resistant design of tailings dams. He pointed out that the peak cyclic strain has significant influence on peak undrained strength of fine refuse. In 2003, an International Workshop on Seismic Stability of Tailings Dams was held (Zeng, 2004).

TEST DESCRIPTION AND INDEX PROPERTIES

The tailings dam studied in this paper is located in the Appalachian coalfield. It is about 100 meters tall and was built entirely by the upstream method. It has been in operation for about 30 years. For the coarse refuse, representative samples were brought into the laboratory and passed through a 19.0 mm sieve to eliminate large particles that could not be tested in the laboratory equipment used in the study. Standard Proctor tests were conducted on the refuse. The maximum dry density was found to be 18.2 kN/m^3, and the optimum moisture content was 10.3%. For both triaxial and resonant column tests, samples of coarse refuse were prepared to have 95% of the maximum dry density or 17.3 kN/m^3.

For the fine refuse, undisturbed tube samples were taken from four locations using the Osterberg tube-sampling device which has an inside diameter of 60.3 mm. The vertical effective stresses at these locations were estimated based on the in-situ unit weight of the refuse and the measured phreatic surface in the ground. A summary of the four samples is listed in Table 1. The tube samples were properly sealed after they were taken from the ground. They were then placed into a custom made box with restrictions on movement. The tubes were then encased by foam and carefully transported to the laboratory. Upon arrival to the laboratory, they were placed in a special sample storage room where temperature and humidity were controlled to reduce environmental influences on the samples. For each sample used in these tests, the soil was pushed out of the tube and then trimmed to the standard size for the equipment. For resonant column tests, the diameter of the sample was 60.3 mm and for cyclic triaxial tests, the diameter of the sample was about 35.2 mm.

Table 1. Summary information of samples of fine refuse.

Sample No.	Identification	Recovery (m)	In-Situ Vertical Effective Stress (kPa)
1	Sta.30+50, Lt., 69’-71.5’	0.6	380
2	Sta.30+50, Lt., 84’-86.5’	0.33	407
3	Sta.36+85, Lt., 46.5’-49’	0.75	186
4	Sta.36+85, Lt., 69’-71.5’	0.75	228

All the tests conducted followed ASTM standards such as: moisture content test ASTM D2216-90 (using an oven temperature of 60 ^{0}C for 48 hours to avoid burning of organic materials), resonant column test ASTM D4015-87, and cyclic triaxial test ASTM D3999-91. For resonant column and cyclic triaxial tests on the fine refuse, the estimated confining pressure that the in-situ soil experienced was applied to the samples. For tests on the coarse refuse, confining pressures of 69 kPa and 138 kPa (10 and 20 psi) were used. The resonant column device used in the tests was a Drnevich

type (Drnevich, 1985) and the cyclic triaxial device was an automated one similar to that described by Li et al. (1988).

Index property tests were conducted on both coarse and fine refuse to determine the particle size distribution and soil classification of the refuse. The particle size distribution curves of the original coarse refuse and those after passing the 19 mm sieve is shown in Fig.2, which shows that the soil is a mixture of sand and gravel with a small fraction of fine grains. The original soil is classified as clayey gravel with sand while those passed through the 19 mm sieve is classified as clayey sand with gravel. The fines portion (those that pass #40 sieve) of the coarse refuse had a plasticity index of 11. A specific gravity of 2.5 was determined for the coarse refuse. The particle size distribution of the four samples of fine refuse is shown in Fig.3, and the results of the index property tests are summarized in Table 2. These data show that fine refuse is typically a mixture of sand, silt, and clay with a low plasticity. There is some variation in terms of soil classifications for the four samples as they are all near the borderlines of different soil groups. The specific gravity of the soil is slightly larger than 2, which is much lower than typical soils. The fines content for the four fine refuse samples are between 40 to 60%, far above the limit used in a typical liquefaction potential study.

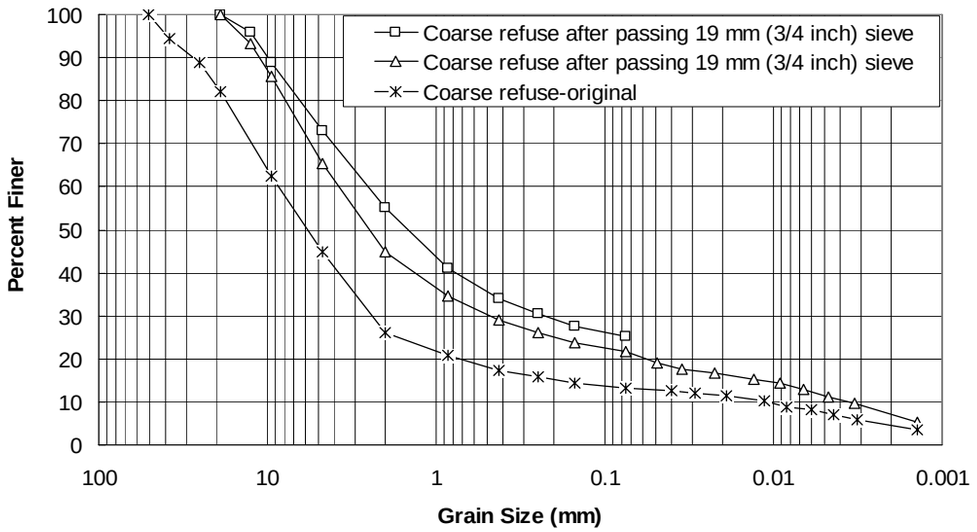


FIG. 2. Particle size distribution curve for coarse refuse.

SHEAR MODULUS

The shear moduli of the samples of refuse undergoing small strain were measured using a resonant column device. When the samples were loaded under large strain conditions, the moduli were measured using a cyclic triaxial device. The normalized shear modulus versus shear strain curves for the coarse refuse under two different confining pressures are shown in Fig.4, together with the empirical relationship for sand suggested by Seed et al. (1986). There is a variation between the results of resonant column tests and cyclic triaxial tests at similar strain level, which was likely caused by system compliance (ASTM D3999). Clearly, the shear modulus shows significant degradation as the shear strain increases, just as in conventional soils.

While the normalized curves for the coarse refuse under the two confining pressures are almost identical, they are slightly different from the empirical relationship for sand. At a very small strain, the coarse refuse seems to have a higher normalized modulus, while at a large strain, the degradation in stiffness is more significant. These data indicate that coal processing refuse have unique characteristics in mechanical properties. A relationship between normalized shear modulus and damping ratio versus shear strain that covers a wide variety of soils such as the one proposed by Vucetic and Dobry (1991) may be more suitable for this type of soil.

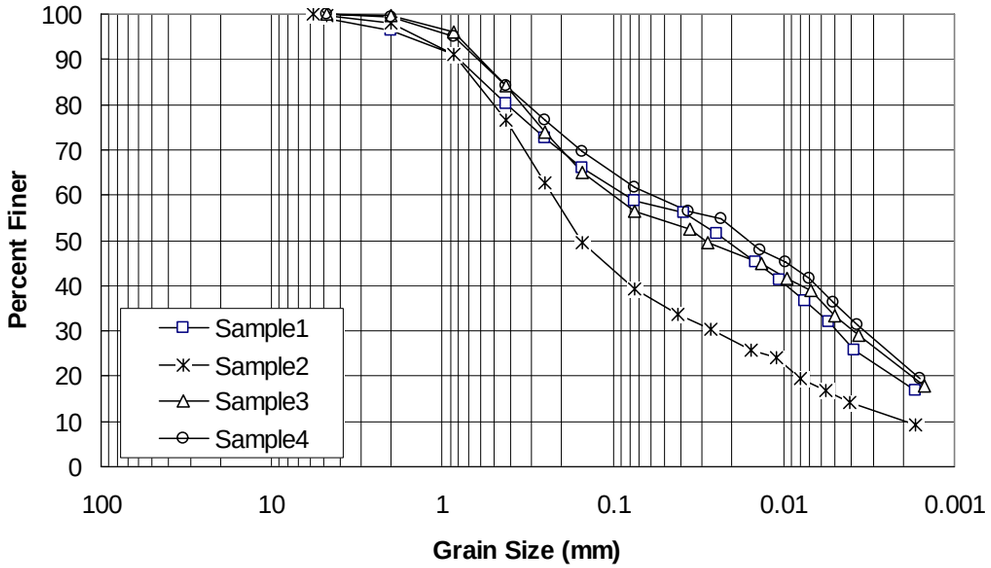


FIG. 3. Particle size distribution curve for four fine refuse samples.

Table 2. Index properties of fine and coarse refuse samples

Sample No	1	2	3	4	Coarse refuse
Water content (%)	13.5	13.6	8.7	12.5	11.2
Wet density (kN/m^3)	15.2	16.5	17.0	15.7	19.2
Liquid limit	36	27	32	34	31
Plastic limit	26	24	21	23	20
Plasticity index	10	3	11	11	11
Specific gravity	2.02	2.02	2.16	2.10	2.50
Soil classification	Sandy silt (ML)	Silty sand (SM)	Sandy lean clay (CL)	Sandy lean clay (CL)	Clayey sand with gravel (SC)

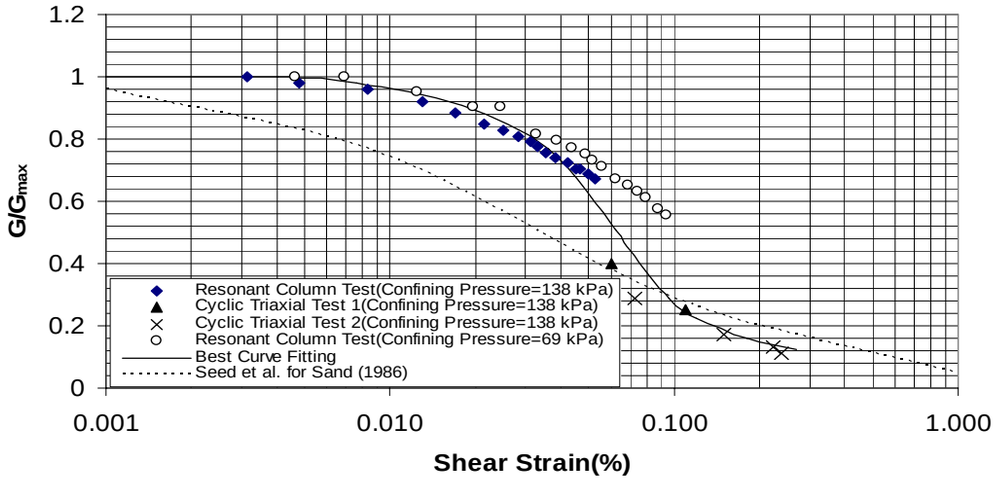


FIG.4. Normalized shear modulus versus shear strain for coarse refuse.
(G_{max} = 114 MPa and 174 MPa when confining pressure = 69 kPa and 138 kPa, respectively)

For the four fine refuse samples, the shear modulus versus shear strain is similar to that of typical sand. The normalized shear modulus versus shear strain curves as well as the empirical relationship for sand suggested by Seed et al. (1986) are presented in Fig.5. The overall trend of the experimental data matches the empirical relationship quite well, especially for samples 1, 3 and 4. This is not surprising since, as shown in Fig.3, the grain size distribution curve of these three samples are close to one another. In addition, all the four samples contain significant portions of sand.

During the resonant column tests on both coarse and fine refuse, the Young's moduli of the soils were also measured when cyclic axial stresses were applied to the samples. From the small strain shear moduli and Young's moduli of the two soils, Poisson's ratio was calculated. It was found that the coarse refuse has a Poisson's ratio of 0.3, and the fine refuse has a Poisson's ratio between 0.26 and 0.39.

DAMPING RATIO

As with the measurements of shear moduli, the damping ratios of the refuse undergoing small strains were measured using resonant column tests while samples undergoing large strain were measured with cyclic triaxial tests. The damping ratio versus shear strain curves for the coarse refuse under two confining pressures are plotted in Fig.6. Also shown in the figure is the empirical relationship between the damping ratio and shear strain for sand proposed by Seed et al. (1986). Once again, there is a variation of damping ratio measured by the two different methods due to system compliance. There are also some differences between the experimental data and the empirical relationship. At a small strain level, the experimental data of damping ratio are slightly lower; at large strain, it is the opposite.

The damping ratio versus shear strain curves of the four fine refuse samples are shown in Fig.7, together with the empirical relationship for sand proposed by Seed at al. (1986). Just as in the shear modulus tests, the experimental results match the empirical relationship very well.

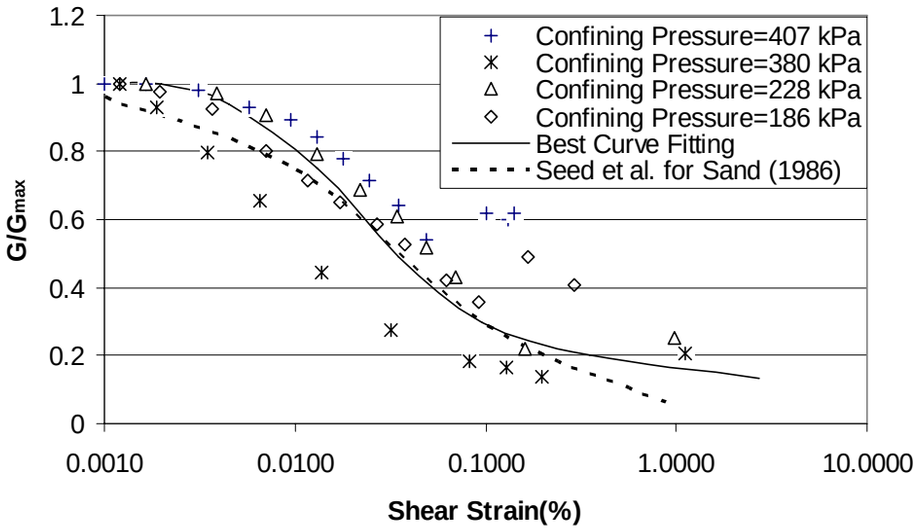


FIG. 5. Normalized shear modulus versus shear strain for fine refuse.
(G_{max} = 22, 44, 50, and 85 MPa when confining pressure = 186, 228, 380, and 407 kPa, respectively)

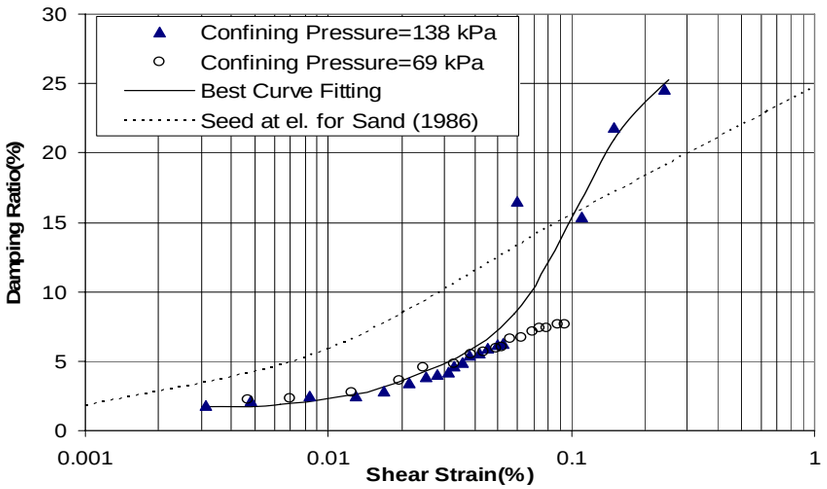


FIG. 6. Damping ratio versus shear strain for coarse refuse.
(The four data points with high damping ratio were from cyclic triaxial tests which the others were from resonant column tests)

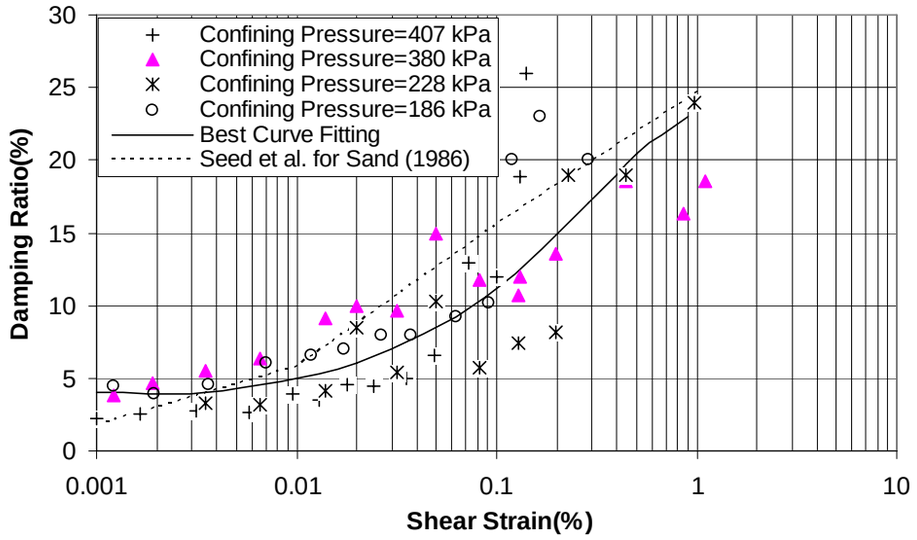


FIG. 7. Damping ratio versus shear strain for fine refuse.

RESPONSE TO CYCLIC LOADING

As discussed earlier, liquefaction of fine refuse is one of the major concerns in seismically resistant design of tailings dams. A comprehensive cyclic testing program was carried out to evaluate the possibility of liquefaction for the four fine refuse samples. In each test, a sample was pushed out of the tube and trimmed to the standard size for the cyclic triaxial device. Then the sample was isotropically consolidated to an effective confining pressure the same as the in-situ effective vertical stress. It needs to be pointed out that the in-situ refuse is typically consolidated anisotropically. Therefore, their resistance to liquefaction will be higher than that tested in the laboratory. After consolidation, the sample was saturated under vacuum for two days and de-aired water was introduced slowly. Then, a back pressure up to 400 kPa was applied to the sample to ensure a high degree of saturation for the samples. Only after B-value reached higher than 0.9, were cyclic loading tests conducted.

For each sample prepared, a series of cyclic loading was applied. The first was the cyclic loading anticipated for a 6.3 Moment Magnitude design earthquake, which includes 9 cycles of ± 20% cyclic loading. That was followed by a sequence of 5 cyclic loadings with a gradual increase in loading intensity. During each test, the cyclic deviator stress, axial strain, and excess pore pressure were measured. For example, the time history of the cyclic deviator stress during loading #6 for sample 3 is shown in Fig.8. This test included 49 cycles of ± 64% deviator stress applied at a frequency of 0.1 Hz. The axial strain recorded under the cyclic loading is shown in Fig.9, indicating a non-symmetric response and gradual buildup of permanent strains. At the end of the test, the peak-to-peak axial strain reached a level of 5.5%. The excess pore pressure response is presented in Fig.10. This shows a gradual accumulation of

excess pore pressure; however, by the end of the test, the average excess pore pressure is still only about 48% of the initial effective confining pressure. The deviator stress versus axial strain during the cyclic loading is shown in Fig.11. There is clear evidence of stiffness degradation as pore pressure increases. The response of this sample of fine refuse is similar to that of a typical silty sand.

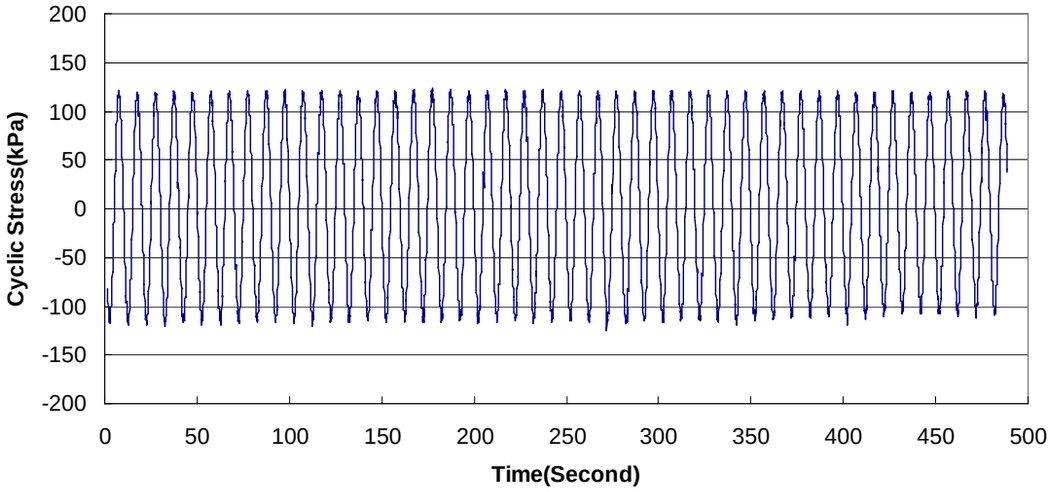


FIG. 8. Cyclic deviator stress applied to a fine refuse sample (initial effective confining pressure σ_c' = 186 kPa, cyclic deviator stress $\Delta\sigma_d = \pm 64\% \sigma_c$').

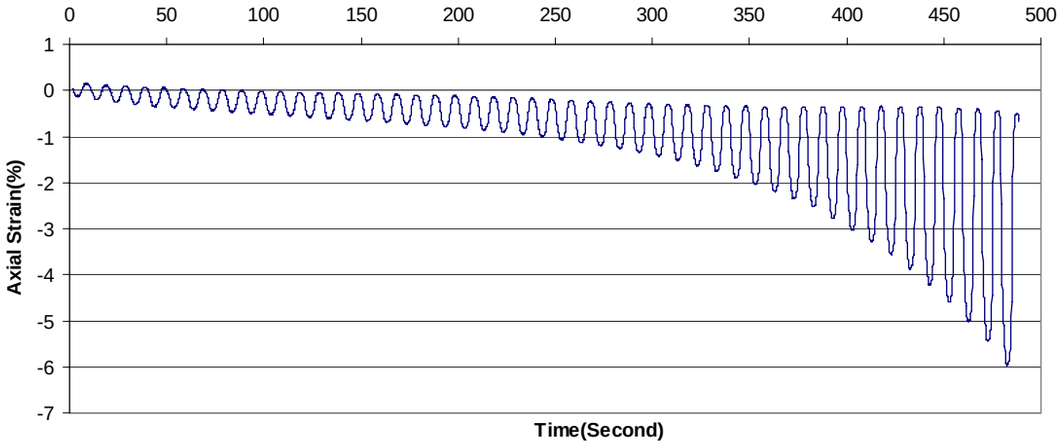


FIG. 9. Cyclic shear strain recorded in the cyclic triaxial test.

The results of all the undrained cyclic triaxial tests conducted on the four fine refuse samples are summarized in Table 3. According to the definition by the ASCE Committee on Soil Dynamics (1978), liquefaction is the process of transforming any

substance into liquid. In soils, liquefaction means a zero effective stress state due to the buildup of excess pore pressure. For the four fine refuse samples subjected to the design earthquake, very little excess pore pressure (excess pore pressure ratio less than 4.5%) was recorded. It can be concluded that the fine refuse at these locations would not liquefy during the design earthquake. In fact, even under much larger cyclic loading including the extremely large amplitude of ± 65% deviator stress of many cycles, the highest pore pressure ratio recorded was only 58%.

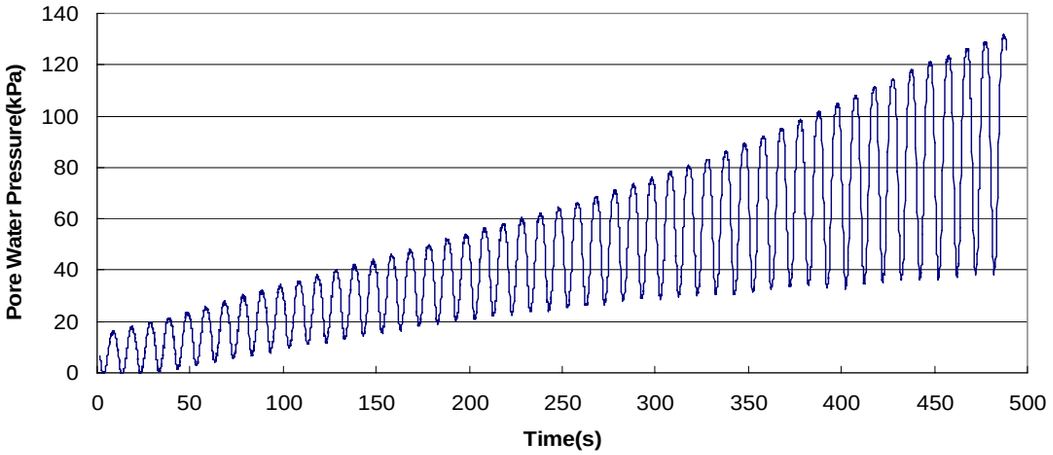


FIG. 10. Excess pore pressure recorded in the cyclic triaxial test.

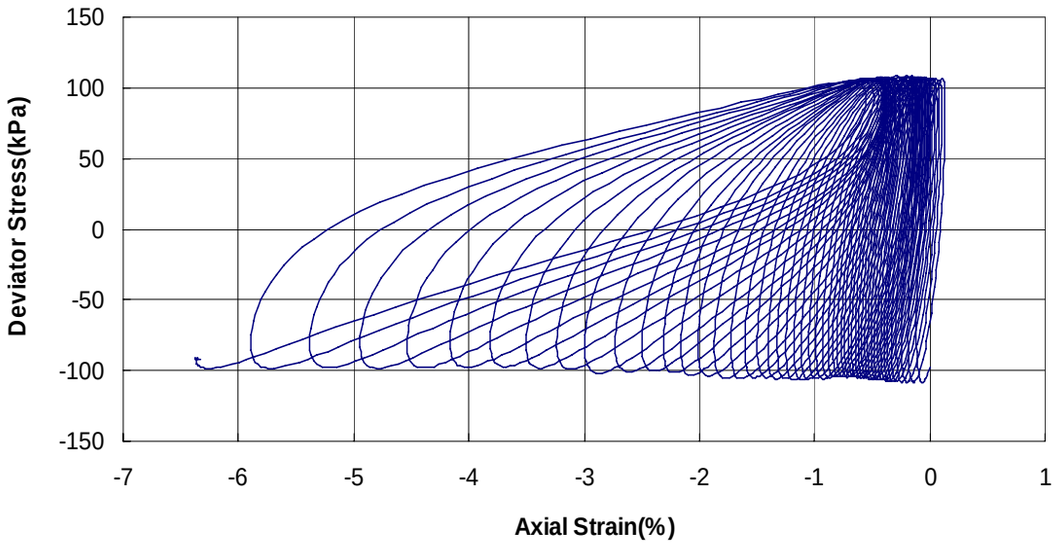


FIG. 11. Deviator stress versus axial strain recorded in the cyclic triaxial test.

In addition to liquefaction failure due to the zero effective stress, the Army Corps of Engineers also defines failure induced by cyclic loading as 5-10 percent peak-to-peak strain. Using this definition, all four samples reached failure under the highest cyclic loading applied. However, under the design earthquake, the maximum peak-to-peak strain recorded was only 0.04%, much less than the strain level defined as failure. Thus, cyclic loading induced failure would not occur at the locations of the samples under the design earthquake.

Table 3 Summary of results of cyclic triaxial tests.

Sample No.	Test No.	Cyclic loading applied	Average excess pore pressure ratio at the end of test	Maximum peak-to-peak axial strain
1	1	± 20%, 9 cycles	0.55%	0.04%
1	2	± 10%, 80 cycles	0.73%	0.01%
1	3	± 20%, 80 cycles	0.72%	0.04%
1	4	± 30%, 80 cycles	2.7%	0.08%
1	5	± 50%, 80 cycles	15%	0.36%
1	6	± 66%, 45 cycles	58%	7.2%
2	1	± 20%, 8 cycles	0.59%	0.04%
2	2	± 10%, 60 cycles	0.63%	0.015%
2	3	± 20%, 45 cycles	1.3%	0.06%
2	4	± 30%, 45 cycles	4.2%	0.14%
2	5	± 50%, 45 cycles	25%	0.55%
2	6	± 64%, 18 cycles	29%	8.5%
3	1	± 20%, 9 cycles	1.9%	0.013%
3	2	± 10%, 80 cycles	5.9%	0.004%
3	3	± 20%, 80 cycles	4.8%	0.013%
3	4	± 30%, 80 cycles	7.4%	0.05%
3	5	± 50%, 80 cycles	18%	0.17%
3	6	± 64%, 49 cycles	48%	5.5%
4	1	± 20%, 9 cycles	4.5%	0.035%
4	2	± 10%, 80 cycles	0.6%	0.012%
4	3	± 20%, 80 cycles	1.5%	0.032%
4	4	± 30%, 80 cycles	6.7%	0.055%
4	5	± 50%, 80 cycles	12%	0.18%
4	6	± 65%, 95 cycles	45%	4.8%

CONCLUSIONS

A comprehensive laboratory testing program was carried out on coarse and fine waste refuse obtained from a coal waste tailings dam in the Appalachian coalfield. From the results of the tests, the following conclusions can be drawn:

1) The coarse refuse is predominantly a mixture of particles of gravel and sand sizes, while the fine refuse is mostly a combination of sand, silt, and clay-sized

particles with a low plasticity. The specific gravity of these particles is about 2 to 2.5, which is much lower than typical soils.

2) The shear modulus versus shear strain and damping ratio versus shear strain curves of both fine and coarse refuse have characteristics similar to that of conventional soils. The relationship for fine refuse was found to be quite similar to the empirical relationship for sand proposed by Seed at al. (1986).

3) Excess pore pressure was recorded in undrained cyclic triaxial tests conducted on saturated samples of fine refuse, but no liquefaction was observed even under the largest cyclic loading applied. On the other hand, significant peak-to-peak axial strain approaching or exceeding that defined as failure was recorded when the largest cyclic loading was applied, indicating the possibility of failure induced by large cyclic loading.

Even though liquefaction was not observed in the laboratory tests on the four fine refuse samples studied here, it should be noted in this project as well as tests at other sites that there can be significant variations in the index properties of fine refuse between different locations. In addition, the four samples were taken from locations underneath the embankments of coarse refuse, which have quite high initial effective confining pressure. For the same materials under lower effective confining pressure, such as at locations in front of the embankment, it can not be completely ruled out the possibility of liquefaction under large earthquake loading. Therefore, it is important in the design that an adequate amount of testing be conducted.

REFERENCES

Casagrande, A. (1950). “Notes on the design of earth dams.” *Journal of Boston Society of Civil Engineers*, Oct., 231-255.

Castro, G. (2003). “Evaluation of seismic stability of tailings dams.” Proc., 12th Panamerican Conference on Soil Mechanics and Geotechnical Engineering, Cambridge, Massachusetts, Volume 2, 2229-2234.

Committee on Soil Dynamics of the Geotechnical Engineering Division (1978). “Definition of terms related to liquefaction.” *Journal of the Geotechnical Engineering Division*, Vol.104, No. GT9, 1197-1200.

Dobry, R. and L. Alvarez (1967). “Seismic failures of Chilean tailing dams.” *Journal of the Soil Mechanics and Foundations Division*, ASCE, Vol. 93, No. SM6, 237-260.

Drnevich, V.P. (1985). “Recent developments in resonant column testing.” *Proceedings of Richart Commemorative Lectures*, ASCE, 79-107.

Gardner, G.H. and Wu, K.K. (2002). “Evaluating the liquefaction potential of coal waste impoundments.” Geo-Strata, April 2002, 10-14.

Huang, Y.H. and Li, J. (1987). “Strength and consolidation characteristics of fine coal refuse.” Report to Office of Surface Mining, Department of Interior.

Ishihara, K. (1992). “Post-earthquake failure of a tailing dam due to liquefaction of the pond deposite.” *Proceedings of the International Conference on Case Histories in Geotechnical Engineering*, Vol. 3, University of Missouri, Rolla, Missouri.

Li, X.S., Chan, C.K., and Shen, C.K. (1988). “An automated triaxial testing system, advanced triaxial testing of soil and rock.” ASTM STP 977, Philadelphia, 95-106.

Marcuson, W.F. III, Ballard, R.F., Jr., and R.H. Ledbetter (1979). "Liquefaction failure of tailings dams resulting from the Near Izu Oshima Earthquake, 14 and 15 January." 1978. *Proc., 6th Pan-American Conference of Soil Mechanics and Foundation Engineering*, Lima.

National Research Council (1985). "Liquefaction of soils during earthquakes." National Academy Press, Washington, D.C.

Seed, H.B. and Idriss, I.M. (1971). "Simplified procedure for evaluating soil liquefaction potential." ASCE Journal of Geotechnical Engineering, Vol.97, No.9, pp.1249-1273.

Seed, H.B., Wong, R.T., Idriss, I.M., and K. Tokimatsu (1986). "Moduli and damping factors for dynamic analyses of cohesionless soils." ASCE Journal of Geotechnical Engineering, Vol. 112, No. 11, 1016-1032.

Thacker, B.K., C.R. Ullrich, J.G. Athanasakes, and G. Smith (1988). "Evaluation of a coal refuse impoundment built by the upstream method." *ASCE Geotechnical Special Publication No. 21*, 730-749.

Vucetic, M. and Dobry, R. (1991). "Effect of soil plasticity on cyclic response." ASCE Journal of Geotechnical Engineering, ASCE, Vol.117, No.1, 89-107.

Zeng, X., Wu, J. and R.A. Rohlf (1998a). "Seismic stability of coal-waste tailings dams." *ASCE Geotechnical Special Publication No. 75*, Vol. 2, 950-961.

Zeng, X., Wu, J. and R.A. Rohlf (1998b). "Modeling the seismic response of coal-waste tailings dams." *Geotechnical News*, June, 30-32.

Zeng, X., Wu, J. and R.A. Rohlf (1998c). "Response of coal-waste tailings dams under simulated earthquake loading." *Proceedings of Centrifuge 98*, Tokyo, Japan, 255-260.

Zeng, X. (editor) (2004). Proceedings of International Workshop on Seismic Stability of Tailings Dams, Cleveland, Ohio, http://ecivwww.cwru.edu/civil/xxz16/tailings dam/index.htm.

Dynamic Properties of Saturated Compacted soils

Chia-Pin Wu[1], Jin-Hung Hwang[2] and Tsai-Kuey Chien[3]

[1] Ph.D. student, Department of Civil Engineering, National Central University, No.300, Jhongda Rd., Jhongli City, Taoyuan County 32054, Taiwan, ROC; TEL: +886-3-4227151-34163; FAX: +886-3-4252960; E-mail: 92322030@cc.ncu.edu.tw.

[2] Professor, Department of Civil Engineering, National Central University, Taiwan, ROC. E-mail: hwangjin@cc.ncu.edu.tw.

[3] Master, Department of Civil Engineering, National Central University, Taiwan, ROC.

Abstract: Dynamic properties of saturated compacted soils are very important parameters used for analyzing seismic responses of compacted earth dams. The complete test results of them are rare since that saturating the compacted soil specimens is time-consuming and laborious by using traditional saturation methods. In this study, two vacuum-saturation methods were proposed to improve saturating the compacted SM, ML and CL specimens. Both methods can reliably make their Skempton coefficient B greater than 0.95. Their complete dynamic properties were then measured by resonant column test (RCT). The test results showed that their G/G_{max} versus strain relationships and damping ratio curves are much different from those of ordinary soils. The empirical equations correlating the maximum shear modulus, void ratio and effective confining pressure were also suggested for different compacted soils.

Keywords: earth dam, compacted soil, vacuum saturation, shear modulus, damping ratio

1. INTRODUCTION

Dynamic properties of saturated compacted soils are very important for performing seismic response analysis of earth dam. However, their complete test results are rarely found in the literatures. It is primarily due to the difficulties in saturating compacted soils using traditional method. The void ratio of compacted soil is very low that water can not pass through it easily. In addition, suction in compacted soil often absorbs too much de-aired water. This softens specimen and will cause it failure. Some researchers introduced increasing back pressure to increase degree of saturation (Ampadu and Tatsuoka, 1993; Santucci et al., 1998). However, most air compressors in laboratories have limited capacity, so the applied cell pressures are also limited. Increasing back pressure will reduce the effective confining pressure that can be applied on the specimen under a constant cell pressure. Thus, complete dynamic properties of compacted soils are difficult to obtain within limited test time and budget using traditional saturating process due to the above difficulties.

This paper presents two vacuum-saturation methods for improving saturating processes of compacted soils. The test results showed that the proposed methods can achieve the required degree of saturation within an acceptable time. A series of the

resonant column tests were then performed on the saturated compacted specimens. It is found that the maximum shear modulus, the normalized modulus and damping ratio curves of them are much different from those of ordinary soils. This paper proposes a useful guide to saturating compacted soils and provides high quality test data of dynamic property for performing seismic response analysis of compacted earth dam.

2. TESTING SCHEME

2.1 Test materials

The test materials were obtained from the borrow areas of a planned earth dam by spiral auger boring and pit excavating. According to the USCS classification system, the soils were classified as the three types, SM, ML and CL, which will be the shell and core materials of the dam. The results of the physical property test were listed in Table 1.

Table1 Physical properties of the compacted soils

		Classification (USCS)		
		SM	ML	CL
Specific gravity G_s		2.71	2.69	2.74
Fines content (%)		17.03	78.56	93.52
Liquid limit LL (%)		NA	20.89	34.84
Plasticity limit PL (%)		NA	17.13	20.89
Plasticity index PI (%)		NA	3.75	13.95
Standard Proctor	γ_{dmax} (kN/m^3)	19.50	19.01	17.25
(ASTM D698)	O.M.C. (%)	11.59	12.64	19.03
Modified Proctor	γ_{dmax} (kN/m^3)	20.48	20.38	19.21
(ASTM D1557 C)	O.M.C. (%)	8.19	9.39	10.33

2.2 Resonant column tests

A “fixed-free” resonant column apparatus was used to perform the dynamic property tests. The SM, ML and CL specimens were prepared by means of the standard and modified compaction effort. They were consolidated at the isotropic pressures of 49, 98, 196 and 294 kPa. When consolidation was completed, the drained valves were closed and the shear modulus G and the damping ratio D were measured by applying different shear strain γ. The investigation focused on the influences of different compaction energies and confining pressures on the dynamic properties.

2.3 Specimen preparation

The soil specimens were prepared by moist tamping for non-cohesive soils and slurry consolidation for fine-graded soils. It is hard to estimate how much compaction energy was applied to the specimens when using traditional triaxial mold. Furthermore, pushing the compacted specimen out of the mold and then trimming it into the size of a cylindrical one may cause serious disturbance and form a specimen of non-uniform size. For this reason, a special split-mold, which has a height of 15 cm and a diameter of 7.12 cm, was designed to match the specimen size of the

resonant column test, as shown in Fig. 1. The volume of the split-mold was much smaller than that of the standard or modified Proctor molds. Thus, the dropping blows per layer had to be calibrated to maintain the same compaction energy per unit volume as in the Proctor tests. Before compacting, silicon oil was smeared on the internal wall of the mold. This could reduce the friction between the specimen and mold. By doing that, it is easy to dismantle the split-mold to get the high-quality compacted specimens.



(a) before assembly (b) after assembly

Fig. 1 The special split-mold

2.4 Specimen saturation

Since the void ratio and permeability of compacted specimens are much lower than those of ordinary soils, the traditional saturating procedures can not achieve the required degree of saturation within an acceptable time. If using high back pressure to increase the degree of saturation, it will has a serious disadvantage that the tests can not be conducted at higher effective confining pressure due to the limited cell pressure that can be applied by the limited air pressure capacity of compressor. Therefore, this paper proposed vacuum-saturation concept to improve these disadvantages.

The vacuum-saturation equipment is shown in Fig.2. The air-extracting motor and vacuum switching apparatus were connected with the valve at the top, the vacuum pressure is controlled in the range of 2.94~5.88 kPa. At the same time, CO_2 or the distilled water was used to pass through the specimen from the valve at the bottom. The proposed method can speed up de-aired water to flow through the specimen and increase its saturation degree. The following are the detailed procedures.

Ⅰ. CO_2 aerating

About a CO_2 bubble per 5 seconds is aerated from the valve at the bottom. This takes about six hours.

Ⅱ. Air-extracting and CO_2 aerating

CO_2 is aerated from the valve at the bottom and the air-extracting motor is connected with the valve at the top to speed up CO_2 seeping into the specimen by suction. It takes about 1-2 hours.

Ⅲ. Air-extracting and de-aired water infiltrating

The de-aired water infiltrates the specimen about a bubble per 5 seconds from

the valve at the bottom and the air-extracting motor is connected with the valve at the top to speed up the water seeping into the specimen by suction. It takes about 1-2 hours.

Ⅳ. De-aired water infiltrating

Turn off the air-extracting motor and naturally infiltrate the de-aired water into specimen. Let the de-aired water seep from the valve at the bottom to the top. The purpose is to make the de-aired water flow steadily into and out of the specimen. It takes at least four hours.

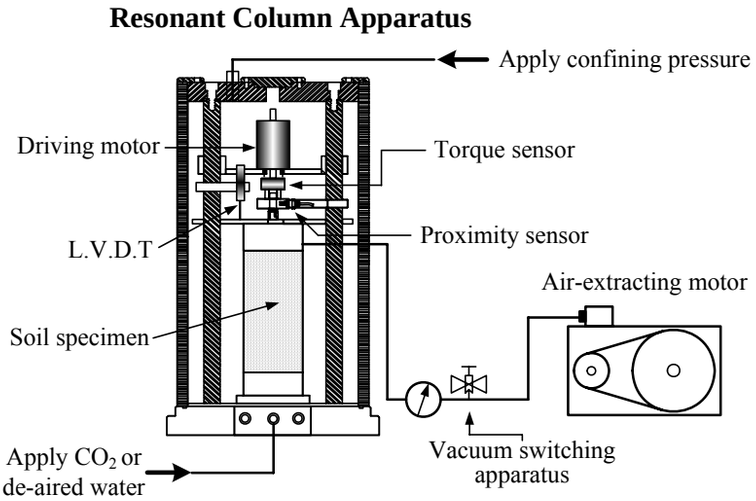


Fig. 2 Configuration of RCT with vacuum-saturation equipment

The above saturating procedures can be combined into two methods which are used according to initial saturation degree of compacted specimen. Both methods, can assure specimen's Skempton coefficient B greater than 0.95. Fig. 3 shows the flowchart of the proposed saturation methods. The followings are the details of the methods:

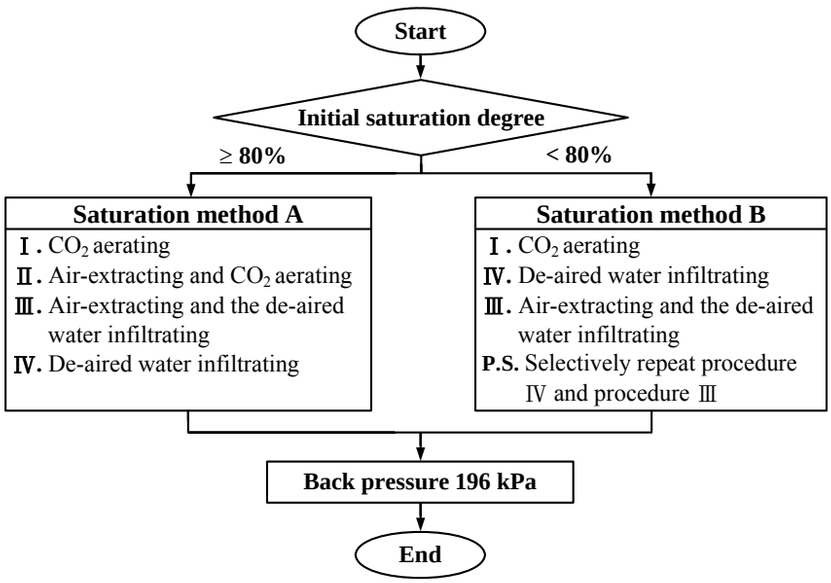


Fig. 3 Flowchart of the proposed saturation methods

(1) Saturation method A

Saturation method A followed the above saturating procedures in sequence. It was used in the cases of the initial saturation degree greater than 80% and was suitable to all specimens with standard compaction effort and the ML specimens with modified compaction effort. The initial saturation degree is defined as the saturation degree after compaction. This method takes about 14 hours and the measured B values were approximately 0.97 ± 0.01.

(2) Saturation method B

This method was used in the cases of the initial saturation degree of the compacted specimen smaller than 80%, such as the SM and CL specimens with modified compaction effort. The method followed the same above procedures, but with a little change in sequence. The sequence was procedure Ⅰ, procedure Ⅳ and procedure Ⅲ, and opportunely repeated the procedure Ⅳ and procedure Ⅲ. This method spends approximately about 24-36 hours and the measured B values were 0.98 ± 0.01.

When using method A to saturate specimens with low degree of saturation, the specimen will absorb much water to soften itself, and finally excessively deform and collapse. For this reason, saturation method B was designed to keep the specimen in good condition during the process of saturation. The idea is to slowly infiltrate a little de-aired water into the specimen, and then, applying a partial vacuum to accelerate water seepage. By repeating procedure Ⅳ and Ⅲ for several cycles, the distilled water can steadily flow throughout the specimen, which can remain in a good shape with a high degree of saturation.

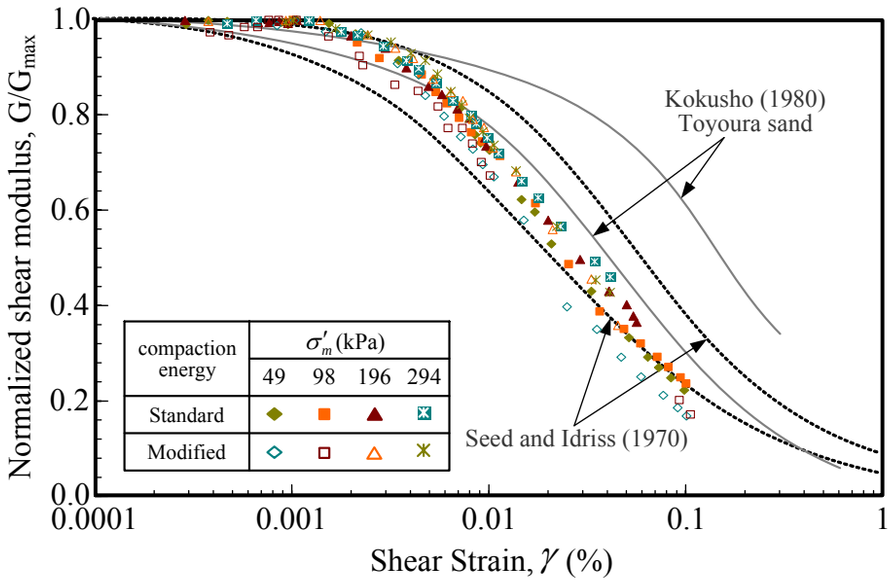
3. DYNAMIC TEST RESULTS AND DISCUSSIONS

3.1 Relationship between shear modulus and shear strain amplitude

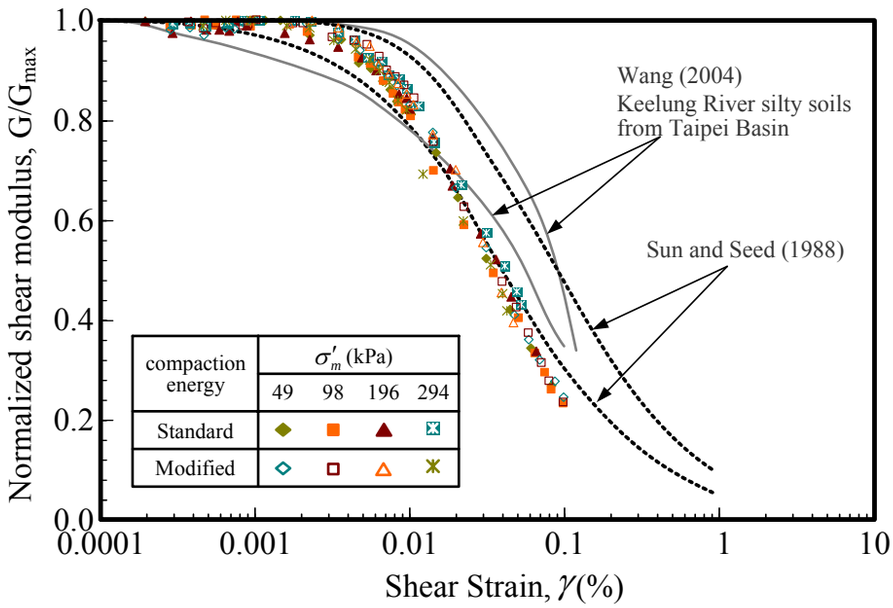
Fig. 4 shows the modulus reduction curves for the SM, ML and CL specimens compacted by standard and modified energies at four isotropic consolidation pressures. In this study, the threshold shear strain of the SM soil was about 0.001%, ML was about 0.002% and CL was 0.01%. Both the threshold shear strain and the rate of modulus reduction increase with increasing plasticity index.

Shibata and Soelarno (1975) showed that the modulus reduction curves for sands were slightly influenced by the confining pressure, the curves only gradually move to the right and upward with increasing confining pressure. The SM soils in this study also have the same tendency, especially for the case of the modified compaction energy. In the strain range greater than 0.004%, the SM modulus reduction curves are below the lower bound curve of Japanese Toyoura sand. This significant difference is shown in Fig. 4(a). The compacted SM soils have greater threshold strain and faster reduction rate than those curves suggested by Seed and Idriss (1970). Fig. 4(b) shows the modulus reduction curves of the compacted ML specimens. These curves are quite similar for different compaction efforts or confining pressures. They look like as linear curves in the strain range greater than the threshold strain. It can be seen that in the shear strain range greater than 0.02 %, the G/G_{max} versus strain relationships for the ML soils are below the lower bound curves suggested by Sun and Seed (1988) and Wang (2004) for cohesive soils. Fig. 4(c) shows the modulus reduction curves of the compacted CL specimens. Their

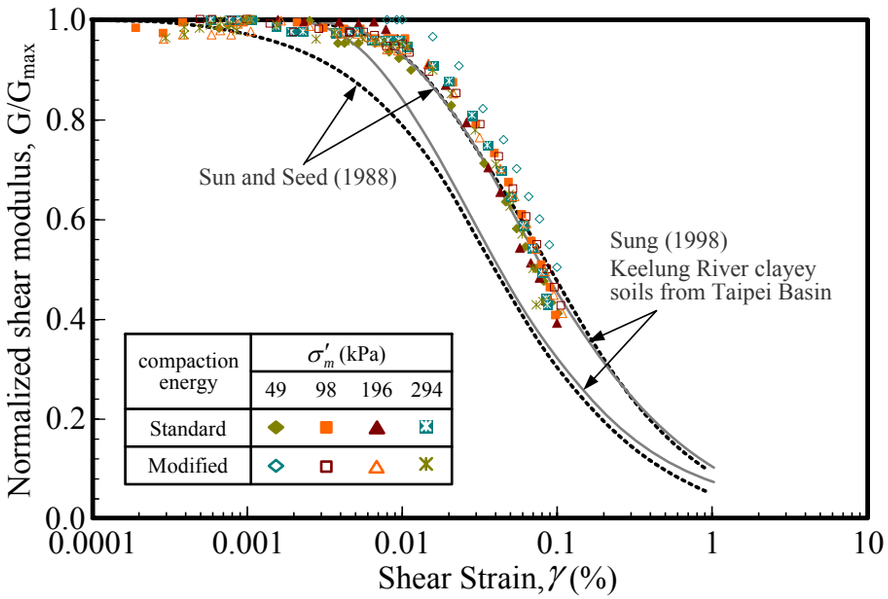
G/G_{max} versus strain relationships also display linear logarithm reduction trend and were above the upper bound curves suggested by Sun and Seed (1988) and Sung (1998) for cohesive soils. Confining pressure has a very limited influence on the G/G_{max} versus strain relationships of the compacted CL soils, which is consistent with the finding of Isenhower and Stoke's work(1981).



(a) SM soils



(b) ML soils



(c) CL soils

Fig. 4 Comparison of modulus reduction curves of saturated compacted soils with those of other soils in previous investigations

3.2 Relationship between maximum shear modulus and confining pressure

Hardin and Richart (1963) indicated that the maximum shear modulus, G_{max}, is primarily related to the void ratio and confining pressure and soil type. Their empirical formula was used to fit the test data. The formula is in a form as below.

$$G_{max} = A \cdot F(e) \cdot (\sigma'_m)^n \quad (1)$$

where A is an empirical coefficient representing the influence of soil type; $F(e)$ is the function of void ratio; σ'_m is the mean confining pressure; n is the power of the confining pressure. A summary of these empirical formulae has been arranged by Kokusho (1987), where it can be seen that, in the majority of the cases, the n value is about 0.5, whereas the value of A varies over a wide range reflecting variability of different soils. In this study, the regressive parameters of equation (1) were listed in Table 2. Since all R-squares were greater than 0.99, the empirical equation well fitted the test data.

Table 2 Regressive parameters of the empirical equation[a]

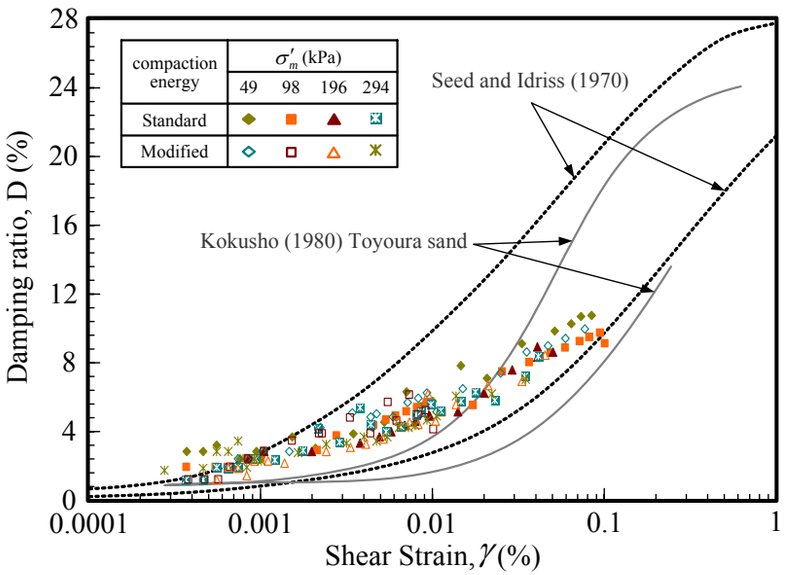
Compaction effort	Soil type	$F(e) = (2.17- e)^2/(1 + e)$			$F(e) = (2.97- e)^2/(1 + e)$		
		A	n	R-square	A	n	R-square
Standard	SM	2100	0.65	0.996	1000	0.66	0.994
	ML	2400	0.60	0.990	1100	0.62	0.993
	CL	1500	0.65	0.998	650	0.67	0.994
Modified	SM	1800	0.68	0.990	900	0.68	0.990
	ML	1400	0.70	0.991	650	0.71	0.996
	CL	600	0.77	0.997	260	0.78	0.997

[a]G_{max}: kpa

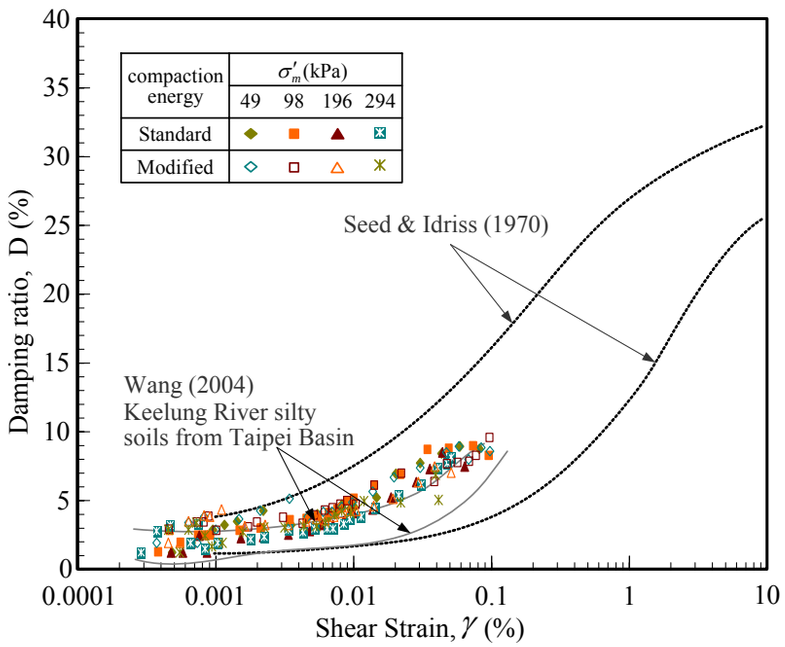
The values of n increase with increasing compaction effort and increasing soil plasticity, and the values of A decrease with increasing compaction effort. However, it is found that the power n of the compacted soils in this study is greater than 0.5, a typical value of ordinary soils from previous researches.

3.3 Relationship between damping ratio and shear strain amplitude

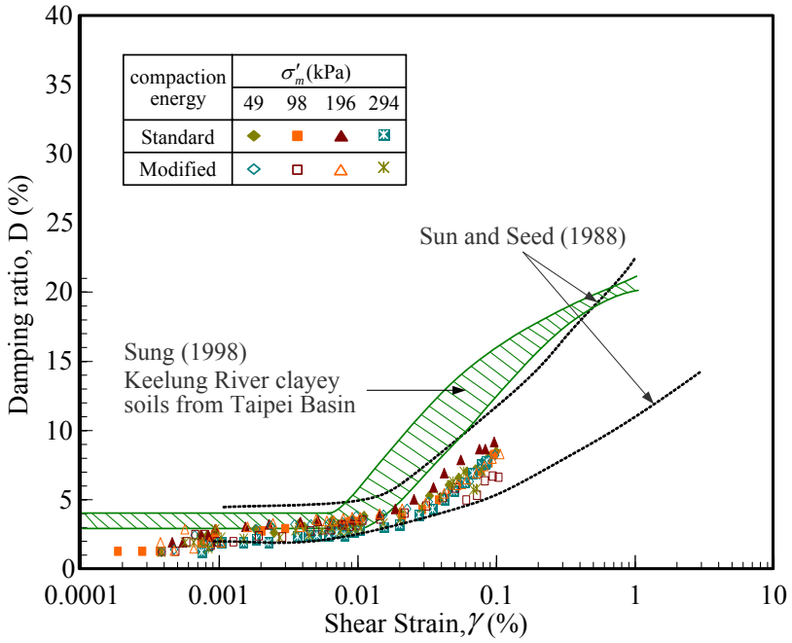
The free vibration decay method was used to estimate the damping ratio D in the resonant column test. Seed and Idriss (1970) indicated that the main factor affecting the strain-dependent relationship of the damping ratio is the confining pressure.



(a) SM soils



(b) ML soils



(c) CL soils

Fig. 5 Comparison of damping ratio curves of saturated compacted soils with those of other soils in previous investigations

Fig. 5 shows the damping ratio curves of the compacted soils. A similar decrease of the damping ratio with increasing confining pressure is observed for the SM soil and not seen for the ML and CL soils. It is very interesting to note that the damping ratio is nearly linearly related with increasing logarithmic strain in the strain range larger than 0.001% for the SM soils, 0.003% for the ML soils, and 0.02% for the CL soils.

4. CONCLUSIONS

The following conclusions can be derived from the test results presented here.

1. The proposed special split mold can prepare compacted specimen quickly and cleanly without sample disturbance.
2. The proposed two saturation methods can reliably saturate the compacted specimens to the degree with the measured Skempton's coefficient B greater than 0.95 using less time and back pressure than those used in previous researches.
3. The strain-dependent shear modulus and damping ratio of the saturated compacted soils are quite different from those of ordinary soils reported in the previous literatures.
4. For the ML and CL soils, the shear modulus approximately linearly decreases with logarithmic strain in the strain range greater than the threshold strain. The damping ratio versus strain relationship approximates to a linear curve in a semi-logarithmic plot for all soil types. These behaviors might be due to the inherent characteristics of saturated compacted soils.

ACKNOWLEDGEMENTS

The authors would like to express their gratitude to the geotechnical engineering research center of Sinotech engineering consultants, INC. for offering earth dam materials from borrow areas. Mr. Ming-Shu, Li, at the C & M Hi-Tech engineering Company, is also highly appreciated for his technical guidance.

REFERENCES

Ampadu, S., and Tatsuoka, F. (1993). "Effect of Setting method on the behaviour of clays in triaxial compression from saturation to undrained shear." *Soils and Foundations*, 33(2), 14-34.

Hardin, B.O., and Richart F.E.Jr. (1963). "Elastic wave velocities in granular soils." *Journal of the Soil Mechanics and Foundations Division,* ASCE, 89(1), 33-65.

Isenhower, W.M., and Stoke, K.H. (1981). "Strain rate dependent shear modulus of San Francisco bay mud." *Proceedings of the International Conference on Recent Advances in Geotechnical Earthquake Engineering and Soil Dynamics*, University of Missouri-Rolla, Vol. 2, 597-602.

Kokusho, T. (1980). "Cyclic triaxial test of dynamic soil properties for wide strain range." *Soils and Foundations*, 20(2), 45-60.

Kokusho, T. (1987). "In situ dynamic soil properties and their evaluation." *Proc. of 8th Asian Regional Conference on Soil Mechanics and Foundation Engineering*, Kyoto, Vol. 2, 215-235.

Santucci de Magistris, F., Silverstri, F., and Vinale, F. (1998). "The influence of compacted on the mechanical behaviour of a silty sand." *Soils and Foundations*, 38(4), 41-56.

Shibata, T., and Soelarno, D.S. (1975). "Stress-strain characteristics of sands under cyclic loading." *Proceedings of the Japanese Society of Civil Engineers*, No. 239.

Seed, H.B., and Idriss, I.M. (1970). "Shear moduli and damping factor for dynamic response analysis." *Report* No. EERC 70-10, Earthquake Engineering Research Center, Univ. of California, Berkeley, California.

Sun, J.I., Golesorkhi, R., and Seed., H.B. (1988). "Dynamic moduli and damping ratios for cohesive soils." *Report* No. EERC 88-15, Earthquake Engineering Research Center, Univ. of California, Berkeley, California.

Sung, Y.W. (1997). "The dynamic properties of Keelung River Clay of Peitou region in Taipei Basin." *Thesis*, Department of Civil Engineering, National Central University, Taiwan. (*in Chinese*)

Wang, J.S. (2004). "Soil dynamic properties of the resonant column test." *Thesis*, Department of Civil Engineering, National Central University, Taiwan. (*in Chinese*)

Dynamic Response of Unsaturated Soils Using Resonant Column and Bender Element Testing Techniques

L.R. Hoyos[1], P. Takkabutr[2], A.J. Puppala[3], and MD.S. Hossain[4]

[1] Associate Professor, University of Texas at Arlington, Texas, 76019, E-mail: lhoyos@uta.edu
[2] Former GRA, University of Texas at Arlington, Texas, 76019, E-mail: jobphayak@hotmail.com
[3] Professor, University of Texas at Arlington, Texas, 76019, E-mail: anand@uta.edu
[4] Assistant Professor, University of Texas at Arlington, Texas, 76019, E-mail: hossain@uta.edu

ABSTRACT: The main objective of this work was to experimentally investigate the influence of key environmental factors, including compaction-induced matric suction and confining pressure, on small-strain stiffness properties of partially saturated sandy and clayey soils using the pressure plate, resonant column, and bender element testing techniques. To achieve this goal, a comprehensive series of resonant column (ASTM D 2325-68), bender element (ASTM C 778), pressure plate (ASTM D 4015-92), and filter paper (ASTM D 5298) tests were conducted on several identically prepared specimens of loose, poorly graded sand (SP) and compacted, high plasticity clay (CH) subject to different compaction-induced (post-compaction) suction and confining stress states prior to resonant column and bender element testing. Compaction-induced suctions in all specimens were assessed prior to testing via a full set of previously calibrated soil-water characteristic curves (SWCC). Compaction-induced matric suction was found to exert a significant effect on the small-strain stiffness response of partially saturated SP and CH soils both from bender element and resonant column testing techniques.

INTRODUCTION

Extensive research efforts have been focused on field and laboratory measurements of soil suction, assessment of soil-water characteristic curve (SWCC), and analyses of swell-collapse behavior. However, very few efforts have been focused on small-strain response of unsaturated soils and their dynamic characterization at small strains. The critical role of soil stiffness at small strains in the design and analysis of geotechnical infrastructure (e.g., earthdams, embankments, foundations) is now widely accepted. As most soils involved in these structures are unsaturated and the real strains are small, there is a need for a better understanding of the small-strain behavior of such soils.

Conventional testing techniques cannot capture this small-strain behavior and, hence, vastly underestimate the true soil stiffness, mainly due to errors in small strain measurements. Recently, bender element based techniques have proved a viable way

to investigate soil stiffness at very small strains, and they are starting to be used more widely for saturated soils. However, very limited use of bender element technique has been reported for unsaturated soils, and the results are very far from conclusive (e.g., Picornell and Nazarian 1998, Cho and Santamarina 2001, Cabarkapa and Cuccovillo 2006). Hence, there is a need for assessing the true feasibility of bender element based techniques in partially saturated soils as compared to more reliable, fully standardized procedures, such as resonant column and/or simple shear based methods. The present work is motivated by this research need.

OBJECTIVE AND SCOPE

The main objective of this work was to experimentally investigate the influence of key environmental factors, including compaction-induced suction, confining pressure, and K_o stress states, on small-strain stiffness properties of partially saturated sand and clay using the pressure plate, resonant column, and bender element testing techniques. To accomplish this goal, a series of resonant column (ASTM D 2325-68), bender element (ASTM C 778), pressure plate (ASTM D 4015-92), and filter paper (ASTM D 5298) tests were conducted on identically prepared specimens of loose, poorly graded sand (SP) and compacted, high plasticity clay (CH) subject to different compaction-induced (post-compaction) suction and confining stress states prior to resonant column (RC) and bender element (BE) testing. Compaction-induced suction in all specimens, prior to RC and BE testing, was assessed via soil-water characteristic curves (SWCC).

ASSESSMENT OF SOIL-WATER CHARACTERISTIC CURVES

In this work, an attempt has been made to develop a modified pressure plate extractor (MPPE) device for assessing the SWCC of unsaturated soils under anisotropic stress states. The MPPE features independent control of net radial confinement ($\sigma_r - u_a$) and vertical pressure ($\sigma_v - u_a$). An original PPE device was modified to accommodate a 2.8 in (7.2 cm) diameter, 1.5 in (3.8 cm) height, stainless steel, confining ring: Figure 1(A). The assembled ring seats directly on top of a 15-bar plate: Figure 1(B). A coarse porous stone, tightly secured onto the top edge of the ring, facilitates the flow of air pressure (suction) in the vessel towards the soil pores (Hoyos et al. 2006).

Figure 2 shows the SWCC response of SP soil for a limited range of isotropic confining pressures. Data points represent actual experimental data (corresponding to 1.25, 2.5 and 5-psi confinement in the MPPE device), whereas the solid lines represent the best-fitting SWCC devised using Fredlund and Xing's (1994) model equation:

$$\theta_v = \frac{\theta_s}{\left\{ \ln\left[e + \left(\frac{\psi}{a} \right)^b \right] \right\}^c} \quad (1)$$

where, θ_v = volumetric water content; θ_s = saturated water content (volumetric water content at suction = 0 kPa); ψ = soil suction (kPa); e = 2.718 (natural number); a = model parameter related to air-entry value (suction value at which air starts to enter largest pores in the soil); b = model parameter related to pore size distribution of the soil; c = model parameter related to the asymmetry of the SWCC model curve.

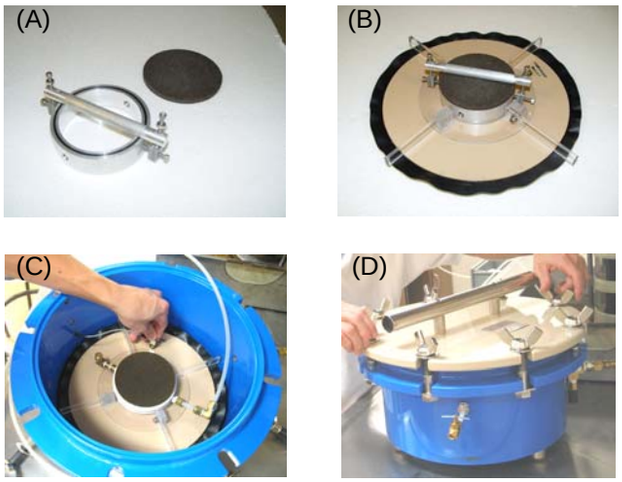


Figure 1. A 15-Bar Modified Pressure Plate Extractor (MPPE) device

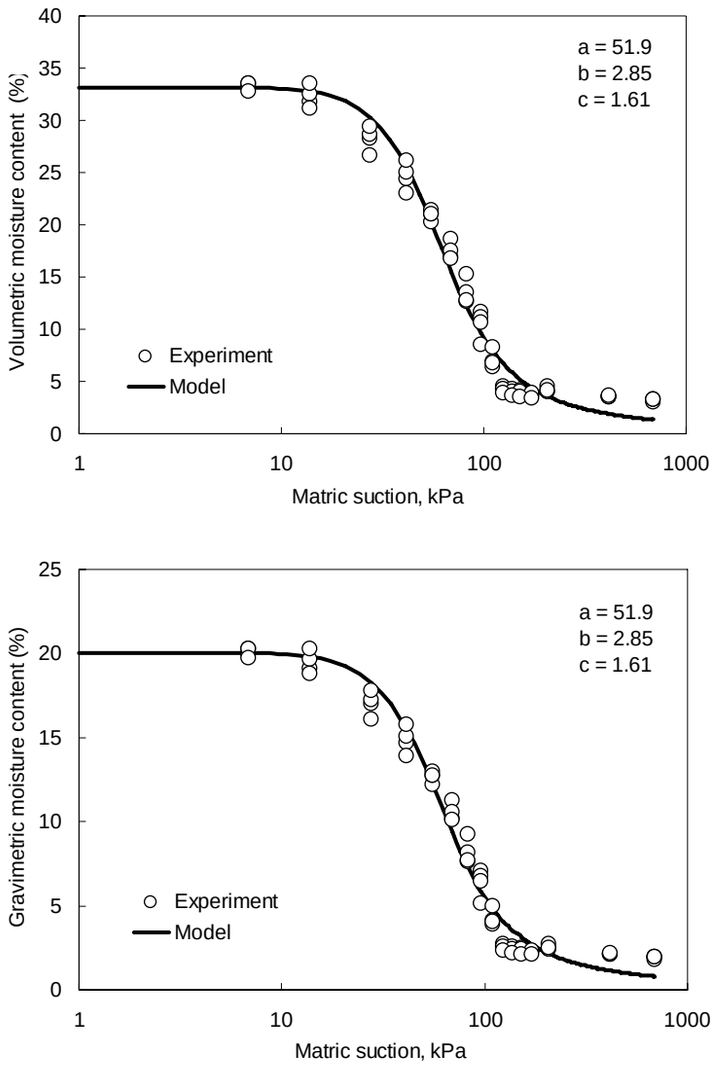


Figure 2. SWCC response of poorly-graded sand from MPPE device

From Figure 2, the induced stress states (up to a 5-psi confinement) are found to exert no significant influence on the SWCC response of SP soil. Similar results were found for CH soil (Hoyos et al. 2006). In this work, the selected range of experimental variables was intended to reproduce in-situ stress state conditions within subgrade or shallow foundation systems. It is expected that higher levels of stress will have a considerably greater effect on SWCC responses. SWCC models obtained for SP and CH soils, via Equation (1), were used to devise empirical correlations between small-strain stiffness properties (shear modulus and damping ratio) and suction, based on values of initial compaction moisture content, as shown in the following sections.

RESONANT COLUMN (RC) AND BENDER ELEMENT (BE) TEST SETUPS

As previously mentioned, limited use of BE based technique has been reported for unsaturated soils, and the results are very far from conclusive. In this work, BE test results on partially saturated sand and clay were compared to those from RC tests in order to assess the feasibility of the BE technique for unsaturated soils compacted at different initial suction states. Figures 3 and 4 show photographs of the RC and BE test setups available at UTA geotechnical laboratories, respectively. Measurements of material damping from bender elements were accomplished in the frequency domain (Brocanelli and Rinaldi 1998).

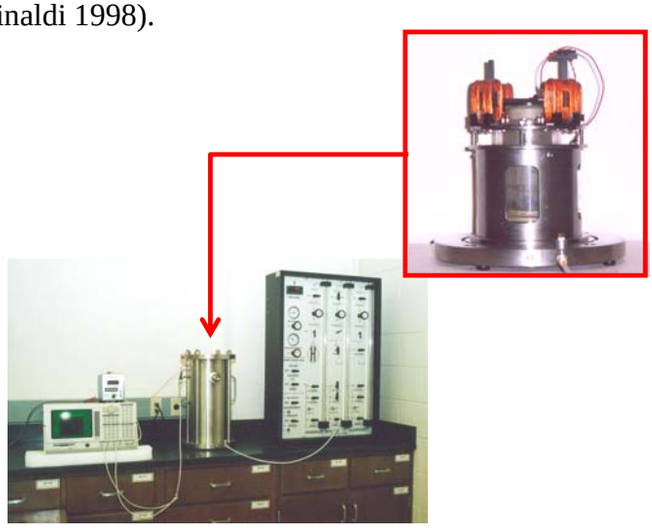


Figure 3. Resonant Column test setup at UTA geotechnical laboratories

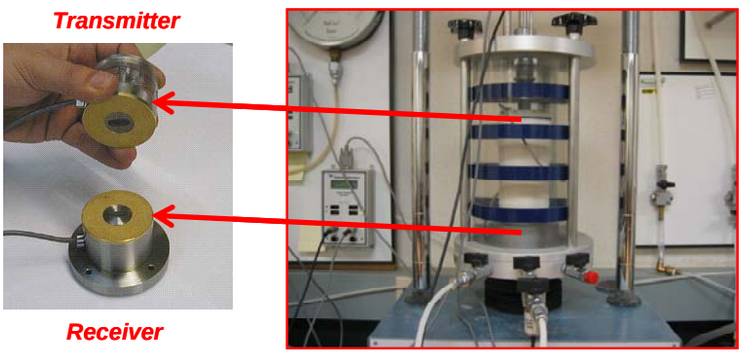


Figure 4. Bender Element test setup at UTA geotechnical laboratories

SMALL-STRAIN STIFFNESS RESPONSE FROM RC/BE TESTS

Figure 5 shows values of normalized small-strain shear modulus G_{max}/σ_o and material damping ratio D_{min}/σ_o from RC tests presented as functions of compaction-induced suction, where σ_o = total confining pressure. As expected, the level of confinement has a significant effect on stiffness response of SP soil. It can also be noted the relatively significant influence of compaction-induced suction, with a considerable increase in shear modulus G_{max} at higher values of suction. Likewise, there is a steady decrease in damping ratio D_{min} at higher values of suction, which can be attributed to the higher effective stresses from compaction-induced negative pore water pressures. Solid lines in Figure 5 represent the best-fit empirical correlations devised for the normalized shear modulus and damping ratio via the SWCC model in Equation (1). Formulations of these empirical correlations are presented by Takkabutr (2006).

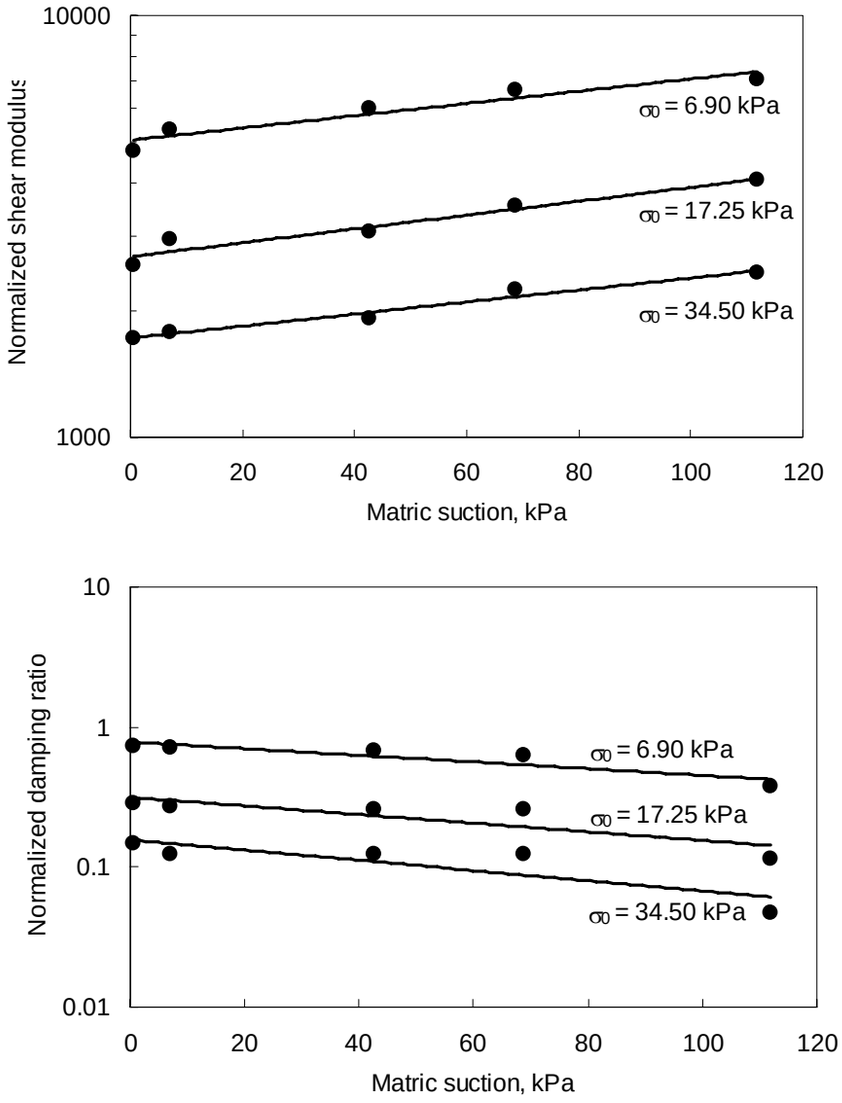


Figure 5. Normalized shear modulus and damping ratio from RC tests in SP soil

Successful correlations as those shown in Figure 5 were also devised for the normalized shear modulus and damping ratio from bender element (BE) tests. Figure 6 shows comparisons between experimental and empirically predicted values of small-strain shear modulus and damping ratio obtained from both techniques. Results from RC and BE tests on high plasticity clay (CH) are also included.

A more pronounced scattering is observed for higher values of shear modulus from bender element (BE) tests, which can be indicative of a deficient performance of the bender elements at higher values of confinement or compaction-induced suction. It can also be observed that the empirical correlations are less effective in reproducing experimental data when it comes to damping ratio.

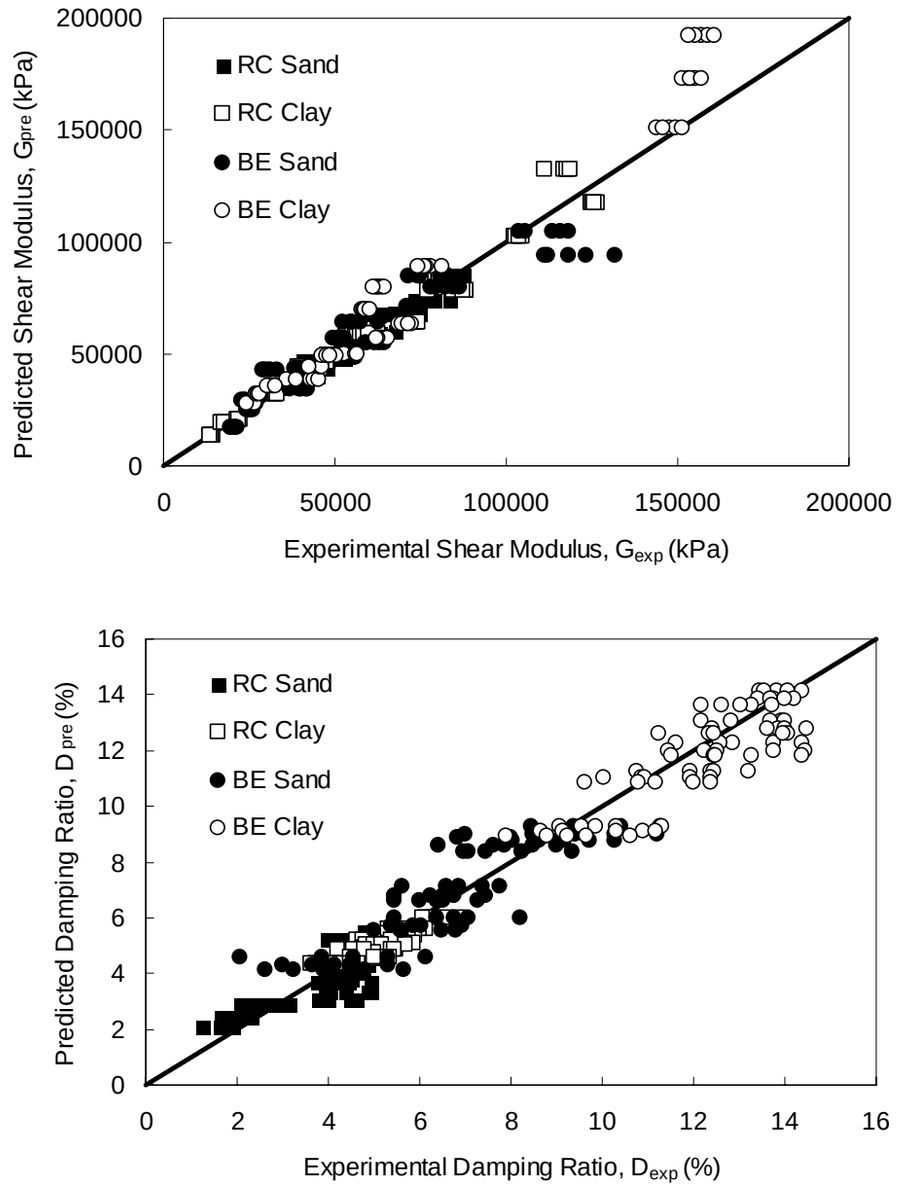


Figure 6. Experimental and empirically-predicted values from RC and BE tests

Figure 7 shows comparisons of all the average experimental values of small-strain shear modulus from RC and BE test techniques. Results from RC and BE tests on CH soil are also included. The BE technique appears to considerably overestimate the RC based values of shear modulus at higher confinements or compaction-induced suction levels, i.e. for G_{max} values greater than approximately 75 MPa (75,000 kPa). It can be observed that the overestimation can be as high as 50%.

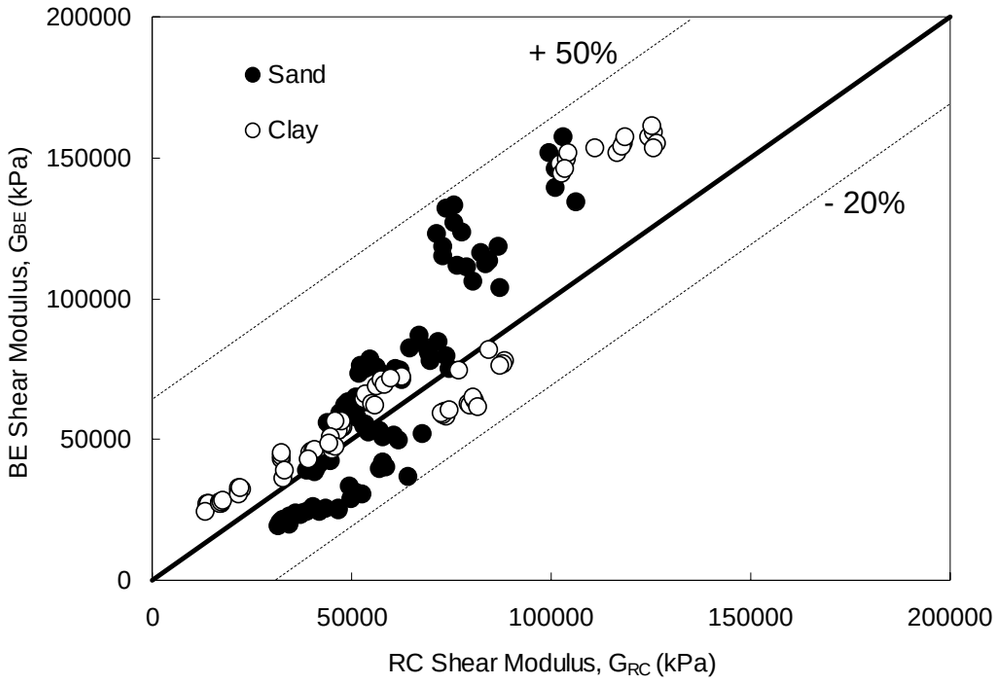


Figure 7. Comparison of all average experimental values from RC and BE tests

CONCLUDING REMARKS

Results from a comprehensive series of pressure plate, filter paper, resonant column, and bender element tests undertaken in this research work have been used to devise empirical correlations for small-strain stiffness properties, such as shear modulus and material damping ratio, and key environmental factors, such as compaction-induced matric suction and stress state, in sandy and clayey soils. The range of experimental variables, as well as the scope of the experimental program, was intended to reproduce in-situ stress states within pavement subgrade or shallow foundation systems that remain under partially saturated conditions throughout any given year. Compaction-induced suction was found to exert a significant influence on small-strain stiffness response of sandy and clayey soils from both bender element (BE) and resonant column (RC) testing techniques. The BE based technique, however, was found to overestimate RC based values of small-strain shear modulus at higher confinements or compaction-induced suction levels.

The recent focus of most State Departments of Transportation in the United States has been primarily towards proposing pavement design procedures based on a mechanistic-empirical approach using resilient modulus as the primary soil parameter. However, a more rational procedure should be based on a thorough understanding of the effects of season-dependent matric suction (i.e., seasonal variations that include wet-dry and freeze-thaw cycles) on the small-strain stiffness properties of unsaturated soils. The present work is a preliminary attempt to contribute towards this goal.

REFERENCES

Brocanelli, D., and Rinaldi, V. (1998). "Measurement of low-strain material damping and wave velocity with bender elements in the frequency domain". Canadian Geotechnical J., vol. 35, pp. 1032-1040.

Cabarkapa, Z., and Cuccovillo, T. (2006). "Automated triaxial apparatus for testing unsaturated soils". Geotechnical Testing J., ASTM, vol. 29(1).

Cho, G.C., and Santamarina, J.C. (2001). "Unsaturated particulate materials – Particle level studies". J. Geotechnical and Geoenvironmenal Engineering, ASCE, vol. 127, pp. 84-96.

Fredlund, D.G., and Xing, A. (1994). "Equations for the soil-water characteristic curve". Canadian Geotechnical J., vol. 31, pp. 521-532.

Hoyos, L.R., Takkabutr, P., and Puppala, A.J. (2006). "A modified pressure plate device for SWCC testing under anisotropic stress states". In: *Unsaturated Soils 2006*, GSP 147, ASCE Geo-Institute, Proceedings of the Fourth International Conference on Unsaturated Soils, April 2-5, 2006, Carefree, Arizona, Eds: G.A. Miller, C.E. Zapata, S.L. Houston, and D.G. Fredlund, vol. 2, pp. 1753-1763.

Picornell, M., and Nazarian, S. (1998). "Effects of soil suction on the low-strain shear modulus of soils". Proceedings of the Second International Conference on Unsaturated Soils, UNSAT'98, Beijing, China, vol. 2, pp. 102-107.

Takkabutr, P. (2006). "Experimental investigations on small-strain stiffness properties of partially saturated soils via resonant column and bender element testing". Ph.D. Dissertation, University of Texas at Arlington, July 2006, 289 pp.

Effective Soil Density for Small Strain Shear Wave Propagation

Tong Qiu[1] and Patrick J. Fox[2]

[1]Assistant Professor, Department of Civil & Environmental Engineering, Clarkson University, Potsdam, New York 13699-5710; tqiu@clarkson.edu
[2]Professor, Department of Civil and Environmental Engineering and Geodetic Science, Ohio State University, Columbus, Ohio 43210; fox.407@osu.edu

ABSTRACT: This paper presents an investigation of the value of soil density that controls the velocity of small strain shear waves in saturated soil. An "effective soil density" is defined that is related to the fraction of pore water that moves with the solid skeleton during shear wave propagation. Biot theory indicates that the ratio of effective soil density to saturated soil density is always ≤ 1 and is a function of the specific gravity of solids, porosity, hydraulic conductivity, and shear wave frequency. Except for extreme cases, the effective density ratio will range from 0.75 to 1.0. For many geotechnical applications, effective soil density will be equal to saturated soil density for low hydraulic conductivity materials (clays and silts). On the other hand, consideration of effective soil density may be important for high hydraulic conductivity materials (clean sands and gravels) in some cases. The findings are relevant to applications involving the propagation of small strain shear waves through saturated soil, and in particular for laboratory and field tests in which shear modulus is back-calculated from measured shear wave velocity.

INTRODUCTION

In geotechnical earthquake engineering and soil dynamics, shear modulus G and shear wave velocity V are important soil properties and are required as input data for many analyses. In particular, G is often back-calculated from measured values of V in laboratory tests (e.g., resonant column) and field tests (e.g., seismic CPT). This is based on the following fundamental relationship,

$$G = \rho V^2 \tag{1}$$

where ρ is soil density. Although derived from elastic theory of a continuum, (1) is used for general analyses involving inelastic and multiphase soils. Inelastic behavior can be accommodated by defining a secant shear modulus as a function of shear strain amplitude as typically used in equivalent linear ground motion analyses (Idriss and

Seed 1968). The application of (1) to multiphase soil requires an assumption regarding material density. If the soil is dry, ρ is equal to the dry density ρ_d because the density of air in the voids is negligible. If the soil is saturated, the density of the pore water is not negligible and the value of ρ is generally taken as the saturated density ρ_{sat} (e.g., Richart et al. 1970, Kramer 1996). This paper is concerned with the validity of the latter assumption.

The use of ρ_{sat} in (1) assumes that the pore water and solid skeleton move together such that the soil mass can be treated as a single phase. The validity of this assumption depends on the magnitude of fluid motion relative to the solid skeleton during the passage of a shear wave. Relative fluid motion can occur from two mechanisms – Biot flow (Biot 1956) and squirt flow (Mavko and Nur 1979, Dvorkin and Nur 1993). Squirt flow effects become more important as grain size decreases (Mavko et al. 1998, Ellis et al. 2000) and for partially saturated soils in the absence of a continuous fluid phase. In the current paper, the concept of effective density is evaluated for saturated soils and will be shown to be primarily important for highly permeable (coarse) materials; hence, the analysis is conducted using Biot theory and squirt flow effects are neglected.

SHEAR WAVE VELOCITY

Biot (1956) derived analytical solutions for the propagation of sinusoidal shear waves in saturated poroelastic media. Shear wave velocity V is,

$$V = \frac{\omega}{\left|\mathrm{Re}(l)\right|} \tag{2}$$

where Re(l) is the real part of complex wave number l and ω is the circular frequency. A reference shear wave velocity V^* can also be defined that corresponds to ρ_{sat},

$$V^* = \sqrt{\frac{G}{\rho_{sat}}} \tag{3}$$

where $\rho_{sat} = (1-n)\rho_s + n\rho_f$, n is the porosity, ρ_s is the solids density ($= G_s \rho_w$), ρ_f is the fluid density, G_s is the specific gravity of solids, and ρ_w is the density of water. A dimensionless shear wave velocity can therefore be defined as,

$$\frac{V}{V^*} = \sqrt{\frac{2}{E_r + \sqrt{E_r^2 + E_i^2}}} \tag{4}$$

where,

$$E_r = \frac{\frac{1}{\rho_{sat}}\left(\rho_{11}\rho_{22} - \rho_{12}^2\right)\left(\rho_{22} + \varepsilon_2\right) + \rho_{22}\varepsilon_2 + \varepsilon_1^2 + \varepsilon_2^2}{\left(\rho_{22} + \varepsilon_2\right)^2 + \varepsilon_1^2} \tag{5}$$

$$E_i = \frac{\frac{\varepsilon_1}{\rho_{sat}} n^2 \rho_f^2}{\left(\rho_{22} + \varepsilon_2\right)^2 + \varepsilon_1^2} \tag{6}$$

$$\varepsilon_1 = n\rho_f \frac{\mathrm{Re}(F)}{\bar{f}} \tag{7}$$

$$\varepsilon_2 = n\rho_f \frac{\mathrm{Im}(F)}{\bar{f}} \tag{8}$$

$$F = \frac{\eta^2 T}{4\eta + i8T} \tag{9}$$

$$T = \frac{ber'(\eta) + ibei'(\eta)}{ber(\eta) + ibei(\eta)} \tag{10}$$

$$\eta = \delta_2 \sqrt{\bar{f}} \tag{11}$$

$$\bar{f} = \frac{f}{f_c} = \frac{2\pi f k}{ng} \tag{12}$$

In the above equations, f is the frequency ($=\omega/2\pi$), $\bar{f}$ is a normalized frequency, f_c is the characteristic frequency ($=ng/2\pi k$), k is the hydraulic conductivity in the plane perpendicular to the direction of wave propagation, g is the acceleration of gravity, $\delta_2 = \sqrt{8}$ for circular and slit-like pores, *ber* and *bei* are Kelvin functions of the first kind and zero order, the prime operator denotes differentiation (i.e., $ber'(\eta) = dber(\eta)/d\eta$), $i = \sqrt{-1}$, Im(F) denotes the imaginary part of F, and ρ_{11}, ρ_{12}, and ρ_{22} are mass coupling coefficients. Biot (1956) provided the following equations for the mass coupling coefficients,

$$\rho_{11} + \rho_{12} = (1-n)\rho_s \tag{13}$$

$$\rho_{12} + \rho_{22} = n\rho_f \tag{14}$$

Biot (1962) also proposed the following expression for coefficient ρ_{12},

$$\rho_{12} = n\rho_f(1-\delta) \tag{15}$$

where δ is a structural factor representing the "added mass" caused by the tortuosity of the pore space (Stoll and Bryan 1970). Sen *et al*. (1981) proposed the following power relationship,

$$\delta = n^{-\bar{\beta}} \tag{16}$$

where $\bar{\beta} = 0.5$ for a random array of spheres and $\bar{\beta} > 0.5$ for a random array of platy particles. Gajo (1996) compared various theoretical models and found that (16) gave the best overall estimate for δ. In the current paper, $\bar{\beta} = 0.5$ is used to approximate mass coupling between fluid and solid phases.

EFFECTIVE DENSITY

In saturated soil, the shear wave velocity is dependent on the relative motion between the pore fluid and solid skeleton. The magnitude of this relative motion depends on the relative magnitudes of driving forces (i.e., inertial forces) and resisting forces (i.e., mass coupling and viscous coupling forces). To quantify this effect, a new term called "effective soil density" ρ_{eff} is defined as,

$$\rho_{eff} = \frac{G}{V^2} \tag{17}$$

Combining (3), (4), and (17) yields an effective density ratio,

$$\frac{\rho_{eff}}{\rho_{sat}} = \frac{E_r + \sqrt{E_r^2 + E_i^2}}{2} \tag{18}$$

A clear advantage of (18) is that the effective density ratio is independent of shear modulus, which results from the small strain assumption. Effective density is related to the fraction of pore water that "effectively" moves with the solid skeleton during shear wave propagation. Effective density is bounded by two cases (Qiu 2005):

$$\rho_{eff} = \rho_{sat} \qquad \bar{f} \to 0 \tag{19}$$

$$\rho_{eff} = \rho_d\left[\frac{n(\delta-1)}{G_s\delta(1-n)} + 1\right] \qquad \bar{f} \to \infty \tag{20}$$

where ρ_d is the dry density. (19) corresponds to low frequency ($f \to 0$) and/or low hydraulic conductivity ($k \to 0$). Under this condition, relative motion between the two phases is negligible due to the strong viscous coupling forces and the effective density

is equal to the saturated density (i.e., upper bound value). (20) corresponds to high frequency ($f \to \infty$) and/or high hydraulic conductivity ($k \to \infty$). In this case, viscous coupling forces are negligible and motions of the two phases are coupled only through mass coupling forces. Relative motion between the two phases yields the lower bound value of effective density. If mass coupling is neglected by specifying $\delta = 1$, solid and fluid motions are completely decoupled and the effective density is equal to the dry density.

The effective density ratio ρ_{eff} / ρ_{sat} is a function of n, G_s, and $\bar{f}$. Fig. 1 shows a dimensionless plot of effective density ratio vs. $\bar{f}$ and n for G_s = 2.7. A detailed view in the low $\bar{f}$ range, which is relevant to many geotechnical applications, is given in Fig. 2. The value $\bar{f} = 0$ corresponds to the upper bound case and indicates $\rho_{eff} / \rho_{sat} = 1$ for all porosity values. As $\bar{f}$ increases, values of ρ_{eff} / ρ_{sat} decrease due to the effect of increasing relative fluid motion. Values of ρ_{eff} / ρ_{sat} also decrease with increasing n. At large $\bar{f}$, each curve approaches its lower bound value. Both Poiseuille flow (i.e., governed by Darcy's law) at low frequencies and non-Poiseuille flow at high frequencies are considered in the above solutions. At low frequencies, $\mathrm{Im}(F)$ is essentially zero, $F \approx 1$, and Poiseuille flow occurs. At high frequencies, the imaginary part of F is non-zero and non-Poiseuille flow occurs. The importance of non-Poiseuille flow and mass coupling effects is discussed by Qiu (2005).

The concept of effective soil density was evaluated using experimental data from test series Ia and IIIa presented by Hardin and Richart (1963). Torsional resonant

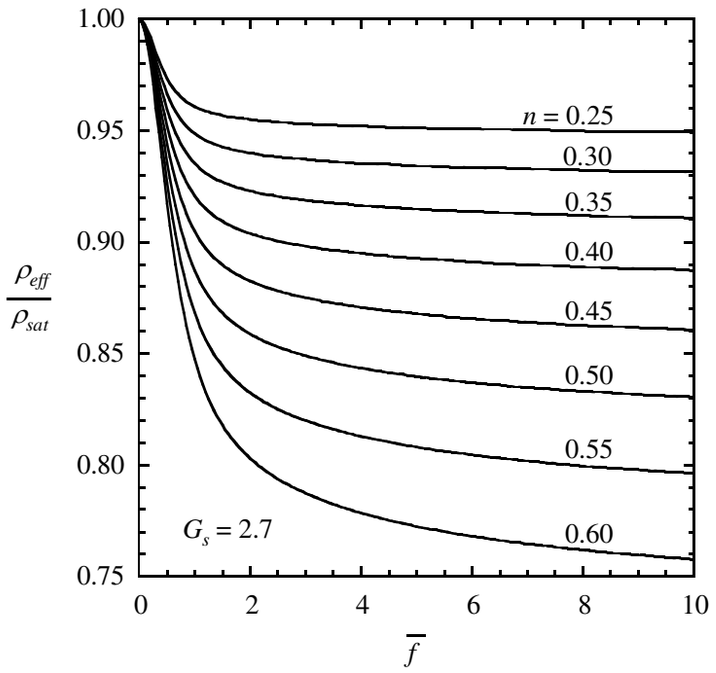


FIG. 1. Effective density ratio for G_s = 2.7.

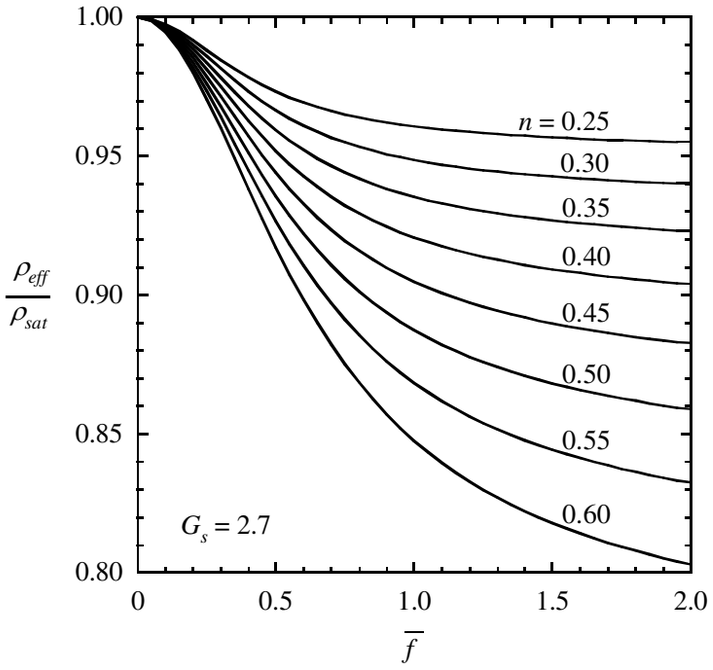


FIG. 2. Detail view of Fig. 1 in the low $\bar{f}$ range.

column tests were conducted on single specimens in both the dry and saturated condition. The tests in series Ia were conducted on 20-30 Ottawa sand and the tests in series IIIa were conducted on 20-30 crushed quartz sand, both having G_s = 2.66. The approximate peak-to-peak amplitude for these tests was 1×10^{-3} radians, giving a shear strain amplitude of 0.05%.

Fig. 3 compares the theoretical values of effective density ratio with the values interpreted from the Hardin and Richart (1963) data. Effective density ratios for these tests were calculated using the following procedure. Figure 7, for example, of Hardin and Richart (1963) presented measured shear wave velocities of Ottawa sand in dry and drained (saturated) conditions for different confining pressures. Measured values of V for the dry sand were used to calculate G. Based on this modulus, the effective density was calculated using the measured V for the drained condition. The underlying assumption is that the dry and drained specimens have the same shear modulus at the same confining pressure and void ratio, which is generally valid. The dimensionless excitation frequency $\bar{f}$ was calculated using measured values of specimen length and shear wave velocity and estimated values of hydraulic conductivity from the Chapuis (2004) equation. Figure 3 indicates that theoretical values of effective density ratio are in reasonable agreement with values calculated from these resonant column tests. The lack of close agreement in Figure 3 may be due in part to errors associated with the estimation of hydraulic conductivity.

Fig. 4 presents a chart that allows a user to rapidly determine if consideration of effective density is necessary for a given application. The chart corresponds to full solutions (i.e., including effects of mass coupling and non-Poiseuille flow) and

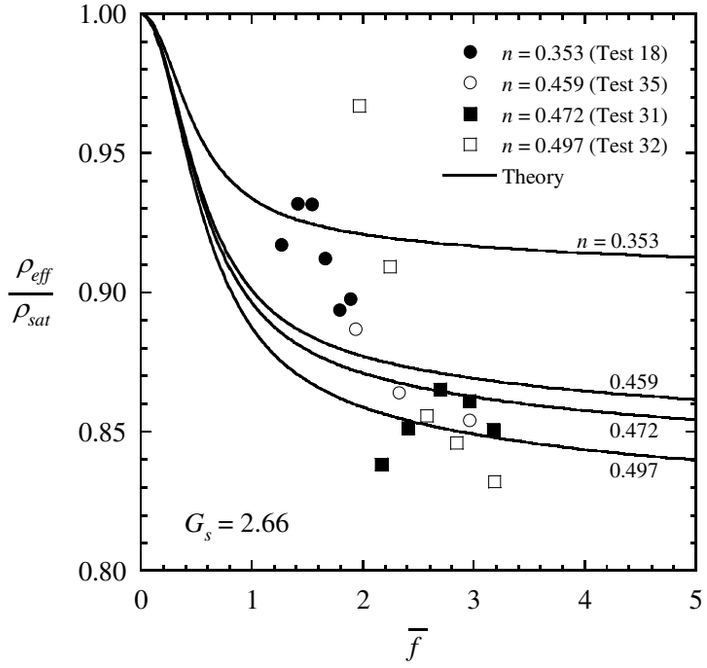


FIG. 3. Theoretical and experimental values of effective density ratio for resonant column tests conducted on Ottawa sand and crushed quartz sand.

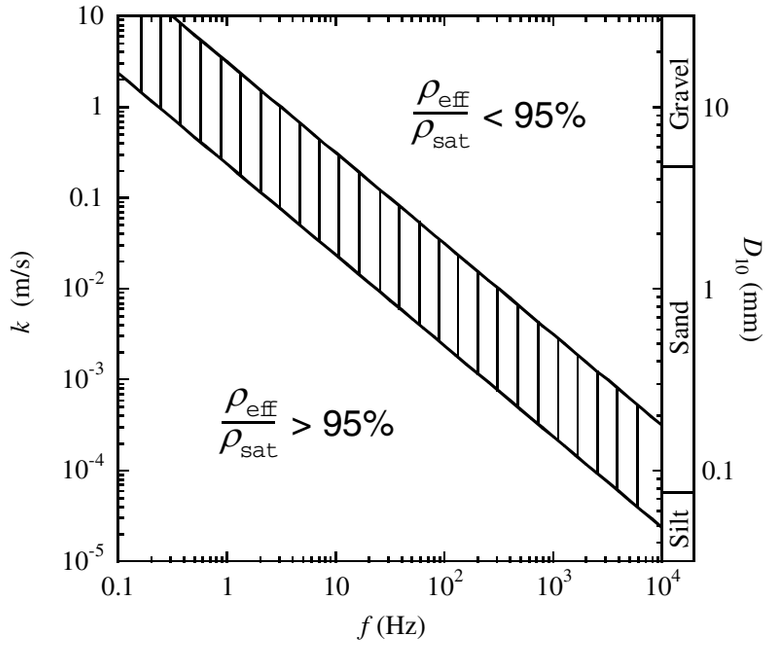


FIG. 4. Chart for quick determination of importance of effective density for a given application.

assumes G_s = 2.7, which will be acceptable for most conditions. The hatched zone in Fig. 4 represents combinations of k and f for practical ranges of n (= 0.25 to 0.6) that yield ρ_{eff}/ρ_{sat} = 0.95. If a given combination of k and f falls above the hatched area, $\rho_{eff}/\rho_{sat} < 0.95$ and consideration of effective density may be important. If a combination falls below the hatched area, $\rho_{eff}/\rho_{sat} > 0.95$ and effective density will be nearly equal to the saturated density. If a combination falls within the hatched area, ρ_{eff}/ρ_{sat} may be larger or smaller than 0.95, depending on the value of n. The right-side axis gives values of effective grain size D_{10} as calculated from k (left-side axis) using the Hazen (1911) equation.

Fig. 4 indicates that consideration of effective density will not be important for clays and is unlikely to be important for coarse clean silts unless the frequency is very high (f > 10 kHz). For clean sands, consideration of effective density may be important for frequencies as low as 10 Hz. Fine and medium sands may be affected under high-frequency excitations such from bender elements or suspension logging (Chen and Wu 2003, Lee and Santamarina 2005). Coarse clean sands may be affected at lower frequencies such for resonant column tests or seismic CPT. Consideration of effective density may be important for clean gravels at essentially all frequencies of geotechnical interest. For each of these applications, the appropriate value of effective density would be based on the dominant shear wave frequency.

The primary importance of the effective density concept is that it accounts for an additional frequency-dependent dispersive characteristic of shear wave velocity that is not generally considered for soil dynamics applications. Higher frequency shear waves (with lower ρ_{eff}) will travel faster than lower frequency shear waves (with higher ρ_{eff}) in the same soil. This effect may be important for applications in which the shear modulus of a saturated coarse soil is back-calculated from a high frequency test (e.g., suspension logging) and then used for a low frequency analysis. In such cases, the use of ρ_{sat} will produce incorrectly high values of G and predicted shear wave velocity, with the maximum error being up to approximately 30% for G_s = 2.7.

CONCLUSIONS

This paper defines an “effective soil density” that governs the velocity of small strain shear waves in saturated soil. The value of effective density is related to the fraction of pore water that moves with the solid skeleton during shear wave propagation. Results based on Biot theory indicate that the effective density ratio (i.e., effective soil density/saturated soil density) is ≤ 1 and is a function of specific gravity of solids, porosity, hydraulic conductivity, and shear wave frequency. Dimensionless charts are provided to allow routine calculation of this ratio. The charts indicate that, except for extreme cases, the effective density ratio will range from 0.75 to 1. Good agreement is found between the theoretical values of effective density ratio and the values interpreted based on four resonant column tests reported in literature.

Consideration of effective density will not be important for clays and is unlikely to be important for clean coarse silts unless the shear wave frequency is very high (> 10

kHz). For clean sands, consideration of effective density may be important for frequencies as low as 10 Hz. Consideration of effective density may be important for clean gravels for essentially all frequencies of geotechnical interest.

REFERENCES

Biot, M. A. (1956). "Theory of propagation of elastic waves in a fluid-saturated porous solid. I. Low-frequency range. II. Higher frequency range." *J. Acoust. Soc. Amer.*, 28(2): 168-191.

Biot, M. A. (1962). "Mechanics of deformation and acoustic propagation in porous media." *J. Appl. Phys.*, 33(4): 1482-1498.

Chapuis, R. P. (2004). "Predicting the saturated hydraulic conductivity of sand and gravel using effective diameter and void ratio." *Can. Geo. J.*, 41(5): 787-795.

Chen, M.-H., and Wu, B.-R. (2003). "The engineering geological database for strong motion stations in Taiwan." *International Collaboration on Earthquake Disaster Mitigation Research*, Joint NCREE/JRC Workshop, Taiwan, 403-408.

Dvorkin, J., and Nur, A. (1993). "Dynamic poroelasticity: A unified model with the squirt and the Biot mechanisms." *Geophys.*, 58(4): 524-533.

Ellis, E. A., Soga, K., Bransby, M. F., and Sato, M. (2000). "Resonant Column Testing of Sands with Different Viscosity Pore Fluids." *J. Geo. Geoenv. Eng.*, 126(1): 10-17.

Gajo, A. (1996). "The effects of inertial coupling in the interpretation of dynamic soil tests." *Geotechnique*, 46(2): 245-257.

Hardin, B. O., and Richart F. E. (1963). "Elastic wave velocities in granular soils." *J. Soil Mech. Fnd. Div.*, 89(SM1): 33-65.

Hazen, A. (1911). Discussion of "Dams on sand foundations" by A. C. Koenig, *Trans. Am. Soc. Civ. Eng.*, 73: 199-203.

Idriss, I. M., and Seed, H. B. (1968). "Seismic response of horizontal soil layers." *J. Soil Mech. Fnd. Div.*, 94(SM4): 1003-1031.

Kramer, S. L. (1996). *Geotechnical Earthquake Engineering*. Prentice Hall, Upper Saddle River, NJ.

Lee, J.-S., and Santamarina, J. C. (2005). "Bender elements: Performance and signal interpretation." *J. Geo. Geoenv. Eng.*, 131(9): 1063-1070.

Mavko, G., and Nur, A. (1979). "Wave attenuation in partially saturated rocks." *Geophys.*, 44(1): 161-178.

Mavko, G., Mukerji, T., and Dvorkin, J. (1998). *The Rock Physics Handbook*. Cambridge University Press, New York.

Qiu, T. (2005). *Theoretical and Numerical Investigations of the Effects of Pore Fluid on the Dynamic Behavior of Saturated Soils*. Ph.D. Dissertation, UCLA.

Richart, F. E., Jr., Hall, J. R., Jr., and Woods, R. D. (1970). *Vibrations of Soils and Foundations*. Prentice-Hall, Englewood Cliffs, NJ.

Sen, P. N., Scala, C., and Cohen, J. H. (1981). "A self-similar model for sedimentary rocks with application to the dielectric constant of fused glass beads." *Geophys.*, 46(5): 781-795.

Stoll, R. D., and Bryan, G. M. (1970). "Wave attenuation in saturated sediments." *J. Acoust. Soc. Amer.*, 47(5): 1440-1447.

This page intentionally left blank

Effects of Cyclic Rotation of Principal Stress Axes and Intermediate Principal Stress Parameter on the Deformation Behavior of Sands

Jian-Min Zhang[1], Zhao-Xia Tong[2] and Yi-Lin Yu[2]

[1]Professor, Institute of Geotechnical Engineering, School of Civil Engineering, Tsinghua University, P.R.China, 100084; zhangjm@tsinghua.edu.cn
[2]Graduate Student, Institute of Geotechnical Engineering, School of Civil Engineering, Tsinghua University, P.R.China, 100084; tongzhaoxia00@mails.tsinghua.edu.cn

ABSTRACT: Four series of drained tests on sands were performed with a hollow cylinder apparatus in order to investigate the fundamental deformation behavior of sands and the effects of the intermediate principal stress parameter b during cyclic rotation of principal stress axes. The test condition that principal stress axes rotated cyclically from 0° to 180° relative to vertical under constant effective principal stresses was maintained. The experimental results indicated that strains were accumulated steadily with the increasing number of cycles, while b had considerable influences on their changes during the process of cyclic rotation. The increase rate of the maximum contractive volumetric strain within each cycle was lowered with its progressive accumulation. It was found from four test series that the magnitude of the volumetric strain at the same number of cycles increased with the increase of b. The hysteretic loop in shear stress-strain curves was observed to be unclosed for the first several cycles but tend to become closed with the increase of the number of cycles. The test results in this paper also demonstrated the significant effects of the density, the effective mean normal stress and deviatoric stress on the deformation behavior of sands under cyclic rotation of principal stress axes.

INTRODUCTION

In engineering practice the stress state of soils induced by various loadings in the ground is very complex. The loadings such as earthquake, traffic and wave loadings may induce not only the change of the magnitude of principal stresses but also the rotation of principal stress axes. The deformation behavior of soils under the conditions of the complex stress state involving rotation of principal stress axes needs to be studied comprehensively for reliable prediction of the behavior of soils in the field.

The undrained deformation behavior of sands under cyclic rotation of principal stress axes while keeping magnitude of principal stresses constant had been investigated

experimentally by researchers such as Symes et al. (1984) and Nakata et al. (1998). Their test results indicated that pore water pressure and plastic strain were accumulated steadily with the cyclic rotation of principal stress axes. Moreover, most of the current researches on the drained deformation behavior of sands due to principal stress axes rotation were conducted under the conditions of monotonic rotation of principal stress axes, such as Miura et al. (1986), Symes et al. (1988) and Wijewickreme et al. (1993). It was found from their test results that rotation of principal stress axes resulted in the contraction of sand samples. However, it should be noted that the intermediate principal stress parameter characterized by b **(** $b = (\sigma_2 - \sigma_3)/(\sigma_1 - \sigma_3)$ **)** was kept to be 0.5 for all above tests performed. The effects of b on the stress-strain-strength characteristics of sands under fixed principal stress axes were investigated by researchers such as Lade et al. (1973), Yamada et al. (1979) and Sayão et al. (1996). Yang et al. (2007) was the first to study intensively the effects of b on the undrained deformation behavior of sands during the cyclic rotation of principal stress axes and found that the generation rate of pore water pressure under $b = 0.0$ was much slower than that under $b = 1.0$.

Presented in this paper is an experimental investigation on the drained deformation behavior of sands and the effects of b during cyclic rotation of principal stress axes through conducting a series of drained tests with a hollow cylinder apparatus. The principal stress axes rotate cyclically from 0° to 180° relative to vertical while keeping constant principal stresses is controlled in all the tests. The effects of the density, effective mean normal stress and deviatoric stress are also examined.

EQUIPMENT AND TEST SCHEME

A hollow cylinder apparatus (HCA) at the Hong Kong University of Science and Technology (HKUST) was used, which has been described in detail by Yang et al. (2007). The loadings of axial load W, torque T, inner pressure P_i and outer pressure P_o and the corresponding vertical stress σ_z, radial stress σ_r, circumferential stress σ_θ and shear stress $\sigma_{z\theta}$ acting on a sand sample are shown in Fig. 1. The equations used to calculate the stress and strain parameters were the same as those in Yang et al. (2007).

Toyoura standard sands (G_s =2.645, $e_{\max}$ =0.975, $e_{\min}$ =0.635) were used for all the tests. The weighted dry sands were poured into the hollow cylinder space between the inner and outer membranes by keeping zero falling head with a spoon and a funnel and then a rubber mallet was used to tap the outer mould gently to adjust the density layer by layer (10 layers totally). The degree of saturation was checked by assuring B greater than 0.97 under the confining pressure increase of 50kPa.

The effective stress paths in effective mean normal stress p' ($p' = (\sigma_1' + \sigma_2' + \sigma_3')/3$) –deviatoric stress q ($q = \sqrt{\left[(\sigma_1 - \sigma_2)^2 + (\sigma_1 - \sigma_3)^2 + (\sigma_2 - \sigma_3)^2\right]}/2$) and deviatoric stress space are shown in Fig.2. The sample was anisotropically consolidated to a desired stress state (point C) from the initial isotropic stress state of 30kPa (point A). And then the cyclic rotation of principal stress axes from 0° to 180° with constant effective principal stresses was commenced in drained conditions. To ensure full discharge of water from the sample, the rate of angular distortion was controlled to be

very slow at $d\theta = 0.04°/\min$, corresponding to a shear strain rate ($d\varepsilon_{z\theta}$) of 0.01%/min. The test conditions for 12 drained tests totally in four series are shown in Table.1.

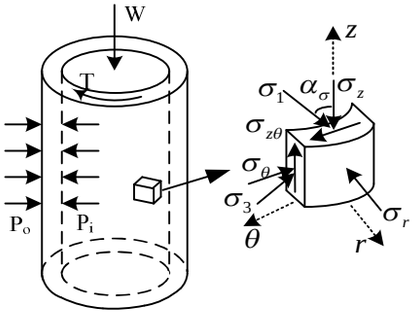


FIG. 1. Element in hollow cylinder specimen and stresses

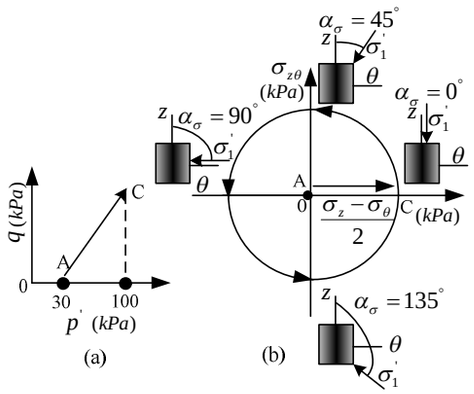


FIG. 2. Stress paths for drained principal stress axes rotation tests

Table 1. Conditions for drained principal stress axes rotation tests

Test ID	*Dr* (%)	p' (kPa)	*b*	*q* (kPa)
Series Ⅰ	50±2	100	0.1 0.5 1.0	69.3
Series Ⅱ	70±2	100	0.1 0.5 1.0	86.6
Series Ⅲ	70±2	100	0.1 0.5 1.0	99.4
Series Ⅳ	70±2	50	0.1 0.5 1.0	49.7

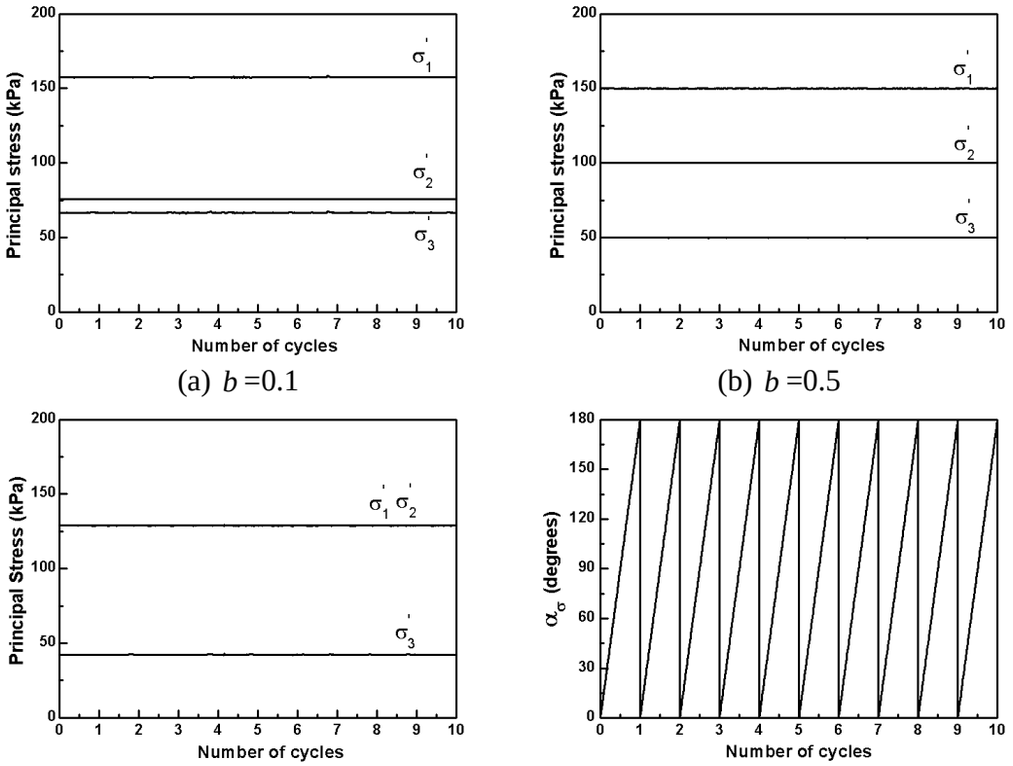
Note: *Dr* , the relative density after consolidation.

TEST RESULTS AND DISCUSSION

Applied stress paths

Shown in Fig.3 are the variations of three principal stresses and rotation angle α_σ ($\alpha_\sigma = arctg[2\sigma_{z\theta}/(\sigma_z - \sigma_\theta)]/2$) for the first 10 cycles in test series Ⅱ. It can be seen that the stress paths that the principal stress axes rotate cyclically from 0° to 180° with constant effective principal stresses could be accomplished well by HCA at HKUST. The stress paths in deviatoric stress plane $(\sigma_z - \sigma_\theta)/2$ - $\sigma_{z\theta}$ plotted in Fig.4 are seen to

approach a circle though the unsmoothed curve occurs during the unloading process of $\sigma_{z\theta}$, showing the reason that unloading of shear stress is much easier than loading.



(a) b =0.1 (b) b =0.5

(c) b =1.0 (d) Variation of α_σ for b =0.1, 0.5 and 1.0

FIG.3. Variations of principal stresses and α_σ

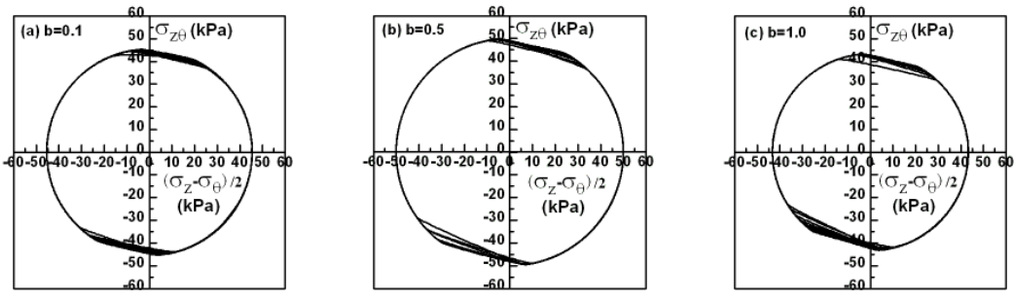
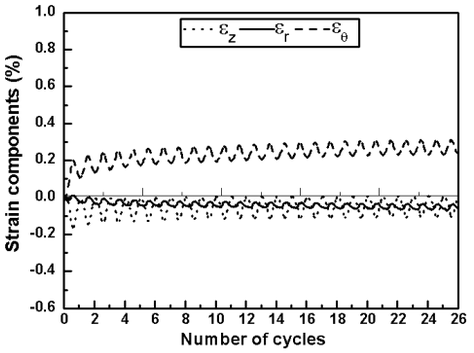


FIG.4. Stress paths in deviatoric stress plane $\sigma_{z\theta}$ - $(\sigma_z - \sigma_\theta)/2$

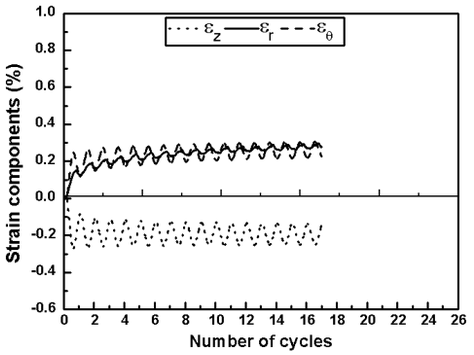
Variations of strain components and strain paths

Fig. 5 and 6 show the variations of three normal strain components with the number of cycles under three cases of b for the test series Ⅱ and Ⅳ. It is observed that the relative strain components have a significant tendency to increase gradually during cyclic rotation of principal stress axes with constant principal stresses kept. Comparing

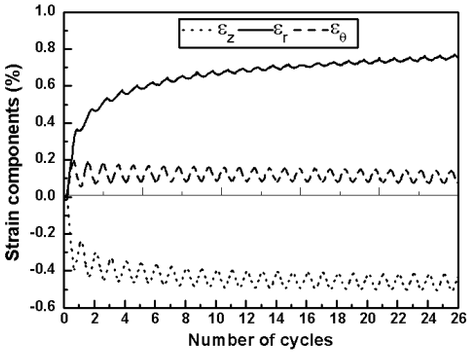
the changes of the strain components with the increasing number of cycles under b =0.1, 0.5 and 1.0 for these two tests series shown in Fig. 5 and 6, the magnitude of b is shown to have considerable effects on their changes without the significant differences in the other test conditions, which will be detailed in the following.



(a) b =0.1

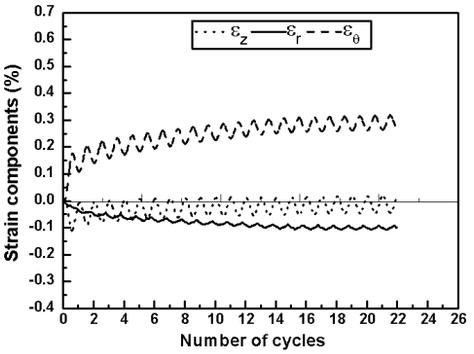


(b) b =0.5

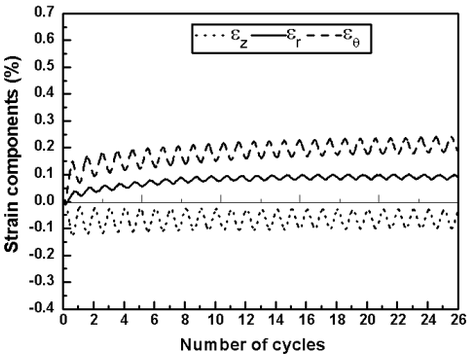


(c) b =1.0

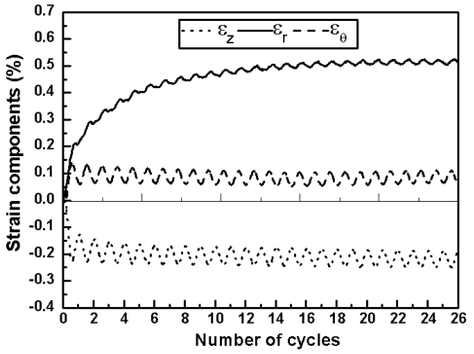
FIG.5. Variation of strain components for test series Ⅱ



(a) b =0.1



(b) b =0.5



(c) b =1.0

FIG.6. Variation of strain components for test series Ⅳ

The vertical strain ε_z reaches its maximum extensive strain in the first cycle and approaches to the emergence of the vertical contractive strain during cyclic rotation of principal stress axes under $b = 0.1$. However, under $b = 1.0$, the magnitude of the

vertical extensive strain ε_z increases gradually with the increasing number of cycles. The development of ε_z seems to be more stable under $b = 0.5$ in comparison with those under $b = 0.1$ and 1.0. The maximum vertical extensive and contractive strains occur in the first cycle and the double magnitude of ε_z tends to reduce with the increasing number of cycles, which is induced due to the densification of the sand sample. In addition, the radial strain ε_r changes from the extensive to the contractive strain with the increase of b from 0.1 to 0.5, and it tends to contract and develop more significantly under $b = 1.0$. Based on the variation of ε_r with b, it can be drawn reasonably that the plane strain state of $\varepsilon_r = 0$ could be achieved at b between 0.1 and 0.5. The circumferential strain ε_θ changes almost in the same phase of ε_z, while the circumferential stress σ_θ varies corresponding to the vertical stress σ_z under the condition of constant principal stresses. The peak values of ε_θ and ε_z are achieved almost at the same time. The effects of b on ε_θ seem not so obvious as on the other two components.

The strain paths in the deviatoric strain plane $(\varepsilon_z - \varepsilon_\theta)/2$ - $\varepsilon_{z\theta}$ for test series Ⅱ with three cases of b are shown in Fig.7. To observe their changes more clearly, the strain paths for the first cycle and tenth cycle are also given in the same figure. It is shown that the strain paths in the deviatoric strain plane are not as closed and circular as the stress paths in the deviatoric stress plane for the first cycle, which is consistent with the test results conducted by Miura et al. (1986). However, with the increasing number of cycles, the strain paths tend to become closed and their shape to approximately an ellipse.

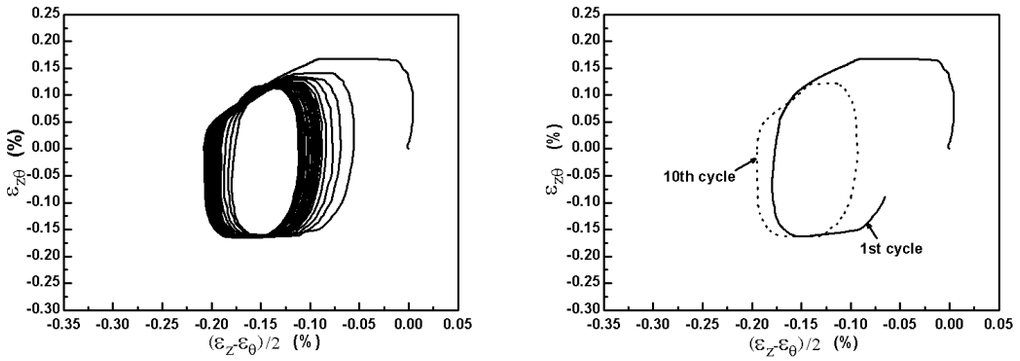
Variation of the volumetric strain

The variations of the volumetric strain ε_v and the maximum volumetric strain within each cycle $\varepsilon_{v,\max}$ with the increasing number of cycles for all test series are shown in Fig. 8. For sands with the medium and dense density, the volumetric strain induced by the rotation is mainly contractive and no obvious dilation is observed, showing consistent with the test results by Miura et al. (1986) and Symes et al. (1988). The $\varepsilon_{v,\max}$ develops gradually with the increasing number of cycles although the change of ε_v shows an obvious oscillation. It should be noted that the developing rate of $\varepsilon_{v,\max}$ tends to decrease as the number cycles increase and most of the volumetric strain is induced during the first several cycles.

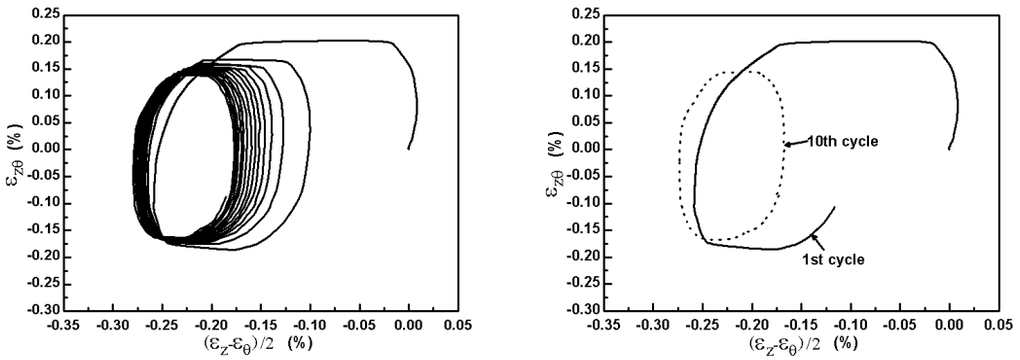
The effects of b on the development of the volumetric strain can be seen clearly in Fig. 8. The volumetric strain at the same number of cycles increases with the increase of b and the developing rate of the volumetric strain under $b = 1.0$ is much higher than that under $b = 0.1$ for all the test series. Since the volumetric strain in drained tests is essentially corresponding to the excess pore water pressure in undrained tests, the above results of the experimental observation are identical with the experimental findings of Yang et al. (2007) that the developing rate of the excess pore water pressure under $b = 0.1$ is much slower than those under $b = 0.5$ and 1.0.

From Fig. 8, the other parameters including D_r, p' and q are also found to have considerable effects on the development of the volumetric strain. Although the

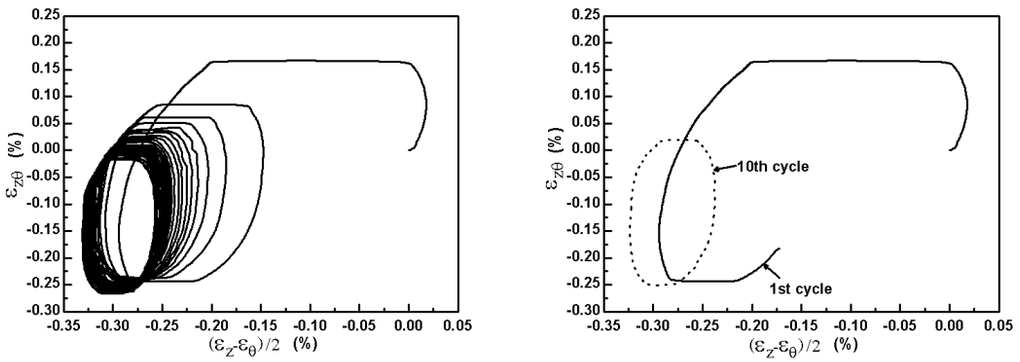
magnitude of q in test series Ⅰ is much lower than that in series Ⅱ, the volumetric strain in series Ⅰ with $D_r \approx 50\%$ is much larger than that in series Ⅱ with $D_r \approx 70\%$. A larger increment of the volumetric strain is induced due to a smaller increase of q from 86.6kPa in series Ⅱ to 99.4kPa in series Ⅲ. For the test series Ⅲ and Ⅳ with the condition that the same ratio of q to p' is kept, the amount of the volumetric strain in test series Ⅲ with higher p' of 100kPa is much higher than that in test series Ⅳ with lower p' of 50kPa.



(a) b =0.1

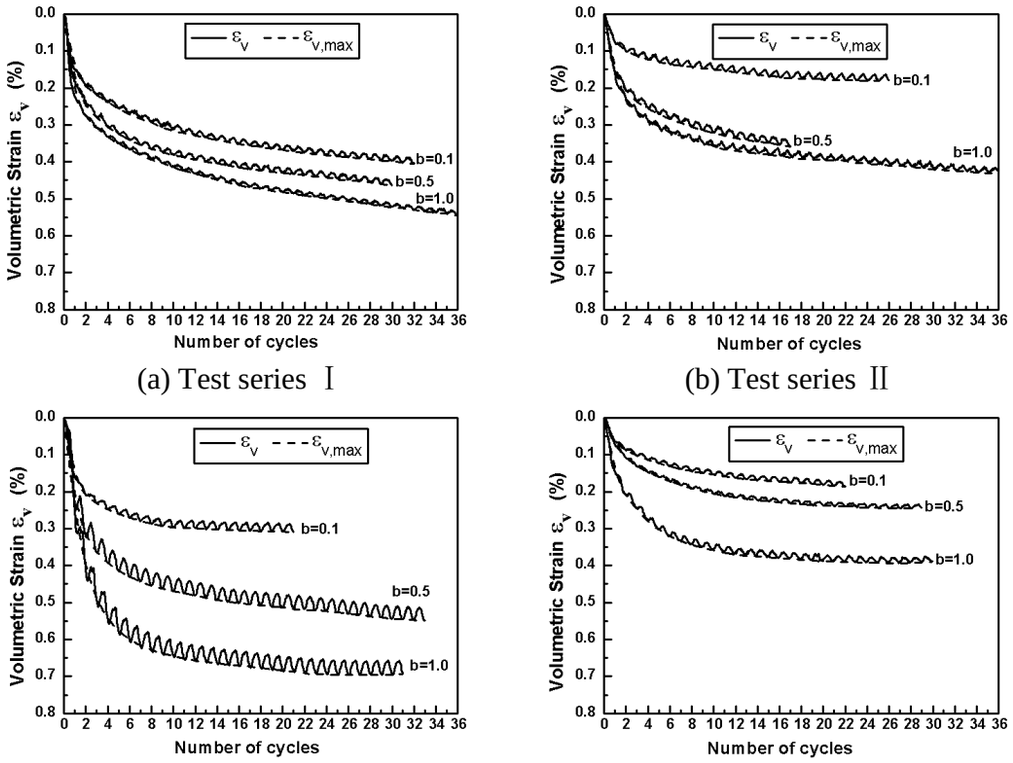


(b) b =0.5



(c) b =1.0

FIG.7. Strain paths in deviatoric strain plane $\varepsilon_{z\theta}$-$(\varepsilon_z-\varepsilon_\theta)/2$ for series Ⅱ



(a) Test series Ⅰ (b) Test series Ⅱ

(c) Test series Ⅲ (d) Test series Ⅳ

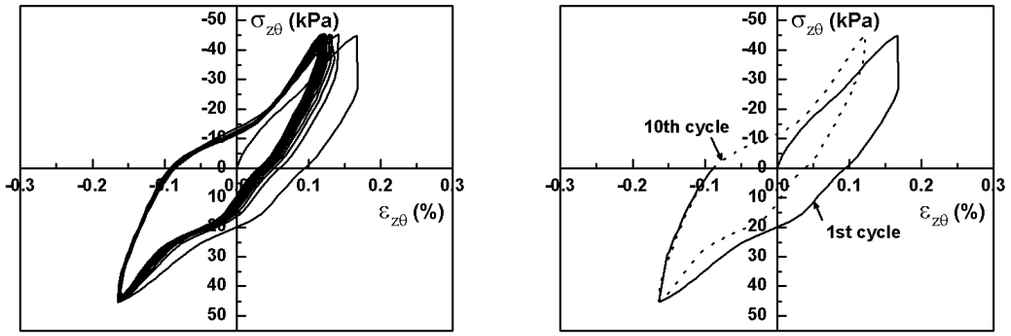
FIG.8. Variation of the volumetric strain for four test series

Shear stress-strain relationship

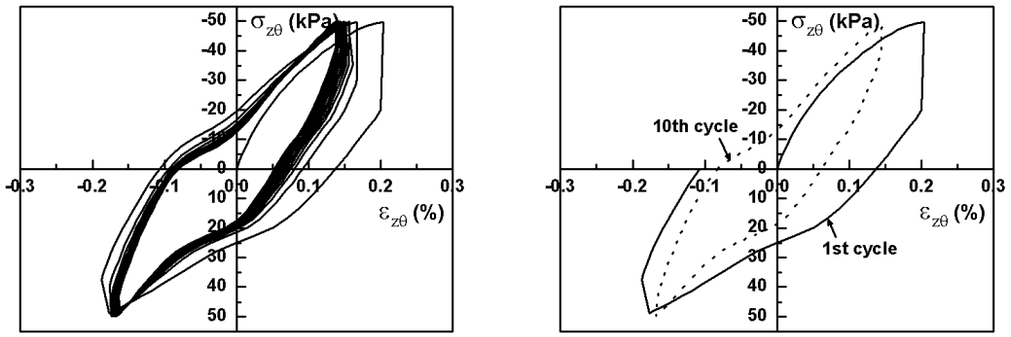
To have a better understanding of the shear stress-strain behavior, the shear stress-strain relationships for the first and tenth cycles are also given in Fig.9 for the test series Ⅱ. The hysteretic loops of the shear stress-strain curves are seen to change during the cyclic rotation of principal stress axes. The hysteretic loop appears unclosed for the first cycle, indicating the occurrence of the plastic deformation though the effective principal stresses were kept constant, and however, it tends to become closed with the increasing number of cycles. The following reasons could be given to explain this phenomenon. Under a given cyclic stress paths, the structure of sands will change gradually and the most stable structure to the current repetitive stress paths may be achieved after a certain number of cycles. With the further increase of number of cycles, the responds of sands will be almost the same within each single cycle number. As far as the shear stress-strain curves are considered, the closeness of the hysteretic loops will occur.

CONCLUSIONS

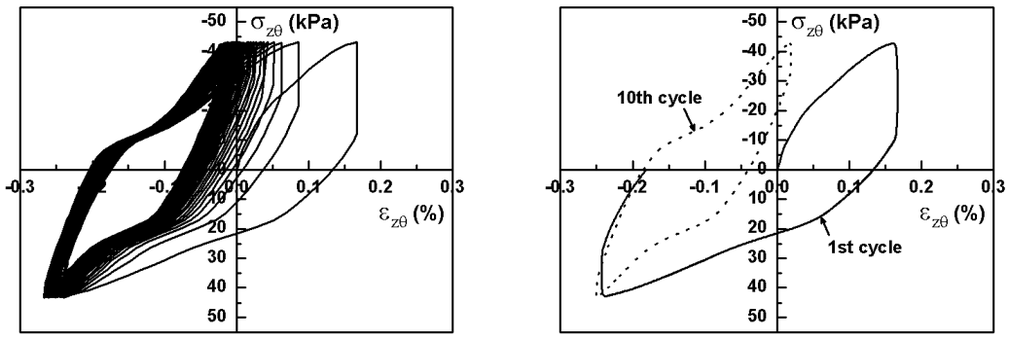
Four series of drained tests on Toyoura standard sands were conducted to investigate the drained deformation behavior of sands under cyclic rotation of principal stress axes with different values of the intermediate principal stress parameter b. The



(a) b =0.1



(b) b =0.5



(c) b =1.0

FIG. 9. Shear stress-strain relationships for test series Ⅱ

major experimental observations and conclusions can be summarized as follows.

(1) Strains are accumulated gradually during cyclic rotation of principal stress axes under the constant effective principal stresses. And the magnitude of b has considerable effects on their evolution.

(2) The vertical strain approaches to the emergence of the contractive strain under b =0.1 and the vertical extensive strain is accumulated progressively under b =1.0 with the increasing number of cycles. The radial strain changes from the extensive to the contractive strain with the increase of b from 0.1 to 0.5 and the larger contractive radial

strain develops for b =1.0. The effect of b on the circumferential strain is not so obvious as on the other two normal strain components.

(3) The contractive volumetric strain increases gradually with the increasing number of cycles. The increase rate of the maximum contractive volumetric strain within each cycle tends to decrease with its steady accumulation. The increase of b induces the increase of the volumetric strain produced within the same number of cycle.

(4) The hysteretic loop of the shear stress-strain relationship shows unclosed for the first several cycles and then becomes closed with the increasing number of cycles due to densification of the sand sample.

(5) The other parameters including the relative density, the effective mean normal stress and the deviatoric stress also have significant effects on the deformation behavior of sands subjected to cyclic rotation of principal stress axes.

ACKNOWLEDGMENTS

The present study was undertaken by the financial supports of the National Natural Science Foundation of China (No.50478016) and the Ministry of Science and Technology of PRC (No. 2007CB714108). The authors wish to express their sincere gratitude to Prof. C.W.W. Ng in HKUST for his help during the experimental work.

REFERENCES

Lade P.V. and Duncan J.M.(1973). "Cubical triaxial tests on cohesionless soil." *Journal of the Soil Mechanics and Foundation Division, ASCE*, Vol.99 (SM10): 793-811.

Miura K., Miura S. and Toki S.(1986). "Deformation behavior of anisotropic sand under principal stress axes rotation." *Soils and Foundations*, Vol.26 (1):36-52.

Nakata Y., Hyodo M., Murata H. and et al.(1998). "Flow deformation of sands subjected to principal stress rotation." *Soils and Foundations*, Vol.38 (2): 115-128.

Symes M.J.P.R., Gens A and Hight D.W.(1984). "Undrained anisotropy and principal stress rotation in saturated sand." *Geotechnique*, Vol.34 (1): 11-27.

Symes M.J., Gens A and Hight D.W.(1988). "Drained principal stress rotation in saturated sand. " *Geotechnique*, Vol.38 (1): 59-81.

Sayão A. and Vaid Y.P.(1996). "Effect of intermediate principal stress on the deformation response of sand." *Can.Geotech.J.*, Vol.33: 822-828.

Wijewickreme D. and Vaid Y.P.(1993). "Behavior of loose sand under simultaneous increase in stress ratio and principal stress rotation." *Can.Geotech.J.*, Vol.30: 953-364.

Yamada Y. and Ishihara K.(1979). "Anisotropic deformation characteristics of sand under three dimensional stress conditions." *Soils and Foundations*, Vol.19 (2): 79-94.

Yang Z.X., Li X.S. and Yang J.(2007). "Undrained anisotropy and rotational shear in granular soil." *Geotechnique*, Vol.57 (4): 371-384.

Evaluation of Dynamic Properties of a Calcite Cemented Gravely Sand

S. Mohsen Haeri[1], Mohammad Reza Shakeri[2] and S. Ali Shahcheraghi[3]

[1]Professor, School of Civil Engineering, Sharif University of Technology, Tehran, Iran, smhaeri@sharif.edu
[2]Ph.D. Student, School of Civil Engineering, Sharif University of Technology, Tehran, Iran, shakeri@civil.sharif.edu
[3]M.Sc. Student, School of Civil Engineering, Sharif University of Technology, Tehran, Iran, shahcheraghy@civil.sharif.edu

ABSTRACT: Understanding of the effect of cementation on dynamic behaviour of cemented soil in an earthquake prone area could be crucial for earthquake resistance design. The major section of the city of Tehran has been developed on cemented coarse-grained alluvium. In order to understand the dynamic behaviour of this soil, a series of undrained cyclic triaxial tests were performed on uncemented and artificially calcite-cemented samples. In this paper, two dynamic parameters including dynamic shear modulus and damping ratio based on different definitions are investigated. In this regard the effects of cement content, confining pressure and cyclic deviatoric stress were studied as well. In general by increase in the amount of cementation, maximum shear modulus increases and damping ratio show no significant variation. Also, increase in deviatoric strain results in the increase in damping ratio and decrease in shear modulus. In addition the higher confining pressures lead to higher shear modulus and lower damping ratio. Furthermore the shear modulus decreases with increase in number of cycles.

INTRODUCTION

Most of the alluvial deposit of Tehran, the capital city of Iran, has a soil with a cemented nature. The amount and characteristics of the cementation of the deposit varies in different parts from highly cemented in the north to non-cemented in the south. This deposit consists of gravely sand to sandy gravel with some cobbles and is dominantly cemented by calcite with carbonate origin (Haeri et al., 2002). On the other hand, Tehran is situated in a seismic region. Thus, characterization of dynamic behaviour of the deposit is inevitable. On the other hand, undisturbed sampling from this soil for triaxial testing is virtually impossible. Therefore, a study on the dynamic behaviour of Tehran deposit, cemented artificially with calcite, has planed.

Previous studies conducted by Haeri and his co-workers on the static behaviour of Tehran cemented gravely sand using different cementing agent like lime, Portland cement, gypsum and calcite show that cementation generally increases the static shear strength parameters and the brittleness of the soil, especially in low confining

pressures (Haeri et al., 2002; Haeri et al., 2005; Haeri and Hamidi, 2005; Haeri et al., 2007b). However the influence of the cementation decreases as the confining pressure increases which could be a result of degradation of cemented bonds. The increase in shear strength mostly affects the cohesion and also slightly the friction angle. However, the increase in brittleness may have reverse effects as the sudden bond breakage and consequent sudden decrease in strength and increase in deformation might be unjustifiable for cuts in, or structures supported on, cemented soils.

In cyclic loading, it is widely accepted that the stress–strain curve shows hysteresis and accumulation of irreversible strains with increasing number of cycles if the stress imposed during cyclic loading lies outside the true elastic range (Kokusho, 1980; Lo Presti et al., 1997). Using the hysteresis loop, and applying geometrical calculations, it is possible to obtain dynamic shear modulus and damping ratio of the soil for compression and extension sections of loading. The procedure used in this paper will be explained later.

From further examination of the hysteresis loop of each cycle, dynamic shear modulus decreases with increase in the strain or the number of cycles. This subject is especially due to bond degradation and increase in pore water pressure for cemented and uncemented soils, respectively. Sharma and Fahey (2003) and Ribay et al. (2004) have showed the increasing trend in shear modulus by increasing the confining pressure. Various researchers have shown that shear modulus increases with the power form of effective confining pressure (Acar and El-Tahir, 1986; Saxena et al., 1988; Chang and Woods, 1986). However, Baig et al. (1997) showed that G_{max} is independent on effective confining pressure for cemented sands. They found that degree of cementation and characteristics of grains skeleton along with cemented bonds strength are the most effective parameters on shear modulus. On the other hand, the increase in cement content leads to higher dynamic shear modulus (Acar and El-Tahir, 1986). Acar and El-Tahir (1986) also showed that degree of cementation and density highly control the stiffness degradation of cemented sands; and increase in shear strains due to consecutive failure of cementing bonds, decreases shear modulus. Ribay et al. (2004) showed that effect of cementation on stiffness is considerable especially in small strains ($<10^{-2}$%). In large strains due to degradation of cementation bonds, shear modulus of cemented samples approach to uncemented samples (Ribay et al., 2004). To investigate decrease in the stiffness through increase in cycles, a degradation index (δ) has been proposed by Idriss et al., (1978) and Yasuhara et al. (1997) based on the ratio of the current shear modulus to the initial shear modulus. The change in cyclic stress ratio changes the pattern of stiffness degradation. For the samples subjected to the lower cyclic stress ratio, the rate of degradation of stiffness is slower than that for samples subjected to higher cyclic stress ratio (Sharma and Fahey, 2003).

In spite of large number of studies on damping of cemented soils no significant outlines are concluded. Acar and El-Tahir (1986) showed that cementing of the soil reduces the damping ratio but Ribay et al. (2004) inversely present an increasing trend. Considering the effect of confining pressure on damping ratio of cemented soils, the results of investigations by various authors do not completely support each

other. Although, confining pressure could reduce the damping ratio (Cai and Liang, 2004). Ribey et al. (2004) reported independency of damping from effective confining pressure

Studies on dynamic behaviour of limy cemented gravely sand samples performed by Haeri et al. (2007a) show that shear modulus increases with increase in cement content up to 4.5% lime content and then the shear modulus decreases for 6% lime. However, damping ratio does not show any clear trend with change in cement content; although a minimum value for damping ratio could be seen at about 3.0 to 4.5 % cement content. The studies also show that shear modulus increases with increase in confining pressure (in the range of 100 to 700 kPa). On the other hand, performed tests indicate a downward trend for damping ratio versus confining pressures. Degradation index has a decreasing linear relation to the number of cycles in semi-logarithmic scale for limy cemented gravely sand samples.

In this paper, the results of a series undrained cyclic triaxial tests performed on uncemented and calcite cemented gravely sands are presented to examine the effect of cementation, confining pressure and cyclic stress ratio on shear modulus and damping ratio of the uncemented and cemented gravely soils.

TEST METHOD

The undisturbed sampling of naturally cemented coarse-grained alluvium of Tehran is extremely difficult and for triaxial testing is virtually impossible. Moreover, the deposit is heterogeneous both in grading and cementation. Therefore dynamic properties of this soil including dynamic shear modulus and damping ratio were investigated using artificially calcite-cemented samples. Cement content (C_C = 0.0 to 3.0%), effective confining pressure (σ_3 = 100 to 500 kPa) and single amplitude of cyclic axial deviatoric stress ($\sigma_{d,c}$) are the main controlling factors considered and tested in this research.

Tested Material

Tehran alluvium alters highly in gradation and cementation. The soil used in this research is obtained from the northern part of Tehran alluvium. An average grain size distribution of Tehran alluvium, which is called the base soil, is applied for reconstituted samples (Haeri et al., 2002). Maximum grain size is limited to 12.5 mm to comply with 100 mm diameter and 200 mm height of the samples. The base soil is sandy gravel that classifies as SW-SM based on the Unified Soil Classification System. The index characteristics of the base soil are also given in Table 1.

Table 1. Index Properties for Tested Material.

F_C [i] (%)	S_C [ii] (%)	G_C [iii] (%)	D_{10} [iv] (mm)	D_{50} [v] (mm)	C_U [vi]	C_Z [vii]	G_s	$\gamma_{d,min}$ (kN/m^3)	$\gamma_{d,max}$ (kN/m^3)	γ_d (kN/m^3)
6	49	45	0.2	4.0	28	1.8	2.57	16.14	18.78	17.75

[i] F_C: Fine Content
[ii] S_C: Sand Content
[iii] G_C: Gravel Content
[iv] D_{10}: Effective Grain Size
[v] D_{50}: Medium Grain Size
[vi] C_U: Uniformity Coefficient
[vii] C_Z: Curvature Coefficient

Testing Procedure

Consolidated undrained cyclic triaxial tests on uncemented and artificially cemented samples of the base soil were planned. Each specimen was compacted in four layers with determined gradation and density using wet tamping method. Under-compaction of lower layers was also considered during preparation (Ladd, 1978). Based on the preliminary cyclic test results, under-compaction percent (U_n) varied linearly between 3.0% for the first layer and 0.0% for the forth layer.

Uncemented samples were directly prepared on the pedestal by a two-split mould. Conversely, cementation with calcite is a time-consuming process that needs particular equipments. This process includes three stages. The first stage is the preparation of cemented samples with hydrated lime. Passing CO_2 through the moist sample for 7 days is the second stage. Finally, samples were cured under water in a curing tank filled with distilled water at 25ºC for 27 days for crystallisation and precipitation of calcite. Four special units including aluminium base, ring, porous disk and cap were designed for preparation of calcite-cemented samples (Figure 1). High strength PVC tubes of 100 mm diameter and 275 mm long were used as mould for calcite cemented samples.

The cemented samples were extracted from the mould with an extruder after curing time and installed on the pedestal in triaxial apparatus. Prior to cover the specimen with rubber membrane, its periphery was coated with a very thin layer of sandy clayey mortar in order to prevent membrane penetration and compliance.

After installation of the specimen, the samples were saturated by flushing CO_2 before gravitational flushing de-aired water. During this process a maximum cell pressure of 30 kPa was maintained on the sample. Saturation stage is then conducted to reach a B-value of greater than 0.95 by applying back pressure. After saturation, the samples were isotropically consolidated and then cyclically sheared under undrained condition in stress control mode with a frequency of 1 Hz. Principal stress reversal is also occurred during cyclic loading for all tests. Some tests were re-examined to evaluate the repeatability of the tests.

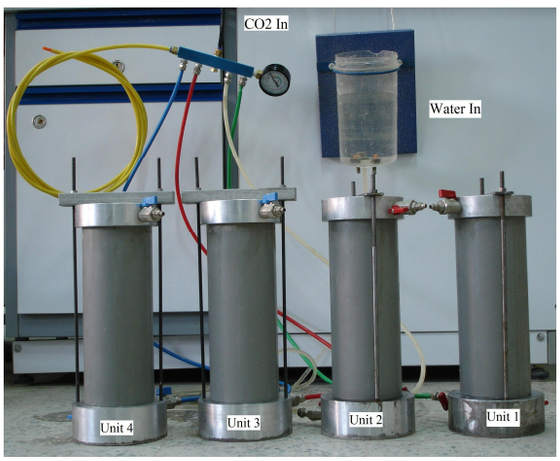
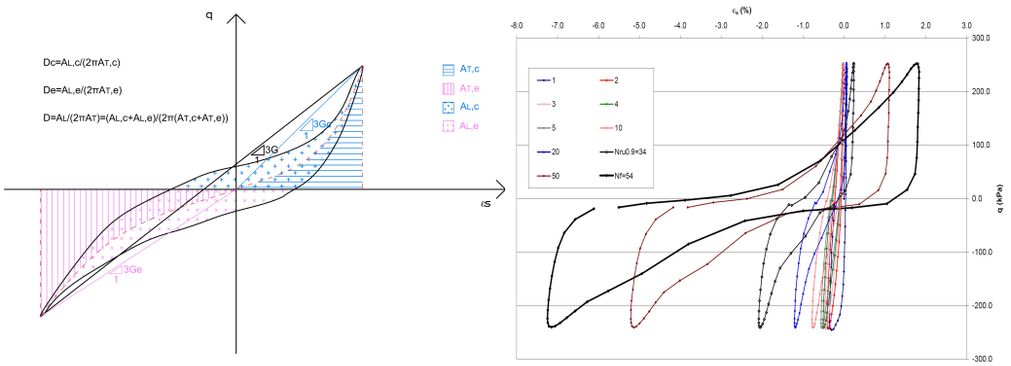


FIG. 1. Cementation Units for Four Sample Preparation.

TEST RESULTS AND DISCUSSIONS

Based on the obtained cyclic results, dynamic shear modulus and damping ratio were defined as shown in Figure 2. In this figure, q is the stress invariant or cyclic deviatoric stress as $q = \sigma'_1 - \sigma'_3 = \sigma_d$, where, σ'_1 and σ'_3 are effective major and minor principal stresses and ε_s is corresponding shear strain invariant that is equal to axial deviatoric strain in undrained condition as $\varepsilon_s = 2/3(\varepsilon'_1 - \varepsilon'_3) = \varepsilon_a$, where, ε'_1 and ε'_3 are effective major and minor principal strains.

In Figure 2-(a), A_T represents the stored energy and A_L is the area of the corresponding hysteresis loop which used for calculation of damping ratio. Since the behaviour is completely different in compression and extension phases (Figure 2-(b)), G and D are defined separately for compression and extension with indices of "c" and "e", respectively. Similar definitions were also used in the previous study (Haeri et al., 2007a). Namely, the upper half of the loop and associated triangle are considered for compression and those for lower half are considered for extension. The necessity of these definitions has been clearly shown in Figure 2-(b) for a representative test that illustrates asymmetric deformations relative to zero axis with trend toward an extension state (the leftward shift). As it can be seen, the amplitude of strain increases as the number of cycles increases. This is mainly due to increase in pore pressure, decrease in stiffness and increase in degradation of cemented bonds by increase in the number of cycles.



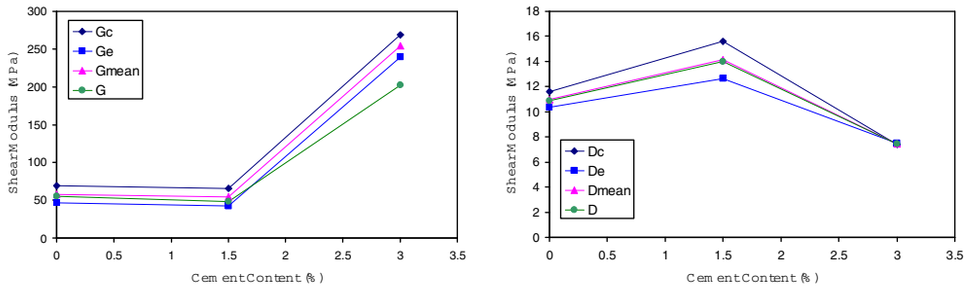
(a) **(b)**

FIG. 2. (a) Schematic Hysteresis Loop and the Method of Calculation of Parameters in This Study and (b) Obtained Hysteresis Loops for a 3.0% Cemented Sample (σ_3=300 kPa and $\sigma_{d,cyc,DA}$=500 kPa).

Effect of Cement Content

The effect of cement content on the dynamic parameters is a major concern in this research. Figure 3 shows the variation of different types of dynamic shear modulus and damping ratio described before versus the cement content. G_{mean} and D_{mean} are the mean values of compression and extension of corresponding parameters, respectively. As it can be seen in this graph and based on the other obtained results,

the higher cement content generally leads to higher shear modulus, and consequently, stiffer samples. On the other hand, the results show that the damping ratio does not follow a decisive trend. It is important to note that cemented samples with 1.5% cement have a very weak inter-particle bonding that leads to a similar stiffness to uncemented samples. Comparing different types of modulus (and damping), it is notable that G_c (and D_c) is the highest and G_e (and D_e) the lowest value. However G (and D) and G_{mean} (and D_{mean}) have approximately the same values. Note that the common modulus and damping are G and D. However, other types are useful depending on the stress path of the loading in the real world.



(a) **(b)**

FIG 3. Variation of (a) Various Shear Moduli and (b) Various Damping Ratios with the Cement Content at the 10th Cycle (σ_3=300 kPa and $\sigma_{d,cyc,DA}$=250 kPa).

Variations of G and D versus single amplitude of axial strain are presented in Figure 4 in semi logarithmic scale. The tests are conducted from small to large strains to get to failure. The legends show the test names constituted from three parts that represent cement content, effective confining pressure and double amplitude deviatoric stress, respectively. During the tests, with increase in the number of cycles, axial strain or shear strain gradually increases. As it is expected, the increase in amplitude of axial strain leads to decrease in shear modulus and increase in damping ratio by progressive degradation of cemented bonds. As mentioned above, cementation has a significant effect on the shear modulus. This effect can also be seen in Figures 4-(a), 4-(c) and 4-(e). Since the amplitude of strain is very low in most cycles up to about failure, the density and scattering of the points regarding the damping ratios are very high in small strain range. At larger strains, damping ratio shows a rising trend with strain in semi-logarithmic scale. The maximum damping ratio obtained is about 27% at the failure cycle. Comparison of Figures 4-(b), 4-(d) and 4-(f) indicates that cement content does not clearly influence on the damping ratio. Note that the single amplitude of axial strain at failure is in the range of 3.5% to 4.5%.

Effect of Confining Pressure

Increase in confining pressure results in the increase in shear modulus irrespective of the type of calculation of shear modulus. However, there could be seen no trend of change in damping ratio with change in confining pressure. Figure 5 shows the

results for 10th cycle of the tests with CSR = 1 ($CSR = \sigma_{d,c}/2\sigma_3$) that confirms the above statement. Confining pressure constrains the sample laterally and as a result, axial strain decreases showing stiffer behavior. However, very high confining pressure can break the bonds and decrease the shear modulus. Therefore the shear modulus for different cemented samples may converge in very high confining pressures. However, because of the level of applied confining pressures in this study, this phenomenon has not been observed.

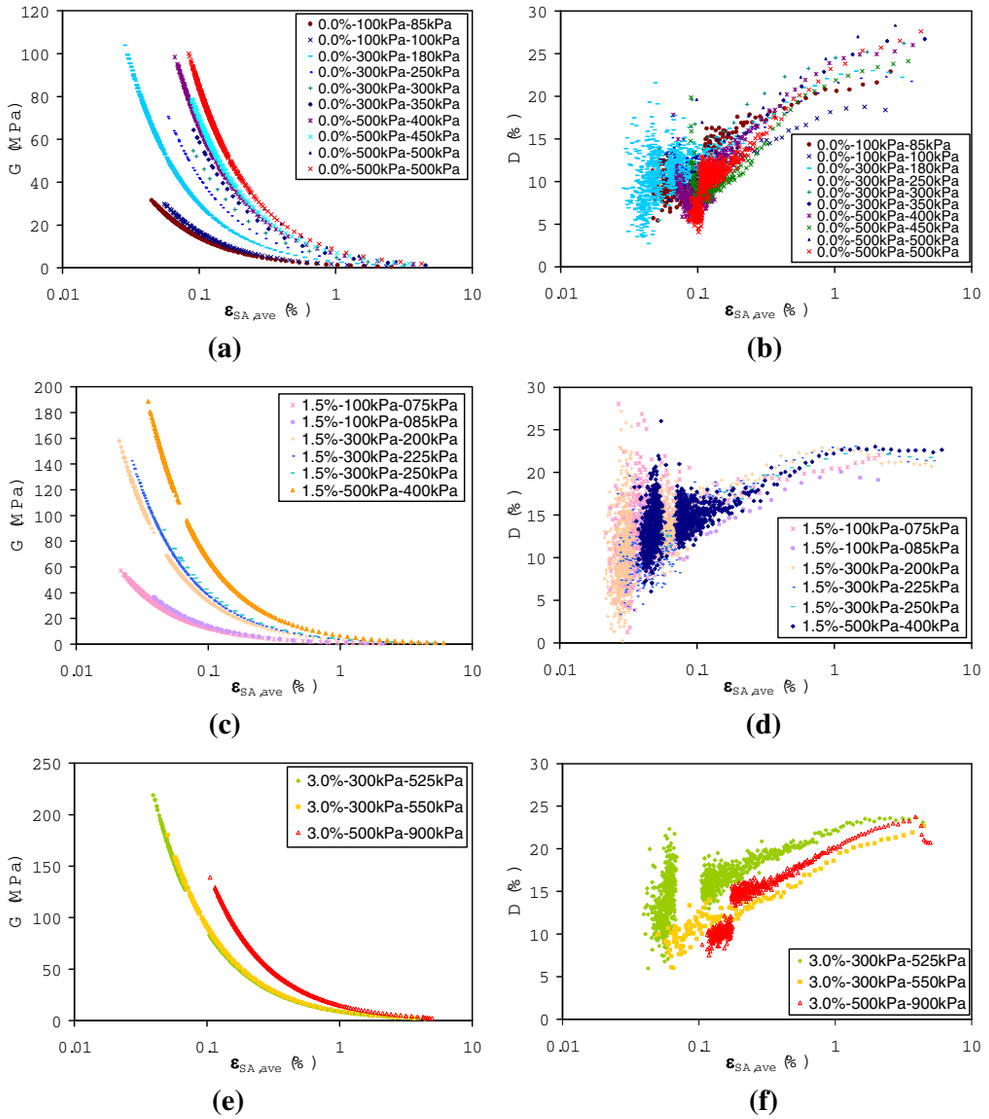
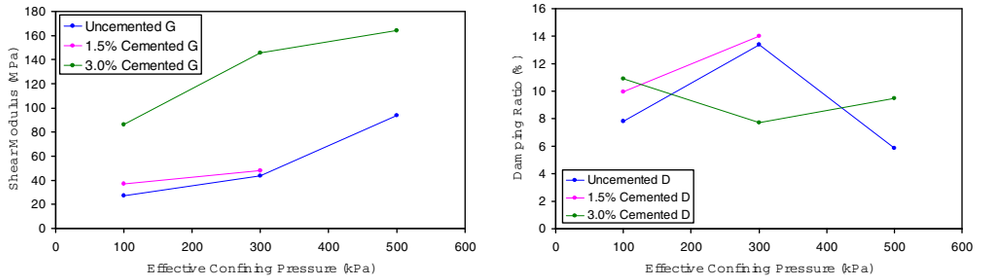


FIG 4. Variation of G and D with Single Amplitude Axial Strain for (a) and (b) Uncemented Samples, (c) and (d) 1.5% Cement and (e) and (f) 3.0% Cement.



(a) **(b)**

FIG. 5. Variation of (a) G and (b) D with Confining Pressure at 10th Cycle for Different Cement Contents (CSR≈1.0).

Degradation

The decrease in stiffness and strength with the number of load cycles is named degradation. This phenomenon is clearly observed in Figure 4 due mainly to the building up of pore water pressure and bonding breakage. However, the cemented samples are not much affected by low amplitude cyclic loadings and depending on the amplitude of the cyclic load and the amount of cement content, degradation may happen. This fact is illustrated in Figure 6 for uncemented to 3.0% cemented samples. In this figure, the degradation index, is plotted against normalized number of cycle i.e. N/N_f and $r_{u,max}$; where the degradation index is the normalized shear modulus or G/G_{max}, G_{max} is maximum shear modulus, N_f is the number of cycles associated with the failure, $r_{u,max} = u_{max}/\sigma'_3$, u_{max} is the maximum excess pore water pressure in each cycle and σ'_3 is the effective confining pressure.
Yasuhara et al. (1997) suggested a linear relationship between degradation index and the number of cycles in logarithmic scale (i.e.: $\delta = 1 - \alpha \text{ Log } N$). However, the results in this study show that almost a nonlinear relation for all samples is more appropriate. Figure 6 illustrates the relation between degradation index and the maximum pore pressure ratio that represents a rational trend.

CONCLUSIONS

Considering the results obtained from the tests, the following items can be concluded:

- Dynamic shear modulus of tested calcite cemented gravely sands increases with increase in cement content.
- Damping ratio does not show a decisive trend with change in cement content.
- Shear modulus rises continuously with increase in confining pressure. However, the performed tests show no clear trend for damping ratio versus confining pressure.
- In contrast to shear modulus, damping ratio increases with amplitude of axial strain.
- Comparing different definitions of shear modulus, compression and extension

modules are the highest and the lowest modulus, respectively. Average and secant modulus are approximately equal in the performed tests.

- Degradation index has a decreasing nonlinear relation to the number of cycles.

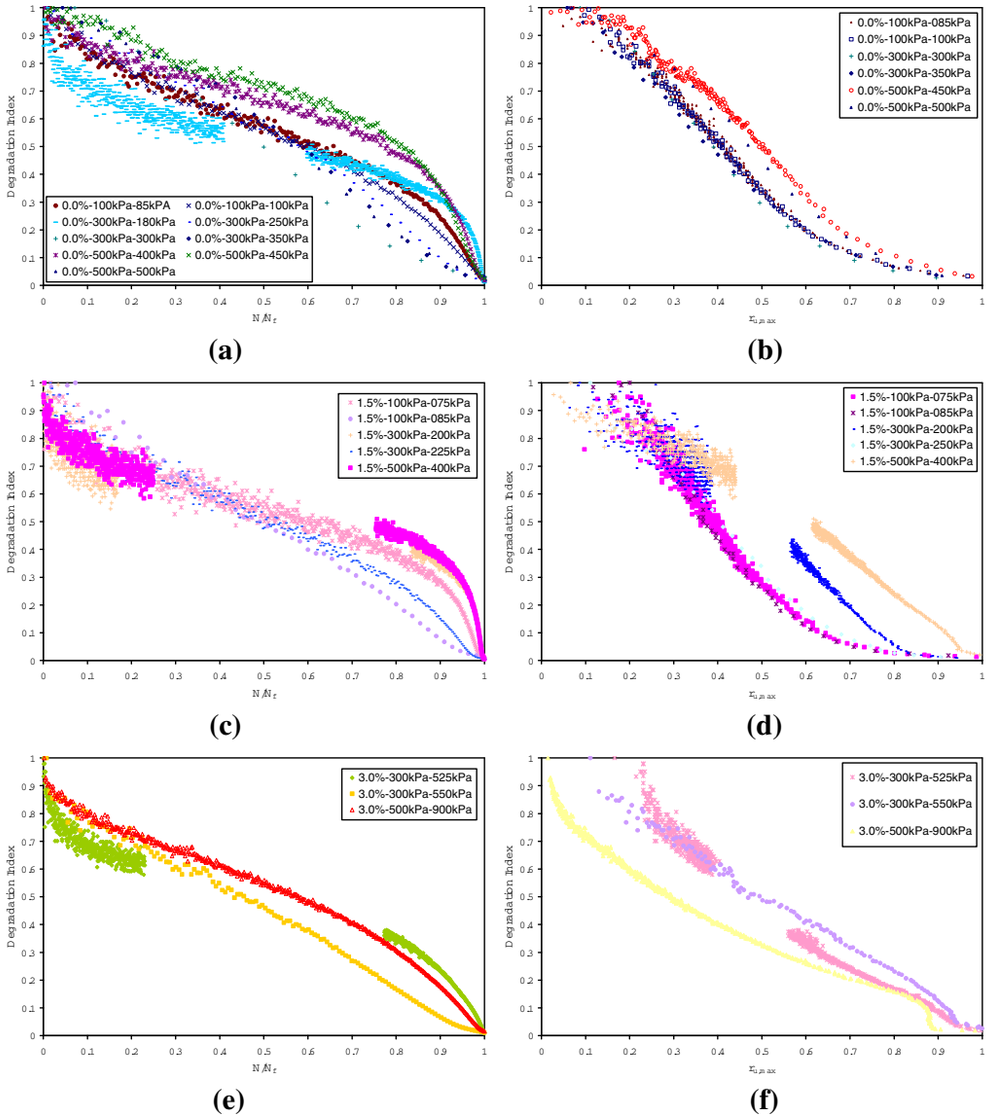


FIG. 6. Variation of degradation index with N/N_f and $r_{u,max}$ (a) and (b) uncemented sample, (c) and (d) 1.5% cement and (e) and (f) 3.0% cement.

AKNOWLEDGEMENTS

All cyclic triaxial tests are conducted in the Advanced Geotechnical Engineering Laboratory of Civil Engineering Department and financially supported by Vice Presidencies in Research and Graduate Studies of Sharif University of Technology.

REFERENCES

Acar, Y. B., El-Tahir, A. E., "Low strain dynamic properties of artificially cemented sand", Journal of Geotechnical Engineering Division, ASCE, Vol. 112, No. 11, 1001-1015, 1986.

Baig, S., Picornell, M., and Nazarian, S., "Low Strain Shear Moduli of Cemented Sands," ASCE Journal of Geotechnical Engineering, Vol. 123, No. 6. pp. 540-545, 1997.

Cai, Y. Q., and Liang, X., "Dynamic properties of composite cemented clay", Journal of Zhejiang University Science, Vol. 5, No. 3, 309-316, 2004.

Chang, T. S., and Woods, R. D., "Effect of particle contact bond on shear modulus", Journal of Geotechnical Engineering, ASCE, 118 (8), 1216-1233, 1992.

Haeri, S.M., Yasrebi, S. and Asghari, E., "Effects of cementation on the shear strength parameters of Tehran alluvium using large direct shear test", Proceedings 9th IAEG Congress, Durban, South Africa, PP. 519-525, 2002.

Haeri, S. M., Hamidi, A., "The effect of gypsum cementation on mechanical behaviour of cemented gravely sands", Geotechnical Testing Journal, Vol. 28, No. 4, 380-390, 2005.

Haeri, S. M., Hosseini, S. M., Toll, D. G. and Yasrebi, S. S., "Experimental study of the behavior of a cemented gravely sand," Geotechnical and Geological Engineering Journal, Vol. 23, No. 5, 537-560, 2005.

Haeri, S. M., Shakeri, M. R., and Ghayoomi, M., Dynamic properties of a limy cemented gravely sand, 4th International Conference on Earthquake Geotechnical Engineering, Greece, 2007a.

Haeri, S. M., Rahmati, A., and Seyphoori, Static behaviour of a cemented gravely sand-case study of Tehran alluvium, 3rd Congress on Civil Engineering, Iran, 2007b.

Idriss, I.M., Dobry, R. & Singh, R.D., "Nonlinear behaviour of soft clays during cyclic loading," Journal of Geotech-nical Engineering, ASCE, 104 (GT12), 1427-1447, 1978.

Kokusho, T., "Cyclic triaxial test on dynamic soil properties for wide strain range", Soils and Foundations, 20 (2), 45-60, 1980.

Ladd, R. S., 1978, Preparing test specimens using undercompaction, Geotechnical Testing Journal, Vol. 1, No. 1, 16-23.

Lo Presti, D. C. F., Jamiolkowski, M., Pallara, O., Cavallaro, A. and Pedroni, S., "Shear modulus and damping of soils", Géotechnique, 47 (3), 603-617, 1997.

Ribay-Delfosse, E., Maigre-Djeran, I., Cabrillac, R., and Gouvenot, D., "Shear modulus and damping ratio of grouted sand," Soil Dynamic and Earthquake Engineering, Vol. 24, 461-471, 2004.

Saxena, S., Avramidis, A. S., and Reddy, K. R., "Dynamic moduli and damping ratios for cemented sands at low strains", Canadian Geotechnical Journal, 25, 353-368, 1988.

Sharma, S. S., and Fahey, M., "Degradation of stiffness of cemented calcareous soil in cyclic triaxial tests," ASCE Journal of Geotechnical and Geoenvironmental Engineering, Vol. 129, No. 7, 619-629, 2003.

Yasuhara, Y., Hyde, A.F.L., Toyota, N. & Murakami, S., "Cyclic stiffness of plastic silt with an initial drained shear stress," Géotechnique Symposium on Pre-failure Deformation Behaviour of Geomaterials, Jardine, R. J. Davies, M. C. R., Hight, D. W., Smith, A. K. & Stallebrass, S. E. (eds), 373-382, 1997.

Pore Fluid Induced Damping of Saturated Soil in Resonant Column Tests

Tong Qiu[1], A.M. ASCE

[1]Assistant Professor, Department of Civil & Environmental Engineering, Clarkson University, Potsdam, NY 13699-5710; tqiu@clarkson.edu

ABSTRACT: This paper presents a theoretical study of pore fluid induced damping of saturated soil in resonant column tests. The solid skeleton is treated as equivalent linear. Pore fluid induced damping due to Biot flow is evaluated based on the spectral response of the soil column under harmonic excitations. Closed-form analytical solution indicates that pore fluid induced damping is frequency and hydraulic conductivity dependant. At the first resonance, pore fluid induced damping is dependent on a dimensionless hydraulic conductivity parameter K. For K within the range of 10^{-3} to 10, corresponding to coarse sands and gravels, pore fluid induced damping may have an important contribution to total soil damping, especially at small strain levels.

INTRODUCTION

It has long been recognized that saturated soils exhibit higher damping than the same soils in the dry state (Hall and Richart 1963, Bolton *et al*. 1990, Ellis *et al*. 1998, Ellis *et al*. 2000). In addition to solid skeleton damping, energy dissipation is induced due to the relative motion between viscous pore fluid and solid particles in saturated soils. Pore fluid induced damping can be conceptually divided into two mechanisms: Biot flow and squirt flow. Biot flow is relative fluid motion that, on average, occurs parallel to the direction of solid motion and results from pore fluid moving past soil particles. Squirt flow is relative fluid motion that occurs as fluid is forced out of small cracks and voids at contacts between solid particles due to solid skeleton deformation (Dvorkin and Nur 1993). Research has shown that consideration of squirt flow in addition to Biot flow results in higher energy losses and produces more realistic attenuation values in sedimentary materials for both p- and s-waves (Mavko and Nur 1979, Murphy *et al*. 1986, Wang and Nur 1990). Though they occur simultaneously and are related, Biot flow and squirt flow are often modeled separately. Biot flow is often treated in a macroscopic sense (Biot 1956), whereas squirt flow is typically treated in a microscopic sense based on microfabric properties such as geometry of individual pores (Mavko and Nur 1979, Miksis 1988). Pore fluid induced damping due to squirt flow is therefore difficult to asses theoretically and is generally evaluated

using laboratory tests. Pore fluid induced damping due to Biot flow, on the other hand, can be evaluated analytically using macroscopic parameters (e.g., porosity and hydraulic conductivity).

Bardet (1995) presented the only major theoretical investigation on pore fluid induced damping due to Biot flow. In his work, the spectral response of a two-phase poroelastic soil column subjected to harmonic compression waves was obtained analytically, and the equivalent damping ratio of the system was evaluated based on the theory of a damped single-degree-of-freedom system. Following Bardet's work, this paper presents a theoretical investigation on pore fluid induced damping for a soil column under shear excitation that is of particular interest to geotechnical earthquake engineering and soil dynamics. In this study, the solid skeleton is treated as equivalent linear assuming that shear strain and volumetric strain are decoupled. This assumption limits this study applicable to small strain levels.

GOVERNING EQUATIONS AND SOLUTIONS

Following Biot theory, the governing equations for shear waves in a saturated equivalent linear soil column can be presented as,

$$\left[(1-n)\rho_s + \rho_a\right]\frac{\partial^2\theta_s}{\partial t^2} - \rho_a\frac{\partial^2\theta_f}{\partial t^2} = G\frac{\partial^2\theta_s}{\partial x^2} + \eta\frac{\partial^3\theta_s}{\partial x^2\partial t} - \frac{n^2\rho_f g}{k}\frac{\partial}{\partial t}(\theta_s - \theta_f) \tag{1a}$$

$$-\rho_a\frac{\partial^2\theta_s}{\partial t^2} + \left(n\rho_f + \rho_a\right)\frac{\partial^2\theta_f}{\partial t^2} = \frac{n^2\rho_f g}{k}\frac{\partial}{\partial t}(\theta_s - \theta_f) \tag{1b}$$

where n, ρ, θ, t, G, η, g and k denote porosity, density, angular displacement, time, shear modulus, shear coefficient of viscosity, acceleration of gravity and hydraulic conductivity, respectively. Subscripts s and f indicates solid phase and fluid phase, respectively. Coefficient ρ_a represents the mass coupling between the solid and fluid phases. Biot (1962) proposed the following relationship,

$$\rho_a = n\rho_f\left(\delta - 1\right) \tag{2}$$

where δ is a structural factor representing the "added mass" caused by the tortuosity of the pore space (Stoll and Bryan 1970). Sen *et al*. (1981) proposed $\delta = n^{-0.5}$ for a random array of spheres. In Eq. (1), fluid flow relative to the solid phase is assumed to be of the Darcy type (i.e., governed by Poiseuille's law). This assumption breaks down above a certain excitation frequency which depends on the kinematic viscosity of fluid and the pore size (Biot 1956). For most cases of interest, the Darcy assumption is reasonable.

In Hall's (1962) fixed base model, a soil column with length L is fixed at its base ($x = 0$) and subject to a torsional excitation at its top ($x = L$). For harmonic excitation, the loading function can be expressed as,

$$T = T_o e^{i\omega t} \tag{3}$$

where $i = \sqrt{-1}$ and T, T_o and ω are the applied torque, torque amplitude and circular frequency, respectively.

The general solution for the steady-state response of the soil column can be expressed as,

$$\theta_s(x,t) = \phi_s(x) e^{i\omega t} \tag{4a}$$

$$\theta_f(x,t) = \phi_f(x) e^{i\omega t} \tag{4b}$$

where $\phi_s(x)$ and $\phi_f(x)$ are the amplitudes of torsional displacement for solid and fluid phases, respectively. Based on Qiu and Fox's work (2006), the solution for $\phi_s(x)$ can be expressed as,

$$\phi_s(x) = \frac{T_o L}{GJ} \frac{\sin\left(\dfrac{\omega}{\alpha_2 \overline{V}_s} x\right)}{(1+2i\xi_s)\dfrac{\omega L}{\alpha_2 \overline{V}_s}\cos\left(\dfrac{\omega L}{\alpha_2 \overline{V}_s}\right) - \dfrac{I_t}{I}\dfrac{\omega^2 L^2}{\overline{V}_s^{\,2}}\sin\left(\dfrac{\omega L}{\alpha_2 \overline{V}_s}\right)} \tag{5}$$

where J is the polar moment of inertia of the soil specimen, $\overline{V}_s$ is the shear wave velocity in the soil when $k = 0$ (i.e., no relative motion between solid and fluid), I_t is the mass polar moment of inertia of the loading system connected to the specimen, and α_2 is a dimensionless parameter,

$$\overline{V}_s = \sqrt{\frac{G}{\rho_{sat}}} \tag{6}$$

$$\alpha_2 = \sqrt{(1+2i\xi_s)\frac{ng + i\omega k\delta}{ng + i(\delta - n\beta)\omega k}} \tag{7}$$

$$\xi_s = \frac{\omega\eta}{2G} \tag{8}$$

$$I = \rho_{sat} L J \tag{9}$$

where ρ_{sat} is the saturated soil density and

$$\beta = \frac{1}{n + (1-n)G_s} \tag{10}$$

The parameter ξ_s is the soil skeleton damping ratio commonly defined in geotechnical engineering and G_s is the specific gravity of solids. Equations (5) and (7) can be normalized as,

$$\phi_s(x) = \frac{T_o L}{GJ} \frac{\sin\left(\frac{\Omega}{\alpha_2}\frac{x}{L}\right)}{(1+2i\xi_s)\frac{\Omega}{\alpha_2}\cos\left(\frac{\Omega}{\alpha_2}\right) - \frac{I_t}{I}\Omega^2 \sin\left(\frac{\Omega}{\alpha_2}\right)} \tag{11}$$

$$\alpha_2 = \sqrt{(1+2i\xi_s)\frac{n + i\Omega \mathrm{K}\delta}{n + i(\delta - n\beta)\Omega \mathrm{K}}} \tag{12}$$

where Ω and K are normalized frequency and hydraulic conductivity,

$$\Omega = \frac{\omega L}{\overline{V}_s} \tag{13}$$

$$\mathrm{K} = \frac{k\overline{V}_s}{gL} \tag{14}$$

Typical values of soil parameters used in this study are based on the values given by Bardet (1995) and Mei and Foda (1981) and are presented in Table 1. The height of the test specimen is assumed to be 0.2 m (i.e., $L = 0.2$ m) in the calculation of K. The pore fluid is assumed to be water as in most cases in geotechnical engineering, however, other types of pore fluid can be considered with the corresponding values of k and K (e.g., silicone-saturated soil in centrifuge testing).

Table 1. Values of Soil Properties and Dimensionless Parameters

Soil Type	n	G_s	k (m/s)	G (MPa)	$\overline{V}_s$ (m/s)	K
Gravel	0.3	2.66	1×10^{-2}	200	300	1.5
Coarse Sand	0.3	2.66	1×10^{-4}	100	200	1×10^{-2}
Fine Sand	0.3	2.66	1×10^{-6}	30	100	5×10^{-5}
Silt	0.3	2.66	1×10^{-8}	10	60	3×10^{-7}

SPECTRAL RESPONSE AND ENERGY DISSIPATION

The dynamic amplification factor at the top of the specimen can be expressed as $|A(\Omega)|$ where,

$$A(\Omega)=\frac{\sin\left(\frac{\Omega}{\alpha_2}\right)}{(1+2i\xi_s)\frac{\Omega}{\alpha_2}\cos\left(\frac{\Omega}{\alpha_2}\right)-\frac{I_t}{I}\Omega^2\sin\left(\frac{\Omega}{\alpha_2}\right)} \tag{15}$$

The energy dissipation in the test specimen can be evaluated using a damping ratio ξ defined as,

$$\xi=\frac{W_D}{4\pi W_s} \tag{16}$$

where W_D and W_s are the energy dissipated in one loading cycle and the peak energy stored in the system at the maximum displacement, respectively. The energy dissipated in one loading cycle is equal to the work done by the externally applied torque in one loading period,

$$W_D=\int_0^{2\pi/\omega} R\left(T_o e^{i\omega t}\right)R\left(\frac{d\phi_s(L)}{dt}e^{i\omega t}\right)dt=-\pi\frac{T_o^2 L}{GJ}I\{A(\Omega)\} \tag{17}$$

where functions $R(z)$ and $I(z)$ return the real part and imaginary part of z, respectively. The peak energy stored in the system at the maximum displacement can be expressed as,

$$W_s=\frac{1}{2}GJ\left|\int_0^L\left(\frac{d\phi_s(x)}{dx}\right)^2dx\right|=\frac{1}{2}\frac{T_o^2 L}{GJ}\left|\frac{\frac{1}{4}\frac{\Omega}{\alpha_2}\sin\left(\frac{2\Omega}{\alpha_2}\right)+\frac{1}{2}\left(\frac{\Omega}{\alpha_2}\right)^2}{\left[(1+2i\xi_s)\frac{\Omega}{\alpha_2}\cos\left(\frac{\Omega}{\alpha_2}\right)-\frac{I_t}{I}\Omega^2\sin\left(\frac{\Omega}{\alpha_2}\right)\right]^2}\right| \tag{18}$$

A closed-form solution of ξ can be obtained by substituting (17) and (18) into (16). Both pore fluid induced damping and solid skeleton damping contribute to the total energy dissipation in the test specimen. Therefore, an equivalent damping ratio for pore fluid induced damping ξ_h can be obtained as,

$$\xi_h=\xi-\xi_s \tag{19}$$

Fig. 1 presents the spectral response of $|A|$ and ξ for a soil specimen with $\xi_s = 0.02$ and $I_t/I = 0$. Values of $\mathrm{K} = 10^{-4}$ and 0.1 correspond to a 0.2 m tall column of fine sand and coarse sand/gravel, respectively. Value of $\mathrm{K} = 10^{2}$ corresponds to a material with hydraulic conductivity much higher than gravel.

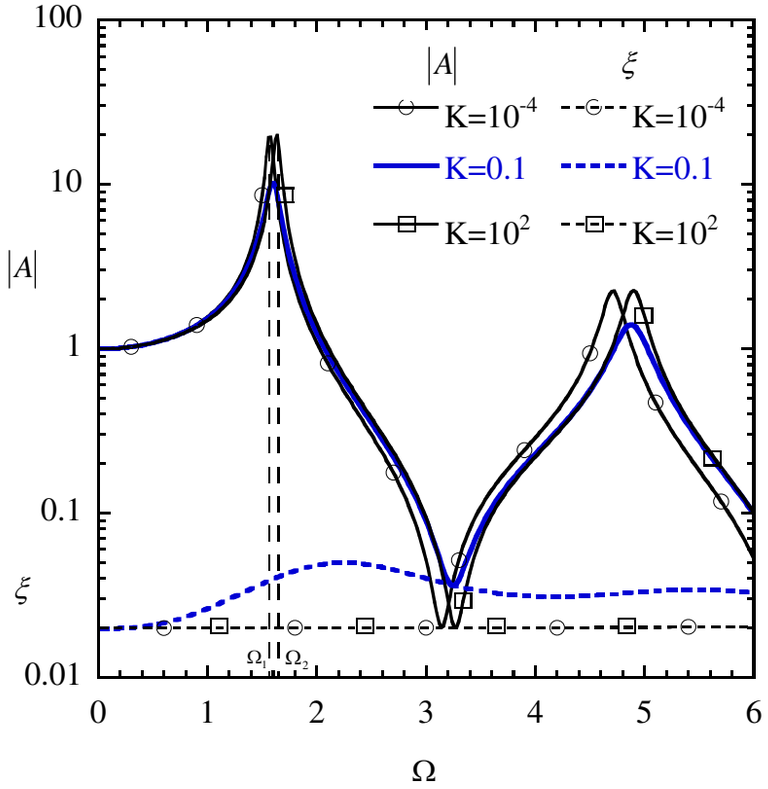


FIG. 1. $|A|$ and ξ *vs.* Ω for various K ($\xi_s = 0.02$ $I_t/I = 0$).

Fig.1 indicates that resonant frequencies are different for cases of $\mathrm{K} = 10^{-4}$ and 10^{2}. This can be explained using two extreme cases: impermeable soil specimen (i.e., $\mathrm{K} = 0$) and infinitely permeable soil specimen (i.e., $\mathrm{K} = \infty$). For the impermeable specimen, there is no relative motion between solid and fluid phases and the shear wave velocity is $\overline{V}_s$. Conversely, there is no viscous coupling between the two phases for the infinitely permeable column and a shear wave propagates at velocity $\overline{V}_s\sqrt{\delta/(\delta - n\beta)}$. Please note that mass coupling is an intrinsic characteristic of porous media and always exists. The different shear wave velocities produce different resonant frequencies; $\Omega_1 = \pi/2$ for $\mathrm{K}_s = 0$ and $\Omega_2 = \Omega_1\sqrt{\delta/(\delta - n\beta)} = 1.63$ for $\mathrm{K}_s = \infty$. In Fig. 1, the first resonance occurs at near Ω_1 for fine sands, indicating that the response of this material with regard to fundamental frequency resembles that of an impermeable soil. For $\mathrm{K} = 10^{2}$, the first resonance occurs at near Ω_2, indicating

that the response of this material resembles that of an infinitely permeable soil. For $\mathrm{K} = 0.1$, the first resonance occurs between Ω_1 and Ω_2 with a much lower amplitude indicating a higher energy dissipation.

Fig.1 also indicates that the damping ratio ξ for the specimen is essentially equal to the damping ratio of the solid skeleton ξ_s for cases of $\mathrm{K} = 10^{-4}$ and 10^2. In these two cases, pore fluid does not contribute to the energy dissipation of the system. For soil specimens with low K values (find sands and less permeable soils), there is essentially no relative motion between the solid and fluid phases due to the strong viscous coupling. Pore fluid induced damping is thus negligible because energy dissipation is proportional to the product of viscous force and relative displacement. For soil specimens with large K values (materials more permeable than gravels), viscous coupling forces are negligible and the resulting damping is also negligible. Large pore fluid induced damping occurs in soils with moderate K values (coarse sands), in which viscous coupling forces and inertial forces are of similar magnitude. Fig. 1 indicates that pore fluid induced damping has a significant contribution to the total damping of the soil specimen for $\mathrm{K} = 0.1$ (coarse sand).

Pore fluid induced damping is frequency dependant and the maximum value occurs at a frequency between the first and second resonances as shown in Fig. 1. In geotechnical engineering, resonant column tests are often carried out at the first resonance. Fig. 2 presents ξ_h *vs.* K for $n = 0.3$ and 0.4 at the first resonance with $\xi_s = 0.02$ and $I_t/I = 0$. Both curves reach maximum values of ξ_h when K is in the range of 0.1 to 0.2, which corresponds to a specimen of coarse sand/gravel. Pore fluid induced damping is essentially zero for K values outside the range of 10^{-3} to 10. Considering that soil skeleton damping ratio is generally less than 2% at small strain levels, pore fluid induced damping may have important contribution to total soil damping for K values in the range of 10^{-3} to 10. Fig. 3 presents ξ_h *vs.* K for $I_t/I = 0$ and 0.5 at the first resonance with $\xi_s = 0.02$ and $n = 0.3$. The maximum value of ξ_h decreases considerably as I_t/I increases from 0 to 0.5. The decrease of ξ_h is likely due to the decrease of first resonance frequency as I_t/I increases.

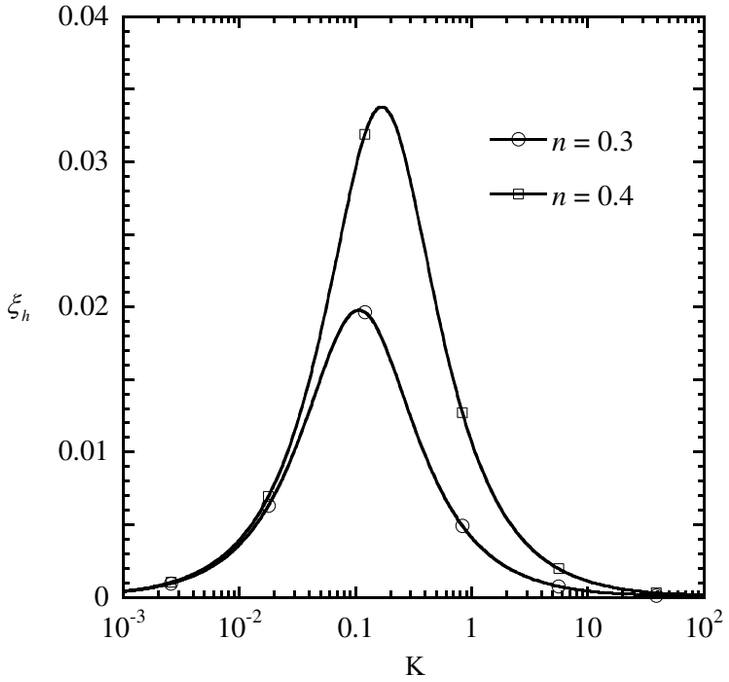


FIG. 2. ξ_h ***vs.*** K **for** $n = 0.3$ **and** 0.4 **at the first resonance** ($\xi_s = 0.02$ $I_t/I = 0$)**.**

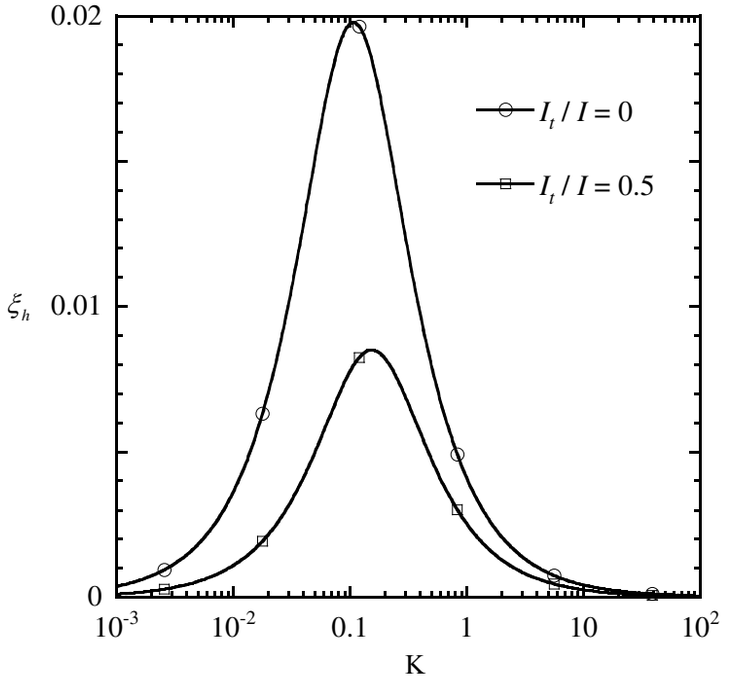


FIG. 3. ξ_h ***vs.*** K **for** $I_t/I = 0$ **and** 0.5 **at the first resonance** ($\xi_s = 0.02$ $n = 0.3$)**.**

CONCLUSIONS

Pore fluid induced damping is a manifestation of internal coupling forces that occur due to relative motion between solid and fluid phases in a porous medium. This paper presents a theoretical investigation on pore fluid induced damping in saturated soil under harmonic torsional excitations. The equivalent damping ratio of the system is evaluated based on the energy dissipated in one loading cycle and the energy stored at the maximum displacement. A closed-form analytical solution of pore fluid induced damping is derived.

The magnitude of pore fluid induced damping is a function of soil hydraulic conductivity, porosity, specific gravity of solids, and excitation frequency. At the first resonance, pore fluid induced damping is dependant on a dimensionless parameter K. Pore fluid induced damping may provide an important contribution to total soil damping when K is in the range of 10^{-3} to 10 corresponding to coarse sand and gravels, but can be practically neglected with K outside of this range.

REFERENCES

Bardet, J.P. (1995). "The Damping of Saturated Poroelastic Soils during Steady-State Vibrations." *Applied Mathematics and Computation*, Vol. 67: 3-31.

Bolton, M. D. and Wilson, J. N. (1990). "Soil Stiffness and Damping." *Structural Dynamics*, Kratzig, W. B., Beskos, D. E., and Vardoulakis, I. G. eds., Balkema, Rotterdam, Netherlands, 209-216.

Biot, M.A. (1956). "Theory of Propagation of Elastic Waves in a Fluid-Saturated Porous Solid. I. Low-Frequency Range. II. Higher Frequency Range." *Journal of the Acoustical Society of America*, Vol. 28 (2): 168-191.

Biot, M.A. (1962). "Mechanics of deformation and acoustic propagation in porous media," *Journal of Applied Physics*, Vol. 33 (4): 1482-1498.

Dvorkin, J. and Nur, A. (1993). "Dynamic poroelasticity: A unified model with the squirt and the Biot mechanisms." *Geophysics*, Vol. 58 (4): 524-533.

Ellis, E.A., Soga, K., Bransby, M.F., and Sato, M. (1998). "Effect of Pore Fluid Viscosity on the Cyclic Behavior of Sands." *Proceedings, Centrifuge 98*, T. Kimura, O. Kusakabe, and J. Takemura, eds., Balkema, Rotterdam, Netherlands, 217-222.

Ellis, E.A., Soga, K., Bransby, M.F., and Sato, M. (2000). "Resonant Column Testing of Sands with Different Viscosity Pore Fluids." *Journal of Geotechnical and Geoenvironmental Engineering*, Vol. 126 (1): 10-17.

Hall, J.R. (1962): "Effect of Amplitude on Damping and Wave Propagation in Granular Materials," Ph.D. dissertation, University of Florida , Gainesville.

Hall, J.R. and Richart, F.E. (1963). "Dissipation of Elastic Wave Energy in Granular Soils." *Journal of the Soil Mechanics and Foundations Division*, Vol. 89 (6): 27-56.

Mavko, G. and Nur, A. (1979). "Wave Attenuation in Partially Saturated Rocks." *Geophysics*, Vol 44 (2): 161-178.

Mei, C.C. and Foda, M.A. (1981). "Wave-Induced Responses in a Fluid-Filled Poroelastic Solid with a Free Surface-a Boundary Layer Theory." *Geophysical Journal of the Royal Astronomical Society*, Vol. 66: 597-631.

Miksis, M.J. (1988). "Effect of Contact Line Movement on the Dissipation of Waves in Partially Saturated Rocks." *Journal of Geophysical Research*, Vol. 93 (6): 6624-6634.

Murphy, W.F., Winkler, K.W., and Kleinberg, R.L. (1986). "Acoustic Relaxation in Sedimentary Rocks: Dependence on Grain Contacts and Fluid Saturation." *Geophysics*, Vol. 51 (3): 757-766.

Qiu, T. and Fox, P.J. (2006). "Hydraulic damping of saturated poroelastic soils during steady-state vibration," *Journal of Engineering Mechanics*, Vol. 132 (8): 859-870.

Sen, P.N., Scala, C., and Cohen, J.H. (1981). "A self-similar model for sedimentary rocks with application to the dielectric constant of fused glass beads," *Geophysics*, Vol. 46 (5): 781-795.

Stoll, R.D. and Bryan, G.M. (1970). "Wave attenuation in saturated sediments," *Journal of the Acoustical Society of America*, Vol. 47 (5): 1440-1447.

Wang, Z. and Nur, A. (1990). "Dispersion Analysis of Acoustic Velocities in Rocks." *Journal of the Acoustical Society of America*, Vol. 87 (6): 2384-2395.

Sand Aging Field Study

R.A. Green[1], M. ASCE, P.E., R.D. Hryciw[2], M. ASCE, D.A. Saftner[3], S.M. ASCE, C.D.P. Baxter[4], M. ASCE, P.E., Y. Jung[3], and T. Jirathanathaworn[3]

[1]Associate Professor, Department of Civil and Environmental Engineering, University of Michigan, 2372 G.G. Brown, Ann Arbor, MI 48109-2125; rugreen@umich.edu
[2]Professor, Department of Civil and Environmental Engineering, University of Michigan, 2366 G.G. Brown, Ann Arbor, MI 48109-2125; romanh@umich.edu
[3]Graduate Student Research Assistant, Department of Civil and Environmental Engineering, University of Michigan, 2340 G.G. Brown, Ann Arbor, MI 48109-2125; dsaftner@umich.edu; yongsub@umich.edu; jirathan@umich.edu
[4]Associate Professor, Departments of Ocean/Civil and Environmental Engineering, University of Rhode Island, Narragansett, RI 02882; baxter@oce.uri.edu

ABSTRACT: Aging effects in sand, such as increases in penetration resistance with time after deposition, densification, and/or liquefaction, are known to occur *in situ*, but the causes of these effects are not fully understood. Nonetheless, these effects have important ramifications in earthquake engineering. First, the lack of understanding of the phenomenon is an impediment to quality assurance/quality control (QA/QC) for ground densification projects aimed at mitigating the damaging effects of liquefaction. This can be understood by considering that most liquefaction evaluation procedures correlate liquefaction susceptibility to *in situ* indices, such as penetration resistance (SPT and CPT) and small strain shear wave velocity (V_s), all of which are influenced by aging. Consequently, it is unclear as to how long after ground densification QA/QC *in situ* tests should be performed to ensure that the densification was sufficient to mitigate liquefaction susceptibility. Presented herein is an overview of an ongoing sand aging field study where liquefaction is being induced by explosives, vibrocompaction (using a vibroflot), and a NEES vibroseis in a heavily instrumented sand deposit. The state and properties of the sand are being monitored as a function of time after the disruption of the soil structure.

INTRODUCTION

Presented herein is an overview of an ongoing field study, the objective of which is to develop a better understanding of the mechanisms and engineering implications of time-dependent changes, commonly referred to as "aging," in the state and properties of recently deposited, liquefied, and/or densified sands. The research study is collaborative and synergistic in nature and involves researchers from the University of

Michigan (UM) and the University of Rhode Island (URI). Additionally, Nicholson Construction is a corporate partner in the project, donating equipment time and use, and Dr. James K. Mitchell (Virginia Tech) is a project consultant.

Numerous field case histories in the literature attest to the existence of the aging phenomenon, which manifests itself through increases in *in situ* test indices such as CPT and SPT penetration resistances and small strain shear wave velocity (V_s) after deposition, densification, and/or liquefaction (e.g., Mitchell and Solymar, 1984; Dumas and Beaton, 1988; Jefferies et al., 1988; Schmertmann, 1991; Charlie et al., 1992; Ng et al., 1996; Stokoe and Santamarina, 2000; Howie et al., 2000, 2001; Amini et al., 2002; Ashford et al., 2004a,b). Several differing hypotheses have been proposed for the underlying mechanisms for the aging phenomenon, including secondary compression and microstructural changes (Mesri et al., 1990; Schmertmann, 1991; Bowman and Soga, 2003), chemistry (Mitchell and Solymar, 1984; Joshi et al., 1995), blast gas dissipation (Dowding and Hryciw, 1986), and biological activity (Martin et al., 1996). However, laboratory investigations have been inconclusive in determining the controlling mechanism (Baxter and Mitchell, 2004), and no study has been able to replicate in the laboratory the large increases in penetration resistance and shear wave velocity observed *in situ*. Impeding the understanding of the mechanisms underlying the aging phenomenon is that most published field case histories lack sufficient detail about spatial variability of soil properties, soil and pore water chemistry, and long-term property changes (> 1 yr). Nevertheless, field case histories provide ample empirical evidence of the phenomenon, and under controlled conditions, field investigations represent the best opportunity to study the aging process and to develop and test a quality assurance/quality control (QA/QC) metric for remedially densified sand.

In the remaining portions of this paper, an overview of previous studies examining the sand aging phenomenon is given first. This information was used to design the current field study, an overview of which is then presented.

PREVIOUS SAND AGING STUDIES

Published data showing the existence of sand aging come primarily from remedial ground densification case histories (explosive compaction, vibrocompaction, and deep dynamic compaction), supplemented in part by data from laboratory investigations. Because liquefaction is typically induced as the first step in the remedial ground densification process, it is logically surmised that aging also occurs in sand deposits following liquefaction by earthquake shaking (e.g., Arango and Migues, 1996; Lewis et al., 1999; Arango et al., 2000; Olson et al., 2001; Gassman et al., 2004). Extensive summaries of aging investigations are given by Mitchell et al. (1997) and Baxter (1999). The following brief review is excerpted from C. Baxter's contribution to Mitchell et al. (1997).

Field Investigations

The Jebba Dam project on the Niger River, Nigeria, was the first well documented field study where aging effects in sands were both significant and widespread

(Mitchell and Solymar, 1984). The project involved the treatment of foundation soils beneath a 42 m high dam and seepage blanket. The foundation soils consisted of deep deposits of alluvial medium to coarse silica sand. In some areas the depth to bedrock was greater than 70 m. Due to the large depths of loose sand requiring improvement, densification was performed in two stages. The upper 25 m of sand (and a 5 to 10 m thick sand pad placed by hydraulic filling of the river) was densified using vibrocompaction, while the deposits between 25 to 40 m were densified by blasting.

Following the blasting operations, it was observed that the sand exhibited both sensitivity (i.e., strength loss on disturbance) and aging effects after redeposition and/or densification. This phenomenon occurred throughout the site. Initially after improvement, there was a decrease in penetration resistance, despite the fact that surface settlements ranging from 0.3 to 1.1 m were measured. With time (measured up to 124 days after improvement), however, the cone penetration resistance was found to increase to approximately 150-200 % of the pre-densification values.

Aging effects were also observed after placement of hydraulic fill working platforms and after densification by vibrocompaction. In the case of vibrocompaction, however, there was considerable variability in the degree of aging throughout the site. Because of the greater increase in density and lateral stress caused by vibrocompaction than by blast-densification, no initial decrease in the penetration resistance (sensitivity) was observed following compaction.

A more recent example of aging effects in sand was reported by Ng et al. (1996) during construction of the Chek Lap Kok airport in Hong Kong. Vibrocompaction was performed in specific areas to improve the penetration resistance of the hydraulically placed sand. Cone penetration testing was performed at one location at different times, up to 47 days after improvement. A clear increase in penetration resistance was observed. As with the Jebba Dam project, the time-dependent increase in cone penetration resistance after vibrocompaction occurred with no detectable increase in density (i.e., surface settlement).

Laboratory Investigations

Although most of the examples of aging in sands reported in the literature are from field studies, some observations have been made in the laboratory as well. Afifi and Richart (1973) showed that when sand specimens are maintained under a constant confining pressure, the shear modulus determined at small strains increased with time of confinement. Thomann and Hryciw (1992) furthermore showed that a moderate shear straining following an initial aging period will decrease the small strain shear modulus, (i.e. negate the aging effects) only to be regained during a subsequent aging period. Daramola (1980) investigated the effects of aging on both the stiffness and shear strength of Ham River sand. Four consolidated drained triaxial tests were performed on samples with the same relative density and confining pressure (400 kPa), but consolidated for different periods of time (0, 10, 30, and 152 days). The test results showed that the stiffness increased and the strain to failure decreased with increasing time of consolidation. The samples consolidated for long periods of time also exhibited greater volumetric expansion (dilatancy) for given values of axial strain. Daramola concluded that a 50 % increase in modulus occurred for each log cycle of

time under stress. Despite the increase in modulus and dilatancy, however, there was no increase in peak shear strength with time of aging. More recent studies by Howie et al. (2001) and Bowman and Soga (2003) present results showing similar trends.

A laboratory study on the effect of time on penetration resistance was performed by Joshi et al. (1995). The influences of both sand type and pore fluid composition on the magnitude of aging effects were investigated. Two different sands were tested: a river sand and Beaufort Sea sand. Three different pore fluids were used: air, distilled water, and sea water. Specimens were prepared by pluviating the sand through either air or water (depending on the pore fluid to be used) into fixed wall cells and vibrated under a static vertical stress of 100 kPa until a desired density was achieved. This method resulted in very dense samples, ranging from 87 to 100 % relative density.

After loading, the specimens were aged for two years, and values of penetration resistance were obtained at various times in each specimen using a series of four, 1 cm diameter penetrometers so that redundant data could be obtained at each time. Aging effects were observed in all cases, but the effects were greater for submerged sand than for dry specimens. Scanning electron micrographs of the aged specimens in distilled water and sea water showed the presence of precipitates on and in between sand grains. An energy dispersive x-ray analyzer was used to determine the composition of the precipitate. For the river sand in distilled water, the precipitates contained calcium and possibly silica. For the river sand in sea water, the precipitates contained sodium, silica, calcium, and chlorine.

Baxter and Mitchell (2004) present the results of an extensive laboratory investigation that examined the influence of different combinations of relative density, temperature, and pore fluid on the aging effects of two different sands: Evanston Beach sand and Density sand. Evanston Beach sand is a tan, sub-angular, poorly graded fine sand and was selected because it had been used in a previous aging study by Dowding and Hryciw (1986). Density sand is a white, rounded, poorly graded, fine to medium sand used for sand-cone tests, and was chosen because its chemical composition (almost pure quartz) and grain shape are markedly different than those of Evanston Beach sand. The results from this study showed increases in the small strain shear modulus throughout most of the tests, and chemical analyses suggested that precipitation of carbonate and silica occurred in two tests. However, despite these changes, there was no corresponding increase in the mini-cone penetration resistance with time in any of the tests. The dichotomy between their laboratory results and the field observations of others lead to the following statement: "…some condition in natural deposits is not replicated in small-scale laboratory testing. Possible conditions that may be different in the field include the introduction of air and gas into the soil during ground improvement, heterogeneity of the deposit, energy imparted by ground improvement, and biological activity."

Hypothesized Aging Mechanisms

Historically, the most widespread theory used to explain aging effects in sand has involved interparticle bonding. Terzaghi originally referred to a "bond strength" in connection with the presence of a quasi-preconsolidation pressure in the field (Schmertmann, 1991). Generally, this bonding mechanism has been thought of as

cementation, which would increase the cohesion of a soil without affecting its friction angle. The cementing agent has commonly been thought to be silica-acid gel, which has an amorphous structure and would form a precipitate at particle contacts (Mitchell and Solymar, 1984). There is little direct evidence that cementation of sand particles by silica precipitation occurs after ground improvement. However, in a laboratory-scale blasting study, Hryciw (1986) demonstrated that explosive generated gases produce a significant fluctuation in pore fluid pH, which enhances dissolution and precipitation of silica and thus possibly assists the early diagenesis of sands. The strongest evidence to date of a chemical mechanism being responsible for aging effects is the work done by Joshi et al. (1995) presented earlier. A precipitate was observed on aged specimens of sand. In addition, the composition of the precipitate in the samples of river sand was found to contain calcium (the much more soluble fraction of the sand), possibly silica, and sodium and chlorine when sea water was the pore fluid.

Mesri et al. (1990) proposed that aging effects in sands are mechanical in nature and are due entirely to an increased frictional resistance which develops during secondary compression. However, this increased resistance does not occur solely from the change in density that occurs during drained secondary compression. Rather, it is due to a continued rearrangement of particles resulting in increased macro-interlocking of particles and increased micro-interlocking of surface roughness. These mechanisms are postulated to cause an increase in both stiffness and horizontal effective stress. Although no direct evidence was presented supporting their hypothesis, Mesri et al. (1990) used the triaxial test data from Daramola (1980) to argue against a chemical mechanism responsible for aging effects in sands. Specimens of Ham River sand that underwent drained secondary compression for up to 152 days had an increased modulus up to approximately 3 % strain. According to Mesri et al. (1990), this large strain would destroy any cementation and another less brittle mechanism must be responsible for the increase in stiffness.

Schmertmann (1991) also hypothesized that aging effects in sands are caused by mechanical effects. Like Mesri et al. (1990), increased interlocking between particles with time was proposed by Schmertmann as a significant factor. He also suggested that small particle movements during secondary compression would lead to internal stress arching and a more stable arrangement of particles. Bowman and Soga (2003) recently measured such particle movements in samples of dense sand. They showed that microstructural changes during secondary compression, including particle rotation and variations in local void ratio distributions, leads to the development of load chains and increased dilatancy.

CURRENT SAND AGING FIELD STUDY

As evident from previous studies, the underlying mechanisms of sand aging remain uncertain. The present study builds on the previous research and involves a field investigation where liquefaction/densification is being induced by explosives, a vibroflot, and a NEES vibroseis in a heavily instrumented sand profile and the state and properties of the sand are being monitored as a function of time after disruption of the soil structure. Explosives and vibrocompaction were selected because they are

ground densification methods in which the aging phenomenon has been observed in the past. However, both methods introduce foreign elements into the soil, as explosives generate gases and vibroflotation introduces heavily aerated water. The dissipation of the blast gases and air from the ground water with time after treatment may be one of the contributors to aging in sand. Also, as noted above, the blast gases change the pH of the pore fluid, which may contribute to the aging effects. To determine whether the dissipation of gases from pore water and the change in pH of pore water influences aging, liquefaction will be induced in the third region using a vibroseis from the University of Texas (i.e., NEES equipment). The vibroseis only introduces seismic waves into the ground and have been known to induce liquefaction, even unintentionally, in deposits of loose, saturated sand (e.g., Hryciw et al., 1990).

The site where the field aging study is being carried out is an active sand quarry owned by Mulzer Crushed Stone, Inc. and is located in southwestern Indiana. The authors characterized the field study site using vision cone penetration tests (VisCPT) (Hryciw and Shin, 2004; Jung et al., 2008), Marchetti dilatometer tests (DMT), seismic cone penetration tests (SCPT), and grain size analysis. The site profile consists of a clay cap of approximately 2 m overlying a thick deposit of sand. The water table at the time of the site investigation was approximately 1.75 m below the ground surface. Figure 1 shows a representative CPT sounding from the site. As may be observed from this figure, there is a loose sand layer from 2.5 to 3.2 m below the ground surface. Immediately below the loose sand layer is a dense sand layer, which will allow the influence of density on the aging phenomenon to be investigated.

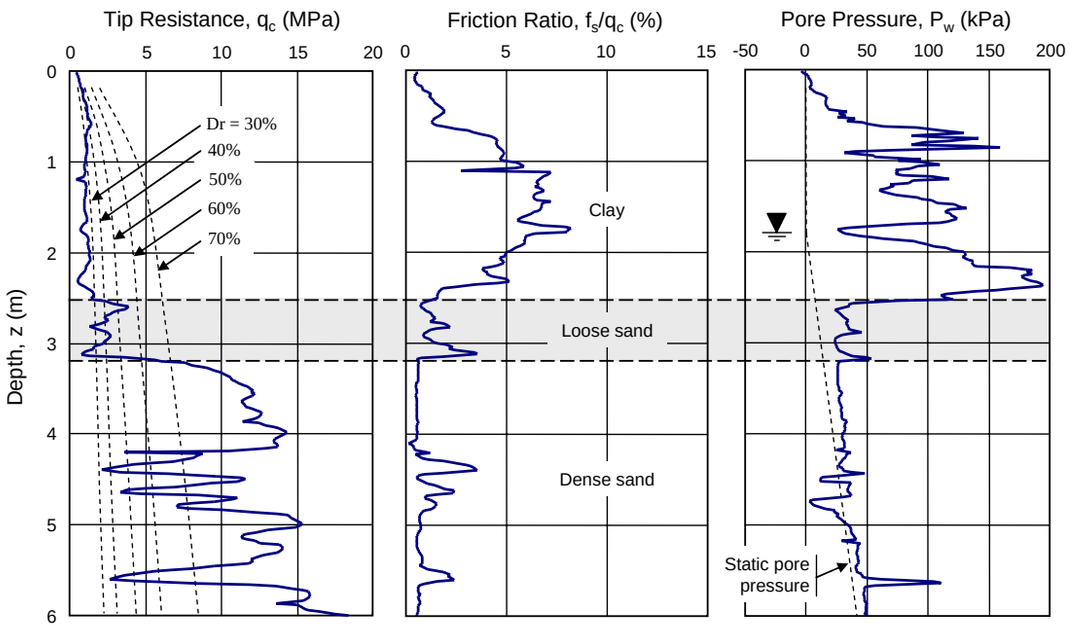


FIG. 1. CPT logs from the field test site. Superimposed on the tip resistance log are contours of equivalent relative density per Jamiolkowski et al. (1985).

The sand at the test site is "poorly graded" (SP), with a coefficient of uniformity of 2.05 and a coefficient of gradation of 0.78. Figure 2 shows the grain size distribution

for the sand. As observed, the grain size curve falls close to the "coarse boundary" that defines "most liquefiable soil." The VisCPT recorded movement of sand (or boiling) as the CPT probe advanced through the loose sand layer, clearly indicating that this soil is liquefiable.

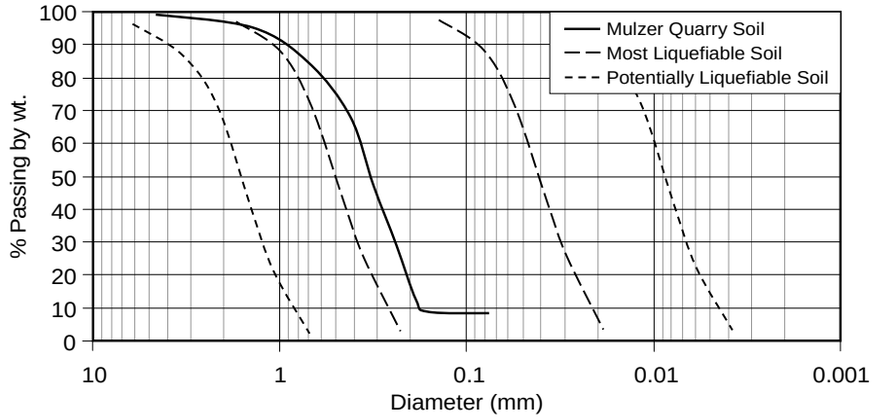


FIG. 2. Grain size distribution of sand from the loose sand layer. Superimposed on the plot are ranges of the grain size distributions of "Most Liquefiable Soil" and "Potentially Liquefiable Soil," per Tsuchida (1970).

At the site, liquefaction/densification will be induced by the three methods (i.e., explosives, vibrocompaction, and vibroseis) in three, non-overlapping regions. It is estimated that each region should have a minimum 15 m radius to ensure the energy imparted to induce liquefaction in one region does not influence an adjacent region, as well as to ensure that elevated pore water pressures do not migrate among adjacent regions. A plan view of the site test layout is shown in Figure 3, wherein the compaction/blast/shake points (labeled as energy points in Figures 3 and 5) are arranged in a diamond pattern with approximately 2.5 m between the points. The purpose for using multiple points is to replicate actual conditions for remedial densification projects. For the explosives test region, the four charges will be detonated sequentially, with a 0.5 sec delay between detonations 1 & 2 and 3 & 4, with a 4 hr delay between detonations 2 & 3. The selected delays are to ensure that the soil is subjected to multiple "hits," similar to actual explosive densification projects.

Within each of the regions, pore pressure transducers, accelerometers, and settlement tubes will be installed. The purpose of the pore pressure transducers is to confirm that liquefaction has been induced (i.e., excess pore pressure equal to the initial effective overburden pressure), and to allow the temporal and spatial monitoring of the excess pore pressure generation and dissipation. The accelerometers will allow the induced strains to be computed (e.g., Rathje et al., 2002, 2004). Also, using a similar approach to that of Zeghal and Elgamal (1994) or Davis and Berrill (1998, 2000) the accelerometers at different depths can be used to calculate the energy dissipated in the soil during the liquefaction process, which will allow an assessment of whether the amount of energy imparted in the soil influences the magnitude of aging effects (e.g., Baxter and Mitchell, 2004). Settlement tubes will provide settlement data as a function of depth and distance from the energy source.

Additionally, a light detection and ranging (LIDAR) system will be used to survey the ground surface before and at various times after the disruption of the soil structure, which will provide temporal and spatial ground surface settlement information.

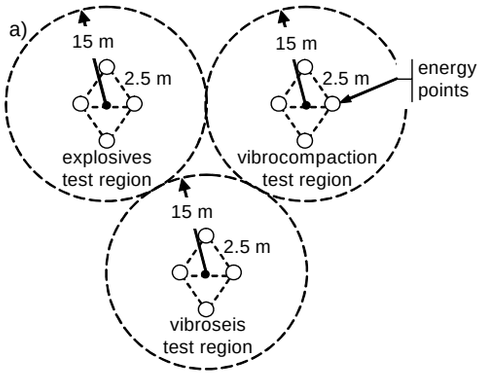


FIG. 3. Plan view of the site test layout: three non-overlapping regions will be used, one for each method by which liquefaction will be induced. The "energy points" are the location where liquefaction will be induced via vibro-compaction, explosive compaction, or using the vibroseis.

Two data acquisition systems will be used in the field study, with different types of data being collected by each. The first acquisition system is a series of wireless sensors that are being integrated with the MEMS accelerometers and pore pressure transducers. The wireless sensors were developed at the University of Michigan by Professor Jerome Lynch (Figure 4).

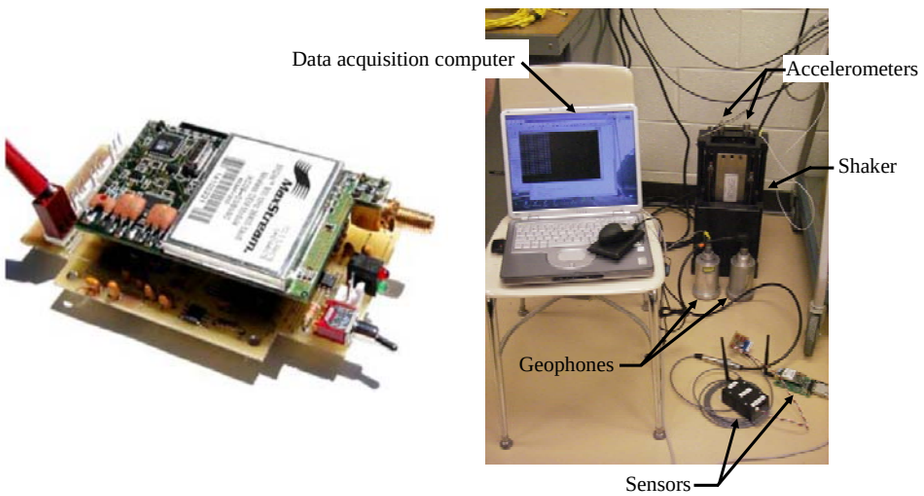


FIG. 4. Wireless sensing unit prototype developed at the University of Michigan by Prof. J.P. Lynch. Right: Sensor without battery and external container (Dimensions of the fully assembled unit are approximately 8 × 15 × 3 cm.). Left: Laboratory calibration of sensors with geophones and accelerometers.

The second data acquisition system being used is a tethered monitoring system by Olson Instruments, Inc. (i.e., the Freedom Data Acquisition System PC). This system

uses SHM Version 2.1 software and has 16 channels. Presently, the authors are performing comparisons of data acquired by the wireless and Olson systems.

A layout of the post-liquefaction *in situ* test plan is shown in Figure 5. The purpose for this plan is to monitor for aging effects in each of the three regions. The use of different techniques for inducing liquefaction/densification will allow chemical versus mechanical mechanisms to be discerned, to some extent. For example, if larger aging effects manifest in the region in which explosive compaction is performed relative to the other two regions, one possible explanation may the change in the pH of the groundwater due to the blast gases. However, conclusive discernment of the chemical versus mechanical aging mechanisms will be made from the synergistic laboratory study using soil and groundwater from the field site. In large part, the laboratory study will be driven by the field observations. The laboratory will provide a more controlled environment wherein the boundary conditions can be systematically varied so that the influence of each on aging can be ascertained, with the field investigation providing a comparative baseline of the cumulative influence of the various testing conditions and parameters.

Using the test plan shown in Figure 5, the *in situ* indices will be measured on a regular basis for the first four weeks after liquefaction/densification. However, the time interval between the radial sets of soundings will increase as the changes in the values of the *in situ* indices with time decrease. Monitoring of the aging effects will continue for the duration of the project.

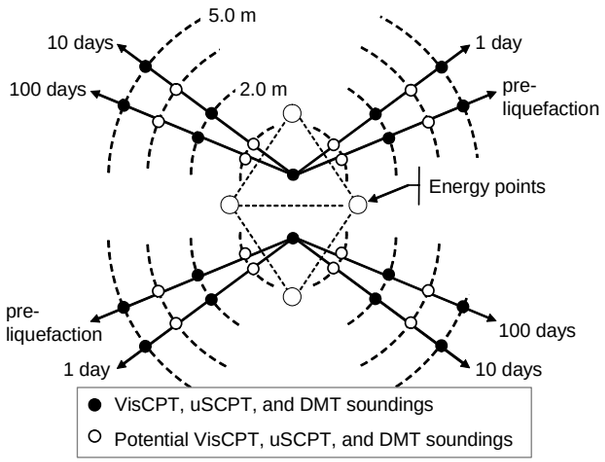


FIG. 5. Idealized plan view of *in situ* sounding locations for monitoring post-liquefaction/densification aging effects. In this figure, the four "energy points" indicate the locations of the vibrocompaction points, the explosives, or the vibroseis. At a given time after liquefaction/densification, *in situ* soundings will be performed at the prescribed radial distances from the center of the energy points.

As currently scheduled, explosive densification will be performed in Spring, 2008. This method of inducing liquefaction is being performed first because it will be the most demanding on the instrumentation and will serve to debug the test setup (and will be repeated if needed as a result of any experienced equipment failure). Vibrocompaction and vibroseis will be performed during the Summer or Fall of 2008.

CONCLUSIONS

The sand aging phenomenon posses an impediment to remedial ground densification programs, as it is uncertain how long after ground densification *in situ* index tests should be performed to ensure the soil is sufficiently densified. An ongoing field study and synergistic laboratory study is being conducted to improve the understanding of the mechanisms underlying the aging phenomenon and their quantitative influences on engineering properties. An increased understanding of sand aging will lead to greater efficiency in site improvement projects aimed at mitigating the risk of seismically induced liquefaction.

ACKNOWLEDGEMENTS

Support for the research presented herein came in part from the NSF grants CMMI 0530378 and CMMI 0636710. Mulzer Crushed Stone, Inc. is donating the use of its quarry and the expertise of its employees, and Nicholson Construction is donating the vibroflot equipment time and the expertise of its employees. Drs. Richard Woods, Jerome P. Lynch, and Kyle Rollins provided valuable assistance in the selection of field instrumentation and data acquisition systems. Mr. Jan Pantolin, Mr. Ayman Ibrahim, and Capt. Theresa White, USAF, provided valuable assistance in performing the preliminary site characterization. This support and assistance is gratefully acknowledged

REFERENCES

Afifi, S.S. and Richart, F.E., Jr. (1973). "Stress-History Effects on Shear Modulus of Soils." *Soils and Foundations*, Vol. 13(1): 77-95.

Amini, A., Howie, J.A., Woeller, D., and Beaton, N. (2002). "Effect of Ground Improvement on CPT Response." *Ground and Water: Theory to Practice*, Proc. 55th Canadian Geotechnical and 3rd Joint IAH-CNC and CGS Groundwater Specialty Conf. (D. Stolle, A.R. Piggott, and J.J. Crowder, eds.), Southern Ontario Section of the Canadian Geotechnical Society, 827-834.

Arango, I. and Migues, R.E. (1996). "Investigation of the Seismic Liquefaction of Old Sand Deposits." Report on Research, Bechtel Corporation, NSF Grant No. CMS-94-16169, San Francisco, CA.

Arango, I., Lewis, M.R., and Kramer, C. (2000). "Updated Liquefaction Potential Analysis Eliminates Foundation Retrofitting of Two Critical Structures." *Soil Dynamics and Earthquake Engineering*, Vol. 20: 17-25.

Ashford, S.A., Rollins, K.M., and Lane, J.D. (2004a). "Blast-Induced Liquefaction for Full-Scale Foundation Testing." *J. Geotechnical & Geoenv. Engrg*, Vol. 130(8): 798-806.

Ashford, S.A., Rollins, K.M., and Lane, J.D. (2004b). "Errata for Blast-Induced Liquefaction for Full-Scale Foundation Testing." *J. Geotechnical & Geoenv. Engrg*, Vol. 130(12): 1350.

Baxter, C.D.P. (1999). "An experimental study on the aging of sands," Ph.D.

Dissertation, Virginia Tech, Blacksburg, VA, 303 pp.
Baxter, C.D.P. and Mitchell, J.K. (2004). "An Experimental Study on Aging." *J. Geotechnical & Geoenv. Engrg*, Vol. 130(10): 1051-1062.
Bowman, E.T. and Soga, K. (2003). "Creep, Ageing and Microstructural Change in Dense Granular Materials." *Soils and Foundations*, vol. 43(4): 107-117.
Charlie, W.A., Rwebyogo, M.F.J., and Doehring, D. O. (1992). "Time-dependent cone penetration resistance due to blasting." *J. Geotechnical Engrg*, Vol. 118(8): 1200-1215.
Daramola, O. (1980). "Effect of consolidation age on stiffness of sand." *Geotechnique*, Vol. 30(2): 213-216.
Davis R.O. and Berrill, J.B. (1998). "Energy Dissipation and Liquefaction at Port Island, Kobe." *Bulletin of the New Zealand National Society for Earthquake Engrg*, Vol. 31(1): 33-50.
Davis, R.O. and Berrill, J.B. (2000). "Wildlife Revisited." *Developments in Theoretical Geomechanics* – The John Booker Memorial Symposium, A.A. Balkema, Rotterdam, Netherlands, 355-370.
Dowding, C.H., and Hryciw, R.D. (1986). "A laboratory study of blast densification of saturated sand." *J. Geotechnical Engrg*, Vol. 112(2): 187-199.
Dumas, J.C., and Beaton, N.F. (1988). "Discussion of "Practical Problems from Surprising Soil Behavior" by J.K. Mitchell." *J. Geotechnical Engrg*, Vol. 114(3): 367-368.
Gassman, S.L., Leon, E., and Talwani, P. (2004). "A Method to Assess the Liquefaction Potential of Aged Sediments." *Proc. 13th World Conference on Earthquake Engineering*, Paper No. 2843, 12pp.
Howie, J.A., Daniel, C., Asalemi, A.A., and Campanella, R.G. (2000). "Combinations of In-Situ Tests for Control of Ground Modification in Silts and Sands." *Innovations and Applications in Geotechnical Site Characterization*, Proc. of Sessions of Geo-Denver 2000 (P.W. Mayne and R. Hryciw, eds.), ASCE Geotechnical Special Publication No. 97, 181-198.
Howie, J.A., Asalemi, A.A., Shozen, T., and Vaid, Y.P. (2001). "Effects of Time on In Situ Test Results after Ground Improvement – New Insights from Laboratory and Field Data." *Proc. 2001 An Earth Odyssey*, The Intern. Assoc. of Hydrogeologists and The Canadian Geotechnical Society, 467-474.
Hryciw, R.D. (1986). "A study of the physical and chemical aspects of blast densification of sand." Ph.D. Dissertation, Northwestern University, Evanston, IL.
Hryciw, R.D., Vitton, S., Thomann, T.G. (1990). "Liquefaction and Flow Failure During Seismic Exploration, *J. Geotechnical Engrg*, Vol. 116(12): 1881-1899.
Hryciw, R.D. and Shin, S. (2004) "Thin Layer and Interface Characterization by VisCPT", Proceedings of the Second International Conference on Site Characterization (ISC'2), Porto, Portugal, pp. 701-706.
Jamiolkowski, M., Ladd, C.C., Germain, J.T. and Lacellotta, R. (1985). "New Developments in Field and Laboratory Testing of Soils," *Proc. 11th Intern. Conf. on Soil Mechanics and Foundation Engineering*, Vol. 1, San Francisco, 57-153.
Jefferies, M.G., Rogers, B.T., Stewart, H.R., Shinde, S., Williams-Fitzpatrick, D.J., and Williams-Fitzpatrick, S. (1988). "Island construction in the Canadian Beaufort Sea." *Hydraulic Fill Structures* (D.J.A. VanZyl and S.G. Vick, eds.), GSP No. 21,

816-883.
Joshi, R.C., Achari, G., Kaniraj, S.R., and Wijiweera, H. (1995). "Effect of aging on the penetration resistance of sands." *Canadian Geotechnical J.*, Vol. 32(5): 767-782.
Jung, Y., Hryciw, R. D., and Elsworth, D. (2008) "Vision Cone Penetrometer Calibration for Soil Grain Size", to be published in the Proceedings of the Third International Conference on Site Characterization (ISC'3), Taipei, Taiwan.
Lewis, M.R., Arango, I., Kimball, J.K., and Ross, T.E. (1999). "Liquefaction Resistance of Old Sand Deposits." *Proc. 11th Panamerican Conference on Soil Mechanics and Geotechnical Engineering*, Foz do Iguassu, Brasil, 821-829.
Martin, G.R., Yen, T.F., and Karimi, S. (1996). "Application of biopolymer technology in silty soil matrices to form impervious barriers." *Proc. 7th Austrailian-New Zealand Conference on Geomechanics*, Adelaide, Austrailia.
Mesri, G., Feng, T.W., and Benak, J.M. (1990). "Postdensification Penetration Resistance of Clean Sands." *J. Geotechnical Engrg*, Vol. 116(7): 1095-1115.
Mitchell, J.K., and Solymar, Z.V. (1984). "Time-dependent strength gain in freshly deposited or densified sand." *J. Geotechnical Engrg*, Vol. 110(11): 1559-1576.
Mitchell, J.K., Baxter, C.D.P., and Soga, K. (1997). "Time Effects on the Stress-Deformation Behavior of Soils." *Proc. Memorial Symposium for Professor Sakuro Murayama*, Kyoto University.
Ng, N., Berner, P., and Covil, C. (1996). "The ageing effects of sands." *Ground Engrg*, Geotechnical aspects of Hong Kong's new airport, December, 21.
Rathje, E.M., Chang, W.-J., Stokoe II, K.H. (2002) "Direct Evaluation of the Liquefaction Characteristics of Soil In Situ." *Proc. 8th US-Japan Workshop on Earthquake Resistant Design of Lifeline Facilities and Countermeasures against Liquefaction*, Tokyo, Japan.
Rathje, E.M., Chang, W.-J., Stokoe II, K.H., and Cox, B.R. (2004) "Evaluation of Ground Strain from In Situ Dynamic Response." *Proc. 13th World Conference on Earthquake Engineering*, Paper No. 3099, 15pp.
Schmertmann, J.H. (1991). " The mechanical aging of soils." *J. Geotechnical Engrg*, Vol. 117(9): 1288-1330.
Solymar, Z.V. (1984). "Earth foundation treatment at Jebba Dam site." *J. Geotechnical Engrg*, Vol. 110(10): 1415-1430.
Stokoe, K.H., II and Santamarina, J.C. (2000). "Seismic-Wave-Based Testing in Geotechnical Engineering." *Proc. GeoEng2000: An International Conference on Geotechnical & Geological Engineering*, Technomic Publishing Co., Inc., Vol. 1: 1490-1536.
Thomann, T. G. and Hryciw, R. D. (1992) "Stiffness and Strength Changes in Cohesion-less Soils due to Disturbance," Canadian Geotech. Jour., Vol. 29, No. 5. pp. 853-861.
Tsuchida, H. (1970). "Prediction and Countermeasure against the Liquefaction in Sand Deposits." *Abstract of the Seminar in the Port and Harbor Research Institute*, 3.1-3.33 (in Japanese).
Zeghal, M. and Elgamal, A.-W., (1994). "Analysis of Site Liquefaction Using Earthquake Records, *J. Geotechnical & Geoenv. Engrg*, Vol. 120: 996-1017.

Stress Integration Approach for Soil Damping Measurements in Torsional Testing

Inthuorn Sasanakul[1], A. M. ASCE, James A. Bay[2], M. ASCE, and Yoon-Shin Bae[3]

[1]Technical Manager, Center for Earthquake Engineering Simulation, Rensselaer Polytechnic Institute, Troy, NY 12180, sasani@rpi.edu
[2]Associate Professor, Civil and Environmental Engineering Department, Utah State University, Logan, UT, 84321; jim.bay@usu.edu
[3]Graduate Research Assistance, Civil and Environmental Engineering Department, Utah State University, Logan, UT, 84321; yoshbae@hanmail.net

ABSTRACT: Determination of strain associated with shear modulus and damping from hysteresis loops generated on torque-rotation plane during torsional test is complicated. This is due to nonuniform stress-strain variation occurring linearly with radius in a soil specimen in torsion. A conventional equivalent radius approach proposed by Chen and Stokoe (1979) is adequate for evaluating strain associated with shear modulus at low to intermediate strain levels. The approach is less accurate for damping measurement, as well as measurements at high strain. Stress integration developed by Sasanakul and Bay (2008) is used to account for the nonuniform stress-strain effect more precisely. The approach involving integration of an assumed soil stress-strain model is used to generate a plot of equivalent radius ratio versus strains based on shear modulus and damping separately. This paper presents the development of equivalent radius ratio curves used for damping measurement. The stress integration approach is applied for hyperbolic, modified hyperbolic, and Ramberg-Osgood models. Variation of equivalent radius ratio with normalized rotation for each model is presented. The results illustrate the usefulness of the stress integration approach and suggest that using a single value of equivalent radius ratio to calculate strains is not appropriate.

INTRODUCTION

When a soil specimen is subjected to cyclic loading in torsional tests, hysteresis loops generated on torque-rotation relationship represent the nonlinear stress-strain behavior and energy dissipating characteristics of the soil. Several approaches have been proposed to identify a specific strain associated with shear modulus and effective damping at a given rotation (Hardin and Drnevich 1972, Taylor and Parton 1973, Chen and Stokoe 1979).

An equivalent radius approach dealing with the nonuniform distribution of strain

in soil specimen was developed by Chen and Stokoe (1979). The approach is based on the assumption that the representative stress and strain in soil specimen in torsion occurs at a radius called the equivalent radius. To apply the equivalent radius approach, an equivalent radius ratio, R_{eq}, which is defined as the ratio of the equivalent radius, r, and the outside radius of soil specimen, R, is used to calculate the stress and strain at a given rotation. Shear strain is calculated from:

$$\gamma = \frac{\theta r}{L} = \frac{r}{R}\gamma_{max} = R_{eq} \times \gamma_{max} . \quad (1)$$

Shear strain at the outer surface or maximum shear strain, γ_{max} can be expressed as:

$$\gamma_{max} = \frac{\theta R}{L}, \quad (2)$$

where θ = rotational angle, R = radius of the soil specimen, and L = length of the soil specimen.

Chen and Stokoe (1979) obtained R_{eq} from a correction of the corresponded θ from the effective shear modulus (G_{eff}) calculated from the total torque-rotation relationship and γ from the equal value of shear modulus (G) from the theoretical stress-strain relationship. More details on this approach can be found in Chen and Stokoe (1979) and Sasanakul (2005). According to Chen and Stokoe, R_{eq} value varies from 0.82 for strains below 10^{-3} % to 0.79 for strains at 10^{-1} % for a solid specimen. In practice, a single value of R_{eq} has been used for range of strains as shown in FIG.1 (Hwang 1997, and Kim 1991).

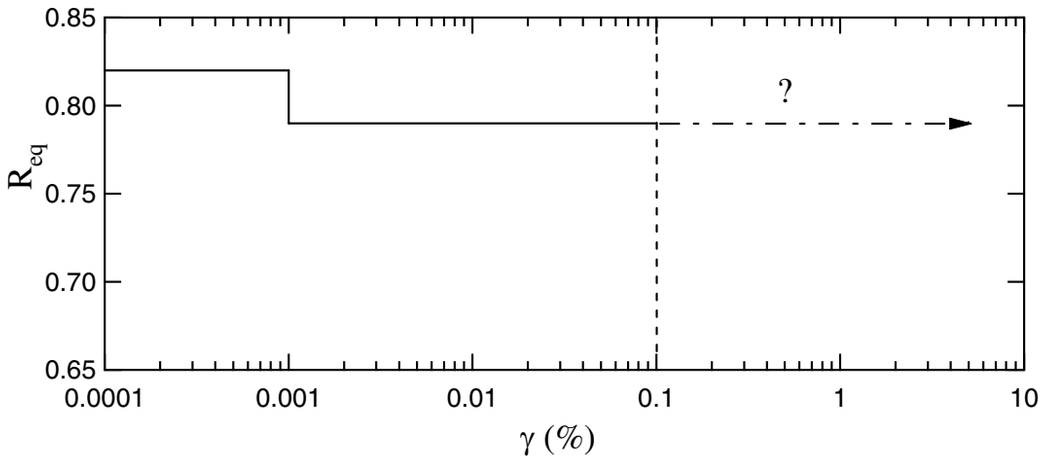


FIG. 1. R_{eq} values suggested by Chen and Stokoe (1979)

The equivalent radius ratio values suggested by Chen and Stokoe (1979) is adequate for evaluating strains corresponded to shear modulus at low to intermediate strain levels but the approach does not account for soil nonlinearity and appear to be less accurate at high strains (Sasanakul and Bay 2008). In addition, the same value of R_{eq} from FIG.1 was suggested for calculation of strain for damping. However, the equivalent radius at which a soil specimen contributes the most damping is not necessarily the same as the equivalent radius at which the representative shear

modulus was contributed. Using less accurate R_{eq} will result in misinterpretation of strain corresponding to a measured damping. Sasanakul and Bay (2008) reported that using a single value of R_{eq} as suggested by Chen and Stokoe (1979) is adequate for shear modulus and damping measurement at strain levels below 0.1%. For higher strains, the error in evaluating strain can be as high as 14.6% for damping measurements.

A new, more general approach called stress integration was developed by Sasanakul and Bay (2008) to account for the nonuniform stress-strain more precisely. In this paper, the approach is adopted to investigate the variation of R_{eq} versus rotation for damping measurement using three stress-strain soil models. These models are hyperbolic, modified hyperbolic, and Ramberg-Osgood. Results and discussions of each model are presented as followed.

STRESS INTEGRATION APPROACH

For a more general approach to account for nonuniform stress-strain than the conventional equivalent radius approach, the stress integration approach was proposed. The nonuniform stress-strain effect was accounted for by integrating the stress over the radius of soil specimen to obtain a torque-rotation relationship.

Stress integration starts by relating the shear stress acting on a circular section to the applied torque, T, using a basic equation of mechanics:

$$T = \int_A dM = \int \tau r dA = \int_0^R 2\pi r^2 \tau dr \text{ ,} \quad (3)$$

where M = resultant moment over the entire cross section area, r = interior radius, A = cross section area, and τ = shear stress.

If the stress-strain relationship is known, then for any given value of θ, the shear stress at any point in the specimen can be determined. This requires using the first part of Equation 1 to calculate the shear strain and calculating the corresponding shear stress from the known stress-strain relationship. Thus, the distribution of shear stress and strain over the entire cross section of the soil can be evaluated. Since the shear strain varies linearly with the radius, the distribution of the shear stresses has the same shape as the stress-strain relation. Torque can be obtained from the integral of Equation 3. As a result, the theoretical torque-rotation relationship can be developed. Curve fitting techniques are then used to match the theoretical torque-rotation relationship with the measured torque-rotation relationship from torsional testing to obtain the best fit model parameters. These model parameters are used to develop the stress-strain relationship for soil. More details description of the stress integration approach can be found in Sasanakul and Bay (2008).

EQUIVLENT RADIUS APPROACH FOR DAMPING MEASUREMENTS

In torsional testing, the torque-rotation relationship is measured directly and a hysteresis loop is developed in the torque-rotation plane. The effective hysteretic damping, D_{eff}, can be calculated similarly to the hysteretic damping, D, from the stress-strain plane except that the D_{eff} is associated with a given rotation, θ. The

values of R_{eq} based on damping can be obtained by matching D-γ relationship with the D_{eff} - θ relationship similar to the conventional equivalent radius approach used to calculate R_{eq} based on shear modulus. In this study, the stress integration approach improves this procedure because the D_{eff} -θ relationship (or G_{eff}-θ relationship) can be generated using either a closed form integration or numerically integration. Procedures for developing R_{eq} based on damping for three different soil models are described as followed.

Hyperbolic Model

For the hyperbolic model, the theoretical torque-rotation relationship can be calculated using the closed form solution presented by Sasanakul and Bay (2008). The hyperbolic stress-strain soil model and the closed form solution for torque-rotation relationship are presented in Equation 4 and 5, respectively.

$$\tau = \frac{G_{max}\gamma}{1+\left(\frac{\gamma}{\gamma_r}\right)} \tag{4}$$

where G_{max} = shear modulus at small strain, and γ_r = reference strain.

$$T = \frac{1}{3}\pi G_{max}\gamma_r R\left[2R^2 - 3R(\frac{\gamma_r L}{\theta}) + 6(\frac{\gamma_r L}{\theta})^2\right] + 2\pi G_{max}\gamma_r^4(\frac{L}{\theta})^3\left[\ln(\gamma_r) - \ln(\gamma_r + \frac{\theta R}{L})\right] \tag{5}$$

It is believed that the damping in soil consists of both hysteretic and linear, viscous-like damping. There is no single damping model available for soils that can fully describe both hysteretic and viscous-like damping behavior. As a result, only a hysteretic damping model was used in this study. The hysteretic loop is developed by applying the Masing rules. This assumption has some limitations. At low strains, the hysteretic damping approaches zero and at high strains the hysteretic damping may become very large. For example, the asymptote of hysteretic damping at high strains has a value of 2/π or 63.7% for the hyperbolic model. Neither of these behaviors exactly describes typical soil behavior. More research is needed to identify the best damping model for soils and the stress integration approach can then be utilized.

The hysteretic damping in the stress-strain plane is obtained as (Ishihara, 1996):

$$D = \frac{2}{\pi}\left[\frac{2\int_0^{\gamma}\tau(\gamma)d\gamma}{\gamma\tau(\gamma)} - 1\right] \tag{6}$$

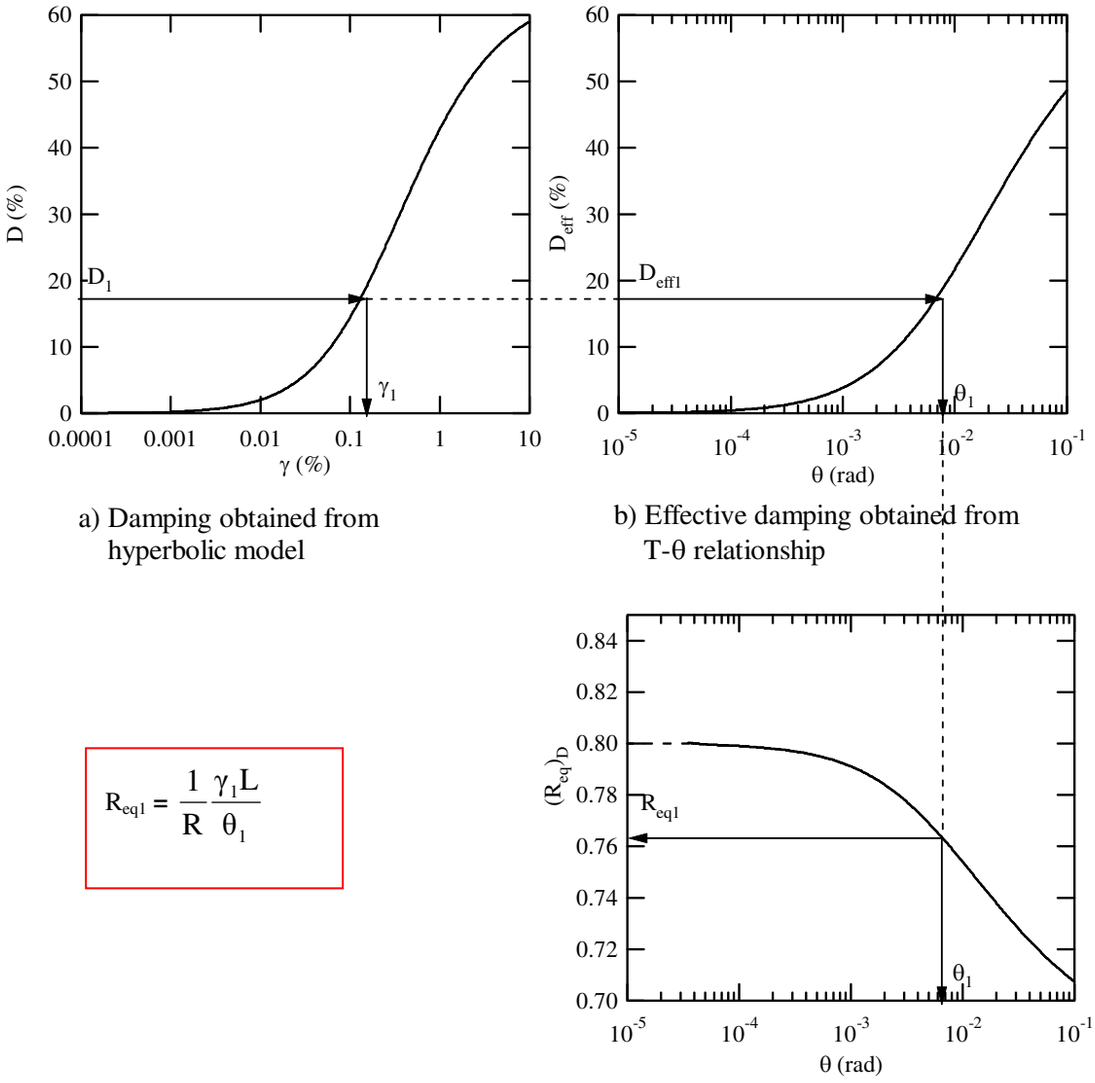
By introducing Equation 4 into Equation 6, the damping, D can be obtained from:

$$D = \frac{4}{\pi}\left[1+\frac{1}{\gamma/\gamma_r}\right]\left[1-\frac{\ln(1+\gamma/\gamma_r)}{\gamma/\gamma_r}\right] - \frac{2}{\pi} \tag{7}$$

Equation 7 is used to generate the D-γ relationship for the hyperbolic model shown in FIG. 2a.

In this case, a theoretical soil is used hence the model parameters; G_{max} and γ_r are known, thus the torque-rotation relationship is obtained directly from the closed form solution presented in Equation 5. Equation 6 can be transformed to obtain the effective damping, D_{eff} obtained from the torque-rotation plane thus the D_{eff} is calculated from:

$$D_{eff} = \frac{2}{\pi}\left[\frac{2\int_0^{\theta} T(\theta(\theta)}{\theta T(\theta)} - 1\right] \quad (8)$$



a) Damping obtained from hyperbolic model

b) Effective damping obtained from T-θ relationship

$$R_{eq1} = \frac{1}{R}\frac{\gamma_1 L}{\theta_1}$$

c) $(R_{eq})_D$ ratio curve based on damping

FIG.2. Determination of R_{eq} based on damping

Equation 8 was used to generate the D_{eff}-θ curve shown in FIG. 2b. The procedure to obtain values of R_{eq} is as follows. The damping, D_1 corresponding to a given shear strain, γ_1 can be obtained from FIG. 2a. A value θ_1 that is associated with the D_{eff} value equal to D_1 is determined in FIG. 2b. Then using Equation 9, a value of R_{eq} is calculated from:

$$R_{eq} = \frac{1}{R}\frac{\gamma L}{\theta}. \tag{9}$$

The R_{eq} values can be obtained and plotted for wide range of strains as shown in FIG. 2c.

It is observed that the R_{eq} curves for soils with different G_{max} and γ_r always merge to the same value of 0.8 at low strains and the R_{eq} value decreases as the strain increases. Effect of soil nonlinearity can be accounted for by plotting the R_{eq} versus normalized rotation as presented in FIG. 3. The term θ_r is a reference rotation defined as:

$$\theta_r = \frac{\gamma_r L}{R} \tag{10}$$

The R_{eq} curve based on damping is also compared with the R_{eq} curves based on shear modulus. The procedure to determine R_{eq} curves based on shear modulus can be found in Sasanakul and Bay (2008). As shown in FIG. 3, the R_{eq} curve based on damping is significantly lower than the R_{eq} curves based on shear modulus, especially at high strains. The R_{eq} values suggested by Chen and Stokoe (1979) approximate R_{eq} values for shear modulus, but significantly over-predict R_{eq} for damping at higher strains. These results also suggest that using a singe value of R_{eq} for a wide range of strains is not appropriate for damping.

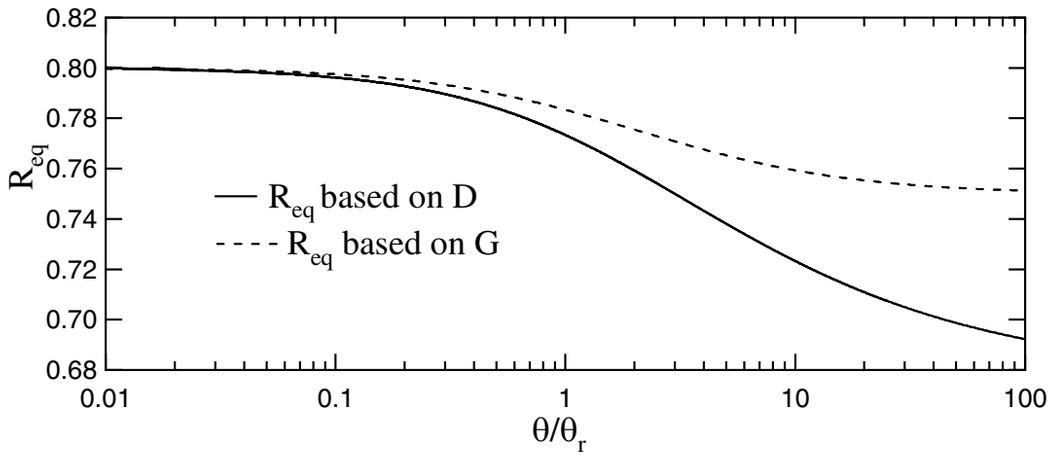


FIG. 3. Normalized R_{eq} curves based on both shear modulus and damping obtained from the hyperbolic model

Modified Hyperbolic Model

Stress integration approach is extended to generate R_{eq} values for damping using modified hyperbolic model. The modified hyperbolic model proposed by Darendeli and Stokoe (1997) is presented as;

$$\tau = \frac{G_{max}\gamma}{1+\left(\frac{\gamma}{\gamma_r}\right)^a} \quad (11)$$

where a = curvature coefficient.

Theoretical soils with the different curvature coefficients are used to generate the D-γ relationship. The D-γ relationship is developed by introducing Equation 11 into Equation 6 and performing integration. FIG. 4 shows the D-γ curve for modified hyperbolic model.

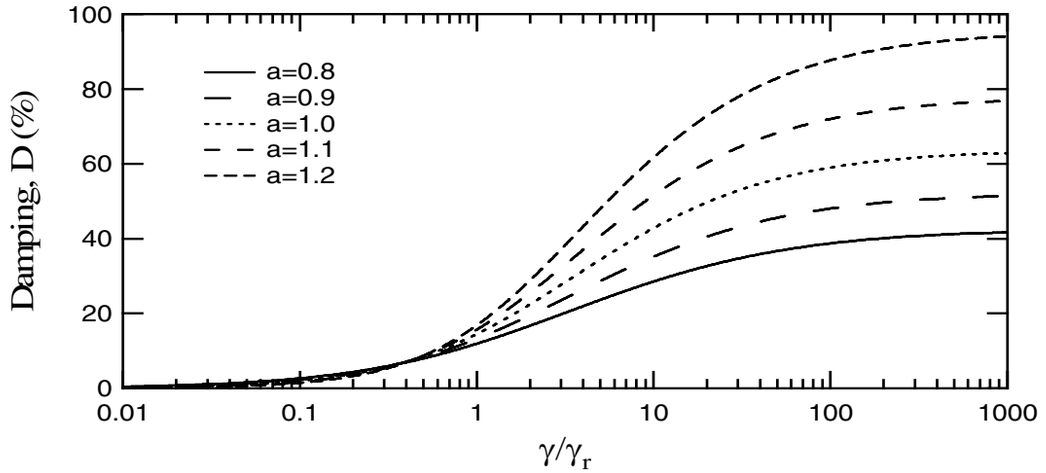


FIG. 4. Damping for the modified hyperbolic model

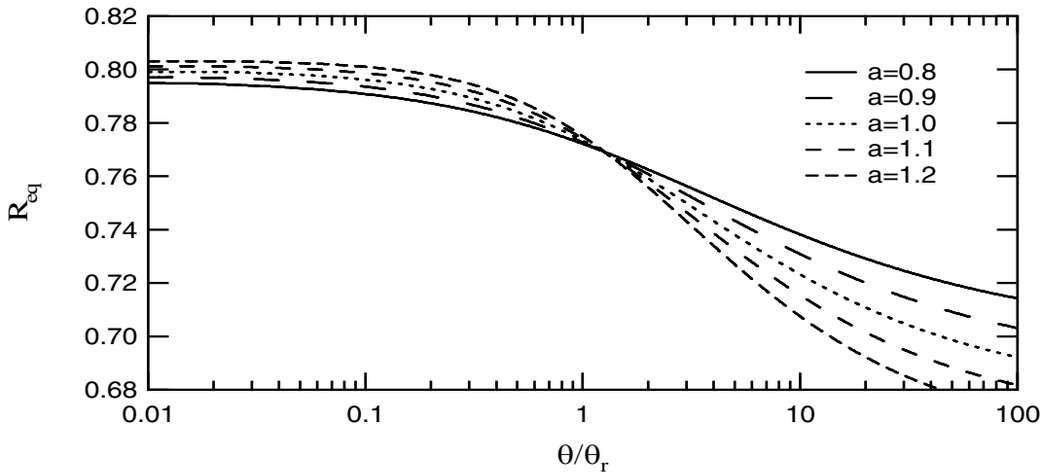


FIG. 5. R_{eq} curves based on damping for the modified hyperbolic model

The torque-rotation relationship can be established by numerically integration of Equation 3 using the stress-strain relationship from Equation 11. As presented in Sasanakul and Bay (2008), the method of numerical integration relative to strain can be employed for the modified hyperbolic model. The D_{eff}-θ curve can be obtained from Equation 8. Same procedure as the hyperbolic model is applied to determine the R_{eq} value presented in FIG.2. FIG. 5 shows the R_{eq} based on damping for the modified hyperbolic model using different curvature coefficients. The values of R_{eq} merge to

approximately 0.8 at low strain similar to the conventional hyperbolic model. More variation is observed for different curvature coefficients at high strain level.

Ramberg-Osgood Model

Stress integration approach was also extended to generate R_{eq} values for damping using the Ramberg-Osgood model. The stress-strain relationship described by the Ramberg-Osgood model is presented as;

$$\gamma = \frac{\tau}{G_{max}}\left(1+\alpha\left|\frac{\tau}{G_{max}\gamma_r}\right|^{b-1}\right) \tag{12}$$

Theoretical soils with different model parameters: α and b are used to develop the D-γ relationships presented in FIG. 6. It is noted that the value of damping approaches lower value at high strain when comparing with the other two soil models. Numerical integration is performed to generate the torque-rotation relationship and similar procedure as the other two soil models is used to obtain the R_{eq} value for the Ramberg-Osgood model. FIG. 7 presents the R_{eq} based on damping for the Ramberg-Osgood model using different model parameters (α and b). Overall the value of R_{eq} for the Ramberg-Osgood model is in the same range as the other two models. Less variation of R_{eq} at high strain is observed in comparison with the modified hyperbolic models.

IMPLEMENTATION OF STRESS INTEGRATION APPROACH FOR DAMPING MEASUREMENTS

A torsional shear test directly measures a torque-rotation curve. Additionally, an effective damping, D_{eff}, can be determined at various rotations, θ, as shown in FIG 2b. Theoretical torque-rotation curves can be determined from closed form integration of the hyperbolic stress-strain model, or numerical integration of the modified hyperbolic

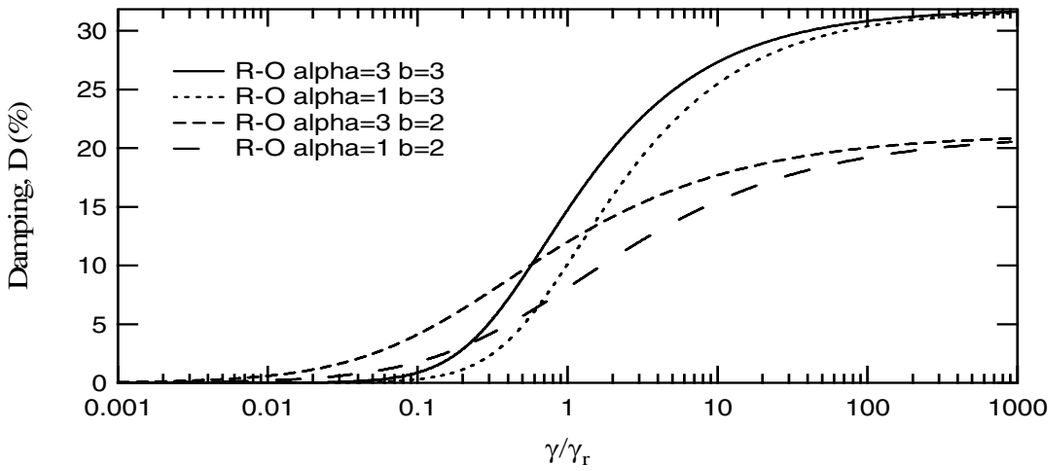


FIG. 6. Damping for Ramberg-Osgood model

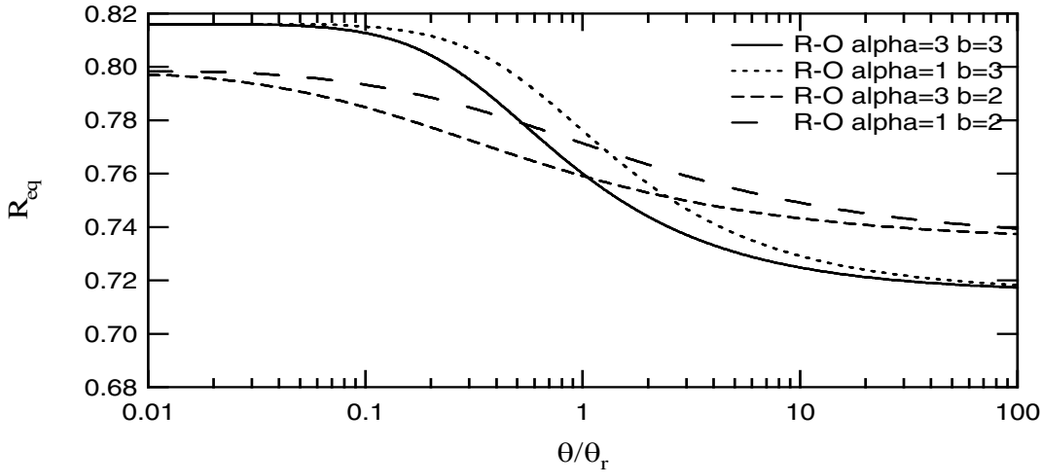


FIG. 7. R_{eq} curves based on damping for the Ramberg-Osgood model

and Ramberg-Osgood stress-strain models. By using curve-fitting methods, model parameters from each model can be determined to best match the measured torque-rotation curve, and the model giving the best match can be identified.

If the hyperbolic model is used to describe the stress-strain relationship for soil, the reference strain, γ_r, determined from curve fitting, will be representative of the soil nonlinearity. Using that value of γ_r, θ_r can then be determined using Equation 10, and the R_{eq} value based on damping shown in FIG. 3 to determine the strain, γ, at any rotation, θ. If the hyperbolic model is not the best stress-stain model for a particular soil, an analysis of R_{eq} for the other soil models such as the modified hyperbolic and Ramberg-Osgood models presented in this paper may be necessary. For routine torsional tests when performing the analysis of R_{eq} curves is not practical, it is recommended that the stress integration for the hyperbolic model should be performed to identify the model parameters. While this is not the best model to predict the stress-strain relationship of the soil being tested, this solution is considered good practice and no major errors are created.

SUMMARY AND CONCLUSIONS

The stress integration approach provides improvement from the conventional equivalent radius approach for damping measurement in torsional tests, especially at high strain levels. Sasanakul and Bay (2008) reported that using a single value of R_{eq} as suggested by Chen and Stokoe (1979) is adequate for shear modulus and damping measurement at strain levels below 0.1%. For higher strains, the error in evaluating strain can be as high as 14.6% for damping measurements. It is clear that using a single value of R_{eq} to calculate strains corresponding to shear modulus and damping for a wide range of strains is not appropriate. In this study, the stress integration approach accounts for the variation of R_{eq} over the range of strains and the soil nonlinearity. Three different stress-strain soil models provide differences in values of R_{eq}. The parameters for each model represent the nonlinearity of soil. Error in evaluating strains can be more pronounced if the soil nonlinearity is not taken into

account precisely.

The stress integration approach makes it possible to very accurately evaluate shear modulus and damping at any strain level. The approach provides flexibility to select the best model that shows the best match to the experimental data to represent the stress-strain relationship for a soil specimen. The limitation of this approach is that hysteretic damping model is used; therefore it does not fully describe the damping behavior of soils. If a more suitable damping model for soils is available, the stress integration approach can be applied using the same procedure.

REFERENCES

Chen, A.T.F., and Stokoe, K. H., II. (1979). "Interpretation of strain dependent modulus and damping from torsional soil tests." *Report No. USGS-GD-79-002.*, NTIS No. PB-298479, U.S. Geological Survey.

Darendeli, M.B. and Stokoe, K.H., II (1997). "Dynamic properties of soils subjected to the 1994 Northridge earthquake." *Geotechnical Engineering Report GR97-5*, Civil Engineering Department, University of Texas at Austin

Hardin, B.O. and Drnevich, V.P. (1972). "Shear modulus and damping in soils: measurement and parameter effects." *Journal of Soil Mechanics and Foundation Engineering Div*., ASCE, Vol. 98 No.SM6, June, 603-624.

Hwang, S. K. (1997). "Investigation of the dynamic properties of natural soils." *Phd Dissertation*, University of Texas at Austin.

Kim, D.S. (1991). "Deformational characteristics of soils at small strains from cyclic tests". *Ph.D. Dissertation*, University of Texas at Austin.

Ishihara, K. (1996). *Soil Behavior in Earthquake Geotechnics.* Oxford Science Publication.

Sasanakul, I. (2005). "Development of an electromagnetic and mechanical model for a resonant column and torsional shear testing for soils", *PhD. Dissertation*, Utah State University.

Sasanakul, I. and Bay, J.A. (2008). "Stress integration approach accounting for nonuniform stress-strain in resonant column and torsional shear testing for soils" *Journal of Geotechnical & Geoenvironmental Engineering,* in review.

Taylor. P. W., and Parton, I.M. (1973). "Seismic torsion testing of soils." *Proceedings of the 8th International Conference on Soil Mechanics and Foundation Engineering*. Moscow, U.S.S.R.

Water, Inertial Damping, and the Complex Shear Modulus

Paul Michaels, M. ASCE, P.E.

Professor, engineering geophysics, Boise State University, Boise, ID 83725-1535; pm@cgiss.boisestate.edu

ABSTRACT:

The author proposes an alternative to the traditional representation of soil damping. Rather than using damping ratio, this author advocates using viscosity as the specific soil property, especially for saturated permeable soils. Thus represented, the imaginary part of the complex shear modulus will vary directly with frequency. The point is particularly relevant in cases where the water table may change, thus affecting the dynamic design of foundations or structures composed of soils.

INTRODUCTION

Beginning around 1965, “equivalent viscosity” was conceived. Because resonant column studies performed on dry soil samples showed little or no viscous behavior, the sample viscosity was assumed to vary inversely with frequency (Hardin, 1965). This was done in order to continue using the Kelvin-Voigt (KV), viscous representation of the soil (which has become required under ASTM D4015). However, “equivalent viscosity” corresponds to a non-viscous viscosity. Approximately 20 years later, resonant column studies on both water saturated and dry soils revealed that the presence of water introduced a truly viscous behavior (Stoll, 1985). More recently, a Kelvin-Voigt-Maxwell-Biot (KVMB) representation of soils was published which is capable of representing damping in terms of soil permeability, porosity, and the presence of water (Michaels, 2006b). A map between the KV and KVMB representations was presented to permit the continued use of the KV formulation while taking into account the inertial coupling between soil solids and pore fluids. Such coupling is fundamental to the Biot (1956) view of wave propagation. Both the KV or KVMB models are truly viscous (friction increases with frequency).

Two Points of View, Waves and Vibrations

We begin by considering the equation for a plane, shear, S-wave in a Kelvin-Voigt (KV) continuum. The derivation appears in many text books. Let ρ be mass density, G be shear modulus, and η be viscosity. The inelastic S-wave equation is given as (Kramer, 1996)

$$\rho \frac{\partial^2 u}{\partial t^2} = G \frac{\partial^2 u}{\partial z^2} + \eta \frac{\partial^3 u}{\partial z^2 \partial t} \quad , \tag{1}$$

where u is particle displacement orthogonal to z, the spatial axis in the direction of wave propagation. Time is represented by t. One can divide through by mass density and this produces two constant coefficients on the right hand side,

$$C_1 = \frac{G}{\rho}, \qquad C_2 = \frac{\eta}{\rho} \quad . \tag{2}$$

The constant, C_1 (m^2/s^2) is the square of the elastic S-wave velocity, and C_2 (m^2/s) is the viscous damping of the wave. When C_2 is non-zero, C_1 is the square of the wave's phase velocity at the limit of zero frequency.

If we move to a vibrator point of view, Kramer (1996) gives a derivation for the damping ratio, ξ, as

$$\xi = \frac{\eta \omega}{2G} = \frac{C_2 \omega}{2C_1} \quad . \tag{3}$$

The shear modulus, G, may also be expressed in terms of complex numbers. Using Kramer's notation, the complex shear modulus is given as

$$G^* = G + i\omega\eta \quad . \tag{4}$$

The loss tangent is the ratio of the imaginary to real component in Eq. 4. For a truly viscous KV medium, η is a constant, and both the complex modulus and the loss tangent will vary with frequency ω. In the case of a vibrator, the oscillator frequency will be inversely proportional to the length of a given soil volume.

The concept of “equivalent viscosity” results from assuming that the viscosity, η, is no longer constant. Rather, damping ratio is assumed constant. This new viscosity is,

$$\eta = \frac{2G}{\omega} \xi \quad . \tag{5}$$

Essentially, this is a non-viscous viscosity, a mathematical convenience which introduces other issues. It is those issues which this paper is about. The convenience is that the complex shear modulus can now be written in terms of a constant damping ratio,

$$G^* = G\left(1 + i2\xi\right) \quad . \tag{6}$$

Engineering practice has been to treat damping ratio as a specific material constant (like density or the real part of the shear modulus).

Historical Background

The continuum representation can also be recast in terms of lumped parameters. This permits springs and dashpots to be employed in the analysis. Fundamentally, soils are represented by both stiffness (spring) and viscous damping (dashpot). Viscous behavior is evident when the resistance to motion varies with the particle velocity. Since particle velocity will increase with oscillatory frequency, we expect frequency dependence for key measures of motion, like damping ratio, loss tangent, phase velocity, and amplitude decay of a wave.

Fig. 1 (a) and (b) shows the KV representation for both the vibrator and wave points of view. In the case of a vibrating soil mass, we expect a sinusoidal exponential decay with time of the

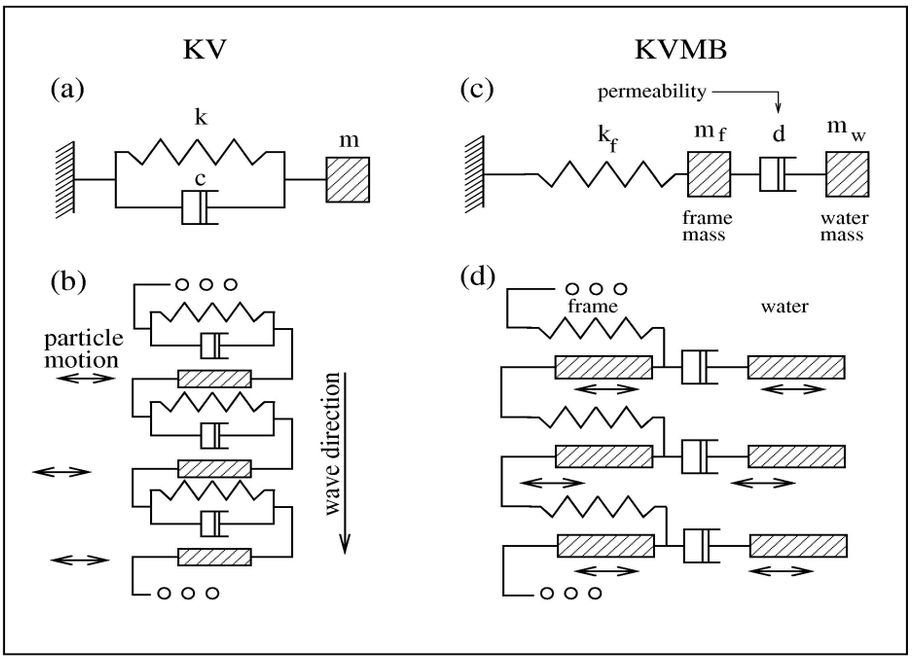


Fig. 1. KV (a) vibrator, (b) wave assemblage and KVMB (c) vibrator, (d) wave assemblage.

motion due to an impulsive excitation. The center frequency of vibration will depend on the length of the soil volume.

Assemblages of the single degree of freedom element may be used to represent the wave point of view. In the wave view, we expect the wave to exponentially decay in amplitude as a function of distance propagated. Further, we expect that the phase velocity and rate of decay to be both functions of frequency.

However, early attempts to measure the viscous behavior of soils showed little or no measurable frequency dependence of the motion. Hardin (1965) found that dry soils evaluated with what has become known as the resonant column test, ASTM-D4015 (ASTM, 1996) did not present the expected viscous behavior. Engineers conducting soil testing found themselves caught between a desirable mathematical representation and the conflicting reality of the measurements. Hardin proposed a solution in the synopsis of his 1965 paper.

> ". . . the viscosity should be assumed to decrease with frequency such that the ratio, viscosity times frequency divided by shear modulus, is a constant with frequency, in order to use this model. Values of the ratio for dry sands are given."

This solution is essentially Eq. 5 above. The model Hardin referred to was the KV representation, and the measured sands were dry. The soil cylinder was strained in rotational shear. This became the standard way of doing the test, and the conclusion about viscosity lead to the definition of "equivalent viscosity". The concept of equivalent viscosity also worked its way into computer software like SHAKE (Schnabel et al., 1972).

Applying resonant-column tests on water saturated samples would occur later. Stoll (1985) compared the shear behavior of resonant-column tests on both dry and saturated soils. While the loss tangent was constant with frequency for dry soils, the same soils, when water saturated, demonstrated measurable variation of loss tangent with frequency. Thus, damping ratio could no longer be held as a constant.

This author has observed these same, behaviors between dry and saturated soils in down-hole shear wave surveys (Michaels, 1998; Michaels, 2006a). The long held contention that pore fluids may interact with the soil frame producing a viscous damping makes particular sense when the medium is permeable. Further, the amount of friction due to relative fluid-frame motion might be expected to be greater with increasing pore size, up to some limit where the friction might begin to drop off in very large pore spaces. Stoll's (1985) measurements demonstrated greater viscous behavior for the sand than was observed for the silt.

KVMB, An Alternative Representation

An alternative representation to the Kelvin-Voigt (KV) model was published for the specific case of shear strain (Michaels, 2006b). The representation was termed Kelvin-Voigt-Maxwell-Biot (KVMB) since it was based on the ideas of those authors. The KVMB representation splits the combined mass into two components (pore fluid and solid frame). These two masses are connected by a dashpot which can then be related to permeability. The KVMB model can also be used to represent both vibrations and wave propagation, Fig. 1 (c) and (d). A mapping between the KV and KVMB representations is included in Michaels (2006b). With this mapping, one may continue to use the KV model, and the mapping provides a connection to soil properties like permeability and porosity.

DOMAINS OF APPLICATION

Pore Fluid Density and Inertial Coupling

One might expect that, since air is also a viscous fluid, viscous behavior should also be observed for dry soils. Indeed, this seems to be the case when the soil is subjected to compressive strain (Michaels, 2006a). However, in the case of shear, the mechanism is inertial, and the low density of air significantly reduces the resistance to motion that an air mass can produce. An analogy would be this. Consider squeezing a sponge to remove either the air or water in the pores. Then consider shaking the sponge. Squeezing (compression) is far more effective in producing a relative motion between the fluid and the solid. The image of a dog shaking its wet fur dry may also be helpful.

Using a truly viscous representation is important in shear when the pore fluid is dense, and permeability is in a range that will permit relative motion between the fluid and frame under an inertial drive. Thus, water saturated and permeable soils require a truly viscous representation, while dry soils apparently do not.

Damping Ratio vs. Viscosity as a Soil Property

Engineering practice tends to follow the equivalent viscosity model and represent the soil damping property in terms of a constant damping ratio (Rix et al., 2000). Often, numerous studies are cited for this decision. For those numerous studies which were conducted on dry samples, or samples of low permeability, this is easy to understand. Most resonant column work is done on dry (air saturated) samples, so it is not surprising that damping ratio has

been considered a constant. The thesis of this paper is two fold:

1. Water saturated soils are not well represented by a constant damping ratio, but by constant viscosity if they are permeable. Water saturated soils are different from dry soils, and engineering design needs to consider the water table.
2. One should refrain from using the damping measurements taken from tests on dry soils when the field conditions are expected to be water saturated and permeable. If tests are done on saturated samples, one may either overestimate or underestimate the damping. Under the constant damping ratio assumption, these possibilities exist due to the frequency dependence of damping ratio under saturated conditions.

In this author's view, using a truly viscous representation will always be best, even when not necessary. Dry soil viscosities can always be represented by very small viscosities. The “equivalent viscosity” representation does not enjoy the same breadth of applicability, and can not represent the frequency effects presented by permeable, water saturated soils.

FIELD DATA EXPERIENCE

As mentioned above, a mapping was derived between the KV and KVMB representations (Michaels, 2006b). This mathematical map is achieved by eigenvalue decomposition of the governing differential equations for the two vibrator representations. Fig. 2 illustrates how a traditional KV damping ratio can be related to hydraulic conductivity under the KVMB model for the down-hole field data published in Michaels (1998). There are a number of steps.

1. Invert the wave measurements of velocity dispersion and amplitude decay to obtain C_1 and C_2 (Michaels, 1998).
2. Use Eq. 3. to compute a KV damping ratio for a vibrator of some defined thickness of soil (and hence frequency). The choice of length can be set to match the center frequency of the seismic wavelet. It is not a critical decision as long as one is on the coupled side of the mapping (Fig. 2).
3. For a given porosity and frequency, find the point on the KVMB mapping curve with an ordinate equal to the KV damping ratio of step (2).

The field data from Michaels (1998) were applied to the above procedure, and cases for a silt, sand, and gravel are shown in Fig. 2 (and Table 1). Several possible porosity curves are shown, since

Mapping of published down-hole data (Michaels, 1998)

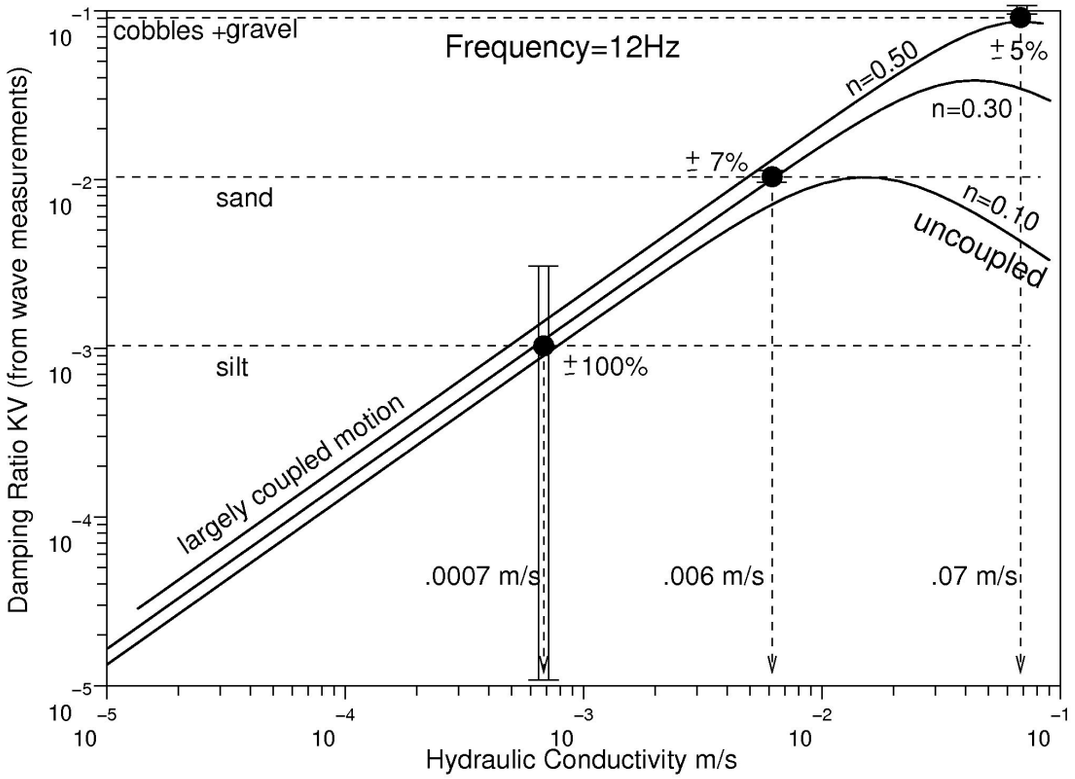


Fig. 2. Plot of 3 soil samples on the computed map between KV damping ratio and hydraulic conductivity. Mapping is for 3 possible porosity cases (10%, 30%, 50%). Confidence limits are 95% for KV damping ratio computations.

Table 1. KV Damping Ratio from C_1 and C_2 at 12 Hz (Michaels, 1998)

Soil	C1 (95%conf.)	C2 (95%conf.)	KV D. Ratio	D.R. 95% Conf.
Logan Silt	25567 +/-218	1 +/- 1	.00147	+/-100%
Logan Sand	51343 +/-375	14 +/- 1	.01028	+/- 7.2%
Idaho Gravel	94917 +/-2913	255 +/- 9	.10128	+/- 4.6%

measurements of soil porosity were not available. In the case of the Geologan 1997 data, soil type was determined from cone penetrometer soil behavior type (SBT). Soil sampling was done in the case of the Idaho data. At 12 Hz, silts are at the limit of detection for damping (large error bars). Also, the degree of water saturation may have been less than 100% at the Logan site. Thus, silts could easily be considered non-viscous at these and lower

frequencies. Sands and gravel, on the other hand, produce measurable damping effects. The 95% error bars on the computed damping ratio are 7.2% and 4.6% of the measured value for these soils respectively.

Domain of Equivalent Viscosity

From Fig. 2 we see that, at 12 Hz, the mathematics predicts largely coupled motion between the soil water and solid frame regardless of grain size. Fine grained soils, like silt, will be less permeable than the granular soils, and we expect far less friction to develop, making soils like silt comparable to dry soil in terms of dynamic behavior. This map is for a 12Hz vibrator. For a silt, significantly higher frequencies would be needed to shake the water into motion relative to the frame. Given that most earthquake motions are at lower frequencies, it is not likely that much harm would be done with an equivalent viscosity analysis in the case of a silt. Vibrations from blasting might be a different matter.

Domain of True Viscosity

We can see from Fig. 2 that as grain size increases, the degree of damping also increases (larger KV damping ratio). The advantage of specifying the soil profile in terms of viscosity instead of damping ratio is that dynamic calculations will automatically adjust for what ever frequencies are expected during an earthquake. The importance of this varies with pore fluid. Using viscosity instead of a single damping ratio benefits one most when water is the fluid, and permeability is large. In any case, a truly viscous representation will work for all soils. When the soil is of low permeability, the viscosity will just be a very small number.

Another observation might be that laboratory tests on water saturated samples of low permeability might require forced excitation at high frequencies to obtain a good measurement. At low frequencies, the damping ratio will be difficult to measure, and quite small in value. Fig. 3 illustrates how shaking the water saturated silt at about 100 Hz should produce the same degree of frictional loss as the sand shaken at 12 Hz.

CONCLUSIONS

The current use of “equivalent viscosity” will certainly serve the engineering communities needs when the pore fluids are of low density (ie. air), or if the soil is so impermeable that viscous effects are prevented by lack of relative motion between the pore fluid and

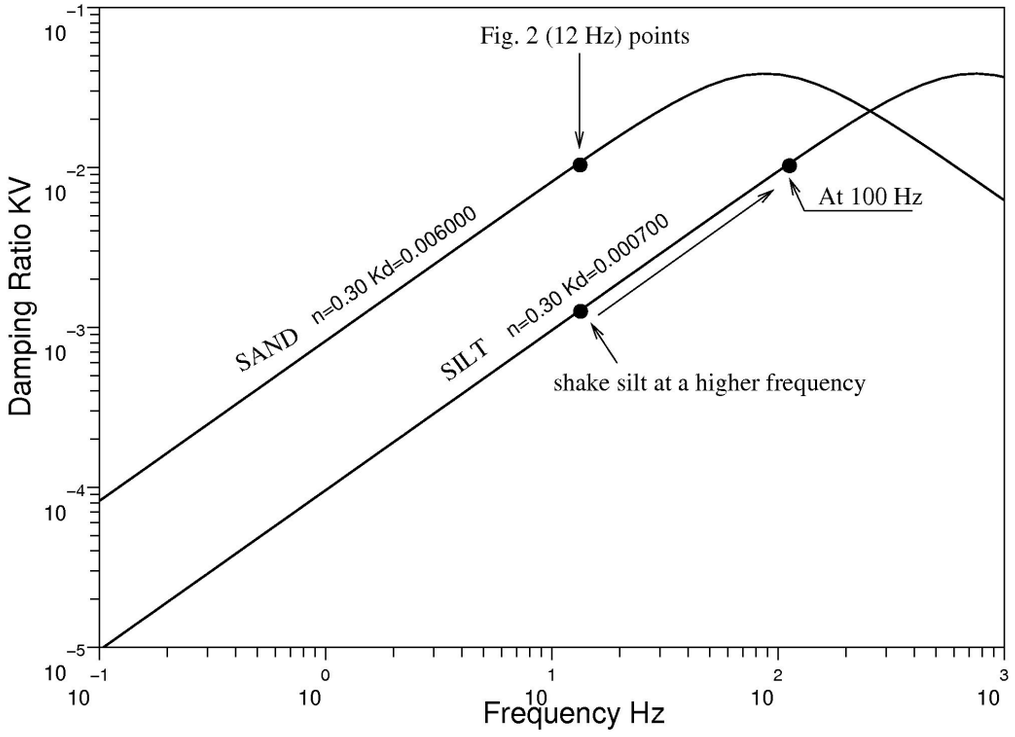


Fig. 3. Improved confidence in the measurement of a silt's damping is predicted by the KVMB model if the frequency is increased.

frame. However, in permeable soils, the equivalent viscosity approach will not be able to capture the variation in damping ratio as a function of frequency. The worse case would be to measure a damping ratio on a dry sample of a granular soil, and then apply that result to a water saturated design problem.

Using a “truly viscous” representation will be appropriate over all domains. Dry or impermeable soils would just present very small values of viscosity, η, or damping coefficient C_2. However, best results would occur by determinations of soil stiffness and damping under the conditions of the field design problem. This requires knowledge of the water table and its variation with time.

Improvements in the measurement of damping can be had by selecting a vibration frequency that results in a large value of damping. At low frequencies, the less permeable soils may present damping values below reliable measurement capabilities.

ACKNOWLEDGMENTS

The author would like to thank the ASCE GeoInstitute and Utah State University for providing the field site and borehole at the Geologan 1997 conference. In particular, Dr. Caliendo of the Utah State Civil Engineering Department did a great job supervising the drilling and management of the field day. Thanks also go to S-Sixteen Inc., Anderson Associates Inc. and Dr. Warren Barrash for providing access to the Idaho borehole.

Computer data processing was done using open source software running in the Linux operating system. There are too many contributors to give individual credit.

REFERENCES

ASTM. (1996). “Standard test methods for modulus and damping of soils by the resonant-column method.” *D4015*, West Conshohocken, Pa.

Biot, M. (1956). “Theory of propagation of elastic waves in a fluid saturated porous solid. I: Low-frequency range” *J. Acoust. Soc. Am.*, 28(2), 168-178.

Hardin, B.O. (1965). “The nature of damping in sands.” *J. Soil Mech. Found. Div.*, Vol. 91 (1), 63-97.

Kramer, S.L. (1996), *Geotechnical earthquake engineering*, 1st Ed., Prentice-Hall, Upper Saddle River, N.J.

Michaels, P. (1998). “In situ determination of soil stiffness and damping.” *J. Geotech. Geoenviron. Eng.*, Vol. 124 (8), 709-719.

Michaels, P. (2006a). "Comparison of Viscous Damping in Unsaturated Soils, Compression and Shear." *Unsaturated Soils 2006, Vol. 1, Proceedings of the Fourth International Conference on Unsaturated Soils,* (GSP 147), ASCE, Reston, VA. 565-576.

Michaels, P. (2006b). “Relating damping to soil permeability” *Int. J. of Geomechanics*, Vol. 6 (3), 158-165.

Rix, G.J., Lai, C.G., and Spang Jr., A.W. (2000). “In situ measurement of damping ratio using surface waves.” *J. Geotech. Geoenviron. Eng.* Vol. 126 (5), 472-480.

Schnabel, P.B., Lysmer, J., and Seed, H.B. (1972). “Shake, A computer program for earthquake response analysis of horizontally layered sites.” *Report No. EERC 72-12*, U. of California, Berkeley

Stoll, R. (1985). “Computer-aided studies of complex soil moduli.” *Proc., Measurement and Use of Shear Wave Velocity for Evaluating Dynamic Soil Properties*, ASCE, New York, 18-33.

Dynamic Properties of Naturally-Cemented Silts

Ravi Murthy, MASCE[1], Soheil Nazarian, MASCE, [2] and Miguel Picornell, MASCE[3]

[1] RM Geoconsultants, L.L.C., Phoenix, Arizona, 3217 E. Desert Cove Ave, Phoenix, AZ 85028; rmgeoconsultants@att.net
[2] Professor, Department of Civil Engineering, University of Texas at El Paso, El Paso, TX 79968; nazarian@utep.edu
[3] Miguel Picornell, Ph.D., P.E., Professor, North Carolina A&T State University; mpicorne@ncat.edu

ABSTRACT

Large deposits of naturally-cemented soils occur in the semi-arid regions of the Southwest, United States. Some of these soils have relatively large void ratios and often exhibit unique characteristics under static and dynamic loads. The dynamic properties of these cemented soils with large void ratios have received little attention in technical literature, mainly due to the difficulty associated with recovering undisturbed specimens of this type of material. This paper presents the results of a cyclic triaxial test program performed on relatively undisturbed samples of cemented silts obtained from block samples. Tests were carried out both under natural moisture contents and after saturation. The results of this study show that the Young's modulus of the soil increases with the degree of cementation, while the damping ratio is relatively insensitive to the degree of cementation.

INTRODUCTION

This paper describes a laboratory testing program conducted to evaluate the dynamic properties of naturally-cemented silts from a site in West Texas. The unique aspect of these silts is their relatively large void ratio – on the order of 0.9. Although soils of this type are fairly common in the arid desert regions of the Southwest US, few investigators have studied and reported the dynamic properties of these soils. The difficulty in obtaining undisturbed specimens is the primary reason for this lack of information. The effects of strain level, confining pressure, and the degree of saturation on the Young's modulus and damping ratio were studied. Two series of tests were performed on specimens at in-situ water content. The objectives of these tests were to verify the repeatability of the test results, and to study the stress-strain behavior of the soil at high strain levels. A third series of tests was performed on saturated specimens. These specimens were consolidated before testing to high strain levels.

GENERAL CONDITIONS

The site was located in the Trans-Pecos region of Texas, in the Basin and Range Physiographic region, about 60 miles Southeast of El Paso, and about 12 miles Northeast of Fort Hancock in Hudspeth County.

The specimens tested during this program were obtained from an exploratory trench excavated at the site. This trench was about 200 ft long, and four ft wide. At the deepest point, the trench was approximately 20 ft deep with vertical walls. The upper six feet of the soil generally comprised of a light brown silty sand, with low cementation. The next four ft were sandy gravel. Below this was a layer of cemented silt, about three ft in thickness. All specimens were obtained from this layer. The layer of cemented silt was underlain by an aggregate of coarse sand, gravel and cobbles, held together by a moderate to strong cementation, and typically locally referred to as "caliche". The soils were characterized as sandy silts of low plasticity with fines content (finer than No. 200 sieve) of approximately 60% and a plasticity index of approximately 6. The calcium carbonate content was used as a surrogate for the degree of cementation of the specimens. The degree of cementation of the specimens was highly variable (varying between 5 and 47%). All specimens had high void ratios ranging from 0.81 to 0.91.

Block samples were first hand-carved from the walls of the exploratory trench. Each block was individually wrapped in plastic film and cheesecloth. The sample was then coated with wax, and carefully transported to the testing laboratory. The individual samples for the cyclic triaxial tests were carved from the block samples using small hand tools.

CYCLIC TRIAXIAL TEST PROGRAM

This paper describes three series of tests performed during this program. The relevant information about the specimens tested is included in Table 1. The procedures followed in each of the series are briefly described below.

Repeatability Tests

Four specimens at in-situ moisture content (RD1 through RD4 in Table 1) were tested at four different confining pressures ranging from 5 to 40 psi over a strain range from 0.03 to 0.12% (peak-to-peak). Each specimen was tested at increasing strains at a constant confining pressure and in-situ moisture content. After each strain increment, the specimen was tested at the lowest strain and the modulus was estimated. The modulus measured at the lowest strain after each increment of strain was compared to the modulus of the specimen at the lowest strain at the start of the test program. If the modulus obtained was noticeably less than the modulus initially measured at the same strain level the specimen was considered to be at the onset of degradation. After testing at the maximum strain level was completed, the confining pressure was raised to the next increment, and the testing procedure repeated. After testing at a confining pressure of 40 psi, the confining pressure was reduced to 5 psi, and the specimen was checked for degradation once more.

Table 1 - Summary of Tested Specimens

SAMPLE ID	CEMENT Content (%)	COMMENTS ON TEST
RD1	25	Tested to assess repeatability of test methods. Tests at low to moderate strains. Each sample tested at in-situ moisture content at confining pressures of 5, 10, 20, and 40 psi.
RD2	47	
RD3	22	
RD4	Not Tested	
SD1	12	In-situ moisture, confining pressure = 5 psi. Tested to strains > 0.5%.
SD2	14	In-situ moisture, confining pressure = 10 psi. Tested to strains > 0.5%.
SD3	5	In-situ moisture, confining pressure = 20 psi. Tested to strains > 0.5%.
SD4	11	In-situ moisture, confining pressure = 40 psi. Tested to strains > 0.5%.
SW1	16	Saturated, confining pressure = 5 psi. Tested to strains > 0.5%. Undrained.
SW2	10	Saturated, confining pressure = 10 psi. Tested to strains > 0.5%. Undrained.
SW3	Not Tested	Saturated, confining pressure = 20 psi. Tested to strains > 0.5%. Undrained.
SW4	13	Saturated, confining pressure = 40 psi. Tested to strains > 0.5%. Undrained.

Tests to Failure

Four other specimens at in-situ moisture content (SD1 through SD4 in Table 1) were tested in the second series of tests. The objective of these tests was to study the variation in modulus with strain at higher strain levels. A different specimen was used for each confining pressure and each specimen was tested to "failure." The specimen was considered to be in a state of "failure" when the strains were so large that the variation of load with time was no longer sinusoidal. This occurred at strain levels of approximately 1%. When testing was complete at each increment of strain, the strain amplitude was reduced to about 0.03%, and the specimen was checked for degradation.

Tests on Saturated Specimens

The final four specimens were tested after saturation (SW1 through SW4 in Table 1). Each specimen was saturated at an effective confining pressure of 5 psi, and then consolidated at the effective confining pressure at which the test was to be performed (i.e. 5, 10, 20, and 40 psi). The specimens were then tested at increasing strain levels.

RESULTS

Young's Modulus

Repeatability Tests

The variation in modulus with strain amplitude for four specimens (RD1 through RD4), at a confining pressure of 5 psi is shown in Figure 1. The fifth set of data in the Figure (Test SD1) is from a specimen tested to failure at a confining pressure of 5 psi. Data from 4 of the 5 specimens plots within a relatively narrow band. Specimen RD2 exhibited a higher stiffness than the other four specimens, probably due to a higher degree of cementation (47% carbonate content). Similar behavior was observed at confining pressures of 10, 20 and 40 psi.

Figure 2 depicts the variation in modulus with cementation for confining pressures of 10 and 40 psi at a strain level of 0.04%. As expected, at a given confining pressure, the modulus increases with increasing cementation. This relationship is fairly linear, albeit with some scatter in the data.

It appears that the effect of cementation on modulus decreases as the strain level increases. This trend can be seen in Figure 3 which depicts the variation of modulus with cementation at strain levels of approximately 0.03, 0.06, and 0.12%. These results were obtained from tests performed at an effective confining pressure of 20 psi. Similar trends are also observed at other confining pressures used in the test program.

Tests to Failure

Figure 4 depicts the variation in modulus with strain amplitude and confining pressure for samples tested to high strains. The modulus decreases with strain, and generally increases with increasing confining pressure. One discrepancy is evident in the data. For confining pressures of 10 psi and 20 psi, no appreciable differences can be seen in the moduli. This discrepancy may be attributed to the variation in the degree of cementation of the two specimens. The specimen tested at a confining pressure of 20 psi had a calcium carbonate content of about 5%, while the specimen tested at a confining pressure of 10 psi had a calcium carbonate content of about 14%. Therefore, the expected increase in modulus with confining pressure may have been offset by a substantial decrease in the degree of cementation.

The relationship between confining pressure and modulus is plotted in Figure 5. This relationship is nearly linear with some scatter. The scatter is likely caused by variability in the cementation of the samples tested. The scatter also appears to increase with increasing strain amplitude. The reason for this increased scatter is not apparent.

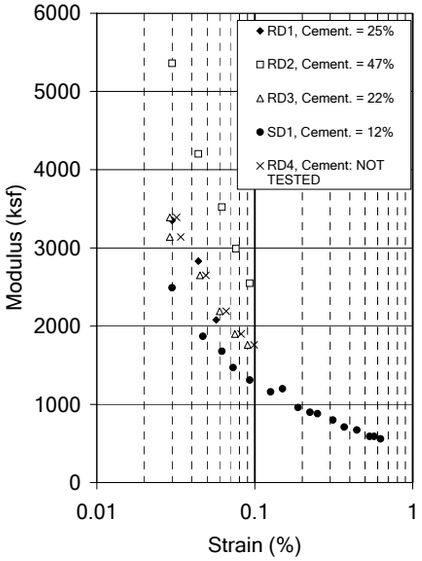


Figure 1: Modulus vs. Strain, Conf. Press = 5 psi

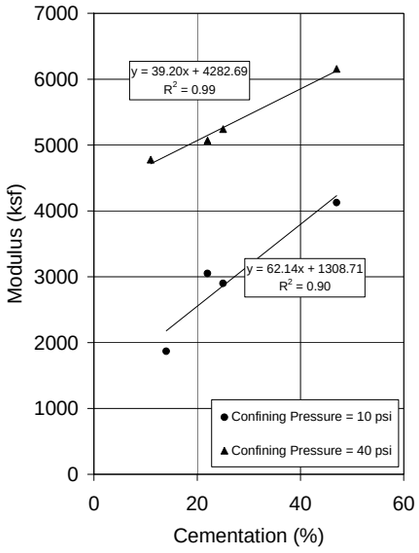


Figure 2: Modulus vs. Cementation, Strain = 0.04%

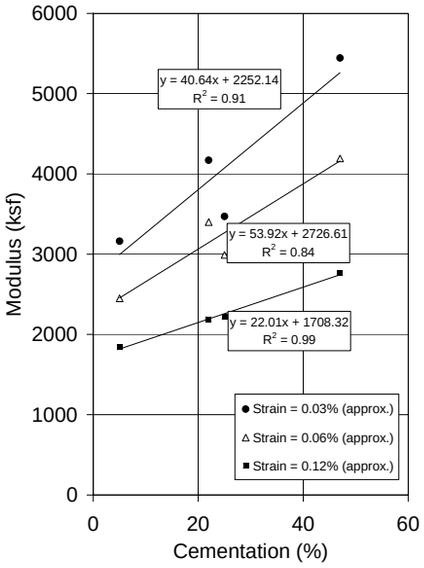


Figure 3: Modulus vs. Cementation, Conf. Press = 20 psi

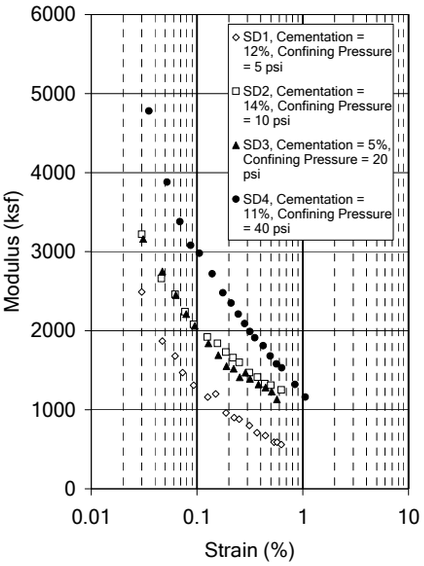


Figure 4: Modulus vs. Strain (Samples tested to failure)

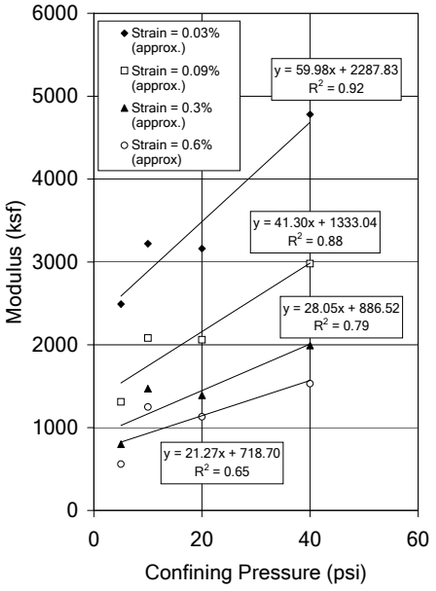


Figure 5: Modulus vs. Confining Pressure (In-situ moisture content)

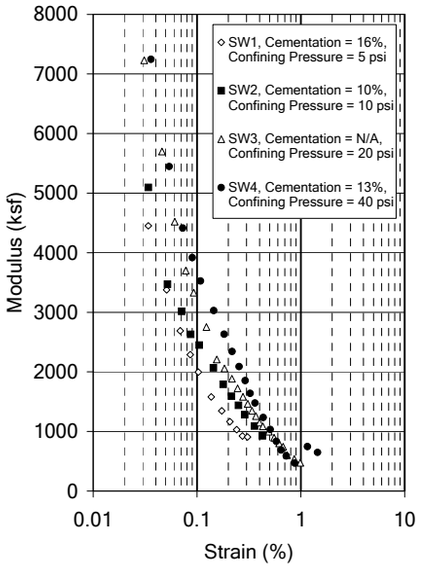


Figure 6: Modulus vs. Strain (Saturated Samples)

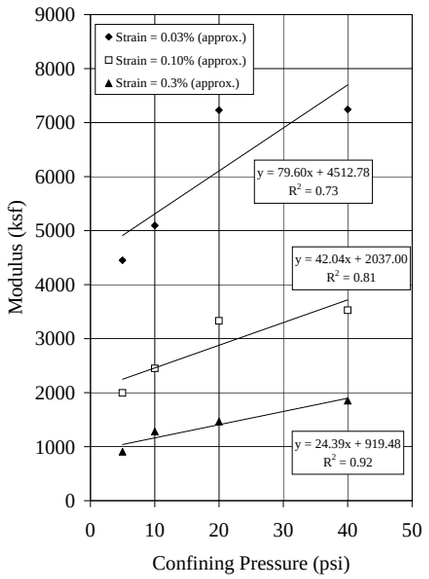


Figure 7: Modulus vs. Confining Pressure (Saturated Samples)

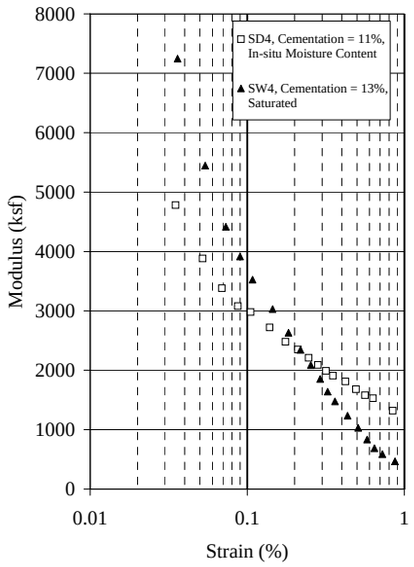


Figure 8: Modulus vs. Strain

Tests on Saturated Specimens

The variation in modulus with strain amplitude and confining pressure is shown in Figure 6. For a given confining pressure, the modulus decreases with strain. The data is well behaved and little scatter is evident.

A plot of modulus as a function of confining pressure, and strain level is shown in Figure 7. The relationship between the modulus and the confining pressure is almost linear albeit with a moderate amount of scatter.

Figure 8 compares moduli obtained from tests on samples at in-situ moisture content, and a saturated sample. At low strain levels, the moduli from the saturated specimens were higher than those of the specimen tested at in-situ water content. But at higher strain levels, the modulus obtained from the specimens at in-situ water content was higher than those of the saturated specimen. This behavior is also observed at confining pressures of 5, 10, and 20 psi. The friction in the testing device at high confining pressures may be a contributing factor to this behavior. When dealing with saturated specimens, the total confining pressure in the cell is of the order of 200 psi, which is much higher than pressures used for testing specimens at in-situ water content. This greater confining pressure would cause a greater friction at the bearing where the actuator rod enters the triaxial cell. Nevertheless, the higher confining pressures were needed to allow for backpressure saturation of the specimens.

Damping Ratios

The damping ratio generally increases with increasing strain (see Figure 9), although some scatter is evident in the data. The scatter was usually larger for lower confining pressures. The damping ratio for samples tested at in-situ moisture content increased with strain, up to a strain of about 0.2%. At higher strains, the damping ratio decreased slightly with increase in strain.

Figure 10 depicts the variation in damping ratio with cementation for four samples tested at in-situ moisture content and an effective confining pressure of 20 psi at a strain of approximately 0.1 percent. Although there appears to be a general trend of decreasing damping ratio with increasing cementation, the relationship in relatively week.

The samples that were saturated prior to testing yielded damping ratios that generally increased monotonically with increasing strains, for the strain levels used in this program. Furthermore, these saturated samples exhibited higher damping ratios than samples tested at in-situ moisture content.

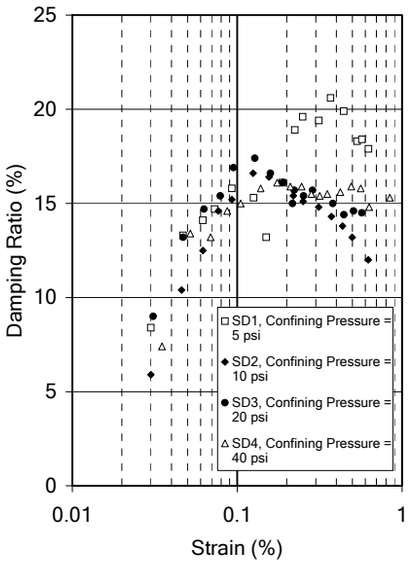


Figure 9: Damping Ratio vs. Strain (In-situ Moisture Content)

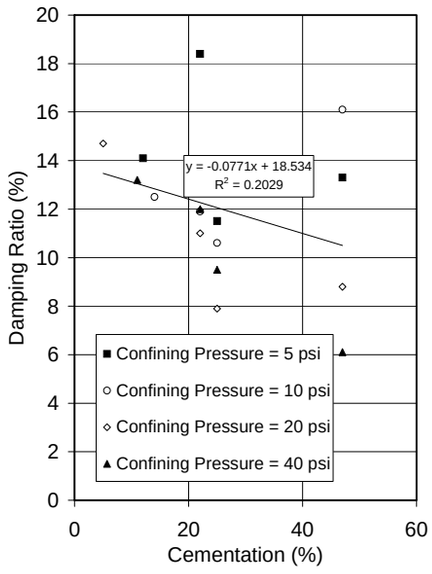


Figure 10: Damping Ratio vs. Cementation (In-situ Moisture Content, Strain Level approx. 0.06%)

CONCLUSIONS

This paper documents the results of a comprehensive laboratory testing program to evaluate the dynamic characteristics of a naturally-cemented silt from a site in West Texas. Based on the results discussed, the authors conclude the following:

1. The results from all sets of repeatability tests are consistent, indicating that the method of specimen preparation and test procedures followed are satisfactory.

2. The modulus of the soil at in-situ moisture content is strongly affected by the degree of cementation of the soil. In contrast, the damping ratio appears relatively insensitive to the degree of cementation.

3. For the levels of cementation encountered in this test program, and the strain levels used in the tests, there is a near-linear relationship between the modulus of the intact soil at in-situ moisture content, and the degree of cementation.

A Comparison of Shear Wave Velocity Profiles from SASW, MASW, and ReMi Techniques

Khiem T. Tran[1] and Dennis R. Hiltunen, M. ASCE, P.E. [2]

[1]Graduate Student, University of Florida, Department of Civil and Coastal Engineering, 365 Weil Hall, P. O. Box 116580, Gainesville, FL 32611; ttk@ufl.edu
[2]Associate Professor, University of Florida, Department of Civil and Coastal Engineering, 365 Weil Hall, P. O. Box 116580, Gainesville, FL 32611; dhilt@ce.ufl.edu

ABSTRACT: Three surface wave techniques, SASW, active MASW, and passive MASW, were conducted at a well-characterized test site. Crosshole shear wave velocity, SPT N-value, and geotechnical boring logs were also available for the test site. For the multi-sensor active test data, it was observed that the cylindrical beamformer transform provided the best resolution in dispersion data over a wide range of frequencies. The dispersion data obtained from all three surface wave techniques was generally in good agreement, and the inverted shear wave profiles were consistent with the crosshole, SPT N-value, and material log results.

INTRODUCTION

Near surface soil conditions control the responses of foundations and structures to earthquake and dynamic motions. To get the optimum engineering design, the shear modulus (G) of underlying layers must be determined correctly. A popular method to obtain shear modulus is nondestructive in situ testing via surface waves. An important attribute of this testing method is ability to determine shear wave velocity (V_s) profile from ground surface measurements, and then shear modulus is calculated from $G=\rho V_s^2$. Three popular techniques, spectral analysis of surface waves (SASW), multi-channel analysis of active surface waves (active MASW), and multi-channel analysis of passive surface waves (passive MASW), have been developed for nondestructive in situ testing, but their accuracy remains a question. This research will apply these three techniques to characterize the soil profile at a well characterized test site. The accuracy will be appraised by comparing the soil profiles derived from these techniques with the soil profile derived from a crosshole test, a highly accurate but invasive testing technique.

SURFACE WAVE METHODS

The motivation for using surface waves for soil characterization originates from the inherent nature of this kind of wave. Surface waves propagate along a free surface, so it is relatively easy to measure the associated motions, and carry the important information about the mechanical properties of the medium.

The SASW technique was introduced by Nazarian (1984) to the engineering community. Advantages of SASW are a simple field test operation and a straightforward theory of signal analysis, but it also has some disadvantages. This method assumes that the most energetic arrivals are Rayleigh waves. When noise overwhelms the power of active sources, such as in urban areas, or where body waves are more energetic than Rayleigh waves, SASW will not yield reliable results. Also during the processing of data, this method requires some subjective judgments that can sometimes influence the final results.

The active MASW technique (Park, et al. [1999]) was developed to overcome the shortcomings of SASW in the presence of noise. The most vital advantage of active MASW is that the transformed data allow identification and elimination of non-fundamental mode Rayleigh waves such as body waves, non-source generated surface waves, higher-mode surface waves, and other coherent noise from the analysis. As a consequence, the dispersion curve of fundamental Rayleigh waves can be picked directly from the mode-separated signal image. The obtained dispersion curve is expected to be more credible than that of SASW, and the method can be automated so that it does not require an experienced operator. An additional advantage of active MASW is the speed and redundancy of the measurement process due to multi-channel recording.

For the active MASW technique, many signal-processing methods have been developed to separate Rayleigh waves from other wave types and background noise. The traditional f-k and f-p transforms well described by Foti (2000) and O'Neill (2003), and the Park, et al. (1998) transform all treat the multi-channel record as a plane wavefield, while a cylindrical beamformer (Zywicki [1999]) uses the cylindrical wave equations to transform and identify Rayleigh waves. It is clear that the cylindrical wave equations describe active surface wavefields more properly than do plane wave equations, since the source is a finite distance from the receivers. This allows estimating phase velocities for relatively long wavelengths compared to the array length of receivers (Zywicki [1999]). In this paper, dispersion curves of surface waves on multi-channel records are imaged by applying these four signal processing methods. The resolution of the resulting dispersion curves will be discussed and the best method will be selected for extracting the final dispersion curve.

The passive MASW technique uses Rayleigh surface wave energy created by ambient energy sources such as highway and railroad traffic, ocean waves, and industrial and construction activity. The most important advantage of using passive waves is the ability to obtain low frequency surface wave energy and thus large depths of characterization with very little field effort. However, because the passive waves can arrive from any direction, this method requires more complicated treatment in data analysis than the active wave methods. Louie (2001) describes a 1-D receiver array method that uses a frequency-slowness (f-p) transform to separate

Rayleigh waves from other seismic arrivals, and to recognize true phase velocity against apparent velocities. Any wave that arrives obliquely to the receiver line has an apparent velocity higher than the true velocity of inline waves, and the dispersion curve is extracted by manual picking the relatively strong signals at the lowest velocities. Another more rigorous method uses 2-D receiver arrays (Park, et al. [2004]), and checks energy for different azimuths of arriving surface waves. For a given frequency and phase velocity, the energy is obtained by summing up that of all azimuths, and the energy is used to map the signal spectra for extracting dispersion curves.

SITE CHARACTERIZATION

Site Description and Tests Conducted

The data were collected at a well-documented test site that consists of an upper layer of approximately 10 m of medium dense, fine, silty sand followed by hard clay. The water table is approximately 5 m below the ground surface. Due to space limitations at the site, all the testing was conducted with 1-D receiver layouts along a straight line of nearly 400 ft. The positions were marked in one-foot increments from 0 to 400 as TestSite0_400. On the mentioned line, three kinds of tests, SASW, active MASW, and passive MASW, were conducted for comparison.

SASW tests were conducted following standard common receivers midpoint (CRMP) geometry at two positions along the 1-D test line, TestSite61 and TestSite128, where the station number refers to the location of the receiver centerline. At each position, tests were conducted at several receiver spacings from 4 ft to 122 ft, and for shot positions on each side of the centerline to generate forward and reverse wave propagation. The active sources were sledgehammers for receiver spacings up to 16 ft, and a vibration shaker for larger receiver spacings.

The active MASW tests were conducted using 62 receivers at a spacing of 2 ft, giving a total receiver spread of 122 ft. Two receiver layouts were established at positions TestSite0_122 and TestSite98_220. For each receiver layout, five sets of data were recorded accordingly to five positions of the sledgehammer active source at 10, 20, 30, 40, and 50 ft away from the first receiver.

The passive MASW tests were recorded by 32 receivers deployed at a spacing of 10 ft at site positions TestSite0_310. For these tests, good passive signals were not always available at the site, thus many sets of data were obtained for combining spectra in the dispersion analysis.

The crosshole test was conducted at a set of nearby cased boreholes spaced approximately 10 ft apart.

Dispersion Analysis

For SASW, 12 sets of data from six receiver spacings and for both forward and reverse records were used for dispersion analysis. Each set provides the dispersion relationship in a certain range of frequencies. Assembling the information from the 12 sets of data, the combined dispersion curve was derived, and the “supsmooth”

smoothing algorithm available in Mathcad was used to obtain the final dispersion curve.

For active MASW, the recorded data were used to check and compare the signal processing methods, f-k, f-p, Park, et al. transform, and cylindrical beamformer. For comparison, the spectra were all imaged in the same domain (figure 1). The frequency interval, velocity interval, number of frequency steps, and number of velocity steps on these spectra are identical. Also, the spectral values in all images were unity normalized, i.e., the highest value in each spectrum is equal to 1.0, and all other values are relatively compared to one. From these data it is apparent that the Park, et al. transform and the cylindrical beamformer have better imaged dispersion curves at low frequencies (<15Hz) than that of the f-k and f-p transforms. Overall, the spectrum obtained from the cylindrical beamformer has the highest resolution. Resolution of spectra in the frequency-phase velocity (f-v) domain can be separated into 2 components: resolution along the frequency axis and resolution along the phase velocity axis. All four methods apply a 1-D Fourier transform along the time direction to discriminate among frequencies for a given phase velocity, thus the resolutions along the frequency axis for each method are not much different. However, for the resolution along the phase velocity axis, the cylindrical beamformer appears best able to separate phase velocities for a given frequency.

To provide further illustration of resolution capabilities, figure 2 shows the normalized spectral values at 4 frequencies: 10, 20, 30, and 40 Hz. For each frequency, the spectral values are normalized to unity, i.e. the maximum value along the phase velocity axis is equal to 1. Even though the strongest peak for each method occurs at similar phase velocities for each frequency, the highest peak of the cylindrical beamformer is most dominant to other local peaks on its spectrum, i.e., the cylindrical beamformer reduces side ripples, and most of the energy concentrates at the strongest peak. The sharpest peak of the cylindrical beamformer allows the best separation of phase velocities for any given frequency. Thus, the high resolution along the phase velocity axis contributes to the highest overall resolution of the cylindrical beamformer. This can be understood that the cylindrical wavefield equations present the motions of waves created by an active source more properly than do plane wavefield equations. Based on these comparisons, the spectrum obtained by the cylindrical beamformer was selected for extracting the final dispersion curve for active MASW shown in figure 3.

For passive MASW, the data from the 1-D receiver array were analyzed using the commercial software SeisOpt ReMi that uses the Louie (2001) method of data analysis. The combined spectrum from several passive records allows obtaining the dispersion curve over a larger range of frequencies (figure 3).

It is observed from figure 3 that the dispersion data from all three techniques is generally in good agreement, particularly at the high and low frequency ranges. However, active MASW dispersion data appear to be higher in a middle frequency range. It is also observed that the active and passive MASW data is smoother than the SASW data. The ripples in the SASW data are mostly produced by slight mismatches in the combined dispersion data from multiple receiver spacings. Each spacing samples a slightly different zone of soil, and lateral variability of soil properties will produce a mismatch in dispersion data.

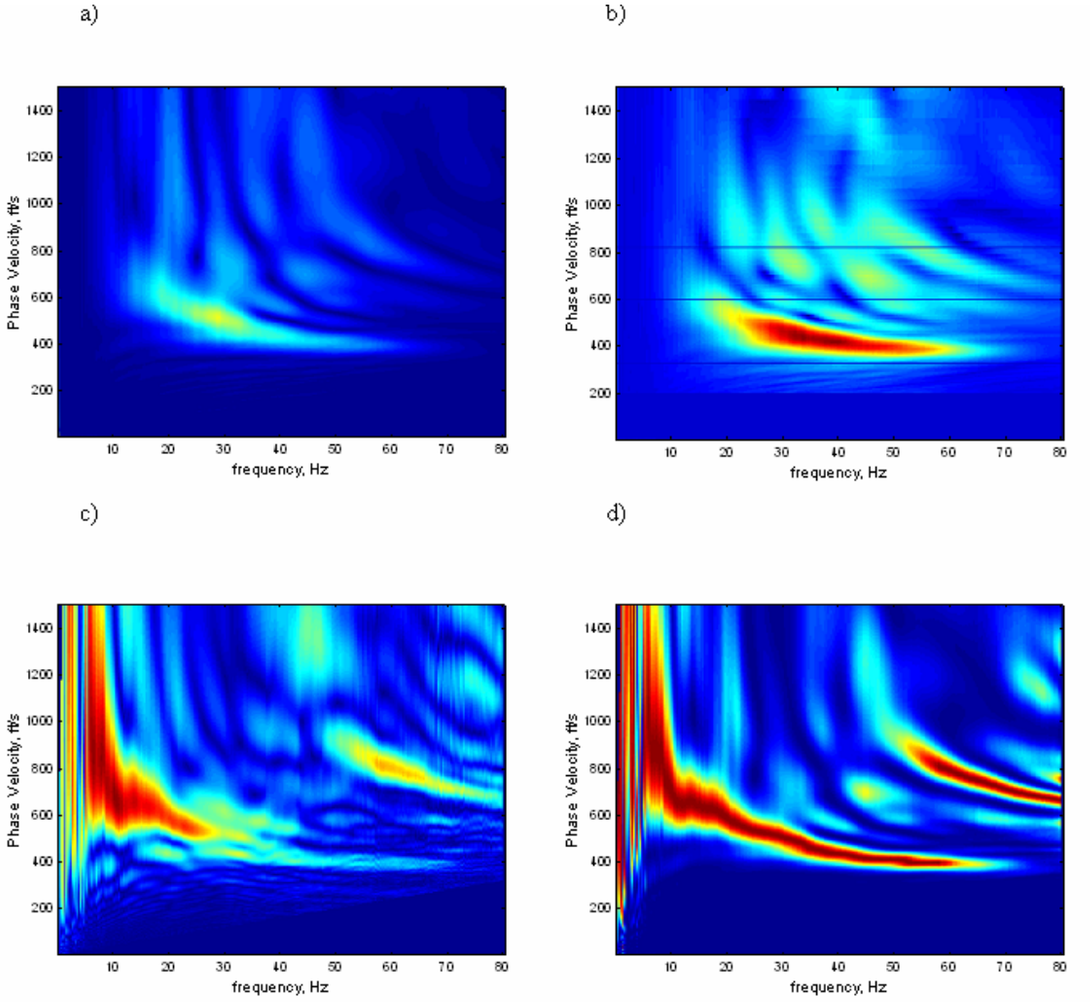


FIG. 1. Spectra of active MASW obtained by: a) f-k transform, b) f-p transform, c) Park, et al. transform, and d) cylindrical beamformer.

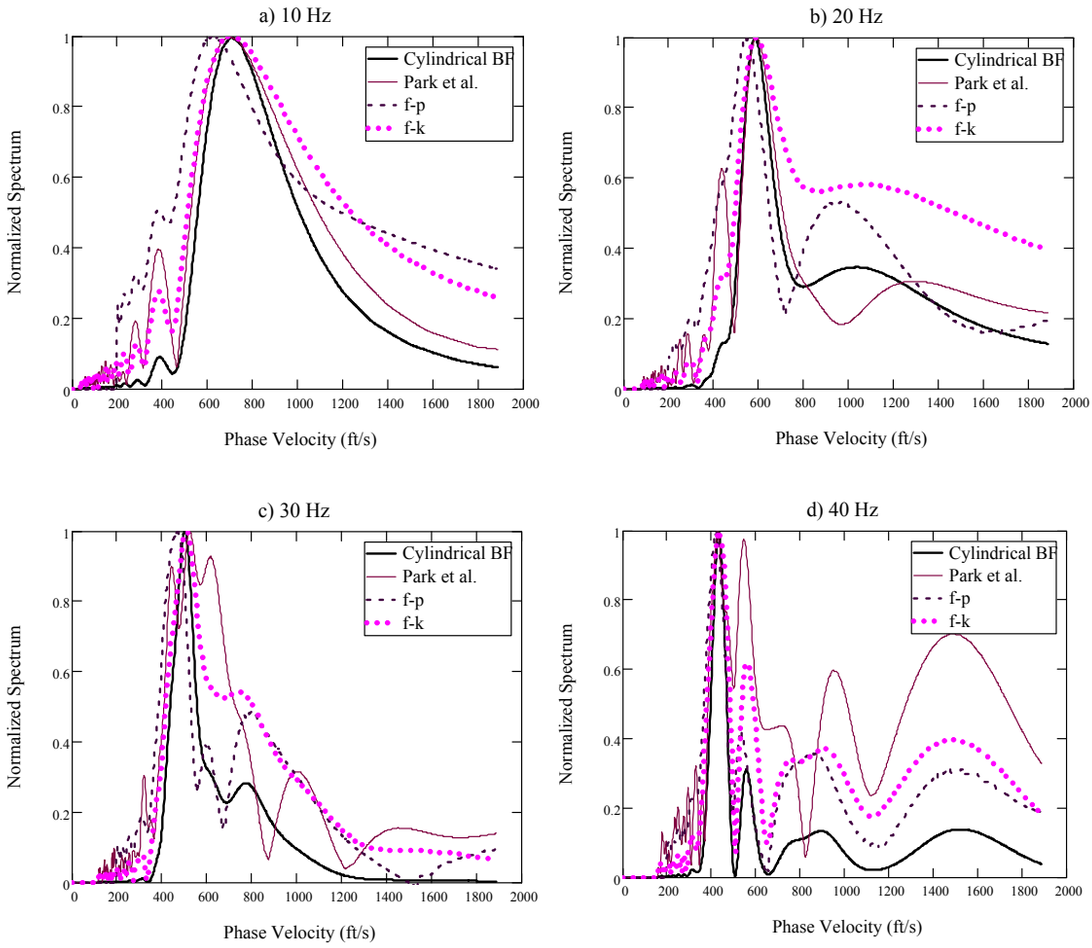


FIG. 2. Normalized spectra at different frequencies.

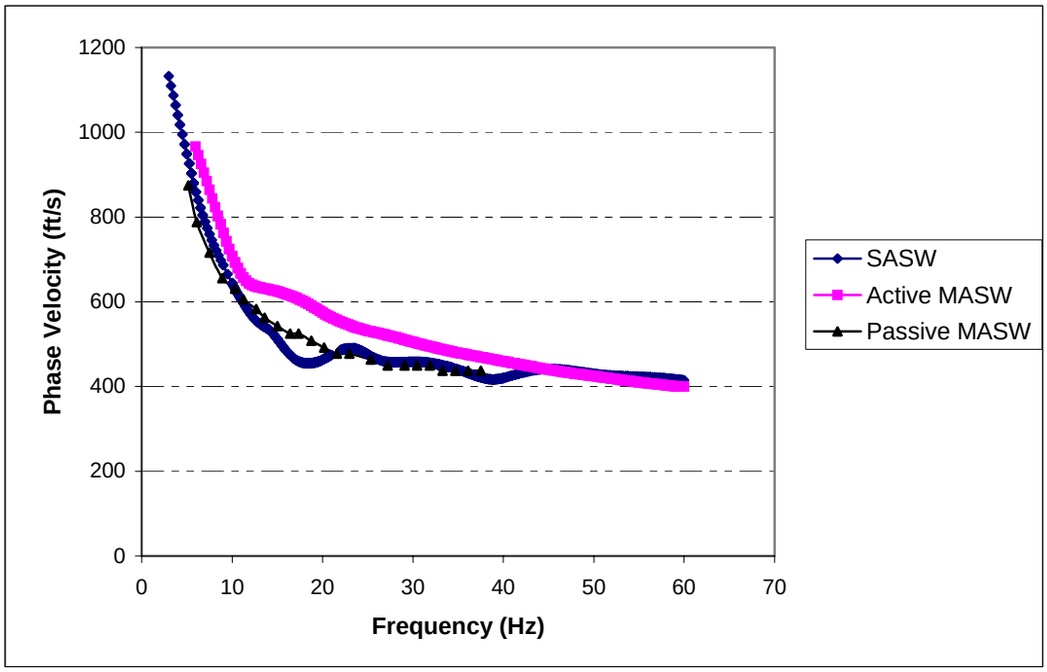


FIG. 3. Dispersion curves obtained by three methods.

Soil Profile Comparison

An inversion routine available in the SeisOpt ReMi commercial software was used to produce shear wave velocity profiles from the dispersion curves presented in the previous section. In all three cases, the inversion routine was able to match the experimental data very well, and the resulting profiles are shown in figure 4. Also shown in figure 4 are results from crosshole measurements, SPT N-values, and material logs from nearby geotechnical borings conducted at the site.

First, regarding the shear wave velocity profiles from the three surface wave techniques, it is observed that they are generally in good agreement. Consistent with the dispersion curves, the SASW and passive MASW are in particularly good agreement. However, the active MASW is slightly stiffer (higher velocity) at some depths which is also consistent with the dispersion data.

Second, it is observed that the surface wave based shear wave velocity profiles compare well with the crosshole results, especially at depths from 30 to 50 ft. Above 30 ft, a reversal occurs in the profile attained from the crosshole tests that is not detected by the surface wave tests. The surface wave tests are conducted over a relatively long array length that samples and averages over a large volume of material, whereas the crosshole results are based upon wave propagation between two boreholes that are only 10 ft apart, and thus these data represent a more local condition at the site.

Lastly, there appears to be reasonable consistently between the shear wave velocity results and the SPT N-values and material log. In the sand layer above a depth of

about 30 ft, the shear wave velocities and the N-values are approximately uniform. Below 30 ft, the shear wave velocities and the N-values increase in the hard clay material.

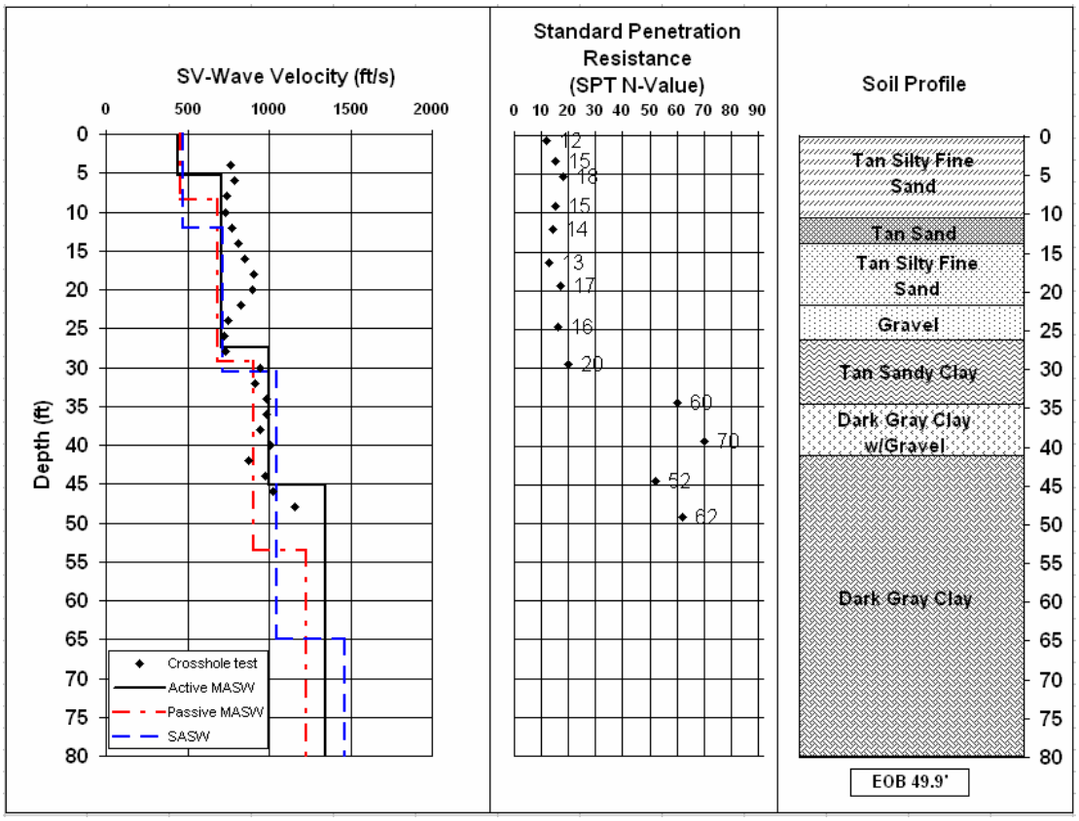


FIG. 4. Composite soil profile of test site.

CONCLUSIONS

Based upon the results presented herein, the following conclusions appear to be appropriate:

- For active multi-channel records, the cylindrical beamformer is the best method of signal processing as compared to f-k, f-p, and Park, et al. transforms. The beamformer provides the highest resolution of imaged dispersion curves, and its dominance of resolution at low frequencies over other methods allows achieving a reliable dispersion curve over a broad range of frequencies.
- There is generally good agreement between dispersion results from SASW, active MASW, and passive MASW surface wave tests.
- The surface wave-based shear wave velocities are in good agreement with the crosshole results, and the shear wave velocities appear consistent with SPT N-values and material logs.

REFERENCES

Aki, K. and Richards, P. G. (1980), *Quantitative Seismology: Theory and Methods,* W. H. Freeman and Company, San Francisco, 932 pp.

Foti, S. (2000), "Multistation Methods for Geotechnical Characterization Using Surface Waves," Ph.D. Thesis, Politecnico di Torino, 229 pp.

Louie, J. N. (2001), "Faster, Better, Shear-Wave Velocity to 100 Meters Depth from Refraction Microtremor Arrays," *Bulletin of Seismological Society of America*, Vol. 91, No. 2, pp. 347-364.

McMechan, G. A. and Yedlin, M. J. (1981), "Analysis of Dispersive Waves by Wave Field Transformation," *Geophysics*, Vol. 46, No. 6, pp. 869-871.

Nazarian, S. (1984), "In Situ Determination of Elastic Moduli of Soil Deposits and Pavement Systems by Spectral-Analysis-Of-Surface-Waves Method," Ph.D. Dissertation, The University of Texas at Austin, 453 pp.

O'Neill, A. (2003), "Full-Waveform Reflectivity for Modelling, Inversion and Appraisal of Seismic Surface Wave Dispersion in Shallow Site Investigations," Ph.D. Thesis, University of Western Australia, 420 pp.

Park, C. B., Miller, R. D., and Xia, J. (1999), "Multi-Channel Analysis of Surface Wave (MASW)," *Geophysics*, Vol. 64, No. 3, pp. 800-808.

Park, C. B., Xia, J., and Miller, R. D. (1998), "Imaging Dispersion Curves of Surface Waves on Multi-Channel Record," *Expanded Abstracts, 68th Annual Meeting of Society of Exploration Geophysicists*, pp. 1377-1380.

Park, C. B., Miller, R. D., Xia, J., and Ivanov J. (2004), "Imaging Dispersion Curves of Passive Surface Waves," *Expanded Abstracts, 74th Annual Meeting of Society of Exploration Geophysicists*, Proceedings on CD ROM.

Zywicki, D. J. (1999), "Advanced Signal Processing Methods Applied to Engineering Analysis of Seismic Surface Waves," Ph.D. Thesis, Georgia Institute of Technology, 357 pp.

This page intentionally left blank

Deep Shear Wave Velocity Profiling of Poorly Characterized Soils Using the NEES Low-Frequency Vibrator

Brent L. Rosenblad[1], A.M. ASCE, Kenneth H. Stokoe, II[2] M. ASCE, Jianhua Li[3], Brad Wilder[4], and Farn-Yuh Menq[5]

[1]Asst. Professor, University of Missouri, Columbia, MO, rosenbladb@missouri.edu
[2]Professor, University of Texas at Austin, Austin, TX, k.stokoe@utexas.edu
[3]Graduate Research Assistant, University of Missouri, Columbia, MO, jlfk4@mizzou.edu
[4]Graduate Research Assistant, University of Texas at Austin, Austin, TX, wilderbradley@gmail.com
[5]Research Associate, University of Texas at Austin, Austin, TX, fymenq@utexas.edu

ABSTRACT: Surface wave velocity measurements have recently been performed in the Salt Lake Valley region in northern Utah and the Mississippi Embayment region of the Central United States using equipment from the Network for Earthquake Engineering Simulation (NEES) program. A unique, low-frequency servo-hydraulic vibrator (termed Liquidator), developed at the University of Texas at Austin as part of the NEES program, was used to excite the requisite low-frequency energy for these studies. These measurements are the first application of this unique equipment for deep (200 m and greater) shear wave velocity (V_S) profiling of soil sites. This profiling depth was achieved because of the field performance of Liquidator in the 1- to 4-Hz frequency range. Profiles from these studies have contributed to a better understanding of the V_S structure and variability of the deep sediments in these seismically vulnerable regions. The field performance of Liquidator, the shear wave velocity structures, and the importance of such profiles in developing community velocity models for use in earthquake engineering are discussed.

INTRODUCTION

Many seismically vulnerable locations in the United States are located on soil deposits that are hundreds of meters thick. The presence of these deep sediment layers can have a significant effect on the amplitude and frequency content of earthquake motions (Hashash and Park, 2001). Accurate prediction of earthquake ground motions in these regions requires reliable information about the shear wave velocity (V_S) profile. Due to the high cost of measuring V_S profiles to great depths using conventional borehole methods, these deep soil deposits are often poorly characterized. Surface wave velocity measurements offer a comparatively inexpensive and non-intrusive means to determine V_S profiles (Stokoe et al., 1994). Until recently it was not possible to actively generate the low-frequencies required to

develop deep V_S profiles from surface wave measurements. Recently, a unique low-frequency field vibrator (termed Liquidator) was developed at the University of Texas at Austin as part of the Network for Earthquake Engineering Simulation (NEES) program (Stokoe et al., 2004). This equipment was designed specifically to address the problem of exciting energy in the frequency band of 1 to 4 Hz, a range where the performance of conventional Vibroseis equipment is greatly compromised. Surface wave energy excited in this frequency band allows generation of very long wavelengths which penetrate deep into the subsurface, often doubling or tripling the penetration depth achieved with a conventional Vibroseis. Utilization of this equipment makes possible the generation of V_S profiles to depths of 200 m and greater at deep soil sites.

In the Summer of 2006, Liquidator was utilized for deep V_S profiling using surface waves in the Salt Lake Valley region of Utah and the Mississippi Embayment region of the Central United States. These studies were the first applications of this equipment for the purpose of obtaining deep V_S profiles at soil sites. The primary objective of this paper is to report on the field performance of Liquidator in these applications. Representative results obtained from the field studies are presented to demonstrate the contribution these measurements are making to a better understanding of the deep V_S structure in these seismically vulnerable regions.

NEES LOW-FREQUENCY VIBRATOR

Liquidator, shown in Figure 1, is one of three field vibrators developed at the University of Texas at Austin, as part of the Network for Earthquake Engineering Simulation (NEES) program. This vibrator was designed with the objective of improving the output at very low frequencies, as compared to conventional Vibroseis equipment used in the exploration industry. The improved performance at low frequencies was achieved by dramatically increasing both the weight and stroke of the reaction mass. Operating the vibrator to such low frequencies also required a redesign of the baseplate isolation system. Table 1 presents a comparison of the characteristics of Liquidator to those of a conventional Vibroseis. Figure 2 presents a comparison of the theoretical force output of Liquidator and a conventional Vibroseis. It can be observed from this figure that Liquidator achieves substantially higher force output levels in the frequency range of 4 Hz and below. The longer stroke extends the flat portion of the force plot down to a frequency of 1.3 Hz, as which point the output levels begin to decrease. Extension of the low-frequency operating range of the equipment results in a substantial increase in the penetration depth of surface wave energy and greatly extends the depth of the V_S profile. For example, extending the frequency range from 4 Hz down to 1 Hz, results in about a four-fold increase in penetrating depth of the surface wave and the resulting V_S profile.

The field studies in Utah and the Mississippi Embayment required transport and mobilization of Liquidator at multiple sites on a daily basis. Liquidator is a large piece of equipment with a length of 9.8 m, a width of 2.4 m, and a total weight of approximately 32,000 kg. It is transported to field sites on a tractor-trailer with a total loaded weight of over 54,000 kg. Logistical issues involved in the deployment of this equipment included: (1) acquiring highway permits for overweight load (2) assuring

adequate capacity of bridge crossings (especially at rural sites), (3) assuring adequate space for loading and unloading, (4) assuring sufficient bearing capacity of ground, especially under wet conditions and (5) providing sufficient offset distance to adjacent structures. Successful deployment and operation of the equipment at multiple sites required advanced site reconnaissance and planning prior to mobilization.



FIG. 1. Low-frequency NEES vibrator (Liquidator).

Table 1. Comparison of Liquidator and Conventional Vibroseis Characteristics.

	Liquidator	Vibroseis
Reaction Mass (kg)	5900	1680
Stroke (cm)	40	10
Peak Force (kN)	89	155
Force at 1Hz (kN)	48	3.3
Isolation Resonance (Hz)	0.3	1.5

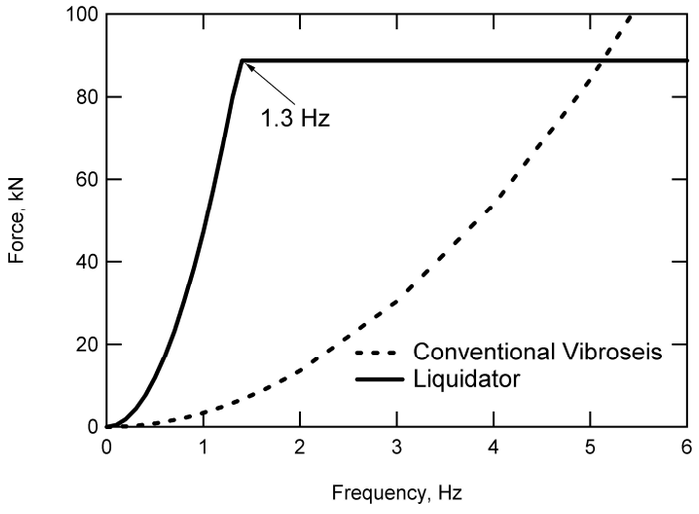


FIG. 2. Theoretical force output of Liquidator at low frequencies compared to a conventional Vibroseis.

STUDY AREAS

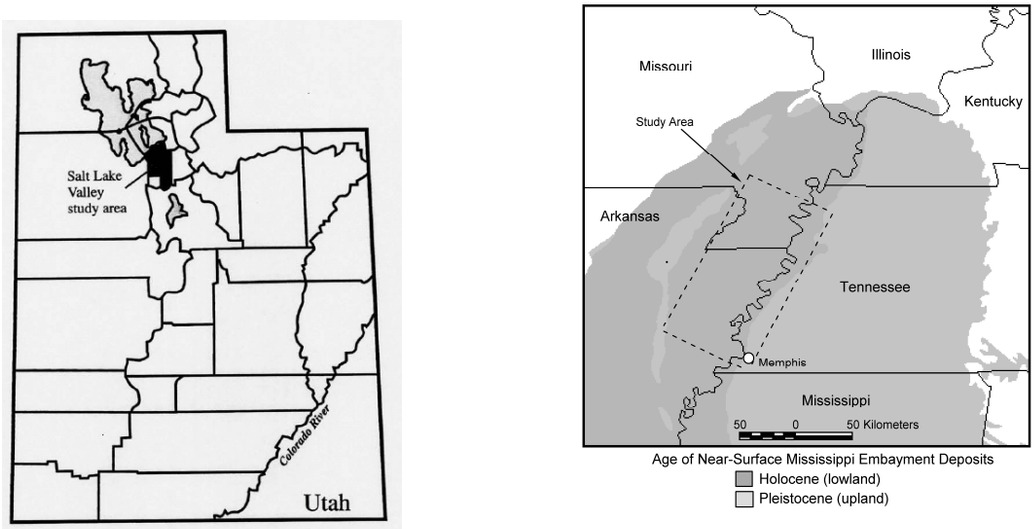
Surface wave velocity measurements utilizing Liquidator were performed in the Salt Lake Valley region of Utah and the Mississippi Embayment region of the Central United States. An overview of the geology and state-of-knowledge of the V_S structure in these regions is presented below.

Salt Lake Valley

The Salt Lake Valley is a highly populated region in northern Utah (Figure 3a) which is situated along the seismically active Wasatch Fault. The Wasatch Fault is considered a major active fault capable of producing powerful earthquakes. The geology of this region consists of unconsolidated Quaternary sediments overlying semi-consolidated Tertiary deposits which overlie consolidated rock. The thickness of the Quaternary deposits is generally less than 250 m (Wong et al., 2002) but exceeds 670 m in the northern part of the valley. The combined thickness of the Quaternary and Tertiary basin-fill deposits exceeds 1000 m in some areas (Arnow and Mattick, 1968). Recent shallow investigations have been performed to determine the V_S to depths of about 50 m (Bay, 2005), but little information is known about the V_S at greater depths. Of particular interest is the identification of the depth to the boundary between the Quaternary and Tertiary deposits, termed the R1 boundary. Surface wave velocity measurements were performed at eleven sites located throughout the valley.

Mississippi Embayment

The Mississippi Embayment is a trough of very deep sediments encompassing portions of Arkansas, Missouri, Kentucky, Tennessee and Mississippi in the Central United States, as shown in Figure 3b. This region overlies the seismically active New Madrid Seismic Zone which was the source of the largest earthquakes in the contiguous United States. Sediment thickness in this region extends to depths of approximately 1000 m near Memphis, Tennessee (Van Arsdale and TenBrink, 2000). The general soil stratigraphy consists of Quaternary alluvial (lowlands), loess (uplands), and gravel deposits underlain by stiffer Tertiary deposits which include the thick Memphis Sand formation. Deeper Cretaceous deposits overlie dolomitic limestone of Paleozoic age. As in the case of Salt Lake Valley, the near-surface Quaternary deposits are generally well characterized in the top 50 m, but little information is available at greater depths (Romero and Rix, 2001). Site response studies in this region have often utilized a single reference V_S profile to represent the deep properties of the embayment (Park and Hashash, 2005; Cramer, 2006). The objectives of the study in the embayment are to: (1) provide information on the variability of the deep V_S structure and (2) develop relationships between V_S and soil formations. Surface wave velocity measurements have been completed at eleven sites located throughout the embayment.



(a) Salt Lake Valley (b) Mississippi Embayment

FIG. 3. General extent of study areas where surface wave measurements were performed in: (a) Salt Lake Valley and (b) Mississippi Embayment.

FIELD PROCEDURES

Both the Salt Lake Valley study and the Mississippi Embayment study utilized the Spectral-Analysis-of-Surface-Waves (SASW) method to develop V_S profiles (Stokoe et al., 1994). The SASW method involves measuring the phase difference as a function of frequency between two sensors located in-line with the source, as shown in Figure 4. The phase is unwrapped by identifying 360-degree "jumps" in phase, and the apparent surface wave velocity, V_R, is calculated from:

$$V_R = f \times (2\pi/\phi) \times d \quad (1)$$

where, f is the frequency, ϕ is the unwrapped phase angle, and d is the spacing between receivers. The measurement is repeated with successively larger receiver spacings, d, and a lowering of the excitation frequencies. Generally, two or more receiver spacings are recorded at each source location. Measurements from all receiver spacings are combined to create an experimental dispersion curve for the site, which relates the surface wave velocity to wavelength or frequency. A forward modeling or inversion procedure is then performed to find a V_S profile that provides a matching theoretical dispersion curve to the experimental dispersion curve.

For deep profiling applications using surface waves, long source offsets and receiver spacings are required. In the Mississippi Embayment study, receiver spacings of up to 300 m were used with a source offset of about 300 m. In the Salt Lake Valley study, source offsets of up to 300 m were used with maximum receiver spacings of about 150 m. This smaller receiver spacing was used in most cases due to limited space for the longest array. The total distance between the source and farthest receiver in these studies, therefore, was typically 450 to 600 m. Ground motions were recorded with vertically-oriented 1-Hz geophones with a sensitivity of 2.8 V/(cm/sec). Liquidator was driven in a stepped-sine mode using a dynamic signal analyzer. At the longest

receiver spacing, the source was operated down to frequencies of less than 1 Hz. The field procedures used in these studies are discussed in greater detail in Wilder (2007) and Rosenblad et al. (2007). The performance of Liquidator in these applications is discussed below.

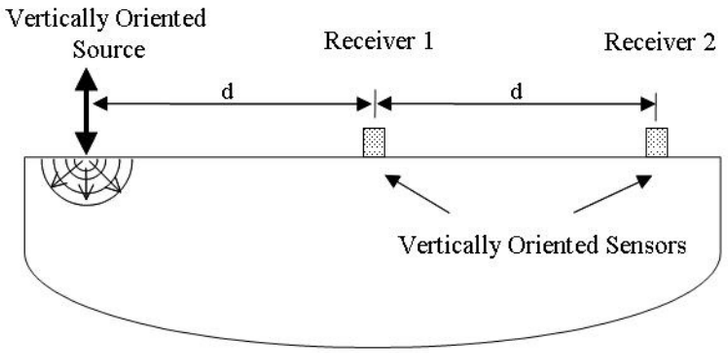
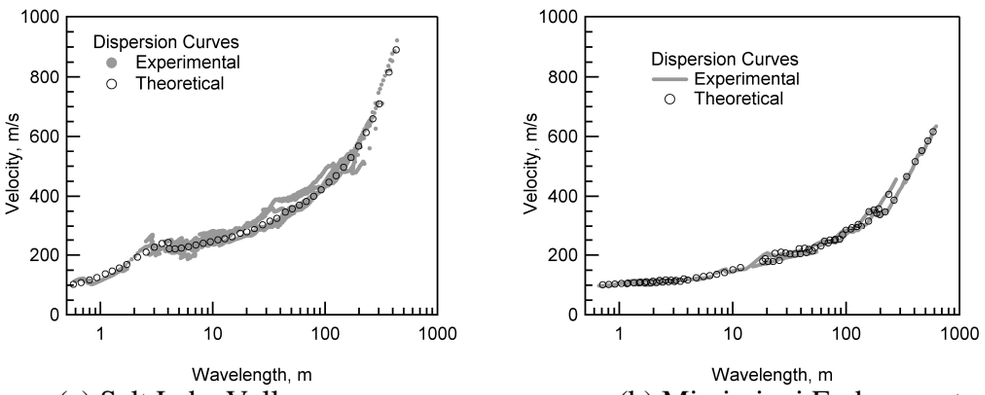


FIG. 4. Experimental set-up of one receiver pair for the SASW method.

FIELD PERFORMANCE OF NEES EQUIPMENT

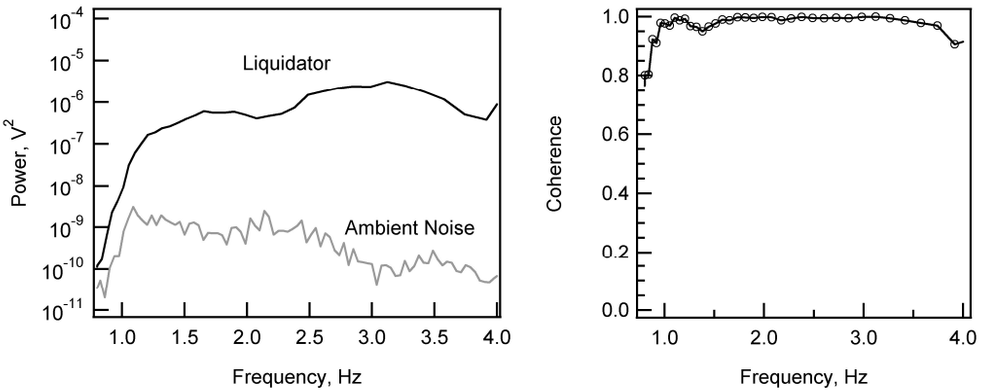
In both the Salt Lake Valley study and the Mississippi Embayment study, surface wave energy at frequencies down to 1 Hz was successful generated and measured. Surface wave dispersion data were generated to wavelengths of approximately 500 to 600 m, resulting in V_S profiles to depths of 200 m and greater. Example dispersion curves generated in the Salt Lake Valley study and the Mississippi Embayment study are shown in Figures 5a and 5b, respectively. It should be noted that the dispersion curve shown in Figure 5b was measured in the Mississippi Embayment at a lowland site consisting of very soft, near-surface alluvial deposits (V_S of approximately 150 m/s in top 10 m). Low-frequency energy was successfully coupled through this soft layer and measured at distances of 600 m from the source.



(a) Salt Lake Valley (b) Mississippi Embayment

FIG. 5. Example dispersion curves recorded in: (a) Salt Lake Valley and (b) Mississippi Embayment.

High-quality phase velocity measurements require a large signal-to-noise ratio which reduces the uncertainty in the phase measurements and subsequent velocity calculations. Figure 6a presents the power spectrum over a frequency range of 0.8 to 4 Hz that was recorded at a receiver located 544 m from Liquidator at a site in the Mississippi Embayment. The power spectrum from background noise alone is also presented in this plot. It can be observed that the output recorded with Liquidator operating is several orders of magnitude greater than the background noise levels at frequencies down to about 1 Hz. The decreased output below 1 Hz is due both to the decreased performance of Liquidator at these frequencies (see Figure 2) and the lower output of the geophones below their resonant frequencies. Another good indicator of signal quality is the coherence function calculated between the signal generated by the source and the recorded signal. Figure 6b shows the coherence measurement recorded at a distance of 544 m from the source at the same site in the Mississippi Embayment. Coherence values of greater than 0.95 are observed over most of the frequency range, indicting high signal-to-noise ratios and hence reliable phase measurements.



(a) Power Spectra (b) Coherence

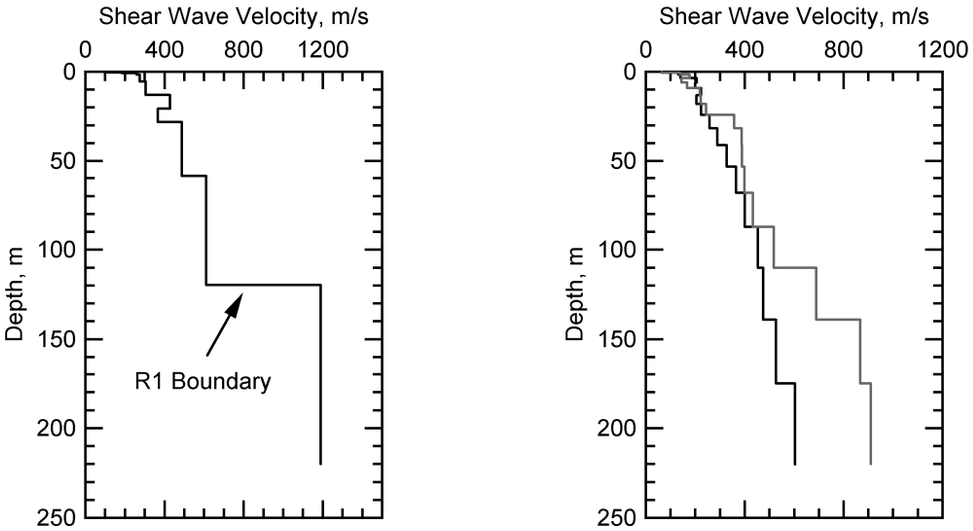
FIG. 6. Recording at a distance of 544 m from the source showing (a) power spectra with and without Liquidator operating and (b) coherence function measured between source signal and recorded signal.

REPRESENTATIVE RESULTS

The high output of Liquidator at low frequencies allowed V_S profiles to be determined to depths of over 200 m in the Salt Lake Valley and the Mississippi Embayment. As previously mentioned, soil properties at these depths are currently very poorly characterized in both of these regions. The profiles generated from these studies will contribute to development of community velocity models, for use by engineers, geologists and seismologists, by providing valuable information on the deep V_S structure in these regions. In the case of the Salt Lake Valley, the depth to the R1 interface (between unconsolidated and semi-consolidated layers) is of great interest. The R1 interface was detected at depths ranging from 35 m to 205 m in all profiles determined in the Salt Lake Valley (Wilder, 2007). Figure 7a shows an example V_S profile recorded at a site located towards the middle of the Salt Lake

Valley. The deep R1 interface is clearly identified by the large increase in V_S at a depth of about 120 m. A detailed presentation of all results from the Salt Lake Valley study can be found in Wilder (2007).

In the case of the Mississippi Embayment, information on the variability of the deep V_S structure throughout the embayment is currently lacking. Five deep profiles measured in May 2006 and an additional six profiles measured in May 2007 are providing valuable information on V_S variability and the correlation with soil formations. Figure 7b presents a comparison of two V_S profiles measured at sites separated by about 50 km. The results demonstrate the potential variability of V_S at depth in this region. Work is ongoing to relate the observed variability with changes in soil formation depths and thicknesses. A detailed presentation of the results from measurements at the first five sites measured in May 2006 can be found in Rosenblad et al. (2007).



(a) Salt Lake Valley Site (b) Mississippi Embayment Sites

FIG. 7. Examples of deep V_S profiles measured at sites in (a) Salt Lake Valley showing the detection of the R1 interface and (b) Mississippi Embayment showing the variability at depth between two sites.

CONCLUSIONS

The low-frequency vibrator (Liquidator) developed as part of the Network for Earthquake Engineering Simulation (NEES) program has been successfully used to measure V_S profiles to depths of 200 m and greater in two regions of the United States with poorly characterized deep soils. Field experience with Liquidator at sites in the Salt Lake Valley and the Mississippi Embayment has demonstrated good performance of the vibrator in the frequency range of 1 to 4 Hz, a range that is critical for high-quality measurements with deeply penetrating surface waves. The profiles developed from these studies are contributing to the development of community velocity models for these regions by providing valuable information on the deep V_S structure and

variability in these seismically vulnerable regions.

ACKNOWLEDGMENTS

Financial support for the development of the NEES field equipment was provided by the National Science Foundation (NSF) under grant CMS-0086605. Financial support for the research program in the Salt Lake Valley was provided by the U.S. Geological Survey (USGS) under award 06-HQGR0050. Financial support for the research program in the Mississippi Embayment was provided by NSF under grant CMS-0530140 and by USGS under award 06-HQGR0131.

REFERENCES

Arnow, T. and Mattick, R. E. (1968). "Thickness of valley fill in the Jordan valley east of the Great Salt Lake." Utah, *U.S. Geol. Surv. Profess. Paper* 600-B, 79-82.

Bay, J.A. (2005) *Shallow Shear Wave Velocity Profiling of poorly Characterized Earthquake Site-Response Units in Urban Salt Lake Valley*, Utah Geological Society, USGS/NEHRP Award 03HQGR0049.

Cramer, C. (2006). "Quantifying the uncertainty in site amplification modeling and its effects on site specific seismic hazard estimation in the upper Mississippi Embayment and adjacent areas." *Bull. Seismol. Soc. Am.*, **96**, No. 6, pp 2008-2020.

Hashash, M.A. and Park, D. (2001). "Non-linear one-dimensional seismic ground motion propagation in the Mississippi Embayment." *Engineering Geology*, **62**, pp. 185-206.

Park, D. and Hashash, M.A. (2005). "Evaluation of seismic site factors in the Mississippi Embayment. I. Estimation of dynamic properties." *Soil Dyn. Earthquake Eng.*, **25**, pp. 133-144.

Romero S.M. and Rix, G.J. (2001). *Ground Motion Amplification of Soil in the Upper Mississippi Embayment*, Mid-America Earthquake Center, Report No. GIT-CEE/GEO-01-1.

Rosenblad, B.L., Li, J., Menq, F.Y., and Stokoe, K.H. (2007). "Deep Shear Wave Velocity Profiles from Surface Wave Measurements in the Mississippi Embayment." *Earthquake Spectra,* EERI (accepted).

Stokoe, K.H. II, Rathje, E.M., Wilson, C.R., and Rosenblad, B.L. (2004). "Development of Large-scale Mobile Shakers and Associated Instrumentation for In-situ Evaluation of Nonlinear Characteristics and Liquefaction Resistance of Soils." *Proceedings, 13th World Conference on Earthquake Engineering*, August.

Stokoe, K.H., II, Wright, S.G., Bay, J.A., and Roesset, J.M. (1994). "Characterization of geotechnical sites by SASW method." *Technical Review: Geophysical Characterization of Sites,* ISSMFE Technical Committee 10, edited by R.D. Woods, Oxford Publishers, New Delhi, India.

Van Arsdale, R.B., and TenBrink, R.K. (2000). "Late Cretaceous and Cenozoic geology of the New Madrid Seismic Zone." *Bull. Seismol. Soc. Am.*, **90**, No. 2, pp. 345–356.

Wilder, B. (2007). *SASW Testing in Salt Lake Valley, UT*, M.S. Thesis, University of Texas at Austin, Department of Civil Engineering.

Wong , I.G., Silva, W., Olig, S., Thomas, P., Ashland, F., Wright, D., Ashland, F., Gregor, N., Peshmann, J., Dober, M., Christenson, G., and Gerth, R. (2002). *Earthquake Scenario and Probabilistic Ground Shaking Maps for the Salt Lake City, Utah, Metropolitan Area*, Miscellaneous Publication 02-5, Utah Geological Survey.

Development and Applications of In-Hole Seismic Method to Measure Shear Wave Velocity of Subsurface Materials

Chul Soo Park[1], Jae Woo Jung[1], and Young Jin Mok[2], P.E.

[1]Research Assistant, Dept. of Civil Eng., Kyunghee University, Korea; charlespark@khu.ac.kr
[2]Professor, Dept. of Civil Eng., Kyunghee University, Korea; yjmok@khu.ac.kr, Corresponding Author

ABSTRACT: The dynamic stiffness of the ground is one of the key parameters in earthquake-resistant designs involving local ground response and in assessment of geotechnical structures subjected to various man-made vibrations. Its use is being extended even to static settlement and deformation problems. Its importance and extended usage require a more manageable method than conventional seismic techniques such as crosshole, downhole test, and suspension logging. In general, conventional borehole seismic methods are expensive and technically complex. This paper presents a new method which has been developed to reduce testing cost and to improve the easiness in its use. An in-hole probe has been developed to be fit in three-inch boreholes with functional improvements including a pair of mechanical couplings driven with two servomotors, and a servomotor triggering device. The in-hole seismic method was adopted at various sites such as compaction fills of railroad subgrade, bedrocks of tunnel construction sites, tunnel-face rock mass, and abutment of rock fill dam. In-hole seismic test results were verified by comparing with reliable crosshole results. Presently, the method is very cost effective and easy to use in residual soils, compaction fills and bedrock where uncased boreholes can stay open.

INTRODUCTION

The dynamic stiffness of the ground is one of the key parameters in earthquake-resistant designs involving local ground response and in assessment of geotechnical structures subjected to various man-made vibrations. Its use is being extended even to static settlement and deformation problems. Its importance and extended usage require a more manageable method than conventional seismic techniques.

The in-situ seismic techniques are divided into non-destructive surface methods and borehole seismic methods. Borehole seismic methods have been diversified into the three techniques such as crosshole, downhole and suspension logging test according to their devices and testing configurations. These field techniques have been improved, in terms of equipment and testing procedures, and are very valuable in site

characterization (Mok 1987; Nigbor and Imai 1994; Stokoe and Woods 1972). Each method has its own advantages and disadvantages in terms of data quality, cost and technical complexity as mentioned briefly in the following part of the paper. An in-hole probe and a testing procedure has been developed in past five years to reduce testing cost and to improve the easiness in the use (Mok et al. 2003; Mok and Park 2007). The key features of the probe are the spring-servomotor source and the mechanical coupling device (Mok et al. 2007). The in-hole method has been adopted at several construction sites including soil fills for highway and railroad, bedrock for bridge and dam foundations, and tunnelling. The test results were verified with the crosshole and down-hole testing accompanied at six sites.

IN-HOLE SEISMIC METHOD

The crosshole seismic method results in more accurate and detailed profiles than any other methods and is yet most expensive because two or more boreholes have to be drilled, cased and inclinated for their verticality (Mok 1987; Stokoe and Woods 1972; Stokoe and Hoar 1978; Wilson et al. 1978). Moreover, meticulous procedures in grouting to ensure intimate bonding between casing and surrounding soil, which is decisive to data quality, hinder its use.

The downhole seismic method is less expensive and needs less testing effort than the crosshole test because it uses only one borehole and much simpler source at the surface. The method results in rather smooth velocity profiles, especially when compared with the more detailed profiles determined by the crosshole method (Mok 1987). Also, as the measurement depth increases, the resolution and data quality decrease because the ray paths are becoming longer and longer.

The suspension logging system includes an in-hole tool, consisting of an energy source, isolation tubes and two biaxial geophone receivers. The energy source is a solenoid whose activation causes a “hammer” to strike the tool casing, producing an impulsive pressure wave in the fluid-filled borehole. This pressure wave transmits energy to the borehole wall, producing both P- and S- waves that travel through the geologic formation. The distance from the energy source to the near receiver is often approximately 2 to 3 meters. The distance between the receivers is about 1 m. The total length of the tool is approximately 7 meters, with the center point between the two receivers approximately 3 to 4 meters above the bottom of the tool. Two drawbacks of the method are that it generally can not be performed in a steel or thick plastic casing if soft soils are to be tested, and it does not work well within 7 meters of the ground surface (Stokoe et al. 2003).

The basic concepts behind the in-hole probe are illustrated in Figure 1. The probe consists of three modules of a spring-servomotor source, one horizontal 1-D receiver aligned with source impact direction, and a rubber connecting rod (or isolator, which contradicts literally, filters out the noise transmitted through the rod from the source) can be combined according to the testing conditions and applications. The overall length of the probe including one source and one receiver is about 1.5 meters. The probe is pushed against the borehole wall by two mechanical coupling devices to measure direct waves through geologic materials. Therefore, the borehole does not have to be filled with fluid (as needed by the suspension logging) and more energy can be delivered to the geologic material by direct impact on the wall.

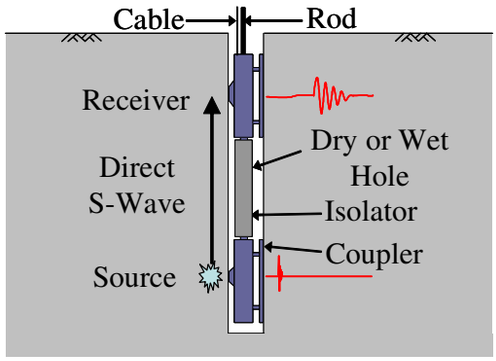


Figure 1. Conceptional diagram of in-hole seismic method

IN-HOLE PROBE AND CONTROL UNIT

The in-hole probe consists of three modules of the source, a receiver, and a connecting rod. The most important and difficult module is the source which can generate seismic energy. The basic operating principles of the first primitive source are such that the trigger-cam releases a spring-loaded impact-pestle by pulling the trigger-wire, thereby impacting the borehole wall and reloading the impact-pestle automatically by a return-spring (Mok et al. 2003). The inflated air bag ensures intimate contact between impact shoe and borehole wall and enhances impact energy delivered into geologic material.

The prototype source has been modified by replacing the manual pulling-wire triggering with a gear-servomotor device and the air-bag coupling with a mechanical packer. The latest version of the source consists of a spring-loaded impact pestle, a gear-servomotor triggering device, and a mechanical packer which is powered by two servomotors. Thus, the source can be operated by pushing buttons of the control unit. Figure 2 shows the in-hole probe (assembled with a source, a receiver, and an isolator), control unit, and a schematic diagram of the source. The same source and the receiver also can be used in crosshole tests.

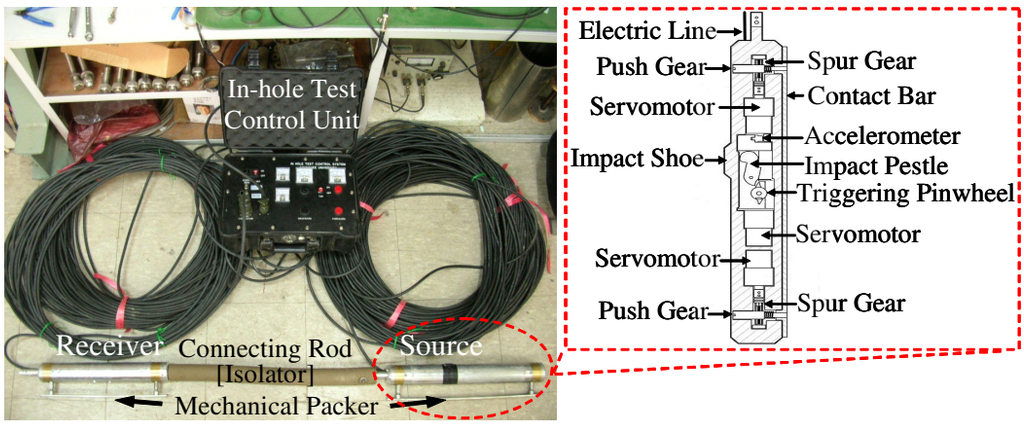


Figure 2. In-hole probe and control unit, and schematic diagram of spring-servomotor source

IN-HOLE TESTING

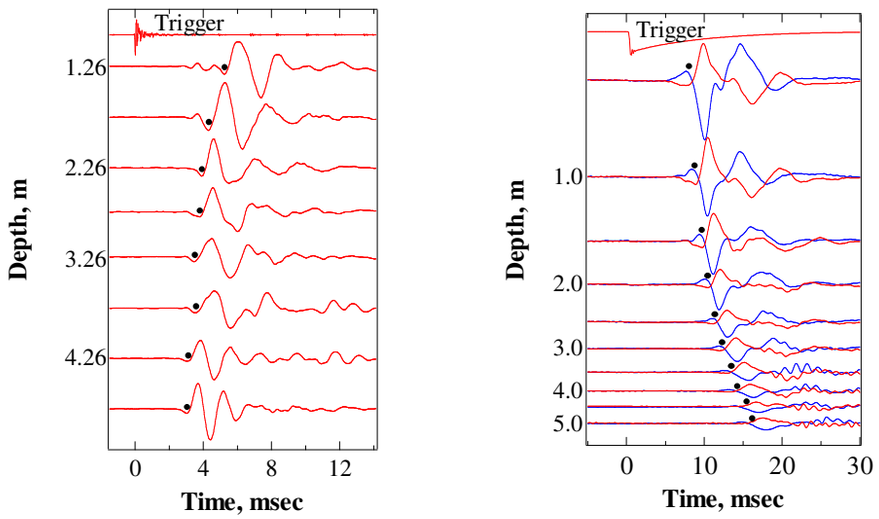
The in-hole method has been adopted at various sites for various engineering purposes. The testing was carried out with uncased boreholes in non-collapsing geologic materials including compaction fills, weathered soil and bedrock. Test results are presented herein.

Subgrade of Railroad Trackbed

Associated with the evaluation of resilient modulus for trackbed design, in-situ seismic testing was performed at two sites near Asan-city, Korea. One uncased borehole was drilled on cutting site of weathered soil (called site AS-1). Another uncased borehole was drilled on compaction fill site (called site AS-2). In-hole and downhole testing was performed at site AS-1, and in-hole and crosshole tests were performed with the same source and receiver at site AS-2. The distance between source and receiver of the in-hole probe was 1 meter. Shear wave signals for each site are shown in Figure 3 and 4. The dot symbols indicate the arrival times of shear waves. The most in-hole data show the "signature wavelet" of the shear wave energy, even though the bottom-most record at AS-2 is unidentifiable of the first shear wave arrival. Stiffness profiles are shown in Figure 5 with crosshole and downhole results. Shear wave velocities of the weathered soil increase from about 200 m/sec to 400 m/sec with depth, whereas those of fill are around 250 m/sec. The in-hole data agree well with data from crosshole and downhole, respectively.

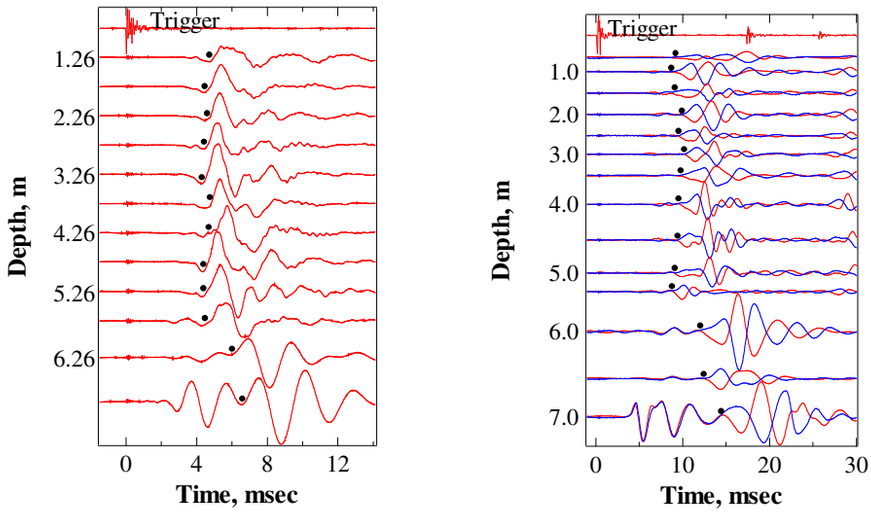
Compaction Fill at Bridge

To assess the quality of compaction fill near a bridge, shear wave velocities were measured using in-hole and crosshole tests at two sites. Two uncased boreholes were drilled to 6 meters at site HS-1 and 3 meters at site HS-2. The shear waves were



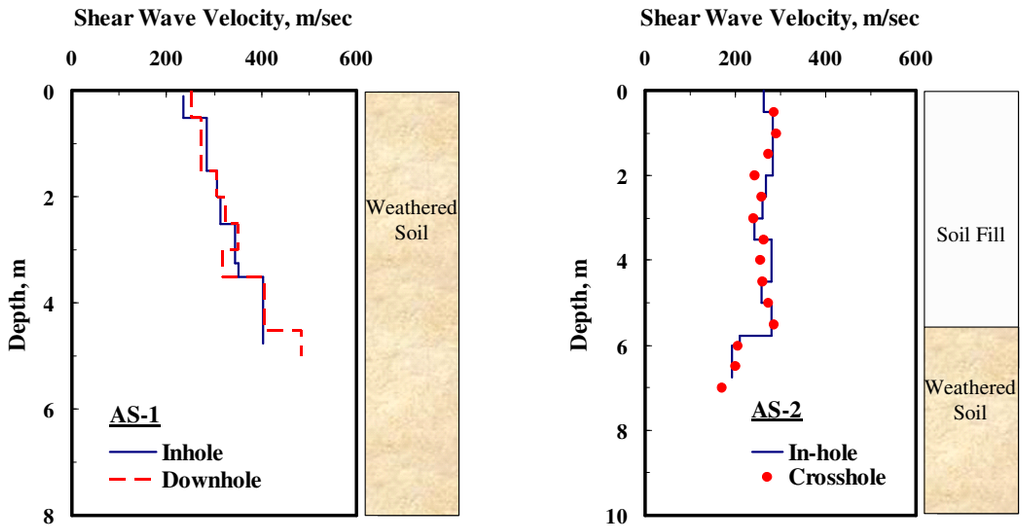
(a) In-hole seismic test (b) Downhole seismic test

Figure 3. Shear wave signals at site AS-1



(a) In-hole seismic test (b) Crosshole seismic test

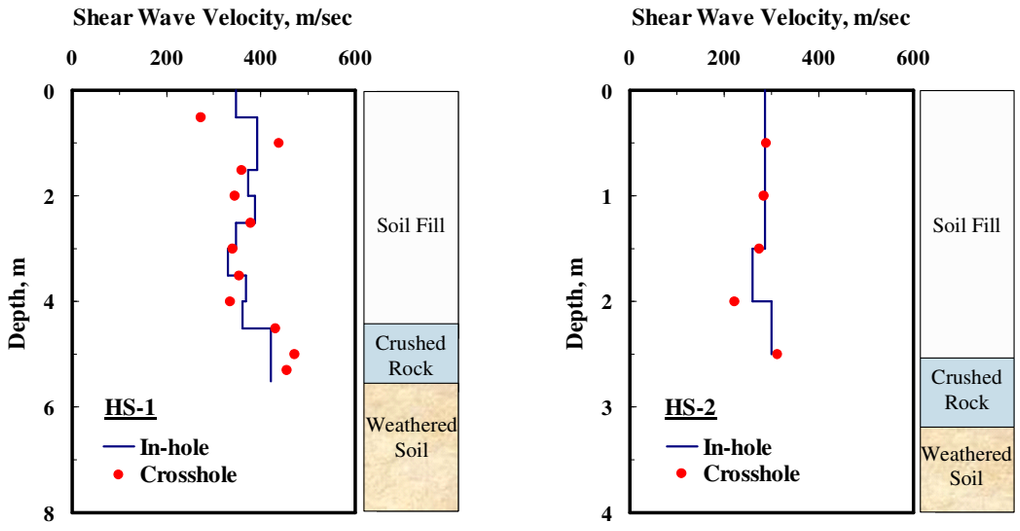
Figure 4. Shear wave signals at site AS-2



(a) Cutting Site (b) Fill Site

Figure 5. Shear wave velocity profiles of subgrade

measured at every 0.5 meters. The soil of the fill was classified as SM, and the boreholes stayed open without casing. Shear wave velocities of the compaction fill (site HS-1) were 300-400 m/sec. At site HS-2, shear wave velocities were about 280 m/sec. Poisson's ratios (ν) of compaction fills were determined using compression wave velocities measured from crosshole tests, and the results were nearly same as 0.28 at two compaction fill sites. Shear wave velocity profiles of compaction fills were determined from in-hole and crosshole tests as shown in Figure 6. Shear wave velocities from in-hole agree well with those from crosshole tests using the same source developed in this study. Despite well agreement, a little difference exists. This



(a) Site HS-1 (b) Site HS-2

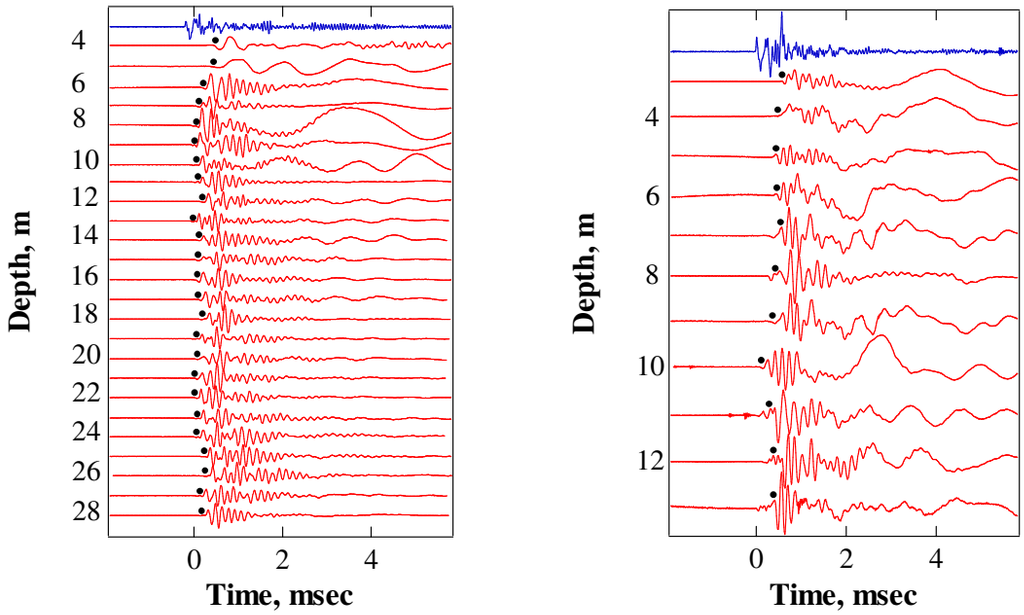
Figure 6. Shear wave velocity profiles of compaction fills

can be accounted for anisotropy of soil layers and the different directions of wave propagation according to the testing methods.

Bedrock of Tunnel and Bridge

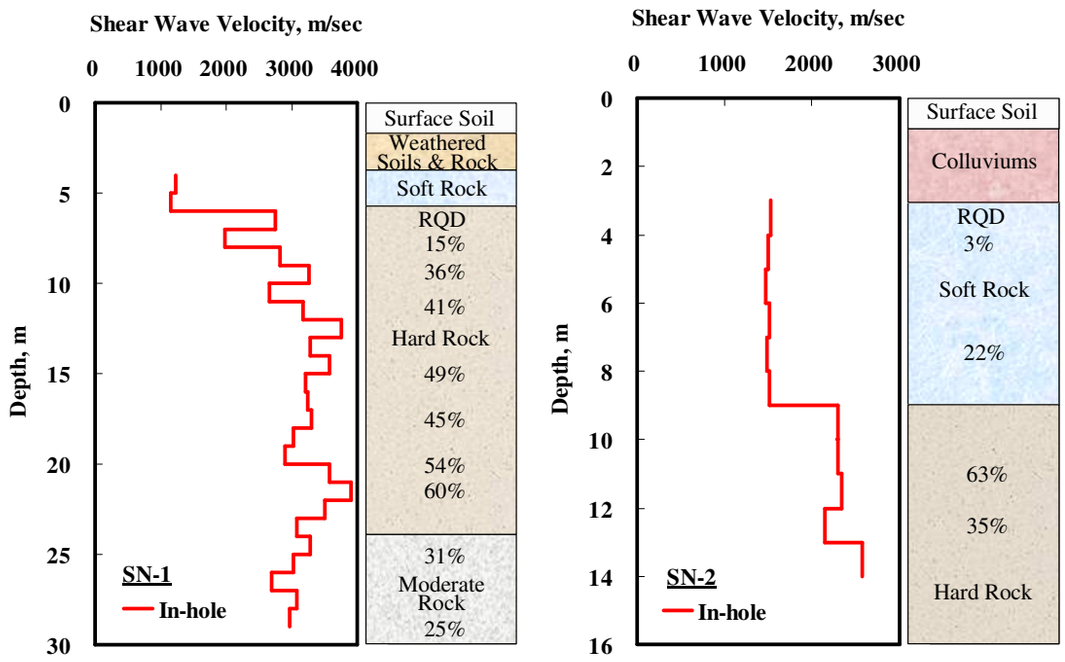
Earthquake-resistant designs are necessary for important structures such as tunnels and bridges. Shear wave velocities of bedrock were evaluated using the in-hole seismic tests at tunnel (called SN-1) and bridge (called SN-2) sites, which were located at Seongnam-city. The geological formation of tunnel site consists of surface soil, weathered residual soil, weathered rock, soft (2.9-5.9m) rock, hard (5.9-24m), and moderate rock (24-32m) of gneiss in sequence. The bedrock of bridge site was layered with surface soil and colluviums (3.4m), soft rock (3.4-9.2m), and hard rock (9.2-15m). Shear wave measurements were carried out at every 1 meter from soft rock layers of site SN-1 and SN-2. The measured shear wave signals are shown in Figure 7. The shear wave signals are distinctive enough to pick up the first arrival of shear energy (denoted by dot symbols). The distance between the source and the receiver of the in-hole probe is one meter, and generally shear wave velocities of rock mass are thousands of meters per second. Hence, the first arrival times of shear waves were picked by expanding the records.

Shear wave velocity profiles and boring profiles including rock quality designation (RQD) proposed by Deere (1964) are presented in Figure 8. Shear wave velocities of the soft rock layer were 1,200 m/sec, those of the hard rock layer were 2,000-3,500 m/sec with depth, and those of moderate rock layer were of the order of 3,000 m/sec at bedrock of tunnel site. Shear wave velocities of the soft rock layer were nearly 1,500 m/sec, and those of the hard rock layer about 2,300 m/sec at bedrock of bridge site. The shear wave velocities were correlated with rock quality designation with a linearly increasing tendency (Figure 9). These results were to be used to evaluate the deformational property of the rock mass for input data in tunnel design.



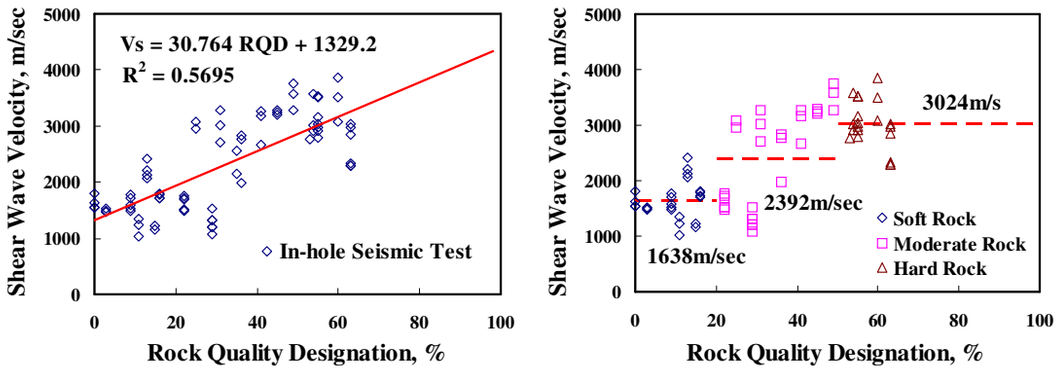
(a) Bedrock of Tunnel (b) Bedrock of Bridge

Figure 7. Shear wave signals measured from in-hole seismic test at tunnel and bridge



(a) Bedrock of Tunnel (b) Bedrock of Bridge

Figure 8. Shear wave velocity profiles of bedrock of tunnel and bridge



(a) Linear Regression (b) Average with RQD

Figure 9. Relationship of shear wave velocity with RQD

Bedrock of Rock Fill Dam

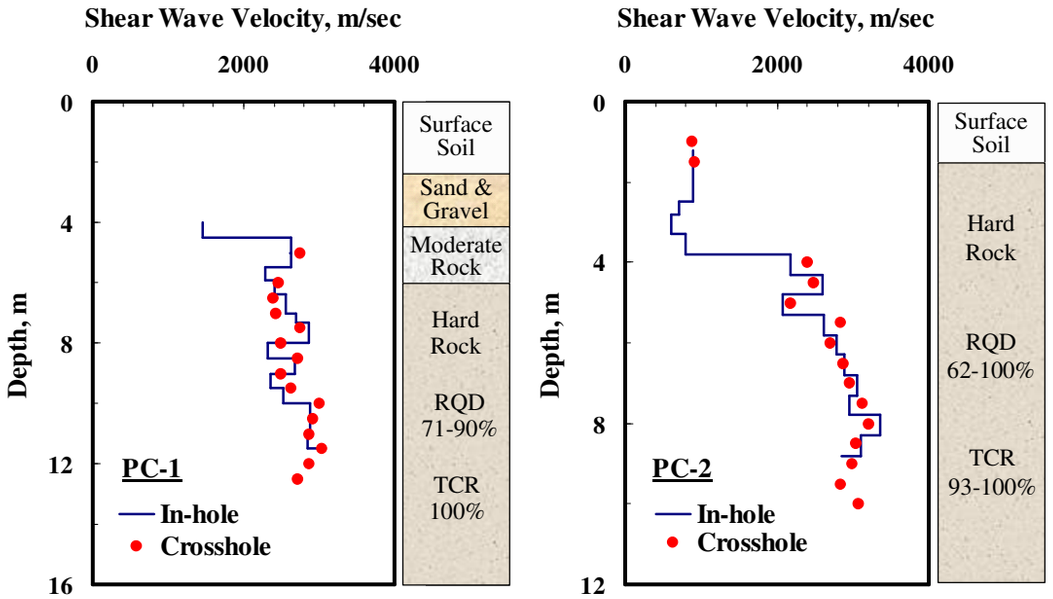
Shear wave velocities were measured to evaluate dynamic stiffness of bedrock at Doam rock fill dam in Korea, using in-hole and crosshole seismic test. The testing locations were bedrock foundation (called site PC-1) and right side abutment (called site PC-2) of the rock fill dam. The geological profile of bedrock foundation consists of surface soil, sedimentary layer of sand and gravel, moderate and hard limestone with increasing depth as in Figure 10. The geological formation of the abutment consists of surface soil and hard limestone. In the surface soil and sedimentary layers, shear wave measurements were not possible because of the noise transmitted through the PVC casing. Two more boreholes were drilled 2.5 meter apart from the original boreholes (PC-1 and PC-2, respectively) to conduct crosshole testing, in which the same source and the receiver were used.

The probe was lowered in a 7.5 cm diameter uncased borehole and shear waves were measured at every 0.5 meters at the rock foundation and the right side abutment of dam, respectively. Shear wave velocities of the hard rock layer at foundation and right abutment were in the range of 2,500-3,000 m/sec. Comparison of the shear wave velocity profiles with companion crosshole tests is presented in Figure 10 and shows good agreement.

Tunnel-Face Rock Mass

To evaluate the dynamic stiffness of rock mass, in-hole seismic tests were performed at tunneling site of road construction. The size of in-hole probe used in this tests was reduced to be fit in 45mm diameter holes (or BX) drilled by a jumbo-drill, which is used to drill holes to install explosives for tunneling. These modifications are to adjust the probe for the unfavorable environment inside of tunnels and to test without any further drilling cost. The lateral length of the drilled holes at tunnel-face was 4 meters. Shear wave velocities of rock mass were measured at the 4 holes (BE-1 ~ BE-4) of tunnel-face, and those were from 800 m/sec to 1,200 m/sec. Shear wave signals with lateral depth of the hole BE-2 and velocity profiles of rock behind tunnel-face are shown in Figure 11. The measured shear wave velocities can be used to

estimate deformation properties of rock mass for tunnel analyses. The probe and testing procedure were successfully adopted with lateral holes drilled by a jumbo-drill at a tunnel-face to evaluate the stiffness of rock mass.



(a) Foundation of Rock Fill Dam (b) Right Abutment of Rock Fill Dam

Figure 10. Shear wave velocity profiles determined from in-hole and crosshole seismic tests

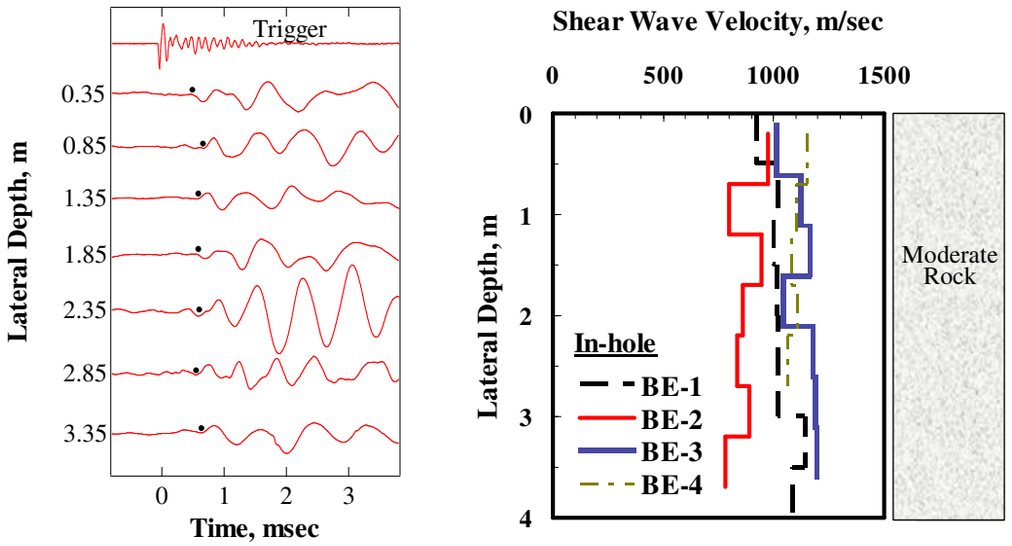


Figure 11. Shear wave signals at borehole BE-2(left) and shear wave velocities with lateral depth at tunnel-face(right)

CONCLUSIONS

The dynamic stiffness of geologic materials is the key parameter for earthquake-resistant designs. Its use is being extended even to static settlement and deformation problems. Its importance and extended usage require a more manageable method than conventional seismic techniques. An in-hole probe and testing method have been developed to be a cost-effective and easy-to-use survey in engineering practice. The in-hole seismic method has been adopted and validated at residual soils, compaction fills and bedrock where uncased boreholes can stay open.

ACKNOWLEDGMENTS

This research was supported by a grant (C105B1000008-06B010000612) from Research Policy & Infrastructure Development Program (RPIDP) funded by Ministry of Construction & Transportation of Korean government.

REFERENCES

Deere, D.U. (1964). "Technical Description of Rock Cores for Engineering Purposes." *Rock Mech. and Rock Engrg.*, 1: 107-116.

Mok, Y.J. (1987). Analytical and Experimental Studies of Borehole Seismic Methods. *Ph.D. Dissertation*, The University of Texas at Austin, 272 p.

Mok, Y.J., Kim, J.H., and Kang, B.S. (2003). "A Pilot Study of In-Hole Seismic Method." *Journal of the Korean Geotechnical Society*, Vol.19, No.3: 23-31.

Mok, Y.J., Park, C.S., and Kong, B.C. (2007). "The Relationship between RQD and Shear Wave Velocity of Rock Mass Using In-hole Seismic Testing." *Proc. of the Korean Geotechnical Society Spring '07 National Conference*, Seoul, Korea: 1079-1088.

Mok, Y.J. and Park, C.S. (2007). "In-Hole Seismic Method for Dynamic stiffness Measurements of Geomaterials." *Proc. 4th International Conference on Earthquake Geotechnical Engineering* (CD-ROM), Thessaloniki, Greece.

Nigbor, R.J. and Imai, T. (1994). "The Suspension P-S Velocity Logging Method." *ISSMFE Technical Committee 10 for XIII ICSMFE, Geophysical Characterization of Sites*, A. A. Balkema Publishers/ Rotterdam & Brookfield, Netherland: 57-61.

Stokoe, K.H., II and Woods, R.D. (1972). "In-Situ Wave Velocity by Cross-Hole Method." *Journal of the Soil Mechanics and Foundation Division, Proceedings*, ASCE, Vol. 98, No. SM5: 356-359.

Stokoe, K.H., II and Hoar, R.J. (1978). "Variables Affecting In Situ Seismic Measurements." *Proceedings of the Conferences on Earthquake Engineering and Soil Dynamics*, ASCE, Geotechnical Engineering Division, Vol. II: 919-939.

Stokoe, K.H., II, Bay, J.A., Redpath, B., Diehl, J.G., Steller, R.A., Wong, I.G., Thomas, P.A., and Luebbers, M. (2003). "Comparison of V_S Profiles from Three Seismic Methods at Yucca Mountain." *12th Panamerican Conference on Soil Mechanics and Geotechnical Engineering*, Cambridge, MA.

Wilson, S.D., Brown, F.R., Jr., and Schwarz, S.D. (1978). "In Situ Determination of Dynamic Soil Properties." *Dynamic Geotechnical Testing*, ASTM STP 654, American Society for Testing and Materials: 295-317.

Use of Shear Wave Velocity to Estimate Settlement Potential in Mine Spoils

Michael E. Kalinski, Ph.D., P. E.[1]

ABSTRACT

Mine spoils are crushed rock fragments resulting from mountaintop removal mining. Mine spoils are typically placed in valleys as fill, but are susceptible to large amounts of differential settlement. Settlement mechanisms in mine spoil are different than those in soil, and include 1) stress-induced settlement due to particle crushing under increased confinement, and 2) hydrocompression due to wetting of the material. Herein, a method has been developed to quantitatively predict settlement in mine spoils by measuring the effect of confining stress and wetting on void ratio in reconstituted laboratory specimens. Settlement potential was found to be much more severe for dry specimens that had not been previously wetted. Upon wetting, the dry specimens experienced almost instant volume change corresponding to vertical strains of around 8%. Resonant column testing revealed that wetted specimens had lower shear wave velocities (v_s) than specimens that had not been wetted. Thus, v_s can be used to indicate whether or not spoils have been previously wetted, and settlement potential can be estimated based on deformation observations made in the laboratory specimens. With this method, mine spoil sites can be screened, and sites less susceptible to excessive amounts of settlement can be identified.

INTRODUCTION

Mountaintop removal is an efficient and widespread method to mine coal in eastern Kentucky and other coal mining regions. During mountaintop removal, overburden rocks are removed to expose coal deposits for easy recovery. The removed material, referred to as mine spoil, consists of crushed rock fragments, and is placed in adjacent valleys to depths of up to hundreds of feet. Mine spoil valley fills create large, flat expanses of potentially valuable level land. These areas have been used for construction of schools, housing, and light commercial development.

Mine spoil has the potential to settle significantly, which, coupled with its heterogeneous nature and varying thickness, causes structures on mine spoil sites to be susceptible to differential settlement. Mine spoil material does not exhibit consolidation settlement associated with the time-dependent dissipation of excess pore pressure, but there are two primary mechanisms that cause settlement of mine spoils: stress-induced crushing and hydrocompression. The first mechanism is stress-induced crushing of mine spoil either under its own weight, or under the weight

[1] University of Kentucky, Department of Civil Engineering, 161 Raymond Bldg., Lexington, KY 40506-0281; PH (859) 257-6117, FAX (859) 257-4404; email: kalinski@engr.uky.edu

of structures on the ground surface. Stress-induced crushing occurs as inter-particle stresses become large enough to crush the particles at points of contact. However, when mine spoils are wetted, the second mechanism, hydrocompression, is enabled where significant settlement can rapidly occur. When the rock fragments in mine spoils are silty, shaly, and angular, they slake when wetted and crush at inter-particle points of contact where stresses are high, resulting in an overall reduction in volume. This mechanism has been widely observed and recognized as a limiting factor in the commercial development of mine spoil valley fills. As a result, development of mine spoil valley fills is often considered to be uneconomical.

Numerous structures in eastern Kentucky have suffered from significant settlement-induced damage attributed to hydrocompression. However, hydrocompression has also been observed in other areas, and the problem is not unique to eastern Kentucky. Wade and Peterson (1993) in their research on two sites in Canada found that settlement due to hydrocompression equal to about 4% of the mine spoil's wetted thickness could occur upon groundwater recharge. Krebs and Zipper (1997) observed at sites in Virginia that settlement of mine spoil fill due to hydrocompression may be accelerated by the introduction of water from septic systems, runoff from roof drains and gutters, and surface runoff. Krebs and Zipper also observed that settlement from hydrocompression occurs almost immediately upon wetting of the material. Once the material has become wetted, further significant amounts of settlement are unlikely.

As mine spoil material settles, a reduction in void ratio (e) occurs as the overall volume of the material decreases. For a given site, settlement can be expressed for the two mechanisms in terms of change in void ratio (Δe):

$$\Delta e = \Delta e_s + \Delta e_h, \tag{1}$$

where Δe_s and Δe_h are changes in void ratio as a result of stress-induced crushing and hydrocompression, respectively. For a layer of material with initial height H_o, settlement (S) is:

$$S = H_o \frac{\Delta e}{1 + e_i}, \tag{2}$$

where e_i is the initial void ratio of the material prior to volume change.

Equation 2 demonstrates that to predict settlement in mine spoils, two pieces of information are required: 1) a quantitative understanding of how changes in state of stress and wetting affect Δe and 2) knowledge of e_i The objective of the research presented in this paper was to develop a method to predict settlement in mine spoils by 1) reconstituting a series of laboratory specimens to measure and quantify the effect of changes in confining stress and wetting on Δe and 2) performing shear wave velocity (v_s) measurements to develop a relationship between v_s and e for estimating

e_i. Shear wave velocity can be correlated to e using the following generic relationship:

$$v_s = f(e)(\sigma_o')^{0.25}, \quad (3)$$

where σ_o' is mean effective confining stress, and $f(e)$ is a soil-specific void ratio function. In general, v_s increases with increasing σ_o' and decreases with increasing e. Thus, if v_s can be measured at a mine spoil site and correlated to e_i using an expression similar to Eqn. 3, and Δe can be predicted based on anticipated changes in σ_o' and wetting at the site, then S can be predicted and mine spoil sites can be screened based on their potential for excessive settlement.

METHODS

Mine spoils used for this study were recovered from six different locations at the Gateway Industrial Park near Jenkins, Kentucky. The spoils at this site originate from the mining of upper Paleozoic coal seams, and consist of a mixture of mudstones, siltstones, and sandstones. The mine spoils were removed by blasting, and placed using Caterpillar D10N bulldozers and 777B dump trucks. The 6 different locations were distributed over the park, and were all within about 0.75 miles (1.2 km) of each other.

Spoils were recovered from a depth interval of approximately 4.0-8.0 ft (1.2-2.4 m) below the ground surface using a backhoe, and placed in 5-gallon (0.2-m^3) plastic buckets for transport to the lab. During excavation, numerous large boulders, with dimensions up to 3 ft (1 m), were encountered. However, only smaller boulders (less than 20 cm) were brought back to the lab due to the size restrictions of the buckets. It is estimated that the boulders that were too large for the buckets comprised approximately 30% of the total material.

The mine spoil was transported to the laboratory and dried in a soil drying oven. After drying, the material was passed through a 0.5-in. (12.7-mm) sieve, and the fine fraction was used to reconstitute specimens for testing. Since resonant column testing was to be performed using 4.0-in. (102-mm) diameter specimens, the material coarser than 0.5 in. (12.7 mm) was excluded to maintain a maximum grain size/specimen diameter ratio less than 1/6 in accordance with the ASTM D4015 standard for resonant column testing. Information regarding the average properties of the materials recovered at the site is summarized in Table 1.

Specimens of oven-dried mine spoil with lengths and diameters of 8.0 in. (20.3 cm) and 4.0 in (10.2 cm), respectively, were reconstituted using the material passing the 0.5-in. (12.7-mm) sieve. Materials were reconstituted in a latex membrane, which was placed in an aluminum mold to maintain a cylindrical shape. The material was placed by dry pluviation from a height of approximately 1.0 in. (2.5 cm), and the material was distributed to minimize segregation. After the material was placed in the membrane, PVC end caps were placed on each end of the membrane,

and the membrane was sealed to the end caps using O-rings. A pore vacuum of 3.0 psi (21 kPa) was applied so that the specimens maintained a right circular cylindrical shape after removal of the mold.

Table 1. Range in properties of the mine spoils used in this study.

	***w* (%)**	**G_s**	***LL* (%)**	***PI* (%)**	**%** fines
Minimum value	4.0	2.64	21.9	0.0 (NP)	20.6
Maximum value	7.5	2.72	26.9	0.5	34.7
Average	5.7	2.68	23.9	5.7	26.5

Three specimens were reconstituted from each of the six locations. Pore vacuum was increased incrementally from 3.0 psi (21 kPa) to 6.0 psi (41 kPa) to 9.0 psi (62 kPa). Specimen volume was measured at each increment by measuring the average length and diameter of each specimen, and e was calculated at each vacuum level to measure the effect of mean effective confining stress (σ_o'; equal to pore vacuum) on Δe_s due to stress-induced crushing.

Tap water was permeated through the dry specimens to measure the effect of wetting. There were three specimens prepared for each location, and each specimen was wetted at a vacuum of either 3.0 psi (21 kPa), 6.0 psi (41 kPa), or 9.0 psi (62 kPa). Specimens were wetted by permeating tap water using a pressure board at a low (between 5 and 10) hydraulic gradient. Specimen volume was measured, and e was calculated to measure the effect of wetting on Δe_h due to hydrocompression.

Free-free resonant column testing was performed at the end of each vacuum/wetting stage for each specimen to measure v_s for correlation with e_i in the specimens. The free-free resonant column method (Kalinski and Thummaluru, 2005) involves the suspension of a right circular cylindrical specimen of material as depicted in Fig. 1. The specimen is excited at one end using a transient torsional pulse, and torsional motion is measured at the other end using two accelerometers. The specimen resonates at a torsional resonant frequency of f_n, which is derived by performing spectral analysis of the time-domain accelerometer output signal. Shear wave velocity is calculated using the following equation:

$$\beta = \frac{2\pi f_n L}{v_s}, \tag{4}$$

where L is the specimen length, and β is calculated using the relationship:

$$\tan\beta = \frac{(\mu_1 + \mu_2)\beta}{\mu_1\mu_2\beta^2 - 1}. \tag{5}$$

In Eqn. 5,

$$\mu_1 = \frac{I_1}{I} \tag{6}$$

and

$$\mu_2 = \frac{I_2}{I}, \tag{7}$$

where I_1 and I_2 are the polar mass moments of inertia of the masses fixed to each end of the specimen, and I is the polar mass moment of inertia of the specimen. After v_s was calculated for each vacuum and wetting stage, the data were analyzed to establish a relationship between v_s and e_i.

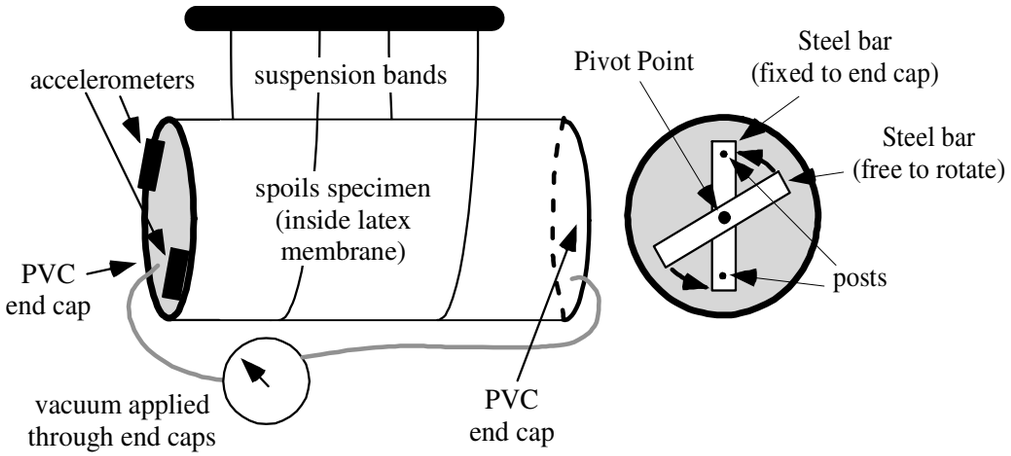


Figure 1. Free-free resonant column test configuration.

RESULTS

A total of 18 specimens were reconstituted and tested. Mean effective confining stress (σ_o'; equal to pore vacuum) was increased incrementally, and e was measured at each increment. During one of the stress increments, the specimen was wetted by permeating tap water through the specimen with a pressure board, and changes in e resulting from wetting were calculated. When wetted, volume change occurred more or less instantly, and was visibly noticeable. Average void ratios before and after wetting were 0.68 and 0.54, respectively

Typical results from measurement of a single specimen are illustrated in Fig. 2. These data demonstrate that increasing the confining stress caused a corresponding reduction in e. These data also demonstrate the dramatic effect of wetting on e.

To quantify the effects of stress-induced crushing on Δe, all of the $e - \sigma_o'$ data were plotted for each location as illustrated in Fig. 3. The data in this figure illustrate that there is a consistent relationship between σ_o', wetting of the spoils, and e.

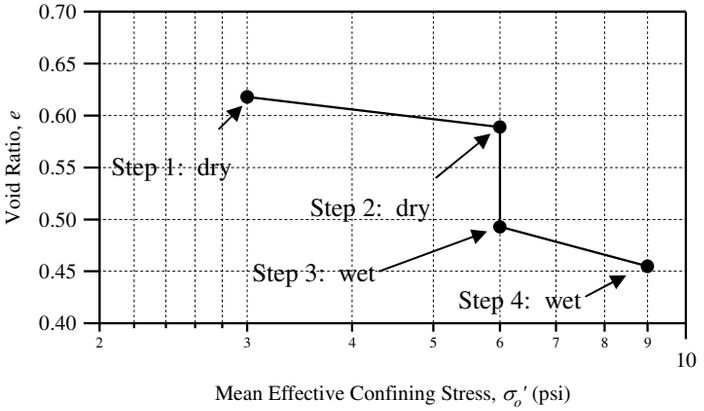


Figure 2. Typical relationship between e and σ_o' with stress/wetting sequence indicated (specimen wetted at 6.0 psi).

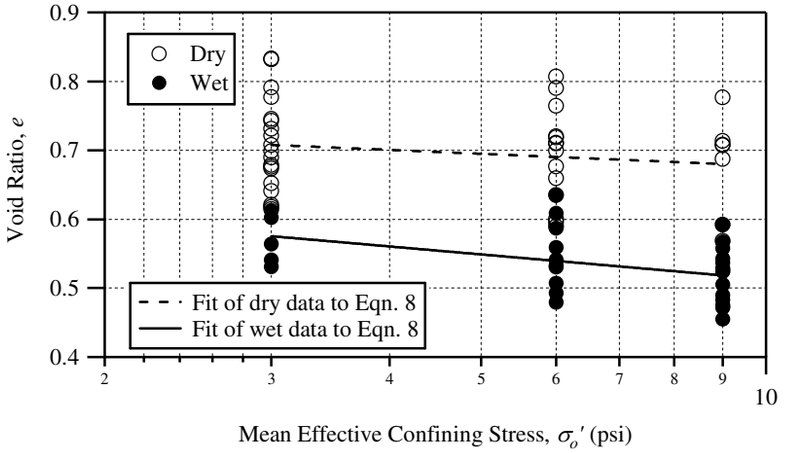


Figure 3. Summary of e - σ_o' data

Regression analysis was performed to fit the data in Fig. 3 to the relationship:

$$e = C_s[\log(\sigma_o')] + b, \tag{8}$$

where C_s and b are regression coefficients. The coefficient C_s can be defined as the stress-induced crushing index, which can be used to estimate settlement caused by stress-induced crushing of mine spoils, S_s:

$$S_s = \frac{H_o}{1+e_i} C_s \log\left(\frac{\sigma_f'}{\sigma_i'}\right), \tag{9}$$

where σ_i' and σ_f' are the in situ vertical effective stress before and after loading.

Results of the regression analysis indicate that wetted spoils are susceptible to slightly greater amounts of stress-induced crushing settlement than dry spoils (i.e. C_s is higher for wetted spoils). When fitting the data from Fig. 3 to Eqn. 8, average values of C_s for dry and wet specimens are 0.058 and 0.12, respectively.

Vertical strain, ε, is expressed as:

$$\varepsilon = \frac{e_i - e_f}{1 + e_i}. \tag{10}$$

Given the average values for void ratio before and after wetting, an average strain of 0.083 is calculated, and settlement caused by hydrocompression, S_h, is expressed as:

$$S_h = H_o \varepsilon, \tag{11}$$

Total settlement caused by stress-induced crushing and hydrocompression is expressed by combining Eqns. 9 and 11:

$$S = S_s + S_h. \tag{12}$$

Shear wave velocity was measured by performing free-free resonant column testing on each specimen. A typical auto power spectrum is illustrated in Fig. 4, and values for v_s for all the specimens are plotted versus σ_o' in Fig. 5. As expected, v_s increases with increasing σ_o'. To identify a relationship between v_s and e, the v_s data were normalized with respect to the quarter root of σ_o' to derive a stress-corrected shear wave velocity, v_s':

$$v_s' = \frac{v_s}{(\sigma_o')^{0.25}}. \tag{13}$$

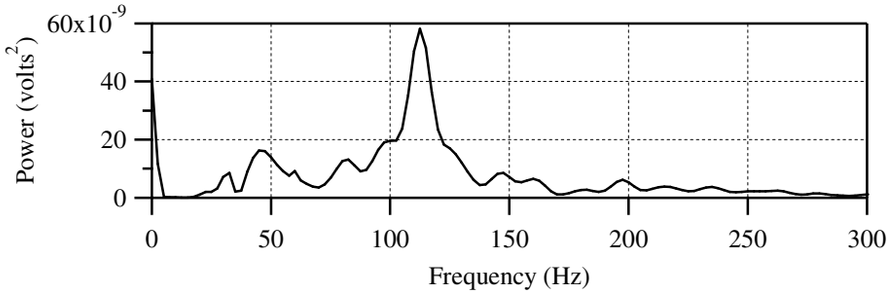


Figure 4. Typical auto power spectrum derived from free-free resonant column testing (specimen tested wet at 6 psi with f_n = 112.5 Hz)

The resulting data (Fig. 6) indicate that v_s generally decreases when the material is wetted due to softening of the rock particles. The large amount of variation in the data is an indication of the heterogeneous nature of the mine spoil.

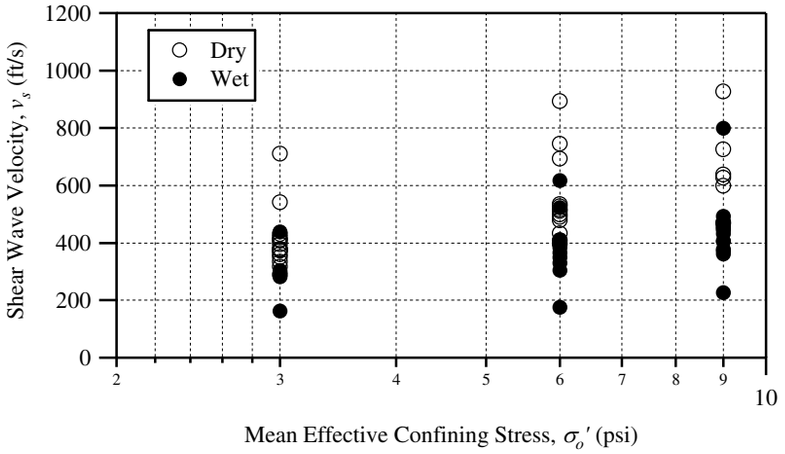


Figure 5. Relationship between v_s and σ_o' for all test specimens.

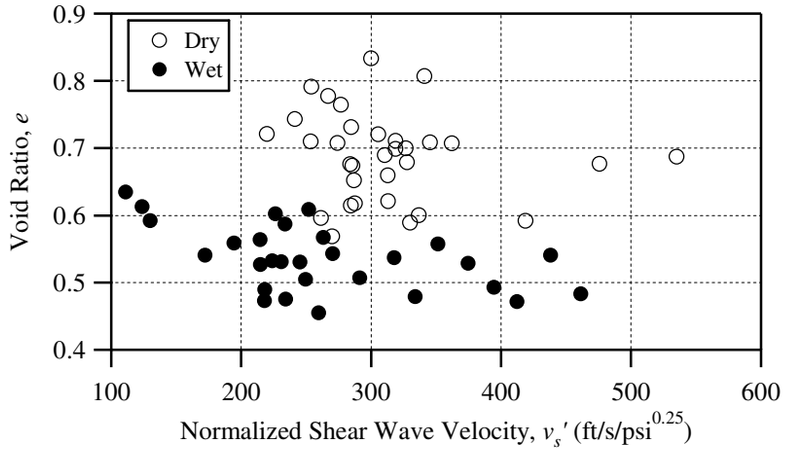


Figure 6. Relationship between v_s' and e for all test specimens.

PROCEDURE FOR SCREENING MINE SPOILS SITES

As a result of this study, a procedure has been developed to screen potential construction sites based on settlement potential. The procedure is described in the following paragraphs.

Step 1 -- Characterization of Mine Spoil Profile. Perform in situ v_s testing using a nonintrusive geophysical method to measure variations in v_s versus depth and define the mine spoil profile. For each interval in the profile, calculate v_s' using Eqn.

13. Mean effective confining stress can be expressed as a function of vertical effective stress (σ_v') and coefficient of earth pressure at rest (K_o):

$$\sigma_o' = \sigma_v' \left(\frac{1+2K_o}{3} \right). \quad (14)$$

If v_s' < 210 ft/s/psi$^{0.25}$ (39.5 m/s/kPa$^{0.25}$), then the material can be considered wet. If v_s' > 210 ft/s/psi$^{0.25}$ (39.5 m/s/kPa$^{0.25}$), then the material is either wet or dry. In the latter case, it is conservative to assume that the material is dry.

Step 2 – Calculation of Settlement Potential. For each layer, settlement can be estimated depending on whether the material is considered wet or dry based on shear wave velocity. For wet material, only stress-induced crushing will occur. The expression for settlement of wet material, S_w, is a form of Eqn. 9 where the average post-wetted value for void ratio of 0.54 is used for e_i, along the average post-wetted value of 0.12 for C_s:

$$S_w = 0.077 H_o \log\left(\frac{\sigma_f'}{\sigma_i'} \right). \quad (15)$$

For dry material, settlement will result from a combination of stress-induced crushing and hydrocompression. The expression for settlement of dry material, S_d, is derived by substituting the measured dry spoil values of 0.68 and 0.058 for e_i and C_s, respectively, into Eqn. 9, and combining Eqns. 9 and 11:

$$S_d = 0.035 H_o \log\left(\frac{\sigma_f'}{\sigma_i'} \right) + 0.083 H_o. \quad (16)$$

In Eqn. 16, the average value for vertical strain of 0.083 is used for ε.

CONCLUSIONS

The results of this study demonstrate that mine spoil sites may be screened for settlement potential by using a combination of in situ shear wave velocity testing and laboratory-based observations. Shear wave velocity measurement can be used to interpret whether or not mine spoil layers have been previously wetted, and settlement can then be estimated for each layer in the profile. This calculation can be performed for numerous sites, and desirable sites with lower settlement potential can be identified.

There are two distinct settlement mechanisms in mine spoil: stress-induced crushing caused by increasing the confining stress, and hydrocompression caused by wetting of the material. Of these two mechanisms, hydrocompression of layers that have not been previously wetted is the most severe, with vertical strains of around

8%. This seems extreme, but is consistent with observations of settlement and damage to structures built on mine spoil sites (Karem, 2005; Karem et al., 2007).

It is important to note that the grain size distribution of the material tested herein was different than the grain size distribution in the in situ material. Much of the coarse fraction (cobble- and boulder-sized particles) was excluded to facilitate lab testing, but the coarse fraction is present in field. In the field, it is likely that the material possessing this coarse fraction would have inflated values of v_s relative to the values presented herein, and would probably exhibit less hydrocompression-induced settlement than the lab material. As a result, there would probably be less separation between the dry and wet data points in Fig. 6, and all of the data points in Fig. 6 would be shifted to the right towards higher velocity. Nevertheless, it is likely that the method presented herein would still be helpful to screen mine spoil sites.

It is also important to note that the regression coefficient C_s used to estimate stress-induced crushing is specific to the material used in this experiment. The values for C_s presented herein are applicable to materials with similar lithologies and origins (i.e. Appalachian Paleozoic clastic sedimentary rocks). For different lithologies, it is recommended that the procedures presented herein be applied to develop site- and lithology-specific values for C_s.

ACKNOWLEDGMENTS

The author would like to thank the Kentucky Science and Engineering Foundation for sponsoring this project under Award #KSEF-633-RDE-007.

REFERENCES

Kalinski, M. E., and Thummaluru, M. S. R. (2005), "A New Free-Free Resonant Column Device for Measurement of G_{max} and D_{min} at Higher Confining Stresses," *Geotechnical Testing Journal*, Vol. 28, No. 2, pp. 180-187.

Karem, W. A., 2005, *Development of a Predictive Model to Evaluate Mine Spoil Fills for Industrial Development*, Ph.D. Dissertation, University of Kentucky, Department of Civil Engineering.

Karem, W. A., Kalinski, M. E., and Hancher, D. E., 2007, "Settlement of Mine Spoil Fill from Water Infiltration: A Case Study in Eastern Kentucky," *Journal of Performance of Constructed Facilities,* Vol. 21, No. 5.

Krebs, R. D., and Zipper, C. E., 1997, "Foundation for Housing on Reclaimed Land Mined Lands", *Publication No. 460*-115, Virginia Cooperative Extension.

Wade, N. H., and Peterson, T. W. P., 1993, "Collapse and Consolidation Settlement in Mine Spoil Due to Saturation and Preloading," *Proceedings of the 46th Annual Canadian Geotechnical Conference*, pp. 185-192.

Inversion Algorithm to Evaluate Velocity Profiles from Downhole Seismic Tests

J. Alfredo Fernandez[1], Glenn J. Rix[2] and Savannah Gowdy[3]

[1] Graduate Research Assistant, Georgia Institute of Technology, School of Civil and Environmental Engineering, 790 Atlantic Dr. Atlanta, GA 30332; jafernandez@gatech.edu
[2] Professor, Georgia Institute of Technology, School of Civil and Environmental Engineering, 790 Atlantic Dr. Atlanta, GA 30332; glenn.rix@ce.gatech.edu
[3] Undergraduate Research Assistant, Georgia Institute of Technology, School of Civil and Environmental Engineering, 790 Atlantic Dr. Atlanta, GA 30332; savannah.gowdy@gatech.edu

ABSTRACT

The downhole seismic test is a widely used method to evaluate in-situ seismic wave velocity profiles. In this test, elastic waves are propagated from a stationary source point that is placed at the ground surface to the receivers, which are placed down in a borehole. The wave velocities are usually determined by evaluating the travel times either between the source and each of the receivers, called the direct method, or between receivers, called the true interval or pseudo-interval method. These conventional approaches of determining wave velocities make simplifying assumptions including a straight raypath between the source and the receivers and velocity isotropy. In a layered and anisotropic media, these assumptions can result in errors in the velocity profile. An inversion algorithm is presented to evaluate the velocity profile from downhole seismic test data. It models the soil profile as a stack of horizontal layers with elliptical velocity anisotropy. The raypaths are calculated using a nonlinear iterative algorithm based on the bending method, fulfilling Fermat's principle of minimum travel time and Snell's Law. The inversion algorithm models wave propagation in real soil media more accurately and thus enables a more robust estimate of the seismic wave velocity profile.

INTRODUCTION

Ground response analyses are used to estimate surface earthquake ground motions for development of design response spectra and liquefaction hazard assessments. The evaluation of the ground response to seismic loads requires the specification of the dynamic properties of the local soil profile that may affect the wave propagation including stiffness, damping, Poisson's ratio, and density. Among these properties, stiffness and damping have the largest influence on the soil response (Kramer, 1996).

The low-strain stiffness or shear modulus G_{max} of the soil is directly related to the shear-wave velocity, and thus many field tests have been developed to measure this parameter. The downhole seismic test is a widely used method to evaluate in-situ seismic wave velocity profiles. In this test, elastic waves are propagated from a stationary source point that is placed at the ground surface to the receivers, which are placed down in a borehole. The wave velocities are usually determined by evaluating the travel times either between the source and each of the receivers, called the direct method, or between receivers, called the true interval or pseudo-interval method.

These conventional approaches of determining wave velocities make simplifying assumptions including a straight raypath between the source and the receivers and velocity isotropy, and might result in large errors in the estimate of the velocities at the boundaries of two layers with high velocity contrast (Kim et al., 2004). An inversion algorithm is presented to evaluate the velocity profile from downhole seismic test data. It models the soil profile as a stack of horizontal layers with elliptical velocity anisotropy. The raypaths are calculated using a nonlinear iterative algorithm based on the bending method, fulfilling Fermat's principle of minimum travel time and Snell's Law. The inversion algorithm models wave propagation in real soil media more accurately and thus enables a more robust estimate of the seismic wave velocity profile. Mok et al. (1988) proposed a similar method to analyze downhole seismic data based on inverse theory; however an advantage of the algorithm proposed herein is the incorporation of velocity anisotropy in the analysis.

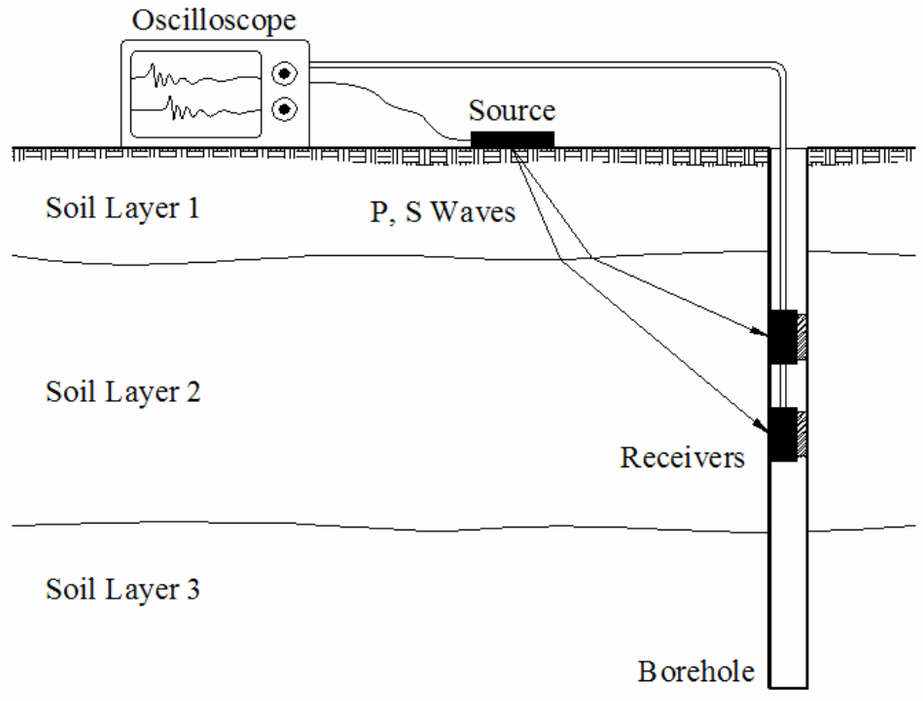


FIG. 1. Downhole seismic test.

DOWNHOLE SEISMIC TEST

The downhole seismic test consists in placing an impulse source at the ground surface adjacent to a borehole. A single or multiple receivers are attached to the wall of the borehole at a given depth. The objective of the test is measure the time required for waves generated at the source to travel to the receivers. The observed travel time is directly related to the wave velocity of the soil. The process is repeated for different depths to obtain a velocity profile of the site. The downhole seismic test can be used to evaluate in situ compression- and shear-wave velocity profiles. Figure 1 illustrates a diagram of the test.

The three most common procedures to calculate the travel time are first shear wave arrival, crossover method, and cross-correlation method (Sully and Campanella, 1995). The first shear wave arrival approach consists of visually calculating the arrival time of the shear wave at the receiver (Stokoe and Woods, 1972; Woods, 1986). The crossover method enhances the previous approach by superimposing oppositely polarized shear wave signals to determine the shear wave arrival time (Campanella et al., 1986; Woods, 1978). The last method calculates the cross-correlation of time histories at adjacent depths to estimate the time delay between receivers and the interval velocity (Woods, 1978, 1986). There are other methods to calculate the travel time (i.e. cross spectral density function method (Campanella et al., 1994; Woods, 1986)); however it is outside the scope of this paper to review and discuss these methods.

The conventional approaches of determining wave velocity profiles are the direct method and the true interval or pseudo-interval methods. The direct method corrects the inclined travel path to a vertical path to calculate the corrected travel time (Auld, 1977; Boore and Thompson, 2007):

$$t_c = t \cdot \frac{H}{R} \tag{1}$$

where t is the observed travel time, H is the depth of the receiver, and R is the length of the straight raypath from source to receiver. The velocity profile can be obtained from the slope of a straight line fitted to the data points having a similar trend in the plot of corrected travel times versus depth. An estimate of the velocity in each depth interval can be calculated by:

$$v = \frac{\Delta H}{\Delta t_c} \tag{2}$$

The true interval method is applicable when the test is performed using two receivers as shown in Figure 1. The velocity between receivers is given by (Woods, 1986):

$$v = \frac{R_L - R_U}{t_L - t_U} \tag{3}$$

where R is the length of the straight raypath from the source to the receiver, t is the observed travel time, and subscripts U and L refer to the upper and lower receivers respectively. The pseudo-interval method uses a similar approach when only a single receiver is used in the test, but the distance and travel time differences in (3) are calculated from two successive depth locations (Campanella et al., 1986; Woods, 1986). The interval methods can not evaluate velocities when the time difference in (3) is negative (Kim et al., 2004), i.e., when the lower receiver is located in a higher velocity layer.

Conventional methods assume a straight raypath between source and receivers with no refraction at layer interfaces. This assumption can not be valid due to Snell's Law which states that the angles of incidence and refraction are different when waves pass through a boundary between two media with different wave velocities. For the case of the downhole seismic test, the straight raypath assumption might be valid when the velocity decreases with depth or when the depth of the receiver is large compared to the offset of the source that the difference between the straight and refracted raypath is not significant, because the angle of incidence is normal to the layer interfaces.

DOWNHOLE INVERSION ALGORITHM

An inversion algorithm is presented to evaluate the velocity profile from downhole seismic test data. It models the soil profile as a stack of horizontal layers with elliptical velocity anisotropy. The raypaths are calculated using a nonlinear iterative algorithm based on the bending method, fulfilling Fermat's principle of minimum travel time and Snell's Law.

The algorithm requires the following input data: observed travel times and their standard deviation, location of source and receivers, depth of the soil layers, initial estimate of the wave velocities and their standard deviation, and the vertical to horizontal velocity ratio to include velocity anisotropy. Layering information can be obtained from geological data, slope changes in the plot of travel times versus depth, or by using the iterative procedure proposed by Boore and Thompson (2007) where the determination of interface depths is based on the minimization and elimination of trends in the travel times residuals. The values of the velocity anisotropy ratio range from 1.0 to 1.1 (Yan and Byrne, 1990).

The inversion algorithm consists in the following steps:

Step 1. The straight raypath is calculated from the source to each of the receivers.

Step 2. The refracted raypath are calculated for each receiver using an iterative algorithm based on the bending method, where the end points of the ray (i.e. source

and receiver) are known, and the raypath and travel time are determined given a velocity profile (Santamarina and Fratta, 1998).

The raypath is calculated based on the Fermat's principle whereby the wave travels on the path that minimizes the travel time between two points (Santamarina and Fratta, 1998). The straight raypath calculated in Step 1 is used as the initial guess, and then the raypath is gradually modified, changing the x-coordinate of the vertices by solving the following equation for every layer interface crossed by the raypath (Chander, 1977):

$$\frac{dt}{dx} = \left(\frac{v_v}{v_h}\right)_j^2 \cdot \frac{x - x_{j-1}}{\sqrt{\left(\frac{v_v}{v_h}\right)_j^2 \cdot (x - x_{j-1})^2 + (z_j - z_{j-1})^2}} \cdot \frac{1}{v_{s\,j}} + \cdots$$
$$\cdots \left(\frac{v_v}{v_h}\right)_{j+1}^2 \cdot \frac{x - x_{j+1}}{\sqrt{\left(\frac{v_v}{v_h}\right)_{j+1}^2 \cdot (x - x_{j+1})^2 + (z_j - z_{j+1})^2}} \cdot \frac{1}{v_{s\,j+1}} = 0 \quad (4)$$

where t is the travel time, x and z are the vertices of the raypath, v_v/v_h is the vertical-to-horizontal velocity ratio, v_s is the wave velocity, and subindex j refers to layer j. The z-coordinate is the depth of the layer interface crossed by the raypath. An elliptical velocity anisotropy model, where wavefronts are ellipses with axes v_h and v_v, is incorporated in the formulation due to its simplicity and ability to model observed data (Lee and Stokoe II, 1986; Slawinski et al., 2004). Figure 2 illustrates the notation used in (4). The procedure is iterative until the difference between the x-coordinate of two successive iterations is less than a specified tolerance. The refracted raypath calculated by this method also satisfies Snell's Law.

Step 3. The x and z coordinates of the refracted raypath are used to calculate the length of the travel path in each layer for each receiver. These values are used to define an N x M matrix **G**, where N is the total number of receivers and M is the total number of soil layers. Thus $G_{i,j}$ is the distance traveled by the raypath to receiver i in layer j.

Step 4. New estimates of the slowness s (i.e. the inverse of the velocity) are computed by solving the following system of equations:

$$\mathbf{A} \cdot \mathbf{s} = \mathbf{b} \quad (5)$$

The elements of matrix **A** and vector **b** are given by:

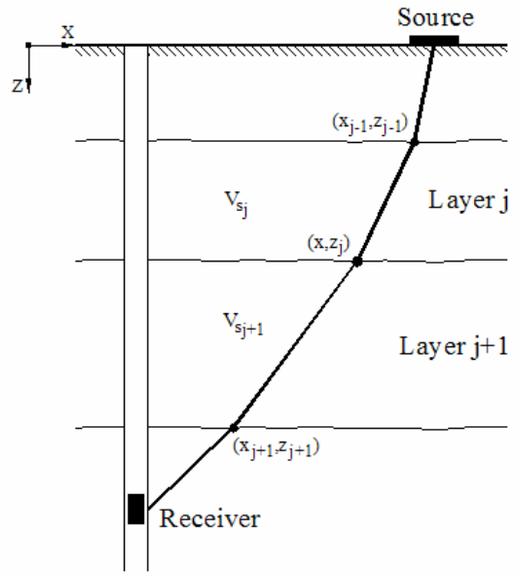


FIG. 2. Raypath illustrating the notation used in (4).

$$A_{j,k} = \sum_{i=1}^{N} \frac{G_{i,j} \cdot G_{i,k}}{\sigma_t{}^2{}_i} \quad j \neq k \quad (j,k = 1,2,\cdots M)$$
$$A_{j,j} = \sum_{i=1}^{N} \frac{G_{i,j} \cdot G_{i,j}}{\sigma_t{}^2{}_i} + \frac{1}{\sigma_S{}^2{}_j} \quad (j = 1,2,\cdots M) \tag{6}$$

$$b_j = \sum_{i=1}^{N} \left(G_{i,j} \cdot \frac{t_i}{\sigma_t{}^2{}_i} \right) + \frac{s_j}{\sigma_S{}^2{}_j} \quad (j = 1,2,\cdots M) \tag{7}$$

where t_i is the observed travel time at receiver i, $\sigma_{t_i}{}^2$ is the variance of t_i, s_j is the estimate of slowness of layer j, and $\sigma_{S_j}{}^2$ is the variance of s_j.

Steps 2 to 4 are repeated until the difference between the estimates of the slowness profile of two successive iterations is less than a specified tolerance. Usually three or four iterations are necessary to obtain convergence.

Step 5. The variance of the final estimation of the velocities in each layer j is calculated by:

$$\sigma_v{}^2{}_j = \left(\mathbf{A}^{-1}\right)_{j,j} \tag{8}$$

EXAMPLE

An example is presented to demonstrate the advantages of the inversion algorithm. The site selected is part of the U.S. Geological Survey program to acquire seismic velocity and geologic data at locations of earthquake strong ground motions stations

(Gibbs et al., 2000). The station selected for the example is Brentwood VA Hospital (BVA) (Lat: 34.06, Lon: -118.46). Gibbs et al. (2000) provides the downhole test data for this site including observed travel times and soil layering. The source was located 4 m from the borehole, and downhole measurements were made at 2.5 m intervals, starting at 2 m depth. The test was performed using compression and shear waves, but only the latter was used in this example. However the inversion algorithm is also applicable to obtain compression-wave velocity profiles. The shear-wave velocity profiles were calculated using the direct method, the pseudo-interval method, and the inversion algorithm proposed herein.

Figure 3 compares the shear-wave velocity profiles calculated by the three methods along with the location of receivers and soil layers and the refracted raypath calculated by the inversion algorithm. Figure 3b shows the mean of the velocity profile calculated by the inversion algorithm and its associated variability along with discrete values of velocity estimated by the conventional methods. The estimates of the variance calculated by (8) do not include the model variability, and therefore these values might be small. The discrete slownesses values calculated by the direct and pseudo-interval methods for each receiver depth shown in Figure 3b were averaged over each layer to obtain an estimate of the velocity for that layer as shown in Figure 3c. Figure 4 compares the observed and predicted travel times by the three methods.

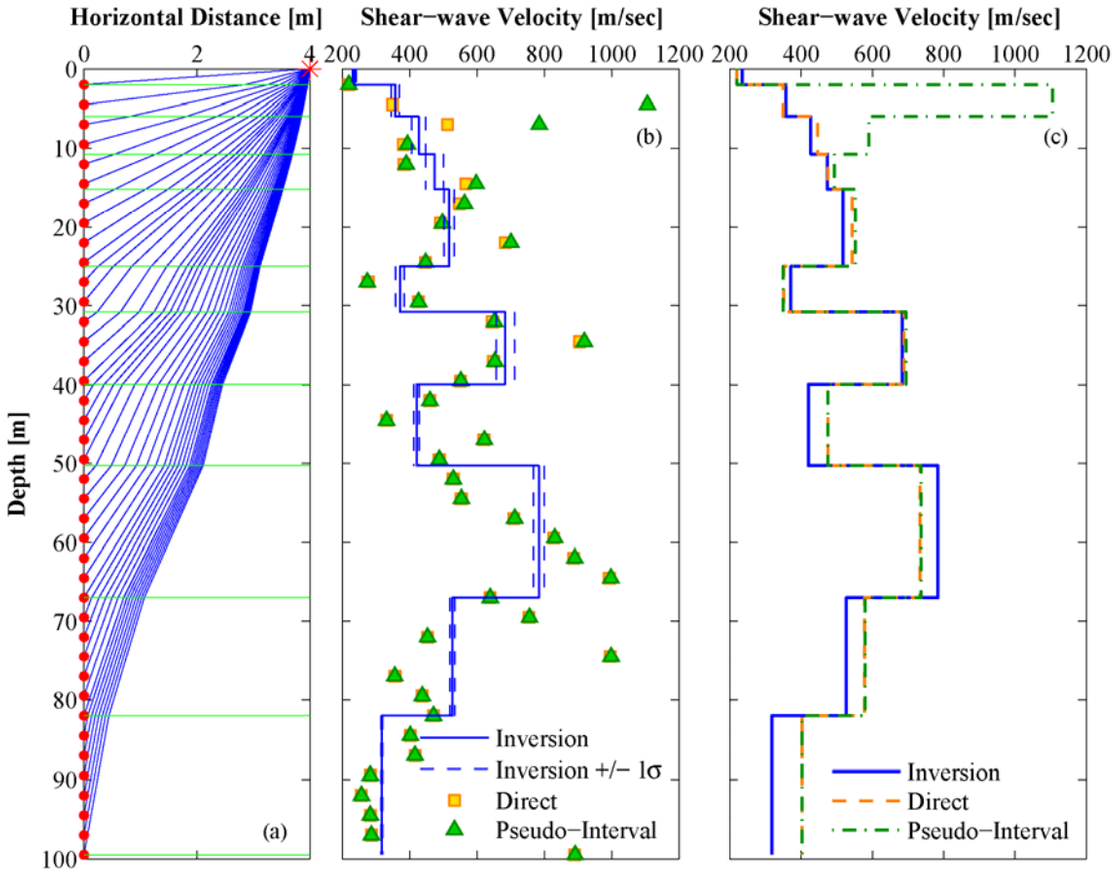


FIG. 3. Refracted raypath and shear-wave velocity profiles.

The travel times predicted by the direct and pseudo-interval methods were calculated assuming a straight raypath.

The large difference in the shear-wave velocity of the second layer calculated by the pseudo-interval method occurs because the upper and lower receivers used in (3) are located in different layers. The method does not consider velocities of upper layers and therefore it assumes that both receivers are in the same layer (Kim et al., 2004). Thus the difference in the observed travel times in (3) is not consistent with the difference in the length of the travel path yielding a higher velocity. This high-velocity layer near the surface affects the predicted travel times as observed in Figure 4. The assumption made by the pseudo-interval method is less evident in the estimated velocities of the third and fourth layer. In those cases there are two receivers in the same layer, and when the velocity estimated using these receivers is averaged with the higher velocity calculated with the receiver located in the upper layer, the effect is reduced. When the depth of the receivers is large compared to the source offset, the vertical travel path assumed by the direct method and the inclined straight raypath assumed by the pseudo-interval method are similar and therefore both methods predict the same velocity as shown in the deeper receivers in Figure 3.

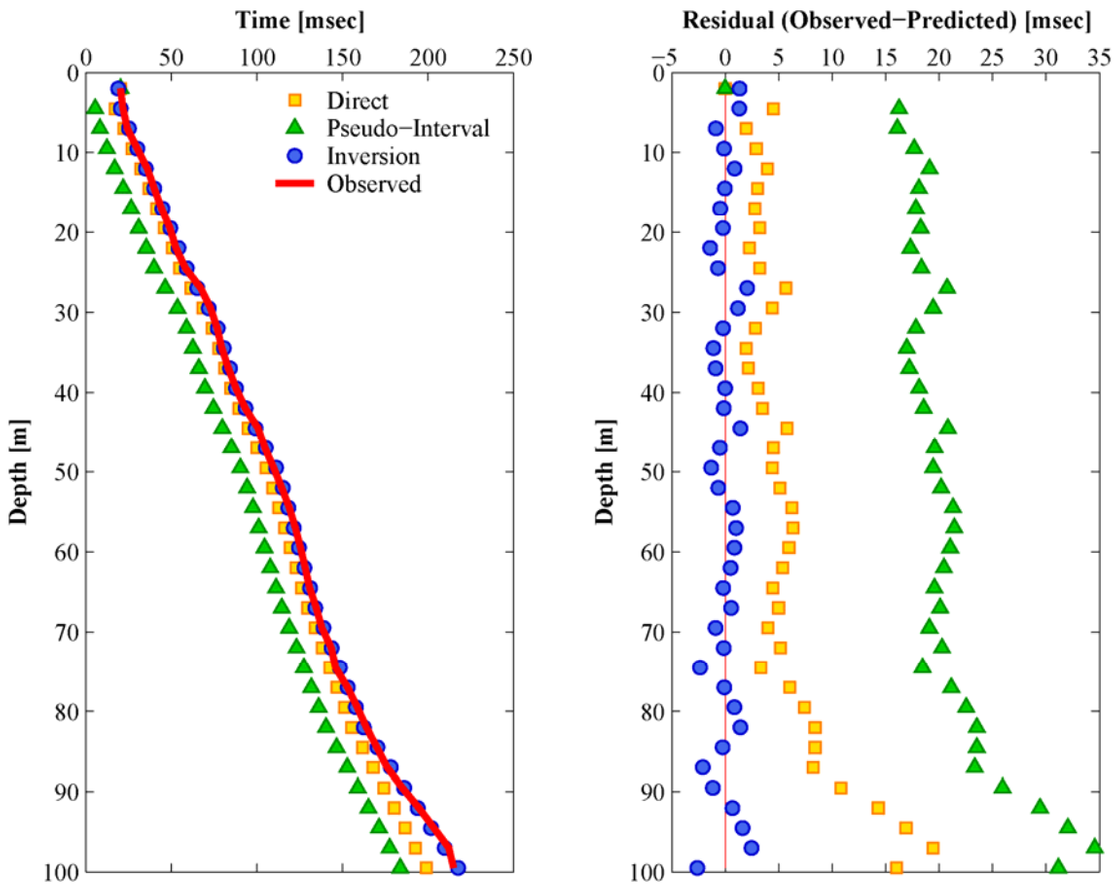


FIG. 4. Refracted raypath and shear-wave velocity profiles.

Figure 4 shows the robustness of the inversion algorithm in predicting the observed travel times at each receiver. The inversion algorithm models wave propagation in real soil media more accurately and thus enables a more robust estimate of the shear-wave velocity profile. The difference in velocities and predicted travel times between the inversion and the conventional methods are mainly due to the assumption of straight raypath and the lack of consideration of upper layers in the estimation of velocities by the conventional methods. Figure 3 illustrates how different the raypath is when refraction at each layer interface is considered in the analysis.

In general the conventional methods give large errors at the interface between two layers with high velocity contrast. However the error can be reduced if the velocity of each layer is estimated as the average of the slownesses calculated for the receivers located in the same layer as shown in Figure 3. A direct conclusion of this observation is that a small test interval will improve the velocity prediction by the conventional methods. The same conclusion applies to the inversion algorithm; however it is not a critical issue. The inversion method uses all the travel paths crossing each layer to estimate its velocity (see Steps 3 and 4). Thus the method does not rely only on single receivers as in the case of conventional methods, but it considers all test data at the same time to estimate the velocity profile. Figures 3 and 4 show that the inversion method is able to converge to the velocity of the upper layers, where only few receivers are located. An additional advantage of the inversion algorithm not presented here is that it can incorporate the velocity anisotropy directly in the analysis as indicated in (4).

CONCLUSIONS

An inversion algorithm has been presented to evaluate the velocity profile from downhole seismic test data. It models the soil profile as a stack of horizontal layers with elliptical velocity anisotropy. The raypaths are calculated using a nonlinear iterative algorithm based on the bending method, fulfilling Fermat's principle of minimum travel time and Snell's Law. The inversion algorithm models wave propagation in real soil media more accurately and thus enables a more robust estimate of the seismic wave velocity profile than conventional methods. The inversion algorithm was presented here to analyze downhole seismic test data however it is also applicable to seismic cone penetrations tests (SCPT).

REFERENCES

Auld, B. (1977). "Cross-Hole and Down-Hole Vs by Mechanical Impulse." *American Society of Civil Engineers, Journal of the Geotechnical Engineering Division*, 103(12), 1381-1398.

Boore, D. M., and Thompson, E. M. (2007). "On using Surface-Source Downhole-Receiver Logging to Determine Seismic Slownesses." *Soil Dynamics and Earthquake Engineering*, 27(11), 971-985.

Campanella, R. G., Robertson, P. K., and Gillespie, D. (1986). "Seismic Cone Penetration Test." *Use of In Situ Tests in Geotechnical Engineering, Proceedings*

of In Situ '86, ASCE Geotechnical Special Publication No. 6, Blacksburg, VA, USA, 116-130.

Campanella, R. G., Stewart, W. P., Roy, D., and Davies, M. P. (1994). "Low Strain Dynamic Characteristics of Soils with the Downhole Seismic Piezocone Penetrometer." *Proceedings of the Symposium on Dynamic Geotechnical Testing II, ASTM Special Technical Publication No. 1213*, San Francisco, CA, USA, 73-87.

Chander, R. (1977). "On Tracing Seismic Rays with Specified End Points in Layers of Constant Velocity and Plane Interfaces." *Geophysical Prospecting*, 25, 120-124.

Gibbs, J. F., Tinsley, J. C., Boore, D. M., and Joyner, W. B. (2000). "Borehole Velocity Measurements and Geological Conditions at Thirteen Sites in the Los Angeles, California Region." *U.S. Geological Survey Open-File Report OF 00-470*.

Kim, D.-S., Bang, E.-S., and Kim, W.-C. (2004). "Evaluation of Various Downhole Data Reduction Methods for Obtaining Reliable Vs Profiles." *Geotechnical Testing Journal*, 27(6), 585-597.

Kramer, S. L. (1996). *Geotechnical Earthquake Engineering*, Prentice-Hall, Inc., Upper Saddle River, NJ.

Lee, S. H. H., and Stokoe II, K. H. (1986). "Investigation of Low-Amplitude Shear Wave Velocity in Anisotropic Material." *Geotechnical Engineering Report GR86-6*, Geotechnical Engineering Center, The University of Texas at Austin.

Mok, Y.-J., Stokoe II, K. H., and Wilson, C. R. (1988). "Analysis of Downhole Seismic Data using Inverse Theory." *Proceedings of Ninth World Conference on Earthquake Engineering*, Tokyo-Kyoto, Japan, III-65 - III-70.

Santamarina, J. C., and Fratta, D. (1998). *Introduction to Discrete Signals and Inverse Problems in Civil Engineering*, ASCE Press, Reston, VA.

Slawinski, M. A., Wheaton, C. J., and Powojowski, M. (2004). "VSP Traveltime Inversion for Linear Inhomogeneity and Elliptical Anisotropy." *Geophysics*, 69(2), 373-377.

Stokoe, K. H., II, and Woods, R. D. (1972). "In Situ Shear Wave Velocity by Cross-Hole Method." *American Society of Civil Engineers, Journal of the Soil Mechanics and Foundations Division*, 98(SM5), 443-460.

Sully, J. P., and Campanella, R. G. (1995). "Evaluation of In Situ Anisotropy from Crosshole and Downhole Shear Wave Velocity Measurements." *Geotechnique*, 45(2), 267-282.

Woods, R. D. (1978). "Measurement of Dynamic Soil Properties." *Proceedings of the ASCE Geotech Engineering Division Specialty Conference, Earthquake Engineering and Soil Dynamics*, Pasadena, CA, 91-178.

Woods, R. D. (1986). "In Situ Tests for Foundation Vibrations." *Use of In Situ Tests in Geotechnical Engineering, Proceedings of In Situ '86, ASCE Geotechnical Special Publication No. 6*, Blacksburg, VA, USA, 336-375.

Yan, L., and Byrne, P. M. (1990). "Simulation of Downhole and Crosshole Seismic Tests on Sand using the Hydraulic Gradient Similitude Method." *Canadian Geotechnical Journal*, 27(4), 441-460.

Characterizing the Liquefaction Resistance of Aged Soils

Hossein Hayati[1], S.M. ASCE; Ronald D. Andrus[2], M. ASCE, P.E.; Sarah L. Gassman[3], M. ASCE, P.E.; Michael Hasek[4]; William M. Camp[5], M. ASCE, P.E.; and Pradeep Talwani[6]

[1]Graduate Research Assistant, Dept. of Civil Engineering, Clemson Univ., Clemson, SC 29634-0911; hhayati@clemson.edu
[2]Associate Professor, Dept. of Civil Engineering, Clemson Univ., Clemson, SC 29634-0911; randrus@clemson.edu
[3]Associate Professor, Dept. of Civil and Environmental Engineering, University of South Carolina, Columbia, SC 29208; gassman@engr.sc.edu
[4]Graduate Research Assistant, Dept. of Civil and Environmental Engineering, University of South Carolina, Columbia, SC 29208; mjhasek@bellsouth.net
[5]Technical Principal, S&ME Inc., Mount Pleasant, SC 29464; bcamp@smeinc.com
[6]Professor, Dept. of Geological Sciences, University of South Carolina, Columbia, SC 29208; talwani@geol.sc.edu

ABSTRACT: The occurrence of liquefaction in soils is often evaluated using the simplified procedure originally proposed by Seed and Idriss based on in situ indices. Although numerous studies have been conducted to improve and extend this procedure, the effect of age on liquefaction resistance is still poorly understood and correction factors have not been generally accepted. Nine published studies on the effect of age are reviewed in this paper. A regression line representing the average variation in liquefaction strength grain with time was developed from cases where strength was expressed based on recommended liquefaction resistance curves. This regression line is considered an update of the previously proposed relationship by Arango et al. The results indicate that commonly used liquefaction evaluation procedures can be overly conservative in many natural soil deposits.

INTRODUCTION

The resistance of soil to liquefaction is often expressed in terms of a variable called the cyclic resistance ratio. The cyclic resistance ratio, *CRR*, is commonly estimated using semi-empirical charts based on the simplified procedure originally proposed by Seed and Idriss (1971). Required input for the charts include the standard penetration test (SPT) blow count, the cone penetration test (CPT) tip resistance, or the small-

strain shear-wave velocity (V_s). A limitation of the charts is that they were derived primarily from field case histories involving soils less than a few thousand years old and there is no generally accepted guideline for evaluating the liquefaction resistance of older soils (Youd et al. 2001).

Youd and Perkins (1978) presented qualitative estimates of liquefaction susceptibility of soils by age of deposit based on field observations following earthquakes. According to their assessment, deposits <500 years old generally have high to very high susceptibility. For older deposits, the susceptibility to liquefaction is generally moderate to high for Holocene age (<10,000 years) sediments, low to very low for Pleistocene age (10,000 to 1.8 million years) sediments, and very low for pre-Pleistocene age sediments.

Since 1978, several studies have been conducted to quantify the effect of age on *CRR* (e.g., Seed 1979; Troncoso et al. 1988; Arango and Migues 1996; Lewis et al. 1999, 2004; Arango et al. 2000; Robertson et al. 2000; Leon et al. 2006; Hayati and Andrus 2008). These previous studies are reviewed in this paper and a new relationship for correcting *CRR* for older soils is developed.

PREVIOUS STUDIES

Seed (1979)

Seed (1979) reported results of laboratory tests conducted on identical specimens of Monterey No. 0 sand at 0.1 to 100 days after sample construction. He also reported results for tests conducted on undisturbed specimens of four sand deposits ranging in age from about 60 to 3,000 years. The Monterey No. 0 sand is clean quartz sand, containing <5 % fines (silt and clay). No information was given for the fines content of the undisturbed specimens.

The strengths of the Monterey No. 0 sand at 10 days and 100 days were 12 % and 25 % higher, respectively, than the strength at 1 day. The older undisturbed specimens exhibited strengths 50 to 100 % greater than the 1-day Monterey sand specimen.

Troncoso et al. (1988)

Troncoso et al. (1988) investigated the influence of time on strength by conducting cyclic triaxial tests on undisturbed block samples from two tailings dams in El Cobre, Chile. One of the dams failed during the 1965 Chilean earthquake. The test samples consisted of sands with fines contents around 25 %, void ratios, *e*, of 0.8 to 0.92, and ages of about 1, 5 and 30 years. *CRR* was defined as the stress ratio causing 5 % double-amplitude axial strain under 20 cycles of loading.

The test results for the El Cobre sand showed the sample from the 5- and 30-year-old deposits had cyclic strengths that were 40 % and 80 %, respectively, greater than the strength of the 1-year-old deposit. The cyclic strength of the reconstituted sample was about 60 % of strength of the 1-year-old deposit.

Arango and Migues (1996)

Arango and Migues (1996) considered the performance of old sand deposits that did not liquefy during the 1994 Northridge earthquake in Southern California. After a detailed evaluation of candidate sites, the Gillibrand Quarry site in the Tapo Canyon area was selected for borehole and block sampling. This non-liquefaction site was located close to areas that did liquefy. The Gillibrand Quarry sand was deposited about 1 million years ago. It was characterized as slightly cemented, consisting of predominantly quartz and a lesser amount of feldspar with no carbonates, micas or clay minerals. Grain size distribution curves were relatively uniform, with maximum grain size of 1 mm and fines content of less than 5 %. The average value of corrected SPT blow count, $(N_1)_{60}$, for the sand was about 30. Eighteen stress-controlled cyclic triaxial tests were conducted on undisturbed specimens obtained from three block samples collected in the quarry.

The results of the cyclic triaxial tests showed the field *CRR* falls in the range of 0.8 to 1.4. These values were obtained by applying correction factors of 1.15 for the effect of loss of strength due to sampling and 1.7 to take into account the difference between stress conditions in the field and in the triaxial test device. Using peak ground acceleration data from Chang et al. (1994), the quarry site experienced cyclic stress ratio, *CSR*, values between 0.5 and 0.6 during the 1994 earthquake. Thus, the *CRR* values obtained are indicative of non-liquefiable soils, consistent with the fact that the Gillibrand Quarry sand did not liquefy. Assuming that *CRR* corresponding to $(N_1)_{60}$ of 30 in the chart of Seed et al. (1985) is 0.5, Arango and Migues (1996) estimated the cyclic strength of the Gillibrand Quarry sand to be 1.6 to 2.7 times greater than the Holocene sands used to develop the evaluation chart.

Lewis et al. (1999)

Lewis et al. (1999) studied dynamic strength of aged soils using field performance data from the 1886 Charleston, South Carolina earthquake originally compiled by Dickenson et al. (1988) and Martin and Clough (1990). They selected 33 cases for which detailed information regarding field performance was available. These cases involved sand layers that were generally described as fairly uniform and clean (<5 % fines) with median grain sizes, D_{50}, of 0.1 to 0.2 mm. The age of the sand deposits ranged from 85,000 to 200,000 years.

For each of the 33 sand layers, the induced *CSR* was calculated assuming an approximate attenuation relationship and peak ground accelerations of 0.5 g and 0.3 g in the meizoseismal zone. Lewis et al. (1999) estimated that the cyclic strengths of the 85,000 to 200,000 year old sand deposits were 2 to 3 and 1.3 to 1.8 times greater than Holocene sands for meizoseismal accelerations of 0.5 g and 0.3 g, respectively.

Arango et al. (2000)

Arango et al. (2000) considered many of the studies previously discussed as well as data from the Tobacco Road Formation at the Department of Energy's Savannah River Site (SRS), South Carolina. The Tobacco Road Formation is about 30 million years old. It consists of poorly-graded clean sands to clayey sands, with corrected SPT blow

counts ranging from 3 to 15 and CPT tip resistances between 2 and 38 MPa. Forty-two stress-controlled cyclic triaxial tests were conducted on undisturbed specimens of the Tobacco Road Formation obtained using a fixed-piston sampler.

The adjusted *CRR* values obtained from the cyclic triaxial tests on the Tobacco Road Formation specimens were 2 to 3 times greater than *CRR* values predicted by the Seed et al. (1985) chart for clean sands. Arango et al. (2000) combined these results with previous studies and proposed the relationship between strength gain and age presented in Figure 1. The data for the Tobacco Road Formation are noted as "Bechtel 1993, 1996" in the figure. The average strength gain relationship proposed by Arango et al. (2000) passes through the range of factors determined by Seed (1979), Lewis et al. (1999), and Arango and Migues (1996). The other relationship shown in the figure by Skempton (1986) and by Kulhawy and Mayne (1990) represent the approximate increase in penetration resistance with time.

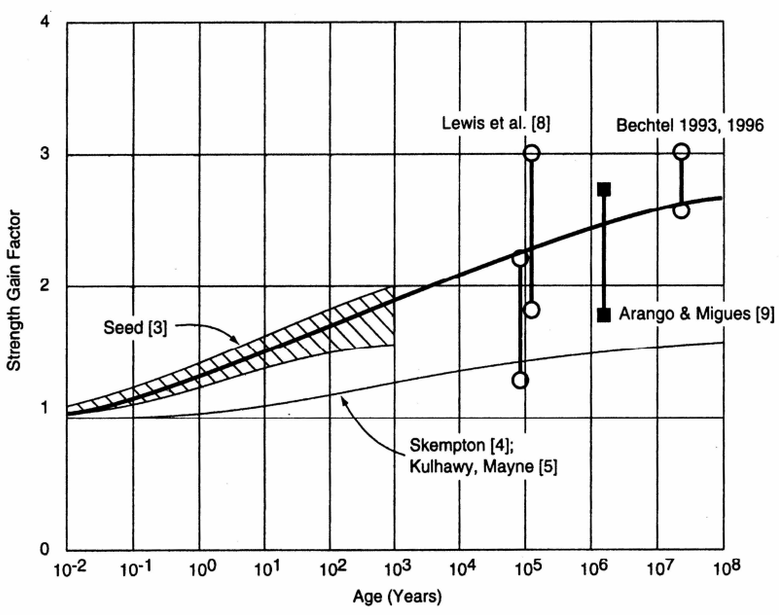


Figure 1. Relationship between strength gain and age by Arango et al. (2000). (Reproduced with permission from Elsevier Limited.)

Lewis et al. (2004)

Lewis et al. (2004) extended and reanalyzed the data from the Tobacco Road Formation at SRS. The three data points plotted on the SPT-based chart in Figure 2a are derived from 17 stress-controlled cyclic triaxial tests on undisturbed samples obtained by fixed piston sampler. The ten data points plotted on the CPT-based chart in Figure 2b are derived from 35 cyclic triaxial tests on undisturbed samples obtained in the same way. The fines content for the tested specimens ranged from 8 to 34 %.

The results presented in Figure 2 suggest strength gain factors of 1.4 to 1.6 based on the SPT curves and 1.3 to 2.8 based on the CPT curves, depending on fines content. It

is noted that these strength gain factors are lower than values reported by Arango et al. (2000), which were calculated using the clean sand curve. Based on these findings, Lewis et al (2000) presented the set of *CRR* curves shown in Figure 2b for Tobacco Road soils with fines contents ranging from 5 to 30 %.

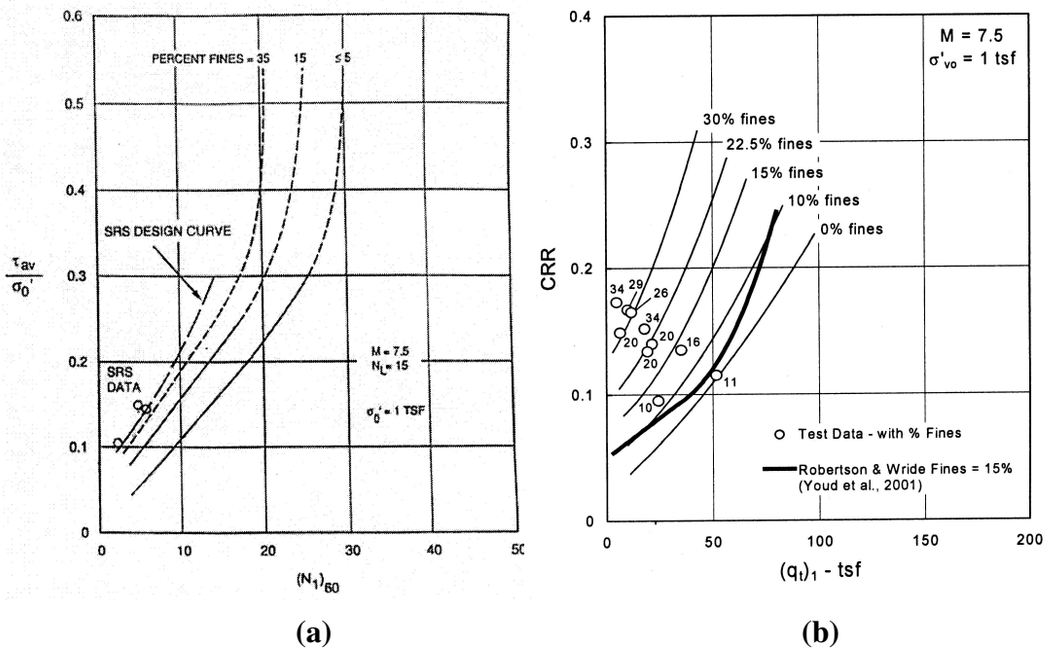


Figure 2. Liquefaction resistance charts based on (a) SPT (Seed et al. 1985) and (b) CPT (Robertson and Wride 1998) with data and modified curves for the Tobacco Road Formation presented by Lewis et al. (2004). (Reproduced with permission from University of Missouri-Rolla.)

Robertson et al. (2000)

Robertson et al. (2000) reported results of six sites in western Canada investigated as part of the Canadian Liquefaction Experiment (CANLEX) project. The six CANLEX sites, plus the Duncan dam, are listed in Table 1. Soils at these seven sites included young hydraulically-placed fills and natural deposits, ranging in age from <1 year to about 10,000 years. The deposits consisted of sub-rounded to angular, primarily quartz sand with D_{50} values of 0.16 to 0.25 mm and fines contents of 5 to15 %. Ground freezing was used to obtain undisturbed samples for cyclic triaxial and cyclic simple shear testing.

Presented in Table 1 are strength gain factors for the seven sites based on SPT, CPT and shear wave velocity measurements and the liquefaction resistance curves recommended by Youd et al. (2001). The strength gain factors range from 0.68 to 1.43 using the SPT as reference; 0.86 to 1.47 using the CPT; and 0.88 to 2.49 using the shear wave velocity measurements.

Table 1. Age, fines content, and strength gain factor for seven Canadian sands (adapted from Robertson et al. 2000).

Site	Approximate age (years)	Fines content (%)	Strength gain factor		
			SPT	CPT	V_S
Mildred Lake	12	10	1.00	1.47	2.49[1]
Massey	200	5	0.91	1.04	1.02
Kidd	4,000	5	0.68	0.93	0.88
J-pit	0.17	15	1.00	0.86	1.49
LL Dam	5	8	1.43	1.31	1.34
Highmont Dam	15	10	1.30	1.19	1.53
Duncan Dam	10,000	5	1.08	1.36	0.97

[1]Velocity measurements at Mildred Lake could be in error due to high testing depths.

Leon et al. (2006)

Leon et al. (2006) considered four paleoliquefaction sites in the South Carolina Coastal Plain (Ten Mile Hill A, Ten Mile Hill B, Sampit, and Gapway) as well as the data reported by Lewis et al. (2004) for the Tobacco Road Formation. The Ten Mile Hill sites are located on barrier-island sands deposited about 200,000 years ago. The Sampit and Gapway sites are located on similar sands deposited about 450,000 years ago. Sand blows were found in freshly cut drainage ditches at the four paleoliquefaction sites. Leon et al. (2006) reported that the most recent liquefaction events occurred about 550 years ago at the Sampit site and 3,500 years ago at the other sites. Sands at the paleoliquefaction sites were characterized as having fines contents <5 % and D_{50} values of 0.15 to 0.2 mm.

Leon et al. (2006) suggested a four-step procedure to establish the *CRR* curves for aged soils. The procedure is based on the fact that aging affects both the cyclic shear strength and the in situ properties (e.g., SPT blow count, CPT tip resistance, V_s). In the first step, values of in situ field indices are corrected using a relationship such as the one proposed by Kulhawy and Mayne (1990) shown in Figure. 1. The first step provides in situ indices analogous to the freshly deposited or post-earthquake state, which are assumed as equivalent states. This first step was not included in the method used by Lewis et al. (1999, 2004) and Arango et al. (2000), who directly applied the simplified procedure. In the second step, a *CRR* curve such as the one suggested by Youd et al. (2001) is assumed to estimate the corresponding *CRR* of freshly deposited soil. In the third step, the *CRR* value for aged soils is obtained using the strength gain relationship suggested by Arango et al. (2000) in Figure 1. In the fourth step, in situ indices obtained in the first step are plotted with *CRR* values obtained in the third step. Leon et al. (2006) followed these four steps to develop three liquefaction resistance curves for soils of 546 to 5,038 years old, 200,000 years old, and 450,000 years old.

Hayati and Andrus (2008)

Hayati and Andrus (2008) developed a liquefaction potential map of Charleston peninsula using CPT profiles and considering the field performance of soils during 1886 earthquake. Natural sands on the peninsula include Holocene to late Pleistocene beach deposits that flank older barrier-island beach deposits of the Wando Formation. The Wando Formation is 70,000 to 130,000 years old. The beach sands are characterized as fine-grained, poorly graded, and consisting primarily of quartz. Hayati and Andrus (2008) found that most of the reported cases of 1886 liquefaction occurred in the younger beach sands. They also found only one reported case of marginal liquefaction occurred in the Wando Formation on the peninsula.

Using the CPT-based liquefaction resistance chart recommended by Youd et al. (2001) directly and the liquefaction potential index (*LPI*) approach developed by Iwasaki et al. (1978, 1982), Hayati and Andrus (2008) characterized the liquefaction potential of both beach sands. They calculated similarly high liquefaction potential for both sands assuming no strength gain factors. To match the field performance, a correction factor was applied to *CRR* as follows (Andrus et al. 2004):

$$CRR_{DR} = CRR \times K_{DR} \tag{1}$$

where CRR_{DR} is the deposit resistance-corrected cyclic resistance ratio, and K_{DR} is a strength gain factor to correct for influence of age, cementation and/or compressibility. The value of K_{DR} was assumed 1.0 for the younger beach deposits that liquefied in 1886. A back-calculated K_{DR} value of 1.8 was obtained to match the *LPI* values with the field performance of the Wando sand. Given the uncertainty in the magnitude and ground acceleration associated with the 1886 earthquake, values of K_{DR} between 1.3 and 2.3 were also considered possible for the Wando Formation.

DISCUSSION

Plotted in Figure 3 are the strength gain factors from the previous studies determined using the *CRR* curves recommended by Youd et al. (2001) as reference. The factors suggested by Seed (1979) and Troncoso et al. (1988) are not plotted because the reference age of 1 day or 1 year was used. The factors denoted as "Bechtel 1993, 1996" in Figure 1 have been replaced using the values reported in Lewis et al. (2004) and the recommended *CRR* curves for various fines content. The soil deposits studied by Arango and Migues (1996) and Lewis et al. (1999) were described as clean sand and, thus, the *CRR* curve for a fines content <5 % was used as reference. In the studies by Robertson et al. (2000) and Hayati and Andrus (2008), the influence of fines was considered. Ages of the soil deposits are expressed in terms of time since initial deposition or critical disturbance. Previous liquefaction is assumed to be a critical disturbance event, when the grain-to-grain contacts were broken and reformed.

The solid line plotted in Figure 3 represents the approximate average variation in the strength gain factor with time. This regression line can be expressed as:

$$K_{DR} = 0.17 \log_{10}(t) + 0.83 \tag{2}$$

where t is the time since initial deposition or critical disturbance in years. In addition to the plotted strength gain factors, Equation 2 is obtained by assuming $K_{DR} = 1$ at $t =$ 10 years. A t value of 10 years is assumed because the *CRR* curves (Youd et al. 2001) were developed using case history data with the time since the last liquefaction mostly within the range of 1 to 100 years. Thus, an approximate geometric average age of 10 years is assumed as the reference age. Without this assumption, the regression would provide $K_{DR} = 1$ at $t = 1$ year, which does not agree with the ages of the case histories.

Also plotted in Figure 3 is the relationship for strength gain factor versus age by Arango et al. (2000) represented by the dashed line. It can be seen that the relationship developed in this study falls below the relationship by Arango et al. (2000), but exhibits a similar slope. Thus, the primary difference between their relationship and this study relationship is the reference age assumed (1 day versus 10 years). Both relationships suggest a strength gain around 0.17 per log cycle of time.

An alternative interpretation of the data shown in Figure 3 is a constant K_{DR} of 1.0 during the Holocene and a constant K_{DR} of 2.0 during the Pleistocene. While climatic conditions were different during the two geologic epochs, the laboratory strength data (e.g., Seed 1979; Troncoso et al. 1988) support the use of Equation 2.

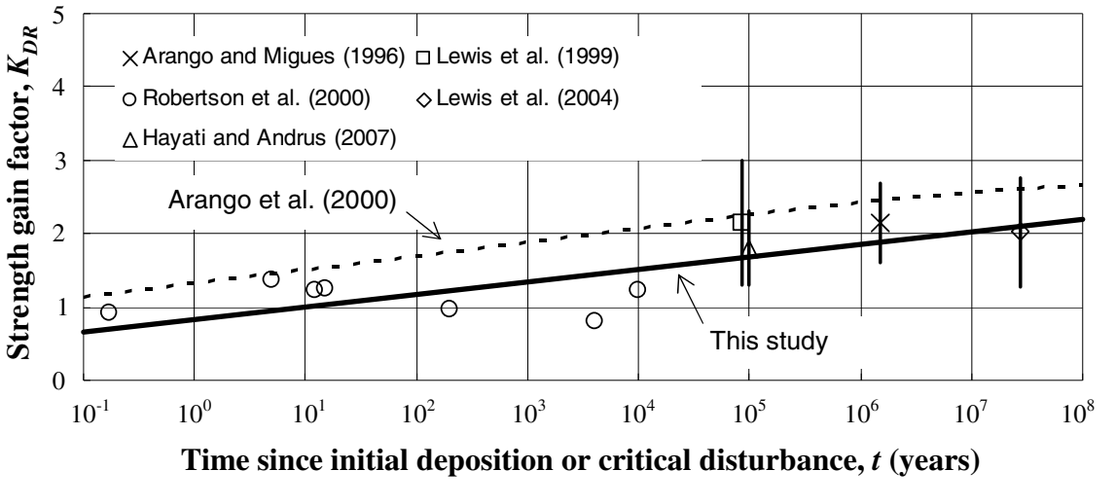


Figure 3. Relationship between strength gain factor and time.

CONCLUSIONS

Based on the results of nine previous studies and using recommended liquefaction resistance curves (Youd et al. 2000) as reference, a new relationship is derived for estimating liquefaction strength gain with time. The relationship, expressed by Equation 2, is obtained by performing linear regression on eleven data points and assuming a strength gain factor of 1 at $t = 10$ years. This reference time is adopted as an average age of the soil deposits for the liquefaction case histories that define commonly used *CRR* curves. Because Equation 2 is based on the penetration-based *CRR* curves, there is no need to adjust penetration resistances for any effect of age.

The relationship between strength gain and time indicates liquefaction resistance increases by a factor of 0.17 per log cycle of time. This amount of increase generally agrees with the results of Seed (1979) and Troncoso et al. (1988), which are based solely on laboratory measurements. The new relationship plots below the relationship proposed by Arango et al. (2000) and, thus, is more conservative. Additional data are needed to validate the proposed relationship.

ACKNOWLEDGMENTS

This research was supported by the National Science Foundation, under grant number CMS-0556006. Any opinions, findings, and conclusions or recommendations expressed in this material are those of the authors and do not necessarily reflect the views of the National Science Foundation.

REFERENCES

Andrus, R. D., Stokoe, K. H. II, and Juang, C. H. (2004). "Guide for shear-wave-based liquefaction potential evaluation," *Earthquake Spectra*, 20(2): 285-308.

Arango, I., Lewis, M. R., and Kramer, C. (2000). "Updated liquefaction potential analysis eliminates foundation retrofitting of two critical structures," *Soil Dynamics Earthquake Engrg.*, Elsevier Limited, 20: 17–25.

Arango, I., and Migues, R. E. (1996). "Investigation of the seismic liquefaction of old sand deposits," Report on Research, Bechtel Corporation, National Science Foundation Grant No. CMS-94-16169, San Francisco, CA.

Chang, S. W., Bray, J. D., and Seed, R. B. (1994). "Ground motions and local site effects," *Preliminary Report on the Principal Geotechnical Aspects of the January 17, 1994 Northridge Earthquake*, Stewart, J. P., Bray, J. D., Seed, R. B. and Sitar, N., eds., *Report No. UCB/EERC-9408*, Univ. of California, Berkeley CA.

Dickenson, S. E., Clough, G. W., and Martin, J. R. (1988). "Evaluation of the engineering properties of sand deposits associated with liquefaction sites in the Charleston, South Carolina area--A report of first year findings," Submitted to the U. S. Geological Survey, Virginia Tech, VA.

Hayati, H., and Andrus, R. D. (2008). "Liquefaction potential map of Charleston, South Carolina based on the 1886 earthquake," *Journal of Geotechnical and Geoenvironmental Engrg.,* accepted for publication.

Iwasaki, T., Tatsuoka, F., Tokida, K.-I., and Yasuda, S. (1978). "A practical method for assessing soil liquefaction potential based on case studies at various sites in Japan," *Proc., 2nd Int. Conf. on Microzonation*, San Francisco, CA: 885-896.

Iwasaki, T., Tokida, K., Tatsuoka, F., Watanabe, S., Yasuda, S. and Sato, H. (1982). Microzonation for soil liquefaction potential using simplified methods, *Proc., 3rd Int. Earthquake Microzonation Conf.*, Seattle, WA: 1319-1330.

Kulhawy, F. H., and Mayne, P. W. (1990). "Manual on estimating soil properties for foundation design," *Final Rep. 1493-6, EL-6800*, Electric Power Research Institute, Palo Alto, CA.

Lewis, M. R., Arango, I., Kimball, J. K., and Ross, T. E. (1999). "Liquefaction resistance of old sand deposits," *Proc., 11th Panamerican Conf. on Soil Mechanics*

and Geotechnical Engineering, Foz do Iguassu, Brazil: 821–829.

Lewis, M. R., McHood, M. D., and Arango, I. (2004). "Liquefaction evaluations at the Savannah River Site, A Case History," *Proc., Fifth Int. Conf. on Case Histories in Geotechnical Engineering*, New York, NY.

Leon, E., Gassman, S. L., and Talwani, P. (2006). "Accounting for soil aging when assessing liquefaction potential," *Journal of Geotechnical and Geoenvironmental Engrg.*, 132(3): 363-377.

Martin, J. R., and Clough, G. W. (1990). "Geotechnical setting for liquefaction events in the Charleston, South Carolina vicinity," *H. Bolton Seed Memorial Symposium*, Vol. 2: page 313.

Robertson, P. K, and Wride, C. E. (1998). "Evaluating cyclic liquefaction potential using the cone penetration test," *Canadian Geotechnical Journal*, 35(3): 442-459.

Robertson, P. K, Wride, C. E. (Fear), List, B. R., Atukorala, U., Biggar, K. W., Byrne, P. M., Campanella, R. G., Cathro, D. C., Chan, D. H., Czajewski, K., Finn, W. D. L., Gu, W. H., Hammamji, Y., Hofmann, B. A., Howie, J. A., Hughes, J., Imrie, A. S., Konrad, J.-M., Küpper, A., Law, T., Lord, E. R. F., Monahan, P. A., Morgenstern, N. R., Phillips, R. , Piché, R. , Plewes, H. D., Scott, D. , Sego, D. C., Sobkowicz, J., Stewart, R. A., Watts, B. D., Woeller, D. J., Youd, T. L., and Zavodni, Z. (2000). "The CANLEX project: summary and conclusions," *Canadian Geotechnical Journal*, 37: 563–591.

Seed, H. B. (1979). "Soil liquefaction and cyclic mobility evaluation for level ground during earthquakes," *Journal of the Geotechnical Eng. Div.,* 105(2): 201–255.

Seed, H. B., and Idriss, I. M. (1971). "Simplified procedure for evaluating soil liquefaction potential," *Journal of the Geotechnical Engrg. Div.*, 97(9), 1249-1273.

Seed, H. B., Tokimatsu, K., Harder, L. F., and Chung, R. M. (1985). "Influence of SPT procedures in soil liquefaction resistance evaluations," *Journal of Geotechnical Engrg.*, 111(12), 1425-1445.

Skempton A. W. (1986). "Standard penetration test procedures and the effects in sands of overburden pressure, relative density, particle size, aging and overconsolidation." *Geotechnique*, 36(3):425-47

Talwani, P., and Schaeffer, W. T. (2001). "Recurrence rates of large earthquakes in the South Carolina Coastal Plain based on paleoliquefaction data," *Journal of Geophysical Research*, 106: 6621-6642.

Troncoso, J., Ishihara, K., and Verdugo, R. (1988). "Aging effects on cyclic shear strength of tailing materials," *Proc., Ninth World Conf. on Earthquake Engineering*, Vol. III: 121-126.

Youd, T. L., Idriss, I. M., Andrus, R. D., Arango, I., Castro, G., Christian, J. T., Dobry, R., Finn, W. D. L., Harder, L. F. Jr., Hynes, M. E., Ishihara, K., Koester, J. P., Liao, S. S. C., Marcuson, W. F. III, Martin, G. R., Mitchell, J. K., Moriwaki, Y., Power, M. S., Robertson, P. K., Seed, R. B., and Stokoe, K. H. II, (2001). "Liquefaction resistance of soils: summary report from the 1996 NCEER and 1998 NCEER/NSF workshops on evaluation of liquefaction resistance of soils," *Journal Geotechnical & Geoenvironmental Engrg.*, 127(10): 817-833.

Youd, T. L. and Perkins, D. M. (1978). "Mapping of liquefaction induced ground failure potential," *Journal of the Geotechnical Engrg. Div.*, 104(GT4): 433-446.

Comparison of Recently Developed Liquefaction Analysis Methods at Two Fluvial Sand Sites

Tianfei Liao[1], John R. Davie[2], Hazem A. Sarhan[3], Emre Biringen[4]

[1, 2, 4] Ph.D., Bechtel Power Corporation, 5295 Westview Drive, Frederick, MD 21703;
[1]tliao@bechtel.com; [2]jdavie@bechtel.com; [4]ebiringe@bechtel.com
[3] Ph.D., Bechtel Corporation, 3000 Post Oak Blvd., Houston, TX 77056; hasarhan@bechtel.com

ABSTRACT: A number of newer liquefaction evaluation methods have been proposed since the consensus on liquefaction analysis procedures was reached by Youd et al. (2001). These methods are compared and applied to two candidate sites for construction of a power plant along the Ohio River. Comprehensive subsurface investigations were carried out and indicated primarily clean fluvial sands at both sites. Assessment of soil liquefaction susceptibility was made using field measurements consisting of SPT N-values, cone tip stress q_T, and shear wave velocity V_s. By comparing the results given by the various newly proposed liquefaction analysis methods, their relative conservatism is evaluated. At these two sites, it was concluded that the methods based on SPT N-value and cone tip resistance q_T are more conservative than the methods based on shear wave velocity V_s.

INTRODUCTION

Construction of a power plant is being considered at two candidate sites, each approximately 400 m × 500 m in area, and located on the floodplain of the Ohio River. The sites are about 10 km apart. Comprehensive subsurface investigation programs were carried out at each site, including standard penetration tests (SPT), cone penetration tests (CPT), seismic CPTs, and laboratory tests.

From the field tests, three types of measurement were obtained, namely the SPT N-value, the CPT cone tip resistance q_T, and the shear wave velocity V_s from the seismic CPT. Based on these types of field data, researchers have proposed various methods to determine the cyclic resistance ratio (CRR) for liquefaction evaluation. Youd et al. (2001) reached a consensus and recommended three widely used methods (i.e., Seed et al., 1985; Robertson & Wride, 1998; and Andrus & Stokoe, 2000) for practitioners to adopt. In more recent evaluations, some improvements have been suggested (i.e, Idriss & Boulanger, 2006), and various CRR curves of different probabilities of occurrence have been developed from updated databases using methods such as logistic regression or Bayesian mapping (e.g., Juang et al., 2002; Cetin et al., 2004; Lai et al.,

2006; and Moss et al., 2006). Calibration and ground-truthing are necessary for these newer methods to achieve a consensus that practitioners can adopt as they did with the Youd et al. (2001) procedures.

Fig. 1 presents the CRR curves for clean sands based on normalized SPT blow count $(N_1)_{60}$, normalized cone tip resistance q_{T1}, and normalized shear wave velocity V_{s1}. They include the deterministic curves suggested by Youd et al. (2001) and Idriss & Boulanger (2006), as well as the recently developed probabilistic curves corresponding to 50% liquefaction probability (PL = 50%). For comparison purposes, the effective overburden pressure is assumed to be one atmosphere for the Cetin et al. (2004) curve, and the normalization exponent of the effective overburden stress is taken to be 0.5 for the Moss et al. (2006) curve, consistent with the normalization procedure adopted in the other methods.

Since all of the deterministic and probabilistic methods can be applied to liquefaction analysis at the two candidate sites for the power plant, there is an excellent opportunity to compare these newly proposed methods and evaluate the effects of these methods on liquefaction analysis results.

SITE CONDITIONS

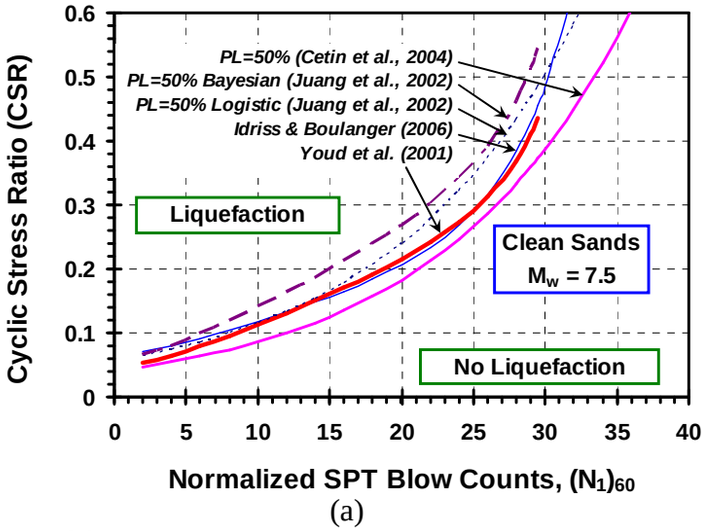
The two sites, referred to here as Site A and Site B, are fairly similar in terms of topography and subsurface profile. Bounded on one side by the Ohio River, each site slopes gently towards the river, with an elevation difference of less than 3 m across each site. Soil at the ground surface is predominantly silty clay with occasional gravels. At the time of field testing, Site A was planted with soy beans and corn, while Site B was grass land adjacent to an existing fossil power plant.

The results of sieve analysis on SPT soil samples from the subsurface investigation at the two sites are presented in Fig. 2, which shows that Site A consists generally of silty clay and silty sand in the top 5 m, overlying a post-glacial deposit of fluvial sand that is about 25 m thick, which in turn overlies Paleozoic bedrock consisting of sandstones, conglomerates, shales, and limestones (Liao et al., 2007). Similarly, at Site B there is a 6.5-m thick layer of silty clay on top of a 6.5-m thick gravelly sandy deposit, which overlies a 13-m thick sand layer, as shown in Fig. 2 (b). The bedrock of Site B underlies the sand layer at about 26 m depth.

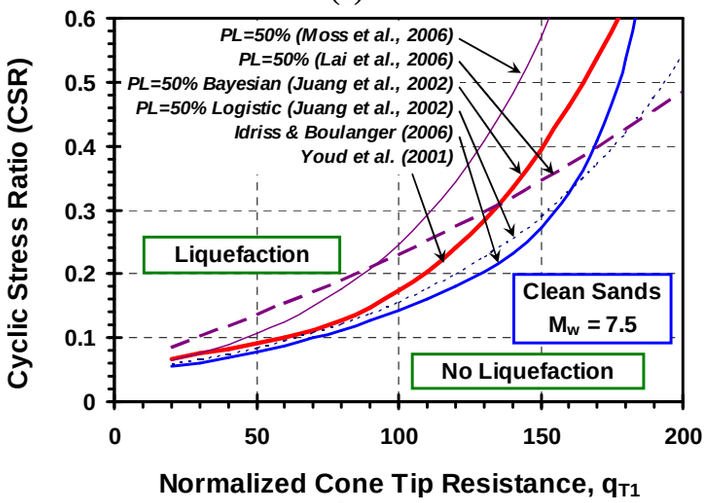
At both sites, interleaved thin layers of fine sand and clayey silt were observed from the SPT soil samples from the top layer of silty clay/sand, probably resulting from sequential deposition after the area was flooded. The average recorded ground water level was about 12 m and 14 m below the ground surface at Site A and Site B, respectively.

FIELD MEASUREMENTS FOR LIQUEFACTION ANALYSIS

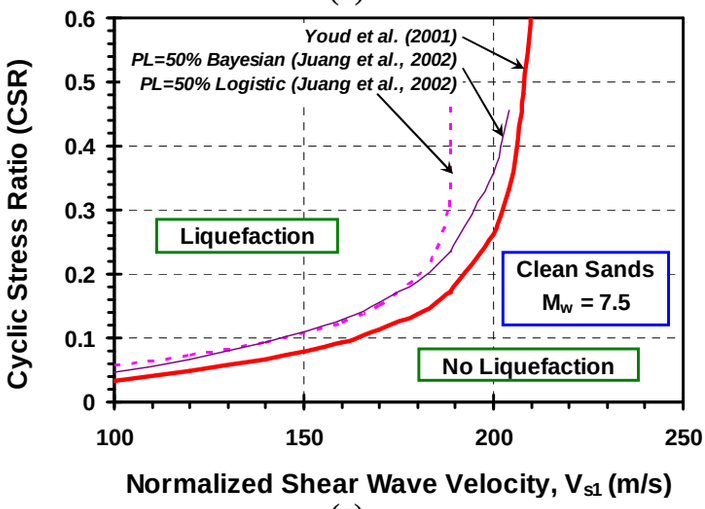
A total of 16 SPT borings and 66 CPTs (including 8 seismic CPTs) were performed at Site A, while 36 SPT borings and 45 CPTs (including 5 seismic CPTs) were carried out at Site B. Since the field test locations were spread fairly evenly across each site, the results can be reasonably assumed to represent the general soil response of each site.



(a)

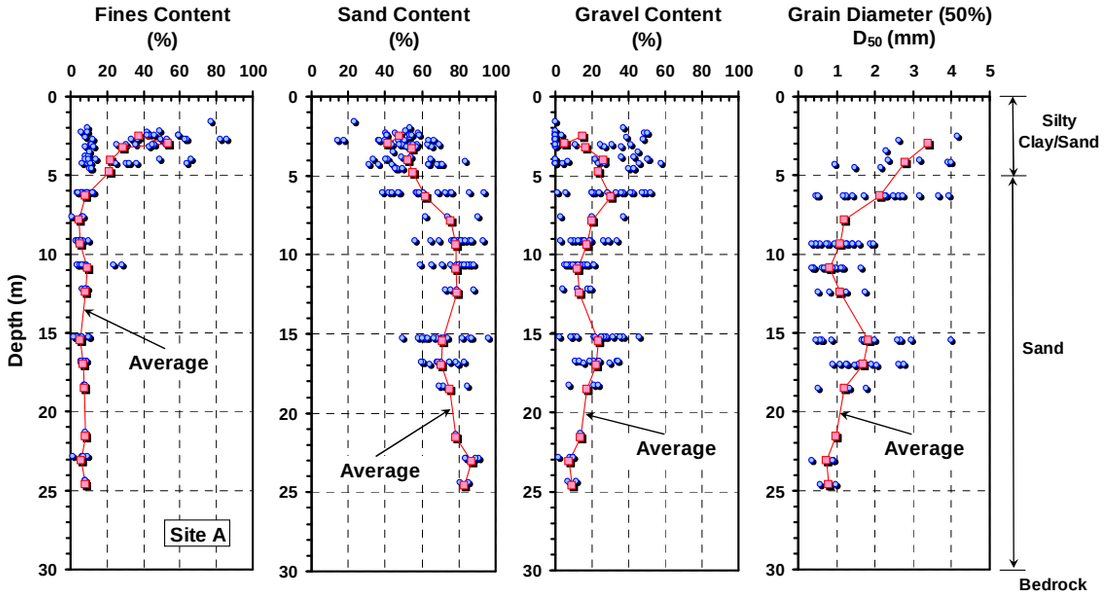


(b)

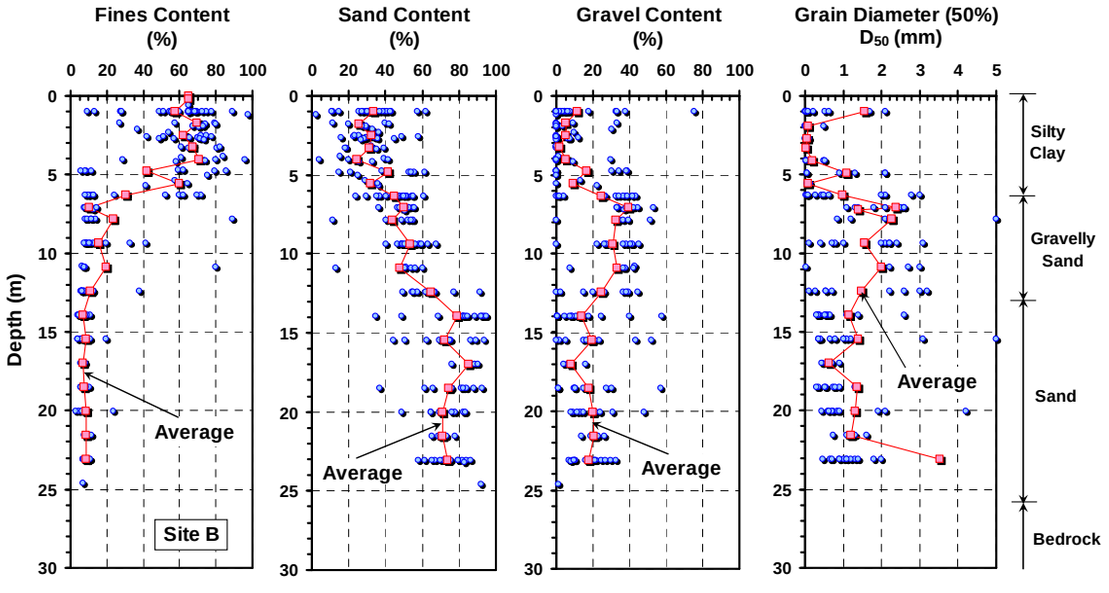


(c)

FIG. 1. Comparison of CRR curves: (a) Based on SPT N-value; (b) Based on cone tip resistance; (c) Based on shear wave velocity.



(a)



(b)

FIG. 2. Results of sieve analysis: (a) Site A; (b) Site B.

The SPTs were performed using the mud rotary method, with the SPT N-value being recorded in the borehole full of bentonite mud. The measured SPT N-values for each site are presented separately in Fig. 3, along with the average N-values at 1.5-m intervals below the top 5 m. At Site A, the average N-value is about 10 blows/0.3 m in the top silty clay/sand layer. It increases to 20 blows/0.3 m at around 12.5 m depth, and then remains almost constant until bedrock is reached. Relatively higher N-values were observed in the sandy deposit of Site B with the average N-value varying from around 20 to 30 blows/0.3 m, especially in the gravelly sand zone where the average

N-value was consistently close to 30 blows/0.3 m. Assuming the energy efficiency is 80% for the automatic hammer used in these tests, the energy-efficiency-corrected SPT blow count N_{60} can be derived by multiplying the measured value by a coefficient of 80% / 60% = 1.33.

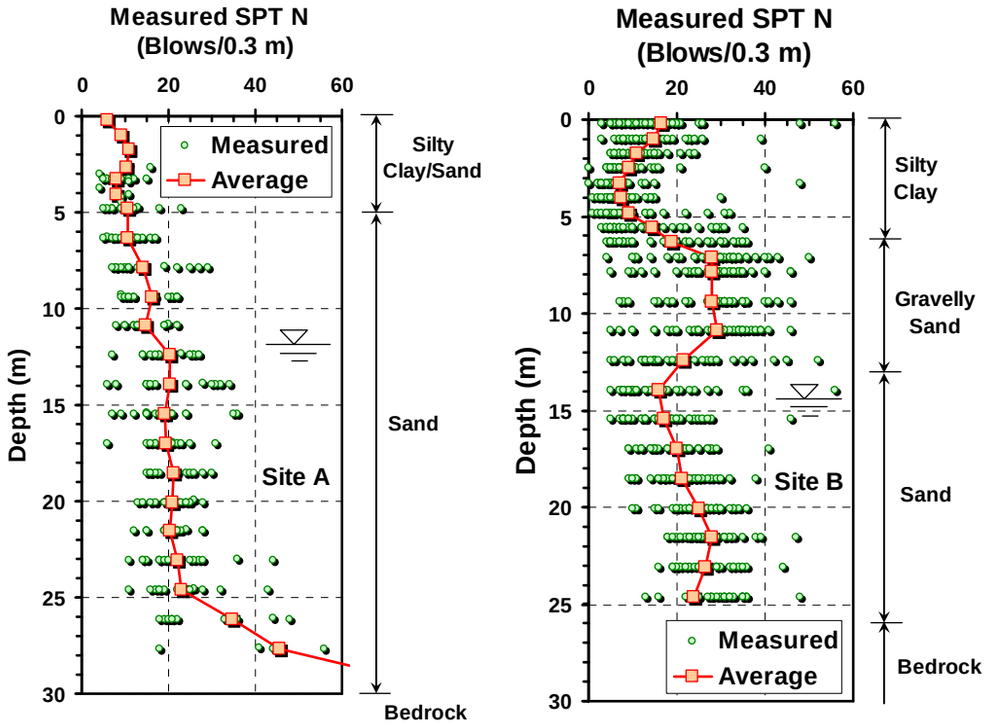


FIG. 3. Results of measured SPT blow counts: (a) Site A; (b) Site B.

The averages of the CPT (including seismic CPT) measurements are presented in Fig. 4, including cone tip resistance q_T, sleeve friction f_s, friction ratio FR, and shear wave velocity V_s. The average value of q_T exhibits a trend similar to that of the SPT N-value with respect to depth. At Site A, the average q_T increases almost linearly from nearly zero at the ground surface to about 20 MPa at 12.5 m depth, and then it remains almost constant until bedrock is reached. The average q_T from the sandy deposits of Site B varies between 10 to 40 MPa, with that in the gravelly sand zone being consistently close to 40 MPa. The V_s from the sand layers at both sites is about 300 m/sec, while the gravelly sand zone of Site B has V_s around 400 m/sec.

LIQUEFACTION ANALYSIS

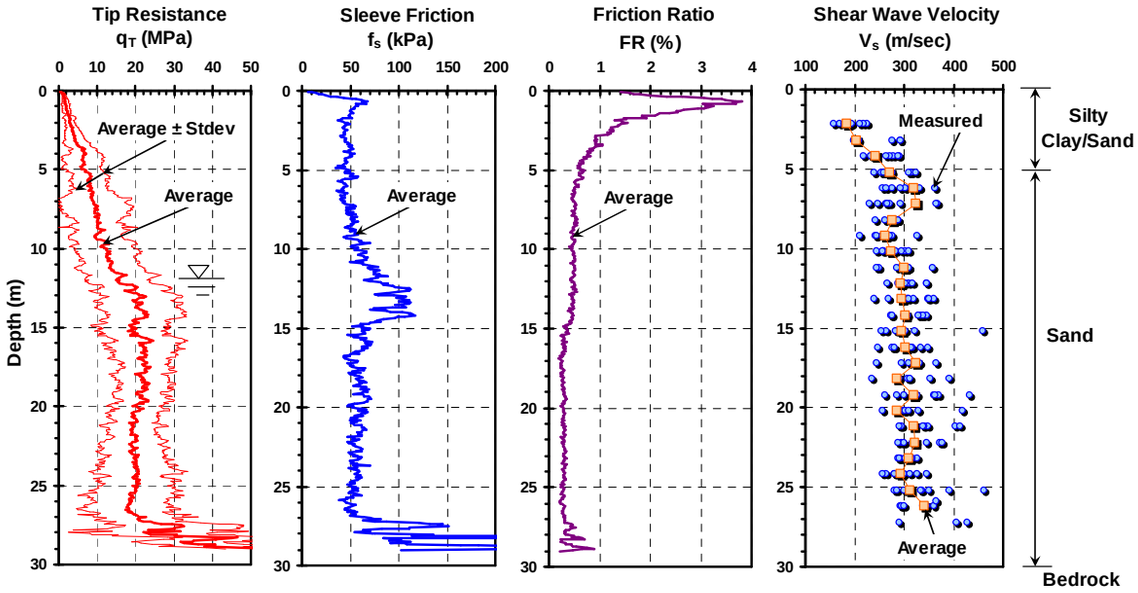
For liquefaction analysis, the cyclic resistance ratio (CRR) is usually determined from field measurements normalized by effective overburden stress. In most methods, the normalization procedure for sands is as follows:

$$(N_1)_{60} = (N_{60})/(\sigma_{v0}' / p_a)^{0.5} \quad (1)$$

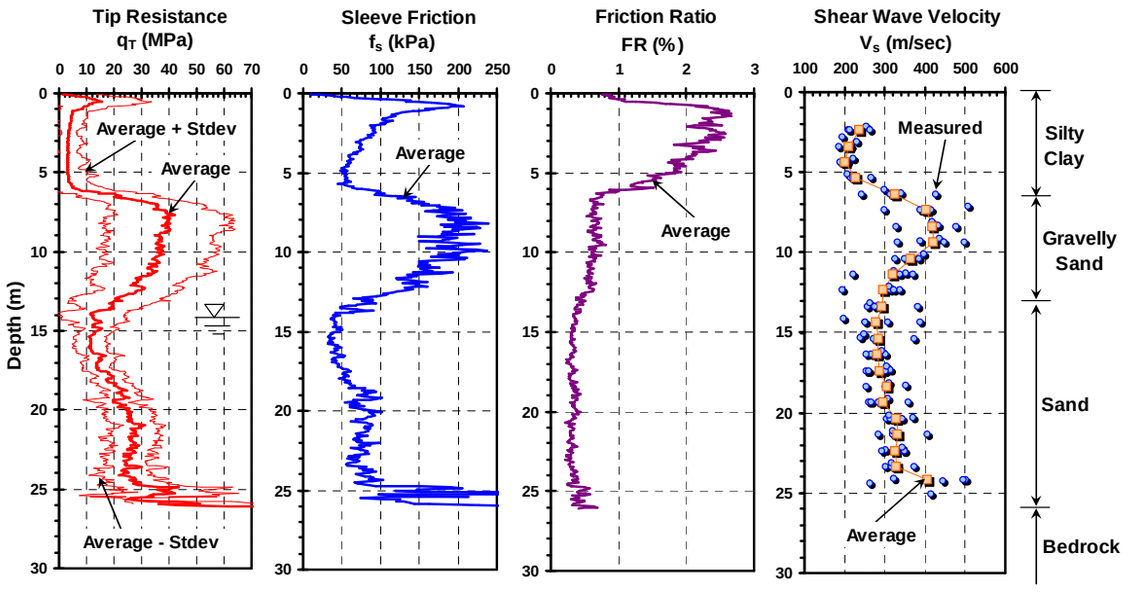
$$q_{T1} = q_T / (\sigma_{v0}' / p_a)^{0.5} \quad (2)$$

$$V_{s1} = V_s / (\sigma_{v0}' / p_a)^{0.25} \quad (3)$$

where $(N_1)_{60}$, q_{T1}, and V_{s1} are the normalized measurements, σ_{v0}' is the effective overburden stress, and p_a is the atmospheric pressure.



(a)



(b)

FIG. 4. Results of cone penetration tests: (a) Site A; (b) Site B.

Here, liquefaction analysis will be performed based on the average values of the measured data. Since discrete layers with relatively low liquefaction resistance might

be masked by the averaging process, the analysis results should be interpreted only as an indicator of the overall liquefaction resistance of each site.

Fig. 2 shows that the fines content is about 10% in the sand layers at both sites, indicating quite clean sand, while it is about 20% in the gravelly sand layer of Site B. The fines content of soils can also be estimated using the soil behavioral type index I_c, which increases with increasing apparent fines content and soil plasticity (Jefferies & Davies, 1993). For liquefaction analysis, the soil behavior index I_c can be expressed as follows (Robertson & Wride, 1998):

$$I_c = \left[(3.47 - \log Q)^2 + (\log F + 1.22)^2\right]^{0.5} \quad (4)$$

where $Q = (q_T - \sigma_{vo})/\sigma_{vo}'$, $F = f_s/(q_T - \sigma_{vo}) \times 100\%$, and σ_{vo} is the total overburden stress.

As shown in Fig. 5, the calculated value of I_c is about 1.5 for most of the depth ranges in the sand deposits at both of the sites, confirming they are in the category of clean sand for liquefaction analysis. Also plotted in Fig. 5 are the normalized field measurements [$(N_1)_{60}$, q_{T1}, and V_{s1}]. Below about 12.5 m depth, these normalized field measurements from the two sites generally agree well. However, those from the gravelly sand zone of Site B have significantly higher values.

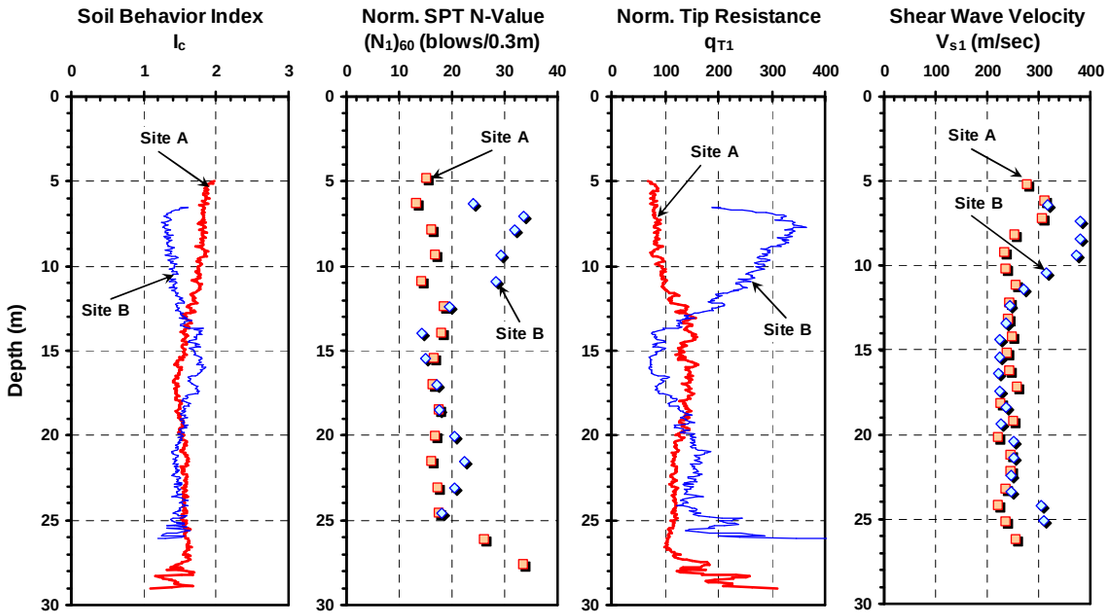


FIG. 5. Presentation of parameters for liquefaction analysis

With a design earthquake of moment magnitude M_w = 7.5, the $CRR_{7.5}$ based on $(N_1)_{60}$ and q_{T1} can be taken directly from the deterministic CRR curves presented in Fig. 1, and they are plotted in Fig. 6 for both the sites.

In liquefaction analyses, the seismic loading is typically expressed in terms of the cyclic stress ratio (CSR), which is a function of the peak ground acceleration a_{max} in the common simplified procedure (Seed & Idriss, 1971). With the deterministic methods, the critical a_{max} triggering liquefaction can be back-calculated assuming the factor of safety against liquefaction is 1.0 (i.e., CSR = CRR), as shown in Fig. 6. The

values of $CRR_{7.5}$ and a_{max} calculated from SPT N-values using the Idriss & Boulanger (2006) method agrees well with that based on the Youd et al. (2001) method, as the corresponding liquefaction criteria (i.e., CRR curves) agree well with each other [Fig. 1 (a)]. Both of them indicate that at Site A the critical a_{max} is about 0.25g in the depth range from 5 m to 12 m, and is about 0.35g below 12 m depth. At Site B, the critical a_{max} derived from N-values is relatively high (0.4g to 0.7g) in the gravelly sand layer (i.e., in the depth range from 6 m to 12.5 m), and varies from 0.3 g to 0.5 g in the lower sand layer.

With respect to the analyses based on q_T, the results from the Idriss & Boulanger (2006) generally match well those based on N_{60}, as shown in Fig. 6. However, the Youd et al. (2001) method gives a less conservative evaluation of liquefaction resistance, particularly where the measured q_T (Fig. 4) is relatively high. Overall, the methods based on N-values give more conservative results than those based on q_T.

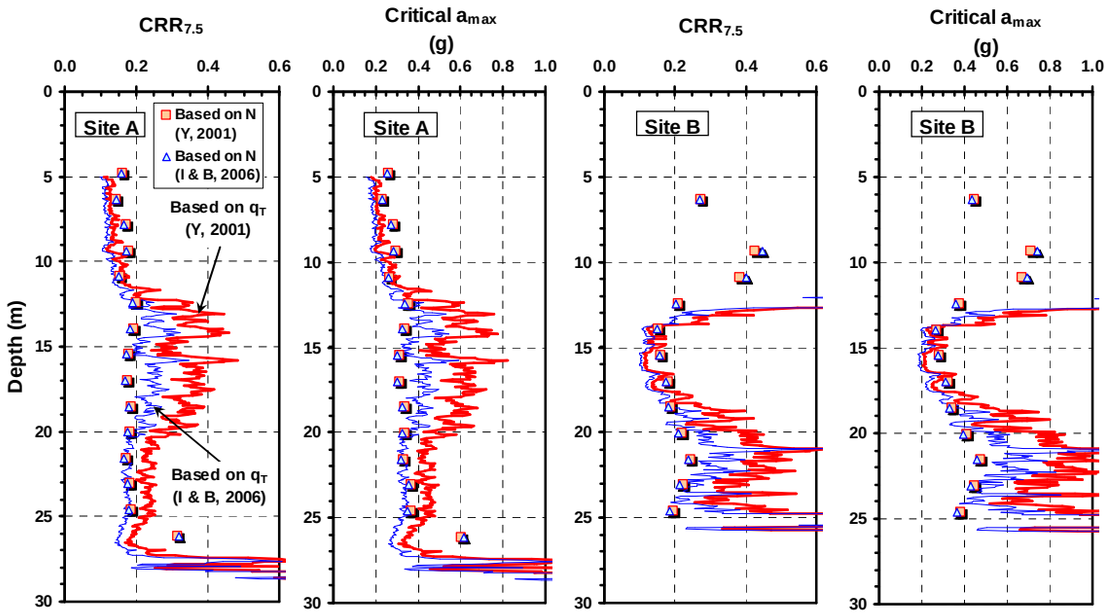


FIG. 6. Comparison of liquefaction analysis results based on deterministic methods

Similarly, the CRR probability curves shown on Fig. 1 (Juang et al., 2002; Cetin et al., 2004; Lai et al., 2006; Moss et al., 2006) can be applied to the field test data from the two fluvial sand sites. With the peak ground acceleration a_{peak} = 0.25 g, the results of probabilistic procedures are presented as the corresponding liquefaction probabilities versus depth in Fig. 7. The results indicate that the probabilities of liquefaction calculated with the Bayesian mapping and logistic regression approaches (Juang et al., 2002) are comparable with each other. For analysis based on N-values, the probability of liquefaction computed using the Juang et al. (2002) methods is generally lower than that based on the Cetin et al. (2004) method. However, among those based on q_T, the Juang et al. (2002) methods give higher probabilities of liquefaction.

Since the V_{s1} values at both sites are higher than 215 m/sec, which is the maximum

value for liquefaction to occur in clean sands (Youd et al., 2001), the $CRR_{7.5}$ value based on V_{s1} does not exist for the deterministic method. Although the liquefaction probability based on the high V_{s1} values from the two sites can be derived using the logistic regression method (Juang et al., 2002), the calculated value is very small (less than 10%), and thus is not presented here. As indicated by Idriss & Boulanger (2006), since the V_s is the least sensitive measurement for distinguishing the relative density of soils (which in turn has a strong effect on the cyclic and post-cyclic loading behavior of cohesionless soils), it may be more appropriate to use the liquefaction criteria based on V_s to identify only extreme conditions where liquefaction is highly likely or highly unlikely.

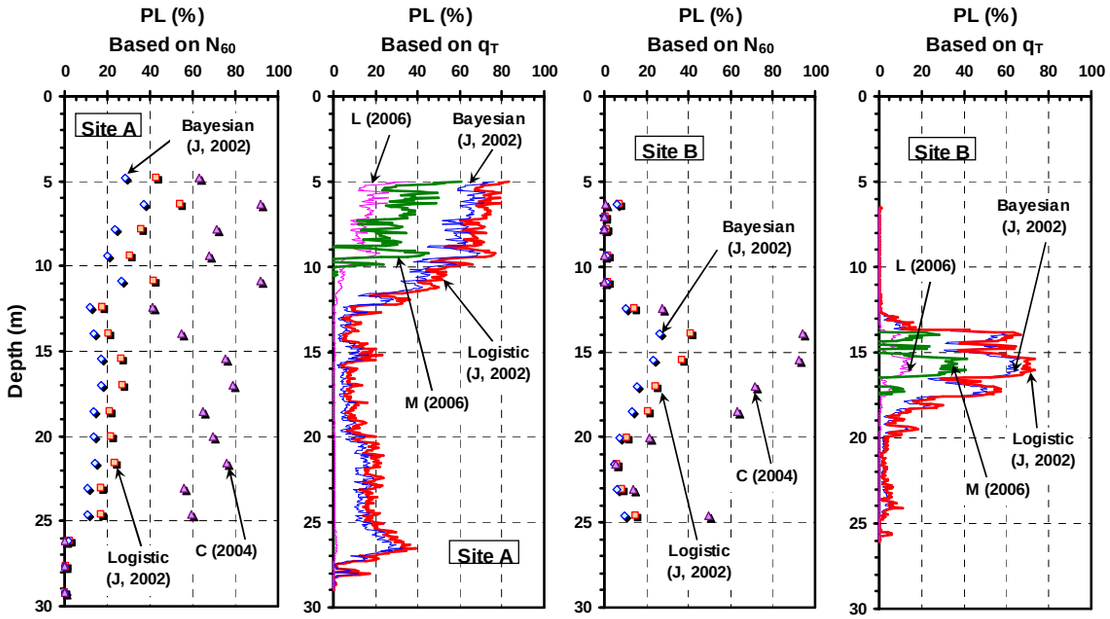


FIG. 7. Comparison of liquefaction analysis results based on probabilistic methods: (a) Site A based on N_{60}; (b) Site A based on q_T; (c) Site B based on N_{60}; (d) Site B based on q_T.

CONCLUSIONS

Three types of field measurements (N-value, q_T, and V_s) are used for liquefaction potential evaluation at two fluvial sand sites, using both deterministic and probabilistic procedures proposed since the consensus on liquefaction evaluation procedures was achieved by Youd et al. (2001). Comparison of these liquefaction evaluation results indicates that the Idriss & Boulanger (2006) method gives almost identical results to Youd et al. (2001) based on SPT N-values, but based on the cone tip resistance q_T, the Idriss & Boulanger (2006) method is more conservative. For the probabilistic approaches, the Juang et al. (2002) methods give more conservative results (i.e., higher probability of liquefaction) than other methods (i.e., Lai et al., 2006, and Moss et al., 2006) based on cone tip resistance q_T. However, based on SPT N-values, the Juang et al. (2002) methods are less conservative than the Cetin et al. (2004) method.

Results of liquefaction analysis at the two sites also indicate that the methods based on SPT N-values and cone tip resistance q_T are more conservative than the methods based on shear wave velocity V_s.

REFERENCES

Andrus, R.D. and Stokoe, K.H. (2000). "Liquefaction resistance of soils based on shear wave velocity." *J. Geotech. & Geoenv. Engrg.*, ASCE, Vol. 126(11): 1015-1026.

Cetin, K.O., Seed, R.B., Der Kiureghian, A., Tokimatsu, K., Harder, L.F., Jr., Kayen, R.E., and Moss, R.E.S. (2004). "Standard penetration test-based probabilistic and deterministic assessment of seismic soil liquefaction potential." *J. Geotech. & Geoenv. Engrg.*, ASCE, Vol. 130(12): 1314-1340.

Idriss, I. M., and Boulanger, R. W. (2006). "Semi-empirical procedures for evaluating liquefaction potential during earthquakes." *J. Soil Dynamics & Earthquake Engrg*, Elsevier, Vol. 26, 115-130.

Jefferies, M.G., Davies, M.P. (1993). "Use of the CPTu to Estimate Equivalent SPT N60," *Geotech. Testing J.*, 16(4): 458-468.

Juang, C.H., Jiang, T., and Andrus, R.D. (2002), "Assessing probability-based methods for liquefaction evaluation." *J. Geotech. & Geoenv. Engrg.*, ASCE, Vol. 128(7): 580-589.

Lai, S., Chang, W., Lin, P. (2006). "Logistic regression model for evaluating soil liquefaction probability using CPT data." *J. Geotech. & Geoenv. Engrg.*, ASCE, 132(6): 694-704.

Liao, T., Davie, J.R., Sarhan, H.A., and Viyanant, C. (2007). "Procedural effects on SPT results at a fluvial sand site." *Proceedings, the 7th International Symposium on Field Measurement in Geomechanics*, Boston, Massachusetts.

Moss, R.E.S, Seed, R.B., Kayen, R.E., Stewart, J.P., Der Kiureghian, A., and Cetin, K.O. (2006). "CPT-based probabilistic and deterministic assessment of in situ seismic soil liquefaction potential." *J. Geotech. & Geoenv. Engrg.*, ASCE, 132 (8): 1032-1051.

Robertson, P.K. and Wride, C.E. (1998). "Evaluating cyclic liquefaction potential using the cone penetration test." *Canadian Geotech. J.*, 35(3): 442-459.

Seed, H.B. and Idriss, I.M. (1971). "Simplified procedure for evaluating soil liquefaction potential." *J. of the Soil Mechanics & Foundations Division*, ASCE, 97(9): 1249-1273.

Seed, H.B., Tokimatsu, K., Harder, L.F., and Chung, R.M. (1985). "Influence of SPT procedures in soil liquefaction resistance evaluations." *J. of Geotech. Engrg.*, ASCE, 111(12): 1425-1445.

Youd, T. L., Idriss, I. M., Andrus, R. D., Arango, I., Castro, G., Christian, J. T., Dobry, R., Liam Finn, W. D., Harder, L. F., Jr., Hynes, M. E., Ishihara, K., Koester, J. P., Laio, S. S. C., Marcuson, III,W. F., Martin, G. R., Mitchell, J. K., Moriwaki, Y., Power, M. S., Robertson, P. K., Seed, R. B., Stokoe, II, K. H. (2001). ''Liquefaction resistance of soils: Summary report from the 1996 NCEER and 1998 NCEER/NSF workshops on evaluation of liquefaction resistance of soils.'' *J. Geotech. & Geoenv. Engrg.*, 127(10): 817–833.

Cyclic Response of a Sand with Thixotropic Pore Fluid

C.S. El Mohtar[1], J. Clarke[1], A. Bobet[1], M. Santagata[1], V. Drnevich[1] and C. Johnston[2]
[1]School of Civil Engineering, Purdue University, West Lafayette, IN
[2]Department of Agronomy, Purdue University, West Lafayette, IN

ABSTRACT

Saturated specimens of Ottawa sand prepared with 0%, 3% and 5% bentonite by dry mass of sand are tested under cyclic loading to investigate the effects of bentonite on the cyclic response. For the same skeleton relative density and cyclic stress ratio (CSR), the cyclic tests on the sand-bentonite mixtures show a significant increase of the number of cycles required for liquefaction compared to the clean sand. This is caused , as observed in resonant column tests, by an increase of the elastic threshold due to the presence of bentonite, which delays the generation of excess pore pressure. Such behavior can be explained by the rheological properties of the pore fluid. Oscillatory tests conducted with a rheometer on bentonite slurries show that for shear strains as large as 1% these materials exhibit elastic behavior with a constant shear modulus. Moreover, due to the thixotropic nature of the bentonite slurries, their storage modulus shows a marked increase with time. This observation is consistent with the increase in the liquefaction resistance of the sand-bentonite mixtures with time also observed in cyclic triaxial experiments.

INTRODUCTION

Liquefaction is an important cause of damage to civil infrastructures during earthquakes. Notable examples are: the collapse of apartment buildings in Niigata, Japan, in 1964; the destruction of the waterfront in Seward, Whittier, and Valdez during the Great Alaskan Earthquake in 1964; the slide at the Lower Van Norman Dam during the San Fernando earthquake in 1971; the damage caused by the earthquake in the Imperial Valley of California in 1979; the failure of a dam in Cerro Negro, Chile, after the 1985 earthquake; the large damage caused to quay walls at Kobe port during the Hyogoken-Nambu earthquake in 1995; the collapse of buildings in Adapazari during the August 1999 earthquake in Turkey; and, most recently, the numerous liquefaction failures caused by the 2007 Pisco, earthquake in Peru.

The sand properties (relative density, stress history, particle size, particle shape and gradation) and the characteristics of the cyclic loading are critical factors that determine the liquefaction susceptibility of a sand deposit (Youd et al., 2001). Observations in the field after an earthquake indicate that the presence of plastic fines increases the resistance to liquefaction (Wang, 1979; Ishihara and Koseki; 1989; Ishihara, 1993; Ishihara, 1996). This observation is the premise for considering the use of bentonite – a highly plastic, widely available clay – as a candidate for treating sand deposits to increase liquefaction resistance.

Preliminary work performed by Haldavnekar et al. (2003) on sand-bentonite mixtures showed that the addition of 5% bentonite to a clean sand specimen increased its liquefaction resistance significantly. The work presented in this paper is the result of additional research performed to evaluate the effects of the addition of bentonite to

clean sand under a broader range of testing conditions, and to gain insight on the mechanisms responsible for the improved resistance to liquefaction of the sand.

The paper presents results of cyclic triaxial and resonant column tests conducted on sand-bentonite mixtures, with 0%, 3% and 5% bentonite by dry mass of the sand. Additionally, it provides results of dynamic oscillatory tests performed on bentonite slurries as a means to gain insight on the behavior of the pore fluid. Our assumption is that the enhanced resistance to cyclic loading of sand-bentonite mixtures is the result of the mechanical properties of the pore fluid: a concentrated bentonite gel, characterized by an elastic response even at large strains. This is supported by additional experimental results that indicate that, due to the thixotropy of the gel, the liquefaction resistance improves with time.

EXPERIMENTAL PROGRAM

Materials

The tests are performed on sand specimens in which the bentonite is mixed with the sand prior to forming the specimen ("wished in place bentonite") following the procedures presented by Haldavnekar et al. (2003). The sand used for the tests is Ottawa sand C 778, a uniform (coefficient of uniformity, C_u=1.7) and clean fine to medium sand, with 2 to 5% finer than the No. 200 sieve. The specific gravity is G_s = 2.65, and the maximum and minimum void ratios are e_{max} = 0.78 and e_{min} = 0.48 (following ASTM standards).

The bentonite used is a Wyoming bentonite (CP-200), commercialized by VOLCLAY, with at least 70% passing the No. 200 sieve, and minimum free swell of 8 ml/g. This commercially available bentonite was selected for its availability in mass quantities for field applications as compared to more purified forms of bentonite. Deionized filtered deaired water was used to flush and saturate the triaxial specimens and to prepare the bentonite slurries.

Testing Methods

Tests on sand-bentonite specimens

Two types of tests are conducted on sand-bentonite specimens: cyclic triaxial tests and resonant column tests. Cyclic tests are conducted using a MTS testing system equipped with a 5000 lb hydraulic actuator. External regulators are used to control the cell and pore pressures, and an external load cell was added to measure the cyclic stresses applied. All cyclic tests are performed using a sinusoidal wave form applied at a rate of 1 cycle per second with stress reversal, starting with compression loading. Undrained conditions are chosen to simulate dynamic earthquake loading in the field. Pore pressure generation is monitored with continuous loading cycles at the base of the soil specimen. Different criteria are employed in the literature to identify the number of cycles leading to liquefaction. In this work, the number of cycles to liquefaction is defined as that corresponding to a loss of effective confining stresses to less than 10% of the initial value.

The Drnevich resonant column is used to investigate the small strain behavior of the sand-bentonite specimens. Tests are performed both at very small strains (approximately 10^{-4} %) to determine the initial shear modulus (G_{max}), as well as at higher shear strains (up to 0.01%) to describe the shear modulus degradation behavior.

All resonant column tests presented in this paper are conducted under undrained conditions, while the pore pressure at the base of the soil specimen is measured along with the resonant frequencies and the shear strains.

Similar procedures are used for specimen preparation and for saturation and consolidation of the specimens, for both the cyclic and resonant column tests. The specimen preparation method has been modified from standard procedures (ASTM D 5322 and ASTM D 4015) to accommodate the specific nature of the tested materials. In this method, the sand and the desired percentage of bentonite are dry mixed in an airtight container for 15 minutes and air-pluviated using a funnel in a triaxial split mold (diameter=70 mm, height=200 mm), which allows for preparation of 160 mm high specimens. The mold is then tapped on the sides to achieve the desired skeletal void ratio. All the tests presented in this paper have the same skeletal relative density (35% ± 5%). The skeleton void ratio is calculated as the volume of voids and bentonite divided by the volume of the sand; the skeletal relative density is calculated using the skeletal void ratio and e_{min} and e_{max} of the clean sand.

Specimens are set under 25 kPa effective confining pressure, and then flushed from bottom to top first with carbon dioxide (CO_2), and then with deionized deaired water. During flushing the gradient is kept low to prevent local liquefaction and bentonite migration (gradient less than 5).

Following flushing and prior to back pressure saturation, specimens are allowed to rest for 72 hours to ensure full hydration and swelling of the bentonite inside the sand pores. The selection of the duration of the rest phase is based on a preliminary study of the swelling time and swelling pressure of sand-bentonite mixtures. This work showed that a minimum time of 36 hours was needed for the bentonite in the pores to hydrate and swell under atmospheric pressure. After the rest period the specimens are back-pressure saturated for 24 hours with a back pressure of 200 to 400 kPa to achieve B-values $\geq$ 0.95 (based on the recommendations by Black and Lee, 1973), and then consolidated to the desired effective consolidation stress.

The cyclic triaxial specimens are isotropically consolidated in two increments to an effective confining stress of 100 kPa to represent shallow soil (5 to 7 m of depth) field conditions. While the majority of the cyclic specimens are allowed 22 hours of secondary compression at 100 kPa, a limited number of specimens are tested after a longer time to investigate thixotropy effects on the response of the sand–bentonite specimens.

Resonant column tests are performed at three different consolidation stresses: 50, 100, and 193 kPa. The homogeneity of tested specimens was checked to insure consistent void ratio and bentonite content. The void ratio was found to be within ± 3% of the target value and the bentonite content was within 0.5% by dry mass of sand throughout the height of the specimen.

Rheological tests on bentonite slurries

The rheological tests are carried out to gain insight on the mechanical properties of the pore fluid that is formed inside the sand specimen as the bentonite hydrates and gels. These tests are performed on bentonite slurries using an Anton Paar Physica MCR301 rheometer, equipped with a 50 mm, 1° angle cone-plate geometry. Bentonite slurries are prepared by mixing bentonite powder (screened to entirely pass

the No. 200 sieve) with deionized filtered water at a concentration of 10% (by mass of the slurry) using a high shear mixer for 20 minutes. The 10% bentonite slurries are equivalent to the pore fluid formed inside a sand specimen with 3% bentonite by dry mass of the sand prepared at a skeletal void ratio equivalent to 35% relative density. Note that this calculation assumes that all the dry bentonite in the specimen fully hydrates and is allowed to swell uniformly within the pore space.

Rheological tests presented in this paper are oscillatory tests measuring the visco-elastic properties of the slurries with increasing shear strain (also referred to as "strain sweeps"). In these tests, the slurry is subjected to an oscillatory shear strain ($\gamma=\gamma_0 \sin[\omega t]$, γ_0 is the maximum applied shear strain) of increasing amplitude at constant frequency (1 Hz in this testing program) while measuring the resulting shear stress τ. The shear stress may be shifted by a phase angle δ with respect to the applied strain. The shear stress can be expressed as the sum of an elastic component, in phase with the applied strain, and a viscous component, out-of-phase, as shown in eq. 1,

$$\tau = \gamma_0 \{G' \sin(\omega t) + G'' \cos(\omega t)\} \qquad \text{eq. 1}$$

Where G' and G'' are the storage (elastic) and the loss (viscous) moduli, respectively, and ω is the frequency (e.g. Barnes et al. 1989).

RESULTS

Cyclic Response

Twenty nine cyclic tests are performed, with cyclic stress ratio (CSR) varying between 0.1 and 0.25, on specimens with 0%, 3% and 5% bentonite by mass of sand. All specimens are prepared at the same skeletal void ratio (corresponding to a skeletal relative density of 35% ± 5%), and consolidated to an effective confining stress of 100 kPa.

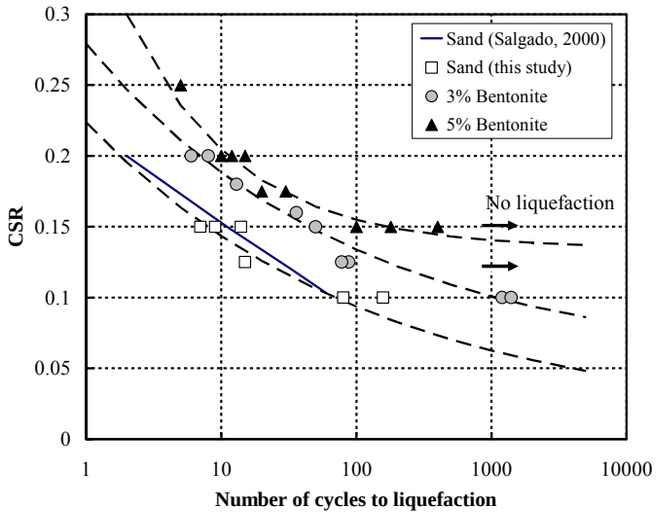


Figure 1 CSR versus number of cycles to liquefaction

Figure 1 shows the number of cycles to liquefaction determined from 27 tests as a function of the applied CSR. The figure also includes the regression proposed by

Salgado et al. (2000) based on tests conducted on the same sand at a slightly higher relative density (D_r = 40%) and using a different cyclic testing apparatus. Note that Salgado et al. (2000) used of a different criterion for determining the number of cycles to liquefaction (5% double strain amplitude criterion). Despite this, the data from the two testing programs are consistent, and the results from the two data sets are within the experimental error for cyclic triaxial tests. This is in agreement with what is reported by other researchers (e.g. Ladd, 1977).

Figure 1 shows that at any CSR, the addition of 3% and 5% bentonite increases the number of cycles to liquefaction by approximately one order of magnitude. For any given CSR, the specimens with 5% bentonite show a greater resistance to liquefaction. For values of CSR $\geq$ 0.15, the difference between the results for 3% and 5% bentonite is relatively small. However, the difference between 3% and 5% bentonite increases at lower CSRs. For all the 3% bentonite tests shown in Figure 1 liquefaction is always reached even though in some cases after over 1000 loading cycles. For CSR=0.125 and 0.15, the 5% bentonite specimens (data indicated in Figure 1 by the horizontal arrows) are able to withstand up to 1000 loading cycles without approaching liquefaction.

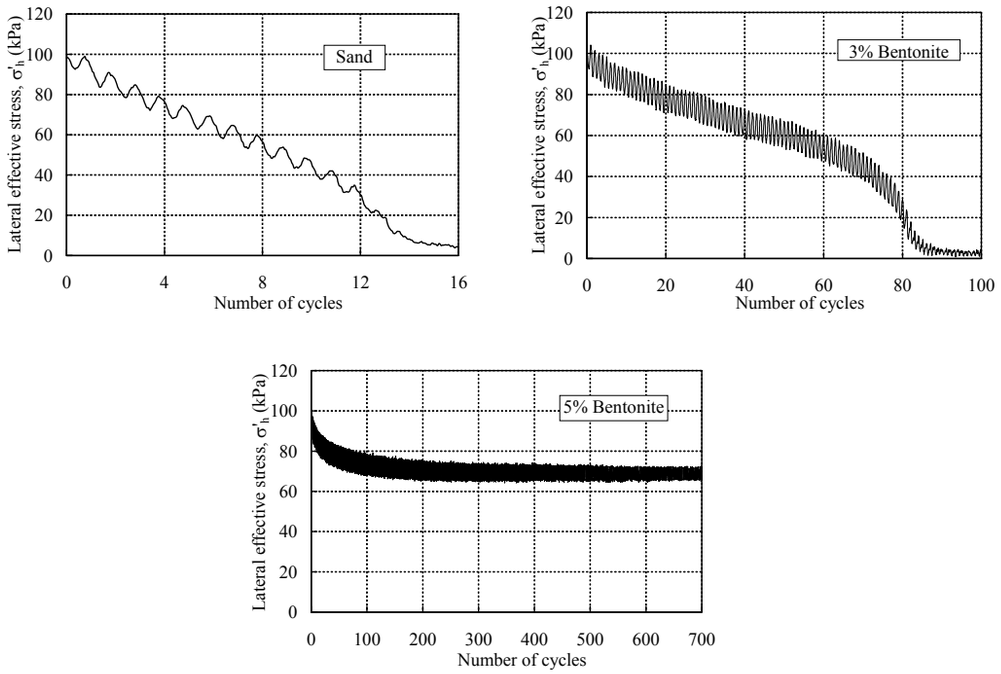


Figure 2 Loss of effective stresses with continuous cyclic loading (CSR = 0.125) for 0%, 3% and 5% bentonite specimens

For sands, there is a threshold strain level below which no liquefaction takes place regardless of the number of loading cycles (e.g. Drnevich and Richart 1970). This strain threshold corresponds to a CSR low enough such that there is no pore pressure buildup from one cycle to the next. Figure 1 suggests that in the presence of bentonite, this threshold increases with increasing bentonite content. This is supported by the cyclic stress results shown in Figure 2. The figure shows the change in effective

confining stress with increasing loading cycles for 0%, 3% and 5% bentonite specimens tested at CSR=0.125. As shown in the figure, the 5% bentonite specimen does not liquefy. The pore pressure increases initially with loading cycles but ultimately reaches a steady condition (corresponding to ~40% effective stress loss). The axial strains (not reported here) are also very small (<0.02% double amplitude strain after 1000 cycles, when the test was stopped). The clean sand specimen and the 3% bentonite specimens do reach liquefaction. The rate of excess pore pressure generation in the clean sand specimen is fast and the loss of effective confining pressure is reached after 15 cycles. The 3% bentonite specimen shows a slower rate of excess pore pressure generation, with 50% of the effective confinement stresses lost after approximately 65 cycles. As the confining pressure is reduced, the soil stiffness decreases resulting in the accumulation of strain and the acceleration of the excess pore pressure buildup. The specimen liquefies at 88 cycles. This is the same type of behavior observed during cyclic loading of clean sand at low CSR. Comparison of the response of the clean and 3% bentonite specimens indicates that the presence of bentonite delays the excess pore pressure generation. This limits the loss of stiffness and results in higher cyclic resistance. More details on the effect of bentonite on pore pressure generation and stiffness degradation are presented in the next section.

Small Strain Behavior

Resonant column tests are typically conducted drained at a constant confining stress to evaluate the shear modulus degradation with shear strain. However, the resonant column tests presented in this paper are performed undrained. The goal of these tests is to observe how the linear threshold strain (critical strain) and excess pore pressure generation change with the addition of bentonite.

Figure 3 shows the shear modulus degradation curves for specimens with 0%, 3% and 5% bentonite, all prepared at the same skeletal void ratio, which are tested at 50, 100 and 193 kPa. It is observed, as expected, that the stiffness increases with effective confining stress. Additionally, at any given confining stress, the results show a small drop in the initial stiffness (G_{max}) of the specimens containing bentonite, relative to the data for the clean sand. It is hypothesized that this reduction in G_{max} is a result of the "lubricating" action of bentonite particles at the particle to particle contacts (note that this effect is likely a by-product of the dry mixing specimen preparation procedure). Figure 3 shows that for all specimens, there is stiffness degradation with increasing shear strain. This is in part a result of the reduction in the effective confining stress due to the excess pore pressures generated under undrained conditions (Figure 4).

The shear stiffness data presented in Figure 3 for 50 and 100 kPa confinement are replotted in Figure 4 and normalized by G_{max}. The figure shows that the curves for the bentonite specimens lie above those of the clean sand, with differences increasing with higher shear strains. Figure 4 also presents the excess pore pressures normalized by the initial effective confining stresses. The data indicate that, at the same confining stress, excess pore pressures are generated much earlier in the clean sand specimens. These results are consistent with an extension of the linear range and a smaller

reduction of shear modulus degradation for the specimens treated with bentonite as compared to clean sand specimens.

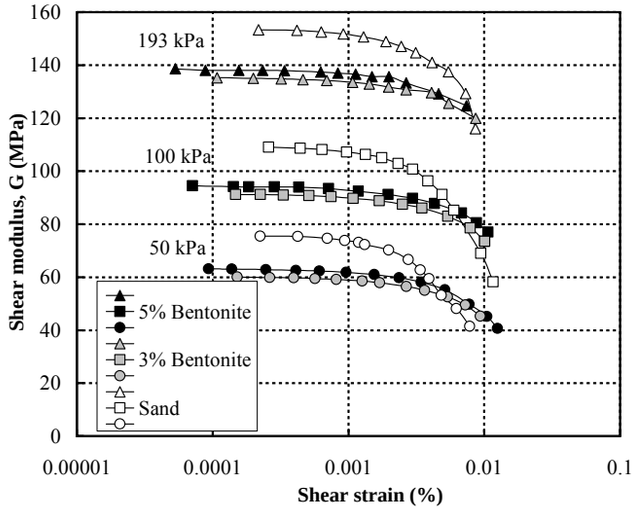


Figure 3 Shear Modulus degradation for 0%, 3% and 5% bentonite at 50, 100 and 193 kPa

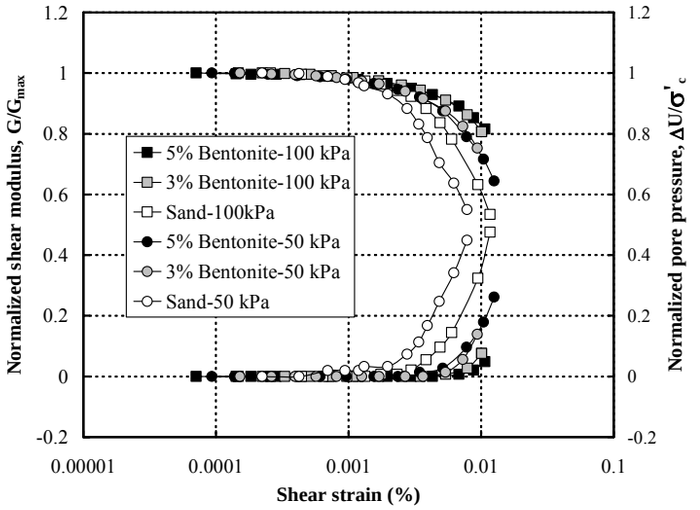


Figure 4 Normalized shear modulus and excess pore pressure for 0%, 3% and 5% bentonite at 50 and 100 kPa

Pore Fluid Rheology

Dynamic oscillatory strain sweep tests are performed to gain insight on the mechanical properties of the pore fluid formed inside specimens prepared with bentonite. Figure 5 shows the results of a strain sweep test conducted at atmospheric pressure on a 10% slurry immediately after mixing.

As shown in Figure 5, for shear strains as large as 1% (linear visco-elastic region), G′ remains basically constant. An elastic response is defined by low value of δ and as the region where G′>>G″. Once the shear strain exceeds a critical value

(approximately 1% for the test shown), the storage modulus drops significantly and the behavior of the material becomes increasingly viscous.

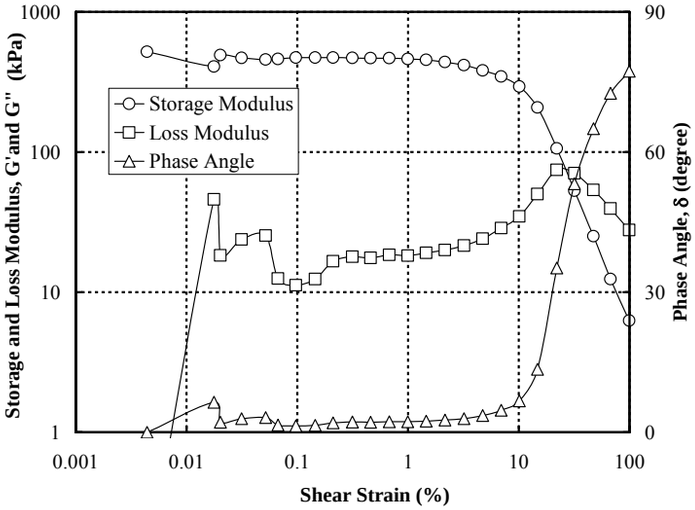


Figure 5 Amplitude sweep test on 10% bentonite slurry

A common occurrence in many colloidal suspensions is the rebuilding of its internal structure after it has been broken by shearing. After the applied shear stress is reduced or completely removed, the internal structure begins to rebuild with time. This time-dependent behavior is referred to as thixotropy (Barnes, 1997).

The thixotropic nature of clay slurries is shown in Figure 6 which plots the storage modulus (G′) measured in the initial portion of an oscillatory test as a function of the age of the slurry (up to 1440 hours). The values of G′ shown in Figure 6 are obtained by averaging G′ values within the linear range. For each ageing time, 4 to 5 strain sweep tests are performed to insure repeatability. The tests show an increase in G′ with time (at 600 hours G′ is about 2.5 times the value at t=0).

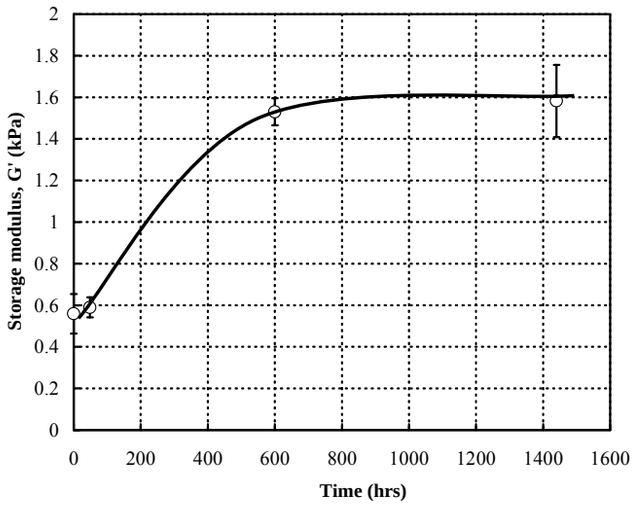


Figure 6 Storage modulus of 10% bentonite slurry versus time after preparation

Thixotropic Effects

Since it is assumed that the pore fluid is responsible for the improved cyclic resistance of sand-bentonite specimens, it is expected that the thixotropic nature of the pore fluid will improve liquefaction resistance with time. Two 3% bentonite cyclic triaxial specimens are prepared as described earlier, but with additional secondary consolidation time: 94 hours and 238 hours, respectively. The specimens are then tested at a CSR = 0.2. The number of cycles to liquefaction is presented in Figure 7 along with the results for clean sand and the reference 3% bentonite (22 hours consolidation) at similar CSR. The results show a significant increase in cyclic resistance with time. The specimen with 238 hours of secondary consolidation does not liquefy and shows a pore pressure generation curve similar to that shown in Figure 2 for 5% bentonite.

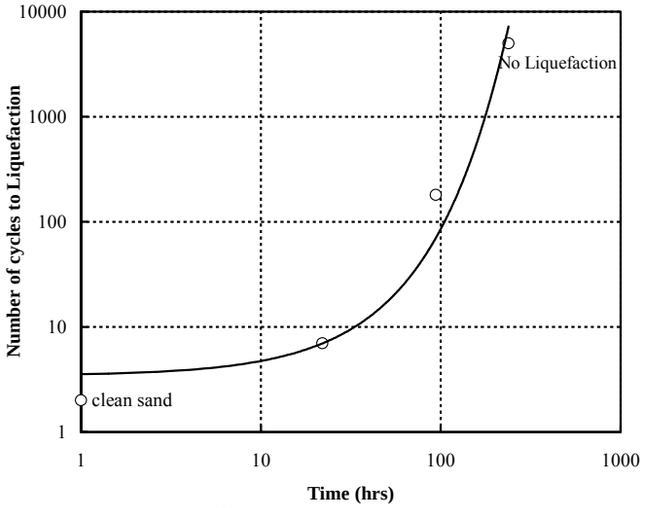


Figure 7 Cyclic resistance of 3% bentonite specimens versus secondary consolidation time at CSR = 0.2

CONCLUSIONS

The paper presents the results of cyclic triaxial and resonant column tests performed on dry-mixed, sand–bentonite specimens with 0, 3, and 5% bentonite. In addition, it includes rheological tests conducted on bentonite slurries representing the pore fluid formed inside the sand with 3% bentonite.

The results demonstrate that in the presence of bentonite there is an order of magnitude increase in the number of cycles that produce liquefaction at any given CSR, and an increase in the minimum cyclic loading required to produce liquefaction. This behavior is a result of the delayed generation of excess pore pressures. Resonant column test results show an increase of the strains required to initiate excess pore pressure generation.

The response of the sand-bentonite mixtures is tied to the pore fluid that is formed: a bentonite gel with essentially elastic response up to 1% shear strain. The thixotropic nature of the pore fluid is reflected in the increased cyclic resistance measured over time. In addition to supporting the use of bentonite for mitigating the liquefaction susceptibility of sands, the work provides increased insight into the role played by plastic fines in the cyclic response of natural soils.

ACKNOWLEDGEMENTS

This research was supported by the National Science Foundation, Geomechanics and Geotechnical Systems Program, under grant CMS-0408739. This support is gratefully acknowledged.

REFERENCES

Barnes, H. A., Hutton, J.F., and Walters, K. (1989). "An Introduction to Rheology". *Elsevier Science Publishers*, Amsterdam, The Netherlands, 199 p.

Barnes, H. A. (1997). "Thixotropy - a review." *Journal of Non-Newtonian Fluid Mechanics*, 70(1-2), pp. 1-33.

Black, D. K. and Lee, K. L. (1973) "Saturating Laboratory Samples by Back Pressure" *Journal of Soil Mechanics and Foundations Division*, ASCE, Vol. 99, No. SM1, pp. 75-93.

Drnevich, V.P., and Richart, Jr., F.E. (1970). "Dynamic prestraining of dry sand" *Journal of the Soil Mechanics and Foundations Division, ASCE*, Vol. 96, No. SM2, pp. 435-469.

Haldavnekar, V., Bobet, A., Santagata, M., and Drnevich, V. (2003). "Soil treatment with a thixotropic fluid: an autoadaptive design for liquefaction prevention." *Proceedings of the 11th International Conference on Soil Dynamics & Earthquake Engineering and 3rd International Conference on Earthquake Geotechnical Engineering*, Vol. II, pp. 553-560.

Ishihara, K. and Koseki, J. (1989). "Discussion of cyclic shear strength of fines-containing sands." *Earthquake Geotechnical Engineering, 12th International Conference on Soil Mechanics and Foundation Engineering*, Rio de Janeiro, pp. 101-106.

Ishihara, K. (1993). "Liquefaction and flow failure during earthquakes." *Géotechnique*, Vol. 43, No. 3, pp. 351-415.

Ishihara, K. (1996). Soil Behaviour in Earthquake Geotechnics. *1st edition, Oxford, Claredon Press*, 350 p.

Ladd, R.S. (1977). "Specimen preparation and cyclic stability of sands." *Journal of the Geotechnical Engineering Division, ASCE*, Vol. 103, No. 6, pp. 535-547.

Salgado, R., Bandini, P., and Karim, A. (2000). "Shear strength and stiffness of silty sand" *Journal of Geotechnical and Geoenvironmental Engineering, ASCE*, Vol. 126, pp. 451-462.

Youd, T.L., Idriss, I.M., Andrus, R.D., Arango, I., Castro, G., Christian, J.T., Dobry, R., Finn, W.D.L., Harder Jr., L.F., Hynes, M.E., Ishihara, K., Koester, J.P., Liao, S.S.C., Marcuson III, W.F., Martin, G.R., Mitchell, J.K., Moriwaki, Y., Power, M.S., Robertson, P.K., Seed, R.B., and Stokoe, K.H. (2001). "Liquefaction Resistance of Soils: Summary Report from the 1996 NCEER and 1998 NCEER/NSF Workshop on Evaluation of Liquefaction Resistance of Soil" *Journal of Geotechnical and Geoenvironmental Engineering, ASCE*, Vol. 127, No. 10, pp. 817-833.

Wang, W. (1979). "Some findings in soil liquefaction." *Water Conservancy and Hydroelectric Power Scientific Research Institute*, Beijing, China.

Effect of High Confining Stresses on Static and Cyclic Strengths of Mine Tailing Materials

Michael Riemer[1] M. ASCE, Yoshi Moriwaki[2] M.ASCE, P.E., James Obermeyer[3]

[1] Assoc. Adj. Professor, UC Berkeley, 451 Davis Hall, Berkeley CA 94703; riemer@ce.berkeley.edu
[2] Principal, GeoPentech, 525 N. Cabrillo Park Dr. #280, Santa Ana, CA 92701; yoshi_moriwaki@geopentech.com
[3] Principal and Vice President, MWH, 1801 California Street, Suite 2900, Denver, CO 80202; james.obermeyer@mwhglobal.com

ABSTRACT

This paper presents the results of static and cyclic undrained triaxial testing on underflow (coarse fraction) tailing materials for a very high proposed tailing storage facility in seismically active southern Peru. The results of these tests, ranging in initial effective confining pressures from about 0.1 to 5.8 MPa, showed contractive but generally ductile behavior at higher initial effective confining pressures likely caused by grain breakage. These test results formed an important part of the design of the tailing storage facility.

1. INTRODUCTION

As part of expanded mining operations, a large tailing storage facility (TSF) has been designed and was placed into operation in November 2006 at the Cerro Verde Mine in southern Peru. The mine is located in a region of high seismicity dominated by earthquakes occurring along the Peru-Chile Subduction Zone, which has a history of producing very large earthquakes that could cause significant shaking at the TSF site. The maximum credible earthquake (MCE) for design is a moment magnitude 9.0 (Mw) megathrust event estimated to be capable of producing a peak horizontal acceleration at the top of bedrock of 0.47g. The TSF includes a starter dam that will be raised over a 22-year period to its ultimate height by the "centerline construction method". This method involves separating the whole tailing materials produced by the milling process into a coarse fraction (tailing underflow) and a fine fraction (tailing overflow) by a cycloning process. The underflow materials are then placed in relatively thin lifts and compacted to high density to construct an embankment that provides drainage and strength characteristics to enhance static and dynamic stability. The overflow tailing materials are hydraulically deposited upstream of the compacted underflow embankment. The design envisioned a maximum fines content of 15% and a compaction specification of 98% of Standard Proctor Density (ASTM D698) for the underflow material used to construct the embankment.

The large anticipated stresses toward the base of the very tall ultimate embankment and the high seismicity environment underscore the need to understand the likely undrained response of these materials to both static and cyclic loading conditions. This paper describes static and cyclic undrained triaxial tests performed during design of the TSF on reconstituted specimens of the tailing underflow materials, presents results of the study, and summarizes outcomes from testing that were important to the design.

2. TESTING PROGRAM

2.1 Material

The soils being investigated are underflow mine tailing materials from the Cerro Verde project, which had been processed to contain a particular fraction of non-plastic fines. Tests were performed primarily on material having approximately 15% by weight finer than the #200 sieve (0.075 mm), although additional tests were performed on similar material, except with 18% by weight fines. Both soils classify as poorly graded, fine grained silty sands (SM) by USCS designation. Nearly all particles are finer than 0.6 mm, while the mean grain size (D_{50}) is 0.15 mm, and the D_{10} size is 0.06 mm . Due to their origin as mine tailing materials, the individual particles are quite angular. As part of the soil preparation, all of the soil of each type was mixed thoroughly to a moisture content of 7%, and stored in sealed bags, so that capillarity would prevent the settling of the fines and minimize segregation.

Table 1: Triaxial tests, including type, fines content, density and stress, and results.

		Consolidation			Mobilized ϕ'	Mobilized ϕ'
	Nominal	Stress	Dry Density		at ε = 3%	at ε = 10%
Test	Fines	(kPa)	(g/cm3)		(degrees)	(degrees)
ICU 2	15	2793	1.65		34.5	37.9
ICU 3	15	470	1.59		37.9	38.0
ICU 4	15	5795	1.72		33.4	37.0
ICU 5	15	1445	1.62		35.8	37.6
ICU 9	18	480	1.66		39.3	39.1
ICU 10	18	5600	1.77		33.8	37.4
ICU 6	15	470	1.55		37.4	38.0
ICU 7	15	1390	1.59		35.8	37.9
ICU 8	15	5590	1.71		33.0	37.1
					(N) Cycles to liquefaction	
				CSR	r_u = 100%	ε = 5% d.a.
CTX 7	15	97	1.57	0.31	8	11
CTX 5	15	97	1.57	0.24	285	n.a.
CTX 6	15	97	1.57	0.36	10	14
CTX 11	15	97	1.58	0.26	112	n.a.
CTX 9	15	1400	1.62	0.184	28	27
CTX 8	15	1400	1.62	0.222	10	9
CTX 10	15	1400	1.62	0.155	84	83
CTX 1	15	5285	1.71	0.18	18	17
CTX 2	15	5280	1.71	0.215	6	5
CTX 3	15	5300	1.72	0.14	83	82

Notes: ε = *axial strain;* ϕ' = *effective stress friction angle;* CSR = *cyclic stress ratio (see 3.2)*

2.2 Scope

The triaxial testing program presented here includes 9 Isotropically Consolidated, Undrained (ICU) static strength tests, performed over a wide range of confining stresses, and 10 Cyclic Triaxial tests (CTX) designed to characterize the liquefaction behavior, also performed on isotropically consolidated specimens. Table 1 summarizes the test numbers, the material, and the consolidation stress and density. All of the specimens tested were prepared using moist tamping procedures (described in detail below), were tested in the same high-pressure cell using the same hydraulic loading system and instrumentation, and all tests were performed by the lead author. In addition to the conventional results from such tests, which include the axial stress, strain and pore pressure histories during the static and cyclic loading, and the number of cycles to liquefaction in cyclic loading, additional data was recorded on the volumetric strain of the liquefaction samples during reconsolidation to their initial effective stress, and on the percentage of fines present in the specimens after testing at high stresses, in order to assess the degree of grain breakage occurring during consolidation and loading.

2.3 Equipment

All of the triaxial testing was performed using a high-pressure triaxial cell which was originally developed by Williams (1982) to accommodate elevated cell pressures in excess of 10 MPa. A new set of stainless steel triaxial caps (5.3 cm in diameter) were designed and fabricated for this testing project, with a single drainage line incorporated in the base cap. The triaxial loading system utilizes an MTS hydraulic actuator, controlled by the "Automated Testing System" software platform. The high confining stresses were supplied with bottled nitrogen applied over water in the triaxial chamber, while the relatively modest back pressures required for saturation were supplied by the conventional compressed air system in the laboratory. Effective stresses were measured using a Validyne differential pressure transducer with a high-range (very stiff) diaphragm. Axial loads and deformations were measured externally using an Interface load cell and Linear Variable Differential Transformer (LVDT), respectively. The triaxial cell design utilizes a double O-ring seal around the loading rod, to minimize leakage associated with the high pressure gradient, and the modest resulting friction was measured across the full range of cell pressures. The cyclic data have been corrected to account for this. Double thickness (t = 0.063 cm) cylindrical membranes were used, and the conventional O-rings utilized to seal the membrane around the caps were supplemented with hose clamps. The very fine effective grain size of the tailing materials prevented membrane penetration issues from being significant, even for the large effective consolidation stresses applied, while the effects of membrane stiffness were also calculated to be insignificant for the stress levels applied in this study.

2.4 Procedures

Individual specimens were prepared using the undercompaction method of moist tamping (Ladd, 1978), an approach for mitigating the tendency for lower layers of the specimen to densify further under the compactive effort of overlying layers. To achieve

a more uniform density following completion of all the layers, therefore, the mass of each subsequent layer is increased slightly from that of the previous layer. Specifically, the specimens in this program were compacted using five layers, with successive layers containing 0.3% more dry mass than the layer below. The nominal diameter of the resulting specimens was 5.33 cm, with a nominal height of 12.5 cm. The target dry densities were identified based on percentages of the maximum values measured during compaction testing. The tailing underflow material with 15% fines was compacted to approximately 1.58 g/cm^3, which represented 98% of the Standard Proctor maximum dry density, and the 18% fines tailing materials were compacted to approximately 1.66 g/cm^3, corresponding to 98% of the maximum value for that material. All specimens were compacted at a moisture content of 17% which was slightly dry of optimum moisture content for the 15% fines material, and slightly wet for the 18% fines material. Substantial effort was required with the tamping device to achieve the target densities, especially for the 18% fines material, which had a significantly higher target density.

Following compaction, the specimens were mounted on the testing caps in the cell, sealed into place, and vacuum saturated at an effective stress of approximately 95 kPa. Initial measurements of height and diameter were recorded under these conditions. Once the chamber was sealed and moved to the loading device, vacuum stresses were replaced by positive cell and back pressures, saturating the sample at essentially constant effective stress until a B value of at least 0.9 was achieved. Specimens were then isotropically consolidated in stages to stresses of approximately 470 kPa; 1400 kPa; 2800 kPa; and 5600 kPa (though some specimens were tested at the lower stress levels as well).

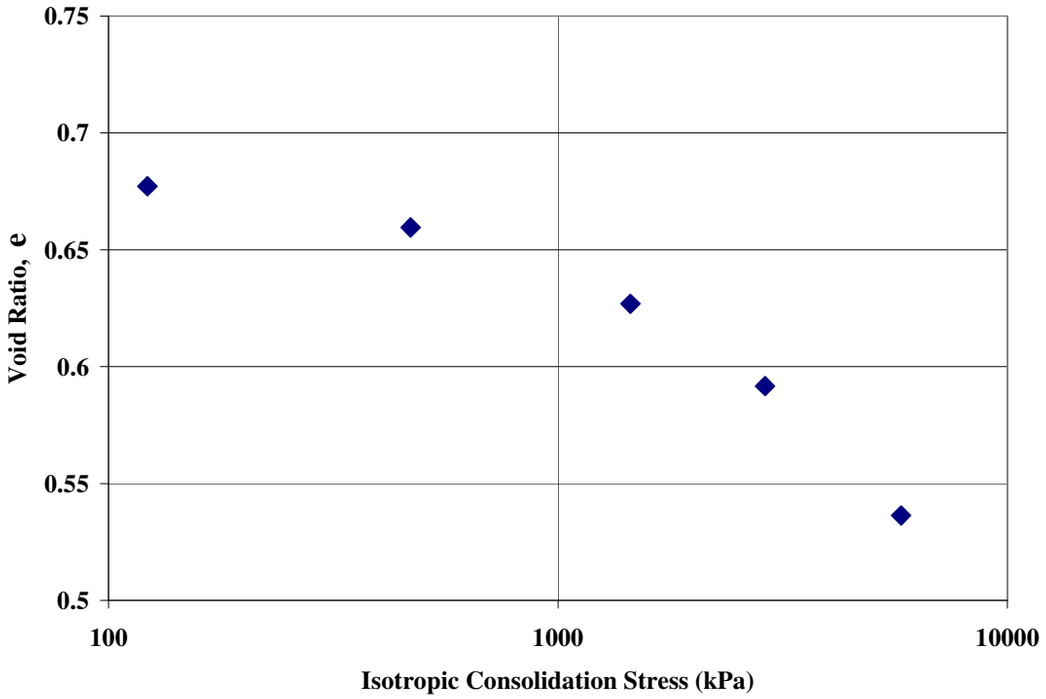


Figure 1: Consolidation of dense tailings specimen (ICU 4) to very high stresses.

Despite the significant fines content, the permeability of the tailings is such that consolidation was completed quickly at each stress, although it was noted that both the axial and volumetric readings continued changing slowly for substantially longer time periods at the highest stress levels compared to the initial increments: is it suspected that this "creeping" is related to continuing densification related to grain breakage and reorientation at the high stress levels. Grain breakage is also suspected to contribute to the large magnitude of strains at the highest stress levels, where the conventional plot of void ratio and effective stress (Figure 1) takes the concave-down shape more typically associated with cohesive soils with a preconsolidation pressure. Sandy soils have also been shown to exhibit such curves at elevated stress levels (Vesic and Clough, 1968).

3. TESTING AND RESULTS

3.1 Static Triaxial Testing

Following consolidation to the desired isotropic stress state, the drainage valve to the burette was closed, and the specimens were sheared at a constant deformation rate of 1 mm/minute, which corresponds to a strain rate of approximately 0.8%/minute. During shearing, the deviatoric load, vertical deformation and effective stress were recorded by the computer. Loading was typically continued to between 10% and 12% axial strain. From the parameters measured during the test, the shear stress, shear strain and other parameters of interest were directly calculated. The cross-sectional area was corrected as a function of strain using the conventional constant-volume assumption of deformation as a right circular cylinder.

Two examples of the stress-strain plots are shown in Figures 2(a) and (b), both of which were performed on tailing materials with 15% fines, but which were consolidated to different stress levels. Figure 2(a) shows the response for ICU 3, which was sheared following consolidation to 470 kPa. Although compacted to a relatively high initial density, the undrained response is still mildly contractive, as evidenced by the initial drop in effective stress up to strains of about 1.5%, after which the specimen shows dilative tendencies (drop in pore pressure) during subsequent shearing to the completion of the test at 12% strain. This sort of response produces a shear stress-strain curve which is monotonically increasing throughout and which therefore shows no clear peak value of shear stress, although the values are clearly leveling out at larger strains.

In contrast, Figure 2(b) shows the response of a specimen prepared to the same density, but isotropically consolidated to 5,795 kPa. Although the specimen is substantially denser in absolute terms following consolidation, its response is very contractive under the high levels of confining stress, as the effective confining stress drops dramatically, leveling out at a value less than 20% of the initial value, and shows no tendency for dilation at large strains. The effect of this contractive response on the stress-strain curve is a peak stress at an axial strain of 1.5%, after which the shear stress declines slightly over the remainder of the test. Similar undrained behavior has been observed for sands at high confining pressures (Bishop, 1966; Vesic and Clough, 1968).

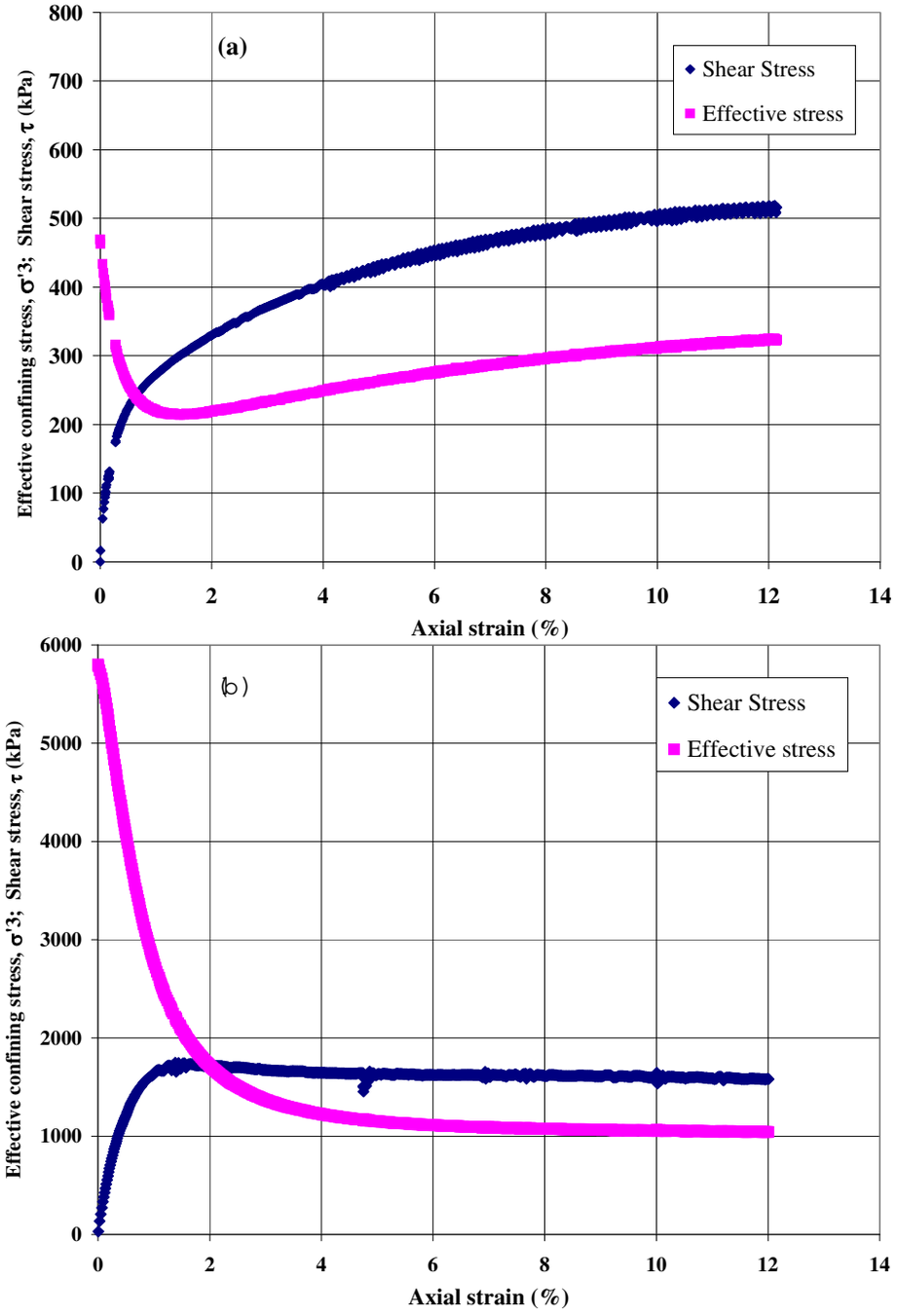


Figure 2: Contrast in static response for (a) moderate and (b) high stress levels.

The effective stress paths corresponding to these and the other static shearing tests are compiled in Figure 3. The tests consistently show that at very high stress levels, all specimens exhibit contractive behavior, with stress paths that move from initial values at the right side of the plot up to some peak value, then continue moving to lower mean effective stresses as the shear stress declines until the specimen reaches a stable stress state. At the lowest consolidation stresses applied, the stress paths reach a limiting ratio of shear to mean stress relatively quickly, then climb up along the failure envelope with continued straining. Specimens tested at intermediate stress levels show a transition

behavior that is between the specimens at either extreme. It should be noted that although the denser specimens are producing higher shear strengths at larger strains, all of the specimens are converging to a similar friction angle: the failure envelope shown on Figure 3 corresponds to an effective friction angle of approximately 37°. Table 1 includes results of the testing in terms of the mobilized effective friction angle at two different strain levels, ϕ' at 3% and 10% axial strain. These tabulated values show that there is a significant difference at the smaller strain level, with the specimens at higher stresses exhibiting lower friction angles, consistent with a greater degree of dilation. This difference diminishes substantially by the time 10% axial strain is reached, with only a slight tendency for higher friction angles at lower stresses.

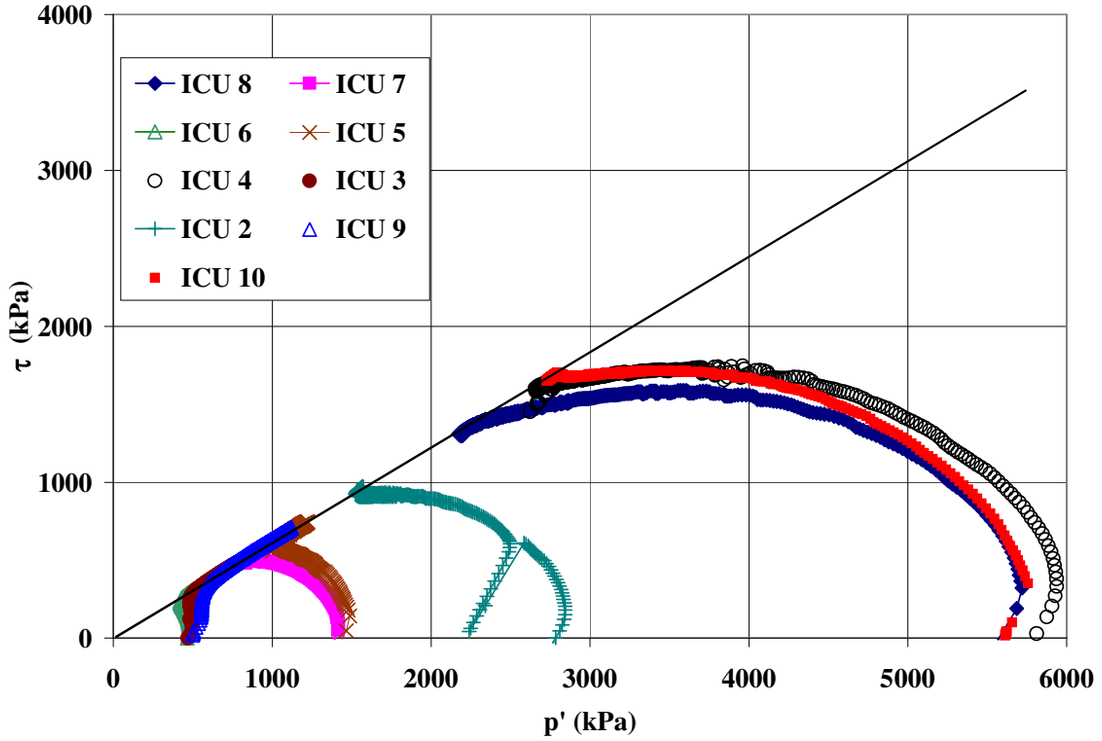


Figure 3: Effective stress paths of static tests consolidated to varying stress levels.

3.2 Cyclic Testing

Cyclic testing was also conducted under undrained conditions, but under stress control. At a frequency of 0.2 Hz, the deviatoric load was cycled sinusoidally around the isotropic consolidation stress level. The amplitude of cyclic loading in such tests is usually characterized by the Cyclic Stress Ratio (CSR), where:

$$CSR = \tau_{max} / \sigma'_{consol} \quad (1)$$

in which τ_{max} is the single amplitude shear stress applied, and σ'_{consol} is the isotropic consolidation stress. Measurements of deviatoric load, axial deformation and effective stress were typically recorded 100 times per cycle. Loading was continued until either sufficient pore pressure was generated to temporarily reduce the effective stress to zero, or sufficiently large strains were observed to consider the material liquefied. In some cases, this required performing multiple identical "tests" in sequence on the specimens, without allowing any drainage of pore pressures between them, to keep the data acquisition system functioning properly for large numbers of cycles (well over 100).

Three suites of such liquefaction tests were performed, to define the relationship between the number of cycles to liquefaction (N) as a function of the applied CSR at three very different consolidation stress levels. Table 1 includes the results of the tests interpreted both in terms of the number of cycles to development of 100% pore pressure, as well as the development of 5% double amplitude strain. The results are plotted graphically in Figure 4, which illustrates the effect of confining stress on the resulting liquefaction resistance: at higher stress levels, a lower CSR is needed to reach liquefaction in a given number of cycles, despite the considerably higher density of those heavily consolidated specimens. It is also interesting to note, however, that there is only a small shift in the curves from the 1,400 kPa level to 5,300 kPa. From Figure 4, the K_σ value needed in liquefaction triggering assessment can be obtained for this material (e.g., Idriss and Boulanger, 2006).

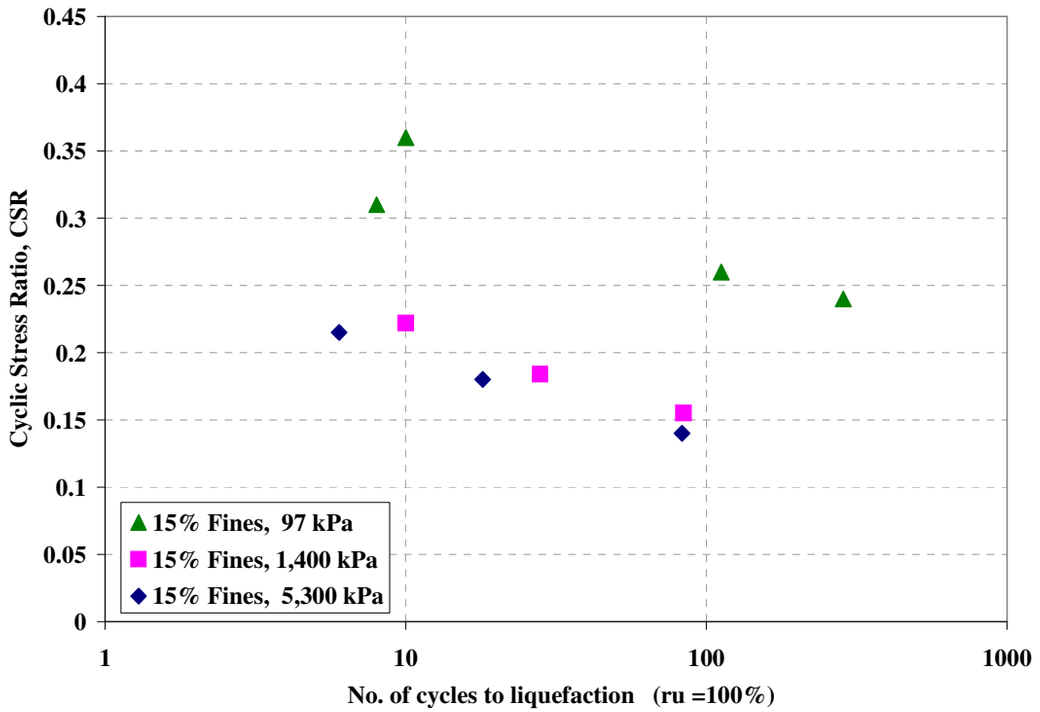


Figure 4: Summary curves of cyclic testing, emphasizing influence of stress level.

4. GRAIN BREAKAGE

Following the triaxial testing, portions of the specimens were wet-sieved over a #200 mesh, in an effort to identify the degree of grain breakage that had occurred by monitoring the increased percentage of fines. A summary graph of these results is shown in Figure 5. While the absolute value of the fines content appears low relative to the "nominal" values reported for the untested material (perhaps relating to different procedures and equipment), the trend for increased fines content with elevated testing stresses is clear. It is also useful to note that at the highest testing stresses, the specimens sheared statically showed greater fines contents after testing – probably related to the fact that these specimens were sheared to large strains under substantial effective stresses, whereas the liquefaction specimens experienced smaller strain levels, at least until the effective stresses were nearly eliminated by the development of pore pressures. Grain breakage effects have been well documented at least for monotonic triaxial loading (Bishop, 1966; Vesic and Clough, 1968; Lade and Yamamuro, 1996).

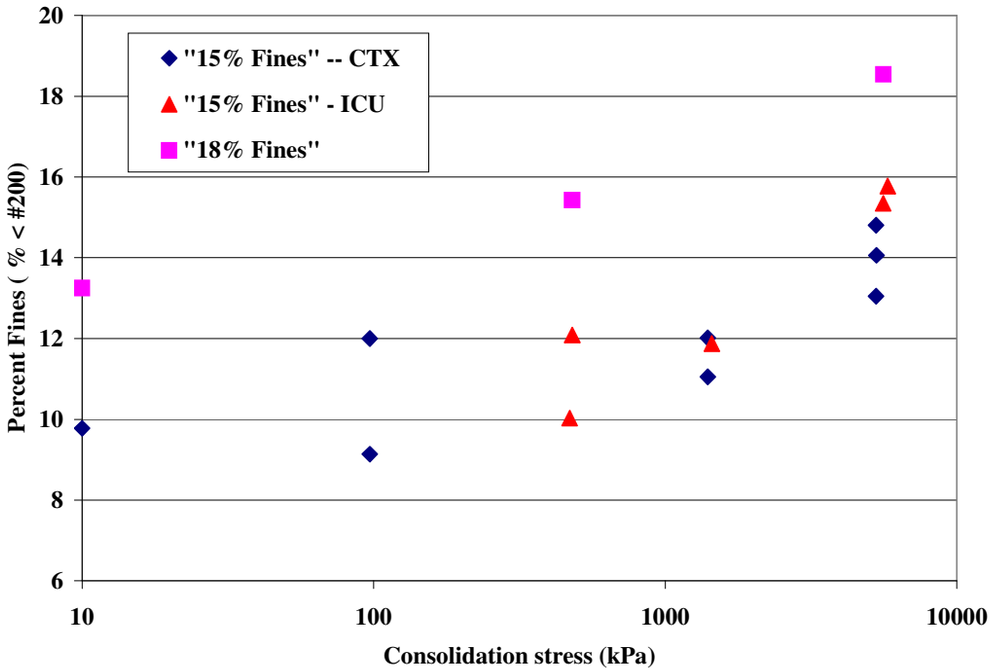


Figure 5: Fines content as a function of consolidation stress in triaxial testing.

5. SUMMARY AND IMPLICATIONS FOR DESIGN

The data obtained from this testing provides information on the likely behavior that the tailing underflow materials will exhibit under the very large overburden stresses anticipated by the design. In accordance with the design specifications, the tailing underflow materials will initially be compacted in the field. They will subsequently consolidate to higher densities under the large anticipated stresses as the embankment increases in height. Despite this densification, the materials will change from being

relatively dilatant and resistant to liquefaction under cyclic loads at shallow depths, to being substantially contractive, and less cyclically resistant at very large depths.

Presumably due to its angular nature and high densities, however, the effective stress friction angle remains quite high across the full range of testing stresses and strains. Furthermore, the testing showed that the undrained shear resistance of the underflow material was essentially non-strain softening (ductile) under the high initial effective confining pressures expected for the project. Such ductile behavior is expected for the underflow material even after the application of significant cyclic loading postulated for the project site. These test results were used in seismic stability and deformation evaluations of the TSF embankment under the postulated earthquake shaking conditions to show that the designed TSF embankment is seismically adequate.

It is of interest to note that available undrained triaxial test data of sands at much higher initial effective confining pressures sometimes show more strain softening undrained behavior than that observed herein (e.g., Lade and Yamamuro, 1996). This emphasizes the importance of site-specific testing of appropriate materials under appropriate conditions when static and seismic undrained behavior of soils under high initial confining pressures are involved in the project.

6. ACKNOWLEDGMENTS

The authors wish to acknowledge Phelps Dodge Corporation (now Freeport McMoRan Copper and Gold Inc.) for their support of this testing program as a part or the final design activities for the Cerro Verde TSF. Special recognition is given to Mr. Jim Venderbeek for his assistance in providing the sample for testing and for his insights into the whole tailing gradation that was expected to be produced by the milling process. Professor R. Boulanger reviewed some aspects of the tests.

7. REFERENCES

Bishop, A.W. (1966). “The strength of soils as engineering materials.” *Geotechnique*, 16(2), 89-130.

Idriss, I. M., and Boulanger, R. W. (2006). "Semi-empirical procedures for evaluating liquefaction potential during earthquakes." Journal of Soil Dynamics and Earthquake Engineering, Elsevier, 26, 115-130.

Ladd, R.S. (1978). “Preparing test specimens using Undercompaction,” *Geotechnical Testing Journal*, ASTM, Vol. 1, No. 1 pp 16-23/

Lade, P.V., and Yamamuro, J.A. (1996). “Undrained sand behavior in axisymmetric tests at high pressures.” *J. Geotech. Engrg*., ASCE, 122(2), 120-129.

Vesic, A.S., Clough, G.W. (1968). “Behavior of granular materials under high stresses.” *J. Soil Mech. and Found. Div*., ASCE, 94(3), 661-688.

Williams, N. (1982), The effects of elevated temperature on the engineering properties of seafloor sediments, *PhD. Thesis*, Dept. of Civil Engineering, UC Berkeley, CA.

Effects of Mica Content on Cyclic Resistance of Poorly-Graded Sand

Kimberly Schmidt[1], M. ASCE

[1] Staff Engineer, Treadwell & Rollo, Inc., 777 Campus Commons Road, Suite 200, Sacramento, Ca 95825; kischmidt@treadwellrollo.com

Abstract: In California several geotechnical projects located in seismically active areas have encountered recent alluvial deposits with varying mica contents. Post-construction liquefaction susceptibility evaluations can be made, however case histories do not exist for soils with considerable mica contents, so it is difficult to evaluate if the results from the post-construction investigation are accurate. Cyclic triaxial tests on isotropically consolidated specimens were performed to evaluate the effect of mica content on the liquefaction of poorly-graded sand. The results show that fewer cycles are required to initiate liquefaction for specimens with higher mica contents. It should be noted that the impact of mica particles on the maximum and minimum void ratio suggests that the maximum compacted density of mica-sand mixtures decreases with an increase in mica content. Therefore, if relative density is used as an indicator of liquefaction potential for sands with varying mica contents, than a correction factor should be applied to the in-situ field tests, such as SPT blow counts or CPT tip resistance and sleeve friction values.

INTRODUCTION

Investigated as part of this study was the mechanism of liquefaction in mica-sand mixtures. Five cyclic tests were performed on sand with no mica and four tests were performed on the same sand with mica contents of 2, 5, and 10 percent mica, for a total of seventeen tests.

Each specimen was isotropically consolidated to an effective confining pressure of 940 pounds per square foot (psf), using a sufficient back-pressure to help ensure saturation. While undrained, each specimen was subjected to a sine waveform at a frequency of 1 Hz until liquefaction occurred. The deviator stresses were varied to produce different cyclic stress ratios (CSR) for each mica-sand mixture.

Test response was monitored using the data acquisition system developed by Geotechnical Consulting and Testing Systems (GCTS). Data from the tests was used to construct liquefaction curves for each mica-sand mixture. Based on the liquefaction curves, an attempt has been made to evaluate the influence of mica content on the liquefaction potential of sand.

PREVIOUS STUDIES

To date, a limited number of studies have focused on the relationship of mica content and sands, especially liquefaction behavior. Conner (2005) ran maximum and minimum density (ASTM D 4253 and D 4254), consolidation (ASTM D 2435), and direct shear (ASTM D 3080) experiments on artificially mixed mica-sand mixtures prepared with 0, 1, 2, 5, and 10 percent mica content by weight. The results from the study showed that the maximum and minimum void ratio increased with percent mica. The compression, C_c, and recompression, C_r, indices evaluated from the consolidation test results increased with percent mica. The friction angle, however, decreased with percent mica.

Another study (Harris et al., 1984a) examined the effects of mica content on engineering properties of mica-sand mixtures with 5, 10, 15, 25, and 50 percent mica content by weight. Engineering properties were examined by performing compaction tests using the miniature Harvard procedure and undrained multistage triaxial tests with differing confining pressures.

The results from the study showed the maximum compacted densities decreased approximately linearly as mica percentage increased. Harris et al. (1984a) suggested that the elastic rebound of mica particles may prevent compaction upon unloading and particles may align parallel to the shear plane during shear, resulting in low bulk shear resistance.

Triaxial test results showed that the initial tangent compression modulii decreased logarithmically with increasing mica percentage. The reduction in the compression modulii was greatest for the mica-sand mixtures with less than 10 percent mica. The frictional angle decreased logarithmically with increasing mica percentage. This property was also affected more in mica-sand mixtures with less than 10 percent mica. Based on these results, Harris et al. (1984a) suggested that mica-sand mixtures with greater than 10 percent mica behave like continuous micaceous mixtures.

An additional study performed by Harris et al. (1984b) showed as the weight fraction of platy minerals increased the friction angle and California bearing ratio (CBR) decreased and the compressibility (C_c) increased. Conversely, the friction angle and CBR increased and the compressibility decreased as the weight fraction of non-platy minerals (quartz and feldspars) increased. The results show that platy materials can collectively reduce the strength and increase the compressibility of a soil. However, platy-mineral effects may be less in soils where non-platy grains are coarse enough to form a skeletal network.

MICA-SAND MATERIAL

The micaceous material tested for this study was obtained in 25-gallon bulk samples of mica slurry purchased from Georgia Industrial Minerals. The mica slurry was dried prior to testing. Conner (2005) performed a particle size analysis on the micaceous material. The mica was found to contain 47% fines content (particle size < 0.075 mm) and had a mean grain size diameter, D_{50} of approximately 0.09. Conner (2005)

also performed a specific gravity analysis on the mica. The mica was found to have a specific gravity of 2.69.

In general, fine-grained particles have been shown to influence liquefaction resistance. Therefore, the fine grained particles of the mica soil were removed prior to mixing in an attempt to isolate the relationship of mica content and liquefaction resistance. The fines were removed by washing the mica through a #200 sieve. Once the mica was dried it was run through another #200 sieve using a sieve shaker to remove the remaining fines.

Tests for particle size analysis, specific gravity, and maximum and minimum density experiments were performed on the sand-mica mixtures in accordance with the ASTM Standard Test Method for Particle Size Analysis of Soils (D 422), ASTM Standard Test Method for Specific Gravity of Soils (D 854), ASTM Standard Test Method for Maximum Index Density of Soils Using a Vibratory Table (D 4253) and Minimum Index Density of Soils and Calculation of Relative Density (D 4254), respectively. The results are presented in below Table 1.

Table 1. Laboratory Test Results

Percent Sand	Percent Mica	Maximum Void Ratio ASTM D4253	Minimum Void Ratio ASTM D4254	Maximum Index Density ASTM D4253	Minimum Index Density ASTM D4254	Specific Gravity ASTM D854
		e_{min}	e_{max}	γ_{dmin} (pcf)	γ_{dmin} (pcf)	GS
1.00	0	0.77	0.93	88.06	95.93	2.72
0.99	1	0.81	0.97	85.94	93.62	2.71
0.98	2	0.86	1.02	83.65	91.13	2.71
0.95	5	0.96	1.14	78.87	85.96	2.70
0.90	10	1.23	1.43	69.59	75.85	2.69

SAMPLE PREPERATION

Several specimen reconstitution techniques are in use in current practice. The primary objective of all of these techniques is to replicate a uniform sand specimen at a desired void ratio. Several methods of sample placement were investigated for this study, including wet and dry pluviation, high and low frequency vibration, moist and dry rodding, and moist tamping.

During wet pluviation, Kolbuszewski (1948) showed that when mica powder was introduced to experiments vertical channels were formed by water moving up and being replaced by settling material. Therefore, the moist tamping method was chosen. The moist tamping method requires a known weight of moist soil be placed in a mold. A tamping pedestal is used to compact the soil to the desired height by moving in a circular motion.

Moist tamping method tends to produce samples that are less uniform (Castro, 1969). However, the undercompaction method attempts to correct for this nonuniformity. Undercompaction was originally recognized by Chen (1948). Ladd

(1978) incorporated the undercompaction theory into the moist tamping method. Instead of compacting each layer to the same height, the layers are compacted to a selected percentage of the layer height, with thicker layers at the bottom. In general, when sand is compacted in layers, the compaction of each succeeding layer can further densify the sand below.

Each layer is compacted to a lower density than the final desired value by a predetermined amount defined as the percent undercompaction, U_n. The percent undercompaction value for each layer is linearly varied from the bottom to the top layer, with the bottom layer having the maximum percent undercompaction, ten percent for this study, and the top layer having zero (0) percent undercompaction.

The specimens tested were approximately 2.8 inches in diameter and 6 inches in height. The desired average relative density of the specimens was 50 percent.

Deaered water was used to saturate the specimens. Incomplete saturation of a specimen can arise when air bubbles are present within the soil mass, the porous stones, between the specimen and the porous stones, or in the drainage lines and pore-water pressure measuring system. After the specimens had been constructed in the triaxial cell, a vacuum was applied to the top of the specimen to move deaered water from the bottom to the top of the specimen. In order not to over consolidate the test specimen a vacuum was applied in incremental stages while concurrently applying an equal vacuum to the triaxial cell.

After the vacuum had been released from the specimen and the triaxial cell, the bottom drainage line was connected to the volume change device. The volume change device allows the measurement of the pore-water pressure and confining pressure, which must be measured accurately when evaluating the B-value. The set-up also allows for the determination of the change in specimen volume due to consolidation.

Solution of air in the specimen or the drainage lines is accomplished by applying a back pressure through the drainage lines concurrently with an equal increase in the cell pressure. The pore-water pressure in the specimen lags behind the applied back pressure and varies with time and location within the specimen. Due to this lag, care must be taken to prevent overconsolidation of the specimen, or allowing the effective stress to approach the final desired effective consolidation stress.

Each specimen was isotropically consolidated to an effective confining pressure of 940 pounds per square foot (psf), using a sufficient back-pressure to help ensure saturation (an effective confining stress of 940 psf was chosen to model a specimen at ten feet below ground surface with a dry unit weight of 100 pcf). While undrained, each specimen was subjected to a sine waveform at a frequency of 1 Hz until liquefaction occurred. The deviator stresses were varied to produce different cyclic stress ratios (CSR) for each mica-sand mixture.

CYCLIC TRIAXIAL TESTING

The triaxial cell consists of a cell base plate, cell wall, three cell tie rods, cell top plate and cell holder ring. The triaxial cell is placed on the loading frame, which consists of a double acting loader, load cell, and a linear variable differential transformer (LVDT). The triaxial cell has two drainage lines, one through the cell

top plate and one through the cell bottom plate and the specimen has two drainage lines, one through the top platen and cell bottom plate which connects the top of the specimen to the volume change device, and one through the bottom platen and cell bottom plate which connects the bottom of the specimen to the volume change device. The confining pressure chamber is connected to the cell pressure regulator on the pressure control panel.

Test response was monitored using the data acquisition system developed by Geotechnical Consulting and Testing Systems (GCTS). The cyclic tests were set-up using the Universal module in the GCTS program and were stress controlled. The cyclic stress applied to the specimen was selected by estimating the stress level required to produce approximate cyclic stress ratios of 0.28, 0.30, 0.35, and 0.40. Therefore, cyclic deviator stresses (σ'_d) equal to approximately 526.3, 563.9, 657.9, and 751.9 psf, respectively, were used. A cyclic frequency of 1 Hz was used.

For this study, liquefaction was assumed to have occurred when the resistance to deformation was approximately zero over wide strain amplitude. In sands, this occurs when the effective confining stress is approximately zero. Therefore, recognition of liquefaction during cyclic loading of loose sands is a relatively simple matter: the development of a condition in which the pore-water pressure is approximately equal to the applied confining pressure.

CONCLUSIONS

Data from the tests was used to construct liquefaction curves for each mica-sand mixture. Based on the liquefaction curves, an attempt has been made to evaluate the influence of mica content on the liquefaction potential of sand.

A liquefaction plot shows the relationship between the cyclic stress ratio (CSR) and the number of cycles to liquefaction. The liquefaction data for the specimens tested in this study are shown on Figure 1. The semi-log graph shows CSR on the vertical axis and the approximate number of cycles to liquefaction on the horizontal axis. The horizontal axis is a logarithmic scale, while the vertical axis is normal. The cyclic stress ratio is the applied deviator stress divided by double the effective confining stress.

The general trend of a liquefaction plot is for the number of cycles to liquefaction to increase with decreasing deviator stress, or decreasing CSR. The liquefaction data shown on Figure 1 appear reasonable since the number of cycles to liquefaction increase with decreasing CSR. In theory, the lower the deviator stress, the slower the pore-water pressure build-up and the longer it takes for liquefaction to occur.

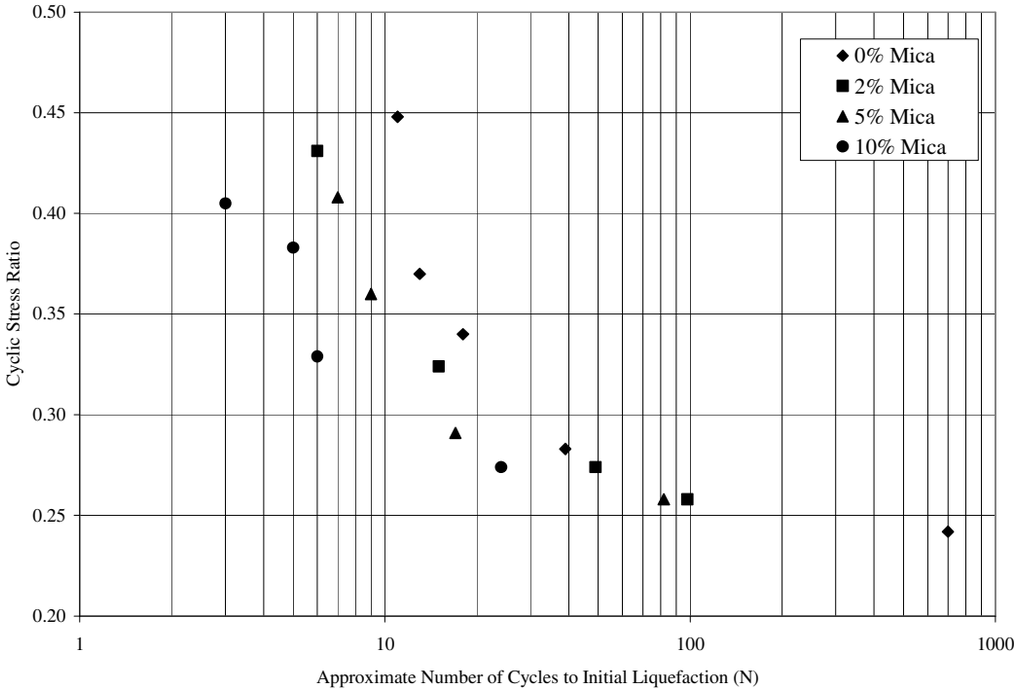


Figure 1. Liquefaction Results

The 0 percent mica specimens were more resistant to liquefaction than the two percent mica, five percent mica, and ten percent mica specimens. In general, the liquefaction resistance of the specimens decreased from the 0 percent mica to ten percent mica specimens. The difference in the liquefaction resistance of the two percent mica and five percent mica specimens appears to be less than the difference between the 0 percent mica and two percent micas specimens and five percent mica and ten percent mica specimens.

However, it should be noted that while the initial relative density for each test specimen was approximately 50 percent, the void ratios for the 0 percent mica, two percent mica, five percent mica, and ten percent mica specimens varied. The maximum and minimum void ratio increased as the mica content increased.

For this study, as the mica content increased, the maximum dry density decreased. Therefore, less mica-sand material was used for specimens with increasing mica content using the moist tamping with undercompaction procedure presented in Ladd (1978).

Since less mica-sand mixture was used to prepare the test specimens as mica content increased, the void ratio, porosity, and volume of voids also increased with mica content. Therefore, the ten percent mica specimens were placed looser than the 0 percent mica specimens, with the same approximate initial relatively density. Just as a soil with a lower blow count is more susceptible to liquefaction than a soil with a higher blow count, a looser test specimen should be more susceptible to liquefaction in the laboratory, which is shown in this study.

Harris et al. (1984a) showed that compressibility of mica quartz mixtures were markedly affected by mica. The effect of mica becomes more pronounced at higher

confining pressures due to the mobilization of frictional forces which dominate stress-strain behavior of cohesionless mica. Interparticle forces result in small particles adhering to each other. Therefore, rather than slipping into the voids and fitting into the larger particles, the small particles stick together and form loose chains and honeycomb structures with high void ratios.

Therefore, if relative density is used as an indicator of liquefaction potential for sands with varying mica contents, than a correction factor may need to be applied to the in-situ field tests, such as SPT blow count or CPT tip resistance and sleeve friction values. A method presented by the National Center for Earthquake Engineering Research (NCEER) has been used in recent practice when evaluating liquefaction susceptibility of sands with appreciable fines content. In general, a soil's resistance to liquefaction increases with increasing fines content. This study found that a soil's resistance to liquefaction decreased with increasing mica content. However, more research should be completed on this topic to provide recommendations for professional geotechnical engineers.

DISCUSSION

It is apparent from this study that mica particles retained on the #200 sieve have a significant affect on the in-situ or laboratory replicated void ratio and dry density of the soil. Further, Conner (2005) showed that mica particles not washed through the #200 sieve also have a significant affect on the void ratio and dry unit weight of the soil. In order to place the M0 specimens at the void ratio corresponding to 50 percent initial relative density for the M2, M5, and M10 specimens, the M0 specimens would have to be placed at 35.0, 7.5, and -26.2 percents relative density, respectively, when following ASTM relative density experiment procedures.

Harris et al. (1984a) showed that compressibility of mica quartz mixtures were markedly affected by mica. The effect of mica becomes more pronounced at higher confining pressures due to the mobilization of frictional forces which dominate stress-strain behavior of cohesionless mica. Interparticle forces result in small particles adhering to each other

Therefore, rather than slipping into the voids and fitting into the larger particles, the small particles stick together and form loose chains and honeycomb structures with high void ratios. Therefore, if relative density is used as an indicator of liquefaction potential for sands with varying mica contents, than a correction factor may need to be applied to the in-situ field tests, such as SPT blow count or CPT tip resistance and sleeve friction values. A method presented by the National Center for Earthquake Engineering Research (NCEER) has been used in recent practice when evaluating liquefaction susceptibility of sands with appreciable fines content.

In general, a soil's resistance to liquefaction increases with increasing fines content. This study found that a soil's resistance to liquefaction decreased with increasing mica content. However, more research should be completed on this topic to provide recommendations for professional geotechnical engineers.

REFERENCES

Castro, G. (1969). "Liquefaction of Sands," *Harvard Soil Mechanics Series No. 81*, Harvard University, Cambridge, Mass.

Chen, L.S. (1948). "An Investigation of Stress-Strain and Strength Characteristics of Cohenionless Soils by Triaxial Compression Tests," *2nd International Conference of Soil Mechanics and Foundation Engineering*, Rotterdam.

Conner, Michael, A. (2005). "Influence of Mica Content on Engineering Properties of Sand." Senior Project. California Polytechnic State University, San Luis Obispo.

Harris, W.G., Parker, J.C., and Zelany, L.W. (1984a). "Effects of Mica Content on Engineering Properties of Sand." *Soil Science Society American Journal,* 48: 501-505.

Harris, W.G., Zelanzy, L.W., Parker, J.C., Baker, J.C., Weber, R.S., and Elder, J.H. (1984b). "Engineering Properties of Soils as Related to Mineralogy and Particle-Size Distribution," *Soil Science Society American Journal*, 48: 978-982.

Kolbuszeski, J.J. (1948). "An Experimental Study of the Maximum and Minimum Porosities of Sands," *2nd International Conference of Soil Mechanics and Foundation Engineering*, Volume 1.

Ladd, R.S. (1978). "Preparing Test Specimens Using Undercompaction," *Geotechnical Testing Journal*, ASCE, 1(1): 16-23.

Effects of Stress Reduction Factors on Liquefaction Analysis

Gökçe Tönük[1] and Atilla Ansal, M. ASCE[2]

[1] Ph.D. Candidate; Bogazici University, Kandilli Observatory and Earthquake Research Institute, Earthquake Engineering Department, Cengelkoy 34684 Istanbul, Turkey; gokce.tonuk@boun.edu.tr
[2] Professor; Bogazici University, Kandilli Observatory and Earthquake Research Institute, Earthquake Engineering Department, Cengelkoy 34684 Istanbul, Turkey; ansal@boun.edu.tr

ABSTRACT: Two variables are essential for the assessment of liquefaction susceptibility of sandy soil layers; the seismic demand expressed in terms of cyclic stress ratio, CSR; and the capacity of the soil layers to resist liquefaction, expressed in terms of cyclic resistance ratio, CRR. The variation of the safety factors (CRR/CSR) with depth were determined for set of soil profiles where CSRs were calculated using stress reduction factors proposed in the literature and CRRs based on SPT blow counts. In addition, CSRs were also determined based on site response analyses. A total stress approach (Shake91) and an effective stress approach (Cyclic1D) were used for site response analysis. Safety factors for effective stress analysis were calculated using the CSRs and CRRs both based on the calculated excess pore water pressures for the analyzed soil profiles. A relationship between CSR and number of cycles with respect to excess pore water pressure ratio, r_u was derived based on previously conducted cyclic laboratory test results. In the second stage of the study, the effects of input motion on liquefaction susceptibility were evaluated. Site response analyses were conducted using 24 previously recorded acceleration time histories that are compatible with the earthquake hazard for the investigated site scaled to the same PGA. All the results are compared and the differences are discussed in terms of the final assessment of the liquefaction susceptibility.

INTRODUCTION

Liquefaction of soil layers has been a major cause of damage to soil structures, lifeline facilities and building foundations during the past earthquakes. The approach that has gained wide acceptance within the framework of urban planning is to establish liquefaction susceptibility microzonation maps to mitigate possible earthquake damage related to liquefaction (Ansal and Tönük, 2006, 2005; Ansal et al., 2004; Todorovska, 1998, Yasuda et al., 1995; Kavazanjian et al., 1985).

Two variables are essential for the assessment of liquefaction susceptibility: (1) seismic demand on the soil layers, expressed in terms of cyclic stress ratio, CSR; and (2) capacity of the soil layers to resist liquefaction, expressed in terms of cyclic

resistance ratio, CRR. Cyclic stress ratio is defined as the ratio of the average cyclic shear stress induced by earthquake excitations to the initial effective normal stress acting on the same plane (Seed and Idriss, 1971).

The site response analysis codes Shake91, originally developed by Schnabel et al. (1972) later updated by Idriss and Sun (1992) and Cyclic1D, developed by Yang and Elgamal (2001) were used to evaluate the effects of local soil stratification as well as the variation of maximum shear stress (from Shake91) and excess pore water pressure (from Cyclic1D) with depth. The peak horizontal accelerations on the ground surface were calculated from Shake91. Previously recorded hazard compatible (in terms of estimated magnitude, rupture distance and fault mechanism) acceleration records were used as outcrop motion for site response analyses. These input acceleration time histories were scaled with respect to the same peak ground acceleration estimated by the earthquake hazard study conducted for the region (Ansal et al., 2006; Durukal et al., 2006).

EVALUATION OF LIQUEFACTION SUSCEPTIBILITY

The oldest and still the most widely used approach is the simplified procedure for assessing liquefaction susceptibility proposed by Seed and Idriss (1971) based on SPT N-values and cyclic stress ratio calculated using stress reduction factor. The cyclic stress ratio, CSR, is expressed as;

$$CSR = \frac{\tau_{av}}{\sigma_v'} = 0.65 \frac{a_{\max}}{g} \frac{\sigma_v}{\sigma_v'} r_d \tag{1}$$

where τ_{av} = average cyclic shear stress amplitude, a_{max}= peak horizontal acceleration on the ground surface; g = acceleration of gravity; σ_v = total vertical overburden stress; σ'_v = effective vertical overburden stress; r_d = stress reduction factor.

There have been various studies concerning the definition of stress reduction factor in the literature (Cetin, et al., 2004; Idriss and Boulanger, 2003; Youd et al., 2001; Liao and Whitman, 1986). In most of these studies, different formulations were proposed to calculate the variation of cyclic stress ratio that would be induced by the design earthquake and almost all of them are only dependent on the depth in the soil profile. In the recent formulation proposed by Cetin et al. (2004), the effects of other factors such as peak acceleration on the ground surface, magnitude of the design earthquake, and soil stiffness at the top 12m in addition to the depth from the ground surface were considered as factors controlling the variation of stress reduction factor or in more general terms variation of maximum shear stresses with depth. Some of these different definitions for the stress reduction factor, r_d, may be given as;

a) by Liao and Whitman (1986)

$$\begin{aligned} r_d &= (1.00 - 0.00765z) \qquad for \qquad z \le 9.15m \\ r_d &= (1.174 - 0.0267z) \qquad for \qquad 9.15m < z < 23m \end{aligned} \tag{2}$$

b) by Idriss (1999) and Idriss and Boulanger (2003)

$$
\begin{aligned}
&Ln(r_d) = \alpha(z) + \beta(z)M \qquad for \qquad z \le 34m \\
&\alpha(z) = -1.012 - 1.126\sin\left(\frac{z}{11.73} + 5.133\right) \\
&\beta(z) = 0.106 + 0.118\sin\left(\frac{z}{11.28} + 5.142\right) \\
&r_d = 0.12\exp(0.22M) \qquad for \qquad z > 34m
\end{aligned}
\tag{3}
$$

c) by Youd et al. (2001)

$$
r_d = \frac{(1.00 - 0.4113z^{0.5} + 0.04052z + 0.001753z^{1.5})}{(1.00 - 0.4177z^{0.5} + 0.05729z - 0.006205z^{1.5} + 0.00121z^{2})} \tag{4}
$$

d. by Cetin et al. (2004)

$$
r_d = \frac{\left\{1.00 + \dfrac{-23.013 - 2.949PGA/g + 0.999M + 0.0525V_{s12}}{16.258 + 0.201e^{0.341(-z+0.0785V_{s12}+7.586)}}\right\}}{\left\{1.00 + \dfrac{-23.013 - 2.949PGA/g + 0.999M + 0.0525V_{s12}}{16.258 + 0.201e^{0.341(0.0785V_{s12}+7.586)}}\right\}} \tag{5}
$$

where, z is the depth below ground surface in meters, velocity (V_{s12}) is the average shear wave velocity at top 12m in m/s, PGA is peak horizontal acceleration, M is the magnitude.

In the first stage of the study a set of borings selected from a previously performed microzonation project (Ansal et al., 2005) were analyzed to observe the variation of safety factors (CRR/CSR) with depth based on CSRs with different definitions for r_d and based on CSRs obtained from two different site response analyses codes. CRR values were calculated based on SPT blow counts according to Youd et al. (2001). Earthquake hazard compatible three acceleration records were used as outcrop motion for the site response analyses. These records were scaled with respect to same peak ground acceleration determined by the earthquake hazard study conducted for the region. The CSR variations were calculated as the average of the CSRs from three site response analyses.

The CSRs calculated by the procedure suggested by Youd et al. (2001) depend only on depth of the element and ground water level and incapable to account for the changes in the soil profile. Depending on the soil stratification and stiffness of the soil layers the variation of CSRs obtained by site response analysis could be considered more realistic (Figure 1).

Using Shake91 analysis results, CSRs were calculated as the ratio of average shear stress over effective overburden stress, $CSR = 0.65\tau_{\max}/\sigma_v^{'}$ where the variation of $\tau_{\max}$ with depth is obtained from the output of the analysis.

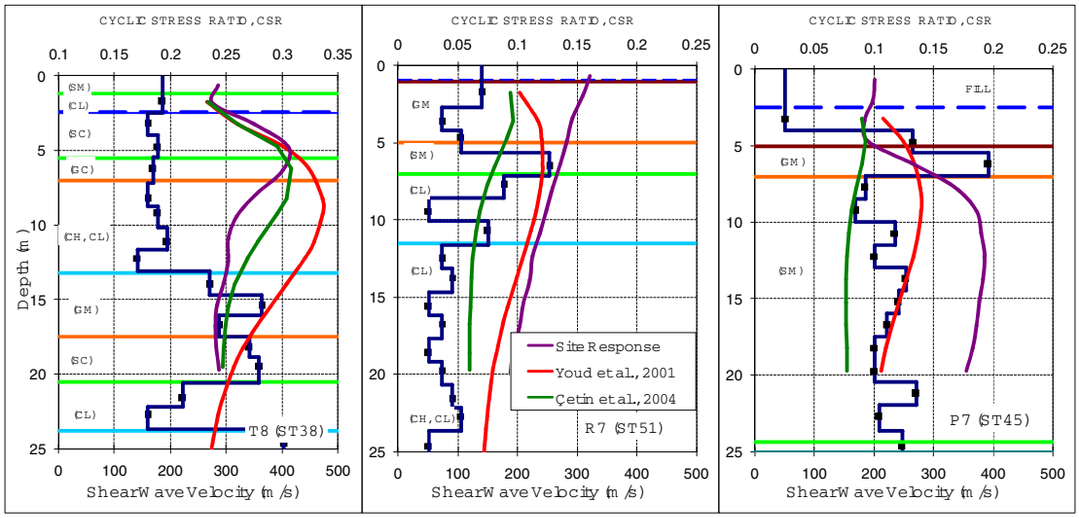


FIG. 1. CSR by site response analyses and by the simplified procedures according to Youd et al. (2001) and Cetin et al. (2004)

Cyclic1D (Yang and Elgamal, 2001) is a nonlinear Finite Element program for one-dimensional site response analysis and liquefaction simulations. CSRs were evaluated from Cyclic1D based on the excess pore water pressure ratios, r_u. The program gives as output the variation of excess pore water pressure with depth. Factor of safety is defined as the ratio of CSR for $r_u = 1$, which is assumed as the CRR of the soil sample, over CSR for r_u generated during excitation. For $r_u<1.0$ safety factor becomes larger than 1.0, which means lower liquefaction susceptibility, FS=1 implies the initiation of liquefaction since at that moment excess pore water pressure is equal to initial effective stress, i.e. $r_u = 1$. In order to derive a relationship between CSR and r_u, previously performed cyclic simple shear test results for the soil samples of sand with 11% of fines content were used (Ansal and Erken, 1990, Erken and Ansal, 1994). The tests were performed for three different shear stress amplitudes corresponding to CSR values of 0.479, 0.284 and 0.209. The test data were used to derive a relationship between r_u and number of cycles as shown in Figure 2. The regression coefficients being relatively high indicate that the empirical modeling is sufficiently accurate.

For r_u changing from 0.4 to 1.0, numbers of cycles were calculated from the equations obtained for three CSR values and these numbers of cycles were plotted versus CSRs for the defined r_u range (Figure 3). A new equation (6) was derived from these curve fits between CSR and number of cycles based on excess pore water pressure ratio.

$$CSR = \left(0.5032 \cdot \ln r_u + 0.7752\right) \cdot N^{\left(0.5295 \cdot \ln r_u - 0.2122\right)} \tag{6}$$

This equation was used to calculate CSRs for r_u obtained from Cyclic1D results, for a constant number of cycles, N = 15.

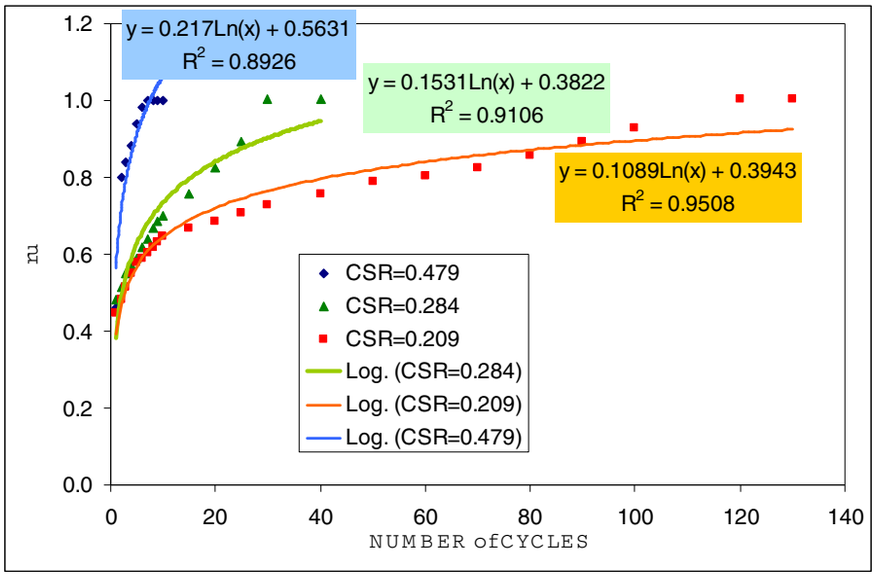


FIG. 2. Simple shear test results on a sand sample with 11% FC for varying CSR amplitudes and the regression equations that fit the data

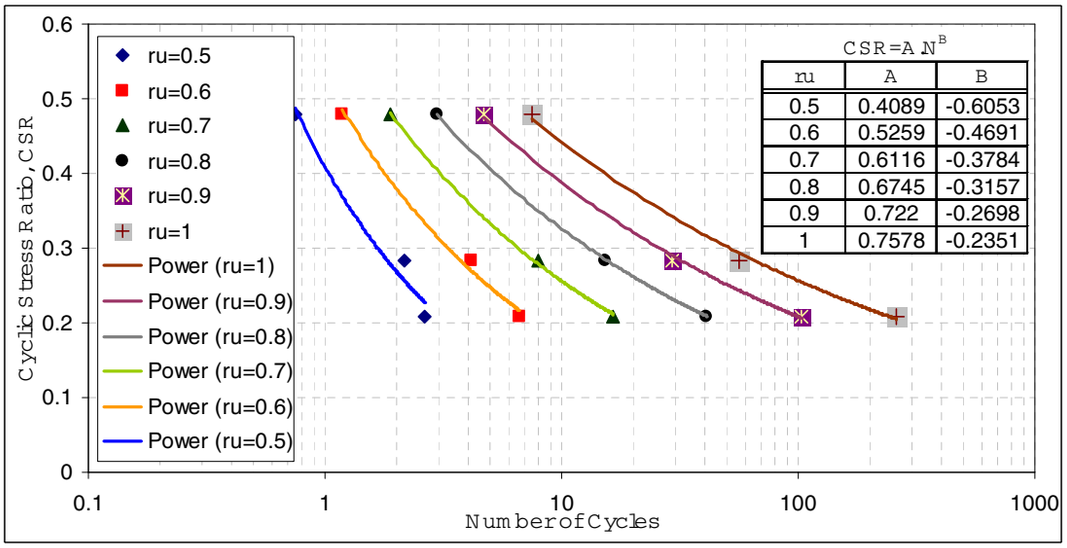


FIG. 3. CSR versus number of cycles from simple shear test results on a sand sample with 11% FC and the regression equations that fit the data

It was interesting to observe the variation of safety factors with respect to liquefaction susceptibility calculated using the r_d formulation proposed by Youd et al. (2001) and Cetin et al. (2004) in comparison to site response analyses as shown in Figure 4 for the selected soil profiles. Even though the differences in the calculated CSR variations appear significant, these differences are not reflected in the safety factor variations except in one case (Boring P7) where the safety factors calculated by site response analysis and using stress reduction factors are radically different.

In Figure 4, the red and green shaded areas are the liquefied and not liquefied areas obtained from the nonlinear analysis (Cyclic1D). The safety factors found as explained previously based on r_u are also plotted on the figure. It should be noted that FS=1 for Cyclic1D results should be considered as liquefaction due to the definition. All the results obtained based on different definitions of r_d and based on Shake91 could be interpreted with respect to nonlinear analysis results that are assumed capable of modeling liquefaction (Elgamal and Yang, 2002) even though the results of Cyclic 1D still require some more verification. The safety factors calculated by site response analysis are closer to Cyclic 1D results than the safety factors using stress reduction factors.

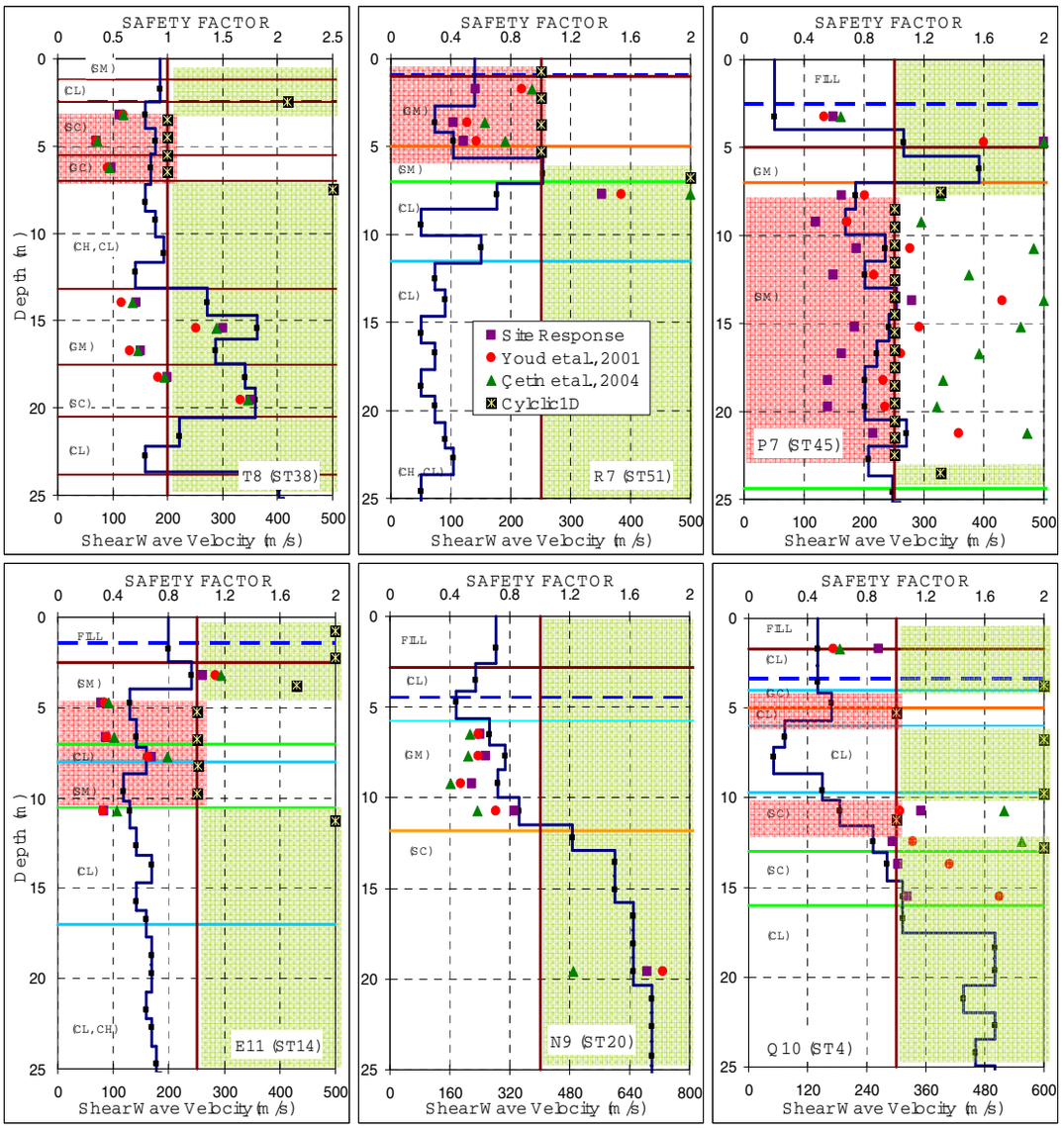


FIG. 4. Safety factors with respect to liquefaction susceptibility by site response analyses (Shake and Cyclic1D) and by the simplified procedures according to Youd et al. (2001) and Cetin et al. (2004)

In the second stage of the study, the effects of input motion characteristics on liquefaction susceptibility were evaluated. In this case as shown in Figure 5, the variation of SPT blow counts as well as shear wave velocity profile determined by PS Logging in-hole seismic survey was utilised for the selected soil profile. Site response analyses were conducted using 24 previously recorded acceleration time histories that are compatible with the earthquake hazard for the investigated site. All of these acceleration records were scaled to the same rock outcrop peak ground acceleration estimated by the earthquake hazard study for the region. The variations of stress reduction factor with depth back calculated from the site response analyses are also shown in Figure 5. It is interesting to observe that even though all the real records selected are compatible with the earthquake hazard for the investigated site and they were all scaled to the same peak ground acceleration, the calculated cyclic stress ratio CSRs and stress reduction factors show some variability with respect to input motion.

The variation of cyclic stress ratios calculated by using r_d proposed by Youd et al. (2001), Liao and Whitman (1986), Idriss (1999) and by site response analysis (Shake91) using DZCew (Duzce earthquake 11/12/1999) and 375ew (Kocaeli earthquake 8/17/1999) acceleration time histories that yielded the highest and lowest r_ds, respectively (Figure 5b) are given in Figure 6(a) along with the respective safety factors calculated. The variation of safety factors calculated based on site response analyses for sandy soil layers given in Figure 5(a) for 24 different input motions are shown in Figure 6(b) with respect to the variation of SPT blow counts.

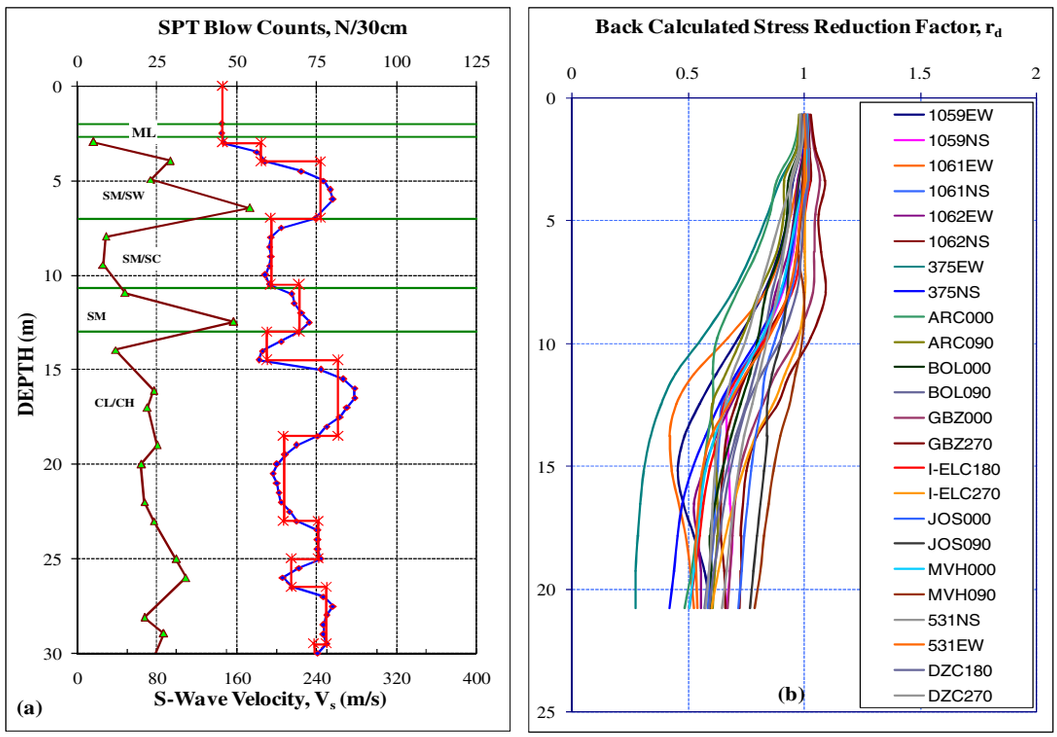


FIG. 5. (a) A soil profile and (b) the variation of CSR with depth with respect to input acceleration records

It is interesting to observe that in terms of safety factors, the end results do not reflect the effects of the variability observed in CSRs as shown in Figure 6(a) or in stress reduction factors as shown in Figure 5(b) on the safety factors calculated shown in Figure 6(c).

There is a variability concerning the peak ground accelerations calculated by site response analyses which generates the variability range. For example in the case of 24 site response analyses conducted for the soil profile given in Figure 5(a), the calculated PGAs on the ground surface varied between the maximum of 0.738g and minimum of 0.31g, with the average of 0.52g and standard deviation of 0.13g.

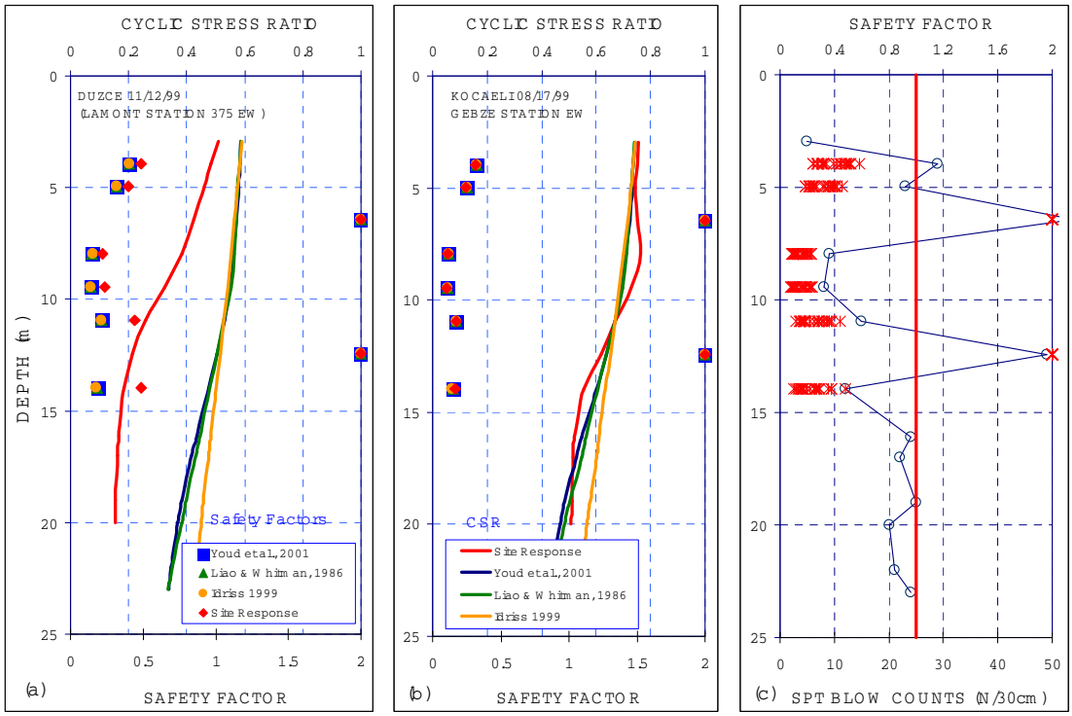


FIG. 6. (a,b)Variation of CSRs and Safety Factors for liquefaction susceptibility with respect to different formulations for two acceleration records (c) Variation of Safety Factors for liquefaction susceptibility based on 24 site response analyses

CONCLUSIONS

The evaluation of liquefaction susceptibility of soil layers in nature for engineering purposes is performed based on empirical procedures developed using Standard Penetration Test results obtained by in-situ testing. One of the most popular procedures was originally developed by Seed and Idriss (1971) and later summarized by Youd et al. (2001). Two variables are required for the assessment of liquefaction resistance of sandy soil layers; the seismic demand expressed in terms of cyclic stress ratio, CSR; and the capacity of the soil layers to resist liquefaction, expressed in terms

of cyclic resistance ratio, CRR. The variation of the safety factors with depth were determined for set of boreholes where CSR is calculated using stress reduction factors proposed by Youd et al.(2001) and Cetin et al. (2004) and CRR based on SPT blow counts. In addition CSRs were calculated based on site response analyses (Shake91 and Cyclic1D). As expected all procedures gave slightly different results. The differences are not consistent and it depends very much on the properties of the soil stratification, shear wave velocity profiles and peak ground accelerations. Assuming that site response analyses would yield more reliable results, the two procedures suggested by Youd et al. (2001) and Cetin et al. (2004) yielded results on the unsafe side. Thus even though r_d procedures to estimate the variation of CSR with depth are simpler and could be applied much faster, the calculated safety factors may not always be on the safe side and it would be preferable to base the final decision concerning liquefaction susceptibility after one dimensional site response analysis.

The effects of input motion characteristics on liquefaction susceptibility were evaluated based on site response analysis using seismic hazard compatible 24 previously recorded acceleration records scaled to same peak ground acceleration. The results indicate that input motion characteristics may be important if only few acceleration records are used for liquefaction assessment and thus it would be preferable to conduct large number site response analysis and use the average of all site response results.

REFERENCES

Ansal, A. and Tönük, G. (2006). "Evaluation of Liquefaction Susceptibility for Microzonation and Urban Planning." *Proceedings of Int. Conf. on Geohazards - Technical, Economical and Social Risks*, Lillihammer, Norway.

Ansal, A, Durukal E, Tönük G (2006). "Selection and Scaling of Real Acceleration Time Histories for Site Response Analyses." *Proc. of ETC12 Workshop*, Athens, Greece.

Ansal, A. and Tönük, G. (2005). "Liquefaction Susceptibility and Microzonation." *Proceedings of Int. Con. on Problematic Soils*, Eastern Mediterranean University, Famagusta, N. Cyprus.

Ansal, A., Tönük, G., and Bayrakli, Y. (2005). "Microzonation for Site Conditions for Bakirköy, Gemlik, Bandırma, Tekirdağ, Eskisehir and Körfez, Microzonation and Hazard Vulnerability Studies for Disaster Mitigation in Pilot Municipalities." *Project Report*, Bogazici Uni., Kandilli Observatory and Earthquake Engineering Research Institute, Turkey.

Ansal, A., Erdik, M., Studer, J., Springman, S., Laue, J., Buchheister, J., Giardini, D., Faeh, D., Koksal, D. (2004). "Seismic Microzonation for Earthquake Risk Mitigation in Turkey." *Proceedings of 13th World Conference of Earthquake Engineering*, Paper.1428. Canada.

Ansal, A., Erken, A. (1990) "Liquefaction Potential of Silty Sand Deposits." *Proc. of 9th European Conference on Earthquake Engineering*, Moscow, 4B, 71-80.

Cetin, K.O., Seed, R.B., and Der Kiureghian, A., Tokimatsu, K., Harder, L.F:, Kayen, R.E. Moss, R.E.S. (2004). "Standard penetration Test-Based Probabilistic and Deterministic Assessment of Seismic Soil Liquefaction Potential." *J. Geotechnical*

& Geoenv. Engrg., Vol. 130(12): 1314-1340.

Durukal,E., Ansal,A., and Tönük,G. (2006). "Effect of Ground Motion Scaling and Uncertainties in Site Characterisation on Site Response Analyses." *Proceedings of the 100th Anniversary Earthquake Con. Commemorating the 1906 San Francisco Earthquake*, USA.

Elgamal, A. and Yang, Z. (2002). "Computational Modeling of Liquefaction-Induced Deformations. " *Proceedings of the 12th European Conference on Earthquake Engineering,* Paper reference:648.

Erken, A., Ansal, A. (1994). "Liquefaction Characteristics of Undisturbed Sands. Performance of Ground and Soil Structure During Earthquakes." *13th ICSMFE*, New Delhi, 165-170.

Idriss, I. M. and Boulanger, R. W. (2003). "Semi-Empirical Procedures For Evaluating Liquefaction Potential During Earthquakes." *Proceedings of the 11th ICSDEE*: 32 – 56.

Idriss, I.M. (1999). "TRB Workshop on New Approaches to Liquefaction Analysis." *Publ. No. FHWA-RD-99-165*, Transportation Research Board (TRB), Federal Highway Administration, Washington, D. C. (on CD-ROM).

Idriss, I. M. and Sun J. I. (1992) "Shake91, A Computer Program for Conducting Equivalent Linear Seismic Response Analysis of Horizontally Layered Soil Deposits." Modified based on the original SHAKE program by Schnabel, Lysmer and Seed, 1972.

Kavazanjian, E. Jr., Roth, R.A., and Echezuria, H. (1985). "Liquefaction potential mapping for San Francisco." *J. Geotech. Eng. ASCE*, Vol. 111(l): 54-76.

Liao, S.S.C. and Whitman, R.V. (1986). "Overburden correction factor OS for SPT in sand." *J. Geotech. Eng. ASCE*, Vol. 112(3): 373-377.

Schnabel, P.B., Lysmer, J. and Seed, H.B. (1972). "Shake-A Computer Program for Earthquake Analysis of Horizontally Layered Sites." *EERC Report No.72-12*, Uni.of Cal.,Berkeley.

Seed, H.B., Idriss, I.M. (1971). "Simplified Procedure for Evaluating Soil Liquefaction Potential." *Journal of the Soil Mechanics and Foundations Div. ASCE*, Vol. 97: 1249-1273.

Todorovska, M.I. (1998). "Quick reference liquefaction opportunity map for a metropolitan area." *Proceedings of 3rd ASCE Speciality Conf. on Geotech. Earthquake Eng. Soil Dynamics*, ASCE Spl. Pub. No., 75(1): 116-127.

Yasuda,S., Negishi, S., Yoshikawa, Y., and Moromoto, I. (1995). "Microzonation for liquefaction to detect liquefaction sites immediately aftere an earthquake." *Proceedings of the 5th Int. Conference on Seismic Zonation*, Nice, FRANCE.

Yang, Z. and Elgamal, A. (2001). "Cyclic1D Pre-release Beta Version (November 2001)." *http://cyclic.ucsd.edu*.

Youd, T.L., Idriss, I.M., Andrus, R.D., Arango, I., Castro, G., Christian, J.T., Dobry, R., Finn, L.W.D., Harder Jr., L.F., Hynes, M.E., Ishihara, K., Koester, J.P., Liao, S.S.C., Marcuson III, W.F., Martin, G.R., Mitchell, J.K., Moriwaki, Y., Power, M.S., Robertson, P.K., Seed, R.B., Stokoe II., K.H. (2001). "Liquefaction Resistance of Soils: Summary Report from the 1996 NCEER and 1998 NCEER/NSF Workshops on Evaluation of Liquefaction Resistance of Soils." *J. Geotechnical & Geoenv. Engrg.*, Vol. 127(10).

Influence of Aging on Liquefaction Potential: Preliminary Results

Robb Eric S. Moss[1], Ph.D., P.E., M.ASCE, David M. Thornhill[2],
Ashley I. Nelson[2], S.M.ASCE, and Darcie A. Levulett[2], S.M.ASCE.

1. Asst. Prof., Dept. Civil and Environmental Engineering, Cal Poly San Luis Obispo, CA 93407. email: rmoss@calpoly.edu phone: 805-756-6427
2. Researcher, Dept. Civil and Environmental Engineering, Cal Poly San Luis Obispo, CA 93407.

ABSTRACT

This paper describes laboratory-based liquefaction testing of aged soil deposits to address the need for quantifying the influence of aging on liquefaction potential. The *in situ* aging of liquefiable soil deposits has been qualitatively shown to result in an increase in liquefaction resistance. For example, Pleistocene age sandy soils will generally have a higher resistance to seismic induced liquefaction than similar sandy soils of Holocene age. However, a quantitative measure of this liquefaction resistance increase for use in liquefaction analysis is still unrealized. Cyclic simple shear testing is used in this study to systematically quantify the influence of aging on liquefaction potential. The influence of aging is then measured as the difference between liquefaction triggering of an aged sample versus a similar reconstituted sample. Uncertainty in the field and lab testing results is explicitly defined in a probabilistic manner so that the age-based correction factor can be used in performance-based analysis. Preliminary results from this ongoing research project are presented.

INTRODUCTION

The potential for soil liquefaction is commonly assessed using empirical methods that are based on post-earthquake field case histories of liquefaction/nonliquefaction (Youd et al. 2001; Cetin et al. 2004; Moss et al. 2006). The existing worldwide databases of SPT- and CPT-based post-liquefaction case histories (Cetin et al. 2000; Moss et al. 2003) are limited to soil deposits of late-Holocene age, where the Holocene defines the time span from the present to the last 11,500 years. In practice it is not uncommon to encounter soils with characteristics that fall outside the existing case history database. This research project addresses a particular group of outliers, sandy soils that are older than late-Holocene age. These aged soil deposits are commonly found in active tectonic regions, and some means of quantifying the liquefaction resistance is urgently needed.

In general, soils older than late-Holocene age have shown higher resistance to liquefaction due to aging effects. As stated in the summary report of the NCEER

workshop on liquefaction (Youd et al. 2001), "Although qualitative increases in liquefaction resistance have been well documented, insufficient quantitative data have been assembled from which correction factors for age can be defined." As a result, it is difficult to accurately assess the liquefaction potential of soils older than late-Holocene in age. This is reason for concern in metropolitan areas, such as San Francisco and Los Angeles, where portions of the built environment are located on various soil deposits older than late-Holocene and are expected to experience high levels of seismic ground shaking.

Research into the influence of aging on liquefaction has resulted in inconclusive and sometimes contradictory results. There is agreement that soil aging results in increased penetration and cyclic resistance but what causes this increase and how this increase translates to liquefaction potential is currently uncertain. Mechanisms that have been suggested include both mechanical mechanisms such as particle interlocking/rearrangement (Schmertman 1991), and chemical mechanisms such as the precipitation of silica or similar bonding agents (Joshi et al. 1995).

There have been generally two paths of research, one path addressing short-term aging (10^{-2} to 10^{1} years) usually related to blasting or ground densification procedures (Mitchell and Solymar 1984; Hryciw 1986; Schmertman et al. 1986; Mesri et al. 1990; Charlie et al. 1992; Joshi et al. 1995). The other path evaluating long-term aging (10^{1} to 10^{6} years) related to naturally buried and exhumed deposits (Arango et al. 2000; Arango and Migues 1996; Olson et al. 2001; Youd and Hoose 1977; Lewis et al. 1999).

These two paths are complimentary and the results can be combined to bridge between short-term and long-term aging (Kulhawy and Mayne 1990), however there is currently not enough data for a quantitative analysis. Leon et al. (2005) compiled an age-based correction factor for liquefaction analysis using existing data. This study presented an interesting approach but was again limited by the lack of data.

Lab testing has been inconclusive in determining the nature of soil aging. Joshi et al. (1995) explored both mechanical and chemical mechanisms of soil aging and produced some useful results. Yet Baxter and Mitchell (2004) have shown that all manner of tests to mimic the aging process in a laboratory environment fail to systematically capture the phenomena that cause aging effects (e.g., cementation, soil fabric, influence of pore fluid chemistry, particle bonding, etc.).

In summarizing existing research results; (a) lab testing that mimics the effects of aging have been inconclusive, (b) lab testing of field-aged samples has provided useful data but the database is limited, and (c) the tests that have been conducted to date neglect the error sources to the detriment of the study. This study addresses items (b) and (c), and will eventually provide a quantified answer to how aging influences liquefaction.

RESEARCH METHODOLOGY

Aged deposits of liquefiable material generally exhibit some "cementation" thereby making these deposits candidates for undisturbed block sampling [note: in this study the term "cemented" will be used to describe a mechanical grain to grain contact that allows a block of dry sandy soil to remain intact when unconfined therefore maintaining the *in situ* void ratio and soil fabric]. Here we retrieve and test block soil samples at selected sites and evaluate penetration resistance in the field and in the lab.

A number of selected field test sites have been identified that are underlain by potentially liquefiable soils exhibiting a wide age range, generally from early-Holocene to early-Miocene (10^4 to 10^7 years), and are accessible and amenable to the proposed field testing and block sampling. To date one site has been fully explored. The following is a general list of the steps performed in this research;

- At each site a block sample of the aged soil is acquired for laboratory testing.
- Field measurement of the *in situ* soil resistance is made using the Cone Penetration Test (CPT) in the immediate vicinity of where the block sample is acquired. The representative mean and standard deviation of the CPT tip resistance are calculated.
- In the lab Cyclic Simple Shear (CSS) tests are performed on hand carved samples to estimate the liquefaction resistance of the aged soil deposit.
- CSS tests are then performed on reconstituted samples at e_{min} to evaluate the difference in liquefaction resistance between the aged soil and a freshly deposited soil of the same source material and density.
- Estimates of the representative mean and standard deviation of the CPT tip resistance for the reconstituted soil are made using a theoretical model based on cavity expansion theory (Salgado and Randolph 2001). The model is calibrated to the site specific soil using fundamental soil properties measured in the lab.
- By pairing the CPT tip resistance measurements to the CSS results we arrive at an indexed measure of the change in liquefiability with age.
- Uncertainty in the age date, number of cycles to liquefaction, CPT index measurements, and other variables are explicitly quantified so that the age-based correction factor can be presented probabilistically for use in performance-based engineering.

LAB EQUIPMENT AND TESTING

A Cyclic Simple Shear (CSS) device (left picture in Figure 1) is used in this study to perform liquefaction tests on the “cemented” and reconstituted sand samples. Our cyclic simple shear testing procedures and protocols closely follow the work by Kammerer et al. (2001) and Wu et al. (2003) which built on the work of previous researchers (Bjerrum and Landva 1966; Boulanger et al. 1993; Franke et al. 1979; Ishihara and Yamazaki 1980; Roscoe 1953). Where we diverge from the previous research is in addressing specifics that pertain to “cemented” sands. Additional guidance was provided by Dr. Mike Riemer at U.C. Berkeley who has experience testing this type of material. The liquefaction testing is performed using NGI-type wire reinforced membranes. These membranes ensure consistent effective lateral stresses and good compliance with zero lateral strain boundary conditions. Back saturation is achieved by repeated flushing with de-aired water. A B-value of 0.96 is achieved before liquefaction testing can proceed.

Liquefaction can be ambiguous when defined by the excess pore pressure ratio, for example in some tests reduction of shear strength begins much prior to achieving 100% excess pore pressure ratio. In keeping with the procedures used by Kammerer et al. (2001) we use a strain threshold to define the point of soil deformation where consistent measurements can be made. In this study the strain threshold is defined by 5% peak to peak shear strain, or 2.5% double amplitude shear strain for symmetric failure. This

provides a consistent threshold to compare different materials being subjected to undrained cyclic simple shear loading. This threshold is the lower bound at which liquefaction initiates as indicated by the rapid increase in shear strains and excess pore pressures.

We have developed a technique for hand carving the "cemented" samples using a template and a high speed drill that provides tight control on the quality of our carved test specimens. The right picture in Figure 1 shows the carving station that consists of a base for mounting the sample and CSS platen, a turntable to rotate the specimen, and a frame-mounted high speed drill for controlled carving of "cemented" sand specimens.

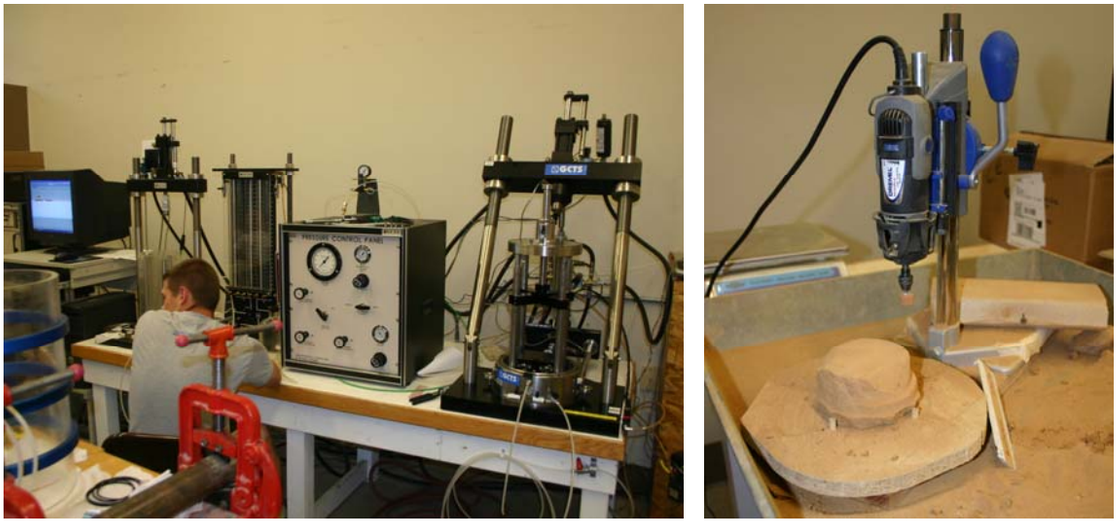


Figure 1. The left photo shows the CSS device with the cell wall removed awaiting a new sample. The right photo shows the hand-carving apparatus used to prepare "cemented" sand samples.

PRELIMINARY RESULTS

The initial results shown in this paper are for potentially liquefiable material hereafter called the Los Osos tan deposit. This material is a relatively clean medium sand (USCS class SP with a range of 5% to 9% fines content) that because of the aging process behaves as a "cemented" material. A weak hydrochloric acid solution was used to verify that there is no calcium bonding between the sand grains, and when a dry sample of this material is placed in water it completely disassociates confirming that there is no bonding other than tight grain packing that holds the material together. Shown in Figure 2 are the results from a single typical liquefaction test of a sample of "cemented" Los Osos tan deposit. This test was conducted at a cyclic stress ratio (CSR=τ/σ_v') of 0.35.

These four plots from upper left in a counter-clockwise direction are: normalized effective vertical stress versus normalized shear stress, shear strain versus normalized shear stress, shear strain versus number of cycles, and excess pore pressure ratio versus number of cycles. These results provide one data point for the relative age of the material and the number of cycles to achieve liquefaction. As discussed previously the threshold strain is defined as 5% peak to peak, or equivalently 2.5% double amplitude shear strain.

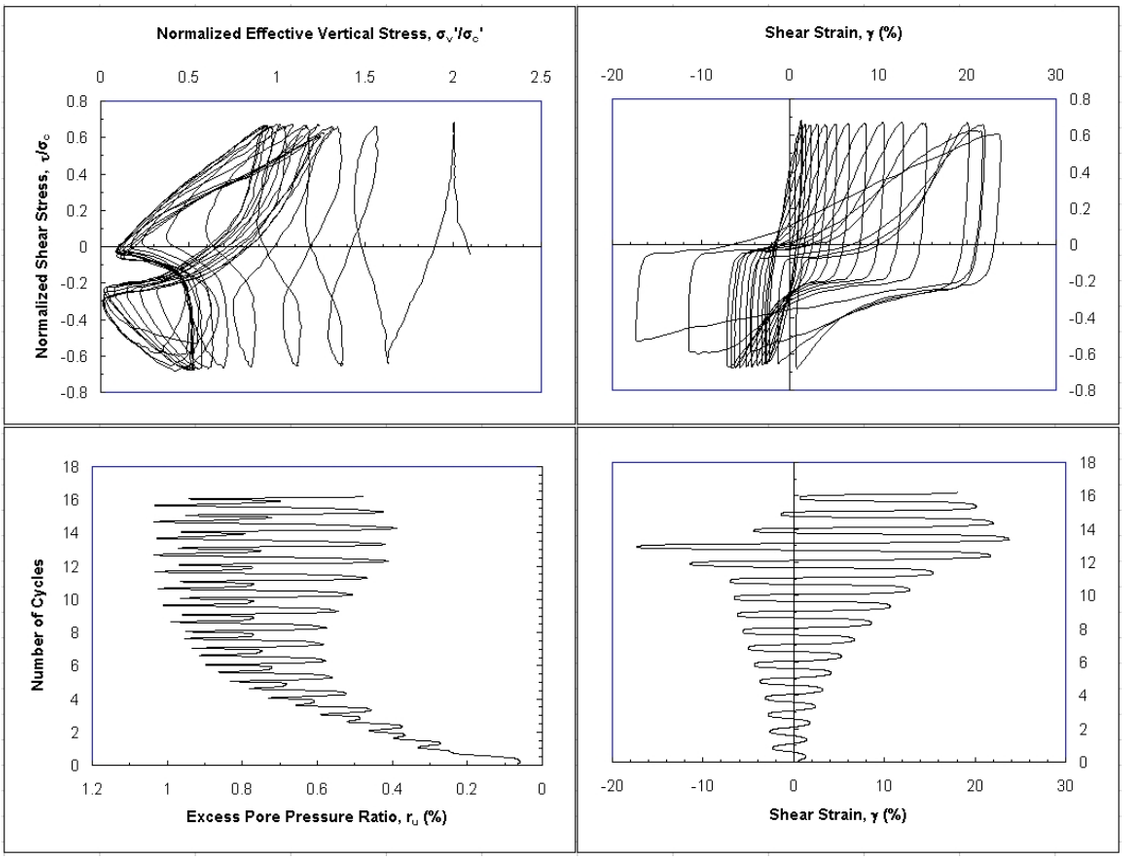


Figure 2. Typical CSS test results for a "cemented" sand deposit. These plots from upper left in a counter-clockwise direction show: normalized effective vertical stress versus normalized shear stress, shear strain versus normalized shear stress, shear strain versus number of cycles, and excess pore pressure ratio versus number of cycles (Los Osos tan specimen, CSR 0.33, σ_{vo}'=100 kPa).

Figure 3 shows conceptually how individual CSS tests are used to develop the relationship between age and cyclic resistance. A number of tests will be run on "cemented" and reconstituted specimens to generate a pair of CSR versus number-of-cycles-to-liquefaction curves for this particular material. The resulting difference between these two curves, when combined with a correlation between magnitude and equivalent number of cycles, will provide a magnitude specific measurement of the increase of liquefaction resistance as a function of the age of the material.

The upper plot in Figure 3 shows the results of CSS liquefaction testing for one "cemented" sample. The number of cycles to liquefaction is where 5% peak to peak shear strain amplitude is achieved for a given CSR. This results in one data point on the middle plot. After testing "cemented" and reconstituted samples at different levels of CSR, curves can be fit to the data to define the trends of both. The mean and standard deviation of the difference between the two trends is used to define the additional liquefaction resistance as a function of the deposits age. This can be taken at 15 cycles (which is roughly correlated to M_w=7.5) to create a data point on the lower plot. After testing many aged soil deposits, the data points and the associated uncertainties can be

used to develop the age-based correction for liquefaction triggering. This correction factor can be expressed as a ratio of CRR (CSR at liquefaction) for the "cemented" and reconstituted samples, or equivalently as a ratio of tip resistance.

To date a suite of tests have been performed on the Los Osos tan deposit. Figure 4 shows the CSS liquefaction results for the "cemented" and reconstituted specimens. A linear trend is fit to each data set using regression. The figure shows the mean and ± one standard deviation lines. The age of the Los Osos tan deposit is estimated from detailed geologic mapping of the area (Alterman et al. 1994), with this particular "cemented" sand unit corresponding to an age of late-Pliocene.

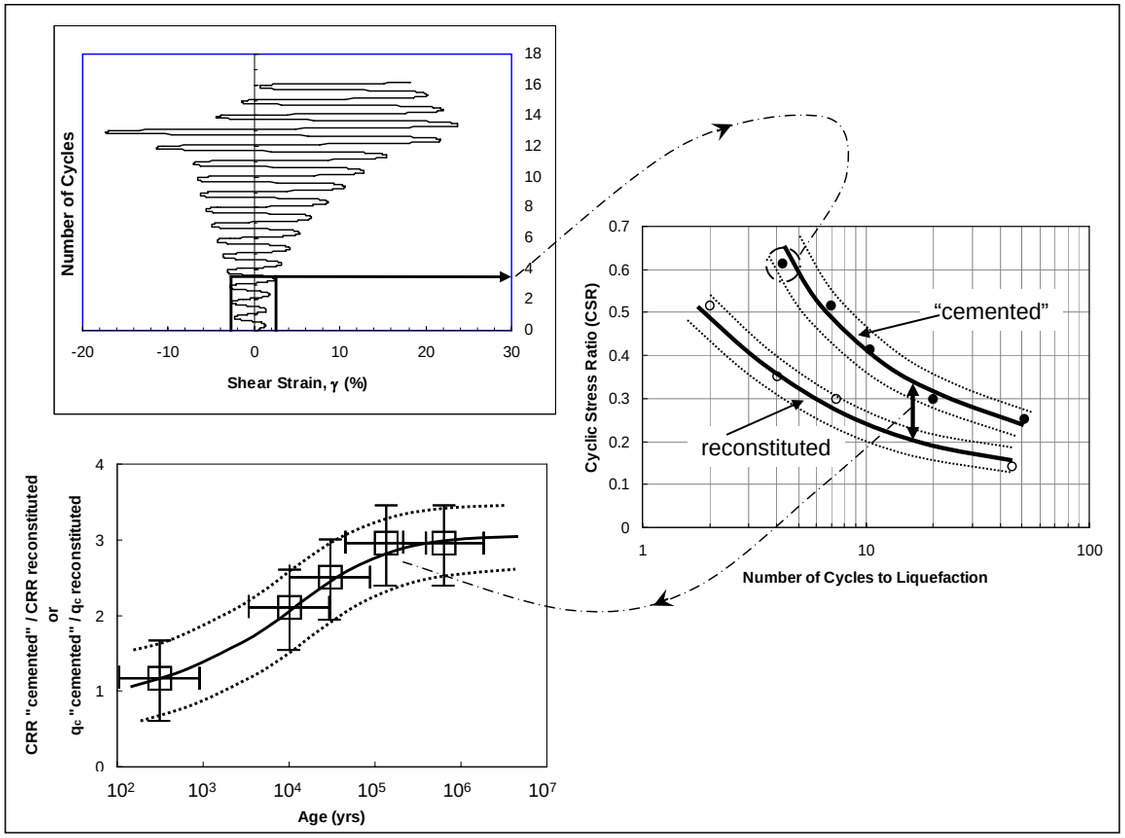


Figure 3. This shows conceptually the research goal, progressing from results of a single liquefaction test (upper plot), to the results from many liquefaction tests on a single aged soil deposit (middle plot), to the final results which shows the increased liquefaction resistance between "cemented" and reconstituted deposits for several aged soil deposits expressed as a ratio of CSR increase or alternatively q_c (CPT tip resistance) increase (lower plot).

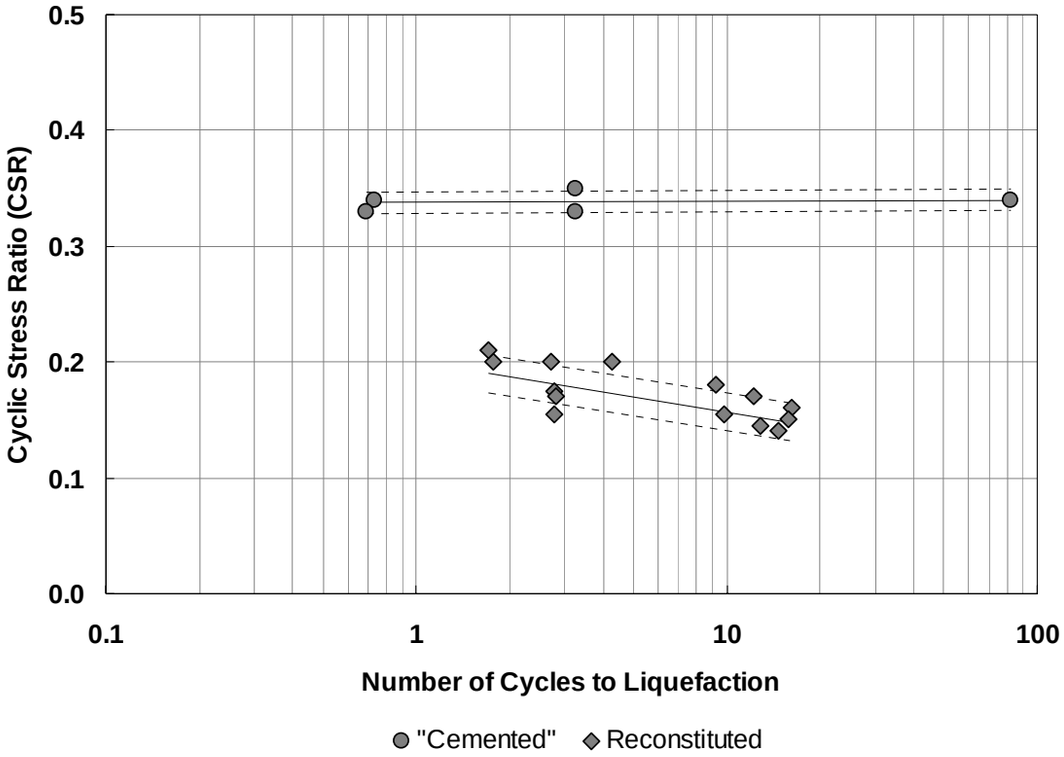


Figure 4. Preliminary results of the Los Osos tan deposits. The circles show the CSS results of the "cemented samples, the diamonds show the reconstituted specimen. Linear trend lines were fit to the results using least squares regression, and the mean and one sigma lines are shown.

This ratio of CRR for the "cemented" versus the reconstituted samples is plotted against the age of the deposit on Figure 5 resulting in one cumulative data point with the associated uncertainty. This data point is plotted with results from Arango and Migues (1996) for comparison. As research progresses CPT tip resistance will be added to Figure 5 showing the ratio of the field measured tip resistance of the "cemented" material with respect to the cavity expansion estimated tip resistance of the reconstituted material. The long-term goal of this research is to populate Figure 5 with as many data points as feasible to better quantify the influence of aging on liquefaction potential.

FUTURE RESEARCH

In the coming year two more sites will visited, block samples will be acquired, and lab testing will commence to generate CSS results for comparing "cemented" versus reconstituted liquefaction resistance. It is our hope to test two sites a year for several years eventually presenting data on over a half a dozen different "cemented" deposits of varying age. The data from previous studies (e.g., Arango et al. 2000; Arango and Migues 1996; Kulhawy and Mayne 1990; Leon et al. 2005) will be evaluated for compatibility with the criteria used in this study. Care will be taken to compare compatible data so that mechanisms other than mechanical bonding can be removed from the pool. The overall project results will be an age-based correction plot presenting

previous relevant data as well as new data generated from this study. Results will be shown as the ratio of CRR, as in Figure 5, as well as the ratio of CPT tip resistance. All the results will explicitly include the uncertainty in the number of cycles to liquefaction, age, and difference in liquefaction resistance to provide a correction factor that is expressed as a probability distribution. This will allow the results to be used seamlessly in performance-based engineering design.

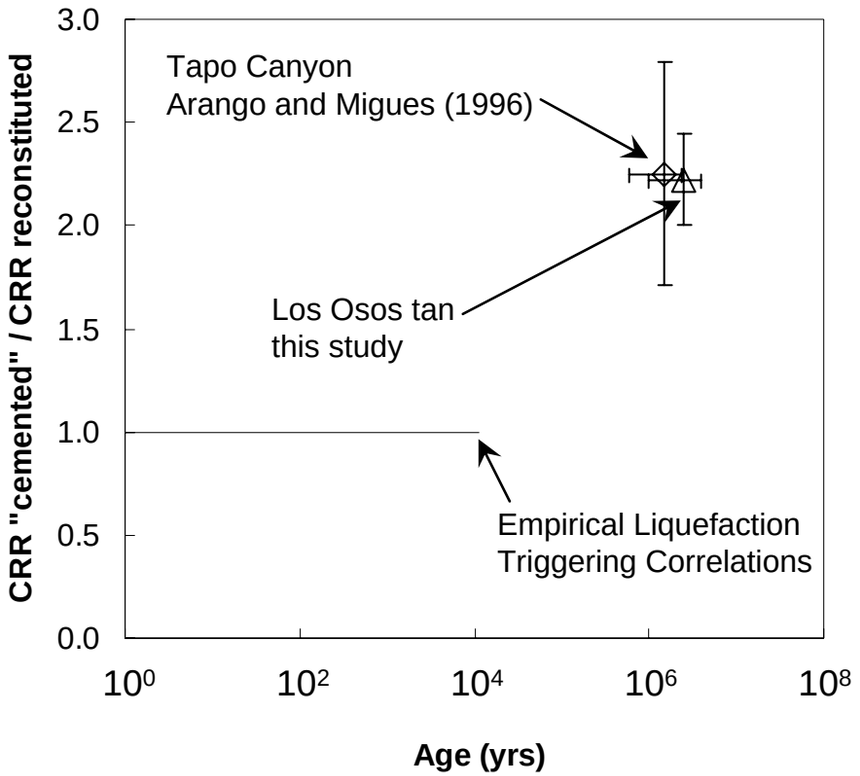


Figure 5. Preliminary results showing Los Osos tan deposit along with Tapo Canyon deposit from Arango and Migues (1996).

AKNOWLDEGEMENTS

Funding for this project has been provided by the Office of Naval Research through C^3RP Project No. 53963. Purchase of the simple shear device was funded by the Cal Poly SFI (student fee initiative) program. This support is gratefully acknowledged. Many people have contributed to the success of this project so far and deserve thanks. Dr. Annie Kammerer was invaluable in providing guidance on initiating the testing program and educating us on the nuances of liquefaction testing. Prof. Gregg Fiegel has provided his insight, guidance, and support from concept to implementation of this project. Tamas Vicsocsean and Manuel Padilla at GCTS have provided ongoing technical support of the equipment. Keith Knudsen, Tom Blake, Jon Blanchard, and Ron Richman have provided assistance in locating viable test sites. Prof. Mike Riemer has provided guidance on the testing of “cemented” materials and has supplied us with unused block samples from a previous study.

REFERENCES

Alterman, I.B. ed. (1994) Seismotectonics of the central California coast ranges. GSA Special Paper 292.

Arango, I., Lewis, M. R., and Kramer, C. (2000). "Updated liquefaction potential analysis eliminates foundation retrofitting of two critical structures." *Soil Dynamics and Earthquake Engineering*, 20, 17-25.

Arango, I., and Migues, R. E. (1996). "Investigation on the Seismic Liquefaction of Old Sand Deposits." NSF Research Report, Grant No. CMS-9416169.

Baxter, C. D. P., and Mitchell, J. K. (2004). "Experimental Study on the Aging of Sands." *Journal of Geotechnical and Geoenvironmental Engineering*, 130(10).

Bjerrum, L., and Landva, A. (1966). "Direct simple-shear tests on a Norwegian quick clay." *Geotechnique*, 16(1), 1-20.

Boulanger, R. W., Chan, C. K., Seed, H. B., and Seed, R. B. (1993). "A low-compliance bi-directional cyclic simple shear apparatus." *Geotechnical Testing Journal*, 16(1), 36-45.

Cetin, K. O., Seed, R. B., Der Kiureghian, A., Tokimatsu, K., Harder, L. F., Kayen, R. E., and Moss, R. E. S. (2004). "SPT-Based Probabilistic and Deterministic Assessment of Seismic Soil Liquefaction Potential." *Journal of Geotechnical and Geoenvironmental Engineering*, 130(12).

Cetin, K. O., Seed, R. B., Moss, R. E. S., Der Kiureghian, A., Tokimatsu, K., Harder, L. F., and Kayen, R. E. (2000). "Field Case Histories for SPT-Based In Situ Liquefaction Potential Evaluation."

Charlie, W. A., Rwebyogo, M. F. J., and Doehring, D. O. (1992). "Time-Dependent Cone Penetration Resistance Due to Blasting." *Journal of Geotechnical Engineering*, 118(8), 1200-1215.

Franke, E., Kiekbusch, M., and Schuppener, B. (1979). "A new direct simple shear device." *Geotechnical Testing Journal*, 2(4), 190-199.

Hryciw, R. D. (1986). "A study of the Physical and Chemical Aspects of Blast Densification of Sand," Ph.D. Dissertation, Northwestern University.

Ishihara, K., and Yamazaki, F. (1980). "Cyclic simple shear tests on saturated sand in multi-directional loading." *Soils and Foundations*, 20(1), 45.

Joshi, R. C., Achari, G., Kaniraj, S. R., and Wijeweera, H. (1995). "Effect of Aging on the Penetration Reistance of Sands." *Canadian Geotechnical Journal*, 32(5), 767-782.

Kammerer, A. M., Wu, J., Riemer, M. F., Pestana, J. M., and Seed, R. B. (2001) "Use of Cyclic Simple Shear Testing in Evaluation of the Deformation Potential of Liquefiable Soils." *4th Internation Conference on Recent Advances in Geotechnical Earthquake Engineering*, San Diego.

Kulhawy, F. H., and Mayne, P. W. (1990). "Manual on Estimating Soil Properties for Foundation Design." *EPRI Report EL-6800*.

Leon, E., Gassman, S. L., and Talwani, P. (2005). "Effect of Soil Aging on Assessing Magnitude and Accelerations." *Earthquake Spectra*, 21(3).

Lewis, M. R., Arango, I., Kimball, J. K., and Ross, T. E. (1999) "Liquefaction resistance of old sand deposits." *Proc 11th Panamerican Conf. on Soil Mechanics and Geotechnical Engineering*, Brasil, 821-829.

Mesri, G., Feng, T. W., and Benak, J. M. (1990). "Postdensification penetration resistance of clean sands." *Journal of Geotechnical Engineering*, 116(7), 1095-1115.

Mitchell, J. K., and Solymar, Z. V. (1984). "Time-Dependent Strength Gain in Freshly Deposited or Densified Sand." *Journal of Geotechnical Engineering*, 110(11), 1559-1576.

Moss, R. E. S., Seed, R. B., Kayen, R. E., Stewart, J. P., Der Kiureghian, A., and Cetin, K. O. (2006). "Probabilistic Seismic Soil Liquefaction Triggering Using the CPT." *Journal of Geotechnical and Geoenvironmental Engineering*, 132(8).

Moss, R. E. S., Seed, R. B., Kayen, R. E., Stewart, J. P., Youd, T. L., and Tokimatsu, K. (2003). "Field Case Histories for CPT-Based In Situ Liquefaction Potential Evaluation." Berkeley Geoengineering Research Report No. UCB/GE-2003/04.

Olson, S. M., Oberbeier, S. F., and Stark, T. D. (2001). "Interpretation of Penetration Resistance for Back-Analysis at Site of Previous Liquefaction." *Seismological Research Letters*, 72(1), 46-59.

Roscoe, K. H. (1953) "An apparatus for the application of simple shear to soil samples." *3rd Internation Conf. on Soil Mechanics and Foundation Engineering*.

Salgado, R., and Randolph, M. F. (2001). "Analysis of Cavity Expansion in Sand." *International Journal of Geomechanics*, 1(2).

Schmertman, J. H. (1991). "The mechanical aging of soils. 25th Terzaghi Lecture." *Journal of Geotechnical Engineering*, 117(9), 1288-1330.

Schmertman, J. H., Baker, W., Gupta, R., and Kessler, K. (1986). "CPT/DMT QC of Ground Modification at a Power Plant." Use of In Situ Tests in Geotechnical Engineering, ASCE STP No. 6.

Wu, J., Seed, R. B., and Pestana, J. M. (2003). "Liquefaction Triggering and Post Liquefaction Deformation of Monterey 0/30 Sand Under Uni-Directional Cyclic Simple Shear Loading." *Geotechnical Engineering Report No. UCB/GE-2003/01*.

Youd, T. L., and Hoose, S. N. "Liquefaction susceptiblility and geologic setting." *Proc. 6th World Conference on Earthqauke Engineering*, New Delhi, India, Vol 6, 37-42.

Youd, T. L., Idriss, I. M., Andrus, R. D., Arango, I., Castro, G., Christian, J. T., Dobry, R., Finn, W. D. L., Harder, L. F., Hynes, M. E., Ishihara, K., Koester, J. P., Liao, S. S. C., Marcuson, W. F., III, Martin, G. R., Mitchell, J. K., Moriwaki, Y., Power, M. S., Robertson, P. K., Seed, R. B., and Stokoe, K. H., II,. (2001). "Liquefaction Resistance of Soils: Summary Report from the 1996 NCEER and 1998 NCEER/NSF Workshops on Evaluation of Liquefaction Resistance of Soils." *Journal of Geotechnical and Geoenvironmental Engineering*, 127(10).

Investigating the Critical State using Laboratory Ring Shear Tests

Abouzar Sadrekarimi[1], S.M. ASCE and Scott M. Olson[2], M. ASCE, P.E.

[1]Ph.D. Student, Department of Civil & Environmental Engineering, University of Illinois at Urbana-Champaign, IL 61801; asadrek2@uiuc.edu
[2]Assistant Professor, Department of Civil & Environmental Engineering, University of Illinois at Urbana-Champaign, IL 61801; olsons@uiuc.edu

ABSTRACT: The critical state is the state at which a mass of soil is sheared at a constant volume, constant effective stress, and constant shear stress. This state is reached at an undrained or constant volume condition and at large strains at which all potential net particle reorientation and crushing are complete. Triaxial compression tests are most commonly used to assess critical state conditions; however, as a result of the limited displacement of the device, triaxial testing may not reach a true critical state. In contrast, the ring shear test allows very large shear displacements where all net particle reorientation and crushing are complete. At the large displacements achieved in the ring shear, particle damage and grain crushing can lead to contractive behavior in initially dense materials. These effects result in critical state conditions that can differ significantly between the triaxial and ring shear devices.

INTRODUCTION

Casagrande (1936) first reported that both loose and dense sands sheared to large strains achieve a constant porosity, termed the critical density, that is independent of the initial condition (i.e., the initial void ratio and initial consolidation stress). Taylor (1948) later termed the density corresponding to a constant volume and constant shear resistance the critical void ratio. Roscoe et al. (1958) extended Casagrande's critical void ratio concept to a "critical void ratio state" at which any further arbitrary increment of shear deformation would not result in any further change in void ratio (in a drained test) or any further change in effective stress (in an undrained test). Thus the critical void ratio state, or simply "critical state," defines a state during unidirectional shearing where the void ratio, effective stress, and shear stress on the failure plane remain constant; and this implies that all net grain rearrangements and particle crushing must be complete (Coop et al. 2004). Poulos (1981) termed this condition the "steady state of deformation" and added a constant velocity criterion. Since the 1980s, many studies have investigated the critical or steady state of sands, and Been et al. (1991) concluded that these conditions are practically the same since

the velocity term is not defined and generally would not be constant in a field flow failure. However, the criteria of statistically complete net grain rearrangements and particle crushing have not been systematically investigated, in part due to conventional testing equipment limitations.

Under plane strain conditions, deformation in frictional materials localizes along well-defined shear planes or "shear bands" and these materials fail by bifurcation (Lee, 1970). Such localizations also have been observed in ring shear (Mandl et al., 1977) and biaxial tests (Vardoulakis and Graf, 1985). In contrast to plane strain tests, Desrues et al. (1996) indicated that the triaxial compression mode of shearing induces complex internal deformation patterns, which leads to bulging, localized shear plane development, and diffuse bifurcation. Furthermore, the triaxial device is capable of reaching only limited displacements, thus limiting the shear strain mobilized on individual shear planes. Despite these limitations, the many advantages of the triaxial device have led many researchers to use triaxial compression tests to define the critical state behavior of potentially liquefiable sands.

To partly overcome these limitations, many researchers have used moist tamping to prepare very loose specimens that are sufficiently contractive to reach a critical state. However, other researchers (e.g., Vaid et al. 1999) argue that moist tamping results in an unrealistically contractive soil fabric that does not mimic natural depositional environments. Vaid et al. (1999) showed that the water pluviation sample preparation method better reproduced the stress-strain response of a specific undisturbed sand (at least at the strain levels available in the triaxial device), and generally yielded a more dilative stress-strain response. But as a result of the dilative response and the limited displacement capacity during undrained triaxial compression, it may not be possible to interpret unequivocally the critical state condition. Occasionally, the critical state interpreted from triaxial tests is only a transient state of constant volume for the strain levels accessible in the triaxial device (Jefferies and Been, 2006). At the critical state, a sand should reach a stable gradation at which the particle contact stresses are insufficient to cause further breakage (Coop et al., 2004); that is, this state represents a balance between volumetric compression arising from particle damage and volumetric dilation from particle rearrangement (Chandler, 1985; Lobo-Guerrero and Vallejo, 2006).

In contrast to the triaxial device, the ring shear apparatus can reach virtually unlimited shear strains and may be able to clarify the critical state condition for many sands. In this paper, we present the results from a comparative study of two sandy soils tested in undrained triaxial compression and constant volume ring shear. We then discuss the implications of these results with respect to field behavior.

TESTING PROGRAM

Two sands were tested in this study: an Illinois River sand and a Mississippi River sand. The Illinois River sand is an alluvial sediment that has been processed for use as fine aggregate in concrete. Processing consisted of washing the sand on a U.S. Standard #200 sieve to remove nearly the entire fine-grained fraction. The resulting sand is medium-grained and uniform, and is comprised mainly of quartz and feldspar with traces of muscovite, chlorite, and hematite. The grains are rounded to sub-

rounded with G_S = 2.63, C_U = 2.6, e_{max} = 0.788, and e_{min} = 0.464 (Mueller 2000). The Mississippi River sand is a very fine-grained silty sand containing about 70% quartz, 21% feldspar and 5% carbonates that we sampled near Cape Girardeau, Missouri. Figure 1 presents the average grain size distributions of these sands.

We prepared reconstituted specimens of Illinois River sand by moist tamping and air pluviation. In the moist tamping method, the sand was moistened and thoroughly mixed with 5% water, and then poured and gently tamped the sand in 20 layers into the specimen container. We used under-compaction as proposed by Mulilis et al. (1978) to achieve a relatively uniform density throughout the specimen. In the air pluviation method, oven dried sand was poured into a funnel whose tip was resting on the bottom of the specimen mold. We then gently raised the funnel to deposit the sand with nearly zero drop height. This method produced a very loose fabric and reduced segregation between the fine and coarse grains. We prepared Mississippi River sand specimens by air pluviation alone because the moist tamped triaxial specimens of this sand deformed severely even under the small vacuum used to hold the specimen.

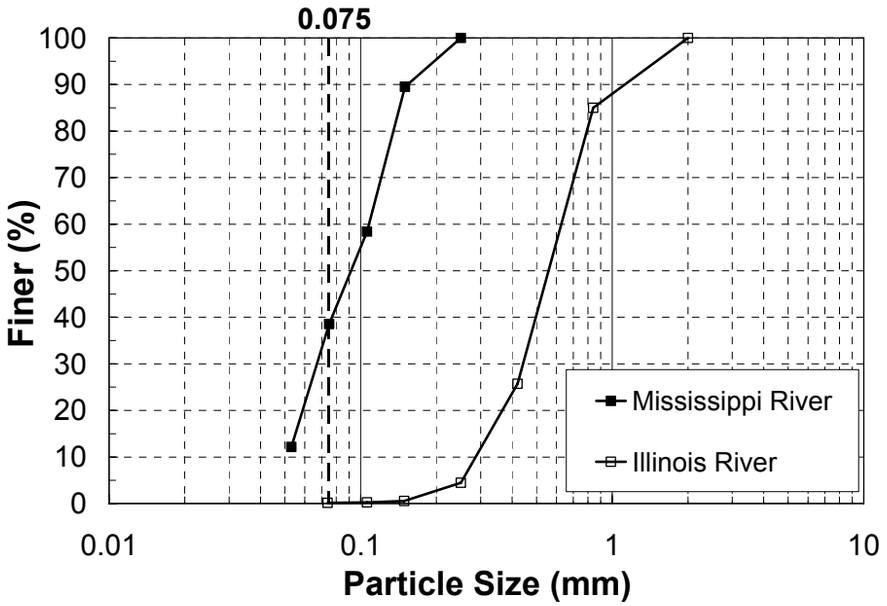


FIG. 1. Average grain size distributions of the sands tested in this study

For the undrained triaxial tests, we lubricated the end platens to reduce end restraint and flushed the specimen with carbon dioxide followed by de-aired water. To ensure saturation, we back-pressured each specimen until a pore pressure parameter (B) of at least 0.97 was obtained. After consolidation, the drainage lines were closed and the specimen was sheared under undrained conditions at a rate of 0.127 cm/min up to an axial strain of 25%. We performed constant volume ring shear tests in a new solid confining ring type machine designed and built at the University of Illinois. Shearing was induced by rotating the bottom disc, which was deeply serrated to prevent slippage. In the ring shear tests, a constant volume condition was imposed by locking the loading plates of the apparatus after consolidating the specimen. The specimens

were sheared at a rate of 18.6 cm/min. The normal and shear friction developed on the sidewalls were measured by independent load and torque cells, respectively; and these measurements were subtracted from the separately-measured total normal and shear forces. Sadrekarimi and Olson (2007) provide further details of the ring shear apparatus and testing procedures. Table 1 summarizes the preparation methods and consolidation conditions for each test of this study.

RESULTS AND DISCUSSION

Figures 2 through 5 present the stress paths and stress-displacement plots of the triaxial compression and ring shear tests listed in Table 1. To facilitate comparison, we present similar triaxial and ring shear tests side-by-side, with the effective and shear stresses normalized to the equal all-around (isotropic) or normal consolidation stress (respectively) prior to shearing.

TABLE 1. Specifications of the Tests Reported in this Study

Test No.[a]	Sand	Preparation method	Consolidation stress[b] (kPa)	Consolidation void ratio
TxC1	Illinois River	Moist tamping	359	0.707
TxC2	Illinois River	Air pluviation	265	0.658
TxC3	Illinois River	Air pluviation	573	0.627
TxC4	Mississippi River	Air pluviation	397	0.760
RS1	Illinois River	Moist tamping	266	0.672
RS2	Illinois River	Air pluviation	272	0.653
RS3	Illinois River	Air pluviation	562	0.645
RS4	Mississippi River	Air pluviation	395	0.756

NOTES: [a]TxC = undrained triaxial compression; RS = constant volume ring shear
[b]Isotropic stress in triaxial tests and normal stress in ring shear tests

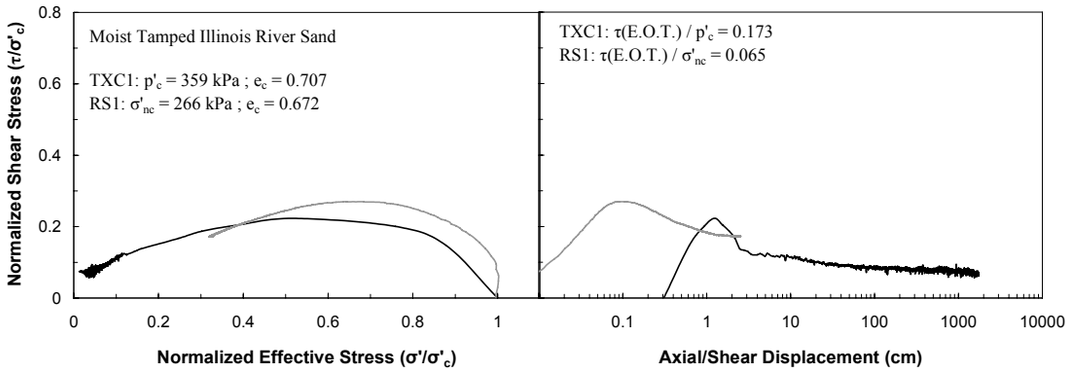


FIG. 2. Normalized stress paths and normalized stress-displacement plots for tests TxC1 (grey) and RS1 (black)

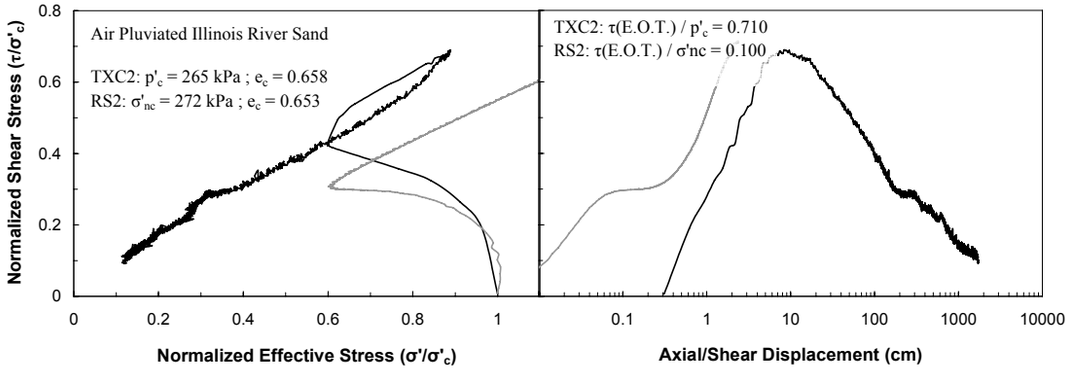


FIG. 3. Normalized stress paths and normalized stress-displacement plots for tests TxC2 (grey) and RS2 (black)

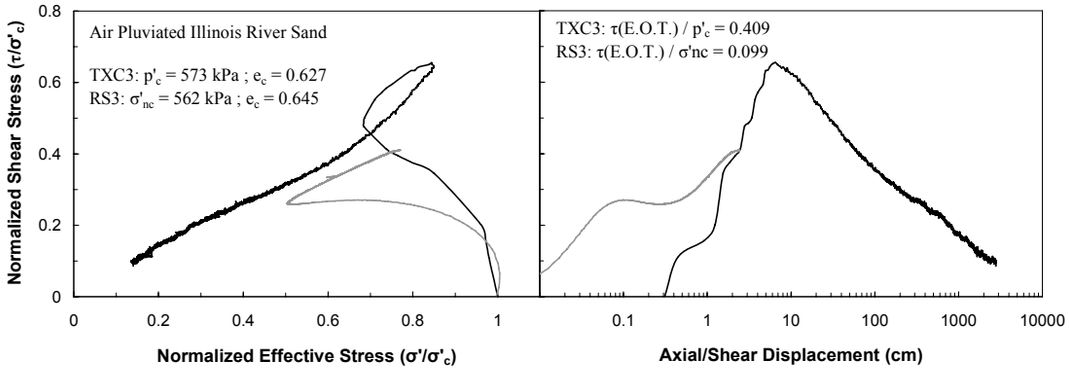


FIG. 4. Normalized stress paths and normalized stress-displacement plots for tests TxC3 (grey) and RS3 (black)

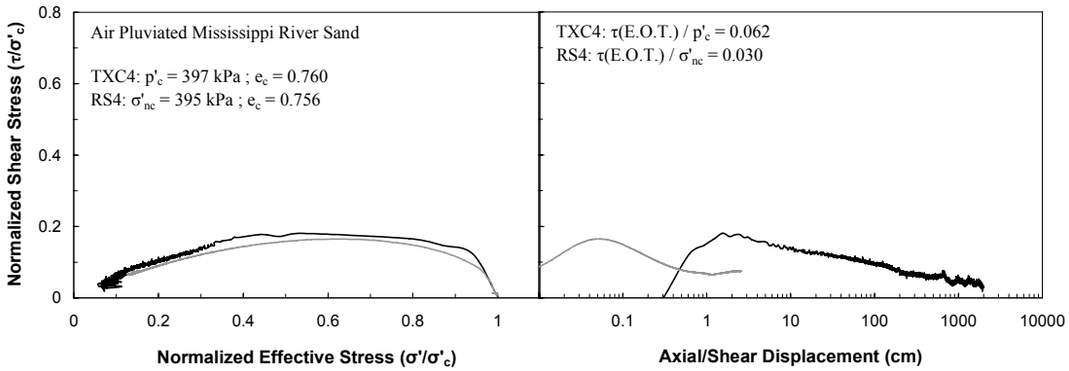


FIG. 5. Normalized stress paths and normalized stress-displacement plots for tests TxC4 (grey) and RS4 (black)

We also plotted the results in terms of shear stress vs. axial (in triaxial)/shear (in ring shear) displacement (rather than the more conventional shear stress vs. strain) and we noted the shear stress ratio mobilized at the end of each test (EOT condition).

Figure 2 compares moist tamped Illinois River specimens. As illustrated in the figure, only moist tamped Illinois River specimens were loose enough to contract in

triaxial compression (TxC1). Here, TxC1 reached a condition at a displacement of ~2.5 cm (i.e., 25% axial strain) that generally would be considered a critical state. Test RS1 involved a slightly denser sample (lower void ratio and lower consolidation stress), yet this test mobilized a considerably lower large strain shear stress ratio, even at comparable shear displacements. This result calls into question whether TxC1 actually reaches a critical state, which we discuss in more detail below.

Figure 3 compares denser air pluviated Illinois River specimens. As illustrated in the figure, both TxC2 and RS2 exhibit strain-hardening behavior to moderate displacements. In TxC2, the specimen bulged considerably at a displacement of ~2.5 cm (25% axial strain), producing complicated stress and strain states and precluding further (meaningful) shearing. However, the shear resistance in TxC2 reached a plateau at an axial strain from 23 – 25%, which could be potentially misinterpreted as a critical state. Similar to TxC2, RS2 initially strain-hardened during shear, and reached a similar maximum shear stress ratio of about 0.7 (Figure 3). However, in contrast to TxC2, during continued shearing, RS2 experienced considerable net contraction to a shear displacement of about 1500 cm. The shear resistance then leveled off at larger displacements (from 1500 to 2000 cm) and yielded a large strain shear stress ratio of about 0.1.

Figure 4 shows another set of tests on dense air pluviated Illinois River sand. Similar to TxC2, TxC3 reached a shear stress plateau at axial strains from about 20 – 25% (i.e., the displacement limit for the triaxial device), which again could be potentially misinterpreted as a critical state. However, unlike the previous comparison, the shear stress plateau in TxC3 was much smaller than the maximum shear stress mobilized in RS3. Test RS3 (like RS2) exhibited strain hardening behavior to a shear displacement of about 10 cm, after which the specimen experienced significant net contraction. After a displacement of about 2000 cm, the RS3 specimen yielded a large strain shear stress ratio of about 0.1.

Figure 5 compares two tests performed on air pluviated Mississippi River sand, which contracted in both triaxial compression and ring shear. Here, both tests appear to reach a critical state; however, the large strain shear stress ratio in RS4 is only about ½ of that of TxC4. We also note that RS4 reached a temporary plateau for shear stress ratio from about 200 to 600 cm that approximates the end-of-test shear stress ratio in TxC4. But with continued shearing, RS4 continued to experience net contraction and mobilized a large strain shear stress ratio of about 0.03.

While part of the difference in end-of-test shear stress ratios (which in all tests could be interpreted as “critical states”) is related to different modes of shear, we anticipate that shear band formation and grain crushing play a much more significant role at large shear displacements. For example, we did not observe any shear zone development or bifurcation in the triaxial compression tests. To examine shear band evolution in the ring shear, we ran two additional tests that were identical to tests RS2 and RS4, but we replaced the stainless steel outer confining ring with a clear Plexiglas ring. Figures 6 and 7 show the final shear zones in these two tests after displacements exceeding 1700 cm. Test RS2b on air pluviated Illinois River sand exhibited a distinct shear zone that measured 5.4 mm thick. Similarly, test RS4b on air pluviated Mississippi River sand exhibited a 1.3 mm thick shear zone.

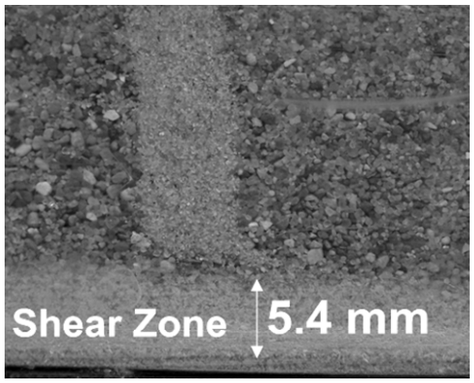


FIG. 6. Shear zone in test RS2b

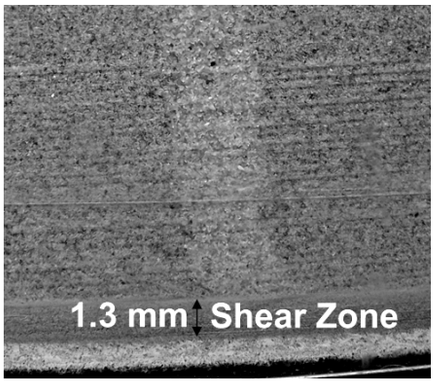


FIG. 7. Shear zone in test RS4b

Many investigators have related shear band thickness in granular soils to median grain size, D_{50} (e.g., Mühlhaus and Vardoulakis, 1987). For example, Roscoe (1970) directly measured shear band thickness in simple shear tests and concluded that shear band thickness is about 10 x D_{50}. Vardoulakis and Graf (1985) and Vardoulakis et al. (1985) measured shear band thickness in biaxial tests using X-ray photographs and they suggested a shear band thickness that was about 16 x D_{50}. Alshibli and Sture (1999) observed that shear bands formed in plane strain tests were approximately 13 - 14 x D_{50} for fine-grained sand, 11 - 12 x D_{50} for medium-grained sand, and 10 - 11 x D_{50} for coarse grained sand. Here, the Illinois River and Mississippi River sand exhibited shear band thicknesses of 10 x D_{50} and 14 x D_{50}, respectively.

In addition, when we compared the grain size distributions of the sands before and after shearing, we did not observe any evidence of crushing in the TxC tests. In contrast, we observed significant grain crushing after each ring shear test, even at the lowest consolidation stress of about 270 kPa in test RS2. Subsequent tests with consolidation stresses lower than 150 kPa also experienced significant grain crushing. To illustrate the significance of grain crushing, Figure 8 presents the grain size distributions of Illinois River sand before and after test RS2. Figure 8 also includes the grain size distribution of the sand collected solely from the shear zone, where considerable grain damage and crushing occurs. Figure 8 includes a photo of the sand (in the shear zone) before and after shearing. The photo illustrates the significant change in color and texture.

We anticipate that grain crushing within the shear zone was primarily responsible for the contraction of the dense Illinois River sands that occurred following dilation in tests RS2 and RS3, as well as for the continued contraction at large shear displacements of the Illinois River and Mississippi River sands in tests RS1 and RS4, respectively. In tests RS2 and RS3, the specimen responds to competing shearing mechanisms: (1) dilation of the original grain structure that leads to increased shear resistance; and (2) particle damage and crushing that leads to increased compressibility, local contraction, and decreased shear resistance. Initially (as also observed in TxC2 and TxC3), grain dilation dominates and shear resistance increases. However, at displacements near 10 cm, a sufficient volume of sand within the shear zone has been damaged to result in a net contraction. Continued contraction occurs as more grains are damaged and grain dilation decreases. The specimens continued to experience net contraction until the effective normal stress decreased to a value below

which grain crushing ceases. At this condition, the soil mobilizes a constant shear resistance and meets all of the criteria for the critical state.

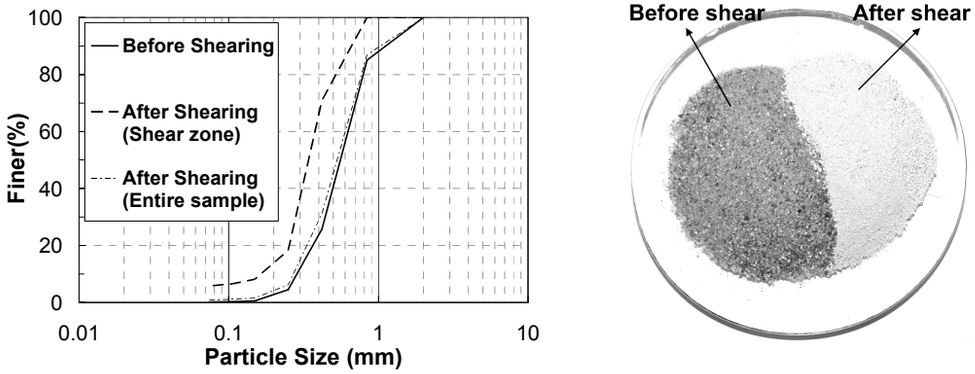


FIG. 8. Grain size distribution after test RS2 and grain crushing

Jeyapalan et al. (1983; among others) have stated that very large shear strains develop during many large run-out landslides/flowslides that could not be properly captured by triaxial compression testing. For example, Sassa et al. (1984) suggested that grain crushing-induced contractive behavior was chiefly responsible for the large runout (up to 1800 m) of the 1903 Franc landslide in Canada (Cruden and Krahn, 1978). Similarly Sassa (1995) and Sassa et al. (2005) suggested that this mechanism was largely the cause of the rapid Nikawa landslide triggered by the 1995 Hyogoken-Nambu earthquake, as well as the Higashi Takezawa and the Terano landslides triggered by the 2004 Mid-Niigata Prefecture earthquake. In contrast to the triaxial device, the ring shear produces a discrete shear zone where grain crushing readily occurs, and may be useful to understand the failures mentioned above. We are currently performing a detailed study to investigate the critical state obtained in the ring shear device, evaluate the stress ratios mobilized in the ring shear, and relate these results to field case histories of flow failures and long run-out landslides.

CONCLUSIONS

The critical state is defined as a condition where soil continuously deforms at constant volume, constant normal effective stress, and constant shear stress after all net particle reorientation and crushing is complete. The results of this study suggest that the triaxial compression test may not produce a true critical state, even in very loose samples, because the test is terminated at limited displacements before particle reorientation and crushing are complete. In contrast, the ring shear device can achieve the very large shear displacements, which may be required to reach a true critical state where particle reorientation and crushing are complete. As a result, the ring shear device may be very useful in analyzing some liquefaction flow failures and other rapid, large run-out landslides that develop relatively thin shear zones.

REFERENCES

Alshibli, K. and Sture, S. (1999). "Sand shear band thickness measurements by digital image techniques." *Journal of Computing in Civil Engineering*, 13(2): 103 – 109.

Been, K., Jefferies, M.G. and Hachey, J. (1991). "The critical state of sand." *Geotechnique*, 41(3): 365-381.

Casagrande, A. (1936). "Characteristic of cohesionless soils affecting the stability of slopes and earth fills." *Journal of Boston Society of Civil Engineers*, 23(1): 13-32.

Chandler, H.W. (1985). "A plasticity theory without Drucker's postulate, suitable for granular materials." *Journal of Mechanics and Physics of Solids*, 33: 215-226.

Coop, M.R., Sorensen, K.K., Bodas Freitas, T. and Georgoutsos, G. (2004). "Particle breakage during shearing of a carbonate sand." *Geotechnique*, 54(3): 157-163.

Cruden, D.M. & Krahn, J. (1978). "Franc rockslide, Alberta, Canada." *Rockslides and Avalanches*, I., Voight B. Ed., Elsevier, 97-112.

Desrues, J., Chambon, R., Mokni, M. and Mazerolle, F. (1996). "Void ratio evolution inside shear bands in triaxial sand specimens studied by computed tomography." *Geotechnique*, 46(3): 529-546.

Jefferies, M. and Been, K. (2006). Soil liquefaction: a critical state approach. *Taylor & Francis*, New York, London, 479p.

Jeyapalan, J.K., Duncan, J.M., and Seed, H.B. (1983). "Analyses of flow failures of mine tailings dams." *Journal of the Geotechnical Engineering Division, ASCE*, 109(2): 150–171.

Lee, K. (1970). "Comparison of plane strain and triaxial tests on sand." *J. Soil Mech. and Found. Div., ASCE*, 96(3): 901-923.

Lobo-Guerrero, S. and Vallejo, L. E. (2006). "Modeling granular crushing in ring shear tests: experimental and numerical analyses." *Soils & Foundations*, 46(2): 147 – 158.

Mandl, G, de Jong, LNJ, Maltha, A (1977). "Shear zones in granular material: An experimental study of their structure and mechanical genesis." *Rock Mechanics,* 9, 95–144

Mueller, C. G. (2000). "Load and Deformation Response of Tieback Walls." *Ph.D. Thesis*, University of Illinois at Urbana-Champaign, 554pp.

Mühlhaus, H. B. and Vardoulakis, I. (1987). "The thickness of shear bands in granular materials." *Geotechnique*, 37(3): 271-283.

Mulilis, J. P., Townsend, F. C. and Horz, R. C. (1978). "Triaxial testing techniques and sand liquefaction." *Dynamic Geotechnical Testing*, ASTM STP 654, American Society for Testing and Materials: 265-279.

Poulos, J. (1981). "The steady state of deformation." *Journal of Geotechnical Engineering Division*, ASCE, 107(GT5): 553-562.

Roscoe, K. H. (1970). "The influence of strains in soil mechanics." 10th Rankine Lecture, *Geotechnique* 20(2): 129-170.

Roscoe, K.H., Schofield, A.N. and Wroth, C.P. (1958). On yielding of soils, *Geotechnique*, 8(1): 22-53.

Sadrekarimi, A. and Olson, S. (2007). "Development of an improved ring shear device to measure liquefied shear strength of sandy soils." *4th International*

Conference on Earthquake Geotechnical Engineering, Thessaloniki, Greece, paper no. 1330.

Sassa, K., Shima, M., Hiura, H., Nakagawa, A. and Suemine, A. (1984). "Development of ring shear type debris flow apparatus." Report of Grant-in-Aid for Scientific Research by Japanese Ministry of Education, Science and Culture (No. 57860028).

Sassa, K. (1995). "Keynote lecture: Access to the dynamics of landslides during earthquakes by a new cyclic loading high-speed ring shear apparatus." *Proc. 6th International Symposium on Landslides*, In "Landslides", Balkema, 3: 1919-1939.

Sassa, K., Fukuoka, H., Wang, F. and Wang, G. (2005). "Dynamic properties of earthquake-induced large-scale rapid landslides within past landslide masses." *Landslides,* 2: 125-134.

Taylor, D. W. (1948). *Fundamentals of Soil Mechanics*, New York, John Wiley and Sons, 700 pp.

Vaid, Y.P., Sivathayalan, S., and Stedman, D. (1999). "Influence of specimen-reconstituting method on the undrained response of sand." *Geotechnical Testing Journal*, ASTM, 22(3): 187–195.

Vardoulakis, I., and Graf, B. (1985). "Calibration of constitutive models for granular materials using data from biaxial experiments." *Geotechnique*, 25(3): 299-317.

Vardoulakis, I., Graf, B., and Hettler, A. (1985). "Shear band formation in a fine-grained sand." *Proc. 5th International Conference on Numerical Methods in Geomechanics,* Nagoya, 1: 517-521.

Wride, C. E. and Robertson, P. K. (1999). *CANLEX, the Canadian liquefaction experiment*, Bi Tech Publishers, Richmond B.C.

Liquefaction Resistance Recovered From "On-the-Fly" CPTu-Measured Pore Pressures

Michael Fitzgerald
110 Hosler Bldg. University Park, PA 16802. Department of Energy and Mineral Engineering, The Pennsylvania State University, University Park, PA, USA

Derek Elsworth
110 Hosler Bldg. University Park, PA 16802. Department of Energy and Mineral Engineering, The Pennsylvania State University, University Park, PA, USA

ABSTRACT: The liquefaction resistance of soils has been noted to be influenced by fines content. At present piezocone measurements are not capable of providing accurate predictions of fines content and are therefore open to uncertainty. The work presented herein, extends previous analyses of liquefaction resistance and develops the framework for prediction of liquefaction resistance through the CPT recovered parameter of excess pore pressure (u_2) measured in flight. The main driving force behind liquefaction is the build-up of excess pore pressure in the soil structure; therefore the use of the piezocone measured excess pore pressure is a preferred variable to fines content in the analysis of liquefaction resistance.

1 INTRODUCTION

Correlations of cone penetration test (CPT)-based end-bearing have been established with cyclic stress ratios (CSR) estimated at liquefied and non-liquefied sites (Ishihara et al. 1993; Stark and Olson 1995). For a given cyclic resistance ratio (CRR), increased fines content or a related reduction in median grain size, are observed to reduce CPT-based end-bearing and require correction (Robertson and Campanella, 1985; Robertson and Wride, 1998) if accurate evaluations of liquefaction resistance are to be projected. Where samples are not recovered, fines content may be estimated through correlations with other cone metrics – most notably those that define the soil type relative to grain size parameters (Robertson and Wride, 1998). These match CPT-based end-bearing and sleeve friction data with empirical correlations of soil type, through a soil behavior index (Robertson and Wride, 1998). A main drawback of this procedure is the limited ability to accurately and independently define the fines content, absent sampling.

The following presents an alternate path to define liquefaction resistance – a rational method is presented to define the set of CPTu-measured parameters, which better represent the active processes that contribute to the nebulous "effect of fines" observed during CPT soundings. We hypothesize that the principal process contributing to the proxy effect of "increased fines" is one of enhanced pore fluid pressures generated in the tip-local process zone, in addition to the secondary effect of reducing cone penetration resistance via increased plasticity. Pore pressures are elevated by both the increased compressibility, and the reduced permeability (Elsworth and Lee 2005), of the penetrated soil – each occasioned by the presence of fines. We hypothesize that at the low fines contents typically observed in liquefiable soils, the effect of permeability is the more important factor, as the main driving force behind liquefaction is pore pressure induced by the collapsing soil layer, which is a function of the permeability of the soil matrix. In the following we link anticipated conditions of tip-local drainage, occasioned by fines content, to define correlations of corrected cone resistance with CRR. This is accomplished via magnitudes of measured tip-local pore pressures.

2 METHOD

Existing correlations of liquefaction resistance primarily relate the normalized corrected end-bearing resistance with the cyclic stress ratio required to induce liquefaction (CRR). The corrected end bearing parameter is normalized to a standard in-situ vertical effective stress of 100 kPa. The expression (Olsen 1997)

$$q_{c1N} = \left(\frac{q_c}{\sigma_{ref}} \right) \left(\frac{\sigma_{ref}}{\sigma_{vo}'} \right)^n \tag{1}$$

relates the corrected end bearing parameter (q_c) to the normalized cone penetration resistance (end-bearing) parameter (q_{c1N}) through an overburden reference stress ($\sigma_{ref} = 100\,\mathrm{kPa}$) and a soil-type exponent (n) that varies from 0.5 for clean sands to 1.0 for clayey soils (silty sands ~0.7) (Olsen, 1997).

A broad suite of observational field data was used to develop semi-empirical correlations directly or indirectly between q_{c1N} and calculated CSR magnitudes, relative to other indices of soil gradation – these include median grain size (D_{50}) or fines content ($FC\,(\%)$) (Stark and Olson, 1995). Apparent from these data are different $CRR - q_{c1N}$ relationships for clean sands, silty sands, and sandy silts. Semi-empirical curves delimit the different D_{50} zones that separate the liquefied from the non-liquefied data. The semi-empirical liquefaction-threshold for clean sands, under a normalized earthquake moment magnitude of 7.5, is expressed for $q_{c1N} < 50$ as (Robertson and Wride, 1998)

$$CRR_{CS} = 0.833\left(\frac{q_{c1N}}{1000}\right) + 0.05 \tag{2}$$

and for $50 \le q_{c1N} \le 160$ as

$$CRR_{CS} = 93\left(\frac{q_{c1N}}{1000}\right)^3 + 0.08\,. \tag{3}$$

2.1 CORRELATIONS OF CPT END-BEARING WITH RELATIVE DENSITY

In addition to correlations of CPT-based end-bearing and CRR for the clean sand condition, as noted in equations (2) and (3), end-bearing may also be linked to relative density (D_r). Data relating q_c, of Hokksund, Ticino, Sacramento, and Monterey #0 sands (Tseng 1989) note the dependence on both D_r, and σ_{mo}', defined in terms of the vertical (σ_{v0}') and horizontal (σ_{h0}') effective stress components as $\sigma_{mo}' = \frac{1}{3}\left(\sigma_{vo}' + 2\sigma_{ho}'\right)$. Estimates of the mean effective stress can be found using the passive earth pressure coefficient ($K_0 = \sigma_{ho}'/\sigma_{vo}' = 1 - \sin\phi$), where ϕ is the angle of internal friction which ranges from ~27° for soft silt to ~42° for dense sand (Lunne et al. 1997), combined with the expression for mean effective stress to form

$$\sigma_{mo}' = \sigma_{vo}' - \left((2/3)\,\sigma_{vo}'\sin\phi\right). \tag{4}$$

This provides an approximate method to estimate the mean effective stress of normally consolidated soils from the vertical effective stress. In the development of the following sections a median angle of internal friction ($\phi = 35°$) was used, and equation (4) reduces to $\sigma_{mo}' \cong 0.62\,\sigma_{vo}'$. (Note, in further analysis not shown here, the influence of ϕ on the resulting CRR curves, within the specified range is not significant.)

Correlations that link cone penetration resistance with prescribed magnitudes of σ_{mo}' and D_r have been developed using calibration tests and can be expressed as

$$q_c = 2.05\,\sigma_{ref}\left(\frac{100\,\sigma_{mo}'}{\sigma_{ref}}\right)^{0.51}\exp(2.93\,D_r) \tag{5}$$

(Jamiolkowski et al. 1988) where $\sigma_{ref} = 100\,\text{kPa}$ and the relative density is defined as a decimal. Normalized cone penetration resistance can be defined jointly as a function of mean effective stress and relative density, by substituting equation (5) into equation (1) to yield

$$q_{c1N} = \left(2.05\,\sigma_{ref}\left(\frac{100\,\sigma_{mo}'}{\sigma_{ref}}\right)^{0.51}\exp\left(2.93\,D_r\right)\right)\left(\frac{\sigma_{ref}}{\sigma_{vo}'}\right)^n. \tag{6}$$

Equation (6) can then be combined with equations (2) and (3) to define the clean sand threshold limit for liquefaction (Robertson and Wride 1998) as a function of the soils mean stress and relative density and is expressed for $q_{c1N} < 50$ as

$$CRR_{CS} = \frac{0.833}{1000}\left[\left(2.05\,\sigma_{ref}\left(\frac{100\,\sigma_{mo}'}{\sigma_{ref}}\right)^{0.51}\exp\left(2.93\,D_r\right)\right)\left(\frac{\sigma_{ref}}{\sigma_{vo}'}\right)^{n}\right] + 0.05 \tag{7}$$

and for $50 \le q_{c1N} \le 160$ as

$$CRR_{CS} = \frac{93}{(1000)^3}\left[\left(2.05\,\sigma_{ref}\left(\frac{100\,\sigma_{mo}'}{\sigma_{ref}}\right)^{0.51}\exp\left(2.93\,D_r\right)\right)\left(\frac{\sigma_{ref}}{\sigma_{vo}'}\right)^{n}\right]^3 + 0.08\,. \tag{8}$$

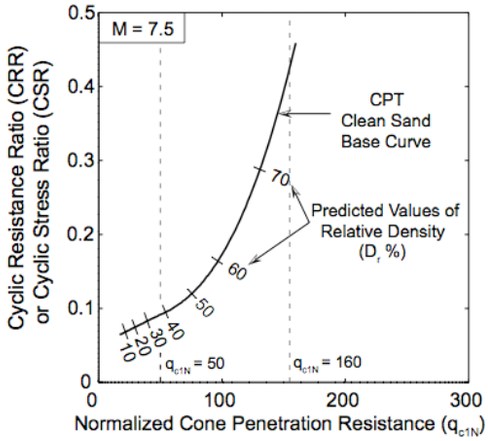


FIG 1. Cyclic resistance ratio versus normalized cone penetration resistance as a function of relative density and mean normal effective stresses produced from equations (7) and (8).

The resulting solutions cover the full range of D_r, and allow CRR to be defined for any magnitude of q_{c1N}. Figure 1 shows the clean sand reference curve for $\sigma_{mo}' = 100\ kPa$, with magnitudes of relative density overlain.

2.2 Evaluation of $CRR - q_{c1N}$ Mediated by CPTu-Generated Excess Pore Pressures

The clean sand curves for $CRR - q_{c1N}$, recovered from equations (7) and (8), and represented in Figure 1, may be corrected for the presence of fines. Assuming that the principal influence of fines is in reducing the penetration resistance via elevated excess CPT-generated pore pressures, then the clean sand curve may be corrected for the influence of impeded drainage at the cone tip. This impeded drainage is manifest as elevated pore pressures, recorded at the shoulder position (u_2), enabling excess pore pressures to be feasibly substituted for the proxy of fines content, when modulating the $CRR - q_{c1N}$ relationship. This approach is applied generically to the expression relating cone penetration resistance to mean effective stress (equation (5)).

Consider, first, penetration in clean sand, where the penetration-induced pore fluid pressures at the tip are null. If the relative density of the sand is $D_r = 60\%$, and the mean effective overburden stress is $\sigma_{mo}' = 65\,\text{kPa}$, then the cone resistance would be $q_c \sim 10\,\text{MPa}$, as illustrated in Figure 2. If drainage at the tip is impeded, then with all else equivalent, for a penetration-induced excess pore pressure of $\Delta P = 30\,\text{kPa}$ the total cone penetration resistance is now reduced to $q_c \sim 7\,\text{MPa}$, a net difference of $\sim 3\,\text{MPa}$.

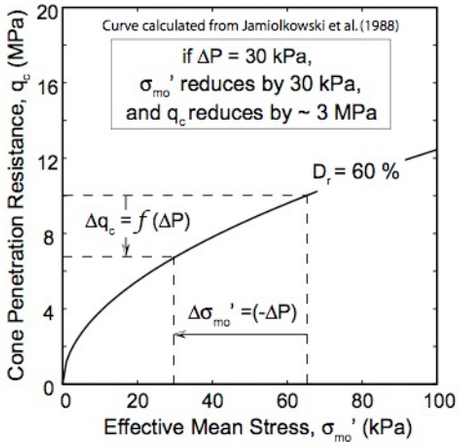


FIG 2. Plot of cone penetration resistance with mean normal stress for $D_r = 60\%$ showing the effect of pore pressure on reducing the mean effective stress and subsequently the CPT cone penetration resistance.

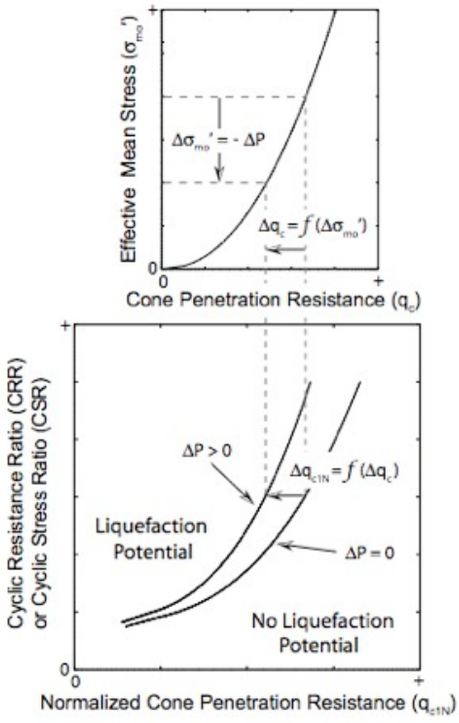


FIG 3. Schematic representing the theoretical adjustment of the CRR_{CS} curve under a given magnitude of excess pore pressure.

Correspondingly, this reduction in the end-bearing stress correlates with a reduction in the normalized end-bearing stress, q_{c1N}, resulting in the translation of the CRR boundary curve to the left, as illustrated in Figure 3.

This procedure may be expressed to define the curves that represent different magnitudes of excess pore fluid pressure. These pore pressures directly correspond to different magnitudes of in situ permeability, as a preferred variable to the usually selected proxy variable of fines content. The clean sand curve represents conditions consisting of $0.25 < D_{50}(mm) < 2.0$ and fines content $FC(\%) < 5$, and may be evaluated using equations (2) and (3) as noted in Figure 4. For each value of q_{c1N}, between 0 and 300, it is possible to determine a value of CRR that is unique to it. To incorporate the influence of pore-pressure, measured at the u_2 position, acting on the mean effective stress, equation (6) has been recast as

$$q_{c1N} = \left(2.05\, \sigma_{ref} \left(\frac{100\sigma_{mo}' - \Delta P}{\sigma_{ref}} \right)^{0.51} \exp\left(2.93 D_r\right) \right) \left(\frac{\sigma_{ref}}{\sigma_{vo}'} \right)^{n} . \quad (9)$$

The location of the additional curves representing different fines contents are obtained by the following procedure:

1. Calculate q_{c1N}, using equation (6), for a selected value of σ_{mo}' with D_r varied in a range so that the maximum value q_{c1N} equals 160, the maximum value given by Robertson and Wride (1998).
2. Using equations (7) and (8) calculate CRR values that uniquely correlate to the calculated values of q_{c1N} from step (1). Plot the values of $CRR - q_{c1N}$ to graphically illustrate the location of the clean sand curve (CRR_{CS}).
3. For the desired curves under the condition $\Delta P > 0$, use equation (9) to calculate the reduced q_{c1N} values that are unique to the selected values of σ_{mo}' and ΔP. The new set of q_{c1N} values should then be plotted against the CRR values found in step (2).
4. Repeat step (3) for each selected value of excess pore pressure for which a CRR curve is desired.

This procedure enables the field curves of CRR versus q_{c1N} to be evaluated and plotted in a modified form in Figure 4 and are plotted for selected percent ratios (0%, 25%, 50%, and 75%) of $\Delta P / \sigma_{mo}'$, where the values of ΔP were selected to achieve the ratios. This procedure was followed as a way of normalizing the curves for different values of σ_{mo}'. An important note is that the curves generated for the same

ratio will overlie additional curves generated using a different value of σ_{mo}' for the clean sand condition $(\Delta P/\sigma_{mo}' = 0)$ and in Figure 4 for the two selected values of mean effective stress ($\sigma_{mo}' = 33, 41$ kPa) calculated from equation (4) with $\sigma_{vo}' = 60$ kPa (median value from Stark and Olson (1995)), and $\phi = 42°, 28°$. The values of ΔP that correspond to these ratios are also given for reference.

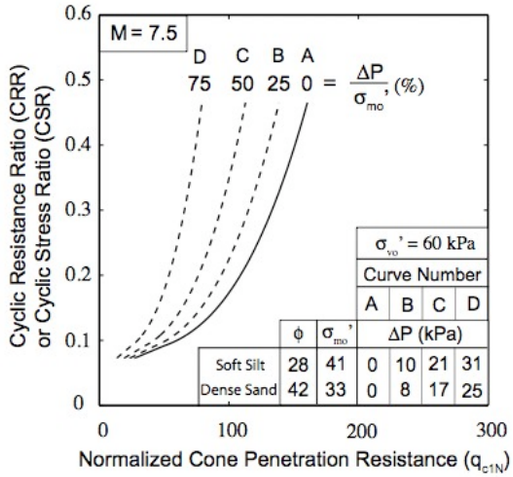


FIG 4. $CRR - q_{c1N}$ curves generated for $\Delta P/\sigma_{mo}'$ ratios of 0, 25, 50, and 75%. This shows the adjustment made to the clean sand curve ($\Delta P/\sigma_{mo}' = 0\%$) using the pore pressure correction procedure.

3 FIELD DATA AND VALIDATION

Meager data exist with which to comprehensively validate the proposed relationships. Historically, few pore pressure data are available for cross correlation, despite the observation that the primary mechanism causing the lateral shift in the CRR liquefaction-threshold curves is the impeded drainage at the tip. Despite this lack of data an indirect procedure is presented to provide partial validation of the model where fitting of the boundaries between liquefied and non-liquefied soils, for different categories of soil classification (clean sand, silty sand, and sandy silt), is done to see if uniform threshold excess pore pressures are capable of defining that boundary.

The pore-pressure-derived CRR boundary curves are plotted in Figure 5 using available CPT-correlated liquefaction data (Stark & Olson (1995)). Analysis of the data was performed by separating the data using the D_{50} selection criteria set forth in Stark & Olson (1995), then plotted to express the $CRR - q_{c1N}$ relationship. The data were delimited using ΔP-mediated CRR curves by manually tuning the $\Delta P/\sigma_{mo}'$ parameter, introduced earlier, until a decent fit was made with the data. This yields a unique value of $\Delta P/\sigma_{mo}'$ which defines the location of the CRR curve for each sand

gradation (for clean sand, silty sand, and sandy silt the parameter $\Delta P/\sigma_{mo}' = 0, 30, \text{and } 70\ \%$ respectively). To explore this relationship further, a means of independently estimating in-situ permeabilities is necessary. For this, a relationship between D_{50} and K has been employed (Shepherd 1989) to calculate values of permeability uniquely related to D_{50} through the expression $K = C(D_{50})^n$, where K is the coefficient of permeability (m/s), C is a sand type coefficient (ranging from 100 for consolidated sediments to 40,000 for glass spheres), n is a soil type exponent, and D_{50} is defined in mm. In the work presented here, the coefficients were selected for "channel deposit" type sand with $C = 450 \text{ and } n = 1.65$, where selection was based on the authors' estimation of liquefiable soils in comparison with the available "sand type" classifications. This procedure now yields an estimated permeability range for each sand gradation classification. For comparison of the $\Delta P/\sigma_{mo}'$ parameter with the estimated permeability range, a separate procedure is employed to directly estimate K from CPT sounding metrics.

A relationship for estimating K using a non-dimensional soil permeability, K_D, may be recovered from the CPT sounding metrics of end-bearing (Q_t) and pore pressure ratio (B_q) as

$$K_D = 1/B_q Q_t \tag{10}$$

where, $B_q = \Delta P/(q_t - \sigma_{v0})$ and $Q_t = (q_t - \sigma_{v0})/\sigma_{v0}'$ (Elsworth and Lee 2005). Substitution of B_q and Q_t into equation (11) yields,

$$K_D = \sigma_{vo}'/\Delta P \tag{11}$$

where,

$$K_D = 4\,K\,\sigma_{vo}'/U\,a\,\gamma_w \tag{12}$$

where, U is the CPTu advance rate (typically constant at 2 cm/sec), a is the radius of the cone penetrometer (1.79 cm), and γ_w is the unit weight of water (9.8 kN/m^3). Further substitution of equation (11) into (12) enables the coefficient of permeability, K, to be defined in terms of excess pore pressure, ΔP, as $K = U\,a\,\gamma_w/4\,\Delta P$.

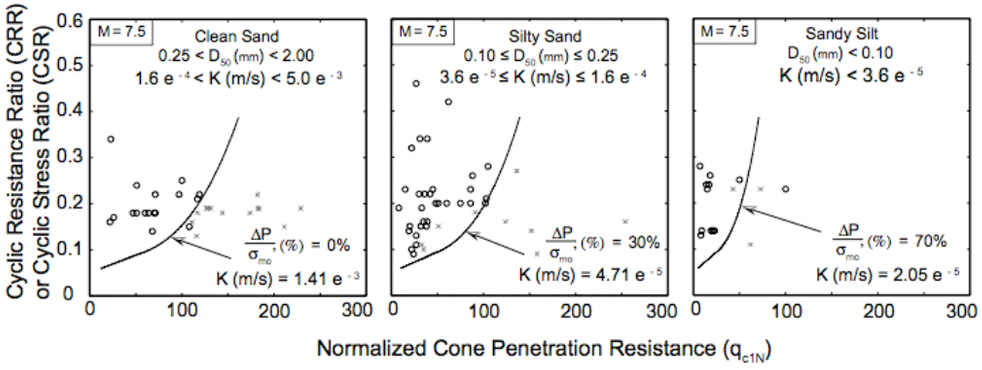


FIG 5. Results of curve matching between proposed procedure and Stark & Olson (1995) data. (Note: (x, o) represent non-liquefied and liquefied data points, respectively.)

Unique values of permeability that relate to the $\Delta P/\sigma_{mo}'$ values, as found for the three sand gradations of Stark & Olson (1995), can be determined and cross-checked with the values obtained from the direct comparison of the D_{50} range given for each sand gradation. Permeability values for each sand gradation are:

- Clean Sand - $0.25 < D_{50}(\text{mm}) < 2.00$ relates to $1.6e^{-4} < K(\text{m/s}) < 5.0e^{-3}$ and $\Delta P/\sigma_{mo}' = 0\%$ relates to $K(\text{m/s}) = 1.41e^{-3}$.
- Silty Sand - $0.10 \le D_{50}(\text{mm}) \le 0.25$ relates to $3.6e^{-5} < K(\text{m/s}) < 1.6e^{-4}$ and $\Delta P/\sigma_{mo}' = 30\%$ relates to $K(\text{m/s}) = 4.71e^{-5}$.
- Sandy Silt - $D_{50}(\text{mm}) < 0.10$ relates to $K(\text{m/s}) < 3.6e^{-5}$ and $\Delta P/\sigma_{mo}' = 70\%$ relates to $K(\text{m/s}) = 2.05e^{-5}$.

From this analysis, it is shown that the manual tuning of the ΔP-mediated CRR boundary curves is capable of matching the available field data and also produces an estimation of permeability within the range of the independently calculated permeability values, found using the median grain size relationship.

4 DISCUSSION AND CONCLUSIONS

This work explores the connection between soil permeability and fines content, to enable liquefaction resistance to be resolved in terms of a true state variable – that of permeability or of penetration-induced excess pore pressure. The linkage with penetration-induced pore pressures is direct since increased tip-local pore pressures reduce effective stresses. Thus, excess pore pressures directly shift the CRR threshold curve to the left, as illustrated in Figures 3 & 4. The form of these shifted curves, for prescribed excess pore pressures, closely approximate the boundaries evident between liquefied and non-liquefied soils. For the soil gradation boundaries identified by Stark and Olson (1995) these boundaries are represented by $\Delta P/\sigma_{mo}'$ ratios of 0, 30,

and 70% for clean sands, silty sands, and sandy silts, respectively in Figure 5. Conversion of the median grain size boundary and threshold curve values into an estimated permeability, by independent methods yield a permeability value, for the curve, which lies within the estimated range of permeability based on median grain size for all three soil gradations. Thus, measured magnitudes of excess pore pressure may be substituted for fines content, in locating the threshold behavior for liquefaction.

Direct validation of the model will require a data set that contains independently measured CPTu-generated excess pore pressures, together with liquefaction resistance indices. However, the feasibility of defining liquefaction resistance without *a priori* knowledge of fines content is an important advance in reducing ambiguities inherent within methods of site characterization developed to date.

Acknowledgements: This work is a partial result of support from the National Science Foundation under grant CMS-0409002. This support is gratefully acknowledged.

5 REFERENCES

Elsworth, D., and Lee, D. S. (2005). "Permeability Determination from On-the-Fly Piezocone Sounding." *Journal of Geotechnical and Geoenvironmental Engineering*, 131(5), 643-652.

Ishihara, K., Acacio, A. A., and Towhata, I. (1993). "Liquefaction-induced ground damage in Dagupan in the July 16, 1990 Luzon Earthquake." *Soils and Foundation*, 33(1), 133-154.

Jamiolkowski, M., Ghionna, V. N., Lancellotta, R., and Pasqualini, E. (1988). "New correlations of penetration tests for design practice." *Proceedings of the First International Symposium on Penetration Testing (ISOPT-1)*, Orlando, FL, USA, 263-293.

Lunne, T., Robertson, P. K., and Powell, J. J. M. (1997). *Cone Penetration Testing in Geotechnical Practice*, Blackie Academic and Professional.

Olsen, R. S. (1997). "Cyclic liquefaction based on the cone penetration test." *Proceedings of the NCEER Workshop on Evaluation of Liquefaction Resistance of Soils*, State University of New York at Buffalo, 225-276.

Robertson, P. K., and Campanella, R. G. (1985). "Liquefaction Potential of Sands Using the CPT." *Journal of Geotechnical Engineering*, 111(3), 384-403.

Robertson, P. K., and Wride, C. E. (1998). "Evaluating cyclic liquefaction potential using the cone penetration test." *Canadian Geotechnical Journal*, 35(3), 442-459.

Shepherd, R. G. (1989). "Correlations of Permeability and Grain Size." *Ground Water*, 27(5), 633-638.

Stark, T. D., and Olson, S. M. (1995). "Liquefaction Resistance Using CPT and Field Case Histories." *Journal of Geotechnical Engineering*, 121(12), 856 - 869.

Tseng, D. J. (1989). "Prediction of Cone Penetration Resistance and its Application to Liquefaction Assessment," Ph.D. Dissertation, University of California, Berkeley.

Numerical and Physical Modeling of Liquefaction Mechanisms In Layered Sands

Pelin Tohumcu Özener[1], S.M. ASCE; Kutay Özaydın[2], M.ASCE;
Mehmet Berilgen[3]

[1]Assistant Professor, Yıldız Technical University, Geotechnical Engineering Department, 34349, Beşiktaş, İstanbul, Turkey; tohumcu@yildiz.edu.tr
[2]Professor, Yıldız Technical University, Geotechnical Engineering Department, 34349, Beşiktaş, İstanbul, Turkey; ozaydin@yildiz.edu.tr
[3]Associate Professor, Yıldız Technical University, Geotechnical Engineering Department, 34349, Beşiktaş, İstanbul, Turkey; berilgen@yildiz.edu.tr

ABSTRACT: This paper presents the results of shaking table model tests and numerical modelling studies which were carried out to gain insight to liquefaction mechanisms in layered sand deposits. The experiments were performed by means of a shaking table testing system on uniform sand columns, silt interlayered sand columns and two layered sand columns deposited at various relative densities and subjected to different input excitations. Excess pore water pressures generated during dynamic loading were measured by pore water pressure transducers installed at three different depths. The physical model tests are also numerically modelled to analyse the dynamic behavior of uniform and layered sand columns by using the Towhata-Iai liquefaction model. The experimental and numerical analysis results revealed that the presence of a less permeable silt interlayer within the sand deposit and existence of a loose sand layer underlying dense sand deposits can have significant effect on the liquefaction behavior.

INTRODUCTION

Site investigations show that sandy soil deposits in the field are generally not uniform and homogenous. They are often composed of sand sublayers having different relative densities and may contain silt and clay interlayers. Since layered structure or stratification in sand deposits are known to have significant influence on the liquefaction response of soil systems, several investigations have been carried out to study the effect of soil stratification on the evolution of liquefaction mechanism. Scott and Zuckerman (1972), Huishan and Taiping (1984), Liu and Qiau (1984), Elgamal et al. (1989), Adalıer

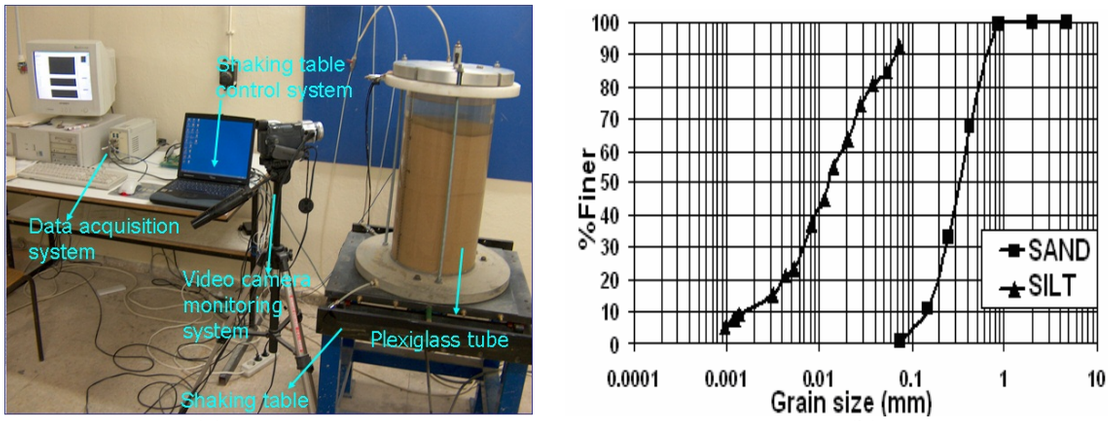
(1992), Fiegel and Kutter (1994), Kokusho (1999, 2002) and Özener Tohumcu et.al (2006) performed studies which focused on liquefaction and its consequences in multilayer sandy soil systems. These studies showed that the presence of a less permeable soil layer (silt or clay) within a liquefiable sand layer may lead to development of a waterfilm beneath the silt or clay layer. The behaviour of dense sand layers underlaid by loose sand layers was experimentally investigated by Steedman and Sharp (2001) and it was observed that dense overlying sand layers are also capable of liquefying due to rapid transmission of excess pore pressures from the lower loose sand layers.

In this paper, the liquefaction behavior of layered sands is investigated both numerically and experimentally, and the results are presented. In order to be able simulate some field liquefaction situations and provide general insight into the basic mechanisms and parameters influencing liquefaction, the experiments are carried out on uniform sand columns, silt interlayered sand columns and two layered sand columns deposited at various relative densities and subjected to different input excitations. The experiments are performed by using a testing system consisting of a cylindrical plexi-glass container and a shaking table on which the plexi-glass container is mounted. Excess pore water pressures generated during dynamic loading are measured using pore water pressure transducers installed at three different depths. The physical model tests are also numerically modelled to analyse the dynamic behavior of uniform and layered sand columns by using the Towhata-Iai liquefaction model, excess pore water pressures are computed and compared with the experimental results.

EXPERIMENTAL STUDY

Shaking Table Model Tests

The experimental set-up was designed at Yıldız Technical University Soil Mechanics Laboratory. The dynamic excitations are generated by means of a shaking table system which is triggered by a frequency-controlled electric motor producing sinusoidal motions. The general view of the experimental set-up is shown in Figure 1a. All the test models are prepared by pouring dry sand into water in a plexiglass cylinder (Fig.1a) of 24cm in diameter and 60 cm in height. The sand deposition is achieved through a sand pluviation system which is designed for preparing target relative densities. For the silt-interlayered test models, a 1 cm thick silt seam is placed within the sand column. Three pore water pressure transducers are installed at three different levels to measure time-dependent variation of excess pore water pressures under dynamic excitations. The surface settlement and the water film thickness are measured by a digital video camera which is controlled by an image processing computer program to record images at 1 second time intervals. The grain size curves of the sand (D_{50}=0.31mm, e_{max}=0.88 and e_{min}=0.53) and silt used in the model tests are shown in Figure 1b.



(a) (b)

FIG. 1. a) The general view of the experimental set-up (b) Grain size distribution curves for the soils used in the experiments

Model Configurations

To investigate liquefaction mechanisms in layered soils, 3 series of shaking table tests are carried out. The characteristics of each are summarized in Table 1. The test models consist of uniform sand columns and various types of layered sand columns which correspond to different field situations. All the models are subjected to sinosodial base motions (consisted of 300 cycles) with 20 Hz, 25 Hz and 30 Hz which correspond to 0.23g, 0.30g and 0.40g peak accelerations, respectively. These high loading intensities were chosen in order to be able to trigger the soil system to reach liquefaction.

Table 1. Summary Description of Shaking Table Model Tests

Model Series	Model Code	Model Height (cm)	Acceleration (g)	Relative Density (%)	
				Upper Layer	Lower Layer
Uniform Sand	U1A, U1B,U1C	45	0.23, 0.30, 0.40	40	
	U2A, U2B,U2C	45	0.23, 0.30, 0.40	72	
Silt-Interlayered Sand	S1A, S1B, S1C	45	0.23, 0.30, 0.40	40	40
	S2A, S2B, S2C	45	0.23, 0.30, 0.40	72	72
Layered Sand	L1A, L1B, L1C	45	0.23, 0.30, 0.40	72	40
	L2A, L2B, L2C	45	0.23, 0.30, 0.40	40	72

The uniform sand models included soil columns with two different relative densities (Dr=%40 and %72) subjected to sinusodial input motions with peak accelerations of 0.23g, 0.30g and 0.40g. The silt-interlayered models were constructed to examine the effect of a less-permeable sand layer within a liquefable sand layer and its consequences on the generation of excess pore water pressures. In these models (S1 and S3) the 45 cm sand column at relative densities of %40 and %72 included a 1 cm thick silt seam. Additionally, the behavior of layered sand deposits are investigated using layered sand columns consisting of loose sand layers overlying dense sand layers and

dense sand layers underlain by loose sand layers.

Experimental Results

In this paper, the results of three series of shaking table model tests are presented. Because the main objective of the experimental study was to explore the development of excess pore water pressures in layered sand deposits, the test results are presented in terms of maximum excess pore water pressure ratio ($r_u=\Delta u/\sigma_{vo}'$), surface settlement and generation of water film under a less permeable seam. The time histories of input base accelerations, excess pore water pressures and settlements as measured on models U1B and S1B subjected to a 0.30g peak acceleration are shown in Figures 2 and 3, corresponding to the cases with and without a silt seam, respectively. The instants of reaching maximum excess pore water pressures (indicated by t_L) are also shown in these figures indicating that there is a time lag in reaching maximum excess pore water pressures from bottom to top. As it is seen, the maximum excess pore water pressures are reached first at the deepest transducer (PPT3) and then proceed upward towards the surface.

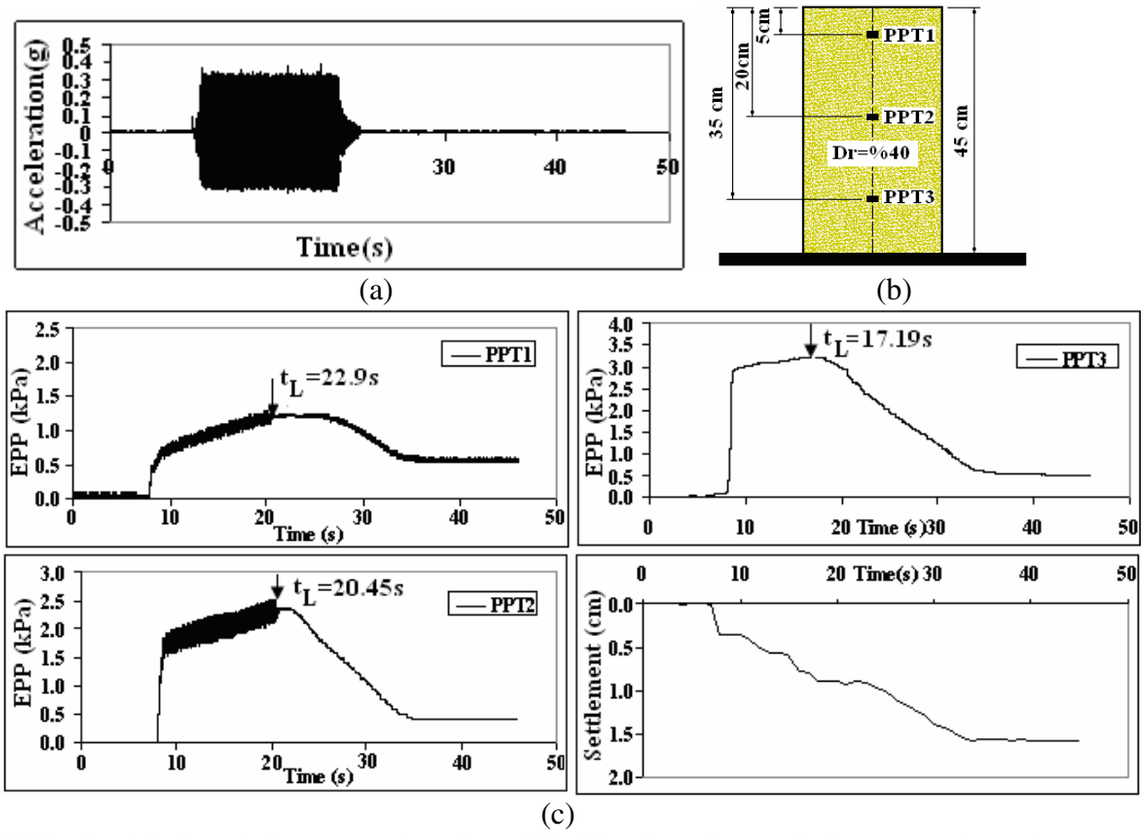


FIG. 2. (a) Input base acceleration (b) The locations of the pwp transducers (c) excess pore water pressures and surface settlement measured in a uniform sand column (Model U1B)

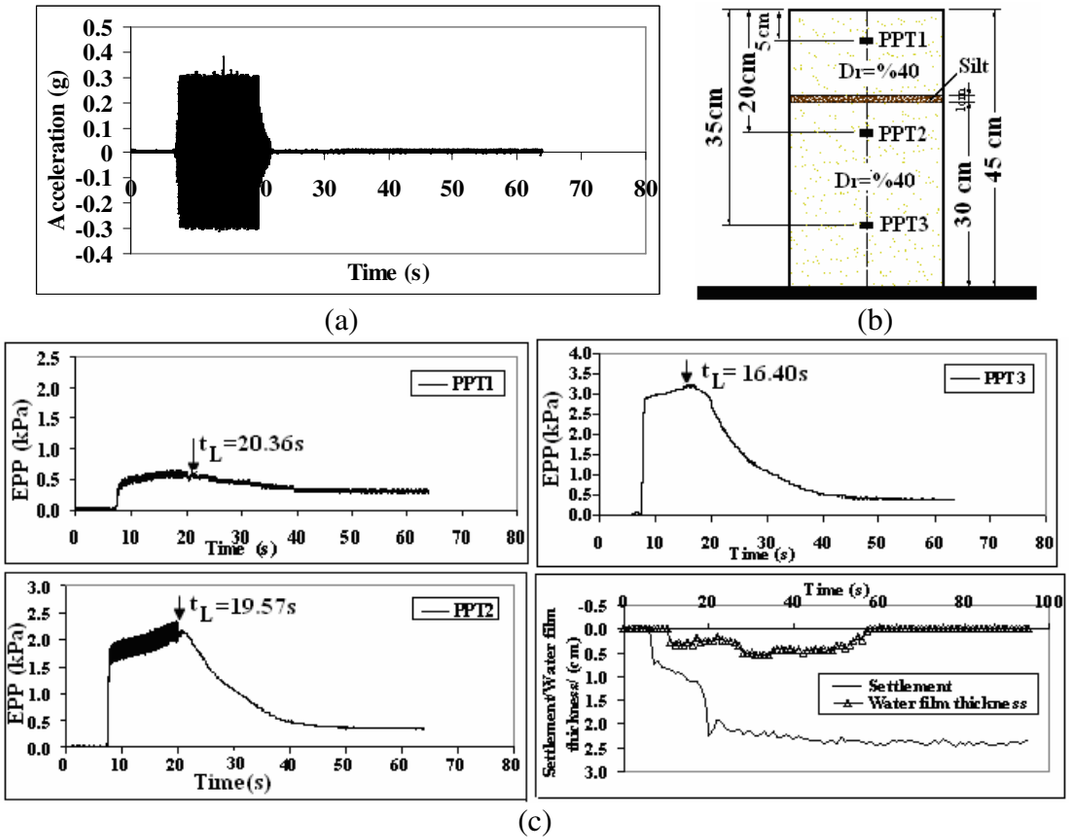


FIG. 3. (a) Input base acceleration (b) The locations of the pwp transducers (c) excess pore water pressures, surface settlement and water film thickness for sand column with a silt seam (Model S1B)

Figure 3 also shows the variation of water film thickness with time. It is observed that excess pore water pressures and water film beneath the silt seam started to develop as soon as the shaking began and state of liquefaction has developed. Although even after the excess pore water pressures leading to liquefaction have dissipated and post liquefaction settlements have ended, the water film continued to exist for a longer period of time (about 97 secs). From the experimental observations, it is concluded that the presence of a thin silt layer inhibits excess pore water pressure dissipation after liquefaction and causes the formation of water film at the interface. As seen in Figures 2 and 3, after the shaking stopped, the pore water pressure readings have not returned to their initial values and some residual values remained due to some inevitable settlements that the transducers have suffered during shaking.

The experimental studies also discovered that the accelaration level has a significant influence on the generation of water film. In some of the silt interlayered models (S1C, and S2C) video camera observations showed that due to a sudden turbulence that took place during shaking, silt layer has ruptured and the most of the water film vented to the surface by carrying silt particles together. From these observations, it is concluded that

in silt interlayered sand deposits under low confining stresses, development of a water film may not be possible at strong ground shaking levels.

Comparison of Silt Interlayered and Uniform Sand Model Behavior

In order to be able to demonstrate the influence of a less permeable soil layer in a sand strata, the peak excess pore water pressure ratios (r_u) at three different depths are compared with the ones measured in uniform sand models. Figure 4 shows the variation of peak r_u values with depth at three different acceleration levels for the cases with and without the silt seam at relative densities of %40 and %72.

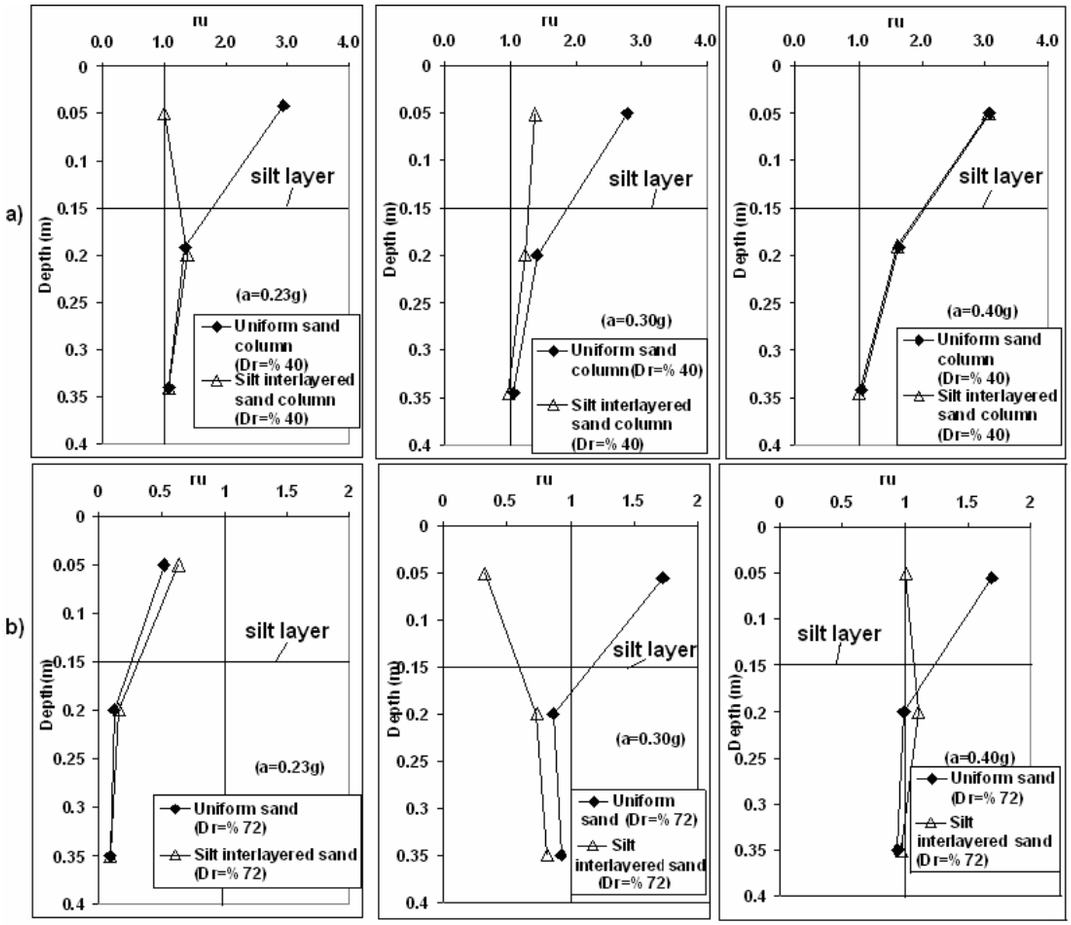


FIG. 4. Comparison of variation of maximum r_u values with depth for the cases with silt and without the silt seam a) Dr= %40 b) Dr=%72

As can be seen in these figures, while the excess pore water pressures measured underneath the silt layer are close to the values measured at uniform sand columns, lower values are measured above the silt seam than the values measured in uniform sand column. This implies that the presence of silt layer reduces the excess pore water pressures above the silt layer most probably by inhibiting upward migration of the pore

water pressures into the upper layer. It is also worth to note that excess pore pressures leading to r_u values excceding unity are measured especially in uniform sand columns at shallow depths. Since the models are subjected to vibrations at the base, excess pore water pressures migrate upwards leading to high hydraulic gradients. High hydraulic gradients cause upward water flows and seepage forces causing additional increases in pore water pressures.

Comparison of Layered and Uniform Sand Model Behavior

Two layered sand columns at various relative densities are subjected to different input excitations to study the generation of excess pore water pressures in layered sands during earthquakes, and the measured maximum excess pore water pressure ratios (r_u) are compared with the ones measured in uniform sand models. Figures 5 shows the variation of maximum r_u values with depth in a layered sand model (L1) comprising of a loose sand layer overlaid by a dense sand layer, with the values measured in uniform loose sand model (U1) at three different acceleration levels. It is observed that the migration of high excess pore water pressures from the lower loose layers into the upper dense layers have led to development of higher than expected excess pore water pressures in the upper dense layer, consistent with the observations made in the centrifuge tests carried out by Steedman and Sharp (2001). The development of high excess pore water pressures in the overlying dense sand layer due to the transmission of excess pore pressures from the underlying loose sand layer is better demonstrated in Figure 6 where experimental results for densely deposited layered (L1) and uniform (U2) sand models are presented with the data indicating the times (t_L) when maximum excess pore water pressures are reached at each transducer elevation. The time lags in reaching maximum excess pore water pressures are also indicative of the pore water pressure transmission from bottom to top.

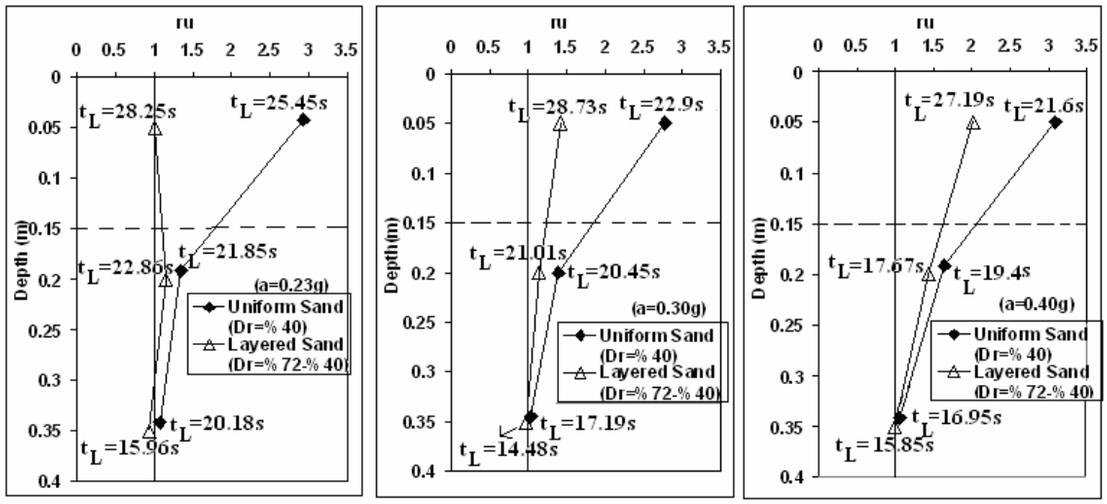


FIG. 5. Comparison of variation of maximum r_u values with depth for a layered sand model (L1) and a uniform loose sand model (U1)

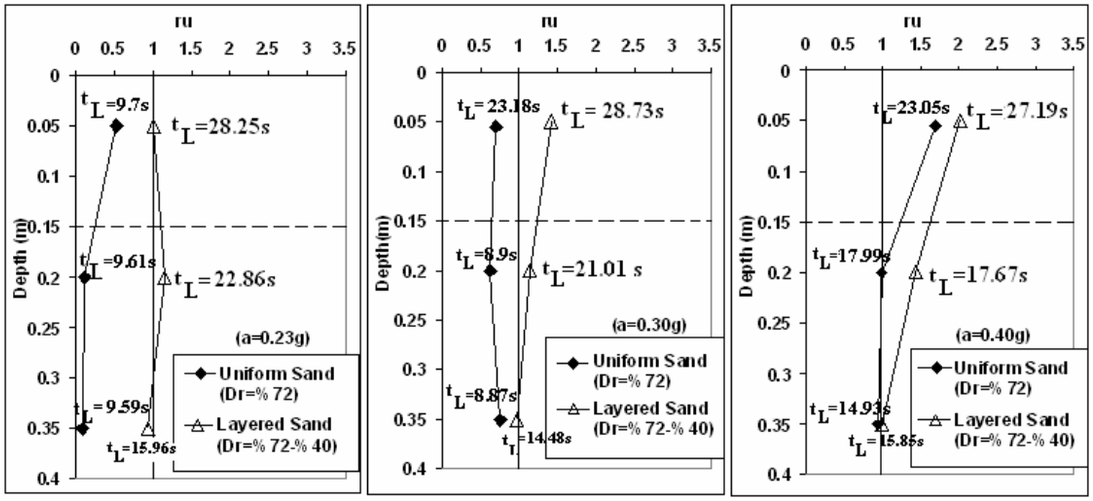


FIG. 6. Comparison of variation of maximum r_u values with depth for a layered sand model (L1) and a uniform dense sand model (U2)

In Figure 7, the behavior of dense sand layers overlaid by loose sand layers during dynamic loading are demonstared by comparing the of excess pore water pressure ratios measured in a layered sand model (loose sand layer at 40% relative density overlying a dense sand layer at 72% relative density) and a uniform sand model (at 40% relative density). It is observed that the excess pore water pressures developed in the upper loose sand layer are highly influenced by the relative density of the underlying dense sand layer, demonstrating that pore water pressure transmission plays an important role in the generation of excess pore water pressures during earthquakes.

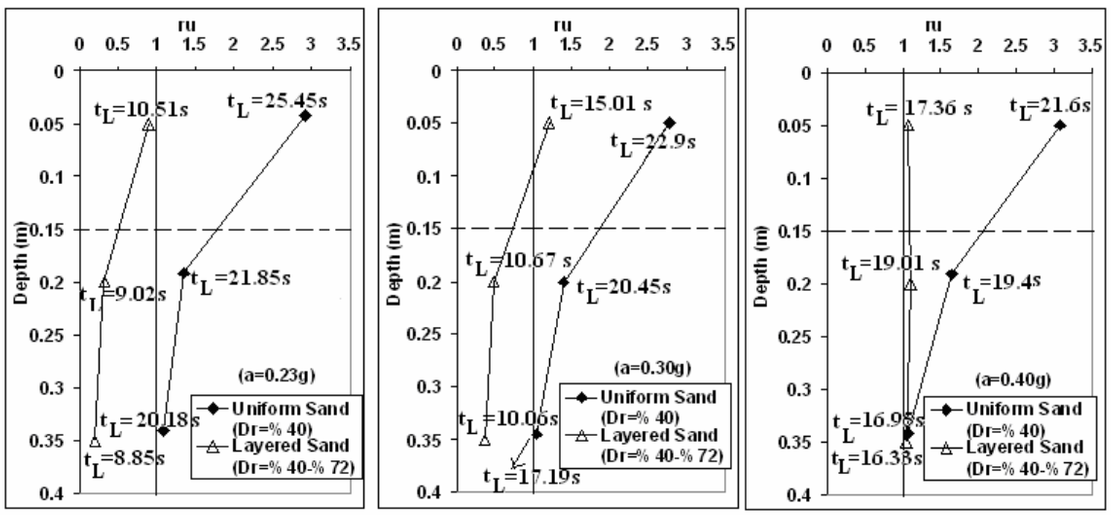


FIG. 7. Comparison of variation of maximum r_u values with depth for a layered sand model (L2) and a uniform loose sand model (U1)

NUMERICAL STUDY

The physical model tests are also numerically modelled in finite element program DIANA by using the Towhata-Iai liquefaction model (Towhata and Ishiara 1985, Iai et al. 1990) to analyse the dynamic behavior of uniform and layered sand columns. The numerical models are created by using 2D quadrilateral elements. The left and right boundaries of the models were restricted in the horizontal direction by allowing only vertical displacements in the nodes in order to be able to consider the rigid confinement effects present in the experiments. The non-linear constitutive model employed in the numerical analysis is based on the plasticity theory and includes the effect of rotation of the effective principal stress axes, the effect of anisotropic consolidation and the loading history of the soil. These factors are taken into account by the liquefaction front and multiple shear mechanism concepts which enable to compute the excess pore water pressure generation during cyclic loading as a function of plastic shear work. The model parameters used in the analysis are outlined in Table 2. Here, ϕ_f and ϕ_p are the shear resistance angle and phase transformation angle of the soil, respectively, S_1, w_1, p_1, p_2, c_1 are dilatancy parameters of the soil and h_{max} is the maximum damping factor. The procedure to calibrate these parameters can be found in Iai et al. (1990) and Tohumcu Özener (2007).

Table 2. Model Parameters for the Analyses

Soil Type	Relative Density (%)	ϕ_f (°)	ϕ_p (°)	S_1	w_1	p_1	p_2	c_1	h_{max}
Sand	40	34	29.6	0.0005	2.0	0.75	0.72	1.8	0.24
	60	37	33.4	0.0005	5.0	2.0	0.72	1.8	0.24
	72	39	35.0	0.0005	15.0	4.0	0.72	1.8	0.24
Silt	-	37	33.4	0.0005	30.0	1.0	4.0	1.8	0.20

Comparison of Experimental Results and Numerical Simulations

As a result of the numerical analyses, the excess pore water pressure time histories were computed and compared with the experimental results. The computed and measured time histories of excess pore water pressures are shown in Figure 8 for a uniform sand column (U1B) at 40% relative density. It is seen that the computed excess pore water pressure time histories are in close aggrement with the measured values except the one at shallow depth. This inconsistency is thought to be due to the fact that numerical model is incapable of modelling the upward migration of water flow leading to higher pore water pressure accumulation observed during the experiments especially at shallower depths.

The existence of a less permeable silt layer in a sand deposit and the behavior of dense sand layers overlying loose sand layers or dense sand layers overlaid by loose sand layers are also simulated by Towhata-Iai numerical model and compared with the numerical results for uniform sand models. In Figure 9, the variation of computed excess pore water pressure ratios with depth for the cases representing a silt interlayered sand column and two layered sand columns are compared with the values computed for the

uniform sand model at 40% relative density.

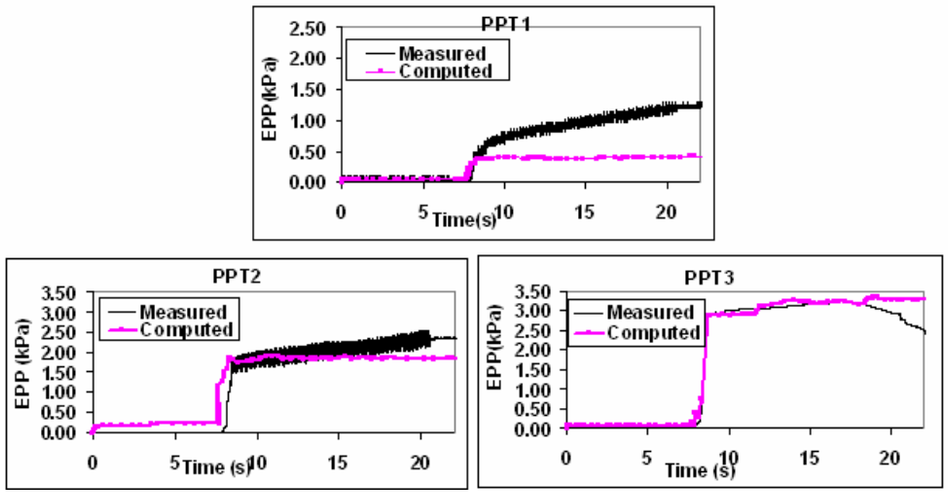


FIG. 8. The time histories of computed and measured excess pore water pressures in a uniform sand model (U1B)

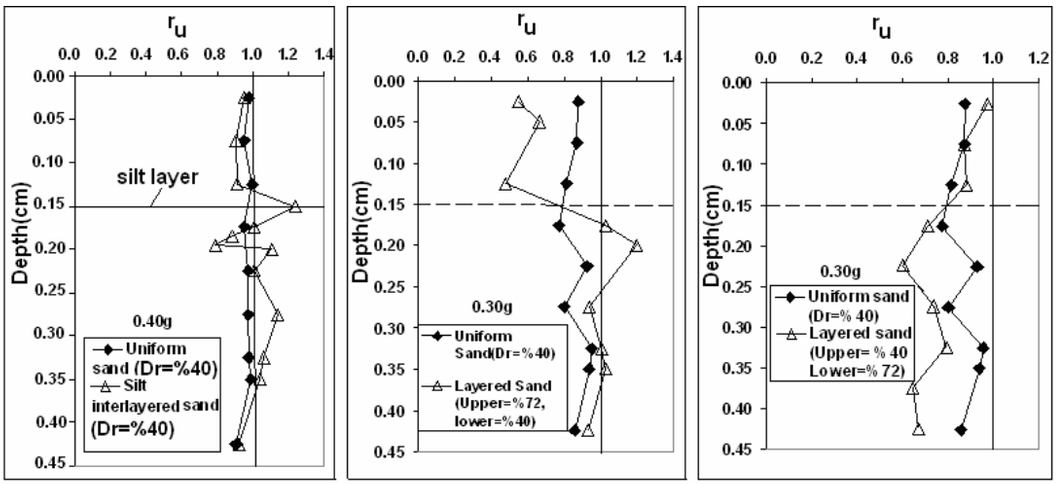


FIG. 9. Comparison of variation of computed r_u values with depth a) for a silt interlayered sand model (S1C) with a uniform sand model (U1C) b) for a layered sand model (L1B) with a uniform sand model (U1B) c) for a layered sand model (L2B) with a uniform sand model (U1B)

It is observed from Figure 9a that, while the computed peak values of r_u for the uniform sand column vary uniformly with depth, there is a small increase in the r_u values for the silt interlayered case below the silt seam, demonstrating the accumulation of pore water pressures below the silt seam. From the comparison shown in Figure 9b, it is seen that the presence of an overlying dense sand layer has an increasing effect on the excess pore water pressures developed in the lower loose sand layer, but contrary to the experimental observations, the development of high excess pore water pressures in the

upper dense sand layer due to the migration of excess pore water pressures from the bottom loose sand layer is not predicted. In Figure 9c where the computed r_u values of layered sand model comprising of dense sand layers overlaid by loose sand layers are compared with the uniform sand model, it is seen that the excess pore water pressures generated in the upper sand layer are not influenced from the presence of underlying dense sand layers.

From the results of numerical analyses, the effect of a silt seam on the generation of pore water pressures, formation of a water film and the development of excess pore water pressures in layered sand columns (which are clearly observed in the model tests) are not satisfactorily simulated in the numerical analysis. It is believed that this is due to the fact that the constitutive model employed in the analysis can not capture the migration of upward water flow resulting from excess pore water pressures. Therefore, it is believed that a constitutive model coupled with a ground water flow analysis is needed to be used to simulate the generation of excess pore water pressures especially in layered sand deposits.

CONCLUSIONS

In this paper, the results of shaking table model tests and numerical analyses which were carried out to investigate the liquefaction mechanism in layered sands are presented.

Based on the observations in the shaking table tests on uniform sand, silt interlayered sand and two layered sand models, it is concluded that the generation of excess pore water pressures are highly influenced by the pore water pressure transmission. In silt- interlayered sand models, it is observed that the presence of a thin silt layer which prevents drainage and dissipation of excess pore water pressure can cause formation of a water film at the interface between silt and sand layers. This water film may continue to be maintained even after the excess pore water pressures have dissipated and post liquefaction settlements have ended. The silt seam is also seen to reduce the excess pore water pressures above the silt layer by inhibiting the upward migration of pore water pressures into the upper layer. The experimental results from two layered sand columns comprising of loose sand layers overlaid by a dense sand layer or loose sand layers overlying dense sand layers also demonstrated the significant role of pore water transmission in the development of excess pore water pressures during earthquakes. The transmission of excess pore water pressures from bottom loose sand layers is observed to liquefy the dense overlying sand layers.

The numerical modelling of silt interlayered sand model tests showed that there is a small amount of increase in the r_u values below the silt seam demonstrating the accumulation of pore water pressures at that depth due to the presence of a silt seam. On the other hand, some contradictions are observed between the experimental and numerical results of layered soils which are believed to be due to the insufficiency of the constitutive model in modelling the upward migration of pore water during the generation of excess pore water pressures. Therefore, it is believed that a constitutive

model coupled with a ground water flow analysis is needed to more accurately simulate the generation of excess pore water pressures especially in layered sand deposits.

ACKNOWLEDGMENTS

The authors gratefully appreciate the financial support of the Yıldız Technical University Research Fund and Scientific and Technological Research Council of Turkey for this study.

REFERENCES

Adalıer, K. (1992). "Post-liquefaction behavior of soil systems". MS thesis dissertation, Renssealer Polytechnic Institute, Troy, N.Y

Elgamal, A.W., Dobry, R., and Adalıer, K. (1989). Small scale shaking table tests of saturated layered sand-silt deposits. *2nd U.S.-Japan Workshop on Soil Liquefaction, Buffalo, N.Y., NCEER Rep. No. 89-0032, 233-245.*

Fiegel, G.L. & Kutter, B.L. (1994).Liquefaction mechanism for layered soils. *J.Geotech. Engrg., ASCE*, 120(4):737-755.

Huishan, L.and Taiping, Q. (1984). "Liquefaction potential of saturated sand deposits underlying foundation of structure". *Proc.8th World Conf. Earthquake Engineering,* Prentice Hall : 199-206.

Iai, S., Matsunaga, Y., Kameoka, T. (1992). "Parameter identification for a cyclic mobility model." *Report of the Port and Harbour Research Inst.*, Vol.29 (4): 57-83.

Kokusho, T.(1999). "Water film in liquefied sand and its effects on lateral spread." *J.Geotech. Engrg., ASCE,* 125(10):817-826.

Kokusho,T. (2002). "Mechanism for postliquefaction water film generation in layered sand" *J.Geotech. Engrg., ASCE,* 128(2):129-137.

Liu, H., and Qiao, T. (1984). "Liquefaction potential of saturated sand depoists underlying foundation of sturucture." *Proc. 8th World Conf. Earthquake Engineering, Vol.3*, Prentice Hall, Englewood Cliffs, N.J. : 199-206

Özener Tohumcu, P., Berilgen, M., Özaydin, K. (2006). "Investigation of liquefaction in layered sands by means of shaking table tests" *The 6th International Conference in Geotechnics (6th ICMPG)*, Hong Kong, Vol.1 : 475-480.

Özener Tohumcu, P. (2007). "Investigation of liquefaction and postliquefaction behavior of layered sands during earthquakes by means of model tests" *Ph.D thesis dissertation*, Yıldız Technical University, İstanbul.

Scott, R.F. & Zuckerman, K.A. (1972). "Sandblows and liquefaction in the Great Alaskan Earthquake of 1964". *Engineering publication 1606, National Academy of Sciences*, Washington, D.C.: 170-189

Steedman, R.S.and Sharp, M. (1995). " Liquefaction of deep saturated sands under high effective confining stress." *Proc. 4th Intern. Conf. on Earth. Eng.,* G. Duma, ed., Balkema, Rotterdam: 441-446.

Towhata, I., Ishiara, K., (1985), "Shear work and pore water pressure in undrained shear", *Soils and Foundations*, Vol.25(3):73-84.

Observations on Sand Boils from Simple Model Tests

Andrew Brennan[1]

[1]University of Dundee, UK. a.j.brennan@dundee.ac.uk

ABSTRACT: Sand boils are a long-recognized phenomenon associated with soil liquefaction. Deep liquefied sand is acknowledged to be able to burst through overlying impermeable layers. However, the exact conditions required to produce sand boils are unclear, as is their relative importance to engineering structures. To investigate the phenomenon further, a series of simple model tests were performed. The models consisted of small sand samples containing one or more layers of consolidated silt, visible in profile, which are then vibrated. Visual monitoring was taken of structural settlement and the influence of multiple layering, and the ensuing water films and sand boils observed. It was found that relatively heavy foundations over relatively thin silt layers were susceptible to sand boils. If the silt layer was too thick to be unduly strained by the foundation then the occurrence of water films was suppressed. Buried silt layers were seen to experience a hitherto unobserved phenomenon whereby silt was carried up towards the soil surface with the pore fluid during shaking. It is concluded that the relative importance of sand boils and associated layered-soil phenomena is an area requiring further investigation.

INTRODUCTION

Earthquake-induced soil liquefaction has been recognized as a hazard for over forty years (e.g. Seed and Lee, 1966; Ishihara, 1985) and static liquefaction for longer (e.g. Koppejan et al., 1948). Loose saturated sands attempting to settle during shaking are unable to dissipate fluid from the contracting void spaces quickly enough, and individual soil grains lose contact with each other and go into suspension (as observed by, e.g., Sasaki et al., 2001). The soil consequently loses strength and dramatic failures occur via a number of mechanisms such as the soil's loss of strength (Fig. 1a) or sand boils (Fig. 1b), bursts of liquefied sand spilling over the ground surface, for example.

Most studies have concentrated on the case where the entire soil mass is liquefiable. However, as natural soils can often contain stratifications of sands and clays. The presence of layers of low permeability materials through liquefiable soils has been shown to create problems and failure mechanisms additional to the unstratified case. Some laboratory element tests have been carried out on layered small samples (e.g. Amini and Sama, 1999), as well as rudimentary 1-g models (Butterfield and Bolton,

2003) and centrifuge tests (e.g. Fiegel and Kutter, 1994; Brennan and Madabhushi, 2005). Thin water films can form at the inter-soil boundary as impermeable layers hinder fluid dissipation (Kokusho, 1999). Based on current understanding, sand boils seem to occur when trapped pore water at elevated pressure bursts through weaknesses in overlying low-permeability layers.

Beyond the qualitative basics outlined above, there have been relatively few studies performed specifically to investigate sand boil formation, possibly due to their perceived low engineering importance. However, sand boils are commonly taken as evidence for liquefaction after an earthquake, so from this point of view it is important to understand a little more about the conditions which are favorable or otherwise for sand boil occurrence. This research therefore aims to understand the factors leading to sand boil occurrence better. The following specific objectives are given for this paper:-

- to develop a means of creating sand boils in a simple laboratory experiment,
- to observe the influence of multiple soil layers, and
- to observe the influence of surface loads on sand boil occurrence.



FIG. 1. a) Liquefaction-induced building settlement, Niigata. b) Sand boil, California. Photographs: Karl V. Steinbrugge Collection, Earthquake Engineering Research Center, University of California, Berkeley.

METHODOLOGY

To investigate the above objectives, a series of simple 1-g model tests were carried out. Two test series are reported in this paper, taken from the wider series performed at Dundee University by Ritchie (2006) and Moran (2007). Tests by Ritchie are labeled "NR" and investigate shallow foundation settlements. Tests by Moran are labeled "DM" and investigate multiple layers. Six tests, shown in Fig. 2, form the basis for the observations presented in this paper. The soil sample was placed in a simple Perspex-fronted aluminium container which was then clamped to a sieve-shaker. Vibration was applied for a period up to two seconds. This is shown below to be sufficient to cause liquefaction conditions in the sand. The applied vibration is difficult to characterize as it occurs both horizontally and vertically. It is not measured, but is believed to be at frequencies of the order of 10 Hz and amplitudes of the order 2 mm. An obliquely-

mounted digital video camera recorded the soil behavior during and after shaking.

Soil used for the tests was a fine Congleton sand and a uniform HPF5 silt. The sand is uniform with an internal friction angle of 31^0 and reference void ratios e_{min} = 0.49 and e_{max} = 0.85. Model construction was slightly different for test series NR and DM. Test series NR were formed by dry-pluviating sand to a void ratio of around 0.75 (relative density ~ 30%), then saturating with water through the base of the container. Silt was mixed at 30% moisture content, just above the liquid limit, and spread on the soil surface as evenly as possible. To ensure some strength in the layer, a 4 kg mass was applied through a sheet of porous plastic for drainage and load spreading and the sample allowed to consolidate for 24 hours. The preload and the porous plastic were removed prior to testing. Test series DM differ in that to accommodate multiple silt layers the sand could not always be saturated through the model base. Sand in these experiments was therefore wet-pluviated through predetermined amounts of water to a similar void ratio.

It should be noted that the experiments do not attempt to simulate an earthquake but to examine the fluid-driven interactions between liquefied/reconsolidating sands and their less permeable crusts. Also, these are not scale models of larger prototypes but small prototypes in themselves and should be interpreted as such.

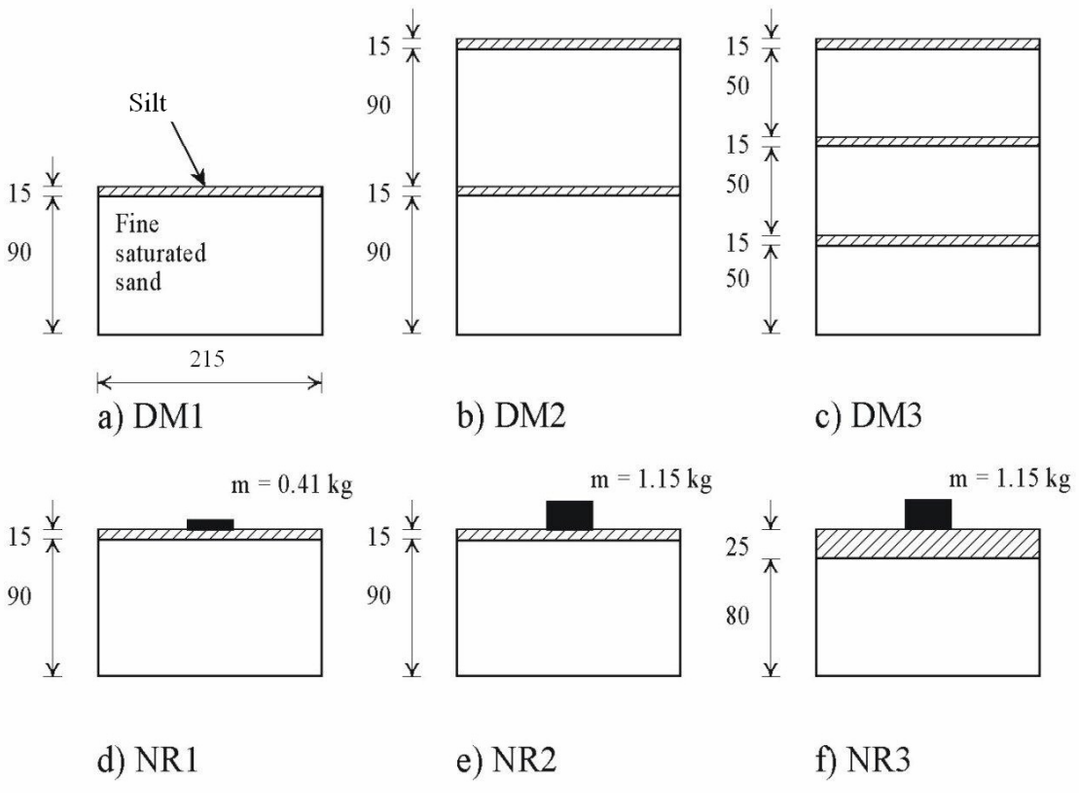


FIG. 2. Models employed in two test series. All dimensions in millimeters. Not to scale. DM tests from Moran (2007). NR tests from Ritchie (2006). Plan area 215 mm wide by 105 mm deep.

PORE PRESSURES

Pore pressure transducers (PPTs) were not available for the whole test series, but an initial test was carried out in order to confirm that the experimental conditions did achieve liquefaction in the sand layer. This test was performed in a sand sample 200 mm deep without a surface crust. Fig. 3 shows the excess pore pressures (total pore pressure – hydrostatic pore pressure) recorded at four depths. Also plotted is an approximate value of initial vertical effective stress σ_{v0}'. This is based on the final PPT position, so small changes in instrument location will affect the accuracy of this value. Such differences manifest as a difference between the initial and final value of excess pore pressure, which is seen in Fig. 3b and Fig. 3c.

All instruments record large transient pore pressures due to the intense shaking. This can exceed σ_{v0}' due to a significant vertical acceleration. Shaking is followed by a period of prolonged high excess pore pressure while deeper soil layers drain. These values are close to σ_{v0}' which, together with their prolonged nature, suggests that the soil is in a state of liquefaction. A second experiment (not presented) showed identical results, in line with the similar test of Florin and Ivanov (1961).

Based on this, it is concluded that this shaking applied to this sand at this density causes it to liquefy. Therefore, by keeping these variables constant, sand in the following experiments would also have liquefied.

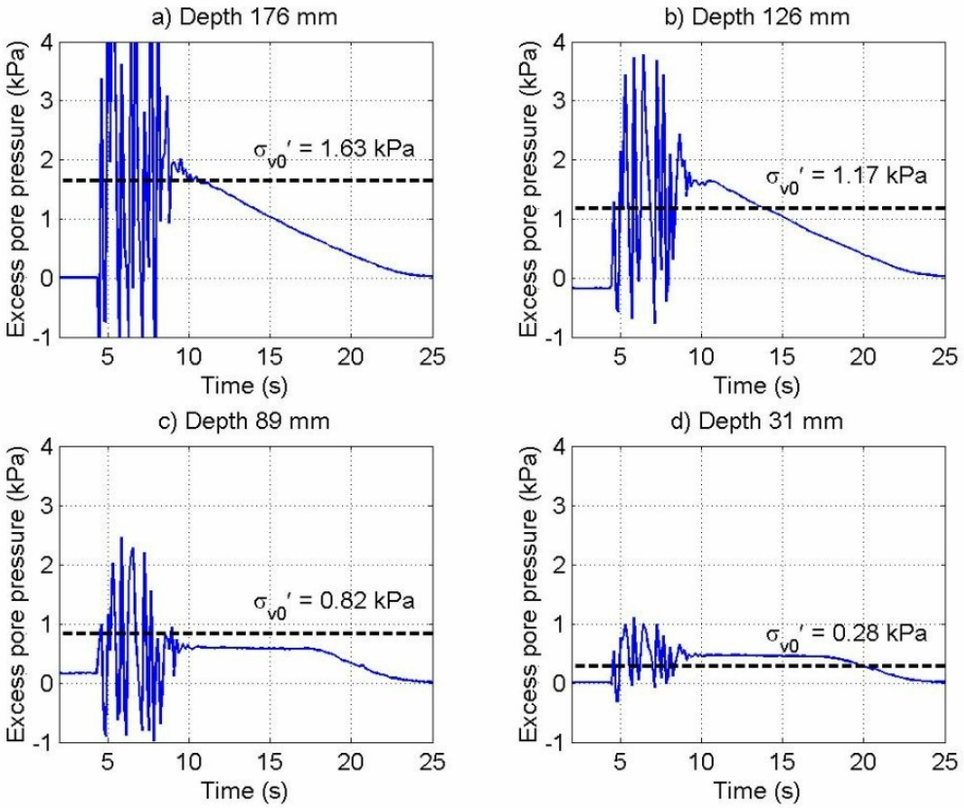


FIG. 3. Excess pore pressures recorded in a 200 mm sand sample, without silt layers.

OBSERVED PHENOMENA IN STRATIFIED SOILS

Water Films

As expected, water films visibly formed at the silt-sand boundaries in all tests, with thicknesses of the order of 1 mm. Similar observations have been made by, e.g., Kokusho (1999). Video images were insufficiently high resolution to distinguish any differences between water films arising during different tests. What was clear, however, was that in multiple-layer tests then water films were invariably first seen at the shallowest layer, followed by formation at successive depths (Moran, 2007). This would sometimes occur during shaking and sometimes after shaking had finished, depending on the duration of shaking.

Sand Boils

Sand boils were observed in all tests. Fig. 4 shows how these appeared during testing, as thin vertical channels through the silt layer that may or may not contain sand. These often appeared to widen as they approached the surface. Ejection was often sufficiently violent to disturb the surface of the water (which was always above the soil surface) indicating great speed and pressure release despite the small-scale nature of the test. These always occurred *after* the two seconds applied shaking had finished. Further experiments (not presented - Ritchie, 2006; Moran, 2007) in which the same and similar models were subjected to increasingly longer duration shaking showed that an exceptionally long duration of shaking was required to cause boiling during shaking. This may be because the required redistribution of fluid required a much greater length of time than the duration of shaking. This correlates with many eyewitness accounts of earthquakes.

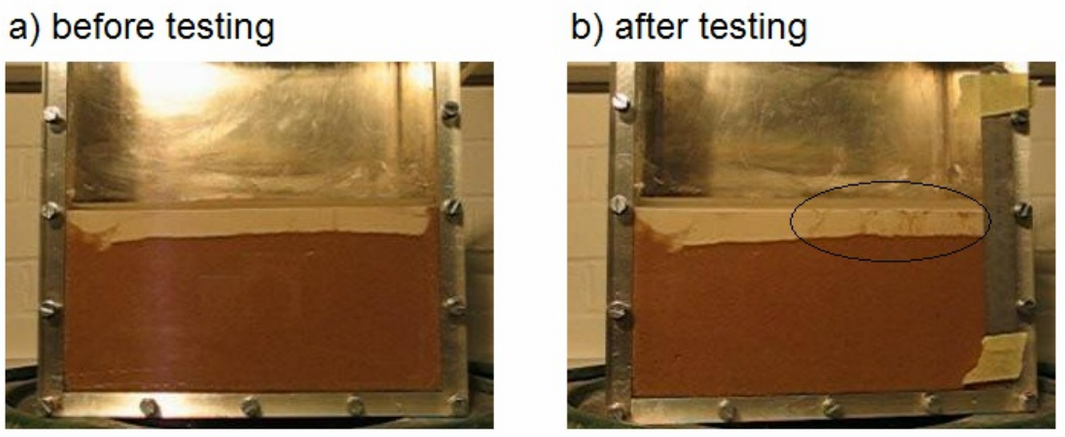


Fig. 4. Illustration of sand boils using before and after images of test DM1.

Silt Clouds

In the experiments with sub-surface silt layers, repeated shaking was seen to induce a further hitherto unobserved phenomenon. Material from this sub-surface silt layer was entrained in the pore fluid and traveled vertically upwards towards the soil

surface. Fig 5 shows examples of these "silt clouds". In these tests, these began very soon after the start of shaking and were *not* seen to continue for a long time after shaking, relative to the other phenomena of water films and sand boils.

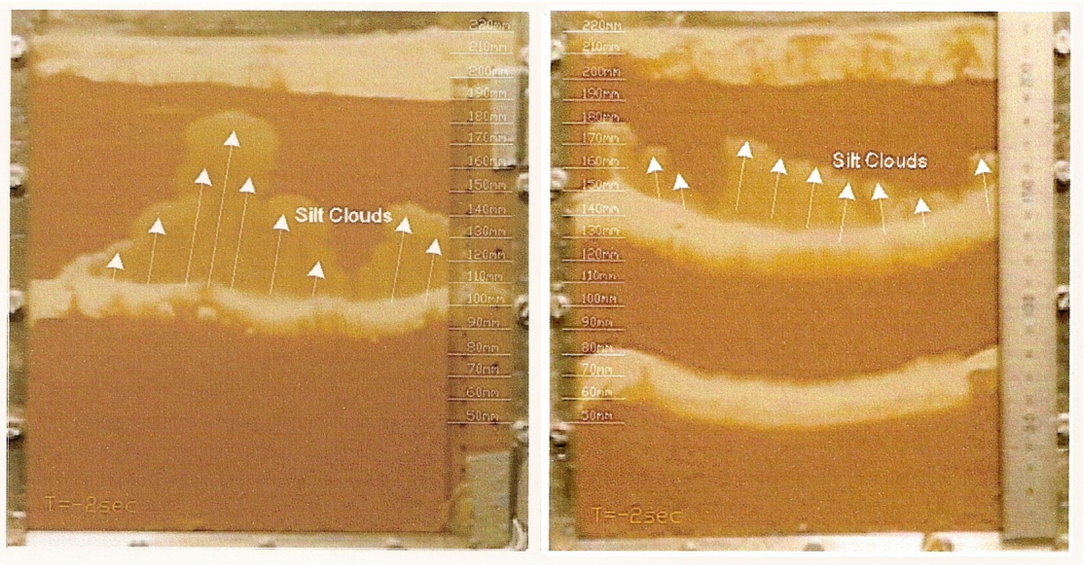


FIG. 5 Illustration of "silt clouds" from tests a) DM2; b) DM3.

Silt clouds appeared to be due to the top surface of the silt being entrained in suspension by the pore fluid. This may have been caused by the high shaking intensity liquefying the silt, or by the high excess pore pressures causing seepage into the silt at a large hydraulic gradient and raising the local pore pressures in the silt (i.e. liquefying the silt). Whether different levels of shaking intensity or conditions of silt would also produce silt clouds is not known, as these variables were kept constant for this study. Particle and void sizes may also be important variables. Therefore, silt clouds are here noted as an observation and are the subject of further research.

On the one occasion that a silt cloud hit the base of the surface layer, a sand boil began at the place and moment of impact. This suggests that silt clouds, while not necessarily of engineering importance, have information to give that can be utilized in the future.

INFLUENCE OF SHALLOW FOUNDATIONS ON SAND BOILS

Test series NR (Fig. 2) observed the effect of a shallow foundation on such layered soil profiles. Snapshots of behavior following the end of shaking are shown in Fig. 6. In Fig. 6, a single image is taken from each test with the (difficult to see) water films ringed on the left hand figures and the locations of observed sand boils ringed on the right hand figures.

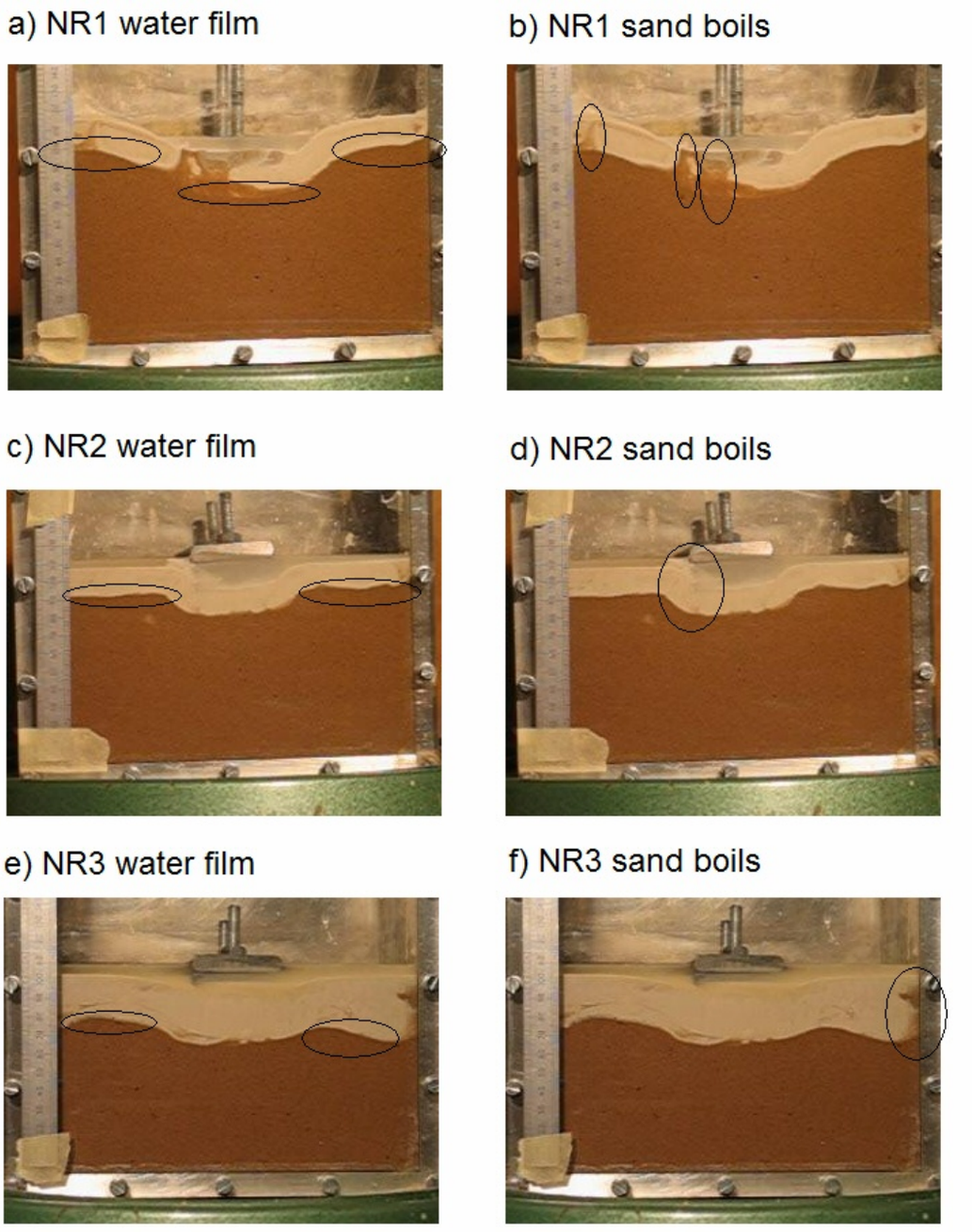


Fig. 6. Snapshots from tests series NR, with indications of the locations of water films (a, c, e) and sand boils (b, d, f).

For the 0.41 kg foundation test NR1, the foundation mass did not affect the water film which formed along the base of the silt layer (Fig. 6a). Significant sand boiling followed around the edge of the foundation (Fig. 6b), as it deformed under the foundation weight. When the foundation mass was increased to 1.15 kg (test NR2) the mass similarly sank, and although it is unclear whether or not a water film was present

beneath the foundation following shaking (Fig. 6c) sand boil evidence again collected around the edge of the foundation (Fig. 6d). With a thicker silt layer, however, a different response resulted. The punch-through failure of the other models was not observed and there was no water film directly beneath the foundation (Fig. 6e) although water films were clearly present elsewhere. The little sand boil activity in this model was restricted to the furthest reaches of the container.

With the water film suppressed immediately beneath the foundation in test NR3, no sand boils were observed near the structure, and they would only occur far from the footing where the water film was present. When punch through occurred with the heavier foundation (test NR2), significant amounts of sand boiling were observed where the shear strain was greatest, as the increased shear stresses in the soil created a weaker zone where fluid could puncture through to the surface. A schematic figure (Fig. 7) has been created to illustrate the two observed regimes of behavior – "sand boils far" implies the water film was suppressed, while "sand boils near" implies that punch-through failure could be expected.

It might be noted that water films are not always a precursor to sand boils (e.g. left hand side, Fig. 6e and 6f, and data of other researchers e.g. Kokusho, 1999). It is unclear if sand boils can form if excess pore pressures are insufficient to allow a water film to form.

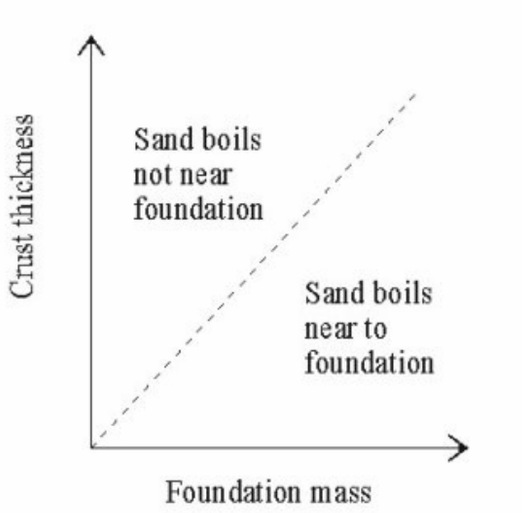


FIG. 7. Qualitative view of observed behavior.

It would be expected that, in a refined form, Fig. 7 would change when accounting for different properties of the impermeable layer. It might be expected that undrained strength would have a significant influence, as well as the moisture content of the soil relative to its Atterberg limits. However, this preliminary test series has only examined one value of each of these variables, and the extension is currently being carried out. The characteristics of shaking would be less likely to change this graph; these characteristics might determine whether or not sand boils occur, but not affect their location.

DISCUSSION

The tests presented have been rudimentary in nature and intended purely to provide qualitative observations of the behavior that might arise in various circumstances associated with layering of liquefiable and low-permeability soils. With increasingly affordable high resolution and high speed video technology becoming available, it is anticipated that quality of successive tests can be improved in these departments.

It has been seen that the simple experiments performed in this series have produced some interesting observations. For the foundation model, shallow footings over thicker surface silt crusts suppressed the formation of water films immediately beneath the foundation. This may be advantageous if there is a risk of sliding failure akin to that possible near Niigata following the 1964 earthquake (Kokusho and Fujita, 2001), or if boiling sand is likely to cause an increase in the structural settlement. Once the sand liquefies there is limited support for the footing, and heavier footings were observed to "punch-through" thinner silt layers. This latter case is the concern of Bouckovalas and Dakoulas (2007) who perform settlement calculations of such cases using the finite element method. To determine whether the displacement and boiling of sand and water increases the settlement from that calculated using numerical models cannot be quantitatively identified from these experiments and requires a carefully controlled centrifuge model.

Of undetermined usefulness is the identification of "silt clouds". They appear to travel with the pore fluid and were linked to sand boils where they touched the surface, so they could at least act as markers for future experiments. It is possible that by removing material from the buried silt layer, its capacity decreases; this could not be ascertained in the available time. Nor could a variety of shaking intensities or silt conditions be tested in order to ascertain whether silt clouds were a general or a special occurrence.

Although accurate quantification of foundation settlement and influence of input motion were not made and require more sophisticated models, such as a centrifuge, both the expected and the unexpected outcomes of the experiments presented show that there is value in performing simplified tests.

CONCLUSIONS

Following these simple experiments, it can be concluded that the phenomena of water films and sand boils can be readily reproduced in a laboratory. By varying simple parameters, the effect of such variations on the occurrence of sand boils were determined. In the test series presented, multiple layers were seen to undergo sand boiling from the shallowest layer first. These models were also susceptible to the upward transmission of silt from deeper layers, which was highly visible and here termed "silt clouds". Finally, shallow foundations on thick silt crusts were seen to suppress water films and consequent sand boil was some distance from the foundation. However, when the structure became heavy relative to the thickness of the crust, a punch-through failure was observed.

ACKNOWLEDGMENTS

Testing performed by Nikholas Ritchie and Donna Moran as part of their BEng projects formed the basis for the research presented. Technical support was provided by Mark Trusswell at the University of Dundee.

REFERENCES

Amini, F. and Sama, K.M. (1999). "Behavior of stratified sand-silt-gravel composites under seismic liquefaction conditions". *Soil Dynamics and Earthquake Engineering*, 18(6): 445-455.

Bouckovalas, G. and Dakoulas, P. (2007) "Liquefaction performance of shallow foundations in presence of a soil crust". *4th Int. Conf. on Earthquake Geotechnical Engineering - Invited Lectures.* pub. Springer. 245-276.

Brennan, A.J. and Madabhushi, S.P.G. (2005) "Liquefaction and Drainage in Stratified Soil". *J. Geotech. & Geoenv. Engrg.*, Vol. 131 (7): 876-885.

Butterfield, K. and Bolton, M.D. (2003). "Modelling pore fluid migration in layered, liquefied soils". Proc. Pacific Conf. on Earthquake Engineering, Christchurch, NZ. Paper no. 131

Fiegel, G. & Kutter, B.L. (1994). "Liquefaction mechanism for layered soils". *J. Geotech. Eng.*, 120(4): 737-755.

Florin, V.A. and Ivanov, P.L. (1961). "Liquefaction of saturated sands". *Proc. V ICSMFE,* Paris, France. Vol. 1: 107-112.

Ishihara, K. (1985). "Stability of natural deposits during earthquakes". *Proc. XI ICSMFE,* San Francisco, CA, USA. pub. Balkema, Rotterdam. 1: 321-376.

Kokusho, T. (1999). "Water film on liquefied sand and its effect on lateral spread". *J. Geotech. & Geoenv. Engrg.*, 125(10): 817-826.

Kokusho, T. and Fujita, K. (2001). "Water films involved in post-liquefaction flow failure in Niigata City during the 1964 Niigata earthquake". *Proc. Fourth Int. Conf. on Recent Advances in Geotechnical Earthquake Engineering and Soil Dynamics,* San Diego, CA, USA. Paper no. 5.38.

Koppejan, A.W., van Wamelen, B.M. and Weinberg, L.J.H. (1948). "Coastal flow slides in the Dutch province of Zeeland". *Proc. 2nd ICSMFE*, Rotterdam, Netherlands. Vol. 5: 89-96.

Moran, D. (2007). "An investigation of the effects of liquefaction during earthquakes". Honours year project, University of Dundee, UK.

Ritchie, N. (2006). "Investigation of the pattern of sand boils around shallow foundations and their associated settlements". Honours year project, University of Dundee, UK.

Sasaki, Y., Ohbayashi, J. and Ogata, Y. (2001). "Compressibility of liquefied sand". *Proc. Fourth Int. Conf. on Recent Advances in Geotechnical Earthquake Engineering and Soil Dynamics*, San Diego, CA, USA. Paper 1.62.

Seed, H.B and Lee, K.L. (1966) "Liquefaction of saturated sands during cyclic loading". *J. Soil Mech. & Foundations Div.,* Vol. 92 (6): 105-134.

Pore Structure Variation of Porous Media under Vibrations

Ming Xiao[1], M. ASCE, Lakshmi N. Reddi[2]. M. ASCE

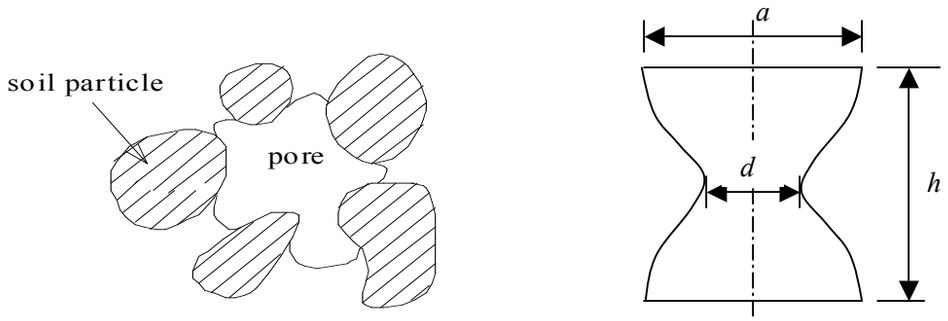
[1]Assistant Professor, Department of Civil and Geomatics Engineering and Construction, M/S EE94. California State University, Fresno, California 93740. Phone: (559) 278-7588. Email: mxiao@csufresno.edu
[2]Professor and Chair, Department of Civil and Environmental Engineering, University of Central Florida, Orlando, FL 32816.

ABSTRACT: Variation of pore structures of soils due to seismic activities affects density and fluid distribution in the pores, which in turn could affect the strength and liquefaction potential of the porous media. This paper, based on experimental investigation, studied the effect of vibrations on pore sizes of porous media. A monolayer of glass beads of different sizes under full saturation condition was used to simulate porous media, and the glass beads were subjected to the vibrations provided by a small-scale shaking table. A microscopic camera, which was positioned above the glass beads and connected to a computer, captured the pore variations during the vibration at 1sec interval. Then, graphical software was employed to analyze the changes of pore size distributions before, during, and after the vibrations. The experimental study revealed that the pore size distributions of saturated and densely packed glass beads changed little before and after the vibration. During the vibration, however, the number of bigger pores decreased and the number of smaller pores increased. It may be concluded from this preliminary experimental study that although the pore structure of dense subsoil may remain relatively unchanged before and after seismic activity, the soil could experience significant change of pore structure *during* the vibration, which could affect the soil's density, strength, and liquefaction potential.

INTRODUCTION

Seismic induced soil failure is a major geohazard. Earthquakes could result in strength reduction, liquefaction, and large ground deformation of subsoil. For instance, Makdisi and Seed (1977) found that the dynamic yield strength can reduce to 80% of the static undrained strength for clayey soils, dry or partially saturated cohesionless soils, or dense saturated cohesionless soils. Also, pore water pressure was shown to increase with the amplitude of shear strain in cyclic shear tests (Ohara and Matsuda, 1988; Dobry, 1989). Pore pressure increase in saturated sand or silt due to seismic loading can result in the loss of bearing capacity and consequently

catastrophic failure of a structure. Soil behaviors during vibrations have been widely studied using macro-scale characteristics, such as porosity, density, deformation, and strength. The soil behaviors under vibrations in pore scale, on the other hand, have been less explored, probably owing to the complex geometry, tortuosity, and irregularity of interconnected pores. Understanding the pore structure variations before, during, and after seismic loading in micro-scale could facilitate the understanding of the effect of seismicity on the density and the pore water pressure in the sample and field scales.



(a) 2D illustration of a pore in porous medium

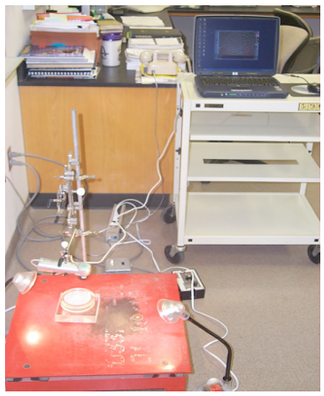
(b) 2D conceptual model of an idealized pore (From Payatakes et al., 1980)

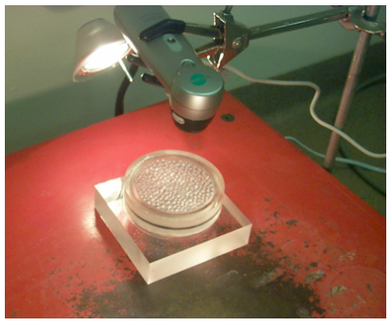
Figure 1. Conceptualization of pore geometry

Conceptualization of pore geometry was proposed by many researchers. An example of an idealized pore structure was shown in Figure 1 (Payatakes et al., 1980). A pore formed by the surrounding grains is comprised of a pore body (measured by pore diameter, *a*) and the constraints (defined as pore throats and measured by pore throat diameter, *d*). The wall profile of a pore is assumed to be a sinusoidal function, and *h* is the pore length. Idealization of pore geometry was used in pore network models to study pore fluid transport and fate in porous media. Xiao et al. (2006) conducted experimental and model study on the effect of vibrations on the fate of discontinuous pore fluids and found the size distribution of discontinuous pore fluid after vibrations was less uniform than that before the vibration. In this study, pore geometry variation and the size distribution of the pores of a saturated porous medium under vibrations was explored experimentally. The purpose of this study is to provide a fundamental understanding of the effect of vibrations on the pore structure of porous media.

VIBRATION TESTS

To measure the pore structure variation under idealized conditions of pore geometry, spherical glass beads were used as the porous media. Three sizes of glass beads were used: 3mm, 4mm, and 5mm. They were mixed with equal mass and tightly packed in a transparent cell made of transparent Plexiglas. In order to clearly monitor the possible pore geometry change under vibrations, a monolayer of glass beads was used. The glass beads sample was saturated with water in the cell, and the cell was capped to prevent spill of glass beads and water in the cell during vibrations. The cell

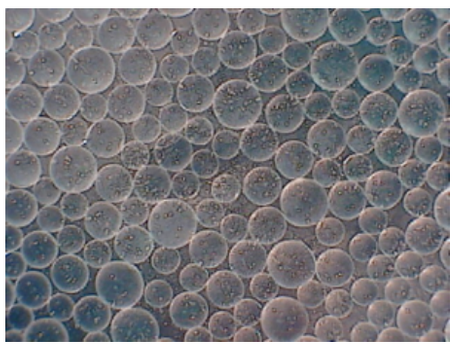


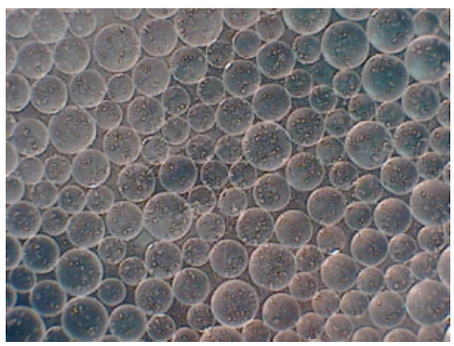


(b) Microscope and glass beads in a cell

(a) Experimental Setup

Figure 2. Experimental setup of the vibration tests





(a) Before vibration (b) At 10 seconds of vibration

Figure 3. Glass beads and pore structures

was fastened on the top of a small- scale shaking table (Model: VP51D1; Frequency: 60Hz or 3600 vibrations/min; Amplitude: 0.33mm; Manufacture: FMC Technologies), as shown in Figure 2. A portable digital microscope (Proscope®) was mounted on the top of the cell to record the pore geometry variation before, during, and after the vibrations. The microscope can take 1.3 Mega-pixels image at 12 frames per second for 30 min. The microscope was connected to a computer so that the images could be instantly displayed and stored for later analysis. The saturated glass beads were shaken for 30sec on the shaking table using the vibration characteristics mentioned above. The microscope was set to capture one image per second. During the vibration, it was observed that the individual pores dilated, shrank, merged, or broke up into smaller pores. Two representative images of the pore structures of the monolayer glass beads before and during the vibration are shown in Figure 3. In order to quantify the pore geometry change before, during, and after the vibration, a graphical software, Sigma Scan®, was used to measure the pore sizes. For an

idealized pore (Figure 1), the pore length and the pore body diameter can be determined by the pore throat diameter (Payatakes et al, 1980). Thus, in this study, the individual pore geometry was represented using pore throat diameter, as identified in Figure 4. It is noted that the Proscope® software can only take square images that are inscribed in the circular cell. Therefore, the two photographs in Figure 3 showed the major area of the glass beads.

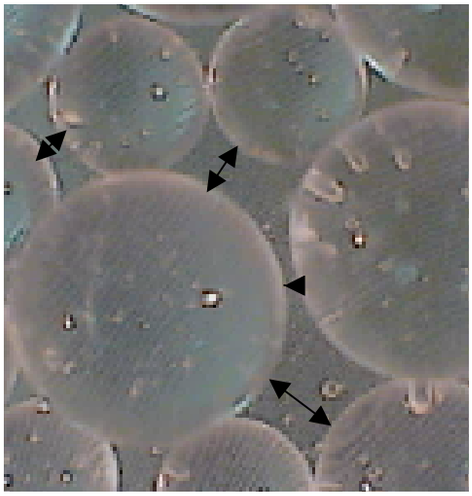


Figure 4. Identification of pore throats, as shown by the arrows.

TEST RESULTS AND DISCUSSION

Four images of the pore configurations of the glass beads were selected for quantitative analysis: one image taken immediately before the vibration, one at 10 seconds of the vibration, one at 20 seconds of the vibration, and the last image taken immediately after the vibration (at the end of the 30-second period). Each pore throat of the pores in the four images was visually identified (as demonstrated in Figure 4) and measured using the graphical software. The pore structure of the entire glass beads sample was presented using *pore throat distribution* (PTD), as illustrated in Figure 5. The PTD is expressed using pore throat diameter and the percentage of the number of pore throats of each size. The results in Figure 5 showed that the PTDs before and after the vibration had the similar size range of pore throats, and the numbers of different pore throats after the vibration were slightly more uniform than those before the vibration. Figure 5 also prominently revealed significant variation of PTDs *during* the vibration, as compared to the PTDs before and after the vibration. At the moments of 10sec and 20sec of the vibration, less data points in the bigger size range were present, indicating reduced number of larger pores in the porous media. Meanwhile, the results showed that more pores in smaller size range were created as a result of the vibration. Duplicate tests were conducted and the same analysis was performed. The PTD variation demonstrated the same trend as described above.

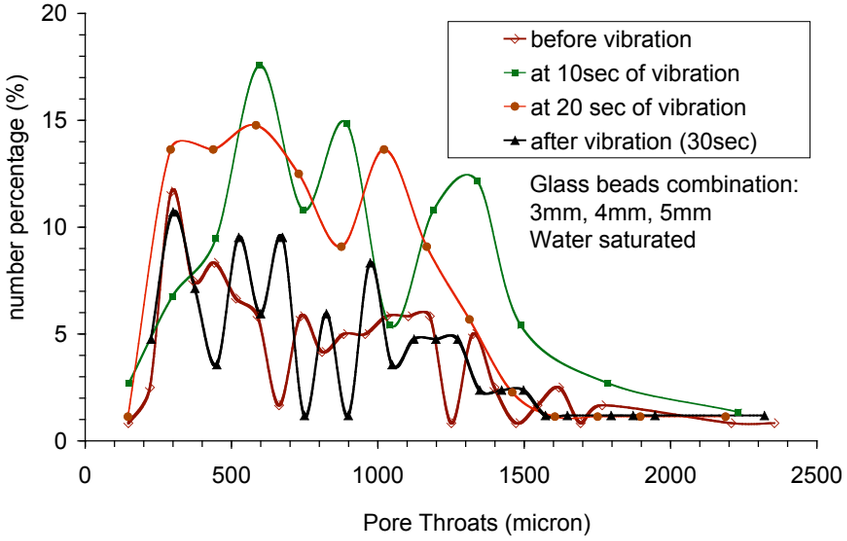


Figure 5. Effect of vibrations on pore throat distributions

The effect of vibrations on soil pore structure may be extended to subsoil performances in the field, using the capillarity theory as expressed in Equation (1).

$$p = \frac{2\sigma \cdot \cos\alpha}{r} \tag{1}$$

The capillary pressure (p) is related to surface tension (σ), contact angle (α), and pore radius (r). Capillary pressure increases with smaller pore size. In order to drain the pore water in the reduced pores caused by seismic activity, a larger hydraulic gradient is required to overcome the increased capillary pressure. Reduced drainage capability may contribute to the difficulty of reducing pore water pressure and increasing effective stress, thus causing reduced strength.

As initial steps in studying the pore structure variations due to vibrations were taken, limitations of this study should be noted. The conclusions are based on the study that used spherical glass beads. In addition, seismic characteristics of the small-scale shaking table are different from those of actual earthquakes (for example, the earthquake frequency is usually 0.2~2 Hz, lower than that of the shaking table). Further studies on real soil samples under real or simulated ground shakings may be needed to verify the conclusions of this study. In addition, the image analysis employed in this study can only measure the pore sizes in the *plan* view, and it only works for uniform or narrow-size-range porous media. This is a limitation of most image analysis of soil pore structure. In this study, narrow size range (3, 4, and 5mm) of glass beads was used. In a monolayer of different sizes of grains, large pores may occur on top of the small glass beads. Three-dimensional pore size variation was not investigated in this study.

CONCLUSIONS

This paper presented a simple experimental study on the pore structure variations due to vibration. The study shows that vibrations can cause larger pores to reduce in size; meanwhile, more pores of smaller sizes can be created during vibration. It may be concluded from this preliminary experimental study that although the pore structure of dense subsoil may remain relatively unchanged before and after seismic activity, the soil could experience significant change in pore structure *during* the vibration, which could affect the soil's density, strength, and liquefaction potential.

ACKNOWLEDGMENTS

This research is a portion of a project funded by the Advanced Life Support Program of NASA John Space Center (Project Number: NAG9-1399). The support from this agency is gratefully acknowledged. The authors thank the anonymous reviewers for their constructive comments that help to improve the paper.

REFERENCES

Dobry, R. (1989). "Some basic aspects of soil liquefaction during earthquakes." Earthquake hazards and the design of constructed facilities in the Eastern United states. Annals of the New York Academy of Sciences. 558: 172-182.

Makdisi, F.I. and Seed, H.B. (1977). "A simplified procedure for estimating earthquake-induced deformation in dams and embankments." Report UCB/EERC-7719, Earthquake Engineering Research Center, University of California, Berkeley, CA.

Ohara, S. and Matsuda, H. (1988). "Study on the settlement of saturated clay layer induced by cyclic shear." *Soils and Foundations*, 28: 103-113.

Payatakes, A.C., Ng, K.M., and R.W.Flumerfelt (1980). "Oil ganglion dynamics during immiscible displacement: model formulation." *AIChe Journal*, 26(3):430-442.

Xiao, M., Reddi, L.N., and Steinberg, S. (2006). "Effect of vibrations on pore fluid distribution in porous media." *Transport in Porous Media,* 62(2):187-204.

The Effect of the Hammer Energy Efficiency Ratio on SPT-Based Liquefaction Evaluation

Troy Hull, P.E., G.E., M. ASCE[1]; Jason Butler-Brown, P.E., M. ASCE [2]; and Travis Willis, E.I. [3]

[1] Principal Geotechnical Engineer, Earth Engineers, Inc., 713 Northeast 152nd Avenue, Vancouver, Washington 98684; troy@earth-engineers.com
[2] Engineer - Geotechnical, City of Portland Office, Bureau of Development Services, 1900 SW Fourth Avenue, Suite 5000, Portland, Oregon 97201; BrownJ@ci.portland.or.us
[3] Geotechnical Engineering Associate, Earth Engineers, Inc., 713 Northeast 152nd Avenue, Vancouver, Washington 98684; travis@earth-engineers.com

ABSTRACT: The Standard Penetration Test (SPT) has long been used by the geotechnical community to evaluate the factor of safety (FOS) against liquefaction and to estimate liquefaction induced soil strength loss, vertical settlement and lateral spread. There are other investigative methods of evaluating liquefaction risk, the most common being the cone penetration test (CPT). However, the SPT method is often the first choice for geotechnical professionals because the testing is economical, the equipment readily available, and it returns physical samples that can be tested in the laboratory.

The public and governing jurisdictions trust that the geotechnical community is using field-testing methods that provide relatively accurate soil strength data, which is critical to liquefaction evaluation. Because most jurisdictions in the United States do not require the use of calibrated SPT hammers, the majority of SPT liquefaction analyses are based on uncalibrated SPT hammer data. There appears to be a perception by governing jurisdictions that it is acceptable for geotechnical engineers to rely on their engineering judgment to determine SPT hammer energy. However, numerous past studies demonstrate that SPT hammer energy varies widely depending upon the hammer type, manufacturer and lifting mechanism. The variance in energy can be as much as 200 to 250 percent, which is too large to reasonably estimate using engineering judgment alone.

This paper focuses on the influence of hammer energy on the SPT liquefaction analyses results. We examine the variability within the results as a function of measured hammer energy. Finally, the paper encourages public agencies to require the use of calibrated SPT hammers in the evaluation of liquefaction triggering, strength loss, dynamic settlement and lateral spread hazards. It is our hope that this practice will be adopted in local and state building codes.

INTRODUCTION

There are scores of published technical papers that discuss the liquefaction phenomenon. Of significant debate recently are the types of soil conditions that are potentially liquefiable, as well as the triggering level of liquefaction. However, the focus of this paper is the evaluation of a common method of characterizing the soil strength—the Standard Penetration Test—not whether a particular soil type (i.e. silt or clay) liquefies. Soil strength is an important engineering property to focus on because it directly impacts the determination of liquefaction potential. As a general characterization, a weaker soil is more likely to be liquefiable while a stronger soil has less risk of liquefaction. If the soil strength data collected by the geotechnical engineer is not accurate, then it impairs the engineer's ability to determine whether or not a site may liquefy.

Having a clear understanding of the liquefaction susceptibility of a particular site is important to protecting the public and property. It also has great economical impact. Misidentifying a site as being liquefiable—when it is not—can lead to unnecessarily higher construction cost. Conversely, classifying a liquefiable site as being non-liquefiable can lead to unanticipated building damage and risk to life-safety.

There are a number of field investigation methods to assist the engineer in evaluating the factor of safety (FOS) against liquefaction and estimating liquefaction induced soil strength loss, vertical settlement and lateral spread. Four in-situ test methods are recommended for use (Seed et al., 2003): the Standard Penetration Test (SPT), Cone Penetration Test (CPT), in-situ shear wave velocity measurement (Vs), and the Becker Penetration Test (BPT). Because SPT testing is economical, the equipment is readily available, and the testing returns soil samples that can then be tested in the laboratory, it is often the first choice for geotechnical professionals when they plan their subsurface investigation.

The Standard Penetration Test (ASTM D1586, revised 1999) consists of driving a standard split-tube sampler a distance of 18-inches into the soil at the bottom of a borehole and counting the number of blows required to drive the device three consecutive 6-inch intervals (18 inches total). The sampler is driven with a 140-pound weight falling a distance of 30 inches. The number of blows required to drive the initial 6 inches is typically recorded but ignored as this interval seats the sampler below disturbed soil at the bottom of the borehole. The actual number of blows required to drive the sampler the final 12 inches is the standard penetration resistance, or N value. The N value is not to be confused with the N_1 and $(N_1)_{60}$ values, which are discussed later in more detail.

The lifting and dropping mechanisms used to drive an SPT hammer include automatic trip, safety rope and pulley, donut rope and pulley, and wire winch line. Ideally, with all of these methods, the 140-pound SPT hammer falling 30 inches would transfer 350 foot-pounds of energy to the sampler (i.e. 2.5 feet times 140 pounds). In actuality, essentially no SPT hammers generate the full 350 foot-pounds

of energy due to energy loss. Various studies have shown that the actual SPT hammer energy is typically much less—as low as about 20 to 30 percent of the theoretical hammer energy.

The N values are used to determine the resistance to liquefaction in the SPT-based liquefaction analysis. Therefore, it is extremely important to understand the actual SPT hammer energy when measuring N values in the field. The liquefaction evaluation procedure consists of calculating (1) the earthquake load, or Cyclic Stress Ratio (CSR), and (2) the soil resistance load, or Cyclic Resistance Ratio (CRR). The ratio of the resistance load (CRR) divided by the earthquake load (CSR) then provides a factor of safety against liquefaction, which is used by the geotechnical engineer to evaluate whether a site is liquefiable or not. The CRR value is calculated based on the N values obtained in the field.

Early studies of hammer energy variability (i.e. Kovacs et al., 1983) eventually resulted in the recommendation to account for SPT hammer energy efficiency when evaluating liquefaction potential (Seed et al., 1985). NCEER (1997) provided a method to account for SPT hammer energy variation as well as other SPT factors including effective overburden stress, equipment, and procedural effects. N values corrected for energy, effective overburden stress, equipment and procedural effects are referred to as $(N_1)_{60}$ values. The equation for $(N_1)_{60}$ is as follows:

$$(N_1)_{60} = N * C_N * C_R * C_S * C_B * C_E \quad (1)$$

where N = blow counts obtained in the field
C_N = correction for overburden effects
C_R = correction for "short" rod length
C_S = correction for non-standardized SPT sampler
C_B = correction for borehole diameter
C_E = correction for hammer energy efficiency

C_N, C_R, C_S and C_B are correction factors that can be found in the NCEER (1997) proceedings and are not presented in detail in this paper. C_E is the correction to account for rod energy and is obtained by dividing the hammer energy ratio, ER, by 0.60. The hammer energy ratio can only be known if the SPT hammer is calibrated. If the SPT hammer is not calibrated, then the hammer energy is unknown and it must be assumed based on the hammer type.

Numerous studies (i.e. Batchelor et al., 1995; Davidson et al., 1999; Sjoblom et al., 2002) have measured the actual variability in energy within SPT hammers, focusing on differences between manufacturers, models, and duration of use. These studies have defined the expected maximum and minimum energy efficiency ratios. Table 1 below outlines the SPT hammer energy efficiency ratio ranges for 4 studies that we considered. It should be noted that the Utah and Seattle studies do not necessarily represent the maximum potential range of hammer energy efficiency variation. The

energy efficiency ranges reported in these 2 reports and summarized in the table below are the ranges for a limited number of hammers tested.

Table 1. SPT Hammer Energy Efficiency Variance Data

SOURCE	SPT HAMMER TYPE	SPT HAMMER ENERGY EFFICIENCY RATIO (ER) RANGE
LiquefyPro, Version 5.5b computer program input options	Automatic trip Safety rope and pulley Donut rope and pulley Winch wire line	0.54 – 0.96 0.36 – 0.70 0.27 – 0.60 no data presented
Seed et al., 2003	Automatic trip Safety rope and pulley Donut rope and pulley Winch wire line	0.5 – 0.8 0.4 – 0.7 0.3 – 0.6 no data presented
Utah DOT Study (Sjoblom et al., 2002)	Automatic trip Safety rope and pulley Donut rope and pulley Winch wire line	0.46 – 0.95 0.55 – 0.76 no data presented 0.50
Seattle ASCE Study (Batchelor et al., 1995)	Automatic trip Safety rope and pulley Donut rope and pulley Winch wire line	0.91 – 0.99 0.64 – 0.75 no data presented 0.25

As is demonstrated in Table 1 above, the SPT hammer energy efficiency ratio can vary by up to a factor of about 2. So the geotechnical engineer who is using an uncalibrated SPT hammer for their site investigation must assume a hammer energy efficiency ratio with an expected wide range of potential error.

There is no dispute in the geotechnical community that hammer energies vary from drill rig to drill rig. Even though hammer energy variance has been acknowledged by the geotechnical engineers that use it in their liquefaction analyses and by the jurisdictions that review the geotechnical analyses prior to approving developments, very little has been done by governing jurisdictions (i.e. states, counties, cities and departments of transportation) to require calibrated hammers in an effort to limit the potential for inaccurate assessment of liquefaction potential.

An informal survey of jurisdictions across the United States (U.S.) revealed only one that currently requires SPT hammer calibration—Minnesota Department of Transportation. The common response from jurisdictions when questioned about why they don't require calibrated SPT data was that it was their assumption that geotechnical engineers should use their engineering judgment to determine the appropriate SPT hammer energy efficiency ratio. To evaluate how the variance in hammer energy ratio impacts the FOS against liquefaction, we performed a parametric study as presented below.

PARAMETRIC STUDY

LiquefyPro, Version 5.5b computer software by CivilTech Software of Bellevue, Washington was used to demonstrate the variability in calculating the FOS against liquefaction due to SPT hammer energy variance. As discussed earlier in this paper, the procedure for calculating the FOS against liquefaction consists of calculating the earthquake load (CSR) and the soil resistance load (CRR). The CRR values are dependent upon the SPT $(N_1)_{60}$ values (Eq. (1) above). The FOS against liquefaction is determined by dividing the CRR by the CSR. In this study, a soil layer was deemed liquefiable if it had a FOS less than or equal to 1.3. This is supported by the recommendation in California Division of Mines and Geology's Special Publication 117 which is widely used as a guideline for liquefaction evaluation (California Division of Mines and Geology and others, 1997).

There are an infinite number of soil and groundwater conditions that could be modeled for liquefaction potential. For the purposes of this limited study, we selected 2 models. Model 1 represents a relatively thin liquefiable layer of 5 feet while Model 2 represents a relatively thick liquefiable layer of 15 feet. For both models, the soil properties and SPT N values were held constant. The soil models are presented in Figure 1 below.

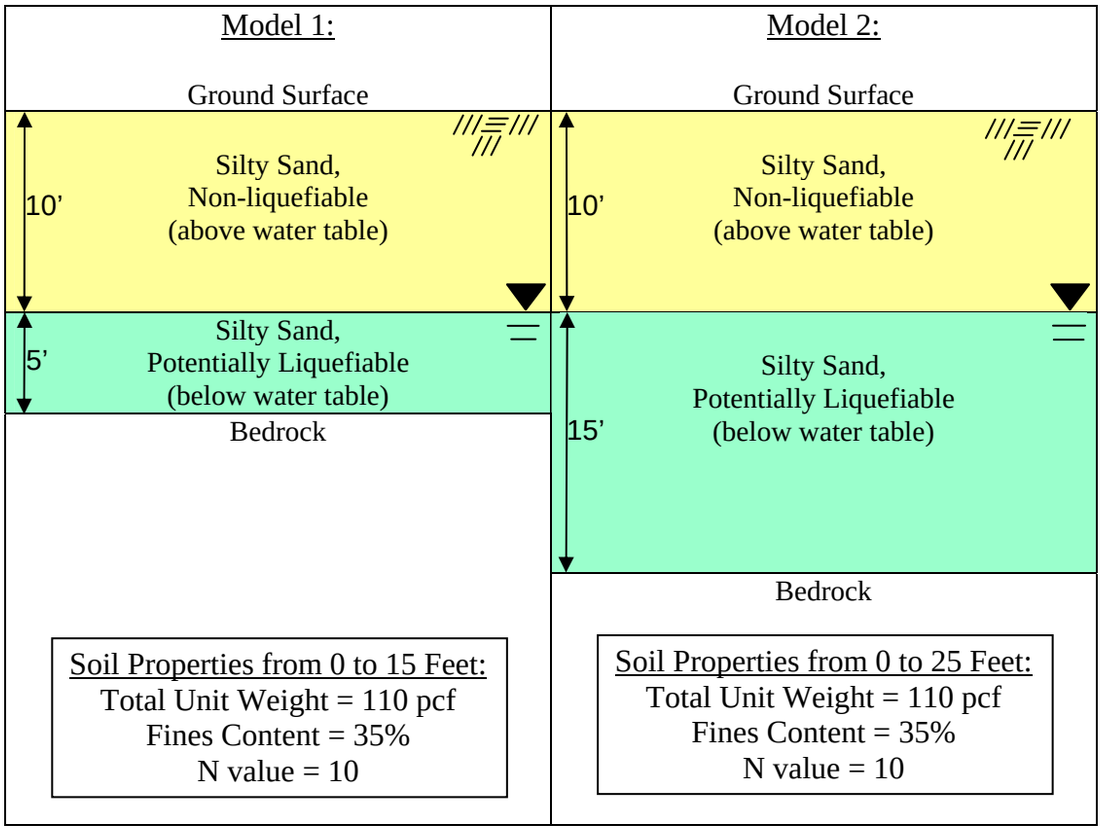


FIG. 1. Summary of Soil Conditions for Models 1 and 2.

The analysis is based on the earthquake magnitude and peak ground acceleration. These values were selected following a review of the 2002 US Geological Survey (USGS) probabilistic seismic hazard deaggregation data for major cities in the U.S. (see Table 2 below). The data was generated using the 2002 Interactive Deaggregation Tool from the USGS website (http://eqint.cr.usgs.gov/deaggint/2002/index.php). The following input parameters were held constant: frequency = 0 hertz (i.e. PGA) and return period = 2475 years (i.e. 2 percent probability of exceedance in 50 years). The return period is consistent with the 2006 International Building Code (International Code Council, Inc., 2006).

Table 2. Summary of USGS Deaggregation Data for Selected Cities

LOCATION	MEAN EQ MAGNITUDE	PEAK HORIZONTAL GROUND ACCELERATION (g)
Atlanta, Georgia	6.25	0.10
Boise, Idaho	6.00	0.21
Chicago, Illinois	5.66	0.08
Columbia, South Carolina	6.35	0.28
Dallas, Texas	6.20	0.05
Denver, Colorado	5.71	0.11
Las Vegas, Nevada	6.06	0.24
Los Angeles, California	6.71	0.72
Memphis, Tennessee	7.28	0.72
Minneapolis, Minnesota	5.81	0.03
New York, New York	5.71	0.22
Phoenix, Arizona	5.96	0.08
Portland, Oregon	6.74	0.41
Sacramento, California	6.16	0.24
Salt Lake City, Utah	6.78	0.76
San Diego, California	6.12	0.41
San Francisco, California	7.39	0.73
Seattle, Washington	6.70	0.63
Washington, D.C.	4.80	0.07
AVERAGE	6.23	0.32

An earthquake magnitude of 6.5 and a peak horizontal ground acceleration of 0.25g were selected for both Models 1 and 2, respectively, based on the available data. These values are generally low for the higher seismicity areas along the west coast of the U.S. and are somewhat higher than typical for low-seismicity areas of the country.

After considering the hammer efficiencies outlined in Table 1 above, the upper and lower bounds were selected for the automatic, safety and winch hammers. The upper bound of the winch hammer was modified from 0.50 to 0.60 to represent a theoretical worst-case correction for hammer energy efficiency (C_E) of 1. The hammer efficiency values used in our LiquefyPro calculations are shown in Table 3 below. The donut hammer was not modeled separately because the upper and lower bounds were essentially the same as the winch hammer as demonstrated in Table 1.

Table 3. SPT Hammer Energy Efficiency Ranges Modeled in LiquefyPro

SPT HAMMER TYPE	SPT HAMMER ENERGY EFFICIENCY RATIO (ER) RANGE
Automatic trip	0.46 and 0.99
Safety rope and pulley	0.36 and 0.7
Donut rope and pulley	0.27 and 0.6
Winch wire line	0.25 and 0.6

Once the two soil profiles, the earthquake loading, and SPT hammer energy efficiency values were selected, the FOS against liquefaction was calculated using the LiquefyPro software. Table 4 presents a summary of the input variables used in the LiquefyPro analyses.

Table 4. Summary of LiquefyPro Input

EARTHQUAKE PGA (g):	0.25	**SETTLEMENT CALCULATION:**	Liquefiable zone only
EARTHQUAKE MAGNITUDE:	6.5	**GROUND IMPROVEMENT OF FILL ON GROUND SURFACE:**	not applicable ("0" feet of fill height)
HOLE DEPTH:	Model 1: 15 feet Model 2: 25 feet	**IN-SITU TEST DATA:**	Refer to Fig. 1 above
WATER TABLE (DURING EARTHQUAKE AND IN-SITU TESTING):	10 feet	**HAMMER ENERGY RATIO:**	Refer to Table 3 above
SETTLEMENT ANALYSIS (WET):	Tokimatsu/Seed	**BOREHOLE DIAMETER:**	2.5 to 4.5 inches
FINES CORRECTION (LIQUEFACTION):	Idriss/Seed (SPT only)	**SAMPLING METHOD:**	Standard sampler
FINES CORRECTION (SETTLEMENT):	During liquefaction	**FACTOR OF SAFETY:**	1.3
Note: The LiquefyPro computer program reference to Idriss/Seed for fines correction should actually reference NCEER (1997), page 7.			

The results of the analyses are presented below for Model 1 and Model 2 in graphical and tabular form in Fig. 2, Fig. 3, Table 5 and Table 6, respectively. The results demonstrate that the hammer energy efficiency ratio significantly impacts whether a site is determined to be potentially liquefiable—when based on the SPT liquefaction evaluation. For example, if a drill rig equipped with a safety hammer were used to evaluate liquefaction on a site similar to Model 1, the site could be classified as "not liquefiable," liquefiable from 10 to 15 feet below grade, or

somewhere in between depending upon the energy efficiency ratio assumed by the geotechnical engineer.

For Model 2, the discrepancy in identifying the liquefiable layer was much worse, especially for the automatic and safety hammers. The automatic hammer results range from "not liquefiable" to about 12 feet of liquefiable soil. The safety hammer ranged from 1 to 15 feet of liquefiable soil.

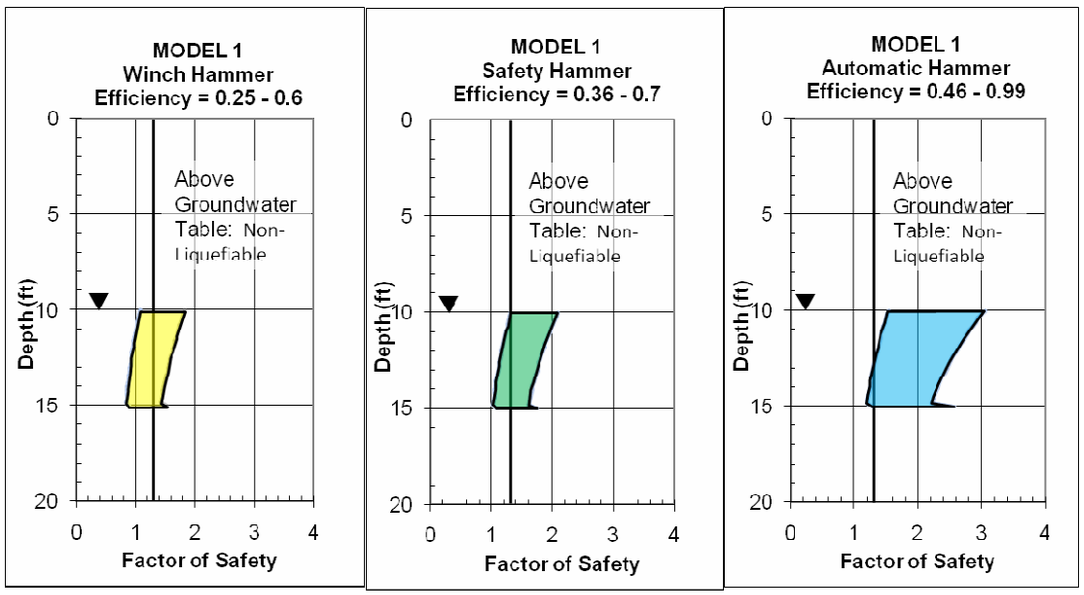


FIG. 2. Liquefaction FOS Calculations for Model 1 (bold vertical line represents FOS of 1.3).

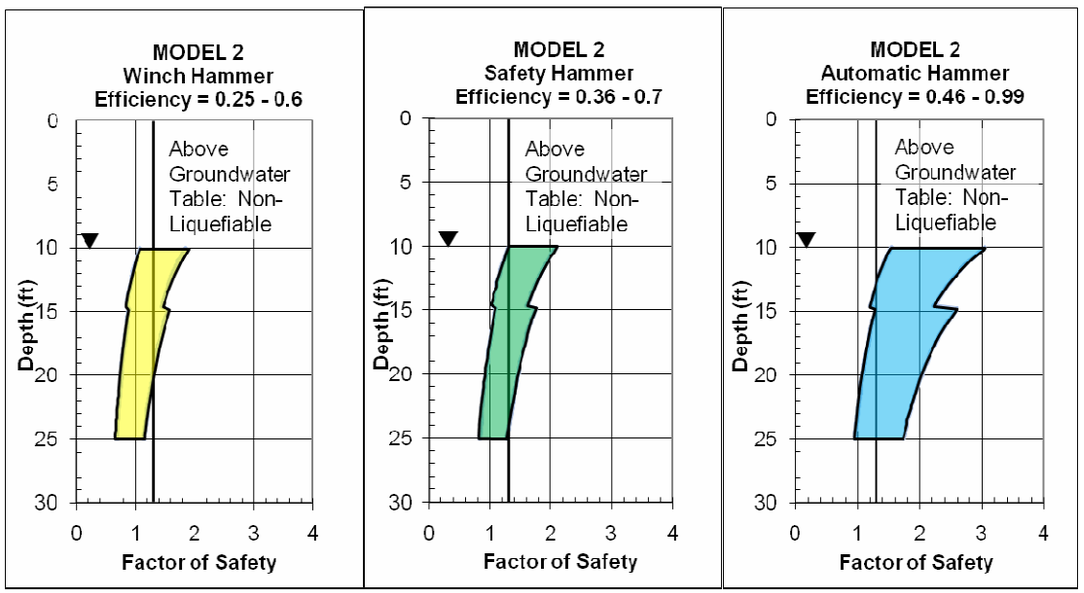


FIG. 3. Liquefaction FOS Calculations for Model 2 (bold vertical line represents FOS of 1.3).

Table 5. Summary of LiquefyPro Output for Model 1

HAMMER	CALCULATED LIQUEFIABLE LAYER THICKNESS
Automatic	At the lower bound hammer energy efficiency ratio of 0.46, **2.2 feet** of the soil was liquefiable (i.e. from 12.8 to 15 foot depth). At the upper bound hammer energy efficiency ratio of 0.99, **none** of the soil was determined to be liquefiable.
Safety	At the lower bound hammer energy efficiency ratio of 0.36, **all 5 feet** of the soil was liquefiable (i.e. from 10 to 15 foot depth). At the upper bound hammer energy efficiency ratio of 0.70, **none** of the soil was liquefiable.
Winch/Donut	At the lower bound hammer energy efficiency ratio of 0.25, **all 5 feet** of the soil was liquefiable (i.e. from 10 to 15 foot depth). At the upper bound hammer energy efficiency ratio of 0.60, **none** of the soil was liquefiable.

Table 6. Summary of LiquefyPro Output for Model 2

HAMMER	CALCULATED LIQUEFIABLE LAYER THICKNESS
Automatic	At the lower bound hammer energy efficiency ratio of 0.46, **12.2 feet** of the soil was liquefiable (i.e. from 12.8 to 25 foot depth). At the upper bound hammer energy efficiency ratio of 0.99, **none** of the soil was determined to be liquefiable.
Safety	At the lower bound hammer energy efficiency ratio of 0.36, **all 15 feet** of the soil was liquefiable (i.e. from 10 to 25 foot depth). At the upper bound hammer energy efficiency ratio of 0.70, **1 foot** of the soil was liquefiable (i.e. from 24 to 25 foot depth).
Winch/Donut	At the lower bound hammer energy efficiency ratio of 0.25, **all 15 feet** of the soil was liquefiable (i.e. from 10 to 25 foot depth). At the upper bound hammer energy efficiency ratio of 0.60, **5.6 feet** of the soil was liquefiable (i.e. from 19.4 to 25 foot depth).

CONCLUSIONS

This limited study demonstrates that for the same SPT N value, each hammer type (automatic, safety, donut and winch) can potentially over or under predict the occurrence of liquefaction. Under-predicting the occurrence of liquefaction could result in severe consequences (i.e. damage to property and loss of life) should a site experience liquefaction during an earthquake. This study demonstrates that hammer calibration could help to reduce that risk.

It is our opinion that public agencies should require calibrated SPT hammer test results when evaluating liquefaction, strength loss, dynamic settlement, and lateral spread hazards. It is our hope that this practice will be adopted by the engineering community as the Standard of Practice and compulsory by local and state building codes.

It should be noted that while this study included analyses for a winch hammer, this hammer type is not recommended for SPT-based liquefaction studies due to its inability to produce repeatable test results. Additionally, ASTM does not sanction the use of the winched wireline SPT hammer.

REFERENCES

ASTM D 1586-99, Revised 1999. "Standard Test Method for Penetration Test and Split-Barrel Sampling of Soils." ASTM International, West Conshohocken, Pennsylvania, Volume 4.08.

Batchelor, C., Goble, G., Berger, J., and Miner, R. (1995). "Standard Penetration Test Energy Measurements on the Seattle ASCE Field Testing Program." Report for the Seattle Section of the American Society of Civil Engineers.

California Division of Mines and Geology and others (1997). "Guidelines for evaluating and mitigating seismic hazards in California." California Division of Mines and Geology Special Publication 117.

Davidson, J.L., Maultsby, J.P., and Spoor, K.B. (1999). "Standard Penetration Test Energy Calibrations. Final Report and Appendices." Florida University, Gainesville; Florida Department of Transportation; and Federal Highway Administration.

International Code Council, Inc. (2006). "2006 International Building Code."

Kovacs, W.D., Salomone, L.A., and Yokel, F.Y. (1983). "Comparison of Energy Measurements in the Standard Penetration Test Using the Cathead and Rope Method." National Bureau of Standards Report to the US Nuclear Regulatory Commission, November, 1983.

NCEER (1997). "Proceedings of the NCEER Workshop on Evaluation of Liquefaction Resistance of Soils." Edited by Youd, T.L. Idriss, I.M., Technical Report No. NCEER-97-0022, December 31, 1997.

Seed, H.B., Tokimatsu, K., Harder, L.F., and Chung, R.M. (1985). "Influence of SPT Procedures in Soil Liquefaction Resistance Evaluations." *ASCE Journal of Geotechnical Engineering*, Volume 11, No. 12, December: pp. 1425-1445.

Seed, R.B., Cetin, K.O., Moss, R.E.S., Kammerer, A.M., Wu, J., Pestana, J.M., Riemer, M.F., Sancio, R.B., Bray, J.D., Kayen, R.E., and Faris, A. (2003). "Recent advances in soil liquefaction engineering: a unified and consistent framework." *Report No. EERC 2003-06*, Earthquake Engineering Research Center.

Sjoblom, D., Bischoff, J., Cox, K. (2002). "SPT Energy Measurements with the PDA," presented at the 2nd International Conference on the Application of Geophysical and NDT Methodologies to Transportation Facilities and Infrastructure, Los Angeles, California, May 15, 19, 2002.

The Rigidity Recovery of Post Liquefied Soils

Seiji Kano[1], Hiroshi Kidera[2] and Yasushi Sasaki[3], Takashi Ikeoka[4] and Koichi Ichii[5]

[1]Assistant Professor, Department of Social and Environmental Engineering, Hiroshima University, 1-4-1, Kagamiyama, Higashihiroshima, 7398529, Japan; skano@hirosihma-u.ac.jp
[2]Engineer, Kunisaki Construction Office, Oita Prefecture, 786-1 Ankokuji, Kunisaki-cho, Higashi-Kunisaki, Oita, 873-0504, Japan
[3]Adviser, Japan Institute of Construction Engineering, 3-12-11, Toranomon, Minato-ku, Tokyo, 105-0001, Japan; y.sasaki@jice.or.jp
[4]Engineer, Kajima Corporation, 5-30, Akasaka 6-chome, Minato-ku, Tokyo 107-8502, Japan, ikeokat@kajima.com
[5]Associate Professor, Department of Social and Environmental Engineering, Hiroshima University, 1-4-1, Kagamiyama, Higashihiroshima, 7398529, Japan; ichiikoji@hirosihma-u.ac.jp

ABSTRACT: On the performance based design, it is very important to predict the deformation of structures. In order to predict the deformation of structures, we have to know how much the ground will move or how much earth pressure will work. Especially, a prediction of behavior of a liquefied ground beneath structures is very important because of its large deformation. Many studies on the behavior of liquefied soil were conducted to evaluate the characteristics of soil in the post liquefaction stage. There are two kinds of idea about the characteristics of post liquefied soil. Some papers demonstrate that the liquefied soil behaves like a solid which has very low shear strength. In the other idea the soil is considered as a liquid. At the first stage of deformation, the soil behaves like a very weak solid or a liquid. However, it recovers the shear strength after the large deformation due to dilatancy caused by the deformation.

This study aims to clarify the effects of some factors on the rigidity recovery of post liquefied soil. This paper describes results of a series of torsional hollow cylinder shearing tests to evaluate the shear stress – strain relationship of liquefied soil. Effects of fine particles content, relative density, overburden pressure, and maximum shear strain during the shaking are discussed.

1. INTRODUCTION

After Hyogoken-nanbu earthquake, design codes of structures are being developed for the performance based design. The design code of earth structures, for example, embankments, levees etc, is also being developed to the performance based design.

On the performance based design, it is very important to predict the deformation of structures. In order to predict the deformation of structures, we have to know how much the ground will move or how much earth pressure will work. Especially, a prediction of behavior of a liquefied ground beneath structures is very important because of its large deformation.

Recently, many studies on the behavior of liquefied soil were conducted to evaluate the characteristics of soil in the post liquefaction stage. There are two kinds of idea about the characteristics of post liquefied soil. Some papers demonstrate that the liquefied soil behaves like a solid which has very low shear strength. In the other idea the soil is considered as a liquid. At the first stage of deformation, the soil behaves like a very weak solid or a liquid. But it recovers the shear strength after the large deformation due to dilatancy caused by the deformation. The reason that the post liquefied soil is being regarded as a weak solid is mainly because the prediction of the change between a liquid state and solid state is very difficult. However, a way to evaluate the shear strength of liquefied soil has not been clearly identified yet. Yasuda et al.,(1993) showed a way to predict the behavior of post liquefied soil by using the F_L value. He defined a small resistance area as shown in Fig. 1.

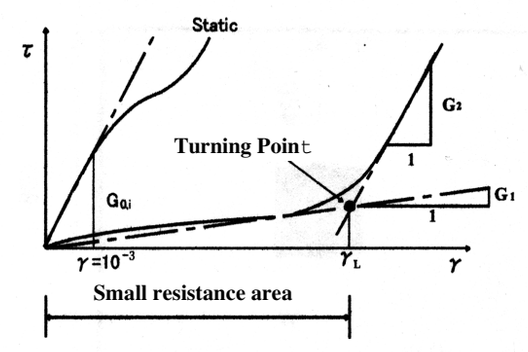


FIG. 1. Small resistance area of post liquefied soil

They said, “the coefficient of shear stiffness of soil was very small in the small resistance area”. However, the small resistance area was not defined clearly. Therefore this study aims to clarify the effects of some factors on the rigidity recovery of post liquefied soil.

The maximum shear strain, γ_{max} were applied to each specimen after the liquefaction induced by cyclic loading. This maximum shear strain was given as one cycle sinusoidal wave. This stands for a scale of ground motion. In this study, the maximum shear strain ranged from 0.40 % to 12.90 %.

2. TORSIONAL HOLLOW CYLINDER SHAERING TESTS

In order to clarify the recovery process of post liquefied soil, a series of torsional hollow cylinder shearing tests were conducted. Specimens were 7 cm in Outside diameter and 3 cm in inside diameter, 10cm in height. Specimens were made by water poring method. Relative density of them ranged from 30 % to 60 %. Silica sand was used in this study. The crushed stone powder and Kibushi clay were also mixed to examine the influence of fine particle contents. Stone powder is non plastic fine particle which is non-cohesive and Kibushi clay is cohesive clay. Table 1 shows the conditions of tests. Fig. 2 shows an example of the pattern of loading process.

Table 1. Test conditions

No	Initial relative density Dr (%)	Dr after consolidation (%)	Initial effective stress σ'_0 (kPa)	FC (%)		Cyclic shear strain (%)	Maximum strain γ_{max} (%)
Test-1	50	52.3	100	0		0.386	0.40
Test-2		52.5				0.614	2.31
Test-3		53.0				0.722	4.48
Test-4		53.6				0.557	8.03
Test-5		52.8				0.609	12.90
Test-6	30	31.5	30	0		1.460	5.80
Test-7		32.8	50			1.452	5.74
Test-8		33.1	100			1.302	5.64
Test-9		34.7	150			1.482	5.83
Test-10	40	41.1	30	0		1.340	5.71
Test-11		41.9	50			1.461	5.68
Test-12		43.5	100			1.306	5.64
Test-13		44.0	150			1.468	5.69
Test-14	50	57.5	30	0		1.332	5.44
Test-15		51.9	50			1.381	5.61
Test-16		52.7	100			1.275	5.08
Test-17		52.4	150			1.222	5.18
Test-18	60	60.8	30	0		1.253	5.16
Test-19		61.5	50			1.328	5.15
Test-20		62.4	100			1.347	5.06
Test-21		63.5	150			1.086	4.85
Test-22	50	50.9	30	10	SP	1.400	5.77
Test-23		51.8	50	10	SP	1.332	5.53
Test-24		50.7	100	5	SP	1.351	5.54
Test-25		51.2		10	SP	1.223	5.35
Test-26		53.5		15	SP	1.238	5.52
Test-27		56.6		20	SP	1.313	5.70
Test-28		55.5		25	SP	1.287	5.45
Test-29		52.8		30	SP	1.382	5.68
Test-30		54.4	150	10	SP	1.264	5.34
Test-31	50	53.9	100	5	KC	1.355	5.74
Test-32		-		10	KC	1.230	5.30
Test-33		51.4		20	KC	1.158	5.44

SP: Crushed stone powder, KC: Kibushi Clay

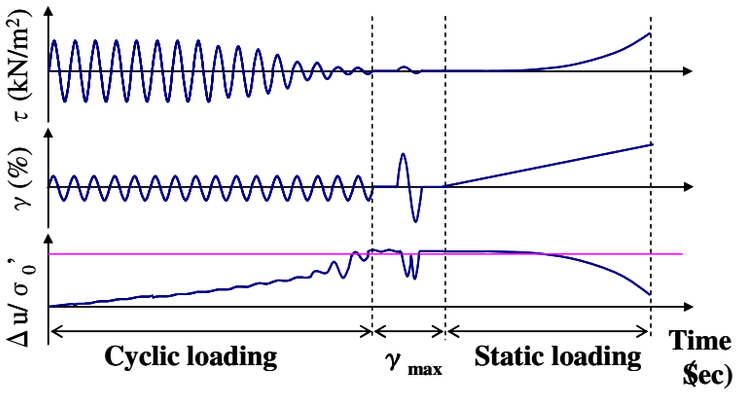


FIG. 2. Pattern diagrams of loading process

3. RESULTS OF TESTS

3.1 Definition of a small resistance

Figure 3 shows the relationship between the shear stress and shear strain in Test-1 to Test-5. According to this, it is found that larger the maximum shear strain was, larger the shear strain needed to recover the strength was. And, it is also found that the relationships between the shear stress and the shear strain after the small resistance area were almost the same to each test.

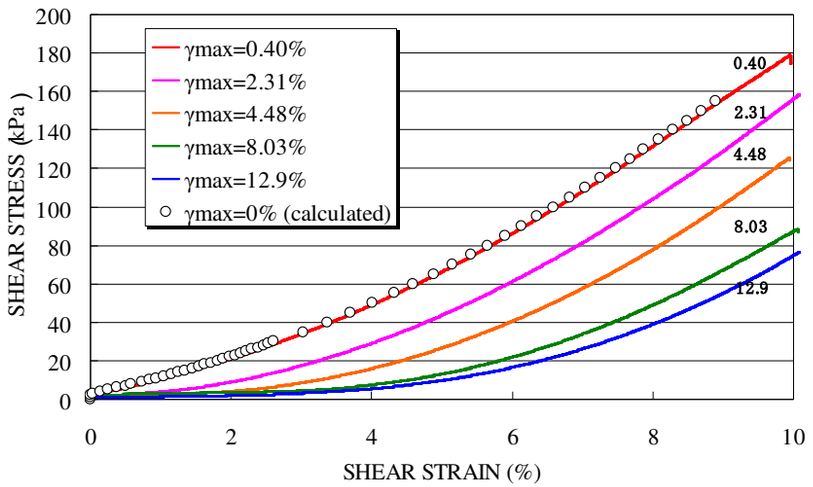


FIG. 3. Relationships between the shear stress and the shear strain

When the ground liquefaction was caused during an earthquake, the reason why a large deformation of ground was caused is mainly by the decreasing of strength in the small resistance area. So it is very important to evaluate this small resistance area. But the definition of this is not cleared as mentioned above. Therefore the small resistance area is defined as the shear strain which the shear strength increases to a certain level in this paper. The relationships between the maximum shear strain and the shear strain at same shear stress were calculated from FIG. 3 and the relationships between the shear stress and the shear strain at the maximum shear strain γ_{max} becomes 0% were calculated as shown in FIG. 3. It is found that the stress - strain curve at γ_{max} = 0 kPa is almost the same as the curve at γ_{max} =0.40 %.

Based on the curve at γ_{max} = 0.40 %, the difference of the shear strains in each case from the curve at γ_{max} = 0.40 %, $\Delta\gamma$, was calculated. The relationships between $\Delta\gamma/\Delta\gamma_{max}$ and the shear stress were shown in FIG. 4. Here $\Delta\gamma_{max}$ is defined as the maximum $\Delta\gamma$ in each case.

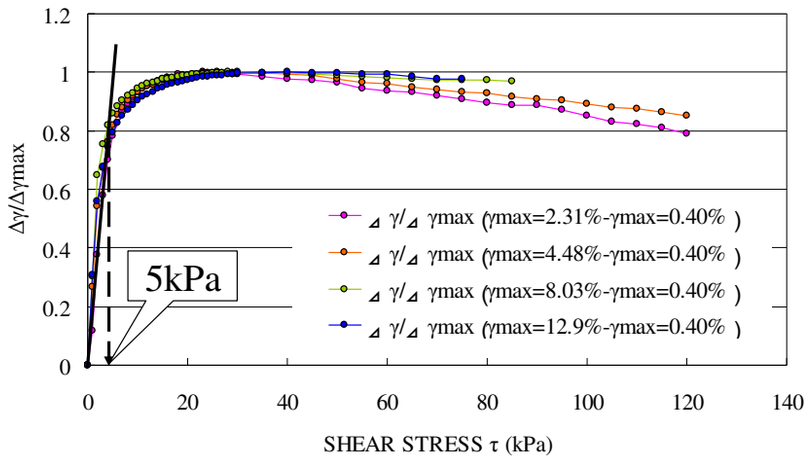


FIG. 4. Relationships between $\Delta\gamma/\Delta\gamma_{max}$ and Shear stress

According to this figure, the curves of $\Delta\gamma/\Delta\gamma_{max}$ and shear stress in each case are almost the same. So the small resistance area is defined as the area that this relationship keeps linear and the shear stress at the small resistance area is smaller than 5 kPa. $\gamma_{5kPa,}$ is defined as the maximum shear strain at shear stress is 5 kpa.

Figure 5 shows the relationships between the shear strains, γ_{5kPa} and the maximum shear strain, $\gamma_{max.}$ It is found from this figure that larger the γ_{max} is, larger the γ_{5kPa} is. And the shear strain, γ_{5kPa}, increases linearly at the small $\gamma_{max.}$ But the increase of γ_{5kPa} becomes smaller at large γ_{max} values.

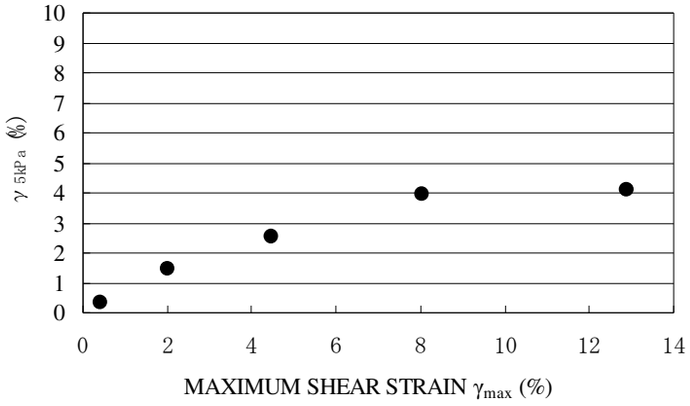


FIG. 5. Relationships between γ_{5kPa} and γ_{max}

3.2 Influence of the relative density and overburden pressure on the rigidity recovery process

Figure 6 shows the relationships between the shear stress and the shear strain at the static loading process in the tests which initial effective stress is 30 kPa (Test-6, Test-10, Test-14 and Test-18). It is found that the stress-strain curve depends on the relative density and the shear strength at higher density is recovered faster than at the lower one. Larger shear strain is needed to recover the shear strength at lower density. Furthermore, the shear strength at the steady state depends also on the relative density. This tendency is observed in all cases from Test -6 to Test-21. Figure 7 shows the relationships between the relative density and $\gamma_{5kPa.}$ It is also found that the influence of confining pressure becomes smaller at the higher density.

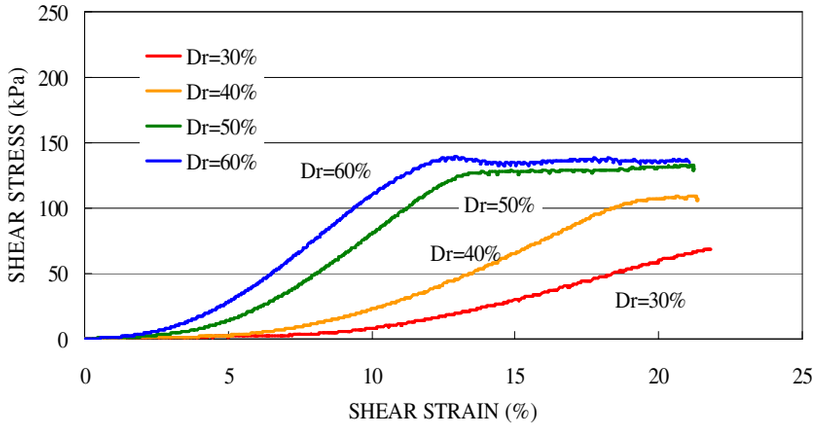


FIG. 6. Relationships between the shear stress and the shear strain at σ'_o = 30 kPa

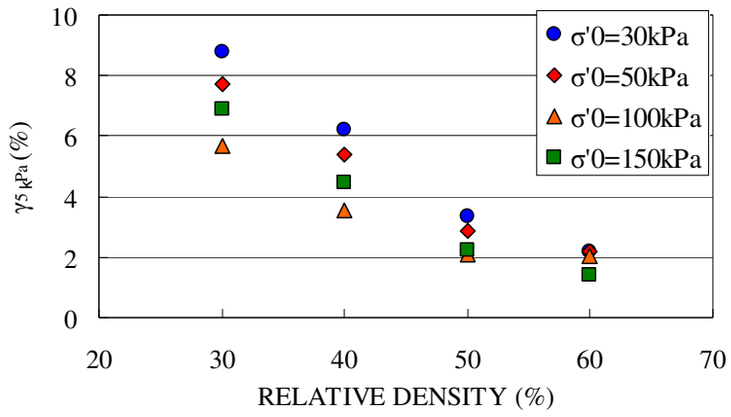


FIG. 7. Relationships between the relative density and γ_{5kPa}

Figure 8 shows the relationships between the shear stress at the steady state τ_{ss} and the relative density. It is clear that the shear stress τ_{ss} depends on the relative density and the shear stress becomes larger in the higher relative density. The shear stress τ_{ss} also depends on the overburden stressσ'_o but the shear stress τ_{ss} at σ'_o = 100 kPa is close to the one at σ'_o = 150 kPa. The reason why the difference of the shear stress is caused is not clear yet. It is possible that the specimen of lower overburden pressure does not reach the steady state. But it is clear that the specimen of higher density reached to the steady state according to their shear stress – shear strain curve.

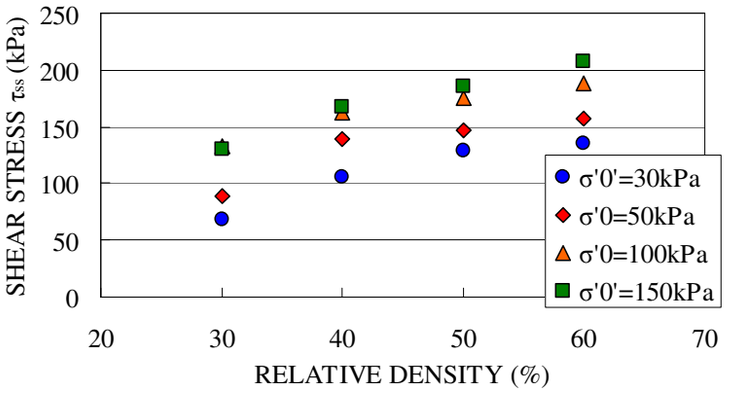


FIG. 8. Relationships between the shear stress and the relative density

3.3 Influence the fine fraction contents on the rigidity recovery process

Figure 9 shows that relationships between the shear stress and the shear strain in Test-24 to Test-29. To compare the results of silica sand, the results of Test-16 is also shown in FIG. 9. In these tests, the crushed stone powder was used as non plastic fine particles. According to this figure, the shear strain that needs to recover the shear stress becomes larger in the higher fine fraction contents.

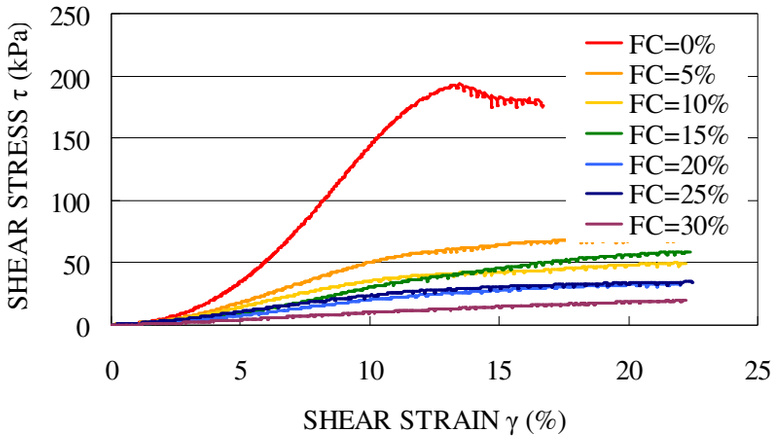


FIG. 9. Relationships between the shear stress and the relative density

Figure 10 shows the relationships between the shear stress and the shear strain in the case of Kibushi clay. Kibushi Clay is one of the cohesive clay. It is found from this figure that the specimen of FC =5% was recovered faster than the crushed stone powder. However in the case of FC =10 %, the relationship is the same to the one of crushed stone powder. In the area that the shear stress is small, it seems that the shear stress of the high fine fraction content is recovered quickly.

Two reasons of this are considerable. One is that fine particles spread the distance of particles and keep the void ratio in the specimen widely. So fine particles keep the relative density be small. The other is that the fine particles keep the soil structure be strong. It seems that the reason of that difference between the non plastic particle and the cohesion clay is latter. Furthermore the influence of the soil structure becomes smaller in the case of high fine fraction content (FC = 10% or 20%) and characteristics of fine particles become predominant. The reason of the quick recovery in the high fine fraction content is considered that the characteristics of fine particles become predominant.

Figure 11 shows the relationships between the small resistance area, γ_{5kPa} and the fine fraction contents FC. From this figure, it is found that the small resistance area with the crushed stone powder, γ_{5kPa} become larger than without the fine particles. However the small resistance area with the cohesion clay, Kibushi clay, does not become large. The reason of this is considered as follows. The specimen with the cohesion clay can keep its stiffness. Therefore the influence of disturbance of soil

structure becomes smaller and the influence of increase of void ratio becomes smaller. Even if the FC is increased, the small resistance area does not become large because these two influences are counterbalanced.

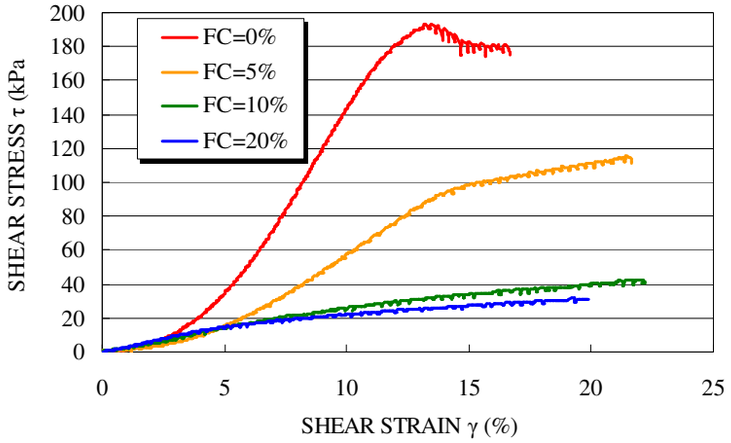


FIG. 10. Relationships between the shear stress and the shear strain

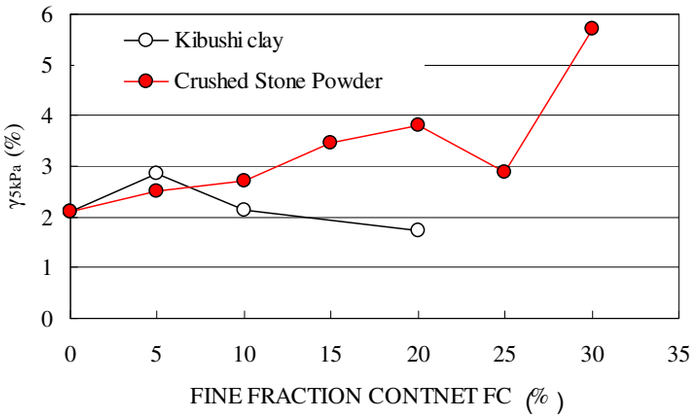


FIG. 11. Relationships between γ_{5kPa} and the fine fraction content

Figure 12 shows the relationship between the shear stress at the steady state, τ_{ss} and the fine fraction content FC. It is also clear that the shear strength with the fine particles becomes small. The shear stress in the case of low FC sand becomes small linearly; however the trend of the reducing of the shear stress becomes gentle in the case of high FC sand. It implies that the fine particles have an influence on the rigidity recovery process when the soil structure is influenced by the fine particles.

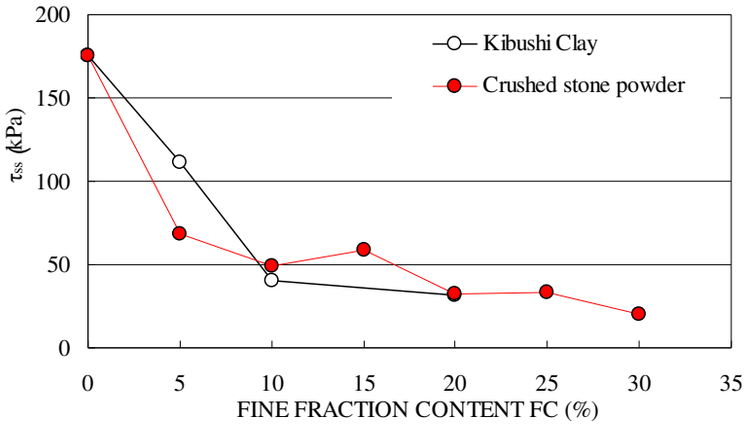


FIG. 12. Relationships between the shear stress τ_{ss} and the fine fraction content

4. CONCLUSIONS

This study aims to clarify the effects of some factors on the rigidity recovery of post liquefied soil. This paper describes results of a series of torsional hollow cylinder shearing tests to evaluate the shear stress – shear strain relationship of liquefied soil. Effects of fine fraction content, relative density, overburden pressure, and maximum shear strain during the shaking were discussed. Results revealed the following:
1) The rigidity recovery process is influenced by the maximum shear strain when the maximum shear strain is less than 8%.
2) It is also found that the recovery process is influenced by the relative density and the degree of influence is larger in the case of lower relative density.
3) The overburden pressure has also an influence on the rigidity recovery process.
4) The rigidity recovery process is influenced by the fine fraction content, FC. But the small resistance area of the sand with the cohesion clay is almost constant. Furthermore, the degree of the influence depends on the FC and when the FC is larger than 10%, the influence is small.

REFERENCES

Yasuda, S., Masuda, T., Kiku. H and Itafuji, S. (1993). "Several torsional shear tests on deformation characteristics of soil before and after liquefaction," *Proceedings of the 28th Japan national conference on soil mechanics and foundation engineering*, JGS, 929-930.

The Seismic Dilatometer Marchetti Test (SDMT) for Evaluating Liquefaction Potential Under Cyclic Loading

S. Grasso[1] and M. Maugeri[2]

[1] Ph. D. in Geotechnical Engineering, University of Catania, Faculty of Engineering, Viale Andrea Doria n. 6, 95125 Catania (Italy).
[2] Full Professor in Geotechnical Engineering, University of Catania, Faculty of Engineering, Viale Andrea Doria n. 6, 95125 Catania (Italy).

ABSTRACT: This paper present a K_D-CRR corrected relation for sandy soils potential liquefaction evaluation under cyclic loading, on the basis of previous tentative CRR-K_D curves proposed. The new tentative correlation for evaluating CRR from K_D, was formulated by combining previous CRR-K_D correlations with the vast experience incorporated in current methods based on CPT and SPT for the evaluation of liquefaction potential. The Seismic Dilatometer Marchetti Test (SDMT) has the advantage, in comparison with CPT and SPT tests, to measure independent parameters, such as the Horizontal Stress Index (K_D). A re-evaluation of CRR-K_D correlation has been also made taking into account the numerous recent SDMT.
The results show that the Horizontal Stress Index (K_D) is a key-parameter and is very sensitive to potential liquefaction behaviour under cyclic loading. The plotted correlation with critical values of K_D is very simple to use for detecting liquefaction potential of soils.
CPT, SPT and SDMT data have been then used in the evaluation of the potential liquefaction at San Giuseppe La Rena site in Catania (Sicily, Italy), which is recognized as a typical Mediterranean city at high seismic risk.

INTRODUCTION

The Seismic Dilatometer Marchetti Test (SDMT) is gradually entering into use in routine geotechnical investigations, allowing therefore the accumulation of numerous data. The SDMT provides, among other measurements, a parameter that previous experience indicated as bearing a significant relationship with soil liquefaction. Such parameter is the Horizontal Stress Index (K_D), whose relationship with CRR has been illustrated by several authors (Monaco et al., 2005; Grasso and Maugeri, 2006). The Authors have collected in the recent years a large amount of measurements of K_D using SDMT in different sandy soils.
The coastal plain of the city of Catania (Sicily, Italy), which is recognized as a typical Mediterranean city at high seismic risk, was investigated by Seismic Dilatometer Marchetti Test (SDMT). Seismic liquefaction phenomena were reported by historical

sources following the 1693 (Ms = 7.0-7.3, Io = X-XI MCS) and 1818 (Ms = 6.2, Io = IX MCS) Sicilian strong earthquakes. The most significant liquefaction features seem to have occurred in the Catania area, near Saint Giuseppe La Rena site, situated in the meisoseismal region of both events. These effects are significant for the implications on hazard assessment mainly for the alluvial flood plain just south of the city, where most industry and facilities are located.

In the site No.11 (Saint Giuseppe La Rena site) eight borings (No. 418÷425 of the database) were made and for all of them SPT data are available. Near the borings eleven CPT (No. 1÷11) tests were also made. The subsoil exploration revealed the presence of a sand with a content of fine particles less then 30% for a depth of about 10 meters.

For a new commercial building, deep site investigations have been performed, which included borings, SPT and CPT. More recently, at the same site, SDMT has been performed. The locations of the SPT, CPT and SDMT are reported in Fig. 1. SPT and CPT were located in the area where the commercial building has been built. The SDMT was performed after the construction of the building, and was located outside the construction area.

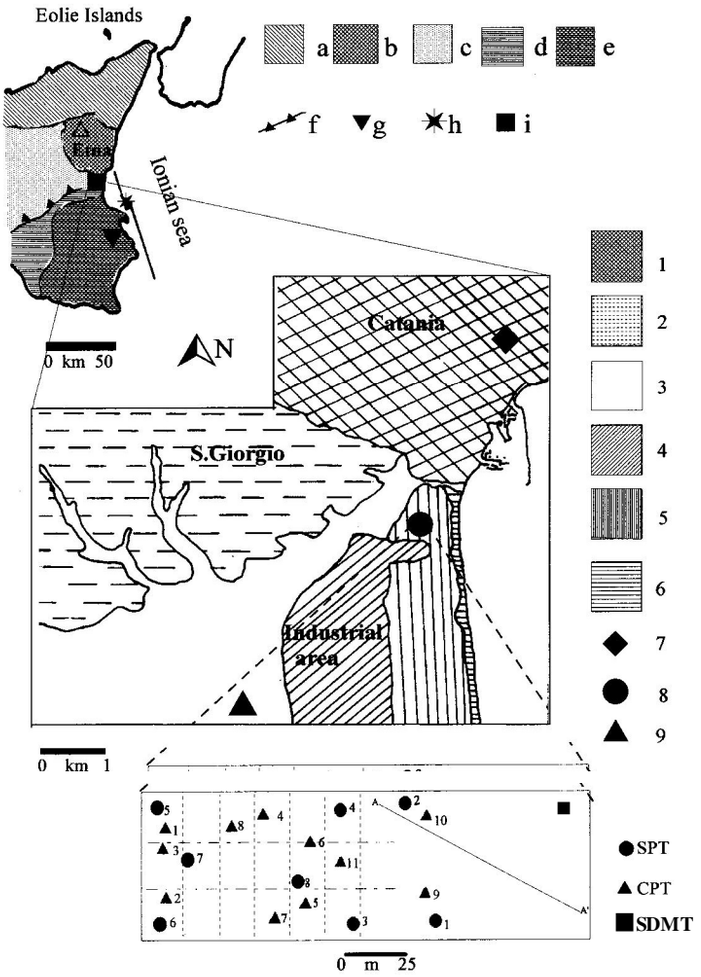


FIG. 1. Location of SPT, CPT and SDMT tests.

CYCLIC SHEAR STRESS RATIOS INDUCED BY EARTHQUAKE GROUND MOTIONS

During cyclic undrained loading, like those imposed by earthquake shaking, almost all saturated cohesionless soils are subjected to significant pore pressure build-up due to the contractive response of the soil at low strain levels. If there is shear stress reversal, the effective stress state can drop rapidly to zero. When a soil element reaches the condition of essentially zero effective stress, the soil has very little stiffness and large deformations can develop during cyclic loading. This phenomenon is generally referred to as liquefaction.

The susceptibility of a site to seismic-induced liquefaction may be assessed comparing the cyclic soil resistance to the cyclic shear stresses due to the ground motion. The latter is of course a function of the design earthquake parameters, while the former depends on the soil shear strength and can be computed using results from in situ tests. The traditional procedure, introduced by Seed & Idriss (1971), has been applied for evaluating the liquefaction resistance of San Giuseppe La Rena sandy soil. This method requires the calculation of the cyclic stress ratio CSR, and cyclic resistance ratio CRR. If CSR is greater than CRR, liquefaction can occur.

The cyclic stress ratio CSR is calculated by the following equation (Seed & Idriss 1971):

$$\mathbf{CSR = \tau_{av} / \sigma'_{vo} = 0.65\,(a_{max}/g)\,(\sigma_{vo}/\sigma'_{vo})\,r_d / MSF}$$

where τ_{av} = average cyclic shear stress, a_{max} = peak horizontal acceleration at the ground surface generated by the earthquake, g = acceleration of gravity, σ_{vo} and σ'_{vo} = total and effective overburden stresses, r_d = stress reduction coefficient depending on depth and MSF is magnitude scaling factor. Seed and Idriss (1971) introduced the stress reduction coefficient r_d as a parameter describing the ratio of cyclic stresses for a flexible soil column to the cyclic stresses for a rigid soil column.

As the shear stresses induced at any point in a level soil deposit during an earthquake are primarily due to the vertical propagation of shear waves in the deposit, these stresses can be calculated using analytical procedures and are particularly dependent on the earthquake ground motion characteristics (e.g., intensity and frequency content), the shear wave velocity profile of the site, and the dynamic soil properties (Idriss and Boulanger, 2004). So, the parameter C could be adequately expressed as a function of depth and earthquake magnitude (M) as reported in Idriss (1999), in extending the work of Golesorkhi (1989):

$$\mathbf{Ln(r_d) = \alpha(z) + \beta(z)M}$$

$$\mathbf{\alpha(z) = -1.012 - 1.126\sin(z/11.73 + 5.133)}$$

$$\mathbf{\beta(z) = 0.106 + 0.118\sin(z/11.28 + 5.142)}$$

in which z is depth in meters and M is moment magnitude. These equations are considered appropriate to a depth $z \leq 34$ m. Plots of r_d calculated using previous equation for M = 5½, 6½, 7½ and 8 are presented in Figure 2. Also shown in this figure is the average of the range published by Seed and Idriss in 1971.

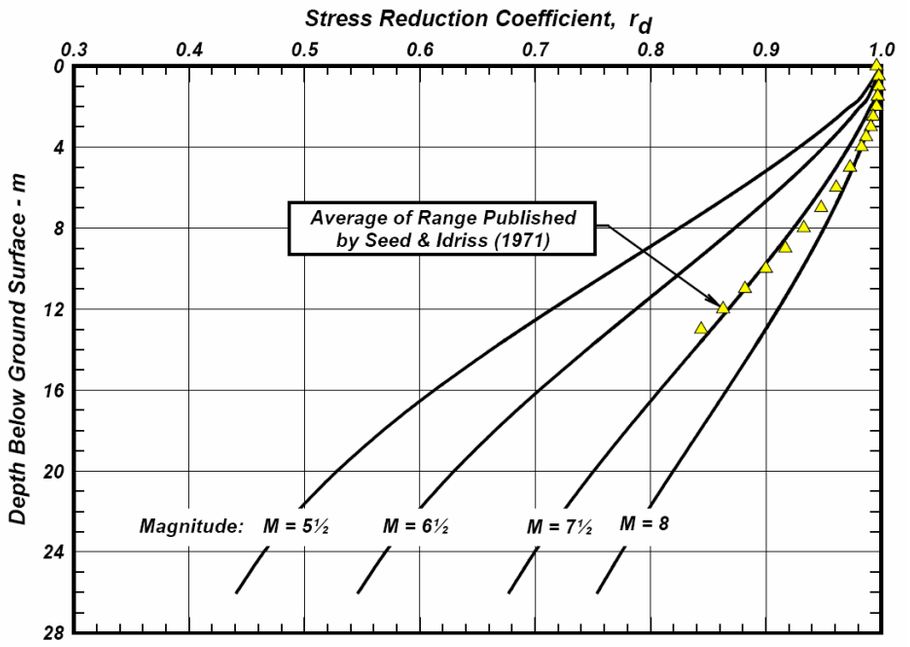


FIG. 2: Variations of stress reduction coefficient with depth and earthquake magnitude (from Idriss 1999).

The magnitude scaling factor, MSF , has been used to adjust the induced CSR during earthquake magnitude M to an equivalent CSR for an earthquake magnitude, M = 7½. The MSF relation used was then expressed by Idriss (1999) as:

MSF = -6.9 exp(-M/4) -0.058
MSF≤1.8

CPT-BASED PROCEDURE FOR EVALUATING SOIL LIQUEFACTION

A primary advantage of the CPT is that a nearly continuous profile of penetration resistance is developed for stratigraphic interpretation. The CPT results are generally more consistent and repeatable than results from other penetration tests. The continuous profile also allows a more detailed interpretation of soil layers and soil types. This stratigraphic capability makes the CPT particularly advantageous for reconnaissance investigations. In addition, CPT data can be used to estimate liquefaction resistance of penetrated soil layers. Thus the CPT can be used to develop preliminary soil and liquefaction resistance profiles for site investigations. In recent years, increased field performance data have become available at liquefaction sites investigated with CPT (Robertson and Wride, 1997). These data have facilitated the development of CPT-based liquefaction resistance correlations. These correlations allow direct calculation of CRR, rather than through conversion of CPT measurements to equivalent SPT blowcounts and then applying SPT criteria, a technique that was commonly applied in the past.

The revised $\boldsymbol{CRR - q_{CIN}}$ relation is shown in Fig. 3 with the case history points or cohesionless soils having $\boldsymbol{FC}$ 5%. The derived relation can be conveniently expressed as (Idriss and Boulanger, 2004):

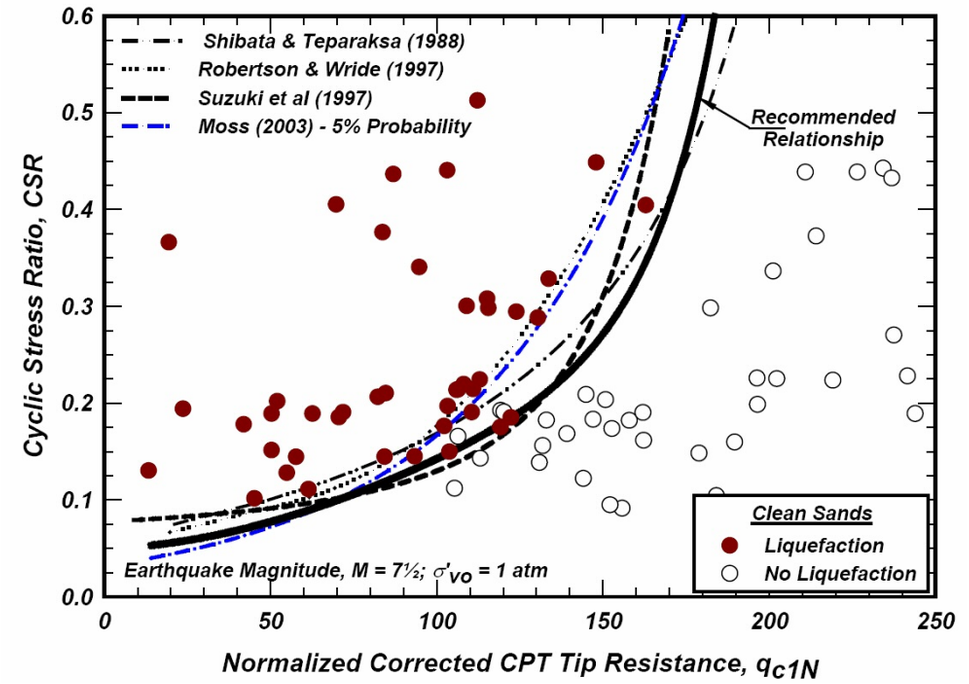


FIG. 3. CPT-based case histories and recommended relation for clean sands for M = 7½ and σo ' = 1 atm (1 tsf).

$$CRR = \exp\left\{\frac{q_{c1N}}{540} + \left(\frac{q_{c1N}}{67}\right)^2 - \left(\frac{q_{c1N}}{80}\right)^3 + \left(\frac{q_{c1N}}{114}\right)^4 - 3\right\}$$

The derived relation is comparable to the curve proposed by Suzuki et al (1997) for clean sands. It is more conservative than the corresponding curves by Robertson and Wride (1997) and by Seed et al. (2003) for almost the entire range of q_{C1N} . The curve proposed by Shibata and Teparaksa (1988) is less conservative than the derived relation except for q_{C1N} greater than about 165.

The results of 11 CPT tests executed in the San Giuseppe La Rena site are reported in Fig. 4, while $(qc_{1N})_{cs}$ values according to Robertson and Wride (1997) are reported in Fig. 5.

SPT-BASED PROCEDURE FOR EVALUATING SOIL LIQUEFACTION

Semi-empirical procedures for liquefaction evaluations originally were developed using the Standard Penetration Test (SPT), beginning with efforts in Japan to differentiate between liquefiable and nonliquefiable sites. Criteria for evaluation of liquefaction resistance based on standard penetration test (SPT) blowcounts have been rather robust over the years. Those criteria are largely embodied in the CSR versus $(N_1)_{60}$.

The value of CRR for a magnitude M =7½ earthquake and an effective vertical stress σ'_{vo}=1atm (≅1 tsf) can be calculated based on $(N_1)_{60}$cs using the following expression:

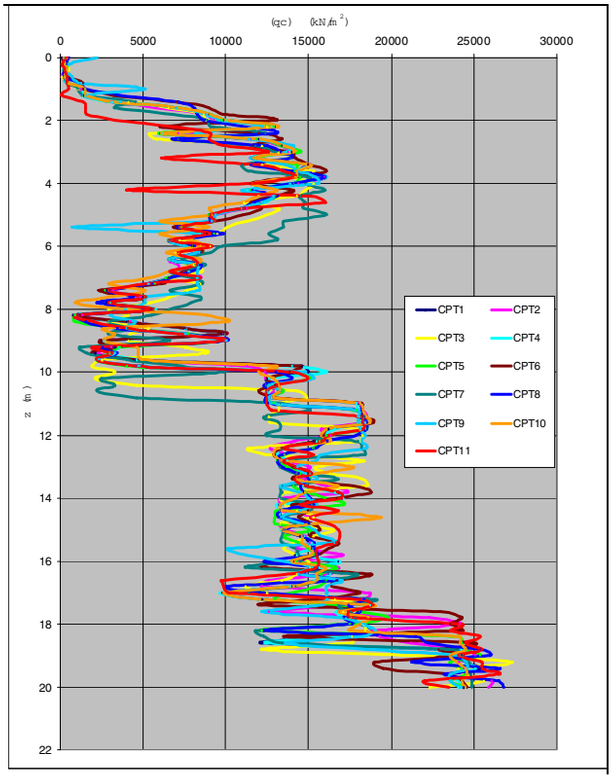


FIG. 4. qc test results versus depth (11 profiles).

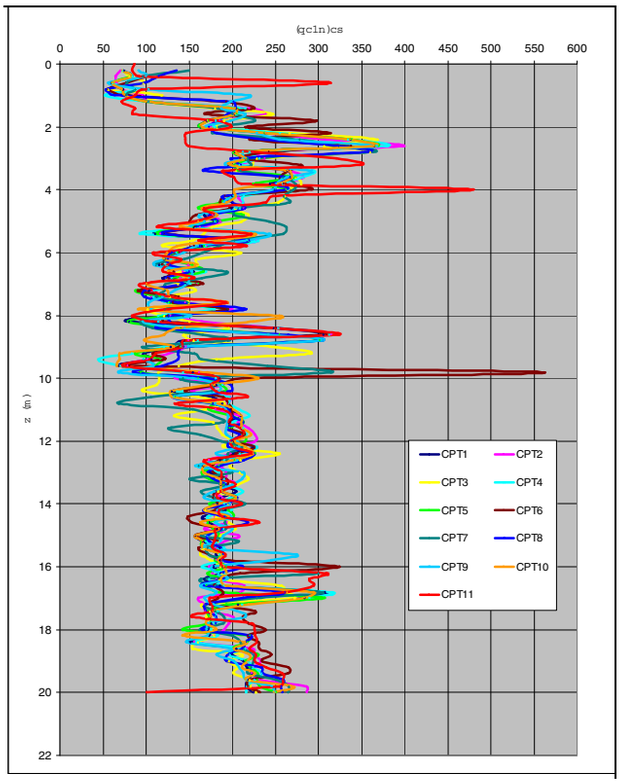


FIG. 5. $(qc_{1N})_{cs}$ test results versus depth (11 profiles).

$$CRR = exp\left\{\frac{(N_1)_{60cs}}{14.1} + \left(\frac{(N_1)_{60cs}}{126}\right)^2 - \left(\frac{(N_1)_{60cs}}{23.6}\right)^3 + \left(\frac{(N_1)_{60cs}}{25.4}\right)^4 - 2.8\right\}$$

The use of these equations provides a convenient means for evaluating the cyclic stress ratio required to cause liquefaction for a cohesionless soils with any fines content (Idriss and Boulanger, 2004).
The results of the SPT in terms of $(N_1)60cs$ assuming Ks= 1.5 according to Robertson and Wride (1997) are reported in Fig. 6.

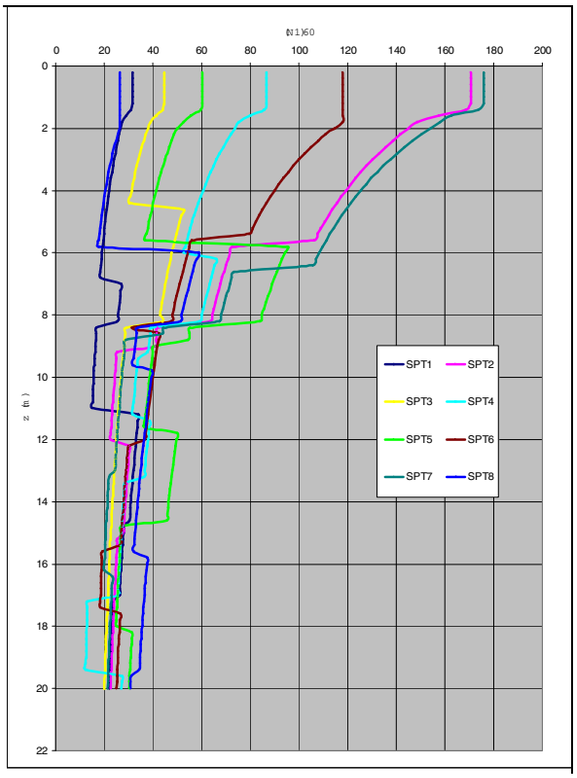


FIG. 6. $(N_1)60cs$ test results versus depth assuming Ks= 1.5.

The ratio CSR to CRR is called the liquefaction resistance factor (F_{SL}). Then is possible to evaluate the liquefaction potential index P_L (Iwasaki et al., 1978), given by the following expression:

$$\mathbf{P_L} = \int_0^{20} F(z)w(z)dz$$

where w(z)= 10 – 0.5z and F(z) is a function of the liquefaction resistance factor (F_{SL}) and its values are: F(z)= 0 for $F_{SL} \geq 1$ and F(z)= 1 - F_{SL} for $F_{SL} < 1$. The liquefaction potential index, P_L, is more conservative for SPT data; it reaches the average value of 30 than the CPT data, which reaches the average value of 15. From these values the liquefaction potential is very high for SPT data and high for CPT data.

SDMT-BASED PROCEDURE FOR EVALUATING SOIL LIQUEFACTION

Evaluation of CRR from shear waves velocity Vs measured by different methods

Shear wave velocity can be measured in-situ by down-hole (D-H), cross-hole (C-H) and the new Seismic Dilatometer Marchetti test (SDMT). Shear wave velocity measurements have been incorporated within a Marchetti flat dilatometer (DMT) by placing a velocity transducer in a connecting rod just above the blade. The hybrid of combining down-hole seismic with flat dilatometer, termed the Seismic Dilatometer Marchetti Test (SDMT), has the superior advantages of determining both the routine estimates of soil properties and stratigraphic information, while also measuring the small-strain stiffness within a single sounding. The SDMT is rapid, simple, and cost effective, requiring essentially no more time than a conventional dilatometer sounding. The seismic modulus is an instrumented tube, located above the blade, housing two receivers at a distance of 0.50 m. The test configuration "two receivers"/"true interval" avoids the problem connected with the possible inaccurate determination of the "first arrival" time sometimes met with the "pseudo interval" configuration (just one receiver). Also the pair of sismograms at the two receivers corresponds to the same blow, rather than at two successive blows - not necessarily identical. The adoption of the "true interval" configuration considerably enhances the repeatability in the Vs measurement. The energization is obtained by a swinging hammer, hitting horizontally a steel parallelepipedal base, pressed vertically against the soil surface to insure a strong contact. The longitudinal axis of the base is oriented parallel to the axis of the receivers, to maximize sensitivity to the shear wave. The shear wave velocity Vs is the ratio between the difference of distance between the energy source and the two receivers and the measured delay time of the pulse from the upper to the lower receiver. Vs may be converted into the initial shear modulus Go. The combined knowledge of Go and of the one dimensional modulus M (from DMT) may be helpful in the construction of the G-γ modulus degradation curves. The Vs determinations are executed at 0.50 m depth intervals.

The use of the shear wave velocity, V_S, as an index of liquefaction resistance has been illustrated by several authors. The correlation between V_S and CRR given by Andrus et al. (2004):

$$CRR_{7.5}=\left[0.022\left(\frac{K_{a1}V_{S1}}{100}\right)^2+2.8\left(\frac{1}{V^*_{S1}-(K_{a1}V_{S1})}-\frac{1}{V^*_{S1}}\right)\right]K_{a2}$$

where V^*_{S1} = limiting upper value of V_{S1} for liquefaction occurrence, assumed to vary linearly from 200 m/s for soils with fines content of 35% to 215 m/s for soils with fines content of 5% or less. K_{a1} is a factor to correct for high V_{S1} values caused by aging, K_{a2} is a factor to correct for influence of age on CRR. Both K_{a1} and K_{a2} are 1.0 for uncemented soils of Holocene age. For older soils the SPT- V_{S1} suggest average

K_{a1} values of 0.76 and 0.61, respectively, for Pleistocene soils (10,000 years to 1.8 million years).

Evaluation of CRR from the DMT horizontal stress index K_D

Marchetti (1982) and later studies suggested that the horizontal stress index K_D from DMT ($K_D = (p_o – u_o)/\sigma'_{vo}$) is a suitable parameter to evaluate the liquefaction resistance of sands. Comparative studies have indicated that K_D is noticeably reactive to factors such as stress state/history (σ_h, OCR), pure prestraining, aging, cementation, structure – all factors increasing liquefaction resistance. Such factors are scarcely felt e.g. by q_c from CPT (see e.g. Huang & Ma 1994) and, in general, by cylindrical-conical probes. As noted by Robertson & Campanella (1986), it is not possible to separate the individual contribution of each factor on K_D. On the other hand, when K_D is low, none of the above factors is high, i.e. the sand is loose, uncemented, in a low σ_h environment and has little stress history. A sand under these conditions may liquefy or develop large strains under cyclic loading. The most significant factors supporting the use of K_D as an index of liquefaction resistance are:

– *Sensitivity of DMT in monitoring soil densification*

The high sensitivity of the DMT in monitoring densification, demonstrated by several studies (e.g. Schmertmann et al. 1986 and Jendeby 1992 found DMT ≈ twice more sensitive than CPT to densification), suggests that the DMT may also sense sand liquefiability. In fact a liquefiable sand may be regarded as a sort of "negatively compacted" sand, and it appears plausible that the DMT sensitivity holds both in the positive and in the negative range;

– *Sensitivity of DMT to prestraining*

CC research on Ticino sand (Jamiolkowski & Lo Presti 1998, Fig. 7) has shown that K_D is much more sensitive to prestraining – one of the most difficult effects to detect by any method – than the penetration resistance (the increase in K_D caused by prestraining was found ≈ 3 to 7 times the increase in penetration resistance q_D). On the other hand, was already observed that reliable predictions of liquefaction resistance of sand deposits of complex stress-strain history require the development of some new in situ device (other than CPT or SPT), more sensitive to the effects of past stress-strain histories;

– *Correlation K_D - Relative density*

In NC uncemented sands, the relative density D_R can be derived from K_D according to the correlation by Reyna & Chameau (1991) shown in Fig. 8. This correlation has been soundly confirmed by datapoints added by subsequent research, in particular by additional K_D –D_R datapoints obtained by Tanaka & Tanaka (1998) at the sites of Ohgishima and Kemigawa, where DR was determined on high quality frozen samples;

– *Correlation K_D - In situ state parameter*

The state parameter concept is an important step forward from the conventional relative density concept in characterizing soil behavior, combining the effects of both relative density and stress level in a rational way. The state parameter (vertical distance between the current state and the critical state line in the usual v - ln p' plot) governs the attitude of a sand to increase or decrease in volume when sheared, hence it is strongly related to liquefaction resistance. More rational methods for evaluating CRR would require the use of the state parameter (see e.g. studies by Boulanger & Idriss 2004).

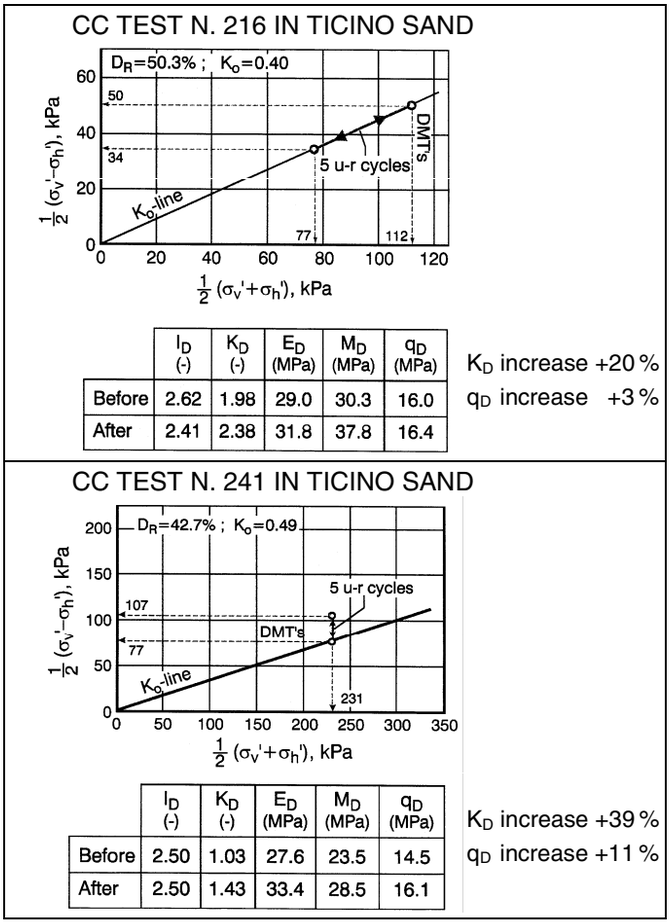


Fig. 7. Results of CC testing (prestraining cycles) showing the higher sensitivity of KD to prestraining than penetration resistance (Jamiolkowski & Lo Presti 1998).

Recent research supports viewing K_D from DMT as an index reflecting the in situ state parameter ξ_o. Yu (2004) identified the average correlation K_D - ξ_o shown in Fig. 9 (study on four well-known reference sands). Clearly relations K_D - ξ_o as the one shown by Yu (2004) strongly encourage efforts to develop methods to assess liquefiability by DMT.

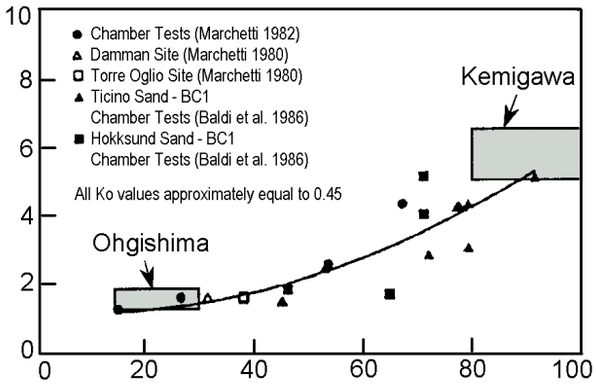


Fig. 8. Correlation K_D - D_R for NC uncemented sands (Reyna & Chameau 1991).

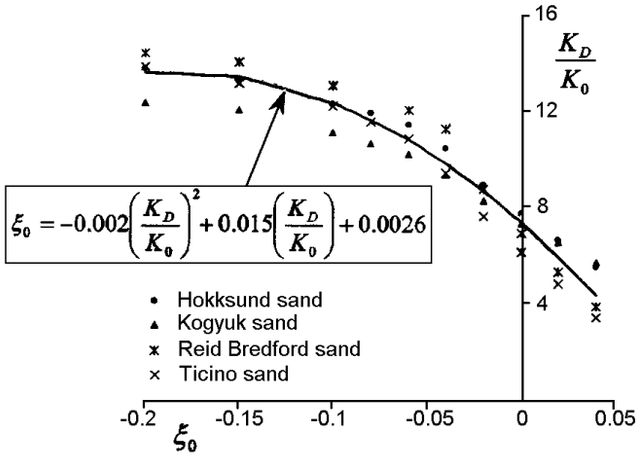


Fig. 9. Average correlation K_D - in situ state parameter ξo (Yu 2004).

Fig. 10 (Monaco et al. 2005) summarizes the various correlations developed to estimate CRR from K_D, expressed in form of CRR-K_D boundary curves separating possible "liquefaction" and "no liquefaction" regions.

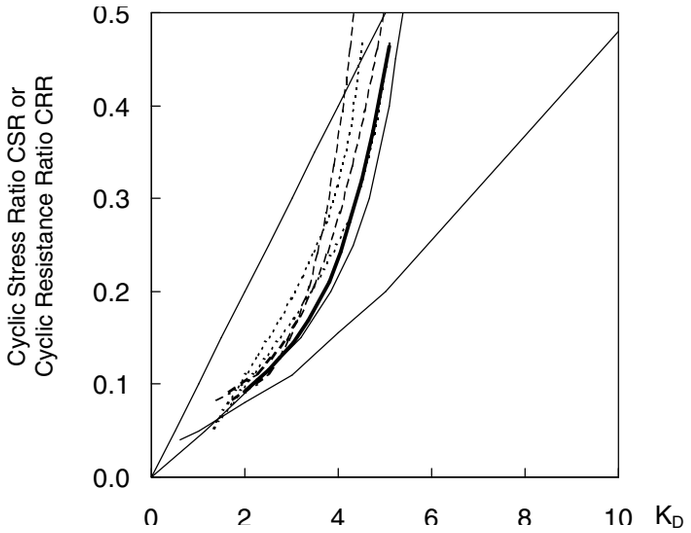


FIG. 10. CRR-K_D curves for evaluating liquefaction resistance from SDMT.

A new tentative CRR-K_D curve approximated by the equation:

$$\mathbf{CRR = 0.0908\,K_D^3 - 1.0174\,K_D^2 + 3.8466\,K_D - 4.5369}$$

has been proposed by the authors as interpolation of the K_D curves derived from SPT and CPT for the site of Saint Giuseppe La Rena. The proposed CRR-K_D curve should be used in the same way as other methods based on the Seed & Idriss (1971) procedure: (1) Enter K_D in equation to evaluate CRR. (2) Compare CRR with the cyclic stress ratio CSR generated by the earthquake.
Fig. 11 shows the variation with depth of CRR given by correlation with K_D from previous equation and from CRR obtained from shear waves velocity Vs, according to

Andrus et al. (2004), using Vs values obtained by Seismic Dilatometer Marchetti Test (SDMT). It shows that the method proposed by Andrus et al. (2004) using Vs gives lower and more conservative CRR values than the procedure using K_D in the evaluation of the same parameter.
Fig. 12 and 13 show respectively the variation with depth of CRR given by correlation with CPT and SPT.
The liquefaction potential index, P_L, using K_D data is less than 5 because this method took into consideration the presence of the rigid upper crust. Therefore, the liquefaction potential is low for K_D data, while it was high for CPT data and very high for SPT and Vs data.

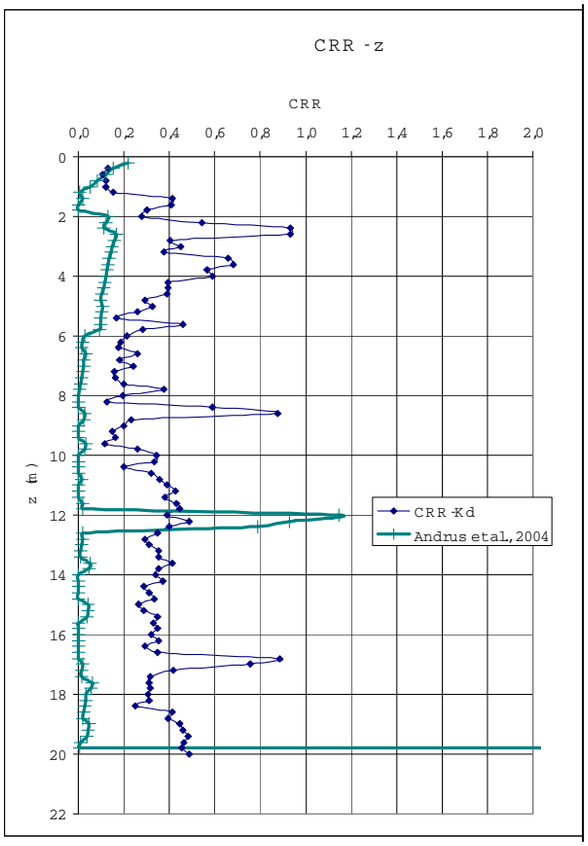


FIG. 11. CRR- with depth, from K_D and V_S data from SDMT, at Saint Giuseppe la Rena test site.

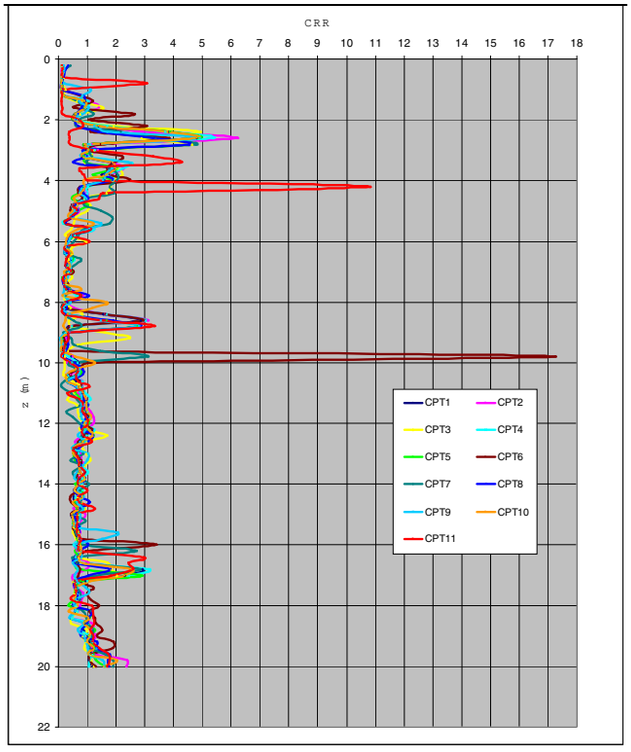


Fig. 12. CRR for CPT data versus depth (11 profiles).

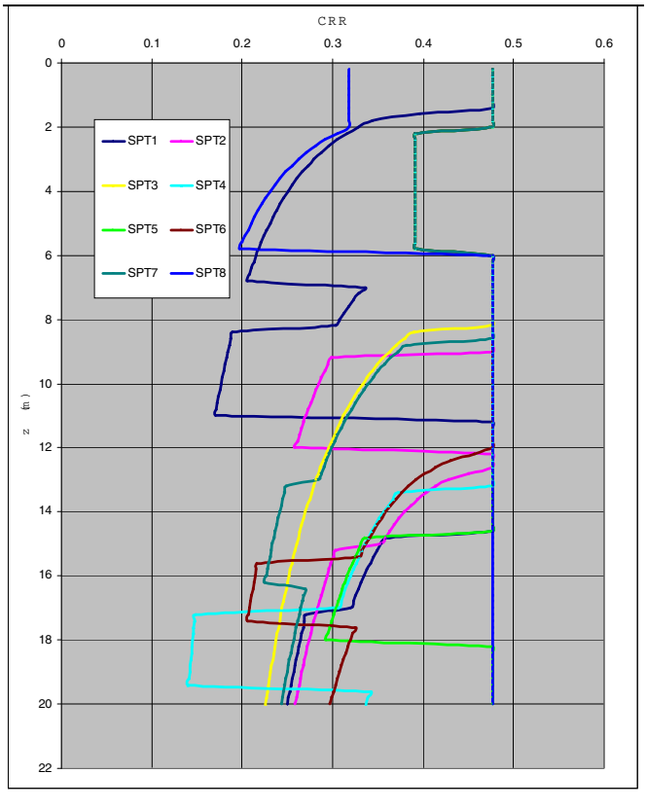


Fig. 13. CRR for SPT data versus depth (8 profiles).

CONCLUSIONS

SDMT gives the possibility to use two independent measurements Vs and K_D for evaluating soil liquefaction. The Seismic Dilatometer Marchetti Test (SDMT) has the advantage, in comparison with CPT and SPT tests, to measure independent parameters, such as the Horizontal Stress Index (K_D). The most significant factors supporting the use of K_D as an index of liquefaction resistance than CPT and SPT are the sensitivity of DMT in monitoring soil densification and the sensitivity of DMT to prestraining.

The tests performed at San Giuseppe La Rena, Catania, Italy, gave some contrasting results in the evaluation of liquefaction potential. When using the Vs or SPT data, the liquefaction potential index, P_L, is very high, and P_L is high for the CPT data. When using K_D data, however, P_L is low because K_D detected the upper rigid crust, which was overlooked by Vs, SPT and CPT measurements.

REFERENCES

Andrus, R.D., Stokoe, K.H., II, & Juang, C.H. (2004). Guide for Shear-Wave-Based Liquefaction Potential Evaluation. Earthquake Spectra, 20(2), 285-305.

Golesorkhi R. (1989). Factors influencing the computational determination of earthquake-induced shear stresses in sandy soils, Ph.D. thesis, University of California, Berkeley, 395 pp., 1989.

Grasso S., Maugeri M., Monaco P. (2006): "Using K_D And Vs From Seismic Dilatometer (SDMT) For Evaluating Soil Liquefaction". Proc. of the Second International Conference on the Flat Dilatometer, Washington, April 2 – 5, 2006.

Huang, A.B. & Ma, M.Y. (1994). An analytical study of cone penetration tests in granular material. *Canadian Geotech. Jnl*, 31(1), 91-103.

Idriss I. M. (1999). "An update to the Seed-Idriss simplified procedure for evaluating liquefaction potential", Proc., TRB Workshop on New Approaches to Liquefaction, January, Publication No. FHWA-RD-99-165, Federal Highway Administration, 1999.

Idriss I. M. and Boulanger R. W. (2004). Semi-Empirical Procedures For Evaluating Liquefaction Potential During Earthquakes. Invited Paper Presented at The Joint 11th International Conference on Soil Dynamics & Earthquake Engineering (ICSDEE) and The 3rd International Conference on Earthquake Geotechnical Engineering (ICEGE). January 7 – 9, 2004 Berkeley, California, USA.

Iwasaki, T., Tatsuoka, F., Tokida, K. & Yasuda, S. (1978). A practical method for assessing soil liquefaction potential based on case studies at various sites in Japan. Proc 2nd Int Conf on Microzonation for Safer Construction, Research and Application, San Francisco, California, 2, 885-896.

Jamiolkowski, M. & Lo Presti, D.C.F. (1998). Oral presentation. 1st Int. Conf. on Site Characterization ISC'98, Atlanta.

Jendeby, L. (1992). Deep Compaction by Vibrowing. Proc. Nor-dic Geotechnical Meeting NGM-92, 1, 19-24.

Marchetti, S. (1982). Detection of liquefiable sand layers by means of quasi-static penetration tests. Proc. 2nd European Symp. on Penetration Testing, Amsterdam, 2, 689-695.

Monaco, P., Marchetti, S., Totani, G. & Calabrese, M. (2005). Sand liquefiability

assessment by Flat Dilatometer Test (DMT). Proc. XVI ICSMGE, Osaka, 4, 2693-2697.

Reyna, F. & Chameau, J.L. (1991). Dilatometer Based Liquefaction Potential of Sites in the Imperial Valley. Proc. 2nd Int. Conf. on Recent Adv. in Geot. Earthquake Engrg. and Soil Dyn., St. Louis, 385-392.

Robertson, P.K. & Campanella, R.G. (1986). Estimating Liquefaction Potential of Sands Using the Flat Plate Dilatometer. *ASTM Geotechn. Testing Journal*, 9(1), 38-40.

Robertson, P.K. & Wride, C.E. (1997). Cyclic liquefaction and its evaluation based on SPT and CPT. Proc. NCEER Work-shop on Evaluation of Liquefaction Resistance of Soils, Technical Report NCEER-97-0022, T.L. Youd & I.M. Idriss, eds., National Center for Earthquake Engineering Research, Buffalo, 41-88.

Schmertmann, J.H., Baker, W., Gupta, R. & Kessler, K. (1986). CPT/DMT Quality Control of Ground Modification at a Power Plant. Proc. In Situ '86, ASCE Spec. Conf. on "Use of In Situ Tests in Geotechn. Engineering", Virginia Tech, Blacksburg, ASCE Geotechn. Special Publ. No. 6, 985-1001.

Seed, H.B. & Idriss, I.M. (1971). Simplified procedure for evaluating soil liquefaction potential. Jnl GED, ASCE, 97(9), 1249-1273.

Seed R. B., Cetin K. O., Moss R. E. S., A. Kammerer, J. Wu, J. Pestana, M. Riemer, R. B. Sancio, J. D. Bray, R. E. Kayen, and A. Faris. (2003). "Recent advances in soil liquefaction engineering: A unified and consistent framework." Keynote presentation, 26th Annual ASCE Los Angeles.

T. Shibata, and W. Teparaksa (1988). "Evaluation of liquefaction potentials of soils using cone penetration tests," Soils and Foundations, Tokyo, Japan, 28(2), pp 49-60, 1988.

Suzuki, K. Koyamada, and K. Tokimatsu (1997). "Prediction of Liquefaction Resistance Based on CPT Tip Resistance and Sleeve Friction," Proceedings, 14th International Conference on Soil Mechanics and Foundation Engineering, Hamburg, Germany, Vol. 1, pp 603 – 606, 1997.

Yu, H.S. (2004). In situ soil testing: from mechanics to interpretation. Proc. 2nd Int. Conf. on Site Characterization ISC-2, Porto, 1, 3-38.

This page intentionally left blank

Using Decision-Tree Learning to Assess Liquefaction Potential from CPT and V_s

Gary Livingston[1], Michael Piantedosi[2], Pradeep Kurup[3], and T. G. Sitharam[4]

[1]Department of Computer Science, University of Massachusetts Lowell; gary@cs.uml.edu
[2]Department of Computer Science, University of Massachusetts Lowell; michael@dogsolitude.org
[3]Department of Civil Engineering, University of Massachusetts Lowell; Pradeep_Kurup@uml.edu
[4]Department of Civil Engineering, Indian Institute of Science, Bangalore, India; proftgs@gmail.com

ABSTRACT: Damages attributed to earthquake-induced liquefaction have resulted in substantial loss of lives and property around the globe. This paper reports on a study that evaluates the effectiveness of bagged and boosted decision-tree machine learning methods to develop models for assessing liquefaction potential. Major advantages of decision tree learning include their ease of use and their production of easily inspected models with which engineers can better understand the mechanism of the liquefaction phenomenon and verify the trained models.

This study demonstrates that the accuracies of the models learned by either bagged or boosted decision-tree learning are competitive with accuracies reported for other learning methods, such as neural network learning. Test-set accuracies of the models learned in this study were 96% on a dataset of 178 cone penetrometer soundings and 89% on a dataset of 225 shear wave velocity soundings, with combined training and testing accuracies of these models on the datasets of 98% and 96%, respectively.

INTRODUCTION

One of the major causes of destruction during an earthquake is the loss of strength and stiffness of cohesionless soils (Yuan et al. 2004). This phenomenon, called liquefaction, occurs mainly in loose and saturated sands. Liquefaction of sandy soils during earthquakes can cause devastating loss of life and extensive damage to buildings, bridges, highway embankments, and other civil infrastructure systems. Recent earthquakes, such as the 2005 Indonesia, 2004 Indian Ocean, 2003 Tangshan, 2001 Bhuj, and the 1999 Chi-Chi earthquakes have resulted in extensive damage associated with soil liquefaction. These events emphasize the need for robust and reliable methods to characterize the liquefaction potential of deposits in the earthquake prone regions of the world.

BACKGROUND

The liquefaction potential or susceptibility of any given soil is determined by a combination of soil properties, environmental features and earthquake characteristics such as the intensity of earthquake and its duration, location of ground water table,

soil type, soil density, particle shape and size, gradation, drainage conditions, confining pressures, aging and cementation, depositional environment of the soil deposit and additional loads on these deposits. Site specific evaluation of liquefaction susceptibility is a measure of the inherent resistance of a deposit to liquefaction and can range from highly susceptible to not susceptible. Susceptibility can be estimated by comparing the properties of a given deposit of soil to other soil deposits where liquefaction has been observed in the past. Several methods have been suggested to evaluate liquefaction susceptibility based on large data from earthquake sites where the soil has experienced liquefaction or no-liquefaction. A brief review of some of these methods is presented below.

The traditional "simplified" procedure for assessing the liquefaction potential of sand using the blow counts (N) from the standard penetration test (SPT) was developed by Seed and Idriss (1971). This procedure has undergone several revisions since it was first proposed, and some of these revisions have been discussed in the 1996 NCEER Workshop report (Youd and Idriss 1996). The use of SPT for evaluating liquefaction potential led researchers to use other types of in situ test data, such as cone resistance (q_c), obtained from the cone penetration test (CPT), and shear wave velocity (V_s), that may be obtained from the seismic cone penetration test and various geophysical methods such as seismic refraction, seismic reflection, and Spectral Analysis of Surface Waves (SASW). CPT gives continuous, detailed soil profiles with depth and is capable of locating thin liquefiable seams of sand or silts. This capability is important in sand and silts because of their non-uniformity. The deterministic approach for evaluating liquefaction potential using q_c and V_s is essentially the same as for using the SPT N value in the simplified procedure. These methods involve calculation of the *cyclic stress ratio* (CSR), formulated by Seed and Idriss (1971) as:

$$\mathrm{CSR} = 0.65 \cdot \frac{a_{max}}{g} \cdot \frac{\sigma_{vo}}{\sigma'_{vo}} \cdot r_d \qquad (1)$$

where a_{max} is the peak acceleration at the ground surface of the site, σ_{vo} is the total stress at the depth under consideration, σ'_{vo} is the effective stress at the same depth, and r_d is the stress reduction coefficient (Youd and Idriss 1996). A graph is drawn between CSR and corrected and normalized in situ test data (N_{160}, q_{c1N}, or V_{s1}). Boundary curves are used to separate the regions with data indicative of liquefaction from the regions with data indicative of no liquefaction. These curves represent the cyclic resistance of soil during an earthquake, known as cyclic resistance ratio (CRR). The ratio of CRR to CSR, if less than 1, indicates 'liquefaction', and if greater than 1, indicates 'no liquefaction'. These traditional methods have been discussed in detail by various investigators (Seed and Idriss 1971, Youd and Idriss 1996, Robertson and Wride 1998, Andrus and Stokoe 1999).

In the traditional soil liquefaction evaluation methods like the ones described above (deterministic approach), it is very difficult, if not impossible, to accurately incorporate the influence of various soil and in situ state parameters, such as percent plastic and non-plastic fines, plasticity index, cementation, and overconsolidation effects. V_s and q_c are both influenced by these parameters in a complex manner. For example, q_c tends to decrease with increasing fines content and increases with

increasing overconsolidation and cementation. Similarly V_s increases with cementation and overconsolidation. If the fines content exceeds 10%, the shear wave velocity decreases as the fines content increases (Chien and Oh 2000).

Alternate techniques based on instance-based learning, artificial neural networks (ANN), logistic regression, and probabilistic methods have also been developed for evaluating liquefaction potential. ANN models were developed using an SPT database from past case histories (Goh 1994). The predictions made by the ANN model showed improvement over the procedure proposed by Seed et al. (1985). Probabilistic neural networks were also applied using the CPT q_c and V_s case values to train and test the networks (Goh 1996, Goh 2002). The models showed very good predictions with both types of in situ data, bettering the performance of corresponding deterministic procedures. Kurup and Dudani (2001) used an ANN with CPT case values, making 96% correct predictions. Instance-based learning models have also been developed for evaluating liquefaction potential (Barai and Agarwal 2002). Various probabilistic methods based on logistic regression techniques (Juang et al. 2001) and a Bayesian mapping approach (Juang et al. 2002) have been developed for predicting the probability of occurrence of liquefaction. Fuzzy Adaptive Resonance Theory (Fuzzy ARTMAP) based neural networks have also been used for the prediction of liquefaction potential (Kurup and Garg 2005).

Machine learning methods such as the ANN method can learn to account for the complex influence of fines content, plasticity index and overconsolidation ratio if these values are available for input to the networks. If these parameters are not readily available for training, it may still be possible that the trained models can learn the influence of these parameters through their impact on q_c and V_s. This supposition is verified by the success of studies using q_c and V_s to predict liquefaction potential (Goh 1996, Goh 2002, Kurup and Dudani 2001, Kurup and Garg 2005).

Additionally, none of these learning methods require normalization of their input variables prior to computation as long as the components of the normalization process are given as input. For example, in the traditional approach q_c is normalized to q_{c1N} using the vertical effective stress (σ'_{v0}) and a reference pressure of 1 atmosphere. As long as both q_c and σ'_{v0} values are passed to the learning algorithm, the learned models will implicitly contain any necessary normalization.

This paper explores the feasibility of using bagged and boosted decision-tree learning methods for predicting liquefaction potential.

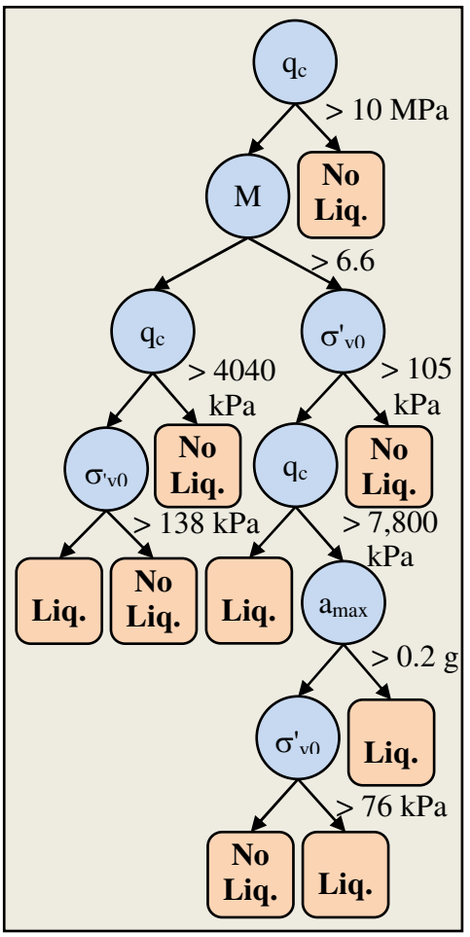


FIG. 1. Decision tree trained for predicting liquefaction

DECISION TREES

Learning Decision Trees

Figure 1 presents a decision tree trained for predicting liquefaction. The internal nodes represent tests on a variable's values, and the leaf nodes are assigned to classes, with the internal nodes being arranged in a tree-like structure. A case is classified using the tree by traversing from the top node, called the root node, down to a leaf node, using the values of the case's variables to determine the path taken to reach that node. The class assigned to this leaf node would be the class predicted for the case.

For example, the decision tree given in Figure 1 would classify a site with $q_c = 5000$ kPa, $M = 7$, $\sigma'_{v0} = 100$ kPa, and $a_{max} = 0.4$ g as follows: first, at the root node, because the site's value for q_c is 5000 kPa, the first left branch would be followed, leading to a node testing the value of M. Because this value is 7, the right branch would be taken. Following that branch leads to a node testing the value of σ'_{v0}. Since this value is 100 kPa, the left branch of the node labeled σ_{v0} would be taken, leading to a node again testing the value of q_c. The site's value for q_c is 5000 kPa, so the left branch of that node would be taken which leads to a leaf node that is assigned to the class "Liq." Thus, the site would be predicted to liquefy.

Decision trees are learned by recursively selecting the variables that "best" sort the data into non-overlapping subsets. As the splitting continues, the variables chosen for splitting the data are arranged into a tree, with the first variable forming the root of the tree, and the variables used to split the subsets formed by the values of the first variable becoming child nodes of the first variable, and so on. This recursive splitting of subsets of cases and forming nodes from the variables used to perform the splits continues until a subset's members have the same class or the subset's size is less than a user-supplied threshold.

Due to their ability to represent complex functions, decision trees can be learned that *overfit* the training data, fitting not only the general relationships found in the training data, but also the noise contained in the data. *Pruning* is a process that attempts to remove the nodes of a decision tree that are overfitting the training data.

Bagging and Boosting

Bagging and boosting of tree learning methods are recent and significant developments in machine learning (Witten and Frank 2005) that greatly enhance the performance of decision trees. Recent research has shown that bagged and boosted decision tree learning has better or similar performance on many problems than most other machine learning methods (Caruana and Niculescu-Mizil 2006).

Bagging

Because slight changes to the training set can produce very different trees, the tree-learning process is unstable (Witten and Frank 2005). Bagging mitigates this instability by repeatedly inducing trees using altered versions of the original training set and then combining the predictions made by the trees. The altered versions of the training set are created by randomly resampling the training set with replacement, where some of the original training cases are deleted and other cases are replicated, to create a new training set of the same size. A tree is then learned for each new version

of the training set. When using these trees to make a prediction, a single value is predicted by using majority voting to combine the individual predictions made by the trees into a single prediction (Witten and Frank 2005).

Boosting

Similarly, boosting (Witten and Frank 2005) generates many variations of the original training sets, learns decision trees from the altered versions, and then combines the predictions from the many decision trees into a single decision tree. The differences are: (1) creating new training sets by preferring incorrectly predicted cases when randomly selecting cases from the original training set and (2) using weighted voting instead of majority voting to combine the individual predictions into a single prediction, with the weights being proportional to the performance of the corresponding trees. Although boosting can overfit noise contained in the training set, such as experimental error, the benefits gained by boosting often exceed the problems caused by overfitting, and if overfitting is a problem it can be diminished by reducing the number of trees used in the boosting process.

Evaluation of Decision Trees

Two common methods for evaluating classification models are holdout and *cross-validation.* In the holdout method the original data set is randomly partitioned into the training set and a *testing set* that is used to test the performance of the trained models.

In the cross-validation method, the original dataset is partitioned into n subsets, and then n iterations are performed as follows: for the *ith* iteration, cases from all subsets except for the *ith* subset are used for training a model and the *ith* subset is used to test the trained model. The n performance measures are averaged into a final performance measure that has a smaller variance than the original measures, producing a more reliable estimate (Witten and Frank 2005).

One of the primary advantages of using decision tree learning is that the trained trees are easy to inspect in order to evaluate their soundness or to identify "nuggets" of information about the liquefaction phenomenon. For example, in the decision tree given in Figure 1, q_c is used in the root node, suggesting that q_c is a major parameter for predicting of liquefaction potential. This is theoretically correct because of q_c's relationship to many soil parameters known to influence liquefaction. Decision tree learning is also easy to use: there are few learning parameters to adjust, and the performance of the trained models changes little when small changes are made to the parameters. Thus, tuning these parameters is relatively simple.

PREDICTING LIQUEFACTION POTENTIAL USING DECISION-TREE LEARNING

Field Test Data: q_c and V_s Datasets

The q_c dataset used in this project is from Stark and Olsen (1995) and Kurup and Garg (2005). The dataset consists of 178 CPT soundings from nine different earthquake events (109 sounding records of sites that liquefied and 69 sounding records of sites that did not liquefy). Six variables were measured for the soundings: earthquake magnitude on the Richter scale (M), maximum horizontal acceleration

(a_{max}), effective stress (σ'_{v0}), total stress (σ_{v0}), cone tip resistance (q_c), and mean particle diameter (D_{50}). Out of the 178 CPT soundings, 108 soundings were selected and used for training the model, and the remaining 70 were used for testing the model. TABLE No. 1 summarizes the soundings contained in this dataset.

TABLE No. 1. Summary of Soundings in the q_c Dataset

Event No.	Earthquake Event	Location	Number of Soundings	
			Training	Testing
1	1964, Niigata	Japan	6	3
2	1971, San Fernando Valley	California, USA	17	12
3	1975, Haicheng	China	4	2
4	1976, Tangshan	China	46	33
5	1977, Vrancea	Romania	3	2
6	1979, Imperial Valley	California, USA	6	3
7	1983, Nihonkai-Chubu	Japan	5	2
8	1988, Saguenay	Canada	5	2
9	1989, Loma Prieta	California, USA	16	11
	Total		**108**	**70**

The V_s dataset is from Andrus and Stokoe (1999) and Kurup and Garg (2005). The dataset consists of 225 V_s soundings from eighteen different earthquake events (96 sounding records of sites that liquefied and 129 sounding records of sites that did not liquefy). Six variables were measured for the soundings: shear wave velocity (V_s), earthquake magnitude (M), effective stress (σ'_{v0}), total stress (σ_{v0}), maximum horizontal ground acceleration (a_{max}), and fines content ($\%F$). Out of the 225 V_s soundings, 142 soundings were selected for training the model, and the remaining 83 were used for testing. TABLE No. 2 summarizes the soundings in this dataset.

Application of Decision Tree Learning to the q_c and V_s Datasets

The Weka machine learning package, named after a flightless bird found in New Zealand (Witten and Frank 2005), was used extensively in this study. The specific components used were J4.8 (version 4.8 of Weka's Java implementation of the classical decision tree learner described above), Weka's bagging implementation for training bagged decision trees, and Weka's Adaboost M1 implementation for training boosted decision trees. When bagging was used, 10 trees were bagged, and when boosting was used, 10 trees were used for each set of boosted trees.

The models were trained and tested using the q_c and V_s data described earlier using two different approaches: the training and testing sets described earlier and ten-fold cross validation. For each of these approaches, three types of tuning were performed:

- *Default*—default parameters provided by Weka for learning decision trees were used. These values are: Pruning = 'On', Minimum Leaf Size = 2, and Confidence = 0.25.
- *Unpruned*—the trained trees were not pruned. For bagged decision trees on the q_c data set, a setting of 2 for Minimum Leaf Size produced the best results, and for all other combinations of learning methods and datasets, a setting of 1

for Minimum Leaf Size produced the best results. When pruning is not used, the confidence parameter is not used.

- *Tuned*—the parameters were adjusted to maximize accuracy on the training set. Only minimal changes to the default parameters were needed to maximize accuracy.

TABLE No. 2. Summary of Soundings in the V_s Dataset

Event No.	Earthquake Event	Location	Number of Soundings	
			Training	Testing
1	1906, San Francisco	California, USA	7	5
2	1957, Daly City	California, USA	2	3
3	1964, Niigata	Japan	3	1
4	1975, Haicheng	China	3	3
5	1979, Imperial Valley	California, USA	7	4
6	1980, Mid Chiba	Japan	1	1
7	1981, Westmoreland	California, USA	7	4
8	1983, Borah Peak	Idaho, USA	12	6
9	1985, Chiba-Ibaraagi	Japan	0	2
10	1985, Taiwan	Taiwan	20	16
11	1987, Chiba-Toho Oki	Japan	0	1
12	1987, Elmore Ranch	California, USA	7	4
13	1987, Superstition Hill	California, USA	6	5
14	1989, Loma Prieta	USA	48	19
15	1993, Kushiro-Oki	Japan	1	1
16	1993, Hokkaido	Japan	3	1
17	1994, Northridge	California, USA	2	1
18	1995, Hyogoken-Nanbu	Japan	13	6
	Total		**142**	**83**

RESULTS

Figures 2 and 3 present the accuracies obtained on the q_c and V_s datasets, respectively, using single, bagged, and boosted decision tree learning, along with the accuracy for Fuzzy ARTMAP-based neural network learners (Fuzzy ArtMap) as reported in (Kurup and Garg 2005).

No pairwise significant differences (significance level of 0.01) exist between test-set accuracies on either the q_c dataset or the V_s dataset. The p value (the probability of seeing the observed difference between a pair of accuracies) for the difference between the accuracies on the q_c testing subset between single decision tree learning using the default settings (89%) and either Fuzzy ArtMap or tuned boosted decision tree learning (96%) is 0.056. The p value for the difference between the accuracies on the V_s testing subset between either unpruned single decision tree learning or unpruned boosted decision tree learning (86%) and Fuzzy ArtMap (93%) is 0.033. The p values given above were calculated using a standard z-test (Mendenhall 1987).

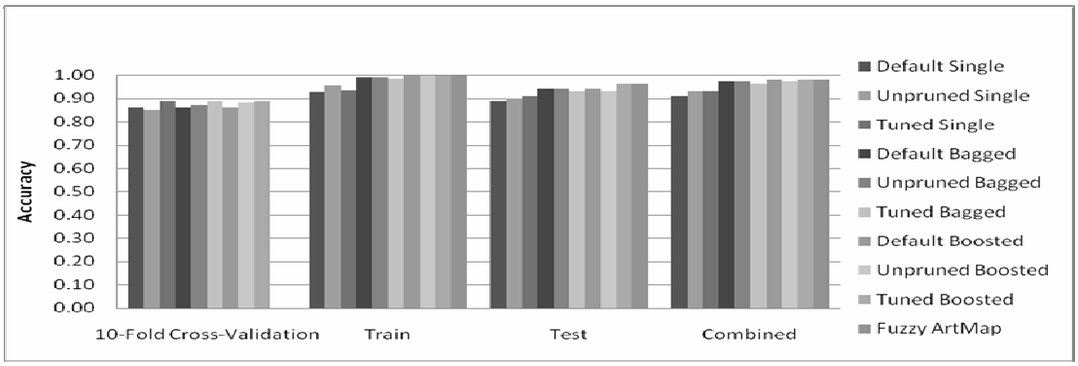


FIG. 2. Bar chart of the accuracies of the learning methods on the q_c dataset

DISCUSSION

Our results show that tuned boosted decision trees can achieve the same predictive performance as Fuzzy ArtMap learning on the q_c dataset and slightly (but not statistically significantly) lower predictive performance on the V_s dataset. The results also show that simply using the Weka-provided default settings generates only slightly lower accuracies. Thus, little tuning of the parameters controlling decision tree learning, bagging, or boosting is needed to achieve good performance.

Generally speaking, more pruning usually generated better accuracy. However, for all single and bagged decision tree V_s models the accuracy was highest when almost no pruning (confidence of 46%) was used.

In related research, Stark and Olsen (1995) used their simplified deterministic method to achieve 90% accuracy on the q_c dataset (no training and testing split was performed); Kurup and Dudani (2001), using feed-forward neural networks with backpropagation for training the networks, achieved 98% accuracy on the q_c training set, 94% accuracy on the q_c testing set, and 96% overall accuracy (on the combined training and testing sets); Barai and Agarwal (2002), using instance based learning (IBL), achieved 100% accuracy using a subset of the q_c dataset (109 cases); and Goh (2002), using a probabilistic neural network (PNN), achieved 100% accuracy on 170 cases of the q_c dataset.

Using the V_s data set, the simplified deterministic method devised by Andrus and

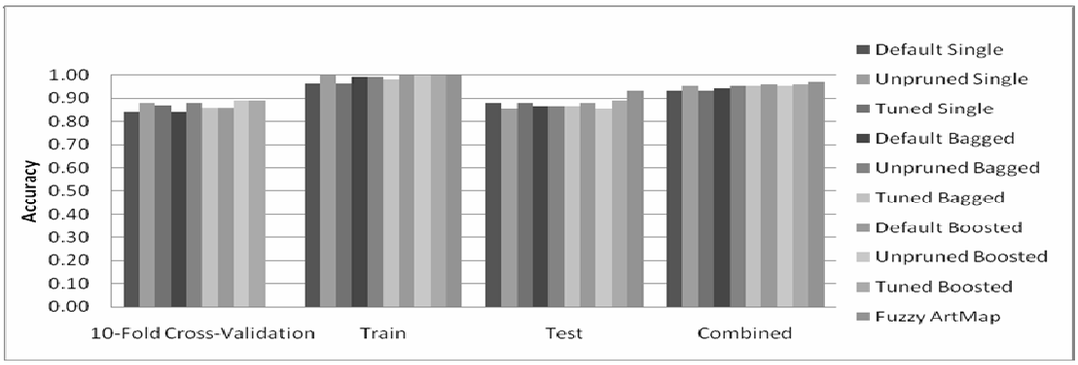


FIG. 3. Bar chart of the accuracies of the learning methods on the V_s dataset

Stokoe (1999) is highly conservative and has an overall accuracy of 68% (with only 1% false negatives); Goh (2002), using PNN on the V_s data set, achieved 98% training accuracy, 97% testing accuracy, and 98% overall accuracy; and Kurup and Garg (2005) applied Fuzzy ArtMap learning to the V_s dataset to achieve 100% training accuracy, 93% testing accuracy, and 97% overall accuracy.

Both training a decision tree and using the tree to make predictions are fast, with each of these tasks requiring less than a few seconds. Additionally, the computational complexity of decision tree learning methods will allow them to scale up easily to larger datasets. In contrast, IBL and PNN methods perform most of their computation at prediction time. This forces the majority of the computation on the end user, hampering adoption and scalability, especially on larger, more encompassing datasets.

Another benefit of decision tree learning is that the trained decision trees are easily understood, allowing an expert to examine the model to ensure that it is theoretically correct and allowing "nuggets" of knowledge to be learned from the model. In contrast, the previously used neural network methods generate "opaque" models: that is, the trained models are difficult to inspect in such a manner and are usually simply treated as black boxes. Thus, neither can the trained models be evaluated for their theoretical soundness nor can much knowledge about the process of liquefaction be learned from the trained models.

CONCLUSION

This study primarily focused on applying bagged and boosted decision tree learning to the problem of liquefaction prediction. Although there is little or no published literature reporting on the use of decision tree learning to train models for assessing liquefaction potential, decision tree learning combined with bagging and boosting was equal to or competitive with other methods that have been used to evaluate liquefaction potential, achieving 98% accuracy on a q_c data set containing 178 cases and 97% accuracy on a V_s data set containing 225 cases. Little tuning of the learning parameters used in decision tree learning was needed to maximize performance. Moreover, the learned models were easy to inspect to determine their fit with what is known about earthquake-induced liquefaction. Thus, decision-tree learning combined with bagging and boosting is a viable and easy to use method for assessing earthquake-induced liquefaction.

ACKNOWLEDGEMENTS

The authors acknowledge the financial support of the National Science Foundation, Award CMS 0409594, and the UML Healey and Public Service Award (H50060000000001). Any opinions, findings, and conclusions or recommendations expressed in this paper are those of the authors and do not necessarily reflect the views of the funding agencies.

REFERENCES

Andrus, R. D., and Stokoe, K. H. (1999). "A liquefaction evaluation procedure based on shear wave velocity." *Wind and Seismic Effects*, *Proceedings of the US/Japan*

Natural Resources Development Program (UJNR) Joint meeting, 31st Technical Memorandum of PWRI 3653. Proceedings. May 11-14, Tsukuba, Japan: 71-78.

Barai, S. V., and Agarwal, G. (2002). "Studies on instance based learning models for liquefaction potential assessment." *EJGE*, paper 0235: 1-17.

Chien, L. and Oh, Y. (2000). "Laboratory and Field Shear Wave Measurement at a Reclaimed Site in West Taiwan." *Geotech. Testing Journal* 23 (1): 21-35.

Caruana, R. and Niculescu-Mizil, A. (2006). "An empirical comparison of supervised learning algorithms." *ICML '06: Proceedings of the 23rd International Conference on Machine Learning,* ACM Press, Pittsburgh, PA: 161-168.

Goh, A. T. C. (1994). "Seismic liquefaction potential assessed by neural networks." *Journal of Geotech. Engrg*., ASCE, 120 (9): 1467-1480.

Goh, A. T. C. (1996). "Neural-network modeling of CPT seismic liquefaction data." *Journal of Geotech. Engrg.,* ASCE, 122 (1): 70-73.

Goh, A. T. C. (2002). "Probabilistic neural network for evaluation seismic liquefaction potential." *Canadian Geotechnical Journal*, 39: 219-232.

Juang, C. H., Chen, C. J., and Jiang, T. (2001). "Probabilistic framework for liquefaction potential by shear wave velocity." *Journal of Geotech. And Geoenv. Engrg.,* ASCE, 127 (8): 670-678.

Juang, C. H., Jiang, T. and Andrus, R. D. (2002). "Assessing probability-based methods for liquefaction potential evaluation." *Journal of Geotech. and Geoenv. Engrg.*, ASCE, 128 (7): 580-589.

Kurup, P. U., and Dudani, N. K. (2001). "CPT evaluation of liquefaction potential using neural networks." *Proceedings of the Fourth International Conference on Recent Advances in Geotechnical Earthquake Engineering and Soil Dynamics,* CD ID: 4.36.

Kurup, P. U., and Garg, A. (2005). "Evaluation of liquefaction potential using neural networks based on adaptive resonance theory." *Transportation Research Record* 1936: 192-200.

Mendenhall, W. (1987). *Introduction to Probability and Statistics,* 7th Ed., Duxbury Press, Boston, 883 p.

Robertson, P. K., and Wride, C. E. (1998). "Evaluating cyclic liquefaction potential using the cone penetration test." *Canadian Geotechnical Journal* 35 (3): 441-459.

Seed, H. B., and Idriss, I. M. (1971). "Simplified procedure for evaluating soil liquefaction potential." *Journal of the Soil Mechanics and Foundations Division*, ASCE, 97 (SM9): 1249-1273.

Seed, H. B., Tokimatsu, K, Harder, L. F., and Chung, R. (1985). "Influence of SPT procedures in soil liquefaction resistance evaluations." *Journal of Geotech. Engrg*. ASCE, 111 (12): 861-878.

Stark, T. D., and Olsen, S. M. (1995). "Liquefaction resistance using CPT and field case histories." *Journal of Geotech. Engrg.* ASCE, 121 (12): 856-869.

Witten, I. H., and Frank, E. (2005). *Data Mining: Practical Machine Learning Tools and Techniques, Second Edition,* Morgan Kaufmann, 560 p.

Youd, T. L., Idriss, I. M. (1996). *Proceedings of the NCEER Workshop on Evaluation of Liquefaction Resistance of Soils*. January 5-6, Inn at Temple Square, Salt Lake City, UT.

Yuan, H., Yang, S., Andrus, R., and Juang, C. H. (2004), "Liquefaction-induced ground failure: A study of the Chi-Chi earthquake cases," Eng. Geol. 71 (1-2), 141-155.

An Experimental Study of the Effect of Seepage Force on Liquefaction of Soil in Embankments

Gang Liu[1], Xiangwu Zeng[2], M. ASCE, and Xiangsong Li[3], Fellow, ASCE

[1]Graduate Student, Department of Civil Engineering, Case Western Reserve University, 10900 Euclid Avenue, Cleveland, OH 44106-7201; gxl48@cwru.edu
[2] Professor, Department of Civil Engineering, Case Western Reserve University, 10900 Euclid Avenue, Cleveland, OH 44106-7201; xxz16@cwru.edu
[3] Professor, Department of Civil Engineering, Hong Kong University of Science and Technology, Clear Water Bay, Kowloon, Hong Kong, China; xsli@ust.hk

ABSTRACT: An experimental study on the effect of seepage force on liquefaction of soil in embankments was performed using centrifuge modeling. A total of 5 model tests were conducted on the centrifuge at Case Western Reserve University. The model configuration was an embankment made of sand overlying a sand foundation. Three of the models were submerged while the other two had pore fluid only on one side of the embankment with seepage in the embankment. In the tests, the relative densities of the sand making the embankments were varied while the density of the soil in the foundation was kept the same. Model preparation techniques and test procedures are described. Pore pressure transducers, accelerometers and LVDTs were used to record the response during the earthquakes. The settlement of embankment was measured and profiles of the embankment before and after earthquakes were compared. In two of the tests, a viscous pore fluid was used to satisfy scaling laws for centrifuge modeling. The effect of the pore fluid viscosity on liquefaction behavior was investigated by comparing the results with that from model tests with water as pore fluid. The study found no conclusive evidence that seepage force affects the liquefaction of soil in embankments.

INTRODUCTION

Failure of embankment dams during earthquakes occurred several times in the past, causing significant losses of life and properties. Therefore, much effort has been placed on the safety of embankment dams subjected to earthquakes over the past few decades. Early pioneering research (Seed et al., 1969; Seed et al., 1975) concluded that a major factor contributing to the failure of embankments during earthquakes was the buildup of excess pore pressures in saturated soils. In the worst cases, liquefaction of soils led to a

complete loss of shear strength, resulting in flow failure of portion of an earth dam, such as that occurred to the Lower San Fernando Dam. As such failure can be catastrophic, seismic rehabilitation of earth dams has been a priority in the USA (Marcuson, et al., 1996).

It is generally accepted in soil liquefaction studies that when the driving shear stress on a potential slip surface through a liquefiable material is greater than its residual strength, the soil mass will move after liquefaction is trigged. Since seepage force is one of the driving forces acting on the soil skeleton, it should be taken into account in the analysis of embankment dams. However, it has not been explicitly examined in the past the effect of seepage force on liquefaction of soils, due to the complication of the dynamic analysis of embankments with seepage forces (Li and Ming, 2004)

An experimental study on the effect of seepage force on liquefaction of soil in an embankment was performed using dynamic centrifuge modeling. The model configuration was an embankment made of sand overlying a sand foundation. Three of the models were submerged while the other two had water or viscous fluid only on one side of the embankment with seepage in the soils. In the tests, relative densities of the embankment were varied while the density of the soil in the foundation was kept the same. The effect of pore fluid viscosity on liquefaction behavior in sand was investigated. Data from the tests are used to investigate the relationship between density of soils, seepage force, pore fluid viscosity, and liquefaction during earthquakes.

FACILITIES AND INSTRUMENTATION

Centrifuge

The centrifuge tests reported here were conducted on the geotechnical centrifuge at Case Western Reserve University that has an effective radius of 1.37m. The centrifuge payload capacity is 20 g-ton with a maximum acceleration of 200g for static tests and 100g for dynamics tests. The centrifuge is equipped with a hydraulic shaker designed by the TEAM Corporation. The laminar box used in the tests consists of 13 rectangular aluminum rings separated by linear bearings. The internal dimensions of the box are 53.3 cm (length) $\times$ 24.1 cm (width) $\times$ 17.7 cm (height). Details about the facility were reported by Figueroa, et al. (1998).

Earthquake Shaker

The simulated earthquakes were generated by a hydraulic shaker, which was programmed to achieve the required input motion. The direction of shaking was perpendicular to the vector of rotation of the centrifuge. Before conducting the tests a calibration test was performed on a box so as to simulate the earthquake that would have the desired amplitude and frequency. The earthquake input motion generated by the shaker was recorded by an accelerometer fixed on the base plate of the model container.

Instrumentation

Three types of transducers were used in the tests: pore pressure transducers (PPT), accelerometers (ACC), and linear variable displacement transformers (LVDT). Pore pressure transducers were placed with the axis of the transducer perpendicular to the direction of shaking so as to minimize the effect of inertia force.

Viscous Fluid

The viscous fluid used in this study is a solution of water and methylcellulose powder with the commercial name of "METHOCEL Cellulose Ethers", product "K100-LV" by DOW Chemical Company. The preparation procedures for the viscous fluid are as following:

- Heat approximately 1/3 the required volume of water to at least 90 ^{o}C.
- Add the METHOCEL powder to the heated water.
- Agitate the mixture until the particles are thoroughly wetted and evenly dispersed.
- For complete solubilization, add the remainder of the water as ice water mixture to lower the temperature of the dispersion. Once the dispersion reaches the temperature at which KV100-LV becomes water soluble, the powder begins to hydrate and viscosity increases.
- Continue agitation for at least 30 minutes after the proper temperature is reached.

Now the viscous fluid is ready to be tested for viscosity. A Cannon Fenske Routine Viscometer is used to measure the viscosity. If the viscosity is more than the desired value, add some water in the viscous fluid and agitate again. If the viscosity is less than the desired, discard them and prepare another one.

MODEL MATERIALS

Nevada sand was used in the model tests. The sand has been widely used in laboratories around US for liquefaction studies. For example, it was used in the VELACS project (Arulanandan and Scott, 1993) for dynamic centrifuge tests. The index properties of the sand are shown in Table 1.

Table 1. Index properties of Nevada Sand.

Parameter	Value
D_{50}	0.17 mm
D_{10}	0.09 mm
C_u	2.0
C_c	1.0
Specific gravity	2.67
Maximum dry unit weight	17.33 (kN/m^3)
Minimum dry unit weight	13.87 (kN/m^3)
Maximum void ratio	0.887
Minimum void ratio	0.511

MODEL PREPARATION

Air pluviation method was selected for sample preparation in combination with a funnel. The apparatus consisted of a plastic conical hopper connected to a 20 cm long rigid tube (Dief, 2000). Sand pouring was placed in thin layers by raising the rigid tube the same amount to obtain a constant height of pluviation for each layer with the help of

a reference bar. The relative density of sand was controlled by the height and rate of pouring. Calibration tests were performed in advance to achieve the required relative density. A sealed wooden box with an airtight cover was used as a chamber around the model. Two types of air tight covers were used, the first one had an open access to pour the soil, while the second one had a closed lid with pipe connections to saturate the soil and a clear window with sealed edges to monitor the saturation process. Pore pressure transducers were soaked up in fluid for at least 48 hours prior to sample preparation.

The total weight of the dry sand was obtained before pluviation. The transducer locations were determined before the tests. When the sand reached the selected height for transducer placement, pouring was stopped to place the accelerometer and the pore pressure transducers at the center point along the box. The accelerometers were placed in the prototype-horizontal direction to record the horizontal accelerations of the model at the selected depths and the pore pressure transducers were placed in the prototype-vertical direction at the selected depths.

When the model construction was finished, the airtight cover was placed with the sealed top. Valves were opened to replace the air in the soil by carbon-dioxide which dissolves easily in water and viscous fluid. Afterwards, all valves were closed and de-aired water/viscous fluid was allowed to pass slowly in the soil from the bottom to the top. When the water/viscous fluid reached the required level, vacuum was applied from the top of the box and maintained for at least 6 hours to obtain complete saturation. The remaining dry sand was weighed to obtain the total weight of soil used in the model preparation.

TEST PROCEDURES

The centrifuge tests followed the following procedures:

- The profile of the model was measured so that the cross-section view of the model before the test could be compared to that after the application of the earthquake motion.
- After saturation was finished, the laminar box was carefully moved from the saturation box and fastened on the shake table of the centrifuge. The counter weight was added to the other side of the swing arm. All of the transducers were properly connected. Before starting the centrifuge, a complete checkup of all equipments and connections on the arm was done.
- The centrifuge was then spun up to 50g and maintained at that speed for 5 minutes so that excess pore pressures due to the increased vertical stress would dissipate. The input motion was then applied.
- The centrifuge was spun down and post-test measurements were performed. The final locations of the transducers were measured.

In order to convert the results obtained in a centrifuge test from model scale into prototype scale, scaling relationship for centrifuge modeling is used. The most commonly used scaling relationship for centrifuge modeling is shown in Table 2.

EXPERIMENTAL RESULTS

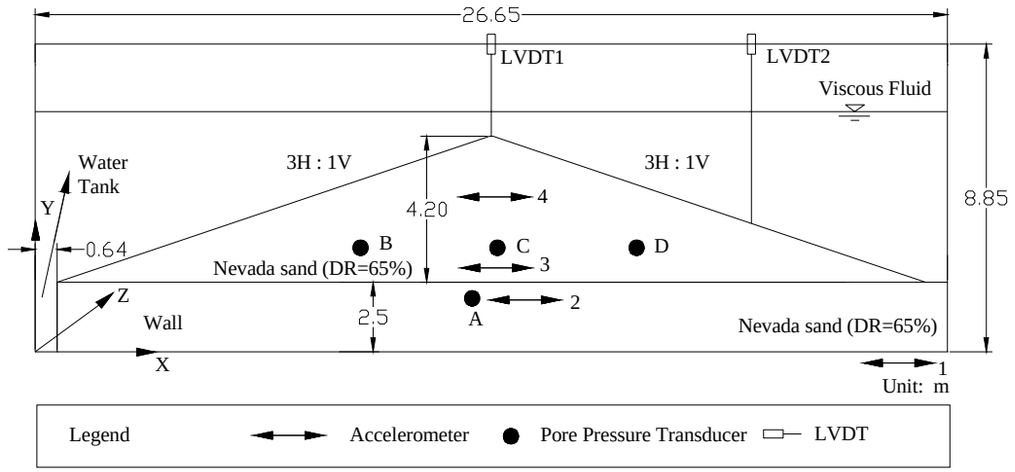
All the data here are reported in prototype scale and the original data are reported with no data processing technique used. An example of cross-sectional view of the model and the initial and final locations of the transducers is shown in Fig. 1. This

model was an embankment made of dense sand (relative density 65%) overlying a dense sand foundation (relative density 65%). The model was submerged under the viscous fluid.

Test conditions and some results are summarized in Table 3. Among the five tests, two used viscous pore fluid while the remaining three used water. Also in two of the tests, water or viscous fluid was placed on only one side of the embankment while on the other side, a small reservoir was built to collect fluid that seeped through the embankment. Thus, a seepage condition existed in these two model tests. For comparison purpose, the targeted input motion in all tests was kept the same, which was shown in Figure 2. It consisted of 20 cycles of a 2 Hz sinusoidal wave, with variable amplitude and maximum peak acceleration of 0.235 g. A zero vertical acceleration time history was targeted and in general, the vertical acceleration recorded was very small. Horizontal accelerations at the base and in the soil, excess pore pressures in the soil and vertical settlements of the soil surface at the center point and at one point on the side were measured (see Fig. 1).

Table 2. Scaling Relationship for Centrifuge Test (After Taylor, 1995)
(N = centrifugal acceleration/gravitational acceleration)

Parameter	Prototype	Model
Length	N	1
Area	N^2	1
Volume	N^3	1
Velocity	1	1
Acceleration	1	N
Mass	N^3	1
Force	N^2	1
Energy	N^3	1
Stress	1	1
Strain	1	1
Mass Density	1	1
Energy Density	1	1
Time (Dynamic)	N	1
Time (Diffusion)	N^2	1
Frequency	1	N



Initial Location of Transducers

Transducer	Coordinates (m)		
	X	Y	Z
1			
2	12.07	1.9	6
3	13.33	3.35	6
4	13.33	5.0	6
A	14.61	1.9	6
B	4.45	3.35	6
C	13.33	3.35	6
D	22.22	3.35	6
LVDT1	13.25	6.6	6
LVDT2	20.9	3.65	6

Final Location of Transducers

Transducer	Coordinates (m)		
	X	Y	Z
1			
2	12.07	1.5	6
3	13.33	2.9	6
4	13.33	4.75	6
A	14.61	1.5	6
B	4.45	3.0	6
C	13.33	3.0	6
D	22.22	3.1	6
LVDT1	13.25	5.85	6
LVDT2	20.9	3.45	6

FIG. 1. Cross-Sectional View of Centrifuge Model, Test1.

Table 3. Test Conditions and Some Results.

Model No.	Foundation Relative Density	Embankment Relative Density	Pore Fluid Viscosity	Seepage Force	Liquefaction	Top Settlement (cm)
1	65%	65%	50	No	Yes	75
2	65%	65%	50	Yes	Yes	80
3	65%	40%	1	No	Yes	145
4	65%	65%	1	No	Yes	90
5	65%	65%	1	Yes	Yes	80

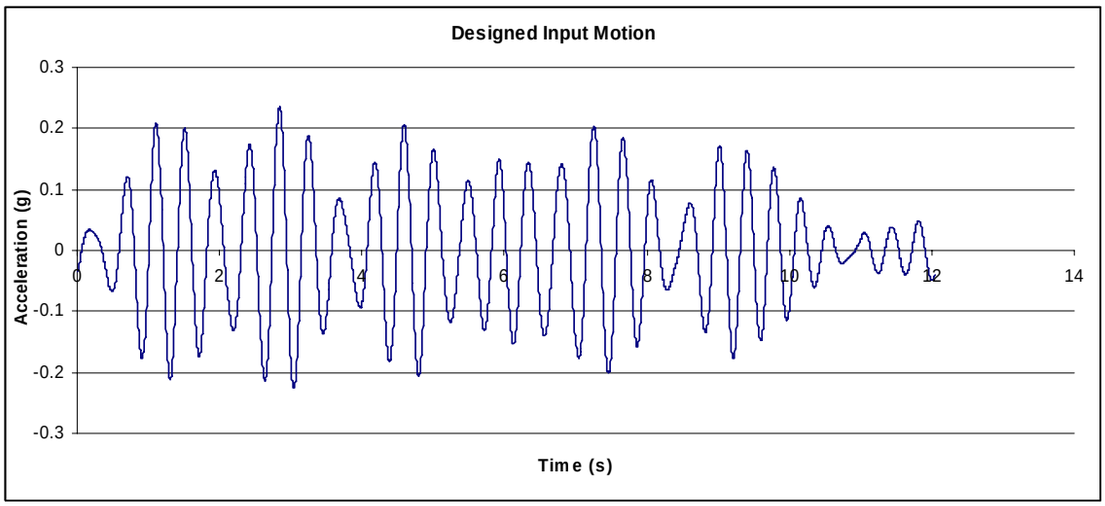


FIG. 2. Time history of the targeted horizontal acceleration.

Typical test results of time history of acceleration in the model embankment are shown in Fig. 3. When compared with input acceleration, the peak acceleration dropped as shear wave propagate upward. This is the results of pore pressure built up in the soil and initiation of liquefaction after the initial few cycles of vibration. As shown in Fig. 4, excess pore pressure started to accumulate at the second wave and was raised quickly to the level of initial effective vertical stress, indicating the liquefaction of the soil. Fig. 5 shows an example of profile of the embankment before and after the earthquake. The embankment had a large surface settlement. The top of the slope settled about 75 cm as the consequence of soil liquefaction.

Influence of Pore Fluid

As shown in Table 3, the settlements recorded in the tests using viscous pore fluid were about the same as those in tests using water. The only difference was that when viscous pore fluid was used, pore water pressures rose up slightly faster. However, since significant excess pore pressure was recorded in all the tests, the influence on the total settlement was insignificant.

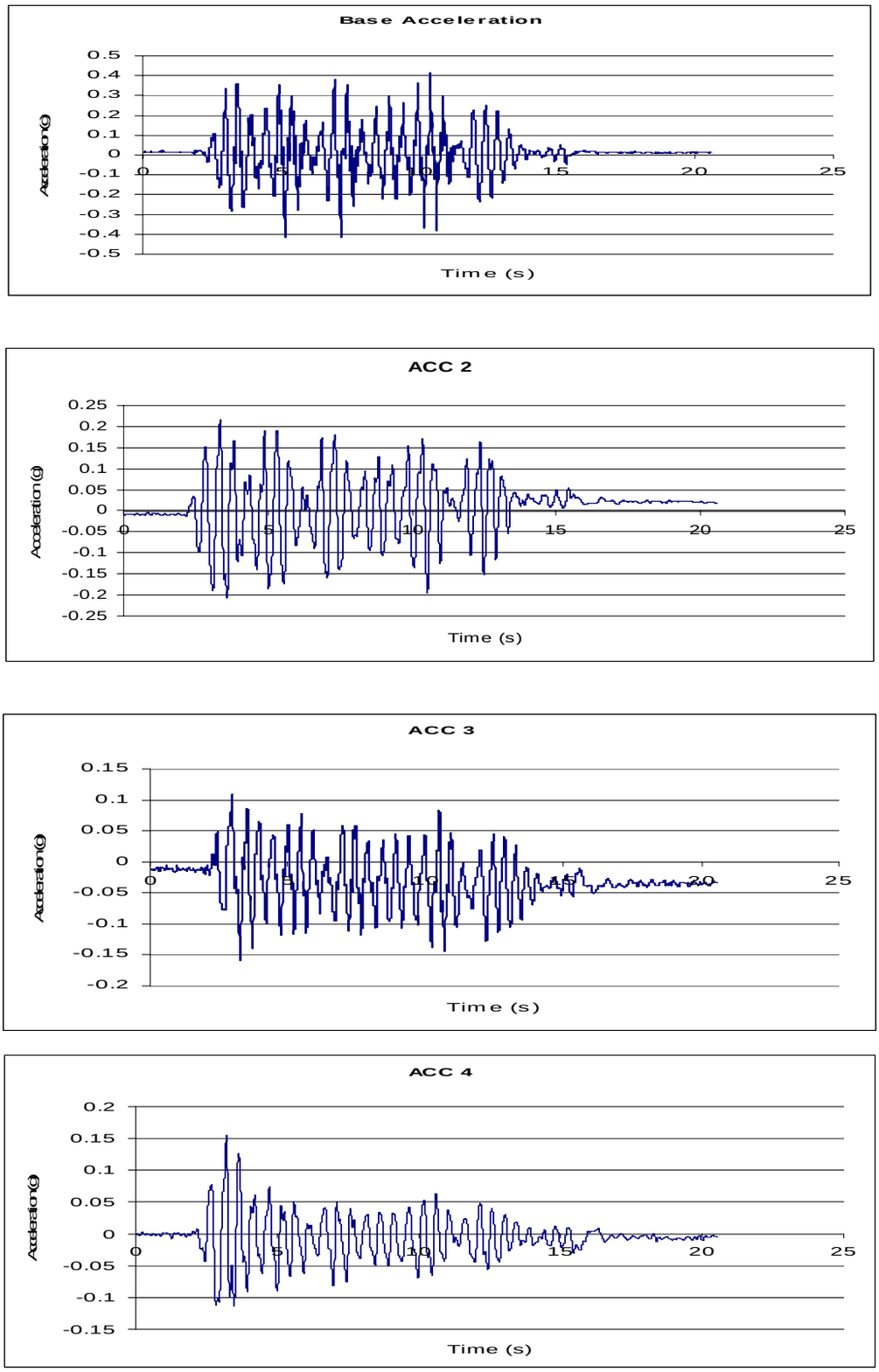
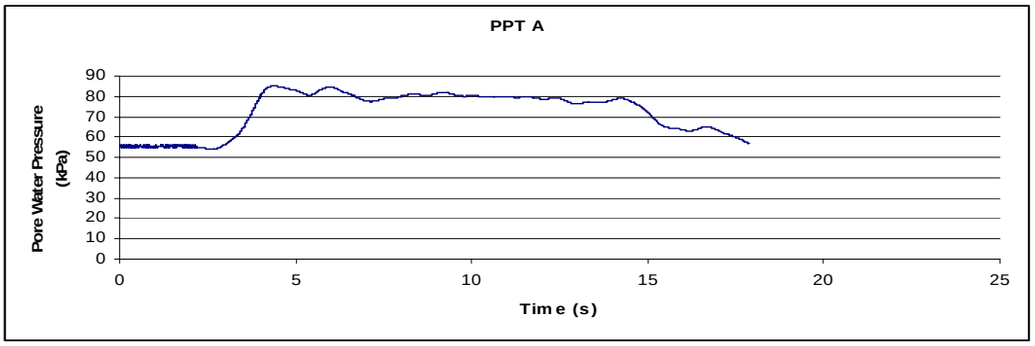
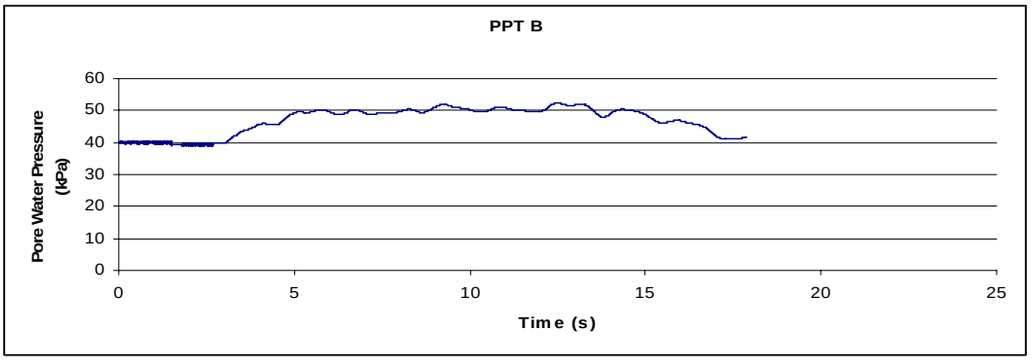
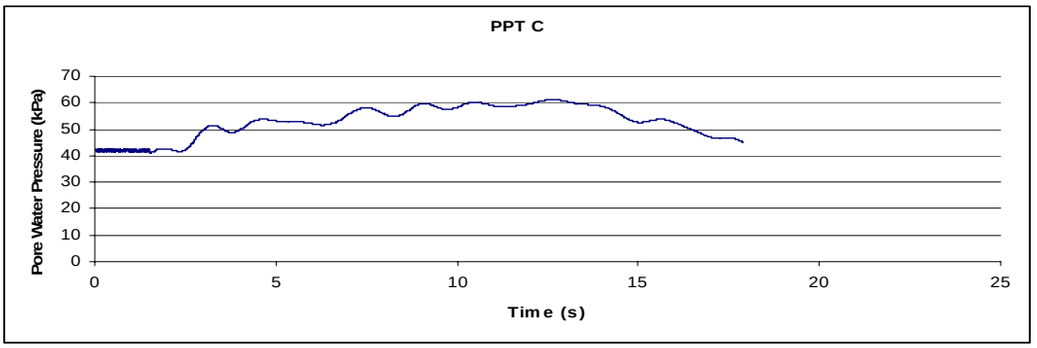


FIG. 3. Accelerations recorded during the earthquake, Model 1.







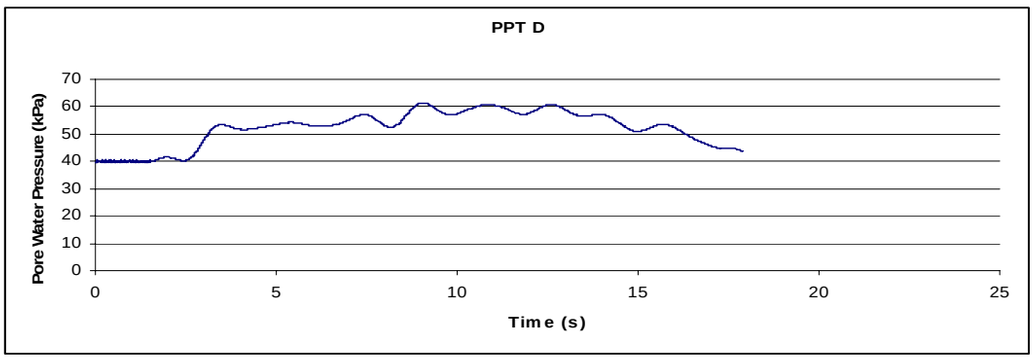


FIG. 4. Pore water pressure recorded in Model 1.

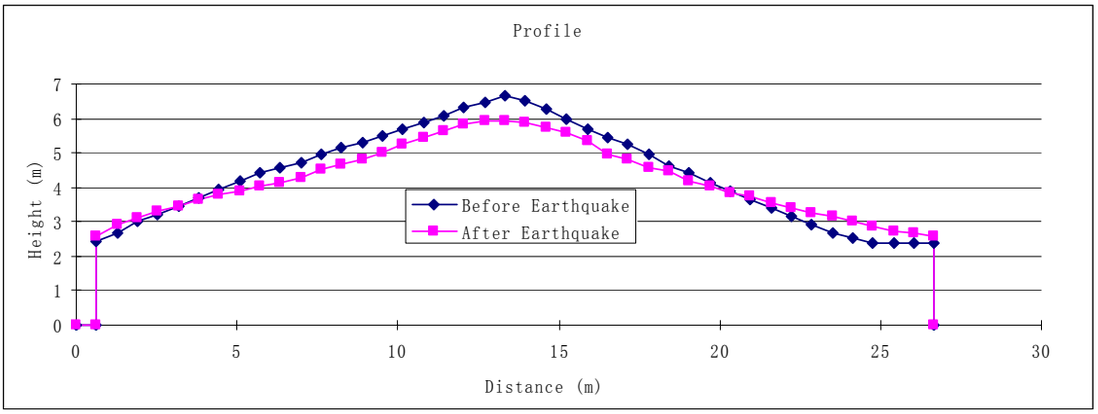


FIG. 5. Profile of the embankment before and after earthquake test, Model 1.

Influence of Soil Density

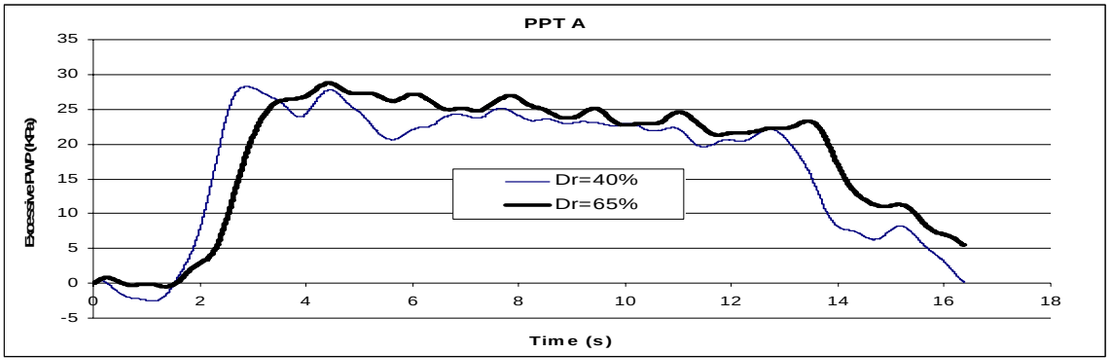
The only difference between Model #3 and #4 was the initial density of the sand in the embankment, with a relative density of 40% and 65%, respectively. The recorded excess pore pressures are shown in Fig.6. In both tests, liquefaction of sand was recorded. However, for the model with lower relative density, the excess pore pressure buildup was quicker and, after earthquakes, the dissipation was faster too. Since the looser sample was more compressible, the resulting settlement was about 60% more.

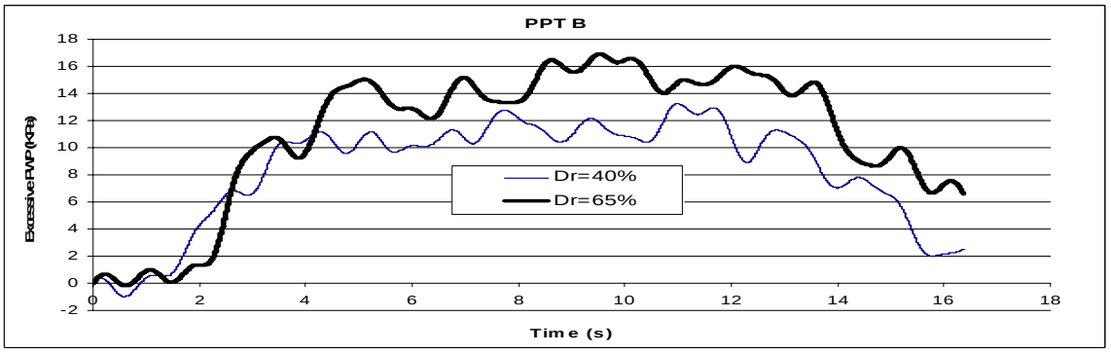
Influence of Seepage Force

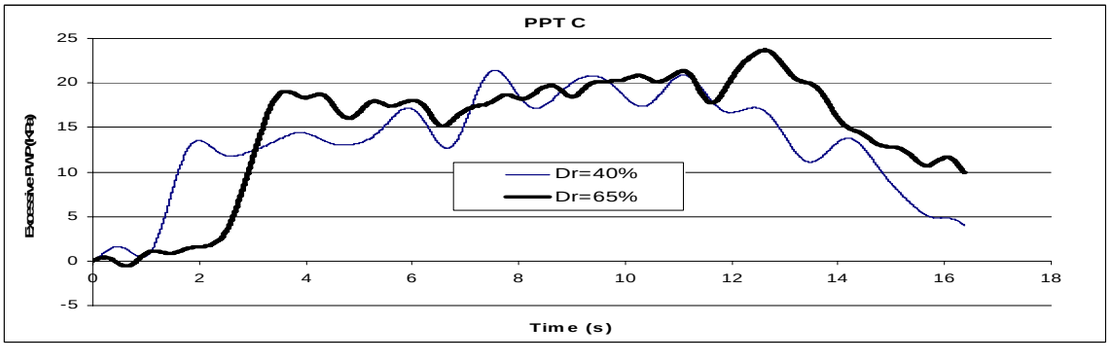
As shown in Table 3, there was no obvious difference in the total settlement of the embankment whether there was seepage force in the embankment. The recorded excess pore pressures during the earthquake are shown in Fig.7. The recording of PPTA, which was located in the foundation of the embankment, was about the same in the two tests. This is not surprising since seepage force had less influence there. On the other hand, the recorded excess pore pressure recorded by the three transducers in the embankment was significantly lower when there was seepage force. There may be two explanations for this result, Seed and Lee (1966). First, as seepage force in the embankment had a vertical component that tends to increase the vertical effective stress. As a result, the excess pore pressure recorded was lower. Secondly, the horizontal component of the seepage force would increase the initial static shear stress on an element of sand in the embankment. This could also reduce the excess pore pressure generated. However, at the same time, because the seepage force was a driving force that pushes the embankment in the downstream direction, the embankment did move more laterally during the earthquake. These two effects seemed to counter each other and resulted in about the same magnitude of total settlement for the tests reported here. On the other hand, this condition may not apply if a different geometry, soil, or input motion is used.

CONCLUSIONS

The effect of seepage force, viscous pore fluid, and density of sand in the embankment on earthquake response of embankments was examined using centrifuge tests. From the results of this study, the following conclusions can be drawn:







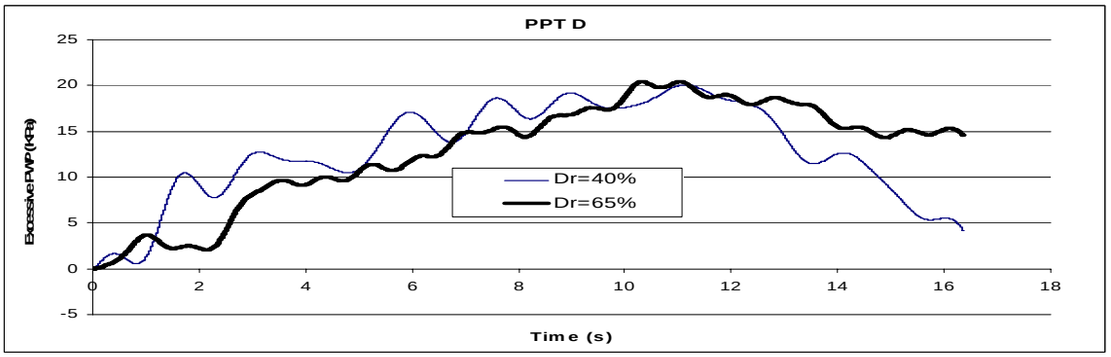


FIG. 6. Excess pore pressure recorded in Models 3 and 4.

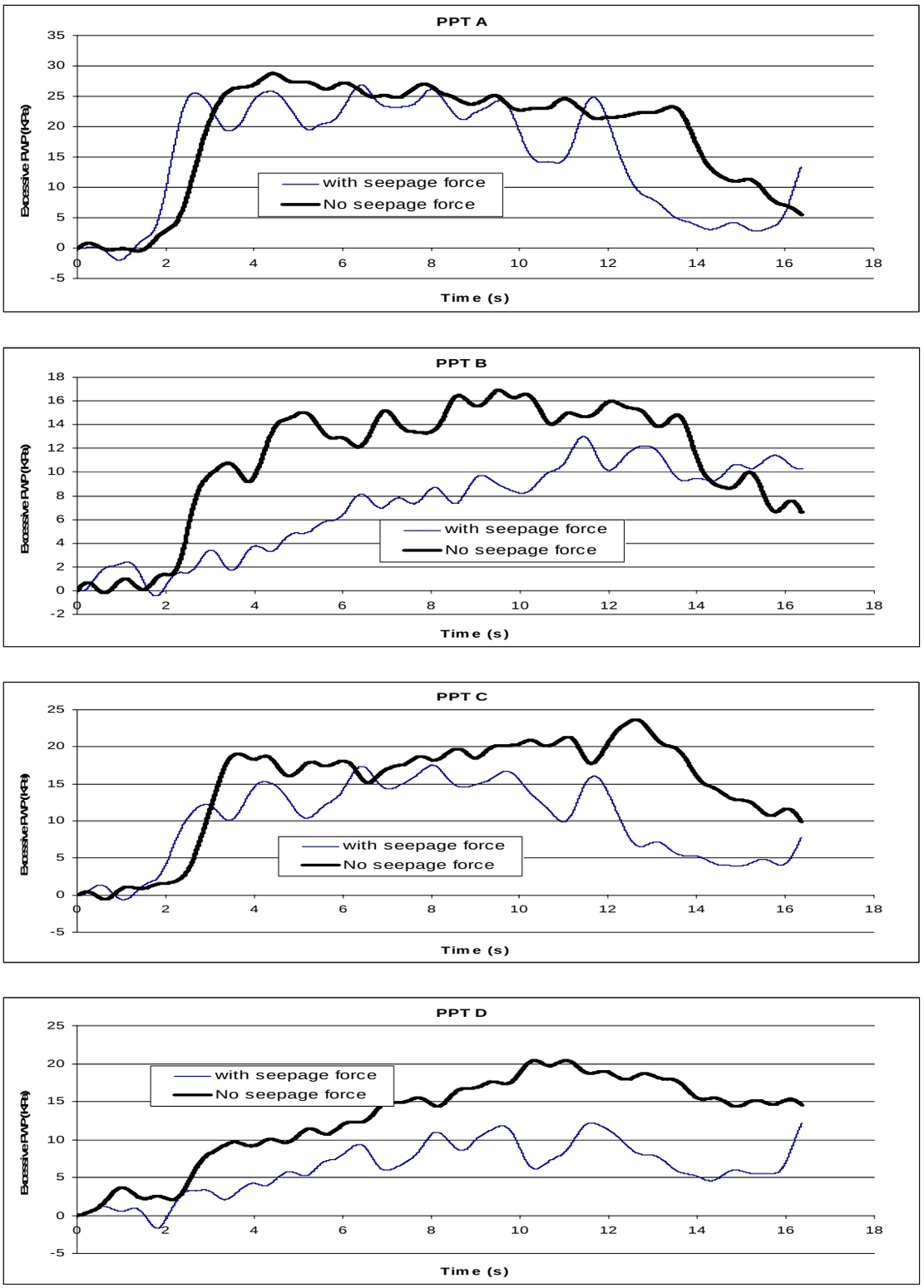


FIG. 7. Excess pore pressure recorded in Models 4 and 5

1. The centrifuge tests generated useful data about the seismic response of embankments with or without seepage.

2. The seepage force acts as driving force and may have effects on the deformation of an embankment. However, it also reduces excess pore pressure generated. As a result, the overall settlement recorded was about the same with or without seepage force.

3. In this study, high viscous pore fluid was used in two tests. It showed that the total settlement of the embankment was not affected by the viscosity of pore fluid for Nevada Sand. However, the viscosity of the fluids influenced the speed of buildup and dissipation of excess pore pressure.

4. Density of embankment soil greatly affected the total settlement of embankment during earthquake.

REFERENCES

Arulanandan, K. and Scott, R.F. (ed.) (1993), "Verification of Numerical Procedures for the Analysis of Soil Liquefaction Problems", A.A. Balkema, Rotterdam**.**

Dief, H.M. (2000), "Evaluating the liquefaction potential of soils by the energy method in the centrifuge", Ph.D. Dissertation, Department of Civil Engineering, Case Western Reserve University, Ohio.

Figueroa, J.L., Saada, A.S. and Dief, H. (1998), "Development of the Geotechnical Centrifuge at Case Western Reserve University", Centrifuge 98, Vol. 1, pp3-8.

Li, Xiang Song and Ming, H.Y. (2004), "Seepage driving effect on deformations of San Fernando Dams", Soil Dynamics and Earthquake Engineering, Vol. 24, pp979-992.

Marcuson, W.F., Hadala, P.F. and Ledbetter, R.H. (1996), "Seismic Rehabilitation of Earth Dam," J. Geotech. Engrg. Div., ASCE, 122(1), 7-20.

Seed H.B.., Lee, K.L., and Idriss, I.M. (1969), "Analysis of Sheffield Dam Failure," Journal of the Soil Mechanics and Foundations Division, ASCE, Vol.95, No. SM6, 1453-1490.

Seed H.B., Lee K.L., Idriss I.M., and Makdisi, F.I. (1975), "The Slides in the San Fernando Dams during the Earthquake of February 9, 1971," Journal of Geotechnical Engineering Division, ASCE, Vol. 101, No.GT7, 651-688.

Seed, H.B. and Lee, K.L. (1966), "Liquefaction of saturated sands during cyclic loading," Journal of Soil Mechanics and Foundations Division, ASCE, Vol.92, No. SM6, 105-134.

Taylor R. N. (1995), "Geotechnical Centrifuge Technology," Blackie Academic and Professional, Glasgow, pp.19-33.

This page intentionally left blank

Assessment of Structure-Induced Liquefaction Triggering

Berna Unutmaz[1], and K. Onder Cetin[2], M. ASCE

1Graduate Student Researcher, Civil Engineering Department, Middle East Technical University, 06531, Ankara, Turkey bunutmaz@metu.edu.tr
2Associate Professor Doctor, Civil Engineering Department, Middle East Technical University, 06531, Ankara, Turkey onder@ce.metu.edu.tr

ABSTRACT

Although there exists some consensus regarding seismic soil liquefaction triggering assessment of free field soil sites, assessing liquefaction triggering potential beneath building foundations still stays as a controversial and a difficult issue. Liquefaction triggering potential under building foundations is affected by both the static and cyclic stress state of the soil medium. As part of these studies, conventionally used normalized cyclic demand term, cyclic stress ratio corrected for K_α and K_σ effects adjacent to and under building foundations are to be estimated. For this purpose series of 3-D numerical simulations have been performed for a number of generic soil-structure systems. A representative CSR value, $CSR_{SSEI,rep}$ varying with depth was defined, which has potential use in assessing liquefaction-induced bearing capacity failures. Then a simplified, semi empirical procedure was recommended for the estimation of $CSR_{SSEI,rep}$ values which was further calibrated through the results of 3-D numerical simulations. Good match between the predictions of the recommended semi-empirical procedure and the results of numerical simulations are concluded to be convincing and promising for the assessment of liquefaction triggering potential for foundation soils.

INTRODUCTION

Evaluation of the in situ cyclic shear stress time history induced within any soil element (or stratum) is a key component of any well-based method for the assessment of the likelihood of “triggering” seismically-induced soil liquefaction. The seismically-induced cyclic shear stress time history is, in most analysis methods, normalized by some measure of the initial normal effective stress in the soil, to calculate the earthquake-induced cyclic shear stress ratio (CSR). At most soil sites, the cyclic shear stresses acting on horizontal planes due to seismic loading are largely dominated by cyclic shear stresses induced by vertically propagating, or nearly vertically propagating shear waves. This gives rise to the "simplified" procedure for evaluation of induced cyclic shear stresses at depth (Seed and Idriss, 1971). When this “equivalent uniform cyclic shear stress” is normalized by the initial effective overburden stress, the result is an estimate of the “equivalent uniform cyclic stress ratio” (CSR) as:

$$CSR = 0.65 \cdot \frac{a_{max}}{g} \cdot \frac{\gamma \cdot h}{\sigma'_v} \cdot r_d \quad \textbf{(1)}$$

The stress reduction coefficient, r_d, is a function of site stratigraphy, soil properties, and characteristics of the "input" motions (excitations). It has a value of 1.0 by definition at the ground surface. Cyclic stress ratio; CSR was chosen as demand term for liquefaction triggering assessment of Seed et al (1984). Since then, numerous researchers, still adopting CSR as the demand term (Liao et al., 1988, Liao and Lum, 1998, Youd and Noble, 1997, Toprak et al., 1999, Juang et al, 2002, Cetin et al., 2004) have attempted to improve the accuracy of liquefaction triggering relationships. However, all these methods founded on "simplified procedure" suffer from a major limitation that they are all applicable to the liquefaction triggering assessment of free field soil sites. Direct applicability of these methods to foundation soils underlying structural systems is not possible, unless, in the estimation of CSR, structure-soil-earthquake interaction is properly addressed. More specifically, compared to a free field soil site, under static conditions, due to the presence of an overlying structural system i) overburden stresses acting on the underlying foundation soils are higher, ii) nonzero shear stresses act on the horizontal soil planes. Similarly during earthquake shaking, presence of iii) foundation elements (e.g.: footings or mat) forms usually a sharp impedance contrast which causes deviations from the free field vertical propagation pattern of shear waves (i.e. : kinematic interaction), iv) an overlying structure due its inertia will exert additional cyclic shear stresses onto foundation soils. Issues referred to in (i) and (ii) can be handled by introducing series of correction factors known as K_α, and K_σ, respectively applied on CSR_{eq} as given in Equation (2).

$$CSR_{eq,\alpha=0,\sigma_v'=100kPa} = \frac{CSR_{eq,\alpha,\sigma_v'}}{K_\alpha \cdot K_\sigma} \quad \textbf{(2)}$$

where $CSR_{eq,\alpha,\sigma v'}$ is the equivalent cyclic stress ratio at the current stress state, K_α and K_σ are the correction factors for initial shear stresses and vertical effective stress respectively. $CSR_{eq,\alpha=0,\sigma v=100kPa'}$ is the cyclic stress ratio at the reference state.

K_α factors as a function of relative density, D_R, and α as defined in Equation (3) were introduced by Seed (1983) to assess the effects of initial static shear stresses on liquefaction triggering resistance. Since then, number of researchers have studied this issue and have shown that K_α is mainly dependent on soil stiffness and confining stress conditions. A review of the literature was presented by Harder and Boulanger (1997) as part of NCEER (1997). More recently, Boulanger (2003, 1) proposed a new set of K_α corrections as a function of relative dilatancy index (ξ_R). Based upon currently available K_α corrections, it can be concluded that from only K_α point of view, due to the presence of an overlying structure, decrease in liquefaction triggering resistance of loose foundation soils is expected especially near the foundation edges. Figure 1 presents a typical α and Figure 2 shows K_α fields developed along the center line of a 4 story residential structure founded on a mat underlain by a sand layer with relative densities of 30 % and 70 %, respectively. As can be interpreted from Figure 2, K_α effects increase seismic demand (i.e. CSR) for "loose" soils.

$$\alpha = \frac{\text{InitialStatic Shear Stress}}{\text{Vertical Effective Stress}} = \frac{\tau_{\text{static,horizontal}}}{\sigma_v'} \quad \textbf{(3)}$$

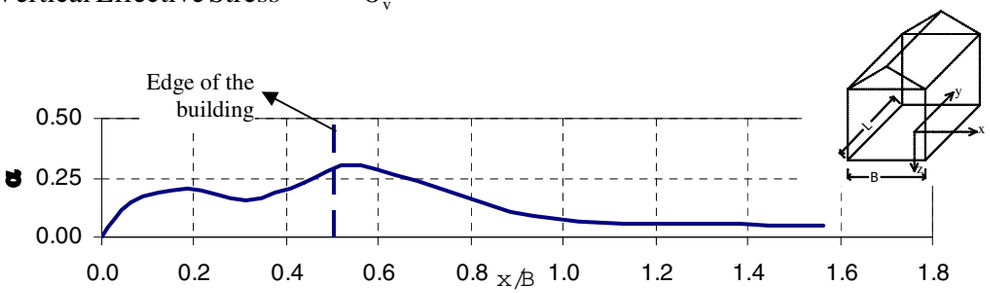
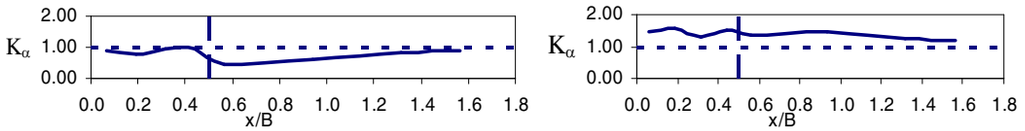


Figure 1. Variation of "α" along the width of the structure at z/B = 0 and y/L = 0



(a) (b)

Figure 2. K_α along the width of the structure, for (a)D_R = 30%, (b) D_R = 70% z/B = 0 and y/L = 0

The additional effect of reduction of normalized liquefaction resistance with increased initial effective overburden stress (σ_v') has been demonstrated by means of laboratory testing, and is a manifestation of "critical state" type of behavior (suppression of dilatancy at increased effective confining stress).

K_σ concept has been addressed by a number of researchers (i.e., NCEER Working Group 1997, Youd et al., 2001; Boulanger, 2003(2); Cetin et al., 2004; Idriss and Boulanger, 2006). Equation (4) presents the recommendations of Idriss and Boulanger, 2006 for the correction factor K_σ:

$$K_\sigma = 1 - C_\sigma \ln\left(\frac{\sigma_{v0}'}{P_a}\right) \quad \textbf{4 (a)}$$

$$C_\sigma = \frac{1}{18.9 - 2.55\sqrt{(N_1)_{60}}} \quad \textbf{4 (b)}$$

where P_a is the atmospheric pressure, $(N_1)_{60}$ is the energy and overburden corrected SPT-N blow-count.

As evident by the available literature, even though there exist some disagreements on the actual values of K_α and K_σ factors, yet it is still possible to compare the free field soil CSR (i.e.: CSR_{FF}) values to the CSR value estimated for a soil, structure and earthquake interacting system (i.e.: CSR_{SSEI}) through currently available K_α, and K_σ correction factors, if both kinematic and inertial interaction components are put aside.

The kinematic and inertial interactions defined previously in iii) and iv) are rather complex and deserve further attention to the soil structure and earthquake interaction (SSEI) problem from liquefaction triggering point of view. Veletsos and Meek (1974)

suggested that the critical factors controlling SSEI are; a) σ (ratio of structure-to-soil stiffness) as defined in Equation (5), b) the ratio of structure height to foundation radius (width) and c) the interaction of the fixed-base natural frequency of the structure to the frequency regions of the design spectrum. By Veletsos and Meek (1974), it was concluded that for σ values in the range of 3-20, soil-structure interaction becomes critical.

$$\sigma = \frac{V_{s,final} \times T_{str}}{h_{effective}} \quad \textbf{(5)}$$

where $V_{s,final}$ is the shear wave velocity of the soil profile after earthquake excitation, T_{str} is the first mode period of the structure and $h_{effective}$ is the effective height of the structure generally taken as two thirds of the total height.

In addition to the ones listed above, Yoshimi and Tokimatsu (1977), Finn and Yodengrakumar (1987), Popescu and Prevost (1993), Jun-Tsai Hwang et al. (1994), Liu and Dobry (1997), Yoshiaki et al, (1997), Stewart et al. (1999), Travasarou et al. (2006) have also studied on the effects of structures on liquefaction triggering of soil sites. A detailed review for these studies can be found in Unutmaz and Cetin (2007). However, there are contradicting arguments regarding the effects and the assessment of liquefaction triggering potential of foundation soils overlain by structural systems. Within the confines of this paper, it is attempted to present the preliminary results of our research studies aiming to comparatively quantify the effects of SSEI on liquefaction triggering potential, more specifically on CSR. The scope of our studies includes 3-D numerical simulation of SSEI.

NUMERICAL SIMULATIONS

3-D finite difference-based simulations were performed for the purpose of assessing SSEI. For verification purposes, additional 1-D soil site response analyses were performed by SHAKE91 software. The numerical assessment scheme included i) 3-D static assessment of soil-structure system for the purpose of estimating horizontal shear stresses and vertical effective stresses, which will be further used in the calculation of K_α and K_σ correction factors, ii) 3-D seismic assessment of soil-structure system for the purpose of estimating both structural and soil mass-induced shear stresses acting on the horizontal plane, which will be further used in the calculation of CSR, iii) 3-D seismic assessment of the free field soil site (without the structural system) for the purpose of enabling direct comparisons with 1-D SHAKE 91 simulations, useful for the calibration of the 3-D model. In the development of the 3-D finite difference mesh, mesh window and element sizes were selected in such a way that the results of FLAC 3-D free field simulations match with SHAKE 91 results, as illustrated in Figure 3, Figure 4 and Figure 5.

Figure 6 presents a typical mesh adopted for the numerical simulations. In FLAC 3-D simulations, to be consistent with the available liquefaction triggering methods (e.g.: NCEER, 1997, Cetin et al., 2004), total stress based equivalent linear model with hysteretic degradation and damping curves as recommended by Vucetic and Dobry (1991) for clean sands (i.e.: PI = 0) was adopted for the purpose of estimating induced shear stresses. The spatial element size is selected to be smaller than approximately one-tenth of the wavelength associated with the highest frequency

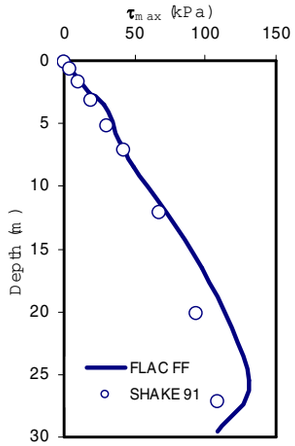


Figure 3. Variation of shear stress (τ) with depth (d)

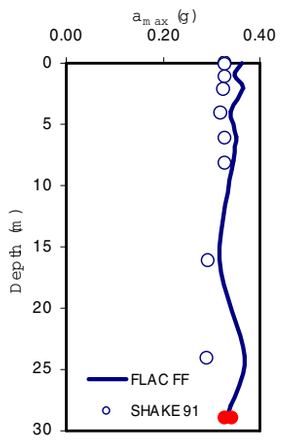


Figure 4. Variation of a_{max} with depth (d)

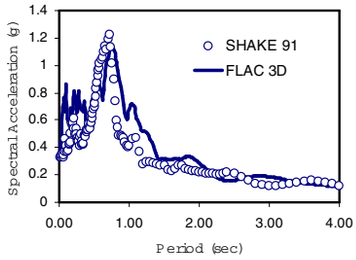


Figure 5. Comparison of elastic response spectra

component of the input wave, which is 15 Hz, to prevent numerical distortion of the propagating wave in dynamic analyses. The boundary condition at the sides of the model is selected as free field which accounts for the free field motion that would exist in the absence of the structure.

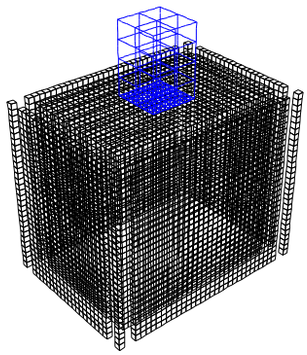


Figure 6. Finite Difference 3D Mesh

Four generic 30 m thick homogeneous soil profiles with shear wave velocity values V_s=100 m/sec, V_s=150 m/sec, V_s=200 m/sec and V_s=300 m/sec, overlain by two different structural systems with fixed base natural periods ranging between 0.22 and 0.50 seconds are shaken by 1999 Kocaeli Earthquake, M_w = 7.4, Sakarya (SKR) record, 1989 Loma Prieta Earthquake, M_w = 7.0 Santa Cruz USCS Lick Observatory Station (LP) and 1995 Kobe Earthquake, M_w = 6.9, Chihaya Station (CHY) records. Foundation systems are defined as 30 cm thick surficial mats, overlain by a regular concrete column-beam system with column and beam dimensions of 40 x 40 and 30 x 30 cm, respectively. Column spacing and storey heights were selected as 4 and 3 m respectively. The storey masses were concentrated at the floor levels.

About 45 sets of numerical simulations were performed corresponding to different combinations of generic soil sites, structures and earthquake records. The results of these simulations are presented in the form of corrected CSR values. As shown in Equation (6), for estimating the CSR values of the soil-structure-earthquake

interacting model, initial static horizontal shear stresses, $\tau_{static,h}$, were subtracted from the estimated maximum horizontal cyclic shear stresses, $\tau_{SSEI,h}$, further normalized by static vertical effective stresses leading to CSR_{SSEI} values. CSR_{SSEI} was then corrected by K_α and K_σ factors to eliminate the variabilities due to initial static vertical effective and horizontal shear stresses.

$$CSR_{SSEI,\alpha=0,\sigma_v'=100kPa} = \frac{0.65 \cdot \left(\tau_{SSEI,h} - \tau_{static,h}\right) / \sigma_{v,static}'}{K_\alpha \cdot K_\sigma} \quad \textbf{(6)}$$

For illustration purposes, variation of the numerically estimated CSR_{SSEI} values along the axis of a 4 story structure founded on interbedded soft clays and loose to medium dense sands, shaken by Kocaeli earthquake is shown in Figure 7. As the figure implies, demand term CSR_{SSEI} varies along the structure axis and has the highest value at the edges of the structure. For the purpose of representing this variation by only two sets of CSR values, which have potential use in foundation performance assessments from bearing capacity, post cyclic volumetric and deviatoric strain points of views, representative and maximum CSR terms designated by $CSR_{SSEI,rep}$ and $CSR_{SSEI,max}$ are defined. The estimation of the maximum CSR value is trivial and conveniently picked as the highest CSR value-induced during cyclic loading at a certain depth z. However, definition and potential use of representative CSR is rather complex and deserve further explanation. $CSR_{SSEI,rep}$ values are estimated through a weighting scheme based on the increase in the vertical stress level of soils due to overlying structure (i.e., $\Delta\sigma$) In simpler terms the soils carrying the most of the weight of the overlying structure will have a higher contribution in the $CSR_{SSEI,rep}$ estimation process. Equation (7) summarizes this calculation process where $\Delta\sigma'_v$ is structural-induced vertical stress difference, τ_{cyc} is cyclic shear stress, τ_{cyc} is the static shear stress induced by structure.

$$CSR_{SSEI,rep}(x,y,z) = \frac{\int_{-\infty}^{\infty} 0.65 \frac{\left(\tau_{cyc}(x,y,z) - \tau_{st}(x,y,z)\right) \cdot \Delta\sigma(x,y,z)}{\sigma_v'(x,y,z)} dx}{\int_{-\infty}^{\infty} \Delta\sigma(x,y,z) dx} \quad \textbf{(7)}$$

Thus, it is believed that $CSR_{SSEI,rep}$ is an effective parameter for the assessment of overall general performance of foundation soils from liquefaction point of view. The horizontal dashed line in Figure 7 represents this representative CSR_{SSEI} value.

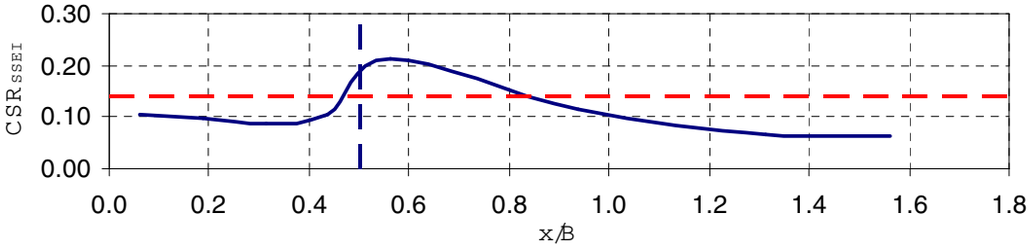


Figure 7. Variation of CSR_{SSEI} along the structure axis

$CSR_{SSEI,rep}$ values can be estimated using the results of numerical soil-structure-earthquake assessments as defined formerly. However, to avoid lengthy, complex and difficult dynamic analyses, a simplified procedure for the estimation of $CSR_{SSEI,rep}$ will be defined next. As a conclusion the comparisons with the predictions of the proposed simplified procedure and numerical analyses will be presented.

SIMPLIFIED PROCEDURE FOR $CSR_{SSEI,rep}$

Cyclic shear stresses induced on the horizontal planes of foundation soils are mainly due to seismic response of the structural and soil masses represented by maximum base shear, τ_b and τ_{soil}. Due to complex nature of the interaction as well as possibly out of phase occurrences of the maximum shear stresses due to structure and soil masses, simple sum of these components is not possible. Thus, the weighting of these shear components are attempted to be modeled as given in Equation (8):

$$CSR_{SSEI,representative} = \frac{f(\sigma)\cdot f\left(\frac{S_A}{PGA}\right)\cdot f\left(\frac{H}{B}\right)\cdot \tau_b + \tau_{soil}}{\sigma_{SSI}\cdot K_\alpha \cdot K_\sigma} \quad \textbf{(8)}$$

where $f(\sigma)$, $f\left(\frac{S_A}{PGA}\right)$ and $f\left(\frac{H}{B}\right)$ are weighting functions modeling SSEI or in simpler terms the contribution of the base shear to the induced overall total shear stresses. In these equations, S_A refers the spectral acceleration corresponding to the period of the structure and PGA is the peak ground acceleration of the earthquake. These weighting functions are estimated through statistical assessments and the forms that produced the best fit to FLAC 3D results are presented in Equation (9):

$$f(\sigma) = 14.79 \times \exp(-0.003\cdot(\sigma)) \quad \textbf{(9a)}$$

$$f\left(\frac{S_A}{PGA}\right) = 0.74 \times \exp\left(-0.683\cdot\left(\frac{S_A}{PGA}\right)\right) \quad \textbf{(9b)}$$

$$f\left(\frac{H}{B}\right) = \exp\left(-0.612\cdot\left(\frac{H}{B}\right)\right) \quad \textbf{(9c)}$$

Maximum base shear force immediately beneath the foundation depth forms the nominator of Equation (10) which decays rapidly with depth, derivation and discussion of which are skipped due to page limitations.

$$\tau_b(z) = 0.65\frac{0.80\cdot S_A\cdot\sigma_b\cdot(B\cdot L)}{(B+1.6\cdot z)\cdot(L+1.6\cdot z)} \quad \textbf{(10)}$$

Shear stress contribution due to soil mass itself can be estimated consistent with Seed and Idriss (1971) simplified procedure as given in Equation (11):

$$\tau_{soil}(z) = 0.65\cdot\frac{a_{max}}{g}\cdot\gamma\cdot z\cdot r_d \quad \textbf{(11)}$$

σ_{SSI} is the vertical effective stress induced by both the structure and the soil and can be easily estimated through simple 2:1 rule, elastic solutions or more complex 3D static soil-structure finite element models .

Last but not least, to account for the variability in vertical and shear stress conditions under static conditions, K_α and K_σ corrections are applied. For the application of K_σ correction, estimation of vertical effective stresses under static conditions are needed, and estimation of them are trivial as discussed in the previous paragraph. In K_σ calculations, the methodology proposed by Idriss and Boulanger (2006), (Equations 4) can be utilized. Similarly, for the application of K_α corrections, a representative α field under the structures is needed. However, static α values are difficult to estimate unless static 3D soil-structure model results are available. For empirical assessment of the α field, a simplified formulation is presented in Equation (12).

$$\alpha_{rep} = \exp\left(\frac{z-1.48}{-4.36}\right) \times \frac{T_{str}^{-0.12}}{10.03} \times (N_1)_{60}^{0.04} \quad \textbf{(12)}$$

where z is the depth from ground surface, T_{str} is natural period of the structure, $(N_1)_{60}$ is the overburden and energy corrected SPT-N blow count. For K_α predictions, chart proposed by NCEER 1997 can be used.

The success of the outlined methodology for the estimation of $CSR_{SSEI,rep}$ values is illustrated by Figure 8 which compares them by the predictions of FLAC 3D analyses results. The unbiased trend as well as all data pairs falling in the 2:1 and 1:2 bounds is concluded to be convincing.

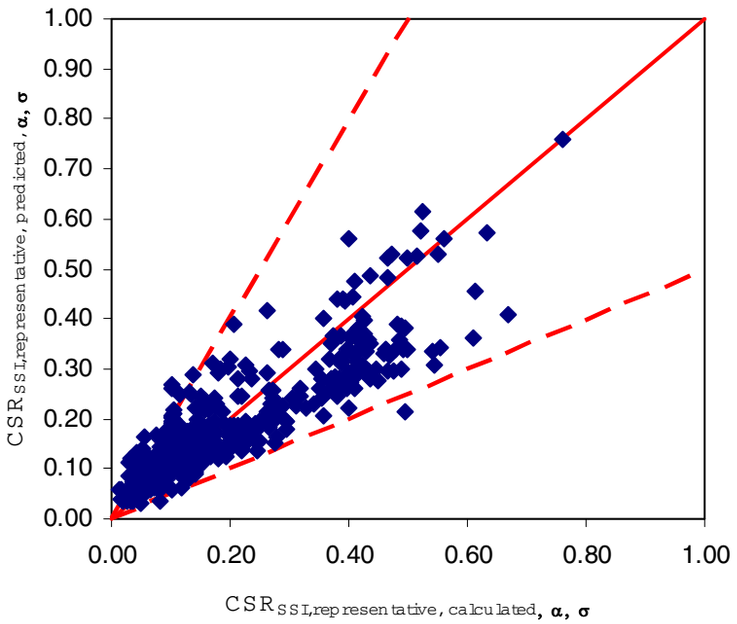


Figure 8. Comparison of calculated and predicted $CSR_{SSEI, rep}$ values

SUMMARY AND CONCLUSIONS

Within the confined of this paper, a review on seismic soil structure interaction problem, emphasis on its effects to seismic soil liquefaction triggering, is presented. Motivated by lack of available methodology for the purpose of assessing liquefaction triggering potential of soils overlain by a structure, it is intended to develop an empirically-based relationship to estimate CSR values of such soil structure, earthquake interacting system as compared to the values of a free field soil site. Thus, series of 3D numerical simulations of generic soil-structure systems shaken by three ground motions obtained from three different earthquakes were performed. A simplified formulation for estimating $CSR_{SSEI,rep}$ has been proposed. In the estimation of this representative term, contributions to the induced shear stresses both from the overlying structure as well as the soil body itself are included. In depth analyses of the proposed methodology revealed that liquefaction triggering potential of foundation soils depends both on the soil-structure-earthquake parameters σ and S_A/PGA and the aspect ratio of the structure (H/B). Good agreement between the estimates of the proposed methodology and 3-D SSEI models is concluded to be convincing and encouraging. As a concluding remark, we need to clarify our intention: as part of our on-going studies, the number of numerical simulations will be increased to cover a wider spectrum of building, soil and earthquake characteristics along with verification of the proposed model both from liquefaction triggering and post liquefaction foundation soil displacement points of views. These limited numerical assessments within a probabilistic framework revealed that the proposed semi-empirical methodology is promising and has potential use assessing liquefaction potential of foundation soils and foundation deformations.

REFERENCES

Boulanger, R.W. (2003(1)). "Relating K_α to Relative State Parameter Index." Technical note, *J. Geotech. and Geoenv Engrg, ASCE*, Vol.129(8), 770-773.

Boulanger, R.W. (2003(2)). "High Overburden Stress Effects in Liquefaction Analyses," *J. Geotech. and Geoenv Engrg, ASCE*, Vol.129(12), 1071-1082.

Cetin, K.O., Seed, R.B., Kiureghian, A.D., Tokimatsu, K., Harder, L.F. Jr, Kayen, R.E., Moss, R.E.S. (2004) "SPT-Based Probabilistic and Deterministic Assessment of Seismic Soil Liquefaction Potential." *ASCE, J. of Geotechnical and Geoenv Engrg*, Vol. 130(12), pp. 1314-1340.

Finn, W.D.L. and Yodengrakumar, M. (1987) "Analysis of pore water pressure in seismic centrifuge tests. " *Soil Dynamics and Liquefaction*, Elsevier, Amsterdam.

FLAC3D, (2005) "Fast Lagrangian Analysis of Continua in 3 Dimensions" *Itasca Consulting Group*, Minnesota.

Harder, L.F., Jr., and Boulanger, R.W. (1997) "Application of K_σ and K_α correction factors." *Proc., NCEER Workshop on Evaluation of Liquefaction Resistance of Soils, Rep. NCEER-97-0022*, National Center for Earthquake Engineering Research, SUNY Buffalo, Buffalo, N.Y., 167–190.

Hwang J. et al. (1994) "Seismic analysis of liquefaction considering soil-structure interaction. " *10th ECCE*, Vol. I, Vienna.

Idriss, I.M., Boulanger, R.W. (2006) "Semi-empirical procedures for evaluating liquefaction potential during earthquakes. " *Soil Dynamics and Earthquake Eng.*, Vol. 26, 115-130.

Juang, C.H., Jiang, T. and Andrus, R.D. (2002) "Assessing the probability-based methods for liquefaction potential evaluation. " *J. Geotech. Geoenv. Eng.*, 128(7), 580–589.

Liao, S.S.C., Veneziano, D. and Whitman, R.V. (1988) "Regression models for evaluating liquefaction probability. " *J. Geotech. Eng.*, 114(4), 389–411.

Liao, S.S.C. and Lum, K.Y. (1998) "Statistical analysis and application of the magnitude scaling factor in liquefaction analysis." *Proc., ASCE 3rd Specialty Conf. in Geotechnical Earthquake Engineering and Soil Dynamics*, Vol. 1, 410–421.

Liu, L. and Dobry, R. (1997) "Seismic response of shallow foundation on liqueifable sand. " *J. Geotech. and Geoenvironmental Engrg, ASCE*, Vol.123(6), 557-567.

NCEER (1997), "Proceedings of the NCEER Workshop on Evaluation of Liquefaction Resistance of Soils", Edited by Youd, T. L., Idriss, I. M., Technical Report No. NCEER-97-0022, December 31, 1997.

Popescu, R. and Prevost, J.H. (1993) "Centrifuge validation of numerical model for dynamic soil liquefaction. " *Soil Dyn. and Earthquake Engrg*., pp.73-90.

Schnabel, P.B., Lysmer, J. and Seed, H.B. (1973) SHAKE: A Computer Program for Earthquake Response Analysis of Horizontally Layered Sites. *Report No. EERC/72-12*, EERC, University of California at Berkeley, p88.

Seed, H.B. (1983) "Earthquake resistant design of earth dams. " *Proc., Seismic Design of Embankments and Caverns*, Philadelphia, ASCE, New York, 46–64.

Seed, H.B., Idriss, M.I. (1971) "Simplified procedure for evaluating soil liquefaction potential." *J. Soil Mech. and Found. Div., ASCE,* 97(9), 1249-1273.

Seed, H.B., Tokimatsu, K., Harder, L.F., Chung, R.M. (1984) "The Influence of SPT Procedures in Soil Liquefaction Resistance Evaluations. " *Earthquake Engineering Research Center Report No. UCB/EERC-84/15*, University of California at Berkeley, October.

Stewart, J.P., Fenves, G.L. and Seed, R.B. (1999) "Seismic soil-structure interaction in buildings. I: Analytical methods. ", *J. Geotech. and Geoenvironmental Engrg, ASCE*, Vol.125(1), 26-377.

Toprak, S., Holzer, T.L., Bennett, M.J. and Tinsley, J.C. (1999) "CPT-and SPT-based probabilistic assessment of liquefaction potential." *Proc., 7th U.S.–Japan Workshop on Earthquake Resistant Design of Lifeline Facilities and Countermeasures against Liquefaction*, Seattle.

Travasarou, T., Bray, J.D., Sancio, R.B. (2006) "Soil-structure interaction analyses of building responses during the 1999 Kocaeli earthquake." *Proc. 8th U.S. National Conference on Earthquake Eng*., Paper No.1877.

Unutmaz, B., Cetin, K.O., "Effects of soil-structure-earthquake-interaction on seismic soil liquefaction triggering", *Proc. 4th International Conference on Earthquake Geotechnical Eng.*, Paper No.1412, 2007.

Veletsos, A.S. and Meek, J.W. (1974) "Dynamic behavior of building-foundation systems. " *Earthquake Eng. and Structural Dynamics*, Vol. 3, pp.121-138.

Vucetic, M., Dobry, R. (1991), "Effect of Soil Plasticity on Cyclic Response", " *J. Geotech. and Geoenv. Eng* ASCE, Vol. 117(1).

Y. Yoshiaki et al. (1997) Settlement of building on saturated sand during earthquake. *Soils and Found.*, 17(1).

Yoshimi, Y.K., and Tokimatsu, K. (1977) "Settlement of buildings on saturated sand during earthquakes. " *Soils and Found.*, Tokyo.

Youd, T.L. and Noble, S.K. (1997) "Liquefaction criteria based on statistical and probabilistic analyses. " *Proc., NCEER Workshop on Evaluation of Liquefaction Resistance of Soils, NCEER Technical Rep. No: NCEER-97-0022*, 201–205.

Youd, T. L. et al. (2001) "Liquefaction resistance of soils: Summary report from the 1996 NCEER and 1998 NCEER/NSF workshops on valuation of liquefaction resistance of soils. " *J. Geotech. and Geoenv. Eng, ASCE*, Vol.127(10), 817-833.

Centrifuge Experimentation of Building Performance on Liquefied Ground

Shideh Dashti[1], Jonathan Bray[2], Michael Riemer[3], and Dan Wilson[4]

[1]PhD Student Researcher (shideh@berkeley.edu), [2]Professor (bray@ce.berkeley.edu), [3]Associate Adjunct Professor (riemer@ce.berkeley.edu), Dept. of Civil and Environmental Engineering, University of California at Berkeley, and [4] Manager (dxwilson@ucdavis.edu), Center for Geotechnical Modeling, University of California at Davis

ABSTRACT: Centrifuge experiments were performed at the NEES@Davis Geotechnical Centrifuge Facility to develop insight into the seismic performance of structures at sites undergoing liquefaction. Three structural models, each representing simple structures founded on shallow rigid mats, were placed on each soil model. The soil profile contained a shallow layer of potentially liquefiable sand to investigate the effects of foundation width and contact pressure on building performance at sites with soil liquefaction. The base of the model container was excited by a sequence of three horizontal shakings, simulating increasing intensities of the Port Island down-hole recordings from the 1995 Kobe Earthquake. Two experiments are described wherein the liquefiable saturated, loose Nevada Sand layer varied in thickness from 3 m to 6 m (prototype scale). A summary of building and free-field movements observed in each experiment is presented with a comparison of the centrifuge results with actual building settlements observed in previous earthquakes. The results from these experiments provide valuable insight, because engineers generally apply methods developed for estimating free-field seismic settlement of clean sand deposits in evaluation of potential building movements at sites prone to liquefaction.

INTRODUCTION

Recent earthquakes such as the August 17, 1999, Kocaeli Earthquake, have provided countless examples of the damaging effects of liquefaction on the built environment. Observations of building performance include punching/settlement, bearing failure, and lateral shifting of buildings. Many of these structures were affected by ground failure due to liquefaction of shallow and relatively thin soil deposits. The occurrence of structural damage was found to be related to the occurrence of ground failure (e.g., Sancio et al. 2002).

In Niigata, Japan, during the 1964 earthquake and in Dagupan City, Philippines, during the 1990 Luzon earthquake, where most of the buildings were two to four stories with shallow foundations, average contact pressure of the building was found to affect the amount of settlement greatly, outweighing other characteristics of the

individual footings. However, there are currently no widely accepted engineering methods to estimate foundation settlement as a result of soil liquefaction.

Soil-foundation-structure-interaction (SFSI) plays a significant role in soil response and structure performance when ground softening occurs. Detailed documentation of the sequence of liquefaction, ground failure, and the resulting impacts on the performance of the structures is generally not available at key sites that have been affected by ground softening. Therefore, the connections between ground response and building response are not well understood. This is a necessary, yet missing, step in the development of advanced soil response models and building performance analytical procedures. In small-scale centrifuge test series, the input motion, surface motion, ground conditions, ground response, and structural response can be carefully documented and analyzed, which will enhance our understanding of ground failure and its resulting impacts on structures.

A series of four centrifuge tests will eventually be performed with the goal of generating well documented "case histories" of building response on liquefied ground. The centrifuge tests are investigating the relative importance of the thickness of the liquefiable soil layer and its void ratio, and the effects of different buildings and foundation conditions on the response of the liquefiable soils and building performance. The goal of this research project is to move beyond the practice of predicting free-field liquefaction to predicting building movements by considering the timing, sequence, and location of soil strength loss near structures.

Two comprehensive centrifuge experiments are described in this paper. In each experiment, three structures are placed atop a soil profile that contains a layer of liquefiable saturated, loose Nevada Sand. The layer thickness is 6 m in one test and 3 m in the other test (in prototype scale). A summary of building and free-field movements observed in each experiment is presented with a comparison of the centrifuge results with actual building settlements observed in previous earthquakes.

PURPOSE AND CONFIGURATION OF THE CENTRIFUGE MODELS

Centrifuge experiments TEST-1 and TEST-2 investigate the seismic performance of three scale models of SFSI systems at liquefied ground sites, with liquefiable layer thickness of 6 m and 3 m, respectively. Nevada Sand, a well characterized clean fine sand, is used as liquefiable model soil in this experiment. A series of four shaking events was applied to the model at a centrifuge acceleration of 55 g. This shaking was applied transversely with respect to the direction of the structural models.

The 9 m radius centrifuge at U.C. Davis can carry a 4,500 kg pay load at up to 75 g acceleration. The flexible shear beam container has internal dimensions of approximately 1.65 m x 0.79 m x 0.58 m (L x W x H). Using 55 g of spin acceleration, the internal dimensions of the shear beam container becomes equivalent to a prototype soil deposit of 91 m x 43 m x 32 m (L x W x H). The soil model in these tests was 26 m deep in prototype scale. The model was shaken with a uniaxial (horizontal) earthquake simulator. Figures 1 and 2 provide schematic plan and cross section views of a typical model. Unless otherwise indicated, all unit used in this paper are prototype units.

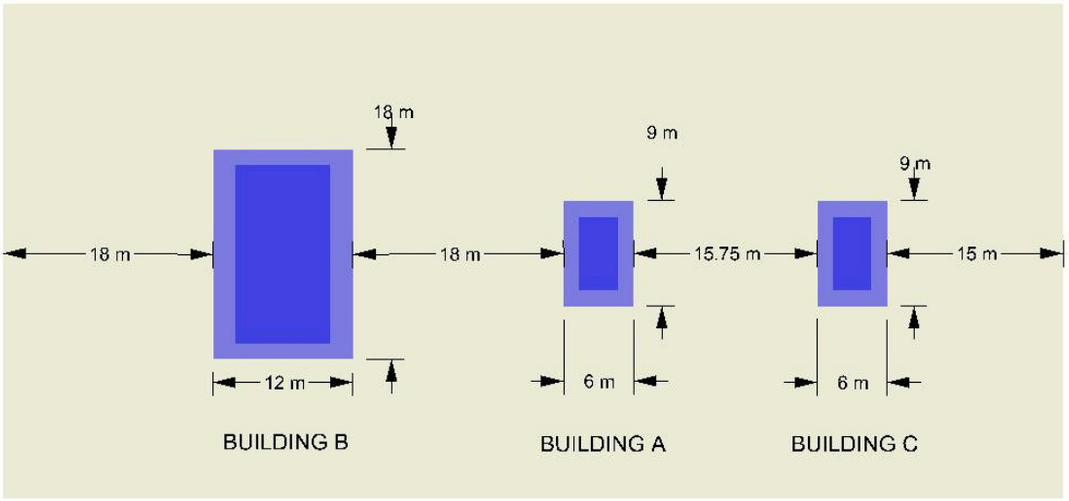


FIG. 1. Plan view of a typical model with prototype dimensions (shaking direction is to left and right in this view)

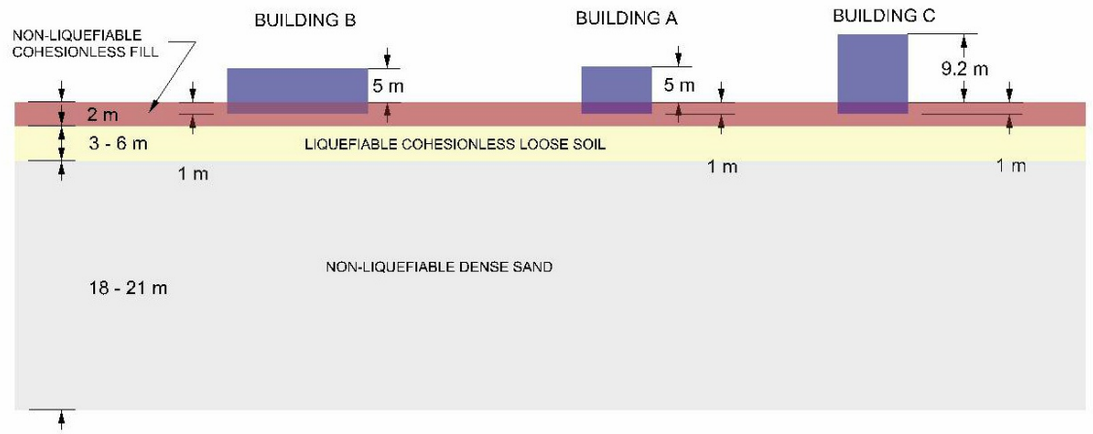


FIG. 2. Cross section view of a typical model; Structure A is a prototype 2-story building on a rigid mat foundation; Structure B has increased width and length; and Structure C is a taller 4-story building. The water level was kept at approximately 1.1 m (prototype) below ground surface after spinning up.

MODEL PREPARATION

Soil layers were placed using a barrel hopper. The placed density was controlled by maintaining a nearly constant drop height, rate, and mesh size. The non-liquefiable dense base sand layer and the liquefiable sand were prepared using dry-pluviation with subsequent saturation. Monterey sand was placed by dry-pluviation for the surficial fill soil. Soil was pluviated into the model container in successive layers, with each layer followed by leveling of the surface using a vacuum. Each lift corresponded to the elevation of a horizontal instrument array.

The model was saturated with a de-aired methyl cellulose solution of a viscosity higher than water to obtain realistic pore-pressure dissipation in the centrifuge model (Stewart et al., 1998). The kinematic viscosity of the fluid should be scaled by a factor of 55 to match the gravitational acceleration. However, using a pore fluid with such high kinematic viscosity significantly increases the amount of time required for saturation of the model and presents other workability problems. As a result, a pore fluid with a viscosity of approximately 20 times that of water was used. The relationship between kinematic viscosity and HPMC concentration developed by Stewart et al. (1998) was used to determine the amount of methyl cellulose that was needed to be added to water.

For saturation, the model container was placed on the centrifuge arm and metal saturation troughs were placed at both ends. Plastic tubes were extended to the bottom of the model container to ensure that the saturation proceeds from the bottom and ends toward the middle and upward. Before saturation, the model was placed under vacuum and the voids were flooded with CO_2.

Model Soil Properties

Nevada Sand is a fine, uniform, angular sand with mean grain size between 0.14 and 0.17 mm, a coefficient of uniformity of 1.67, and less than 5% fines. Nevada Sand with a relative density (D_r) of approximately 30% was used for the liquefiable material in both experiments. The relative density of the non-liquefiable sand layer was approximately 80% and 95% in TEST-1 and TEST-2, respectively. The estimated values of minimum and maximum dry densities (according to ASTM D4253-83 and D4254-83) of Nevada Sand are summarized in Table 1.

Monterey 0/30 Sand, a uniform coarse sand with mean grain size of approximately 0.4 mm, was placed on top of the liquefiable Nevada Sand layer as the unsaturated fill material. The purpose for using this layer was to minimize capillary rise and liquefaction directly below the structures and to provide adequate bearing pressure at the foundation level of the buildings. This soil was placed using a hand held hopper at an established relative density of 85%. Table 1 also provides estimates of minimum and maximum dry densities for Monterey Sand.

Table 1. Properties of Nevada Sand and Monterey Sand 0/30

Source	Soil Type	G_s	e_{min}	e_{max}	$\gamma_{d,\,min}$ (kN/m^3)	$\gamma_{d,\,max}$ (kN/m^3)	k (cm/s)
Cooper Lab	Nevada Sand	2.67	0.535	0.808	14.47	17.05	1.7e-3
Wu (1999)	Monterey 0/30	2.64	0.541	0.855	13.96	16.80	-

Properties of Structural Models

All structural models were single-degree-of-freedom structures made of steel and aluminum. The foundations were made of solid blocks of aluminum and were assumed to be rigid. The blocks representing the mass of the structures and the two side walls holding the mass were made of steel, due to steel's relatively high density and yield strength. Three structures were used in each test, each representing a mat foundation with bearing pressures of approximately 80 kPa, 80 kPa, and 130 kPa for structures A, B, and C, respectively. Table 2 summarizes the properties and dimensions of these structures in prototype scale.

Table 2. A summary of the properties of the three structural models

Structure	Structure Dimensions (WxLxH), m	Foundation Dimensions (WxLxH), m	Foundation Contact Pressure (kPa)	Fixed-Base Structure Natural Period, T_n (sec)
A	6 x 9 x 5	6 x 9 x 1	80	0.21
B	12 x 18 x 5	12 x 18 x 1	80	0.26
C	6 x 9 x 9.2	6 x 9 x 1	130	0.33

Ground Motions

The same sequence of shaking events was applied to the model at a centrifugal acceleration of 55 g during the two experiments. The shaking direction was parallel to the width of the structures. The first event applied to the model was a step wave that was used to evaluate the small strain elastic response of the model and to verify that the instruments and the data acquisition systems functioned properly. The next events were a sequence of scaled versions of the fault-normal component (north-south) of the ground motion recorded at a depth of 83 m in the Kobe Port Island down-hole array during the 1995 Kobe Earthquake. The sequence of ground motions that were applied to the test model is summarized in Table 3. Figure 3 presents the horizontal acceleration, velocity, and displacement-time histories, as well as the 5% damped elastic acceleration response spectrum of the input motion used for the Large Port Island event in the centrifuge experiments.

Table 3. Summary of ground motion sequence in TEST-1

Name of Motion	Centrifuge Acceleration (g)	Peak Base Acceleration (g)	Primary Purpose
Step Wave	55	0.01	Elastic Characterization
Small Port Island	55	0.045	No Liquefaction
Mod. Port Island.	55	0.19	Slight Liquefaction
Large Port Island	55	0.60	Significant Liquefaction

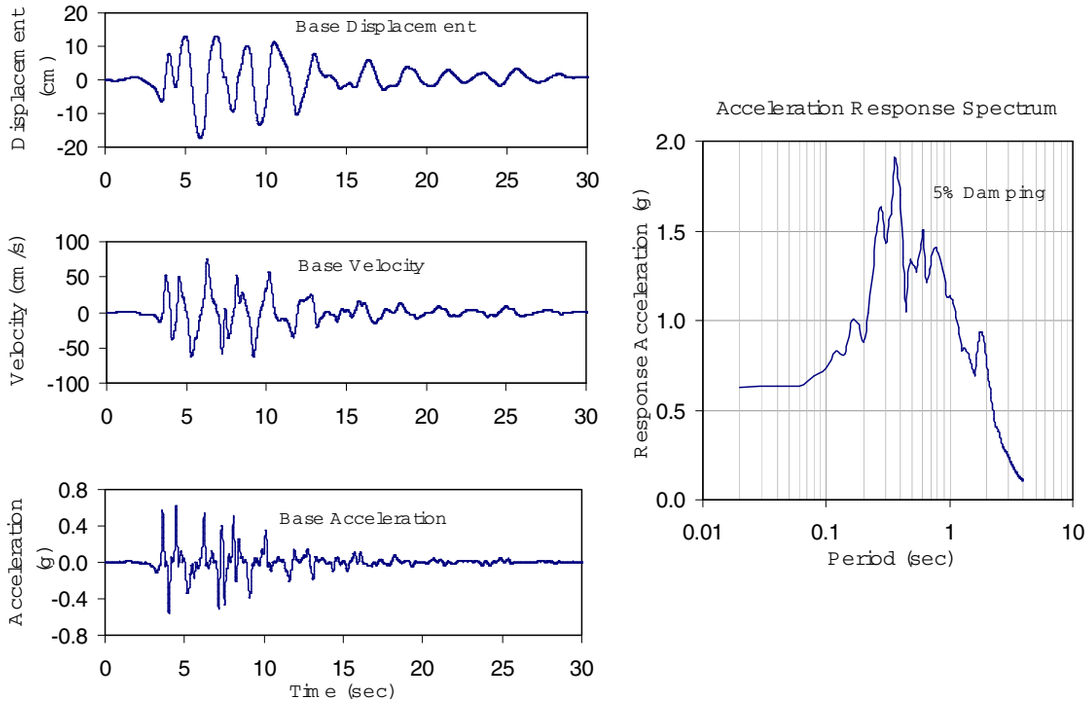


FIG. 3. Acceleration, velocity, displacement-time histories, and the 5% damped acceleration response spectrum of the Large Port Island shake (PGA = 0.6 g)

Instrumentation and Measurements

Thorough descriptions of the centrifuge facilities and instrumentation at UC Davis are provided at their website: http://nees.ucdavis.edu. A logical combination of wired pore pressure transducers, accelerometers, and LVDTs with wireless accelerometers and an array of high-speed video cameras available at UC Davis were used to record data during the first two test series, which are available as streaming data archived as part of the NEES data repository on NEES Central (http://central.nees.org). In addition to these instruments, colored sand grids were used to facilitate measuring vertical strains when excavating each model at the end of the shaking events.

EXPERIMENT RESULTS

Figure 5 shows representative vertical arrays of excess pore pressure ratio-time histories in the free-field and under a structural model during the Large Port Island event in TEST-1. These plots indicate that pore water pressures measured within the liquefiable layer away from the structures reached initial liquefaction (that is, pore water pressures approached the initial overburden effective stress) within 1 to 2 seconds of shaking. Excess pore water ratios generally tended to be smaller under the foundations compared to the free-field due to the additional load imposed by the structures, which increased the initial vertical effective stress. However, the absolute values of pore water pressure were generally higher under the buildings.

Building downward movement was observed to be a rapid and violent process that occurred mostly during strong ground shaking. The rate of building movement as well as free-field ground settlement during the Large Port Island event in both experiments can be observed in the settlement-time history plots in Figure 6. Positive displacement in these plots indicates settlement. It can be observed that structures sank rapidly, mostly within the 8 to 12 second period of strong shaking that followed the initial 3 to 4 sec of strong shaking. Building settlements after strong shaking were observed to slow down through the end of shaking followed by a relatively slow, time-dependent process consistent with theories of post-liquefaction re-consolidation. This post-earthquake settlement is only a small portion of the total building movement (i.e., about 1 to 4% of the total settlement). It was, however, of much higher significance in the free-field in both experiments (i.e., about 20-30% of the total free-field settlement).

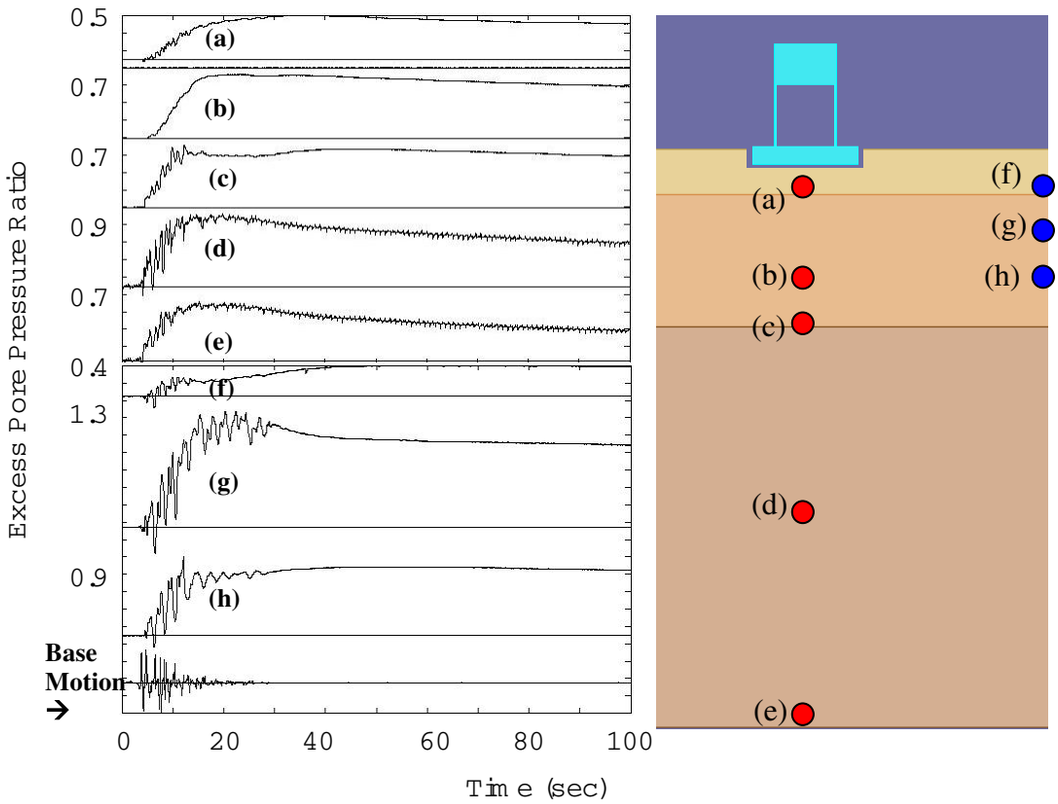


FIG. 5. A few representative excess pore pressure ratio time histories during the Large Port Island event in TEST-1, under a structure and in the free-field. (Values to the left of the plots are the maximum excess pore pressure ratios)

Table 4 provides a summary of the permanent soil movements in the free-field as well as the average permanent structure movements after each shaking event, from both experiments, obtained from the displacement transducers. The settlements reported in this table are total raw values that also include the downward movement of the dense Nevada Sand layer at the bottom of the soil profile. The average total

permanent downward movement of dense Nevada Sand was measured to be about 30 cm and 15cm in TEST-1 and TEST-2, respectively.

A comparison of the normalized average permanent settlement of each structure during the Large Port Island event (after subtracting the movement of the lower deposit of Dense Nevada Sand) with the available case histories and previous centrifuge experimental results are shown in Figure 7. Although the results of the first experiment (TEST-1) with the relatively thick liquefiable layer of 6 m are consistent with the available data, the results of the second experiment (TEST-2) with the thinner liquefiable layer (i.e., 3 m) are not consistent. Although the thickness of the liquefiable layer is larger for TEST-1, the amount of building movement is similar for both of these tests, which suggests that much of the vertical building movement is likely due to liquefied sand being pushed horizontally from underneath the buildings and water flowing out from under the buildings due to the large hydraulic gradients.

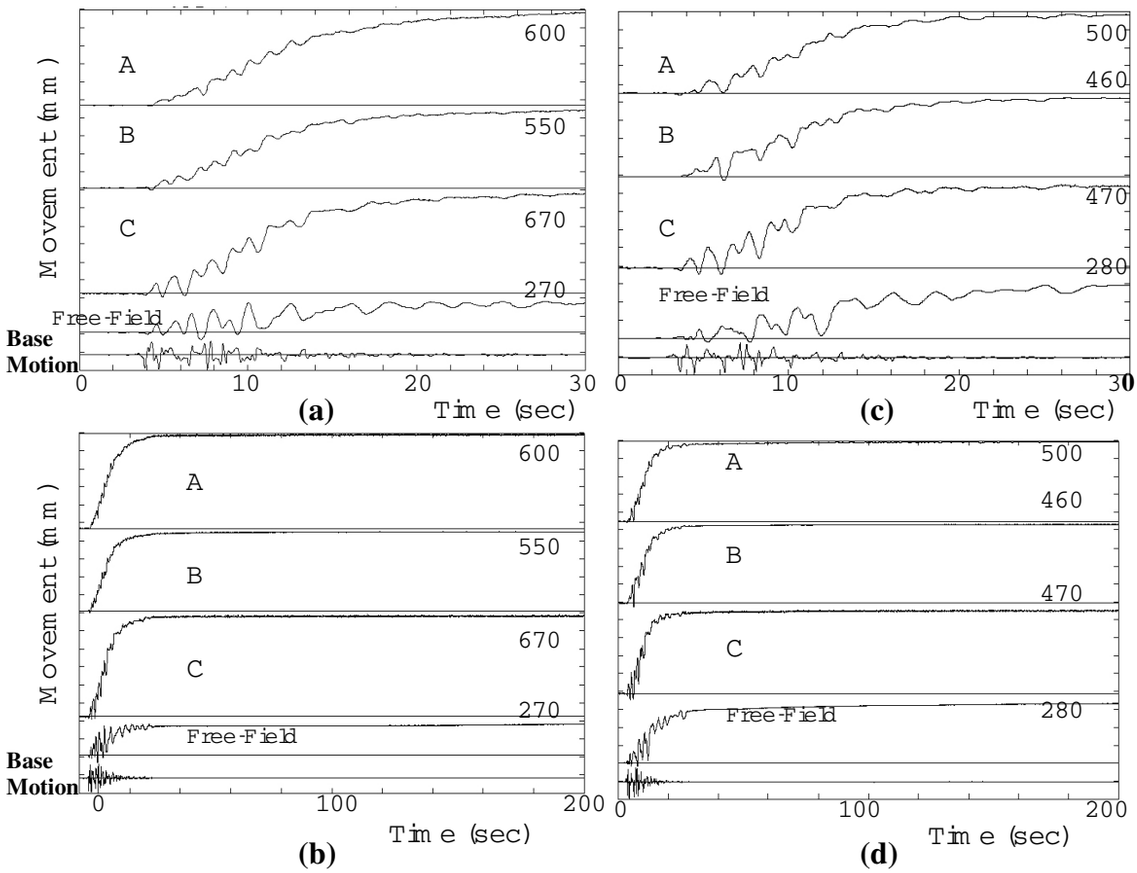


FIG. 6. Recorded time histories of average structure and free-field soil surface downward movement during the Large Port Island event: (a) TEST-1 records at beginning of shaking; (b) TEST-1 records for long term; (c) TEST-2 records at beginning of shaking; (d) TEST-2 records for long term. (values at the right of the plots are the final permanent downward movements in the units of mm)

The previous centrifuge tests were performed with thick, homogenous layers of liquefiable soil, and the Niigata and Luzon earthquake data are from deep deposits of

liquefiable material. The TEST-2 experiment provides the only centrifuge data for a case with a relatively thin liquefiable soil layer. It can be seen that the commonly used normalization by thickness of the liquefiable layer is not appropriate for this case. A significant portion of the building's downward movement appears to be deviatorically-induced in addition to volumetric settlements resulted from vertical and horizontal flow of pore water due to the significant hydraulic gradients that develop as result of earthquake shaking and the soil's response to cyclic loading.

Table 4. A summary of structure and free-field average permanent settlements

	TEST-1 Average Settlements (cm)				TEST-2 Average Settlements (cm)			
Event	**Free-Field**	**Struc. A**	**Struc. B**	**Struc. C**	**Free-Field**	**Struc. A**	**Struc. B**	**Struc. C**
Step Wave	0	0	0	0	0	0	0	0
Small P.I.	0	0	0	0	0	0	0	0
Mod. P.I.	11	9	11	11	20	28	20	17
Large P.I.	24	60	55	67	28	50	46	47
Total Settlements	35	69	66	79	48	78	66	64
% Due to Large Shake	68%	86%	84%	85%	58%	64%	70%	73%

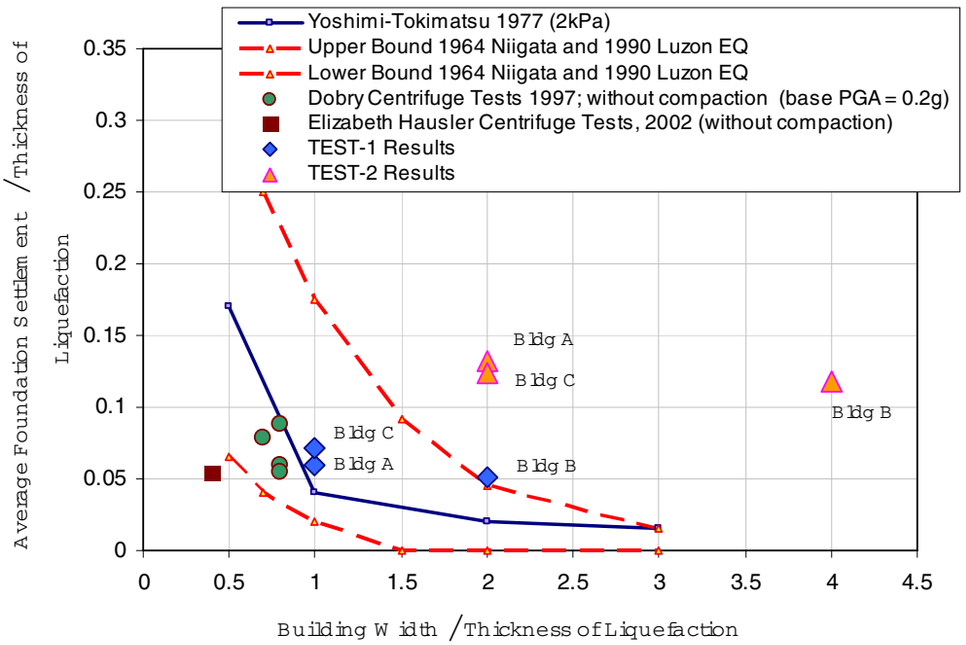


FIG. 7. Comparison of normalized foundation movement in centrifuge tests of this study due to Large Port Island event with case histories from 1964 Niigata and 1990 Luzon Philippines earthquakes and previous centrifuge experiments

CONCLUSIONS

Liquefaction occurred during the Moderate and Large Port Island events in the free-field for both centrifuge experiments as expected. The results summarized in Table 4 show that the Large Port Island event was responsible for approximately 85% and 70% of the total structural downward movements in TEST-1 and TEST-2, respectively. It is evident that the downward movement of the structures and the ground surface adjacent to the structures are greater than those measured in the free-field. Although the thickness of the liquefiable layer decreased from 6 m in TEST-1 to 3 m in TEST-2, the absolute amounts of building settlements were similar in both tests. Building settlements are not directly proportional to the thickness of the liquefiable layer.

It was also observed that as prototype building width increased from 6 m to 12 m at the same contact pressure, the total footing settlement decreased only slightly. Increasing the footing contact pressure from 80 kPa to 130 kPa did not seem to have a consistent effect on structural movements but seemed to significantly increase the structural tilt. These types of responses are not captured well by available analytical methods, and the commonly used normalization by thickness of the liquefiable layer is not appropriate for cases involving relatively thin layers of liquefiable soil.

ACKNOWLEDGEMENTS

This material is based upon work supported by the National Science Foundation under Grant No. CMS-0530714. Any opinions, findings, and conclusions or recommendations expressed in this material are those of the authors and do not necessarily reflect the views of the NSF. This project was also partially supported by the NSF through the George E. Brown, Jr. Network for Earthquake Engineering Simulation (NEES) UC Davis Grant No. CMS-0402490. We would also like to thank the staff at the UC Davis for their technical assistance and patience.

REFERENCES

Hausler, E.A. (2002). “Influence of Ground Improvement on Settlement and Liquefaction: A Study Based on Field Case History Evidence and Dynamic Geotechnical Centrifuge Tests.” PhD Thesis, Univ. Calif. Berkeley, Ch. 5: 85-271.

Kammerer, A.M., Wu, J., Pestana, J.M., Riemer, M.F., and Seed, R.B. (2000). “Cyclic Simple Shear Testing of Nevada Sand for PEER Center Project 2051999.” Geotechnical Engineering Report No UCB/GT/00-01.

Liu, L. and Dobry, R. (1997). “Seismic Response of Shallow Foundation on Liquefiable Sand.” *J. Geot.& Geo-environ. Engrg.*, ASCE, 123(6), 557-567.

Sancio et al. (2002). “Correlation Between Ground Failure And Soil Conditions in Adapazari, Turkey.” *Soil Dyn.& EQ Engrg.* J., 22, 1093-1102.

Stewart, D.P., Chen, Y.R., and Kutter, B.L. (1998). “Experience with the Use of Methylcellulose as a Viscous Pore Fluid in Centrifuge Models.” ASTM *Geotechnical Testing Journal*, GTJODJ, 21(4), 365-369.

Yoshimi, Y., and Tokimatsu, K. (1977). “Settlement of Buildings on Saturated Sand during Earthquakes.” *Soils and Found.*, 17(1), 23-38.

Components of Dynamic Subgrade Reaction on Pile in Saturated Sand

Hideki Funahara[1]

[1] Senior Research Engineer, Technology Center, Taisei Corporation, 344-1, Nase-cho, Totsuka-ku, Yokohama, JAPAN 245-0051; hideki.funahara@sakura.taisei.co.jp

ABSTRACT: The dynamic lateral subgrade reaction generated on a pile foundation in saturated ground consists of an effective stress component and a pore water pressure component. These components were measured through a shaking table test using a centrifuge facility. The total stress and the pore water pressure acting on the pile surface were measured directly using earth pressure meters and pore pressure meters, respectively. These components were measured on opposing sides of the pile in the direction of shaking. The effective stress was evaluated as the difference between the total stress and the pore water pressure. It was found that the compressive effective stress dominates on the side of a pile where the adjacent soil is under compression. On the other hand, the tensile pore water pressure dominates on the side of a pile where the adjacent soil is under extension.

INTRODUCTION

It is important to understand the generation mechanism of the dynamic horizontal subgrade reaction on a pile for the rational seismic design of pile foundations.

Usually, the ground surrounding piles is saturated with underground water. As shown in Fig. 1. , the surface of a pile in saturated soil is subjected to an effective stress of soil particles and pore water pressure at the same time. In other words, the total horizontal subgrade reaction in saturated soil consists of an effective stress component and a pore water pressure component.

Tokimatsu et al.(2004) already pointed out that the tensile pore water pressure plays an important role in the generation of the subgrade reaction in liquefied ground.

In this study, not only the pore water pressure but also the effective stress of the soil skeleton is taken into consideration to understand the generation mechanism of the dynamic subgrade reaction on a pile in saturated sandy ground. With this objective, a dynamic centrifuge test on piles in saturated ground was conducted to observe those components of the dynamic subgrade reaction on a pile.

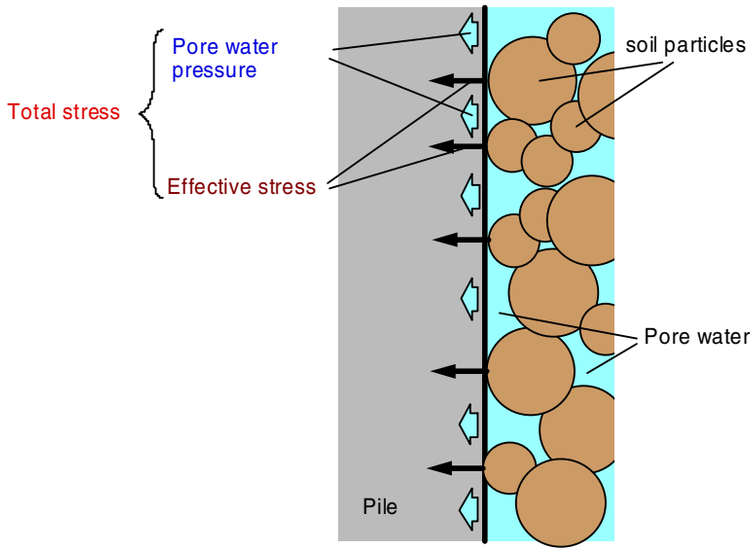


FIG. 1. Microscopic view of subgrade reaction components

DISTRIBUTION OF THE SUBGRADE REACTION COMPONENTS

For simplicity, we consider the equilibrium of horizontal force on a pile in only left and right directions.

An effective stress component and a pore water pressure component for each depth act on the left side and on the right side of the pile simultaneously. Under the normal (not seismic) state, the right component and the left component at the same depth are the same. Therefore, the total subgrade reaction on a pile in the normal state becomes zero, as shown in Fig. 2.

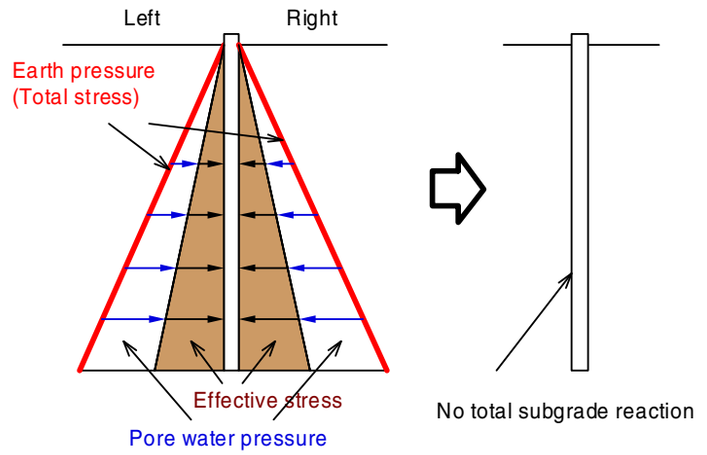


FIG. 2. Components of subgrade reaction in normal state

Fig. 3. shows the concept of the dynamic subgrade reaction components under the seismic state. The lateral force from the super-structure acts at the pile head, and some total subgrade reaction is generated on the pile to balance with the force at the pile head. The total subgrade reaction can be divided into the left component and the right component of the total stress. Moreover, each side component can be divided into the effective stress component and the pore water pressure component.

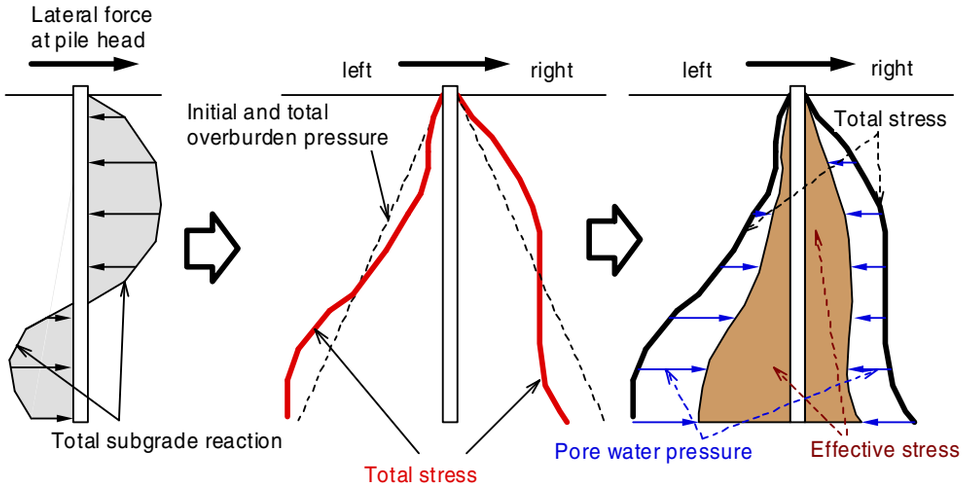


FIG. 3. Components of subgrade reaction under seismic excitation

OUTLINE OF THE SHAKING TABLE TEST IN CENTRIFUGAL FIELD

In order to observe the dynamic behavior of the subgrade reaction components mentioned above, a shaking table test in a centrifugal field was conducted. Schematic view of the test model and the measurements is shown in Fig. 4.

A saturated sand deposit and a structure model are set in the laminar shear box. The sand deposit is made in Toyoura silica sand (D_{50}: 0.19mm, e_{max}: 0.988, e_{min}: 0.616) and is compacted up to 90% of relative density. The structure model consists of steel mass (6.2kg) and four steel pipe piles (diameter: 9.5mm, thickness: 0.21mm, bending stiffness EI: $1.3*10^{-2}$kNm^2).

Accelerations are measured at the shaking table, at the ground surface, in the ground, on the pile, and at the super-structure. The ground surface acceleration is used to evaluate the ground displacement. The super-structure acceleration is used to evaluate the inertial force of the super-structure. The pile acceleration and the ground acceleration are used to evaluate the relative displacement between the pile and the ground at the depth of the "shallow" part as shown in the figure.

The bending strains are measured at eight depths for every pile. By the differentiation of the bending moments with respect to the length of the pile, the shear forces and the total subgrade reactions can be evaluated.

In order to evaluate the subgrade reaction components of the pile, some pressure meters are set on the pile surface. The pore water pressure meters are set on Pile-1 and the total earth pressure meters are set on Pile-3. These pressure meters are set at the

shallow part and the deep part as shown in the figure. They are set on the left side and the right side of the piles.

A synthetic wave called ' RINKAI wave ' was employed as the input motion for the shaking table. The input motion measured at the shaking table is shown in Fig. 5.

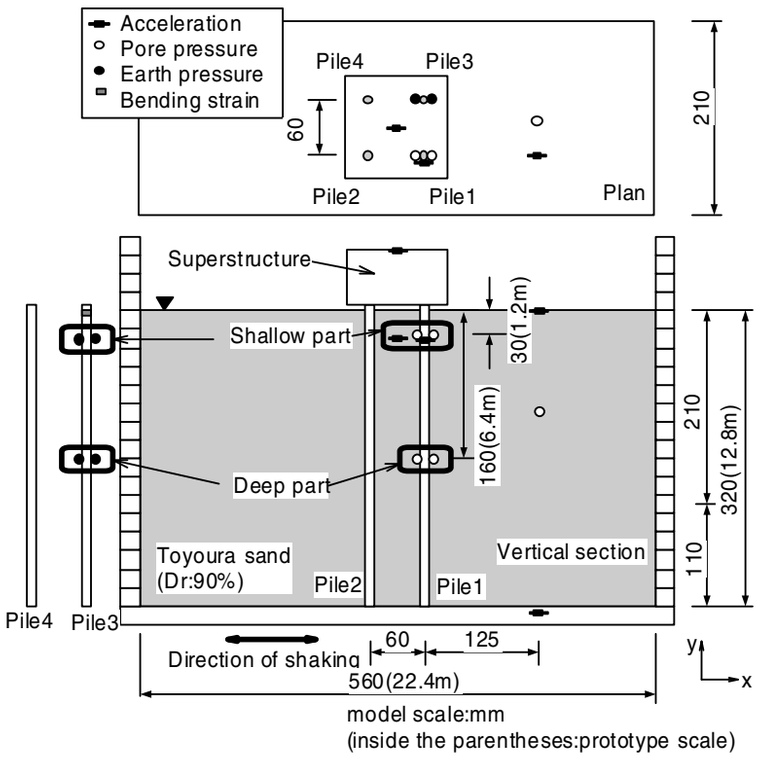


FIG. 4. Schematic view of the test model

REPRESENTATIVE RESPONSES

In order to grasp the overall behavior of the test model, representative responses of the model are shown in Fig.5. The shown time histories are the inertial force of the super-structure, the bending moment at the pile head, the displacement of the ground surface, the pore water pressure in the ground which is apart from the piles, and the acceleration of the shaking table.

The pore water pressure built up and reached the initial effective overburden pressure at around 22 seconds. In other words, the ground liquefied at around 22 seconds. The inertial force of the super-structure was large until that time and after that time the amplitude of the inertial force decreased and the dominant period elongated. On the other hand, the displacement of the ground surface was small at first but the amplitude of the displacement increased after the liquefaction.

As is well known, the bending moment of the pile is affected by the inertial force from the super-structure and the ground deformation. The time history of the bending

moment at the pile head implies that before the liquefaction the bending is affected by the inertial force mainly but after the liquefaction it is affected by the ground deformation also.

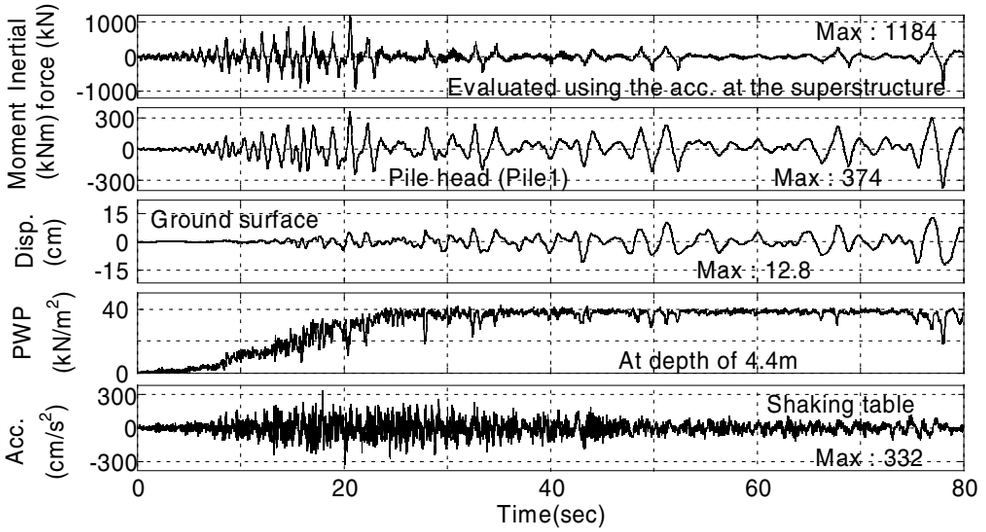


FIG. 5. Time histories of measured responses

EVALUATION OF EFFECTIVE STRESS COMPONENT

The effective stress can not be measured directly. But if the total stress and the pore water pressure are measured properly, the effective stress can be evaluated as the difference between the total stress and the pore water pressure. Since the total subgrade reaction evaluated from the earth pressure meter and that evaluated from the strain gauges were judged to be almost the same and since the behavior of pile-1 and pile-3 were judged to be almost the same based on the comparison of the total subgrade reactions derived from the bending moment (Funahara et al. (2005)), the effective stress component of the subgrade reaction was evaluated as the difference between the total stress of pile-3 and the pore water pressure of pile-1.

OBSERVED SUBGRADE REACTION COMPONENTS

Fig. 6 and Fig. 7 show the measured and evaluated components of the subgrade reaction on a pile. Fig. 6 shows the components at the shallow part, and Fig. 7 shows ones at the deep part.

Each figure consists of the total stress components, the pore water pressure components, and the effective stress components. Moreover, each component is shown as the total value of the left and right sides, and as the left component and the right component.

The plus sign of the subgrade reaction components indicates that the direction of the

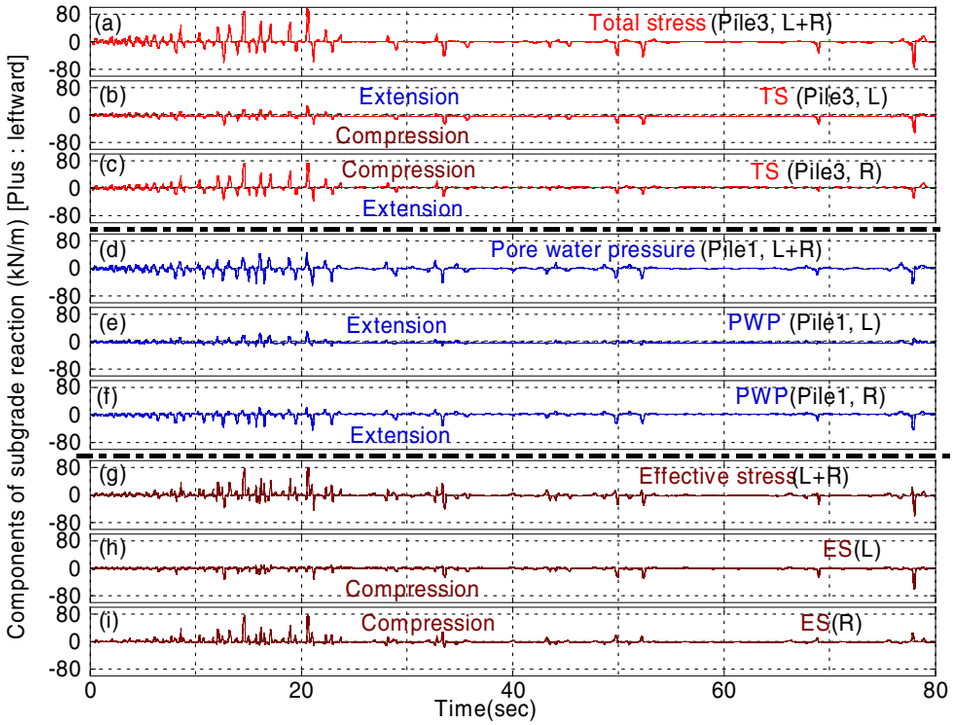


FIG. 6. Measured components of subgrade reaction (shallow part)

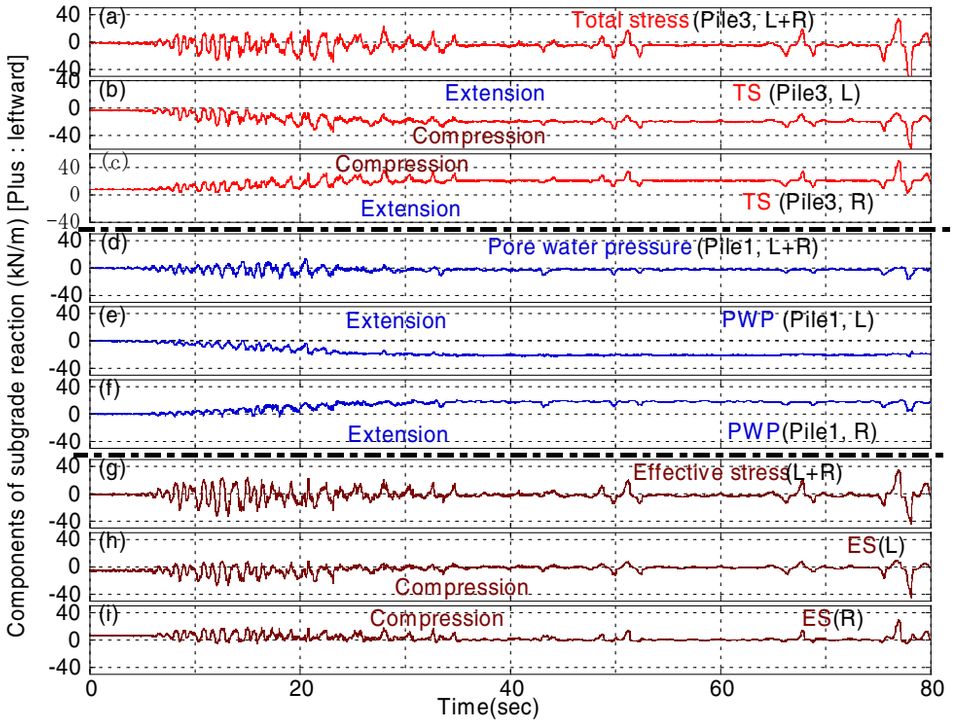


FIG. 7. Measured components of subgrade reaction (deep part)

force is leftward. In the case that the subgrade reaction is divided into the left and the right components, the sign of each component indicates whether the adjacent soil is under the compression state or under the extension state. In Fig. 6 and Fig. 7, the adjacent soil's states are also described.

Based on Fig. 6 and Fig. 7, the following can be pointed out. Firstly, the pore water pressure (PWP) components tend to be generated when the adjacent soil is under the extension state (e, f). On the other hand, the effective stress components tend to be generated when the adjacent soil is under the compression state (h, i).

CORRELATION WITH RELATIVE DISPLACEMENT

In order to confirm the tendencies mentioned above, the correlations of the subgrade reaction components with the relative displacement between the pile and the surrounding ground will be examined next.

Fig. 8 shows the time history of the relative displacement between the pile and the ground at the shallow part. Each displacement is evaluated by the double integration of the acceleration record.

At the deep part, no positive correlation between the evaluated relative displacement and the subgrade reaction components was seen. This is possibly because of the effect of the long-term components in the measured acceleration. Therefore only the result for the shallow part is shown.

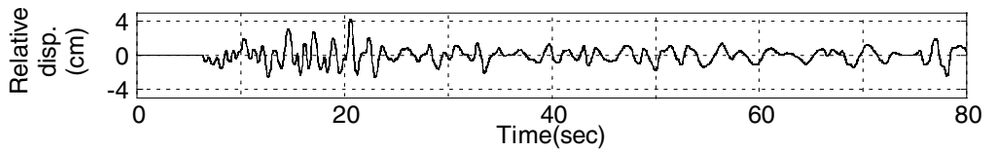


FIG. 8. Relative displacement between pile and ground (shallow part)

Fig. 9 shows the correlations between each subgrade reaction component and the relative displacement shown above. The relative displacement also indicates the adjacent soil's state on the left and the right side, respectively.

There is a positive correlation between all the components and the relative displacement. These figures show the same tendencies mentioned above more clearly, namely, the pore water pressure components tend to be generated on the extension side (e, f) and the effective stress components tend to be generated on the compression side (h, i).

Instantaneous coefficients of subgrade reaction change extensively hour by hour (a). When large lateral loads are being applied cyclically on the pile, the coefficient of subgrade reaction is small while the relative displacement is relatively small, and then the subgrade reaction recovers rapidly accompanied by the increase of the relative displacement. As a result of this, the hysteretic loops appear like an inverse S character. The three dotted lines in the figure (a) indicate the three different coefficients of subgrade reaction. It can be said that the coefficient of subgrade reaction changes over two orders.

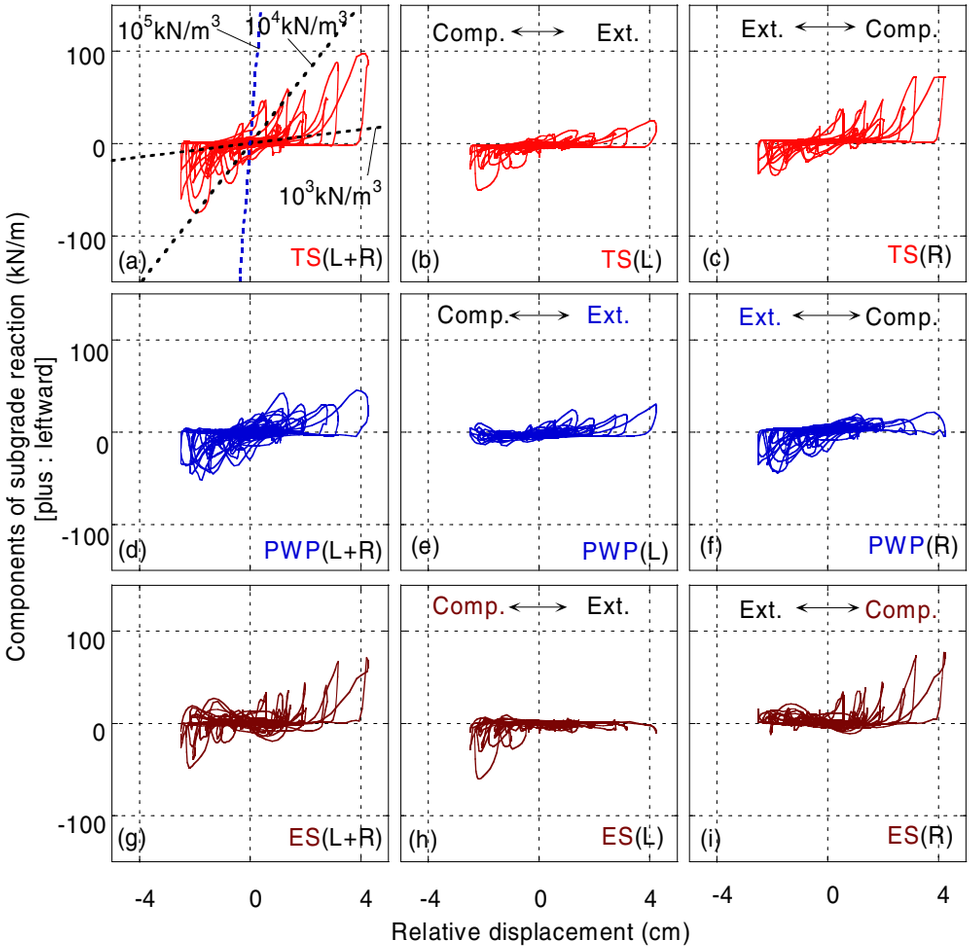


FIG. 9. Relationship between components of subgrade reaction and relative displacement

MECHANISM OF SUBGRADE REACTION GENERATION

Fig. 10 shows the schematic view of the effective stress generation on the compression side and the pore water pressure generation on the extension side after the excess pore water pressure reaches the initial effective overburden pressure. The soil skeleton pushes the pile surface on the compression side. On the other hand, the pore water which is being suctioned pulls the pile surface on the extension side at the same time.

Fig. 11 shows the state around the pile just after the direction of the subgrade reaction reversed. On the right side, the contact between the soil particles and the pile is lost due to the very small relative displacement, and the small pore water pressure which pulls the pile surface is generated. The tensile pore water pressure at this stage is small because the effective confining stress is almost zero and therefore the stiffness of

the soil skeleton on the extension side is very small. On the other hand, the lost contact on the left side can not be recovered immediately because of the gap between the soil particles and the pile generated during the former suction, so the compressive effective stress does not recover immediately. Moreover, just after the recovery of the contact between the soil particles and the pile surface, the soil skeleton is still loose and the effective confining stress is small. Therefore, the stiffness of the soil skeleton is still small. This is the reason why the instantaneous coefficients are very small while the relative displacement is small.

The larger the relative displacement, the larger both the compressive effective stress and the tensile pore water pressure. Then the state like Fig. 10 is reproduced.

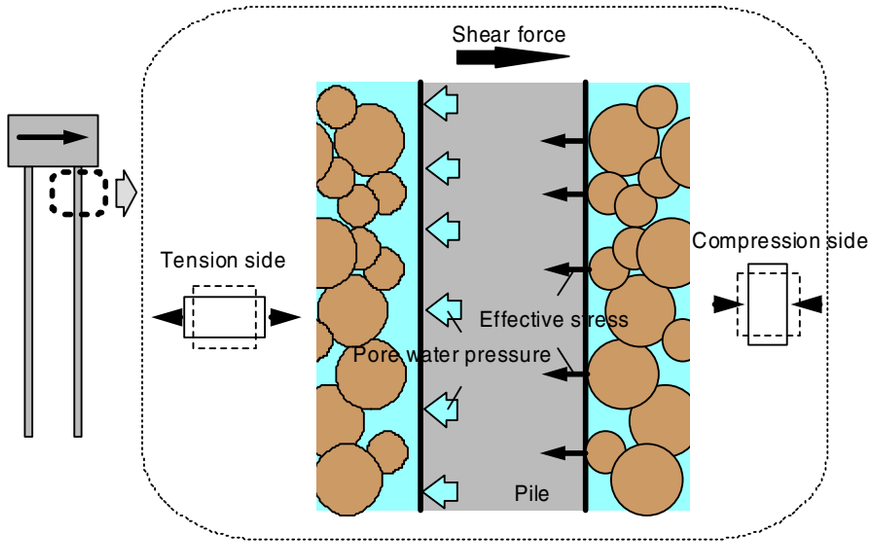


FIG. 10. Schematic view of effective stress on compression side and pore water pressure on tension side

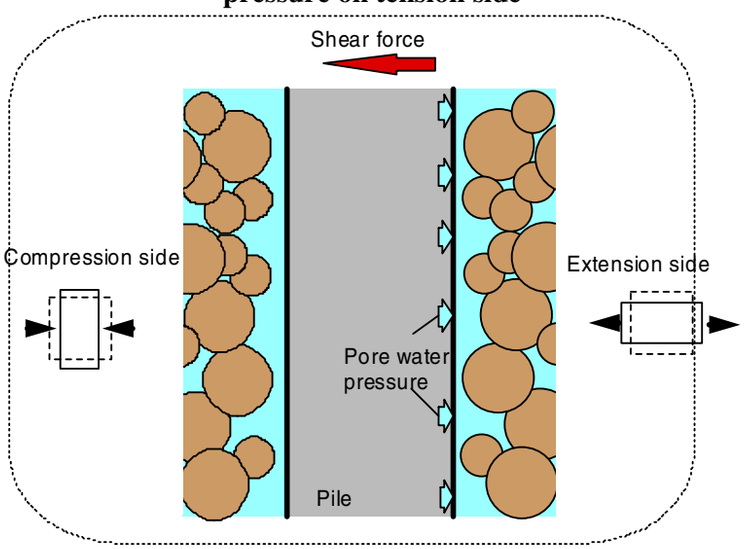


FIG. 11. Microscopic state around pile just after the reversal of the subgrade reaction

CONCLUSIONS

Conclusive remarks are the following.

If the soil is dense, a significant amount of effective stress component and pore water pressure component are generated due to the large relative displacement even after the soil is liquefied.

The compressive effective stress dominates on the side of a pile where the adjacent soil is under the compression state. On the other hand, the tensile pore water pressure dominates on the side of a pile where the adjacent soil is under the extension state.

Just after the reversal of the subgrade reaction direction, the water in the gap between the soil skeleton and the pile surface which was suctioned during the former extension hardly push the pile surface on the compression side. At the same time, the pore water on the extension side pulls the pile surface weakly, because the stiffness of the adjacent soil skeleton is small.

Numerical simulations of this experiment are now being conducted using a two-phase effective stress method. These results will be reported and discussed in another paper.

REFERENCES

Funahara, H. (2005) " Subgrade reaction components of pile on liquefying soil based on centrifuge test." *Summaries of technical papers of annual meeting,* Architectural Institute of Japan, 513-514. (in Japanese)

Funahara, H. (2006) " Dynamic horizontal subgrade reaction on pile in saturated sandy ground." *8th. symposium on dynamic soil-structure interaction*, Architectural Institute of Japan, 29-36. (in Japanese)

Funahara, H. and Shibata K. (2007) " Centrifuge tests and effective stress analyses on *dynamic* horizontal subgrade reaction components of pile in saturated sandy ground Part.1 Centrifuge tests" *42th. Meeting for reading research papers of the Japanese Geotechnical Society*, 1673-1674. (in Japanese)

Shibata K. and Funahara, H. (2007) " Centrifuge tests and effective stress analyses on dynamic horizontal subgrade reaction components of pile in saturated sandy ground Part.2 *Effective* stress analyses" *42th. Meeting for reading research papers of the Japanese Geotechnical Society*, 1675-1676. (in Japanese)

Tokimatsu, K. and Suzuki, H. (2004). " Pore water pressure response around pile and its effects on P-Y behavior during soil liquefaction." *SOILS AND FOUNDATIONS*, JGS, Vol.44, No.6, 101-110.

Effect of Soil Liquefaction on Flexural Behavior of Axially and Laterally Loaded Piles

R. S. Meera[1] and P. K. Basudhar[2] A. M. ASCE

[1]Assistant Systems Engineer, TATA Consultancy Services Ltd.
Techno Park Campus, Trivandrum – 695581, India
E-mail: rsmeera@rediffmail.com

[2]Professor, Department of Civil Engineering
IIT Kanpur, Kanpur – 208016, India
E-mail: pkbd@iitk.ac.in

ABSTRACT: The paper presents a brief outline of a simplified analysis procedure to analyze the flexural response of axially and laterally loaded piles under liquefied soil condition. Parametric study has also been presented in this paper to bring out in to focus the influence of various factors like gradient of surface topography, depth of liquefied zone, pile boundary condition, presence of axial and lateral loads etc, controlling the pile behavior under such condition.

INTRODUCTION

Damaging effect of lateral spreading of loose saturated sands on pile foundations during earthquakes have been reported by several investigators (Hamada, 1986; Tokimatsu et al., 1998; Tokimatsu, 1999; Tsukamoto et al., 1999). Analysis has been carried out to study the effect of lateral force, exerted on the piles due to spreading of soils, on the deflection of piles (Mishra, 1992; O'Rourke, 1994; Ishihara and Cubrinovski, 1998). Meera et al. (2007) presented an analysis procedure to predict the response of an axially and laterally loaded pile based on the information available in literature and demonstrated the success of the developed method with reference to the observed pile deformation (O'Rourke,1994). However, a detailed parametric study affecting the behavior of such piles was not presented. In this paper, an effort is made to present the same.

STATEMENT OF THE PROBLEM

The idealization of the pile and the soil profile surrounding the pile for the assessment of the soil-pile interaction is shown in Fig.1. A pile of length (L) and diameter (D) is embedded in a homogeneous saturated sand deposit. The water table is at the top of a liquefiable stratum of thickness, L_2, above which is the non-liquefiable soil cover of thickness, L_1. Below the liquefiable stratum, there is a firm, non-liquefiable soil layer. The pile is further embedded by a distance L_3 into this non-liquefiable stratum. Over the depth L_2, the soil is in a liquefied state and the pile has lost the support of the soil either completely or partially. The pile is subjected to a lateral load, H_T and a moment, M_T along with an axial load, P at the top.

In this problem, the possible movement of the liquefied soil in the liquefied zone has also been considered. The liquefied soil flows with a maximum velocity at the ground

level, the maximum soil displacement, g_x is at the ground surface and it varies to zero at the lower end of the liquefied zone. Here it is assumed that the top nonliquefied soil layer moves with the same velocity in continuity with the moving liquefied soil layer lying beneath it. The velocity distribution within the liquefied soil in fact will be nonlinear and can be theoretically predicted considering flow of viscous liquids over a stationary soil boundary. However, for the sake of simplicity the velocity distribution is assumed linear as shown its value being zero at an elevation where the top of the stationary nonliquefied soil-layer zone exists. This flowing mass will cause a drag force on the pile. There are various possible distributions of soil displacement. A trapezoidal distribution is applied in the figure.

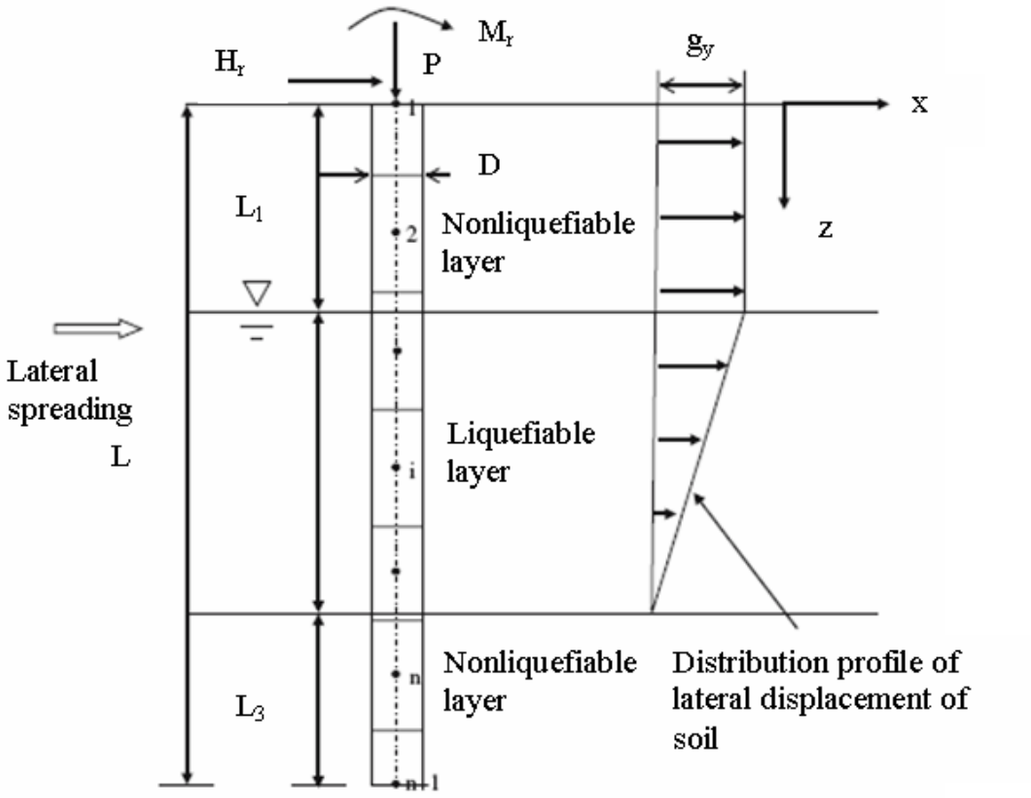


FIG. 1. Definition Sketch

ANALYSIS

Behavior of liquefied soil is complex and imprecisely understood and, therfore, a relatively simple pseudo-static design method developed by Meera et al.(2007) has been adopted in this paper for parametric studies. The method based on the concept of modulus of subgrade reaction and helps in the evaluation of important parameters without introducing unnecessary complexity in the formulation of the problem. For the sake of completeness, the method is briefly described here with out giving the details except the basic concepts that are essential for understanding the present paper with out reference to the original works.

Variation of the horizontal modulus of subgrade reaction, k_h, with depth in the soil deposits is correlated with the Standard Penetration Test (SPT), N values. The modulus of subgrade reaction for nonliquefied soils, k_{hn} proposed by Architecture Institute of Japan 2001, and Japan Road Association 1997 is assumed valid,

$$k_{hn}=80E_0D^{(-0.75)} \quad (1)$$

$$E_0=0.7N \quad (2)$$

in which k_{hn} is the modulus of subgrade reaction in MN/m^3, E_0 is the modulus of deformation in MN/m^2, N is the SPT N-value, and D is the diameter of the pile in centimeters.

As soil liquefies, the stiffness of soil degrades. It has been found from case studies that the modulus of subgrade reaction for the laterally spreading soils can be reduced by a scaling factor, termed as Stiffness degradation parameter, S_f varying from 0.001 to 0.01 (Ishihara and Cubrinovski, 1998) as compared to the normal soil condition where there is no liquefaction. The degree of stiffness degradation in the laterally flowing soil deposits is related to the displacement of the pile relative to the surrounding soil. The degradation of k_{hn} with increasing displacement is expressed as (Tokimatsu et al 1998; Tokimatsu, 1999)

$$k_h = (k_{hn} S_f) \frac{1}{1+\left|y_r / y_1\right|} \quad (3)$$

where, y_r is the relative displacement between ground and pile and y_1 is the reference value of y_r, S_f is the scaling factor for the liquefied soil.

For large ground displacements, the soil is assumed a Winkler-type material with lateral soil force proportional to the relative displacement between pile and soil. Thus,

$$p=k_h (y-g(z, x)) \quad (4)$$

where, g (z, x) is the permanent ground displacement profile with depth, z, near the pile.

When lateral spreading occurs near the waterfront, the permanent horizontal ground displacement generally decreases towards inland with a maximum value at the waterfront. The affected distance of such lateral spreading from the waterfront, L_s is given as (Tokimatsu et al 1998),

$$L_s/L_2=(25\sim100)\, g_0/L_2 \quad (5)$$

where, g_0 is the permanent horizontal ground displacement at the waterfront and is defined as,

$$g_0= min (g_{max}, g_w) \quad (6)$$

in which g_w is the displacement of the quay wall and g_{max} is the maximum possible permanent ground surface displacement of the liquefied soil. g_{max} is found out using the relation (Hamada et al., 1986),

$$g_{max}=0.75 (L_2)^{0.5} (sl)^{0.33} \quad (7)$$

where, g_{max} and L_2 are in meters and *sl* is the slope of the base of the liquefied layer or the gradient of the surface topography whichever is maximum.

The horizontal ground displacement at a distance; x from the waterfront, g_x is expressed in a normalized form as shown in Fig. 2 and 3 and defined as (Shamato et al 1998)

$$g_x/g_0=(0.5)^{(5x/Ls)}+\{1-(0.5)^{(5x/Ls)}\}g_{rs}/g_0 \quad (8)$$

where g_{rs} is the permanent horizontal displacement of the level ground far away from the waterfront and may be assumed to be zero.

The permanent horizontal ground displacement profile with depth, z at a distance, x of a laterally spreading deposit, g(z,x) may be approximated as (Tokimatsu 1999),

For $z<L_1$, $g(z,x)=g_x$

For $z>L_1$ *and* $z<(L_1+L_2)$, $g(z,x)=g_x\left[\cos\left\{\frac{\pi(z-L_1)}{2L_2}\right\}\right]$

For $z>(L_1+L_2)$, $g(z,x)=0$ (9)

For an elastic pile of constant stiffness E_pI_p and diameter D embedded in a Winkler medium and subjected to an axial load, P at the pile head, the governing differential equation for the horizontal deflection, y along the pile is (Hetenyi 1946)

$$E_pI_p\frac{d^4y}{dz^4}+\frac{d}{dz}\left[P_z\frac{dy}{dz}\right]=-pD \tag{10}$$

in which E_p and I_p are Young's modulus and moment of inertia of pile respectively.

Substituting equation (4) in equation (10), we get

$$E_pI_p\frac{d^4y}{dz^4}+\frac{d}{dz}\left[P_z\frac{dy}{dz}\right]+k_hD(y-g(z,x))=0 \tag{11}$$

For arbitrary distribution of k_h and appropriate boundary condition, the above equation is solved conveniently by using finite difference method. Using central difference technique, the governing differential equation can be expressed in finite difference form in terms of the nodal deflections. The details of the developed method can be obtained from Meera et al. (2007).

Using MATLAB, computer programs were developed for the analysis. The developed program had been first calibrated with a synthetic problem then validated with reference to a field problem. The same was reported elsewhere (Meera et al. 2007).

RESULTS AND DISCUSSIONS

Parametric study has been made and presented to bring out the influence of various parameters, such as, non-liquefied depth factor (r = L1/L), liquefied depth factor (s = L_2/L), embedded depth factor (t = L_3/L), pile flexibility factor R, ratio of the Young's modulus of pile and non-liquefied soil (k = E_p/E_s), the pile length to pile diameter ratio, i.e., the slenderness ratio (λ = L/D), soil modulus to soil strength ratio Q, vertical load factor (V =$4P/\pi D^2Es$), horizontal load factor (H = H_T/S_uD^2), moment factor ($M=M_T/S_uD^3$), ratio of distance of the location of the pile from the waterfront to affected distance of lateral spreading, i.e., Location factor (L_x= x /L_s), scale factor for liquefied soil (Sf), and gradient of the surface topography (*sl*) on the flexural behavior of pile. Analysis has been done using the following range of parameters unless otherwise specified. R = 0.0001, K = 500, λ = 25, Q = 200, V = 0–9, H = 0–25, M = 0–120, S_f = 0.01, , L_x= 0 , Standard penetration test value, N≤10(for liquefied soil) and N≥60 (for nonliquefied soil) and sl = 1%. The effect of these parameters are studied and the results are presented in the form of non-dimensional charts correlating nondimensional depth coefficient, Z=z/L, nondimensional deflection coefficient, Y=y/D, and nondimensional bending moment coefficient, $M'=M_D/S_uD^3$ where M_D is the developed bending moment.

The maximum deflection coefficient and the maximum positive bending moment coefficient are referred as Y^* and M^* respectively.

Effect of Gradient of Surface Topography

The gradient of the surface topography, *sl*, has an appreciable influence on the deflection and bending moment of the pile, as the ground displacements are directly proportional to it. The observed behavior is shown in Fig.2 and Fig.3; it is observed that both Y* and M* nonlinearly increased with the slope. This is because the steepness of the slope itself triggers the liquefied soil to spread and subsequently cause the soil layer to move. The values of Y* and M* at different values of ground slopes are also shown in Table.1; however, it should be noted that additional results corresponding to *sl* equals to 1 has been reported in the table that has not been shown in the graph. The table further indicates that there is a substantial increase (more than double) in the values of Y^* and M^* when *sl* is increased from 1% to 10%.

Table 1. Variation of Y* and M* with slope

	Free-Free Pile		Fixed-Free Pile	
sl (%)	Y*	M*	Y*	M*
1	1.044	100.425	1.0225	103.1691
10	2.2321	214.7037	2.1861	220.5716
20	2.8057	269.8855	2.748	277.2615
30	3.2074	308.5245	3.1414	316.9565
40	3.5268	339.2497	3.4542	348.5214
50	3.7963	365.1739	3.7182	375.1541

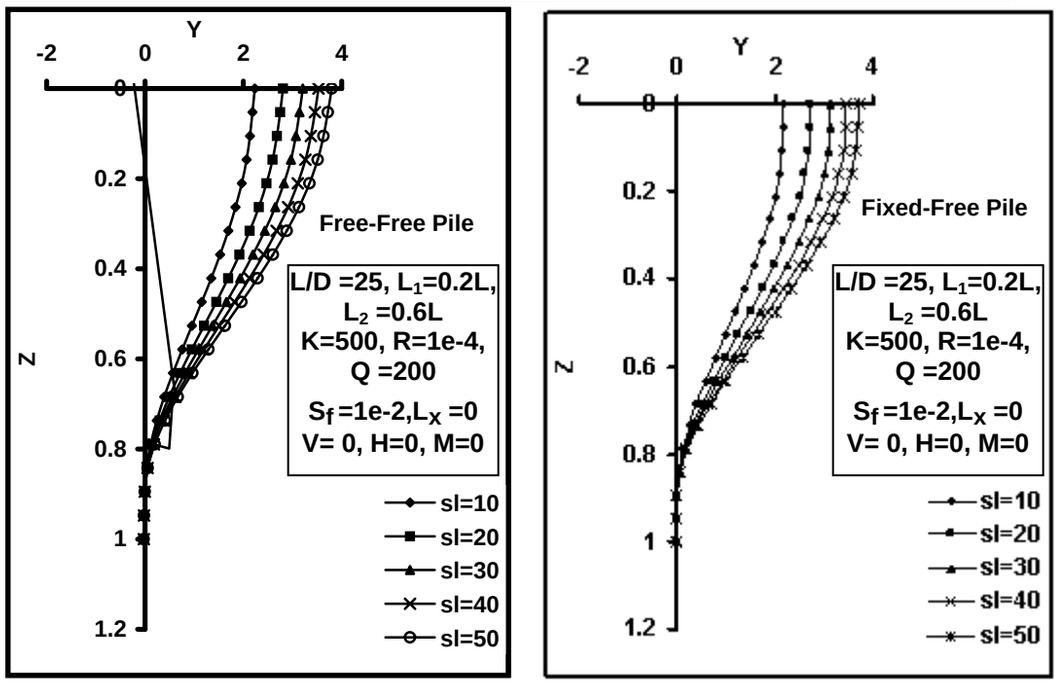


FIG. 2. Variation of Y with Z for different *sl*

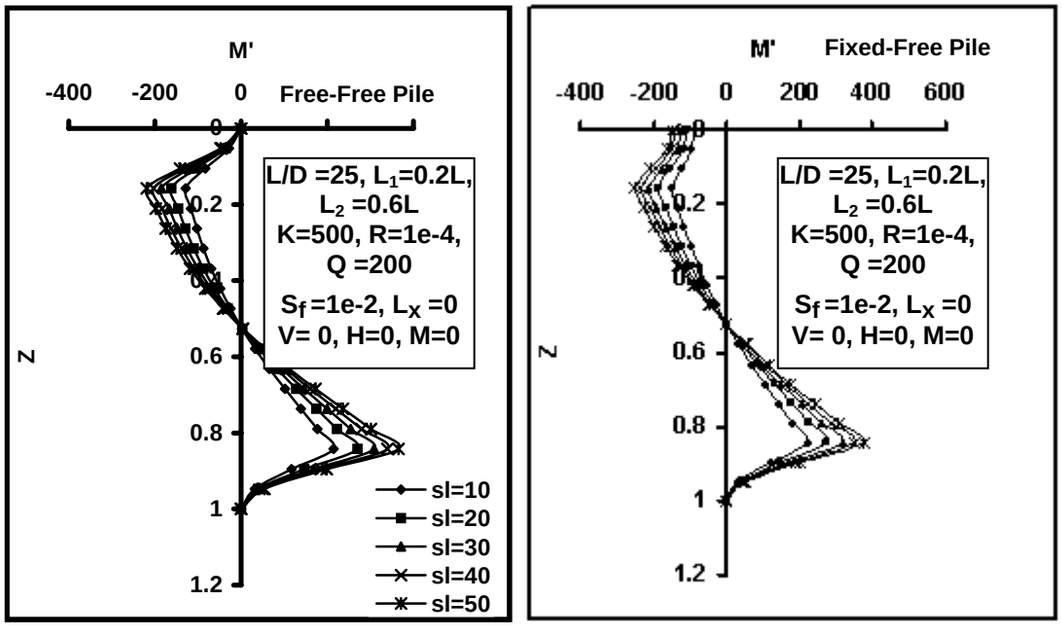


FIG. 3. Variation of M' with Z for different *sl*

Effect Of Depth Of Liquefaction

The non-liquefied depth factor, r is varied from 0 to 0.8. The embedded depth is taken to be constant throughout the analysis as 20% of the length of the pile. When there is no liquefaction i.e. when r=0.8, the pile shows zero values of Y and M', which validates the correctness of the developed program (Meera et al. 2007). As the non-liquefied depth factor decreases to zero, i.e. when the liquefaction is starting from the ground surface itself, the Y at the pile top increases to its maximum value, which is around 1.2D compared to zero when there was no soil liquefaction at all. But the Y in liquefied region is more when the non-liquefied depth is larger. This is because the relative displacement of the pile and the soil is more when the non-liquefied depth is larger and this results in the increase of lateral soil pressure. It will lead to the increase of deflection in the liquefied zone and also an increase in the values of M* from 82 to 168, which occurs at Z=0.8. Thus M* increases with r and suddenly drops to zero when r=0.8. For both the end conditions Y* decreases and M* increases with increase in r. Only in the range r=0 to r=0.2, the end condition will influence the flexural behavior of pile. In this range Free-Free pile will have more Y* than that of Fixed-Free pile and reverse is the case for M*. Table 2 shows the values of Y* and M* at different depth of liquefaction.

Table 2. Variation of Y* and M* with r under no external loading condition

	Free-Free Pile		Fixed-Free Pile	
r	Y*	M*	Y*	M*
0	1.1712	82.2762	1.1503	101.2597
0.2	1.044	100.425	1.0225	103.1691
0.4	0.8319	128.573	0.831	128.6744
0.6	0.5944	168.698	0.5944	168.7142
0.8	0	0	0	0

The effect during combined loading condition is given in Fig.4 and Fig.5. When V and H acts on the Free-Free pile, Y* decreases from 1.3 to 0.84 as r increases from 0 to 0.4 .The critical range of V reduces as r reduces. This is because the supporting capacity of the soil becomes increasingly smaller over greater length with the reduction in r. M* does not show appreciable variation with r, at lower values of V. But for V greater than 4, M* considerably reduces. The influence of combined loading in Fixed-Free pile has also been studied (Fig.6 and Fig.7). At r=0, Y* and M* increases with increase in H. At r=0.4, Y* increases with V and H and finally reaches a constant value of 0.84. M* decreases with H as V varies from 0 to 4 beyond which it starts increasing. When V is greater than 4, the negative moments are higher due to the higher relative displacement in the top interface.

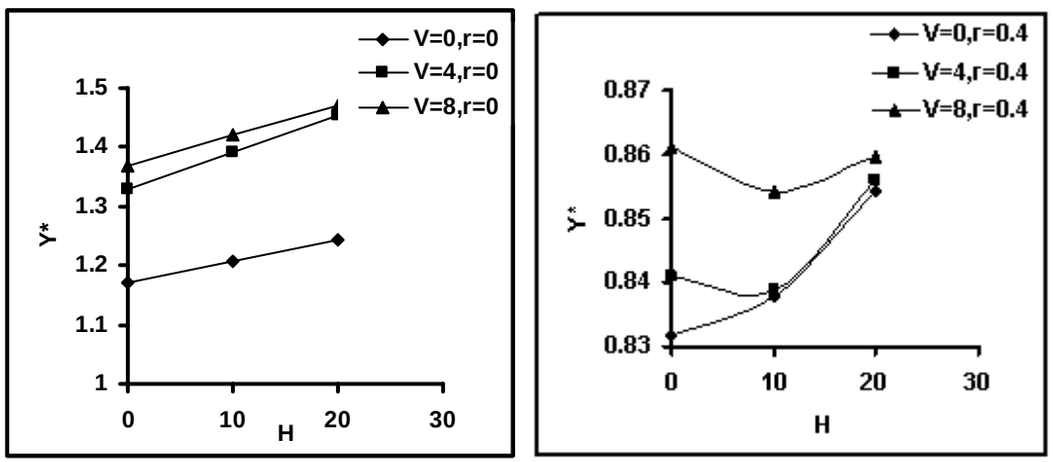


FIG. 3. Effect of H on Y* of Free-Free pile for different V and r

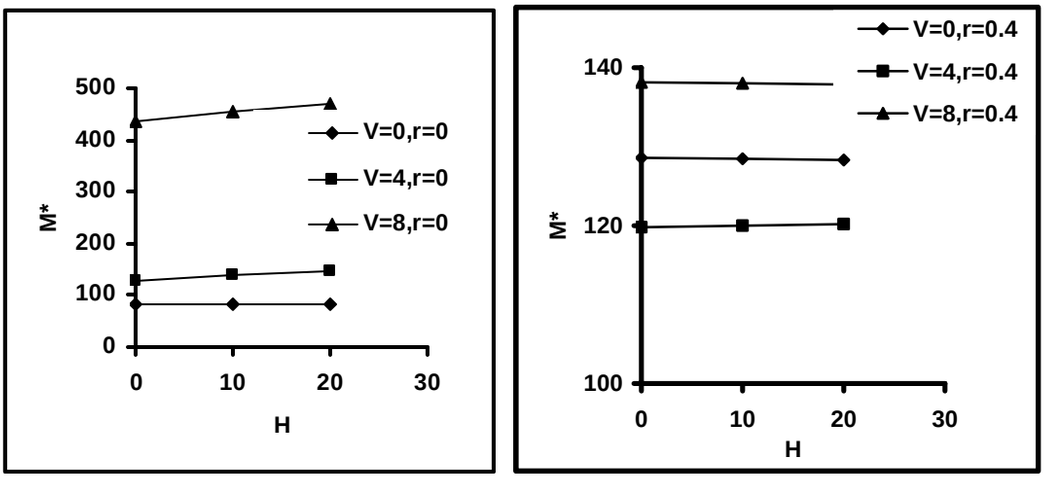


FIG. 5. Effect of H on M* of Free-Free pile for different V and r

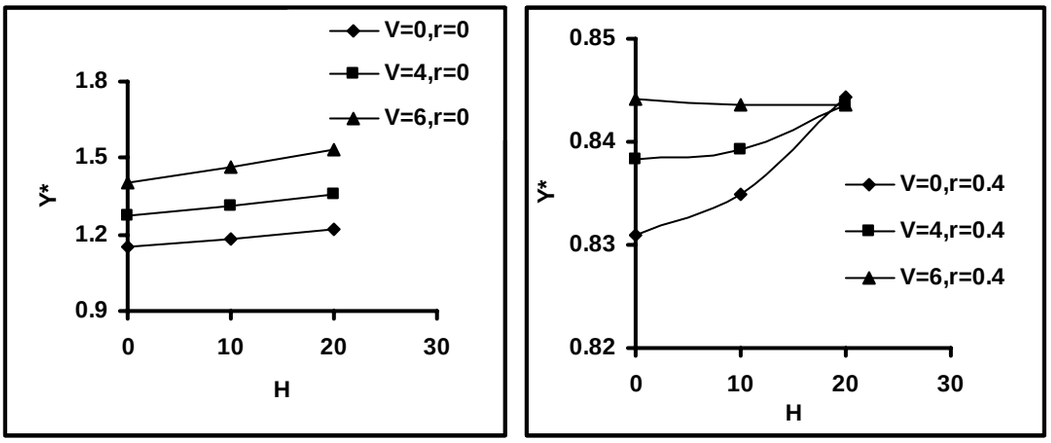


FIG. 6. Effect of H on Y* of Fixed-Free pile for different V and r

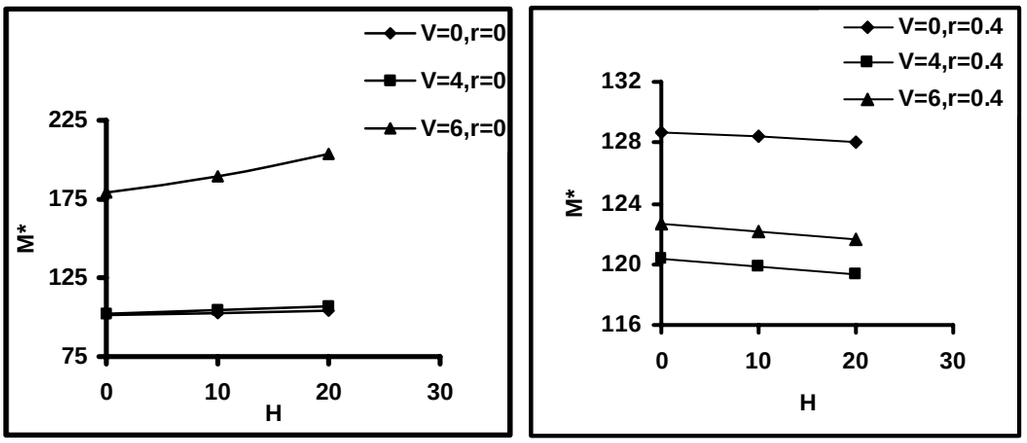


FIG. 7. Effect of H on M* of Fixed-Free pile for different V and r

Effect of Location Factor

The effect of location factor (L_x) designated by the ratio of the distance from the waterfront to the total lateral spreading length has been studied. It has been observed from case studies that worst conditions of ground deformation exist near the waterfront. The results of no external loading condition are shown in Fig.8. As the distance from waterfront (x) increases Y as well as M' decreases. The Y* as well as M* shows a nonlinear decrease with increase in L_x with Y* decreasing from 1.04 to 0.03 and M* decreasing from 100 to 3 as L_x increases from 0 to 1.

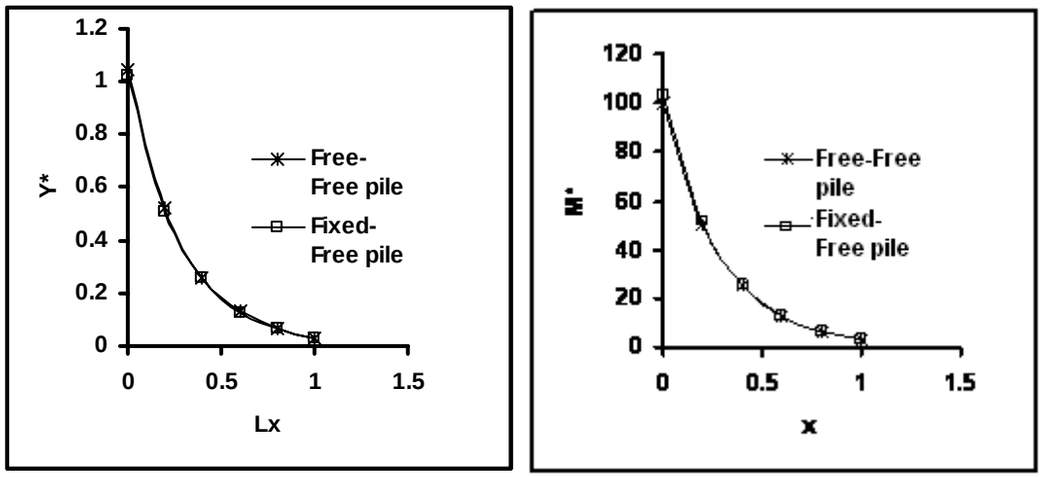


FIG. 8. Effect of L_x on Y* and M*

CONCLUSIONS

The following conclusions can be drawn based on the present study:

1. The developed computer program can be used effectively to predict the deflection and bending moment of the piles under various conditions of loading, soil profile, and pile characteristics. It has been shown earlier by Meera et al.(2007) that the use of the method leads to a reasonable compliance between the predicted results and the field observations.
2. The deflection and bending moment of the pile in lateral spreading areas are directly proportional to the gradient of surface topography. As the gradient varies from 1% to 50%, the maximum nondimensional deflection and bending moment coefficient increases by three to four times.
3. The depth of top non-liquefied layer plays an important role in the flexural behavior of piles in liquefiable areas. As the top nonliquefied depth increases from zero to 40% of the length of the pile, then the reduction in maximum deflection is around 30%. The densification of the soil in the liquefiable areas and a proper top nonliquefied soil cover will cause an appreciable reduction in the destruction. In addition, it has been seen that compared to Free-Free piles, Fixed-Free piles are more suitable in sites with sufficient top non-liquefied cover due to

reduced deflection and moments.

4. The piles near waterfront suffer more damage, and hence the design should take care of the location factor. The Free-Free piles located at places away from waterfront (i.e. at L_x=0.5 in the present study) are experiencing 80% lesser deflection and 50% lesser bending moment compared to that at the waterfront.

REFERENCES

Hamada, M. Yasuda, S. Isoyama, R and Emoto, K. (1986).” Study on liquefaction-induced permanent ground displacements.”*Association for the development of earthquake prediction*, Tokyo, Japan.

Hetenyi, M. (1946).” Beams on elastic foundations”. *University of Michigan Press*, Ann Arbor, Mich.

Ishihara,K. and Cubrinovski, M.(1998).”Soil–pile interaction in liquefied deposits undergoing lateral spreading.” *In: Maric B et al (eds) Geotechnical hazards*. Balkema: 51–64.

Meera, R.S. Shanker, K and Basudhar, P.K. (2007). “Flexural response of piles under liquefied soil conditions." *J. Geotechnical & Geological Engineering.*, 25:409-422.

Mishra, S.K (1992) “Analysis of laterally loaded piles under liquefied soil conditions.” *M. Tech thesis*, Indian Institute of Technology, Kanpur.

O’Rourke,T,D. Meyersohn, W.D. Shiba, Y. and Chaudhuri ,D.(1994).” Evaluation of pile response to liquefaction-induced lateral spread.” *Technical Report NCEER-94– 0026*, NCEER, Buffalo, NY: 457–479.

Shamato, Y. Zhang, J.M . and Tokimatsu , K. (1998).”Methods for predicting residual post-liquefaction ground settlement and lateral spreading.” *Soils Found 38(special issue)*:69–83.

Tokimatsu, K. Oh-oka, H. Satake, K. Shamoto,Y. and AsakaY (1998).”Effects of lateral ground movements on failure patterns of piles in the 1995 Hyogoken-Nambu earthquake” *Geotecnical earthquake Engrg and soil dynamics 3rd Conference*, ASCE: 1175–1186.

Tokimatsu ,K. (1999).” Performance of pile foundations in laterally spreading soils.” *Proc 2nd international conf. on Earthquake Geotechnical Engineering*, Lisbon, Portugal: 957–964.

Tokimatsu, K. and Suzuki,H. (2004). “Effects of dynamic soil-structure interaction on pile stress in large shaking table tests.” *First International Conference on Urban Earthquake Engineering,* Tokyo, Japan: 331-338.

Tsukamoto,Y. Ishihara,K. Yamabe,S. and Hyodo,J. (1999). “Behaviour of piles in the liquefied deposit undergoing lateral spreading.” *Proc 2nd international conf. on Earthquake Geotechnical Engineering*, Lisbon, Portugal: 377-382.

FD Solutions for Static and Dynamic Winkler Models with Lateral Spread Induced Earth Pressures on Piles

D.W. Chang[1], B.S. Lin[2], C.H. Yeh[2] and S.H. Cheng[2]

[1] Professor, Department of Civil Engineering, Tamkang University, Tamsui, Taiwan 25137; dwchang@mail.tku.edu.tw

[2] Research Assistant, Department of Civil Engineering, Tamkang University, Tamsui, Taiwan 25137

ABSTRACT: Finite difference (FD) solutions for static and dynamic Winkler's foundation models are applicable in modeling pile responses. In this paper, relevant solutions on liquefaction induced lateral spreading are presented. Direct and indirect earth-pressure approximations and implementations are introduced. Pile foundation failures of 1995 Kobe earthquake were examined using these models. It was found that both the static and dynamic analyses could provide rational pile displacements in agreement with field observations. The largest pile displacements were found at the pile head from static modeling and the dynamic one using indirect earth pressures. For dynamic solutions with direct earth pressure approximations, maximum pile displacements were found at pile tip. These solutions seem reasonable to model different types of lateral spreading. The mechanism of ground motion, strongly affected by geologic and geographic site conditions as well as the soil-foundation-structure interactions, needs to be carefully verified before applying these solutions.

INTRODUCTION

Pile foundations subjected to liquefaction-induced lateral spreading under the earthquake have been extensively studied in the past decade. Seismic pile performance with this concern can be analyzed utilizing a rigorous FE technique, or much simpler one representing by Winkler foundation model. For static solutions of the later, the ground forces acting on pile could be obtained from two alternatives, 1. Direct earth pressure approach, available as the one suggested by Japan Road Association (1990), 2. Indirect earth pressure approach, in which the earth pressures are obtained from prescribed ground displacements and soil springs. The displacement profile could be represented by the one proposed by Tokimatsu and Asaka (1998). The static Winkler model and nonlinear moment-curvature relationships of piles are often used for analysis of nonlinear pile responses. For dynamic solutions of the Winkler model, a two-step computational procedure has been suggested. It can be found that Chang et al. (2001, 2003), Boulanger et al. (2003, 2007), Arduino et al. (2005), Lin et al. (2005) and

Liyanapathirana and Poulos (2005) have all pointed out that free-field ground motions can be obtained first and then used to solve for the pile responses. Pseudo static pile displacements at any specific time can be obtained from the corresponding ground displacement profile. This simulation was found comparable to the static ones.

To analyze the seismic pile responses under earthquake, the authors have suggested discrete FD solutions for the dynamic Winkler model. For lateral spreading effects, preliminary study (2007) was made using the seismic earth pressures suggested by Zhang et al. (1998). This model initially suggested for retaining structure was adopted ignoring the differences of geometry and structure/material rigidity. As the results, deformed shape and magnitude of the pile displacement were found compatible to the field observations of Ishihara and Cubrinovski (2004), where the piles tilted to yield large displacements at the bottom.

For dynamic analysis using the indirect earth pressure approach, the permanent ground displacement profile (Tokimatsu and Asaka, 1998) is adopted and modified in this paper. Other than that, any feasible solution could be obtained from proper ground deformational analysis. Figure 1 illustrates available numerical schemes for the task problem. The discrete equations based on difference formulas of the static/dynamic modeling and the corresponding earth pressure approaches were presented next. Preliminary comparisons of these solutions were discussed for case studies on 1995 Kobe earthquake.

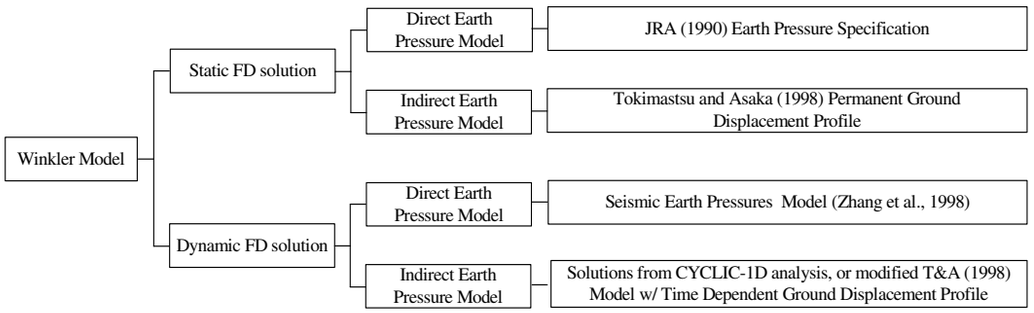


FIG. 1. Available numerical schemes of the task problem.

STATIC AND DYNAMIC FD FORMULATIONS

For static Winkler's foundation model, the governing equation and corresponding finite difference formulation are written as follows,

$$EI\frac{d^4u(z)}{dz^4}+P_x\frac{d^2u(z)}{dz^2}=q(z)\cong\beta k_h\left(f(z)-u(z)\right) \tag{1}$$

In Equation (1), $E=$ Young's modulus of pile, $I=$ pile's moment of inertia, $P_x=$ axial load, $q(z)=$ earth pressures (units in *F/L*), $u(z)=$ pile displacement, $k_h=$ modulus of subgrade reaction (units in F/L^2; for OC clay, $k_h=k_{ch}D$; for NC clay or sand, $k_h=nz$, where $k_{ch}=$ coefficient of subgrade reaction, $n=$ constant of subgrade reaction), $\beta=$ ratio for nonlinearity, $f(z)=$ ground displacement, $z=$ spatial variable along the pile, $D=$ pile diameter. The earth pressures could be evaluated using direct and indirect

models with the prescribed ground displacements. Corresponding FD solutions are respectively presented as follows,

$$A_1u(i-2)+(-4A_1+B_1)u(i-1)+(6A_1-2B_1)u(i)+(-4A_1+B_1)u(i+1)+A_1u(i+2)=q(i) \quad (2)$$

$$A_1u(i-2)+(-4A_1+B_1)u(i-1)+(6A_1-2B_1+\beta k_h)u(i)+(-4A_1+B_1)u(i+1)+A_1u(i+2)=\beta k_h f(i) \quad (3)$$

where $A_1=\frac{EI}{(\Delta z)^4}$; $B_1=\frac{P_x}{(\Delta z)^2}$; i is the *ith* node along the pile. Boundary conditions at pile head and pile tip would change the discrete formulation accordingly. To solve the equations representing for a single pile and the surrounding soils, one need to conduct a matrix analysis.

For dynamic solution of the Winkler's foundation model, governing equation is written as follows.

$$EI\frac{\partial^4u(z,t)}{\partial z^4}+\rho A\frac{\partial^2u(z,t)}{\partial t^2}+P_x\frac{\partial^2u(z,t)}{\partial z^2}=q(z,t) \cong \beta k_h\left(f(z,t)-u(z,t)\right) \quad (4)$$

where $\rho=$ mass density of the pile, $A=$ area of pile's cross section. Similarly, Equation (4) could be evaluated using direct and indirect earth pressures. If the seismic earth pressures were known already, then Eq. (4) could be written as

$$u(i,j+1)=\frac{1}{A_2}\begin{bmatrix}-u(i+2,j)+(4-B_2)\cdot u(i+1,j)\\+(2A_2+2B_2-6)\cdot u(i,j)\\+(4-B_2)\cdot u(i-1,j)-u(i-2,j)\\-A_2\cdot u(i,j-1)+C_2\end{bmatrix} \quad (5)$$

where $A_2=\frac{\rho A(\Delta z)^4}{EI(\Delta t)^2}$; $B_2=\frac{P_x(\Delta z)^2}{EI}$; $C_2=\frac{q(z,t)(\Delta z)^4}{EI}$; j is the *jth* time step.

For prescribed ground motions applied to the indirect earth pressures, Eq. (4) can be solved as follows:

$$u(i,j+1)=\frac{1}{A_2}\begin{bmatrix}-u(i+2,j)+(4-B_2)\cdot u(i+1,j)\\+(2A_2+2B_2-C_3-6)\cdot u(i,j)\\+(4-B_2)\cdot u(i-1,j)-u(i-2,j)\\-A_2\cdot u(i,j-1)+C_3\cdot f(i,j)\end{bmatrix} \quad (6)$$

where $C_3=\frac{\beta k_h(\Delta z)^4}{EI}$. It is necessary to point out that the modulus of subgrade reaction, k_h could be found in *p-y* models or simply determined from SPT-N values and undrained shear strength, C_u for sands and clays, respectively.

Again boundary conditions at the pile head and tip would affect these formulations. Long pile conditions were usually assumed at bottom of the pile. Modified equations

need to be derived for boundary nodes and their neighboring nodes in pile shaft. The independent equations can save considerable time of computations. Details of the derivations and all the numerical formulations can be found in Lin (2006) and Yeh (2006). Pile nonlinearities could be properly simulated using rigorous modeling or a simple treatment based on iterative analysis and moment-curvature relations of the pile (Ishihara and Cubrinovski, 2004). A recent study conducted by Rajaparthy and Hutchinson (2006) using the program LPILE (Reese and Wang, 2000) to show useful performance measures for plastic hinge and maximum moment of the pile was also founded on moment-curvature behavior of the piles.

DIRECT AND INDIRECT EARTH PRESSURE MODELS

The direct earth pressure model has been suggested by Japan Road Association (1990). Earth pressures of the upper crust and the liquefied layer were suggested as follows,

$$\begin{cases} q_{NL} = c_s \cdot c_{NL} \cdot K_p \cdot \gamma_{NL} \cdot z & \left(0 \le z \le H_{NL}\right) \\ q_L = c_s \cdot c_L \cdot \left\{\gamma_{NL} \cdot H_{NL} + \gamma_L \cdot \left(z - H_{NL}\right)\right\} & \left(H_{NL} \le z \le H_{NL} + H_L\right) \end{cases} \tag{7}$$

where $K_p = \dfrac{1+\sin\phi}{1-\sin\phi}$; γ_{NL}, γ_L, H_{NL}, H_L are the unit weights and thickness of the layers. Note that the coefficients c_s, c_{NL}, c_L are to be determined according to the distance to waterfront, the liquefaction potential index, P_L and the engineering judgment. Pile shaft underneath the liquefied layer could be assumed either rigid or flexural. Eqs. (2) and (7) are combined to solve for the pile deformations. One must multiply Eq. (7) with the pile diameter to obtain corresponding loads for solutions. Ishihara and Cubrinovski (2004) adopted this method to analyze pile responses. For static modeling with the indirect earth pressures, the permanent ground displacement profile proposed by Tokimatsu and Asaka (T&A, 1998) are as follows,

$$L/H = \left(25 \sim 100\right) D_0 / H \tag{8}$$

$$D\left(x\right)/D_0 = \left(\frac{1}{2}\right)^{5x/L} \tag{9}$$

$$\begin{cases} f_{LS}\left(z,x\right) = D\left(x\right) & \left(z \le z_w\right) \\ f_{LS}\left(z,x\right) = D\left(x\right)\cos\left[\dfrac{\pi\left(z-z_w\right)}{2H}\right] \cong D\left(x\right)\left[1 - \dfrac{\left(z-z_w\right)}{H}\right] & \left(z \ge z_w\right) \end{cases} \tag{10}$$

where $L =$ length of lateral spreading zone, $H =$ thickness of liquefied layer, $D_0 =$ maximum ground displacement at the waterfront, $x =$ site distance to waterfront, $D\left(x\right) =$ maximum ground displacement at the site, $f_{LS}\left(z,x\right) =$ ground displacement profile, $z =$ depth, $z_w =$ depth of water table. Note that in using this model, ground displacements are only applicable to the zone of lateral spreading. Soils underneath the zone are assumed stable, where no soil displacement would exist.

For dynamic modeling using Eq. (4), it is rather difficult to find proper direct and indirect earth pressure models as those discussed in static modeling. Ignoring the

structural geometry and rigidity differences, seismic earth pressure model (Zhang et al., 1998) used for the embedded pile cap (Tokimatsu, 2003) may be used. The seismic earth pressures are simply modeled as follows.

$$\begin{cases} p_E = p_{EP} - p_{EA} \\ p_{EP} = K_{EP}\gamma_s h\left(1 \pm K_v\right) = \gamma_s h\left(1 \pm K_v\right) f_{EP}\left(\phi, l, \delta_p, I_E = \tan^{-1}\left[K_h / \left(1 \pm K_v\right)\right], \alpha\right) \\ p_{EA} = K_{EA}\gamma_s h\left(1 \pm K_v\right) = \gamma_s h\left(1 \pm K_v\right) f_{EA}\left(\phi, l, \delta_a, I_E = \tan^{-1}\left[K_h / \left(1 \pm K_v\right)\right], \alpha\right) \end{cases} \quad (11)$$

where p_E = net seismic pressure, p_{EA} = active earth pressure, p_{EP} = passive earth pressure, K_h, K_v = seismic coefficients in horizontal and vertical directions, γ_s = unit weight of soil, h = depth of soil, f_{EP} and f_{EA} are time-dependent potential function, ϕ = soil's friction angle, l = pile length, δ_a and δ_p = friction angel between soil and pile for active and passive earth pressures, I_E = angle of seismic forces, α = inclination angle of ground surface. In applying this model, the sloping ground amenable for the lateral spreading occurrence is able to monitor. For adequate loadings, Eq. (11) needs to be multiplied with the pile diameter too. One could modify the corresponding equations according to 3D pile geometry and the pile-to-pile interaction effects such as those suggested on *p-y* relationships (Reese and Van Impe, 2001).

For dynamic modeling using indirect earth pressure model, time-dependent ground displacement profiles ought to be obtained first. One may conduct a proper seismic analysis for the ground displacements and then use them to solve for the corresponding pile displacements. Computer program CYCLIC-1D (Elgamal et al., 2002) is available for the ground displacements affected by lateral spreading. For simplicity and to elaborate the use of indirect earth pressure mode, the liquefaction-induced permanent ground displacements suggested by Tokimatsu and Asaka (1998) is considered. A time dependent normalized equation, $\overline{H}(t)$ is proposed herein. This function is suggested by integrating the normalized ground accelerations, $\overline{a}(t)$ $(= a(t)/a_{max})$ twice with time. Then, normalize and multiply it with original static displacement function, $f(z,x)$ as follows,

$$\overline{H}(t) = \int\int \frac{a(t)}{a_{max}} dt / H_{peak} \quad (12)$$

$$f(z,x,t) = f(z,x) \cdot \overline{H}(t) \quad (13)$$

where H_{peak} = peak of the integral, a_{max} = peak ground acceleration. Displacement-time history of the soils at different depths will then have the same variations but different quantities according to this approximation.

CASE STUDIES ON 1995 KOBE EARTHQUAKE

Pile foundation damages reported by Ishihara and Cubrinovski (2004) on Oil-storage tank TA72 located about 20*m* from the waterfront in Mikagehama island during the 1995 Kobe earthquake are studied herein. The tank, having a diameter of 14.95 *m* and

storage capacity about 2450 kl, is supported on 69 precast concrete piles with length of 23~24 m and diameter of 45 cm. The water table is estimated at the depths of 2~3 m. Sand compaction pile has been conducted to increase the SPT-N values for the Masado layer around Tank TA72. Figure 2 shows the reported relations for the bending moment (M) and curvature (φ) of the piles where D_0 is pile diameter and N is axial load on pile. The cracking moment (M_{cr}), the yield moment (M_y) and the ultimate moment (M_u) are known as 105, 200 and 234 $kN-m$ respectively. The ultimate shear strength is 232 kN according to ACI specifications (1998). Initial EI of pile is 58330 kN/m^2. Soil properties in use are listed in Table 1. Bore-hole cameras and inclinometers were used to inspect the damages of the piles. Deteriorating of No. 2 and No. 9 piles are shown in Figure 3. The main cracks along the shaft were found at the depths of 8~14m. Pile No. 2 have scraped wounds, and pile No. 9 was sheared off at the depth about 10.5 m. Both piles were found damaged by lateral spreading of the soils at the foundation site.

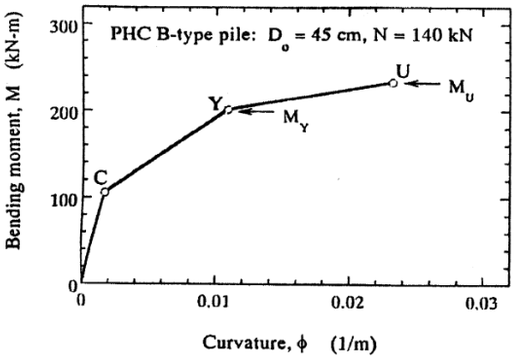


FIG. 2. Relationships of bending moment and curvature of pile (from Ishihara and Cubrinovski, 2004).

Table 1. Fundamental properties of soils used in case studies.

Soil layers	Z (m)	γ (kN/m^3)	ϕ (deg)
Masado soil	0~13.5	18	33
Silty sand	13.5~14	18	36
Silty sand	14~20	19	36
Fine sand	20~23.5	20	39
Gravel	23.5~26	20	40

In the simulations, seismic record of the NS-component of 1995 Kobe Earthquake is used. Table 2 depicts all the parameters used for the comparative analyses. Note that iterative technique is used to simulate the pile nonlinearities based on moment-curvature relationships shown in Figure 2. Figures 4 shows the pile displacements from the static modeling using direct and indirect earth pressures for tank TA72. It can be seen that the maximum pile displacement from direct solution is lager than the one from indirect solution. The deviations between these solutions and the one made by Ishihara and Cubrinovski are caused by material parameters and boundary conditions. The maximum pile displacements are found at pile head rather than the

bottom. Nevertheless, their magnitudes are similar to those shown in Figure 3. On the other hand, Figure 5 depicts the ultimate pile displacements from the dynamic modeling where the direct pressure model was used. Note that in Figure 5 the difference of the peak displacements between pile head and pile tip is about the same order of field displacements. Unlike the static modeling, maximum pile displacements from the dynamic analysis are found at the bottom of piles. Although the pile displacement profiles from the static and dynamic solutions are quite different, their magnitudes are about the same. Furthermore, Figure 6 depicts the results from dynamic analysis using indirect earth pressure approach where modified Tokimatsu and Asaka model was adopted. The maximum pile displacement appearing at the pile head is found greater than the static ones.

It can be seen that all these modeling can provide rational solutions for pile displacements with liquefaction-induced lateral spreading concerns. The static analysis would predict largest displacements at pile head because the earth pressures/ground motions applied are decreasing with the depth. Similarly, the dynamic modeling using modified indirect earth pressures would give largest pile displacements at pile head. Pile deformations at arbitrary time could also be reviewed. If the site was amplified by earthquake shaking and the surface ground motions are pronounced to cause shallow spreading, then one can use JRA and T&A models to analyze the pile foundation. In the contrast, dynamic modeling using seismic earth pressures would yield largest pile displacements at the bottom according to the depth-increased earth pressures. This approach implies that the lateral spreading can be modeled as a massive motion of the layered soils, in which the earth pressures could be increased with the depth. If the lateral spreading could affect the deep soils, then one should use the seismic earth pressure model for the modeling. As a result, the mechanics of lateral spreading and the soil-foundation-structure interactions should be examined prior to the analysis.

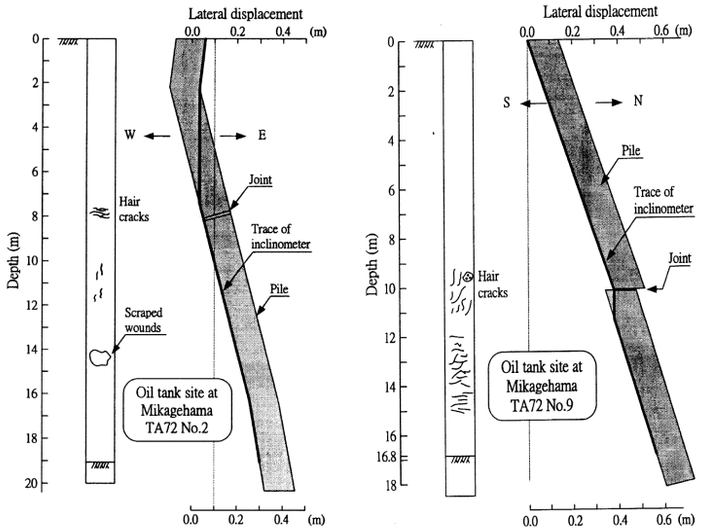
Table 2. Parameters used in various numerical solutions for the case studies.

Method	Parameters in use
Static / Direct	$H_{NL} = 2.5m$, $H_L = 11m$, $c_s = 1.0$, $c_{NL} = 0.133$, $c_L = 0.3$
Static and Dynamic / Indirect	$D_0 = 1.75m$, $L = 76m$, $H = 11m$, $x = 28m$, $z_w = 2m$, β= 1.0
Dynamic / Direct	$K_h = 0.83$, $K_v = 0$, $\theta = 90^\circ$, $\alpha = 5^\circ$, $\delta_a = 0.6\phi$, $\delta_p = 0.8\phi$, $\delta_{moba} = \delta_a$, $\delta_{mobp} = \delta_p$

CONCLUDING REMARKS

This paper discusses the static and dynamic FD solutions for Winkler's models on piles under lateral spreading. Direct and indirect earth-pressure models are both presented. Nonlinear pile responses could be obtained using iterative analysis with prescribed pile moment-curvature relationships. It was shown that the lateral spreading could be monitored through these solutions with careful calibrations for model parameters. Static modeling with direct and indirect earth pressures would result in maximum pile displacements at pile head. Dynamic modeling using modified indirect earth pressures can provide similar results and the pile deformations at a specified time. On the other

hand, dynamic analysis using direct earth pressures would yield largest pile displacement at the tip. Nevertheless, all the solutions can provide similar pile displacements to those observed in the field. The differences are mainly caused by the earth pressures and ground displacements in use. For routine design applications, one must understand that these simplified solutions are good for first approximation. They may lead significant errors by neglecting the complexities of the physical mechanism. For proper use of these solutions, the geological and geographic site conditions as well as the soil-foundation-structure interactions must be evaluated carefully prior to the analysis.



(a) Pile No.2 (b) Pile No.9

FIG. 3. Lateral displacements and observed cracks of Pile No. 2 and Pile No. 9 (from Ishihara and Cubrinovski, 2004).

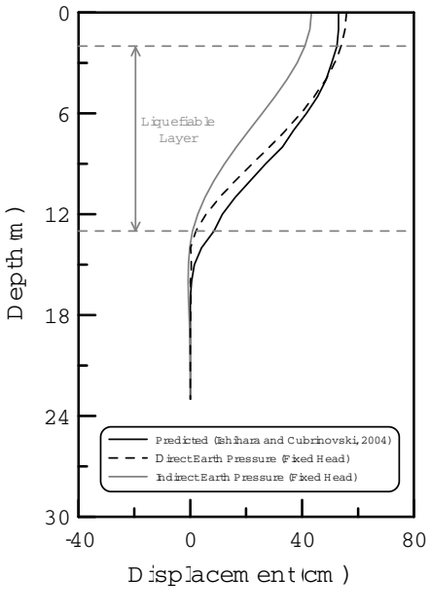


FIG. 4. Pile displacements from the static modeling using direct and

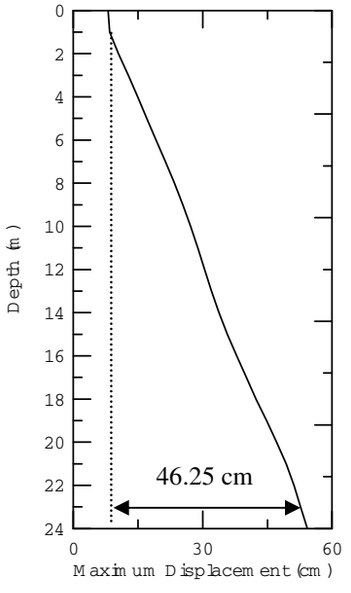


FIG. 5. Peak displacements from dynamic modeling using direct

indirect earth pressures. **seismic earth pressures.**

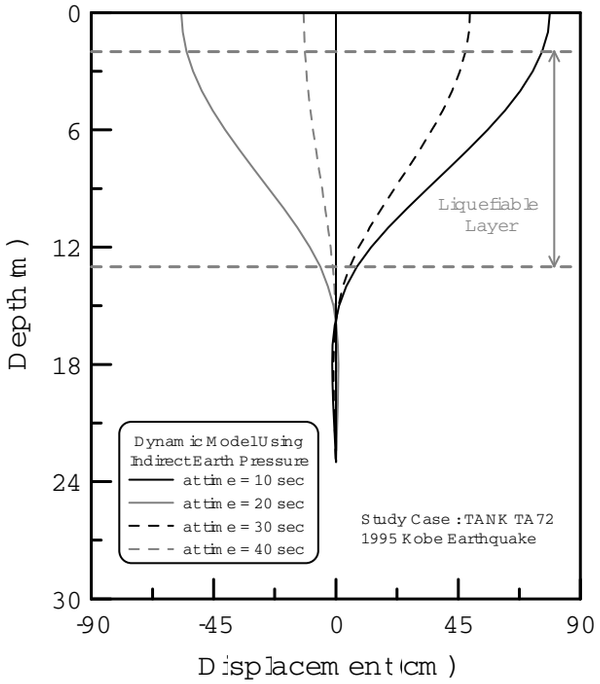


FIG. 6. Pile displacements from the dynamic modeling using indirect earth pressures of modified T&A displacement profile.

ACKNOWLEDGEMENTS

This work is a partial result of the studies through research contract NSC95-2211-E032-043 from National Science Council in ROC. The authors express their sincere gratitude for the support.

REFERENCES

American Concrete Institute (1998). "Building Code Requirements for Structural Concrete." ASCE, U. S. A.

Arduino, P., Kramer, S.L., Li, P. and Home, J. (2005), "Stiffness of Piles in Liquefiable Soils." *Procds.*, ASCE Conf. on Seismic Performance and Simulation of Pile Foundations in Liquefied and Laterally Spreading Ground, Davis, University of California, U.S.A., pp. 135-148.

Brangenberg, S.J., Boulanger, R.W., Kutter B.L., Chang, D. (2007). "Liquefaction-induced Softening of Load Transfer Between Pile Groups and Laterally Spreading Crusts." *J. Geotechnical & Geoenvironmental Engrg*, Vol. 133 (1), pp. 91-103.

Boulanger, R.W., Kutter B.L., Brangenberg, S.J., Singh, P., Chang, D. (2003). "Pile Foundations in Liquefied and Laterally Spreading Ground: Centrifuge Experiments and Analyses." Report UCD/CGM-03/01, Center for Geotechnical Modeling, University of California, Davis, 205 pp.

Chang, D.W. and Lin, B.S. (2003). "Wave Equation Analyses on Seismic Responses of Grouped Piles." *Procds.*, 12th Asian Regional Conference on Soil Mechanics and Geotechnical Engineering, Singapore, pp. 581-586.

Chang, D.W. and Lin, B.S. (2006). "*EQWEAP*~a Simplified Procedure to Analyze Dynamic Pile-Soil Interaction with Soil Liquefaction Concerns." *Procds.*, Second Taiwan-Japan Joint Workshop on Geotechnical Hazards from Large Earthquake and Heavy Rainfall, Nagaoka, Japan, pp. 155-162.

Chang, D.W., Lin, B.S. and Cheng, S.H. (2007). "Seismic Earth Pressure Induced Pile Response from Discrete Wave Equation Analysis." *Procds.*, 16th Southeast Asian Geotechnical Conference, Malaysia, PP. 663-668.

Elgamal, A., Yang, Z. and Parra, E. (2002). "Computational Modeling of Cyclic Mobility and Post-Liquefaction Site Response." *Soil dynamic and Earthquake Engineering*, Vol. 22 (4), pp. 259-271.

Ishihara, K. and Cubrinovski, M. (2004). "Case Studies on Pile Foundations undergoing Lateral Spreading in Liquefied Deposits." *Procds.*, 5th International Conference on Case Histories in Geotechnical Engineering, New York, Paper SOAP 5.

Japan Road Association (JRA) (1990). - *Specification for Highway Bridges, Part V, Seismic Design*.

Lin, B.S. (2006) "Structural Analysis for Pile Foundations Subjected to Soil Liquefaction and Lateral Spreading." PhD Thesis, Dept. of Civil Engr., Tamkang University.

Lin, S.S., Tseng, Y.J., Chiang, C.C. and Hung, C.L. (2005). "Damage of Piles Caused by Laterally Spreading – Back Study of Three Cases." *Procds.*, ASCE Conf. on Seismic Performance and Simulation of Pile Foundations in Liquefied and Laterally Spreading Ground, Davis, University of California, U.S.A., pp. 121-133.

Liyanapathirana, P.S. and Poulos, H.G. (2005). "Pseudostatic Approach for Seismic Analysis of Piles in Liquefying Soil." *J. Geotechnical & Geoenvironmental Engrg*, Vol. 131(12), pp. 1480-1487.

Rajaparthy, S.R. and Hutchinson, T.C. (2006). "Evaluation of Methods for Analyzing the Seismic Response of Piles Subjected to Liquefaction-Induced Loads." *Procds.*, 5th International Conference on Bridges and Highways, San Francisco.

Reese, L.C. and Wang, S.T. (2000). *Documentation of Computer Program* LPILE PLUS 4.0. Ensoft, Inc., Austin, Texas.

Reese, L.C. and Van Impe, W.F. (2001). *Single Piles and Pile Groups under Lateral Loading*. A. A. Balkema, Rotterdam, Brookfield.

Tokimatsu, K. and Asaka, Y. (1998). "Effects of Liquefaction-Induced Ground Displacement on Pile Performance in the 1995 Hyogoken-Nambu Earthquake." *Soils and Foundations*, Special Issue, No. 2, pp. 163-178.

Tokimatsu, K. (2003). "Behavior and Design of Pile Foundations Subjected to Earthquakes." *Procds.,* 12th Asian Regional Conf. on Soil Mechanics and Geotechnical Engineering, pp 1065-1096.

Yeh, C.H. (2006). "Study on Static Modeling of Pile Foundation in Liquefied Soils." Master Thesis, Dept. of Civil Engr., Tamkang University.

Zhang, J. M., Shamoto, Y., and Tokimatsu, K. (1998). "Seismic Earth Pressure for Retaining Walls under Any Lateral Displacement." *Soils and Foundations*, Vol. 38(2), pp. 143-163.

Mechanism of pile group settlement in liquefiable soils

Jonathan Knappett[1], and Gopal Madabhushi[2]

[1]Lecturer, Division of Civil Engineering, University of Dundee, Dundee, DD1 4HN, Scotland, UK; j.a.knappett@dundee.ac.uk
[2]Reader, Schofield Centre, University of Cambridge, High Cross, Madingly Road, Cambridge, CB3 0EL, UK; mspg1@eng.cam.ac.uk

ABSTRACT: This paper examines the settlement of instrumented 2 × 2 model pile groups in liquefiable soil based on the results of dynamic centrifuge tests. The piles are end-bearing in dense sand, and are instrumented such that base, shaft and total pile load components can be measured. The data suggest that the overall co-seismic group settlement is accrued from incremental settlements of the individual piles as the group rocks under the action of the kinematic and inertial lateral loads. A Newmarkian framework for describing this behaviour is presented in which permanent settlement is incremented whenever the load in any of the piles exceeds the capacity of the soil to support the pile. This bearing capacity of the piles in liquefied soil is estimated based on measured dynamic soil properties during shaking and observations of the changes in load carried by the piles. The contribution of the pile cap in reducing settlement is also discussed.

INTRODUCTION

Over the past few decades, a great amount of attention has been focused on observing and predicting the horizontal response of piled foundations during earthquakes in liquefiable ground (e.g. Brandenberg et al., 2005 and Dobry et al., 2003 respectively). While permanent horizontal displacement of such foundations can be very damaging to the structures they support, particularly those with tight tolerances on alignment such as bridges (Orense et al. 2002), permanent settlements which may arise due to the loss of bearing capacity with liquefaction are often overlooked. These however can be similarly damaging to structures (Zhang and Ng, 2005), particularly if the structure is to remain serviceable following the earthquake. Gross settlement is damaging in itself, but differential settlement may similarly cause problems, particularly for long structures, such as rotation of bridge decks or damage to walls and facades.

This paper aims to demonstrate that significant settlement of piled foundations may occur with continued shaking in liquefiable soil and to investigate the mechanism by which this settlement occurs. This is achieved by observing the behaviour of instrumented model pile groups in dynamic centrifuge tests.

CENTRIFUGE TESTING

Test layout and procedures

Dynamic centrifuge testing was undertaken on two 2 × 2 pile groups at 80g using the 10 m diameter beam centrifuge at the Schofield Centre, University of Cambridge. These were installed in a two-layer sand profile consisting of an upper layer of loose liquefiable silica sand (relative density, $D_r \approx 35\%$) 10.4 m thick (prototype units are used throughout), overlying a dense layer of the same sand ($D_r \approx 85\%$). The sand has a $D_{10} \approx 0.1$ mm and $\phi = 32°$. The two pile groups were tested within the same profile such that the dynamic excitation and soil properties were identical for both. The soil was prepared within a flexible equivalent shear-beam (ESB) container to model a semi-infinite soil profile. The entire soil bed was saturated to ground level with 80 cS methyl-cellulose solution. The use of a viscous fluid allows for pore-fluid seepage to be correctly modeled during dynamic events (Schofield, 1981 and Stewart et al., 1998).

Each pile group consisted of four closed-ended tubular piles made from aluminium-alloy, having an outside diameter (D_0) of 0.496 m at prototype scale. These were installed at a centre-to-centre spacing of $5.6D_0$. Further mechanical properties for this pile section are given in Table 1. Figure 1 shows schematically the layout for the test. The two groups were installed such that the pile tips were founded at a depth of 15.2 m. The piles in group S1, which was used to investigate the behaviour of the piles alone, were a further 2 m longer to provide clearance between the underside of the connecting pile cap and the surface of the loose sand. This group was vertically loaded at the cap by rigid aluminium blocks so that the approximate load per pile was ~ 450 kN. Group S3 was formed of piles 15.2 m long and was installed such that the underside of the pile cap was just in contact with the surface of the sand. This was loaded identically to group S1.

TABLE 1. Mechanical and geometric properties of pile section

Property	Nomenclature	Value (prototype scale)
Outside diameter	D_0	0.496 m
Base area	A_b	0.19 m^2
Pile length (in soil)	L_p	15.2 m
Bending stiffness	EI	164 MNm^2
Axial stiffness	EA/L_p	0.96 MN/m

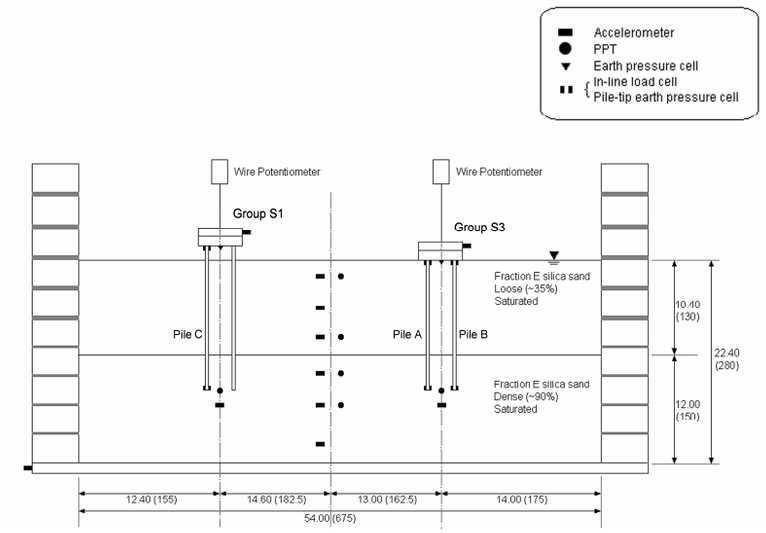


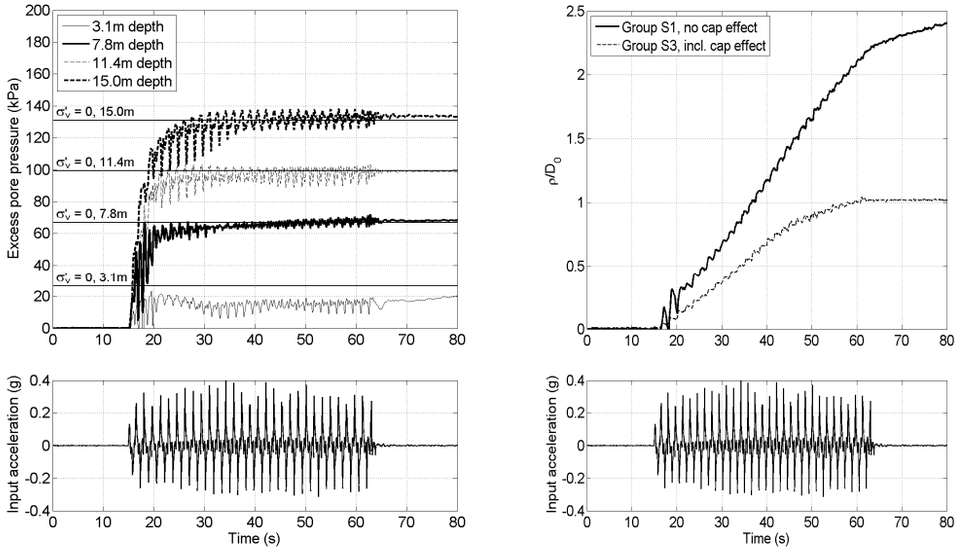
FIG. 1. Cross-section of centrifuge model, dimensions in m, prototype scale (mm model scale)

Settlement of the pile groups was measured using draw-wire potentiometers at the pile group centerline. Surface-mount earth pressure cells were installed beneath the centerline of the pile caps to measure bearing pressure. In the case of group S1, this instrument was used to verify that the pile cap did not contact the soil during shaking. Three of the eight piles used in the test were instrumented with miniature tension-compression in-line load cells at the interface between the pile head and the cap. Sub-miniature earth pressure cells were installed into the tips of the piles with the same area as the base of the pile. These were used to measure pile tip load, and from the difference between the two sensor values, the integrated pile shaft load along the length of the pile was obtained. Two of the instrumented piles were used in group S3 (denoted piles A and B) such that load transfer during rocking of the foundation could be investigated, with the remaining pile being used in group S3 (pile C). This arrangement is shown in Figure 1.

Liquefaction-induced pile group response

Sinusoidal excitation was imparted to the model using the stored angular momentum (SAM) actuator; this is described in detail by Madabhushi et al. (1998). Thirty cycles of shaking were applied at a frequency of 0.63 Hz with a nominal peak magnitude of 0.31g. This was sufficient to cause full liquefaction to a depth of 15 m (i.e. the maximum measured depth of the soil) though the low confining stress towards the surface of the sand reduced the excess pore pressures generated at a depth of 3.1 m, as shown in Figure 2(a). As the soil liquefied, both pile groups were observed to suffer extensive settlement as shown in Figure 2(b). It is clear from Figure 2(b) that the settlement of each of the pile groups is accrued in a series of steps. In this Figure, settlement (ρ) is normalized by the outside diameter of the pile

(D_0). It is also clear from the same Figure that the settlement is significant after only a few cycles of strong shaking. At 20 s, the settlement of group S3 has exceeded 50 mm, while that of group S1 (without any effect of the pile cap) is closer to 150 mm.



(a) Excess pore pressure (b) Pile group settlement

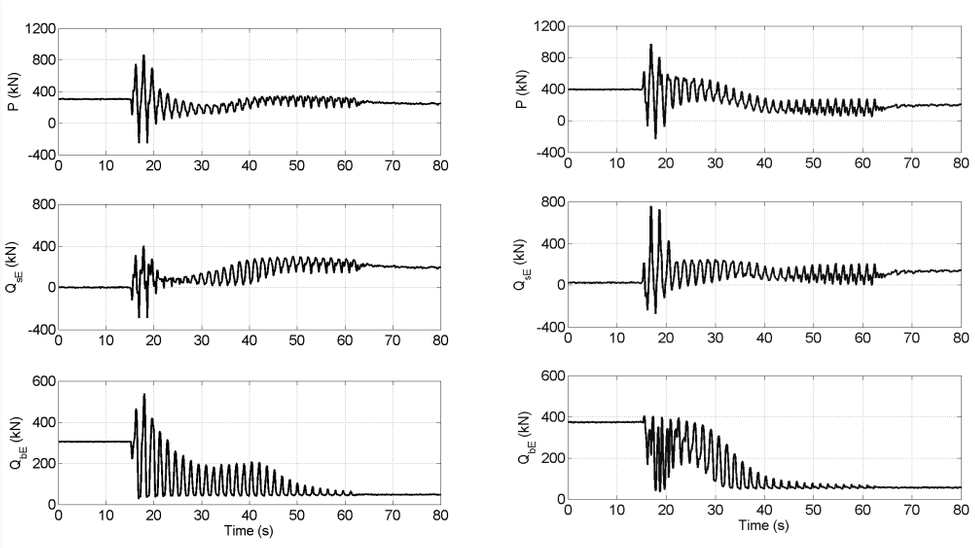
FIG. 2. Liquefaction-induced settlement during seismic excitation

Pile loads in liquefied soil

As the pile groups settle, the loads carried by the different sections of the pile change. This is shown for group S3 in Figure 3. As liquefaction begins, the total loads carried by the piles at the head (P) reduce. This is chiefly due to a drop in load carried by the piles at the base (Q_{bE}), as the shaft loads (Q_{sE}) increase with increasing settlement. As the base load carried reduces with increasing settlement, this may be interpreted as a drop in bearing capacity as the dense soil beneath the piles liquefies.

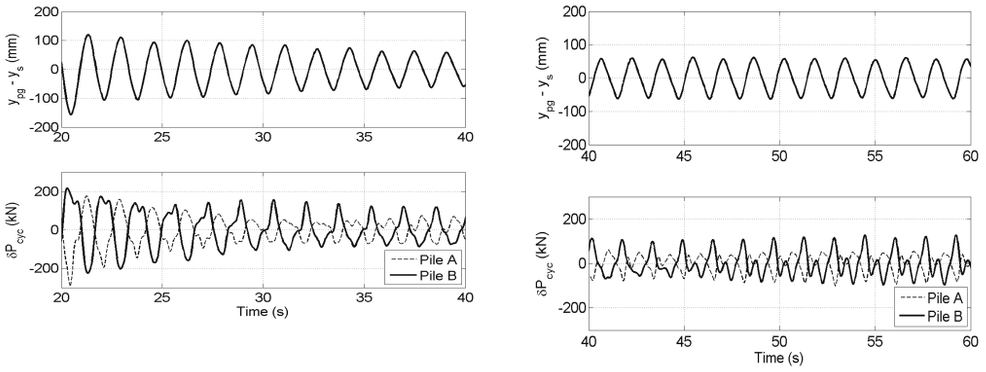
The cyclic variation in pile load which is evident from Figure 3 arises due to rocking of the pile group during the earthquake, and this is shown in Figure 4. In this figure the cyclic relative displacement of the pile cap (y_{pg}) relative to that of the soil at the tip of the pile (y_s) has been computed by integrating carefully filtered acceleration time histories at the two points. This is compared with the cyclic component of the total pile load (δP_{cyc}), obtained by high-pass filtering the load P to remove the monotonically varying component. When $y_{pg} - y_s$ is positive, the pile cap is moving towards pile A (as indicated in Figure 1) generating a rotation of the group and causing pile A to settle. Negative values correspond to the pile cap moving towards pile B, leading to settlement of pile B. From Figure 4 it can be inferred that positive local settlement of each of the piles is correlated with transient peaks in the load carried by the respective piles.

If the average variation in P from Figure 3 relates to the capacity of the liquefied soil to support the pile, then positive values of δP_{cyc} would indicate time periods at which the capacity is being exceeded which may correlate to an increment of permanent settlement. In this way, the pile group would 'stamp' its way into the soil as it rocks during the earthquake, with the settlement increasing whenever the capacity is exceeded in any of the piles. This is similar in principle to the accumulation of permanent displacement in slopes during earthquakes when a yield acceleration is exceeded (Newmark 1965).



(a) Pile A (b) Pile B

FIG. 3. Variation in pile loads during shaking and liquefaction, group S3



(a) Early in the earthquake (20 – 40 s) (b) Late in the earthquake (40 – 60 s)

FIG. 4. Dynamic vertical loading of piles due to lateral foundation movement, group S3

MECHANISM OF SETTLEMENT – NEWMARKIAN 'STAMPING'

The capacity of a pile in liquefying soil may be separated into components at the base and along the shaft of the pile. Base capacity was computed using a modified form of the spherical cavity solution originally proposed by Vesic (1970):

$$q_{bE,ult} = \frac{(1+\sin\phi)(1+2K_0)}{(1-\sin\phi)(3-\sin\phi)} \cdot \left(\frac{I_r}{1+\varepsilon_v I_r} \right)^{\frac{4\sin\phi}{3(1+\sin\phi)}} \cdot \sigma'_v \tag{1}$$

in which

$$I_r = \frac{3G}{(1+2K_0)\tan\phi \cdot \sigma'_v}. \tag{2}$$

During liquefaction both the shear modulus (G) and the instantaneous vertical effective stress (σ'_v) will reduce as excess pore pressures increase. Secant values of G for each cycle of the seismic shaking were obtained based on stress strain loops for the soil mid-way between the tip of the piles and base of the container. These were obtained from the accelerometer records using the method detailed by Brennan et al. (2004). Average values of vertical effective stress at pile tip depth in the free-field, consistent with the measurements of G, were computed based on the measured excess pore pressures. Volumetric compression (ε_v) was assumed to be zero (undrained). Predictions of base capacity obtained using Equation (1) have been shown to match the average reduction in base load measured in the centrifuge tests (c.f. Figure 3) reasonably well by Knappett (2006).

Shaft capacity ($Q_{sE,ult}$) was estimated empirically based on the observed shaft loads from the centrifuge testing. The instrumented pile in group S1 was observed to reach a maximum value as it settled during swing-up of the centrifuge which did not increase with further settlement. This was interpreted to be the static shaft capacity of the pile and was consistent with simple predictions. Despite a significant dynamic component, the average shaft load for this pile was observed to steadily reduce as the soil liquefied, which was interpreted as a drop in the shaft capacity of the pile. This is shown in Figure 5(a), along with a bi-linear fit defined by:

$$\frac{Q_{sE,ult}}{Q_{s0,ult}} = \begin{cases} 1 & N < 7 \\ -0.022N + 1.16 & N \geq 7 \end{cases} \tag{3}$$

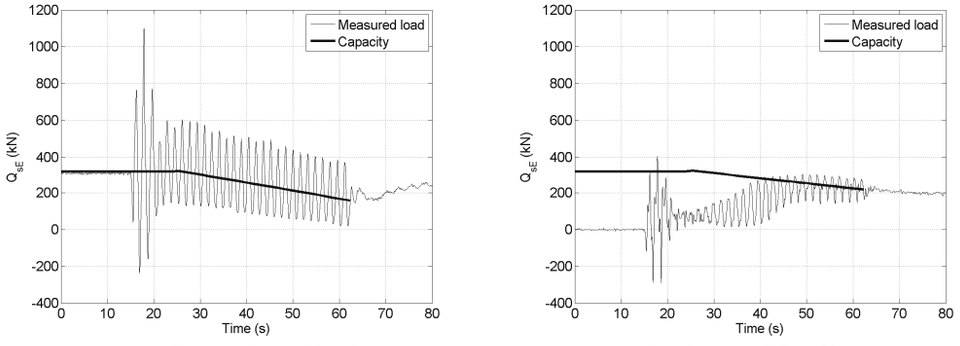
where N is the number of cycles. This residual capacity is likely to arise from cyclic stiffening at the pile shaft – soil interface in the dense sand.

When applying this capacity envelope to pile A of group S3, it was noted that the cyclic variation in Q_{sE} was much less than that observed for pile C in group S1 (Figure 5(b)). It is commonly understood that reduction in shaft capacity under

cyclic loading is affected by the magnitude of the load cycles, with a lower reduction in capacity for smaller loading cycles. As shown in Figure 5(b), Q_{sE} for group S3 was observed to increase until approximately 45 – 50 s at which point it began to decrease, but less rapidly than for group S1. The capacity was therefore taken to be:

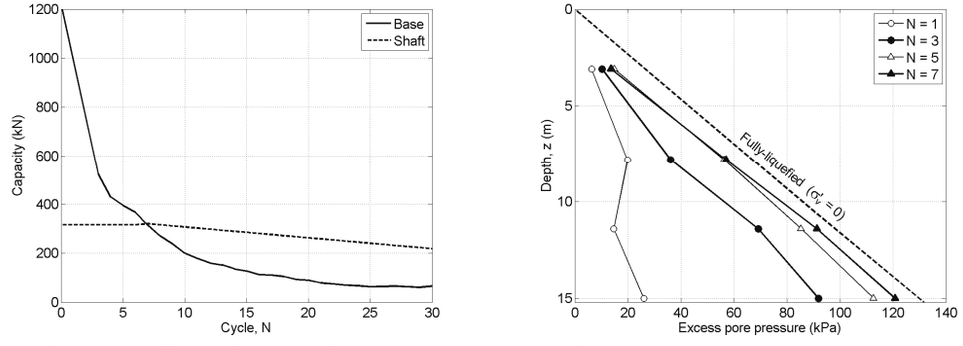
$$\frac{Q_{sE,ult}}{Q_{s0,ult}} = \begin{cases} 1 & N < 7 \\ -0.014N + 1.11 & N \geq 7 \end{cases}. \quad (4)$$

It should be noted that the initial shaft load prior to the earthquake for group S3 was approximately zero. With liquefaction-induced settlement, shaft friction is mobilized within the capacity envelope defined by Equation (4). This is different to the behaviour observed for group S1 in which the shaft friction had reached its maximum value prior to the earthquake, and therefore immediately decreases as liquefaction reduces the capacity according to Equation (3).



(a) Group S1, pile C (b) Group S3, pile A

FIG. 5. Measured shaft loads and predicted capacity in liquefied soil



(a) Pile capacity estimate (liquefied soil) (b) Isochrones of excess pore pressure

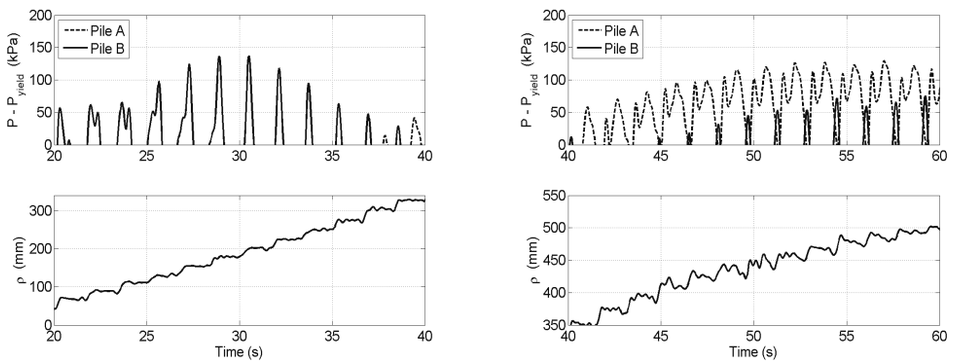
FIG. 6. Base and shaft capacity of pile in liquefied soil

The resulting base and shaft capacities for the piles in group S3 are shown in Figure 6(a). Figure 6(b) shows isochrones of excess pore pressure with depth. It is interesting to note that as the soil becomes approximately fully liquefied over its entire depth at around N = 5 – 7, The base capacity reduces below that of the shaft such that the piles will behave more like friction piles instead of end-bearing piles. The dramatic reduction in base capacity is coincident with the rise of excess pore pressure in the bearing layer.

The predicted total pile capacity at which the pile will 'yield' through the soil (i.e. suffer permanent settlement), P_{yield}, is obtained from the addition of the two curves in Figure 6(a). However, this capacity estimate is based on soil parameters measured in the free-field. Local soil response beneath the pile group may vary somewhat from this, depending on the influence of the piles on the soil. This has been accounted for here to a first-order estimate by taking the pile capacity to be:

$$P_{yield} = \alpha\left(Q_{bE,ult} + Q_{sE,ult}\right). \tag{5}$$

Figure 7 shows a correlation between $P - P_{yield}$ and the increments in group settlement. A value of $\alpha = 0.7$ was found to provide a positive spike of $P - P_{yield}$ for each stepwise increment of group settlement. This value of α was used in producing Figure 7. It will be seen that the times at which settlements occur correlate with one or other pile exceeding P_{yield}. It is also interesting to note that in this case, the more heavily loaded pile initially (pile B, c.f. initial values of P in Figure 3) is responsible for the settlement early in the earthquake, with pile A responsible for the settlement later in the earthquake.



(a) Early in the earthquake (20 – 40 s) (b) Late in the earthquake (40 – 60 s)

FIG. 7. Correlation of settlement increments with times at which pile capacity is exceeded.

CONCLUSIONS

The effects of simplified earthquake shaking and liquefaction on the vertical load transfer in end-bearing pile groups in saturated sand have been investigated using dynamic centrifuge testing. Particular attention has been paid to the permanent settlement of the group which may exceed 50 – 100 mm even after only a few cycles of strong shaking, when excess pore pressures may still be relatively low. The pile cap has been shown to play an important role in resisting settlement. The influence of a 4.4 × 4.4 m square pile cap bearing on the surface of loose sand was observed to approximately double the stiffness of the four pile group considered herein.

A Newmarkian framework has been presented to account for the settlement behaviour of the pile groups observed in the centrifuge test. As the pile group rocks back and forth under the action of inertial and kinematic lateral loads, high transient loads are applied to the piles on either side of the group in turn. When these loads exceed the capacity of the pile in the liquefied soil, the pile group suffers an increment of permanent settlement. Further research is required to improve the estimates of pile capacity presented herein and to provide a means of estimating the increment of settlement for a given magnitude of cyclic load. Nonetheless, this has been shown to be a viable mechanism for the development of permanent pile group settlement in liquefiable soils and is an important first step towards being able to predict the vertical response of piled foundations in a performance-based framework.

ACKNOWLEDGMENTS

The authors appreciate the support and advice of the technical staff at the Schofield Centre, University of Cambridge, UK for their help with the centrifuge testing. The first author is also grateful for the financial support provided by the EPSRC, UK to support his PhD studies on which this work is based.

REFERENCES

Brandenberg, S.J., Boulanger, R.W., Kutter, B.L. and Chang, D. (2005). "Behaviour of pile foundations in laterally spreading ground during centrifuge tests." *J. Geotechnical & Geoenv. Engng.*, Vol. 131 (11): 1378-1391.

Brennan, A.J., Thusyanthan, N.I. and Madabhushi, S.P.G. (2005). "Evaluation of shear modulus and damping in dynamic centrifuge tests." *J. Geotechnical & Geoenv. Engrg.*, Vol. 131 (12): 1488-1497.

Dobry, R., Abdoun, T., O'Rourke, T.D. and Goh, S.H. (2003). "Single piles in lateral spreads: field bending moment evaluation." *J. Geotechnical & Geoenv. Engrg.*, Vol. 129 (10): 879-889.

Knappett, J.A. (2006). "Piled foundations in liquefiable soils: accounting for axial loads." *PhD Thesis*, University of Cambridge, UK.

Madabhushi, S.P.G., Schofield, A.N. and Lesley, S. (1998). "A new stored angular momentum based earthquake actuator." *Proc. Centrifuge '98*, Tokyo, Japan: 111-116.

Orense, R.P., Vargas-Monge, W. and Cepeda, J. (2002). "Geotechnical aspects of the January 13, 2001 El Salvador earthquake." *Soils & Found.*, Vol. 42 (4): 57-68.

Newmark, N.M. (1965). "Effects of earthquakes on dams and embankments." *Géotechnique*, Vol. 15 (2): 139-160.

Schofield, A.N. (1981). "Dynamic and earthquake geotechnical centrifuge modelling." *Technical Report CUED/D-SOILS/TR104*, University of Cambridge, UK.

Stewart, D.P., Chen, Y.R. and Kutter, B.L. (1998). "Experience with the use of methylcellulose as a viscous pore fluid in centrifuge models." *ASTM Geotechnical Testing J.*, Vol. 21 (4): 365-369.

Vesic, A.S. (1972). "Expansion of cavities in infinite soil mass." *J. Soil Mech. & Found. Div.*, Vol. 98 (SM3): 265-289.

Zhang, L.M. and Ng, A.M.Y. (2005). "Probabilistic limiting tolerable displacements for serviceability limit state of foundations." *Géotechnique*, Vol. 55 (2): 151-161.

Performance-based Seismic Response of Pile Foundations

Brendon A. Bradley[1], Misko Cubrinovski[2], Rajesh P. Dhakal[3].

[1]PhD Candidate, Department of Civil Engineering, University of Canterbury, New Zealand; bab54@student.canterbury.ac.nz
[2]Associate Professor, Department of Civil Engineering, University of Canterbury, New Zealand; misko.cubrinovski@canterbury.ac.nz
[3]Senior Lecturer, Department of Civil Engineering, University of Canterbury, New Zealand; rajesh.dhakal@canterbury.ac.nz

ABSTRACT: Investigation of the correlation between so-called engineering demand parameters (EDPs) and various intensity measures (IMs) has received substantial attention in structural earthquake engineering, as accurate prediction of seismic demand is desired in performance-based seismic evaluation of structures. Little work however has been performed quantifying the seismic response of pile foundations within a performance-based context. In this study the seismic demands of pile foundations are investigated in a performance-based approach. A simple soil-pile-structure model consisting of a two layer soil deposit with a single pile and a single-degree of freedom superstructure is used in a parametric study to determine the salient features in the seismic response of the soil-pile foundation system. A suite of 40 'ordinary' ground motion records were scaled to various ranges of intensity to probabilistically investigate the full range of pile behaviour, from initial elastic response to failure. Various IMs are used to inspect their correlation with the seismic demand, which is measured in terms of: peak lateral displacement of the pile head (relative to pile toe) and peak pile curvature. The lowest scatter in the prediction of pile response was observed when seismic intensity was measured in terms of velocity-based IMs.

INTRODUCTION

Within the context of emerging trends in performance-based earthquake engineering (PBEE), seismic performance is measured with respect to the demand (and its associated consequences) of engineering systems during a seismic event, as opposed to the conventional factor of safety approach. The low – frequency high – consequence nature of seismic events coupled with randomness and uncertainty in response behaviour and modelling, requires that a probabilistic stance is also

endeavored when seismic performance is assessed. In such a probabilistic framework system performance is principally affected by the uncertainty in each of the variables comprising the system, which are generally differentiated as being either aleatory or epistemic. Kramer and Mitchell (2006) give a good overview of the effect of uncertainties in PBEE.

Significant research over the past decade has focused on determining IMs which correlate well with the prediction of structural response due to ground motion excitation (e.g. Shome and Cornell, 1999; Baker and Cornell, 2005; Tothong and Luco, 2007). Recently, Kramer and Mitchell (2006) investigated the correlation of various IMs with the occurrence of liquefaction in a soil deposit. They found that compared to traditional ground motion parameters, such as PGA and Arias intensity, a new parameter, CAV_5, defined as the cumulative absolute velocity for velocities above 5 cm/sec provided a significantly reduced uncertainty in the prediction of peak pore pressure ratio (the EDP used in this case).

In this paper the performance-based response of pile foundations is investigated considering the correlation of various IMs with the seismic demand on pile foundations embedded in non-liquefiable soils. Firstly, discussion is given to the determination of which measures of demand (EDP) should be used to describe the seismic response of the pile(s). Next, various candidate IMs are examined and ranked based on their efficiency in predicting the EDP, and their independence from the rupture magnitude and propagation distance to the recorded site.

PREDICTION OF SEISMIC DEMAND FOR PILES

It is well known that the seismic demands on pile foundations arise due to both inertial effects from the superstructure and kinematic effects imposed by cyclic lateral ground displacements (Gazetas and Mylonakis, 1998). The vibratory motion in the vicinity of the pile foundation is complex and differs significantly from the free-field motion due to the flexural rigidity of the piles, which causes refraction and scattering of the incident seismic waves. Prediction of seismic demands considering both inertial and kinematic effects requires a rigorous dynamic analysis of the soil-pile-structure system. Experience from recent strong earthquakes and observations from benchmarking experiments on piles have shown that pile foundations are subjected to very large lateral loads leading to serious damage and collapse of piles. Hence a key requirement in the analysis is estimation of the inelastic response and damage to the pile(s). While a pseudo-static analysis of a simple beam-spring model provides a convenient design-oriented approach for preliminary assessment of pile response, a dynamic time-step analysis based on the effective stress principle allows modelling of the salient features of soil-pile-structure interaction including the complex effects of excess pore pressures and soil non-linearity. This approach permits more accurate prediction of the seismic demand on piles and was therefore adopted in this study. Since assessment of pile response in the performance-based framework has not been scrutinized to date, first attention is given to the identification of adequate seismic demand and intensity measures for piles.

OPTIMAL INTENSITY MEASURES FOR PILE RESPONSE

The determination of an optimal IM for prediction of a level of seismic demand is

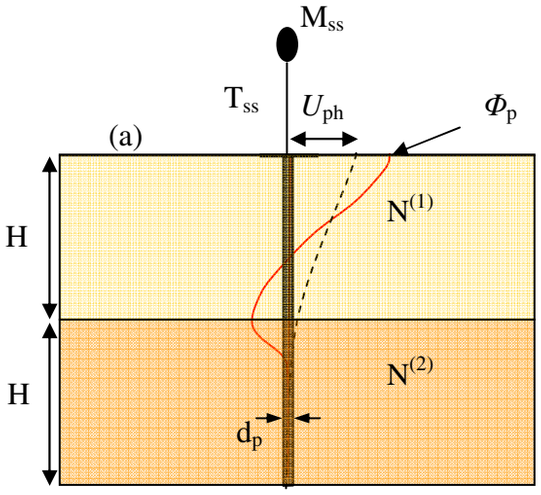
guided by the concepts of 'efficiency' and 'sufficiency', as defined by Shome and Cornell (1999). 'Efficiency' gives a measure of correlation of IM with EDP, and is typically measured via the standard deviation of the logarithm of the residuals, $\beta_{lnEDP|IM}$ (herein denoted simply as β). The residuals, $\varepsilon_i = y_i - y(x_i)$, represent the error between the raw data and some trend line (typically from regression). The better the efficiency of the IM, the smaller the value of β, which consequently reduces the number of analyses (i.e. EDP-IM data points) required to estimate the mean demand with a certain level of confidence.

The term 'sufficiency' refers to the independence of the residuals, ε_i, with respect to typical ground motion characteristics such as rupture magnitude and source distance. For example, if an IM is sufficient with respect to magnitude and distance, then effects of magnitude and distance can be ignored when predicting EDP without any loss in the accuracy of the prediction.

A suite of 40 ground motion records complied by Medina and Krawinkler (2003) were used for conducting the non-linear time history analyses. The suite contains ground motions recorded on stiff soil with magnitude and distance ranges of 6.5-6.9 and 13.3-39.3 km, respectively. The suite is termed 'ordinary' by Medina and Krawinkler, as none of the records show effects of near-fault motions (i.e. directivity or 'fling' effects), and all motions were recorded on stiff soils. This suite has been used by several other researchers (e.g. Tothong and Luco, 2007).

ADOPTED SOIL-PILE-STRUCTURE MODEL

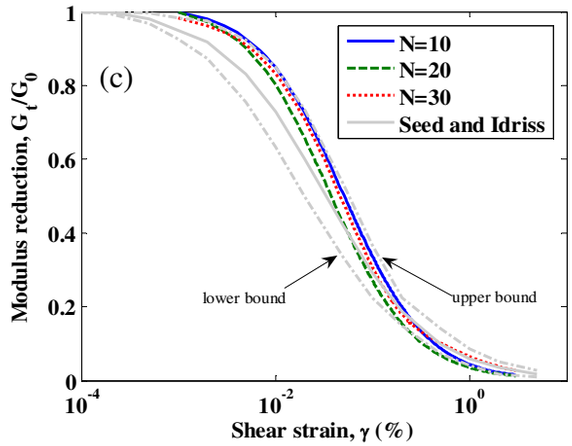
A conceptually simplified numerical model was used in this investigation, to try and capture the salient features of the pile response without onerous complexity. As shown schematically in Figure 1a the model consisted of a two-layer soil deposit with a single pile, rigid footing, and single degree-of-freedom (SDOF) superstructure. To investigate the effects of different material and geometrical properties, several different scenarios were considered (Figure 1b), which involved variations in the soil stiffness, pile properties, weight and period of the superstructure, based on typically observed configurations in engineering practice. Only the results of the first scenario is presented in this paper, an in-depth discussion of all six scenarios is given in Bradley et al, (2008). A finite element code was used which allows for direct effective stress analysis with pore water pressure development and dissipation. The Stress-Density (S-D) model of Cubrinovski and Ishihara (1998) was used as the constitutive model for the soil. The S-D model parameters were set such that the occurrence of liquefaction was suppressed in the scenarios considered herein. Effects of excess pore pressures and liquefaction were conducted in additional analyses which are beyond the scope of this paper. The shear modulus reduction curves for the soil were calibrated based on the well-known generalised curves of Seed and Idriss (1970) (Figure 1c). The pile and superstructure were modeled using beam elements with a hyperbolic moment-curvature relationship as an approximation to the 'exact' M-φ relationship of the 120 cm diameter RC pile, as shown in Figure 1d. The model was subjected to a base input motion scaled to peak ground accelerations between 0.1 and 1.0g in steps of 0.1g. Thus, using the 40 different ground motion records previously discussed a total of 400 analyses were performed for each of the scenarios listed in Figure 1b.



(b)

Scenario	1	2	3	4	5	6
$N^{(1)}$	10	20	10	20	10	10
$N^{(2)}$	30	30	30	30	30	30
W_{ss} (kN)	2500	2500	400	400	-	-
T_{ss} (s)	1.8	1.8	0.8	0.8	-	-
d_p (cm)	120	120	40	40	120	40
H (m)	10	10	10	10	10	10

($N^{(i)}$=SPT blow count of layer *i*)



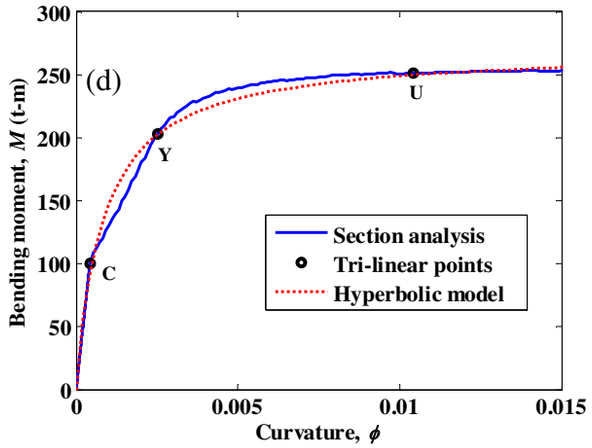


FIG. 1. Soil-pile-structure model used in investigation: (a) schematic illustration of model; (b) scenarios considered; (c) modulus reduction curves; (d) hyperbolic approximation of M-*Φ* relationship for the pile.

MEASURE OF SEISMIC DEMAND ON PILES

The first question which must be asked when determining which ground motion intensity measures correlate well with seismic demand on piles, is how is the seismic demand measured? Ideally, the so-called engineering demand parameter (EDP) that is used would correlate perfectly with the occurrence of damage in the component. In comparison to the research attention that the EDP-IM relationship has received, little research has focused on determining optimal EDPs which correlate well with damage states (DS) in components. This is particularly true for foundations.

As with any engineering material, the seismic demand on a pile is generally related to the hysteretic energy released due to inelastic behaviour during ground shaking. Hysteretic energy is typically expressed as a function of both peak and cumulative deformations, one obvious example being the damage index of Park and Ang (1985). In the performance-based assessment of structural systems, typically cumulative plastic rotation and peak interstorey drift are used as the engineering demand

parameters. When considering which EDP to use, consideration must also be given to the complexity in obtaining the EDP from engineering analyses. For example, while increasing numbers of finite element programs have the capability to compute damage indices (DIs), there are still some that do not, and also if simplified (i.e. not non-linear dynamic) analyses are to be used, then the computation of DIs is most likely not considered. For this reason peak response measures (e.g. peak floor acceleration, peak interstorey drift.) have been commonly adopted as the EDP for use in the fragility curve development of structural components (e.g. Tothong and Luco, 2007; Baker and Cornell, 2005). Following the same reasoning, only a peak response quantity will be used to quantify the seismic demand on the pile foundation in this study.

The peak pile curvature, Φ_p, would seem the most obvious candidate to use for pile demand, as it directly provides the peak strain at the critical section of the pile and hence the damage level. However, in order to determine the peak pile curvature, the rotations at pile nodes throughout the length of the pile are required for each integration time step in the analysis. The curvature for each pile element is first computed and then the maximum must be identified along the length of the pile. It is not easily understood how this peak curvature relates to the global response of the pile. The peak lateral displacement of the pile head (i.e. at the foundation of the structure), U_{ph}, is such an EDP which is conceptually easier to understand. To make the EDP applicable to pile foundations of different geometry and soil stratification we will use a normalized peak lateral displacement of the pile head. The normalized peak lateral displacement of the pile head (herein referred to as pile head displacement for brevity) is defined as:

$$U_{ph}^{N} = \frac{U_{ph}}{h_{eff}} \tag{1}$$

where: h_{eff} = effective height of the pile, which is the length between the location of the peak curvatures (potential plastic hinges) along the pile length. In this sense, U_{ph}^{N} relates directly to inelastic rotation of the potential plastic hinges and therefore will correlate well with the occurrence of different damage states (e.g. cracking, yeilding, failure) in the pile. Note that as determination of the effective length of the pile is not the focus of this study, it has merely been taken as 10m (the depth of the upper soil layer) in further discussions. In other words, it has been assumed that the peak curvatures occur at the pile head and the interface between the soil layers. This is in agreement with observed damage to piles in past strong earthquakes.

It is intuitive that the peak pile head drift and the peak pile curvature are well correlated based on the likely first mode-dominated deformed shape of the pile during seismic excitation. Figure 2 illustrates the correlation between peak pile drift and peak pile curvature (for Scenario 1) from the 400 non-linear finite element analyses conducted in this study. The correlation indicates that U_{ph}^{N} can be used to predict the deformation and hence damage of the pile.

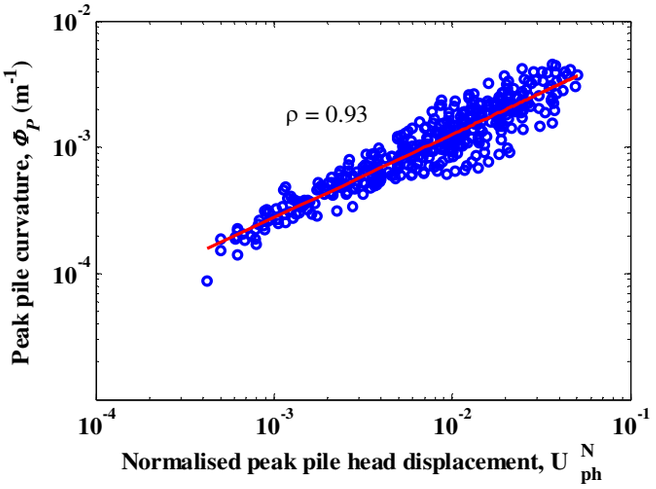


FIG. 2: Correlation between normalized peak pile displacement and peak pile curvature from 400 nonlinear FE analyses for scenario 1

INTENSITY MEASURES INVESTIGATED

A total of 19 different candidate IMs were considered for correlation with the pile response (measured in terms of the normalized peak lateral pile head displacement), which are presented in Table 1. Definitions of all the IMs can be found in Riddell (2007). The list of candidate IMs cover acceleration-, velocity-, and displacement-based intensity measures, which include both peak and cumulative quantities. The periods of 0.4, 0.6, 0.8, and 1.8s which the spectral accelerations of IM 16-19 are computed at are selected to capture separately inertial and kinematic effects due to the vibration of the superstructure and imposed ground deformations, respectively.

Table 1. Candidate IMs used in correlation analyses

ID	IM name	ID	IM name
1	Peak ground acceleration, PGA	11	Cumulative absolute velocity, CAV
2	Peak ground velocity, PGV	12	Acceleration spectrum intensity, ASI
3	Peak ground displacement, PGD	13	Velocity spectrum intensity, VSI
4	Significant duration, D	14	Sustained maximum acceleration, SMA
5	PGV/PGA, V_{max}/A_{max}	15	Sustained maximum velocity, SMV
6	RMS acceleration, RMS_a	16	Spectral acceleration, S_a(T=0.4s,5%)
7	RMS velocity, RMS_v	17	Spectral acceleration, S_a (T=0.6s,5%)
8	RMS displacement, RMS_d	18	Spectral acceleration, S_a (T=0.8s,5%)
9	Arias intensity, I_a	19	Spectral acceleration, S_a (T=1.8 s,5%)
10	Specific energy density, dE		

RESULTS

Efficiency

Firstly the efficiency of the candidate IMs was evaluated in an effort to reduce the

number of IMs to focus on. For scenario 1 (see Figure 1b), Figure 3a depicts the efficiency of the candidate IMs (in-terms of β), with the numerical values of β given in the third column of Table 2. Inspection of the results for scenario 2 showed similar trends as those for scenario 1, with values of β typically varying by ±0.02. It becomes immediately apparent that the velocity-based IMs (e.g. PGV, RMS_v, SMV, VSI) all have good efficiency (smallest β values) with respect to predicting the normalized peak pile displacement. The efficiency of the acceleration- and displacement-based IMs is noticeably less than the velocity-based IMs. Other IMs such as Arias Intensity (β=*0.402*) and *CAV* (β=*0.383*) are in the middle of the range of β values. Also it is noted that while the efficiency of the spectral acceleration IMs (IM 16-19) is not poor, it is noticeably less efficient than the velocity-based IMs. As mentioned, Sa(1.8s,5%) was used to capture the inertial effects of the superstructure, and Sa(0.4-0.6s,5%) was used for the kinematic effects of the soil. As none of these IMs was able to efficiently (relative to the lower β values observed) capture the pile response then it can be concluded that both inertial and kinematic effects are significant in this problem.

Over all of the six scenarios considered in this study it was found that VSI was consistently the most efficient IM, while the efficiency of PGV was dependent on the scenario considered (Bradley et al, 2008). As VSI is the integral of the velocity spectra (which is directly related to the acceleration spectra), then a ground motion prediction (attenuation) relationship (which describes the temporal occurrence of VSI), can be determined from ground motion prediction equations for spectral acceleration (Bradley et al, 2008). The availability of numerous attenuation equations for S_a means that VSI will also be a predictable IM (i.e. a small scatter in the attenuation relation) (Kramer and Mitchell, 2006). For the above reasons we will use VSI as the optimal IM in further discussions, and we will also use PGA for comparison because of its conventional use as an IM. Figures 3b and 3c show the EDP-IM correlations for PGA and VSI, respectively. It should be noted that the reason the data points in Figure 3b are in 'strips' of constant IM is that the ground motion scaling factors for the records were based on scaling to PGA values. A significant difference in the scatter between the PGA- and VSI-based EDP-IM plots is clearly evident. A more rigorous evaluation of these IMs for a wider range of scenarios is given in Bradley et al, (2008).

Sufficiency

As previously mentioned an IM should be sufficient (Shome and Cornell, 1998) with respect to rupture magnitude and source distance, in order to prevent bias when results are determined based on a finite ensemble of ground motions records. If an IM is sufficient with respect to a given ground motion parameter then it indicates that the results of the analysis are independent of that ground motion parameter. Since a finite ensemble of ground motion records is used to predict the response, if an IM is insufficient with respect a particular parameter then the response prediction will be sensitive to the distribution of this parameter in the ensemble of motions used.

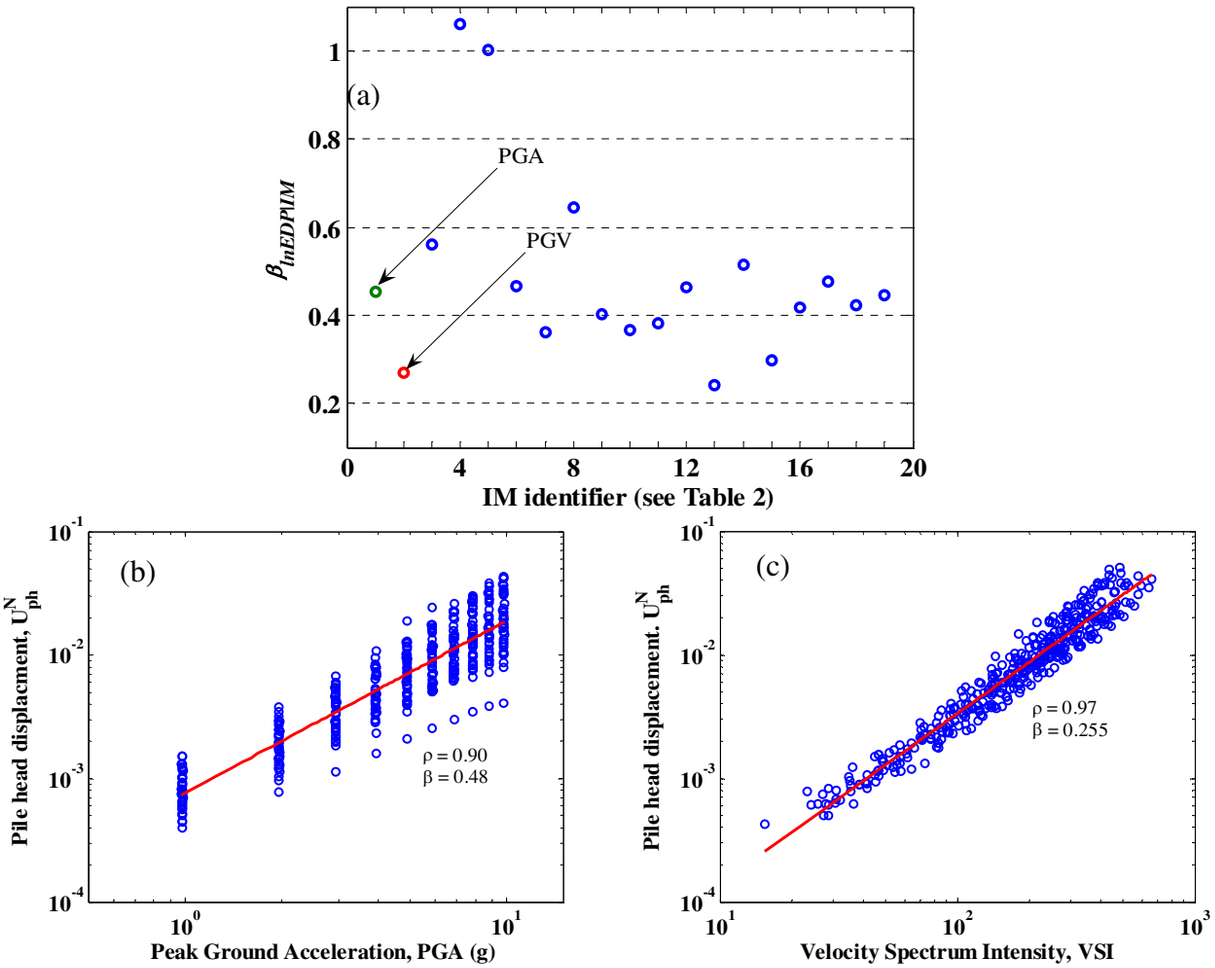


FIG. 3: Efficiency of the candidate IMs. (a) Efficiency of all IMs as a function of $\beta_{lnEDP|IM}$; (b)&(c) EDP-IM scatter plots for PGA and VSI, respectively.

In order to determine if an IM is sufficient with respect to a ground motion parameter, first the residuals, ε_i, have to be computed for the respective IMs. Here, the residual represents the error in the prediction by the regression model with respect to the actually computed EDP. Therefore, based on the previous statements if an IM is sufficient with respect to a given ground motion parameter there should be no trend in the residuals as a function of the ground motion parameter, that is, the residuals should be statistically independent of the ground motion parameter. Such independence is typically quantified by determining the 'p-value' (Ang and Tang, 1975), which corresponds to the probability that the slope, b, of the regression line through the epsilon-ground motion parameter is equal to zero. Typically if the p-value is less than 0.05 then there is evidence to reject the null hypothesis that the slope (b) of the regression line is zero. If $p < 0.01$ then it is said there is significant evidence to reject the null hypothesis.

Table 2. Efficiency and Sufficiency of IMs from analysis (scenario 1)

			Magnitude		Distance		Scale factor	
IM	ρ	$\beta_{\ln EDP\|IM}$	***b***	***p*-value**	***b***	***p*-value**	***b***	***p*-value**
1	0.898	0.475	0.66	0	-0.19	0.007	0.05	0.052
2	0.97	0.261	0.25	0.010	0.07	0.062	0.02	0.244
3	0.864	0.542	0.98	0	0.4	0	0.21	0
4	0.168	1.062	0.9	0.013	-0.2	0.209	0.93	0
5	0.38	0.997	0.36	0.291	0.03	0.859	0.89	0
6	0.891	0.488	0.81	0	-0.17	0.023	0.01	0.671
7	0.946	0.35	0.75	0	0.2	0	0.03	0.198
8	0.812	0.628	1.4	0	0.35	0	0.25	0
9	0.919	0.424	0.64	0	-0.14	0.029	-0.01	0.596
10	0.945	0.351	0.6	0	0.21	0	0.05	0.011
11	0.929	0.399	0.75	0	-0.11	0.071	-0.03	0.2
12	0.892	0.486	0.64	0	-0.17	0.018	0.05	0.092
13	0.972	0.255	-0.05	0.565	0.02	0.546	0.04	0.003
14	0.866	0.539	0.47	0.011	-0.22	0.006	0.07	0.017
15	0.962	0.294	0.24	0.017	0.13	0.003	-0.01	0.719
16	0.911	0.443	0.33	0.031	-0.2	0.003	0.07	0.008
17	0.886	0.499	-0.45	0.008	-0.23	0.002	0.25	0
18	0.913	0.439	-0.73	0	-0.3	0	0.19	0
19	0.918	0.427	0.28	0.057	0.09	0.183	0.13	0

Figures 4a and 4b give the magnitude sufficiency plots for VSI and PGA, respectively. It can be seen that the dependence of magnitude on the PGA-based residuals is significantly larger than that for VSI. It should be noted that some care should be taken when viewing Figure 4 since the magnitude distribution of the as-recorded ground motions is very coarse. Figure 4a indicates that the b-value (the slope of the regression line) is 0.25 and a corresponding probability of 56% that the slope of the trend line is zero. Therefore it can be stated that the VSI-based prediction is independent of magnitude (over the limited range considered).

Figures 4c and 4d illustrate the sufficiency of VSI and PGA with respect to source distance. As for sufficiency based on magnitude, the dependence of the VSI-based prediction on source distance is less than that for the PGA-based prediction. Hence, in addition to a better efficiency, VSI is also more sufficient than PGA with respect to rupture magnitude and source distance.

CONCLUSIONS

From the results of this investigation the following conclusions can be drawn:

1. Good correlation between the normalized peak lateral displacement of the pile head and the peak curvature of the pile was obtained from a series of 400 non-linear FE analyses indicating the use of the peak pile displacement as a rational EDP for piles under lateral loading
2. By considering a simple soil-pile-structure model it was found that for the scenarios investigated in this study, velocity-based measures of intensity (such as velocity spectrum intensity, VSI) correlate best with the seismic demand on pile foundations.
3. VSI was found to be more efficient than PGA and was also sufficient

(independent) with respect to rupture magnitude and source distance.

The model used in this study considered only a single pile and a SDOF supersturucture. Therefore, pile group effects and higher mode effects were ignored in this study. Also, the IMs considered were all of a scalar form. If use of a vector-based IM may improve the prediction of the pile response (EDP) through more sophisticated treatment of the inertial and kinematic effects of the pile response.

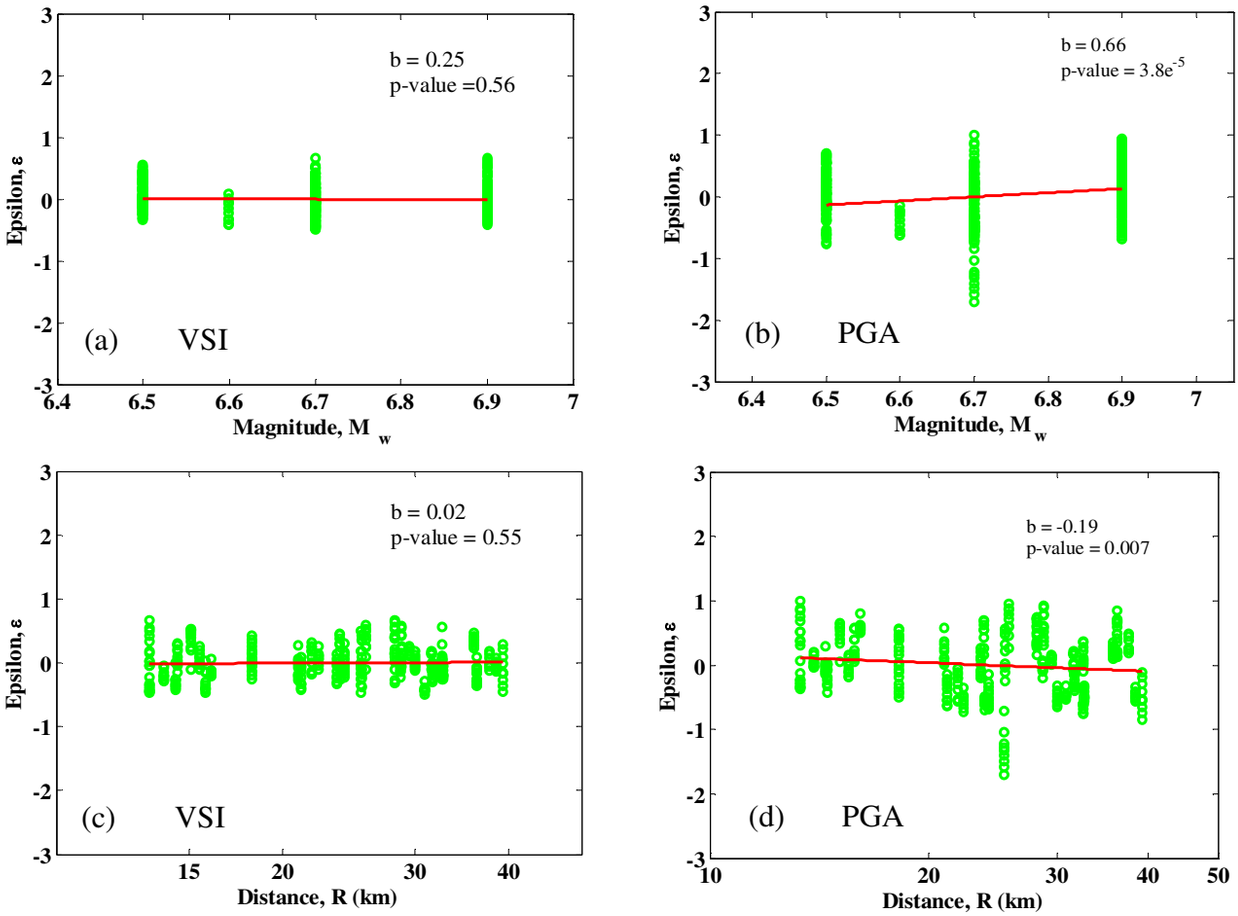


FIG. 4: Sufficiency of velocity spectrum intensity and peak ground acceleration with respect to magnitude and distance

REFERENCES

Ang, A.H.S. Tang, W.H. (1975). "Probability Concepts in Engineering Planning and Design: Volume I – Basic Principles." John Wiley & Sons, Inc.

Baker, J. and Cornell, C.A. (2005). "A vector-valued ground motion intensity measure consisting of spectral acceleration and eplison." *Earthquake Engineering and Structural Dynamics*. Vol 34. (10): 1193-1217.

Bradley, B.A. Cubrinovski, M. (2008). "Performance-based seismic response of pile foundations in non-liquefiable soils". *Soil Dynamics and Earthquake Engineering*, Submitted

Cubrinovski, M and Ishihara, K. (1998). "State Concept and Modified Elastoplasticity for Sand Modelling". *Soils and Foundations*; Vol 38. (4): 213-225

Gazetas, G. and Mylonakis, G. (1998). "Seismic soil-structure interaction: new evidence and emerging issues." *Geotechnical Earthquake Engineering and Soil Dynamics III* (GSP 72,2), ASCE, 1119-1174.

Kramer, S.L. and Mitchell, R.A. (2006). "Ground motion intensity measures for liquefaction hazard evaluation." *Earthquake Spectra*, Vol. 22 (2): 413-438.

Medina, R.A. and Krawinkler, H. (2003) "Seismic demands for nondeteriorating frame structures and their dependence on ground motions." *Report No. 144*, John A. Blume Earthquake Engineering Center, Department of Civil and Environmental Engineering, Stanford University, Stanford, CA; 347pp.

Park, Y.J. and Ang, A.H.S. (1985). "Mechanistic Seismic Damage Model for Reinforced Concete." *Journal of Structural Division, ASCE*. Vol. 111 (4):722-739.

Riddell, R. (2007). "On ground motion intensity measures." *Earthquake Spectra.* Vol 23. (1):147–173.

Seed, R.B and Idriss, I.M. (1970): "Soil moduli and damping factors for dynamic response analysis", Report UCB/EERC-70/10, Earthquake Engineering Research Center, UC, Berkeley, 48p.

Shome, N. and Cornell, C.A. (1999). "Probabilistic seismic demand analysis of nonlinear structures". Report No. RMS-35, RMS Program, Stanford University, Stanford, CA.

Tothong, P. and Luco, N. (2007). "Probabilistic seismic demand analysis with advanced ground motion intensity measures." *Earthquake Engineering and Structural Dynamics* (in press)

This page intentionally left blank

Plastic Hinge Formation in Pile Foundations due to Liquefaction-Induced Loads

Rajaparthy, S.R., Zhang, Z., Hutchinson, T.C., and Lang, F.[1]

[1]Post Doctoral Researcher (SRS, JZ), Associate Professor (TCH), and PhD Student (AL), Department of Structural Engineering, University of California, San Diego, La Jolla, CA 92093; corresponding author: tara@ucsd.edu.

ABSTRACT: Liquefaction induced soil pressures and lateral spreading demands are often the major cause of pile foundation failures. Review of case studies and data indicate that: (i) liquefaction-induced loads include soil pressures and potentially large displacements due to laterally spreading soil, both of which impose significant deformation demands on below-ground piles, (ii) these large deformation demands may result in plastic hinging of the piles, and (iii) the magnitude, location, and spread of the plastic hinging has not been comprehensively investigated.

This numerical study evaluates the inelastic behavior of reinforced concrete pile foundations under liquefiable and lateral spreading soil conditions. The parametric study considers different structural and soil details, as well as different simplified analyses methods commonly used for applying liquefaction-induced demands. The application of liquefaction-induced demands is studied using either (i) applied pressures or (ii) applied lateral spread displacements. Of the available methods for estimating lateral spread displacements, the four parameter empirical model proposed by Bardet et al. (2002), is used and observed to be conservative in comparison with other empirical and analytical models. This investigation reveals that the most pronounced variation in inelastic demands, as characterized by maximum bending moment depth and plastic hinge length, is attributed to the strength and stiffness of the pile as well as the layering condition of the soil. In particular, the existence of a non-liquefiable layer (crust) at the ground surface significantly affects the demands on the pile shaft.

INTRODUCTION

Numerous case histories of pile performance after earthquakes indicate severe to minor damage to the piles (e.g., Alaska 1964, Niigata 1964, Loma Prieta 1989, Kobe 1995). Damage to the pile shaft region can primarily be attributed to loss of lateral soil support, excessive soil pressures, lateral spreading of the soil due to liquefaction and poor structural detailing of the pile. While modern design has largely minimized the potential hazards of poor structural detailing, the former issues related to imposed soil pressures or displacements remain poorly understood. Although post-earthquake studies have been conducted to evaluate below-ground damage patterns, substructure damage is

hidden from observation following an earthquake, making it difficult to clearly identify the damage distribution and mechanism. Clearly it is undesirable for a structure to remain in service without knowledge of its defective foundation. It is therefore important for design engineers to assess below ground damage characteristics due to scenario earthquake demands using both robust and simple simulation tools. Although there a number of design methods exist in the literature to account for liquefaction-induced demands on piles, there is limited study whereby explicit attention is given to the pile sectional design and its resulting plastic behavioral characteristics.

LITERATURE REVIEW

Detailed case histories describing pile foundations damaged due to liquefaction induced demands are summarized in for example, Hamada and O'Rourke (1992), Barlett and Youd (1992), Mizuno et al., (1996), Berrill and Yasuda (2002) and Boulanger et al. (2003). From these and other literature, is recognized that there are two major causes of pile failure due to liquefaction-induced demands: (i) loss and/or reduction of strength and stiffness of the soil and (ii) movements of the soil exerting damaging pressures or displacements on the pile. A recent summary of modeling methods to account for these causes may be found in Dobry and Abdoun (2001), Boulanger et al. (2003) and Finn (2005). While these reports cover the state of the art regarding pile foundations in liquefied and laterally spreading ground, they also particularly emphasize the need for development of simplified design procedures. Therefore, in the present study, three different simplified p-y based design methods have been used to evaluate the performance of the pile under liquefiable conditions, namely: (i) the p-y reduction method, (ii) lateral earth pressure method and (iii) the ground displacement method.

p-y Reduction Method – Perhaps the most useful simplified method from a design practice perspective is the p-y reduction method, whereby discrete springs are used along the length of the pile to capture the soil resistance under lateral earthquake demands. The resistance of these springs is then modified to account for the reduction in stiffness and strength anticipated when the soil surrounding the pile liquefies (e.g. Wilson et al., 1999; Tokimatsu et al., 2001). Although use of the p-y reduction method has been widespread (largely due to its simplicity and commonality with the well known p-y method), it warrants validation against other methods of analysis. In this study, the p-y reduction factors are selected based on test results of Wilson et al. (1999), where single piles were embedded in sands with different relative densities, D_r ranging from 35-60%.

Lateral Earth Pressure Method – This method was adopted by the Japanese Road Association (2002) based on the analysis of case histories of pile performance in the 1995 Kobe earthquake. The approach represents kinematic loading on the pile due to lateral spreading as uniform lateral pressure applied to the pile within the liquefied soil zone (where $p = 0.3\sigma_v D$, where, p = pressure applied to the pile from the liquefied soil, σ_v = overburden pressure and D = pile diameter).

Ground Displacement Method – Soil deformations can be applied directly to the pile within the zone of liquefied soil, and/or within stiff crustal layers, as deemed

appropriate. This method is termed the *ground displacement method*. LRFD guidelines for seismic design of highway bridges (MCEER, 2003) provide guidance for use of this method for bridge foundations. Most commonly, Newmark's sliding block analysis is used to estimate surface ground displacements, and these are applied to the soil-pile foundation system. The system is then analyzed under the imposed displacements and inertial loads as applicable. There are, however, a number of methods available for estimating the ground displacement magnitude and distribution. In this work, a several commonly used empirical methods are considered for estimating the displacement magnitude and distribution.

NUMERICAL ANALYSIS

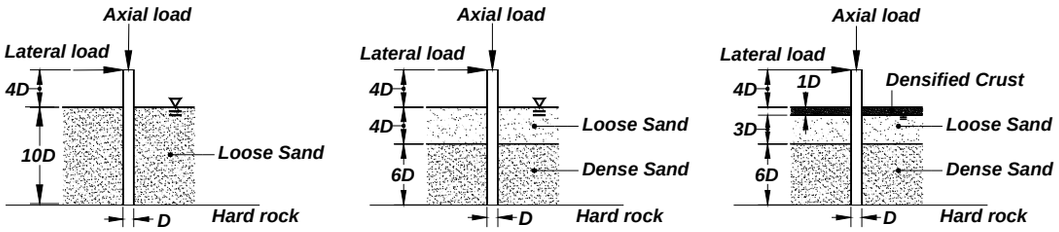
In this study, the above simplified design methods are evaluated through a numerical case study investigation, considering a single reinforced concrete pile shaft embedded in a variety of soil conditions and subjected to different liquefaction-induced demands. Pile sectional modeling is conducted using the program XTRACT (2004) and the soil-pile system is loaded pseudo-statically under uni-directional lateral loading using the program LPILE (Reese et al., 2000). Simulations are intended to account for both inertial and kinematic effects by prescribing lateral load on the structure and lateral spread induced displacements.

Pile Modeling – Nonlinear behavior is modeled using the moment curvature (M-ϕ) sectional behavior of the pile as calculated using the program XTRACT (2004). XTRACT evaluates force equilibrium across the section under increasing bending strains. The increase in core strength and strain capacity due to confinement is accounted for using Mander's model (Mander et al., 1988). A 1.0 m diameter reinforced concrete pile is considered for the study, constructed of concrete with an unconfined compressive strength of 24 MPa and elastic modulus of 2.32×10^4 MPa. The pile is reinforced with steel bars of yield strength 415 MPa and ultimate strength 620 MPa. A design axial load is selected to range from 0 to 20% of $f'_c A_g$ (where f'_c = unconfined compressive strength and A_g = gross sectional area). Longitudinal reinforcing steel ratios of ρ_l = 1%, 2% and 4% and transverse steel ratios of ρ_s = 1% and 2%, corresponding to Caltrans and ACI specifications, are used. In the present study, the pile is assumed to extend 4D above ground level and 10D below ground level.

Soil Modeling – Three different liquefiable soil conditions are considered as shown in Figure 1, namely; a fully saturated loose condition, a layered loose and dense condition, and a crustal layer above the loose-dense layering model. The saturated loose sand is assumed to have a friction angle of 28°, unit weight of 18 kN/m^3 and sub-grade modulus of 5.4 MPa/m, while the saturated dense sand is assumed to have a friction angle of 38°, unit weight of 19 kN/m^3 and sub-grade modulus of 34 MPa/m. The crustal layer is assumed to have a friction angle of 42°, 19kN/m^3 unit weight and a sub-grade modulus approximately that of dry dense sand at 61 MPa/m.

Soil-Pile Modeling – Modeling of the soil-pile system is conducted using the program LPILE$^+$ (Reese et al., 2000). Load conditions include combined axial and lateral inertial loading, as well as ground-imposed displacements and pressures, all applied under a

static, monotonic condition. By increasing the lateral loading applied to the soil-pile model, and monitoring the moment-curvature response, the first yield point of the soil-pile system is identified. The piles are then each pushed to a displacement ductility of μ_Δ = 3.0 (where $\mu_\Delta = \Delta_{max}$ at the pile head / Δ_y), as this a target design recommended by ATC-32 (1996) for extended pile shafts.



(a) (b) (c)

Figure 1. Schematic of soil-pile conditions considered: (a) homogenous liquefiable, (b) layered liquefiable, and (c) liquefiable with crust.

RESULTS AND DISCUSSION

Capacity Assessment – Pile capacity can be assessed in terms of its sectional M-ϕ characteristics, namely, the yield moment (M_y), effective yield curvature (ϕ'_y), and the curvature ductility (μ_ϕ) for different axial load and reinforcement ratio combinations considered in the study. In addition, global parameters such as lateral strength at yield (yield strength V_y), period of the soil-pile system (T_n), and seismic yield coefficient (α_y) characterize the soil-pile system (Figures 2a and b). In this case, the period of the soil-pile system is associated with the secant stiffness at first yield. The soil-pile systems considered are fairly flexible, with yield drift ratios ranging from 2.3 – 4.1%, and corresponding periods at first yield of T_n = 1.04 – 2.61 seconds. The range of normalized strength is within conventional seismic design space, ranging from 0.06 – 0.52, with larger strength attributed to the higher ρ_s and ρ_l design cases. From Figure 2(a), four quadrants of capacity can be observed, separated by those with higher strengths (upper two quadrants), and higher axial loads (right two quadrants). As may be anticipated, lower axial load carrying soil-pile models ($5\%f'_cA_g$) have lower periods (1.04 – 1.49 sec), while higher axial loads (20% of P_A) result in larger periods (2.01 – 2.61 sec). A plot of seismic yield coefficient as a function of the soil-pile system periods is also shown in Figure 2(b). This plot shows that the larger period systems yield at a lower seismic coefficient and vice versa, as expected. Notice that the liquefiable with crust cases have consistently larger yield strengths and lower periods, for a given pile section and axial load condition. This can be attributed to the additional strength and stiffness provided to the system by the crust layer.

Estimating Lateral Spread-Induced Displacements – Upon development of full liquefaction, it can be expected that lateral displacement will be induced on the pile due to the ground spread. The distribution and magnitude of this lateral spread displacement is needed to superimpose on the soil-pile system. It is noted that there are a number of methods available for calculating lateral spread displacements, each of which have been calibrated using different datasets and also with different underlying physical assumptions. The focus herein is on use of empirical methods,

which are simple and straight forward to implement in design. To evaluate the different methods, a dataset from 28 different earthquakes (resulting in 101 ground motions) is developed and lateral spread-induced displacements are calculated using the methods proposed by: (i) Newmark (1965), (ii) Ambraseys and Menu (1988), (iii) Yegian et al. (1991), (iv) Youd et al. (2002), and (v) Bardet et al. (2002). Methods (i), (ii) and (iii) are based on the Newmark's sliding block analysis whereas, (iv) and (v) are based on calibration against case histories using a multiple linear regression approach. While Newmark's sliding block analysis is perhaps the most predominantly used analysis method for determining sloping ground movements, recent methods based on calibration against field data are attractive to practitioners, as they typically involve a few simple calculations; thus comparison is warranted.

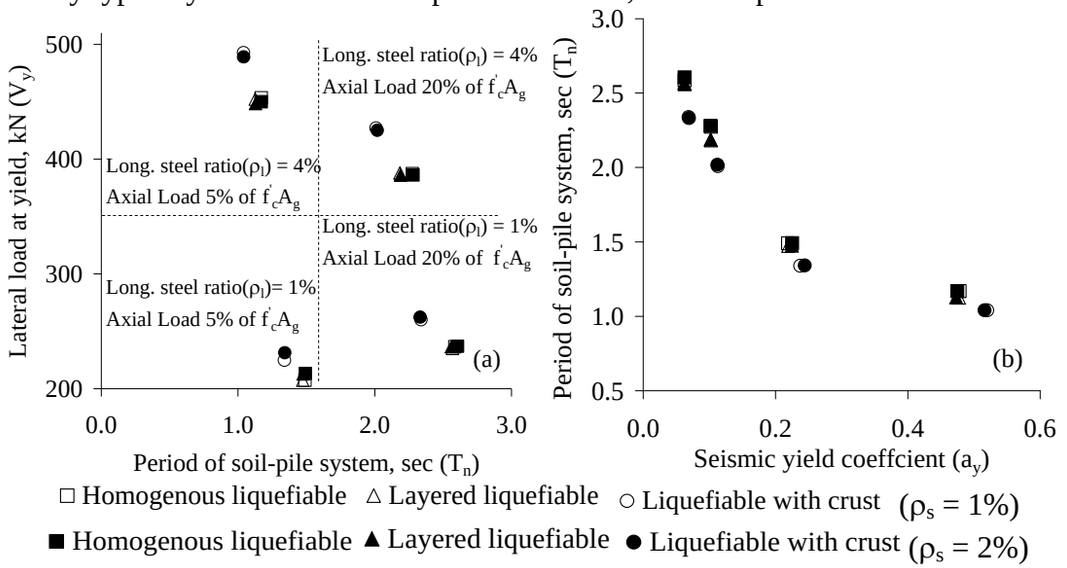


Figure 2: Capacity of soil-pile systems considered in this study.

Table 1: Characteristics of the ground motions selected for this work.

	M_w –	Neq –	Closest Distance (km)	Hypocenter Depth (km)	PGA (g)	Fourier Amplitude (cm/s^2)	Period (sec)
Maximum	7.5	15	39	18	1.50	1000	2.93
Minimum	6.0	5	3	5	0.12	39	0.06
Average	6.6	7	17	13	0.33	190	0.61

The search criterion for selecting the ground motions is based on the parametric range used in development of the various empirical methods investigated, namely: (a) moment magnitude between M_w = 6.0-7.5, (b) epicenter distance less than 40 km, (c) ASCE (2005) site classification 'C' and (d) maximum acceleration exceeding the yield acceleration. The dataset is compiled using the NGA[1] database. The majority of these records (statistics Table 1) are from the Western United States (about 30% from Northridge earthquake, 11% from Loma Prieta, and 10% from San Fernando and Morgan Hill). Note that the validity of the selected empirical methods is limited to gently sloping ground conditions (between 0.1% and 6% slope). In this article, results are presented for a 6% slope condition.

[1] NGA is the Next Generation Attenuation of Ground Motion Project (http://peer.berkeley.edu/nga/)

Using the various methods and the selected ground motions, permanent displacements at the ground surface are calculated. To evaluate the various ground displacement methods, each approach is compared with Newmark's upper bound solution for unsymmetrical resistance (Figure 3, Table 2). Unsymmetrical resistance considers the movement induced by the sliding mass in addition to the movement due to sliding resistance. The following observations are made from Figure 3:

- At low a_y/a_{max} values, Newmark's time integration method results in the lowest displacements compared to other methods.
- For higher a_y/a_{max} values, Yegian et al. (1991) indicates the lowest displacement estimates. However, this model has significant dispersion (σ = 233 cm). This may be attributed to derived parameters used in the calculation, such as equivalent number of cycles (N_{eq}) or predominant period (T).
- Youd et al. (2002) also indicates a wide range of displacements from 3.5 cm to 24 m and large dispersion (σ = 377 cm). The large dispersion might be due to ignoring select input soil parameters ($_{D50}$ and fines content).
- Bardet et al. (2002) predicts displacements in the range of 3.5 cm to 5 m with a reasonably low dispersion (σ = 84 cm) compared with other methods.
- Although the Yegian et al. and Youd et al. methods predict greater than 10 m displacement, they were not calibrated to this extent by the authors.

Table 2: Ground displacements obtained by the various methods (in cm).

Method adopted	Newmark Simplified	NM Time Integration	Ambraseys and Menu (1988)	Yegian et al. (1991)	Bardet et al. (2002)	Youd et al. (2002)
Maximum	902	129	130	2010	505	2376
Mean (μ)	37	8	22	69	73	223
Std Dev (σ)	117	19	24	233	83	377

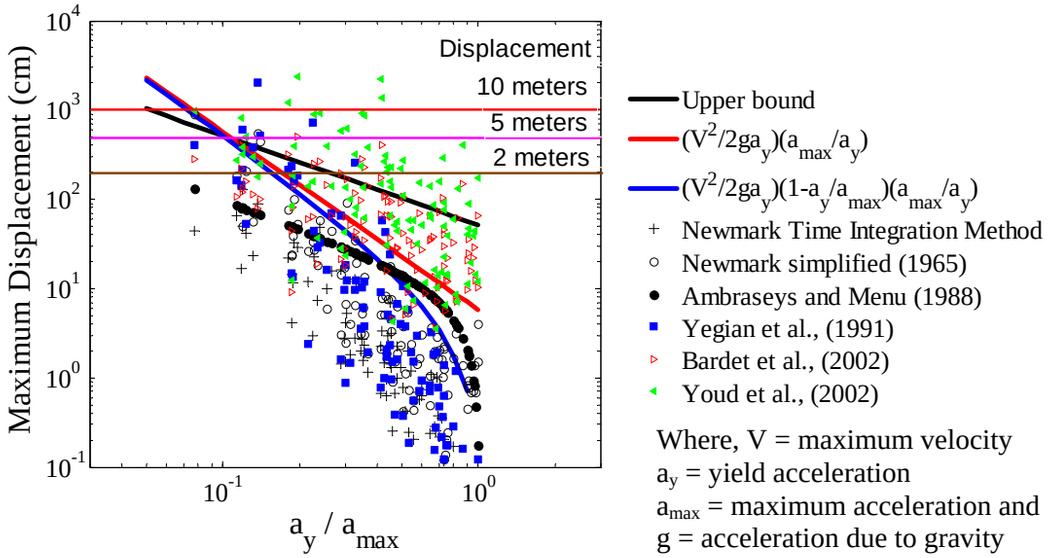


Figure 3: Newmark's bounded curves (Unsymmetrical resistance)

The large variation of displacement estimates for select models may be due to the broad range of earthquake records selected for these analyses and/or the soil

parameters selected. Nonetheless, in this work, the model by Bardet et al. (2002) is used in subsequent analysis for several reasons:

- The dispersion in displacement demand estimates as compared with the magnitude of displacement is reasonably low.
- The method is a function of the liquefiable layer depth and can be used to calculate the displacements along the layer depth.
- The model is simple, robust and has a broad calibration basis (467 case histories were used in the four parameter regression).
- The estimates using the Bardet et al. model are bounded by Newmark's simplified expression, which is readily used in design, and has been obtained from sliding block analysis.

Soil-Pile Performance under Liquefaction Loading – Using the three different simplified design methods and for the range of pile detailing conditions, the pile performance in terms of normalized plastic hinge length ($\lambda_p = L_p/D$, where L_p = length of the plastic hinge) and depth of maximum bending moment ($\lambda_m = L_m/D$, where L_m = depth to maximum moment) is assessed (Tables 3 and 4). These values are presented considering a global displacement ductility demand of $\mu_\Delta = 3.0$. Note that while the amplitude of displacement imposed on the soil-pile system varies, the displacement ductility is consistent for each case. However, this is not strictly the case when considering an applied ground displacement. The application of ground displacement imposes a different boundary condition on the soil-pile system; therefore one may expect these results to be inconsistent, when compared with applied pressures or p-multipliers. For these analyses, the ground displacement profile as determined by the method of Bardet et al. (2002) is used, assuming an earthquake with R = 22 km, M_w = 6.6, slope = 6% (Figure 4).

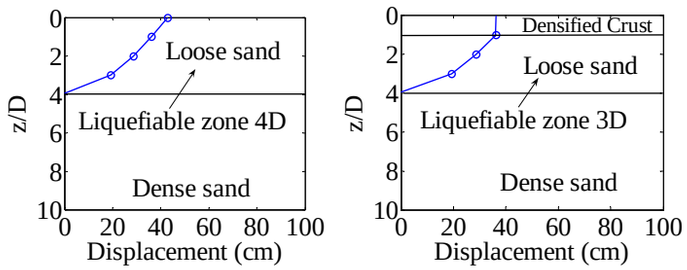


Figure 4. Applied soil displacements for the layered soil conditions considered in this study using the method of Bardet et al. (2002).

Excluding the results of analyses considering an imposed ground displacement, the following observations can be made from results summarized in Table 3 and 4:

- The maximum bending moment occurs at a reasonably shallow depth, λ_m ranges from 1.4-3.2), with 2/3 of the cases below 3.0.
- The range of damaged region, as characterized by λ_p is 1.3-3.2, however, 95% of the cases are below 3.0. More than 85% of the cases indicate a plastic hinge length greater than 1.5D. In general, these values are larger than those suggested for dry sand conditions (e.g. Budek et al., 2000; Chai and Hutchinson, 2002). This might be expected as the softer surrounding soils tend to spread the damage over a larger region.

- In general, application of axial load increases the depth to maximum moment for weaker piles, and has little effect for stronger piles. This is to be expected as the moment capacity and stiffness is larger for confined sections with larger axial loads. The plastic hinge length is generally smaller for axially loaded piles, indicating a more concentrated damaged region.
- There is little difference between the *p-y reduction* analysis and that with applied *soil pressures*, indicating the magnitude of the pressures is consistent with the reductions in strengths applied when using the *p-y reduction* method.
- Due to inconsistent boundary conditions when considering applied *soil displacements* the normalized depth to maximum moment λ_m and plastic hinge length λ_p are significantly different than the former two methods. On average λ_m is twice that of the p-y reduction and soil pressures analyses cases, and λ_p values vary depending on the soil condition and pile strength.
- In general, for the soil displacement cases, stronger piles (ρ_l = 4%) indicate larger λ_m values at a given displacement ductility demand. The location of the plastic hinge for stronger piles is below the liquefiable layer for both with and without crust soil conditions. However, weaker piles (ρ_l = 1%) result in plastic hinge formation concentrated completely within the liquefiable layer for with crust condition and at the interface of liquefiable and non-liquefiable layer for the layered without crust condition.
- A liquefiable crust soil condition generally results in lower λ_m and λ_p values, as compared with a homogeneous or layered liquefiable condition, indicating that the more concentrated damaged region migrates towards the ground surface, as would be anticipated since the crust is stiff in comparison with the liquefied sublayers. The plastic hinge is concentrated below the liquefiable layer for strong-stiff piles, irrespective of soil condition, and at the interface of the soil layers for weak-soft piles.

It should be noted that the above observations are dependent on other factors such as boundary conditions, above ground height of the pile, and distribution of soil layering and/or crust conditions relative to pile diameter.

Table 3: Non-dimensional depth of maximum bending moment (λ_m)

	ρ_l	ρ_s	P_A	p-y Reduction	Soil pressure	Soil displacement	Soil condition
Weak-Soft Piles	1	1	No load	1.92	1.88	NA[1]	Homogenous liquefiable
	1	1	20% load	1.97	2.02	NA	Homogenous liquefiable
	1	1	No load	1.92	1.92	4.07	Layered liquefiable
	1	1	20% load	2.06	2.06	4.03	Layered liquefiable
	1	1	No load	1.36	1.36	1.60/3.80	Liquefiable with crust
	1	1	20% load	1.55	1.55	3.61	Liquefiable with crust
Strong-Stiff Piles	4	2	No load	3.09	3.18	NA	Homogenous liquefiable
	4	2	20% load	2.90	3.14	NA	Homogenous liquefiable
	4	2	No load	3.09	3.14	5.01	Layered liquefiable
	4	2	20% load	3.09	3.14	5.10	Layered liquefiable
	4	2	No load	2.62	2.67	5.10	Liquefiable with crust
	4	2	20% load	2.62	2.67	5.19	Liquefiable with crust

[1] Soil movements across a 10m deep layer may not be realized in practice therefore are not considered.

Table 4: Non-dimensional plastic hinge length (λ_p)

	ρ_l	ρ_s	P_A	p-y reduction	Soil pressure	Soil movement	Soil condition
Weak-Soft Piles	1	1	No load	2.52	1.68	NA	Homogenous liquefiable
	1	1	20% f'_cA_g	1.82	1.31	NA	Homogenous liquefiable
	1	1	No load	1.73	1.77	1.45	Layered liquefiable
	1	1	20% f'_cA_g	1.35	1.35	2.10	Layered liquefiable
	1	1	No load	1.59	1.63	1.54 / 1.07	Liquefiable with crust
	1	1	20% f'_cA_g	1.31	1.35	3.17	Liquefiable with crust
Strong-Stiff Piles	4	2	No load	3.17	2.38	NA	Homogenous liquefiable
	4	2	20% f'_cA_g	2.33	2.01	NA	Homogenous liquefiable
	4	2	No load	2.38	2.38	1.63	Layered liquefiable
	4	2	20% f'_cA_g	2.05	2.10	1.40	Layered liquefiable
	4	2	No load	2.38	2.38	1.59	Liquefiable with crust
	4	2	20% f'_cA_g	2.01	2.01	1.40	Liquefiable with crust

CONCLUSIONS

The performance of a single pile, embedded in a variety of liquefiable soil conditions is evaluated. The case study pile is taken as 1.0 m diameter, extending 10D into the ground and 4D above ground, and embedded in (i) homogeneous liquefiable sand, (ii) layered liquefiable sand, and (iii) layered liquefiable sand with a dense crust. The nonlinear moment-curvature behavior of the pile is modeled, considering piles with detailing resulting in strong-stiff and weak-soft behavior, with the pile unloaded and heavily loaded (axially). The pile is analyzed under pseudo-static lateral loading to a displacement ductility of $\mu_\Delta = 3.0$ and considering different liquefaction induced pressures and displacements. Most notable conclusions include the following: (i) maximum bending moments occur within the upper 1-3D from the ground surface (where D = pile diameter), which is fairly consistent with typical lateral pile response in stable soils, however, (ii) the spread of damage is larger than predicted considering stable soils, typically greater than 1.5D, (iii) of the different analyses methods, applying soil displacements due to lateral spreading of the ground results in a different boundary condition applied to the soil-pile system, thus resulting in inconsistent values when compared to applying pressures or reducing the soils capacity, consequently, application of soil displacements results in deeper maximum moments and more concentrated regions of plasticity, and (iv) a liquefiable crust soil condition generally results in lower λ_m and λ_p values, as compared with a homogeneous or layered liquefiable condition. While these results need to be evaluated against experimental data and extended to consider other above-ground heights and soil layering geometries, the general trends provide useful insight for design engineers when evaluating damage to the substructure foundation system.

ACKNOWLEDGMENTS

The research support by the National Science Foundation (NSF) under the CAREER program, grant number CMS-0348144 is greatly acknowledged. Any opinions, findings, and conclusions expressed are those of the authors, and do not necessarily reflect those of the sponsoring organization.

REFERENCES

ASCE (2005). *Minimum design loads for buildings and other structures*: *ASCE Standard SEI 7-05*.

Ambraseys, N.N., and Menu, J.M., 1988. Earthquake-induced ground displacements: *Earthquake Engineering and Structural Dynamics*, John Wiley & Sons, Vol. 16: 985-1006.

Applied Technology Council (ATC), 1996. *Improved seismic design criteria for California bridges: Provisional Recommendations*. ATC-32, Redwood City, CA. June.

Bardet, J.-P., Tobita, T., Mace, N., and Hu, J., 2002. Regional modeling of liquefaction-induced ground deformation. *Earthquake Spectra*, Vol. 18(1): 19-46.

Bartlett, S.F and Youd, T.L., 1992. Empirical analysis of horizontal ground displacement generated by liquefaction-induced lateral spreads, *NCEER-92-0021*, State University of New York, Buffalo.

Berrill, J and Yasuda, S., 2002 Liquefaction and piled foundations: Some issues *Journal of Earthquake Engineering*, Vol. 6(1): 1-41.

Boulanger, R. W., Kutter, B. L., Brandenberg, S. J., Singh, P., Chang, D., 2003. *Pile foundations in liquefied and laterally spreading ground during earthquakes: Centrifuge Experiments & Analyses. Report No. UCD/CGM-03/01*, Center for Geotechnical Modeling, Department of Civil & Environmental Engineering, University of California Davis, California.

Budek, A. M., Priestley, M. J. N., and Benzoni, G., 2000. Inelastic Seismic Response of Bridge Drilled-Shaft RC Pile/Columns, *Journal of Structural Engg.*, ASCE, Vol. 126, No. 4, pp. 510-517.

Chai, Y.H., and Hutchinson, T. C., 2002. Flexural strength and ductility of extended pile-shafts-II: experimental study, *Journal of Structural Engineering*, ASCE, Vol. 128, No. 5, pp. 595-602.

Dobry, R. and Abdoun, T., 2001. Recent studies on seismic centrifuge modeling of liquefaction and its effect on deep foundations. *In Proceedings of the 4th International Conference on Recent Advances in Geotechnical Earthquake Engineering and Soil Dynamics*. San Diego, California.

Finn, W. D. L., 2005. A study of piles during earthquakes: issues of design and analysis. *Bulletin of Earthquake Engineering*, Vol. 3: 141–234.

Hamada, M. and O'Rourke, T., 1992. *Case Studies of Liquefaction and Lifeline Performance during Past Earthquakes. Vol. – 1*, Technical Report NCEER-92-0001, Buffalo NY.

Japanese Road Association. 2002. *Specifications for highway bridges, Japan Road Association (JRA)*, English-prepared by PWRI and CRL Japan.

Mander, J.B., Priestley, M. J. N., Park, R., 1988. Theoretical stress-strain model for confined concrete, *Journal of Structural Engineering*, ASCE, Vol. 114, No. 8, pp. 1804-1826.

MCEER (ATC-49), 2003. *Recommended LRFD guidelines for seismic design of highway bridges.*

Mizuno, H., M., Iiba, and T. Hirade., 1996. Pile damage during the 1995 Hyogoken-Nanbu earthquake in Japan, *Proc. 11th World Conf. Earthquake Eng., Acapulco*, Paper No. 977.

Newmark, N.M., 1965. Effects of earthquakes on dams and embankments: Fifth Rankine Lecture, *Geotechnique*, Vol. 15: 139-159.

Reese, L. C., Wang, S. T., Isenhower, W. M., Arrelaga, J.A., and Hendrix, J. A., 2000. *LPILE Plus technical manual version 4.0m*, Ensoft, Inc. Austin, TX.

Tokimatsu, K., Suzuki, H., and Suzuki, Y., 2001. Back-calculated p-y relation of liquefied soils from large shaking table tests. *4th Int. Conference on Recent Advances in Geotechnical Earthquake Engineering and Soil Dynamics*, S. Prakash, ed, University of Missouri, Rolla, paper 6.24.

Wilson, D. W., Boulanger, R. W., and Kutter, B. L., 1999. Lateral resistance of piles in liquefying sand *OTRC'99 Conf. on Analysis, Design, Construction and Testing of Deep Foundations*, J. M. Roesset, ed., ASCE, Geotechnical Special Publication, No. 88, pp. 165–179.

XTRACT, 2004. *Cross-sectional structural analysis of components*, Imbsen software systems, ver. 3.0.1, Sacramento.

Yegian, M.K., Marciano, E.A., and Ghahraman, V.G., 1991. Earthquake-induced permanent deformations: Probabilistic approach: *Journal of Geotechnical Engineering*, ASCE, Vol. 117(1): 35-50.

Youd, T.L., Hansen, C.M. and Bartlett, S.F., 2002. Revised multilinear regression equations for prediction of lateral spread displacement, *Journal of Geotechnical and Geoenvironmental Engineering*, ASCE, Vol. 128(12): 1007-1017.

The role of soil compressibility in centrifuge model tests of piles foundation undergoing lateral spreading of liquefied soil

Marcelo González[1], Javier Ubilla[2], Tarek Abdoun[3] and Ricardo Dobry[4].

[1]ASCE Student Member, Graduate Student, RPI, 110 8th Street, Troy, NY, 12180. gonzam2@rpi.edu
[2]ASCE Student Member, Graduate Student, RPI, 110 8th Street, Troy, NY, 12180. ubillj@rpi.edu
[3]Associate Professor and Associate Director, NEES-NSF Geotechnical Centrifuge Research Center, Rensselaer Polytechnic Institute, 110 8th Street, Troy, NY, 12180. abdout@rpi.edu
[4]Professor and Director, NEES-NSF Geotechnical Centrifuge Research Center, Rensselaer Polytechnic Institute, 110 8th Street, Troy, NY, 12180. dobryr@rpi.edu

ABSTRACT: Two centrifuge model tests at 40g level were examined in order to evaluate the use of particle size reduction as an alternative method to construct centrifuge model tests of a pile foundation undergoing lateral spreading of liquefied soil. The main difference between both tests was the method used to match the prototype permeability coefficient: (1) viscous pore fluid instead of water and (2) reduction of the particle size while using water as pore fluid. The two soils were placed at the same relative density, which resulted in two very different soil compressibilities and different model responses. Other centrifuge tests reported elsewhere (Gonzalez M., 2007), indicate that when compressibility rather than relative density is matched, particle size reduction produces the correct soil and pile response that agrees. Therefore, both permeability and compressibility need to be matched when using the particle size reduction technique.

INTRODUCTION

The permeability coefficient of a clean sand deposit in the field usually can be achieved in a centrifuge model test by two methods: (1) using viscous pore fluid instead of water and (2) reducing of the particle size while using water as pore fluid. Increasing the viscosity of the pore fluid by N times than that of the water, a saturated clean sand deposit can be tested in an Ng level environment assuring the same permeability coefficient that it would have in the 1g level environment. The same effect in the permeability coefficient can also be achieved in the Ng level environment tests by using water and reducing uniformly the particle size of the soil deposit $N^{0.5}$ times.

In most cases, the viscous fluid is preferred over the particle size reduction method because it is easy to implement and uses the same soil as in the field (prototype). On the other hand, it has been argued that the use of viscous fluid while keeping the same particle size may change aspects of the soil and foundation response such as shear band development and bearing capacity (Tatsuoka F., 1997). Use of particle size reduction becomes an alternative solution to these potential problems, but also brings new challenges to the researchers when a soil with a different grain size distribution is used to simulate the behavior of the field soil deposit including its response close to a foundation (prototype model).

This paper compares the results of two centrifuge tests that replicate the case of a single pile foundation undergoing lateral spreading of liquefied soil. All the results are presented in prototype units.

The soil deposit in both tests corresponds to saturated loose sand with a gentle- slope of 4.5 degrees. The soil deposit was liquefied by applying a uniform sinusoidal input base motion of amplitude 0.35g and frequency of 2Hz.

CENTRIFUGE TESTS

Two centrifuge model tests: CMT1 and CMT2, with the same prototype permeability and relative density were analyzed by using the 3 m radius centrifuge installation of Rensselaer Polytechnic Institute. CMT1 was created by using coarse sand and viscous fluid. On the other hand, CMT2 was formed with a combination of Nevada sand and non-plastic silt. The grain size distribution curves for both soils are compared in Fig.1. Both tests were conducted in a flexible shear beam container spun at a 40g level. Fig.2 shows the location of the instrumentation and dimension of the piles used in tests CMT1 and CMT2.

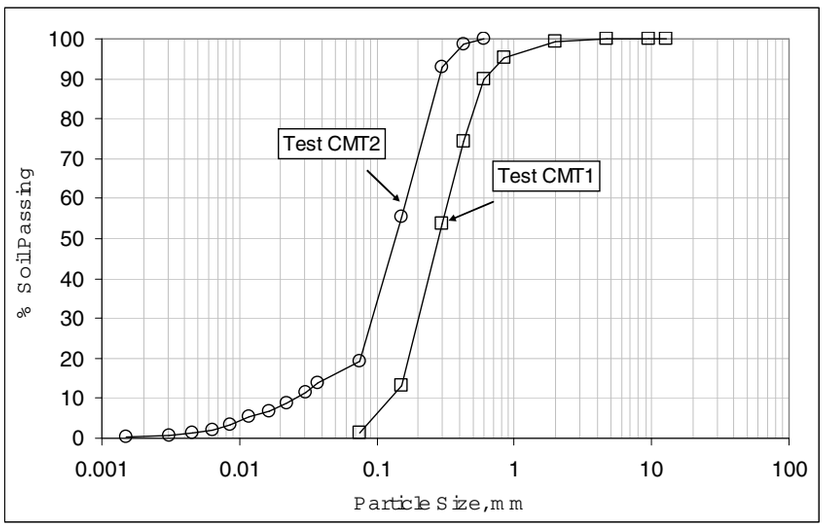


FIG.1 Particle grain size distribution for the soil deposit in model tests CMT1 and CMT2

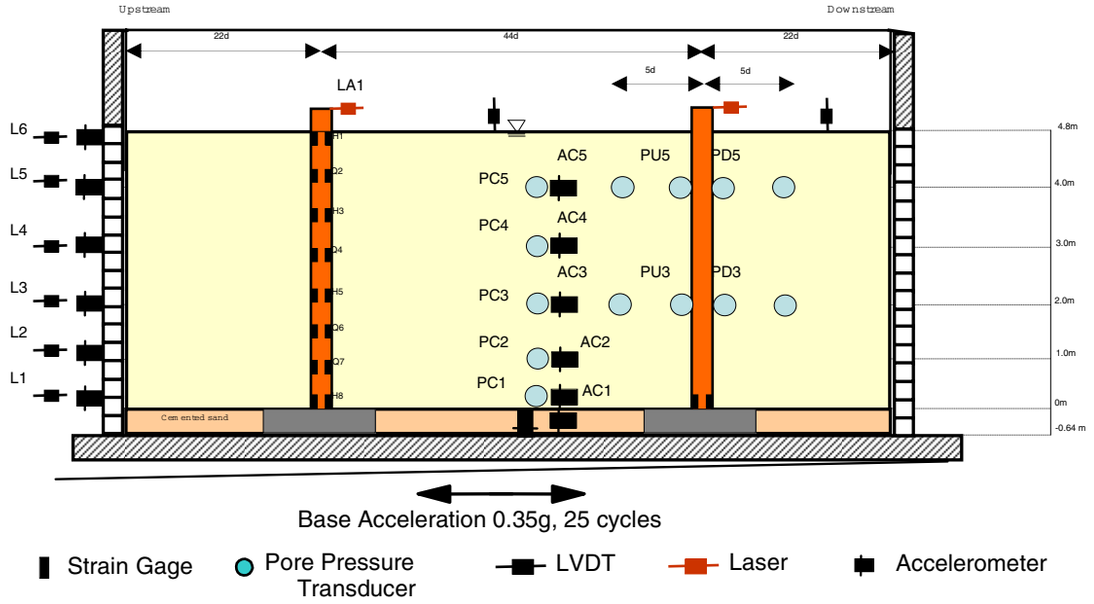


FIG. 2 Schematic diagram of centrifuge model test CMT1 and CMT2

Soil and model Properties

In both tests CMT1 and CMT2, the soil profile includes a cemented sand layer of 0.64m thickness located at bottom of the model, with a uniform saturated loose sand deposit with a thickness of 4.8 m placed over the cemented layer. The soil was placed in the container by using a dry pluviation method and saturated in a high vacuum condition. More details of the model preparation and saturation processes can be found in Gonzalez L. (2005).

Table 1 and 2 summarize the main index properties of the soils and their characteristics as placed in the centrifuge model tests, respectively.

Table 1. Soil index Properties

SOIL PROPERTIES	Test CMT1	Test CMT2
D_{50} , mm	0.30	0.15
D_{10} , mm	0.12	0.025
FC , %	1.4	20
Minimum void ratio	0.555	0.390
Maximum void ratio	0.806	0.954
Gs	2.700	2.671

Table 2. Centrifuge model test properties

TEST PROPERTIES	Test CMT1	Test CMT2
Gravity Level, g	40	40
Initial Void Ratio	0.705	0.714
Relative Density, %	40	42
Permeability Coefficient, cm/sec	1.28×10^{-2}	1.70×10^{-2}
Compression Index (C_c)	0.0064	0.0150

CMT1 and CMT2 have a very similar prototype permeability coefficient; in addition, the sand in test CMT2 was placed controlling the void ratio intending to match the same relative density of test CMT1. However, as a consequence the sand in test CMT2 was more compressible than in test CMT1 (C_c =0.015 versus 0.0064).

Pile Foundation

Each model test has attached two identical piles foundation. The solid circular piles are 0.25m diameter with a bending stiffness (EI) of 14,000 kNm^2. The pile was placed in the model before the soil was pluviated, attempting to simulate the case of a pre – excavated pile installation. Bending moment and excess pore water pressure were monitored in the piles located at upper and down slope, respectively (Fig. 1). Displacement of the Pile Foundation was measured by a laser sensor.

Both piles were fixed at the bottom of the container and cemented soil was used to create the base of the model. The rotational spring at the bottom of the upper pile was estimated at 25,000 kN-m/ rad.

EXPERIMENTAL RESULTS

Acceleration measured in the soil

Fig.3 shows the acceleration time history measured in the soil (refer to Fig.2). It is observed that the stiffness degradation starts at the top of the model at around 1.5 sec and is propagated to the bottom where the phenomena of the stiffness degradation takes place at about 2.5sec. The stiffness degradation can be usually associated with the beginning of the soil liquefaction. The results of the soil acceleration show in Test CMT1 a high presence of upslope negative spikes which are associated with a dilative response of the soil (Taboada, 1995). In the case of test CMT2, non high frequency spikes are observed up to 3.8m depth.

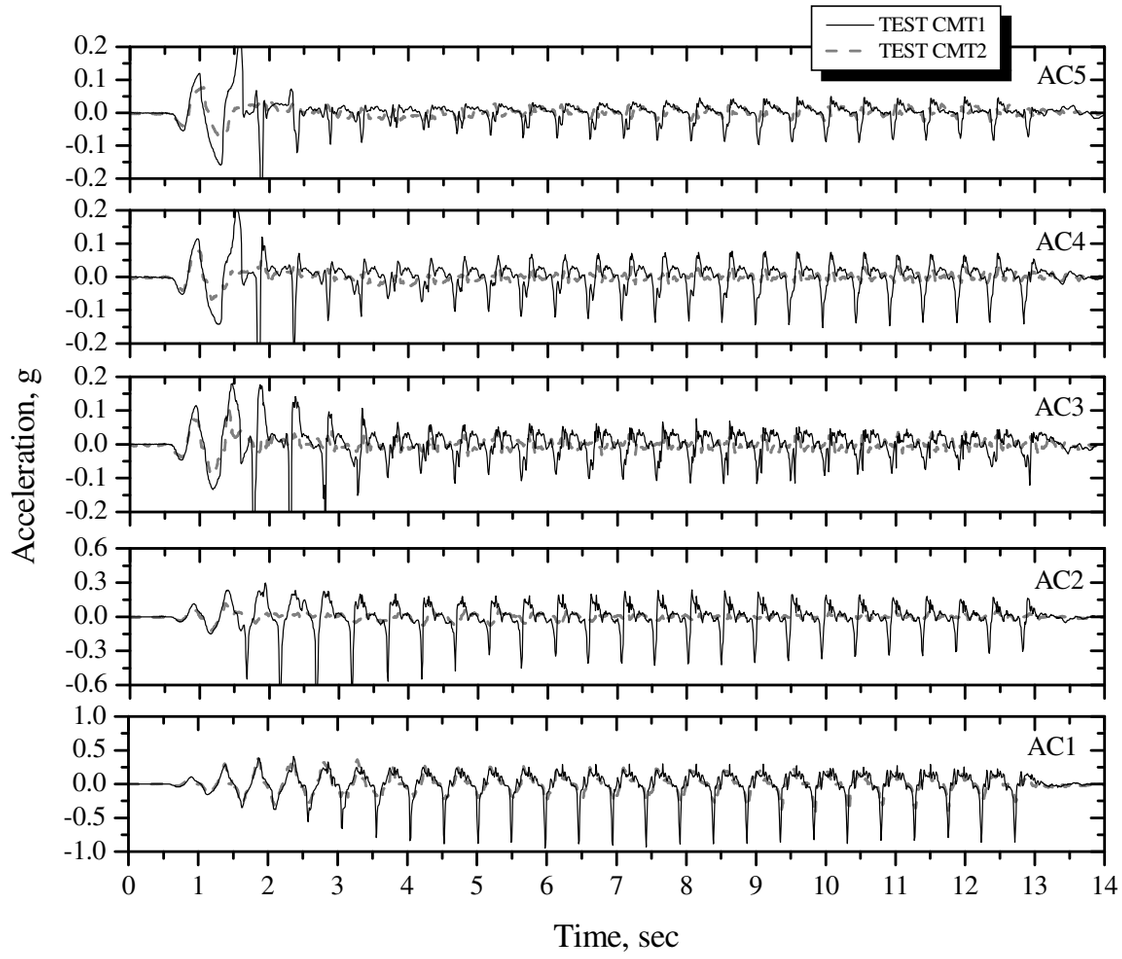


FIG. 3. Time history of the acceleration measured in the soil

Excess pore water pressure

The excess pore water pressure was measured close to the pile as well as far from the pile. Fig.4 shows the time history of the excess pore pressure attached to the down slope pile at 0.8m and 2.8m depth. In this figure, negative excess pore pressures at shallow depths in the piles (suction forces) are observed; this has also been noted by researchers Gonzalez L. (2005) and Ubilla J. (2007). These suction forces disappear at deep depths (see pore pressure transducers PU3 and PD3[1]).

It is interesting to observe in Fig.4 that suction forces are greater in value and dissipate at a slower rate in test CMT1 than in test CMT2, which has a complete dissipation of the suction forces when shaking ends.

[1] PU and PD refer to the Pore Water Pressure Instrumentation located at Up and Down Stream side of the Pile Foundation, respectively.

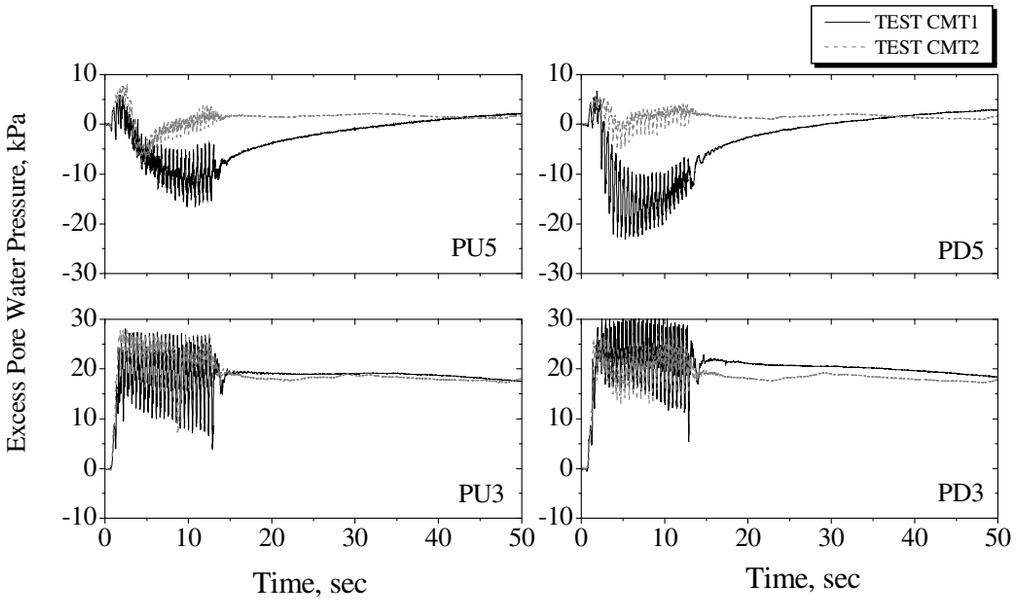


FIG. 4. Excess pore water pressure history measured in the pile foundation located at down slope side of the model

Fig.5 shows the excess pore water pressure dissipation measured at a far distance from the pile. In this figure, it is noted that test CMT1 tends to dissipate the excess pore water pressure faster at shallow depths than in test CMT2. It is also noted that at bottom depths the rate of dissipation in both experiments is similar, which is an indirect indication that the permeability coefficient of the soil deposits is also similar in both tests.

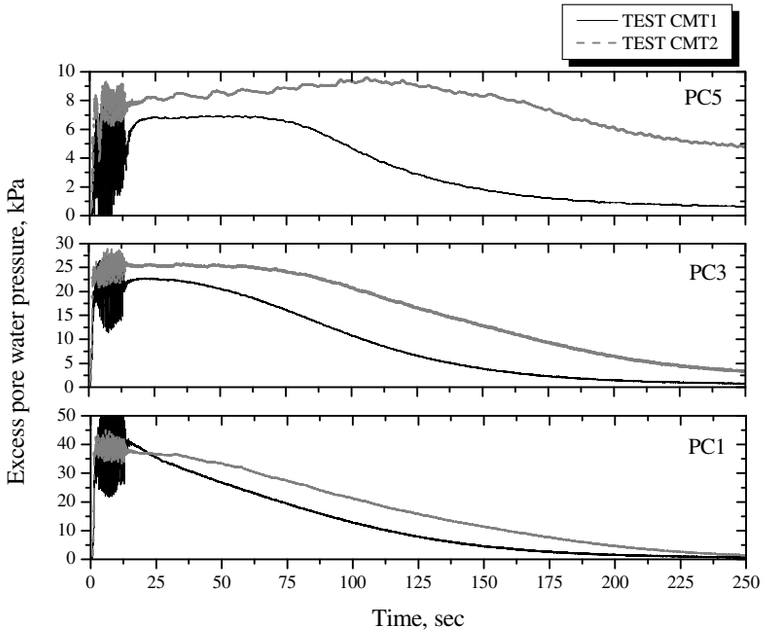


Fig.5: Time history of the Excess pore water pressure measured in the soil

Lateral Displacement of the soil

The lateral displacement was measured by using LVDTs attached to the laminar pieces of the container. Fig.6 shows the time history of the lateral displacement for top, middle and bottom model levels. The lateral displacement at the surface in test CMT2 was calculated at 1.30m, almost 50% more displacement than measured in test CMT1. It is known that more dilative soil behavior prevents bigger flow failure displacement (Elgamal, 1998).

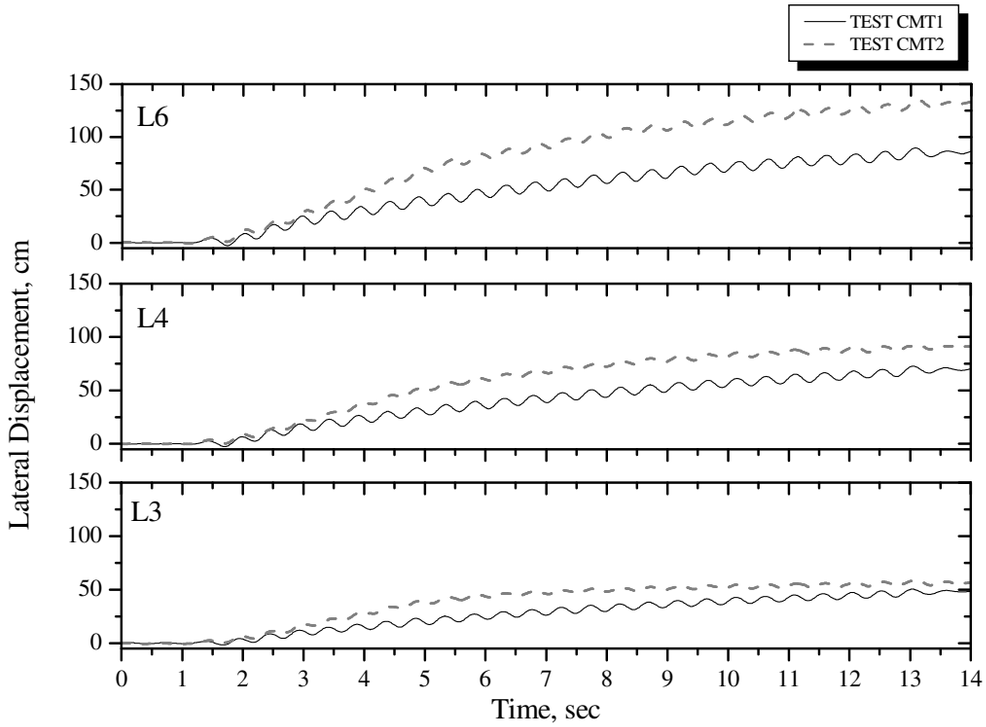


FIG. 6. Time History of Lateral displacement of the soil

Bending moment in the pile

Bending moments in the upper pile were measured by using strain gauges. The pile displacement was also measured by using a laser sensor LA1. Fig.7 describes the time history of the measurements previously mentioned. One very interesting observation extracted from Fig.7 is that the upper pile in Test CMT1 is clearly dragged beyond the shaker end time unlike of the upper pile in test CMT2, which rebounded during the shaking. This observation is supported by the pile displacement.

The fact that one pile rebounded and the other did not, is due to the reduced existing suction forces and faster dissipation in one of the tests. The higher compressibility of the soil in test CMT2 produces high values and long duration of the excess pore water pressure at shallow depths, which helps in the dissipation of the suction forces around the pile and allows the pile to rebound during the shaking.

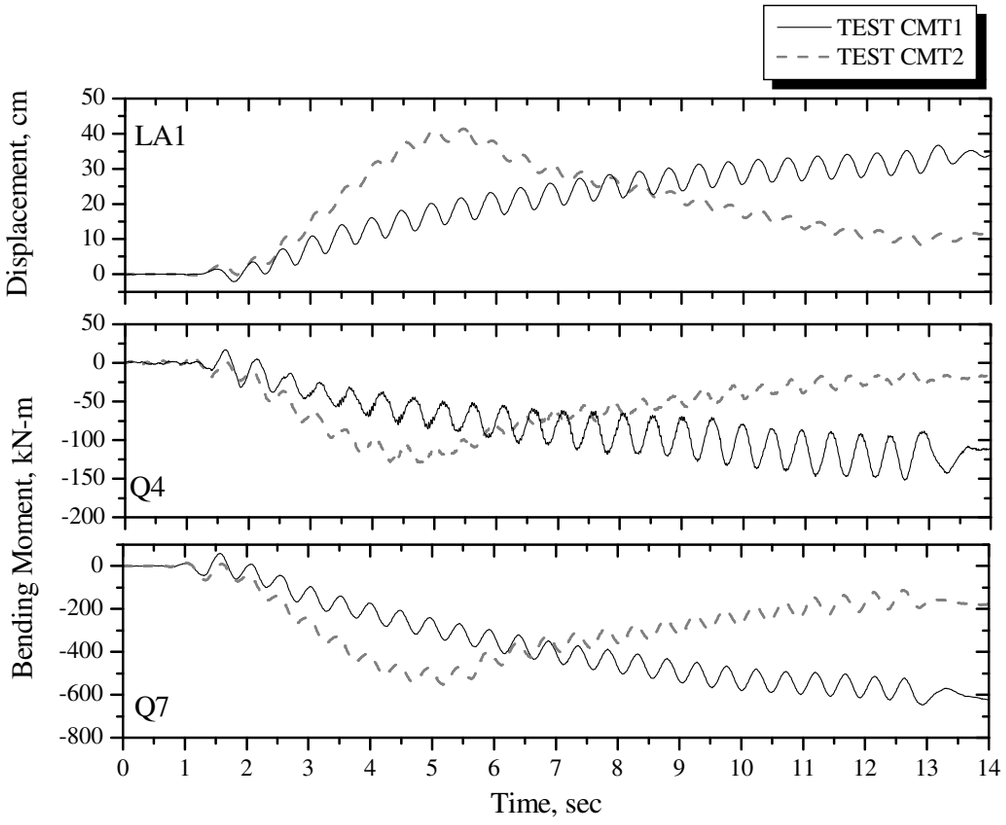


FIG. 7. Pile displacement and bending moment measured in the pile located at upper slope side of the model

CONCLUSIONS

In this research, two centrifuge model tests were examined in order to evaluate the use of particle size reduction as an alternative method of construction for model tests of piles foundation undergoing lateral spreading of liquefied soil. The two soils were placed at the same relative density and permeability, which resulted in two very different soil compressibilities and different model responses.

The responses in both tests in terms of acceleration, excess pore water pressure, displacement and pile bending moments are completely different. The high compressibility of the soil in test CMT2 produces small values and faster dissipation of the negative excess pore water pressure around the pile; it also increases the lateral soil displacements and makes the pile rebound during shaking. On the other hand, test CMT1 behaves in a completely contrary way to test CMT2.

This research illustrates that permeability and compressibility need to be matched when the particle size reduction technique is used.

REFERENCES

Elgamal A., Dobry R., Parra E., Yang Z., (1998) "Soil Dilation and Shear Deformations during Liquefaction", *Proc. 4th Intl. Conf. on Case Histories in Geotechnical Engineering*, March 8-15, 1998, Prakash, Ed., St. Louis, Missouri

Gonzalez, L. (2005) "Centrifuge Modeling of Permeability and Pinning Reinforcement Effects on Pile Response to Lateral Spreading" *Ph.D. Thesis, Department Civil Engineering, Rensselaer Polytechnic Institute*, Troy, NY

Gonzalez, M. (2007) "Use of particle size reduction as a construction technique for centrifuge model tests in pile foundation undergoing lateral spreading of liquefied soil". *Paper in Progress*

Taboada, V. (1995) "Centrifuge Modeling of Earthquakes – Induced Lateral Spreading in Sand using Laminar Box", *Ph.D. Thesis, Department Civil Engineering, Rensselaer Polytechnic Institute*. Troy, NY

Tatsuoka, F., Goto, S., Tanaka, T., Tani, K., and Kimura, Y. (1997) "Particle size effects on bearing capacity of footing on granular material" *Proc., Deformation and Progressive Failure in Geomechanics*, IS-Nagoya '97; A. Asaoka, T. Adachi, and F. Oka, eds., Pergamon, 133–138. JGGE © ASCE / MAY 2003 / 449

Ubilla, J. (2007) "Physical modeling of the effects of natural hazards on soil-structure interaction" *Ph.D. Thesis, Department Civil Engineering, Rensselaer Polytechnic Institute*, Troy, NY

This page intentionally left blank

Cyclic Failure of Fine-grained Soils During the 1999 Kocaeli Earthquake

Volkan Okur[1], M. ASCE, Selim Altun[2], M. ASCE and Atilla Ansal[3], M. ASCE,

[1]Eskisehir Osmangazi University, Dept. of Civil Engineering, Eskisehir/Turkey; vokur@ogu.edu.tr
[2]Ege University, Dept. of Civil Engineering, Izmir/Turkey; selim.altun@ege.edu.tr
[3]Bogazici University, Kandilli Obs. & Earthquake Res. Ins., Istanbul/Turkey; ansal@boun.edu.tr

ABSTRACT: The 1999 Kocaeli earthquake caused severe damages, most notably in areas closer to the epicenter. Most of the major property damage resulted from liquefaction and cyclic failure. Many buildings settled and tilted due to the liquefaction and bearing capacity failures. Damages of loss of coastal lands and subsidence of the ground occurred at several sites along Izmit Bay due to liquefaction and cyclic failure. Several site surveys, soil investigations and static and dynamic laboratory soil tests were conducted covering most of the affected area. The results presented in this paper are part of an investigation including series of tests on the behavior of saturated natural fine-grained soil samples, taken from the area. The samples were tested using stress-controlled cyclic triaxial and cyclic torsional apparatuses. The results were analyzed for the assessment of dynamic instability of fine-grained soils by using the energy criteria, which is frequently used for liquefaction analysis. Analysis of cyclic test data suggests that portions of fine-grained soil deposits, i.e. silts and silty clays, likely developed relatively high excess pore pressures and significant shear strains during the earthquake that led to particle structure breakdown and strain softening, and thus, likely contributed to the observed overall stability problems.

INTRODUCTION

Until recent earthquakes like the 1999 Kocaeli, the liquefaction phenomena of saturated sands have continued to receive much more attention than any other problem in geotechnical earthquake engineering. Extensive research has been conducted to understand the mechanisms leading to liquefaction, and according to these studies and their results, new methods were proposed for evaluating the liquefaction susceptibility of saturated sandy soils (Youd et al. 2001).

Besides the liquefaction susceptibility of coarse-grained soils, cyclic failure of fine-grained soils was also considered for much of the damage observed after the1999 Kocaeli earthquake (Bray and Sancio, 2006). The Chinese criteria, commonly

recommended to evaluate liquefaction susceptibility of fine-grained soils with clay contents seem not adequate.

This study presents the results from a preliminary experimental study of cyclic failure of fine-grained soils using dynamic triaxial and dynamic hollow cylinder torsional shear tests. The study also includes the use of activation energy in fine-grained soils, an energy concept introduced by Nemat-Nasser and Shokooh (1979) for evaluating the liquefaction susceptibility of coarse-grained soils. The approach is based on the assumption that, part of the energy is dissipated throughout the soil during deformation under cyclic loads, and part of the energy is dissipated into the soils.

One of the main problems during cyclic tests with fine-grained soils in laboratory environment is the accurate measurement of pore water pressures. Generally, the measurements are made from top or bottom pedestals and sometimes from the middle which probably disturbs the soil. Also, for the equalization of excess pore water pressure throughout the sample, one must conduct tests at slow rates, like between 0.001Hz-0.01Hz. However, seismic loading frequency is much higher than these values and cyclic loading at higher frequencies prevents the equalization of pore pressure throughout the sample. Consequently, pore pressure may not be a reliable parameter in evaluating the cyclic response of fine-grained soils under different seismic loading rates. In that case, if pore pressure measurements are inaccurate, it seems reasonable to use some kind of energy criteria for the assessment of dynamic instability of fine-grained soils. There are a number of evaluation methods based on material ability to absorb the applied energy which increases the internal energy and change its strength (Law et al.,, 1990; Figueroa and Dahasaria, 1991; Liang et al., 1995; Voznesensky and Steinar, 1999). Among these, unit dissipated and unit activation energy methods are the most promising methods for identifying potential problems during cyclic loading.

Both methods are based on the definition of a critical strain and the calculation of unit energy required to be dissipated by the soil to reach to this specified state. Unit activation energy, also called threshold energy, E_a, is defined as the minimum energy that the system must overcome before it can undergo the appropriate changes. Unless the accumulated energy reaches this minimum level, activation energy may, otherwise, indicate that material behavior is nonlinear elastic. It is independent of anything but the nature of the soil particles bonding, and as such it is very desirable to use unit activation energy as the instability criteria. The shape of hysteresis loops for the initial cycles has the same area for every cycle that indicates the non-linear elastic response of the soil. Actually those material response thresholds already identified, but just considering straining and degradation effects (Okur and Ansal, 2005; Vucetic and Dobry, 1991). Further accumulation of internal energy over the level beyond this threshold eventually results in plastic alteration in the structure of the material which means degradation of soil's rigidity. The area of the loops begins to increase and appears as an open stress strain loop (Fig 1).

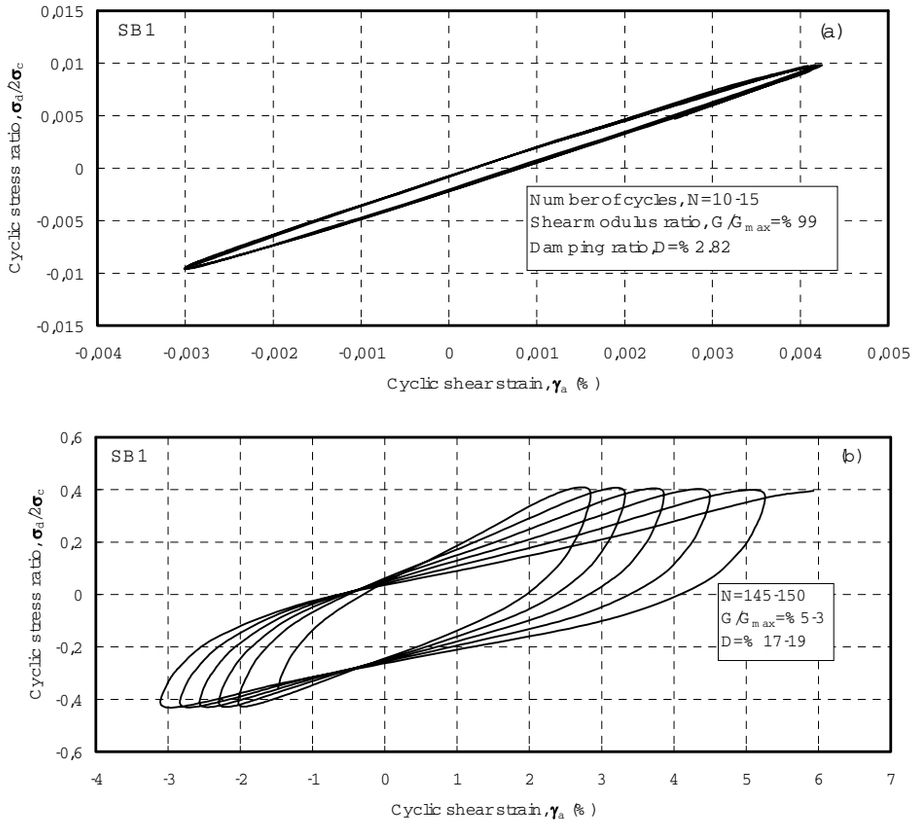


FIG. 1. Actual test records during a) nonlinear elastic response, and b) cyclic failure

The other energy criteria used in this study is the unit dissipated energy. The total energy accumulated per unit volume (ΔW) absorbed by the specimen is actually "the cumulative energy" dissipated in the unit volume of soil in all cycles at an instant like liquefaction in saturated coarse-grained soils or cyclic failure in fine-grained soils. For triaxial compression-extension and as well as torsional shear, it can be evaluated by (Figueroa and Dahasaria, 1991):

$$\Delta W = \sum_{i=1}^{n-1} 0.5(\sigma_{i+1} + \sigma_i)(\varepsilon_{i+1} - \varepsilon_i) \qquad (1a)$$

$$\Delta W = \sum_{i=1}^{n-1} 0.5(\tau_{i+1} + \tau_i)(\gamma_{i+1} - \gamma_i) \quad (1b)$$

where σ is the deviator stress, ε is the axial strain, τ is the shear stress and γ is the shear strain, n is the number of points recorded to a specified instant in loading history.

The accumulated dissipated energy per unit volume up to cyclic failure is affected by both cyclic stress strain amplitudes and the number of cycles. Various relationships were also proposed between pore pressure development and the dissipated energy during the dynamic loading (Berrill et al., 1985; Law et al., 1990; Liang et al.,, 1995; Figueroa and Dahasaria,1991).

Compared with other existing evaluation methods, there are several advantages of the energy-based approaches. Among the most important are listed as follows: a) Energy is directly related to the intensity of dynamic loading. b) It is not necessary to decompose the shear stress history to find the equivalent number of uniform cycles for selected stress or strain levels. c) It is practically independent of the load waveform and since there is no need to model a complicated random stress history in laboratory experiments, a simple sinusoidal pattern of loading could be used in all cases. d) It is generally independent of the type of testing device which facilitates the comparison of results obtained in different laboratories (Law et al., 1990; Liang et al., 1995; Voznesensky and Steinar, 1999).

This paper discusses the evaluation and analysis of dynamic instability of fine-grained soils during cyclic loading using the two above mentioned energy criteria.

GEOTECHNICAL SITE CONDITONS

The soil specimens selected for this study were obtained from the town of Gölcük, a province of Kocaeli (Izmit) City that suffered a major earthquake (M_w=7.4) in 1999. Damaging ground shaking intensities affected approximately 2000 square kilometers. The epicenter was very close to Gölcük, located along the coastal areas of Izmit Bay. Site effects played an important role in the localized damage concentrations, as well as inadequate provision for seismic forces in the designs or poor construction practices. An important percentage of the structural damage was due to the liquefaction and cyclic bearing capacity failures. Also, subsidence of a large area close to the shorelines caused flooding and extensive damage to buildings.

The geological profile of the south shores of Izmit bay consists of Tertiary marine sediments overlain by Pliocene continental deposits and marine terrace and marine terrace deposits. Gölcük is located on Holocene alluvium deposits.

After the earthquake, several borings were performed within the investigated site (Fig 2), (Ansal et al., 2000). The results indicated a heterogeneous soil profile consisting mostly of marine sediments with gravels and shells. However, it is possible to identify five layers within the soil profile: soft silty clay, loose to medium dense gravel and sand, medium/stiff clay, dense gravel, and stiff clay layers. As shown in Figure 2; dense and stiff clay layers are encountered below 20 meters depth in all boreholes. Special precautions were taken in recovering the samples, especially below the groundwater table.

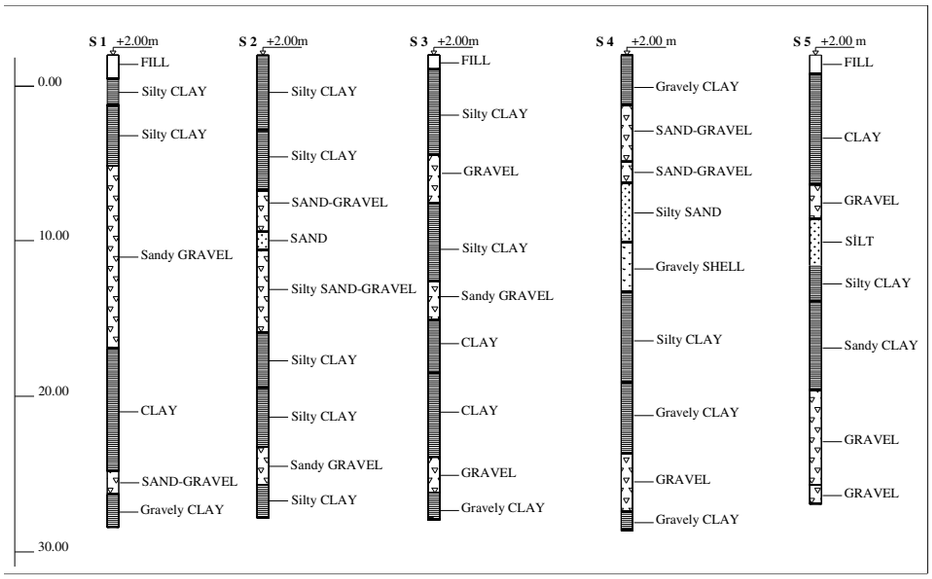


FIG. 2. Two dimensional stratigraphic characteristics of the investigated site

TESTING DEVICES AND TEST PROGRAM

For the evaluation of cyclic failure of fine-grained dynamic triaxial and dynamic hollow torsional tests were conducted. The details of the test systems and specimen preparation guidelines are similar with Okur and Ansal (2007). The specimens for dynamic triaxial tests had a height of 105mm and a diameter of 50mm. Dynamic hollow torsional test specimens had a height of 200 mm and an outer diameter of 100mm and an inner diameter of 60mm. The characteristics of tested material are given in Table 1. After applying back pressures between 100-250 kPa, Skempton's B parameter was checked and values greater than 0.95 were achieved. The samples were then consolidated to initial confining stress levels ranging from 50kPa to 250kPa. In both testing systems, the samples were sheared under undrained conditions using a stress-controlled procedure. Two different testing systems were used in this investigation to observe the influence of the boundary conditions such as loading directions, specimen sizes on the test results.

In dynamic hollow torsional test, the height of the specimen was fixed, so during dynamic loading, only torsional deformation takes place, but the dimensions of the specimen remains unchanged. The torque is applied with a constant torsional shear rate while the specimen and inner cell were kept undrained. In this condition, the dimensions of the specimen do not change, but only torsional deformation is possible.

Table 1. Properties of tested samples

Depth (m)	w_o (%)	e_o	w_L (%)	PI (%)	Soil Type
6-20	28-40	0.81-1.08	41-70	10-40	CL, ML, ML-MH

w_o: natural water content, e_o: natural void ratio
w_L: Liquid limit, PI: plasticity index

Tests were conducted on samples having various water contents and plasticity indices. All tests were conducted using a stress-controlled loading type and under sinusoidal loading at a frequency of 0.1 Hz. Cyclic loading stages are composed of multi stress loadings that were generally used where the numbers of test samples are limited. In these tests, samples were first consolidated, and then were subjected to 5 cycles of cyclic axial or shear stresses starting from quite low cyclic stress amplitudes under undrained conditions. The samples were cyclically loaded step by step with gradually increasing stress amplitudes covering a wide strain range of 10^{-3}to10^{1} % under a constant confining pressure.

TEST RESULTS

A characteristic test is selected to explain the representative results. The sample had a plasticity index of 22% and a water content of 30%. Fig. 3 shows the strain and pore pressure response. Due to the strain rate, pore water pressure build-up begins at the very initial cycles but the specimen is rigid and strain is almost negligible until cycle 40. Despite confirmed saturation of the sample before cyclic loading, pore pressure ratio never exceeds 0.7 although cyclic strain reaches to a value of 5% double amplitude (defined as cyclic failure) which means pore water pressure values may not be a consistent parameter to determine cyclic loading response of fine-grained soils at this or higher loading rates.

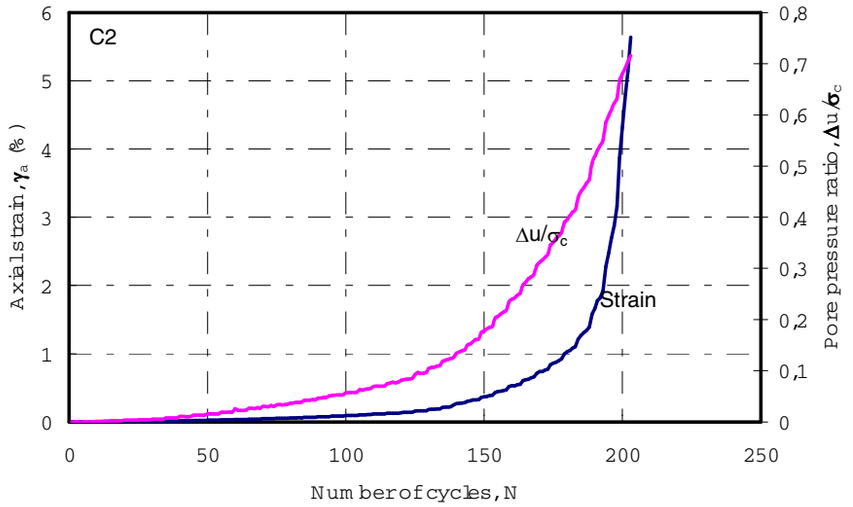


FIG. 3. Cyclic strain and pore water accumulation during cyclic loading

Critical thresholds may be defined either using the cyclic strain versus time or shear modulus cyclic strain response curves. The first threshold is related with the axial strain between 0.5-1% (Figure 4) and the second one is actually the point where plastic deformation or otherwise stated cyclic failure occurs which is around an axial strain of 3%.

Based on the test results, two threshold states named above selected for analysis and dissipated energy values were evaluated (Figure 5) for these critical strain levels. The activation energy, E_a were evaluated for the cyclic strain levels ranging between 0.01-0.06% depending on effective confining pressure and plasticity index of the sample.

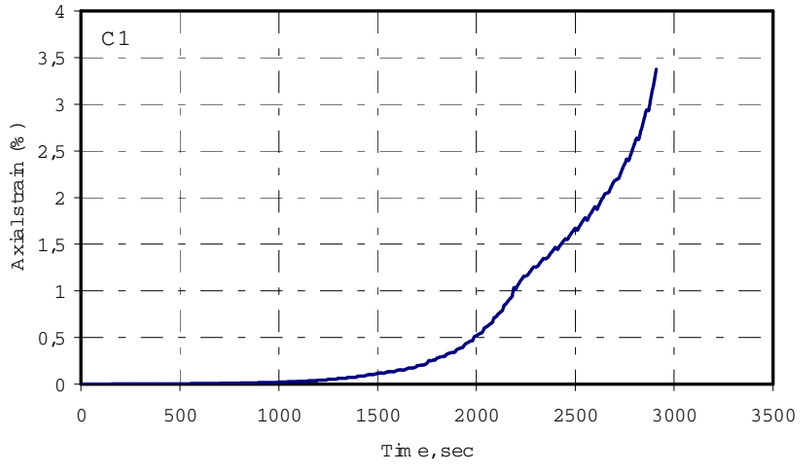


FIG. 4. Cyclic strain accumulation vs time

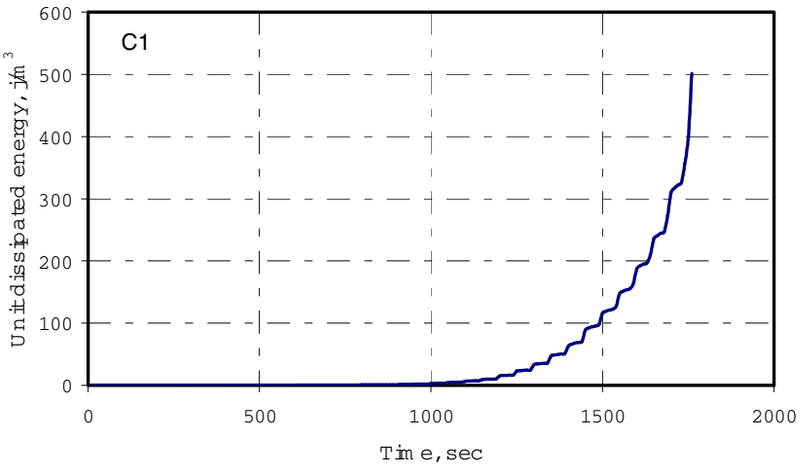


FIG. 5. Buildup of dissipated energy with time

Figure 6 shows the unit energy difference between consecutive cycles. Increasing cyclic stress ratio in every five cycles generates almost same hysteresis loops until 1400th sec. As can be expected the value is almost zero that could mean that energy dissipation is almost zero which actually verifies that the response of the soil sample is in nonlinear elastic state. After 1400th sec, the dissipation between consecutive cycles begins to increase in a slow rate until 1750-1800th sec. The point where the plastic deformation becomes significant, the dissipated energy difference reaches to a value on the order of 2000-3000 J/m^3 before 1750-1800th sec.

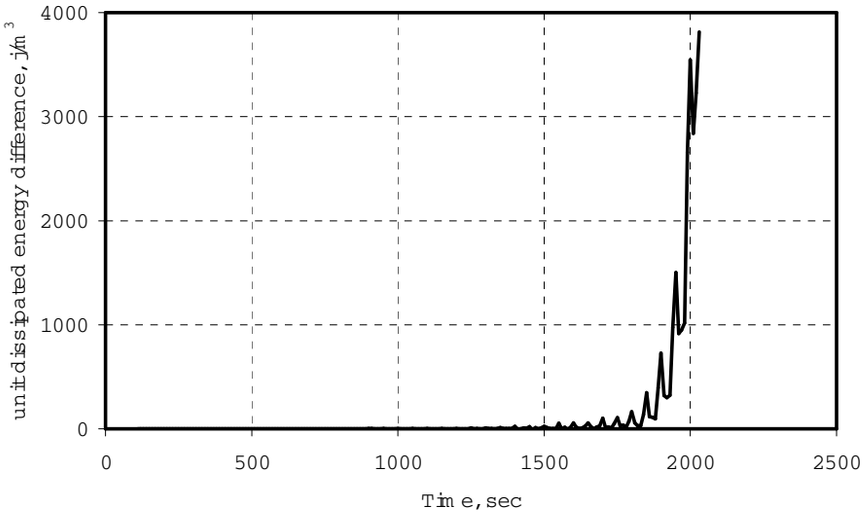


FIG. 6. Energy difference between consecutive cycles

The amount of energy per unit volume related with two different cyclic strain levels and different confining pressures were calculated and compared with plasticity index values. Confining stress values were grouped between 50-100 and 100-250 kPa. It appears that, for the same initial effective confining pressure, the dissipated energy per unit volume increases with the plasticity index of the sample. Higher amount of energy is needed for samples having higher plasticity indices in order for cyclic failure to take place. Also, increase in the confining stress for the same plasticity index requires more energy either for transforming from nonlinear elastic to elasto-plastic response or to cyclic failure (Figure 7). The effect of confining pressure is not so significant in evaluating dissipated energy in small strain levels where confining stress is between 50-100 kPa (Figure 8). There are almost negligible differences due to the testing devices and loading directions which could be a result of assumptions in Poisson's ratios.

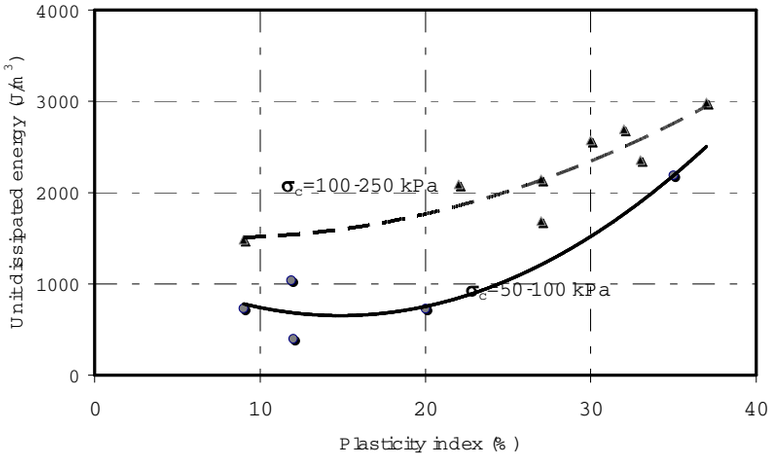


FIG.6. Unit dissipated energy values during cyclic failure with respect to plasticity index and confining pressure

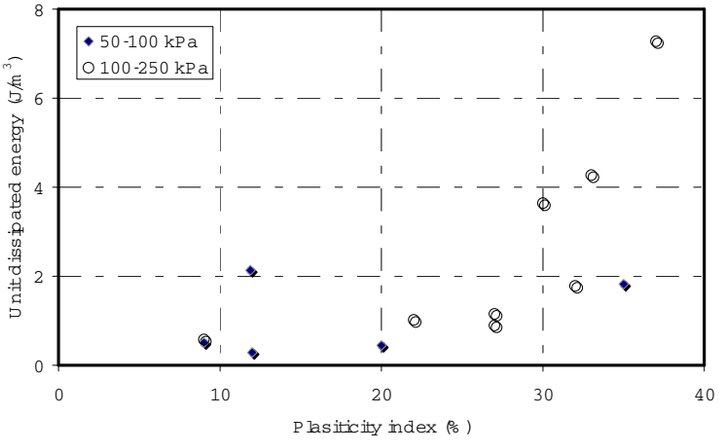


FIG.7. Energy values for nonlinear elastic to elasto-plastic response

CONCLUSIONS

An energy concept which is used for liquefaction of coarse-grained soils has been adopted to define the cyclic failure of fine-grained soils. The theory has been examined through a series of two different laboratory dynamic tests with different loading directions and specimen sizes. Even though the number of cyclic tests conducted are limited, the results indicate that the energy per unit volume needed to induce cyclic failure is dependent on loading history and physical characteristics like

plasticity index but independent of loading directions and, as well as, specimen dimensions. If the energy during seismic loading per unit volume is higher than the energy evaluated from the dynamic laboratory tests, then cyclic failure of the soil deposit would be expected.

ACKNOWLEDGMENTS

The authors appreciate the significant resources that were provided by JICA and consulting firms that took part in this research. Special recognition is also given to Prof. Ayfer Erken for her help in the testing program.

REFERENCES

Ansal, A., Toğrol, E., Kurtuluş, A., Iyisan, R. and Okur, D.V., (2000). Near fault site effects in Gölcük, *Proceedings of the 3rd Japan-Turkey Workshop on Earthquake Engineering,* Istanbul, 21-25 February, Turkey, p. 251-262.

Berrill, J.B. and Davis, R.O. (1985). Energy dissipation and seismic liquefaction of sands: revised model. Soils and Foundations 25(2), 106-118

Bray, J.D., Sancio, R.B., (2006). Assessment of the liquefaction susceptibility of fine grained soils" *Journal of the Geotechnical and Geoenviromental Eng.* 132(9), 1165-1177

Figueroa, J.L. and Dahasaria, M.N. (1991). Evaluation of soil liquefaction by energy principles, *Journal of the Geotechnical Engineering*, ASCE, 120(9), 1554-1569.

Law, K.T., Cao, Y.L. and He, G. N. (1990). An energy approach for assessing seismic liquefaction potential. Canadian Geotechnical Journal, 27, 320-329

Liang, L, Figueroa, J.L., Saada, A.S. (1995). Liquefaction under random loading: unit energy approach. *Journal of the Geotechnical Engineering Division,* ASCE, 121, 776-781

Nemat-Nasser, S., Shokooh, (1979). A unified approach to densification and liquefaction of cohesionless sand in cyclic shearing, Canadian Geotechnical Journal, 16, 659-678

Okur, D.V., Ansal, A. (2007). Stiffness degradation of natural fine grained soils during cyclic loading, *Soil Dynamics and Earthquake Engineering*, 27: 843-854

Vucetic, M. and Dobry, R., (1991). Effect of soil plasticity on cyclic response, *Journal of the Geotechnical Engineering Division,* ASCE, 117, 89-107.

Youd, T,L., et al. (2001). "Liquefaction resistance of soils: Summary report from the 1996 NCEER and 1998 NCEER/NSF workshops on evaluation of liquefaction resistance of soils" *Journal of the Geotechnical and Geoenviromental Eng.* 127(10), 817-833

Voznesensky, E.A., Steinar, N. (1999). Dynamic instability of clays: an energy approach. *Soil Dynamics and Earthquake Engineering*, 18: 125-133.

Cyclic shear response of undisturbed and reconstituted low-plastic Fraser River silt

Dharma Wijewickreme[1], M. ASCE and Maria V. Sanín[2]

[1]Associate Professor, Department of Civil Engineering, University of British Columbia, 6250 Applied Science Lane, Vancouver, B.C. V6T 1Z4 Canada; dwije@civil.ubc.ca
[2]Graduate Student, Department of Civil Engineering, University of British Columbia, 6250 Applied Science Lane, Vancouver, B.C. V6T 1Z4 Canada; msanin@civil.ubc.ca

ABSTRACT: The cyclic shear response of natural low-plastic Fraser River silt was investigated using constant volume direct simple shear tests, employing specimens prepared from undisturbed field samples and by reconstitution of the same silt material. The specimens of undisturbed silt, despite having a looser density under identical consolidation stress conditions, exhibited extensively more dilative response and larger shear resistance in comparison to those displayed by counterpart reconstituted specimens. In addition to consolidation stress conditions and resulting void ratios, it appears that other naturally inherited parameters such as soil fabric and aging effects would critically influence the shear response of natural silt. Since the shear response observed from reconstituted specimens seem to result in conservative design parameters, it would be prudent to use specimens from undisturbed samples to assess the expected field behavior of natural silt.

INTRODUCTION

Fine-grained silty soils with high levels of saturation are commonly found in natural river deposits, and they also originate as a man-made waste product in tailings derived from the processing of ore in the mining industry. Recent evidence of ground failure during strong earthquakes has indicated that certain saturated fine-grained soils can be susceptible to earthquake-induced softening and strength reduction as much as clean sands. The commonly used Chinese criteria to evaluate the liquefaction susceptibility of fine-grained soils are now clearly noted as unacceptable (USNCEE, 2006), and alternate criteria for this purpose have been proposed by Boulanger and Idriss (2006) and Bray et al. (2006). These criteria, again based on grain size and index parameters, also suggest the increased potential of low-plastic fine-grained soils to be susceptible to liquefaction and/or cyclic mobility; however, these criteria are relatively new and require validation. As such, there is a need for understanding the response of the low-plastic fine-grained soils (i.e., silts) under cyclic loading in a fundamental manner, and laboratory testing plays an important role in this regard.

The response of a given soil to cyclic loading is controlled by many parameters such as packing density, microstructure, fabric, level/duration of cyclic loading, confining stress, initial static bias, etc. These parameters have been noted to primarily govern the development of excess pore water pressures, stiffness, and strength in a soil mass during earthquake shaking and, in turn, controlling the overall seismic response. Due to the difficulties associated with field sampling, most of the laboratory research on sands has been conducted using reconstituted soil specimens. The influence of specimen reconstitution technique on laboratory observed soil behavior, and the differences in the fabric and mechanical response between undisturbed and reconstituted samples of sand and silty sands has been widely studied (e.g., Oda 1972; Vaid et al. 1999). The effect of specimen reconstitution on the performance of silty soils has also been studied and significant differences in behavior have been found between undisturbed and reconstituted specimens (e.g., Høeg et al. 2000; Long et al. 2001).

In general, it is fair to state that the behavior of a given field soil condition is best examined in the laboratory by testing of good quality "undisturbed" soil specimens. The possibility to obtain reasonably undisturbed samples of certain low-plastic silts has been already demonstrated (e.g., Bray et al. 2004, Sanin and Wijewickreme 2006); in spite of this, due to increased costs and difficulties with such undisturbed field sampling, there is a tendency to use reconstituted specimens for assessing the shear response of silts. Therefore, it would be suitable to compare the performance observed in undisturbed specimens of silt with that from reconstituted material.

With this background, a series of monotonic and cyclic direct simple shear (DSS) tests were undertaken at the University of British Columbia (UBC), Canada, to study the response of a naturally occurring fine-grained low-plastic silt. The tests were conducted on specimens prepared from "undisturbed" field tube samples as well as those derived from the reconstitution of the same soils. The observed response between the two types of silt specimens is compared, and the findings are discussed in this paper.

MATERIALS TESTED AND TEST PROGRAM

The database included in this study comprises results from monotonic and cyclic constant volume DSS tests performed on relatively young, uniform channel-fill silt obtained from the Fraser River Delta of the Province of British Columbia, Canada. The Fraser Delta sediments have a thickness of up to 300 m, and consist of: surficial fills of variable depth, overbank silts extending up to 6 m in thickness overlying up to 15 m in thickness of deltaic sands, which are then underlain by inter-layered sand and fine-grained materials. For the present study, undisturbed samples of the upper natural silt were obtained using fixed piston tube sampling with a specially fabricated stainless steel, thin-walled tube with no inside clearance (~75 mm diameter, 5-degree cutting edge and 1.5 mm wall thickness). The use of these thin, sharp-edged tubes has been shown to offer an acceptable method to obtain good quality specimens of low-plastic Fraser River silt for laboratory testing (Sanin and Wijewickreme, 2006). The samples were shipped to the laboratory in secured light-weight packing with instructions to minimize disturbance, and they were carefully stored in a moisture-controlled room until the time of sample extrusion and preparation for testing.

Gradation curves of the material included in this study are presented in Figure 1, along with some key physical characteristics given in Table 1.

Table 1. Physical characteristics of low-plastic, channel-fill Fraser River silt

G_s	Sand %	Silt %	Clay %	LL	PI	Consolidation Void Ratio (e_c)	
						(Undisturbed)	(Reconstituted)
2.69	10	80	10	31	4	0.88 – 0.99	0.84 - 0.87

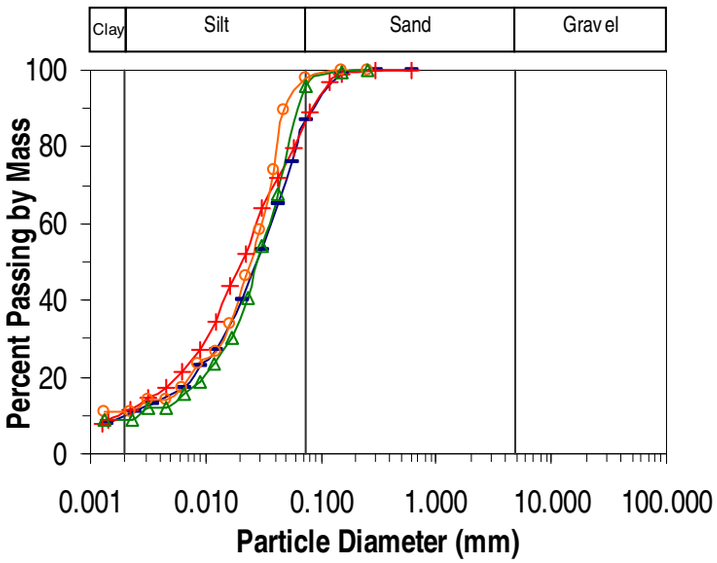


FIG. 1. Grain size distribution – Fraser River silt

The device used for DSS testing is NGI-type (Bjerrum and Landva 1966), and it allows the testing of a specimen having a diameter of ~70 mm and height of 20 to 25 mm. In DSS tests, as an alternative to suspending the drainage of a saturated specimen, a constant volume condition can be enforced even in a dry soil by constraining the specimen boundaries (diameter and height) against changes. The specimen diameter is constrained against lateral strain using a steel-wire reinforced rubber membrane, and the height constraint is obtained by clamping the top and bottom loading caps against vertical movement. It has been shown that the decrease (or increase) of vertical stress in a constant volume DSS test is essentially equal to the increase (or decrease) of pore water pressure in an undrained DSS test where the near constant volume condition is maintained by not allowing the mass of pore water to change (Finn et al. 1978; Dyvik et al. 1987).

After extrusion from the sample tube, the specimens of the natural undisturbed silt were secured in the DSS device with assistance from a polished-stainless steel sharpened-edge cutting-ring. On the other hand, reconstituted DSS specimens were

prepared by placing the Fraser River silt in the form of thick slurry in a specimen mold containing the reinforced-rubber DSS membrane. Since the material was placed in a slurry state, care was exercised to consolidate the reconstituted specimens in several stages of loading to avoid loss of material due to squeezing.

All the DSS specimens were initially consolidated to a vertical effective stress (σ'_{vo}) of approximately 100 kPa with no applied static shear stress (i.e., simulating level-ground field condition) prior to commencement of constant volume shear loading. The preconsolidation pressure ($\sigma'_{p\text{-}1D}$) derived from two one-dimensional consolidation tests on undisturbed specimens of this silt were 80 and 88 kPa, respectively; the corresponding estimated in situ overburden pressures ($\sigma'_{v\text{-}insitu}$) for these two specimens were 79 kPa and 84 kPa, respectively, based on the field depths of the two specimens. The close agreement between $\sigma'_{v\text{-}insitu}$ and $\sigma'_{p\text{-}1D}$ suggested that the in situ silt deposit at the sampled location is essentially in a normally consolidated state. The observation is consistent with the knowledge that the tested silt material originates from a relatively recent channel-fill deposit in the Fraser River Delta. With this background, it is reasonable to infer that the undisturbed DSS specimens consolidated to $\sigma'_{vo} \approx 100$ kPa would also be in a normally consolidated (NC) state. The reconstituted DSS specimens can invariably be considered normally consolidated since the consolidation was commenced from an approximate zero stress (thick slurry) state to reach the target $\sigma'_{vo} \approx 100$ kPa stress level.

The range of void ratios observed for the undisturbed and reconstituted specimens at the end of consolidation are presented in Table 1. As may be noted, the end-of-consolidation void ratios observed for the reconstituted specimens were somewhat lower than those noted for the undisturbed specimens under similar consolidation stress levels (i.e., density of specimens obtained using reconstitution was observed to be higher than that of undisturbed specimens).

Upon completion of the consolidation phase, the specimens (both undisturbed and reconstituted) were subject to monotonic or cyclic constant volume shear loading as desired. Monotonic loading tests were conducted in a strain-controlled manner using a shear strain rate of 10% per hour. Cyclic loading was applied in a stress-controlled manner at a frequency of 0.1 Hz; this consisted of a symmetrical sinusoidal pulse at constant cyclic stress ratio (CSR = τ_{cy} / σ'_{vo}) amplitude. A continuous record of test data was obtained by a computer interfaced data acquisition system. The test variables monitored consisted of full time-histories of horizontal shear stress (τ_h), decrease in vertical stress (= induced excess pore water pressure, Δu) and horizontal shear strain (γ %).

MONOTONIC SHEAR RESPONSE

The stress path and stress-strain response observed from constant volume, monotonic, strain-controlled DSS tests on undisturbed and reconstituted specimens of Fraser River silt are presented in Figure 2. Data have been normalized in relation to the initial consolidation effective stress for ease of comparison.

The undisturbed specimen initially deformed in a contractive manner followed by a dilative response that commenced around 5% shear strain. The specimen exhibited increasing shear resistance with increasing strain. Except for the initial shear strain

levels (say up to ~1%) where the behaviors were almost identical, reconstituted specimen exhibited a response more contractive than that observed for the undisturbed specimen. Moreover, the reconstituted specimen experienced a mild strain-softening response before regaining its shear resistance at a strain close to 8%. In an overall sense, the reconstituted specimen, despite having a slightly lower void ratio, exhibited a weaker stress-strain response than displayed by the undisturbed specimen.

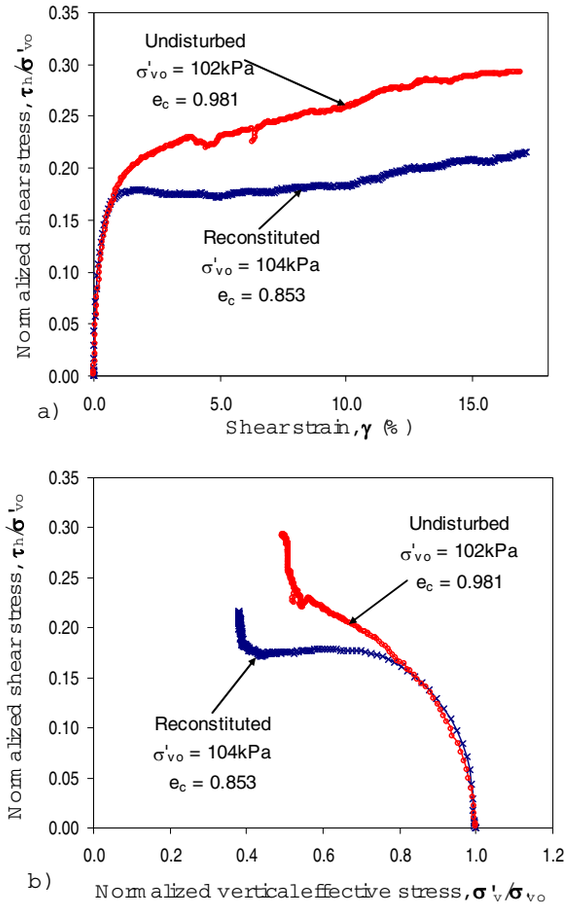


FIG. 2. Typical (a) stress-strain and (b) stress path response of undisturbed versus reconstituted specimens of NC Fraser River silt under constant volume monotonic DSS shear loading ($\sigma'_{vo} \approx 100$ kPa).

CYCLIC SHEAR RESPONSE

Stress path, stress-strain, and excess pore water pressure response

Typical stress path and stress-strain relationships observed for undisturbed and reconstituted Fraser River silt during cyclic DSS loading, under constant CSR amplitude, are shown in Figure 3.

In a general sense, both the specimens seem to exhibit gradual increase in excess pore water pressure and degradation of shear stiffness with increasing number of load

cycles. Typically, the shear stiffness experienced its transient minimum when the applied shear stress is close to zero. This "cyclic mobility type" response is generally similar in form to the undrained (constant-volume) cyclic shear responses observed from cyclic shear tests on fine-grained mine tailings, and clays, and compact to dense reconstituted sand (Wijewickreme et al. 2005a, 2005b; Wijewickreme and Sanin 2007).

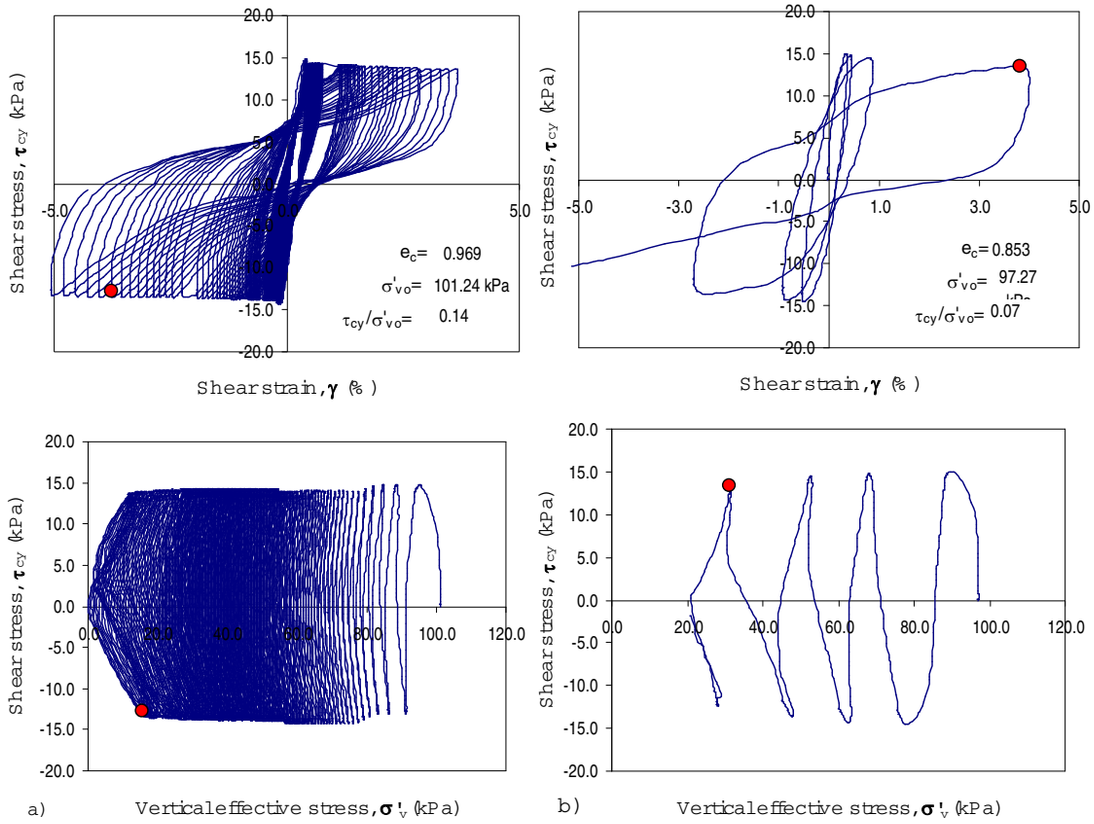


FIG. 3. Typical stress-strain and stress path response of undisturbed versus reconstituted specimens of NC Fraser River silt under constant volume cyclic DSS shear loading ($\sigma'_{vo} \approx 100$ kPa and CSR ≈ 0.14): a) undisturbed specimen; and b) reconstituted specimen.

In spite of the observed similarity of the strain development mechanism, there is a dramatic difference in the cyclic shear behavior between undisturbed and reconstituted specimens under identical CSR amplitudes. Both the undisturbed and reconstituted specimens displayed completely contractive response during the 1st half cycle of loading. Beyond that point, the undisturbed specimen exhibited dilative tendency during "loading" (or increasing shear stress) and contractive response during "unloading" (or decreasing shear stress). Whereas, the reconstituted specimen continued to develop excess pore water pressures at a much faster rate (i.e., perform in a contractive manner) leading to a rapid degradation of shear stiffness with increasing number of cycles – particularly, in comparison to that for the case of the undisturbed

specimen.

The generation of excess pore water pressure ratio r_u [= ($\Delta u/\sigma'_{vo}$)] with the number of cycles observed from two undisturbed silt specimens tested with differing CSR amplitudes are presented in Figure 4. The response observed from counterpart tests conducted on reconstituted silt under identical consolidation and CSR loadings are also superimposed in the same figure for direct comparison. As previously noted from the stress path plots in Figure 3, the gradual increase of r_u with increasing number of load cycles can be noted from all the tests, and the rate of generation of r_u with number of load cycles increases with increasing CSR. From the point of view of this study, again, it is important to note the remarkably high contractive tendency in reconstituted silt specimens in comparison to undisturbed silt specimens under identical initial consolidation stress and subsequent cyclic shear loading conditions.

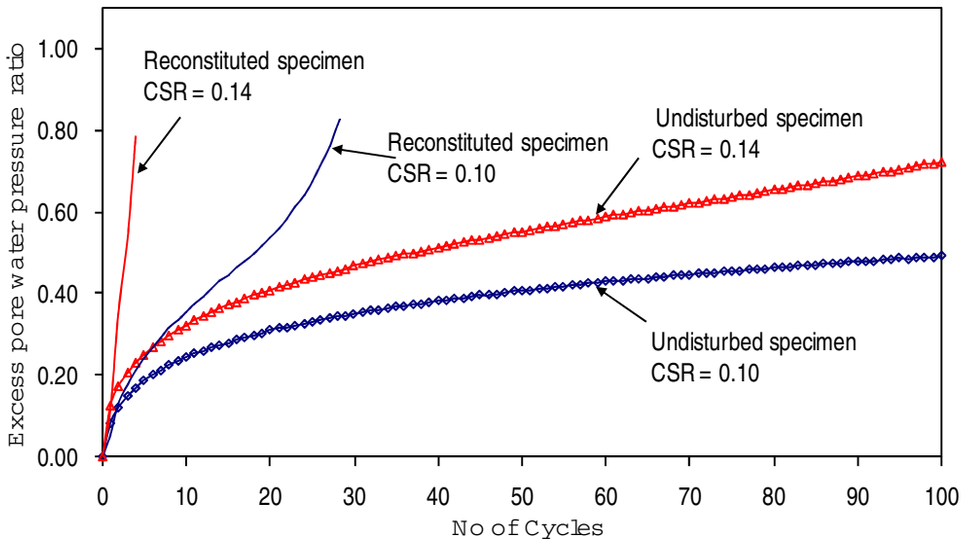


FIG. 4. Typical excess pore water pressure ratio (r_u) vs. number of cycles response of undisturbed versus reconstituted specimens of NC Fraser River silt under constant volume cyclic DSS shear loading ($\sigma'_{vo} \approx 100$ kPa and varying CSR amplitudes).

Cyclic Shear Resistance

It is also of interest to examine the cyclic shear resistance by comparing the response observed from DSS testing under different applied cyclic loadings. In order to facilitate this comparison, the number of load cycles required to reach a single-amplitude horizontal shear strain $\gamma = 3.75\%$, in a given constant volume DSS test under a given applied CSR, was defined as $N_{\gamma=3.75\%}$. This $\gamma = 3.75\%$ condition in a DSS specimen is essentially equivalent to reaching a 2.5% single-amplitude axial strain in a triaxial soil specimen. An identical definition has been previously used to assess the cyclic shear resistance of sands by the U.S. National Research Council (US NRC 1985), and it also has been adopted in many previous liquefaction studies at UBC.

The cyclic resistance ratio [CRR = (τ_{cyc}/σ'_{vo})] versus number of cycles to reach single-amplitude $\gamma = 3.75\%$ derived from a series of tests (with different cyclic load

amplitudes) conducted on undisturbed and reconstituted specimens of Fraser River silt are shown in Figure 5. Despite having a higher density (see Table 1), again, it is evident that all reconstituted specimens consistently exhibited a significantly lower CRR vs. number of cycles characteristic in comparison to the undisturbed specimens.

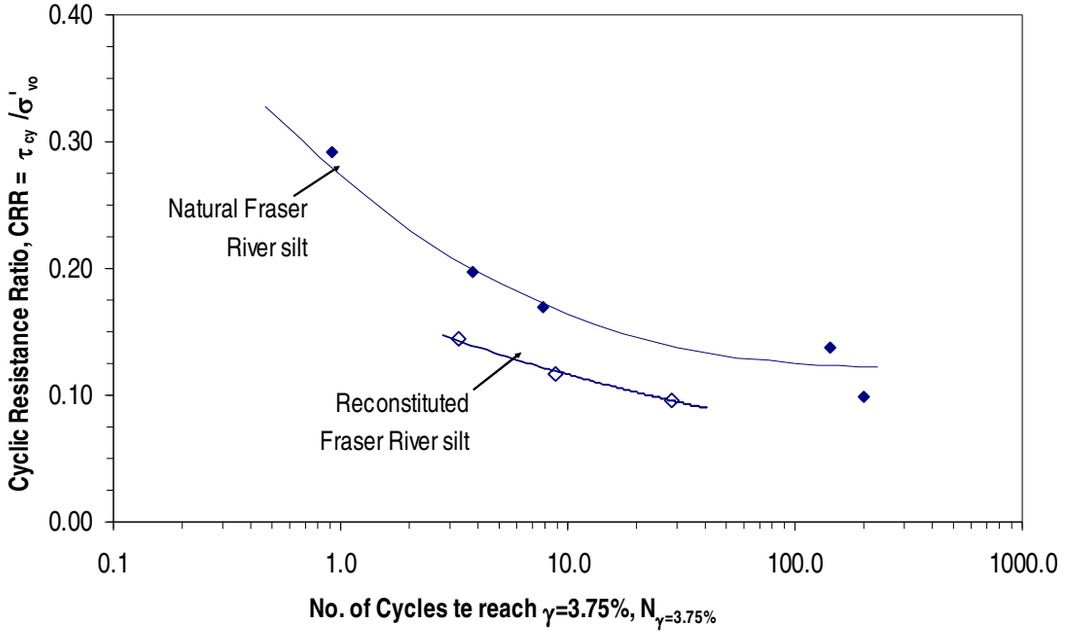


FIG. 5. Cyclic resistance ratio (CRR) versus number of cycles to reach shear strain γ = 3.75% for undisturbed and reconstituted Fraser River silt.

SUMMARY AND DISCUSSION

The constant-volume shear response of low-plastic, normally consolidated fine-grained natural silt (Fraser River silt) was examined using data from constant volume monotonic and cyclic direct simple shear (DSS) tests. The intent was to compare the response of undisturbed specimens versus reconstituted specimens of the same material tested under essentially identical consolidation stress conditions.

Under monotonic loading conditions, the undisturbed specimens generally exhibited a more dilative response and higher shear resistance compared to that derived from the reconstituted specimens.

With respect to constant volume cyclic DSS loading, Fraser River silt (both undisturbed and reconstituted) exhibited cumulative decrease in effective stress (or increase in excess pore water pressure) with increasing number of load cycles; the observed behavior was also associated with progressive degradation of shear stiffness. This observed cyclic mobility type stress-strain response is conceptually in accord with the responses previously observed on a number of natural silts (Wijewickreme and Sanin 2007).

The overall cyclic shear stress-strain response of the undisturbed specimens, however, was dramatically more dilative than that observed for the counterpart

reconstituted specimens; this, in turn, led to a significantly larger cyclic resistance ratio (CRR) for the former compared to the latter. It is also worthwhile noting this strong resistance exhibited by the undisturbed silt was in spite of having a density lower than its reconstituted counterpart under same consolidation stress conditions.

The void ratio (e_c) and corresponding consolidation stress state (σ'_{vo}) are commonly considered as suitable variables to represent the state of a soil. The results from the laboratory research work presented herein suggest that these two variables (e_c-σ'_{vo}) alone are not sufficient to define/determine the monotonic and cyclic shear behavior of the tested natural silt. The dramatic difference in the shear response between the undisturbed and reconstituted silt can be reasonably attributed to other considerations such as the difference in particle structure (soil fabric) and the age; it is fair to assume that the natural fabric and aging effects in the undisturbed silt would have been destroyed in the preparation of reconstituted silt specimens commencing from a slurry state. These deductions are in accord with the observations made by Leroueil and Hight (2003) with respect to the performance of several other natural soils.

It is also worthwhile noting the following inferences that could be made based on the above experimental observations: (i) if testing were to be undertaken at a consolidation stress level significantly higher than the in situ preconsolidation stress ($\sigma'_{p\text{-}1D}$), due to possible destructuration of "undisturbed" silt, the shear response between "undisturbed" and reconstituted specimens will probably be less contrasting compared to the shear response between the specimens from testing at consolidation stress levels in the vicinity of $\sigma'_{p\text{-}1D}$ as shown in Figures 2 and 3; (ii) if testing were to be undertaken with reconstituted specimens allowed to "age" after consolidation (and prior to shearing), the cyclic performance of such specimens will likely improve due to the "aging effects"; this again, will potentially reduce the contrast in shear response between "undisturbed" and counterpart reconstituted specimens.

Due to costs and difficulties associated with field "undisturbed sampling", there is a tendency to use reconstituted specimens for assessing the shear response of silts. This is based on the assumption that reconstituted laboratory specimens would reasonably represent the field material as long as the e_c-σ'_{vo} conditions are suitably matched. The findings from the present study indicate that such an approach of using reconstituted specimens does not necessarily reflect the characteristics of natural material, and it would likely generate overly conservative parameters for design purposes. As such, it appears that there is merit in obtaining undisturbed samples to assess the field behavior of fine-grained silts such as Fraser River silt.

ACKNOWLEDGMENTS

The data analysis presented herein was supported by research funding from the Natural Sciences and Engineering Research Council of Canada (NSERC).

REFERENCES

Bjerrum, L., and Landva, A. (1966). "Direct simple-shear tests on a Norwegian quick clay." *Geotechnique,* 16(1), 1-20.

Boulanger, R. W., and Idriss, I. M. (2006). "Liquefaction susceptibility criteria for silts and clays." *J.Geotech.Geoenviron.Eng.,* 132(11), 1413-1426.

Bray, J. D., Sancio, R. B., Riemer, M. F., and Durgunoglu, T. (2004). "Liquefaction susceptibility of fine-grained soils." *Proceedings of the 11th International Conference on Soil Dynamics and Earthquake Engineering and 3rd International Conference on Earthquake Geotechnical Engineering,* Berkeley, CA, 7–9.

Bray, J. D., and Sancio, R. B. (2006). "Assessment of the liquefaction susceptibility of fine-grained soils." *J.Geotech.Geoenviron.Eng.,* 132(9), 1165-1177.

Dyvik, R., Berre, T., Lacasse, S., and Raadim, B. (1987). "Comparison of truly undrained and constant volume direct simple shear tests." *Geotechnique,* 37(1), 3-10.

Finn, W. D. L., Vaid, Y. P., and Bhatia, S. K. (1978). "Constant volume simple shear testing." *Proceedings of the 2nd International Conference on Microzonation for Safer Construction—Research and Application,* San Francisco, CA, 839–851.

Høeg, K., Dyvik, R., and Sandbæ kken, G. (2000). "Strength of undisturbed versus reconstituted silt and silty sand specimens." *J.Geotech.Geoenviron.Eng.,* 126(7), 606-617.

Leroueil, S., and Hight, D. W. (2003). "Behaviour and properties of natural soils and soft rocks." *Characterisation and engineering properties of natural soils,* T. S. Tan, K. K. Phoon, D. W. Hight, and S. Leroueil, eds., A.A. Balkema, United States (USA), .

Long, M., Vaid, Y. P., Sivathayalan, G., Hoeg, K., Dyvik, R., and Sandbaekken, G. (2001). "Strength of undisturbed versus reconstituted silt and silty sand specimens; discussion and reply." *J.Geotech.Geoenviron.Eng.,* 127(11), 991-994.

Oda, M. (1972). "The mechanism of fabric changes during compressional deformation of sand." *Soils and Foundations,* 12(2), 1-18.

Sanin, M. V., and Wijewickreme, D. (2006). "Cyclic shear response of channel-fill Fraser River Delta " *Soil Dynamics and Earthquake Engineering,* 26(9), 854-869.

U.S. National Conference on Earthquake Engineering, NCEE (2006), "Session on Liquefaction", *Proceedings of 8th US NCEE, 2006*, San Francisco, CA, April 18-22, 2006.

U. S. National Research Council, Committee on Earthquake Engineering, Washington, DC, United States (USA). (1985). *Liquefaction of soils during earthquakes.* Natl. Acad. Press, Washington, DC, United States (USA).

Vaid, Y. P., Sivathayalan, S., and Stedman, D. (1999). "Influence of Specimen-Reconstituting Method on the Undrained Response of Sand." *Geotech Test J,* 22(3), 187-195.

Wijewickreme, D., and Sanin, M. V. (2007). "Effect of Plasticity on the Laboratory Cyclic Shear Response of Fine-grained Soils." *Fourth International Conference on Earthquake Geotechnical Engineering*, Thessaloniki, Greece.

Wijewickreme, D., Sanin, M., and Greenaway, G. (2005a). "Cyclic Shear Response of Fine-grained Mine Tailings", *Canadian Geotechnical Journal*, 42(5), 1408-1421.

Wijewickreme, D., Sriskandakumar, S., Byrne, P.M., (2005b), "Cyclic Loading Response of Loose Air-pluviated Fraser River Sand for Validation of Numerical Models Simulating Centrifuge Tests", *Canadian Geotechnical Journal*, 42(2), 550-561.

Effect of Fines on Sand Residual Strength after Liquefaction

Pedro de Alba, M. ASCE and Thomas P. Ballestero, M. ASCE, P. E.

Department of Civil Engineering, Kingsbury Hall, University of New Hampshire, Durham, NH 03824-3591. PH (603) 862-1417; email: pedro.dealba@unh.edu; tom.ballestero@unh.edu.

ABSTRACT

The shear force on a metal coupon dragged through liquefied sand was measured in a modified triaxial apparatus. This device allowed much larger strains and strain rates to be imposed than in a conventional triaxial liquefaction test. The effect of varying fines content on the post-liquefaction large-strain residual shear resistance was measured for specimens prepared at a range of different densities, and compared with residual strength values back-calculated from field liquefaction slope failures. Increasing fines content was found to decrease the residual strength compared to that of clean sand under similar placement conditions. Values measured in the laboratory under truly undrained conditions were comparable to lower-bound values obtained from field cases, suggesting that the laboratory values represent a conservative lower bound for fully-undrained conditions during sliding.

INTRODUCTION

Earthquake stability analyses of existing earth structures may reveal zones within the structure or its foundation with a high probability of liquefaction. Engineers are then faced with the problem of deciding on remedial measures, which generally involve estimating the strength remaining in the liquefied material: the residual strength (S_r). Selecting values of residual strength remains a challenging problem, requiring a great deal of engineering judgment. Current practice relies basically on S_r values back-calculated from collections of case histories of liquefaction failures, as originally proposed by H. B. Seed (1986) and later expanded by other researchers, (e.g. Olson and Stark, 2002, Idriss and Boulanger, 2007).

These S_r values are then plotted against normalized SPT or CPT values obtained in the liquefied zones. There is, unfortunately, a considerable scatter in these plots, even with a rigorous selection of the most well-documented cases. One contributing factor that must be investigated is the influence of a wide range of fines contents in the liquefied materials. For example, of the 18 cases examined by Idriss and Boulanger (2007), representative fines contents ranged from 3% to 85%, with

only 3 having less than 5% fines. In order to compare the calculated S_r - values on a common basis, the majority of studies have corrected normalized SPT or CPT values to an equivalent 'clean sand' value; Olson and Stark (2002), on the other hand, in an extensive study involving 33 case histories, reported no clearly discernible effect of fines on the resulting values, and have not corrected the normalized SPT's.

The effect of fines on the triggering of liquefaction has been studied by a number of researchers, with apparently contradictory results as to the effects of increasing fines content. Polito and Martin (2003) reconciled these effects by comparing results on the basis of relative density and pointing out that the maximum and minimum index void ratios (calculated from the maximum and minimum relative densities) change with fines content, so that tests carried out at constant overall void ratio have a progressively decreasing relative density, and thus a decreasing resistance, as the fines content increases, up to the point of limiting silt content, which is the maximum percentage of silt that permits grain-to-grain contact of the sand skeleton (the limiting silt content generally tends to be on the order of 30-45% for many sands).

While the triggering of liquefaction can be adequately simulated with conventional laboratory equipment, and the effects of such factors as fines content studied as described above, it is much more difficult to properly simulate residual strength behavior. The great majority of residual strength studies have been carried out using triaxial compression equipment, which is extremely limited in this regard; a conventional triaxial test cannot impose axial strains of more than about 25% at shear strain rates on the order of 2 rad/sec (Bryant et al. 1983), whereas liquefaction flow slides involve shear strains of several hundred percent at shear strain rates on the order of 10 to 100 rad/sec.

The writers measured large strain and strain rate behavior for a clean sand using the specialized experimental setup described below, and concluded that liquefied clean sand under conditions of zero effective stress behaves as a non-Newtonian viscoplastic material with stress-thinning characteristics, i.e., its viscosity decreases as the strain rate increases, and consequently resistance to flow increases with flow velocity, but at a continuously decreasing rate. The effect of fines on this behavior, however, remained to be explored.

EXPERIMENTAL APPARATUS

In order to study the evolution of S_r at high velocities and strain levels, the writers originally carried out experiments in which a small sphere was embedded in a long triaxial specimen, which was liquefied by cyclic loading. The behavior of the sphere was observed as it was drawn lengthwise through the liquefied soil by a deadweight system, and the hydrodynamic behavior of the sphere was analyzed modeling the liquefied soil as a viscous fluid (de Alba and Ballestero, 2004). However, in many cases the Reynolds number approached the limit for laminar flow, which made the analysis more difficult, so in a subsequent series of experiments, the

sphere was replaced by a smooth square coupon, drawn with its flat sides parallel to the direction of motion (de Alba and Ballestero, 2005). Hydrodynamically, the coupon was easier to analyze because the flow remains laminar over a much larger range of velocities.

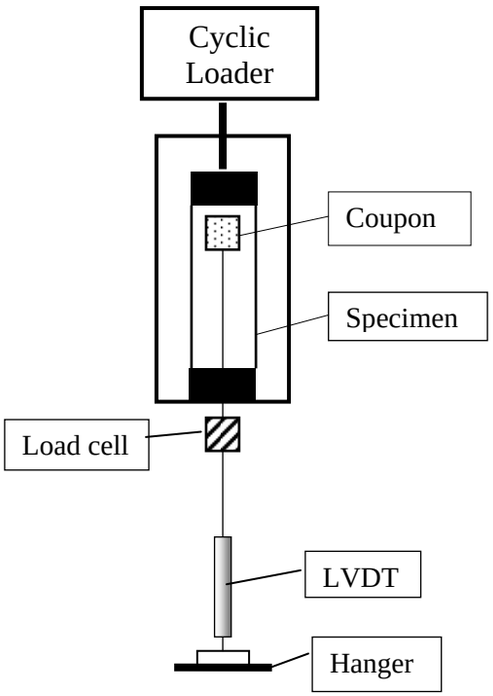


FIG. 1. Test System Schematic (not to scale)

Figure 1 (left) is a schematic of the experimental device; tests were carried out by forming triaxial specimens of sand around a 2.54-cm smooth square titanium coupon, 0.16 cm thick, attached to a fine (0.081 cm-diameter) wire which could slide through an o-ring seal in the chamber base.

Triaxial specimens were approximately 24 cm (9.5 in) high and 7.1 cm (2.8 in) in diameter. The coupon was placed in the specimen so that it could travel approximately 17.8 cm (7 in) before the weight hanger hit its support, thus stopping the coupon about 2.5 cm (1 in) above the base of the specimen. The coupon's displacement and resistance to motion were measured by a load cell and LVDT arrangement as shown in the figure.

MATERIALS

A uniform clean fine sand with a mean grain diameter of approximately 0.3 mm was used for all tests. To study the effect of non-plastic fines, two series of tests were carried out, in which the base sand was mixed with 10% and 30% by weight sil-co-sil 90® ground quartz silt (97.5 % passing #200 sieve, 89% finer than 53 microns). Another series was carried out using 10% Kaolin (LL = 55, PI =23). Maximum and minimum index void ratios of the different materials were determined from relative density tests by Japanese standard test method JIS A 1224, as summarized in Table 1. While this test is not rigorously applicable to materials with 30% fines, the values were found to be useful indicators, as discussed below.

Table No. 1: Index Void Ratios

Material	Maximum e	Minimum e	$e_{max} - e_{min}$
0% Fines	0.856	0.574	0.282
10% Non-Plastic Fines	0.859	0.449	0.410
10 % Kaolin	1.202	0.544	0.658
30% Non-Plastic Fines	1.281	0.517	0.764

SPECIMEN PREPARATION

The test setup required that the coupon be initially located at the correct height (approximately 1.25 cm below the top cap) and then the specimen formed around it. To produce a uniform distribution of fines through the material, specimens were made by first placing a sleeve, with a metal hex grid (0.71 cm opening) at its base, inside the sample mold and then gradually depositing the sand/fines mixture in the sleeve using a 'zero drop height' procedure with a long-stemmed funnel. The sleeve, which had a central slot in the base grid to allow passage of the coupon, was then slowly withdrawn from the mold to form the specimen. For the 30% fines and Kaolin specimens, it was found that a low intensity vibration had to be applied to the sleeve to keep the grid from clogging. Sectioning of trial specimens showed a uniform distribution of fines (within 1 % of target fines content). Forming specimens of 30% fines content with the coupon in place proved extremely challenging, and only two truly satisfactory tests are reported. The differences in formation process were not considered to affect the S_r measurements, since any differences in initial structure were considered to be erased at large strains in the liquefied material.

Specimens were saturated and tested using the conventional cyclic triaxial test procedure; specimens with 10% Kaolin were allowed to hydrate after saturation for 24 hours before testing. For comparison purposes, a series of clean sand tests, with specimens formed by air pluviation, as described by de Alba and Ballestero (2005, 2006) are also discussed. It is important to note that all tests were carried out at the same initial effective confining pressure of 140 kPa.

RESULTS

For all tests, the triaxial system was set up to stop cycling when axial strains exceeded $\pm$ 2 %, one to two cycles after initial liquefaction (pore pressure ratio, $\mathbf{r_u}$= 100%). Typical results for a test with 10% non-plastic fines are shown in Figure 2.

The coupon was seen to plunge at point A on the LVDT trace (curve 1) as the effective stress (curve 2) went to zero. It dropped, at increasing velocity, until the hanger stopped moving, about 2.5 cm above the specimen base, at (B). It is important to note that the effective stress remained essentially equal to zero during coupon displacement. This was typical of all tests reported. As the coupon started to plunge, the load cell reading (curve 3; 'apparent drag') dropped to a low value (point C), then started to increase as the coupon strained further, finally leveling off shortly before the load hanger reached the end of its stroke. The test was considered to end at point D, as the LVDT reached the end of its linear range and the presence of the rigid specimen base was seen to affect the load cell reading. Figure 3 shows the apparent drag plotted against coupon velocity between points (A) and (D) in Figure 2. This behavior is typical of all tests reported, with the drag reaching a minimum and then exhibiting a regain in drag resistance which typically stabilizes when the bottom

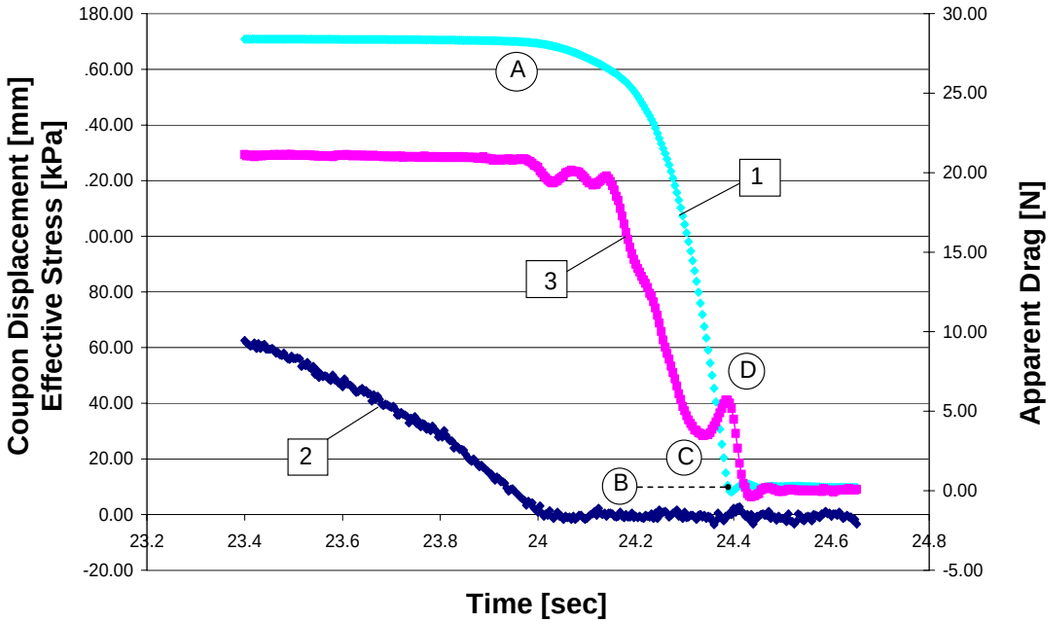


FIG. 2. Coupon Behavior at liquefaction, test 10%-J. Curve [1] Coupon displacement. [2], Effective stress. [3] Load cell reading: 'Apparent Drag'

edge of the coupon reaches a height of about 5 cm above the sample base. These stabilized values were the ones used to calculate the residual shear strengths reported.

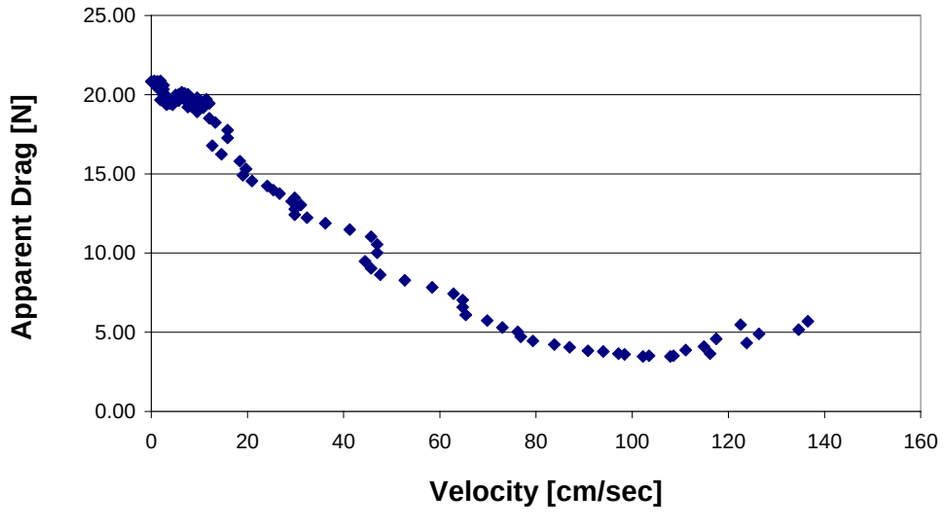


FIG. 3. Measured apparent drag vs. coupon velocity

ANALYSIS

As previously noted, the relative motion of liquefied sand around a solid is best modeled as a viscous flow. In order to obtain the shear stress exerted against the coupon, and the viscosity of the equivalent fluid, it is necessary to carry out a hydrodynamic analysis of the coupon movement, with emphasis on its behavior when it reached high strain rates and a 'stabilized' shear strain range.

In order to obtain correct drag values and viscosities, the dynamic equilibrium of the coupon/sphere system for each time step had to be considered. A free body diagram of the testing apparatus was drawn from above the coupon to just above the load cell (Fig. 1). From this free body diagram, a force balance equation in the vertical direction was prepared in which the sum of the vertical forces was set equal to the mass of testing apparatus in the free body diagram times its acceleration. Forces that acted included buoyant force, weight, wire seal resistance, frictional drag on the wire, and the load cell reading (apparent drag). From the time histories of apparent drag and coupon displacement (Fig. 2) the coupon velocity and acceleration were computed. The force balance allowed calculation of the corrected drag force as described by de Alba and Ballestero (2005). From the drag force calculations, the stabilized drag forces at large strains, and thus the shear stresses on the faces of the coupon, could readily be calculated. Figure 4 compares the results of two tests carried out at similar void ratios, albeit at different relative densities, as shown in

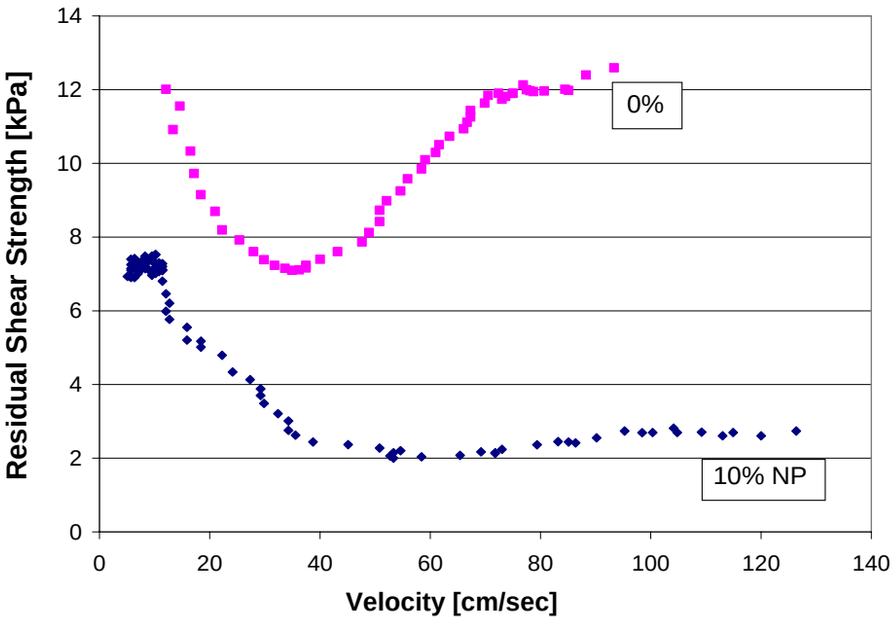


FIG. 4. Coupon shear stress vs. velocity, tests at similar void ratios

Table 2 (below). As will be discussed below, overall void ratio was found to be the

best basis for comparison of results, given the wide range of relative densities obtained in the test samples.

It is evident that, on the basis of void ratio, residual shear resistance decreases with fines content. The recovery in residual strength before final stabilization at large strains is most noticeable in the 0% fines test. In general , all clean sand tests displayed this behavior more markedly than tests with fines, with the amount of recovery increasing as relative density increased. Although this resembles dilatant behavior, it was not accompanied by an instrumentally detectable decrease in the pore pressure coefficient, $\mathbf{r_u}$.

Table No. 2: Test Conditions, Figure 4 Specimens

Test	Fines content	Void ratio, e	Relative density [%]
14	0	0.770	49.00
10%-C	10%NP	0.773	21.8

Figure 5 (next page) compares S_r values on the basis of overall void ratio after saturation and consolidation. It is obvious that, to obtain a given S_r, a significantly lower void ratio is required as the fines content increases. It should be noted that the clean-sand test result at point (A) is for a sample prepared by a modified air pluviation method, in which the clean sand was dampened before pluviation, to obtain a very high void ratio (de Alba and Ballestero, 2005). This result suggests that the overall trend curves for all fine contents should show the same concave-upward behavior, exhibiting a small resistance at high void ratios.

The same results are compared on the basis of relative density (Dr) in Figure 6. While on the basis of void ratio the results are seen to group by fines content, in terms of Dr, clean sand and 10% non-plastic fines material will produce approximately the same S_r at the same Dr, whereas a material with the same content of plastic fines will require a significantly higher Dr for the same strength, and the 30% NP fines sand would need to be at close to the densest packing obtainable by the JIS test. In considering these results, however, it is well to remember that the relative densities are being calculated on the basis of significantly different index void ratios (Table 1).

DISCUSSION

Material densities can be roughly converted to standard penetration test (SPT) results, and the S_r-values from this study compared with the values back-calculated from field case histories. The most reasonable SPT values were found to be obtained using lower-bound values of the conversion suggested by Cubrinovski and Ishihara (1999):

$$\mathbf{N_1 = C_d\,(Dr)^{\,2}} \qquad (1)$$

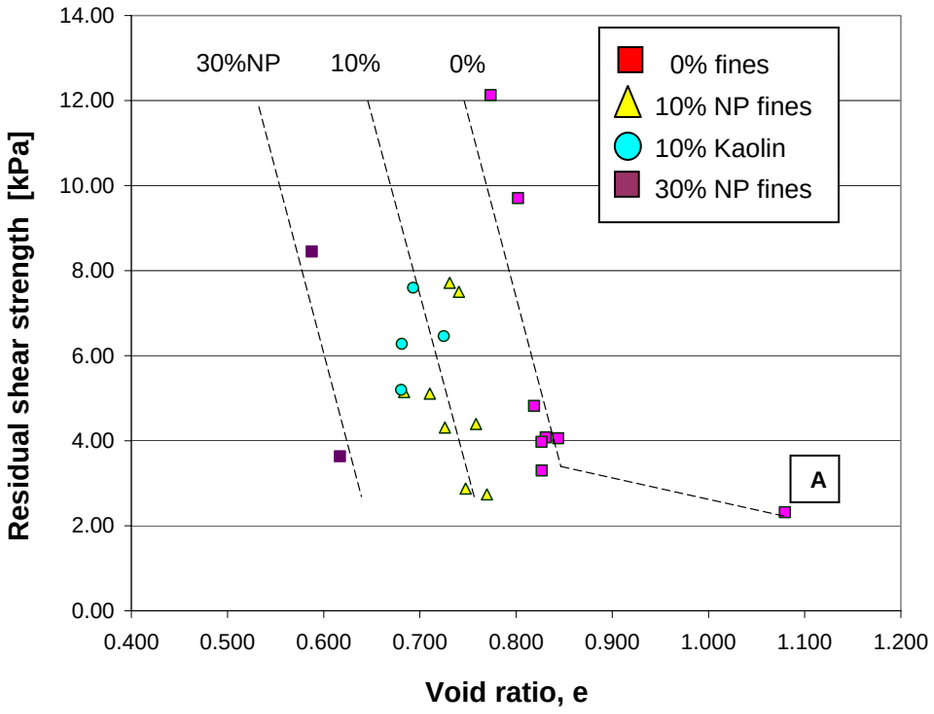


FIG. 5. Residual strength vs. overall void ratio

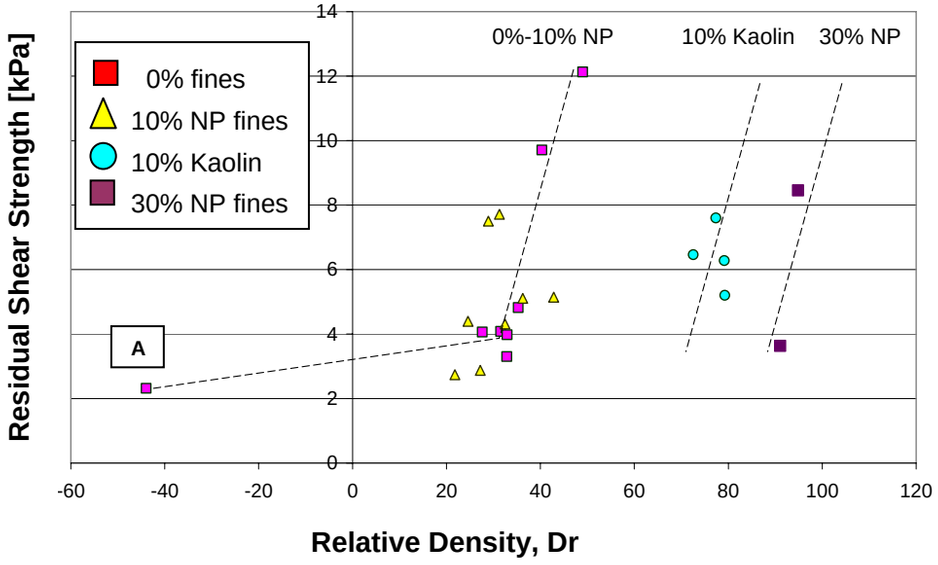


FIG. 6. Residual strength vs. relative density

in which Dr is a ratio, not a percentage, and C_d values depend on the difference in index void ratios, e_{max} and e_{min}. Table 4 summarizes the C_d values used to convert the

test relative densities to SPT values. Since these values were obtained for an energy ratio of 78%, a further normalization was required to obtain $N_1)_{60}$.

Table No. 4: C_d-Values

Fines Content	$e_{max} - e_{min}$	C_d
0%	0.282	46
10% NP	0.410	25.5
10% Kaolin	0.658	10.9
30% NP	0.764	8.4

Finally, in order to convert to equivalent clean sand values, the correction suggested by Cetin et al. (2004) was used:

$$C_{fines} = (1 + 0.004FC) + 0.05\,(FC/\,N_1)_{60}) \qquad (2)$$

where FC is the fines content as an integer. Figure 7 compares the laboratory residual shear strengths, normalized by the initial effective confining pressure of 140 kPa, with the lower bound of case history S_r- values proposed by Olson and Stark (2002). For this case, $N_1)_{60}$ values are not corrected to equivalent clean sand values, as Olson and Stark combined all 33 of their field cases, detecting no significant differences between clean sands and those with fines. Finally, Figure 8 compares the laboratory results with the lower bound residual strength curve proposed by Idriss and Boulanger (2007). In this case, laboratory relative densities were converted to $N_1)_{60\text{-cs}}$ values.

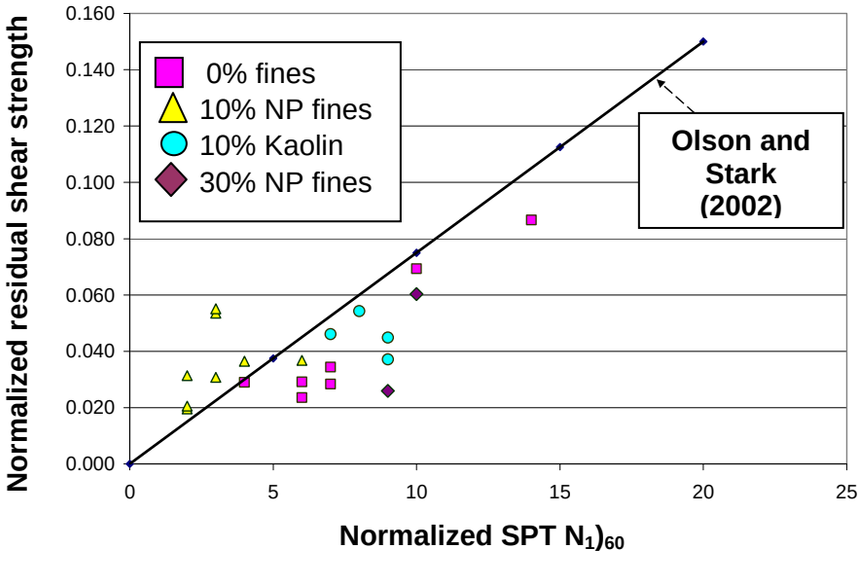


FIG. 7. Laboratory residual strengths compared with lower bound of Olson and Stark (2002)

The laboratory S_r values are seen to form a reasonably consistent pattern at all fines contents when compared to the proposed field lower bounds, with a somewhat closer fit to the more conservative Olsen and Stark boundary. These results suggest that a

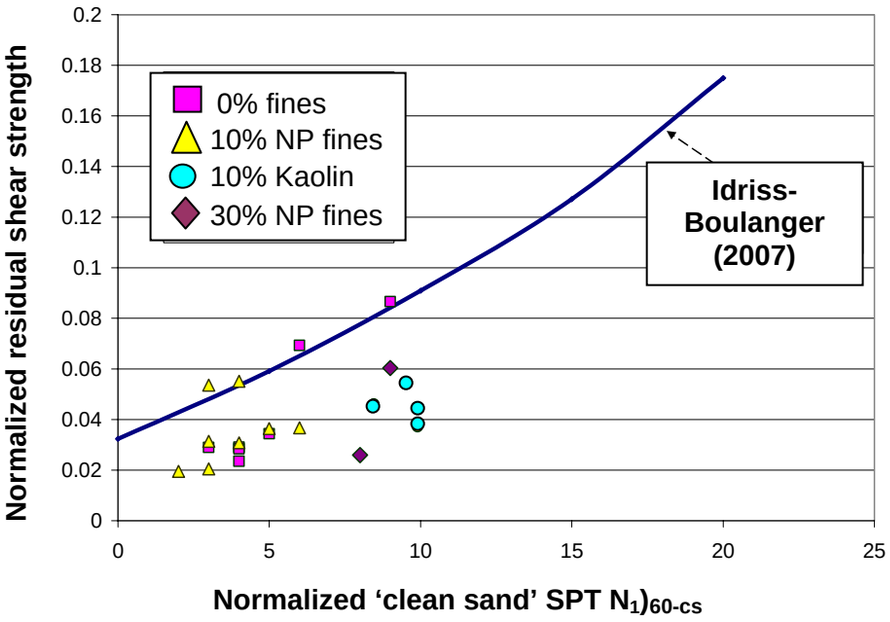


FIG. 8. Laboratory residual strengths compared with lower bound of Idriss and Boulanger (2007)

relative density-SPT conversion based on the index void ratio range for the particular material, as described above, may adequately account for fines content without further correction.

CONCLUSIONS

For the materials tested, a significant decrease in void ratio is required to obtain the same S_r as fines content increases. With regard to the actual values, it should be noted that the measured residual strengths were obtained with a smooth coupon under conditions of zero effective stress, at much higher shear strains and shear strain rates than are possible in conventional laboratory liquefaction tests, and thus may approximate true minimum values.

From a practical point of view, when compared to field case histories, and assuming the Dr to SPT conversion is reasonable, the S_r-values from this study tend to plot at or below proposed lower bound envelopes of back-calculated values. It has been suggested (e.g. Idriss and Boulanger, 2007) that these lower bounds are for failure conditions in which drainage is impeded, for example by an overlying low-permeability layer, which may produce a void ratio redistribution and consequent loosening of the upper part of the confined sliding mass. As previously noted, the laboratory S_r-values were obtained essentially for zero effective stress; this suggests

that even the lower bound of the field cases represents situations where some level of drainage was possible; indeed, it is difficult to visualize a sliding mass subjected to large deformations that will not break up in such a way to allow some dissipation of pore pressure during sliding. Consequently, S_r-values obtained from tests such as those described in this paper would represent a conservative lower bound to those that might occur in the field.

ACKNOWLEDGEMENTS

The writers appreciate the reviewers' comments which improved the clarity of the paper. Equipment development was funded by a Small Grant for Exploratory Research (SGER) from the National Science Foundation Geoenvironmental Engineering and Geohazards Mitigation Program.

REFERENCES

Bryant S. M., Duncan J. M., Seed H. B. (1983), "Application of tailings flow analyses to field conditions." *Report UCB/GT/83-03 to U.S. Bureau of Mines*, Department of Civil Engineering, University of California, Berkeley. 312 p.

Cetin, K. O., Seed, R. B., Der Kiureghian, A., Tokimatsu, K., Harder, L. Kayen, R. E. and Moss, E. S.(2004), "Standard-penetration based probabilistic and deterministic assessment of seismic soil liquefaction potential," JGGE 130 (4) 1314-1340.

Cubrinovski, M and Ishihara, I. (1999) "Empirical correlation between SPT N-value and relative density for sandy soils." *Soils and Foundations*, 39 (5) 61-71.

de Alba, P. and Ballestero, T.P.(2004) "Residual strength after liquefaction: a rheological approach," *Proc., 11th International Conference on Soil Dynamics and Earthquake Engineering and 3d International Conference on Earthquake Geotechnical Engineering*, Vol. 2 , 513-520.

de Alba, P. and Ballestero, T.P.(2005),"Liquefied granular materials as non-Newtonian fluids: a laboratory study." *Proc., Geo-Frontiers 2005, GSP 133*, ASCE.

de Alba, P. and Ballestero, T.P. (2006)."Residual strength after liquefaction: a rheological approach," *Soil Dynamics and Earthquake Engineering* 26, 143-151.

Idriss, I.M and Boulanger, R. (2007), "SPT and CPT-based relationships for the residual shear strength of liquefied soils." *Proc. 4th Int. Conf. on Geotechnical Earthquake Engineering-Invited lectures*, 1-21, Springer.

Olson S. M., Stark T. D. (2002). "Liquefied strength ratio from liquefaction flow failure case histories." *Canadian Geotechnical Journal*, 39: 629-647.

Polito, C. P. and Martin, J. R. II (2003),"A reconciliation of the effects of non-plastic fines on the liquefaction resistance of sands reported in the literature." *Earthquake Spectra* 19 (3) 635-651.

Seed, H. B. (1986). "Design problems in soil liquefaction." *Journal of the Geotechnical Engineering Division,* ASCE, 113 (8), 827-845.

This page intentionally left blank

Effect of Sand Gradation and Fines Type on Liquefaction Behaviour of Sand-fines Mixture

Md. Mizanur Rahman[1], S.M. ASCE and Sik-Cheung Robert Lo[2]

[1]PhD Student, University of New South Wales at Australian Defence Force Academy, ACT-2600 Australia; mmrahman@adfa.edu.au
[2]Associate professor, University of New South Wales at Australian Defence Force Academy, ACT-2600 Australia; r.lo@adfa.edu.au

ABSTRACT: Equivalent granular void ratio and equivalent granular steady state line was used as the common basis for synthesizing test results. In isolating the influence of host sand, two sand-fines mixes with different host sand, but the same fines type and content, were tested. The influence of fines type was then investigated by testing Sydney sand mixed with three different types of fines. Scanning Electron Microscope (SEM) photography was also used to elucidate the role of angularity of fines. This led to the finding that the angularity of fines may need to be considered in determining equivalent granular void ratio.

INTRODUCTION

The factors that control the liquefaction of clean sand are well-understood. However, the understanding of liquefaction behaviour of sand with fines is less complete. There is a lack of concensus of opinion on whether the inclusion of fines will increase or reduce the liquefaction tendency. Unexpected behaviour trend was reported Yamamuro and Lade (1998) and independently confirmed by Bobei and Lo (2005). Some researchers suggested that void ratio may not serve as a consistent basis for comparison because the fine particles may be trapped in between sand particle and remain inactive on sand force structure (Georgiannou et al. 1990; Kuerbis et al. 1988; Thevanayagam 1998). Alternate state variables such as inter-granular void ratio or equivalent granular void ratio have been proposed for unifying the liquefaction behaviour of clean sand and sand with fines. However, these studies mainly concentrated on studying the influence of fines content. As such, both the host sand and fines type were fixed in these studies. This paper presents some preliminary findings on the influence of both host sand gradation and fines type on the liquefaction behaviour of sand-fines mixture where the “fines in sand” model is still valid.

BACKGROUND

Three important aspects on the liquefaction behaviour of sand-fines mixture will be discussed in this section.

Equivalent Granular Steady State Line

The critical state soil mechanics (CSSM) framework has been used to characterize the liquefaction behaviour of sand. This methodology relies on knowing the Steady State Line of the soil (SSL). Note that the SSL may be curved even though it is still referred to as "line". However, location of the SSL can be strongly dependent on fines content. This lead to some practical difficulties in applying the CSSM framework to sand-fines mix, because each fines content requires its own SSL.

There is a potential problem in the use of void ratio as a state variable because the fines may simply get trapped in the void space between the sand particles and remain inactive in the force chain of the solid skeleton. Mitchell (1976) may be the first publication that suggested that the clay particles in a coarse matrix may not play any active role in the force chain of a granular phase structure. This rationale was confirmed by Kenny (1977) and Troncoso and Verdugo (1985). By considering fines as inactive, ie as void space, Thevanayagam and co-workers (1998; 1999; 2000) proposed, in lieu of void ratio, inter-granular void ratio e_g, defined by Eqn (1) below as the alternative state parameter.

$$e_g = \frac{e + f_c}{1 - f_c} \tag{1}$$

where e = void ratio and f_c = fines content in decimal. The assumption that fines can be treated as void space is not universally applicable. For higher f_c or larger fines size relative to host sand, some fraction of fines will have to get between the host sand grains and participate in force structure. Thevanayagam et al. (1999; 2000) proposed the general concept of equivalent granular void ratio, e^*, defined as:

$$e^* = \frac{e + (1-b) f_c}{1 - (1-b) f_c} \tag{2}$$

where b = fraction of fines which actively take part in the force structure of the solid skeleton. When b = 0, equivalent granular void ratio reduces to inter-granular void ratio. However, most literature deduced the "b" values by back-analysis, as such test results for a range of fines content has to be known as a priori. Rahman and Lo (2007b), recognizing the analogy between "b"-value and binary packing, suggested that "b" should be a function of both particles size ratio, (r) and fines content, (f_c), i.e. $b = B(r, f_c)$. The size ratio, r, is defined by $r = (d_{50}/ D_{10})$ where d_{50} = median size for fines and D_{10} = particle size at 10% fractile for host sand. Based on a synthesis of existing studies on binary packing, it was revealed that this functional relationship has to possess certain mathematical attributes. The details can be found in Rahman and Lo

(2007b; Rahman et al. 2007). The following equation was found to possess the attributes required:

$$b = \left(1 - e^{\left(m[f_c]^n / k\right)}\right)\left(\frac{rf_c}{f_{thre}}\right)^r \quad (3)$$

Where m and n are empirical constant, $k = (1 - r^{0.25})$, f_{thre} = threshold fines content, which is the fines content where the behaviour of sand-fines mix changes from "fines in sand" to "sand in fines". Thus the value of f_{thre} is the point where the behaviour trend reverses with further increase in fines content. Eqn. (3) is applicable for $f_c < f_{thre}$ so that the mixture remains as 'fines in sand". Eqn (3) requires two fitting constants, m and n. Rahman and Lo (2007a; 2007b), by calibrating Eqn (3) against nine databases, reported that setting $m = n = 1.5$ will yield an approximately unique SSL for sand in the e^*-log(p') space, or a unique correlation between cyclic resistance and e^*. The former finding can be idealized into the concept of a unique equivalent granular SSL (in the triaxial compression plane). This idealization provides a simple means for predicting the SSL of sand with any fines content (less than that of the threshold value) from that of clean sand by the following procedure.

1. For any p'_{SS}, on the SSL of clean sand, determine the corresponding void ratio. This void ratio is in fact e^* of sand with fines because the SSL of clean sand is in fact the equivalent granular SSL.
2. Calculate the corresponding global void ratio, e, of the sand with fines by:
    - First calculate "b" using Eqn. (3)
    - Calculate e from e^* with Eqn. (2)
3. Repeat steps 1 and 2 for other values of p'_{SS} so that a complete SSL for sand with fines is generated.

However, the above findings were established for non-plastic fines. It is pertinent to examine the effect of angularity and plasticity on the above conceptual framework.

Effect of Host sand Gradation

Chang et al. (1982) reported that cyclic liquefaction resistance of a clean sand was strongly affected by the mean diameter, D_{50}, and coefficient of uniformity, CU, provided that $D_{50} < 0.23$mm. However, the individual effects of D_{50} and CU were not isolated. Vaid at el. (1991) examined the effect of CU by testing three clean sands with identical mineralogy, D_{50}. Furthermore the grading curves of these three sands were linear. They found that cyclic liquefaction resistance of clean sand increases with CU, at low relative density and the trend was reversed at high relative density. However, there is a scarcity of test data on the influence of CU for sand-fines mix, the subject of this paper.

Effect of Fines Type

Most of the published literatures on the liquefaction behaviour on sand fines mixture are based on non-plastic fines. Perlea et al. (1999) reported any increase in plasticity

of fines resulted in decrease in liquefaction resistance for f_c <15% and the trend reversed when f_c >20%. Ghahremani and Ghalandarzadeh (2006) reported that, for sand with 16% fines, cyclic liquefaction resistance increased when the plasticity index, PI, was increased from 20 to 40. Ghahremani et al. (2006) also reported for sand with 30% fines, the steady state strength of the sand-fines mix increased with increase in PI (from PI =19 to PI=48). However, Sadek and Saleh (2007) reported, for a sand with 10% fines, the influence of PI on cyclic liquefaction resistance depended on the value of PI relative to a threshold value (which was about 11%). For PI < 11%, liquefaction resistance decreased with PI, but for PI > 11% liquefaction resistance increased with PI at an insignificant rate. Thus, our understanding of the effect of plasticity of fines is far from adequate.

EXPERIMEMTAL STUDY

Experimental studies were conducted on sand-fines mixtures using two types of host sand and three types of fines. The two types of host sand are: a well-graded sand denoted as WG-sand and a uniform size sand referred to as Sydney sand. The three types of fines are: M-Silt-II, S-Silt-I and S-Silt-II. The notation "II" denotes that the fines was synthesized from two types of fines materials. The fines content were kept at 15%. The particle size distributions of the host sands and fines are plotted in Figure 1. It is evident that a size gap between the host sand and the fines is always maintained and the intrinsic assumption of a "fines in sand" model is always satisfied.

Sydney sand is a medium quartz clean sand (SP), with a coefficient of uniformity, CU = 1.26 and it's index properties can be found in Lo et al. (1989). WG-sand is commercially available sand used in concrete industry. It has a coefficient of uniformity of 4.16. Three different fines: M-Silt-II, S-Silt-I and S-Silt-II, are used to study the effect of fines. M-Silt-II is a specially designed low plasticity fines with a coefficient of uniformity 12.56. It is composed of 2/3 of well-graded silt (CL) from the Majura River (PL=23, PI=18) and 1/3 commercial kaolin (PL=32, PI=31). S-Silt-I is a non-plastic fines that is obtained by milling Sydney sand. S-Silt-II is synthesized from 2/3 S-Silt-I and 1/3 kaolin. A summary of the sand-fines composition and their relevance in this study are given in the Table 1.

Table 1. Summary of fines used on the study

<table>
<tr><th>Fines</th><th colspan="2">Composition</th><th colspan="2">Comparative study</th></tr>
<tr><td>S-Silt-I</td><td colspan="2">Milled Sydney Sand (MSS)</td><td rowspan="2">Effect of fines Plasticity</td><td></td></tr>
<tr><td>S-Silt-II</td><td>2/3 MS Sand</td><td>1/3 kaolin</td><td rowspan="2">Effect fines angularity & mineralogy</td></tr>
<tr><td>M-Silt-II</td><td>2/3 Majura Silt</td><td>1/3 kaolin</td><td></td></tr>
</table>

Specimen Preparation

A specimen was formed by a modified moist tamping method. A pre-determined quantity of moist soil was carefully placed and then tamped lightly into a prescribed

thickness using a standardised plastic strip with a tamping area of 8.5 X 20 mm. A total of 10 layers were placed. The dimensions of as placed soil specimens were 100mm in both diameter and height. Free ends with enlarged platens were used to minimize end restraint. This technique has been proven to be successful in achieving essentially uniform deformation for a range of soil type (Lo et al. 2003; Lo and Wardani 2002). Bedding and membrane penetration errors were reduced to an insignificant value by using the liquid rubber technique developed by Lo et al. (1989). Saturation was achieved by vacuum flushing with a low head followed by back pressure saturation, both in a manner that ensured the effective stress in a specimen was less than 20 kPa. Details of the specimen preparation method are contained in Bobei and Lo (2005).

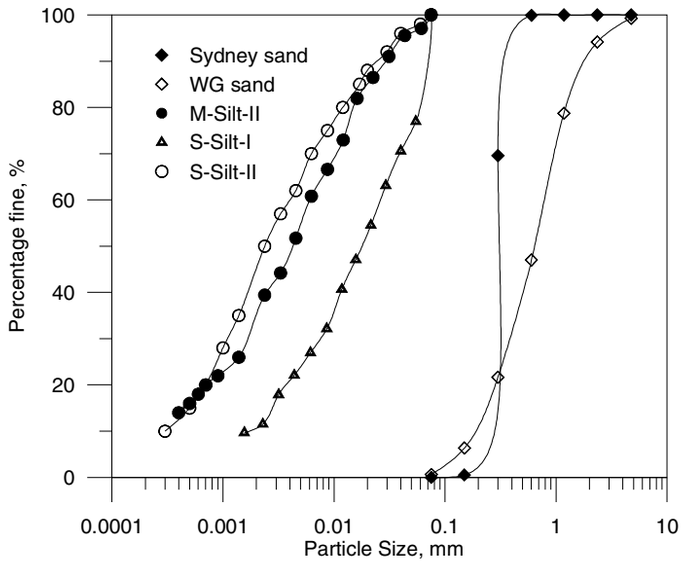


FIG. 1. Grain size distribution curve of host sand and fines.

Experiment Setup

A strain controlled triaxial loading system with fully automated data logging facilities was used for this study. Axial load was measured with an internal load cell. The axial deformation was measured by a pair of internal LVDTs mounted directly across the top platen and an external LVDT. The former was used in the early stage of shearing whereas the latter was used at large deformation. Cell pressure was controlled by a large capacity Digital Pressure Volume Controller (DPVC). The pore pressure line was connected to a small capacity DPVC for controlling back pressure (and measuring the volume change) at the consolidation stage, and for imposing an undrained condition and measuring the resultant pore pressure response. Two pressure transducers mounted on the top and bottom platen respectively were also used to verify pore pressure equilibrium.

RESULT AND DISCUSSION

Effect of Host sand Gradation

To study the influence of host sand gradation on static liquefaction behaviour, isotropically consolidated undrained (ICU) tests were conducted on two sand-fines mix. The host sand was either Sydney sand or WG-sand, but the fines type and content was fixed: 15% M-Silt-II. All specimens were prepared with exactly same amount of material so that the as-placed void ratio measured at a standardized confining stress of 20 kPa was essentially same for all tests. The consolidation stress, p'_0, was in the range of 350 to 850 kPa, and therefore the void ratios at start of shearing were dependent on p'_0. However, for tests with the same p'_0, WG-sand with fines attained a smaller void ratio than Sydney sand with fines. The ratio of peak deviatoric stress to deviatoric stress at steady state, q_{peak}/q_{ss}, was used to interpret the liquefaction susceptibility of sand-fines mix. Higher q_{peak}/q_{ss} indicates more liquefaction susceptibility than lower value of q_{peak}/q_{ss}. The tests results in the form of effective stress path (ESP) and q-ε_1 curves in Figure 2(a-d). It is evident that all the tests approached the SS closely at end of shearing.

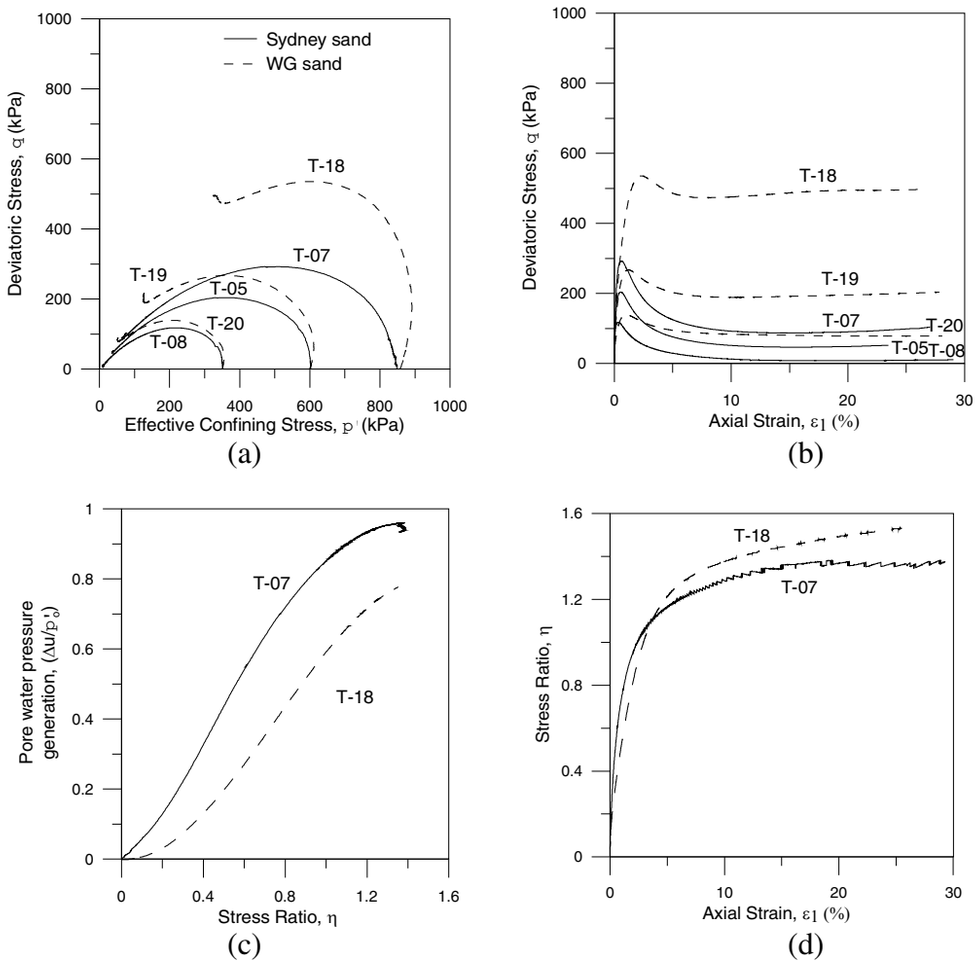


FIG. 2. Effect of host sand gradation on: (a) q-p' space, (b) q-axial strain, (c) pore water pressure generation ($\Delta u/p'_o$), (d) η-axial strain

The ratio, q_{peak}/q_{ss}, of WG-sand with fines varied from 1.10 for shearing from p'_0 of 850kPa to 1.80 for shearing from p'_0 of 350kPa. The ratio, q_{peak}/q_{ss} for Sydney sand with fines varied from 3.50 for shearing from p'_0 of 850 kPa to 11.50 for shearing from 350 kPa. So for both types of host sand (with very different CU), liquefaction susceptibility decreased with p'_o. However, Sydney sand with fines showed lower q_{SS} than WG-sand with fines irrespective of p'_o. This finding is consistent with Vaid et al. (1991), liquefaction resistance increases with CU of host sand. The details experimental results are given in Table 2.

Figure 2(c) compares pore water pressure generation in a normalized form, $\Delta u/p'_o$, for T-18 (WG sand) and T-07 (Sydney sand). The pore water pressure generation of Sydney sand is much higher than that of WG-sand throughout undrained shearing. This is a main reason of the lower q_{SS} of Sydney sand with fines. Figure 2(d) compares the mobilization of effective stress ratio with axial strain. Evidently the difference between T-18 (WG sand) and T-07 (Sydney sand) was small. Therefore, the influence has to be attributed to the gradation (not the inter-particle friction).

Table 2. Summary of tests used on the study

Test Name	Initial p'_o(kPa)	Sand	Fines	Comparison	q_{SS} (kPa)	q_{peak}/q_{SS}
T-08	350	Sydney	M-Silt-II	Types of host sand	9.10	11.50
T-05	600	Sydney	M-Silt-II		46.50	4.50
T-07	850	Sydney	M-Silt-II		91.60	3.50
T-20	350	WG sand	M-Silt-II		78.10	1.80
T-19	600	WG sand	M-Silt-II		189.00	1.45
T-18	850	WG sand	M-Silt-II		486.00	1.10
NTC-01	600	Sydney	No fines	Types of fines	278.10	1.40
NTC-08	600	Sydney	S-Silt-I		153.80	2.67
NTC-11	600	Sydney	S-Silt-II		139.60	2.56
T-05	600	Sydney	M-Silt-II		46.50	4.50

Effect of Fines Type

The influence of fines type was investigated by testing Sydney sand mixed with different types of fines, viz, S-Silt-I, S-Silt-II and M-Silt-II. Fines content was fixed at 15%. ICU test results are presented in Figs. 3(a-d) in the form of ESP, q-ε_1 curves, pore water pressure responses and η-ε_1 curve. Flow liquefaction was manifested in all three tests of sand-fines mix. However, the peak deviator strength and pre-peak ESP of sand with S-Silt-I and sand with S-Silt-II, and clean sand are similar, although the host sand only manifested limited flow. The peak strength of sand with M-Silt-II is considerably lower. The Steady State deviatoric strength, q_{SS}, of these three sand-fines mix followed a similar trend. The deviatoric stress at steady state, q_{SS} for sand with S-Silt-I fines is 153.80kPa which is slightly higher than that of sand with S-Silt-II at 139.60kPa. However, the deviatoric stress at steady state, q_{SS} for sand with M-Silt-II is at a significantly lower value of 46.50kPa.

The only difference between S-Silt-I and S-Silt-II is that the latter was derived from the former by replacing 1/3 of the synthetic silt with Kaolin, and thus introduced a small and controlled amount of plasticity to the fines. This only led to slight reduction in q_{peak} and q_{ss}. Therefore, the considerably inferior behaviour (lower q_{peak} and lower q_{ss}) for sand with M-Silt-II has to be attributed to factors other than plasticity for characterizing fines type.

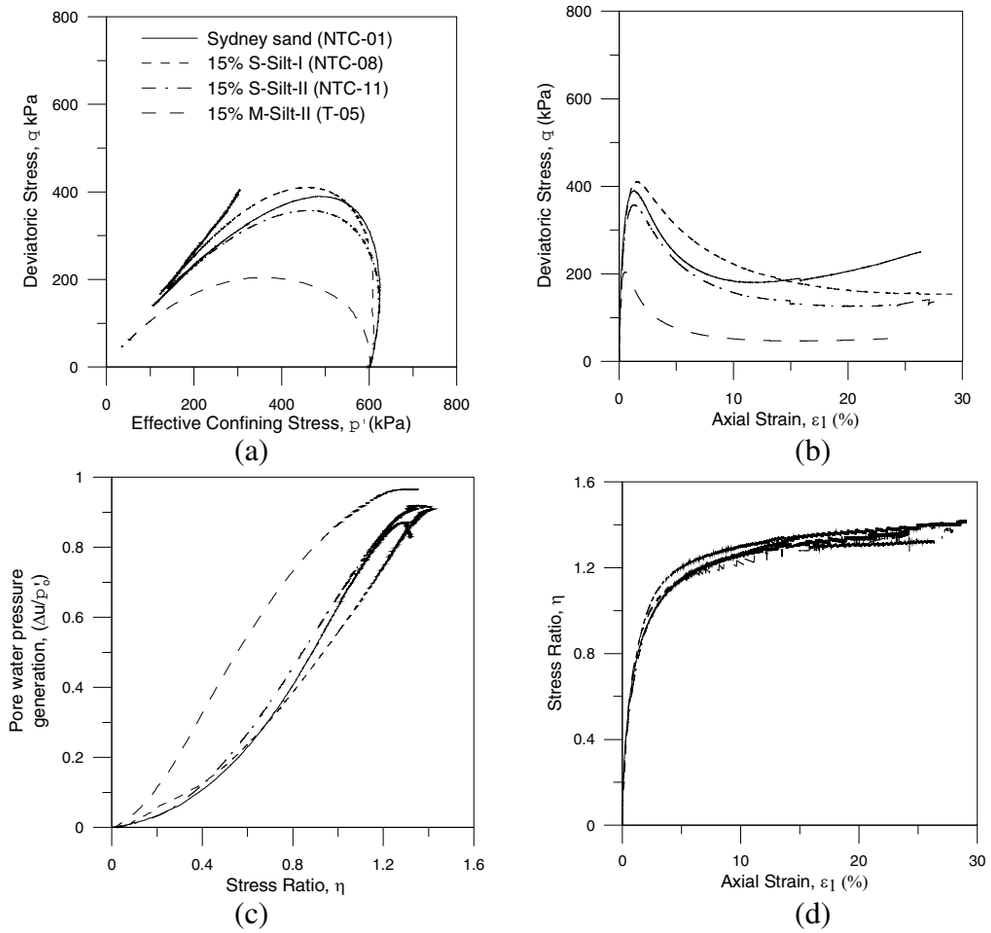
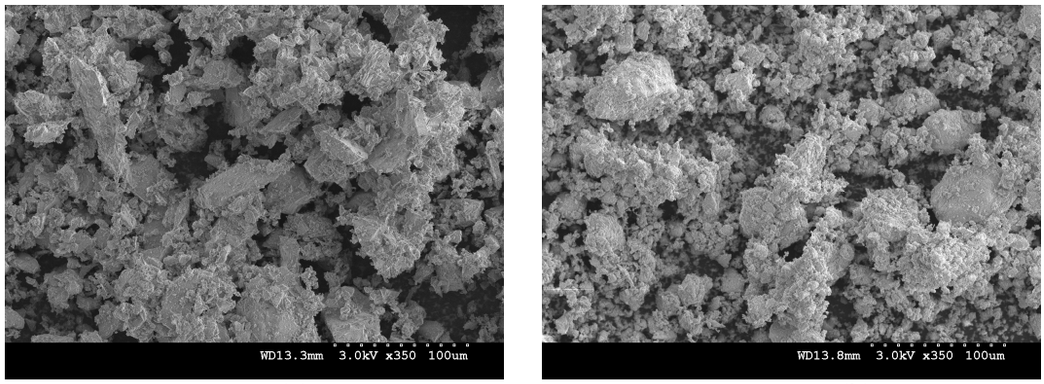


FIG. 3. Effect of fines type on Sydney sand: (a) q-p' space, (b) q-axial strain, (c) pore water pressure generation ($\Delta u/p'_o$), (d) η-axial strain

Scanning Electron Microscope (SEM) Photography

To investigate the reason for the significant inferior behaviour (lower q_{peak} and lower q_{SS}) for sand with M-Silt-II, SEM photographs of S-Silt-I and M-Silt-II were taken. Two such photos were compared in Fig. 4. S-Silt-I consists of sharp, angular particle with a spiky surface; where as M-Silt-II is rounded and coated with "spongy" kaolin particles. It can be concluded from the photograph that angularity of fines plays an important role on the behaviour of a sand-fines mix. However, the adverse effect of S-Silt-II on strength is not as much as M-Silt-II, though both of them contain one-third of kaolin. It indicates that angularity of fines may play higher contribution on sand-fines mix strength than kaolin.

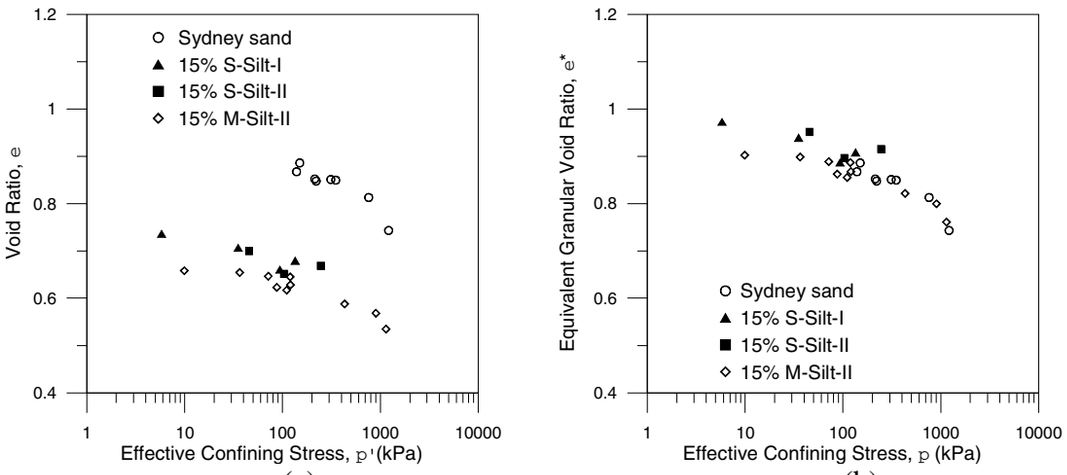


(a) (b)

FIG. 4. SEM photograph of (a) S-Silt-I, (b) M-Silt-II

Effect of Fines Type on Equivalent Granular Steady State Line

The SSLs in e-log(p') space were plotted in Figure 5a, which showed that the addition of 15% fines, for all three fines type, the SSL shifted downward. This is consistent with previous studies. However the extent of downward shift depends on fines type. According to Rahman and Lo (2007b), the extent of shift depends on the particles diameter ratio, r. If this hypothesis can be extended to different fines type, a unique equivalent granular SSL line can be achieve irrespective of fines type, angularity and plasticity. Figure 4b showed that SS points of Sydney sand and Sydney sand with different types of fines. The data points all clustered around a narrow band and the concept of a unique equivalent granular SSL appears to be still applicable for capturing the effects of different type of fines. However, careful observation of the data points shows that some scatter from a unique relationship at low effective mean stress. It is considered that the angularity of fines may be the reason of the scatter and thus is another parameter for the determining of e^*.



(a) (b)

FIG. 5. (a) Effect of fines type on SSLs, (b) Unique equivalent granular SSL independent of fines type.

CONCLUSIONS

The effect of sand gradation and fines type on liquefaction behaviour and their effect on equivalent granular void ratio formula were studied. The findings are as follows.

- The liquefaction behaviour of a sand fines mix, for a given fines type and content, depends on host sand gradation as represented by CU. It general, q_{SS} increases with CU.
- Angularity and plasticity of fines in a sand-fines mix play important role in liquefaction potential and SS strength. q_{SS} increases with angularity of fines and it can be attributed that angularity may have higher influence than plasticity on q_{SS}. Again, liquefaction resistance decreases with increasing plasticity which is consistent with Sadek and Saleh (2007) but contradictory with Ghahremani et al. (2006) findings. Existence of threshold plasticity could be the reason of contradictory findings. Extensive investigation may need to draw a conclusion. However, liquefaction resistance of sand-fines mix always decreases with fines, no matter what is their type.
- The equation proposed by Rahman and Lo (2007b) for calculating "*b*" and thus *e**, plus the conceptual framework of a unique equivalent granular SSL, can be used for sand with different types of fines. However, angularity of fines led to some scatter from a unique relationship in the *e**-log(*p′*) space at low confining pressure. Thus, the equations used for determining *e** may be further improved by considering angularity of fines.

REFERENCES

Bobei, D. C., and Lo, S. R. (2005). "Reverse behaviour and critical state of sand with small amount of fines." *The Proceedings of the 16th International Conference on Soil Mechanics and Geotechnical Engineering (16ICSMGE)*, Japan, 475-478.

Chang, N. Y., Yey, S. T., and Kaufman, L. P. (1982). "Liquefaction potential of clean and silty sand." Proc. 3rd International Earthquake Microzonation Conference, 1018-1032.

Georgiannou, V. N., Burland, J. B., and Hight, D. W. (1990). "The undrained behaviour of clayey sands in triaxial compression and extension." *Géotechnique*, Vol. 40(3), 431-449.

Ghahremani, M., and Ghalandarzadeh, A. (2006). "Effect of plastic fines on cyclic resistance of sands." *Soil and Rock Behavior and Modeling* (GSP 150), Shanghai, China, 406-412.

Ghahremani, M., Ghalandarzadeh, A., and Moradi, M. (2006). "Effect of plastic fines on the undrained behavior of sands." *Soil and Rock Behavior and Modeling* (GSP 150), Shanghai, China, 48-54.

Kenney, T. C. (1977). "Residual strength of mineral mixture." *Proc. 9th International Conference of Soil Mechanics and Foundation Engineering*, 155-160.

Kuerbis, R., Negussey, D., and Vaid, Y. P. (1988). "Effect of gradation and fine content on the undrained response of sand." *Hydraulic fill structure* (GSP 21)*, ASCE*, New York, 330-345.

Lo, S. R., Chu, J., and Lee, I. K. (1989). "A Technique for reducing membrane

penetration and bedding errors." *Geotechnical Testing Journal*, Vol. 12(4), 311-316.

Lo, S. R., Lade, P. V., and Wardani, S. P. R. (2003). "An experimental study of the mechanics of two weakly cemented soils." *Geotechnical Testing Journal*, Vol. 26(3), 328-341.

Lo, S. R., and Wardani, S. P. R. (2002). "Strength and dilatancy of a silt stabilized by cement and fly ash mixture." *Canadian Geotechnical Journal*, Vol. 39(1), 77.

Mitchell, J. K. (1976). *Fundamental of soil behaviour*, 1st edition, John Wiley & Sons, Inc.

Perlea, V. G., Koester, J. P., and Prakasha, K. S. (1999). "How liquefiable are cohesive soils." *Second International Conference on Earthquake Geotechnical Engineering and Soil Dynamics*, Lisbon, Portugal, 611-618.

Rahman, M. M., and Lo, S. R. (2007a). "Equivalent granular void ratio and state parameters for loose clean sand with small amount of fines." *10Th Australia New Zealand Conference on Geomechanics*, Brisbane, Australia, 674-679.

Rahman, M. M., and Lo, S. R. (2007b). "On intergranular void ratio of loose sand with small amount of fines." *16th South East Asian Geotechnical Conference*, Kuala Lumpur, Malaysia, 255-260.

Rahman, M. M., Lo, S. R., and Gnanendran, C. T. (2007). "On equivalent granular void ratio and steady state behaviour of loose sand with fines." *Canadian Geotechnical Journal*, under second review.

Sadek, S., and Saleh, M. (2007). "The effect of carbonaceous fines on the cyclic resistance of poorly graded sands." *Geotechnical and Geological Engineering*, Vol. 25, 257-264.

Thevanayagam, S. (1998). "Effect of fines and confining stress on undrained shear strength of silty sands." *Journal of Geotechnical and Geoenvironmental Engineering*, Vol. 124(6), 479-491.

Thevanayagam, S. (1999). "Effect of fines and confining stress on the undrained shear strength of silty sands - Closure." *Journal of Geotechnical and Geoenvironmental Engineering*, Vol. 125(11), 1024-1027.

Thevanayagam, S., Fiorillo, M., and Laing, L. (2000). "Effect of non-plastic fines on undrained cyclic strength of silty sands." *ASCE Geotechnical Special Publication*, 99-91.

Thevanayagam, S., and Mohan, S. (2000). "Intergranular state variables and stress-strain behaviour of silty sands." *Géotechnique*, Vol. 50(1), 1-23.

Troncoso, J. H., and Verdugo, R. (1985). "Silt content and dynamic behaviour of tailing sands." *Proc. 11th International Conference on Soil Mechanics and Foundation Engineering*, 1311-1314.

Vaid, Y. P., Fisher, J. M., and Kuerbis, R. H. (1991). "Particle gradation and liquefaction." *Journal of Geotechnical Engineering*, Vol. 116(4), 698-703.

Yamamuro, J. A., and Lade, P. V. (1998). "Steady-State Concepts and Static Liquefaction of Silty Sands." *Journal of Geotechnical and Geoenvironmental Engineering*, Vol. 124(9), 868-877.

This page intentionally left blank

Effects of Fines on Undrained Behaviour of Sands

Misko Cubrinovski[1] and Sean Rees[2]

[1] Associate Professor, Department of Civil and Natural Resources Engineering, University of Canterbury, New Zealand; misko.cubrinovski@canterbury.ac.nz

[2] PhD Candidate, Department of Civil and Natural Resources Engineering, University of Canterbury, New Zealand; sdr40@student.canterbury.ac.nz

ABSTRACT: A series of monotonic and cyclic triaxial tests were performed on a sand with fines sourced from Christchurch, New Zealand. The sand was sieved and then mixed to give three soils with different fines contents. The undrained tests were used to examine the effects of fines on the strain softening behaviour under monotonic loading and liquefaction resistance in cyclic loading. Two reference states were used as a basis for evaluation of the effects of fines: the relative density and the steady state line within the state-concept framework for sand characterization. The addition of fines to the sand base caused downward movement of the steady state line in the D_r-p' plane (e-p' plane), and this effectively increased the potential for strain softening or flow deformation. Samples prepared at an identical relative density showed decreasing cyclic strength with increasing fines content. Conversely, samples at an identical initial state relative to the steady state line showed increasing cyclic strength with the fines content.

INTRODUCTION

Case histories from strong earthquakes and laboratory studies show clearly that fines have significant influence on both monotonic and cyclic undrained behaviour of sands (Lade and Yamamuro, 1997; Thevanayagam, 1998; Polito and Martin, 2001). These effects are particularly relevant when evaluating the potential for strain softening or flow deformation during monotonic loading and liquefaction resistance in cyclic loading. When comparing the liquefaction resistance of fines-containing sand with that of a clean sand, one encounters the problem of a lack of proper basis for comparison. For example, in the conventional procedure for liquefaction evaluation based on the penetration resistance (Youd and Idriss, 1998), fines-containing sands show greater liquefaction resistance as compared to clean sands. In these criteria, however, the penetration resistance, e.g. normalized SPT blow count N_1, is used as a basis for comparison. Since the penetration resistance is affected by the grain size and fines content, these criteria do not show only the effects of fines on the liquefaction resistance but rather they depict the combined effects of fines on

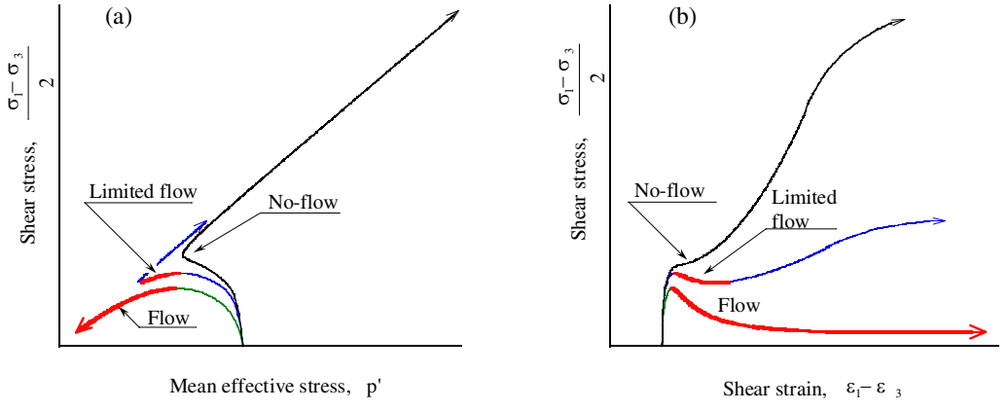


FIG. 1. Undrained behaviour of sand in monotonic tests

both penetration resistance and liquefaction resistance. Thus, it is not straightforward from these charts whether the fines per se increase the liquefaction resistance or not. In order to investigate the effects of fines in more detail, a series of undrained triaxial tests were conducted on natural sands recovered from a site in Christchurch, New Zealand. In the interpretation of the effects of fines on undrained behaviour both the relative density of the soil and the initial state of the soil relative to its steady state line (state-concept interpretation) were used as a basis for comparison.

EFFECTS OF FINES ON UNDRAINED MONOTONIC BEHAVIOUR

Background

Three types of response characterize undrained behaviour of sands under monotonic shearing, as outlined in Figure 1. Very loose sand shows fully contractive behaviour and strain softening until the steady state or critical state is reached at large strains. The strain-softening phase of the response resembles flow-type behaviour and therefore it is often referred to as flow or flow deformation. If the density of the sand is somewhat higher, then the strain softening takes place over a limited range, and limited flow occurs followed by strain hardening and steady state of deformation. Finally, in the case of medium dense and dense sands, a strain-hardening response associated with strong dilation towards the steady state is observed.

The undrained behaviour of a given sand changes within the three types of response outlined in Figure 1 and shows different degrees of strain softening and strain hardening depending upon the density of the sand and confining stress at the initial state, prior to shearing. It is possible, therefore, to distinguish between initial density-stress states that are associated with strain-softening behaviour (flow deformation) and those entirely exhibiting strain-hardening behaviour in monotonic undrained loading. In this context, Ishihara (1993) defined a so-called initial dividing line (ID-line) that marks the boundary between flow and no-flow conditions in the *e-p'* diagram (void ratio-mean effective stress diagram). As illustrated in Figure 2, samples lying above the ID-line are contractive and exhibit flow-type behaviour while all of the initial density-stress combinations lying below the ID-line exhibit strain-hardening behaviour upon monotonic shearing under undrained conditions.

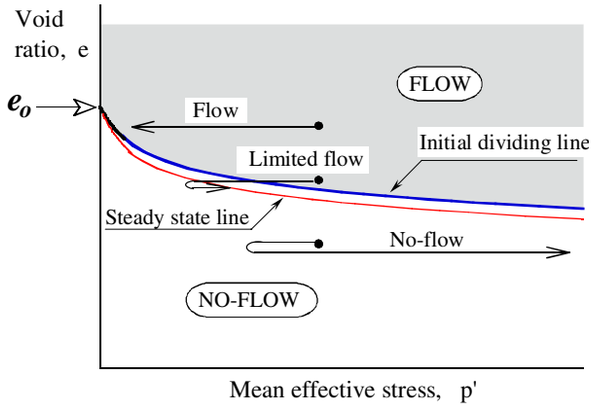


FIG. 2. Characterization of monotonic undrained behaviour based on state concept

This illustrates the essence of the state-concept interpretation of sand behaviour where a particular type of behaviour is associated with the initial *e-p′* state of the soil relative to a reference state.

As depicted in Figure 2, the projection of the steady state line in the *e-p′* plane is relatively close to the initial dividing line, and therefore, it could be used as its approximation when identifying whether the sand behaviour upon monotonic undrained shearing is of strain-softening or strain-hardening type. Two features of the steady state line make this line a particularly suitable reference state. Firstly, the steady state line is unique for a given sand, and therefore, the position of the steady state line is uniquely defined in the *e-p′* plane. Secondly, any soil sample subjected to monotonic shearing will eventually reach the steady state of deformation; in other words, the ultimate *e-p′* state will end up on the steady state line irrespective of the initial *e-p′* state of the soil. Hence, the ultimate level of dilation/contraction or excess pore water pressure development in monotonic undrained shearing is practically defined by the initial *e-p′* state of the soil relative to the steady state line. All initial states above the steady state line will show contractive behaviour or positive excess pore water pressure. The contractive tendency or excess pore pressure level will increase with the distance from the steady state line. Note that initial states with a void ratio greater than e_o will end up at $p' = 0$ and exhibit zero steady state strength upon monotonic undrained loading.

The position and slope of the steady state line of sandy soils are affected by a number of factors including the grain-size characteristics, fines content and grain shape of sands. Figure 3 summarizes the effects of grain-size composition and fines content on the steady state line of sandy soils. Here, the circular symbols show published data on 52 sandy soils obtained from triaxial compression tests on reconstituted samples of clean sands and sands with non-plastic fines (Cubrinovski and Ishihara, 2000). The figure also includes recently summarized data by Jefferies and Been (2006) and results for the three soils tested in this study. Note that D_{ro} indicates the relative density corresponding to e_o (see Figure 2) and hence defines the threshold relative density below which soils exhibit a zero steady state strength. Figure 3 shows that the position of the steady state line in the *e-p′* plot or D_r-*p′* plot is

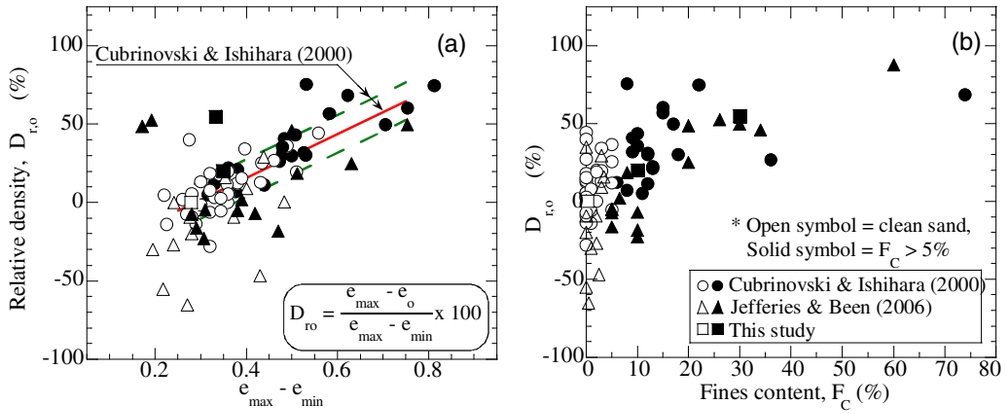


FIG. 3. Position of the steady state line of sandy soils as a function of: (a) Void ratio range, *(e_{max} -e_{min})*; (b) Fines content, *F_C*

related to the grain-size composition, as represented by the void ratio range *(e_{max}-e_{min})*, and fines content, *F_C*. As the fines content or *(e_{max}-e_{min})* increases, the steady state shifts downwards in the *e-p'* plot or the relative density *D_{ro}* corresponding to *e_o*, defined in Figure 2, increases. This implies that, at a given relative density, loose samples containing fines are more contractive and show greater potential for strain softening than clean sands. This feature of the undrained behaviour of sands was further investigated by testing samples of Christchurch soils with different fines content using conventional triaxial compression tests.

Materials Tested

Three soils were tested in this study all based on a host sandy soil obtained from a single layer at the Fitzgerald Bridge Avenue site in Christchurch, New Zealand. We will call the host material as well as the soils derived from it Fitzgerald Bridge Mixture (FBM) and will distinguish between them based on the fines content, as follows. The host soil FBM-10 was created by mixing "undisturbed" samples obtained from the Fitzgerald Avenue Bridge site. The initial soil mixture created in this way was a silty sand containing approximately 10% fines by weight (FBM-10), with the fines determined to be non-plastic. This material was dry-sieved after testing to isolate the clean-sand base and create the second material that happened to have 1% fines by weight (FBM-1). Finally, the third soil was produced by reintroducing the fines to the clean-sand base, and creating a silty sand with approximately 30% fines by weight (FBM-30). Material properties of the tested soils are summarised in Table 1 while their grain-size curves are shown in Figure 4. Note that e_{max} and e_{min}

Table 1. Properties of the tested soils

Material	F_C (%)	G_s	e_{max}	e_{min}	$e_{max} - e_{min}$
FBM-1	1	-	0.907	0.628	0.279
FBM-10	10	2.664	0.945	0.597	0.348
FBM-30	30	-	0.860	0.527	0.333

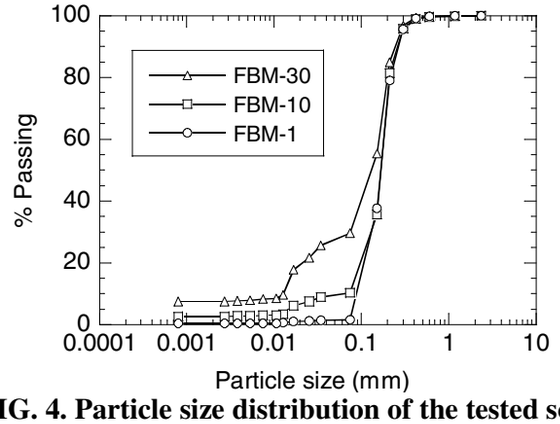


FIG. 4. Particle size distribution of the tested soils

were obtained for all soils using the British standard procedures for minimum and maximum densities of sands (BSI, 2002). Whereas one should be cautious when applying these procedures to soils with relatively high fines contents, Cubrinovski and Ishihara (2002) presented evidence based on 300 natural soils that the procedures stipulated by the Japanese Geotechnical Society for clean sands (JGS, 2000) provide reasonably consistent e_{max} and e_{min} values for sands with a fines content of up to 30%.

Each of the three soils required re-use during the monotonic and cyclic triaxial testing. This was due to the limited amount of material available. The tested soil was dried overnight at 104ºC and then gently ground to allow a return to a homogenous material. This soil was placed in a separate container and only re-used once the original material mixture had been exhausted. An effort was made during these steps to retain as much material (particularly fines) as possible. Particle size distributions taken of the re-used material varied insignificantly from the original grain-size curves shown in Figure 4.

Results from Monotonic Tests

In total, 28 undrained monotonic tests in triaxial compression were performed on the three materials created from the Fitzgerald Bridge soils. All specimens were prepared using the moist-tamping method by firstly preparing the sand to a moisture content of approximately 9%, placing the soil in 6 equal layers, and applying an appropriate amount of tamping for the target specimen density. The specimens had conventional dimensions of approximately 50mm in diameter and 100mm in height. All specimens had CO_2 percolated through them before saturation for varying amounts of time, with the amount of time increasing with the fines content. The samples were isotropically consolidated to an initial mean effective stress of 100 kPa, except for two tests in which p' = 200 kPa was used. The tests were conducted in a strain-controlled manner at an axial strain rate of 0.3 %/min.

Figure 5 shows stress-strain curves and effective stress paths for each of the three soils tested. In this case, all three specimens exhibited either limited flow or flow deformation. The stress-strain relationships shown in Figure 5(a) give good indication of how fines can affect undrained behaviour of sand. All specimens peak at approximately the same stress level, around 80kPa to 90kPa, but the steady state

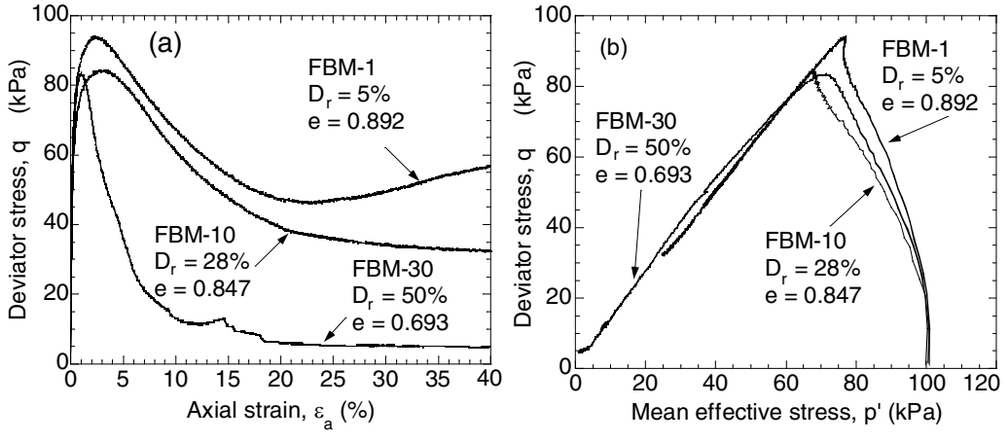


FIG. 5. Stress-strain curves and effective stress paths observed in monotonic undrained tests on sands with different fines content

stresses vary significantly. The clean sand mixture (FBM-1) has the highest stress at steady state, being close to q = 55kPa, whilst having the lowest relative density of D_r = 5%. The specimen prepared using the FBM-30 mixture has the lowest stress at steady state, with q = 5kPa, yet is the densest specimen with a relative density of D_r = 50%. These responses demonstrate that the addition of fines to the clean sand base increased the potential for flow deformation during undrained monotonic loading. The sand with 30% fines (FBM-30) shows greater drop in the shear stress during the strain softening at a relative density of D_r = 50% than the clean sand (FBM-1) at a relative density of D_r = 5%. This result is in agreement with findings from previous studies summarized in Figure 3.

Another way to consider these effects is to depict the position of the steady state line for each of the tested soils in the *e-p'* plot or even more suitably in the D_r-*p'* plot, as shown in Figure 6. Here, the steady state condition of a given test is defined by the

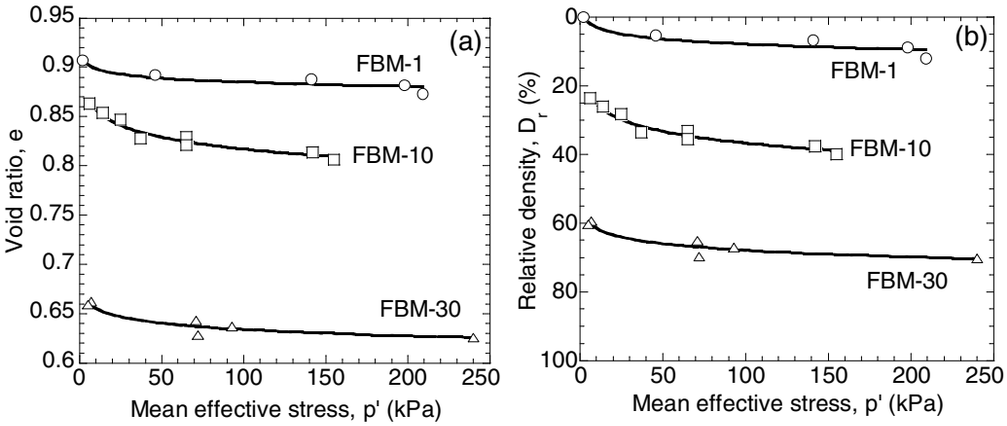


FIG. 6. Effects of fines on the position of the steady-state line: (a) *e-p'* plane; (b) D_r-*p'* plane

state at 40% strain. The downward shift in the steady state line as the fines content increases can be clearly seen in Figures 6(a) and (b); the steady state line for FBM-1 is at relative densities of 0% to 10% while the corresponding relative density for FBM-30 is 60% to 70%. In view of the state-concept interpretation of sand behaviour introduced previously, the downward shift in the steady-state line with increasing fines content in effect implies that fines tend to increase the flow potential and make the sand more contractive during undrained monotonic loading, at least when the relative density is used as a basis for comparison.

EFFECTS OF FINES ON UNDRAINED CYCLIC BEHAVIOUR

Results from Cyclic Tests

In addition to the monotonic tests, undrained cyclic triaxial tests were performed on the three tested soils. In total 43 cyclic tests were conducted including three series of tests on FBM-1, four series of tests on FBM-10 and two series of tests on FBM-30. Each of these test series was used to determine the liquefaction resistance curve for a selected relative density of the respective soil. All specimens were prepared using the previously described moist-tamping technique and were isotropically consolidated to an initial mean effective stress of $p' = 100$ kPa. Figure 7 shows typical effective stress path and stress-strain response observed in one of the cyclic tests.

For each soil, four or five specimens were prepared at a nearly identical relative density (void ratio), and then the specimens were subjected to cyclic stresses at different cyclic stress ratios (CSR) allowing liquefaction resistance or cyclic strength curves to be generated for each test void ratio (relative density). Liquefaction resistance curves determined in this way are shown in Figure 8 where the cyclic stress ratio is plotted against the number of cycles required to cause 5% double amplitude strain. As expected, for each soil, the liquefaction resistance increases with the relative density of the soil. The effects of fines on the liquefaction resistance are not apparent in these plots. In order to scrutinize these effects, in what follows the liquefaction resistance of soils FBM-1, FBM-10 and FBM-30 is examined using two reference states: the relative density of the sand and the steady state line respectively.

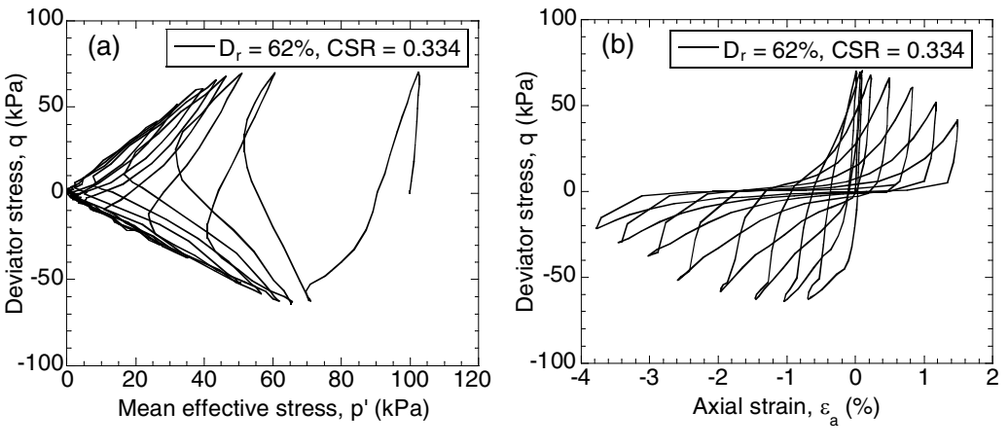


FIG. 7. Stress path and stress-strain curve observed in a cyclic test on FBM-1

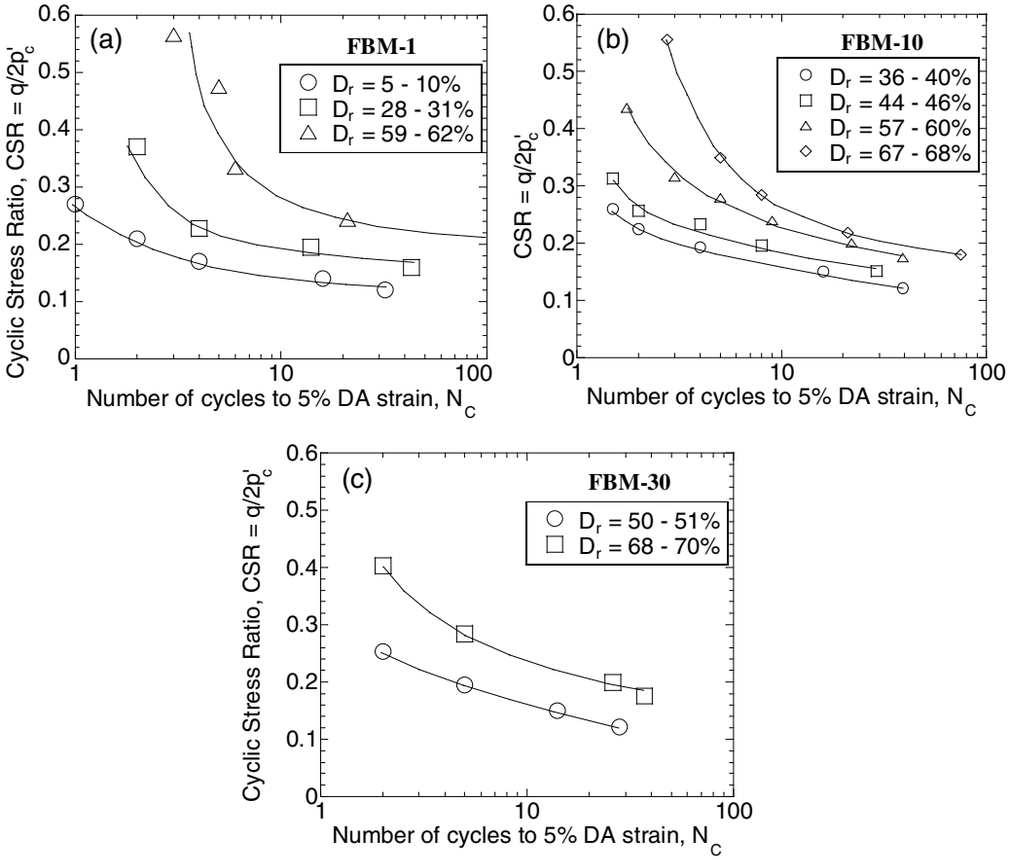


FIG. 8. Liquefaction curves for the tested soils at different relative densities: (a) FBM-1; (b) FBM-10; (c) FBM-30;

The cyclic strength data is re-plotted in Figure 9 where cyclic stress ratios at 5 cycles and 15 cycles, $CSR_{Nc=5}$ and $CSR_{Nc=15}$ respectively, are plotted against the relative density of the soil. These plots allow comparison of the liquefaction resistance of soils with different fines content, at the same relative density. Clearly, at any relative density within the range considered, the clean sand shows higher cyclic strength than the sand containing 10% or 30% fines. In other words, when the relative density is used as a reference for comparison, the liquefaction resistance of FBM soils decreases with increasing fines content.

The state concept approach has already been shown to be useful in describing the undrained monotonic behaviour of sand. Parameters such as the state parameter (Been and Jefferies, 1986; Roscoe and Poorooshasb, 1963) and state index (Ishihara, 1993) quantify the initial state of the soil relative to the steady state line, whilst taking into account combined effects of density and stress on sand behaviour. Therefore, it is interesting to examine how this concept works in describing the undrained cyclic behaviour of sands, and in particular the effects of fines on the liquefaction resistance.

The most straightforward way to assess the suitability of the state concept in

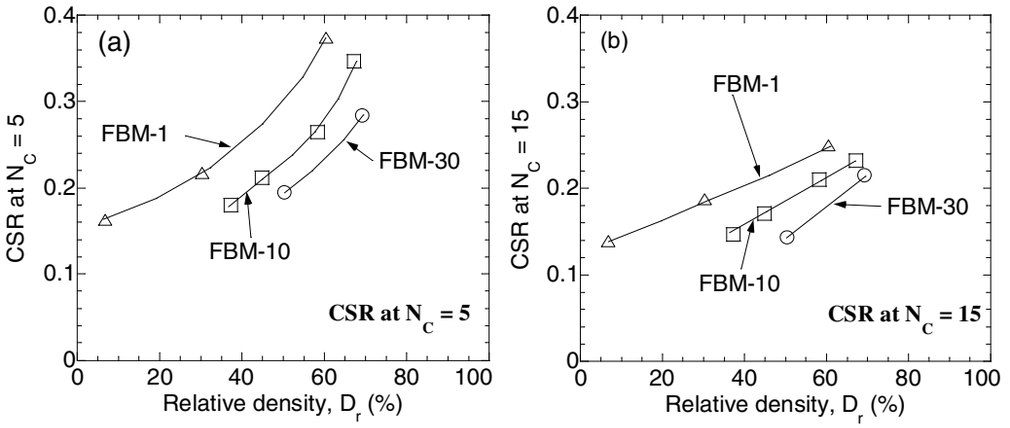


FIG. 9. Cyclic stress ratio required to cause 5% DA strain in 5 cycles (a) and 15 cycles (b) as a function of relative density

describing undrained cyclic behaviour is to compare the cyclic response for initial states lying on the steady state line itself. Both the state index (I_s) and the state parameter (ψ) have a constant value along the steady state line, I_s = 1 and $\psi = 0$ respectively, and this suggests that the monotonic behaviour for all initial states lying along the steady state line should be similar. This is readily apparent for an undrained test because in such a case the initial state prior to shearing and the ultimate state achieved upon monotonic shearing will be identical. In other words, the pore pressure due to the contractive tendency and dilation will be identical when a sample with an initial state at the projection of the steady state line is subjected to undrained monotonic shearing.

Figure 10 shows the cyclic strength curves for the three tested soils, for specimens with initial states on the steady state line. Here, all samples had an initial mean

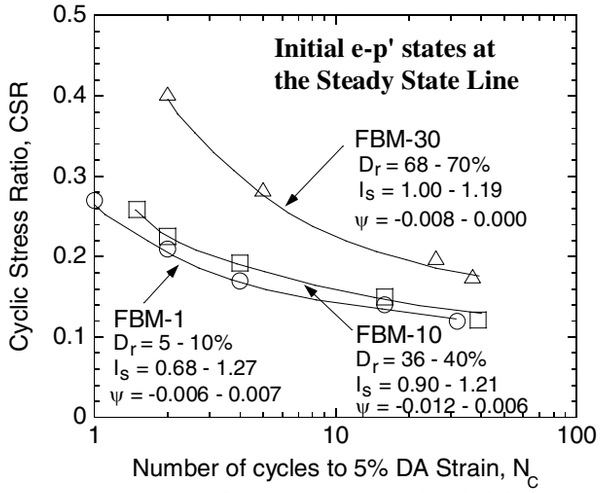


FIG. 10. Cyclic strength curves for specimens with initial states on the steady state line

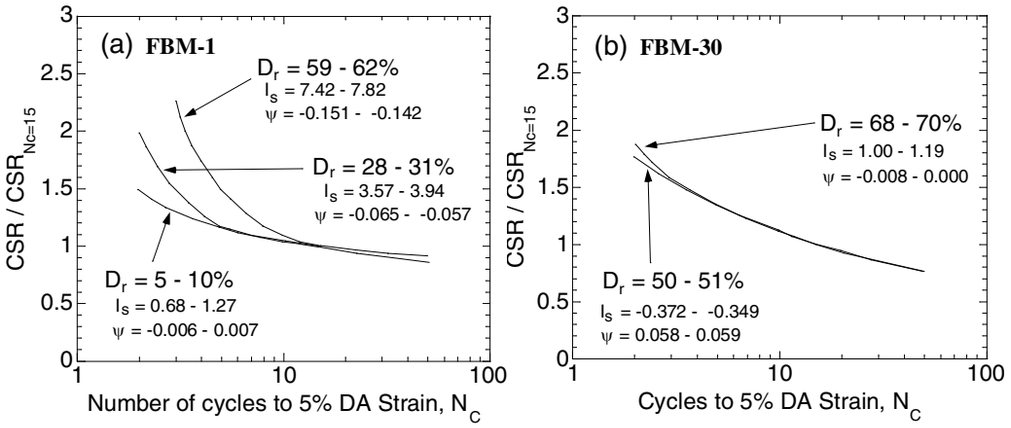


FIG.11. Cyclic liquefaction curves for FBM-1 (a) and FBM-30 (b) normalised by $CSR_{Nc=15}$

effective stress of p' = 100kPa and quite different relative density of D_r=5-10%, 36-40% and 68-70%, for FBM-1, FBM-10 and FBM-30 respectively, in accordance with the position of the steady state line of these soils shown in Figure 6b. Figure 10 shows clear effects of fines on the liquefaction resistance of samples having identical initial states relative to the steady state line. There is a small increase in the cyclic stress ratios for the sand containing 10% fines (FBM-10) as compared to the clean sand (FBM-1), and furthermore a significant increase in CSR as the fines content reaches 30% (FBM-30). Clearly, the liquefaction resistance of FBM soils increases with the fines content when initial states on the steady state line or more generally when the state concept is used as a basis for comparison. As the specimens were all prepared using the same technique, effects of fabric are most likely not significant and any differences in fabric would be due to the effects of fines content on fabric.

In order to examine the effects of relative density, state of the soil and fines content on the shape of the liquefaction resistance curve, the cyclic stress ratio was normalized by the CSR at 15 cycles ($CSR_{Nc=15}$), as shown in Figure 11 for FBM-1 and FBM-30. The clean sand (FBM-1) curves show an increase in the liquefaction resistance with increasing density or corresponding change in the state measure, in the region below 10 cycles. The normalised curves for FBM-10 (not shown) were similar to the FBM-1 curves. In the case of FBM-30, however, the effects of density or state of the soil on the shape of the curve are not pronounced, though one should acknowledge that the range of densities/states considered was relatively small for this soil. Further testing both at low densities high above the steady state line and at high densities well below the steady state line are needed to quantify the effects of fines in this regard.

CONCLUSIONS

A series of monotonic and cyclic triaxial tests on FBM soils were used to investigate the effects of non-plastic fines on undrained behaviour of sand. The key findings can be summarized as follows:

(a) The steady state line shifts downwards in the e-p' (D_r-p') plot as fines are added to a clean-sand base. This effectively increases the flow potential of the fines-containing soil, as there are more initial states in the e-p' plane above the steady state line showing contractive behaviour associated with strain softening.

(b) When the relative density (D_r) is used as a basis for comparison of cyclic behaviour, the cyclic strength decreases with increasing fines content. At a given relative density, the liquefaction resistance of the clean sand (FBM-1) was the highest while the sand with 30% fines (FBM-30) showed the lowest resistance.

(c) The liquefaction resistance of FBM soils increases with the fines content when initial states on the steady state line or more generally the state concept is used as a basis for comparison.

(d) The shape of the cyclic strength curve of FBM soils is affected by the relative density and initial state of the soil. The extent of these effects, in turn, depends on the fines content.

REFERENCES

Been, K., and Jefferies, M. G. (1985). "A state parameter for sand." *Geotechnique.* 35 (2): 99-112.

BSI (2002). *BS 1377-4:1990 Methods of tests for soils for civil engineering purposes. Part 4: Compaction-related tests*.

Cubrinovski and Ishihara (2000). "Flow potential of sandy soils with different grain compositions," *Soils and Foundations*, 40 (4): 103-119.

Cubrinovski and Ishihara (2002). "Maximum and minimum void ratio characteristics of sands," *Soils and Foundations*, 42 (6): 65-78.

Ishihara, K. (1993). "Liquefaction and flow failure during earthquakes." *33-rd Rankine Lecture, Geotechnique*. 43 (3): 351-415.

Japanese Geotechnical Society (2000). *Test methods for minimum and maximum densities of sands, Soil Testing Standards*. (in Japanese).

Jefferies, M. G. and Been, K. (2006). *Soil liquefaction: a critical state approach*. Taylor&Francis, New York.

Lade, P.V. and Yamamuro, J. (1997). "Effects of nonplastic fines on static liquefaction of sands." *Canadian Geotechnical Journal*, 34, 918-928.

Polito, C.P. and Martin II J.R. (2001). "Effects of nonplastic fines on the liquefaction resistance of sands." *ASCE Journal of Geotechnical and Geoenvironmental Engineering*, 127 (5), 408-415.

Roscoe, K. H., and Poorooshasb, H. B. (1963). "A fundamental principle of similarity in model tests for earth pressure problems." *Proceedings of the 2nd Asian Regional Conference on Soil Mechanics,* Vol. 1, Tokyo: 134-140.

Thevanayagam, S. (1998). "Effects of fines and confining stress on undrained shear strength of silty sands." *ASCE Journal of Geotechnical and Geoenvironmental Engineering*, 124 (6), 479-491.

Youd, T.L. and Idriss, I.M. (1998). "Liquefaction resistance of soils: summary report from the 1996 NCEER and 1998 NCEER/NSF Workshops on Evaluation of LiquefactionResistance of Soils " *Journal of Getoechnical and Geoenvironmental Engineering,* 127 (4): 297-313.

This page intentionally left blank

Effects of Permeability on Liquefaction Resistance and Cone Resistance

S. Thevanayagam[1], and N. Ecemis[2]

[1]Associate Professor, University at Buffalo, State University of New York, Buffalo, NY 14260; Tel: 716 645 2114 ext: 2430; theva@eng.buffalo.edu
[2]Graduate Student, University at Buffalo, State University of New York, Buffalo, NY 14260; necemis@eng.buffalo.edu

ABSTRACT: Sands and silty sands with the same liquefaction resistance can have significantly different hydraulic conductivity and coefficient of consolidation. Numerical simulations of cone penetration resistance taking into account the effects of silt content and consolidation characteristics show that the penetration resistances are significantly affected by consolidation characteristics for sands and sand-silt mixes with similar liquefaction resistances. The influence of permeability and consolidation characteristics on cone penetration resistances are presented. Relationships between liquefaction resistance, cone penetration resistance, and a normalized penetration rate are presented and compared with current field-based CPT-liquefaction screening methods.

INTRODUCTION

Current liquefaction screening techniques rely on knowledge from extensive laboratory research conducted on liquefaction resistance of clean sands, and extrapolations of observed field performance during past earthquakes. Such observations have been documented in the form of normalized penetration resistance (SPT $(N_1)_{60}$, CPT q_{c1N}) (Seed et al. 1983, Robertson and Wride 1997), and shear wave velocity (v_{s1}) (Andrus and Stokoe, 2000) versus cyclic stress ratio (CSR) induced by the earthquakes, corrected for magnitude, for many sites where occurrence or non-occurrence of liquefaction were recorded during the earthquakes. Cyclic resistance ratio (CRR), applicable for a standard earthquake magnitude of 7.5, of a soil deposit with a known value of q_{c1N} is obtained from a demarcation line drawn between the field-observation-based data points which correspond to liquefied sites and those that did not liquefy in Fig.1. This is denoted as $CRR_{7.5}$. This CRR is compared against the anticipated cyclic stress ratio (CSR) for that deposit due to a design earthquake of the same magnitude to determine whether or not that deposit would liquefy. Factor of safety (FS) against liquefaction is defined as $FS=CRR_{7.5}/CSR$. If a different design earthquake magnitude is expected, the $CRR_{7.5}$ is multiplied by a magnitude scaling factor (MSF) to account for the differences in number of cycles, frequency content,

etc. (FS= MSF*$CRR_{7.5}$/CSR). Researchers have observed that the CRR determined in this manner depends on fines content of the soil for a given q_{c1N}.

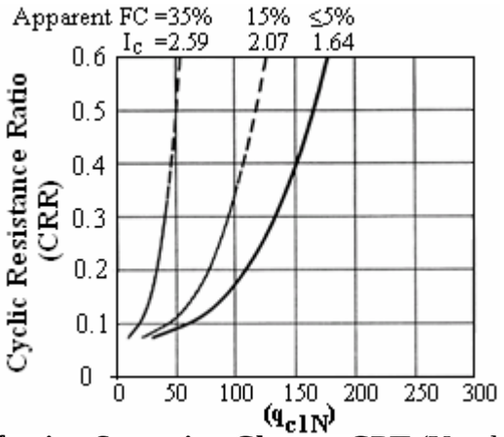


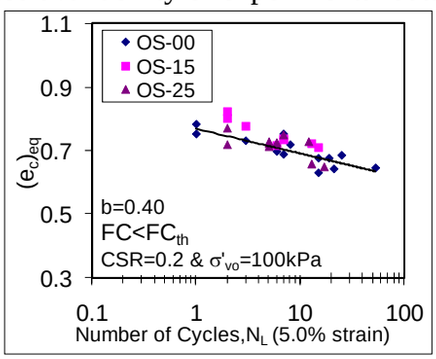
FIG.1 Field Liquefaction Screening Charts –CPT (Youd et al. 2001, Robertson and Wride 1997)

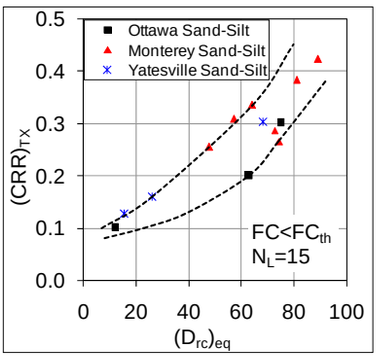
This has sparked numerous researches on the effects of fines on cyclic resistance of silty sands (e.g. Chang et al. 1982, Kuerbis et al. 1988, Vaid 1994, Koester 1994, Zlatovic and Ishihara 1997, Polito and Martin 2001) and its effects on liquefaction screening (Carraro et al. 2003). Recently it has been shown that silt content affects permeability, compressibility, and consolidation characteristics of silty sands and therefore influences the penetration resistance. Two soils with the same stress-strain characteristics and cyclic liquefaction resistance may have different silt contents and different permeabilities, compressibility, and coefficients of consolidation. Their cone resistance could be different due to different degrees of partial drainage, which occurs around the cone. A unique correlation between cyclic liquefaction resistance and penetration resistance is not possible without considering the effects of coefficient of consolidation on penetration resistance (Thevanayagam and Martin 2002, Thevanayagam et al. 2003, 2006). The authors' previous work in 2006 focused on the numerical simulation of the effects of consolidation characteristics of silty sands on cone penetration resistance and a possible correlation between the cyclic liquefaction resistance, cone penetration resistance and a non-dimensional parameter T (vd/c_h) where v=penetration rate, d=cone diameter, and c_h=coefficient of consolidation. Several numerical simulations were carried out on sands and silty sands for a range of equivalent relative densities, $(D_{rc})_{eq}$. CRR values corresponding to 15 cycles of uniform loading obtained from undrained cyclic triaxial experiments were correlated with q_{c1N} obtained from the above numerical simulations at the corresponding $(D_{rc})_{eq}$. An interesting correlation similar to the field-based correlation shown in Fig.1 was observed. However, the numerical simulations reported in that study ignored possible effects of soil dilation on q_{c1N}. Dilation angle was assumed to be zero in the numerical simulations. This paper focuses on the effects of permeability and consolidation characteristics of silty sands on cone penetration resistance with due consideration of the effects of dilation angle. A revised liquefaction-screening chart that takes into account the effects of consolidation characteristics on penetration resistance is presented.

EFFECTS OF FINES

Undrained liquefaction resistance

Recently, Thevanayagam and co-workers (2002, 2003) proposed that mechanical properties such as liquefaction resistance of granular soils containing non-plastic fines are dependent on the intergrain contact density of a soil. Silty sand and sand at the same void ratio are not expected to have the same intergrain contact density. Therefore, it is not appropriate to compare the liquefaction resistance of silty soil with that of clean sand using global void ratio. A soil classification system based on contact density was developed (Thevanayagam et al. 2002) and two contact density indices, $(e_c)_{eq}$ and $(e_f)_{eq}$, respectively, were introduced for soils at silt content (FC) less than a threshold silt content FC_{th} and more than FC_{th}, respectively. $(e_c)_{eq}$ and $(e_f)_{eq}$ have been defined as $(e_c)_{eq}=[e+(1-b)fc]/(1-(1-b)fc)]$ and $(e_f)_{eq}=[e/(fc+(1-fc)/R_d m)]$, respectively. Where fc = fines content by weight, R_d= ratio of the d_{50}'s of the host sand and silt in the soil mix, and b and m are constants depending on grain size characteristics of the soil (Thevanayagam 2007a,b). It has been shown that sand and silty sand have similar liquefaction resistance, undrained shear strength, and stress-strain characteristics if compared at the same contact density indices $(e_c)_{eq}$ or $(e_f)_{eq}$. One set of result is shown in Fig.2a for Ottawa sand-silt mixes prepared at $FC<FC_{th}$. The cyclic resistance correlates well with the respective contact density index. This classification system has been shown to be valid for many soils (Ni et al. 2004). Based on experimental data for a number of soils reported in the literature a relationship between $(CRR)_{tx}$ required to cause liquefaction in 15 cycles and equivalent intergranular contact relative density, $(D_{rc})_{eq}$ has been developed for silty sands at $FC<FC_{th}$ as shown in Fig.2b (Ecemis, 2008). $(D_{rc})_{eq}$ has been defined as $(D_{rc})_{eq}=[e_{max,HS}-(e_c)_{eq}]/[\ e_{max,HS}-(e_{min,HS})]$, where $e_{max,HS}$ = maximum void ratio of the coarse grains, $e_{min,HS}$ = minimum void ratio of the coarse grains. Such a relationship has not yet been developed for soils at $FC>FC_{th}$ due to limited availability of experimental data.





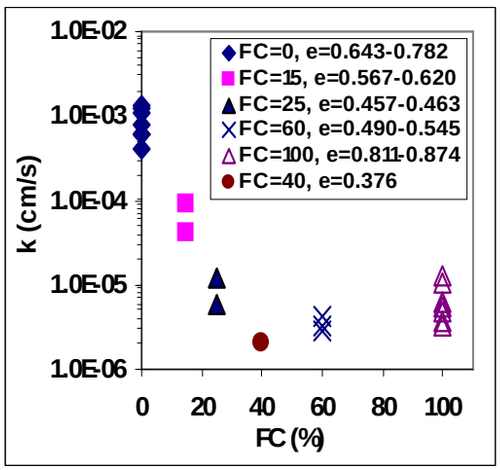
(a) $(e_c)_{eq}$ versus N_L **(b) $(CRR)_{tx}$ versus $(D_{rc})_{eq}$**

FIG.2 Effect of silt content on liquefaction resistance

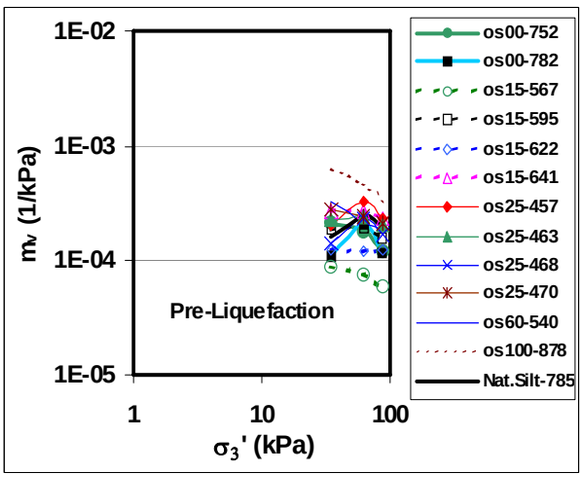
Hydraulic conductivity and coefficient of consolidation

Fig.3a shows the variation of hydraulic conductivity k against silt content for Ottawa sand-silt mixes (Thevanayagam et al. 2001). The notation "FC=15, e=0.567-0.620"

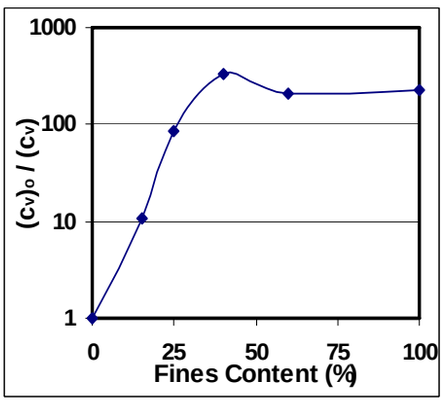
refers to silty sand at 15% silt content and a range of void ratio of 0.567 to 0.620. At each silt content, k varies depending on the void ratio. With an increase in silt content up to threshold value of FC, k decreases with an increase in silt content and decrease in void ratio. The primary influence on k is however the reduced pore size with an increase in silt content. Following threshold fines content, the effect of void ratio becomes important. A slight increase in k is observed with an increase in void ratio and silt content beyond FC_{th}. Fig.3b shows the relationship between compressibility m_v and confining stress at different silt contents. The notation "os15-595" refers to silty sand specimen at 15% silt content and void ratio of 0.595. There is some variability in m_v with silt content. The effect of silt content in m_v is much smaller compared to its effect on k. Fig.3c shows the normalized (c_{vo}/c_v) values at nearly the same $(e)_{eq}$ versus silt content, where c_v and c_{vo} are the coefficient of consolidation of Ottawa sand-silt mix and clean Ottawa sand, respectively. c_v decreases with increasing silt content. (c_{vo}/c_v) increases steadily with an increase in silt content up to a threshold value of silt content (FC_{th}) and it is little affected with further increase in silt content.



(a) k



(b) m_v



(c) c_v

FIG.3 Effect of non-plastic fines on k, m_v and c_v

The above combined observations indicate that a sand and sand-silt mix show similar cyclic resistance (CRR), as the host sand or silt, when compared at the same contact density indices $(e_c)_{eq}$ or $(e_f)_{eq}$, respectively or at the same $(D_{rc})_{eq}$. But there is a major difference in k and c_v between sand and sand-silt mixes even if compared at the same contact density indices.

Penetration resistance with possible partial drainage

Consider penetration of a CPT cone into a saturated sand or silty sand. The penetration causes loads on the soil around the probe and shear strains around the probe. The spatial distribution of shear strain and the excess pore pressures around the probe are highly non-uniform. Therefore, depending on the rate of penetration, geometry of the penetrating object, and stress-strain and consolidation characteristics of the soil a different degree of partial dissipation of excess pore pressures and consolidation may occur around the cone. Therefore the penetration resistance is expected to differ for two soils with identical stress-strain characteristics, but different permeability and consolidation characteristics. If the stress-strain characteristics of a sand and a silty sand are the same, the penetration resistance would be identical in both soils if the penetration rate is fast enough such that the penetration is fully undrained or slow enough such that the penetration is fully drained. In reality however, even if the stress-strain characteristics and the liquefaction resistance of the two soils are the same, the degree of drainages around the probe are not the same for the same rate of penetration due to major differences in coefficient of consolidation between the two soils. Therefore the penetration resistances would be different. The solution to the phenomenon observed in Fig.1 depends on this critical difference in the consolidation behaviour of the soils.

CONE PENETRATION RESISTANCE

Finite Element Model

In order to study the effect of k and c_v and the associated partial drainage conditions around the cone tip on cone penetration resistance of sand and silty soils a numerical simulation study was conducted using finite element code ABAQUS (2000). During penetration of the cone, cavity expansion occurs, the stress fields around the cone changes, excess pore pressures were induced, and fluid flow and consolidation occur. These aspects of the problem can be treated in ABAQUS. The soil around the cone penetrometer was simulated using Drucker-Prager model. An axis-symmetric model of a cone and the surrounding soil with the finite element mesh used in the analysis is given in Fig.4. A vertical effective stress of 100 kPa was imposed at the top surface of the mesh to simulate the cone at a depth with about 100 kPa effective vertical stress. The diameter d of the cone was 4.37cm, and the cone tip was placed at 36cm from the top surface of the finite element mesh. The mesh extended to a distance of 54cm (about 15d) below the cone tip and 40 cm away horizontally (about 18d) from the cone axis. Such large distances were chosen to alleviate any boundary effects.

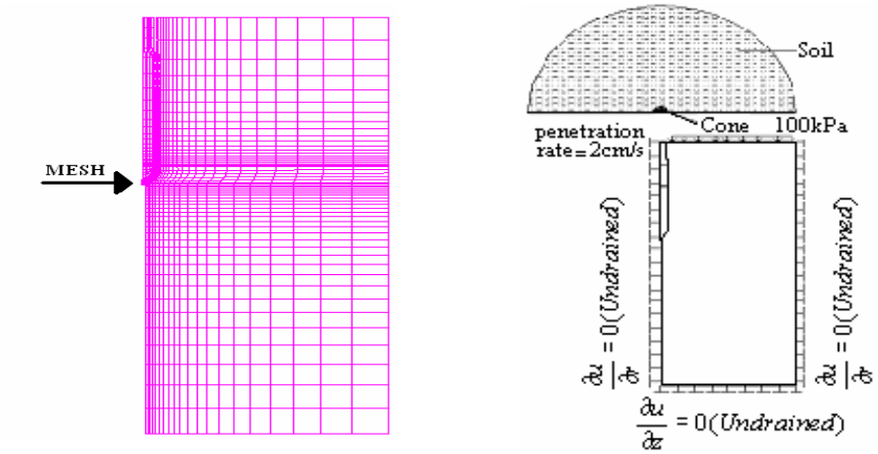


FIG.4 Finite element mesh – CPT model

Soil was modelled using elements with eight displacement nodes, whereas elements with four displacement nodes were used to model the cone. Axis-symmetric elements were used since both the geometry of the model and loadings were axis-symmetric. The soil was fully saturated. Fig.4 also shows the boundary conditions used in the finite element model for a site having uniform soil. On the bottom and two vertical sides, the normal component of displacement and fluid flow were fixed at zero. No pore fluid flow was permitted across cone body.

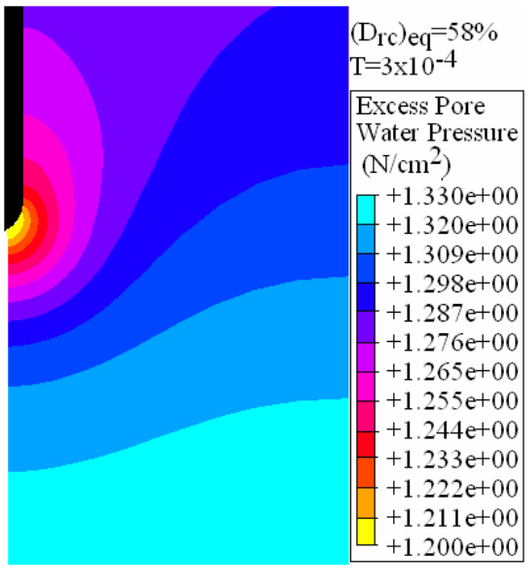
Soil Parameters

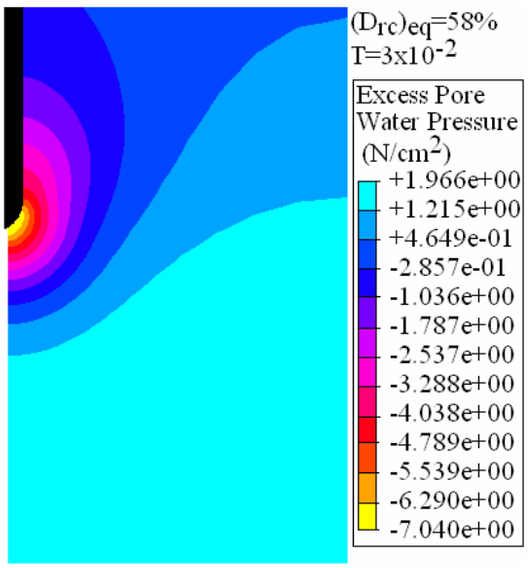
Several sets of cone penetration simulations were made using ABAQUS. As a first step, material properties, including dilation angles, required for numerical simulation of cone penetration were obtained from several sets of triaxial test data on Ottawa sand and sand-silt mixes (Ecemis 2008, Thevanayagam et al. 2003). Each of the triaxial tests was simulated using ABAQUS and compared with actual triaxial test data to assess the effectiveness of ABAQUS to model soil behavior. Using such a procedure described above, a set of soil parameters were derived for a number of soils used in the triaxial test program at different densities and fines contents. These parameters were than used to simulate cone penetration in each of these soils. Pore pressure responses and cone penetration resistances were monitored with penetration of the cone at a constant penetration speed of v = 2 cm/s (ASTM D3441) until a steady state was reached. In each case, several parametric simulations were done by varying the hydraulic conductivities to study the effect of permeability on cone resistance.

Effect of permeability on normalized cone tip resistance

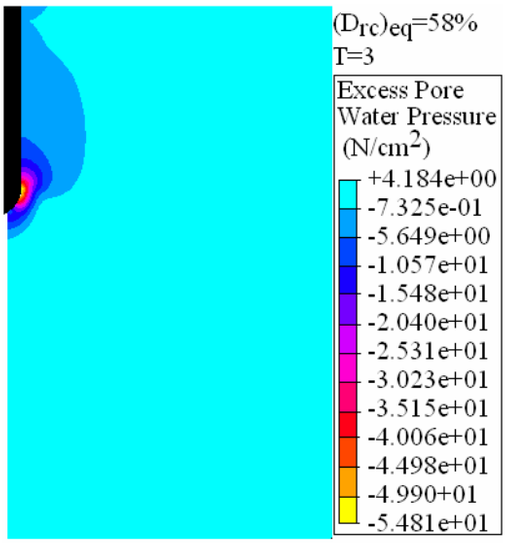
Figs.5a-c show the excess pore water pressures around the cone tip for a medium-dense soil at $(D_{rc})_{eq}$=58% the excess pore pressure at the cone tip are 11.4kPa for $k=10^{-3}$m/sec ($T=3x10^{-4}$), -35kPa for $k=10^{-5}$m/sec ($T=3x10^{-2}$), and - 41kPa for $k=10^{-7}$m/sec (T=3). The corresponding q_{c1N} values are 117 for $k=10^{-3}$m/sec ($T=3x10^{-4}$), 90 for $k=10^{-5}$m/sec ($T=3x10^{-2}$), and 48 for $k=10^{-7}$m/sec (T=3). A similar trend was

observed for dense soil. For a medium dense or dense soil there was a significant decrease in q_{c1N} with a decrease in k. For loose soils there was only a slight difference in q_{c1N} with decrease in k (increase in T). The effect of permeability on q_{c1N} is high for medium-dense soils in contrast with a loose soil.





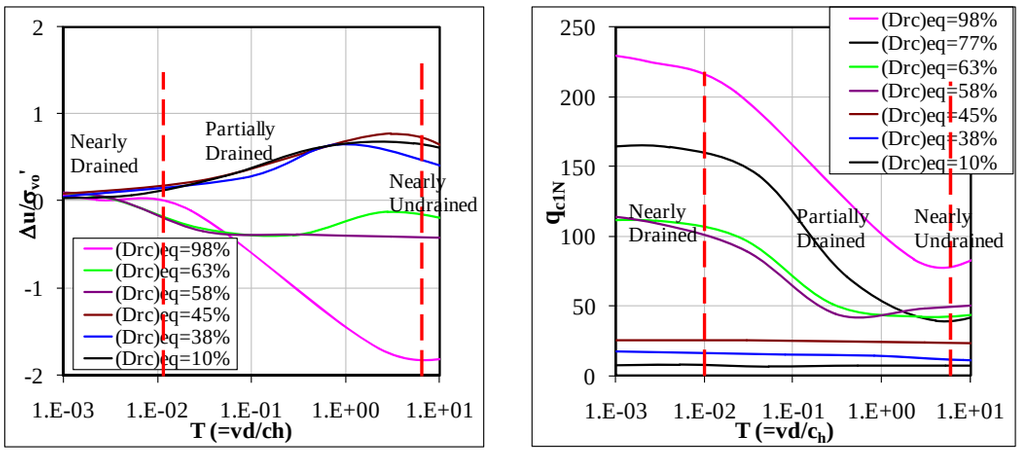
(a) T=3x10^{-4} (k=10^{-3} m/sec) (b) T=3x10^{-2} (k=10^{-5} m/sec)



(c) T=3 (k=10^{-7} m/sec)
(Dilation angle = 13 degrees)
FIG.5 Excess pore pressure response at cone tip for medium-dense soil

The normaized excess pore pressure at the tip of the cone was plotted against a normalized penetration rate ($T=vd/c_h$) and equivalent relative density $(D_{rc})_{eq}$ in Fig.6a. The normalized cone resistance, q_{c1N} was also plotted against T and $(D_{rc})_{eq}$ in Fig.6b.

The cone tip force was calculated by integrating the vertical components of stresses and pore pressures at elements in contact with the cone. The tip force is then divided by cone area to obtain the tip resistance. q_{c1N} is then obtained by dividing the tip resistance by 100kPa. It was found that the q_{c1N} and excess pore water pressure values around the cone for a given $(D_{rc})_{eq}$ depend on T. For loose soils, the excess pore pressure at the cone tip steadily increases with an increase in T as shown in Fig.6a. Beyond a value of T in the range of about 5 to 10, the excess pore pressure ratio reaches a high value and remains little affected by further increase in T, indicating nearly undrained penetration. Similarly at values of T less than about 0.05 to 0.01 the excess pore pressure is small and is little affected by further decrease in T, indicating a highly drained condition around the probe. A partially drained condition prevails at intermediate T values of about 5 to 0.01. In the case of dense soils, the excess pore pressure is small for T values less than about 0.05 to 0.01, indicating drained soil response during cone penetration. At high values of T in the range of about 5 to 10, the excess pore pressure is negative and remains unaffected by further increase in T. This is indicative of highly dilative response of the soil and undrained conditions around the cone. For intermediate values of T, the excess pore pressure is affected by T, indicating existence of partial drainage effects around the cone tip. The q_{c1N} at the cone tip steadily decrease with an increase in T as shown in Fig.6b. For each case, beyond a value of T in the range of about 5 to 10, the q_{c1N} reaches a low value and remains little affected by further increase in T, indicating nearly undrained penetration. Similarly at values of T less than about 0.05 to 0.01 the q_{c1N} is high and is little affected by further decrease in T, indicating a highly drained condition around the probe. A partially drained condition prevails at intermediate T values of about 5 to 0.01. These effects are reflected in the normalized cone penetration resistance in Fig.6b.



(a) $\Delta u/\sigma_{vo}$' versus T **(b) q_{c1N} versus T**

FIG.6 Excess pore pressure and normalized cone tip resistance

Observations from Fig.6 imply that, q_{c1N} for a low permeable silty sand would be smaller than that of highly permeable clean sand at the same $(D_{rc})_{eq}$. This difference is attributable to the presence of fines, which causes low permeability and undrained or

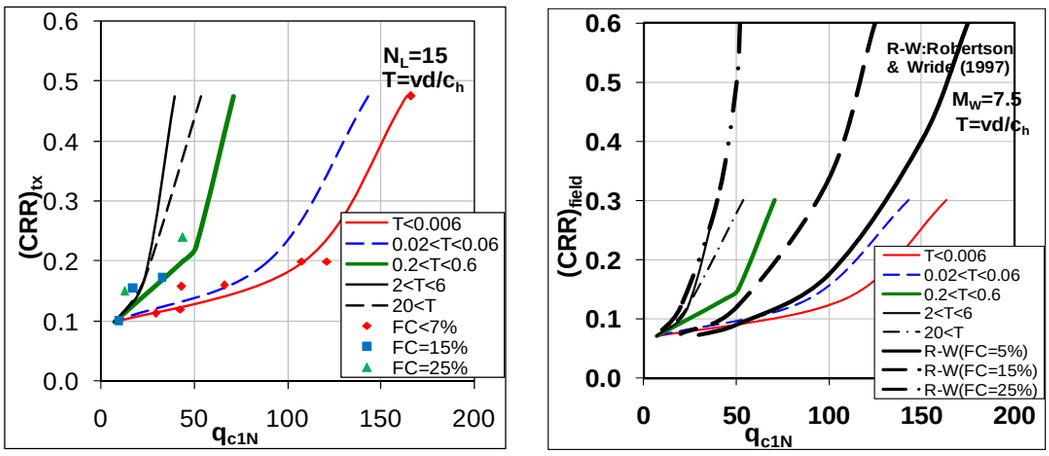
partially drained conditions during penetration in silty sands leading to a decrease in tip resistance compared to highly permeable sand.

LIQUEFACTION RESISTANCE AND PENETRATION RESISTANCE

CRR versus q_{c1N}

The q_{c1N} values obtained from the above numerical simulations for each soil at a range of distinct $(D_{rc})_{eq}$ values were also plotted against the corresponding undrained cyclic resistance ratio (CRR) required to cause liquefaction in 15 cycles for that soil at the corresponding $(D_{rc})_{eq}$ obtained from laboratory undrained cyclic triaxial compression tests (Thevanayagam et al. 2003). The solid points in Fig.7a shows this relationship for q_{c1N}-$(CRR)_{TX}$. Based on these "data points" and additional parametric studies where the permeability were varied for each soil, a generic relationship for q_{c1N} versus $(CRR)_{TX}$ was obtained. This is shown by solid lines. Each solid line refers to a narrow range of T values. As T increases, the CRR versus q_{c1N} curves shift to the left. With further increase in T, the curves merge together.

The relationship shown in Fig.7a was further modified to obtain $(CRR)_{field\text{-}7.5}$ applicable for an earthquake of magnitude 7.5 by correcting the $(CRR)_{TX}$ for 15 cycles using the relationship between $(CRR)_{field}$ and $(CRR)_{TX}$ proposed by Castro (1975), and Seed et al. (1978). The resulting $(CRR)_{field\text{-}7.5}$ versus q_{c1N} relationship is shown in Fig.7b. Fig.7b compares this relationship with the CPT based liquefaction screening chart proposed by Robertson and Wride 1997 corresponding to nearly clean sands, silty sands at nearly 15% silt content and 35% silt content, respectively. The curves corresponding to T<0.006 tend to follow the R-W curves for clean sands. The curves corresponding to 0.02<T<0.06 tend to follow the R-W curve for 15% silt content. The remaining curves tend to follow the R-W curve for 35% silt content. It appears from Fig.7a-b that the ranges of T greater than about 0.2 could be bundled together.



(a) $(CRR)_{tx}$ versus q_{c1N} **(b) $(CRR)_{feild}$ versus q_{c1N}**

FIG.7 Liquefaction Resistance, q_{c1N} and T

Although the T-dependent q_{c1N}-CRR relationships depict the same trend as observed in the field-based liquefaction screening procedures, additional numerical and physical

simulation or field verification studies are needed to validate and refine this trend using penetration tests involving large scale soil model tests, or field tests at past earthquake sites.

CONCLUSIONS

Sands and silty sands with the same liquefaction resistance have significantly different hydraulic conductivity and coefficient of consolidation characteristics. Pore pressure response around the cone tip during penetration and normalized cone tip resistances are significantly different for sand and silty sand with similar or nearly the same equivalent relative density $(D_{rc})_{eq}$. For the same $(D_{rc})_{eq}$, q_{c1N} increases with a decrease in T (=vd/c_h) (or increase in permeability). At large values of T, q_{c1N} represents an undrained cone resistance of the soil. At low T values, q_{c1N} is derived from a nearly drained response of a soil. Undrained cyclic resistance is primarily governed by $(D_{rc})_{eq}$ irrespective of permeability of the soil and T. Relationship between liquefaction resistance (CRR at 15 cycles) and q_{c1N} is dependent on the normalized cone penetration rate, T. A permeability and c_v dependent liquefaction-screening chart based on normalized cone penetration resistance and T is proposed.

ACKNOWLEDGEMENT

Financial support for this work was provided by the USGS/NEHRP program. It is gratefully appreciated.

REFERENCES

ABAQUS, 2000. User's manual, Hibbitt, Karlsson & Sorensen, Inc., Fremont, CA.

Andrus, R. D. and Stokoe, K. H. (2000) "Liquefaction resistance of soils from shear-wave velocity", *J. Geotech. and Geoenv. Eng., ASCE*, Vol.126(11), 1015-25

ASTM (1993) "Designation D3441 – Standard test method for deep quasi-static, cone, and friction cone penetration tests of soil. In soil and rock: Building Stones" *Annual Book of ASTM Standards*, Vol. 4.08, American Society for Testing and Materials, Philedalphia, PA

Carraro, J.A.H., Bandini, P., and Salgado, R. (2003) "Liquefaction resistance of clean and nonplastic silty sands based on cone penetration resistance", *J, Geotech. and Geoenv. Eng., ASCE*, Vol.129(11), 965-976.

Castro, G. (1975) "Liquefaction and cyclic mobility of saturated sands", *J. Geotech. Eng. Div., ASCE*, Vol. 101(6), 551-569.

Chang, N. Y., Yeh, S. T., and Kaufman, L. P. (1982) "Liquefaction potential of clean and silty sands" *Proc., 3rd Int. Earthquake Microzonation Conf.*, Vol. 2, 1017-1032

Ecemis, N. (2008). "Effects of soil permeability and compressibility on liquefaction screening using cone penetration resistance", *Ph.D. Dissertation (in preparation), University at Buffalo*, Buffalo, NY.

Koester, J. P. (1994) "The influence of fines type and content on cyclic resistance" *Ground Failures under seismic conditions, Geotech Spec. Publ.* No. 44, ASCE, New York, 17-33.

Kuerbis, R., Negussey, D., and Vaid, V. P. (1988) "Effect of gradation and fines content on the undrained response of sand" *Proc., Hydr. Fill Struct.*, 330-345

Ni, Q., Tan, T. S., Dasari, G.R., and Hight, D.W. (2004) "Contribution of fines to the compressive strength of mixed soils" *Geotechnique*, Vol. 54(9), 561-569

Polito, C. P. and Martin II, J. R. (2001) "Effects of nonplastic fines on the liquefaction resistance of sands" *J. Geotech. and Geoenv. Eng. Div., ASCE*, Vol. 127(5), 408-415

Robertson, P.K. and Wride, C.E. (1997) "Evaluation of cyclic liquefaction potential based on the CPT", *Seis. Behavior of Ground & Geotech Struct., Balkema Publs.*, 269-278.

Seed, H. B., Martin, G. R., and Pyke, C. K. (1978) "Effects of multi-directional shaking on pore pressure development in sands", *J. Geotech. Eng. Div., ASCE*, Vol. 104(1), 27-44.

Seed, H. B., Idriss, I. M, and Arango, I. (1983) "Evaluation of liquefaction potential using field performance data", *J. Geotech. Eng., ASCE*, 109(3), 458-482

Thevanayagam, S. Martin, G.R, Shenthan, T. and Liang J. (2001) "Post-liquefaction pore pressure dissipation and densification in silty soils", *Proc., 4th Intl. Conf. Recent Adv. Geot. Earthq. Eng. & Soil Dyn.*, ed. S. Prakash, Paper# 4.28.

Thevanayagam, S., Shenthan, T., Mohan, S. and Liang, J. (2002), "Undrained fragility of sands, silty sands and silt", *ASCE, J. Geotech. & Geoenv. Eng.*, 128 (10), 849-859.

Thevanayagam, S. and Martin, G. R. (2002) "Liquefaction in silty soils - screening and remediation issues", *Soil Dyn. and Earthq. Eng.*, 22, 1034-1042.

Thevanayagam, S., Shenthan, T., and Kanagalingam, T., (2003). "Role of intergranular contacts on mechanisms causing liquefaction and slope failures in silty sands" *Final Report, USGS Award No. 01HQGR0032 and 99HQGR0021, US Geological Survey, Department of Interior, USA*, http://erp-web.er.usgs.gov/reports/abstract/2001/pt/01hqgr0032-report.pdf, 396p.

Thevanayagam, S., Ecemis, N., Kanagalingam, T., and Martin, G. R., (2006) "Effects of fines on liquefaction screening using penetration resistance" *8th U.S. National Conference on Earthquake Engineering*, San Francisco, CA, April

Thevanayagam, S. (2007a) "Intergrain contact density indices for granular mixes–I: Framework", *J. Earthquake Eng. and Eng. Vibrations*, Vol.6 (2), 123-134.

Thevanayagam, S. (2007b) "Intergrain contact density indices for granular mixes–II: Liquefaction resistance", *J. Earthquake Eng. and Eng. Vibrations*, Vol.6 (2), 135-146.

Vaid, V. P. (1994), "Liquefaction of silty soils" *Gound failures under seismic conditions, Geotech. Spec. Publ.*, No.44, ASCE, New York, 1-16.

Youd, T. L. and Idriss, I. M. (2001) "Liquefaction resistance of soils: Summary report from the 1996 NCEER and 1998 NCEER/NSF workshops on evaluation of liquefaction resistance of soils." *J. Geotech. and Geoenv. Eng.*, Vol. 127(4), 297-313

Zlatovic, S. and Ishihara, K. (1997) "Normalized behavior of very loose non-plastic soils: Effects of fabric", *Soils and Foundations*, Tokyo, Vol. 37(4), 47-56.

This page intentionally left blank

Liquefaction Behavior of Mississippi River Silts

Ali M. Izadi[1], Ronaldo Luna[2] and Richard W. Stephenson[3]

[1] Graduate Research Assistant, University of Missouri-Rolla, Rolla, 65409; amiq32@umr.edu

[2] Associate Professor, University of Missouri-Rolla, Rolla, 65409; rluna@umr.edu

[3] Professor, University of Missouri-Rolla, Rolla, 65409; stephens@umr.edu

ABSTRACT: Civil infrastructure built on alluviums and recent deposits, such as dams, contain significant amount of silts. The static and dynamic behavior of these fine-grained soils has been investigated less than the clay-like or sand-like soils. Low plasticity silts (PI = 6) obtained east of St. Louis in Illinois are known as loess that has been re-deposited by water in the floodplains of the Mississippi River. These silts were reconstituted in the laboratory by slurry at water content above the liquid limit and then consolidated to an initial effective stress. The initial laboratory characterization under monotonic loading included a series of consolidated undrained triaxial compression tests at different effective confinement to determine the critical state parameters. A series of stress-controlled cyclic triaxial compression tests were run under normally and overconsolidated conditions. The liquefaction behavior of the silt at different over consolidation ratios and its relationship to the monotonic behavior is presented and discussed.

INTRODUCTION

The determination of the liquefaction potential of low plasticity silts has been a challenge in geotechnical engineering. Liquefaction is a phenomenon that is typically associated with sands, loss of strength, and large deformations often induced by dynamic loading. In late 1990s, more evidence during and after earthquakes has indicated that liquefaction also can occur in both non-plastic and plastic fine-grained soils. Several criteria have been suggested to assess the liquefaction potential of these soils. One of the first of these was the Chinese Criteria, which has been modified several times. It was recognized early on that as the plasticity of the soil decreases the potential to liquefaction. Some of these modifications are not associated with a magnitude of earthquake or loading intensity. Several researchers in the past 10 years have been focusing on the static and dynamic behavior of non-plastic silts (Brandon, et al. 2006; Boulanger and Idriss, 2004; Fleming and Duncan, 1990; Guo and Prakash, 1999).

Non-plastic silts have characteristics that are common to both sands and clays (Brandon, et al. 2006). Silts are more affected by compression than are sands. However, silts become denser under vibration more easily than do clays. Normally consolidated silts, unlike normally

consolidated clays, tend to dilate upon shearing, and the deviator stress continues to increase with increasing strain (Fleming and Duncan, 1990).

Obtaining undisturbed samples of non-plastic silts for triaxial and consolidation testing is very difficult (Fleming and Duncan, 1990). Unlike clays, no apparent cohesion exists to hold the sample together as it is being transferred to a laboratory facility. In addition, methods such as the moist tamped method, which are commonly used to prepare sand specimens, do not produce a silt structure that is comparable to the structure observed in nature. The disturbance of silt samples highly influences their shear strength.

It has been observed that the strong dilation of low plasticity silts in triaxial compression can cause adsorbed gases to escape the pore water (Penman, 1953). This phenomenon has been known to be a major source of error and miscalculation. Also, because of the high absolute dilation of low plasticity silts, determining the undrained shear strength and failure is very complex (Fleming and Duncan, 1990).

LABORATORY TESTS (EXPERIMENTAL PROGRAM)

Description of Materials & Equipment

The soil material being tested is a low plasticity silt which was originally deposited by wind as the upland loesses on the east bank of the Mississippi River in Collinsville, Illinois. The materials were obtained from a dry bank and transported to the UMR laboratories in bulk for testing. The liquid limit is 28 and the PI is equal to 6 with a percent clay fraction of about 16.5%. The soil classifies as a ML, close to the border of the CL-ML region in the plasticity chart.

The experimental program was carried out using a servo-controlled triaxial compression system developed by GCTS, Inc. The equipment is controlled by a program that receives feedback from the multiple sensors on the system. The chamber has a capacity of about 180 psi and the pneumatic actuator that can apply axial load at frequencies of about 5 Hz. The advanced programming capability to stop the test after cyclic loading (when liquefaction is reached) and then perform a static test were very helpful to assess the post-liquefaction behavior of the silt material. A network webcam is mounted inside the geotechnical laboratories and aimed at the cyclic triaxial equipment for public viewing and can be found at: http://geotech.umr.edu/geolab.html

Preparation of Specimens

The specimen preparation techniques for this experimental program were varied and they were evaluated to examine their quality and uniformity. All samples were prepared from silt slurry with a water content of 44%. The amount of water content is very important and has a considerable amount of influence on the uniformity of the samples. As seen by Kuerbis and Vaid (1988) and Romero (1995), if the water content is too low, then air voids can form within the specimen. If the water content is too high, stratification within the silt can be a problem.

Initially a large specimen was prepared in a large diameter consolidometer using radial consolidation and later using thin-walled tubes triaxial specimens were extracted. Additionally, another series of specimens were prepared on a 2-inch diameter split mold with top loading only. The uniformity of the specimens were obtained by examining the change in water content across the sample, since the water content can be directly correlated to the initial density.

It was observed that when specimens were consolidated using only top loading, a significant change in water content ($\Delta w = 3.5\%$) was found from top to bottom. The friction between the silt and the membrane causes a non-uniform density distribution. The problem caused by the friction is more evident were the silt is more distant from the loading source. In order to solve this problem a vacuum pressure equal to the consolidation pressure was applied to bottom of the specimen to equalize stresses. The vacuum pressure was applied after the initial consolidation of the sample was performed using top loading. With this method changes in water content ($\Delta w = 1.4\%$) throughout the sample were reduced.

Static tests and determination of shear strength parameters

A series of tests was conducted on low plasticity silts. The results showed that the undrained stress-strain behavior changed as the OCR was varied. The silt specimens' initial contractive behavior changed to dilative behavior as the OCR increased. The boundary between dilative behavior and contractive behavior was seen at an OCR of about 2. This has been illustrated in Figure 1. The normally consolidated specimen (F2G) shows contractive behavior, while the silt with an OCR of four (F2I) shows dilative behavior. The sample that has OCR of 2 (F2H) shows neither contractive nor dilative behavior. It is important to note that the OCR did not have an effect on the failure criteria and did not change the friction angle. On the other hand, the initial density was the most important factor defining failure and the friction angle.

Another important finding was that the classical steady-state behavior was not seen in the tested silt, even though the pore water pressure stabilized at very high strains. The stabilization of the pore water pressure was caused by cavitation of the pore fluid. This happened when the pore water pressure fell below the initial back pressure used for saturation. Therefore, it is very important to control and monitor the amount of back pressure and the pore water pressure generated in order to ensure the sample stays in its saturated state.

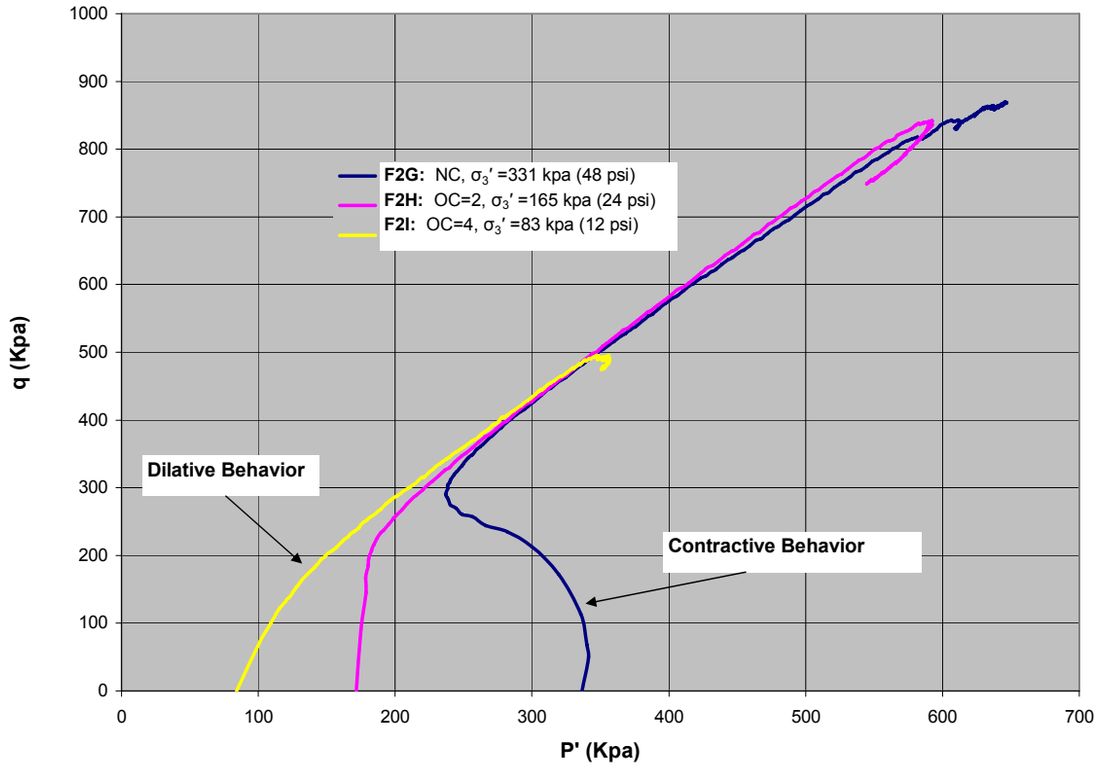
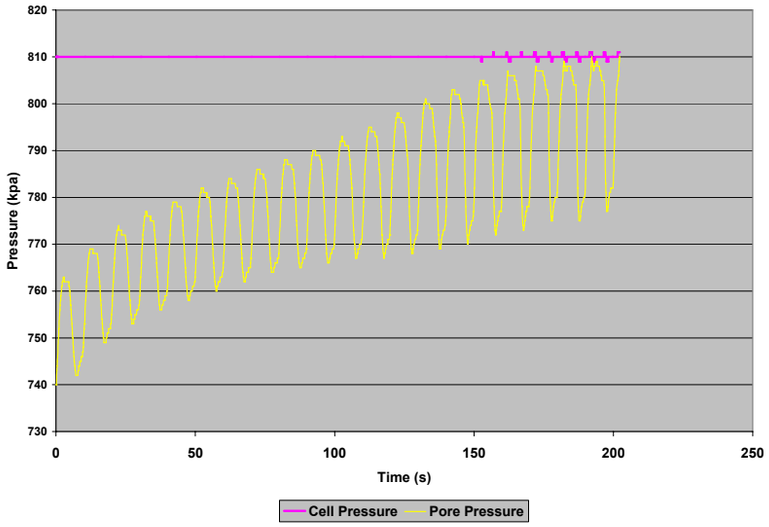


Fig. 1. Stress Paths of Monotonically loaded undrained triaxial tests performed on low plasticity silts with varying OCR

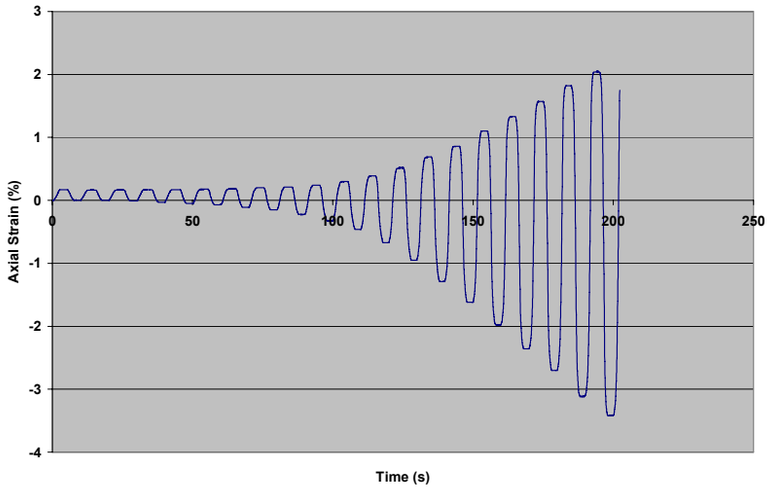
Based on extensive triaxial testing of the subject silt materials, the state parameters were determined for monotonic loading. The normally consolidated line was determined by plotting the void ratio vs. effective stress and the stress paths were traced to find the critical state line. The slope of the NCL or (λ) was found to be 0.05 and the slope of the recompression line (κ) was found to be 0.007. The effective internal angle of friction (ϕ) was determined to be about 35 degrees. This information was used to determine the objectives of the cyclic loading from a wet and dry of critical conditions. Therefore, the cyclic tests were run at corresponding OCR of 1, 1.5, 2 and 4 to capture the different behavior at different initial conditions.

Cyclic Triaxial Testing

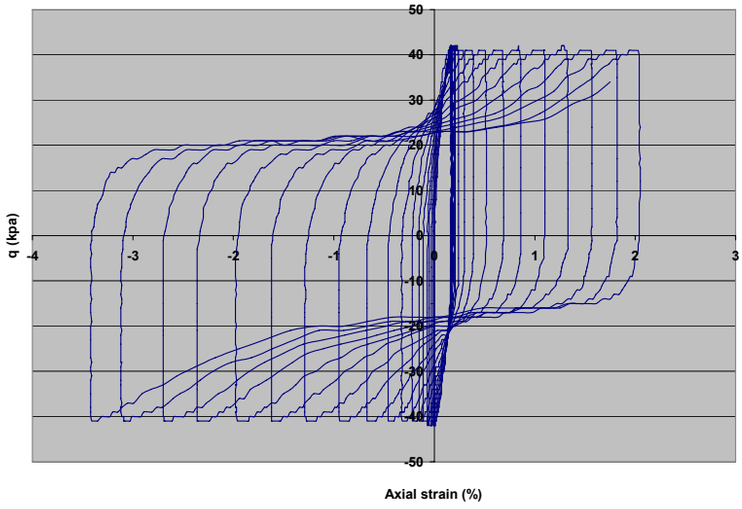
The cyclic triaxial test data are presented herein as typical results of the series of stress-controlled liquefaction tests. The test setup applies a constant cyclic stress to the specimen and measures the response of the deformation and pore pressure buildup. For example, a specimen consolidated to 10 psi tested at a frequency of 0.1 Hz at a cyclic stress ratio of 0.3 are shown for the entire duration of the test in Figure 2a and 2b, respectively. The pore pressure buildup and axial stress vs. time are captured by the data acquisition system and a liquefaction condition can be easily identified. Additionally, the hysterisis curve and degradation of the shear modulus are shown in Figure 2c.



(a)



(b)



(c)

Fig. 3. Typical Results of cyclic testing conducted on NC low plasticity silt

Cyclic tests at different over-consolidation ratios

The effects of overconsolidation and stress history on the liquefaction potential of soils have not received the needed attention. This is partially do to fact that overconsolidation is not a major player in dynamic properties of sands. Even though the effect of overconsolidation has been studied extensively for clay like material less emphasis has been on the liquefaction potential of overconsolidated clay-like soils. Due to the lack of information on stress history with regards to cyclic strength of soils, an experimental study was conducted to analyze the effect of OCR in low plasticity silts.

In an effort to isolate the effect of overconsolidation, the effective confinement pressure at the time of cyclic loading was the same for all the tests. This was achieved by consolidating the specimens to a higher confinement pressure and then lowering the confinement pressure to the base confinement pressure used for all the tests. Overconsolidation ratios of 1.5, 2, and 4 specimens were prepared and tested and the results were compared to the normally consolidated specimens. The overconsolidated tests are summarized in Table 2.

Table 2. Summary of Cyclic Triaxial Testing Program

TEST	Initial confinement pressure σ_3'	Cyclic confinement pressure σ_3'	OCR	CSR	Time to Liquefaction (sec)
D11	52kpa (≈7.5 psi)	35kpa (≈5 psi)	1.5	0.45	22.5
D12	70kpa (≈10 psi)	35kpa (≈5 psi)	2	0.45	31.9
D13	70kpa (≈10 psi)	35kpa (≈5 psi)	2	0.35	212.1
D14	70kpa (≈10 psi)	35kpa (≈5 psi)	2	0.30	461.9
D15	140kpa (≈20 psi)	35kpa (≈5 psi)	4	0.45	211.9
D16	140kpa (≈20 psi)	35kpa (≈5 psi)	4	0.35	-

DISCUSSION OF RESULTS

The ability to perform more sophisticated stress paths is now possible with the servo-controlled equipment. For example, specimens can be consolidated to a desired effective confining pressure and then cyclic loading applied until liquefaction is reached. Then after this failure condition is reached, a static shear test can be performed on the liquefied soil to obtain the post-liquefaction shear strength. Judgment is needed to determine at what state of reconsolidation should the tests be performed, since the liquefaction stage is a transient condition. With time the pore-pressure build-up due to cyclic loading will eventually dissipate.

This process can be examined in the stress path shown in Figure 3. After the specimens were consolidated isotropically to the desired effective confining pressure (e.g., 70 psi), the drainage paths are closed and the cyclic axial loading starts until the specimen liquefies. The GCTS control program is configured to automatically stop the cyclic load when the effective pore water pressure reaches the effective confinement pressure. This section of the test is illustrated in blue in Figure 3. The deviator stress is slowly lowered to zero and the bottom drainage line is opened

while keeping the same 70 psi consolidation pressure as the back pressure. The excess pore water pressure slowly dissipates back to 70 psi (illustrated in red). By monitoring the pressure on top of the sample, one can determine when the sample has dissipated all of the excess pore water pressure. Next, the drainage valves are closed in order to perform an undrained monotonic test on the specimen (illustrated in yellow). This procedure can be refined to perform static tests at post-liquefaction conditions, which is being presented in a separate publication by the authors.

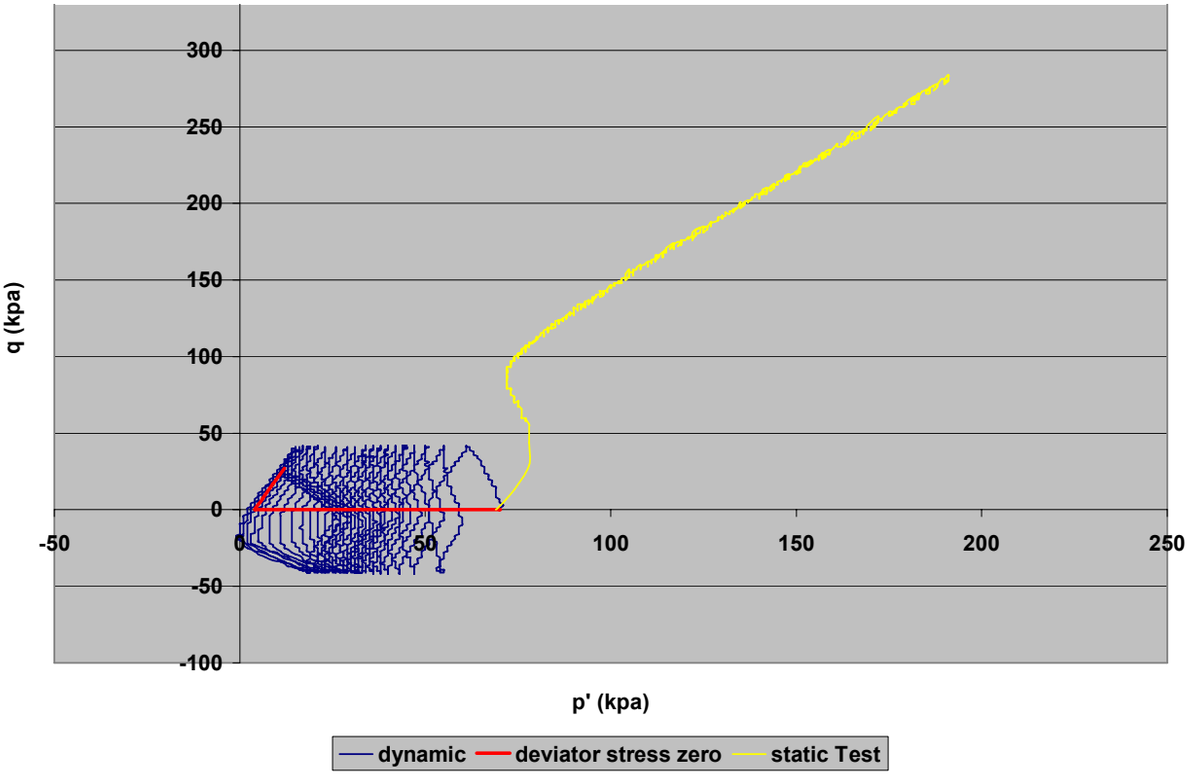


Fig. 3. Result of cyclic and static test conducted on low plasticity silt (Izadi, 2007)

Cyclic stress ratios to liquefaction and the effect of OCR

In order to analyze and compare the effect OCR, the results for the normally consolidated specimens were plotted together with the overconsolidated test results. Figure 4 shows the cyclic stress ratio versus number of cycles to liquefaction for both NC and OC specimens. The normally consolidated specimens were duplicated to ensure the testing procedures are repeatable and accurate, they are very close to each other. Then, the OCR was increased and consequently the resistance to liquefaction increased accordingly. Similarly, the decrease in cyclic strength was also evident with the decrease in cyclic stress ratio (CSR). For the specimens with an OCR of 4 and cyclic stress ratio of 0.35 liquefaction was not reached and there was no evident buildup of pore water pressure. Therefore, further increase of OCR (> 4) was deemed unnecessary.

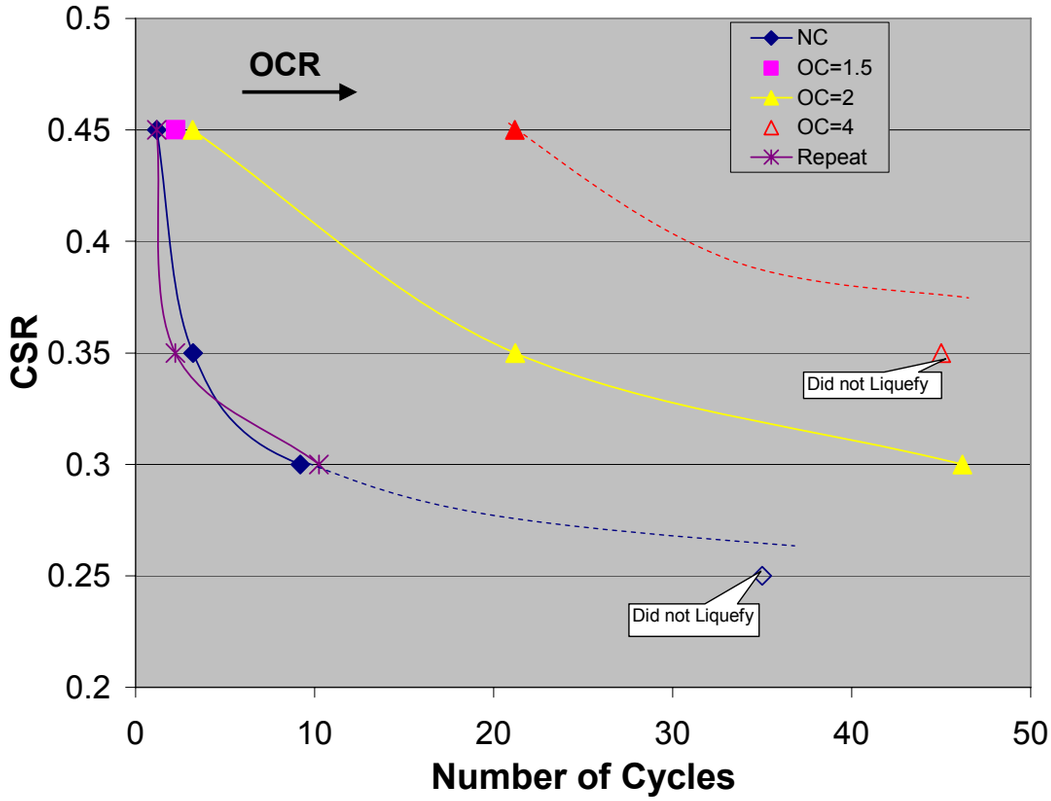


Fig. 4. The effect of Overconsolidation on the Resistance to Liquefaction

Figure 5 illustrates the pore pressure ratio $\left(r_u = \frac{\Delta u}{\sigma'} \right)$ versus time to liquefaction for different specimens consolidated at different effective confining stress and different cyclic stress ratios. The p′ - q (Cambridge stress space) plots of a liquefied (D13) specimen and a specimen that did not liquefy (D16) are illustrated in Figure 6 and clearly shows the effect of overconsolidation. It can be noted that the stress path for the NC specimen (D13) moves to the left towards failure as the pore water pressure builds up and the stress path of the specimen (D16) with higher OCR remains stationary over several cycles.

SUMMARY AND CONCLUSIONS

The results presented in this paper are part of a project that studies the fundamental behavior of silts under dynamic loading. Much care was taken in developing the procedure to reconstitute specimens from a slurry. Small variations in water content result on changes in soil density that are directly related to the shear strength of the material. The proposed method using top loading and vacuum from both ends ensures a more uniform specimen density.

Silts have both clay-like and sand-like tendencies from different points of view. Overconsolidation can be induced quite readily and pore pressure builds up easily like in clays. However, dilative behavior in its dense condition can be observed at low levels of deviator stress. The

behavior of this low plasticity silts is quite dependent on the level of overconsolidation and clearly the normally consolidated clays particularly are vulnerable to undrained loading. At an OCR of 2.0 the silt starts having a dilative behavior and develops negative pore pressure during static shear. Near this level of overconsolidation is where the phase transformation takes place and the material continues to dilate at large strains. These results are similar to the data shown in Brandon, et al. (2006) and were also repeatable in the UMR laboratories. At an OCR greater than 2.0 the silt has a dilative behavior at low strain. When the deviator stress reaches the failure envelope the stress path moves along the failure envelope or K_f line, but the specimens continue to dilate. Hence, liquefaction will take place at both low CSR and low number of cycles for low OCR silts. However, slight increases in OCR are enough to make the specimen resistant to liquefaction.

Non-plastic or low plasticity silts continue to be difficult to test and their behavior difficult to understand in dynamic loading. It is clear that the effect of OCR on these Mississippian silts impacts their susceptibility to liquefaction.

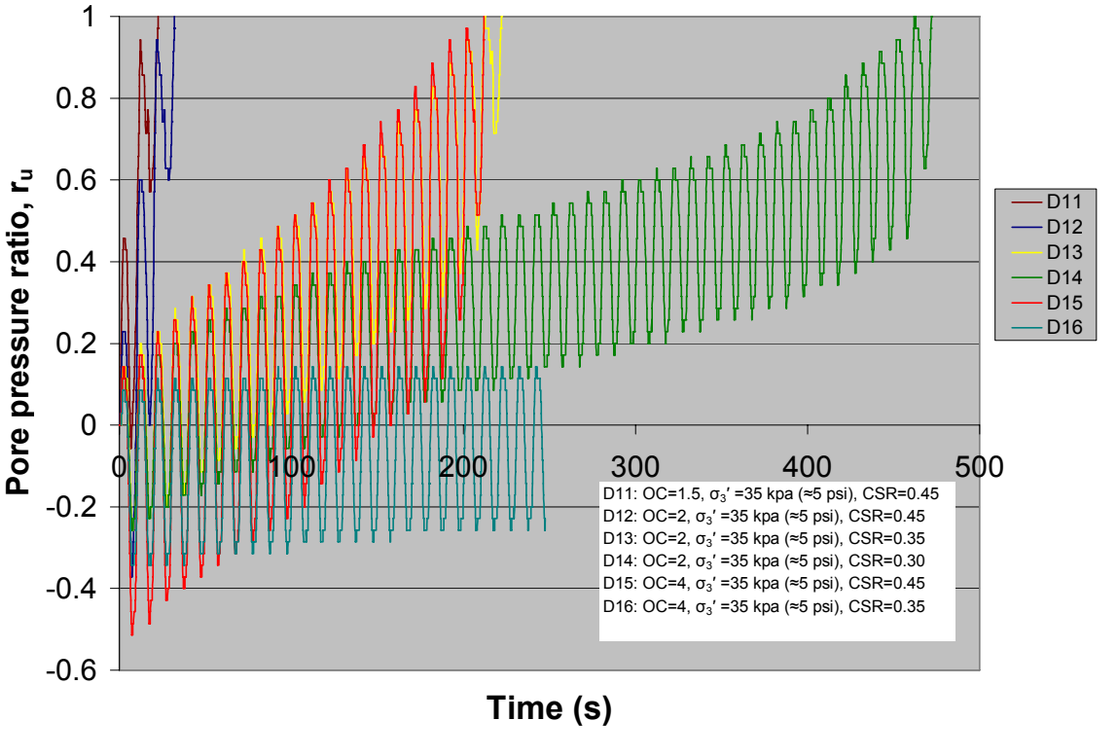


Fig. 5. Build-up of pore pressure ratio vs. time (notice D16 does not liquefy)

ACKNOWLEDGEMENTS

The experimental program presented herein is a portion of a more broad study sponsored by the US Bureau of Reclamation under the technical direction of Jeff Farrar. The financial and technical support is sincerely appreciated. The technical staff under the direction of Jeff Bradshaw and graduate students that helped during the test program are also acknowledged as contributors to this paper.

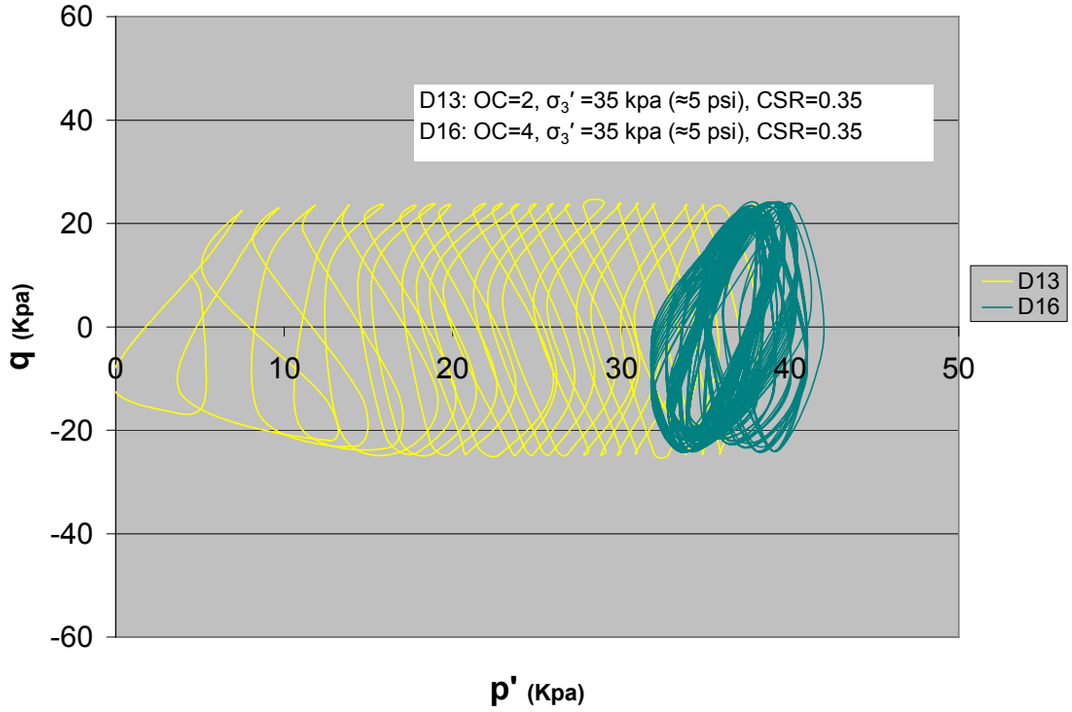


Fig. 6. Specimen D13 and D-16 at the same initial confining pressure and CSR, but different OCR (D13 liquefies and stress path moved to the left).

REFERENCES

Boulanger, R.W. and Idriss, I.M. (2004). "Evaluating the Potential for Liquefaction for Cyclic Failure of Silts and Clays." Center for Geotechnical Modeling, University of California Davis, Report No. UCD/CGM-04/01.

Brandon, T.L., Rose, A.T., Duncan J.M. (2006). "Drained and Undrained Strength Interpretation for Low-Plasticity Silts." *Journal of Geotechnical and Geoenvironmental Engineering*, 132, 250-257pp.

Fleming, L.N., and Duncan, J.M. (1990). "Stress-deformation characteristics of an Alaskan silt." *Journal of Geotechnical Engineering*, 116(3), 377-393.

Guo, T., and Prakash, S., (1999), "Liquefaction of Silts and Silt-Clay Mixtures." *Journal of Geotechnical and Geoenvironmental Engineering*, Vol. 125, No. 8, 706-710.

Izadi, A., (2007), "Static Behavior of Silts", MS Thesis, University of Missouri-Rolla, 82 pp.

Kuerbis, R., and Vaid, Y.P. (1988), "Sand Sample Preparation-The Slurry Deposition Method." *Soils and foundations*, Vol. 28, No. 4, 107-118.

Penman, A.D.M. (1953). "Shear characteristics of a saturated silt measured in triaxial compression." *Geotechnique*, 3, 312–328.

Romero, S. (1995). "The Behavior of Silts as Clay Content is Increased. MS Thesis, University of California-Davis, 108 pp.

Liquefaction Resistance of Sands Containing Varying Amounts of Fines

G.A.Athanasopoulos[1], M. ASCE. and V.C.Xenaki[2]

[1]Professor, Dept of Civil Engineering, University of Patras, Patras Greece (gaa@upatras.gr)
[2]Soils Engineer, MSc, PhD, Edafomichaniki S.A., Athens, Greece

ABSTRACT: Results of undrained cyclic triaxial tests on sand-(nonplastic) silt mixtures (under conditions of constant global void ratio) reported by Xenaki and Athanasopoulos (2003) are further analyzed in the framework of recent advances on the subject of liquefaction behavior of fine-grained soils. The observed behavior, for all values of fines content (0% to 100%), is found to have the characteristics of the "sand-like" behavior described in the literature. The same characteristics are also exhibited by plastic sand-clay mixtures with plasticity index ranging from 2 to 11. The undrained initial modulus of the specimens and the amplitude of pre-liquefaction strains were found to decrease and increase, respectively, with increasing fines content, thus negating the beneficial effects of dilatancy in this type of soils. The existence of a critical value of fines content, FC_{cr}, at which liquefaction resistance is minimized, is confirmed and shown to be useful in describing the behavior of the mixtures in terms of their relative density.

INTRODUCTION

In current practice the evaluation of soil liquefaction/cyclic softening potential follows the successive steps of applying criteria for (a) liquefaction susceptibility, (b) liquefaction triggering and (c) expected magnitude of ground deformations (Kramer, 1996). For coarse-grained soils containing small amounts of nonplastic or low-plasticity fines, the procedures recommended by Youd et al. (2001) have been found to adequately (and safely) predict the behavior of this type of soils under earthquake loading. For fine-grained soils (silts and clays), however, recent experience with strong earthquakes has shown that the existing liquefaction criteria (e.g. the Chinese criteria) are inadequate and unsafe (Bray et al., 2004, Boulanger et al., 1998, Ghalandarzadeh et al., 2007). The above findings have attracted the interest of many investigators into the subject of liquefaction behavior of fine-grained soils and on the effects of the amount and plasticity index of the fines fraction. During the last ten years the pertinent research has followed three main directions: (1) laboratory testing of sand-silt-clay mixtures under monotonic and cyclic undrained (or drained) loading, (2) laboratory testing of undisturbed or reconstituted samples retrieved from liquefaction sites, and (3) analyses of case histories involving the occurrence of liquefaction/cyclic softening in fine-grained soils.

The objective of the present study is to present a brief overview of the behavior of saturated sands containing varying amounts of fines under cyclic (or monotonic) loading and to further analyze results of cyclic triaxial tests on sand-silt mixtures reported by Xenaki and Athanasopoulos (2003). The discussion focuses on the effects of fines content and relative density of sand-silt or sand-clay mixtures on their liquefaction resistance and the magnitude of strains developing prior to the onset of material instability. The role of the critical value of fines content, FC_{cr}, in describing the material behavior is also discussed in the paper.

REVIEW OF LITERATURE

The behavior of sands containing varying amounts of nonplastic (as well as plastic) fines under monotonic and cyclic loading, has been investigated experimentally by several authors, who have presented and interpreted their results in the framework of critical state soil mechanics (Jefferies and Been, 2006). Yamamuro and Lade (1998) and Yamamuro and Covert (2001) on the basis of results of tests on sands containing two different amounts (7% and 40%) of nonplastic silt, concluded that silty sand (a) may not be characterized by a unique steady-state line (SSL) and (b) its behavior is unconventional (or reverse) in the sense that it develops increased dilatancy with increasing confining pressure. The above behavior is the result of the compressible particle structure created by the complex interaction of sand and silt grains. Yamamuro and Lade (1998) has used the volumetric compressibility of silty sands as an index for the liquefaction potential and summarized their test results (for confining pressure=25kPa) in the form of the 3-D diagram depicted in Fig.1. The diagram of Fig.1 presents the combined effects of void ratio and fines content on the compressibility (or the liquefaction potential) of the material, and indicates that under conditions of constant void ratio the liquefaction resistance of the material decreases with increasing fines content up to a critical value FC_{cr}. For fines content > FC_{cr} the silty sand starts recovering the losses in liquefaction resistance, although it never regains the resistance of clean sand. It is worth mentioning that Georgiannou (2006) has recently presented experimental evidence indicating that the behavior of sands containing small amounts of fines depends on the shape (i.e. round vs. platy) and size (compared to the size of sand grains) of the fine particles.

Other investigators have found that the SSL of silty (or even clay) sands is changing location with increasing fines content. Yang et al. 2006 and Ghahremani et al. 2006 have shown that for increasing fines content the SSL moves downward-in a parallel fashion-in the e-lnp′ space up to the critical value, FC_{cr}, after which it starts returning to their initial position. On the other hand, Bouckovalas et al. (2003) have compiled data from the literature showing a clockwise rotation of the SSL with increasing fines content. The monotonic (peak or steady-state) and cyclic strength of silty or clayey sands have been

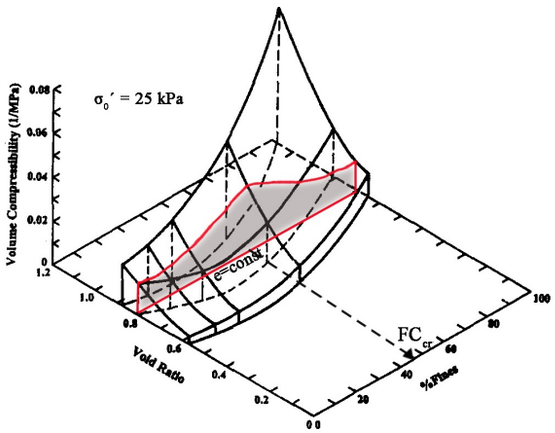


Figure 1. Effect of void ratio and fines content on the compressibility (or liquefaction potential) of sand-silt mixtures (adopted from Yamamuro and Lade, 1998)

found by the above and other investigators (e.g. Yang et al. 2006 and Wang et al. 2007) to first increase (for FC< FC_{cr}) and then decrease (for FC> $FC_{cr)}$) with increasing fines content. It has also been found that by utilizing the concept of "effective" void ratio (intergranular, e_s or interfine, e_f, void ratio), as presented by Thevanayagam (1998), Thevanayagam and Mohan (2000) Thevanayagam et al. (2002) and Thevanayagam and Martin (2002), two unique relationships can be established for the shear strength and the location of SSL (irrespectively of the exact amount of fines content) for the two ranges of fines content i.e. for FC<FC_{cr} or FC> FC_{cr}.

The dependence of the liquefaction resistance of silty or clayey sands and sandy silts on the fines content has been investigated in the past by several researchers as discussed by Thevanayagam and Mohan (2000) and Thevanayagam et al. (2002). A number of recent studies have also been conducted -under conditions of constant (global) void ratio (Polito and Martin, 2001, Xenaki and Athanasopoulos, 2003, Ghahremani and Ghalandarzadeh, 2006, Yang et al., 2006, Ghahremani et al. 2007, Papadopoulou and Tika, 2007, Kokusho, 2007). The findings of the above investigators, in agreement with the trend indicated in Fig.1, indicate the existence of a critical value of fines content, FC_{cr}, (ranging from 30% to 40%) such that when FC< FC_{cr} the liquefaction resistance decreases with increasing fines content whereas in the range FC> FC_{cr}, the liquefaction resistance increases slowly with increasing fines content. Several studies have also shown that the liquefaction resistance of sands containing fines, increases with the plasticity of fines (Ghahremani and Ghalandarzadeh, 2006, Ghahremani et al., 2007, Wijewickreme and Sanin, 2007). The above findings indicate that soils consisting of sands, silts and clays in different proportions, when saturated, may be particularly susceptible to liquefaction/cyclic softening, especially when their fines content is close to the critical value, FC_{cr}. Thus, the amount of fines contained in a sandy soil may be an important parameter to consider, in addition to the plasticity of fines, when evaluating the liquefaction susceptibility of this type of soils.

As mentioned in the **Introduction**, experiences of liquefaction failures of fine-grained soils in recent earthquakes has shown the inadequacy of existing liquefaction criteria and motivated the development of new ones. Bray and Sancio (2006) performed cyclic triaxial and simple shear tests on undisturbed specimens of natural soils sampled from liquefied sites in Adapazari, Turkey, in the 1999 Kocaeli earthquake. Their results-and other more recent results on reconstituted specimens (Donahue et al. 2007)-indicate that the liquefaction resistance increases with increasing plasticity and that the "Chinese criteria" are unsafe and their use should be discontinued. Instead, they proposed new criteria as follows: PI<12 and w_c/LL>0.85 $\rightarrow$ soil susceptible to liquefaction, 12<PI<18 and w_c/LL>0.8 $\rightarrow$ moderately susceptible, and PI>18, w_c/LL<0.8 $\rightarrow$ not susceptible. On the other hand, Boulanger and Idriss (2006), have proposed the classification of fine-grained soils into "sand-like" materials (susceptible to liquefaction) when PI<7 and "clay-like" materials (susceptible to cyclic softening) when PI$\geq$7. They recommend the use of conventional liquefaction evaluation procedures for the sand-like soils (e.g. Youd et al.,2001), whereas for the case of PI$\geq$7 they propose the use of procedures that have been developed for evaluating the cyclic softening potential of cohesive soils (Boulanger and Idriss (2007). The above investigators also suggest the discontinuance of using the Chinese criteria.

The review presented above indicates that silty or clayey sands, sandy silts and silts/clays are characterized by a peculiar particle structure resulting from the interaction between grains of different sizes. The behavior of the above soils, when saturated, under cyclic (or monotonic) loading cannot be described by the global void ratio alone without the aid of fines content and the critical value FC_{cr} or the "effective" void ratio. The stability of the above soils increases with the plasticity of the fine-grained fraction whereas the value of their water content-compared to the value of liquid limit- is a critical parameter in evaluating the liquefaction/cyclic softening potential.

TEST MATERIALS AND EXPERIMENTAL PROCEDURE

The materials used in the present study include a fine sand with D_{50}=0.12 mm and C_u=1.7, and a nonplastic silt having D_{50}=0.02mm and C_u=10. The grain size curves of the two materials are shown in Fig.2. Undrained stress-controlled cyclic triaxial tests were conducted using an automated, PC-driven system, on dry-compacted and then fully saturated mixtures of the above materials, with fines content ranging from 0% (clean sand) to 100% (pure silt). The test specimens had a diameter of 50mm, a height of 100mm and their high degree of saturation was confirmed by the results of appropriate B-checks (0.97 to 1.0). The consolidation pressure of specimens was σ_o'=200kPa, whereas the value of global void ratio was kept equal to $e \approx 0.66$ in all tests, with the exception of the tests conducted on (pure) silt specimens in which the global void ratio was $e \approx 0.78$. As the global void ratio of a soil is the most common parameter used in current geotechnical engineering practice it was decided in this study to use it as the basis for comparing the behavior of the different sand-silt mixtures. Other alternatives used as a basis for comparison in pertinent studies include the granular void ratio, relative density, depositional method of specimen formation etc. (Lade and Yamamuro, 1997). The results obtained in this study from the silt specimens were subsequently corrected to a void ratio of $e \approx 0.66$, by utilizing the liquefaction resistance vs. relative density relationship derived from the test results and discussed in the next section.

In all tests the specimens were loaded with uniform sinusoidal cycles with a frequency of 0.1Hz. The cyclic stress, excess pore water pressure and axial strain of each specimen were continuously recorded during testing. The effect of loading frequency on the behavior of clay specimens has been much discussed in the literature (e.g. Boulanger et

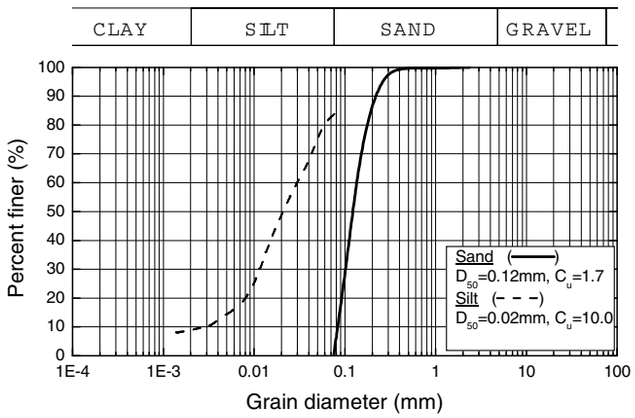


Figure 2. Grain size distribution curves of the two soils used in the present study.

al., 1998, Zergoun and Vaid, 1994). The use of low frequencies is generally suggested to assure pore water pressure equalization throughout the specimen and a correct interpretation of results in terms of effective stress. In the present study the loading frequency of 0.1Hz is considered slow enough on the basis of the following observations : (a) the sand-silt mixtures are much more permeable (at least two orders of magnitude) compared to plastic clays, (b) the pattern of excess pore water pressure development during cyclic loading was in all tested specimens (even in the case of 100% silt) similar to the typical one for sands, as explained by Boulanger et al. (1998), i.e. two peaks during the compression half-cycle (each of the peaks corresponding to the instant of zero deviator stress) followed by a negative pressure during the extension half-cycle of loading, and (c) the calculated p´-q´ diagrams for all tested specimens were realistic. On the basis of above observations it is expected that the distribution of the excess pore water pressure throughout the specimen was uniform and that initial liquefaction occurs when the pore water pressure ratio becomes r_u=100%. The cyclic stress ratios, CSR, applied to tested specimens ranged from 0.07 to 0.49.

TEST RESULTS AND DISCUSSION

Examples of cyclic stress-strain curves from the results of the present study (accompanied by the corresponding plots of excess pore water pressure and axial strain as a function of number of cycles of loading as well as p'-q' diagrams) are shown in Fig.3. These results correspond to mixtures having fines content equal to 0%, 42% and 55%, for CSR $\approx$ 0.25. In each of the stress-strain diagrams, two loops are shown i.e. the loop for the first cycle of loading (N=1) and the loop corresponding to initial liquefaction ($N=N_L$). An observation of the diagram of Fig.3 can lead to the following comments:

(1) The observed behavior is in agreement with the behavior of "sand-like" soils described by Boulanger and Idriss (2006) i.e. the stress-strain loops at initial liquefaction have a flat middle portion combined with strain-hardening (due to dilatancy) ends. In addition, the tested mixtures are nonplastic (i.e. PI<7) and the pore water pressure ratio reached the value r_u=100% in all tests. In the case of silt specimens the large magnitude of axial strains developed during the very first cycle of loading, exceeded the capability of the system to maintain a constant cyclic stress ratio and for this reason an inverted S-shaped loop could not be observed in these results.

(2) The liquefaction resistance of the mixtures (expressed as the number of cycles to induce initial liquefaction, i.e. r_u=100%) decreases with increasing fines content as shown in Fig.4 for CSR=0.23, and reaches a minimum value at a critical value, FC_{cr}=42%. This critical value was found not to vary appreciably for other CSR values. A further increase of fines content beyond the critical value results in an increase of the stability of the mixture, although the liquefaction resistance remains always lower than that of clean sand. In the diagram of Fig.4, the number of cycles to liquefaction for pure silt (FC=100%) has been corrected to correspond to the common value of void ratio ($e \approx 0.66$) by utilizing the diagram of Fig.6 discussed later in this section. As mentioned in the previous section, several other investigators have reported experimental results for the case of nonplastic fines similar to the ones described in Fig.4 (e.g. Polito and Martin, 2001, Papadopoulou and Tika, 2007). Xenaki and Athanasopoulos (2003) have also expressed the results of their tests in terms of constant intergranular, e_s and interfine, e_f, void ratio and have shown that the liquefaction resistance, for a constant value of e_s,

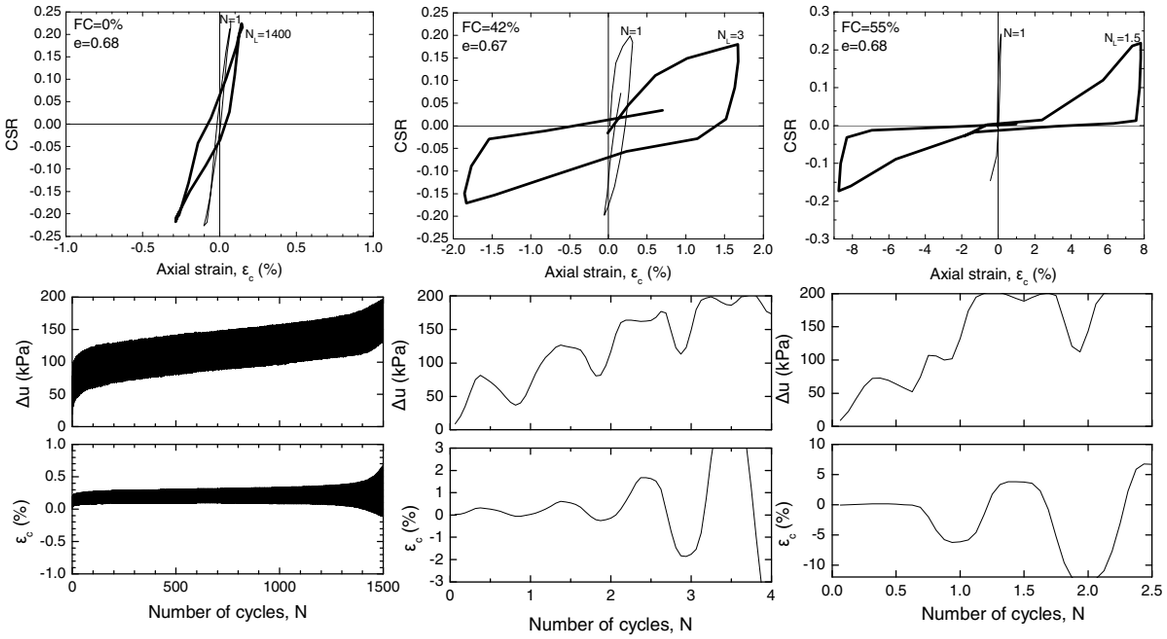


Figure 3. Results of cyclic triaxial tests on sand-silt mixtures with fines content of 0%, 42% and 55% under conditions of constant global void ratio.

increases with increasing fines content whereas the behavior is reversed for constant values of e_f. Ghahremani and Ghalandarzadeh (2006) and Ghahermani et al. (2007) have reported results indicating that the above "sand-like" behavior is also manifested in the case of plastic (clay) fines. The plasticity of sand-clay mixtures tested by the above investigators ranged from PI=2 to11, thus exceeding the limit value of PI=7 proposed by Boulanger and Idriss (2006), while falling in the "liquefaction" range (PI<12) proposed by Bray and Sancio (2006).

(3) The pre-liquefaction strains of the sand-silt mixture increase significantly with the fines content as shown in Fig.5 (0.2% for sand, 1% for FC=10%, 2% for FC=30% to 24%, 8% for FC=55% and >10% for pure silt). Thus, an increasing amount of fines inhibits the early development of dilatancy and contributes to accumulation of excessive strains. It is worth mentioning that from the diagrams of Fig.3 (and other similar diagrams not shown here) the initial stiffness E_u of each mixture can be determined from the average slope of the loop corresponding to the first cycle of loading. The diagram of Fig.6 depicts the E_u vs. FC relation for the tested soils and indicates a significant decrease of initial stiffness with increasing fines content. It should be mentioned that the values of E_u depicted in Fig.6 were determined for an average axial strain amplitude $\varepsilon_c \approx 10^{-3}$, with the exception of the case for FC=100%, in which $\varepsilon_c \approx 10^{-2}$ (and $e \approx 0.78$). For this case, the value of E_u has been corrected, as shown in Fig.7, to correspond to e=0.66 and $\varepsilon_c \approx 10^{-3}$. The test results depicted in Fig.6 indicate that the effect of fines in reducing the initial stiffness of mixture is more pronounced for fines content up to critical value, FC_{cr}.

It was mentioned in the previous section that several investigators have recently reported experimental results indicating a change of behavior of saturated sand-silt mixtures under monotonic or cyclic loading, depending on whether the amount of fines is lower or higher than the critical value, FC_{cr}. In the present study, in an attempt to present the results in a unified way, the liquefaction resistance of the tested sand-silt mixtures is

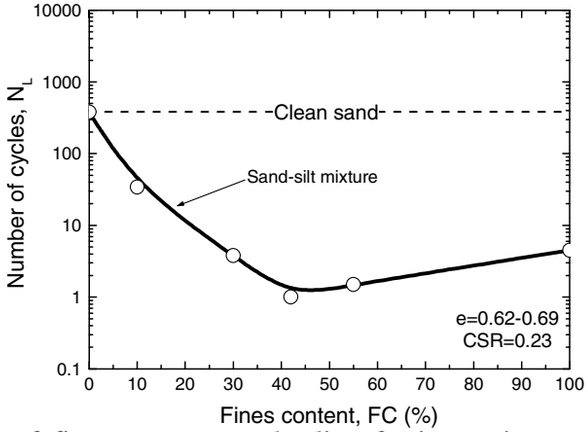


Figure 4. Effect of fines content on the liquefaction resistance of sand-silt mixtures, under conditions of constant global void ratio.

expressed as a function of global relative density, D_r, of material for a constant value of global void ratio ($\varepsilon_c \approx 0.66$) and CSR ≈ 0.23. The relative density of each mixture was estimated by using the corresponding values of e_{max} and e_{min} reported by Xenaki and Athanasopoulos (2003). In the diagram of Fig.7 the liquefaction resistance of sand-silt mixtures is plotted vs. the corresponding values of relative density, D_r. The plot indicates that the N_L vs. D_r curve is composed of two unique (i.e. independent of FC) branches intersecting at the point corresponding to the critical value of fines content. One of the branches describes the liquefaction behavior for FC<FC_{cr} whereas a second branch – having a much lower slope- holds for FC> FC_{cr}. As shown in the above diagram the extrapolation of the second branch of the CRR vs. D_r relationship (i.e. for FC>FC_{cr}) up to a value of D_r=100% was used to correct the number of cycles N_L corresponding to a void ratio $e \approx 0.66$. The differentiation of liquefaction behavior, depending on the relation of FC to the value of FC_{cr}, is evident in Fig.7 and it bears great similarity to the relations reported by Yang et al.(2006 a, b) and Wang et al.(2007) between the undrained strength and the effective void ratio (e_s or e_f) or relative density. Thus, the relative density of a soil (appropriately evaluated for fines content greater than 15%) may be a useful parameter for assessing its liquefaction susceptibility (or resistance), provided the fines content and the critical value FC_{cr} are known.

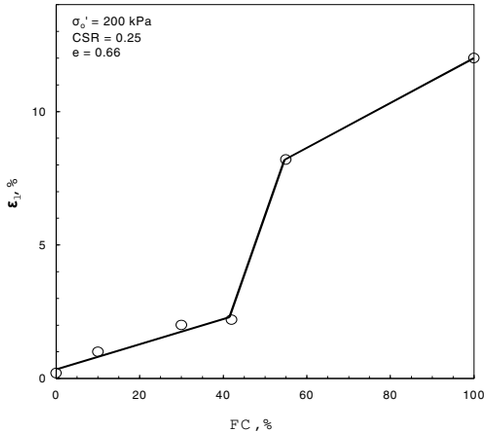


Figure 5. Effect of fines content on the amplitude of pre-liquefaction strains of sand-silt mixtures under cyclic loading and conditions of constant global void ratio.

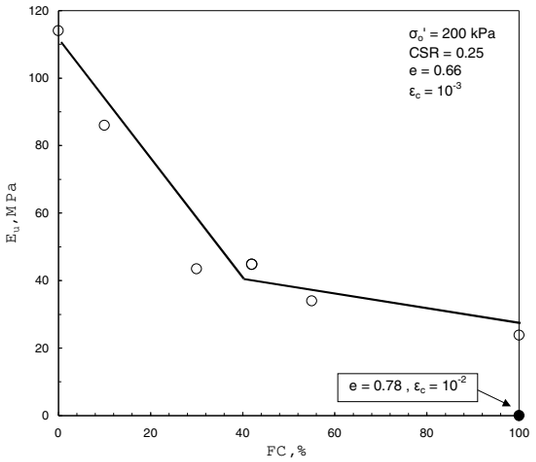


Figure 6. Effect of fines content on the initial (during first cycle of loading) stiffness of sand-silt mixtures under cyclic loading and conditions of constant global void ratio.

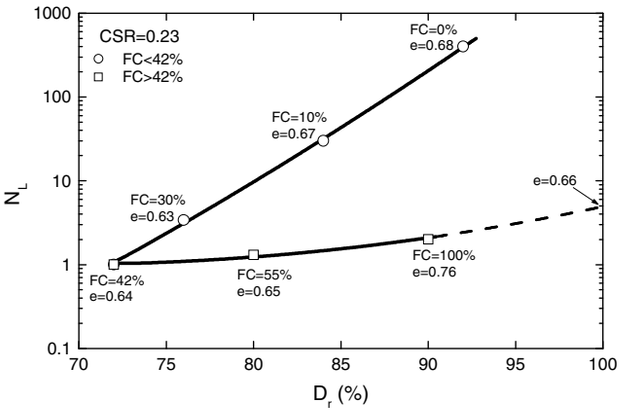


Figure 7. Relation of liquefaction resistance of sand-silt mixtures with varying fines content and constant global void ratio to the relative density of mixtures.

CONCLUSIONS

On the basis of the results of the present study and of other recently reported results the following conclusions can be drawn:

(1) The behavior of saturated nonplastic reconstituted sand-silt mixtures (having fines content ranging from 0% to 100%) under cyclic loading, is very similar to the behavior of natural fine-grained soils and to the behavior attributed in the literature to "sand-like" soils.
(2) The behavior of saturated plastic reconstituted sand-clay mixtures (having fines content ranging from 0% to 50%) under cyclic loading is consistent with the behavior attributed to "sand-like" soils, although their plasticity index may take values higher than the limit value (PI=7) proposed in the literature.
(3) The undrained initial (i.e. upon the first cycle of cyclic loading) stiffness of sand-silt mixtures, under conditions of constant void ratio, is decreasing significantly for increasing nonplastic fines content, compared to the case of clean sand. The decrease is more pronounced for fines content ranging from 0% to FC_{cr}.
(4) Pre-liquefaction cyclic strains of sand-silt and sand-clay mixtures (behaving similarly to the "sand-like" soils described in the literature), increase significantly with increasing fines content, especially in the range where $FC \approx FC_{cr}$. This behavior may negate the beneficial effect of post-liquefaction dilatancy of these soils.
(5) The critical value of fines content, FC_{cr}, is an important parameter for describing the behavior of soils containing fines, in terms of relative density or "effective" void ratio of the mixture. Its importance is extended to the cases of any pair of mixed materials having significantly different mean particle sizes (e.g. gravel-sand, sand-silt, sand-clay, silt-clay etc.). Further study is therefore warranted on the dependence of FC_{cr} on void ratio and

particle size of the host material, effective confining stress and type, shape and size of additive material.

REFERENCES

Bouckovalas, G.D., Andrianopoulos, K.I. and Papadimitriou, A.E. (2003), "A Critical State Interpretation for the Cyclic Liquefaction Resistance of Silty Sands", *Soil Dynamics and Earthquake Engineering*, 23 (2003), 115-125.

Boulanger, R.W. and Idriss, I.M. (2006), "Liquefaction Susceptibility Criteria for Silts and Clays", *Journal of Geotechnical and Geoenviromental Engineering*, ASCE, 132(11), 2006, pp. 1413-1426.

Boulanger, R.W. and Idriss, I.M. (2007), "Evaluation of Cyclic Softering in Silts and Clays", *ASCE Journal of Geotechnical and Geoenvironmental Engineering*, 133 (6), June 2007, pp.641-652.

Boulanger, R.W., Meyers, M.W., Mejia, L.H. and Idriss, I.M. (1998), "Behavior of Fine-grained Soil During the Loma Prieta Earthquake", *Canadian Geotechnical Journal*, 35, pp. 146-158.

Bray J.D. and 11 more authors, (2004), "Subsurface Characterization at Ground Failure Sites in Adapazari, Turkey", *ASCE Journal of Geotechnical and Geoenvironmental Engineering*, 130(7), July 2004, pp.673-685.

Bray, J.D. and Sancio, R.B. (2006), "Assessment of the Liquefaction Susceptibility of Fine-Grained Soils", *Journal of Geotechnical and Geoenviromental Engineering*, ASCE, 132(9), 2006, pp.1165-1177.

Donahue, I., Bray, I. and Riemer, M. (2007), "Liquefaction Testing of Fine-Grained Soil Prepared Using Slurry Deposition", *Proceedings of 4ICEGE*, Thessaloniki, Greece, June 2007, Paper No. 1226

Georgiannou, V. N. (2006), "The Undrained Response of Sands with Additions of Particles of Various Shapes and Sizes", *Geotechnique,* 56(9), pp. 639-649

Ghahremani, M. and Ghalandarzadeh, A. (2006), "Effect of Plastic Fines on Cyclic Resistance of Sands", *ASCE (GSP 150): Soil and Rock Behavior and Modeling* (Eds.R.Luna, Z.Hong, G.Ma and M.Huang), pp. 406-412.

Ghahremani, M., Chalandarzadeh, A.and Moradi, M. (2006), "Effect of Fines on the Undrained Behavior of Sands", *ASCE (GSP 150): Soil and Rock Behavior and Modeling* (Eds. R. Luna, Z.Hong, G.Ma and M.Huang) pp.48-54.

Ghahremani,M., Ghalandrorzadeh, A. and Ghahremani, K. (2007), "Laboratory Investigation of the Effects of Plastic Fines on Cyclic Resistance of Sand-Clay Mixtures", *Proceedings of 4ICEGE*, Thessaloniki, Greece, June 2007, Paper No.1166.

Ghalandarzadeh A., Ghahremani M. and Konagai, K. (2007), "Investigation on the Liquefaction of a Clayey-Sandy Soil During Changureh Earthquake", *Proceedings of 4ICEGE*, Thessaloniki, Greece, June 2007, Paper No.1165.

Jefferies, M. and Been, K. (2006) *"Soil Liquefaction: A Critical State Approach"*, Taylor and Francis, London and New York, 479p.

Kokusho, T. (2007), "Liquefaction Strengths of Poorly – Graded and Well-Graded Granular Soils Investigated by Lab Tests, *"Earthquake Geotechnical Engineering, Proceedings of 4ICEGE- Invited Lectures*, (K.D.Pitilakis, E1), Springer, pp. 159-184.

Kramer, S.L. (1996), *"Geotechnical Earthquake Engineering"*, Upper Saddle River, NI.: Prentice Hall, 1996.

Papadopoulou, A. and Tika, Th. (2007) "The Effect of Non-Plastic Fines on the Liquefaction Resistance of Sands", *Proceedings of 4ICEGE*, Thessaloniki, Greece, June 2007, Paper No.1414.

Polito, C.P. and Martin, J.R. (2001), "Effects of Nonplastic Fines on the Liquefaction Resistance of Sands", *ASCE Journal of Geotechnical and Geoenvironemental Engineering*, 127 (5), May 2001, pp. 408-415.

Thevanayagam, S. (1998)", Effect of Fines and Confining Stress on Undrained Shear Strenght of Silty Sands", *ASCE Journal of Geotechnical and Geoenvironmental Engineering*, 124 (6), June 1998, pp. 479-491.

Thevanayagam, S. and Martin, G.R. (2002), "Liquefaction in Silty Soils-Screening and Remediation Issues", *Soil Dynamics and Earthquake Engineering*, 22 (2002) pp. 1035-1042.

Thevanayagam, S. and Mohan, S. (2000), "Intergranular State Variables and Stress-Strain Behaviour of Silty Sands", *Geotechnique 50(1)*, pp. 1-23.

Thevanayagam, S., Shenthan, T., Mohan, S. and Liang, J. (2002), "Undrained Fragility of Clean Sands, Silty Sands and Sandy Silts", *ASCE Journal of Geotechnical and Geoenvironemental Engineering*, 128 (10), Oct. 2002, pp. 843-859.

Wang, G., Sassa, K. Foukuoka,It. And Tada, T. (2007), "Experimental Study on the Shearing Behavior of Saturated Silty Soils Based on Ring-Shear Tests", *ASCE Journal of Geotechnical and Geoenvironmental Engineering*, 133(3), March 2007, pp. 319-333.

Wijewickreme, D. and Sanin, M. (2007), "Effect of Plasticity on the Laboratory Cyclic Shear Response of Fine-grained Soils", *Proceedings of 4ICEGE, Thessaloniki*, Greece, June 2007, Paper No. 1321.

Xenaki, V.C. and Athanasopoulos, G.A. (2003), "Liquefaction Resistance of Sand-Silt Mixtures: An Experimental Investigation of the Effects of Fines", *Soil Dynamics and Earthquake Engineering*, 23 (2003), 183-194.

Xenaki, V.C. and Athanasopoulos, G.A. (2003), Discussion of "Effects of Nonplastic Fines on the Liquefaction Resistance of Sands", by C.P. Polito and J.R. Martin II, ASCE of May 2001, Vol. 127, No. 5 pp. 408-415., *ASCE Journal of Geotechnical and Geoenvironmental Engineering*, 129 (4), 2003, pp. 387-389.

Yamamuro, J.A. and Lade, P.V. (1998), "Steady-State Concepts and Static Liquefaction of Silty Sands", *ASCE Journal of Geotechnical and Geoenvironmental Engineering*, 124(9) 1998, pp. 868-877.

Yamamuro, I.A. and Covert, K. M. (2001), "Monotonic and Cyclic Liquefaction of Very Loose Sands with High Silt Content", *ASCE Journal of Geotechnical and Geoenvironmental Engineering*, 127(4), 2001, pp. 314-324.

Yang, S.L. Sandren, R. and Grande, L. (2006b), "Steady-state Lines of Sand-Silt Mixtures", *Canadian Geotechnical Journal*, 43, 1213-1219.

Yang, S.L., Sandven, R. and Grande, L. (2006a), "Instability of Sand-Silt Mixtures", *Soil Dynamics and Earthquake Engineering*, 26 (2006), 183-190.

Youd, et al. "Liquefaction Resistance of Soils: Summary Report from the 1996 NCEER and 1998 NCEER/NSF Workshops on Evaluation of Liquefaction Resistance of Soils", *ASCE Journal of Geotechnical and Geoenvironmental Engineering*, 127 (10), pp. 817-33.

Zergoun, M. and Vaid, Y.P. (1994), "Effective Stress Response of Clay to Undrained Cyclic Loading", *Canadian Geotechnical Journal*, 31, pp.714-727.

Post-liquefaction Shear Behavior of Bonneville Silty-Sand

Zahra A. Amini[1] and Aurelian C. Trandafir[2]

[1]Graduate Student, Department of Geology and Geophysics, University of Utah, 135 South 1460 East Rm 717, Salt Lake City, Utah 84112-0111; zahra.amini@utah.edu
[2]Assistant Professor, Department of Geology and Geophysics, University of Utah, 135 South 1460 East Rm 717, Salt Lake City, Utah 84112-0111; a.trandafir@utah.edu

ABSTRACT: This paper presents the results of a laboratory study addressing the post-liquefaction undrained shear behavior of a silty-sand characterizing the main liquefiable layer within Bonneville sediments at the Farmington Siding Landslide Complex (FSLC). FSLC is located in Davis County, Utah where liquefaction flow-slides associated with past earthquake activity in the region have been documented. Undrained cyclic triaxial tests to trigger liquefaction in water-pluviated samples of Bonnevile silty-sand consolidated isotropically under various effective confining stresses were followed by undrained monotonic triaxial compression tests on the liquefied specimens. The experimental results revealed a dilative behavior of the liquefied soil element, and the post-liquefaction undrained shear strength showed an increase with increasing initial effective consolidation stress. An infinite slope analysis addressing the onset of flow-slide in a liquefied Bonneville silty-sand deposit, using the post-liquefaction undrained shear strength data from laboratory testing, resulted in required minimum slope inclinations much greater than the actual slope gradient at the FSLC.

INTRODUCTION

Farmington siding landslide complex (FSLC) in Davis County, Utah has long been recognized as an area of recurrent, prehistoric liquefaction-induced ground deformation characterized by flow and lateral spread on very gentle slopes with an average topographic gradient ranging from 0.4 to 0.8% (Hylland 1997). Stratified sand, silt, and clay deposited in Lake Bonneville and Great Salt Lake form the upper Pleistocene to Holocene lacustrine sediments on which FSLC lies. The Weber segment of the Wasatch fault which is located less than 1 km east of the head of the landslide complex is responsible for the past earthquakes of the area.

Examination of data from an exploratory borehole (Fig.1) drilled by the United States Geological Survey (USGS) at the FSLC (Miller et al. 1981) revealed that the

predominant liquefiable material is a silty-sand encountered in Bonneville sediments (denoted here as Bonneville silty-sand). The present study addresses the post-liquefaction monotonic shear response of reconstituted silty-sand specimens collected from a surface exposure of Bonneville sediments in Farmington. As shown in Figure 1, the characteristics of the grain size distribution of the material analyzed in this study (shown by dashed lines) are quite similar to those of the sandy soils encountered in the USGS borehole indicating that median size of the material is 0.1 mm and there is 1.32%-5.26% clay fraction. Investigations on the shear behavior of this material can therefore provide valuable insight into the mechanism of liquefaction induced lateral ground deformations associated with past earthquake activity in the region.

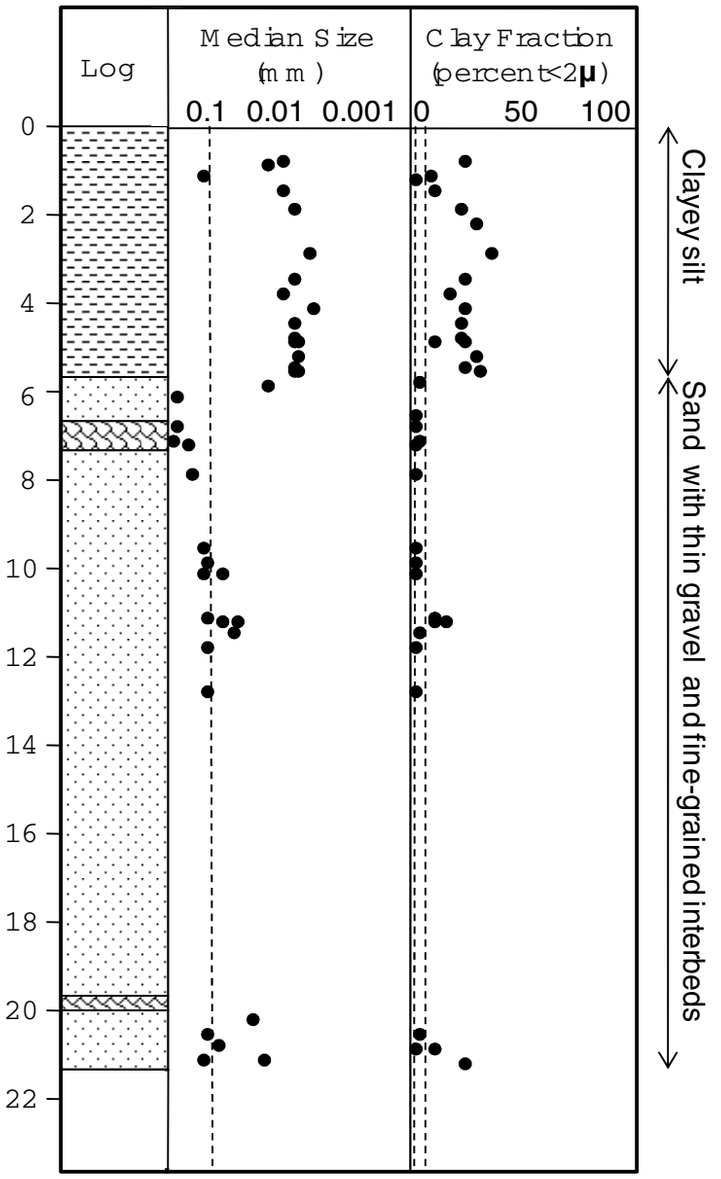


FIG. 1. Characteristics of subsurface soils associated with the USGS borehole data at the FSLC (after Miller et al. 1981).

MATERIAL PROPERTIES AND SAMPLE PREPARATION PROCEDURE

According to the grain size analysis (Fig. 2) and Atterberg's limits (PL=LL=25%) test results, the investigated soil can be qualified as a nonplastic silty-sand consisting of 77-88% sand and 12-23% fines (with 4-8% particles finer than 0.005 mm). The soil has a specific gravity (G_s) of 2.62.

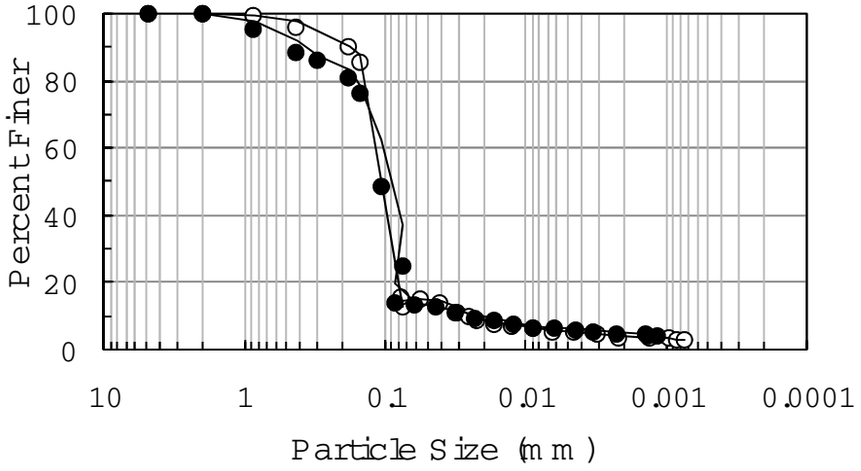


FIG. 2. Grain size distribution of Bonneville silty-sand.

Water sedimentation technique described by Ishihara (1993) has been used for sample preparation of laboratory triaxial specimens in this investigation in order to reproduce the lake environment in which the sediments were geologically formed; thus, the observed shear response is representative for the ground conditions associated with the occurrence of first-time liquefaction due to past earthquakes at this site. The tested cylindrical soil specimens were 50 mm in diameter and had an initial height of 120 mm. The samples were backpressure saturated at relatively low back-pressures (<200 kPa), ensuring a Skempton's *B* pore pressure parameter of 0.95 prior to consolidation. The specimens' void ratio after consolidation was 0.52 ± 0.02 associated with a relative density of $32.8\% \pm 6.2\%$.

EXPERIMENTAL PROGRAM

A fully automated cyclic triaxial equipment manufactured by Geocomp Corporation and currently available in the Department of Geology & Geophysics at the University of Utah was employed to study the post-liquefaction shear behavior of Bonneville silty-sand. The experimental program consisted of a series of two-phase triaxial tests involving a cyclic phase to trigger liquefaction of the soil element followed by an undrained monotonic shear phase on the liquefied soil specimen. The experiments were conducted on isotropically consolidated samples at initial effective confining

stresses (σ_0') of 50, 100 and 200 kPa.

The cyclic triaxial tests were performed at a loading frequency of 0.5 Hz. The applied cyclic stress ratio (CSR), defined as the maximum applied shear stress ($\sigma_d/2$) divided by the initial effective consolidation stress (σ_0') ranged within 0.2-0.45. Liquefaction during cyclic testing was assumed to occur when the effective normal stress attained a zero value (i.e., the excess pore pressure ratio (r_u) defined as the excess pore water pressure (Δu) divided by the initial effective consolidation stress (σ_0') reached 100%). Figure 3 shows representative time histories of cyclic shear resistance $q=(\sigma_1-\sigma_3)/2$ (with σ_1 and σ_3 representing the vertical and horizontal principal normal stresses), axial strain, (ε_a) and excess pore pressure ratio (r_u) for the last thirteen cycles before liquefaction in a cyclic triaxial test with σ_0' = 200 kPa and CSR=0.3. For most tested soil samples, the r_u = 100% condition was achieved at approximately 5% axial strain which typically occurred in extension (Fig. 3). The final pore water pressure in the liquefied soil element at the end of the undrained cyclic process together with the total confining stress acting on the specimen at the beginning of the cyclic triaxial testing represent the initial conditions for the second phase of the experiment, i.e., undrained monotonic shearing of the liquefied soil sample.

POST-LIQUEFACTION MONOTONIC TRIAXIAL TEST RESULTS AND RELATED IMPLICATIONS ON LATERAL GROUND DISPLACEMENTS AT FSLC

The response of liquefied Bonneville silty-sand subjected to undrained monotonic triaxial compression tests is illustrated in Figure 4 in terms of effective stress path, stress and pore water pressure relations with strain. Apparently, the liquefied soil exhibited a dilative behavior associated with gain in shear resistance due to decrease in excess pore water pressure with increasing axial strain in spite of a zero effective normal stress in the soil at the beginning of the monotonic phase. A similar behavior has been reported for Fraser River sand by Vaid and Thomas (1995) based on post-liquefaction triaxial monotonic test results. It is noteworthy though that during the initial stages of post-liquefaction undrained shear deformation, the soil experienced a perfectly plastic behavior under nearly zero shear stress for a range of axial strains up to approximately 2% (Fig.4*b*). This behavior of sand has been interpreted by Shamoto et al. (1998) indicating that once liquefaction takes place during cyclic loading soil grains lose contact due to the pore water pressure increase to the point that it equals the initial confining pressures therefore leading to zero effective confining stresses. However, during the application of monotonic shear, the liquefied specimen will undergo rearrangement of the grains under zero effective confining stresses for the range of plastic axial strains within 0-2%, as shown in Figure 4*b*. With increasing axial strain, the grains will eventually regain contact, subsequently the pore water pressure starts to decrease and a dilative behavior is seen in the soil response associated with the increase in effective confining stresses. The post-liquefaction undrained shear strength (S_u) in Figure 4 seems to be sensitive to the initial effective

consolidation stress (σ_0'). A very good positive linear correlation (R^2=0.998) between S_u and σ_0' can be noticed in Figure 5.

The S_u-σ_0' relationship derived from laboratory testing (Fig. 5) has been employed in an infinite slope analysis addressing the flow-slide susceptibility of a liquefied Bonneville silty-sand deposit. The safety factor against flow-slide for an infinite slope of angle β and depth of sliding surface H (Fig. 6) can be expressed as

$$F_s = S_u / \tau_0 \quad (1)$$

where τ_0 represents the static driving shear stress along the sliding surface.

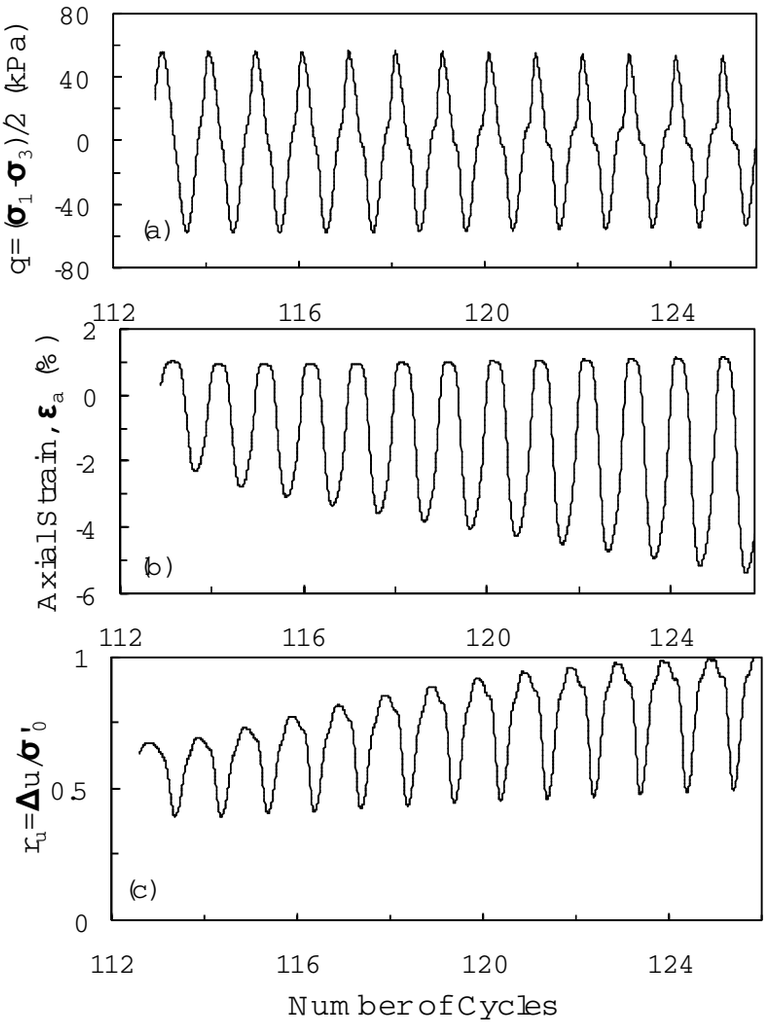


FIG. 3. Typical response of the analyzed silty-sand to cyclic loading: (a) variation of *q*, (b) variation of axial strain (ε_a), and (c) variation of excess pore pressure ratio $r_u = \Delta u / \sigma_0'$ versus the number of cycles.

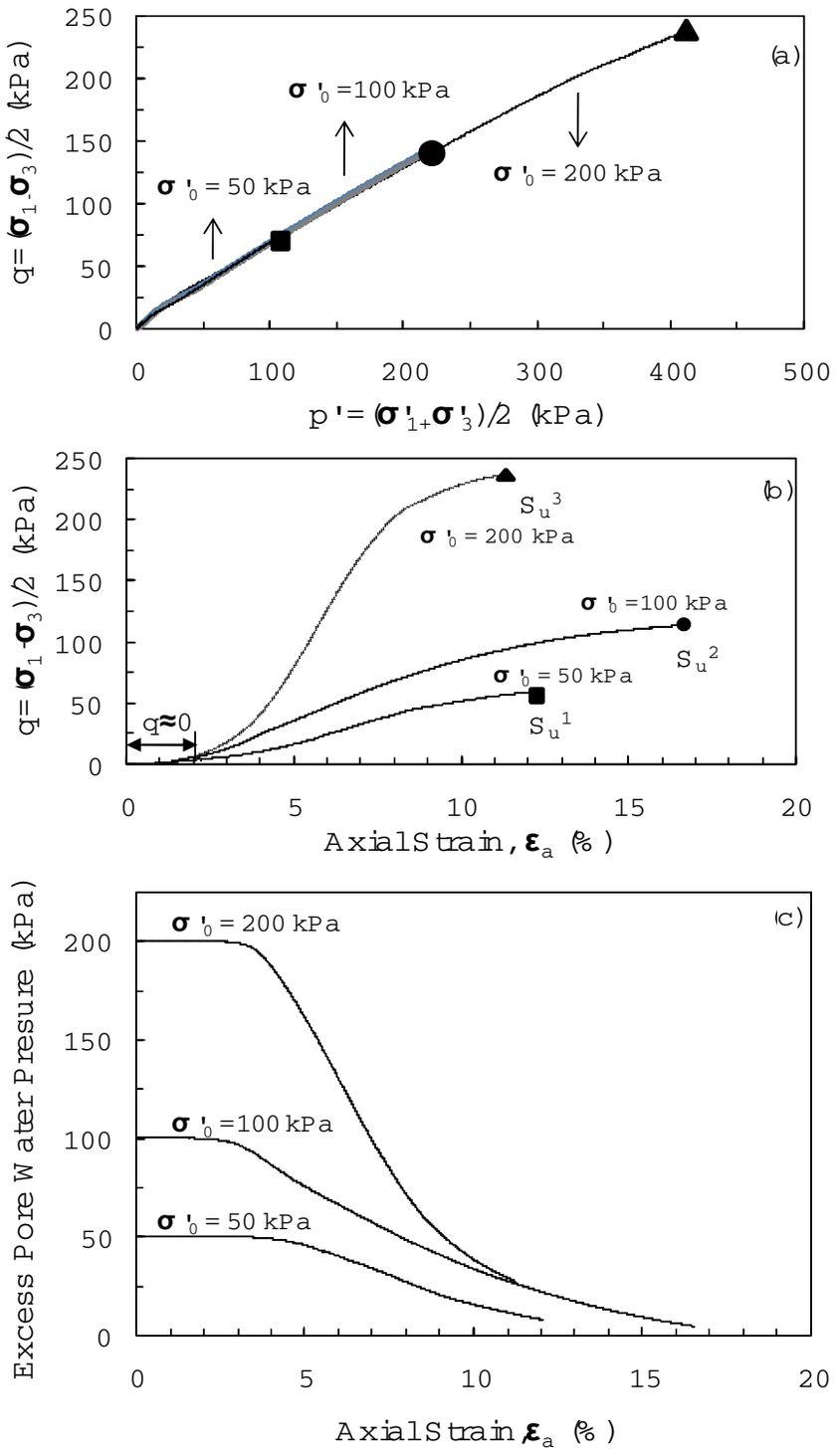


FIG. 4. Post-liquefaction monotonic shear response of Bonneville silty-sand: (a) effective stress path; (b) stress-strain response; (c) excess pore water pressure versus axial strain.

By combining the regression relationship in Figure 5

$$S_u = 1.174\sigma_0' \tag{2}$$

with the equations of τ_0 and σ_0' for a fully saturated infinite slope model (Fig. 6)

$$\tau_0 = \gamma H \sin\beta\cos\beta \tag{3}$$

$$\sigma_0' = (\gamma - \gamma_w) H \cos^2\beta \tag{4}$$

Equation (1) becomes

$$F_s = (\frac{\gamma - \gamma_w}{\gamma})(\frac{1.174}{\tan\beta}) \tag{5}$$

$$F_s = \frac{0.587}{\tan\beta} \tag{6}$$

where γ = 20 kN/m^3 is the unit weight of the sliding mass and γ_w = 10 kN/m^3 is the unit weight of water.

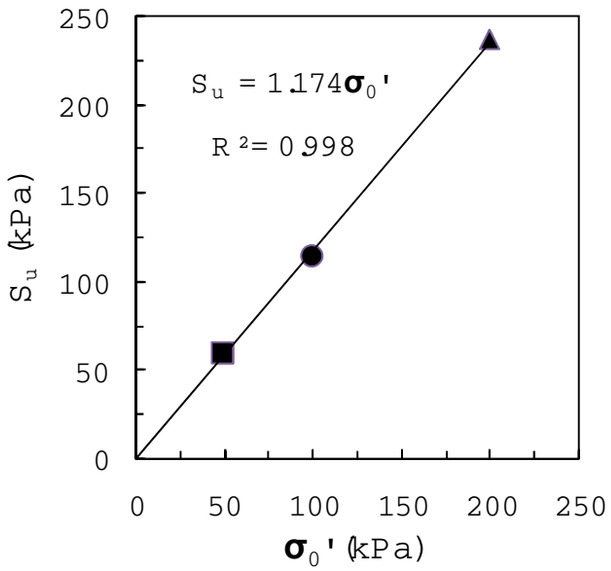


FIG. 5. Post-liquefaction shear strength (S_u) from monotonic triaxial tests in relation to initial effective consolidation stress (σ_0').

According to Equation (6), a flow-slide may be initiated under static conditions in liquefied Bonneville silty-sand when $\beta \geq 30.4°$. The average slope angle at the FSLC is however less than1°, thus much smaller than the minimum slope angle (30.4°) required for the onset of a flow-slide based on the post-liquefaction shear strength

from laboratory triaxial testing. For the nearly horizontal ground conditions, translated into $\tau_0 \approx 0$, characterizing the site surface topography at the FSLC, a 15 m thick liquefied Bonneville silty-sand deposit (as encountered in the USGS exploratory borehole at the Farmington site) would experience a lateral deformation not greater than 0.3 m based on a limited plastic shear strain of less than 2% under nearly zero shear stress as shown by the post-liquefaction triaxial test results (Fig. 4*b*).

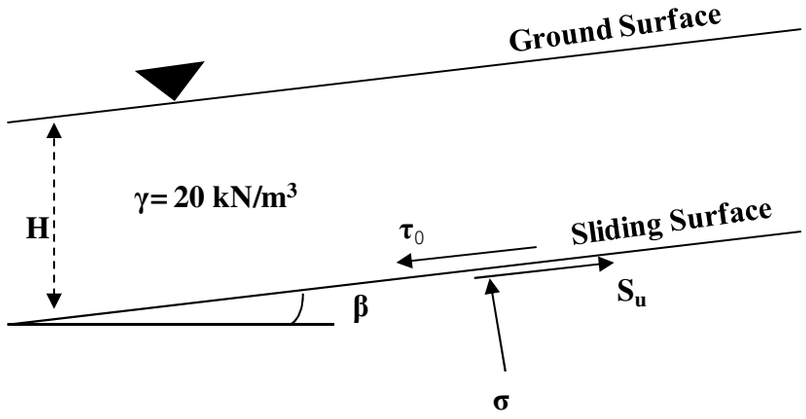


FIG. 6. Infinite slope model for flow-slide susceptibility assessment in a liquefied deposit.

CONCLUSIONS

Undrained monotonic triaxial compression tests on liquefied Bonneville silty-sand showed a dilative soil behavior and sensitivity of the post-liquefaction undrained shear strength to the initial effective consolidation stress. An infinite slope analysis based on the post-liquefaction undrained shear strength from laboratory testing resulted in a minimum slope angle required for the onset of a flow-slide much greater than the actual slope at the FSLC, Davis County, Utah. The interpretation based on the shear response of liquefied Bonneville silty-sand can explain the past earthquake-induced lateral spread phenomena in Farmington area. However further studies are required to address the mechanism associated with the occurrence of large lateral displacements due to the past earthquake-induced ground liquefaction at the FSLC characterized by a mild topography with an average slope gradient not greater than 1%.

REFERENCES

Hylland, M.D. (1997). "Hazard assessment of the Farmington siding landslide complex, Davis County, Utah." *Survey Notes*, UGS, Vol. 29 (2):1-2.

Ishihara, K. (1993). "Liquefaction and flow failure during earthquakes." Géotechnique, 43(3): 351–415.

Miller, R.D., Olsen, H.W., Erickson, G.S., Miller, C.H., and Odum, J.K. (1981).

"Basic data report of selected samples collected from six test holes at five sites in the Great Salt Lake and Utah Lake valleys, Utah." *U.S. Geological Survey Open-File Report* 81-179, 49 pp.

Shamoto, Y., Zhang, J., and Tokimatsu, K. (1998). "New Charts for Predicting Large Residual Post- Liquefaction Ground Deformation." *Soil Dynamics and Earthquake Engineering*, Elsevier, Vol. 17: 427-438.

Vaid, Y.P., and Thomas, J. (1995). "Liquefaction and postliquefaction behavior of sand." *Journal of Geotechnical Engineering*, ASCE 121(2), 163-173.

This page intentionally left blank

Probabilistic Assessment of Cyclic Soil Straining in Fine-Grained Soils

H. Tolga Bilge[1], and K. Onder Cetin[2].

[1]Graduate Student Researcher, Civil Engineering Dept., Middle East Technical University, 06531, Ankara, Turkey; htbilge@metu.edu.tr
[2]Assoc. Prof. Dr., Civil Engineering Dept., Middle East Technical University, 06531, Ankara, Turkey; onder@ce.metu.edu.tr

ABSTRACT: This paper presents a probabilistically-based semi-empirical model for the assessment of cyclically-induced shear and post-cyclic volumetric (reconsolidation) straining of saturated fine-grained soils. Consolidated-undrained, strain-controlled static, and stress-controlled cyclic triaxial tests have been performed on undisturbed silty and clayey samples for the purpose of compiling a database composed of induced maximum cyclic shear and post-cyclic volumetric strains along with Atterberg limits, natural moisture content, undrained static shear strength. The maximum likelihood methodology is used to develop limit-state models incorporating the selected descriptive variables for the estimation of cyclically-induced soil straining. Results are summarized in the form of a semi-empirical stochastic model which enables the estimation of cyclically-induced maximum shear and post-cyclic volumetric straining as a function of liquid limit, plasticity index, natural moisture content, undrained shear strength, cyclic shear stresses.

INTRODUCTION

Four decades have been passed since the pioneer studies were performed on cyclic behavior of fine-grained soils. Initially, cohesive soils had been considered to be resistant to cyclic loading due to cohesional component of shear strength. For fine-grained soils potential problems under dynamic loading were generally associated to the degradation of their stiffnesses (Thiers and Seed, 1968; Castro and Christian, 1976; Idriss et al., 1978; etc.). Increasing research interest was drawn in understanding their cyclic response, motivated after ground failure case histories of fine-grained soil sites following 1975 Haicheng and 1979 Tangshan earthquakes in China. As a result, Chinese Criteria (Wang, 1979) have been proposed to assess liquefaction susceptibility of clayey soils and these criteria had been widely used with further modifications (Seed et al., 1983; Finn et al., 1994). More recently, ground failure case histories after 1989 Loma-Prieta, 1994 Northridge, and more importantly, 1999 Kocaeli and 1999 Chi-Chi earthquakes have re-accelerated research studies on assessing cyclic mobility response of clayey soils as case histories from these

earthquakes highlighted that low plasticity silt-clay mixtures might significantly strain-soften which may in turn cause significant damage to overlying structural systems. As an alternative to Chinese Criteria, based on field observations and laboratory cyclic test results, Seed et al. (2003), Bray and Sancio (2006) and Boulanger and Idriss (2006) have recently recommended new criteria for the assessment of liquefaction triggering potential of fine-grained soils. Bray and Sancio (2006) have indicated that strength loss is significantly affected by the ratio (w_c / LL). Whereas, as an alternative Boulanger and Idriss (2006) have proposed liquidity index (LI) term defined as the ratio of the difference ($w_c - PL$) to PI. More recently, Boulanger and Idriss (2007) have also presented a methodology to asses triggering of "cyclic failure" in clayey soils. As discussed, previous efforts were confined to improve ability to assess identification of fine-grained soils susceptible to liquefaction. Meanwhile, on a separate stream, number of studies was performed aiming to determine the important factors affecting dynamic response of cohesive soils (Ishihara, 1986; Sun et al., 1988; etc). Vucetic and Dobry (1991) summarized earlier efforts and concluded that the most influential factor affecting dynamic behavior of cohesive soils was plasticity index (PI), they also proposed shear modulus degradation relationships as a function of PI.

As also illustrated by the presented literature, there exist a significant gap in the assessment of cyclically-induced deviatoric and volumetric straining of fine-grained soils. Previous studies mostly focused on cohesionless soils, due to significant cyclic straining potential of them. Some of these studies produced semi-empirical models for the assessment of cyclic straining in clean sands (e.g. Tokimatsu and Seed, 1984; Ishihara and Yoshimine, 1992). On the other hand, only a few attempts can be listed for the estimation of cyclically-induced straining in fine-grained soils. Ohara and Matsuda (1988) and Yasuhara et al. (2001) have proposed new constitutive models founded on cyclic test results along with one-dimensional consolidation theory for the prediction of cyclically induced ground settlements in normally- or over-consolidated clayey soils. The former method was primarily based on the generation of excess pore water pressure due to applied uniform strain cycles. Inspired by the theory of 1-D consolidation, volumetric strains were estimated in terms of excess pore water pressure, initial void ratio and the compression index induced by cyclic loading. However, due to difficulties in the estimation of model input parameters, which require cyclic soil testing, the proposed method had a limited impact on practical applications. Similarly, Yasuhara et al. (2001) proposed an alternative methodology which enabled the assessment of both immediate and post-cyclic settlements. In this method, volumetric strain is expressed as a function of cyclically-induced excess pore water pressure, PI and factor of safety against bearing capacity. Within the framework of one-dimensional consolidation theory, a constitutive model as well as chart solutions were presented, which require unpractical and time consuming, 2- or 3D dynamic numerical analyses for the determination of excess pore water pressure distribution within a soil media. As clearly presented, most studies have focused on volumetric straining and very few attempts exist regarding quantifying cyclically-induced shear straining in fine-grained soils.

Inspired by this gap, the aim of this study is defined as the development of a probabilistically-based semi-empirical, practical to use, model for the assessment of

maximum shear and post-cyclic volumetric straining of saturated fine-grained soils subjected to 20 uniform loading cycles, corresponding to equivalent number of cycles of a moment magnitude, M_w, 7.5 earthquake would produce (Liu et al., 2001). For this purpose, series of static and cyclic triaxial tests have been performed on undisturbed fine-grained soil samples. Details of the compilation and assessment efforts, as well as triaxial testing along with the presentation of the applied probabilistic framework, will be discussed in following sections.

TRIAXIAL TESTING PROGRAM AND EXPERIMENTAL RESULTS

In this study, undisturbed fine-grained soil specimens, sampled from variety of locations in Adapazari and Ordu cities of Turkey were used. Samples were by large diameter, thin-wall Shelby tubes which enabled the extraction of two identical specimens from each cross-section by using cylindrical thin-walled pipes. On the first specimen, consolidated undrained strain-controlled static triaxial test was performed while the second specimen was used for the stress-controlled cyclic triaxial test. At least one oedometer test was performed for each Shelby tube for the aim of understanding the stress history of specimens. Besides, simple index tests were performed to classify soil samples including Atterberg limits, specific gravity, grain size distribution and natural moisture content. The (LL) and (PI) values of the samples varied in the ranges of 27 to 83, and 5 to 53, respectively. Average values of the tested specimens LL and PI are 47 and 22, respectively. The ratio (w_c / LL) was documented to be in range of 0.4 to 1.1 with an average value of 0.72.

Static Triaxial Testing

Strain controlled static triaxial tests have been performed on 3.6 cm diameter and 7.1 cm long specimens, aiming to estimate undrained shear strengths, s_u. Consistent with ASTM D4767-88, the specimens were saturated by back-pressure until a B-value of minimum 0.96 is achieved. Specimens were normally-consolidated to a horizontal to vertical effective stress ratio varied in the range of 0.4 to 1.0, where the upper limit indicates isotropical consolidation. Horizontal effective consolidation stresses varied in the range of 60 to 150 kPa. Following the saturation and consolidation phases, axial stain at a rate of 1%/min is applied until the sample fails. During monotonic straining of specimens; change in i) cell pressure, ii) pore water pressure, iii) axial deformation in specimen, and iv) axial load were recorded at a sampling rate of 2 seconds.

For strain softening specimens, defining the peak undrained shear strength was rather trivial due to a well-defined peak deviatoric stress. Due to lack of a well defined peak deviatoric stress for strain-hardening materials, maximum stress obliquity (σ'_1 / σ'_3) criterion, consistent with the recommendations of ASTM D4767-88, was adopted. Estimated s_u values ranged from 30 to 220 kPa covering soft to stiff soil range. Each test has been carried until specimen exhibited a pronounced contractive or dilative response.

An illustrative test result of an ML ($LL = 31$ and $PI = 6$) type specimen, consolidated isotropically under an effective confinement pressure of 100 kPa is

presented in Figure 1. Peak deviatoric stress was observed at around 12 % axial strain, and estimated as 277 kPa. The maximum stress obliquity was recorded as 5.5 % axial strain and corresponding deviatoric stress was determined as 205 kPa from the corresponding stress-strain plot. Luckily, both the peak deviatoric stress and maximum obliquity criteria produced comparable s_u values (~ 138 kPa).

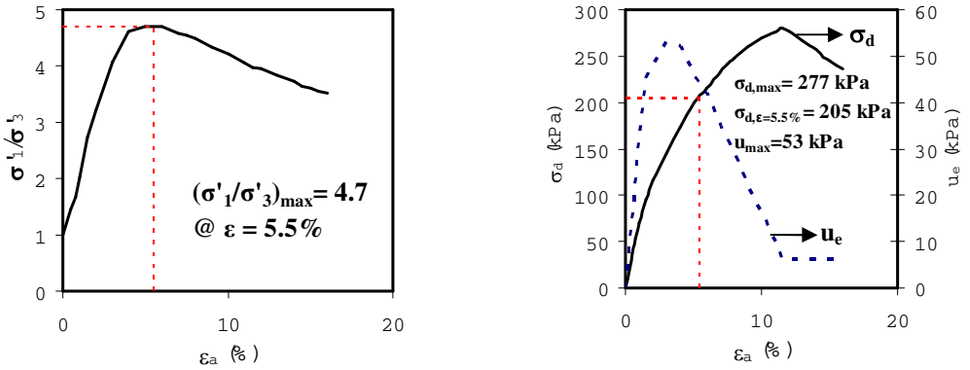


FIG. 1. A sample static triaxial test on ML type specimen (LL=31, PI=6)

Cyclic Triaxial Testing

Stress-controlled cyclic triaxial tests were performed to assess cyclic straining behavior of fine- grained soil samples. Compared to static testing, for the cyclic testing identical specimen saturation and consolidation stages were followed hoping to lead to identical stress states for the identical soil. In cyclic loading stage, the deviatoric loads were applied as a fraction of the undrained shear strength, which had already been determined by static tests performed on the identical sample. The frequency of cyclic loading was selected as 1 Hz. As previously stated by various researchers (e.g.: Zergoun and Vaid, 1994), for high frequency loading, it is unfortunately not possible to monitor the effective stress response in fine-grained soils due to delayed pore water pressure equalization. Unfortunately, a slower loading might let the creep-induced dominate over cyclic straining of high plasticity soils (Zavoral and Campanella, 1994). 1 Hz loading was judged to be the optimum value to the solution of problem. Samples were subjected to 20 deviatoric loading cycles simulating the duration of an moment magnitude 7.5 earthquake. During cyclic loading, change in i) cell pressure, ii) pore water pressure, iii) axial deformation in specimen and iv) applied axial load were recorded. After 20th cycle, loading was stopped and sample was reconsolidated to its initial confining stress state, during which volumetric straining was continued to be recorded. Recorded axial strain measurements were scaled by a factor of 1.5 to convert them to equivalent shear strain values, as recommended by Ishihara and Yoshimine (1992).

An illustrative cyclic test result is presented in Figure 2 for an ML soil specimen with PI of 9. Its w_c / LL value was estimated as 0.9, fulfilling potentially liquefiable criteria of Seed et al. (2003) and Bray and Sancio (2006). The sample was consolidated isotropically under a confinement pressure of 110 kPa, and subjected to cyclic deviatoric stress of 65 kPa. In the presented four-way plots, cyclic response of

the sample in the form of pore water pressure generation, shear strain accumulation as well as dilation and contraction transitions under cyclic shearing can be followed. Load term, τ_{cyc}/s_u, is expressed as the ratio of applied cyclic shear stress to undrained shear strength. Maximum double amplitude cyclic shear strain is determined from the lower-right figure as 20.1 %.

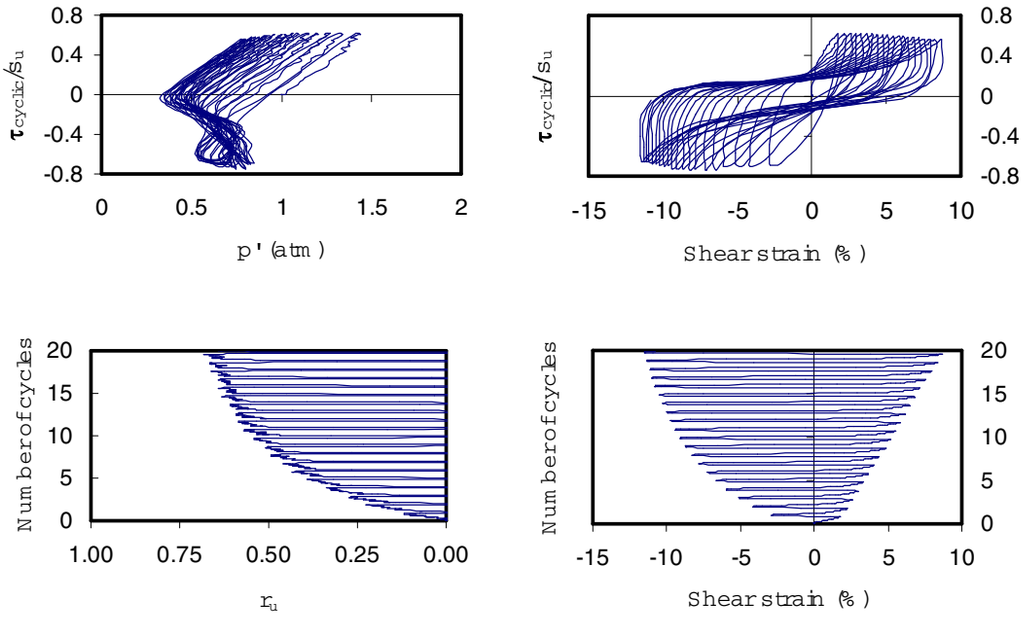


FIG. 2. A sample cyclic triaxial test on ML type specimen (PI=9, w_c/LL=0.9)

For anisotropically consolidated specimens, static shear stress (τ_{st}) existed besides applied cyclic shear stress (τ_{cyc}). The ratio of static to cyclic shear stresses ranged from 0.0 to 2.0 where 0.0 has meant isotropical consolidation.

Figure 3 summarizes the resulting database including the maximum double amplitude cyclic shear strain (γ_{max}) and post-cyclic volumetric strain (ε_v) values recorded during and after 20 loading cycles, PI, w_c/LL. If the undrained shear strengths of samples are selected as the capacity term, then the ratio of τ_{cyc}/s_u (x-axes) and the ratio of τ_{st}/s_u (y-axes) on Figure 3, indicate the percentage of capacity used during cyclic and static loading phases, respectively.

Discussion of Experimental Results

Due to inevitable variability in controlling parameters, (i.e.: PI, w_c/LL, τ_{cyc}/s_u, τ_{st}/s_u) of natural soil samples, unfortunately interpretations of results were not easy compared to the ones of controlled tests where only one controlling factor was typically changed at a time. However, after studying test results which were presented in Figure 3 carefully, following observations could be made.

i. Consistent with previous findings in literature, it is observed that PI is a controlling parameter for cyclic straining. As PI increases, resistance of material to cyclic stresses also increases and resulting strains decrease. Based upon our preliminary test results, specimens having $PI > 15$, cyclic shear strains do not exceed 7.5 % for $\tau_{cyc} / s_u \leq 0.50$.

ii. The amplitude of τ_{cyc} / s_u is important as it is the cyclic demand term. Below a threshold τ_{cyc} / s_u value of 0.45, cyclic stresses can not accumulate significant shear strains (i.e. $\gamma_{max} < 2.5$ %).

iii. The ratio of applied static stress to cyclic stress is important as it determines the occurrence of stress reversal. As indicated in previous studies (e.g.: Konrad and Wagg, 1993) presence of stress reversals may significantly increase cyclically-induced shear strains. Beyond a value of 0.6, the amplitude of cyclic shear strains is limited.

Last but not least, the ratio of soil samples' natural moisture content to its liquid limit (w_c / LL) was found to be a significant parameter for the estimation of shear strain (or flow) potential of soils, consistent with the findings of recent liquefaction triggering studies. It was concluded that shear straining become smaller as w_c / LL decreases, and below a value of 0.7, no significant soil shear straining was observed.

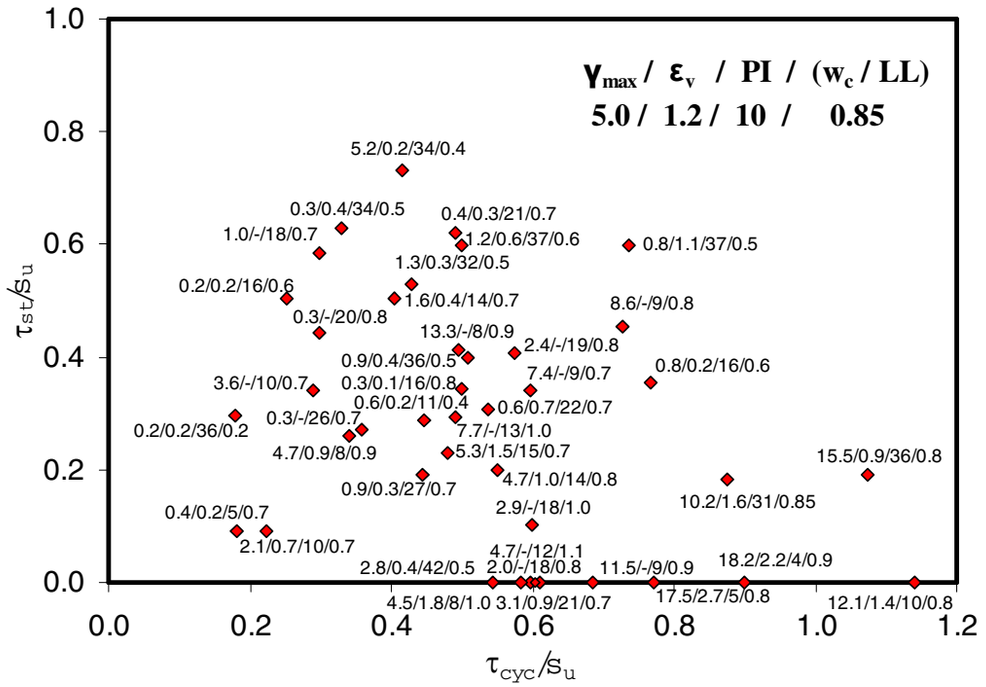


FIG. 3. Cyclically-induced strain database used in this study.

As illustrated in Figure 4, post-cyclic volumetric straining is strongly correlated to the maximum cyclic shear straining as also observed in cohesionless soil response (Ishihara and Yoshimine, 1992). Thus, if γ_{max} is estimated, as will be discussed next, ε_v can also be calculated through the relationship given in Figure 4.

Despite limited number of available test results of this ongoing study, it is attempted to develop a probabilistic framework for the illustrative assessment of cyclic soil straining in fine-grained soils as it will be discussed next.

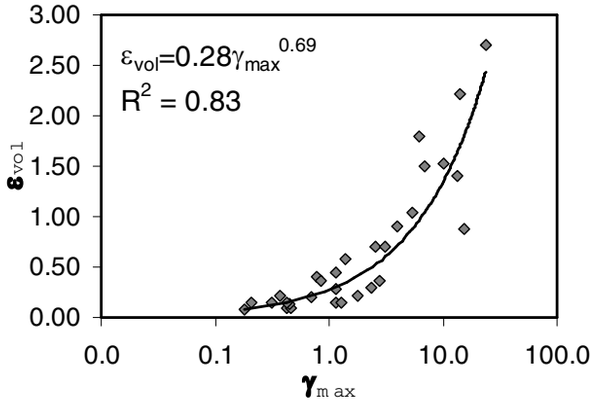


FIG. 4. Relationship between γ_{max} and ε_v.

DEVELOPMENT OF PROBABILISTIC MODELS FOR CYCLIC STRAIN PREDICTION

The first step in developing a probabilistic model is to select a limit state expression that captures the essential parameters of the problem. The model for the limit state function has the general form g = g (**x, Θ**) where x is a set of descriptive parameters and Θ is the set of unknown model parameters. Inspired by trends in the presented database, controlling parameters are selected and then following model is adopted as the limit state function for maximum cyclic double amplitude shear strain (γ_{max}):

$$g_{\gamma_{max}}\left(\frac{w_c}{LL}, PI, \frac{\tau_{cyc}}{s_u}, \frac{\tau_{st}}{s_u}, \gamma_{max}, \Theta\right) = ln(\gamma_{max}) - ln\left(\theta_1 \cdot \frac{\theta_2^{\left(\theta_3 \cdot \frac{w_c}{LL}\right)}}{ln(PI)} \cdot \frac{\theta_4 - \sqrt{\left(\frac{\tau_{st}}{s_u} - \theta_5\right)^2 + \left(\frac{\tau_{cyc}}{s_u} - \theta_6\right)^2}}{\theta_4 - \theta_7}\right) \pm \varepsilon_{\gamma_{max}} \quad \textbf{(1)}$$

where θ_i are the set of unknown model parameters.

The proposed model include a random model correction term (ε) to account for the facts that i) possible missing descriptive parameters with influence on cyclic straining may exist; and ii) the adopted mathematical expression may not have the ideal functional form (various models were tested and the functional form producing the best fit to observed behavioral trends were adopted). It is reasonable and also convenient to assume that ε has normal distribution with zero mean for the aim of producing an unbiased model (i.e., one that in the average makes correct predictions). The standard deviation of ε, denoted as σ_ε, however is unknown and must be estimated. The set of unknown parameters of the model, therefore, is $\Theta = (\boldsymbol{\theta}, \sigma_\varepsilon)$.

Assuming the maximum shear strain values of each cyclic shear test to be statistically independent, the likelihood function for "n" tests can be written as the product of possibilities of the observations, i.e.,

$$L_{\gamma_{max}}(\boldsymbol{\theta},\sigma_{\varepsilon}) = \prod_{i=1}^{n} P\left[g_{\gamma_{max}}\left(\frac{w_c}{LL_i}, PI_i, \frac{\tau_{st}}{s_{u\ i}}, \frac{\tau_{cyc}}{s_{u\ i}}, \varepsilon_{\gamma_{max},i}, \boldsymbol{\theta}\right) = 0 \right] \quad \textbf{(2)}$$

Suppose the values of $(w_c / LL)_i$, PI_i, $(\tau_{st} / s_u)_i$, and $(\tau_{cyc} / s_u)_i$ at the each data point are exact, i.e. no measurement error is present, noting that $g(...) = \hat{g}(...) + \varepsilon_i$ has the normal distribution with mean $\hat{g}$ and standard deviation σ_ε, then the likelihood function can be written as:

$$L_{\gamma_{max}}(\boldsymbol{\theta},\sigma_{\varepsilon}) = \prod_{i=1}^{n} \varphi\left[\frac{\hat{g}_{\gamma_{max}}\left(\frac{w_c}{LL_i}, PI_i, \frac{\tau_{st}}{s_{u\ i}}, \frac{\tau_{cyc}}{s_{u\ i}}, \boldsymbol{\theta}\right)}{\sigma_{\varepsilon_{\gamma_{max}}}} \right] \quad \textbf{(3)}$$

where $\varphi[.]$ is the standard normal probability density function. Note that the above is a function of the unknown parameters. As part of maximum likelihood methodology, the coefficients which are estimated to maximize the likelihood functions given in Equation 3 are presented in Table 1. Cetin et al. (2002) have further discussed application of maximum likelihood methodology and model parameter determination.

Table 1. Maximum Shear Strain Model Parameters

Θ_1	θ_2	θ_3	θ_4	θ_5	θ_6	θ_7	σ_ε
20.17	22.88	0.75	0.84	0.72	-0.60	6.04	0.73

CONCLUSIONS

Within the confines of this paper it is intended to develop a probabilistically- based semi-empirical model to predict cyclically induced maximum shear strains and post-cyclic volumetric strains in fine-grained soils. For this purpose, series of strain-controlled static and stress-controlled cyclic triaxial tests were performed on undisturbed silty and clayey samples. The important controlling parameters (descriptive variables) of the cyclic straining problem were concluded to be PI, w_c / LL, τ_{cyc} / s_u, and τ_{st} / s_u. The maximum likelihood methodology was used to develop limit-state model incorporating these important descriptive variables for the assessment of cyclically-induced straining problem. The proposed model for the estimation of maximum double amplitude shear strains is given in Equation 4. The comparisons of predicted and observed maximum shear strain values were presented in Figure 5. Predictions within an accuracy factor of 2 were judged to be promising. Proposed model yields slightly overestimated predictions in small strain range ($\gamma_{max} < 2.5\%$), whereas for moderate and large strain ranges (i.e., $2.5 \le \gamma_{max} \le 15\%$ and $\gamma_{max} > 15\%$ respectively) proposed method slightly underestimates the actual measured strains. However, in the overall the proposed model captured the general trend.

$$ln(\gamma_{max}) = ln\left(20.17 \cdot \frac{22.88^{\left(0.75\cdot\frac{w_c}{LL}\right)}}{ln(PI)} \cdot \frac{0.84 - \sqrt{\left(\frac{\tau_{st}}{s_u} - 0.72\right)^2 + \left(\frac{\tau_{cyc}}{s_u} - (-0.60)\right)^2}}{0.84 - 6.04} \right) \pm 0.73 \qquad \textbf{(4)}$$

Following the estimation of maximum double amplitude shear strain, post-cyclic volumetric strain , ε_v can be estimated as follows , as also shown in Figure 4;

$$\varepsilon_v = 0.28 \cdot \gamma_{max}^{0.68} \qquad \textbf{(5)}$$

In Figure 6, predicted and measured post-cyclic volumetric strains are compared based on maximum cyclic shear strain observations.

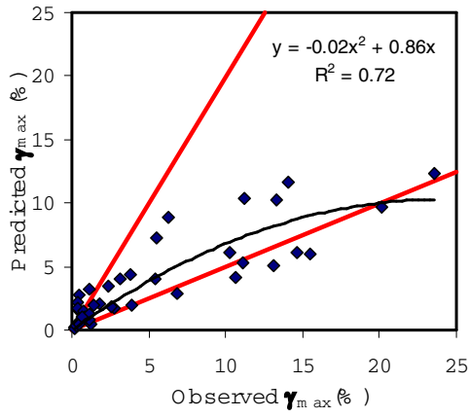


FIG. 5. Comparison between observed and predicted γ_{max}.

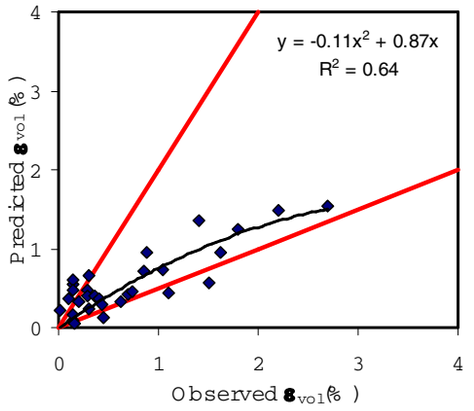


FIG. 6. Comparison between observed and predicted ε_{vol}.

As the concluding remark, we would like to clarify our intention. All these preliminary findings were based on limited number of test results as part of our ongoing research studies. More samples are going to be tested at the i) plasticity ranges of 20< PI <60, and ii) stress conditions corresponding to (τ_{cyc} / s_u >0.8) and (τ_{st} / s_u >0.7) where our current database has slight gaps. After these, we believe that the resulting model will be more general and powerful and help us to estimate the extent of lateral deformations (spreading) and reconsolidation settlements at soft cohesive soil sites subjected to cyclic loading. However, even these limited test results assessed within a probabilistic framework revealed that the proposed semi-empirical model is promising.

REFERENCES

ASTM D4767-88 Standard Test Method for Consolidated-Undrained Triaxial Test on Cohesive Soils.

Boulanger, R.W. and Idriss, I.M. (2006). "Liquefaction susceptibility criteria for silts and clays." *J. Geotechnical & Geoenv. Engrg.*, Vol. 132 (11): 1413-1426.

Boulanger, R.W. and Idriss I.M. (2007). "Evaluation of cyclic softening in silts and clays." *J. Geotechnical & Geoenv. Engrg.*, Vol. 133 (6): 641-652.

Bray, J.D. and Sancio B.S. (2006). "Assessment of the liquefaction susceptibility of fine-grained soils." *J. Geotechnical & Geoenv. Engrg.*, Vol. 132 (9): 1165-1177.

Castro, G. and Christian, J.T. (1976). "Shear strength of soils and cyclic loading." *J. Geotechnical Engrg.*, Vol. 102 (9): 887-894.

Cetin, K.O., DerKiureghian, A., and Seed, R.B. (2002). "Probabilistic models for the initiation of seismic soil liquefaction." *Struct.* Safety, 24(1), 67-82.

Finn, W.D.L., Ledbetter, R. H., and Wu, G. (1994). "Liquefaction in silty soils: design and analysis." Ground Failures under Seismic Conditions, GSP 44, ASCE, 51-76.

Idriss, I.M., Dobry, R. and Singh, R.D. (1978). "Nonlinear behavior of soft clays during cyclic loading." *J. Geotechnical Engrg.*, Vol. 104 (12): 1427-1447.

Ishihara K. (1986). "Evaluation of soil properties for use in earthquake response analysis." Geomechanical Modeling in Engineering Practice, Dingar R and Studer JA, eds., A. Balkema, Rotterdam, Netherlands, 241-275.

Ishihara K and Yoshimine M. (1992). "Evaluation of settlements in sand deposits following liquefaction during earthquakes." *Soils & Foundations*, 32(1): 861-878.

Liu, H., Stewart, J.P., Abrahamson N. A., and Moriwaki, Y. (2001). "Equivalent number of stress cycles for stress cycles for soil liquefaction analysis." *J. Geotechnical & Geoenv. Engrg.*, Vol. 127(12): 1017-1026.

Ohara, S. and Matsuda, H. (1988). "Study on the settlement of saturated clay layer induced by cyclic shear." *Soils & Foundations*, 28(3): 103-113.

Seed, H. B., Idriss, I. M., and Arango, I. (1983). "Evaluation of liquefaction potential using field performance data." *J. Geotechnical Engrg.,* 109(3): 458-482.

Seed, R.B., Cetin, K.O., Moss, R.E.S., Kammerer, A. Wu, J., Pestana, J., Riemer, M., Sancio, R.B., Bray, R.E. and Faris, A. (2003). "Recent advances in soil liquefaction engineering: A unified and consistent framework." Keynote presentation, 26th Annual ASCE Los Angeles Geotechnical Spring Seminar, Long Beach, California.

Sun, J.I., Golesorkhi, R. and Seed, H.B. (1988). "Dynamic moduli and damping ratios for cohesive soils." Report No. EERC 88-15, Univ. of California, Berkeley.

Thiers, G.R. and Seed, H.B. (1968). "Strength and stress-strain characteristics of clays subjected to seismic loading conditions." Vibration Effects of Earthquakes on Soils and Foundations, ASTM STP 450, American Society for Testing and Materials.

Tokimatsu, K. and Seed, H.B. (1984). "Simplified procedure for the evaluation of settlements in clean sands." Report No. UCB/EERC-84/16, Earthquake Engineering Research Center, Univ. of California, Berkeley.

Vucetic, M. and Dobry, R. (1991). "Effect of soil plasticity on cyclic response." *J. Geotechnical Engrg.*, Vol. 117(1): 89-107

Wang, W. (1979). "Some findings in soil liquefaction engineering." Water Conservancy and Hydroelectric Power Scientific Research Institute, Beijing, China.

Yasuhara, K., Murakami, S., Toyota, N. and Hyde, A.F.L. (2001). "Settlements in fine-grained soils under cyclic loading." *Soils & Foundations*, 41(6) 25-36.

Zavoral, D.Z. and Campanella, R.G. (1994). "Frequency effects on damping modulus of cohesive soil," Dynamic Geotechnical Testing II, ASTM STP 1213, eds., Ebelhar, R.J., Drnevich, V.P. and Kutter, B.L.

Zergoun, M and Vaid, Y.P. (1994). "Effective stress response of clay to undrained cyclic loading." *Canadian Geotechnical Journal*, 31: 714-727.

Shaking Table Test on a Large Specimen of Mailiao Silty Sand

Tzou-Shin Ueng[1], M.ASCE, Chia-Han Chen[2], Cheng-Fu Tsou[3] and Yi-Cheng Chen[3]

[1] Professor, Department of Civil Engineering, National Taiwan University, Taipei, Taiwan; ueng@ntu.edu.tw
[2] PhD Student, Department of Civil Engineering, National Taiwan University, Taipei, Taiwan; chiaham@ncree.org.tw
[3] Former Graduate Students, Department of Civil Engineering, National Taiwan University, Taipei, Taiwan.

ABSTRACT: Based on the results of assessment of various preparation methods, the specimen of the Mailiao silty sand was prepared by the staged sedimentation method in the large biaxial laminar shear box of 1880 × 1880 × 1520 mm (L × W × H) at the National Center for Research on Earthquake Engineering (NCREE). It was found that there is no significant difference of the densities and fines contents of sand at various depths, except a very thin layer (< 1 mm) of soil with a higher fines content at the top of the specimen. The P-wave velocity measurement confirmed the saturation of the silty sand specimen. The relatively low permeability and high compressibility of the Mailiao silty sand resulted in a longer duration of dissipation of generated pore water pressure and a larger volumetric strain after shaking compared with those of the clean Vietnam sand. Sand boils were observed when water rushed out through the thin relatively impervious layer on the surface of the specimen.

INTRODUCTION

In the past, the studies on the undrained stress-strain behavior and seismic behavior of clean sand have been studied in the laboratory. However, natural sandy soils usually contain some amount of fines that may result in a different behavior from that of clean sand. Sand with fines has been tested in the laboratory using triaxial apparatus, simple shear device, and torsional shear apparatus under regular or irregular dynamic loads in recently years (e.g., Yamamuro and Lade 1997; Thevanayagam et al. 2000; Amini and Qi 2000; Huang et al. 2005). The stress conditions and deformations in the small soil elements in these types of tests are significantly affected by the boundary condition due to the limitations of the loading devices and the size of the specimens. A large-scale laminar biaxial shear box on the 5 m × 5 m shaking table at the National Center for Research on Earthquake Engineering (NCREE) in Taiwan has thus been developed to test a large soil specimen under one- and two-dimensional (multidirectional) earthquake shakings. This study presents the preparation method and preliminary shaking table test

results of large specimens of Mailiao silty sand in the biaxial laminar shear box.

BIAXIAL LAMINAR SHEAR BOX

The biaxial laminar shear box developed at NCREE, as shown schematically in Fig. 1 is composed of 15 layers of sliding frames. Each layer consists of two nested frames, an inner frame (1880 mm × 1880 mm) and an outer frame (1940 mm × 2340 mm). Both frames are made of a special aluminum alloy with 30 mm in thickness and 80 mm in height, except the uppermost layer that has a height of 100 mm. These 15 layers of frames are separately supported on the surrounding rigid steel walls with a gap of 20 mm between adjacent layers. A 2-mm thick silicone membrane was placed inside the box to provide a watertight shear box to contain saturated sand. Thus, a sand specimen of 1880 mm × 1880 mm × 1520 mm can be placed inside the inner frames.

Linear guideways consisting of sliding rails and bearing blocks are used to allow an almost frictionless horizontal movement without vertical motions. Each outer frame is supported by the sliding rails built on two opposite sides of the outer rigid walls. The bearing blocks on the outer frame allow its movement in the X direction with minimal friction. Similarly, sliding rails are also provided for each outer frame to support the inner frame of the same layer such that the inner frame can move in the Y direction with respect to the outer frame. With these 15 nested layers of inner and outer frames supported independently on the rigid walls, the soil at each depth can move in a multidirectional fashion in the horizontal plane without torsion in response to the wave actions induced by the shaking table.

Details of the design, manufacturing, and tests of the performance of the laminar shear box can be found in Ueng et al. (2006).

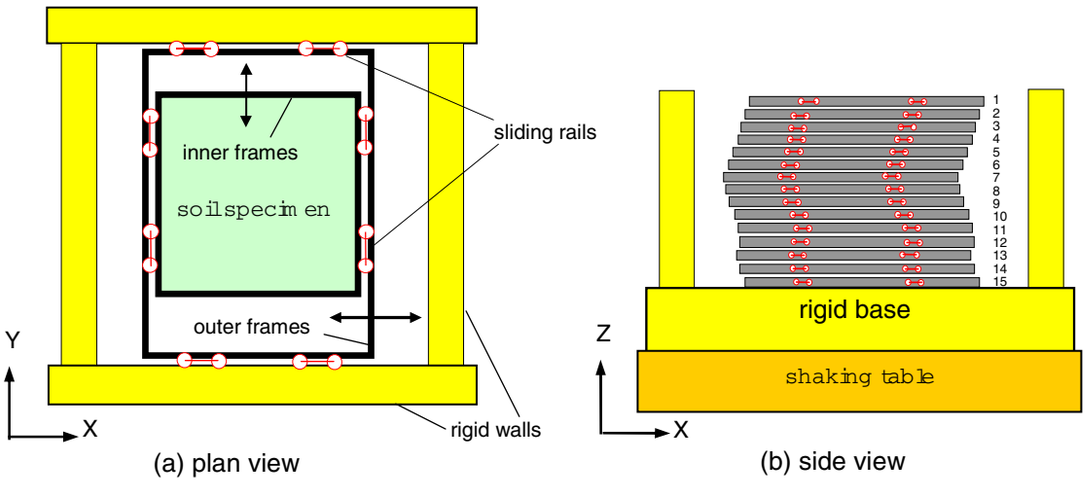


FIG. 1. Schematic drawings of the biaxial laminar shear box

SAMPLE PREPARATION

Mailiao silty sand is a typical soil in the reclamation industrial sites in the western coastal area of Taiwan. The grain shape of the sand is mainly sub-angular and flaky. It is more compressible and friable than silica sand. Depending on the location and depth, this soil at site contains a wide range of fines from about 5 % up to 80% with a lower fines content mostly 8 – 30 % in the shallower (< 15 m) depth (Chen and Huang 1997). The fines content of the sand obtained for this study is about 6 – 9 %. The representative grain size distribution of the sand is shown in Figure 2. The minimum and maximum void ratio of this sand are 0.586 and 1.162, respectively, according to ASTM D4253 Method 1B (wet method) and ASTM D4254 Method C. The fines content was obtained according to ASTM D1140 because of the crumbly characteristic of Mailiao silty sand.

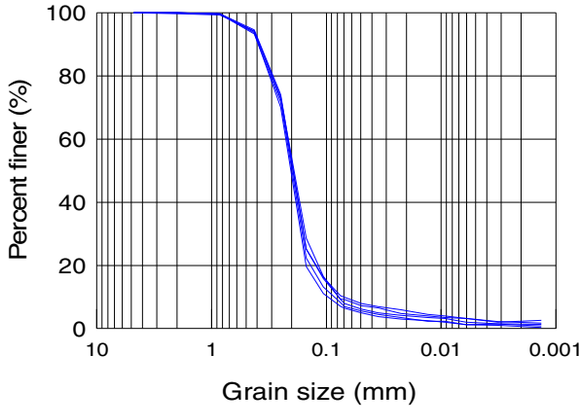


FIG. 2. Grain size distribution of Mailiao silty sand in this study

Preparation methods for a large saturation specimen of clean sand to obtain a uniform and saturated specimen have been reported by many researchers (e.g., Chang 2002; Ueng et al. 2003). However, very little information is available for preparing a large saturated specimen of silty sand to obtain the desired uniformity and density. In order to evaluate the preparation method for a large saturated specimen in the laminar shear box using the moist Mailiao silty sand, a series of experiments in a smaller glass container (500 mm × 230 mm × 350 mm) were conducted using various preparation methods, including wet sedimentation method using dry or moist silty sand, pre-mixture filled method and staged sedimentation method. It was found that the staged sedimentation method could obtain a better specimen according to the experiment results (Tsou 2006). Except a thin layer of sand with a higher fines content on the top of specimen, there was no significant difference of fines content at other depths of sand specimen. Thus, the staged sedimentation method was adopted in this study. The preparation of a large specimen in the laminar shear box is as follows.

A special pluviator with internal dimensions of 1600 mm × 1600 mm × 600 mm (L × W × H) was designed for preparing the Mailiao silty sand specimen into the laminar shear box by using the staged sedimentation method. The pluviator, as shown in Figs 3 and 4, is composed of:

- A container to house the needed volume of sand (about 1.0 Mg in mass at each stage) to fill the shear box. The bottom of the container is consisted of eight vanes with dimensions of 1600 mm × 200 mm.
- Eight vanes hinged on single side of the internal reinforcements in longitudinal direction to rotate rapidly when the hooks are released.
- Two transmission shafts consisted of two rods and sixteen hooks to control the hinged vanes to open simultaneously to dump the sand uniformly into the shear box.

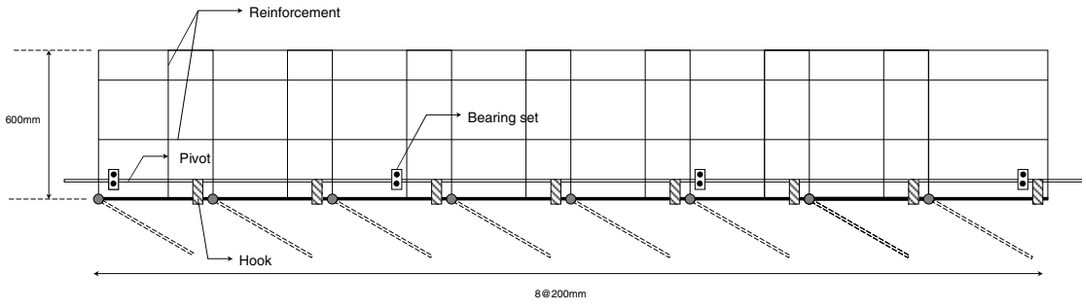


FIG. 3. Schematic drawing of the pluviator



FIG. 4. The picture of the pluviator with opened vanes

The moist Mailiao silty sand with a mass of 1.0 Mg and an average water content of 7.2% were dropped into the laminar shear box filled with water to a pre-calculated depth at first as shown in Fig. 5. After an interval of about 30 minutes for the major sedimentation, the laminar box was filled with water slowly to the calculated depth based on the measurements of water level and the height of the sand specimen after the first step. Another stage of preparation was conducted by repeating the aforementioned sand dumping and water filling. It took seven stages to complete a Mailiao silty sand specimen of about 1.350 m in height in this study. The saturation of the specimen prepared by this method was verified by measuring P-wave velocity across the specimen horizontally at different depths. A small steel ball hit the sand specimen at the

20-mm gaps between the frames and the arrival times of the P-wave were measured using the accelerometers close to the hitting point and across the specimen. Figure 6 shows the results of P-wave velocity measurements at two vertical sections of the sand specimen. It can be seen that the sand was well saturated with the P-wave velocities between 1450 m/s and 1566 m/s at various depths including the water above the sand surface. In order to directly measure the density, fines content and uniformity of the large sand specimen, short thin-walled tube samples (≈ 150 mm in length and 73 mm in diameter) were taken at various locations and depths inside the shear box. These thin-walled tubes were pushed into the sand at various elevations during the excavation of the sand from the shear box, and the samples were taken by carefully removing the surrounding soil. Figure 7 shows the dry densities and fines contents of the sand specimen at different depths immediately after specimen preparation. The results indicated that the sample was well saturated and the uniformity of density and fines content of the sample was acceptable.



FIG. 5. Setup of the pluviator during sample preparation

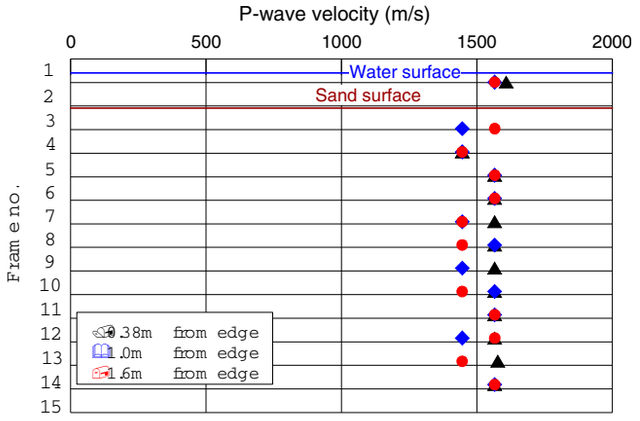


FIG. 6. P-wave velocities of sand specimen after preparation

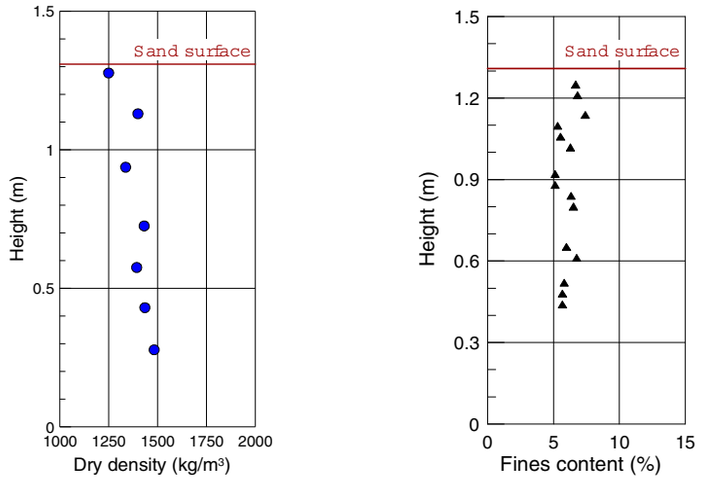


FIG. 7. Density and fines content of Mailiao silty sand after preparation

SHAKING TABLE TEST

Transducers for displacement and acceleration measurements were placed at various locations and depths on the outside rigid walls, the outer frames for X-direction motions, and the inner frames for Y-direction motions. In addition, mini-piezometers and mini-accelerometers were installed inside the box for pore water pressure and acceleration measurements at different locations and depths before placing the sand into the shear box. Two settlement plates were also placed to measure the surface settlements during the shakings. The height of the sand surface was also measured manually after each shaking test so that the settlement of the sand specimen can be calculated. Figure 8 shows Mailiao silty sand specimen on the shaking table.

A series of shaking table tests have been conducted on Mailiao silty sand specimen in the biaxial laminar shear box at NCREE on two separate dates, May and November 2006. Various one- and multi-directional input motions were imposed by the shaking table. The input motions included sinusoidal (1 Hz, 2 Hz, 4 Hz and 8 Hz) accelerations, with amplitudes (A_{max}) from 0.03g to 0.2g in X and/or Y directions. In the two-dimensional (multidirectional) shaking, there is a 90° phase difference between the input acceleration in X and Y directions, i.e., a circular or ellipse motion was applied. The acceleration, full and reduced amplitudes, recorded at seismograph stations in Chi-Chi Earthquake and Kobe Earthquake were also applied in X and/or Y directions.

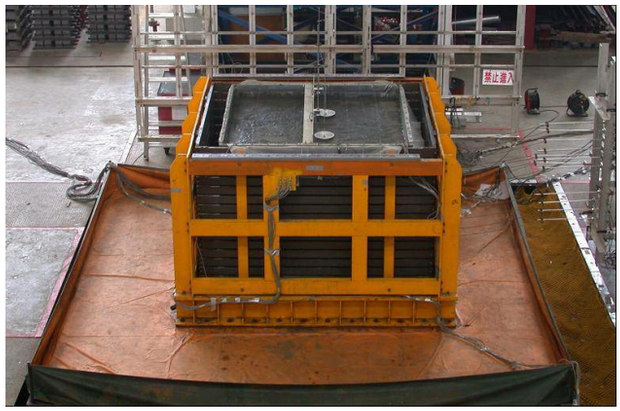


FIG. 8. Mailiao silty sand specimen in the shear box on the shaking table

TEST RESULTS

Liquefaction Phenomenon

Sand boil is a well-known feature after liquefaction owing to the expelled water carrying sand particles with it to the ground surface through volcano-like vents. It is rarely seen in the uniform saturated specimen of clean sand under any kind of shakings due to its high permeability and uniformity. Figure 9 shows that sand boils occurred on the surface of the Mailiao silty sand specimen after liquefaction. The thin layer of sand with a high fines content on the top of the sand specimen would possibly be one of the reasons for this phenomenon. Hence, the thin layer of sand containing high fines was scraped from the surface of sand specimen before the shaking table tests in November 2006. The phenomenon of sand boil did not occur at the beginning of shaking but reappeared after a thin layer of high-fines-content sand was formed due to the fines carried up from the specimen during water pressure dissipation.

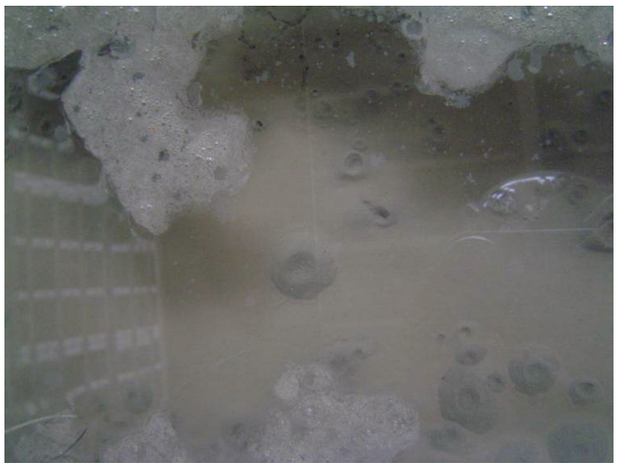
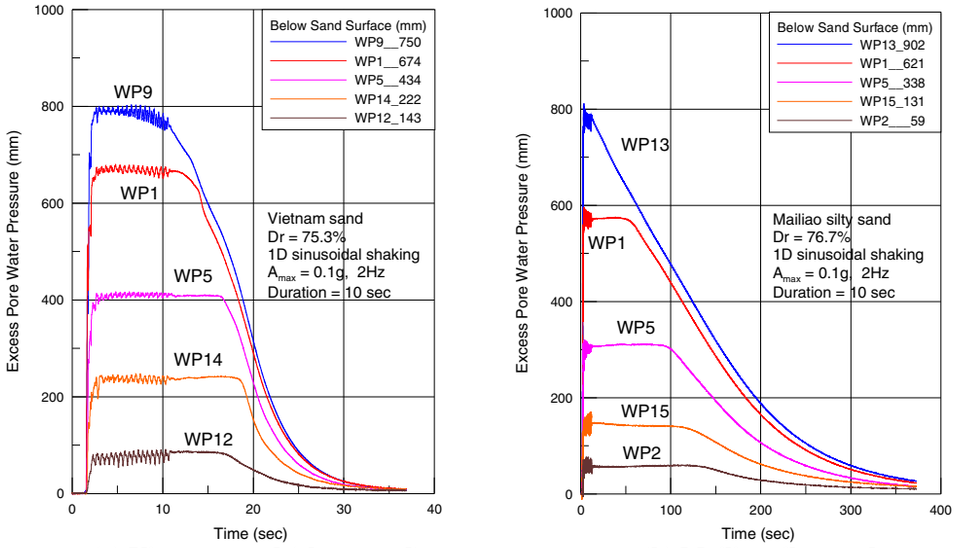


FIG. 9. Sand boils on the sand surface of the specimen

Pore Water Pressure Generation and Settlement

A comparison of pore water pressure changes at five different depths in the specimens of clean Vietnam silica sand and Mailiao silty sand during one-dimensional sinusoidal shaking with an amplitude of A_{max} = 0.1g is shown in Fig. 10. It can be seen that the excess pore water pressure in Mailiao silty sand takes a longer time to dissipate than that in Vietnam sand. According to the measurements of the mini-piezometers, the time of pore water pressure dissipation of Mailiao silty sand is about 15 times longer than that of Vietnam sand. The permeability test results also show that the ratio of permeability of Vietnam sand to that of Mailiao silty sand is approximate 15 (Chen 2007). It illustrates the significant effect of permeability on pore water pressure dissipation after shaking.

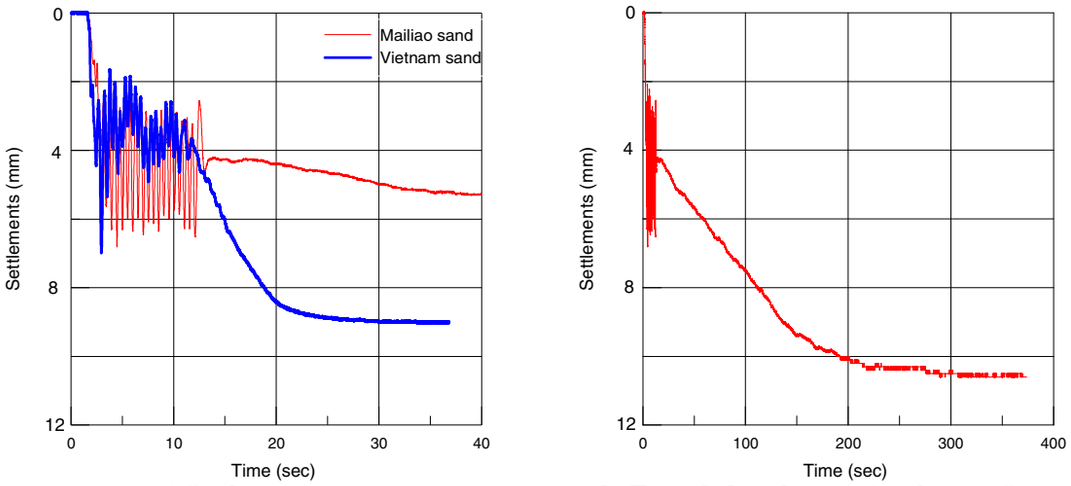


(a) Vietnam sand (clean sand) **(b) Mailiao silty sand**

FIG. 10. Water pressure changes during 1D shaking

Under the same shaking conditions, the measured surface settlements of Vietnam sand and Mailiao silty sand specimens are also shown in Fig. 11 with final settlements of 9.0 mm and 10.6 mm, respectively after dissipation of excess pore water pressure. Comparing with Fig. 10, the rate of the settlement after shaking is related to the rate of dissipation of excess pore water pressure.

The liquefaction depth of the specimen is determined based on the measurements of mini-piezometers and accelerometers on the inner frames (Ueng et al. 2007). They are 1050 mm and 767 mm for Vietnam sand and Mailiao silty sand specimens, respectively. This implies a higher liquefaction resistance for Mailiao silty sand. With consideration of the liquefaction depth, the volumetric strains induced by liquefaction are 0.85 % for Vietnam sand and 1.38 % for Mailiao silty sand. The greater volumetric strain of Mailiao silty sand could be due to its higher compressibility.



(a) Settlement versus time

(b) Extended settlement time history for Mailiao sand specimen

FIG. 11. Surface settlement of sand specimen during 1D shaking

CONCLUSIONS

A large laminar shear box with a specimen size of 1880 mm × 1880 mm × 1520 mm at NCREE was used to study the dynamic response of Mailiao silty sand with fines. A special pluviator was designed to prepare the Mailiao silty sand specimen by the staged sedimentation method. The uniformity, density, fines content and saturation were checked by thin-walled tube sampling and P-wave velocity measurements, and found satisfactory. A series of one- and multi-directional shaking table tests were performed on saturated Mailiao silty sand in the shear box. The test results show that the relatively low permeability of the Mailiao silty sand resulted in longer duration of dissipation of generated pore water pressure and surface settlement compared with those of the clean Vietnam silica sand. The sand boils were observed when there was liquefaction of the Mailiao silty sand. Further analyses of the test results and more shaking table test are under way.

ACKNOWLEDGMENTS

This study is supported by National Center for Research on Earthquake Engineering, Taiwan. The authors wish to thank the assistances of Mr. S. Y. Wang and engineers at NCREE in conducting tests on the shaking table.

REFERENCES

Amini, F., and Qi, G.Z. (2000). "Liquefaction testing of stratified silty sands," *J. Geotechnical and Geoenvironmental Engineering*, 126(3): 208-217.

Chang, W.J. (2002) "Development of an in situ dynamic liquefaction test", *PhD Dissertation*, University of Texas at Austin.

Chen Y.C. (2007). "Shaking table test on large saturated Mailiao sand specimens," *MS Thesis,* Department of Civil Engineering, National Taiwan University, Taipei, Taiwan. (in Chinese)

Chen, C.H. and Huang, F.K. (1997) "Liquefaction Risk Evaluation and Microtremor Measurements and Analyses for Reclaimed Soils in the Yunlin Industrial Area," National Center for Research on Earthquake Engineering, Report No. NCREE-97-013. (in Chinese)

Huang, A.B., Lin, C.P., Ku, C.S., Tsai, J.S., Lee, D.H. and Lin. P.S. (2005) "Cyclic behavior analysis of the silty sand in central western Taiwan," *Sino-Geotechnics*, 103: 5-30. (in Chinese)

Thevanayagam, S., Fiorillo, M., and Liang, J. (2000). "Effect of non-plastic fines on undrained cyclic strength of silty sands," *Soil Dynamics and Liquefaction 2000*, GSP No. 107, ASCE: 77-91.

Tsou C.F. (2006). "Sample preparation of Mailiao sand in large scale biaxial shear box on shaking table," *MS Thesis*, Department of Civil Engineering, National Taiwan University, Taipei, Taiwan. (in Chinese)

Ueng, T.S., Chen, C.H., Peng, L.H. and Li, W.C. (2003). "Large-Scale Shear Box Soil Liquefaction Tests on Shaking Table (II)—Preparation of Large Sand Specimen and Preliminary Shaking Table Tests," *Report No. NCREE-03-042,* National Center for Research on Earthquake Engineering, Taipei, Taiwan. (in Chinese)

Ueng, T.S., Wang, M.H., Chen, M.H., Chen, C.H. and Peng, L.H. (2006). "A large biaxial shear box for shaking table tests on saturated sand," *Geotechnical Testing J.* ASTM, 29(1): 1-8.

Ueng, T.S., Wu, C.W., Cheng, H.W. and Chen, C.H. (2007). "Settlements of saturated clean sand deposits in shaking table tests," Under preparation.

Yamamuro, J.A. and Lade, P.V. (1997). "Static liquefaction of very loose sands," *Canadian Geotechnical J.* 34(6): 905-917.

Recent Developments in Ground Improvement for Mitigation of Seismic Risk to Existing Embankment Dams

James K. Mitchell[1], Distinguished M. ASCE

[1]University Distinguished Prof. Emeritus, Virginia Tech; Patton Hall, Blacksburg, VA 24061-0105, jkm@vt.edu

ABSTRACT: The majority of large embankment dams in the United States in operation today were constructed over half a century ago – before major earthquakes in 1964 jump-started geotechnical earthquake engineering and initiated systematic evaluations of the seismic stability of these earth structures and the soil deposits on which they are built. Many dams have required strengthening owing to increased levels of anticipated shaking or inadequate resistance of the embankment or foundation materials. Soil stabilization and ground improvement methods have included buttress fills, removal and replacement of weak foundation soils, deep dynamic compaction, vibro-compaction, vibro-replacement, explosive compaction, deep soil mixing, jet grouting, compaction grouting, and permeation grouting. In most cases the design strategy is to strengthen the dam to prevent vertical crest deformations that would exceed the freeboard and transverse cracking to depths greater than the remaining freeboard after the earthquake. Special attention must also be given to assuring that seepage paths cannot form along conduits or other discontinuities. In many cases stabilization to prevent excessive upstream deformations is costly and difficult, so in recent years there have been several cases where ground improvement and construction of stabilizing trenches and berms has been confined to the downstream slope and foundation area.

INTRODUCTION

The majority of major dams in operation today were constructed many years ago – well before the earthquakes of 1964 in Anchorage Alaska and Niigata, Japan, jump-started geotechnical earthquake engineering. Accordingly, only thereafter was it realized that there could be severe risks to dams that had not been appreciated at the time of their original design and construction. The near catastrophe following the failure of the Lower San Fernando Dam in California in 1971 served to accelerate the re-evaluation of the seismic stability of many dams. Mitigation of seismic risk has now become one of the major applications of different methods of soil stabilization and ground improvement, and this is the subject of this paper.

The scope of this paper includes:

- Types of dam failure or distress that can develop under seismic loading
- Why so many embankment dams require remediation and the basis for prioritizing them for fixing
- The process that is usually followed in selecting among the available ground improvement methods.
- Trends in mitigation strategy and ground improvement that have developed in recent years.
- Some unresolved issues in dam safety and risk mitigation that impact ground improvement decisions and designs.
- Some thoughts about future developments – both with respect to the methods of ground improvement and the remediation strategies.

Case history information is used to illustrate points under discussion. The evaluation of site seismicity and the details of liquefaction and ground response analysis, except as they relate to the case history examples, are beyond the scope of this paper.

TYPES OF DAMAGE TO EMBANKMENT DAMS CAUSED BY EARTHQUAKES

Seismic shaking of an embankment dam can cause settlements, liquefaction, and deformations. These damages can, in turn, lead to:

- Loss of freeboard and reservoir over topping as a result of:
  - Compression of embankment and foundation materials
  - Crest settlement resulting from loss of embankment stability
  - Crest settlement resulting from liquefaction in the foundation and lateral spreading
  - Combinations of the above three effects
- Seepage and piping through the embankment as a result of cracking of the core
- Seepage and piping through the foundation as a result of cracking of cutoffs and seepage control blankets
- Piping along conduits as a result of differential ground movements
- Loss of reservoir control as a result of spillway and spillway gate malfunction
- Loss of reservoir control as a result of damage to intake and outlets works structures

Focus in this paper is on ground improvement for mitigation of liquefaction risk and prevention of dam failures resulting from stability failure, lateral spreading, and excessive crest settlement leading to overtopping and/or the formation of transverse cracks that extend below the reservoir water level.

The results of a study of 54 embankment dams by Swaisgood (1998) indicated the correlation between crest settlement and peak ground acceleration shown in Fig. 1. Earthquake shaking for four additional cases, where there were liquefaction failures, resulted in considerably greater crest settlement than shown in Fig. 1. Overall, vertical crest settlement appears to provide a good measure of the damage sustained by an embankment dam, and even in the absence of liquefaction, the settlements can exceed a foot or two for high embankments on thick layers of alluvium subjected to high peak

ground acceleration.

Several types of ground modification are available for preventing excessive compression, liquefaction, and loss of stability, and in principle, therefore, for preventing each of the listed failure modes. For each project, specific attention must be directed at each failure mode to be sure that there is compatibility between the method, its implementation, and the goals to be achieved.

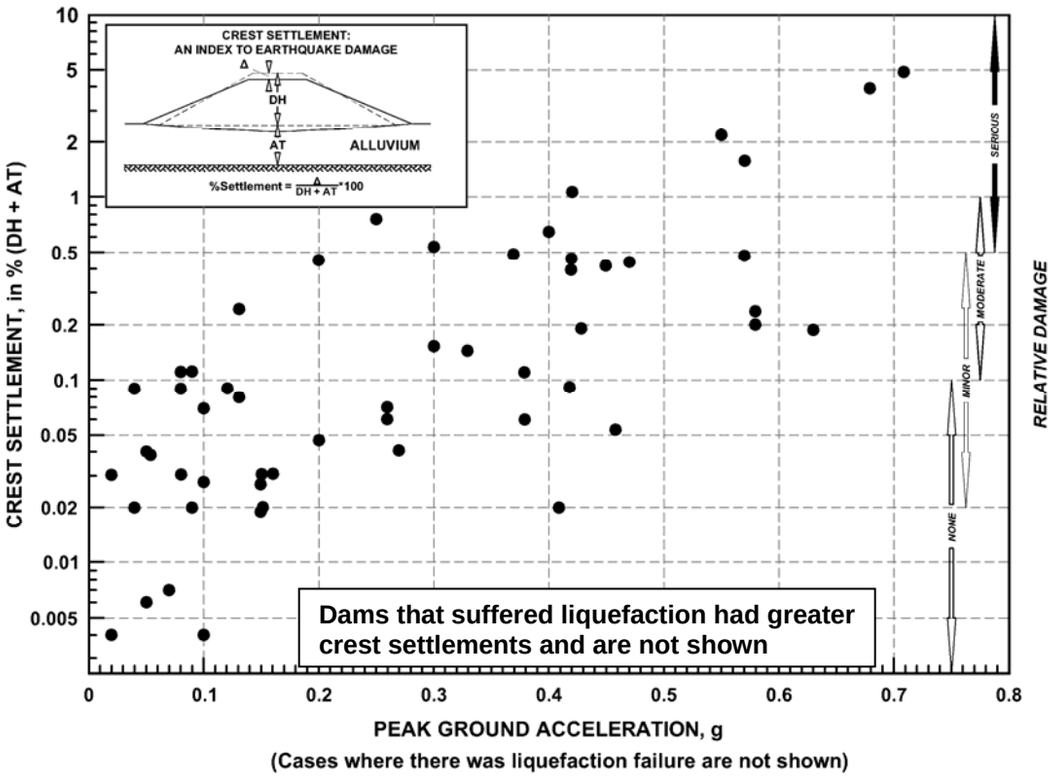


Fig. 1. Embankment dam crest settlement as a function of peak acceleration. (Modified and redrawn from Swaisgood, 1998)

WHY MORE DAMS REQUIRE STRENGTHENING

Within the past 40 years seismic safety evaluations of existing flood control and water storage embankment dams by government owners and operators; e.g., the U.S. Army Corps of Engineers, the U.S. Bureau of Reclamation, and by federal and state regulatory agencies, public and private dam owners and providers of hydropower and water supplies, have identified many dams that require modification to assure adequate life safety, minimal property damage and environmental protection. There are several reasons for this, including:

- Many dams were built on sedimentary deposits that are now known to be susceptible to liquefaction.
- Many dams were built using methods and materials that are now known to be especially vulnerable to liquefaction and large deformations, most notably hydraulic fill dams. A photograph of San Pablo Dam near Oakland, California during construction in 1919 is shown in Fig. 2. This process of dumping the

materials from suspension produces a coarser-grained shell with finer-grained core materials. These materials remain loose and unconsolidated and, if cohesionless, they are susceptible to liquefaction and large deformations in earthquakes.

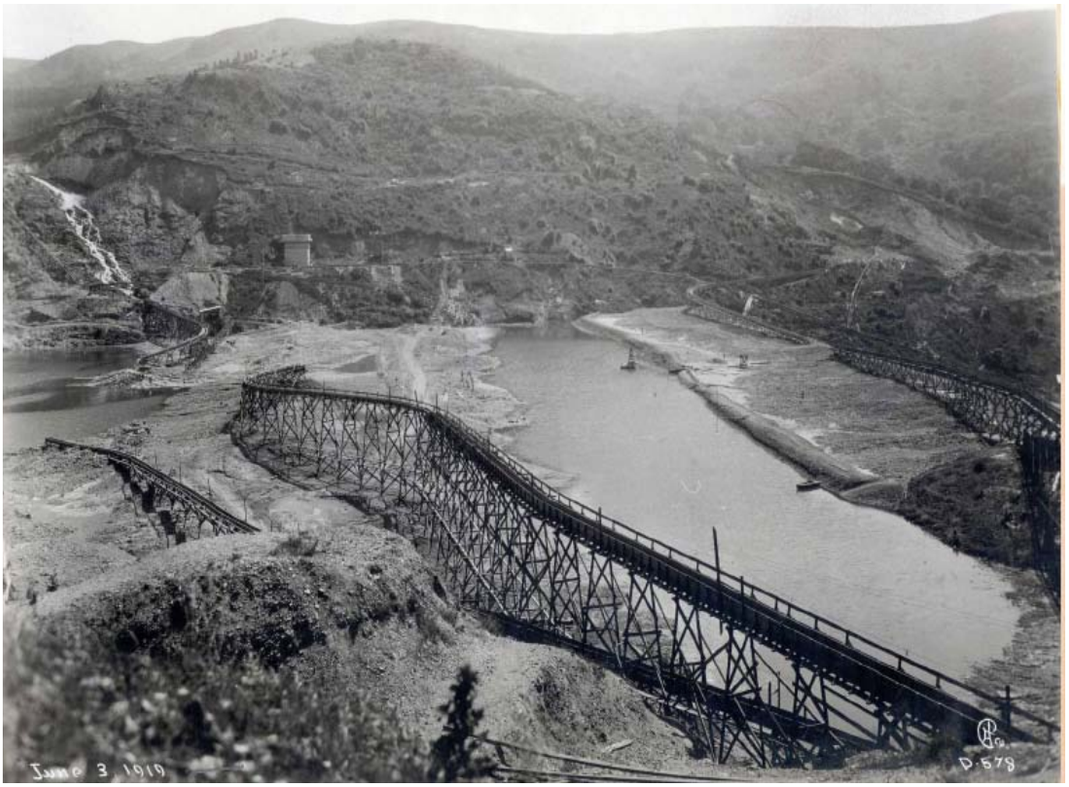


Fig. 2. Hydraulic filling during construction of San Pablo Dam near Oakland, CA in 1919 (Photo courtesy of East Bay Municipal Utility District)

- Better understanding of embankment response and the failure modes that can develop as a result of earthquake shaking.
- Escalation of estimated seismic risk, resulting from:
  - Better (and usually more conservative) seismic hazard evaluation
  - Better site characterization
  - Better identification of critical conditions and improved understanding of conditions that can lead to failure
- Escalation of required levels of protection. In recognition of the great life loss that could be caused by most catastrophic dam failures, higher standards of performance have been established; i.e., acceptable factors of safety have increased and acceptable failure probabilities have decreased.
- Larger populations now reside in the floodplains downstream of many dams
- Aging dam inventory. Many of the dams in the U.S. that have been and are now being remediated were constructed during the period 1940-1960.
- Stricter regulatory requirements

STEPS IN THE EVALUATION OF DAM SAFETY

There are more embankment dams with seismic safety deficiencies than it has been possible to remediate with available time and resources. Most agencies have established procedures for periodic evaluation of their dam inventory and prioritizing those requiring modification. A logical series of steps to do this includes the following:

1. Review the project history – site conditions, construction records, as-built conditions, maintenance records, etc.
2. Assess the current conditions of the embankment and appurtenant structures
3. Determine the site seismicity and estimate the ground motions using state-of-knowledge procedures.
4. Develop best estimate characterization models for the dam and its foundation
5. Do simple, approximate analyses for estimation of possible liquefaction, deformation, and cracking failure modes.
6. If the results indicate the possibility of failure or near-failure by any conceivable failure mode, then more refined analyses may be required
7. If it is evident that further analyses will not make the problem go away, then the seriousness of the problems must be assessed using more detailed investigations and analyses and development of remedial strategies initiated.

Formal risk analyses, used by some agencies, are very helpful in helping risk analysis team members identify and focus on all conceivable failure modes, quantify the levels of risk reduction that can be achieved by different remediation strategies, and prioritize the different projects for construction as resources become available.

PROBLEMS IN EXISITING SITE AND DAM CHARACTERIZATION

Accurate identification and characterization of the materials, their current properties, and their locations within an existing dam and its foundation are perhaps the most important elements of any dam safety assessment. This information is essential to the design, development, and implementation of ground improvement for correction of seismic deficiencies. Original design and construction reports and subsequent inspection records are the usual starting points. Information from these sources is supplemented by geophysical measurements, sampling and testing, and in-situ testing. Standard penetration tests (SPT) and cone penetration tests (CPT) are most commonly used, with Becker penetration tests (BPT) used when potentially liquefiable soils containing gravel and cobbles are encountered. Shear wave velocity measurements are often made to provide supplemental, corroborating data.

The data from different sources and in-situ test results do not always provide a clear, or even consistent, indication of liquefaction potential or post liquefaction residual strength, both of which are essential for reliable analysis of current seismic stability and prediction of post-treatment deformations and dam safety. The problem is exacerbated by the uncertainties in correlations between the penetration resistance values derived from different test types and the many empirical corrections used to deduce the needed parameters. In such situations it may be necessary to accept the most pessimistic view, leading to overly-conservative remedial treatments.

An Illustrative Case History about Characterization

San Pablo Dam, a 170 ft high hydraulic fill dam near Oakland, California was constructed between 1916 and 1920. Hydraulic filling operations during 1919 are shown in Fig. 2. Prior seismic safety evaluations of this dam were based on the assumption that much of the material in both the embankment fill and in the alluvial/colluvial foundation was potentially liquefiable. Compacted fill buttresses were constructed on the downstream embankment slope in 1967 and on the upstream embankment slope in 1979. More recent studies led to the conclusion that the dam is unsafe for the currently specified earthquake loading. A feasibility level upgrade modification was developed that consists of a larger downstream buttress fill and foundation strengthening using cement deep soil mixing panels (CDSM).

As a part of the development of suitable final design, a comprehensive field investigation was made that included CPT tests, SPT tests, boring and sampling, and laboratory tests. The results of this program indicated that the embankment, except for the fine-grained impervious core, consists largely of a "lumpy", overconsolidated clay material that is not at all similar to liquefiable hydraulic fill sand. Almost all of the samples classified as (CL), (CH), or (ML). The alluvial/colluvial foundation has been shown to be much more clayey than had been anticipated as well.

Based on this new characterization, liquefaction within the embankment is considered unlikely, and potential liquefaction zone in the foundation is not as large as had been anticipated. Dynamic deformation analyses using FLAC have shown that embankment movements can be kept within acceptable levels using a smaller buttress than originally proposed, leading to significant material, cost, and time savings for the necessary construction. A currently proposed cross section showing the location of the new buttress and CDSM treatment zone is shown in Fig. 3. Descriptions of the site investigations, materials characterization, and recommended design details are given by Moriwaki, et al. (2007) in a separate paper to this conference.

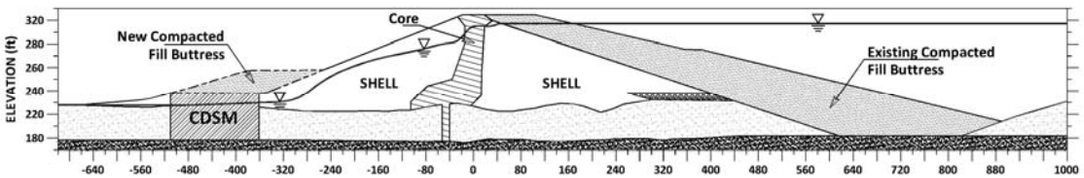


Fig. 3. Proposed buttress fill and CDSM foundation improvement for assuring seismic safety at San Pablo Dam (modified from TNM, 2007)

GROUND IMPROVEMENT METHODS AND DESIGN

Available Methods

Ground treatment methods used for strengthening existing embankment dams and their foundations are shown in Fig. 4 in relation to different soil types, and listed in Table 1 along with some relevant characteristics and considerations that influence their selection for specific projects. Comprehensive information describing the technology of all of these methods is readily accessible; e.g., Mitchell (1981), USACE (1999), ASCE (1978, 1987, 1997), Moseley and Kirsch (2004), and literature provided by ground improvement specialty contractors.

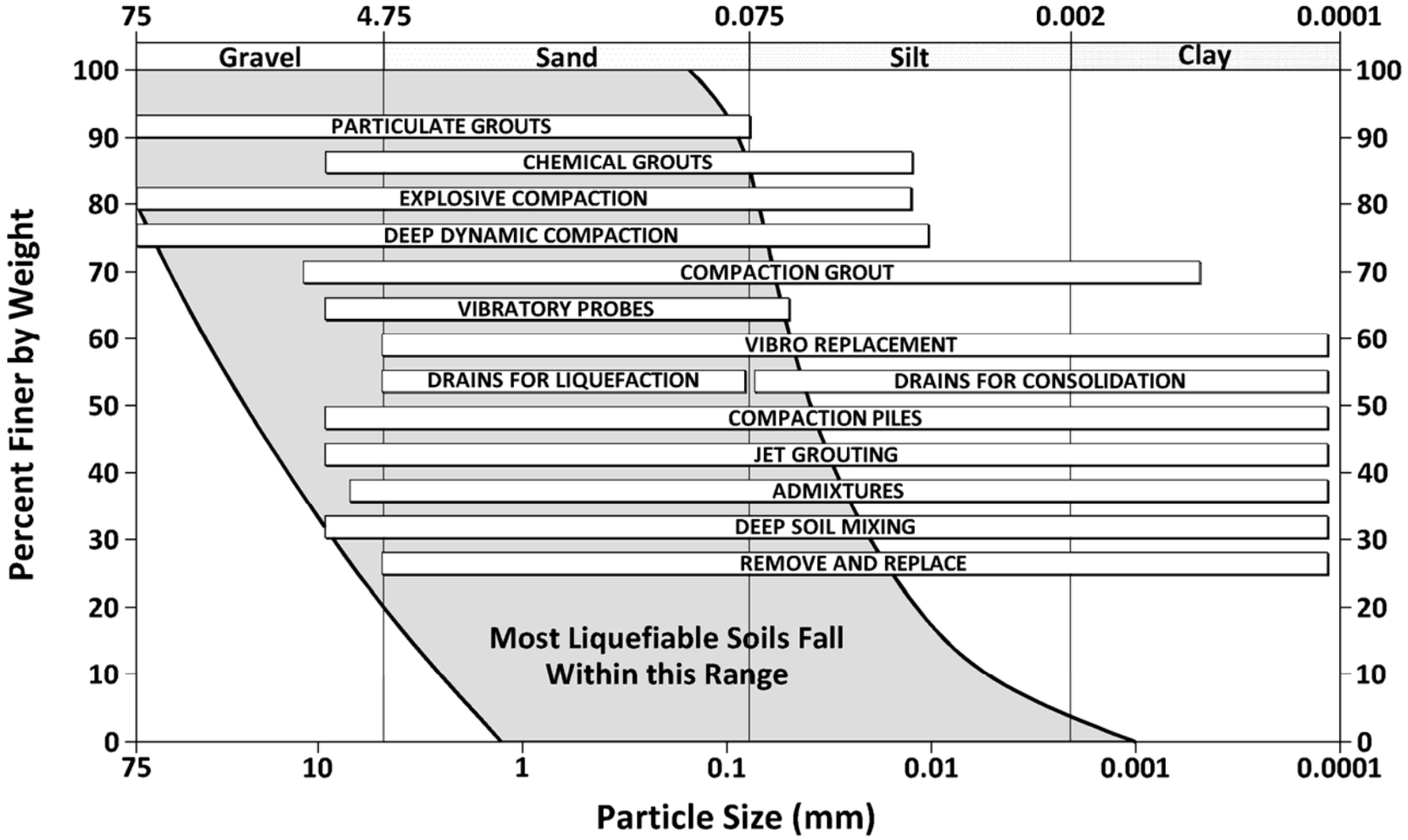


Fig. 4. Ground Improvement Methods for Mitigation of Seismic Risk to Existing Embankment Dams and Their Foundations

Table 1. Characteristics of Ground Improvement Methods in Relation to Mitigation of Seismic Risk to Existing Embankment Dams and Their Foundations

Method	Most Suitable Soil Types	Effective Depth	Attainable Maximum Improvement	Advantages	Limitations
Gravel Drains (GD)	Sands, silty sands	20 m (?)	Reduce pore pressure buildup during shaking, Intercept pore pressure plumes	• Inexpensive • Full area treatment not required	• Require close spacing • EQ-induced settlement not prevented • Treated ground must have high hydraulic conductivity • Limited performance record
Penetration Grouting (PG)	Sands and coarser materials, rocks	Unlimited	Void and crack filling and solidification	• No excess pore pressure or liquefaction in treated zone • Can localize treatment area	• High cost • Excessive fines content prevents use in many soils
Deep Dynamic Compaction (DDC)	Saturated sands and silty sands; partly saturated materials	Up to 10 m	D_r = 80 % $(N_1)_{60}$ = 25 q_{c1} = 10-15 MPa	• Low cost • Simple • Good for large areas	• Limited effective depth • Clearance required • High mobilization cost • Vibrations can impact adjacent structures
Explosive Compaction (EC)	Saturated clean sands and gravels	>30 m	D_r = 75 % $(N_1)_{60}$ = 20-25 q_{c1} = 10-12 MPa	• Inexpensive • Simple technology • Can use at greater depths than other dynamic methods • Can use in soils with cobbles and boulders	• Vibrations • Safety issues • Psychological barriers

Method	Most Suitable Soil Types	Effective Depth	Attainable Maximum Improvement	Advantages	Limitations
Vibro-compaction (VC)	Sands, silty sands, gravelly sands < 20% fines	30 m	D_r = 80+ % $(N_1)_{60}$ = 25 q_{c1} = 10-15 MPa	• Uniformity with depth in a given soil type • Moderate cost	• Special equipment needed • Best in clean sand • Unsuitable in soils with cobbles and boulders • Backfill required in most cases
Compaction Grouting (CG)	Any rapidly consolidating, compressible soil	Unlimited	Up to D_r=80+% $(N_1)_{60}$ = 25 q_{c1} = 10-15 MPa (Soil type dependent)	• Controllable treatment zone • Useful in soils with fines	• High cost • Post-treatment loss of prestress • Slow
Vibro-replacement Stone Columns (SC)	Silty sands, silts, clayey silts; close-spaced vertical drains enhance effectiveness	30 m	$(N_1)_{60}$ = 20 q_{c1} = 10-12 MPa	• Provides drainage and reinforcement • Uniformity with depth in a given soil • Bottom feed dry process puts fill where needed	• Special equipment needed • Unsuitable in soil with cobbles and boulders • Fines may intermix with and clog columns • Backfill may be costly • Difficult QA/QC
Sand and Gravel Compaction Piles (CP)	Can use in most soil types	20 m (?)	Up to $(N_1)_{60}$ = 25-30, q_{c1} = 10-15 MPa, depending on soil type	• Proven effectiveness • Provides drainage and reinforcement • Uniformity with depth	• Special equipment needed • Slow • High cost

Method	Most Suitable Soil Types	Effective Depth	Attainable Maximum Improvement	Advantages	Limitations
Cement Deep Soil Mixing (DSM)	Most soil types	Can be used to depths >30 m; 20 m typical in U.S.A.	Depends on size, strength and configuration of DSM elements; design compressive strengths of 150-200 psi	• Positive ground reinforcement • Can contain liquefiable soil within high strength grid walls	• Requires special equipment • Brittle elements • Expensive • Difficult QA/QC
Jet Grouting (JG)	Any soil; difficult in highly plastic clays	Unlimited	Depends on size, strength and configuration of high strength jetted elements; design compressive strengths of 150-200 psi	• Controllable treatment depth range • Useful in soils with fines • High strength columns • Large treatment depth possible	• High cost • Difficult to QA/QC • Uncertain keying into underlying stratum • Can induce hydraulic fracture in grouted formation
Remove and Replace, with or without admixtures (RR)	All soils	A few m	High density fills to strong, cemented materials, including roller compacted concrete	• Can design to desired improvement level • Easy to QA/QC	• May be expensive • May require dewatering • Excavations may impair stability of adjacent ground • Temporary support of existing structures may be needed

Vibratory and impact methods; e.g., vibro-compaction, deep dynamic compaction, vibro-replacement stone columns, explosive compaction, are usually the most economical methods for densification of liquefiable soil deposits; however, they may be ineffective if the fines content (<0.074 mm particles) exceeds more than about 20 percent. This is because the hydraulic conductivity of these materials is too low to permit significant rapid escape of water during the treatment process. Some benefit can still be achieved if vibro-replacement is used even if there is no densification of the treated soil, because the resulting stone columns provide both reinforcement and drainage. Some organizations will not take these two types of improvement into account, however.

Recent experience has shown that it is possible to densify higher fines content liquefiable materials by installation of closely spaced vertical drains prior to vibratory or impact treatment. Successful improvement of an up to 18 m (60 ft) thick deposit of interbedded, generally cohesionless, fluvial-lacustrine sandy and silty foundation material beneath Salmon Lake Dam in Washington State, Luehring, et al (2001), is a good example. Both extensive SPT and CPT testing indicated that this material was susceptible to liquefaction under the design earthquake. Fines contents ranged up to more than 60 percent. Prefabricated vertical drains (wick drains) were installed on 3 or 6 ft spacing to the full 58 to 61 ft target depths of stone columns throughout the treatment area. Dry, bottom feed stone columns were spaced 6.0 ft on centers, and the drains were located at the mid-points of the sides of the triangles formed by the stone column pattern. Stone column area replacement ratios of 22 and 35 percent were used. The column diameters were 3.0 ft or 3.75 ft, with the larger diameter specified for the area underlain by the finer-grained soils.

The vertical drains enabled rapid drainage of the ground during the stone column installation process, with accompanying densification and large increases in both the SPT and CPT penetration resistances, as may be seen in Table 2, adapted from Luehring, et al. (2001). The values in Table 2 are also consistent with past findings that the upper bound on the penetration resistance that can be attained by densification decreases as the fines content increases. Dise, et al., (1994) report the effective treatment of silty sands (SM) and sandy silts (ML) at three dams (Jackson Lake Dam, Mormon Island Auxiliary Dam, and Steinaker Dam) using methods to enhance the pore pressure dissipation in conjunction with deep dynamic compaction. These included wick drains, drainage trenches, controlled sequencing patterns for the weight drops during DDC, increased time between passes, and reduced energy per drop in confined areas. As is the case for vibro-replacement stone columns, the wick drains should be installed to the full depth of ground requiring improvement.

Deep soil mixing (DSM) and jet grouting (JG) are relatively newer methods of ground improvement used for increasing the seismic stability of embankment dams. The reconstruction of Jackson Lake Dam, Wyoming in the late 1980's marked the first major use of deep soil mixing for a dam in the U.S. Both DSM and JG enable construction of strong and continuous walls and cells of high strength, as well as individual columns, in-situ. The high strength of the treated soil means DSM and JG can be used for construction of stabilizing blocks in soils that cannot be densified and strengthened effectively using vibro-compaction and vibro-replacement methods.

Table 2. SPT Penetration Resistance Increases by Combined Stone Columns and Wick Drains in Salmon Lake Dam Foundation Materials (after Luehring, et al., 2001)

Soil Type	Average percent fines	Average percent clay (<0.005mm)	Average pre-treatment $(N_1)_{60}$	Average post-treatment $(N_1)_{60}$	Percent Increase
Silt	65	11	12	23	88
Silty sand	49	5	17	33	95
Poorly graded sand with silt (SP-SM)	10	2	21	40	92
Silty gravel with sand	12	3	15	52	236

DSM and JG are different technologies. Wet deep soil mixing involves mechanical cutting and mixing with low pressure injection of cement slurry and produces columns of uniform diameter in all soil types equal to that of the mixing auger. Jet grouting involves transfer of kinetic energy into cutting, eroding and mixing by jetting from a set of nozzles on the monitor. Accordingly, the size and properties of the resulting JG columns are much more greatly influenced by the soil type and state than are the DSM columns. A comparison between soil columns installed by both deep soil mixing and jet grouting into the same soil profile is shown in Fig. 5. Both methods suffer from problems associated with insuring adequate keying of stabilizing columns, walls, and cells into underlying hard strata, brittleness, and reliable quality assurance methods.



Fig. 5. Deep soil mix columns (right) and jet grout columns (left) in a test section at the downstream toe of Tuttle Creek Dam, Kansas.

Considerations in Selection of Method(s)

Project design and performance requirements dictate some of the needed design parameters, including the required stability and the allowable deformation of treated ground under both static and dynamic loading. The subsurface conditions set other design criteria, such as the suitability of different ground improvement methods and the required depth and areal extent of treatment. Collectively, these factors determine the level of improvement required to assure satisfactory performance. Site constraints play a role in design, as do the construction schedule, the available construction budget, and the availability of experienced specialty contractors.

Answers to the following questions aid in selecting suitable methods and determining the size and depth of treatment zones:

1. What type of soil needs to be improved?
2. What methods are appropriate for improving it?
3. At what depth and how thick is the layer that needs to be treated?
4. What length and width of treatment zone is needed?
5. Does more than one layer or material type require treatment?
6. At what depth is the ground water table?
7. Will over-water construction be required?
8. How much improvement is needed?
9. What filter and drainage requirements must be satisfied?
10. Are QC/QA procedures available, and can they be implemented to be sure that the design objectives have been met?
11. Can procedures be incorporated for long-term condition and performance monitoring?

Current dam safety practice often considers two earthquake loadings, the Operating Basis Earthquake (OBE) and the Maximum Credible Earthquake (MCE). Following an OBE, the facility must remain operational. To provide safety against the MCE, or the largest conceivable earthquake shaking at the site, the dam must not fail catastrophically; however, some damage may occur, provided the reservoir can be drawn down in time to protect against subsequent life loss. When applied to remediation of deficient dams, these criteria usually translate into different allowable crest settlements and lateral displacements. Differences in required level and extent of treatment needed for a given improvement method to provide protection against MCE loading as well as OBE loading may be important considerations in the selection of method.

Time requirements and construction scheduling often limit the potentially applicable ground improvement methods, especially if they impact normal reservoir operations. For example, if excavation into the downstream embankment slope and/or foundation is required to enable construction of a buttress fill or access for deep foundation treatment, then lowering of the reservoir may be mandated to maintain an adequate margin of safety against slope failure. Reservoir restrictions usually have negative water user impacts that must be considered in the decision process.

Design Procedures

With the aid of answers to the foregoing questions, the following steps can be followed to select the methods and design the ground improvement program:

1. Identify remedial design concepts and strategies for implementation.
2. Identify potentially applicable improvement methods that will fit the design concept.
3. List the pros and cons for each strategy and method.
4. Choose one or more methods for further study, preliminary design, cost estimating, and construction time and procedure evaluation.
5. Compare the results and select the best one(s).
6. Do sufficient field testing to be sure that the selected method(s) will work.
7. Perform final designs.
8. Develop specifications and QA/QC programs.

On many projects brainstorming workshop sessions are held to assist in completing steps 1-5. Participants usually include engineers from the responsible design organization who embrace the required areas of expertise; e.g., seismic, geologic, geotechnical, hydraulic, construction, materials, often augmented by outside experts.

QA/QC Considerations

Verifying that the specified level of improvement has been obtained is a difficult but critical aspect of ground improvement. Quality assurance and quality control consist of two phases: observations during construction and verification testing after construction is completed. Observations should be made and recorded during construction at each improvement location. Things to be noted include ground surface movements, backfill quantities, injected material quantities, consistency, unit weight, viscosity of mixed in-situ materials, and spoils returned to the ground surface. After construction, in-situ test methods such as SPT and/or CPT penetration resistance and shear wave velocity testing are usually used to verify that the level of improvement is achieved. Hydraulic conductivity measurements may be required as part of the assessment of pore pressure, seepage quantity, and hydraulic gradient determinations. Sampling and laboratory testing can also be used to verify some types of improvement, such as jet grouting and deep soil mixing.

Invariably problems arise in the post-treatment evaluation of the improved ground. They include:

- Specification of test types, location, and frequency
- Whether samples are representative
- Variability in the treatment and uncertainty about how much variability is acceptable without compromising the effectiveness
- Accounting for the time-dependency of properties that is common following treatment
- Correlating in-situ measurements to the relevant properties
- How to deal with failure to meet specifications
- Differing soil conditions, both real and perceived.

An Illustrative Case History

Morman Island Auxiliary Dam (MIAD), a part of the Folsom Project on the American River near Sacramento, California, completed in 1956, is an excellent example illustrating difficulties in site characterization, innovative ground improvement methods and challenges in their implementation, difficulties in QA/QC,

subsequent re-evaluation of dam safety, and remaining challenges for additional remediation to assure long-term seismic stability.

Approximately 940 feet of the 4820 ft long, 110 ft high MIAD were constructed on top of loose tailings that were deposited from placer gold mining done from floating dredges. Analysis in the 1980's showed that the tailings were liquefiable under the recommended design earthquake loading, and it was concluded that the liquefaction would lead to large deformations in the dam, ultimately resulting in a catastrophic release of the reservoir and large loss of life downstream. Low reservoir levels in 1990 presented an opportunity to work at the upstream toe of the dam. Deep dynamic compaction (DDC) was used to densify the tailings, and a berm was constructed to buttress the upstream slope and apply weight to the treated foundation. DDC was selected because of the limited time available for construction before the reservoir would fill again. At the same time it was recognized that the dynamic compaction might not densify the full thickness of the loose tailings material sufficiently to preclude liquefaction under the recommended design earthquake, and that it might prove necessary to treat the deepest material later with compaction grouting or some other method. A cross section through the upstream treated zone is shown in Fig. 6.

Following an extensive test program of several methods, bottom-feed stone columns (BFSC) to a depth of 20 m (60 ft) were selected to densify the liquefiable deposits beneath the downstream toe of MIAD. Zones of small-diameter (0.25 m) drainage columns were installed immediately upstream and downstream of the BFSC to prevent excess pore-water pressure migration into the densified zone in the event of liquefaction of untreated tailings. A cross section through the downstream treated zone is shown in Fig. 7. This work was done during 1993-94. Construction activities were monitored by visual inspection, computer logging of the BFSC installation, and Becker Penetration Tests (BPTs). BPT results were used to evaluate whether density requirements were achieved. Owing to the presence of much higher fines contents than had been anticipated in the lower 6 m (20 ft) of the improvement zone, the acceptance level for post-treatment penetration resistance was reduced. Lack of site specific correlation between the BPT penetration resistance values and the corresponding values of $(N_1)_{60}$ for the Standard Penetration Test (SPT) used for liquefaction potential evaluation added to subsequent uncertainties about the overall effectiveness of treatment.

Reevaluations of the improvement zones by field explorations and testing, as well as stability and deformation analyses carried out during the past few years, have indicated that liquefaction beneath the upstream DDC zone and within the lower part of the downstream BFSC zone have high enough probability of occurrence that a stabilizing berm and additional foundation treatment are needed to reduce the failure risk to an acceptable level. The scheme under evaluation includes 1) a downstream overlay in the area of the liquefiable alluvium, 2) a system of filters and drains beneath the overlay along the entire length of the dam, and 3) either jet grouting an 80-ft wide by 900-ft long strip of liquefiable soil to bedrock beneath the downstream toe, or excavating and replacing the downstream liquefiable alluvium within a strip of approximately similar dimensions and location.

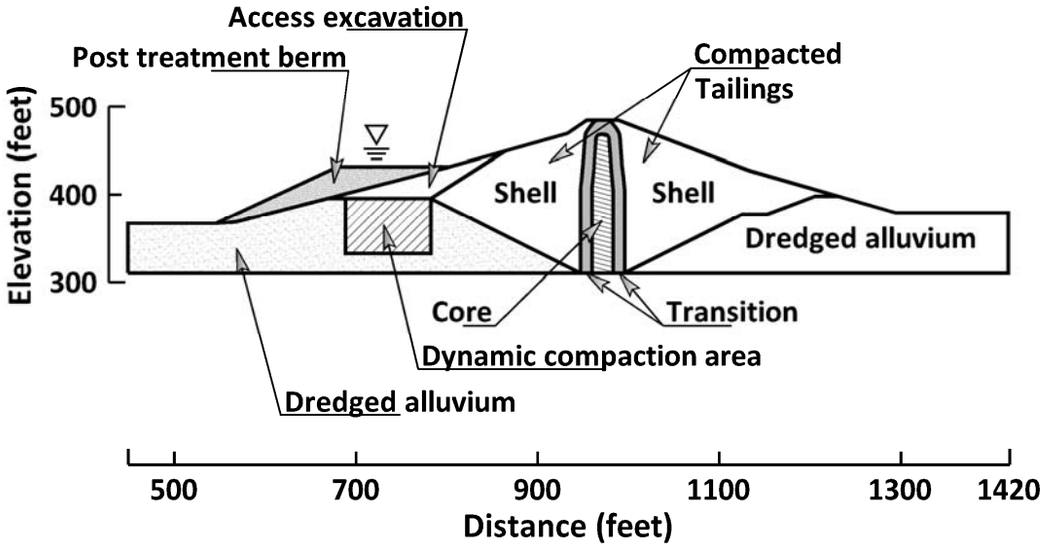


Fig. 6. Ground improvement design for stabilization of the upstream embankment of Mormon Island Auxiliary Dam done in 1990.

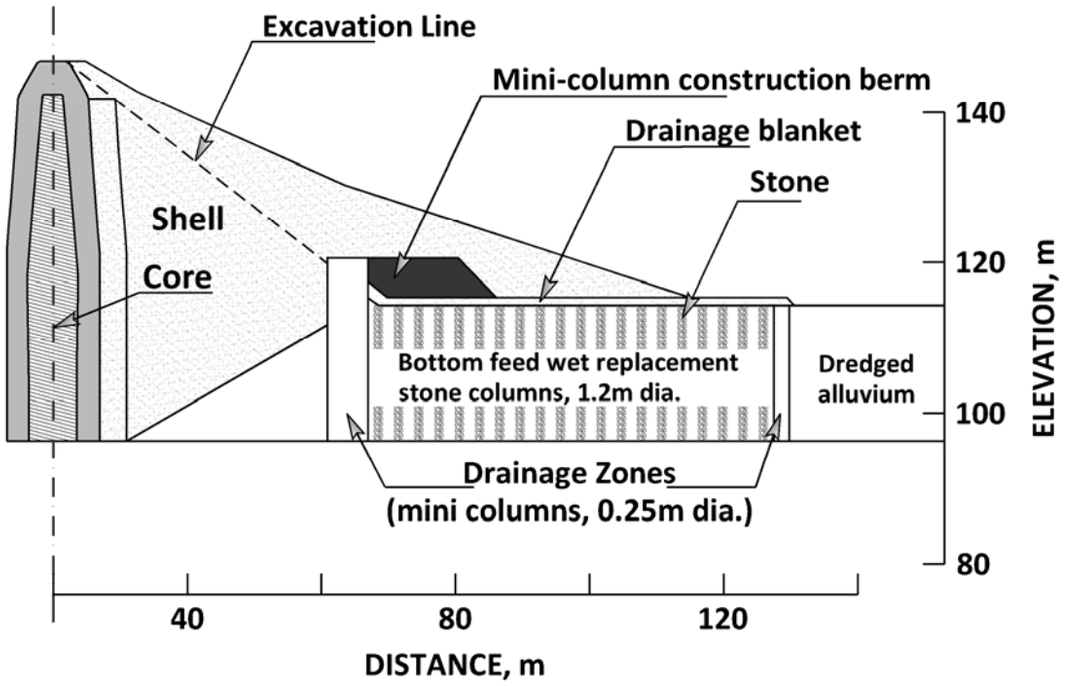


Fig. 7. Ground improvement design for stabilization of the downstream embankment of Mormon Island Auxiliary Dam done in 1993-94.

The ultimate risk reduction would be about the same for either the jet grout or excavate and replace option. Jet grouting was initially selected as the preferred alternative, because the estimated cost for jet grouting is lower and the downstream embankment failure risk during construction is significantly less than for the excavate

and replace option. However, there is much more uncertainty associated with the jet grouting option as to whether the needed soil improvement can be attained. Accordingly, a jet grouting test program was designed in anticipation that the necessary information could be obtained to 1) develop procedures that will yield homogeneous jet grout columns that have specified dimensions, verticality, and location; 2) produce a minimum specified shear strength of 100 psi; 3) assure a shear resistance along the grout column-bedrock interface of at least 100 psi; and 4) demonstrate that the high pressure injection of the cement-water grout would not produce unacceptable environmental impacts. At the time of writing, the test program has not been completed; however, preliminary indications are that the desired results are not being obtained. If this is confirmed, then attention will need to be refocused on the removal and replacement of the liquefiable soil in the region beneath the overlay berm.

TRENDS IN GROUND IMPROVEMENT FOR DAM SAFETY

Beginning with applications to such projects as Sardis Dam, Rye Patch Dam, and Mormon Island Auxiliary Dam in the 1980's, dynamic deformation analyses have become widely used for estimation of earthquake-induced deformations in existing embankment dams and for parametric studies of how properties, dimensions, and locations of improved soil zones within embankments and their foundation strata combine to provide the needed added resistance to assure post-earthquake stability. Programs such as FLAC and PLAXIS are now widely used for this purpose. Overall confidence in the accuracy of predictions using these methods, however, seems to remain only at about plus or minus a factor of 2. Difficulties in the constitutive modeling of liquefiable soil, in estimating the extent of liquefaction, in determining the time at which liquefaction is triggered during shaking and in estimating the post-liquefaction residual strength are major contributors to this uncertainty.

When space and fill materials are available, stabilizing berms have been, and continue to be used extensively for preventing extensive lateral spreading, both upstream and downstream, in the event of foundation layer liquefaction. Use of berms on upstream slopes may be impractical, however, unless the reservoir can be drawn down to provide the necessary construction access and to avoid underwater fill placement. Accordingly, alternative upstream treatment strategies have evolved. Some examples are the use of deep dynamic compaction at Mormon Island Auxiliary Dam, California, and large driven prestressed concrete piles at Sardis Dam, Mississippi. At the latter site, the function of the 24-in square piles is to anchor the embankment across a 5 to 10-ft thick potentially liquefiable silt layer to the underlying resistant strata.

After analyses showed that densification or other in-situ upstream embankment and foundation treatment would be unable to limit upstream deformations and crest settlement sufficiently to prevent overtopping at Rye Patch Dam, Nevada, a new strategy was developed and implemented. Rye Patch Dam is a 78-ft high homogeneous earth fill dam with a crest length of 700 ft founded on a 30 to 38-ft thick potentially liquefiable alluvial foundation. In addition, the lower 20-30 ft of the embankment material had an estimated steady state post-earthquake strength of only

550 psf. Dynamic deformation analyses of the existing conditions gave the results shown in Fig. 8. The computed deformations were unacceptably large in both the vertical and downstream directions, and the factor of safety against upstream stability failure was only 1.02. Attempts to design an upstream improved ground restraining block that would limit movements sufficiently to prevent overtopping were unsuccessful. The decision was made, therefore, to construct a downstream combination soil-cement shear key and buttress fill that would limit crest settlements sufficiently to avoid overtopping. This design and the computed post-treatment deformations are shown in Fig. 9.

This concept of letting the upstream embankment deform while increasing the crest width and confining the ground treatment to the downstream side of the embankment has now been adopted at other dams. However, it is conditional on there being space and materials available to accommodate the needed buttress fill and there not being intake structures, spillways, conduits, or other appurtenant structures located adjacent to, on, or in the upstream embankment.

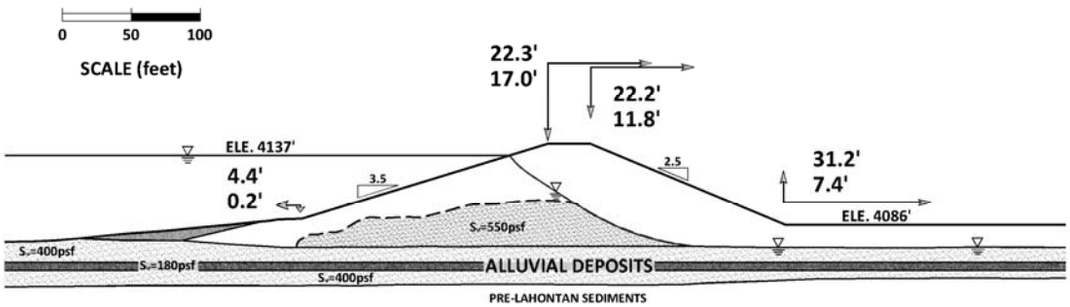


Fig. 8. Computed dynamic vertical and horizontal displacements for the existing conditions at Rye Patch Dam (modified from Woodward-Clyde Consultants - URS Corporation)

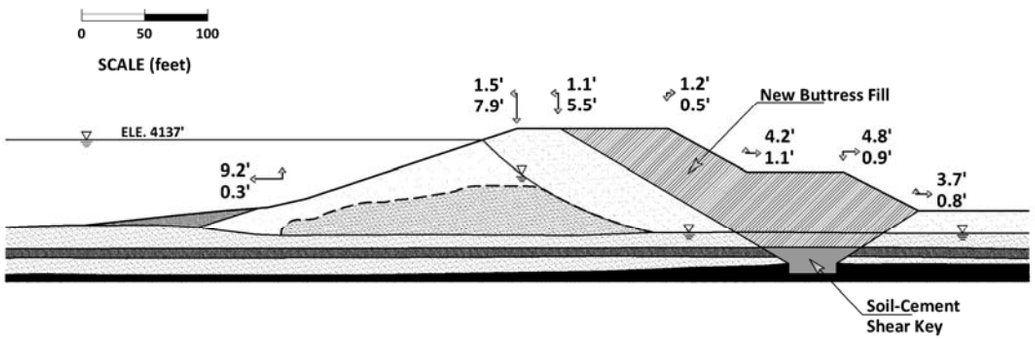


Fig. 9. Computed dynamic vertical and horizontal displacements for the remediated Rye Patch Dam (modified from Woodward-Clyde Consultants - URS Corporation)

SOME UNRESOLVED PROBLEMS IN EMBANKMENT DAM SAFETY EVALUATION AND RISK MITIGATION

Although not directly focused on ground improvement technologies, there are several aspects of embankment dam seismic safety evaluations that impact mitigation strategies and the choice and implementation of ground improvement methods for any project. These include:

- Assessing the liquefaction potential of soils with cobbles and gravel
- Assessing the liquefaction potential of silty soils
- Assessing the post-liquefaction residual strength
- Interpreting the results of a risk analysis
- Deciding the acceptable level of risk
- Selecting and implementing, through the choice of representative properties and parameters, the appropriate constitutive model for liquefaction and dynamic deformation analyses
- Assessing the reliability and accuracy of the results of dynamic deformation analyses
- Assessing and controlling conservatism
- Assessing compliance with specifications

CONCLUDING COMMENTS

Dam stability during and after an earthquake is a critical life safety issue.

Although the basic concepts and approaches to soil stabilization and ground improvement – densification, drainage, cementation, reinforcement, removal and replacement – are very old, new ways to implement them for mitigation of liquefaction risk to embankment dams continue to be developed. As a result, many strategies and methods for improving the ground at existing dams are possible. Different ground improvement methods are likely to be the most suitable for different soils, different purposes, and different site and project constraints. Optimal designs may justify use of more than a single method of ground treatment for a project. Whatever the methods chosen, success is largely dependent on accurate characterization of the existing embankment and subsurface conditions, and this characterization may be the most challenging part of a project.

Predictions of liquefaction and post-liquefaction deformations should be based on realistic (unfactored) loads and best estimates of average soil properties. More conservative estimates of loading conditions and properties should be used when predicting the probable deformations and displacements after ground improvement.

Full-scale field tests yield the most reliable verification that the needed ground improvement can be obtained and that the design is feasible. Such tests should be a required part of all major projects. Once feasibility has been established, a QC/QA program should be designed that verifies the most critical aspects of the work. Evaluating the results of the QA/QC testing may be challenging.

Soil improvement will continue to play an important role in the mitigation of seismic risk to existing dams. Current trends and recent experiences support the “simpler is better” approach to ground improvement designs.

ACKNOWLEDGMENTS

I thank Nestor Suarez for assistance in preparation of several of the figures. Professor Ross Boulanger contributed to the development of Fig. 4, which is updated from similar versions used in previous publications by the author. John France kindly made available information about the Rye Patch Dam remediation project.

REFERENCES

ASCE (1978). *Soil Improvement – History, Capabilities and Outlook,* Committee on Placement and Improvement of Soils, Geotechnical Engineering Division, 182 pp.

ASCE (1987). *Soil Improvement – A Ten Year Update*, J.P. Welsh, ed., Geotechnical Special Publication No. 12, 329 pp.

ASCE (1997). *Ground Improvement, Ground Reinforcement, Ground Treatment: Developments 1987 – 1997,* V. R. Schaefer, ed., GSP No. 69.

Dise, K., Stevens, M.,G., and Von Thun, J.L. (1994), "USBR Experiences Using DDC at 3 Dams for Mitigation of Liquefaction Risk, ASCE GSP No.45, 1-23.

Luehring, R., Snortland, N., Stevens, M. and Mejia, L. (2001). Liquefaction Mitigation of a Silty Dam Foundation Using Vibro-Stone Columns and Drainage Wicks: A Case History at Salmon Lake Dam," Bureau of Reclamation *Water Operation and Maintenance Bulletin,* No. 198, 1-15. http://www.usbr.gov/infrastr/waterbull

Mitchell, J. K. (1981). "Soil Improvement: State of the Art," *Proc. Tenth Intl. Conf. on Soil Mechs. & Found. Engrg.*, Stockholm, Sweden, Vol. 4, 509-565.

Swaisgood, J.R. (1998) "Seismically-Induced Deformation of Embankment Dams,) *Proc. 6th U.S. National Conference on Earthquake Engineering,* Washington, DC.

Moriwaki, Y., Dinsick, A., Barneich, J.A., Roussel, G., Yiadom, A., Starr, F., and Tan, P. (2007). "Seismic Characterization and Evaluation of San Pablo Dam", *Proc. GEESD IV.*

Moseley, M.P. and Kirsch, K.(2004). *Ground Improvement*. 2nd ed. Spon Press. NY.

USACE (1999)."Engineering and Design Guidelines on Ground Improvement for Structures and Facilities," Publication No. ETL 1110-1-185, U.S. Army Corps of Engineers, Engineering Division, Directorate of Civil Works, Washington, DC. http://www.usace.army.mil/inet/usace-docs/eng-tech-ltrs/etl1110-1-185/toc.htm

Application of Deep Dynamic Compaction to U.S. Route 44 Relocation Project

Yong Tan

WPC, Inc., 2201 Rowland Avenue, Savannah, GA 31404; PH (912) 629-4000; FAX (912) 629-4001; Email: tanyong21th@hotmail.com

Abstract: In order to reduce potential settlements and liquefaction susceptibility, two passes of deep dynamic compaction (DDC) were adopted to densify the loose, saturated granular backfill between steel sheet pile walls in peat bogs at the relocated U.S. Route 44 in Carver, Massachusetts. Piezocone penetration tests (CPTu) were performed before and after DDC to verify compaction effects. The comparison of pre- and post-compaction CPTu results indicated that the strength and stiffness of the backfill were significantly improved after each pass of dynamic compaction. Under the design load, around 40 percent of the estimated settlements in the backfill could be reduced after one pass of DDC, and up to 84 percent after two passes. At the same time, the backfill was densified to the level of resisting potential liquefaction under the design earthquake motions.

INTRODUCTION

The relocated U.S. Route 44 in Massachusetts was a four-lane divided highway with a typical median width of 18.3 m. It started from the existing Route 44 at Carver, Mass. to the existing Route 3 near Plymouth, Mass. Many areas of this project required embankments to accommodate the proposed roadway. Unfortunately, a large portion of the proposed embankments would be located in cranberry bogs and water ponds featuring deep peat deposits overlying sands. At some stations, peat deposits were up to 10.5 m deep. Water table levels were near the existing ground surface. The in-situ peat mainly consists of decomposition of plants or animal bodies over long time. It shows extremely high compressibility, low bearing capacity, and significant creep behavior. According to Ernst et al. (1996), more than 60 percent of settlements in the peat deposits were estimated to take place in the secondary compression phase. The existence of peat deposits really challenged the roadway design and construction in these wetland areas. If embankments were built without peat removal, as the peat deposits varied in thickness, long-term settlements beneath the embankments would not be uniform and would vary sharply between the areas overlying peat and the areas overlying sands. Differential embankment settlements would induce local depressions in roadway and thus cause maintenance problems. Also, leaving peat in-place would

cause uncertainties to the global embankment stability. On the basis of above considerations, finally it was determined to replace all the peat deposits under the proposed embankments with granular soils. In order to mitigate the impacts of embankment construction on the wetland environment, steel sheet pile walls were installed along the both sides of the proposed roadway in the wetlands, as retaining structures for peat removal and embankment construction later. Figure 1 presents typical roadway construction in the wetland areas. The removal of the peat between sheet pile walls was accomplished using a crane outfitted with a dragline bucket. After peat removal, the site was backfilled with granular soils without dewatering. As the backfill was placed in a fairly loose saturated state, potential settlements and liquefaction susceptibility were great concerns for the site studied. Therefore, two passes of deep dynamic compaction (DDC) were carried out to reduce potential settlements and increase liquefaction resistance via densifying the backfill.

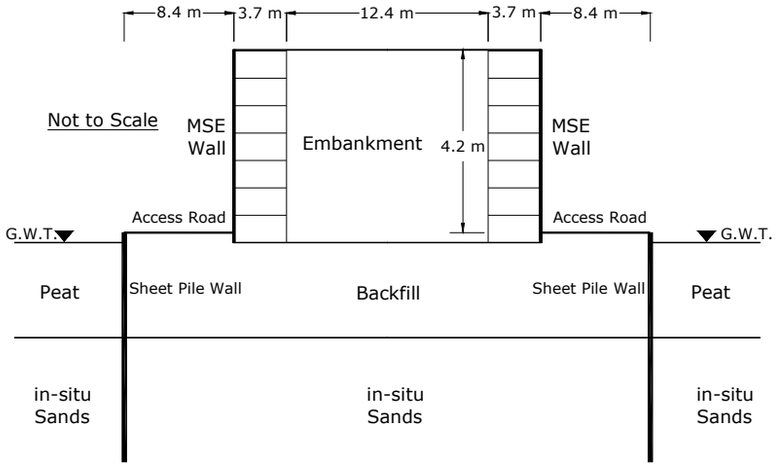


FIG. 1. Typical roadway construction in the wetland areas

In order to verify compaction effects, piezocone penetration tests (CPTu) were performed before and after DDC. The comparison of pre- and post-DDC CPTu results indicated that the strength and stiffness of the backfill were significantly improved after each pass of DDC. Under the design load, around 40 percent of the estimated settlement in the backfill could be reduced after one pass of DDC, and up to 84 percent after two passes. Meanwhile, the liquefaction susceptibility of the backfill subjected to earthquake motions was significantly reduced. The aims to reduce potential settlements and mitigate liquefaction hazards were satisfied.

SITE CONDITIONS

The backfill depth at the project site ranged between 2.5 and 10.5 m, overlying medium to dense in-situ sands. Figure 2 presents the grain-size distribution curves of the backfill at Route 44. According to sieve analysis results, the backfill mainly consists of fine to coarse sands, with a trace of gravels and silts. Based on the triaxial

tests on the representative backfill samples, its effective friction angle, ϕ', was around 32^o. Before DDC was implemented, it was very important to determine whether the backfill could be improved by DDC. Mitchell (1982) identified soils according to grain size distribution and suggested that most granular soils with a fine content (particles sizes < 0.064 mm) lower than 10% could be improved by vibratory or impact methods. According to his criterion, the backfill at Route 44 lied in the region of compactable.

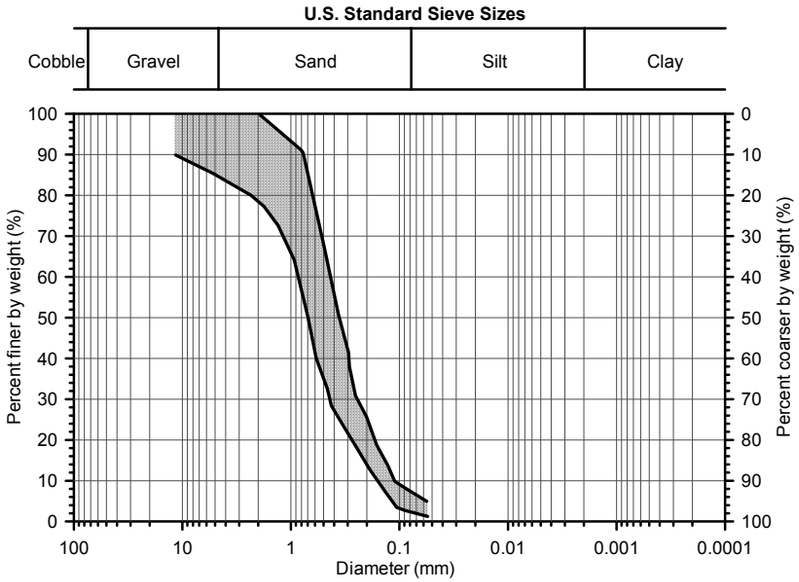


FIG. 2. Grain-size distribution of the backfill

DEEP DYNAMIC COMPACTION (DDC)

As a widely used ground improvement method, DDC was "rediscovered" by Mr. Louis Menard in French in 1965, who transformed the crude tamping method into a rational compaction procedure. This method is carried out essentially by repeatedly dropping a very heavy tamper onto the soil surface from a relatively great height. DDC can be used for both unsaturated and saturated granular soils. The densification process in unsaturated soils is the process of expelling air out from voids, thereby decreasing void volume and making soil denser. The mechanism of densifying saturated soils is based on dynamic consolidation (Ye et al. 1992). The energy produced by DDC in soils destroys the soil structure and causes the water trapped between soil particles to be expelled out. Thus, cracks are formed, allowing rapid dissipation of pore pressure generated in DDC. Then, the soil consolidates, and the soil particles are forced into a denser state. As a result of densification, soil bearing capacity is improved via increasing soil strength and in-situ density, soil stiffness is increased to reduce potential total and differential settlements, and the risk of liquefaction hazards of the soils is mitigated via reducing soil particle voids and increasing confining stresses.

For the areas between stations 139+00 and 166+00 with deep peat deposits, the backfill beyond 6.9 m from the sheet pile walls was impacted by a 14.4-ton tamper, dropped from a height of 18.3 m. For the backfill within 6.9 m from the sheet pile walls, the dropped height was reduced to 9.2 m. Each tamping point was repeatedly impacted nine drops. The second pass of DDC was conducted at the center spacing of the first pass. To ensure complete dissipation of excess pore pressure generated in the first DDC, the second pass was conducted six days later. The distance between tamping points and sheet pile walls was no less than 4.6 m to avoid unexpected large sheet pile wall deflections during DDC. Figure 3 presents a typical DDC grid-pattern along with the investigated CPTu sounding locations at the project site.

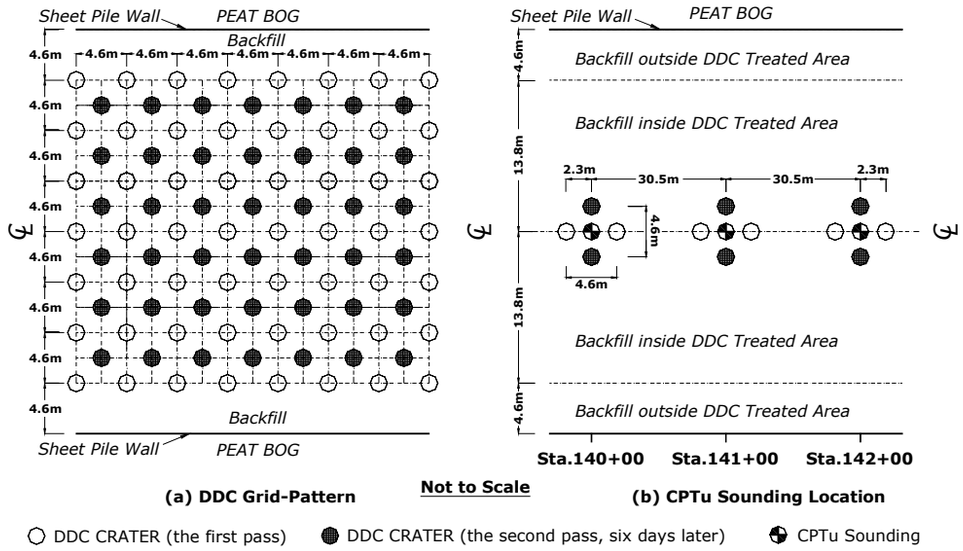


FIG. 3. Typical DDC grid-pattern at U.S. Route 44

PIEZOCONE PENETRATION TEST (CPTu)

A series of piezocone penetration tests (CPTu) were carried out to verify compaction effects. The initial evaluation tests were conducted prior to DDC. The second tests were conducted following the completion of the first pass of DDC. The subsequent third tests were conducted following the completion of the second pass. The CPTu soundings were located at the center spacing of the first and second pass of tamping points, and were spaced 30.5 m apart along the central line of the constructed roadway (see Fig. 3).

VERIFICATION OF DDC EFFECTS

After two passes of DDC, the determined densification depths which were based on the measured cone tip resistance reached as deep as 11 m at some stations. The detailed investigation of densification depth can be found in Tan et al. (2007). This

paper mainly focuses on the study of the effects of DDC on the mitigation of potential settlement and liquefaction susceptibility via improving the backfill engineering properties.

Typical CPTu Data

Figure 4 presents typical CPTu results achieved before and after DDC at station 140+00. The backfill mainly consisted of clean sands and gravelly sands. Except for the topsoil near the ground surface, the cone tip resistance, q_t, and side friction, f_s, of the backfill were significantly improved after each pass of DDC. For most of the backfill, the q_t values were increased by up to 4 times after the first pass, and up to 7 times after two passes. The water table levels did not show significant changes because of the cut-holes in the steel sheeting, which were designed to allow the water table level on both sides of the sheet pile walls to be at the same level to keep the retaining structures in balance. The distribution of friction ratio, R_f, versus depth was more uniform after DDC. Following the completion of the first pass of DDC, the estimated total vertical stress, σ_{v0}, along depth had some increase, while, the second pass did not cause apparent changes. The CPTu results also indicated that the compaction did not induce significant densification effects on the in-situ medium to dense sands underneath the backfill.

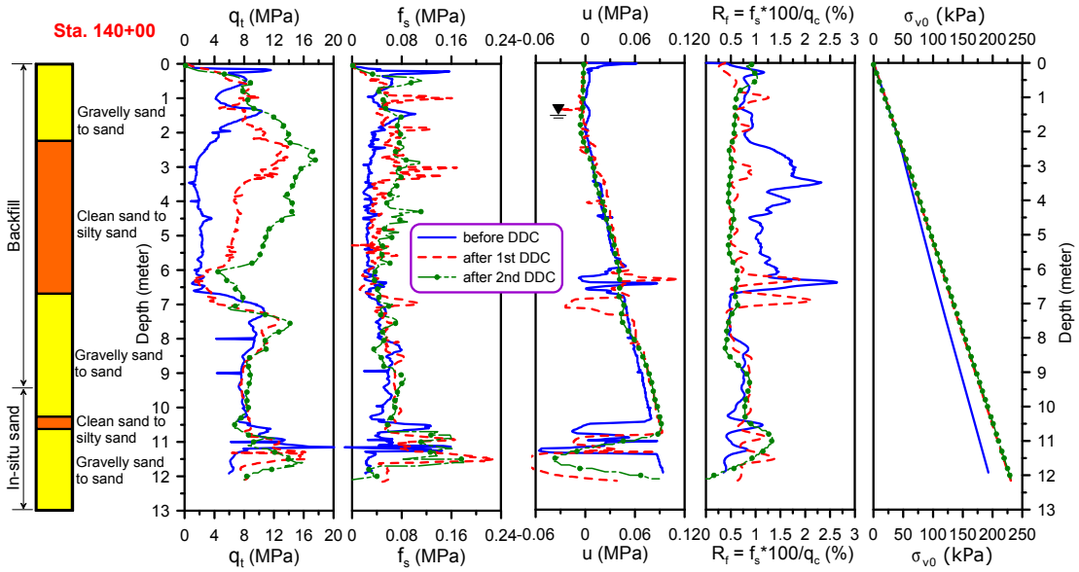


FIG. 4 Typical CPTu results at station 140+00

Comparison of Backfill Engineering Properties before and after DDC

Figure 5 presents the comparison of pre- and post-compaction backfill engineering properties at station 140+00, in which the unit weight, γ, was estimated by CPTu, relatively density, D_r, was calculated by the procedure proposed by Jamiolkowski et al. (1985), effective friction angle, ϕ', was estimated by the correlation developed by Meyerhof (1976), and constrained modulus, M, was

calculated based on the procedure proposed by Massarch (1994). For the unit weight of the backfill, γ, it was around 16 to 18 kN/m^3 before DDC, while around 19 to 20 kN/m^3 after two passes of DDC. Prior to DDC, most of the backfill at depths of 1.5 to 6.5 m was in a loose to medium dense state. While, it was densified to the state of medium dense to dense after the first pass of DDC and to the state of dense to very dense after two passes. For the medium dense to very dense backfill in the upper 1.5 m and at depths of 6.5 below, DDC did not show significant densifications effects. For the backfill at depths of 1.5 to 6.5 m, its effective friction angle, ϕ', was around 32^o to 36^o before DDC, and around 35^o to 38^o after one pass of DDC and around 36^o to 39^o after two passes. Similar to D_r, the estimated ϕ' in the upper 1.5 m and at depths of 6.5 m below did not show significant changes after DDC. The estimated constrained modulus, *M*, in the upper 6.5 m was around 10 MPa before DDC. After the first pass of DDC, it was increased to 20 to 25 MPa, and around 30 MPa after two passes. For the backfill at depths of 6.5 m below, *M* has about 5 MPa increase after the first pass, and the second pass did not induce significant changes. The analyses of the pre- and post-DDC backfill engineering properties indicated that the in-situ density, strength and stiffness of the backfill were significantly improved after DDC, especially for those in a loose to medium dense state. The improvement in the backfill density, strength and stiffness indicated increase in the soil bearing capacity, i.e. the stability of foundation soils and reduction of total and differential settlements.

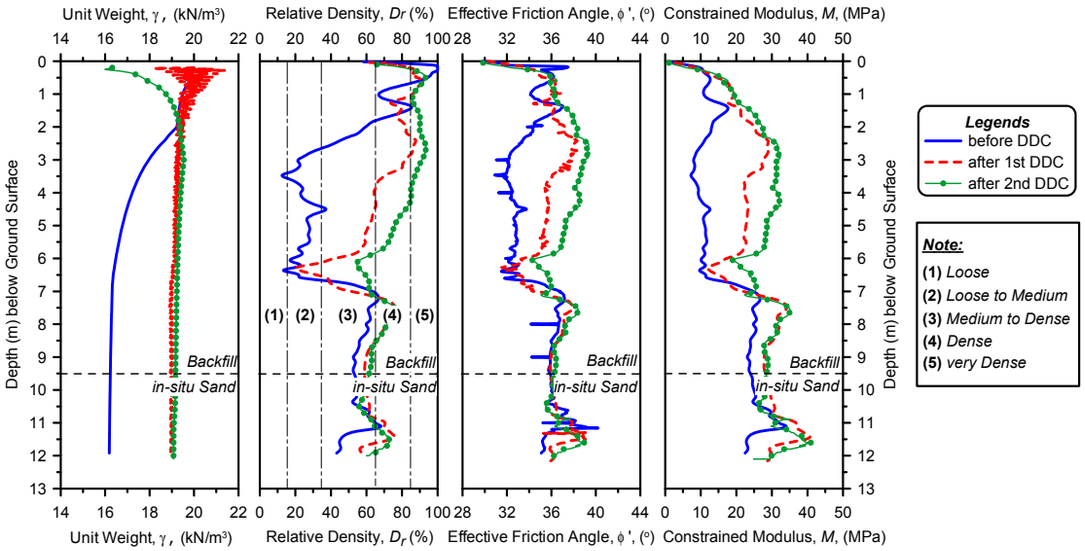


FIG. 5 Comparison of the backfill engineering properties before and after DDC

Settlement Evaluation

After DDC, embankments with an average height of 4.2 m would be built on the compacted backfill. Intolerable total or differential settlements below the embankments would cause local depression in roadway and instability of the embankments, which would induce long-term maintenance problems. Therefore, it was necessary to evaluate the potential settlements in the backfill induced by the

proposed embankments. The settlement calculation method based on constrained modulus, *M*, proposed by Janbu (1974) was used for settlement estimation, and *M* was calculated by the procedure developed by Massarch (1994). In the settlement estimation, the load induced by embankments on the backfill was treated as a strip loading with a value of 80 kPa and the stress distribution along depth in the soils below embankments was estimated by Boussinesq's solution. Figure 6 presents the comparison of the estimated settlements in the backfill before and after the ground treatment, in which the settlements were the averages based on the CPTu soundings at twelve stations. Prior to DDC, the estimated embankment-induced settlement was around 7.0 cm. While, it was reduced to 4.3 cm after one pass of DDC, and to 1.0 cm after two passes. This comparison implied that after one pass of DDC, about 40 percent of potential settlement could be reduced and up to 84 percent after two passes. The aim to reduce potential settlements was achieved.

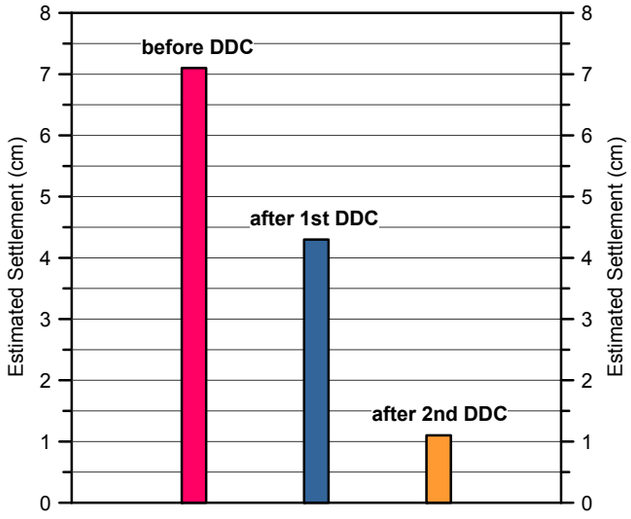


FIG. 6 Comparison of the estimated settlements before and after DDC

Potentional Liquefaction Evaluation

As mentioned previously, the backfill was placed in a loose saturated state and might be at a risk of liquefaction when it was subjected to earthquake shaking. Therefore, it was important to investigate whether the backfill was still liquefiable after the ground improvement. The method based on the in-situ CPT data developed by Robertson and Wride (1998) was adopted in the liquefaction evaluation. It assumes liquefaction to occur if F_S is less than 1.0 and no liquefaction occurs if F_S is greater than or equal to 1.0. The safety factor F_S is defined as the ratio of cyclic resistance ratio (*CRR*) to cyclic stress ratio (*CSR*):

$$F_S = CRR/CSR = MSF * CRR_{7.5}/CSR \quad (1)$$

in which, *MSF* is magnitude scaling factor, $CRR_{7.5}$ is cyclic resistance ratio determined for magnitude 7.5 earthquake, and *CSR* is cyclic stress ratio. $CRR_{7.5}$ is calculated as (Robertson and Wride 1998):

$$\text{if } (q_{c1N})_{cs} < 50,\ CRR_{7.5} = 0.833[(q_{c1N})_{cs}/1000] + 0.05 \quad (2a)$$

$$\text{if } 50 \le (q_{c1N})_{cs} < 160,\ CRR_{7.5} = 93[(q_{c1N})_{cs}/1000]^3 + 0.08 \quad (2b)$$

where, $(q_{c1N})_{cs}$ is clean-sand cone penetration resistance normalized by approximately 100 kPa (1 atm). *CSR* is calculated as (Seed and Idriss 1971):

$$CSR = 0.65 \times (a_{\max}/g) \times (\sigma_{v0}/\sigma'_{vo}) \times r_d \quad (3)$$

where, $a_{\max}$ is peak horizontal acceleration at the ground surface generated by earthquake; g is acceleration of gravity; σ_{v0} and σ'_{v0} are total and effective vertical overburden stresses, respectively; and r_d is shear stress reduction coefficient. The value of r_d in equation (3) is estimated by the equations (Cetin et al. 2004):

For $d < 20$ m,

$$r_d(d, M_w, a_{\max}, V^*_{s,12m}) = \frac{[1 + \frac{-23.013 - 2.949 \cdot a_{\max} + 0.999 \cdot M_w + 0.0525 \cdot V^*_{s,12m}}{16.258 + 0.201 \cdot e^{0.341 \cdot (-d + 0.0785 \cdot V^*_{s,12m} + 7.586)}}]}{[1 + \frac{-23.013 - 2.949 \cdot a_{\max} + 0.999 \cdot M_w + 0.0525 \cdot V^*_{s,12m}}{16.258 + 0.201 \cdot e^{0.341 \cdot (0.0785 \cdot V^*_{s,12m} + 7.586)}}]} \pm \sigma_{\varepsilon_{rd}} \quad (4a)$$

For $d \ge 20$ m,

$$r_d(d, M_w, a_{\max}, V^*_{s,12m}) = \frac{[1 + \frac{-23.013 - 2.949 \cdot a_{\max} + 0.999 \cdot M_w + 0.0525 \cdot V^*_{s,12m}}{16.258 + 0.201 \cdot e^{0.341 \cdot (-d + 0.0785 \cdot V^*_{s,12m} + 7.586)}}]}{[1 + \frac{-23.013 - 2.949 \cdot a_{\max} + 0.999 \cdot M_w + 0.0525 \cdot V^*_{s,12m}}{16.258 + 0.201 \cdot e^{0.341 \cdot (0.0785 \cdot V^*_{s,12m} + 7.586)}}]} - 0.0046 \cdot (d - 20) \pm \sigma_{\varepsilon_{rd}} \quad (4b)$$

As $d < 12$ m,

$$\sigma_{\varepsilon_{rd}}(d) = d^{0.8500} \cdot 0.0198 \quad (5a)$$

As $d \ge 12$ m,

$$\sigma_{\varepsilon_{rd}}(d) = 12^{0.8500} \cdot 0.0198 \quad (5b)$$

Where, d is depth below the ground surface in meter, $a_{\max}$ is in gravitational acceleration (g/s), $V^*_{s,12m}$ is the representative site shear wave velocity over the top 12 m in m/s, M_w is earthquake magnitude. The measured $V^*_{s,12m}$ by the in-situ seismic cone penetration tests (SCPT) at station 140+00 was around 150 m/s prior to DDC, and was around 160 m/s after the first and second pass of DDC. The site studied was designed to withstand a maximum earthquake magnitude M_w of 5.5 with two percent of probability of being exceeded in 50 years (this implies a mean recurrence interval of about 2500 years). A magnitude scaling factor (*MSF*) value equal to 1.43 recommended by Seed and Idriss (1982) for the magnitude 5.5 earthquake was used in equation (1). Accord to USGS seismic hazard map, a maximum horizontal ground acceleration $a_{\max}$ equal to 0.136g was used in the liquefaction analyses.

Figure 7 presents typical liquefaction analysis results at station 140+00, in which the red-color shade areas represents liquefaction. Before DDC, the backfill at depths of 3 to 8.5 m would liquefy under the design earthquake motions. Following the completion of the first pass, the backfill at depths of 4 to 8.5 m were still at a risk of liquefaction with a factor of safety (F_S) around 1.0. While, after two passes of DDC, the backfill along depths was densified to the state of unliquefiable. In order to resist

potential liquefaction, a minimum cone resistance, q_t, value equal to 8 to 9 MPa was required to be achieved after DDC.

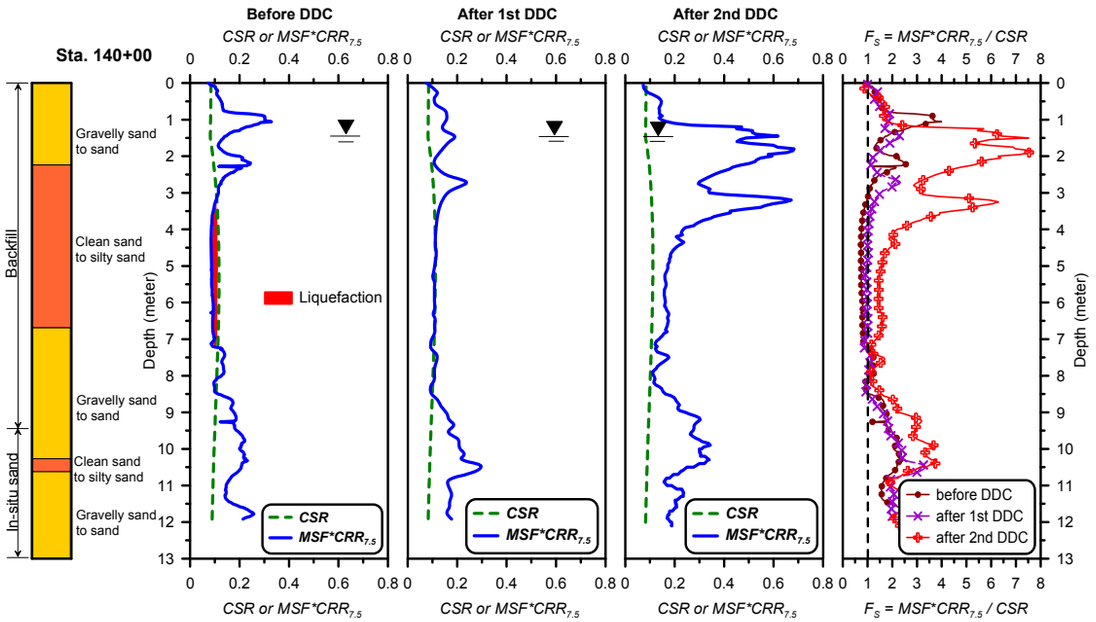


FIG. 7. Results of the liquefaction analyses at station 140+00

CONCLUSIONS

Based on the analyses of pre- and post-DDC CPTu results carried out at the site of U.S. Route 44 relocation project, the following conclusions can be reached:

(1) DDC is an effective ground improvement method for densifying loose to medium dense saturated granular soils. After two passes of DDC, cone tip resistance q_t of the backfill was increased by five to seven times, which resulted in 4^o to 6^o increase in the estimated strength ϕ' and 200 percent increase in the estimated constrained modulus M. However, for the medium dense to dense backfill and the underlying in-situ sands, DDC did not or only showed very limited densification effects.

(2) DDC was very effective in reducing potential settlements. The estimated settlements induced by embankments could be reduced by 40 percent after one pass of DDC and up to 84 percent after two passes.

(3) DDC was also very effective in mitigating potential liquefaction hazards. After two passes of DDC, the backfill was densified to the level of resisting potential liquefaction when it was subjected to the design earthquake motions.

ACKNOWLEDGEMENT

The author would like to express appreciation to the following people and organizations for providing related information: Dr. E. L. Hajduk of WPC, Inc.; Dr. N.

Hourani and Mr. P. Connors of Massachusetts Highway Department (MHD); P. A. Landers, Inc., Massachusetts; TerraSystems, Virginia; and WPC, Inc. Finally, the author would like to thank the reviewers' comments and suggestions.

REFERENCS

Cetin, K. O., Seed, R. B., Kiureghian, A. D., Tokimatsu, K., Harder, L. F., Kayen, R. E., and Moss, R. E. S. (2004). *Journal of Geotechnical and Geoenvironmental Engineering*, ASCE, 130(12), pp. 1314-1340.

Ernst, H., Connors, P., and Pettis, J. (1996). Geotechnical Report for Relocated Route 44, Section I Carver, Plympton and Kingston. Aug.1996, Massachusetts Highway Department (MHD), Geotechnical Section, Boston.

Jamiolkowski, M., Ladd, C. C., Germaine, J. T., and Lancellotta, R. (1985). "New developments in field and laboratory testing of soils." *Proceeding 11th International Conference on Soil Mechanics and Foundation Engineering,* San Francisco, Vol. 1, pp. 57-153.

Janbu, N. (1974). "Relationship between tangent modulus and cone resistance". *In Proceedings of the European Symposium on Cone Penetration Testing,* ESOPT, Vol. 2:1, pp. 132-134.

Massarch, K. R. (1994). "Settlement analysis of compacted fill". *In Proceedings of the 13th International Conference on Soil Mechanics and Foundation Engineering,* ICSMFE, New Delhi, Vol. 1, pp. 325-328.

Meyerhof, G. G. (1976). "Bearing capacity and settlement of pile foundations." *Journal of the Geotechnical Engineering Division,* ASCE, 102(1), pp. 197-259.

Mitchell, J. K. (1982). "Soil improvement-state of the art." *Proc. 10th ICSMFE, Stockholm,* Vol. 4, pp. 509-565.

Robertson, P. K., and Wride, C. E. (1998). "Evaluation cyclic liquefaction potential using the cone penetration test." *Canadian Geotechnical Journal,* 35(3), pp. 442-459.

Seed, H. B., and Idriss, I. M. (1971). "Simplified procedure for evaluating soil liquefaction potential." *Journal of the Geotechnical Engineering Division,* ASCE, 97(9), pp.1249-1273.

Seed, H. B., and Idriss, I. M. (1982). "Ground motions and soil liquefaction during earthquakes." Earthquake Engineering Research Institute Monograph.

Tan, Y., Lin, G., Paikowsky, S. G., and Fang, J. (2007). "Evaluation of compaction effects on granular backfill using CPT." *Geotechnical Special Publication: Soil Improvement,* GSP172, ASCE, pp. 1-10.

Ye, S. L., Ye, G. B., and Han, J. (1992). *Ground Treatment (in Chinese)*. Tongji University, Shanghai, China.

Centrifuge Testing of Prefabricated Vertical Drains for Liquefaction Remediation

Antonio Marinucci[1], M. ASCE, P.E., Ellen Rathje[2], M. ASCE, P.E.,
Seiji Kano[3], Ronnie Kamai[4], Carolyn Conlee[5], Rachelle Howell[6],
Ross Boulanger[7], M. ASCE, P.E., and Patricia Gallagher[8], M.ASCE, P.E.

[1] Doctoral Candidate, Dept. of Civil, Architectural, and Environmental Engineering, University of Texas at Austin, Austin, TX 78712-0280; marinucci@mail.utexas.edu
[2] Associate Professor, Dept. of Civil, Architectural, and Environmental Engineering, University of Texas at Austin, Austin, TX 78712-0280; e.rathje@mail.utexas.edu
[3] Assistant Professor, Dept. of Social and Environmental Engineering, Graduate School of Engineering, Hiroshima University, Hiroshima, Japan; skano@hiroshima-u.ac.jp
[4] Graduate Student, Dept. of Civil & Environmental Engineering, University of California at Davis, Davis, CA 95616-5294; rkamai@ucdavis.edu
[5] Doctoral Candidate, Department of Civil, Architectural, and Environmental Engineering, Drexel University, Philadelphia, PA 19104; cc428@drexel.edu
[6] Graduate Student, Dept. of Civil, Architectural, and Environmental Engineering, University of Texas at Austin, Austin, TX 78712-0280; rhowell@mail.utexas.edu
[7] Professor, Dept. of Civil & Environmental Engineering, University of California at Davis, Davis, CA 95616-5294; rwboulanger@ucdavis.edu
[8] Assistant Professor, Department of Civil, Architectural, and Environmental Engineering, Drexel University, Philadelphia, PA 19104; pmg@drexel.edu

ABSTRACT: One potential method for soil improvement against soil liquefaction is accelerated drainage through in situ vertical drains. Vertical drains are utilized to expedite the dissipation of excess pore water pressures by reducing the length of the pore water drainage path. For more than thirty years, gravel drains have been employed to ensure the excess pore water pressure ratio ($r_U = \Delta u/\sigma'_V$) remains below a prescribed maximum value. Recently, interest in the use of prefabricated vertical drains has increased because these elements can be installed with less site disruption than with other soil improvement methods. This paper presents the results from initial centrifuge experiments intended to evaluate the effectiveness of prefabricated vertical drains for liquefaction remediation. The centrifuge model includes sloping ground towards a central channel. Prefabricated vertical drains were installed in the soil upslope of one side of the central channel, while the other side was left untreated. Based on the results of the experiment, the prefabricated vertical drains were effective at draining and dissipating the excess pore water pressures, as well as significantly reducing the horizontal and vertical deformations.

INTRODUCTION

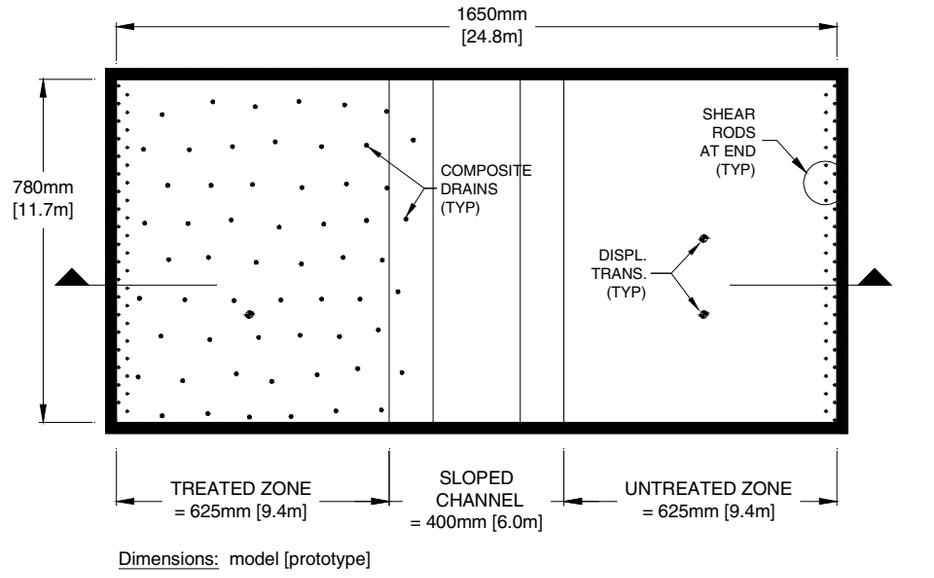
Various ground improvement methods are available for treating potentially liquefiable sites. When considering sites with previous development, such as pile-supported wharf structures constructed adjacent to hydraulic fills, the options for soil improvement are limited. Traditional methods, such as compaction and vibratory techniques, are difficult to employ because of adverse effects on adjacent structures. As part of a NEESR Grand Challenge project, centrifuge testing is being performed to investigate two innovative and less-invasive soil improvement methods suitable for developed sites: prefabricated vertical drains (e.g. Rollins et al 2004) and passive site stabilization (e.g. Gallagher et al 2007). This paper presents results from initial centrifuge experiments performed to evaluate prefabricated vertical drains. The centrifuge model consisted of sloping ground with a free-face at a central channel, such that two opposing lateral spread sections were tested. This configuration allowed one side to be treated with prefabricated vertical drains, while the other side remained untreated.

CENTRIFUGE MODEL

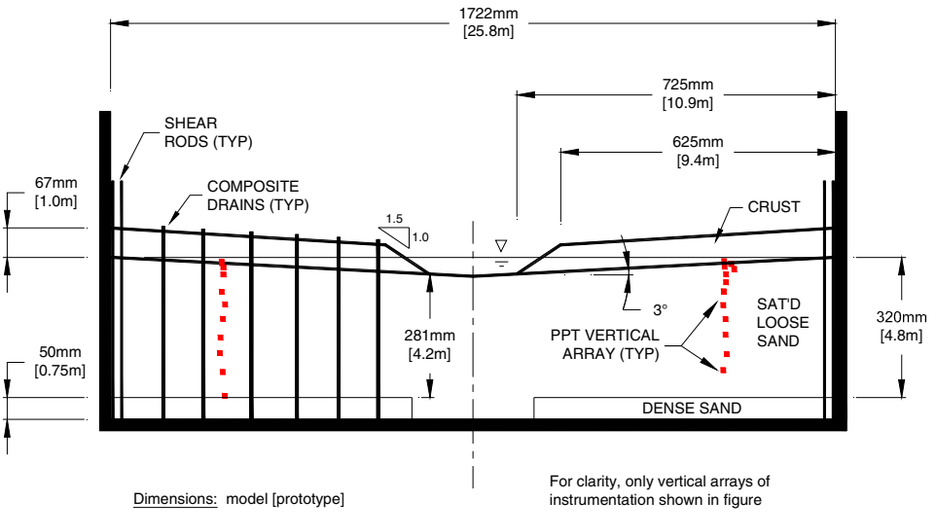
Centrifuge testing was performed at the NEES Equipment Site at the University of California at Davis in a flexible shear beam model container. The centrifugal acceleration was approximately 15 g, which is relatively small but allowed for reasonably sized model drains and drain spacing. The soil profile (Figure 1) slopes at approximately 3° toward a central channel and is comprised of two main layers: (1) a 4.8 m thick (prototype) liquefiable layer of loose Nevada sand (D_R~40%) overlain by (2) a 1 m thick crust of compacted Yolo Loam. The crust impedes vertical dissipation of pore water pressure from the underlying liquefiable sand, compels the generation of a water film at the sand-clay boundary, and promotes lateral spread deformations. Additional soil information is presented in Kamai et al. (2007). The soil upslope of the central channel on one side was treated with prefabricated vertical drains. The untreated zone on the other side of the channel contained no vertical drains.

The treated zone contained 58 vertical drains in a triangular pattern at a center-to-center spacing of approximately 1.5 m prototype scale (100 mm model scale). The drains were modeled using nylon tubes with an inside diameter of 7 mm, which translates into a prototype diameter of approximately 100 mm (Figure 2). The nylon tubes were perforated and covered with a thin fabric to prevent soil migration.

Because fluid flow is central to the drain problem being modeled in the centrifuge, it is important to consider the flow characteristics of the prototype soil. Generally, a viscous pore fluid is used in centrifuge flow modeling to maintain similitude between the hydraulic conductivity (k) of the model and prototype soils. In this study, water was used as the pore fluid because of the relatively small centrifugal acceleration and the relatively small k of the Nevada sand. The resulting k for the prototype soil was 10^{-1} cm/s, which is still realistic for sands, and thus the centrifuge test results are considered valid.



(a)



(b)

FIG. 1. (a) Plan View of Centrifuge Model within Container FSB-03 and (b) Cross-Section



(a) (b)

FIG 2. Photograph of (a) 7mm Model Drain with filter fabric and (b) actual 100mm drain with geosynthetic filter

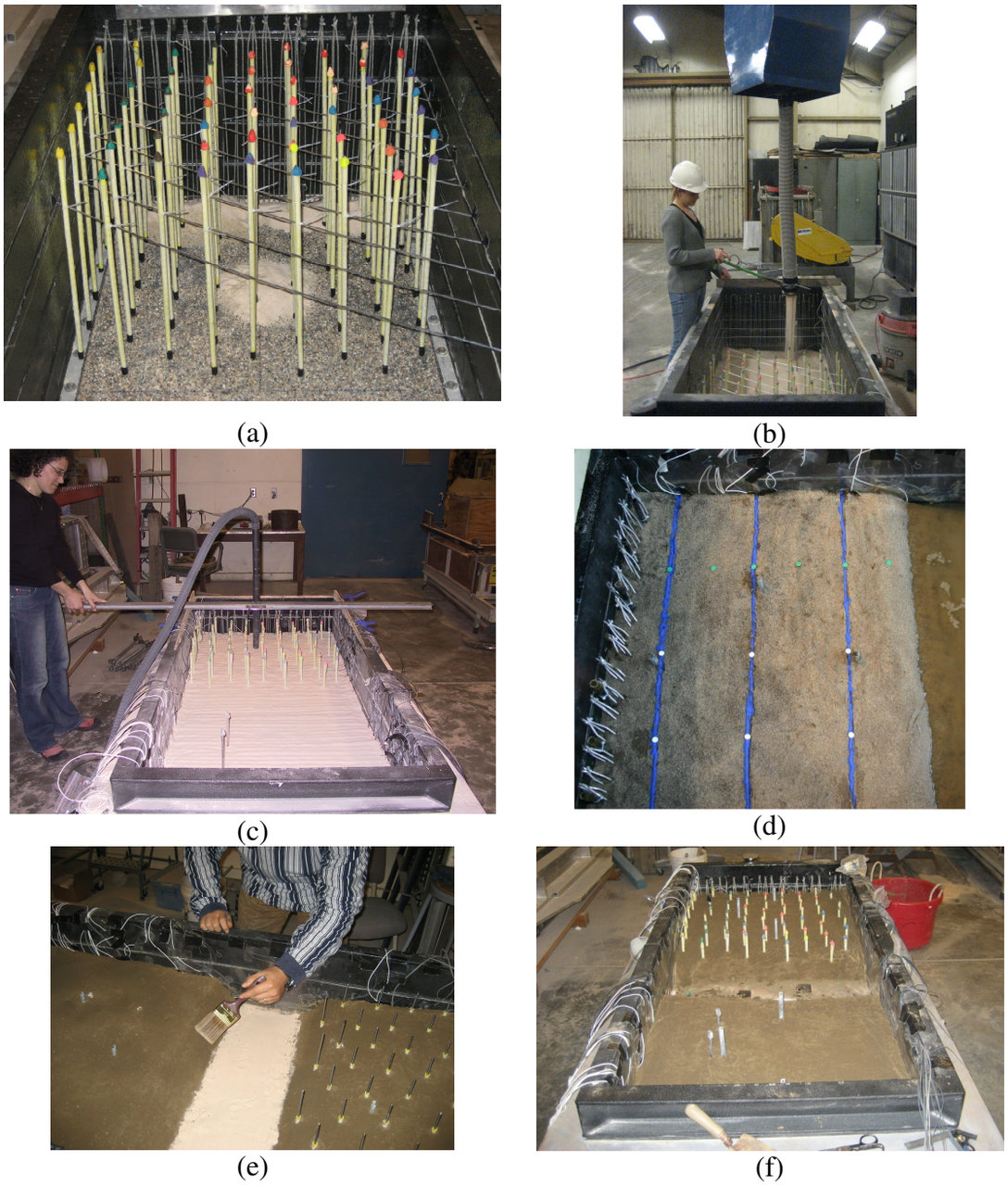


FIG 3. (a) Drains placed before Pluviation, (b) Pluviation of Sand, (c) Vacuuming to Ensure Proper Elevations, (d) Surface Markers on Untreated Side, (e) Construction of the Crust Layer, and (f) View of Completed Model

Specimen construction included placing the model drains before soil pluviation and supporting each drain by a steel rod connected to a wire grid on top of the container (Figure 3a). The sand was placed around the drains using dry pluviation (Figures 3b and 3c). The crust, compacted at 15% moisture content, was placed in 3 lifts using a specially designed roller that imparted a normal stress of 9 kPa on the surface. Selected photographs taken during stages of model construction are presented in Figure 3.

Saturation of the model was a two-fold process. The model was flooded with carbon dioxide (CO_2) gas while under a vacuum to remove air within the soil. The model was then saturated with water from the bottom upward. Water was placed to a depth such that the entire loose sand layer was saturated. As a result, the crust had portions that were either saturated or unsaturated prior to spin up. The height of the water within the model was readily observed within the central channel (Figures 1 and 3e).

A total of 12 shaking events were applied to the model, each consisting of 20 cycles of sinusoidal motion at a frequency of 2 Hz (prototype). The input base peak ground acceleration (PGA) ranged from 0.01 to 0.28 g. The early events were used to verify proper equipment and instrument response, only the last 5 shaking events (0.01 g, 0.028 g, 0.063 g, 0.11 g and 0.28 g) were used to evaluate the drains.

An extensive array of instrumentation was used to measure and record the behavior of the model during and after each shaking event. The instrumentation included 88 accelerometers, 57 pore pressure transducers (PPTs), 13 linear potentiometers, 3 vertical colored sand markers, and 6 colored sand surface markers.

CENTRIFUGE TEST RESULTS

Results from Low Amplitude Shaking (Base PGA = 0.028 g)

Selected excess pore pressure ratio ($r_U = \Delta u/\sigma'_V$) -time histories from the vertical PPT arrays (Figure 1) are presented in Figure 4 for Shake Event No. 9 (Base PGA = 0.028 g). At this low level of shaking, excess pore water pressure generation was small ($r_U < 0.1$ to 0.2) and full liquefaction did not occur. As anticipated, slightly larger values of r_U were realized on the untreated side as compared to the treated side. The generation and dissipation curves for the PPTs on the treated side were nearly linear as compared to the curvilinear ones on the untreated side. Settlement and lateral deformations for both sides of the model were negligible.

Results from High Amplitude Shaking (Base PGA = 0.28g)

Selected r_U -time histories from the vertical PPT arrays are presented in Figure 5 for Shake Event No. 12 (Base PGA = 0.28 g). The soil on the untreated side liquefied ($r_U = 1.0$) at all depths within a few cycles and maintained large values of r_U long after shaking ended. Large values of r_U (in excess of 0.5) were also observed on the treated side, but $r_U = 1.0$ was not reached at depths below about 3 m. Additionally, large dilatant cycles of smaller r_U were observed on the treated side due to the rapid dissipation of pore water pressure during shaking. Finally, the drains quickly dissipated the excess pore water pressures after shaking ended. A photograph depicting water exiting from the drains and shooting into the air is shown in Figure 6.

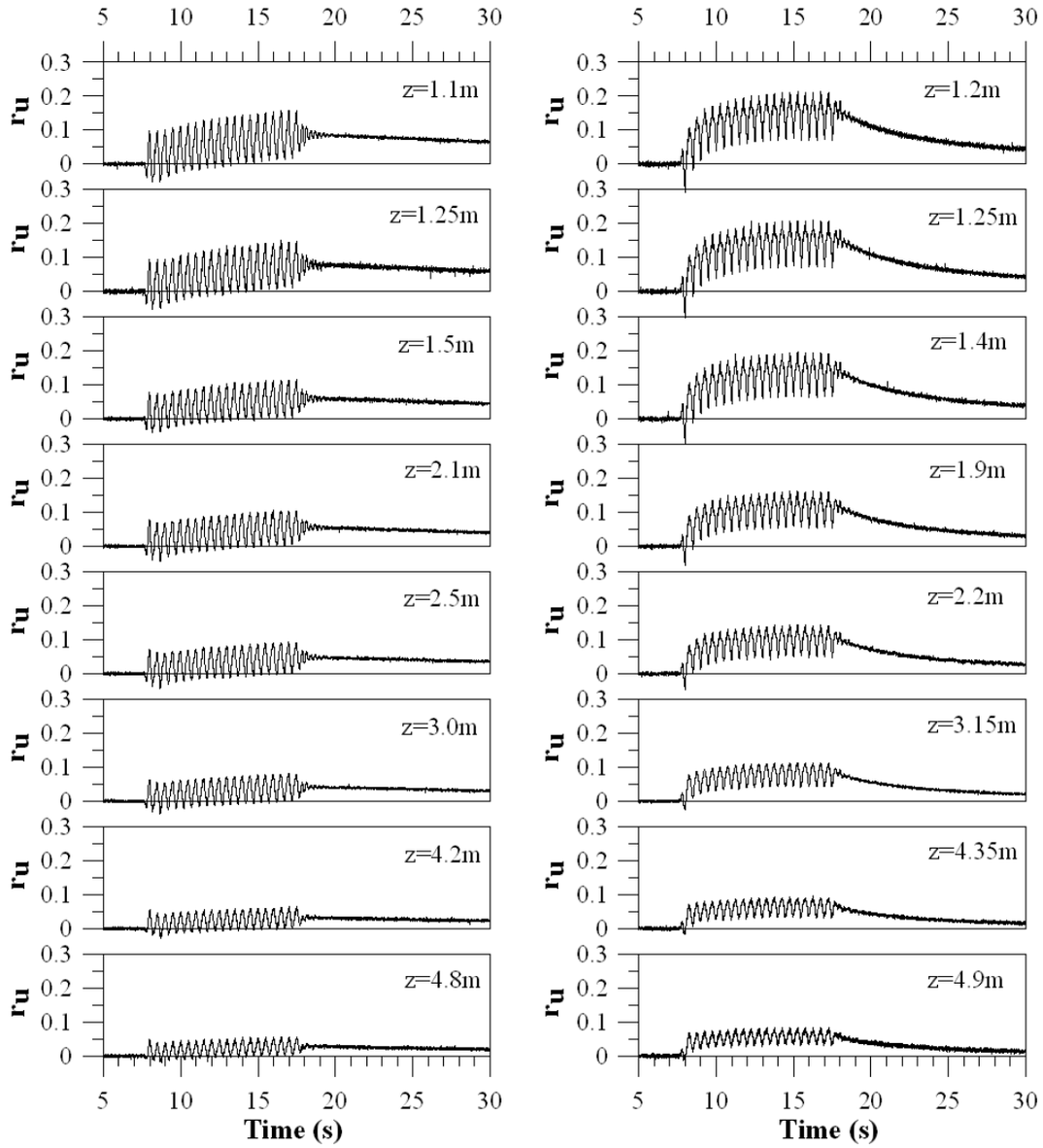


FIG 4. Excess Pore Pressure Ratio vs. Time for Base PGA=0.028g (Shake Event No. 9) for (a) Treated and (b) Untreated Sides

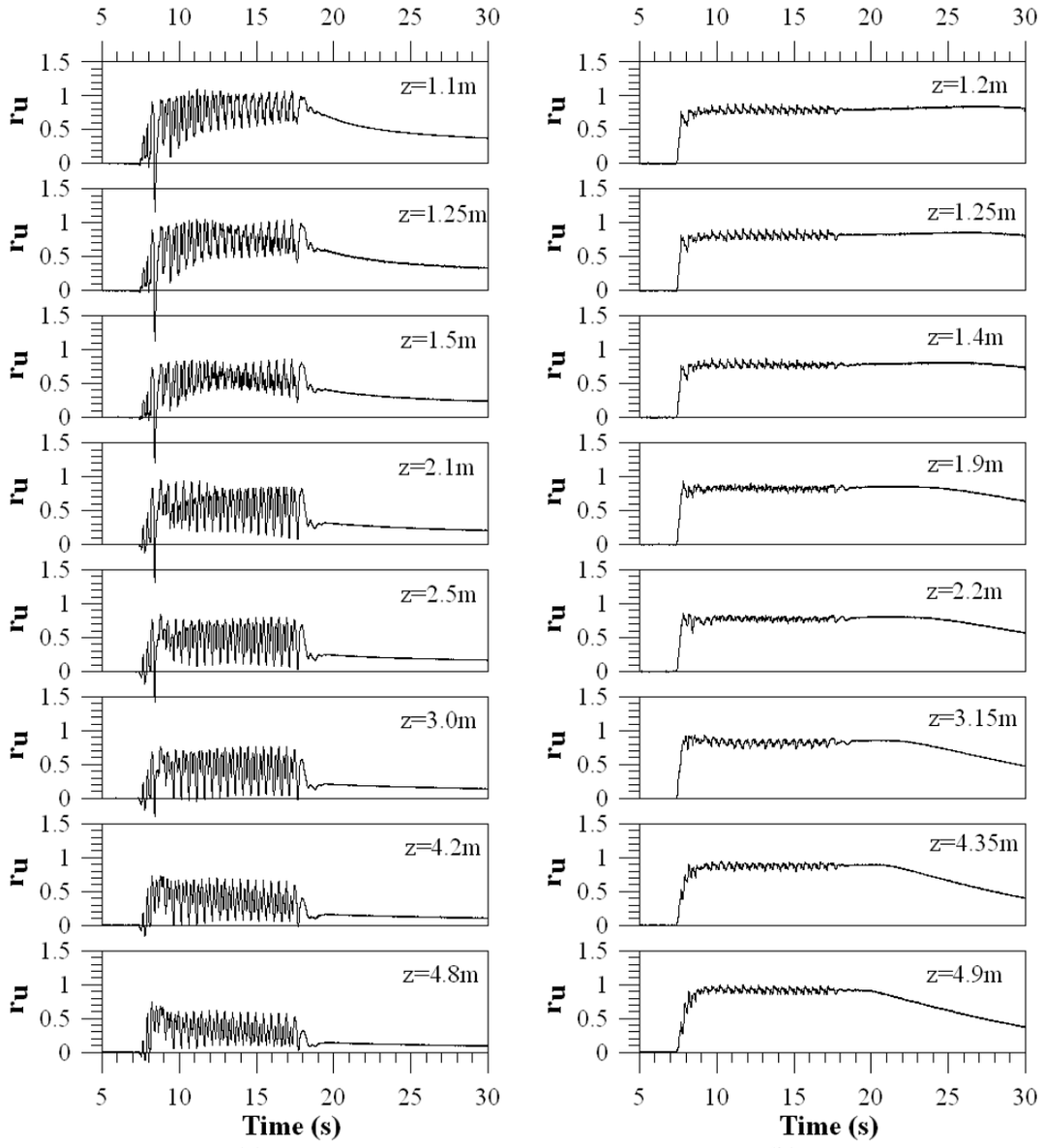


FIG 5. Excess Pore Pressure Ratio vs. Time for Base PGA=0.28g (Shake Event No. 12) for (a) Treated and (b) Untreated Sides

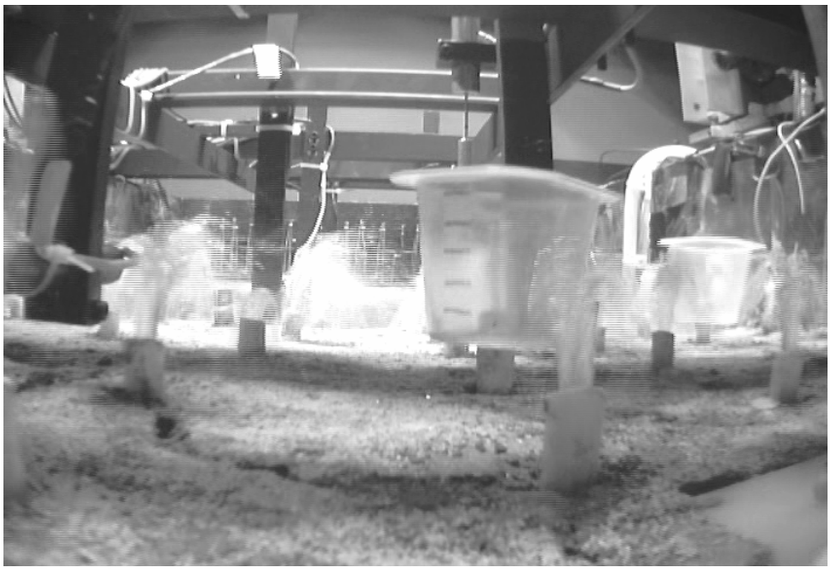


FIG 6. Photograph taken with Onboard Camera during Shake Event 12 (PGA=0.28g). Note the Water Discharging from Top of Drains.

Excess pore water pressure profiles for both the treated and untreated sides of the model at different times are presented in Figure 7. On the treated side, excess pore water pressures toward the top of the sand layer approached the initial effective stress during excitation but rapidly dissipated after shaking ended. Toward the bottom of the sand layer, the excess pore water pressures reached only about half the value of the initial effective stress. On the untreated side, excess pore water pressures throughout the profile quickly approached (in fewer than 3 cycles of shaking) the initial effective stress and, near the surface, remained there even 10 s after shaking had ended (t = 20 s in Figure 7). At the same time, excess pore water pressures toward the bottom of the sand layer were about one-half the value of the initial effective stress, indicating that the excess pore water pressures dissipated from the bottom of the specimen. For comparison, on the treated side, the excess pore pressures had dissipated significantly by t = 20 s, and the excess pore pressure distribution was almost constant with depth.

Shaking-induced displacement-time histories for the horizontal and vertical directions for both the treated and untreated sides of the model are presented in Figure 8 for all five shaking events. The horizontal and vertical displacements were negligible for the two lower-level shaking events. At 0.063 g, displacements became noticeable. At the end of the entire shaking sequence, the permanent horizontal displacement on the treated side, was only one-fifth (20%) of that measured at a similar location on the untreated side (Figure 8a). The vertical displacement on the treated side was about one-half of that measured at a similar location on the untreated side (Figure 8b). Selected photographs indicating location-specific deformations and sand boils were taken during various stages of model dissection and are presented in Figure 9. Interesting to note is the localization of horizontal displacement at the sand-clay interface for the untreated side (Figures 9a and b).

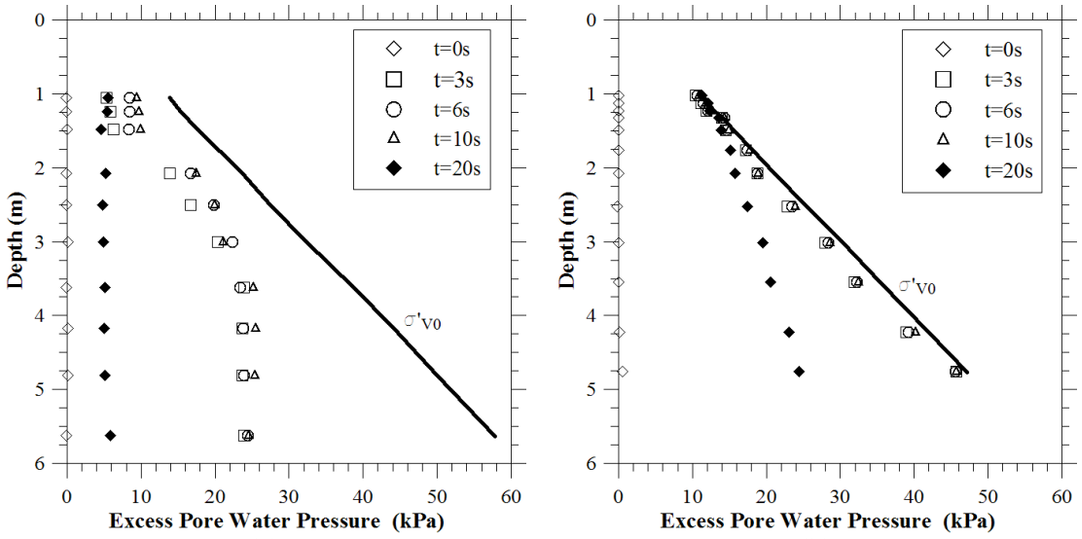


FIG 7. Excess Pore Water Pressure Profile for Varying Times for PGA=0.28g (Shake Event No. 12) for (a) Treated and (b) Untreated Sides. (Note: "t=0s" corresponds to the start of shaking.)

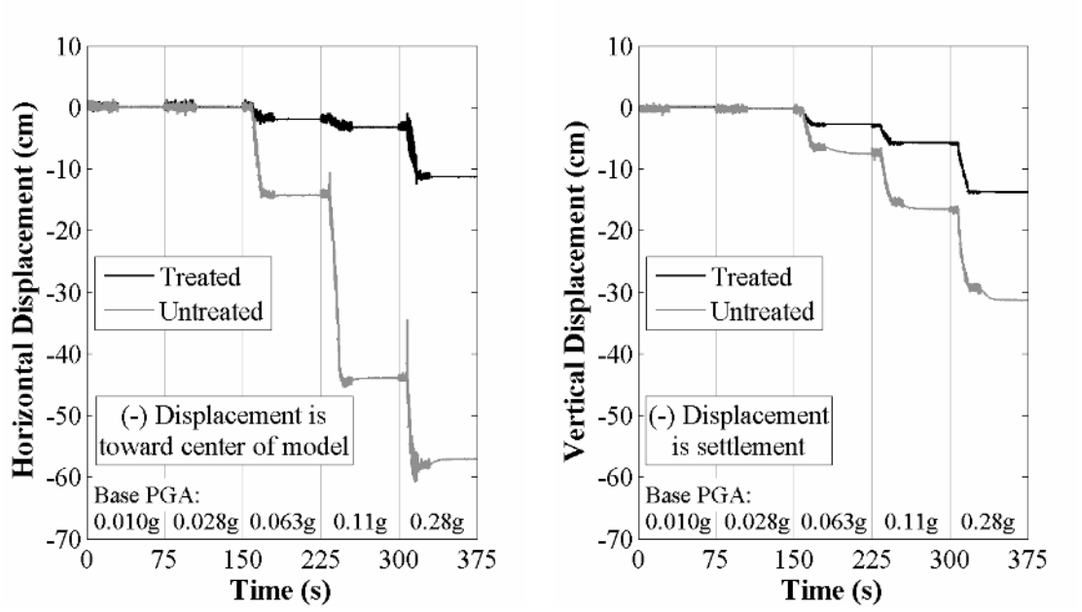
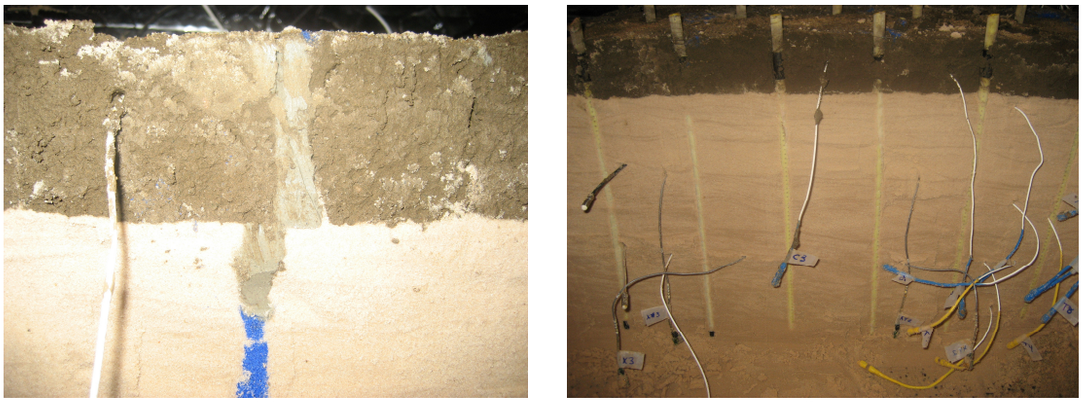


FIG 8. Shaking-Induced Deformation: (a) Horizontal and (b) Vertical Directions. Measurement locations shown in Figure 1.



(a) (b)

FIG 9. (a) Localization of Horizontal Displacement at Sand-Clay Interface on Untreated Side, (b) Absence of Localization on Treated Side

CONCLUSIONS

The first experiment in a series of centrifuge tests to evaluate the effectiveness of prefabricated vertical drains for liquefaction remediation was performed. The response of two similar slopes, one treated with drains and the other left untreated, at two levels of excitation was presented. Results from these tests indicate that prefabricated vertical drains were effective at dissipating excess pore water pressures during shaking of a loose soil. Permanent horizontal and vertical displacements on the treated side were significantly smaller than those at similar locations on the untreated side. These results demonstrate that prefabricated vertical drains can reduce excess pore pressures, as well as associated deformations at liquefiable sites.

ACKNOWLEDGMENTS

This research is part of the NEES Grand Challenge project for Seismic Risk Management of Port Systems, directed by Dr. Glenn Rix of the Georgia Institute of Technology. The authors wish to acknowledge the assistance of Dr. Brady Cox, Dr. Dan Wilson, Chad Justice, Peter Rojas, Ray Gerhard, Nick Sinikas, and Lars Pederson.

REFERENCES

Gallagher, P.M., Conlee, C.T. and Rollins, K.M. (2007). "Full-Scale Field Testing of Colloidal Silica Grouting for Mitigation of Liquefaction Risk." *Journal of Geotechnical and Geoenvironmental Engineering*, 133(2), p. 186–196.

Kamai, R., Kano, S., Conlee, C. Marinucci, A., Rathje, E., Boulanger, R. and Rix, G. (2007). "Evaluation of the Effectiveness of Prefabricated Vertical Drains for Liquefaction Remediation – Centrifuge Data Report for SSK01," Center for Geotechnical Modeling Data Report UCD/CGMDR. Univ. of California, Davis.

Rollins, K.M., Goughnour, R.R., Anderson, J.K.S and Wade, S.F. (2004). "Liquefaction Hazard Mitigation by Prefabricated Vertical Drains." *Proc., Fifth Int'l Conference on Case Histories in Geotechnical Engineering*, N.Y., 8pp.

Colloidal Silica Gel and Sand Mixture Dynamic Properties

Laura Spencer[1], Glenn J. Rix[2], A.M. ASCE, and Patricia Gallagher[3], A.M. ASCE, P.E.

[1] Graduate Research Assistant, School of Civil and Environmental Engineering, Georgia Institute of Technology, Atlanta, GA 30332-0355; laura.spencer@ce.gatech.edu
[2] Professor, School of Civil and Environmental Engineering, Georgia Institute of Technology, Atlanta, GA 30332-0355; glenn.rix@ce.gatech.edu
[3] Associate Professor, Department of Civil, Architectural and Environmental Engineering, Drexel University, Philadelphia, PA 19104; pmg24@drexel.edu

ABSTRACT: A comparative study of two different concentrations of colloidal silica gel and sand mixtures is presented. The dynamic properties, shear modulus and damping ratio, of No. 120 Nevada sand permeated with colloidal silica gel were determined using resonant column tests. The behaviour of the gelled samples is compared to untreated sand samples. The effects of the concentration of colloidal silica gel by percent weight, cyclic shear strain and aging on the dynamic properties of the gel-sand mixtures were studied. Results show there is a small difference in shear modulus with concentration of colloidal silica gel by percent weight and the gel-sand mixtures have a slightly higher shear modulus than untreated sand. The presence of the silica gel does not greatly affect the damping ratio. A 5% by weight gel-sand sample subjected to a long-term, small-strain cyclic shear resonant column test for a duration of 28 days after gelation shows an increase of 6 MPa in the shear modulus.

INTRODUCTION

Grouting with colloidal silica gel, as a method of passive soil improvement, has shown promise as a liquefaction mitigation technique. Passive soil improvement methods are an attractive alternative for situations requiring minimal disruption. Passive site stabilization involves slow injection of stabilizing materials at the up-gradient edge of a site and delivery of the stabilizer to the target location using natural or augmented groundwater flow. Prior studies of candidate stabilizing materials (Gallagher and Mitchell, 2002; Gallagher et al., 2007; Persoff et al., 1999) have identified colloidal silica (Iler, 1979) as an ideal, environmentally benign grouting material with low initial viscosity, controllable gel times, and good long-term mechanical stability. Colloidal silica is an aqueous dispersion of silica nanoparticles that can be made to gel by adjusting the pH and ionic strength of the solution. Upon delivery to the target location, the stabilizer starts to gel or set rapidly at a predetermined time to bind the soil particles. In concentrations of 5

percent by weight, it significantly improves the deformation resistance of loose sands to cyclic loading (Gallagher, 2000; Gallagher and Mitchell, 2002; Whittle, 2007).

Previous work on the applicability of colloidal silica gel as a passive liquefaction mitigation method has focused on the ability of the gel to resist deformations. However, no research has been conducted on the dynamic properties of sand treated with colloidal silica gel in the small and intermediate strain range. To accurately characterize the response of the sand and gel mixtures to seismic loading, the dynamic properties of the mixture are essential. The purpose of this experimental study is to determine the influence the colloidal silica gel has on the shear modulus and damping ratio and to investigate the effect of cyclic shear strain and aging on these properties.

Colloidal Silica Gel

Colloidal silica is an aqueous dispersion of silica nanoparticles (Iler, 1979). The solutions used in these experiments are Ludox SM-30, diluted to colloidal silica weight percent concentrations of 5, 7 and 9. The silica particles are approximately 7nm in size in the stabilized solution before gelation begins (DuPont, 1997). The structure of the silica molecules are polymer spheres (Scott, 1993) with negatively charged surfaces as shown in Figure 1.

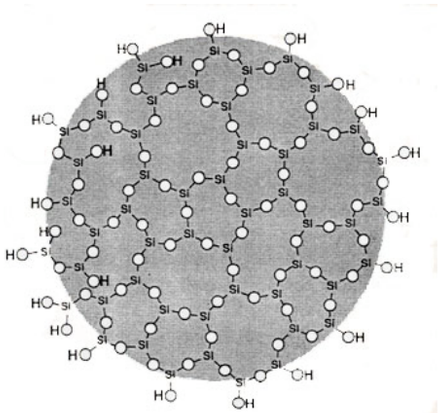


FIG. 1. Schematic of colloidal silica particle (Silco International, 2005).

Due to the small size and surface charge of the silica particles, electrical interparticle forces dictate the behavior and fabric formation of the particles (Santamarina et al., 2001; Scott, 1993). Aggregation, or gelation, is induced by altering the repulsive forces of the silica particles in solution. The addition of NaCl to the water used to dilute the silica sol increases the salt concentration of the solution and reduces the double layer thickness of the silica particles. This reduces the repulsive forces and allows the particles to move close enough together to form siloxane bonds and dissociate an H_2O molecule. The dissociated water caused by multiple bonds remains within the pore space of the gelled silica particle network. A simplified chemical bond is shown in Figure 2. The chemical bonding continues after the initial resonating gel state is reached. The continuing bonding causes an increase in the strength of the gel over time (Axelsson, 2006; Hench and West, 1990).

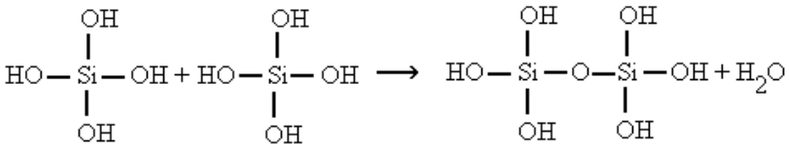


FIG. 2. Simplified schematic of siloxane bonding.

In order to characterize the long-term performance of the gel-sand mixtures, it is necessary to investigate the shear modulus changes due to the increase of interparticle cross-linking within the gel. The purpose of a long-term test is to determine how the colloidal silica gel aging affects the dynamic properties.

TEST PROCEDURE

Sample Preparation

Samples of No. 120 Nevada sand were prepared using an air pluviation device. The index properties of No. 120 Nevada sand are shown in Table 1. A schematic of the device is shown in Figure 3. Samples prepared by air pluviation are more uniform than other preparation methods and result in a uniform local void ratio (Jang, 1997; Park, 1999). To maintain a constant fall height during pluviation, the pluviation container was raised continuously at the same rate as the rise in the surface of the sand being deposited in the specimen mold.

Table 1. Index Properties of No. 120 Nevada Sand

Supplier	Gordon Sand Co., Compton, CA
USCS Classification	Uniform, fine sand, SP
D_{50} (mm)	0.15
Coefficient of Uniformity, C_u	1.6
Maximum dry unit weight (kN/m^3)	16.76
Minimum dry unit weight (kN/m^3)	13.98

The pluviator was calibrated to obtain 50% relative density No. 120 Nevada sand for samples with a nominal diameter of 7.1 cm and height of 14.2 cm. Following pluviation, the samples were consolidated using vacuum to an effective confining pressure of 50 kPa. While under confinement, colloidal silica gel solution was permeated into the sample under a low gradient. To perform sample permeation, a resonant column cell and end platens were modified so only disposable items were exposed to the colloidal silica solution as shown in Figure 4. The sample was pluviated, permeated and tested on the modified resonant column to minimize disturbance of the sample. Ionic concentrations of the colloidal silica solutions were chosen to achieve gel times of approximately two to three hours. After permeating, the sample was left to cure for a period of 10 times the gel time to ensure the sample was at a resonating gel state before testing and to test each

sample at the same progression of bond formation to make accurate comparisons between the different colloidal silica concentrations (Gallagher, 2000).

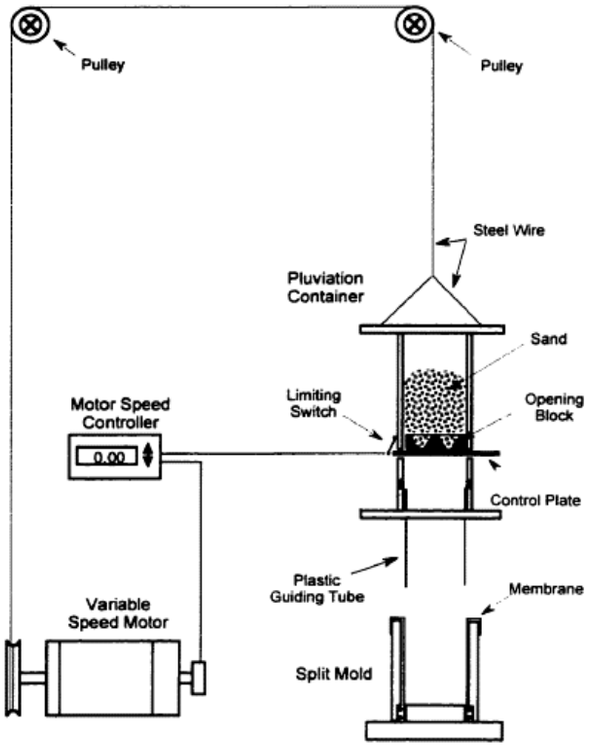


FIG. 3. Schematic of air pluviation device (after Park, 1999).

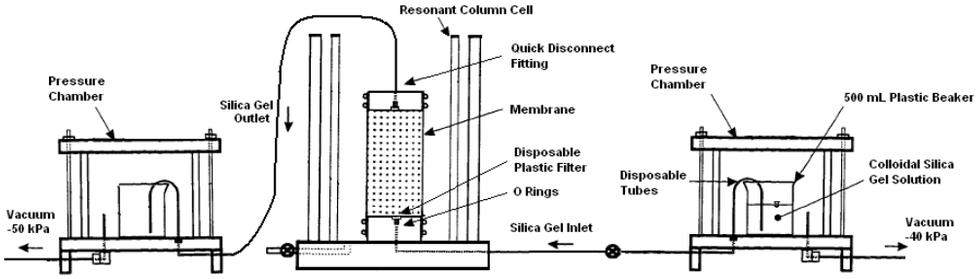


FIG. 4. Schematic of colloidal silica gel permeation device (after Jang, 1997).

Resonant Column Test Procedure

The resonant column test is a widely used test that employs the torsional vibrational method to measure the dynamic properties of soils (Ni, 1987; Woods, 1994). The resonant frequency of each specimen for a particular shear strain level was determined by measuring the frequency response between the voltage applied to the coils of the resonant column and the output of the accelerometer used to monitor the angular acceleration of the top of the specimen. The resonant frequency was used to determine the shear wave velocity of the specimen using:

$$\frac{I}{I_o} = \frac{\omega_r \cdot L}{V_s} \cdot \tan\left(\frac{\omega_r \cdot L}{V_s}\right) \quad (1)$$

where:
I = mass polar moment of inertia of the soil specimen,
I_0 = mass polar moment of inertia of the drive system determined via calibration,
ω_r = circular resonant frequency of the system in torsion (= $2\pi f_r$),
L = length of the soil specimen, and
V_s = shear wave velocity of the specimen.

The corresponding value of shear strain was determined using:

$$\gamma_{avg} = 0.79 \cdot \frac{r_o \cdot \theta}{L} \quad (2)$$

where r_0 is the radius of the specimen and θ is the angle of rotation.

The material damping ratio of the specimen was calculated using the half-power bandwidth method:

$$D = \frac{f_2 - f_1}{2f_r} \quad (3)$$

where f_1 and f_2 are the frequencies of the half-power points defined as 0.707 times the amplitude of the resonant peak (ASTM D4015, 2001).

Equipment-generated damping in the resonant column test due to the interaction between the magnets and solenoids results in a bias error in the measurement of material damping. Meng and Rix (2003) demonstrated that a current-mode source significantly reduces equipment-generated damping in comparison to a conventional voltage-mode source. In this study, a current-mode source was implemented via a voltage-to-current converter.

The resonant column tests were performed starting at low cyclic shear strain amplitudes and increasing to a maximum strain of approximately 0.03%, depending on the stiffness of the sample. A final low-strain test was performed after the higher-strain testing was completed. Cyclic prestraining tends to cause a small increase in the shear modulus (Alarcon-Guzman et al., 1989; Drnevich and Richart, 1970); however, the final low-strain tests for both the treated and untreated samples resulted in a negligible difference. In addition, the shear moduli at shear strain amplitudes larger than the previous maximum strain are not affected by cyclic prestraining (Alarcon-Guzman et al., 1989).

To investigate the effect of aging, a 5% gel-sand sample was subjected to small-strain resonant column tests performed at pre-determined time intervals over 28 days. A cyclic shear strain of approximately 2.5 x 10^{-4}% was used for all the tests. Three tests were performed at each time interval to evaluate the repeatability of the measurements.

RESULTS

The effect of strain amplitude on the dynamic properties was investigated by testing two concentrations of colloidal silica gel and sand mixtures. Untreated sand samples were tested as a reference. Two specimens of each weight percent colloidal silica gel were

tested at the same time interval (gel time multiple) after gelling to evaluate the repeatability of the measurements. Shown below in Figure 5 are the results for the 5 weight percent colloidal silica and sand mixture samples. This data is representative of results of the gel-sand samples.

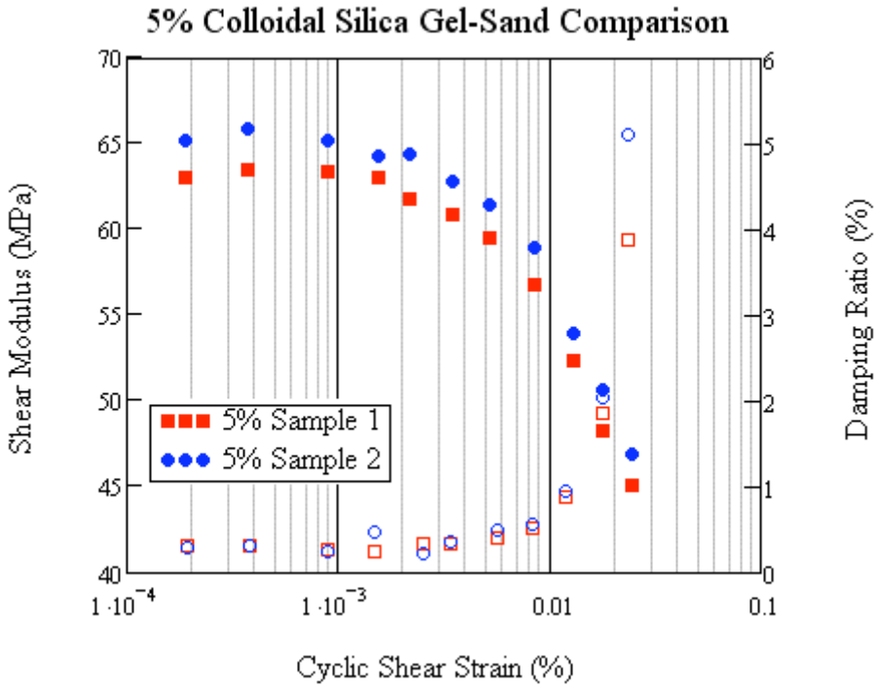


FIG. 5. Typical results of colloidal silica and sand mixture resonant column tests. Shown is data from 2 separate 5% CS-sand specimens.

A summary plot of the effect of the colloidal silica gel on the shear modulus is shown in Figure 6. The varying concentrations are compared to the untreated sand sample. Multiple tests for a particular concentration have been averaged. It is observed that there is a small difference in the shear modulus with increasing concentration of colloidal silica in the gel-sand mixtures. The shear modulus of all colloidal silica gel-sand mixtures is slightly higher than the shear modulus of untreated sand in the low cyclic strain region.

The damping ratio of different concentrations of colloidal silica and sand mixtures and untreated sand are shown in Figure 7. The values shown are the average of multiple tests. The effect of introducing colloidal silica into the soil matrix on the damping ratio is negligible.

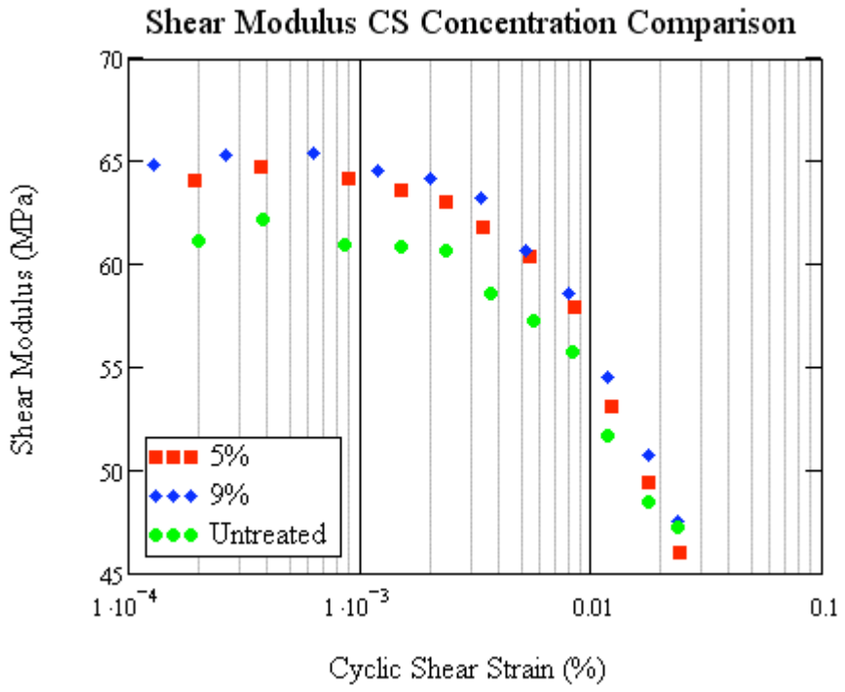


FIG. 6. Shear modulus comparison of CS mixtures to untreated sand.

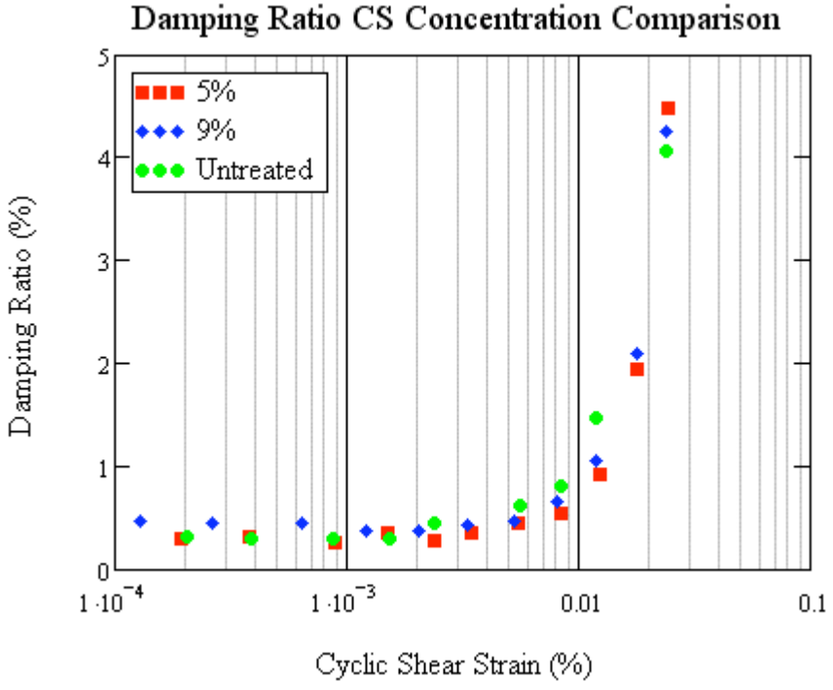


FIG. 7. Damping ratio comparison of CS mixtures to untreated sand.

A summary plot of the effect of aging on the shear modulus of colloidal silica gel-sand samples is shown in Figure 8. The small-strain shear modulus of a 5% by weight gel-sand mixture was measured at time intervals over a period of 28 days. Three trials were run at each time interval to identify repeatability and the resonant frequency observed during each trial was the same. It should be noted this sample was tested at an effective confining pressure of 26 kPa due to a regulator malfunction. Over a period of 28 days after gelling, the shear modulus of the gelled sand samples increased by approximately 6 MPa. However, the shear modulus is still increasing and has not reached an apparent ultimate G_{max} value.

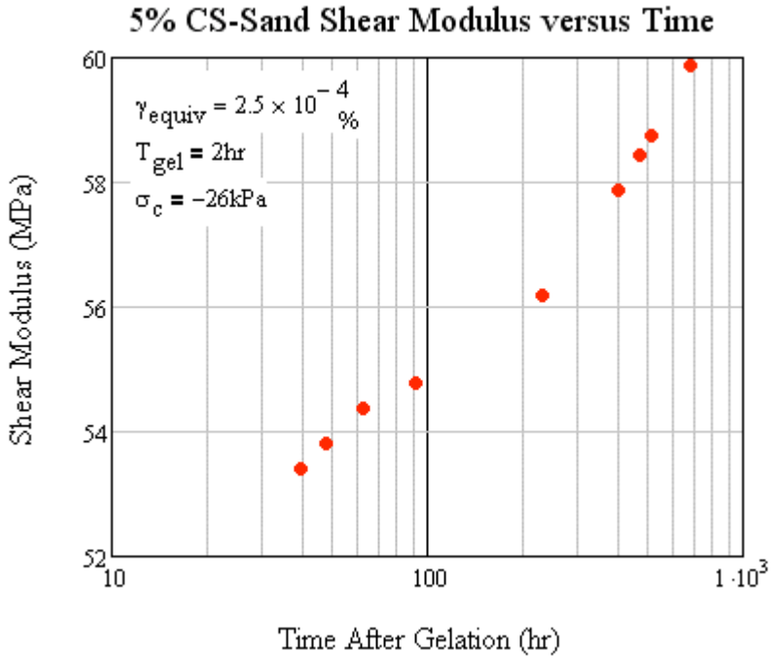


FIG. 8. Small-strain shear modulus of 5% CS-sand sample over 28 days.

CONCLUSIONS

The shear modulus and damping ratio of No. 120 Nevada sand treated with two different concentrations of colloidal silica were determined using resonant column tests. The effects of the concentration of the colloidal silica gel were investigated. Based on the results, it can be concluded that there is a small difference in the shear modulus with increasing concentration of colloidal silica in the grouting solution and the gel-sand mixtures have slightly higher shear modulus than untreated sand in the low strain region. The influence of colloidal silica on the damping ratio is negligible over the strain range investigated.

The effect of aging on the small strain shear modulus of No. 120 Nevada sand permeated with 5% weight colloidal silica solution was determined using resonant column tests. The results show the shear modulus increases approximately 6 MPa over 28 days and has not reached an apparent ultimate G_{max}.

ACKNOWLEDGMENTS

This material is based upon work supported by the National Science Foundation under Grant No. CMS-0530478. The authors would like to thank Dr. Jiewu Meng for his assistance with the voltage-to-current converter.

REFERENCES

Alarcon-Guzman, A., Chameau, J. L., Leonards, G. A., and Frost, J. D. (1989). "Shear modulus and cyclic undrained behavior of sands." *Soils and Foundations*, Vol. 29 (4): 105-119.

ASTM D4015. (2001). "Standard test methods for modulus and damping of soils by the resonant-column method. Designation D-4015." ASTM International, West Conshohocken, PA.

Axelsson, M. (2006). "Mechanical tests on a new non-cementitious grout, silica sol: A laboratory study of the material characteristics." *Tunnelling and Underground Space Technology*, Vol. 21: 554-600.

Drnevich, V. P., and Richart, F. E., Jr. (1970). "Dynamic prestraining of dry sand." *Journal of Soil Mechanics and Foundations Division, ASCE*, Vol. 96 (SM 6): 1917-1934.

DuPont. (1997). "Ludox Colloidal Silica: Properties, Usage, Storage and Handling." Product Information, DuPont, Wilmington, DE.

Gallagher, P. M. (2000). "Passive site remediation for mitigation of liquefaction risk," PhD Dissertation, Virginia Polytechnic Institute and State University, Blacksburg, VA.

Gallagher, P. M., and Mitchell, J. K. (2002). "Influence of colloidal silica grout on liquefaction potential and cyclic undrained behavior of loose sand." *Soil Dynamics and Earthquake Engineering*, Vol. 22: 1017-1026.

Gallagher, P. M., Pamuk, A., and Abdoun, T. H. (2007). "Stabilization of liquefiable soils using colloidal silica grout." *Journal of Materials in Civil Engineering*, Vol. 19(1), 33-40.

Hench, L. L., and West, J. K. (1990). "The sol-gel process." *Chemical Reviews*, Vol. 90 (1): 33-72.

Iler, R. K. (1979). *The Chemistry of Silica: Solubility, Polymerization, Colloid and Surface Properties, and Biochemistry*, John Wiley & Sons, New York, NY.

Jang, D.-J. (1997). "Quantification of sand structure and its evolution during shearing using image analysis," PhD Dissertation, Georgia Institute of Technology, Atlanta, GA.

Meng, J., and Rix, G. J. (2003). "Reduction of equipment-generated damping in resonant column measurements." *Geotechnique*, Vol. 53 (5): 503-512.

Ni, S. (1987). "Dynamic properties of sand under true triaxial stress states from resonant column/torsional shear tests," Ph.D. Dissertation, The University of Texas at Austin, Austin, TX.

Park, J.-Y. (1999). "A critical assessment of moist tamping and its effect on the initial and evolving structure of dilatant triaxial specimens," PhD Dissertation, Georgia Institute of Technology, Atlanta, GA.

Persoff, P., Apps, J., Moridis, G., and Whang, J. M. (1999). "Effect of dilution and contaminants on sand grouted with colloidal silica." *Journal of Geotechnical and Geoenvironmental Engineering*, Vol. 125 (6): 461-469.

Santamarina, J. C., Klein, K. A., and Fam, M. A. (2001). *Soils and Waves*, John Wiley & Sons, New York, NY.

Scott, R. P. W. (1993). *Silica Gel and Bonded Phases: Their production, properties and use in LC*, John Wiley & Sons, New York, NY.

Silco International. (2005). "Colloidal Silica Technical Information." Silco International, LLC, Portland, OR, http://www.silco-intl.com/technical/index.html.

Whittle, A. (2007). Personal communication.

Woods, R. D. (1994). "Laboratory measurements of dynamic soil properties." *Dynamic Geotechnical Testing II*, ASTM STP 1213, Ebelhar, R. J., Drnevich, V. P. and Kutter, B. L., Eds., American Society for Testing and Materials, West Conshohocken, PA, 165-190.

Compaction Grouting to Mitigate Liquefaction For a New Medical Retail Building

Mark Russell[1], M. ASCE, P.E., G.E., Jeff Geraci[2], M. G-I, C.E.G. and David Murray[3]

[1] Senior Geotechnical Engineer, Earth Systems Southern California, 2114 East Walnut St., Pasadena, CA 91107; phone 626-356-0955; mrussell@earthsystems.com.
[2] Manager, Moore & Taber, 1290 N. Hancock St., Suite 102, Anaheim, CA 92807; phone 714-779-0681; j.geraci@mooreandtaber.com.
[3] Principal, Earth Systems Southern California, 14550 Haynes St., Suite 202, Van Nuys, CA 91411; phone 818-901-8075; dmurray@earthsystems.com.

ABSTRACT: This paper presents a case study of compaction grouting used as a mitigation measure for soil liquefaction beneath a proposed two-story retail building with integral parking structure. The site is in an area that experienced significant seismic shaking, liquefaction, and structural damage during the 1994 "Northridge" earthquake. Analysis suggested potential for a lateral spreading hazard into the adjacent Los Angeles River. Compaction grouting was used to treat loose to medium dense saturated alluvium to a depth of 17.1 m. A test grout section was conducted prior to production to help determine optimum spacing of grout injection locations. Records of injected grout quantities were maintained in order to provide an indication of relative soil displacement with respect to treatment depth. A grout flow logger was used periodically to acquire real-time pressure and flow data during production grouting. Evaluation of these data provided a means of detecting soil response, providing a basis for establishing practical quantity limits when working near a buried storm drain pipe and a concrete-lined embankment. Comparison of pre-grouting and post-grouting soil test data showed significant improvement in liquefaction resistance, and estimated total and differential settlement was reduced from approximately 280 to 35 mm. Ground improvement was sufficient to allow the local building department to approve a previously infeasible project and to allow an alternate (more conventional) foundation system, representing significant project economy.

INTRODUCTION

The skyrocketing value of land in southern California has allowed developers a second look at sites where the cost of mitigating adverse soil conditions would have previously been considered prohibitive. Such was the case of a parcel in the Reseda area of the San Fernando Valley. Although ideally suited in many respects for commercial development,

the site was located in an area designated by the State of California as a "liquefaction hazard zone", and an engineered approach was required. The site is located along the south bank of the Los Angeles River channel in an area that had experienced severe damage during the 1994 Northridge earthquake, largely due to soil liquefaction.

Project plans called for construction of a two-story reinforced concrete commercial structure in the northwesterly portion of a 1.5 acre site with an approximate plan-view footprint of 1,550 m^2. The lowest level (ground level) is scheduled for retail space, while the second and roof levels have been designed for automobile parking, with a pedestrian access bridge to the existing adjacent medical facility. An automobile ramp is planned along the north side of the building to allow access to the roof.

The challenge facing the owner/developer was how to construct the building to meet current building code requirements and mitigate potential damage in the event of a liquefaction-producing earthquake, while maintaining an economically-viable project. Other restrictions imposed included limits on noise and vibration during construction, due to adjacent residential neighborhoods and an active five-story medical office building located within approximately 6 m of the site (Figure 1).

Recommendations for mitigation of liquefaction potential were developed based on the geotechnical consultant's subsurface investigation. Exploratory borings revealed that the southern part of the site was underlain by silts and clays, while the northern part was underlain by loose sandy sediments deposited during past meanderings of the Los Angeles River channel.



FIG. 1 – Photo of jobsite taken from the adjacent five-story medical office building. Image was obtained approximately one year after completion of grouting, and shows new building under construction. LAR = Los Angeles River, TA = Tampa Avenue.

Groundwater was present at a depth of approximately 6 m, with a potential to rise to within 4.6 m from the ground surface. Due to the loose, sandy, saturated nature of these soils, the site was determined to possess significant potential for liquefaction-induced settlement and lateral spreading (toward the adjacent channel) in the event of another sizable earthquake.

Several remedial options were presented to allow site development, including deep foundations, mat foundations, and ground improvement. After review and comparison of available options, it was determined that ground improvement using compaction grouting would provide the most economic and appropriate means of mitigation based on site geometry and soil conditions, as well as cultural sensitivity to noise and ground vibration intrinsic to other remedial options.

LIQUEFACTION RELATED HAZARDS

Prior to compaction grouting, sandy soils at the project site between 4.6 m and 17.1 m were found to possess a significant potential for liquefaction, with total maximum potential for earthquake-induced ground subsidence predicted to range from approximately 58 mm to 280 mm for CPT-based and SPT-based analyses, respectively. Procedures used for estimating these potential settlements were in accordance with those of Tokamatsu & Seed (1987), Robertson & Wride (1997), and Pradel (1988).

These relatively large estimated settlements were identified toward the northern part of the site, closer to the Los Angeles River, as depicted in the cross section shown in Figure 2. In addition, lateral spreading of the soil in a northward direction toward the Los Angeles River flood control channel also posed a potential hazard in the event of another significant earthquake.

The extent of potential lateral spreading was estimated using the multi linear regression procedures provided by Youd (2002) and also by a "Newmark sliding block" type evaluation (MCEER, 2001). Potential lateral displacements were determined to be approximately 0.4 to 0.8 m (Earth Systems, 2005).

Seismic settlement criteria established by the City of Los Angeles for conventional spread footing systems were for total predicted settlement of less than 38 mm and predicted differential settlement of less than 19 mm in a 9.1 m span. For mat foundations, the City's maximum acceptable values were for total predicted settlement not exceeding 76 mm and predicted differential settlement not exceeding 38 mm in a 9.1 m span. The reader should note that all settlement values herein have been converted to metric units for consistency, and should not be interpreted to imply the accuracy of measurements.

Since the predicted settlement and lateral ground movement values exceeded City allowable levels and levels tolerable for structural design, it was determined that ground improvement would be required in order to develop the proposed structure. Initial project objectives were to mitigate predicted soil liquefaction potential to allow use of a mat foundation, without the need for deep foundation elements. The project owner elected to use compaction grouting as the mitigation/ground improvement method, since noise and dynamic vibrations associated with other methods were considered to pose a nuisance to nearby commercial tenants and residents.

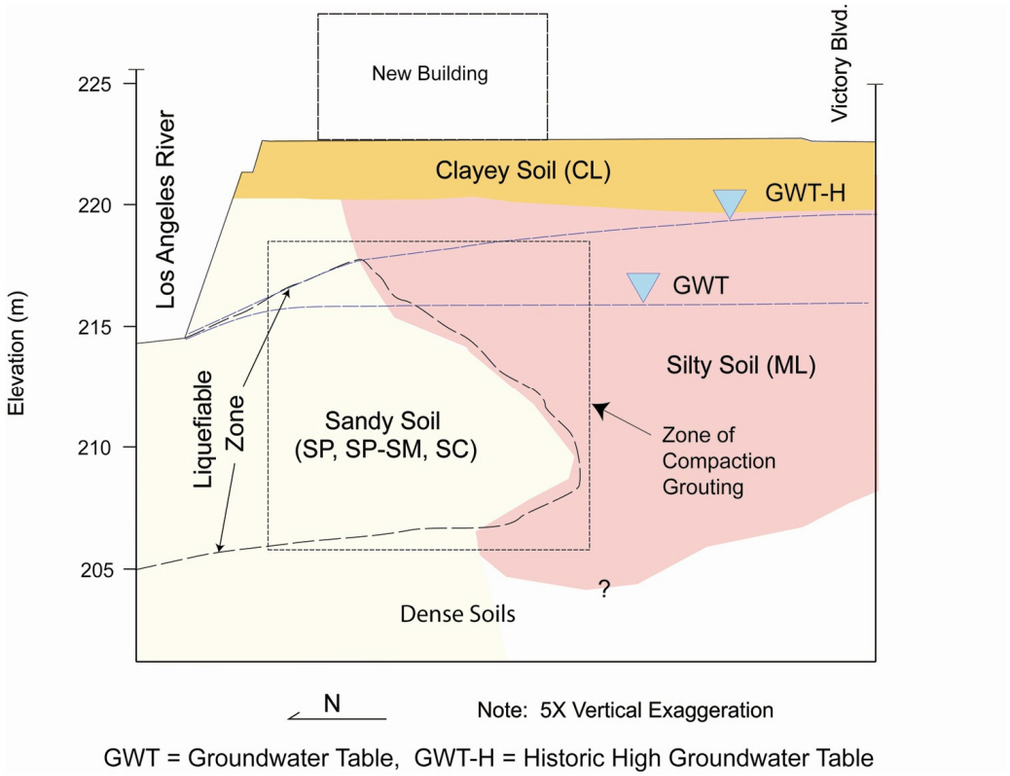


FIG. 2 – Generalized cross section showing site soil profile, liquefiable zone and compaction grouting treatment zone.

COMPACTION GROUTING

Compaction grouting is a well-established method of improving soil density in-situ through pressure-displacement. Mechanical energy from a high-pressure pump is transferred to surrounding soils at depth by emplacing very-stiff mortar-like grout through small-diameter, relatively confined delivery lines and a steel casing set to the target treatment interval depth. This ground improvement technique, first described by Graf (1969), and by Brown and Warner (1973), allows for work in and around operational facilities and other structures or infrastructure elements.

The procedure involves advancement of a small-diameter steel casing to the base of the treatment interval, slight withdrawal of the casing to open the first pumping interval (also called a "stage"), and initiation of grout flow. Grout is injected into surrounding soils at each stage until injection pressure is determined to exceed local effective overburden stress, typically interpreted as the point at which uplift is detected at the ground surface. The casing is then withdrawn to the next planned stage and the process is repeated up to the top of the target treatment interval. Other criteria for termination of pumping at a given stage are also implemented, and commonly include measurement of sustained high injection pressure (indicative of a "tight" formation), rapid changes in injection pressure (indicating a potential fracture), or upon emplacement of a prescriptive maximum quantity of grout.

The compaction grouting treatment interval for this project extended from 17.1 m to 4.6 m below the ground surface (BGS). Each grout probe was advanced to17.1 m BGS, considered to be the deepest extent of liquefiable soil. Compaction grouting was then performed using a "stage-up" (bottom-to-top) injection sequence, beginning at the top of the denser soil and proceeding upward in stages of up to1.2 m. Grout was injected at each stage at a constant flow rate of 0.057 m^3 per minute until surface response was detected.

An initial test program was conducted to evaluate effective grid spacing of grout injection points, and consisted of eight probes spaced at 3.1 m and another eight probes at 2.4 m. Average injection pressure was 3,540 kPa, and a total of 112 m^3 of grout was injected for the test program. The grout mix used consisted of fine to coarse silty sand aggregate with 10 to 30 percent fines (passing the #200 sieve), approximately 8 percent portland cement, and sufficient water to achieve a slump of typically 40 mm or less.

Both pre- and post-grouting CPT testing was conducted, including two comparative probes in each of the test grids. Initial (pre-grouting) average tip resistance (Qc) for the 12.5 m treatment interval was measured at 10.8 MPa in the area of the 2.4 m grid, and at 13.9 MPa in the area of the 3.1 m-spaced grid. Post-treatment average Qc values were identical for each of the test grids at 16.5 MPa, and corresponded to 19 percent improvement within the 3.1 m test grid, and 53 percent improvement in the 2.4 m grid. Accordingly, the 2.4 m spacing was selected as the prescriptive grout probe spacing for the remainder of the project, which included 472 grout injection locations on a plan-view grid spacing of 2.4 m. A diagram showing the proposed building outline and limits of grouting treatment is shown in Figure 3.

VERIFICATION AND MONITORING

Verification consisted of both quality control (QC) and quality assurance (QA) procedures. Quality control procedures were implemented by the contractor and included monitoring, regulating and recording grout mix consistency and injection rate; monitoring and recording injection pressure, grout quantity and surface response at each stage. Daily records of all grout constituents consumed (sand, cement and water) were also maintained.

The engineer's QA procedures included observation of contractor procedures, verification of grout unit weight and compressive strength, and post-treatment subsurface exploration; including SPT, CPT, and in-situ sampling. Records of grout production and consumption were corroborated by comparison of pump stroke counts with daily material balance and measured grout unit weight.

Measurement of ground surface uplift is considered to provide sufficient verification that grouting-induced stresses have exceeded local effective stress in the underlying soil. Monitoring of the ground surface was conducted constantly during production grouting, and consisted of measuring uplift with manometers, as well as visual observations of surface response. Vertical ground deflection was limited to approximately 1 mm per stage, with maximum cumulative uplift of 13 mm resulting from each injection location.

Lateral ground deflection was monitored at the surface where adjacent to the Los Angeles River channel, as well as the Tampa Avenue right-of-way. A grid of temporary survey monuments was established in these areas, and the project owner retained a surveyor to provide continuous real-time monitoring during proximal grouting operations. In-pipe photography by plumber's camera was used to help document the existing conditions for a storm drain lateral along the easterly portion of Tampa Avenue.

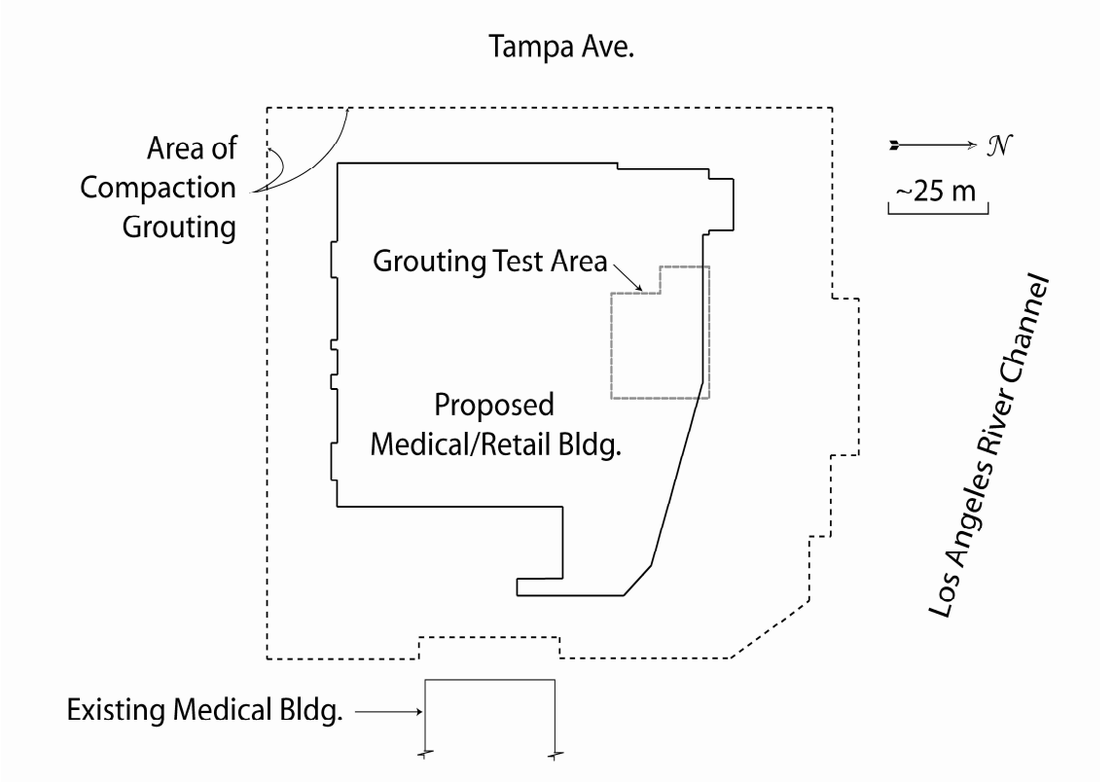


FIG. 3 – Location of proposed building, and limits of compaction grouting. Initial investigation included 7 borings and 20 CPT soundings at arbitrary locations throughout the site. Final confirmation testing included 6 borings and 16 CPT soundings at arbitrary locations within the area of treatment.

One of the challenges encountered during this project was the need to detect lateral grout-induced strain at depth to mitigate off-site subsurface response. This was initially accomplished by placing vertically-installed small-diameter PVC sleeves in the ground between the area of grout injection and the adjacent Tampa Avenue right-of-way. An approximately 0.5 m long steel cylinder of slightly smaller outer-diameter would then be attached to a rigid steel tape and lowered down the sleeve and retrieved repeatedly while grouting at a nearby injection probe. Increasing resistance to the cylinder passing through the sleeve indicated lateral migration of grout-induced strain, and was used as another criterion for pumping cessation for a particular injection stage. The device associated with this method is often referred to as a "poor-man".

Another method used to mitigate lateral strain in sensitive areas was to establish practical limits on injected grout quantity. This was initially accomplished through empirical observation of grout quantity as a function of depth required to provoke a response at the poor-man. However, careful observation of pressure-take behavior as measured with the grout flowlogger allowed further refinement of these limits due to the ability to recognize grout-induced ground fractures in real-time.

The flowlogger used for this project included an in-line ultrasonic flowmeter and a pressure transducer at the grout injection header. Data were collected at either 1- or 2-second intervals, transmitted to a laptop computer via a wireless spread-spectrum connection, and displayed on-screen in graphic format over a time domain. Visual inspection of the graphic information allowed for real-time identification and interpretation of soil response resulting from grout injection.

Figure 4 is a graph of compaction grouting pressure-take behavior plotted on a volume domain for data collected at a stage depth of 9.8 m to 11.0 m BGS. The associated injection point was located in a predominantly sandy zone near the river channel. A pressure drop from 4,960 kPa to 1,255 kPa had occurred upon injection of 0.16 m^3 of grout, and was observed to occur within a span of less than 20 seconds. Such rapid drops in pressure are common during compaction grouting, and are representative of localized ground fracture. An additional 0.1 m^3 of grout was injected following initiation of the soil fracture, until 1 mm uplift was detected with a manometer at the ground surface. Injection pressure was observed to rebuild to 4,250 kPa in the final sequence. The behavior observed in this record is similar to that described by Geraci (2007), and is interpreted as post-fracture redistribution of the grouting-induced stress field. Consequently, grout quantity limitations to mitigate unwanted lateral strain for this project were based empirically on the grout volume associated with initiation of a soil fracture.

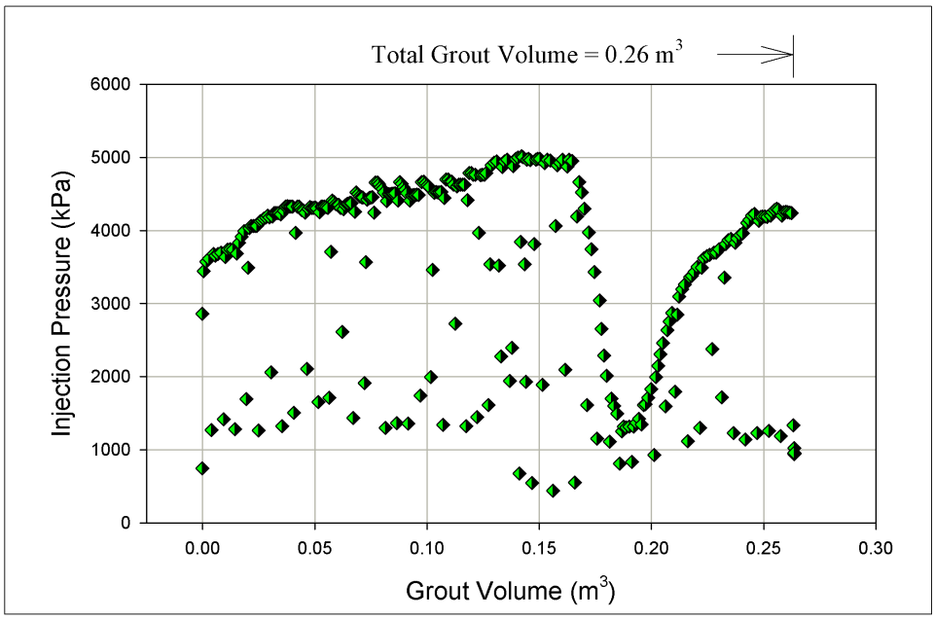


FIG. 4 – Graph of compaction grouting pressure-take response for an injection stage interval of 9.8 m to 11.0 m BGS

EFFECTS OF SITE COMPACTION GROUTING

Since compaction grouting relies on pressure-displacement, soil improvement is typically expressed as a displacement ratio, representing the net volumetric strain resulting from grout emplacement. When considering the volume of soil treated by the grouting process,

that volume can be taken as either the plan view limits of grouting multiplied by the average treatment interval; or as a the hypothetical volume of soil surrounding each injection probe within the treatment interval, with a rectangular prism dimension equal to the probe-to-probe spacing. Consideration of a plan-view treatment area of 3,364 m^2 with an average treatment interval of 12.5 m yields a total treatment volume of approximately 40,700 m^3. Using the alternate method, 472 injection points on a rectangular grid with an average treatment depth interval of 12.5 m and a hypothetical grout prism dimension of 2.4 m yields an effective volume of treated soil of 34,000 m^3. If the total effective grout volume for this project is taken as 2,033 m^3 (2,075 m^3 total grout volume minus an expansion volume of 44 m^3 resulting from an average surface heave of 13 mm), then soil improvement as a function of grout-induced strain would be in the range of 5.0 to 6.0 percent, depending on which method is considered.

The average soil dry unit weight as determined from ring samples retrieved from post-treatment borings was 1.79 g/cm^3, as contrasted to the pre-treatment value of 1.67 g/cm^3, suggesting an average increase in density of 7.2 percent, and is in reasonable agreement with strain-based calculations.

Tip resistance from confirmation CPT soundings and average SPT $(N_1)_{60}$ blow counts from the confirmation borings show a distinct increase over those obtained from pre-treatment exploration (Figure 5).

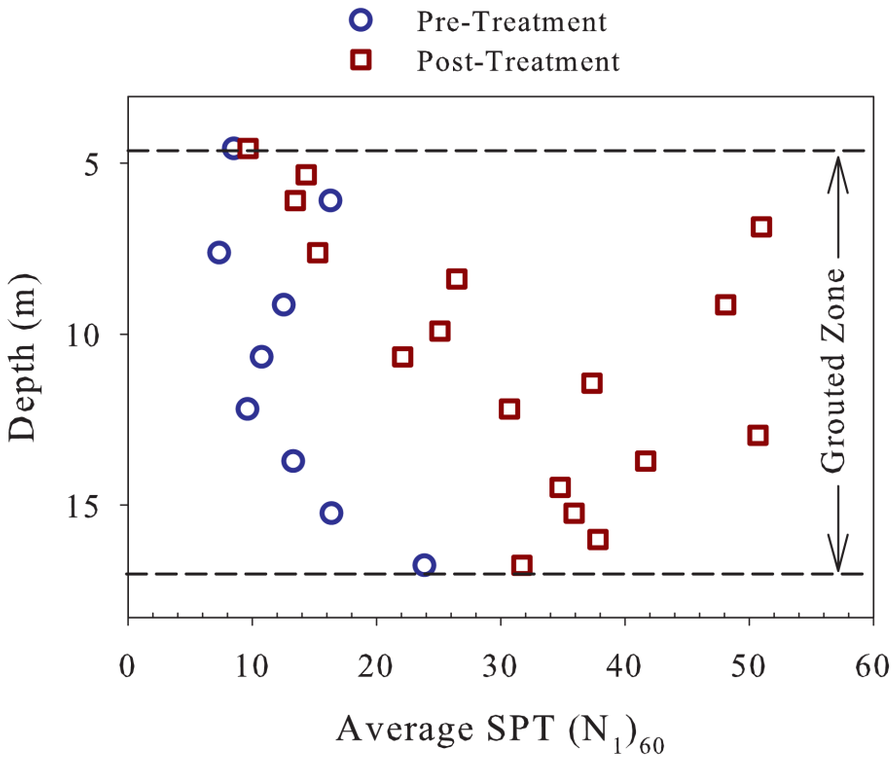


FIG. 5 – Graph of pre- and post-treatment SPT data obtained from 5 pre-treatment borings and 6 post-treatment borings, located arbitrarily throughout the area grouted

Liquefaction potential of the soil zone treated by compaction grouting was evaluated in accordance with guidelines established by Youd (1997). The soil profiles from the CPT soundings, in particular, were evaluated by the procedures of Robertson & Wride (1997). Data from each of 16 confirmation CPT soundings, as well as each of the six confirmation borings were evaluated, and only a few thin lenses of soil were determined to remain as potentially liquefiable zones.

Ground settlement due to liquefaction was evaluated according to the procedures outlined by Tokimatsu & Seed (1987), Robertson & Wride (1997), and Pradel (1998). According to those procedures, the remaining few thin lenses of potentially-liquefiable soils beneath the site were predicted to be capable of volumetric strains of up to approximately 2 percent, with estimated total maximum earthquake-induced ground subsidence ranging from zero to 8 mm for CPT-based analyses and 3 mm to 36 mm for SPT-based analyses. Differential settlement was estimated as ½ the maximum settlement (in this case 18 mm) or as the difference in total settlements between points. The worst-case differential settlement calculated using the latter method would be 19 mm over a span of 9.1 m (Earth Systems, 2006).

Corrected blow counts $(N_1)_{60}$ for potentially liquefiable lenses remaining above the depth of the Los Angeles River channel were found to be greater than 15 blows per foot. Consequently, the potential for lateral spreading under post-grouting site conditions is considered to have been effectively mitigated based on criteria by Youd (2002).

CONCLUSIONS

Sandy saturated sites vulnerable to liquefaction and lateral spreading can be successfully treated using compaction grouting. Sufficient density can be achieved to effectively mitigate earthquake-related ground deformation hazards.

Compaction grouting treatment for this site resulted in sufficient improvement to allow the proposed structure to be supported by a conventional spread footings foundation system, provided all column pads were restrained laterally with grade beams and remedial grading (shallow soil removal and recompaction) was performed as recommended. Ground improvement attributed to the compaction grouting was sufficient to preclude a mat foundation.

Evaluation of pressure-take data during the compaction grouting process is indicative of elastic-plastic ground response, and can be used to establish effective grout injection quantity limits and control undesired ground deformation.

ACKNOWLEDGEMENT

It is with heartfelt respect and admiration that the authors would like to posthumously acknowledge Frank Nonamaker, whose lifetime commitment to the practical application of compaction grouting technology contributed largely to the success of this project.

REFERENCES

Brown, D. R. and Warner, J. (1973). "Compaction Grouting". Journal of the Soil Mechanics and Foundation Division 99(SM8): p. 589-601., ASCE.

Earth Systems Southern California (2005), Preliminary Geotechnical Engineering Report, Tract 25145, Lots 1 and 2, 19215 to 19231 Victory Boulevard at Tampa Avenue, Reseda, California, PL-05718-01, dated July 22, 2005.

Earth Systems Southern California (2006). "Results of Compaction Grouting Report, Tract 25145, Lots 1 and 2, 19215 to 19231 Victory Boulevard at Tampa Avenue, Reseda, California", LA-01035-01, dated October 19, 2006.

Geraci, J. (2007). "Time-History Compaction Grouting Data Obtained through Instrumentation", Proc., Geo-Denver 2007: New Peaks in Geotechnics, GSP 168, edited Harold W. Olsen, February 18-21, Denver, Colorado, ASCE, 157-174.

Graf, E. D. (1969). "Compaction Grouting Technique and Observations". Journal of the Soil Mechanics and Foundation Division ASCE, 95(SM5), pp. 1151-1158, ASCE

Idriss, I.M. and R.W. Boulanger (2004). "Semi-Empirical Procedures for Evaluating Liquefaction Potential During Earthquakes", Invited Paper – 11th SDEE and 3rd ICEGE, Univ. of California, Berkeley, 2004.

Ishihara, K. (1985). "Stability of Natural Deposits During Earthquakes", Proceedings of the International Conference on Soil Mechanics and Foundation Engineering.

Multidisciplinary Center for Earthquake Engineering Research (MCEER) (2001). "Recommended LRFD Guidelines for the Seismic Design or Highway Bridges", Part II: Commentary and Appendices – Appendix D, Prepared under the MCEER Highway Project, Project 094, Task F3-1, April 9, 2001.

Pradel, Daniel (1998). "Procedure to Evaluate Earthquake-Induced Settlements in Dry Sandy Soils", Journal of Geotechnical and Geoenvironmental Engineering, v. 124, n. 4, p. 364-368, with Erratum October 1998.

Robertson P.K. and Campanella, R.G. (1985). "Liquefaction Potential of Sands Using the CPT", American Society of Civil Engineers, Journal of Geotechnical Engineer, v. 111, n. 3, p. 384-403.

Robertson and Wride (1997). "Cyclic Liquefaction and its Evaluation Based on SPT and CPT", in NCEER Proceedings, 1997, p. 41-48.

Tokimatsu, K., and Seed, H. B. (1987). "Evaluation of Settlements in Sands Due to Earthquake Shaking", Journal of Geotechnical Engineering, American Society of Civil Engineers, v. 113:8, p. 861-878."

Youd, T. Leslie, Corbett M. Hansen, and Steven F. Bartlett (2002). "Revised Multilinear Regression Equations for Prediction of Lateral Spread Displacement", Journal of Geotechnical and Geoenvironmental Engineering, Vol. 128, No. 12, December 2002.

Youd, T. L., and Idriss, I.M. (1997). "Proceedings of the NCEER Workshop on Evaluation of Liquefaction Resistance of Soils", Salt Lake City, Utah, January 5-6, 1996, NCEER Technical Report NCEER-97-0022, Buffalo, New York.

Cone Penetration Resistance Variation with Time After Blast Liquefaction Testing

Kyle M Rollins[1], Ph.D., M. ASCE and Joshua K.S. Anderson[2], M. ASCE

[1]Prof., Civ. & Env. Engrg. Dept., Brigham Young Univ. 368 CB, Provo, UT 84602; rollinsk@byu.edu.
[2]Staff Engr., LEI Consulting Engineers and Surveyors, Inc., 3302 N. Main St., Spanish Fork, UT 84660, jkasqrd@yahoo.com

ABSTRACT: Blast liquefaction testing was used to evaluate the effectiveness of vertical drains in preventing liquefaction. As part of the study, settlements associated with drain installation and blasting were measured. In addition, CPT soundings were made before and after drain installation and at 1, 2, 4, and 8 weeks after blasting. Drains installed with high vibration produced 350 mm of settlement while drains installed with low vibration produced only 100 mm of settlement. Despite the settlement, CPT soundings 3 to 5 days after drain installation showed decreases of 66% to 50% in the cone resistance at the low and high vibration test areas, respectively. In contrast, 13 days after drain installation and 7 days after blasting, which produced another 300 to 400 mm of settlement, the cone tip resistance was 30% to 60% higher than prior to treatment. Although there was some evidence of increased penetration resistance at times greater than 7 days, the trends were inconsistent.

INTRODUCTION

A number of investigators have observed increases in the penetration resistance of clean sands as a function of time after treatment with various soil improvement techniques (Mitchell and Solymar 1984, Mesri et al. 1990, Schmertmann 1991, Thomann and Hryciw 1992). These observations suggest that penetration tests for quality control should be conducted weeks after treatment to properly determine the improvement that was produced. However, time constraints imposed by the construction schedule often make this approach undesirable. For example, if a test section is used to validate a soil improvement strategy, the contractor would prefer to continue with production treatment work without delay to minimize downtime for equipment and personnel. Similarly, the construction schedule for an embankment might be delayed if testing to evaluate the success of a foundation treatment cannot be performed soon after treatment. As an alternative, quality control testing could be completed shortly after treatment if it were possible to accurately predict the increase in penetration resistance that could be expected in the future. In cases where the

penetration resistance did meet specifications, the expected increase could be predicted without the need for additional penetration testing. Unfortunately, at present an insufficient number of case histories are available on which to base a predictive equation. In addition, recent studies have also presented cases where little or no strength gain has been observed with time (Liao and Mayne 2005, Baxter and Mitchell 2004). These inconsistencies further complicate attempts to predict strength gain with time in clean sands.

To provide field data regarding the variation of penetration resistance with time after blast-induced liquefaction, cone penetration tests were performed at approximately 1, 2, 4, and 8 weeks after blast-induced liquefaction at a test site south of the Massey Tunnel near Vancouver, B.C., Canada. The blasting was used to evaluate the effectiveness of pre-fabricated vertical drains (EQ drains) in preventing liquefaction. A total of 35 vertical drains were installed at each of two test sites prior to blast testing using a vibrating steel mandrel. At one site the drains were installed with maximum vibration, while at the other site a minimum vibration was used. This paper summarizes the settlement resulting from drain installation and blasting at these sites and compares the change in penetration resistance at each site as a function of time.

TEST LAYOUT AND SITE CONDITIONS

A plan view drawing showing the locations of the drains, blasthole, pore pressure transducers and CPT soundings for the two test areas is shown in Fig. 1. At each test site a total of 35 drains were installed in a triangular pattern with a spacing of 1.22 m. The drains consisted of slotted corrugated pipe with an inside diameter of 100 mm which were encased in a filter fabric “sock” to prevent soil infiltration. In one test area the drains were installed using a steel pipe mandrel with a minimum of vibration to prevent sand densification so that improved performance would be primarily due to drainage. At the other site, the drains were installed with maximum vibration energy using a pipe mandrel with three fins to create maximum densification of the surrounding sand. The drains extended to a depth of 12.8 m at each site.

Four blast holes were located at a distance of 5 m from the center of the drain pattern. In each blast hole, charge weights of 3.0, 1.8, 1.8 and 1.8 kg were centered at depths of approximately 14, 11, 8, and 5 m, respectively with gravel stemming between each charge. Piezometers which could survive the transient blast pressure yet still accurately measure the residual pore water pressure were installed at depths of 6.7, 9.1, 11.6, and 14.0 m below the ground using techniques described by Rollins et al (2005).

Six CPT soundings were eventually made at each test area at locations shown in Fig. 1. CPT test results for the two test areas prior to drain installation are provided in

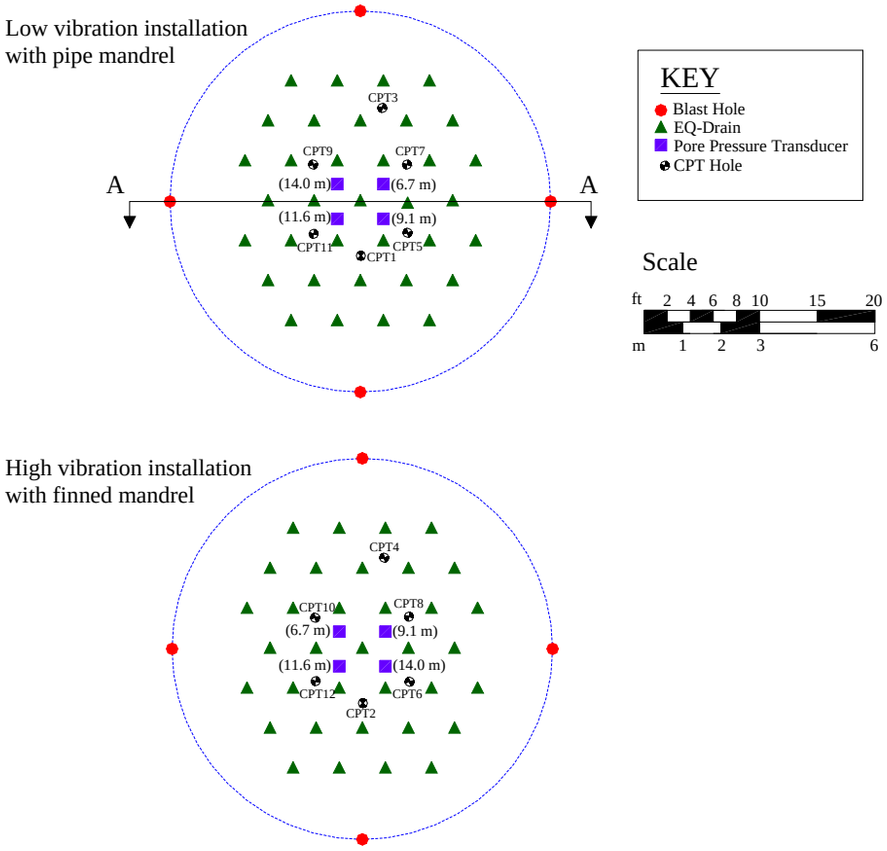


Fig. 1. Layout of drains, blast holes and CPT soundings for each test area.

Fig. 2. Generally, the agreement between the two soundings is very good. Based on CPT soundings and supplemental borings the soil profile shown in Fig. 2 was defined The profile consists of three units; a surface layer of silty sand to a depth of 2.6 m, a layer of silt to clayey silt from 2.6 to 4.6 m, and a clean fine sand from 4.6 to 15 m.

The sand from 5 to 13 m below the ground was identified as liquefiable in CANLEX experiments (Wride et al. 2000) conducted at the site and was the focus of this blast liquefaction test. The relative density of the sand was estimated using a correlation developed by Kulhawy and Mayne (1990) for unaged, normally consolidated sand. Monahan (1995) indicates that the alluvial sand at the site is less than 200 years old. The relative density in the sand from 5 to 13 m depth generally ranges between 35% and 45% with an average of about 40%. During the CANLEX project frozen samples of the clean sand were obtained at this test site and the average void ratio was found to be approximately 0.95 (Wride et al. 2000). Fraser river sand is composed of 40% quartz, quartzite, and chert, 11% feldspar, and 45% unstable rock fragments, with 4% miscellaneous detritus (Garrison et al. 1969). Grain size distribution curves for sand and silt layers in the profile are provided in Fig. 3 along with typical ranges for Fraser River sand.

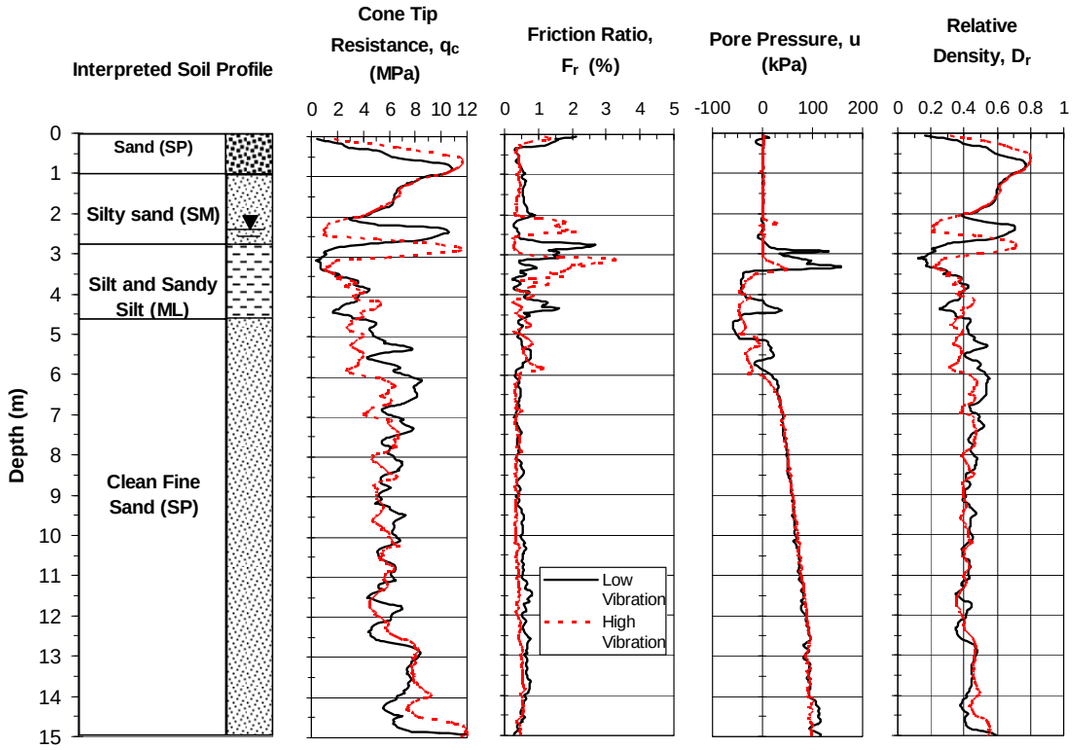


Fig. 2. Results from CPT soundings for two test sites at Massey Tunnel test site prior to drain installation and blasting.

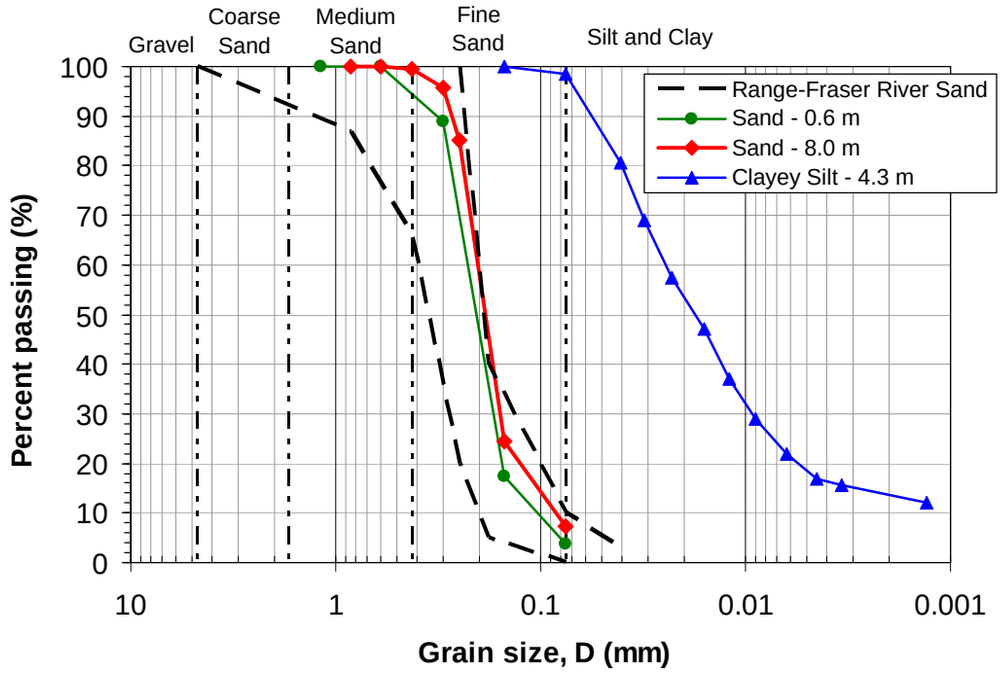


Fig. 3. Grain size distribution curves for sand and silt layers in the profile along with typical range for Fraser River sand.

BLAST LIQUEFACTION TESTING

The explosive charges were detonated one at a time from the bottom up with delays of 0.5 seconds between charges. Therefore, the total blast sequence took about 7.5 seconds. At both sites, large volumes of water began flowing from the drains within about 2 to 3 seconds after the initial charge detonation suggesting that liquefaction, or at least significant excess pore pressures, had been produced. Pore pressure transducers were located at four depths within the profile and indicated that excess residual pore pressures were nearly equal to the initial vertical effective stress in the ground at both sites. Although the drains were not capable of relieving the excess pore pressures produced by the blasting, subsequent analyses suggest that they may still be effective for earthquakes where pore pressures would be generated at slower rates. The pore pressure measurements clearly showed that the vertical drains did increase the rate of pore pressure dissipation relative to a blast test on an adjacent untreated site (Rollins et al. 2004). Pore pressures returned to near static levels within about 45 minutes after the blast.

SETTLEMENT MEASUREMENTS

To evaluate ground surface settlement produced by drain installation and subsequent blasting, survey points were installed along eight rays which extended outward from the center of the test area at 45 degree angles. Measurement points along these rays were at 0.61-meter intervals for the first 3.66 meters, and then at 1.22-meter intervals to 14.6 meters. Before and after drain installation elevation surveys were performed and the average settlement profiles for the two test areas are presented in Fig. 4(a) as a function of distance from the center at each test area. Nearly 350 mm of settlement occurred at the center of the test area where the finned-mandrel was used with high vibration to install the drains. The settlement decreased to about 50 mm at the periphery of the drain cluster. This differential settlement is likely due to arching against the surrounding untreated soil. In contrast, the maximum settlement was only 100 mm at the center of test area where drains were installed with a smooth pipe mandrel and low vibration. Therefore, the finned mandrel installation produced 250% more settlement than the pipe mandrel installation.

Before and after blasting, an elevation survey was also performed on the points along the rays extending from the center of the drain cluster to evaluate the liquefaction-induced settlement. Post-blast surveys were conducted within about an hour after the blast and then again 18 to 24 hours after the blast. The surveys consistently indicated that essentially all of the settlement occurred within 1 hour after the blast. Fig. 4(b) presents a plot of the average settlement versus distance from the center of the test area resulting from blasting in the two test areas. Although liquefaction occurred at both sites, the maximum liquefaction induced settlement was 25% lower for the test area where drains were installed using the finned-mandrel with high vibration than for the test area where drains were installed with the pile mandrel and low vibration. Nevertheless, settlement was significant in both cases. The

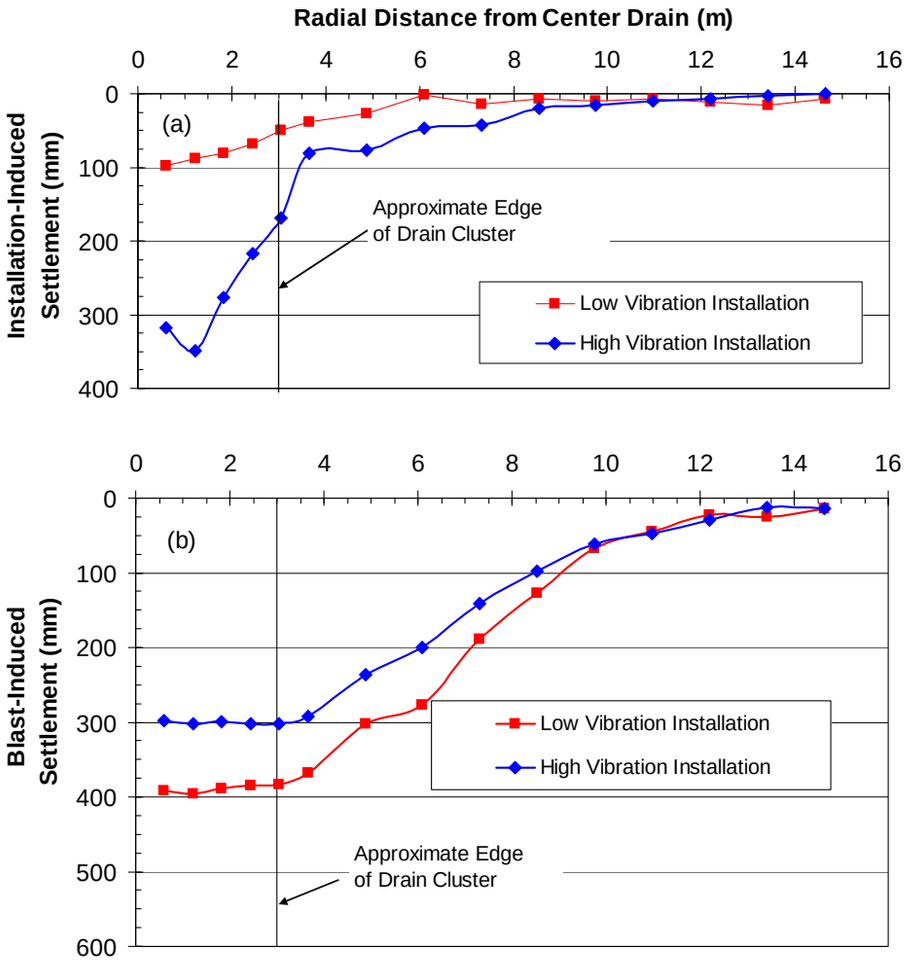


Fig. 4. Plots of (a) installation induced settlement and (b) blast-induced settlement as a function of distance from the center drain for the two test areas.

settlement was quite uniform within the area treated with the drains and then gradually decreased to less than 20 mm beyond 12 m.

The total settlement due to drain installation and blasting amounted to a maximum of about 500 mm at the low vibration site and 650 mm at the high vibration site. Sondex measurements at an adjacent untreated site suggest that about half of the observed settlement is in the 7 m-thick clean sand zone from 6 to 13 m in depth (Rollins et al, 2004). Based on this assessment, the volumetric strain due to drain installation would be 0.7% and 2.5% for low and high vibration test areas, respectively. The blast-induced volumetric strain in the high vibration area would be 2.1% while the volumetric strain in the low vibration area would be 2.9%.

CONE PENETRATION TESTING

At each test area, CPT soundings performed shortly after the installation of the drains indicated a reduction in cone tip resistance. Three days after drain installation the cone tip resistance at the test site with low vibration was only about 35% of its original resistance. Five days after drain installation, the cone tip resistance at the test site with high vibration was about 50% to 60% of its initial value. It is unclear whether the higher resistance at the site with high vibration is due to the increased densification or the additional 2 days prior to testing, as both could have contributed.

CPT soundings were also made at intervals of approximately 1, 2, 4, and 8 weeks after the blasting to evaluate potential increases in cone tip resistance with time. The CPT holes were distributed around the center drain as shown in Fig 1. Plots of the cone tip resistance as a function of depth are presented for each of the soundings at each test area in Fig. 5. Thirteen days after installation and seven days after blasting the CPT soundings show a considerable increase in tip resistance at both sites. At the high vibration site, the cone resistance also increased modestly up to 28 days after blasting, but the sounding at 56 days either showed no further increase or, at most depths, a decrease in resistance. The decrease in resistance at 56 days suggests that the increases in cone tip resistance may simply be due to random variations in sand properties rather than consistent trends. This conclusion seems to be borne out by the CPT soundings for the site with low vibration drain installation. While significant inc-

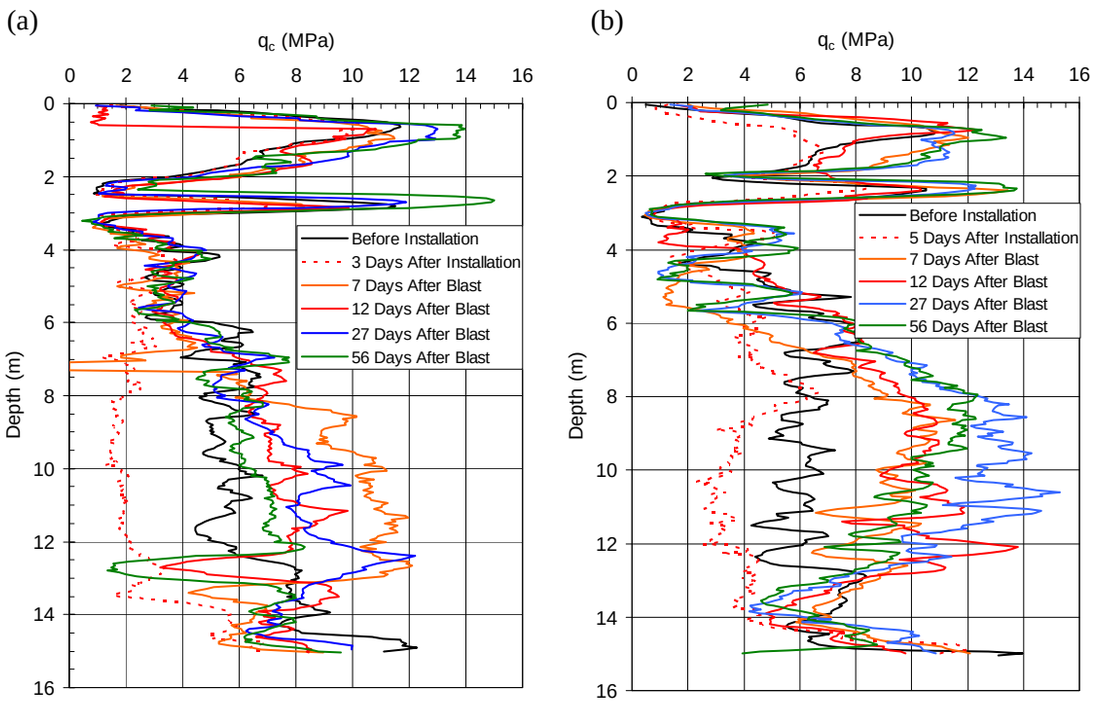


Fig. 5. Cone penetration test soundings before drain installation, after drain installation and at 1, 2, 4, and 8 weeks after blasting for (a) test area with low vibration, and (b) test area with high vibration drain installation.

reases in cone tip resistance were observed after 7 days, the soundings at 14, 28 and 56 days each show much smaller increases with the smallest increase observed after 56 days. Although there was some minor increase in the friction ratio at both sites, there was no pattern relative to time after blasting. Taken as a whole, the data generally indicate that there is no consistent increase in resistance with time after blasting. However, the results also point out the need for conducting multiple soundings at each time interval to better identify trends.

Although consistent increases with respect to time were not generally observed, some trends between pre- and post-blast penetration resistance are apparent in the data. For example, Fig. 6 presents the average cone tip resistance profiles for each site following blasting along with profiles prior to drain installation and shortly after drain installation. At both test areas the post-blast penetration resistance in the clean sand is generally higher than the pre-installation resistance and considerably higher than the resistance immediately following installation. A comparison of the average post-blast CPT profiles at both test areas indicates that the resistance in the clean sand layer is considerably higher for the test area where the finned mandrel was used with high vibration than for test area where a pipe mandrel with low vibration was used. Since both test areas were subjected to the same blast induced stresses, the increased cone tip resistance must be attributed to the densification provided by the installation of the drains. Based on the average post-blast CPT profiles at each site shown in Fig. 6, the

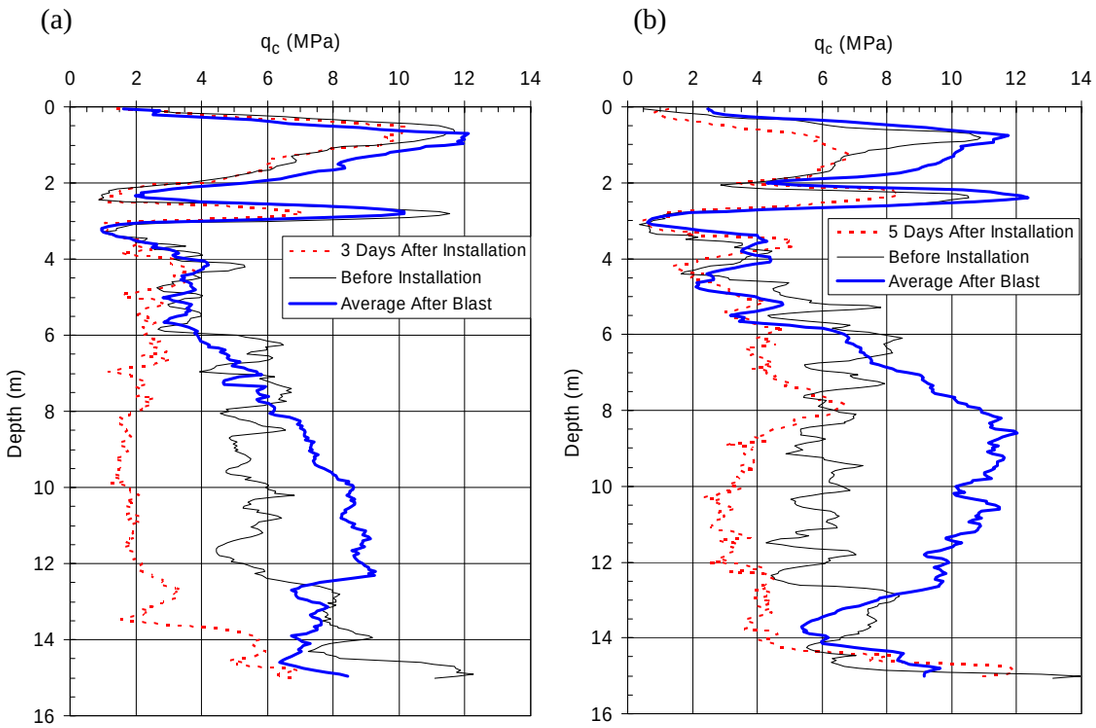


Fig. 6. Comparison of cone tip resistance before drain installation, shortly after drain installation, and after blasting for (a) test area with low vibration, and (b) test area with high vibration drain installation.

relative density was also computed using the Kulhawy and Mayne (1990) equation. Because of the densification provided by the drain installation and the blasting, the relative density was increased from about 40% prior to treatment to about 50% in the low vibration test area and to about 60% in the high vibration test area. Since both sites were subjected to the same blast densification, the additional 10 percentage point change in relative density at the high vibration test area can be attributed to drain installation effects.

CONCLUSIONS

Based on the results of the field testing and analysis of the test data the following conclusions can be drawn.

1. Placement of the vertical drains in the clean sand at 40% relative density produced volumetric strain of 0.7% when a pipe mandrel was used with low vibration and a volumetric strain of 2.5% when a finned mandrel was used with high vibration.
2. Blasting, which produced liquefaction in a zone from 6 to 13 m, led to volumetric strains of 2.9% and 2.1% in the low-vibration and high-vibration test sites, respectively.
3. Despite the settlement produced by drain installation, CPT tests conducted 3 to 5 days after installation showed cone tip resistance reductions of 66% and 50% in the low and high vibration test areas, respectively.
4. Fourteen days after drain installation and seven days after blasting, significant increases in penetration resistance were observed for both test sites. Some additional increases with time were observed in some cases, but the trends were not consistent.
5. Drain installation using a finned mandrel with high vibration increased the relative density from 40% to 50%, while blasting increased the relative density to about 60%.
6. We recommend that CPT soundings to evaluate improvement after blasting or drain installation be conducted at least 14 days after treatment and that multiple soundings be performed to account for local variations.

ACKNOWLEDGMENTS

Funding for this study was provided by a grant from the National Cooperative Highway Research Program-Ideas Deserving Exploratory Analysis (NCHRP-IDEA) program (Project 94). This support is gratefully acknowledged. Nilex, Inc. donated all equipment, personnel and materials necessary to install the drains at the test site which made this project possible. Advanced Drainage Systems, Inc. donated the drain pipes installed at the two test areas. ConeTec, Inc. donated CPT time for performing post-blast soundings. These donations made this project feasible. The conclusions from this study do not necessarily reflect the views of the sponsors. Finally, we express appreciation to the British Columbia Ministry of Transportation for allowing us to use the Vancouver test site.

REFERENCES

Baxter, C.D.P. and Mitchell, J.K. (2004). "Experimental Study on the Aging of Sands." *J. Geotechnical and Geoenv. Engrg.*, ASCE, Vol. 130(10), 1051-1062.

Garrison, R.E., Luternauer, J.L., Grill, E.V., MacDonald, R.D., and Murray, J.W. (1969). "Early diagenetic cementation of recent sands, Fraser River Delta, British Columbia," *Sedimentology*, 12: 27-46.

Joshi, R. C., Achari, G., Kaniraj, S. R., and Wijiweera, H. (1995). "Effect of aging on the penetration resistance of sands," *Canadian Geotechnical Journal*, 32(5), pp. 767-782.

Liao, T. and Mayne, P.W. (2005). "Cone penetrometer measurements during Mississippi embayment seismic excitation experiment", *Proceedings, GeoFrontiers*, ASCE GSP 133, Austin, TX.

Kulhawy, F.H. and Mayne, P.W. (1990). Manual on Estimating Soil Properties for Foundation Design, Electric Power Research Institute, Palo Alto, CA.

Mesri, G., Feng, T.W., and Benak, J.M. (1990). "Postdensification penetration resistance of clean sands," *J. Geotechnical Engineering*, 116(7): 1095-1115.

Mitchell, J.K., and Solymar, Z.V., (1984). "Time-dependent strength gain in freshly deposited or densified sand." *J. Geotechnical Engineering* 110(11): 1559-1576.

Monahan, P.A., Luternauers, J.L., and Barrie, J.V. (1995). "The geology of the CANLEX Phase II sites in Delta and Richmond, British Columbia." Procs, *48th Canadian Geotechnical Conference*, Vancouver, 152-160.

Rollins, K.M. (2004). "Liquefaction mitigation using vertical composite drains: full scale testing." NCHRP-IDEA Project 94 Report, Transportation Research Board, Washington, DC, 107 p.

Rollins, K.M., Goughnour, R.R., Anderson J.K.S. and McCain, A. (2004). "Liquefaction hazard mitigation using vertical composite drains." *Procs. 13th World Conf. on earthquake Engineering*, EERI.

Schmertmann, J.H. (1991). "The mechanical aging of soils." *J. Geotechnical Engineering* 117(9): 1288-1330.

Thomann, T. G. and Hryciw, R. D. (1992). "Stiffness and Strength Changes in Cohesionless Soils due to Disturbance." *Canadian Geotechnical Journal*, 29(5): 853-861.

Wride, C.E., Robertson, P.K., Biggar, K.W., Campanella, R.G., Hofmann, B.A., Hughes, J.M.G., Kuppper, A., and Woeller, D.J. (2000). "Interpretation of In-Situ Test Results from the CANLEX Sites", *Canadian Geotechnical Journal*, NRC, 37: 505-529.

Cone Penetration Testing Before, During, and After Blast-Induced Liquefaction

William M. Camp, III, M. ASCE, P.E.[1], Paul W. Mayne, PhD, M. ASCE, P.E.[2] and Kyle M. Rollins, PhD, M. ASCE[3]

[1]Technical Principal/Vice-President, S&ME, Inc., 620 Wando Park Blvd., Mt. Pleasant, SC 29464; bcamp@smeinc.com

[2]Professor, Georgia Institute of Technology, School of Civil and Environmental Engineering, Atlanta, GA 30332-0355; paul.mayne@ce.gatech.edu

[3]Professor, Brigham Young University, Civil and Environmental Engineering, 368 CB, Provo, UT 84602; rollinsk@byu.edu

ABSTRACT: To investigate the consequences of liquefaction with regard to foundation performance, subsurface blasting was used to induce liquefaction around a test shaft for a major foundation load testing program in Charleston, South Carolina, USA. Cone penetration test data were recorded before blasting, immediately following two blast-induced liquefaction events while pore pressures were still elevated, one month after the blasting, and again, seven years after the blasting. All testing was located inside of the blast array (i.e., within the liquefied area). Tip resistance, sleeve friction, and u_2 porewater pressure measurements were all lower in the two soundings that were performed while the sands were still liquefied. The post-blast soundings performed one month later and again seven years later indicated that the upper portion of the liquefied deposit (immediately below an impermeable clay cap) had been loosened. There was little change between the data collected one month after blasting and those data collected 7 years after blasting. Densification was not apparent. However, the sand was Pleistocene Age and the destruction of aging effects may have countered blast-induced densification effects in the CPT data.

INTRODUCTION

Historically, surficial deposits of Holocene sands indicated widespread evidence of liquefaction during the 1886 Charleston earthquake event. To investigate the consequences of liquefaction with regard to foundation performance, subsurface blasting, similar to the Treasure Island Load Test Program (Ashford et al, 2004) was used to induce liquefaction around a test shaft for a major foundation design-phase load testing program in Charleston, South Carolina, USA. Subsurface conditions were characterized prior to the blasting via soil test borings, seismic cone penetration testing (SCPTu), and laboratory grain size analyses (Camp, 2004). A generalized profile of the conditions at the test site is shown in Fig. 1. The sands between depths of 3m and

13m were the target zone for the blast-induced liquefaction.

As illustrated in Fig. 2, three circular arrays, each consisting of eight 12-m deep blast holes, were installed at radial distances of 4-m, 4.6-m, and 5.2-m from the center of a 2.4m diameter drilled test shaft. Explosives were loaded into each blast hole and the three arrays were detonated at approximately 1 hour intervals. The first and third blast series used a 0.68 kg (1.5 lb) charge at 3.05, 6.1, 9.14, and 11.73 m below the ground surface in each hole. The second blast series used 0.91 kg (2 lb) charges at 4.57, 7.62, and 10.67 m depths. The charges were binary explosives consisting of a mixture of ammonium nitrate and nitro-methane, and the weights are given in equivalent weights of TNT. For each blast sequence, the charges were detonated two at a time with a delay of 250 milliseconds between detonations. The charges were detonated beginning around the bottom ring and then moved upward around each subsequent ring to the top. Porewater pressures were continuously monitored by 20 piezometers that were installed at various depths and distances from the test shaft. Immediately following the detonation of a blast hole array, a lateral statnamic device was used to load the test shaft. Three cycles of blasting and statnamic loading were performed. Details of the test program are summarized in Brown and Camp (2002).

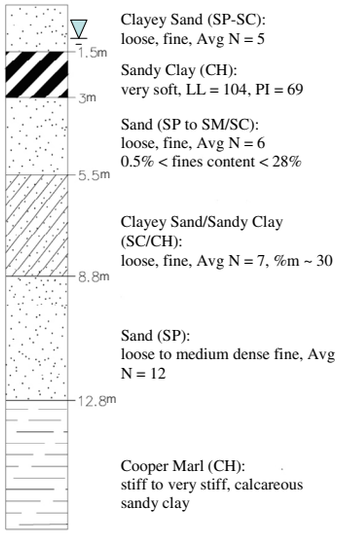


Fig. 1 – Generalized subsurface conditions.

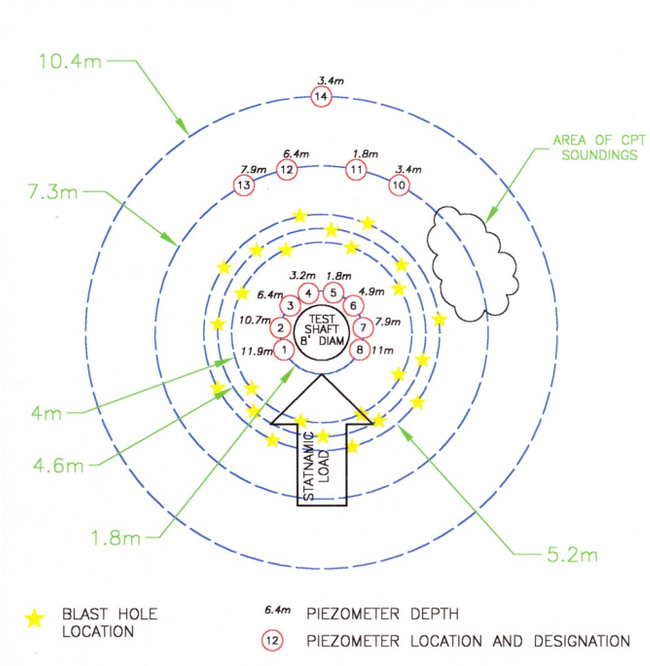


Fig. 2 – Layout showing test shaft, blast holes, piezometers, and area of CPT soundings.

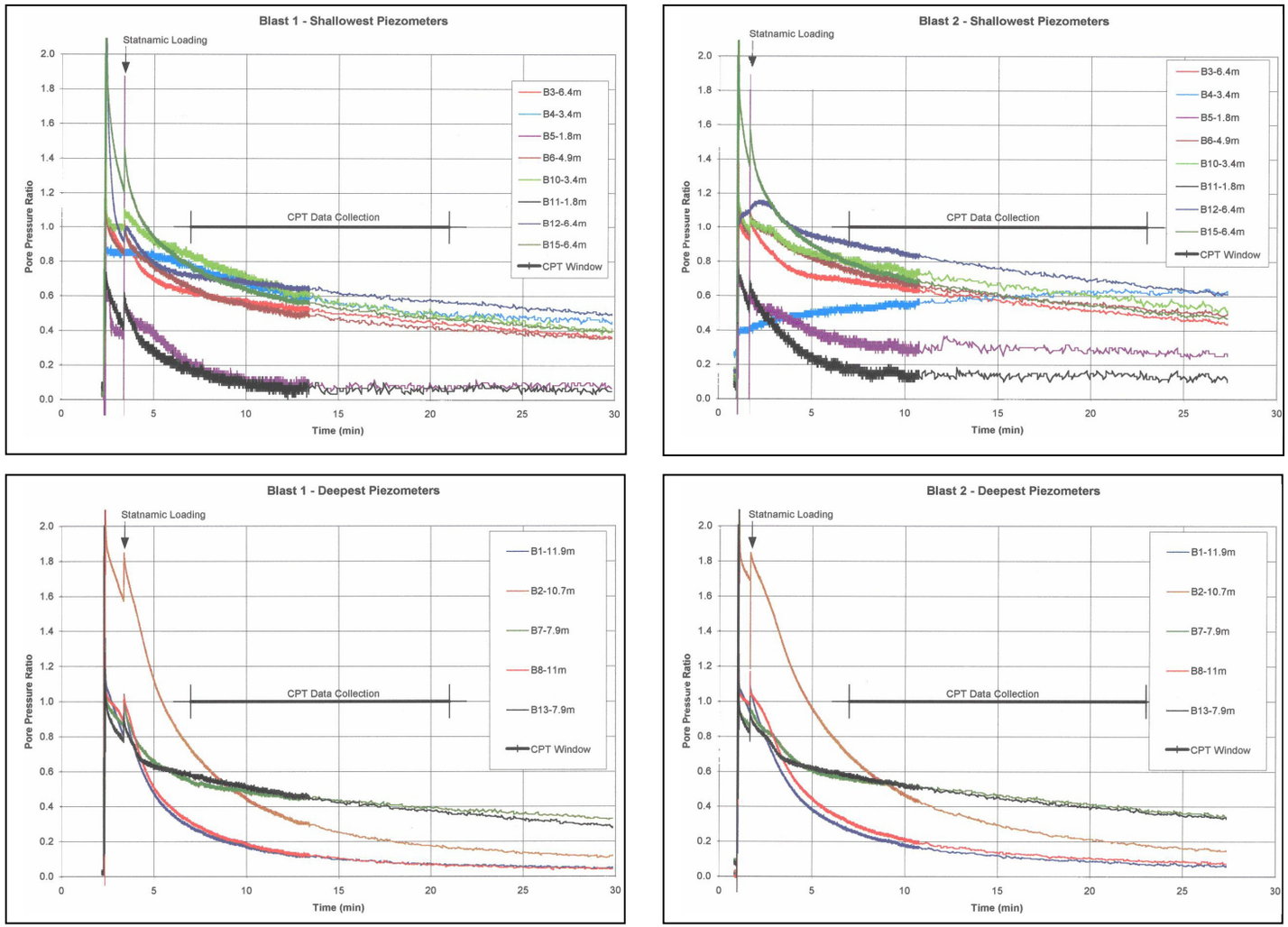


Fig. 3 – Pore Pressure Ratio (u_e/σ_v') versus time for the first two blast events. Window of cone penetration testing also shown on the plots.

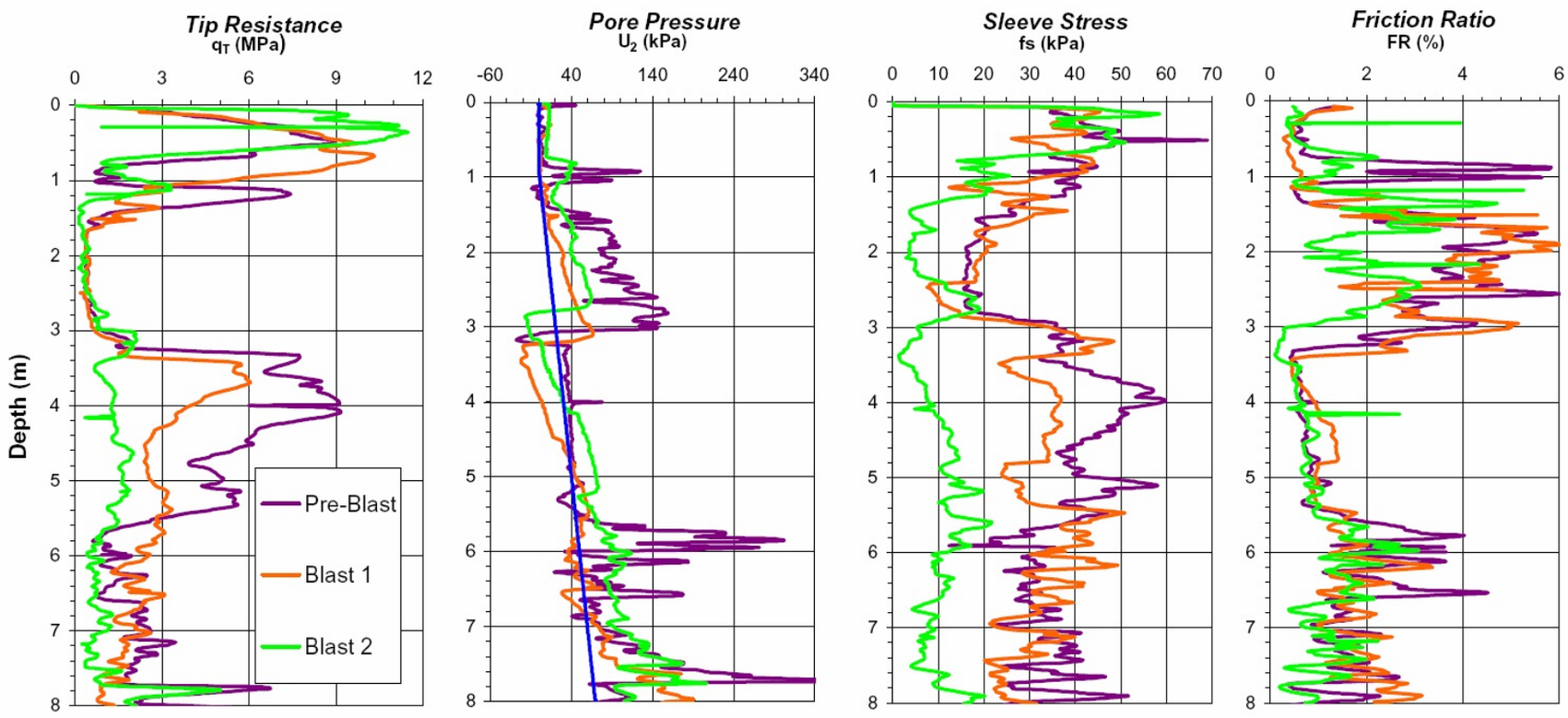


Fig. 4 – CPT data from pre-blasting, immediately following blast 1, and immediately following blast 2 at Charleston SC site. (extra line on pore pressure plot is hydrostatic pressure)

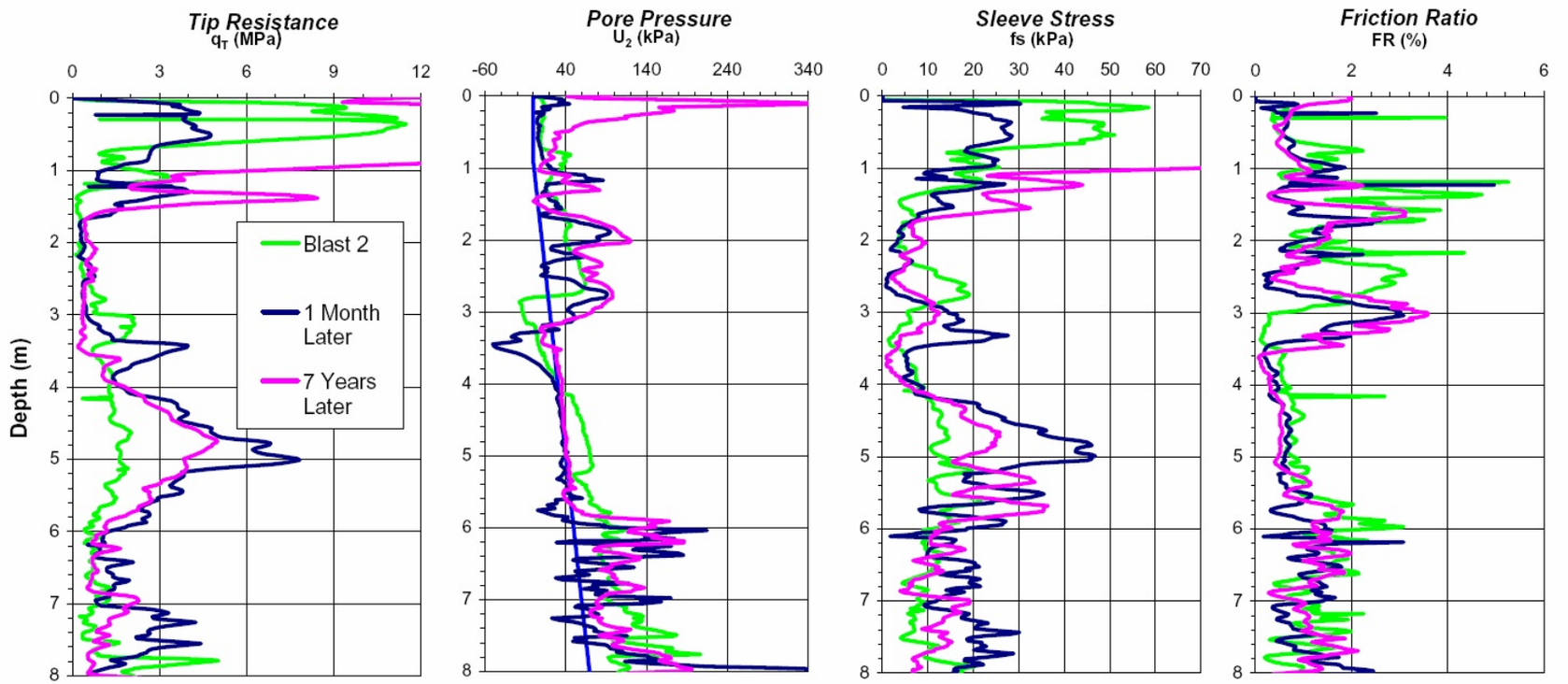


Fig 5 – CPT data immediately following blast 2 and then 1 month after blasting and 7 years after blasting at Charleston SC site. (extra line on pore pressure plot is hydrostatic pressure)

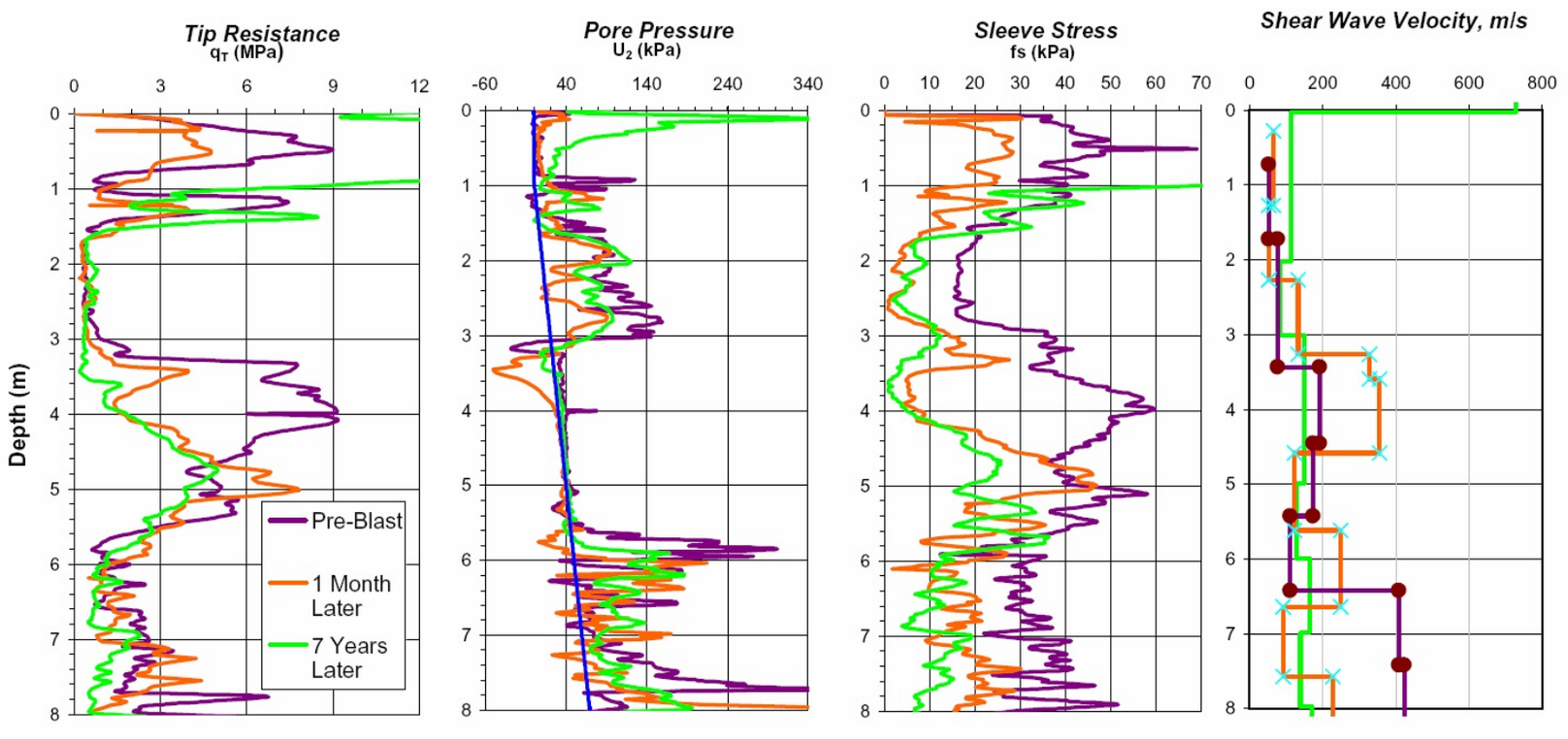


Fig. 6 – Pre-blast CPT data compared to 1 month and 7 year CPT data at Charleston SC site. (extra line on pore pressure plot is hydrostatic pressure)

CONE PENETRATION TESTING, PIEZOMETER, AND SETTLEMENT DATA

Immediately following the first two lateral statnamic tests (approximately 30 seconds after blasting), cone penetration testing (CPT) was performed at a radial distance of approximately 7.3m from the test shaft or about 3.3m to 2.7m from the two detonated blast hole arrays. The piezometer responses from both blast events, and the time period during which CPT data were collected, are shown in Fig. 3. The piezometer data, presented as a pore pressure ratio, r_u (where r_u = excess porewater pressure/initial vertical effective stress), indicated that liquefaction was triggered and pore pressures were substantially elevated for periods of more than 30 minutes, which was greater than the length of time required to perform the CPT sounding. Cone penetration testing was not performed immediately after the third blast event but additional CPT soundings and seismic CPT soundings were made at the same location approximately one month after and seven years after the blasting. The CPT measurements are summarized in Figures 4 through 6. The surface topography was surveyed after each blast event and the computed settlements are shown in Fig. 7.

RESULTS

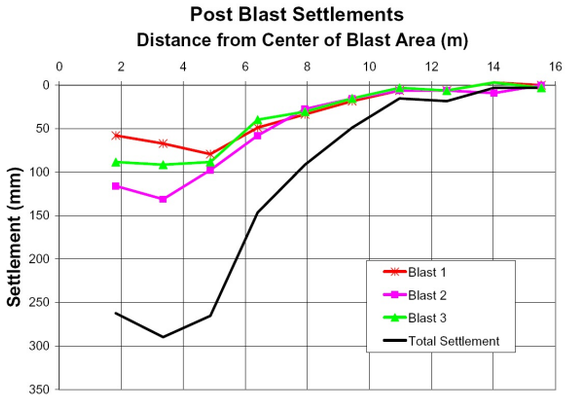


Fig. 7 – Settlements after blast-induced liquefaction events

As compared to the pre-blast data, differences in the CPT readings as a result of the blast-induced liquefaction were mainly limited to the soils between depths of 3m to 6m. This zone contained the cleanest sands, which were most susceptible to liquefaction and was located beneath a relatively impermeable cap. After each blast event, there was a marked decrease in tip stress, u_2 pore pressure (measured behind the tip), and sleeve stress. The tip and sleeve stress reductions are expected since the elevated pore pressures had significantly reduced the effective stress. The reduced pore pressure – even negative at times – may seem surprising since the piezometer data indicates a substantial pore pressure increase. However, the pore pressure measurement at the u_2 position is an interface measurement. At the interface, the pore pressure response is influenced by both octahedral stresses and shear stresses (Burns & Mayne, 2002). The octahedral stresses will always generate positive pore pressures but shear stresses may generate positive or negative pore pressure changes. As evidenced by pore pressure data recorded at the Wildlife site during the 1987 Superstition Hills earthquake (Youd and Holzer, 1994), liquefied soils may dilate during shearing thereby reducing the porewater pressure. Similarly, the strain-hardening load-deflection response observed during the lateral load-testing of piles and shafts in liquefied soils indicates that liquefied soils dilate under large shear strains (Rollins et al 2005). The cone

measurements are consistent with this behavior.

In practice, a liquefied soil is frequently modeled as an undrained material with a residual shear strength in accordance with a correlation proposed by Seed and Harder (1990). The correlation relates an undrained residual shear strength, S_{uSPT}, to a corrected Standard Penetration Test (SPT) N-value. Using the mid-range of the Seed and Harder correlation, the estimated S_{uSPT} based on the N-values measured before blasting were computed and plotted in Fig. 8. Also shown on Fig. 8 are estimated undrained shear strengths based on a CPT correlation: $S_{uCPT} = (q_t - \sigma_v)/N_{kt}$ where q_t is the cone tip resistance, σ_v is the total vertical stress, and N_{kt} is an empirical factor ranging from 10 to 20 (e.g., Lunne, et al. 1997). The CPT-based shear strengths shown in Fig. 8 for each blast event were computed using an N_{kt} of 15. Although use of the CPT undrained strength correlation for a sand may be questionable, the observed agreement with the N-value correlation appears reasonable.

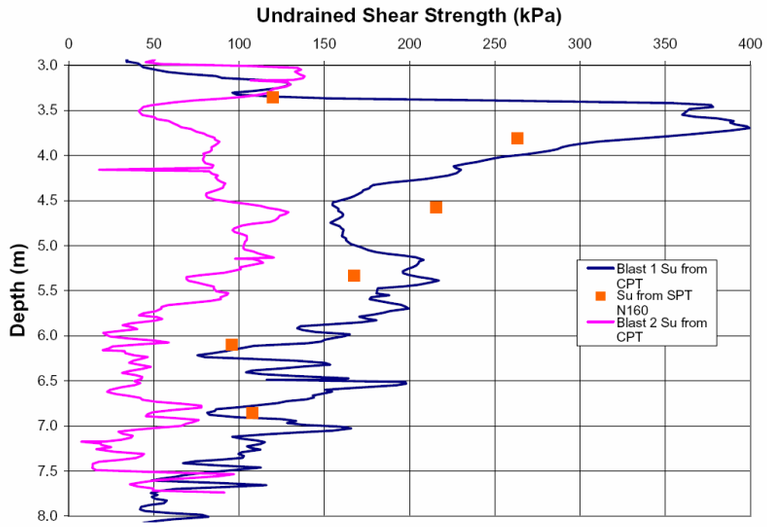


Fig. 8 – Residual undrained shear strength according to Seed & Harder (1990) compared to undrained shear strength using CPT correlation with data obtained during blast-induced liquefaction.

Focusing on the 3m to 6m zone that was most affected by the blasting, the soundings performed one month after blasting indicate an increase in both tip resistance and sleeve friction relative to the values just after blast 2 (see Fig. 5). However, in comparison with the pre-blast data, the tip resistance in the upper half of this zone is still less than the initial value and approximately equal to the initial value in the lower half (see Fig. 6). The pore pressure and friction ratios were generally unchanged. There is a layer of low permeability clayey sand or sandy clay between a depth of 1.5m to 3m. In such situations, as indicated by Youd (1984), the upper portion of a liquefied stratum is often left in a loose state after liquefaction. This is a result of void redistribution as discussed by Malvick et al 2006, among others. Porewater flowing upward from the lower portion of the liquefied layer is trapped beneath the lower permeability cap resulting in a volume increase. The data collected 7 years after blasting are very similar to the one month data. Again, the upper portion of the critical

zone still appears to be loose while the lower portion appears to be relatively unchanged relative to pre-blast conditions.

At the location of the CPT soundings, approximately 120mm of settlement was recorded. Although some of the settlement may have occurred as a result of ejection, the visible sand boils alone were not large enough to explain this level of settlement. Therefore, some densification likely occurred even though it is not apparent from the CPT data. It should be noted that this sand deposit is of Pleistocene Age and is more than 100,000 years old. The blast-induced liquefaction would have destroyed any aging effects and even if the lower zone was densified as a result of the blasting, the corresponding tip stress increase may be less than the decrease due to the loss of the 100,000 years of aging effects.

SUMMARY

Cone penetration testing was performed before, during and after two blast-induced liquefaction events, covering up to 7 years time. Two soundings were obtained shortly after blasting while excess pore pressures were still elevated. As compared to the pre-blast CPT data, the data collected immediately following blasting exhibited lower tip stresses, sleeve friction, and shoulder pore pressures. The observed pore pressure reduction is consistent with the nature of the measurement and the behavior of liquefied sand. A comparison of the N-value based undrained residual shear strength following liquefaction and undrained shear strengths based on the cone tip stresses appear reasonable. Additional data collected one month later and again, seven years later indicated that despite increases in tip resistance relative to post-blast conditions, the zone of liquefied soil immediately below an impermeable layer was permanently loosened relative to pre-blast conditions. This behavior is consistent with observations by Youd (1984) in post-earthquake investigations and with void redistribution (Malvick et al, 2006). Significant densification was not evident in the later soundings despite the observed surface settlement of 120 mm. There was little change between the one month and seven year data. However, the liquefied deposit is of Pleistocene age and the blasting would have likely destroyed structural gains due to any aging effects.

ACKNOWLEDGMENTS

The load test program that generated these data was funded by the South Carolina Department of Transportation. Prof. Dan Brown and Mr. Tim Siegel designed the over-all test program. Prof. Kyle Rollins and Prof. Scott Ashford implemented the blast-induced liquefaction program. S&ME, Inc. and Dan Brown provided technical oversight and data interpretation. Additional funding for the lead author was provided by ADSC. The authors also thank the reviewers for their very helpful comments and suggestions.

REFERENCES

Ashford, S.A., Rollins, K.M., and Lane, J.D. (2004). "Blast-induced liquefaction for full-scale foundation testing", *Journal of Geotechnical and Geoenvironmental Engineering*, ASCE, Vol. 130, No. 8, August, pp 798-806.

Brown, D.A. and Camp, W.M. (2002). "Lateral load testing for the Cooper River Bridge, Charleston, SC" *Proceedings of the International Deep Foundations Congress*, Vol. 1 (GSP 116), ASCE, Reston,VA: 95-109.

Burns, S.E. and Mayne, P.W. (2002). "Analytical cavity expansion-critical state model for piezocone dissipation in fine-grained soils." Soils & Foundations 42 (2): 131-137.

Camp, W.M. (2004). "Site characterization and subsurface conditions for the Cooper River Bridge." *Proceedings of Geo-Trans – Geotechnical Engineering for Transportation Projects*, GSP No. 126, Vol 1., ASCE, Reston, VA, pp 347-360.

Lunne, T., Robertson, P.K. and Powell, J.J.M. (1997). "Cone Penetration Testing in Geotechnical Practice." EF Spon/Blackie Academic, London, 312 p.

Malvick, E.J., Kutter, B.L., Boulanger, R.W., and Kulasingam, R. (2006), "Shear Localization Due to Liquefaction-Induced Void Redistribution in a Layered Finite Slope", *Journal of Geotechnical and Geoenvironmental Engineering*, ASCE, Vol. 132, No. 10, October, pp 1293-1303.

Rollins, K.M., Gerber, T.M., Lane, J.D. and Ashford, S.A. (2005), "Lateral Resistance of a Full-Scale Pile Group in Liquefied Sand", *Journal of Geotechnical and Geoenvironmental Engineering*, ASCE, Vol. 131, No. 1, January, pp 115-125.

Seed, R.B. and Harder, L.R., Jr. (1990). "SPT-based analysis of cyclic pore pressure generation and undrained residual strength." Proceedings, H.B. Seed Memorial Symposium, Vol. 2, BiTech Publishers, Vancouver: 351-376.

Youd, T.L. (1984). "Recurrence of liquefaction at the same site." *Proceedings of the 8th World Conference on Earthquake Engineering*, San Francisco, Vol. 3, pp 231-238.

Youd, T.L. and Holzer, T.L., (1994). "Piezometer Performance at Wildlife Liquefaction Site, California", *Journal of Geotechnical Engineering*, ASCE, Vol. 120, No. 6, June, pp 975-995.

Dynamic Response of an Embankment during Stone-Column Piling

Dario Rosidi[1], M. ASCE, P.E, Areq Gharabegian[2], P.E, and Deh-Jeng Jang[3], P.E.

[1]Principal Technologist, CH2M HILL, Oakland, CA 94612; dario.rosidi@ch2m.com
[2]Vibration and Noise Section Manager, Parsons, Pasadena, CA 91124; areg.gharabegian@parsons.com
[3]Transportation Engineer, Caltrans, Sacramento, CA 95819; deh-jeng_jang@dot.ca.gov

ABSTRACT: Stone-columns were used as part of Interstate 5 (I-5)/Interstate 805 (I-805) Highway Widening Project undertaken by the California Department of Transportation (Caltrans). During the stone-column construction, excessive slope movements were observed. Since no measurements were taken during construction, it was not known if the movements were caused by the vibration generated during the stone-column installation. A series of dynamic response analyses was conducted using the 2-D finite element computer program Plaxis (Plaxis b.v., Version.8 Professional, 2002) to determine the probable causes of the observed slope movements by evaluating the possible correlations between the observed movements and the nearby stone-column installation activities.

The overall study consisted of a test stone-column piling vibration measurement program and dynamic responses analyses. The piling measurement program was conducted to gather vibration data at various embankment points due to pilings. Two sets of dynamic response analysis were performed. The first set involved the embankment response analysis during the June 15, 2004, San Clemente Island earthquake. The results of the analysis were used to calibrate the dynamic soil parameters. The second set of analysis was carried out to assess the potential adverse impacts of the stone-column installation to the embankment stability. The second set of analysis included calibration of the dynamic soil parameters using the recorded vibrations from the test stone-column piling program. The results of the analyses indicate that the potential for excessive slope movements and failure due to stone-column piling exists.

INTRODUCTION

Stone-columns were used to improve the foundation soils of I-5, due to the presence of liquefiable soils. The construction was part of the I-5/I-805 Highway Widening Project undertaken by Caltrans in San Diego. During the stone-column construction, excessive slope movements that require shoring were observed on the I-5 embankment between Wall Stations 14+40 and 15+80; with the worst movements

observed at approximately Station 15+10. Unfortunately, no vibration and slope movements were measured at the time of construction. Therefore, it was not immediately known if the movements were caused by the vibration generated during the stone-column installation or by other causes.

This study was carried out to assess the possible correlations between the observed embankment movements and the nearby stone-column installation activities. The study approach consisted of the following activities: 1) conducted a test stone-column piling vibration measurement study to gather vibration data on the embankment due to pilings, 2) developed cross sections and characterized the soil dynamic parameters using the logs of borings and field as well as laboratory testing results, 3) calibrated the soil dynamic parameters by performing dynamic embankment response analysis using the earthquake motions recorded at a nearby seismograph station during the June 15, 2004, San Clemente Island earthquake, 4) further calibrated the soil dynamic parameters by performing additional dynamic response analysis using the results of a more "problem-specific" test stone-column piling, 5) performed dynamic vibration analysis for the embankment subject to stone-column pilings. In this analysis, the recorded vibrations closest to the test stone-column installation and the above soil parameters were used as inputs to the analysis, and 6) assessed the potential impacts of the stone-column installation to the embankment stability and slope movements.

TEST STONE-COLUMN PILING VIBRATION MEASUREMENTS

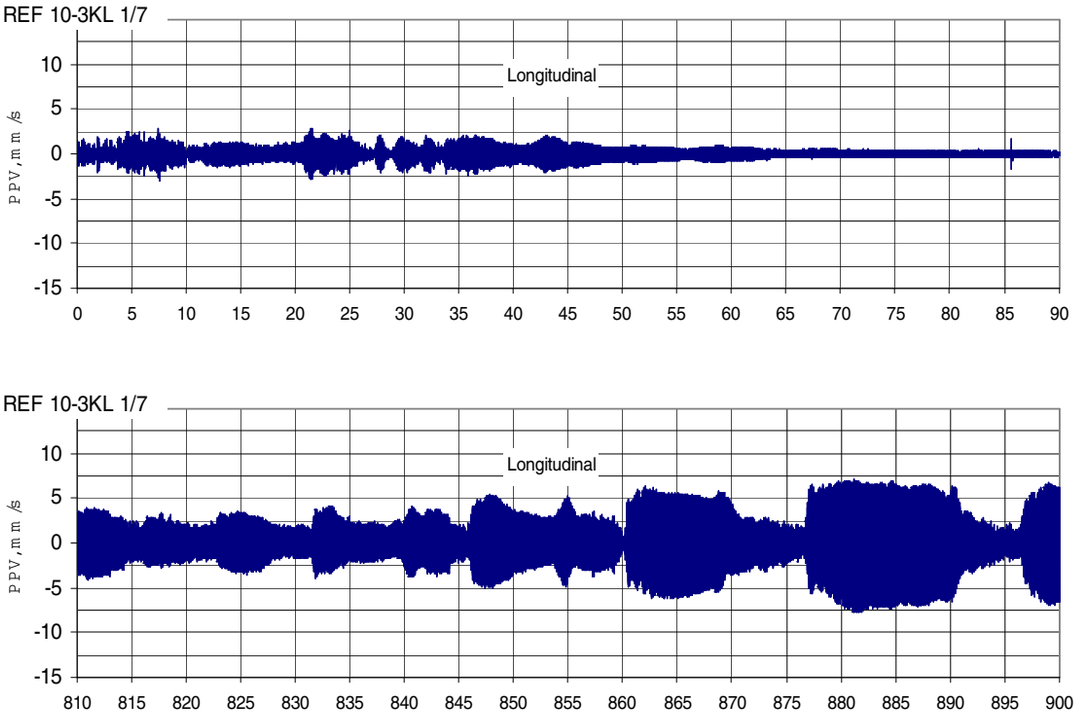
A test stone-column piling vibration measurement study was conducted on the I-5 embankment. The purpose of this test program was to gather vibration attenuation data generated by stone-column piling and traffic on the embankment. The measurements were taken at two locations (Pilings 10-3KL and 9-14KL) with similar geological conditions to the area where the embankment settlements had occurred. At each station, vibrations were measured at four locations: a reference point closest to the installed stone-column, as well as at the embankment toe, mid-slope, and top.

The sensors at the reference and toe-of-slope positions were placed 2.0 and 5.5 meters from the center of the pile, respectively. The mid-slope sensors were placed approximately midway up the highway embankment slope, and the top-of-slope recordings were positioned at the top of the highway embankment slope, closest to the traveled way. Vibrations were recorded simultaneously at the four measurement locations for each test stone piling using Geosonics 3000 seismograph units equipped with tri-axial geophones. Vibratory ground velocities in the longitudinal, transverse, and vertical directions were recorded at the rate of 333 samples per second for a total duration of 900 seconds. The longitudinal (L) and transverse (T) axes measure the motions perpendicular and parallel to the longitudinal axis of the embankment, respectively. Typical plots of the time history of the recorded ground particle velocity in the longitudinal axis at the reference point are shown in Figure 1.

The results of measurement indicate that vibrations at the top-of-slope sensor are low, and they are generally below the noise level of the sensor (approximately 0.08

millimeters per second [mm/s]). Also, because of their positions with respect to the traveled way, the recorded motions at the mid-slope and top-of-slope locations have more contributions of vibration from the highway traffic than stone pilling.

Figure 1. Vibratory Ground Velocity Recorded at the Reference Point (Stone-Column 10-3KL at Wall Station 20+20)



Note: The figure does not show the complete records. It only shows the data over two selected time periods (0 – 90 seconds and 810 – 900 seconds).

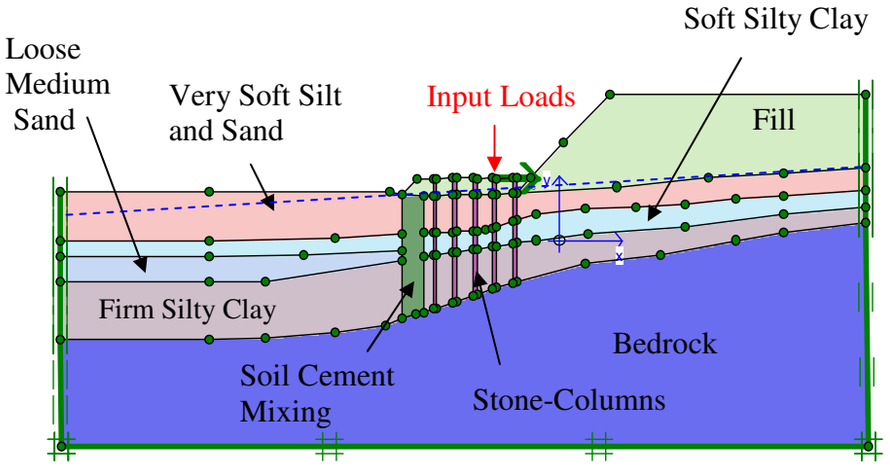
CROSS SECTIONS AND SOIL PARAMETERS FOR DYNAMIC ANALYSIS

A detailed review of the existing soil information and embankment conditions was performed to develop the cross sections and dynamic soil characteristics of the various embankment and foundation soils. The logs of the boring indicate that the highway embankment was built on alluvial soils, consisting of silt, sand, and clay of varying density.

Two cross sections along the embankment were developed for the analysis based on the available logs of boring. The embankment cross section at the location where the worse settlements were observed (Sta. 15+00) during the piling is shown in Figure 2. Note that the cross section reflects the condition at the time when the excessive slope movements occurred during the stone-column construction, including the soil cement mixing wall that was included in the analysis.

The Mohr-coulomb elastic-perfectly plastic soil model was used for the dynamic analysis. Soil shear strength parameters and the elastic moduli were developed utilizing empirical relationships that relate soil characteristics (primarily the field Standard Penetration Test (SPT) N-value) to these parameters. The friction angles for the sandy and silty soil deposits were estimated using the relationship of Schmertmann (1975) from the N-values. Similarly, the empirical relationship proposed by Terzaghi and Peck (1967, taken from Djoenaidi, 1985) that relates the undrained shear strength (S_u) and N-value was used for the cohesive soils.

Figure 2. Cross Section Used for Analysis (Wall Station 15+00)



Other parameters include the Young's Modulus (E) or Shear Modulus (G) and Poisson's Ratio (ν). These moduli can be correlated to the shear-wave (V_s) and compressive-wave (V_p) velocities. It should be noted that for the proposed dynamic analysis, which involves relatively rapid, low-intensity loadings from the stone-column construction and small magnitude and distant earthquake, soil responses are primarily defined by undrained behavior and higher elastic moduli at small stress and strain levels. Accordingly, the small-strain Young's Moduli for the cohesive soils were developed using the relationships of Wroth, *et al.* (1979) and Dickenson (1994). For the sandy and silty soil deposits, the relationship of Seed *et al.* (1984) was utilized.

Table 1 summarizes the estimated values of the undrained shear strength parameters and the Young's Modulus for the various major embankment soil deposits. These Young's Modulus values were calibrated (adjusted) based on the results of the earthquake and test stone-column piling vibration response analyses (discussed in the following sections). The adjusted Young's Modulus values are listed in Table 1; column (e) for the earthquake and column (f) for the test stone-column piling vibration analyses. Note that in Plaxis program, additional bulk stiffness for

pore fluid is automatically added, resulting in an effective Poisson's Ratio of less than 0.5 for undrained case.

Table 1. Estimated Soil Parameters for Plaxis Dynamic Analysis

Soil Type	γ	ν	E	E_1[1]	E_2[2]	c[3]	ϕ	S_u
	[kN/m^3]	[-]	[kPa]	[kPa]	[kPa]	[kPa]	[°]	[kPa]
	(b)	(c)	(d)	(e)	(f)	(g)	(h)	(i)
Embankment Fill	20.5	0.32	4E+5	2E+5	2E+5	-	-	160
Very Soft Silt and Sand	18	0.30	3.7E+5	2E+4	4E+4	10	29	-
Soft Silty Clay	19	0.30	1.9E+5	1.5E+4	2E+4	-	-	75
Loose Medium Sand	18	0.30	3.9E+5	3E+04	4E+04	10	33	-
Firm Silty Clay	19	0.35	3E+5	4E+4	1E+5	-	-	120
Bedrock	20	0.35	1E+6	1E+6	1E+6	10	38	-
Stone-Column	20.5	0.35	5E+5	5E+5	5E+4	5	40	-

Notes:
[1]Adjusted Young's Moduli, based on the results of earthquake analysis.
[2]Adjusted Young's Moduli, based on the results of test piling analysis.
[3]Small cohesions were assigned to the non-plastic soils for numerical modeling stability.

ANALYSIS FOR THE 2004 SAN CLEMENTE ISLAND EARTHQUAKE

The responses of the highway embankment were recorded during the June 15, 2004, San Clemente Island earthquake. The hypocenter of this magnitude 5.2 earthquake was located approximately 80 km southwest of the project site. The earthquake was recorded at the nearby I-5/Highway 52 Interchange Bridge, located approximately 7 km south of the project site and approximately 77 km from its hypocenter. The subsurface soils that underlie the free-field seismograph consist of fill over alluvium, similar to the subsurface soils underlying the project site.

Responses were recorded at a number of monuments located along the top of the embankment near Wall Stations 15+00 and 15+50. Changes in the monument's northing and easting, as well as the elevation, were surveyed and recorded by Caltrans before and after the earthquake. The embankment slope movements at Wall Station 15+00 were also recorded by two inclinometers to depths of approximately 30 m. The recorded data indicate that the embankment top along this section moved outward up to approximately 1.0×10^{-2} m during the earthquake. The inclinometers suggest that the embankment mass experienced displacements or movements of approximately 2.0×10^{-3} m, relative to the inclinometer bottom.

The calibration analyses were performed for the two cross sections where the measurements were made using embankment conditions at the time when the earthquake occurred (June 15, 2004). The time-history analysis utilized the 2-D finite element computer program Plaxis to estimate the responses of the highway embankment due to the earthquake. The two horizontal motions recorded at the nearby bridge were inputted to the models. Special nonreflecting boundaries were applied at the model boundaries to minimize spurious wave reflections. Material damping was modeled using Rayleigh damping.

A series of iterative analyses was performed. At each iteration, the dynamic parameters of the various embankment soils were adjusted such that an overall agreement was achieved between the calculated embankment slope displacements and those recorded on the monuments and inclinometers. The adjusted Young's Modulus values used in the last iterative analyses are listed in Table 1, column (e). These soil dynamic parameters were further calibrated using the data recorded during the test stone-column piling vibration measurement study.

ANALYSIS FOR THE STONE-COLUMN VIBRATIONS

The dynamic vibration analyses were conducted using the 2-D Plaxis program to further calibrate the soil parameters with the "problem-specific" test stone-column piling data and to assess the potential impacts of the stone-column installation to the embankment stability and slope movements. The recorded vibrations at the reference point (located at 2 m from the test stone column piling) were used as inputs to the analysis. Only the longitudinal component of the vibrations was considered, as it will cause larger movements to the embankment.

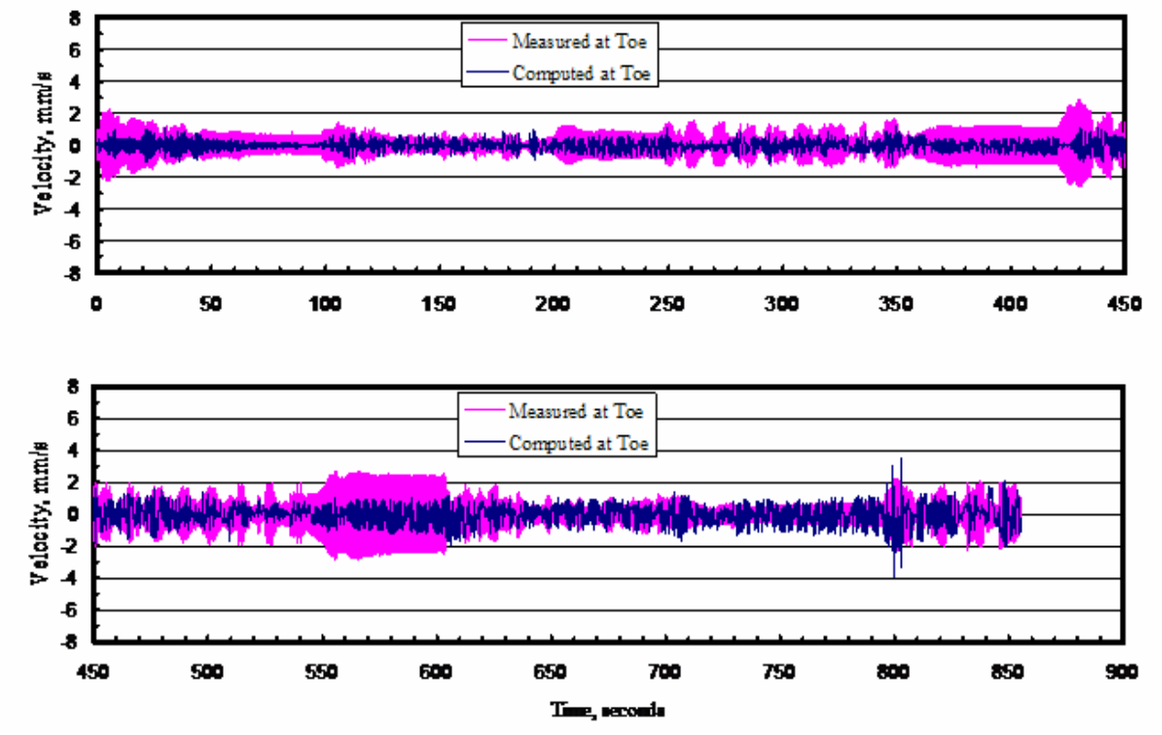
Model Calibration Using Stone-Column Vibration Measurements

Similar to the earthquake calibration, a series of iterative analyses was performed using the two test stone-column piling vibration measurements. The Young's modulus and the Rayleigh damping values of the various embankment soils obtained from the previous earthquake analysis (Table 1 column [e]) were further adjusted until an overall "good" agreement was achieved between the computed particle velocities and those recorded. The comparisons were made using the computed and measured velocities at the toe of the embankment slope. The adjusted Young's Modulus values are listed in Table 1, column (f).

Figure 3 shows the comparison of particle velocity time histories between those predicted by the model and recorded during the test stone-column piling (10-3KL piling) at the toe of the embankment slope. The model generally under-predicted the measured velocities, especially within the following time periods: the first 120 seconds, between 260 to 280 seconds, 360 to 450 seconds, and 525 to 600 seconds. Good predictions are achieved between 120 to 200 seconds, 450 to 525 seconds, and 600 to 850 seconds.

In the analysis, the vibration measurements at the reference location were input at the ground surface, representing the dynamic loads induced by the nearby stone-column installation. In actuality, the stone-column was constructed by first "drilling" to its maximum depth, and then stones were poured in stages filling the column from the bottom to the ground surface. At each stage or depth, the stones were compacted, and loads (vibrations) were generated. In this way, the piling generated vibrations at various depths along the stone-column length. The Plaxis computer program; however, does not have the capability to consider a moving source under the ground surface. Therefore, for the analysis, it was assumed that the vibration source is at the ground surface. This could be one of the reasons why the measured and the predicted results do not match well in some areas.

Figure 3. Comparison of Computed vs. Measured Velocities at Slope Toe



To evaluate the overall goodness-of-fit of the model predictions, a parameter, I_t, was defined as follow:

$$I_t = \sum_{t=0}^{T} |V_t| \Delta t$$

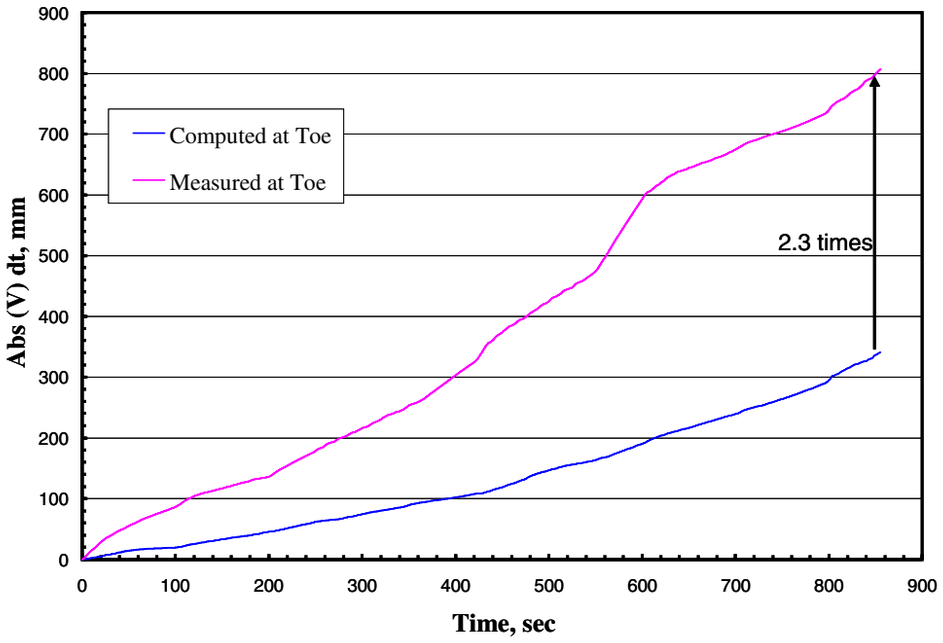
where V_t is the velocity at time t, and the summation is carried out over the total duration of interest, T. I_t represents the (absolute) sum of the areas under velocity as a function of time, and it can be interpreted as a measure of displacement. The computed I_t of the predicted velocities is plotted with that of the measurements at the

toe in Figure 4 for the 10-3KL piling. As the figure shows, the model under-predicts the parameter I_t by a factor of approximately 2.0.

Slope Movements due to Stone-Column Installation

In this analysis, the vibration data recorded at the reference locations were used as inputs, assuming that a stone-column installation at the testing location would produce the same vibrations at the wall location where failures were observed. The computed embankment displacements after 900 seconds of stone piling are shown in Figure 5 for the 10-3KL test pile. The time histories of the cumulative displacements at the toe, middle, and top of the embankment slope are plotted in Figure 6, showing maximum slope displacements of approximately 0.023-m (23 mm) for the 10-3KL piling. The figure also indicates significant increases in slope displacements after approximately 770 seconds of piling, indicating a progressive slope failure at the end of the piling.

Figure 4. Computed I vs. Time at Toe for Stone Piling 10-3KL



As discussed previously, the analysis model represents a simplified loading condition, and it under-predicted the measurements; hence, the induced slope displacements are likely to be greater than those calculated by the model.

An examination of the vibration data recorded at the reference location indicates that the 10-3KL piling produced ground particle velocities of up to approximately 3.5 mm/s, for the first 800 seconds of piling, and up to approximately 8 mm/s thereafter. The higher vibrations recorded toward the end of piling correspond to the stone-column installation closer to the ground surface.

CONCLUSIONS

Embankment dynamic time-history response analyses were performed using the vibrations generated by the stone-column installation. These analyses were carried out to evaluate the potential of embankment slope movements due to these vibrations.

For the stone-column analyses, the recorded vibrations from the test pilings were used. The vibrations recorded at the reference locations located approximately 5.5 m from the toe were used as inputs. The sensors at the reference locations were situated approximately 2 m from the installed stone-columns. Therefore, the vibrations recorded at these locations are assumed to be representative of those at the stone-column installation locations.

The results of the analyses suggest that the propagation of vibrations from the stone-column installation could potentially induce stresses and strains large enough to initiate excessive slope movements and failure. The analysis considered only the vibrations from the construction of a stone-column for a total duration of approximately 850 to 900 seconds (this is the duration for a typical stone piling). In the actual construction, the embankment slope was subject to repeated loadings from the construction of many stone-columns, and each of them can be expected to induce incremental slope movements. The cumulative movements resulting from multiple pilings, therefore, are expected to be large enough to cause slope failure.

In conclusion, the results of the dynamic response analyses suggest that the stone-column construction between Wall Stations 14+40 and 15+80 in late March 2004 most likely caused the excessive settlements and slope movements on the I-5 embankment.

REFERENCES

Dickenson, S.E. 1994. Dynamic Response of Soft and Deep Cohesive Soils during the Loma Prieta Earthquake of October 17, 1989.

Djoenaidi, W.J. 1985. A Compendium of Soil Properties and Correlations, M. Eng. Thesis, University of Sydney.

Plaxis b.v., Finite Element Code for Soil and Rock Analyses, Version.8.2 Professional. 2002.

Schmertmann, J.H. 1975. Measurement of In-situ Shear Strength, Proceedings, ASCE Specialty Conference on In-Situ Measurement of Soil Properties, Vol. 2. Raleigh, North Carolina.

Seed, H.B., Wong, R.T., Idriss, I.M. and Tokimatsu. K. 1984. Moduli and Damping Factors for Dynamic Analyses of Cohesionless Soils, Report No. UCB/EERC-84/14, September.

Wroth, C.P., Randolph, M.F., Houlsby, G.T. and Fahey, M. 1979. A Review of the Engineering Properties of Soils with Particular Reference to the Shear Modulus, CUED/D – SOILS TR 75, University of Cambridge.

Figure 5. Calculated Displacements after 900 Seconds of Stone Piling

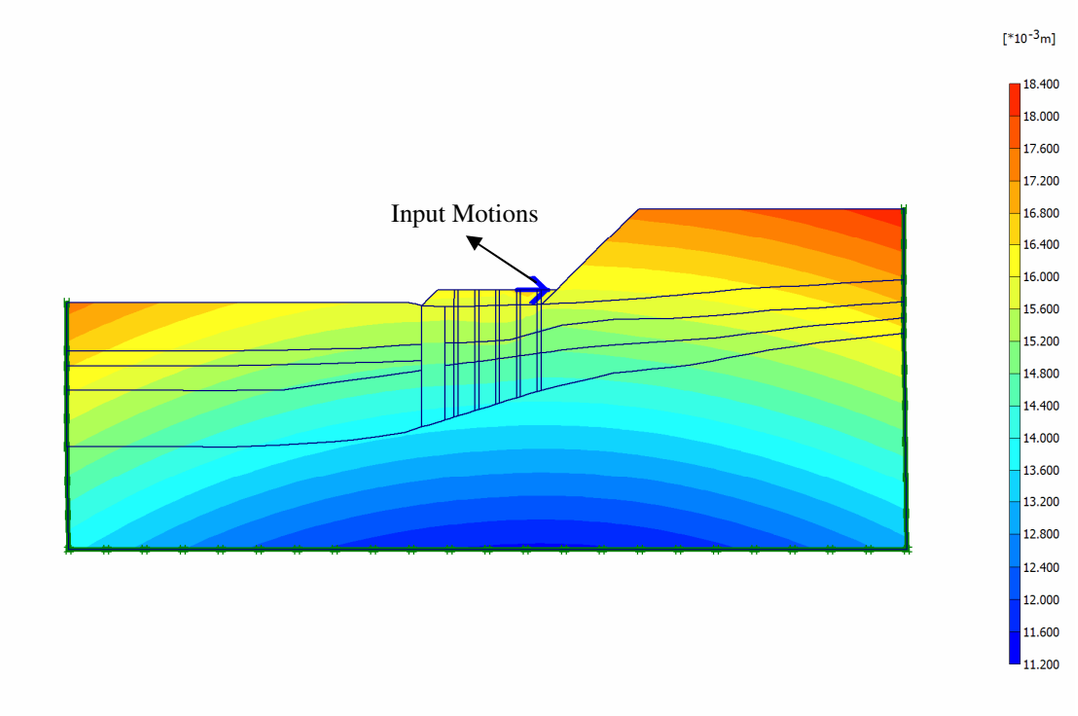
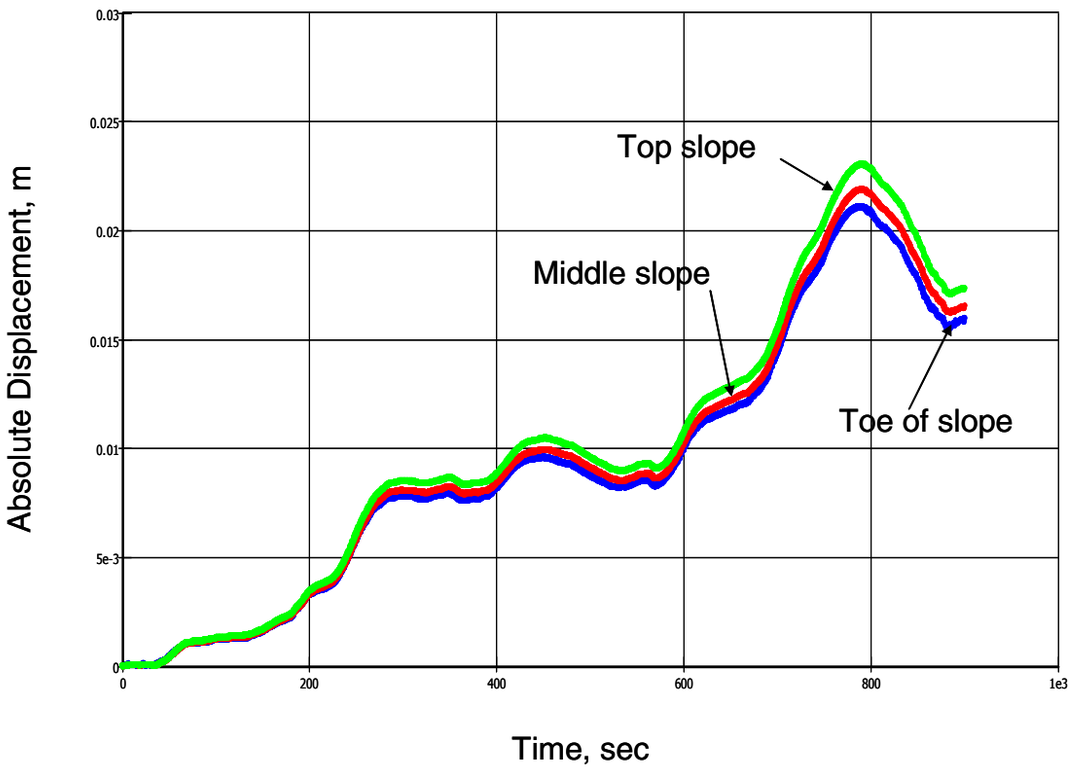


Figure 6. Time-History Plot of Slope Displacements



Evaluation of a Geogrid-Reinforced Soil Mat to Mitigate Post-Liquefaction Settlements – A Case Study

James R. Gingery[1], PE, GE, M. ASCE and Scott M. Merry[2], PhD, PE, M. ASCE

[1]Senior Engineer, Kleinfelder, 5015 Shoreham Place, San Diego, CA 92122, jgingery@kleinfelder.com
[2]Senior Engineer, Kleinfelder, 2015 N. Forbes Rd, Ste 103, Tucson, AZ 85746, smerry@kleinfelder.com

ABSTRACT: The use of geogrid reinforced soil mats has become a viable method to mitigate differential settlements caused by deformations in the underlying soils, including those resulting from fault rupture and seismically induced settlements. In this paper a case study is presented where numerical modeling was used to evaluate the effectiveness of geogrid reinforced soil to mitigate as much as 100 mm of differential seismic settlement. The subsurface investigation, which made extensive use of the cone penetration test, is first presented. Using this information, numerical models were then developed. Descriptions of the modeling procedures are presented and important/sensitive aspects of the models are discussed. The results of the modeling are presented and observations are made regarding performance of the geogrid-reinforced soil system. Areas where additional studies are warranted are identified.

INTRODUCTION

Numerous case histories have demonstrated that settlement from excess pore water pressure dissipation and reconsolidation following soil liquefaction (or excess pore water pressure ratios near unity) can lead to damage of man-made improvements (Kramer 1995). This is also true, though to a lesser degree, of settlement from contractive volumetric strains induced in unsaturated soil by earthquake shaking. Collectively, these two modes of settlement are referred to herein as "seismically induced settlement".

There are many methods available for mitigation of liquefaction hazards, including in-situ ground densification techniques (e.g., vibro-replacement and solidification techniques, such as jet grouting), and structural approaches (e.g., deep foundations). We have observed that geogrid reinforced soil mats constructed near the ground surface above the liquefiable layer(s) have increasingly been recommended by consulting geotechnical engineers in the western U.S. These mats typically consist of two or more layers of geogrid placed below the lowest foundation elevations within compacted fill, and their use is mostly limited to mitigation of seismically induced settlement (as opposed to other liquefaction hazards such as lateral spreading).

Geogrid reinforced soil has been employed for many years to strengthen foundation soils and increase the bearing capacity of embankment or building foundations (Gabr & Han 2005) and also to span over zones of localized settlement (Giroud et al. 1990). Relatively simple techniques for the analysis and design of foundation bearing capacity enhancement have been developed and are commonly used in practice. Previous work by Bray et al. (1993) and Bray (2001) concluded that reinforced soil mats can be effective in spreading differential displacements and reducing angular distortions relative to a distinct offset in an underlying normal or reverse bedrock fault. However, to the authors' knowledge, a simple, rational and quantitative technique to analyze and design geogrid reinforced soil mats for mitigation of seismically induced settlements has not been developed. In practice, the "design" of these soil mats has frequently relied heavily on engineering judgment.

This paper presents a case study where a combination of more extensive site characterization and numerical modeling was used to evaluate the efficacy of a geogrid reinforced soil mat to mitigate seismically induced differential settlement.

SUBJECT PROJECT BACKGROUND

The project consisted of a proposed warehouse that measured approximately 123 by 98 meters in plan dimension constructed using concrete masonry walls, steel columns, and a steel truss roof. Ancillary improvements included loading docks, parking lot, and landscaping areas. The maximum anticipated wall and column loads were 65 kN/m and 310 kN, respectively. Floor loads were typically 20 kPa. Approximately 4 meters of new fill was necessary to bring the site to the building pad grade.

INITIAL SUBSURFACE AND LIQUEFACTION CHARACTERIZATION

An initial geotechnical and geologic investigation was performed consisting of 16 borings, 16 cone penetrometer tests with pore water pressure measurement (CPTu), and geologic mapping. In the borings, samples were obtained using Standard Penetration Test (SPT) and California samplers. An array of geotechnical laboratory testing was also performed. The field and laboratory investigations revealed that the site is underlain by approximately 19 meters of alluvium consisting of poorly graded sands, silty sands, sandy silts, clayey silts, clays and gravel. Groundwater was present at a depth of approximately 2.1 meters below the existing ground surface. In the upper 13 meters of the alluvium, the sands, silty sands and gravels were typically loose to medium dense, and the silts and clays were soft to medium stiff. The lower 6 meters of granular materials became dense and the cohesive materials became medium stiff to very stiff. Dense to very dense, weakly cemented sandstone was encountered underlying the alluvium. The first two plots in Fig. 1 present soil behavior type index (I_c) and tip resistance from a sample CPTu trace that are illustrative of the interbedded sandy and clayey alluvial deposits at the site.

The 2001 California Building Code (CBC) (CBSC 2001), which was the governing code for development at this site, requires seismic design be performed for an earthquake having a 10 percent probability of exceedance in 50 years. For the purpose of geotechnical earthquake engineering analyses, a peak ground acceleration (PGA) of

rock at the site of 0.24g was estimated based on the USGS (2002) probabilistic seismic hazard analysis (PSHA) maps. The ground surface PGA was estimated to be 0.30g by accounting for site amplifications effects using the method of Seed et al. (2001). A design moment magnitude of 7.0 was used based on deaggregation of the PSHA.

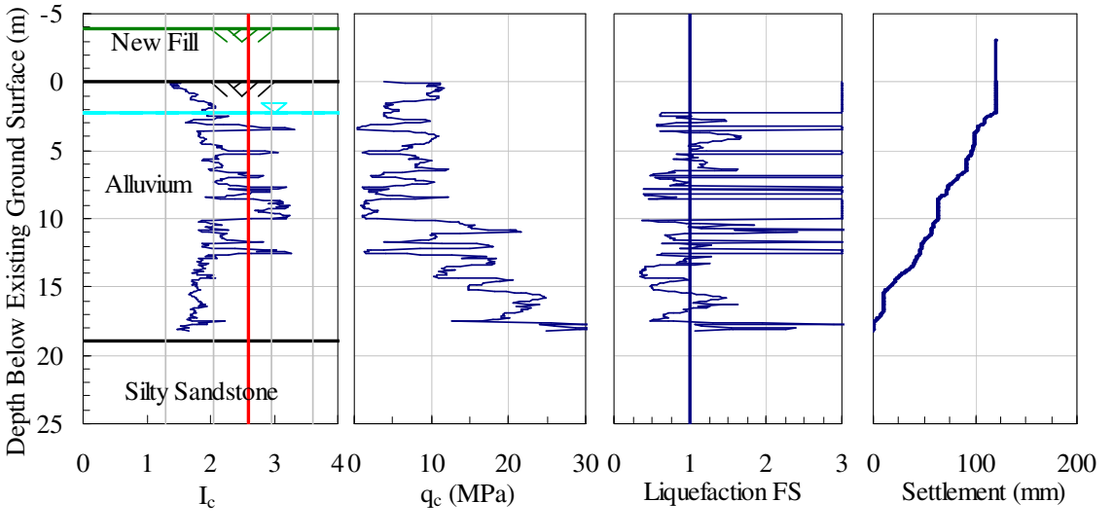


FIG. 1. Sample soil profile, and liquefaction and seismic settlement plot.

Liquefaction triggering analyses were performed using the techniques outlined by NCEER 1997 / Youd et al. (2001), except for compositional criteria evaluations where the recommendations presented by Bray & Sancio (2006) were used rather than the Modified Chinese Criteria, which are now widely recognized as unreliable. While more recent/updated proposed triggering analyses are available (e.g., Idriss and Boulanger 2004; Cetin et al. 2004), the many consultants elect to use the Youd et al. (2001) procedures since it is the latest "expert consensus" technique available and allows designers and contractors to more readily agree on a uniform standard to base performance criteria for ground improvement in construction documents. Post-liquefaction reconsolidation settlement and seismic compaction settlements were estimated using Tokimatsu and Seed (1987). The unsaturated soil settlements were negligible compared to the post-liquefaction reconsolidation settlements.

CPTu data were used in the evaluations of CRR at the site due to its advantage of providing continuous profiling and its avoidance of uncertainties in hammer energy that are inherent in the SPT method. Samples from borings were checked for compositional criteria (Bray & Sancio 2006) and cross correlated against I_c values.

The results of liquefaction triggering evaluations indicated that layers within the alluvium below the groundwater table were susceptible to liquefaction under the design earthquake ground motion. The liquefied layers were present at great enough depth below the finished ground surface so as not to result in reduced bearing capacity of the foundations. However, the calculated seismically induced settlements of 100 to 200 mm were judged to be too severe to be left unmitigated; hence, a preliminary vibro-replacement (stone column) ground improvement design was developed. The relative high cost of the stone column ground improvement provided the impetus to evaluate more cost effective alternative mitigation techniques. Reinforcement of the 4

meters of new fill with geogrid was considered. The following sections of this paper describe the engineering analyses performed to evaluate the effectiveness of using geogrid reinforced soil mat for this site.

NUMERICAL MODEL DEVELOPMENT

A numerical model was developed for the purpose of aiding the design of a geogrid reinforced soil mat and gaining insight into its expected performance. As the focus from this study was on response of these materials to the seismically induced settlements in the underlying materials, only the geogrid reinforced soil mat and the underlying unsaturated native soils were modeled.

A two dimensional plane strain explicit finite difference (EFD) model was developed using the computer code FLAC (Itasca 2005). The model included 2.1 meters of existing unsaturated native soil overlain by the 4 meters of new engineered fill. The model is a total of 164 meters long, with a 122-meter long building area centered laterally within it. A nominal mesh element size of 600 mm by 600 mm was used. Three horizontal layers of geogrid were positioned at depths of 1.2, 2.4 and 3.5 meters below the ground surface. The geogrid layers extended 3 meters laterally beyond the building pad edge. A schematic diagram of the model geometry and initial boundary conditions is presented in Fig. 2.

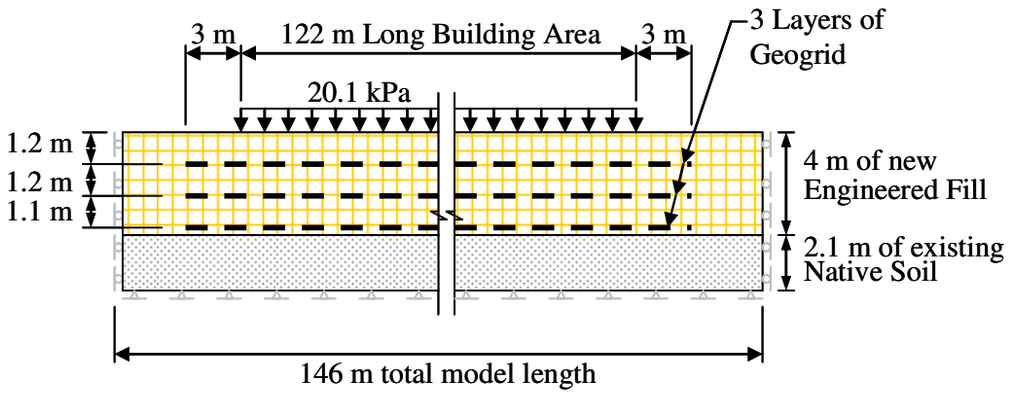


FIG. 2. Model geometry and initial fixity.

The response of the geogrid reinforced soil mat was evaluated by imposing a "seismic settlement profile" at the base of the model and allowing it to come to equilibrium. The magnitude and distribution of the imposed settlement profile is an important boundary condition for the model. Since the initial field investigation did not provide sufficient data to develop a settlement profile, a supplemental field investigation and additional seismic settlement calculations were performed. The supplemental field investigation consisted of performing a row of relatively closely spaced (10± meters) CPTs across the proposed building envelope. This CPT profiling provided further insight into the variability of the alluvial stratigraphy across the site. The settlements calculated at each CPT along the profile are shown as points in Fig. 3.

The fluvial depositional environment at the site suggested that liquefiable layers may taper at their boundaries (more gradual differential settlement) or could be abruptly truncated by erosion and redeposition (more abrupt differential settlement). The

interpreted settlement profile was constructed essentially as a step function, with differential settlement occurring between the finite difference grid points (600 mm apart) as shown on Fig. 3. The assumption of abrupt differential settlement between discrete CPT settlement data points was considered conservative but reasonable since the concentrated differential settlement that are expected at some locations at the site would be critical to the reinforced mat performance.

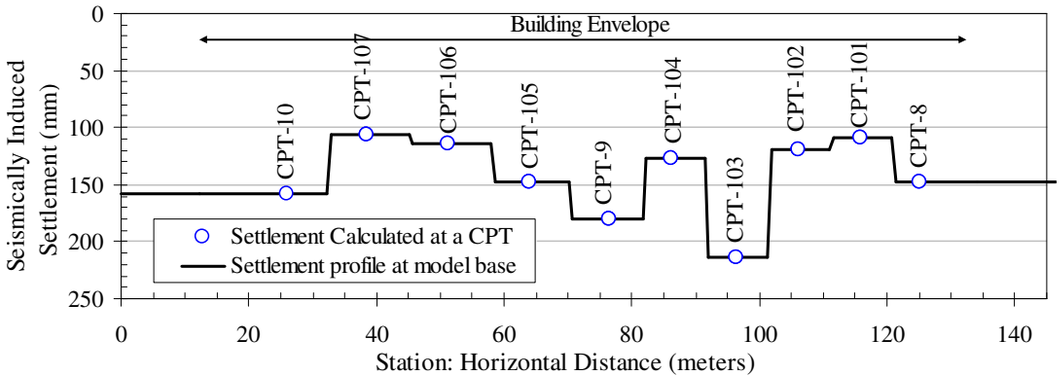


FIG. 3. Settlement calculated for CPTs and interpreted settlement profile.

The "Duncan-Chang" (Duncan et al. 1980) constitutive model was used to represent the soil behavior. The Duncan-Chang model uses a hyperbolic stress-strain relationship, stress dependent bulk and initial Young's moduli and a stiffer unloading-reloading modulus. It has been used previously in numerical modeling of fault rupture propagation through geogrid reinforced and unreinforced fill (Bray 1993, 2001), which is analogous to this study of seismic settlement.

The source of the proposed imported fill was not ascertained at the time this study was performed. However, recommended imported fill specifications were provided that were intended to be flexible enough to permit the fill to be obtained in an economical and timely fashion, while providing favorable strength, compressibility and other engineering characteristics. A minimum relative compaction of 90 percent with a moisture content of 0 to 3 percent above optimum (based on ASTM D 1557) was specified. Two sets of constitutive model parameters were developed that were considered representative of the range of the fill specifications from granular materials (gravelly sand / sandy gravel) to silty sand. Since the specific engineered fill materials were not yet know and not available for laboratory testing, typical constitutive soil model parameter values reported in Duncan et al. (1980) for the material types and compaction levels were used. The constitutive soil model parameters used in the analyses are presented in Table 1.

FLAC's "Strip Structural Element" was used to model the layers of geogrid reinforcement. The tensile behavior of the Strip element is linear elastic, perfectly plastic, with rupture at a prescribed strain. The Strip's interface elements can be programmed for linear elastic perfectly plastic shear resistance. The Strip parameters were developed based on a commercially available polypropylene biaxial geogrid. An allowable tensile strength was established based on the manufacturer's published value for ultimate strength (T_{ult}) in the machine direction and by considering reduction factors due to installation damage (RF_{ID}), biological/chemical degradation (RF_D) and

long term creep (RF_{CR}) using Eq. (1) referenced from Elias et al. (2001):

$$T_{all} = \frac{Tult}{RF_{CR} \cdot RF_{D} \cdot RF_{ID}} \qquad \text{Eq. (1)}$$

Table 1. Summary of constitutive soil model parameters

Material Description	Depth Range (meters)	Density ρ (kg/m^3)	ϕ_0 (deg)	$\Delta\phi$ (deg)	c (kPa)	K	K_{ur}	K_b	n	R_f	m
Engineered Fill - Granular	0-4	2243	36	0	1	300	600	75	0.40	0.7	0.2
Engineered Fill - Silty to Clayey Sand	0-4	2243	33	0	5	450	900	350	0.25	0.7	0
Native Soil - Silty Sand	4-6	1922	30	0	0	150	300	150	0.25	0.7	0.0

Values of 1.1 and 1.0 were used for RF_{ID} and RF_{D}, respectively, based on the manufacturer's data. A value of 1.0 was used for RF_{CR} since the re-stiffening of soil beneath the geogrid reinforced matt after excess porewater pressure dissipation was interpreted as a temporary loading condition for the geogrid. The manufacturer's load-strain data was also reduced in the same fashion as T_{ult} in developing the modeled load-strain behavior. Fig. 4 presents the manufacturer's reduced load-strain data against the results of a pull test simulation performed with FLAC. The modeled geogrid parameters include an elastic-range EA of 229 kN/m, a T_{allow} of 11.5 kN/m and a rupture strain of 12.1 percent. FLAC's Strip element attaches to the soil grid through interface elements that permit modeling of confining pressure-dependent stiffness and strength of the soil-strip interface. In this study, the interface stiffness was set to a high value so that elastic shear displacement between the soil and geogrid was negligible. The interface strength was conservatively set equal to 2/3 of the soil strength as suggested by Elias et al. (2001).

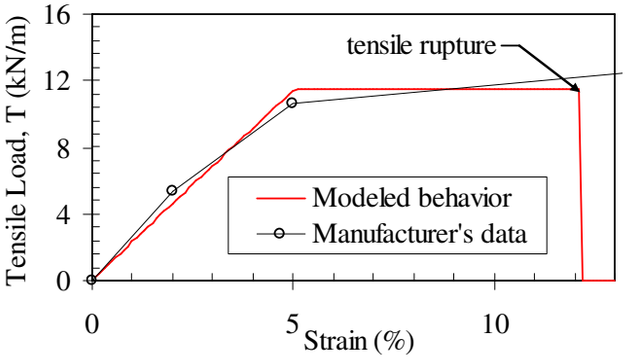


FIG. 4. Tensile behavior of geogrid: manufacturer data and FLAC pull test results.

The modeling included three stages as described below:

1. The geometry of the soil layers and geogrid were established and the soil and

strip parameters were assigned. Initial static stresses (based on a K_0 of 0.8 for fill and 0.5 for native soil) were assigned to the model and it was allowed to come to equilibrium under the acceleration of gravity.

2. A vertical pressure of 20.1 kPa was applied to the ground surface in the building area to account for foundation and floor slab loads. The model was allowed to come to equilibrium and the displacements were reset to zero. The end of stage 2 is considered the initial, pre-earthquake condition.

3. The seismic settlement profile was imposed at the bottom of the model. Since FLAC employs a time-marching EFD solutions scheme, the displacements were achieved by assigning displacement-proportional velocities, then stepping until the ultimate displacements were achieved. Since post-liquefaction settlements occur relatively slowly as excess porewater pressures dissipates, the velocities were selected to be low enough so that the inertial effects were believed to be negligible. After the ultimate settlements were achieved the velocities were set back to zero and the model was allowed to come to equilibrium.

MODELING RESULTS

Fig. 5 presents a plot of the input settlement profile along with surface settlement profiles calculated for the case where granular fill was used with and without geogrid reinforcement. The geogrid-reinforced and unreinforced results for the case where silty sand fill was used are shown in Fig. 6. Based on observational comparison of these results, these two cases are expected to have very similar levels of field performance. Fig. 7 shows an example of vertical displacement contours for the granular fill with-geogrid condition in an area of the model where the largest differential settlement was imposed. As anticipated, the concentrated differential displacements introduced at the base of the model are spread to a wider area as they propagate toward the ground surface. For example, Figure 7 shows the abrupt differential settlement at the base of the model of 90 mm (210 – 120 mm) at about Station 102 m is spread to a width of about 10 m when it reaches the ground surface. There is a significant reduction of angular distortions at the ground surface relative to the base of model. There is a 15 percent reduction of the total differential settlement observed for all cases across the input differential step at the 92 meter station; otherwise the total differential settlements are essentially the same at the base and the ground surface of the model. Notably, there is very little difference between the surface settlement profile calculated for the geogrid reinforced cases and their unreinforced counterpart. An additional case (which is not fully reported herein due to space restrictions) was run with 4 layers of geogrid and still the resulting surface settlement profile was the same as the unreinforced case.

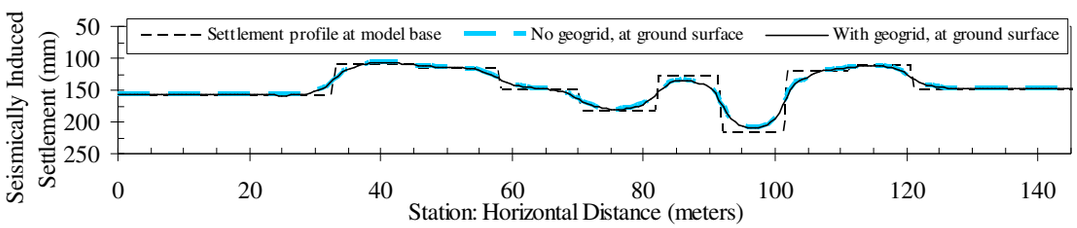


FIG. 5. Plot of input settlement profile and resulting surface settlement profiles from numerical modeling, granular fill case.

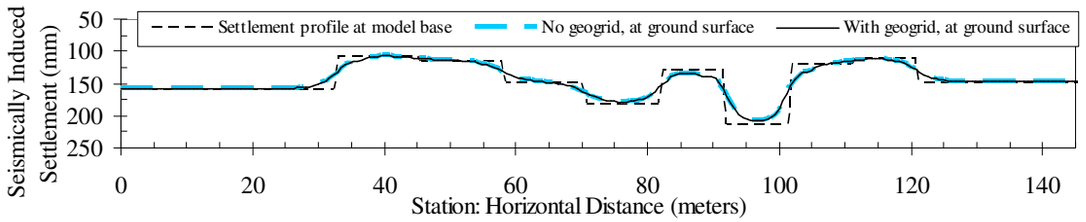


FIG. 6. Plot of input settlement profile and resulting surface settlement profiles from numerical modeling, silty sand fill case.

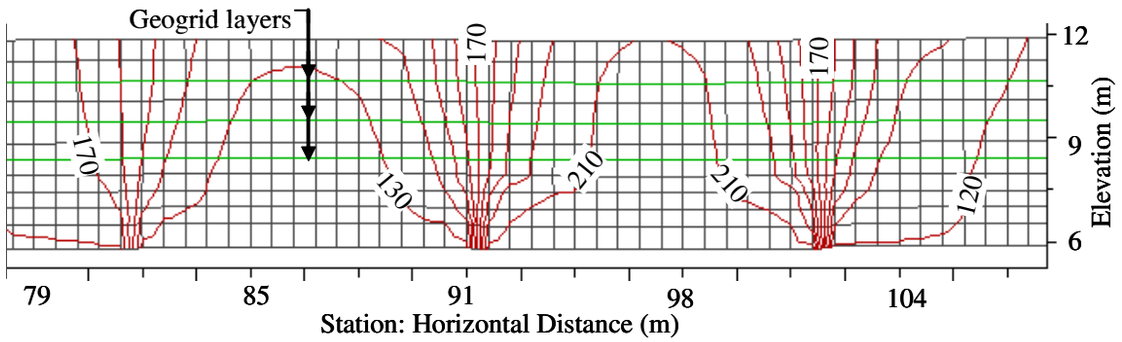


FIG. 7. Plot of vertical displacement contours (in mm) for area of model where the largest differential settlement was imposed (granular fill with geogrid case). Plot also shows the distorted EFD grid and the geogrid layers.

DISCUSSION

While the modeling results showed a significant reduction in angular distortions for all cases, the geogrid reinforced cases did not result in additional reduction of angular distortions compared to the corresponding unreinforced cases. This seemingly counterintuitive result is, upon closer inspection, reasonable and generally consistent with previous studies. Geogrid can sustain tensile loads but has essentially no bending or axial compressive stiffness. Therefore, in order for geogrid reinforcement to contribute significantly to the redistribution of stresses and strains within a reinforced soil mass, a mechanism must be present that introduces extensional strain in the geogrid. In this study, the seismically induced settlements at the base of the model were imposed with no horizontal movement. With displacements occurring in a direction normal to the geogrid layers and with spreading of the differential settlement occurring within the soil below the first layer of geogrid, very little extensional strain is introduced in the geogrid layers. In finite element modeling of normal fault rupture propagation through geogrid reinforced and unreinforced soil by Bray (2001), little to no difference in angular distortion reduction was reported for 3 to 4.5 meter thick fill when an 85 degree dipping (close to vertical) fault was considered. For the case of a 65 degree dipping normal fault, which directly introduces extensional strain in the geogrid, greater reduction of angular distortion was reported by Bray (2001). It is

possible that different geogrid reinforcement layouts, such as more geogrid layers at closer spacing, could result in lesser angular distortions compared to the unreinforced case.

Cracking of non-liquefiable soil "crust" and the formation of blocks that can move differentially is a damaging mechanism that has been observed in many earthquakes (Seed et al. 2001). The development of these cracks is difficult to predict and this behavior cannot be modeled in the continuum model used in this study. Owing to its strength in tension, it is evident that the geogrid reinforcement can help mitigate the ground cracking hazard. Despite the modeling results showing that angular distortions were not reduced with the geogrid reinforced fill compared to the unreinforced fill, geogrid reinforcement was recommended for the soil mat design alternative because of the geogrid's potential to mitigate ground cracking. Ultimately the project owner elected to pursue the stone column design alternative because it afforded a higher level of expected field performance and increased the likelihood that the facility could remain functional with little or no repair required after the design earthquake.

CONCLUSIONS

A case study has been presented that illustrates an approach to evaluating differential seismic settlement hazard and its mitigation using an unreinforced and geogrid reinforced fill mat. Performing liquefaction and seismically induced settlement analyses for the closely spaced CPT profile provided a more quantitative characterization of the expected differential settlement at the site. The calculated seismic settlements were conservatively interpreted to develop a seismic settlement profile that was used as a boundary condition for numerical modeling of geogrid reinforced and unreinforced fill. The modeling results showed that the unreinforced and reinforced fill mats were effective in reducing angular distortions at the ground surface. For the geogrid layout considered in this study, there was no additional reduction of angular distortions observed in the geogrid reinforced case compared to the unreinforced case.

REFERENCES

Bray, J.D., Ashmawy, A., Mukhopadhyay, G. and Gath, E.M. (1993). "Use of Geosynthetics to Mitigate Earthquake Fault Rupture Propagation Through Compacted Fill", *Proceedings of the Geosynthetics '93 Conference*, Vol. 1, 379-392.

Bray, J.D. (2001). "Developing Mitigation Measures for Hazards Associated with Earthquake Surface Fault Rupture", *A Workshop on Seismic Fault-Induced Failures – Possible Remedies for Damage to Urban Facilities*, Japan Society for the Promotion of Science, Japan, pp. 55-79, January 11-12, 2001.

California Building Standards Commission (CBSC) (2001). *2001 California Building Code (CBC), California Code of Regulations, Title 24, Part 2, Volume 2.*

Bray, J.D., Sancio, R.B. (2006). "Assessment of the Liquefaction Susceptibility of Fine-Grained Soils", *JGGE*, Vol. 132, No. 9, September 2006, pp. 1165-1177.

Cetin, K.O., Seed, R.B., Der Kiureghian, A., Tokimatsu, K., Harder, L.F., Kayen, R.E., Moss, R.E. (2004). "Standard Penetration Testing-Based Probabilistic and Deterministic Assessment of Seismic Soil Liquefaction Potential", *JGGE*, Vol. 130, No. 12, Dec. 2004, pp. 1314-1340.

Elias, V., Christopher, B.R., Berg, R.R. (2001). *Mechanically Stabilized Earth Walls and Reinforced Soil Slopes Design and Construction Guidelines*, Federal Highway Administration Pub. No. FHWA-NHI-00-043.

Duncan, J.M., Byrne, P., Wong. K.S., Mabry, P. (1980). *Strength, Stress-Strain and Bulk Modulus Parameters of Finite Element Analyses of Stresses and Movements in Soil Masses*, U.C. Berkeley Geotechnical Engineering Report No. UCB/GT/80-01.

Gabr, M. and Han, J. (2005). "Geosynthetic reinforcement for soft foundations: US perspectives." *ASCE GSP No. 141: International Perspectives on soil reinforcement applications, ASCE GeoFrontiers*, Jan. 24-26, 2005, Austin, TX.

Giroud, J.P., Bonaparte, R., Beech, J.F. and Gross, B. (1990). "Design of Soil Layer-Geosynthetic Systems Overlying Voids," *Geotext. and Geomem.,* V9#1, pp. 11-50.

Idriss, I.M. and Boulanger, R.W. (2004). "Semi-empirical Procedures for Evaluating Liquefaction Potential During Earthquakes", *Proc. of the 11th Intrnl. Conf. on Soil Dyn. and Earthquake Engnr. and 3rd Intrnl. Conf. on Earthquake Geotech. Engrn.*, Volume 1, University and California, Berkeley, January 2004.

Itasca Consulting Group, Inc. (2005). Fast Lagrange Analysis of Continua Ver. 5.00.

Kramer, S.L. (1995). *Geotechnical Earthquake Engineering,* Prentice Hall, NJ.

Seed, R.B., Cetin, K.O., Moss, R., Kammerer, A., Wu, J., Pestana, J., and Riemer, M. (2001). "Recent Advances on Soil Liquefaction Engineering and Seismic Site Response Evaluation," *4th Intrnl. Conf. and Sympsm. on Recent Advances in Geotech. Earthquake Engineering and Soil Dynamics*, Paper SPL-2, March 26, San Diego, CA.

Tokimatsu, K. and Seed, H.B. (1987). "Evaluation of Settlements in Sands Due to Earthquake Shaking," *J. of Geotech. Engr. Div.*, ASCE, Vol. 113, No.8, 1987.

USGS (2002). NSHMP http://earthquake.usgs.gov/research/hazmaps/

First Applications of the SAVE Compozer Method (Non-Vibratory Stone Columns) for Soil Densification in the U.S.

Jun Mukai[1], Masaru Sakakibara[2], Juan I. Baez, Ph.D., P.E[3],
Sean G. Callan, P.E[4] and Hideo Tsuboi, Dr.Eng[5]

[1]Staff Engineer, Fudo Construction Inc., 2555 Flores Street Suite 490 San Mateo, CA 94403, jun@fudo-const.com
[2]President, Fudo Construction Inc., 2555 Flores Street Suite 490 San Mateo, CA 94403, masaru@fudo-const.com
[3]President, Advanced Geosolutions, Inc., 11400 West Olympic Blvd., Suite 200 Los Angeles, CA 90064, jibaez@advgeosolutions.com
[4]Vice President, Advanced Geosolutions, Inc., 11400 West Olympic Blvd., Suite 200 Los Angeles, CA 90064, sgcallan@advgeosolutions.com
[5]General Manager, Fudo Tetra Corporation, 7-2 Nihonbashi-Koami-Chou Chuou-Ku, Tokyo 103-0016 Japan, hideo.tsuboi@fudotetra.co.jp

ABSTRACT: The Vibro-Replacement Method, also known as Stone Columns is one of the most prevalent liquefaction mitigation measure used in the U.S. However, difficulties have been encountered occasionally when applying this method in urban or residential environments because of the potential for negative impacts such as noise and vibration on project neighbors, and the potential for structural damage when it is applied too close to the exiting structures. The SAVE (Silent, Advanced, Vibration-Erasing) Compozer is a newly developed Non-Vibratory Replacement method that does not induce vibration and creates very little noise. The same degree of densification can be achieved when using the SAVE Compozer as can be achieved with conventional Vibro-replacement without the negative impacts of noise or vibration. This paper presents case histories of the first two applications of the SAVE Compozer in the U.S. including verification results of densification performance and vibration monitoring records, together with an overview of the SAVE Compozer method including densification concept, equipment, and execution.

INTRODUTION

When using Vibro-replacement, densification of the subsurface soils is achieved by a combination of vibratory force and enforced placement of coarse grained materials into the ground. As a result of the soil densification and stone placement, the bearing capacity is increased while static settlement is reduced, and for a seismic event, liquefaction is mitigated and dynamic settlements are reduced.

Although Vibro-replacement is suitable for a wide range of soil types, difficulties have been encountered occasionally when applying this method in urban or residential areas. Vibration and noise during the installation of stone columns are generally found to cause discomfort to neighbors in close proximity to the project site. To deal with this issue, the development of new soil densification methods with less vibration and noise has been considered a priority, especially in Japan, a densely populated country with frequent occurrence of earthquakes.

In 1998, shortly after the Hyogoken Nambu Earthquake in Kobe, Japan, the SAVE Compozer method was developed by Fudo Construction Co., Ltd. as the first Non-Vibratory Replacement method.

SAVE COMPOZER METHOD

Figure 1 shows the SAVE Compozer rig operating at an urban site in Japan. The rig is equipped with a new type of forced driving / lifting mechanism. Figure 2 shows the operational sequence. The SAVE Compozer does not require vibration for either initial penetration or column construction. Both operations are completed using a combination of rotational force and downward crowd pressure. By using the SAVE Compozer, the same degree of densification can be achieved as would be expected with conventional Vibro-replacement. Development of the SAVE Compozer has allowed for dependable subsurface soil densification in urban and residential areas. Since its inception, the SAVE Compozer has been applied widely in Japan and has recently been used on two projects in the U.S.



FIG. 1. SAVE Compozer Rig

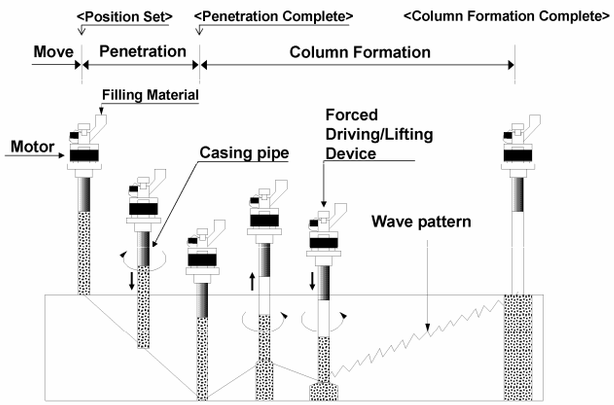


FIG. 2. Densification Sequence

SAVE Compozer has many advantages including::

- *No negative impact to surrounding environment.*
  No vibration and low noise during operation of the SAVE Compozer allows stone column construction in urban and residential environments. Figure 3 shows vibration and noise as a function of distance from the equipment for

both the SAVE Compozer and conventional Vibro-replacement.

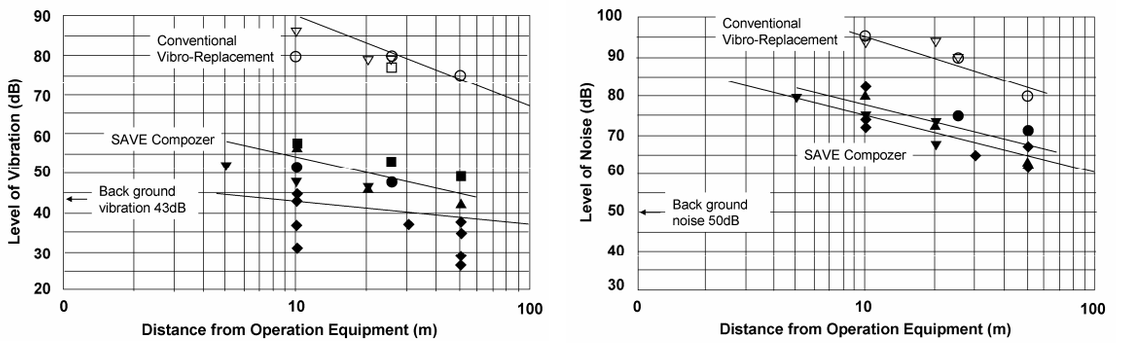


FIG. 3. Decrease over Distance of Noise and Vibration

・*Wide range of filling materials are usable.*

Figure 4 shows the applicable grain size range of suitable backfill materials. The SAVE Compozer can be used to install traditional crushed stone, sand or recycled materials, another added environmental advantage.

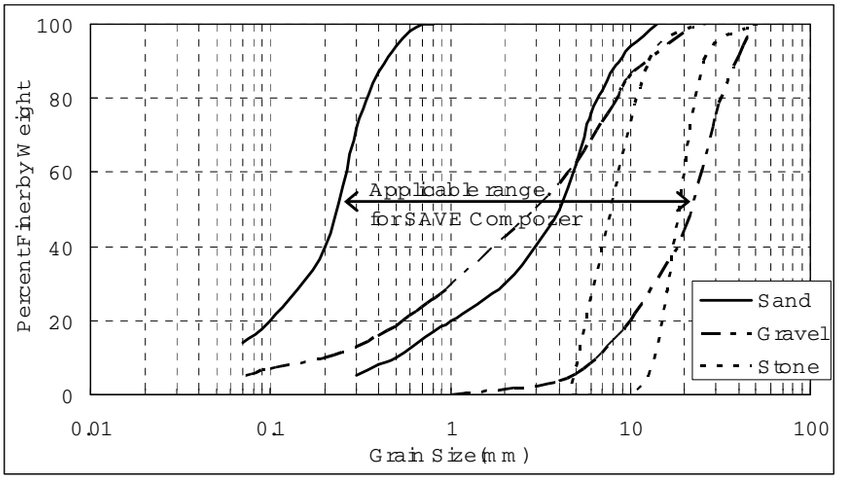


FIG. 4. Applicable Range of Materials

・*Same densification as Vibro-replacement.*

There is no difference in densification effect between vibratory and non-vibratory methods.

・*Excellent reputation in Japan.*

During various earthquakes, the ground improved by the SAVE Compozer has performed very well.

SOUTHERN CALIFORNIA INDUSTRIAL SITE

On this project, ground improvement using stone columns was specified to mitigate liquefaction, reduce static and seismic settlement and increase bearing capacity for a multi-storey parking structure. The stone column layout is shown in Figure 5. The ground improvement adjacent to the existing building located on the east side of the project site was required to be vibration-free. The SAVE Compozer method was chosen to improve the soils within 40-feet of this existing structure. The method was also used adjacent to utility lines located in the public street, while the conventional Vibratory Replacement method was used for the remainder of the site.

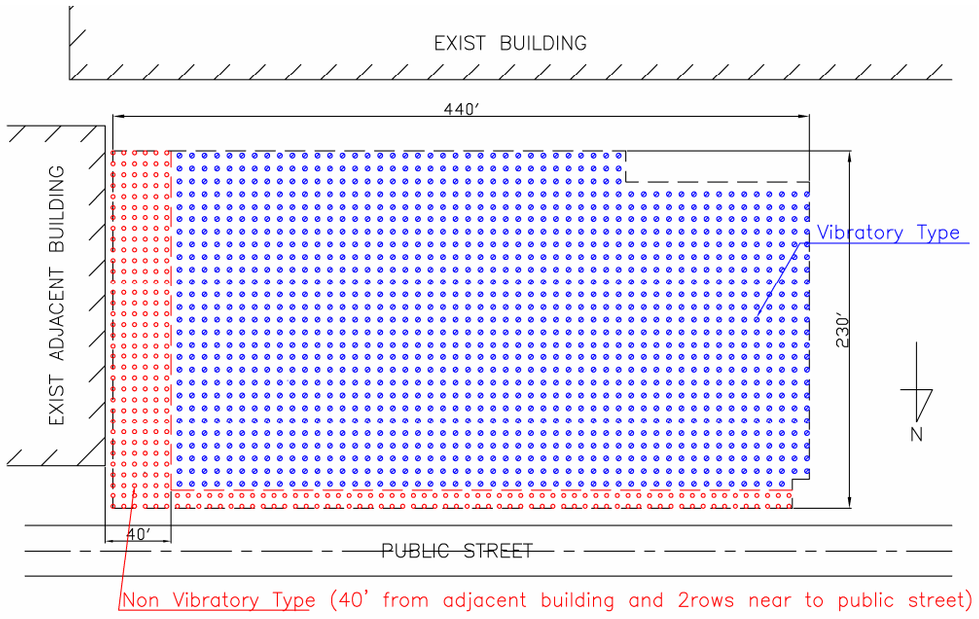


FIG. 5. Drawing of Southern California Industrial Site

Soil Condition and Performance Criteria

The pre-improvement soils investigation consisted of thirteen Standard Penetration Tests (SPT) and sixteen Cone Penetration Tests (CPT). The soils at the site can be characterized as follows:

- Undocumented fill with a thickness varying between 5-feet and 7-feet. The fill consists of sandy silt to silty sand and contains wood and construction debris.
- Predominantly loose to medium dense sand zone with silt layers extended from below the undocumented fill to a variable depth averaging about 33-feet below existing ground surface.
- Interbedded layers of predominantly silts and clays or silty sand layers existed below an approximate depth of 41 feet from the existing ground surface.
- Ground water was encountered at a depth of 8 and 10 feet below the existing ground surface.

The liquefaction analysis was performed using the procedure of Youd and Idriss (1996 NCEER and 1998 NCEER/NSF workshops) using the site design earthquake of Mw 7.5 and PGA of 0.3g. The seismic induced settlement calculations were performed using the procedures of Tokimatsu and Seed (1984) and static settlement calculation was performed using the Schmertmann (1970) procedure. The untreated seismic settlement was calculated to be about 5-inches, and the static settlement at the foundations was calculated to be 4-inches.

The performance criteria for the contractor-designed ground improvement program required that the post-improvement total static and dynamic settlements be limited to 1-inch in each case. In addition the post-treatment clean sand equivalent $(q_{c1N})_{cs}$ tip resistance had to be greater than 100 at a depth of 7-feet below ground surface increasing to 135 at a depth of 41-feet below ground surface.

Construction

Figure 6 shows the SAVE Compozer at work adjacent to the existing building. Although the center-line of the nearest SAVE location was only 10-feet from the wall, the installation of columns was successfully performed without producing any cracks to the wall or other discernible damage to the structure. In this project, recycled concrete materials were used for the filling materials due to economic consideration.



FIG. 6. Adjacent Installation

Result of Post-CPT Tests

A total of seventeen post-improvement verification CPT's were performed. Figure 7 shows the results at the areas improved using the SAVE Compozer. Adjacent pre-improvement test results are also presented. The tip resistance (q_c), sleeve friction (f_s), soil behavior type index (Ic), and normalized tip resistance $(q_{c1N})_{cs}$, respectively, versus depth from ground surface are shown. A comparison between pre-improvement and post-improvement results can be summarized as follows.

- $(q_{c1N})_{cs}$ increased in most of the target treatment zone.
- The increase in f_s is significant. The state of stress (K_0) has been changed as a result of the ground improvement.
- There are some spots that q_c after the densification was smaller than one at pre-densification. The reason of this reduction in q_c is that the soil contained much fines and this made Ic larger than 2.6. Such a high fines contents layer is non-liquefiable layer.
- Seismic settlements were calculated as 0.2-inches at the SAVE Compozer area and 0.9- inches at the Vibo-replacement area.

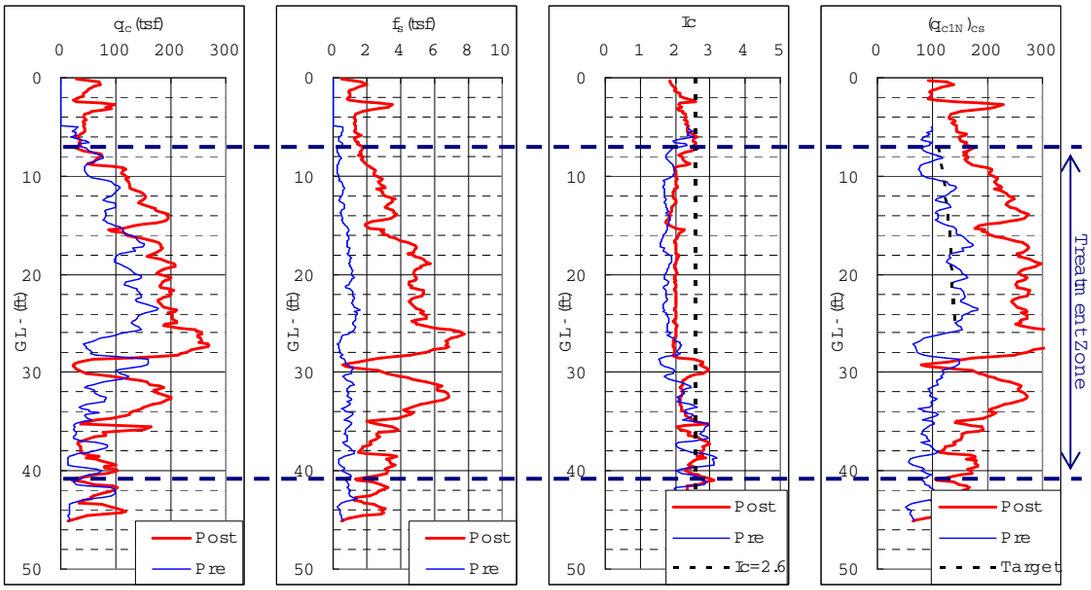


FIG. 7. Pre & Post CPT Result for SAVE Compoze (From GL-7 to GL-41feet)

All post-improvement CPT results, both in the SAVE Compozer and the Vibro-replacement treated areas, satisfied the project criteria. This demonstrates that the SAVE Compozer can achieve improvement results similar to Vibro-replacement results, as has previously been shown with similar comparisons studies conducted in Japan.

Figure 8 shows a comparison of normalized pre- and post-tip resistance with clean sand equivalent $(q_{c1N})_{cs}$ between vibratory and non-vibratory installation methods. To compare the densification data in the same condition, data from similar depths and where the soil behavior type index (Ic) was lower than 2.0 was used. From Figure 8, it can be seen that both the non-vibratory and the vibratory method successfully densified soils that without improvement would not meet the project criteria and there was virtually no difference in the effectiveness of either method.

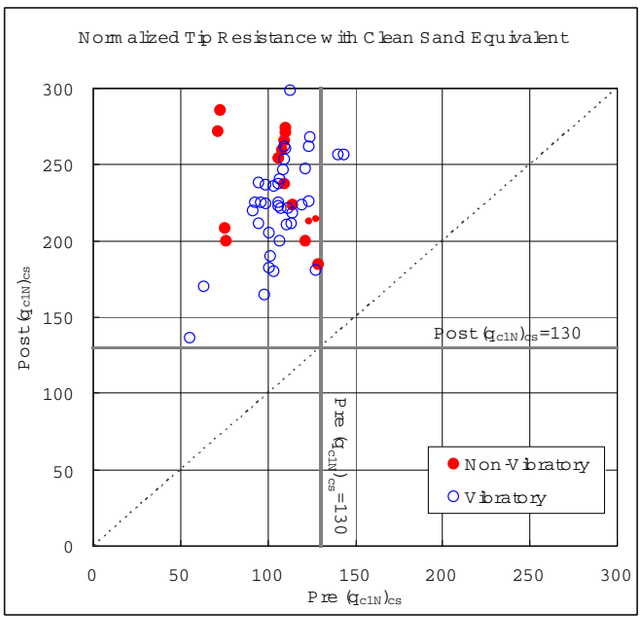


FIG. 8. Comparison of Densification Effect

NORTHERN CALIFORNIA COMMERCIAL SITE

On this project, soil densification by stone columns was planned to mitigate liquefaction and lateral spreading in hydraulically placed fills. The improvement area consisted of a strip of land 2,800-feet long by 40-feet wide alongside a lagoon with a residential neighborhood on the opposite side of the lagoon. A cross section of the site is shown in Figure 9. The project was contractor designed and although the actual method of installation was not specified, the owner was concerned about the impact vibrations might have on the surrounding residences. When the contractor proposed the SAVE-Compozer non-vibratory installation method the owner chose this method over the more traditional vibratory method.

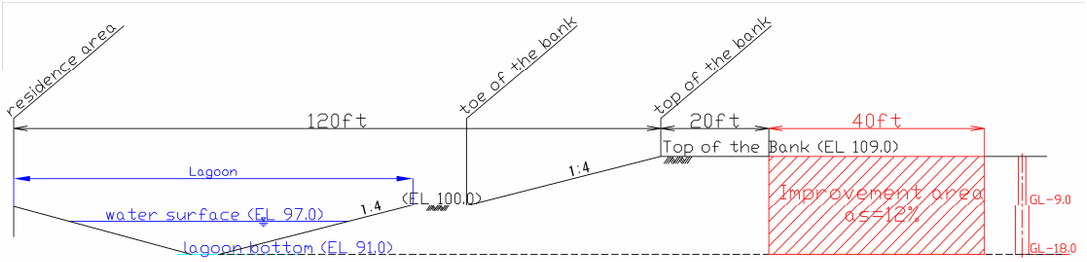


FIG. 9. Cross Section of Northern California Commercial Site

Soil Condition and Performance Criteria

Based on the results of pre-improvement soil investigation tests of the site (two Standard Penetration Tests and twenty-eight Cone Penetration Tests), the subsurface materials were characterized as follows:

- The treatment zone was comprised primarily of fine sands and silty sands, with occasionally sandy silts. These sands were generally fine grained and uniformly graded and were commonly interspersed with layers of soft, plastic clays and some silts.
- The ground water level was the same as the lagoon water level and was encountered at a depth of between 10 and 12 feet below the existing ground surface.

The ground improvement portion of this project was contactor design-build. The performance-based specification required that the soils in the improvement zone must obtain a minimum normalized cone penetration tip resistance $(q_{c1N})_{cs}$ of 130. The column diameter and spacing was selected by the contractor based on the results of the pre-improvement CPT program.

Vibration Monitoring

In order to confirm that the SAVE-Compozer method did not negatively impact he neighborhood, the owner carried out continuous vibration monitoring at the residences while the installation work was in progress. The location of the monitoring points and the proximity of the construction activities at the time the monitoring was performed are shown in Figure 10. The owner had established two monitoring points and the minimum distance between the production operation and monitoring point was 140-feet.

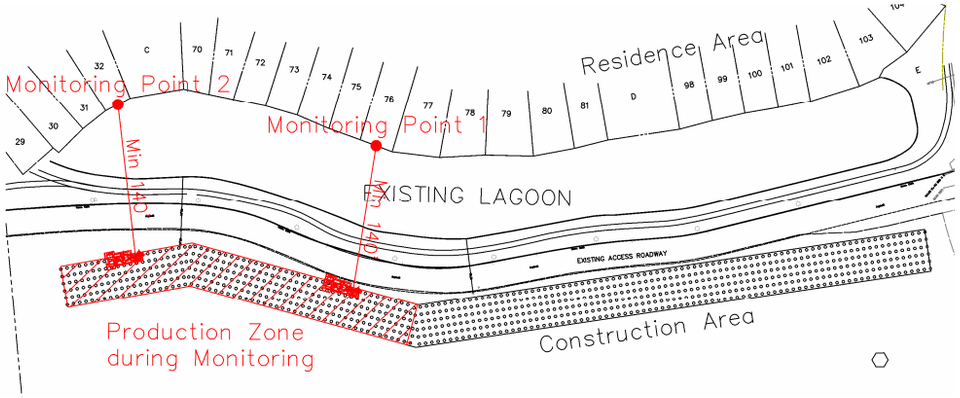


FIG. 10. Vibration Monitoring Point

Figure 11 shows the Peak Particle Velocity (vertical) for the SAVE rig at this project, the historical data for the SAVE rig in Japan, and data for the vibratory method, all plotted versus distance from the source The straight line indicates the average vibration level by the SAVE Compozer vibrations based on studies performed in Japan. From this graph, the monitoring results of vibration at this project were lower than the average vibration level caused by the SAVE Compozer work in Japan.

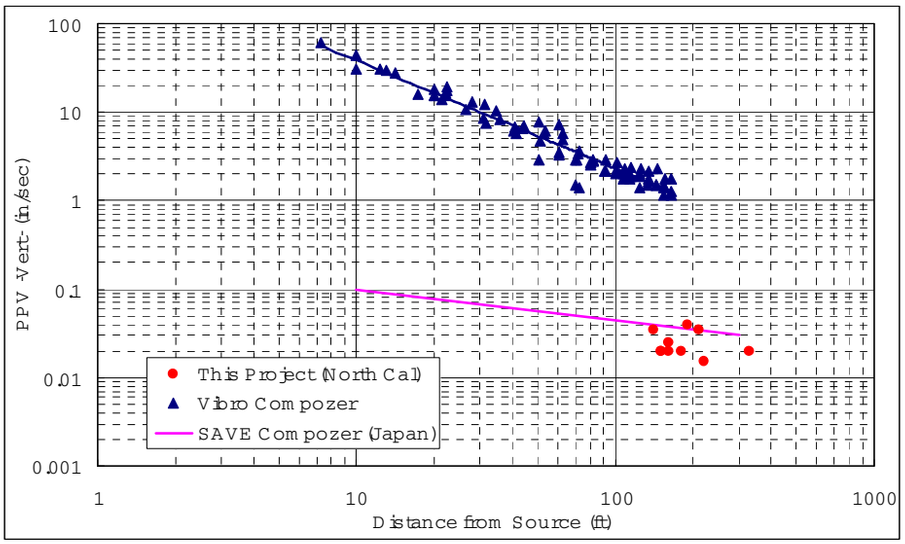


FIG. 11. Vibration vs. Distance from Source

Result of Post CPT Tests

A total of fifty-five post-improvement CPT's were performed on the soils improved with the SAVE Compozer method. Figure 12 shows the pre- and post-improvement CPT results for the site including; tip resistance (q_c), sleeve friction (f_s), soil behavior type index (Ic) and normalized tip resistance with clean sand evaluation $(q_{c1N})_{cs}$, all versus depth from the ground surface (GL).

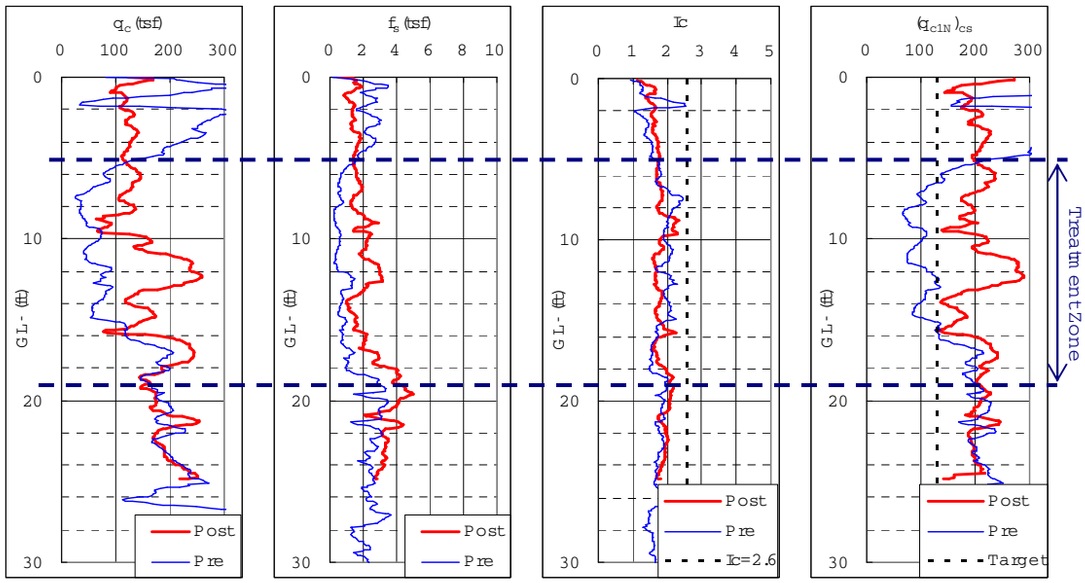


FIG. 12. Pre & Post CPT Results (Treatment Zone GL-5 to GL-19feet)

A comparison of the pre- and post-improvement test results can be summarized as follows.

- $(q_{c1N})_{cs}$ increased in most of the target treatment zone.
- The increase in f_s was smaller than at the Southern California site.
- The upper 5-feet (GL to GL-5feet) was not intended to be improved with the SAVE method. The results indicate a lower q_c than in the pre-improvement condition due to disturbance from SAVE production.

The subsurface soils were successfully densified to meet the project performance criteria except for a very small area where the soils contained a high percentage of fines and were considered unsuitable for improvement using the stone column method. The successful densification of the soils at this site confirms the SAVE Compozer's ability to densify soils similar to the Vibro-replacement method.

CONCLUSIONS

In Japan, demand for the SAVE Compozer is increasing due to increased building construction in urban areas. Since its introduction in 1998, the SAVE Compozer has been used on more than 500 projects in Japan with a total installed linear footage in

excess of 190,000 feet.

This paper presents information on the first two applications of the SAVE Compozer in the U.S. The test results presented here demonstrate the SAVE Compozer can achieve densification comparable to that which can be achieved using vibratory methods, but without the negative impacts of noise and vibration. These results and conclusions are similar to experiences gained from use of the SAVE Compozer method in Japan over the past ten years.

REFERENCES

Kenji Harada et al. (2004) "Case Histories and Recent Development of the Sand Compaction Pile Method as a Countermeasure against Liquefaction" *Fifth International Conference on Case Histories in Geotechnical Engineering New York*

Youd, T. L. et al. (2001) "Liquefaction resistance of soils; summary report from the 1996 NCEER and 1998 NCEER/NSF workshops on evaluation of liquefaction resistance of soils" *Journal of Geotechnical and Geoenvironmental Engineering, ASCE, Volume 127, October*

Tokimatsu, K. and H.B. Seed (1987) "Evaluation of Settlement in Sands due to Earthquake Shaking" *Journal of the Geotechnical Engineering Division, ASCE, Vol.113, August*

John H. Schmertmann (1970) "Static Cone to Compute Static Settlement over Sand" *Journal of the Soil Mechanics and Foundations Division, ASCE*

Minoru Yamamoto et al. (2000) "Effects on environmental aspect of new sand compaction pile method for soft soil" *Coastal Geotecnical Engineering in Practice*

Hideo Tsuboi et al. (1998) "Development and Application of Non-Vibratory Sand Compaction Pile Method" *8th International Offshore and Polar Engineering Conference*

Imaging a Grouted Column in a Centrifuge Model using Shear Wave Velocity Tomography

Scott J. Brandenberg[1], A.M. ASCE

[1] Assistant Professor, Department of Civil and Environmental Engineering, University of California, 5731 Boelter Hall, Los Angeles, CA 90095-1593, sjbrandenberg@ucla.edu

ABSTRACT: Bender elements embedded in a centrifuge model were used to image a concrete column grouted in sand. The bender elements were oriented in a polar array with the center of the column near the center of the array, and travel-time based tomographic inversion clearly identified the presence of the high-shear wave velocity anomaly. Tomographic imaging was performed using a pixel-based representation, in which the domain is divided into pixels and the shear wave velocity of each pixel is solved by inversion, and using a parametric-based representation, in which the geometry of the domain is assumed and the domain parameters are varied to minimize inversion error. Elimination of time delay present in the system was required to reduce inversion errors. Though the inversion is sensitive to input parameters and data quality, the grouted column was evident in the center of the array for a range of inversion techniques.

INTRODUCTION

Tomography is the process by which the interior properties of a region are non-invasively imaged by inversion of measurements collected at the region's boundaries. The most notable application of tomography is in the field of medicine. Allan Cormack (1963, 1964) and Godfrey Newbold Hounsfield (1973) received the Nobel Prize for Medicine in 1979 for independently developing the Computed Axial Tomography (CAT) scanning approach, which revolutionized medical diagnostic capabilities. Application of tomography in geotechnical engineering has been limited. Examples include cross-hole sonic tomography used to image defects in drilled shafts (e.g., Olson et al. 1998), and laboratory implementation by Lee et al. (2005), which constituted a proof-of-concept study of tomographic imaging using shear wave velocity. The limited application of tomographic imaging in geotechnical engineering is surprising considering that the biggest problem we face is our inability to sufficiently understand the properties of the subsurface. As asserted by the Terzaghi (1947): “The theories of soil mechanics provide us only with working hypotheses, because our knowledge of the average physical properties of the subsoil and of the orientation of the boundaries between the individual strata is always incomplete and often utterly inadequate.” Tomographic imaging is a promising method by which we may be able to improve our understanding of the subsurface, but research is required to advance our use of tomography.

This paper presents tomographic imaging of a concrete column grouted in dry sand by inversion of shear wave velocity measurements obtained using an array of bender elements embedded in the soil around the perimeter of the column. The bender element instrumentation layout is briefly discussed, followed by a detailed discussion of the pixel-based and parametric based imaging approaches. Both methods reasonably rendered the position and size of the embedded column, while the shear wave velocity of the inclusion could not be accurately measured. Finally, several limitations of tomographic imaging are discussed, along with potential approaches that could improve the resolution and accuracy of the images.

MEASUREMENTS USING BENDER ELEMENT SYSTEM

Brandenberg et al. (2006) described the bender element system implemented on the 9-m radius geotechnical centrifuge at UC Davis, including data processing methods required to recover high-quality signals in the difficult centrifuge environment where ambient vibrations have higher amplitude than the desired shear wave signals. Hence, the system is described in this paper only to the extent required to explain the application to the grouted columns. The system was used to collect shear wave velocity measurements from a test described by Bian et al. (2007) in which helical grouted columns were installed in a model of dry sand. Fig. 1 shows a polar array of bender elements that was placed on the surface of the sand during construction of the model, and was subsequently buried as more sand was placed on top of the bender elements. A concrete column with a diameter of 38*mm* was later grouted near the center of the array. The diameter of the polar array was 152*mm*, with eight receivers spaced at equal 45° angles (Fig. 1). Source benders were placed adjacent to the receivers at four locations to provide sufficient spatial coverage of the interior region of the array. Eight benders would have provided better spatial coverage, but the limited number of source bender element channels combined with placement of bender elements at other locations in the model (not shown in Fig. 1) prevented the use of the full array. Nevertheless, four source locations proved sufficient to image the column as shown later.

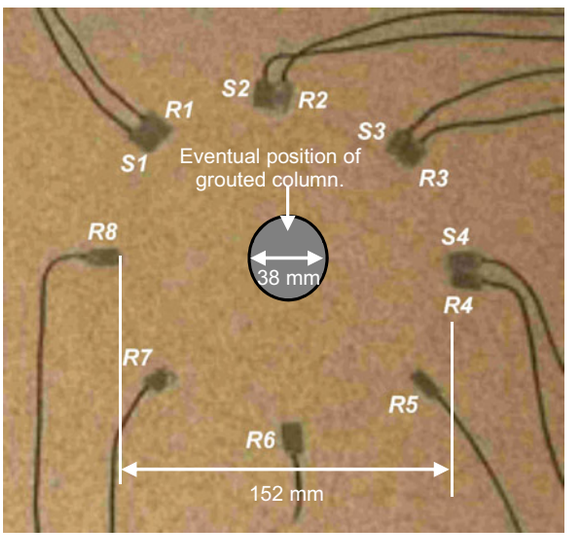


Figure 1: Polar array of four source bender elements (S1 - S4) and eight receiver bender elements (R1 - R8).

As the centrifuge spun the model to 15*g*, each source bender element was excited by supplying a square wave high-amplitude voltage signal, and the elastic waves were recorded by every receiver. The helical piers were then grouted and the concrete was given sufficient time to cure, and the process was repeated. Fig. 2 shows example signals recorded before and after grouting using S1 as the source and R5 as the receiver. The straight ray path between the sensors passes through the center of the array, and therefore the waves after grouting were influenced by the presence of the column. The signal to noise ratio in the recorded signals is excellent because signal stacking was used to reduce the amplitude of the noise.

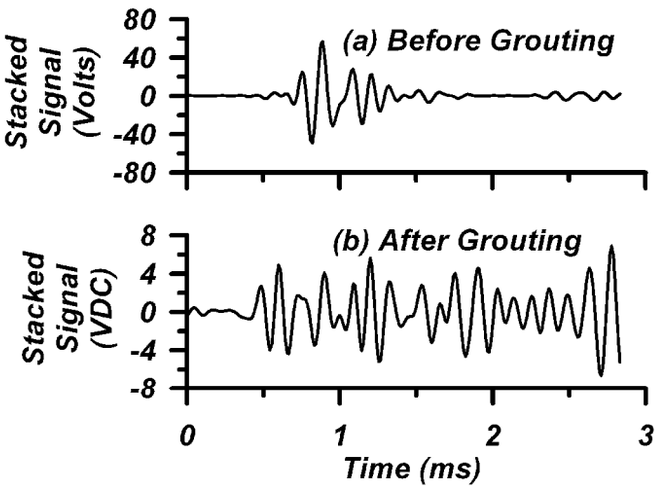


Figure 2: Signals recorded along ray path S1-R5 (a) before grouting and (b) after grouting

The signal recorded before grouting clearly shows the arrival of an elastic wave at approximately 0.7*ms*, and the pulse duration continues until about 1.3*ms*. The small-amplitude wiggles in the signal at about 2.5*ms* are likely caused by a reflection from one of the walls of the container, but the reflection does not interfere with the first arrival and has no bearing on travel time selection. The signal recorded after grouting exhibits a number of significant differences from the one before grouting. First, the first arrival is earlier because the shear wave velocity of the grouted column is higher than that of the soil. Second, the amplitude of the signal was about an order of magnitude smaller even though the number of stacked signals was about the same. The probable explanation for this observation is that the high-impedance contrast at the soil-concrete interface causes reflection of seismic energy, thereby scattering wave energy and reducing the amplitude of the wave transmitted through the grout column. Third, the signal is much more complex, showing arrivals of multiple waves, with the largest-amplitude wave arriving after 2.5 *ms*. The arrival of multiple waves is caused by the scattering effect of the grouted column, where scattered waves arrive at the receiver via complex ray paths. The high-amplitude wave after 2.5 *ms* is also present in Fig. 2a due to the reflection from the container boundary, but the reflection appears to have smaller amplitude in Fig. 2a compared with Fig. 2b due to the difference in scales between the two plots.

TOMOGRAPHIC IMAGING

The polar array of bender elements in Fig. 1 was used to construct tomographic images of a concrete pier that was grouted near the center of the array using procedures described by Santamarina and Fratta (2005). The first step was to construct a vector of 28 travel times $\underline{t}$ between each source/receiver pair (with the exception of source/receiver pairs immediately adjacent to each other, e.g., S1-R1). Travel time picks were made at the

peaks of the signals by correlation with a Morlet wavelet that was time-shifted to empirically fit the data well. Travel time was taken as the time shift that optimized the correlation. Lee and Santamarina (2005) used correlation with wavelets convolved through analytical wave propagation solutions to improve travel time picks that exhibit near field effects, such as those collected in the study presented in this paper. Fig. 3 shows a plot of travel time versus path length for the 28 travel times collected before grouting the column. The nonzero intercept of travel time at zero ray path length implies that some time delay error is present in the raw measurements. The time delay is attributed to phase lag caused by peripheral electronics and by dynamic soil-bender interaction. Hence, the intercept was subtracted from the vector of travel times. Taking travel time picks at the first arrival instead of the peak could decrease this error, but first-arrival picks are often more difficult to accurately measure from the waveforms due to near-field effects and wiggles in the signal that can precede the shear wave. The slope of the relation in Fig. 3 is 4.70 *ms/m*, the inverse of which is the average shear wave velocity of 213 *m/s*. Determining average shear wave velocity as a linear regression of ray length versus travel time inherently eliminates time delay errors and provides a check on the reasonableness of the shear wave velocities in the tomograms.

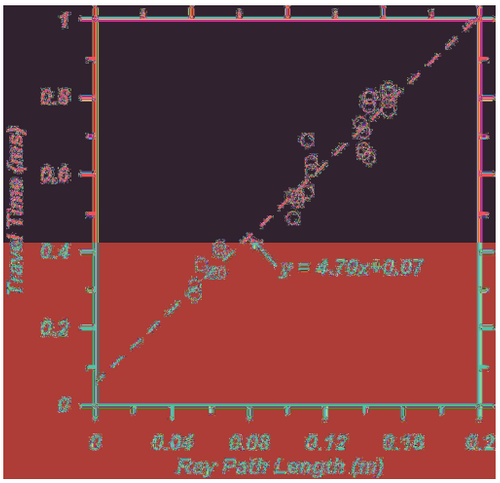


Figure 3: Travel time versus ray path length.

The second step in the tomographic inversion was to discretize the region inside the polar array into 24 polar pixels with dr = 25.4*mm* and dθ = 45°, where dr is the pixel size in the radial direction and dθ is angle subtended by each pixel. Fig. 4 shows the ray paths between each source-receiver combination, and the spatial distribution of coverage information in each pixel. The length of each ray path in each pixel was computed and organized into a 28 x 24 element matrix $\underline{\underline{h}}$.

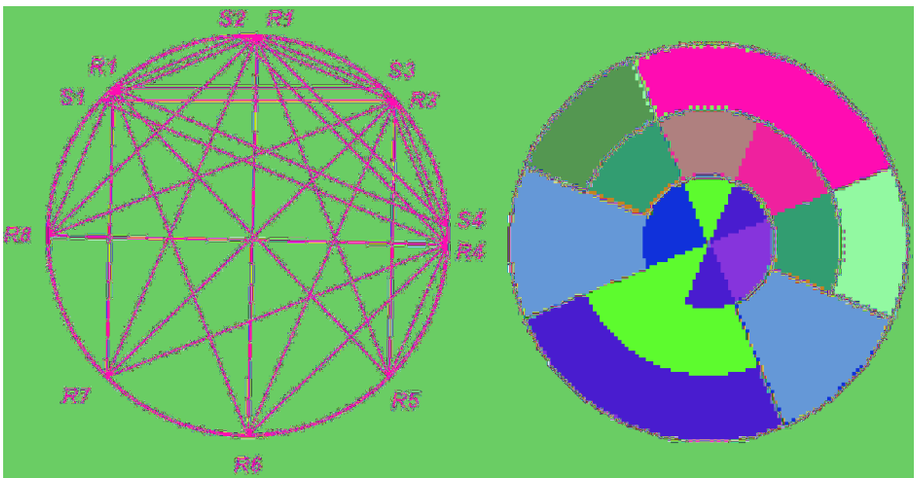


Figure 4: Ray paths and spatial coverage density for tomographic image, where darker pixels exhibit higher coverage.

The third and final step was to solve for the vector of pixel slowness values $\underline{s}$ (slowness is the inverse of shear wave velocity, $s_i = 1/Vs_i$) by inversion of Eq. 1.

$$\underline{t} = \underline{\underline{h}} \cdot \underline{s} \tag{1}$$

The matrix $\underline{\underline{h}}$ cannot be inverted because the system of equations is ill-conditioned, so the inverse problem was solved by constructing a pseudo-inverse using the regularized least squares solution (e.g., see Santamarina and Fratta 2005) in Eq. 2, where λ is the nonnegative regularization coefficient and $\underline{\underline{R}}$ is the regularization matrix.

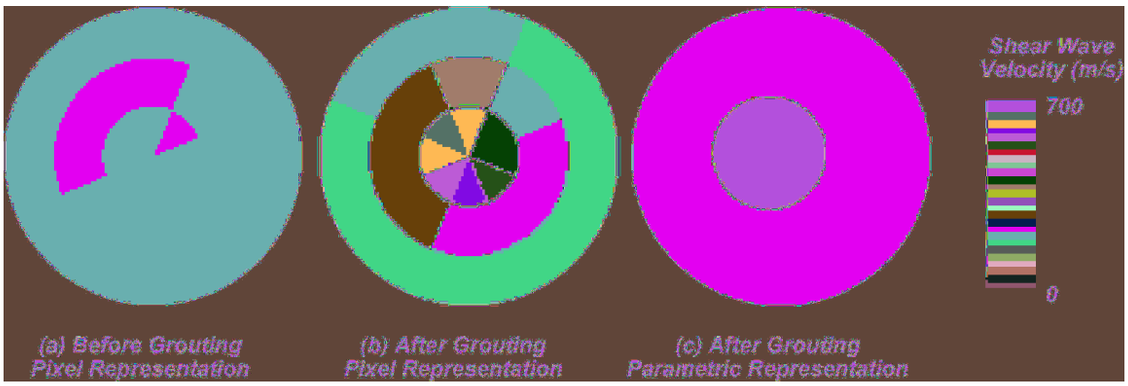


Figure 5: Shear wave velocity tomograms.

$$\underline{s} = \left(\underline{\underline{h}}^T \cdot \underline{\underline{h}} + \lambda \cdot \underline{\underline{R}}^T \cdot \underline{\underline{R}}\right)^{-1} \underline{\underline{h}}^T \cdot \underline{t} \tag{2}$$

A Laplacian 2-D regularization matrix $\underline{\underline{R}}$ was selected to minimize second derivatives of pixel slowness in the r- and θ- directions (i.e. the local variation of pixel slowness was assumed to be linear in the r- and θ- directions). The regularization coefficient must be selected on a problem-specific basis. A value of regularization coefficient $\lambda = 0.01$ was selected for this study, and the influence of λ on the results is discussed later.

Tomograms of shear wave velocity are shown before and after grouting in Fig. 5. Before grouting, the shear wave velocity is nearly constant with a median value of 213 m/s. After grouting a high velocity region in the interior of the array shows some pixels approaching shear wave velocities near 700 m/s. Some pixels in the middle ring also exhibited an increase in shear wave velocity compared with the before-grouting tomogram, even though the grouted column was entirely contained within the center ring. This increase could be explained by densification of the sand during grouting, by mechanics of wave propagation around the grouted column, or as an artifact of the tomographic inversion, as discussed later. The outer ring of pixels had nearly the same shear wave velocity as before grouting.

The inverse problem was also solved using a parametric-based representation, wherein the grout bulb was assumed to have a circular cross-section, and the following parameters were selected to minimize the error between measured and computed travel times: the shear wave velocity of the sand, the shear wave velocity of the grout bulb, the radius of

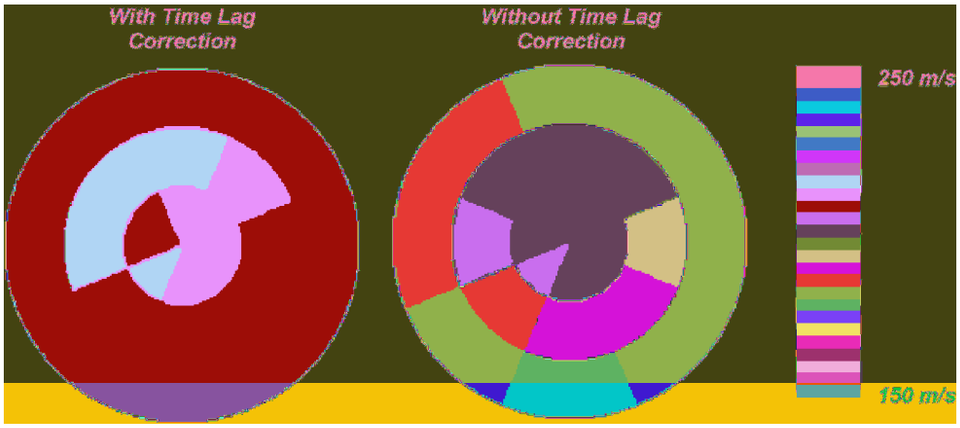
the grout bulb, and the two coordinates of the center of the grout bulb. The parametric-based solution predicted that the grout bulb diameter was 57*mm*, which is 50% larger than the measured value of 38*mm*. The grout bulb was slightly off center toward the left of the center of the array. These observations are consistent with the pixel-based representation that showed some increase in shear wave velocity in the middle ring of pixels to the left of the center of the array.

There are several limitations of tomographic imaging that should be considered when interpreting the tomograms. First, the shear wave velocity of the inclusion could not be accurately resolved by the measured data. For example, doubling the shear wave velocity of the inclusion causes only about a 10% increase in the error of the solution (for comparison, doubling the shear wave velocity of the outer ring of soil elements causes the error to increase by about 700%). The waves travel quickly through the high-velocity anomaly, and the travel time of the wave through the inclusion is small compared with the travel time through the softer soil, hence the resolution with which travel time tomography can resolve the shear wave velocity of the inclusion is poor for the sensor configuration adopted in this study. Furthermore, the shear wave velocity of the inclusion is sensitive to the selection of λ for the pixel-based representation, as discussed later. Bian et al. (2007) estimated that the shear wave velocity of the grout is about 1570-1800 m/s based on correlations between unconfined compressive strength and small-strain stiffness. Second, ray paths were assumed to be straight lines while they are known to bend when the direction of particle motion is not parallel to the interface of an impedance contrast. The implications of this model assumption are not known. Finally, the inaccuracy in the diameter predicted by the parametric-based representation is likely caused by the diameter being only about 1.5x the wavelength of the waves induced by the bender elements. Resolution is commonly estimated as being equal to one wavelength, hence the anomaly is somewhat small to be accurately imaged using the bender elements in this study. Lee et al. (2005) experienced an analogous problem when they found that the diameter of a hole in a plexiglass plate was under-predicted by parametric inversion of travel times from bender elements, in their case due to diffraction healing of waves around the low-velocity inclusion. Nevertheless, the presence of the anomaly could clearly be identified, which can be important information regardless of inaccuracies in the images. For example, whether grout had been injected into the sand during the test was sometimes unclear since the grout pumps were operated remotely during centrifuge spinning. The bender elements could provide a check on whether the grout had been placed in the sand, though the bender element data was processed after the testing was completed in this prototype application.

DISCUSSION

The importance of removing time delay errors from the measurements prior to tomographic inversion is illustrated in Fig. 6, which shows tomograms before grouting the column with the time delay correction (Fig. 6a) and without the time delay correction (Fig. 6b). Fig. 6a is the same as Fig. 5a, but appears darker because the pixel shades have been distributed over a smaller range of shear wave velocities to more clearly show details in the tomograms. Fig. 6a exhibits a reasonably constant shear wave velocity, with pixel values ranging from 211 *m/s* to 218 *m/s*, and a median of 213 *m/s*. These

results agree well with the average shear wave velocity of 213 *m/s* estimated by linear regression of ray path length versus travel time (see Fig. 3). The results without the correction show more dispersion in the shear wave velocity values, with pixel values



(a) **(b)**

Figure 6: Tomograms constructed before grouting with (a) with time lag error correction and (b) without time lag error correction.

ranging from 182 *m/s* to 206 *m/s*, and a median of 198 *m/s*. Two sources of error in Fig. 6b are particularly interesting. First, the median shear wave velocity is under-predicted because the time delay error causes an over-prediction of travel time, implying a slower medium. Second, the shear wave velocity appears larger in the center of the array and smaller at the perimeter. This spatial distribution of the error is related to the fact that 1. a constant time delay error causes larger errors in measured shear wave velocity for shorter travel distances, and 2. ray paths that illuminate the outer ring of pixels are shorter than those that illuminate the center ring of pixels (see Fig. 4). This example clearly demonstrates how errors in data interpretation can propagate through the tomographic inversion and potentially lead to false inferences.

The regularized least-squares solution adopted in the pixel-based representation introduces smoothing to the data to render the ill-conditioned inverse problem solvable. As the regularization coefficient (λ) decreases, resolution improves but errors can arise from a poorly-conditioned system of equations. As λ increases, stability of the system of equations improves at the expense of resolution. Fig. 7 shows tomograms produced with λ = 0.001, 0.01, and 0.1. Fig. 7a, with λ=0.001, shows the largest contrast between the sand and grouted column, but also predicts a large variation of shear wave velocity within the sand and within the grouted column even though these regions were relatively uniform. Fig. 7c exhibits a clear velocity gradient, with high velocity in the center, intermediate velocity in the middle ring of pixels, and lowest velocity on the outside, and significantly under-predicts the shear wave velocity of the inclusion. This pattern would be expected with large smoothing. Fig. 7b is intermediate and clearly shows a high-velocity center region while maintaining a relatively uniform shear wave velocity in the sand. The shear wave velocity of the anomaly varies considerably as λ changes, further supporting the conclusion that the available information was insufficient to resolve the velocity of the inclusion. The non-uniformities in the center of the array at the position

of the grouted column are unrealistic, and slightly resemble the image showing spatial coverage of the ray paths through the pixels (see Fig. 4). Similarities between the spatial coverage image and the tomograms can be an indication that the data was not sufficient to fully resolve the domain (Santamarina and Fratta 2005). Though the three tomograms have differences, all three clearly reflect the high-velocity anomaly present at the center of the array, which indicates that the regularized least-squares solution is adequate for determining the presence of the anomaly.

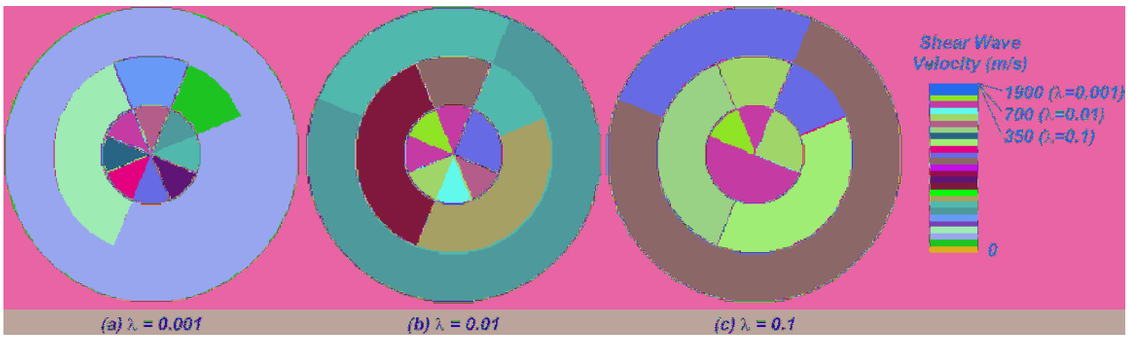


Figure 7: Influence of regularization coefficient, λ, on resulting tomograms. Note that different scales of shear wave velocity are used to show detail in the tomograms.

Travel time tomography disregards a large amount of data in the recorded signals. For example, the manner in which the waves were scattered in Fig. 2b contains information about the sand and grouted column that is not utilized since travel time is the only information extracted from the signal. Utilizing the amplitude of the signals can provide additional information, particularly about the value of impedance contrasts. Utilizing the entire waveform (e.g., Pratt and Goulty 1991) can significantly improve resolution by solving for a physical domain that minimizes errors in the recorded signals rather than just the travel time. This approach has not yet been explored for the example presented in this paper.

CONCLUSION

A grouted column was imaged by shear wave velocity tomography using the bender element system on the 9-m radius geotechnical centrifuge at the Center for Geotechnical Modeling at UC Davis. This example application is a demonstration of how geophysical tomographic imaging can non-invasively improve our understanding of the subsurface. The centrifuge is an excellent tool for performing such proof-of-concept experiments, and geophysical imaging has improved our ability to characterize and monitor centrifuge models. More research is required to improve the resolution and accuracy of the tomographic methods in the centrifuge models as the use of geophysical methods becomes more widely adopted and integrated into centrifuge test programs. Similar geophysical methods also show tremendous potential for application in the field to help us understand subsurface properties at a scale typical for geotechnical projects. Additional research needs to be devoted to sensor development and inversion methods to make use of this valuable tool at the geotechnical field scale.

ACKNOWLEDGMENTS

The development and implementation of the bender element system was funded under NSF Award No. CMS-0086566 through the George E. Brown, Jr. Network for Earthquake Engineering Simulation (NEES). The Center for Geotechnical Modeling is managed by Bruce L. Kutter and Daniel W. Wilson, who oversaw implementation of the bender element system. Seokhyeon Choi helped implement the hardware and develop the signal processing software. Advice regarding bender elements and preliminary testing in 1-g laboratory specimens at Georgia Tech were provided by Jong-Sub Lee and Carlos Santamarina. The grouted pier test that contained the polar array of bender elements was performed by Yueying Bian and Tara Hutchinson under NSF Award No. CMS-0513972. The work would not have been possible without the able assistance of UC Davis centrifuge staff Chad Justice, Nick Sinikas, Tom Coker, Ray Gerhard, and Peter Rojas. The contents of this paper do not necessarily represent a policy of NEES or NSF or endorsement by federal government.

REFERENCES

Bian, Y., Hutchinson, T.C., Wilson, D., Laefer, D., and Brandenberg, S. (2007). "Experimental investigation of grouted helical piers for use in foundation rehabilitation." *4th International Conference on Earthquake Geotechnical Engineering*. Thessaloniki, Greece. Paper No. 1471.

Brandenberg, S.J., Choi, S., Kutter, B.L., Wilson, D.W., and Santamarina, J.C. (2006). "A bender element system for measuring shear wave velocities in centrifuge models." *International Conference of Physical Modeling in Geotechnics*. Hong Kong, August 2006. Accepted.

Cormack, A.M. (1963). "Representation of a function by its line integrals, with some radiological applications." *J. Appl. Physics.* No. 34. pp. 2722-2727.

Cormack, A.M. (1964). "Representation of a function by its line integrals, with some radiological applications. II" *J. Appl. Physics.* No. 35. pp. 2908-2913.

Hounsfield, G.N. (1973). "Computerized transverse axial scanning (tomography): part 1. Description of system." *Br. J. Radiol.* No. 46, pp. 1016-1022.

Lee, J.S., Fernandez, A.L., and Santamarina, J.C. (2005). "S-wave velocity tomography: small-scale laboratory application." *Geotechnical Testing Journal*. ASTM. 28(4). 336-344.

Lee, J.S. and Santamarina, J.C. (2005). "Bender elements: performance and signal interpretation." *J. of Geotech. Geoenviron. Eng., 131(9)*, 1063-1070.

Olson, L.D., Aouad, M.F., and Sack, D.A. (1998). "NDT Diagnosis of Drilled Shaft Foundations." *Transportation Research Board, 77th Annual Meeting,* Washington, D.C., January 11-15.

Pratt, G.R., and Goulty, N.R. (1991). "Combining wave-equation imaging with traveltime tomography to form high-resolution images from crosshole data." *Geophysics*. 56(2). 208-224.

Santamarina, J.C., and Fratta, D. (2005). "Discrete signals and inverse problems. An introduction for engineers and scientists." John Wiley & Sons Ltd. West Sussex, England. 350 p.

Terzaghi, K. (1947) “Theoretical soil mechanics.” Fourth Printing. John Wiley and Sons, Inc., New York. 510 pp.

Increase in Cyclic Liquefaction Resistance of Sandy Soil Due to Installation of Drilled Displacement Piles

Timothy C. Siegel[1], M. ASCE, P.E., Willie M. NeSmith[2], M. ASCE, P.E., and W. Morgan NeSmith[3], M. ASCE

[1]Senior Geotechnical Engineer, Berkel & Company Contractors, Inc., 1808 Northshore Hills Boulevard, Knoxville, TN 37922; tcsiegel@knology.net
[2]Chief Geotechnical Engineer, Berkel & Company Contractors, Inc., 1503 Milner Crescent, Birmingham, AL 35205; wnesmith@bellsouth.net
[3]Senior Geotechnical Engineer, Berkel & Company Contractors, Inc., 834 Dekalb Avenue, Unit B, Atlanta, GA 30307; morgan_nesmith@comcast.net

ABSTRACT: Drilled displacement piles are installed by the displacement of soil and subsequent placement of fluid cement grout within the evacuated volume. Depending on the soil grain-size characteristics, soil behavior, *in situ* soil density, pile spacing, and pile diameter, the installation process can result in measurable densification and an increase in lateral stress. Thus, it follows that the drilled displacement process may be used to mitigate cyclic liquefaction in sandy soils. In an effort to quantify the increase in cyclic liquefaction resistance resulting from drilled displacement piles, the authors performed pre- and post-installation cone penetration testing at a site in North Myrtle Beach, South Carolina. The results support that the installation of drilled displacement piles generally increases the liquefaction resistance of the surrounding soil. For a specific area replacement ratio, the trend is that improvement decreases with increasing pre-installation $(q_{t1N})_{cs}$ and approaches unity at very high values of pre-installation $(q_{t1N})_{cs}$. The improvement can be significant for values of pre-installation $(q_{t1N})_{cs}$ generally as high as 250. Overall, the degree of improvement is greater for higher area replacement ratios.

INTRODUCTION

As described by NeSmith (2002), drilled displacement piles (also known as augered cast-in-place displacement or augered, pressure grouted displacement piles) are installed by the displacement of soil and subsequent placement of fluid grout within the evacuated volume. Siegel *et al.* (2007a; 2007b) showed that the installation process can result in ground improvement as characterized by measurable increases in cone tip resistance and sleeve friction in sandy soils. Thus, it follows that the potential for liquefaction can be intentionally reduced by the installation of drilled displacement piles in sandy soils.

This paper examines the reduction in cyclic liquefaction potential due to the ground improvement within groups of drilled displacement piles. To characterize the soil conditions, the authors' performed cone penetration testing (CPT) prior to and following the installation of drilled displacement piles at a site in North Myrtle Beach, South Carolina. Using the CPT data, the normalized (equivalent) cone tip resistance for clean sands [$(q_{t1N})_{cs}$] is used to graphically represent the reduction in cyclic liquefaction potential in sandy soils resulting from the installation of drilled displacement piles.

INSTALLATION PROCESS

The Berkel tool (Figure 1) used in the drilled displacement process consists of a bottom auger section with a length of 0.9 m (3 ft), a displacement section that is equal to the nominal diameter of the pile, and few flights of reverse auger above the displacement section. As this tool is advanced to the pile tip depth, the soil in the pile volume is displaced horizontally. Once the tool has reached the pile tip depth, then fluid cement grout is pumped downward through the hollow stem and tool, and introduced into the hole through the grout port at the tip of the tool. Once a sufficient amount of grout has been pumped to fill the volume between the tool and the hole, then the tool is extracted in a controlled manner while grout is pumped at a rate sufficient to fill the hole. The drilled displacement process typically results in somewhat lower grout factors (*i.e.,* the ratio of the actual grout volume to the theoretical hole volume) than typically used for conventional augered, cast-in-place piles.

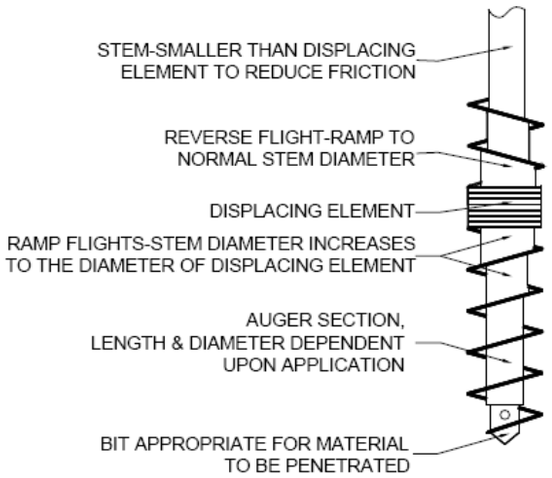


Figure 1. Berkel Drilled Displacement Pile Tool

The installation platform (Figure 2) is typical of those used in European continuous flight auger (CFA) applications. It includes a vertical mast with an attached turntable capable of producing 25 meter-tons (180,000 ft-lbs) of torque and a cabling system that allows a downward force (or crowd) of 356 kN (40 tons). Pile lengths greater than 17 m (56 ft) with diameters of up to 457 mm (18 inches) are routinely installed with this system. The system is also adaptable to larger equipment that can increase the maximum pile length and the practical pile diameter.

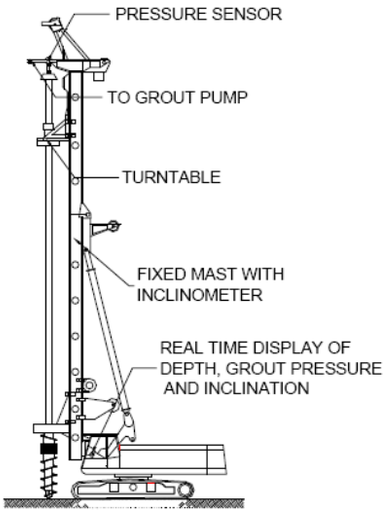


Figure 2. Installation Platform for Drilled Displacement Piles

NORTH MYRTLE BEACH (SC) TEST SITE

The test site is a beachfront development in North Myrtle Beach, South Carolina, which is located within the Coastal Plain Physiographic Province. The upper 8.5 m (28 ft) of the subsurface profile consist of beach sands and shell hash that are Pleistocene age deposits. Locally, these sands and shell hash are underlain by the Pee Dee Formation. The testing at this site focused on the conditions in the upper beach sands and shell hash because the presence of limestone lenses within Pee Dee Formation was expected to present significant difficulties with respect to testing and interpretation. Figure 3 presents a CPT profile of the beach sands and shell hash. Note that the majority of the profile for the pre-installation data classifies as sands and sand mixtures (I_c < 2.60) according to the classification system by Robertson and Wride (1998). There are thin clay layers at depths of 4.5 m to 5.5 m (14.8 ft to 18 ft) and 7 m to 8 m (23 ft to 26.2 ft).

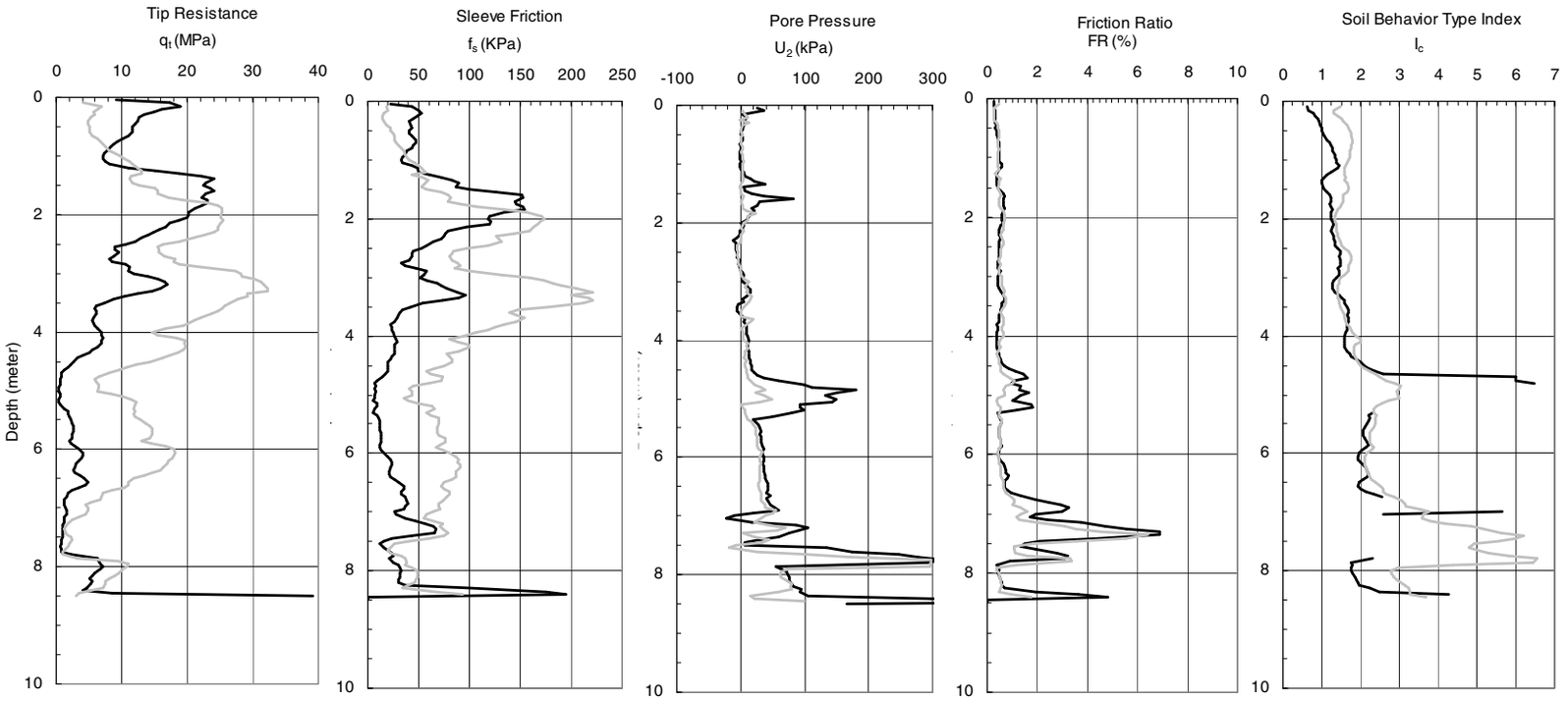


Figure 3. CPT Profiles for Original Site Conditions (Dark Lines) and for a Pile Group with a_s=0.068 (Light Lines)

The testing was performed in the area of planned 4 x 3 pile cap of 406 mm (16 in) diameter drilled displacement piles. Figure 4 shows the various pile group configurations included in this study. The piles were installed with a Bauer BG 25 drilling platform. As previously discussed in detail, the installation involves advancing the displacement tool to the design depth and then extracting the displacement tool at a slow forward rotation while pumping a pressurized grout through a port at the tip of the displacement tool. Typical of this displacement system, the upper soils (approximately 1.5 m) are displaced upward during the initial penetration of the displacement tool and otherwise the spoil generation is negligible. Observations by the authors of extracted piles from other sites confirm that this process results in a very uniform cross-section with a diameter equivalent to that of the displacement tool.

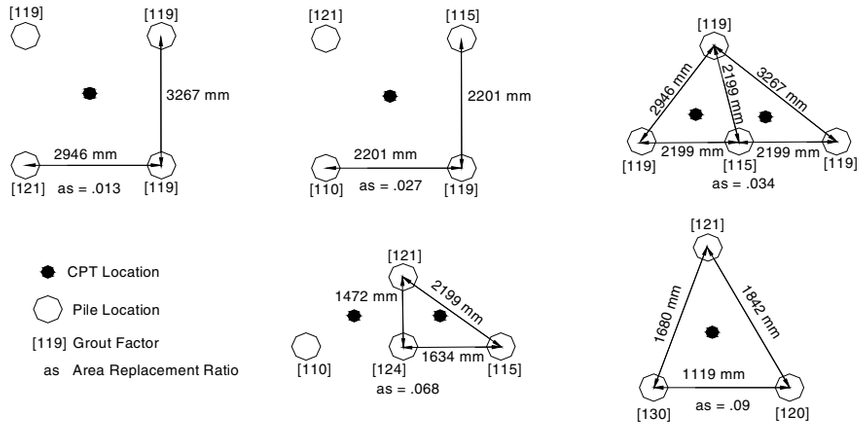


Figure 4. Configurations of Drilled Displacement Pile Groups and Relative CPT Locations

DATA ANALYSIS

Liquefaction is the soil behavior phenomenon in which saturated sand softens and loses strength due to the development of high pore water pressures during strong ground shaking (Seed and Idriss; Silver and Seed, 1971). In this study, the reduction in cyclic liquefaction potential is quantified using the normalized (equivalent) cone tip resistance for clean sands $(q_{t1N})_{cs}$ computed using the CPT-based cyclic liquefaction prediction method by Robertson and Wride (1998) and the recommendations by NCEER (Youd *et al.*, 2001). The advantages of using $(q_{t1N})_{cs}$ are that it considers both tip resistance and sleeve friction in a single value, it may be calculated for soils with a range of fines content, and it may be used to directly estimate the cyclic resistance ratio (CRR) from published charts (Robertson and Wride, 1998; Youd *et al.*, 2001).

DATA PRESENTATION

The influence of displacement pile installation is represented by the ratio post-installation $(q_{t1N})_{cs}$ to the pre-installation $(q_{t1N})_{cs}$. The Improvement Ratio $[R_{(qt1N)cs}]$ is defined by the following expression:

$$\text{Improvement Ratio: } R_{(qt1N)cs} = \frac{(q_{t1N})_{cs_post_installation}}{(q_{t1N})_{cs_pre_installation}}$$

The Improvement Ratio, $R_{(qt1N)cs}$, was computed at each measurement depth increment of 50 mm (2 in). The water table was assumed to be at the ground surface in computing $R_{(qt1N)cs}$. Only data collected below 1.5 m (5 ft) were considered because the lack of confinement (as illustrated by the observed soil displacement previously described by the authors) precludes densification very near the working ground surface. Note that the testing was performed in the center of the pile group with the exception of the configuration with an $a_s = 0.068$. For this exception, the CPT location was shifted slightly to one side of the triangular pile arrangement.

The relationship between pile cross-sectional area and pile spacing are represented by the area replacement ratio (a_s) which is defined as the cross-sectional area of the pile divided by the tributary area for each pile. Because this is an actual project, the pile group configurations were dictated by the design. The area replacement ratios, which range from 0.013 to 0.09, were computed by graphically determining the total area and pile area bounded by the pile groups.

RESULTS AND DISCUSSION

The plots presented in Figure 5 summarize the results of this study and show the pre-installation $(q_{t1N})_{cs}$ versus the Improvement Ratio, $R_{(qt1)cs}$ for the various area replacement ratios. The plots indicate that installation of drilled displacement piles generally results in an increase in liquefaction resistance. For a specific area replacement ratio, the trend is that $R_{(qt1N)cs}$ decreases with increasing pre-installation $(q_{t1N})_{cs}$ and approaches unity at very high values of pre-installation $(q_{t1N})_{cs}$. The improvement can be significant for values of pre-installation $(q_{t1N})_{cs}$ generally as high as 250. Overall, the degree of improvement is greater for higher area replacement ratios.

It is proposed that the increases in liquefaction resistance, in terms of the Improvement Ratio, due to the installation of drilled displacement piles in sandy soils are conservatively represented in Figure 5. The testing within the pile groups was performed near or at the midpoint of the pile configurations which is believed to provide conservatism to the application of these values as an estimate for the entire soil volume. Recent field observations and numerical analyses by Martin and Olgun (2006) support that stiff inclusions were effective at mitigation liquefaction-induced settlement as a result of a high vertical composite stiffness. This suggests that there is a beneficial reinforcement aspect not considered by the Improvement Ratio.

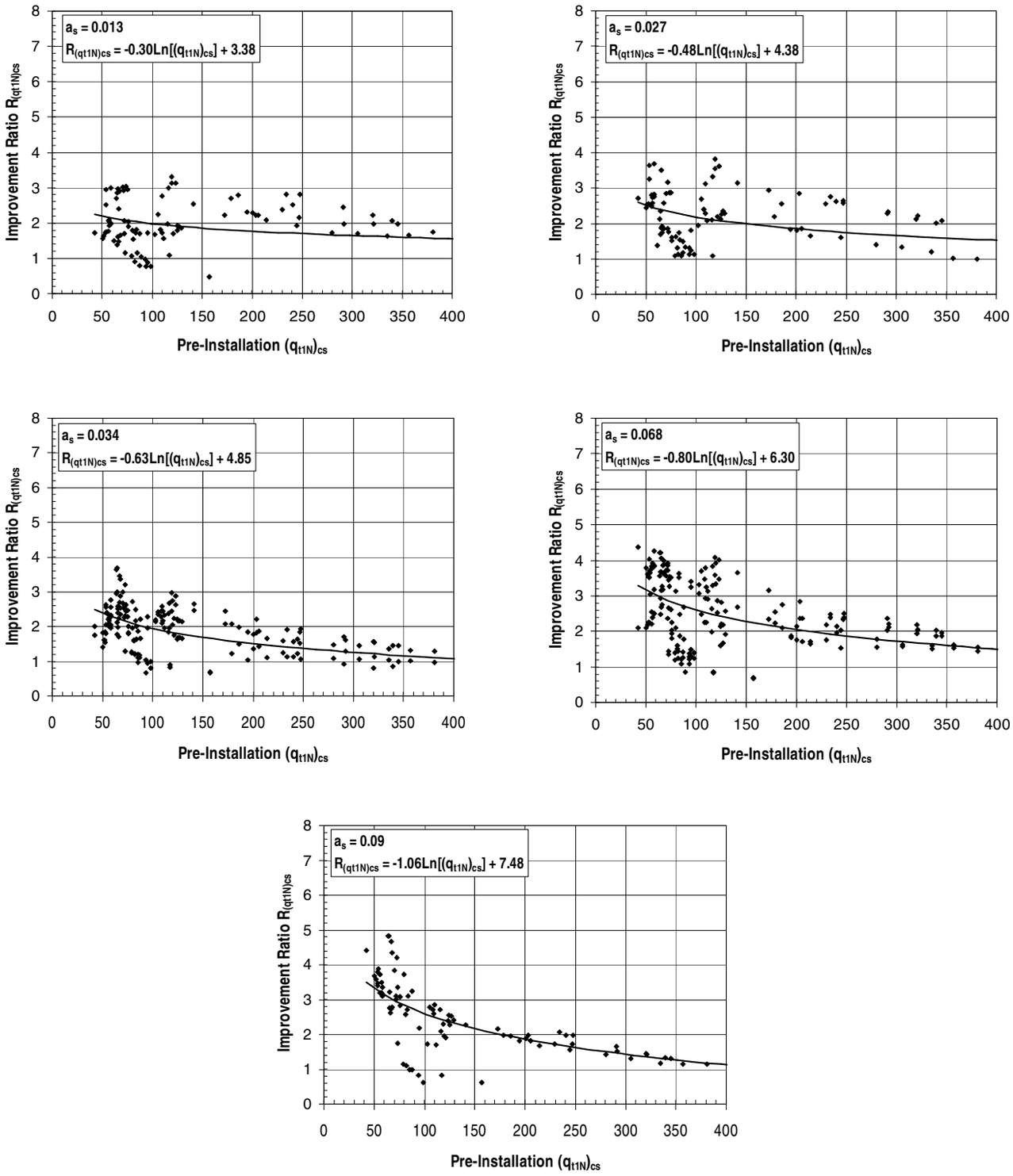


Figure 5. Improvement Ratios for Various Area Replacement Ratios

In the application of the plots presented in Figure 5, it may be helpful to discuss the limitations of the CPT-based liquefaction methodology. While a number of field studies (Mitchell and Solymar, 1984; Schmertmann, 1987; Mesri *et al*., 1990; Charlie *et al*., 1992) have shown that the tip resistance continues to increase for some time after the application of a variety of ground improvement techniques, the effect of time on the CPT resistances is not well understood. The data presented in this paper is based on testing performed within one or two days after installation and there has been no adjustment made for the influence of time on the cone penetration test data.

As illustrated in Figure 3, this study shows that there is a measurable reduction in friction ratio between the pre-installation data and the post-installation data. Greater changes in friction ratio have been reported after ground improvement by dynamic compaction (Tan *et al.*, 2007). This raises a pertinent question as to appropriate consideration where the Soil Behavior Type Index (I_c) changes based on the post-installation (or post-improvement) CPT data. A strict evaluation of I_c indicates that post-installation soils have a higher fines content. It is more likely that there is actually no change in soil type, but that the post-installation soil conditions are not well calibrated with the friction ratio-based classification systems. While this study used both pre- and post-installation values of I_c computed from the respective testing, such an approach may lead to inappropriate conclusions regarding liquefaction potential where there is a more dramatic change in I_c.

The CPT-based liquefaction prediction and the associated calculation of $(q_{t1N})_{cs}$ does not consider effects of aging, overconsolidation, geologic setting and depositional conditions (Pyke, 2003; Youd *et al.*, 2003). In general, the absence of such considerations is conservative; however, this conservatism may be reduced or eliminated by the disturbance induced by the ground improvement process. Therefore, the results of this study are most appropriately considered along with all of the other pertinent factors when determining whether to implement the drilled displacement process to increase the liquefaction resistance at a particular site.

CONCLUSIONS

Cone penetration testing was performed at a beachfront site in North Myrtle Beach, South Carolina. Baseline data were collected for the natural ground conditions and compared to data collected within groups of drilled displacement piles. The reduction in cyclic liquefaction potential was quantified using the normalized (equivalent) cone tip resistance for clean sands $(q_{t1N})_{cs}$ computed using the CPT-based cyclic liquefaction prediction method. The results support that the installation of drilled displacement piles generally increases the liquefaction resistance of the surrounding soil. For a specific area replacement ratio, the trend is that improvement decreases with increasing pre-installation $(q_{t1N})_{cs}$ and approaches unity at very high values of pre-installation $(q_{t1N})_{cs}$. The improvement can be significant for values of pre-installation $(q_{t1N})_{cs}$ generally as high as 250. Overall, the degree of improvement is greater for higher area replacement ratios.

REFERENCES

Charlie, W.A., Rwebyogo, M.F.J. and Doehring, D.O. (1992). "Time-dependent cone penetration resistance due to blasting", *J. Geotech. Engrg*, ASCE, Vol. 118(8), 1200-1215.

Martin, J.R. II and Olgun, C.G. (2006). "Liquefaction mitigation using jet-grout colums – 1999 Kocaeli earthquake case history," *Ground Modification and Seismic Mitigation* (GSP 152), Porbaha, A., Shen, S-L., Wartman, J., and Chai, J-C., Editors, 349-358.

Mesri, G., Feng, T.W. and Benak, J.M. (1990). "Postdensification penetration resistance in clean sands", *J. Geotech. Engrg*, ASCE, Vol. 116(7), 1095-1115.

Mitchell, J.K. and Solymar, Z.V. (1984). "Time-dependent strength gain in freshly deposited or densified sand", *J.Geotech. Engrg*, ASCE, Vol. 110(11), 1559-1576.

NeSmith, W.M. (2002). "Static capacity analysis of augered, pressure-injected displacement piles," *Deep Foundations 2002* (GSP 116), ASCE, 1174-1186.

Pyke, R. (2003). "Discussion of 'Liquefaction resistance of soils: Summary report from the 1996 NCEER and 1998 NCEER/NSF workshops on evaluation of liquefaction resistance of soils' by T.L. Youd, *J. Geotech. Geoenviron. Engrg.*, Vol. 129(3), 283-284.

Robertson, P.K. and Wride (Fear), C.E. (1998). "Cyclic liquefaction and its evaluation based on the CPT and SPT," *Proceedings, 1996 NCEER Workshop on Evaluation of Liquefaction Resistance of Soils*, Youd, T.L. and Idriss, I.M., Editors, NCEER-97-0022.

Seed, H.B. and Idriss, I.M. (1971). "Simplified procedure for evaluating soil liquefaction potential," *J. Soil Mech. & Fdns Div*., Vol. 97(SM9), 1249-1273.

Schmertmann, J.H. (1987) Discussion on "Time-dependent strength gain in freshly deposited or densified sand," by J.K. Mitchell and Z.V. Solymar. *J. Geotech. Engrg*, ASCE, Vol. 117(9), 171-176.

Siegel, T.C., Cargill, P.E. and NeSmith, W.M. (2007a). "CPT measurements near drilled displacement piles," *Proceedings, 7th International Symposium on Field Measurements in Geomechanics,* (GSP 175).

Siegel, T.C., NeSmith, W.M., NeSmith, W.M. and Cargill, P.E. (2007b). "Ground improvement resulting from installation of drilled displacement piles," *Proceedings, 32nd Annual Conference on Deep Foundations*, 131-138.

Silver, M.L. and Seed, H.B. (1971). "Volume changes in sand during cyclic loading," *Journal of Soil Mech. & Fdns Div*., Vol. 97(SM9), 1171-1182.

Tan, Y., Lin, G., Paikowsky, S.G. and Fang, J. (2007). "Evaluation of compaction effects on granular backfill using CPT," *Soil Improvement* (GSP 174).

Youd, T.L., Idriss, I.M., Andrus, R.D., Arango, I., Castro, G., Christian, J.T., Dobry, R., Finn, W.D.L., Harder, L.F., Jr., Hynes, M.E., Ishihara, K., Koester, J.P., Liao, S.S.C., Marcuson, W.F., III, Martin, G.R., Mitchell, J.K., Moriwaki, Y., Power, M.S., Robertson, P.K., Seed, R.B., Stokoe, K.H., II. (2001) Liquefaction resistance of soils: Summary report from the 1996 NCEER and 1998 NCEER/NSF workshop on evaluation of liquefaction resistance of soils, *J. Geotech. Geoenv. Engrg.,* Vol. 127(10), 817-833.

Youd, T.L., Idriss, I.M., Andrus, R.D., Arango, I., Castro, G., Christian, J.T., Dobry, R., Finn, W.D.L., Harder, L.F., Jr., Hynes, M.E., Ishihara, K., Koester, J.P., Liao, S.S.C., Marcuson, W.F., III, Martin, G.R., Mitchell, J.K., Moriwaki, Y., Power, M.S., Robertson, P.K., Seed, R.B., Stokoe, K.H., II. (2003) "Closure to'Liquefaction resistance of soils: Summary report from the 1996 NCEER and 1998 NCEER/NSF workshop on evaluation of liquefaction resistance of soils', *J. Geotech. Geoenv. Engrg.,* Vol. 129(3), 284-286.

Liquefaction Potential Mitigation using Rapid Impact Compaction

Lori A. Simpson,[1] M. ASCE, G.E., Serena T. Jang,[2] M. ASCE, G.E.,
Cary E. Ronan,[3] M. ASCE, G.E., and Lisa M. Splitter,[4] M. ASCE, P.E.

[1] Principal, Treadwell & Rollo, Inc., 501 14th St 3rd Fl, Oakland, California 94612; lasimpson@treadwellrollo.com
[2] Senior Engineer, Treadwell & Rollo, Inc., 555 Montgomery St #1300, San Francisco, California 94111; stjang@treadwellrollo.com
[3] Senior Engineer, Treadwell & Rollo, Inc., 555 Montgomery St. #1300, San Francisco, California 94111; ceronan@treadwellrollo.com
[4] Project Engineer, Treadwell & Rollo, Inc., 501 14th St 3rd Fl, Oakland, California 94612; lmsplitter@treadwellrollo.com

ABSTRACT: Mission Bay is a 1.21-square-kilometer (300-acre) reclaimed site in San Francisco, California, that is currently being redeveloped. The composition of the fill varies and includes loose sand, loose to medium dense silty and clayey sand, and loose to medium dense sandy gravel with clay. The fill is liquefiable throughout much of Mission Bay. The groundwater is typically 1 to 3 meters (3 to 10 feet) below the ground surface. This paper will present case studies of the mitigation of liquefaction potential at two sites using Rapid Impact Compaction (RIC). RIC is a method of soil improvement using a track-mounted machine that imparts energy by dropping an approximately 6,800 kilogram (7.5-ton) weight from a controlled height, about 1 meter, onto a patented foot. The energy is delivered at a rate of 40 to 60 blows per minute. Drop height, number of blows, and penetration per blow are monitored and/or controlled by an on-board data acquisition system. Case studies will include results of pre-treatment borings and/or CPTs, results of post-treatment CPTs, and a comparison of before and after liquefaction potential. In addition, the results of vibration monitoring performed during RIC will be discussed.

INTRODUCTION

Mission Bay is a 1.21-square-kilometer (300-acre) site in San Francisco that is currently being redeveloped (Figure 1). Mission Bay fronts on the San Francisco Bay and is adjacent to AT&T Park (home of the Giants).



FIG. 1. Map of San Francisco and Mission Bay

It was formerly a shallow bay (Figure 2) that was reclaimed beginning in the 1880s and continuing through the 1920s. Reclamation of the shallow bay coincided with booming development in San Francisco. The bay was reclaimed using earth materials from construction and excavation sites throughout the city: rock excavated from Telegraph Hill and Potrero Hill, sand removed from dunes along current Market Street, and building rubble from the 1906 Great Earthquake and Fire. Portions of the bay were used as the city dump. Upon completion of reclamation, the land had extended to the limits shown on Figure 3. Currently, Mission Bay is relatively flat, with site elevations ranging from 29 to 34 meters (95 to 111 feet)[1].

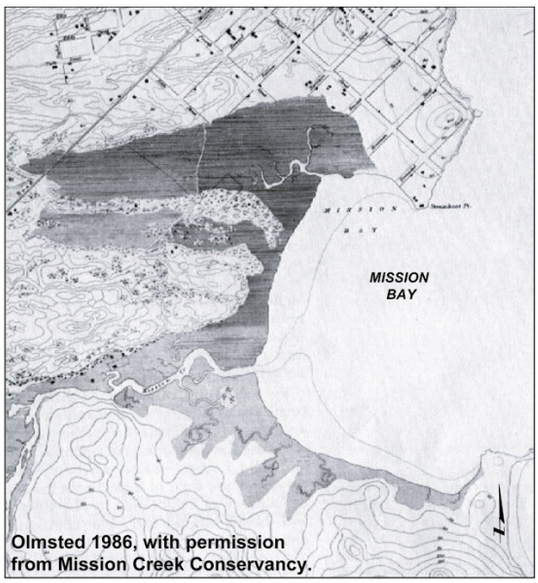


FIG. 2. Historic Shoreline Map

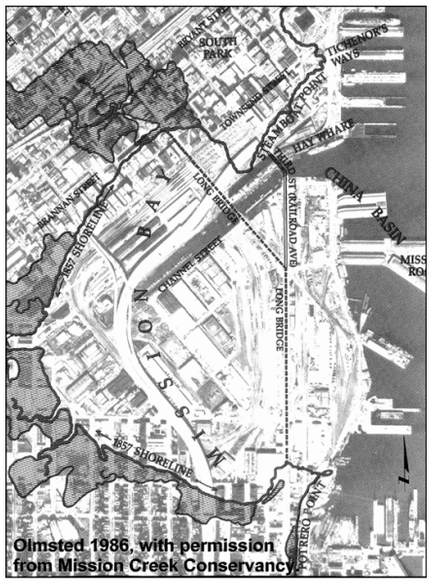


FIG. 3. Current & Historical Shoreline Map

[1] All elevations reference San Francisco City Datum plus 30.5 meters (100 feet) (SFCD = Mean Sea Level – 2.63 meters (8.616 feet)).

Since the 1990s, Mission Bay has been under redevelopment, with planned new residential, commercial, community, and research buildings. In addition, the area is being re-mapped with new streets, requiring new infrastructure. This paper will focus on two projects in Mission Bay that are currently under construction:

- Site A, a 52- by 76-meter (170- by 250-foot) site with a residential development of 3 to 13 stories over a 3-level podium
- Site B, an 84- by 198-meter (275- by 650-foot) site; site development consists of two residential buildings, both comprised of 2 to 13 stories above a 3-level podium

SEISMICITY AND FAULTING

Mission Bay is in a seismically active region. The major active faults in the area are the San Andreas, San Gregorio, Hayward, and Calaveras Faults. For each of the major active faults, the distance from the site and estimated maximum or mean characteristic Moment magnitude[2] [Working Group on California Earthquake Probabilities (WGCEP) (2003) and Cao et al. (2003)] are summarized in Table 1.

Table 1. Regional Faults and Seismicity

Fault Segment	Approximate Distance from Site (km)	Direction from Site	Mean Characteristic Moment Magnitude
San Andreas	13	Southwest	7.9
Hayward	16	Northeast	6.7
San Gregorio	19	West	7.3
Calaveras	34	East	6.8

WGCEP estimates there is a 62 percent likelihood of a major earthquake (Moment Magnitude 6.7 or greater) occurring by 2031 in the San Francisco Bay Area.

SUBSURFACE CONDITIONS

In general, the subsurface conditions in Mission Bay consist of fill, Bay Mud, Colma Formation sand, Old Bay Clay, sand and clay, and Franciscan Formation bedrock. Because of the various materials used during reclamation, the fill in Mission Bay is heterogeneous, generally containing sand and gravel mixtures, with some silt and clay; its density varies from loose to very dense. Rubble and rock boulders are present in the fill in many areas of Mission Bay. Liquefiable soil is encountered in the fill throughout much of Mission Bay. The fill thickness varies

[2] Moment magnitude is an energy-based scale and provides a physically meaningful measure of the size of a faulting event. Moment magnitude is directly related to average slip and fault rupture area.

from about 1.5 to 13.7 meters (5 to 45 feet). These extremely different thicknesses can occur within short distances and are typical of conditions where a "mudwave" has occurred. Mudwaves occur when a large amount of fill is rapidly placed on a soft clay layer, causing a bearing capacity failure.

Bay Mud is a soft, weak, and compressible marine clay; it varies throughout Mission Bay from 0 to 42.7 meters (0 to 140 feet) thick. The Colma Formation, beneath the Bay Mud, consists of medium dense to very dense sand, silty sand, and clayey sand. Old Bay Clay, which is a medium stiff to hard overconsolidated clay, underlies the Bay Mud and Colma Formation. Dense to very dense sand and gravel and stiff to hard clay and sandy clay are sometimes encountered below the Old Bay Clay. Bedrock within Mission Bay is of the Franciscan Formation and has been encountered at depths ranging from 1.5 to 64 meters (5 to 210 feet) below the ground surface (bgs). Groundwater has been found from about 1 to 3 meters (3 to 10 feet) bgs (Elevations 26.2 to 29.6 meters (86 to 97 feet)).

LIQUEFACTION HAZARD

Liquefaction is a phenomenon in which saturated soil temporarily loses strength resulting from the buildup of excess pore water pressure, and can occur during earthquake-induced cyclic loading. Soil susceptible to liquefaction includes loose to medium dense sand and gravel, low-plasticity silt, and some low-plasticity clay deposits.

As previously discussed, a major earthquake is predicted in the Bay Area; strong to violent ground shaking is expected to occur in Mission Bay. Mission Bay is within a designated liquefaction hazard zone as designated by the California Geological Survey (CGS) seismic hazard zone map for the area titled *State of California Seismic Hazard Zones, City and County of San Francisco, Official Map,* dated 17 November 2001.

Site-specific geotechnical investigations, which included Cone Penetration Tests (CPTs) and/or rotary wash borings, were performed to evaluate liquefaction potential at each site discussed in this paper. Borings were drilled using the rotary wash drilling method and soil samples were obtained in potentially liquefiable layers mainly using a Standard Penetration Test (SPT) sampler without liners. The SPT sampler was driven with a rope-and-pulley system and a 63.5-kilogram (140-pound) safety hammer falling about 760 millimeters (30 inches).

Based on the presence of liquefiable fill and the predicted consolidation settlement of the Bay Mud from new building loads, the buildings at Sites A and B are supported on steel H-piles driven to rock. Because the fill is susceptible to liquefaction at these sites, as presented in more detail below, lateral resistance in these layers is low, thus requiring a significant number of piles to resist the base shear. To decrease foundation costs, the project teams evaluated the benefit of improving the sites to mitigate liquefaction potential and increase lateral resistance. After evaluating more traditional site improvement methods, such as compaction grouting, stone columns, and vibroflotation, Rapid Impact Compaction (RIC) was selected because of its relative speed and economy.

RAPID IMPACT COMPACTION

RIC is a method of soil improvement using a track-mounted machine that imparts energy by dropping an approximately 6,800-kilogram (7.5-ton) weight from a height of about 1 meter onto a 1.5-meter (5-foot) diameter steel plate. The RIC equipment is shown on Figure 4. The energy is delivered at a rate of 40 to 60 blows per minute. Drop height, number of blows, and penetration per blow are monitored and/or controlled by an on-board data acquisition system. RIC treatment typically consists of performing 13 compaction points per 6–by-6-meter (20-by-20-foot) area. The dropping of the weight at each point is ceased when one of the following criteria is met: 1) a set of 5 mm for the last blow, or 2) 40 total blows, whichever occurs first. A set of 5 mm for the last blow is desirable, whereas a set of greater than 10 mm for the last blow is considered to be "soft".

Craters are formed at each point; typical craters are shown on Figure 5. Crater depths typically range from about 150 to 610 millimeters (6 to 24 inches). Craters deeper than about 460 millimeters (18 inches) indicate the near surface soil may be so loose that the energy cannot propagate sufficiently deep to improve the soil below the water table. In these areas, retreatment is performed. If deep craters are created during the second round, shallow soft soil may be present.

Generally, recommendations include retreating areas where craters are greater than 18 inches deep with an additional 13 compaction points per 6-by-6-meter (20-by-20-foot) area no sooner than 24 hours after the initial treatment to allow pore pressures to dissipate. Acceptance criteria for improved fill (where classified as sand, clayey sand, or silty sand) included meeting minimum and average tip resistances $(q_{c1N})_{CS}$, over an interval of 1 meter (3 feet), of at least 7,660 and 9,580 kilopascals (kPa) (80 and 100 tons per square foot (tsf)), respectively, corresponding to SPT $(N_1)_{60cs}$ values of 20 and 25 blows per 305 millimeters (blows per foot), respectively. While soil layers may meet the site improvement criteria after RIC is performed, some liquefaction potential may still be present and it is up to the judgment of the engineer to alter lateral pile capacities and change the code site soil profile type on a case-by-case basis.



FIG. 4. RIC Rig



FIG. 5. RIC Craters

SITE A

Subsurface Conditions

Subsurface exploration indicates the site is blanketed by heterogeneous fill, which is approximately 4.3 to 7.3 meters (14 to 24 feet) thick. Measured groundwater levels range from 1.5 meters (5 feet) bgs (Elevation 27.7 meters (91 feet)) to 3 meters (10 feet) bgs (Elevation 26.2 (86 feet)).

The fill consists of gravel, sand, and clay mixtures, with abundant amount of rubble, such as concrete, brick, and wood. Loose to medium dense sand and gravel with varying silt and clay content (2 to 14 percent fines where tested) is present just above or below the water table, with thicknesses ranging from 0.5 to 4.3 meters (1.5 to 14 feet). Using Youd and Idriss (2001), the analyses indicate these layers could liquefy in a major earthquake. The Tokimatsu and Seed (1984) method for evaluating earthquake-induced liquefaction settlement, predicts approximately 13 to 76 millimeters (½ to 3 inches) of settlement.

RIC Program

Because of the construction schedule, the test program for the RIC was incorporated into the production RIC program. During the RIC program for this project, the contractor could not get the data acquisition system functioning. Therefore, the contractor adapted a criterion of 50 blows at each compaction point. If the penetration depth after 50 blows was greater than 460 millimeters (18 inches) deep, the area was to be retreated. Based on observations of the crater depths and the field conditions, no areas required retreatment.

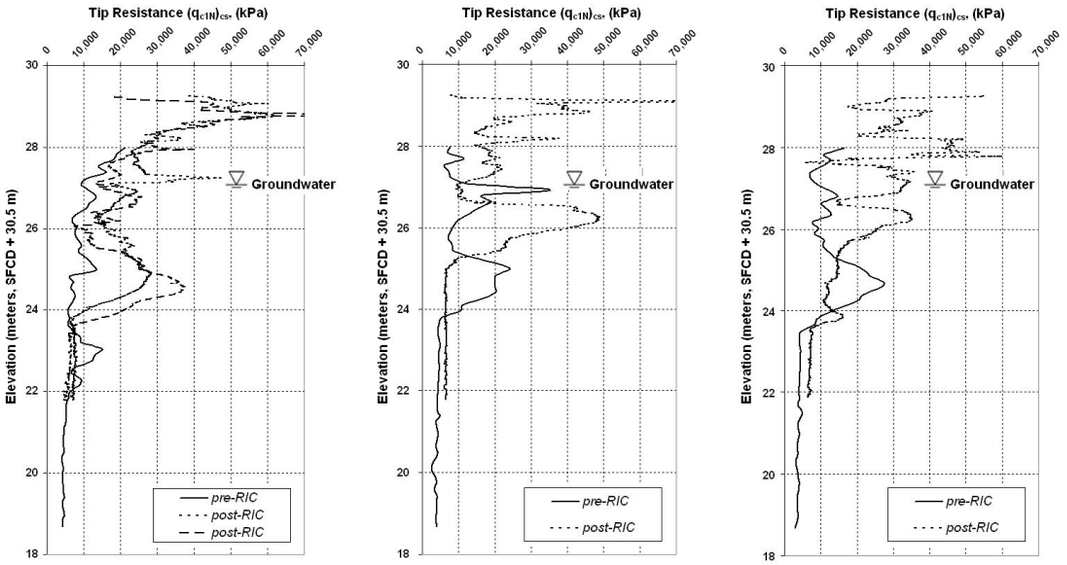
At the start of the program, the contractor used a compaction pattern of 41 points within a 6-by-6-meter (20-by-20-foot) square area. However, after reevaluation by the contractor, the production RIC treatment was changed to consist of performing compaction with 13 points within a 6-by-6-meter (20-by-20-foot) square area. This pattern was used for the remainder of the site.

Vibrations were monitored during RIC to evaluate the potential for damage to nearby utilities. Seismographs were placed at distances ranging from 1.8 to 76.2 meters (6 to 250 feet) away from the RIC to measure the peak particle velocity (PPV), which is the parameter most commonly used to evaluate the effects of vibrations on structures. The attenuation data compiled during RIC at one location indicates the maximum PPV recorded was about 135 millimeters per second (mm/sec) (5.3 inches per second (ips)) at a distance of 2.4 meters (8 feet) from the RIC; the best-fit attenuation curve for the PPV data dropped below 127 mm/sec (5 ips) at a distance of about 3 to 4.6 meters (10 to 15 feet) from the RIC and below 51 mm/sec (2 ips) at a distance of about 10.7 meters (35 feet) from the RIC. At another location, the maximum PPV was 58 mm/sec (2.3 ips) at a distance of 1.8 meters (6 feet) and the attenuation curve indicates the PPV is below 25 mm/sec (1 ips) at a distance of 12.2 meters (40 feet) (Municon, 2006).

Confirmation Testing

CPTs were used to confirm the level of improvement by the RIC. The CPTs performed for the site investigation were used as the pre-treatment CPTs. At the start of the RIC production program, the contractor performed RIC around the locations of three pretreatment CPTs. Following the RIC work, four CPTs were performed to provide post-treatment evaluation of the improvements provided by the RIC. The post-treatment CPTs were advanced to depths of about 7.6 meters (25 feet) bgs approximately 2½ to 6 days after the RIC treatment, near each pre-treatment CPT.

Two pre-treatment CPTs encountered liquefiable soil from the water table to a depth of approximately 4 meters (13 feet); one encountered liquefiable soil from the water table to the top of the Bay Mud. The corresponding post-treatment CPTs indicate an increase in the tip resistance within these same depths up to about 200 percent. Figures 6a through 6c compares the results of the pre- and post-treatment CPTs.



FIGS 6a, 6b and 6c. Results of pre- and post-RIC CPTs at Site A

While the analyses indicate some liquefaction potential remains after improvement by RIC, the remaining liquefiable deposits are thin, intermittent and non-continuous. Therefore, it was concluded the fill was sufficiently improved to increase the lateral pile capacity, thereby reducing the foundation cost. The savings in foundation costs exceeded the cost to improve the site.

SITE B

Subsurface Conditions

The results of the subsurface investigation indicate the site is underlain by between 1.8 to 15 meters (6 and 49 feet) of fill. Groundwater was encountered at the time of the investigation in the borings at depths of between 1.4 to 2.3 meters (4-1/2 to 7-1/2 feet) bgs.

The fill consists of gravel, sand, silt, and clay mixtures. The sand and gravel ranges in density from loose to very dense and the clay and silt are soft to stiff. The upper few feet of the fill across most of the site is medium dense to very dense, while the remaining fill is generally loose to medium dense. The fill contains rubble, such as concrete, brick, wood, and abundant rock fragments.

Loose to medium dense sand with between about 5 and 29 percent fines (clay and silt) was encountered in the fill below the water table in several borings across the site with thicknesses ranging from about 2.1 to 6.1 meters (7 to 20 feet). Results of liquefaction analyses following the procedures outlined in the 1996 NCEER and 1998 NCEER/NSF workshops (Youd and Idriss 2001) indicate these layers could liquefy in a major earthquake. Using the Tokimatsu and Seed (1984) method for evaluating earthquake-induced liquefaction settlement, approximately 13 to 51 millimeters (1/2 to 2 inches) of settlement is predicted.

RIC Program

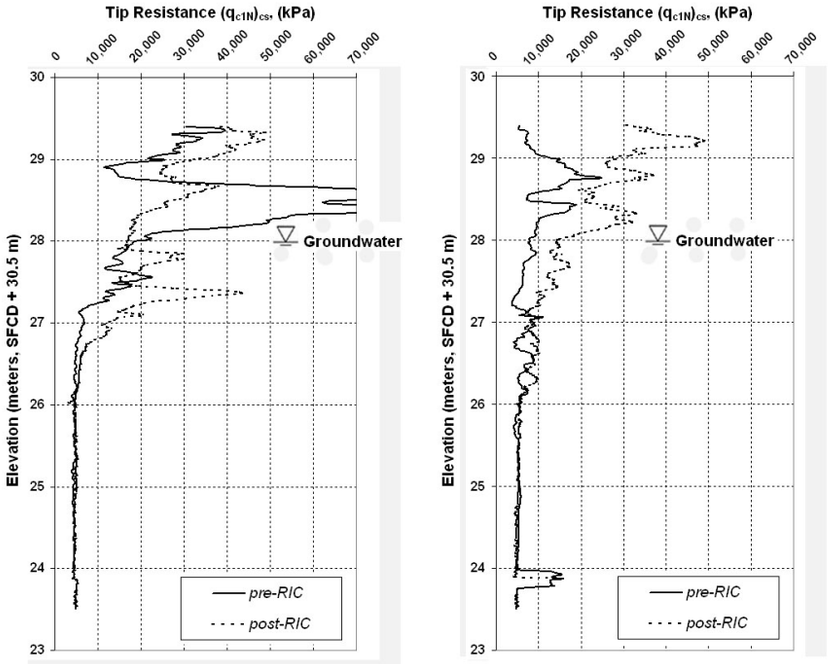
The RIC program was performed on a 3-meter (10-foot) on-center grid pattern in the first pass; the second pass consisted of points at 3-meter (10-foot) on-center midway between points of the first pass. Craters deeper than about 460 millimeters (18 inches) were created in an area approximately 30.5 by 30.5 meters (100 by 100 feet) in the northeast corner of Site B; this area was retreated and the resulting craters were less than 460 millimeters (18 inches) deep.

Vibration monitoring was performed on 31 January 2006 at three RIC locations while RIC was being performed. Vibrations were recorded at distances of 3, 6.1, 9.1, 15.2, 22.9, 30.5, 61, and 91.4 meters (10, 20, 30, 50, 75, 100, 200, and 300 feet). The results indicate the PPV ranged from about 24 mm/sec (0.95 ips) to 36 mm/sec (1.4 ips) at a distance of 3 meters (10 feet), 14 mm/sec (0.55 ips) to 25 mm/sec (1.0 ips) at a distance of 6.1 meters (20 feet), and 6.4 mm/sec (0.25 ips) to 19 mm/sec (0.75 ips) at a distance of 9.1 meters (30 feet). Beyond a distance of about 15.2 meters (50 feet), the maximum ppv measured dropped to less than about 5 mm/sec (0.2 ips) (Municon, 2006).

Confirmation Testing

Four test sections were performed near four test borings where the analysis indicated the fill was potentially liquefiable. CPTs were performed in these test sections prior to RIC, followed by CPTs advanced between 2 and 14 days after RIC treatment. Figures 7a and 7b show $(q_{c1N})_{cs}$ versus elevation at two test locations for pre- and post-RIC treated CPTs.

Figures 7a and 7b show the RIC treatment was effective in increasing the tip resistance of the granular fill beneath the groundwater table, thus reducing the potential for liquefaction in these layers. Based on our analysis, some liquefaction potential remains, although the remaining potentially liquefiable layers are significantly thinner and the post-treatment tip resistances are significantly higher than the pre-treatment values. Therefore, the overall results indicate fill at the site was sufficiently improved such that the liquefaction potential was reduced and lateral pile capacity was increased by about 30 to 35 percent.



FIGS 7a and 7b. Results of pre- and post-RIC CPTs at Site B

CONCLUSIONS

RIC is a viable and economical method of ground improvement. The projects presented herein benefited from its use, mainly by a reduction in the foundation costs. The cost and time to perform RIC provided a savings to the project versus the cost of the foundation system without it. Results indicate improvement of fill to depths of up to 5.2 meters (17 feet) below the ground surface at these sites.

The potential effect of the vibrations from RIC on nearby improvements should be considered. At one site where monitoring was performed, some vibrations measured were relatively high (127 mm/sec within 3 meters (5 ips within 10 feet)), although no known damage to nearby utilities has occurred. At the time RIC was performed at each site, existing above-ground structures were at least 30.5 meters (100 feet) from the sites. Vibration monitoring indicates vibrations were less than 15 mm/sec (0.6 ips) at these distances. No known damage to above-ground improvements occurred.

To date, RIC has been successfully performed at eight other sites in Mission Bay. At this time, however, RIC test programs at two other sites in Mission Bay have not

indicated improvement of the fill. Additional measures, such as ripping the upper 760 millimeters (30 inches) of subgrade (to prevent too much spreading of the energy in the medium dense to dense upper soil) and treating the test sections twice, were unsuccessful. The liquefiable layers at these sites have more fines (up to 33 percent fines where tested) and/or are interbedded with clay layers. Layers with higher fines content are not ideal for improvement by RIC and interbedded clay layers may attenuate the energy, making it difficult to improve deeper layers.

ACKNOWLEDGEMENTS

The authors would like to thank Craig S. Shields, M. ASCE, G.E. for his peer review of this paper.

REFERENCES

California Geological Survey (2001). State Of California Seismic Hazards Zones City and County Of San Francisco, Official Map.

Cao, T., Bryant, W.A., Rowshandel, B., Branum D. and Wills, C. J., (2003). The Revised 2002 California Probabilistic Seismic Hazard Maps.

Municon Consultants (2006). Mission Bay Block N4 Parcel 1, San Francisco, California, Vibration Monitoring During Rapid Impact Compaction.

Municon Consultants (2006). RIC Test, Mission Bay Block 10A, San Francisco, California, Vibration Data and Attenuation Curve.

Olmsted (1986). Vanished Waters: A History of San Francisco's Mission Bay.

Tokimatsu, K. and Seed, H.B. (1984). "Simplified procedures for the evaluation of settlements in sands due to earthquake shaking." Report no. UCB/EERC-84/16.

Working Group on California Earthquake Probabilities (WGCEP) (2003) "Earthquake probabilities in the San Francisco Bay region: 2002 to 2031". Open File Report 03-214.

Youd, T.L, and Idriss, I.M. (2001). "Liquefaction Resistance of Soils: Summary Report from 1996 NCEER and 1998 NCEER/NSF Workshops on Evaluation of Liquefaction Resistance of Soils". Journal of Geotechnical and Geoenvironmental Engineering, Vol. 127 (4): 297-313.

Monitoring for Successful Site Improvement

Brian D. Bauldry[1], G.E., Lisheng Shao[2], PhD, G.E., and Francis B. Gularte[3], G.E.

[1]Principal Engineer – Bauldry Engineering, 718 Soquel Avenue, Santa Cruz, CA 95062 (831) 457-1223; brian@bauldryengineering.com
[2]Chief Engineer – Western Region, Hayward Baker Inc., 1780 Lemonwood Dr., Santa Paula, CA 93060 (805) 933-1331; LShao@HaywardBaker.com
[3]Sr. Vice President, Hayward Baker Inc., 1780 Lemonwood Dr., Santa Paula, CA 93060 (805) 933-1331; FBGularte@HaywardBaker.com

ABSTRACT: Computer aided installation of stone columns combined with insitu instrumented surcharging provided the necessary feedback to improve a difficult site for support of a new gymnasium and health center. The low lying site consists of an ancient landslide with loose sands over bedrock which is overlain by peaty soils. Both liquefaction of the loose saturated sands and settlement of the organic soils needed improvement. Vibro-displacement stone columns combined with surcharging was employed to improve both types of soil present, thus providing the long term performance needed. Computer monitored vibro-replacement provided the necessary real-time information to confirm the stratigraphy, and control the diameter of column installed within the softer surface soils. Final improvement of the surface organic soils was provided by surcharge. An in-situ vibrating wire water level system was installed after the vibro improvement, providing the necessary feedback to confirm completion of the primary consolidation.

INTRODUCTION

Vibro-compaction is a soil improvement technique that uses a specially developed depth vibrator to direct compactive energy throughout the required improvement depth. Improvement is achieved by rearranging the soil matrix to a tighter packing, resulting in an increase in the in-situ density and shear strength of the soil mass.

Vibro-replacement/displacement uses the same depth vibrator; however, it also introduces gravels to fill the void caused by the vibro densification. Therefore, the vibro-replacement/displacement method is often referred to as the Vibro Stone Column technique. These Vibro soil improvement methods are widely used for site liquefaction mitigation, increasing foundation bearing capacity and settlement reduction, roadway embankment foundation reinforcement, and slope stabilization.

The key factors of a successful Vibro project, since the 1930s, are the operator's use of voltage and current meters to measure the vibrator power consumption as an indication of improvement. They also measure the volume of sand backfilled into the surface vibro-crater to estimate the degree of soil densification. Today, the quality control of stone column installation includes monitoring, recording, and displaying vibrator penetration depth, energy consumption, gravel consumption, and air pressure to continuously aid the operator and the inspector. In the past 15 years, with the advance of electronic and computer technology, the data acquisition and recording system for vibro stone column construction has been developed and widely used in many projects.

i-VIBRO SYSTEM

Hayward Baker developed the first vibro instrumentation system in 1992, using a data logger to record the vibrator current consumption and the vibrator penetration depth. In 1994, the data logger was connected with a 386 portable computer to provide a real time graphical display. The weight of stone was measured by an electronic system on the loader, which transferred the measurement through radio link to the data logger. This vibro instrumentation system was successfully used in many vibro stone column projects, including Mormon Island Dike near Sacramento, California, Salmon Lake Dam (Luehring, *et al.*, 1998), Utah, Lopez Dam seismic mitigation project (Callan, *et al.,* 2004*)*, Arroyo Grande, Califronia, and California Interstate I5/56/I805 intersection extension project, along with numerous other projects.

The most recent "i-Vibro" instrumentation system was developed in 2003. The i-Vibro system collects, stores, and displays relevant vibro stone column data (Figures 1 and 2). This Windows-based system has a user-friendly interface, which displays column name, depth, time, hydraulic pressure or AC current, air pressure, stone weight, volume, and accumulated stone volume, along with installation duration. The column depth, diameter, current, air pressure, and volumes are shown numerically as well as graphically. The stone column data can later be retrieved from the computer hard drive for further analysis, graphical presentation and/or for QA/QC records. These programs allow real-time monitoring, analysis, and assessment, thus greatly improving field control of vibro stone operations. The data acquisition unit is shown mounted on the side of a crane in Figure 1.



FIG.1. Typical ground improvement operation showing monitoring system mounted on side of crane.

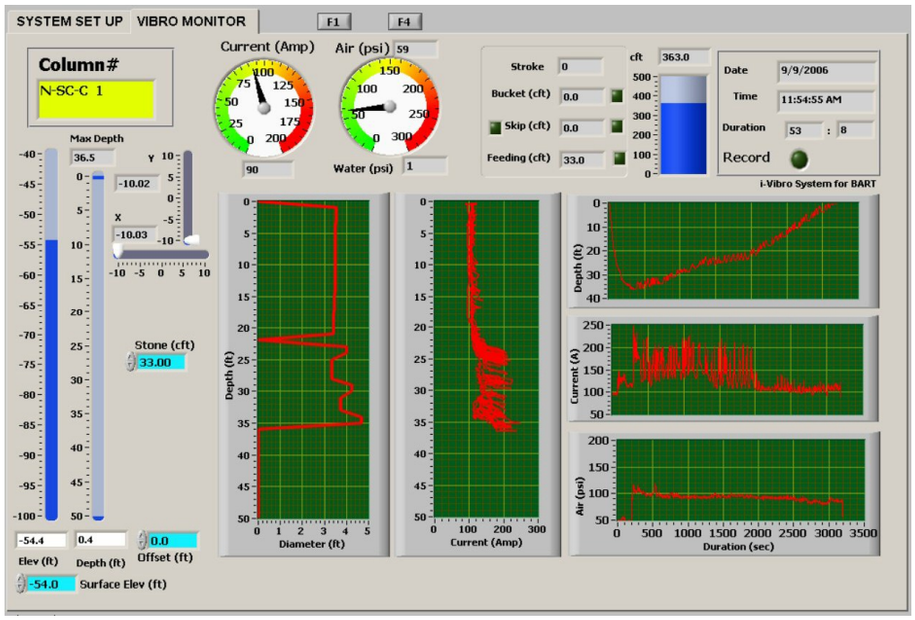


FIG.2. i-Vibro system collects parameters from the vibrator, the crane, and the loader, integrating this information into a graphics-based user interface.

Mount Hermon Project

A new field house was planned in the beautiful Santa Cruz, California coastal mountain area. The soils consist of 0.9 to 3.0 m (3 to 10 ft) of very soft organic (peaty) clay over loose to medium dense sand, extending up to 12.1 m (40 ft) deep, as shown in a typical Cone Penetration Test (CPT) profile in Figure 3. This mix of

granular and cohesive stratigraphy presented a combination of long term static and seismic settlement problems.

Under the site design earthquake of magnitude 7.9 and peak ground surface acceleration (PGA) of 0.4 g, the loose to medium dense sand layer could liquefy and create 75 to 175 mm (3 to 7 in) of dynamic settlement. Static settlement was estimated up to 250 mm (10 in) under the foundation dead load and live load.

The liquefaction analysis was performed in accordance with the procedures of Youd and Idriss (NCEER, 1997), and Martin and Lew (SCEC, 1999), under the site design earthquake. The dynamic settlement was calculated following Tokimatsu and Seed (1984), after converting the CPT tip resistance into SPT blow count based on Robertson (1998) method. As shown in Figure 3, one of the pre-treatment CPT, Pre-CPT-3, found about 95 mm (3.75 in) of dynamic settlement under the design earthquake.

The geotechnical engineers and specialty contractor teamed up to design a three-fold solution. The liquefiable sands would be densified by the vibratory process and the cohesive peaty soils by a combination of stone columns and surcharge. The stone columns provide a dual role of improving drainage during the surcharge period and providing reinforcement to the softer clayey soils. In addition, a gravel/geo-textile pad constructed over the improved soils and stone columns would help distribute the transfer of building loads more uniformly to the underlying improved soils, as well as horizontal drainage path during surcharge program.

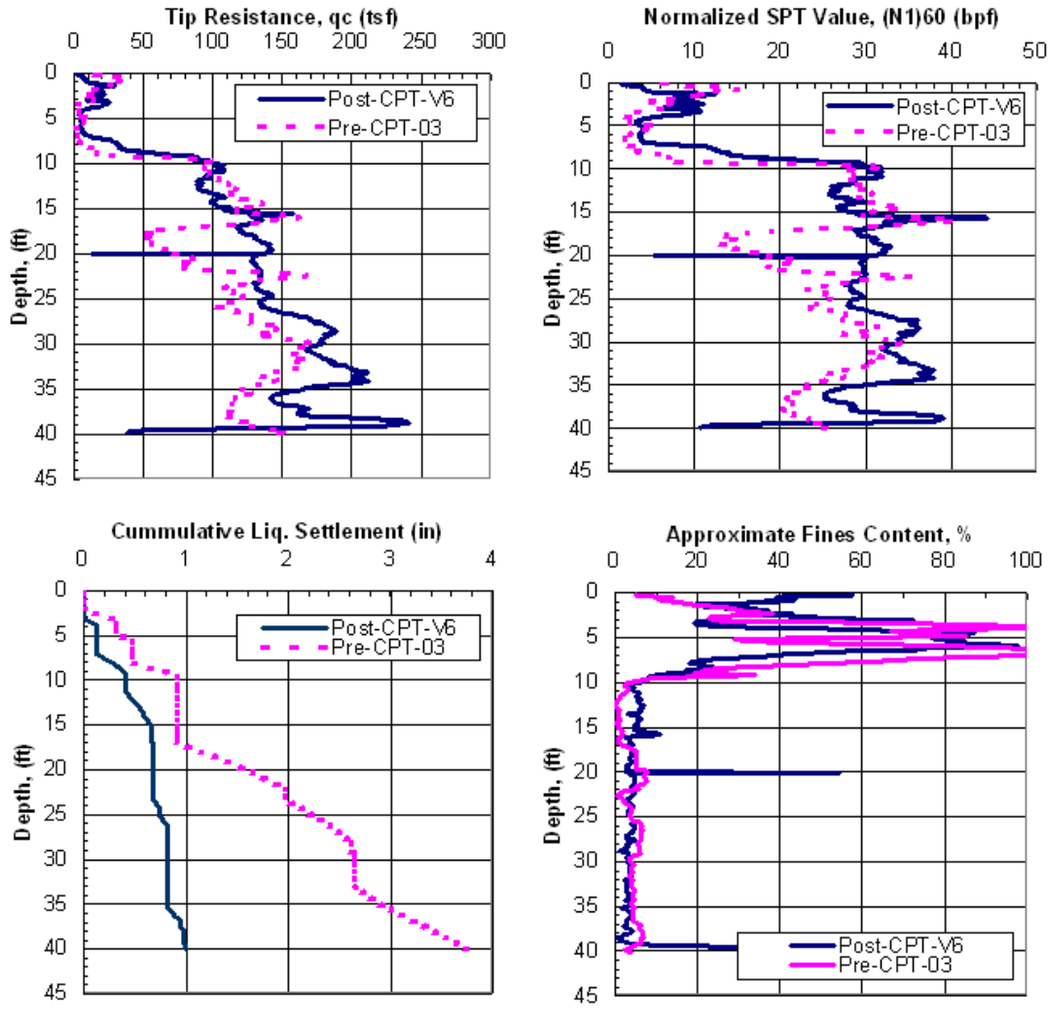


FIG.3. Comparison of CPT tests before and after vibro stone column treatment. The locations of these two CPTs are plotted in Figure 6.

The liquefiable sand was densified by a depth vibrator suspended from a crane, which penetrated by means of its own weight, vibrations, and air jetting. Once design depth of 12.2 m (40 ft) was reached, the vibrator was lifted in stages as the stone backfill was fed from an overhead hopper through follower side pipes and expelled at the vibrator tip. These actions continued until the column was complete. For this project, the nominal 1.07 m (3.5 ft) diameter stone columns were installed at 2.75 m x 2.75 m (9 ft x 9 ft) square grid, and achieved a replacement ratio of 11.9% (Figure 4).

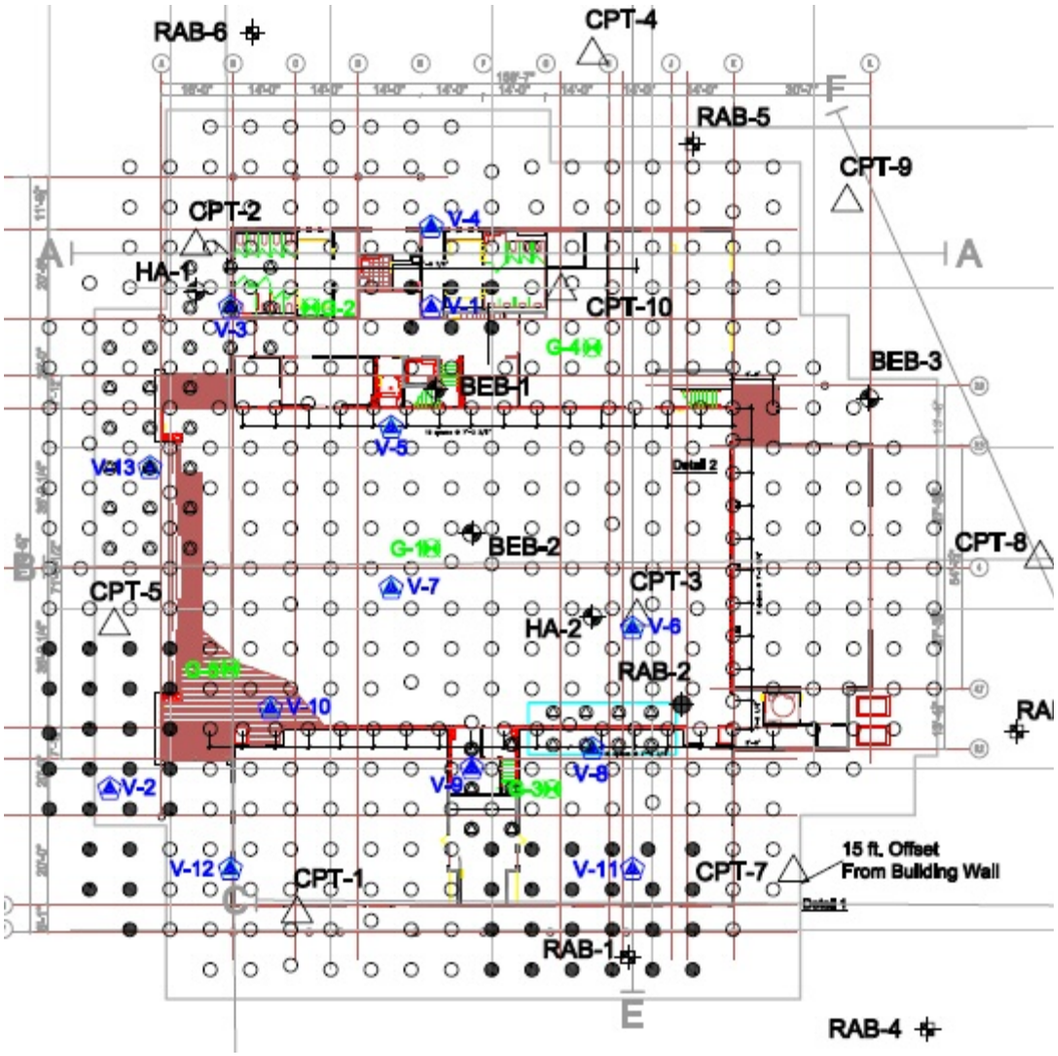


FIG.4. Plan layout at Mount Hermon.

The effectiveness of the vibro stone column treatment was evaluated by the post-treatment CPT tests. Figure 3 shows the comparison of the Pre-CPT-3 and Post-CPT-V6 at the same location. The vibro stone column treatment significantly increased the CPT tip resistance in the sand layer, and reduced the calculated dynamic settlement value from the pre-treatment 95 mm (3.75 in) to the post-treatment 25 mm (1 in).

For better control of this complicated soil improvement project, the i-Vibro system was used to monitor and record the stone column installation process. A typical i-Vibro record is presented in Figure 5.

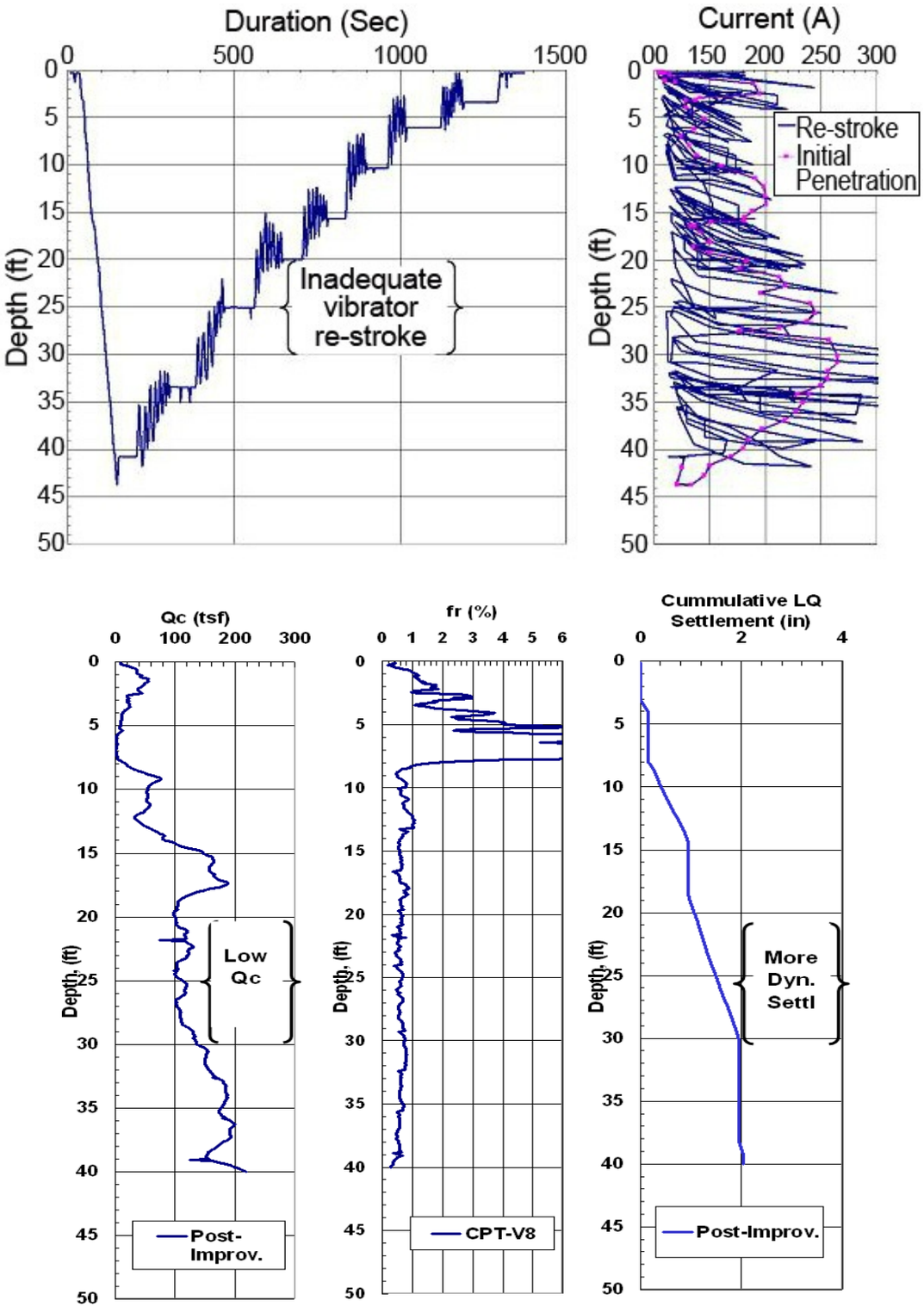


FIG.5. i-Vibro record compared with post-treatment CPT results. Inadequate re-strokes and relative low current value between 6.0 to 9.1 m (20 to 30 ft) at stone column #4859 yielded low post-treatment CPT tip resistance.

The i-Vibro system allowed the engineers to analyze the data on a real-time basis, making needed adjustments to the densification program during field operations. Usually the electric current passing through the vibro motor relates to the vibro probe confinement in the soil. The denser the sand, the higher the current value measured by i-Vibro system. Combined with periodic CPT tests, one can verify the effectiveness of the soil densification by the vibro stone column treatment. For example, Figure 5 shows a zone between 6.0 to 9.1 m (20 to 30 ft) deep that has not been adequately treated. At the depth of 25 ft and after, gravel was re-loaded into the pressure chamber, the vibrator then penetrated 3 ft below 25 ft, then was pull up 4 ft and down 3 ft repeatedly.

The adjacent CPT test indicates relatively low tip resistance of about 10 MPa (100 tsf). The dynamic settlement calculation, following Tokimatsu and Seed (1984) found about 50 mm (2 in) of dynamic settlement after the initial stone column treatment. In order to satisfy the site liquefaction mitigation criteria, additional stone columns were installed in this area to further densify the soil. The continuous feedback from the i-Vibro instrumentation system significantly enhanced the technical quality of this project.

In the clayey soil layer, which is not sensitive to vibration, the post-treatment CPT tip resistance shows only a little improvement. Based on Priebe (1995) method, the stone column replacement ratio at about 12% will reduce the static settlement by half of its pre-treatment settlement value due to the stone column reinforcement effect. The calculated pre-treatment static settlement under the building was 250 mm (10 in); however, even half of this value would not satisfy the structural requirement. Therefore, a surcharge program was developed to further reduce the static settlement.

To consolidate the surface clays, silts and organic soils that underlay the site approximately 3 m (10 ft) of soil was placed over the stone column grid to surcharge the compressible soils. The surcharge extended 1.2 m (4 ft) above the design finish grade. To accelerate the settlement a gravel blanket was constructed between the base of the surcharge and the top of the stone columns. The gravel blanket in conjunction with the stone columns provided a drainage path for water expelled from the consolidating soil. Settlement was monitored using 5 vibrating wire soil settlement gages. Pressure transducers were attached to base plates and embedded in the soil. Liquid filled tubes connected the pressure transducers to reservoirs located on stable ground. The gages were located in the center and near the four corners of the building. The bulk of the settlement occurred during the 19 days it took to place the surcharge. The CPT soundings as well as the settlement gages indicated that the thickness of the compressible soils increased from the rear of the building to the front. Settlement at the rear of the building stabilized after approximately 3 weeks. Settlement at the front of the building stabilized after approximately 9 weeks. Because of the significant difference in settlement characteristics between the front and rear of the building, the upper 1.2 m (4 ft) of surcharge was taken from the rear of the building and repositioned over the front half of the building resulting in an additional episode of settlement beneath the front half of the building. After 2 additional weeks the surcharge was removed.

Settlement of up to 140 mm (5.5 in) was detected under the front of the building, as shown in Figure 6. Settlement under the rear of the building was limited to 25 mm

(1 in) or less. Following construction of the footings, the general contractor placed a mark on the footings and episodically monitored the foundation for settlement as the building was constructed, including after the raising of tilt-up walls and the construction of the roof. The contractor reported that they did not detect any settlement throughout construction. After two years, the client reports that the building has shown no signs of differential settlement. Post-construction monitoring indicates that total settlement is less than 12 mm (0.5 in) and differential settlement is negligible.

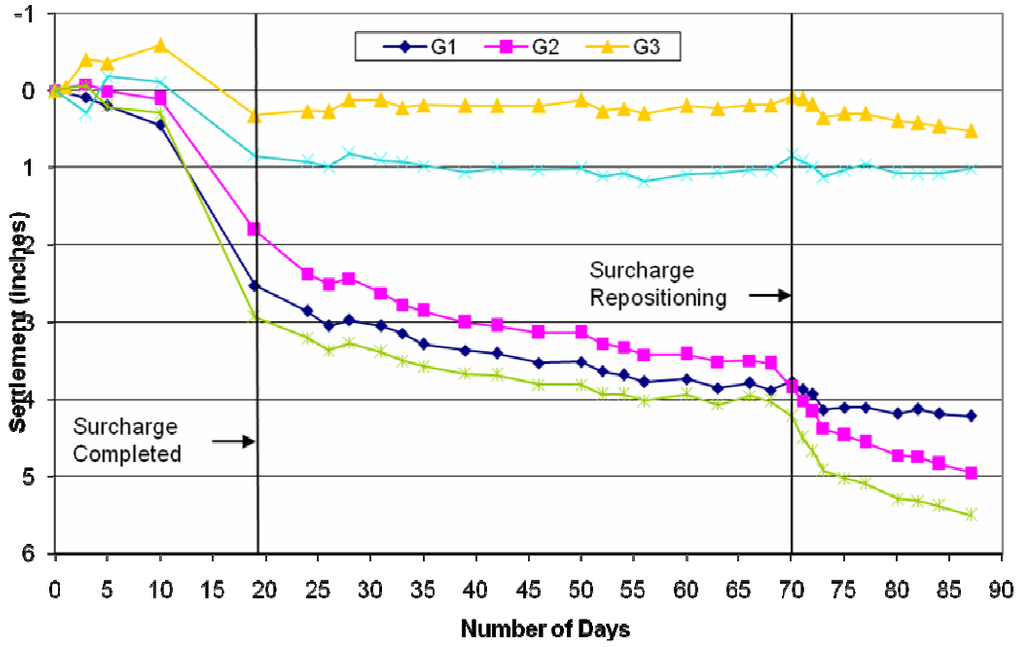


FIG.6. Mount Hermon field house settlement monitoring

CONCLUSION

Many of the inter-urban building sites remaining today offer challenges to our engineering skills. Many sites not only have poor soils, but have different types and thicknesses. With careful evaluation of boring data various ground improvement methods can be employed to improve difficult sites with regard to static and dynamic and/or lateral concerns.

The use of state of the practice computer systems to acquire the data, reduce the data, and present it in a meaningful way on a real-time basis provide the control necessary to "tailor" the ground improvement method to the difficult soils conditions present. In addition, combining state of the practice instrumentation systems in situ provide the ability to evaluate and predict the performance. The success of this project was clearly due to the composite use of vibro improvement with surcharging,

guided by the instrumentation systems that allowed real-time observation and adjustments to be made in the field.

The continuing advancement of computer and instrumentation systems offers numerous possibilities for the future. With regard to vibro methods it is possible that variable speed vibrators combined with ground accelerometers can be compared and/or integrated with specific energy calculations on a real-time basis in an effort to optimize the process to a higher degree. Perhaps more graphical presentation of the collected data, such as comparing the specific energy of penetration to confirm and/or better define the stratigraphy, will provide evaluation of the variations in the stratigraphy, allowing better calculations and predictions in differential settlement not available today.

REFERENCES

Baez, J., Dewey, B., Luehring, D., Mejia, L., and Stevens, M. (1998), "Liquefaction mitigation of silty dam foundation using vibro-stone columns and drainage wick drains: A test section case history at Salmon Lake Dam." *Proceedings of Dam Safety 1998*, Association of State Dam Safety Officials Annual Conference, Las Vegas, Nevada.

Idriss, I.M and Youd, T.L. (1997). National Center for Earthquake Engineering Research (NCEER). *Proceedings of the NCEER Workshop on Evaluation of Liquefaction Resistance of Soils*, NCEER Technical Publication 97.

Martin, G.R. and M. Lew. (1999). "Recommended Procedures for Implementation of DMG Special Publication 117 –Guidelines for Analyzing and Mitigating Liquefaction in California." Southern California Earthquake Center.

Priebe, H. J. (1995) "The Design of Vibro Replacement". *Ground Engineering*, December, 1995.

Robertson, P.K. (2004). "Evaluating soil liquefaction and post-earthquake deformations using the CPT." Proceedings ISC-2 on Geotechnical and Geophysical Site Characterization, Viana da Fonseca & Mayne (eds.) Millpress, Rotterdam, ISBN 90 5966 009 9

Robertson, P.K. and Wride, C.E. (1998). "Evaluating cyclic liquefaction potential using the cone penetration test." *Can. Geotech J.* 35: 442-459.

Shao, L and Gularte, F. (2007) "Instrumentation for Vibro Stone Columns" *7th International Symposium on Field Measurements in Geomechanics*, Boston, MA

Tokimatsu, K., and H.B. Seed. (1984). "Simplified Procedures for the Evaluation of Settlements in Clean Sands," Report No. UCB/GT-84/16, Earthquake Engineering Research Center, University of California, Berkeley.

Numerical Modeling of the Seismic Response of Columnar Reinforced Ground

C. Guney Olgun[1] and James R. Martin II[2]

[1]Research Scientist, Via Department of Civil and Environmental Engineering, Virginia Tech, 111 Patton Hall, Blacksburg, VA 24061; olgun@vt.edu
[2]Professor, Via Department of Civil and Environmental Engineering, Virginia Tech, 111-B Patton Hall, Blacksburg, VA 24061; jrm@vt.edu

ABSTRACT : Ground improvement using stiff columnar reinforcement, such as stone, jet-grout, and soil-mix columns, is commonly used for mitigation of seismic damage in weak ground. Seismic shear stress reduction in the reinforced soil mass is often counted on for reducing liquefaction potential. Current design methods assume composite behavior of the reinforced soil, where the shear stress reduction is based on the ratio of the columnar stiffness relative to the soil as well as the area replacement ratio. This implicitly assumes the stiff columns will deform in pure shear along with the soil. We performed 3-D dynamic finite element modeling to better understand the column deformation and shear stress reduction behavior. We found that the columns deform in both shear and flexure, providing little seismic shear stress reduction and current methods may be unconservative.

INTRODUCTION

Ground improvement using stiff columnar reinforcement, such as stone columns, jet grout and soil-mix columns is commonly used for mitigation of seismic ground damage in soils susceptible to significant seismic-induced deformation. A number of benefits are gained, such as in-situ densification of loose granular soils where stone columns are installed, and increased bearing support where jet-grout or soil–mix columns are constructed in fine-grained soils that cannot be effectively densified. Current engineering practices often consider shear stress reduction in the reinforced soil mass a key factor in reducing the liquefaction susceptibility of soils improved with stiff columns. The shear stress reduction mechanism of stiff columns is based on the presumption that the stiff columns attract more of the seismically-induced shear stress than the surrounding softer soil mass. The idea that the column carries larger shear stress, in proportion to the stiffness ratio, is implicitly based on the assumption that both the soil and the stiff columns deform compatibly in shear, namely undergoing the same shear deformation. This assumption is further utilized in calculating the reduction of seismically induced shear stresses on the soil (Baez and Martin 1994).

Recent studies by the authors (Martin and Olgun 2007), along with Goughnour and Pestana (1998) for stone columns, suggest that current design methods for shear stress reduction should be more closely examined. We performed dynamic numerical analyses of reinforced ground to investigate the potential mechanisms of shear stress reduction in columnar reinforced ground.

Our analyses showed that the seismic behavior of columnar reinforced ground is more complicated than widely thought, and importantly, that current design methods may greatly over-estimate the shear stress reduction the columns provide. The study found that stiff columns do not behave as pure shear beams as implicitly assumed by current methods, but that their behavior is a combination of shear and flexural behavior. Further, the results indicate that the mode of deformation of the columns significantly influences their effectiveness in reducing shear stresses in the reinforced soil, with shear deformation being the most effective, and flexural being the least. For most common field conditions, the shear stress reduction of the stiff columns was found to be significantly less than predicted by the current design methods such as Baez and Martin (1994) and Priebe (1995). This paper presents the findings from these analyses and describes the mechanisms associated with the shear stress reduction.

ANALYTICAL STUDY AND NUMERICAL MODELING

Mechanics of Columnar Behavior

Studies in the literature differ in their explanation of columnar reinforced ground behavior. As mentioned above, current design methods such as Baez and Martin (1994) implicitly assume that the columns behave as shear beams during ground shaking, as the predicted reduction of shear stress in the soil is assumed to be proportional to the area and stiffness of the columns relative to the soil. More recent studies, such as Goughnour and Pestana (1998), suggest that columns behave as flexural beams. If so, this implies that little to no additional shear stress is carried by the columns. Thus, for the current analysis, it was important to first clearly understand the basic mechanics of column behavior, and the fundamental differences between deformation modes. Figure 1, illustrates shear and flexural deformation modes of a column; the left side of the figure shows pure shear deformation, and the right side shows flexure. The modes of column deformation were a major focus in our numerical study of columnar reinforced ground. Clarification of the deformation modes during shaking was a fundamental step in determining how the soil mass responds seismically, and ultimately, how much shear stress reduction is achieved in the soil.

Numerical Modeling

The modeling involved three-dimensional dynamic finite element analyses that simulated the seismic response of soft ground reinforced with columnar elements. The analyses were performed using the computer code DYNAFLOW (Prevost 1981). Shown in Figure 2 is plan view of the finite element mesh used to model the representative profile developed for this study. The mesh was 1.8 m x 1.8 m in plan view, 12 m deep, and contained approximately 14,000 elements. The soil profile consisted of 6 meters of soft soil underlain by 6 m of relatively stiff material. Shear wave velocities of the soil in the upper and the lower 6 m of the profile were 150 m/s

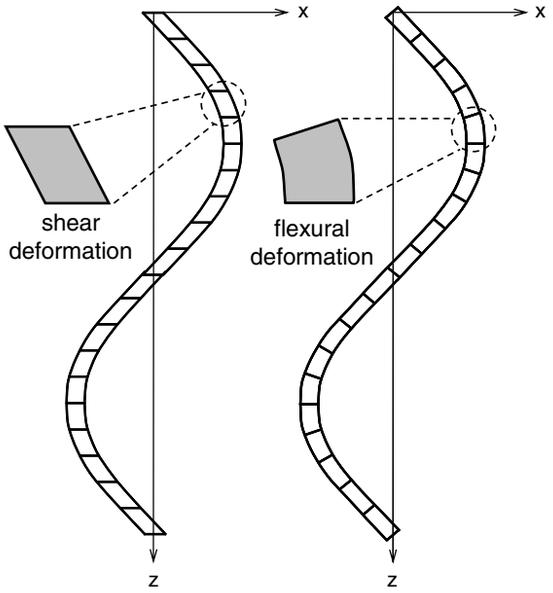


FIG. 1. Shear and flexural deformation modes of a column (Adapted from Goughnour and Pestana 1998).

and 250 m/s with unit weights of 16.7 kN/m^3 and 17.6 kN/m^3, respectively. The upper 6 m of the soil profile was reinforced with 6-m long columns, 90-cm in diameter with a 180 cm center-to-center spacing, corresponding to a spacing-to-diameter (S/D) ratio of 2 and an area replacement ratio of about 20%. This geometry and stiffness ratio is typical of stone-column reinforced ground. This representative profile was used for the benchmark analyses to understand the basic mechanisms of column behavior related to shear stress reduction. Subsequently, after the behavior was understood for this base case, key parameters such as column-to-soil stiffness ratio and column diameter were varied in an additional set of parametric analyses to show their effect on shear stress reduction. The analyses considered a linear elastic stress-strain relationship for the soil and the stiff column. Linear elastic modeling was preferred mainly due to its

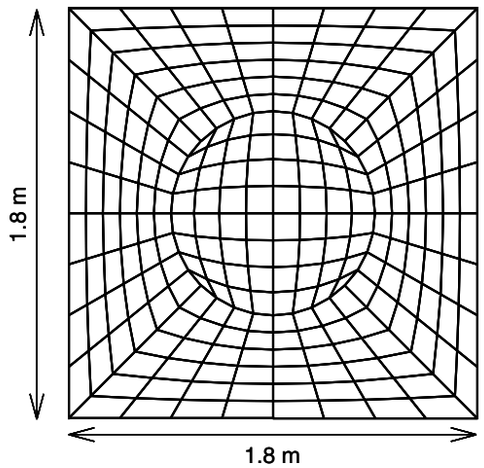


FIG. 2. Plan view of the finite element mesh used in the analyses

simplicity, and because the main issues we were concerned with for this particular study are sufficiently captured by linear behavior assumptions. Any further sophistication in modeling the material behavior probably would not have added to the findings. The analyses were performed with total stress analyses where pore pressure generation in the soil was not considered.

In terms of boundary conditions along the sides, the three-dimensional model was assumed to be surrounded by an infinitely repeating sequence of identical 1.8 m x 1.8 m reinforced soil sections. This was achieved by assigning the opposite nodes on each face of the model to be equivalent. By assigning nodal equivalency to node couples at the same elevation they share the same set of equations of motion, and therefore undergo the same motion in each direction. This equivalency imposes dynamic symmetry along each vertical face of the model, creating a repeating sequence in plan view. The model was shaken in two horizontal directions simultaneously. The EW and NS horizontal components of the strong ground motions recorded in Izmit (IZT station) during the 1999 Kocaeli Earthquake were used for this purpose.

Numerical Analysis Results

The mechanics of deformation and the interaction of the stiff column with the surrounding soil during shaking were of primary interest of the analytical study. Schematic of the deformed soil-column system during the dynamic analysis is shown in Figure 3. Shown is a simplified sketch of the two-dimensional planar section of the finite element mesh. As can be seen, the stiff column bends within the soft soil mass while the soil elements within the reinforced zone mainly deform in shear. Rotation of the column base causes additional shearing of the soil beneath as seen in the figure. A closer look at the modes of shear and flexural deformation is necessary to identify the mechanics of columnar behavior.

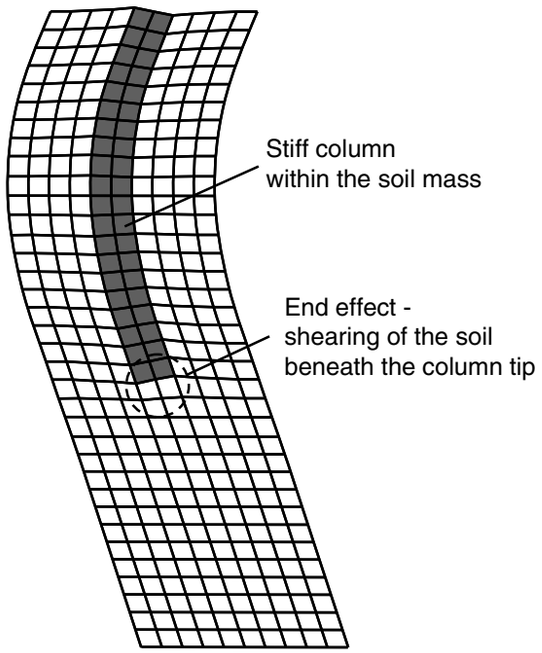


FIG. 3. Deformed shape of the soil-column system

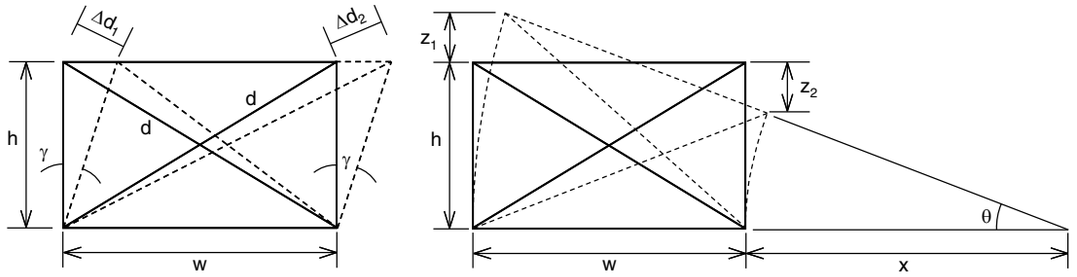


FIG. 4. Shear and flexural deformations - schematic

In our effort to understand the modes of deformation along the column we took sets of four quadrilateral points along the center of the model and investigated the shear and flexural deformations as illustrated in Figure 4. The shear deformation (γ) and flexural deformation (θ) were calculated using Equations (1) and (2) below along the height of the 6-m column, as well as the lower half of the model that was unreinforced.

$$\gamma = \frac{\gamma_L + \gamma_R}{2} \approx \frac{\Delta d_1 - \Delta d_2}{2} \cdot \frac{d}{h \cdot w} \qquad \text{shear deformation} \qquad (1)$$

$$\theta = \frac{z_2 - z_1}{w} \qquad \text{flexural deformation} \qquad (2)$$

The cumulative shear and flexural deformations were computed by integrating the absolute values of γ and θ over the course of shaking. Progression of shear and flexural deformations along both directions at three elevations along the column is shown in Figure 5. The relative magnitude of shear and flexural deformations throughout shaking remains unchanged as a constant ratio between the two parameters is maintained. As can be seen, near the top of the column at a depth of 1.1m, flexural deformation is considerable, about slightly more than half the shear deformation along both horizontal directions. The relative magnitude of flexural deformation in proportion to shear deformation is smaller at mid-depth and near the bottom end of the stiff column. The contribution of shear deformation with respect to the total of shear and flexural deformation is calculated along the length of the 6-m columns, and continuing along a vertical section through the underlying unreinforced soil down to a depth of 12 m. Shear deformation contribution is defined using Equation 3 below using the respective magnitudes shear (γ) and flexural (θ) deformations. Had the assumption of pure shear beam behavior that forms the basis of current design procedures held, we would expect the shear deformation contribution to be 100%.

$$\text{Shear deformation contribution}\,(\%) = \frac{\gamma}{\gamma + \theta} \cdot 100(\%) \qquad (3)$$

Calculated values of shear deformation contribution are shown in Figure 6 along the height of the finite element model. Contribution of shear deformation along the stiff column increases with depth, indicating it behaves more as a shear beam at deeper levels. Additionally, the contribution of shear deformation beneath the column below a ~1 m transition zone base quickly reaches 100% as expected. With the exception of

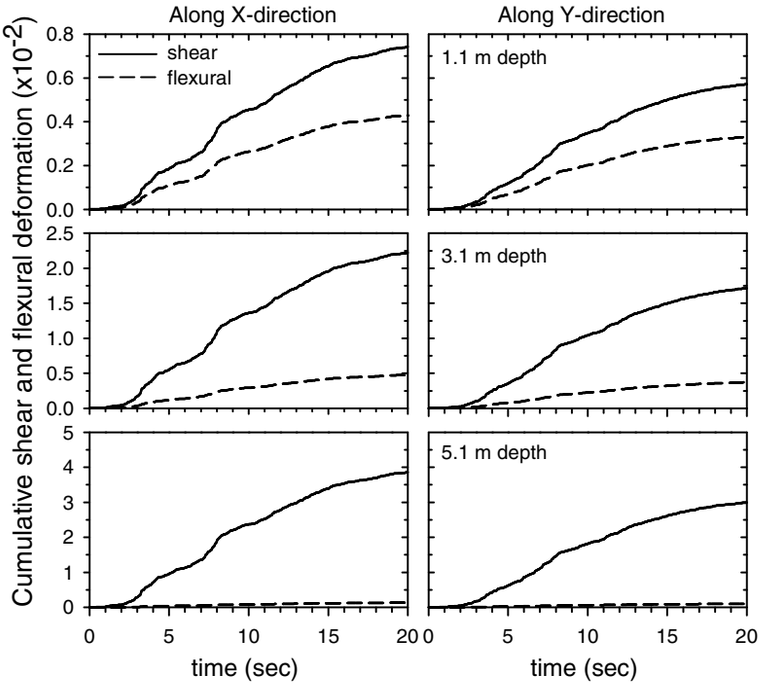


FIG. 5. Progression of shear and flexural deformations along the column

this transition zone, which we attribute to the end effects imposed by the 90 cm diameter column to the soil underneath, the unreinforced soil acts like a pure shear beam as expected.

These results indicate that for the considered geometry (90 cm diameter column with 180 cm center-to-center spacing) and column-to-soil stiffness ratio of 10, the stiff reinforcement element behaves differently than a pure shear beam which is the underlying assumption in the current design guidelines (Baez and Martin, 1994). We are primarily interested in the effects of such deviations on the stress transfer mechanisms of the soil-column system. Of practical concern is the effect of these unanticipated flexural deformations on the relative magnitudes of shear stresses carried by the soil and the stiff column. If pure shear behavior assumption held, we would expect the stiff column and the soil carry shear stresses in proportion to their stiffnesses. Even though the magnitudes of flexural deformations are small compared to the shear deformations for the stiffness ratio investigated, as presented below, even such small values of flexural deformation have significant implications in terms of the shear stresses carried by the stiff columns.

Average values of shear strain and shear stress within the column and the soil at each elevation are calculated and the maximum values of these average strains and stresses throughout shaking are plotted in Figure 7. As can be seen in plot (c), the stiff columns were not strained as hard as the soil around them – they experienced negligible shear strains, while peak strains in the reinforced soil mass approached 0.1%. If the stiff column behaved as a pure shear beam, the column and the soil would deform compatibly and would undergo the same magnitude of shear strains. However, as seen in plot (d), the stiff column on average is deforming 5 times less than the soil. The stiff

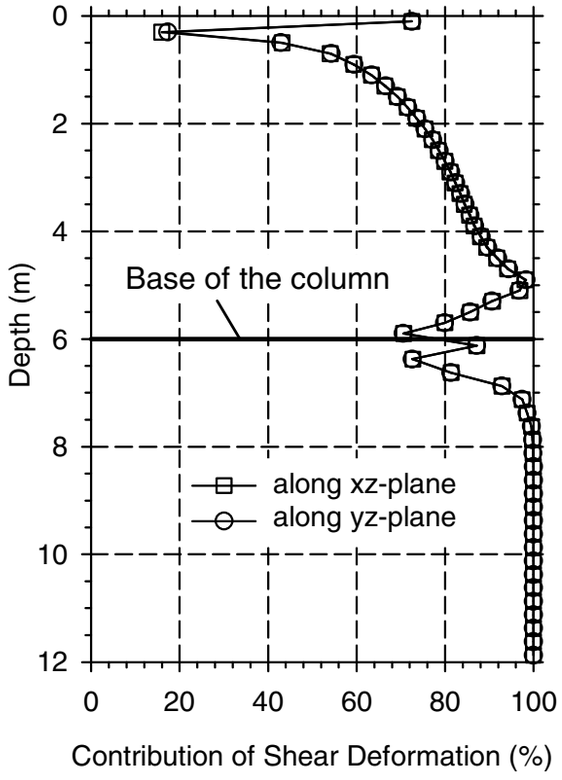


FIG. 6. Percent contribution of shear deformation along the center of the model

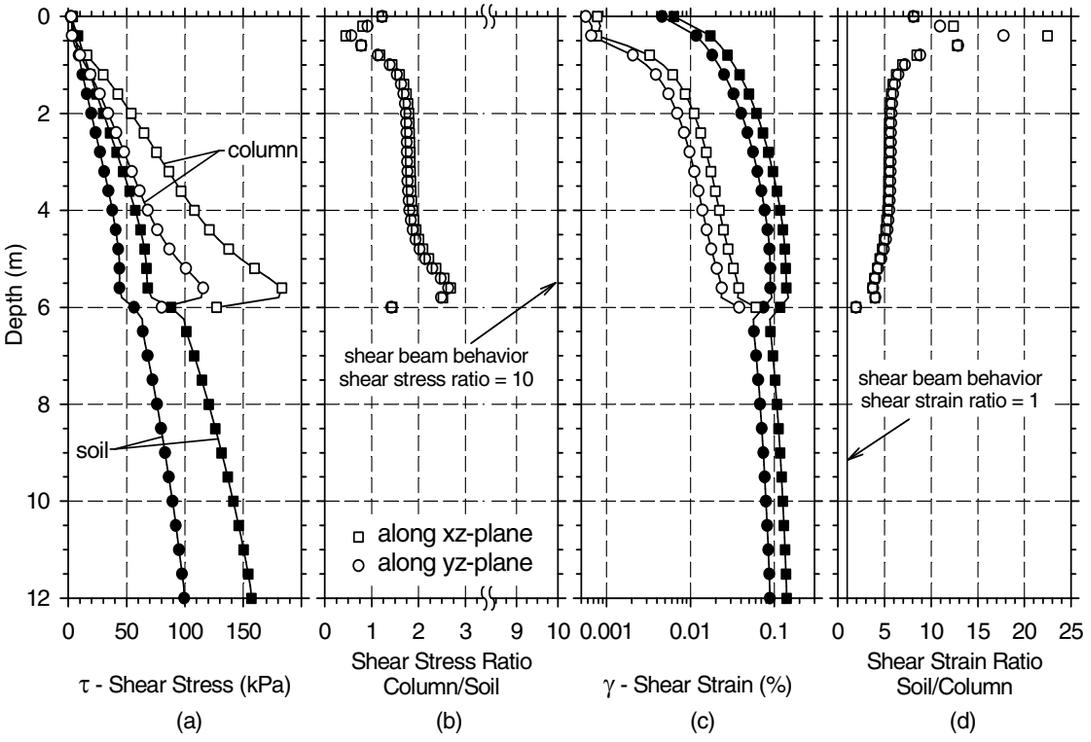


FIG. 7. Peak values of shear stresses and strains within the soil and the column

column is not being strained as hard as it would be strained as a pure shear beam. As a result, it is not attracting as much stress as anticipated by current design methods.

Predicted peak seismic shear stresses are shown in plot (a) in Figure 7. The peak stresses in the stiff columns (120-180 Pa) were consistently higher than those in the soil mass (50-70 kPa) in the reinforced zone, as would be expected because the columns are stiffer and attracted more load; however, they did not attract nearly enough shear stress to significantly reduce the shear stresses in the reinforced soil mass. The stiff columns picked up only a small percentage of the shear stresses implied by methods such as Baez and Martin (1994) that assume composite shear behavior. That is, if the basic assumptions behind the shear stress reduction for composite behavior were valid then the stiff column should have carried 10 times more shear stress than the soil. The peak value of seismic shear stress on the column is only about two-to-three times larger than the shear stress induced on the soil as seen in plot (b). In essence, one might say this behavior indicates that the column is not very "efficient" in reducing seismic shear stresses as anticipated by Baez and Martin (1994). This finding is consistent with results reported by Goughnour and Pestana (1998) based on their analysis of ground reinforced with stone columns. They also suggested that the columns should provide little, if any, shear stress reduction in most cases. The main implication is that commonly-used design approaches based on assumptions of composite behavior for ground reinforced with discrete columnar elements may greatly over-estimate seismic shear stress reduction.

The analyses suggest significant strain incompatibility between the soil and columns which were 10 times stiffer in shear relative to the soil. Such incompatibility was also evident in the deformed mesh shapes as shown earlier, which showed that the columns tended to flex back and forth within the soil profile and rotate at the ends during shaking rather than shearing along with the surrounding soil. As such, they clearly did not behave as shear beams as tacitly assumed. Therefore, even though the columns were much stiffer, they did not strain sufficiently in shear to attract a significant portion of the shear loading.

Parametric Analyses

After establishing and understanding basic column-soil behavior using the representative case above, we performed detailed parametric studies to better understand the effects of reinforcement-to-soil stiffness ratio and column diameter on seismic shear stress reduction. The results are summarized in the following figures. Contribution of shear deformation along the length of the column for a variety of stiffness ratios is presented in Figure 8. The graph is shown for stiffness ratios ranging from 2 to 200. (For reference, typical column-to-soil stiffness ratios for stone columns are about 5-10, and about 50-100 for soil-mix columns, and 100-150 for jet-grout columns). The case for the stiffness ratio of 10, shown with a dashed line, corresponds to the base case presented earlier. It is shown in the figure that as column stiffness increases, the column progressively behaves more as a flexural beam, and the contribution of shear deformation decreases. The column behavior consistently also changes with depth, having more shear beam behavior toward the bottom of columns, and more flexural behavior near the top.

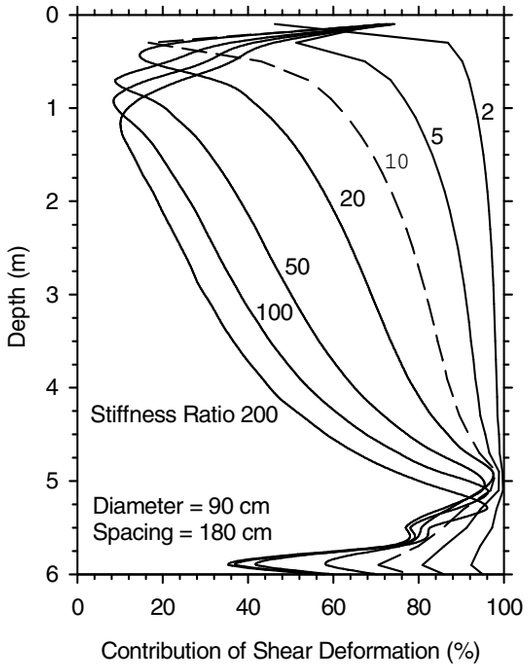


FIG. 8. Shear contribution for a series of stiffness ratios

As the contribution of shear deformation varies along the column length we computed the average percentage of shear deformation occurring in the columns, and plotted this versus column diameter and stiffness ratio in Figure 9. As shown, stiffness ratio has a significant effect for ratios less than about 20. In particular, for stiffness ratios of less than 5, the columns have more than 80% shear beam behavior, and exponentially approach 100% as the stiffness further decreases. As stiffness ratios increase, especially after about 20, increased stiffness ratio has little effect on shear deformation in the columns. Column diameter was found to have some effect on column behavior.

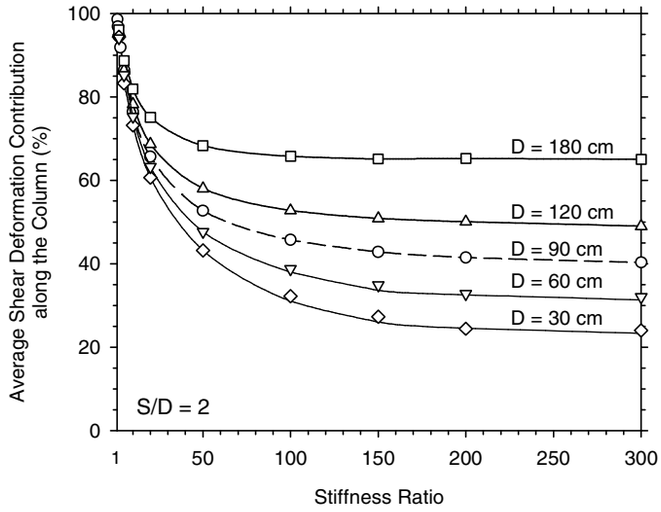


FIG. 9. Average shear contribution for a series of stiffness ratios and a variety of column diameters

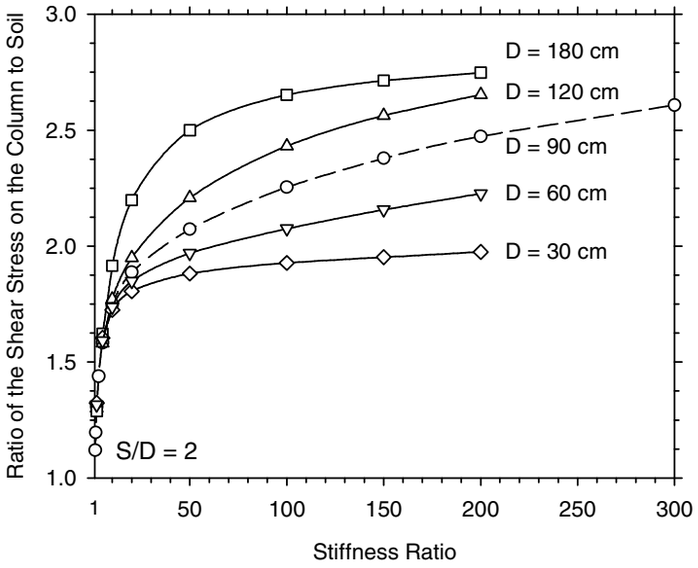


FIG. 10. Average column-to-soil stress ratio for a series of stiffness ratios and a variety of column diameters

For smaller columns in the range of 30 cm diameter, there was a maximum of 20% shear beam contribution for a range of stiffnesses. For larger columns of 180 cm diameter, there was at least 70%-80% shear beam behavior for most stiffnesses. This is consistent with what would be expected. An infinitely wide column would correspond to a pure shear beam, and thus larger diameter columns behave more like shear beams than smaller columns.

Because shear stress was the main interest, we computed the ratio of the average shear stress in the columns relative to the shear stress in the soil mass. We computed this ratio for various stiffnesses and column diameters. As shown in Figure 10, the column shear stresses are only up to about 2.5 times higher than those in the soil for a wide range of stiffnesses and column diameters. Only a modest amount of shear stress was attracted by the stiffer reinforcement. This is a key finding, because if pure shear beam behavior were occurring, the shear stresses in the stiff column relative to the soil mass would be in proportion to the column-to-soil stiffness ratio. In other words, the column which is 100 times stiffer than the soil (about typical of a soil-mix column in loose sand) would attract 100 times the stress carried by the soil if the column behaved as a pure shear beam and assumptions made by Baez and Martin (1994) were valid. However the results presented in this figure indicate that such a column would only carry 1.8 to 2.6 times the shear stress carried by the soil for the range of column diameters investigated.

CONCLUSIONS

Current methods used to predict seismic shear stress reduction in soils reinforced with columnar elements assume composite behavior. This implicitly assumes a shear mode of deformation of the columns as well as the soil. Three-dimensional dynamic finite element modeling using DYNAFLOW was performed for a 12-m deep soft soil profile

reinforced with stiff columnar elements. An S/D = 2 was assumed, along with a column diameter of 90 cm, a soil-to-stiffness ratio of 10, and column lengths of 6 m. These improvement geometries and stiffnesses are typical of stone-column reinforced ground. Analyses were first performed for this representative case to investigate the essential behavior. This was followed by parametric analyses to show the effects of column diameter and column-to-soil stiffness ratio.

The deformation behavior of the columnar elements is more complicated than thought. The columns deform in a combination of both shear and flexure during seismic loading. The net effect is that stiff columns typically achieve only a small percentage of the shear stress reduction implied by area-replacement ratio methods, such as Baez and Martin (1994) that assume composite behavior for reinforced ground. Parametric analyses show that as the column-to-soil stiffness ratio increases, the tendency for flexural deformation of the columns increases, and thus the shear contribution of the columns becomes less. The "efficiency" of the columns to behave as shear beams and produce shear stress reduction decreases with increasing column stiffness.

For the spacings (i.e., S/D=2), diameters, and column-to-soil stiffnesses ratios seen in most common field situations, such as for stone columns and jet-grout columns, there is relatively little shear stress reduction achieved in the soil mass. Commonly-used design approaches based on assumptions of composite behavior for ground reinforced may greatly over-estimate the actual level of seismic improvement in terms of shear stress reduction.

REFERENCES

Baez, J.I. and Martin, G.R. (1994). "Advances in the Design of Vibro Systems for the Improvement of Liquefaction Resistance," The 2nd Seismic Short Course on Evaluation and Mitigation of Earthquake Induced Liquefaction Hazards, *Division of Engineering, San Francisco State University and Department of Civil Engineering University of Southern California*, Los Angeles and San Francisco.

Goughnour, R.R., and Pestana, J. M. (1998) "Mechanical Behavior of Stone Columns Under Seismic Loading," *Proceedings, 2nd International Conference on Ground Improvement Techniques*, October 1998, Singapore, pp. 157-162.

Martin, J.R., and Olgun, C.G. (2007) "Liquefaction Mitigation Using Jet-Grout Columns – 1999 Kocaeli Earthquake Case History And Numerical Modeling," 4th International Conference on Earthquake Geotechnical Engineering, Paper ID: 1273, Thessaloniki, Greece, June 2007.

Prevost, J.H. (1981) "DYNAFLOW: A Nonlinear Transient Finite Element Analysis Program," Technical Report, Department of Civil Engineering and Operations Research, *Princeton University*, Princeton, New Jersey.

Priebe, H.J. (1995). "The Design of Vibro Replacement." *Ground Engineering*, December, pp. 31-37.

This page intentionally left blank

Relations between Penetration Resistance and Cyclic Strength to Liquefaction as Affected by K_C-conditions

Kenji Harada[1], Kenji Ishihara[2], Rolando P. Orense[3], M. ASCE, P.E., and Jun Mukai[4]

[1]General Manager, Research and Engineering Department, Fudo Tetra Corporation, 6-1, Nihonbashi-Koami-cho Chuo-ku, Tokyo, 103-8543, Japan kenji.harada@fudotetra.co.jp
[2]Professor, Department of Civil Engineering, Chuo University, 1-13-27 Kasuga, Bunkyo-ku, Tokyo 112-8551, Japan ishihara.kenji@kiso.co.jp
[3]Senior Lecturer, Department of Civil and Environmental Engineering, University of Auckland, Private Bag 92019, Auckland, New Zealand r.orense@auckland.ac.nz
[4]Senior Engineer, Fudo Construction Inc., 2555 Flores St., Suite 490, San Mateo, CA U.S.A jun@fudo-const.com

ABSTRACT: The effectiveness of ground improvement by the sand compaction pile (SCP) method is generally evaluated through penetration resistances, such as cone resistance (q_c) and *N*-values of the standard penetration test (SPT), measured at the center point in-between piles before and after the pile installation. However, it is known that the penetration resistance of the ground adjacent to piles does not only increase, but the lateral stress increases as well, resulting in increase in the resistance to liquefaction. Therefore, in order to evaluate the effectiveness of the ground improvement on compacted soils, it is necessary to quantify the effect of K_C-values on the penetration resistance and the resistance to liquefaction. In this paper, based on the results of SPT and CPT performed in chamber box in the laboratory, the relationships between penetration resistance, resistance to liquefaction and relative density were re-examined, and the influence of K_C was investigated. Although the results indicated that generally the resistance to liquefaction increases with increasing K_C-value, little difference was noted when the density of the deposit was high. Based on the results, recommended charts incorporating the effect of K_C were proposed.

1. INTRODUCTION

In practice, it has been customary to evaluate the resistance to liquefaction or the liquefaction strength of ground through the penetration resistance obtained using standard penetration tests (SPT) or cone penetration tests (CPT). In North America, this type of relation has been established by correlating the penetration resistance with the field liquefaction behavior during past earthquakes. (e.g., Youd and Idriss, 2001). In compiling the field performance data as to whether a given deposit has or has not

developed liquefaction, the looseness or denseness of the in-situ deposit was judged via the SPT conducted nearby. Since the SPT was conducted at natural deposits which were not compacted, it may be assumed that the K_C-values at these sites would have been nearly equal to 0.40-0.50. In Japan, on the other hand, the penetration resistance was correlated with the liquefaction strength obtained from the triaxial tests on high-quality undisturbed samples (e.g., JRA, 1996; AIJ, 2001). In expressing the cyclic strength for the design formula, the test results were corrected for the condition of K_C=0.5. Thus, the formulations in U.S. and Japan are both considered applicable to natural or uncompacted reclaimed sand deposits with the lateral stress conditions of about K_C=0.5.

Sand compaction pile (SCP) method is one of the popular methods for improving grounds to resist against liquefaction. This involves the installation of well-compacted sand piles of large diameters through the process of repeated driving down and extracting motion of a vibrating steel pipe. As the sand pile is compacted and enlarged, the adjacent ground is pushed laterally and compacted, resulting in increase in the density of the ground. The effectiveness of ground improvement is usually evaluated by the increase in the penetration resistance at the center-point between the sand piles, which mainly reflects the increase in density of the ground. However, it is also known that the pile installation and the associated pile enlargement during SCP operation result in increased lateral stress; therefore, it is also important to investigate the effect of K_C-values on the liquefaction strength of the ground.

Unfortunately, it is difficult to explicitly investigate the effects of the K_C-conditions on the relation between penetration resistance and relative density for natural ground. Thus, there is no alternative way to investigate this aspect except by relying on the results of chamber tests in the laboratory. Thus, an attempt is made in the present study to seek such relations by compiling the outcome of the chamber tests that have been reported so far where the effect of K_C-conditions was examined explicitly. The study in this context was made and presented in a previous paper by Ishihara and Harada (2008). The present paper is intended to illustrate the more generalized concept and procedures to take into account the effects of K_C-condition, based on the empirical correlations proposed plus some new test data.

2. BASIC METHODOLOGY

The methodology adopted in this study is based on the concepts and a series of steps as described below.

(1) The relation between the resistance to liquefaction or cyclic strength R_ℓ and the penetration resistance of SPT N_1-value or q_{c1}-value of cone penetration tests have been proposed and used both in Japan and in North America. These are based on a number of laboratory tests and field performance data during past earthquakes and therefore they will be used here as a seminal basis of further study to examine the effects of K_C-conditions. It will be assumed with good reasons as mentioned above that all the relations between R_ℓ and N_1 or q_{c1} both in Japan and North America are applicable for the deposits consolidated under K_C=0.5 condition, where N_1 and q_{c1} refer to the penetration resistance normalized to an effective overburden pressure of

σ'_v=1 kgf/cm^2. It is to be noticed that in all these relations, the cyclic strength R_ℓ is directly related to N_1 or q_{c1} values, and that the R_ℓ-N_1 relation and the R_ℓ-q_{c1} relation have been addressed with reference to the relative density, D_r.

(2) In all of the chamber tests ever reported, the relative density D_r was utilized to express the state of looseness or denseness of the sand used in the tests. The tests were conducted by controlling the K_C-value. Then, the q_{c1} or N_1 values of the penetration resistance were expressed in terms of the relative density and K_C-value.

(3) Thus, in order to examine the influence of K_C-conditions on the relations between R_ℓ and N_1 or q_{c1}, it was necessary, first of all, to express both R_ℓ and N_1 or q_{c1} value as a function of the relative density for K_C=0.5 condition. The study of this context was made first as presented in this paper.

(4) In the final steps, the effects of K_C-conditions on the cyclic strength R_ℓ and N_1 or q_{c1} need to be known. There is a relation reported for the K_C-effects on cyclic strength as reported by Ishihara and Takatsu (1979). Also there are relations correlating q_{c1} under K_C=0.5 with those under different K_C-conditions. These will be used to eliminate the influence of relative density and to derive final results for each of the Japan- and U.S.-proposed correlations between R_ℓ and N_1 or q_{c1}.

3. PENETRATION RESISTANCE AND RELATIVE DENSITY RELATION

In this section, the relation between penetration resistance and relative density is discussed. Note that in these cases, K_C=0.5 is tacitly assumed. Firstly, considering various types of soils, Cubrinovski and Ishihara (1999) proposed a relation between the mean grain size, D_{50}, and the void ratio range, e_{max}-e_{min}, as shown below, where e_{max} and e_{min} are the maximum and minimum void ratios, respectively.

$$e_{\max} - e_{\min} = 0.23 + \frac{0.06}{D_{50}} \tag{1}$$

In the analysis presented herein, only the results for clean sands are considered, and the sands are classified roughly as being either fine sand or coarse sand. For fine sand, the mean grain diameter will be taken as D_{50}=0.2~0.3 mm with e_{max}-e_{min}=0.4~0.5 (average=0.45) while values of D_{50}=0.3~0.5 mm and e_{max}-e_{min}=0.35~0.4 (average= 0.375) will be assumed for coarse sand.

3.1 Corrected *N*-value and Relative Density

Several researchers have investigated the relation between SPT *N*-value and relative density, D_r. Among these, the data compiled by Fujita (1968) are considered most comprehensive and these are shown in Fig. 1(a). Additional data points are plotted from the results of chamber tests conducted by Yoshida et al. (1988), Yasuda et al. (1996) and other investigators. In the figure, N_1 value is the corrected SPT *N*-value for an effective overburden pressure, σ'_v=1 kgf/cm^2 by way of the formula $N_1 = 1.7N/(0.7+\sigma'_v)$. Since all the data were obtained from chamber tests, the energy transfer ratio in the

hammer dropping is considered approximately equal and assumed as 80%. Thus the blow count number is indicated as $(N_1)_{80}$. Note that both fine and coarse sands are included in the figure, as well as saturated and dry/wet soils. It may be observed that a linear relation can be roughly established between $(N_1)_{80}$ and the square of D_r expressed as a ratio, not a percentage, with fine and dry sands showing higher gradients than coarse sands and dry/wet samples. It is to be recalled that the linearity between N_1 and D_r^2 is consistent with the relation of $N_1=40D_r^2$, proposed by Meyerhof (1957).

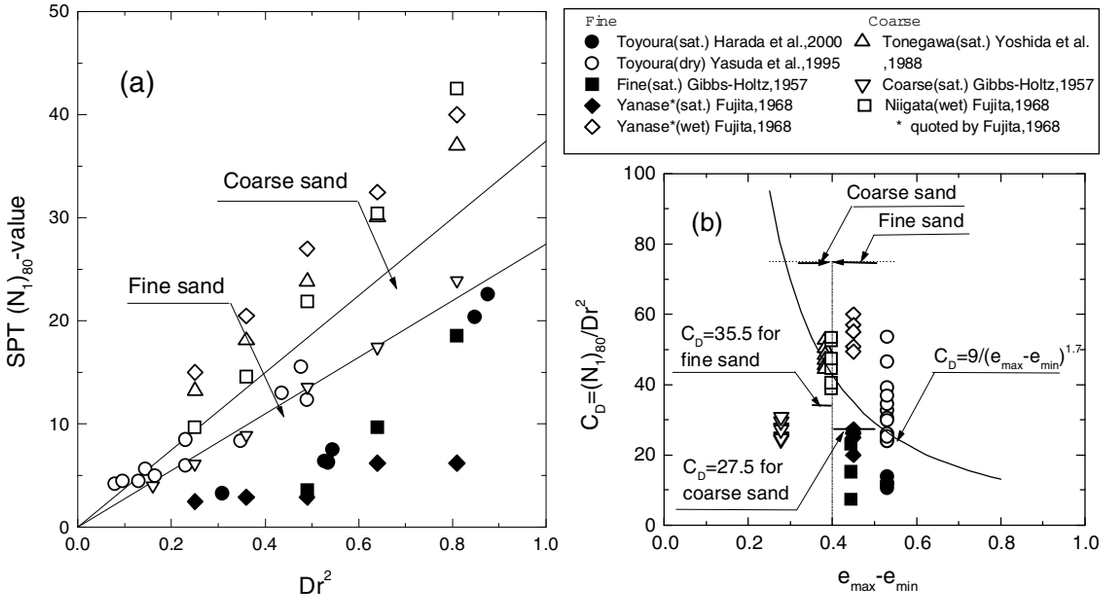


FIG 1. (a) Relationship between SPT $(N_1)_{80}$-value and relative density, D_r; and (b) Relationship between $(N_1)_{80}/D_r^2$ and void ratio range

Next, the slope of a straight line connecting the zero point and each of the data point in Fig. 1(a) is read off and plotted versus the value of e_{max}-e_{min} for each of the sands used in the chamber tests. This slope, as indicated by $C_D = (N_1)_{80} / D_r^{\,2}$, is shown in the ordinate of Fig. 1(b). The solid curve in Fig. 1(b) is the average of the data points compiled by Cubrinovski and Ishihara (1999). It can be observed that although the data points for saturated and dry/wet samples show different trends, all the data points may be represented roughly by the following expression as proposed by Cubrinovski and Ishihara (1999):

$$\left(N_1\right)_{80} = C_D \cdot D_r^{\,2} = \frac{9}{\left(e_{\max} - e_{\min}\right)^{1.7}} \cdot D_r^{\,2} = \frac{9}{\left(0.23 + \dfrac{0.06}{D_{50}}\right)^{1.7}} \cdot D_r^{\,2} \qquad (2)$$

where the relation of Eq. (1) is used to account for the gradation effects of each sand. It can be seen in Fig. 1(b) that there are considerable scatters in the data points but, for practical purposes, the values of C_D may be taken roughly as 27.5 and 35.5 for fine and coarse sands, respectively.

3. 2 Corrected q_c-value and Relative Density

Similar to that performed for SPT *N*-values, the data of cone resistance corrected for an effective overburden pressure, σ'_v=1 kgf/cm^2 with the equation $q_{c1} = q_c / \sqrt{\sigma'_v}$ are shown in Fig. 2(a) versus D_r^2. These were obtained from various test results (Jamiolkowski et al., 1988; Huang and Hsu, 2005). All the data points indicated in the figure are for dry samples. Note that unlike the case shown in Fig. 1(a), there is no significant difference between the trends for fine sands and coarse sands. The relation between the slope of this plot (q_{c1}/D_r^2) and the void ratio range similarly established is shown in Fig. 2(b). For each of the data points, it may be seen that the effect of grain diameter is insignificant. Thus, similar to the empirical equation of Eq. (2), the relation between q_{c1} and D_r may be expressed as follows:

$$q_{c1} = C_{Dq} \cdot D_r^{\,2} = \frac{12}{\left(e_{\max} - e_{\min}\right)^{0.8}} \cdot D_r^{\,2} = \frac{12}{\left(0.23 + \dfrac{0.06}{D_{50}}\right)^{0.8}} \cdot D_r^{\,2} \qquad (3)$$

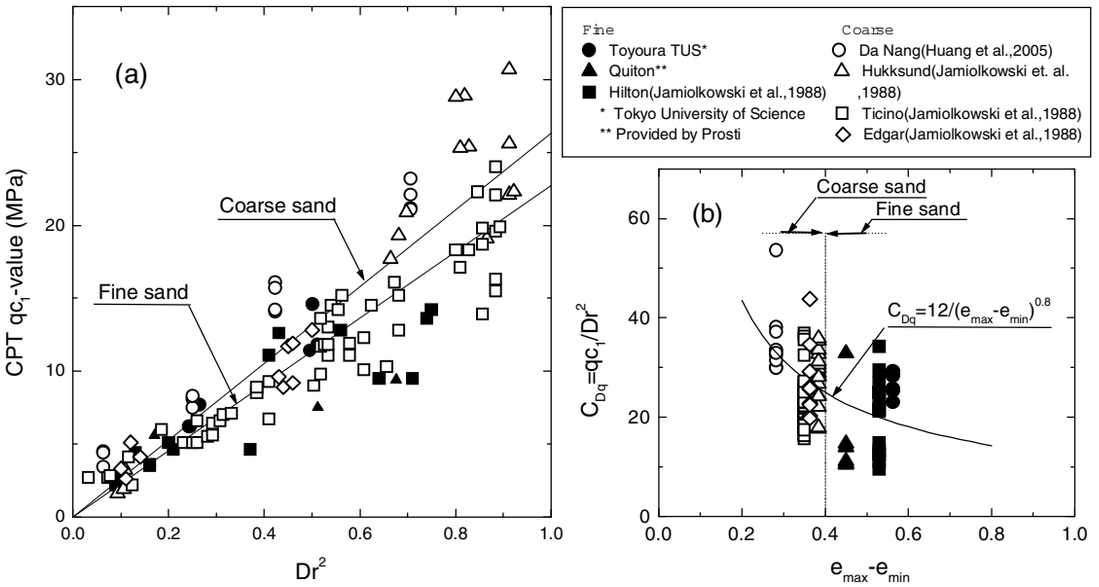


FIG 2. (a) Relationship between q_{c1}-value and relative density, D_r; and (b) Relationship between q_{c1}/D_r^2 and void ratio range

It is to be noted that there are relations of the form D_r versus log q_{c1} proposed by Jamiolkowski et al. (1988), but the form of Eq. (3) will be used instead in this study.

4. LIQUEFACTION STRENGTH AND RELATIVE DENSITY RELATION

4.1 Liquefaction Strength and Relative Density Relation through Corrected *N*-value

In the formula incorporated in the Japanese code, the basic cyclic strength, R_ℓ, is expressed as a function of SPT $(N_1)_{80}$-value as follows (JRA, 1996).

$$R_\ell = \begin{cases} 0.0882\sqrt{(N_1)_{80}/1.7} & \text{for } (N_1)_{80} < 14 \\ 0.0882\sqrt{(N_1)_{80}/1.7} + 1.6\times10^{-6}((N_1)_{80}-14)^{4.5} & \text{for } (N_1)_{80} \geq 14 \end{cases} \quad (4)$$

In terms of the cyclic resistance ratio (*CRR*) which is commonly used in North America, the basic cyclic strength can also be expressed as (Youd and Idriss, 2001):

$$R_\ell = \frac{CRR}{0.65} = \frac{1}{0.65}\left[\frac{1}{34-(N_1)_{60}} + \frac{(N_1)_{60}}{135} + \frac{50}{[10-(N_1)_{60}+45]^2} - \frac{1}{200}\right] \quad (5)$$

Note that in the above equation, which is valid for $(N_1)_{60}$<30, an approximate relation $(N_1)_{80}$=1.3$(N_1)_{60}$ can be incorporated to correct for the difference in energy transfer between the Japanese and American SPT practice. Moreover, the correcting factor 0.65 entering Eq. (5) was used to take into account the fact that the liquefaction strength in Japanese code is expressed in terms of the maximum value of acceleration, while the average value of acceleration during seismic shaking is used in American practice.

The relation between $(N_1)_{80}$ and D_r, given by Eq. (2), is substituted into Eq. (4) to obtain the relation between R_ℓ and D_r. The plots thus obtained from Eq. (4) are displayed in Fig. 3(a) corresponding to fine sand and coarse sand for the Japanese code. Similar plots can be obtained from Eq. (5), but they are not shown here. It can be observed in Fig. 3(a) that the cyclic strength shows sudden increase when the relative density is greater than about D_r=90% for fine sand and when D_r is larger than 80% for coarse sand.

4.2 Liquefaction Strength and Relative Density Relation through Corrected q_c-value

In similar vein, the formula for the basic cyclic strength, R_ℓ, as a function of q_{c1}-value as proposed by Suzuki and Tokimatsu (2003) is expressed as follows,

$$R_\ell = \frac{1}{0.65}\frac{\tau_\ell}{\sigma_o'} = \frac{1}{0.65}\left\{0.45\times0.57\times\left[\frac{16\sqrt{N_c}}{100} + \left(\frac{16\sqrt{N_c}}{83.7}\right)^{14}\right]\right\} \quad (6)$$

where $$N_c = \begin{cases} 0.341 I_c^{\,1.94}(q_{c1}-0.2)^{1.34-0.0927 I_c} & q_{c1} > 0.2\,\text{MPa} \\ 0 & q_{c1} \leq 0.2\,\text{MPa} \end{cases}$$

On the other hand, the relation between R_ℓ and q_{c1} based on North American practice is given by Robertson and Wride (1998). When expressed in SI units, the curve can be approximated by the following equations:

$$R_\ell = \frac{CRR}{0.65} = \begin{cases} 0.0134(q_{c1}) + 0.077 & \text{for } q_{c1} < 4.8\,\text{MPa} \\ 1.63\times10^{-4}(q_{c1})^3 + 0.123 & \text{for } 4.8 \leq q_{c1} < 15.3\,\text{MPa} \end{cases} \quad (7)$$

Similarly, the relation between q_{c1} value and D_r given by Eq. (3) is substituted into Eqs. (6) and (7) to obtain the relation between R_ℓ and D_r. The plots thus obtained from Eq. (7) are shown in Fig. 3(b) for fine and coarse sands. The relation from Eq. (6) can be similarly obtained, but not shown here. It is seen in Fig. 3(b) that the cyclic strength shows sudden increase when the density exceeds D_r=60% for both fine and coarse sands.

As there is not much difference between the curves for fine and coarse sands in both figures, the average curves shown by the solid lines in Fig. 3 will be adopted hereafter.

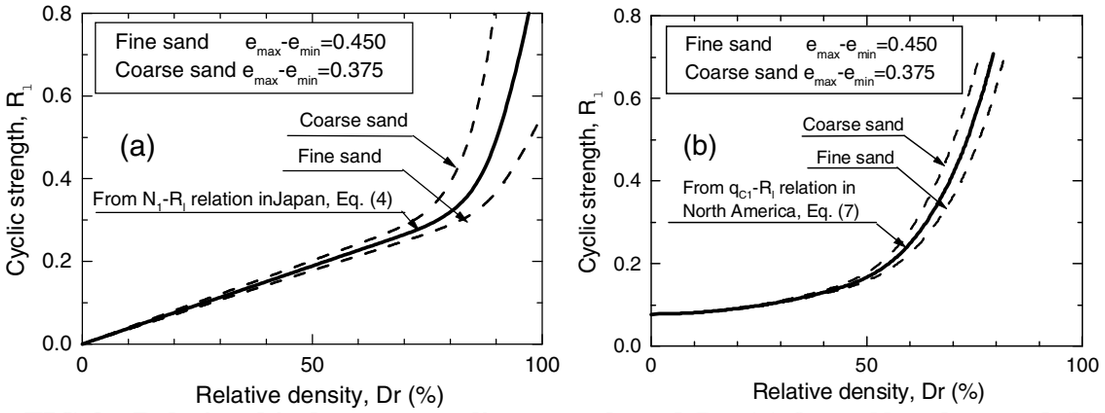


FIG 3. Relationship between cyclic strength and D_r: (a) from N_1 value; and (b) from q_{c1} value

5. EFFECT OF K_C ON PENETRATION RESISTANCE AND LIQUEFACTION STRENGTH

5.1 Effect of K_C on Penetration Resistance

(a) K_C-effect on SPT

There has been no data ever reported in the literature on the effects of K_C-conditions on SPT N-values, except for the recent data obtained at the Tokyo Denki University. These data are shown in Fig. 4(a) in terms of C_{SPH} defined as the increase in standard penetration resistance associated with increase in K_C value, i.e., $C_{SPH}=(N_1)_{KC}/(N_1)_{KC=0.5}$ which is plotted versus the relative density. One set of data pertains to the values of C_{SPH} when K_C was increased from 0.5 to 1.0 and another set was for the case of K_C=0.5 to 1.5. From the data, the following relation given by Eq. (8) is proposed. This relation is shown by the lines in Fig. 4(a). Note that these lines were drawn to best-fit the data points for denser state of saturated Toyoura sand in Fig. 1(a).

$$C_{SPH}=\left(\frac{K_C}{K_{C,NC}}\right)^{0.80-0.75(D_r/100)} \tag{8}$$

(b) K_C-effect on CPT

Various relations have been proposed based on the chamber test results indicating the effect of K_C on the q_c-values of CPT. These are as follows:

$$C_{CPH} = \sqrt{\frac{K_C}{K_{C,NC}}} \qquad \text{(Salgado, 1997)} \qquad (9)$$

$$C_{CPH} = \sqrt{\frac{1+2K_C}{1+2K_{C,NC}}} \qquad \text{(Jamiolkowski et al., 1988; Huang \& Hsu, 2005)} \qquad (10)$$

$$C_{CPH} = \left(\frac{K_C}{K_{C,NC}}\right)^{0.7066-0.5208(D_r/100)} \qquad \text{(Boulanger, 2003)} \qquad (11)$$

where C_{CPH} indicates the increase in cone penetration resistance associated with an increase in K_C-value, i.e., $C_{CPH} = (q_{c1})_{KC}/(q_{c1})_{KC=0.5}$. The subscript *NC* represents normally consolidated condition (i.e., K_C=0.5). Eqs. (9) and (10) indicate constant values for any changes in the value of K_C irrespective of the relative density. However, Eq. (11) indicates that the parameter C_{CPH} tends to decrease with increasing relative density, which appear more reasonable in the light of the results of recent tests.

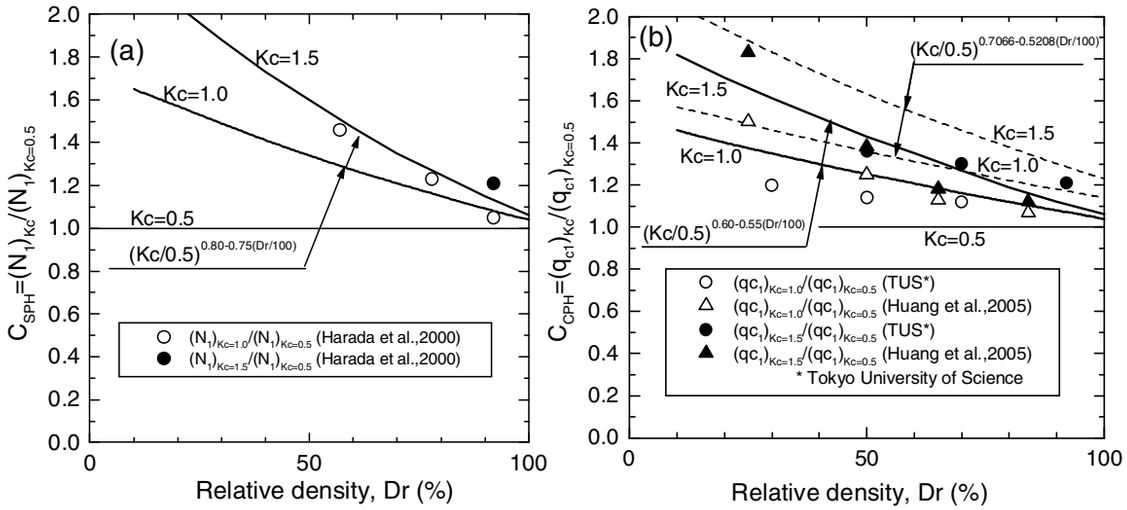


FIG 4. Relation between relative density and increase in penetration resistance

The values of C_{CPH} as given by Eq. (11) are plotted against relative density in Fig. 4(b) by dashed lines. Also plotted in the same figures are the data obtained from the recent chamber tests at the Tokyo University of Science and at Chao Tung University in Taiwan. It can be seen that for q_{c1}, the rate of increase in penetration resistance tends to decrease with increase in D_r. Looking over the new data together with the trends given by Eq. (11), it might be possible to draw new lines as shown by solid lines in Fig. 4(b). This is expressed by

$$C_{CPH} = \left(\frac{K_C}{K_{C,NC}} \right)^{0.60-0.55(D_r/100)} \tag{12}$$

5.2 Effect of K_C on Liquefaction Strength

Ishihara and Takatsu (1979) have shown that the effect of K_C on liquefaction strength can be expressed as follows:

$$\frac{R_\ell}{R_{\ell,NC}} = \frac{1+2K_C}{1+2K_{C,NC}} \tag{13}$$

By applying Eq. (13) on the average curves of the liquefaction strength - relative density relations for fine and coarse sands (see Fig. 3), which can be considered as the reference curves (K_C =0.5), the effects of K_C on R_ℓ can be obtained, as shown in Fig. 5, for example.

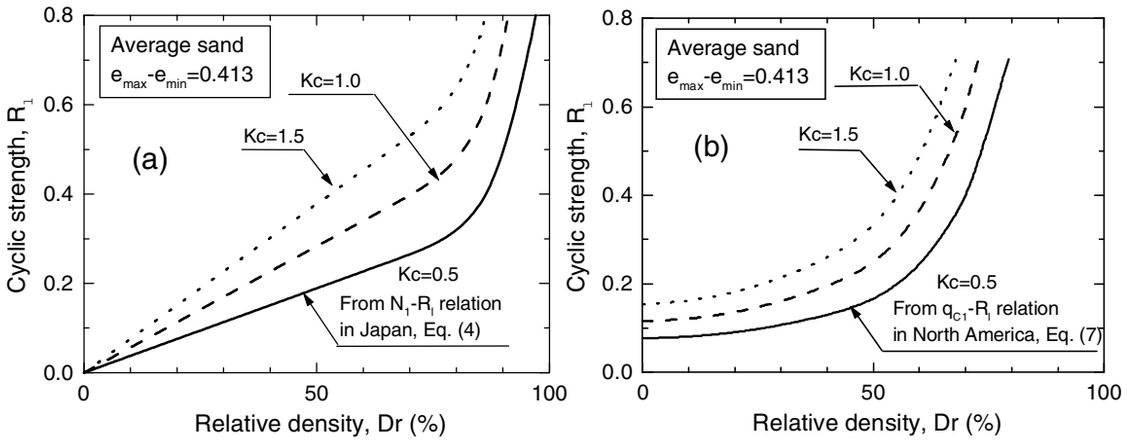


FIG 5. Effect of K_C on liquefaction strength: (a) from Eq. (4); and (b) from Eq. (7)

6. RELATION BETWEEN PENETRATION RESISTANCE AND CYCLIC STRENGTH TO LIQUEFACTION

As mentioned in Sections 3 and 4, it was possible to establish the basic relation between penetration resistance and liquefaction strength at K_C=0.5 using relative density. Moreover, the effects of K_C on penetration resistance and on liquefaction strength have been discussed in Section 5. Therefore, the relation between penetration resistance and liquefaction strength for different K_C-values can now be established. The liquefaction strength curves expressed in terms of K_C values can be formulated by substituting Eqs. (8) and (13) into Eqs. (4) and (5) for N_1 values, and Eqs. (12) and (13) into Eqs. (6) and (7) for q_{c1} values. The plots thus obtained are shown in Figs. 6 and 7, respectively. It can be seen from the figures that as K_C increases, the liquefaction strength also increases. It may also be seen that all the curves generally tend to merge to be a curve close to each other at large values of penetration resistance, indicating that the effect of K_C tends to decrease in denser deposits.

To explain this tendency, schematic diagrams showing the effect of K_C on the relation between liquefaction strength and penetration resistance are shown in Figs. 8(a) and 8(b) for deposits with low and high penetration resistance, respectively. Suppose the penetration resistance is increased from a value at point *a* to point *b* while keeping K_C=0.5, the cyclic resistance R_ℓ is increased from point *b* to *e*. If the K_C-value is increased, then additional increase in R_ℓ is expected as indicated by the shift from point *e* to *d*. It can also be observed that the gradient of the liquefaction curve at point *a* for K_C=0.5 is smaller than the gradient due to combined increase in K_C and N_1 or q_{c1} (point *a* to *d*). Hence, the liquefaction curve is shifted upwards.

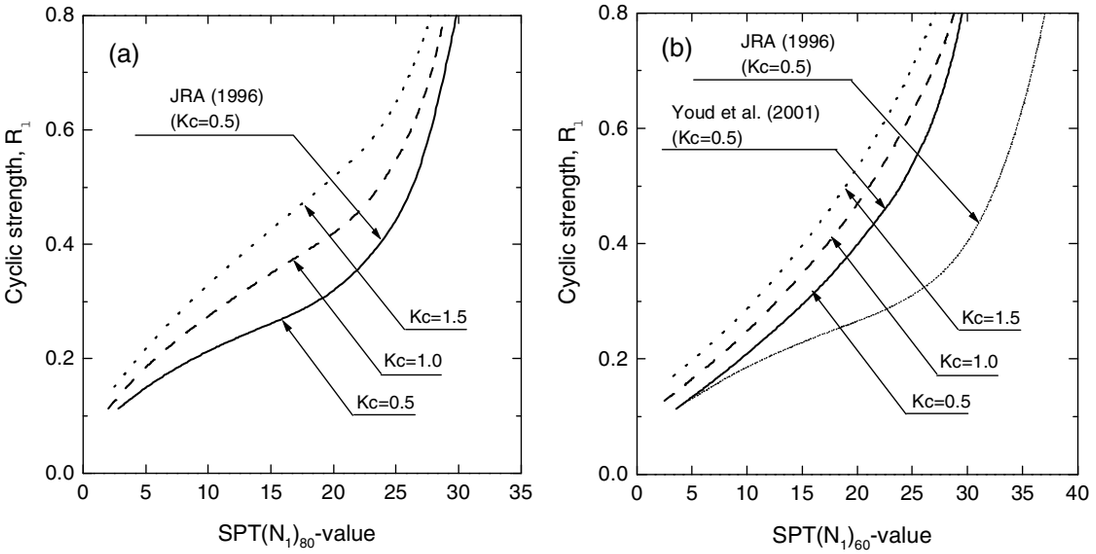


FIG 6. Recommended chart correlating corrected *N* value and liquefaction strength through K_C (Based on Eqs. (4) and (5))

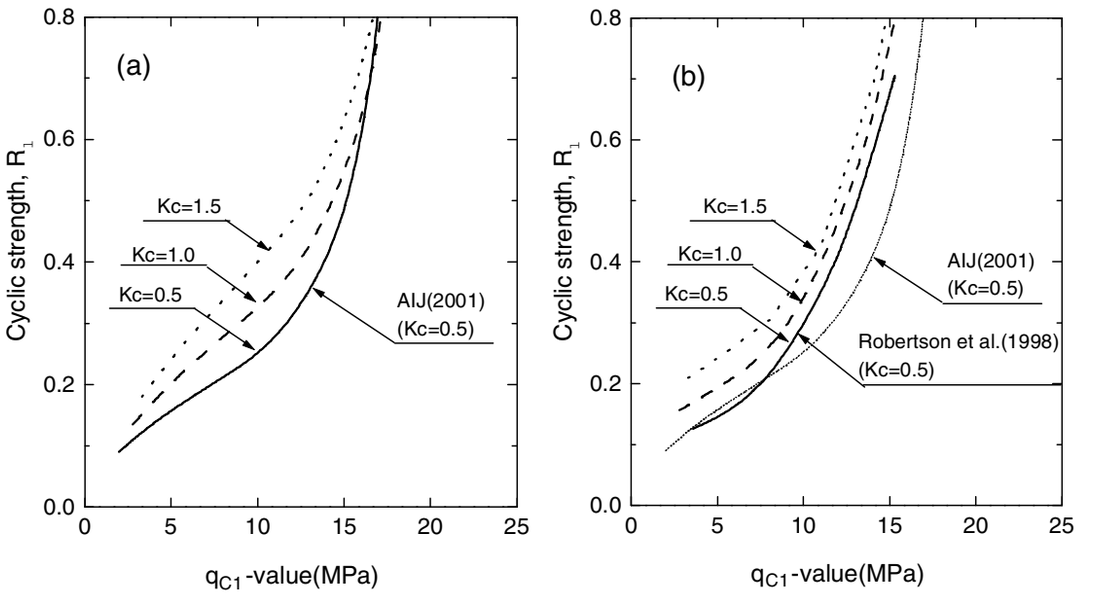


FIG 7. Recommended chart correlating corrected q_c value and liquefaction strength through K_C (Based on Eqs. (6) and (7))

When the ground has low penetration resistance (loose deposit), the gradient due to increase in K_C is much greater than the gradient coming from the density increase alone. This indicates that the effect of K_C on R_ℓ is more significant than the effect of penetration resistance for a loose state of deposits as shown in Fig. 8(a). On the other hand, when the ground has high penetration resistance (dense deposit), the gradient of the liquefaction curve for K_C=0.5 is generally high, indicating that the effect of penetration resistance is much more significant than the effect of K_C as illustrated in Fig. 8(b).Thus, it can be said that with increasing K_C-value, the liquefaction strength increases, but its effect becomes smaller at higher density.

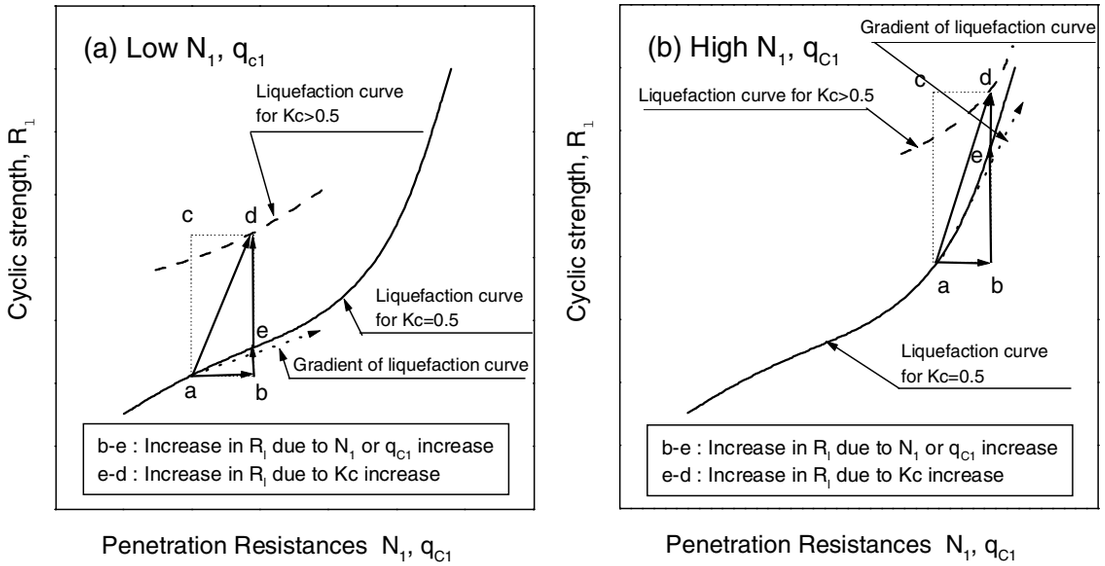


FIG 8. Schematic diagram showing the effect of K_C on penetration resistance and liquefaction strength

7. CONCLUDING REMARKS

In order to examine the effects of K_C on the penetration resistances and liquefaction strengths of grounds improved by compaction method, experimental data from chamber tests with controlled K_C values were compiled and arranged. From the curves relating penetration resistances (N_1 and q_{c1}) and relative density, as well as those relating liquefaction strengths and relative density, charts were formulated showing the relation between liquefaction strengths and penetration resistances as functions of K_C-values. Thus, the methodology presented herein can incorporate the effects of K_C-values on the relations between penetration resistance and liquefaction strengths. These charts can be used to quantify the effects of increase in lateral stress on the liquefaction strength of grounds improved by sand compaction pile method.

REFERENCES

Architectural Institute of Japan, AIJ. (2001) *Recommendations for Design of Building Foundations*, p.65.

Boulanger, R. W. (2003). "High overburden stress effects in liquefaction analysis," *J. Geot Eng, ASCE,* 129 (12), 1071-1082.

Cubrinovski, M. and Ishihara, K. (1999). "Empirical correlation between SPT N-value and relative density for sandy soils," *Soils and Found.*, 39 (5), 61-71.

Fujita, K. (1968). "Standard penetration test," *Interpretation of Soil Investigation Test Results and Example Application*, JSSMFE, 29-76 (in Japanese).

Harada, K., Yasuda, S., Yamamoto, M., Arai, D. and Uda, M. (2000). "Influence of earth pressure coefficient on SPT-N value and liquefaction resistance of the ground improved by compaction methods," *Proc., GeoEng2000*.

Huang, A.B. and Hsu, H.H. (2005). "Cone penetration tests under simulated field conditions," *Geotechnique*, 55 (5), 345-354.

Ishihara, K. and Takatsu, H. (1979). "Effects of overconsolidation and K_O conditions on the liquefaction characteristics of sands", *Soils & Foun.*, 19 (4), 59-68.

Ishihara, K. and Harada, K. (2008). "Effect of lateral stress on relations between penetration resistances and cyclic strength to liquefaction," *Proc. 3rd International Conference on Site Characterization*, Taiwan (to appear).

Ishihara, K. (1996). *Soil Behaviour in Earthquake Geotechnics*, Oxford Press, 209-218.

Jamiolkowski, M., Ghionna, V.N., Lancellotta, R. and Paqualisis, E. (1988). "New correlations of penetration tests for design practice," *Proc. Int Symp on Penetration Testing, ISOPT-1*, Orlando, Balkema, 263-296.

Japan Road Association, JRA (1996). *Specifications for Highway Bridges,* Part V, Seismic Design.

Meyerhof, G.G. (1957). "Discussion on research on determining the density of sands by penetration testing," *Proc., 4th International Conference on Soil Mechanics and Foundation Engineering*, London, U.K., Vol. III, 110.

Robertson, P.K. and Wride, C.E. (1998). "Evaluating cyclic liquefaction potential using the cone penetration test," *Can Geot Journal*, 35(3), 442-459.

Salgado, R., Boulanger R.W. and Mitchell, J.K. (1997). "Lateral stress effects on CPT liquefaction resistance correlations," *J. Geot Eng,* ASCE, 123 (8), 726-735.

Suzuki, Y. and Tokimatsu, K. (2003). "Correlations between CPT data and liquefaction resistance of in-situ frozen samples," *J. Struct Constr Eng*, AIJ, 566, 81-88 (in Japanese).

Yasuda, S. Nishikawa, O., Kobayashi, T., Asaka, H. and Naito, F. (1996). "Model tests on the relation between relative density and SPT N-value," *Proc., 51st Annual Conference of JSCE*, 290-291 (in Japanese).

Yoshida, T. and Kokusho, T. (1988). "Proposal on the method of application of penetration test on sandy ground," *CRIEPI Report* (in Japanese).

Youd, T.L. and Idriss, I.M. (2001). "Liquefaction resistance of soils: Summary report from the 1996 NCEER and 1998 NCEER/NSF workshops on evaluation of liquefaction resistance of soils," *J. Geot Eng,* ASCE, 127 (4), 297-313.

Seismic Response Evaluation of an Onshore Building Site Improved by Deep Mixed Foundation System

Raj V. Siddharthan[1] and Ali Porbaha[2]

[1]Department of Civil Engineering; Mail Stop 258, University of Nevada, Reno, NV 89557, USA; siddhart@unr.edu
[2]Department of Civil Engineering; California State University, Sacramento; 6000 J Street, Sacramento, California 95819-6029, USA; porbaha@ecs.csus.edu

Abstract: This study presents the seismic response of a deep mixed (DM) treated foundation under the fourteen-story Oriental Hotel building in Japan using a simplified method proposed by Siddharthan and Porbaha (2008). This hotel was subjected to intensive shaking during the 1995 Hyogoken-Nanbu (Kobe) Earthquake (M = 6.9) and extensive liquefaction and ground movement at locations near the building have been observed. The hotel that was retrofitted with grid type deep mixing method survived the earthquake with little or no damage. The proposed simplified approach showed clearly the effectiveness of treated columns in reducing the pore water pressure response at locations closer to DM treated zone. The effectiveness of treatment is significant, especially near the surface. Absence of liquefaction within the cells and at locations within up to 2.7 m from the edge column would have played a positive role relative to the accepted performance of the Oriental Hotel during the 1995 Hyogoken-Nanbu earthquake. Accordingly, the proposed simplified approach can be effectively used to analyse various DM configurations, site and excitation conditions. The soil responses are needed within and around the DM columns to ascertain the effectiveness of DM treatment and obtain an optimum design.

INTRODUCTION

Construction on poor or marginal soil requires some kind of remedial measures either by improving the compressible soil foundation near the surface or by installing deep foundations. Deep mixing (DM) is one remedial measure that mixes soil in situ with a binder, such as cement, using a specially designed machinery equipped with paddles and augers. Many details on this technique, including its historical development, applicability, and design have been well documented by Porbaha (1998), Porbaha et al. (1998), Porbaha et al. (1999) and O'Rourke and Goh (1997), among others.

The objective of this study is to apply the method proposed by Siddharthan and Porbaha (2008) to evaluate the residual pore water pressure response under the oriental hotel building during 1995 Kobe earthquake. A summary of the proposed approach and

the details of the analysis are presented in detail.

SUMMARY OF THE PROPOSED APPROACH

The seismic response characteristics of the DM sites have been assessed based on the residual pore water pressure response (or liquefaction) since this is a widely-used engineering response indicator. Other important seismic design issues such as residual strength, permanent lateral deformation (e.g. lateral spread), and ground failure (e.g. sand boils) can be investigated based on the liquefaction analysis. The design issues can be assessed based on empirical relations that have been developed specifically addressing each of the failure modes. Well-documented guidelines for this undertaking are available in the literature and have been incorporated into many design guides such as Special Publication No. 117 developed by Division of Mines and Geology and the Southern California Earthquake Center (CDMG 1997; SCEC 1999).

Siddharthan and Porbaha (2008) proposed a method to evaluate the residual pore water pressure response of DM treated sites. A summary of the steps is presented here:

Step 1: Evaluate soil response of DM sites at various locations within and adjacent to DM treated soil and in the free-field for a variety of pre-selected "test cases" with different DM treatments (configurations and properties), untreated soil conditions, and excitations. The database of as many as 216 test cases analyzed includes consideration of two levels of overburden (3 and 8m). Therefore, the influence of overburden on liquefaction soil response has been accounted for. The result of this investigation is the establishment of a database of pore water pressure response ratios (PWPRs), normalized with respect to the free-field response. These response ratios are computed at various depths along many vertical sections (within and adjacent to DM columns).

Step 2: Evaluate level ground seismic soil response in the free-field in terms of pore water pressure at various depths using simplified liquefaction procedures outlined by Youd *et al*. (2001). Unlike Step 1, this is a site-specific analysis performed for the given untreated soil mass, which is to be provided with DM treatment. This step requires many input requirements such as soil layering and properties (e.g. thicknesses, SPT values, density etc.), and excitation characteristics (e.g. acceleration strength and earthquake magnitude).

Step 3: Establish pore water pressure ratios (PWPRs) that are appropriate for the problem under consideration based on the case-specific untreated soil conditions, DM treatment, and excitation characteristics from the database established in Step 1. Multiply the free-field responses computed in Step 2 by these "equivalent" factors to obtain the pore water response at various locations within and adjacent to the DM columns.

The seismic response evaluation model is simple and realistic since it appropriately accounts for many important factors that affect the DM treated soil response. More details on these steps are discussed by Siddharthan and Porbaha (2008).

PROJECT SUMMARY

Porbaha et al. (1999) discussed acceptable DM treated foundation soil performance observed in the case of fourteen-story Oriental Hotel building in Japan during the 1995 Hyogoken-Nanbu (Kobe) Earthquake (M = 6.9). This hotel building was subjected to intensive shaking during the earthquake and extensive liquefaction and ground movement at locations near the building have been observed.

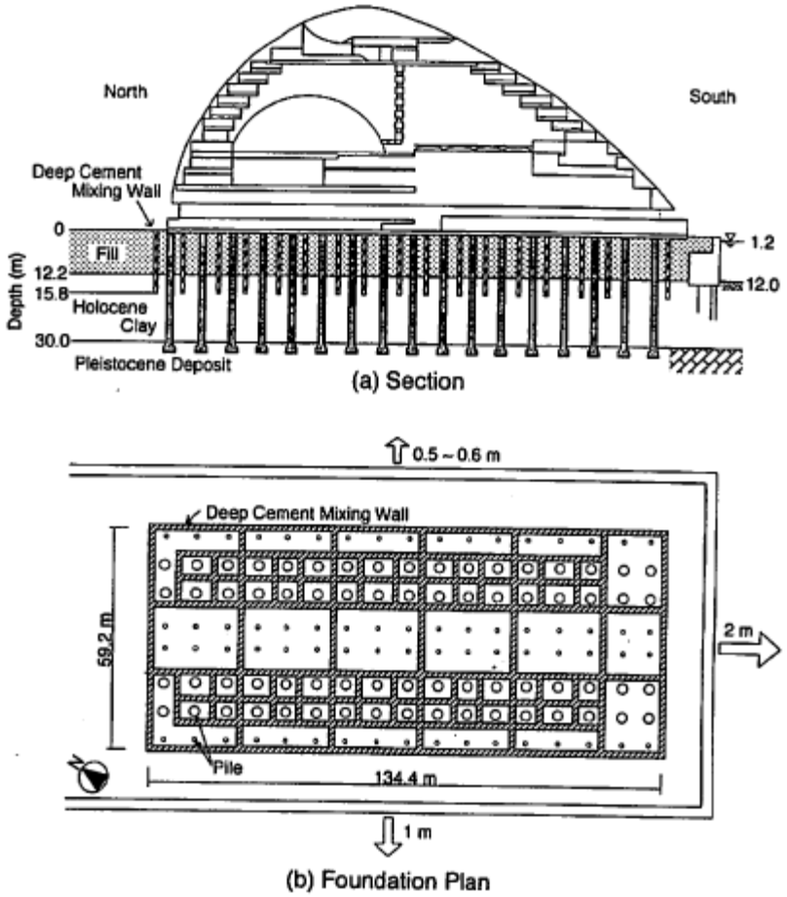


Fig. 1: Cement-Soil Mix Treatment at the Oriental Hotel Site, Kobe

As shown in Figure 1, deep mixing method with grid patterns was applied to improve the lateral resistance of the pile foundation of this hotel. The DM treatment consists of soil-cement walls, which were founded on Holocene clay extended to 15.8 m below the

ground surface through the liquefiable soil layer. The building was supported on concrete piles of 2.5 m in diameter and 33 m long. The DM walls were installed to encapsulate the piles to a depth of 15.8 m as shown in the Figure 1. During the 1995 Hyogoken-Nanbu earthquake, the locations near the hotel experienced lateral deformations and settlement in excess of 2.3 m and 1.5 m, respectively. Such large deformations are indicative of lateral spreading in the surface fill and it was observed along many kilometers surrounding the waterfront quay facilities (Elgamal *et al.* 1996). This building, nevertheless, survived without damage to either the superstructure or its pile foundations, while many other buildings in the vicinity suffered severe damage. Excavation of the foundation after the earthquake indicated no sign of liquefaction or lateral flow (Suzuki *et al*. 1996).

INPUT PARAMETERS

Table 1 shows the input parameters used with the proposed simplified approach to evaluate the seismic response. Many of the input values were selected from publications that provided data on the soil conditions at a well-documented instrumented down-hole array site located at the Port Island in Kobe.

Table 1: Input Parameters Used in the Field Verification: Oriental Hotel Site.

Input Parameter	Selected Value
Properties of liquefiable surface layer	
a) Unit weight, γ_{soil} (kN/m^3)	19.2
b) SPT N_1 value	11.4
c) Fines content (%)	0
d) Thickness (m)	12.2
Properties of bottom clay layer	
a) Unit weight, γ_{clay} (kN/m^3)	17.1
b) Max. shear modulus (kPa)	1.6×10^5
c) Fines content (%)	0
d) Thickness (m)	3.6
Properties of DM column	
a) Max. shear modulus, G_{dm} (MPa)	2208
b) Thickness, d (m)	0.9
c) Length, L (m)	15.8
d) Spacing, b (m)	5.5
Characteristics of excitation	
a) Max. surface acceleration, a_{max}	0.31g
b) Magnitude of earthquake, M	6.9

Madabhushi (1995) and Elgamal *et al.* (1996) reported on the soil layer properties that included SPT and shear wave velocity measurements at the Port Island site. Field investigations revealed that the surface layer at this reclaimed site is a fill (Masa soil) mined from nearby Rokko mountain and this layer was constructed mainly by bottom dumping from barges with no compaction, except for the upper few meters of soil above the ground water level. The surface layer consists of decomposed granite fill mixed with sand and occasional gravel. The SPT testing at the site revealed that SPT values varied between 5 and 8 with representative average uncorrected value of 6.0 (Elgamal *et al.* 1996). Taking note of SPT impact energy level is about 15% higher in Japan than in the US, the corrected (for overburden) average SPT N_1 value for the surface fill has been estimated as,

$$N_1 = 11.4 \tag{1}$$

This corresponds to an equivalent sand relative density D_r (eq. 1) of about 51%, which is within the range of relative densities considered in the database that was developed as a part of the proposed approach.

The underlying clay layer on which the DM cells were founded has an average shear wave velocity of about V_s = 303 m/s (Madabhushi 1995; Elgamal *et al.* 1996). The corresponding maximum shear modulus of the clay layer is given by,

$$G_{clay} = \rho V_s^2 = \frac{17.1\,(303)^2}{9.8} = 1.6\text{x}10^5 \text{ kPa} \tag{2}$$

The data on the stiffness of DM treated soil is not readily available. Suzuki *et al.* (1996) reported that the axial compressive strength of the soil-cement mix was in the order of dozens of kgf/cm2 (note: 1 kgf/cm2=98 kPa). Assuming a conservative value of 20 kgf/cm^2 (equivalent to 1960 kPa) for the axial strength and using the empirical relationship that relates Young's modulus to axial strength (Nilson et al. 2004), an estimate of the shear modulus for DM treated soil is as,

$$G_{dm} = 2208 \text{ MPa} \tag{3}$$

This value of shear modulus is consistent with the range of data on shear modulus of soil cement reported by Shibuya *et al*. (1992) and Porbaha *et al*. (1998). The average thickness (wall thickness) and the spacing within cells were estimated from Suzuki *et al.* (1996) as 0.9 m and 5.5 m, respectively.

Surface measurements of acceleration response were made at the Port Island down hole array site using a three component accelerometer. The East-West (EW) and North-South (NS) components showed maximum values of 0.28g and 0.34g, respectively (Madabhushi 1995; Elgamal *et al.* 1996). This means that the average maximum acceleration the surface, which is an input to the proposed simplified approach is,

$$(a_{max})_{surface} = 0.31g \quad (4)$$

Table 1 lists all the input values used in the prediction of soil response.

COMPUTED PORE WATER PRESSURE RATIOS

Maximum computed pore water pressures ratios for this field case along three vertical sections (Sections P-P, Q-Q, and R-R; see Fig. 2) located between the free-field and treated edge column are presented in Fig. 3. Only the response in the reclaimed soil is shown. For the level of excitation considered in the prediction (a_{max} = 0.31g), liquefaction in the free-field was widespread. A closer examination of Fig. 3 reveals that the vertical section closest to the edge column (Section P-P) showed the lowest amount of pore water pressure response, while the Section R-R located the farthest showed the highest. The farthest vertical section (R-R) showed liquefaction to a depth of as much as 7 m and at other sections (P-P and Q-Q), no liquefaction was indicated. This observation indicates the effectiveness of the treated columns in reducing the pore water pressure response at locations closer to DM treated zone. The effectiveness of treatment is significant, especially near the surface.

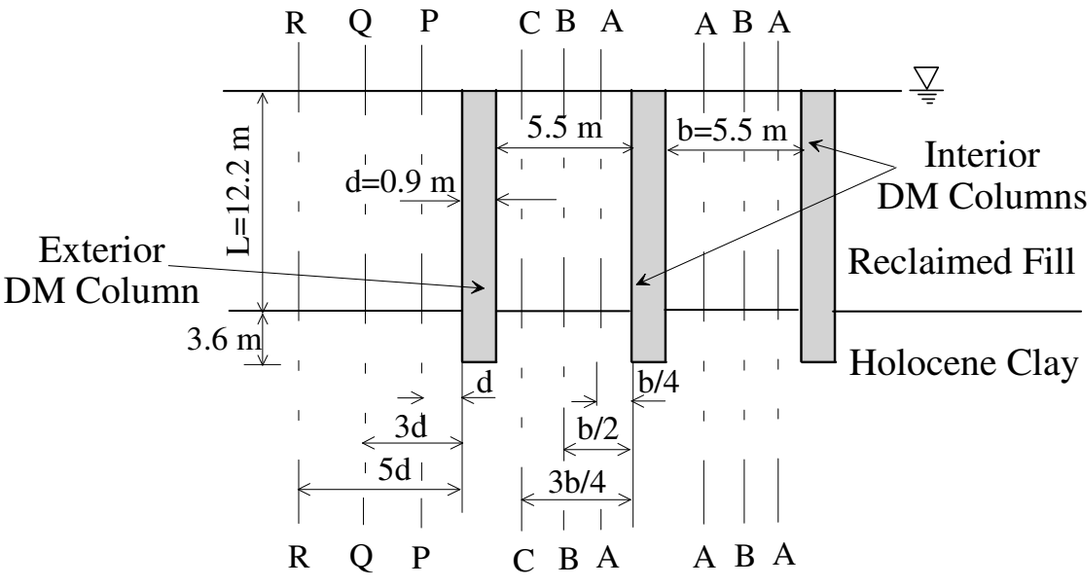


Fig. 2: DM Configuration Considered in the Field Case Study

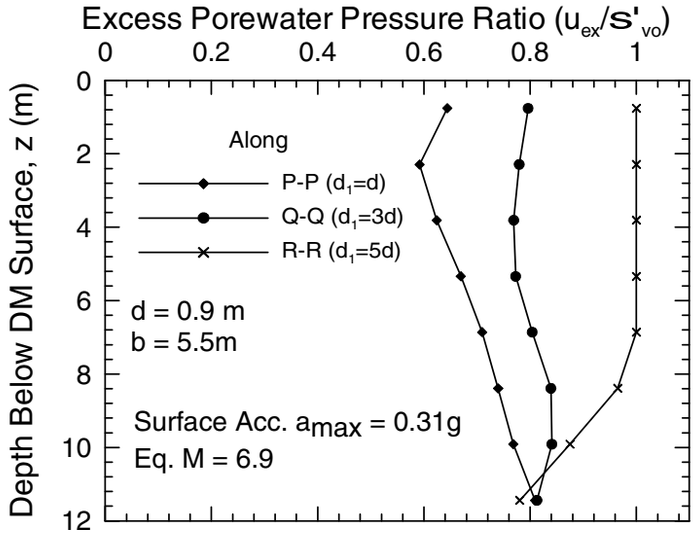


Fig. 3: Excess Pore water Pressure Adjacent to Edge DM Column

The observations relative to pore water pressure response between the treated columns can be made from Fig. 4. The vertical sections here are equally spaced at b/4, as shown in Fig. 2. In general, the following observations can be made: (1) the pore water pressure within the treated zone is smaller than those computed in the free-field, (2) the pore water pressure response is consistently lower along Section C-C, which is located closest to the edge column, (3) highest pore water pressure responses are computed near the middle of the DM columns. The reason for the third observation above can be attributed to the fact that unlike the soil elements near the DM columns, the elements away from the columns are less affected by the presence of columns.

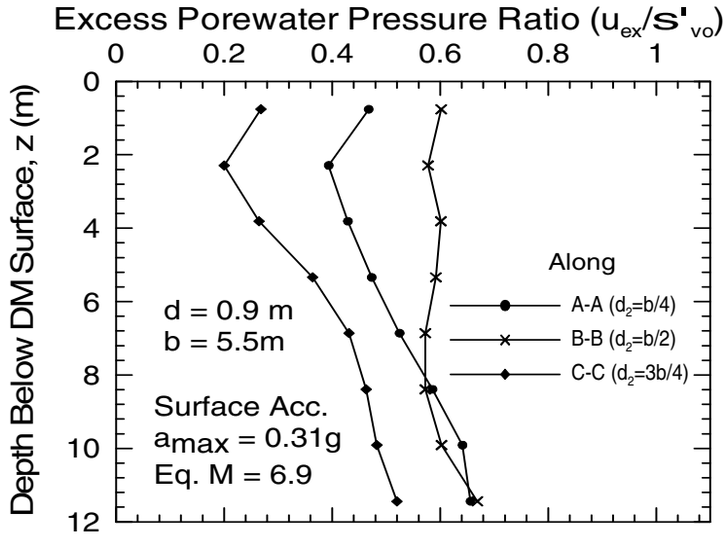


Fig. 4: Excess Pore water Pressure within DM Cell

Absence of liquefaction within the cells and at locations within up to 2.7 m from the edge column would have played a positive role relative to the accepted performance of the Oriental Hotel in the 1995 Hyogoken-Nanbu earthquake.

CONCLUSIONS

In this study the seismic response characteristics of an onshore hotel building on deep mixed column foundation was assessed based on the residual pore water pressure response (or liquefaction). Other important seismic design issues such as residual strength, permanent lateral deformation (e.g. lateral spread), and ground failure (e.g. sand boiling) can be investigated based on the liquefaction analysis. This study is based on a parametric study that focused on the influence of many variables that affect seismic soil response (Siddharthan and Porbaha 2008). The oriental hotel studied here was subjected to intensive shaking during the 1995 Hyogoken-Nanbu Earthquake and extensive liquefaction and ground movement at locations near the building have been observed. The effectiveness of treatment is significant, especially near the surface. This field case example verifies that the proposed simplified approach can be effectively used to analyse various DM configurations, site and excitation conditions.

ACKNOWLEDGEMENTS

The authors would like to express their sincere appreciation to Tom Shantz of Caltrans for his help with the selection of input acceleration histories and for his valuable discussions and suggestions relative to the formulation of the approach presented here. Appreciation is extended to N. Suthahar for technical assistance.

REFERENCES

Elgamal, A.W., Zeghal, M., and Parra, E. (1996). “Liquefaction of Reclaimed Island in Kobe, Japan.” *J. of Geotech. Engrg.*. Vol. 122(1), ASCE, 39 -49.

Madabhushi, S.P.G. (1995). “Strong motion at Port Island during the Kobe Earthquake,” Cambridge University Publication CUED/D-SOILS/TR285, Cambridge, UK.

Martin, G.R., Finn, W.D.L, and Seed, H.B. (1975). “Fundamentals of liquefaction under cyclic loading,” J. Geotech. Engrg., Vol. 101(5), ASCE, 423-438.

Nilson, A.H., Darwin, D., and Dolan, C.W. (2004). Design of Concrete Structures, 13th Edition, McGraw Hill Book Co., New York, NY.

O’Rourke, T.D., and Goh, S.H. (1997). “Reduction of liquefaction hazard by deep soil mixing,” Proc. Earthquake Engrg. Frontiers in Transportation Facilities, Editors: Lee, G. C., and Friedland, I. M., NCEER Technical Report 97-0005, 87-105.

Porbaha, A. (1998). “State-of-the-art in deep mixing technology: part I. Basic concepts and overview,” *Ground Improvement*, Vol. 2, 81-92.

Porbaha, A., Tanaka, H., and Kobayashi, M. (1998). “State-of-the-art in deep mixing technology: part II. Applications,” *Ground Improvement*, Vol. 2, 125-139.

Porbaha, A., Zen K., and Kobayashi, M. (1999). "Deep mixing technology for liquefaction mitigation," *J. of Infrastructure Systems*, Vol. 5(1), ASCE, 21-33.

Shibuya, S., Tatsuoka, F., Teachavorasinskun S., King, X.J., Abe, F., Kim, Y.S., and Park, C.S. (1992). "Elastic deformation properties of geomaterials," *Soils and Foundations*, Vol. 32(3), 26-46.

Siddharthan, R. V., and Porbaha, A. (2005) "Pore pressure response of treated sites due to strong excitations", International Conference on Deep Mixing and Best Practices, Proceedings of Deep Mixing 05, May 23-25, Stockholm, Sweden, 297-304.

Siddharthan, R. V. and Porbaha, A. (2008) "Seismic response evaluation of deep mixing improved ground", *Ground Improvement*, Thomas Telford, UK (approved for publication)

Suzuki, Y., Onimaru, S., Uchida, A., Saitoh, S., and Kimura, T. (1996). "Grid-shaped stabilized ground improved by Deep Cement Mixing Method against liquefaction for a building foundation," Tsuchi-to-Kiso, Vol. 44(3), No. 458, 46-48 (in Japanese).

Tokimatsu, K., Mizuno, H., and Kakurai, M. (1996) "Building damage associated with geotechnical problems", *Soils and Foundations*, special issue, 219-234, January 1996., Japanese Geotechnical Society, Tokyo, Japan.

Youd, T.L., Idriss, I., M., Andrus, R.D., Arango, I., Castro, G., Christian, J. T., Dobry, R. Liam Finn, W.D., Harder, L., F., Hynes, M. L., Ishihara, K., Koester, J. P., Liao, S. C. Marcuson, III, W.F., Martin, G. R. Mitchell, J.K., Moriwaki, Y. Power, M.S., Robertson, P.K., Seed, R.B., and Stokoe, K.H. (2001). "Liquefaction resistance of soils: summary report from the 1996 NCEER and 1998 NCER/NSF Workshops on evaluation of liquefaction resistance of soils," *J. Geotech. and Geoenvironmental Engrg*., Vol. 127(10), ASCE, 817-833.

This page intentionally left blank

Shear Stress Redistribution as a Mechanism to Mitigate the Risk of Liquefaction

Russell A. Green[1], M. ASCE, P.E., C. Guney Olgun[2], and Kord J. Wissmann[3], M. ASCE, P.E.

[1]Associate Professor, Department of Civil and Environmental Engineering, University of Michigan, 2372 G.G. Brown, Ann Arbor, MI 48109-2125; rugreen@umich.edu
[2]Research Scientist, Via Department of Civil and Environmental Engineering, Virginia Tech, 111 Patton Hall, Blacksburg, VA 24061; olgun@vt.edu
[3]President, Geopier Foundation Company, Inc., 150 Fairview Road Suite 335, Mooresville, NC 28117; kwissmann@geopier.com

ABSTRACT: The installation of stone columns or piers in a loose, saturated sand deposit can potentially mitigate the risk of liquefaction by decreasing the seismic demand on the soil by redistributing the induced shear stresses from the sand to the columns or piers. In calculating the shear stress redistribution, it is commonly assumed that both the soil and the columns or piers respond as shear beams. Although less common, it has also been assumed that the soil responds as a shear beam and that the columns or piers respond as flexural beams, with the redistribution of the shear stresses computed accordingly. However, the results presented herein show that the columns or piers, and the soil immediately surrounding the column/pier, deform in a combination of shear and flexure. The percent contribution of shear versus flexural deformation of the column or pier varies with depth, with the column/pier deforming predominantly in flexure near the ground surface and predominantly in shear at depth. The percent contribution of each mode of deformation governs the redistribution of the shear stresses from the soil to the pier. The distribution of the shear stresses between the soil and columns or piers are quantified for "typical" properties of a loose, saturated sand profile reinforced with Impact™ Rammed Aggregate Piers™.

INTRODUCTION

Presented herein are the results of numerical analyses performed to quantify the distribution of seismically induced shear stresses between liquefiable soil and stone columns or piers. The motivation for the study is the development of a procedure for determining the maximum allowable spacing of columns/piers for mitigating the risk of liquefaction. The installation of stone columns or piers in a loose, saturated sand deposit can mitigate the risk of seismically induced liquefaction by several mechanisms. The columns/piers potentially increase the soil's ability to resist liquefaction by: (1) increasing the soil's density during installation, (2) increasing the

lateral effective confining stress in the soil, and (3) providing a mechanism for rapid dissipation of excess pore pressure. Additionally, the seismic load can potentially be decreased by redistributing the induced shear stresses from the soil to the columns/piers. With respect to this latter mechanism, it is commonly assumed that both the soil and the columns/piers respond as shear beams, with the distribution of the seismically induced stresses computed accordingly (e.g., Priebe 1995, Baez 1995). Although less common, in computing the stress redistribution it has also been assumed that the soil responds as a shear beam, while the columns/piers respond as flexural beams (Goughnour and Pestana 1998). Using these two sets of assumptions, it can be clearly demonstrated that the mode of deformation of the columns/piers significantly influences their effectiveness to mitigate the risk of liquefaction, with shear deformation being the most effective and flexural being the least, to the point of being ineffective and possibly detrimental.

To better quantify the deformation behavior of columns/piers (and hence, their effectiveness to mitigate the risk of liquefaction), a liquefiable sand deposit reinforced with Impact^{TM} (*Impact*) Rammed Aggregate Piers^{TM} (RAPs) and subjected to earthquake motions was modeled using finite elements. The results of the analyses were used to compute the relative percentages of shear and flexural deformations experienced by the *Impact* RAPs as a function of depth. This information is then used to determine an "equivalent" shear modulus for the soil-pier system (i.e., the shear modulus of an unreinforced soil profile having an equivalent shear stiffness as the soil profile reinforced with *Impact* RAPs.), which is required in the standard design procedures for determining the column/pier spacing.

In the following sections of this paper, first an overview of the numerical analyses is presented, followed by a discussion of data reduction and interpretation. Next, the results are used to quantify the percent contribution of shear and flexural deformation in the *Impact* RAPs as a function of depth. Finally, equations are given for computing an equivalent shear modulus for the soil-pier system.

NUMERICAL ANALYSES

A 2-D, total stress, plane strain finite element analysis (FEA) of a saturated, loose sand deposit reinforced with *Impact* RAPs and subjected to earthquake motions was modeled using the software Dynaflow (Prevost 2007). The analyses consisted of a series of two-dimensional site response analyses of soil-pier system. The shear wave velocity profile of the deposit analyzed is shown in Figure 1. The increase in shear wave velocity with depth for this profile varies proportionally to $(\sigma'_m)^{0.25}$, where σ'_m is the mean effective confining stress. In computing σ'_m, the at rest lateral earth pressure coefficient (K_o) and the total unit weight (γ_t) of the sand were assumed equal to 0.5 and 19.65 kN/m^3 (125 pcf), respectively, and the ground water table was assumed to be located 1 m (3.28 ft) below the ground surface.

The overall dimensions of the finite element model used in this study are given in Figure 2. In the model, both the soil and pier are linear elastic and a "welded" interface was used between the pier and the soil. To minimize numerical distortion of seismic waves having frequencies of engineering interest, the finite element mesh was discretized into approximately 0.3m × 0.3m size elements. Using the approach

outlined in Itasca (2000) and Green and Ebeling (2002), the maximum frequency (f_{max}) that the mesh for the profile can pass without numerical distortion is approximately 30 Hz. This limiting frequency is significantly greater than the first two modes of vibration of the profile, which are ~3.4 and ~9.2 Hz, respectively.

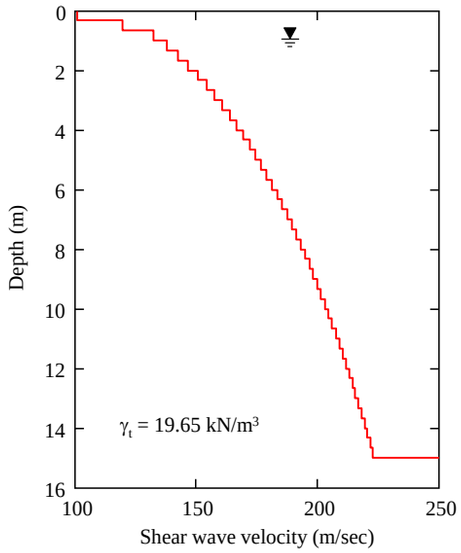


FIG. 1. Shear wave velocity profile for the loose sand deposit modeled in the finite element analyses.

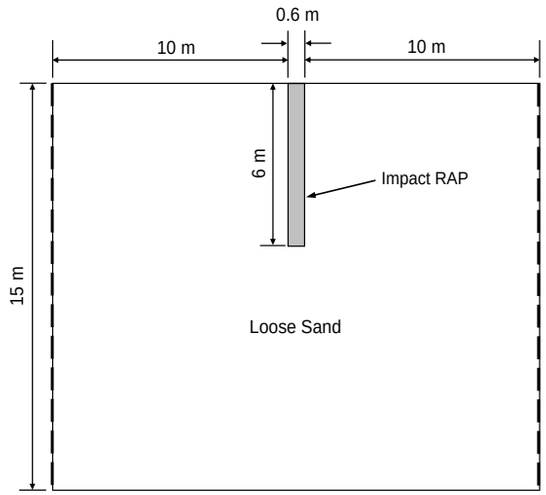


FIG. 2. Dimensions of the finite element model used in the parametric study.

In the site response analyses, the vertical and horizontal displacements of the lateral boundaries of the model were forced equal to each other, thus simulating a continual repeating of the mesh in the lateral direction (i.e., ~20 m center-to-center spacing of the piers). [Note: It was desired in these analyses to have the piers spaced far enough apart that halfway between the piers was essentially free-field conditions.] To validate the appropriateness of this imposed lateral boundary condition, the theoretical free-field transfer function from the base rock to the soil surface was computed. The

theoretical transfer function was compared with that computed by taking the ratio of the Fourier amplitude spectra (FAS) of the input base rock motion and FEA computed soil surface motion at the lateral boundary; 10 % damping was assumed in computing both transfer functions (Rayleigh damping was used in the FEA, centered at 5 Hz). The resulting transfer functions are shown in Figure 3. As may be observed from this figure, there is very good agreement between the transfer functions up to approximately 12.5 Hz (i.e., the first two modes of vibration of the profile are adequately modeled in the analyses.). Beyond ~12.5 Hz, the transfer function computed from the FEA motions is suppressed by the Rayleigh damping.

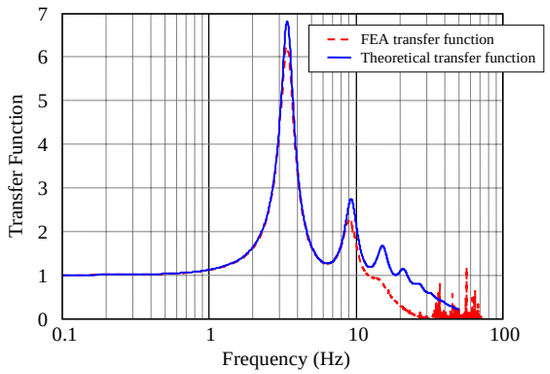


FIG. 3. Comparison of the theoretical and FEA base rock to the soil surface transfer functions.

A synthetic base rock motion was generated and used in the site response analyses. The reason for using a synthetic motion, versus a recorded motion, was to ensure that the motion had sufficient bandwidth to excite as many modes as possible in the soil profile. A plot of the synthetic base rock motion (scaled to 0.3g) and the computed soil surface motion at the lateral boundary are shown in Figure 4, as well as a plot of the variation of the peak ground acceleration (pga) up through the soil column.

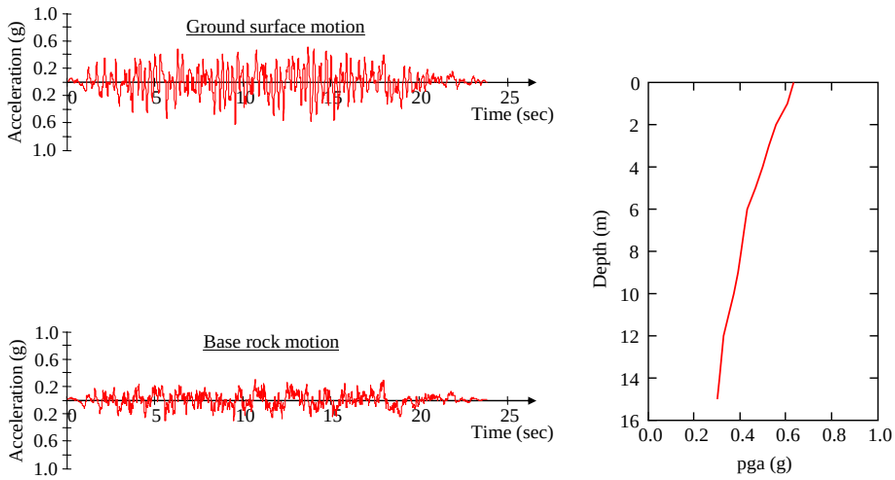


FIG. 4. Synthetic base rock motion and computed soil surface motions at the lateral boundary and the variation of the compute pga up through the profile.

DATA REDUCTION AND INTERPRETATION

In post-processing the FEA results, a grid was superimposed on the FEA mesh (Figure 5) and the computed horizontal and vertical displacement time histories were extracted at the corners of each of the grid elements. [Note: The grid elements labeled 1 through 4 are discussed below.]

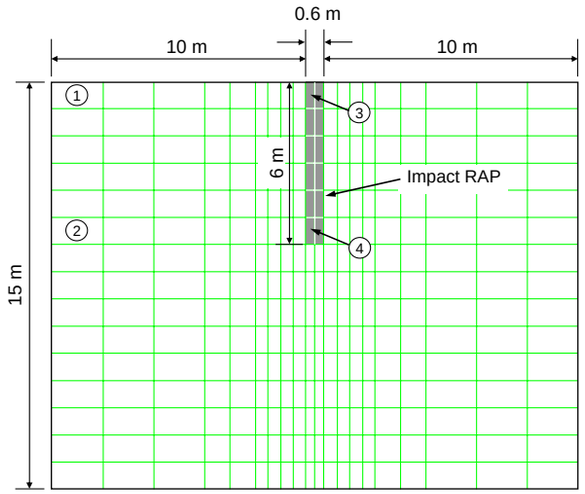


FIG. 5. Grid superimposed on the finite element mesh showing the locations where computed horizontal and vertical displacement time histories were extracted in the post processing of the FEA results.

The shear (γ) and flexural (θ) deformations for the grid elements were computed as a function of time using Eqs.1 and 2, respectively.

$$\gamma_{avg}(t) = \frac{\gamma_L(t) + \gamma_R(t)}{2} \approx \frac{\delta_1(t) - \delta_2(t)}{2} \cdot \frac{d}{h \cdot w} \tag{1}$$

$$\theta(t) = \frac{z_2(t) - z_1(t)}{w} \tag{2}$$

where all the variables in these expressions are defined in Figure 6. The cumulative shear and flexural deformations (*CSD* and *CFD*, respectively) were computed by integrating the absolute values of $\gamma_{avg}(t)$ and $\theta(t)$ over time, i.e.:

$$CSD = \int_0^{t_{dur}} \left|\gamma_{avg}(t)\right| dt \tag{3}$$

$$CFD = \int_0^{t_{dur}} \left|\theta(t)\right| dt \tag{4}$$

where t is elapsed time and t_{dur} is the total duration of the earthquake shaking. The

CSD and *CFD* for grid elements 1 through 4 (Figure 5) for a pier-to-soil stiffness ratio of 10 are plotted as a function of time in Figure 7. As may be observed from Figure 5, grid element 1 is at the profile surface at the lateral boundary of the model and grid element 2 is at a depth of ~5.6 m (~18.5 ft), also at the lateral boundary of the model. As discussed above, both of these elements can be treated as being in the free field (i.e., their response will be not be influenced by the pier). Grid elements 3 and 4 are at the top and bottom of the pier, respectively. Note: Elements 1 and 3 and elements 2 and 4 are at corresponding depths. From Figure 7, it can be observed that *CSD* and *CFD* are approximately linear functions of time. This inherently implies that the contributions to the pier deformations from shear and flexural modes are relatively constant through out shaking.

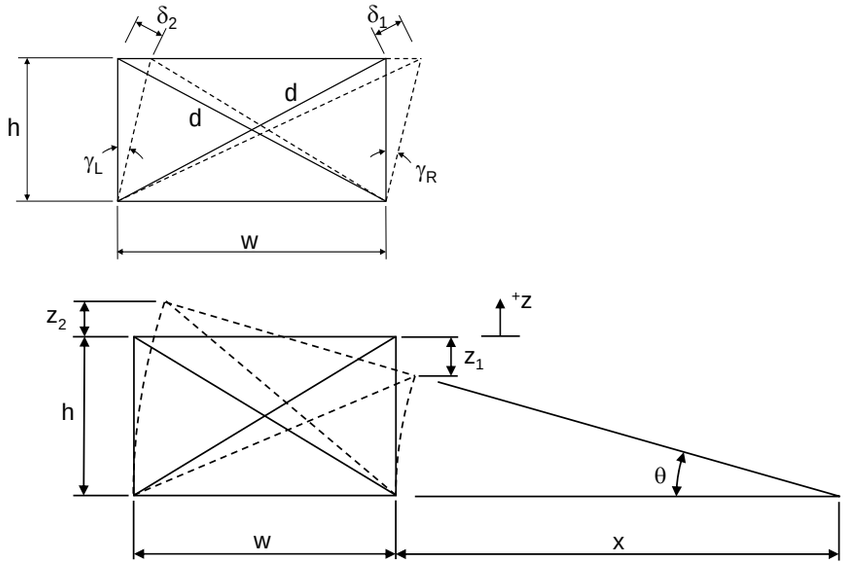


FIG. 6. Shear and flexural deformation of grid elements. The dotted lines represent the deformed shape of the elements. (Adapted from Oesterle et al. 1979 and Shiu et al. 1981).

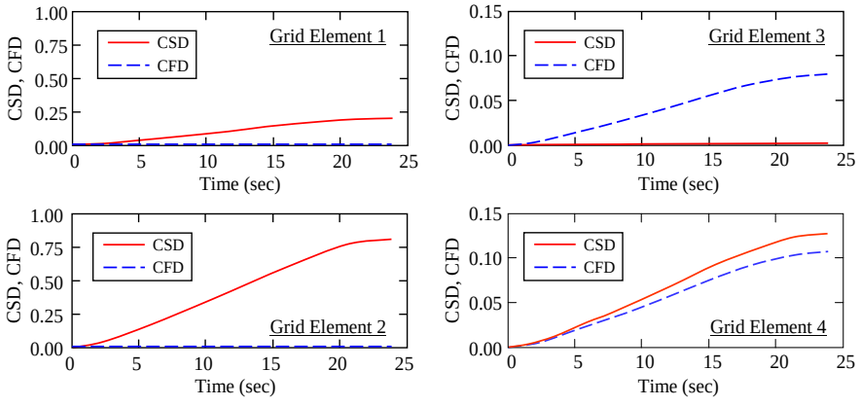


FIG. 7. Cumulative shear and flexural deformation of grid elements 1 through 4 (see Figure 5). Note: The vertical scale for elements 1 and 2 differs from that for elements 3 and 4.

As may be observed from Figure 7, both elements 1 and 2 deform completely in shear, which is what is expected for free field conditions. However, element 3 deforms predominately in flexure and element 4 deforms in a combination of shear and flexure. (Figure 8 illustrates the difference between shear and flexural deformation. As may be observed in this figure, horizontal planes in the *Impact* PAR deforming in pure shear remain horizontal, while they do not in the *Impact* PAR deforming in pure flexure.) The percent contribution of each mode of deformation governs the redistribution of the shear stress from the soil to the pier.

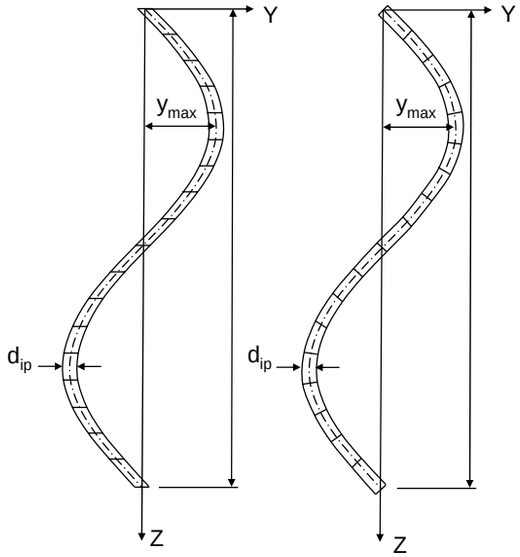


FIG. 8. *Impact* RAPs deforming in pure shear (left) and pure flexure (right). (Adapted from Goughnour and Pestana 1998).

Using Eqs. 3 and 4, *CSD* and *CFD* were computed for the vertical line of grid elements from the top of the pier down to bed rock. The percent contribution of each mode of deformation was computed as follows:

$$PC_{CSD} = \frac{CSD}{CSD + CFD} \times 100\% \tag{5a}$$

$$PC_{CFD} = \frac{CFD}{CSD + CFD} \times 100\% \tag{5b}$$

where PC_{CSD} = percent contribution of shear deformation, and PC_{CFD} = percent contribution of flexural deformation. The results from the analyses are shown in Figure 9. As may be observed from this figure, PC_{CSD} increases (and correspondingly PC_{CFD} decreases) with depth. Also, below the bottom of the pier, the soil PC_{CFD} fast approaches 0% and PC_{CSD} fast approaches 100% (i.e., the soil behaves as a shear beam).

EQUIVALENT SHEAR MODULUS

Following the current design procedure for determining the spacing of stone columns or *Impact* RAPs required to mitigate the risk of liquefaction, an "equivalent shear modulus" of the reinforced profile is required (e.g., Priebe 1995, Baez 1995, Goughnour and Pestana 1998). In this approach, the equivalent shear modulus is the shear modulus of a "homogenized" profile that has a shear stiffness equal to the composite stiffness of a soil profile reinforced with columns/piers (Olgun 2003). If both the soil and columns/piers behave as shear beams, the equivalent shear modulus of the homogenized profile is simply a weighted average of soil and column/pier shear moduli, with the weighting being based on the replacement ratio of the reinforced profile. However, the computation of the equivalent shear modulus of the homogenized profile is less straightforward if the columns/piers do not behave as shear beams, but rather deform as a combination of shear and flexure (as shown in Figure 9) or in pure flexure. For the latter case, Goughnour and Pestana (1998) derived the following expression for computing the pseudo shear modulus ($G_{IP\ flex}$) of a column/pier, which is defined as the shear stress carried by the column/pier divided by the shear strain experienced by the column/pier (i.e., dy/dz in Figure 8):

$$G_{IP\ flex} = \frac{1}{2} \cdot \left(\frac{\pi \cdot d_{IP}}{V_{S\ avg} \cdot T} \right)^2 \cdot (1+\nu) \cdot G_{IP\ shear} \qquad (6)$$

In this expression, d_{IP} = diameter of stone column or *Impact* RAP, $V_{S\ avg}$ = average shear velocity of the composite column/pier-soil reinforced profile down to depth corresponding to the bottom of the piers, T = period of the ground motion (e.g., Rathje et al. 2004), ν = Poisson's ratio of the *Impact* RAP, and $G_{IP\ shear}$ = shear modulus of the *Impact* RAP (White et al. 2004).

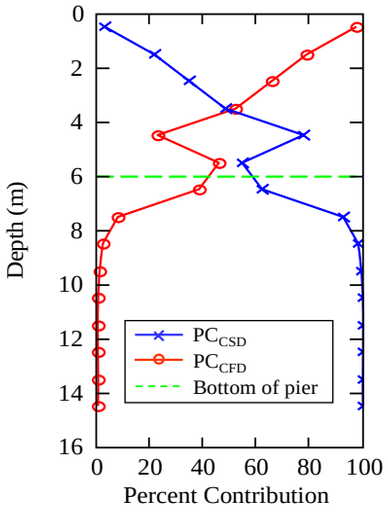


FIG. 9. Percent contributions of shear and flexural modes of deformation of *Impact* RAPs as a function of depth.

Using Eq. 6 and the information given in Figure 9, the pseudo shear modulus ($G_{IP\ flex+\ shear}$) of a column/pier that deforms in a combination of flexure and shear can be determined. This is done by taking a weighted average of $G_{IP\ flex}$ and $G_{IP\ shear}$, using PC_{CFD} and PC_{CSD} as the respective weighting factors, i.e.:

$$G_{IP\ flex+shear} = PC_{CFD} \cdot G_{IP\ flex} + PC_{CSD} \cdot G_{IP\ shear} \quad (7)$$

Because both $G_{IP\ shear}$ and $G_{IP\ flex}$ will vary as a function of mean effective confining stress, $G_{IP\ flex+\ shear}$ will also vary as a function of mean effective confining stress (or synonymously, as a function of depth). Additional analyses are currently being performed to further validate the assumed linear variations of the contributions of $G_{IP\ shear}$ and $G_{IP\ flex}$ to $G_{IP\ flex+\ shear}$ inherent to Equation 7.

Once the pseudo shear modulus of the column or pier is determined using Eq. 7, the equivalent shear modulus of the profile reinforced with stone columns or *Impact* RAPs can be computed assuming both the soil and column/pier behave as shear beams (i.e., a weighted average of soil and column/pier shear moduli can be computed with weighting factors being based on the replacement ratio of the reinforced profile) (e.g., Priebe 1995, Baez 1995). The resulting column/pier spacing will be smaller than that computed assuming the columns/piers deform in pure shear (e.g., Priebe 1995, Baez 1995) and larger than assuming the columns/piers deform in pure flexure (e.g., Goughnour and Pestana 1998).

CONCLUSIONS

One way in which stone columns or *Impact* RAPs mitigate the risk of liquefaction is by redistributing the seismically induced shear stresses from the soil to column/pier. However, the effectiveness of this mechanism is governed by the deformation behavior of the column/pier. Two assumptions used in the past have been that columns/piers deform in pure shear and pure flexure, with the former being a much more common assumption than the latter. However, the results from FEA presented herein show that the columns/piers deform in a combination of shear and flexure. The percent contribution shear versus flexural deformation of the column or pier varies with depth, with the column/pier deforming predominantly in flexure near the ground surface and predominantly in shear at depth. The resulting column/pier spacing will be smaller than that computed assuming the columns/piers deform in pure shear and larger than assuming the columns/piers deform in pure flexure.

ACKNOWLEDGEMENTS

The authors gratefully acknowledge the financial support of this study by Geopier Foundation Company, Inc. and the review comments of Dr. Manuel Gutierriez, Mr. Jongwon Lee, and Capt. Theresa White, USAF. Also, the authors acknowledge the involvement and contributions of Dr. Sherrif El-Tawill during the early stages of this study.

REFERENCES

Baez, J.I. (1995). *A Design Model for the Reduction of Soil Liquefaction by Vibro-Stone Columns.* Ph.D Thesis (G.R. Martin, Advisor), University of Southern California.

Goughnour, R.R. and Pestana, J.M. (1998). "Mechanical Behavior of Stone Columns Under Seismic Loading." *Proc. 2nd International Conference on Ground Improvement Techniques*, Singapore.

Green, R.A. and Ebeling, R.M. (2002). *Seismic Analysis of Cantilever Retaining Walls, Phase I.* ERDC/ITL TR-02-3, Information Technology Laboratory, US Army Corps of Engineers Engineering Research and Development Center, Vicksburg, MS.

Itasca Consulting Group, Inc. (2000). *FLAC (Fast Lagrangian Analysis of Continua) User's Manuals*, Minneapolis, MN.

Oesterle, R.G., Aristizabal-Ochoa, J.D., Fiorato, A.E., Russell, H.G., and Corley, W.G. (1979). *Earthquake Resistant Structural Walls – Tests of Isolated Walls – Phase II.* PCA R&D Serial No. 1629, Construction Technology Laboratories, Skokie IL.

Olgun, C.G. (2003). *Performance of Improved Ground and Reinforced Soil Structures during Earthquakes – Case Studies and Numerical Analyses*, Ph.D Thesis (J.R. Martin, Advisor), Virginia Tech.

Prevost, J.H. (2007). Dynaflow™, http://www.princeton.edu/~dynaflow/description_df.htm

Priebe, H.J. (1995). "Vibro Replacement to Prevent Earthquake Induced Liquefaction." *Ground Engineering*, September, 30-33.

Rathje, E.M., Faraj, F., Russell, S., and Bray, J.D. (2004). "Empirical Relationships for Frequency Content Parameters of Earthquake Ground Motions." *Earthquake Spectra*, EERI, 20(1): 119-144.

Shiu, K.N., Daniel, J.I., Aristizabal-Ochoa, J.D., Fiorato, A.E., and Corley, W.G. (1981). *Earthquake Resistant Structural Walls – Tests of Walls with and without Openings.* PCA R&D Serial No. 1679, Construction Technology Laboratories, Skokie IL.

White, D.J., Suleiman, M.T., and Pham, H. (2004). *Field Determination of Shear Modulus for Geopier Foundations.* Report No. ISU-ERI-05226, Iowa State University.

Study on Uplift Behaviour of Plate Anchor in Geogrid Reinforced Sand Bed

Ilamparuthi K[1]., Ravichandran P.T[2]., and Mohammed Toufeeq M[3].

[1]Professor, Div. of Soil Mechanics., Anna University, Chennai-25, India, kanniilam@hotmail.com
[2]Asst. Professor, Dept. of Civil Engg, SRM University, Chennai- 603 203, India,ptrsrm@yahoo.com
[3]PG Student, Div. of Soil Mechanics, Anna University, Chennai-25, India, mmtoufeeq @yahoo.com

ABSTRACT: Two series of pullout loads tests were conducted on anchors embedded in submerged sand in this study. First series of tests were in submerged sand and the second series of test were in submerged sand reinforced with single layer of geogrid. The geogrid was positioned directly on the anchor and its width ratio was varied (Br/B = 2, 3 and 4). Other parameters varied in both monotonic and cyclic mode of loading were embedment ratio of anchor (H/B=2, 3 and 4) and density of sand (loose, medium and dense conditions). All the cyclic load tests were conducted for the cyclic load ratio of 60%. From the results of study it was found that the load - displacement response of unreinforced and reinforced sand for a given density and depth of embedment are similar except higher peak and residual loads due to the inclusion of geogrid reinforcement. Both peak and residual pullout loads increased with width ratio of reinforcement for the densities and embedment ratios studied in this investigation. In the case of cyclic load, the displacement of anchor was increased with decreasing rate and reached almost a constant value after 350 cycles. The post cyclic peak pullout load was marginally higher than the peak pullout load of monotonic condition for all the comparable test conditions.

INTRODUCTION

An anchor is a foundation system that is capable of resisting tensile force with the support of surrounding soil in which anchor is embedded. It is used in various civil engineering structures as a structural member, primarily to resist uplift loads and overturning moments; and to ensure the structural stability. A wide variety of anchor systems (plate, belled, under reamed pile, pedestal, pyramid, grillage and helical anchors) have been developed in order to satisfy the increase in demand for foundations to resist the pullout loads.

Researchers proved that the uplift capacity can be improved by grouping the anchors, increasing the unit weight of back fill, depth of embedment and the size of anchor. Innovation of geosynthetics in the field of geotechnical engineering as reinforcement found to be possible alternative in enhancing anchor capacity. Its behaviour on anchor system was first documented by Subbarao et al. (1988). Polypropylene strip as ties was found to increase the uplift capacity of anchors.

Selvadurai (1993) studied the performance of uplift capacity of buried pipelines by the use of geogrid in sand bed. The increase in uplift capacity of the reinforced system was around 100% and also reported that reinforcement increased the pullout load with increase in displacement indicating an improvement in ductility of the system. Krishnaswamy and Parashar (1994) studied the uplift behaviour of plate anchors embedded in cohesive and cohesionless soil media, with and without geosynthetics. Placing the geosynthetics directly on the anchor foundation was proved to be beneficial in achieving maximum increase in the uplift capacity. Further they reported that two layers of geogrid reinforcement does not increase the uplift capacity predominantly. Ilamparuthi and Dickin (2001 a and b) carried out an extensive study on the behaviour of belled pile anchors in reinforced sand bed and formulated a hyperbolic theory for the breakout factor. Ravichandran and Ilamparuthi (2004) studied the behaviour of rectangular plate anchors in the unreinforced and reinforced (horizontal and vertical) sand bed. Vertical reinforcement showed higher increase in the uplift capacity of the anchors than the horizontal reinforcement, since vertical reinforcement was found to attribute better interlocking resistance than that of the horizontal reinforcement. Kingshri et al. (2005) carried out two series of tests to understand the influence of stiffness and opening size of geosynthetic reinforcement on the enhancement of uplift capacity of rectangular anchor. First series of tests were on combination of geocomposite and geogrid and the second series of tests were on two layers of geogrid as reinforcements and concluded that the performance of geocomposite & geogrid (two layer) combination was found to be effective in resisting uplift force than two combined layers of geogrids. Limited work was reported on the effect of submergence under uplift loading. Andreadis and Harvey (1981), Ghaly et al. (1991), Krishnaswamy and Parashar (1992), Ilamaparuthi and Muthukrishnaiah (2001) are some among the few known researchers in this field. Krishnaswamy and Parashar (1992) performed the test in reinforced sand bed and others in unreinforced conditions. Further the research on the effect of cyclic load on anchor embedded against pullout is very rare in reinforced sand bed.

The behaviour of anchors in submerged sand subjected to cyclic loading is a complex interaction problem involving the water, the sand, the anchor and the loading pattern. Although quite a good amount of research has been carried out to understand the behaviour of plate anchors under monotonic loading, the effects of cyclic loading on anchor behaviour has drawn little attention from the investigators particularly in sand. A review of these works indicates that due to lack of sufficient information the design of anchors under repeated loading is generally based on high factor of safety. Keeping this in view in this paper, an attempt has been made to study the behaviour of plate anchors in submerged sand both under monotonic and cyclic loads.

TEST PROGRAMME

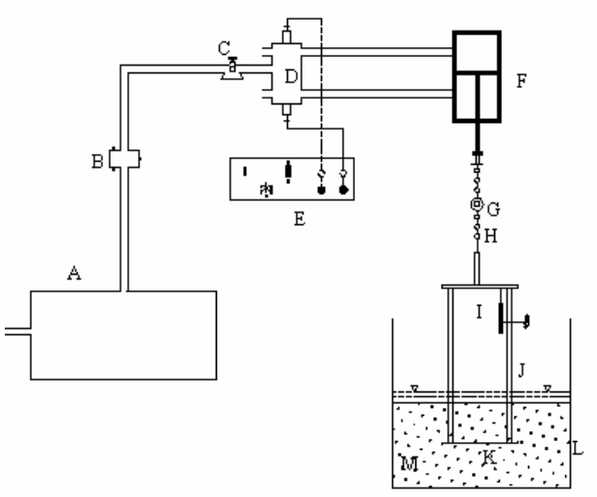
The test programme involved monotonic and cyclic pullout tests on rectangular anchors of size 50mm×350mm×5mm (L/B=7, L=length and B=width of anchor) at

embedment ratios (H/B, where H=depth of embedment and B=width of anchor) of 2, 3 and 4 in dense (γ'=10.81kN/m^3), medium dense (γ'=10.41kN/m^3) and loose (γ'= 9.47kN/m^3) sand beds under submerged condition. Submergence of sand was achieved by allowing water to flow from the bottom of the bed to top and water level of 50mm above the top level of sand bed was maintained in all the tests. Model anchors were tested on unreinforced and reinforced systems. All the tests were carried in submerged conditions. In this study the parameters investigated are the depth of embedment (H), the unit weight of sand bed (γ') and the width of reinforcement (B_r).

The arrangement of the test set up for monotonic and cyclic loading is shown in the Fig.1. This setup consists of a loading frame of 30kN capacity with a hydraulic jack arrangement other than pressure cylinder, timer and monitoring devices required for cyclic load. The anchor was placed inside the model tank of size 740 mm x 740 mm x 560 mm and the anchor was pulled monotonically through the loading yoke connecting the proving ring, the hydraulic jack and the anchor. In the case of cyclic load tests, embedded plate anchors in submerged sand were subjected to a constant cyclic load ratio (CLR) of 60% (ratio of intensity of cyclic load to peak pullout load of anchor under monotonic loading condition) and uniform rectangular cyclic loading of 6 seconds period. Anchors were subjected to a maximum of 1000 cycles. At the end of cyclic load, pullout tests were conducted to find out the post-cyclic pullout capacity of anchors. In this investigation one way vertical cyclic pullout load on anchors were imparted through a pneumatic loading apparatus developed in house by the authors and its arrangement is as shown in Fig.1. Stress controlled cyclic loading tests were conducted as it is more appropriate for simulating field conditions. In this system, a predetermined cyclic pull was applied on the model anchor at the desired frequency. The cyclic load on the anchor was applied using a double acting pneumatic power cylinder which was connected to the anchor rod by a chain of required length. The piston of the pneumatic power cylinder is actuated by regulated filtered compressed air, passing through a solenoid valve system controlled by an electronic timer. Desired cyclic load to the anchor is imparted by regulating pressure and setting loading and unloading time intervals in the timer. A strain gauge load cell of 3 kN connected to the pullout arrangement was used to monitor the cyclic and post cyclic pullout loads. The displacement of the anchor was measured using LVDT'S. Monitoring devices were used for measuring load and displacements.

Properties of sand and reinforcement material

The sand used in this study was tested for index properties. It contains traces of fines with medium and fine sand contents of 80% and 19% respectively. Its minimum and maximum void ratios are 0.497 and 0.897 respectively. Its specific gravity is 2.69 and it is classified as poorly graded sand (SP) as per unified soil classification. A NETLON (CE-121) geogrid was used as reinforcement in all the tests. Its aperture shape and size are Diamond and 8mm x 6 mm respectively. Thickness of reinforcement at the joint is 3.1mm and its maximum strength is 7.68 kN/m.



A - Compressor
B – Air filter
C– Pressure regulator with pressure guage
D- Solenoid valve
E – Electronic timer
F – Double acting pneumatic cylinder
G – Load cell
H – Chain connector
I – Dial Guages
J – Anchor rod
K – Plate anchor
L – Test tank
M – Sand bed

Fig. 1 Test set up for monotonic and cyclic loads

BEHAVIOUR OF ANCHOR UNDER MONOTONIC LOADING

Effects of width ratio (Br/B) on pullout loads

Fig.2 shows the pullout response of anchors for an embedment ratio of 4 and reinforcement width ratios of 2, 3 and 4 in medium dense sand bed. In this figure, the effect of width ratio of reinforcement was compared with unreinforced condition. The load-displacement response of anchor in reinforced sand was almost identical to that of unreinforced sand except that the pullout load was higher for a given displacement of anchor.

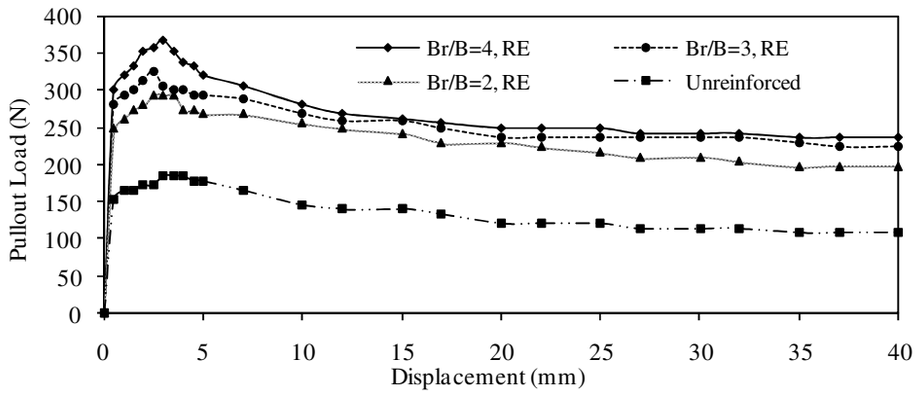


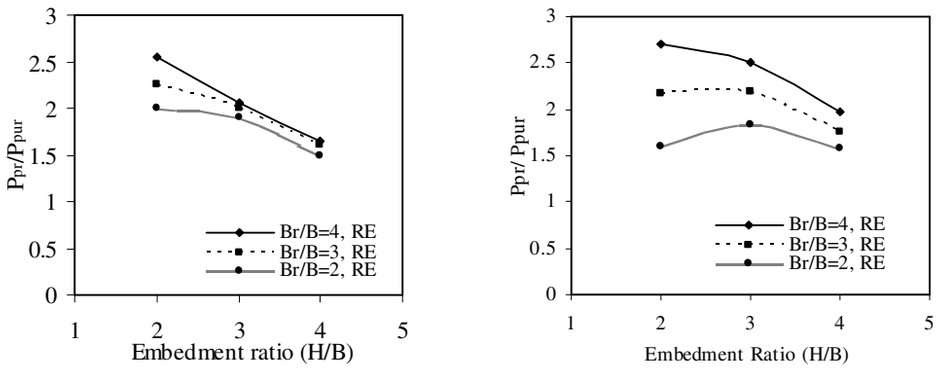
Fig. 2 Pullout response on anchor in medium dense sand bed for H/B = 4

The increase in peak pullout loads for the embedment ratio of 4 with B_r/B ratios 2, 3 and 4 were 59%, 76% and 96% respectively, over unreinforced medium dense sand. It was also found that increase in peak pullout load values for corresponding

B_r/B ratios (2, 3 and 4) of reinforcement were 59%, 118% and 171% respectively in medium dense sand for an embedment ratio of 2. This variation in peak load indicates that the percentage increase in peak pullout load reduces with increase in embedment ratio. Though the magnitude of pullout resistance was high for deeper embedments, the contribution from the reinforcement to peak pullout load is better for the anchor embedded at shallower depth. Further, reinforcement increased the residual pullout load and let a gradual decrease in pullout load for further displacement of anchor after the peak pullout was reached. The increase in residual pullout load for the embedment ratio 2 was 166%, 200% and 433% for the width ratios of 2, 3 and 4 respectively in medium dense sand over unreinforced sand. The increase in residual pullout load due to the introduction of reinforcement reduced with increase in embedment ratio. For an embedment ratio of 4 and Br/B of 2, the increase was about 82% and this value was almost around 160% for embedment ratio of 2 and 3. Almost similar behaviour was observed in the case of tests in dense and loose sand conditions.

From the observations made in submerged sand bed condition, it was found that the reinforcement provides substantial increase in peak and residual pullout loads. The percentage increase in pullout load was higher in case of loose sand bed than in medium dense and dense sand bed. Increase in width ratio (Br/B) provides better improvement in peak and residual pullout loads for an embedment ratio 2 and 3 in medium dense sand. But this effect converges with increase in embedment ratio. The improvement was also found to decrease with increase in density of sand bed irrespective of depth of embedment and width ratio of reinforcement.

Effects of the depth of embedment on pullout loads



(a) Dense sand **(b) Medium dense sand**

Fig. 3 Variation of pullout load ratio with embedment ratio (H/B)

The ratio between peak pullout load of anchor embedded in reinforced (P_{pr})and unreinforced (P_{pur}) bed are presented for various embedment ratios in Fig.3 for dense and medium dense conditions. It decreases with H/B ratio irrespective of width ratios of reinforcement and densities of sand bed. The P_{pr} /P_{pur} is maximum for the width ratio 4 and minimum for width ratio 2 irrespective of the depth of embedments

studied. Further for a given H/B ratio, higher the density, lower is the peak pullout load ratio. The peak pullout loads in reinforced bed are 1.5 to 2.55 times the peak pullout load in unreinforced bed for the dense sand and the width ratio of 2. The corresponding ranges for medium dense condition are 1.58 to 1.83 respectively.

BEHAVIOUR OF ANCHOR UNDER CYCLIC LOADING

Effects of the width ratio (Br/B) on pullout loads

Fig.4 shows the cyclic response of anchors for the embedment ratio of 2 in medium dense sand bed. The effect of width ratio of reinforcement was compared with unreinforced condition. The anchor movement was high initially as observed in unreinforced sand and it was increasing with number of cycles and after 350 cycles the rate of movement of anchor was almost constant and also negligibly small. It was found that the anchor movement after 1000 cycles for Br/B ratio 3 and 4 were around 1.85 and 2.53 times the unreinforced condition for the embedment ratio of 2 and for the embedment ratio of 4 the respective anchor movements were 1.77 and 2 times the unreinforced condition. Thus the movement of anchor decreases with embedment ratio as expected. However anchor movement was higher in denser bed despite the tests were conducted at CLR value of 60% because intensity of cyclic load was higher for denser condition.

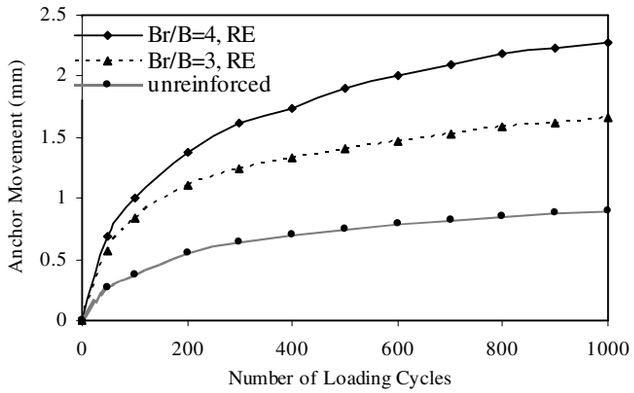


Fig. 4 Cyclic response of anchors in medium dense bed for embedment ratio 2

Degree of anchor movement

The anchor movement at different cycles of loading expressed as a percentage of movement corresponding to 1000 cycles and is referred to as the degree of anchor movement. Typical variations of degree of anchor movement with number of loading cycles are compared in Fig.5 for Br/B=3, H/B=4 and densities of loose, medium and dense conditions. Almost a unique relation is obtained both for unreinforced and reinforced conditions which is independent of the density and embedment ratios of sand bed. The test results on other width ratios of reinforcement also showed identical trend.

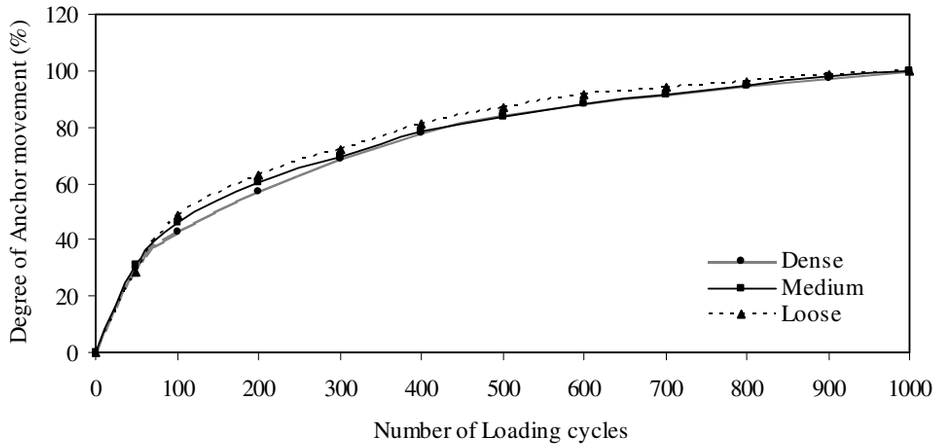


Fig. 5 The variation of degree of anchor movement with number of loading cycles for a width ratio (Br/B) of 3 and H/B=3

The degree of anchor movement increases with the number of cycles, but at decreasing rate. Around 90% of movement is reached within 500 cycles (i.e. 50% of targeted cycle) in all the three densities of sand bed for the CLR of 0.6. For the test conditions analysed in this study, the loading cycles more than 500 is insignificant in increasing the movement of the anchor, indicating that the anchor tends to attain an equilibrium displacement (constant displacement) at lesser number of loading cycles. Curves of these types are extremely useful in estimating the movement of anchors during storm periods. However, for estimation of movement of anchor for actual field situations, data of similar type, based on long-term cyclic loading tests under different CLR ratios are required.

POST-CYCLIC MONOTONIC PULLOUT TESTS

Fig. 6 compares the monotonic and post cyclic monotonic response of anchors in dense sand bed for width ratio 3. In post cyclic monotonic pullout test the peak pullout load of 153.8N, 268.4N and 380.6N for embedment ratios 2, 3 and 4 were observed in dense sand bed. The displacements corresponding to the peak pullout load were 3.7mm, 3.3mm and 3.8mm respectively. For the same density condition and embedment ratio, the peak pullout load of 143.8N, 255.6N and 270N were obtained in case of monotonic pullout tests. The displacements corresponding to the peak pullout load were 3.5mm, 3mm and 3.5mm respectively.

The post cyclic pullout load and monotonic pullout load of anchors for Br/B ratio 3 and the embedment ratios 2, 3 and 4 were compared in the Table 1 for medium dense condition. It is clear from the results, the post cyclic pullout capacities are marginally higher (maximum 10% and average 6%) than monotonic pullout capacities and the displacement required to develop peak resistance in cyclic loading was also higher than that of monotonic pull. Marginal increase in capacity may be attributed to negative pore water pressure (suction pressure) at the base of the anchor.

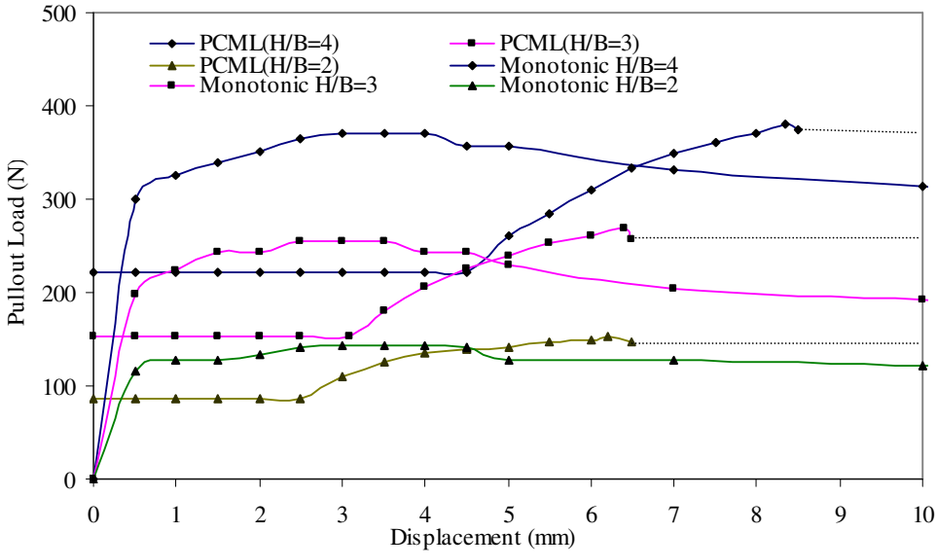


Fig. 6 Comparison of monotonic and post cyclic monotonic response of anchors in dense sand bed for width ratio 3

Ilamparuthi (1991) recorded negative pore water pressure at different levels of failed mass during pullout and also reported that the negative pore water pressures are higher for higher rate of pull. However post cyclic resistance was less when compared with the response of monotonic pull particularly for the displacements less than the displacement corresponds to peak pullout load of monotonic loading condition. Further, the rate of increase of resistance with displacement in the post cyclic phase was lesser than the monotonic pull. This may be attributed to gradual collapse of sand towards the gap created at the bottom of anchor during cyclic load, loss of resistance in sand due to adjustment of particles and change in the pore pressure

Table 1 Comparison between monotonic and post cyclic peak pullout loads for Medium dense (Br/B=3)

Nature	H/B=2		H/B=3		H/B=4	
	P_u (N)	δ_u (mm)	P_u (N)	δ_u (mm)	P_u (N)	δ_u (mm)
Monotonic	118.2	3.0	210.9	3.0	325.9	2.5
Cyclic	128.4	4.9	224.2	5.6	337.0	6.1

CONCLUSIONS

The shape of the load-displacement curves for anchors embedded in reinforced and unreinforced beds are similar. However the rate of increase of pullout resistance (Pre-peak phase) is higher for reinforced condition.

The peak pullout load increases with embedment ratio and density of sand bed for both reinforced and unreinforced conditions and is higher for reinforced sand than unreinforced condition irrespective of density and embedment ratio. Friction along the reinforcement is the main contributing factor for the higher pullout capacity.

The increase in the width ratio (Br/B) of the reinforcement increased the pullout capacity of the anchor owing to the fact that the friction along the reinforcement increases with the increase in anchorage length of the reinforcement. The effect of reinforcement is more pronounced at lower embedment ratio and density irrespective of the width of reinforcement.

In the case of cyclic loading, the upward movement of anchor per loading cycle decreases with the increase in the number of load cycles and the movement of anchor gets stabilized after 350 cycles. The displacements of the anchors increase with the increase in density and depth of embedment. Though the tests were conducted at same CLR value (60%) in all the densities, the movement is higher in denser beds because absolute cyclic load is higher for higher densities and deeper embedments.

The post cyclic peak pullout loads are marginally higher (< 10%) than monotonic peak pullout loads for all the three states of sand and embedment ratios in unreinforced and reinforced sand beds. But the displacement corresponding to post cyclic peak pullout load is 1.5 to 2 times higher than the displacement of the monotonic peak pullout load.

REFERENCES

Andreadis, A. and Harvey, R.C. (1981). "A design procedure for embedded anchors." *Applied Ocean Res*.3, No.4, 117-182.

Ghaly, A. M., Hanna, A. M. and Hanna, M. (1991). "Uplift Behaviour of Screw Anchors in Sand II: Hydrostatic and Flow Conditions", *Journal of Geotechnical Engineering*, ASCE, Vol. 117, No.5, 794-808.

Ilamparuthi, K. and Dickin, E.A. (2001a). "Predictions of the uplift response of model belled piles in geogrid-cell-reinforced sand." *Geotextiles and Geomembranes*, 19, 89-109.

Ilamparuthi, K. and Dickin, E.A. (2001b). "The influence of soil reinforcement on the uplift behaviour of belled piles embedded in sand bed." *Geotextiles and Geomembranes*, 19, 1-22.

Ilamparuthi, K and Muthukrishnaiah, K. (2001). "Breakout capacity of seabed anchors due to snap loading." *Proceedings of International Conference in Ocean Engineering,* IIT Madras, Chennai, India, 393 – 400.

Kingshri, A., Ilamparuthi, K., and Ravichandran, P. T. (2005). "Enhancement of uplift capacity of anchors with Geocomposite." *Proceeding of National Symposium on Geotechnical prediction methods*(Geopredict 2005), IIT Madras, Chennai, 148-152.

Krishnaswamy, N.R. and Parashar, S.P. (1994). "Uplift behaviour of plate anchors with Geosynthetics." *Geotextiles and Geomembranes*, 13, 67-89.

Krishnaswamy, N.R. and Parashar, S.P. (1992). "Effect of submergence on the uplift resistance of footings with geosynthetic inclusion." *Proceedings of Indian geotechnical conference*, Surat, India, 333-336.

Ravichandran, P.T. and Ilamparuthi, K. (2004). "Behaviour of rectangular plate anchors in reinforced and unreinforced sand beds." *Proceedings of International Conference on Geoenvironmental Engineering(ICGGE),* IIT Bombay, Mumbai, 123-128.

Selvadurai, A.P.S. (1993). "Uplift behaviour of strata-grid anchored pipelines embedded in granular soils." *Geotechnical Engineering*, 24(1), 39-55.

Subbarao, C., Mukhopadhyay, S., and Sinha, J., (1988), "Geotextile ties to improve uplift resistance of anchors." *Proc. of the first Indian Geotextile Conference on Reinforced soil and Geotextiles*, Bombay, India, F3-F8.

Uplift Testing of Rammed Aggregate Pier® Systems

Tom Farrell[1] GE, MASCE, Brendan FitzPatrick[2] PE, William Kenney[3] GE MASCE.

[1]President, Farrell Design-Build Companies, Inc., 685 Placerville Drive, Placerville, CA 95667 USA, tom@farrellinc.com. [2]Director of Engineering, North America Geopier Foundation Company, Inc., 150 Fairview Road, Suite 335, Mooresville, NC 28117, USA, bfitzpatrick@geopier.com. [3]Project Manager, Farrell Design-Build Companies, Inc., 685 Placerville Drive, Placerville, CA 95667 USA, bill@farrellinc.com.

ABSTRACT: Recent changes and consolidation in building codes across the U.S. have put a larger emphasis on the need for cost-effective foundation support of both bearing and uplift foundation loads resulting from wind and seismic forces. The Rammed Aggregate Pier (RAP) system is a commonly-accepted soil reinforcement method that results in highly-densified aggregate columns for liquefaction mitigation, bearing capacity enhancement, and uniform settlement control for conventional shallow foundations. The RAP system provides a cost beneficial alternative to deep foundations such as pre-cast driven piles, auger-cast piles, or concrete piers and to mass excavation and replacement for shallow foundations. In high seismic and wind areas, uplift loads created by overturning forces on foundations are resisted with uplift RAPs that are equipped with a structurally designed steel anchor assembly. Typical uplift capacities in California range from 178 to 445 kN (40 to 100 kips) for 762 to 838 mm (30 to 33 inch), 3.6 to 7.0 m (12 to 23 feet) meter long RAP elements using ASD (allowable stress design) and incorporating a minimum factor of safety of 2. Full scale load tests on uplift RAPs show repeatable tangent stiffness after multiple overstress load cycles. This paper presents the first published results of psuedo-cyclic uplift load tests on uplift RAPs installed on projects in California.

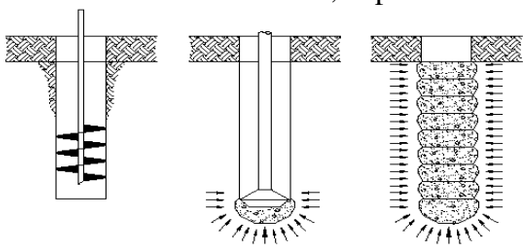
INTRODUCTION

The nationwide adoption of the International Building Code in the US and recently in California presents challenges to engineers now faced with often higher seismic and wind forces updated by current events and research. Increased seismic forces in California are of particular concern in building design, construction, and performance. Seismic forces resulting in large short term bearing and uplift loads on a building foundation can be challenging and expensive to solve in California. This paper discusses the engineering, construction, performance, and load test results of Uplift Rammed Aggregate Pier systems (uplift RAPs). The limit states and

mechanisms considered for friction capacity along the sides of the RAP shaft are discussed along with the structural design considerations of the steel anchors. Of particular importance, the results of multiple pseudo-cyclic uplift load tests are presented and discussed for differing soil conditions in California.

RAMMED AGGREGATE PIER CONSTRUCTION

Rammed aggregate pier systems are constructed by installing thin lifts of highly-densified aggregate using vertical ramming energy. Two different installation methods are typically used depending on the site specific soil conditions. The first method is a replacement RAP method (aka Geopier® RAP). This method involves removing soft and weak soil or fill by drilling shafts measuring 762 to 838 mm (30 to 33 inch) in diameter to depths ranging from 2 to 9 m (6 to 30 feet), see Figure 1. After drilling is complete, aggregate is added to the shaft and rammed in place. The ramming equipment consists of a 200 kN (45,000 pound) hydraulic excavator equipped with a 15.6 kN (3,500 pound) hydraulic break hammer and a specially designed 45° beveled ram to form the thin, expanded rock lifts (Majchrzak, 2004).



A. Drill 762 to 838 mm (30 and 33 inch) diameter shafts to design depth
B. Ram 51 mm (2 inch) crushed rock into the "bottom bulb", then ram thin lifts
C. Ram 19 mm (¾ inch) crushed rock in 305 mm (12 inch) lifts to form a Geopier RAP.

Fig. 1 Geopier Rammed Aggregate Pier Construction Process

The second method is a displacement RAP method (aka Impact® RAP) which densifies and displaces soil by driving a hollow pipe mandrel into the ground. Aggregate is introduced to the bottom of the displaced hole through the pipe mandrel. The mandrel is raised and then driven back down to vertically densify thin lifts of aggregate. Aggregate and sand densification is achieved during installation using both vertical static crowd pressure and vertical impact ramming energy delivered by a high-frequency, vibratory, pile driving hammer. This RAP method is unlike vibro-replacement stone column methods where horizontal vibrations, that are produced by eccentric weights in a vibrating probe, are used to compact the stone. Displacement RAP elements are typically 508 to 610 mm (20 to 24 inch) in constructed diameter and extend to depths ranging from 3 to 15 m (10 to 50 feet). For greater densification and improvement, re-ramming of rock lifts often results in diameters over 762 mm (30 inches). The ramming equipment consists of a 445 to 624 kN (100 to 146 kip) piling rig equipped with a 1,350 kN (152 ton) vibratory hammer, pipe mandrel, and an expanded beveled ram. See Figure 2 for the Impact RAP method of construction.

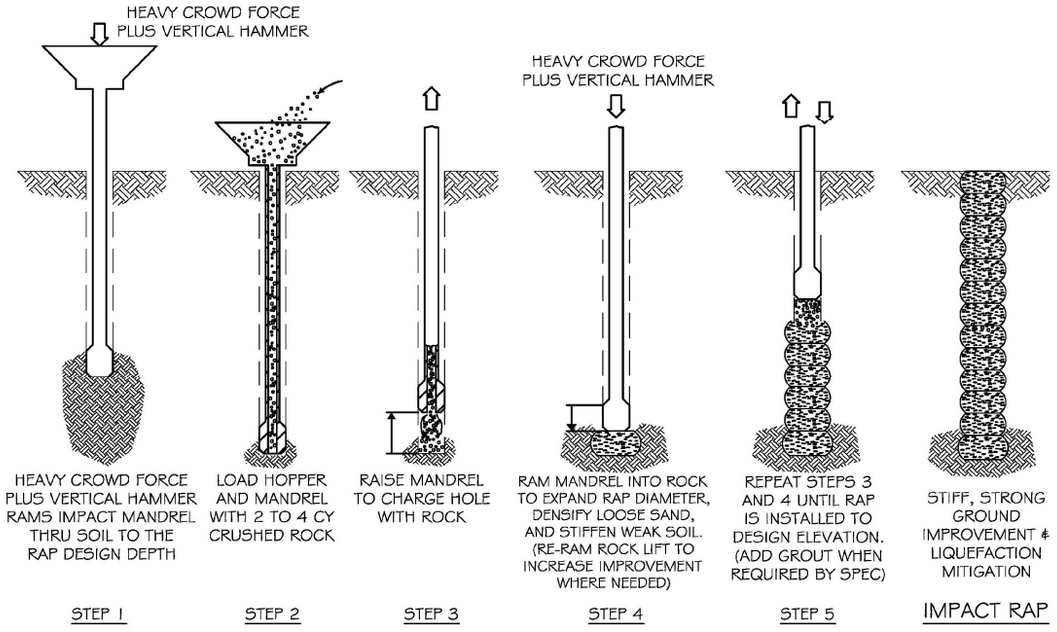


Fig. 2 Impact Rammed Aggregate Pier Construction Process

As a result of heavy crowd force and vertical ramming during installation, both RAP construction methods result in expansion of the aggregate at the edge of the pier (cavity expansion). These installation processes and resulting cavity expansion form undulated sides along the pier perimeter and significantly increase the lateral stress in the matrix soil. The combination of high lateral stress and undulated shape results in enhanced coupling of the RAP aggregate to the matrix soil providing an efficient mechanism for shear resistance along the sides of the RAP element (Handy 2001, White et al 2002). This development of high shear resistance is the basis for providing both high bearing and uplift resistance using RAPs for foundation support.

Both RAP construction methods deliver uplift resistance with the addition of a structurally designed steel anchor assembly. An uplift RAP is constructed by installing a vertical "dead-man" anchor at the "bottom bulb" elevation during construction of the RAP. In California, the structural steel anchor typically consists of two bard for Impact RAPs or four bars for Geopier RAPs. Williams Form Engineering #7 all-thread rebars with a minimum ultimate strength of 267 kN (60 kips) are used in most uplift RAP applications. Figure 3 shows an uplift anchor assembly and properties of the all thread rebar.

At the bottom of the anchor, the all thread bar are bolted to a 25 mm (1-inch) thick, hot dip galvanized, A36 steel plate. For permanent installations, the uplift assembly is corrosion protected. A robust corrosion protection system is used in California as follows: 1) oversized and hot dip galvanized steel bars, 2) asphaltic coating on the bars, 3) a heat-shrink polyurethane coating of 0.8 to 1.6 mm (30 to 60 mils) thick over the asphalt coating on the bars. The 25 mm plate nut assembly are also covered with a poly urethane coating. The tops of the all thread bar receive 102 mm (4 inch) square bearing plates, which provide the necessary anchorage in the concrete footing.



All Thread Structural Properties	
Minimum Yield Stress	Ultimate Tensile Stress
517 MPa (75 ksi)	698.5 MPa (100 ksi)

Fig. 3 RAP Uplift Assembly and All Thread Rebar Properties and Threads

UPLIFT RAP PERFORMANCE

Uplift RAP strength and stiffness performance is affected by several design parameters and the construction process. The most considered performance parameter by practicing engineers is typically "embedment depth," which the authors have observed by numerous load tests does not solely control the ultimate capacity and performance of the uplift RAP. The basic design and construction parameters to be considered for reliable uplift RAP strength and stiffness are:

1. Density of Rammed Aggregate directly above the bottom plate
2. Embedment depth "D" (distance between bottom of footing and bottom plate)
3. Shear resistance by skin friction in sand or undrained shear strength in clay
4. Stiffness of steel rods ($\Sigma AE/D$)
5. Group effects (multiple uplift RAPs)
6. Adjacent bearing RAPs (which increase confinement)
7. Number of load cycles
8. Uplift load

Expected seismic performance requires an equivalent spring stiffness from between 5.7 to 56.5 kN/m (50 to 500 kips/inch). Current uplift RAP design methods are based on well accepted limit states of embedment depth and shear resistance at the shaft edges. However, these limit states are based on strength and not deflection. Based on the performance of numerous load tests, the authors have observed that the

parameter with the most influence on uplift RAP stiffness is the density and expansion of the rammed aggregate directly above the bottom plate. This parameter is also the most sensitive to the construction process and requires a specially trained and highly experienced operator on the ramming equipment.

Based on the author's observation and experience with numerous uplift RAP tests, the soil strength and rammed aggregate within the bottom 1/3 of the RAP often limits the RAP deflection response to load. Engineers can use judgment during design to increase the RAP tension capacity by specifying cement treated aggregate. When a stiffer response is needed or softer soils are observed within 1.5 m (5 feet) of the bottom plate, cement can be mixed with the aggregate and installed on and above the plate. The cement treated aggregate is placed from to 0.9 to 1.5 m (3 to 5 feet) above the plate, where vertical stresses induced in the pier from the applied uplift loads are highest – on the order of 1,915 kPa (40 ksf).

UPLIFT RAP ENGINEERING CALCULATIONS

The design for uplift RAPs must consider the limit states for the system. These limit states may be divided into 1) geotechnical design considerations which incorporate not only the behavior of the RAP element, but also relate the anticipated performance to the site-specific soil conditions as well as 2) structural design considerations focusing on the structural design of the high-strength rods and anchor plate. These limit states are described below.

Geotechnical Limit State Considerations

Uplift RAPs generate capacity by developing shear resistance along the perimeter of the shaft. The shear resistance is enhanced by the high lateral stress imparted by cavity expansion at the edges of the shaft (Wissmann et. al. 2001, Caskey 2001). The increase in lateral stress or horizontal pressure in the matrix soil as a result of ramming aggregate into the soil provides for the benefit of greater capacity and greater load diffusion in the matrix soil (Schmertmann 2005).

Figure 4 shows a typical 4-bar uplift RAP detail. The limit state of unit shaft resistance is computed as the unit resistance (f_s) to vertical movement as:

1. The product of the effective horizontal earth pressure ($\sigma'_h = K_p\sigma'_v$) and the tangent of the unimproved soil friction angle (ϕ'_s) for sandy soil or over-consolidated, clay soil as shown in Equation 1, where σ'_v is the effective vertical stress and K_p is the Rankine passive earth pressure coefficient (Lawton et al. 1994). The Rankine passive earth pressure coefficient is used in design up to a maximum pressure often limited to 120 to 144 kPa (2,500 to 3,000 psf). This limit is based on field measurements of lateral stress using the Ko-Stepped Blade next to installed RAPs (Handy 2001, Wissmann, 2001).

   for sand or over-consolidated clay soil: $f_s = \sigma'_h \tan(\phi'_s)$ (1)

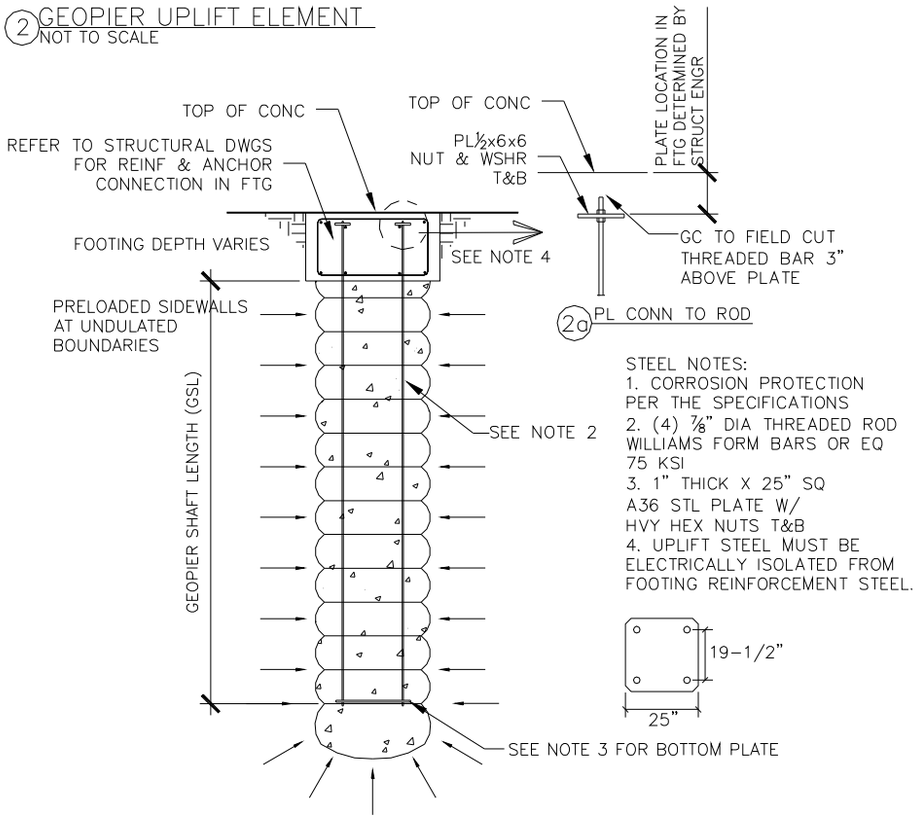


Fig.4. Typical Detail of a 4-bar RAP Uplift Element

2. The undrained shear strength (s_u) for normally-consolidated to slightly over-consolidated clay soil as shown in Equation 2. The RAP installation process results in lateral stress increases (Handy 2001). Although this increase in lateral stress causes consolidation and subsequently an increase in the undrained shear strength of the matrix soil, a conservative pre-installation estimate of undrained shear strength is used for design.

for normally- to slightly over-consolidated clay soil: $f_s = s_u$ (2)

The ultimate uplift capacity (T_{ult}) is computed by integrating the unit uplift resistance (f_s) over the assumed cylindrical perimeter area (A_s) of the RAP plus the weight of the uplift RAP (W_{RAP}):

$$T_{ult} = f_s A_s + W_{RAP} \quad (3)$$

A factor of safety of 2 is commonly applied to the theoretical ultimate uplift capacity to assign the allowable capacity for design. Typical geotechnical uplift capacities of 222.4 to 355.8 kN (50 to 80 kips) ASD are calculated and tested in California. While an additional geotechnical limit state that addresses uplift capacity of a RAP group as described in Wissmann et al. (2001) is checked, the single pier capacity is typically the controlling consideration.

Structural Limit State Considerations

The structural design of the RAP uplift anchor must take into account these structural limit states: 1) the tensile load capacity of the anchor rods, 2) the bending of the bottom plate, and 3) anchorage of the rod in the concrete footing.

Anchor rod capacity (Q_{yield}) is calculated by either Load and Resistance Factor Design (LRFD) or Allowable Stress Design (ASD) design approach.

$$Q_{yield} = F_{yield} \sum A_{rod} \tag{4}$$

where Q_{yield} is the yield strength of the threaded rod group, F_{yield} is the yield stress, and ΣA_{rod} is the sum of the minimum cross sectional area of the threaded rod. In most environments, corrosion protection is taken into account using procedures outlined in FHWA-NHI-00-044 (Elias, 2000). Typically a design life of 75 years is considered for permanent structures. Additional width is then added to the rod diameter to enhance the corrosion protection measures described above.

For Allowable Stress Design (ASD):

$$Q < Q_A \tag{5}$$

$$\text{where } Q_A = 0.60\ Q_{yield} \tag{6}$$

where Q equals uplift demand at "working stress" levels

For Load and Resistance Factor Design (LRFD):

$$Ru < \phi Rn \tag{7}$$

$$\text{where } \phi Rn = 0.9\ Q_{yield}, \text{ and} \tag{8}$$

Ru is the critical factored load based on the governing load combination

The minimum plate thickness with regard to bending of the bottom plate can be estimated with a closed-form equation. However, this tends to over-estimate the plate thickness. A finite element analysis using "thick" plates provides for an optimized solution. The typical uplift RAP application consists of an 838 mm (33 inch) drilled diameter RAP equipped with four #7 all-thread bars of 22.2 mm (7/8 inch) in diameter, 517 MPa (75 ksi) that extend 3.7 to 6.4 m (12 to 21 feet) to the bottom plate with a minimum plate thickness of 25 mm (1 inch). The plate thickness is also increased to enhance the required corrosion protection measures.

Anchorage of the rods in the footing is determined using conventional concrete procedures. To reduce embedment length in the concrete footing, 102 mm (4-inch) square steel plates are used on the anchor bars in the footing.

UPLIFT RAP LOAD TEST RESULTS

Uplift RAP elements are tested under single load cycles and multiple load cycles in general accordance with ASTM pile uplift test method D3689 Standard Test Method (1995). Cyclic testing protocols are generally non-standard for the geo-structures industry, however, these tests provide useful data to understand the RAP load deformation relationship. The following section presents the continuous load, cyclic axial uplift test results for projects in Sacramento and Pleasant Hill, California.

The results of two consecutive cyclic uplift load tests at 1801 L Street project in Sacramento, CA are shown in Fig. 6. The soil profile at this site consists of alluvial, loose sandy silt extending 9.5 m (30 feet) below the ground surface (bgs). Groundwater was encountered at about 2 m (6.5 feet) bgs. Standard penetration test (SPT) "N- values" ranged from 2 to 10. Moisture contents ranged from 24 % to 33% for soil above and below the groundwater, respectively.

The maximum applied load during the test was 534 kN (120 kips). The tests indicate an initial deflection of about 5 mm (0.2 inch) at the design load of 267 kN (60 kips). As the test continued, a maximum deflection of about 17 mm (0.67 inch) was observed after 5 load cycles under twice the design load 534 kN (120 kips). This test shows the repeatability of stiffness of the uplift RAP in tension in soft soil after two multiple cycle events. Based on the deflection data, it is observed that almost 50% of the initial elastic deflection is attributed to elongation of the steel anchor bars.

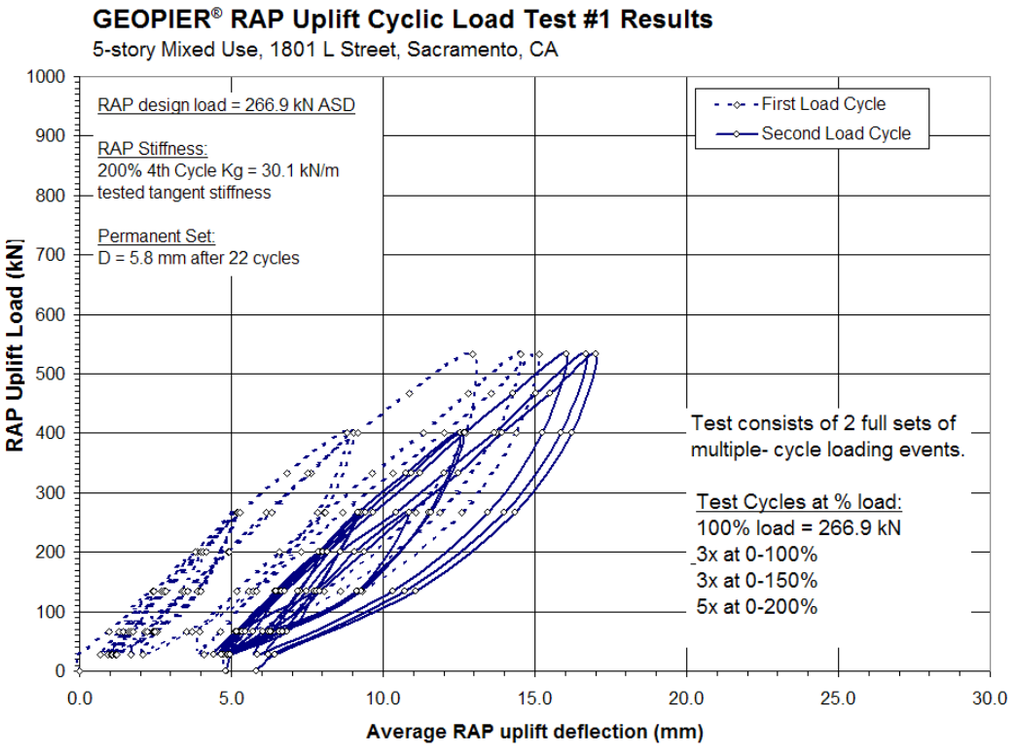


Fig. 6 Cyclic Load Test on 838 mm dia. by 4.6 m deep uplift RAP

This uplift RAP maintained linear tangent stiffness after multiple cycles performed to levels of 200% of the design load.

Cyclic uplift tests were also performed at the BART Parking Structure project located in Pleasant Hill, California. The soil profile at this site consists of alluvial soil deposits of stiff clay interbedded with medium dense sand to depths of 12.2 to 13.7 m (40 to 45 feet). Groundwater was observed at 4.6 m (15 feet) bgs. Siltstone (bedrock) was encountered at depths of 13.7 to 16.8 m (45 to 55 feet) bgs. The soil exhibited SPT N-values ranging from 6 to 10 and undrained shear strengths between 50 and 110 kPa (1044 to 2300 psf) to depths of 9.1 m (30 feet) bgs. Figure 7 shows the average undrained shear strength estimated from 3 cone penetration tests performed at the BART site.

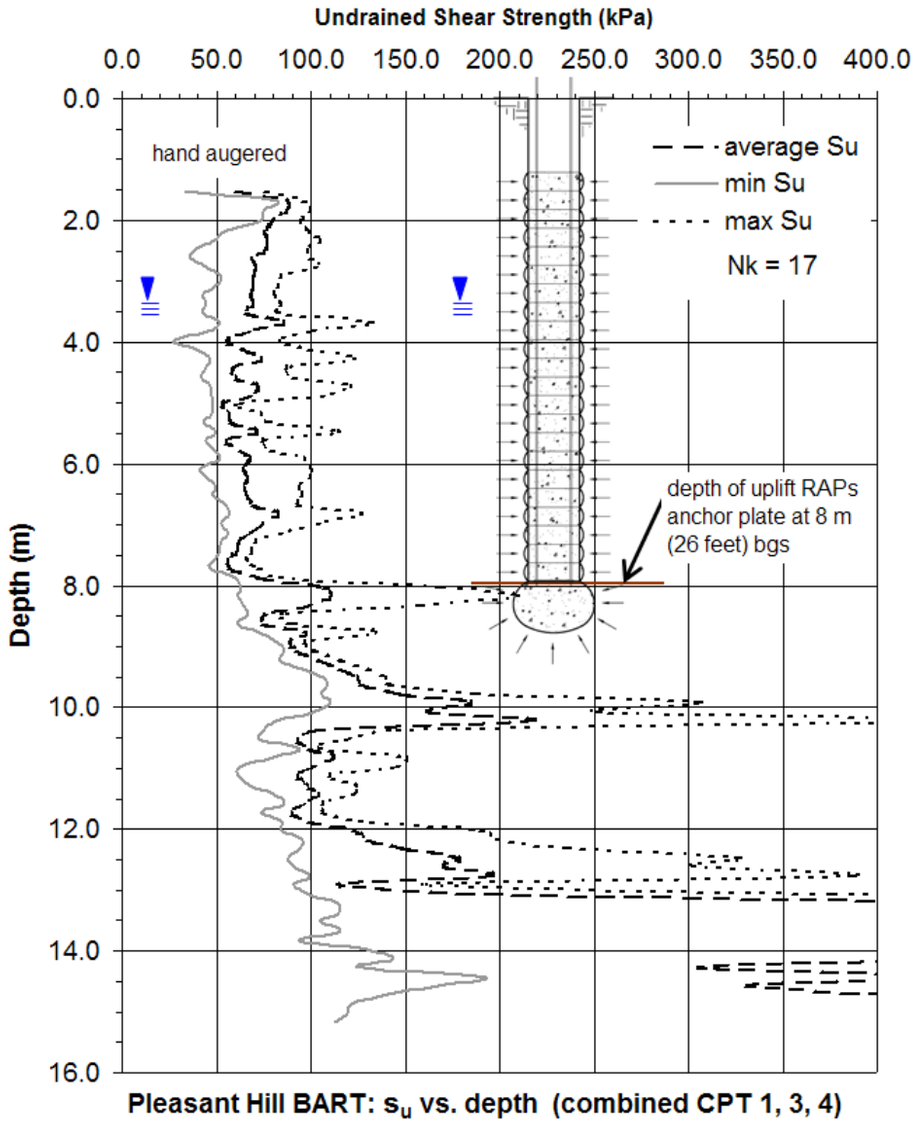


Fig. 7 Average undrained shear strength at BART Parking Structure.

The BART project required multiple full scale bearing and uplift tests at different test locations across the large site. Cyclic loading was performed on two of the uplift tests and plots of the results are shown in Figures 8 and 9. The maximum applied load during the tests was 890 kN (200 kips).

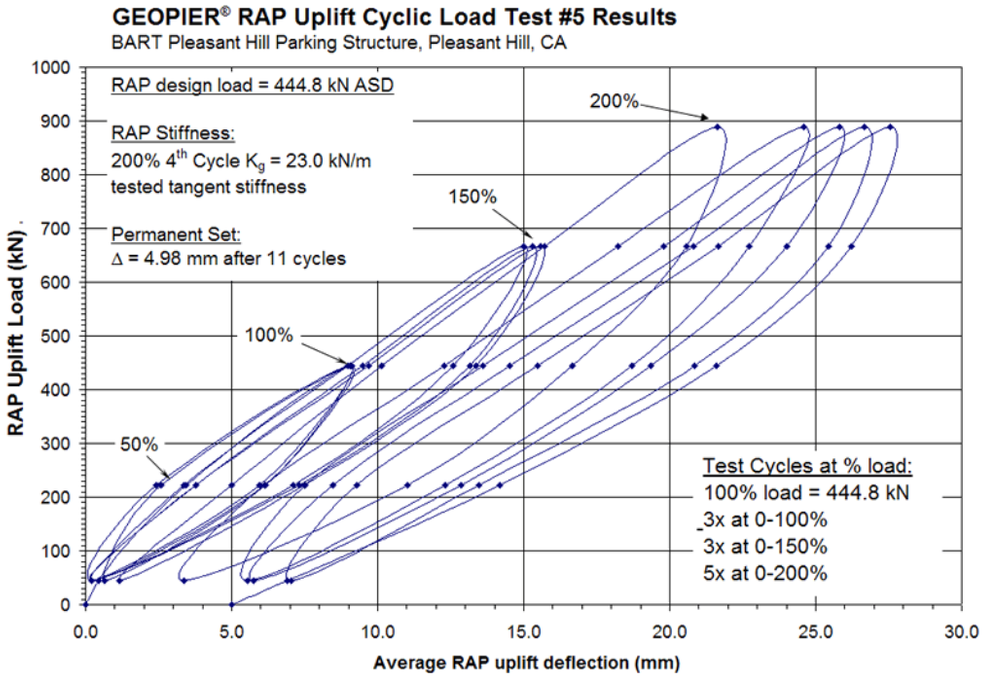


Fig. 8 Cyclic Load Test #5 on 838 mm dia. by 6.1 m deep uplift RAP

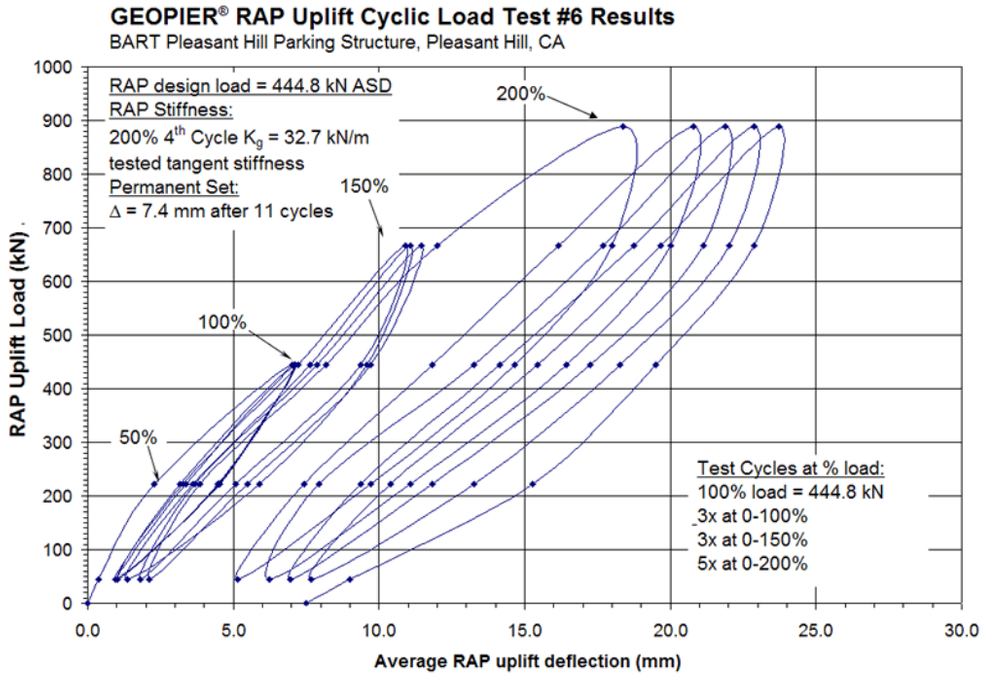


Fig. 9 Cyclic Load Test #6 on 838 mm dia. by 6.1 m deep uplift RAP

The BART test results indicate deflections of less than 10 mm (0.39 inch) at the design load of 445 kN (100 kips) and typically less than 25 mm (1 inch) of deflection after repeated cycles at 200% of the design load. Once again these tests show the repeatability of linear stiffness of between 23 to 33 kN/m (204 to 292 kips/inch) of the uplift RAP in tension in stiff clay and medium dense silty sand after multiple load cycles. Figure 10 shows a group of uplift RAPS in a shearwall mat at the BART site in Pleasant Hill.



Fig. 10 Group of uplift RAPs at BART in Pleasant Hill, CA.

SUMMARY OF UPLIFT RAP CYCLIC TENSION TESTS

Table 1 summarizes the RAP Design Parameter values and Uplift Test data for pseudo-cyclic uplift tests performed in Sacramento and Pleasant Hill, CA. The results of the data indicate the piers exhibit a relatively consistent load-deflection behavior under multiple loading cycles performed up to 200% of the allowable design capacity. Additionally, while the cyclic deflections observed during testing were up to 27 mm (1.1 inch), the permanent deflections measured after the conclusion of the cyclic testing are less than 8 mm (0.3 in). It is also interesting to observe that a significant contribution to the total deflection of the uplift RAPs at 200% design load is related to elongation of the anchor bars.

These pseudo-cyclic tests were performed as a part of research efforts to better understand the load-deformation relationship of uplift RAP elements. While the

relationship between number of cycles and deformation is not specifically included as a design parameter, it is interesting to note from these test results that the stiffness does not degrade with additional load cycles. In addition, while each load cycle produces incremental plastic deformation (set) of the soil/bottom-plate zone, the increment of plastic deformation generally decreases with increased load cycles. This behavior is likely related to the cavity expansion and lateral stress increases imparted during RAP installation. This behavior also results in repeatable tangent stiffness with virtually no degradation after as many as 22 continuous load cycles.

Table 1. Summary of RAP Design Parameters and Uplift Tests

Soil and Test Parameters	1801 L Street	BART Test 5	BART Test 6
Soil Profile, m (feet)	ML to 9.5 (30)	CL to 12.2 (40)	CL to 12.2 (40)
Unit weight, kN/m^3 (1b/ft^3)	18.1 (115)	19.6 (125)	19.6 (125)
Ground Water, m (feet)	1.5 (5)	3.0 (10)	3.0 (10)
N_1 - mid depth, blows/0.3m	5	10	10
N_1 - Low/Hi, blows/0.3m	2/10	6/21	6/21
Su (Hi/Lo), kPa (psf)	0	71 (1,250)	71 (1,250)
Phi angle, degrees	34	0	0
RAP Installation Method	Replacement	Replacement	Replacement
RAP Diameter, m (feet)	0.83 (33)	0.83 (33)	0.83 (33)
Footing Depth, m (feet)	0.9 (3)	1.8 (6)	1.8 (6)
RAP Shaft Length, m (feet)	4.6 (15)	6.7 (22)	6.7 (22)
Total Drill Depth, m (feet)	5.6 (18)	5.6 (18)	5.6 (18)
Est. Capacity, kN (kip)	934 (210)	961 (216)	961 (216)
FS for Design Capacity	3.5	2	2
ASD Capacity, kN (kip)	267 (60)	445 (100)	445 (100)
Tested Capacity, kN (kip)	534 (120)	890 (200)	890 (200)
Bar Strain, mm (inch)	9.6 (0.38)	14.1 (0.56)	14.1 (0.56)
Tested RAP Deflection at 200% ASD Cap., mm (inch)	13.5 (0.53)	27.6 (1.09)	23.7 (0.93)
Actual Plate Deflection at 200% ASD Cap., mm (inch)	3.9 (0.15)	13.5 (0.53)	9.6 (0.38)
Permanent Plate Deflection at end of test, mm (inch)	5.8 (0.2)	5.0 (0.2)	7.4 (0.3)
RAP Stiffness at 200% ASD Cap., kN/m (kip/inch)	30.1 (266.4)	23.0 (203.6)	32.7 (289.4)

CONCLUSIONS

As building codes have consolidated into the IBC and with California's adoption of the 2007 California Building Code, the California version of the IBC, the need for cost-effective foundation solutions to resist high seismic foundation loads can be mitigated using Rammed Aggregate Pier solutions. In high seismic and wind regions,

the resulting overturning forces are effectively resisted with uplift RAPs. RAP installation methods increase the lateral stress in the soil, thereby increasing the RAP uplift capacity at shallow depths. Full scale load test data presented herein demonstrate the performance of uplift RAP elements for the resistance of uplift forces on foundations. Typical RAP ASD uplift capacities in California range from 178 to 445 kN (40 to 100 kips) for 762 to 838 mm (30 to 33 inch), 3.6 to 7.0 m (12 to 23 feet) long RAP elements and incorporate a minimum factor of safety of 2. The load test results show repeatable tangent stiffness after multiple overstress load cycles to 200% of the allowable design load. Tangent stiffness exhibited by uplift RAPs ranged between 23 and 33 kN/m (204 to 292 kips/inch). A robust corrosion protection system incorporated in the design of uplift RAPs is also described. Coupling the demonstrated repeatable stiffness at high loads with multiple layers of corrosion protection on the uplift RAP components, designers and engineers can be assured of reliable hold-down resistance and long lasting performance.

ACKNOWLEDGMENTS

The authors appreciate the support of the practicing geotechnical engineers and structural engineers in California that have recommended and supported the use of rammed aggregate pier supported foundations. Particular thanks are made to Watry Design Inc. and Treadwell & Rollo Inc. for their support in multiple uplift tests at the Pleasant Hill BART project and Point 2 Structural Engineers and Wallace Kuhl & Associates for their support in uplift tests at the 1801 L Street project in Sacramento.

REFERENCES

ASTM Test Standards (1995)

Caskey, J.M. (2001). “Uplift Capacity of Rammed Aggregate Pier Soil Reinforcing Elements.” University of Memphis.

Elias, Victor (2000). “Corrosion/Degradation of Soil Reinforcements for Mechanically Stabilized Earth Walls and Reinforced Soil Slopes”, Publication FHWA-NHI-00-044

Geotechnical Report BART Pleasant Hill, Treadwell & Rollo Inc. (2004)

Geotechnical Report 1801 L Street, Wallace Kuhl & Associates (2000)

Handy, R.L. (2001). “Does lateral stress really influence settlement?” Journal of Geotechnical and Geoenvironmental Engineering. 127(7), 623-626.

Lawton, E. C. (2000). “Performance of Geopier Foundations During Simulated Seismic Tests at South Temple Bridge on Interstate 15, Salt Lake City, Utah.” *Final Report, No. UUCVEEN 00-03*, University of Utah, Salt Lake City, Utah.

Lawton E. C. and N. S. Fox. (1994). "Settlement of structures supported on marginal or inadequate soils stiffened with short aggregate piers." *Vertical and Horizontal Deformations of Foundations and Embankments,* A.T. Yeung and G.Y. Fello (Editors), American Society of Civil Engineers, 2, 962-74.

Lawton, E.C., Fox, N. S., and R. L. Handy. (1994). "Control of settlement and uplift of structures using short aggregate piers." *In-situ Deep Soil Improvement*, K.M. Rollins (Editor), American Society of Civil Engineers, 121-132.

Majchrzak, M., Lew, M., Sorensen, K., and Farrell, T. (2004). "Settlement of Shallow Foundations Constructed Over Reinforced Soil: Design Estimates vs. Measurements." Fifth International Conference on Case Histories in Geotechnical Engineering, April 2004.

Robertson, PK, Campanella, RG, Gillespie, D, Greig, J, (1986). "Use of Piezometer Cone Data." Proceedings of inSitu 86, ASCE Specialty Conference, Blacksburg, VA

Schmertmann, J.H. (2005). "Stress Diffusion Experiment in Sand." Journal of Geotechnical and Geoenvironmental Engineering. 131(1), 1-10.

White, D.J., Wissmann, K.J., Barnes, A.G., and Gaul, A.J. (2002). "Embankment Support: A Comparison of Stone Column and Rammed Aggregate Pier Soil Reinforcement." Presented, Transportation Research Board. 81st Meeting, Washington, D.C. January 13-17.

Wissmann, K.J., J.M. Caskey, and B.T. FitzPatrick. (2001). "Geopier® Uplift Resistance." Technical Bulletin No. 3. Geopier® Foundation Company, Inc., Scottsdale, AZ.

DEM SIMULATION OF THE SEISMIC RESPONSE OF SHALLOW FOUNDATION ON LIQUEFIABLE SOIL

U. El Shamy[1]

[1]Environmental and Civil Engineering Dept., Southern Methodist University, PO Box 750340, Dallas, TX 75275, E-mail: uelshamy@engr.smu.edu

ABSTRACT

This paper presents an attempt to model the seismic response of a spread footings system founded on liquefiable granular soil deposit using a three-dimensional transient fully-coupled hydromechanical model and taking into account the effects of soil-foundation interaction. The porous soil medium is modeled as a mixture of two interpenetrating phases, namely the fluid phase (water) and the particulate solid phase. The fluid is idealized as a continuum by using averaged Navier-Stokes equations that accounts for the presence of the solid particles. The Discrete Element Method (DEM) is employed to model the assemblage of these particles. The interphase momentum transfer is modeled using established relationship that accounts for the dynamic change in porosity. The spread footing is modeled as a rigid block and its motion is described by the resultant forces and moments acting upon it. A computational simulation is conducted to investigate the response of spread-footings on a saturated granular deposit when subjected to a dynamic excitation. Results of the conducted simulation showed that the foundation sustained excessive settlement as the ground shaking progressed and the underlying soil liquefied. The conducted simulation appears to capture essential dynamic response patterns typically observed in such systems.

INTRODUCTION

Liquefaction-induced settlement of shallow foundations is a major form of failure for buildings in saturated sand deposits. Examples of such failure were noticed during the 1964 Niigata, Japan earthquake. Despite of the importance of such foundation systems, there appear to be very little work done to investigate the response of such systems particularly on the computational front. This is perhaps due to the complexity of such systems as opposed to analyzing free-field deposits which has received a great deal of attention over the past two decades (e.g., Arulanandan and Scott, 1993). Most of the analytical framework available in the literature deals with the seismic response of shallow foundations on dry deposits or saturated soils (excited at low strain levels) within the context of the "equivalent linear approach" (see for example Mylonakis et al., 2006, for a comprehenssive compilation of work in this area). Seismic analysis of soil-foundation systems encompasses several issues such as soil nonlinearities and dynamic

soil-foundation interaction as well as the development of pore-water pressure as shaking progresses and its impact on soil stiffness degradation, among other factors. Most of the available computational models rely on continuum-based approaches with constitutive relations that usually include parameters that are difficult to predict (Kramer, 1996).

The Discrete Element Method (DEM) emerged as a powerful tool to analyze granular materials (Cundall and Strack, 1979). Recent simulations of the seismic response of saturated granular deposits (free-field) have shown the seamless capabilities of DEM to capture essential characteristics that are commonly observed in physical modeling (Zeghal and El Shamy, 2004; El Shamy and Zeghal, 2005b). In this paper, a DEM-based approach is utilized to investigate the response of a saturated soil-foundation system to seismic excitations. As shown below, the approach inherently accounts for the modeling issues described above and thus provides a powerful tool to model such complex systems.

COMPUTATIONAL MODEL

Conceptually, in presented computational simulation, the mixture of solid particles and pore fluid is viewed as two interpenetrating media, namely the solid phase and the fluid phase. The fluid is idealized as a continuum by using a homogenized form of Navier-Stokes equations that accounts for the presence of the solid particles. These particles are modeled at a micro scale using DEM. Averaged fluid-particle interactions are quantified using a semi-empirical relationship. The shallow foundation is idealized as a rigid block by generating a group of particles glued to each other, and subsequently interact with the surrounding deposit particles.

Fluid Phase

The averaged Navier-Stokes continuity and momentum equations for an incompressible inviscid pore fluid are given by (e.g., Jackson, 2000):

$$\frac{\partial n}{\partial t} + \nabla \cdot (n\bar{\mathbf{v}}_\mathrm{f}) = 0 \tag{1}$$

$$\rho_\mathrm{f}\left(\frac{\partial (n\bar{\mathbf{v}}_\mathrm{f})}{\partial t} + \nabla \cdot (n\bar{\mathbf{v}}_\mathrm{f}\bar{\mathbf{v}}_\mathrm{f})\right) = -n\nabla \bar{p}_\mathrm{f}\boldsymbol{\delta} - \bar{\mathbf{f}}_i + n\rho_\mathrm{f}\mathbf{f}_g \tag{2}$$

where $n = n(\mathbf{x},t)$ is porosity (in which $\mathbf{x}$ and t are space and time coordinates), $\bar{\mathbf{v}}_\mathrm{f} = \bar{\mathbf{v}}_\mathrm{f}(\mathbf{x},t)$ is averaged fluid velocity vector, $\bar{p}_\mathrm{f} = \bar{p}_\mathrm{f}(\mathbf{x},t)$ is averaged fluid pressure, ∇ is gradient operator, ρ_f is fluid density, $\mathbf{f}_g$ is gravitational acceleration vector, and $\bar{\mathbf{f}}_i = \bar{\mathbf{f}}_i(\mathbf{x},t)$ is averaged fluid-particle interaction vector. The associated boundary conditions consists of fluid velocity and/or pressure constraints.

Averaged fluid-particle interactions may be quantified using a number relationships. In this study, the semi empirical equation developed and calibrated by Ergun (1952) was employed.

Solid Phase

The discrete element method (Cundall and Strack, 1979) was used to idealize the assemblage of soil particles using distinct spheres. The motion of a particle p is

dictated by the momentum equations:

$$m_p \dot{\mathbf{v}}_p = m_p \mathbf{f}_g + \sum_c \mathbf{f}_c + \mathbf{f}_d \quad (3)$$

$$I_p \dot{\boldsymbol{\omega}}_p = \sum_c \mathbf{r}_c \times \mathbf{f}_c \quad (4)$$

where $\mathbf{v}_p$ and $\boldsymbol{\omega}_p$ are translational and rotational velocity vectors (a superposed dot indicates time derivative), m_p is particle mass, I_p is particle moment of inertia, $\mathbf{f}_c$ refers to inter-particle force at contact c ($c = 1, 2, \cdots$), $\mathbf{r}_c$ is vector connecting the center of the particle to the location of the contact c, and $\mathbf{f}_d$ is drag force exerted by the fluid on the particle p which includes buoyancy and fluid-particle interaction terms. The inter-particle forces are dictated by contact laws which are direct functions of grain stiffness properties and relative movements at the contacts. The normal component was idealized using a linear spring stiffness which is connected in parallel to a viscous dashpot. The shear contact force was modeled using an elastic spring in series with a frictional slider. The shear and normal forces are related by a slip Coulomb model (Itasca, 2005). More details of the coupled fluid-particle model may be found in Zeghal and El Shamy (2004) and El Shamy and Zeghal (2005a).

COMPUTATIONAL SIMULATION

The proposed approach was used to investigate the response of a spread footings foundation system founded on liquefiable granular deposit. The was assumed to be composed of square footings (2.4 m$\times$2.4 m) equally spaced at 5.6 m in the lateral directions. The foundation depth is 1.2 m below ground surface and the soil profile at the site is composed of 1.5 m of dry granular soil underlain by a 5 m thick saturated granular material. The granular deposit is resting on a rigid bedrock.

Some assumptions were made in order to simulate such a boundary value problem based on micro-mechanical considerations. Periodic boundaries (El Shamy, 2004) were employed to simulate an intermediate spread footing of the system described above along with the portion of soil deposit "serving" this footing (Fig. 1). Furthermore, use was made of the high g-level concept commonly used in centrifuge testing to reduce the dimensions of the domain that needs to be filled with particles and to benefit from the shorter time scaling law within witch the simulation has to be conducted. Finally, relatively large particle diameters are used to bring the number of particles in the system to a manageable size. In order to compensate for the employed high g-level and large particle size, viscous fluid was used in the simulation (Kutter, 1992).

The deposit shown in Fig. 1 was created as follows. Soil particles were generated at a larger space and then allowed to settle under gravity. Once settled, the high gravitational field (50 g) was introduced and the particles were allowed to reach equilibrium. Next, the particles occupying the space where the foundation would be installed were deleted and the foundation structure is formed as described in the next section. The system was then allowed to reach equilibrium under the static load from the foundation.

Modeling the Foundation System

The spread footing was modeled as a rigid block that is composed of clumped spherical particles. That is, regardless of the forces acting upon it, the block will not break

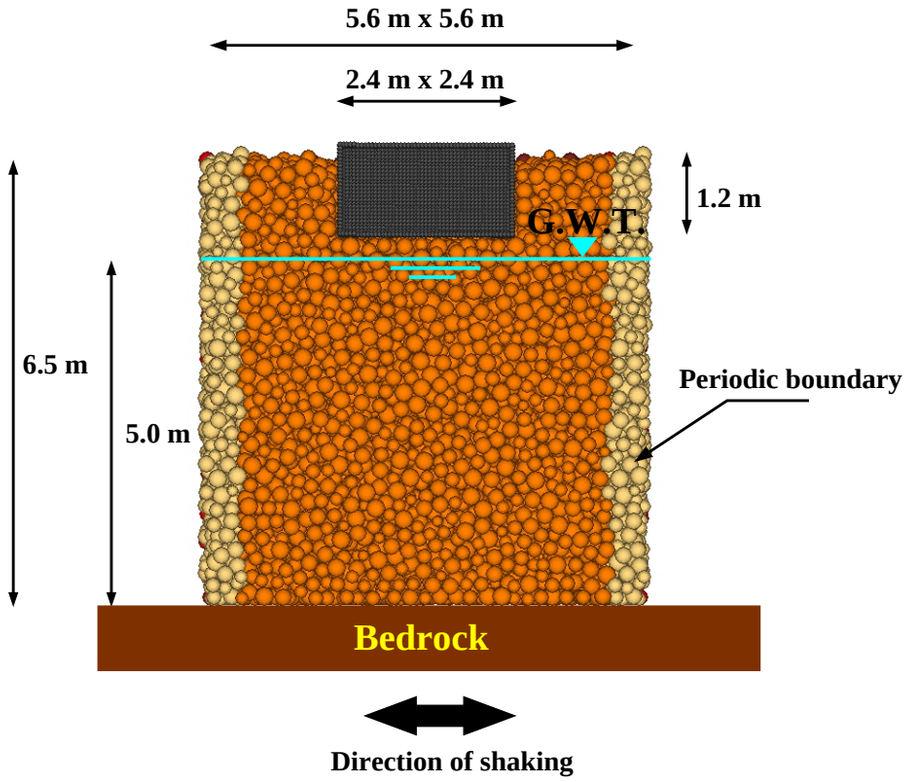


FIG. 1. Analyzed particulate deposit in the conducted simulation.

apart. The contact forces between the clumped particles are not taken into account. However, the interactions between the clumped particles and soil particles are considered. The spherical clumped particles were assembled to resemble near-realistic conditions between the foundation and the soil particles. The block was formed as a parallelpiped structure that its walls are made of particles arranged next to each other. These particles were smaller than the particles composing the deposit to resemble the typical contact surface between a foundation and the underlying soil. The stress applied by the foundation on the underlying soil was about 100 kPa (a typical value for spread footing systems). Such stress was achieved by specifying the density of the clumped particles such that the weight of the block over its area produces the desired average stress.

Since the clumped particles in PFC^{3D} behave as a rigid body, translational and rotational motion equations are sufficient to describe its motion (Eqs. 5 and 6). The translational motion of the center of mass is described in terms of its position (x_i), velocity ($\dot{x}_i$) and acceleration ($\ddot{x}_i$). The rotational motion of the block is described in terms of its angular velocity and acceleration (Itasca, 2005).

$$F_i = M_{cl} \times (\ddot{x}_i - g_i) \tag{5}$$

$$M_i = \dot{H}_i \tag{6}$$

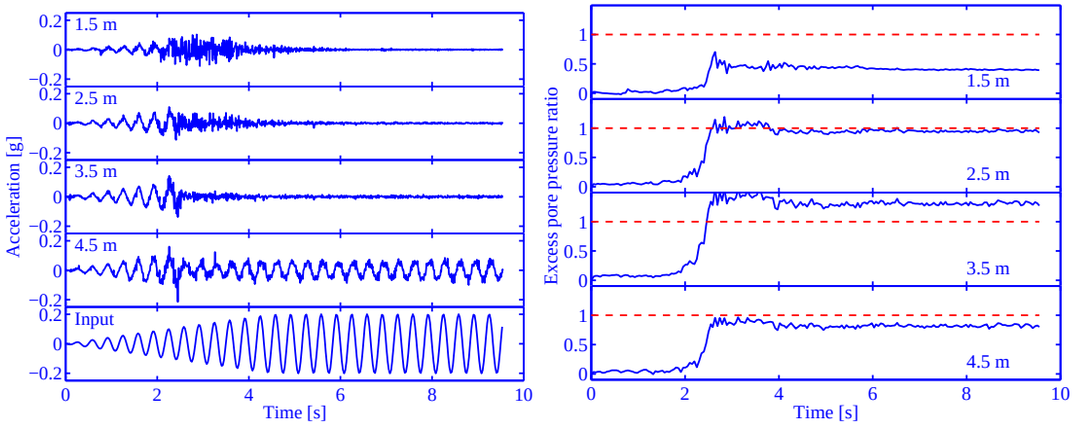


FIG. 2. Time histories for computed accelerations (left) and pore pressure ratios (right) at selected depth locations along the centerline of the foundation below the ground water level.

In the above equations, F_i is the resultant force (the sum of all externally applied forces acting on the clump), g_i is the gravitational acceleration vector, M_i is the resultant moment about the center of mass and $\dot{H}_i$ is the time rate-of-change of the angular momentum of the block.

The resultant force and moment for the block are computed by the following equations in PFC^{3D}.

$$F_i = \sum_{b=1}^{N_b} (\tilde{F}_i^{[b]} + \sum_{c=1}^{N_c} F_i^{[b,c]}) \tag{7}$$

$$M_i = \sum_{b=1}^{N_b} (\tilde{M}_i^{[b]} + \varepsilon_{ijk}(x_j^{[b]} - x_j^{[G]})F_k^{[b]} + \sum_{c=1}^{N_c} \varepsilon_{ijk}(x_j^{[c]} - x_j^{[b]})F_k^{[b,c]}) \tag{8}$$

where, N_b is the number of block balls (particles), $\tilde{F}_i^{[b]}$ is the externally applied force acting on ball (b), $F_i^{[b,c]}$ is the force acting on ball (b) at contact (c), $\tilde{M}_i^{[b]}$ is the externally applied moment acting on ball (b), $F_k^{[b]}$ is the resultant force acting on ball (b) at its centroid, $F_k^{[b,c]}$ is the force acting on ball (b) at contact (c), $x^{[b]}$ is the centroid location of ball (b) and $x^{[G]}$ is the location of center of mass of the block.

The deposit and the foundation are then subjected to a dynamic base excitation that gradually increases to reach a maximum acceleration of 0.2 g. The fluid phase boundary conditions are such that the pressure is constant (atmospheric) at the water level and no flow across the impermeable base (the bedrock). Periodic boundaries along the four lateral sides of the domain were also enforced for the solution of averaged Navier-Stokes equations. Multiple solid and pore-fluid state variables were monitored during the course of the simulation. Table 1 summarizes the computational data for the solid and fluid phases as well as other computational details. Results are presented in prototype units exclusively.

TABLE 1. Simulation data in model units.

Particles	
Diameter	3.8 mm to 5.8 mm
Normal/Shear Stiffness	1e6 N/m
Critical damping ratio	0.10
Friction coefficient	0.5
Density	2650 kg/m^3
Number of particles	28,310
Foundation	
Width	48 mm
Length	48 mm
Height	25 mm
Number of clump particles (n_{cl})	2,208
Density of a clump particle (ρ_{cl})	1,169 kg/m^3
diameter of a clump particle	2 mm
Fluid	
Density	1000 kg/m^3
Viscosity	4.75 Pa s
Boundaries	
Width	112 mm
Length	112 mm
Depth	130 mm
Computation parameters	
Time steps for DEM	1×10^{-6} s
Time steps for fluid	5×10^{-5} s
Number of fluid cells	$7\times7\times5$
Applied 'g' level	50

Saturated Soil Layer Response

Fig. 2 shows the computed accelerations and excess pore-pressure ratios for selected depth locations within the saturated portion of the deposit. The accelerations and the pore-pressure ratios suggest that liquefaction of the saturated deposit took place after about 2.5 s from the start of shaking (during the gradual increase of the input motion). The lower two thirds of the saturated layer appears to have fully liquefied. The top one third of the layer did not fully liquefy as indicated by the pore-pressure ratio smaller than one at the 1.5 m depth location. Note that the value of pore-pressure ratio at the 3.5 m location was higher than 1.0. The increase in pressure at this location is necessary to generate a pressure gradient capable of overcoming the weight of the particles at this location and the non-liquefied zones above it. Note also that the high frequency components observed in the computed accelerations of the upper one third of the saturated layer are due to the inertia forces induced by the motion of the massive foundation

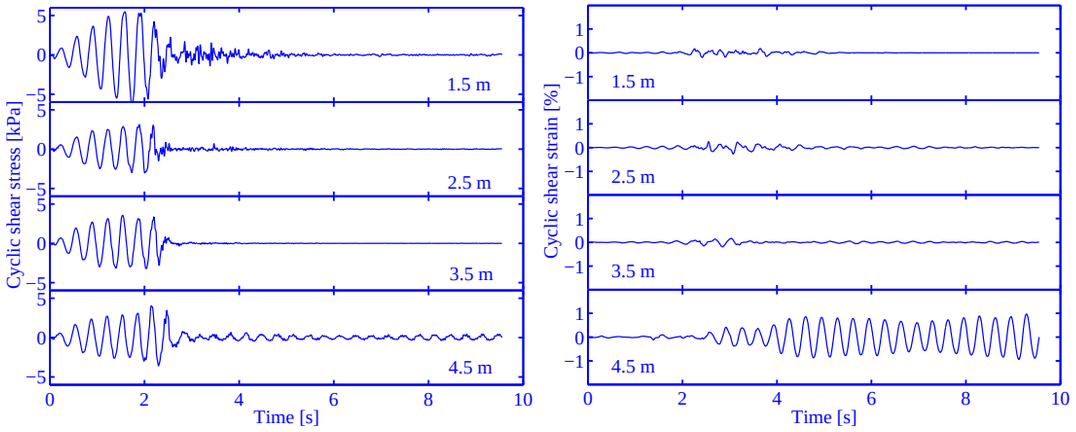


FIG. 3. Time histories for shear stresses (left) and shear strains (right) at selected depth locations along the centerline of the foundation below the ground water level.

block (which is actually a representative of a foundation system extending in the two lateral directions) and the enclosed mass of dry soil between the foundation blocks prior to liquefaction. This motion continues for some time after liquefaction takes place in the saturated layer and isolates the transmission of the input motion to the upper layers.

The shear stresses and shear strains at corresponding locations are presented in Fig. 3 where it can be seen that for the upper 4 m of the saturated deposit, the shear stresses vanished as the soil liquefied. Liquefaction of this portion of the deposit can also be verified by inspecting the micro-scale quantity known as the coordination number (average number of contacts per particle, Fig. 4). A minimum coordination number value of 4 is needed to have a stable packing of frictional spheres (Edwards, 1998). Liquefaction then can be said to take place at a particular location if the coordination number reaches values below 4. As can be seen, for the lower two thirds of the deposit, the coordination number decreased significantly below 4. However, the coordination number at the top of the saturated layer (the top 1.5 m) the coordination number increased to a value more than 4 after about 5 s. As noted in Fig. 2, the pore-pressure ratio did not reach a value of 1.0 at this location, indicating that the particles did not fully liquefy.

Foundation Response

The foundation acceleration was monitored during the course of the simulation and is provided in Fig. 5 where it is compared to the base input motion. As can ne seen, significant deamplification of the input motion was observed at the foundation level prior to the instant when liquefaction took place (2.5 s), after which the ground acceleration was not transmitted to the foundation . This is due to having a layered soil system where the wave is traveling through a relatively soft system (saturated) into a relatively stiffer system (dry). In addition, the fact that the foundation is embedded at 1.2 m below the ground surface increases its stiffness and reduces its displacement.

During shaking, the foundation experienced a settlement of about 280 mm (Fig. 6). The long-term settlement that includes post liquefaction deformation was about 350 mm.

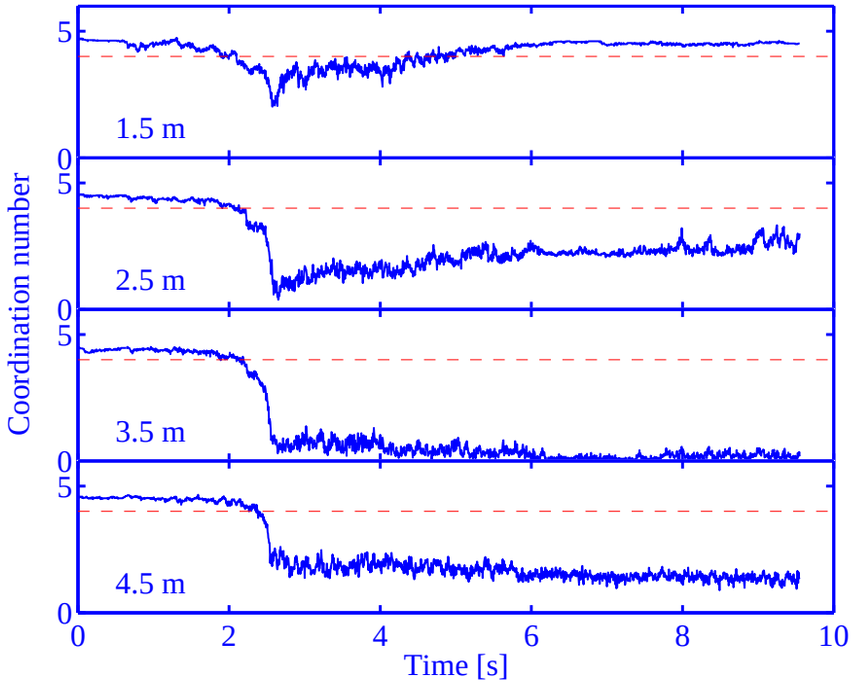


FIG. 4. Variation of coordination number with time at selected depth locations along the centerline of the foundation below the ground water level.

More results and analysis of the conducted simulation as well as other planned simulations will be presented in future publications.

CONCLUSIONS

This paper presents preliminary results of an attempt to investigate the dynamic response of a coupled soil-foundation system using a DEM-based approach. The computational framework accounts for soil nonlinearity as well as the possible buildup of pore pressure due to cyclic loading. In addition, the foundation is modeled as an embedded rigid block with frictional side walls and base. This block is allowed to undergo deformation in any of the associated six degrees of freedoms. All these features are presented in a fully-coupled transient formulation that appears to be a very promising tool to analyze soil-foundation systems subjected to seismic loads.

REFERENCES

K. Arulanandan and R. Scott, eds. (1993). *Verification of numerical procedures for the analysis of soil liquefaction problems. Proceedings of the International Conference on the Verification of numerical procedures for the analysis of soil liquefaction problems.* A.A.Balkema, Davis, California.

Cundall, P. and Strack, O. (1979). "A discrete numerical model for granular assemblies." *Geotechnique*, 29(1), 47–65.

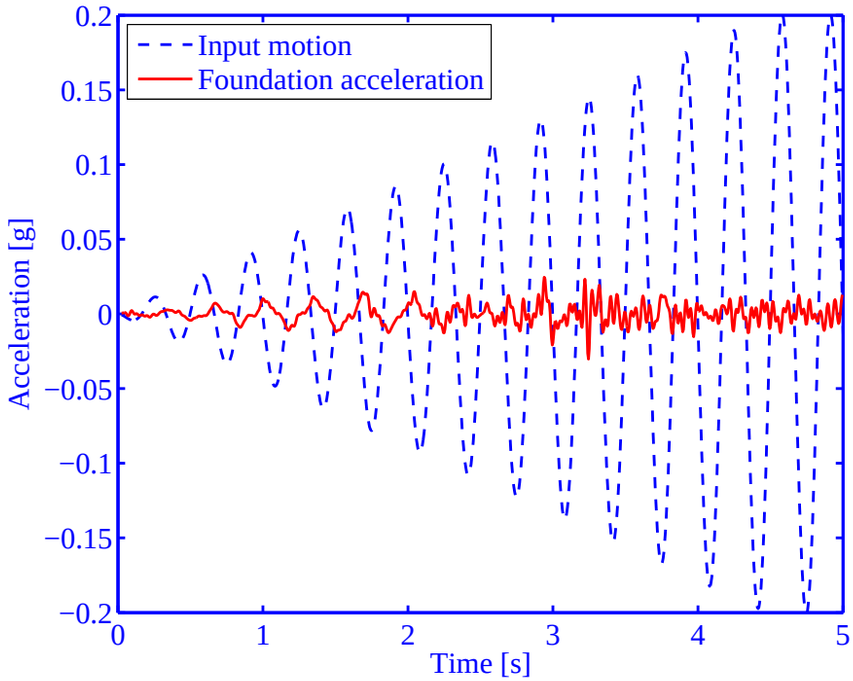


FIG. 5. Time history of the computed acceleration of the foundation in comparison with the input motion.

Edwards, S. (1998). "The equations of stress in a granular material." *Physica A*, 249, 226–231.

El Shamy, U. (2004). "A coupled continuum-discrete fluid-particle model for granular soil liquefaction," PhD Thesis, Rensselaer Polytechnic Institute, Troy, NY.

El Shamy, U. and Zeghal, M. (2005a). "A coupled continuum-discrete model for saturated granular soils." *Journal of Engineering Mechanics*, ASCE, 131(4), 413–426.

El Shamy, U. and Zeghal, M. (2005b). "A micro-mechanical study of the seismic response of saturated cemented deposits." *Journal of Earthquake Engineering*, 9. Special Issue 1 on Geotechnical Earthquake Engineering.

Ergun, S. (1952). "Fluid flow through packed columns." *Chemical Engineering Progress*, 43(2), 89–94.

Itasca (2005). *Particle Flow Code, PFC3D, release 3.1*. Itasca Consulting Group, Inc., Minneapolis, Minnesota.

Jackson, R. (2000). *The dynamics of fluidized particles*. Cambridge, U.K.; New York: Cambridge University Press.

Kramer, S. (1996). *Geotechnical earthquake engineering*. Prentice-Hall, Englewood Cliffs, NJ.

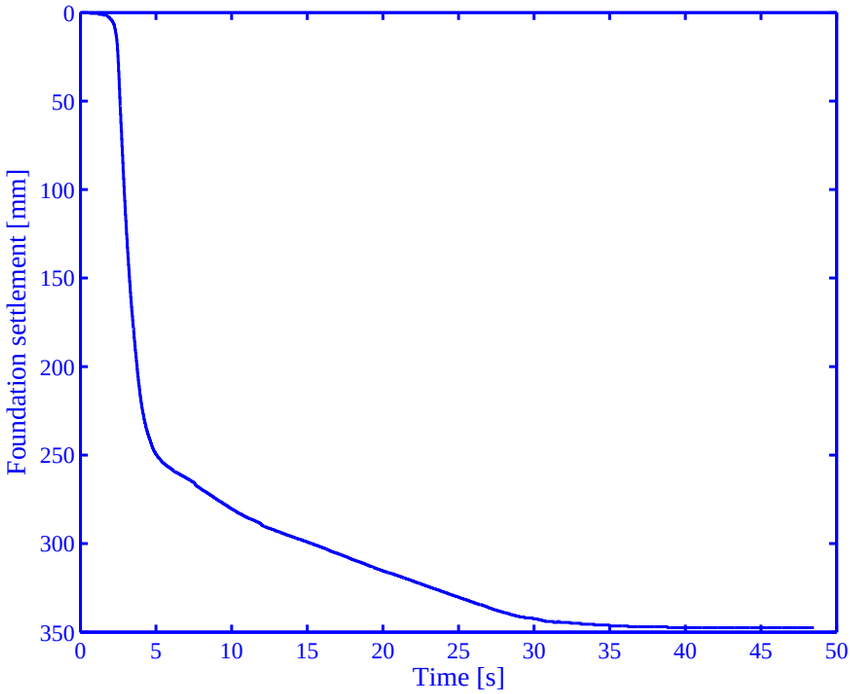


FIG. 6. Time history of foundation settlement.

Kutter, B. (1992). "Dynamic centrifuge modeling of geotechnical structures." *Transportation research record*, (1336), 24–30.

Mylonakis, G., Nikolaou, S., and Gazetas, G. (2006). "Footings under seismic loading: Analysis and design issues with emphasis on bridge foundations." *Journal of Soil Dynamics and Earthquake Engineering*, 26, 824–853.

Zeghal, M. and El Shamy, U. (2004). "A continuum-discrete hydromechanical analysis of granular deposit liquefaction." *International Journal for Numerical and Analytical Methods in Geomechanics*, 28, 1361–1383.

Efficient Numerical Modeling of Liquefaction-Induced Deformations of Soil Structures

Achilleas Papadimitriou[1], M. ASCE, Konstantinos Andrianopoulos[2] and George Bouckovalas[3], M. ASCE

[1] Lecturer, Department of Civil Engineering, University of Thessaly, Greece; apapad@civ.uth.gr
[2] Post-Doctoral Researcher, School of Civil Engineering, National Technical University of Athens, Greece; kandrian@tee.gr
[3] Professor, School of Civil Engineering, National Technical University of Athens, Greece; gbouck@central.ntua.gr

ABSTRACT: A new numerical methodology is presented for the simulation of the non cohesive soil response under small, medium and large cyclic shear strains, with special interest given to liquefaction phenomena. The new methodology is based on a recently proposed elastoplastic bounding surface model, which has been implemented to the 2D finite difference code *FLAC*, via its User-Defined-Model capability. In particular, the emphasis in this paper is on comparing measurements to numerical results for the seismic response of a liquefiable sand layer that has a mild slope leading to the detrimental phenomenon of lateral spreading. The new methodology is proved capable of accurately predicting the time-histories of ground acceleration, excess pore pressure buildup and accumulation of displacements at all depths within the mildly-sloping liquefiable layer. Moreover, the new methodology provides insight to the mechanism of accumulation of displacement during lateral spreading.

INTRODUCTION

The simulation of soil response during a strong earthquake is still a subject of significant research in the field of Earthquake Geotechnical Engineering. The bulk of this research is performed via numerical analysis, which can deal with complicated situations where simple analytical or empirical solutions are too crude. The very large majority of currently available constitutive models implemented in commercial boundary value problem codes oriented towards Geotechnical Engineering are not able to quantitatively capture this response and this is mainly due to its complicated nature. In particular, features of this response like the accumulation of permanent deformations, the generation of excess pore pressures, the degradation of deformation moduli, the increase of hysteretic damping and the evolution of soil fabric anisotropy as a function of the imposed cyclic shear straining require advanced constitutive

modeling (e.g. Papadimitriou & Bouckovalas 2002, Elgamal et al. 2002, Dafalias & Manzari 2004), which may prove extremely difficult to implement in commercial codes. Hence, most often the solution to this problem is given via in-house codes, which are developed in various research institutes and universities and are not readily available to the technical community and have sometimes a narrow range of applicability.

This paper presents the implementation and validation of a new constitutive model for cyclic shearing in the 2D finite difference code *FLAC* (Itasca, 1998). This model takes advantage of the UDM (User-Defined Model) capability of this code and has been developed with the goal to overcome the foregoing shortcomings. It is based on incremental elasto-plasticity and aims at performing realistic fully coupled dynamic analyses for practical problems of Earthquake Geotechnical Engineering. As an application, in this paper the emphasis is on the phenomenon of lateral spreading and on the mechanism of accumulation of the related lateral displacement.

PLASTICITY MODEL AND IMPLEMENTATION TO FLAC

The new UDM (Andrianopoulos, 2006) is a bounding surface model with a vanished elastic region that incorporates the framework of Critical State Soil Mechanics. It is based on a recently proposed model (Papadimitriou et al., 2001; Papadimitriou & Bouckovalas, 2002), which has been proven capable of simulating the cyclic behavior of non-cohesive soils (sands and silts), under any (small-medium-large) cyclic shear strain amplitude using a single (sand-specific) set of constants, irrespective of the initial stress and density conditions.

In its current form, the model incorporates three (3) open cone-type surfaces with apex at the origin of stress space: (i) the Critical State surface at which deformation develops for fixed stresses and zero volumetric strain, (ii) the Bounding surface which locates the (ever-current) peak stress ratio states and (iii) the Dilatancy surface which dictates the sign of the plastic volumetric strain rate during loading. Figure 1 presents the shape of these surfaces in the triaxial [q-p] space. Its basic feature is the direct association of shear behavior to the state parameter ψ (Been and Jefferies, 1985). This is accomplished by correlating the 'opening' of the Bounding and the Dilatancy surfaces to the ever-current value of the state parameter ψ, an idea first proposed by Manzari & Dafalias (1997).

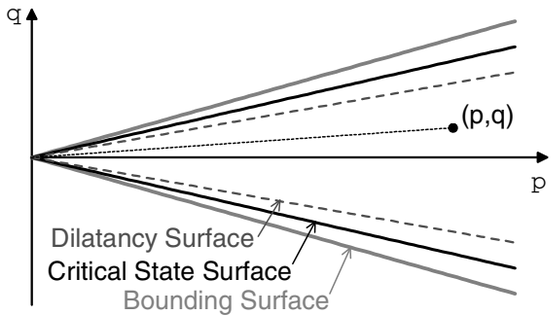


FIG. 1. Model surfaces in the triaxial [q-p] space

The non-linear soil response under small to medium cyclic strain amplitudes is simulated mainly by introducing a Ramberg-Osgood type non-linear hysteretic formulation on the otherwise hypoelastic moduli, thus requiring the memory of the last shear reversal point in stress space. At larger cyclic strain amplitudes elasto-plasticity governs the behavior and a properly defined scalar-valued variable is introduced, which reflects macroscopically the effect of sand fabric evolution during shearing on the magnitude of plastic strains.

Note that there is no purely elastic region and thus the response of soil during loading is continuously elastoplastic, i.e. irrecoverable deformations occur at every incremental step. The choice of a vanished elastic region provides a smoother transition from smaller to larger strains and hence improves the numerical robustness and efficiency of the code (Naylor, 1985; Andrianopoulos, 2006). In this way, it was made possible to alleviate a number of issues that would significantly increase the required computational effort, i.e. the stress point crossing of the yield surface, the drift correction resulting from the weak enforcement of the consistency condition, and the subsequent sub-stepping in the integration scheme. The adoption of a vanished elastic region differentiates the proposed model from the original of Papadimitriou & Bouckovalas (2002) and leads to a number of other modifications as well, namely: (i) the introduction of a new mapping rule (Andrianopoulos et al., 2005) and (ii) modification of the existing interpolation rule. However, the basic constitutive equations of the original model were preserved, so that the reader can readily refer to the respective publications for more details. Due to space limitations, the calibration process is not included in this paper. It is merely stated here that the model requires the calibration of thirteen (13) model constants and that information on the calibration procedure can be found in Andrianopoulos et al (2006b), as well as in the original paper of Papadimitriou & Bouckovalas (2002).

In the current work, the sub-stepping technique with automatic error control proposed by Sloan et al. (2001) was adopted, which belongs to the family of effective explicit algorithms, after appropriate modifications to account for the complexity of the constitutive equations. In brief, this algorithm divides automatically the applied strain increment into sub-increments, using an estimate of the local error and attempts to control the global integration error in the computed stresses. It uses a modified Euler scheme, which consists of two basic steps. Namely, in the first step, an approximate stress increment $\Delta\sigma_1$ is calculated by using the initial matrix of elastoplastic moduli D_{ep}. In the second step, the matrix of elastoplastic moduli D_{ep} is temporarily updated and a new approximation of the stress increment $\Delta\sigma_2$ is calculated. Next, the relative error between these two approximations is estimated and, if required, sub-stepping is activated. The size of each sub-step is continuously updated so that the relative error is less than a specified tolerance level. At the end of each successful sub-step, the stress increment $\Delta\sigma_n$ is computed as the average of $\Delta\sigma_1$ and $\Delta\sigma_2$ and similar averaging is used for the hardening parameters. Further details can be found in Andrianopoulos et al. (2006b).

For the coupling of fluid-mechanical response and hence the performance of fully-coupled dynamic analyses, the process proposed in *FLAC* is adopted. Namely, the framework of quasi-static Biot theory is applied, while diffusion is controlled by single-phase Darcy equations (Itasca, 1998).

NUMERICAL MODELING OF LATERAL SPREADING

The proposed numerical methodology has been validated against results from the well-known VELACS experimental project (Arulmoli et al., 1992). This paper emphasizes on liquefaction-induced soil displacements and therefore results from model tests No. 2 are used, which simulate the practically one-dimensional (1D) seismic response of a mildly sloping liquefiable soil layer. Such a layer exhibits lateral displacement during seismic shaking, a phenomenon widely referred to as *lateral spreading*, and on which background reading can be found in Youd et al. (2002). It should be underlined, that the same numerical methodology has also been validated against results from model test No. 1 for a purely horizontal liquefiable layer, as well as model test No. 12 for a shallow foundation on liquefiable soil. Details on the foregoing validation runs can be found in Andrianopoulos et al (2007) and Andrianopoulos et al. (2006a), respectively.

The test arrangement and the instrumentation for Model test No. 2 is shown in Figure 2. In prototype scale, the experiment refers to a 10m deep Nevada Sand layer with 40% relative density. The centrifuge model was built inside a laminar box, which was tested at 50g centrifugal acceleration, and was tilted by 2^o in order to simulate lateral spreading conditions. The excitation applied at the base of the laminar box had a peak horizontal acceleration amplitude of 0.235g, a strong motion duration of approximately 11sec and a predominant frequency of 2Hz. The response of the mildly-sloping ground was monitored with ten (10) accelerometers, eight (8) pore pressure transducers and six (6) LVDTs measuring displacements. The grid used for the numerical analysis was uniform with 1.0m thick square elements. The horizontal acceleration time-history was applied at the bottom of the mesh, while the lateral boundaries were tied to one-another in order to ensure the same horizontal and vertical displacements of the two boundaries, as imposed by the laminar box device in the centrifuge test. The vertical acceleration during the experiments was minimal and was not taken into account during the numerical simulation. In the simulation of the prototype, the soil permeability was appropriately increased to account for the difference in the scaling of the dynamic time and the diffusion time.

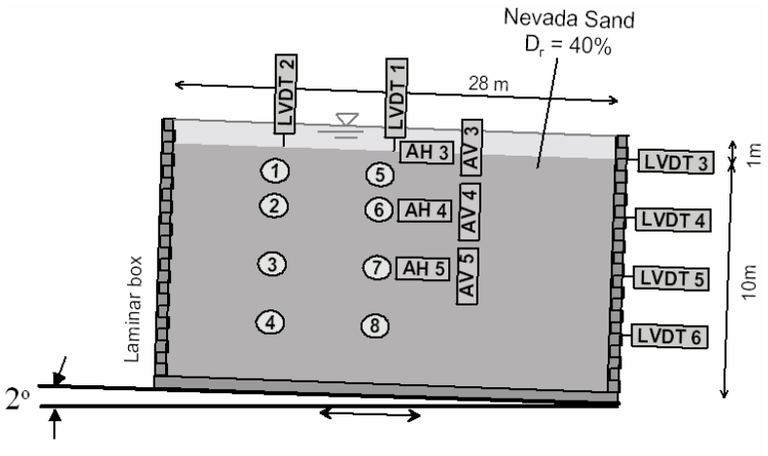


FIG. 2. Schematic illustration of testing configuration of VELACS Model No 2

Figure 3 compares the time histories of the excess pore pressure ratio $r_u = \Delta u/\sigma'_{vo}$ from the centrifuge test recordings to their numerically simulated counterparts, at various depths (-1.45m, -2.6m, -5.0m, -7.5m) of the sand layer and along the axis of the centrifuge model. As in the case of level ground conditions, both recordings and simulations show initial liquefaction ($r_u = 1.0$) in the upper 5m and smaller values of r_u at deeper locations. Again, very high values of r_u develop from the first seconds of the shaking in the upper 2.5m, while deeper locations develop similarly high values of r_u at later stages of the shaking. The rates of excess pore pressure buildup and dissipation are satisfactorily simulated, with the possible exception of the first 2 loading cycles during which the model shows more intense buildup than the data. Unlike the case of the level ground, the time histories of excess pore pressures show instant drops at the depths where initial liquefaction has been attained. This trait illustrates enhanced dilative response following a condition of $r_u \cong 1$ and is attributed to the small shear stress offset originating from the static equilibrium of a mildly sloping ground.

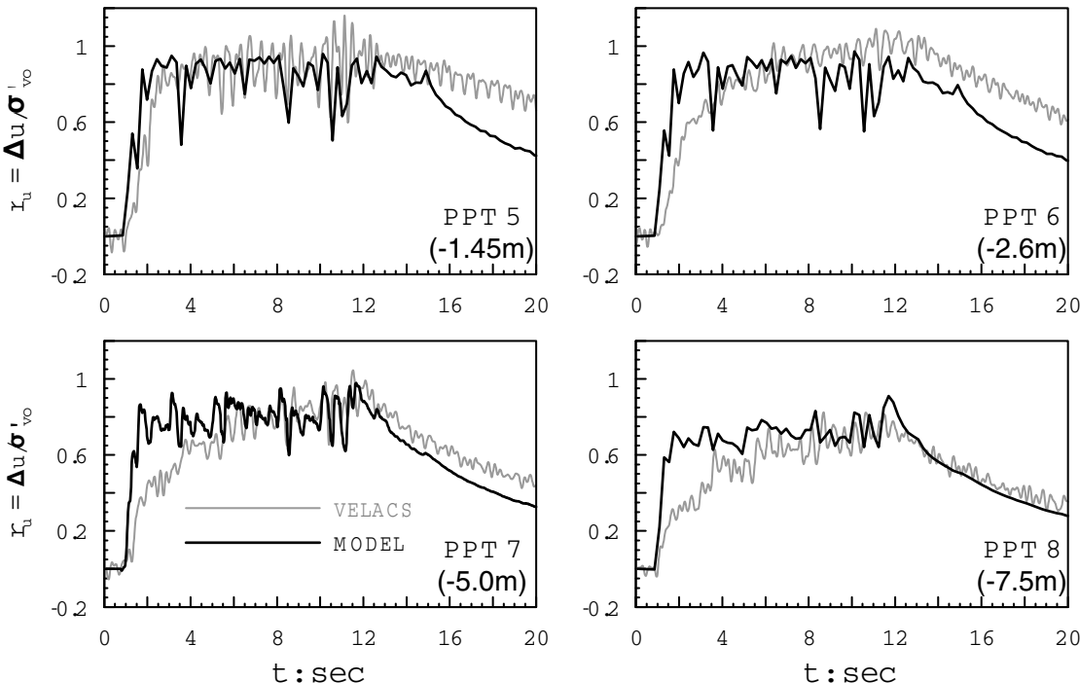


FIG. 3. Comparison of data to simulations for the time history of the excess pore pressure ratio $r_u = \Delta u/\sigma'_{vo}$ developed at various depths along the axis of VELACS Model No 2

Figure 4 compares the time histories of ground acceleration (in percent of g) from the centrifuge test recordings to their numerically simulated counterparts, at the ground surface (AH3) and at the mid-depth (AH5) of the sand layer, always along the axis of the centrifuge model. Satisfactory agreement is observed, since both the recording and the simulation show a liquefaction-induced deamplification of the acceleration at the ground surface (peak values of 0.10 – 0.12g, neglecting very high-frequency spikes), as compared to the 0.235g applied at the base. Unlike the case of

the level ground, the acceleration does not nullify at the ground surface and this is attributed to the foregoing enhanced dilative response due to the mildly sloping ground. Similarly, the accelerations from the recording and the simulation at mid-depth are again higher than their respective counterparts of the level ground case.

Figure 5 compares snapshots of the (relative to the base) lateral displacements of the soil layer from the centrifuge test recordings to their numerically simulated counterparts at t = 3, 6, 9 and 12sec. In both the simulation and the recording the soil layer shows to have increased lateral displacements in the upper 5.0m, a fact attributed to the higher excess pore pressures and the ensuing lower shear strength of the upper layer. Close investigation of the results (in Figure 6) reveals an almost linear increase of the lateral displacement with time at any depth for the applied almost harmonic base excitation, an increase that is terminated at the end of the strong shaking (at t=12s). An index of the overall satisfactory simulation is that the final lateral displacement of the surface of the sand layer (LVDT3) was found equal to 42.7cm in the simulation versus 46.8cm in the centrifuge test, whereas at mid-depth the respective values are 19.4 and 14.3cm (LVDT5).

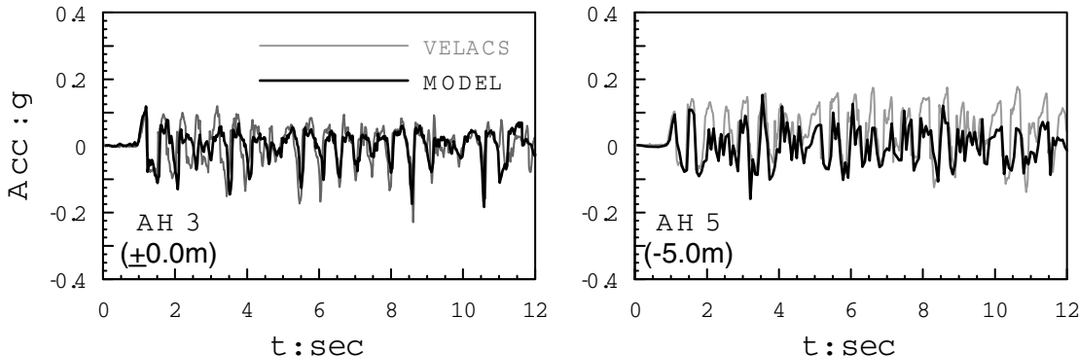


FIG. 4. Comparison of data to simulations for the time history of ground acceleration developed at various depths along the axis of VELACS Model No 2

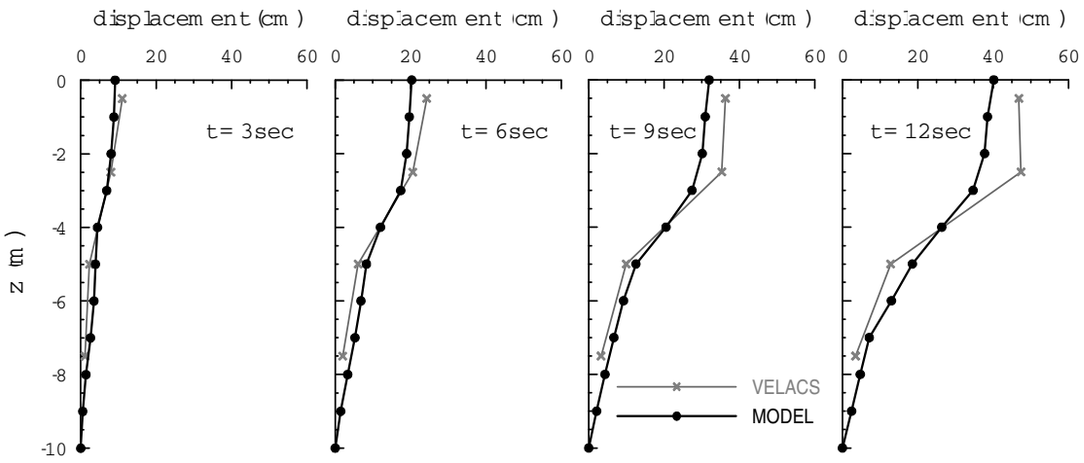


FIG. 5. Comparison of data to simulations for the (relative to the base) lateral displacement profile at various times of the shaking for the VELACS Model No 2

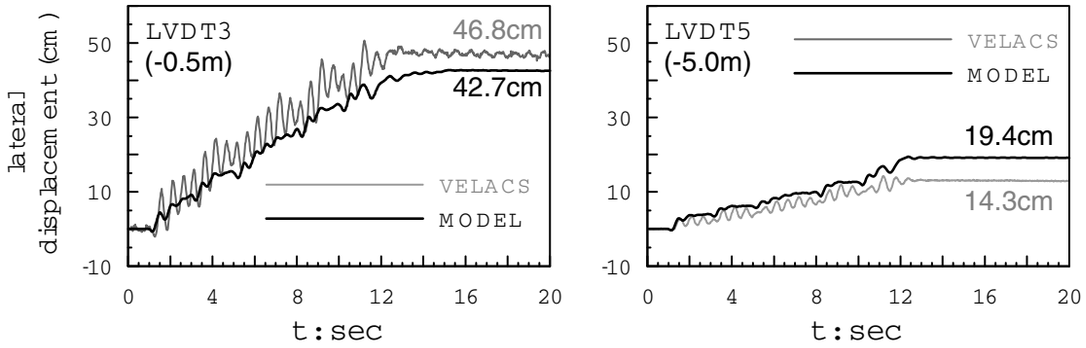


FIG. 6. Comparison of data to simulations for the time history of the (relative to the base) lateral displacement at various depths of the VELACS Model No 2

Further details for the foregoing and additional comparisons for VELACS Model test No 2 are not shown here for reasons of brevity and can be found in Andrianopoulos (2006). What is of importance in this paper is to underline that the ascertained level of accuracy in simulating Model test No 2 is similar to the level of accuracy in the simulations of VELACS Model tests No 1 and 12, as shown in Andrianopoulos et al (2007) and Andrianopoulos et al. (2006a), respectively. More importantly, these successful simulations of very different boundary value problems on the same (Nevada) sand were achieved with the same set of (sand-specific) model constants, thus underlining the efficiency of the proposed numerical methodology.

MECHANISM OF ACCUMULATION OF LATERAL DISPLACEMENTS

Given its accuracy, the new numerical tool can be used for an in depth analysis of liquefaction-related phenomena. Of interest here is the mechanism of accumulation of displacements in the lateral spreading phenomenon. The basis for this analysis is the simulation of the VELACS Model No 2 presented above. Of particular interest here are the effects of the enhanced dilative response following a condition of $r_u = 1$ that was observed in Figures 3 and 4 and was attributed to the small shear stress offset originating from the static equilibrium of a mildly sloping ground. Hence, Figure 7 focuses on the time-histories of acceleration (7a), velocity (7b), excess pore pressure ratio (7c) and their relation to the respective time-history of the (relative to the base) lateral displacement at the ground surface (7d). In this figure, the shaded areas denote the duration of two sequential dilation spikes initiating at t=3.56sec and t=4.11sec. Observe that the sharp dilation spikes (Fig 7c) correspond to acceleration pulses towards the upslope direction (negative sign in Fig 7a), which result in a decrease of the down slope velocity of the sand layer (positive sign in Fig 7b). As expected, the foregoing decrease of down slope velocity produces a reduction of the down slope displacement accumulation rate of the laterally spreading sand layer. Hence, during shaking, the accumulation of down slope displacement (attributed to the reduced shear strength produced from very high r_u values near liquefaction) is temporarily obstructed by successive dilation spikes (see Fig 7d), that may even lead to temporary upslope movement if the respective shaking is strong enough.

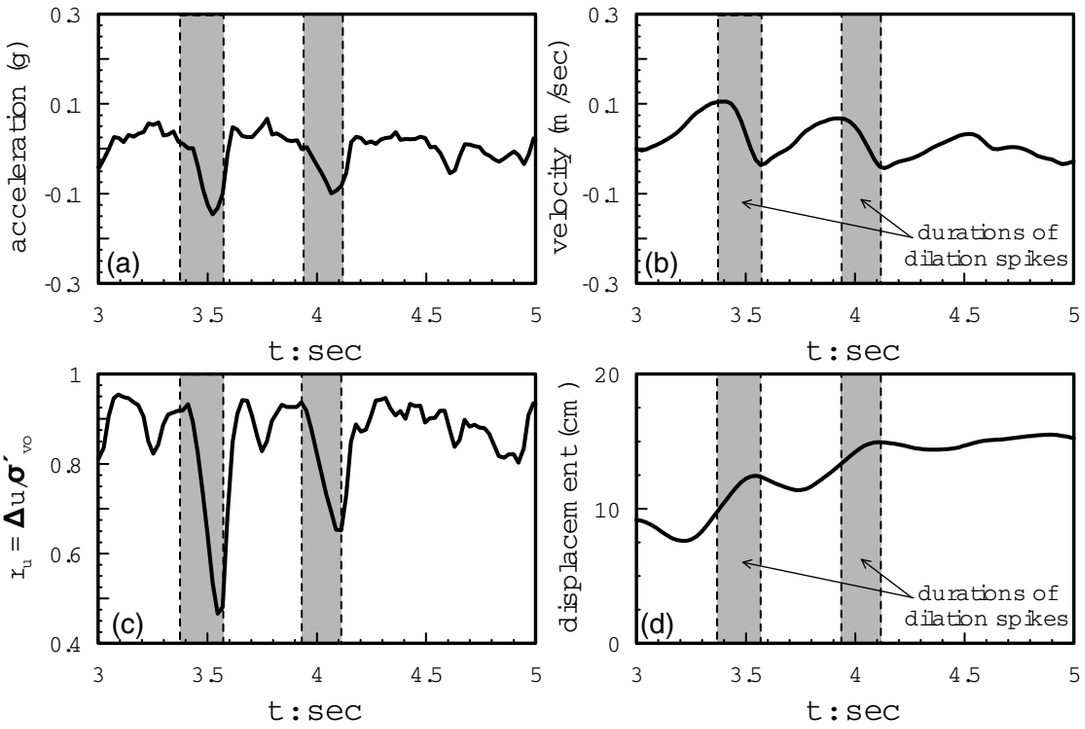


FIG. 7. Description of the surface response with time of a laterally-spreading sand layer in terms of: a) acceleration, b) velocity, c) excess pore pressure ratio r_u and d) the (relative to the base) lateral displacement, based on the simulation of VELACS Model No 2

Interestingly, the successive dilation spikes have a recurrence period of 0.56sec, a value that may be considered as the elongated predominant period of the applied base motion of 2Hz. This period elongation may be attributed to the overall reduction of the effective stress-level dependent stiffness of the sand due to excess pore pressure buildup during strong seismic shaking (e.g. $r_u \geq 0.8$ in the time window of 3 to 5sec of Fig. 7, except for the "shaded" duration of the dilation spikes which again do not reduce the r_u below 0.45). Based on all the above, the accumulation of displacement due to lateral spreading is reminiscent of a "*stick-slip*" physical mechanism, with a recurrence period that is somewhat larger than the predominant period of the applied seismic excitation.

CONCLUSIONS

On the basis of the comparisons of data to simulations presented herein it may be concluded that the proposed numerical tool (a new constitutive model implemented in *FLAC*, as a User-Defined-Model) simulates with accuracy the stress-strain response of non-cohesive soils (sands and silts) during earthquake loading. Of special importance is the fact that the model formulation emphasizes on the response under small, medium and large cyclic strain amplitudes by specific constitutive ingredients.

From a practical point of view, the most important asset of the proposed methodology is its efficiency, attributed to the fact that:

a. the constitutive model requires a single soil-specific set of model constants, irrespective of drainage, density and loading conditions, as well as the boundary value problem at hand (see Andrianopoulos et al 2006b and Papadimitriou & Bouckovalas 2002 for the calibration process), and that
b. the new numerical tool can be readily used by both researchers and practitioners that have experience in using *FLAC*, thus establishing the widest possible potential use of the proposed methodology.

Furthermore, the accuracy of the new numerical tool makes it ideal for in-depth analysis of complicated problems of Earthquake Geotechnical Engineering. In this perspective, this paper shows evidence that the accumulation of displacement due to lateral spreading is reminiscent of a "*stick-slip*" physical mechanism, with a recurrence period that is somewhat larger than the predominant period of the applied seismic excitation.

ACKNOWLEDGEMENTS

The work presented herein has been financially supported by the University of Thessaly in Greece, through a research project entitled "*Optimization of non-linear dynamic coupled numerical analysis of soil structures in 2 dimensions*" (Code No. 3538). This contribution is gratefully acknowledged.

REFERENCES

Andrianopoulos, K.I. (2006). "Numerical modeling of static and dynamic behavior of elastoplastic soils", *Doctorate Thesis*, Department of Geotechnical Engineering, School of Civil Engineering, National Technical University of Athens (in Greek)

Andrianopoulos, K.I., Papadimitriou, A.G. and Bouckovalas, G.D. (2005). "Bounding surface models of sands: Pitfalls of mapping rules for cyclic loading", *Proceedings, 11th International Conference on Computer Methods and Advances in Geomechanics*, Torino, June, Vol. 1: 241-248

Andrianopoulos, K.I., Bouckovalas, G.D., Karamitros D.K., Papadimitriou, A.G. (2006). "Effective stress analyses for the seismic response of shallow foundations on liquefiable sand", *Proceedings, 6th European Conference on Numerical Methods in Geotechnical Engineering*, Graz, September

Andrianopoulos, K.I., Papadimitriou, A.G., Bouckovalas, G.D. (2006). "Implementation of a bounding surface model for seismic response of sands", *Proceedings, 4th International FLAC Symposium on Numerical Modeling in Geomechanics*, Madrid, May

Andrianopoulos, K.I., Papadimitriou, A.G., Bouckovalas, G.D. (2007). "Use of a new bounding surface model for the analysis of earthquake-induced liquefaction phenomena", *Proceedings, 4th International Conference on Earthquake Geotechnical Engineering*, Thessaloniki, June

Arulmoli, K., Muraleetharan, K.K., Hossain, M.M. and Fruth, L.S. (1992). "VELACS: verification of liquefaction analyses by centrifuge studies; Laboratory Testing Program – Soil Data Report", *Research Report*, The Earth Technology Corporation

Been, K. & Jefferies, M.G. (1985), "A state parameter for sands", *Geotechnique*, 35(2): 99-112

Dafalias, Y.F. and Manzari, M.T. (2004). "Simple plasticity sand model accounting for fabric change effects", *Journal of Engineering Mechanics*, ASCE, 130(6): 622-634

Elgamal A., Yang Z., Parra E. (2002). "Computational modeling of cyclic mobility and post-liquefaction site response", *Soil Dynamics and Earthquake Engineering,* 22 (4): 259-271

Itasca Consulting Group, Inc. (1998). "FLAC – Fast Lagrangian Analysis of Continua", Version 3.4, *User's Manual*, Minneapolis: Itasca

Manzari, M.T. and Dafalias, Y.F. (1997). "A critical state two-surface plasticity model for sands", *Geotechnique*, 47(2): 255-272

Naylor, D.J., "A continuous plasticity version of the critical state model", *International Journal of Numerical Methods in Engineering*, 21: 1187-1204, 1985

Papadimitriou, A.G., Bouckovalas, G.D. and Dafalias, Y.F. (2001). "Plasticity model for sand under small and large cyclic strains", *Journal of Geotechnical and Geoenvironmental Engineering*, ASCE, 127(11): 973-983

Papadimitriou, A.G. and Bouckovalas, G.D. (2002). "Plasticity model for sand under small and large cyclic strains: a multiaxial formulation", *Soil Dynamics and Earthquake Engineering*, 22: 191-204

Sloan, S.W., Abbo, A. J. and Sheng, D. (2001). "Refined explicit integration of elastoplastic models with automatic error control", *Engineering Computations,* 18 (1/2), 121-154

Youd, T.L., Hansen, C.M. and Bartlett, S.F. (2002). "Revised multilinear regression equations for prediction of lateral spread displacement", *Journal of Geotechnical and Geoenvironmental Engineering*, ASCE, 128(12): 1007-1017

Numerical Simulation of Seismic Ground Motion Isolation Using Fully Coupled Nonlinear Response in Saturated Sands

Mahdi Taiebat[1], Boris Jeremić[2], Zhao Cheng[3], and Yannis Dafalias[4]

[1]Graduate Student Researcher, Department of Civil and Environmental Engineering, University of California, Davis, CA 95616; email: mtaiebat@ucdavis.edu

[2]Associate Professor, Department of Civil and Environmental Engineering, University of California, Davis, CA 95616; email: jeremic@ucdavis.edu

[3]Staff Engineer, Earth Mechanics Inc. Oakland, CA 94621

[4]Professor, Department of Civil and Environmental Engineering, University of California, Davis, CA 95616 and Department of Mechanics, National Technical University of Athens, Zographou 15780, Greece;

ABSTRACT: A fully coupled nonlinear dynamic numerical approach and an advanced constitutive model have been implemented in a three dimensional finite element computer code to predict the response of saturated porous media under different types of loading conditions including earthquake loading. The formulation and implementation are already verified and validate, and were then applied to the problem of sand liquefaction and cyclic mobility phenomena for investigation on a specific configuration of layered soil column, where liquefaction of the deeper loose elements prevents transmission of earthquake induced shear stresses to the upper layers.

INTRODUCTION

Modeling and simulations of soil behavior induced by earthquakes, that can be related to liquefaction and cyclic mobility, continue to challenge engineering research and practice. Such behavior commonly occurs in loose to medium dense sands which are fully saturated and will result in almost complete loss of strength (liquefaction), or partial loss of strength (cyclic mobility). Fully coupled transient response of the saturated system and the constitutive behavior of the soil skeleton play equally important roles in successful numerical simulation of soil liquefaction. To model these complex phenomena one needs to utilize, a) a consistent and efficient coupled formulation, and b) an accurate single-phase constitutive model for soil. In addition to these the numerical tool should be capable to do all the simulations in three-dimensional geometry which is what engineers really need for simulation of the real life systems.

Having a reliable tool for realistic simulation of saturated sands, a number of challenging issues can be investigated. The results rely on verified formulation and implementation of behavior of a porous media fully coupled with pore fluid, and on validated constitutive material modeling. Issues of verification and validation are fundamental to the process of prediction of mechanical behavior in computational science and engineering (Jeremić et al., 2007; Oberkampf et al., 2002). Prediction of mechanical behavior comprises use of computational model to foretell the state of a physical system under consideration under conditions for which the computational model has not been validated. Confidence in predictions relies heavily on proper Verification and Validation (V&V) process. In the current paper an interesting issue about isolation of system from transmission of earthquake induced shear waves is briefly examined. A 1D sand column example is used as the system of interest in this example.

GENERAL FORMULATION

Three general continuum formulations (Zienkiewicz and Shiomi, 1984) are possible for modeling of the fully coupled problem (soil skeleton – pore fluid) in geomechanics, namely the (a) $u-p$, (b) $u-U$, and (c) $u-p-U$ formulations. Here, the unknowns are the soil skeleton displacements u; the pore fluid (water) pressure p; and the pore fluid (water) displacements U. In this paper coupled dynamic field equations with $u-p-U$ formulation are used to determine pore fluid and soil skeleton responses (Zienkiewicz and Shiomi, 1984; Argyris and Mlejnek, 1991). Each node of the $u-p-U$ element has thus seven degrees of freedoms in three dimensions (three for solid displacements, one for pore fluid pressures and three for pore fluid displacements). It should be noted that it is possible to use same shape functions for both displacement and pore pressure unknown field as $u-p-U$ formulation with compressible fluid allows that without volumetric locking (Zienkiewicz and Shiomi, 1984). Despite it's power, the $u-p-U$ formulation has rarely been implemented into finite element code. Details of the formulation, finite element discretization, and implementation can be found in Jeremić et al. (2007). In addition to that a set of verification examples are presented there to determine that formulation and the implementation accurately represent conceptual description of porous media behavior.

Development and evaluation of comprehensive constitutive models which can reliably simulate complex stress-strain behavior of sands and yet are conceptually simple and computationally efficient is an iterative process. SANISAND is the name used for a family of Simple ANIsotropic SAND constitutive models (the name resulting from the foregoing uppercase letters) developed over the past few years (Manzari and Dafalias, 1997; Li and Dafalias, 2000; Dafalias and Manzari, 2004; Dafalias et al., 2004), within the framework of critical state soil mechanics and bounding surface plasticity. The latest members of the SANISAND family of models are implemented and used in the current research (Taiebat and Dafalias, 2007). It is basically a critical-state plasticity model within the concept of the bounding surface. The model consists of a close-ended narrow yield surface in $p-q$ space which can capture the plastic response for constant and variable stress-ratio loading. Figure 1 shows the yield, critical, bounding and dilatancy surfaces of the model both in $p-q$ space and in general stress-ratio π-plane. Using the concept of critical state soil mechanics, the

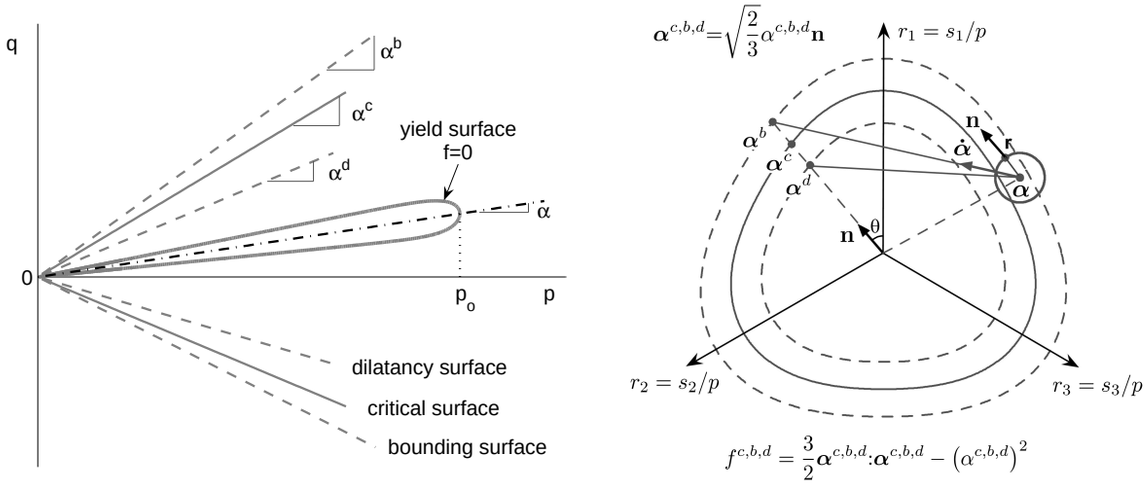


Figure 1. Schematic illustration of the SANISNAD model surfaces in triaxial stress space and in stress ratio π-plane (Taiebat and Dafalias, 2007).

model is capable for capturing the response of sand in a wide range of confining pressure and densities with a unique set of model constants. Additional constitutive ingredient addressing issues of inherent and evolving fabric anisotropy are simple add-ons features and the later one is incorporated in the present work (Dafalias et al., 2004; Dafalias and Manzari, 2004). Detailed calibration procedure for the model constants is already presented in the reference papers, while successful simulation of both drained and undrained behavior of sands under constant and variable stress-ratio loadings at various densities and confining pressures is obtained by the model. The validation process is important in determining the degree to which a model is accurate representation of the real world from the perspective of the intended uses of the model.

MODEL DESCRIPTION

In order to examine the problem of interest in this research, a vertical column of saturated sand consisting of ten $u-p-U$ 8-node brick elements is considered subjected to an earthquake shaking. The soil is assumed to be Toyoura sand. For tracking convenience, the mesh elements are labeled from E01 (bottom) to E10 (surface). The boundary conditions are such that the soil and water displacement degree of freedom (DOF) at the bottom surface are fixed, while the pore pressure DOFs are free; the soil and water displacement DOFs at the upper surface are free upwards to simulate the upward drainage. The pore pressure DOFs are fixed at surface thus setting pore pressure to be zero. On the sides, soil skeleton and water are prevented from moving in horizontal directions while vertical movement of both is free. It is emphasized that those displacements (of soil skeleton and pore fluid) are different. In order to simulate the 1D behavior, all DOFs at the same depth level are connected in a master–slave fashion. The permeability is assumed to be isotropic $k = 5.0\times10^{-4}$ m/s. A static application of gravity analysis is performed before seismic excitation.

It should be noted that the self weight loading is performed on an initially zero stress (unloaded) soil column and that the material model and numerical integration algorithms are

powerful enough to follow through this early loading with proper evolution. Input acceleration time history (Figure 2) is taken from the recorded horizontal acceleration of Model No.1 of VELACS project by Rensselaer Polytechnic Institute (Arulanandan and Scott, 1993). The peak acceleration of the motion is close to 0.2 g, while main shaking lasts for about 12 seconds (from 1 s to 13 s). Two distinct cases are considered in this study. In the first case the whole soil column is assumed to be uniformly dense Toyoura sand with $e = 0.75$. In the second case, however, the deepest two elements of the soil column are assumed to be at very loose state with $e = 0.95$. The rest of the soil column, i.e. the upper eight element are at the same density as the first case ($e = 0.75$). The formulation and implementation takes into account velocity proportional damping (usually called viscous damping) by proper modeling of coupling of pore fluid and solid skeleton, while the displacement proportional damping is appropriately modeled using the advanced material model. No additional damping is used in FEM model.

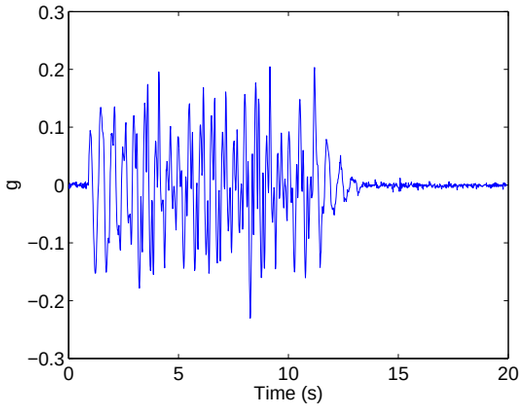


Figure 2. Input earthquake ground motion for the soil column.

SIMULATION RESULTS AND DISCUSSIONS

Results of the analysis for both cases of interest are presented in Figure 3. Three sets of plots are shown in this figure: a) variations of effective vertical stress σ'_v v.s. shear stress τ_h; b) variations of r_u[1] v.s. time; and c) variations of shear stress τ_h v.s. shear strain γ.

For Case 1, where all ten elements are initially in dense state ($e = 0.75$), this figure shows the typical mechanism of cyclic decrease in effective vertical stress. Signs of the partial butterfly shape in the effective stress path can be observed from early stages of shaking. The butterfly is more evident in the upper layers with the lower confining pressures, i.e. more dilative response. In later stages of the shaking, i.e. when the confining pressure reduces to smaller values the butterfly shape of the stress path gets more pronounced due to having more dilative response in the lower confining pressure based on Critical State Soil Mechanics concept. It can be observed that the vertical effective stress in most of the upper

[1] $r_u = [(\sigma'_v)_{in} - \sigma'_v] / (\sigma'_v)_{in}$ and therefore is equal to 0 for zero excess pore pressure and is equal to 1 for the fully liquefied state, i.e. when the vertical effective stress is negligible.

layers gets pretty much close to zero and as a result the value of r_u approaches to 1. Although because of having partial segments of dilative response sand column has not completely lost its strength, one can still observe some horizontal strains in a number of the layers due to partial liquefaction.

For Case 2, as mentioned before elements E01 and E02 are very loose ($e = 0.95$) and elements E03-E10 are at same density as what they are in case 1 ($e = 0.75$). The very loose initial state of elements E01 and E02 causes very fast decrease in the effective stress ratio and brings these two elements to fully liquefied state almost at the end of the first cycle. In the first half-cycle when E01 and E02 are still not liquefied the stress path in the upper layers look similar to what it used to be in case 1, however once E01 and E02 approach the fully liquefied at the end of the first cycle, almost no shear stress can be transmitted to the upper layers and so the value of shear stress in these elements remains very close to zero. This is isolation of the upper layers from transmission of earthquake induced shear waves coming from the base. The shear stress-strain path clearly shows that for the second case where the upper layers do not feel the shear stresses after the first cycle of loading, the resulting shear stains are almost negligible comparing to case 1. Of course the very loose elements E01 and E02 (and their adducent element E03) show considerable value of shear strain due to liquefaction.

Despite the absence of transmission of earthquake loading to the upper layers after the first cycle, one can still observed decrease in the effective vertical stress for the upper layers after this point. This indeed is due to the transient pore water flux that enters these elements from the liquefied bottom elements and forces the upper elements toward low effective stresses. After all, looking at the middle plot for variations of r_u it can be observed that the outcome of isolation in one way and water flux in the other way still keeps the upper layer more away from the $r_u = 1$ comparing to what they used to behave in case 1.

Regardless of the mentioned distinctions between the two cases of simulations, the top section of the model has remained closer to liquefied well past the end of shaking. This is explained by the large supply of pore fluid from lower layers, for which the dissipation starts earlier. For example, for the lowest layer, the observable drop in excess pore pressure start as soon as the shaking ends, while, the upper layers then receive this dissipated pore fluid from lower layers and as a result their effective stress keep approaching to (or remain at) smaller values well past end of shaking (which happens at approximately 13 seconds). It is very important to note the significance of this incoming pore water flux on the pore water pressure of the top layers.

CONCLUSIONS

Using fully coupled nonlinear finite element analysis, it was shown that in a specific configuration of the layered system liquefaction of the deeper loose elements prevents transmission of the earthquake induced shear stresses to the upper layers. Absence of these shear stresses in the upper layers during the earthquake helps in having almost negligible shear strain in these layers, however on the other hand the water flux coming from the liquefied bottom layers will force the upper layers toward lower effective stress even in absence of earthquake induced shear stresses.

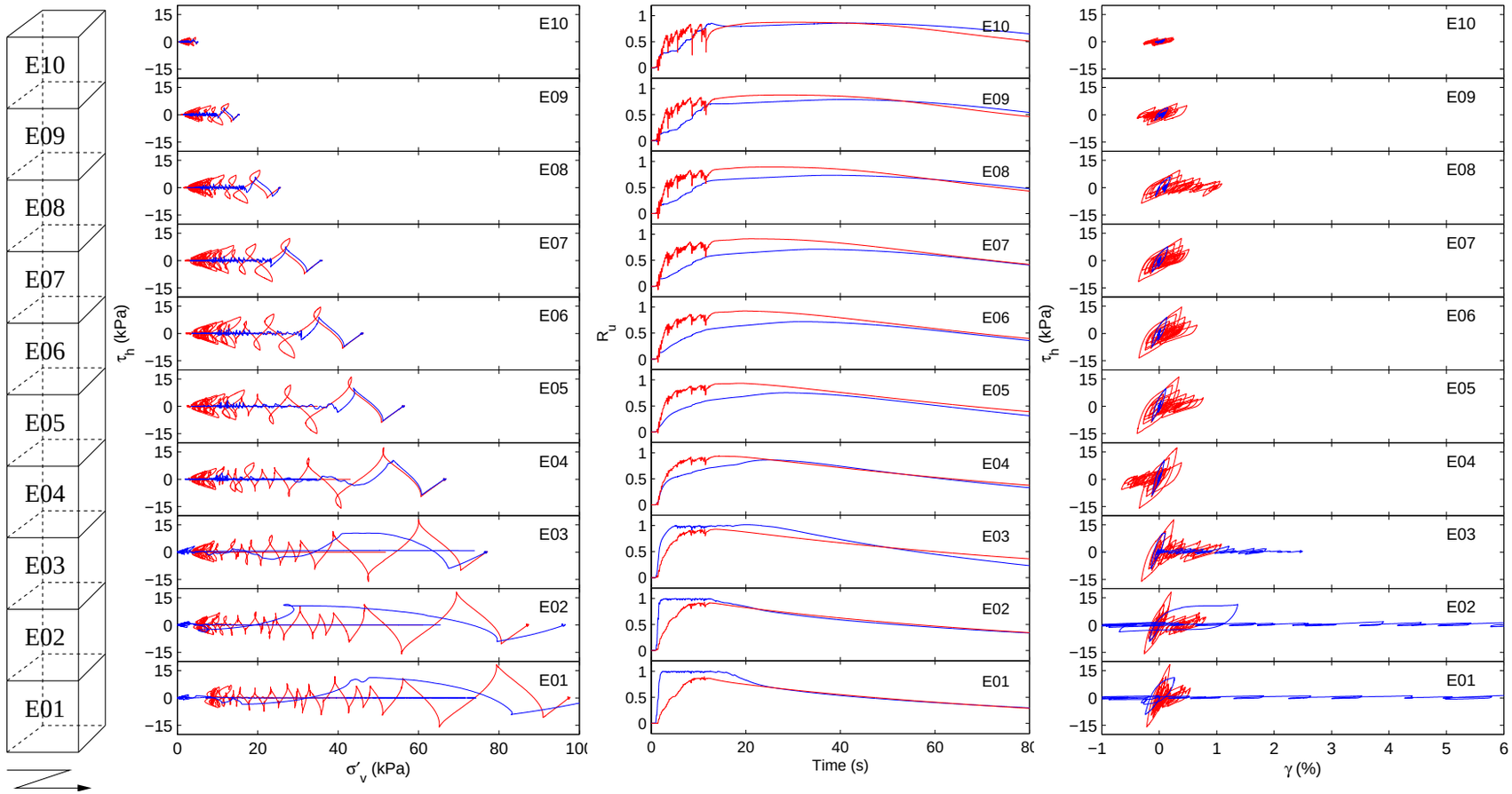


Figure 3. Seismic response of uniform (E01-E10 with $e = 0.75$, red) and layered (E01-E02 with $e = 0.95$, and E03-E10 with $e = 0.75$, blue) soil columns. a) variations of effective vertical stress σ'_v v.s. shear stress τ_h; b) variations of r_u v.s. time; and c) variations of shear stress τ_h v.s. shear strain γ.

ACKNOWLEDGMENTS

The work presented in this paper was supported in part by grants NSF–EEC–9701568, NSF–CMS–0337811, and NSF–CMS–0201231 from National Science Foundation. These supports are gratefully acknowledged.

REFERENCES

Argyris, J. and Mlejnek, H.-P. (1991). "Dynamics of Structures". *North Holland in USA Elsevier*.

Arulanandan, K. and Scott, R. F., eds. (1993). "Verification of Numerical Procedures for the Analysis of Soil Liquefaction Problems". *A. A. Balkema*.

Dafalias, Y. F. and Manzari, M. T. (2004). "Simple plasticity sand model accounting for fabric change effects." *Journal of Engineering Mechanics*, 130(6), 622–634.

Dafalias, Y. F., Papadimitriou, A. G., and Li, X. S. (2004). "Sand plasticity model accounting for inherent fabric anisotropy." *Journal of Engineering Mechanics*, 130(11), 1319–1333.

Jeremić, B., Cheng, Z., Taiebat, M., and Dafalias, Y. F. (2007). "Numerical simulation of fully saturated porous materials." *International Journal for Numerical and Analytical Methods in Geomechanics*. DOI: 10.1002/nag.687. (In press).

Li, X. S. and Dafalias, Y. F. (2000). "Dilatancy for cohesionless soils." *Géotechnique*, 54(4), 449–460.

Manzari, M. T. and Dafalias, Y. F. (1997). "A critical state two–surface plasticity model for sands." *Géotechnique*, 47(2), 255–272.

Oberkampf, W. L., Trucano, T. G., and Hirsch, C. (2002). "Verification, validation and predictive capability in computational engineering and physics." *Proceedings of the Foundations for Verification and Validation on the 21st Century Workshop*, Johns Hopkins University / Applied Physics Laboratory, Laurel, Maryland. 1–74.

Taiebat, M. and Dafalias, Y. F. (2007). "SANISAND: simple anisotropic sand plasticity model." *International Journal for Numerical and Analytical Methods in Geomechanics*, DOI: 10.1002/nag.651. (in press).

Zienkiewicz, O. C. and Shiomi, T. (1984). "Dynamic behaviour of saturated porous media; the generalized Biot formulation and its numerical solution." *International Journal for Numerical Methods in Engineering*, 8, 71–96.

This page intentionally left blank

Transient Boundary Integral Equation of Dynamic Unsaturated Poroelastic Media

Iman Ashayeri[1], Mohsen Kamalian[2], Mohammad Kazem Jafari[3]

[1]Ph.D. Student, International Institute of Earthquake Engineering and Seismology (IIEES), Tehran, Iran, P.O.Box: 19537-14453; i.ashayeri@iiees.ac.ir
[2]Ph.D., Assistant Professor, IIEES, Tehran, Iran, P.O.Box: 19537-14453; kamalian@iiees.ac.ir
[3]Ph.D., Professor, IIEES, Tehran, Iran, P.O.Box: 19537-14453; jafari@iiees.ac.ir

ABSTRACT: The dynamics of saturated poroelastic media has received attention of several investigators from the mid twentieth century but problems concerning unsaturated soils necessitate the theoretical developments for mechanics of unsaturated media. By the development of high speed digital computers numerical methods are used to solve complex engineering problems. One of the most common problems in geotechnical earthquake engineering is the seismic wave propagation from the seismic source to the structure's foundation, throughout the stratified sedimentations. The well known boundary element method (BEM) is an effective boundary type numerical method for dynamic analysis of linear elastic bounded and unbounded media. The BEM consists of two key ingredients: the governing boundary integral equation and the corresponding fundamental solutions. This paper presents the full dynamic boundary integral equation of unsaturated isotropic poro-elastic media for the first time. The introduced boundary integral equation can be solved by BEM once the corresponding fundamental solutions are determined.

INTRODUCTION

The mechanics of fluid saturated porous media has received attention of researchers for more than one century and a half. Darcy's law (Darcy 1856) for liquid transport in porous media is an outstanding evidence. However, the first theoretical works were introduced by Terzaghi (1923), pioneering one dimensional theory of consolidation in cohesive soils. Afterward, Biot used a macro-mechanical approach based on the quantities like stress and strain that hold at macro-level and published series of papers concerning a general theory of poroelastic materials (Biot 1941, 1955, 1956a).

More recently, Truesdell and Toupin (1960) and Green and Naghdi (1965) introduced theory of mixtures that provides the mechanics of deformable porous media using averaging procedures to represent the microscopic quantities in macro level. These theories are well-suited to take the complex interactions between

constituents into action. Coussy et al. (1998) presented detail comparison of Boit's theory with theory of mixtures.

The Pioneer works of Biot (1956b,c, 1962) that presented a full dynamic theory for study of wave propagation in fluid saturated porous media was the onset of dynamic poro-elasticity. Later, owing to increasing interest in non-linear applications, an extension of Biot's theory into non-linear material behaviour was presented by Zienkiewicz et al (1980) and Prevost (1982). In their approach soil is viewed as a multiphase medium and the theory of mixtures is applied. Schrefler et al. (1990) extended a similar approach to derive the governing equations of unsaturated porous media and presented the discretization of the governing equations for finite element method (FEM).

A similar approach for saturated porous media can be applied for unsaturated media. The unsaturated porous media are known and treated as the superposition in time and space of at least three phases; solid skeleton and two fluids that are immiscible. In soil mechanics context, solid skeleton is formed by soil particles (solid matrix) and the free space between it and the fluids (commonly water and air) that saturate the voids. Therefore, the mechanics of unsaturated porous media are viewed as a multiphase interacting continuum mechanics which the conservation and conduction laws and momentum balance equations are derived based on this concept (Coussy 1995). More recently, Muraleetharan and Wei (1999) and Wei and Muraleetharan (2002a,b) applied a continuum theory, which explicitly considers the interfaces between bulk phases, to develop the governing equations of unsaturated porous media.

Fortunately, with the development of high-speed computers, more engineering problems are analyzed using numerical methods such as FEM, BEM (Boundary Element Method) and FDM (Finite Difference Method). One of the most common problems in geotechnical earthquake engineering is the seismic wave propagation from the seismic source to the structure's foundation throughout the stratified sedimentations. It is apparent that wave propagation in unsaturated porous media is a complex problem, which can only be solved accurately, economically and under realistic conditions, with the aid of numerical methods.

The well known BEM is an effective boundary type numerical method for dynamic analysis of linear elastic bounded and unbounded media. The method is attractive for wave propagation problems, because the discretization is done only on the boundary, yielding smaller meshes and systems of equations compared to other domain type numerical methods. Another advantage is that it efficiently represents the outgoing waves through infinite domains, which is useful when dealing with waves scattered by irregular structures. When this method is applied to problems with semi-infinite domains, there is no need to model the far field. Obviously, formulating the numerical procedure entirely in time domain enables one to combine the effective characteristics of BEM with other numerical methods like finite element method (FEM) to solve also non-linear wave propagation problems.

BEM encompasses the governing boundary integral equation and the corresponding fundamental solutions. Probably the first attempt to obtain integral equations of saturated poro-elastic media was presented by Predeleanu (1981). Since his equations were formulated based on the velocity instead of displacement, they have not received much attention. Cheng and Liggett (1984) presented an integral equation for a quasi-

static poroelastic medium based on the displacement of solid and fluid. Integral equation for dynamic poroelastic medium was also presented by Manolis and Beskos (1989) in Laplace domain based on the same variables. Bonnet (1987) showed that, in poroelastic problems in the frequency domain, the fluid displacement is irrotational and therefore only the solid displacement and the fluid pressure are independent. Dominguez (1991) presented frequency domain integral equations for dynamic poro-elasticity in terms of solid displacement and fluid pressure. Finally, Chen (1994a,b) presented the most complete integral formulation of dynamic poro-elastic medium.

The present work presents the full dynamic integral equations of unsaturated isotropic poroelastic media for the first time. The unsaturated media is formulated based on the recent works of mixture theory and the developed mechanics of porous media (Coussy 1995). It is shown that, as in saturated media, solid displacement and liquid and gas pressure is sufficient to derive basic equations. All volume integrals are eliminated by assuming zero actual body force and fluid injection rate and assigning proper Heaviside point force and impulse scalar fluid source to virtual body force and fluid injection rate. The introduced boundary integral equation introduced can be utilized by BEM once the corresponding fundamental solutions are determined.

GOVERNING DIFFERENTIAL EQUATIONS

Governing differential equations consist of mass balance laws of constituents, momentum balance and fluids mass conduction. The differential equations are derived based on the assumption of infinitesimal transformation and incompressibility of soil particles. The final differential equations in time domain yield

$$\sigma_{ij,j} + \rho F_i - \rho \ddot{u}_i - \rho^{lq}\phi^{lq}\ddot{v}_i - \rho^{g}\phi^{g}\ddot{w}_i = 0 \tag{1}$$

$$q^{lq} = \phi^{lq}\dot{v}_i = k^{lq}(-p^{lq}_{,i} - \rho^{lq}\ddot{u}_i - \rho^{lq}\ddot{v}_i) \tag{2}$$

$$q^{g} = \phi^{g}\dot{w}_i = k^{g}(-p^{g}_{,i} - \rho^{g}\ddot{u}_i - \rho^{g}\ddot{w}_i) \tag{3}$$

$$\frac{(1+\varepsilon)\phi^{lq}}{D^{lq}}\dot{p}^{lq} + (1+\varepsilon)\dot{\phi}^{lq} + \phi^{lq}\dot{u}_{i,i} + q^{lq}_{i,i} = \gamma^{lq} \tag{4}$$

$$\frac{(1+\varepsilon)(\phi^{g})}{D^{g}}\dot{p}^{g} - (1+\varepsilon)\dot{\phi}^{lq} + (1-\phi^{lq})\dot{u}_{i,i} + q^{g}_{i,i} = \gamma^{g} \tag{5}$$

Where ρ is the apparent mass density of the whole medium, $\rho^{\alpha}_{\alpha=lq,g}$ is the intrinsic mass density of the liquid or gas, $\phi^{\alpha}_{\alpha=lq,g}$ is the volume fraction or porosity of liquid or gas, F_i is the body force density per mass unit, u_i is the displacement vector of skeleton particle, v_i, w_i are the relative displacement vectors of liquid and gas particles respect to skeleton particle, $k^{\alpha}_{\alpha=lq,g}$ is the isotropic permeability coefficient of the liquid

phase, $q^{\alpha}_{\alpha=lq,g}$ is the liquid or gas flux vector, $p^{\alpha}_{\alpha=lq,g}$ is the liquid or gas pressure, $D^{\alpha}_{\alpha=lq,g}$ is the bulk modulus of liquid or gas, ε, ϕ^{lq} are the volume dilation and liquid porosity that are constant in the time step and $\gamma^{\alpha}_{\alpha=lq,g}$ is the rate of liquid or gas injection to the medium.

The other required relation is the constitutive relations of skeleton. Following to the assumption of isotropic linear elastic behaviour the relation between stress and strain in the skeleton reads

$$\sigma_{ij} = \lambda\varepsilon_{kk}\delta_{ij} + 2\mu\varepsilon_{ij} + b^{lq}p_c\delta_{ij} - p^{g}\delta_{ij} \tag{6}$$

Where λ, μ are Lame coefficients, $p_c = p^g - p^{lq}$ is the capillary pressure and δ_{ij} is the Kronecker delta.

The next constitutive relation presents variation of liquid and gas volume fraction. Assuming solid matrix incompressibility, the capillary pressure constitutive relation will present this variation as follows

$$c^{lq}\dot{p}_c + (b^{lq} - \phi^{lq})\dot{u}_{i,i} = (1+\varepsilon)\dot{\phi}^{lq} \tag{7}$$

Where b^{lq} is the Biot's coefficient for liquid, and $c^{lq} = (1+\varepsilon)\dfrac{\phi^{lq}}{D^{lq}} - N$, with N being the modulus linking liquid pressure change to the liquid mass. Substituting (7) into (4), (5) yields the final relation for mass balance

$$c^{lq}\dot{p}^{g} + N\dot{p}^{lq} + b^{lq}\dot{u}_{i,i} + \phi^{lq}\dot{v}_{i,i} = \gamma^{lq} \tag{8}$$

$$(c^{g} - c^{lq})\dot{p}^{g} + c^{lq}\dot{p}^{lq} + (1 - b^{lq})\dot{u}_{i,i} + \phi^{g}\dot{w}_{i,i} = \gamma^{g} \tag{9}$$

Where; $c^{g} = \dfrac{(1+\varepsilon)(\phi^{g})}{D^{g}}$.

LAPLACE DOMAIN GOVERNING EQUATIONS

Laplace transform is very common in solving differential equations. Therefore, the equations (1), (2), (3), (8) and (9) in the Laplace domain are

Momentum Balance

$$\tilde{\sigma}_{ij,j} + \rho\tilde{F}_i - \rho s^2\tilde{u}_i - \rho^{lq}\phi^{lq}s^2\tilde{v}_i - \rho^{g}\phi^{g}s^2\tilde{w}_i = 0 \tag{10}$$

Mass Conduction (Darcy's law) of liquid and gaseous phases

$$\tilde{v}_i = \frac{\eta^{lq}}{s}(-\tilde{p}^{lq}_{,i} - \rho^{lq} s^2 \tilde{u}_i) \tag{11}$$

$$\tilde{w}_i = \frac{\eta^{g}}{s}(-\tilde{p}^{g}_{,i} - \rho^{g} s^2 \tilde{u}_i) \tag{12}$$

Introducing the $\eta^{lq} = \dfrac{1}{\dfrac{\phi^{lq}}{k^{lq}} + \rho^{lq} s}, \eta^{g} = \dfrac{1}{\dfrac{\phi^{g}}{k^{g}} + \rho^{g} s}$

Mass Balance (Liquid and gas)

$$c^{lq} s\tilde{p}^{g} + Ns\tilde{p}^{lq} + b^{lq} s\tilde{u}_{i,i} + \phi^{lq} s\tilde{v}_{i,i} = \tilde{\gamma}^{lq} \tag{13}$$

$$(c^{g} - c^{lq}) s\tilde{p}^{g} + c^{lq} s\tilde{p}^{lq} + (1 - b^{lq}) s\tilde{u}_{i,i} + \phi^{g} s\tilde{w}_{i,i} = \tilde{\gamma}^{g} \tag{14}$$

Now one can take divergence from the mass conduction equations (11) and (12) and substitute into mass balance equations (13) and (14), respectively. This yields

$$\phi^{lq}\eta^{lq}\tilde{p}^{lq}_{,ii} - c^{lq} s\tilde{p}^{g} - Ns\tilde{p}^{lq} - (b^{lq} - \rho^{lq}\phi^{lq}\eta^{lq} s) s\tilde{u}_{i,i} + \tilde{\gamma}^{lq} = 0 \tag{15}$$

$$\phi^{g}\eta^{g}\tilde{p}^{g}_{,ii} - (c^{g} - c^{lq}) s\tilde{p}^{g} - c^{lq} s\tilde{p}^{lq} - (1 - b^{lq} - \rho^{g}\phi^{g}\eta^{g} s) s\tilde{u}_{i,i} + \tilde{\gamma}^{g} = 0 \tag{16}$$

One also can eliminate $\tilde{v}, \tilde{w}$ between equations (10), (11) and (12) and find

$$\tilde{\sigma}_{ij,j} - (\rho - \rho^{lq}\rho_{lq}\eta^{lq} s - \rho^{g}\rho_{g}\eta^{g} s) s^2 \tilde{u}_i + \rho_{lq}\eta^{lq} s\tilde{p}^{lq}_{,i} + \rho_{g}\eta^{g} s\tilde{p}^{g}_{,i} + \rho\tilde{F}_i = 0 \tag{17}$$

Where $\rho_\alpha = \rho^\alpha \phi^\alpha$ is the apparent mass density of fluid phase "α". Using these substitutions mass balance and mass conduction are reduced to one equation for each fluid phase (Eqs. 15, 16) and meanwhile all the governing equations are expressed by only 5 (4 in 2D) unknowns in Laplace domain. These unknowns are the three components of u_i (2 components in 2D), p^{lq} and p^{g}.

BASIC INTEGRAL EQUATION (LAPLACE DOMAIN)

The basic integral equation are derived by defining two force and displacement fields; the actual and virtual one. It is worth noting that all equations are obtained with the assumption of zero initial conditions.

Basic Integral Equation of Motion Equation

The equation of motion (17) is weighted by a virtual displacement field $\hat{u}_i$ and is

integrated over the volume Ω of the medium. Since the integrant is zero the integral is equal to zero too.

$$A = \int_{\Omega} \{ \tilde{\sigma}_{ij,j} - (\rho - \rho^{lq} \rho_{lq} \eta^{lq} s - \rho^{g} \rho_{g} \eta^{g} s) s^2 \tilde{u}_i + \rho_{lq} \eta^{lq} s \tilde{p}^{lq}_{,i} + \rho_{g} \eta^{g} s \tilde{p}^{g}_{,i} + \rho \tilde{F}_i \} . \tilde{\hat{u}}_i d\Omega = 0 \quad (18)$$

The first right hand side (r.h.s) term of equation (18) can be rewritten by taking integration by parts and using divergence theorem and definition of traction forces $t_i = \sigma_{ij} . n_j$, where n_j is the normal to the boundary Γ.

$$A_1 = \int_{\Omega} \tilde{\sigma}_{ij,j} . \tilde{\hat{u}}_i d\Omega = \int_{\Gamma} \tilde{\sigma}_{ij} . \tilde{\hat{u}}_i . n_j d\Gamma - \int_{\Omega} \tilde{\sigma}_{ij} . \tilde{\hat{u}}_{i,j} d\Omega = \int_{\Gamma} \tilde{t}_i . \tilde{\hat{u}}_i d\Gamma - \int_{\Omega} \tilde{\sigma}_{ij} . \tilde{\hat{\varepsilon}}_{ij} d\Omega \quad (19)$$

The second r.h.s term of equation (19) now can be rewritten introducing the isotropic linear elastic constitutive equation (6). Hence;

$$A_{12} = \int_{\Omega} \tilde{\sigma}_{ij} . \tilde{\hat{\varepsilon}}_{ij} d\Omega = \int_{\Omega} (\lambda \tilde{\varepsilon}_{kk} \delta_{ij} + 2\mu \tilde{\varepsilon}_{ij} + b^{lq} \tilde{p}_c \delta_{ij} - \tilde{p}^{g} \delta_{ij}) . \tilde{\hat{\varepsilon}}_{ij} d\Omega =$$

$$\int_{\Omega} (\lambda \tilde{\hat{\varepsilon}}_{kk} \delta_{ij} + 2\mu \tilde{\hat{\varepsilon}}_{ij} + b^{lq} \tilde{\hat{p}}_c \delta_{ij} - \tilde{\hat{p}}^{g} \delta_{ij}) . \tilde{\varepsilon}_{ij} d\Omega + \int_{\Omega} b^{lq} (\tilde{p}_c . \tilde{\hat{\varepsilon}}_{ii} - \tilde{\hat{p}}_c . \tilde{\varepsilon}_{ii}) d\Omega - \int_{\Omega} (\tilde{p}^{g} . \tilde{\hat{\varepsilon}}_{ii} - \tilde{\hat{p}}^{g} . \tilde{\varepsilon}_{ii}) d\Omega$$

$$A_{12} = \int_{\Omega} \tilde{\hat{\sigma}}_{ij} . \tilde{\varepsilon}_{ij} d\Omega + \int_{\Omega} b^{lq} (\tilde{p}_c . \tilde{\hat{\varepsilon}}_{ii} - \tilde{\hat{p}}_c . \tilde{\varepsilon}_{ii}) d\Omega - \int_{\Omega} (\tilde{p}^{g} . \tilde{\hat{\varepsilon}}_{ii} - \tilde{\hat{p}}^{g} . \tilde{\varepsilon}_{ii}) d\Omega \quad (20)$$

Once again rewriting first r.h.s term of (20) using integration by parts and virtual traction force definition, A_{12} reads;

$$A_{12} = \int_{\Gamma} \tilde{\hat{t}}_i . \tilde{u}_i d\Gamma - \int_{\Omega} \tilde{\hat{\sigma}}_{ij,j} . \tilde{u}_i d\Omega + \int_{\Omega} b^{lq} (\tilde{p}_c . \tilde{\hat{\varepsilon}}_{ii} - \tilde{\hat{p}}_c . \tilde{\varepsilon}_{ii}) d\Omega - \int_{\Omega} (\tilde{p}^{g} . \tilde{\hat{\varepsilon}}_{ii} - \tilde{\hat{p}}^{g} . \tilde{\varepsilon}_{ii}) d\Omega \quad (21)$$

Consequently

$$A_1 = \int_{\Gamma} \tilde{t}_i . \tilde{\hat{u}}_i d\Gamma - \int_{\Gamma} \tilde{\hat{t}}_i . \tilde{u}_i d\Gamma + \int_{\Omega} \tilde{\hat{\sigma}}_{ij,j} . \tilde{u}_i d\Omega - \int_{\Omega} b^{lq} (\tilde{p}_c . \tilde{\hat{\varepsilon}}_{ii} - \tilde{\hat{p}}_c . \tilde{\varepsilon}_{ii}) d\Omega + \int_{\Omega} (\tilde{p}^{g} . \tilde{\hat{\varepsilon}}_{ii} - \tilde{\hat{p}}^{g} . \tilde{\varepsilon}_{ii}) d\Omega \quad (22)$$

The second integral term of equation (18) reads

$$A_2 = \int_{\Omega} (\rho - \rho^{lq} \rho_{lq} \eta^{lq} s - \rho^{g} \rho_{g} \eta^{g} s) s^2 \tilde{u}_i . \tilde{\hat{u}}_i d\Omega = \int_{\Omega} (\rho - \rho^{lq} \rho_{lq} \eta^{lq} s - \rho^{g} \rho_{g} \eta^{g} s) s^2 \tilde{\hat{u}}_i . \tilde{u}_i d\Omega \quad (23)$$

And the other integral terms of (20) are

$$A_3 = \int_{\Omega} \rho_{lq} \eta^{lq} s \tilde{\hat{p}}^{lq}_{,i} . \tilde{u}_i d\Omega - \int_{\Gamma} \rho_{lq} \eta^{lq} s (\tilde{\hat{p}}^{lq} \delta_{ij} . \tilde{u}_i - \tilde{p}^{lq} \delta_{ij} . \tilde{\hat{u}}_i) . n_j d\Gamma + \int_{\Omega} \rho_{lq} \eta^{lq} s (\tilde{\hat{p}}^{lq} . \tilde{\varepsilon}_{ii} - \tilde{p}^{lq} . \tilde{\hat{\varepsilon}}_{ii}) d\Omega \quad (24)$$

$$A_4 = \int_\Omega \rho_g \eta^g s \tilde{\hat{p}}^g_{,i} . \tilde{u}_i d\Omega - \int_\Gamma \rho_g \eta^g s(\tilde{\hat{p}}^g \delta_{ij} . \tilde{u}_i - \tilde{p}^g \delta_{ij} . \tilde{\hat{u}}_i) . n_j d\Gamma$$
$$+ \int_\Omega \rho_g \eta^g s(\tilde{\hat{p}}^g . \tilde{\varepsilon}_{ii} - \tilde{p}^g . \tilde{\hat{\varepsilon}}_{ii}) d\Omega \quad (25)$$

$$A_5 = \int_\Omega \rho \tilde{F}_i . \tilde{\hat{u}}_i d\Omega = \int_\Omega \rho \tilde{\hat{F}}_i . \tilde{u}_i d\Omega - \int_\Omega \rho(\tilde{\hat{F}}_i . \tilde{u}_i - \tilde{F}_i . \tilde{\hat{u}}_i) d\Omega \quad (26)$$

And finally, knowing that
$\tilde{\hat{\sigma}}_{ij,j} - (\rho - \rho^{lq} \rho_{lq} \eta^{lq} s - \rho^g \rho_g \eta^g s) s^2 \tilde{\hat{u}}_i + \rho_{lq} \eta^{lq} s \tilde{\hat{p}}^{lq}_{,i} + \rho_g \eta^g s \tilde{\hat{p}}^g_{,i} + \rho \tilde{\hat{F}}_i = 0$, the integral A yields

$$A = A_1 - A_2 + A_3 + A_4 + A_5 =$$
$$\int_\Gamma (\tilde{t}_i . \tilde{\hat{u}}_i - \tilde{\hat{t}}_i . \tilde{u}_i) d\Gamma + \int_\Omega (b^{lq} - \rho_{lq} \eta^{lq} s)(\tilde{p}^{lq} . \tilde{\hat{\varepsilon}}_{ii} - \tilde{\hat{p}}^{lq} . \tilde{\varepsilon}_{ii}) d\Omega$$
$$+ \int_\Omega (1 - b^{lq} - \rho_g \eta^g s)(\tilde{p}^g . \tilde{\hat{\varepsilon}}_{ii} - \tilde{\hat{p}}^g . \tilde{\varepsilon}_{ii}) d\Omega - \int_\Gamma \rho_{lq} \eta^{lq} s(\tilde{\hat{p}}^{lq} \delta_{ij} . \tilde{u}_i - \tilde{p}^{lq} \delta_{ij} . \tilde{\hat{u}}_i) . n_j d\Gamma \quad (27)$$
$$- \int_\Gamma \rho_g \eta^g s(\tilde{\hat{p}}^g \delta_{ij} . \tilde{u}_i - \tilde{p}^g \delta_{ij} . \tilde{\hat{u}}_i) . n_j d\Gamma - \int_\Omega \rho(\tilde{\hat{F}}_i . \tilde{u}_i - \tilde{F}_i . \tilde{\hat{u}}_i) d\Omega = 0$$

Basic Integral Equation of Mass Conduction and Balance (liquid)

This time the equation (15) is weighted by a virtual liquid pressure $\hat{p}^{lq}$ and is integrated over the volume Ω.

$$B = \int_\Omega (\phi^{lq} \eta^{lq} \tilde{p}^{lq}_{,ii} - c^{lq} s \tilde{p}^g - N s \tilde{p}^{lq} - (b^{lq} - \rho^{lq} \phi^{lq} \eta^{lq} s) s \tilde{u}_{i,i} + \tilde{\gamma}^{lq}) . \tilde{\hat{p}}^{lq} d\Omega \quad (28)$$

The first r.h.s term can be expanded using Green theorem (29)

$$\int_\Omega u \cdot \nabla^2 v \cdot d\Omega = \int_\Omega \left(u \cdot \nabla v - v \cdot \nabla u \right) \cdot n d\Gamma + \int_\Omega v \cdot \nabla^2 u \cdot d\Omega \quad (29)$$

$$B_1 = \int_\Omega \phi^{lq} \eta^{lq} \tilde{p}^{lq}_{,ii} . \tilde{\hat{p}}^{lq} d\Omega = \int_\Gamma \phi^{lq} \eta^{lq} (\tilde{\hat{p}}^{lq} . \tilde{p}^{lq}_{,i} - \tilde{p}^{lq} . \tilde{\hat{p}}^{lq}_{,i}) . n_j d\Gamma + \int_\Omega \phi^{lq} \eta^{lq} \tilde{\hat{p}}^{lq}_{,ii} . \tilde{p}^{lq} d\Omega \quad (30)$$

And the other terms are

$$B_2 = \int_\Omega c^{lq} s \tilde{p}^g . \tilde{\hat{p}}^{lq} d\Omega = \int_\Omega c^{lq} s \tilde{\hat{p}}^g . \tilde{p}^{lq} d\Omega - \int_\Omega c^{lq} s(\tilde{\hat{p}}^g . \tilde{p}^{lq} - \tilde{p}^g . \tilde{\hat{p}}^{lq}) d\Omega \quad (31)$$

$$B_3 = \int_\Omega N s \tilde{p}^{lq} . \tilde{\hat{p}}^{lq} d\Omega = \int_\Omega N s \tilde{\hat{p}}^{lq} . \tilde{p}^{lq} d\Omega \quad (32)$$

$$B_4 = \int_\Omega (b^{lq} - \rho^{lq}\phi^{lq}\eta^{lq}s)s\tilde{u}_{i,i}.\tilde{\hat{p}}^{lq}d\Omega = \int_\Omega (b^{lq} - \rho^{lq}\phi^{lq}\eta^{lq}s)s\tilde{p}^{lq}.\tilde{\hat{u}}_{i,i}d\Omega - \int_\Omega (b^{lq} - \rho^{lq}\phi^{lq}\eta^{lq}s)s(\tilde{p}^{lq}.\tilde{\hat{\varepsilon}}_{ii} - \tilde{\hat{p}}^{lq}.\tilde{\varepsilon}_{ii})d\Omega \quad (33)$$

$$B_5 = \int_\Omega \tilde{\gamma}^{lq}.\tilde{\hat{p}}^{lq}d\Omega = \int_\Omega \tilde{p}^{lq}.\tilde{\hat{\gamma}}^{lq}d\Omega - \int_\Omega (\tilde{p}^{lq}.\tilde{\hat{\gamma}}^{lq} - \tilde{\hat{p}}^{lq}.\tilde{\gamma}^{lq})d\Omega \quad (34)$$

And finally, $B = B_1 - B_2 - B_3 - B_4 + B_5$ by knowing that $\phi^{lq}\eta^{lq}\tilde{\hat{p}}^{lq}_{,ii} - c^{lq}s\tilde{\hat{p}}^{g} - Ns\tilde{\hat{p}}^{lq} - (b^{lq} - \rho^{lq}\phi^{lq}\eta^{lq}s)s\tilde{\hat{u}}_{i,i} + \tilde{\hat{\gamma}}^{lq} = 0$,
the integral B yields

$$\int_\Gamma \phi^{lq}\eta^{lq}(\tilde{\hat{p}}^{lq}.\tilde{p}^{lq}_{,i} - \tilde{p}^{lq}.\tilde{\hat{p}}^{lq}_{,i}).n_j d\Gamma + \int_\Omega c^{lq}s(\tilde{\hat{p}}^{g}.\tilde{p}^{lq} - \tilde{p}^{g}.\tilde{\hat{p}}^{lq})d\Omega + \int_\Omega (b^{lq} - \rho^{lq}\phi^{lq}\eta^{lq}s)s(\tilde{p}^{lq}.\tilde{\hat{\varepsilon}}_{ii} - \tilde{\hat{p}}^{lq}.\tilde{\varepsilon}_{ii})d\Omega - \int_\Omega (\tilde{p}^{lq}.\tilde{\hat{\gamma}}^{lq} - \tilde{\hat{p}}^{lq}.\tilde{\gamma}^{lq})d\Omega = 0 \quad (35)$$

Basic Integral Equation of Mass Conduction and Balance (gas)

In the same way of liquid phase, equation (16) is weighted by a virtual gas pressure $\hat{p}^g$ and is integrated over the volume Ω.

$$C = \int_\Omega (\phi^g\eta^g\tilde{p}^g_{,ii} - (c^g - c^{lq})s\tilde{p}^g - c^{lq}s\tilde{p}^{lq} - (1 - b^{lq} - \rho^g\phi^g\eta^g s)s\tilde{u}_{i,i} + \tilde{\gamma}^g).\tilde{\hat{p}}^g d\Omega \quad (36)$$

The first r.h.s term can be expanded using Green theorem

$$C_1 = \int_\Omega \phi^g\eta^g\tilde{p}^g_{,ii}.\tilde{\hat{p}}^g d\Omega = \int_\Gamma \phi^g\eta^g(\tilde{\hat{p}}^g.\tilde{p}^g_{,i} - \tilde{p}^g.\tilde{\hat{p}}^g_{,i}).n_j d\Gamma + \int_\Omega \phi^g\eta^g\tilde{\hat{p}}^g_{,ii}.\tilde{p}^g d\Omega \quad (37)$$

And the other terms are

$$C_2 = \int_\Omega (c^g - c^{lq})s\tilde{p}^g.\tilde{\hat{p}}^g d\Omega = \int_\Omega (c^g - c^{lq})s\tilde{\hat{p}}^g.\tilde{p}^g d\Omega \quad (38)$$

$$C_3 = \int_\Omega c^{lq}s\tilde{p}^{lq}.\tilde{\hat{p}}^g d\Omega = \int_\Omega c^{lq}s\tilde{\hat{p}}^{lq}.\tilde{p}^g d\Omega - \int_\Omega c^{lq}s(\tilde{\hat{p}}^{lq}.\tilde{p}^g - \tilde{p}^{lq}.\tilde{\hat{p}}^g)d\Omega \quad (39)$$

$$C_4 = \int_\Omega (1 - b^{lq} - \rho^g\phi^g\eta^g s)s\tilde{u}_{i,i}.\tilde{\hat{p}}^g d\Omega = \int_\Omega (1 - b^{lq} - \rho^g\phi^g\eta^g s)s\tilde{p}^g.\tilde{\hat{u}}_{i,i}d\Omega - \int_\Omega (1 - b^{lq} - \rho^g\phi^g\eta^g s)s(\tilde{p}^g.\tilde{\hat{\varepsilon}}_{ii} - \tilde{\hat{p}}^g.\tilde{\varepsilon}_{ii})d\Omega \quad (40)$$

$$C_5 = \int_\Omega \tilde{\gamma}^g.\tilde{\hat{p}}^g d\Omega = \int_\Omega \tilde{p}^g.\tilde{\hat{\gamma}}^g d\Omega - \int_\Omega (\tilde{p}^g.\tilde{\hat{\gamma}}^g - \tilde{\hat{p}}^g.\tilde{\gamma}^g)d\Omega \quad (41)$$

And finally; $C = C_1 - C_2 - C_3 - C_4 + C_5$ by knowing that

$$\phi^g \eta^g \tilde{\tilde{p}}^g_{,ii} - (c^g - c^{lq}) s\tilde{\tilde{p}}^g - c^{lq} s\tilde{\tilde{p}}^{lq} - (1 - b^{lq} - \rho^g \phi^g \eta^g s) s\tilde{\tilde{u}}_{i,i} + \tilde{\tilde{\gamma}}^g = 0$$

the integral C yields

$$\begin{aligned} &\int_\Gamma \phi^g \eta^g (\tilde{\tilde{p}}^g . \tilde{p}^g_{,i} - \tilde{p}^g . \tilde{\tilde{p}}^g_{,i}) . n_j d\Gamma + \int_\Omega c^{lq} s(\tilde{\tilde{p}}^{lq} . \tilde{p}^g - \tilde{p}^{lq} . \tilde{\tilde{p}}^g) d\Omega + \\ &\int_\Omega (1 - b^{lq} - \rho^g \phi^g \eta^g s) s(\tilde{p}^g . \tilde{\tilde{\varepsilon}}_{ii} - \tilde{\tilde{p}}^g . \tilde{\varepsilon}_{ii}) d\Omega - \int_\Omega (\tilde{p}^g . \tilde{\tilde{\gamma}}^g - \tilde{\tilde{p}}^g . \tilde{\gamma}^g) d\Omega = 0 \end{aligned} \tag{42}$$

One can eliminate the similar terms in integrals between (35) , (42) by summing them up.

$$\begin{aligned} B + C = &\int_\Gamma \phi^{lq} \eta^{lq} (\tilde{\tilde{p}}^{lq} . \tilde{p}^{lq}_{,i} - \tilde{p}^{lq} . \tilde{\tilde{p}}^{lq}_{,i}) . n_j d\Gamma + \int_\Gamma \phi^g \eta^g (\tilde{\tilde{p}}^g . \tilde{p}^g_{,i} - \tilde{p}^g . \tilde{\tilde{p}}^g_{,i}) . n_j d\Gamma \\ &+ \int_\Omega (b^{lq} - \rho_{lq} \eta^{lq} s) s(\tilde{p}^{lq} . \tilde{\tilde{\varepsilon}}_{ii} - \tilde{\tilde{p}}^{lq} . \tilde{\varepsilon}_{ii}) d\Omega + \int_\Omega (1 - b^{lq} - \rho_g \eta^g s) s(\tilde{p}^g . \tilde{\tilde{\varepsilon}}_{ii} - \tilde{\tilde{p}}^g . \tilde{\varepsilon}_{ii}) d\Omega \\ &- \int_\Omega (\tilde{p}^{lq} . \tilde{\tilde{\gamma}}^{lq} - \tilde{\tilde{p}}^{lq} . \tilde{\gamma}^{lq}) d\Omega - \int_\Omega (\tilde{p}^g . \tilde{\tilde{\gamma}}^g - \tilde{\tilde{p}}^g . \tilde{\gamma}^g) d\Omega \end{aligned} \tag{43}$$

Now similar terms can be eliminated between equations (27) and (43)

$$\begin{aligned} A = &s\int_\Gamma (\tilde{t}_i . \tilde{\tilde{u}}_i - \tilde{\tilde{t}}_i . \tilde{u}_i) d\Gamma - s\int_\Omega \rho(\tilde{\tilde{F}}_i . \tilde{u}_i - \tilde{F}_i . \tilde{\tilde{u}}_i) d\Omega \\ &+ \int_\Gamma [\tilde{\tilde{p}}^{lq} . (-\phi^{lq} \eta^{lq} \tilde{p}^{lq}_{,i} - \rho_{lq} \eta^{lq} s^2 \tilde{u}_i) - \tilde{p}^{lq} . (-\phi^{lq} \eta^{lq} \tilde{\tilde{p}}^{lq}_{,i} - \rho_{lq} \eta^{lq} s^2 \tilde{\tilde{u}}_i)] . n_j d\Gamma \\ &+ \int_\Gamma [\tilde{\tilde{p}}^g . (-\phi^g \eta^g \tilde{p}^g_{,i} - \rho_g \eta^g s^2 \tilde{u}_i) - \tilde{p}^g . (-\phi^g \eta^g \tilde{\tilde{p}}^g_{,i} - \rho_g \eta^g s^2 \tilde{\tilde{u}}_i)] . n_j d\Gamma \\ &+ \int_\Omega (\tilde{p}^{lq} . \tilde{\tilde{\gamma}}^{lq} - \tilde{\tilde{p}}^{lq} . \tilde{\gamma}^{lq}) d\Omega + \int_\Omega (\tilde{p}^g . \tilde{\tilde{\gamma}}^g - \tilde{\tilde{p}}^g . \tilde{\gamma}^g) d\Omega \end{aligned} \tag{44}$$

Rewriting (44) using equations (4), (5), (13) and (14)

$$\begin{aligned} &s\int_\Gamma (\tilde{t}_i . \tilde{\tilde{u}}_i - \tilde{\tilde{t}}_i . \tilde{u}_i) d\Gamma - \int_\Gamma (\tilde{p}^{lq} . \tilde{\tilde{q}}^{lq}_i - \tilde{\tilde{p}}^{lq} . \tilde{q}^{lq}_i) d\Gamma - \int_\Gamma (\tilde{p}^g . \tilde{\tilde{q}}^g_i - \tilde{\tilde{p}}^g . \tilde{q}^g_i) d\Gamma \\ &+ \int_\Omega (\tilde{p}^{lq} . \tilde{\tilde{\gamma}}^{lq} - \tilde{\tilde{p}}^{lq} . \tilde{\gamma}^{lq}) d\Omega + \int_\Omega (\tilde{p}^g . \tilde{\tilde{\gamma}}^g - \tilde{\tilde{p}}^g . \tilde{\gamma}^g) d\Omega + s\int_\Omega \rho(\tilde{F}_i . \tilde{\tilde{u}}_i - \tilde{\tilde{F}}_i . \tilde{u}_i) d\Omega = 0 \end{aligned} \tag{45}$$

Equation (45) is the Betti's reciprocal theorem in the Laplace transform domain.

TIME DOMAIN BOUNDARY INTEGRAL EQUATIONS

The integral equation (45) are derived in Laplace domain and then inverse convolution product is used to represent (45) in time domain that is the reciprocal

theorem in time domain.

$$\int_\Gamma (t_i * \hat{u}_i - \hat{t}_i * u_i)d\Gamma - \int_\Gamma (p^{lq} * \hat{q}_i^{lq} - \hat{p}^{lq} * q_i^{lq})d\Gamma - \int_\Gamma (p^g * \hat{q}_i^g - \hat{p}^g * q_i^g)d\Gamma$$
$$+ \int_\Omega (p^{lq} * \hat{\gamma}^{lq} - \hat{p}^{lq} * \gamma^{lq})d\Omega + \int_\Omega (p^g * \hat{\gamma}^g - \hat{p}^g * \gamma^g)d\Omega \quad (46)$$
$$+ \int_\Omega \rho(F_i * \hat{u}_i - \hat{F}_i * u_i)d\Omega = 0$$

Now consider actual body force, the actual liquid and gas injection rate are zero (i.e. $F_i = \gamma^{lq} = \gamma^g = 0$) and the corresponding virtual values are defined $\hat{F}_i = \delta(x).h(t)$ and $\hat{\gamma}^{lq} = \hat{\gamma}^g = 0$, Where; $\delta(x)$ is the Dirac Delta function and $h(t)$ is the Heaviside step function. Then the integral equation (46) results

$$u_i = \int_\Gamma (t_i * \hat{u}_i - \hat{t}_i * u_i)d\Gamma - \int_\Gamma (p^{lq} * \hat{q}_i^{lq} - \hat{p}^{lq} * q_i^{lq})d\Gamma - \int_\Gamma (p^g * \hat{q}_i^g - \hat{p}^g * q_i^g)d\Gamma \quad (47)$$

Once again consider the other virtual loading condition with the same actual loading condition $\hat{F}_i = \hat{\gamma}^g = 0$ and $\hat{\gamma}^{lq} = \delta(x)\delta(t)$ this time the integral equation (46) results

$$-p^{lq} = \int_\Gamma (t_i * \hat{u}_i - \hat{t}_i * u_i)d\Gamma - \int_\Gamma (p^{lq} * \hat{q}_i^{lq} - \hat{p}^{lq} * q_i^{lq})d\Gamma - \int_\Gamma (p^g * \hat{q}_i^g - \hat{p}^g * q_i^g)d\Gamma \quad (48)$$

And for the third time consider $\hat{F}_i = \hat{\gamma}^{lq} = 0$ and $\hat{\gamma}^g = \delta(x)\delta(t)$ to obtain

$$-p^g = \int_\Gamma (t_i * \hat{u}_i - \hat{t}_i * u_i)d\Gamma - \int_\Gamma (p^{lq} * \hat{q}_i^{lq} - \hat{p}^{lq} * q_i^{lq})d\Gamma - \int_\Gamma (p^g * \hat{q}_i^g - \hat{p}^g * q_i^g)d\Gamma \quad (49)$$

In the integral equations (47), (48) and (49) all the integrals are the boundary integrals.

CONCLUSIONS

The boundary integral equation (BIE) and their corresponding fundamental solutions are essential parts of BEM. The time domain BIE for unsaturated poro-elastic media were not presented before. This paper presents full dynamic BIE with variables of solid displacement, liquid and gas pressure.

REFERENCES

Biot, M.A. (1941). "General theory of three-dimensional consolidation." *J. Appl. Phys.* Vol. 12: 155-164.

Biot, M.A. (1955). "Theory of elasticity and consolidation for a porous anisotropic solid." *J. Appl. Phys.* Vol. 26: 182-185.

Biot, M.A. (1956a). "General solution of the equations of elasticity and consolidation

for a porous material." *J. Appl. Mech.* Vol. 23 (1): 91-96.
Biot, M.A. (1956b). "The theory of propagation of elastic waves in a fluid saturated porous solid I. Low frequency range." *J. Acoust. Soc. Am.* Vol. 28: 168-178.
Biot, M.A. (1956c). "The theory of propagation of elastic waves in a fluid saturated porous solid II. Higher frequency range." *J. Acoust. Soc. Am.* Vol. 28: 179-191.
Biot, M.A. (1962). "Mechanics of deformation and acoustic propagation in porous media." *J. Appl. Phys.* Vol. 33: 1482-1498.
Bonnet, G. (1987). "Basic singular solutions for a poroelastic medium in the dynamic range." *J. Acoust. Soc. Am.*, Vol. 82: 1758-1762.
Chen, J. (1994a). "Time domain fundamental solution to Biot's Complete equations of dynamic poroelasticity. Part I. Two dimensional solution." *Int. J. Solids Structures.*, Vol. 31 (10): 1447-1490.
Chen, J. (1994b). "Time domain fundamental solution to Biot's Complete equations of dynamic poroelasticity. Part I. Three dimensional solution." *Int. J. Solids Structures.*, Vol. 31 (2): 169-202.
Cheng, A.H.D. and Liggett, J.A. (1984). "Boundary integral equation method for linear porous-elasticity with applications to soil consolidation." *Int. J. Numer. Meth. Engng.*, Vol. 20: 255-278.
Coussy O. (1995). "Mechanics of Porous Continua", John Wiley & Sons, Ltd.
Coussy O., Dormieux L., and Detournay E. (1998). "From Mixture Theory to Biot's Approach for Porous Media", Elsevier Science Ltd., *Int. J. Solids Structures*, Vol. 35 (34-35): 4619-4635.
Darcy, H. (1856). "Les fontaines publique de la villa de Dijon." Dalmont. Paris.
(3): 119-132.
Dominguez J. (1991). "An integral formulation for dynamic poroelasticity" *J. Appl. Mech.*, Vol. 58: 588-591.
Green, A.E. and Naghdi, P.M. (1965). "A dynamic theory of interacting continua." *Int. J. Engng. Sci.*, Vol. 3: 231-241.
Manolis, G. and Beskos, D. (1989). "Integral formulation and fundamental solutions of dynamic poroelasticity and thermoelasticity." *Acta Mechanica*, Vol. 76: 89-104.
Muraleetharan K. K., Wei C., (1999). "Dynamic Behaviour of Unsaturated Porous Media: Governing Equations Using the Theory of Mixtures with Interfaces (TMI)", *Int. J. Numer. Anal. Meth. Geomech.*, 23, 1579-1608.
Predeleanu, M. (1981). "Boundary element methods." C.A. Brebbia (ed.), Springer Verlag.
Prevost, J.H. (1982). "Nonlinear transient phenomena in saturated porous media." *Comp. Math. In Appl. Mech.*, Vol. 20: 3-8.
Schrefler, B.A., Simoni, L., Xikui, L. and Zienkiewicz, O.C. (1990). "Mechanics of Partially Saturated Porous Media.", in Numerical Methods and Constitutive Modeling in Geomechanics, Desai, C.S., Gioda, G. (eds.), Springer-Verlag.
Terzaghi, K. (1923). "Die berechnung der darchlassigkeit des tones aus dem verlauf der gydromechanischen spannungsercheinungen." *Sitzungsber. Akad. Wiss. (Wein). Math. Naturwiss.*, Kl. Abt. Ha. Vol. 132: 125-138.
Truesdell, C. and Toupin, R. (1960). "The classical field theories." *Handbuch der Physik.*, S. Flugge (Ed.), Springer-Verlag, Berlin, Vol. 3.
Wei C., Muraleetharan K. K., (2002a) "A continuum theory of porous media saturated

by multiple immiscible fluids: I. Linear poroelasticity" *Int. J. Engng. Sci.*, Vol. 40: 1807-1833.

Wei C., Muraleetharan K. K., (2002b) "A continuum theory of porous media saturated by multiple immiscible fluids: II. Lagrangian description and variational structure" *Int. J. Engng. Sci.*, Vol. 40: 1835-1854.

Zienkiewicz, O.C., Chang, C.T. and Bettess, P. (1980). "Drained, undrained, consolidation and dynamic behaviour assumptions in soils." *Geotechnique.*, Vol. 30: 385-395.

DETERMINATION OF SOIL-STRUCTURE INTERACTION EFFECTS FOR A MODEL TEST STRUCTURE USING PARAMETRIC SYSTEM IDENTIFICATION PROCEDURES

Salih Tileylioglu[1], Robert L. Nigbor[2], and Jonathan P. Stewart[3]

[1] PhD. Candidate, Department of Civil and Environmental Engineering, Boelter Hall 6689, University of California, Los Angeles, CA 90095; email: saliht@ucla.edu
[2] Researcher, Department of Civil and Environmental Engineering, Boelter Hall 6689, University of California, Los Angeles, CA 90095; email: nigbor@ucla.edu
[3] Professor and Vice Chair, Department of Civil and Environmental Engineering, Boelter Hall 6689, University of California, Los Angeles, CA 90095; email: jstewart@seas.ucla.edu

ABSTRACT: Earthquake recordings from a model test structure located at Garner Valley California are used to evaluate inertial soil-structure interaction (SSI) effects. The test structure consists of steel columns and bracings 4.06 m in height supporting a $4m \times 4m \times 0.4m$ reinforced concrete roof slab. The structure rests on a $4m \times 4m \times 0.5m$ reinforced concrete foundation with no embedment. Surficial soil conditions consist of organic soil overlying silty sand alluvium with an average shear wave velocity in the upper 15 m of $200m/s$. Seismic monitoring is performed with uni-axial (horizontal) accelerometers on the roof and foundation as well as vertical sensors at the corners of the foundation. Parametric system identification procedures are implemented to evaluate fundamental-mode vibration frequencies for a fixed- and flexible-base condition, from which SSI effects can be inferred. Data is available for the structure with and without bracing from two earthquakes. The lengthening of the fixed-base period due to SSI is a period lengthening of 12% and 74% for the braced and unbraced structure, respectively. The corresponding foundation damping levels for these two cases are about 1% and 5%. The different levels of period lengthening and foundation damping for the two structural configurations reflect the strong increase of inertial SSI effects with the ratio of structure-to-soil stiffness, which is naturally greater for the fixed- base configuration. The observed levels of SSI are reasonably well predicted by available theoretical models.

INTRODUCTION

Both inertial and kinematic soil-structure interaction (SSI) effects can contribute to the response of a structure resting on a compliant geologic medium. Kinematic interaction principally affects the frequency content and amplitude of foundation motions relative to free-field motions (e.g., Veletsos and Prasad, 1989). Inertial interaction is fundamentally related to the foundation rotations and displacements, as well as the energy dissipation, that occurs when base shear and moment is applied to the foundations by the vibrating structure. In some conditions, those foundation

rotations and displacements can represent a significant fraction of the total soil-foundation-structure system flexibility. Similarly, the radiation and hysteretic damping associated with the foundation acting as a wave source into the surrounding geologic medium can significantly contribute to the overall system damping. These inertial interaction effects can be concisely expressed by their impact on modal vibration frequencies and damping ratios. These parameters are termed as "flexible-base" for a structure on a compliant base and "fixed- based" for the fictional case of a structure resting on a rigid base.

Theoretical models have existed for many years to predict inertial SSI effects on the period and damping ratio of a single degree of freedom oscillator (e.g., Bielak, 1975; Veletsos and Nair, 1975). Previous studies have sought to validate those studies using strong motion data from instrumented structures (e.g., Stewart et al., 1999a, b) and forced-vibration data (e.g., Luco and de Barros, 2004). We extend that work by investigating SSI effects on the fundamental-mode period and damping ratio of a well instrumented model test structure. This extends previous work in several respects: (1) the resolution of the sensors and quality of the data acquisition system allows more accurate evaluation of SSI effects than has been possible previously; (2) the test structure is reconfigurable so that SSI effects for different levels of structural stiffness, but constant foundation and soil conditions, can be evaluated; (3) SSI effects can be evaluated for three vibration sources including ambient, a mounted shaker, and earthquakes.

The test structure was constructed in 2004 and is located in Garner Valley, California. It is owned and operated by the NEES site at UCSB (Nigbor et al., 2004; Steidl et al., 2004; http://nees.ucsb.edu).

The paper begins with a general overview of the site and structure. The system identification procedures used to evaluate modal parameters for different base fixity conditions are then presented along with the results. Those results are then interpreted to evaluate SSI effects, which are compared to predictions of a theoretical model.

SITE AND STRUCTURE DESCRIPTION

The test structure is located in a sedimentary basin that is instrumeted as part of the Garner Valley Differential Array (GVDA). Garner Valley, California is in a region of high seismicity. As shown in Figure 1, soil conditions consist of organics at the top and silty sand extending to a depth of 18 *m*, which then transitions to decomposed granite. Relatively intact crystalline bedrock occurs at a depth of 88 *m*. The ground water table is at the surface in rainy seasons and drops to about 3 *m* in dry seasons. Geophysical tests (suspension logging and SASW) have been carried out to measure P- and S-wave velocity profiles. The SASW analysis indicates near-surface shear wave velocity, V_s = 207 *m/s*.

The test structure was constructed specifically to facilitate SSI experiments and hence is referred to as the soil-foundation-structure interaction (SFSI) test structure. As shown in Figure 2, the structure consists of a simple steel frame supporting a roof slab 40 cm in thickness. The foundation consists of a non-embedded reinforced concrete slab 50 cm thick. The height of the structure from base of foundation to top of roof slab is 4.56 m. The plan dimensions of the foundation and roof slabs are 4m x

4m. Reconfigurable bracings can be inserted within the structure to modify its vibration characteristics.

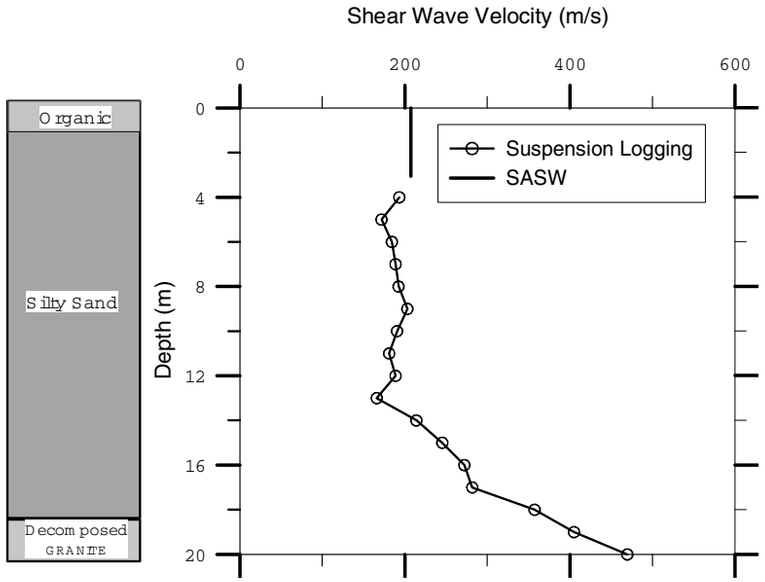


FIG. 1. Near surface soil profile with shear wave velocities obtained from suspension logging and SASW tests



FIG. 2. The SFSI test structure at GVDA with bracings in place

The SFSI test structure is instrumented with triaxial and uniaxial accelometers and pressure sensors. The structure is located within the broader GVDA, which consists of free-field triaxial accelerometers positioned across Garner Valley. A downhole array is also present near the structure. Sensor signals are digitally recorded with a resolution of 24-bits and a sample rate of 200 samples per second. Several earthquakes have been recorded with magnitudes of magnitudes of 5 or less. In this paper we consider two earthquakes with M_L=3.5 and M_w=4.9. Unfortunately, free-field data are not available for these events. Base-of-structure peak accelerations for these two events were 0.008g and 0.05g, respectively. The M_l = 3.5 event is used for system identification without bracing and the M_L = 4.9 event is used for system identification with bracing.

SYSTEM IDENTIFICATION

Ground motion recordings and forced vibration tests may be used in system identification procedures to estimate modal vibration parameters of the soil-structure system. System identification is a process by which the properties of an unknown system are estimated based on a measured input to the system and output from the system. When different input-output pairs are utilized, the system itself changes. Referring to Figure 3, the base-of-structure recording can be visualized as being the sum of the free-field ground motion (u_g) and the relative free-field/foundation motion (u_f). This motion is modified at the roof of the structure as a result of base rotation (θH) and deformations of the structure itself (u). Hence, if u_g is taken as input and roof motion is taken as output, the intervening system has contributions from base translation, base rotation, and structure deformation, and is referred to as the flexible-base condition. Similarly, if the sum of base translation and θH is taken as input and roof translation as output, the intervening system is the structure alone, and the identified properties are referred to as fixed-base. The pseudo flexible-base case is an intervening case that neglects base translation, as indicated in Figure 3. Formal derivations of the above input-output pairs are given in Stewart and Fenves (1998).

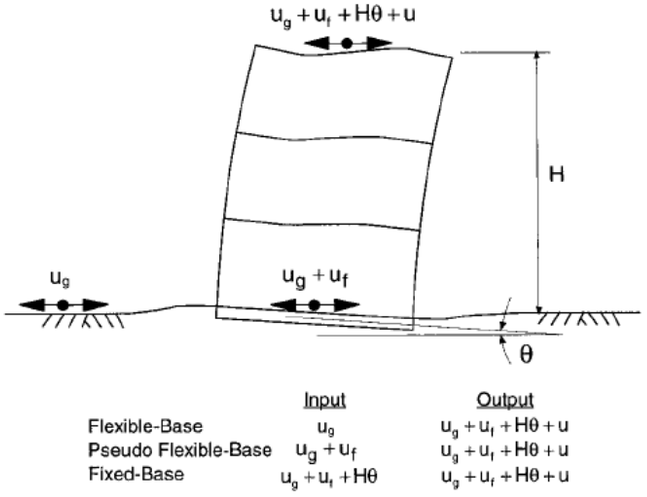


FIG. 3. Inputs and Outputs for System Identification analysis of a building (after Stewart et al., 1999)

A general measure of SSI effects can be obtained by comparing fixed-base and flexible-base parameters. One of the important effects of soil-structure interaction is to increase the system period with respect to the fixed-base case. This phenomenon is called period lengthening. Another important effect of SSI is to introduce foundation damping, which includes contributions from radiation damping and hysteretic material damping. This is expressed by a foundation damping factor (β_f) that is expressed as follows (Bielak, 1975; Veletsos and Nair, 1975):

$$\beta_f = \tilde{\beta} - \frac{\beta}{\left(\tilde{T}/T\right)^3} \tag{1}$$

where $\tilde{\beta}$ =flexible-base damping, β=fixed-base damping, $\tilde{T}$ =flexible-base period, and T=fixed-base period.

We use a parametric system identification procedures described in detail by Stewart and Fenves (1998) to evaluate fundamental-mode frequencies and damping ratios. In this procedure, the system is assumed to consist of a multi degree-of-freedom structure

with lumped masses. The procedure maps inputs to outputs via a transfer function surface defined in the Laplace domain (parametric procedure). The surface is defined as a function of both frequency and damping. The ordinates of the surface are evaluated so as to minimize the cumulative error between the model output and the recorded output. The peaks in the surface define modal frequencies and damping ratios.

Parametric system identification requires two user-specified parameters; the time delay between the input and output signals and the number of modes required to capture the response of the system. This is illustrated in Figure 4 for a particular input-output pair (structure without bracing, pseudo-flexible- base input-output pair). The minimum error occurs at a time delay of 2. The error for the number of modes essentially does not change significantly for number of modes > 4.

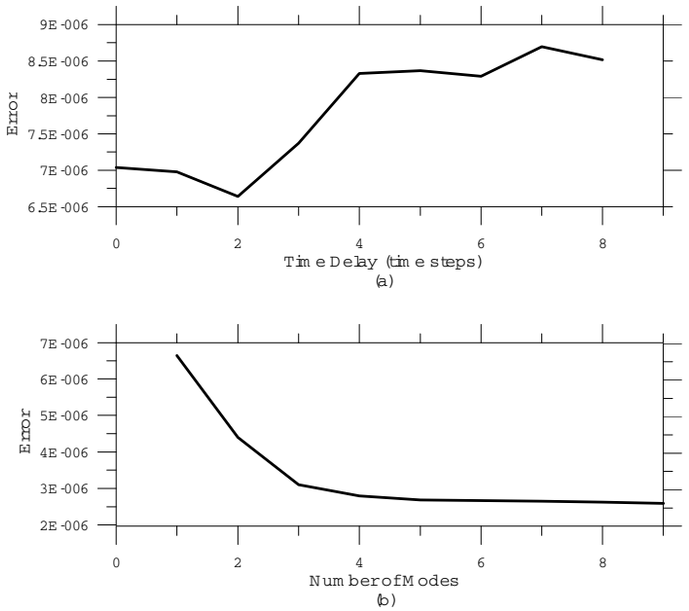


FIG.4. Error of system identification model with respect to (a) Time delay and (b) Number of modes

Using the aforementioned time lag and number of modes, the transfer function surface is identified as shown in Figure 5. Locations of high points ("poles") and low points ("zeros") are obtained that define the modal frequencies and damping ratios. Figure 6 compares a slice through the parametric transfer functions on the frequency axis and its comparison to a transmissibility function defined from smoothed power spectral density functions of the input and output (Pandit, 1991; Stewart and Fenves, 1998). We note that the frequencies of the major peaks match reasonably well. The amplitudes need not match as the transmissibility function depends on the smoothing procedure utilized (Stewart et al. 1999). As shown in Figure 7, another check consists of comparing the time series output of the parametric model to data, which indicates a reasonable match.

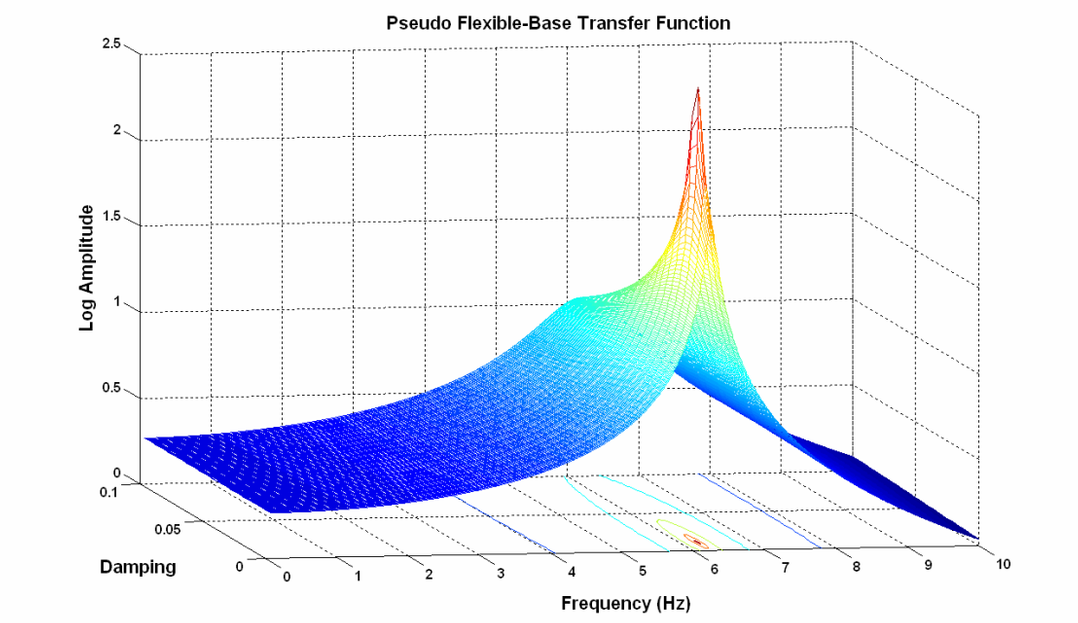


FIG.5. Transfer function surface (pseudo flexible-base case, no bracing)

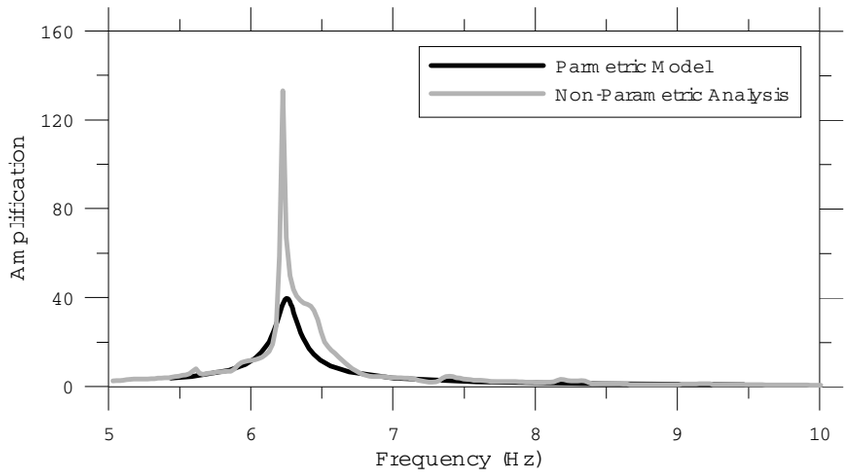


FIG.6. Comparison of transfer function from parametric system identification and transmissibility function obtained from smoothed power spectral densities of input and output signals (pseudo flexible-base case, no bracing)

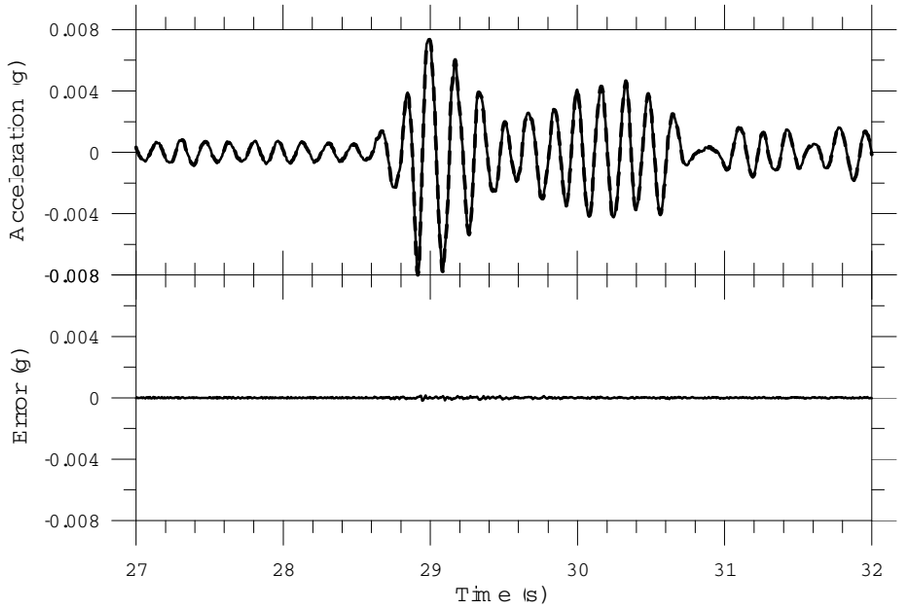


FIG.7. The output recording compared to the model output and the difference between the two motions (bottom)

The result of this analysis is that pseudo flexible-base first-mode frequency and damping ratio are estimated as 6.25 Hz and 1.1%. Repeating these analyses for the fixed-base input-output pair and for the braced structure yields the results given in Table 1. The reduction in frequency and increase of damping of pseudo flexible-base parameters relative to fixed-base parameters indicates an inertial SSI effect for this structure.

Table 1. Summary of system identification from ground motions

		Fixed-Base Parameters		Pseudo Flexible- Base Parameters	
Structural Configuration	**Peak motion at top of structure (g)**	**f (Hz)**	**β (%)**	**f (Hz)**	**β (%)**
Unbraced	0.008	7.0±0.001	0.20±0.003	6.25±0.001	1.10±0.004
Braced	0.05	16.20±0.005	3.0±0.01	9.70±0.001	5.60±0

INTERPRETATION

The lack of free-field data prevented the calculation of flexible- base parameters from system identification. However, those parameters may be estimated using a procedure described by Stewart and Fenves (1998). For the case of known fixed- and pseudo flexible-base parameters, the flexible-base frequency is calculated as follows:

$$\tilde{\omega}^2 = \frac{1}{1/\omega^2 + 1/\omega_\theta^{\,2} + 1/\omega_u^{\,2}} \tag{2}$$

Parameter ω=fixed-base circular frequency, ω_u=vibration frequency related to foundation translation, and ω_θ=vibration frequency related to foundation rotation, which is estimated as:

$$\frac{1}{\omega_\theta^{\,2}} = \frac{1}{(\omega^*)^2} - \frac{1}{\omega^2} \tag{3}$$

where ω^*=pseudo flexible-base circular frequency. Parameter ω_u is calculated from:

$$\left(\frac{\omega_\theta}{\omega_u}\right)^2 = \left(\frac{r_\theta^3}{r_u h^2}\right)\left(\frac{2-\upsilon}{3(1-\upsilon)}\right)\left(\frac{\alpha_\theta}{\alpha_u}\right) \tag{4}$$

Parameters r_θ and r_u are the equivalent radii which match the moment of inertia and area of the foundation, respectively, υ=Poisson's ratio of soil, h=height of structure, and α_θ and α_u represent frequency-dependent dynamic modifactor factors to the static foundation rotational and translational stiffness, respectively (e.g., Veletsos and Verbic, 1973).

Similarly, the flexible-base damping ratio ($\tilde{\beta}$) is calculated from:

$$\tilde{\beta} = \left(\frac{\tilde{\omega}}{\omega_u}\right)^3 \beta_u + \left(\frac{\tilde{\omega}}{\omega}\right)^3 \beta + \left(\frac{\tilde{\omega}}{\omega_\theta}\right)^3 \beta_\theta \tag{5}$$

where β_θ and β_u are given by:

$$\beta_\theta = \frac{\tilde{\beta}^* - \beta(\tilde{\omega}^*/\omega)^3}{(\omega^*/\omega_\theta)^3} \tag{6}$$

$$\beta_u = \beta_\theta \frac{\omega_\theta}{\omega_u}\frac{c_u}{c_\theta}\frac{h^2 r_u^2}{r_\theta^4}\frac{3(1-\upsilon)}{2-\upsilon} \tag{7}$$

in which $\tilde{\beta}^*$ is the pseudo flexible-base damping, β=fixed-base damping, and β_u and β_θ are frequency dependent dynamic factors used for the calculation of the complex-part of foundation impedance functions (e.g., Veletsos and Verbic, 1973).

Table 2 summarizes the flexible-base frequency $\tilde{f}$ and damping ratio $\tilde{\beta}$ estimated using the above process. The flexible-base parameters are similar to the pseudo flexible-base parameters, because foundation rocking is the dominant SSI effect in this case.

Table 2. Estimated flexible-base parameters, SSI effects inferred from data, and SSI effects predicted by model

	Flexible-Base Parameters		SSI Effect: Data		SSI Effect: Model	
Structural Configuration	$\tilde{f}(Hz)$	$\tilde{\beta}(\%)$	$\tilde{T}/T$	$\beta_f(\%)$	$\tilde{T}/T$	$\beta_f(\%)$
Unbraced	6.13	1.11	1.14	0.96	1.10	1.40
Braced	9.20	4.80	1.76	4.20	1.55	5.30

As shown in Table 2, period lengthening and foundation damping (per Eq. 1) are calculated from the fixed-base parameters in Table 1 and the estimated flexible-base parameters in Table 2. The period lengthening and foundation are much larger for the braced configuration because of the stiffer structural system. Those results are compared to theoretical predictions for a rigid circular foundation on viscoelastic halfspace. The theoretical formulation, which is modified from Veletsos and Nair (1975), is described by Kramer and Stewart (2004). The model underpredicts the observed period lengthening and foundation damping in both cases, although the residuals are modest and the model captures well the differences between the unbraced and brace cases.

CONCLUSIONS

In this article, we have described the SFSI test structure in Garner Valley, which is an excellent experimental facility for detailed examination of SSI effects. Parametric system identification procedures were performed to examine the effects of SSI on the fundamental mode period and damping ratio. Results are obtained with the structure in a braced and unbraced configuration, which provides significantly different levels of SSI effects. The foundation damping and period lengthening calculated were found to be 0.96% and 1.14, respectively for the unbraced configuration. The values were 4.2% and 1.76 for the braced configuration. The results obtained from the system identification apply for small-strain conditions due to the weak shaking during the subject earthquakes. Strong ground motions have not yet been recorded by this array.

ACKNOWLEDGMENTS

The authors thank support from CENS. Special thanks to Ali Asghari for his help in the reconfigurations of the bracings in the structure.

REFERENCES

Bielak, J. (1975). “Dynamic behavior of structures with embedded foundations.” *J. Earthquake Engrg. Struct. Dyn.*, 3 (3), 259–274.

Kramer, S.L. and Stewart, J.P. (2004). Chapter 4: “Geotechnical Aspects of Seismic Hazards,” in *Earthquake Engineering. From Engineering Seismology to Performance-Based Engineering*, Y. Bozorgnia and V.V. Bertero (editors), CRC Press, 85 pages.

Luco, J. E and de Barros, F.C.P (2004). “Assessment of predictions of the response of the Hualien containment model during forced vibration tests,” *J. Earthquake Engrg. Struct. Dyn.*, 24 (12), 1013–1035.

Nigbor, R., Asghari, A., McMichael, L., and Mish, K., (2004). "Development of prototype SFSI simulation tool,” *13WCEE*, Vancouver BC.

Pandit, S. M. (1991). *Modal and spectrum analysis.* Wiley, New York.

Steidl, J., Youd, T.L., and Nigbor, R.L. (2004)/ "Research Opportunities at the NEES permanently instrumented field sites," *13WCEE*, Vancouver BC.

Stewart, J.P. and Fenves, G.L. (1998). "System identification for evaluating soil-structure interaction effects in buildings from strong motion recordings," *J. Earthquake Engrg. Struct. Dyn.*, 27 (8), 869-885.

Stewart, J.P., Fenves, G.L. and Seed, R.B. (1999a). "Seismic soil-structure interaction in buildings. I: Analytical aspects," *J. Geotech. & Geoenv. Engrg.*, ASCE, 125 (1), 26-37.

Stewart, J.P., Seed, R.B., and Fenves, G.L. (1999b). "Seismic soil-structure interaction in buildings. II: Empirical findings," *J. Geotech. & Geoenv. Engrg.*, ASCE, 125 (1), 38-48.

Veletsos, A. S., and Nair, V. V. (1975). ''Seismic interaction of structures on hysteretic foundations.'' *J. Struct. Engrg.*, ASCE, 101(1), 109–129.

Veletsos, A.S and Prasad, (1989). "Seismic interaction of structures and soils: stochastic approach*," J. Struct. Engrg,* ASCE,115(4),935-956,

Veletsos, A. S., and Verbic, B. (1973). ''Vibration of viscoelastic foundations.'' *J. Earthquake Engrg. Struct. Dyn.*, 2 (1), 87–102.

Dimensional Analysis of Soil-Foundation-Structure System Subjected to Near Fault Ground Motions

Jian Zhang[1], A.M. ASCE and Yuchuan Tang[2]

[1]Assistant Professor, Department of Civil and Environmental Engineering, University of California, Los Angeles, CA 90095-1593; zhangj@ucla.edu
[2]Graduate Student Researcher, Department of Civil and Environmental Engineering, University of California, Los Angeles, CA 90095-1593; bytang@ucla.edu

ABSTRACT: This paper investigates in depth the dynamic responses of soil-foundation-structure systems using dimensional analysis in order to evaluate the significance of soil-structure interaction effects when subjected to near-fault ground motions. A soil-foundation-structure interacting (SFSI) system is idealized into a simplified 2DOF system where both linear and elastic-plastic structures with flexible foundations are considered. Through rigorous dimensional analysis, the response of superstructure is presented in terms of the dimensionless Π-products. This approach brings forward the self-similarity, the invariance with respect to changes in scale or size, which decisively describe the interactive behaviour of a foundation-structure system. Extensive simulations have been conducted on various foundation-structure systems subjected to pulse-type ground motions to numerically describe the structural response, i.e. dimensionless relative displacement, as function of distinctive properties of superstructure and foundation. Results show that soil-structure interaction is insignificant for a variety of structure-foundation systems in practice. However, there are conditions under which the response of foundation-structure system is significantly higher than that of the fixed-base structure.

INTRODUCTION

It is well recognized that soil-structure interaction (SSI) affects the dynamic responses of structures under earthquake motions. The SSI effects have been identified to affect seismic response of civil structures by various researchers (Moslem and Trifunac 1986; Aviles and Perez-Rocha 1998; Stewart et al. 1999a,b; Mylonakis and Gazetas 2000 among others). Significant efforts have been made to model these complex effects rationally and accurately. Numerous discussions have also emerged on whether, when and how to incorporate the complex SSI effect in analysis and design.

The design procedures contained in FEMA 450 (BSSC 2004) and FEMA 440 (ATC 2005) incorporate SSI effects by modifying the period and damping ratio with respect to the fixed-base value. The lengthened period and increased damping due to

SSI effects result in increment or reduction of the structural response depending on the resonant period in the response spectrum. The design procedures, although simple and practical, have several limitations. First, a direct connection from structural/foundation properties to the response is missing. Secondly, the significance of ground motion regarding the SSI effects is poorly addressed through the response spectra in design procedure. Lastly, the influence of hysteretic nonlinearity possibly occurring in the structure-soil system is only roughly handled via the ductility demand for the system. As pointed out by Mylonkis and Gazetas (2000), SSI effects can be detrimental as well as beneficial and cautions are needed to interpret the results.

In this study, efforts are made to relate the SSI effects on structural responses directly to mechanical properties of soil-foundation-structure system and ground motion characteristics through rigorous dimensional analysis. Simple pulse type excitations representing the near-fault ground motions are used to analyze both linear and yielding structures. The significance of SSI effects is identified in this study.

CHARACTERISTICS OF NEAR-FAULT GROUND MOTIONS

Near-fault ground motions of major earthquakes are particularly destructive to civil structures and they usually contain distinguishable velocity and displacement pulses (Bertero 1976; Bertero et al. 1978; Makris and Black 2004b). Closed-form approximation models which capture the leading kinematic characteristics of near-fault ground motions have been developed by various researchers (Veletsos et al. 1965; Hall et al. 1995; Makris and Chang 2000; Mavroeidis and Papageorgiou 2003 among others). The pulse duration, pulse amplitude as well as the number and phase of half cycles are identified as the main parameters that define the near-fault velocity pulses. Mavroeidis and Papageorgiou (2003) pointed out that pulse duration and amplitude are the controlling parameters for structural response. They also pointed out that the number of half cycles was found to vary within a limited range and the maximum structural response depends more on the main pulse made of several cycles rather than the residual cycles of low amplitude after the main cycles. Given these considerations, the simple pulse-type formulations defined by Makris and Chang (2000) are used in this study to resemble the near-fault ground motions. The model input parameters include the acceleration amplitude, a_p, and duration, T_p. The effect of phase angle and number of cycles are implicitly accounted for by selecting different pulse types. Figure 1 depicts the three distinctive cycloidal pulse types, namely type-A, B and C_1 and their resemblance to recorded near-fault ground motions (Left: type-A pulse and FN acceleration record at Lucerne Valley station, during the 1992 Landers earthquake; Center: type-B pulse and FN acceleration record at Rinaldi station during the 1994 Northridge earthquake; Right: type-C_1 pulse and NS acceleration record at station 39 during the 1977 Bucharest earthquake). The type A and type B pulses are used in this study to explore the SSI effects under near-fault ground motions.

DIMENSIONAL ANALYSIS OF LINEAR SFSI SYSTEM

When neglecting rocking motion, a linear structure-foundation-soil system can be simplified as the lumped 2DOF system shown in Fig. 2a, where m_s, k_s, c_s denotes the mass, stiffness and damping constants of structure respectively, while m_f, k_f, c_f is the

foundation mass, equivalent spring and dashpot values of soil-foundation respectively. Denoting u_s and u_f as the structural and foundation displacement relative to the ground, the equations of motion of this lumped 2DOF system can be written as:

$$\begin{cases} \ddot{u}_s + 2\xi_s\omega_s(\dot{u}_s - \dot{u}_f) + \omega_s^2(u_s - u_f) = -\ddot{u}_g \\ \ddot{u}_f - \dfrac{m_s}{m_f}\cdot 2\xi_s\omega_s\dot{u}_s + \dfrac{m_s}{m_f}\left(1+\dfrac{c_f}{c_s}\right)\cdot 2\xi_s\omega_s\dot{u}_f - \dfrac{m_s}{m_f}\cdot\omega_s^2 u_s + \dfrac{m_s}{m_f}\left(1+\dfrac{k_f}{k_s}\right)\omega_s^2 u_f = -\ddot{u}_g \end{cases} \quad (1)$$

where $\omega_s = \sqrt{k_s / m_s}$ and $\xi_s = c_s / 2m_s\omega_s$ is the frequency and damping coefficient of the correspondent fixed-base structure.

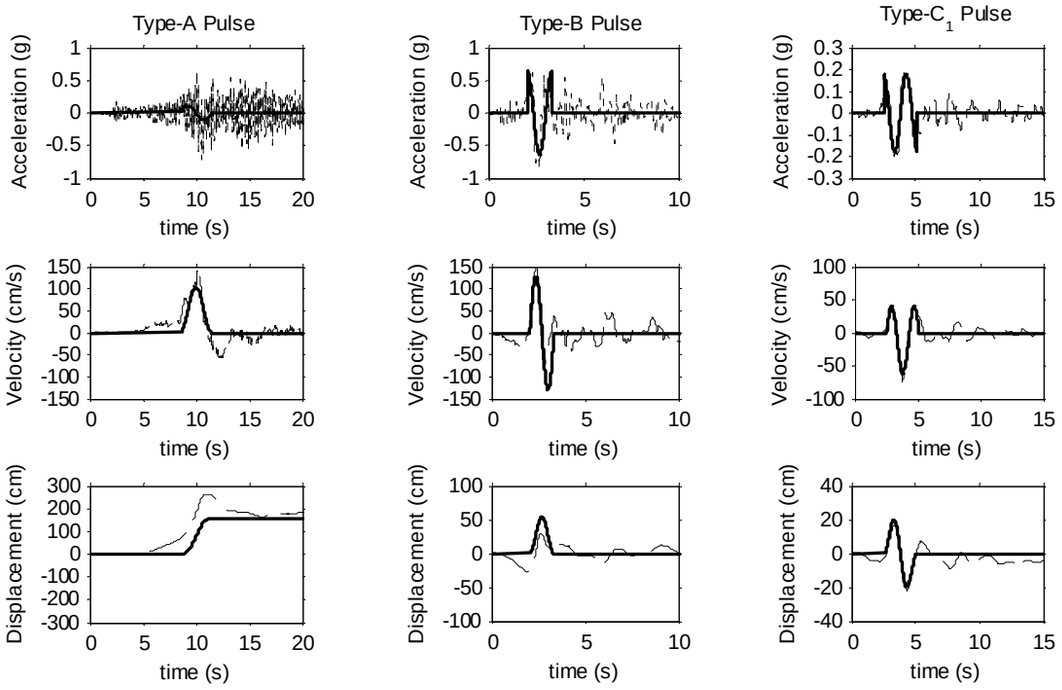


FIG. 1. Near-fault ground motion (dashed line) resemblance to pulse-type motions (solid line). Left: Lucerne Valley (FN), 1992 Landers; Center: Rinaldi (FN), 1994 Northridge; Right: Station 39 (NS), 1977 Bucharest earthquake.

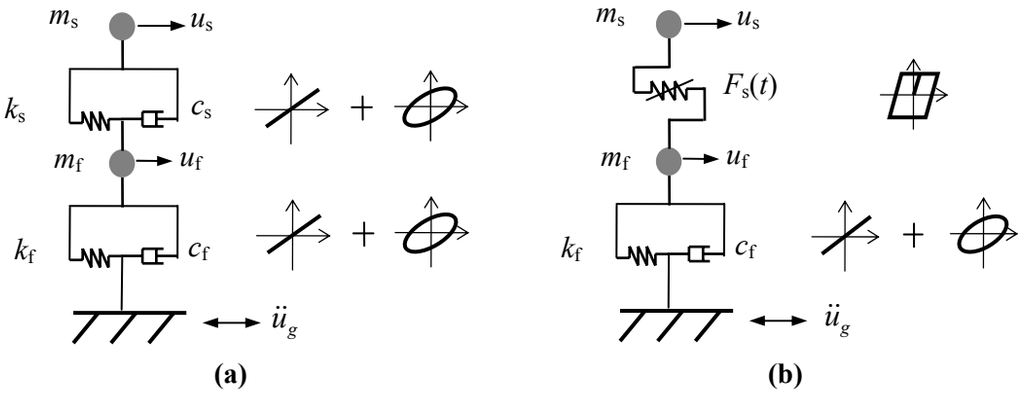


FIG. 2. Schematic 2DOF lumped system representing soil-foundation-structure system: (a) linear structure; (b) elastic-plastic structure.

Under a pulse-type motion of amplitude a_p and duration T_p, the maximum response of the structure, such as structural drift (relative to foundation), $u_{drift}^{\max}$ becomes a function of ω_s, ξ_s, m_f / m_s, k_f / k_s, c_f / c_s, a_p and $\omega_p = 2\pi / T_p$. Accordingly,

$$u_{drift}^{\max} = \max_t \left[\left| u_s(t) - u_f(t) \right| \right] = f\left(\omega_s, \xi_s, \frac{m_f}{m_s}, \frac{k_f}{k_s}, \frac{c_f}{c_s}, a_p, \omega_p \right) \tag{2}$$

The eight terms appearing in Eq. (2) involve only two reference dimensions that are length [L] and time [T]. According to Buckingham's Π-theorem (Langhaar 1951; Barenblatt 1996), the number of independent dimensionless Π-products is now: (8 variables) – (2 reference dimensions) = 6 Π-terms. It is desired to normalize the structural drift, $u_{drift}^{\max}$ to the energetic length scale of ground excitation, $L_e = a_p T_p^2 = 4\pi^2 a_p / \omega_p^2$ (Makris and Black 2004a). Utilizing the dimensional analysis toolbox in MATLAB (Bruckner 2002), Eq. (2) reduces to

$$\frac{u_{drift}^{\max} \omega_p^2}{a_p} = \phi\left(\frac{\omega_s}{\omega_p}, \xi_s, \frac{m_f}{m_s}, \frac{k_f}{k_s}, \frac{c_f}{c_s} \right) \tag{3}$$

Eq. (3) suggests that the normalized maximum structural drift ($\Pi_1 = u_{drift}^{\max} \omega_p^2 / a_p$) is a function of the normalized frequency ($\Pi_2 = \omega_s / \omega_p$), structural damping coefficient ($\Pi_3 = \xi_s$), mass ratio ($\Pi_4 = m_f / m_s$), stiffness ratio ($\Pi_5 = k_f / k_s$) and damping ratio ($\Pi_6 = c_f / c_s$) between foundation and structure. Fig. 3 plots the dimensionless response Π_1 as function of parameter Π_2 when the system is subjected to the type-A and type-B pulses with peak acceleration of $a_p = 2, 5$ and 8 m/s^2. Despite the different intensity of input ground motions, the structural response shows remarkable self-similarity as manifested by the single master curve shown in Fig. 3.

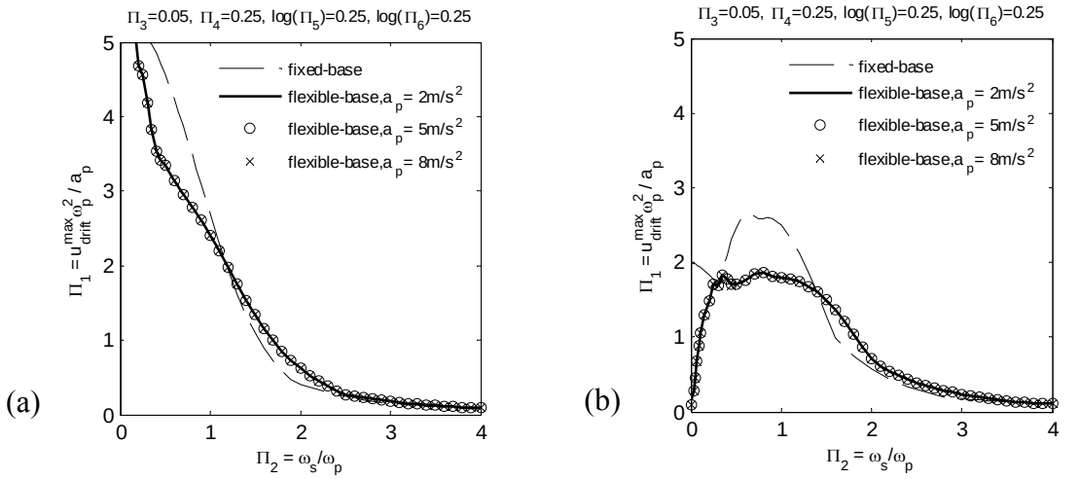


FIG. 3. Self-similar normalized structural drift of fixed- and flexible-base linear structure under cycloidal pulse: (a) Type-A pulse, (b) Type-B pulse.

To quantify the effects of independent Π-terms on the normalized structural drift, the range of interest in practice needs to be determined. In this study, the fixed-base structural damping coefficient, $\Pi_3 = \xi_s$, is taken as constant 5%. The review of typical building structures indicates that the foundation-to-structure mass ratio, $\Pi_4 = m_f / m_s$, is usually in the range of $0.05 \le \Pi_4 \le 0.35$. Occasionally, the mass ratio Π_4 can approach close to one. Therefore, Π_4 = 0.25 and 1.0 are considered in the analyses.

(1) normalized frequency, $\Pi_2 = \omega_s / \omega_p$

The fundamental period, T_s, of most building structures locates in the range of 0.1 s – 5.0 s (Goel and Chopra 1997, 1998; Balkaya and Kalkan 2003). On the other hand, the duration, T_p, of most destructive acceleration pulses may vary from 0.5 s to 1.5 s (Bertero 1976; Makris and Black 2004b). Therefore, the normalized frequency of structure, $\Pi_2 = \omega_s / \omega_p = T_p / T_s$, has practical meaning in the range around 0.1 – 15.

(2) foundation- to-structure stiffness ratio, $\Pi_5 = k_f / k_s$

For any given shallow foundation on linear elastic soil half-space, its complex-valued dynamic stiffness in horizontal direction, $K = k_f + i\omega c_f$, can be calculated with the approximate formulas and charts published in literature (Gazetas 1991; Mylonakis et al. 2006). The real part of dynamic stiffness, k_f, stands for the equivalent foundation stiffness which resists lateral load applied at the top of foundation. The foundation-to-structure stiffness could range within $0.1 \le \Pi_5 \le 1000$ depending on the structure type and site condition.

(3) foundation-to-structure damping ratio, $\Pi_6 = c_f / c_s$

The imaginary part of dynamic stiffness, c_f, represents the energy dissipation of foundation through wave propagating in elastic soil half-space. The foundation-to-structure damping ratio could also range within $0.1 \le \Pi_6 \le 1000$ depending on the structure characteristics and site condition.

Eq. (3) is solved numerically for various combinations of Π_2, Π_4, Π_5 and Π_6 terms to explore the dependency of normalized structural response on Π terms. Terms Π_5 and Π_6 are regarded as primary variables since they are directly related to soil-structure interaction and also vary in a wider range of 0.1 – 1000. The SSI effects can be manifested more directly by taking the ratio of normalized structural drift of flexible-base structure over that of fixed-base structure, i.e. $\Pi_{1,flex}/\Pi_{1,fixed}$. The SSI effects amplify ($\Pi_{1,flex}/\Pi_{1,fixed}>1$) or de-amplify ($\Pi_{1,flex}/\Pi_{1,fixed}<1$) the structural response based on this ratio. Fig. 4 plots the response ratio as function of parameters Π_5 and Π_6 for values of Π_4 = 0.25, 1.0 and Π_2 = 0.1, 1, 2 and 10 respectively under type-A pulse excitations. It is observed that response ratio, $\Pi_{1,flex}/\Pi_{1,fixed}$, approaches unity in each plot when either Π_5 or Π_6 becomes larger than 100, indicating the SSI effects can be neglected in this region. The peaks above the flat plane of unity indicate the region where SSI effects amplify the structural response. On the other hand, the valleys below the flat plane indicate that SSI effects in this region de-amplify the structural response and the fixed-base assumption is conservative. It is the combination of Π_2, Π_5 and Π_6 that determines whether amplification or de-amplification happens. Figure 4 also shows that the larger the mass ratio, Π_4, the more significant is the amplification due to SSI

effects since the peaks are typically higher. SSI is not sensitive to mass ratio, Π_4, when the normalized frequency $\Pi_2 \geq 0.5$. The analysis results reveal that mass ratio, Π_4, influences SSI in the region of $(\Pi_5, \Pi_6) = (1-100, 0.1-100)$ when the normalized frequency of structure $\Pi_2 < 0.5$. SSI effects can be neglected for large values of Π_2 (>10), for which the structure-foundation moves like a rigid body.

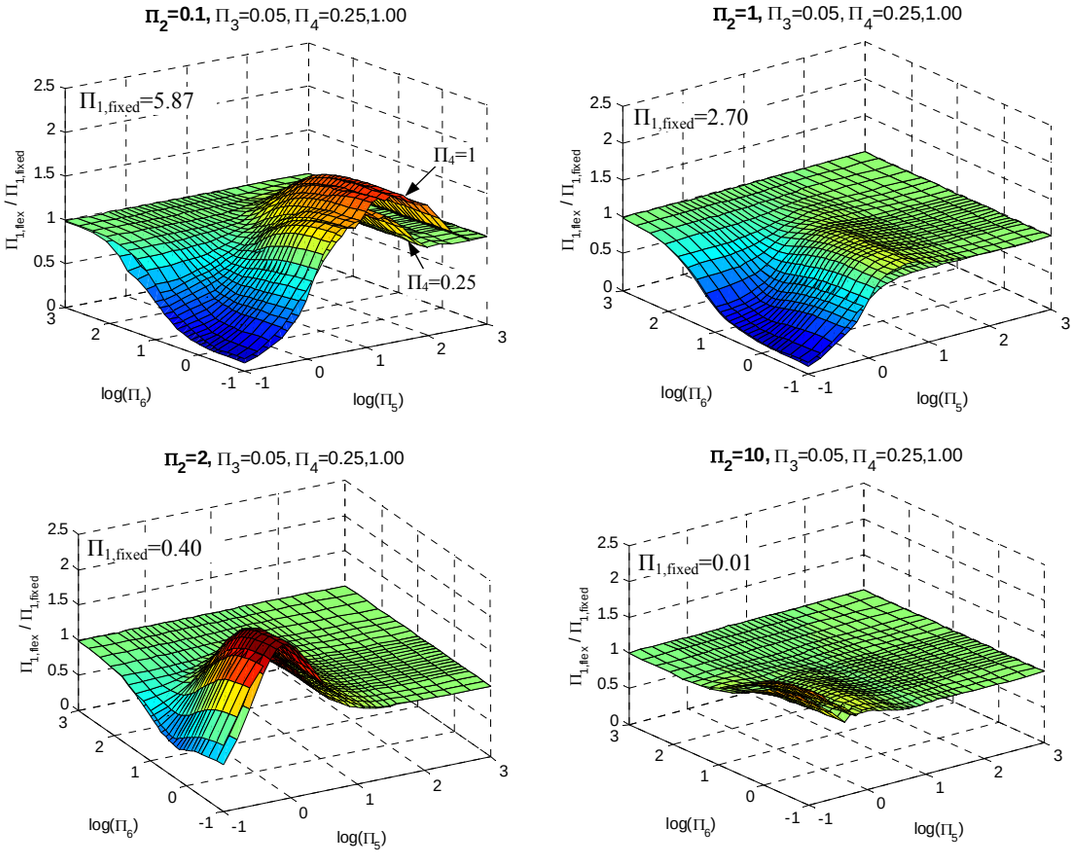


FIG. 4. Response ratio of normalized structural drift between flexible- and fixed-base linear structures for normalized frequency, Π_2=0.1, 1, 2 and 10 under type-A pulse motions.

DIMENSIONAL ANALYSIS OF NONLINEAR SFSI SYSTEM

Structures often behave nonlinearly under strong ground shakings. However, limited studies have been conducted to evaluate the SSI effects for yielding structures (Veletsos and Verbic 1974; Aviles and Perez-Rocha 2003, 2005). In this section, dimensional analysis is applied to a nonlinear structure sitting on flexible foundation, as shown by the lumped 2DOF system in Fig. 2b, where m_s denotes the mass of structure, $F_s(t)$ represents the elastic-plastic behavior of structure, while m_f, k_f, c_f are the foundation mass, equivalent spring and dashpot values of soil-foundation respectively. The Bouc-Wen model (Wen 1976) is used to simulate the elastic-plastic behavior of structure shown in Fig 2b.

The equations of motion of the nonlinear SFSI lumped system are written as:

$$\begin{cases} m_s\ddot{u}_s(t) + Q_s \cdot z(t) = -m_s\ddot{u}_g(t) \\ m_f\ddot{u}_f(t) - Q_s \cdot z(t) + c_f\dot{u}_f(t) + k_f u_f(t) = -m_f\ddot{u}_g(t) \end{cases} \tag{4}$$

where $z(t)$ is the hysteretic parameter in Bouc-Wen model, Q_s and u_{sy} are the yielding strength and yielding displacement of structure respectively. $z(t)$ is governed by:

$$\dot{z}(t) = \frac{\dot{u}_s - \dot{u}_f}{u_{sy}}\left\{1 - \left[\gamma \cdot \text{sign}\left((\dot{u}_s - \dot{u}_f)z(t)\right) + \beta\right] \cdot |z(t)|^n\right\} \tag{5}$$

where the modal parameters are chosen as β=0.5, γ=0.5, and n=20 to simulate elastic-plastic behavior of structures. An equivalent viscous damping coefficient, $c_{s,eq}$ is also defined to describe the energy dissipation capacity of elastic-plastic structure with ductility μ, where $c_{s,eq} = \frac{4m_s(\mu-1)}{\pi\mu\sqrt{\mu}}\sqrt{\frac{Q_s}{m_s u_{sy}}} = 0.477\sqrt{\frac{Q_s m_s}{u_{sy}}}$ when $\mu = 4$.

Defining initial stiffness of structure as $k_{s0} = Q_s / u_{sy}$, the maximum structural drift relative to foundation, $u_{drift}^{\max}$, becomes a function of the coefficient terms in Eq. (4) when $\ddot{u}_g$ is represented by a pulse type motion of amplitude a_p and duration $T_p = 2\pi/\omega_p$. Accordingly,

$$u_{drift}^{\max} = \max_t\left[\left|u_s(t) - u_f(t)\right|\right] = f\left(\frac{Q_s}{m_s}, u_{sy}, \frac{m_f}{m_s}, \frac{k_f}{k_{s0}}, \frac{c_f}{c_{s,eq}}, a_p, \omega_p\right) \tag{6}$$

Applying the formal dimensional analysis similar as for linear system discussed earlier, Eq. (6) reduces to six independent Π-terms as shown below:

$$\frac{u_{drift}^{\max}\omega_p^2}{a_p} = \phi\left(\frac{Q_s}{m_s a_p}, \frac{u_{sy}\omega_p^2}{a_p}, \frac{m_f}{m_s}, \frac{k_f}{k_{s0}}, \frac{c_f}{c_{s,eq}}\right) \tag{7}$$

Eq. (7) indicates that the normalized structural drift ($\Pi_1 = u_{drift}^{\max}\omega_p^2 / a_p$) depends on normalized yielding strength ($\Pi_2 = Q_s / m_s a_p$), normalized yielding displacement ($\Pi_3 = u_{sy}\omega_p^2 / a_p$), foundation-to-structure mass ratio ($\Pi_4 = m_f / m_s$), stiffness ratio ($\Pi_5 = k_f / k_{s0}$) and damping ratio ($\Pi_6 = c_f / c_{s,eq}$). It is noted that the damping ratio, $\Pi_6 = c_f / c_{s,eq}$, is computed using the equivalent viscous damping of the elastic-plastic structure since the real structural behavior is instead nonlinear.

The practical ranges for normalized structure strength and displacement at yielding are estimated as $0.1 \le \Pi_2 \le 4.0$, $0.01 \le \Pi_3 \le 1.00$ based on the building cases studied by Makris and co-workers (Makris and Black 2004a; Makris and Psychogios 2006). The other Π-terms are assumed to locate in the same range as those for linear systems respectively, i.e. $0.05 \le \Pi_4 \le 0.35$, $0.1 \le \Pi_5 \le 1000$, $0.1 \le \Pi_6 \le 1000$.

Similar to linear structure-foundation system, the response ratio between flexible- and fixed-base cases, $\Pi_{1,flex} / \Pi_{1,fixed}$ is presented to evaluate the significance of SSI effects for yielding structures. Fig. 5 plots the response ratio, $\Pi_{1,flex} / \Pi_{1,fixed}$ as function

of parameters Π_5 and Π_6 for values of $\Pi_3 = 0.5$, $\Pi_4 = 0.25$ and Π_2 = 0.1, 1, 2 and 4 respectively under type-A pulse motions. The response of elastic-plastic structure with flexible base is found to approach its fixed-base counterpart when either normalized stiffness ratio or damping ratio is large enough. As normalized strength Π_2 increases, the displacement of the fixed-base structure decreases. However, the SSI effect becomes more significant, which is manifested by the high peak observed on the left-bottom plot in Fig. 5. There is a region of de-amplification for structures with smaller strength, indicating the beneficial effect of SSI. For structures with high normalized strength, the SSI effects are generally insignificant but can become detrimental when structures are founded on soft soil ($\Pi_5 \le 10$ or $\Pi_6 \le 10$). Additional analyses show that the significance of SSI is also influenced by the normalized yielding displacement, Π_3. Generally, SSI effects become weaker when Π_3 decreases, which leads to earlier yielding. When both Π_2 and Π_3 becomes very large, the responses similar to that of linear structure are observed.

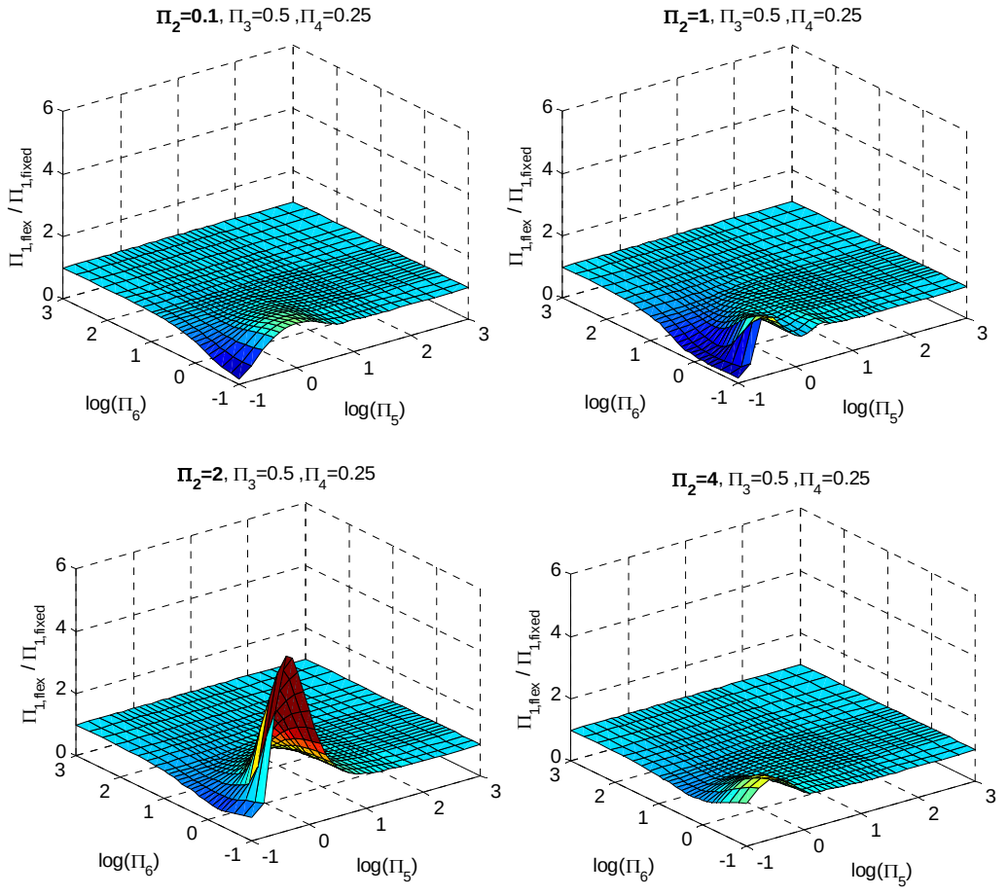


FIG. 5. Response ratio of normalized structural drift between flexible- and fixed-base elastic-plastic structures for normalized strength, Π_2=0.1, 1, 2 and 4 under type-A pulse motions.

CONCLUSIONS

This paper introduces a new way to evaluate the SSI effects of soil-foundation-structure system when subjected to pulse-type near-fault ground motions using rigorous dimensional analysis. This method relates the SSI effects directly and explicitly to both the characteristics of soil-foundation-structure systems and the scales of input ground motions.

For linear structure on flexible foundation, SSI effects depend highly on foundation-to-structure stiffness ratio and damping coefficient ratio, as well as the structure-to-input motion frequency ratio. SSI is insignificant when structure-to-input motion frequency ratio is larger than 10 or the foundation-to-structure stiffness ratio and damping ratio are higher than 100. The foundation-to-structure mass ratio is in general not important except when structure-to-input motion frequency ratio is smaller than 0.5. The SSI can be significant under certain conditions and it is the specific combination of dimensionless Π-terms that governs the amplification or de-amplification of structural response due to SSI effects.

For the elastic-plastic structure on flexible foundation, the SSI effects are controlled by not only the foundation-to-structure stiffness and damping ratios but also the normalized strength and yielding displacement of structure. Compared with the linear structures, the SSI is less significant for majority of the nonlinear structures. In general, the SSI effects become weaker as the normalized strength and yielding displacement of the structure become lower. However, for structures with higher strength but supported on very flexible foundations, the SSI can become very detrimental. The nonlinear foundation behavior including uplifting and local soil yielding will be considered in the future study.

ACKNOWLEDGEMENT

Partial financial support for this study was provided by National Science Foundation under grant NEESR-SG: Seismic Behavior, Analysis and Design of Complex Wall Systems (Award #0421577).

REFERENCES

Applied Technology Council (ATC). (2005). *Improvement of Nonlinear Static Seismic Analysis Procedures* (FEMA 440), FEMA, Washinton, D.C.

Aviles, J. and Perez-Rocha, L.E. (1998), “Site effects and soil-structure interaction in the Valley of Mexico”, *Soil Dynamics & Earthquake Engineering*, 17(1):29-39.

Aviles, J. and Perez-Rocha, L.E. (2003). “Soil-structure interaction in yielding systems.” *Earthquake Eng. & Struct. Dyn.*, 32(11): 1749–1771.

Aviles, J. and Perez-Rocha, L.E. (2005). “Design concepts for yielding structures on flexible foundation.” *Engineering Structures*, 27(3): 443–454.

Balkaya, C. and Kalkan, E. (2003). “Estimation of fundamental periods of shear-wall dominant building structures.” *Earthquake Eng. & Struct. Dyn.*, 32(7): 985–998.

Barenblatt, G.I. (1996). *Scaling, Self-Similarity, and Intermediate Asymptotics*, Cambridge University Press, Cambridge, United Kingdom.

Bertero, V.V. (1976). “Establishment of design earthquakes—Evaluation of present

methods." *Proc., Int. Symp. on Earthquake Structural Engineering*, Vol. 1: 551–580.
Bertero, V.V., Mahin, S.A., and Herrera, R.A. (1978). "Aseismic design implications of near-fault San Fernando earthquake records." *Earthquake Eng. & Struct. Dyn.*, 6(1): 31–42.
Bruckner, S. (2002). *Dimensional Analysis Toolbox for Use with MATLAB® Version 1.04*, http://www.sbrs.net/.
Building Seismic Safety Council (BSSC). (2003). *NEHRP Recommended Provisions and Commentary for Seismic Regulations for New Buildings and Other Structures* (FEMA 450), Federal Emergency Management Agency, Washington, DC.
Gazetas, G. (1991). "Formulas and charts for impedances of surface and embedded foundations." *J. Geotechnical Engineering*, ASCE, 117(9): 1363–1381.
Goel, R.K. and Chopra, A.K. (1997). "Period formulas for moment-resisting frame buildings." *J. Structural Engineering*, ASCE, 123(11): 1454-1461.
Goel, R.K. and Chopra, A.K. (1998). "Period formulas for concrete shear wall buildings." *J. Structural Engineering*, ASCE, 124(4): 425–433.
Hall, J.F., Heaton, T.H., Halling, M.W. and Wald, D.J. (1995). "Near-source ground motion and its effects on flexible buildings." *Earthquake Spectra*, 11(4): 569–605.
Langhaar, H.L. (1951). *Dimensional Analysis and Theory of Models*, Wiley: New York.
Makris, N. and Chang, S. (2000). "Effect of viscous, visco-plastic and friction damping on the response of seismic isolated structures." *Earthquake Eng. & Struct. Dyn.*, 29(1): 85–107.
Makris, N. and Black, C.J. (2004a). "Dimensional analysis of rigid-plastic and elastoplastic structures under pulse-type excitations." *J. Engineering Mechanics*, ASCE, 130(9): 1006-1018.
Makris, N. and Black. C.J. (2004b). "Evaluation of peak ground velocity as a 'good' intensity measure for near-source ground motions." *J. Engineering Mechanics*, ASCE, 130(9): 1032–1044.
Makris, N. and Psychogios, T. (2006). "Dimensional response analysis of yielding structures with first-mode dominated response." *Earthquake Eng. & Struct. Dyn.*, 35(5): 1203-1224.
Moslem K. and Trifunac M.D. (1986), "Effects of soil structure interaction on the response of building during the strong earthquake motion", *Report No. 86-04*, Department of Civil Engineering, University of Southern California.
Mylonakis, G., Nikolaoub, S. and Gazetas, G. (2006). "Footings under seismic loading: Analysis and design issues with emphasis on bridge foundations." *Soil Dynamics and Earthquake Engineering*, 26(9): 824–853.
Mylonakis, g. and Gazetas, G. (2000), "Seismic soil-structure interaction: beneficial or detrimental?", *J. Earthquake Engineering*, 4(3):277-301.
Veletsos, A.S., Newmark, N.M. and Chelapati, C.V. (1965). "Deformation spectra for elastic and elastoplastic systems subjected to ground shock and earthquake motions." *Proc. 3rd World Conference on Earthquake Engineering*, Wellington, New Zealand, Vol. II: 663–682.
Veletsos, A.S. and Verbic, B. (1974). "Dynamics of elastic and yielding structure-foundation systems." *Proc. 5th World Conference on Earthquake Engineering*, Rome, Italy: 2610–2613.
Wen, Y-K. (1976). "Method for random vibration of hysteretic systems." *J. Engineering Mechanics Division*, ASCE, 102(EM2): 249–263.

Dimensional Response Analysis of Inelastic Structures

Nicos Makris[1], and Theodoros Psychogios[2]

[1]Professor, University of Patras, Department of Civil Engineering, 26500 Patras, Greece; nmakris@upatras.gr
[2]Civil Engineer, M.Sc.; theodorospsychogios@yahoo.gr

ABSTRACT: This paper introduces a new way of estimating the inelastic response of yielding structures with behavior that can be approximated with the elastoplastic idealization. The proposed approach emerges from formal dimensional analysis and is liberated from the response of the elastic system. The application of the proposed method hinges upon the existence of a distinct time scale and a length scale that characterize the most energetic component of the ground shaking. The most decisive feature of this work is that the inelastic response curves that result with the proposed approach assume similar shapes for different values of the normalized yield displacement. Because of this similarity the paper proposes a single inelastic response curve which offers directly the maximum inelastic displacement of the structure given the energetic pulse period and pulse amplitude of the ground shaking.

INTRODUCTION

The two most widely used approaches in estimating the earthquake response of yielding structures combine the nonlinear static analysis procedure with results from linear elastic dynamic analysis. They are known as the *inelastic displacement coefficient* method and the *capacity "spectrum"* method.

The inelastic displacement coefficient method has been studied extensively during the last 40 years and has evolved from the early ideas of Veletsos and Newmark (1960). The idea of associating the response of an elastic-plastic system to the response of an elastic system was at that time a logical transition concept from the pre-1960 elastic idealization to the mid-1960's inelastic reality that was made most clear after the 1964 Alaska, USA and Nigata, Japan earthquakes. Following the work of Veletsos and coworkers (1960, 1965) a large number of researchers have elaborated on this approach. A comprehensive introduction to the major past work on this subject can be found in the papers by Miranda (2000, 2001) and Chopra and Chintanapakdee (2004). At present, this approach is deeply rooted in earthquake engineering practice and has been accepted by recent design recommendations (FEMA 1997, FEMA 2000).

The capacity "spectrum" method, initially developed by Freeman (1975) compares the capacity of a structure with the demand of the earthquake ground motion. The base shear force and roof displacement obtained with a nonlinear static (pushover) analysis are converted to spectral accelerations and spectral displacements and are compared with the earthquake demand. Various limitations of the pathological capacity spectrum method have been identified by Bertero et al. (1991), Krawinkler (1995), while the shortcoming of the ATC-40 procedure (ATC 1996) which has adopted the capacity spectrum method have been identified and addressed by Chopra and Goel (2000) and Fajfar (1999).

The lack of consensus on estimating seismic demand was part of the motivation of this paper which hinges upon the idea that there exists a **length scale** and a **time scale** that characterize the earthquake excitation. Seismological studies have shown that the pulse period and pulse amplitude of the most energetic pulse of near source ground motions are directly related to the rise time and slip velocity of faulting and they are expected to scale accordingly to them.

KINEMATIC CHARACTERISTICS OF PULSE-TYPE GROUND MOTIONS

The relative simple form, yet destructive potential of near source ground motions has motivated the development of various closed form expressions which approximate their leading kinematic characteristics. The early work of Veletsos et al. (1965) was followed by the papers of Hall et al. (1995), Heaton et al. (1995), Makris (1997), Makris and Chang (2000), Alavi and Krawinkler (2001) and more recently by the paper of Mavroeidis and Papageorgiou (2003). Physically realizable pulses can adequately describe the impulsive character of near-fault ground motions both qualitatively and quantitatively. The input parameters of the model have an unambiguous physical meaning. The minimum number of parameters is two, which are either the acceleration amplitude, a_p, and duration, T_p, or the velocity amplitude, v_p, and duration, T_p (Makris 1997, Makris and Chang 2000). The more sophisticated model of Mavroeidis and Papageorgiou (2003) involves 4 parameters, which are the pulse period, the pulse amplitude as well as the number and phase of half cycles, and was found to describe a large set of velocity pulses generated due to forward directivity or permanent translation effect. The pulse period, T_p, of the most energetic pulse of strong ground motions is strongly correlated with the moment magnitude, M_w, of the event (Mavroeidis and Papageorgiou 2003, Aki et al. 1977, Papageorgiou and Aki 1983).

The current established methodologies for estimating the pulse characteristics of a wide class of records are of unique value since the product, $\alpha_p T_p^2 = L_p$, is a characteristic length scale of the ground excitation and is a measure of the persistence of the most energetic pulse to generate inelastic deformations (Makris and Black 2004a). Our analysis uses 10 strong ground motions listed in Table 1.

DIMENSIONAL RESPONSE ANALYSIS OF ELASTIC-PLASTIC SYSTEMS

Consider the response of an initially elastic system that exhibits a finite yield displacement before sliding. This is the elastic-plastic idealization shown in Fig. 1

(left) which is a good approximation of the macroscopic behavior of the three structural systems considered in this study. With reference to Fig. 1 the response of an elastic-plastic system with mass m subjected to some acceleration pulse of amplitude a_p and duration T_p, should be a function of the specific strength, Q/m, the yield displacement, u_y, and the characteristics of the pulse, a_p and $\omega_p = 2\pi/T_p$. Accordingly,

$$u_{max} = f\left(\frac{Q}{m}, u_y, a_p, \omega_p\right). \quad (1)$$

Table 1. : Information pertinent to the strong records selected for the study and kinematic characteristics of the associated pulses.

				Makris & coworkers (2004a, 2000, 2004b]			Mavroeidis & Papageorgiou (2003)	
Earthquake (Year)	Station (Component *)	M_w	PGA g	T_p s	v_p m/s	a_p m/s²	T_p s	v_p m/s
San Fernando (1971)	Pacoima Dam (164 or FN)	6.7	1.23	1.3	0.85	4.11	1.47	1.15
Bucharest, Romania (1977)	Bucharest (NS)	7.2	0.20	1.8	0.50	1.75	2.10	0.62
Imperial Valley (1979)	El Centro, Array #5 (230 or FN)	6.6	0.38	3.2	0.70	1.37	3.92	0.84
Imperial Valley (1979)	El Centro, Array #6 (FN)	6.6	0.44	3.7	1.00	1.70	3.85	0.96
Imperial Valley (1979)	El Centro, Array #7 (230 or FN)	6.6	0.46	3.4	0.63	1.16	3.60	0.79
Erzikan, Turkey (1992)	Erzikan (NS)	6.7	0.52	1.8	0.70	2.44	2.44	0.67
Northridge (1994)	Sylmar Converter (FN)	6.7	0.73	2.3	0.60	1.64	3.0	0.80
Northridge (1994)	Rinaldi Receiving (228 or FN)	6.7	0.84	0.8	1.75	6.87	1.25	1.42
Northridge (1994)	Newhall (360 or FP)	6.7	0.59	0.75	0.90	7.54	2.70	0.94
Aigion, Greece (1995)	Aigion (FP)	6.2	0.50	0.60	0.50	5.24	0.71	0.45

* FN: Fault-Normal, FP: Fault-Parallel, NS: North-South.

The five variables appearing in Eq. 1 involve only two reference dimensions that of length [L] and time [T]. According to Buckingham's Π-theorem the number of independent dimensionless Π-products is: (5 variables) – (2 reference dimensions) = 3 Π-terms.

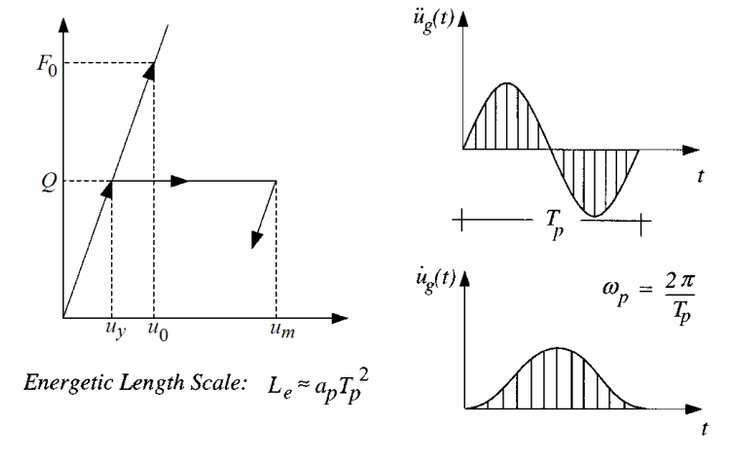


FIG. 1: Left: Elastic and elastic-plastic behavior. Right: The acceleration and velocity time histories of a one-sine acceleration pulse (from Makris and Black, 2004a).

Herein, we select as repeating variables the characteristics of the pulse excitation, a_p and $\omega_p = 2\pi / T_p$, since we desire to normalize the inelastic response, u_{max} to the energetic length scale of the excitation, $L_p = a_p / \omega_p^2 = (1/4\pi^2) a_p T_p^2$. Accordingly, Eq. 2 reduces to:

$$\frac{u_{max}\omega_p^2}{a_p} = \phi\left(\frac{Q}{ma_p}, \frac{u_y\omega_p^2}{a_p}\right). \tag{2}$$

Eq. 2 suggests that the maximum inelastic displacement normalized to the energetic length scale of the pulse excitation ($\Pi_1 = u_{max}\omega_p^2/\alpha_p$) is a function of the normalized strength of the system ($\Pi_2 = Q/m\alpha_p = \eta$ = seismic resistance coefficient according to Bertero et al. 1978) and the yield *displacement* normalized to the energetic length scale of the pulse excitation ($\Pi_3 = u_y\omega_p^2/\alpha_p$). The dotted-curves shown in Fig. 2 illustrate how the response of the elastic- plastic system amplifies as the normalized yield displacement increases. The most notable observation is that the normalized response is invariant with respect to the level of the acceleration amplitude, a_p. This scale invariance between the size of the maximum relative displacement, the size of the yield displacement, and the intensity of the acceleration pulse is known as self-similarity (Langhaar 1951, Barenblatt 1996) which is a special type of symmetry that has unique importance in understanding and ordering nonlinear response.

THREE STRUCTURES OF INTEREST

The proposed new way of estimating and presenting the inelastic response of yielding structures is introduced and evaluated by investigating the inelastic response

of three distinct framing systems: (1) A three-storey Special Moment Resisting Frame (SMRF) that is well-known to the literature since it is the lateral resisting frame of the study-building in the SAC/FEMA Steel Project (SAC 2000). The building is assumed to be located in Los Angeles (seismic zone 4) on UBC soil type S2 and was designed to meet the 1994 UBC provisions. (2) A seven-storey, eight-bay reinforcedconcrete frame from the Van Nuys hotel building located in Los Angeles, California. The building has been studied extensively and is an active PEER test-bed with focus on issues relevant to older commercial buildings for which the primary hazard is earthquake loading. The building was instrumented during the strong shaking from the 1971 San Fernando and the 1994 Northridge earthquakes, which caused severe damage. (3) A lighter moment resisting steel frame equipped with Buckling-Restrained Braces ("unbonded braces"). The lighter braced frame was designed according to the 1994 UBC equivalent static lateral-force provisions for Eccentric Braced Frames (EBF) (Aiken et al. 2000).

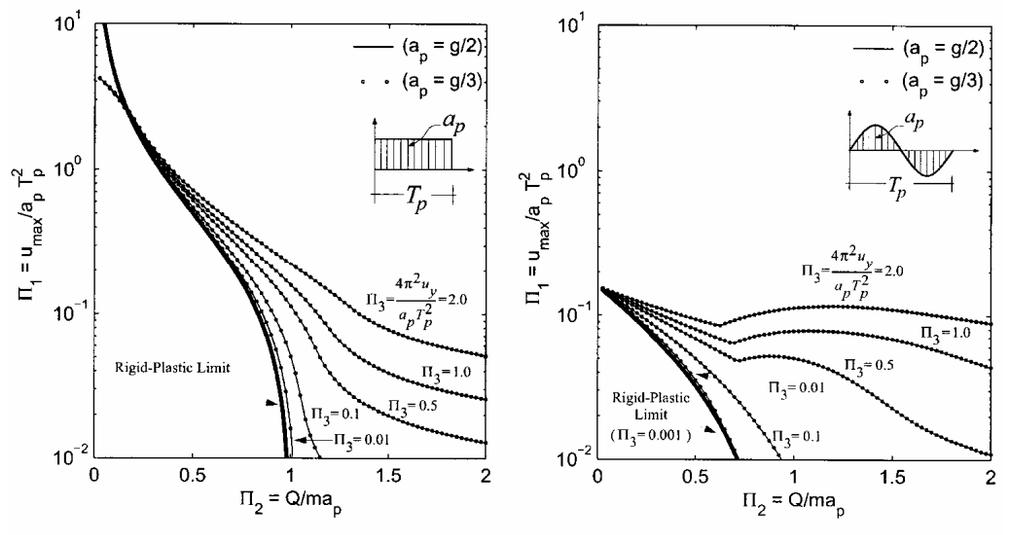


FIG. 2: Normalized relative displacement curves of an elastic-plastic structure subjected to a rectangular and a one-sine acceleration pulse.

Fig. 3 plots the push-over curves of the three frames of interest. They have been computed with the open source software OpenSees (http://opensees.berkeley.edu) which accounts for the influence of distributed inelasticity and P-Delta effects. Note that the computed push-over curves have a post-yielding stiffness close to zero, a situation that makes the elastic-plastic idealization most realistic. The strength Q and yield displacement u_y of the three structures of interest following the bilinear idealization are presented in Table 2.

INELASTIC DEFORMATION RESPONSE CURVES

The inelastic response of the three multistory frames of interest in this study can be expressed via the response of the elastic-plastic system with the three dimensionless Π-products, $\Pi_1 = u_{\max}\omega_p^2 / a_p$, $\Pi_2 = Q / ma_p$ and $\Pi_3 = u_y\omega_p^2 / a_p$ appearing in Eq. 3.

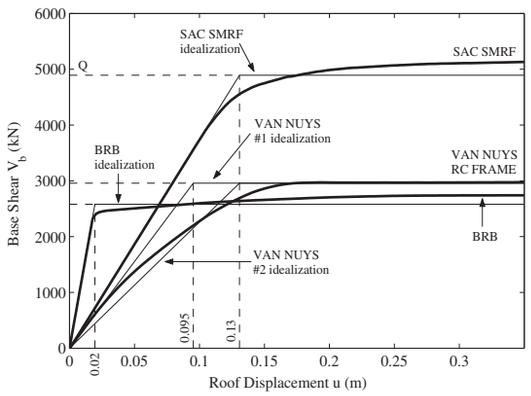


FIG. 3: Push over curves of the three frames of interest and their elastic-plastic idealization.

Table 2. Yield strength and yield displacement of the three frames.

Framing system	Q (kN)	u_y (m)
SAC SMRF	4895	0.13
Van Nuys RC	2960	0.095 or 0.13
MRF with BRB	2580	0.02

The exact value of the Π-products for each frame and a specific earthquake depend on the specific values of the acceleration amplitude and duration of the pulses that have been selected to approximate the most energetic pulse of the ground motion. For instance, Table 1 shows that there are differences between the period, T_p and velocity amplitude, v_p, used by Makris and his coworkers (2004a, 2000, 2004b) and by Mavroeidis and Papageorgiou (2003).

Fig. 4 plots the normalized peak displacement $\Pi_1 = u_{\max}\omega_p^2 / a_p$ as a function of the normalized strength $\Pi_2 = Q / ma_p$ of a bilinear system when excited by two of the strong earthquakes listed in Table 1. The values of $\Pi_3 = u_y\omega_p^2 / a_p$ appearing within the box of each graph are for the yield displacements of the three buildings of interest in this study. With reference to Fig. 3 and Table 2 one can associate two different values for the yield displacement of the Van Nuys building, that of $u_y = 0.095$ m or that of $u_y = 0.13$ m. The three graphs of Fig. 4 show that in general as strength increases the peak displacement decreases. Nevertheless, the larger the yield displacement the less rapid is the decrease in the response with increasing strength. As a result, the stronger SMRF building with a larger yield displacement exhibits a peak response that is larger than the peak response of the less strong frame with buckling restrained braces.

What is most interesting in Fig. 4 is that the inelastic response curves computed for smaller values of Π_3 reach smaller values of Π_1; yet they assume a similar form. Based on this observation this paper proposes a single inelastic response curve which

will decay with Π_2 and scale up with Π_3. A simple expression that is a good candidate to approximate such response is:

$$\hat{\Pi}_1 = \left(p + q\Pi_3^s \right) e^{-\Pi_2^r}, \tag{3}$$

where the parameters $p = -1.4$, $q = 7$, $s = 0.21$ and $r = 0.63$ are determined from nonlinear regression analysis using the Levenberg – Marquardt method (MATLAB, www.mathworks.com). Fig. 5 (top) plots the comparison of the single master curve:

$$\hat{\Pi}_1 = \left(-1.4 + 7.0 \cdot \Pi_3^{0.21} \right) e^{-\Pi_2^{0.63}}, \tag{4}$$

with all the inelastic response curves (10 earthquakes appearing in Table 1, 3 values of Π_3 and 2 sets of pulse parameters). The contained dispersion of the inelastic response curves is most encouraging, while the proposed analytical expression given by Eq. 4 is very close to the mean of all the computed inelastic response curves. Of course the form of Eq. 3 is not unique and one may propose a variation of Eq. 3 when a wider set of earthquake records is examined (Makris and Psychogios 2006).

Regardless of what is the analytical expression of the single-master curve that one will adopt, what is most important in this paper is the concept of self-similarity that emerges from the dimensional analysis developed herein which offers an attractive alternative in estimating inelastic response without referring to the elastic response spectra.

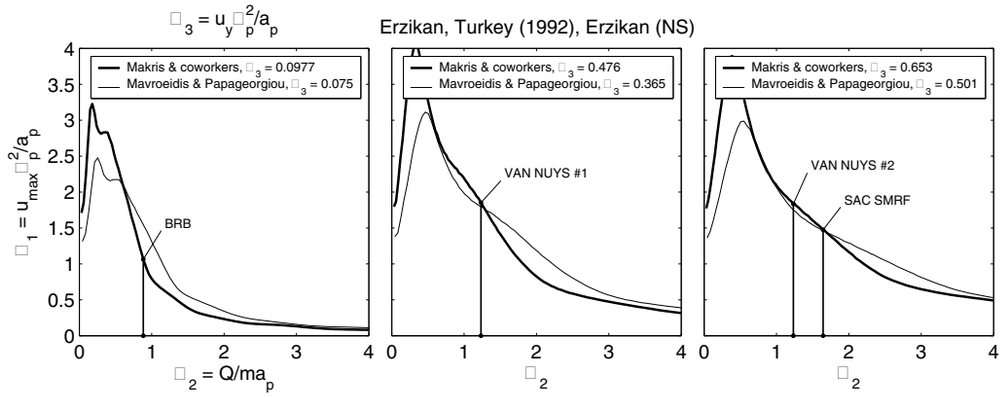


FIG. 4: Inelastic response curves (top) and ductility demand spectra (bottom) of the elastic-plastic system subjected to the 1992 Erzikan, Turkey earthquake.

CONCLUSIONS

This paper introduces a new way of estimating and presenting the inelastic response of yielding structures with behavior that can be approximated with the elastoplastic idealization. The proposed method emerges from formal dimensional analysis and is liberated from the response of the elastic system.

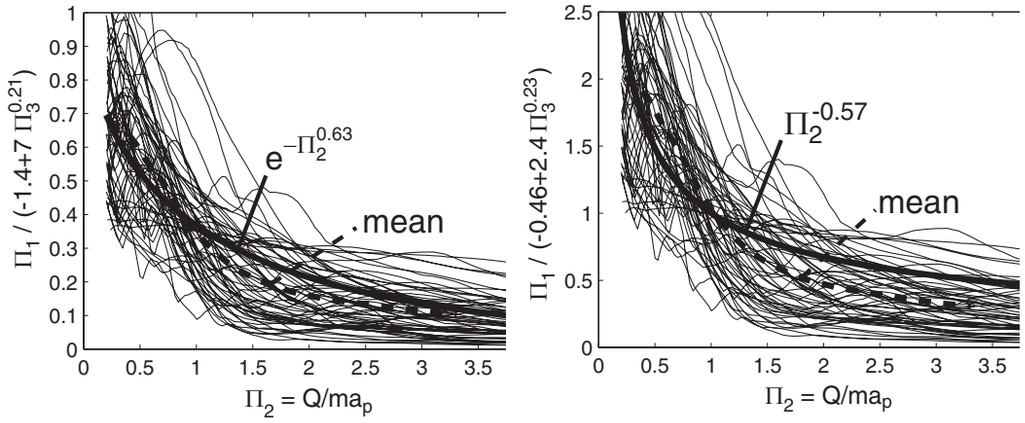


FIG. 5: Comparison of all response curves computed in this study for the three buildings of interest, subjected to the 10 earthquakes listed in Table 1 with a single master curve expressed with an exponential law (left) and a power law (right).

The application of the proposed method hinges upon the existence of a distinct time scale and a length scale that characterize the ground shaking. Such time and length scales emerge naturally from the distinguishable pulses which dominate a wide class of strong earthquake records, they are directly related with the rise time and slip velocity of faulting and can be formally extracted with validated mathematical models published in the literature.

The study shows that the normalized inelastic displacement $\Pi_1 = u_{\max}\omega_p^2 / a_p$ decreases with increasing normalized strength $\Pi_2 = Q / ma_p$, while it scales up with increasing normalized yield displacement, $\Pi_3 = u_y\omega_p^2 / a_p$. Based on these observations the paper proposes a single inelastic response curve (master curve given by Eq. 4) which involves only four parameters that are identified with nonlinear regression analysis. The proposed analytical expressions for the single master curve was found to give dependable predictions for the maximum inelastic displacements of three yielding structures when excited by six strong ground motions which were not used for the calibration of the parameters of the master curve.

ACKNOWLEDGEMENTS

The European Social (ESF), Operational Program for Educational and Vocational Training II (EPEAEK II), and particularly the Program PYTHAGORAS II, is gratefully acknowledged for funding the above work.

REFERENCES

A.S. Veletsos, N.M. Newmark, Effects of inelastic behavior on the response of simple systems to earthquake motions. *Proceedings of the 2nd World Conference on Earthquake Engineering,* Tokyo, Japan, Vol. II, 1960; 895-912.

A.S. Veletsos, N.M. Newmark, C.V. Chelepati, Deformation spectra for elastic and elastoplastic systems subjected to ground shock and earthquake motions. *Proceedings of the 3rd World Conference on Earthquake Engineering,* Wellington, New Zealand, Vol. II, 1965; 663-682.

E. Miranda, Inelastic displacement ratios for structures on firm sites. *Journal of Structural Engineering* (ASCE) 2000; **126**(10): 1150-1159.

E. Miranda, Estimation of inelastic deformation demands of SDOF systems. *Journal of Structural Engineering* (ASCE) 2001; **127**(9): 1005-1012.

A.K. Chopra, C. Chintanapakdee, Inelastic deformation ratios for design and evaluation of structures: single-degree-of-freedom bilinear systems. *Journal of Structural Engineering* (ASCE) 2004; **130**(9): 1309-1319.

Federal Emergency Management Agency (FEMA). NEHRP guidelines for the seismic rehabilitation of buildings. *Report No. FEMA-273 (Guidelines) and Report No. FEMA-274 (Commentary)*, Washington, D.C., 1997.

Federal Emergency Management Agency (FEMA). Prestandard and commentary for the seismic rehabilitation of buildings. *Report No. FEMA-356*, Washington, DC, 2000.

S.A. Freeman, J.P. Nicoletti, J.V. Tyrell, *Evaluation of existing buildings for seismic risk – A case study of Puget Sound Naval Shipyard*. Bremerton, Washington. Proc. 1st National Conf. Earthquake Engineering, EERI, Berkeley, 1975: 113-122.

V.V. Bertero, J.C. Anderson, H. Krawinkler, E. Miranda, Design guidelines for ductility and drift limits. *Report No. EERC/UCB-91/15*, Earthquake Engineering Research Center, University of California, Berkeley, California, 1991.

H. Krawinkler, New trends in seismic design methodology. *Proceedings of the 10th European Conference on Earthquake Engineering*, Vol. 2, Balkema, Rotterdam, The Netherlands, 1995; 821-830.

Applied Technology Council (ATC). Seismic evaluation and retrofit of concrete buildings. *Report No. ATC-40*, Redwood City, California, 1996.

A.K. Chopra, R.K. Goel, Evaluation of NSP to estimate seismic deformation: SDF systems. *Journal of Structural Engineering* (ASCE) 2000; **126**(4): 482-490.

P. Fajfar, Capacity spectrum method based on inelastic demand spectra. *Earthquake Engineering and Structural Dynamics* 1999; **28**(9): 979-993.

J.F. Hall, T.H. Heaton, M.W. Halling, D.J. Wald, Near-source ground motion and its effects on flexible buildings. *Earthquake Spectra* 1995; **11**(4): 569-605.

T.H. Heaton, J.F. Hall, D.J. Wald, M.W. Halling, Response of high-rise and base-isolated buildings to a hypothetical M_w 7.0 blind thrust earthquake. *Science*, 1995; **267**: 206-211.

N. Makris, Rigidity-plasticity-viscosity: Can elecrorheological dampers protect base-isolated structures from near-source ground motions? *Earthquake Engineering and Structural Dynamics*, 1997; **26**: 571-591.

N. Makris, S. Chang, Effect of viscous, visco-plastic and friction damping on the response of seismic isolated structures. *Earthquake Engineering and Structural Dynamics* 2000; **29**: 85-107.

B. Alavi, H. Krawinkler, *Effects of near-source ground motions on frame-structures,* Technical Report No. 138, The John A. Blume Earthquake Engineering Center, Stanford University, 2001.

G.P. Mavroeidis, A.S. Papageorgiou, A mathematical representation of near-fault ground motions. *Bulletin of the Seismological Society of America*, 2003; **93**(3): 1099-1131.

K. Aki, M. Bouchon, B. Chouet, S. Das, Quantitative prediction of strong motion for a potential earthquake fault, *Ann. Geofis*. 1977; **30**: 341-368.

A.S. Papageorgiou, K Aki, A specific barrier model for the quantitative description of inhomogeneous faulting and the prediction of strong ground motion. II. Applications of the model. *Bulletin of the Seismological Society of America*, 1983; **73**: 953-978.

N. Makris, C.J. Black, Dimensional analysis of rigid-plastic and elastoplastic structures under pulse-type excitations. *Journal of Engineering Mechanics* (ASCE) 2004; **130**(9): 1006-1018.

N. Makris, C.J. Black, Evaluation of peak ground velocity as a 'good' intensity measure for near-source ground motions. *Journal of Engineering Mechanics* (ASCE) 2004; **130**(9): 1032-1044.

V.V. Bertero, S.A. Mahin, R.A. Herrera, Aseismic design implications of near-fault San Fernando earthquake records. *Earthquake Engineering and Structural Dynamics* 1978; **6**(1): 31-42.

H.L. Langhaar, *Dimensional Analysis and Theory of Models.* John Wiley, New York, NY, 1951.

G.I. Barenblatt, *Scaling, self-similarity, and intermediate asymptotics,* Cambridge University Press. Cambridge, United Kingdom, 1996.

SAC. State of the art report on system performance of steel moment frames subjected to earthquake ground shaking. *FEMA-355C*, Federal Emergency Management Agency, Washington, DC, 2000.

I.D. Aiken, P. Clark, F. Tajirian, K. Kasai, Unbonded braces in the United States – Design studies, large scale testing and the first building application. *Japan Passive Control Symp.,* Tokyo Institute of Technology, Japan, 2000.

N. Makris, T. Psychogios, Dimensional response analysis of yielding structures. *Earthquake Engineering and Structural Dynamics* 2006; **35**: 1203-1224.

Dynamic effects of impact machine foundations

Mark R. Svinkin, Member, ASCE[1]

[1]VIBRACONSULT, 13821 Cedar Road, #205, Cleveland, OH 44118-2376; PH (216) 397-9625; FAX (216) 397-1175; msvinkin@stratos.net

Abstract

Foundations for machines with impact loads are widespread powerful sources of industrial vibrations. These foundations mostly transmit vertical dynamic loads on the ground and generate ground vibrations which may harmfully affect surrounding buildings. Dynamic effects range from serious disturbances of working conditions for sensitive devices and people to visible structural damage. Natural frequency of vertical machine foundation vibrations and complete vibration records of ground and structure vibrations can be predicted prior to installation of machine foundations. Diverse measures can be used to mitigate dynamic effects of impact machine foundations.

Introduction

Various machines with impact or shock loads are used for production processes at plants and in industrial buildings. As a rule, such machines are installed on massive concrete foundations. Forge and drop hammers are most powerful machines producing impact loads.

Forge hammer production is usually accompanied with high vibration levels of ground vibrations because substantial dynamic loads are transmitted on hammer foundations, and these vibrations may detrimentally affect adjacent and remote structures, sensitive equipment and people. It is likely that structure damage caused by vibrations may occur in close proximity of the dynamic sources. Nevertheless, unacceptable structural vibrations may also be induced at long distances from the sources due to the dynamic effect of low-frequency ground vibrations. Therefore, it is important to predict ground and structure vibrations before erection of foundations under machines with impact loads and consider possible outcomes of vibration effects in the design stage of machine foundations.

Knowledge and experience in understanding the causes of vibration effects of impact machine foundations can be helpful in prevention of detrimental structural vibrations. Each construction site is unique, and vibration mitigation measures before or after construction of machine foundations should be correctly applied at a site because it is possible that eliminating one dynamic excitation can trigger another one.

The paper is based on analysis and generalization of numerous case studies.

Impact Machine Foundations as Sources of Vibrations

Impact machines generate intensive dynamic forces which comprise a single pulse of arbitrary form and relatively short duration. Such dynamic loads are of great importance in the design of impact machine foundations and assessment of vibration effects on adjacent and remote structures.

Impact Machine Foundations

There are various forge and drop hammers. In forge shops, two major types of hammers are used: a counterblow hammer (proper) and a short-stroke drop hammer. The former machine provides free forging operations. The latter machine also called drop hammer for die stamping is applied to the precision of blows required in forging. Besides, diverse punch-presses such as sizing presses, hydraulic presses and others are employed for production of machine parts at industrial plants.

Two other hammers put in practice to remake steel scrap heaps. Sizeable drop hammers break scrap iron, and press-hammers are used to compress and pack lightweight steel scrap.

Research studies of hammer foundation dynamics have been accomplished by Rausch (1950), Barkan (1962), Novak (1987), Prakash and Puri (1988) and others.

Each forge hammer has two major parts: an anvil and a frame. For counter blow hammers, footings under the frame are paced on the anvil foundation at both sides of the anvil with 2-3 cm layers of roofing felt between the frame footing and the anvil foundation. Short-stroke drop hammers are usually installed on a single concrete block to support the anvil and the frame. Such a design decreases stresses in hammer foundations. Also, it is possible to meet the old-designed anvil foundations separated from foundations under the frames. Such separation can result in substantial settlements of the anvil foundation.

Square timbers are used for pads under the anvil. The pad thickness of 0.1 – 1.2 m depends on the weight of hammer dropping parts.

Sizeable drop hammers are installed for breaking scrap iron and large iron blocks. These hammers generate the great energy during impacts and have large foundations with upper parts around the anvils for protection from flying iron pieces. Layers of timber, iron chips and steel plates are used for pads under the anvils and the pad thickness is about 2 m.

Foundations under the press-hammers are relatively small and the anvils are usually installed directly on the foundations without pads.

Punch-presses are installed directly on their foundations.

Dynamic Loads Transmitted on the Ground

For impact machine foundations as the vibration sources, it is important to determine what major foundation vibrations are transmitted on the ground and how these vibrations may have effects upon adjacent and remote structures.

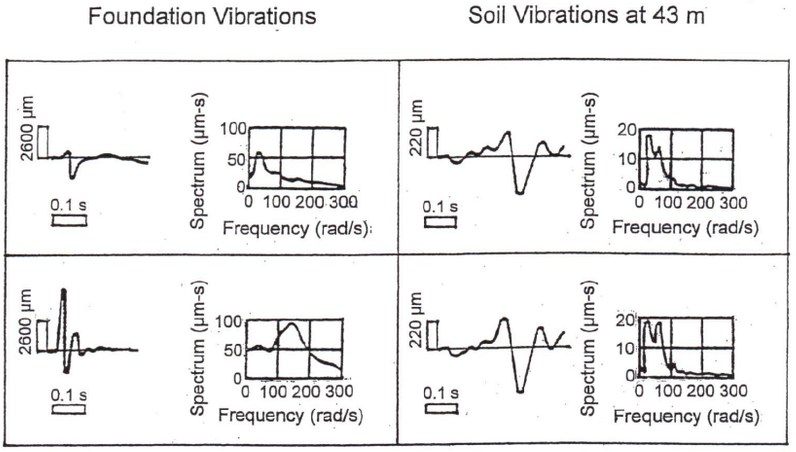


Figure 1. Identical vertical impact loads with different eccentricity induced different foundation vibrations and similar ground vibrations at distance of 43 m from foundation for drop hammer (Svinkin 2002)

Most hammer foundations are undergone only vertical vibrations under applied centered impacts, but some machines with impact loads can cause vertical and rocking foundation vibrations. An experimental study showed that rocking foundation oscillations do not affect soil vibration records with distance from the machine foundation (Figure 1). Identical vertical impact loads with different eccentricity produced vertical foundation vibrations with the frequency of 20 rad/s in one event and rocking foundation vibrations with the frequency of 135 rad/s in another event. However, these impact loads produced similar ground vibrations at a distance of 43 m from the foundation for a drop hammer.

Obviously, only vertical foundation vibrations have to be considered for analysis of impact machine foundations as sources of industrial vibrations.

The hammer foundation and the anvil are modeled as lumped-mass systems with one or two degrees of freedom. In a reality, an anvil mass is substantially less than a foundation mass and stiffness of the anvil pad is much larger than soil stiffness under the hammer foundation. Therefore in most cases, the hammer foundations respond to impact loads generated by hammers as a SDOF system.

Normalized responses of the hammer-foundation-soil systems are presented in Figure 2 for four foundations under different machines producing impact loads: a press-hammer with the ram mass M_R=4 tonnes and the foundation base area A_{FB}=12.3 m^2, a short-stroke drop hammer with M_R=7.25 tonnes and A_{FB}=80 m^2, a counterblow hammer with M_R=6 tonnes and A_{FB}=58.8 m^2 and a sizeable drop hammer with M_R=15 tonnes and A_{FB}=158 m^2. It can be seen that the responses of three hammer foundations are represented by SDOF transfer functions which almost coincide with the corresponding theoretical transfer functions for which parameters were determined from experiments. Only for the counterblow hammer foundations, a transfer function represents the system with two degrees of freedom but with the domination of the first shape. It is acceptable for practical goals to consider the hammer-foundation-soil system as SDOF.

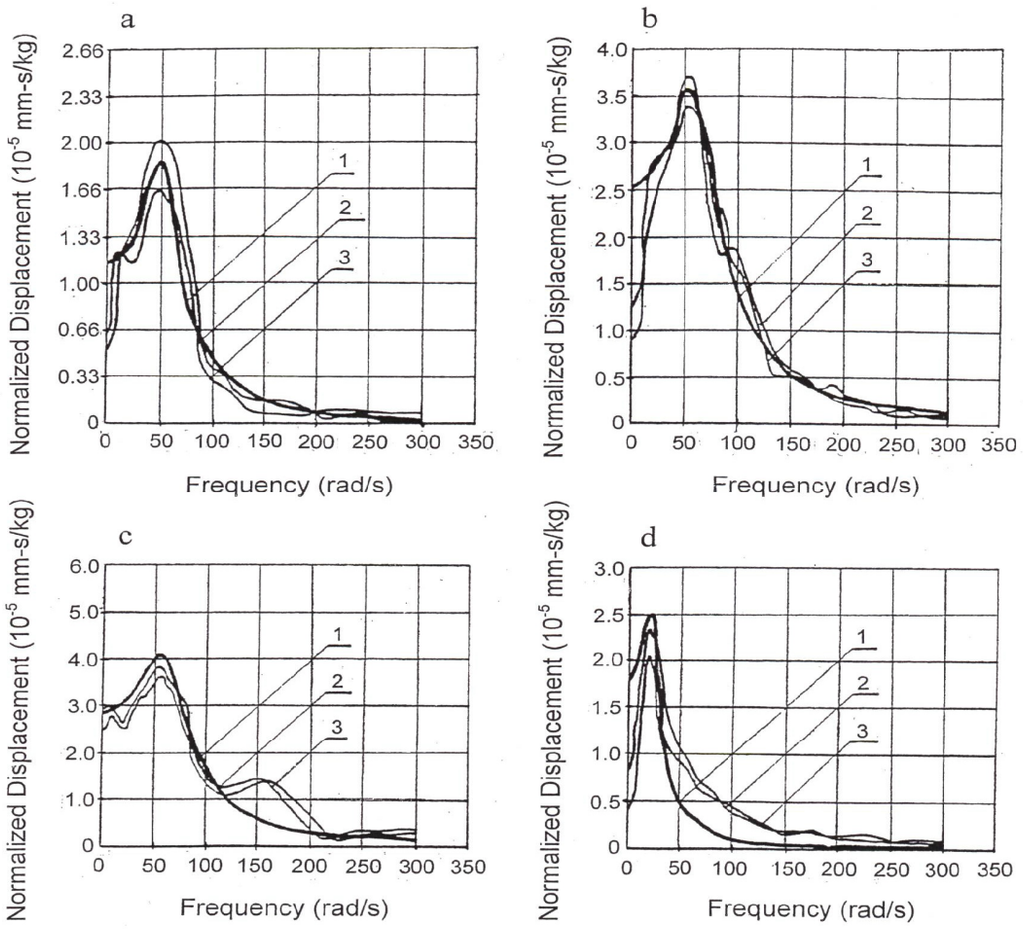


Figure 2. Transfer functions of impact machine foundations; a – foundation for press-hammer with M_R=4 tonnes and A_{FB}=12.3 m^2; b - foundation for short-stroke drop hammer with M_R=7.25 tonnes and A_{FB}=80 m^2; c – foundation for counterblow hammer with M_R=6 tonnes and A_{FB}=58.8 m^2; d - sizeable drop hammer with M_R=15 tonnes and A_{FB}=158 m^2. 1 – Theoretical transfer function for SDOF foundation-soil system with parameters determined from experiments; 2 and 3 – Normalized spectra of free foundation vibrations

Variables of Machine Foundation Vibrations

Variables of hammer foundation vibrations presented in Table 1 for three groups of hammer foundations were gathered on the basis of published data (Rausch 1950; Barkan 1962; Scheglov 1960; Klattso 1965; Glazyrin and Martyshkin 1971) and studies performed by the writer (Svinkin 1980 and 1995).

The first and second groups represent hammer foundations installed on the ground without vibration isolation. These groups gathered foundations under hammers depending on the mass of hammer rams: 5-25 tonnes range for the first group and below 5 tonnes for the second group. Natural angular frequencies of these foundations are in limits of 40-90

rad/s that correspond the periods of free foundation vibrations between 0.16 and 0.07 s. Because of the duration of ram impacts on the anvil is approximately 0.01 s (Rausch 1950), the impact loads on hammer foundations can be considered as instantaneous loading. The impact loads induce transient hammer foundation vibrations consisting of 1-2 cycles with large damping. Foundation vibrations are transferred onto the ground.

Table 1. Variables of Hammer Foundation Vibrations (modified from Svinkin 1995)

Groups of Foundations	Forge Hammers	Variables of Hammer Foundation Vibrations				Energy Transferred onto Soil kJ
		Frequency rad/s	Displacement mm	Velocity cm/s	Acceleration cm/s^2	
1	Large forge hammers with ram mass between 5-25 tonnes	40-60	0.4-1.0	2.0-6.0	120-420	0.8-5.9
2	Forge hammers with ram mass less than 5 tonnes	60-90	0.3-1.0	1.9-8.8	120-980	0.06-1.9
3	Vibration isolated forge hammers	19-38	0.1-0.7	0.4-1.6	14-17	0.01-2.8

Values of the frequencies of free vertical foundation vibrations in certain degree depend on the capacity of forge hammers. The masses of hammer rams and the frequencies of free vertical foundation vibrations are shown in Figure 3. It can be seen the trend that the larger mass of the hammer ram the lower frequency of free vertical foundation vibrations. Foundations for powerful forge hammers have the lowest frequencies, and the highest frequencies were found for foundations under forge hammers with the ram mass of 1-3 tonnes.

This phenomenon has a reasonable explanation. It is obvious that the larger ram mass requires the larger foundation base area, and the larger volume of soil mass is involved in hammer foundation vibrations. An enlargement of the foundation base area increases the soil stiffness under the foundation base area. However, an augmentation of the soil mass is greater than that of the soil stiffness, and consequently it results in decreasing the frequency of free vertical foundation vibrations.

The third group in Table 1 renders vibration isolated foundations for forge hammers. A concrete block with a hammer is mounted on vibroisolators for which springs and dashpots are used. Records of free block vibrations from hammer impact are similar to

low frequency damped sinusoid with small damping. The block vibrations are transmitted onto the foundations and induce elastic waves in the ground.

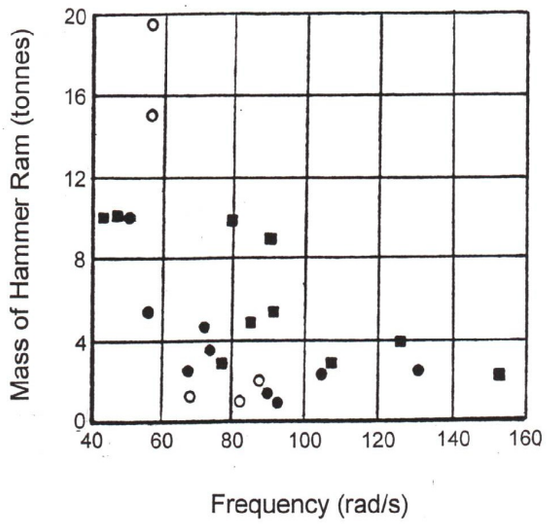


Figure 3. Relationship between mass of hammer ram and frequency of free foundation vibrations for diverse soil conditions: ● - sandy soil, ○ - loess loam, ■ - clayey soil. Data were modified from Svinkin (1995)

It can be seen from Table 1 that displacements are in the similar ranges for all three groups of hammer foundations. The maximum energy transferred onto the ground and big values of velocities and accelerations are observed for foundations under large forge hammers. The greatest velocity of 8.8 cm/s and acceleration of 980 cm/s^2 were obtained at foundations for relatively small forge hammers in group 2 because of comparatively high natural frequencies of these foundations. The minimum values of vibration variables are related to vibration isolated hammer foundations.

In addition to information about forge hammers and their foundations presented in Table 1 and Figure 3, sizeable drop hammers have somewhat different values of dynamic loads and variables of foundation vibrations. The maximum mass of dropping weight is 15 tonnes and the maximum dropping height is 30 m. Frequencies of free vertical foundation vibrations are in limits of 3-8 Hz. Maximum displacements of vertical and rocking foundation vibrations are 3 and 6 mm respectively. Accelerations can reach values up to 600 cm/s^2. Foundations under sizeable drop hammers can transfer much energy up to 35 kJ onto the ground. This considerable amount of energy is 6-14 times higher than energy transferred onto the ground from foundations under hammers with big ram masses.

Displacements of machine foundation vibrations can be calculated using known procedures available in Barkan (1962) for foundations under forge hammers and sizeable drop hammers, in Svinkin (1993) for press-hammer foundations, and in Svinkin (1982)

for punch-press foundations. The permissible displacement values are 1.0-1.2 mm for forge hammer foundations and 0.25-0.50 mm for punch-press foundations.

Vibration Effects on Structures

Forge shop structures, adjacent and remote buildings may be affected by vibrations generated by operating impact machines. Vertical oscillations of impact machine foundations induce elastic waves in the soil medium which trigger vertical and horizontal ground vibrations.

Dynamic Settlements

Vertical ground vibrations from impact machine foundations in sand soils can be the cause of non-uniform dynamic settlements of column footings in forge shops. Column footings are usually designed for static loads transferred on the ground without taking into account the dynamic loads from ground vibrations which increase the pressure on the ground. According to Table 1, accelerations of hammer foundations may reach the value of 980 cm/s^2 or 1.0 g, and consequently the real pressure from column footings on the ground will be up 2 times higher than the static pressure. For foundations under impact machines, this effect is less important because the design of machine foundation provides a smaller static pressure on the ground in comparison with structure footings which support only static loads like column footings.

Accelerations attenuate very fast with distance from the impact machine foundations. Because of attenuation of vertical ground vibrations, dynamic loads under column footings are diverse and that may provoke additional differential settlements of column footings. A similar dominant frequency can be observed at various distances from the source. Therefore, accelerations at most locations of measurements of ground vibrations are proportional to displacements of ground vibrations, and the settlements are proportional to the maximum displacements or the maximum accelerations of vertical ground vibrations.

Barkan (1962) reported three case studies of damaging effects of structure footing settlements caused by ground vibrations from forge hammer foundations. The hammers had dropping weights of 4.5, 2.5 and 3 tonnes. The static pressure on the ground under wall footings was in the 1.75-2.5 kg/cm^2 range. The soil deposits of fine-grained sands were in all three cases. The water tables were at depths of 4.0-8.5 m. In the first study, a three story auxiliary building attached to a forge shop was completely destructed. This brick building was located at a distance of 6 m from the hammer foundation and erected much later than the forge shop. In the second study, ground vibrations from a hammer destroyed the forge shop building which brick walls were supported by continuous footing. In the third study, differential settlements of the shop columns nearest the hammer foundation were observed. These settlements were the cause of crack formation in the reinforced-concrete frame structures of the shop and in the brick walls.

To assess the effect of ground vibration intensity on dynamic settlements, Savinov (1979) suggested the threshold of 15 cm/s^2 for buildings sensitive to differential settlements and 30 cm/s^2 for insensitive buildings.

Differential dynamic settlements of forge shop structures and abutted buildings are the major harmful results of foundation vibrations under forge hammers.

Resonant Vibrations of Adjacent and Remote Structures

A coincidence of the frequency of ground vibrations to one of natural building oscillations may generate the condition of resonance in the building. Even the proximity of those frequencies may strongly increase building vibrations.

Oscillations of impact machine foundations also generate horizontal ground vibrations which have only one-two cycles in relatively small spaces of forge shops. Such horizontal ground vibrations cannot trigger horizontal resonant vibrations of forge shop structures. Displacements of these structural vibrations are usually similar to displacements of horizontal ground vibrations near footings under exterior forge shop structures.

In various soils, waves propagate in all directions from impact machine foundations forming a series of quasi-harmonic waves with the predominant frequency equal or close to the frequency of the source. This phenomenon is particularly well observed in saturated sands. A coincidence of ground and structure frequencies may trigger resonant structural vibrations. Rausch (1950) described a case history where intolerable vibrations were observed in an administrative building located 200 m from the foundation of a hammer with a ram mass of 1.5 tonnes. Probably wave paths had low attenuation at that site. Svinkin (1993) reported resonant horizontal vibrations of one part of a five story apartment building located at approximately 500 m from the foundation under a vibroisolated block for a forge hammer with a ram mass of 16 tonnes.

Direct Vibration Effects on Forge Shop Structures

Damage to masonry of the exterior walls is observed in various forge shops. Such damage can be produced by ground vibrations from impact machine foundations when frequencies of ground vibrations do not match natural frequencies of structures. The experimental studies of ten forge shops were performed because of visible damage in shop exterior structures at sites with diverse soil conditions, Svinkin (1995).

The investigated forge shops had similar structural set-up: one story braced steel frames and exterior walls supported by spread footings or foundation beams installed on column footings. The brick walls were connected to the columns. There were various soil conditions at sites: fine and middle sands with natural moisture, moist and very moist loams, and clays.

Cracks and other damage of exterior walls were found at the time of investigation. The most typical cracks were found in brick walls along the axes of steel columns. A length of cracks changed from 1 to 7 m and a crack width was in the 2-30 mm limits. Oblique cracks were detected at wall corners. The holes from fallen bricks were revealed

at both sides of some parts of exterior walls. Considerable deformations of the masonry were found in the walls of auxiliary buildings abutted to the forge shops.

Horizontal and vertical vibrations were measured on the column footings and brick walls during the operation of 24 forge hammers with a ram mass from 1 to 20 tonnes. Besides, brick wall vibrations from operating bridge cranes were recorded, particularly at the time of motion and braking of bridge cranes and crab motors.

Vertical vibrations of the column footings in the proximity of the hammer foundations had shapes similar to vibrations of the hammer foundations, but their displacements decreased 2-5 times dependently on a distance from the source and soil conditions. Vibrations of the column footings attenuated quickly with distance from the hammer foundations.

Records of horizontal structural vibrations showed that the maximum transverse displacement of 0.7 mm was measured at the upper parts of brick walls in the shop spans against the hammer foundations. Forces vibrations of brick walls had the dominant frequencies between 50-58 rad/s which coincided with the frequencies of free hammer foundation vibrations. At the rest of shop spans, free wall vibrations had frequencies in the 19-34 rad/s range and much smaller displacements. Horizontal displacements in the wall plane were 5-10 times less than the maximum transverse displacements at the same points.

Dynamic loads from bridge cranes induced forced brick wall vibrations with the dominant frequencies in the 17-34 rad/s range and the maximum horizontal wall displacements between columns of the same order like those from operating hammers. Brick wall transverse vibrations had certain features at the locations of wall abutting to the columns. On the wall section located against the hammer foundations, vibrations of the brick wall on both sides of the column had the same phase and close displacements. A phase of these vibrations changed and differences between their displacements increased with moving away from the span with the hammer foundation. This phenomenon was pronounced during operations of bridge cranes.

The performed experimental studies of ten forge shops revealed the causes of crack formation, minor and major masonry damage in shop exterior walls. It is common to consider differential column footing settlements induced by the static pressure and vibrations as the basic cause of cracks and damage in the exterior walls. It is correct for sites with sand deposits at close distances from the hammer foundations. Nevertheless, in numerous cases the masonry damage of the forge shop walls was observed at sites with other soil deposits than sands. Deformations of exterior structures due to non-uniform column footing settlements were not visible at the observed forge shops even built on cohesionless soils.

The analysis of the obtained results showed that cracks and damage of the brick walls bordered with steel columns were caused by to the effects of wall vibrations relatively to the columns. While a part of the brick wall on one side of a steel column moved, a similar part of the wall on other side of the column stayed immovable because a phase of vibrations changed. These vibrations were induced mostly by dynamic loads generated by operating bridge cranes. Simple calculations confirmed that tension stresses in the masonry were greater than the allowable limits. It is necessary to point out that cracks found at the upper part of exterior walls were not dangerous for the masonry in the good condition. However, for the masonry with insufficient quality, vibrations developed

cracks which length reached several meters with a width of 2-3 cm. Such cracks are unacceptable because they split the brick wall into separate parts. The appearance of extensive masonry damage at locations where the shop brick walls were attached to auxiliary buildings can be explained by inadequate quality of expansion joints between buildings and unequal settlements of the attached buildings.

Disturbance of People

Vibrations from impact machines shake working places near machine foundations, disturb people at forge shops and other places at plants, and may be annoying for residents of adjacent and sometimes remote buildings.

According to ANSI S3.29-1983, vibrations from impact machines with respect to human response can be divided into impulsive and intermittent vibrations.

An impulsive vibration is a transient isolated event with the duration less than two seconds. Such dynamic loads are generated by most of hammers in forge shops and hammers for remaking steel scrap heaps. Vibration values at workshop areas with such industrial process are specified in ANSI S3.18-1979, but ANSI S3.29-1983 should apply for assessment of impulsive vibration magnitudes in offices and adjacent building.

Intermittent vibration is a string of vibration incidents with short duration less than two seconds separated with intervals of much lower vibration amplitudes or without vibration at all. Such dynamic loads are generated by various punch presses and some old small forge hammers. ANSI S3.29-1983 should apply for assessment of impulsive vibration magnitudes in offices and adjacent building.

Predicting Vibrations from Impact Machine Foundations

Predicting soil and structure vibrations from impact machine foundations is important for proper assessment of vibration effects on structures, sensitive devices and people. The ground under machine foundations plays the major role in forming the machine foundation response and the ground responses to dynamic loads generated by impact machines.

Natural Frequency of Vertical Foundation Vibrations

Dynamic loads on the ground induce elastic waves in the medium of soil. The spectra of ground vibrations caused by impact loads have few maximums which are the natural frequencies of the soil layers. The experimental study (Svinkin 1996) revealed that values of these frequencies are practically independent of the condition at the contact area where impacts are made directly on the ground.

It has been found that the natural damped frequency of vertical foundation vibrations coincides with the dominant natural frequency of the soil profile, Svinkin (1997a, 2001). This finding is the basis of the method for predicting the natural frequency of vertical foundation vibrations.

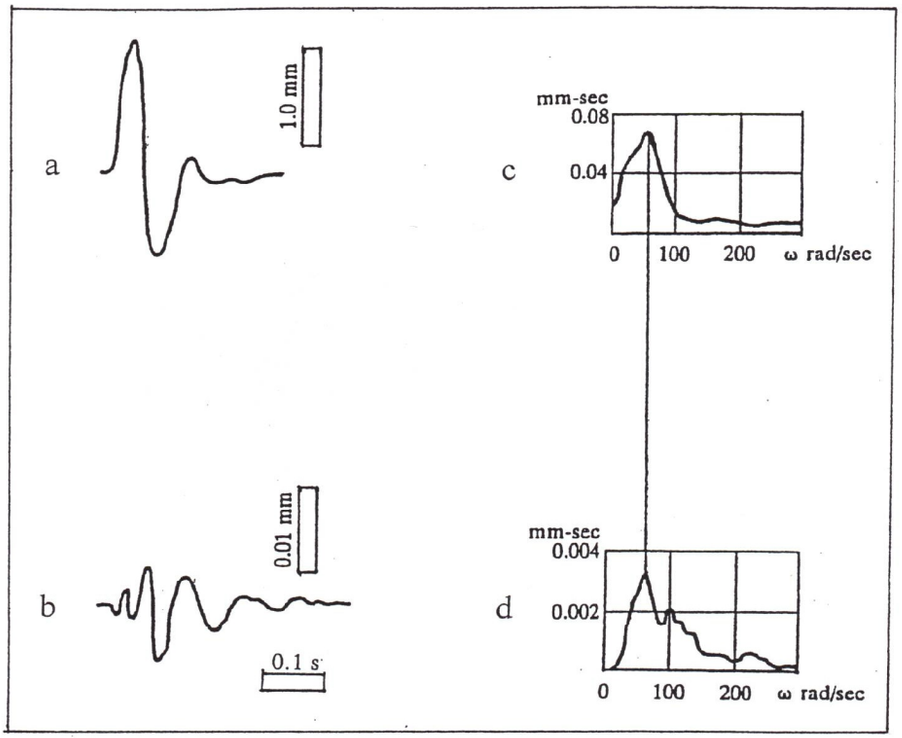


Figure 4. Natural frequency of foundation under press-hammer; a - foundation vibrations and c – their spectrum, b – ground vibrations and d – their spectrum (Svinkin 2001). Reprinted with permission

According to the method, impact loads are applied onto the ground within an area for installation of the machine foundation. Output locations are also at this area but beyond the zone of plastic deformations of the ground caused by impact forces. The dominant frequency of the spectra of ground vibrations at the location for installation of machine foundation is the predicted natural frequency of vertical damped vibrations of the machine foundation for the specified impact machine.

The result of predicting is shown for the foundation under a press-hammer with the ram mass of 4 tonnes and the foundation base area of 12.3 m^2 installed at the site with mostly a fine sand deposit (Figure 4). There is a good coincidence of predicted and measured results.

Ground and Structure Vibrations

An IRFP method can be used to predict complete time-domain records of ground and structure vibrations from impact machines, Svinkin (1997b, 2002). This method is founded on the utilization of the impulse response function technique that eliminates the need to use mathematical models of soil profiles, foundations and structures in practical application. The method takes into consideration the variety of soil and structural

properties and reflects real behavior of soil and structures without investigation of soil and structure properties.

The parameters of a machine foundation system can be determined using the existing theories, e.g. Rausch (1950), Barkan (1962), Lysmer and Richart (1966), Richart et al. (1970), Wong and Luco (1976), Arya et al. (1979), Roesset (1980), Dobry et al. (1986), Novak (1987), Prakash and Puri (1988), Gazetas (1991), Veletsos (1993), Wolf (1994), and others. The reason for the agreement of predicted results with the use of all of these theories is that ground vibration responses are negligibly dependent on the parameters of the foundation-soil system.

The procedure for predicting soil and structures vibrations prior to installation of foundation for impact machines includes experimental and computational parts.

In an experimental part, the place for a machine foundation should be chosen at an industrial site. At the place of installation of the machine foundation, impact forces of known magnitude are applied on the ground. The impact can be created using a rigid steel sphere or pear-shaped weight falling from a bridge or mobile crane. At the moment of impact on the ground, oscillations are recorded at the points of interest, for example, at the locations of instruments and devices sensitive to vibrations. These oscillations are the impulse response functions of the considered system which automatically take into account complicated soil conditions.

In a computational part, after preliminary calculation of the frequencies and the damping constant of soil, a convolution integral is used to compute predicting soil and structure vibrations, Svinkin (2002).

The following example demonstrates the application of the IRFP method for predicting ground surface oscillations excited by vibrations of the foundation under a vibroisolated block for the large forge hammer with a ram mass of 16 tonnes. The foundation base area was 116.4 m². The soil deposit consisted of about 1.5 m of earth fill followed by about 5 m of gray and brown moist soft sandy clay underlain by about 7 m of yellow moist dense sand deposited on green moist soft clay. The water table was not encountered during soil boring at the site. Measured and predicted soil vibrations at distances 7.7 m and 28.8 m from the hammer foundation are shown in Figure 5. The predicted soil vibrations demonstrate a close fit to the measured data.

The IRFP method predicts complete three-dimensional wave forms, vertical and two horizontal, with reasonable accuracy. A comparison of computed and measured records confirms the acceptability of the IRFP method for prediction vibrations in target points prior to installation of foundations for impact machines.

Mitigation of Vibration Outcomes

There are a limited number of means which can mitigate vibrations generated by impact machines. Some ways can be used at a design stage; other ways can be employed before and after construction of impact machine foundations. It is possible that a measure for decreasing one type of structural vibrations will trigger another vibration excitation. A proper analysis is needed for each site.

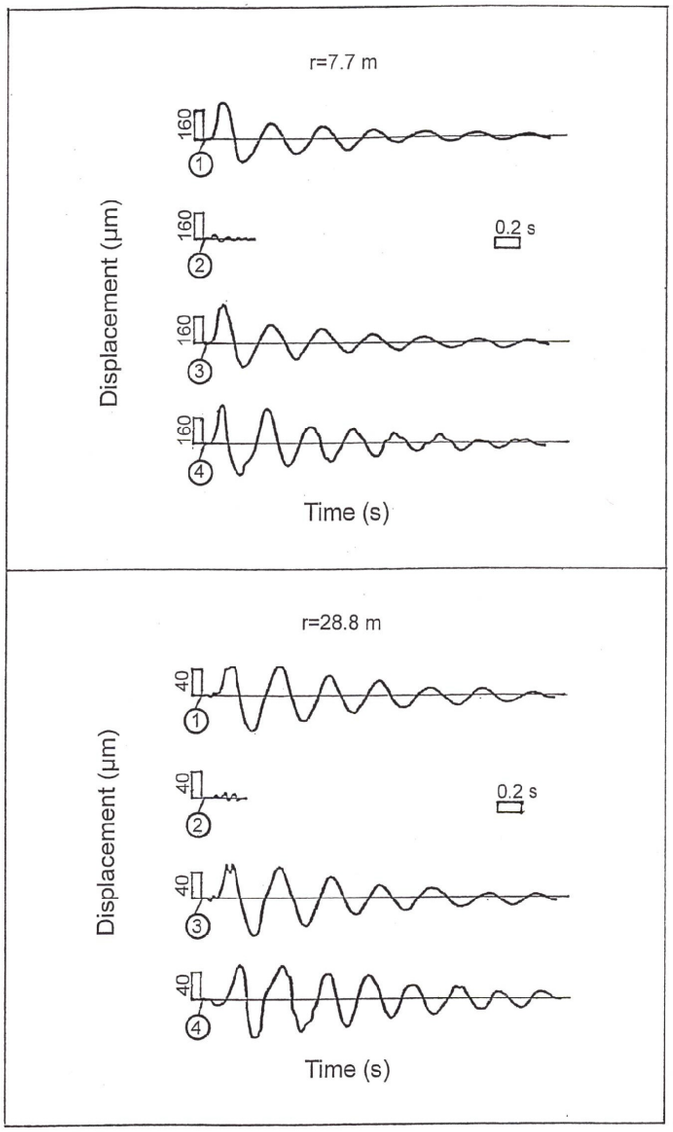


Figure 5. Vertical soil vibrations excited by sizable forge hammer installed on vibroisolated block; predicted vibrations ① – ③: from forced foundation oscillations ①, from free foundation oscillations ②, summary ③; and measures vibrations ④; Svinkin (2002)

Prevention of Differential Settlements

Footings under columns in forge hammer shops are designed for a constant static pressure transferred from structures onto the ground. An additional dynamic pressure from ground vibrations generated by the impact machine foundations depends on a distance from the source. Because the settlements are proportional to the accelerations of vertical ground vibrations, column footings have differential settlements.

To diminish detrimental vibrations effects on building footings, Barkan (1962) proposed to assign the permissible static pressures from column footings on the ground depending on the displacements or the accelerations of ground vibrations at the locations of column footings. The IRFP method (Svinkin 2002) can be used for predicting ground displacements before construction of a hammer foundation.

Resonant Building Vibrations

Low-frequency transient vibrations appear at some distances from machine foundations and may trigger resonant structure vibrations. It occurs seldom and there are no readily apparent means for reducing resonant vibrations. However, resonance problem can be detected in advance with the IRFP method.

Wave Barriers

There are numerous studies of the application of wave barriers for diminishing ground vibrations from different dynamic sources, for example Woods (1968), Haupt (1995), Naggar and Chehab (2005) and others. However, there is no example of the successful application of the wave barriers technique to mitigate ground vibrations from foundations under machines with impact loads, Woods (2007).

Active Vibration Isolation

Vibrating isolation of forge hammers is used at industrial plants in order to diminish harmful vibration effects on adjacent and remote buildings, technological processes, sensitive devices and people. A forge hammer is installed on an isolated concrete block which is supported by steel springs and rubber dashpots.

Natural frequencies of vertical block vibrations usually are in 3-6 Hz range. Low frequencies are typical for sizeable hammers. It is necessary to point out that the first mode of multi-story buildings has frequencies between 2-5 Hz, while for row-rise buildings these limits are 4-10 Hz. The proximity of source frequencies to ones of natural building oscillations may generate resonant building vibrations.

The following is an example of unacceptable building vibrations induced by the foundation under a vibroisolated concrete block and a sizeable forge hammer with a ram mass of 16 tonnes, Svinkin (1993). A five story apartment building was located at a distance about 500 m from the hammer foundation. The building had two perpendicular parts. A major part of the building was oriented in a radial direction from the hammer foundation and had large stiffness in this direction. There were no vibration problems with this building part. In the same direction, a minor part of the building had low stiffness and harmful vibrations particularly sensitive at night.

Vibrations of the hammer foundation induced horizontal transversal structural vibrations with the frequency of 3.1 Hz. This frequency was certainly closed to the natural frequency of horizontal building vibrations. A change of the frequency of vertical

vibrations of the vibroisolated block with the hammer is the simplest and economical way for diminishing building vibrations. To rich this goal, it is necessary to decrease stiffness of vibroisolators by eliminating part of them. A number of steel springs cannot be reduced because they are chosen in accordance with the condition of strength to support the concrete block. Therefore, it is necessary to decrease the quantity of dashpots.

Buildings usually have a narrow resonant zone. In the described case history, the natural frequency of vibroisolated concrete block with hammer was decreased from 3.1 to 2.9 Hz due to elimination of a few dashpots. It was sufficient to diminish structural vibrations to the acceptable limits.

Mitigation of Vibration Effects on People

Impact machine foundations generate high levels of ground vibrations which are considerably bigger than the threshold of human exposure to vibrations in buildings. Therefore, offices have to be located at relatively large distance from the dynamic sources.

Sometimes there is the need for mitigating vibration effects at the existing offices located at distances with perceptible vibrations. It is a complicated problem. For the remedial work at those places, it is reasonable to use passive vibration isolation in the offices. Composite high damping panels for flooring and walls should to be used to decrease vibrations.

Conclusions

Impact machines generate intensive dynamic forces which induce machine foundation and ground vibrations. Forge and drop hammers are most powerful machines producing impact loads.

In most cases, the hammer foundations respond to impact loads generated by hammers as a SDOF system, and only vertical foundation vibrations have to be considered for analysis of impact machine foundations as sources of industrial vibrations.

There is a trend of decreasing the natural frequency of vertical foundation vibrations with increasing the ram mass and the foundation base area.

A real pressure under column footing in forge shops can be up two times higher than the static pressure due to vibrations from hammer foundations. Accelerations attenuate very fast with distance from the impact machine foundations. Therefore, dynamic loads under column footings are diverse and that may provoke additional settlements of column footings. Differential dynamic settlements are the major cause of damage to exterior walls in forge shops at sites with a sand deposit.

Horizontal vibrations of exterior forge shop structures triggered by ground vibrations from impact machine foundations are not dangerous for integrity of these structures. However, low-frequency ground vibrations can trigger resonant building vibrations at relatively large distances from the hammer foundations.

The analysis of the obtained results showed that cracks and damage of the brick walls bordered with steel columns in forge shops had occurred due the effect of wall vibrations

relatively to the columns. These vibrations were induced mostly by dynamic loads from operating bridge cranes.

The natural frequency of vertical machine foundation vibrations can be predicted before installation of a machine foundation. An IRFP method can be used to predict complete time-domain records of ground and structure vibrations from impact machines at the time of design of the machine foundation.

There are a limited number of means which can mitigate vibrations generated by impact machines. Some measures can be used at a design stage; others can be employed before and after construction of impact machine foundations. Mitigation measures should be correctly applied because it is possible that eliminating one dynamic excitation can trigger another one. It is better to mitigate vibration effects on peoples in offices at the time of a design of forge shops and surrounding areas than decrease unacceptable vibrations after construction.

References

ANSI S3.18 (1979). *AMERICAN NATIONAL STANDARD, Guide to the Evaluation of Human Exposure to Whole Body Vibrations*.

ANSI S3.29 (1983). *AMERICAN NATIONAL STANDARD, Guide to the Evaluation of Human Exposure to Vibration in Buildings*.

Arya, S.C., O'Neill, N.M., and Pincus, G. (1979). *Design of structures and foundations for vibrating machines.* Gulf Publishing Company, Houston, Texas.

Barkan, D.D. (1964). *Dynamics of Bases and Foundations*, McGraw Hill Co., New York.

Dobry, R., Gazetas, G, and Stokoe, K.H., II (1986). "Dynamic response of arbitrarily shaped foundations: Experimental verification." *Journal of Geotechnical Engineering*, ASCE, 112, No. 2, 136-149.

Gazetas, G.. (1994). "Foundation vibrations." *Foundation Engineering Handbook*, 2nd Ed., H.Y.Fang, ed, Van Nostrand Reinhold, New York, 553-593.

Glazyrin, V.S. and Martyshkin, B.C. (1971). “Investigation of vibrations of vibration isolated foundations under forge hammers.” *Bases, Foundations and Soil Mechanics*, Stropiizdat, 3 (in Russian).

Haupt, W.A. (1995). “Wave propagation in the ground and isolation measures.” *Proceedings of the Third International Conference on Recent Advances in Geotechnical Earthquake Engineering and Soil Dynamics*, St. Louis, Missouri, V.II, 985-1016.

Lysmer, J. and Richart, F.E., Jr. (1966). "Dynamic response of footings to vertical loading." *Journal of Soil Mechanics and Foundation Division*, ASCE, 92(1), 65-91.

Klattso, M.M. (1965). “Parameters of ground vibrations induced by forge hammers.” *Industrial Construction*, Stropiizdat (in Russian).

Naggar, M.H.E. and Chehab, A.G. (2005). “Vibration barriers for shock-producing equipment.” *Canadian Geotechnical Journal*, 42, 297-306.

Novak, M. (1987). "State of the art in analysis and design of machine foundations." *Soil-Structure Interaction*, Elsevier/CML Publisher, New York, 171-192.

Prakash, S. and Puri, V.K. (1988). *Foundations for machines: analysis and design,* John Wiley and Sons, Inc., New York.

Rausch, E. (1950). *Maschinen Fundamente*, Verlag, Dusseldorf, Germany (in German).

Richart, F.E., Hall, J.R. and Woods, R.D. (1970). *Vibrations of soils and foundations,* Prentice-Hall, Inc., Englewood Cliffs, NJ.

Roesset, J.M. (1980). "The use of simple models in soil-structure interaction." *Civil Engineering and Nuclear Power*, ASCE, No. 1/3, 1-25.

Savinov, O.A. (1979). *Modern construction of machine foundations and their calculations*. Second Edition, Stroiizdat, Leningrad (in Rissian).

Scheglov, V.F. (1960). Soil vibrations from forge hammers with various degree of vibration isolation." *Forge-Punching Production*, Mashinostroenie, 8 (in Russian).

Svinkin, M.R. (1980). "Determination of dynamic loads transmitted to a hammer foundation." *Soil Mechanics and Foundation Engineering*, Publishing Corporation, New York, 17(5), 200-201, a translation of Osnovaniya, Fundamenty i Mekhanika Gruntov in Russian.

Svinkin, M.R. (1982). "Determining the vibration amplitude of foundations supporting crankshaft presses." *Soil Mechanics and Foundation Engineering*, Publishing Corporation, New York, 19(3), 99-102, a translation of Osnovaniya, Fundamenty i Mekhanika Gruntov in Russian.

Svinkin, M.R. (1993). "Analyzing man-made vibrations, diagnostics and monitoring". *Proceedings of the Third International Conference on Case Histories in Geotechnical Engineering*, St. Louis, Missouri, June 1-4, 663-670.

Svinkin, M.R. (1995). "Vibrations of impact machine foundations and footing settlements." *Proceedings of the Third International Conference on Recent Advances in Geotechnical Earthquake Engineering and Soil Dynamics*, St. Louis, Missouri, V. II, 797-802.

Svinkin, M.R. (1996). Discussion of 'Impact of weight falling onto the ground' by Roesset et al." *Journal of the Geotechnical and Geoenvironmental Engineering,* ASCE, 120(8), 414-415.

Svinkin, M.R. (1997a). A method for estimating frequencies of machine foundations. *U.S. Patent No. 5,610,336* issued March 11, 1997.

Svinkin, M.R. (1997b). "Numerical methods with experimental soil response in predicting vibrations from dynamic sources." *Proceedings of the Ninth International Conference of International Association for Computer Methods and Advances in Geomechanics*, A.A. Balkema, Rotterdam, 3, 2263-2268.

Svinkin, M.R. (2001). "Natural frequency of vertical foundation vibrations evaluated from in-situ impact test." *Proceedings of the Fourth International Conference on Recent Advances in Geotechnical Earthquake Engineering and Soil Dynamics*, San Diego, California, March 26-31, Paper No. 2.33, CD-ROM.

Svinkin, M.R. (2002). "Predicting soil and structure vibrations from impact machines." *Journal of the Geotechnical and Geoenvironmental Engineering*, 128(7), 602-612.

Veletsos, A.S. (1993). "Design concepts for dynamics of soil-structure interaction." *Developments in Dynamic Soil-Structure Interaction*, Kluwer Academic Publishers.

Wong, H.L. and Luco, J.E. (1976). "Dynamic response of rigid foundations of arbitrary shape." *Earthquake Engineering and Structural Dynamics*, 4, 579-587.

Wolf, J.P. (1994). *Foundation vibration analysis using simple physical models,* PTR Prentice Hall, Englewood Cliffs, NJ.

Woods, R.D. (1968). "Screening of surface waves in soils." *Journal of the Soil Mechanics and Foundation Division*, ASCE, 94(SM4), 951-979.

Woods, R.D. (2007). Personal communications.

This page intentionally left blank

Physical and Numerical Modeling of Dynamic Soil-Structure Interaction

Mohammad H.T. Rayhani[1], S.M. ASCE and Hesham El Naggar[2], M. ASCE.

[1]Research Associate, Geo-Engineering Center, Queen's University; mrayhani@ce.queensu.ca
[2]Professor, Geotechnical Research Center, University of Western Ontario; helnaggar@eng.uwo.ca

ABSTRACT: A numerical model was developed to simulate the response of two instrumented, centrifuge model tests on soft clay. The centrifuge tests consist of a rigid containment to simulate the behavior of rectangular ten-storey buildings on 30 m uniform and layered soft soils. Each test model was subjected to several earthquake-like shaking events i.e. scaled versions of an artificial western Canada earthquake and the Port Island ground motion recorded during the 1995 Kobe Earthquake at a centrifugal acceleration level of 80g. The centrifuge model was simulated with the 3-D finite-difference-based Fast Lagrangian Analysis of Continua (FLAC) program. The results predicted with the use of nonlinear elastic–plastic models for the soil are shown to be in good agreement with measured acceleration, soil response, and structural behaviour. Numerical results were used to study the effect of soil layering and soil-structure interaction on foundation input motion.

INTRODUCTION

Dynamic centrifuge modeling is an effective approach for studying seismic site response and soil-structure interaction (SSI). An advantage of centrifuge modeling is that it facilitates performing a physical parameter study, and thus allows observing the effects of parameters such as strata thickness, soil properties, earthquake frequency content, and level of shaking. Model test results are often used as calibration benchmarks for analytical methods, or to make quantitative predictions of the prototype response. Such models, when subjected to a controlled base motion, can provide a database for the validation of numerical approaches. Elgamal *et al.* (2005) studied the dynamic shear modulus and damping of saturated Nevada sand using centrifuge tests and conducted a numerical simulation and compared the results with reference data in small and large strain ranges. The effects SSI and nonlinear site response (SR) on the 1994 Northridge earthquake main shock and aftershock motions recorded at two buildings in the Jensen Filtration Plant were investigated by Crouse and Ramirez (2003). Nonlinear SR and kinematic SSI were identified as the main reasons for the differences observed in the three sets of building earthquake records, each with clearly distinct amplitude and duration characteristics. However, models of

inertial SSI, calibrated to the vibration test data, demonstrated that this phenomenon was of secondary importance, even when adjusted for nonlinear behavior of the soil and structure. Stewart et al. (2003) indicated that for stiff structures founded on soil, such as shear wall or braced frame lateral load resisting systems with small aspect ratios, the effects of SSI were found to be most significant. For long period structures like high-rise buildings, the effects of SSI are found to be negligible because of the large structure flexibility.

This paper focuses on the development of a numerical model validated using seismic site response results from centrifuge tests reported by Rayhani and El Naggar (2007a). The program FLAC-3D (Itasca Consulting Group, 2005) was used to develop the numerical models employed to investigate seismic site response and soil-structure interaction in soft soils. Computed and measured results are compared in terms of soil response, horizontal accelerations at different depths, and response spectra of those accelerations. The validated numerical model was then used to perform a parametric study to examine factors affecting site response, accelerations amplification at different depths, and soil-structure interaction.

CENTRIFUGE MODEL TESTS

Centrifuge model tests have been conducted at 80-g on the C-CORE 5.5 m radius beam centrifuge located at Memorial University of Newfoundland. An electro-hydraulic earthquake simulator (EQS) was mounted on the centrifuge to apply a one-dimensional prescribed base input motion. A model container with inner dimensions of 0.73 m in length, 0.3 m in width, and 0.57 m in height was used to contain the soil. Figure 1 shows the configuration and instrumentation layout of the model tests. The total thickness of the soil model is approximately 0.375 m, simulating 30 m on a prototype scale. The building model consisted of a rigid structure box slightly embedded in the soil bed. The average bearing stress beneath the structure model at 80 g was about 95 kPa. This arrangement was considered to represent a reasonable simulation for the behavior of rectangular ten-storey buildings.

Glyben clay with glycerin ratios of 45% and 40% was used to simulate soft and medium stiff clay behavior in model tests. This soil was used due to lack of facility to prepare the clay samples from the slurry in the centrifuge center. The density of glyben with 45% glycerin and 55% bentonite was 1575 Kg/m^3 and its voids ratio is e = 1.36. The density and void ratio for glyben with 40% glycerin were 1593 Kg/m^3 and 1.21, respectively. Detailed characterization of glyben for seismic application was presented by the authors elsewhere (Rayhani and El Naggar 2007b). The models were prepared by tamping the soil in layers to obtain the desired density (90% of maximum dry density). The shear strength profile of each clay layer was evaluated by conducting vane shear tests at depth intervals of 50mm.

The models were instrumented to measure accelerations and displacements. Accelerometers were used to measure the soil acceleration at different depths. The accelerometers were placed within the soil bed by tamping the clay to the required level, placing the instrument in the desired position and then adding more soil to the required level. Accelerometers were also placed on top of the structure and on its walls. The system model was also instrumented with Linear Variable Differential

Transducers (LVDTs) to measure the settlement of the soil surface.

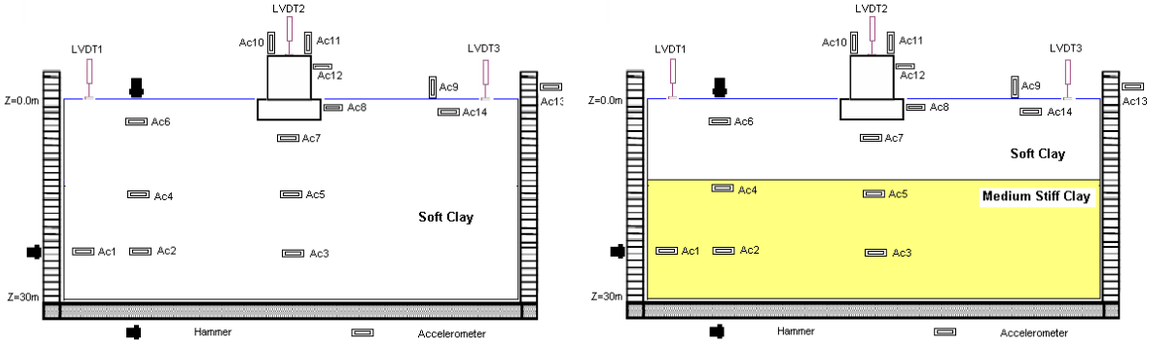


FIG. 1: Centrifuge model configuration in prototype scale

The site stiffness or shear wave velocity profile is a required input for wave propagation site response analyses. The T-bar test was performed in each clay model at 80*g* to determine a continuous profile of the deposits undrained shear strength, S_u. The undrained shear strength measured using the T-bar bearing resistance data varied between 40 and 60 kPa in soft clay (RG-01). The shear strength in model RG-02 was about 40-50 kPa for the upper soft clay and about 85-95 kPa for the medium stiff clay. The shear strength increased slightly with depth in both models. This trend was expected, considering the normal stress level in the test model. The shear wave velocity was measured using the hammer test. Also, the shear wave velocity profile at different depths was estimated using established relations between shear strength and shear wave velocity for glyben clay (Rayhani and El Naggar, 2007b). The shear wave velocity, V_S, varied between 50-90 m/sec in RG-01 (soft clay) and 65-130 m/sec in RG-02 (medium stiff clay). The average shear wave velocity of the 30 m soil profile was about 73 and 100 m/sec for models RG-01 and RG-02, respectively.

Table 1: Shaking events and peak accelerations (units in prototype scale)

Model	Event ID	Base acc. (g)	Peak Acceleration (g)				
			A2	A3	A6	A7	A12
RG-01	WCL	0.1	0.12	0.125	0.15	0.18	0.2
	WCM	0.18	0.185	0.19	0.24	0.28	0.33
	WCH	0.38	0.375	0.385	0.43	0.51	0.6
	KH	0.54	0.54	0.63	0.61	0.72	0.9
RG-02	WCL	0.1	0.12	0.12	0.19	0.19	0.28
	WCM	0.2	0.21	0.19	0.28	0.275	0.41
	WCH	0.38	0.39	0.39	0.4	0.39	0.49
	KL	0.03	0.04	0.04	0.06	0.06	0.08
	KH	0.54	0.63	0.61	0.61	0.65	0.87

* WCL, WCM, WCH are Western Canada and KL and KH are Kobe earthquakes

The models were subjected to earthquake excitations with different peak acceleration and frequency content. Each test model was subjected to several

earthquake-like shaking events at a centrifugal acceleration level of 80*g*. Table 1 presents the input excitations, i.e., scaled versions of an artificial western Canada earthquake (Seid-Karbasi, 2003) and the Port Island ground motion recorded during the 1995 Kobe Earthquake. The model input motions varied from 2.5g to 43g, at target frequencies from 40-200Hz (simulating prototype earthquakes between 0.03g and 0.54g). Table 1 also lists peak accelerations at the accelerometer locations A2 and A3 near the base; A6 near the surface; A7 beneath the structure and A12 on structure wall for all shaking events. The recorded peak acceleration near the model surface in the longitudinal direction ranged from 0.15 to 0.65*g*. This broad range of acceleration magnitudes resulted in soil response covering linear to nonlinear scenarios.

NUMERICAL SIMULATION

The numerical analysis investigated various aspects of the testing, including the soil characteristics on amplification factor and soil-structure interaction. The finite-difference-based program, *FLAC3D* (Itasca Consulting Group, 2005) was used to analyze the centrifuge model tests and to simulate their response under seismic loading. *FLAC3D* is a three-dimensional explicit finite-difference program, which can simulate the behavior of structures built of soil, rock or other materials that may undergo plastic flow when their yield limits are reached. The explicit, Lagrangian, calculation scheme and the mixed-discretization zoning technique used in *FLAC3D* ensure that plastic collapse and flow are modeled accurately. Materials are represented by elements, and each element behaves according to a prescribed linear or nonlinear stress/strain law in response to the applied forces or boundary restraints. A fixed boundary condition in the vertical, z, and y directions was assumed at the numerical grid points on the soil far end boundary, representing the rigid centrifuge container that was used to contain the model soil (i.e. at the sides of the model).

The Mohr-Coulomb plastic constitutive model was used to simulate the nonlinear soil behavior. In FLAC, this model is characterized by its yield function and flow rule. The yield functions define the stress combination for which plastic flow takes place. The failure envelope for this model corresponds to a Mohr-Coulomb criterion (shear yield) with tension cutoff (tension yield function). The position of a stress point on this envelope is controlled by a non-associated flow rule for shear failure, and an associated rule for tension failure. The building structure was modeled as a linearly elastic material.

The soft soil was modeled with continuum zones. The mesh size and the maximum unbalanced force at the grid points (i.e., error tolerance) were selected on the basis of a series of parametric analyses to concurrently optimize accuracy and computation speed. Numerical computations were carried out in both small and large-strain modes to ensure sufficient accuracy in the event of strong earthquake application.

The glyben clay soil was modeled as a nonlinear elastic–plastic material using Mohr–Coulomb failure criterion with non-associated flow rule. The shear strength values of 50 kPa and 90 kPa were used as representative values for the soft and medium stiff clay soils, respectively. A Poisson's ratio of 0.43 for soft clay and 0.42 for medium stiff clay was employed based on resonant column measurements (Rayhani and El Naggar, 2007b). The structure and its foundation were modeled using

linear elastic elements, with an elastic modulus of 100 GPa and Poisson's ratio of 0.25 and were rigidly connected.

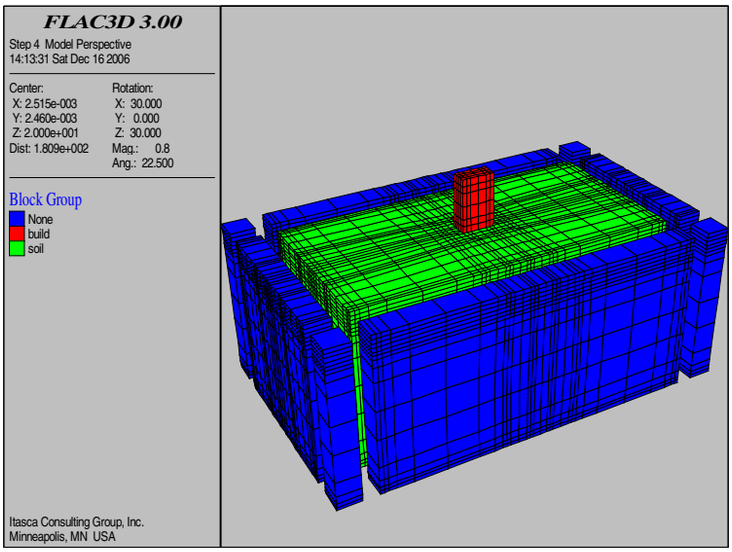


FIG. 2: Numerical grid and model component

The applied earthquake-like shaking events, listed in Table 1, covered linear and nonlinear responses and thus the soil properties used in the numerical analysis had to be consistent with the expected strain ranges. The objective was to define a set of modeling parameters that achieve a satisfactory level of success in matching the recorded site response. The centrifuge shear wave velocity measurements and estimated shear modulus and damping ratios were used as input to these analyses. Since V_S data was measured only for the lower soil layer in centrifuge, the shear wave velocity profile estimated from the shear strength soil profile was used for response analysis (Rayhani and El Naggar, 2007a). Adequacy of the matching process was based on inspection of the recorded and computed acceleration response spectra (5% damping) at all accelerometer locations. Table 2 lists the main parameters used for these models.

Table 2: Major modeling properties of soft and medium stiff clay

Model parameters	Soft clay	Medium stiff clay
ρ, Mass density (kg/m^3)	1575	1595
K, Bulk modulus (kPa)	5.7 x 10^4	9.37 x 10^4
G, Shear modulus (kPa)	8.4 x 10^3	15.9 x 10^3
ν, Poisson's ratio (kPa)	0.43	0.42
E, Elastic modulus (kPa)	2.4 x 10^4	4.5 x 10^4
c, Cohesion intercept (kPa)	45	90
c_{sf}, Interface adhesion (kPa)	30	50
k_n, Interface Normal stiffness (kPa/m)	4.5 x 10^4	7.6 x 10^4
k_s, Interface Shear stiffness (kPa/m)	5 x 10^2	8 x 10^2

The interfaces between the foundation and soil were modeled as linear spring–slider systems, with interface shear strength defined by the Mohr–Coulomb failure criterion. The relative interface movement is controlled by interface stiffness values in the normal (k_n) and tangential (k_s) directions. Based on recommended rule-of-thumb estimates for maximum interface stiffness values given by Itasca Consulting Group (2005), k_n and k_s were set to ten times the equivalent stiffness of the neighboring zone. The maximum interface shear resistance between the foundation and the soil is controlled by the peak soil cohesion, and a reduced value of the soil cohesion was used for this interface (i.e., c_{sf} in Table 2).

NUMERICAL MODEL VERIFICATION

The recorded time history at the base of the centrifuge container was used as the base input motion of the soil profile in the analyses. Representative simulation results of the moderate excitation (Event WCM) for model RG-01 are shown in Figs. 3 in terms of acceleration time histories and the corresponding response spectra (5% damping). In the three cases, the numerical model gives an overall satisfactory match to the experimental counterpart at all accelerometer locations, both in the time and frequency domains in the soil profile. Similar to the observed behavior in experiments, the computed response indicated that the seismic waves were amplified as they propagated from the bedrock to the surface. However, the calculated response spectra for periods ranging from 0.2 to 0.5 second were slightly less than the measured response spectra, for the region close to surface in both free field and underneath the structure. This may be attributed to the approximate modeling of the rigid boundaries (i.e. container) around the soil mass, and the foundation-soil interface.

ANALYSIS AND DISCUSSION

The characteristics of the earthquake motion at the base of a structure are affected by the properties of the underlying soil through soil amplification and soil–structure interaction phenomena. The results obtained from the numerical analysis are discussed with respect to the different soil profiles and different types of earthquake input motions. The results are presented in terms of acceleration, response spectra and amplification factors. Figure 4 depicts free field acceleration amplification computed in both soil profiles for all shaking events. The acceleration amplifications were obtained by normalizing the maximum recorded acceleration at a given elevation by the corresponding peak acceleration of the base excitation.

The accelerations of both free field and underneath the structure were amplified, with larger amplification occurring for the weaker earthquake excitations. The amplification of the earthquake shaking as well as the frequency of the response spectra decreased with increasing earthquake intensity. This is attributed to shear modulus degradation and higher material damping during strong motions. Larger amplification also occurred for the layered soil profile, indicating the importance of layering effect on ground motion.

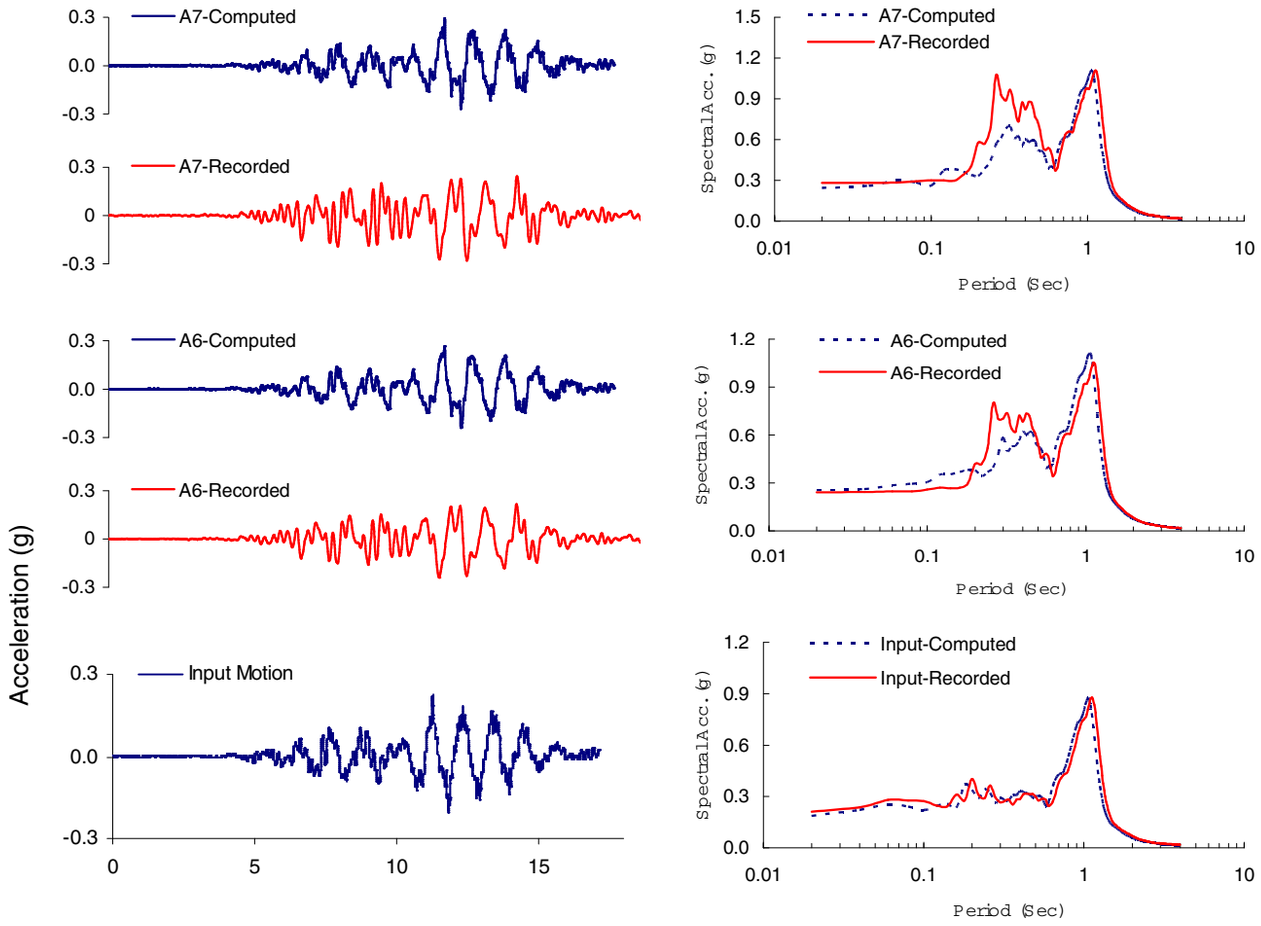


FIG. 3: Calculated and recorded acceleration time histories and response spectra in model RG-01 for event WCM (Amax=0.2g)

Table 3: Amplification factor for different soil strata, event WCM (a_{max}=0.18g)

Soil profile	Depth (m)	V_S (m/s)	Average V_S (m/s)	Peak Acc. (g)	Amplification factor
Lay-E0	30	166	166	0.23	1.28
Lay-E1	10 20	100 250	166	0.275	1.53
Lay-E2	10 10 10	250 100 250	166	0.245	1.36

A series of numerical analysis was also performed to evaluate the layering effect on amplification in the same range of average shear wave velocity. Table 3 shows the amplification factor for three soil profiles that can be categorized in group E of National Building Code of Canada (NBCC, 2005) based on the average shear wave velocity (V_S =166 m/s). It is noted that the amplification factor varied between 1.28

and 1.53 for different profiles. It is also noted that the amplification for soil profiles with an upper soft layer is higher than that of the uniform soil profile. These observations demonstrate the average shear wave velocity of the top 30 m, probably, is not a sufficient indicator for expected amplification as postulated in most seismic codes. The soil layering should be carefully considered.

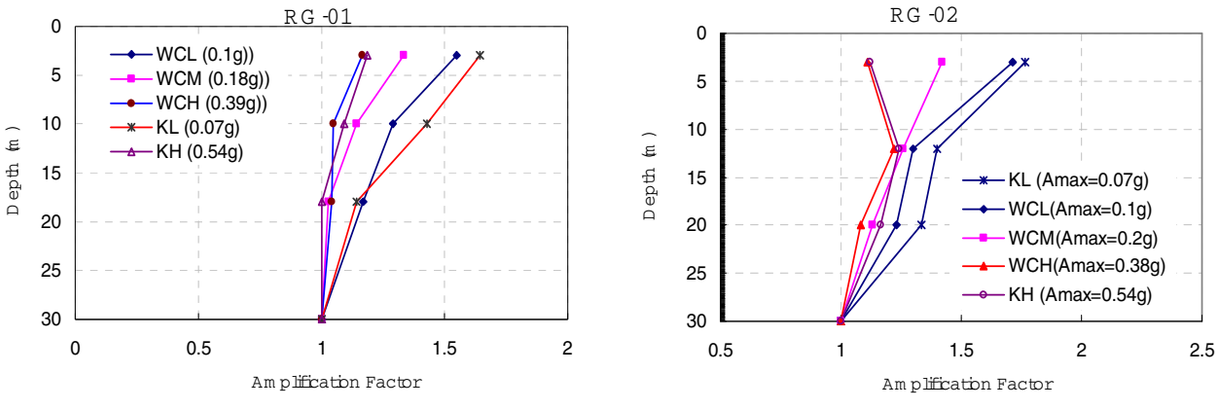


FIG. 4: Calculated free field amplification in both profiles for all shaking events

The amplification beneath the structure was generally higher than that for the free field, indicating the structure feedback and interaction between the soil and foundation during shaking. This is qualitatively similar to estimated soil-structure interaction effects which have been identified by Aviles and Perez-Rocha (1998) for medium and long period structures located on soft soils in Mexico City during the Mexico earthquake of 1985.

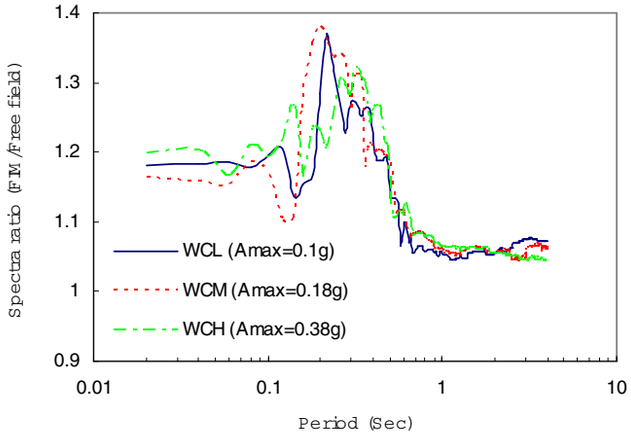


FIG. 5: Spectra ratio of foundation input motion to the free field in model RG-01

The effect of kinematic soil-structure interaction (SSI) on foundation input motion is assessed by comparing the acceleration response underneath the structure with the free field response in model RG-01. The deviation of the foundation input motion

(FIM) from the free-field motion is dependent on the stiffness and geometry of the foundation and soil properties. This deviation is expressed through a transfer function that represents the ratio of foundation and free-field motions in the frequency domain. Figure 5 shows the response spectra ratio of underneath the structure to the free field ($SA_{FIM}/SA_{Free\ field}$).

As noted from Fig. 5, the foundation accelerations are up to 37 percent higher than the free field over the frequency range of 2 Hz to 6 Hz. These differences are most pronounced for the WCL and WCM shaking events. The difference between the free field ground motion and the foundation input motion (in the same level) is not so significant at frequencies less than 2 Hz (5-7%). The parametric analyses indicated that the seismic soil-structure interaction has unfavorable effects on horizontal ground motions for frequencies between 2-6 Hz.

The inertial soil-structure interaction was evaluated by comparing the acceleration response spectra of the structure wall with those of beside the foundation. Figure 6 shows the ratio of response spectra of the structure to the response beside the structure in foundation level. It is noted that the structure experienced higher acceleration up to 34% compared to the response beside the foundation level over the frequency range of 3-5 Hz. This higher response indicates the effect of inertial SSI on structural behavior.

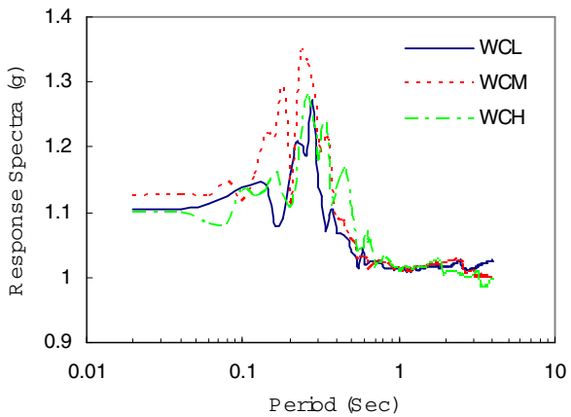


FIG. 6: Spectra ratio of the structure motion to the response beside structure

A series of numerical analysis was also performed on fixed-base structure and its response was compared with response of the structure on different soil profiles to evaluate the effect of SSI (both kinematic and inertial) on structural response. As it can be seen from Figure 7, SSI amplified the fixed-base structural response from 0.3g up to 1.6g in soft soil. Soil-structure interaction also increased the natural period of fixed-base structure from 0.15 seconds to about 0.3 seconds.

The relationship between the vibration frequencies of the model structure, natural frequency of the supporting soil, and predominant frequency of earthquake input motion influences the seismic response of structures. The natural frequency of the soil is close to the vibration frequency of the structure (2-5 Hz), resulting in significant amplification of input motion. However, the predominant frequency of input motion is lower than the natural frequencies of soil and structure.

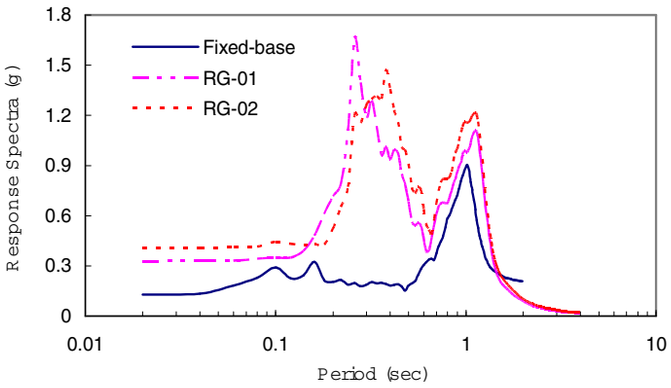


FIG. 7: Response spectra of structure on different foundation soils

CONCLUSIONS

Dynamic centrifuge experiments with one- and two-layer soft clay profiles produced a comprehensive set of data covering linear to highly nonlinear response scenarios. Numerical simulations were conducted for a representative set of weak to strong shaking events, using a fully nonlinear Finite Difference program (FLAC3D) calibrated by the identification results. The predicted responses from the numerical models were calibrated with the measured responses of two centrifuge model tests on homogeneous and layered clay. The resulted model was used to perform a series of numerical analyses on amplification of earthquake motion in clay as well as soil-structure interaction.

The peak surface acceleration and foundation input motions were significantly amplified, especially for low amplitude base acceleration. The amplification of the earthquake shaking as well as the frequency of the response spectra decreased with increasing earthquake intensity. This is associated with shear modulus degradation and higher material damping during strong motions. The results also clearly demonstrate that the layering system has to be considered, and not just the average shear wave velocity, when evaluating the local site effects.

The peak accelerations of soil beneath the structure increased due to strong interaction between the soil and the foundation. For the case considered, the seismic soil-structure interaction significantly increased the horizontal ground motions at frequencies 2-6 Hz.

ACKNOWLEDGEMENT

The authors would like to thank Dr. Ryan Phillips and C-CORE staff for their support during the centrifuge testing phase of this research. Their help is gratefully acknowledged.

REFERENCES

Aviles, J., and Perez-Rocha L.E. Site effects and soil-structure interaction in the Valley of Mexico. J. of Soil Dynamic & Earthquake Engineering, 1998, 17: 29-39.

Crouse, C.B. and Ramirez, J.C. Soil-Structure Interaction and Site Response at the Jensen Filtration Plant during the 1994 Northridge, California. Bulletin of the Seismological Society of America; 2003; v. 93; no. 2; p. 546-556.

Elgamal A, Yang Z, Lai T, Kutter B, Wilson DW. Dynamic response of saturated dense sand in laminated centrifuge container. Journal of Geotechnical and Geoenvironmental Engineering, ASCE 2005; 131(5):598-609.

Itasca. *FLAC3D*: Fast Lagrangian Analysis of Continua in 3 Dimensions, Version 3.0, User Manual, 2005, Itasca Consulting Group, Inc., Minneapolis.

Rayhani MT, and El Naggar MH. Centrifuge modeling of layered soft clay. Bulletin of Earthquake Engineering, Accepted Aug. 2007(a).

Rayhani MT, and El Naggar MH. Characterization of glyben for seismic application. Geotechnical Testing Journal, ASTM, Vol. 31, No. 1, 2007(b).

Seid-Karbasi M. Input motion time histories for dynamic testing in the C-CORE centrifuge facilities. Report No. 2003/01, 2003; University of British Columbia.

Stewart, J.P., Kim, S., Bielak, J., Dobry, R. and Power, M.S. Revisions to soil-structure interaction procedures in NEHRP Design Provisions. Earthquake Spectra, 2003, Vol.19, No.3, pp 677-696.

This page intentionally left blank

Response Sensitivity Analysis of Soil-Structure Interaction (SSI) Systems

Quan Gu[1], M. ASCE and Joel P. Conte[2], M. ASCE, P.E.

[1]Ph.D. Student, Structural Engineering Department, University of California at San Diego, 9500 Gilman Drive, La Jolla, CA 92093-0085; qgu@ucsd.edu

[2]Professor, Structural Engineering Department, University of California at San Diego, 9500 Gilman Drive, La Jolla, CA 92093-0085; jpconte@ucsd.edu

ABSTRACT: This paper presents a framework for finite element response sensitivity analysis of structural and/or geotechnical systems based on the direct differentiation method (DDM). A frame-soil system subjected to both quasi-static pushover and dynamic loads is used as application example. Focus is on the sensitivity of the FE predicted response of this SSI system with respect to the material parameters used to represent the elastoplastic behavior of the various soil and structural materials. The sensitivity analysis results provide the relative importance of the various material parameters for selected global and local response parameters of the SSI system.

INTRODUCTION

Finite element response sensitivities represent an essential ingredient for gradient-based optimization methods needed in various subfields of structural and geotechnical engineering such as structural reliability analysis, structural/geotechnical system identification, and FE model updating (e.g., Ditlevsen and Madsen 1996, Kleiber 1997). In addition, FE response sensitivities are invaluable for gaining insight into the effect and relative importance of system and loading parameters in regards to structural response behavior.

Several methods are available for response sensitivity computation, such as the Finite Difference Method (FDM), the Adjoint Method (AM), the Perturbation Method (PM), and the Direct Differentiation Method (DDM). These methods are described by Zhang and Der Kiureghian (1993), Kleiber et al. (1992, 1997), Conte et al. (2001, 2003, 2004), and Gu and Conte (2003). The FDM is the simplest method for response sensitivity computation, but is computationally expensive and can be negatively affected by numerical noise (i.e., truncation and round-off errors). The AM is extremely efficient for linear and non-linear elastic systems, but is not a competitive method for path-dependent problems. The PM is computationally efficient, but generally not very accurate. The DDM, on the other hand, is very general, accurate and efficient and is applicable to any material constitutive model (both path-independent and path-dependent). The computation of FE response sensitivities to system and loading

parameters based on the DDM requires extension of the FE algorithms for response-only computation (Conte et al. 2003). This paper focuses on finite element response sensitivity analysis of SSI systems based on the DDM.

EXTENTION OF FE RESPONSE SENSITIVITY ANALYSIS FRAMEWORK TO SSI SYSTEMS

In the context of nonlinear FE analysis, the consistent FE response sensitivities based on DDM are computed at each time step, after convergence is achieved for the response computation. This requires differentiation of the FE algorithm for the response computation with respect to each sensitivity parameter θ. Consequently, the response sensitivity computation algorithm involves the various hierarchical layers of FE response analysis, namely: (1) structure level, (2) element level, (3) Gauss point level (or section level), and (4) material level. Details on the derivation of the DDM-based sensitivity equations for classical displacement-based, force-based and mixed finite elements can be found in a number of references (Zhang and Der Kiureghian 1993, Kleiber et al. 1997, Conte et al. 2001, 2003, Gu and Conte 2003).

General Response Sensitivity Analysis Based on DDM

After spatial discretization using the FEM, the equations of motion of a materially-nonlinear-only model of a structural-geotechnical system take the following form:

$$\boldsymbol{M}(\theta)\ddot{\boldsymbol{u}}(t,\theta) + \boldsymbol{C}(\theta)\dot{\boldsymbol{u}}(t,\theta) + \boldsymbol{R}(\boldsymbol{u}(t,\theta),\theta) = \boldsymbol{F}(t,\theta) \tag{1}$$

where t = time, θ = sensitivity parameter, $\boldsymbol{u}(t)$ = vector of nodal displacements, $\boldsymbol{M}$ = mass matrix, $\boldsymbol{C}$ = damping matrix, $\boldsymbol{R}(\boldsymbol{u}, t)$ = history dependent internal (inelastic) resisting force vector, $\boldsymbol{F}(t)$ = applied dynamic load vector, which in the case of earthquake excitation takes the form $\boldsymbol{F}(t,\theta) = -\boldsymbol{M}(\theta)\boldsymbol{L}\ddot{u}_g(t,\theta)$ where $\boldsymbol{L}$ = influence coefficient vector and $\ddot{u}_g(t,\theta)$ = ground acceleration time history. The potential dependence on θ of each term of the equation of motion is shown explicitly in Eq. (1).

The equation of motion in Eq. (1) is integrated numerically in time using the Newmark-β method of structural dynamics. The dynamic residual $\boldsymbol{\Psi}(\mathbf{u}_{n+1})$ expressed at discrete time $t = t_{n+1} = (n+1)\,\Delta t$ (where Δt denotes the constant integration time step) is given by

$$\boldsymbol{\Psi}(\mathbf{u}_{n+1}) = \tilde{\boldsymbol{F}}_{n+1} - \left[\frac{1}{\beta(\Delta t)^2}\boldsymbol{M}\boldsymbol{u}_{n+1} + \frac{\alpha}{\beta(\Delta t)}\boldsymbol{C}\boldsymbol{u}_{n+1} + \boldsymbol{R}(\boldsymbol{u}_{n+1})\right] = \mathbf{0} \tag{2}$$

where
$$\tilde{\boldsymbol{F}}_{n+1} = \boldsymbol{F}_{n+1} + \boldsymbol{M}\left[\frac{1}{\beta(\Delta t)^2}\boldsymbol{u}_n + \frac{1}{\beta(\Delta t)}\dot{\boldsymbol{u}}_n - \left(1-\frac{1}{2\beta}\right)\ddot{\boldsymbol{u}}_n\right] + \boldsymbol{C}\left[\frac{\alpha}{\beta(\Delta t)}\boldsymbol{u}_n - \left(1-\frac{\alpha}{\beta}\right)\dot{\boldsymbol{u}}_n - (\Delta t)\left(1-\frac{\alpha}{2\beta}\right)\ddot{\boldsymbol{u}}_n\right]$$

Differentiating Eq. (2) with respect to θ, recognizing that $\boldsymbol{\sigma} = \boldsymbol{\sigma}(\boldsymbol{\epsilon}(t, \theta), \theta)$,

$$\left[\frac{1}{\beta(\Delta t)^2}\boldsymbol{M} + \frac{\alpha}{\beta(\Delta t)}\boldsymbol{C} + (\boldsymbol{K}_T^{stat})_{n+1}\right]\frac{\partial \boldsymbol{u}_{n+1}}{\partial \theta} = -\left(\frac{1}{\beta(\Delta t)^2}\frac{\partial \boldsymbol{M}}{\partial \theta} + \frac{\alpha}{\beta(\Delta t)}\frac{\partial \boldsymbol{C}}{\partial \theta}\right)\boldsymbol{u}_{n+1} - \frac{\partial \boldsymbol{R}(\boldsymbol{u}_{n+1}(\theta), \theta)}{\partial \theta}\bigg|_{\boldsymbol{u}_{n+1}} + \frac{\partial \tilde{\boldsymbol{F}}_{n+1}}{\partial \theta} \tag{3}$$

where $$\frac{\partial \tilde{\boldsymbol{F}}_{n+1}}{\partial \theta} = \frac{\partial \boldsymbol{F}_{n+1}}{\partial \theta} + \frac{\partial \boldsymbol{M}}{\partial \theta}\left(\frac{1}{\beta(\Delta t)^2}\boldsymbol{u}_n + \frac{1}{\beta(\Delta t)}\dot{\boldsymbol{u}}_n - \left(1 - \frac{1}{2\beta}\right)\ddot{\boldsymbol{u}}_n\right) +$$

$$\boldsymbol{M}\left[\frac{1}{\beta(\Delta t)^2}\frac{\partial \boldsymbol{u}_n}{\partial \theta} + \frac{1}{\beta(\Delta t)}\frac{\partial \dot{\boldsymbol{u}}_n}{\partial \theta} - \left(1 - \frac{1}{2\beta}\right)\frac{\partial \ddot{\boldsymbol{u}}_n}{\partial \theta}\right] +$$

$$\frac{\partial \boldsymbol{C}}{\partial \theta}\left[\frac{\alpha}{\beta(\Delta t)}\boldsymbol{u}_n - \left(1 - \frac{\alpha}{\beta}\right)\dot{\boldsymbol{u}}_n - (\Delta t)\left(1 - \frac{\alpha}{2\beta}\right)\ddot{\boldsymbol{u}}_n\right] +$$

$$\boldsymbol{C}\left[\frac{\alpha}{\beta(\Delta t)}\frac{\partial \boldsymbol{u}_n}{\partial \theta} - \left(1 - \frac{\alpha}{\beta}\right)\frac{\partial \dot{\boldsymbol{u}}_n}{\partial \theta} - (\Delta t)\left(1 - \frac{\alpha}{2\beta}\right)\frac{\partial \ddot{\boldsymbol{u}}_n}{\partial \theta}\right]$$

In Eq. (3), the term $[\partial \boldsymbol{R}(\boldsymbol{u}_{n+1}(\theta), \theta)/\partial\theta]\big|_{\boldsymbol{u}_{n+1}}$ represents the partial derivative of the internal resisting force vector $\boldsymbol{R}(\boldsymbol{u}_{n+1})$ with respect to sensitivity parameter θ under the condition that the displacement vector $\boldsymbol{u}_{n+1}$ remains fixed. This conditional derivative term is expressed as an assembly of contributions from all elements, and thus from all integration/material points.

In Eq. (3), the term $\boldsymbol{K}_T^{dyn} = 1/(\beta(\Delta t)^2)\boldsymbol{M} + \alpha/\beta(\Delta t)\boldsymbol{C} + (\boldsymbol{K}_T^{stat})_{n+1}$ denotes the tangent dynamic stiffness matrix, in which $(\boldsymbol{K}_T^{stat})_{n+1}^{i}$ denotes the *consistent tangent stiffness matrix* defined by $(\boldsymbol{K}_T^{stat})_{n+1} = \partial \boldsymbol{R}_{n+1}/\partial \boldsymbol{u}_{n+1}$. The attribute 'consistent' emphasizes that the tangent operator is obtained through consistent linearization of the the constitutive law integration scheme, which guarantees the quadratic rate of asymptotic convergence of iterative solution strategies based on Newton's method (Simo and Taylor 1985).

Response Sensitivity Algorithm for Multi-Yield Surface J_2 Plasticity Model

The multi-yield surface J_2 plasticity model was first developed by Iwan (1967) and Mroz (1967), then further developed and applied to soil mechanics by Prevost (1977, 1978), and recently implemented in OpenSees by Elgamal et al. (2003). OpenSees is an open source software framework for advanced modeling and analysis of structural and geotechnical systems (Mazzoni and McKenna 2006). In contrast to the classical J_2 plasticity model with a single yield surface, the multi-yield surface J_2 plasticity model

employs the concept of a field of plastic moduli to achieve a more realistic representation of the material plastic behavior under cyclic loading conditions. This field is defined by a collection of nested yield surfaces each of constant size (i.e., no isotropic hardening) in the stress space, which define the regions of constant plastic shear moduli. At each time step, it is not possible to know a priori which and how many yield surfaces will be reached until global equilibrium is achieved at the end of the step. Hence, the expressions for the consistent tangent moduli and the response sensitivities at the current stress point (converged time step) depends on those yield surfaces that have contributed to the change of stress state from the last converged time step.

Yield Surfaces. Each yield surface of this multi-yield-surface J_2 plasticity model is defined in the deviatoric stress space as

$$f = \left\{ \frac{3}{2}((\boldsymbol{\tau} - \boldsymbol{\alpha}):(\boldsymbol{\tau} - \boldsymbol{\alpha})) \right\}^{\frac{1}{2}} - K = 0 \tag{4}$$

where $\boldsymbol{\tau}$ denotes the deviatoric stress tensor, and $\boldsymbol{\alpha}$ denotes the back-stress tensor, which corresponds to the center of the yield surface $\{f = 0\}$ in the deviatoric stress space (Fig. 1). Parameter K represents the size of the yield surface which defines the region of constant plastic shear moduli. The operator ":" denotes the dyadic tensor product.

In geotechnical engineering, the nonlinear shear behavior of soil materials is characterized by a shear stress-strain backbone curve as shown in Fig. 1. The experimentally determined backbone curve can be approximated by the hyperbolic formula of Kondner (1963) as

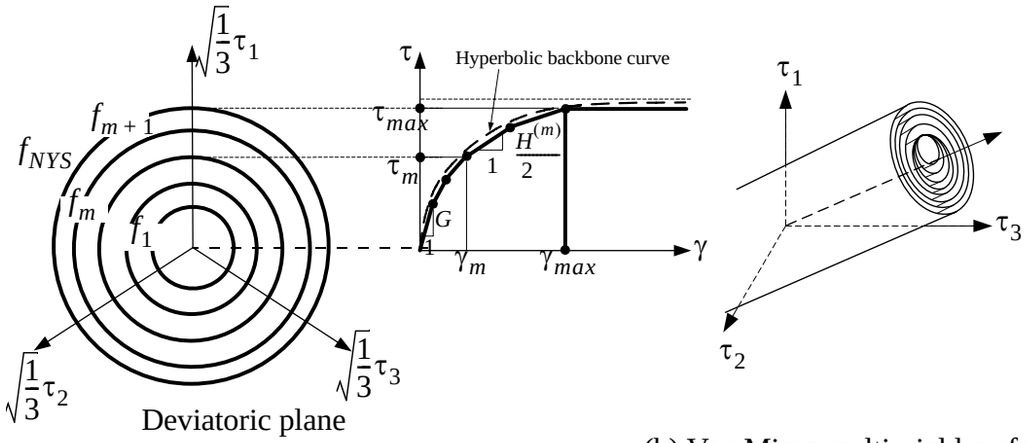
$$\tau = \frac{G\,\gamma}{1 + \gamma / \gamma_r} \tag{5}$$

where τ and γ denote the octahedral shear stress and shear strain, respectively, G is the low-strain shear modulus, and parameter γ_r is a reference shear strain.

Within the framework of multi-yield surface plasticity, the hyperbolic backbone curve in Eq. (5) is replaced by a piecewise linear approximation as shown in Fig. 1. Each line segment represents the domain of a yield surface $\{f_i = 0\}$ of size K_i characterized by an elasto-plastic shear modulus $H^{(i)}$ for i = 1, 2, ..., NYS, where NYS denotes the total number of yield surfaces (Prevost 1977, 1978).

Flow Rule. An associative flow rule is used to compute the plastic strain increments. In the deviatoric stress space, the plastic strain increment tensor is expressed as

$$d\boldsymbol{\epsilon}^p = \frac{1}{H^{(i)}} \boldsymbol{Q} \cdot \langle L \rangle \quad (\text{i} = 1, 2, ..., \text{NYS}) \tag{6}$$



(a) Octahedral shear stress-strain (b) Von Mises multi-yield surfaces

FIG. 1. Yield surfaces of multi-yield-surface J_2 plasticity model in principal deviatoric stress space.

where the constant plastic shear modulus $H^{(i)}$ associated with each yield surface $\{f_i = 0\}$ is defined as $1/H^{(i)} = 1/H^{(i)} - 1/(2G)$. The second-order unit tensor $\boldsymbol{Q}$ is defined as $\boldsymbol{Q} = (1/Q)\partial f/\partial \boldsymbol{\sigma}$, in which $Q = \{(\partial f/\partial \boldsymbol{\sigma}):(\partial f/\partial \boldsymbol{\sigma})\}^{1/2}$ represents the plastic flow direction normal to the yield surface $\{f = 0\}$ at the current stress point. The plastic loading function L in Eq. (6) is defined as the projection of the stress increment vector $d\boldsymbol{\tau}$ onto the direction normal to the yield surface, i.e., $L = \boldsymbol{Q}:d\boldsymbol{\tau}$. The symbol $\langle\ \rangle$ denotes the MacCauley's brackets defined such that $\langle L\rangle = max(L, 0)$.

Numerically, the deviatoric stress $\boldsymbol{\tau}$ is computed by an elastic predictor, followed by several plastic corrector steps, each corresponding to a single yield surface. This correction process continues until the stress point no longer crosses any yield surface.

After convergence of the deviatoric stress $\boldsymbol{\tau}$, the volumetric stress σ^{vol} is computed as $\sigma^{vol} = B(\boldsymbol{\epsilon}:\boldsymbol{I})$ where B denotes the elastic bulk modulus, $\boldsymbol{\epsilon}$ denotes the total strain tensor, and $\boldsymbol{I}$ represents the second order unit tensor. Then, the total stress is obtained as $\boldsymbol{\sigma} = \boldsymbol{\tau} + \sigma^{vol}\boldsymbol{I}$.

Hardening Law. A pure deviatoric kinematic hardening rule is employed to conveniently generate hysteretic cyclic response. The current active yield surface translates in the stress space along a direction $\boldsymbol{\mu}$ until it touches the current stress point $\boldsymbol{\tau}$. This translation is generally governed by the consideration that no overlapping is allowed between yield surfaces. The translation direction $\boldsymbol{\mu}$ is given by (Elgamal 2003)

$$\boldsymbol{\mu} = [\boldsymbol{\tau}_T - \boldsymbol{\alpha}^{(m)}] - \frac{K^{(m)}}{K^{(m+1)}}[\boldsymbol{\tau}_T - \boldsymbol{\alpha}^{(m+1)}] \tag{7}$$

where $\boldsymbol{\tau}_T$ is the deviatoric stress tensor defining the position of the intersection of the yield surface $f_{m+1} = 0$ with the line determined by the center $\boldsymbol{\alpha}^{(m)}$ of the inner surface and the current stress point $\boldsymbol{\tau}$. After the active yield surface $f_m = 0$ is updated, all the inner yield surfaces, f_0, f_1, ..., f_{m-1}, need to be updated such that they are all tangent to each other and to the active surface $f_m = 0$ at the current stress point $\boldsymbol{\tau}$.

Material Consistent Tangent Moduli and Response Sensitivity. Material consistent tangent moduli are obtained by differentiating the discretized constitutive equation $\Delta\boldsymbol{\sigma} = \Delta\boldsymbol{\sigma}(\Delta\boldsymbol{\epsilon})$ with respect to the finite strain increment $\Delta\boldsymbol{\epsilon}$. In the multi-yield surface J_2 plasticity model, these consistent tangent moduli are obtained through differentiating the stress increment with respect to the total strain increment $\Delta\boldsymbol{\epsilon}$ by following the stress computation process. The stress is computed by a predictor multi-corrector scheme and the computation of the consistent tangent moduli follows the same scheme accumulating the contributions from all yield surfaces that have been activated from the last converged time step up to the current stress state.

For material sensitivity parameters, the term $[\partial \boldsymbol{R}(\boldsymbol{u}_{n+1}(\theta), \theta)/\partial\theta]\big|_{\boldsymbol{u}_{n+1}}$ in Eq. (3) simplifies to

$$\left.\frac{\partial \boldsymbol{R}(\boldsymbol{u}_{n+1}(\theta), \theta)}{\partial\theta}\right|_{\boldsymbol{u}_{n+1}} = \left[\sum_{n=1}^{Nel} \int_{\Omega_e} \boldsymbol{B}^T(\boldsymbol{x}) \cdot \left.\frac{\partial\boldsymbol{\sigma}(\boldsymbol{x})}{\partial\theta}\right|_{\boldsymbol{\epsilon}_{n+1}} \cdot d\Omega_e\right] \tag{8}$$

where $\boldsymbol{B}$ is the strain-displacement transformation matrix. The conditional stress sensitivity $[\partial\boldsymbol{\sigma}(\boldsymbol{x})/\partial\theta]\big|_{\boldsymbol{\epsilon}_{n+1}}$ is computed by following the same predictor multi-corrector stress computation scheme as mentioned above.

APPLICATION EXAMPLE

This example consists of the two-dimensional Soil-Structure Interaction (SSI) system described in Fig. 2. The frame component of this SSI system is modeled using displacement-based, fiber-section Euler-Bernoulli frame elements with distributed plasticity and four Gauss integration points each. Section stress resultants and section tangent stiffnesses at the integration points along each frame element are computed by discretizing the frame cross-section into layers (or fibers). Foundation footings and the layered soil medium are modeled using isoparametric four-node quadrilateral finite elements with bilinear displacement interpolation. The constitutive behavior of the steel reinforcement is modeled via the one-dimensional J_2 plasticity model with both linear kinematic and isotropic hardening. The concrete is modeled through the Kent-Scott-Park model with zero tension stiffening as described by Scott et al. (1982). Different material parameters are used for the confined (core) and unconfined (cover) concrete in the beams and the columns. The foundation footings are assumed linear

elastic and the soil is modeled using the multi-yield surface J_2 plasticity model (specialized for plane strain condition) with multiple sets of material parameters.

The material parameters for the concrete core are: compressive strength f_c = 34.5 MPa, crushing strength f_{cu} = 20.7 MPa, strain at maximum (compressive) strength ε_c = 0.004, strain at crushing strength ε_{cu} = 0.014. The concrete cover parameters are: f_c = 27.6 MPa, f_{cu} = 0, ε_c = 0.002, ε_{cu} = 0.008. The steel material properties are: Young's modulus E = 200GPa, yield stress σ_y = 248 MPa, kinematic hardening modulus H_{kin} = 1.61 GPa, isotropic hardening modulus H_{iso}= 0. For the different soil layers (1-4), the low-strain shear moduli are G_1 = 54.45 MPa, G_2 = 33.8 MPa, G_3 = 61.25 MPa, and G_4 = 96.8 MPa, respectively; the maximum shear strengths are $\tau_{max,1}$ = 33 kPa, $\tau_{max,2}$ = 26 kPa, $\tau_{max,3}$ = 35 kPa, and $\tau_{max,4}$ = 44 kPa; and the bulk moduli are K_1 = 160 MPa, K_2 = 100 MPa, K_3 = 180 MPa, and K_4 = 290 MPa. The foundation concrete blocks are modeled as linear elastic with Young's modulus $E_{foundation}$ = 2.0e7 kPa.

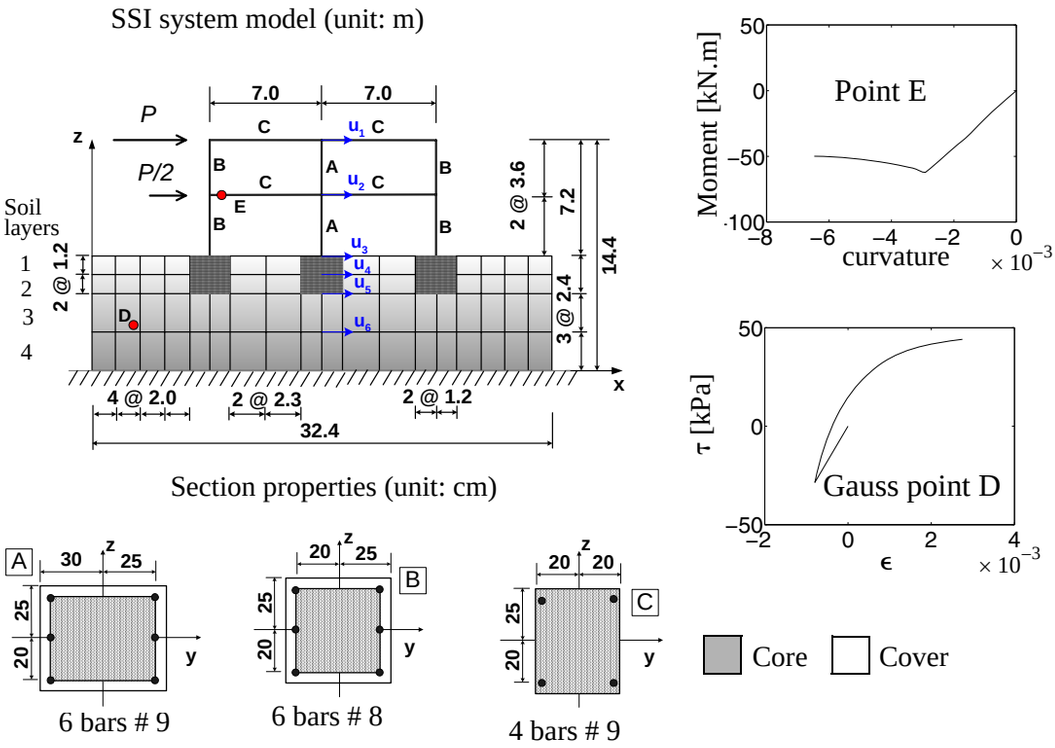


FIG. 2. 2-D model of SSI system.

Quasi-static pushover: After static application of the gravity loads, the frame structure is subjected to a quasi-static pushover analysis, in which an upper triangular distribution of horizontal forces is applied at the floor levels (see Fig. 2). The total applied pushover load (equal to the base shear), P_{tot} = 1.5P, is considered deterministic and is assumed to increase linearly during the analysis from 0 kN to 750 kN (= P_{max}). The moment-curvature response at section E of a second floor beam and the shear stress-

strain response at Gauss point D in the third soil layer are shown in Fig. 2. From these results, it is clear that the system undergoes significant nonlinear material behavior during the pushover. As an illustration of the response sensitivity results, Fig. 3(a) shows the sensitivity of DOF u_1 (see Fig. 2) to the yield strength of steel σ_y. The response sensitivity obtained using DDM (solid line) is verified using FFD analysis (dashed lines). It is observed that the FFD results approach asymptotically the DDM results for decreasing sensitivity parameter perturbation $\Delta\theta/\theta$, thus validating the DDM results. The discontinuities in the response sensivity curve are due to material state transitions from elastic to plastic at various Gauss points. In Fig. 3(b), the response sensitivity results for the first interstory drift $u_{drift} = u_2 - u_3$ are normalized by the nominal values of the sensitivity parameters. These normalized sensitivity results provide a measure of relative importance of the sensitivity parameters for the response quantity of interest. The normalized sensitivity results for f_{cu} of the cover concrete and H_{iso} of steel are not shown in Fig. 3(b), since these two parameters have a zero nominal value.

It is observed that the relative importance of the material parameters (except for f_c and H_{iso}) change with the level of the pushover load. The importance rankings of the material parameters for the first interstory drift at the three load levels $P = 10\%P_{max}$, $50\%P_{max}$, $100\%P_{max}$ are given in Table 1.

Table 1: Importance rankings of the material parameters for the first interstory drift at different load levels

Load level	Steel			Concrete Core Cover				Soil												Foundation
	E	σ_y	H_{kin}	f_c	ε_c	f_c	ε_c	G_1	G_2	G_3	G_4	$\tau_{max,1}$	$\tau_{max,2}$	$\tau_{max,3}$	$\tau_{max,4}$	K_1	K_2	K_3	K_4	E_{found}
10%	1	20	19	8	4	2	3	12	13	9	16	7	11	6	14	15	18	5	10	17
50%	1	7	20	11	12	2	3	14	15	13	16	6	10	4	8	17	19	5	9	18
100%	3	1	14	9	11	4	12	19	18	16	17	8	10	2	7	13	15	5	6	20

It is observed that from load level $P = 10\%P_{max}$ to $P = 100\%P_{max}$: (a) the importance ranking (IR) of the steel σ_y increases dramatically from last to first, while that of steel H_{kin} increases moderately from 19-th to 14-th. (b) The IRs of steel E and soil G_1 to G_4 decrease. (c) The IRs of soil K_1 to K_4, $\tau_{max,3}$ and $\tau_{max,4}$ increase, while those of $\tau_{max,1}$ and $\tau_{max,2}$ do no change. (d) The IRs of concrete ε_c and f_c decrease for both core and cover concrete, while the IR of foundation $E_{foundation}$ remains low. Thus, as the pushover load increases, stiffness related material parameters (such as steel E, soil G_1 to G_4, as well as concrete ε_c and f_c which are closely related to the concrete Young's modulus) become relatively less important, while

strength or post-yield related material parameters (such as steel σ_y and H_{kin}, soil $\tau_{max,3}$ and $\tau_{max,4}$) become relatively more important. (e) The maximum shear strength of the third soil layer $\tau_{max,3}$ becomes the second most important material parameter in regards to the first interstory drift as the load level reaches $P = 100\%P_{max}$.

Earthquake base excitation: After static application of the gravity loads, the structure is subjected to a base excitation taken as the N-S component of the 1940 El Centro earthquake recorded at the SMIP station, scaled by a factor 3.0. The peak ground acceleration (PGA) is 9.39 m/s^2. During this earthquake excitation, the SSI system considered here undergoes significant nonlinear material behavior. As an illustration of the response sensitivity results, Fig. 4(a) shows the sensitivity of DOF u_1 (see Fig. 2) to Young's modulus of steel *E*. This figure also shows that the response sensitivities obtained using FFD analysis (dashed lines) approach asymptotically the DDM result (solid line) for decreasing parameter perturbation $\Delta\theta/\theta$. The normalized response sensitivity results for the first interstory drift u_{drift} and the shear stress τ at Gauss point D (τ_D, see Fig. 4(b)) are used to determine the IRs of the material parameters given in Table 2.

Table 2: Importance rankings of the material parameters for the first interstory drift and the shear stress τ_D

Resp. par.	Steel			Concrete Core Cover				Soil												Foun-dation
	E	σ_y	H_{kin}	f_c	ε_c	f_c	ε_c	G_1	G_2	G_3	G_4	$\tau_{max,1}$	$\tau_{max,2}$	$\tau_{max,3}$	$\tau_{max,4}$	K_1	K_2	K_3	K_4	E_{found}
u_{drift}	4	1	19	13	10	6	14	15	16	9	8	5	7	2	3	17	18	11	12	20
τ_D	4	3	18	13	15	8	12	20	17	10	11	7	9	2	1	16	14	6	5	19

From the results in Table 2, it is observed that the five material parameters to which u_{drift} is most sensitive are (in order of decreasing IR): steel σ_y, soil $\tau_{max,3}$ and $\tau_{max,4}$, steel E, and soil $\tau_{max,1}$. These parameters are mainly steel and soil strength related parameters, except for E. The five parameters to which u_{drift} is least sensitive are (in the order of increasing IR): $E_{foundation}$, H_{kin}, K_2, K_1, and G_2, all five stiffness related parameters. It is interesting to note that parameters σ_y, $\tau_{max,3}$, and E are most important parameters for both cases of earthquake excitation and quasi-static pushover (at full load). For the local response parameter τ_D (in soil layer 3), the six most important parameters are (in order of decreasing IR): $\tau_{max,4}$, $\tau_{max,3}$, σ_y, E, K_4, and K_3. Four of these parameters are stiffness and strength related parameters of the third and fourth soil layers.

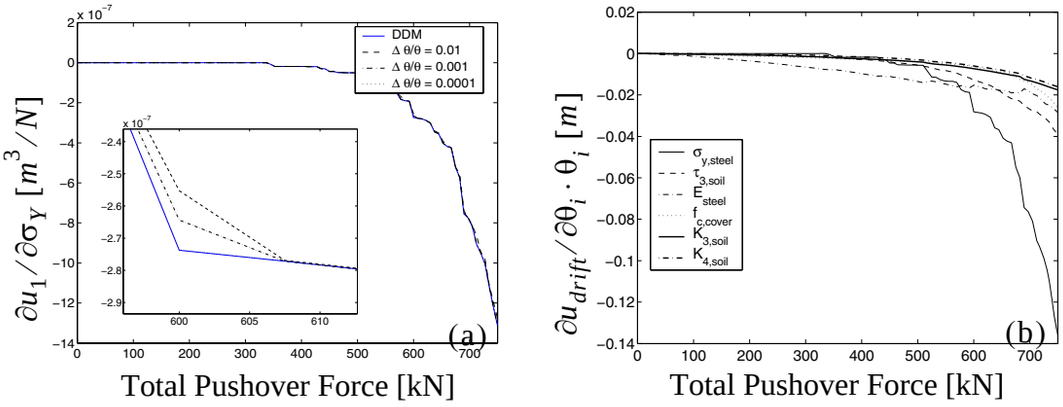


FIG. 3. (a) Sensitivity of response u_1 with respect to steel σ_Y, and (b) relative importance of material parameters on first interstory drift (full pushover load).

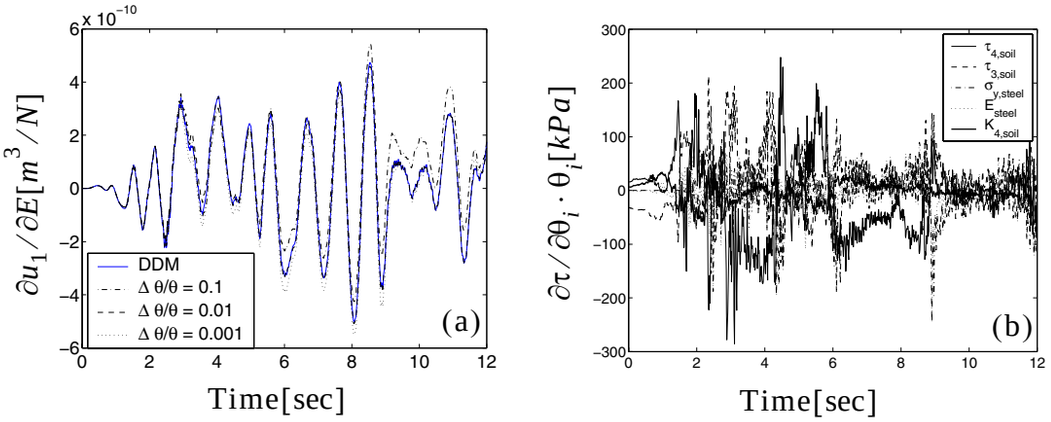


FIG. 4. (a) Sensitivity of response u_1 with respect to steel Young's modulus E, and (b) relative importance of material parameters on shear stress at Gauss point D.

CONCLUSIONS

This paper presents a framework for FE response sensitivity analysis of structural and/or geotechnical systems based on the direct differentiation method (DDM). A 2D SSI example is provided to illustrate the methodology and show how it can be used to evaluate the relative importance of material parameters on the response quantities of interest.

ACKNOWLEDGMENTS

The research presented here was supported by the Pacific Earthquake Engineering Research (PEER) Center through the Earthquake Engineering Research Center Program of the National Science Foundation under Award No. EEC-9701568. This support is gratefully acknowledged. Any opinions, findings, conclusions, or

recommendations expressed in this publication are those of the authors and do not necessarily reflect the views of the sponsor.

REFERENCES

Conte, J. P. (2001). "Finite element response sensitivity analysis in earthquake engineering." *Earthquake Engineering Frontiers in the New Millennium*, Spencer & Hu, Swets & Zeitlinger, 395-401.

Conte, J.P., Vijalapura, P.K. and Meghella, M. (2003). "Consistent finite-element response sensitivity analysis." *Journal of Engineering Mechanics*, (ASCE), 129(12): 1380-1393.

Conte, J.P., Barbato, M., and Spacone, E. (2004). "Finite element response sensitivity analysis using force-based frame models." *International Journal for Numerical Methods in Engineering*, 59 (13): 1781-1820.

Ditlevsen, O., and Madsen, H.O. (1996). Structural Reliability Methods, Wiley, New York.

Elgamal A,Yang Z, Parra E, Ragheb A. (2003). "Modeling of cyclic mobility in saturated cohesionless soils". *Internatinal Journal of Plasticity*, 19:883-905.

Gu, Q., and Conte, J.P. (2003). "Convergence studies in non-linear finite element response sensitivity analysis." *Proceedings of ICASP9*, Berkeley, USA.

Iwan W.D. (1967). "On a class of models for the yielding behavior of continuous and composite systems." *J. Appl. Mech. Trans*, ASME, 34(E3): 612-617.

Mroz A. (1967). "On the description of anisotropic workhardening." *J. Mechanics and Physics of Solids*, 15:163-175.

Kondner R.L. (1963). "Hyperbolic stress-strain response: cohesive soils." *Journal of Soil Mechanics and Foundations Division*, ASCE, 89(SM1):115-143.

Kleiber, M., Antunez, H., Hien, T.D., and Kowalczyk, P. (1997). Parameter Sensitivity in Nonlinear Mechanics: Theory and Finite Element Computations, Wiley, New York.

Kleiber, M., and Hien, T.D. (1992). The Stochastic Finite Element Method. Basic Perturbation Technique and Computer Implementation, Wiley, New York.

Prevost J.H. (1977). "Mathematical modelling of monotonic and cyclic undrained clay behaviour." *International Journal for Numerical and Analytical Methods in Geomechanics*, 1(2):195-216.

Prevost J.H. (1978a). "Plasticity theory for soil stress-strain behavior." *Journal of the Engineering Mechanics Division* ASCE, 104(EM5):1177-1194.

Scott, B.D., Park, P., and Priestley, M.J.N. (1982). Stress-strain behavior of concrete confined by overlapping hoops at low and high-strain rates, J*ournal of the American Concrete Institute*, 79(1):13-27.

Simo J.C., Taylor R.L. (1985). "Consistent tangent operators for rate-independent elastoplasticity." *Computer Methods in Applied Mechanics and Engineering*, 48:101-118.

Zhang, Y., and Der Kiureghian, A. (1993). "Dynamic response sensitivity of inelastic structures." *Computer Methods in Applied Mechanics and Engineering*, 108(1-2):23-36.

This page intentionally left blank

Seasonally Frozen Soil Effects on the Nonlinear Behavior of a Parking Garage

Feng Xiong[1], M. ASCE, Zhaohui (Joey) Yang[2], M. ASCE, Feifei Bai[3], and He Liu[4], M. ASCE

[1]Asst. Professor, University of Alaska Anchorage, 3211 Providence Dr, Anchorage, AK 99508; affx@uaa.alaska.edu; Sichuan University, Chengdu, China
[2]Asst. Professor, University of Alaska Anchorage, 3211 Providence Dr, Anchorage, AK, 99508; afzy@uaa.alaska.edu
[3]Feifei Bai, Staff Engineer, PN&D, Inc, 1506 W. 36th Ave, Anchorage, AK 99503; feifei@pnd-anc.com
[4]He Liu, Professor, University of Alaska Anchorage, 3211 Providence Dr, Anchorage, AK, 99508; afhl@uaa.alaska.edu

ABSTRACT: This paper presents the results of experimental and analytical studies of the seasonally frozen soil effects on a three-story reinforced-concrete parking garage. With a 16-channel portable accelerograph, vibration test data were collected during the winter of 2006-2007. The structural dynamic properties were identified from the recorded data. Meanwhile, a three-dimensional Finite Element (FE) model including both superstructure and soil has been developed in order to verify the frozen soil effects. The FE modeling results indicate that the fundamental frequency of the soil-structure system increases 50% as the frost penetrates from 0 to 1.4 m. It is found by push-over analysis that the system stiffness increases 114% due to soil freezing. Most importantly, the shear distribution between columns and shear walls is significantly changed due to soil freezing. When soil thaws, the shear force taken by columns increases 10~15%, and that taken by shear walls decreases by 10~15%. It also shows that more columns experience yielding at thawing condition. This indicates that crucial zones in the frame-shear wall structures might move from shear walls to columns.

INTRODUCTION

Even though the Soil-Structure Interaction (SSI) effects have been investigated for more than three decades, there has been very little research conducted on SSI accounting for frozen soils. Most of the research conducted on frozen soils mainly focused on the soil properties (e.g. stiffness, shear strength, creep properties, etc.), rather than its impact on structural nonlinear behavior. However, recent studies, e.g. Alampalli (1998), Cornwell et al. (1999), Sohn et al. (1999), and Peeters and De Roeck (2001), have indicated that the environmental variables such as temperature and seasonal frost can significantly change the structural dynamic properties. Several investigators (Han et al.

1991; Sritharan et al. 2006; 2007) have reported significant impact of seasonally frozen ground on pile foundations. Yang et al. (2007a) conducted a study by using a nonlinear monitoring system installed on a steel-girder bridge in Anchorage, Alaska and the results indicate a significant variation in the bridge fundamental frequency (about 12%) from winter to summer season. This study also concluded that the main reason for this change is the seasonally frozen ground. Another study by Yang et al. (2007b) shows that the fundamental frequency of a 20-story office building changes by 4% between winter and summer conditions due to seasonally frozen ground effects, and numerical simulation results indicate that the fundamental frequency of a reinforced-concrete (RC) building of similar geometry could change by as much as 30%. However, this finding regarding RC buildings has not been verified by any experimental data.

This paper presents the experimental and analytical study results of seasonally frozen soil effects on a three-story unheated RC parking garage located on the University of Alaska Anchorage (UAA) campus. This paper is organized as the follow sections: Structure and Site Description, Field Tests, Identification of Dynamic Properties, Finite Element Modeling, Effects on Dynamic Properties, and Impact on the Nonlinear Behavior**.** Finally, conclusions regarding the effects of seasonally frozen soil on the nonlinear behavior of the structure-soil system and future studies are presented.

STRUCTURE AND SITE DESCRIPTION

The selected structure for this study is an unheated parking garage located on the UAA campus. This three-story RC parking garage was designed based on the 1997 Uniform Building Code and constructed in 2001. It has a square base and floor plan with dimension of 59.7 x 60.3 m. The overall building height is approximately 11 m with an average story height of 3.1 m. Its structural system consists of post-tensioned floors supported by columns and shear walls. Main shear walls are connected into three RC tubes (stairway room) of 254 mm thickness. The dimension of most columns is 450 x 450 mm. No frame beams were used to connect columns except at the perimeter. It is noted that the floor in the center is inclined to allow vehicle access. The foundation system consists of RC spread footings (4.5 x 4.5 m) under each column embedded 1.5 m deep.

Subsurface investigation of the parking garage site shows that poor quality fill and peat layers underlie existing ground surface reaching a depth of 2.5 to 5 m. Beneath them lie poorly graded sands and gravels followed by silty sands and gravels to a depth of 10 m. During the construction, the existing fill layer was excavated and backfilled with structural fill to support the spread footings. The frost action can be expected to penetrate as deep as 1.8 m or more during winter season. Considering the cost, the garage has no insulation for the foundation.

FIELD TESTS

In order to investigate the effects of seasonally frozen soil on the nonlinear behavior of the parking garage-foundation system, particularly to study the gradual changes of structural dynamic properties versus the progress of the seasonal frost, five sets of field tests including ambient and forced-vibration tests had been conducted during the winter of 2006-2007. At each test, a Portable Data Acquisition System (PDAQ) connected with 16 high-dynamic range accelerometers (±2 g, 1.25 V/g sensitivity) was used to record vibration response. The accelerometers were deployed from the second to top level, as shown in Fig. 1, to record horizontal vibrations at a sampling frequency of 200 Hz. No sensors had been installed in the ground level since the input motion has been assumed to be white noise. Two types of excitation were used for each test: ambient and forced vibration. The forced vibration was achieved by the braking forces from vehicles driven clockwise on the top floor. During each test, at least 3 sets of ambient or forced vibration data were collected. The duration of recording was about 360 seconds.

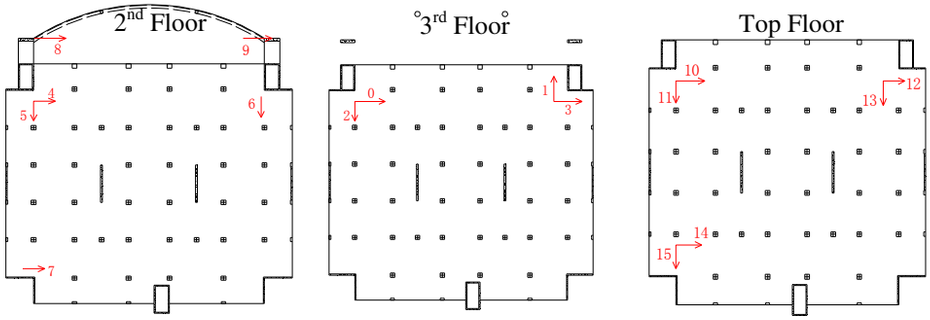


FIG. 1. Sensor distribution for vibration data recording.

Frozen soil depth has to be obtained in order to relate the structural response to the frost penetration. Although a borehole existing near the parking garage is available for measuring frozen ground depth, the surface condition is quite different from that of the garage site. Thus analytical method was used to estimate the depth of frozen ground based on the daily average temperature recorded in a nearby weather station. More specifically, the Modified Berggren Equation (Andersland and Ladanyi, 2004) was applied to determine the frozen depth for each month while the soil temperature profiles measured from the borehole was used as a reference. The estimated frozen depth corresponding to each test date is shown in the second column of Table 1.

IDENTIFICATION OF DYNAMIC PROPERTIES

The vibration response data from the ambient and forced-vibration tests were processed using system identification program ARTeMIS Extractor (Structural Vibration Solution A/S, 2004) to identify the structural dynamic properties. For each set of data, the Enhanced Frequency Domain Decomposition (EFDD) method (Brincker et

al. 2000) implemented in ARTeMIS Extractor has been used and the fundamental frequency (first mode in E-W direction) is listed in Table 1. In some case, it was not able to identify the fundamental frequency due to the weak excitation. It is very interesting to see that the average fundamental frequency increases from 1.16 Hz to 1.74 Hz with frozen depth increasing from 0 to 1.4 m, or 50% change. Although there was about 20^{o}C change in air temperature in the five field tests, it is believed that its contribution to the change of structural dynamic properties is very limited since the reinforced concrete material properties only change slightly in such a small temperate range (Sritharan and Suleiman 2004). Therefore, it is assumed that the change of soil stiffness mainly contributes to the change of fundamental frequency through the soil structure interaction. This assumption will be verified by Finite Element analysis described below.

Table 1. Fundamental Frequency of the Garage Identified from Test Data

Field Test Date		Fundamental Frequency (Hz)						
Date	Frozen Depth (m)	Test #1	Test #2	Test #3	Test #4	Test #5	Test #6	Average
10/22/2006	0	1.15	1.15	1.18	N/A	N/A	N/A	1.16
12/02/2006	0.52	1.39	1.39	1.39	N/A	N/A	N/A	1.39
01/13/2007	0.57	1.39	1.44	1.45	1.37	1.42	1.44	1.42
03/01/2007	1.04	1.76	1.64	1.69	N/A	N/A	N/A	1.69
04/02/2007	1.40	N/A	N/A	1.73	N/A	1.73	1.75	1.74

FINITE ELEMENT MODELING

To verify the test results and analyze the seasonal frozen soil effect on the structural nonlinear behavior, a serial of numerical simulations have been conducted. A three-dimension FE model of the superstructure-soil system was developed by using ANSYS software based on the design plans and geotechnical data. The soils were modeled by solid element, columns by beam element and shear walls by shell element. The nodes at the bottom of the soil model were fully fixed and the boundaries at the sides can move vertically but are fixed in horizontal direction. The rate-independent plasticity theory based Drucker-Prager model, which uses the Drucker-Prager yield criterion with an associated flow rule and no hardening, was used to simulate the elasto-plastic behavior of unfrozen soils. However, the frozen soil layer on the surface was modeled as an elastic material, since it is known to be an extremely stiff material compared with unfrozen soil and the assumption of elastic response is adequate (Stevens, 1973). Meanwhile, the reinforced concrete was modeled as an elasto-plastic material with multilinear kinematic hardening. Saenz curve for plain concrete was employed as the constitutive relation of concrete column and shear wall. The reinforcing effect was considered through equivalent elastic modulus converted by the area ratio of steel to

concrete. Since the floor slab is very stiff in lateral direction, it was treated as an elastic material.

No specific soil properties data other than descriptive information can be found from the geotechnical report. Therefore, it was decided to use the field test results to calibrate the FE model under unfrozen and frozen state, respectively. The soil parameters in unfrozen condition were obtained by adjusting the elastic modulus of the backfill and sandy gravel within a reasonable range until the predicted fundamental frequency matched the identified based on the field tests conducted on Oct. 22, 2006. Similarly, the elastic modulus of frozen soil was obtained based on the field tests conducted on Dec. 2, 2006. The material parameters obtained are summarized in Table 2. These parameters were then used in the subsequent FE analysis. It is seen from this table that the elastic modulus of the frozen backfill layer is 5,600 MPa, which is 40 times that of the same material at unfrozen condition. This is consistent with previous study results obtained by Nakano and Froula (1973) and Stevens (1975).

Table 2. Material Properties used for the Finite Element Analysis

Material Type	Modulus of Elasticity, E (MPa)	Poisson's Ratio, ν	Cohesion (MPa)	Internal Friction Angle (Deg.)	Dilatancy Angle (Deg.)	Mass Density (kg/m^3)
Concrete	28,000	0.2				2,560
Sandy Gravel (Native Soil)	160	0.35	0	40	30	2,300
Sandy Gravel (Backfill, Frozen)	5,600	0.35				2,200
Sandy Gravel (Backfill, Unfrozen)	140	0.35	0	40	30	2,200

EFFECTS ON DYNAMIC PROPERTIES

Modal analysis was conducted using the calibrated FE model. The soil freezing process was modeled by changing the frozen depth and the material properties of soils from unfrozen to frozen state in a layered manner. The results, i.e. the fundamental frequencies for frozen depths corresponding to each field test, have been obtained and plotted in Figure 2. For comparison, the results obtained from field test are also shown. Note that the fundamental frequencies of the structure-soil system for frozen soil depths deeper than the tested cases have also been obtained to study the sensitivity of the system to the frozen depth.

From Figure 2, it is seen that the results obtained from both field testing and numerical analysis agree fairly well. As mentioned above, the first two tests are used as the benchmark to calibrate the FE model. The rest of testing results follows the trend of the numerical simulation results very well. It indicates that the calibrated FE model is

acceptable and could be used in further analysis. Both the field testing and FE analysis results show that the fundamental frequency increases by about 50% when the soils freeze to a depth of 1.4 m. It implies that the frozen soil would influence the structural nonlinear behavior by changing the earthquake energy input. The numerical analysis results also indicate that the sensitivity of fundamental frequency change varies with frozen depths. At the initial presence of frozen soil (0.30 m or 1 foot) in early winter, the frequency increases almost 20%. As the frost penetrates deeper, the effect becomes consistently greater for frozen depths up to abound 1.5 m. However, the frequency versus frozen depth curve flattens and the fundamental frequency becomes less sensitive to the frozen soil at depths beyond 1.5 m. Even if the frozen depth increases to 4.5 m or deeper, the frequency will only increase slightly to 1.95 Hz. This tendency shows that the effects of frozen soils on the dynamic properties of the RC garage structure will be mainly in the shallow soil layers.

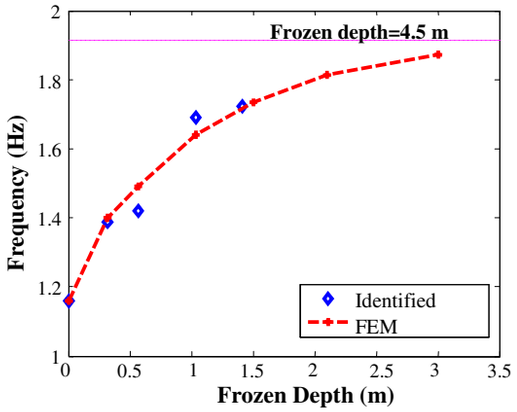


FIG. 2. Fundamental frequency vs. frozen depth.

IMPACT ON THE NONLINEAR BEHAVIOR

Besides the significant effects on the dynamic properties, frozen soils may also have great impact on the nonlinear behavior of structures consisting of shear walls and columns. The general consensus (Comartin et al. 1994) is that some amount of foundation movement or inelastic behavior of the soil materials actually helps the building by dissipating energy. However, a thick frozen crust will allow little foundation movement, therefore unfavorably affect the nonlinear behavior of structures in cold regions. To understand the impact of soil freezing and thawing on structural nonlinear behavior of the parking garage structure, a push-over analysis was conducted using the calibrated model. By applying a successively increasing displacement on the building top in E-W direction, the structure is pushed laterally under the frozen and unfrozen soil condition, respectively. The target displacement was selected to be 25 cm, which is approximately 1/50 of height of the structure and generally regarded as the controlling displacement under the earthquake with 2% exceedance in 50 years.

Fig. 3 shows the relation between lateral force (or base shear) and lateral displacement at the building top under both frozen and unfrozen condition. It is clearly seen from Fig. 3 that the system behaves rather elastically before reaching a lateral displacement of 0.11 m and inelastically beyond that. An obvious difference between the lateral stiffness at frozen and unfrozen condition is also observed. Before reaching the yielding point, the equivalent or secant stiffness is 1.5×10^6 kN/m for frozen soil condition and 0.7×10^6 kN/m for unfrozen soil, or 114% increase in lateral stiffness.

When the structure reaches the target lateral displacement, the required lateral load is 1.96×10^5 kN for frozen condition, and 1.00×10^5 kN for unfrozen condition, or 96% increase. The stiffness change would result in different nonlinear demand that needs to be examined in more detailed analysis.

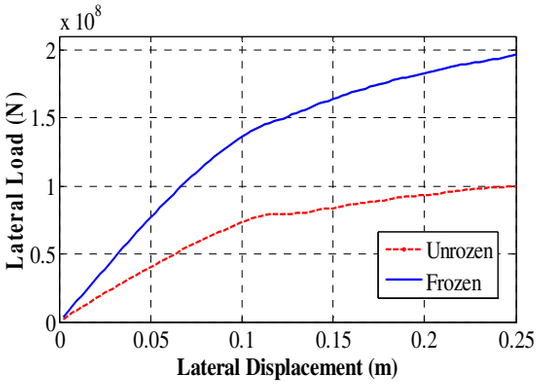


FIG. 3. Lateral load vs. displacement.

The freezing and thawing of soil not only affects the overall stiffness change, but also the shear force distribution between shear walls and columns. Fig. 4 and Fig. 5 show the percentage of shear forces assumed by shear walls and columns, respectively. Under frozen condition, shear walls bear around 70~80% base shear during the push-over analysis process, and columns around 10%. It is noted that some shear force has been assumed by the inclined floor and this portion accounts for about 15% total shear force. Under unfrozen condition, however, the shear walls only assume about 60% total shear force and the columns about 20%. In other words, the portion born by columns increases by 10% from frozen to unfrozen soil condition, and that born by shear walls decreases by about 15%. The reason for this may be that, when soil freezes, it will allow much less rocking in the structure, therefore forcing the shear walls to bear more loads generated by earthquakes. Once soil thaws, rocking could more likely to occur, and the total shear force would redistribute between shear walls and columns. The shear redistribution could also occur during the development of plastic deformation. As shown in Fig. 5, when lateral displacement increases from 0 to 0.25 m, the shear force born by shear walls decreases by 10%, while the column portion remains almost constant.

Further examination of the shear forces of individual columns shows that the shear force redistribution could cause undesirable shear failure in some of the columns. Fig. 6 indicates the yielded columns (marked by circles) at the lateral displacement of 0.25 m

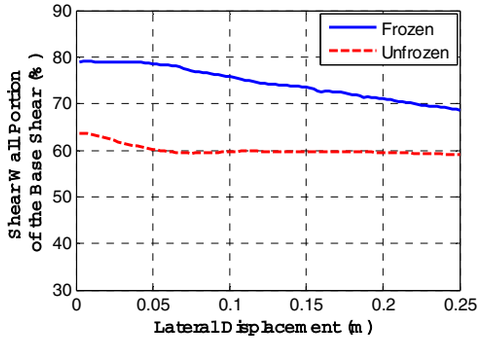


FIG. 4. Shear wall portion of the base shear.

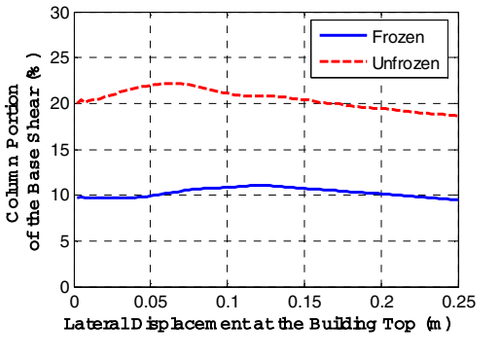


FIG. 5. Column portion of the base shear.

under unfrozen (Fig. 6a) and frozen (Fig. 6b) soil condition. The axial strain corresponding to that of rebar yielding is taken as the yield criterion, at which plastic

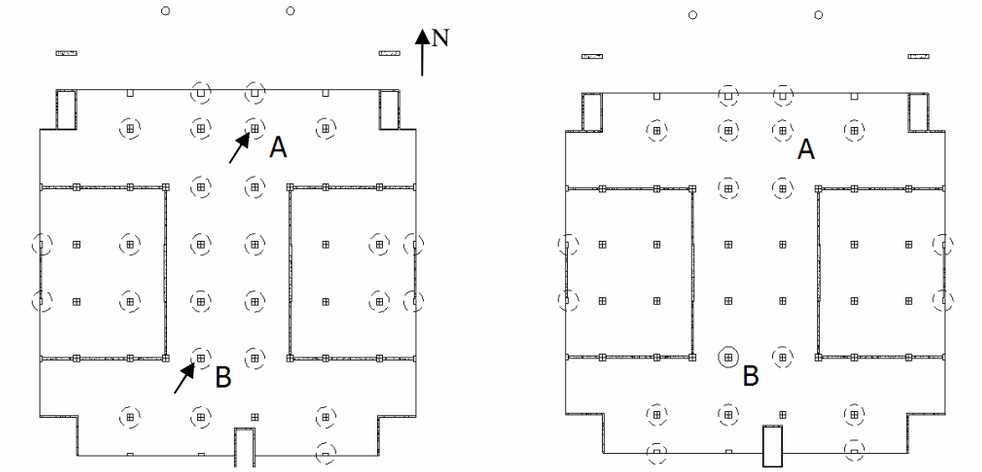


FIG. 6. Yielded columns at unfrozen and frozen soil conditions.

hinge begins to form in column. Fig. 6 indicates that at the same lateral displacement, eight more columns at the central area of the floor plan reach yielding in unfrozen soil condition. In fact, the shear force of individual column at unfrozen soil condition increases significantly than frozen soil condition, although the total base shear for frozen condition is much larger than unfrozen condition. Fig. 7 shows the shear forces of Column A and B (Locations marked in Fig. 6) at different soil conditions. It is seen that

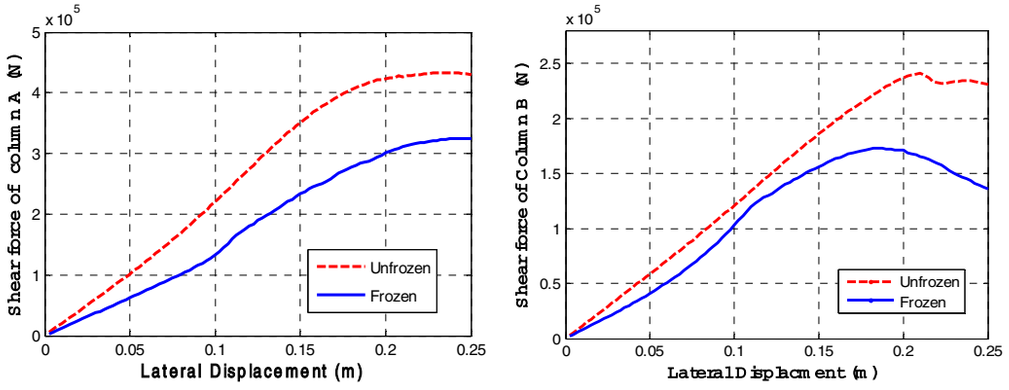


FIG. 7. Shear force on selected columns at unfrozen and frozen soil conditions.

the shear forces of both Column A and B at unfrozen soil condition are larger than frozen condition in the entire push-over analysis process. At the lateral displacement of 0.25 m, the shear at unfrozen condition increases 40% for Column A and 50% for

Column B. This will certainly increase the chance of shear failure for columns at unfrozen condition than frozen condition.

Based on these evidences, it is concluded that the crucial zones in the frame-shear wall structures could move from shear walls to columns at unfrozen soil condition. This is significant since the shear capacity of shear wall receives more attention in current design practice based on the fixed-base assumption; columns generally are designed to resist vertical load. This may be appropriate for designing structures under the frozen soil condition. At unfrozen condition, however, columns would undertake more shear force and become more vulnerable to failure.

CONCLUSION

A three-story unheated parking garage located on the University of Alaska Anchorage campus has been investigated by both experimental and analytical methods to study the effects of seasonally frozen soil on the nonlinear behavior of RC structures. Collected data were processed and analyzed by a system identification method to identify the dynamic properties of the structure. Meanwhile, a three-dimensional FE model of the soil-structure system was developed by using ANSYS software and calibrated with the field test results. A serial of analyses had been conducted based on the FE model to investigate the effects of seasonally frozen soil. The following conclusions can be made:

1. It is found through the field tests that the fundamental frequency of the RC garage soil-structure system increases 50% as the soils freeze from 0 to 1.4 m.
2. The analytical study shows that the fundamental frequency of the soil-structure system can be greatly influenced by the presence of seasonally frozen soils and confirms the results obtained by field test. Analysis also indicates that the dynamic properties of the structure system are only sensitive to the freezing of the shallow soil layers up to a depth of 1.5 to 2 m.
3. The analytical study shows that the stiffness of the soil-structure system increases 114% due to the freezing of soils to a depth of 1.4 m.
4. Seasonally frozen soils would greatly impact the failure modes of RC frame-shear wall structures. For the specific garage structure, the shear force born by columns would increase about 10%, and that by shear walls would decrease 15% from frozen to unfrozen soil condition. More columns experience yielding and greater shear force in unfrozen condition than frozen condition. It indicates that the crucial zone in the frame-shear wall structures could move from shear walls in frozen condition to columns in unfrozen condition.

ACKNOWLEDGEMENT

All the temperature data were retrieved with the help of Dr. Utpal Dutta. Fellow graduate students Mr.Toshifumi Kono and Mr. Rys Miranda provided assistance in instrument installation and tests. Mr. Gang Xu helped with the numerical modeling.

Special thanks go to Dr. Bart Quimby for offering valuable comments. Funding for Feifei Bai and Feng Xiong were provided by Alaska Experimental Program to Stimulate Competitive Research of NSF and the State of Alaska (EPS-0346770).

REFERENCES

Alampalli S. (1998). "Influence of in-service environment on modal parameters." *Proc., IMAC 16,* Santa Barbara, CA, USA, 111-116.

Andersland, O. B., and Ladanyi, B. (2004). "Frozen Ground Engineering." *John Wiley & Sons, Inc.*

Bricker.R, Zhang. L and Anderson, P. (2000). "Output –only Modal Analysis by Frequency Domain Decomposition". *Proceedings of The ISMA 25 Noise and Vibration Engineering,* Leuven, Belgium, Vol. 11: 717-723.

Comartin, C.D., Keaton, J.R., Grant, W.P., Martin, G.R. and Power, M.S. (1994). "Transitions in nonlinear analysis and design procedures for building and their foundation." *Proceedings, 6th U.S.-Japan Workshop on the Improvement of Structural Design and Construction Practices*, ATC-15-5, 325-342

Cornwell, P., Farrar, C., Dowbling, S., and Sohn, H. (1999). "Environmental variability of modal properties." *Experimental Techniques*, Vol. 23 (6): 45–48.

Han, Y.C, Vaziri H.H and Hubble D. (1991). "Dynamic Response of Pile Foundation in Frozen Soils." *Canadian Geotechnical Conference*, pt 1: 40/1-40/7.

Nakano, Y., and Froula, N.H. (1973). "Sound and shock transmission in frozen soils." *In Proceedings of the 2nd International Conference on Permafrost, North American Contribution*, Washington, D.C: 359–369.

Peeters, B., and De Roeck, G. (2001). "One-year monitoring of the z24-bridge: environmental effects versus damage events." *Earthquake Engineering and Structural Dynamics,* Vol. 30: 149–171.

Sohn, H., Dzwonczyk, M., Straser, E., Kiremidjian, A., and Law, K. (1999). "An experimental study of temperature effect on modal parameters of the Alamosa Canyon Bridge." *Earthquake Engineering and Structural Dynamics,* vol. 28: 879–897.

Sritharan S. White J D and Suleiman M.T. (2004), "Bridge Column Foundation-Soil Interaction under Earthquake Loads in Frozen Conditions," *Proceedings of 13th World Conference on Earthquake Engineering,* Vancouver, B.C Canada.

Stevens, H.W. (1975), "The response of frozen soils to vibratory loads." *U.S. Army Cold Regions Research and Engineering Laboratory (CRREL),* Technical Report 265.

Structural Vibration Solutions A/S. ARTeMIS Extractor, ver 3.0 User's Mannual, Aalborg, Denmark. Technical report, 2004. www.svibs.com

Yang, Z., U. Dutta, D. Zhu, E. Marx and N. Biswas (2007a). "Seasonal Frost Effects on Soil-Foundation-Structure Interaction." *ASCE Journal of Cold Regions Engineering*. In press.

Yang, Z., Dutta, U., Xiong, F., Biswas, N. and Benz, H. (2007b). "Seasonal Frost Effects on the Nonlinear Behavior of a Twenty-Story Office Building." *Cold Regions Science and Technology*. In press.

Sliding blocks under Near-Fault Pulses: Closed-Form Solutions

Elia Voyagaki[1], George Mylonakis[2], M. ASCE and Ioannis N. Psycharis[3], M. ASCE

[1] National Technical University, Athens, Greece, evogi@tee.gr
[2] University of Patras, Greece, mylo@upatras.gr
[3] National Technical University, Athens, Greece, ipsych@central.ntua.gr

ABSTRACT: Analytical and numerical solutions are presented for the rigid-plastic response of geo-structures to idealized ground acceleration pulses. These shock-like waveforms are typical of near-fault earthquake motions generated by forward fault-rupture directivity and may inflict large permanent displacements in the absence of substantial residual soil strength. The geo-structures are modeled as rigid blocks resting on inclined frictional planes. Although idealized, these models are widely accepted by geotechnical engineers, for simulating a variety of structures including retaining walls, embankments and slopes.

Four basic simple pulse waveforms are examined: (1) rectangular; (2) sinusoidal; (3) triangular; (4) exponential. An analytical study is presented on the effect of frictional strength and number of excitation cycles on peak displacements.

Results are presented in the form of dimensionless graphs and closed-form expressions that elucidate the salient features of the problem. It is shown that Newmark approaches based on conventional motions may under- or over-estimate peak displacements depending on the circumstances. It is also shown that all three time histories of ground motion (i.e., acceleration, velocity, and displacement) control peak response – contrary to the widespread view that ground velocity alone is of leading importance. Issues related to scaling laws of peak displacement are discussed.

INTRODUCTION

Following pioneering studies by seismologists and earthquake engineers in the 1970's [e.g., Boore & Zoback 1974; Bertero et al, 1978], the destructiveness of near-fault earthquake motions has become a major subject in earthquake engineering research. These motions are generated by fault-rupture directivity, as the rupture propagates towards a site (and slip vector points towards the site), located within approximately ten to twenty kilometers from fault. The resulting ground motions attain the form of high-amplitude, shock-like pulses, polarized in the strike-normal direction, concentrated in the early part of the earthquake record [Sommerville et al, 1997; Rodriguez-Marek 2000]. A number of structural failures have been attributed to near-fault pulses including those of Olive View Hospital in the 1971 San Fernando

Earthquake, Elevated Hanshin Expressway in Kobe, building structures in Northridge, and a weapon industry in Greece during the 1995 Aegion earthquake. Comprehensive catalogues and models of such motions are available in the literature [Mylonakis & Voyagaki, 2006; Mavroeidis & Papageorgiou, 2003].

Most recent studies utilize actual earthquake recordings in conjunction with numerical algorithms to analyze the response of various structural and geotechnical systems to one or several ground motions [Ambraseys & Menu 1988]. On the other hand, idealized pulses that may provide useful insight in the physics of the problem have received less attention [Yegian et al 1989; Conte & Dente 1989, Mavroeidis & Papageorgiou 2003, Mylonakis & Voyagaki, 2006]. Studying simple pulses appears desirable, since there is ample evidence that only a short interval in ground motion, associated with the pulse, contributes to most of the seismic demand. In addition, simple waveforms often allow closed-form solutions to be obtained, which have distinct advantages over numerically constructed solutions.

PROBLEM PRESENTATION & PARAMETER DEFINITION

The problem considered in this study is that of a rigid block of mass m, resting on a rough plane of frictional coefficient μ and yielding strength Q_y, subjected to four idealized ground acceleration pulses, as shown in Figs 1 and 2. The pulses are described by their shape (rectangular, sinusoidal, triangular & exponential), amplitude $A_{g,}$ half-cycle duration t_d (or, equivalently, period $T_p = 2 \times t_d$) and number of cycles (half cycle, full cycle).

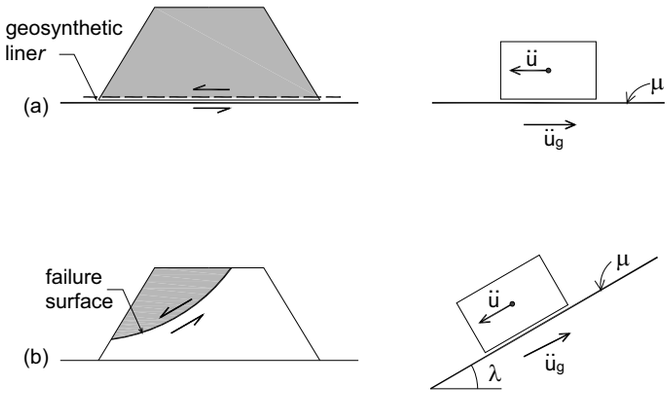


FIG1. Geotechnical problems analyzed by means of sliding block idealizations: (a) sliding of embankment on geosynthetic liner (modeled as block under symmetric friction), (b) failure of embankment (modeled as block under asymmetric friction).

It is well known that, from a seismological viewpoint, velocity pulses have certain advantages over acceleration pulses, as they scale better with source parameters such as moment magnitude and stress drop [Mavroeidis & Papageorgiou, 2003]. On the other hand, acceleration pulses tend to correlate better with engineering parameters such as yield seismic coefficient and inelastic displacement. This can be understood given that the triggering of plastic deformations (termed “yielding” in the ensuing) is

inherently associated with acceleration – not velocity. Thereby, acceleration pulses may be equally suitable – or perhaps advantageous, over velocity pulses when plastic response is of main concern. It should also be noted that velocity and acceleration pulses are interconnected, as, for instance, a full – cycle sinusoidal acceleration pulse corresponds to a half-cycle velocity pulse and a full – cycle box acceleration pulse corresponds to a half-cycle triangular velocity pulse.

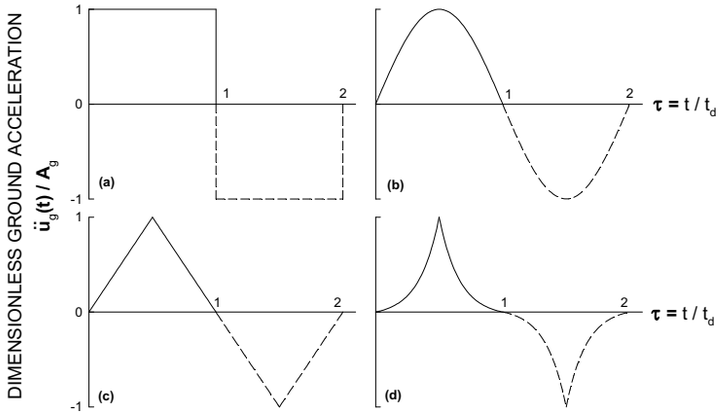


FIG 2. Dimensionless ground acceleration time histories of four idealized ground pulses of different durations (half and full cycles): (a) rectangular; (b) sinusoidal; (c) triangular; (d) exponential.

With reference to Fig 2, both half – and full-cycle pulses are considered, denoted by solid and solid-broken lines, respectively. Strictly speaking, the former are not physically realizable, for ground velocity at the end of the excitation ($\tau = 1$) is not zero. Nevertheless, these incomplete pulses incorporate the large acceleration and velocity excursions observed in actual near-fault recordings and, thereby, are well suited for studying the main features of seismic demand imposed by such motions. In addition, it will be shown that certain sliding systems attain their peak response *before* the end of excitation and, thereby, whether ground velocity tends to zero or not at a later time becomes of less importance.

The following dimensionless quantities are used to describe the results presented below: yielding strength $\eta = Q_y/mA_g$, time of yielding $\tau_y = t_y/t_d$, time of maximum sliding $\tau_m = t_m/t_d$, where Q_y = force necessary to induce sliding, t_y = time of yielding, t_m = time of peak displacement. In addition, peak sliding velocity V_m, maximum sliding displacement u_m, incremental ground displacement during sliding $\Delta u_g = u_g(\tau_m) - u_g(\tau_y)$, t_{vm} = time of V_m, V_g = peak pulse velocity, D_g = peak pulse displacement, are employed in the ensuing.

CLOSED-FORM SOLUTIONS

A: Half – Cycle Pulses

The governing equation of motion of a rigid block sliding on a rough inclined plane under seismic action acting parallel to it is

$$\ddot{u} = \ddot{u}_g - \frac{Q_y}{m}\,\mathrm{sgn}(\dot{u}) \tag{1}$$

where $\ddot{u}$ denotes sliding acceleration relative to the inclined plane. Note that the sign in front of the seismic acceleration term $\ddot{u}_g$ is considered positive for convenience†.

Integrating the above equation twice with respect to time, enforcing the initial conditions of zero sliding velocity and displacement at t = 0, and considering unidirectional sliding in the downhill direction $(\dot{u} \geq 0)$, block velocity and displacement are obtained from the expressions [Mylonakis & Voyagaki 2006]:

$$\dot{u} = \dot{u}_g - \dot{u}_g(t_y) - \frac{Q_y}{m}(t - t_y) \tag{2}$$

$$u = u_g - u_g(t_y) - \dot{u}_g(t_y)(t - t_y) - \frac{Q_y}{2m}(t - t_y)^2 \tag{3}$$

The time of peak deformation is obtained from Eqn (2) by setting block velocity equal to zero

$$t_m = t_y + \frac{m}{Q_y}[\dot{u}_g(t_m) - \dot{u}_g(t_y)] = t_y + \frac{m}{Q_y}\begin{pmatrix} pulse\ area\ \ after \\ initiation\ of\ \ sliding \end{pmatrix} \tag{4}$$

which defines a motion reversal. For half-cycle pulses such as those studied in this section, it is evident that the smallest positive root of Eqn 4, corresponding to the *first* velocity reversal, defines the time of peak sliding. For full cycle pulses, this peak should be distinguished from peak residual response which may take place at a later time.

The above equation elucidates the intimate interconnection between pulse velocity and peak sliding displacement. Indeed, the higher the pulse area after yielding, the longer the block will stay in motion, the higher the ensuing sliding displacement. It should be kept in mind, however, that Eqns 1-4 tacitly assume that the block has slipped. Evidently, initiation of sliding requires considerable levels of ground acceleration and, thereby, ground velocity should not be viewed as the sole descriptor of earthquake destructiveness [Rodriguez-Marek, 2000; Mylonakis & Voyagaki 2006].

Additional support to this suggestion comes from the observation that block displacement in Eqn (3) depends on ground displacement u_g – not on ground velocity. Evidently, a change in ground displacement during sliding will increase or decrease block displacement without altering the restoring force. This suggests that ground displacement may be more important in design against near-fault motions than previously thought.

In terms of dimensionless time, Eqn (2) yields for the four half-cycle pulses in Fig 2:

† This is to ensure positive sliding response for positive ground acceleration. The concept is indicated with the help of the reference systems of Fig 1.

$$\tau_m = \begin{cases} \dfrac{1}{\eta} & \text{rectangular} \quad (5a) \\ \tau_y + \dfrac{1}{\eta\pi}(1+\cos\pi\tau_y) & \text{sinusoidal} \quad (5b) \\ \tau_y - \dfrac{1}{\eta}(\tau_y{}^2 - \dfrac{1}{2}) & \text{triangular} \quad (5c) \\ \tau_y + \dfrac{1}{\eta(1-e^{\pi})}[1+\dfrac{1}{2\pi}(1+e^{2\pi\tau_y}) - \dfrac{e^{\pi}}{\pi} - \tau_y] & \text{exponential} \quad (5d) \end{cases}$$

which correspond to the case $\tau_m \geq 1$.

When maximum response occurs during forced sliding, $\tau_m \leq 1$, time of maximum response can be obtained from Eqn (4). The associated equations are rather complex and will not be provided herein. Note that this case is never true for a rectangular pulse, as maximum displacement for this type of motion always occurs during free sliding.

Setting t equal to t_m in Eqn (3) and after some straightforward algebra, the following explicit solutions are obtained for the normalized maximum displacement response:

- *Rectangular Pulse*

$$\frac{u_{\mathrm{m}}}{\Delta u_g} = 1 - \eta\frac{\tau_m{}^2}{2\tau_m - 1} \quad (6a)$$

- *Sinusoidal Pulse*

$$\frac{u_m}{\Delta u_g} = 1 - \frac{\frac{\eta\pi}{2}(\tau_m - \tau_y)^2 - (\cos\pi\tau_y - 1)(\tau_m - \tau_y)}{[1+H(\tau_m - 1)]\cdot\tau_m - \tau_y - H(\tau_m - 1) - \frac{1}{\pi}[H(\tau_m - 1)\cdot\sin\pi\tau_m - \sin\pi\tau_y]} \quad (6b)$$

- *Triangular Pulse*

$$\frac{u_m}{\Delta u_g} = 1 - \frac{(\tau_m - \tau_y)[\tau_y{}^2 + \frac{\eta}{2}(\tau_m - \tau_y)]}{1/12 - \tau_m/2 + \tau_m{}^2 - \tau_m{}^3/3 - \tau_y{}^3/3 - (1/3 + \tau_m{}^2 - \tau_m{}^3/3 - \tau_m)\cdot H(\tau_m - 1)} \quad (6c)$$

- *Exponential Pulse*

$$\frac{u_m}{\Delta u_g} = 1 - \frac{2\pi(\tau_m - \tau_y)[1 - e^{2\pi\tau_y} + 2\pi\tau_y + \eta\pi(\tau_m - \tau_y)(1 - e^{\pi})]}{-e^{-2\pi(\tau_m - 1)} + e^{2\pi\tau_y} - 2\pi e^{\pi}(2\tau_m - 1) + 2\pi(\tau_m - \tau_y)[1 + \pi(\tau_m + \tau_y)] - [1 - e^{-2\pi(\tau_m - 1)} + 2\pi(\tau_m - 1)(\pi(\tau_m - 1) - 1)]H(\tau_m - 1)} \quad (6d)$$

where *H( )* denotes the Heaviside (step) function. In the above equations, η denotes the ratio of yielding acceleration to peak pulse acceleration (Bertero et al 1978). In the present problem, η is related to μ, λ and A_g as

$$\eta = \frac{\tan[Arc\tan(\mu) - \lambda\, sign(\dot{u})]\, g}{A_g} \tag{7}$$

which defines a problem of *asymmetric* friction with respect to the direction of sliding.

The time of slippage is obtained from the equation:

$$\ddot{u}_g(t_y) = \frac{Q_y}{m} = \eta\, A_g \tag{8}$$

Solving Eqn (8) yields the following solutions for the dimensionless time τ_y

$$\tau_y = \begin{cases} 0 & \text{rectangular} \quad (9a) \\ \frac{1}{\pi}\sin^{-1}\eta & \text{sinusoidal} \quad (9b) \\ \frac{\eta}{2} & \text{triangular} \quad (9c) \\ \frac{1}{2\pi}\ln[1-\eta(1-e^{\pi})] & \text{exponential} \quad (9d) \end{cases}$$

which correspond to a rectangular, sinusoidal, triangular, and exponential pulse, respectively. The dependence of τ_y on η elucidates the sole importance of acceleration content on initiation of yielding.

Note that the above displacements are both peak and residual responses due to the unilateral nature of the pulse.

B: Full – Cycle Pulses

The above analysis can be extended to the case of full-cycle pulses. For the sake of brevity, only final results are presented below. It is noted that these results assume unidirectional sliding in the downhill direction.

- *Rectangular Pulse*

$$\frac{u_m}{\Delta u_g} = 1 - \eta\frac{2}{1-\eta(\eta-2)} \tag{10a}$$

- *Sinusoidal Pulse*

$$\frac{u_m}{\Delta u_g} = 1 - \frac{\eta\pi(\tau_m - \tau_y)^2/2 - (\cos\pi\tau_y - 1)(\tau_m - \tau_y)}{\tau_m - \tau_y - (\sin\pi\tau_m - \sin\pi\tau_y)/\pi} \tag{10b}$$

- *Triangular Pulse*

$$\frac{u_m}{\Delta u_g} = 1 - \frac{12(\tau_m - \tau_y)[{\tau_y}^2 + \frac{\eta}{2}(\tau_m - \tau_y)]}{1 - 6\tau_m + 12{\tau_m}^2 - 4({\tau_m}^3 - {\tau_y}^3) - (2\tau_m - 3)^3\ H(\tau_m - 2/3)} \tag{10c}$$

- *Exponential Pulse*

$$\begin{aligned}\frac{u_m}{\Delta u_g} = 1 - \frac{2\pi(\tau_m - \tau_y)[1 - e^{2\pi\tau_y} + 2\pi\tau_y + \eta\pi(\tau_m - \tau_y)(1 - e^{\pi})]}{\{-e^{-2\pi(\tau_m - 1)} + e^{2\pi\tau_y} - 2\pi e^{\pi}(2\tau_m - 1) + 2\pi(\tau_m - \tau_y)[1 + \pi(\tau_m + \tau_y)] + \\ [e^{-2\pi(\tau_m - 1)} + e^{2\pi(\tau_m - 1)} - 4\pi^2(1 - \tau_m)^2 - 2]\,H(\tau_m - 1) + \\ + [e^{2\pi(\tau_m - 2)} - e^{-2\pi(\tau_m - 1)} + 2\pi e^{\pi}(2\tau_m - 3)]\,H(\tau_m - 3/2)\}\end{aligned} \tag{10d}$$

where τ_m can be obtained by corresponding closed form expressions (not shown).

Numerical results from Eqns 5 to 9 are shown in Fig 3, plotted as functions of sliding strength. Evidently, time of slippage (Fig 3a) is an increasing function of η for all pulses – except for the rectangular one, for which $\tau_y = 0$. The functional dependence of τ_y on sliding strength for the three pulses is relatively simple. As a first approximation, it can be viewed as a mere proportionality (i.e., $\tau_y \propto \eta$).

Time of maximum displacement (Fig 3c) is a decreasing function of sliding strength. The functional dependence of τ_m on η is more complex than in the previous case. In most cases, peak displacement occurs during free sliding. Peak response during forced sliding occurs for $\eta > 0.36$ (exponential pulse), $\eta > 0.59$ (triangular pulse), and $\eta > 0.73$ (sinusoidal pulse).

Peak sliding displacement is shown in Fig 3b, plotted as fraction of incremental base displacement during sliding: $\Delta u_g = u_g(\tau_m) - u_g(\tau_y)$. This ratio is, naturally, always smaller than 1 and decreases with increasing η, reaching zero at $\eta = 1$. As pointed out by Garini & Gazetas (2007), this monotonic behavior may not be true with motions containing multiple pulses of alternating sign. Typical values lie between approximately 0.4 and 0, implying that up to approximately 40% of incremental base displacement becomes sliding displacement. Note that the behavior close to $\eta = 0$ is anomalous (recall that block response under zero friction to a half-cycle pulse is unbounded – regardless of pulse shape), and shall not be discussed here.

A comparison of permanent displacements obtained for half - cycle pulses is compared against established solutions by Newmark (1965), Richard Elms (1979), Whitman & Liao (1985) and Yegian et al (1991), in Figure 4. These solutions have been obtained for conventional (non-impulsive) motions of multiple cycles. The solutions by Newmark and Richard-Elms refer to maximum expected values, whereas those by Whitman-Liao and Yegian et al to average or median values. The herein

proposed solution provides results which are comparable or higher to the median predictions – a remarkable behavior given the half cycle duration of the excitation.

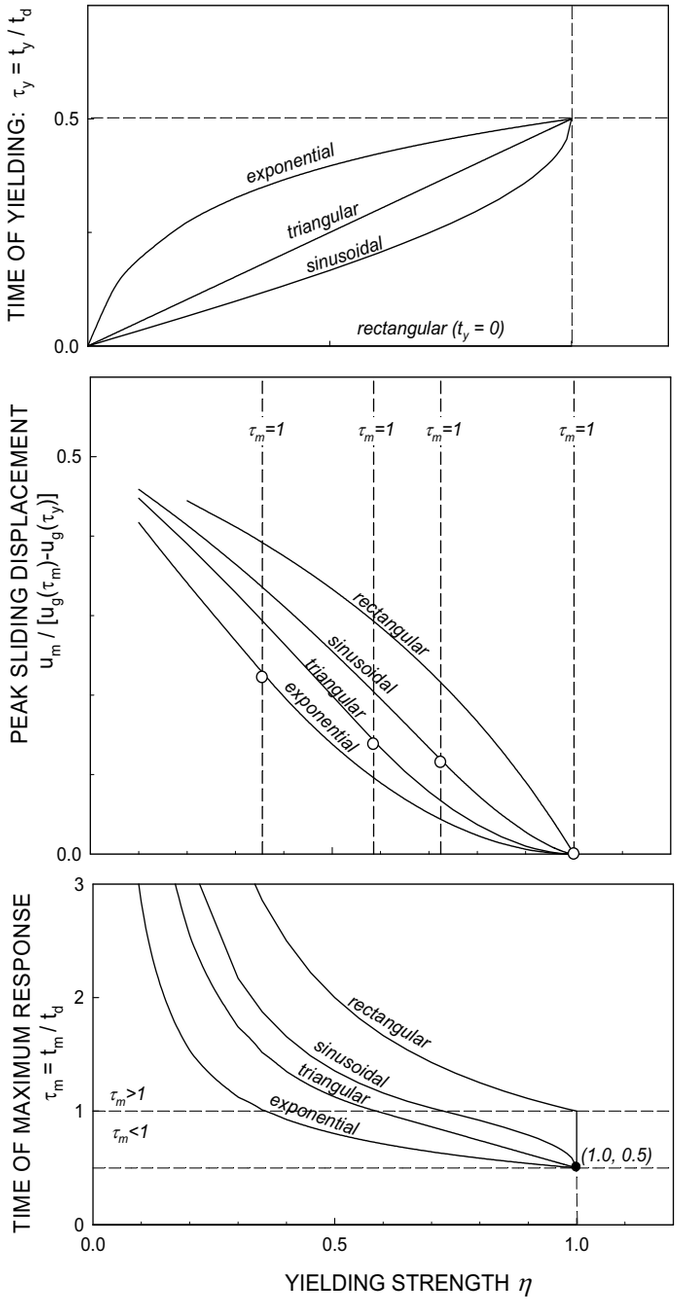


FIG 3. Normalized time of yielding, peak sliding and corresponding time as function of yielding strength for a rigid block on an inclined plane subjected unilateral sliding under four idealized half-cycle acceleration pulses.

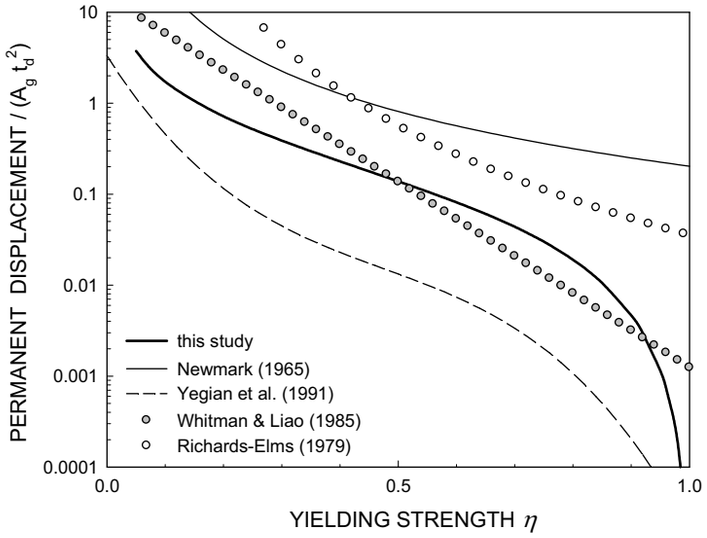


FIG 4. Comparison of permanent displacement for a half-cycle sinusoidal pulse obtained in this study, with established solutions from the literature.

A comparison of permanent displacements for half- and full-cycle pulses obtained from the herein proposed solution is shown in Figure 5. Evidently, half-cycle pulses generate more permanent displacement than their full cycle counterparts. The solutions converge with increasing yielding strength and become identical beyond η = 0.36, 0.59 and 0.73 for an exponential, triangular and sinusoidal pulse, respectively. These limiting values are identical to those shown in Figure 3 and suggest that maximum displacement is often obtained during the first half of the pulse.

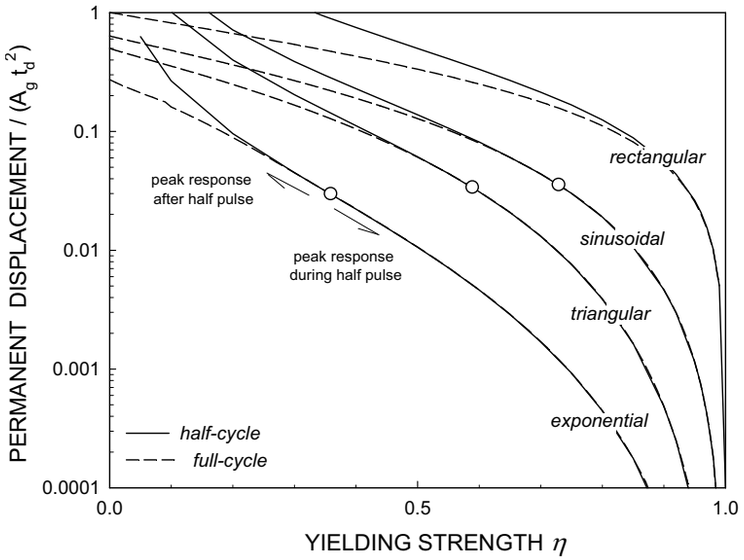


FIG 5. Comparison of permanent displacements for half and full – cycle acceleration pulses.

CONCLUSIONS

The response of rigid blocks on inclined frictional planes subjected to four idealized pulses (rectangular, sinusoidal, triangular & exponential) was obtained analytically. The main conclusions of this study are:

(1) Half-cycle pulses generate higher displacements than full – cycle pulses for equal peak acceleration and frictional strength. This is in contrast to ordinary (non impulsive) motions, for which displacement increases with increasing cycles.
(2) Permanent displacements for the idealized pulses are comparable or higher to mean values obtained by established solutions in the literature. This is remarkable given the limited duration of the idealized motions, and elucidates the fundamental differences between plastic response to ordinary and impulsive ground motions.
(3) The highly complex dependence of peak displacement with frictional strength η is elucidated in equations (6) and (10). This suggests that simple scaling laws of power or exponential nature may not be possible – even for idealized pulses such as those studied in this paper.

REFERENCES

Ambraseys, N.N., Menu, J.M. (1988). "Earthquake-Induced Ground Displacements." *Earthquake Engng and Structural Dynamics*, Vol. 16, pp. 985-1006

Bertero, V.V., Mahin, S.A., Herrera, R.A. (1978). "Aseismic design implications of near-fault San Fernando earthquake records." *Earthquake Engineering and Structural Dynamics*, 6: 31-42.

Boore, D.M., Zoback, M.D. (1974). "Near-field motions from kinematic models of propagating faults." *Bulletin of the Seismological Society of America,* 64: 321-342.

Conte, E., Dente, G. (1989). "An Analytical Solution for Newmark's Sliding Block." *Soils and Foundations*, 29 (3): 152-156.

Garini, E., Gazetas, G. (2007). "Sliding of Rigid Block on Sloping Plane: The Surprising Role of the Sequence of Long – Duration Pulses." *Proc. 2nd Japan – Greece Workshop on Seismic Design, Observation, & Retrofit of Foundations*, April 3~4, Tokyo, Japan.

Mavroeidis, G., Papageorgiou, A. (2003). "A mathematical representation of near-fault ground motions." *BSSA*, 93(3): 1099-1131.

Mylonakis, G., Voyagaki, E. (2006). "Yielding Oscillator subjected to simple pulse waveforms: numerical analysis & closed-form solutions." *Earthquake Engineering and Structural Dynamics*, 35:1949-1974.

Rodriguez-Marek, A. (2000). "*Near-fault seismic site response*." Ph.D. Dissertation, Department of Civil Engineering, University of California, Berkeley.

Somerville, P.G., Smith, N.F., Graves, R.W., Abrahamson, N.A. (1997). "Modification of empirical strong motion attenuation relations to include the amplitude and duration effects of rupture directivity." *Seism. Research Letters,* 68: 199-222.

Yegian, M.K., Marciano, E. A., Gharaman, V.G. (1991) "Earthquake - induced permanent deformations: probabilistic approach." *Journal of Geotechnical Engineering*, ASCE, Vol. 117, No. 1, pp. 35-50.

ADVANCED 3-D SEISMIC SOIL-STRUCTURE INTERACTION ANALYSIS OF A CELLULAR-RAFT FOUNDATION IN SOFT CLAY

Juan M. Mayoral[1], Miguel P. Romo[2], and Sergio Martinez[3].

Associated Professor, Instituto de Ingeniería, UNAM, Mexico City, Mexico, jmayoralv@iingen.unam.mx
[2]Professor and Head of the Geotechnical Group, Instituto de Ingeniería, UNAM, Mexico City, Mexico, mpr@pumas.iingen.unam.mx
[3]PhD Student, Instituto de Ingeniería, UNAM, Mexico City, Mexico

ABSTRACT: Seismic soil-structure interaction performance evaluations of projects located in deep soft clay deposits warrant special attention, particularly when designing strategic infrastructure that must remain operating after a major earthquake. The development of numerical analytical platforms in recent decades, along with faster computing tools, have made possible to include in the state of practice quite sophisticated solution techniques aimed at better representing the physics of the problem at hand. This paper presents the application of a 3-D finite difference model for evaluating the static and dynamic response of a 118 by 100 m cellular-raft foundation to be built in soft clay. The raft foundation is a 2.5 m high box-type foundation embedded 1 m and supported by a grid of peripheral and internal walls, 2.5 m long and 0.40 m thick, which integrates a cellular structure. The model is used to obtain first the static behavior exhibited by the foundation for the construction stages, including long term consolidation, and then the design earthquake is considered and the equation of motion is solved in time domain.

INTRODUCTION

In recent years, the urban and industrial growing of Mexico City has prompt using near by areas for new developments, such as the Texcoco Lake region. Clays in this region, in addition of exhibiting low shear strength and high compressibility, present seasonal desiccation cracks which usually do not reach depths higher than 1.5 m, but that may extend up to 10 to 12 meters, or being randomly interconnected (Mayoral et al., 2006 & 2007). Moreover, very often these clays are interbedded with thin lenses of silty sands and sandy silts. In an attempt to deal with this particular subsoil conditions, a new foundation alternative has been proposed by Romo (Romo et al., 2001) for light to medium weight structures to be located at this region. This foundation alternative is

an open-ended cellular grid of reinforced concrete walls. This paper presents the static and seismic performance evaluation conducted for designing the foundation of a strategic power plant located at the Texcoco Lake area using this foundation alternative. A three dimensional fully coupled finite difference model of the soil and foundation was developed using the code FLAC 3D (HCItasca, 2006). Elastic expansions and settlements along with long term settlements due to consolidation under its own weight were carried out to obtain the initial stress state conditions to be used in the seismic soil-structure interaction, SSI, analysis. The response of the system is evaluated in terms of ground displacements, structure distortions and ground and structure accelerations. Due to the space constrains, only the most important aspects of these studies were included.

PROJECT DESCRIPTION

A major power plant is going to be built in the proximity of an old Solar Evaporator, within the old Texcoco Lake region in Mexico City western side (Figure 1). The power plant will be comprised of an area for heavy electric equipment and transformers, and two one-story buildings A and B, where electronic controlling boards will be located (Figure 2). The power plant will be supported by a 118 by 100m reinforced concrete partially compensated box foundation, stiffened with concrete walls spaced at 5 m in average, which form interconnected cells. Some of these walls have pass through openings to allow access to maintenance crews. The height of the box foundation ranged from 2.5 to 3.0 m. The box foundation embedment depth is 1.0m, and is structurally connected to a reticular array of reinforced concrete walls spaced at distances ranging from 12.0 to 30 m in both longitudinal and transverse directions. These walls are 2.5 m high and 0.45 m wide, as depicted schematically in Figure 2. These wall arrays, which integrate series of open-ended cells, have the purpose of increasing the lateral stiffness of the foundation while reducing its embedment and thus, the corresponding excavation depth. Furthermore, soft deposits found at this depth are incorporated into the foundation by the confinement provided by the skirts (i.e. the internal grid wall). This is equivalent to increasing the box-foundation depth, enlarging its bearing capacity and reducing foundation settlements.

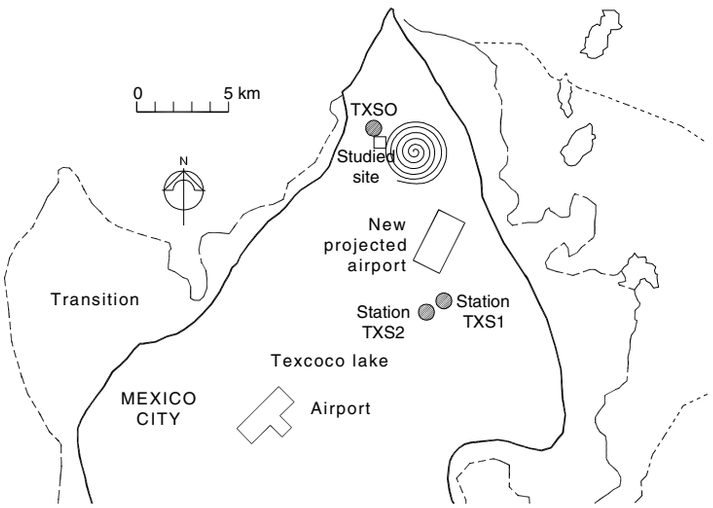


FIG. 1. Project site location at Texcoco Lake Valley (after Mayoral et al., 2007).

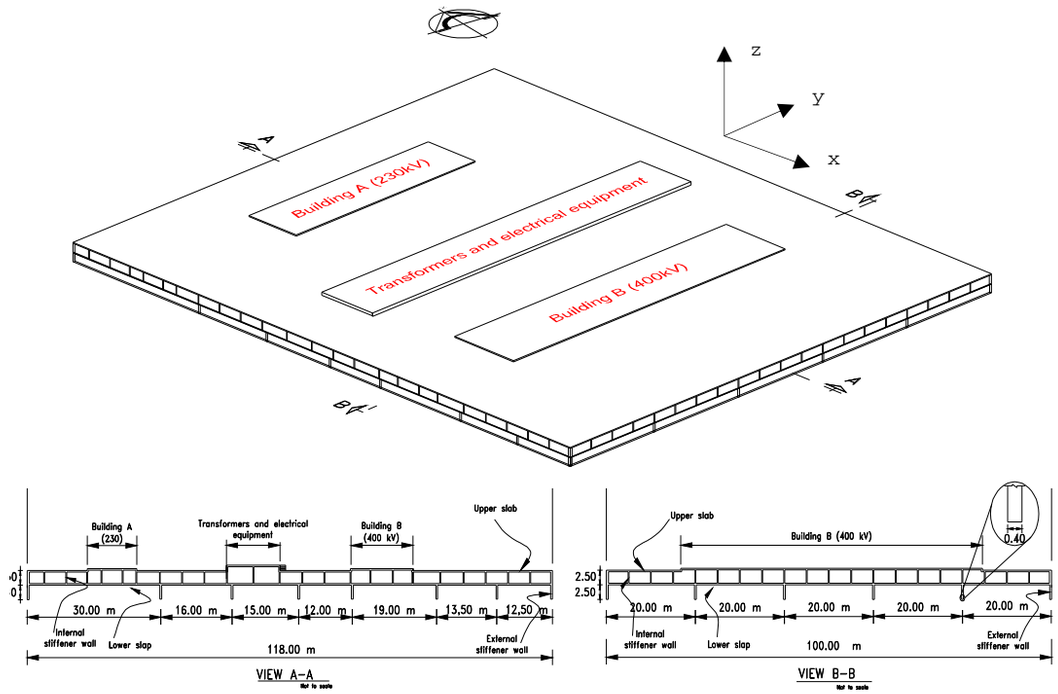


FIG. 2. 3-D general view of the projected soil-foundation system.

Subsoil conditions

The subsoil conditions found at the project site consisted of a desiccated crust of clay at the top extending up to a depth of 1.0 m approximately, which is underlain by a soft clay layer of about 25.0 m thick, with a large number of interbedded lenses of sandy silt, sandy clays and silty sands. The water content of these materials varied from 190 to 295 %, and plasticity index ranging from 139 to 265%. Underlying the clay, there is a 4.0 m average thick layer of very dense sandy silt ($(N1)_{60}$ larger than 65) combined with volcanic ashes, which rests on top of a stiff clay ($(N1)_{60}$ of about 9) layer which goes up to about 60 m depth. Underneath this elevation a competent layer of very dense sandy silts ($(N1)_{60}$ lager than 100) is found. Seasonal desiccation cracks are often observed at the upper clay layers, which usually do not reach depths higher than 1.5 m, but that may occasionally extend up to 10 to 12 meters, or being randomly interconnected. Details of the subsurface exploration and laboratory testing can be found in Mayoral et al. (2006). A three-dimensional interpretation of the subsoil conditions is presented in figure 3 as well as the representative average of the shear wave velocity distribution. Table 1 summarizes the dynamic and static soil properties of the layered system. The dynamic shear stiffness and damping used in the FLAC model corresponds to equivalent linear properties obtained from 1-D wave propagation analysis as described by Mayoral et al. (2007). As an example, the modulus degradation and damping curves used in the site response analysis for clayey soils and those obtained from laboratory testing (Mayoral et al. 2006) are presented in figure 4.

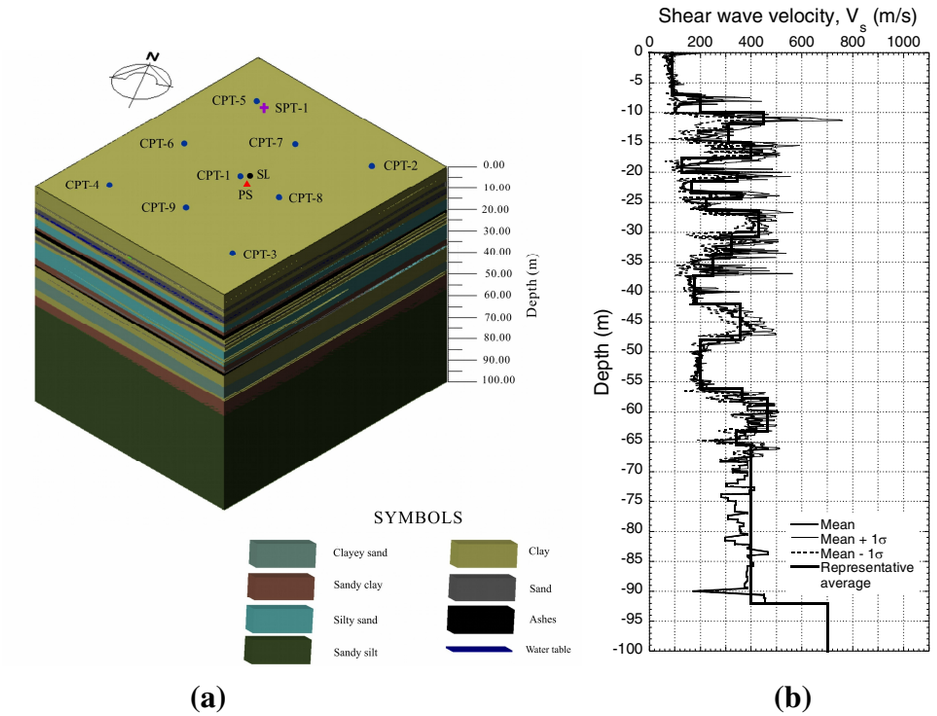


FIG. 3.(a) 3-D representation of subsoil conditions found at the site (after Mayoral et al., 2007), (b) Shear wave velocity distribution.

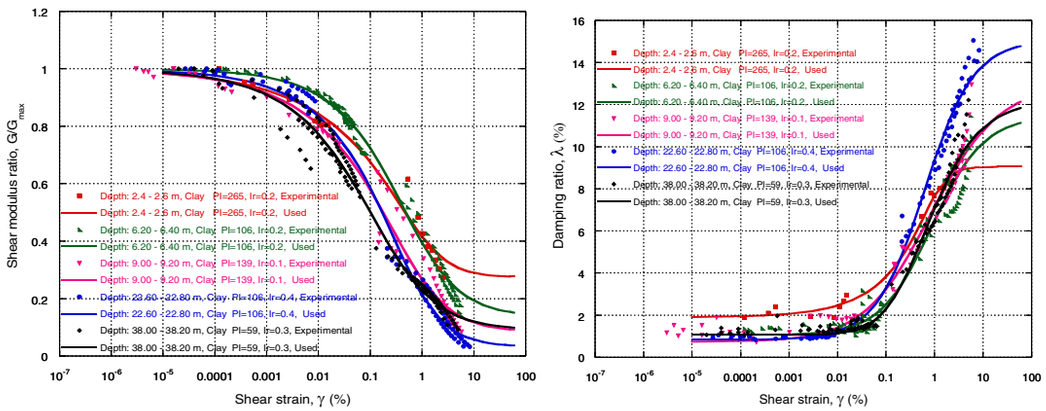


FIG. 4. Modulus degradation (a) and damping (b) curves used in the analysis (after Mayoral et al., 2007).

NUMERICAL MODELING

A 3-D finite difference model of the soil-foundation-structure system was developed (Figure 5). A total of 83,600 sub-domains were used to model the 1 m high, 118 x 100m box-type foundation, and the surrounding soil. The mesh ranged from -150.0 to 150.0 m, in the X direction, from -177.0 to 177.0 m in the Y direction, and from 0 to -100 m in the Z direction. Initial stress conditions were determined solving the static problem first.

Table 1. Dynamic and static soil properties

Layer ID	Thickness (m)	Young Modulus (kN/m^2)		Dynamic Shear Stiffness G (kPa)	Poisson Ratio υ	Unit Weight γ (kN/m^3)
		E_i (initial)	E_f* (final)			
1	6.3	26,830	17	8,910	0.49	11.2
2	1	27,960	17	9,290	0.49	11.6
3	0.6	150,500	150,500	55,970	0.35	13.7
6	2	145,080	17	48,790	0.49	11.9
4	0.7	731,210	24	246,250	0.49	11.9
5	1.2	758,500	758,500	282,590	0.35	13.7
9	2.5	366,250	366,250	135,930	0.35	13.7
6	0.6	353,070	24	118,460	0.49	11.9
7	2.7	601,980	601,980	223,940	0.35	13.7
12	0.7	59,730	59,730	22,260	0.35	13.7
8	1.5	65,150	13	21,790	0.49	13.5
9	1.6	453,030	453,030	168,780	0.35	13.7
15	0.4	102,430	102,430	38,160	0.35	13.7
10	1.2	111,730	18	37,350	0.49	13.5
11	0.4	102,430	102,430	38,160	0.35	13.7
18	1	490,320	490,320	181,900	0.35	13.7
12	1.9	202,260	18	67,220	0.49	13.5
13	4.4	695,670	695,670	259,220	0.35	13.7
22	3	392,530	392,530	145,750	0.35	13.7
14	2.5	256,500	64	85,750	0.49	13.5
15	0.9	235,150	235,150	87,620	0.35	13.7
25	4.8	125,620	64	41,940	0.49	13.4
16	1.1	522,660	85	174,910	0.49	13.4
17	5	484,900	484,900	180,080	0.35	13.7
30	8	162,210	162,210	54,390	0.49	13.4
18	1.7	498,500	498,500	185,340	0.35	13.7
19	5.5	813,520	813,520	302,890	0.35	13.7
36	2.3	434,930	434,930	162,170	0.35	13.7
20	26.4	601,980	601,980	223,940	0.35	13.7
21	8.1	1,843,570	1,843,570	685,740	0.35	13.7

***E_f was computed with the following expression** $E_f = (1+\upsilon)(1-2\upsilon)/m_v(1-\upsilon)$ **, where** υ **: Poisson ratio and** m_v **:coefficient of volume compressibility**

According to the weights of the supported structures and related equipment summarized in Table 2, the foundation self weight and the partial load compensation (i.e. 12 kPa) due to the removed soil (i.e. 1m of embedment depth) the average contact pressure at the embedment depth is 14 kPa. This compensation helps reducing long term settlements. Due to the unusual shape of the foundation, traditional approaches based on elasticity theory to compute stresses and settlement distributions can not be strictly applied. Therefore, a deformation analysis considering the soil as an elastic material and using a 3-D finite difference model of the foundation was conducted, assuming the elastic soil properties summarized in Table 1. For the concrete structure it was considered a Young modulus of 15,500 MPa, a Poisson ratio of 0.3, a unit weight of 23.5 kN/m^3 and a damping ratio of 3 %. This allowed the simulation of each construction stage, including excavation, construction of the cellular structure and box

foundation. Once the soil conditions prior to seismic loading were established, the seismic SSI analysis was undertaken. The seismic load was input to the model through an acceleration time history applied at its base. A dashpot-like transmitting boundary was used at the edges of the model to simulate free field conditions. In order to minimize computing time, a rigid base was assumed at the bottom of the model. However, three layers of elements with larger damping were placed between the rigid base and the modeled soil to dissipate reflected wave's energy. The damping of this region was determined by an iterative process where the response spectrum of an actual ground motion recorded at the site during the Michoacan 1985 earthquake was matched (Mayoral et al., 2006).

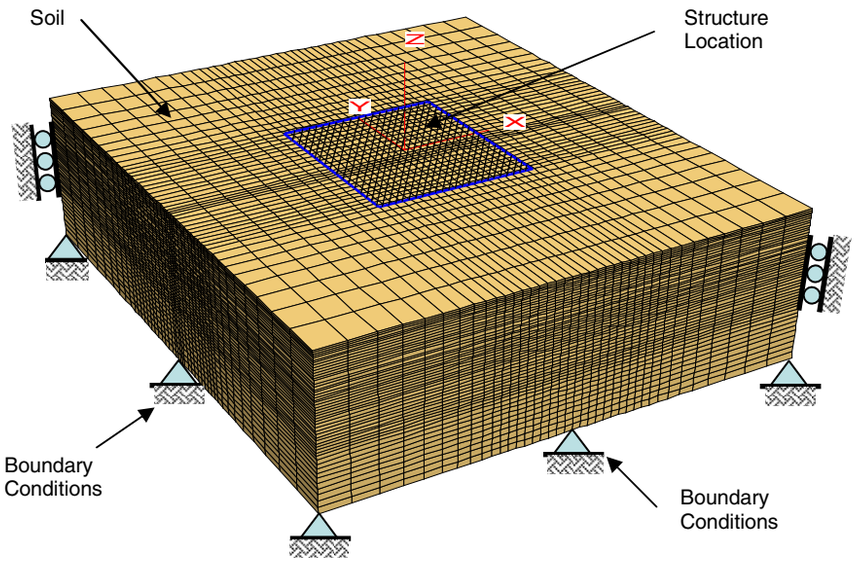


FIG. 5. Finite difference mesh and boundary conditions.

Dynamic properties

Equivalent linear properties (i.e. shear stiffness and damping) were used to model approximately soil nonlinearities. These were computed at each depth through 1-D wave propagation iterative analysis (Mayoral et al., 2007). Soil damping was considered through a Raleigh-type formulation. Equivalent linear properties have been shown to yield good results based on the wide quasi-linear range behavior observed in Mexico City clays even for shear strains as large as 0.3% (Romo et al., 1988, Romo 1995), due to their high plasticity. In fact, even for the near field soil, results obtained through instrumentation of actual structures and back analyses of the gathered data support the fact that nonlinearities a few meters from the soil-foundation interface are significantly low, at least for Mexico City clays, and in consequence, the generation of dynamic excess pore pressure and the corresponding strain softening is also small (Romo, 2000). Furthermore, analytical studies have shown that very approximate predictions can be achieved following similar numerical procedures when analyzing the seismic response of instrumented buildings located at Mexico City clayey area, if the response-controlling parameters are properly modeled. Nonlinearities associated with possible foundation slip and concrete cracking in the external walls was not

accounted for, because for this type of foundation will be difficult to occur, especially when the walls are to be designed to work in their elastic range.

Static loads

The static loads due to self weight of the foundation and walls were accounted for through the unit weight of the concrete. Other loads such as electric equipment, buildings, cables, connectors were applied as uniform pressure or punctual loads on their corresponding location according to the values compiled on Table 2.

Table 2. Equipment weights

Equipment	Weight, kNw
Control board in building A (400 kV)	2600
Control board in building B (230 kV)	820
Transformers	10500
Aereal structure and wall protection walls	2800

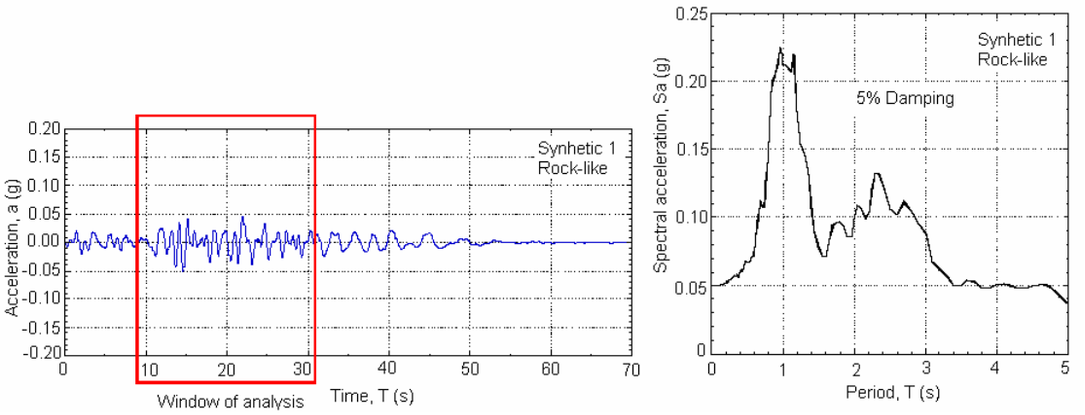
Input earthquake motions

The seismic parameter characterization of the project site was presented in Mayoral et al., (2007). From this investigation, a set of recommended synthetic acceleration time histories for seismic soil structure interaction, SSI, analysis in the Texcoco Lake region, were obtained through time domain spectral matching of empirically derived response spectra and 1-D wave propagation analyses. The results presented herein were obtained using the most critical (larger intensity in a 20 s long window frame) of this ground motions, scaled by 1.5 to account for the importance of the structure as it is stated by the Mexican Building Code (RCDF, 2004) for strategic infrastructure. The acceleration time history and the corresponding response spectrum are presented in figure 6.

Static ground movements

The conditions of the soil-foundation system prior to the seismic SSI study were obtained from a static analysis of the foundation response conducted in stages, considering first the excavation of the foundation, then the construction or placement (i.e. if prefabricated panels are considered) of the external walls and finally the box foundation.

To reduce the computation time, the distribution of settlements due to long term consolidation were evaluated solving the relaxation problem considering the initial E_i and final, E_f, Young Modulus compiled in Table 1, and assuming a linear variation between them. The parameter E_f was obtained based on the increment of stresses due to the surcharge and the compressibility soil parameters, this approach seems to provide results close to those measured in structures located within Mexico City Valley (Romo et al., 2000). A 3-D view of the computed static settlements is presented in Figure 7. This includes elastic expansions and compressions according to the construction stage, as well as long term settlements due to ground consolidation. The maximum settlement is about 33 cm, and it is practically uniform throughout the foundation due to the high flexural stiffness provided mainly by the structural cells, as can be seen in Figure 7. The uniform settlements of the foundation through its service life prevents irregular loading of the power station components.



(a) **(b)**

FIG. 6. Input ground motion: (a) acceleration time history and (b) response spectrum.

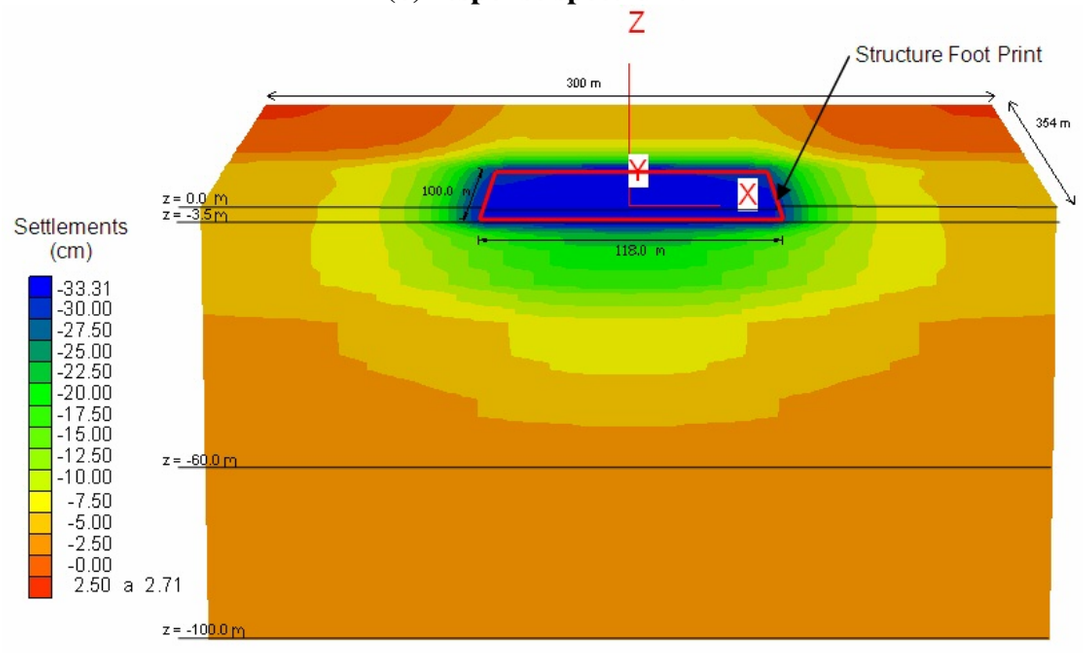


FIG. 7. Long term consolidation settlements 3-D distribution.

Seismic SSI analysis

As it has been mentioned, the seismic SSI analysis was conducted in time domain using equivalent linear properties. The input ground motion was applied at the base of the model and in the X direction, which corresponds to that one with the lower transverse stiffness for the buildings A and B as it is depicted in Figure 2. Only 20 seconds of the acceleration time history, corresponding to the intense part of the event, was considered in order to reduce the computing time (Figure 6). To asses the performance of the new foundation system and in particular the external stiffener walls, the seismic response was obtained at several points within the upper and lower slabs and at the contact with the head of the external stiffener concrete walls

underlying the box foundation, in terms of acceleration time histories of horizontal displacements and accelerations along direction X, bending moments and shear axial forces. Due to space constrains, only plots of acceleration time histories of the computed response at the base, at the free field surface and at the same depth in the geometric center of the structure and at one corner, are presented in Figure 8, along with their corresponding response spectra. As can be noticed, no significant seismic-soil-structure-interaction occurs and the foundation moves as a rigid body, as it was intended to ensure that the electric equipment, including cables and poles will not suffer important damage due to the relative movement of their supports during the design earthquake, and that not differential movement occurred between the electrical station equipment and the incoming and outgoing electrical towers, which are located outside the box foundation. Furthermore, the foundation helps to uniform the structure response, and to reduce the peak observed in the response spectrum at 1 second period. Rocking motion was negligible, as it was expected from the large dimensions and rigidity of the foundation system (i.e. box foundation and internal and external stiffeners walls).

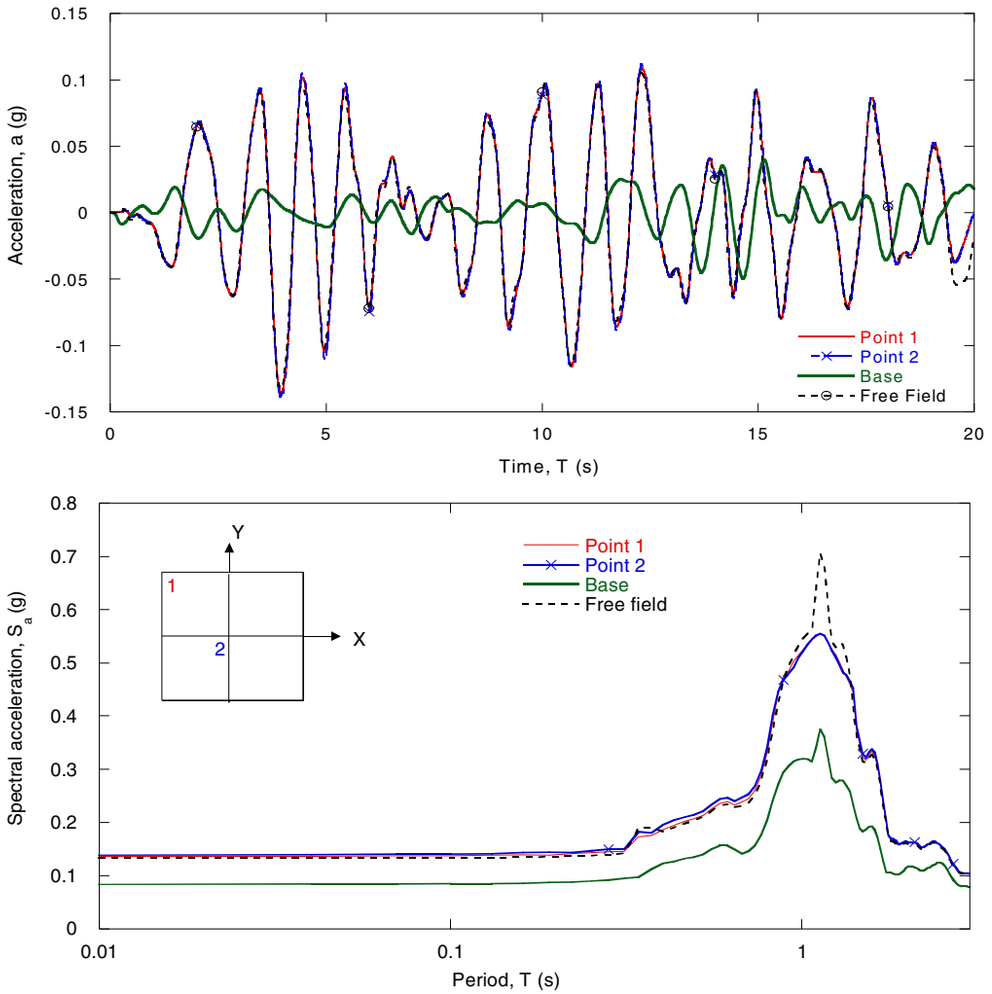


FIG. 8. Acceleration time history and spectral acceleration for free field and structure.

CONCLUSIONS

This paper describes the static and seismic performance evaluation of an unconventional foundation system, comprised by a partially compensated box-foundation structurally tied to an open-ended grid of stiffeners walls. This unconventional system has been proposed as a foundation alternative of light to medium weight structures to be built in the low strength-highly compressible, fissured clays typically found at the Texcoco lake valley, in the Mexico City surrounding areas. Although, there seems to be no technical objection to be used for founding high-rise buildings, more research is required. Quantitatively, it should be expected that wall depth increases with building height and loading level. In this particular case, due to the short length of the underlying grid walls, its influence in the dynamic response was small, although it was very helpful to uniform long term settlements.

REFERENCES

Administración Pública del Distrito Federal, Jefatura de Gobierno (2004). "Normas técnicas complementarias para el diseño por sismos." Reglamento de Construcciones para el Distrito Federal, México.

HCItasca (2006). Advanced Three Dimensional Continuum Modeling for geotechnical analysis of rock, soil, and structural support software, FLAC 3D.

Mayoral J. M., Romo M. P., and Osorio L. (2007), "Seismic parameters characterization at Texcoco Lake, México." Accepted for publication in Journal of Soil Dynamics and Earthquake Engineering.

Mayoral J. M., Romo M. P., and Osorio L. (2006). "Estudios de campo y laboratorio llevados a cabo para la caracterización geo-sísmica en la zona del Lago de Texoco." Informe Interno, Instituto de Ingeniería, UNAM.

Romo M. P., Jaime A. and Reséndiz D. (1988). "General soil conditions and clay properties in the Valley of Mexico." Journal Earthquake SPECTRA, Vol 4, No 2, pp 731 752.

Romo M. P. (1995) "Clay behavior, ground response and soil-structure interaction studies in Mexico City." Lecture and State of the Art paper, Proceedings of the Third International Conference on Recent Advances in Geotechnical Earthquake Engineering and Soil Dynamics, St. Louis Missouri, Vol 2, pp 1039-1051.

Romo M. P., Mendoza M. J. J. y García S. R. (2000). "Geotechnical factors in seismic design of foundations." Lecture and State-of-the-Art paper, Proceedings 12th World Conference on Earthquake Engineering, Paper # 2832, Auckland, New Zealand.

Romo M. P., Auvinet G., Ovando E., Mendoza M. J., Taboada V. M., Lermo J. y Mooser F. (2001). "Ingeniería geotecnia para el nuevo aeropuerto internacional de la Ciudad de México: Soluciones en el ex-Lago de Texcoco y en Zapotlán de Juárez." Informe del Instituto de Ingeniería, UNAM, a Aeropuertos y servicios Auxiliares.

Dynamic Soil-Structure Interaction for SDOF Structures on Footings and Piles

Andreas Maravas[1], George Mylonakis[2] and Dimitris L. Karabalis[3]

[1]Research Assistant, Department of Civil Engineering, University of Patras, anmaravs@upatras.gr
[2]Associate Professor, Department of Civil Engineering, University of Patras, mylo@upatras.gr
[3]Professor, Department of Civil Engineering, University of Patras, karabali@upatras.gr

ABSTRACT:

Novel analytical solutions are presented for single-degree-of-freedom (SDOF) oscillators founded on footings and piles on compliant ground. *First*, exact formulas are derived for the fundamental viscoelastic natural period and effective damping of these structures. It is shown that certain approximations proposed in the literature may be inaccurate for highly-damped systems. *Second*, the influence of foundation mass on natural period and damping is investigated. *Third*, the effect of coupled swaying-rocking oscillations at the pile head is addressed by translating the reference system to the location down the pile, where the resultant soil reaction is applied. This ensures a diagonal foundation impedance matrix and simplifies the solution. *Fourth*, the amount of radiation damping generated from a single pile and a surface footing are compared. To this end, a new concept of statically and geometrically equivalent SSI systems is introduced. It is shown that a structure founded on a pile may generate twice the radiation damping of a similar structure on a spread footing.

INTRODUCTION

Knowledge on the subject of dynamic Soil-Structure Interaction (SSI) has been derived mainly from studies of structures on mat foundations. The seismic response of structures on pile foundations has received considerably less attention. More importantly, the results of these efforts have not yet lead to established design methods and/or code provisions, such as the simple methods developed for structures on surface foundations (NEHRP-03, EC-8). Therefore much is yet to be learned on the subject before a comprehensive understanding is developed on the role of basic problem parameters on the seismic response of flexibly-supported systems.

The goals of this article are: (1) to outline available methods with emphasis on the popular solutions by Veletsos and co-workers (1974, 1975, 1977) and Wolf (1985), (2) to present a new general solution for determining the natural period and effective damping of a simple oscillator supported on a surface foundation and a single pile, (3) to compare radiation damping generated from a surface foundation and a pile foundation.

STRUCTURE ON SURFACE FOOTING

The classical analysis of soil-structure interaction aims at replacing the actual structure by an equivalent simple oscillator supported on a set of frequency-dependent springs and dashpots accounting for the stiffness and damping of the soil (Parmelee 1967; Veletsos et al 1974, 1975; Jennings & Bielak, 1973; Wolf 1985; Aviles et al 1998). An outline of available methods is presented below. Based on these procedures, a new scheme, for finding the exact viscoelastic solution is presented.

The system studied is shown in Figure 1. It involves a simple oscillator on flexible base representing a single storey structure, or a multi storey structure after a pertinent reduction of its degrees-of-freedom.

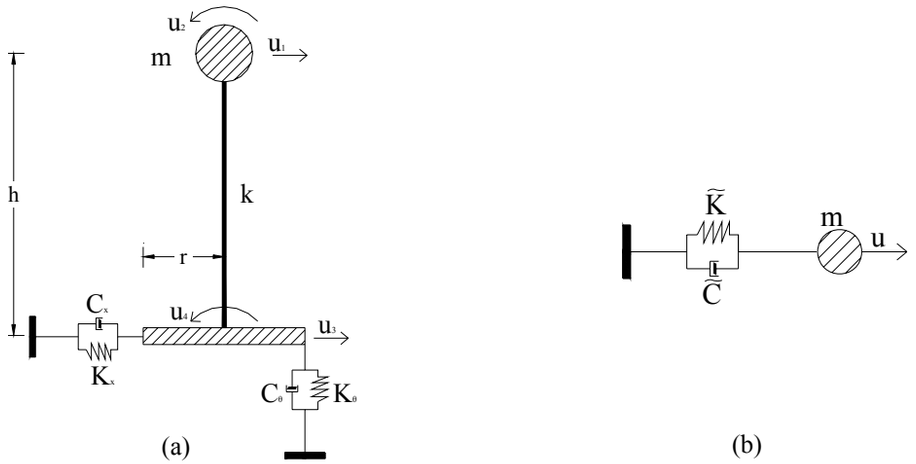


FIG. 1. (a) Structure idealized by a stick model, (b) Reduced SDOF model.

The structure is described by its stiffness k, mass m, height h, and damping ratio ζ, which may be either viscous or linearly hysteretic. The foundation consists of a rigid circular footing of radius r resting on a homogeneous, linearly elastic, isotropic halfspace described by a shear modulus G_s, mass density ρ_s, Poisson's ratio ν_s, and hysteretic damping ratio ζ_s. Foundation stiffness is modeled by frequency-dependent springs K_x and K_θ representing stiffness in translational and rocking oscillations, respectively. Damping is modeled by a pair of dashpots C_x, C_θ, representing energy loss due to wave radiation and hysteretic action (Veletsos & Nair 1974).

In general, the dynamic impedance $K^*(\omega)$ of any degree of freedom can be decomposed as

$$K^*(\omega) = K + i\omega C = K(1 + 2i\zeta) \tag{1}$$

where ω is the cyclic excitation frequency; ζ is an energy loss parameter, which is analogous (yet not identical) to the viscous damping coefficient of a simple oscillator:

$$\zeta(\omega) = \frac{\mathrm{Im}(K^*)}{2\,\mathrm{Re}(K^*)} = \frac{\omega C}{2K} \tag{2}$$

Under seismic excitation, the system displaces and deflects as shown in Figure 2. The translation of the mass relative to ground is composed of three parts: (1) horizontal translation due to swaying motion of footing $u_x(\omega)$, (2) horizontal translation due to rocking motion of footing, $u_\theta(\omega)$ and (3) horizontal deflection of the column, u_c. Based on this nomenclature, the dynamic impedance of the system can be defined as:

$$\tilde{K}^* \equiv \frac{P(\omega)}{u_x + u_\theta h + u_c} \tag{3}$$

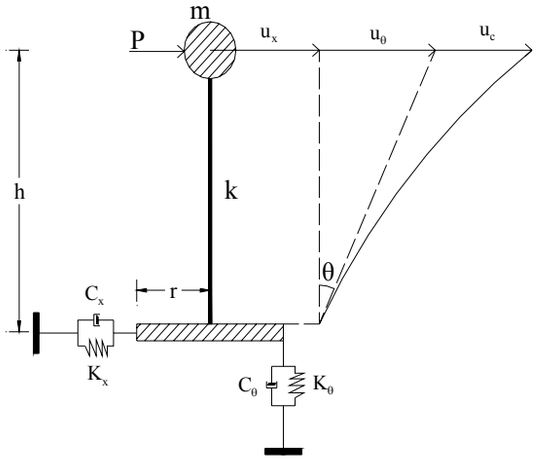


FIG. 2. Deflection diagram for soil-structure system

The response of the system depends on the mechanical properties of the foundation, the soil, the superstructure and the characteristics of the excitation. These are summarized in the following dimensionless parameters (Veletsos, 1977):

(i) The wave parameter σ

$$\sigma = \frac{V_s}{f_c h} \tag{4}$$

where f_c is the natural frequency of the fixed base structure and V_s the shear wave propagation velocity in the soil.

(ii) The relative mass density for the structure and the soil, γ

$$\gamma = \frac{m}{\pi \rho_s h r^2} \tag{5}$$

(iii) The damping ratio ζ of the structure (fixed base), (iv) the slenderness ratio (h/r), (v) the Poisson's ratio ν_s of the soil and (vi) the hysteretic damping ratio ζ_s of the soil.

Solution by Veletsos and co-workers (1974, 1975, 1977)

The aim of these solutions is to connect the properties of the soil-structure system

($\tilde{T}$, $\tilde{\zeta}$) with the properties of the fixed base structure (T, ζ), so that the influence of soil-structure interaction on the dynamic behavior of the structure can be elucidated. This connection is expressed by the following pair of equations (Veletsos 1977):

$$\tilde{T} = T\sqrt{1+\frac{k}{K_x}\left(1+\frac{K_x h^2}{K_\theta}\right)} \tag{6}$$

$$\tilde{\zeta} = \tilde{\zeta}_0 + \left(\tilde{T}/T\right)^{-3}\zeta \tag{7}$$

where ζ represents the viscous damping of the structure and $\tilde{\zeta}_0$ the radiation damping of the footing. An expression for $\tilde{\zeta}_0$ is provided in Veletsos and Nair (1975).

Solution by Wolf (1985)

The system considered by Wolf is identical to that shown in Figures 1 and 2. The main assumption is that frequency-independent moduli are adopted for the foundation. The response of the system is determined by solving a set of three simultaneous algebraic equations for degrees of freedom u_1, u_3, and u_4 (Figure 1). The properties of the replacement oscillator in this solution are given by

$$\tilde{\omega}^2 = \omega_c^2\left(1+\frac{k}{K_x}+\frac{kh^2}{K_\theta}\right) \tag{8}$$

$$\tilde{\zeta} = \left(\frac{\tilde{\omega}}{\omega_c}\right)^2\zeta + \left[1-\left(\frac{\tilde{\omega}}{\omega_c}\right)^2\right]\zeta_s + \left(\frac{\tilde{\omega}}{\omega_x}\right)^2\zeta_x + \left(\frac{\tilde{\omega}}{\omega_\theta}\right)^2\zeta_\theta \tag{9}$$

In the above equations quantities ω_i (where i=θ, x, c) $\omega_\theta = \sqrt{K_\theta r^2/mh^2}$, $\omega_x = \sqrt{K_x/m}$, $\omega_c = \sqrt{k/m}$ define the uncoupled cyclic natural frequencies of the system under rocking oscillations of the base, swaying oscillations of the base, and oscillations of the superstructure, respectively.

Notwithstanding the importance and theoretical appeal of the above pioneering methods, their shortcomings can be summarized as follows:

(a) Both methods neglect products of damping ratios (ζ_i x ζ_j), as 'higher order' terms. This approximation is questionable for highly-damped soil-structure systems.

(b) The effective damping in the Veletsos approach arises from an approximate procedure leading to an expression containing imaginary terms. This limits its suitability for practical applications.

(c) Frequency dependence of foundation impedances is not considered by Wolf.

(d) Both solutions employ rather complex procedures involving either "equivalence" of responses of different dynamic systems (Veletsos), or solutions of simultaneous linear equations (Wolf).

(e) In both solutions, foundation mass and rotational inertia are neglected.

Proposed Exact Viscoelastic Procedure

The total horizontal deflection of the system can be decomposed as sum of the three additive modular displacements shown in Figure 2. This implies that the stiffness terms can be viewed as complex springs attached in parallel and, thereby, the dynamic impedance of the system can be expressed through the summation rule:

$$\frac{1}{\tilde{K}^*} = \frac{1}{K_x^*} + \frac{1}{K_\theta^*}\left(\frac{h}{r}\right)^2 + \frac{1}{k^*} \tag{10}$$

in which the associated impedances are complex valued and frequency dependent. Substituting each complex impedance term in Eq. (10) by meas of Eq. (1) yields the exact linear damping and elastic natural frequency of the system as (Maravas, 2006)

$$\tilde{\zeta} = \frac{\dfrac{\zeta_x}{\omega_x^2\left(1+4\zeta_x^2\right)} + \dfrac{\zeta_\theta}{\omega_\theta^2\left(1+4\zeta_\theta^2\right)} + \dfrac{\zeta}{\omega_c^2\left(1+4\zeta^2\right)}}{\dfrac{1}{\omega_x^2\left(1+4\zeta_x^2\right)} + \dfrac{1}{\omega_\theta^2\left(1+4\zeta_\theta^2\right)} + \dfrac{1}{\omega_c^2\left(1+4\zeta^2\right)}} \tag{11}$$

$$\tilde{\omega}^2 = \left[\frac{1+4\tilde{\zeta}^2}{\omega_x^2\left(1+4\zeta_x^2\right)} + \frac{1+4\tilde{\zeta}^2}{\omega_\theta^2\left(1+4\zeta_\theta^2\right)} + \frac{1+4\tilde{\zeta}^2}{\omega_c^2\left(1+4\zeta^2\right)}\right]^{-1} \tag{12}$$

Given the frequency-dependent nature of foundation impedances, an iterative procedure is generally required to determine ζ and ω from these solutions (Veletsos & Nair 1974). Note that omitting the products ζ_i^2, the above formulas duly reduce to those in Eqns (8) and (9), respectively.

Influence of Foundation Mass

The influence of foundation mass and inertia (m_f, I_f) on dynamic behavior of the system presented in Figures 1 and 2 can be incorporated by using modified frequency-dependent springs K_x and K_θ according to the formulas:

$$\overline{K}_x = K_x - m_f\omega^2 \tag{13}$$

$$\overline{K}_\theta = K_\theta - \mathrm{I}_f\omega^2 \tag{14}$$

This modification does not alter the form of the solution in Eqs (11) and (12). It merely introduces an additional dimensionless parameter, μ, which expresses the ratio of footing mass to superstructure mass.

$$\mu = \frac{m_f}{m} \tag{15}$$

Parametric Analysis and Comparisons with Classical Methods

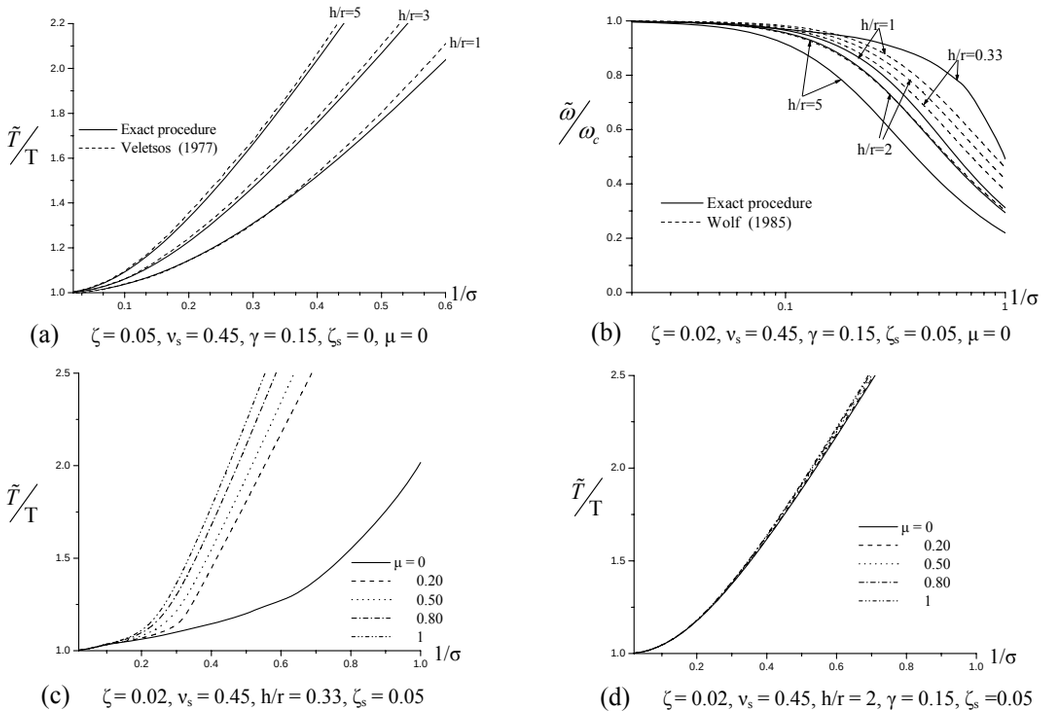
Comparative graphs for the variation of the ratio $\tilde{T}/T$ (inverse of $\tilde{\omega}/\omega_c$) versus the slenderness ratio h/r are presented in Figures 3a and 3b. Using the proposed exact viscoelastic procedure, the influence of mass ratio μ on the period and effective damping of the soil-structure system is presented in Figures 3c and 3d.

It is evident from Figure 3a that the results from the method of Veletsos are in good agreement with those obtained by the proposed procedure. Also in Figure 3b, we observe that results from the method of Wolf are quite different from those of the proposed procedure. This is mainly due to the assumption of frequency-independent springs and dashpots adopted by Wolf, and it is justified by the fact that for low values of $1/\sigma$ (i.e., low values of ω_c) the results of the two methods are nearly identical. Results obtained by Wolf deviate from those of the proposed procedure with decreasing h/r.

In Figure 3(c) it is shown that the variation of mass ratio μ affects the natural period of soil-structure systems with low values of h/r. On the contrary, it does not affect systems with high values of the slenderness ratio, as shown in Figures 3d. System damping is affected at the same manner as shown in Maravas (2006).

STRUCTURE ON PILE FOUNDATION

The system studied is shown in Figure 4. It consists of the SDOF structure described in the previous section, founded on a single flexible, circular solid pile of Young's modulus E_p, diameter d, mass per unit length m_p, and length L.
The soil is considered a linearly elastic homogeneous, halfspace, as described above.



(a) ζ = 0.05, ν_s = 0.45, γ = 0.15, ζ_s = 0, μ = 0

(b) ζ = 0.02, ν_s = 0.45, γ = 0.15, ζ_s = 0.05, μ = 0

(c) ζ = 0.02, ν_s = 0.45, h/r = 0.33, ζ_s = 0.05

(d) ζ = 0.02, ν_s = 0.45, h/r = 2, γ = 0.15, ζ_s =0.05

FIG. 3. (a,b) Comparison of proposed exact elastic solution with those of Veletsos (1977) and Wolf (1985), (c, d) Influence of foundation mass on dynamic behavior

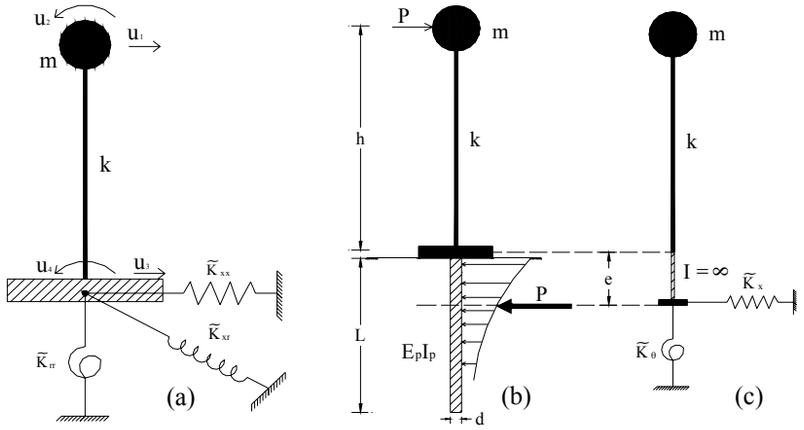


FIG. 4. (a) Model of pile-supported-structure, (b) Distribution of soil reactions due to horizontal loading, (c) Reduced model with two dynamic impedances

Soil-pile system can be represented by three dynamic impedances K_{xx}^*, K_{rr}^*, and K_{xr}^*, corresponding to swaying, rocking, and cross-swaying-rocking of the pile head, respectively. In this study, analytical expressions for the dynamic impedances are used, as derived by Novak, (1974)

$$K_{xx}^* = 4E_p I_p \lambda^3,\ K_{xr}^* = 2E_p I_p \lambda^2,\ K_{rr}^* = 2E_p I_p \lambda \tag{16}$$

$$\lambda = \left[\frac{k_x - m_p \omega^2 + i\omega c_x}{4E_p I_p} \right]^{1/4} \tag{17}$$

where λ is a wave number parameter, I_p is the moment of inertia of the pile cross section, and k_x and c_x are the moduli of distributed springs and dashpots along the pile.

Under horizontal loading the soil reacts in the manner shown in Figure 4b. The resultant of the distributed reactions is applied at depth e below the pile head. Since the reference system is anchored at the pile head, a cross swaying-rocking impedance term $\tilde{K}_{xr}$ is necessary for modeling the compliance of the foundation. This term is not compatible with the analysis of the spread footing presented earlier. To overcome this, the reference system can be translated to a depth e, where the total soil reaction is applied. In this manner, the cross impedance K_{xr}^* vanishes and the impedance matrix of the pile becomes diagonal, as shown in Figure 4c. This transformation is approximate, as it requires the pile to be rigid between the depths z = 0 and z = e. The associated error, however, is relatively minor, since e is usually small compared to the overall pile length. The transformed impedances K_{xxe}^* and K_{rre}^* are given by

$$K_{xxe}^* = K_{xx}^*,\ K_{rre}^* = K_{rr}^* - 2K_{xr}^* e + K_{xx}^* e^2,\ K_{xre}^* = 0 \tag{18}$$

where e is the aforementioned eccentricity.

The transformation shown in Figure 4(c) allows the usage of the exact elastic procedure developed for the analysis of structures on surface footings (Maravas, 2006).

Comparison of two SSI Systems: Footing vs Pile

In this section, the concept of statically and geometrically equivalent interacting systems is introduced, in an effort to compare the damping of systems on pile or surface footing foundations. To achieve this, the stiffness of the two SSI systems should be comparable at the elevation of mass m. Accordingly, the two systems are geometrically equivalent, i.e., h/d=h/2r, if the ratio of Young's moduli for the soil (Maravas 2006):

$$\frac{E_s^{(f)}}{E_s^{(p)}} = \frac{1}{2}\left(\frac{\pi\delta^3}{16}\right)^{1/4}\left(\frac{E_p}{E_s^{(p)}}\right)^{1/4}\frac{(2-\nu_s)(1+\nu_s)\left[1+4\left(h/d\right)^2\right]}{1+\left[1+2\left(\frac{16\delta}{\pi}\right)^{1/4}\left(\frac{E_p}{E_s^{(p)}}\right)^{-1/4}\frac{h}{d}\right]} \tag{19}$$

In the above equation, (f) denotes "footing" and (p) "pile". Because a pile is much stiffer than a footing, the supporting soil of the footing must have a modulus of elasticity $E_s^{(f)}$ quite larger than the modulus of elasticity of the soil around a pile.

Kinematic Response Factor

It is well known that the kinematic part of soil-structure interaction cannot be neglected in the case of embedded foundations (e.g. piles). The influence of kinematic response in SSI is expressed by the following factors

$$I_k = I_u - \frac{h}{a} I_\theta \tag{20}$$

where

$$I_u \equiv \frac{u_k}{u_{ff}},\ I_\theta \equiv \frac{\theta_k}{u_{ff}} \tag{21}$$

in which α is the characteristic length of the foundation, and u_k, θ_k are the response of the foundation due to kinematic soil-structure interaction. For pile foundations, the kinematic response factor I_k is determined by the boundary conditions of the pile head (pile cap), and is given by Nikolaou et al (2001)

$$I_k = \Gamma \text{ (Fixed-head pile)} \tag{22}$$

$$I_k = \Gamma\left[1+\frac{1}{2}\left(\frac{k^*}{\lambda}\right)^2\left(1-\lambda d\right)\frac{h}{d}\right] \text{ (Free-head pile)} \tag{23}$$

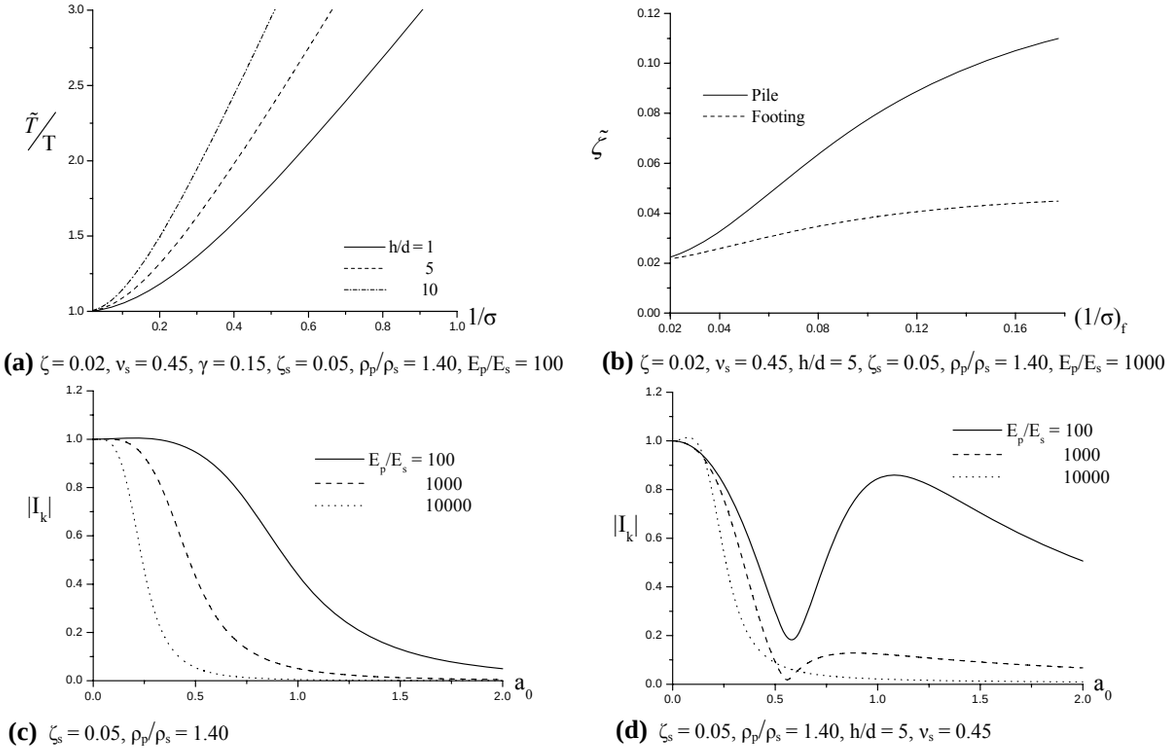
where λ is given by Eqn (17) and Γ, k^* are determined as Nikolaou et al (2001)

$$\Gamma = \frac{k_x + i\omega c_x}{E_p I_p\left(k^{*4} + 4\lambda^4\right)} \tag{24}$$

$$k^* = \frac{\omega}{V_s^*} = \frac{\omega}{V_s}\frac{1}{\sqrt{1+2i\zeta_s}} \tag{25}$$

Results of Parametric Analyses

Figure 5(a) presents the influence of the slenderness ratio (h/d). on the natural period of the interacting system. Evidently, the behavior is similar to the behavior of the soil-footing-structure system presented earlier. The same observation holds for the effective damping, as shown in Maravas (2006).



(a) $\zeta = 0.02$, $\nu_s = 0.45$, $\gamma = 0.15$, $\zeta_s = 0.05$, $\rho_p/\rho_s = 1.40$, $E_p/E_s = 100$

(b) $\zeta = 0.02$, $\nu_s = 0.45$, h/d = 5, $\zeta_s = 0.05$, $\rho_p/\rho_s = 1.40$, $E_p/E_s = 1000$

(c) $\zeta_s = 0.05$, $\rho_p/\rho_s = 1.40$

(d) $\zeta_s = 0.05$, $\rho_p/\rho_s = 1.40$, h/d = 5, $\nu_s = 0.45$

FIG. 5. (a) System period as function of h/d, (b) Effective damping, (c, d) Kinematic response factor for fixed- and free-head piles.

Using the proposed procedure, the effective damping of the two SSI systems is compared in Figure 5b. It is obvious that a structure on a pile may experience three times the damping generated from the same structure on a spread footing. This is justified in view of the two-dimensional nature of wave propagation around a pile, which results to higher energy dissipation. In Figures 5c, 5d the absolute value of kinematic response factor is presented, as function of dimensionless frequency $a_0 = \omega d/V_s$. It is evident that I_k for a fixed-head pile decreases monotonically with frequency (Figure 5c). For a free-head pile, the behavior may be oscillatory (Figure 5d).

CONCLUSIONS

A novel procedure for determining the dynamic characteristics of simple structures founded on surface footings and piles is presented. Using the proposed methodology, the influence of common assumptions on the computation of the mechanical properties of such systems is elucidated. By introducing the concept of statically and geometrically equivalent SSI systems, the amounts of radiation damping generated from a single pile and a footing are compared. The main conclusions of the study are:

(1) The common approximation of neglecting higher-order terms involving products of damping coefficients may be inaccurate for highly-damped SSI systems.

(2) The foundation mass affects considerably the dynamic response of SSI systems with low values of slenderness ratio.

(3) The proposed analysis can easily incorporate embedded foundations, by translating the reference system to the depth where the resultant soil reaction is applied. This ensures a diagonal foundation impedance matrix and greatly simplifies calculations.

(4) A structure founded on a pile may generate 100% more radiation damping than a similar structure on a spread footing. The difference gets more pronounced with high-frequency, squatty structures on stiff soil.

(5) The kinematic part of soil-structure interaction can affect (reduce) considerably the response of structure founded on a single pile.

(6) The proposed solution is more accurate, and general than the classical solutions by Parmelee, Bielak, Veletsos and Wolf.

REFERENCES

Aviles, J. & Perez-Rocha, L. E (1998). “Effects of foundation embedment during building-soil interaction”, *Earthq. Engng & Struct Dyn*, **27**(12), 1523-15400.

Jennings, P.C. & Bielak, J.(1973). "Dynamics of building-soil interaction", *Bulletin of the Seismological Society of America*, **63**(1) 9-48.

Maravas, A. (2006). “Discrete model for dynamic soil-structure interaction of structures on rigid surface or pile foundations*”, MS. Thesis, University of Patras,* (in Greek).

Mylonakis, G. (1995). “Contributions to the static and seismic analysis of pile-supported bridge piers”, *Ph.D. Dissertation,* SUNY-Buffalo. 1995

Nikolaou, S., Mylonakis, G., Gazetas, G., and Tazoh, T. (2001). “Kinematic Pile Bending During Earthquakes: Analysis and Field Measurements”, *Geotechnique,* 51(5), 425-440,

Novak, M. (1974) “Dynamic stiffness and damping of piles”, *Canadian Geotech. Journal,* **11**, 574-591.

Parmelee, R. (1967). “Building-foundation interaction effects”, *Journal of Engineering Mechanics Division*, ASCE, **93**(EM2), 131-152.

Veletsos, A.S. & Meek, J.W. (1974). “Dynamic behavior of building-foundation systems”, *Earthq, Engng & Struct, Dyn,*, **3**(2), 121-138.

Veletsos, A.S. & Nair, V.V. (1975) “Seismic interaction of structures on hysteretic foundations”, *Journal of Structural Engineering*, ASCE, **101**(1), 109-129.

Veletsos, A. S. (1977) “Dynamics of Structure-Foundation Systems”, in: Hall, W. J. (ed.), *Structural & Geotechnical Mech.*, Prentice-Hall.

Wolf, J. P. (1985). *Dynamic Soil-Structure Interaction*, Prentice Hall.

Effect of Critical Contact Area Ratio on Moment Capacity of Rocking Shallow Footings

Sivapalan Gajan[1] and Bruce L Kutter[2]

[1]Assistant Professor, North Dakota State University, Fargo, ND 58105; s.gajan@ndsu.edu
[2]Professor, University of California, Davis, CA 95616; blkutter@ucdavis.edu

ABSTRACT: The rocking of a relatively rigid footing on soil can be visualized as a moving contact problem, with a contact area moving from one side of the footing to the other as the footing rocks. Thus the partial separation of footing (uplift) and the resulting moment capacity can be more closely related to the critical contact area ratio, A/Ac (ratio between the actual footing area (A) and the area required to support the vertical and shear loads (Ac)). This paper compares the moment capacities calculated by using A/Ac with those obtained from centrifuge and 1-g experiments conducted on rocking shallow footings for a range of A/Ac values. It is shown that the moment capacity of a rocking footing is well defined and, unlike bearing capacity, moment capacity is less sensitive to the uncertainty in soil properties as A/Ac increases.

INTRODUCTION

Soil-foundation interaction associated with heavily loaded shear wall structures supported by shallow foundations during large seismic events may produce highly nonlinear load-displacement behavior. It has been shown that the ductility demands on the super structure could be reduced by allowing mobilization of the ultimate capacity and rocking behavior of shallow footings during seismic loading (for e.g., Gajan et al., 2005). However, the perceived lack of certainty in soil properties and the lack of confidence in designing foundations with desired moment capacity have hindered the use of foundation rocking as a primary energy dissipation mechanism.

This paper presents the relationships between ultimate moment capacity of rocking footings and critical contact area ratio (A/Ac), where A is the actual footing area and Ac is the footing area required to be in contact with the soil to support applied vertical and shear loads. The estimation of A/Ac for given arbitrary loading and the difference between A/Ac and the traditionally defined vertical factor of safety (FS_V) are explained using conventional bearing capacity equations and the shape and size of contact area when the footing rocks. The dependence of moment capacity on A/Ac is explained using parametric studies that include the effects of geometry of the footing and soil properties. The moment capacities observed in centrifuge experiments as well

as in 1-g experiments on rocking shallow footings are compared with those predicted by using A/Ac. The effect of uncertainty in soil properties on moment capacity is also presented.

CRITICAL CONTACT AREA RATIO AND MOMENT CAPACITY

The rocking of a relatively rigid footing on soil can be visualized as a moving contact problem, with a contact area moving from one side of the footing to the other with the opening and closing of gaps behind and in front of a contact area that moves based on the geometry of the footing-soil interface. Fig. 1 shows a schematic of a footing-soil interface during foundation rocking; the base of a rigid footing and its contact with the curved soil surface beneath the footing. As the magnitude of rotation increases, the footing contact area with soil becomes smaller and moves towards the edge of the footing due to uplift at the other side. As the contact area decreases, the bearing resistance intensity along the contact area increases in order to satisfy vertical equilibrium.

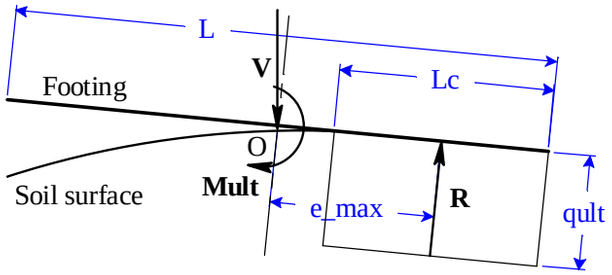


FIG. 1. Footing-soil contact interface and critical contact area ratio.

As shown in Fig. 1, at one stage, the bearing resistance along the whole contact area may become equal to the ultimate bearing resistance; hence, no further reduction in contact area is possible. This minimum contact area is defined as the critical contact area (Ac), which can be calculated from conventional bearing capacity equations and the associated shape and depth factors for the critical contact area. For rectangular footings, with loading in the long (L) direction, the ratio of areas (A/Ac) can be equated to a length ratio, L/Lc, where Lc is referred to as critical contact length. The moment obtained when the contact length reaches Lc (or when the contact area reaches Ac) is referred to as the ultimate moment (M_{ULT}), and can be obtained by,

$$M_{ULT} = \frac{V \cdot L}{2} \cdot \left[1 - \frac{Ac}{A}\right] \quad (1)$$

where V is the applied vertical load at the footing-soil interface. Note that M_{ULT} is the maximum possible moment that the foundation soil can resist for given V, L, A, and Ac, assuming that the bearing pressure distribution beneath the contact area Ac is ultimate and uniform.

CALCULATION OF A/Ac

In this section, the procedure to calculate A/Ac is described. The A/Ac ratio is equal to FS_V, if the maximum bearing pressure is independent of the shape and size of the loaded area (FS_V is the factor of safety with respect to bearing capacity failure for concentric vertical loading). The bearing capacity shape factors (e.g., De Beer, 1970), depth factors (e.g., Hansen, 1970), and the $(1/2)\cdot\gamma\cdot B\cdot N_\gamma$ term in Terzaghi's bearing capacity equation (Terzaghi, 1943, Hanna and Meyerhof, 1981) indicate that A/Ac is different from FS_V, as contact geometry changes during footing rocking. An iterative procedure is used to calculate A/Ac given the applied vertical load, soil properties, footing geometry, direction of rocking and conventional bearing capacity equations.

Get_AoverAc $(V, L, B, D, \phi, \gamma, k_h, k_v, n)$
{
  Set $dV_{min} = V$
  For i = 1 to n
  {
    Get $Lcont = L \cdot \left(\frac{i}{n}\right)$
    If $(Lcont < B)$ then swap Lcont and B
    Get $\theta = f(k_h, k_v)$
    Get $k_p = f(\phi, \theta)$
    Get $N_q, N_\gamma = f(k_p, \phi)$
    Get $F_{qs}, F_{\gamma s}, F_{qd}, F_{\gamma d} = f(Lcont, B, D)$
    Get $V_{trial} = f(N_q, N_\gamma, Lcont, B, D, \gamma, F_{qs}, F_{\gamma s}, F_{qd}, F_{\gamma d})$
    Get $dV = |V - V_{trial}|$
    If $(dV < dV_{min})$
    {
      Set $dV_{min} = dV$
      Get $\frac{A}{Ac} = \frac{L}{Lcont}$
    }
  }
  Return $\frac{A}{Ac}$
}

Fig. 2 Algorithm for calculating A/Ac for footings supported by sandy soils

For dynamic base shaking tests, additional inertial forces in the soil mass during ground shaking have been shown to cause additional stresses in the soil, which, in turn, cause a reduction in bearing capacity (Richards et al., 1993). Therefore the A/Ac values for dynamic tests were calculated using the dynamic bearing capacity factors that correlate the reduction in bearing capacity with the magnitude of shaking. Richards et al. (1993) proposed an expression for the passive earth pressure coefficient that includes the effects of horizontal and vertical shaking magnitudes.

$$K_p = \frac{\cos(\phi - \theta)^2}{\cos(\theta)^2 \cdot \left[1 - \left(\frac{\sin(\phi) \cdot \sin(\phi - \theta)}{\cos(\theta)}\right)^{0.5}\right]^2} \quad (2a)$$

$$\theta = a\tan\left[\frac{k_h}{1 - k_v}\right] \quad (2b)$$

where, k_h and k_v are the horizontal and vertical seismic coefficients. When $\theta = 0$, K_p becomes $\tan(\pi/2 + \varphi/2)^2$, leading to the static bearing capacity factor N_q.

The algorithm shown in Fig.2 explains the calculation of A/Ac values for footing supported by sandy soil. In the algorithm, V is the applied vertical load, L, B, and D are the length, width, and depth of embedment of footing respectively, φ and γ are the friction angle and unit weight of soil respectively, k_h and k_v are the horizontal and vertical seismic coefficients respectively, and n is the number of trials (i.e., number of area increments) to find the accurate contact area Ac so that the maximum possible error in Ac estimate is less than A/n. As can be seen from the algorithm, when the footing is loaded laterally in L direction, the iterative procedure repeats n times, each time increasing the contact length (Lcont) by L/n, to find the best estimate of Lc, and hence A/Ac. A similar algorithm is used to calculate the A/Ac ratios for clay foundations using bearing capacity equations and factors for cohesive soils.

ASSUMPTIONS AND SIMPLIFICATIONS

The following are the assumptions and simplifications employed in the calculation of A/Ac and ultimate moment.

1. Effects of side friction and passive resistance on the side of the footing: The ultimate moment defined in eq. 1 does not take into account the passive resistance and the side frictional resistance of soil on the side of the footing (i.e., eq. 1 is intended for surface footings). However, for shallow embedded footings or after few cycles of loading on a surface footing, there will be soil resistances on the side of the footing. Fig. 3 shows a shallow footing, with depth of embedment $D = h_f$, subject to moment loading and the resistances from soil: bearing resistance (R), side frictional resistance (F), and passive resistance (P). By using vertical and moment equilibrium about the base center point O, one can obtain the following expression for ultimate moment (M_{ULT}) that the soil can support,

$$M_{ULT} = \frac{V \cdot L}{2} \cdot \left[1 - \frac{Ac}{A}\right] + F \cdot \frac{Lc}{2} + P \cdot \frac{h_f}{3} \quad (3)$$

The last two terms in eq. 3, terms with F and P, are neglected in ultimate moment equation. It is shown in the experimental comparison section, that the relative error in M_{ULT} by ignoring the last two terms in eq. 3 is up to about 5% for relatively shallow embedded ($D \leq hf$) footings that were used in experiments presented in this paper.

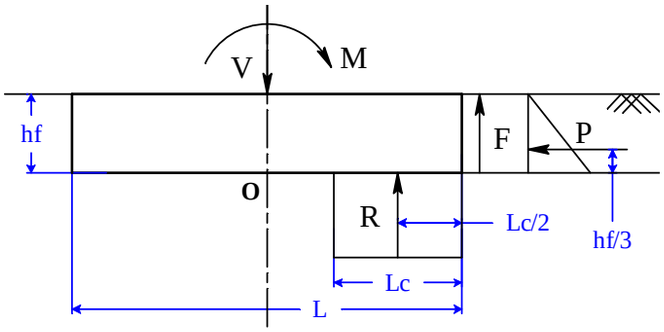


FIG. 3. Footing-soil contact area and the forces and reactions

2. Bearing pressure distribution and its resultant location: The ultimate moment expressions in eq. 1 and 3 are the maximum moment that the foundation soil can support, and thus, it depends on the bearing pressure distribution when the contact area reaches its minimum possible value. It is assumed that the critical contact area is reached when the bearing pressure distribution is ultimate and uniform beneath the contact area. This is the theoretical minimum contact area (according to conventional bearing capacity theory), and this assumption is proven to be reasonable when comparing the calculated M_{ULT} with experimental results in the next section.

3. Effect of base shear on ultimate moment: Many researchers have studied the coupling between moment and shear at the base of the footing and the reduction in ultimate moment due to shear (Gajan, 2006). According to the interaction diagrams (in normalized moment-shear planes) proposed by these researchers and from the experimental evidence presented by Gajan and Kutter (2007), the effect of shear on moment capacity can be neglected for relatively higher moment to shear ratio (M/H > L). However, for shear-dominated behavior (for e.g., low aspect ratio structures), the moment capacity will be reduced due to increased shear. Therefore the proposed expressions for ultimate moment, based on A/Ac, are valid for higher moment-to-shear ratio footing and loading. For shear dominated behavior, the algorithm to calculate A/Ac is modified to include the applied shear (Gajan, 2006) and to calculate the reduced ultimate moment.

COMPARISONS WITH CENTRIFUGE EXPERIMENTAL RESULTS

In this section, experimental results for moment-rotation-settlement behavior of footing-soil interface are presented and the results are used to verify the proposed relationship between M_{ULT} and A/Ac. Most of the experimental results presented in this paper were obtained from a series of centrifuge experiments, conducted in University of California at Davis, each of which consists of several shear wall-shallow foundation models tested under slow lateral cyclic and dynamic loading conditions. Detailed experimental results are available for all the models tested in the centrifuge in data reports (e.g., Gajan et al., 2003). Unless otherwise indicated, the model configurations and all the experimental results are presented using prototype-scale units in this paper.

Fig. 4 compares the footing response in terms of moment-rotation and settlement-rotation at the base center point of the footing during slow lateral cyclic tests (three on sand and one on clay) for different A/Ac footings. Rectangular footings (2.8 m x 0.65 m) were loaded laterally in longer direction of the footing. The normalized moment-to-shear ratio (M/(H·L)) at the base of the footing for all these tests ranges from 1.7 to 1.9. In Fig. 4, moment is normalized by V·L/2 (the overturning moment for a footing on rigid soil (infinite A/Ac)), while the settlement is normalized by the length (L) of the foundation in the direction of rocking. The weight of the structure used in a particular test along with the footing geometry, depth of embedment, and soil properties were used to calculate the A/Ac values for each structure.

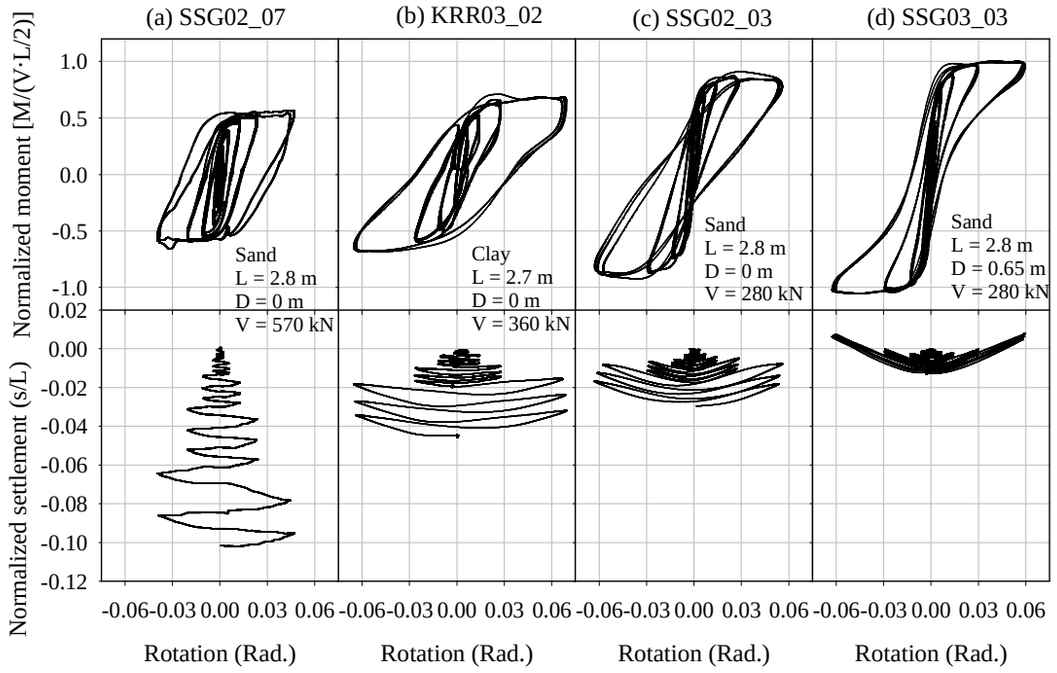


FIG. 4. Moment-rotation-settlement relationships at the base center point of the footing during slow lateral cyclic tests showing the effect of A/Ac: (a) A/Ac = 2.2, (b) A/Ac = 3.0, (c) A/Ac = 3.8, and (d) A/Ac = 12.3

In all four tests presented in Fig. 4, the moment-rotation relationships are highly nonlinear and show stiffer response for low levels of rotation, but as the magnitude of rotation increases, rotational stiffness degrades. Foundation rocking progressively rounds the soil beneath the footing, and this rounding causes a reduction in contact area between the footing and soil thereby causing nonlinearity in moment-rotation relationships. Once the soil beneath the footing contact area yields and the ultimate vertical bearing capacity is mobilized, the footing continues to rotate without significant reduction in moment capacity. The settlement-rotation relationships show the cyclic rotation of the footing with uplift associated with a formation of gap and the accumulation of permanent settlement associated with yielding of the soil on the other side of the footing. The larger A/Ac footings show less permanent settlement and

larger normalized moment capacity, which is consistent with eq. 1. The observed moment-rotation-settlement behavior on clay foundation (Fig. 4.b) is similar to that on sand foundations.

Fig. 5 shows the relationship between the normalized theoretical ultimate moment with A/Ac, as calculated from eq. 1. Also plotted in Fig. 5 are the ultimate moments obtained from several experiments. Experimental data obtained from the slow lateral cyclic and dynamic shaking tests on sand and clay foundations in the centrifuge experiments described in the previous section (plotted as Gajan and Rosebrook). The second set of data in Fig. 5 are the experimentally observed normalized ultimate moments in 1-g experiments conducted in University of Auckland, New Zealand (Bartlett, 1976 and Wiessing, 1979). Experiments conducted by Wiessing (1979) considered the rocking response of foundations resting on dry dense sand, whereas the experiments conducted by Bartlett (1976) included foundations resting on saturated clay. In both series of experiments, cyclic rotation was applied to model rectangular footings (0.25 m x 0.5 m) while the footings were fixed against lateral sliding. The third set of data was obtained from centrifuge experiments conducted on bridge structures supported by shallow foundations in University of California, Davis (Ugalde et al., 2007). Square footings of different sizes (5.4 m, 7.1 m, and 8.9 m) supported by dry Nevada sand and subjected to both slow lateral cyclic and dynamic base shaking tests.

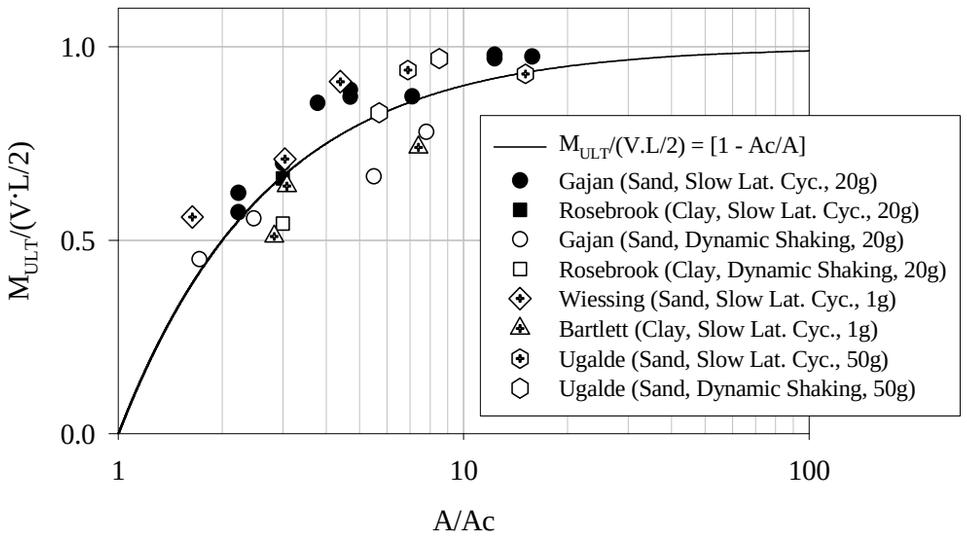


FIG. 5. Variation of experimental normalized ultimate moment and theoretical normalized ultimate moment with A/Ac

As can be seen in Fig. 5, the normalized ultimate moment rapidly increases as A/Ac increases from 1 to 10; 90% of the tip-over moment ($V{\cdot}L/2$) is achieved when A/Ac = 10. Fig. 4 also shows that the moment capacities of the footing obtained in the centrifuge and 1-g experiments, on sand and clay foundations, and on rectangular as well as square footings, are reasonably close to the theoretical ultimate moment calculated by using A/Ac. According to eq. 3, the error in normalized ultimate moment by ignoring the side friction and passive resistance can be obtained as,

$$\text{Error}\left|M_{ULT_Normalized}\right| = \frac{\left(\frac{1}{2}\cdot\gamma\cdot h_f{}^2\cdot K_p\cdot B\right)\left(\tan(\delta)\cdot\frac{Lc}{2}+\frac{h_f}{3}\right)}{\left(\frac{V\cdot L}{2}\right)} \quad (4)$$

Where γ is the unit weight of soil and δ is the friction angle between soil and footing. For the experimental results presented in Fig. 5, the error in normalized ultimate moment, calculated using eq. 4, is up to about 5%. This indicates that the proposed equation for M_{ULT} based on A/Ac can be used to calculate the ultimate moment of shallow embedded footings subjected to relatively higher moment-to-shear ratio loading.

A/Ac VERSUS FS_V

In order to present the effect of L, and hence the effect of A/Ac, on the moment capacity of rocking foundation, a simple parametric study was carried out. Fig. 5 shows a shallow foundation supporting a column that carries 1000 kN axial load. The depth of embedment of the footing is zero and the width of the footing is fixed at 2.0 m. Soil profile consists of dry uniform sand with friction angle 40 degrees and unit weight 15 kN/m^3. For these given conditions, the length of the footing, L, was varied and A/Ac and moment capacity were calculated.

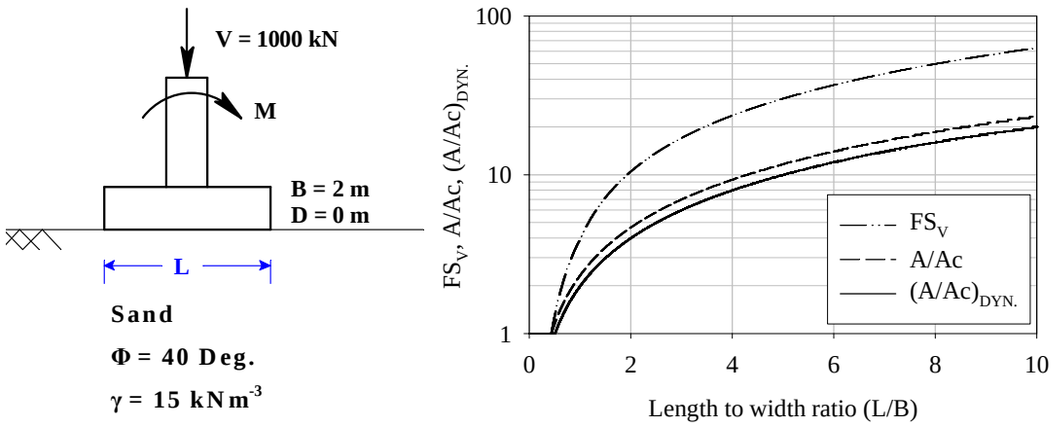


FIG. 6. Effect of L on A/Ac for a surface footing supported by uniform sandy soil

Fig. 6 also presents the calculated values of FS_V, A/Ac, and $(A/Ac)_{Dyn.}$ as a function of footing length to width ratio (L/B). Note that L is the length of the footing in the direction of rocking; not necessarily the larger dimension of the footing. The FS_V values were calculated using bearing capacity equations and the initial geometry of the footing for a given L/B ratio. The A/Ac values were calculated using bearing capacity equations and the geometry of the footing when the contact length is at its critical value, Lc, using an iterative procedure. It is clearly seen from the results that the shape and size of the contact geometry makes a significant difference in A/Ac as opposed to

the traditionally defined FS_V; in this example, A/Ac is about three times smaller than FS_V when L/B > 5. The dynamic A/Ac values were calculated using the dynamic bearing capacity factors, including the effect of shaking on N_q (eq. 2). A/Ac was reduced by about 20% to 25% when a lateral seismic coefficient of 0.5 was used.

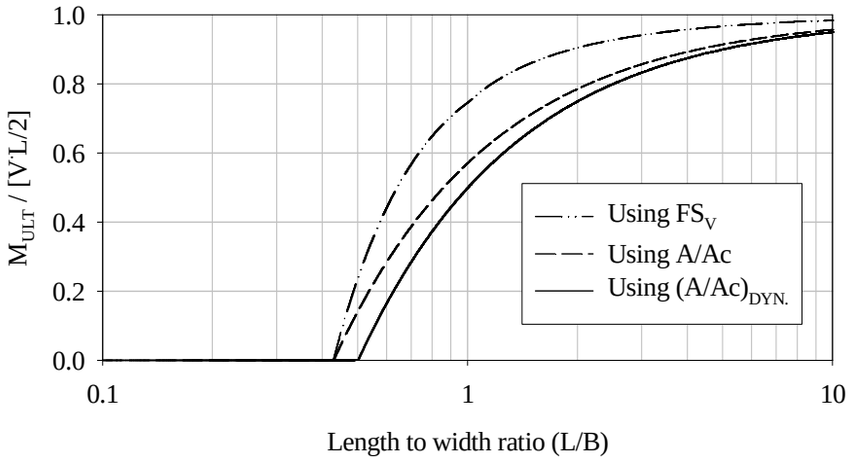


FIG. 7. Normalized moment capacity and footing length

Fig. 7 shows the variation of normalized ultimate moment with the length to width ratio of the footing. Ultimate moments were calculated using FS_V, A/Ac, and $(A/Ac)_{dyn}$ in eq. 1. For the square footing (L/B = 1) in this example, using FS_V to calculate the ultimate moment over predicts the capacity by about 50% (compared to $M_{ULT}_(A/Ac)_{dyn}$). Also, the difference in moment capacities predicted by using A/Ac and $(A/Ac)_{dyn}$ is up to about 25% (for 0.5 g shaking), which is consistent with the centrifuge experimental results (Gajan and Kutter, 2007). Though the difference between FS_V and A/Ac increases as L/B increases, the differences between the ultimate moments calculated by FS_V and A/Ac, and, A/Ac and $(A/Ac)_{dyn}$ decrease as L/B increases.

Note that Fig. 6 and Fig. 7 plot the results for this particular example, where soil properties, applied vertical load, and width and depth of embedment of the footing were fixed and constants. The effect of footing size on A/Ac and M_{ULT} are presented as a function of L/B by varying the length of the footing in the direction of rocking. If any of those fixed parameters change, one will get different sets of curves, however the trend shown with L/B will remain the same.

UNCERTAINTY IN SOIL STRENGTH

To study the effect of uncertainty on ultimate moment capacity, the friction angle of sand was varied and the moment capacities were calculated for a particular footing geometry (L = 10 m and B = 2.0 m). The A/Ac of this footing is about 10 for 40 degrees friction angle sand (Fig. 5). For these calculations, friction angle was varied from 25 degrees to 45 degrees and all other parameters were kept constant as in previous example. Fig. 8 plots both ultimate bearing capacity ($FS_V = V_{ULT}/V$) and moment capacity ($M_{ULT}/V{\cdot}L/2$) against friction angle of the sand.

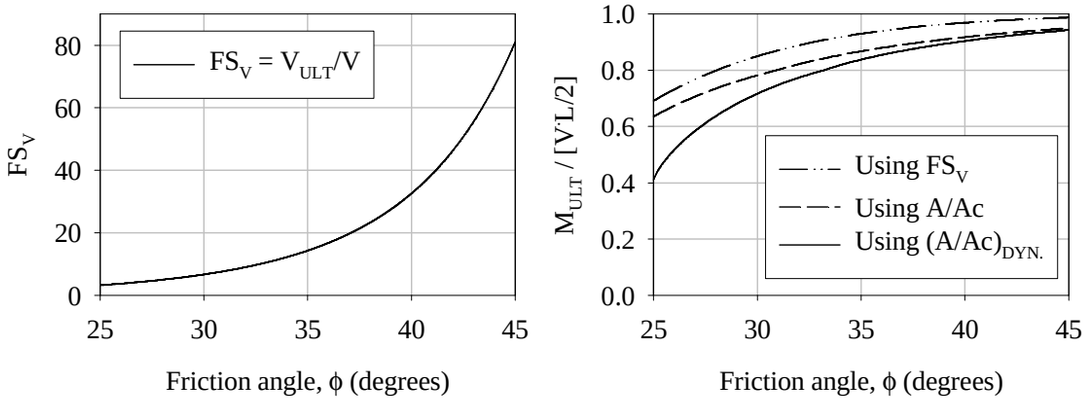


FIG. 8. Variation of ultimate bearing capacity and ultimate moment capacity with friction angle

It is well known that the ultimate bearing capacity of sand is very sensitive to friction angle, as the bearing capacity factor Nq is an exponential function in friction angle. This is shown in FS_V versus friction angle relationship in Fig. 7. On the other hand, Fig. 8 shows that the rocking moment capacity is not that sensitive to the friction angle of sand. For example, when friction angle decreases from 45 to 30 degrees, the ultimate bearing capacity decreases by about 90%, while the reduction in moment capacity is only about 20%. Thus the moment capacity of a rocking foundation with large A/Ac ratio (A/Ac > 10) is well defined and predictable with less uncertainty for typical friction angle values of sand.

CONCLUSIONS

Rocking behavior and mobilization of ultimate bearing capacity of shallow foundations is often not considered to be a usable energy dissipation mechanism during seismic loading in current civil engineering practice. Some of the reasons for avoiding foundation rocking include concerns about permanent settlement and the uncertainty in soil properties and moment capacity. The experimental results presented in this paper shows that the moment capacity of a rocking foundation can well be correlated with critical contact area ratio (A/Ac). The parametric studies presented for a simple foundation on uniform sand shows that the moment capacity is not very sensitive to soil properties for large A/Ac footings. Footings with A/Ac > 10 have a well defined moment capacity, suffer negligible permanent settlement beneath the footing, and dissipate seismic energy at footing-soil interface. Thus there is promise to use rocking foundations in place of or in combination with structural base isolation and energy dissipation devices to improve the performance of the structure during seismic loading. While requiring A/Ac > 10 may sound excessive, it should be noted that the size of large footings is often governed by settlement, not capacity, hence requiring a larger A/Ac does not translate directly to large footings.

ACKNOWLEDGEMENTS

The centrifuge experiments were supported by the Pacific Earthquake Engineering Research (PEER) Centers Program of the National Science Foundation (NSF) under award number EEC-9701568 and PEER project number 2262001. Any opinions, findings and conclusions or recommendations expressed in this paper are those of the authors and do not necessarily reflect those of the NSF. The authors would like to acknowledge the suggestions and contributions of Geoff Martin, Tara Hutchinson, Jonathan Stewart, Ross Boulanger, Boris Jeremic, Dan Wilson, Jose Ugalde, Key Rosebrook, Justin Phalen, and Jeremy Thomas.

REFERENCES

Bartlett, P. E. (1976). "Foundation Rocking on a Clay Soil." M.E. Thesis, School of Engineering, University of Auckland, New Zealand, Report No. 154.

De Beer, E. E., (1970). "Experimental Determination of Shape Factor and Bearing Capacity Factors of Sand," *Geotechnique*, Vol. 20, No. 4, 387-411.

Gajan, S (2006). "Physical and numerical modeling of nonlinear cyclic load-deformation behavior of shallow foundations supporting rocking shear walls". Ph.D. Dissertation, College of Engineering, University of California, Davis, Calif.

Gajan, S. and Kutter, B. L. (2007), "Capacity, settlement, and energy dissipation of rocking shallow foundations," *Journal of Geotechnical and Geoenvironmental Engineering*, ASCE (accepted for publication)

Gajan, S., Phalen, J. D. and Kutter, B. L. (2003). "Soil-foundation-structure interaction: Shallow foundations." *Centrifuge Data Report for test series SSG02*. Report No. UCD/CGMDR-03/01, Center for Geotechnical Modeling, University of California, Davis, Calif.

Gajan, S., Phalen, J. D., Kutter, B. L., Hutchinson, T. C. and Martin, G. (2005). "Centrifuge modeling of load-deformation behavior of rocking shallow foundations", *Journal of Soil Dynamics and Earthquake Engineering*, Vol. 25 (7-10), 773-783.

Hanna, A. M. and Meyerhof, G. G. (1981). "Experimental Evaluation of Bearing Capacity of Footings Subjected to Inclined Loads," *Canadian Geotechnical Journal*, Vol. 18, No. 4, 559-603.

Hansen, J. B. (1970). "A Revised and Extended Formula for Bearing Capacity," *Danish Geotechnical Institute*, Bulletin 28, Copenhagen.

Richards Jr., R., Elms, D. G., and Budhu, M. (1993). "Seismic bearing capacity and settlements of foundations", *Journal of Geotechnical Engineering*, ASCE, Vol. 119, No. 4, pp 662 - 674

Terzaghi, K. (1943). "Theoretical soil mechanics", Wiley, New York

Ugalde, J. A., Kutter, B. L., Jeremic, B., and Gajan, S. (2007), "Centrifuge modeling rocking behavior of structures on shallow foundations", *Proc. 4th Intl. Conf. Earthquake Geotechnical Engineering*, Paper #1484, Thessaloniki, Greece, June 25-28, 2007

Wiessing, P. R. (1979). "Foundation rocking on sand." M.E. Thesis, University of Auckland, School of Engineering, Report No. 203, November, 1979.

This page intentionally left blank

Material Model Parameters for Shallow Foundation Numerical Analysis

Prishati Raychowdhury and Tara Hutchinson
Department of Structural Engineering, University of California, San Diego

ABSTRACT: In material modeling, a number of physical properties such stiffness, strength and post-yield capacity can be directly determined through element-level tests. However, to actually generate a numerically robust representation of a materials response, additional parameters describing the backbone and/or cyclic response (e.g., the shape of transitions from linear to nonlinear regions and the full shape of the post-yield region) are needed. These backbone parameters are difficult to characterize directly from an element-level experiment, and thus are not well correlated with typical soil parameters. However, they may be more readily obtained from system-level tests. Therefore, this study focuses on the parameters needed to describe the nonlinear response of Winkler springs, used in the context of Winkler-based shallow foundation modeling. The foundation subgrade is assumed as a system of discrete, mechanistic, uncoupled springs having nonlinear uplift, sliding and damping capabilities. For this type of modeling problem, elastic-plastic spring representations are commonly used in practice. However, under cyclic rocking, physical changes to the underlying soil occur (mostly due to the densification and shearing at the edges), therefore an elastic-plastic representation will not provide a realistic description of the soil-footing behavior. In this paper, data sets from centrifuge and large-scale footing experiments, whereby the response is controlled in a single degree of freedom, are used to determine the parameters describing the nonlinear backbones of mechanistic springs. For this purpose, models of each test are constructed and through comparison of model results with the experimental response, and isolating one parameter at a time, best-fit parameters are determined. Finally, a sensitivity study is carried out to observe the effect of parameters that describe the spring backbone response.

INTRODUCTION

When a building supported by shallow foundations is subjected to earthquake ground motion, the seismic loading can potentially cause the foundation to rock. If the amplitude of this rocking is sufficient to mobilize nonlinear deformation of the foundation, energy is dissipated through moment-rotation action at the soil-footing interface. This energy dissipation phenomenon has been observed through many centrifuge and one-g experiments. Despite this potential benefit, current building codes discourage designs that allow rocking. Design codes that provide guidance regarding structural rehabilitation, however, do provide minimal guidance in this context [e.g. ATC-40 (1996); ASCE-7 (2003)].

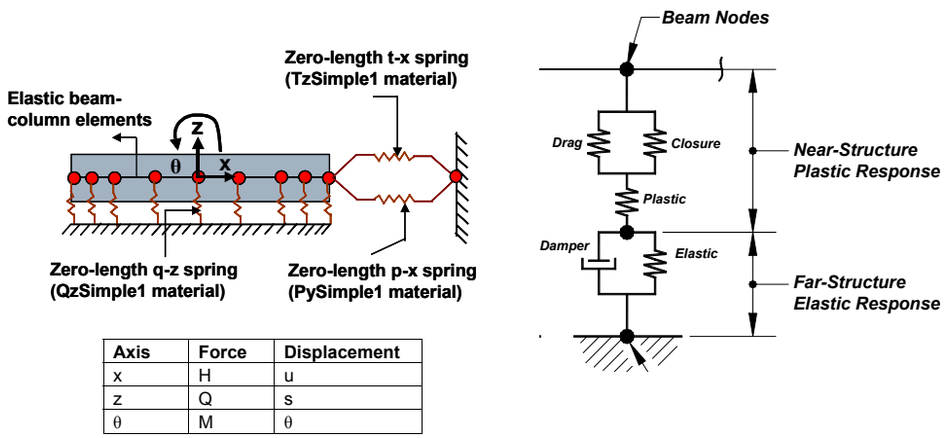
Modeling of this energy dissipation phenomenon has been done by several researchers using mechanistic nonlinear Winkler springs [e.g. Chopra and Yim (1985); Allotey and Naggar (2007)]. However, to-date the spring backbones used

for this purpose were either elastic-plastic or smoothly varying nonlinear curves calibrated against lateral pile load test data [e.g., Matlock (1970); API (1987)]. Although smoothly varying nonlinear backbones are better representation of the soil-footing behavior, it is not clear if the pile-calibrated nonlinear springs are reasonable to represent the response of a soil-shallow footing system. In this work, backbone curves typically used for modeling of pile foundations are used as a baseline and their parameters are calibrated against a variety of shallow foundation load tests.

MODELING APPROACH

In this study, the well-known BNWF (Beam-on-Nonlinear-Winkler-Foundation) model has been adopted to capture shallow foundation behavior. A mesh of nonlinear spring elements is used for vertical and moment resistance, as well as lateral resistances as shown in Figure 1(a). The analysis in this work is conducted using the OpenSees platform (PEER, 2008). Individual springs are modeled with one-dimensional zeroLength elements, where nonlinearity is modeled using the Qzsimple1, PySimple1 and TzSimple1 material models implemented in OpenSees (Boulanger, 2000). Note that the backbone curves of these material models were calibrated using pile load test curves [e.g. Matlock (1970); API (1987)]. Thus, the nomenclature used to describe the material models is based on a coordinate system of a laterally loaded pile (y and z being horizontal and vertical axes, respectively). In the present work, the orientation shown in Figure 1(a) is adopted.

The axial and moment responses are captured by using a mesh of nonlinear q-z springs, while p-x and t-x springs are placed horizontally to capture passive and sliding resistance, respectively. The Qzsimple1 material has an asymmetric hysteresis, with a backbone defined by an ultimate load on the compression side and a reduced strength in tension (a maximum tension capacity of 10% of the ultimate compressive load is considered), as well as the capability to account for soil-footing separation via a gap element placed in series with the elastic and plastic components. The elastic material is intended to capture the "far-field" behav-



Axis	Force	Displacement
x	H	u
z	Q	s
θ	M	θ

FIG. 1. (a) BNWF schematic and (b) typical zero-length element.

ior, while the plastic component is intended to capture the "near-field" permanent displacements (Figure 1b). PySimple1 and TzSimple1 materials are similar to the QzSimple1 material in nature, as they consist of an elastic and plastic material in series, however their backbone curves are symmetric (Figure 2). Equations defining the material model for PySimple1, QzSimple1 and TzSimple1 can be found in Boulanger et al. (1999) and Boulanger (2000). The backbone curve for these

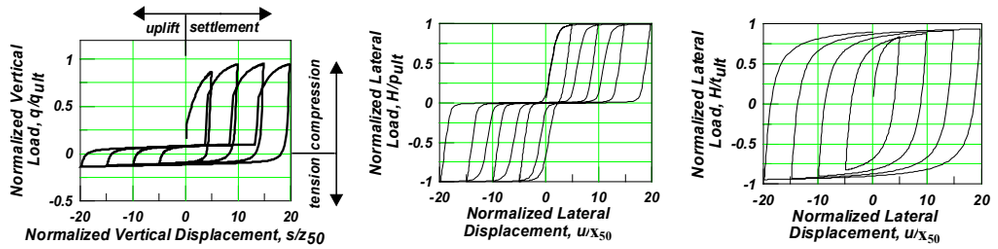


FIG. 2. Cyclic response of springs that are used for (a) axial and moment, (b) passive, and (c) sliding resistance, respectively, of shallow footings

material models are characterized by a linear portion, followed by an increasingly growing nonlinear portion. In the linear portion, the load q is linearly related to the displacement z via the initial elastic (tangent) stiffness k_{in} i.e., $q = k_{in}z$. The elastic region range is defined by relating the ultimate load q_{ult} to the load at the yield point q_0, through a parameter C_r, i.e. $q_0 = C_r q_{ult}$. In the nonlinear (post-yield) portion, the backbone is described by $q = q_{ult} - (q_{ult} - q_0)\left[\frac{cz_{50}}{cz_{50}+(z-z_0)}\right]^n$, where z_{50} = displacement at which 50% of the ultimate load is mobilized, z_0 = displacement at the yield point, c and n = constitutive parameters controlling the shape of the post-yield portion of the backbone curve. The expressions for PySimple1 and TzSimple1 material models are exactly the same as QzSimple1 model with variables representing sliding and passive resistance rather than axial resistance (Boulanger, 2000). The parameters governing the shape of the backbone such as c, n and C_r were determined via best-fit to the relation of Reese and Neill (1988) for drilled shafts in clay and the Vijayvergiya (1977) relation for piles in sand (see Figure 3(a)) and fit to the QzSimple1 backbone by Boulanger (2000) (see Figure 3(b)). Similarly, pile test results by Matlock (1970) and API (1987) are used to calibrate the PySimple1 backbone. The TzSimple1 backbone is best-fit to the models of Reese and Neill (1988) and Mosher (1984).

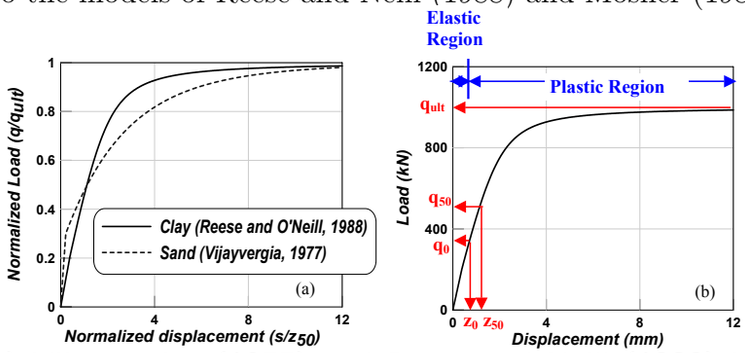


FIG. 3. (a) Vijayvergiya (1977) and Reese and Neill (1988) backbones for clay and sand, respectively and (b) QzSimple1 material backbone

Regression Analysis

Parameters describing the shape of the backbone curves (c, C_r and n), are determined by regression through a number of shallow footing axial and lateral tests. For the q-z springs, a number of axial tests on footings are used, whereas data from laterally loaded footings are used for the t-x and p-x springs. At first, each test model has been analyzed with experimentally recorded input and considering the pile-calibrated values of these parameters as initial values. Subsequently, each parameter is isolated and iteratively modified until a best-fit to the experimental response is obtained. To determine the best-fit response, the sum of the residual of the forces (the sum of the differences between the experimental and the simulation results at all displacement values) is calculated. The parameter set that minimizes the sum of the residual forces is selected as the best-fit value for that particular experiment. The procedure is repeated for all experiments considered and the statistics of the parameter set is calculated (mean μ and standard deviation σ). Using the calculated μ and $\mu \pm \sigma$ values of each parameter, three new backbone curves are defined. Table 1 shows the mean values of these parameters compared with the pile-calibrated values. Note that parameter n and c have similar effect on the backbone curve, thus n was held constant in the study to values suggested by Boulanger (2000), whereas c was varied. The values of the parameters for the PySimple1 and TzSimple1 materials for clay could not be determined due to unavailability of experimental data. Note, in some cases, the mean parameters are significantly different from that of the pile-calibrated parameters. Additional details of the regression analysis and experiments considered can be found in Raychowdhury and Hutchinson (2008).

TABLE 1. Parameters for defining material backbone curves

Material Type	Soil Type	Pile-calibrated values		Proposed shallow foundation-calibrated mean values	
		C_r	c	C_r	c
QzSimple1	clay	0.2	0.35	0.22	0.5
	sand	0.3	12.3	0.36	9.29
PySimple1	clay	0.35	10	-	-
	sand	0.2	0.5	0.33	1.1
TzSimple1	clay	0.5	0.5	-	-
	sand	0.5	0.6	0.48	0.26

EFFECT OF MODIFIED BACKBONES ON FOOTING RESPONSE

The effect of backbone curve calibration is investigated by considering a simple sinusoidal rotational input motion quasi-statically applied at the mid point of a 5m square footing and a 5m x 2.5m strip footing, resting on dry dense sand with a relative density of 80%. Analyses have been conducted using the pile- and mean shallow foundation-calibrated backbone curves. Figures 4 and 5 show the moment–rotation and settlement–rotation curves for the square and strip footings, respectively. It is observed from these figures that the modified backbone has the most significant effect on the settlement response for both footings. The maximum moment and the loading and unloading rotational stiffness are not significantly affected for these footings. The settlement is 21% and 30% lower when the mean regressed backbone curve is used for the square and strip footings, respectively.

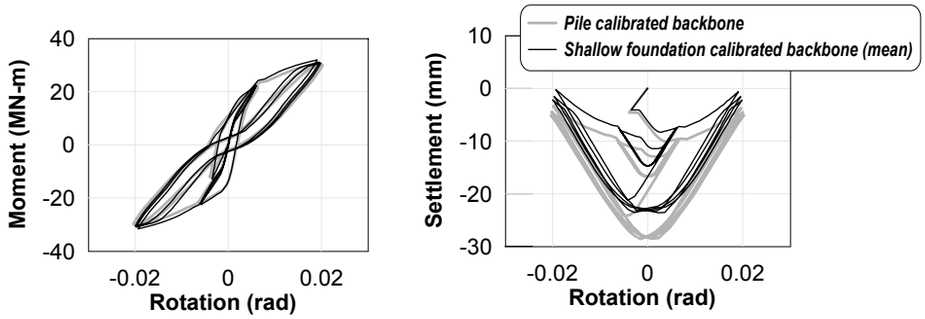


FIG. 4. Effect of modified backbone on the response of a square footing

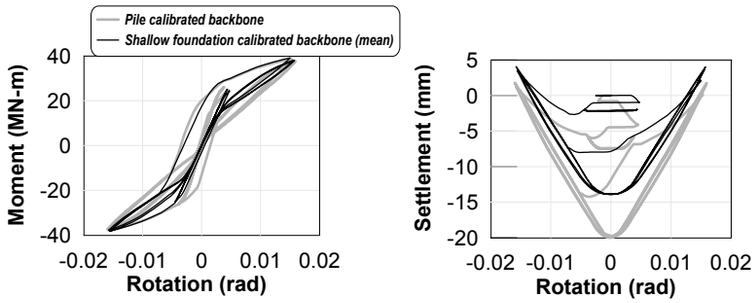


FIG. 5. Effect of modified backbone on the response of a strip footing

The analyses is also repeated for $\mu \pm \sigma$ backbones to get an idea of the range of response. It was observed that the maximum moment and rotational stiffness remain almost unchanged even for the band of $\mu \pm \sigma$ backbones. However, the settlement has a considerably large range of variation. For the square footing, using the upper bound backbone ($\mu + \sigma$), the maximum permanent settlement is obtained as 21mm (25% deviation from the settlement using original backbone curves) compared with a settlement of 26mm for the lower bound ($\mu - \sigma$) case. The settlement deviation for the strip footing is even higher. Using the $\mu + \sigma$ backbone, the settlement is 8.5mm (60% deviation from original settlement), while using the $\mu - \sigma$ backbone, the settlement is 15.5mm (23% deviation from original settlement).

SENSITIVITY STUDY

The sensitivity of the backbone curve parameters on the footing response has been studied using the 5m square footing resting on 80% dry sand and subjected to the same quasi-static reversed cyclic rotational loading. The values of friction angle, unit weight of soil and shear modulus have been assumed as 40^o, 16 kN/m3 and 30 MPa, respectively. Bearing capacity and initial elastic stiffness are calculated after Meyerhof (1963) and Gazetas (1991), respectively. Additional BNWF model parameters such as the elastic range, the post-yield stiffness and the distribution of stiffness along the base of the footing are also considered in the sensitivity study.

1. Bearing capacity

The ultimate bearing capacity Q_{ult} is a function of the footing dimensions, the depth of embedment and the soil strength. It can be calculated based on the

general bearing capacity equations found in foundation design textbook. For the PySimple1 material, the ultimate lateral capacity is taken as the total passive resisting force acting on the front side of the embedded footing. For the TzSimple1 material, the ultimate capacity is taken as the total sliding resistance at the base of the footing (side friction is ignored). Figure 6 shows the effect of Q_{ult} on footing moment–rotation and settlement–rotation responses for a change in bearing capacity. It is observed that using 70% of bearing capacity, the moment capacity is reduced by 25%. The most significant change is in the settlement response, which increased by 125% by this capacity change. Although it may seem countertuitive that the stiffness of the system is affected by change in capacity, but under this demand, Q_{ult} is mobilized in some of the springs, thus the instantaneous stiffness is modified.

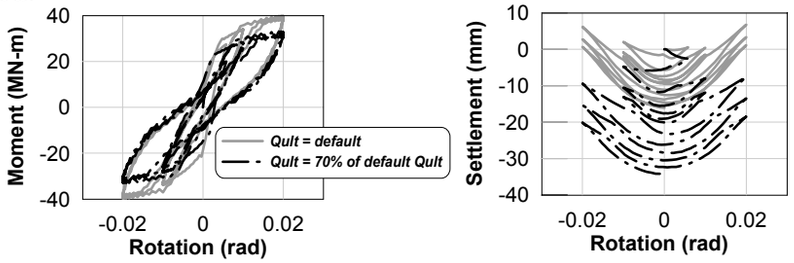


FIG. 6. Effect of bearing capacity on footing response

2. Elastic stiffness

The rotational stiffness of the foundation is implicitly accounted for via the movement of the distributed vertical springs. Figure 7 shows the effect of change in the vertical stiffness K_v on the footing moment-rotation and settlement-rotation response. It is observed that using 70% of K_v, the maximum permanent settlement response is increased by 50%. Note also, a reduction in K_v reduces the maximum moment since some of the springs (near the mid portion of the footing) behave linearly.

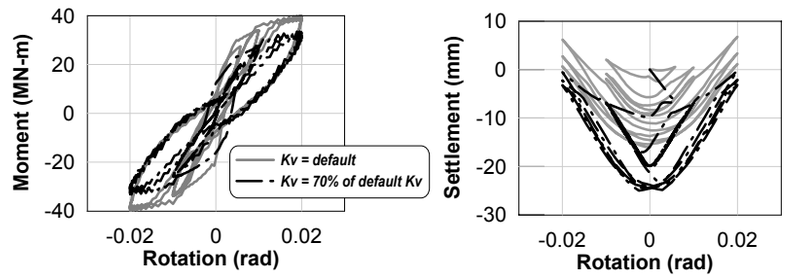


FIG. 7. Effect of vertical stiffness on footing response

3. Elastic Range

One may anticipate that by increasing C_r, and hence increasing the elastic zone, less permanent settlement for a given moment demand would be observed. The effect of changing C_r on a single q-z spring response and on the entire footing response is shown in Figure 8. It is observed from Figure 8, that assuming 2.5 times the C_r value (0.2 to 0.5) results in less than half of the initially calculated settlement.

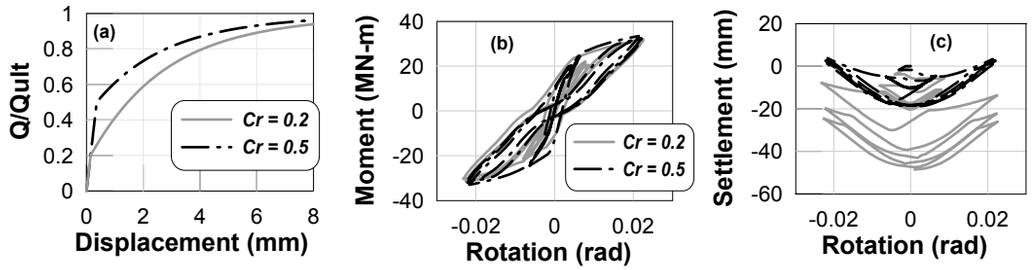


FIG. 8. Effect of C_r on (a) single q-z spring, (b) & (c) footing response

4. Post-yield Stiffness

The shape and instantaneous stiffness of the nonlinear portion of the material model are functions of parameters c and n. The nonlinear stiffness (tangent) is expressed as $k_p = n\,(q_{ult} - q_0)\left[\frac{cz_{50}}{cz_{50}+(z-z_0)}\right]^{n+1}$. Note that any change in c or n modifies k_p. To express k_p as a fraction of initial stiffness k_{in}, a variable α_{80} is introduced, where α_{80} is the ratio of k_p at 80% of q_{ult} to k_{in}. Thus, if k_p is higher, α_{80} is also higher. For three different values of $c = 12.3/4$, 12.3 and 12.3*4, $\alpha_{80} =$ 0.036 (low k_p), 0.078 and 0.094 (high k_p), respectively. Figure 9 shows the effect of change in c of a single q-z spring and the resulting effect on the footing response. One may observe that changing the elastic-plastic transition has a considerable effect on both the rotational stiffness and the settlement response (up to 80%).

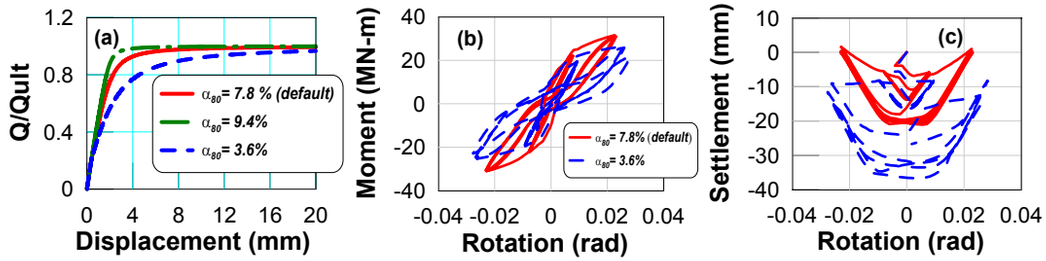


FIG. 9. Effect of c on (a) single q-z spring, (b) & (c) footing response

5. Stiffness ratio

When a foundation is subjected to large cyclic and dynamic loading, the soil under the edge of the footing compacts more than the soil under the middle portion of the foundation. This happens because the edges are loaded much more heavily when the foundation rocks and the other end uplifts. This phenomenon leads to an increase in the end stiffness. Even prior to imposition of cyclic rocking loads, very rigid footings will have larger reactions at the ends of the footing due to imposed boundary conditions at the footing ends. To account for this, ATC-40 (1996) suggests that a higher intensity of springs should be placed at the end region. Harden et al. (2005) developed an analytical solution suggesting that the stiffness intensity ratio (R_k) varies with footing aspect ratio, while ATC-40 (1996) suggests that the end stiffness intensity should be about 9 times the mid stiffness intensity irrespective of the footing dimension and aspect ratio (Figure 10). Figure 11 shows the effect of end to mid stiffness ratio (R_k) on the overall footing response based on these two suggestions. One observes that nearly doubling the stiffness at the ends (while maintaining the same overall global vertical stiffness), results in about half of the total settlement.

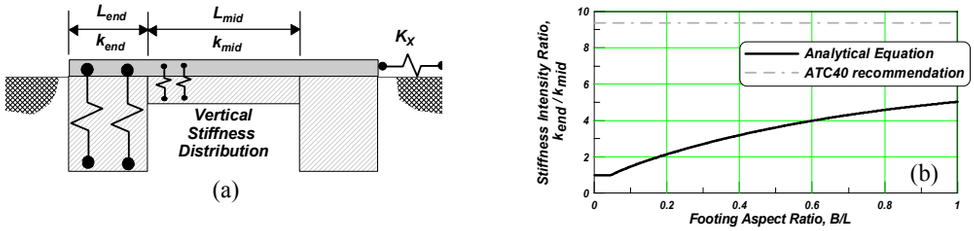


FIG. 10. (a) Vertical stiffness distribution and (b)stiffness ratio versus footing aspect ratio (Harden et al., 2005)

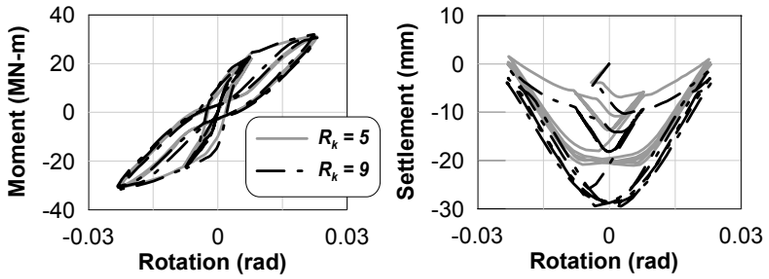


FIG. 11. Effect of stiffness ratio on a 5m square footing response

COMPARISON WITH EXPERIMENTAL DATA

Figure 12 shows the performance of the BNWF model with the newly adopted backbone curves with respect to the centrifuge test series SSG04-06 conducted by Gajan et al. (2006) at the University of California, Davis. This test is a slow laterally loaded cyclic experiment conducted on a 2.8m x 0.65m strip footing supporting a shearwall with a static vertical factor of safety 2.3 and resting on a sand bed of 80% relative density. Results show that the BNWF model captures the maximum moment and shear, rotational stiffness, lateral stiffness and settlement very well. Additional comparisons with centrifuge experiments have indicated similar reasonable comparisons using the suggested parameter input protocol.

CONCLUSIONS

In this study the foundation subgrade is modeled as a Beam-on-Nonlinear-Winkler-Foundation (BNWF) that contains a system of discrete, mechanistic, springs having nonlinear behavior as well as uplift, sliding and damping capabilities. Previous mechanistic spring efforts have mainly focused on calibration against pile load test data, however, in this study, the backbone curves from shallow footing centrifuge and field experiments are used. To demonstrate the effects on footing response when using the newly calibrated backbone curves, a simple sinusoidal rotational motion is input to a model square and strip footing. Subsequently, a sensitivity study is conducted considering model parameter variations. It is observed that settlement is highly sensitive to these parameters. Since accurate prediction of settlement is key to the performance evaluation of the footing, a broader range of footing configurations (sizes, soil types, factors of safety, etc.) should be modeled using the proposed backbone curves and response sensitivity (particularly settlement) should be assessed.

ACKNOWLEDGMENTS

Support for this work was provided by the EERC Program of NSF, under

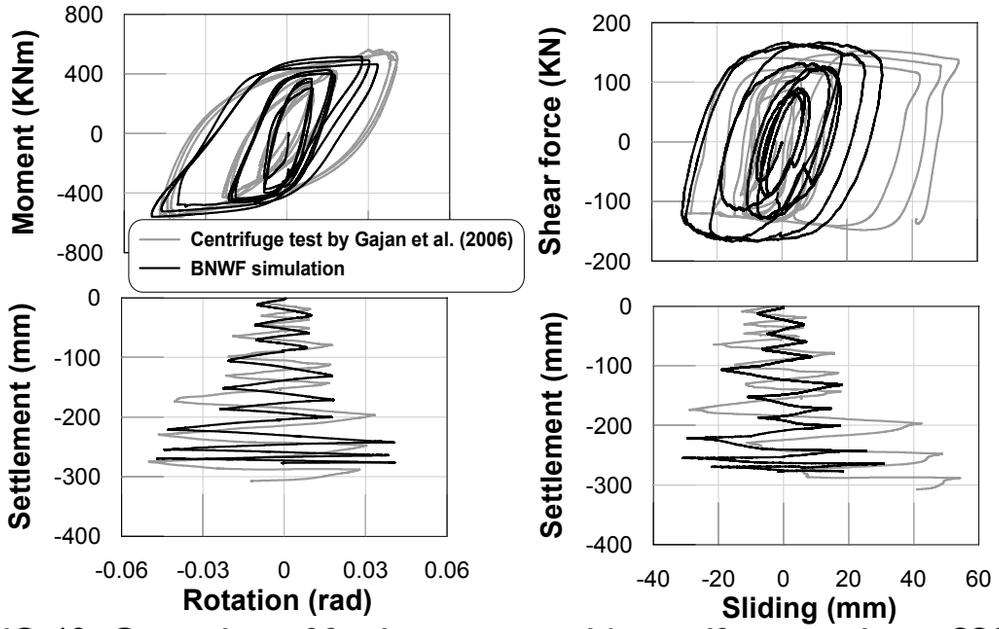


FIG. 12. Comparison of footing response with centrifuge experiment SSG04-06 (Gajan et al., 2006)

Award Number EEC-9701568, through the Pacific Earthquake Engineering Research Center (PEER). The above support is greatly appreciated. Any opinions, findings, and conclusions expressed in this paper are those of the authors, and do not necessarily reflect those of the sponsoring organization. Helpful suggestions of Professors B. Kutter, J. Stewart, and S. Gajan during this study are appreciated.

REFERENCES

Allotey, N. and Naggar, M. H. E. (2007). "An investigation into the winkler modeling of the cyclic response of rigid footings." *Soil Dynamics and Earthquake Engineering*, 28, 44–57.

API (1987)." *American Petrolium Institute, Recommended Practice for Planning, Designing and Constructing Fixed Offshore Platforms API Recommended Practice 2A (RP2A), Seventeenth Edition, April 1.*

ASCE-7 (2003). *Seismic Evaluation and Retrofit of Concrete Buildings.* Structural Engineering Institute (SEI) and American Society of Civil Engineers (ASCE), Reston, Virginia.

ATC-40 (1996). *Seismic Evaluation and Retrofit of Concrete Buildings.* Applied Technolgy Council (ATC).

Boulanger, R. W. (2000). "The pysimple1, qzsimple1 and tzsimple1 material documentation." *Documentation for the OpenSees platform available at: http://opensees.berkeley.edu/.*

Boulanger, R. W., Curras, C. J., Kutter, B. L., Wilson, D. W., and Abghari, A. (1999). "Seismic soil-pile-structure interaction experiments and analyses." *ASCE, Journal of Geotechnical and Geoenvironmental Engineering*, 125(9), 750–759.

Chopra, A. and Yim, S. C. (1985). "Simplified earthquake analysis of structures with foundation uplift." *ASCE Journal of Structural Engineering*, 111(4), 906–930.

Gajan, S., Thomas, J. M., and Kutter, B. L. (2006). "Soil-foundation-structure interaction: Shallow foundations." *Centrifuge Data Report for test series SSG04. UCD/CGMDR, Center for Geotechnical Modeling, University of California, Davis, California.*

Gazetas, G. (1991). "Displacement and soil-structure interaction under dynamic and cyclic loading." *Proceedings of the Tenth European Conference on Soil Mechanics and Foundation Engineering, Florence.*

Harden, C. W., Hutchinson, T., Martin, G. R., and Kutter, B. L. (2005). "Numerical modeling of the nonlinear cyclic response of shallow foundations." *Report for Pacific Earthquake Engineering Research Center, PEER*, 2005/04.

Matlock, H. (1970). "Correlations for design of laterally loaded piles in soft clay." *Proceedings, 2nd Annual Offshore Technological Conference, Houston, Texas*, 1(1204), 577–594.

Meyerhof, G. G. (1963). "Some recent research on the bearing capacity of foundations." *Canadian Geotechnical Journal*, 1(1), 16–26.

Mosher, R. (1984). "Load transfer criteria for numerical analysis of axially loaded piles in sand, technical report k-84." *US Army Engineers Waterways Experiments Station, Vicksburg, MS*, 1.

PEER (2008). "Open system for earthquake engineering simulation." *http://opensees.berkeley.edu/.*

Raychowdhury, P. and Hutchinson, T. (2008). "Nonlinear material models for winkler-based shallow foundation response evaluation." *GeoCongress 2008*, (In press).

Reese, L. C. and Neill, M. (1988). "Field load tests of drilled shafts." *Deep Foundations on Board and Auger Piles, Van IMpe Edited*, Balkema, Rotterdam, 145–191.

Vijayvergiya, V. (1977). "Load-movement characteristics of piles." *Prceeding, Ports 77 Conference, American Society of Civil Engineers, Long Beach, California, March.*

Numerical Simulation of a Soil Model-Model Container-Centrifuge Shaking Table System

Mahadevan Ilankatharan[1], S.M. ASCE and Bruce Kutter[2], M. ASCE

[1]Graduate Student Researcher, University of California at Davis, One Shields Ave., Davis, CA 95616; milankatharan@ucdavis.edu
[2]Professor and Director, Center for Geotechnical Modeling, University of California at Davis; blkutter@ucdavis.edu

ABSTRACT: A numerical model is developed using OpenSees to represent the dynamics of a soil model-model container-centrifuge shaking table system. The centrifuge shaker-system includes soil model, the flexible shear beam model container, shaking table and its reaction mass. All of these different components interact with the soil model during dynamic excitation, with some absorbing energy and others allowing undesired modes to affect the response observed in the experiment. This interaction of soil model and centrifuge/actuation system might attenuate or amplify the discrepancies in the responses of the numerical and physical models. The relative error between a numerical simulation and a physical simulation depends on how the boundary conditions and interaction among different components in the physical model are included in the numerical model. Assessment of the quality of a comparison between a numerical and physical simulation should account for the effects of the boundary conditions and dynamic interaction among different components in the dynamic system. This paper outlines the details of the simulation model, presents some representative results from simulations, discusses the effect of interaction among different components on the responses, and presents how the sensitivity of simulation outputs to uncertainties in the material properties depends on boundary conditions in the physical and numerical simulations.

INTRODUCTION

One of the greatest challenges that earthquake engineers face is the paucity of data available to calibrate the performance of numerical models for varying earthquake characteristics (level of shaking, frequency content, and waveform), soil profile characteristics, and superstructure/substructure characteristics. Dynamic centrifuge modeling with detailed instrumentation is often used to obtain physical data, gain

insight into the mechanisms involved, and perform parametric studies to calibrate numerical models. The Center for Geotechnical Modeling at University of California, Davis operates a 9.1m radius geotechnical centrifuge equipped with a 2 m x 1 m servo hydraulic shaking table to perform realistic earthquake simulations on the soil models at prototype stress field conditions.

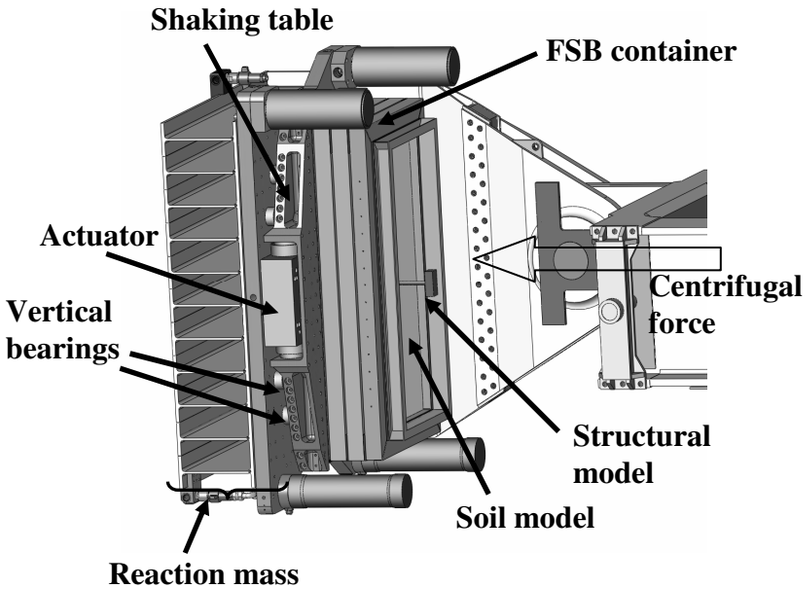


FIG.1. 3D rendering of a soil model-model container-centrifuge shaking table system

A 3D rendering of the UC Davis centrifuge-shaker system is shown in Figure 1. The centrifuge-shaker system includes a soil model, a flexible shear beam model container, a shaking table and its reaction mass. All of these different components, with their own resonance frequencies of vibration, interact with the soil model during dynamic excitation, some absorbing energy, some allowing undesired modes to affect the response observed in the experiment. This interaction of the soil model and the centrifuge/actuation system might attenuate or amplify the discrepancies in responses of the numerical and physical models. Comprehensive understanding of these interactions and accurate modeling of experimental boundary conditions are essential for an unbiased validation of a numerical model. A 2D finite element model is developed using OpenSees (Open System for Earthquake Engineering Simulation, http://opensees.berkeley.edu/index.php) to represent the dynamics of centrifuge-shaking table-model container-soil model system. Data from a series of highly instrumented centrifuge tests that were performed a part of a NEES collaboration project (Ilankatharan et al. 2005) are used to validate the numerical procedure. The dimensions of the finite element domain, all modeling parameters, and the results are presented in centrifuge model scale (52g - gravity level) unless otherwise specified. The centrifuge scaling factors for some physical properties are given in Table 1, more details on the centrifuge scaling laws can be found in Kutter (1992).

Table 1. Centrifuge scaling factors at the centrifuge acceleration (g) level of 52

Quantity	Prototype Scale/Model Scale
Stress	1
Acceleration	1/52
Length	52
Mass	52^3
Time	52
Force	52^2

MODELING SYSTEM COMPONENTS

Soil Model

Dry Nevada sand of a target relative density of 80% (with a thickness of 534mm) is considered to represent the soil profile. The details of soil properties can be found in Ilankatharan et al. (2005). In OpenSees, soil is modeled with 4-node quad elements using PressureDependMultiYield (PDMY) elasto-plastic soil model. A complete description of this material model, and recommended modeling parameters can be found at *http//cyclic.ucsd.edu/opensees/*.

Table 2. Main modeling parameters for dry dense Nevada sand (Dr=80%)

Modeling parameter	Parameter value
Soil mass density (Mg/m^3)	1.66
Reference mean effective confining pressure, p'_r (kPa)	80
Reference low-strain shear modulus at p'_r=80kPa, G_r (kPa)	64284
Reference Bulk Modulus at p'_r=80kPa,	192852
Friction angle, ϕ (deg)	37
Peak shear strain	0.1
Phase transformation angle (deg)	27

Table 2 lists the main modeling parameter for this dry dense Nevada sand stratum. Within the PDMY material, the following equation defines the low-strain shear modulus of soil (G) as a function of instantaneous effective confinement (p').

$$G = G_r \left(\frac{p'}{p'_r} \right)^{0.5}$$

The reference low-strain shear modulus (G_r) of Nevada sand is defined based on the shear wave velocity data available in the literature for 80% relative density dry Nevada sand (Arulnathan et al. 2000). In addition to the hysteric damping generated by the stress-strain loops of PDMY material, very small amount of stiffness-proportional damping is employed for the purpose of numerical stability with an average of 3% over the frequency range of interest (1-500Hz).

Model container

A flexible shear beam container (FSB2) was considered in this study (shown in FIG.1). The FSB2 container consists of an aluminum base plate and five metal rings, with overall dimensions of 1.651×0.788×0.584 m in length, width, and height, respectively. The container rings are sandwiched with 12 mm thick soft neoprene rubber rings providing lateral flexibility. In OpenSees, the container metal rings, neoprene rubber rings, and the base plate are modeled using 2D plane strain finite elements using *elastic nD material*. The shear stiffness of the FSB container was determined by matching data from static lateral loading of the empty container (Stevens, 2001). The mass and stiffness properties of 2D finite element container were calculated to match the mass and stiffness of the real container when the thickness of the plane strain finite element domain set to the width of the container (0.788m). In the FE container, the both ends of the container are connected with a series of 1D truss elements (with axial stiffness matched that of side walls) to force one end of the container to follow the other end, along the longitudinal direction. The shear rods used to provide the complementary shear stresses at the both ends of the container are modeled using elastic beam column elements. At the both ends of the container, soil nodes are slaved with shear rod nodes in both horizontal and vertical directions. The vertical bearing supports at the base of the container are included to incorporate the possibility of rocking of the container; the stiffness of these bearings is modeled using elastic zero-length elements. Some 3-D behavior was approximately accounted by including the weight of the side walls and end walls. Furthermore, one truss element connected the centroid of each ring section, which allowed free twisting of the rings about an axis normal to the plane of the problem. Torsional stiffness and bending of the rings and friction on the sides of the container were not accounted for; these were considered to have a secondary effect on the conclusions of this paper.

Shaker and Reaction mass

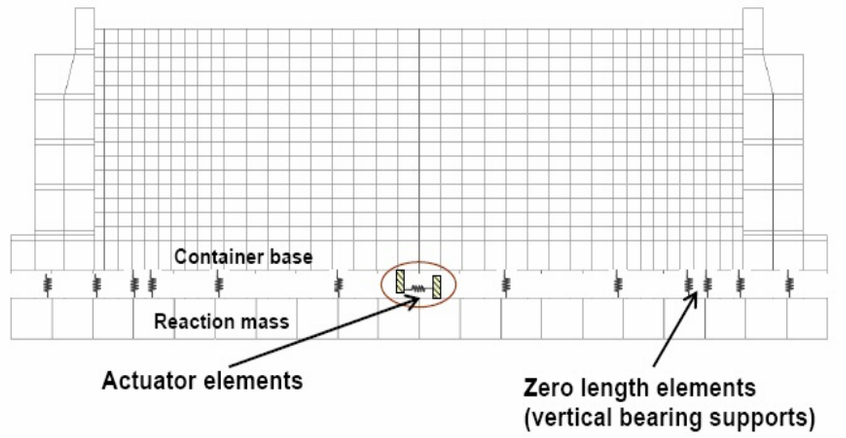


FIG. 2. 2D finite element mesh of the soil model-model container-centrifuge shaker system

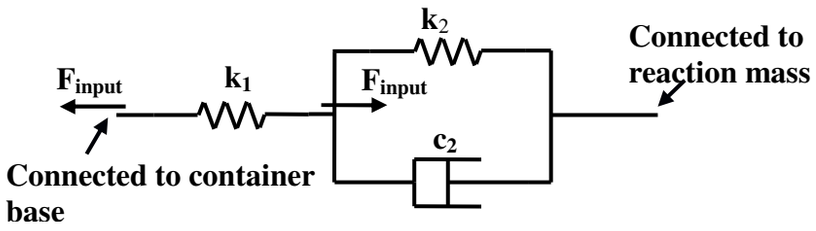


FIG. 3. Configuration of actuator elements

The horizontal shaking table system of the UC Davis centrifuge facility is considered for this present study. The horizontal shaker is driven by two servo-hydraulic actuators, one of which is visible in FIG.1. The design detail and actuator mechanism of the horizontal actuation system is described in Kutter et al. (1994). The 2D finite element mesh of the soil model-container-shaker system is depicted in FIG.2. Zero-length elements, to represent stiffness of the vertical bearing supports, connect the container base and the reaction mass. The reaction mass is modeled as an *elastic nD material*, the mass of the reaction mass is assumed to be two times the payload mass (mass of container and soil). Excitation to the system is applied through the actuator elements. A simplified model of actuator system, illustrated in FIG.3, was used for the analysis. The main components of this actuator model are briefly described below.

k_1 - A stiff spring across which the input excitation is applied – this represents the stiffness of the servo-control system; for the data presented here, we have chosen k_1 = 10 k_2. (k_1 = 8764640 kN/m)

k_2 - A spring to represent stiffness of the actuator due to compressibility of oil and mechanical connections between the actuator and the payload. Assuming that the compressibility of the oil is the most flexible component. k_2 can be calculated using following equation.

$$k_2 = 4\beta\frac{A}{L}$$

where, β is the bulk modulus of oil (10^5 psi); A is the cross sectional area of piston ($A = \frac{\pi}{4}D^2$, D=4inches); L is the stroke of piston (L=0.5 inches for average piston position); and the multiplier four is to account for four pistons-two pistons per actuator (the calculated k_2 is then reduced by 50% to account for the reduction in stiffness due to the volume of trapped oil and mechanical connections).

c_2 – A dashpot representing the damping associated with the actuator spring, k_2. c_2 is calculated as follows.

$$c_2 = \xi c_{crit}$$
$$c_{crit} = 2\sqrt{k_2 m}$$

where, ξ is the damping ratio (ξ =40%, assumed), c_{crit} is the critical damping, and m is the payload mass (i.e., mass of the container and soil).

F_{input} - Excitation force command to the system. F_{input} is calculated as follows.

$$F_{input} = k_1 d$$

where, d is the command displacement.

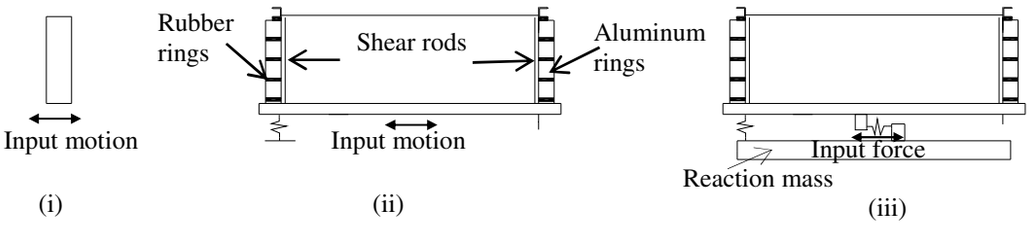


FIG.4. Different boundary conditions in simulation models

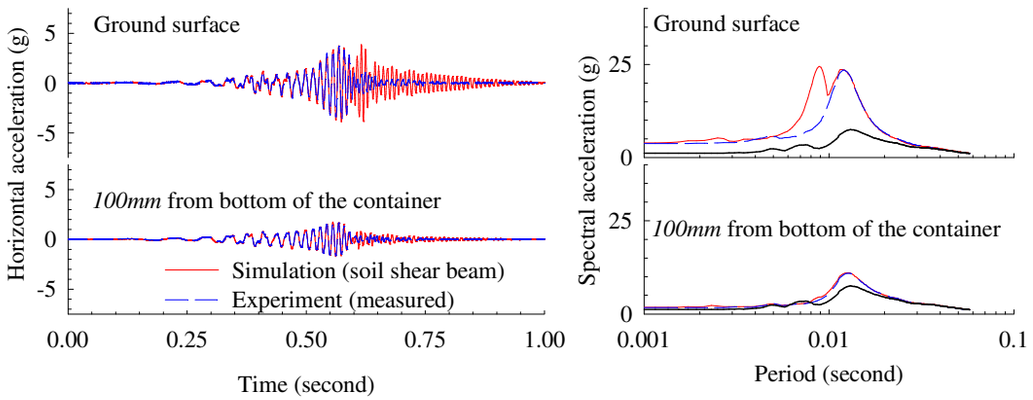


FIG.5. Measured and computed acceleration histories and response spectra (5% damping) from soil shear beam simulations (sweep motion, peak base acc=1.3g)

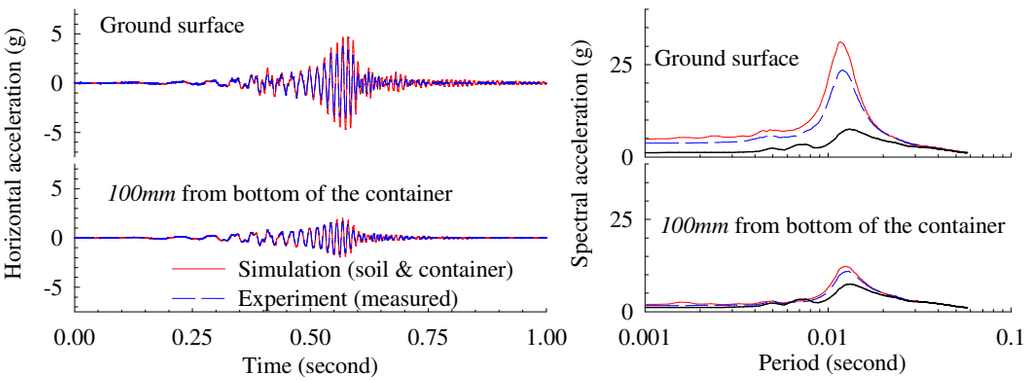


FIG.6. Measured and computed acceleration histories and response spectra (5% damping) from soil and container simulations (sweep motion, peak base acc=1.3g)

Boundary conditions in simulation models

To improve understanding of interactions among soil model, container, and shaker system and to evaluate how the sensitivity of simulation results depends on boundary conditions in experiment and simulation, the boundary conditions were treated with three different levels of detail as described below (and depicted in FIG.4.)

(i) 1-D Simulations of Soil

In this suite of analyses, the container and actuator were excluded; a 1D shear-beam type FE model is employed to simulate soil site response (FIG.4(i)). The unit weight of soil is increased by 30% to account for the effect of container mass (which is 30% of the soil mass) on the inertia forces. Dynamic excitation, equal to the measured acceleration time history at the base of the container, is applied to the bottom soil nodes.

(ii) 2-D Simulations of Soil and Container

The FSB2 container is included in this simulation model. The mass and stiffness of the container, and the vertical bearing supports at the base of the container are taken into account. Dynamic excitation is imparted to the bottom container nodes along horizontal direction (FIG.4(ii)). Measured acceleration time history at the base of the container is used as an input.

(iii) 2-D Simulations of Soil, container, and actuator

The effect of the shaker is included, the flexibility of actuator and the mass of the reaction mass are modeled as indicated in detail in FIG.3 and schematically in FIG.4 (iii). Excitation to the system is applied as force time history through the actuator elements (FIG.3.). To begin the analysis, the command displacement (d) is calculated by double integration of acceleration time history measured at the base of the container. The base acceleration predicted from the simulation is then compared with measured base acceleration in the experiment. A transfer function is calculated between the measured and the predicted responses. This transfer function is then used to modify the initial command displacement, to obtain a reasonable (but still not identical) agreement between the base motion calculated and the input base motion for cases *(i)* and *(ii).*

SIMULATION RESULTS

Soil horizontal accelerations

Representative simulation results of a small sweep motion excitation from soil shear beam simulations and soil and container simulations are shown in Figures 5 and 6, in terms of acceleration time histories and the corresponding response spectra (5% damping) along the soil profile. The computed accelerations closer to base of the container (100mm from bottom of the container) in both simulations are in reasonable agreement with experiment. However, there are significant differences in simulation results at ground surface. For instance, the peak in the response spectra at a period of 0.009 sec in the soil shear beam simulations disappears when the container is included. This shows the effect of the soil model-container interaction. Inclusion of the container in the simulation improves agreement between simulation and experiment.

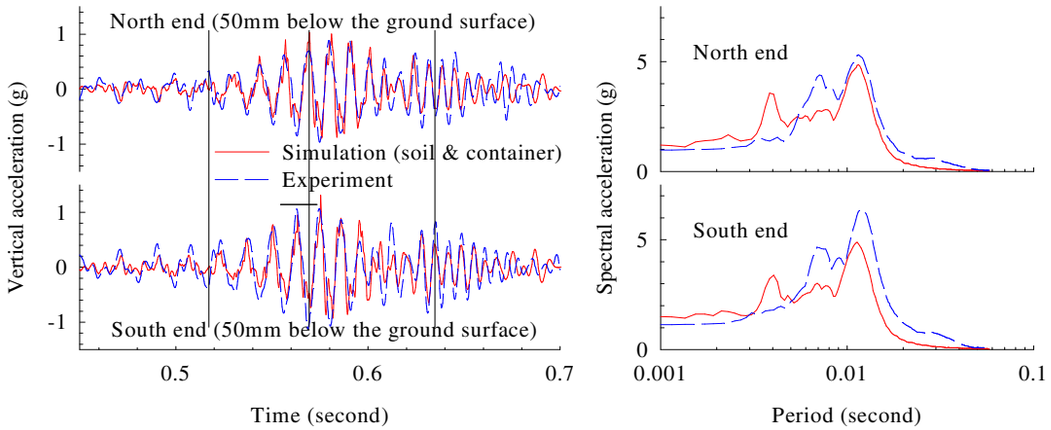


FIG.7. Measured and computed vertical acceleration histories and response spectra (5% damping) from soil and container simulations at 50mm from ground surface (sweep motion, peak base acc=1.3g)

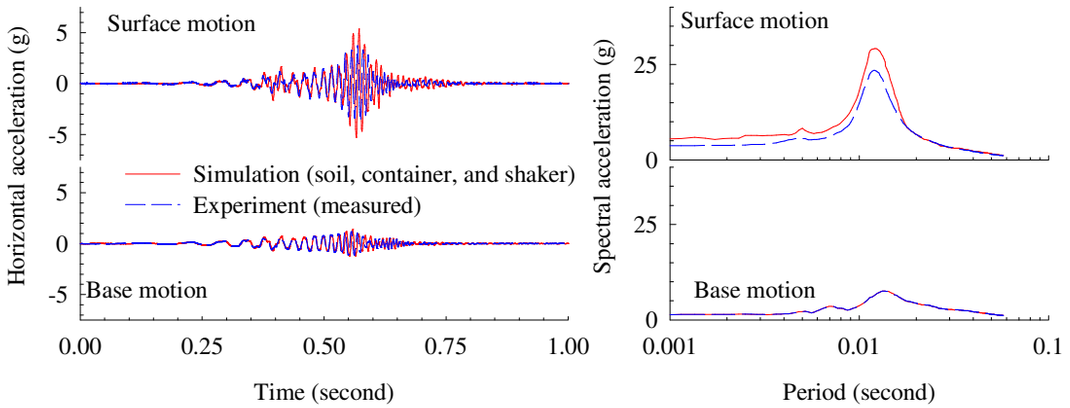


FIG.8. Measured and computed acceleration histories and response spectra (5% damping) from soil, container and shaker simulations (sweep motion, peak base acc=1.3g)

Soil vertical accelerations

FIG.7 shows the time histories and response spectra (5% damping) of soil vertical accelerations at 50mm below the ground surface at both ends of the container. The time histories of accelerations in the experiment are 180 out of phase, show rocking response of the container. Vertical accelerations are better predicted when the flexibility of vertical bearing supports at the base of the container is included in the analysis.

Response of the soil, container, and shaker simulation model

Representative simulation results from soil, container, and shaker simulation model are presented in FIG.8, in terms of acceleration time histories and response spectra (5%

damping) at the container base and ground surface. The calculated base response is identical to the experiment after tuning the command displacement (the tuning procedure is described in the previous section). The presented simplified shaker model (in FIG.3.), with a tuned command displacement, allows a reasonable prediction of the response at the ground surface.

SENSITIVITY ANALYSIS

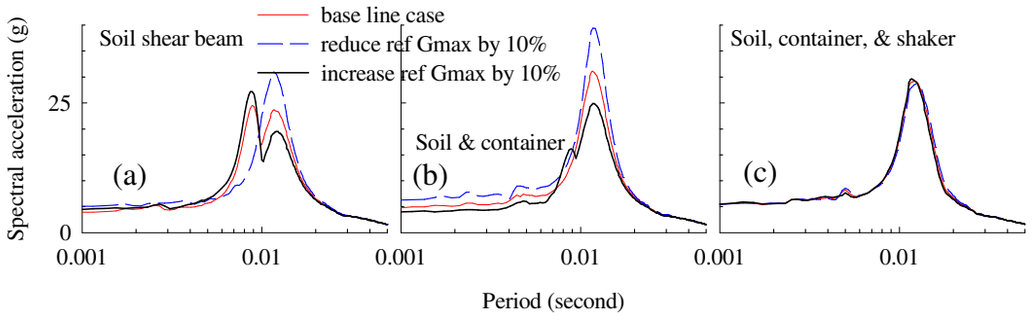


FIG.9. Effect of varying shear modulus on calculated ground surface response spectrum for different boundary conditions (sweep motion, peak base acc=1.3g)

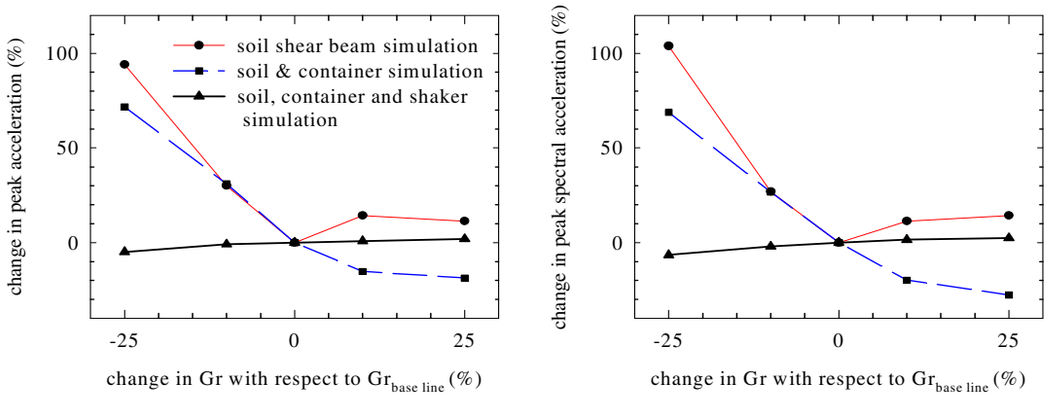


FIG.10. Sensitivity of peak and peak spectral accelerations of surface motion to reference shear modulus of PDMY material (sweep motion, peak base acc=1.3g)

The reference shear modulus of the PDMY material is systematically varied from baseline case (the value shown in Table 2) to determine the sensitivity of results for different boundary conditions. Results are shown in FIG. 9. The percentage change of simulation results (peak acceleration, and peak spectral acceleration), with respect to the base line case, is plotted against the percentage change in reference shear modulus (Gr) from base line case ($Gr_{baseline}$), in FIG. 10. From Figures 9 and 10, it is evident that the sensitivity of simulated ground surface response depends on how the experimental boundary conditions are incorporated in the simulation models. Interestingly, for this example, the results of the simulation are insensitive to the shear modulus when the boundary conditions are more accurately modeled in the simulation (see FIG 9c).

CONCLUDING REMARKS

Modeling of complex dynamics interaction of a centrifuge-shaker system is presented. This modeling incorporates mass and flexibility of the container, the effect of shear rods at both ends of the container, stiffness of the vertical bearing supports at the base of the container, flexibility of the actuator, and the effect of reaction mass. A simplistic approximation of the actuator and control system using springs and dashpots is used to include first-order effects of actuator flexibility on the interaction between the specimen and the shaking table. As expected, more accurate modeling of boundary conditions results in more accurate simulation of the experiment. Results from sensitivity studies show that the sensitivity of computational simulation output to changes in input parameters depends on how boundary conditions are modeled in the simulation; to provide an unbiased validation of a numerical model, it is important to accurately model the boundary conditions in the physical model. Furthermore, it is possible that the results of experiments are more sensitive to uncertainties in boundary conditions than they are to uncertainties in geotechnical material models. This raises fundamental questions about the significance of conclusions drawn from the comparisons between experiments and simulations for dynamic shaking table experiments.

ACKNOWLEDEMENTS

The authors would like to acknowledge Dr. Dan Wilson, Lars Pedersen, and the staff of the UC Davis Center for Geotechnical Modeling, and Prof. Pedro Arduino, Prof. Steve Kramer, Hysung-Suk Shin (University of Washington), and Prof. Scott Brandenberg (UCLA) for their support in the course of this study. The experiments were supported by NSF award # CMS-0324343. The operation and maintenance of the centrifuge including development of a numerical model of the centrifuge shaker is made possible by funding from NSF award # CMS-0402490 through a sub award from NEESinc.

REFERENCES

Arulnathan, R., Boulanger, R. W., Kutter, B. L., and Sluis, W. K. (2000). “New tool for shear wave velocity measurements in model tests.” *Geotechnical testing journal*, 23(4): 444-453.

Ilankatharan, M., Sasaki, T., Shin, H., Kutter, B. L., Arduino, P., and Kramer, S. L., 2005. “A demonstration of NEES system for studying soil-foundation-structure interaction” *Centrifuge data report for MIL01. Rep. No. UCD/CGMDR-05/05*, Ctr. for Geotech. Modeling , Dept. of Civ. and Envir. Engrg., UC Davis.

Kutter, B.L. (1992). "Dynamic centrifuge modeling of geotechnical structures." *Transportation Research Record 1336*, TRB, National Research Council, National Academy Press, Washington, D.C., pp. 24-30.

Kutter, B.L., Idriss, I.M., Kohnke, T., Lakeland, J., Li, X.S., Sluis, W., Zeng, X., Tauscher, R., Goto, Y., and Kubodera, I. (1994). "Design of a large earthquake simulator at UC Davis." *Proceedings, Centrifuge 94*, Leung, Lee, and Tan, Eds., Balkema, Rotterdam, pp. 169-175.

Stevens, D.K. (2001) "Comprehensive investigation of nonlinear site response: Collaborative Research with UC San Diego and UC Davis," *Masters of Science Thesis*, University of California, Davis.

Numerical simulation of displacement functions of strip footings

Abir Jendoubi[1], Frédéric Legeron [2] and Mourad Karray [3]

[1] PhD student, Faculté de génie, Université de Sherbrooke, Québec, Canada, J1K 2R1
[2] Prof., Faculté de génie, Université de Sherbrooke, Québec, Canada, J1K 2R1
[3] Prof., Faculté de génie, Université de Sherbrooke, Québec, Canada, J1K 2R1

ABSTRACT: The risk associated with structures subjected to dynamic loading needs a rigorous analysis that takes into account dynamic soil-structure interaction. A key step of this analysis consists of estimating the dynamic response of the foundations by calculating their impedance (i.e. dynamic stiffness K and damping C) or displacement functions (real part F_1 and imaginary part F_2).

The purpose of this work is to evaluate the displacement functions (inverse of impedance functions) of strip footings on the surface of some homogeneous soil.

Validation studies indicate the accuracy and versatility of the models performed with the software FLAC (Fast Lagrangian Analysis of Continua).

It is known that the assumption of homogenous layer or half space with constant shear modulus G may not be realistic as the shear wave velocity increases as a function of the effective overburden stress. In this paper, three soil models are considered. For each case, the adopted mechanical characteristics correspond to a type of soil with constant or variable shear wave velocity. Calculations are performed over a practically sufficient range of oscillating frequency ratios a_0. Comparison of results obtained with varying and constant shear wave velocity shows the importance to consider this velocity increasing with depth.

Additional calculations conducted on two-layer soil are also presented in order to recommend the thickness of soil that is required in the model to capture soil-structure interaction.

Key words: Impedance function, displacement functions, dynamic soil-structure interaction, strip footings, shear wave velocity, two-layer, numerical simulation, oscillating frequency, FLAC.

INTRODUCTION:

The analysis of foundations vibrations has advanced considerably since the introduction of soil dynamics (Sieffert and Franck 1991). Indeed, the study of the wave propagation in a continuum and the use of computer codes make it possible to

take into account dynamic soil-structure interaction by calculating the displacement and displacement functions representing flexibility and damping effect of foundation.

The dynamic displacement is a complex stiffness defined as the ratio between the force and the resulting displacement (Pecker 2005). The real part represents the true stiffness (Novak and El Sharnouby 1983). The imaginary part describes the out-of-phase component and represents the damping due to energy dissipation in the soil (Novak and El Sharnouby 1983).

Calculations of displacements are carried out using several methods (Sieffert and Cevear 1991, Shekar and Rana 2002, Gazetas 1991, Stewart et al. 1999, Wolf 1985, Veletsos and Vebric 1973 and Novak and El Sharnouby 1983) such as: analytical solutions, semi-analytical and boundary formulations, dynamic finite-element methods and hybrid methods combining analytical and finite element approaches (Jacquart et al. 2005).

In this work, the finite difference method is used to model the soil and foundation. To avoid the reflection of waves, quiet boundaries suggested by Lysmer and Kuhlemeyer (1969), are applied on the limits of models.

The paper presents the results of numerical simulation performed with the software FLAC in order to evaluate the real and imaginary parts of displacement functions of strip footings on the surface of some homogeneous soil with a shear modulus (consequently a shear wave velocity) constant or increasing with depth. A two-layer soil model is also simulated.

With dimensionless displacement functions, it is possible to predict effect of soil-structure interaction on the behaviour of any structure by replacing foundation of a structure by a set of dashpot and springs.

NUMERICAL MODELING OF SOIL-STRUCTURE INTERACTION:

Simulating the soil-structure interaction problem in a layered medium requires the numerical resolution of the equations of motion with respect to appropriate limit conditions. The computer program FLAC (Itasca 2002) is used here, assuming the medium to be homogenous and the soil to be linearly elastic. Model consists of a grid with square elements ($0.5\text{m} \times 0.5\text{m}$). The foundation, vibrating under the action of a harmonic vertical or horizontal exciting force, is modeled with structural beam elements.

The wave propagation problem in a half-space cannot be simulated perfectly by finite-element or finite-difference methods due to the restriction imposed by the model length and the element size (Smith 1973). The model must be large enough to reduce the effect of the reflected waves at the boundary of the model (Rosset and Ettouney 1977) and the elements must be as small as possible to take into account accurately the wave propagation. To solve the problem of reflection at the model boundaries, the method of quiet boundaries suggested by Lysmer and Kuhlemeyer (1969) is used in this study. Boundaries located at the bottom, right and left side of the mesh involve dashpots attached independently to the boundary in the vertical and horizontal directions (figure 1).

In this work, models are between 20 and 100m length and between 15 and 30m thick. A proportional Rayleigh damping is used to simulate the mechanical damping. A value of 5 % that is typically used for soil-structure interaction problems is adopted

in all cases. It is important to note that some numerical distortion of the propagating wave can occur at wavelengths lower than an eighth of the element size (Δl=0.5). Thus, results obtained at higher frequency (>25 Hz for a shear wave velocity V_s=100 m/s and >50 Hz for V_s=200 m/s) must be considered with caution.

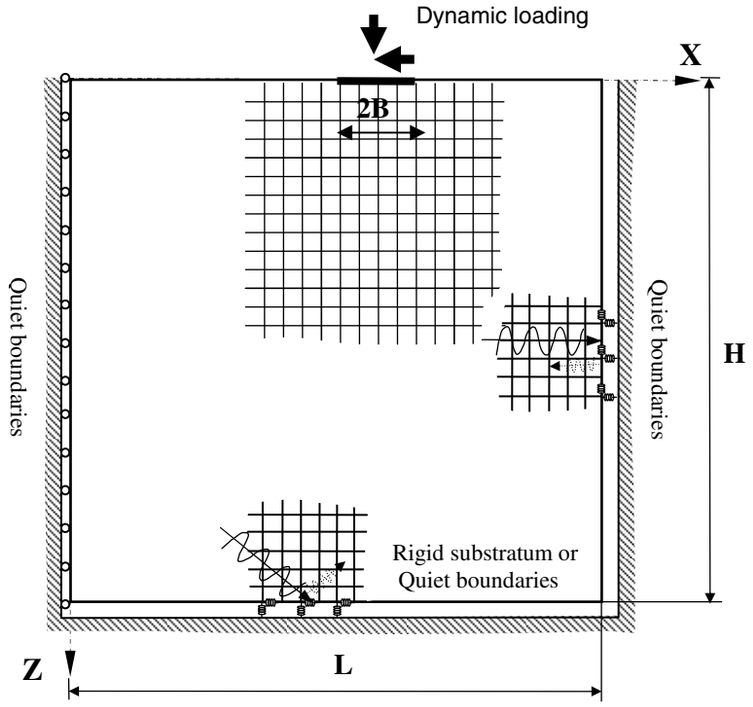


FIG.1. Model for numerical simulations (FLAC) of soil–structure interaction problem

MODEL VALIDATION

In order to validate the FLAC model, results are compared to those of Huh (1986). Huh used the **B**oundary **E**lement **M**ethod based on the discretisation of the boundary only. The BEM is a numerical method that attempts to use the given boundary conditions to fit boundary values into an integral equation. Huh has an important contribution on the calculation of displacement functions of strip footings. His model comprises of homogeneous elastic material with a Poisson's ratio ν=0.4, ρ=2000 kg/m^3 and a damping ratio ξ = 5%. The soil rests on a rigid substratum. A shear wave velocity *(V_s)* of 310 m/s is used for computation. The half width of the strip footing foundation (*B*), subjected to horizontal sinusoidal loading, is 2m and simulations were performed over a range of frequency ratios:

$$a_0 = \frac{\omega B}{V_s} \qquad 0.04 < a_0 < 1.6 \text{ or } 1 < f < 40 \text{ Hz}$$

Case of H/B = 15

The height of the model is *H*=30m and length is *L*=100m. Then the displacement functions are described for *H/B*=15. The soil rests on the surface of a rigid substratum.

The dimensionless real and imaginary parts of the displacement functions are respectively presented in figures 2 and 3. Interested readers can find addition al information in Jendoubi (2007).

Numerical results compare well with those presented by Huh. The agreement is better at the higher values of a_0. The components of the functions of displacement present peaks due to the reflection of the waves on the base of the model.

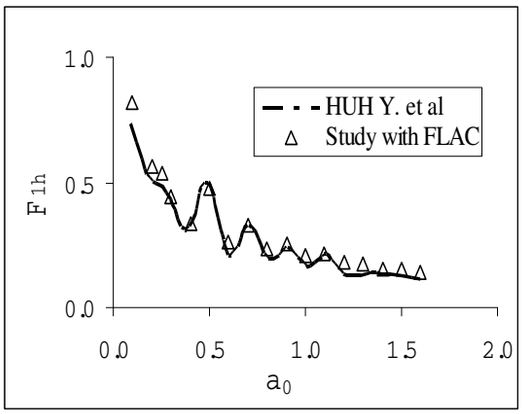


FIG.2. Real part of displacement functions (H/B =15)

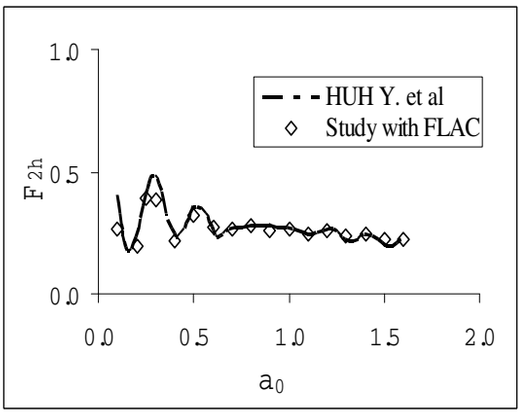


FIG.3. Imaginary part of displacement functions (H/B = 15)

Case of H/B = ∞

The vertical displacement functions are described for *H/B*=∞. The presence of quiet boundaries on the base of the model (figure 1) allows the consideration of the soil as a half-space medium with *L*=30m.

The dimensionless real and imaginary parts of the displacement functions are respectively presented in figures 4 and 5. FLAC results are in good agreement with those of HUH. Quiet boundary on the base of model solves the problem of wave reflection.

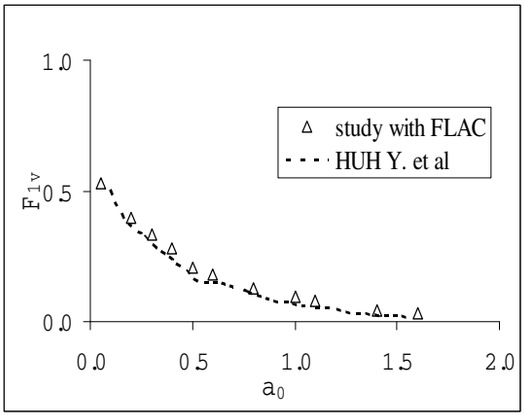


FIG.4. Real part of displacement functions (H/B= ∞)

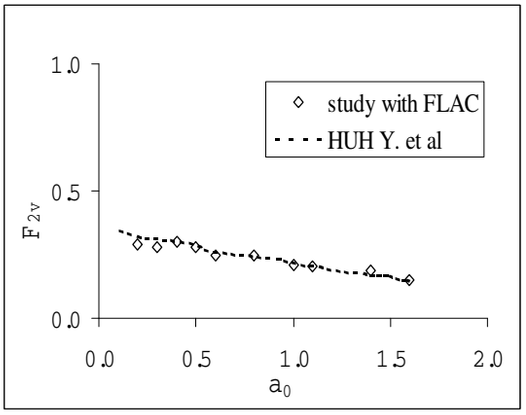


FIG.5. Imaginary part of displacement functions (H/B = ∞)

INFLUENCE OF SHEAR WAVE VELOCITY VARIATION WITH DEPTH:

The usual assumption of homogenous layer or half space with constant shear modulus *G* may not be realistic as the shear wave velocity increases with depth even for homogenous soils. The shear wave velocity increases as a function of the effective overburden stress (σ') and the velocity normalized by a stress of 100 kPa (V_{s1}) according to the following equation (Hardin and Drnevich 1972)

$$V_s = V_{s1}\left(\frac{\sigma'}{100}\right)^{1/4}$$

To study the effect of shear wave velocity variation with depth, numerical simulations are performed for three cases: (i) granular sandy media; (ii) cohesive soil; (iii) granular gravely soil. A 20m width and 15m height model is adopted in all cases. In each case, calculations are carried with constant or variable values of shear wave velocity V_s as shown in the table 1.

When V_s is varying with depth, each soil is divided into five layers with a height of 3m for each layer. V_s is constant for each one of these layers. Its value corresponds to the average value in the medium of the layer. Figure 6 shows the shear wave velocity profiles. For the parametric study purpose, V_s is considered to be equal to V_{s1}.

Table.1. Mechanical characteristics of soils models

Type of soil	Constant shear wave velocity	Variable shear wave velocity	ρ (kg/m^3)	ν
sandy	V_s = 200m/s	V_{s1} = 200m/s	1800	0.33
cohesive	V_s = 100m/s	V_{s1} = 100m/s	1600	0.45
Granular gravely	V_s = 300m/s	V_{s1} = 300m/s	2000	0.33

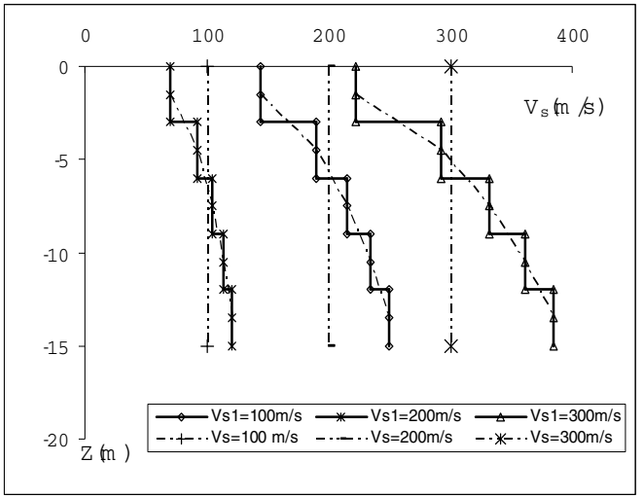


FIG.6. Variation of the shear wave velocity with depth
Results of calculation

Simulation results

Due to space limitation, only the imaginary parts of displacement functions associated with a horizontal vibration are presented in this paper. The results associated with the real part and vertical loading are given in Jendoubi (2007). Figure 7 presents the results for soils with constant shear wave velocity. Figure 8 shows the results for soils with a shear wave velocity increasing with depth.

The comparison of the results obtained with a constant shear wave velocity and those obtained with a variable velocity indicates that:

- In the two cases, the value of the imaginary part of the displacement functions shows that the energy of shear waves dissipated in the soil decreases up to zero when the frequency of vibration tends towards zero. This translated into elastic behaviour of soil with no dissipation when the loading is quasi-static which an exacted result.
- The values of the imaginary part for a soil with constant shear modulus are lower than the values of these parameters in the case of a soil with variable modulus. Indeed, for the cohesive soil, the maximum variation reached 50.2%, while the minimum variation is equal to 8.6% (figure 9).
- Displacement functions are the reverse of impedance functions. Therefore, important values of imaginary part in the case of variable shear wave velocity means lower damping than in the case of constant velocity.
- The curve of the cohesive soil (V_{s1} = 100m/s) deviates even more from the two other curves for the granular soils if we consider variable velocity with depth.
- The use of variable shear wave velocity with the depth induced also a considerable increase in the values of the real part of the functions of displacement especially for low frequencies (Jendoubi 2007).

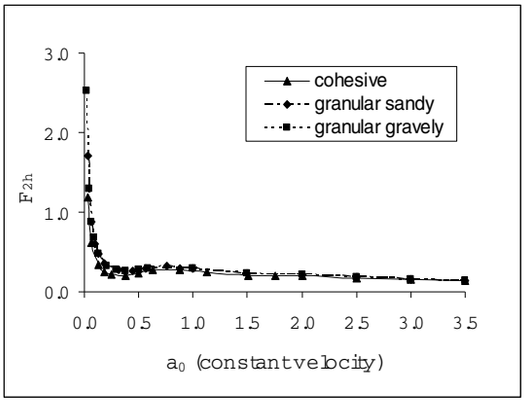


FIG.7. Imaginary parts of displacement functions : constant velocity

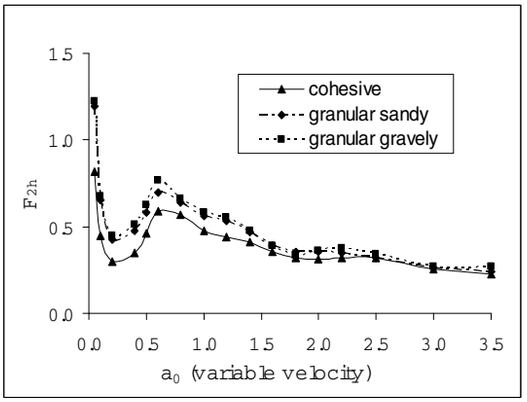


FIG.8. Imaginary parts of displacement functions : variable velocity

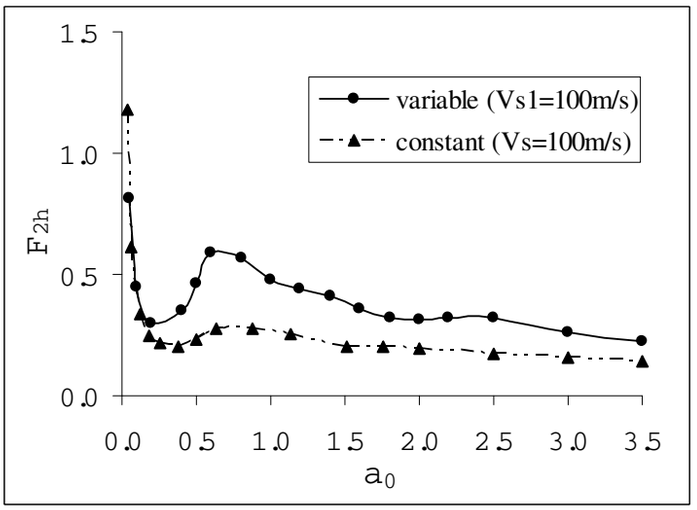


FIG.9. Imaginary parts of displacement functions associated with horizontal loading for cohesive soil

CASE OF A TWO-LAYER SOIL

In order to compare results obtained for two-layer soil to those of single layer, three models are considered. The first model is a two-layer soil deposit that is 15m thick and contains two materials. The top layer consists of granular soil and is 7.5m thick. The bottom layer consists of cohesive soil 7.5m thick. The second model consists only of granular soil that is 15m thick. The third one is cohesive soil deposit that is 15m thick also. In all cases, a Poisson's ratio, ν=0.33 and density ρ=1800 kg/m^3 for the granular soil and ν=0.45 and ρ=1600 kg/m^3 for the cohesive soil.

Figures 10 and 11 show the real and imaginary parts of displacement functions of two-layer, granular and cohesive soils in the case of horizontal vibration. Results associated with vertical loading are presented on figures 12 and 13.

In the case of a horizontal vibration the values of the real and imaginary parts are similar to the values of the top layer. Therefore, modeling of only the top layer is sufficient for the determination of real and imaginary part of displacement functions. If vibration is vertical, one notes the influence of the bottom layer clearly. For frequencies above 10 Hz, real part (figure 12) of displacement for two-layer soil is similar to real part of displacement of top layer. For frequencies below 2Hz, the real part of two-layer is in between top and bottom layer‘s displacement. In between 2 and 10 Hz, it is noted that real part of displacement functions for two-layer soil is below real part of both top and bottom layer. The effect of the cohesive soil is more important at lower frequencies because the lengths of shear waves are larger. For frequencies between 0.5 and 5Hz, dissipated energy *(F_{2v})* in the two-layered soil is lower than that dissipated if the granular soil and higher than what is dissipated in a purely cohesive ground (figure 13).

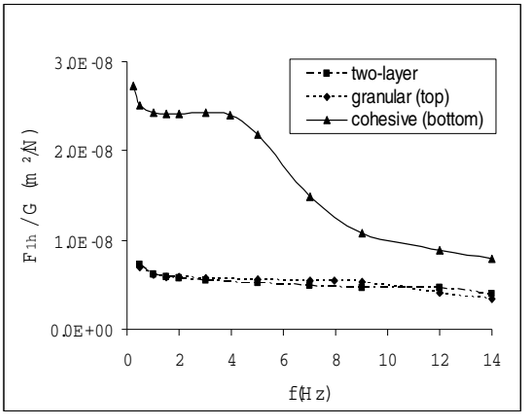


FIG.10. Imaginary part: horizontal vibration

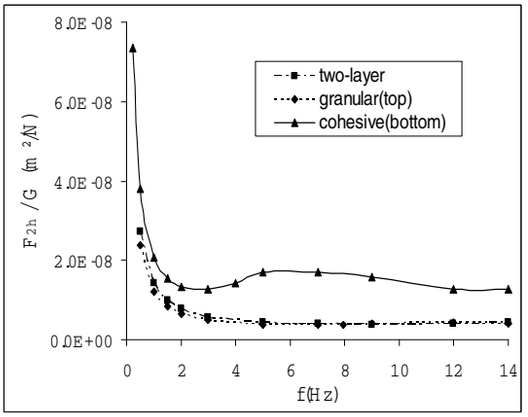


FIG.11. Real part : horizontal vibration

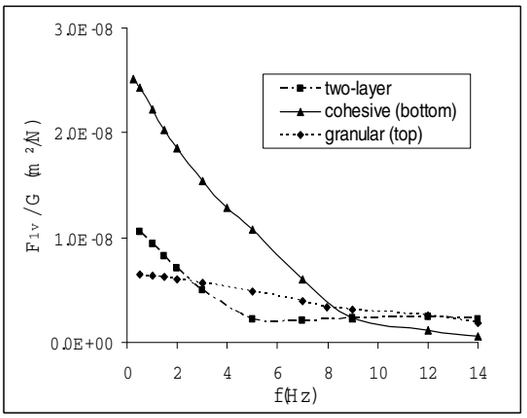


FIG.12. Real part : vertical vibration

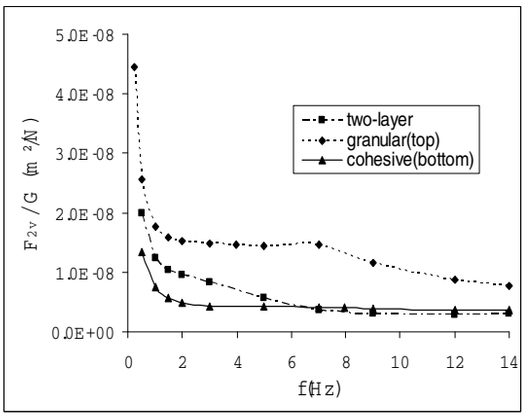


FIG.13. Imaginary part : vertical vibration

CONCLUSIONS

Validation and application studies indicate the accuracy and versatility of our models based on combining finite difference method and quiet boundaries that solve the problem of wave reflection and allow the consideration of the soil as a half-space medium.

Taking into account the variation of the shear modulus with the depth reflects better the reality of a homogeneous soil in which shear wave velocity increases as of function of overburden stress.

Results obtained with variable velocity are different from calculations with a constant shear wave velocity. The values of real and imaginary parts of displacements functions with constant G are lower than values calculated with variable G. This reveals that the ground is less rigid (K), deformations are larger and damping (C) is lower with variable V_s. The differences between displacement functions of strip footings with variable or constant shear wave velocity indicate that displacement should be evaluated with regard to the real profile of soil with increasing shear modulus. Calculations with variable shear wave velocity could also provide displacement functions for foundations on inhomogeneous soils.

In the case of two-layer soil, the top layer with 7.5m thick is sufficient to estimate the displacement functions for horizontal vibrations. For vertical vibrations, the bottom layer must be included in the model.

REFERENCES

Gazetas G. (1991) “Formulas and charts for displacements of surface and embedded foundations.” *Journal of Geotechnical Engineering*, Vol. 117 (9): 1363-1381.

Hardin B.O. and Drnevich V.P. (1972) “Shear modulus and damping in soils: design equation and curves.” *Journal of Soil Mechanics and Foundations Division, ASCE*, Vol. 98 (7): 667-692.

Huh Y. (1986) “Anwendung der Randelmentmethode zur Untersuchung der dynamischen. ” *RUB, SFB* 151- Mitteilung Nr. 86-13.

Jacquart G., Devesa G. and Clouteau D. (2005) “Couplage finite element method-boundary element method”: *Applications en ISS. Technical report 2005,* EDF.

Jendoubi A. (2007) “Étude de l’influence des impédances de fondation sur le comportement dynamique des lignes de transport d’énergie électrique. ” *Mémoire de maîtrise*, Université de Sherbrooke, Faculté de génie.

Lysmer J. and Kuhlemeyer R.L. (1969) “Finite dynamic mode for infinite media.” *Journal of the engineering mechanics division ASCE*, Vol. 95.

Novak M. et El Sharnouby B. (1983) “Stiffness constants of single piles.” *Journal of Geotechnical Engineering*, Vol.109 (7) : 961-974.

Itasca consulting group, Inc. (2002) “FLAC User’s Guide.” *Minneapollis, Minnesota USA.*

Pecker A. (2005) “Dynamique des ouvrages et Dynamique des Structures. ” *Doc pédagogique* (École Nationale des Ponts et Chaussées, France).

Rosset J.M. and Ettouney M.M. (1977) “Transmitting boundaries: comparison.” *Journal of numerical and analytical methods in geomechanics.* ” Vol. 2 (2).

Smith W. (1973)“A non-reflecting place boundary for wave propagation problem. ” *Journal of computer physics*, 1.

Sieffert J.G. et Franck C. (1991) “Manuel des fonctions d'impédance - Fondations superfcielles. ” France, *presses académiques* edition, 175p.

Sekhar C.D et Rana Roy. (2002) “A critical review on idealization and modeling for interaction among soil foundation structure system.” *Computers and Structures*, Vol. 80 (*20*): 1579-1594.

Stewart J.P, Fenves G.L. et Seed R.B. (1999) “Seismic soil-structure interaction in building: analytical methods.” *Journal of geotechnical and geoenvironmental engineering*, ASCE, Vol. 125 (1): 26-37.

Veletsos A.S. and Vebric B. “Vibration of viscoelastic foundations.” (1973) *Earthquake engineering and structural dynamics*, Vol. 2: 87-102.

Wolf J.P. (1985) Dynamic soil structure interaction. *Prentice-Hall Inc*., London. 466p.

This page intentionally left blank

Wave Propagation under Vertically Excited Surface Foundation

Jaehun Ahn[1], Giovanna Biscontin[2], and Jose M. Roësset[3]

[1] Visiting Assistant Professor, Department of Civil, Construction and Environmental Engineering, North Carolina State University, Raleigh, NC 27695-7908; jahn4@ncsu.edu
[2] Assistant Professor, Zachry Department of Civil Engineering, Texas A&M University, College Station, TX 77843-3136; gbiscontin@civil.tamu.edu
[3] Cain Chair Professor, Zachry Department of Civil Engineering, Texas A&M University, College Station, TX 77843-3136; jroesset@civil.tamu.edu

ABSTRACT

Recently developed equipment allows measurement of the shear modulus of soil in situ as a function of level of strain. In these field experiments, the excitation is applied on the ground surface using large scale shakers, and the response of the soil deposit is recorded through embedded receivers. The focus of this paper is on the simulation of signals which would be recorded at the receiver locations in idealized conditions to provide guidelines on the interpretation of field measurements. Discrete and finite element methods are employed to model one dimensional and three dimensional geometries, respectively, under various lateral boundary conditions. When the first times of arrival are detected by receivers under the vertical impulse, they coincide with the arrival of the P wave, related to the constrained modulus of the material, regardless of lateral boundary conditions. If one considers, on the other hand, phase differences between the motions at two receivers the picture is far more complicated and one would obtain propagation velocities, function of frequency and depth, which do not correspond to either the constrained modulus or Young's modulus. It is thus necessary to apply some care when interpreting the data from field tests based on vertical steady state vibrations. The use of inverse analysis can be considered as a way of extracting the shear modulus of soil from the field test measurements.

INTRODUCTION

The recent development of large scale shakers (Stokoe et al., 2006) allows to measure soil properties, such as the shear modulus, in the nonlinear range directly in situ. The method involves applying static and dynamic loads at the surface of the soil deposit and measuring the dynamic response of the soil mass beneath the loaded area with embedded geophones. A description of the test setup is illustrated in Figure 1. The wave propagation velocity can be obtained from interpretation of the recorded soil motions. However, the first times of arrival (or the inter-arrival times between sensors) for vertical motions will coincide with the arrival times of P waves and would provide therefore the P wave velocity for the material, corresponding to its constrained modulus. When

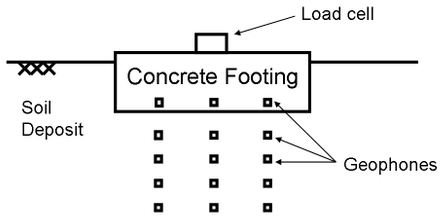


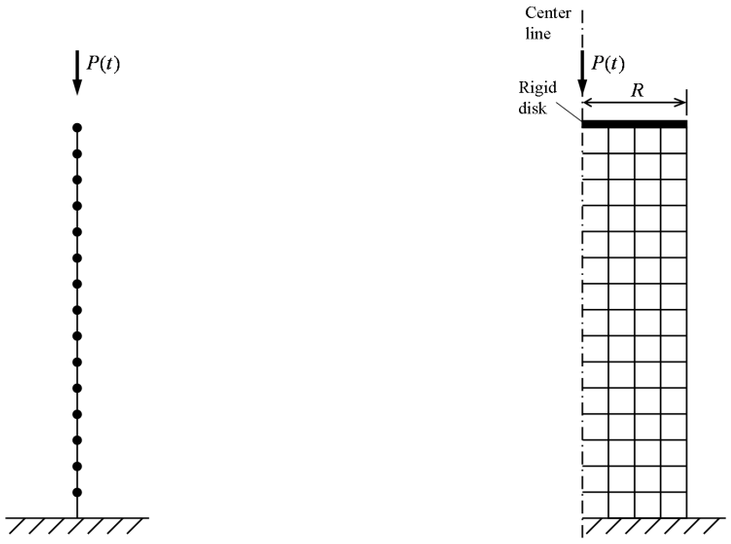
FIG. 1. Test setup

considering, on the other hand, the phase difference between the recorded motions, the resulting propagation velocities will be functions of frequency and depth, and will not correspond exactly to either the constrained modulus or Young's modulus (rod wave velocity). Therefore the records of the measured velocities at different locations below the foundation are not sufficient to estimate the soil moduli or the strain level correctly. Interpretation of the measurements is required to estimate the local strains in the soil, as well as the soil properties of interest, such as the shear modulus. Actual field recordings are difficult to interpret because of noise and the effects of the inherent heterogeneity of the soil, as well as its nonlinearity. The goal of this paper is to simulate the signals which would be recorded at the geophone locations in idealized conditions. The understanding developed through this process can then be applied to the actual recordings as a tool for interpretation. We will evaluate two different strategies to model the system and their effectiveness in capturing the essential characteristics of the motion for a correct interpretation of the field results.

First, the response time histories of waves propagating through a one dimensional column are calculated by discrete modeling. Then, the results obtained with a three dimensional model and different boundary are assessed and compared with previous results. Finally, the paper focuses on wave propagation through an elastic medium using the three dimensional model with consistent transmitting boundary and minimizing the effects of a rigid bottom boundary.

NUMERICAL METHODS AND MATERIAL INPUTS

Wave propagation through a one dimensional column is simulated using a discrete model. The column is represented by a series of lumped masses connected by springs, as shown in Figure 2(a), with $P(t)$ representing the excitation. The dynamic equilibrium equation is formulated in the time domain and solved by the central difference formulation, which requires a time step Δt equal or smaller than T_{min}/π, where T_{min} denotes the smallest natural frequency of the system, for stability. The bottom of the column is fixed. Figure 2(b) shows the column finite element model. The solution takes advantage of the axisymmetry of the problem and is carried out in the frequency domain, using Fourier series expansion in the circumferential direction. The lateral boundary can be free or constrained in the horizontal direction. The consistent transmitting boundary by Kausel and Roesset (1975) is also implemented to absorb propagating waves and simulating more realistic field conditions. All numerical models presented in this paper are coded by the authors.



(a) One dimensional column (b) Three dimensional column

FIG. 2. Discrete and finite element models

The same material inputs are assigned to all cases of the numerical analyses: mass density 2000 kg/m^3, shear wave velocity 100 m/s, and Poisson's ratio 0.45. A Poisson's ratio 0.45 is selected to separate the value of the constrained modulus from that of the Young's modulus, making it easier to compare the calculated wave velocity. Given these material properties, the constrained and Young's moduli become 220 MPa and 58 MPa, respectively.

TIME HISTORIES

In modeling hypothetical field conditions, a one dimensional column of 6 m length is considered first. We assume receivers are placed at depths of 1, 2 and 3 m from the top along. Consider first a vertical load $P(t)$ in the form of a triangular pulse with duration $T_d = 0.01$ s as shown in Figure 3. The displacement time histories at the receiver locations are illustrated in Figure 4(a). The motion starts at the receivers at times of 0.00587, 0.01174 and 0.01762 s coinciding with the arrival of the wave. The wave propagation velocity is 170.4 m/s, corresponding to the rod wave velocity, or the Young modulus of the soil. The displacement increases over the 0.01 s of duration of the pulse, remains constant and then decreases as the reflected pulse from the bottom of the column reaches the receivers. After this, not shown in the figure, there are pulses reflected from the top (free surface) and the displacements reproduce themselves with a negative sign. The arrival of the first pulse and of its reflection from the bottom are clearly seen in the velocity records in Figure 4(b). When the column is constrained laterally, the constrained modulus, rather than the Young's modulus, is the relevant material property, resulting in a wave propagation velocity of 331.66 m/s (P wave velocity). The corresponding displacements and velocities for a one dimensional model are as shown in Figures 5(a) and 5(b), with the same shapes as in the previous case, but different arrival times for the pulses (0.003015, 0.00603 and 0.009045 s at the three receivers).

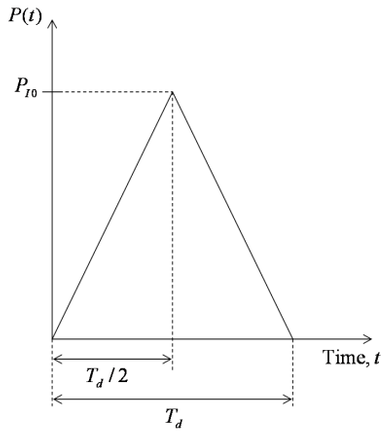
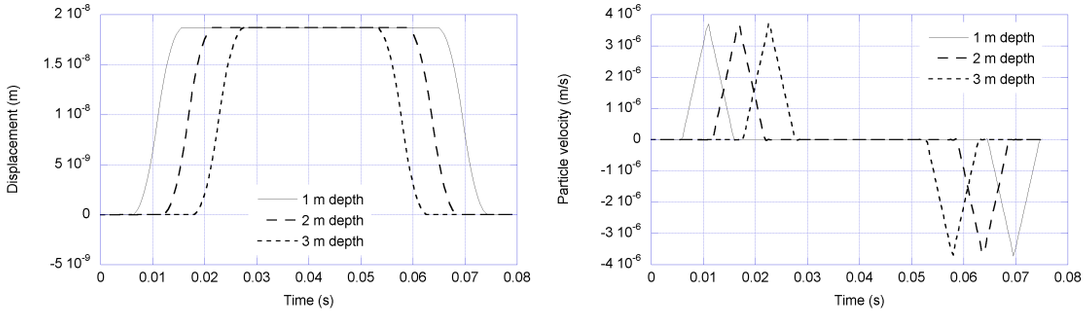


FIG. 3. Triangular pulse

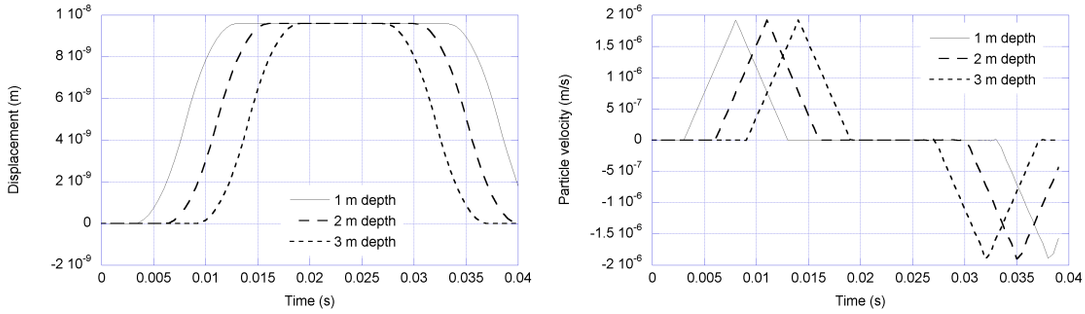


(a) Displacement time histories (b) Particle velocity time histories

FIG. 4. Displacement and particle velocity time histories in one dimensional unconstrained column after impact ($\Delta T_d = 0.01$ s)

The arrivals of the different waves are very easy to identify when the duration of the pulse is very small, as in this case (duration of 0.01 s, corresponding to a predominant frequency of 100 Hz). For longer durations this is not the case. Figure 6 shows, for instance, the displacement histories of the same column under a pulse of duration 0.04 s. The motion starts at the same time at each sensor location, but it is no longer possible to visualize the arrivals of the reflected waves: the column is vibrating at its own natural period (0.074 s, in this case).

The same conditions can be evaluated using the three dimensional finite element model with a radius $R = 0.5$ m as shown in Figure 2(b). The boundary condition on the top of the column assumes uniform vertical displacements, i.e. a rigid disk. Three different boundary conditions are considered in the horizontal direction: free, constrained and absorbing (consistent transmitting) boundary. When a triangular pulse $P(t)$ with duration 0.01 s is applied to the three dimensional column with free lateral boundary, the displacement time histories at the three receiver locations appear as in Figure 7(a). The boundary conditions in this case are analogous to those in the first example for the one dimensional models yielding the results in Figure 4. The displace-



(a) Displacement time histories (b) Particle velocity time histories

FIG. 5. Displacement and particle velocity time histories in one dimensional constrained column after impact ($\Delta T_d = 0.01$ s)

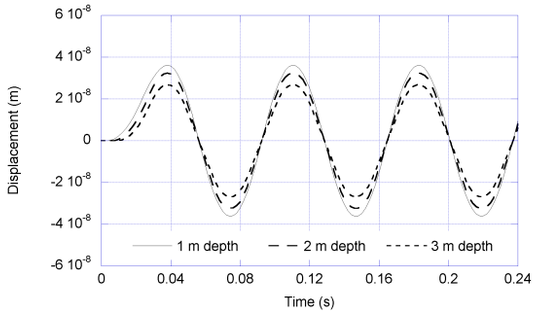
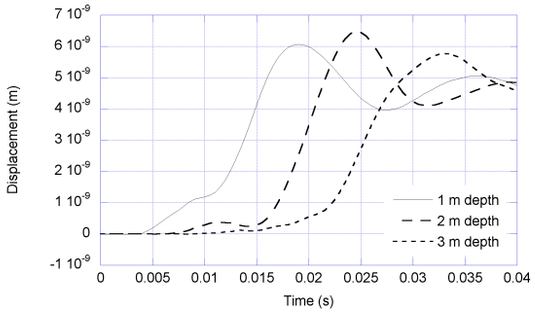


FIG. 6. Displacement time histories in one dimensional constrained column after longer impact ($\Delta T_d = 0.04$ s)

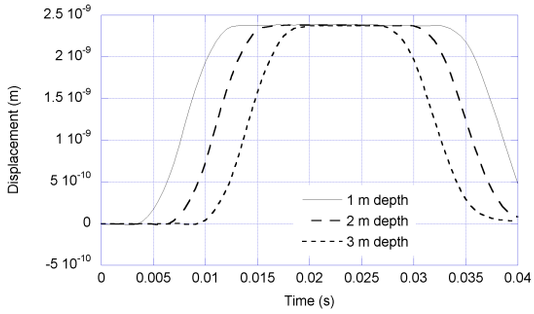
ment histories in Figure 7(b) are obtained when the lateral boundary is constrained (no radial displacements permitted) corresponding to the second example with the one dimensional model. If the load is applied to the three dimensional column with the consistent transmitting boundary, which simulate what would happen in the field most closely, the displacement time histories change as shown in Figure 7(c). The displacements start at the times of arrival of the P wave (0.003015, 0.00603 and 0.009045 s), but the shape of the displacement time histories is very different from those obtained earlier with the one dimensional model. Comparing these three figures, we see that the times at which the motions start are the same for all three cases, corresponding to the arrival of the P wave, irrespective of the lateral boundary conditions. The shape of the displacements is the same as in the one dimensional solution when the lateral boundary is constrained but it is quite different in the other two cases. The differences in the shape of the displacement histories will affect the phase differences between the motions at the receivers.

DISPERSION CURVES

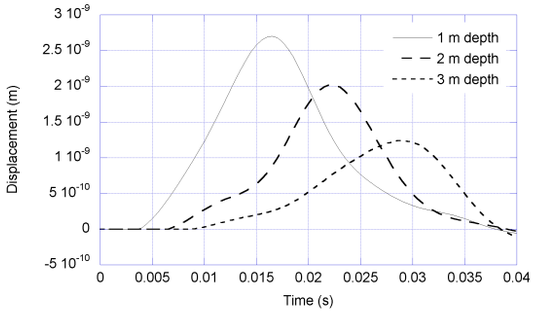
As shown above, accurately measuring the first time of arrival of the waves provides in all cases the velocity of propagation of P waves, and therefore the value of the constrained modulus of the material, assuming its density is known. For field tests,



(a) Three dimensional unconstrained column



(b) Three dimensional constrained column



(c) Three dimensional column with consistent transmitting boundary

FIG. 7. Displacement time histories in three dimensional column with unconstrained, constrained, and consistent transmitting boundary

identifying the arrival time may not be simple and it is preferred sometimes to use the dispersion curve, showing how the phase changes as a function of frequency depending on the location of the recorded motion. The phases can be obtained from the ratio of the Fourier transforms of the motions (displacements, velocities or accelerations) recorded at two receivers. Alternatively, one can obtain analytically or numerically the transfer functions between the motions at the two receivers under a steady state harmonic vibration.

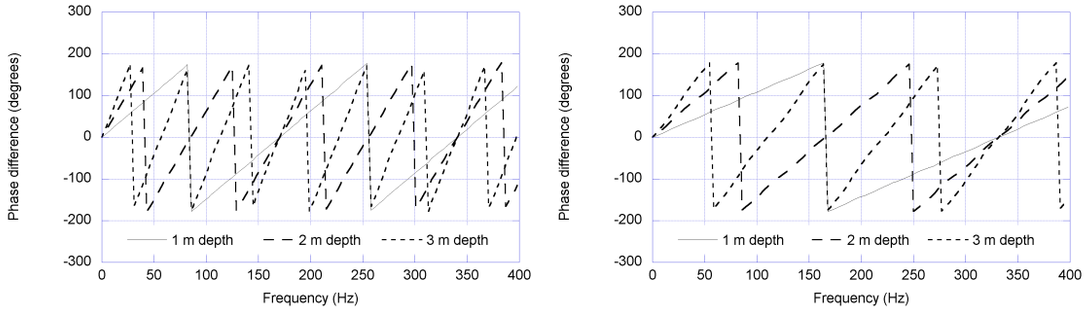
Figure 8(a) shows the phase difference between the input and the motions at the three receiver locations for the one dimensional model with free lateral boundary. The results for the column with constrained boundaries are in Figure 8(b). The phases vary linearly with frequency. If the phases were unfolded one would get straight lines with an equation of the form

$$\varphi = 360 \cdot d \cdot f/c \tag{1}$$

where φ is the phase in degrees, d is the depth of the receiver, f is the cyclic frequency (in Hz), and c is the wave propagation velocity. Alternatively,

$$c = 360 \cdot d \cdot f/\varphi. \tag{2}$$

When the phase difference is a multiple of 360 equal to the distance in units of length



(a) One dimensional unconstrained column (b) One dimensional constrained column

FIG. 8. Phase differences of signals in one dimensional unconstrained and constrained column

between the top of the column and the receiver, the difference in frequency is the wave propagation velocity. The first up-crossing for the first receiver, the second up-crossing for the second receiver and the third up-crossing for the third receiver happen all at the same frequency, resulting in a value of the propagation velocity of roughly 170 m/s for the free column and 331.7 m/s for the constrained one.

In order to simulate field conditions most closely, the three dimensional column finite element model with consistent transmitting boundary is chosen. The rigid bottom boundary is placed deeper, 12 m below the surface, to decrease its effect. The finite element model used in the computations is illustrated in Figure 9. The small squares indicate the locations of the receivers. The results are calculated using different sizes of the square elements $\Delta L = 0.125, 0.0833, 0.0625$ m ($\Delta L = 1/8, 1/12, 1/16$ m). The phase differences between the input and the receiver locations at depths of 1 m, 2 m, and 3 m are presented in Figure 10(a) for the elements size of $\Delta L = 0.125$ m over the range of frequencies of 10 Hz to 25 Hz. For this range of frequencies the plots are nearly, although not exactly, straight lines. The corresponding wave propagation velocities are shown in Figure 10(b). They are nearly constant with frequency but show small variations. The wave velocity tends to be higher at shallower depth, where the level of confinement due to the excitation is higher. In field tests, a certain level of vertical static loading is followed by harmonic excitation. In the vicinity of the foundation, when the vertical excitation is applied, the wave velocity is affected by the confinement due to the initial static load, as well as the vertical excitation. Therefore, the tendency of the calculated wave velocity to decrease with receiver depth could be even greater the field if the dependency of soil properties on confinement is high. In addition, as could be expected, the wave propagation velocities are higher when the mesh size is coarser since the model with coarse elements is stiffer than the one with finer elements. As the relation between wave velocity and mesh size appeared to be almost linear, wave velocities corresponding to mesh size are linearly extrapolated as shown in Figure 11, in an effort to minimize the effect of the mesh size. The average estimated wave velocities are about 225 m/s, 178 m/s, and 164 m/s corresponding to the first, second and third receiver location, respectively.

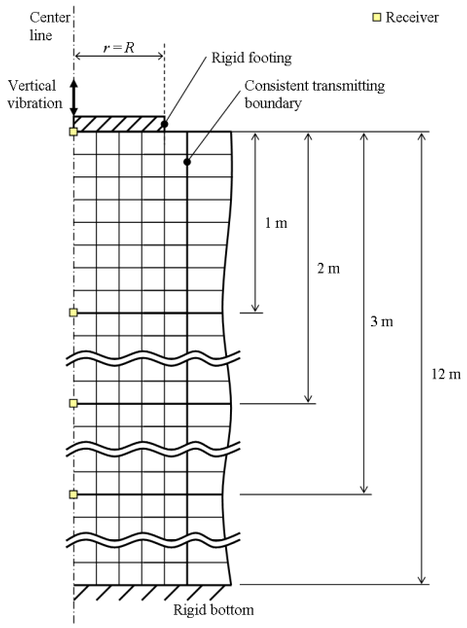
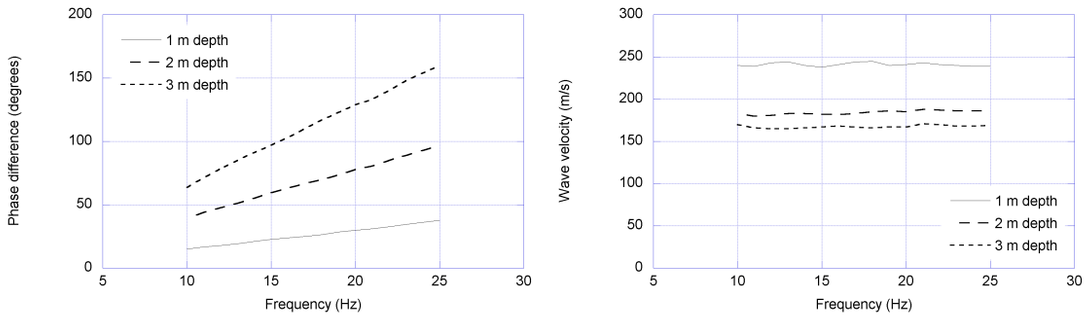


FIG. 9. Description of finite element model



(a) Phase differences of signals under rigid disk using FE analysis ($\Delta L = 0.125$ m)

(b) Wave velocities under rigid disk using FE analysis ($\Delta L = 0.125$ m)

FIG. 10. Phase differences of signals and wave velocities under loaded area using finite element code with consistent transmitting boundary

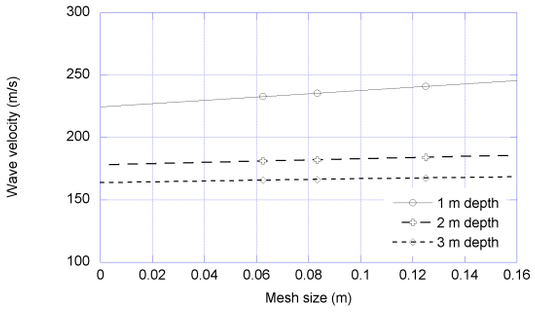


FIG. 11. Variation of wave velocities with mesh size

SUMMARY AND CONCLUSIONS

Wave propagation is simulated on one dimensional models by discrete modeling, and on three dimensional models by the finite element method. The results indicate that when the wave propagation velocities in the vertical direction are calculated from the phase differences between the vertical motions recorded at receivers placed at different depths, the values obtained may change with location and also with frequency. These values will not correspond exactly to either the P wave velocity, associated with the constrained modulus of the material, nor to the rod velocity associated with Young's modulus. They tend to be between these two values but much closer to the latter.

It is thus necessary to apply some care when interpreting the data from field tests based on steady state vibrations. Since the wave velocities do not exactly correspond to either the P or rod wave, the use of inverse analysis would be recommended to extract shear modulus of soils the field test data measured under the vertically excited footing.

ACKNOWLEDGEMENTS

This material is based upon work supported by the National Science Foundation under Grant No. CMS-0421275. The support is gratefully acknowledged.

REFERENCES

Kausel, E. and Roesset, J. (1975). "Dynamic stiffness of circular foundations." *Journal of the Engineering Mechanics Division, ASCE*, 101(EM6), 771–785.

Stokoe, K. H., Kurtulus, A., and Park, K. (2006). "Development of Field Methods to Evaluate the Nonlinear Shear and Compression Moduli of Soil." *Earthquake Geotechnical Engineering Workshop*, Christchurch, New Zealand.

This page intentionally left blank

Analysis of statnamic behavior of full–scale pile group in soft clays and silts

Tetsuo Tobita[1], M. ASCE and Gi Cheon Kang[2], Susumu Iai[3], and Kyle, M., Rollins[4], M. ASCE

[1] Disaster Prevention Research Institute, Kyoto University, Gokasho, Uji, Kyoto, 611–0011, Japan
Email: tobita@geotech.dpri.kyoto–u.ac.jp
[2] Department of Civil and Earth Resources Engineering, Kyoto University, Katsura, Nishi-kyo-ku, Kyoto, 615–8530, Japan, Email: kang@geotech.dpri.kyoto–u.ac.jp
[3] Disaster Prevention Research Institute, Kyoto University, Gokasho, Uji, Kyoto, 611–0011, Japan
Email: iai@geotech.dpri.kyoto–u.ac.jp
[4] Department of Civil and Environmental Engineering, Brigham Young University
Email: rollinsk@byu.edu

ABSTRACT: Dynamic behavior of a pile group is simulated by a two–dimensional finite element analysis. Results of the full–scale lateral–load tests of a 3 × 5 pile group conducted in the Salt Lake City International Airport site are compared with the simulation. The soil profile at the test site generally consisted of cohesive sandy silt and silty sand. Closed–end steel pipe piles were driven to a depth of 11.6 m. Pile head was rotation free. Dynamic lateral loads were applied to pile head with the statnamic device. To conduct numerical analysis, model parameters for soils are taken from the geotechnical investigation data at the test site. Response of five piles in the middle of the 3 × 5 pile group are simulated. Measured dynamic loads are applied at the pile head. Overall load–deflection behavior of the pile group agrees well with the measured ones. Some discrepancies are found on the bending moment profile. In the full–scale dynamic tests, peak moments for larger target deflections occurred at the same depths for all piles, while in computation, the peak moment occurs with greater depths as target deflection increases. Numerical analysis overestimates the group effects in dynamic tests. This calls up further improvement of a numerical modeling.

INTRODUCTION

Fairly reliable methods have been developed for prediction of the lateral load capacity of a single pile, e.g., Reese et al. (2000). However, very little information is known to engineers about the design of closely spaced pile group. Experimental studies, e.g., Brown et al. (1988), Rollins et al. (1998), Tobita et al. (2004), and Rollins et al. (2005), have shown that the pile head displacement of pile groups is significantly larger than that of a single pile under the same amount of loading. This is called the group effects caused by overlap of failure wedges. One method to account for the group effect is to

reduce the single pile *p*–*y* curve using *p*–multipliers. For example, Rollins et al. (1998), and Rollins et al. (2005) derived *p*–multipliers from the full–scale lateral load tests of a pile group of 3 × 3 pattern at three–pile diameter spacing. They applied the *p*–multiplier approach to numerical analysis (Reese and Wang 1996) and obtained good agreement with measured and computed pile group response.

However, considering costs and labors to conduct full–scale lateral load tests on pile groups, it is desirable to develop a simulation method which can predict group pile response including the group effect with the accuracy required for design practice. Using the 2D FEM code developed by Iai et al. (1992), Tobita et al. (2006) analyzed the full− scale group pile behavior under static lateral loads and obtained reasonable results. Objective of the present study is to further investigate the applicability of the FEM code by simulating the statnamic lateral− load tests conducted in a series of the full− scale lateral–load test project (Snyder 2004).

THE FULL–SCALE LATERAL LOAD TESTS OF A 3 × 5 PILE GROUP

Overall layout of the 15–pile group and single pile is shown in Figure 1(a). Figure 1(b) shows the statnamic device for the dynamic load tests. A solid fuel propellant inside the combustion chamber is ignited then the reaction mass and silencer are launched away from the pile group. The term "statnamic" is derived from a notion indicating a hybrid of conventional static and dynamic load tests. Major advantages of the statnamic test are it can be done quickly and mobilized with relative ease compared to other test methods, and high load levels can be reached without the need for a reaction foundation or loading frame (Snyder 2004).

The soil profile of the site (Figure 2) shows a dominance of cohesive sandy silt and silty sand. Piles were driven in 3 × 5 pattern with a spacing of 3.92 pile diameters centre to centre in the direction of loading. The pile is made of steel and has an outer diameter of 324 mm with a wall thickness of 9.5 mm. It was driven closed–ended to a depth of 11.6 m. Lateral load was applied either statically or dynamically. In both cases, a lateral load was applied at 495 mm above the ground surface. Each pile and the load frame were pin–connected so that the rotation was free at the pile head. For static loading, piles were pushed against reaction wall with hydraulic jacks. For dynamic loading, piles were pushed by a 311 kN statnamic device.



(a) 15 pile group and a single pile



(b) Statnamic device

FIG. 1. Photograph of the full− scale lateral− load tests (after Snyder 2004).

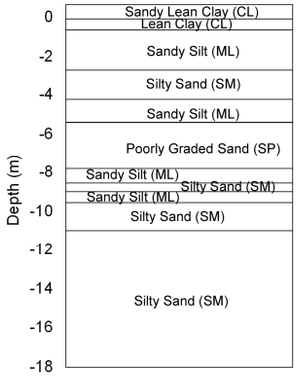


FIG. 2. Ground profile at the Salt Lake City International Airport (after Snyder 2004)

NUMERICAL MODEL

Two dimensional finite element analysis based on the multi–shear mechanism constitutive relationship, FLIP (Finite element analysis program for LIquefaction Process) (Iai, et al. 1992), is employed to simulate the full–scale lateral–load tests of a pile group. To have the same loading condition with the full–scale tests, the present analysis is conducted under drained condition by applying lateral load at the pile head. In the analysis of the dynamic loading tests, measured time histories of statnamic load are applied to the pile head.

Five piles in the middle row shown in Fig. 1 is a target of the analysis. Finite element mesh of the target cross section is shown in Fig. 3. In FLIP, the multi–spring elements (Towhata and Ishihara 1985) are used for modeling visco− plastic behavior of soils. Bilinear beam elements are used for modeling piles. Displacement degrees of freedom of side boundaries are fixed in horizontal direction, while that of the bottom boundary are fixed in both horizontal and vertical direction. Top and bottom of piles are set as displacement and rotation free to keep the same fixity condition as the full–scale tests.

Soil deformation near piles is a major concern when the simulation is carried out in two dimension (Iai et al. 2006). In FLIP, soil–pile interaction springs are adapted between soil and pile nodes to take into account the soil deformation near piles. Values of these spring coefficients are internally determined based on the separately derived empirical relationship Detail can be found in Ozutsumi et al. (2003). To derive these coefficients, an assumption is made that confining stress to piles is high enough so that soils near piles virtually have no vertical movement. Namely, soil–pile interaction is considered in the plane strain condition. It is true if confining stress is high, i.e., nodes are located deep and/or pile movement is small. However, at shallow depth, confining stress is low, therefore, the assumption tends to give large soil–pile interaction spring coefficient in the given frame work of empirical relationship. This may give adverse effect on the behavior of soil deformation near ground surface. To relief this effect, a coefficient called “PFACT” is multiplied to the spring coefficient to reduce the spring force. In the present analysis, PFACT=0.6 is multiplied to the spring coefficients shallower than 3.06 m and PFACT=1.0 is to the rests (Tobita et al. 2006).

Model parameter identification

Soil layers shown in Fig. 2 are adopted in the analysis. Model parameters of the ground and pile are defined, respectively, in Table 1 and 2. They are obtained based on the geotechnical investigation data at the site (Snyder 2004). Parameters for piles are taken from the industrial standard. A value of cohesion of the top layer was slightly changed from that of Snyder (2004), 41.4 kPa, for calibration of single pile behavior. Variation of shear modulus in depth is consistent with the variation of tip resistance and sleeve friction of the CPT test results (Tobita et al. 2006). Rayleigh damping parameters are set as 0.2 % for soil and zero for pile element.

Table 1. Idealized soil layers and model parameter for soil element

Depth (m)	Density	Porosity	Parameter for deformation characteristic							
			G_{max}	E_{max}	Average effectve stress corrsponding to Gr, Kr	Poisson ratio	Exponent of elastic modulus	Internal friction angle	Cohesion	Max. dampin g ratio
	ρ	n	G_r	K_r	p_r	v	m	φ_f	c	h_{max}
	(kg/m^3)		(kPa)	(kPa)	(kPa)			(°)	(kPa)	
0 - 1.22	9.05	0.55	20700	55062	36.72	0.33	0.5	-	51.4	0.2
1.22 - 2.14		0.6	25000	66500	41.98			-	50	
2.14 - 3.06			20000	53200	47.35			-	40	
3.06 - 4.8	8.14		147000	391020	52.93			38	-	
4.8 - 5.33	9.05		28450	75677	62.62			-	56.9	
5.33 - 5.87			12500	33250	67.83			-	25	
5.87 - 6.48			27000	71820	67.83			-	54	
6.48 - 11.6	8.14		169000	449540	77.67			33	-	
11.6 - 18.0			49000	130340	85.5			33	-	

Table 2. Model parameter for pile element

Depth (m)	PFACT	Gs (kPa)	Poisson ratio	Density (kg/m^3)	Area/unit width	Initial flexural rigidity, EI0 (kPa)	Second flexural rigidity, EI2 (kPa)	Full plastic moment (kN-m)
0-3.06	0.6	7.752×10^7	0.29	6.9	0.02897	1.087×10^5	6.52×10^4	874.7
3.06-11.6	1							

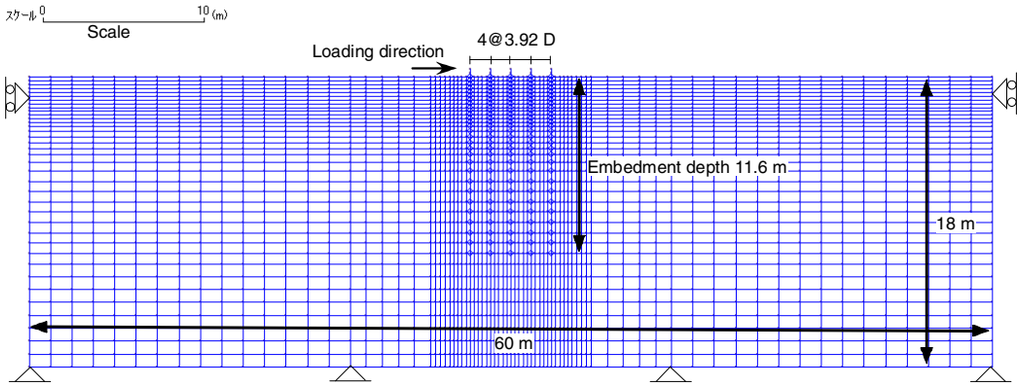


FIG. 3. FEM Mesh for the FLIP analysis

Single pile behavior

A lateral load is statically applied at the pile head (0.495 m above the surface) until the displacement of 90 mm at the loading point is achieved [Fig. 4(a)]. The maximum load at the maximum deflection agrees, however, the load– deflection behavior is slightly over– estimated. The initial slope of the computed load–deflection curve is about 1.5 times larger than that of measured. Computed load at the pile head deflection of 50 mm is about 30 % over– estimated. The maximum moment at a given lateral load shown in Fig. 4(b) is practically in good agreement.

Computed bending moment in depth at 90 mm of the pile head displacement shown in Fig. 5 is consistent with the one measured at the pile head displacement of 89 mm. An anomaly kink at the bottom of the computed moment in Fig. 5 may be due to an error on the mesh set up. Although the effect of this kink is minor, this has to be corrected.

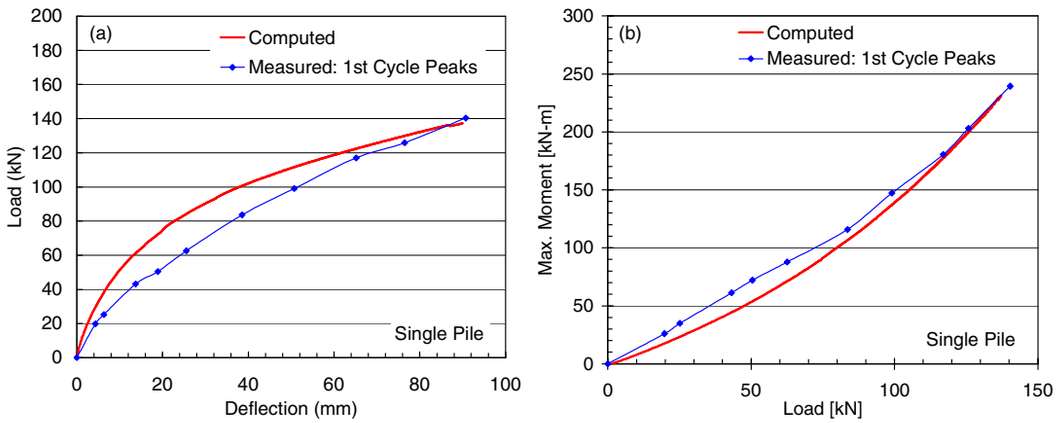


FIG. 4. Single pile: (a) Measured and computed load deflection curve, and (b) Maximum moment load curve.

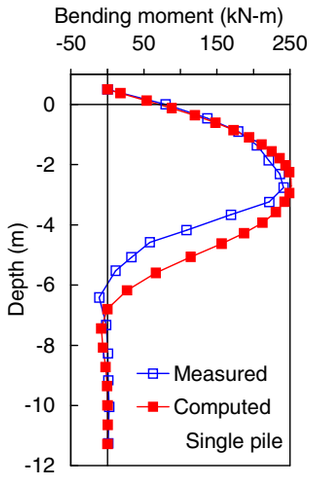


FIG 5. Comparison of bending moment profile of a single pile: Full scale experiment (Snyder 2004) and computation by FLIP

GROUP PILE STATNAMIC LOAD TEST

In the full− scale tests, the statnamic tests on the 15− pile group were conducted simultaneously with the static loading tests. The statnamic tests were performed mainly as final loading cycles. The group pile was cyclically loaded up to certain target deflections after which the statnamic test was performed by loading the pile group to the same target deflection. The dynamic test was performed as a 16th cycle for target deflections of 13 mm and 25 mm, a 15th cycle for 38 mm, and 11th cycle for the 64 mm target deflection. The statnamic test was performed as an initial cycle once to observe the dynamic behavior of the pile group as it was loaded into virgin soil. Thus, the test was conducted as a 1st and 16th cycle for the 89 mm target deflection. This brings the total to six statnamic tests performed on the pile group (Snyder 2004).

In the numerical analysis, six dynamic loads without cyclic static loads were sequentially applied to the pile group [Fig. 6(a)], i.e., for all target deflections, the group pile was loaded into virgin soil. This preserves the simplicity and saves computational time in the numerical analysis. However, deflection levels after the second dynamic loading are evaluated smaller than measured ones [Fig. 6(b)]. This will be discussed in the next section.

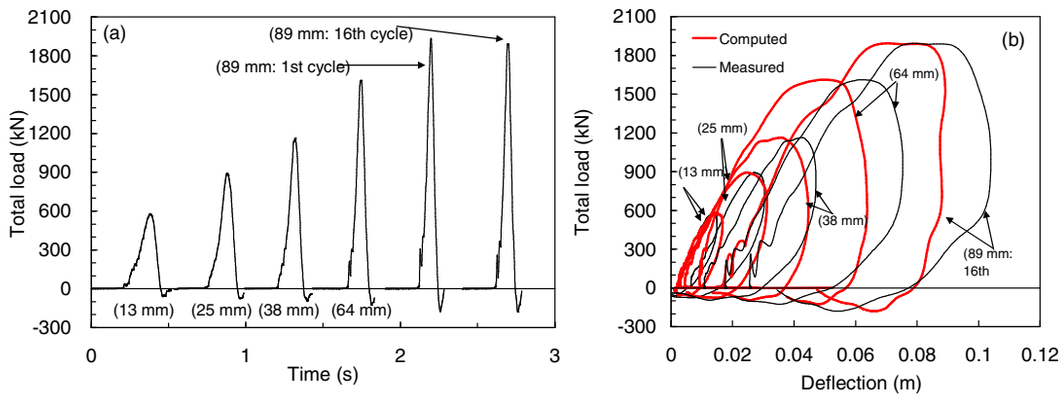


FIG 6. Time sequence of the total load applied to the pile group in the numerical analysis (a), comparison of load− deflection curves except for 1st cycle of a target deflection of 89 mm, (b). Target deflection is specified in parenthesis.

Load versus deflection

Figure 6(b) provides the plot of the measured and computed load− deflection curves for all cases, except for the 1st cycle of the target deflection of 89 mm. In each curve, slope in the loading phase agrees well. However, computed curves are consistently under estimating the deflections, partly because loading condition is different from the full− scale tests as mentioned earlier. In the full− scale tests, gaps between piles and surrounding ground made by static cyclic loads might lead larger deflection, while in the numerical analysis, no gaps are allowed between soil and pile.

Curves shown in Fig. 6(b), and the 1st cycle of the target deflection of 89 mm are separately shown in Fig. 7. Each curve is shifted so that loading starts at zero deflection.

Load− deflection curves during loading phase agree well for all cases. While in the unloading phase, when target deflection is small [Fig. 7(a)− (c)], deflections are over − estimated, because soil elements attached to piles may resist against reverse movement of piles. As target deflection increases, analytical curves show better agreements, because soil resistance behind piles may be reduced due to large strains in soil elements near piles during loading phase.

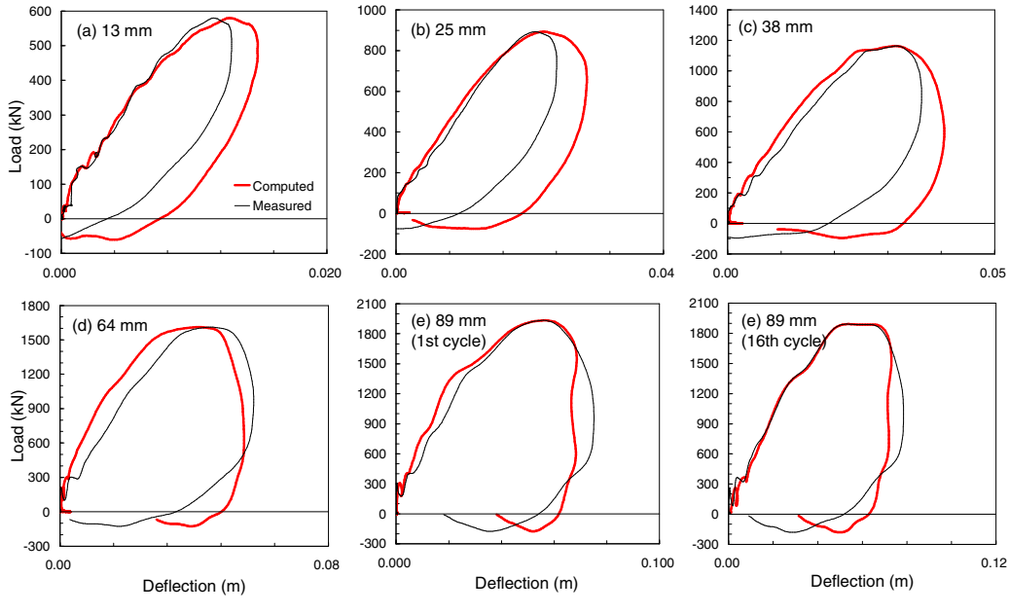


FIG 7. Measured and computed load versus deflection curve: target deflection of (a) 13 mm, (b) 25 mm, (c) 38 mm, (d) 64 mm, (e) 89 mm (1st cycle), and (f) 89 mm (16th cycle).

Bending moment profiles

Bending moment profiles of target deflections of 13, 38, and 89 mm (1st cycle) are compared in Fig. 8. Snyder (2004) reports that, "in the full− scale static load tests, the depth at the maximum bending moment became progressively greater depths with increasing deflection. This was typically not the case with the dynamic tests." For example, in Fig. 8, at a target deflection of 13 mm, the peak moments occurred at a depth of 1.8 m for the trailing rows and a depth of 1.2 m for the lead row (Row 1). The peak moments for a target deflection of 89 mm (1st cycle) generally occurred at the same depths (Fig. 8). The moment in Row 5 were typically greater than all other rows indicating that the reduced soil resistance ahead of these piles forced them to develop more curvature for a given load resulting in higher bending moments despite the fact that lower loads were carried (Snyder 2004).

Computed bending moment curves at peak loads (Fig. 9) shows that trends of the computed curves are much similar to those of the static tests: at a small target deflection of 13 mm, the peak moment occurs on the lead row at the depth of 0.8 m, and as target deflections increase to 38 and 89 mm, the peak moments of the lead row occur at the greater depths of 1.2 m and 1.5 m, respectively. For all cases in the analysis, bending moments of trailing row piles show lower peaks than that of the lead row, which is not the case with the full–scale dynamic tests shown in Fig. 8. Compared with measured

profile, peak moments of trailing rows are significantly underestimated. Also, in the full-scale tests, bending moment of row 3 gives smallest peak, while in the analysis, row 5 is the smallest. These discrepancies have to be minimized to simulate group pile behavior with a reasonable accuracy. Further investigation and improvement of modeling are required in this respect.

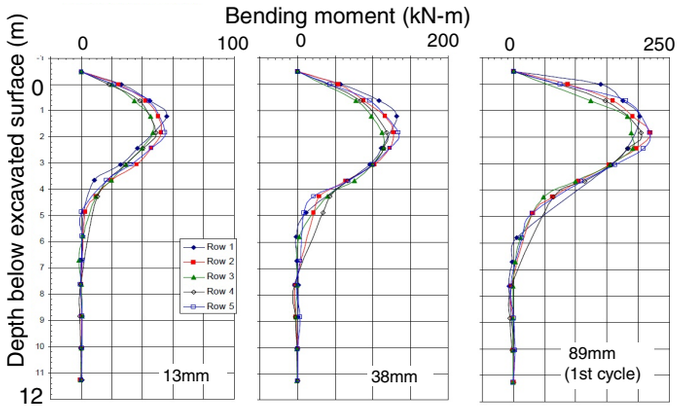


FIG. 8. Measured bending moment curves at peak loads for the 13, 38, and 89 mm (1st cycle) target deflection [after Snyder (2004)].

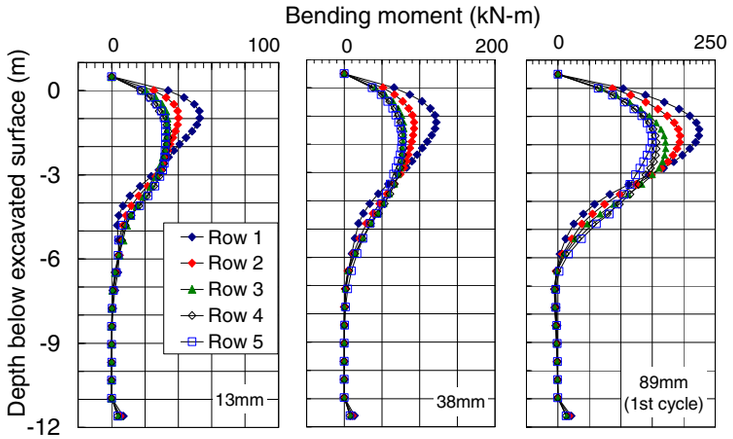


FIG. 9. Computed bending moment curves at peak loads for the 13, 38, 89 mm (1st cycle) target deflection.

Next, the curves are separated by row to illustrate the general trends as the pile group is loaded progressively. Figure 10 shows the measured bending moment curves of Row 1 (lead row), 3, and 5. As noted earlier, in the full–scale tests, the maximum bending moments remained at a constant depth for all target deflections, and the peak values are generally larger in the profile of trailing rows. As shown in Fig. 10, a larger target deflection gives larger peak value for all piles.

On computed curves shown in Fig. 11, however, the peak values of Row 1 are significantly larger than those of the other rows. A larger target deflection gives larger

peak value, except for Row 3 in which the largest peak is obtained on the curve of the 64 mm target deflection.

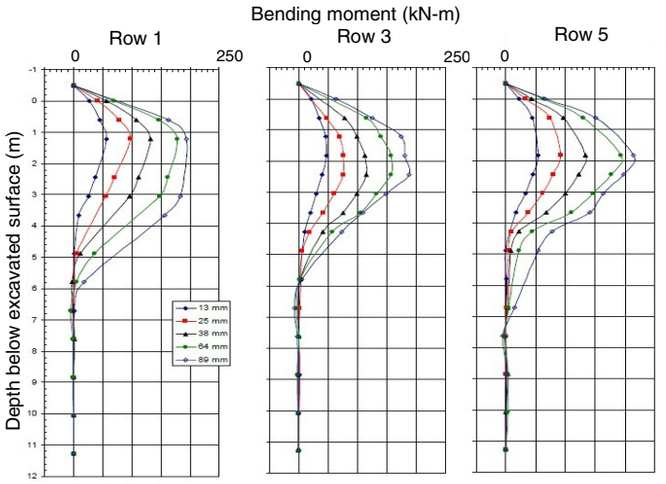


FIG. 10. Measured bending moment profile by row for all target deflections [after Snyder (2004)]

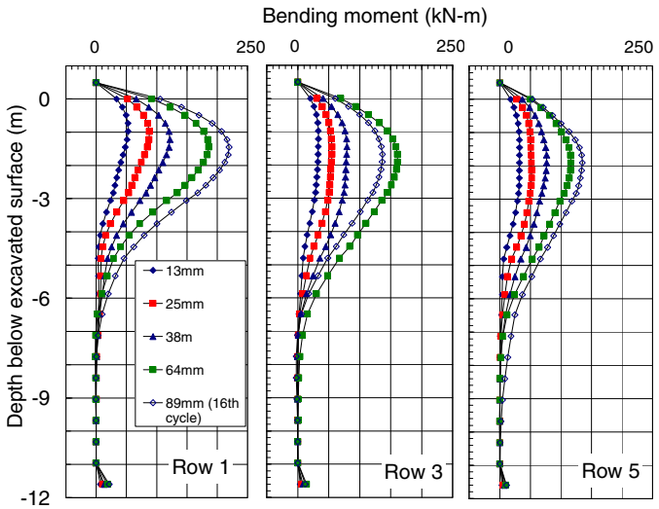


FIG. 11. Computed bending moment profile by row for all target deflection

CONCLUSIONS

Needs of development of a simulation method which can predict group pile response including the group effect with the accuracy required to design practice has been increasing. The computer code called FLIP was applied to simulate the full–scale lateral–load tests of a 3 × 5 pile group conducted in the Salt Lake City International Airport site. The soil profile at the test site generally consisted of cohesive sandy silt and silty sand. A series of tests includes static load tests for single and pile group, and dynamic load tests for pile group. Lateral loads were applied at 0.495 m from the ground surface with the hydraulic jack for the static loading and the statnamic device for the dynamic loading. Closed–end steel pipe piles were driven to a depth of 11.6 m. Pile

head was rotation free.

In the numerical analysis, model parameters for soils are taken from the geotechnical investigation data at the test site. With these model parameters, the full–scale static loading tests of a single pile and the full–scale dynamic loading tests of a pile group was simulated. Overall load–deflection behavior of the pile group agrees well with the measured ones. Some discrepancies are found on the bending moment profile. In the full–scale dynamic tests, peak moments for larger target deflections occurred at the same depths for all piles, while in computation, the peak moment occurs with greater depths as target deflection increases. Numerical analysis overestimates the group effects in dynamic tests. This calls up further improvement of a numerical modeling.

REFERENCES

Brown, D. A., Morrison, C., and Reese, L. C. (1988). "Lateral load behavior of pile group in sand." *Journal of Geotechnical Engineering, ASCE*, 1261–1276.

Iai, S., Matsunaga, Y., and Kameoka, T. (1992). "Strain space plasticity model for cyclic mobility." *Soils and Foundations, Japanese Society of Soil Mechanics and Foundation Engineering*, Vol. 32(2), 1– 15.

Iai, S., Tobita, T., Nakamichi, M., and Kaneko, H. (2006). "Soil–pile interaction in horizontal plane, Seismic Performance and Simulation of Pile Foundations in Liquefied and Laterally Spreading Ground." Geotechnical Special Publication, ASCE, No. 145, 38–49.

Ozutsumi, O., Tamari, Y., Oka, Y., Ichii, K., Iai, S., and Umeki, Y. (2003). "Modeling of soil–pile interaction subjected to soil liquefaction in plane strain analysis." *Proceedings of the 38th Japan national conference on geotechnical engineering*, Akita, Japan, 1899–1990.

Reese, L., C., Wang, S., T., Isenhower, W., M., and Arrellage, J., A. (2000). "Computer program LPILE plus version 4.0 technical manual." Ensoft, Inc, Austin, Texas.

Reese, L. C., and Wang, S. T. (1996). "Technical manual of computer program GROUP 4.0 for Windows." Ensoft, Inc., Austin, Texas.

Rollins, K. M., Lane, D., J., and Gerber, T., M. (2005). "Measured and computed lateral response of a pile group in sand." *Journal of Geotechnical and Environmental Engineering*, Vol. 131(1), 103–114.

Rollins, K. M., Peterson, K. T., and Weaver, T. J. (1998). "Lateral load behavior of full–scale pile group in clay." *Journal of Geotechnical and Geoenvironmental Engineering, ASCE*, Vol. 124(6), 468–478.

Snyder, J., L. (2004). "Full–scale lateral–load tests of a 3x5 pile group in soft clays and silts." *Master thesis submitted to the faculty of Brigham Young University.*

Tobita, T., Iai, S., and Rollins, K., M. (2004). "Group pile behavior under lateral loading in centrifuge model tests." *International Journal of Physical Modelling in Geotechnics*, Vol. 4(4), 1–11.

Tobita, T., Iai, S., and Rollins, K. M. (2006). "Numerical analysis of full–scale lateral–load tests of a 3 X 5 pile group." First European Conference on Earthquake Engineering and Seismology, Geneva, Switzerland, 700.

Towhata, I., and Ishihara, K. (1985). "Shear work and pore water pressure in undrained shear." *Soils and Foundations*, Vol. 25(3), 73–84.

Cyclic P-Y Curves for a Pile in Cohesive Soil

Travis M. Gerber[1], M. ASCE, P.E., and Kyle M. Rollins[2], M. ASCE

[1]Assist. Prof., Dept. of Civil & Environmental Engineering, Brigham Young University, 368 CB, Provo, UT 84602; tgerber@byu.edu
[2]Prof., Dept. of Civil & Environmental Engineering, Brigham Young University, 368 CB, Provo, UT 84602; rollinsk@byu.edu.

ABSTRACT: A lateral load test was performed on a full-scale steel pipe pile installed in a soil profile consisting of cohesive, fine-grained soils with occasional sand layers. The pile was loaded in nine increments from 0 to 89 mm of displacement, with 15 loading cycles applied for each increment. P-y curves representing static monotonic and cyclic loading conditions were derived from strain gauge data using a moving cubic polynomial technique. The results of push-over analyses using the derived p-y curves as input agreed well with the measured load-displacement response. It was observed that the cyclic p-y curves exhibited a sharp concave-up shape which contrasted with the broader concave-down shape of the static p-y curves. The cyclic p-y curves also exhibited lower peak resistances relative to the static p-y curves. The initial portion of the cyclic p-y curves is relatively flat with near-zero resistance which represents gapping of the soil. The displacement at which the soil reaction component of the cyclic p-y curves begins to dramatically increase is a function of the maximum displacement during previous loading cycles. It was also observed that the effects of cyclic loading were more pronounced in shallower soils.

INTRODUCTION

The soil-structure interaction problem of a laterally loaded deep foundation is often treated as a beam interacting with a set of discrete, non-linear springs. P-y curves used to describe the load-displacement response of these soil springs have generally been developed from monotonic lateral load tests conducted on instrumented full-scale deep foundations. While such curves are helpful in conducting static pushover analyses, the curves do not accurately describe soil-structure behavior when the loading is cyclic in nature. For example, during cyclic loading, the soil surrounding a structure may develop gaps and experience strength loss. The engineering modulus of the soil also changes as the load path varies from loading to unloading to reloading. Few cyclic p-y curves have been developed and published, with curves for soft clay

by Matlock (1970), curves for stiff clay by Reese et al. (1975), and curves for sand by Reese et al. (1974) being the most prominent. These curves are based on "intuition and judgment," (Matlock, 1970) coupled with theoretical mechanics adjusted to fit limited empirical data. To augment and further substantiate the few p-y curves that are available, the authors have tested a single full-scale pile and used the resulting data to derive cyclic p-y curves.

TESTING PROGRAM

Site Conditions

Testing of the full-scale pile, as well as two nearby pile groups, is reported in Johnson (2003) and Rollins et al. (2005a, 2005b). Because multiple research projects have been conducted at the site, subsurface conditions are relatively well known. Prior to testing, 1.5 m of imported sandy gravel fill was excavated to expose the original ground surface. A generalized profile of the remaining soil strata is shown in Fig. 1 together with data from a cone penetration test (CPT) performed within 10 m of the pile location. The soil profile consists of multiple silt and clay strata and two sandy strata 1 to 2 m in thickness. Also shown in Fig. 1 is a profile of undrained shear strength as derived in the work of Johnson (2003) and Rollins et al. (2005a, 2005b) based on laboratory unconsolidated undrained triaxial compression tests (UU)

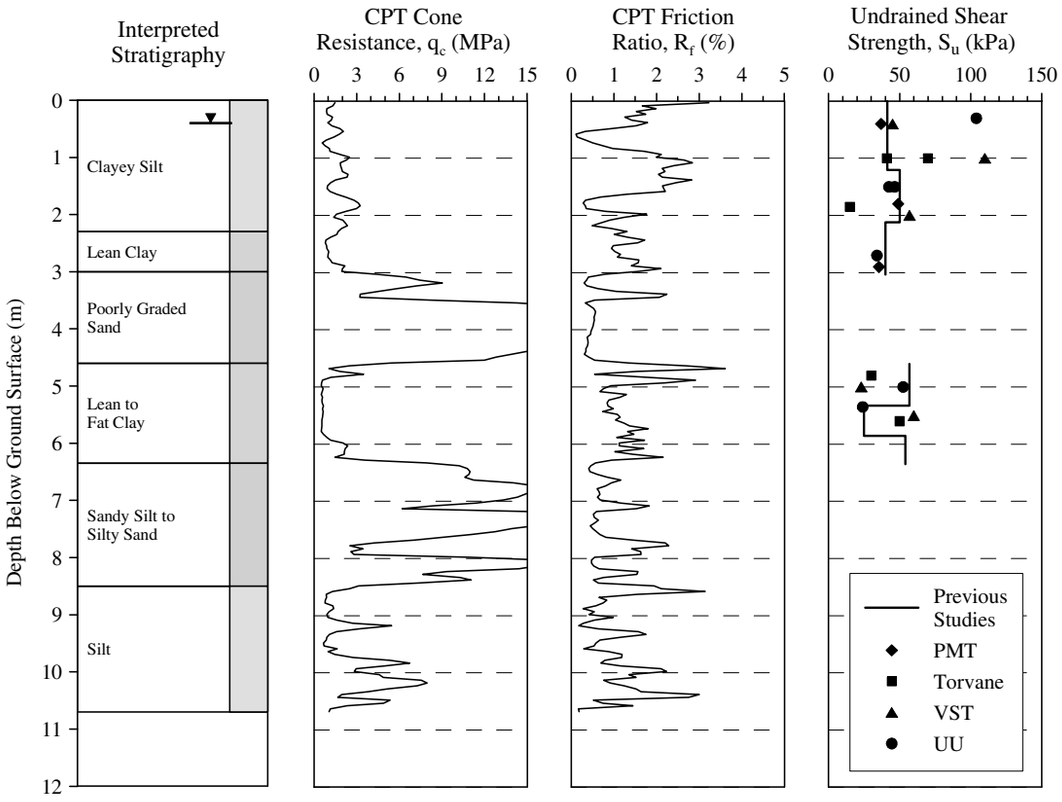


FIG. 1. Subsurface conditions at the test site.

and field tests (vane shear (VST), torvane, and pressuremeter (PMT)). During testing of the pile, the water table was located at a depth of approximately 0.4 m.

Test Components and Testing Procedure

The test pile, consisting of ASTM A252 Grade 3 (i.e., 310 MPa minimum yield strength) steel pipe, had an outside diameter and wall thickness of 324 and 9.5 mm, respectively. To protect externally mounted strain gauges from damage during driving, small continuous steel angles were welded on opposing sides of the pile. A scaled cross-section of the composite pile is shown in Fig. 2. The moment of inertia of the pile section was approximately 1.43×10^8 mm^4. Pairs of strain gauges were spaced along the pile at 457-mm intervals, beginning at a distance of 2.13 m from the top end of the pile and ending at 7.62 m, followed by additional pairs of gauges spaced at 914-mm intervals, extending to 12.19 m. One additional pair of gauges was placed near the bottom of the pile at 13.44 m, for a total of 19 pairs of gauges. After installation of the pile, the uppermost pair of gauges was located approximately at the ground surface.

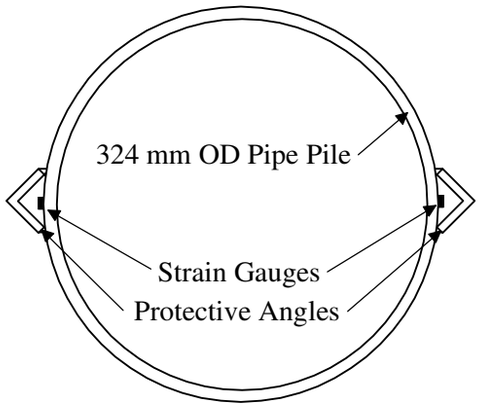


FIG. 2. Cross-section of test pile.

The pile was laterally loaded at a height of 0.48 m above the ground surface using a 1.34-MN hydraulic jack reacting against an adjacent pile group. Swivel plates and pinned-connections were used to prevent eccentric loading and provide a free pile-head condition. A string potentiometer was used to measure displacement of the pile-head relative to an independent reference frame. Load, displacement, and strain data was measured at a frequency of 2 Hz.

The pile was loaded in one direction using manual displacement control. After a single, initial displacement of 4 mm to verify functionality of the equipment, nine series of fifteen loading cycles each were applied. The target displacement of each series was progressively increased from 6.4 to 13, 19, 25, 38, 51, 64, 76, and 89 mm, as measured at the pile-head. During a typical cycle, load was applied at a rate of approximately 3 to 6 kN/s until the target displacement level was reached, after which the load was removed. In the case of the first loading cycle of a series, the peak

displacement was held constant for five minutes before unloading. A continuous plot of the measured load-displacement response of the pile is shown in Fig. 3.

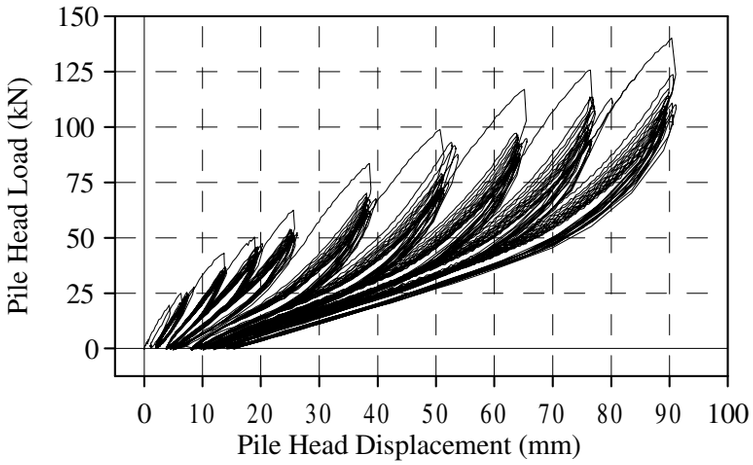


FIG. 3. Continuous plot of the measured load-displacement response of the pile.

ANALYSIS AND INTERPRETATION

Development of P-Y Curves

As part of the process of developing p-y curves, profiles of both pile curvature and bending moment were generated. Curvature was determined by dividing the strain difference between the two sides of the pile by the distance between those gauges. Since peak strains were less than the elastic limit, bending moment was taken as the product of curvature and the flexural stiffness, *EI*, of pile cross-section. Representative bending moment profiles are presented later. To mitigate the effects of gaps and errors in the strain data resulting from the attrition of gauges during installation and testing, missing and errant data was estimated using a quadratic Lagrangian interpolation polynomial based on adjacent measured values.

To determine the displacement component, *y*, of the p-y curves, the curvature-area method from beam mechanics was used, providing a bottom-to-top piecewise double integration of the curvature profile which relies on the fixity of the pile at its toe to define boundary conditions. Because the determination of soil pressure, *p*, (expressed as a reaction force per unit length of foundation) is significantly more problematic than the determination of displacement, *y*, due to the double differentiation required and the accompanying magnification of experimental errors, the cubic polynomial approach proposed by Matlock and Ripperger (1958) and later modified by Gerber (2003) was used. In this approach, cubic polynomials are fit to successive sets of five data points along the bending moment profile. These polynomials are then twice differentiated and evaluate at their mid-points. The resulting values are then averaged using a planar gradient method to develop the soil pressure profile. Corresponding *p* and *y* values were then paired to form p-y curves. The continuous p-y curve

generated for a depth of 0.46 m below the ground surface (bgs) [which corresponds to 0.94 m below the load point (blp) on the pile] is shown in Fig. 4.

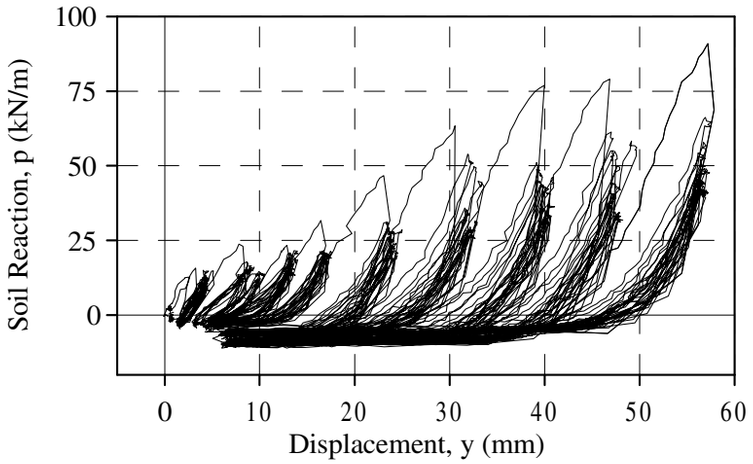


FIG. 4. Continuous p-y curve for a depth of 0.46 m below the ground surface (0.94 m blp).

Two types of discrete p-y curves were produced from the continuous p-y curve data. The first type of p-y curves are 'static backbone' curves. These curves were created by fitting a curve along the peak soil reaction value at the end of the first loading cycle for each displacement series. These curves represent what the soil response would be under a static, monotonic loading. The second type of p-y curves are cyclic curves generated by isolating the load path for each cycle within each displacement series and fitting a curve to the path. Some judgment was required during both fitting processes due to artifacts of the soil pressure computation process. The static p-y curves developed for the six gauge depths from 0.46 to 2.74 m below ground surface, z, are shown in Fig. 5. A depth of 2.74 m corresponds to 8.5 pile diameters, a depth above which soils are commonly assumed to have the greatest influence on the load-displacement response of a free-headed pile. Cyclic p-y curves for the same depths from the second loading cycles of the 25- and 76-mm displacement series are also shown in Fig. 5.

Discussion of P-Y Curves

As seen in Fig. 5, the cyclic p-y curves exhibit a sharp concave-up shape which contrasts with the broader concave-down shape of the static p-y curves. Also evident is the generally lower peak value of the cyclic p-y curves relative to the static p-y curves. Both of these characteristics are mirrored in the load-displacement response of the pile-head shown previously in Fig. 3. The vastly different shapes of the static monotonic and cyclic p-y curves indicate that the loading-unloading-reloading of these soils cannot be described by constitutive models based on Masing-type rules.

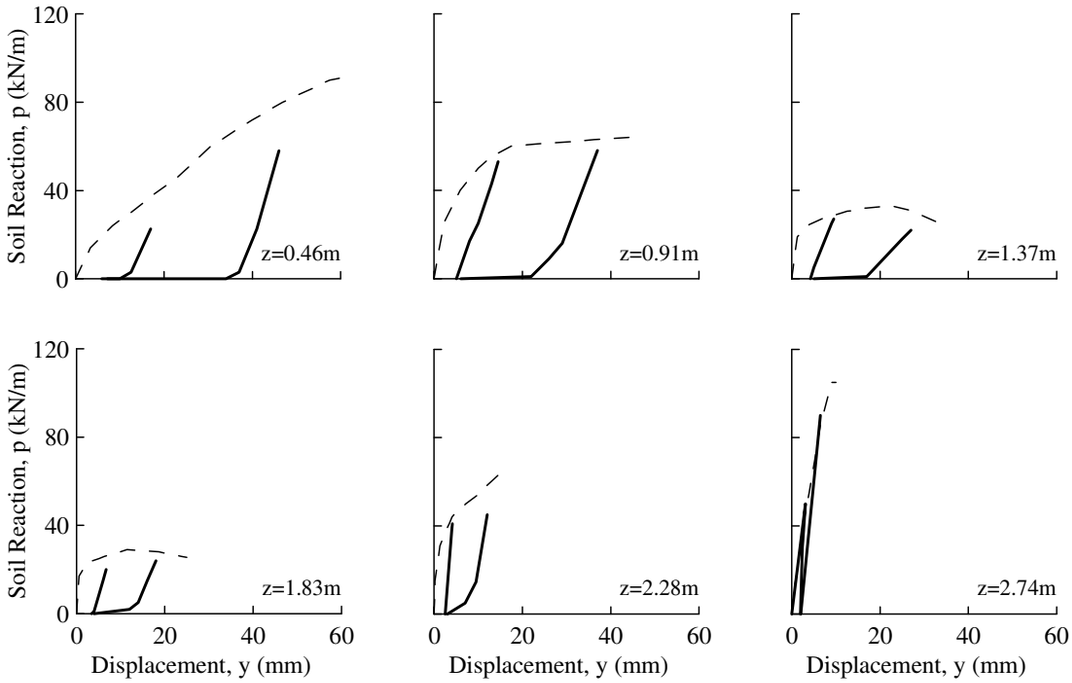


FIG. 5. Comparison of monotonic or static backbone p-y curves (dashed line) and second cycle p-y curves from the 25-and 76-mm displacement series (solid lines, left and right, respectively).

The static curves shown in Fig. 5 depict different types of response. For example, the first curve at a depth of 0.46 m below the ground surface (bgs) exhibits greater resistance to load than the curves immediately below it. This is consistent with this curve being almost above the water table and within a more overconsolidated crust while the deeper curves are well beneath the water table. The three curves from 0.91 to 1.83 m bgs exhibit the same the general shape, consistent with their being within the same silty stratum. Although one might typically expect that resistance should increase with depth, the presence of near-surface overconsolidation produces a profile of strength which decreases with increasing depth. The last two curves from 2.28 and 2.74 m bgs coincide with the lean clay stratum. These curves exhibit greater resistance, consistent with the greater depth and overburden pressure present.

For the second cycle p-y curves, the displacement corresponding to the greatest change in the rate of reaction (i.e., the point where soil reaction begins to rise sharply from near-zero values) appears to be a function of the maximum displacement during previous loadings. It can also be observed that, in general, the reloading stiffness after this transition point is at least as great as the initial loading stiffness of the static p-y curves. In the case of the 25-mm displacement series, the transition point between near-zero and significant soil reaction occurs essentially at the beginning of the curves, indicating that the pile/soil interface experienced a permanent displacement with minimal gapping or “slotting” at depth during the previous 6.4- to

19-mm displacement series. In contrast, the shallower curves from the 76-mm displacement series exhibit a significant amount of displacement before the transition point is encountered, indicating that significant permanent gapping of the soil had developed during the previous displacement series. (This gapping was visible during the pile load test and was determined by probing to extend to a depth exceeding 1 m). At greater depths, the extent of gapping is less evident in the p-y curves.

One can conclude that at large displacement levels, the effects of cyclic loading are more pronounced in shallow soils than in deeper soils. The reason for this occurrence is that, during the first loading cycle, the shallower soils quickly mobilize their full strength in response to pile displacement due to their relatively low ultimate resistance, whereas deeper soils usually have a 'reserve' capacity due to a combination of greater ultimate resistance and smaller pile displacement. During a second or subsequent loading cycle, the effective resistance of the soils has been reduced due to gapping and inherent strength degradation (the latter of which is exhibited in the curves by the lower-than-static peak strengths for a given displacement). Consequently, a similarly loaded pile must, upon its next loading, displace a greater amount to mobilize the same total amount of resistance. Since additional resistance is not available in the shallower soils, the pile continues to displace, forming gaps, until pile displacements in the deeper soils mobilize enough of the soils' remaining capacity to satisfy force equilibrium. This mechanism is also manifest as progressively larger pile bending moments occurring at depth during cyclic loading.

Oft times, quasi-cyclic p-y curves are constructed by connecting the peaks of reaction-displacement loops after a specified number of loading cycles or at a steady-state of load-displacement response. These types of p-y curves can be seen as "degraded" static backbone curves which illustrate how peak soil resistance reduces with cyclic loading. In Fig. 5, comparisons between the peak soil resistances for the cyclic p-y curves and the static backbone curves indicate that peak soil resistance is reduced by 5 to 40% for the second loading cycle relative to the first, but a clear trend of loss with respect to displacement level is not readily discerned.

Validation of P-Y Curves

The computer program LPILE (1997) was used to help verify the correctness of the static and cyclic p-y curves derived from the pile load test. Using measured pile-head loads and the derived p-y curves as inputs, pile displacement and bending moments were calculated. In the case of the cyclic loadings, the initial displacement offsets in the p-y curves were removed when the curves were input into LPILE. This was done so that the program's method of defining p-y curves only using the first quadrant would produce appropriate results when calculating displacements and reactions in the third quadrant. The removed displacements are afterward added back to the calculated pile displacement profile to obtain the pile displacements that would have occurred had the original p-y curves been used. This procedure for addressing non-zero displacements when the pile-head load is zero must also be used for pile bending

moments; non-zero bending moments existing before load is applied to the pile-head must be accounted for in the LPILE analysis by adding the initial moments back to the calculated results.

Fig. 6 presents a comparison of the measured and calculated load-displacement curves for the static monotonic p-y curves as well as for the second cycle p-y curves from the 25- and 76-mm displacements series. (Recall that in the case of the static monotonic data, the measured values are based on the peak values obtained from the first cycle of loading at each displacement level rather than from a single continuous loading) It can be seen that there is good agreement between the two sets of curves, indicating that the derived static and cycle p-y curves are reasonable representations of the actual load-displacement response of the soil.

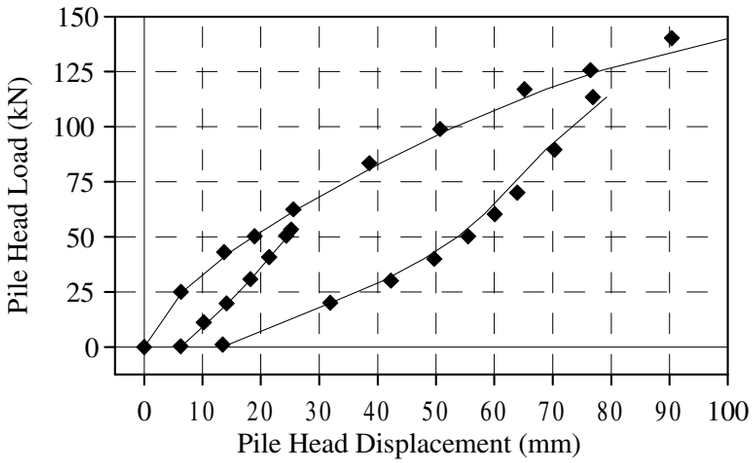


FIG. 6. Comparison of measured (markers) and calculated (solid line) pile head load-displacement response.

An additional validation of the second cycle p-y curves from the 76-mm displacements series is provided in Fig. 7. Figs. 7a through 7c show very good agreement between the measured and calculated bending moment profiles for pile-head loads of 1.1 (the start of the loading cycle), 50.2 (the middle of the loading cycle), and 113.4 kN (the peak load and end of the loading cycle). (Field test data points created from the Lagrangian interpolation polynomial to replace errant or missing bending moment data are indicated by the hollow markers). Fig. 7a exhibits small amounts of residual displacement and bending moment from previous loading cycles which were used to adjust the p-y curves in the LPILE validation analyses as discussed previously. In addition to the very good agreement in bending moment, Fig. 7 also shows similar agreement between calculated pile displacement profiles and measured pile head displacements.

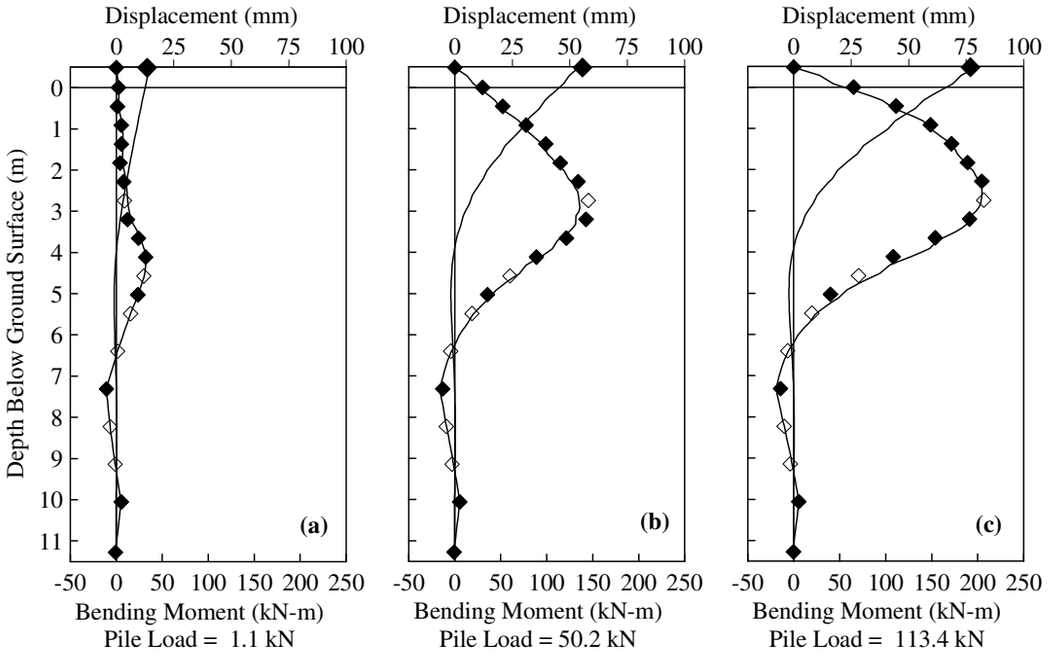


FIG. 7. Comparison of pile bending moment and displacement profiles based on field test data (markers) and p-y curves (lines) for the second cycle p-y curves from the 76-mm displacements series.

CONCLUSION

Based on the results of the pile load test and subsequent analysis of the test data, both static monotonic and cyclic p-y curves have been developed which accurately describe the load-displacement response of the test pile. Based on these curves, the following conclusions are drawn.

1. Cyclic p-y curves exhibit a sharp concave-up shape which contrasts with the broader concave-down shape of the static p-y curves.
2. Cyclic p-y curves exhibit lower peak resistances relative to the static p-y curves.
3. After experiencing a previous load cycle, the initial portion of the cyclic p-y curves becomes relatively flat with near-zero resistance; this behavior represents gapping of the soil.
4. The displacement at which the soil reaction component of a cyclic p-y curve begins to increase dramatically is a function of the maximum displacement during previous loading cycles.
5. The effects of cyclic loading are more pronounced in shallower soils.
6. Cyclic loading reduces peak soil resistance, but a clear trend of loss with respect to displacement level is not readily discerned.

ACKNOWLEDGEMENTS

Support for the pile testing program was provided by the National Science Foundation through grant number CMS-0100363. This support is gratefully acknowledged. The conclusions in this paper do not necessarily reflect the views of the sponsor.

REFERENCES

Gerber, T.M. (2003). "P-y curves for liquefied sand subject to cyclic loading based on testing of full-scale deep foundations." *PhD Dissert.*, Dept. of Civil and Environmental Engineering, Brigham Young University, Provo, Utah.

Johnson, S.R. (2003). "Static lateral load testing a full-scale pile group spaced at 5.65 pile diameters." *MS Thesis*, Dept. of Civil and Environmental Engineering, Brigham Young University, Provo, Utah.

LPILE – version Plus 3.0. (1997). *LPILE – A Program for the Analysis of Piles and Drilled Shafts under Lateral Loads*. Reese, L. C., Wang, S.-T., Arrellaga, J. A., and Hendrix, J., Ensoft, Inc., Houston, Texas.

Matlock, H. (1970). "Correlations for design of laterally loaded piles in soft clay." *Procs. 2nd Annual Offshore Technology Conf.,* Paper No. 1204: 577-594.

Matlock, H. and Ripperger, E. A. (1958). "Measurement of soil pressure on a laterally loaded pile." *Proc. of the American Society for Testing Materials*, Vol. 58: 1245-1260.

Reese, L.C., Cox, W.R., and Koop, F.D. (1974). "Analysis of laterally loaded piles in sand." *Procs. 6th Annual Offshore Technology Conf.*, Vol. 2, Paper No. 2080: 473-484.

Reese, L.C., Cox, W.R., and Koop, F.D. (1975). "Field testing and analysis of laterally loaded piles in stiff clays." *Procs. 7th Annual Offshore Technology Conf.*, Vol. 2, Paper No. 2312: 672-690.

Rollins, K.M., Snyder, J.L., and Broderick, R.D. (2005a). "Static and dynamic lateral response of a 15 pile group." *Procs. 16th Intl. Conf. on Soil Mechanics and Geotechnical Engineering*, Vol. 4, Millpress, Rotterdam, Netherlands: 2035-2040.

Rollins, K.M., King, R., Snyder, J.E., and Johnson, S.R. (2005b). "Full-scale lateral load tests of pile groups and drilled shafts in clay." *Procs. Intl. Conf. on Soil-Structure Interaction, Calculation Methods and Engineering Practice*, Vol. 1, Ulitsky, V.M., Ed., ASV Publishers, Moscow: 287-292.

E-Defense Facility: a Frontier in Geotechnical Physical Modeling

Ramin Motamed [1], Ikuo Towhata [2], and Tsuyoshi Honda [3]

[1] JSPS Postdoctoral Fellow, Department of Civil Engineering, Tokyo Institute of Technology, 2-12-1 Ookayama, Meguro ku, 152-8552, Tokyo, Japan. motamed@cv.titech.ac.jp
[2] Professor, Department of Civil Engineering, The University of Tokyo, 7-3-1, Hongo, Bukyo-ku, Tokyo 113-8656, Japan. towhata@geot.t.u-tokyo.ac.jp
[3] Researcher, Takenaka Corporation, 1-5-1, Ohtsuka, Inzai, Chiba, 270-1395, Japan. honda.tsuyoshi@takenaka.co.jp

ABSTRACT: Recently, a great attention has been devoted to performance based design in geotechnical engineering, and many design codes have initiated applying its concepts. As a result, estimation of deformation of structures subjected to intense loading, earthquake, is becoming more important. In this regard, physical modeling in geotechnics is a key measure to study the behavior of different structures including pile foundation and quay wall. 1-g shaking model test is one of the most common tools in the field of experimental geotechnical engineering. However, limitation of the size of model decreases its efficiency. To overcome the disadvantage of low confining stress, the world's largest shaking table, 20m×15m, which is called E-Defense, was established in the National Research Institute for Earth Science and Disaster Prevention (NIED), Japan where full-scale tests on engineering structures including RC building, quay wall, pile foundation, and masonry house are run. This paper aims to illustrate E-Defense facility by giving an example of a full-scale test on pile group and sheet pile quay wall which was subjected to the liquefaction-induced large ground deformation. The quay wall was displaced laterally, and the pile group, which was placed behind it, was damaged extensively. Over 880 channel data of various parameters were recorded and some of the results are presented in this paper mainly on rate dependency behavior of liquefied sand.

INTRODUCTION

In geotechnical earthquake engineering research, model testing is a popular approach to study the behavior of earth structures under both static and dynamic loadings. More specifically, shaking table model test is one of the most popular tools whose cost is also reasonable. In addition, model preparation is easy. However, there is a question on the level of confining stress. To overcome this disadvantage,

centrifugal model test was introduced and became popular in which same stress level as prototype is reproduced. But, it is very expensive and still there are some discussions on grain size and aging effects. Full scale testing is a solution to some of the aforementioned problems. In this regard, NIED established the Hyogo Earthquake Engineering Research Center in Miki City, Hyogo Prefecture, Japan where in this cutting edge center, the world's largest shaking table (20m × 15m) is located. Two experiments were carried out in geotechnical engineering discipline in 2006, and this paper describes the results of the full scale test on a pile group subjected to lateral spreading of the liquefied sand behind a sheet pile quay wall. In this experiment, a 2×3 pile group was distressed by the liquefaction-induced large ground deformation; as a result, the pile foundation was damaged extensively.

SHAKING TABLE FACILITY IN E-DEFENSE

General view of full scale shaking table facility is shown in Fig. 1. This cutting edge center consists of a 3-D full-scale shaking table and other earthquake related research facilities and is called "E-Defense". This shaking table is supposed to be the world's largest shaking table. Detailed information on construction process can be found in Ogawa et al., (1999), Ohtani et al., (2003), and Sato and Inoue (2003).

A special research project for earthquake disaster mitigation in urban areas was initiated in E-Defense from September 2002 to March 2007. The project was sponsored by the Ministry of Education, Culture, Sports, Science, and Technology (MEXT) and conducted by the NIED. This mega project included six main research topics in which test and analysis of soil-pile-structure systems was the experiment in geotechnical discipline. According to the research plan, two types of geotechnical tests were performed in 2006 (Fig. 2).

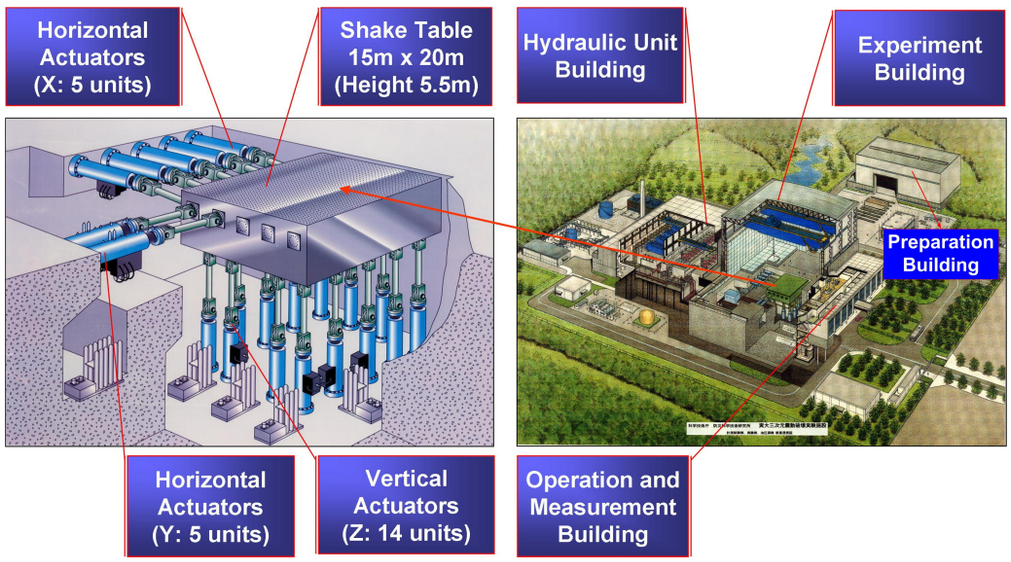


FIG. 1. Units of E-Defense complex (E-Defense website).

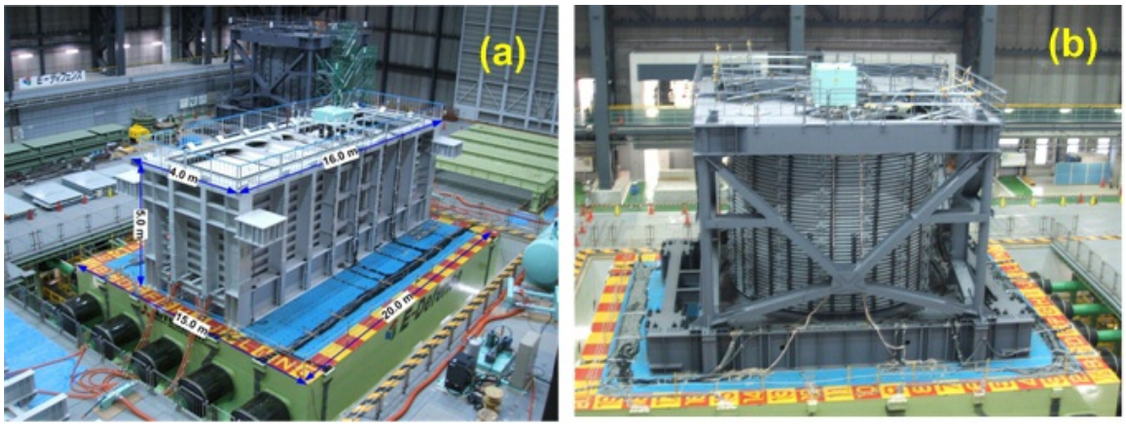


FIG. 2. (a) Test on lateral spreading of liquefied sand behind quay wall, (b) Test on soil-pile-structure interactions

There was a tremendous need for a uniform and cheap testing material in large scale. Therefore, it was decided to import Albany Silica sand from Australia to be used in the geotechnical tests. Table 1 provides basic geotechnical properties of Albany Silica Sand.

Table 1. Basic geotechnical properties of Albany Silica sand (MEXT and NIED, 2006)

Specific gravity (g/cm^3)	2.63
Maximum void ratio, (e_{max})	0.783
Minimum void ratio, (e_{min})	0.513
Mean grain size, D_{50}	0.2
Coefficient of uniformity, U_c	1.64

SHAKING TABLE FULL SCALE TEST ON LATERAL SPREADING OF LIQUEFIED SOIL BEHIND QUAY WALL

The full scale test on lateral spreading of liquefied sand behind the quay wall was conducted in March 2006. Fig. 3 presents a schematic plan and a cross section of the model which consisted of a 2×3 pile group located behind a sheet pile quay wall. The model was constructed in a huge rigid box with the dimensions of 16m×5m×4m. The ground was a liquefiable soil with the relative density of 60% which was constructed by the dry deposition method, and compacted to achieve the desired density. Next, air was removed from the ground by vacuum, and soil was saturated using de-aired water. An extensive range of instruments were employed to record several parameters during the shaking such as strain gauges, accelerometers, laser and wire-type displacement transducers, earth pressure sensors, pore water pressure sensors, and inclinometers. In

total, 883 channel data were recorded for fully understanding of behavior of the model. In the pile group, six hollow steel piles were connected to the base with pin connection, while fixed at the top to the footing. Moreover, a sheet pile was used as quay wall to trigger the liquefaction-induced lateral spreading.

FULL SCALE TEST RESULTS

The full scale model was shaken under two-dimensional input motion: horizontal and vertical components. The input time histories were a scaled-down (80%) version of the records monitored at JR Takatori station during the 1995 Kobe earthquake (Fig. 4). As can be seen, amplitude of the horizontal component (0.6g) was greater than the vertical acceleration (0.23g). In the following sections, some of the results are presented.

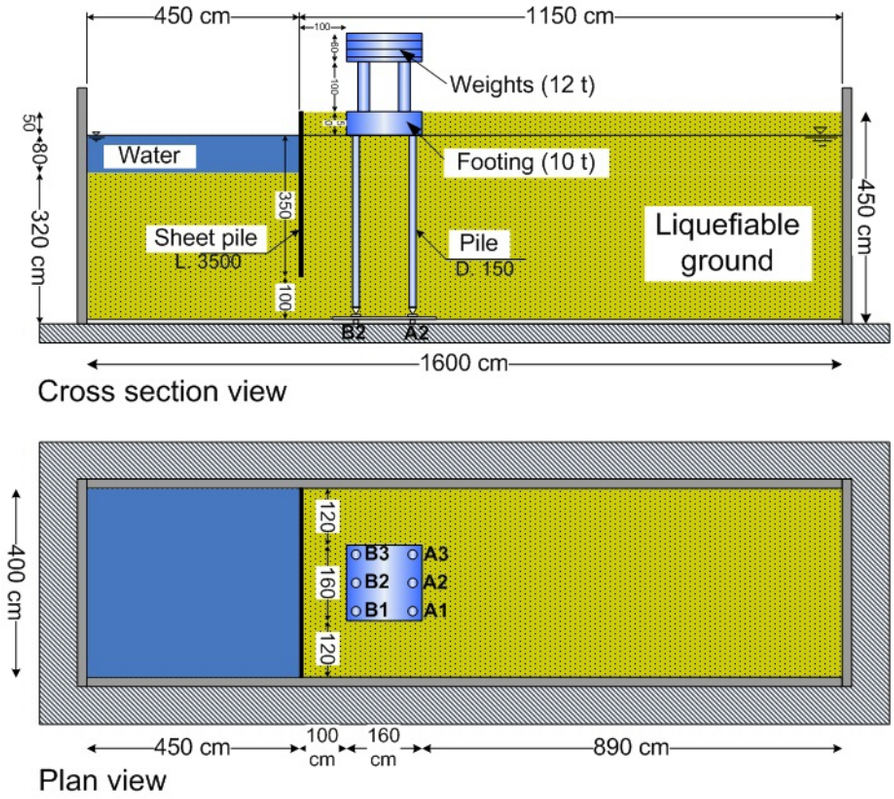


FIG. 3. Cross section and plan view of 2×3 pile group and sheet pile quay wall full scale test in E-Defense (March 2006)

Lateral Soil Displacement

During shaking, extensive liquefaction occurred in the model ground; as a result, liquefaction-induced large ground deformation happened Fig. 5 illustrates the deformed shape of the model after shaking, and arrows with numbers show the

residual ground and pile displacements measured after the test. As can be seen, the sheet pile quay wall moved 1.1 m toward the sea, pile group displaced horizontally between 1.1 m to 1.4 m at the pile heads, and the footing with superstructure tilted 20-degrees toward the land. Observed surface ground displacement indicated that the soil lateral deformation decreased as distance from quay wall increased toward land-side.

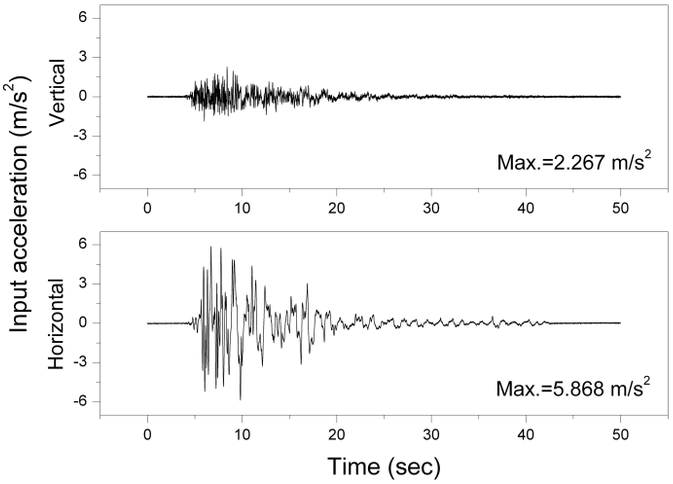


FIG. 4. Acceleration time histories of input motion

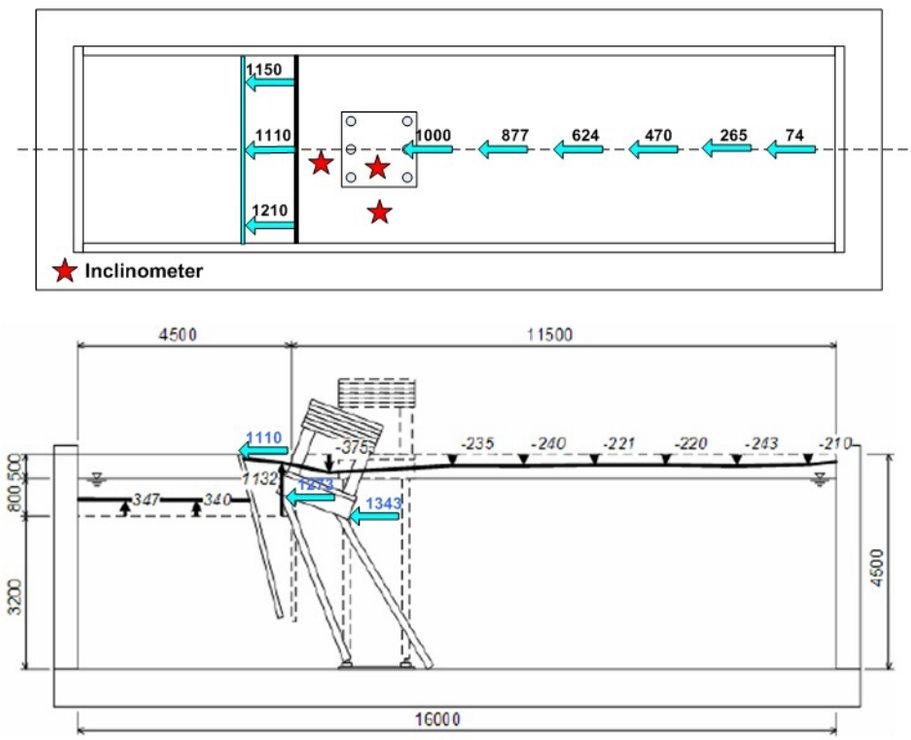


FIG. 5. Deformed shape of model after shaking and residual displacement values together with position of inclinometers (modified from MEXT and NIED, 2006)

Inclinometers were installed to measure the lateral soil displacement at three positions: behind quay wall, inside pile group, and beside pile group (Fig. 5). In each point, soil lateral displacement was recorded at 13 different depths. Fig. 6 demonstrates profiles of soil displacement at two points: behind quay wall and beside pile group, at different time steps. The results show that soil displacement behind quay wall (85 cm) was greater than beside pile group (75 cm), and this is consistent with direct observation of the deformed model. Since soil deformation was measured at different depths, it was possible to calculate the velocity of soil flow by time derivative of displacement. For example, Fig. 7 displays time histories of monotonic component of lateral soil displacement and the velocity of flow at different levels behind quay wall. As can be seen, maximum velocity of soil flow was observed at ground surface.

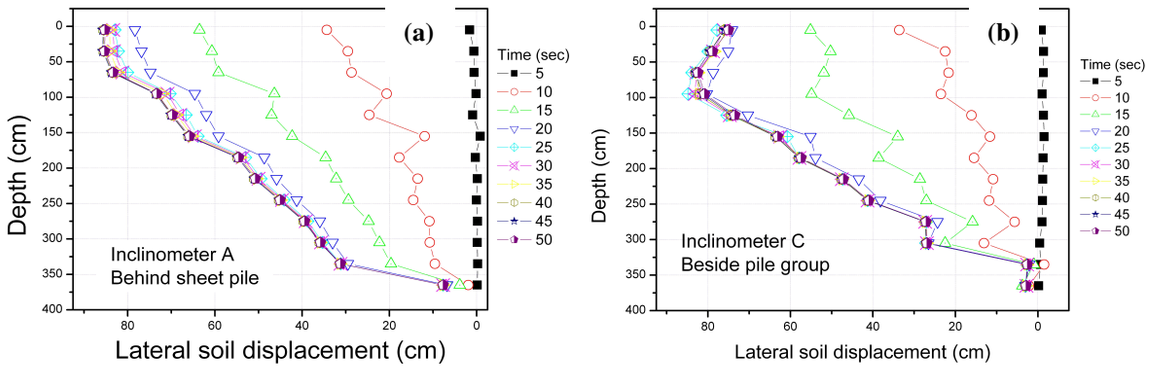


FIG. 6. Profiles of lateral soil displacement by Inclinometers; (a) behind quay wall, (b) beside pile group

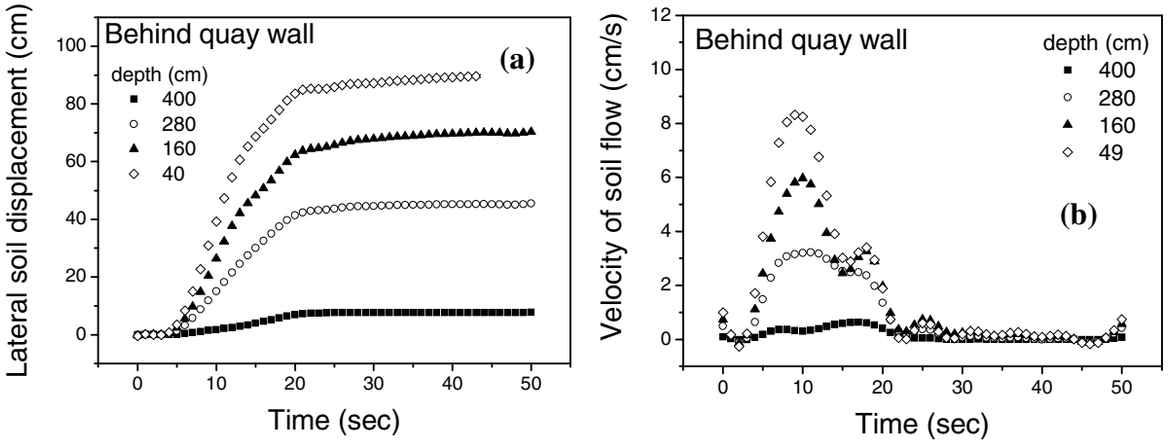


FIG. 7. Time histories of; (a) soil displacement, (b) velocity of soil flow, behind quay wall

Furthermore, displacement (Fig. 9) and velocity of pile lateral movement were calculated using the records of accelerometers which were attached to the piles. Hence, relative displacement and velocity between soil and piles were obtained.

Lateral Earth Pressure of Liquefied Soil

An important objective of this full-scale experiment was to evaluate the lateral force exerted on piles by the liquefied ground. Two different techniques were employed in this study to calculate the lateral earth pressure. First method was to back calculate from strain gauge records, while second approach was through direct measurements by earth pressure sensors. In this paper, back calculated results from strain gauge data are presented.

Several strain gauges were pasted on the piles to record the bending strain, and earth pressure was then back calculated by two times derivative of bending moment along piles using finite differential method. Therefore, it was possible to back calculate earth pressure at different depths. For instance, Fig. 8 presents a time history of back-calculated earth pressure from bending strain records in Pile A1. As is shown, there are some fluctuations in earth pressure during shaking and finally approaching to a residual value. In this figure, thick line represents the monotonic component of earth pressure.

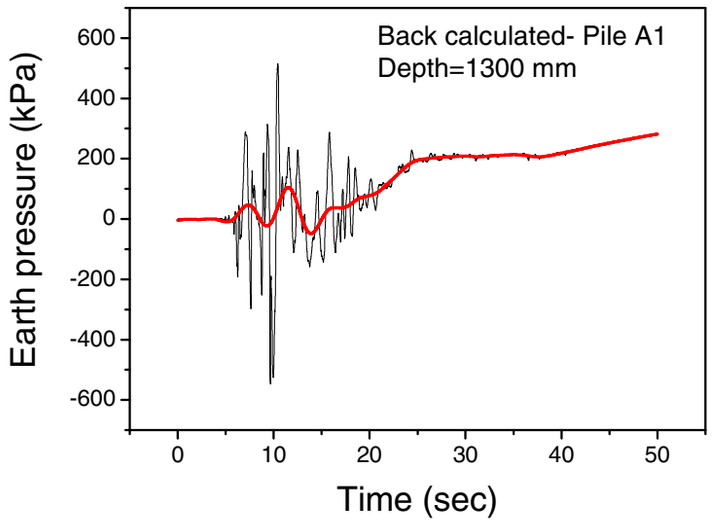


FIG. 8. Time history of lateral earth pressure back calculated from strain gauge data

Rate Dependency of Lateral Soil Pressure

In this section, rate dependency behavior of lateral soil pressure is investigated. According to Fig. 9, both soil and pile lateral displacements increased steadily during the shaking, approaching a residual value at the end. However, lateral soil pressure followed a different pattern; a sudden rise at the early stage of shaking, then some fluctuation, and finally displaying a residual value.

Since the lateral soil pressure showed no correlation with either soil or pile displacements during shaking, relative velocity between soil and pile was calculated,

and an example is illustrated in Fig. 9. As can be seen in Fig. 9, pressure demonstrated fairly good agreement with the relative velocity during shaking period. These results seem to suggest the rate dependency behavior of lateral soil pressure during shaking at which pore water pressure maintains high values. In other words, results demonstrated that liquefied soil during lateral spread is analogous to a viscous liquid, and this conclusion could be applied to the numerical modeling of lateral spreading.

Pore Water Pressure Variation around an Individual Pile

Since many pore water pressure (PWP) sensors were attached to both front and back sides of each pile, it was possible to investigate PWP variation around each pile in detail. As can be seen in Fig. 10, PWP data which were recorded in front and back sides of Pile B2 at depth of 3700 mm are presented, and results seem to suggest that there was no significant differences between front and back side records. Therefore, rate dependency of lateral soil pressure which was explained in the previous section can be attributed to neither PWP variation nor drag force.

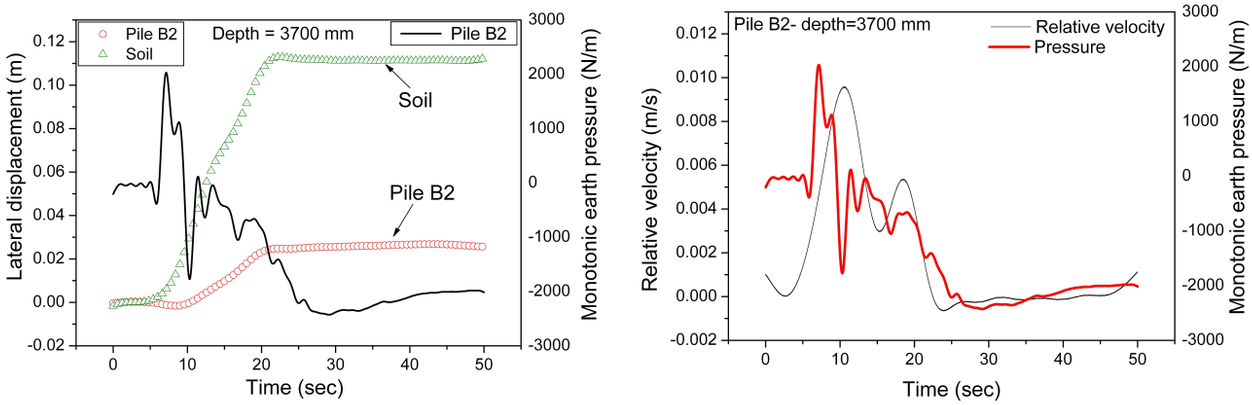


FIG. 9. Time histories of lateral earth pressure, displacements of soil and pile, and relative velocity

CONCLUSIONS

1. Inclinometers were installed to measure the lateral soil displacement, and comparison with the directly observed values showed a close agreement.
2. Soil lateral displacement decreased as distance from the quay wall increased.
3. Lateral soil pressure exerting on piles was back calculated from strain gauge records, and a fairly close correlation was established between the lateral soil pressure and the relative velocity of soil flow. This rate dependency behavior of the liquefied soil is consistent with previous studies by the authors.
4. PWP distribution around each individual pile was studied carefully and no significant difference was observed. This observation showed that the rate dependency behavior of the liquefied sand could be attributed to neither PWP variation nor drag force.

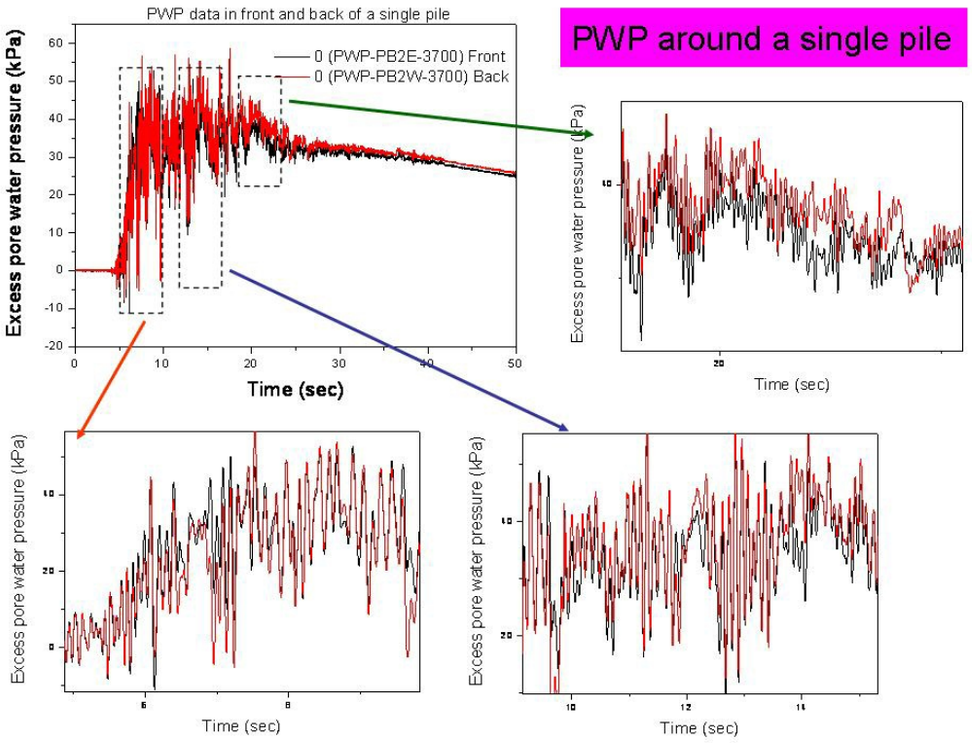


FIG. 10. Time histories of pore water pressure in front and back sides of Pile B2

ACKNOWLEDGMENTS

Full scale experiment was carried out at the National Research Institute for Earth Science and Disaster Prevention, E-Defense Research Center, which is highly acknowledged.

REFERENCES

1- E-Defense-website, http://www.bosai.go.jp/hyogo/ehyogo/index.html.
2- Ogawa, N. and Ohtani, K. and Katayama, T. and Shibata, H. (1999) "World's Largest Shaking Table Takes Shapes in Japan--A Summary of Construction Plan and Technical Development" SmiRT.
3- Ohtani, K. and Ogawa, N. and Katayama, T. and Shibata, H. (2003) "Construction of E-Defense (3-D full-scale earthquake testing facility)" *Proc. of Second International Symposium on New Technologies for Urban Safety of Mega Cities in Asia*, 69-76.
4- Sato, M. and Inoue, T. (2003) "General Framework of Research Topics Utilizing the 3-D Full-Scale Earthquake Testing Facility" *Proc. of the 2nd International Symposium on New Technologies for Urban Safety of Mega Cities in Asia*, 77-86.

5- MEXT and NIED (2006) "Research Theme No.2, Annual Report of the Fiscal Year 2005, Special Project for Earthquake Disaster Mitigation in Urban Areas" Ministry of Education Culture Sports Science and Technology and National Research Institute for Earth Science and Disaster Prevention, 831 pages (in Japanese).

NONLINEAR BEHAVIOR OF SINGLE PILES VIBRATING VERTICALLY

Jin-xing Zha, Ph.D., P.E.[1] and George Gazetas Ph.D., P.E.[2]

ABSTRACT

A numerical method is presented for analyzing the nonlinear behavior of single piles subjected to harmonic vertical or torsional loading. The method combines the finite element method accounting for nonlinear soil behavior in the near field and a semi-analytical formulation for radiation damping in the far field. Nonlinear stress-strain characteristics of soil are considered with a shear modulus degradation model used in soil dynamics and earthquake engineering. Mohr-Coulomb strength criterion is used to approximate the contact property at the pile-soil interface. The method is simplified but versatile, and the soil parameters required are relatively few being all the standard geotechnical parameters. The comparisons between the predictions and the results from field tests and a boundary element method are made to verify the present method. A parametric study indicates that the linear analysis overestimates both the stiffness of piles and the interaction factor for the pile group effect.

INTRODUCTION

Dynamic response of a pile in nonlinear soils is a complicated problem in terms of the interplay between the pile and its surrounding soil and the dynamic boundary conditions. Both the nonlinear behavior of soils and the boundary conditions (including outgoing wave energy) have a significant effect on the response of a pile.

[1] Office of Earthquake Engineering, California Department of Transportation, 1801 30th Street – MS 9-2/5i, Sacramento, CA 95816, U.S.A.
[2] National Technical University of Athens, 36 Asimakopoulou Street, Ag. Paraskevi 15342, Athens, Greece

Field tests of piles have indicated that the natural frequency of a cap-mass supported on piles under forced or free vibration decreases with increase in dynamic force level In order to obtain a good match between the observed and predicted results based on a linear analytical model, reduced values of soil stiffness parameters such as shear modulus have to be used in numerical analysis models.

Alternatively, the t-z curve method or a Winkler foundation method can be used for better approximation of the nonlinearity of soils surrounding a pile subject to dynamic excitation. Although the t-z method was developed based on the calibration from static and/or cyclic test results of piles mostly with diameters of 24 inches or smaller, it still must be determined how well the t-z curve model works for larger diameter piles greater than 36 inches, especially for 60-inch diameter or larger drilled shafts increasingly used for bridge foundations. In addition, the static and cyclic t-z curves are only part of the solution for dynamic cases since the inertia effect of soil is not included. It is uncertain to introduce participating masses for the inertia effect of the surrounding soil. To address these issues rationally, a 3D finite element method is preferred using commercial FEM software such as ANSYS, the OPENSEE model, or some programs developed specifically for dynamic nonlinear pile-soil-structure interaction (Trochanis *et al.* 1991). However, it is not straightforward for a user to find a solution for a dynamic nonlinear pile problem using a FEM program. Special knowledge of elasto-plastic soil models and script programming is required in generating input files for such sophisticated 3D FEM programs as in OPENSEE modeling. It is not unusual that use of these programs is limited due to lack of database of sophisticated model parameters for soil nonlinearity. Therefore, a simplified method is sought by engineers for analyzing nonlinear pile problems.

In this paper a simplified hybrid method to analyze dynamic vertical pile-nonlinear soil interaction is presented. The effects of the following factors on the pile response are taken into account: (a) the nonlinear stress-strain characteristics of soils surrounding the pile; (b) the radiation damping induced by propagating wave away to infinite soil region; and (c) the plastic deformation such as slippage at the pile-soil interface. The procedure combines a finite element method for the near field and a semi-analytical formulation for the far field. Nonlinear stress-strain characteristics of soil are considered with nonlinear relations for shear modulus and damping versus shear strain developed in the soil. The behavior of the interface between pile and soil affects notably the nonlinear response of the pile. In practice, before application of a load there can be no nonlinearity. As the load increases slippage at the pile-soil interface may appear. Herein, the Mohr-Coulomb failure criterion is incorporated into the analysis to approximate the contact property at the interface (Zha 1995).

Conceptually, the method presented here is an extension of the work by Blaney *et al*. (1976) and Angelides and Roesset (1981). Blaney *et al*. (1976) analyzed the linear dynamic stiffness of an end-bearing pile using toroidal finite elements and the consistent transmitting boundaries, which were derived by Waas (1972) and Kausel (1974). A finite element method with the same dynamic consistent transmitting boundary matrix was proposed by Angelides and Roesset (1981) to analyze the

nonlinear horizontal response of a pile. A nonlinear relation of soil modulus with shear strain amplitude was incorporated into the analysis and an equivalent linearization and iteration technique was utilized. However, perfect bond between the pile and soil was still assumed in their model.

FORMULATION OF PROBLEM AND OUTLINE OF SOLUTION

The cap-mass supported by a single pile is subjected to a harmonic vertical excitation as shown in Figure 1. In the figure are also given the geotechnical parameters of each soil layer: mass density ρ_i, (initial) shear modulus G_i, Poisson's ratio ν_i, and damping ratio β_i. The dynamic response of the pile is affected by the nonlinear characteristics of soils. Near the ground surface, the soil surrounding the pile exhibits strong nonlinearity. However, the motion in the soil away from the pile is linear, with waves propagating to infinity. The entire pile-soil system is divided through a cylinder with a radius of $r = r_o$ into two regions: the near field and the far field.

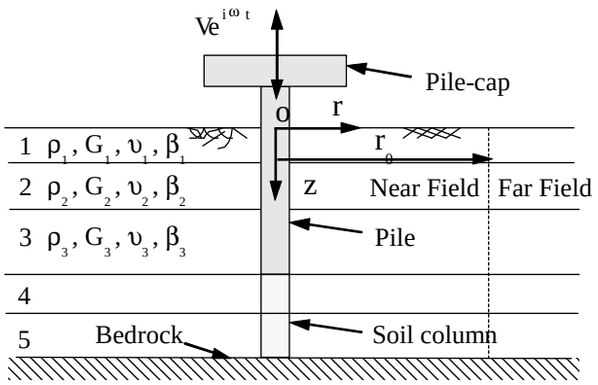


Figure 1. Geometry of Problem

The near field soil is modeled by discrete toroidal finite elements with a Fourier expansion in the circumferential direction. Using a semi-analytical method the effect of the far field is expressed as a boundary stiffness matrix. The pile is discretized into a series of 2-node rod elements with rigid section link to soil element nodes. The axial response of the pile itself is assumed to be linear.

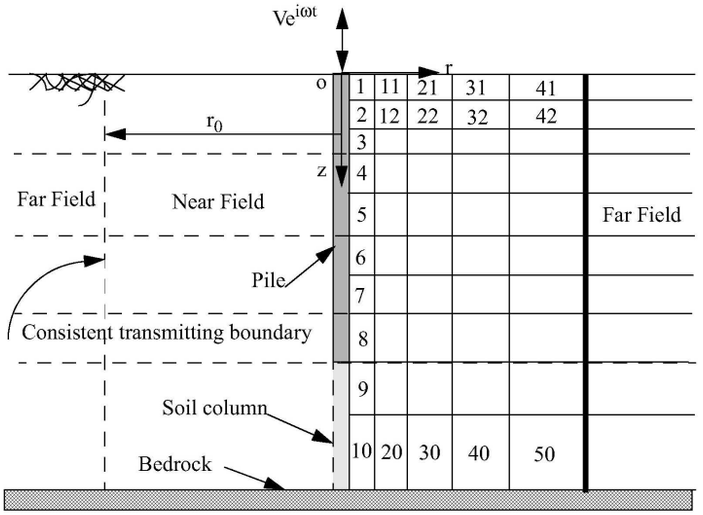


Figure 2. A Discretization of Dynamic FE Model

Numerical implementation for nonlinearity of soils is conducted through an equivalent linearization technique by iterating and using the appropriate values of soil parameters that are compatible to the octahedral shear strain developed in the soil. For each of the elements, the octahedral shear strain is evaluated at the geometric center

of the element. At the pile-soil interface thin interface elements are used to take into account the effect of slippage. There have been few theoretical and experimental investigations on how the slippage is developed at the interface in reality and modeled in analysis. Mohr-Coulomb criterion is used for the interface elements in the proposed procedure. It is assumed that the dynamic response of the pile induced by the soil nonlinearity can be approached by using equivalent linear parameters of soils, such as secant modulus, corresponding to the shear strain level developed in soils. Therefore, the nonlinear pile response can be obtained by application of iteration until the convergence with a given tolerance is reached.

SOIL MODELING

Nonlinearity of a soil is introduced through the variation of shear modulus ratio G/G_{max} with shear strain γ (in percent) developed in the soil. The relation is expressed as the following function of only soil plasticity index PI (Bouckovalas and Gazetas 1992; Vucetic and Dobry 1991). The function can also be applied to saturated cohesionless soils such as gravel and sands if PI = 0 is assumed for them.

$$\frac{G}{G_{\max}} = 1 - \left[27\,\gamma \left(\frac{G}{G_{\max}}\right) \right]^{0.72} 10^{-(PI/\lambda)} \tag{1}$$

where λ is a parameter depending on plasticity index only. It can be obtained from the following table. For any intervening PI, the value of λ can be linearly interpolated.

Table 1. Values of PI and λ

PI	≤ 50	100	180
λ	70	110	180

Damping ratio β of a soil can be approximated by the following expression.

$$\beta = \beta_o + \beta_{\max} (1 - G / G_{\max}) \tag{2}$$

in which β_o and β_{max} are the initial and the maximum value of β, respectively. It can be determined from the experimental data as well as some empirical formulae.

INTERFACE ELEMENTS

In the present study, thin-thickness elements are used which incorporate Mohr-coulomb criterion as shown in Figure 3(b) into the analysis to deal with slippage at the pile-soil interface. That is, the shear stress at the pile-soil interface, τ is limited to the shear strength, τ_f of the soil,

$$\tau \leq \tau_f \qquad \tau_f = c + \sigma_n \tan\phi \tag{3a,b}$$

where c and ϕ are the cohesion and angle of internal friction of the soil, respectively; σ_n is the normal stress in the soil corresponding to the shear stress, τ;

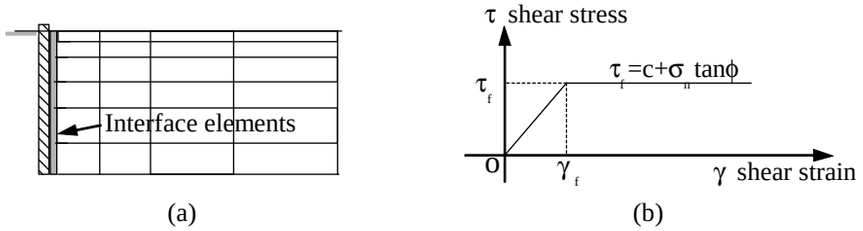


Figure 3. (a) Model with interface elements for pile-soil system (b) Perfect plastic stress-strain relationship

DATA COMPARISONS

Layered half-space

The shear wave velocity is 81 m/s for the surface layer and 332 m/s for the underlying half-space media as shown in Figure 4. The mass densities are 1.5 and 2.0 Mg/m^3, respectively. The Poisson's ratios of 0.49 and 0.475 are used and the damping ratio is 0.05 for both soil materials. A concrete pile with a length of 15.5m and a diameter of 1.3m is used for computation of the vertical impedance. The Young's modulus of pile material is taken as $E_p = 2.0x10^7$ kPa and the damping ratio is neglected. The pile vertical impedances from a boundary element method (Kaynia, 1982) and the present finite element method are in good agreement as shown in Figure 5(a). The stiffness, K_v from the present FEM is larger than that from the BEM because a limited depth of soil layer is used to discretize the half-space in the FEM analysis.

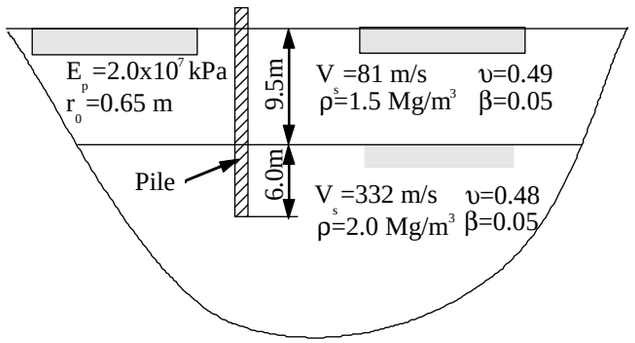


Figure 4. A pile embedded in a layered half-space

Comparison with test results from a site in Mexico City

A square concrete pile with a length of 15 m and a width of 0.3 m was tested statically by applying vertical loads to its head. The soil parameters and profile may be found in the paper by Trochanis *et al* (1991). For the top 5 m soil layer near the ground surface, a freestanding height of 5 m is used in the present analysis since the pile within the layer was encased by a steel pipe with a diameter of 0.5m and a wall thickness of 9mm. The excitation frequency of f = 0.01 Hz is assumed to approach the static case. The load-settlement curve from the present method is close to the measured one as shown in Figure 5(b).

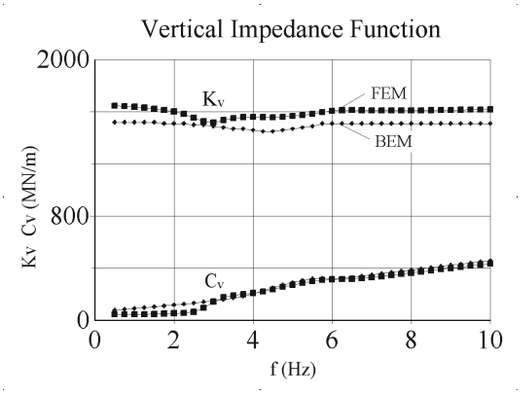


Figure 5a. Comparison of computed dynamic impedances K_V+iC_V

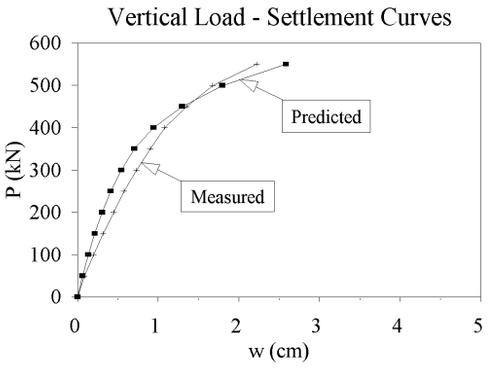


Figure 5b. Comparison of measured and predicted static responses

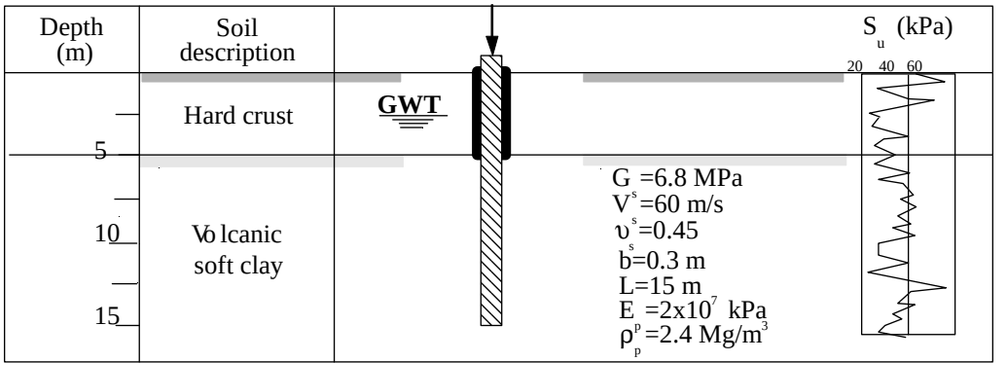


Figure 6. Soil profile and undrained strength, S_u, at test site

PARAMETRIC STUDY

A parametric study is performed to investigate the effect of nonlinear soil behavior on the pile response. A homogeneous half-space is considered as shown in Figure 7. The shear wave velocity of the soil is assumed to be V_s=60, 100, and 150 m/s corresponding to three typical profiles from soft to stiff soils, respectively. Only part of the numerical results from the proposed method is given here due to space limit.

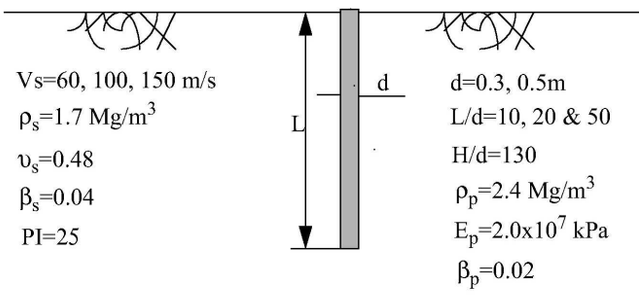


Figure 7. A pile in a homogeneous half-space

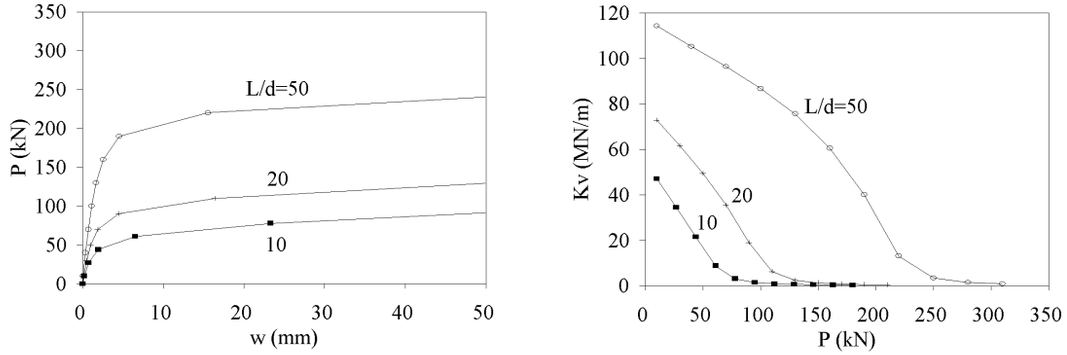


Figure 8. (a) Static load versus settlement curves (b) Static vertical stiffness

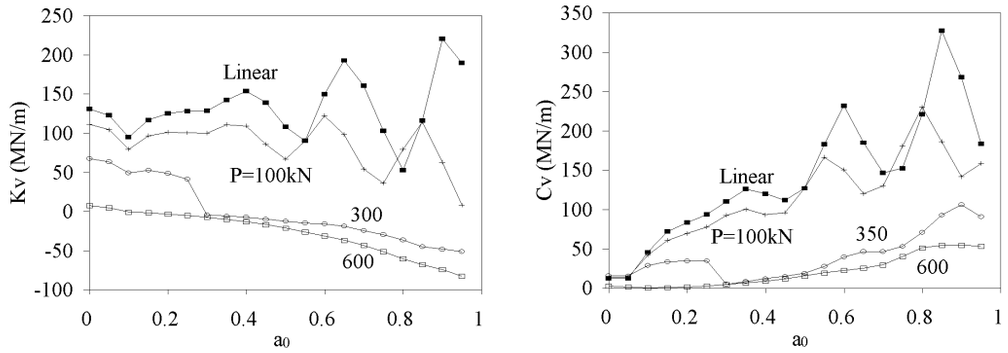


Figure 9. Vertical impedance function (V_s=65m/s, L/d=20)

Static load-settlement curve and stiffness of single pile

The static load versus settlement curves for V_s=65m/s are presented in Figure 8(a). It can be observed that a longer pile bears a larger load without undergoing more settlement. The vertical load capacity of a pile is the combination of the side friction along its length and the base resistance at the tip. Because of a higher vertical stiffness of a pile compared to the soil stiffness, the vertical load at the pile head can be transferred to a deeper part in the soil than a horizontal load. Hence, the piles with different slenderness ratios under consideration have significantly different yielding loads on the load versus settlement curves. From the equivalent linear stiffness shown in Figure 8(b), it can be seen that the longer the pile, the larger the stiffness. As the load increases, the degradation of soil shear modulus mobilizes toward a deeper location, and a shorter pile reaches its failure firstly while a longer pile can carry further increase in load until reaching its ultimate tip resistance. It is observed from the numerical results that the soil shear modulus ratio G/G_{max} is approximately 0.26 in the elements surrounding the top of the pile and the corresponding shear strain is 0.29% for the pile (L/d =50) loaded by a load of 250 kN (the corresponding settlement w = 50mm).

Dynamic stiffness

The soil profile with V_s=65m/s shown in Figure 7 is used for studying the dynamic stiffness of a pile and the displacement distribution along the radial direction at the ground surface. The pile diameter is d = 0.5m and its slenderness ratio L/d = 20. Figure 9 presents the stiffness as a function of frequency with force level as a parameter. The linear stiffness symbolized by "Linear" is also shown on the plot. It can be clearly seen from the figure that the nonlinear stiffness of a pile is strongly dependant of both force level and frequency.

Interaction Factor

The interaction factor, α is defined as the ratio of the displacement of pile 2 induced by the load on pile 1 over the displacement of pile 1 induced by the load on itself, i.e.

$$\alpha = \frac{\text{displacement of pile 2 induced by the load on pile 1}}{\text{displacement of pile 1 induced by the load on itself}} \quad (4)$$

This interaction factor for the pile group effect may be numerically approximated by the normalized displacement of the soil on the ground surface, w(r), with respect to the displacement of a pile at its head, w(0), i.e. w(r)/w(0). However, no such an attempt is made in this paper that the interaction factor can be obtained by the normalized displacement. This approximation is made only in this study for the comparison of linear response of a pile with nonlinear one. The approximation will yield an upper limit of the interaction factor from a pointview of linearly static analysis in which the stiffness of pile 2 is ignored. It will approach to the exact interaction factor if pile 2 has the same stiffness as the soil.

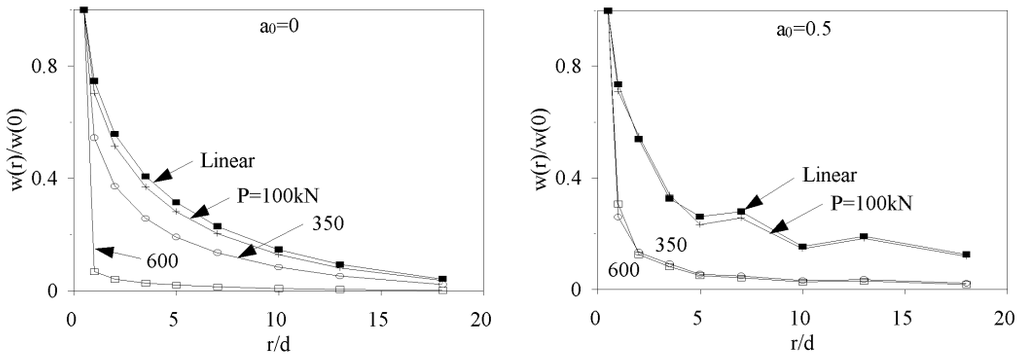


Figure 10. Normalized displacement versus distance curves (V_s=65m/s, L/d=20)

Variation of normalized displacement with distance

Normalized displacement amplitude versus radial distance curves are shown in Figure 10 for different force levels and a dimensionless frequency of $a_o = \omega d/V_s = 0$ and 0.5, in which ω = circular frequency, d = diameter of the pile, and V_s = shear

wave velocity of the soil layer. The linear solution is also presented for comparison. From the results it can be concluded that the normalized displacement decreases rapidly with the increase in distance and that the larger the force level, the more rapid the decrease. The nonlinear solution approaches to the linear one when the force level is small enough.

Figure 11 shows the results of variation of normalized displacement amplitude with force level for different frequencies and radial distances. It can be seen that the normalized displacement reduces with increase in force level. The closer the piles, the more rapid the reduction. In other words, there is more pile-soil-pile interaction for closely spaced piles. This interaction between piles becomes small as the force level increases or the nonlinearity in the soil becomes dominant.

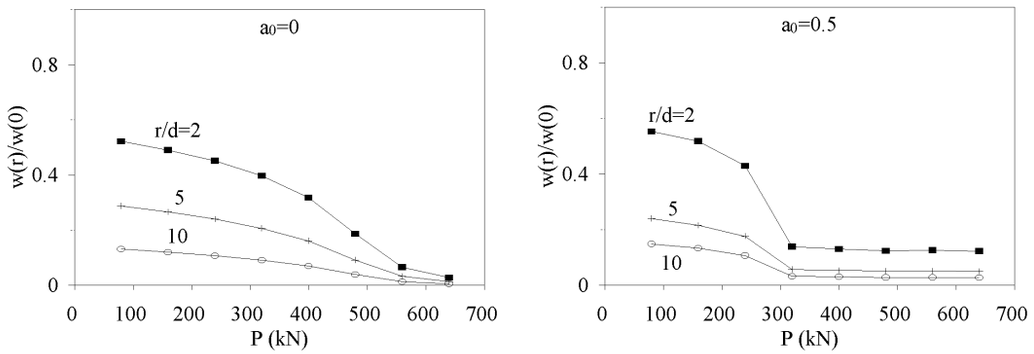


Figure 11. Normalized displacement versus force curves (V_S=65m/s, L/d=20)

SUMMARY AND CONCLUSIONS

The main purpose of this study is to analyze the nonlinear response of a pile subjected to harmonic vertical loading at the pile head by means of a finite element method with consistent boundary condition. Mohr-Coulomb strength criterion is used to model the contact property at the pile-soil interface. Based on the numerical results from a limited parametric study of the nonlinear response of piles, the following conclusions can be drawn.

The nonlinear analysis yields notably different prediction about the dynamic response of a pile from that of linear analysis unless a very small force level is applied. The equivalent linear stiffness of a pile decreases with increase in force level. It is an important behavior of the nonlinear response of a pile that the applied force reduces the natural frequency of a soil-pile-structure system, as verified by previous experimental observations.

The vertical displacement distribution along the radial direction shows a more dramatic decrease than that from linear analysis. The larger the force level, the more the decrease in displacement. Therefore, linear analysis overestimates the interaction between piles through soil, in particular, for a closely spaced pile foundation with

many piles. This may explain the pile test measurements from which less interaction between piles is observed than the prediction from linear analysis. Investigation into the pile group effect with the interaction factor as defined above is to be made in conjunction with verification from sophisticated 3D finite element methods and/or field or laboratory testing, since the two-by-two pile superposition approach tends to overestimate the group effect.

The prediction of nonlinear pile response from the present method is within a limited margin of the measured load – settlement curve for a tested pile. The nonlinear soil behavior is considered in the present analysis with an approximate relation of the soil shear modulus ratio versus shear strain. It is expected that more accurate prediction can be made by incorporating more realistic nonlinear soil stress-strain relations into the model.

Sharp variation of the pile stiffness with frequency can be observed in Figure 9 for $a_o > 0.5$. This may be smoothed by analyzing the problem with finer element meshes at more frequency points than those used in the analysis.

REFERENCES

Angelides, D. C. and Roesset, J. M. (1981). "Non-linear lateral dynamic stiffness of Piles." *Journal of Geotechnical Engineering*, ASCE, 107(11), 1443-1460.

Blaney, C. W., Kausel, E. and Roesset, J. M. (1976). "Dynamic stiffness of piles." *Proc. 2nd Int. Conf. on Num. Methods in Geomech.*, ASCE, Vol.II, 1001-1012.

Bouckovalas, G. and Gazetas, G. (1992). "Soil parameters for nonlinear analysis of axial vibration," *Proc. 2nd Greek Geotechnical Conference*, Thessaloniki, Vol.2.

Kausel, E. (1974). "Forced vibrations of circular foundations on layered media." *Research Report R74-11, Soils Publication No. 336*, Dept. of Civil Engineering, MIT, Cambridge, Massachusetts.

Kaynia, A. M. (1982). "Dynamic stiffness and seismic response of pile groups." *Ph.D. Thesis*, Department of Civil Engineering, MIT, Massachusetts

Trochanis, A. M., Bielak, J. and Christiano, P. (1991). "Three-dimensional nonlinear study of piles." *Journal of Geotechnical Engineering*, ASCE, 117, 429-447.

Vucetic, M., and Dobry, R. (1991). "Effect of soil plasticity on cyclic response." *Journal of Geotechnical Engineering*, ASCE, 117(1), 89-107.

Waas, G. (1972). "Linear two-dimensional analysis of soil dynamics problems in semi-infinite media." *Ph.D. Thesis*, University of California, Berkeley, California.

Zha, J. (1995). "Finite element analysis of nonlinear dynamic pile-soil interaction." *Ph.D. Thesis*, State University of New York at Buffalo.

Non-Linear Dynamic Response of Deepwater Suction Pile Foundation

Fabrizio Ardoino[1], Chiara M. Traverso[2], Eric J. Parker[3] M. ASCE, P.E.

[1]Geotechnical Engineer, D'Appolonia S.p.A., Via San Nazaro 19, 16145 Genoa, Italy; fabrizio.ardoino@dappolonia.it
[2]Geohazard Unit Manager, D'Appolonia S.p.A., Via San Nazaro 19, 16145 Genoa, Italy; chiara.traverso@dappolonia.it
[3]Offshore Division Manager, D'Appolonia S.p.A., Via San Nazaro 19, 16145 Genoa, Italy; eric.parker@dappolonia.it

ABSTRACT: Deepwater subsea petroleum developments present unique challenges for the geotechnical engineer. The combination of very soft soils and moderate to strong seismic ground motion requires innovative foundation solutions. This paper describes the seismic design of suction caisson foundations for subsea infrastructure in a deepwater field. Six-meter diameter, 12-m long suction piles were used to support underwater manifold assemblies. The seismic response of the structures was evaluated using a non-linear analysis in the time domain to predict foundation displacements under the design seismic event. The methodology used to define foundation response and assess structure displacements is presented. Results of the analysis showed that although there was local yielding of the foundation soils, the expected dynamic and permanent displacements were acceptable.

INTRODUCTION

The offshore industry is moving into ever deeper water in the quest for hydrocarbon production. Typically the developments are completely subsea, requiring a significant quantity of infrastructure: manifolds, pipeline end terminations (PLETs) and power/communication distribution assemblies. These are moderate size structures weighing from several tens to a few hundred tons (Figure 1). In deepwater the structures are below the level of wave action, and the principal foundation loads are due to self weight and the mechanical forces from piping temperature, pressure and installation tolerances. Depending on the location, the most severe horizontal loading may well arise from earthquake ground motion.

The foundations of choice for deepwater structures are suction piles, large diameter open ended steel caissons installed by a combination of self weight and underbase suction. This paper discusses the seismic response of suction pile foundations and presents an example of a recent design for a deepwater field offshore North Africa. The foundations were dimensioned using performance based design. Initial sizing was

based on a conventional load factor resistance approach for the gravity and operational loading conditions. The foundation behavior under seismic loading was then evaluated to verify that dynamic and permanent displacements would not have adverse impact on the functionality of the structure. This approach resulted in significant cost savings, both in foundation size and installation requirements.

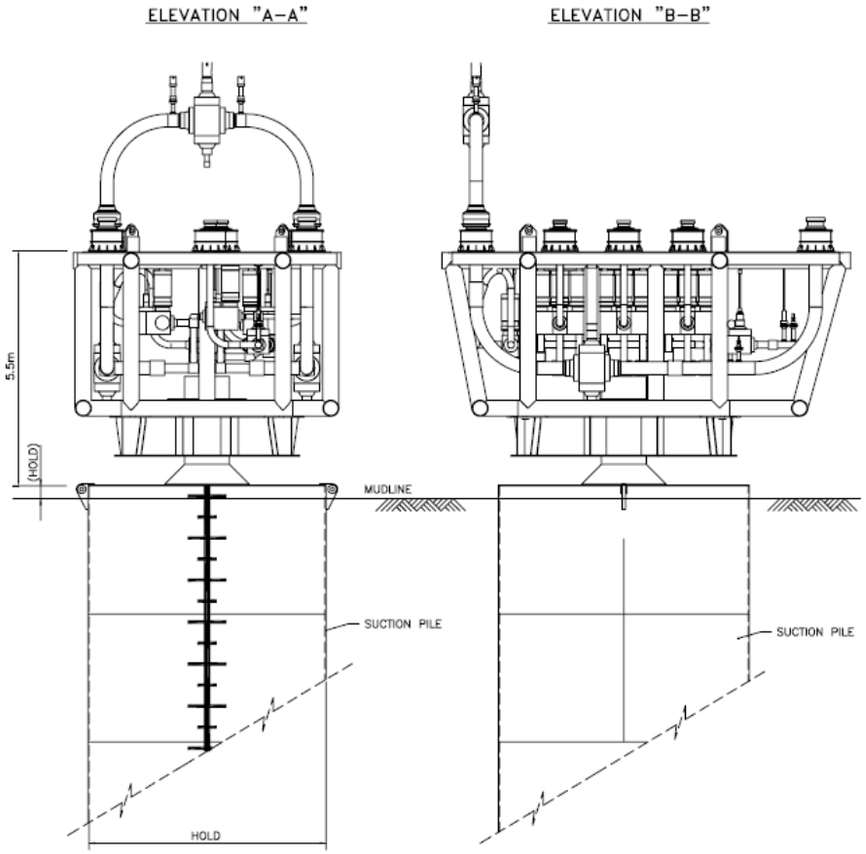


FIG. 1. Typical Deepwater Manifold.

SOIL CONDITIONS

Soils at the location comprise a thick sequence of high plasticity normally consolidated clays. Occasional thin sand layers are present, but generally at depths greater than the expected pile penetration. Figure 2 shows geotechnical data from a borehole at the location. The soils are seen to be high plasticity clays generally classified as CH in the USCS system. The undrained shear strength measurements are somewhat scattered, but there is a clear trend of increasing strength with depth.

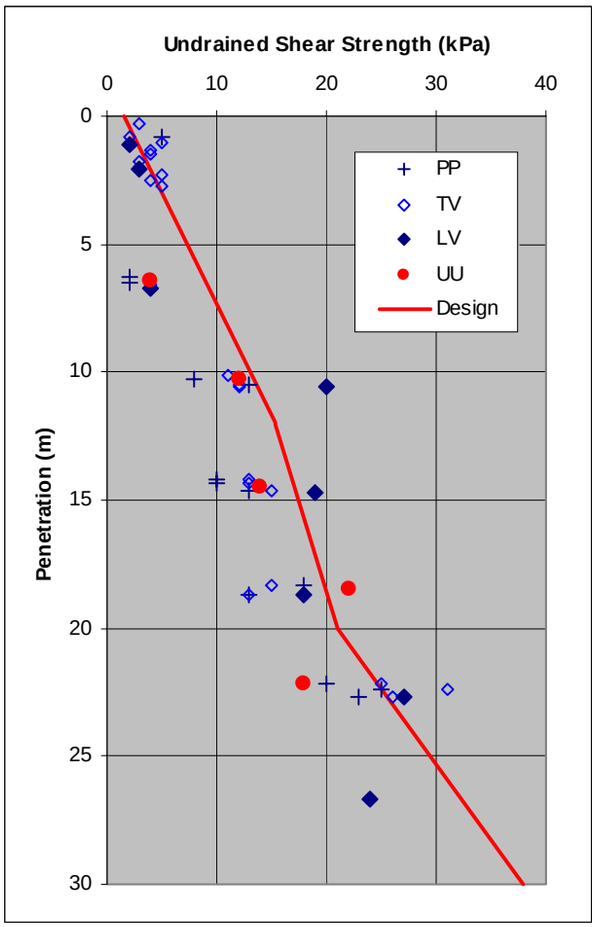


FIG. 2. Geotechnical Data.

The foundation response to dynamic loading is controlled by the soil shear modulus (G) and damping (D). Shear modulus is non-linear, and decreases with soil strain level. The small strain shear modulus is denoted G_{max}. Figure 3 shows the design G_{max} profile at the site. The design profile was developed considering G_{max} = 550 Su. Following the recommendations of ASCE 4-98 (2000), the range of uncertainty on G_{max} was taken as from 2/3 to 3/2 of the design value. The figure also shows values of G_{max} inferred from results of the seismic CPT. These data are believed to provide the best estimate of small strain soil stiffness for the location. The design profile is somewhat lower than the field measurements.

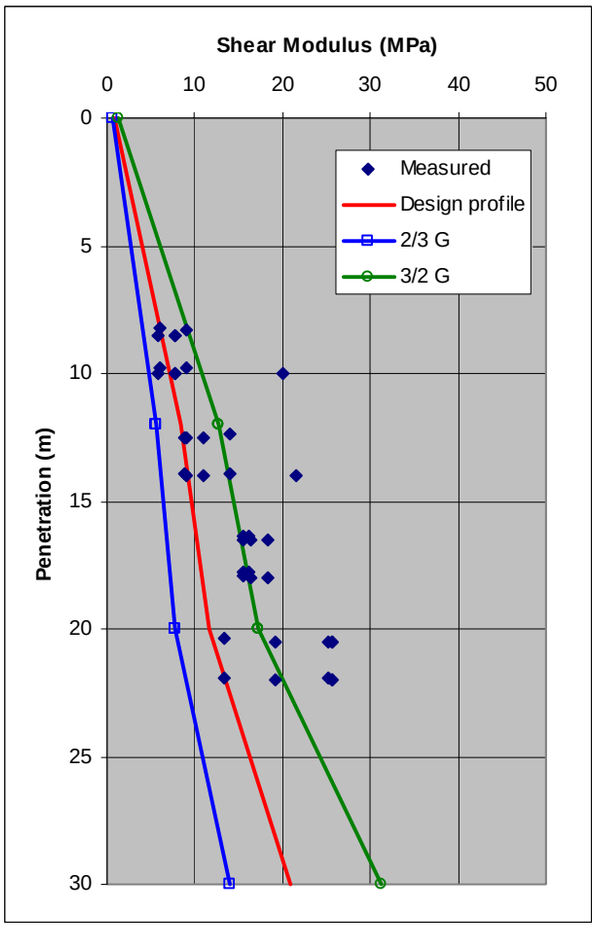


FIG. 3. G_{max} Profile.

DYNAMIC RESPONSE OF FOUNDATION

Foundation response under seismic loading was evaluated by a non-linear soil structure interaction analysis. The analysis predicted the horizontal displacement of the structure under seismic loading, modeling the system as a concentrated mass supported by a viscously damped elasto-plastic spring. Vertical displacements were also considered in design; these aspects are not discussed for brevity. The acceptance criteria for the foundation used the concept of "performance based" design. In this approach the foundation was considered acceptable if it does not experience significant deformations during and after the design seismic event. Two levels of earthquake ground motion were considered, a moderate frequent event and a stronger extreme shaking scenario.

The soil-structure interaction analysis was conducted for a manifold founded on a 6-m diameter 12.5-m penetration suction pile. The weight of the superstructure was of the order of 200 kN and the hydrodynamic added mass in the horizontal direction was approximately 185 kN. The manifold was the heaviest structure in the field and was expected to have the most severe seismic response. The following sections discuss the

evaluation of foundation stiffness and damping, and the foundation verification.

Foundation Model

The foundation was represented by an equivalent elasto-plastic spring with viscous damping. The slope of the elastic portion of the spring was taken as the static foundation stiffness. The plastic resistance was defined as the ultimate capacity of the foundation computed from a conventional static analysis. Damping was computed at the soil structure interaction frequency.

The structure foundations can experience four modes of deformation:

- Lateral displacement;
- Torsional displacement;
- Rocking;
- Vertical displacement.

The main horizontal movements of the suction piles are expected to result from lateral displacements and rocking (tilt) with respect to the vertical. There will also be a minor contribution from torsional displacement. As the inertial loads during an earthquake act at the center of gravity of the structure, there is significant coupling between the rocking and translational modes of deformation. This coupling was captured using the equivalent condensed system described below.

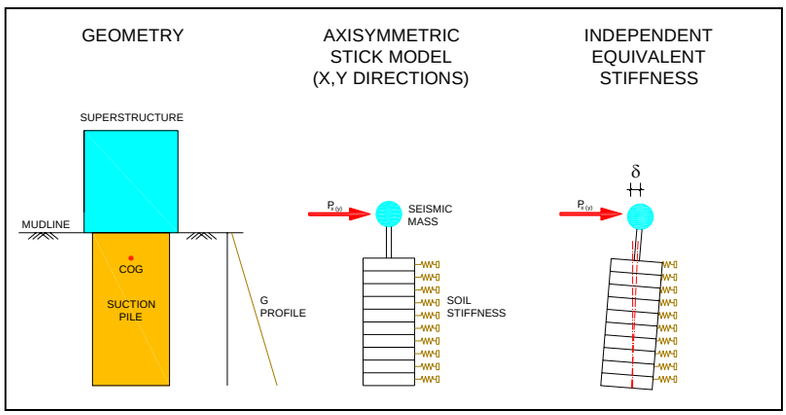


FIG. 4. Horizontal Foundation Model.

Figure 4 shows the schematic development of the foundation model. The pile was modeled as a foundation embedded in an elastic half space. The shear modulus of the half space was taken to increase with depth. The pile was divided into a series of discreet elements, and the stiffness to horizontal displacement was computed for each element. A simple stick model was then evaluated using the ANSYS software to determine displacement at the system center of gravity (COG) for a unit load. The equivalent stiffness of the condensed model was computed as the ratio of applied force to displacement. This approach correctly incorporates both translational and rocking modes. The springs were applied to both the x and y directions.

Given the geometry of the suction pile, in ultimate conditions a significant portion of overturning resistance would be due to shear at the pile base. In dynamic conditions, however, the displacements at base level are small and the contribution to the stiffness is considered less important. Conservatively, the base stiffness was neglected in the analysis.

The soil reaction stiffness for the individual elements was computed as the lateral stiffness of a cylindrical foundation in an elastic medium. The stiffness of the foundation element to lateral displacement was defined following Gazetas (1991). Neglecting the contribution of the base area of the cylinder, the horizontal stiffness K_x (K_y) is:

$$K_x = K_y = \frac{8Gd}{2-\nu} \quad (1)$$

where

G	shear modulus
d	height of segment in contact with soil
ν	Poisson's ratio

An elastic torsional spring was developed for the horizontal condensed system in order to account for potential rotations about the vertical axis. Such rotations could arise from eccentric horizontal inertial forces as the center of gravity of the structure is slightly offset from the vertical axis. The torsional stiffness was computed according to Gazetas as:

$$K_t = 14.2GR^2L \quad (2)$$

where

G	shear modulus
R	pile radius
L	pile length

Radiation damping of the foundation was also computed using the Gazetas approach. The calculated values of damping were typically in excess of 30% for both lateral and rocking modes. Consistently with FEMA 450 (BSSC, 2004) recommendations, damping was limited to 20% of critical. Viscous damping was computed as follows:

$$C_x = C_y = 20\%\ C_{crit} \quad (3)$$

$$C_{crit} = 2\sqrt{Km} \quad (4)$$

where:

C_x	viscous damping
C_{crit}	damping ratio at SSI fundamental frequency (resonance)
K	equivalent stiffness in x and y directions
m	mass of the system

The final foundation model was taken as two elasto-plastic springs and viscous dampers located at the center of gravity of the system, combined with one elastic torsional spring. The stiffness of the elastic portion of the horizontal springs was computed using the stick model described above. The maximum soil resistance was taken as the ultimate lateral resistance of the pile, considering interaction of vertical, horizontal, overturning moment and torsional loading. The degradation of modulus with shear strain was estimated as a function of peak ground acceleration following the FEMA 450 code (BSSC, 2004). The degraded modulus was taken at 81% of G_{max} for moderate level shaking and 42% of G_{max} for extreme ground motion.

Hysteretic damping was considered in the permanent plastic deformations of the foundation spring. A schematic representation of the load displacement behavior of the foundation is shown in Figure 5.

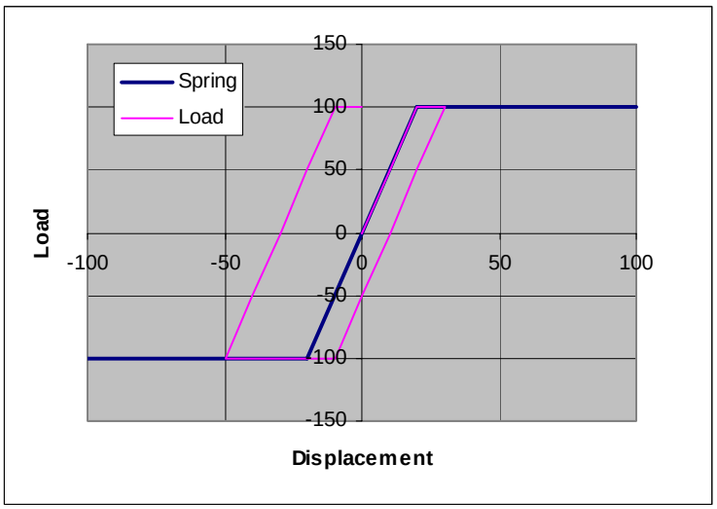


FIG. 5. Elasto-plastic Foundation Spring.

Figure 6 shows the final lumped mass model used for the non-linear soil structure interaction analysis. The structure is represented as a concentrated lumped mass connected to elasto-plastic springs with viscous damping in the X and Y directions. The mass is offset from the connection point by an eccentricity, representing the horizontal eccentricity of the center of gravity of the structure with respect to the vertical axis of the suction pile. An elastic moment-rotation spring is added in this plane to evaluate torsional displacements.

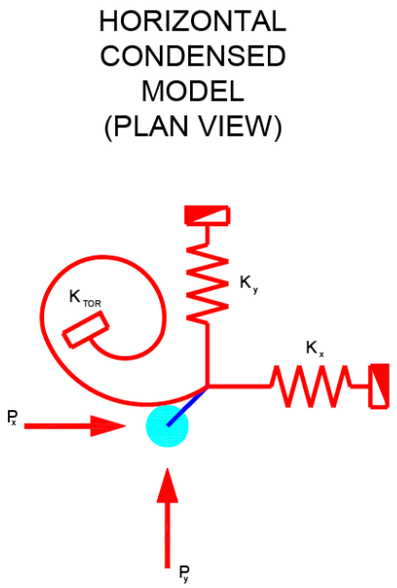


FIG. 6. Final Lumped Mass Model.

Displacement under Earthquake Loading

Foundation displacements under seismic loading were computed by non-linear soil structure interaction (SSI) analysis. A two dimensional analysis was performed considering seismic effects of both in plane and out of plane accelerations. This was achieved by applying two horizontal components of recorded time histories simultaneously to the lumped parameter model.

The steps in the analysis were as follows. An estimated range of the first natural frequency of the structure, the so called "soil-structure interaction frequency" was computed considering uncertainty on soil parameters. A set of eight earthquake time histories were then scaled to match the project design spectra in the range of SSI frequency. Finally, the non-linear interaction analysis was performed in the time domain to estimate structure displacements under moderate and extreme earthquake conditions.

The time histories used in the analyses were selected to watch seismotectonic setting of the project location. Time histories were chosen to watch the most probable combination of earthquake magnitude and source-site distance, based on PSHA hazard deaggregation. Special care was taken to match the soil condition (stiff soil) and source type (actives plate boundary) in the of records. A final verification was that the design response spectra adequately represented in the suite of time histories.

The analysis considered several levels of static horizontal load applied at the center of gravity of the entire system. These loads simulated eventual forces from the piping system. Appropriate reductions to the horizontal ultimate dynamic capacity were applied to consider interaction effects due to overturning moment and torsion during seismic loading.

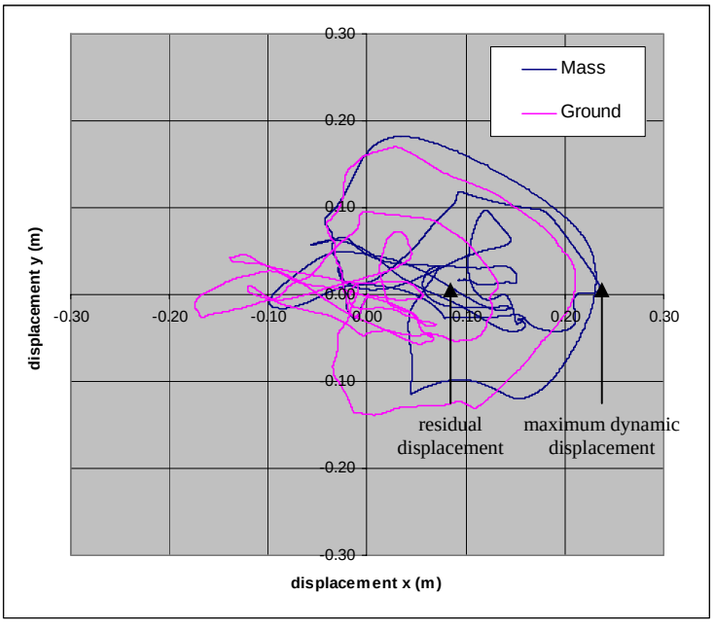


FIG. 7. Horizontal Manifold Displacements – Imperial Valley Time History.

An example of the displacements computed for the manifold is shown in Figure 7. Displacements were computed considering the Imperial Valley time history scaled to the moderate level earthquake and the upper bound stiffness. A permanent horizontal load of 100 kN was assumed. In this case the maximum dynamic displacement is 24 cm, and the residual displacement at the end of the earthquake is 9 cm. Torsional displacements are minimal.

Note that displacements are computed at the center of gravity of the structure. Considering the movement at the upper flange, elevation +8.3 m would increase the displacements by a factor of 2.7. The dynamic displacement at the flange is 64 cm and the residual displacement is 24 cm.

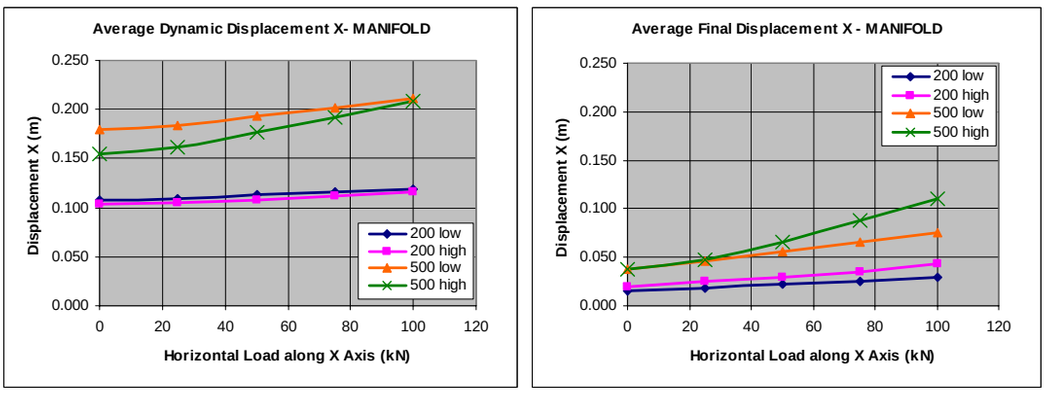


FIG. 8. Average Displacement as Function of Horizontal Load.

Figure 8 shows the average permanent static post-seismic displacement and the maximum dynamic displacements during the event. The individual lines show lower and upper bound hypotheses on soil stiffness (low, high) for the two different levels of ground motion (200 years, 500 years). Following the recommendations of FEMA 450, the average of the results from the eight time history analyses were used in design.

CONCLUSIONS

The main findings of the seismic response analysis were:

- If the structure is not subject to permanent horizontal loads during the earthquake there is virtually no residual displacement;
- For horizontal loads of up to 100 kN the permanent horizontal post-seismic displacement is less than 30 cm for the manifold. This is true for both moderate and extreme level events;
- The maximum dynamic displacement during the event was less than about 65 cm. This is a small value compared to allowable jumper deformations, which are typically of the order of 1 or 2 m. The dynamic displacement is not strongly conditioned by the permanent horizontal load;
- The displacements expected during and after either the moderate or extreme level events are small, and should not compromise function of the structures.

REFERENCES

American Society of Civil Engineers. (ASCE, 2000). *Seismic Analysis of Safety-Related Nuclear Structures and Commentary*, ASCE 4-98, Reston/VA.

Building Seismic Safety Council. (BSSC, 2004). *NEHRP National Earthquake Hazards Reduction Program Recommended Provisions for Seismic Regulations for New Buildings and other Structures (FEMA 450),* 2003 Edition, National Institute of Building Sciences, Washington, D. C.

Gazetas, G. (1991). “Foundation Vibrations”, Chapter 15 of *Foundation Engineering Handbook*, Edited by H-Y Fang, 2nd Edition, Van Nostrand Reinhold, New York/NY.

PILES UNDER EARTHQUAKE LOADS

Shamsher Prakash[1], F. ASCE , PE and Vijay K. Puri[2], M. ASCE

[1]Professor Emeritus, Department of Civil, Architectural and Environmental Engineering University of Missouri Rolla, Rolla, MO 65409, prakash@umr.edu
[2]Professor, Department of Civil and Environment Engineering, Southern Illinois University, Carbondale, IL 62901, puri@engr.siu.edu

ABSTRACT: Piles are preferred type of foundation for supporting structures in seismic areas. Their performance is affected by soil, pile and earthquake related parameters. In non-liquefying soils, the shear modulus may degrade and material damping may increase with increasing strain/displacement. In liquefying soils ,the lateral ground displacement may lead to increased lateral loads and moments on the pile leading to pile failure in bending. The loss of lateral support can also lead to buckling type failure. These issues for pile design in seismic areas are examined.

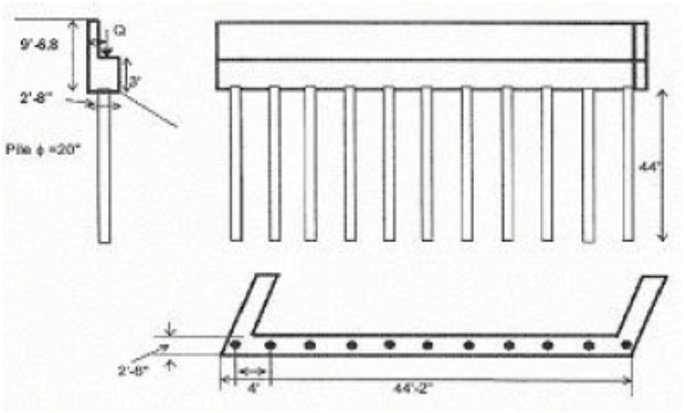
INTRODUCTION

Pile foundations are regarded as a safe alternative for supporting structures in seismic areas. The seismic loading induces large displacements/strains in the soil . The shear modulus of the soil degrades and damping (material) increases with increasing strain. The stiffness of piles should be determined for these strain effects. For piles in non-liquefying soils the stiffness of the pile group is estimated from that of the single piles by using group interaction factors. The contribution of the pile cap, if any, is also included. The response of the single pile or pile groups may then be determined using principles of structural dynamics.

In liquefiable soils, progressive buidup of pore water pressure may result in loss of strength and stiffness resulting in large bending moments and shear forces on the pile. The mechanism of pile behavior in liquefying soil has been investigated by several investigators in the recent years (Liyanapathirana and Poulos, 2005). The behavior and design of piles in liquefying soil is also discussed.

PILES IN NON-LIQUEFYING SOIL

The liquefaction susceptibility of the soil should first be ascertained by appropriate analysis. If the soils are not liquefiable, the following procedures (Prakash and Sharma,1990) may be used:



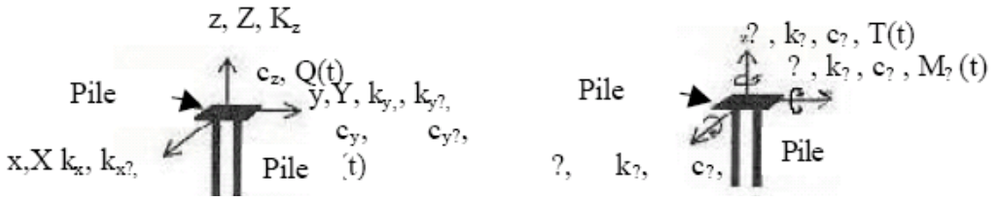


FIG. 1. Old St. Francis River pile layout- Bridge Abutment(Munaf, Prakash and Fennesey, 2003)

Analysis of Pile Groups in Non-Liquefiable soils

Typical section of a pile group is shown in Figure 1.The following steps are involved in analysis of a pile group (Prakash and Sharma 1990)

1. Determine the stiffness and radiation damping of the single pile
2. Determine the stiffness of the pile group by applying appropriate pile-soil-pile interaction factors.
3. Determine natural frequencies of the pile group.
4. Estimate the response of the pile group for the given input motion.

The pile cap displacements (translation and rotation) may be used as input parameters for structural analysis.

Stiffness and Radiation Damping of Single Piles

Stiffness of single piles in horizontal-translation and rotation may be determined as follows: Novak and El-Sharnouby (1983) have recommended expressions for horizontal sliding stiffness ($k_{x\phi}$, rocking stiffness (k_{ϕ}) and cross-coupling stiffness $k_{x\phi}$. Corresponding expressions for radiation damping coefficients C_x, C_{ϕ} and $C_{x\phi}$, cross-damping respectively have been developed (Prakash and Puri 2008).

Stiffness and Radiation Damping of Pile-Group

Novak and El-Sharnouby(1983) have recommended pile-soil-pile interaction factors .

Group Efficiency Factor (ε) is defined as:

$$\in = \frac{\text{Group stiffness } (k_{xg})}{\text{N X Single pile stiffness}(k_x)} \tag{1}$$

where s = Center to center spacing of piles
d = Diameter or width of pile
N = Number of piles in group
Similarly group radiation damping in sliding (C_{xg}) is given by Eq. 2.,

$$Group\ damping(C_{xg}) = N\,X\,Single\,Pile\,Damping \tag{2}$$

The above equation follows from the recommendations for pile group effects by Novak (1974).

Pile Group Natural Frequencies

The next step is to determine natural frequencies of the system, which may be determined from the following equation (Kumar and Prakash, 1995)

$$\left[\left\{\omega^4 - \left(\frac{k_x}{m} + \frac{k_\phi}{M_m} + \frac{C_x C_\phi}{m M_m} - \frac{C_x^2 \phi}{m M_m}\right)\omega^2 + \left(\frac{k_x k_\phi}{m M_m} - \frac{k_x^2 \phi}{m M_m}\right)\right\}^2 + \left\{\left(\frac{k_x C_\phi}{m M_m} + \frac{k_\phi k_x}{m M_m} - \frac{2 k_{x\phi} C_{x\phi}}{m M_m}\right)\omega - \left(\frac{C_\phi}{M_m} + \frac{C_x}{m}\right)\omega^3\right\}^2\right]^{1/2} \tag{3}$$

Pile Group Response

The response of the pile group may be determined by any standard structural dynamic method of analysis (Luna, Prakash et al 2001). A detailed time history solution for a given ground motion may be obtained and the maximum response values be selected for design. The above response may be used as input motion for analysis of the superstructure. Alternatively, a spectral response method be used.

Non-Linear Analysis

The strains in soils during earthquakes may be of the order of 10^{-4} to 10^{-2}. Non-linear analysis may be performed by using step- by- step linear approach and repeating the process until convergence between predicted and assumed strains has been obtained

Strain-Displacement Relationships

Puri and Prakash (2007) have reviewed that shear strain and displacement relationship in many practical problems for use as the basis for evaluating the shear strain in each particular case; For vertically vibrating footings as:

$$\gamma = \frac{\text{Amplitude of foundation vibration}}{\text{Average width of foundation}} \tag{4}$$

Shear strain (γ_x) and horizontal displacement (x);

$$\gamma_x = \frac{(1 + \nu)X}{2.5D} \tag{5}$$

Where, ν = Poisson's ratio
X = horizontal displacement in x-direction
D = diameter of pile

γ_ϕ due to rocking ϕ can be reasonably determined as

$$\gamma_\phi = \frac{\phi}{3} \tag{6}$$

Where, ϕ = rotation of foundation about y axis

The shear strain-displacement relationship for couple sliding and rocking can be determined as

$$\gamma = \frac{(1 + \nu)X}{2.5D} + \frac{\phi}{3} \tag{7}$$

Solution Technique for Displacement Dependent K's and C's

1. OBTAIN Unit weight, shear wave velocity, poisson's ratio, initial shear modulus; shear modulus degradation curve as function of soil shear strain
2. OBTAIN Pile length, pile diameter, elastic modulus of pile, shear wave velocity
3. SELECT relationship for half space stiffness and damping parameters as function of soil parameters, pile dimensions, and piles arrangements.
4. DETERMINE Strain-Displacement Relationship
5. DETERMINE Stiffness and damping factor for single pile at selected displacements
6. CALCULATE Group efficiency factor
7. CALCULATE Group piles stiffness and damping factors
8. REPEAT Steps 5-7 for all desired displacements and plot stiffness (k) and damping (c) parameters versus displacement functions

Figure 2 shows a plot of k's versus non dimensional displacement of a typical pile group. Munaf, Prakash and Fennesey(2003) have analyzed abutment of a bridge (fig. 3) supported on piles. Figure 3 shows the displacements of the abutment for a two synthetic ground motions.

These and similar relationships were used in the analysis of bridge structures at two locations (Anderson, Prakash et al 2001, Luna et al 2001).

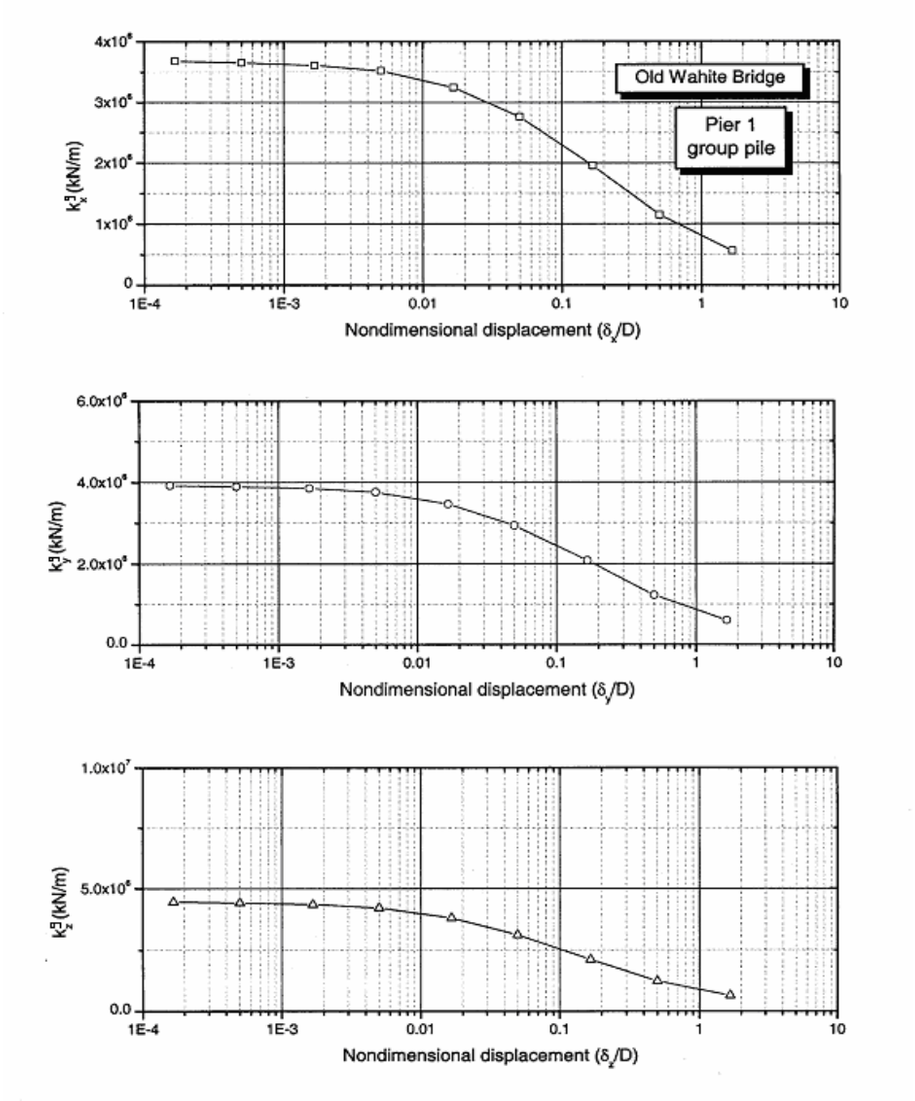
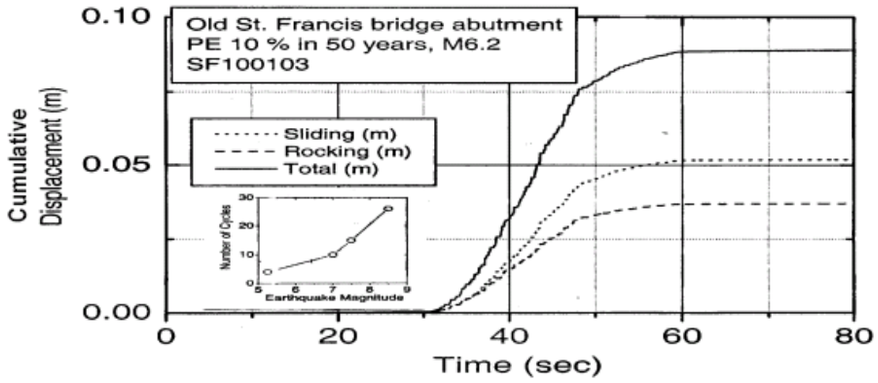


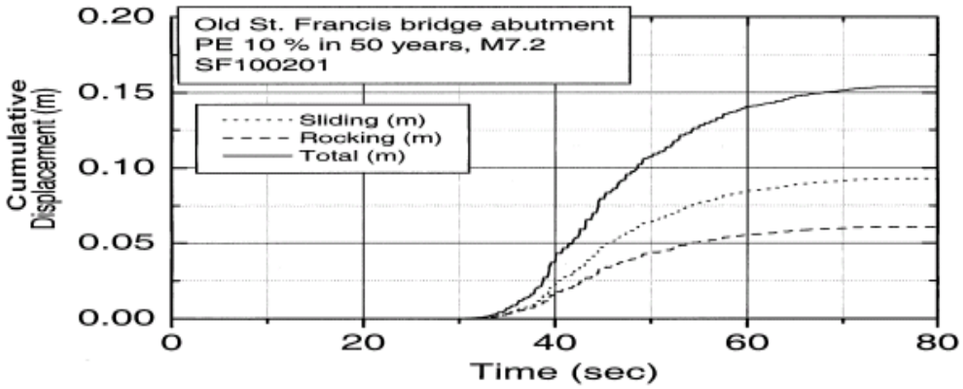
FIG. 2 k_x^g , k_y^g , k_z^g versus, non-dimensional displacement (δ/D)

PILES IN LIQUEFIABLE SOILS

Excess pore pressure during seismic motion may cause lateral spreading resulting in large moments in the piles and settlements and tilt of the pile cap and the superstructure. Excessive lateral pressure may lead to failure of the piles which was experienced in the 1964 Niigata and the 1995 Kobe earthquakes (Finn and Fujita, 2004). Damage to a pile under a building in Niigata caused by about 1m of ground displacement is shown Figure 4(Yasuda et al, 1990). Displacement of Quay wall and damage to piles supporting tank TA72 (Fig. 5, 6 and 7) during 1995 Kobe earthquake has been reported by Ishihara and Cubrinovski, (2004)



(a)



(b)

FIG. 3 Time histories of sliding, rocking and total displacements for (a) M=6.2 and (b) M7.2



FIG. 4. Damage to pile by 2m of lateral ground displacement during 1964 Niigata earthquake (Yoshida et al.1990)

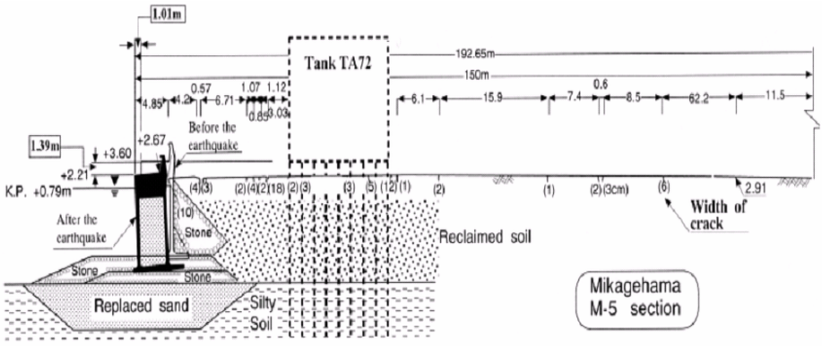


FIG. 5. Detailed profile of the quay wall movement and ground distortion in the backfills at Section M-5 (Ishihara and Cubrinovski, 2004)

The quay wall moved approximately 1m towards the sea. The seaward movement of the quay wall was accompanied by lateral spreading of the backfill soils resulting in a number of cracks on the ground inland from the waterfront. The lateral ground displacement was plotted as a function of the distance from the waterfront. As indicated in the Figure. 8, the permanent lateral ground displacement corresponding to the location of Tank TA72 is seen somewhere between 35 and 55 cm (Ishihara and Cubrinovski, 2004). To inspect the damage to the piles of an oil tank site after Kobe (1995) event 70cm wide and 1m deep trenches were excavated at 4 sections and the upper portion of the pile was exposed. The wall of the cylindrical piles was cut to open a window about 30cm long and 15cm wide. From this window, a bore-hole camera was lowered through the interior hole of the hollow cylindrical piles to examine the damage to the piles throughout the depth .

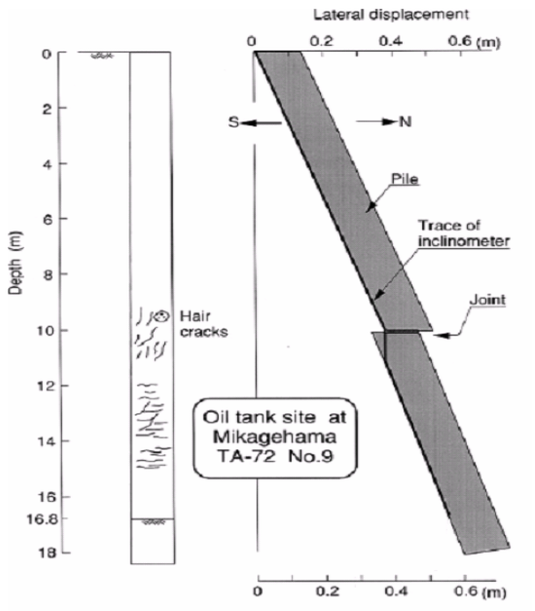


FIG. 6. Lateral displacement and observed cracks on the inside wall of Pile No.9 Kobe 1995 EQ (Ishihara and Cubrinovski, 2004)

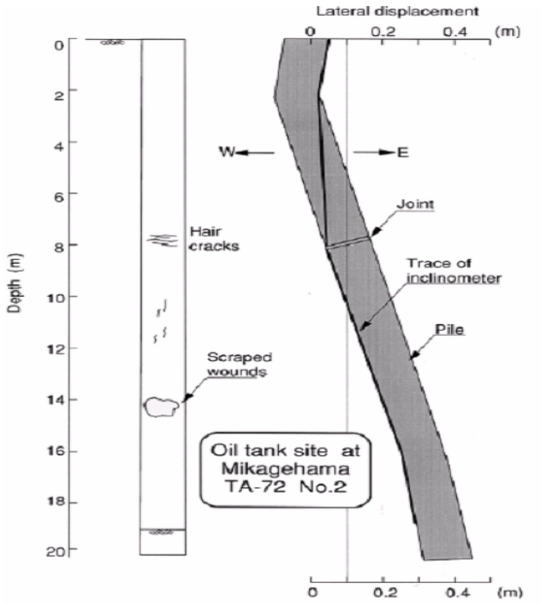


FIG. 7. Lateral displacement and observed cracks on the inside wall of Pile No.2 Kobe 1995 EQ (Ishihara and Cubrinovski, 2004)

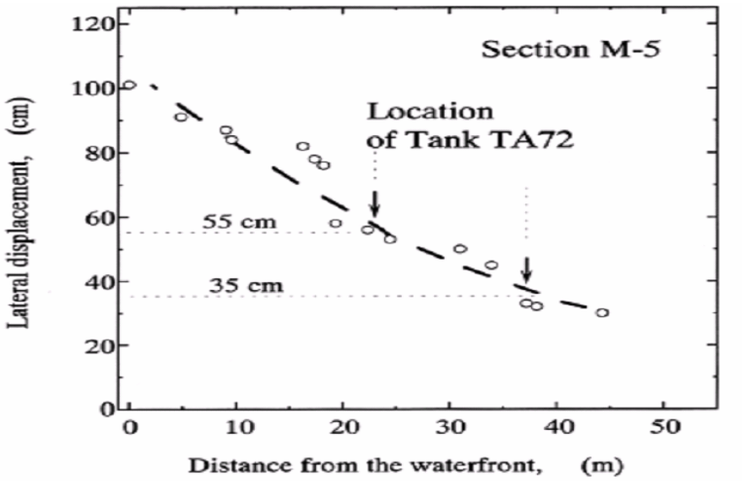


FIG. 8. Lateral ground displacement versus distance from the waterfront along Section M-5, Kobe 1995 EQ (Ishihara and Cubrinovski, 2004)

DESIGN OF PILES IN LIQUEFYING SOIL

The design of pile foundations in liquefied soils requires a reliable method of calculating the effects of earthquake shaking and post liquefaction displacements on pile Foundations (Finn and Fujita, 2004). The methods currently in use for design of piles in liquefying soil are:

1. The force or limit equilibrium analysis and
2. The displacement or p-y analysis.
3. Dynamic analysis.

The Force or Limit Equilibrium Analysis

This method of analysis is recommended in several Japanese design codes for analysis of pile foundations in liquefied soils undergoing lateral spreading (JWWA, 1997 ; JRA, 1996). The method involves estimation of lateral soil pressures on pile and then evaluating the pile response.

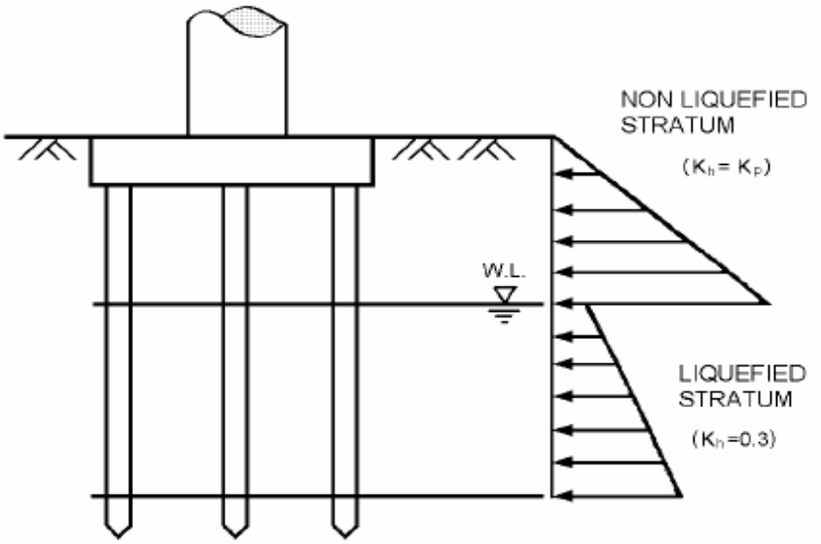


FIG. 9. . Schematic sketch showing pressure distribution against the piles due to lateral soil flow associated with liquefaction (JWWA, 1997)

A schematic sketch showing lateral pressures due a non- liquefied and liquefied soil layers is shown in Figure 9. The non-liquefied top layer is assumed to exert passive pressure on the pile. The liquefied layer is assumed to apply a pressure which is about 30% of the total overburden pressure . This estimation of pressure is based on back calculation of case histories of performance of pile foundations during the Kobe earthquake (Ashford and Juirnarongrit, 2004 and Finn and Fujita, 2004). The maximum is assumed to occur at the interface between the liquefied and non-liquefied soil layer.

Displacement or p-y Analysis

This method involves making Winkler type spring mass model shown schematically in Figure 10. The empirically estimated post liquefaction free field displacements are calculated. These displacements are assumed to vary linearly and applied to the springs of the soil-pile system as shown in Fig. 10 (Finn and Thavaraj, 2001). Degraded p-y curves may be used for this kind of analysis. In the Japanese practice the springs are assumed to be linearly elastic-plastic and can be determined from the elastic modulus of soil using semi-empirical formulas (Finn and Fujita , 2004). The soil modulus can be evaluated from plate load tests or standard penetration tests. Reduction in spring stiffness is recommended by

JRA(1996) to account for the effect of liquefaction. Such reduction is based on $F_{L,}$ (factor of safety against liquefaction). These reduction factors are shown in Table 1

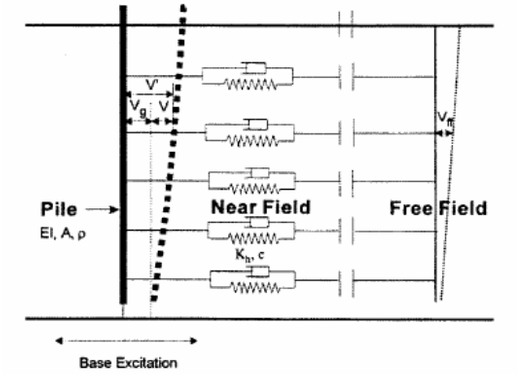


FIG. 10. Schematic sketch for Winkler spring mModel for pile foundation analysis (Finn and Thavaraj, 2001)

Ashford and Juirnarongrit (2004) compared the force based analysis and the displacement based analysis for the case single piles subjected to lateral spreading problems. They observed that the force based analysis reasonably estimated the pile moments but underestimated the pile displacements. The displacement analysis was found to make better prediction about both the pile moment and the pile displacement.

The design of pile foundations in liquefied soil needs an understanding of phenomenon of liquefaction, the behavior of soil following liquefaction and soil-pile interaction.

Table.1 Reduction coefficients for soil constants due to liquefaction(JRA,1996)

Range of F_L	Depth from the Present Ground Surface x (m)	Dynamic Shear Strength Ratio R	
		R ≦ 0.3	0.3 < Ra
$F_L \leqq 1/3$	$0 \leqq x \leqq 10$	0	1/3
	$10 < x \leqq 20$	1/3	1/3
$1/3 < F_L \leqq 2/3$	$0 \leqq x \leqq 10$	1/3	2/3
	$10 < x \leqq 20$	2/3	2/3
$2/3 < F_L \leqq 1$	$0 \leqq x \leqq 10$	1/3	1
	$10 < x \leqq 20$	1	1

North American Practice is to multiply the p-y curves, by a uniform degradation factor p, called the p-multiplier, which ranges in values from 0.3 - 0.1.The values ‘p’ seem to decrease with pore water pressure increase (Dobry et al 1995) and become 0.1 when the excess pore water pressure is 100%. Wilson et al(1999) suggested that

the value of 'p' for a fully liquefied soil also depends on the initial relative density Dr. The values of 'p' range from 0.1 to 0.2 for sand at about 35% relative density and from 0.25 to 0.35 for a relative density of 55%. It was found that the resistance of the loose sand did not pick up even at substantial strains but the denser sand, after an initial strain range in which it showed little strength, picked up strength with increasing strain Fig:9 . This finding suggests that the good performance of the degraded p-y curves which did not include an initial range of low or zero strength ,must be test specific and the p-multiplier may be expected to vary from one design situation to another. Dilatancy effects may reduce the initial p-y response of the dense sands(Yasuda et al 1999). Ashford and Juirnarongrit (2004) compared the force based analysis and the displacement based analysis for the case of single piles subjected to lateral spreading problems. They observed that the force based analysis reasonably estimated the pile moments but underestimated pile displacements. The displacement analysis was found to make better prediction about the pile moment and the pile displacement.

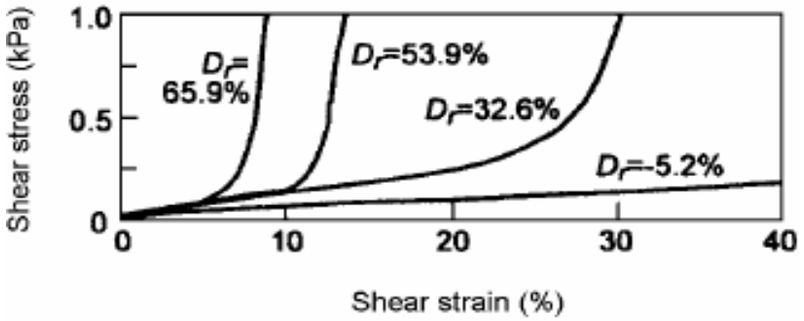


FIG. 11. Post-liquefaction un-drained stress-strain behavior of sand (Yasuda et al 1999)

Liyanapathirana and Poulos (2005) developed a numerical model for simulating the pile performance in liquefying soil . They also studied the effect of nature of earthquake on pile performance and observed that the 'Arias intensity' and he natural frequency of the earthquake strongly influence performance of the pile in liquefying soil. Bhattacharya (2007) re-examined the damage to piles during 1964 Niigta and 1995 and Kobe earthquakes and noted that pile failure in liquefying soil can be better explained as buckling type failures.

CONCLUSIONS

PILES IN NON-LIQUEFIABLE SOILS
1. Soil-pile behavior is strongly strain dependent
2. Simple frequency independent stiffness and damping equations of Novak give reasonably good results.
3. Group interaction factors are also frequency independent, since predominant excitation frequencies may not exceed 6-10 Hz in soft soils
PILES IN NON-LIQUEFIABLE SOILS
1. Liquefaction may result in large pile group displacements.

2. Lateral spreading of soils may cause large bending moments and shears on the pile, which may result in failure of piles below the ground level (as in Niggata and Kobe earth quake)
3. Japanese and North American design practices may not give identical solutions.
4. Considerably more research is needed to refine design methods

REFERENCES

Ashford, S. and Juirnarongrit, T.,(2004),"Evaluation of Force Based and Displacement Based Analysis for Response of Single Piles to Lateral Spreading", Proceedings of 11th International Conference on Soil Dynamics and Earthquake Engineering and 3rd International Conference Earthquake Geotechnical Engineering, University of California, Berkely, Vol. 1, pp. 752-759.

Bhattacharya,S. (2006), "A Review of Methods for Pile Design in Seismically Liquefiable Soil", Design of Foundations in Seismic Areas: Principles and Applications, NICEE, IIT Kanpur.

Cubrinovsky, M. and Ishihara ,K (2005), "Assessment of Pile Group Response to Lateral Spreading by Single Pile Analysis", Proceedings of the Workshop on Seismic Performance and Simulation of Pile Foundations in Liquefied and Laterally Spreading Ground, Geotechnical Special Publication No. 145, March 16-18, pp.242-254.

Dobry, R., Taboda,V. and Liu .L(1995),"Centrifuge Modeling of Liquefaction Effects During Earthquakes",Proc.1st International Conference on Earthquake Engineering,Tokyo,Vol.3.PP.1291-1324.

Finn, W.D.L. and Fujita N.,(2004) ,"Behavior of Piles During Earthquakes : Analysis and design", Proceedings, fifth international Conference on Case Histories in Geotechnical Engineering, New york, N.Y., April 13-17.

Finn, W.D.L. and Thavaraj, T.(2001)," Deep Foundations in liquefiable Soil", ", Proc. 4th Int. Conf. on Recent Adv. in Geotech. Earth. Engrg. And Soil Dynamics, San Diego

Ishihara ,K. and Cubrinovsky, M.,(2004) "Case Studies of pile Foundations Undergoing lateral Spreading in liquefied deposits" , Proceedings, fifth international Conference on Case Histories in Geotechnical Engineering, New york, N.Y., April 13-17

JRA (1996), "Seismic Design Specifications of highway Bridges", Japan Road Association

JWWA(1997), "Seismic Design and Construction Guidelines for Water Supply Facilities, Japan Water Works Association, Tokyo

Kumar, S. and Prakash, S. (1995), Couple horizontal and rocking vibration of block foundations, Proc. III Intern. Conf. on Recent Advances in Geot. Earthquake Eng and Soil Dyn. April, St. Louis, MO Vol. III, pp 1369-1373.

Luna, R., Prakash….et al (2001), "Earthquake Assessment of Critical Structures for Route 66 Missouri, Paper No. 8-13 Proc. 4th International Conf. Recent Advances in Geot. Earthquake Energy Soil Dynamics, San Diego, CA, CD-ROM (March)

Munaf, Y.and Prakash, S. (2002),"Displacement Dependent Spring and Damping Factors of Soil Pile Systems," Proc. 12th ECEE, London Paper No. 763

Munaf. Y, S.Prakash and T.Fennessey (2003) " Geotechnical Seismic Evaluation of Two Briohra in SE Missouri" Proc PEEC, Christchurch NZ Paper No-5, CD-ROM

Novak, M. (1974), Dynamic stiffness and damping of piles, Con. Geot. J. Vol. II No 4, pp. 574-598.

Novak, M. and ElSharnouby, E.B. (1983), Stiffness and damping constrants for single piles, J. Geot. Engg. Dn. ASCE, Vol. 109 No 7, pp 961-974.

Prakash, S., (1981), Soil dynamics, McGraw Hill, New York. Reprinted SP foundation, Rolla, MO

Prakash, S. and Sharma, H.D. (1990), Pile foundations in engineering practice, John Wiley and Sons, NY.

Prakash S and V.K .Puri (2008) " Piles Under Seismic loads of the Art" Proc. Sixth Intern. Conf. on case histories in Geot.Eng. Page No. CD-ROM, Arlington VA

Puri V.K. and S. Prakash(2007) " Foundations for Seismic Loads" Geo-Denver, ASCE Conference, CDROM

Wilson.D.O. Boulanger,R.W. and Kutter,B.L. (2000), "observed lateral resistance of liquefying sand", journal of geotechnical and Geo-Environmental Engineering, ASCE, pp.34-43

Yasuda, Y. N., Kiku, H. and Adachi, K. (1999), "A simplified Practical Method for evaluating Liquefaction Induced flow"' proceedings 7th U.s.- Japan Workshop on Earthquake Resistant design of lifeline facilities and Countermeasures Against Liquefaction, November, pp. 311-320.

This page intentionally left blank

RESPONSE OF CLAY-PILE SYSTEM UNDER EARTHQUAKE LOADING

Subhadeep Banerjee[1], Siang Huat Goh[2] and Fook Hou Lee[3]

[1]Research Scholar, [2]Research Fellow, and [3]Associate Professor
National University of Singapore, 1 Engineering Drive 2, #07-03, Blk E1A, Singapore 117576

ABSTRACT: The response of pile foundations during past earthquakes have shown that piles in firm soils generally perform well, while the performance of piles in soft or liquefied ground can raise some questions (Wilson, 1997). Pile foundations are very frequently used in soft clay to achieve the required bearing in stiff stratum. This paper presents the results of dynamic centrifuge model tests carried out at the National University of Singapore to physically model dynamic soil-pile response in soft clay. The experimental results strongly suggest that there are significant effects arising from stiffness degradation due to imposed inertial loading of surrounding soil on piles with repetitive shaking during earthquake, and corresponding changes in time period and amplification of ground motion. The study also examined the influence of different relative stiffness of the clay-pile system, and different superstructural inertial loads. The centrifuge tests were back-analyzed via 3-D finite element modeling using the general purpose code ABAQUS. The analyses show that the use of simple non-linear hypoelastic soil models can provide reasonable agreement with the experimental observations.

INTRODUCTION

Pile foundations are frequently used in soft clays to achieve the required bearing capacity. The behavior of pile foundations under earthquake loading is an important factor affecting the performance of many essential inland or offshore structures such as bridge, harbors, tall chimney, wharf etc. Performance of pile foundations during past earthquakes have shown that piles in firm soils generally perform well, while the performance of piles in soft or liquefied ground can raise some questions (Wilson., 1997).

It is well known that the mechanical behavior of soil under dynamic loading, such as sea waves, earthquakes and traffic loading, differ significantly from those under quasi-static loading. Nonlinearity associated with soft clays under cyclic loading was experimentally shown by Idriss et al.(1978), Vucetic and Dobry (1988) and Puzrin et al. (1995). Rao and Panda (1997) proposed a one-dimensional nonlinear model to simulate cyclic behavior of soft marine clay, the results of which compared favorably with the experimental observations made by Idriss et al.(1978) and Vucetic and Dobry (1988). Brennan et al. (2005) examined shear modulus and damping in dynamic

centrifuge tests, and showed that soft clay exhibited strain softening, as reflected in reduced G/G_{max} values with increasing strain levels.

The presence of piles in soft clays, however, introduces additional complexity to the problem. Wilson (1997) and Christina et al.(1999) studied performance of pile foundations in clays using the large servo-hydraulic shaking table on the 9-m-radius centrifuge at the University of California at Davis and proposed design charts for the practicing engineer. Snyder (2004) showed that the clay stiffness degraded around the single pile during cyclic lateral load tests in the field. However, the study did not consider the effect of superstructural loadings and the relative stiffness of soil-pile materials on the dynamic ground response.

In this paper, the results from a series of dynamic centrifuge model tests carried out at the National University of Singapore are presented. The centrifuge experiments were performed to examine dynamic soil-pile response in soft clays, with special focus on the stiffness degradation due to earthquake shaking and corresponding changes in time period and amplification of ground motion. The experimental observations were then compared with the results obtained from 3-D finite element modeling utilizing a simple hypoelastic soil model in the software ABAQUS.

EXPERIMENTAL SET-UP

The tests were performed on the geotechnical centrifuge at the National University of Singapore at a centrifugal acceleration of 50g. Soft kaolin clay (bulk unit weight = 16kN/m3, water content = 66%, liquid limit = 80%, plastic limit = 35%) bed models were prepared by pouring clay slurry into the laminar container, followed by a period of consolidation to re-create the desired strength profile and stress history. The base plate of the box is connected to a shaking apparatus consisting of actuator, accumulator and motor pump assembly. More details of the set-up are available in Banerjee et al.(2006). This paper provides the additional details associated with the modeling of the pile-raft system. The model pile-raft system comprises four cylindrical model piles, 2.2 cm in diameter and 18 cm long, connected to a rigid steel base plate with dimensions 25 cm x 15 cm x 1 cm. The minimum clear spacing between adjacent piles was 4.5 times the pile diameter. The minimum clear spacing between the pile and the internal wall of the box is about 4.6 times the pile diameter. These spacings were chosen to keep the pile-to-pile and pile-wall interaction to a minimum. Three different types of model piles were used (Table 1).

The superstructural loads acting on the raft were simulated by means of steel plates placed on top of the raft. Up to 7 steel plates, each of mass 2.4 kg, were added in stages to simulate the effects of above-ground inertial forces on the response of the clay-pile-raft system. The model and prototype masses associated with the three load cases are shown in Table 2.

The input motions used in the centrifuge experiments (Figure 1) were generated using response spectra from earthquakes measured in Singapore from Sumatran events. These typically have long periods and durations. Owing to the limited duration of excitation which the shaking table can generate, low frequency waves with prototype periods exceeding 20s were removed from the earthquake spectra before regeneration. Three different input motions were thus generated, corresponding to a

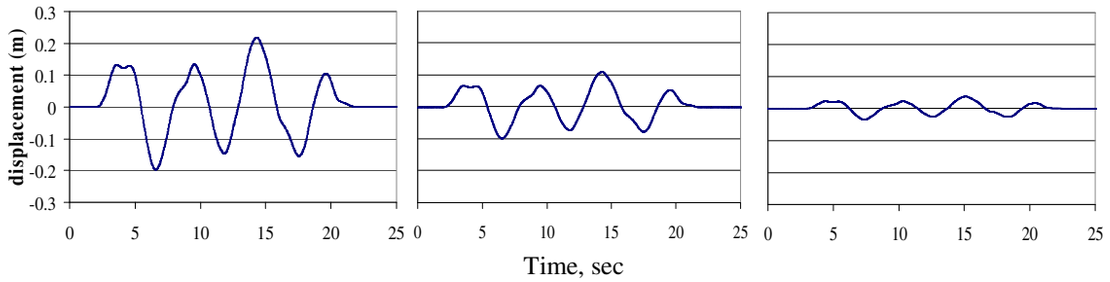
large, medium and small earthquake event. Figure 1 shows the three prescribed input motions, in prototype scale, to the displacement-controlled servo-actuators.

Table 1. Different piles used for the study

Pile material	Model Flexural Rigidity (kN-m^2)	Prototype Flexural Rigidity (kN-m^2)
Solid stainless steel	2.40	15x10^6
Hollow stainless steel	0.765	4.78 x10^6
Hollow stainless steel filled with plain cement concrete	0.95	6 x10^6

Table 2. Mass of the added plates

Superstructural loading configuration	Model mass, kg	Prototype mass, kg
only base plate	6.36	795x10^3
base plate + 3 added plates	11	1375 x10^3
base plate +7 added plates	20.80	2600 x10^3



(a) Large Earthquake (b) Medium Earthquake (c) Small Earthquake

Figure 1 Time Histories of Prototype Displacements Used as the Centrifuge Input Motion

In each centrifuge experiment, the model is subjected to nine earthquake events. These earthquakes were "fired" in three cycles, each comprising a small, medium and large earthquake that were triggered sequentially. The 'rest' periods between consecutive earthquakes were such that the excess pore pressures in the clay generated during each earthquake were fully dissipated.

RESULTS AND OBSERVATIONS

Figure 2 shows a schematic of the centrifuge model with pile-raft foundation, together with the accelerometer locations. The raft was supported on four model piles with inter-pile spacing of about 4.5 times the pile diameter. The raft was also partially embedded in the ground, resulting in some interaction between the raft and the soil.

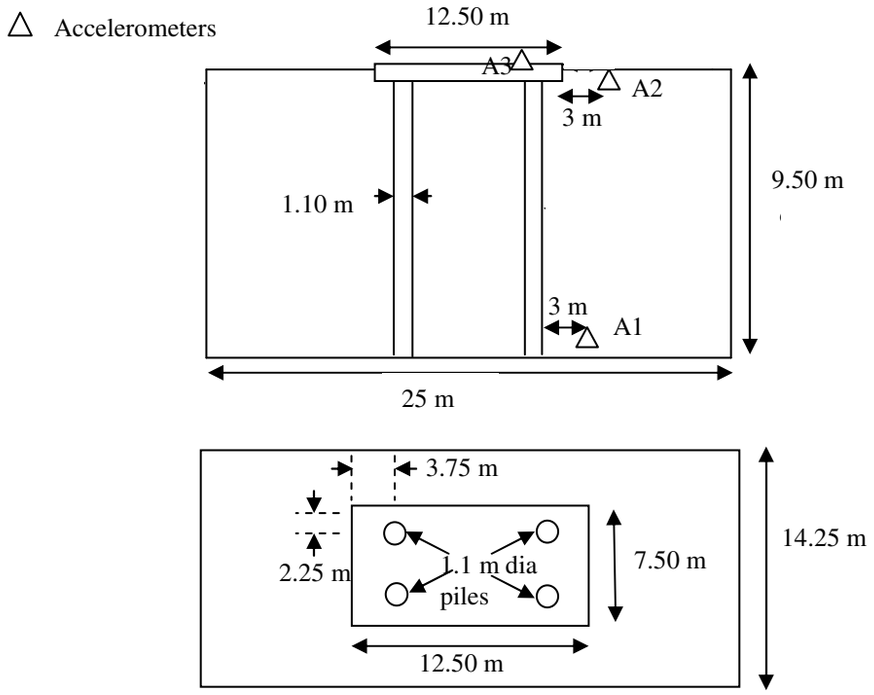


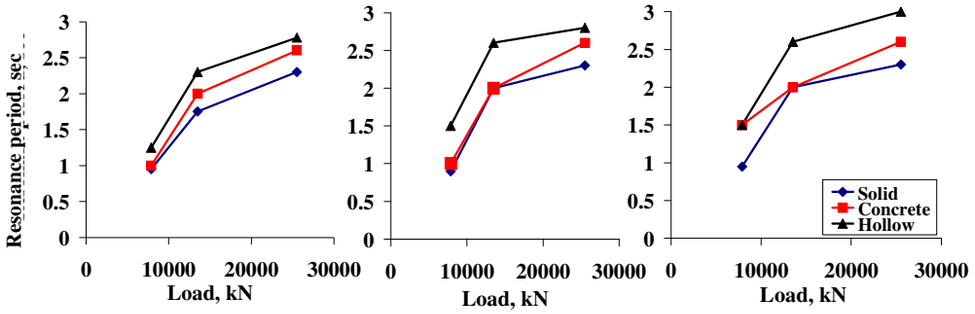
Figure 2 Lay-out and model for all tests with pile-raft structure

Figure 3 summarizes, for the three earthquakes of the first cycle, the resonance periods of the three pile-raft systems for different levels of inertial loadings. The results show that, for a given earthquake level and inertial loading from the superstructure, hollow piles have the largest resonance period, followed by the concrete-infilled piles, and finally, the solid steel pile. This is readily explained by the different flexural rigidities of the different pile types. In all cases, the back-calculated resonance periods from the measured A3 accelerations are much higher than the natural periods of the pile-raft system in the absence of any soil.

Figure 4 shows the resonance periods (obtained from the measured A2 accelerations) at the clay surface adjacent to the raft for different levels of superstructural loading. Comparison with Figure 3 shows that, in almost all cases, the resonance periods in the adjacent clay are higher than those calculated for the embedded pile-raft. This shows that the soil and the pile-raft do not move in tandem. It also indicates that the effect of the soil around the pile is predominantly one of imposing additional inertial loading on the pile-raft structure.

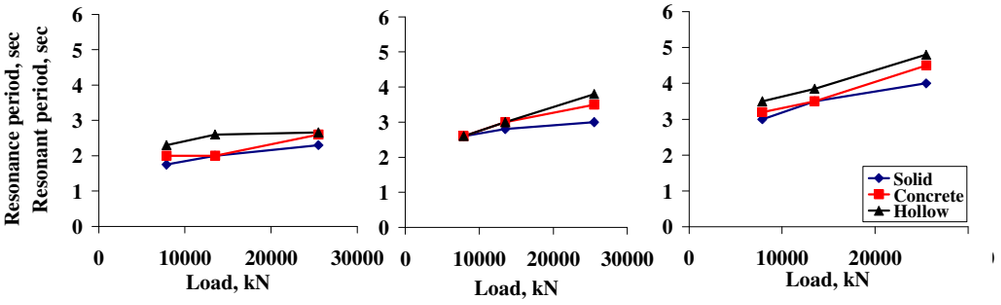
Figure 4 also indicates that the type of piles has some effect on the resonance response of the adjacent soil, although the influence is not as significant as that

reported for the pile-raft response. The ground resonance period is generally higher when the hollow piles are used, and is smaller when the solid steel piles are used. In addition, Figure 4 also shows that, for all the three pile types considered, the resonance period of the adjacent soil increases when the pile-raft is more heavily loaded, the effect being more dominant when the earthquake is large.



(a) Small earthquake (b) Medium earthquake (c) Large earthquake

Figure 3 Effect of different pile types on the resonance period of the pile-raft system, for different earthquake magnitudes and superstructural loadings (first cycle only).



(a) Small earthquake (b) Medium earthquake (c) Large earthquake

Figure 4 Resonance period at the clay surface adjacent to pile-raft, for different earthquake magnitudes and superstructural loadings (first cycle only).

The data of Figure 4 are re-plotted in Figure 5 to show how the resonance period at the clay surface adjacent to the raft varies with the peak ground acceleration (PGA), the pile type and the applied superstructural loadings on the raft. Figure 5 shows that, for all three applied load levels, the soil surface adjacent to the pile group shows a significant increase in the resonance period with PGA. In addition, there is also a consistent increase in resonance period between the first and the second earthquake cycle. This suggests a significant increase in the degree of strain softening and degradation in the clay near the pile-raft which could have resulted from the relative motion between pile, raft and soil. In contrast, no significant changes in resonance period were measured for the raft response between the first and second cycles, indicating that the response of the raft is likely to be dominated by the pile stiffness.

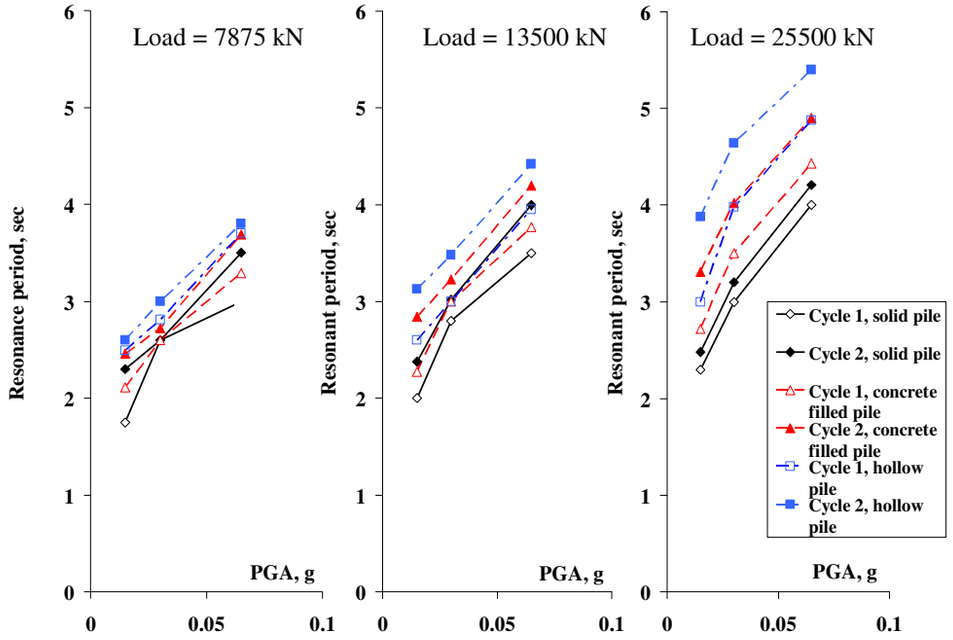


Figure 5 Resonance periods at the clay surface adjacent to the raft for different peak ground accelerations (PGA), pile types and superstructural loadings.

NUMERICAL SIMULATION

Numerical back-analyses of the centrifuge experiments were conducted using the finite element software ABAQUS, wherein the soil and pile domains were discretized into 8-noded brick elements, as shown on Figure 6. To simulate laminar box movements, linear multi-point constraints were applied to the two vertical faces normal to the earthquake motion, so that nodes at opposite ends of the domain and at the same depth move in unison with each other. In addition, vertical displacement restraints were applied at all four vertical faces while the bottom of the mesh is constrained against vertical movement.

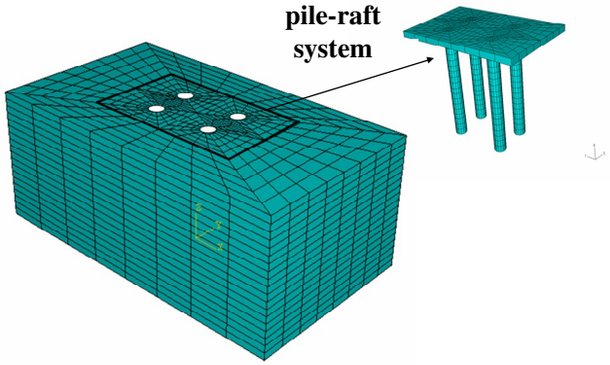


Figure 6 3-D ABAQUS model of clay-pile-raft system

Soil behavior was described by a simple hypoelastic model. In the hypoelastic model, the values of the modulus of elasticity and Poisson's ratio are assumed to be functions of the strain invariants. Hysteretic behavior, however, was not modeled. In this study, the variation of shear stiffness with shear strain was prescribed using Vucetic and Dobry's (1988) curve, as shown on Figure 7.

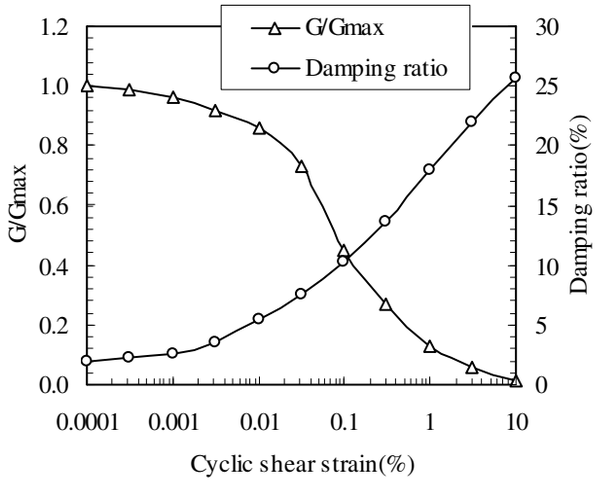


Figure 7 Shear modulus reduction and damping ratios with shear strain levels (after Vucetic & Dobry, 1988)

The geotechnical properties of kaolin clay used in the numerical analyses are summarized in Table 3. Based on resonance column tests on several types of Singapore soils, Chew et al. (1997) suggested that the small strain shear modulus G_{max} is approximately 500 times the undrained shear strength c_u, and c_u is about 0.22-0.25 times the effective overburden stress σ'_o. Hence, Gmax $\approx$ 100 σ'_o. In the numerical simulation, a constant G_{max} of 20 MPa was adopted, corresponding to the average c_u value over a depth of 9.5m (based on Chew et al.'s relationship).

Table 3. Geotechnical properties of kaolin clay

Properties	**Kaolin clay**
Bulk unit weight (kN/m3)	16
Water content	66%
Liquid limit	80%
Plastic limit	40%
Coefficient of permeability (m/s)	1.36x10-8
Initial void ratio	1.74
Angle of friction	25°

Comparison of Centrifuge and Finite Element Results

Figure 8 plots the measured and computed time histories at the clay surface adjacent to the pile raft. As can be seen, the computed response provides a generally good fit to the measured accelerations at both locations, and is able to capture the maximum values quite well.

Figure 9 shows the effect of PGA on the computed resonance period of the clay in the vicinity of the pile-raft, for different levels of applied loads on the raft. The computed trends are similar to those obtained from the 1st cycle earthquakes of the centrifuge experiments, as presented earlier on Figure 5.

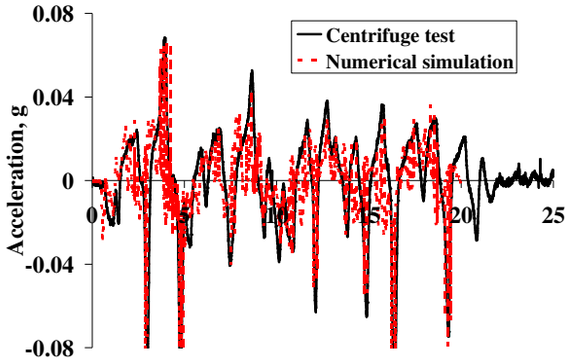


Figure 8 Comparison of typical time histories recorded in centrifuge tests with numerical simulations (at clay surface)

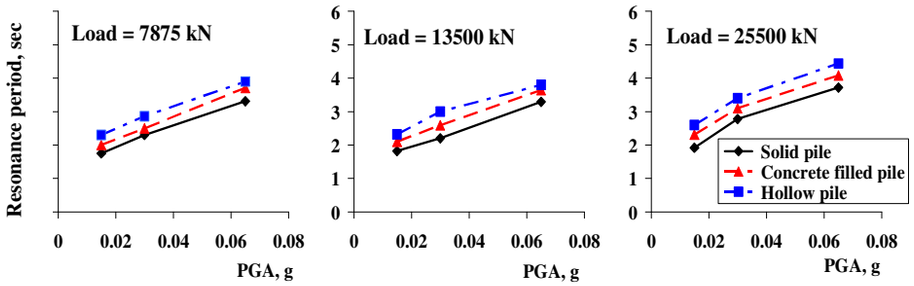


Figure 9 Resonance period from FE analyses vs PGA for different piles in kaolin clay under different load levels

Shear strains

To examine the postulate that the increase in resonance period and amplification response is related to the modulus reduction in clay under earthquake excitation, the results from the numerical analyses were processed to obtain the maximum shear strains, and from there, the effective shear modulus associated with these strains.

For each earthquake, the ABAQUS output was processed to obtain the maximum shear strain at selected successive nodes in the clay, located at 1 m spacing, from the

shorter edge of the raft. As shown on Figure 10a, the small earthquake generates maximum shear strains of about 14% in the immediate vicinity of the raft, which reduces to about 2% at a distance of about 5 m from the edge of the raft. The large earthquake, on the other hand, generates shear strains of about 22% or higher near to the raft, which reduces to about 7% at 5 m away. Figure 10b shows the corresponding shear moduli at different distances from the raft, based on the Vucetic and Dobry (1988) relationship shown on Figure 7. Near the raft, the large shear strains (>10%) that developed in the clay give rise to significant modulus reduction, resulting in G/Gmax ratios that are about 2% or less.

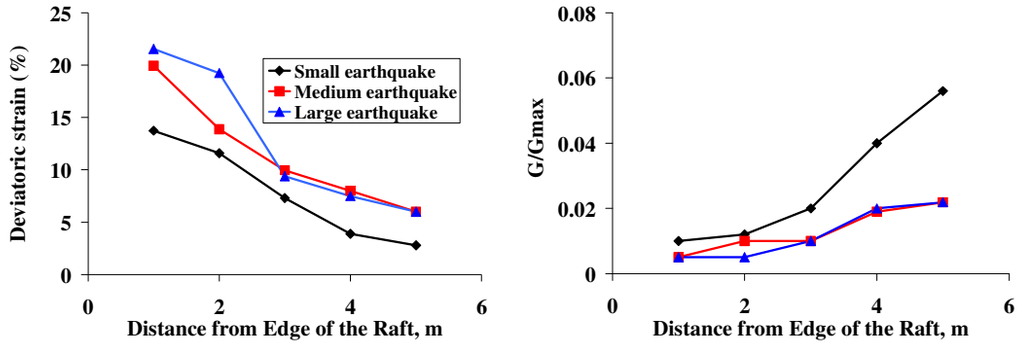


Figure 10. Variation of maximum deviatoric strain and G/G_{max} with increasing distance from the edge of the raft

CONCLUSIONS

The foregoing discussion shows that strain softening and stiffness degradation has a significant effect on clay-pile-raft interaction, as manifested in a lengthening of the resonance period of both the surface ground motion and pile-raft structure, compared to their respective uncoupled values. It is noted that the piles tested in this study are relatively short. The results of the study show that, in such a case, the effect of the surrounding soil is primarily one of imposing inertial loading onto the pile and raft. This leads to a lengthening of the resonance period of the pile-raft structure. Shear strains computed from ABAQUS were found to be as high as 15 to 20% for three different earthquakes, which is consistent with experimental observations. The engineering implication arising from this study is that, for the case of short piles in soft clays, ground surface motions may not be representative of pile-raft motion. This conclusion is only applicable to relatively short piles. More studies are needed to examine the behavior of longer and more flexible piles installed in soft clays subjected to earthquake excitation.

ACKNOWLEDGEMENTS

The centrifuge tests were carried out with the excellent support and assistance of the technical staff at the Centre for Soft Ground Engineering, NUS, which is acknowledged with much gratitude.

REFERENCES

Banerjee, S., Paul, D. K., Lee, F. H. (2006). "Dynamic response of bridge piles on soft ground using NUS geotechnical centrifuge", *ASCE Geotechnical Special Publication*, Vol. 150, 375-382.

Brennan, A. J., Thusyanthan, N. I. and Madabhushi, S. P. G. (2005), "Evaluation of shear modulus and damping in dynamic centrifuge tests". *Journal of Geotechnical and Geoenvironmental Engineering*, ASCE, Vol.131, No.12, 1488-1497.

Chew, C. H., Lee, F. H., Lim, S. C., Lim, S. P., Quek, S. T., Tan, T. S. (1997). "Review of floating slab rack system for North-East line (stage I I); Ground Vibration Study" *Report subjected to Land and Transport Authority*, Singapore.

Christina, J. Curras, Boulanger, Ross W., Kutter Bruce L., Wilson, D. (1999) "Seismic soil-pile-structure interaction experiments and analyses", *Journal of Geotechnical Engineering*, ASCE, Vol-125, No.9, 345-369.

Idriss, I.M., Dobry, R., Doyle, E.H., Singh, R.D. (1978). "Nonlinear behaviour of soft clays during cyclic loading conditions". *Journal of the Geotechnical Engineering Division*, ASCE, Vol. 104, 1427–1447.

Puzrin, A., Frydman, S., Talesnick, M., 1995. "Normalising degrading behaviour of soft clay under cyclic simple shear loading", *Journal of the Geotechnical Engineering Division*, ASCE , Vol. 121, No.12, 836–843.

Rao, S. N. and Panda, A.P. (1999). "Non-linear analysis of undrained cyclic strength of soft marine clay", *Ocean Engineering*, Vol. 26, 241–253.

Snyder, J. L. (2004). "Full scale test lateral load tests of a 3x5 pile group in soft clays and silts", *MSc Thesis*, Brigham Young University.

Vucetic, M., Dobry, R. (1988). "Degradation of marine clays under cyclic loading". *Journal of the Geotechnical Engineering Division*, ASCE, Vol. 114, No.2, 133–149.

Wilson, D. (1995). "Dynamic centrifuge tests of pile supported structures in liquefiable sand," *PhD thesis*, Univ. of California, Davis.

Static and Dynamic Lateral Load Tests on a Pile Cap with Partial Gravel Backfill

Kyle M Rollins[1], Ph.D., M. ASCE and Ku Hyun Kwon[2], and Travis M. Gerber[3], Ph.D, PE, M. ASCE

[1]Prof., Civ. & Env. Engrg. Dept., Brigham Young Univ. 368 CB, Provo, UT 84602; rollinsk@byu.edu.
[2]Staff Engr., GeoEngineers, Inc., 523E 2nd Ave, Spokane, WA 99202; kkwon@geoengineers.com
[3]Asst. Prof., Civ. & Env. Engrg. Dept., Brigham Young University, 368 CB, Provo, UT 84602, tgerber@byu.edu

ABSTRACT: Lateral pile cap tests were performed on a pile cap with two backfills to evaluate its static and dynamic behavior. In one case the backfill was loose silty sand while in the other case, a 0.91-m wide zone of gravel was compacted between the pile cap and the loose silty sand. The relatively thin dense gravel zone increased the lateral resistance by 75 to 150% relative to the loose silty sand backfill. The dense gravel zone also increase lateral resistance to 59% of the resistance that would be provided by a backfill entirely composed of dense gravel. The dynamic stiffness for the pile cap with the gravel zone decreased about 10% after 15 cycles of loading, while the damping ratio remained relatively constant with cycling. Stiffness increased by about 10% at higher deflections, while the damping ratio decreased from an initial value 0.30 to around 0.26 at higher deflections.

INTRODUCTION

Numerical analyses conducted by several investigators indicate that the passive force-deflection relationship for bridge abutments plays a significant role in the seismic response of bridges. For example, in analyses of a bridge using a 3D finite element model, Faraji et al. (2001) found that the change in stiffness associated with switching from a loose to dense abutment backfill produced a two-fold increase in axial load and bending moment in the bridge deck. Analyses conducted by El-Gamal and Siddharthan et al. (1998) as well as Shamshabadi et al. (2007) also indicate significant influences of abutment stiffness on bridge response. Significant lateral resistance could also be provided by the passive pressure on pile caps. Unfortunately, only a few large-scale tests have been performed to define these passive force-deflection relationships for various soil types (Rollins and Sparks 2002; Mokwa and Duncan 2001; Rollins and Cole 2006). In addition, these large-scale tests have only

been performed under static loading conditions so the dynamic behavior has not been well-defined. In the absence of dynamic test data, engineers have often used equivalent static analysis and neglected effects of cyclic loading or increased resistance provided by damping.

To better quantify the static and dynamic passive force-deflection behavior of cohesionless soils, large-scale lateral load tests were performed on a pile cap with and without cohesionless backfill against one side. Load was applied incrementally using a deflection control approach to define the static load-deflection curve. In addition, at each deflection increment 15 cycles of loading were applied dynamically to define dynamic stiffness and damping values. In one test the backfill consisted of loose silty sand, while in another test the backfill consisted of a dense gravel zone 0.91-m wide immediately adjacent to the pile cap with the same loose silty sand beyond it. This geometry was intended to simulate the compaction often required of backfill near a cap and the relatively loose natural material beyond the compacted zone.

TEST LAYOUT

Plan and profile views of the overall layout for the passive load tests are shown in Fig. 1. The main test components were a pile cap against which backfill was compacted and two hydraulic actuators which were used to apply both the static and cyclic loads to the test pile cap as shown in Fig. 1. The actuators reacted against an even larger pile cap. The same 5.18m × 3.05m × 1.12m concrete pile cap constructed previously by Rollins et al (2003) and used by Rollins and Cole (2006) was also used for this field test program. The pile cap was constructed of reinforced concrete with a compressive strength of about 5000 psi and the reinforcing mats consisted of No. 25 bars (soft metric) at 150 mm spacing in the long direction and No. 29 bars at 300 mm spacing in the short direction both top and bottom. The pile cap was supported by twelve 324-mm (12.75 in) OD, 9.5-mm (3/8 in) wall thickness steel pipe piles which were filled with concrete. The piles were connected to the pile cap by a reinforcing cage which consisted of six No. 25 bars with No.13 hoops spaced at 0.3 m on centers. The cage extended to a depth of 1.7 m into the piles and 1.06 m above the piles to tie into the upper reinforcing mat in the pile cap. This connection produced a "fixed-head" condition although some pile head rotation still occurred. The piles were driven closed-ended approximately 12.2 m (40 ft) into the soil profile in a 4 × 3 configuration with 1.42 m and 1.06 m (4.4 and 3.3 pile diameter) center-to-center spacing in the long and short direction under the pile cap. Adjacent to the pile cap was a reaction foundation that was supported by nine steel pipe piles driven open-ended in a 3 × 3 configuration to a depth of about 12.2 m (40 ft). The steel pipe piles had an outside diameter of 610 mm (24 in) and a wall thickness of 12.7 mm (1/2 in).

Lateral load was applied by two 2.7 MN (600 kip) MTS hydraulic load actuators positioned between the test and reaction pile caps. In order to apply the cyclic lateral load, the end of each actuator was centered vertically on the faces of the pile caps. Sixteen high strength threaded bars 50 mm in diameter (four bars for each end of actuators) were used to connect the actuators to the two pile caps.

Applied load was measured by the actuators while pile cap deflection was measured using four string potentiometers located near the corners of the back face of the pile cap which were attached to an independent reference frame. Deflection measurements at the top and bottom of the cap were used to determine pile cap rotation. Data was recorded using a high-speed data acquisition system at a rate of 200 Hz.

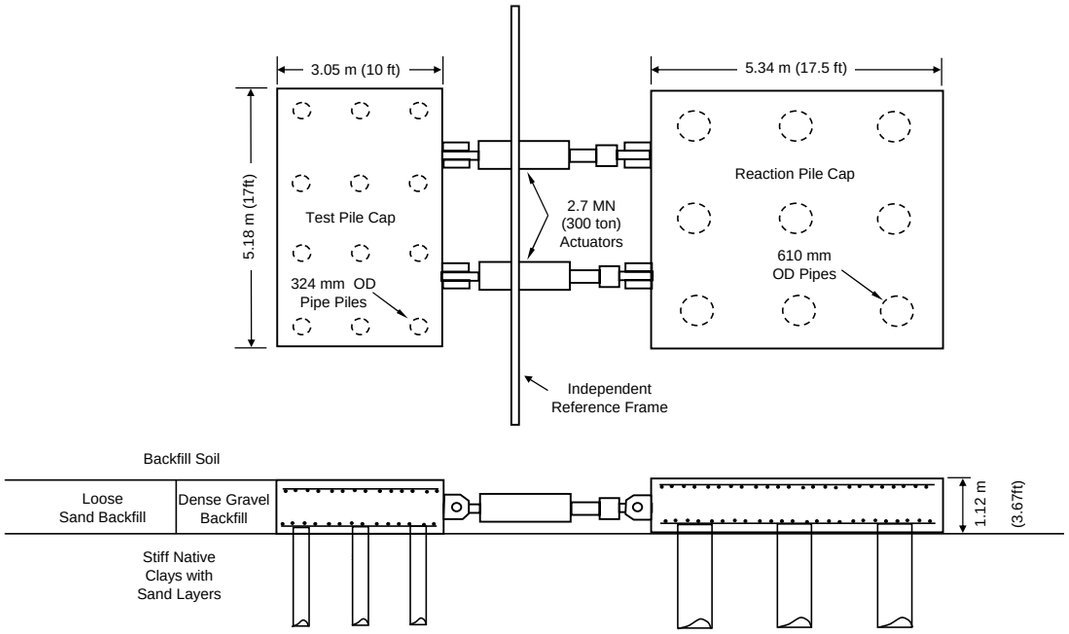


Fig. 1 Plan and profile views of the test layout for the large-scale passive force tests.

Testing Procedure and Testing Sequence

The lateral load testing was performed using a deflection control approach. The actuators applied equal load to each side of the pile cap until a specified target deflection was obtained. This deflection was then held for a few seconds while manual readings were obtained. At each target deflection, 15 deflection-controlled bi-directional cycles were applied with a frequency of 1.50 Hz and an amplitude of about ± 2 mm. At the completion of the cyclic loading, the actuators increased the load until the next target deflection was achieved and the same procedure was repeated. Deflection increments were typically 6.4 mm (0.25 in) and the maximum deflection was about 64 mm (2.5 in).

Initially, a lateral load test was performed without any backfill in place to provide a "baseline" force-deflection relationship for the pile cap itself. Because the pile cap had been loaded a number of times previously (Rollins and Cole, 2006), the baseline force-deflection curve was relatively linear. Subsequently, a lateral load test was performed with the backfill consisting of loose silty sand. The sand backfill was

placed to a height of 1.12 m (3.67 ft) on the front side of the pile cap only and extended a distance of 4.9 m (16 ft) in front of the cap. Finally, a lateral load test was performed after compacting a dense sandy gravel zone from the face of the cap to a distance of 0.91 m (3 ft) in front of the cap, but leaving the loose silty sand in place from 0.91 m to a distance of 4.9 m (16 ft) in front of the cap as shown in Fig. 1. This silty sand zone represents the loose native soil which might exist beyond the compacted granular backfill adjacent to pile cap.

Subsurface and Backfill Characteristics

The silty sand material classifies as SM and A-4 according to the Unified Soil Classification and the AASHTO Classification Systems, respectively. The maximum particle size of the fill was 12.5mm with approximately 90% passing the No. 40 sieve and 45% non-plastic fines. The coefficient of uniformity (C_u) and curvature (C_c) were 14.8 and 2.8, respectively. The specific gravity was 2.68. The modified Proctor unit weight was 17.75 kN/m^3. The fine gravel material classifies as silty, clayey gravel with sand (GC-GM), and A-1-b according to the USCS and AASHTO methods, respectively. The fill had a maximum particle size of 19 mm. C_u and C_c were 454 and 1.2, respectively. The plasticity index (PI) and liquid limit (LL) were 6% and 23%, respectively. The specific gravity was 2.70. The modified Proctor unit weight was 21.68 kN/m^3. The dense sandy gravel was compacted in 100 mm-thick lifts using hand-operated compaction equipment to meet Utah DOT backfill specifications which require a minimum unit weight greater than 92% of the modified Proctor maximum unit weight (ASTM D 1577) with an average unit weight greater than 96% of the Proctor maximum unit weight. Nuclear density tests were performed on each layer of compacted gravel fill. All tests indicated a relative compaction (R_c) greater than 92% and the average relative compaction was 97% which is greater than the required average. This average dry unit weight corresponds to a relative density of about 85% according to correlations developed by Lee and Singh (1971). The loose silty sand was also compacted in 100 mm-thick lifts but with much lower energy. The minimum relative compaction was 84% with an average of 88% of the modified Proctor maximum. This corresponds to a relative density of 40% based on correlations developed by Lee and Singh (1971). In-situ direct shear tests performed on the dense gravel and loose silty sand backfills indicate that the friction angles for these two materials were 42.6º and 27.7º, respectively. Table 1 provides a summary of grain size distribution and other soil properties for the two backfills.

Table 1. Summary of Properties of Backfill Materials

				Modified Proctor		As Compacted				
Backfill Type	Gravel (%)	Sand (%)	Fines (%)	w_{opt} (%)	$(\gamma_d)_{max}$ (kN/m^3)	w (%)	γ_d (kN/m^3)	R_c (%)	D_r (%)	ϕ (º)
Silty sand	2.4	52.9	44.7	11	17.75	11	15.69	88	40	27.7
Gravel	49.7	30.5	19.9	7	21.68	6	20.9	97	85	42.6

TEST RESULTS

Static Load Tests

The peak passive force vs. deflection curves are plotted in Fig. 2 for the pile cap tests involving both the loose silty sand backfill and the 0.91-m wide dense gravel zone between the pile cap and the loose silty sand backfill. Even though the gravel zone is relatively narrow in comparison to the expected length of the shear zone (approximately 2.8 m), the placement of the dense gravel zone had a pronounced effect on the mobilized passive force. With the gravel zone in place, the passive force was 75 to 150% higher than for the silty sand backfill at any given deflection.

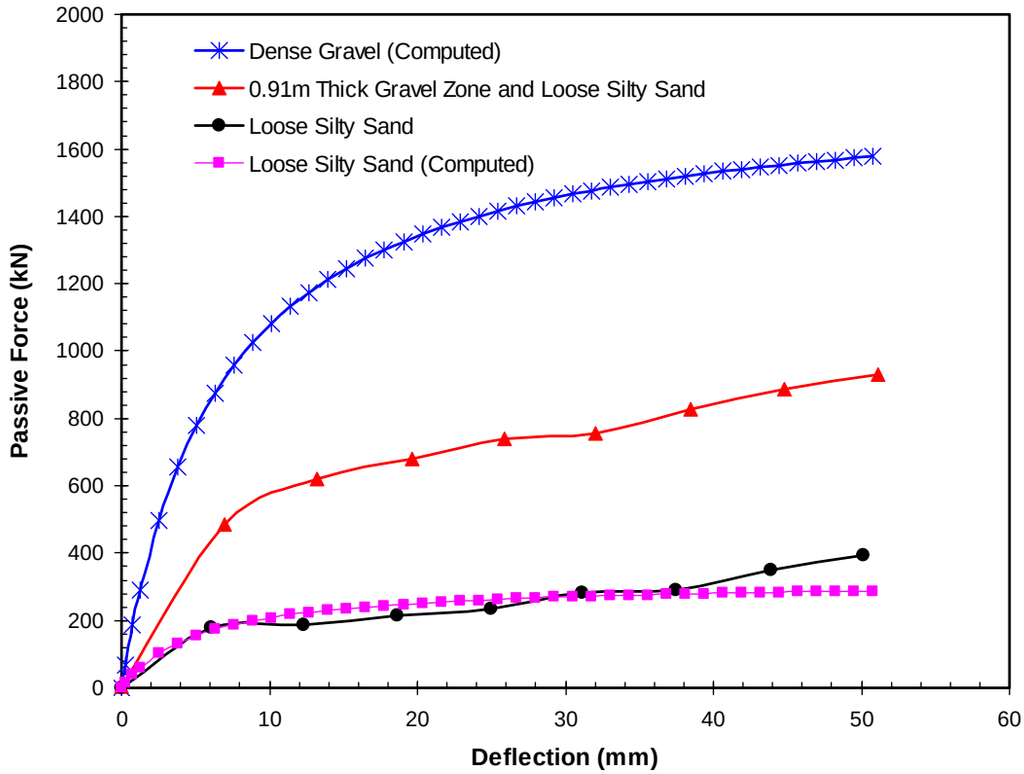


Fig. 2 Measured passive force vs. deflection curves for pile cap with loose silty sand backfill and a 0.91-m wide dense gravel zone with silty sand backfill together with computed curves for backfills composed entirely of loose silty sand and dense gravel.

Using the spreadsheet program PYCAP developed by Duncan and Mokwa (2001), passive force vs. deflection curves were also computed for the pile cap with backfills consisting entirely of loose silty sand and dense gravel. In PYCAP, the ultimate passive force is computed using the log-spiral method and the force vs. deflection curve is based on a hyperbolic relationship that is dependent on the initial elastic modulus of the backfill soil. The parameters used in making these computations are

presented in Table 2. The computed passive force vs. deflection curves are also plotted in Fig. 2 for comparison. The computed curve for the silty sand backfill compares very well with the measured curve. The computed curve for the dense gravel backfill is clearly higher than the measured curves at a given deflection. Nevertheless, placement of the 0.91 m wide gravel zone produced 59% of the resistance provided by the backfill consisting entirely of dense gravel**.** This result clearly illustrates the value of placing a thin, but dense, gravel layer adjacent to a pile cap or an abutment wall when increased lateral resistance is desired, but the cost of using large quantities of select backfill material must be minimized.

Table 2. Summary of backfill soil properties used in PYCAP analysis.

Backfill	Moist Unit Weight (kN/m^3)	Friction Angle ϕ (^{o})	Wall Friction Angle δ (^{o})	Initial Soil Modulus E_i (kN/m^2)	3D Adjustment Factor (R_d)	Deflection at Failure Δ_{max}/H
Silty Sand	17.3	27.7	20.8	9600	1.18	0.05
Gravel	22.15	42.6	32	48,900	1.46	0.05

Dynamic Load Tests

Fig. 3 provides the peak static load-deflection curve for the test with the 0.91-m wide gravel zone. Also shown are the load-deflection curves for the 1st and 15th cycles at each deflection increment. As discussed previously, after the peak static resistance was reached at each deflection increment the deflection was held constant for about one minute after which 15 cycles were applied. During this time interval, creep relaxation in the soil led to a reduction in lateral resistance which ranged from 5 and 18%. As a result, the cyclic load-deflection curves are generally associated with re-loading rather than virgin loading. Therefore, the peak-to-peak secant stiffness of the load-deflection loops is stiffer than the stiffness of the static curve.

A comparison of the 1st and 15th cycle load-deflection loops in Fig. 3 indicates that there is some decrease in the stiffness with cycling; however, the area within the loop appears to remain about the same with cycling. To investigate these observations further, the stiffness and damping ratio were computed for each cycle of loading at each deflection increment. The stiffness, k, was computed by the equation

$$k = \Delta F / \Delta u \quad (1)$$

where ΔF is the change in load and Δu is the change in deflection for the peak points on each cycle. The damping ratio, β, was computed using the equation

$$\beta = \frac{A_{loop}}{2\pi k u^2} \quad (2)$$

where A_{loop} is the area within the load-deflection loop and u is the single amplitude deflection value for a given cycle.

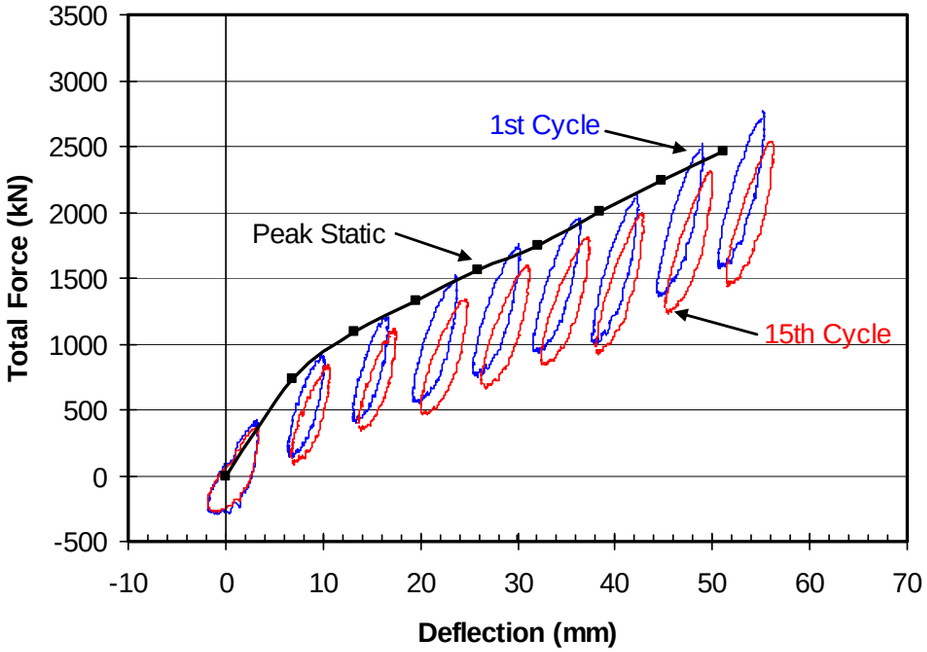


Fig. 3 Plots of peak static load-deflection along with 1st and 15th load cycles at each deflection increment for tests involving 0.91 m wide gravel zone.

Plots of the stiffness and damping ratio as a function of the number of cycles at each deflection increment are provided in Fig. 4. Apart from the cyclic loading at zero deflection, the stiffness values generally plot within a fairly narrow range from about 180 to 240 kN/mm. After 15 cycles, the stiffness is only 8 to 15% lower than the stiffness for the first cycle. In contrast to the static loading where the stiffness tends to decrease with increasing deflection (or load) level, the dynamic stiffness is highest at the highest deflections although the increase is only about 10%. As shown in Fig. 4, the dynamic stiffness in almost all cases is associated with reload conditions rather than virgin loading. The modest increase in dynamic stiffness is likely associated with strain hardening in the loose sand backfill as it becomes progressively denser owing to contraction during shearing as the deflection level increases.

Apart from the cyclic loading at zero deflection, the computed damping ratios typically plot within a narrow range from 0.26 to 0.30. There is no consistent trend in the damping ratio with the number of cycles and for practical purposes the damping ratio remains essentially constant with cycling. The damping ratio from the cyclic load-deflection loops tends to decrease somewhat as the initial deflection level (or load level) increases. For example, the damping ratio was typically about 0.30 at low deflection levels and decreased to about 0.26 at the higher deflection levels.

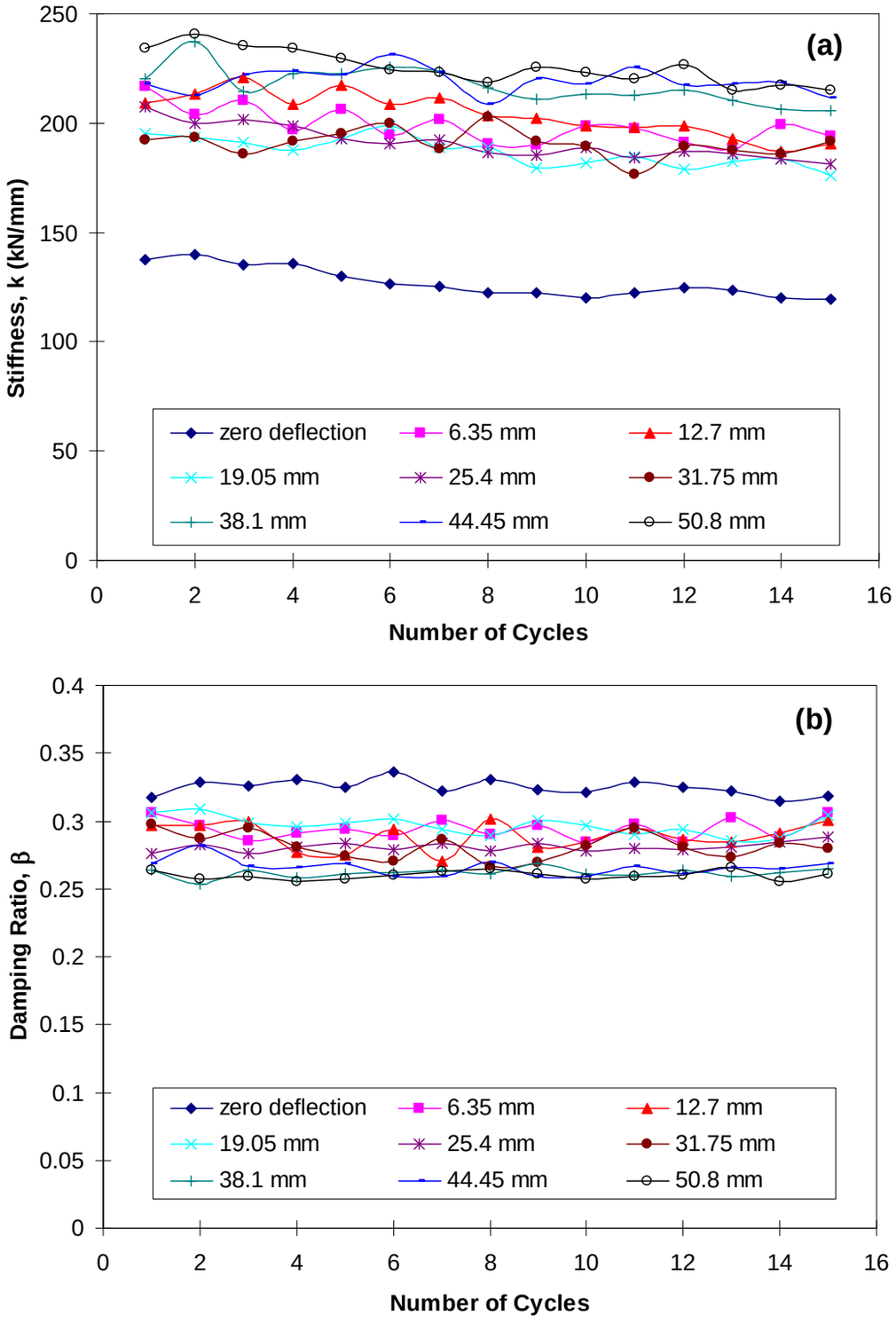


Fig. 4. Plots of (a) dynamic stiffness and (b) damping ratio as a function of number of cycles at each initial deflection increment for the pile cap with a 0.91-m wide dense gravel zone.

CONCLUSIONS

Based on the results of the field testing and analysis of the test data the following conclusions can be drawn.

1. Placement of a relatively thin, but dense, gravel backfill zone between a pile cap or abutment wall and a loose silty sand backfill can significantly increase the static passive force provided by the backfill. Specifically, in these tests with a 5.2 m long, 1.12 m high wall, a 0.91-m wide gravel zone increased the passive force by about 75 to 150% relative to the loose silty sand backfill alone.

2. A thin dense gravel zone in front of loose sand can also produce a significant percentage of the lateral passive resistance that would be obtained if the entire backfill consisted of dense gravel.

3. The dynamic stiffness of the backfill with compacted gravel zones showed a relatively small decrease (approx. 8 to 15 %) after 15 cycles of loading at a given initial deflection level, whereas the damping ratio remained relatively constant after 15 load cycles.

4. Although the static stiffness of the backfill soils with dense gravel zones decreased as the deflection level (or load level increased), the average dynamic stiffness (primarily from reloading) tended to experience a slight increase (approx. 10 %) at higher initial deflection levels likely due to strain hardening in the loose backfill.

5. The average damping ratio from the cyclic load-deflection loops stayed within a fairly narrow range (0.26 to 0.30) but the damping ratio tended to decrease somewhat as the initial deflection level (or load level) increased. For example, the damping ratio was typically about 0.30 at low deflection levels and decreased to about 0.26 at the higher deflection levels.

ACKNOWLEDGMENTS

This research investigation was supported by the National Science Foundation under Award Number CMS-0421312, the George E. Brown, Jr. Network for Earthquake Engineering Simulation (NEES) which operates under NSF Award Number CMS-0402490, and the Departments of Transportation for the states of California, New York, Montana, Oregon, and Utah through an FHWA pooled-fund arrangement. This support is greatly appreciated. The Utah Dept. of Trans. served as the lead agency with Daniel Hsiao as the Project Manager. Nevertheless, the conclusions and recommendations expressed in this paper do not necessarily reflect the views of the sponsors.

REFERENCES

Duncan, J.M. and Mokwa, R. L. (2001). "Passive earth pressures: theories and tests." *J. Geotechnical and Geoenv. Engrg*., ASCE, Vol. 127 (3): 248-257.

El-Gamal, M. and Siddharthan, R.V. (1998). "Stiffness of Abutments of Piles in Seismic Bridge Analyses." *Soils and Foundations*, JGS, Vol. 38 (1): 77-87.

Faraji, S. Ting, J.M., Crovo, D.S., and Ernst, H. (2001). "Nonlinear analysis of integral bridges; finite-element model." *J. Geotechnical & Geoenviron. Engrg*., ASCE, Vol. 127 (5): 454-461.

Lee, K.W. and Singh, A. (1971). "Relative Density and Relative Compaction." *J. Soil Mech. And Found. Div*., ASCE, Vo.. 84 (SM2) 1654-1 to 1654-35.

Mokwa, R. L. and, Duncan, J. M., (2001). "Experimental evaluation of lateral-load resistance of pile caps." *J. Geotechnical and Geoenv. Engrg.*, ASCE Vol. 127, (2): 185-192.

Rollins, K. M. and Cole, R. T., (2006). "Cyclic Lateral Load Behavior of a Pile Cap and Backfill" *J. Geotechnical & Geoenv. Engrg.*, ASCE Vol. 132 (9): 1143-1153.

Rollins, K.M. and Sparks, A.E. (2002) "Lateral Load Capacity of a Full-Scale Fixed-Head Pile Group." *J. Geotechnical and Geoenv, Engrg.,* ASCE, Vol. 128 (9): 711-723.

Shamshabadi, A., Rollins, K.M., Kapaskur, M. (2007). "Nonlinear Soil-Abutment-Bridge Structure Interaction for Seismic Performance-Based Design." *J Geotechnical and Geoenv.*., ASCE, Vol. 133 (6): 707-720.

Undrained Tip Response of Drilled Shaft in Cohesionless Soils

Sherif Elfass[1] A.M. ASCE and Gary Norris[2], M. ASCE

[1]Research Assistant Professor, Department of Civil and Environmental Engineering, University of Nevada, Reno, Reno, NV 89557, elfass@unr.edu
[2]Professor, Department of Civil and Environmental Engineering, University of Nevada, Reno, Reno, NV 89557, norris@unr.edu

ABSTRACT: A method for assessment of the undrained drilled shaft tip load – tip displacement response in sands under earthquake or impact loading has not been available heretofore. Statnamic test results on two WSDOT drilled shaft with the shaft tips in sand below the water table have yielded field evidence with which to compare/calibrate such assessment. A method for tip load – tip displacement evaluation based on the assessed undrained stress-strain-strength of a sand as established from drained tests results and formulation is presented here. It is used to provide assessed response to compare with field recorded behavior

INTRODUCTION

Axial capacity of drilled shafts consists of side shear and tip resistances. However, capacities of these resistances develop at considerably different levels of displacement. O'Neill and Reese (1999) provide normalized load-displacement curves for such resistances for cohesionless and cohesive soils. The curves for cohesive soils represent undrained response, while those for cohesionless soils reflect drained response. Many DOT's will ignore drained tip resistance in sands because of the considerable displacement required to mobilize it. However, under seismic or impact loading the undrained tip and side shear responses of cohesionless soils are also of interest. (Furthermore, undrained tip resistance in sand will likely develop at much less displacement than drained tip resistance.) This paper provides a method of analysis (MOA) of undrained tip load-tip displacement response, unavailable previously. Recent Statnamic tests conducted on two drilled shafts sponsored by the Washington Department of Transportation (WSDOT) were used to validate the proposed MOA.

UNDRAINED TIP LOAD - TIP SETTLEMENT MODEL

As is well accepted, the net ultimate point resistance of a pile or shaft in saturated clay is 9c, where c is the undisturbed undrained shear strength of the clay at and below the pile or shaft tip. The net ultimate pressure can be represented in a Mohr diagram as the distance between the bottom end of the lowermost failure circle (at the apparent effective overburden pressure, P_o, in the soil at the shaft tip) and the upper end of the last 4.5 circles representing different zones of stress in the transition between P_o and the pressure immediately below the shaft tip. At undrained point or tip failure, the circles are of a radius equal to the undrained clay strength. Since the strength is the same in all zones (same radius circle) the deviatoric stress-axial strain curves should likewise be equal. (All apparent effective/total stress circles have in common the same effective stress circle.) Therefore, one is able to imagine at any prefailure state the various zones experience the same major principal strain, ε, corresponding to the same stress level, c_m/c (or σ_{dm}/σ_{df}) as shown in Fig. 1. Such stress level corresponds to a common point on the

undrained stress-strain curve as obtained in an unconsolidated undrained or UU test on an undisturbed sample taken from a distance of half the pile/shaft diameter (B/2) below the tip.

The immediate settlement of a foundation in soil under loading conditions can be assessed as the integration of the vertical strain (= ε_1) over the depth of soil below the centerline of that foundation. If

$$\varepsilon_1 = \frac{\Delta\sigma_1}{E} - \frac{\nu\Delta\sigma_2}{E} - \frac{\nu\Delta\sigma_3}{E} \qquad (1)$$

where $\Delta\sigma_2 = \Delta\sigma_3$ for a square or round foundation, and where ν is taken to be equal to 0.5 corresponding to undrained behavior of sand, the equation above reduces to

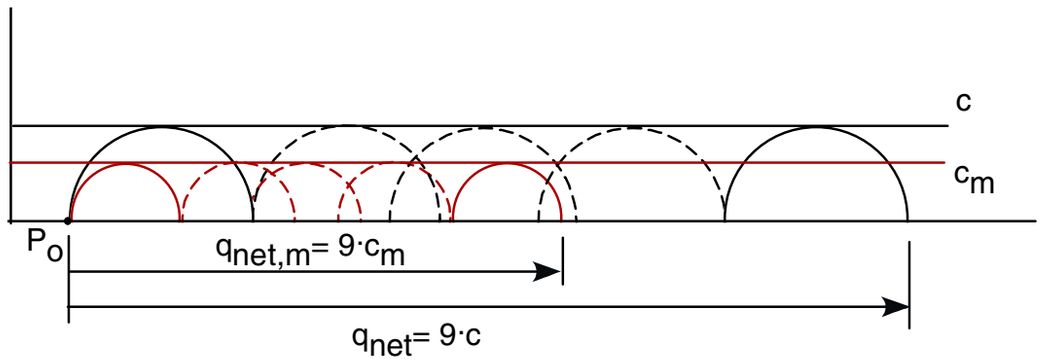


FIG. 1. Undrained mobilized and failure stress states in the different zones at pile tip

$$\varepsilon_1 = \frac{\Delta\sigma_1 - \Delta\sigma_3}{E} = \frac{\sigma_{dm}}{E} \qquad (2)$$

where σ_{dm} is the mobilized deviatoric stress in the zone immediately below pile/shaft tip. Of course, $(\Delta\sigma_1 - \Delta\sigma_3)$ and ε_1 vary in a triangular fashion as shown in Fig. 2. This is Schmertmann's (Schmertmann, et al. (1978) 2B triangle for a square or round foundation of width/diameter B. Ignoring Schmertmann's nonzero value of ε_1 at the base of the foundation, the area of this triangle is equal to ε_1 evaluated at a depth ½B multiplied by the foundation width B. Therefore, if one is able to evaluate ε_1 at a depth ½B below the base of the foundation due to the imposed net pressure $q_{net,m}$, the resulting settlement z_p is

$$z_p = \varepsilon_1 B \qquad (3)$$

Therefore the undrained stress-strain curve can be converted to the load-settlement curve by multiplying the vertical axis ($\sigma_{dm} = 2c_m$) by 4.5 times the cross sectional area (A_p) of the pile/shaft ($Q_{pm} = 9c_m$ or $4.5\sigma_{dm} \cdot A_p$) and the horizontal axis of ε_1 by B ($z_p = \varepsilon_1 B$). While the above discussion was stated for the situation of clay below the pile or shaft tip, it would also apply to the undrained stress-strain curve obtained from a consolidated undrained (CU) test on a sand representing undrained loading of a pile/shaft tip in sand below the water table. The consolidation pressure (σ_3') to which a reconstituted sample of sand would be subjected would be $P_o = \sigma_{vo}$'. Alternatively, the same result might be obtained if the undrained curve is established from drained stress-strain characterization.

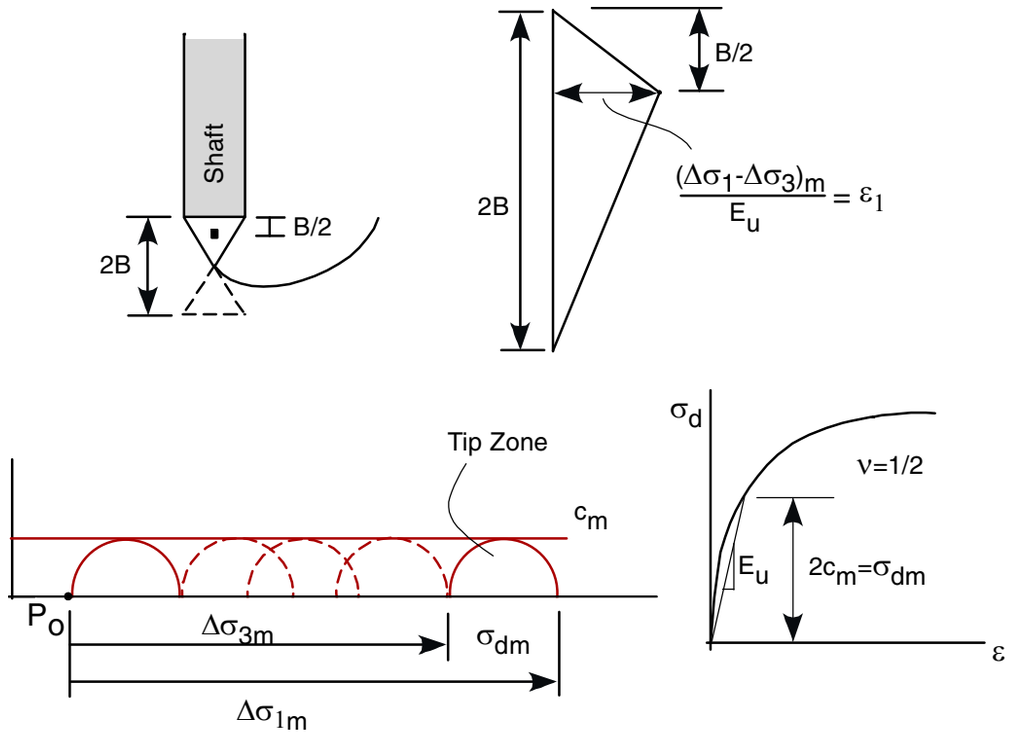


FIG. 2. Strain profile and the associated mobilized stresses immediately below pile tip

UNDRAINED STRESS-STRAIN CHARACTERIZATION OF COHESIONLESS SOIL

The undrained stress-strain response for cohesionless soil is needed for the abovementioned undrained MOA for sand. Such evaluation can be achieved based on the method outlined by Norris et al. (1997) in which isotropically consolidated rebounded drained deviatoric stress-axial strain (σ_d-ε_1) curves and their associated volume change curves ($\varepsilon_{v,shear}$-ε_1) are used in conjunction with the isotropic drained consolidation and rebound response ($\varepsilon_{v,iso}$-σ_3') to construct the undrained response (the undrained deviatoric stress-axial strain, σ_d-ε_1, curve and the undrained effective stress path, $q = \sigma_d/2$ versus $p' = \sigma_3' + \sigma_d/2$).

The undrained response derives from the requirement that volumetric strain in drained isotropic expansion, $\varepsilon_{v,iso}$, be equal and opposite to the volumetric strain in drained shear, $\varepsilon_{v,shear}$, such that the resultant undrained volumetric strain, $\varepsilon_v = \varepsilon_{v,iso} + \varepsilon_{v,shear}$, due to competing effects (effective confining pressure change, $\Delta\sigma_3$', and deviatoric stress, σ_d) equals zero. Ashour and Norris (1999) provide the formulation for the drained stress-strain (σ_d-ε_1) curve, but instead of that paper's empirical volume change formulation for drained shear ($\varepsilon_{v,shear}$-ε_1), the paper by Norris et al. (2008) yields a more fundamental relationship, namely that the drained stress-strain (σ_d-ε_1) and the volume change ($\varepsilon_{v,shear}$-ε_1) responses are directly connected via the phase transformation friction angle, ϕ_{PT}. ϕ_{PT} is the mobilized effective stress friction angle, ϕ_m, where $\varepsilon_{v,shear}$ reaches a maximum ($d\varepsilon_v/d\varepsilon_1 = 0$) before transitioning from compressive to dilative behavior.

The isotropic consolidation and rebound response from the initial effective confining pressure (equal to the vertical effective overburden pressure at the depth of the shaft tip), σ_{3o}' (= σ_{vo}'), is

expressed here in the typical fashion of a consolidation curve, $\varepsilon_{v,iso} = C_{r/c} \ln (\sigma_3'/\sigma_{vo}')$ with the appropriate value for C_c or C_r depending whether σ_3' is greater or smaller than σ_{vo}'.

The proposed MOA requires the input of the peak drained and phase transformation friction angles, ϕ and ϕ_{PT}, the drained strain at 50% stress level (SL), $\varepsilon_{50,ref}$ and its associated confining pressure, $\sigma_{3,ref}'$, slopes C_c and C_r above and below σ_{3o}' (= σ_{vo}'), the effective overburden pressure at pile tip (σ_{vo}') and the shaft diameter (B).

The peak friction angle, ϕ, can be estimated based on the SPT blow count; $\varepsilon_{50@850\ psf}$ can be estimated based on void ratio, e, and uniformity coefficient, C_u (Ashour et al. 1998); and the phase transformation angle can be estimated (for poorly graded clean silica sand) as $\phi_{PT}(^o)$ = 0.60n (where n is the porosity in percent). Void ratio and porosity are related and might also be evaluated based on the water content (w) of a split spoon sample from below the water table (e = wG_s and n = e/1+e). At present, C_r in rebound and reconsolidation is taken by trial and error to cause a close match to the drained effective stress-isotropic volume change ($\varepsilon_{v,iso}$-σ_3') response, as given for example by Ashour and Norris (1999). The value of C_c in consolidation beyond σ_3'= σ_{vo}' has yet to be a factor for undrained tip movement, z_p, that has been observed.

A spreadsheet has been set up with successive columns that yield the undrained stress-strain curve of the cohesionless soil at the shaft tip and according to the abovementioned MOA. The end result is the assessment of Q_p versus z_p as previously described.

COMPARISON WITH WSDOT TESTS

Two 6-ft diameter, ≈ 50-ft long, WSDOT shafts, ≈ 80-ft apart, in a cohesionless soil profile were loaded to 2200 tons using the Statnamic load test method. While the response in such tests is dynamic and undrained, static undrained test results, including tip load-tip displacement response, were provided by the test organization, AFT, after removing rate effects.

Subsurface soil exploration information was provided by WSDOT for the nearby Higgins Slough Bridge at the intersection of SR20 and SR536. An average automatic hammer blow count of 18 at the tip elevation taken in an SP-SM soil from the nearest borehole approximately 200 ft and 300 ft away from shafts 2 and 1, respectively, yields a range in soil properties that might be estimated at the base of the two shafts. The fines contents in representative samples recovered at tip elevation of the two shafts during shaft construction yielded separate values of 1 and 24% (SP and SM sands). For a water table at 7 ft depth, a value of σ_{vo}' of 3600 psf was used.

A run of the program with select parameters ($\phi = 33.5^o$, $\phi_{PT} = 23^o$, $\varepsilon_{50,850\ psf} = 0.006$, Cr = 0.009 and Cc = 0.036) yields the predicted curve, shown in Fig. 3, with comparison to the recorded response for the two shafts. It should be pointed out that the break in the latter part of the predicted response curve derives from the instantaneous change from C_r to C_c consolidation response as σ_3' passes through σ_{vo}'. More likely there would be a gradual change between these values of C_r to C_c over a range in pressure from somewhere below to somewhere in excess of σ_{vo}'. This would yield a smoother predicted curve. While the predicted results compare quite well with the Statnamic responses, reasonable changes in the input values can easily move the predicted curves ±20% or more. This reflects the sensitivity of the material's undrained behavior to the choice of $\varepsilon_{50,ref}$ and ϕ_{PT} that control $\varepsilon_{v,shear}$ and C_r and C_c that control $\varepsilon_{v,iso}$, and the interplay between them (such that $\varepsilon_{v,iso} = -\varepsilon_{v,shear}$). Figure 4 compares the curve from Fig. 3 with curves resulting from changes in input parameter values. Curve 1 reflects a -1^o change in ϕ; Curve 2

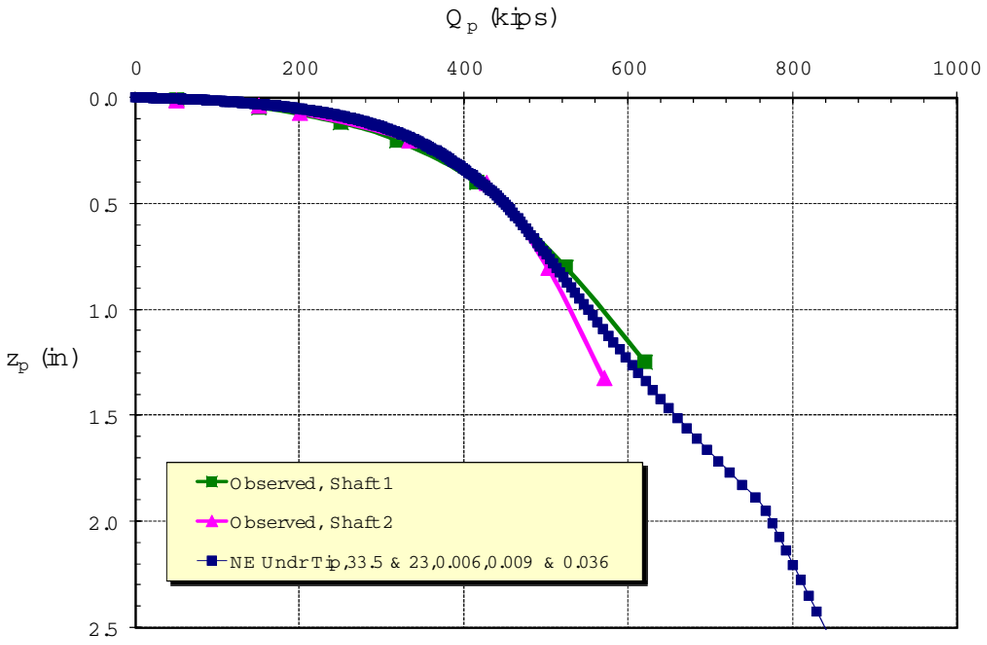


FIG. 3. Observed versus predicted undrained pile tip response

reflects a +1° change in ϕ_{pt}; Curve 3 reflects a -0.001 change on $\varepsilon_{50@850\ psf}$; Curve 4 reflects a -0.002 change in C_r.

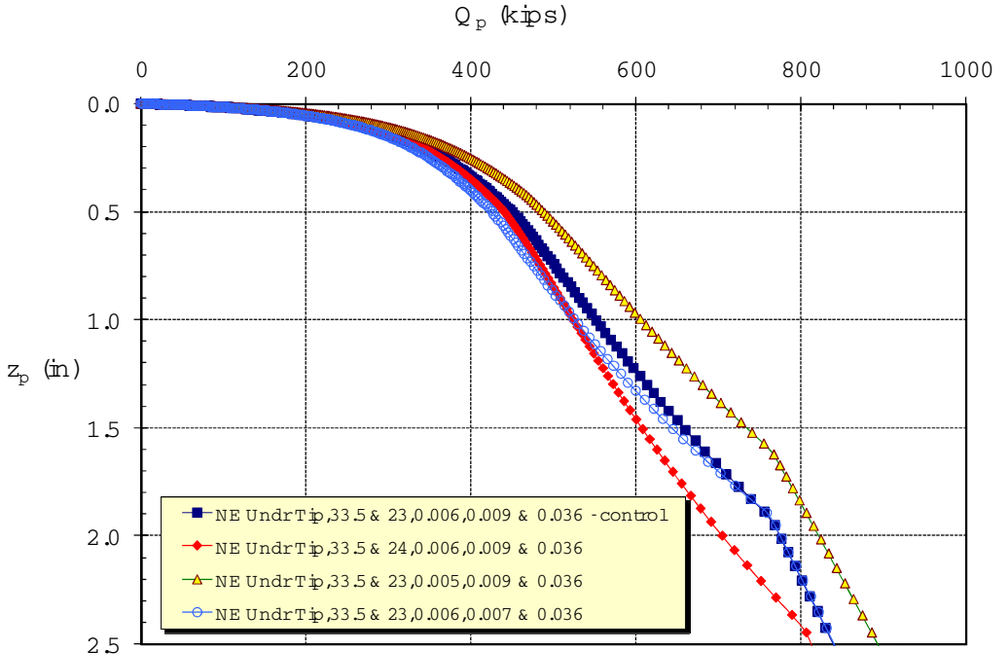


FIG. 4. Parametric variation in predicted behavior

SUMMARY AND CONCLUSION

Undrained tip (and associated side shear) load versus displacement response is required for the analysis and design of drilled shafts in saturated cohesionless soils for earthquake and impact loading conditions. It is required for both the axial response of drilled shafts and for tip behavior of short to intermediate shaft lengths under lateral loading.

The MOA presented provides a basis for assessing undrained tip load – tip displacement behavior in cohesionless soils. As demonstrated in Fig. 4 results vary depending upon the choice of input parameters. Therefore, while the method is useful in capturing the nature of the observed undrained behavior, there is need for an expanded material database along with guidance for consistent selection of the input parameters.

ACKNOWLEDGEMENTS

The authors acknowledge WSDOT and FHWA, in particular Mohammad Sheikhizadeh, for the support of the drilled shaft tests. The analytical work undertaken is in parallel with an ongoing research project funded by the California Department of Transportation (Caltrans). AFT performed the Statnamic tests and provided the static undrained responses. Walt Vanderpool from Terracon and Suthan from UNR provided invaluable assistance.

REFERENCES

Ashour, M. and Norris, G. M. (1999). "Liquefaction and Undrained Response Evaluation of Sands From Drained Formulation," *Journal of Geotechnical and Geoenvironmental Engineering*, ASCE, Vol. 125, No. 8, pp. 649-658.

Ashour, M., Norris, G. M., and Pilling, P. (1998). "Lateral Loading of a Pile in Layered Soil Using the Strain Wedge Model," *Journal of Geotechnical and Geoenvironmental Engineering*, ASCE, Vol. 124, No. 4, pp. 303-315.

Norris, G., Siddharthan, R., Zafir, Z. and Madhu, R. (1997). "Liquefaction and Residual Strength of Sands from Drained Triaxial Tests," *Journal of Geotechnical and Geoenvironmental Engineering*, ASCE, Vol. 123, No. 3, pp. 220-228.

Norris, G., Yang, G.H-J., Elfass, S., and Ashour, M. (2007). "Dilatant Relationship Between Stress-Strain and Volume Change Behaviors**,"** submitted to *Journal of Geotechnical and Geoenvironmental Engineering*, ASCE.

O'Neill, M. and Reese, L. (1999). "Drilled Shafts: Construction Procedures and Design Methods," Publication No. FHWA-IF-99-025.

Schmertmann, J., Hartman, J., and Brown, P. (1978). "Improved Strain Influence Factor Diagrams," Journal of Geotechnical Engineering, ASCE, Vol. 104, No. GT8, pp.1131-1135.

Analysis of the Seismic Behaviour of Propped Retaining Structures

Luigi Callisto[1], Fabio M. Soccodato[2] and Riccardo Conti[3]

[1]University of Rome 'La Sapienza', Italy; luigi.callisto@uniroma1.it
[2]University of Cagliari, Italy; soccodato@unica.it
[3]University of Rome 'Tor Vergata', Italy

ABSTRACT: This paper discusses the results of a dynamic numerical analysis in which a pair of propped retaining walls embedded in a dry coarse-grained soil are subjected to two different earthquakes. The retaining walls have a small embedded length, so that they undergo significant displacements under seismic conditions. Soil behaviour is described with a non-linear elastic-plastic model, with damping resulting from irreversible strains. The seismic input is made of two real acceleration time histories, having a similar Arias intensity but a different frequency content. The response of the soil and the retaining structures to these different inputs is presented, devoting a special attention to the description of soil-wall interaction that occurs during an earthquake.

INTRODUCTION

The mechanical behaviour of embedded retaining structures subjected to seismic loading is still unclear, as it results from a combination of phenomena which can be difficult to model with sufficient accuracy. During the propagation of seismic waves through a continuum in which an excavation has been made, a bi-dimensional amplification occurs, which depends on the spatial distribution of stiffness, on the non-linear soil response and on the hysteretic soil behaviour. Because of the excavation, a significant portion of the soil located in the vicinity of the retaining walls is in a state close to limit equilibrium, and this in turn affects the soil response to the subsequent seismic loading. It follows that a pre-requisite for a reasonable prediction of the seismic behaviour of these structures is a reliable estimate of the stress state produced by the excavation. This poses certain constraints to the constitutive models that can be deemed adequate to study this problem: beyond being able to reproduce non-linearity and hysteretic damping, they should allow for the development of plastic limit conditions.

The seismic design of embedded retaining structures is routinely performed using a pseudo-static approach, in which a constant acceleration field is superimposed to

the gravity acceleration, and safety against a collapse mechanism is checked using limit equilibrium methods. When it comes to the use of more advanced analyses, which account for the variation of acceleration in space and time, the notion of safety against a collapse mechanism becomes meaningless and attention should especially be focused on the permanent displacements undergone by the geotechnical system.

A preceding paper (Callisto & Soccodato 2007) presented the results obtained from an analysis of an ideal pair of cantilever embedded retaining walls subjected to a real acceleration time history. The present paper is aimed to extend this investigation to the case of embedded retaining walls connected to each other by a prop level, subjected to two different seismic inputs.

NUMERICAL MODEL AND SEISMIC INPUT

The dynamic analysis was carried out using the Finite Difference Code FLAC v.5 (Itasca 2005). Figure 1 shows the finite difference grid, together with a schematic layout of the retaining structures. An ideal excavation with a depth of 4 m is supported by a couple of embedded retaining walls connected to each other by an elastic prop hinged at the top. The excavation is carried out in a dry coarse-grained soil with a constant angle of friction $\varphi' = 35°$, density $\rho = 2.04$ Mg/m^3 and a stress-dependent small strain shear modulus $G_0 = 10000 \cdot p'^{0.5}$ (kPa), where p' is the mean effective stress. The bedrock is located at a depth of 30 m from the ground surface. Table 1 lists the values of the key input parameters for the analysis.

The embedded length of the walls, equal to 1.5 m, was computed through a pseudo-static limit equilibrium analysis in which a horizontal seismic coefficient $k_h = 0.1$ was used and a global factor of safety equal to 1.8 was applied to the passive resistance. Active seismic forces were evaluated using the Mononobe-Okabe (M.O.) theory, while the passive ones were computed, assuming a soil-wall angle of friction $\delta = 20°$, with the solution developed by Lancellotta (2007) based on a lower bound limit analysis.

Soil behaviour was described using a non-linear model with hysteretic damping available in the FLAC library. This model is a two-dimensional extension of the one-dimensional non linear models describing hysteresis loops through the Masing (1926) rules; details are given in Itasca (2005). The model parameters were chosen to reproduce the Seed & Idriss (1970) modulus decay and damping curves for sands, as discussed by Callisto & Soccodato (2007). This hysteretic model was used to update at each calculation increment the shear modulus of an elastic-perfectly plastic soil model with a Mohr-Coulomb failure criterion and a non-associated flow rule (dilatancy angle $\psi = 0$). Therefore, plastic strains associated to full strength mobilisation occurring during the analysis provided additional energy dissipation beyond that resulting from the Masing rule. No additional viscous damping was introduced in the analysis.

The soil-wall contact was simulated using elastic-perfectly plastic interfaces with a friction angle $\delta = 20°$. A small cohesion $c' = 0.5$ kPa was used to ensure numerical stability in the calculation.

Zones in the finite difference grid have a size of 0.25 m near the retaining wall

and a maximum size of 1.2 m in the vicinity of the bedrock. The initial stress state was computed assuming an earth pressure coefficient at rest $K_0 = 0.5$. Effects of the installation of the retaining walls were not modelled. The static analysis for the excavation was carried out in four steps, each time removing 1 m of soil; the prop was installed at the beginning of the excavation. In this calculation a reduced shear modulus was used, equal to $0.3\,G_0$, corresponding on the Seed & Idriss (1970) modulus decay curve to a shear strain $\gamma \approx 0.1$ %. During the static stage, the grid was restrained horizontally and vertically at the base, while only horizontal displacements were prevented on the lateral sides.

The dynamic analysis was carried out applying acceleration time-histories to the bedrock nodes. On the lateral sides, standard FLAC dynamic boundary conditions were applied: the grid was connected to "quiet" boundaries (Lysmer & Kuhlemeyer, 1969) that in turn were connected to free-field boundaries, along which a free-field one-dimensional calculation was carried out in parallel with the main grid calculation. The time increment used in the explicit time integration scheme was $\Delta t = 2 \cdot 10^{-7}$ s.

Two real seismic signals recorded in Italy on stiff soils were applied to the bottom boundary of the grid, namely the Tolmezzo (TM) and the Assisi (AS) acceleration time histories. The Tolmezzo record has a peak acceleration $a_{max} = 0.35$ g and an Arias intensity $I_a = 0.79$ m/s. The Assisi record was scaled to $a_{max} = 0.28$ g to obtain a similar Arias intensity as the Tolmezzo record. The significant durations (between 5 and 95 % of I_a) are of 9.9 and 10.5 s respectively. The input signals were low-pass filtered at 15 Hz for compatibility with the dimensions of the larger grid zones. Their Fourier amplitude spectra signals are shown in Figure 2(*a*, *f*) where it is apparent that the two records are characterised by a different frequency content: the Tolmezzo time history shows significant Fourier amplitudes in the range of 1 to 4 Hz, while the Assisi time history shows the highest amplitudes between 2.5 and 6 Hz. The mean period T_m as defined by Rathje et al. (1998) is equal to 0.4 and 0.24 s respectively.

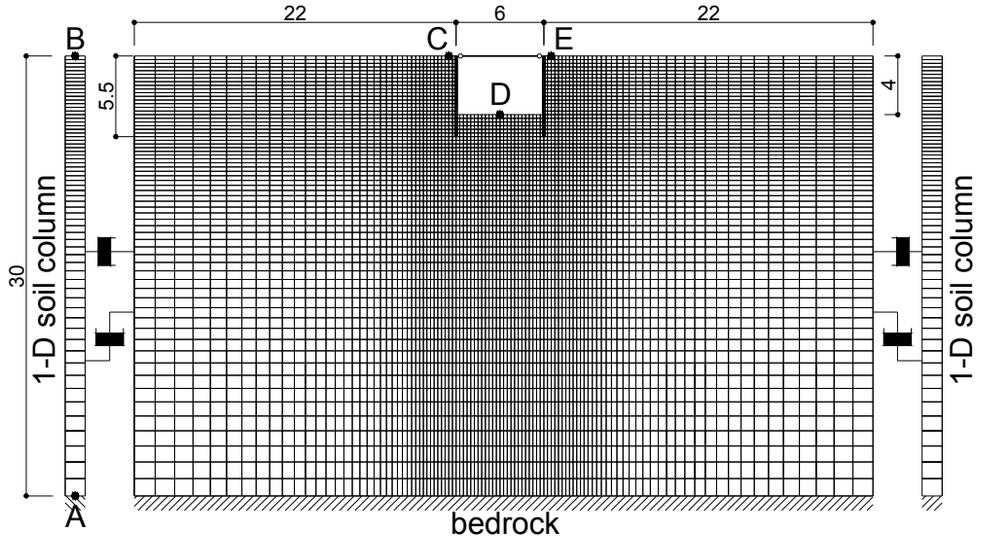


FIG. 1. Problem layout and finite difference grid.

Table 1. Input parameters for the analysis.

							retaining walls		prop level
ρ (Mg/m^3)	c' (kPa)	φ' (°)	ψ	δ (°)	G_0 (kPa)	ν'	EA (kN/m)	EI (kNm^2/m)	EA (kN/m)
2.04	0.5	35	0	20	$10000 \cdot p'^{0.5}$	0.2	$1.21 \cdot 10^7$	$2.72 \cdot 10^5$	$3.0 \cdot 10^6$

RESULTS

Amplification

Table 2 reports some properties of the acceleration time histories computed at specific locations, while the corresponding Fourier spectra are shown in Figure 2. A significant amplification is obtained for $f = 2$ Hz, which is about the fundamental frequency of the deposit. Frequencies in the range of 4 to 6 Hz are also amplified, especially in the soil zones located behind the retaining wall, near the stiff support system. The overall frequency content is modified only slightly by amplification, as shown by the values of the mean period T_m.

For both input records, one-dimensional propagation produces a three-fold increase in the Arias intensity (from 0.79 to 2.4-2.5 m/s). Additional amplification is produced by two-dimensional effects, as shown by a further increase in the Arias intensity close to the retaining walls; this effect is substantial for the Assisi input record, which yields Arias intensities as high as 6.2 m/s. In general, properties of the acceleration time histories computed at points C and E, behind the two retaining walls, are very similar to each other.

The Fourier spectra of Figure 2 show that the computed acceleration time histories contain non-zero amplitudes at large frequencies that are not present in the input records. This effect may be ascribed to insufficient damping produced by the hysteretic soil model at small strains, and might be corrected by introducing a small viscous damping in the analysis. However, a spectral analysis of the displacement time histories of the walls and of the adjacent soil showed that such high frequencies do not produce any additional permanent displacement, therefore their effect appears negligible for practical purposes.

Stress state

Figure 3 shows the distribution of the total horizontal stress σ_h acting against the retaining walls. The figure also shows the theoretical distributions of σ_h for active and passive limit states, evaluated using the static active and passive earth coefficients K_a and K_p obtained by Lancellotta (2002) (solid lines). Under static conditions, active limit state is attained behind the retaining walls down to about 3.5 m, while larger values of σ_h are computed below this depth. In front of the walls, full mobilization of passive resistance is observed down to about 4.5 m, i.e. 0.5 m below the bottom, essentially due to the decrease in vertical stress produced by the excavation. A more complete illustration of the stress state under static conditions can be seen in the plot of Figure 4(*a*) which shows, for the central part of the grid,

Table 2. Properties of acceleration time histories computed at specific locations.

input signal	Tolmezzo					Assisi				
location	A	B	C	D	E	A	B	C	D	E
a_{max} (g)	0.35	0.56	0.93	0.72	0.67	0.28	0.51	1.15	1.25	1.05
I_a [12s] (m/s)	0.79	2.36	3.73	2.24	3.71	0.79	2.54	6.17	2.32	6.24
T_m (s)	0.40	0.46	0.39	0.44	0.39	0.24	0.26	0.23	0.24	0.23
$f_m = T_m^{-1}$ (Hz)	2.50	2.17	2.56	2.27	2.56	4.17	3.84	4.35	4.17	4.35

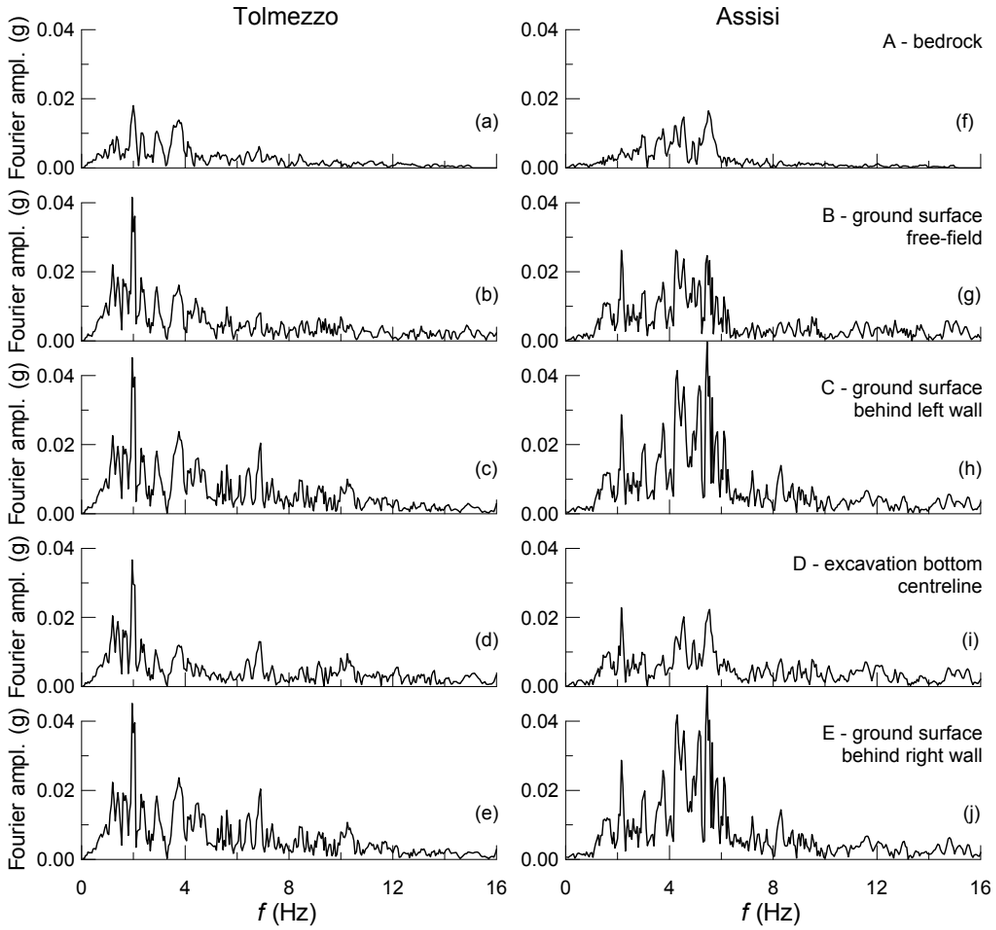


FIG. 2. Fourier spectra of the acceleration time histories computed at specific locations (see Fig. 1).

the contours of the mobilised strength, defined as the ratio τ/τ_{lim} of the maximum shear stress acting at a point and the corresponding available strength.

During the earthquake, the normal stresses acting against the wall change very rapidly in a somewhat erratic way. Nevertheless it is possible to observe specific trends in the distribution of the contact stresses, and these are shown in Figure 3(*a*) at the selected instants of 5.0 s and 5.8 s for the analyses involving the Tolmezzo and the Assisi record respectively. At these instants, contact stresses against the left wall

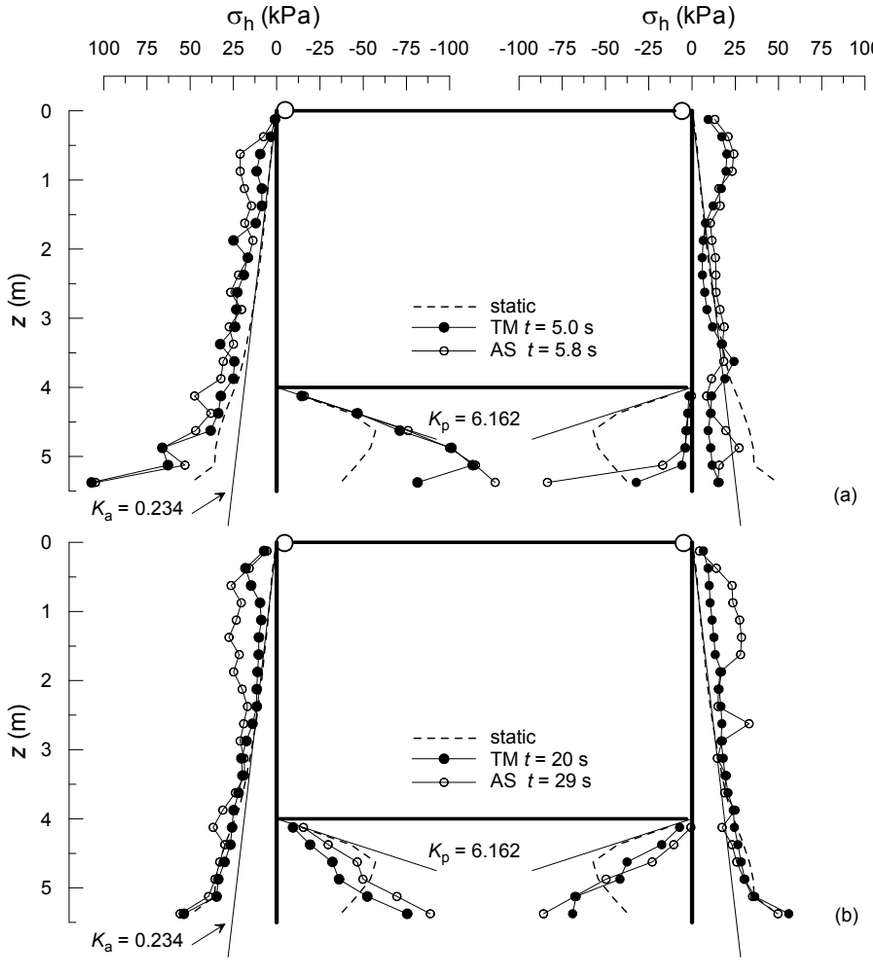


FIG. 3. Computed horizontal stresses acting against the retaining walls during (*a*) and after (*b*) the earthquakes.

are the highest. This implies a low mobilisation of shear strength behind the wall, and an almost full mobilisation of shear strength in front of the wall. Conversely, at the same instants, contact stresses acting against the right wall are the lowest, and this in turn implies full mobilisation of shear strength behind the wall and a 90 degrees rotation of the principal stress directions in front of the wall, where near active limit conditions are attained. During strong motion, contact stresses increase and decrease simultaneously behind and in front of a single wall, and this behaviour occurs in an alternate fashion between the two walls. It is interesting to note that during shaking the contact stresses behind the upper part of the walls become much higher than those computed under static conditions. This effect, which was not observed in the seismic analysis of cantilever walls (Callisto & Soccodato 2007) is probably caused by the stiff prop restraining the relative displacements at the top of the walls. Figure 4(*b*) shows the contour plot of τ/τ_{lim} for the Tolmezzo earthquake at $t = 5$ s. It can be seen that behind the walls there is a spreading of the plastic zones

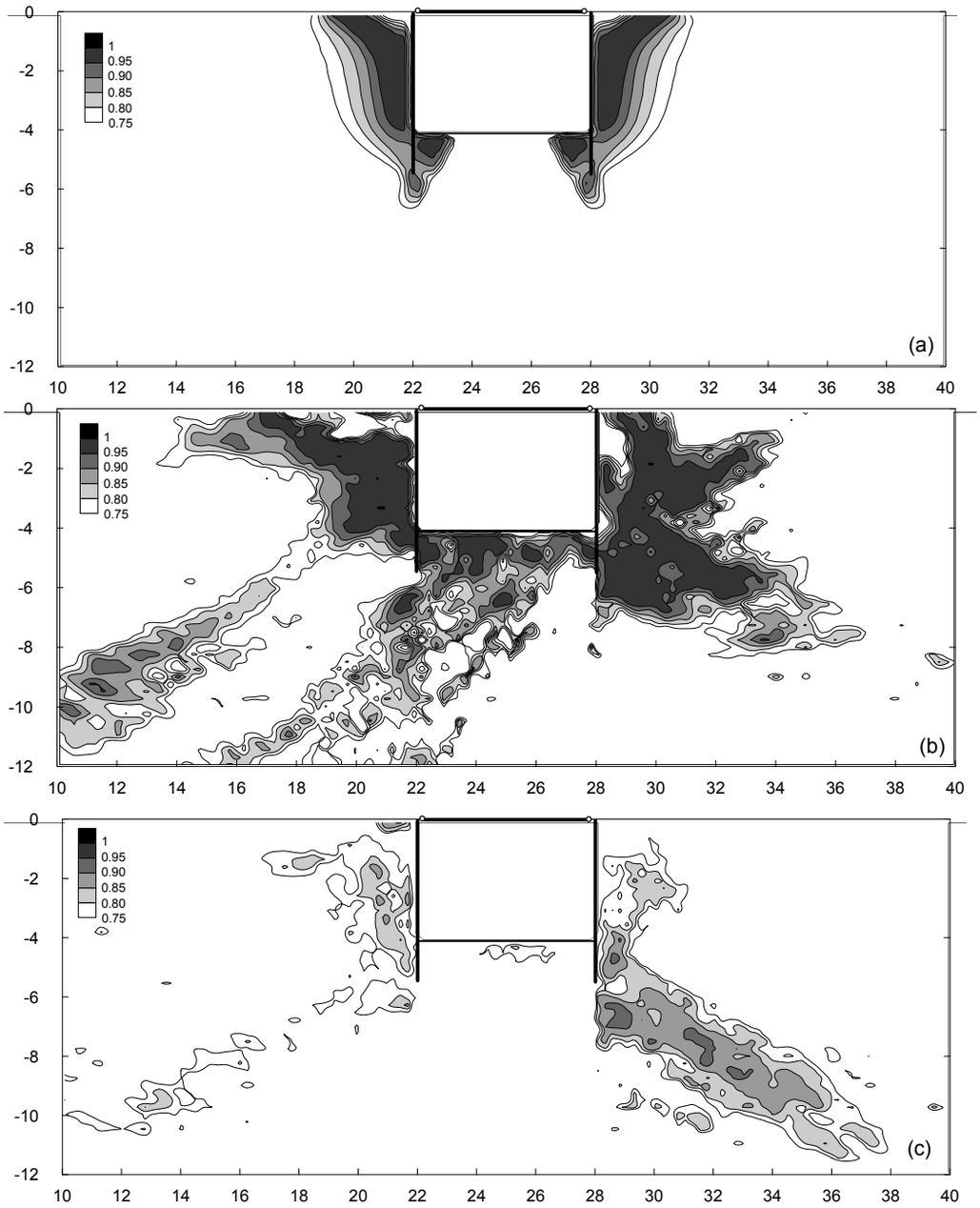


FIG. 4. Contours of the mobilised shear strength in static conditions (*a*); after 5 s of the Tolmezzo record (*b*); at the end of the Tolmezzo record (*c*).

($\tau/\tau_{lim} > 0.95$) that assume wedge-like shapes, while the soil in front of the left wall is close to passive limit conditions, consistent with the distribution of σ_h depicted in Fig. 3(*a*). Note that the plastic zones extend well below the toe of the right wall: the toe is moving towards the excavation (see next section) and this causes a perturbation which is spread downwards because of soil continuity. This is quite different from

the results obtained for a pair of cantilevered walls, in that for such walls the toe was close to the instantaneous rotation point undergoing very small displacements, and the plastic zones were thus confined to an upper portion of soil.

At the end of the earthquake, symmetry in the distribution of σ_h is nearly restored for the Assisi earthquake (Figure 3(*b*)). Conversely, at the end of the Tolmezzo record σ_h values behind the left wall near the prop are significantly larger than those acting against the right wall. Contact stresses in front of the walls show a quasi-linear distribution and are about half of the available static passive pressures: if compared to the initial static conditions, the soil in the lower part of the wall is closer to a limit passive state, while soil elements located right below the bottom of the excavation are more distant from passive conditions. The contour plot of Figure 4(*c*) shows that the soil stress state is now everywhere quite far from a plastic limit state and therefore, in terms of a limit equilibrium analysis, a collapse mechanism appears to be more distant than in the initial conditions. However, this also implies that the net pressures acting against the walls are larger and therefore stresses in the walls are more significant, as discussed in the next section.

Bending moments and axial force

Figure 5 shows the spatial and temporal variation of the bending moments M in the walls and the axial force N in the prop. In static conditions, the computed values of M and N are in a close agreement with those obtained from the limit equilibrium calculation. Seismic shaking produces a significant increment in both M and N, which is seen to occur in a rather different way for the two seismic records: the Tolmezzo earthquake results in a few sharp peaks in M and N occurring between 4 and 6 s, after which both M and N stabilize to somewhat lower values; conversely, the increase in M and N produced by the Assisi earthquake is more gradual, and the final values are quite higher. The post-seismic distribution of bending moments after the Tolmezzo earthquake could be obtained with a pseudostatic analysis using a seismic coefficient $k_h = 0.16$, and this was shown to be the case also for a pair of cantilevered walls. However, the resulting value of the axial force in the prop would be about 30 % smaller that that computed in the numerical analysis. The Assisi earthquake, with a similar Arias intensity and a lower peak acceleration, is seen to be much more damaging for this specific problem.

Displacements

Figure 6 shows the horizontal displacements u of the retaining walls, relative to the free-field lateral boundaries, and the settlements w of the soil located behind the walls, computed at the end of the earthquake. The seismic events produce permanent horizontal displacements of the walls which are an order of magnitude larger than the very small static ones. After the Assisi earthquake symmetrical wall displacements are computed, consisting in a quasi-rigid rotation about the propped top. The ground surface settles accordingly, with maximum vertical displacements occurring right behind the walls. A different behaviour is observed after the Tolmezzo record, whose

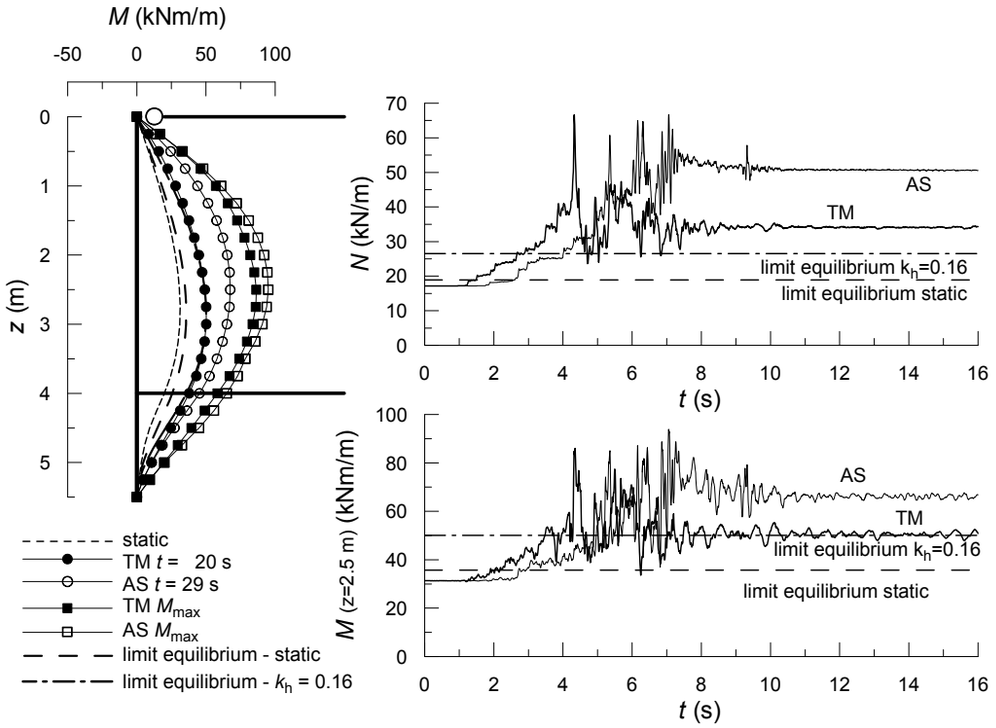


FIG. 5. Spatial and temporal variation of bending moments *M* in the wall and axial force *N* in the prop.

displacement time history is strongly unsymmetrical: after this earthquake the right wall has translated towards the excavation while the left wall shows a rotation about its toe, with permanent displacements directed away from the excavation. Consistently, settlements behind the right wall are larger than those occurring close to the left wall, and are spread to a larger distance from the excavation.

CONCLUSIONS

Propagation of the two seismic records in the vicinity of a pair of propped retaining walls causes instantaneous attainments of the available shear strength in soil zones interacting with the walls, resulting in a progressive increase in bending moments and axial force, and in a gradual accumulation of displacements.

The two real acceleration time histories, applied to the lower boundary of the finite difference grid, are both significantly amplified and this amplification appears to be emphasized by a two-dimensional interaction with the excavation. The Assisi record, characterized by a similar Arias intensity as the Tolmezzo record and by a smaller peak acceleration, causes the strongest effects, particularly in terms of stresses in the walls and in the prop. This may be related to its higher frequency content, and to the consequent larger amplification occurring close to the stiff structures supporting the excavation.

The bedrock seismic input chosen for these analyses is quite severe and would correspond to an ultimate limit state for the worst scenario in the Italian territory.

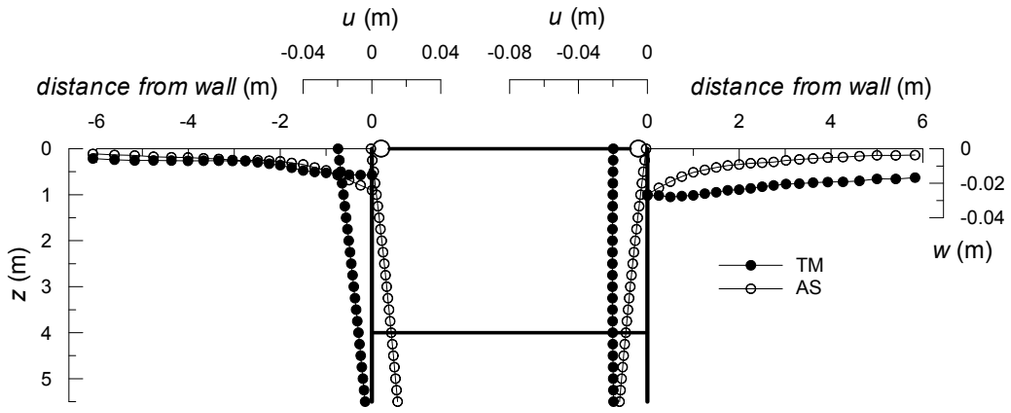


FIG. 6. Computed displacements of retaining walls and ground surface.

Nevertheless the retaining walls, proportioned using a pseudo-static approach with seismic coefficients equal to only a fraction (29-35 %) of the peak bedrock acceleration, undergo displacements smaller than 30 mm, while they are subjected to bending moments that during shaking might produce instantaneous yielding. The most critical component seems to be the prop, with respect to normal stresses and to safety against buckling, since at the end of the Assisi earthquake the prop level is subjected to a compressive axial force equal to about 2.5 times the initial one.

ACKNOWLEDGMENTS

The work presented in this paper is part of the *ReLUIS* research project, funded by the Italian Department of Civil Protection.

REFERENCES

Callisto L. and Soccodato F.M. (2007). Seismic analysis of an embedded retaning structure in coarse-grained soils. *Proc. 4th Int. Conf. on Earthquake Gotechnical Engineering*. Thessaloniki.

Itasca (2005). *FLAC Fast Lagrangian Analysis of Continua* v. 5.0. User's Manual.

Lancellotta R. (2002). "Analytical solution of passive earth pressure". *Géotechnique*, 52 (8): 617-619.

Lancellotta R. (2007). "Lower bound approach for seismic passive earth resistance". *Géotechnique*, 57 (3): 319-321.

Lysmer, J., and Kuhlemeyer R.L. (1969). "Finite dynamic model for infinite media", *Journal of Engineerig Mechanics* 95 (EM4): 859-877.

Masing, G. (1926). "Eigenspannungen und Verfertigung bim Messing". *Proceedings 2nd Int. Congress on Applied Mechanics*, Zurich.

Rathje E.M., Abrahamson N.A. and Bray J.D. (1998). Simplified frequency content estimates of earthquake ground motions. *Journal of geotech. and geoenv. eng.* 124 (2): 150-159.

Seed H.B. and Idriss I.M.(1970). *Soil moduli and damping factors for dynamic analysis*. Report No. EERC 70-10, University of California, Berkeley, 1970.

Distribution of Seismic Earth Pressures on Gravity Walls by Wave-based Stress Limit Analysis

Panos Kloukinas[1], George Mylonakis[2] and Costas Papantonopoulos[3]

[1] Graduate Student, Department of Civil Engineering, University of Patras, Greece; pkloukin@upatras.gr
[2] Associate Professor, Department of Civil Engineering, University of Patras, Greece; mylo@upatras.gr
[3] Associate Professor, Department of Civil Engineering, University of Patras, Greece; cip@upatras.gr

ABSTRACT: A closed-form stress plasticity solution is presented for earthquake-induced earth pressures and distribution of these pressures on inflexible retaining walls. The solution is essentially an approximate yield line approach that over- and under-estimates active and passive pressures, respectively. Results are presented in the form of dimensionless graphs and charts that elucidate the salient features of the problem. Compared to Mononobe-Okabe equations, the proposed solution is simpler, more accurate and safe. In addition, it provides a rational means for determining the distribution of limit thrusts on the wall. It is shown that the pseudo-dynamic seismic problem does not differ fundamentally from the gravitational one, as the former can be derived from the latter by means of a revolution of the reference axes. In the second part of the paper, the solution is extended to determine the distribution of limit pressures on a gravity wall by means of simple wave equations. The proposed approach has advantages over earlier efforts by Steedman and Zeng, as it satisfies the stress boundary conditions of the problem.

INTRODUCTION

The classical equations of Coulomb and Mononobe-Okabe [Okabe, 1926; Mononobe & Matsuo, 1929] are being widely used for determining earth pressures due to gravitational and earthquake loads, respectively. It is well known that both solutions fall into the family of *kinematic* solutions of limit analysis. These solutions are based on kinematically admissible failure mechanisms in conjunction with a yield criterion and a flow rule for the soil material, both of which are enforced along pre-specified failure surfaces [Chen, 1975]. Stresses outside the failure surfaces are not examined and, thereby, equilibrium in the medium is generally not satisfied. In the realm of associative and convex materials, solutions of this type are inherently *unsafe* that is, they underestimate active pressures and overestimate the passive [Green et al., 2003; Ostadan, 2005; Ostadan & White, 1998].

A second group of limit-analysis methods, the *stress* solutions, make use of pertinent

stress fields that satisfy the equilibrium equations and the stress boundary conditions, without violating the failure criterion anywhere in the medium. On the other hand, the kinematics of the problem is not examined and, therefore, compatibility of deformations is generally not satisfied. For convex materials, formulations of this type are inherently *safe* that is, they overestimate active pressures and underestimate the passive. The best known such solution is that of Rankine, the applicability of which is severely limited by the assumptions of horizontal backfill, vertical wall and smooth soil-wall interface. Owing to difficulties in deriving pertinent stress fields for all but the simplest geometries, the vast majority of limit-analysis solutions in geo-engineering are of the kinematic type [Chen, 1975]. With minor exception [Lancellotta 2007, Mylonakis et al 2007], no closed-form stress solutions have been derived for seismic earth pressures.

Notwithstanding the theoretical significance and practical appeal of the Coulomb and Mononobe-Okabe solutions, these formulations can be criticized on the following important aspects: (1) in the context of limit analysis their predictions are unsafe; (2) their accuracy (and safety) diminishes in the case of passive pressures on rough walls, (3) the mathematical expressions are complicated and difficult to verify, (4) the distribution of contact stresses on the wall are not predicted (typically assumed hydrostatic following Rankine's solution), (5) optimization of the failure mechanism is required in the presence of multiple loads, to determine a stationary (optimum) value of soil thrust, and (6) stress boundary conditions are not satisfied, as the yield surface does not generally emerge at the soil surface at angles $45^o \pm \varphi/2$.

In light of the above, it appears that the development of a closed-form solution of the stress type for assessing seismically-induced earth pressures would be desirable. It will be shown that the proposed solution is mathematically simpler than the existing kinematic solutions, offers satisfactory accuracy, yields results on the safe side, satisfies the stress boundary conditions, and predicts the elevation of soil thrust.

PROBLEM DEFINITION AND MODEL DEVELOPMENT

The problem under investigation is depicted in Figure 1: a slope of dry cohesionless soil retained by an inclined gravity wall, is subjected to plane deformations under the combined action of gravity (g) and seismic body forces (a_h x g) and (a_v x g) in the horizontal and vertical direction, respectively. The problem parameters are: the height (H) and inclination (ω) of the wall, the inclination (β) of the slope; the roughness (δ) of the wall-soil interface; the friction angle (φ) and unit weight (γ) of the soil material, and the surface surcharge (q). Since backfills typically consist of granular materials, cohesion in the soil and the soil-wall interface are not considered. Note that the retained soil is considered rigid* before yielding, so the seismic force is uniform within the backfill, so the resultant body force is acting at an angle ψ_e from vertical

$$\tan\psi_e = \frac{a_h}{1 - a_v} \tag{1}$$

* This assuption is not essential from a limit analysis viewpoint. It is merely a convenient assumption regarding earthquake action in the backfill.

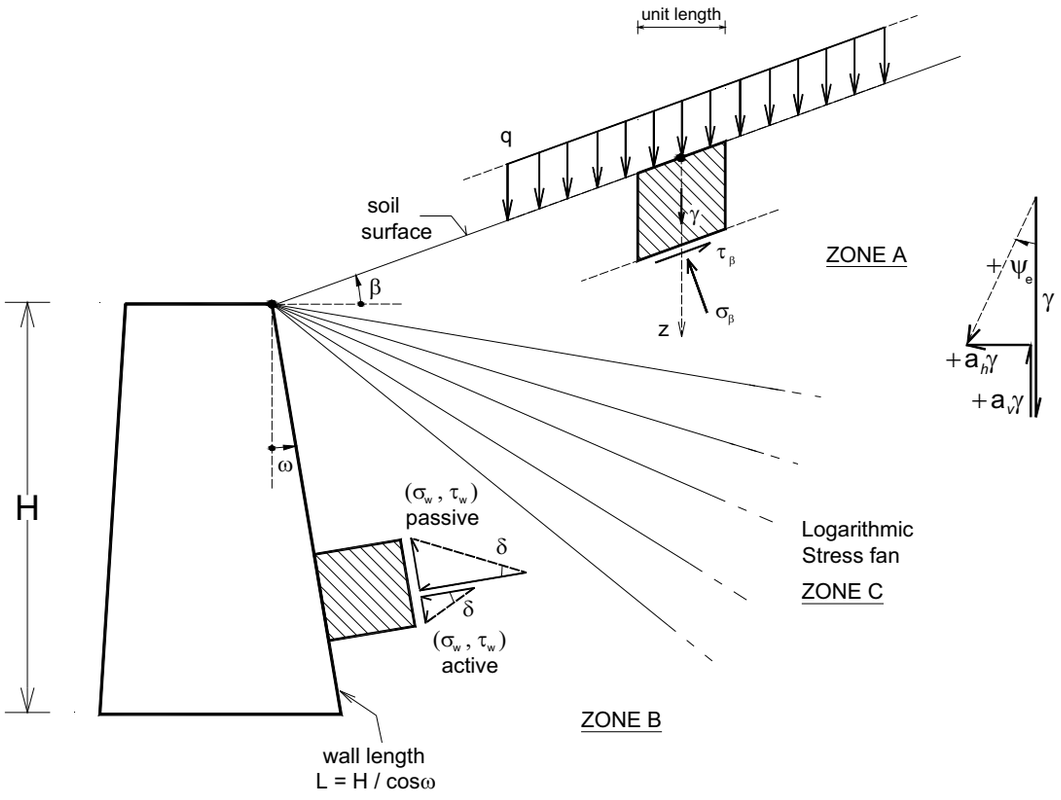


FIG. 1. Stress fields close to soil surface (Zone A), wall (Zone B) and transition zone (Zone C).

To analyze the problem, the backfill is divided into two main regions subjected to different stress fields: the first region (A) is located close to the soil surface, whereas the second (B) close to the wall. In both regions the soil is assumed to be in a condition of impeding yielding under the combined action of gravitational and seismic forces. The same assumption is adopted for the soil-wall interface, which is subjected exclusively to contact stresses. A transition zone between regions A and B is introduced below.

Fundamental to the proposed analysis is the assumption that stresses close to the soil surface can be well approximated by those in an *infinite slope* so the stress boundary conditions at the surface are satisfied. For points in region B, it is assumed that stresses are functions exclusively of the vertical coordinate and obey the strength criterion at the frictional soil-wall interface.

Considering the material to be in a condition of impeding yielding, the Mohr circles of stresses in regions A and B are depicted in Figure 2. It becomes evident that the orientation of principal planes (and thereby stress characteristics) in the two regions is different. In addition, the mean stresses S_A and S_B (Figure 2) generally do not coincide. To determine the separation of mean stresses S_A and S_B and ensure a smooth transition in the orientation of principal planes in the two zones, a logarithmic *stress fan* is adopted (Zone C), centered at the top of the wall (Figure 1).

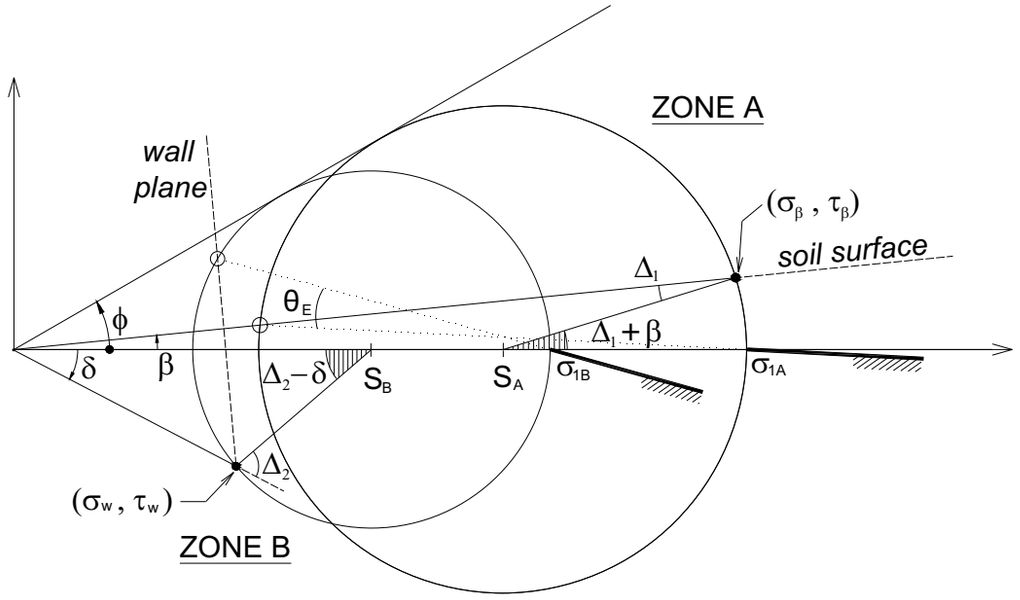


FIG. 2. Mohr circles of stresses and major principal planes in zones A and B.

In the interior of the fan, principal stresses are gradually rotated by the angle θ separating the major principal planes in the two regions, as shown in Fig 1. This additional condition is written as [Chen, 1975]:

$$S_B = S_A \exp\left(-2\theta \tan\phi\right) \tag{2}$$

The negative sign in the above equation pertains to the active case ($S_B < S_A$) and vice versa. Equation (2) is an exact solution of the governing Kötter equations for a weightless material and, thereby, it is only approximate for a fan with weight.

PSEUDO-DYNAMIC SOLUTION FOR EARTHQUAKE LOADING

Recognizing that earthquake action imposes a resultant thrust in the backfill inclined at a *constant* angle ψ_e from vertical (Fig 1), it becomes apparent that the seismic problem does not differ fundamentally from the static problem, as the former can be obtained from the latter through a rotation of the reference axes by the angle ψ_e, as shown in Fig 3. In other words, considering ψ_e does not add an extra physical parameter to the problem, but simply alters the values of the other variables. This property of *similarity* was apparently first employed by Briske and later by Terzaghi and Arango [Seed & Whitman, 1970; Ebeling et al, 1992] for the analysis of related problems. So, the solution to the seismic problem, can be derived from the statics of the gravitational problem. The limit thrust on the wall is given by the well-known expression:

$$P_E = K_{qE}(1 - a_v) q H + \frac{1}{2} K_{\gamma E}(1 - a_v)\gamma H^2 \tag{3}$$

where earth pressure coefficients $K_{\gamma E}$ and K_{qE} are given by (Mylonakis et al 2007)

$$K_{\gamma E} = \frac{\cos(\omega-\beta)\cos(\beta+\psi_e)}{\cos\psi_e \cos\delta \cos^2\omega}\left[\frac{1-\sin\phi\cos(\Delta_2-\delta)}{1+\sin\phi\cos\left[\Delta_1^*+\beta+\psi_e\right]}\right]\exp(-2\theta_E\tan\phi) \quad (4)$$

$$K_{qE} = \frac{\cos\omega}{\cos(\omega-\beta)}K_{\gamma E} \quad (5)$$

In the above equation,

$$2\theta_E = (\Delta_2-\delta)-(\Delta_1^*-\beta)-2\omega-\psi_e \quad (6)$$

is twice the revolution angle of principal stresses in the two regions and Δ^*_1 and Δ_2 denote the two Caquot angles [Caquot, 1934; Sokolovskii, 1965] given by

$$\sin\Delta_1 = \sin(\beta+\psi_e)/\sin\phi, \qquad \sin\Delta_2 = \sin\delta/\sin\phi \quad (7)$$

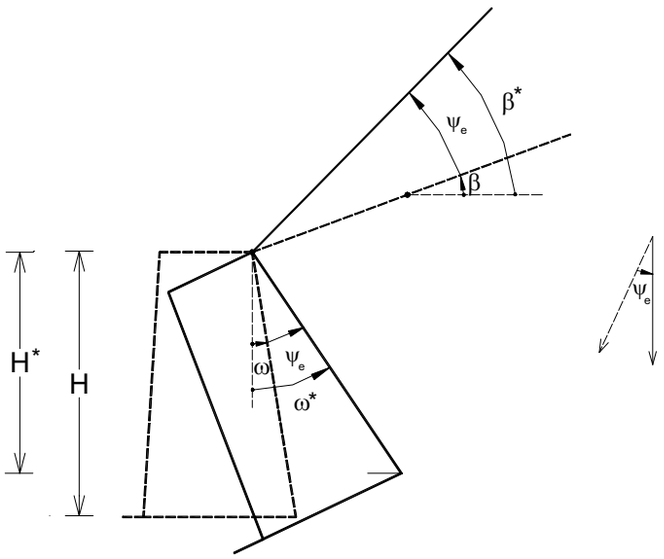


FIG. 3. Similarity transformation based on a rotation of the reference axes for analyzing the seismic case as a gravitational problem.

Results for active seismic earth pressures are given in Figure 4, referring to cases examined in the seminal study of Seed & Whitman [1970], for a reference friction angle of 35°. Naturally, active pressures increase with increasing levels of seismic acceleration and slope inclination and decrease with increasing friction angle and wall roughness. The conservative nature of the proposed analysis versus the Mononobe-Okabe (M-O) solution is evident in the graphs. The trend is more

pronounced for high levels of horizontal seismic coefficient (a_h > 0.25), smooth walls, level backfills, and high friction angles. Conversely, the trend becomes weaker with steep backfills, rough walls, and low friction angles.

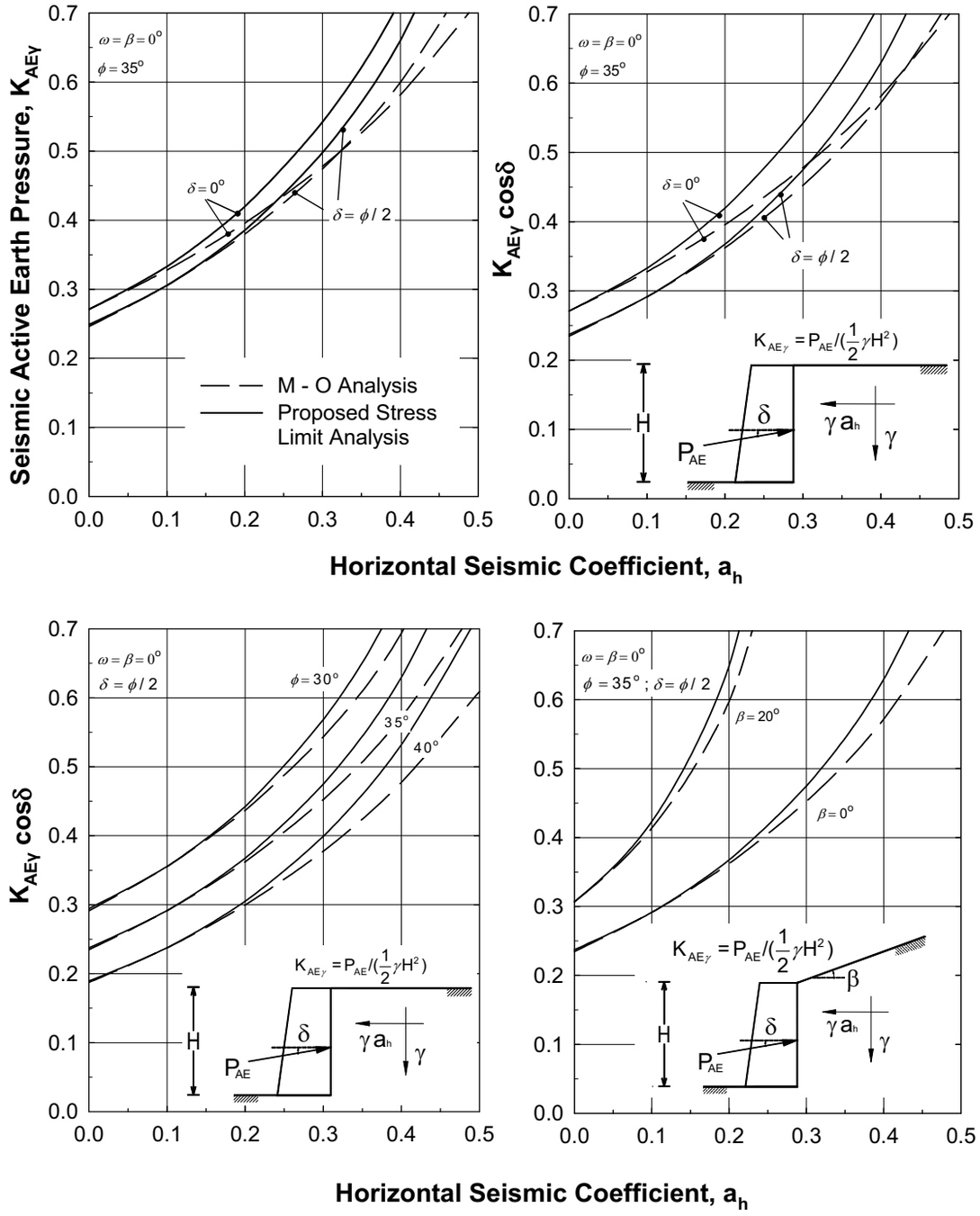


FIG.4. Comparison of active seismic earth pressures predicted by the proposed solution and from conventional M – O analysis, for different geometries, material properties and accelaration levels. (Modified from Seed & Whitman, 1970)

EARTH PRESSURE DISTRIBUTION: SIMPLE WAVE SOLUTION

The classical kinematic-type solutions by Coulomb and Mononobe–Okabe do not provide information on the distribution of stresses with height. They adopt a hydrostatic distribution, as a practical simplification for design purposes. The same limitation applies to more rigorous numerical kinematic solutions pioneered by Chen (1975).

On the other hand, in stress solutions (Terzaghi 1943) the hydrostatic distribution results naturally from the formulation itself. This is due to the linear variation of stresses with depth in the Rankine zone close to the soil surface, which is not altered in the stress fan and close to the wall.

It is experimentally known, however, that the actual distribution of stresses is not hydrostatic. Two major mechanisms are responsible for this. They both relate to the basic assumptions about the behavior of the retained soil and the kinematics of the problem. First, the soil mass responds dynamically and, thereby, the distribution of accelerations (and associated body forces) is not uniform with depth. These effects have been incorporated in elastodynamic solutions (Veletsos & Younan 1994) and some limit analysis solutions (Steedman & Zeng 1990). Secondly, the distribution of earth pressures changes for different kinematic constraints (e.g., rotation about wall base or top), which relate directly to arching in the backfill. The redistribution of stresses due to arching leads to changes in the magnitude and point of application of soil thrust. Only the effect of dynamic response of the backfill is addressed herein.

The proposed approach allows evaluation of dynamic limit thrust on gravity walls by means of the stress solution and the simple wave solution for the response of a homogeneous soil layer to vertically-propagating SH waves shown in Figure 5.

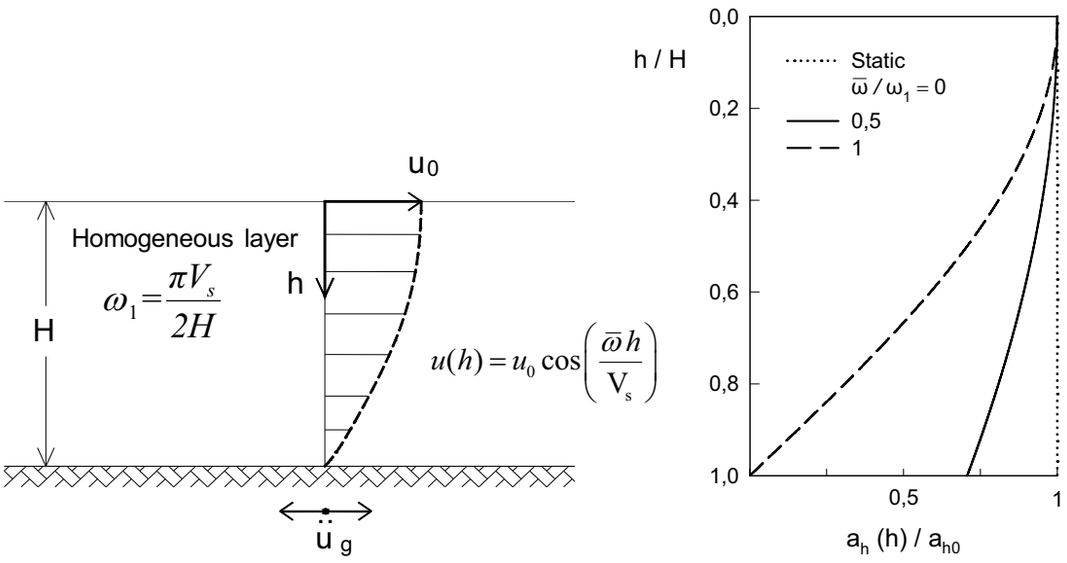


FIG.5. Dynamic response of backfill and distribution of inertial loads with height.

This dynamic response results to a non uniform distribution of inertial accelerations with height and, thereby, seismic angle ψ_e

$$\psi_e(h) = \tan^{-1} a_h(h) = \tan^{-1}\left[a_{h0} \cos\left(\frac{\pi}{2}\frac{\bar{\omega}}{\omega_1}\frac{h}{H}\right)\right] \tag{8}$$

where $\bar{\omega}$ denotes the cyclic excitation frequency. The use of the above elastodynamic function into the proposed plasticity solution is theoretically admissible, as the medium in a condition of impeding yielding, and, thereby, elasticity is valid. Based on the foregoing, the dynamic pressures on the retaining wall are obtained by the expression:

$$p(h) = \frac{\cos(\omega-\beta)\cos(\beta+\psi_e(h))}{\cos\psi_e(h)\cos\delta\cos^2\omega}\left[\frac{1-\sin\phi\cos(\Delta_2-\delta)}{1+\sin\phi\cos\left[\Delta_1^*+\beta+\psi_e(h)\right]}\right]\exp(-2\theta_E(h)\tan\phi) \tag{9}$$

where ψ_e varies with depth, h, according to equation (8).

Distributions of seismic earth pressures along the back of the wall are given in Figure 6. Evidently, the closer the excitation frequency to the fundamental natural frequency of the medium, the larger the deviation from the conventional triangular distribution.

It is important to mention that the dynamic effects lead invariably to a decrease in magnitude of total thrust, as seen in the left graph of Figure 7. It also leads to an increase in the elevation of point of application of active thrust (left graph of Fig 7). The maximum elevation is observed at resonance ($\bar{\omega}/\omega_1 = 1$), and does not exceed H/2 for the purely seismic component of the thrust.

Corresponding results are provided in Figure 8, plotted as function of horizontal ground acceleration a_{ho}. Naturally, total thrust increases with increasing horizontal ground acceleration. The elevation of point of application is affected to a lesser degree by the level of ground shaking.

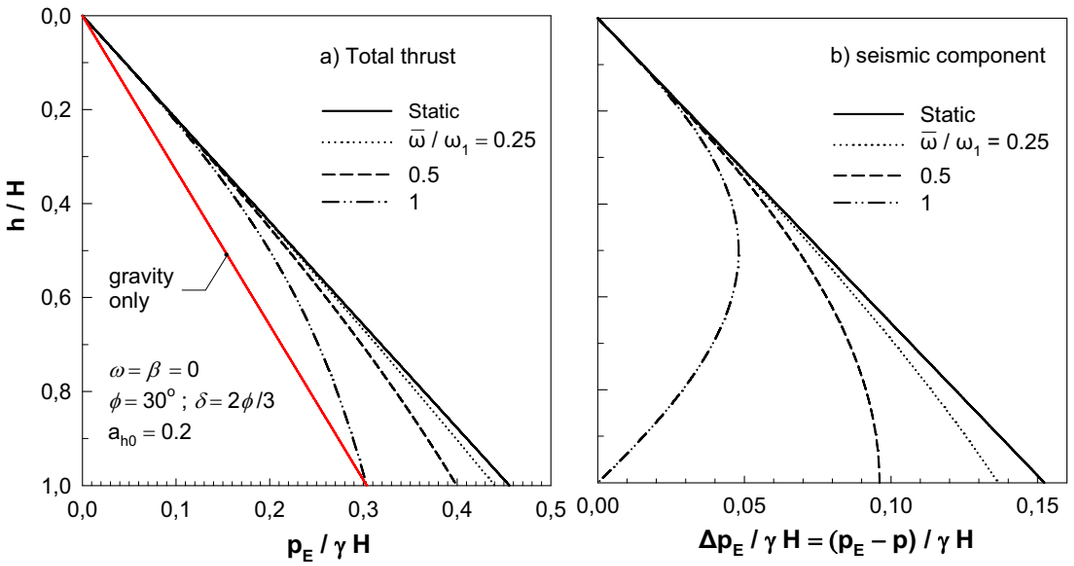


FIG.6. Distribution of earth pressures: a) Total thrust, b) Seismic component only

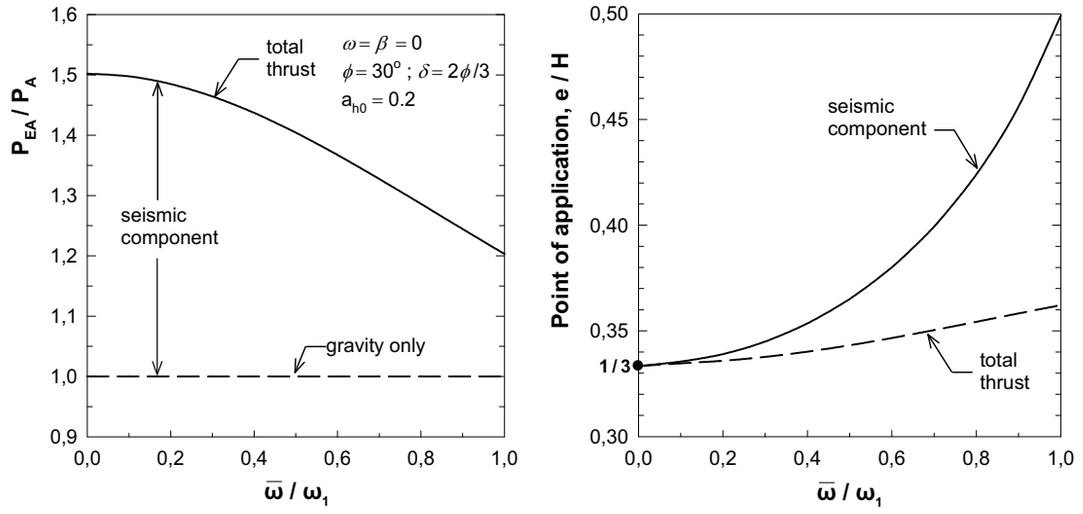


FIG.7. Variation of the magnitude and the point of application of the seismic thrust with respect to exciting frequency.

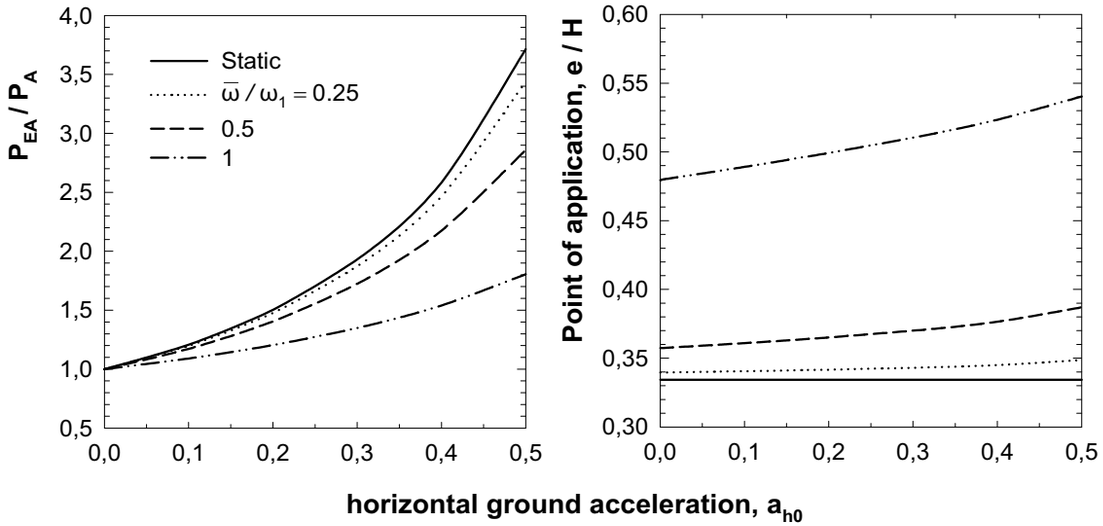


FIG.8. Effect of the peak ground acceleration (PGA) level on the magnitude and the point of application of the seismic thrust, for varying exciting frequency.

CONCLUSIONS

A stress plasticity solution was presented for gravitational and earthquake-induced earth pressures on gravity walls. The following are the main conclusions of the study:
(1) The proposed solution is simpler than the Mononobe-Okabe equations, and safe, as it over-predicts active pressures and under-predicts the passive.
(2) For active pressures, the accuracy of the solution is excellent. The largest deviations

occur for high seismic accelerations, high friction angles and steep backfills.
(3) The pseudo-dynamic seismic problem can be deduced from the gravitational problem through a revolution of the reference axes by the seismic angle ψ_e (Fig 3).
(4) Stress limit analysis is suitable for determining traction distributions on the wall. By incorporating the dynamic response of backfill, the distribution of pressures becomes parabolic and the elevation of the seismic component rises to above 50% of wall height. The deviation from hydrostatic distribution may be important for walls taller than approximately 5m.

REFERENCES

Caquot, A. (1934). "Equilibre des massifs a frottement interne. "*Gauthier-Villars*: Paris.

Chen, W.F. (1975). "Limit analysis and soil plasticity." *Elsevier*, Amsterdam.

Ebeling, R.M., Morrison, E.E., Whitman, R.V., Liam Finn, W.D. (1992). "A Manual for Seismic Design of Waterfront Retaining Structures." *US Army Corps of Engineers*, Tech. Report ITL-92-11.

Green, R.A., Olgun, C.G., Ebeling, R.M. and Cameron, W.I. (2003). "Seismically induced lateral earth pressures on a cantilever retaining wall." *ASCE, Earthquake Engineering,* 133**:** pp. 946–955.

Kramer, S.L., (1996). "Geotechnical Earthquake Engineering." *Prentice Hall*.

Lancellota, R. (2007). "Lower-bound approach for seismic passive earth resistance." *Geotechnique* 57, No3: 319-321.

Mononobe, N., Matsuo, O. (1929). "On the determination of earth pressure during earthquakes." *Proceeding of the World Engineering Congress*, Tokyo, vol 9: 179-187.

Mylonakis, G.E, Kloukinas, P. and Papantonopoulos, C. (2007). "An alternative to the Mononobe–Okabe equations for seismic earth pressures." *Soil Dynamics and Earthquake Engineering*, Volume 27, Issue 10: 957-969

Okabe, S. (1924). "General theory on earth pressure and seismic stability of retaining walls and dams." *Journal of Japanese Society of Civil Engineers,* 10, 6: 1277-1323.

Ostadan, F. (2005). "Seismic soil pressure for building walls - An Updated Approach." *Soil Dynamics and Earthquake Engineering,* 25: 785-793.

Ostadan, F., White,W.H. (1998). "Lateral Seismic Soil Pressure - An Updated Approach." *US-Japan SSI Workshop,* Sept 22-23, USGS.

Seed, HB, Whitman, R.V. (1970). "Design of earth retaining structures for dynamic loads." *Proceedings of specialty conference on lateral stresses in the ground and design of earth retaining structures*, *ASCE*, Ithaca, New York: 103-147.

Sokolovskii, V.V. (1965). "Statics of granular media." *Pergamon Press*, New York.

Steedman, R.S. and Zeng, X. (1990). "The Influence of Phase on the Calculation of Pseudo-Static Earth Pressure on a Retaining Wall." *Geotechnique* 40, No1: 103-112.

Terzaghi, K. (1943). "Theoretical soil mechanics." *John Wiley & Sons Inc.*, New York.

Veletsos, A.S. and Younan, A.H. (1994). "Dynamic soil pressures on rigid retaining walls." *Earthquake Engineering and Structural Dynamics,* 23: 275 – 301.

Dynamic Centrifuge Study of Seismically Induced Lateral Earth Pressures on Retaining Structures

Nicholas Sitar, M. ASCE[1] and Linda Al Atik[2]

[1]Professor, Department of Civil & Environmental Engineering, University of California, Berkeley, 449 Davis Hall, Berkeley, CA 94720; nsitar@ce.berkeley.edu
[2]PhD Student, Department of Civil & Environmental Engineering, University of California, Berkeley, 445 Davis Hall, Berkeley, CA 94720; l_atik@berkeley.edu

ABSTRACT: A set of two dynamic centrifuge experiments on stiff and flexible U-shaped retaining structures with dry medium dense sand backfill was performed in order to evaluate the validity of the various assumptions and analysis procedures currently used for the evaluation of seismically induced forces on retaining structures. The experimental results show that dynamic moments and dynamic earth pressures tend to be overestimated using the current analysis methods. More importantly, the dynamic earth pressure increases monotonically with depth and the maximum measured moments are not necessarily in with maximum measured earth pressure. These results are consistent with results obtained independently for gravity retaining structures (Nakamura, 2006) and call into question the validity of the basic assumptions in the currently used analysis and design procedures.

INTRODUCTION

The problem of seismically induced lateral earth pressures on retaining structures and basement walls has been the topic of considerable research over the last 80 years. The earliest and most widely used method for estimating the magnitude of seismic forces acting on a retaining wall is based on the experimental and analytical work of Okabe (1926) and Mononobe and Matsuo (1929) following the 1923 great Kanto earthquake in Japan. The Mononobe-Okabe (M-O) method, as it is commonly referred to, was originally developed for gravity walls retaining dry cohesionless backfill. It is an extension of Coulomb's static earth pressure theory to include the inertial forces due to the horizontal and vertical backfill accelerations. Since then, the method has been adapted for analysis of all types of retaining structures and many researchers have concluded that the M-O method gives adequate estimates of the magnitude of the dynamic earth pressures on retaining walls (e.g. Prakash and Basavanna 1969, Seed and Whitman 1970, Bolton and Steedman 1982, Sherif. et al. 1982, Ortiz et al. 1983, Ishibashi and Fang 1987, Stadler 1996). However, more recently, analytical studies have led some researchers to suggest that the M-O method underestimates the dynamic earth pressures (e.g. Morrison and Ebeling 1995, Green et al. 2003, Ostadan and White 1998, Ostadan 2004). As a result, there has been a trend toward more and more conservative design recommendations. However, documented failures of basement walls or underground structures in non-liquefiable deposits in recent major earthquakes are exceedingly rare (e.g. Sitar 1995, Al Atik and Sitar 2007) even in locations that were subjected to very strong ground motions and where the retaining structures were not particularly designed to consider seismic loading of that magnitude. In addition, a review of case history data suggests that retaining structures

that are designed with adequate conventional factors of safety under static loading have enough strength reserve to resist seismic loading up to a very substantial levels of seismic shaking (e.g. Clough and Fragaszy 1977).

In order to address this apparent difference between analysis and performance, we embarked on a program of experimental and analytical studies to develop a more refined understanding of the problem. Specifically, the experiments were aimed to obtain data that could be used by the Bay Area Rapid Transit (BART) in assessing the designs of their most frequent cantilever U-shaped retaining structures. To this end, we performed two sets of dynamic centrifuge model experiments aimed at studying the seismic behavior of stiff and flexible retaining structures with dry medium dense sand backfill. The data from these experiments suggests that the distribution and magnitude of the dynamic forces on retaining structures substantially differs from the assumptions made in the current design and analyses procedures (Al Atik and Sitar 2007). The purpose of this paper is to provide a brief overview of the experimental methods and of the results..

EXPERIMENTAL SETUP

Dynamic Geotechnical Centrifuge Testing

The centrifuge experiments were performed on the 400g-ton dynamic centrifuge at the Center for Geotechnical Modeling at the University of California, Davis. The centrifuge has a radius of 9.1m, a maximum payload of 4,500Kg, and an available bucket area of $4m^2$. The shaking table has a maximum payload mass of 2,700Kg and a maximum centrifugal acceleration of 80g. Additional technical specifications for the centrifuge and the shaking table are available in the literature (Kutter et al. 1994, Kutter 1995). The centrifugal acceleration used in the experiments was 36g. All results are presented in terms of prototype units unless otherwise stated.

Model Configuration

The models for these experiments were constructed in a rectangular flexible shear beam container with internal dimensions of 1.65m long by 0.79m wide by approximately 0.58m deep. The model container is designed such that its natural frequency is less that the initial natural frequency of the soil in order to minimize boundary effects.

In prototype scale, the models consist of approximately 12.5m of dry medium dense sand overlaid by two U-shaped retaining wall structures, stiff and flexible, spanning the width of the container. Both structures support dry medium dense sand backfill. The first centrifuge experiment was performed on a two-layer sand model with sand backfill and foundation having relative density of 61% and 73%, respectively. The second centrifuge experiment was performed on a uniform density sand model (Dr = 72%), which configuration is presented in Fig. 1 in model units.

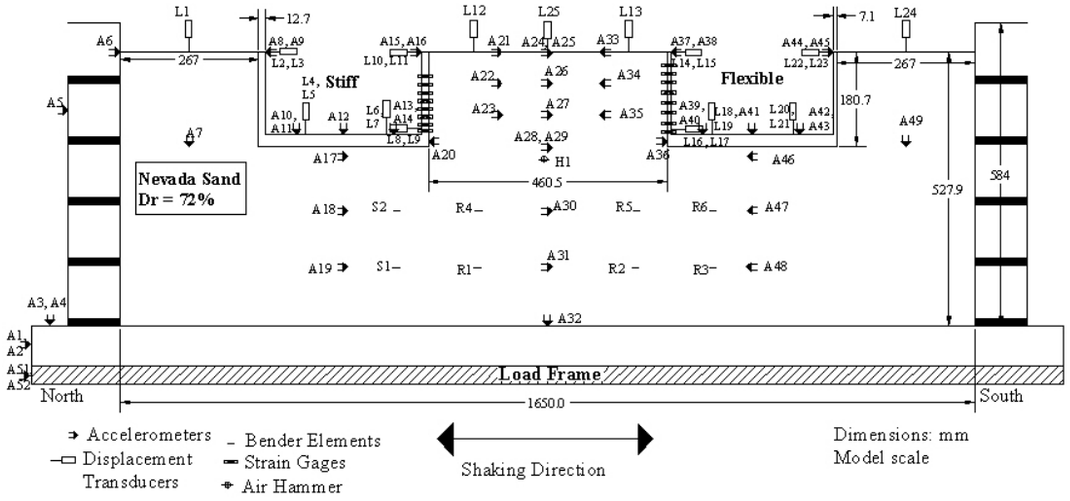


FIG. 1. Model configuration for the second centrifuge experiment, profile view.

Model Preparation

Dry pluviation was used to place the sand in different layers underneath and behind the structures. The different soil densities were produced by calibrating the drop height, mesh opening, and speed of drop for the pluviator. The height of each layer corresponds to a horizontal array of instruments, as shown in Fig. 1. After placement of each layer, the sand surface was smoothed with a vacuum and instruments were placed at their specific locations. Industrial grease was placed between the structures' walls and the model container in order to provide a frictionless boundary and prevent the sand from passing through. Lead was added to the structures in small pieces of 1 in^2 each in order to match the masses of the prototype reinforced concrete structures.

Instrumentation

The two centrifuge models were densely instrumented in order to collect accurate and reliable measurements of accelerations, displacements, shear wave velocities, strains, bending moments and earth pressures. Horizontal and vertical accelerations within the soil and on the structures were measured using miniature ICP and MEMs accelerometers. Soil settlement and structures' deflection and settlement were measured using linear potentiometers and LVDTs. Shear wave velocities of the soil underneath and behind the structures were measured using bender elements and air hammers. The location of accelerometers, air hammers, bender elements, displacement transducers and strain gages for the second centrifuge experiment are shown in Fig. 1.

Lateral soil stresses are probably the most difficult parameter to measure (Dewoolkar et al. 2001). Therefore, three different sets of independent measurements were made. Lateral earth pressures on each wall were directly measured using flexible tactile pressure Flexiforce sensors manufactured by Tekscan. Lateral earth pressures on the south stiff and north flexible walls were also calculated by double differentiating the bending moments measured by the strain gages mounted on the model walls. Finally, direct measurements of the total bending moments at the bases

of the south stiff and north flexible walls were made using force-sensing bolts at the wall-foundation joints.

Shaking Events

Multiple shaking events covering a wide range of predominant periods and peak ground accelerations were applied to each model in flight at a centrifugal acceleration of 36g. The shaking was applied parallel to the long sides of the container. The shaking events consisted of step waves, ground motions recorded at the Santa Cruz (SC) and the Saratoga West Valley College (WVC) stations during the Loma Prieta earthquake, ground motions recorded at the Port Island (PI) and Takatori (TAK) stations during the Kobe earthquake, and ground motions recorded at the Yarmica (YPT) station during the Kocaeli earthquake. The detailed description of the input ground motions can be found in Al Atik and Sitar (2007)

EXPERIMENTAL RESULTS

Accelerations

The acceleration time histories recorded during the experiment at the different accelerometers locations were used to evaluate the amplification and attenuation of the input ground motions. Fig. 2 is a plot of the peak accelerations measured at the base of the model container versus those measured at the top of the soil in the free field, at the top of the south stiff and the north flexible walls during the different shaking events. A 45° line is displayed for reference.

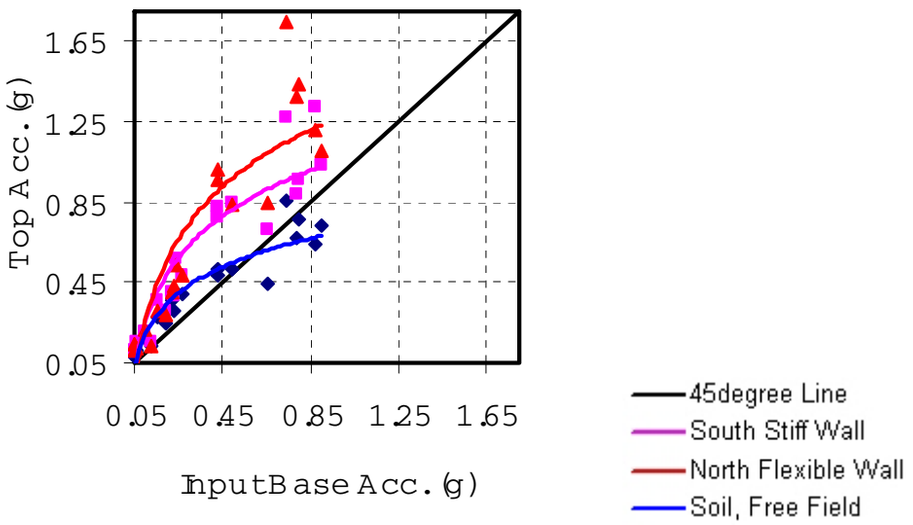


FIG. 2. Base motion amplification/attenuation for the soil, stiff and flexible walls.

Fig. 2 shows that the motions are consistently amplified at the tops of the walls and that the acceleration at the top of the soil crosses the 45° line, indicating attenuation of the large magnitude shaking events. This behavior is consistent with what would be

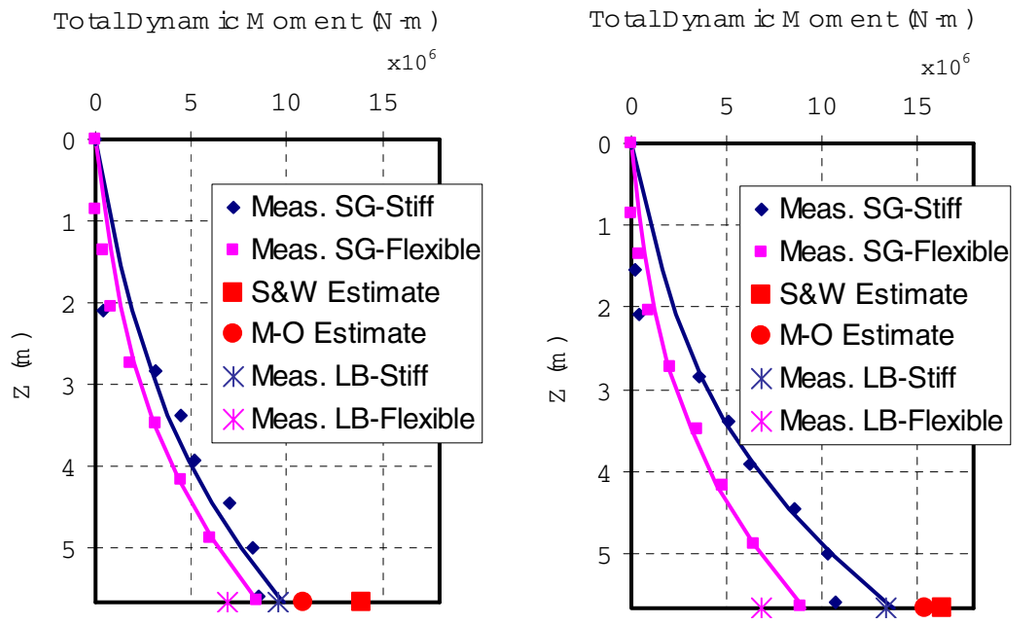
expected in typical soil deposits.

Moment distributions

While it is traditional in geotechnical practice to work in terms of earth pressures, from structural design point of view it is the moment distribution and the moment at the base of the wall that is of paramount interest. As it turns out, it is easier to measure moments than earth pressures and, therefore, moments were measured and analyzed as a part of this study. The south stiff and north flexible walls were instrumented with force sensing bolts and strain gages to measure the moment distributions along the height of the walls as well as the moments at the wall/base joints. Measured maximum total dynamic moments were compared with moment estimates using the M-O pressure distribution with the total resultant force applied at one third the height of the wall above its base and with moment estimates using the Seed and Whitman (1970) method. For the Seed and Whitman (1970) method (S&W), the resultant force of the dynamic pressure increment is applied at two thirds the height of the wall above its base.

The maximum total dynamic moment profiles interpreted from the strain gages (SG) measurements and directly measured by the force sensing bolts (LB) for the south stiff and north flexible walls are presented in Fig. 3 for the Loma Prieta-SC-2 and Kobe-TAK090-2 shaking events. The Loma Prieta-SC-2 and Kobe-TAK090-2 shaking events have peak ground accelerations of 0.49g and 0.87g and mean periods of 0.52 and 0.44sec, respectively. Fig. 4 presents a summary of results for the fifteen shaking events performed during the second centrifuge experiment. Fig. 4 shows the maximum total dynamic moments at the bases of the south stiff and north flexible walls interpreted from the strain gages data versus moment estimates using the M-O and the Seed and Whitman (1970) methods. A 45° line is displayed for reference. The M-O and Seed and Whitman (1970) total dynamic moment estimates presented in Fig. 3 and Fig. 4 are calculated using the peak ground acceleration measured at the soil surface in the free field.

It is apparent in Fig. 3 that the maximum total dynamic moment profiles are cubic in nature. Moreover, Fig. 3 and Fig. 4 show that the M-O and Seed and Whitman (1970) methods used with the total peak ground accelerations generally overestimate the maximum observed moments at the bases of the stiff and the flexible walls for all the shaking events performed during the second centrifuge experiment. As seen in Fig. 4, the ratio of the observed maximum total dynamic moments to the computed values varies for the different shaking events and this ratio appears to be function of the flexibility of the wall, the magnitude of shaking, and the density of the sand backfill. The magnitude of the overestimate is less for the stiff wall.



(a) **(b)**

FIG. 3. Maximum total dynamic moment profiles measured by the strain gages and force sensing bolts and estimated using M-O and Seed and Whitman (1970) methods for (a) Loma Prieta-SC-2 and (b) Kobe-TAK090-2 shaking events.

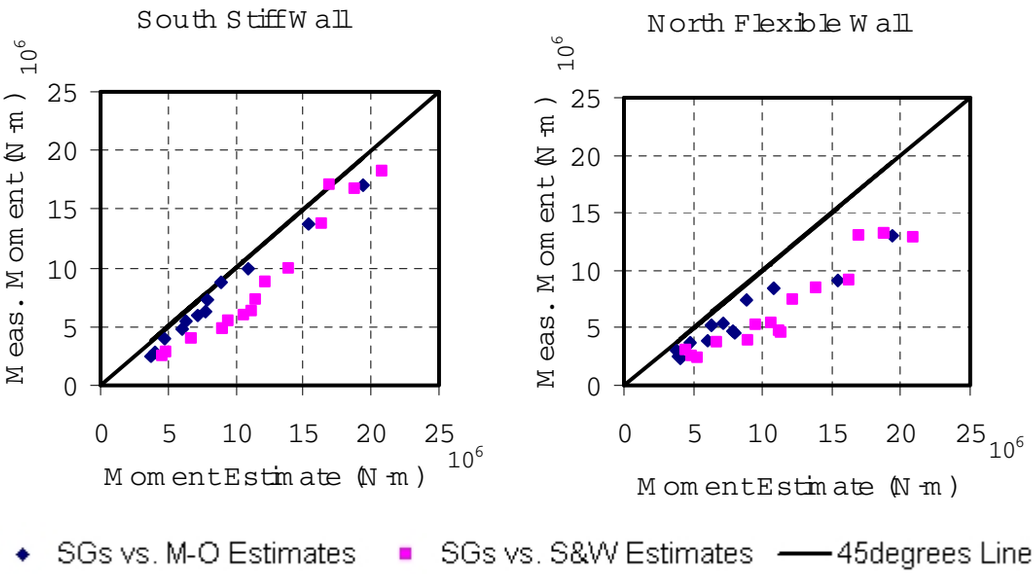


FIG. 4. Summary of maximum total dynamic moments interpreted at the base of the stiff and the flexible walls from the strain gages measurements versus estimated moments using the M-O and Seed and Whitman (1970) methods for all shaking events during the second centrifuge experiment

Lateral Earth Pressures

Lateral earth pressures were directly measured along the height of the four walls by the Flexiforce sensors. A consistent agreement was observed between the dynamic earth pressure profiles measured at the north and the south walls of each structure. Seismically induced lateral earth pressure profiles were also interpreted on the south stiff and north flexible walls by double differentiating the maximum total dynamic moment profiles obtained from the strain gages data. Fig. 5 shows the maximum total dynamic pressure distributions recorded by the Flexiforce sensors and interpreted from the strain gages data on the stiff and flexible walls during Loma Prieta-SC-2 and Kobe-TAK090-2 shaking events. We note that the maximum total dynamic pressure distributions recorded by the Flexiforce sensors and interpreted from the strain gages measurements did not occur at the same time. The pressure distributions estimated by the M-O method using the peak and 65% peak ground accelerations are also plotted in Fig. 5.

Fig. 5 shows that the maximum total dynamic earth pressures increases linearly with depth with magnitudes smaller than the M-O estimates using total peak ground accelerations. Dynamic pressure estimates obtained using 65% of the peak ground acceleration with the M-O method are in better agreement with the maximum measured total dynamic pressure profiles.

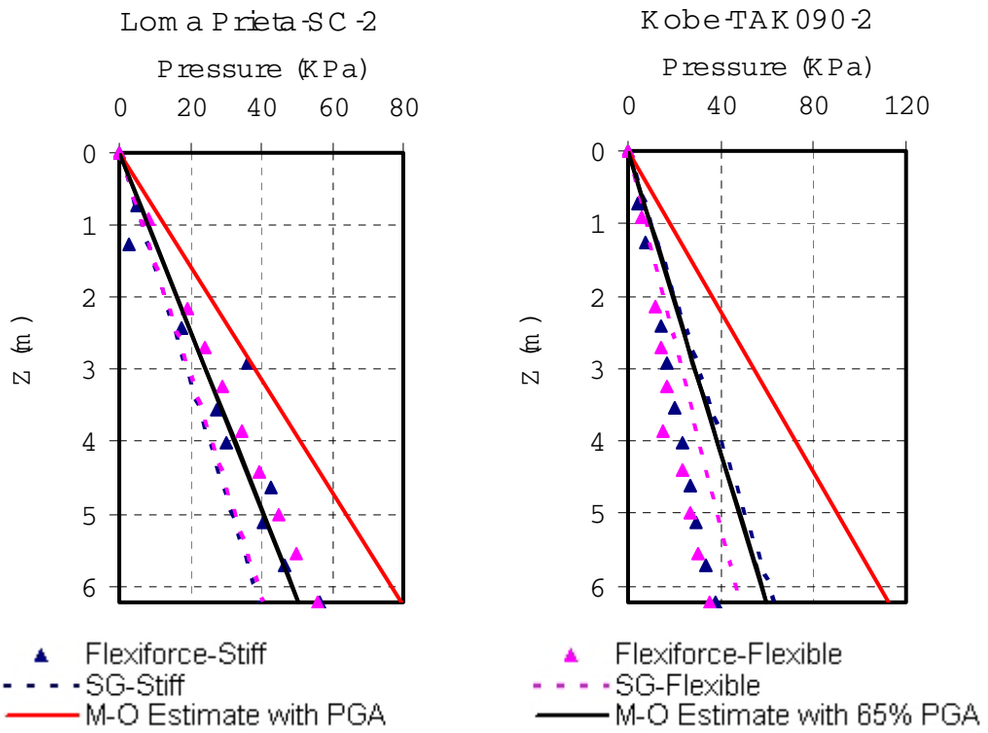


FIG. 5. Maximum total dynamic pressure distributions measured and estimated using M-O method on the south stiff and north flexible walls during Loma Prieta-SC-2 and Kobe-TAK090-2

Wall Inertial Effects on Moment and Pressure Distributions

An important element of structural design of cantilever retaining structures is the moment capacity of the wall to footing connection. The bending moment acting on the wall is not only generated by the dynamic soil pressure but also by the wall inertial force. Fig. 5 shows that the pressure profiles measured by the Flexiforce sensors were generally lower than those interpreted from the strain gage measurements. This difference can be attributed to the fact that the moments measured on the walls include the wall inertial effects while the direct earth pressure measurements only include the soil-wall interaction effects.

The current design methods assume that the earth pressure and inertia force simultaneously take their maximum. In order to investigate the wall inertial effects on the moment and pressure distributions, the authors studied the dynamic moment increment and dynamic pressure increment time series recorded by the strain gages and the Flexiforce sensors and compared them to the inertia force acting on the walls throughout the shaking events. The inertia force time series was estimated by multiplying the negative value of the mass of the walls by the acceleration time series recorded at the top of the walls. Fig. 6 presents a comparison of the time series recorded by a strain gage, a Flexiforce sensor as well as the inertia force on the stiff wall during Loma Prieta-SC-1.

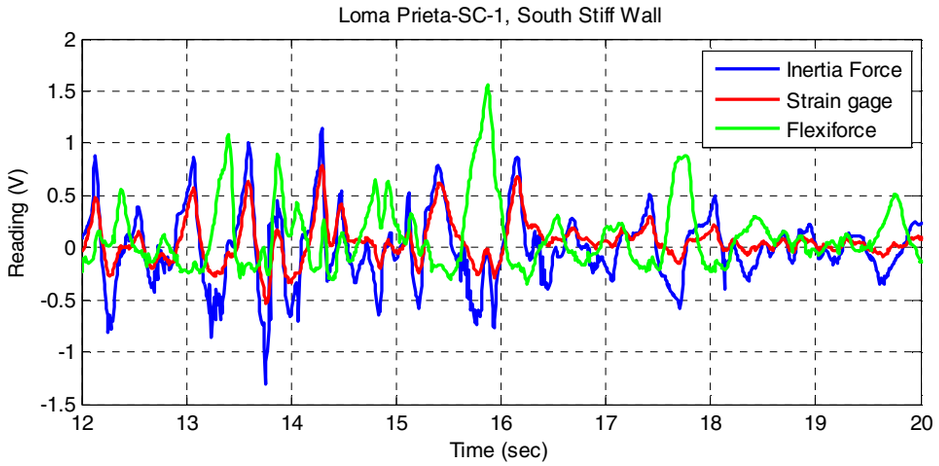


FIG. 6. Dynamic pressure increment recorded by a strain gage, dynamic moment increment recorded by a Flexiforce sensor and inertia force on the south stiff wall during Loma Prieta-SC-1

As seen in Fig. 6, the dynamic moment increment is generally in phase with the inertial force on the wall and but out of phase with the dynamic pressure increment recorded by the Flexiforce sensor. Moreover, Fig. 6 shows that the earth pressure increment is around zero when the inertia force and the dynamic moments are at maximum and vice versa. Nakamura (2006) observed a similar phenomenon for gravity retaining walls and concluded that the earth pressure is nearly equal to its initial value prior to shaking when the inertia force is at its maximum.

Preliminary analyses of the data suggest that the moments at the base of the stiff and

the flexible walls due to wall inertial effects range from about 5 to 26% of the maximum total dynamic moments interpreted from the strain gages data. Therefore, the moments measured by the strain gages and the force sensing bolts are inherently conservative since they include the wall inertial effects.

CONCLUSIONS

We present a brief overview of the results of a series of dynamic centrifuge experiments designed to evaluate the magnitude and distribution of dynamic earth pressures on retaining structures. These results indicate that seismically induced lateral earth pressures of a medium dense sand backfill monotonically increase with depth and can be reasonably approximated by a triangular distribution. Moreover, the magnitude of seismic earth pressures depends on the magnitude and intensity of shaking, the density of the backfill soil, and the flexibility of the retaining structures. In general, total dynamic earth pressures appear to be adequately estimated if not overestimated by the M-O method. Using reduced peak ground accelerations with the M-O method yields predictions of the total dynamic pressures and moments that are closer to the values measured during the experiment. However, since the dynamic earth pressure increment is not in phase with the wall inertia force the fact that the presently used methods of analysis give reasonably conservative results appears to be merely a fortuitous outcome. Therefore, further careful experimental and analytical studies are needed to fully address this problem.

ACKNOWLEDGMENTS

The authors gratefully acknowledge the support and valuable input provided by Prof. Bruce Kutter, Dr. Dan Wilson and all the staff at the Center for Geotechnical Modeling at the University of California, Davis. This research was supported by a grant from the San Francisco Bay Area Rapid Transit (BART) and the Santa Clara Valley Transportation Authority (VTA) to the Pacific Earthquake Engineering Research Center at UC Berkeley. The authors also received valuable input from Mr. Ed Matsuda, Dr. Jose Vallenas at BART and Mr. James Chai at VTA.

Any opinions, findings, and conclusions or recommendations expressed in this paper are those of the authors and do not necessarily reflect those of the funding agencies.

REFERENCES

Al Atik, L. and Sitar, N. (2007). "Development of improved procedures for seismic design of buried and partially buried structures." *PEER Report 2007/06*, College of Engineering, University of California, Berkeley.

Bolton, M.D. and Steedman, R.S. (1982). "Centrifugal testing of micro-concrete retaining walls subject to base shaking." *Proc. of Conference on Soil Dynamics and Earthquake Engineering*, Vol. 1, Southampton, Balkema: 311-329.

Clough, G.W. and Fragaszy, R.F. (1977). "A study of earth loadings on floodway retaining structures in the 1971 San Fernando Valley earthquake." *Proc. of the 6th World Conference on Earthquake Engrg.* Vol. 3.

Dewoolkar, M.M, Ko, H., and Pak R.Y.S. (2001). "Seismic behavior of cantilever retaining walls with liquefiable backfills," J. of Geotechnical and Geoenvironmental Engrg., ASCE, Vol. 127 (5): 424-435.

Green, R.A., Olgun, C.G., Ebeling, R.M. and Cameron, W.I. (2003). "Seismically induced lateral earth pressures on a cantilever retaining wall." *Earthquake Engineering*.

Ishibashi, I. and Fang, Y.S. (1987). "Dynamic earth pressures with different wall movement modes." *Soils and Foundations*, Vol. 27 (4): 11-22.

Kammerer, AM, Wu, J, Pestana, JM, Riemer, M, and Seed, RB. "Cyclic Simple Shear Testing of Nevada Sand for PEER Center Project 2051999," Geotechnical Engineering Report No. UCB/GT/00-01, University of California, Berkeley, CA, 2000.

Kutter, B.L. (1995). "Recent advances in centrifuge modeling of seismic shaking." *Proc. of the 3rd International Conference on Recent Advances in Geotechnical Earthquake Engrg. and Soil Dynamics*, Vol. 2, St. Louis: 927-941.

Kutter, B.L., Idriss, I.M., Kohnke, T., Lakeland, J., Li, X.S., Sluis, W., Zeng, X., Tauscher, R.C., Goto, Y. and Kubodera, I. (1994). "Design of a large earthquake simulator at UC Davis." *Centrifuge 94*, Leung, Lee, and Tan (eds.), Balkema: 169-175.

Mononobe, N. and Matsuo, M. (1929). "On the determination of earth pressures during earthquakes." *Proc. World Engrg. Congress*, Vol. 9: 179-187.

Morrison, E.E. and Ebeling, R.M. (1995). "Limit equilibrium computation of dynamic passive earth pressure." Canadian Journal of Geotechnical Engrg., Vol. 32: 481-487.

Nakamura, S. (2006). "Reexamination of Mononobe-Okabe theory of gravity retaining walls using centrifuge model tests." *Soils and Foundations*, Vol. 46, No. 2: 135-146.

Okabe, S. (1926). "General theory of earth pressures." *J. of the Japanese Society of Civil Engineer*s, 12 (1), Tokyo, Japan.

Ortiz, L.A., Scott, R.F. and Lee, J. (1983). "Dynamic centrifuge testing of a cantilever retaining wall." *Earthquake Engrg. and Structural Dynamics*, Vol. 11: 251-268.

Ostadan, F. (2004). "Seismic soil pressures for building walls an updated approach." *11th International Conference on Soil Dynamics and Earthquake Engrg. (11th ICSDEE) and 3rd International Conference on Earthquake Geotechnical Engrg. 93rd ICEGE)*, University of California, Berkeley.

Ostadan, F. and White, W.H. (1998). "Lateral seismic earth pressure an updated approach." *US-Japan SSI Workshop*, USGS, Menlo Park, California.

Prakash, S. and Basavanna, B.M. (1969). "Earth pressure distribution behind retaining wall during earthquakes." *Proc. of the Fourth World Conference on Earthquake Engrg.*, Santiago, Chile.

Seed, H.B. and Whitman, R.V. (1970). "Design of earth retaining structures for dynamic loads." *Lateral stresses in the ground and design of earth retaining structures*, Vol. 1, New York: 103-147.

Sherif, M.A., Ishibashi, I. and Lee, C.D. (1982). "Earth pressure against stiff retaining walls." *J. of Geotechnical Engrg*., Vol. 108, ASCE: 679-695

Sitar, N. (1995). "Geotechnical reconnaissance of the effects of the January 17, 1995,

Hyogoken-Nanbu earthquake, Japan." *Earthquake Engrg. Research Center*, University of Califronia, News, Vol. 16 (4).

Stadler, A.T. (1996). Dynamic centrifuge testing of cantilever retaining walls. PhD Thesis, Dept. of Civil Engineering, University of Colorado at Boulder.

This page intentionally left blank

Excitation and Flexibility Effects on Dynamic Response of Cantilever Retaining Walls

Özgür L. Ertuğrul[1], Selman Sağlam[2], M. Yener Özkan[3]

[1] PhD Candidate, Dept. of Civil Engineering, Middle East Technical University, Ankara, Turkey; erozgur@metu.edu.tr
[2] PhD Candidate, Dept. of Civil Engineering, Middle East Technical University, Ankara, Turkey; selman@metu.edu.tr
[3] Professor, Dept. of Civil Engineering, Middle East Technical University, Ankara, Turkey; myozkan@metu.edu.tr

ABSTRACT: A series of dynamic response analyses of cantilever retaining walls were conducted in order to assess the effects of ground shaking characteristics (amplitude and frequency) and wall flexibility on the seismically induced lateral earth pressures occurring on the walls. The investigation was focused on the seismically induced thrust and its application point on the wall stem. Idealized backfill-wall systems were modeled by finite element method. Results were compared with solutions obtained by pseudo-static approach of Mononobe-Okabe and pseudo dynamic approach of Steedman-Zeng. The analyses indicate that the acceleration amplitude of the horizontal ground motion is the major effective parameter on magnitude of the dynamic thrust acting on the walls. The difference between the dynamic thrust predicted by finite element and analytical methods becomes more significant for large acceleration amplitudes. Magnitude of the dynamic thrust calculated by finite element method reaches its highest value when the excitation frequency overlaps with the natural frequency of the backfill-wall system Numerical modeling study indicates a decrease in dynamic earth pressures for more flexible walls.

INTRODUCTION

Predicting the magnitude and distribution of the seismically induced lateral earth pressure on retaining walls located in earthquake prone regions is a complex soil-structure interaction problem that depends on several parameters related with structures, geomaterials and ground motions. The seismic analyses of retaining walls have been commonly performed by means of pseudo static methods based on limit equilibrium theory in which the wall is considered to move sufficiently to provide the backfill shear strength mobilization. Mononobe-Okabe (Okabe, 1924; Mononobe and Matsuo, 1929) has become the most commonly used method to design retaining

walls under seismic conditions. In addition to pseudo static considerations, Steedman and Zeng (1990) reported that dynamic amplification and phase difference effects within the soil mass are supposed to be taken into account during the seismic analyses of retaining walls. Retaining systems with constraints that prevent development of limit equilibrium conditions have been recently examined by using theory of elasticity. In such analyses, the wall is considered to be fixed against both deflection and rotation at the base, and the backfill is considered to behave like a linearly elastic or viscoelastic material (Veletsos and Younan, 1994; 1997).

The verification of these theories and methods with full scale structures or scaled models has practical limitations. The most realistic modeling of such soil structure interaction problems can be performed by using centrifuge facilities. Nevertheless, in recent years, use of computer software which facilitates simulation of vibration effects on soils and structures has become widespread in predicting the dynamic response of many engineering structures and retaining walls as well.

In the present paper, the effects of ground shaking characteristics (acceleration amplitude and frequency) and wall flexibility on the seismically induced lateral earth pressures occurring on cantilever retaining walls are to be evaluated through a series of dynamic response analyses. The investigation is focused on the seismically induced thrust and its application point on the wall stem. Idealized backfill-wall systems were modeled by Plaxis 8.2 Finite Element Code with dynamic module. The responses are to be evaluated due to total and incremental dynamic thrust, point of application of the dynamic thrust, and bending moment profile on the wall. The results of finite element analyses are to be compared with the solutions obtained by pseudo static approach of Mononobe-Okabe (M-O), and pseudo dynamic approach of Steedman-Zeng (S-Z).

PRELIMINARIES USED IN NUMERICAL MODELING

Important points about dynamic finite element modeling are summarized as follows:

a. The analyses were performed with plane-strain assumption.
b. Soil was modeled as a strain hardening material. Non-linear stress-strain behavior of the soil is represented by hardening soil model of Schanz et al. (1999).
c. Finite element code used in the analyses solves incremental dynamic equations of each time step by an implicit solver based on Newmark's time integration scheme.
d. Use of ordinary zero displacement boundaries utilized in the static geotechnical analyses is not adequate for dynamic problems. Special conditions were prescribed for absorption of the radiated energy at the boundaries.
e. In Plaxis, soil-wall contacts were modeled by interface elements taking into account of slipping and gapping.
f. Staged construction of the wall-backfill system was simulated to achieve incremental build-up of initial earth pressures.

g. Considered finite element systems were dynamically excited by base motions in terms of harmonic sinusoidal acceleration time histories. Acceleration amplitudes were calculated according to formula $A(t)=\alpha\sin(\omega t)$ where α represents peak amplitude in g, and ω represents circular frequency (rad/sec) of the excitation.

FINITE ELEMENT MODEL

Analyses were performed for the backfill retained by a vertical, flexible wall having foundation with a base width of 4m and a thickness of 0.5m. The model wall of 8m in height was used in all analyses, and in order to investigate effects of wall flexibility, different dimensions were presumed for the thickness of the wall. Subsoil thickness was also considered as 8m. Water table was not taken into account in the analyses. Properties of the backfill and the subsoil used in the model are given in Table 1. Finite element discretization and geometry of the system are demonstrated in Figure 1.

Beam elements utilized to model concrete structural components were set to behave linearly elastic. Material properties of the concrete structural elements are given in Table 2.

The strength properties of interfaces are linked to the strength properties of the soil layer which the wall interacts with. Each interface data set has an associated strength reduction factor (R_{inter}). Interface strength reduction factors of 0.90 and 0.45 were used for wall-backfill and foundation-subsoil interactions respectively. Failure ratio (R_f) was taken as 0.9 which is often a suitable value to use for most soils.

Table 1. Properties for modeling the soil with hardening soil model

Parameter	Value
Unit weight of the backfill material (kN/ m^3)	18
Unit weight of the foundation subsoil (kN/ m^3)	19
Poisson's Ratio (ν) for backfill material	0.33
Poisson's Ratio (ν) for foundation subsoil	0.33
Young's Modulus (E_{50}) for backfill material (kPa)	35000
Young's Modulus (E_{50}) for foundation subsoil (kPa)	40000
Cohesion of the foundation subsoil (kPa)	5
Internal Friction Angle for the backfill material	30^0
Internal Friction Angle for the foundation subsoil	30^0
Dilatancy angle for the backfill	5^0
Dilatancy angle for the foundation subsoil	3^0
R_{inter} for wall-backfill	0.9
R_{inter} for foundation-subsoil	0.45
m (stress dependency of stiffness for the soil model)	0.5
R_f (failure ratio) for both layers	0.9

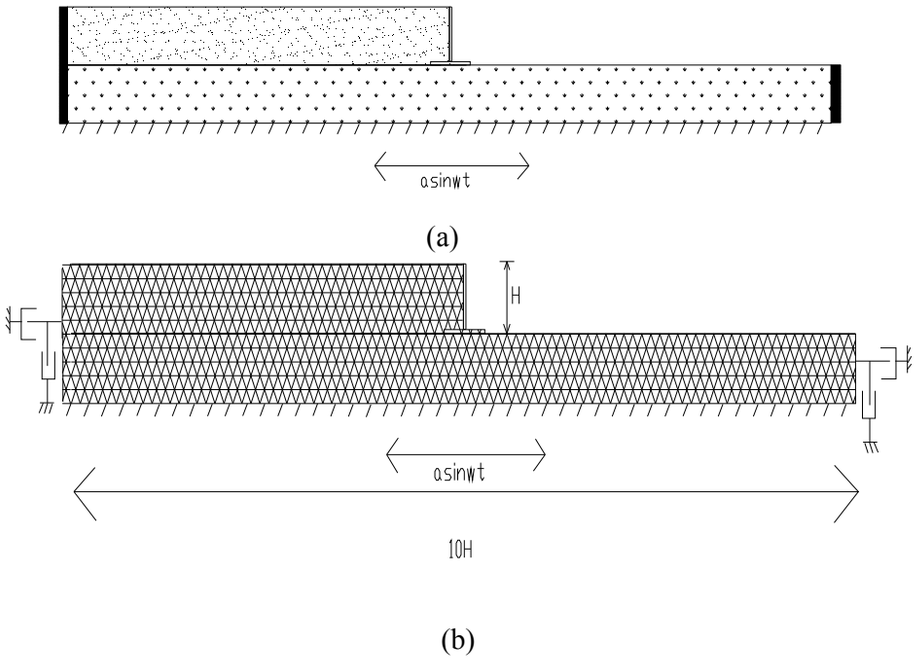


FIG.1. (a) Geometry and (b) finite element discretisation of the model

Table 2. Material properties of concrete structural elements

Parameter	Value
Material	Concrete
Unit weight (kN/m^3)	22
Young's Modulus (E) (Gpa)	230
Poisson's Ratio (ν)	0.2

Excitation was applied by a prescribed acceleration time history at the base of the whole model, and the duration of the analyses were chosen to be long enough for the system to reach steady state conditions. Natural frequency for the two layer system with equal thicknesses of H was calculated by Rayleigh algorithm which was described in detail by Biggs (1964). The formulation is:

$$\omega_1^2 = \frac{4V_s^2 V_{sf}^2 (9V_s^2 + V_{sf}^2)}{H^2 \left[\left(6V_s^2 + V_{sf}^2 \right)^2 + 9V_s^4 \right]} \qquad (1)$$

where V_s and V_{sf} are the shear wave velocities of the backfill and foundation layers respectively. By using Eq. 1, natural frequency of the system for low shaking was calculated as 1.43 Hz.

Effect of Input Excitation Amplitude

The effect of input acceleration is studied by exciting the soil-wall system harmonically at different acceleration values. Analyses were carried out for acceleration amplitudes varying between 0.05g and 0.30g. Frequency was taken as 2 Hz for all harmonic loadings. Maximum incremental dynamic thrust obtained by finite element method (FEM) and the methods of M-O and S-Z are shown in Figure 2. Thrust values are commonly close to the values calculated by analytical methods with a maximum difference of 25% which is reached at the amplitude of 0.30g. It is observed that the thrusts obtained by FEM remain lower than the values of S-Z and higher than the ones of M-O for the all amplitudes.

In Figure 3 incremental bending moments occurring on the wall for various acceleration amplitudes are plotted in normalized format. The vertical axis represents normalized wall height z/H where z is the distance from wall base and H is the height of the wall. Horizontal axis represents normalized bending moment that is calculated by dividing the predicted bending moments by the product of the soil unit weight and the wall height cubed. Incremental moments were obtained by subtracting the moments caused by static lateral pressures from the total moments.

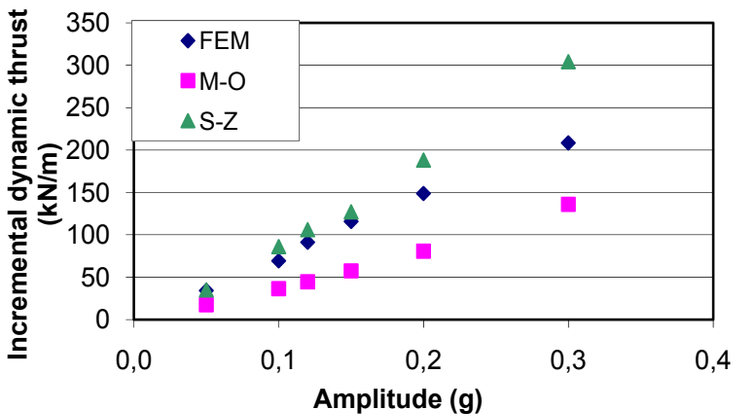


FIG.2. Incremental dynamic thrust versus acceleration amplitude

Application points of the maximum thrusts obtained by FEM are approximately at 0.30H above the base of the wall for the all amplitudes (Fig. 4). For calculating the application points for M-O approach, total active thrust is divided into static and dynamic components. The resultant of the static component is chosen to act at one-third of the wall height above the base of the wall and the resultant of the dynamic load at 0.6H above base as suggested by Seed and Whitman (1970). In figure 4, application point for the M-O solution is calculated for the total thrust which is the

resultant of static and dynamic lateral pressure components. In M-O approach, dynamic thrust is dependent on the horizontal acceleration amplitude and this effectively raises the application point of total thrust for higher acceleration amplitudes.

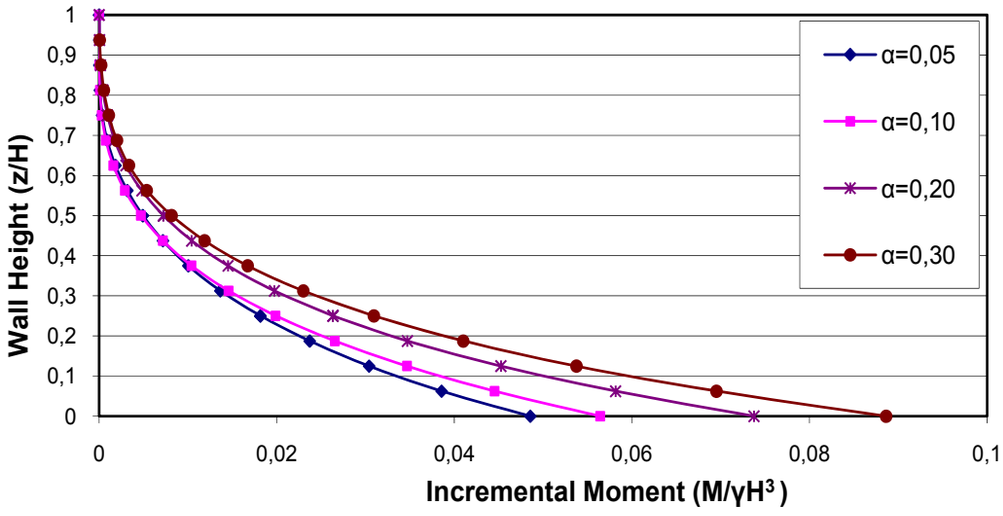


FIG.3. Incremental normalized bending moments for different acceleration amplitudes (α in terms of g)

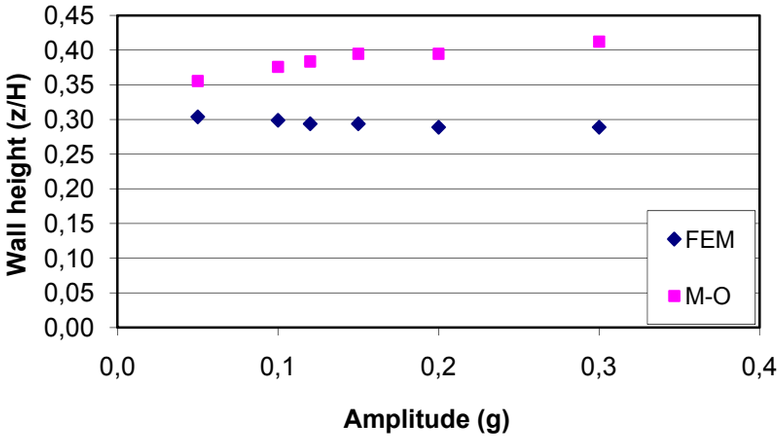


FIG.4. Application point of total thrust (static+dynamic) for different acceleration amplitudes

Effect of Input Excitation Frequency

Effect of input excitation frequency is investigated in a frequency ratio between 1 and 6. Frequency ratio (ξ) is defined as the ratio of base excitation frequency to natural frequency of the system. Analyses were performed by constant base acceleration amplitude of 0.1g. Dynamic thrust gets the greatest value in resonance condition (ξ=1) for FEM and S-Z method, while it is constant for the method of M-O which is not frequency dependent. However, the thrust values are intensely becoming lower than the values of S-Z and M-O methods after frequency ratio of 2 (Fig. 5). Figure 6 also indicates that highest bending moments profile is observed when the system is in resonance condition. Moment profile obtained from M-O solution is similar to FEM predictions when excitation frequency is outside the vicinity of the natural frequency of the system. A third order polynomial approximately fits the bending moment profile obtained from M-O solution. Application points predicted by FEM are varying between the values of 0.28H and 0.38H. As depicted in Figure 7 the point of application is in highest position during resonance case.

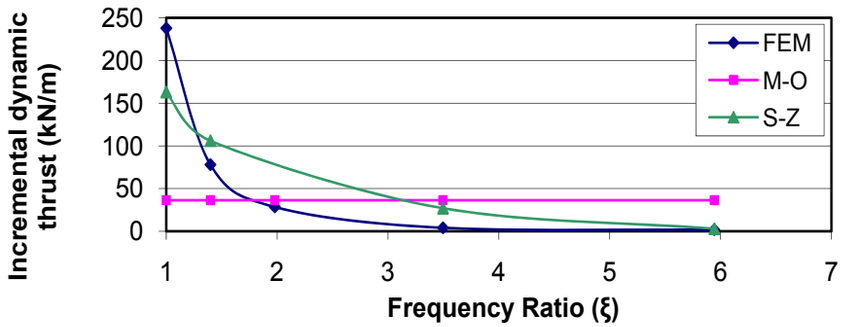


FIG.5. Incremental dynamic thrusts versus frequency ratio

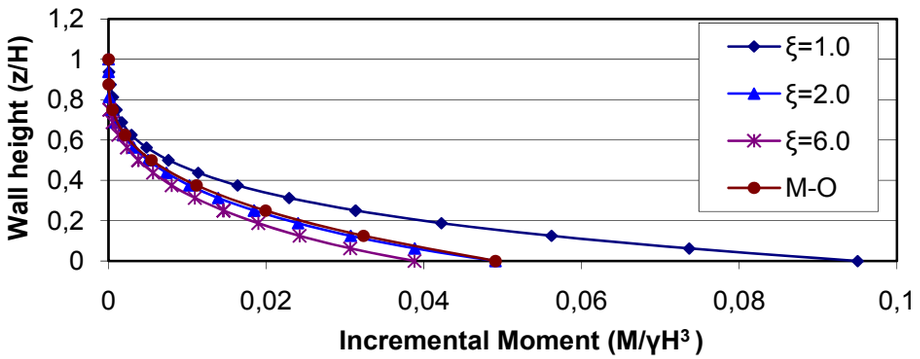


FIG.6. Incremental bending moments for different frequency ratios

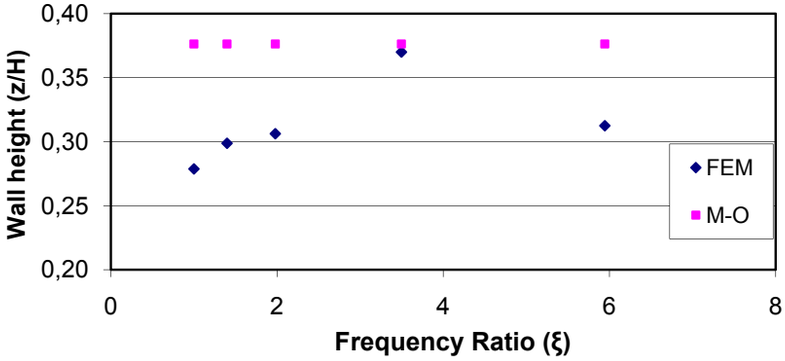


FIG.7. Application point of total thrust (static+dynamic) thrusts at different frequency ratios

Effect of Wall Flexibility

Wall flexibility parameter (f) is defined as the wall stem height raised to the fourth power divided by the product of wall Young's modulus and moment of inertia (H^4/EI). As it is shown in Table 3, different flexibilities were achieved by assigning 5 different values for the wall thickness while the wall height and the other parameters were kept constant.

Table 3. Flexibility parameter as a function of wall thickness

Wall Thickness (m)	0.3	0.4	0.5	0.75	1.0
f (m^2/kN per m)	0.0791	0.0334	0.017	0.0051	0.0021

In Figure 8 incremental dynamic thrust values are plotted against wall flexibility together with M-O and S-Z results. Although flexibility is not a variable in the M-O and S-Z methods, the results of them are included in the figures for comparison purposes. According to FEM analyses, dynamic thrust decreases and approaches to a constant value with the increase in flexibility of the wall.

The moments obtained by FEM analyses are also dependent on wall flexibility. As it is seen in Figure 9, larger moments are occurring at wall base for less flexible walls. Nevertheless, M-O results are nearly identical with the results of FEM analyses for nearly rigid wall of 1m in thickness, but it overestimates the moments for flexible walls.

Figure 10 shows that there is no significant change in application points of thrust obtained for different wall flexibilities.

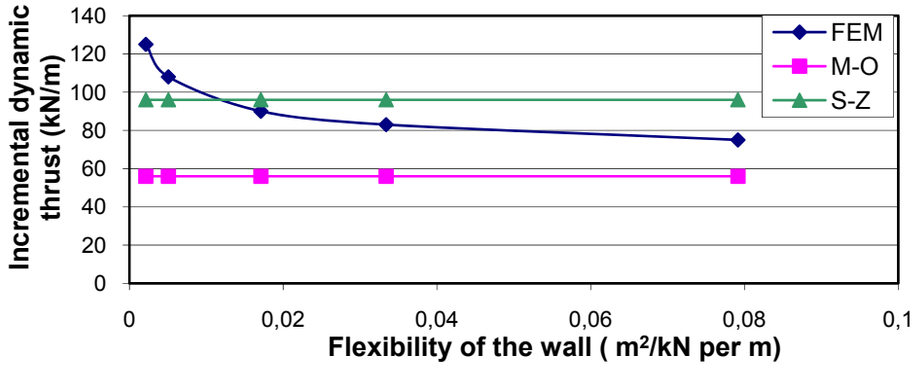


FIG.8. Incremental dynamic thrusts versus wall flexibility

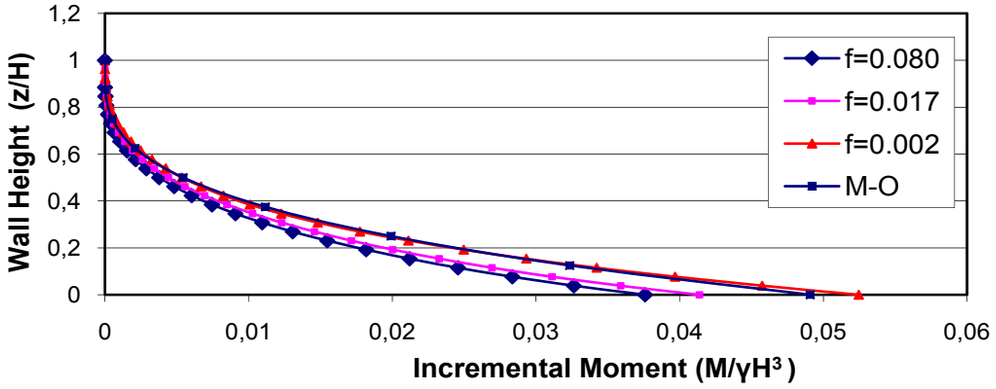


FIG.9. Incremental bending moments for different flexibilities

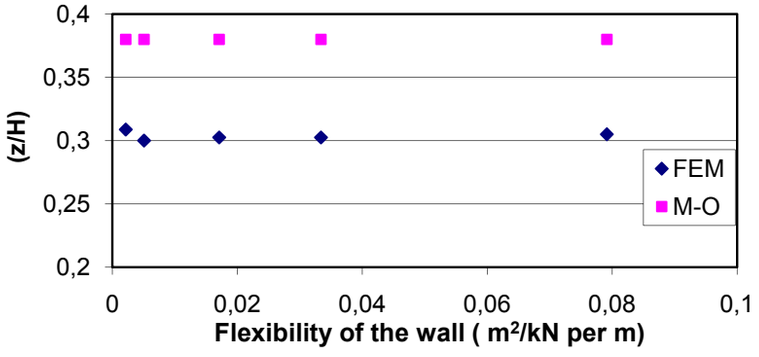


FIG.10. Application point of total thrust (static+dynamic) at different wall flexibilities

CONCLUSIONS

Values of incremental dynamic thrust, point of application and dimensionless bending moment profiles are presented together with commonly used pseudo-static Mononobe-Okabe and pseudo-dynamic Steedman-Zeng approaches. Comparison of analytical and numerical results indicates that base excitation amplitude is the major effective parameter on the dynamic lateral thrust acting on the wall. In the analyses performed by different base excitation amplitudes, it is observed that the dynamic thrust is significantly increasing for higher amplitudes, and the increasing trend is also valid for the results of M-O and S-Z methods. The application point of thrust remains constant at approximately 0.30H above the base for FEM analyses.

Effect of frequency on thrust becomes significant when excitation frequency approaches to the natural frequency of the system. In resonance case, thrust obtained by FEM is remarkably larger than the values obtained by M-O and S-Z methods. Besides, it must be recalled that M-O method does not take into account the effect of excitation frequency. According to FEM and S-Z method, increasing excitation frequency causes dynamic lateral thrust decrease, and predictions of FEM are in better accordance with the ones of analytical methods when excitation frequencies are far from natural frequency of soil-wall system. Application points of the total thrusts obtained by M-O method are approximately at 0.38H above the base of the wall for all of the frequency ratios investigated, whereas application points predicted by FEM are between the values of 0.28H and 0.38H.

Effect of wall flexibility on the dynamic response was investigated through the analyses in which thickness of the wall was changed while height of the wall was kept constant. It is observed that thrust occurring due to dynamic motion is indeed a function of flexibility. The magnitude of dynamic thrust and bending moments decrease as the flexibility increases. S-Z method, which takes into account the amplification of motion through the height of the backfill, predicts dynamic thrust values close to FE solutions for wall flexibilities larger than $0.02 m^2/kN$ per meter. However, it must be noted that these flexibility analyses were performed by a base excitation input of 0.1g in amplitude and 5 Hz in frequency. Evaluation of dynamic response of cantilever retaining walls which are to be imposed by real earthquake acceleration-time histories is left as a further investigation.

REFERENCES

Biggs, J. M. (1964). *Introduction to Structural Dynamics*. McGrawHill, New York.

Mononobe, N. and Matsuo, H. (1929). "On the determination of earth pressure during earthquakes" *Proceedings of World Engineering Conference*, (9), 177-185.

Okabe, S. (1924) "General theory of earth pressure and seismic stability of retaining wall and dam", *J. Japanese Soc. of Civil Eng.*, 10(5).

Schanz, T., Vermeer, P. A., Bonnier P. G. (1999). "The hardening –soil model: Formulation and verification" *Beyond 2000 in Computational Geotechnics* , In R.B.J. Brinkgrieve, Balkema-Rotterdam, 281-290

Seed,H.B.,Whitman,R.V. (1970). "Design of earth retaining structures for dynamic loads", Proceedings, ASCE Specialty Conference on Lateral Stresses in the Ground and Design of Earth Retaining Structures, pp. 103-147

Steedman, R. S. and Zeng, X. (1990). "The influence of phase on the calculation of pseudo-static earth pressure on a retaining wall" *Geotechnique*, (40), 103-112.

Veletsos, A. S. and Younan, A. H. (1994). "Dynamic soil pressures on rigid retaining walls." *Earthquake Engrg. and Struct. Dyn.,* 23(3), 275-301.

Veletsos, A. S. and Younan, A. H. (1997). "Dynamic response of cantilever retaining walls." *Journal of Geotechnical and Geoenv. Engineering,* ASCE 123(2), 161-72.

This page intentionally left blank

Extended Veletsos-Younan Model for Geofoam Compressible Inclusions Behind Rigid, Non-Yielding Earth-Retaining Structures

John S. Horvath[1], Ph.D., P.E., M.ASCE

[1]Professor, Manhattan College, Civil and Environmental Engineering Department, Bronx, NY 10471, U.S.A.; john.horvath@manhattan.edu

ABSTRACT: *Geofoam* is a type of *cellular geosynthetic* that can be used to reduce lateral earth pressures acting on rigid earth-retaining structures (RERSs) under a variety of soil and load conditions. One of the geosynthetically-functional ways in which geofoams do this is as a *compressible inclusion* to allow shear-strength mobilization of retained soil through *controlled yielding* which involves the well-known soil mechanics mechanism of *arching*. This paper describes how a mathematical model developed by Veletsos and Younan for a seismic-load application not involving geofoam was modified and extended to create a novel solution involving the use of geofoam as a compressible inclusion. An illustration of how this Extended Veletsos-Younan model can be applied in practice is also included using a case-history and full-scale, 1-*g* physical tests.

INTRODUCTION

Geofoam is the generic geosynthetic name for any closed-cell foam used in a geotechnical application (Horvath 1995). Contrary to popular, but incorrect, belief the term geofoam is not limited to one specific material or product. Geofoam is now recognized as a type of cellular geosynthetic along with geocombs and geocells.

Geofoams have many and varied functional applications. One with significant potential use worldwide and in a wide variety of ground and loading conditions is to reduce lateral earth pressures on earth-retaining structures (ERSs). A companion paper to this conference (Horvath 2008) addresses this overall geofoam application with an emphasis on seismic loading. This paper focuses on specific, innovative aspects of this broader subject.

BACKGROUND

Terminology

A term used in discussions related to ERSs is *yielding*. In this context, yielding is synonymous with horizontal (lateral) displacement.

Compressible Inclusions: Basic Concept

One of the more theoretically elegant yet practical functional uses of geofoam is as a *compressible inclusion* (Horvath 1995, 1996, 1998a, 2004, 2005). This is a *large-strain* geofoam function as the geofoam product used is designed to undergo relatively large compressive strains under design-load conditions.

The basic concept of a compressible inclusion is one that existed before geofoams were invented. Indeed the concept existed before modern soil mechanics evolved beginning in the 1920s. Simply stated, a compressible inclusion is any material that is intentionally the least-stiff component of a multi-material geotechnical system. As a result, the compressible inclusion readily compresses compared to the other system components under loads applied to the overall system. The net result is improved performance of the system, usually through load reduction (with concomitant safety increase and/or cost reduction) on one or more system components.

The earliest, classical application of the compressible-inclusion concept was using bales of hay or straw above the crown of underground conduits to reduce vertical loads on the conduits (Spangler and Handy 1982). This involved the soil-mechanics mechanism of *vertical arching* that is colloquially referred to as the *trap-door* effect (Terzaghi 1943). Arching can also develop in the horizontal direction (Handy 1985, Harrop-Williams 1989) which means that a compressible inclusion can be used to induce horizontal arching as well as vertical arching. Research has indicated that a durable, 'engineered' material such as geofoam is a superior material for compressible inclusions for both vertical and horizontal arching (Horvath 1995).

Compressible Inclusions: Geofoam Use to Reduce Lateral Earth Pressures on Earth-Retaining Structures

The basic, generic geofoam application of the compressible-inclusion concept with ERSs is known as the *Reduced-Earth-Pressure* (REP) concept and is illustrated in Figure 1. A relatively-thin (of the order of 300 mm (1 ft) thick or less) layer of geofoam that has been engineered and manufactured to have the desired stiffness is placed in a chimney-drain orientation between the back of the ERS and retained soil. In this application, the primary role of the geofoam product is to readily compress in its thickness (horizontal) dimension and allow horizontal displacement of the retained soil mass even if the ERS is rigid and non-yielding (e.g. a below-grade building wall, bridge abutment, or restrained retaining wall). As a result of this process, which is

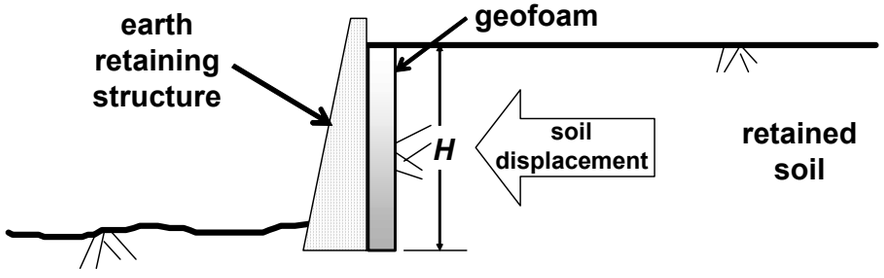


FIG. 1. Generic application of REP concept of compressible-inclusion function.

referred to as *controlled yielding*, the inherent shear strength of the retained soil is mobilized and the lateral earth pressure acting on the ERS decreases from the lateral pressure that would exist had the compressible inclusion not been there. Stated another way, a geofoam compressible inclusion used as shown in Figure 1 allows a retained soil mass to undergo the same horizontal displacement adjacent to a non-yielding RERS as it would have adjacent to a yielding one such as a free-standing retaining wall. This load-reduction benefit can be enjoyed for a variety of soil and loading conditions, as well as for both new construction as well as in the rehabilitation, renovation, or upgrading of existing structures. Of interest and relevance to this conference is use under seismic loading.

ANALYTICAL METHODS

Overview

The concept of using a geofoam compressible inclusion for lateral earth pressure reduction on RERSs has been proven by both research and actual use in practice going back at least to the 1980s. However most applications to date have involved gravity loads. Thus analytical methods for seismic loads are still an active, ongoing area of research and development. It is the primary purpose of this paper to discuss some of this ongoing research in order to encourage others to pursue research and advance the state of knowledge of this useful geotechnology.

Traditional Model

The traditional analytical model used to date for the REP concept illustrated in Figure 1 presumes use of this concept only with non-yielding RERSs that would normally be designed for the at-rest earth pressure state under both gravity and seismic loading. It is further assumed that the stiffness of the geofoam compressible inclusion is intentionally selected so as to allow horizontal displacement of the retained soil mass under the estimated earth loads (gravity or seismic) that is sufficient to mobilize the active earth pressure state within the retained soil. As discussed in Horvath (2004, 2005, 2008), the model concept used to date is that of two horizontally-oriented springs in series. One spring represents the compressive stress versus horizontal displacement in compression of the geofoam compressible inclusion and the other spring represents the compressive stress versus horizontal displacement in extension of the retained soil mass.

In most REP-concept applications, the primary design variable is the compressive stiffness of the compressible-inclusion 'spring'. This is defined as the Young's modulus of the compressible-inclusion material divided by the thickness (horizontal dimension in Figure 1) of the compressible-inclusion product installed. For the purpose of quantifying this stiffness it was found useful to define a new dimensionless parameter, λ, called the *normalized compressible inclusion stiffness* (Horvath 2000, 2004, 2005). This parameter is evaluated numerically using the following equation:

$$\lambda = \frac{E_{ci} \cdot H}{t_{ci} \cdot p_{atm}} \quad \textbf{(1)}$$

where E_{ci} = Young's modulus of the compressible-inclusion material; H = 'geotechnical' height of the RERS (see Figure 1); t_{ci} = thickness of the compressible inclusion; and p_{atm} = atmospheric pressure. Limiting values are $\lambda = 0$ (the 'perfectly compressible' case of horizontal displacement without restraint) and $\lambda = \infty$ (the 'perfectly rigid' case of no horizontal displacement, i.e. infinite restraint). Quantitatively, the smaller the value of λ the more compressible the inclusion is.

In the REP-concept application, the goal is to completely mobilize the inherent shear strength of the retained soil by allowing sufficient ground displacement so that the assumed active earth pressure state develops. This is presumed to occur after a certain magnitude of horizontal displacement, Δ_a, of the retained-soil mass (usually stated in the literature (e.g. Clough and Duncan 1991) as a dimensionless ratio, Δ_a/H). Therefore the stiffness of the compressible inclusion as defined by Equation 1 is matched to the soil stiffness necessary to mobilize the active state.

This simple-but-effective analytical model was first proposed by Partos and Kazaniwsky (1987) for gravity loading and used successfully on a project documented by them, with additional analysis and discussion of this case history by Murphy (1997). This model has gone through several evolutionary changes as discussed in detail in Horvath (2000). The most-useful form of the solution in practice is to solve for the required minimum thickness of the compressible inclusion:

$$t_{ci} = \frac{E_{ci} \cdot \left(\Delta_a / H\right)}{0.75 \cdot K_a \cdot \cos\delta \cdot \gamma_t} \quad \textbf{(2)}$$

where K_a = coefficient of active earth pressure evaluated numerically using either Coulomb or some 'exact' (e.g. log-spiral) theory; δ = friction angle between the retained soil and the geofoam compressible-inclusion material; and γ_t = total unit weight of the retained soil.

Equation 2 can be logically extended to seismic loading and is done so here as one new contribution of this paper:

$$t_{ci} = \frac{E_{ci} \cdot \left(\Delta_a / H\right)}{0.75 \cdot K_{ae} \cdot \cos\delta \cdot \gamma_t} . \quad \textbf{(3)}$$

The only change from Equation 2 to Equation 3 is in the lateral-earth-pressure coefficient that appears in the denominator. K_{ae} in Equation 3 represents the seismic active earth pressure coefficient that could be evaluated, for example, from Mononobe-Okabe theory (Ebeling and Morisson 1992, Kramer 1996).

Alternative Model

While Equation 3 provides a simple, pragmatic model for use in routine practice it is of interest to explore alternative models that might capture the behavior of the

system more accurately yet still retain a simplicity of use that would be attractive in practice. The basis of one such model is the work of Veletsos and Younan (1994) who developed a mathematical model and corresponding numerical solution for a yielding RERS where yielding is restricted to the mode of rotation-about-base. They expressed the relative soil-wall-system stiffness using a dimensionless variable, d_θ, that was defined as follows:

$$d_\theta = \frac{G_{avg} \cdot H^2}{R_\theta} \tag{4}$$

where G_{avg} = average shear modulus of the retained soil (evaluation depends on the variation of shear modulus, G, with depth); H = geotechnical height of the RERS as before (see Figure 1); and R_θ = a rotational-spring stiffness that defines the rotational stiffness of the RERS on its foundation soil.

The author recognized subsequently that the applicability of the Veletsos-Younan model could be extended from its original boundary-value assumptions as their model could alternatively be visualized as a non-yielding RERS with a compressible inclusion placed between the RERS and retained soil as shown in Figure 1. In this case, even though the RERS cannot rotate about its base the retained soil can still go through the same rotational displacement as in the original Veletsos-Younan problem because of the compressible inclusion.

The postulation and detailed derivation of this extension of the Veletsos-Younan model was presented in Horvath (1997, 1998b). The final result (in a form simplified slightly from the original one published) is

$$d_\theta = \frac{2 \cdot G_{avg} \cdot t_{ci}}{H \cdot E_{ci}} \tag{5a}$$

which, when combined with Equation 1, can be expressed as

$$d_\theta = \frac{2 \cdot G_{avg}}{\lambda \cdot p_{atm}} \tag{5b}$$

where all terms have been defined previously.

Other Models

The use of geofoam compressible inclusions to reduce lateral earth pressures on RERSs is receiving increasing attention from both practitioners and researchers. In addition to the traditional and Extended Veletsos-Younan models discussed in this paper, there are other models that have been developed in recent years by others. One such model can be found in Bathurst et al. (2007b). Consideration of this and other models is beyond the scope of this paper.

GEOFOAM MATERIAL AND PRODUCT SELECTION

As discussed in detail in Horvath (1995), there are numerous materials and products that have been used for geofoam applications in general. In particular, the concept of using geofoams as compressible inclusions has been investigated since at least the 1980s. Thus there is significant experience with determining the optimum geofoam materials and products to use for compressible-inclusion functional applications although both material and product refinement continues to the present.

At the present time and for the foreseeable future, expanded polystyrene (EPS) and materials related to it are the geofoam materials of choice for compressible inclusions. EPS is the ubiquitous white polymeric (plastic) foam used for beverage cups and cushion packaging. For the geofoam applications under discussion, EPS has been and can be used in various forms:

- *Block-molded* EPS is the simplest, most-generic product to use. All things being equal, the lower the EPS density the lower the material stiffness so typically the lowest-density EPS that is commercially available is used for compressible-inclusion applications. However, experience indicates that generic block-molded EPS is usually the least efficient choice from both technical and cost perspectives.

- A more-efficient form of block-molded EPS for compressible-inclusion applications is a product that has had a portion of its otherwise-solid cross-section removed so that there is less material per unit area in a direction parallel to the direction of desired displacement (horizontal in the case of Figure 1). A simple way in which this can be achieved is by creating a saw-tooth product (called *castellated* in product literature) by judicious factory cutting or by simply drilling holes (e.g. see Bathurst et al. 2007a, 2007b).

- The most-efficient form of EPS that has been found to date for compressible-inclusion applications is *resilient* (*elasticized*) EPS. This is generic low-density block-molded EPS that has been subjected to additional manufacturing steps to reduce its stiffness significantly below that of normal EPS, especially under relatively low-stress conditions (Horvath 1995).

- There is a geofoam material called *porous-polystyrene block* (PPB) that uses the same raw material (called *expandable polystyrene* or colloquially *bead* or *resin*) as EPS in the initial (*pre-expansion*) stage of it manufacture but with a completely different process used for its final stage of manufacture. Although PPB was developed for a completely different geofoam functional application (as a geosynthetic sheet drain for fluids) by happenstance PPB displays stiffness characteristics very similar to the aforementioned resilient-EPS. Thus PPB can be used for its compressible-inclusion functional characteristics. In fact, by pure happenstance it was the material used for the earliest known published case history involving geofoam compressible inclusions for lateral earth pressure reduction (Partos and Kazaniwsky 1987).

Regardless of the specific material or combination of materials used (e.g. PPB can be factory-laminated to resilient-EPS and a nonwoven geotextile to create a multifunctional geocomposite that acts as a compressible inclusion providing fluid drainage and thermal insulation as well), the products created from these materials for applications as shown in Figure 1 are typically factory-produced panels that are simply attached to the back of the RERS using a special adhesive to create the desired geometry.

CONCEPT VERIFICATION

Introduction

Published research and case-history applications to date involving geofoam compressible inclusions have largely focused on gravity loading. However in recent years there has been increased interest in applications involving seismic loading so it is of interest to review available information in terms of the Extended Veletsos-Younan model discussed in this paper.

Numerical Modeling and Case-History Application

Inglis et al. (1996) presented a case history where low-density (13 kg/m^3 (0.81 lb/ft^3)) block-molded EPS was used around the below-grade portion of a building in Vancouver, British Columbia, Canada. A variety of numerical-modeling techniques were reportedly used during the design phase of the project. Although their published information is subject to some interpretation for the purpose of using Equation 1 to evaluate the relative stiffness of the compressible inclusion, calculations performed by the author resulted in λ values of the order of 50 to 100 for this project. Recall that the closer the value of λ is to zero the more effective the compressible inclusion should be at reducing lateral earth pressures compared to the baseline case of no compressible inclusion.

Using Equation 5b, this range in values of λ produce a relative soil-wall-system stiffness for the Extended Veletsos-Younan model, d_θ, of the order of 5 which suggests that the compressible inclusion in this case should be relatively effective at reducing lateral earth pressures. Note that for comparative purposes $d_\theta = 0$ is the baseline case of no compressible inclusion and thus the larger the value of d_θ the more effective the compressible inclusion in terms of lateral-earth-pressure reduction.

Inglis et al. indicated that their various numerical analyses suggested that the geofoam compressible inclusion reduced design loads by approximately 50% compared to the baseline condition of no compressible inclusion. This order-of-magnitude reduction is consistent with what one would expect for a $d_\theta = 5$ based on figures published in Veletsos and Younan (1994).

Large-Scale Model Testing

Bathurst et al. (2007a) presented the results of 1-*g* laboratory testing involving relatively large-scale shake-table testing of a physical model that consisted of a 1-

metre-high rigid, non-yielding wall with a geofoam compressible inclusion. They tested three different compressible-inclusion materials and products:

- generic normal, moderate-density (16 kg/m^3 (1.0 lb/ft^3)), block-molded EPS;
- resilient-EPS (a proprietary commercial product); and
- generic normal, low-density (12 kg/m^3 (0.75 lb/ft^3)), block-molded EPS that had been modified to have one-half of its cross-sectional area removed by coring holes.

Using Equation 1, the author calculated that the relative stiffnesses of the compressible inclusions, λ, were 317, 86, and 26 respectively. Note that these values cover a larger range than the $\lambda \approx 50$ to 100 for the Inglis et al. (1996) case history discussed previously. Again recall that the smaller the value of λ the more effective the compressible inclusion should be at reducing lateral earth pressures compared to the baseline case of no compressible inclusion ($\lambda = 0$ is the limiting case of zero lateral earth pressure or a 'perfect' compressible inclusion).

The author's calculations using Equation 5b of the relative soil-wall-system stiffness, d_θ, for the Bathurst et al. tests were complicated by the fact that evaluating G_{avg} using the data provided by Bathurst et al. (2007a) was inconclusive. However using additional data in a companion paper (Bathurst et al. 2007b) it was possible to estimate values for $d_\theta = 0.4$, 2, and 5 respectively for the three types of compressible inclusion tested ($\lambda = 317$, 86, and 26 respectively). This is a relatively large range in relative soil-wall stiffness. Again, note that the larger the value of d_θ the more effective the compressible inclusion should be at reducing lateral earth pressures ($d_\theta = 0$ represents the baseline case of no compressible inclusion and no lateral-earth-pressure reduction).

Measurements of wall forces reported by Bathurst et al. (2007a) suggest that the compressible inclusions produced reductions in lateral earth pressures in the range between approximately 15% and 35% relative to the baseline case of no compressible inclusion. The relative magnitude of load reduction was consistent with what would be expected based on the relative values of λ and d_θ, i.e. the least-efficient compressible inclusion (a combination of the largest value of λ and smallest value of d_θ) resulted in the smallest load reduction, etc. The range of load reductions observed were also consistent with what one would expect based on figures published in Veletsos and Younan (1994).

CONCEPT EXTENSION

It is of interest to note that the REP concept shown in Figure 1 can be logically extended by including multiple layers of geosynthetic tensile reinforcement (geotextiles, geogrids, metallic elements) within the retained soil (Horvath 1995, 1996, 1998a, 2004, 2005, 2008). This is referred to as the *Zero-Earth-Pressure* (ZEP) concept because the lateral earth pressures acting on the ERS can be reduced to effectively zero by using appropriate combinations of compressible-inclusion and

reinforcement stiffnesses. This reduction accrues from the mobilization of resistance within the tensile reinforcement in the classic geotechnical mechanism of *mechanically stabilized earth* (MSE).

The ZEP concept is much less advanced than the REP concept in terms of model development, physical testing, and use in practice. However all research to date supports the validity of the basic ZEP concept and it is possible that the Extended Veletsos-Younan model discussed in this paper could be utilized if the horizontal stiffness of the reinforced retained soil mass were properly quantified, perhaps using elastic theory (e.g. Harrison and Gerrard 1972) as noted in Horvath (2008).

CONCLUSIONS

The use of geofoam compressible inclusions consisting of EPS and/or related materials in what is referred to as the REP concept is a proven geotechnology to reduce lateral earth pressures on RERSs under both gravity and seismic loading. The Extended Veletsos-Younan model shows promise as an analytical tool for analyzing and designing geofoam compressible inclusions under seismic loading and deserves further research and verification for this purpose.

One of the things to keep in mind when using compressible inclusions in a REP application is that the reduction in lateral earth pressures is not without limit. In any given application for both gravity and seismic loading there is always a stiffness of compressible inclusion (as characterized by the thickness of the inclusion) beyond which using a thicker inclusion with less stiffness would not have any technical benefit, at least in terms of lateral-earth-pressure reduction (it might in terms of other geofoam functions such as thermal insulation). This was observed in the numerical modeling performed by Inglis et al. (1996) and, importantly, is a feature captured by the Extended Veletsos-Younan model as well as the earlier, simpler traditional model that was also discussed in this paper.

REFERENCES

Bathurst, R. J., Zarnani, S. and Gaskin, A. (2007a). "Shaking table testing of geofoam seismic buffers." *Soil Dyn. & EQ Engrg.*, 27: 324-332.

Bathurst, R. J., Keshavarz, A., Zarnani, S. and Take, W. A. (2007b). "A simple displacement model for response analysis of EPS geofoam seismic buffers." *Soil Dyn. & EQ Engrg.*, 27: 344-353.

Clough, G. W. and Duncan, J. M. (1991). "Earth pressures". Ch. 6 in *Foundation engineering handbook*, 2nd ed., H.-Y. Fang (ed.). Van Nostrand Reinhold, New York, NY.

Ebeling, R. M. and Morrison Jr., E. E. (1992). "The seismic design of waterfront retaining structures." *U.S. Army Tech. Rpt. ITL-92-11/U.S. Navy Tech. Rpt. NCEL TR-939*, USACOE WES, Vicksburg, MS.

Handy, R. L. (1985). "The arch in soil arching." *J. Geotech. Engrg. Div.*, 111 (3): 302-318.

Harrop-Williams, K. O. (1989). "Geostatic wall pressures." *J. Geotech. Engrg. Div.*, 115 (9): 1321-1325.

Harrison, W. J. and Gerrard, C. M. (1972). "Elastic theory applied to reinforced earth." *J. Soil. Mech. and Fndns. Div.*, 98 (SM12): 1325-1345.

Horvath, J. S. (1995). *Geofoam geosynthetic*. Horvath Engrg., P.C., Scarsdale, NY.

Horvath, J. S. (1996). "The compressible inclusion function of EPS geofoam: an overview." *Proc. Intl. Sym. on EPS Construction Method (EPS Tokyo '96)*, Tokyo, Japan: 71-81.

Horvath, J. S. (1997). "The compressible inclusion function of EPS geofoam." *Geotextiles and Geomembranes*, 15 (1-3): 77-120.

Horvath, J. S. (1998a). "The compressible inclusion function of EPS geofoam: an overview of concepts, applications, and products." *Res. Rpt. No. CE/GE-98-1*, Manhattan Coll. Civ. Engrg. Dept., Bronx, NY.

Horvath, J. S. (1998b). "The compressible-inclusion function of EPS geofoam: analysis and design methodologies." *Res. Rpt. No. CE/GE-98-2*, Manhattan Coll. Civ. Engrg. Dept., Bronx, NY.

Horvath, J. S. (2000). "Integral-abutment bridges: problems and innovative solutions using EPS geofoam and other geosynthetics." *Res. Rpt. No. CE/GE-00-2*, Manhattan Coll. Civ. Engrg. Dept., Bronx, NY.

Horvath, J. S. (2004). "Geofoam compressible inclusions: the new frontier in earth retaining structures." *Geotechnical Engineering for Transportation Projects* (GSP 126), ASCE, Reston, VA: 1925-1934.

Horvath, J. S. (2005). "Expanding the use of expanded polystyrene (EPS) geofoam in practice." *Proc. BSCES ASCE Geo-Institute Fall 2005 Geotech. Engrg. Sem.*, Boston Soc. Civ. Engrs. Sec. ASCE, Boston, MA.

Horvath, J. S. (2008). "Seismic lateral earth pressure reduction on earth-retaining structures using geofoams." *Geotechnical Earthquake Engineering and Soil Dynamics IV*, ASCE, Reston, VA.

Inglis, D., Macleod, G., Naesgaard, E. and Zergoun, M. (1996). "Basement wall with seismic earth pressures and novel expanded polystyrene foam buffer layer." *Proc. 10th Ann. Sym.*, Vancouver Geotech. Soc., Canada.

Kramer, S. L. (1996). *Geotechnical earthquake engineering*. Prentice Hall, Upper Saddle River, NJ.

Murphy, G. P. (1997). "The influence of geofoam creep on the performance of a compressible inclusion." *Geotextiles and Geomembranes*, 15 (1-3): 121-131.

Partos, A. M. and P. M. Kazaniwsky (1987). "Geoboard reduces lateral earth pressures." *Proc. Geosynthetics '87*, IFAI, St. Paul, MN: 628-639.

Spangler, M. G. and Handy, R. L. (1982). *Soil engineering* (4th ed.). Harper & Row, New York, NY.

Terzaghi, K. (1943). *Theoretical soil mechanics*. John Wiley and Sons, Inc., New York, NY.

Veletsos, A. S. and Younan, A. H. (1994). "Dynamic modeling and response of soil-wall systems." *J. Geotech. Engrg.*, 120 (12): 2155-2179.

LATERAL SEISMIC SOIL PRESSURES ON SOLDIER PILE WALLS

Jin-xing Zha, Ph.D., P.E.[1]

ABSTRACT

This paper presents a simplified procedure for computing lateral seismic earth pressures on soldier pile retaining walls. This approach is to develop two curves of lateral load versus displacement behavior to consider the soil-pile-wall interaction in a "decoupled" way. A curve of lateral earth driving force versus displacement is first established by slope stability analysis for the sliding soil mass behind the wall based on the Newmark chart that relates the standardized maximum displacement of the soil mass to the limiting acceleration coefficient. A second curve of lateral load versus displacement for the soldier pile/wall is then obtained by lateral analysis of the pile/wall structure under the lateral earth driving force. The intersection between the two load-displacement curves is considered as the lateral earth driving force on the pile/wall. An example of analyzing one soldier pile retaining wall is presented in this paper to illustrate the proposed method. The simplified method of accounting for the soil-pile-wall interaction may be used to estimate the lateral soil seismic driving forces on piles/walls without the uncertainty in determining the seismic coefficient related to the use of the Mononobe-Okabe method and choosing the design wall displacement. However, the simplified method is not validated and the results from the method should be verified against finite element studies or field or model testing.

INTRODUCTION

In current practice for seismic design of bridge abutments or retaining walls, the Mononobe-Okabe method is widely used to determine the soil pressures including

[1] Office of Earthquake Engineering, California Department of Transportation, 1801 30th Street – MS 9-2/5i, Sacramento, CA 95816, U.S.A.

dynamic inertia effect by applying assumed pseudo-static horizontal and/or vertical accelerations. To account for the effect of lateral displacement of a retaining structure on the seismic soil pressure, different intensities of earthquake shaking in terms of a seismic acceleration coefficient are assigned to apply to retaining structures with different restraints that limit lateral displacement. For most design purposes, a value of seismic acceleration coefficient from one-third of the peak ground acceleration (k_h = A/3) (Caltrans, 2003) to one-half of it (k_h = A/2) (AASHTO, 2007) may be used, provided that an outward displacement of up to 5 inches for k_h = A/2 and 15 inches for k_h = A/3 is allowed. This allowed outward displacement, however, is excessive for most retaining walls located in urban areas. One shortcoming with the use of the Mononobe-Okabe method is the uncertainty in determining the seismic acceleration coefficient according to the restraints that prevent the wall from freely moving.

In the latest AASHTO LRFD Bridge Design Specifications (2007) – Section 11, a 'design-for-displacement' approach is recommended for bridge abutments and retaining walls that may undergo significant horizontal displacement. This is a simplified Newmark method that relates the site peak acceleration, the maximum ground velocity, and the maximum wall lateral displacement to the seismic acceleration coefficient. This method converts the determination of the seismic acceleration coefficient to an issue of choice of the desirable wall displacement. As soon as a design value of maximum wall displacement is chosen for the wall design at a site where the peak acceleration and maximum ground velocity are designated, the seismic acceleration coefficient is approximated by an equation given in the LRFD specifications (AASHTO, 2007). Then the estimated seismic acceleration coefficient is used in the Mononobe-Okabe method to obtain the seismic earth pressure on the retaining wall. However, there are cases where choosing a design wall displacement is as difficult or subjective as determining the seismic acceleration coefficient. Also, in instances where the materials behind a retaining wall include fine-grained soils such as clay, it is hard to directly employ the Mononobe-Okabe method to compute the seismic lateral earth pressure (Power *et al*, 2004).

This paper presents a simplified two-curve procedure that may be used for computing lateral seismic earth pressures on bridge abutments or retaining walls supported by piles with or without tieback anchors. For these walls, the structural stiffness can be estimated without much difficulty and the lateral load versus deflection curve can be found by a computer program such as *COM624P* (Wang and Reese 1993) that uses p-y soil spring models for lateral analysis of flexible long piles. The proposed procedure is a displacement-based method which is based on the Newmark chart that relates the standardized maximum displacement of the sliding block/soil mass to the limiting acceleration coefficient. This displacement-based approach is conceptually an extension of the design method suggested by Richards and Elms (1979) for analyzing seismic behavior of gravity retaining walls with a specified limiting wall displacement to which the limiting acceleration coefficient is correlated (Franklin and Chang 1977). For the sake of simplicity, it is assumed in the present analysis that the seismic force acts in the horizontal direction only. In this analysis, the pile-wall-soil interaction is considered in a "decoupled" manner in which

two separate lateral load versus displacement curves are developed from slope stability analysis and lateral wall/pile analysis, respectively. The solution for the interaction is then obtained by combining the two individual load versus displacement curves. To illustrate the proposed method, presented in this paper is also an example of analysis performed for one soldier pile wall designed to create direct access ramp lanes on/off a state highway in the median area south of a bridge site.

PROPOSED PROCEDURE

The simplified two-curve procedure proposed for computing lateral seismic earth pressures on bridge abutments and retaining walls supported by piles that may be restrained by tieback anchors is outlined as follows:

1 Assessment of site seismicity to determine the horizontal Peak Bedrock Acceleration (PBA) and the Peak Ground Acceleration (PGA): This is usually conducted according to the Caltrans California Seismic Hazard Map 1996 – a GIS database of seismicity for California State and Counties bridges. This assessment may be carried out based on seismicity information from government agencies or research institutes such as U.S. Geological Survey (USGS) and Pacific Earthquake Engineering Research Center (PEER). The maximum ground velocity is not needed for the simplified procedure, which however is one required parameter in using the correlation equation (A11.1.1.2-1) (AASHTO, 2007).

2 Slope stability analysis to determine the lateral seismic earth pressure due to cut slope instability during earthquake shaking based on the simplified Janbu method: By this method, the factor of safety (FOS) against shear failure is defined as:

$$FOS = F_R / F_D \quad (1)$$

in which, F_R and F_D are respectively the horizontal component of the soil resistance along the failure surface and the horizontal driving force of the sliding block mass. When the factor of safety, FOS, is smaller than one or a threshold, additional lateral resistance provided by piles is required to maintain the slope stability. The pile lateral resistance to apply to the cut of the slope is so determined that the nominal factor of safety (FOS_{Reinf}) as defined by Equation (2) is greater than one or a threshold. That is:

$$FOS_{Reinf} = (F_{Pile} + F_R)/ F_D \quad (2)$$

in which, F_{Pile} is the pile lateral resistance required to maintain the slope stability with piles for a designated factor of safety, FOS_{Reinf}. The distribution of the pile lateral resistance is to be discussed in Step (4). By combining Equations (1) and (2), one can get:

$$F_{Pile} = F_R (FOS_{Reinf}/FOS - 1) \quad (3)$$

For a given seismic acceleration coefficient (in unit of g, gravity acceleration), a pseudostatic analysis of slope stability based on the simplified Janbu method generates the safety factor (FOS) and the horizontal component (F_R) of the soil resistance along the failure surface. Consequently, the required pile lateral resistance can be obtained from Equation (3) to maintain the slope stability with a designated factor of safety, FOS_{Reinf}.

This slope stability analysis is performed for a unit width of the slope cut in place of the calculation of seismic soil pressure with Mononobe-Okabe formula. Though there is much work in preparing the input file, the 'finite-layer-type' slope stability analysis gives us flexibility to model a soil profile of layered sandy and clayey soils that cannot be considered in Mononobe-Okabe method.

3 Establishment of lateral seismic soil thrust versus displacement curve – Curve 1 as shown in Figure 3 for the sliding slope mass according to the Newmark sliding block model (Newmark 1965): Part of the results by Franklin and Chang (1977) is tabulated in Table 1 for numerical generation of the curve in seven points. For each of the limiting accelerations listed in Column 3, 4, or 5, depending on the moment magnitude of an earthquake, a required pile lateral resistance calculated from Equation (3) and the corresponding permanent displacement in Column 2 make one point on the curve of lateral seismic soil thrust vs. displacement. For more accuracy in analysis or "rare" or Maximum Considered Earthquake events, the curves of sliding displacement versus limiting acceleration coefficient as given in Table 1 should be replaced with results from site-specific time history analysis based on the Newmark sliding block integration.

Table 1. Mean Permanent Displacement of Slide Block as a Function of k/A* for Different Moment Magnitudes of Earthquakes (Soil Sites)

No.	Permanent Displacement mm (inches)	Moment Magnitude of Earthquake		
		5.2-6.0	6.5	7.7
1	1016 (40)	0.14	0.17	0.2
2	178 (7)	0.34	0.37	0.41
3	76 (3)	0.44	0.47	0.51
4	25.4 (1)	0.54	0.6	0.62
5	7.6 (0.3)	0.64	0.7	0.74
6	2.5 (0.1)	0.74	0.79	0.83
7	0.25 (0.01)	1.0	1.0	1.0

* k/A is the ratio of limiting acceleration coefficient to peak ground acceleration coefficient.

4 Development of lateral load – deflection curve – Curve 2 as shown in Figure 3 for the bridge abutments and retaining walls supported by piles: This may be completed in case of a bridge abutment wall by pushover analysis of the global structure model to take advantage of the passive soil pressure behind the wall at the other abutment. In many cases, this can be simplified to a laterally loaded pile

analysis for a pile with an effective retaining width. The pile analysis is performed by incrementally applying the required pile lateral resistance or lateral seismic earth pressure obtained from Equation (3). The point of application for the lateral seismic soil thrust may be approximately at the mid-height of the sliding block/soil mass with an assumption that the seismic earth pressure is uniformly distributed between the pile and the sliding soil mass (Seed and Whitman 1970; Wood 1973; and Richards and Elms 1979). The point at which the displacement is observed is assumed to be the point of application for the lateral seismic soil thrust.

5 Determination of lateral seismic soil thrust as the intersection of the two lateral load – displacement curves – Curves 1 and 2 as shown in Figure 3 developed in Steps 3 and 4: The soil-pile-wall interaction is approximately considered by maintaining the displacement compatibility and the force balance at the mid-height of the wall as indicated by the intersection of Curve 1 for the sliding soil mass and Curve 2 for the pile/wall system. The lateral seismic soil thrust – displacement curve from Step 3 typically approaches an asymptotic value within a displacement of 380 mm (15 inches) as indicated by our case studies for four bridge sites for which this simplified method was applied to estimate lateral seismic soil thrust. An upper bound load value on the curve at a displacement ranging from 25 to 130 mm (1 to 5 inches), depending upon the ductility of the pile, may be defined as the lateral seismic soil thrust without the results from Step 4. In the case in which Curve 2 as shown in Figure 3 is ignored, this procedure can be truly considered a decoupled method that is usually used during initial design phase.

EXAMPLE

To illustrate the proposed method, presented in this section is an example of analysis performed for one soldier pile wall that is part of two 124-meter long retaining walls to create direct access ramp (DAR) lanes on/off the highway in the median area south of a single span bridge located on a California state highway. The wall height or excavation depth into the highway embankment at the bridge abutment is approximately 7.3 meters (24 ft). A typical section of the wall is shown in Figure 1 for locations where soldier piles with tieback anchors are to be used.

Site Peak Ground Acceleration

The horizontal Peak Bedrock Acceleration (PBA) at this site is estimated to be 0.2g (gravity acceleration) based on the 1996 Geomatrix attenuation relationship and to be 0.3g according to the Caltrans California Seismic Hazard Map 1996. For structural design of the bridge, a PBA = 0.3g is conservatively recommended. However, based on the estimated PBA = 0.2g with the attenuation, a Peak Ground Acceleration of PGA = 0.3g may be used for retaining wall design.

Slope Stability of DAR Wall at Abutment

Slope instability of backfills behind the DAR wall under seismic shaking may displace the wall and cause significant differential settlement and cracks/damage in highway pavement. The global slope stability of embankment materials behind the

DAR wall under seismic shaking is evaluated by performing pseudo-static slope stability analysis using the program XSTABL for a slope cut of 7.3 meters (24 ft) height at the southern abutment. It is assumed in the pseudo-static analyses that a seismic acceleration coefficient, k_h = 0.06 to 0.3, up to the peak ground acceleration coefficient, is used while the effect of vertical acceleration is ignored. It is found from the XSTABL results as presented in Table 2 for the embankment cut slope that the retaining wall should be designed adequately to provide a minimum lateral resistance to maintain the cut slope stability.

To maintain the cut slope stability, a minimum lateral static resistance of 534 kN (120 kips) per pile with an effective retaining wall width of 3 meters (10 ft) should be provided. The required minimum lateral resistance is calculated as the force demand on the soldier pile when a factor of safety FS = 1.3 for static case is applied. FS = 1.0 is assumed for seismic cases: k_h = 0.06 to 0.3. The lateral static and seismic forces as shown in Table 2 are for a soldier pile with an effective retaining width of 3 meters (10 ft). For other retaining width or pile center-center spacing, the minimum force demand on a pile can be calculated based on the data of the resistance of the soil wedge and the driving force as presented in the table.

Lateral Seismic Earth Pressure

Following Step 3 discussed above, the first curve of lateral seismic soil thrust versus displacement for the specific retaining width of 3 meters (10 ft) is generated by slope stability analysis for the sliding soil mass behind the wall based on the Newmark chart, as plotted in Figure 3. Calculation of lateral seismic soil thrust on a pile is given in detail in Table 2.

Step 4 is to be followed for developing the second curve. The lateral seismic soil thrust on a pile is incorporated into the analysis of pile lateral load – deflection behavior by applying an approximately uniformly distributed pressure on the upper portion of the pile. However, pushover analysis for the second curve of pile lateral load – deflection behavior is not performed as the first curve approaches an asymptotic value within a displacement of 254mm (10 inches). Nevertheless, a second sample curve is plotted against the first one in Figure 3 for illustration only.

From Figure 3, the lateral seismic soil thrust can be 510kN (115 kips) per pile at a displacement of 30mm (1.2 inches) if an effective retaining width of 3.0 m (10 ft) per pile is configured. It is important to compare it with the minimum static soil thrust of 534 kN (120 kips) for a factor of safety FS = 1.3. In this case, the static soil thrust controls the design.

The difference between the two curves after the intersection as shown in Figure 3 may be viewed as the room for any uncertainty in determination of the lateral load demand on a pile or the pile lateral resistance. When a factor of safety $FOS_{Reinf} > 1.0$ is used for the uncertainty in the pseudo-static slope stability analysis to find the load demand on a pile, Curve 1 will drift up in proportion to FOS_{Reinf} as determined by Equation (3). Hence, the difference or the gap between the two curves becomes small

if the load – deflection behavior of the designed pile remains the same. The gap becomes small too if an undersized pile is used when FOS_{Reinf} = 1.0. It should be pointed out that an undersized pile is never used when Curve 2 is below Curve 1 or the intersection can only be found at a displacement that requires an unsustainable ductility for the pile.

SUMMARY AND DISCUSSION

A displacement-based method for computing lateral seismic earth pressures on bridge abutments and retaining walls supported by piles during earthquake shaking is proposed as a simplified two-curve procedure based on the Newmark sliding block model. One example of a soldier pile retaining wall is presented to illustrate the proposed method. This method avoids the 'engineering judgment' in choosing a design wall displacement for use with the Newmark correlation and eliminates the uncertainty in determining the seismic coefficient with Mononobe-Okabe method to compute lateral seismic earth pressure on bridge abutments and retaining walls supported by piles. With the proposed approach, it is easy to model a multi-layered soil profile of sandy and clayey soils for which the Mononobe-Okabe method is hardly utilized to compute the lateral seismic earth pressure. The procedure is simple to use since the pile-wall-soil interaction is considered in a "decoupled" manner.

The entire system is subdivided into two parts: the soil mass and the pile/wall system. The lateral load – deflection behavior of the soil mass is analyzed by the Newmark sliding block model and the lateral stiffness of the pile/wall is analyzed by a computer program of a laterally loaded pile such as *COM624P*. The soil-pile-wall interaction is approximately considered by maintaining the displacement compatibility and the force balance at the mid-height of the wall as indicated by the intersection of Curve 1 for the sliding soil mass and Curve 2 for the pile/wall system. Although the individual methods for analyzing either the soil mass or the pile/wall are increasingly acceptable, the proposed simplified method of accounting the soil-pile-wall interaction is not validated yet. Results from the method need to be verified with sophisticated finite element analyses and/or field or laboratory model testing.

REFERENCES

AASHTO (American Association of the State Highway and Transportation Officials) (2007). *LRFD Bridge Design Specifications*, 4th Edition – Section 11: Abutments, Piers, and Walls

Caltrans (2003). *LFD Bridge Design Specifications*, – Section 5: Retaining Walls

Franklin, A. G. and Chang, F. K. (1977). "Earthquake Resistance of Earth and Rock-Fill Dams." *Report 5: Permanent Displacements of Earth Embankments by Newmark Sliding Block Analysis, Miscellaneous Paper S-71-17*, Soils and Pavements Laboratory, U.S. Army Engineer Waterways Experiment Station, Vicksburg, Mississippi

Newmark, N. M. (1965). "Effects of Earthquakes on Dams and Embankments." *Geotechnique*, London, England, Vol. 15, No. 2, pp.139-160

Power, M., Fishman, K., Richards, R., Makdisi, F., Musser, S., and Youd, L., (2004). "Seismic Retrofitting Manual for Highway Structures: Part 2 – Retaining Structures, Slopes, Tunnels, Culverts and Roadways." FHWA-HRT-05-067

Richards, R. and Elms, D. (1979). "Seismic Behavior of Gravity Retaining Walls." *Journal of Geotechnical Engineering*, ASCE, pp. 449-464

Seed, H. B. and Whitman, R. V. (1970). "Design of Earth Retaining Structures for Dynamic Loads." *Lateral Stresses in the Ground and Design of Earth Retaining Structures*, pp. 103-147

Wang, S.T. and Reese, R.C. (1993), *COM624P - Laterally Loaded Pile Analysis Program for the Microcomputer*, Report No. FHWA-SA-91-048, Federal Highway Administration, Washington, D.C.

Wood, J. H. (1973). "Earthquake-Induced Soil Pressures on Structures." *Report No. EER: 73-05*, Earthquake Engineering Research Laboratory, California Institute of Technology, Pasadena, California

Zha, J. (2004). "Lateral Spreading Forces on Bridge Abutment Walls/Piles." *Geotechnical Special Publication No. 126*, ASCE, Vol. 2, pp.1711-1720

Zha, J. (2006). "Lateral Spreading Forces on Bridge Piles." *Geotechnical Special Publication No. 145*, ASCE, pp.71-82

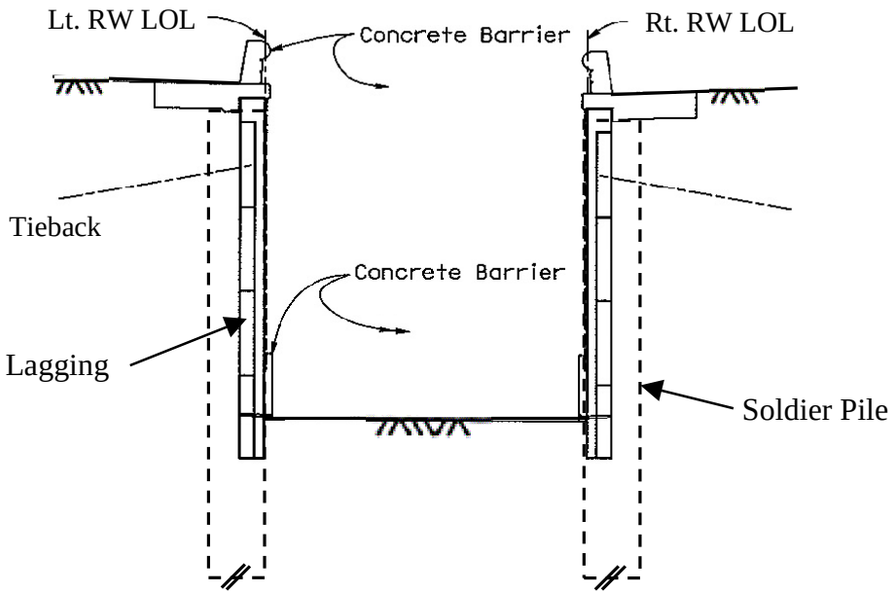


Figure 1. Cross Section of Soldier Pile Retaining Walls

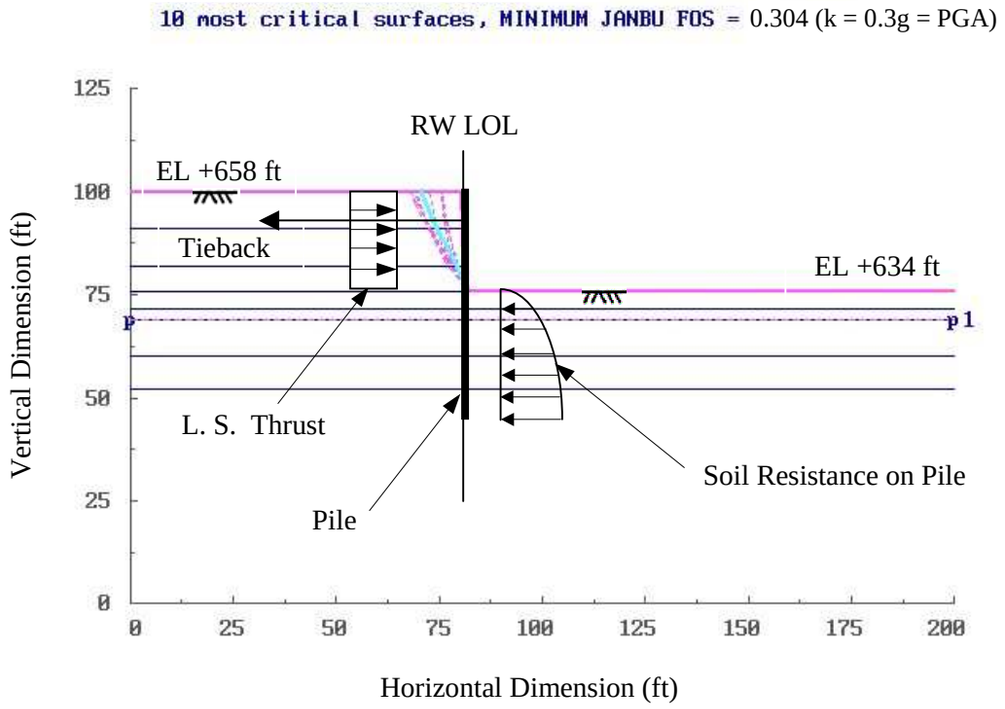


Figure 2. A Schematic of Slope Cut for Slope Stability Analysis

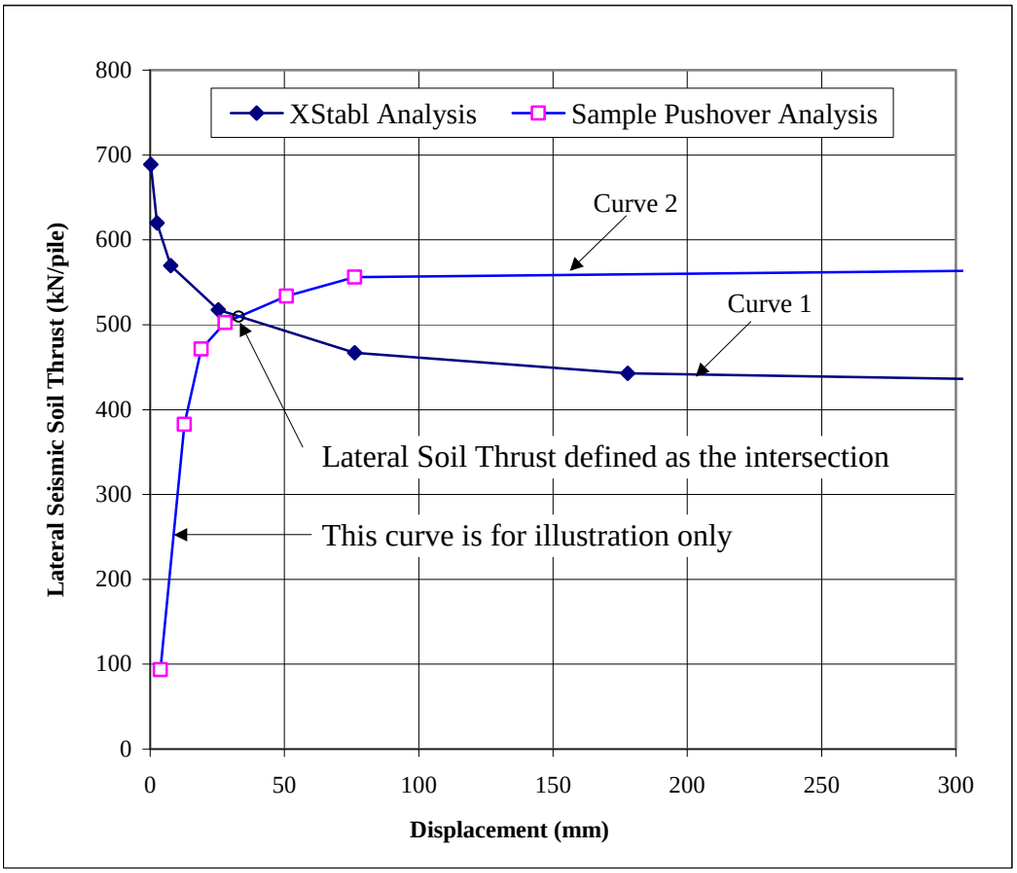


Figure 3. Lateral Seismic Thrust vs. Displacement of a Single Pile

Table 2. Calculation of Lateral Seismic Thrust on a Single Pile

	Acceleration		Displace-ment	Factor of Safety	Resistance	Driving Force	Force Demand
No	a (g)	a/PGA	Δ (mm)	FOS	F_R (kN/m)	F_D (kN/m)	F_P (kN/pile)
0	0	0%		0.412	81.3	197	534
1	0.06	20%	1016	0.359	73.4	204	399
2	0.12	40%	178	0.311	65.6	211	443
3	0.15	50%	76	0.287	61.6	215	467
4	0.20	65%	25	0.552	209.3	379	518
5	0.23	75%	7.6	0.521	203.3	390	570
6	0.26	85%	2.5	0.492	197.0	400	620
7	0.30	100%	0.25	0.455	188.7	415	689
			PGA (g) =	0.3			
			Effective Pile Diameter (mm) =	610			
			Effective Retaining Width per Pile (m) =	3.05			
			Factor of Safety for Seismic Slope Stability =	1.0			
			Factor of Safety for Static Slope Stability =	1.3			

Permanent Seismic Deformation of MSE Walls with Uneven Reinforcement

Raj V. Siddharthan[1], M. ASCE, P.E. and Gopalan Vishnan[2], A.M. ASCE, P.E.

[1]Professor of Civil Engineering, University of Nevada, Reno, NV 89557-0152; siddhart1@unr.edu
[2]Staff Engineer, Fugro West Inc., 502 Guisseppe Court, Roseville, CA 95678; gvishnan@hotmail.com

ABSTRACT: Among the six MSE earth walls tested on the National Geotechnical Centrifuge at the University of California, Davis, one wall (Wall 2) was provided with uneven reinforcement. There was no catastrophic failure observed in any of the six walls, even though the base excitation was as high as 0.9g. Wall 2 showed the lowest lateral displacement. A relatively simple rigid plastic model for predicting the seismic permanent displacement of MSE walls with uneven reinforcement is presented. It extends an existing model that was developed for MSE walls with uniform reinforcement (Siddharthan *et al*. 2004a, b). The variation of the acceleration in the backfill has been included since significant deamplification in acceleration was observed in the backfill in large excitations. The study reveals that the proposed analytical model captures many aspects of the characteristic behavior of MSE walls under seismic loading. Computed and measured lateral MSE wall displacements were compared and the agreement between them is very good.

INTRODUCTION

Almost all damage reports from large earthquakes in the last two decades have ample references relative to the performance of MSE walls. Such cases include the 1994 Northridge, 1995 Kobe, 1999 Chi-Chi, and 1999 Kocaeli earthquakes. For example, Sandri (1994), who conducted a performance survey of MSE walls soon after the 1994 Northridge earthquake (M6.7), found no evidence of visual damage to 9 of 11 structures located within 23 to 113 km of the earthquake's epicenter. The damaged structures did not show any internal instability but exhibited tension cracks within and behind the reinforced soil mass. Tatsuoka *et al.* (1996) reported on the performance of MSE and other types of retaining walls during the 1995 Kobe earthquake (M6.9). Though many traditional retaining walls such as rigid and cantilever walls suffered extensive damage, many MSE walls showed only minor damage. On the other hand, the summary of Huang and Tatsuoka (2001) indicated damage to three MSE walls located within 40 km of the epicenter of the 1999 Chi-Chi earthquake (M7.6). Though these walls were short, measuring less than 3.2 m in height, one of them completely collapsed. The sites at these walls experienced a

maximum acceleration, a_{max} in excess of 0.44g. Damage to 100 m-long MSE wall system (Arifiye Overpass) located in the city of Adapazari, Turkey during the1999 Kocaeli Earthquake (M7.4) was significant. The largest acceleration recorded at a nearby station (4 km away) was about 0.41g. The wall height, H varied to as much as 10 m and a section of the wall with H = 10 m displaced laterally by more than 25 cm. The dominant failure mode was permanent deformations, which occurred between the base and mid-point of the wall. Recently, Gazetas *et al*. (2004) also reported on similar seismic behavior relative to other recent earthquakes.

Up to date methods to design Mechanically Stabilized Earth (MSE) under static loading conditions have been well documented in two recent design manuals (Bathurst and Simac 1997; Elias *et al*. 2001). These guidelines were developed based on extensive field, including full-scale tests, and laboratory tests on individual components. Past seismic performance of MSE walls have revealed that the major design concern is the outward permanent lateral movement away from the backfill. Though MSE walls have been built with uniform reinforcements spanning the entire height of the wall, centrifuge tests have revealed that longer reinforcements near the soil surface can substantially reduce the permanent wall movement (Siddharthan *et al*. 2004a). Presently there is no simple deformation analysis model available to predict lateral permanent seismic displacement of unevenly reinforced MSE walls.

The paper describes a numerical model to evaluate permanent seismic displacement of MSE walls with variable lengths of reinforcement. The model was developed by extending an existing model that was proposed for MSE walls with uniform reinforcement (Siddharthan *et al*. 2004a, b). Subsequently, the predictive capability of the numerical model was verified using centrifuge tests carried out at the large centrifuge at the National Geotechnical Centrifuge at the University of California, Davis.

CENTRIFUGE TESTING OF MSE WALLS

Model Description

In the centrifuge study reported by Siddharthan *et al*. (2004a) three test models were constructed and tested on the large centrifuge at UC Davis. In each test model two wall configurations were constructed so that the walls were back to back (Fig. 1). Among a total of six such walls tested, one wall had uneven reinforcement. Since analysis of the MSE wall behavior with uniform reinforcements has been addressed in detail by Siddharthan *et al*. (2004a, b), only the test results relative to the wall with uneven reinforcement is presented here. The models tested in this study represented 7.32 m (24 ft) high walls in prototype supporting a dry, granular backfill. The scale factor used in these tests was N = 24. Correspondingly the model wall height was 1 ft. It was decided that a bar mats system much like the ones widely used by Caltrans would be modeled. The reinforcement was modeled by using commercially available galvanized steel wire mesh.

In each of the models tested the backfill consisted of fine dry Nevada sand at an initial relative density (D_r) of 65%. The sand was placed by pluviating from the large pluviater at the UC Davis National Geotechnical Centrifuge center. More details on the model description can be found in Howard *et al*. (1998) and Ganeshwara (1998).

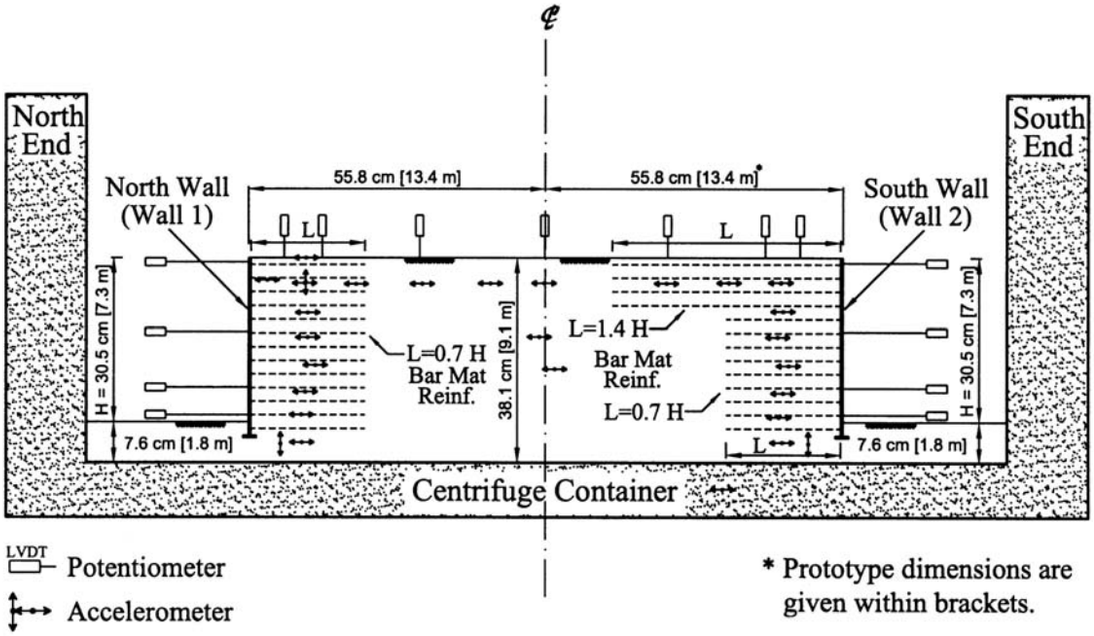


Fig. 1. Centrifuge testing of MSE walls with uniform (Wall 1) and uneven reinforcements (Wall 2).

Instrumentation

The walls tested in test series MSE-01 have uniform (Wall 1) and uneven reinforcements (Wall 2) as shown in Fig. 1. The Wall 1 had a reinforcement length (L) of 0.7 times the height (H), while the Wall 2's L varied from 1.4H near the surface to 0.7H at the bottom. While the layer by layer construction continued, the accelerometers were placed at the pre-determined positions. After the model construction was completed the LVDT's and the linear potentiometers were positioned on the model. The linear potentiometers were mounted on vertical beams attached to the base of the container and they measured the lateral wall deformation along the height of the walls. The LVDT's were mounted from a rack that was fixed to the top ring of the model container. From the LVDT measurements the settlement of the soil can be interpreted at various locations (behind the walls and at the free-field).

Testing of the Models

Once the model was spun up to attain the required gravity level of 24g, several types of base motions, including step waves, cosine sweeps, and recorded earthquake motions were used in the testing program. The test model configuration was shaken by a total of 17 excitations (referred to as events A through Q) back to back. Among the two recorded acceleration records used in this study, one was from the 1995 Hyogogen-Nanbu earthquake (Kobe) and the other was from Santa Cruz, California recorded during the Loma Prieta event of 1989. The typical order of shakes started with small amplitude step wave to verify that the accelerometers were functioning correctly. Subsequently, a base excitation history with strength, a_{max} of as much as

0.9g was used. In MSE-01 series, the number of strong excitations with a_{max} more than 0.3g was three. Only under these higher excitations the walls showed appreciable permanent displacements.

Interpretation of Centrifuge Test Results

Figure 2 shows the measured lateral displacements near the middle of the Wall 1 and 2 in the test series MSE-01, when the model wall subjected to the cosine sweep base excitation from event B. This excitation had an a_{max} of 0.17g with constant amplitude and period (0.4s). Figure 2 shows that the lateral displacement at any time consists of a permanent and a cyclic component. At the end of the excitation, there was only permanent displacement and no cyclic component of displacement.

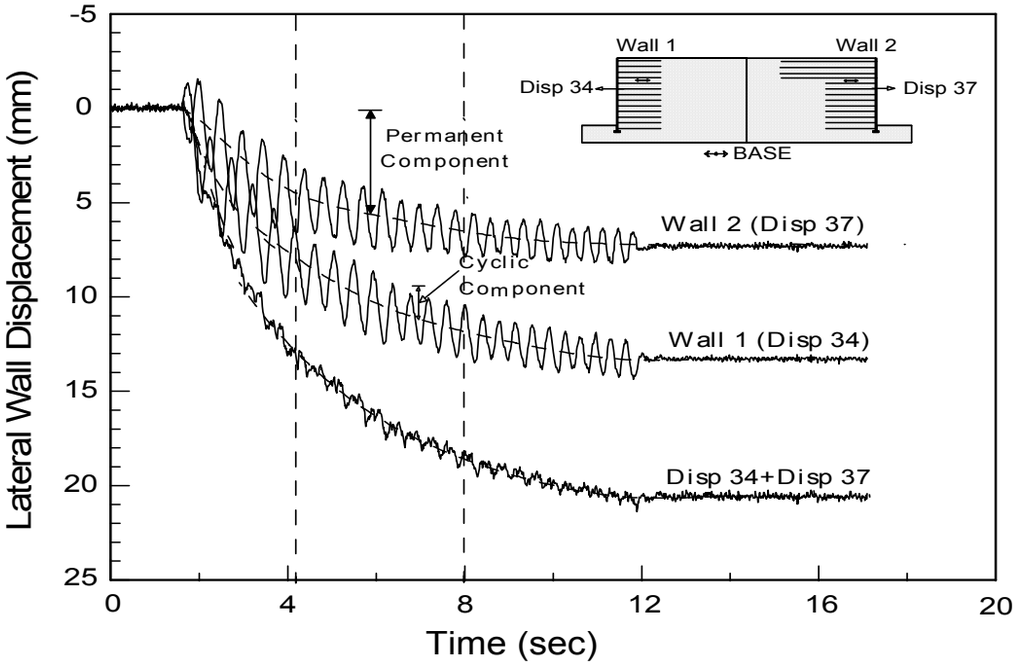


Fig. 2. Measured lateral response in event B (a_{max} = 0.17g).

The permanent component represents the progressive movement of the wall away from the backfill whereas the cyclic components represent the instantaneous response to the base excitation. The vertical arrows drawn on the figures facilitate the comparison of the cyclic component and permanent component of displacements at the middle of Walls 1 and 2. This figure also provides the summation of both wall displacements. Unlike the individual displacement which had significant oscillations, the summation plot displays negligible cyclic component. Such behavior leads to the conclusions that (1) the permanent displacement of the wall stretches laterally in a progressive manner away from the backfill with negligible cyclic components; (2) the cyclic components are indeed a result of the entire test model moving laterally in response to inertia forces generated by the shaking; and (3) wall movement into the backfill (i.e., passive) is negligibly small.

Deformation of Walls

As a typical plot, Fig. 3 shows the cumulative lateral permanent displacements

(prototype scale) of Wall 1 and Wall 2 in the events N, O and P. These events had the a_{max} values of 0.48g, 0.70g, and 0.83g, respectively. These earthquake events were selected because these were the largest excitations in the MSE-01 test series. It is clear from Fig. 3 that the Wall 2 with uneven reinforcement behaved better than the Wall 1 in every shaking event. This was expected because of the additional reinforcement at the top four panels in Wall 2. From the wall deformation shown in Fig. 3, it appears that the bottom part of the wall has translated as well as rotated. The deformation mechanism adopted in the analytical model described subsequently is based on this observation.

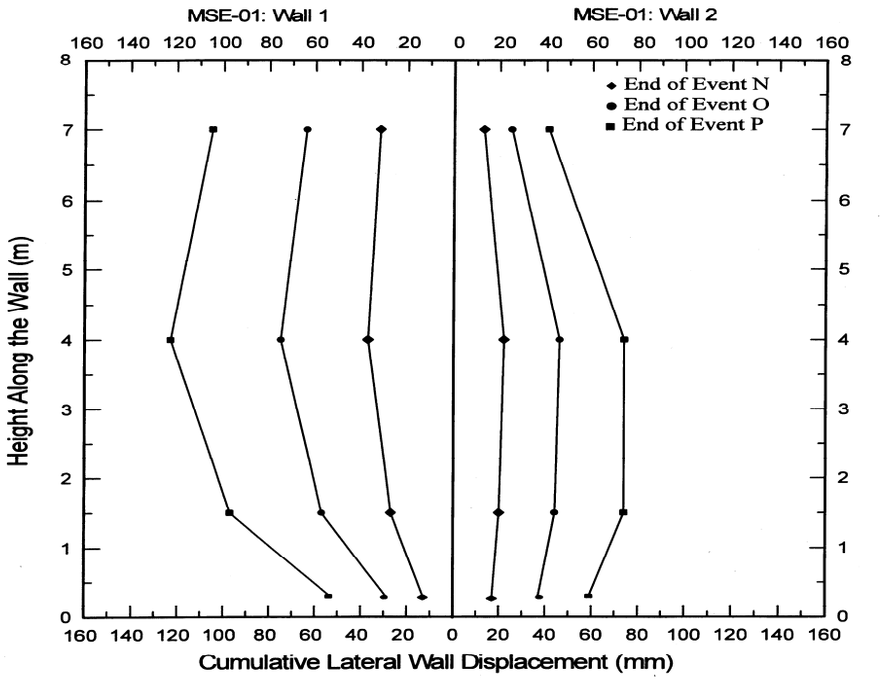


Fig. 3. Cumulative lateral wall displacement in three largest events.

Relative Density Variation during Tests

As the shaking continued in the tests, the relative density is expected to increase since shaking results in compaction of soil (grain slip). Assuming one-dimensional settlement, the relative density changes can be estimated at the end of each test. This calculation requires a knowledge of maximum (e_{max}) and minimum (e_{min}) void ratios of Nevada sand. These values are readily available from the database of Nevada sand reported by Arulmoli *et al*. (1994). They report e_{max} = 0.887 and e_{min} = 0.511 for Nevada sand. Based on the assumption that the initial relative density at the start of all test series is 65%, the relative densities at the start of each shaking event can be evaluated. These computed relative densities are presented in Fig. 4. There are three

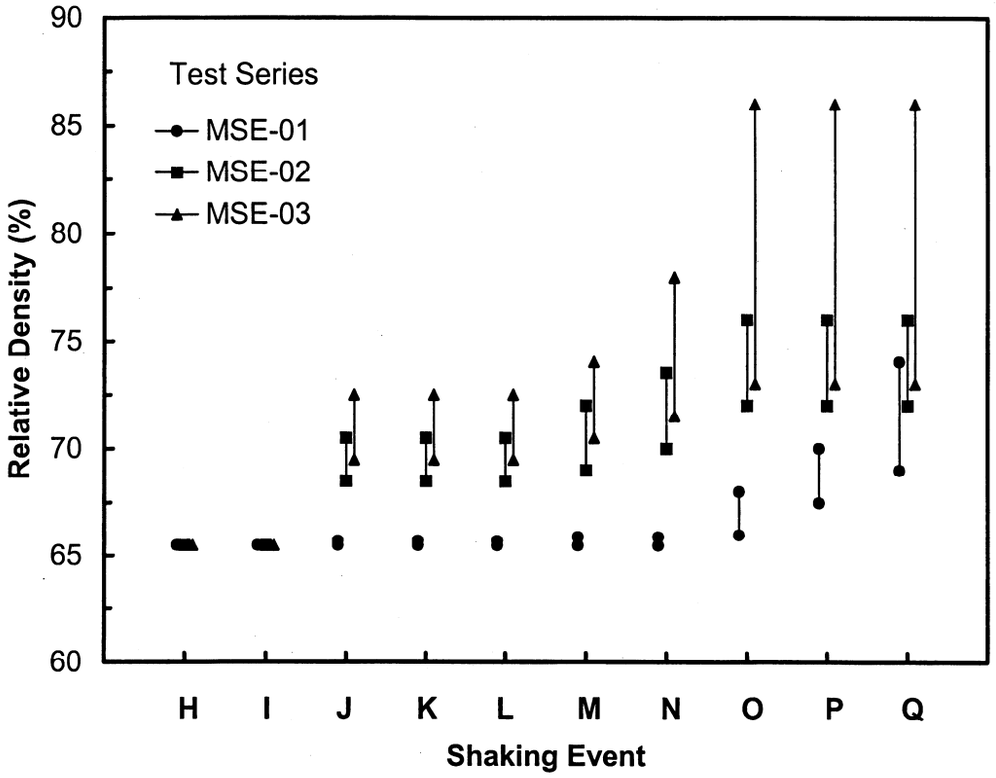


Fig. 4. Estimation of relative density (D_r) changes during testing.

free-field locations and it is believed that these three settlement values will provide a range for the relative densities. Since there was not much change in relative density in the events A through G, the relative densities only for the events H through Q (shown on x axis) are presented for all the three test series (MSE-01, MSE-02, and MSE-03).

It is apparent from Fig. 4 that though the relative densities are similar initially (low level of excitations), they subsequently increased substantially as the test progressed to higher and higher level of excitations. Among all test series, the test series MSE-01 had the lowest initial relative densities. The increase in relative density will lead to an increase in the friction angle of the soil. Therefore, as it will be seen later that when event by event comparison of the measured and computed wall displacements are made, consideration should be given to the changes in relative density.

Amplification of Motion in Free-Field

The analytical model described subsequently uses the acceleration induced in the backfill as an input parameter in the computation of the interaction force between the reinforced zone and the backfill. Therefore, the characteristics of the acceleration response in the free-field are important. In the free-field (middle of the two walls in Fig. 1) there were three accelerometers placed along a vertical plane to study the free-field amplification.

Figure 5 shows the recorded maximum acceleration along the wall in the large three events. The amplification factors shown on x-axis were obtained by normalizing the

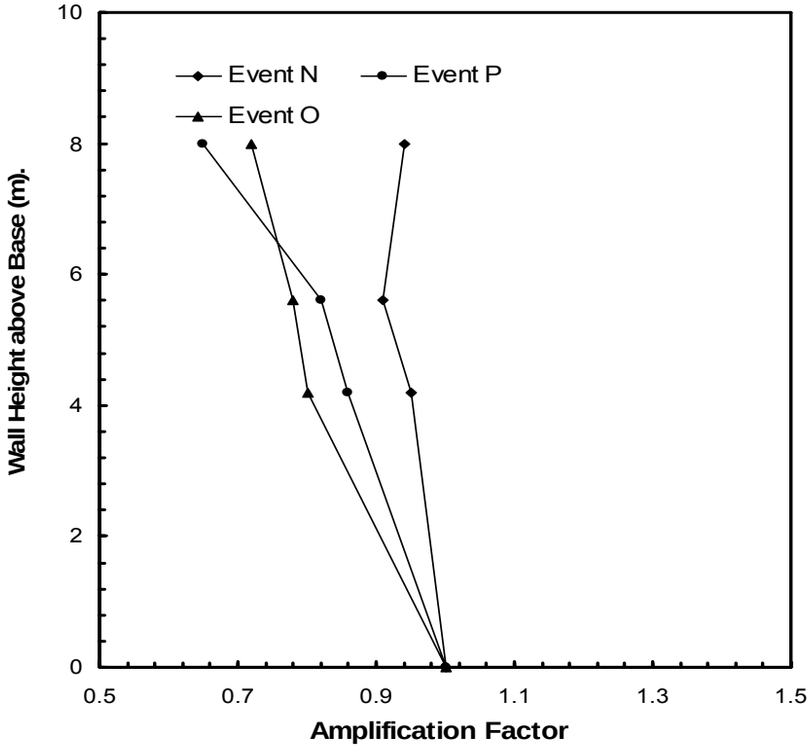


Fig. 5. Amplification in the free-field during the largest events.

maximum-recorded acceleration by the maximum base acceleration. This figure shows that deamplification of base motion occurred in all events and at all locations. The amplification factor was as low as 0.66 and this occurred near the surface in the event P with a_{max} = 0.83g. This type of response is not surprising and it is consistent with nonlinear soil behavior as seen in many measured acceleration responses in large earthquake events (Chin and Aki 1991; Ni *et al*. 1997). These amplification variations will be used subsequently in the prediction of lateral wall displacements.

ANALYTICAL MODEL FOR WALL DEFORMATION

From the centrifuge test results presented thus far, a failure mechanism described below has been selected to study the deformation behavior of MSE walls with uneven reinforcements. The proposed failure mechanism consists of three rigid blocks (Fig. 6); two top blocks that are rectangular and a bottom block that is triangular. The length of the blocks varies depending on the length of the reinforcements. The interface between any two, blocks is horizontal. The bottom block (Block III) is assumed to have both rotational (θ_3) and translational (x_3) degrees of freedom. In order to keep the total degrees of freedom to a minimum, the top two blocks were assigned only translational degrees of freedom (x_1 and x_2). This leads to a total of four degrees of freedom for the failure mechanism. The bottom failure plane associated with Block III is a slope, which starts at the top of the bottom most reinforcement. The length of the top blocks equals the lengths of the reinforcement in

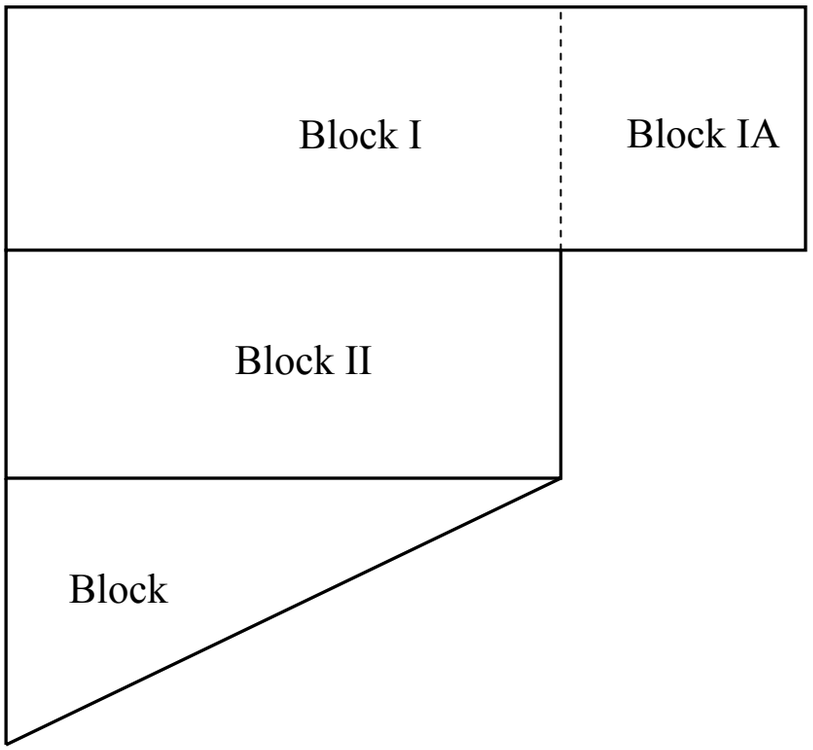


Fig. 6. Proposed three block model for lateral wall displacement.

these blocks. The top block is divided into two parts: Block I and Block IA; but in the deformation analysis both of these blocks are assumed to move as one block, and there is no vertical interface separation between Block I and Block IA. The subdivision of the top block is only necessary when uneven reinforcement is considered. It should be noted that since the face panels are rigid, the interface between blocks, which are horizontal, cannot be arbitrary. Therefore, the interface between failure blocks should coincide with the interface between face panels. An iterative approach has been developed for computational purposes. The slope of the failure plane in Block III and the horizontal interface between the top two blocks are variable, and the wall deformation at the end of a given excitation is computed for each trial combinations. The combination that gives the largest permanent wall face deformation is considered to be the correct failure mechanism.

The failure mechanism adopted above, is based on the observed behavior of many walls in centrifuge tests. Since the bar mat reinforcement may be considered to be inextensible, its flexibility is not included in the model. The focus is on overall permanent wall deformation, which is an external stability issue. Local failure modes such as pull-out of individual reinforcement and failure at the face panel-reinforcement connections, which are issues of internal stability, are not addressed.

Method of Solution

The dynamic equilibrium equations for horizontal and vertical directions for all the blocks and rotation of Block III about the base were assembled to arrive at four equations of motion in terms of the unknowns x_1, x_2, x_3, and θ_3. These equations are

coupled and are ordinary differential equations of second order. A step by step procedure in time domain, similar to the one described by Siddharthan *et al*. (2004b) has been used to obtain the solutions (x_1, x_2, x_3, and θ_3). The acceleration can vary in the backfill due to amplification (or deamplification). The forces on the blocks which are affected by the backfill acceleration have been computed using the appropriate acceleration (average) at the level of the blocks based on the results shown in Fig. 5. A computer program DIS-MSE2, has been developed to compute the block deformations for many failure mechanisms by varying the slope angle of Block III and the location of separation between Blocks I and II. Integration in the time domain was carried out using Newmark's scheme of constant average acceleration.

RESUILTS AND CONCLUSIONS

As typical plots, the computed and measured wall displacements of Wall 2 during events O (a_{max} = 0.7g) and P (a_{max} = 0.83g) are shown in Figs. 7 and 8. Different values for backfill friction angle φ were considered to get a match between the experimental and analytical results. Computed displacements during the event O for φ values of 36^o and 38^o bracket the measured displacement. Similarly, in the case of event P, the corresponding φ values are 38^o and 40^o. Lower value of φ range for fit in the event O than the corresponding φ range in event P is consistent with the relative density changes described earlier (Fig. 4). The comparison between the computed and measured wall displacements is very good, thus validating the applicability of the proposed analytical model. It should be noted that since only one wall with uneven reinforcement was tested in the centrifuge, caution should be exercised in extending the findings of this study to other cases.

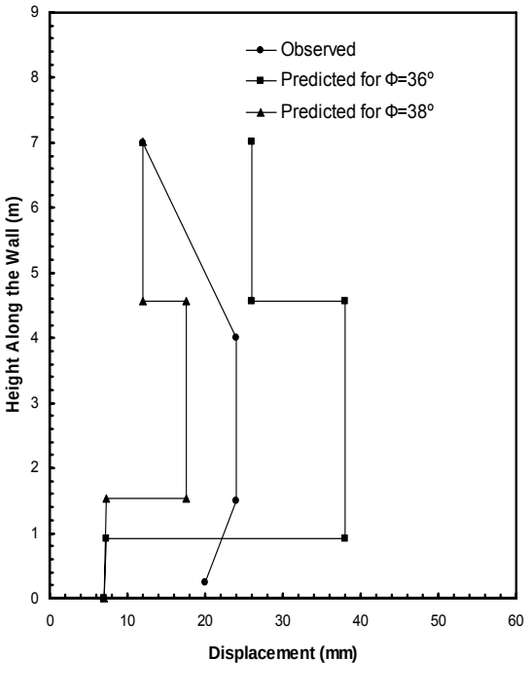


Fig. 7: Lateral wall displacement in event O (a_{max} = 0.7g).

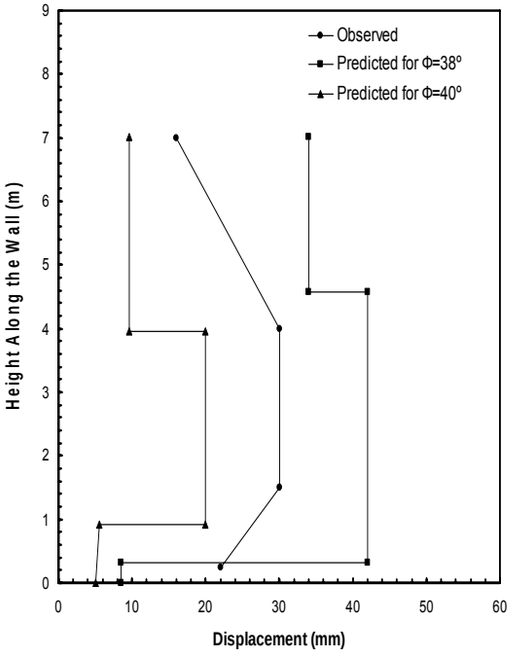


Fig. 8. Lateral wall displacement in event P (a_{max} = 0.83g).

REFERENCES

Arulmoli, K., Muraleetharan, K.K., Hossain, M.M., and Fruth, L.S. (1992). "VELACS: Verification of liquefaction analyses by centrifuge studies - laboratory testing program soil data report," The Earth Technology Corporation, Irvine, CA.

Bathurst, R.J., and M.R. Simac (1997). *Design manual for segmental retaining walls*, Second Edition, National Concrete Masonry Association, VA, 1997.

Chin, B.H., and K. Aki (1991). "Simultaneous study of the source, path, and site effects on strong ground motion during Loma Prieta Earthquake: A preliminary result on pervasive nonlinear site effects," *Bull. of Seism. Soc. of America*, Vol.81: 1859-1884.

Elias, V., B.R. Christopher, and R.R. Berg (2001). "Mechanically stabilized earth walls and reinforced soil slopes: design and construction guidelines," *Report No*. FHWA-NHI-00-043, FHWA.

Ganeshwara, V. (1998). *Seismic analysis of reinforced earth walls*, *M.S. Thesis*, Univ. of Nevada, Reno, NV.

Gazatas G., Psarropoulos, P.N., Anastasopoulos, I., and Gerolymos, N. (2004). "Seismic behavior of flexible retaining systems subjected to short-duration moderately strong excitation," *J. of Soil Dynamics and Eq. Engrg.*, Vol. 24(7), Sept.,: 537-550.

Howard, R.W.A., B.L. Kutter, and R.V. Siddharthan (1998). "Seismic deformation of reinforced soil centrifuge models," *Proc. Geotech. Eq. Engrg. and Soil Dyn., III*, Geotech. Special Pub. 75, ASCE, Vol. I: 446-457.

Huang, C.C. and Tatsuoka, F. (2001). "Stability analysis of the geosynthetic-reinforced modular block walls damaged during the Chi-Chi Earthquake," *Proc. Fourth Int. Conf. on Recent Advances in Geotech. Earthquake Engrg. and Soil Dyn.*, San Diego (CD-ROM).

Ni, S.H., R.V. Siddharthan, and J.G. Anderson (1997). "Characteristics of nonlinear response of deep saturated soil deposits," *Bull. Seism. Soc. of America,* Vol. 87 (2): 342-355

Sandri, D. (1994). "Retaining walls stand up to the Northridge Earthquake," *Geotech. Fabrics Report*, Vol. 12(4), 30-31.

Siddharthan, R.V., Ganeshwara, V., Kutter, B.L., El-Desouky, M., and Whitman, R.V. (2004a). "Seismic deformation of bar mat MSE walls I: Centrifuge tests," *J. of Geotechnical and Geo-Environmental Engrg.*, ASCE, Vol. 130(1): 14-25.

Siddharthan, R.V., Ganeshwara, V., Kutter, B.L., El-Desouky, M., and Whitman, R.V. (2004b). "Seismic deformation of bar mat MSE walls II: A multi-block model," *J. Geotechnical and Geo-Environmental Engrg.,* ASCE, Vol. 130(1): 26-35.

Tatsuoka, F., Tateyama, M., and Koleski, J. (1996). "Performance of soil retaining walls for railway embankments," Special Issue of *Soils and Foundations*, Japanese Geotechnical Society, January: 311-324.

Vishan, G. (2004). *Further Development on MSE Wall Behavior under Seismic Loading*, MS Thesis, submitted to University of Nevada, Reno, Dec.

Seismic Earth Pressures Behind Retaining Walls: Effects of Rigid-body Motions

Chulmin Jung[1], M. ASCE and Antonio Bobet[2], M. ASCE, Sc.D.

[1]Doctoral Student, School of Civil Engineering, Purdue University, West Lafayette, IN 47907-1284; jungc@purdue.edu
[2]Associate Professor, School of Civil Engineering, Purdue University, West Lafayette, IN 47907-1284; bobet@purdue.edu

ABSTRACT: The seismic earth pressures behind a retaining wall that bends, rotates about its base, and translates horizontally and vertically are evaluated numerically using an ideally elastic model. The following factors are analyzed: (1) flexural movements of the wall; (2) rotation of the wall at its base; and (3) horizontal and vertical movements of the wall. The following results are obtained: (1) the flexural flexibility of the wall, the horizontal translation, and the rotation at the base have significant effects on the earth pressures behind the wall; and (2) within the range of relative flexibilities of typical retaining walls (relative between wall and backfill), the effects of the horizontal translation are more significant than those of the vertical translation and rotation. Four extreme cases are also analyzed: rigid wall with stiff foundation, rigid wall with soft foundation, flexible wall with stiff foundation, and flexible wall with soft foundation. The seismic pressures behind a rigid wall with a stiff foundation are the largest, and they are the smallest for a flexible wall with a soft foundation. The pressures behind a rigid wall with a soft foundation are affected the most by the horizontal translation of the wall, while the pressures behind a flexible wall with a soft foundation are affected both by the flexural flexibility of the wall and by the horizontal movements.

INTRODUCTION

It is not appropriate, in general, to simulate the seismic response of a retaining structure using elastic models. This is because elastic models do not capture the cyclic behavior of the soil, nor any failure condition that may be reached. However, elastic models can be very useful to perform conceptual analyses and can be effectively used to identify key parameters that affect the seismic pressures behind a wall. In some cases, elastic models may be even acceptable; for example a gravity-type retaining wall on a rock foundation with a stiff backfill and a small to moderate earthquake.

Scott (1973) and Wood (1973) provided elastic analytical solutions for the seismic response of a rigid retaining wall fixed at its base. The solutions were expanded later on by Veletsos and Younan (1997) for a wall that bends and rotates about its base. From the results obtained with the analytical solutions, the authors concluded that the seismic

earth pressure on the wall was significantly affected by: (1) relative flexural stiffness of the wall with respect to the backfill; and (2) rigid-body rotation of the wall about its base. Psarropoulos et al. (2005) verified numerically the analytical solutions provided by Veletsos and Younan (1997) with a finite-element code.

The Mononobe-Okabe method, which is extensively used in practice, (Mononobe and Matsuo, 1929, and Okabe, 1924) does not account for soil-structure interaction, nor for the effects of the rigid body motions of the wall. This is a key issue for example to assess the seismic behavior of a cantilever retaining wall underlain by a soft foundation, since the wall response tends to be governed by its rigid-body rotation about the base due to an insufficient bearing capacity of the foundation soil. This observation has been supported by field investigations on seismic performance of retaining walls during the Hyoken-Nanbu (Tatsuoka et al., 1996) and the Chi-Chi earthquakes (Fang et al., 2003), and from results from laboratory model tests (Koseki et al., 1998). Also a retaining wall with a low height-to-width ratio on a rigid foundation tends to move horizontally with increasing loads.

In this paper we expand numerically the results obtained by Veletsos and Younan (1997) where, in addition to the relative flexural flexibility of the wall and its rotation about the base, the vertical and horizontal rigid body motions of the wall are included.

DEFINITION OF RELATIVE FLEXIBILITIES

In most cases, a retaining wall has a length much larger than its height or width. As a consequence, the problem can be considered as two- dimensional plane strain. To investigate the effects of the flexural displacements and the rigid-body motions of a wall with height, H, four non-dimensional parameters are introduced (Fig. 1). The parameters are: (1) relative flexural flexibility of the wall with respect to the backfill, d_B, (Veletsos and Younan, 1997); (2) relative flexibility of the rotational constraint at the base of the wall, d_R (Veletsos and Younan, 1997); (3) relative flexibility of the horizontal constraint at the base, d_H; and (4) relative flexibility of the vertical constraint at the base to the backfill, d_V.

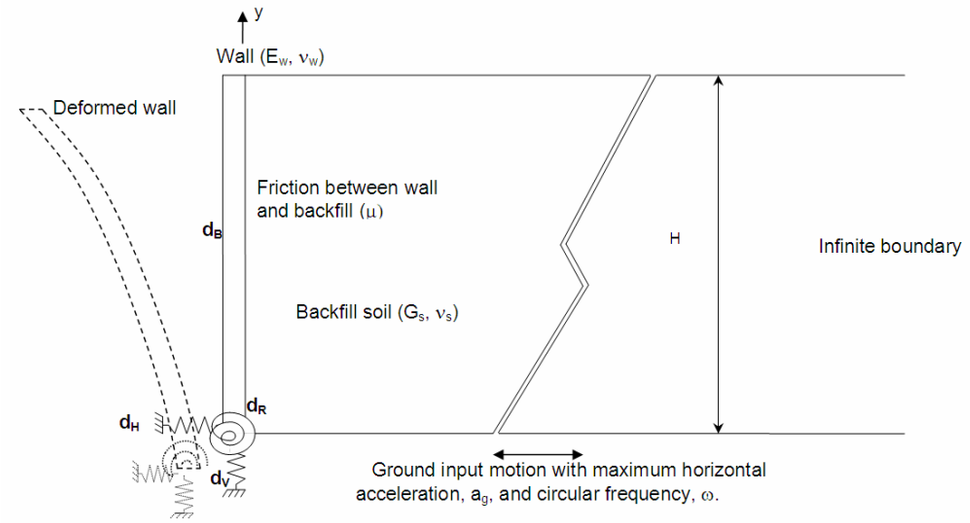


FIG. 1. Model of a flexible retaining wall with three types of rigid-body motion at its base: (1) rotational; (2) horizontal; and (3) vertical movement.

The flexural relative flexibility, d_B, is defined as (Veletsos and Younan, 1997):

$$d_B = \frac{G_s H^3}{D_w} \tag{1}$$

Where G_s is the shear modulus of the backfill soil, H is the height of the wall, and D_w is a measure of the wall rigidity. It is defined as:

$$D_w = \frac{E_w I_w}{12(1-\nu_w^2)} \tag{2}$$

Where E_w is the Young's modulus of the wall; I_w is the moment of inertia of the wall per unit length; and ν_w is the Poisson's ratio of the wall. d_B=0 denotes a perfectly rigid wall that does not bend. As d_B increases, the wall becomes more flexible relative to the backfill.

The rotational flexibility, d_R, is defined as (Veletsos and Younan, 1997):

$$d_R = \frac{G_s H^2}{K_R} \tag{3}$$

Where K_R is the rotational elastic spring constant (Fig. 1). d_R =0 indicates that the wall cannot rotate. As d_R increases, the wall is less constrained to rotate about its base.

The horizontal flexibility is denoted as d_H, which is defined as:

$$d_H = \frac{G_s}{K_H} \tag{4}$$

Where K_H is the horizontal elastic spring constant (Fig. 1). When d_H=0, the wall cannot move horizontally. As d_H increases, the horizontal constraint decreases.

Similarly, the vertical flexibility, d_V, is defined as:

$$d_V = \frac{G_s}{K_V} \tag{5}$$

Where K_V is the vertical elastic spring constant (Fig. 1). d_V=0 applies to a retaining wall that cannot move vertically. As d_V increases, the wall is less constrained to translate vertically.

To evaluate the effects of the relative flexibilities on the seismic earth pressures behind the wall, a parametric analysis is conducted where one of the relative flexibilities is changed while the others remain constant. However, in soils, some of the flexibilities may not be independent. For example, a soft soil at the foundation of a retaining wall would cause the wall to rotate about its base and to move vertically more than a stiff soil. Hence the relative stiffnesses are somewhat related to each other. The effects of such combinations are also investigated, in addition to the parametric study. To do that, the

following four extreme cases are selected: (1) a rigid retaining wall with stiff foundation (Case 1); (2) a rigid retaining wall with soft foundation (Case 2); (3) a flexible retaining wall with stiff foundation (Case 3); and (4) a flexible retaining wall with soft foundation (Case 4).

The wall and backfill are defined by: (1) height, H; (2) width of its base, B; (3) thickness of the wall, t; (4) shear wave velocity of the backfill layer, V_s; and (5) shear wave velocity of the foundation, V_{sf}. The values of geometry and material properties are as follows: (1) $3 \leq H \leq 10$ meters; (2) $0.4H \leq B \leq 0.7H$; (3) $0.08H \leq t \leq 0.125H$; (4) $E_W = 2.4 \times 10^{10}$ Pa; (5) $50 \leq V_s \leq 150$ m/s; and (6) $100 \leq V_{sf} \leq 300$ m/s. For the cases where the combined effect of the different relative flexibilities is investigated, the values of the elastic spring constants, K_R, K_H, and K_V are obtained from static elastic numerical analysis. In the static analysis, a moment, a horizontal or a vertical force, respectively, are applied to a rigid plate with width B, which is placed on the surface of the foundation. The contact between the base of the wall and the foundation is assumed to be completely bonded. With increasing moment and forces, the rotational, horizontal and vertical displacements of the wall are measured. From the force-displacement relations, the elastic spring constants are determined. The values of the non-dimensional parameters for the four extreme cases are: (1) $d_B = 1.1$, $d_R = 0.09$, $d_H = 0.02$, and $d_V = 0.01$ (Case 1); (2) $d_B = 1.1$, $d_R = 0.82$, $d_H = 0.14$, and $d_V = 0.11$ (Case 2); (3) $d_B = 38$, $d_R = 2.5$, $d_H = 0.17$, and $d_V = 0.14$ (Case 3); and (4) $d_B = 38$, $d_R = 23$, $d_H = 1.5$, and $d_V = 1.3$ (Case 4).

NUMERICAL MODEL

Fig.1 shows a schematic of the numerical model used for the investigation. The retaining wall is represented as a uniform linear elastic material with constant damping ratio, ξ_w, which is defined as a fraction of the critical damping coefficient. Due to its flexibility, the wall itself bends with increasing load. In addition to the flexural displacements, the wall can move horizontally, vertically, and it can rotate about its base. The movements of the wall are defined with: (1) rotational constraint, K_R, which has a dimension of force; (2) horizontal constraint, K_H, which has a dimension of force divided by length; and (3) vertical constraint, K_V, also with dimension of force divided by length. The backfill is modeled as a semi-infinite, horizontal, uniform, and elastic stratum, with a thickness, H, the same as the wall height. The material properties of the backfill are: (1) density, ρ_s; (2) shear modulus, G_s; (3) Poisson's ratio, ν_s; and (4) damping ratio, ξ_s. The commercial FEM code, ABAQUS (version 6.6), is used for the investigation. In the model, the wall is discretized with beam elements and the backfill with two-dimensional, four-noded quadrilateral, plan-strain elements. Infinite elements are introduced at the far end to model the infinite boundary. The infinite elements absorb the radiated energy generated by the seismic excitation and prevent body waves from reflecting back towards the wall. The interface between the wall and the backfill is modeled as a frictional contact that can open in tension and slide in compression. The friction coefficient at the interface, μ, is 0.4. A sinusoidal ground input motion is applied at the bottom of the backfill, with maximum acceleration A_g, and circular frequency, ω. In this study, $\omega = \omega_1/6$. Where ω_1 is the fundamental natural circular frequency of the free-field backfill:

$$\omega_1 = \frac{\pi V_s}{2H} \tag{6}$$

Table 1 shows the geometries and material properties investigated with the model.

Table 1. Geometries and material properties used in the numerical model

	Parameter	Symbol	Value	Unit
Ground input motion	Peak acceleration	A_g	0.1	g
	Angular frequency	ω	3.2	radian/sec
Wall	Height	H	8	meter
	Thickness	t	0.2	meter
	Unit weight	γ_w	25	kN/m^3
	Poisson's ratio	ν_w	0.2	
	Damping ratio	ξ_w	2	%
Backfill	Shear wave velocity	V_s	100	m/s
	Fundamental natural frequency	ω_1	19.2	radian/sec
	Unit weight	γ_s	18	kN/m^3
	Poisson's ratio	ν_s	1/3	
	Damping ratio	ξ_s	5	%

RESULTS AND DISCUSSION

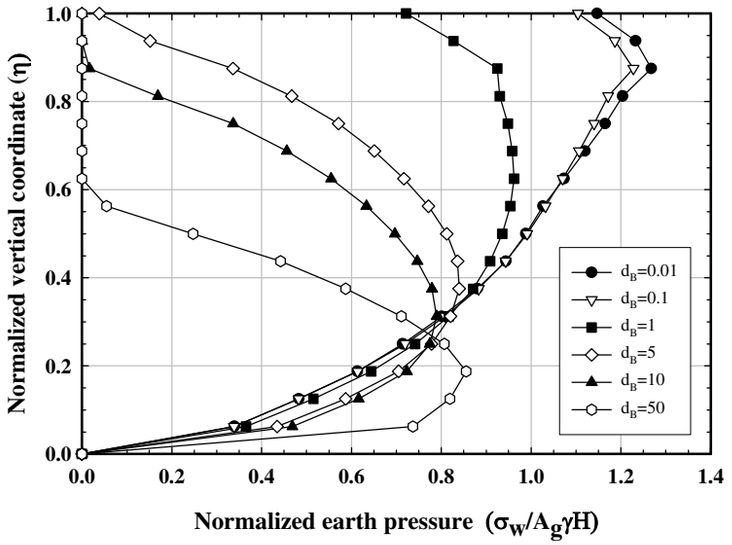
Fig. 2(a) shows the distribution of the normalized seismic earth pressures behind the wall for different d_B. To plot the results, the normalized vertical coordinate, $\eta=y/H$, is used (see Fig. 1). The seismic earth pressure at the back of the wall is divided by $A_g\gamma H$. The normalization is used because in the analytical solutions the seismic earth pressure is proportional to $A_g\gamma H$ (Veletsos and Younan, 1997). The results are obtained for $d_R = d_H = d_V = 0.001$, which correspond to a wall fixed at its base.

As d_B increases, or as the wall becomes more flexible, it is observed from the figure that: (1) the normalized pressure near the top of the wall becomes smaller while the normalized pressure near the base remains nearly constant; (2) the location of the maximum pressure moves towards the base of the wall; and (3) when $d_B = 5$, the wall begins to detach from the backfill at the top of the wall. Note that the area between the earth pressure distribution and the vertical axis is the resultant horizontal force, R_H, acting behind the wall. R_H and its point of application are discussed later.

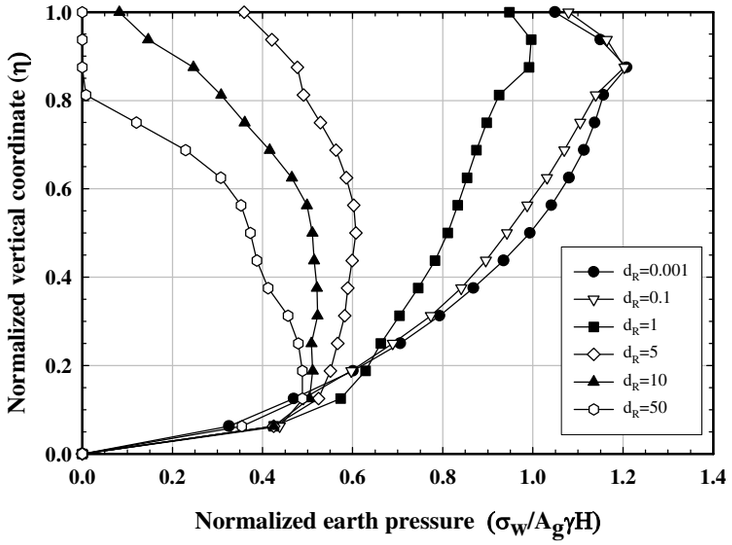
Fig. 2(b) shows the normalized seismic earth pressures behind a rigid wall (d_B=0.1) for different rotational relative flexibilities, d_R. d_B=0.1 represents that the wall is rigid enough such that the flexural displacements of the wall are negligible. In addition the wall is fixed horizontally and vertically at its base (d_H= d_V=0.001). From the figure, one can see that with increasing, d_R: (1) the normalized pressure near the top becomes smaller while the normalized pressure near the base remains nearly constant; (2) the position where the maximum earth pressure occurs moves towards the base; (3) the wall begins to detach from the backfill at the top of the wall when $d_R \geq 10$.

Fig. 2(c) plots the normalized seismic earth pressures at the back of a rigid wall (d_B=0.1) for different horizontal relative flexibilities, d_H. The results are obtained for d_R= d_V=0.001 which correspond to a wall fixed rotationally and vertically at its base. The figure shows that as d_H increases: (1) the normalized pressures near both the top and the base of the wall decrease at a similar rate in such a way that the shape of the curves remains unchanged; (2) the location where the maximum earth pressure occurs moves slightly towards the top of the wall; (3) the wall begins to detach from the backfill at the base of the wall when $d_H \geq 0.1$.

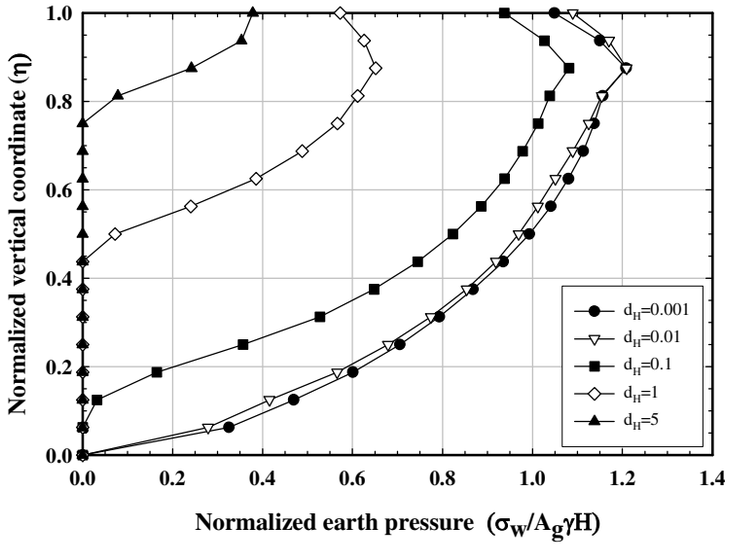
Fig. 2(d) plots the normalized seismic earth pressures at the back of a rigid wall (d_B=0.1) for different vertical relative flexibilities, d_V. The results are obtained for d_R= d_H=0.001 which correspond to a wall fixed rotationally and horizontally at its base. As shown in the figure, the distributions of the normalized pressures are the same regardless of d_V.



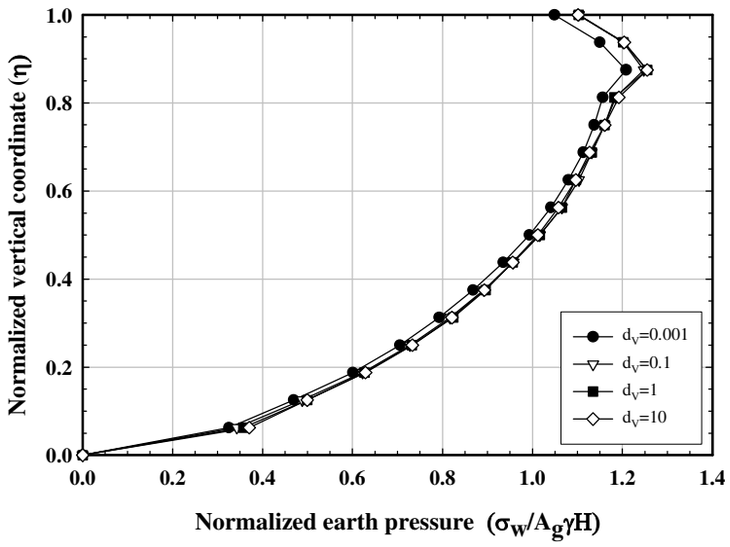
(a)



(b)



(c)

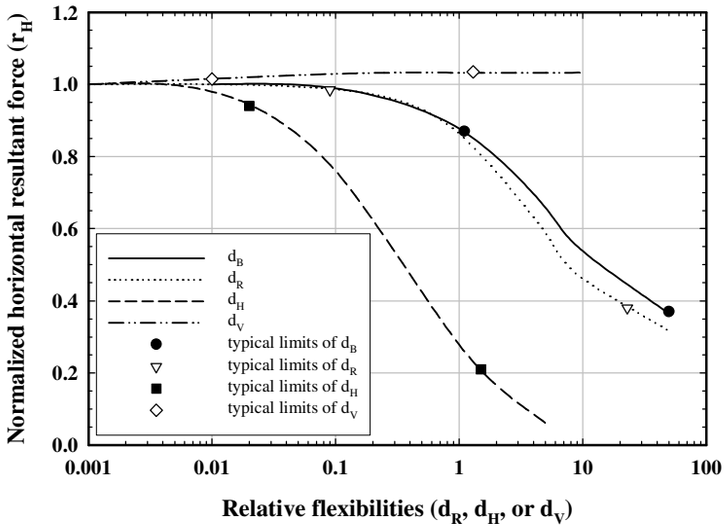


(d)

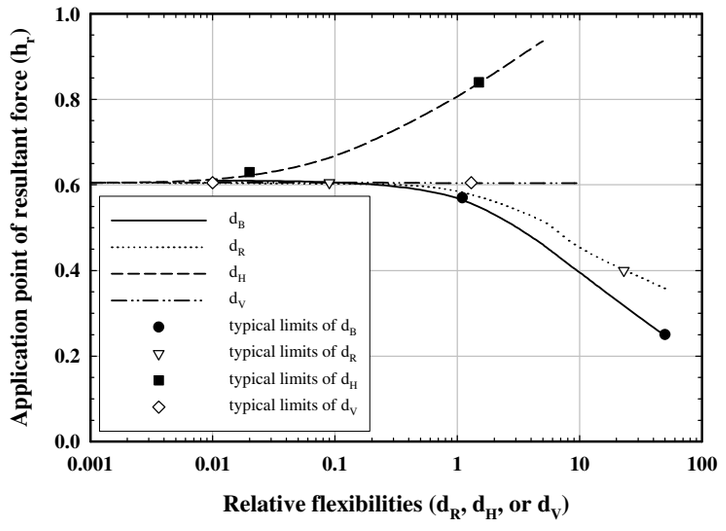
FIG. 2. Distribution of normalized seismic earth pressure behind a wall for: (a) flexural relative flexibility, d_B; (b) rotational relative flexibility, d_R; (c) horizontal relative flexibility, d_H; and (d) vertical relative flexibility, d_V.

Fig. 3 (a) and (b) show, respectively, the horizontal resultant force, R_H, and the point of application of R_H, h_r, which is measured from the base of the wall to the centroid of the earth pressure area. In the figures four pairs of symbols with the same shape denote reasonable upper and lower limits of the relative flexibilities of typical cantilever walls. In Fig. 3(a), the normalized force, r_H, is used instead of R_H; r_H is the ratio of the force R_H obtained in each case and the force R_H computed for the perfectly rigid wall totally fixed at its base. The figure shows that with increasing d_B, d_R, and d_H, r_H decreases. It also shows that the horizontal translation induces the largest reduction of horizontal thrust.

Fig. 3(b) shows that with increasing d_B or d_R, h_r decreases and that with increasing d_H, h_r increases; h_r however remains unchanged with increasing d_V. These results indicate that the horizontal translation of the wall has the largest effect on the magnitude of the seismic earth pressure behind the wall. In addition, the effects of the rotation at its base are similar to those of the flexural displacements of the wall.



(a)



(b)

FIG. 3. Resultant force and its point of application for different relative flexibilities, d_B, d_R, d_H, and d_V. (a) normalized horizontal resultant force, r_H; (b) point of application of horizontal resultant force, h_r (two symbols with the same shape represent upper and lower limits of typical retaining walls for each relative flexibility)

The combined effects of the different parameters are highlighted in Fig. 4. The figure

is a plot of the normalized earth pressures behind the wall for the four extreme cases: rigid wall and stiff foundation (Case 1), rigid wall and soft foundation (Case 2), flexible wall and stiff foundation (Case 3), and flexible wall and soft foundation (Case 4). For Case 1, it is observed that the wall does not detach from the backfill, the normalized pressure near the top of the wall is larger than near the base, and that the maximum earth pressure behind the wall occurs at η=0.6. For Case 2, Fig. 4 shows that the wall detaches from the backfill at the base, the normalized pressure near the top of the wall is larger than near the base, and that the location of the maximum earth pressure along the wall is similar to Case 1. For Case 3, one can see that the wall detaches from the backfill at its top, and that the maximum earth pressure behind the wall occurs at η=0.2. For Case 4, the wall detaches from the backfill both at the top ($\eta \geq 0.5$) and at the base ($\eta \leq 0.2$) and the maximum earth pressure behind the wall occurs at η=0.35. The horizontal resultant force, R_H, is the largest for Case 1, and the smallest for Case 4. The point of application of the horizontal resultant force, h_r for both Case 1 and Case 2 is about 0.6H. h_r for Case 3 and Case 4 is 0.25H and 0.35H, respectively.

These results are due to the interplay between the wall and the foundation. A rigid wall with a soft foundation detaches from the backfill at its base due to the horizontal translation of the wall. In addition, Fig. 4 shows that the shape of the distribution of the earth pressures is similar to that of a rigid wall with a stiff foundation, so the magnitudes of h_r are similar in both cases. The figure also shows that the relative flexibility d_H has the most significant effect on the seismic earth pressures behind a rigid wall with a soft foundation. A flexible wall with a stiff foundation detaches from the backfill only at its top, while a flexible wall with a soft foundation detaches both from the top and the bottom. Hence, it is expected that the key parameter that determines the earth pressures behind a flexible wall is the relative stiffness of the wall, d_B, when the foundation is stiff, and both the relative stiffness d_B and d_H when the foundation is soft.

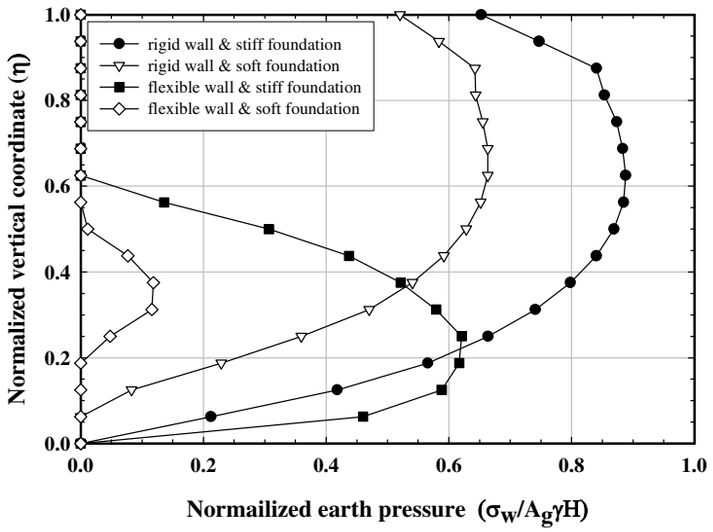


FIG. 4. Distribution of normalized seismic earth pressure behind a wall for: (1) rigid wall with stiff foundation (Case 1); (2) rigid wall with soft foundation (Case 2); (3) flexible wall with stiff foundation (Case 3); and (4) flexible wall with soft foundation (Case 4)

SUMMARY AND CONCLUSIONS

In this study, the seismic response of retaining walls that bend, rotate, and translate horizontally and vertically is evaluated using a numerical model. The model assumes that both the wall and the backfill have an elastic behavior. The results from the numerical analysis show that:

(1) The relative flexural flexibility between the wall and the backfill, and the relative horizontal and rotational flexibilities of the wall all have significant effects on the seismic earth pressures behind the wall.
(2) The effects of the relative flexural flexibility of the wall on the seismic earth pressures are similar to those of its relative rotational flexibility.
(3) Within the range of the relative flexibilities of typical retaining walls, the relative horizontal flexibility has the most significant effect.
(4) Considering the following four extreme cases: rigid-stiff (rigid wall and stiff foundation), rigid-soft, flexible-stiff, and flexible-soft, the seismic earth pressure behind a rigid wall with a stiff foundation is the largest, and the pressure on a flexible wall with a soft foundation is the smallest.
(5) The seismic pressures behind a rigid wall with a soft foundation are very sensitive to the relative horizontal flexibility of the wall. The pressures behind a flexible wall with a stiff foundation depend strongly on the relative flexibility of the wall, while they depend both on relative flexural flexibility and relative horizontal flexibility for a flexible wall with a soft foundation.

REFERENCES

ABAQUS (Ver. 6.6) User's Manual (2006). Hibbit, Karlsson and Sorensen, Inc., 2006.

Fang, YS., Yang, YC., and Chen, TJ. (2003), "Retaining walls damaged in the Chi-Chi earthquake," *Canadian Geotechnical Journal*, National Research Council of Canada, vol. 40, pp 1142-1153.

Koseki, J., Munaf, Y., Tatsuoka, F., Tateyama, M., Kojima K. and Sato, T. (1998), "Shaking table and tilt table tests of geosynthetic –reinforced soil and conventional retaining wall," *Geosynthetic International*, Vol. 5(1-2), pp 73-96.

Mononobe, N. and Matsuo, H. (1929). "On the determination of earth pressure during earthquake," *Proceedings of World Engineering Congress*, Tokyo, Vol. IX, Part 1, pp 177-185.

Okabe, S. (1924). "General theory on earth pressure and seismic stability of retaining wall and dam," *Journal of Japanese Society of Civil Engineering*, Vol. 10(6), pp 1277- 1323.

Psarropoulos, PN., Klonaris, G. and Gazetas, G. (2005), "Seismic earth pressures on rigid and flexible retaining wall," *Soil dynamics and Earthquake Engineering*, vol. 25, pp 795-809.

Scott, RF. (1973), "Earthquake-induced pressures on retaining walls," *Proceedings of the fifth world conference on earthquake engineering*. vol. 2, pp 1611–1620.

Tatsuoka, F., Tateyama, M., and Koseki, J. (1996), "Performance of soil retaining walls for railway embankments," *Soils and Foundations*, Special Issue of Soils and Foundations on Geotechnical Aspects of the January 17, 1995, Hyogoken-Nanbu Earthquake, pp 331-324.

Veletsos, AS., and Younan, AH. (1997), "Dynamic response of cantilever retaining walls," *Journal of Geotechnical and Geoenvironmental Engineering*, ASCE, Vol. 123, No. 2, pp 161-172.

Wood, JH. (1973), "Earthquake-induced soil pressures on structures," *Report EERL 73-05*,

Earthquake Engineering Research Laboratory, California Institute of Technology.

This page intentionally left blank

Seismic Lateral Earth Pressure Reduction on Earth-Retaining Structures Using Geofoams

John S. Horvath[1], Ph.D., P.E., M.ASCE

[1]Professor, Manhattan College, Civil and Environmental Engineering Department, Bronx, NY 10471, U.S.A.; john.horvath@manhattan.edu

ABSTRACT: *Geofoam* is a type of *cellular geosynthetic* that can be used to reduce lateral earth pressures acting on a wide range of earth-retaining structures (ERSs). There are two distinct geosynthetic-functional ways in which geofoams can provide this benefit: as *lightweight fill* and as a *compressible inclusion*. These functions can be implemented either in new construction or retroactively with existing ERSs. Depending on the specific design details chosen, it is possible to reduce lateral earth pressures acting on an ERS to almost zero under both gravity and seismic loading. Unfortunately, the existence and capabilities of this geotechnology, which has the potential to revolutionize the way ERSs are designed, are still not widely known and thus have been significantly underutilized to date. This paper summarizes the state of knowledge concerning the use of geofoams to reduce lateral earth pressures on ERSs and addresses both analytical methods (with an emphasis on seismic loading) as well as geofoam materials and products. It is hoped that this will encourage both usage and research of this intriguing geotechnology.

INTRODUCTION

One of the important advances in geosynthetics geotechnology in the final years of the 20th century was the recognition that there are categories of geosynthetics beyond the traditional two-dimensional/planar types such as geotextiles, geomembranes, and geogrids. In particular, a type of geosynthetic called geofoam was defined that encompasses a wide spectrum of materials, each with a characteristic texture of small, closed, gas-filled cells so relatively numerous that the resulting material has a porosity that is typically greater than 90% (i.e. a void ratio in excess of 1000%) with a concomitant very low density compared to normal earth materials (Horvath 1991; 1992a,b,c; 1995). It is important to note that geofoam is the generic term for all closed-cell synthetic materials used in geotechnical applications and is not limited to one material or product. Geofoams, along with *geocombs* and *geocells*, are now recognized collectively as cellular geosynthetics where product geometry and performance are distinctly three-dimensional in nature.

Some of the geotechnically significant general attributes of geofoams are that they:

- offer geosynthetic functions that, with few exceptions, are not provided by any other type of geosynthetic. Thus geofoams provide the design professional with design alternatives that would otherwise not be available;

- are inherently *multifunctional* which means that one geosynthetic product consisting of or incorporating geofoam can provide two or more distinct geosynthetic functions. This increases the cost effectiveness of using geofoam-based products because more than one technical benefit can be attributed to a single product; and

- synergistically complement traditional planar geosynthetics, especially those that provide tensile reinforcement (geogrids, geotextiles, metallic elements), to provide design professionals with innovative design alternatives that no one geosynthetic alone can provide.

BACKGROUND

Introduction

A comprehensive overview of geosynthetic functions and applications for geofoams was presented in Horvath (1995) with an updated bibliography in Horvath (2001). More recently, a survey was made of the relative state of usage of the various geosynthetic functions of geofoams (Horvath 2005b).

Prominent in these publications was information concerning the use of geofoams to reduce lateral earth pressures as this particular application has the promise to revolutionize how ERSs are designed and constructed (Horvath 2004c). Although this particular geofoam application dates back to at least the 1970s experience indicates that it has been significantly under-researched and underutilized to date. Furthermore, what research and practical application have occurred to date have largely focused on gravity loads. Consequently, the purpose of this paper is to focus on analytical methods used for seismic loads. Both what is already known as well as where improvements in the state of knowledge are needed are identified and discussed. Thus it is hoped that both practitioners and researchers will find this paper of use, and that it will both inform and inspire so that there is both greater utilization of as well as increased research into the use of geofoams with ERSs.

Terminology

A common term used in discussions related to lateral earth pressures and ERSs is *yielding*. In this context, yielding is synonymous with horizontal (lateral) displacement and is used solely in this context throughout this paper.

Types of Earth-Retaining Structures

ERSs are broadly divided into those that are:

- *non-yielding* which defines an ERS that is inherently incapable of and/or constrained against both deformation and displacement in the horizontal direction under design loads. Common examples include below-grade (e.g. basement) walls of buildings, bridge abutments, and free-standing retaining walls that are restrained against horizontal displacement due to physical restraint or structure geometry. The hallmark of non-yielding ERSs is that they are logically designed assuming the *at-rest* earth-pressure state within the retained soil; and

- *yielding* which defines an ERS that can either displace or deform or both in the horizontal direction under design loads. The hallmark of yielding ERSs is that they are assumed to be capable of developing the *active* earth-pressure state within the retained soil.

Not considered in this paper, although noted here for the sake of completeness, is a third type of ERS called *self-yielding*. These are rigid-ERSs that displace horizontally on their own (usually as a result of thermal changes in their surrounding environment) as opposed to displacing (or not) as a reaction from earth loads as in the classic cases of yielding and non-yielding ERSs. Examples include *integral-abutment bridges* as well as various types of circular water- and wastewater-treatment tanks (Horvath 2000, 2004b, 2005a).

Relevant Geofoam Functions

There are two primary mechanisms by which geofoams can be used to reduce the lateral pressures on ERSs, with each utilizing a different geosynthetic function:

- The lightweight-fill function makes use of the fact that geofoams have a density that is considerably less (as low as 1%) than that of soil; are inherently self-supporting even on a vertical slope; and can have a Poisson's ratio that approaches zero. This is a *small-strain function* of geofoams.

- The compressible-inclusion function makes use of the fact that geofoam materials can be designed to be relatively compressible to intentionally induce horizontal displacements and concomitant shear-strength mobilization within the retained-soil mass (called *controlled yielding*). This is a *large-strain function* of geofoams.

It is relevant to note that regardless of the specific type of ERS or geofoam functional application utilized there is practical applicability not only for new construction but with existing structures. The latter is useful in practice as it is often a better design alternative to reduce the loads on an existing ERS as a way of upgrading its current and/or future performance as opposed to modifying or replacing the ERS to accept greater loads. Relevant to the theme of this conference is that this design strategy of load-reduction can be a cost-effective way to seismically upgrade an existing ERS that was not designed originally with a consideration of seismic loads or was designed for seismic loads of smaller magnitude than those required by current design codes or good practice.

LIGHTWEIGHT-FILL FUNCTION

Application Concept

Figure 1 shows a generic cross-section where geofoam is used for its lightweight-fill function. The details of the ERS are irrelevant for the present discussion as this function can be used effectively with both non-yielding and yielding ERSs. Note that nowadays the geofoam would be configured as shown in this figure with a stair-stepped interface between geofoam and retained soil when viewed in cross-section. The importance of this stepped geometry was not always recognized in the past.

Analytical Model

The current state of knowledge indicates that the behavior of the geofoam mass as shown in Figure 1 is much more complex than usually thought. A common perception is that a classical active-earth-pressure 'wedge' forms within the geofoam mass as shown qualitatively by the dotted line in Figure 1. The presumed benefit of the geofoam is that its unit weight is substantially less than that of soil and thus the active earth force that this hypothetical wedge imparts on the back of the ERS is proportionately reduced compared to soil using a classical equivalent-fluid-pressure distribution along the back of the ERS.

However research to date indicates that this behavioral mechanism, although intuitive, is completely incorrect as it is based on a simplistic extrapolation of what occurs with a soil mass of essentially unlimited lateral extent behind an ERS. In reality, as shown in Figure 1 two very different materials (geofoam and soil) are in close proximity behind an ERS and the interaction of these materials must be taken into account to develop the net result on the back of the ERS.

The current state of practice assumes that the geofoam mass acts as a pseudo-ERS independent of, but interacting with, the actual ERS (note that a geofoam mass can be designed to be entirely self-supporting without an ERS in which case it is called a *geofoam wall*). The retained soil is assumed to act on the geofoam mass along an imaginary plane defined by the angle θ and dashed line in Figure 1. Furthermore, it is assumed that the active-earth-pressure state always develops within the retained soil adjacent to the geofoam mass whether the actual ERS is non-yielding or yielding. This is because it is assumed there is always sufficient lateral compression within the geofoam mass to allow the retained soil to displace sufficiently to mobilize the active state. Thus the earth forces applied to the geofoam mass by the retained soil under

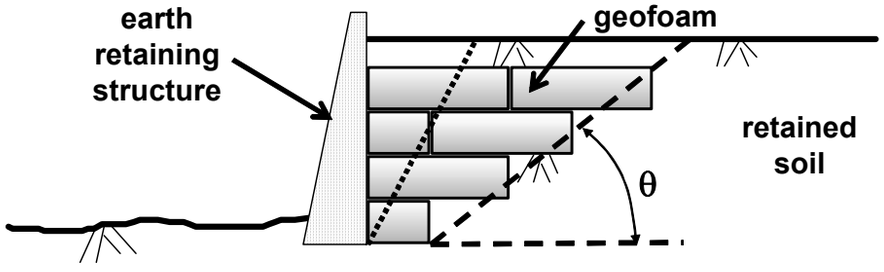


FIG. 1. Generic application of lightweight-fill function.

seismic loads can be estimated in the usual way using, for example, the classical Coulomb and Mononobe-Okabe theories. These earth forces are assumed to be transmitted through the geofoam mass to the back of the ERS.

The magnitude of forces from both the Coulomb and Mononobe-Okabe theories are dependent on the angle θ which is dictated by the geofoam geometry chosen. Thus it is through appropriate selection of the angle θ that geofoams achieve both gravity- and seismic-load reduction using the lightweight-fill function. Note that there is always a magnitude of θ for which both the gravity and seismic earth loads applied to the geofoam mass will be zero, although the θ-values are different. Of course in any project-specific application it is not necessary to reduce these forces to zero but this does indicate the significant reduction in earth forces that can be achieved in concept when using the lightweight-fill function of geofoam, albeit requiring use of a relatively large volume of geofoam to achieve this. Thus in any project-specific application the actual value of θ used needs to be optimized to where the combined costs of the ERS and geofoam material are minimized.

Additional forces are assumed to act on the back of the ERS as a result of the mass of material (soil, pavement, etc.) lying above the geofoam (the mass of the geofoam itself is negligible under both gravity and seismic loading):

- A static component exists under both gravity and seismic loading. It consists of a classical equivalent-fluid-pressure distribution within the thickness of material overlying the geofoam mass (at-rest or active conditions are assumed depending on whether the ERS is non-yielding or yielding respectively) plus a uniform-pressure distribution within the full thickness of the geofoam mass equal to one-tenth of the vertical stress acting on the top of the geofoam mass.

- A dynamic component exists under seismic loading only. It is based on the assumption that the geofoam mass and any overlying material act together as a flexible system modeled as a classical single-degree-of-freedom system where the geofoam acts as the spring and dashpot/damper components and the overlying material represents the lumped mass. Guidelines for numerically evaluating the various model parameters can be found in Horvath (1995, 2004a) and Stark et al. (2004a). For yielding ERSs only this component of load is reduced by a horizontal shear force that is assumed to develop along the horizontal portions of the stepped interface between the geofoam and underlying ground. This shear force is calculated using the vertical stress applied to the top of the geofoam and the friction angle between the geofoam material and underlying ground.

Suggestions for Future Improvements

The above-described analytical model and its various assumptions are the collective result of relatively limited research and observation of actual ERSs, much of which was not well documented in published literature (Horvath 1995). In particular, the assumptions concerning load components attributable to seismic loading, i.e. the uncoupled analysis of forces acting on the ERS from the retained soil versus those from the geofoam with overlying material, are considered particularly tentative at this

time even though they have been in use since the 1990s. Therefore it is suggested that the entire analytical model and concomitant assumptions used to perform an analysis of geofoam used for its lightweight-fill function to reduce lateral earth pressures be critically studied and reviewed using the entire gamut of modern numerical and physical testing.

COMPRESSIBLE-INCLUSION FUNCTION

Application Concept

Overview

Experience indicates that the geosynthetic function of compressible inclusion is not intuitive to many design professionals (Horvath 2005b), even though it utilizes the fundamental soil-mechanics principle of arching (Handy 1985, Harrop-Williams 1989) that was recognized and utilized in the early 20th century, if not before that, to reduce vertical loads on underground conduits (Spangler and Handy 1982; Horvath 1995, 1996, 1998a, 2004c). This coupled with the fact that geofoams are identified so closely and, in many cases, exclusively with the lightweight-fill function has led to an overall lack of knowledge and use of this geofoam functional application to date.

In its most basic form, utilizing a geofoam compressible inclusion produces a benefit only for non-yielding ERSs. However this concept can be extended by incorporating geosynthetic tensile reinforcement within the retained-soil mass. In this latter configuration there are benefits for both non-yielding and yielding ERSs.

The basic concept of a compressible inclusion is that a relatively low-stiffness material is intentionally placed between two stiffer materials. In such conditions the least-stiff material in the system will compress much more easily than the other materials, resulting in load reduction through some soil-mechanics mechanism such as, but not limited to, arching (different mechanisms occur with expansive soil for example). The attraction of this concept is that it is very efficient material-wise as a relatively thin compressible inclusion can result in significant load reductions.

It is of relevance to note that the compressible-inclusion function of geofoams is a *large-strain* geofoam application, i.e. one where relatively large compressive strains of the geofoam product are intended under design loads. This contrasts to the lightweight-fill function such as shown in Figure 1 which is a *small-strain* geofoam application where compressive strains under design loads must be kept relatively small in magnitude for the design life of the structure.

Reduced-Earth-Pressure (REP) Wall Concept

The original, basic concept for using a geofoam compressible inclusion to reduce lateral earth pressures on an ERS is illustrated generically in Figure 2. Again, the ERS details are irrelevant although it is worth noting that this application is used only with non-yielding ERSs. Essentially, the function of the compressible inclusion in this application is to allow a mass of retained soil to displace laterally and mobilize its inherent shear strength even if the ERS does not displace or deform, essentially

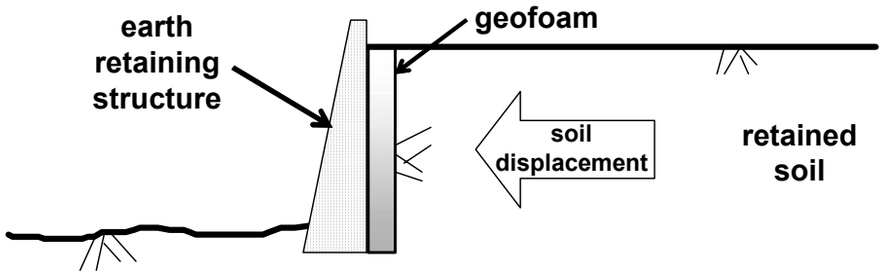


FIG. 2. Generic application of REP concept of compressible-inclusion function.

transforming a non-yielding ERS into a yielding ERS in the process. Because lateral earth pressures reduce in magnitude from the at-rest to active state as the retained soil displaces this is referred to as the *Reduced-Earth-Pressure* (REP) concept.

Zero-Earth-Pressure (ZEP) Wall Concept

The original REP concept was extended circa the 1980s as shown in Figure 3 by incorporating multiple layers of geosynthetic tensile reinforcement (geotextiles, geogrids, metallic elements) within the retained soil in the classical arrangement of *mechanically stabilized earth* (MSE). In this application, compression of the geofoam and resulting horizontal displacement of the reinforced soil mass allows the reinforcement to strain and develop tensile forces even in situations where little or no displacement or deformation of an ERS would not allow this to develop, thus rendering the reinforcement of little or no value. Because the lateral earth pressures in this case can reduce in magnitude from the at-rest state to effectively zero as the retained soil expands horizontally and the tensile reinforcement strains this application is referred to as the *Zero-Earth-Pressure* (ZEP) concept.

Analytical Models

The basic physical model used to date for both REP and ZEP applications is that of a system consisting of two springs in series. Each spring, which may be linear or non-linear as desired, represents the horizontal force-displacement behavior of a system component. Referring to figures 2 and 3:

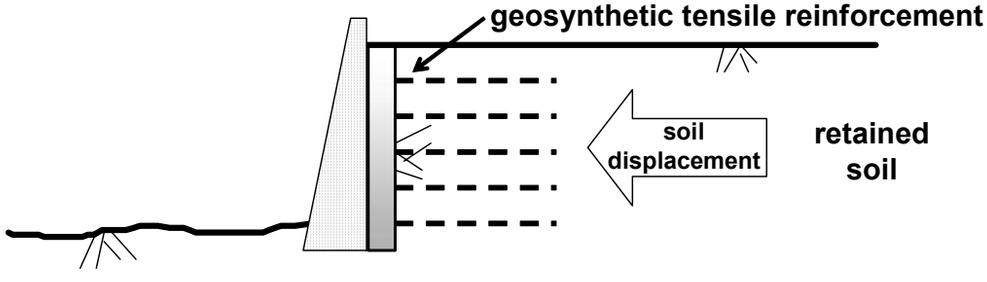


FIG. 3. Generic application of ZEP concept of compressible-inclusion function.

- The unreinforced (REP concept) or reinforced (ZEP concept) mass of retained soil is a spring with an initial horizontal compressive force (typically assumed to be that of the at-rest earth pressure state) that reduces with increasing horizontal displacement to either the active state (REP concept) or zero (ZEP concept).

- The geofoam compressible inclusion is a spring with zero initial force that develops a horizontal compressive force with increasing horizontal displacement.

The solution is found by matching forces and displacements in the springs. The resulting force is that assumed to be acting on the ERS.

The most complex aspect of this model is properly quantifying the force-displacement behavior of the retained soil (Horvath 2000). In the case of the REP concept, the minimum horizontal force assumed to develop corresponds to the active earth pressure state and can be estimated using the classical Coulomb and Mononobe-Okabe theories for gravity and seismic loads. The Veletsos and Younan (1994) solution for a yielding ERS under seismic loading has been extended for use with the REP concept to provide an alternative solution (Horvath 1997, 1998b, 2005b, 2008).

Efforts to date relative to the ZEP concept have been much more limited and have considered gravity loads only (Horvath 2000). A key problem is that MSE design is typically failure-, not displacement-, based so quantifying the force-displacement behavior of a MSE mass is difficult. One item under current consideration is to see if an elasticity-based solution such as that developed by Harrison and Gerrard (1972) might provide useful insight. In any event, one characteristic of the ZEP concept is that the minimum horizontal force assumed to develop within the reinforced soil mass always becomes zero at some finite displacement.

Suggestions for Future Improvements

The analytical models for the compressible-inclusion function of geofoam for use with lateral-earth-pressure reduction are relatively much less researched and developed than those for the lightweight-fill function, especially for the ZEP concept. Therefore as a group they should be considered a work-in-progress and in need of future research to either validate them or develop other models.

GEOFOAM MATERIAL SELECTION

Despite the relatively recent recognition of closed-cell foams as geosynthetics and the use of the term geofoam to identify them generically as a group, such materials have actually been in commercial use since at least the 1950s and used in geotechnical applications since at least the early 1960s. Consequently, geofoams have a longer history of use than most other geosynthetics and there is extensive practical experience concerning both the in-ground performance and relative economics of various closed-cell foams as geofoam geosynthetic. A comprehensive discussion of geofoam materials can be found in Horvath (1995).

This collective experience indicates that the geofoam material of choice worldwide for most functional applications is *expanded polystyrene* (EPS). This is the familiar

white polymeric (plastic) foam commonly known for its various consumer applications for beverage cups and cushion packaging. For geofoam applications it is typically used in the form of prismatic blocks or panels created in a process called *block molding*.

Consistent with the dominance of block-molded EPS as the overall geofoam material of choice is that it is the material of choice when using the lightweight-fill function for lateral-earth-pressure reduction as shown in Figure 1. Detailed guidance on how to rationally design for this application can be found in Stark et al. (2004a). It is important to note that EPS used for this application is a generic, commodity material that is typically bid on a price-competitive basis in practice. Experience has clearly demonstrated the need for, and rigorous enforcement of, detailed project-specific specifications based on appropriate standards such as contained in Stark et al. (2004b) or ASTM (2004, 2005) as the basis for helping ensure delivery of technically acceptable material for a project. This includes the need for independent manufacturing quality assurance (MQA) of all EPS blocks delivered for a project.

While block-molded EPS geofoam has been used for compressible-inclusion applications experience indicates that it is far more efficient and cost-effective to use a more-compressible material. Both *resilient* (*elasticized*) EPS and *porous-polystyrene block* have been used successfully for this application. These materials are discussed in detail in Horvath (1995). When sold alone or in combination as panel-shaped products for the geofoam market these are both proprietary in nature.

REFERENCES

ASTM (2004). "Standard specification for rigid cellular polystyrene geofoam." *Standard D6817-04*, ASTM Intl., Conshohocken, PA.

ASTM (2005). "Standard guide for use of expanded polystyrene (EPS) geofoam in geotechnical projects." *Standard D7180-05*, ASTM Intl., Conshohocken, PA.

Handy, R. L. (1985). "The arch in soil arching." *J. Geotech. Engrg. Div.*, 111 (3): 302-318.

Harrison, W. J. and Gerrard, C. M. (1972). "Elastic theory applied to reinforced earth." *J. Soil. Mech. and Fndns. Div.*, 98 (SM12): 1325-1345.

Harrop-Williams, K. O. (1989). "Geostatic wall pressures." *J. Geotech. Engrg. Div.*, 115 (9): 1321-1325.

Horvath, J. S. (1991). "The case for an additional function." *IGS News*, 7 (3): 17-18.

Horvath, J. S. (1992a). "'Lite' products come of age; new developments in geosynthetics." *Standardization News*, 20 (9): 50-53.

Horvath, J. S. (1992b). "Dark, no sugar: a well-known material enters the geosynthetic mainstream." *Geotechnical Fabrics Report*, 10 (7): 18-23.

Horvath, J. S. (1992c). "Geofoam - the next geosynthetic material?" *Proc. Soc. of the Plastics Industry Expanded Polystyrene Div. Tech XIII Conf.*, San Francisco, CA.

Horvath, J. S. (1995). *Geofoam geosynthetic*. Horvath Engrg., P.C., Scarsdale, NY.

Horvath, J. S. (1996). "The compressible inclusion function of EPS geofoam: an overview." *Proc. Intl. Sym. on EPS Construction Method (EPS Tokyo '96)*, Tokyo, Japan: 71-81.

Horvath, J. S. (1997). "The compressible inclusion function of EPS geofoam." *Geotextiles and Geomembranes*, 15 (1-3): 77-120.

Horvath, J. S. (1998a). "The compressible inclusion function of EPS geofoam: an overview of concepts, applications, and products." *Res. Rpt. No. CE/GE-98-1*, Manhattan Coll. Civ. Engrg. Dept., Bronx, NY.

Horvath, J. S. (1998b). "The compressible-inclusion function of EPS geofoam: analysis and design methodologies." *Res. Rpt. No. CE/GE-98-2*, Manhattan Coll. Civ. Engrg. Dept., Bronx, NY.

Horvath, J. S. (1999). Discussion of "Status of ASCE standard on design and construction of frost protected shallow foundations" by L. S. Danyluk and J. H. Crandell. *J. Geotechnical and Geoenvironmental Engrg.*, 125 (2): 166-167.

Horvath, J. S. (2000). "Integral-abutment bridges: problems and innovative solutions using EPS geofoam and other geosynthetics." *Res. Rpt. No. CE/GE-00-2*, Manhattan Coll. Civ. Engrg. Dept., Bronx, NY.

Horvath, J. S. (2001). "Geomaterials research project - geofoam and geocomb geosynthetics: a bibliography through the second millennium A.D." *Res. Rpt. No. CGT-2001-1*, Manhattan Coll. Ctr. for Geotechnology, Bronx, NY.

Horvath, J. S. (2004a). "Geomaterials research project - a technical note re calculating the fundamental period of an EPS-block-geofoam embankment." *Res. Rpt. No. CGT-2004-1*, Manhattan Coll. Ctr. for Geotechnology, Bronx, NY.

Horvath, J. S. (2004b). "Integral-abutment bridges: a complex soil-structure interaction challenge." *Geotechnical Engineering for Transportation Projects* (GSP 126), ASCE, Reston, VA: 460-469.

Horvath, J. S. (2004c). "Geofoam compressible inclusions: the new frontier in earth retaining structures." *Geotechnical Engineering for Transportation Projects* (GSP 126), ASCE, Reston, VA: 1925-1934.

Horvath, J. S. (2005a). "Integral-abutment bridges: geotechnical problems and solutions using geosynthetics and ground improvement." *Proc. IAJB 2005: The 2005 FHwA Conference on Integral Abutment and Jointless Bridges*, Baltimore, MD: 281-291.

Horvath, J. S. (2005b). "Expanding the use of expanded polystyrene (EPS) geofoam in practice." *Proc. BSCES ASCE Geo-Institute Fall 2005 Geotech. Engrg. Sem.*

Horvath, J. S. (2008). "Extended Veletsos-Younan model for geofoam compressible inclusions behind rigid, non-yielding earth-retaining structures." *Geotechnical Earthquake Engineering and Soil Dynamics IV*, ASCE, Reston, VA.

Spangler, M. G. and Handy, R. L. (1982). *Soil engineering* (4th ed.). Harper & Row, New York, NY.

Stark, T. D., Arellano, D., Horvath, J. S. and Leshchinsky, D. (2004a). "Geofoam applications in the design and construction of highway embankments." *NCHRP Web Document 65*, Transp. Res. Board, Wash., DC.

Stark, T. D., Arellano, D., Horvath, J. S. and Leshchinsky, D. (2004b). "Guideline and recommended standard for geofoam applications in highway embankments." *NCHRP Report 529*, Transp. Res. Board, Wash., DC.

Veletsos, A. S. and Younan, A. H. (1994). "Dynamic modeling and response of soil-wall systems." *J. Geotech. Engrg.*, 120 (12): 2155-2179.

Seismic Modeling of a 135-Foot-Tall MSE Wall

D. D. Lindquist, PE[1]

[1]Hart Crowser, Inc., 1700 Westlake Avenue North, Suite 200, Seattle, WA 98109; PH (206) 324-9530; FAX (206) 328-5581; email: Doug.Lindquist@hartcrowser.com

Abstract

This paper describes the seismic modeling performed for the design of a 135-foot-tall mechanically stabilized earth (MSE) wall for the Third Runway Project at the Seattle-Tacoma International Airport. The FLAC finite difference program was used to model the MSE wall under construction and seismic loading conditions. This wall was constructed in 2005 and is the tallest MSE wall in North America. The wall was built of granular fill reinforced with steel strips. Wall fascia consists of concrete facing panels. The wall was designed in accordance with the 1996 AASHTO standard guidelines incorporating the interim revisions through 2000. The numerical modeling was performed to provide the design team with additional insight into the static and seismic performance of the MSE wall.

Project Introduction

The Third Runway project consisted of the construction of a new 8,500-foot-long dependent runway. The new runway was located offset from and adjacent to the two existing runways, which are too close together to allow dependent operation during inclement weather. The runway project included placement of 17,000,000 cubic yards of compacted fill and 3,000,000 cubic yards of excavation. To complete the project while minimizing impact to adjacent wetland ecosystems and a creek, three MSE walls were constructed with heights ranging from 40 to 135 feet. The West Wall is the tallest MSE wall and was constructed to maintain a setback between fill placement and the existing creek located near the base of the wall. The West Wall is 1,425 feet long and transitions into 2H:1V slopes at each end. Figure 1 illustrates the location of the new Third Runway and West Wall. Figure 2 is a close up view of the West Wall, with the individual 5 feet by 5 feet concrete facing panels visible. The was design was done collaboratively by Hart Crowser and the Reinforced Earth Company (RCEo). Hart Crowser analyzed the external and combined (internal/ external) stability of the walls, RECo analyzed the internal stability of the walls, HNTB was the lead civil engineer, and the Port of Seattle was the owner. Other papers have been written on this project by Chen and Bailey (2004) regarding ground improvement and Stuedlein et al.(2007) regarding instrumentation.

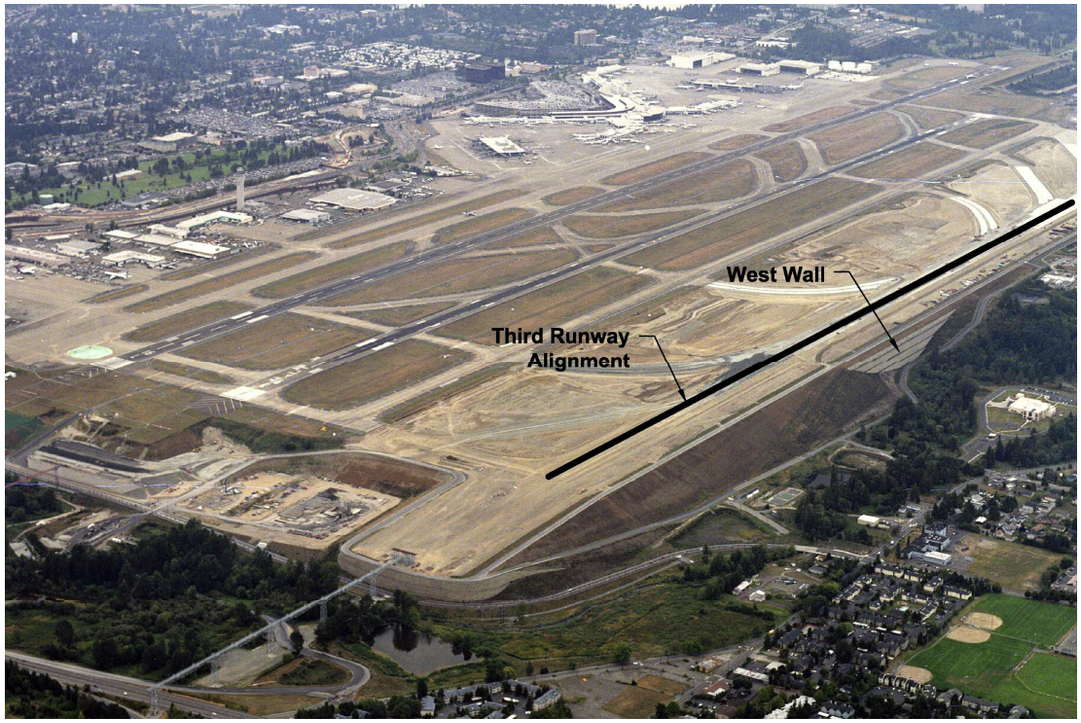


Figure 1. Location of West Wall



Figure 2. Close Up View of West Wall

Seismic Performance Goals

The Third Runway Project was designed as a "structure of ordinary importance" similar to large public buildings and other transportation infrastructure (e.g., bridges and highways). The project components were designed to accommodate a seismic

design event with a 10 percent probability of being exceeded in 50 years, which corresponds to an average return period of 475 years. Specific performance goals for the Third Runway Project were to meet the following conditions for this design level event:

- The MSE walls and embankment fill will remain stable. Some deformation is acceptable (up to a few feet) provided stresses in the retaining wall materials remain typically below the values allowed by the AASHTO code;
- There will be no wetland or creek impacts due to seismic shaking of the embankment or MSE walls; and
- There will be no operational impacts to the new runway related to movement of the embankment slopes and walls during an earthquake.

To achieve these goals, satisfy limit equilibrium factor of safety requirements, and optimize MSE wall performance, design modifications were made to the extent of ground improvement (i.e., excavation and replacement of sections of the subgrade soils with compacted granular fill) and to the length and spacing of reinforcement.

Modeling Philosophy

The finite difference software FLAC Version 4.0 (Itasca 2000) was used to perform displacement-based analysis of the West Wall. This was the current version of FLAC during the period of time this work was performed (2001). Details of the specific soil and structural input properties used in the analysis are described in the following sections.

The purpose of the numerical modeling was to provide the design team insight into the performance of the MSE walls under static and seismic loading. Displacement-based analyses were performed to provide information on wall performance at the end of construction and during and after a design level earthquake. Results of the analyses include horizontal and vertical deformations of the walls and areas adjacent to the walls, and stresses in the reinforcing strips for various load conditions.

The static analysis calculated the distribution of deformation and baseline stresses prior to the seismic analysis. The seismic analysis and liquefied analysis were performed to evaluate performance during and after a seismic event. Portions of the existing subgrade soils beneath the wall were determined to be susceptible to liquefaction in the design level seismic event. Prior to wall construction, the liquefiable soils below the wall were removed and replaced with densely compacted granular fill. The potential effects of liquefaction in liquefiable soils left in front of the wall and behind the reinforced zone were included in the modeling. The analyses bounded the initiation of liquefaction by modeling its initiation at the beginning and end of the ground shaking time history, in separate analyses. Residual strength soil properties were applied within the finite difference model at the time of liquefaction initiation for each of these analyses.

Model Input

Soil Properties. The soil properties were based on soil explorations, laboratory tests, *in situ* tests, specifications for the fill to be placed, and consideration of the expected level of strain in that soil unit. In addition to index and strength testing, pressuremeter and shear wave velocity tests were used to obtain a better understanding of the moduli of the site soils. A parametric analysis was performed to evaluate the influence/significance of variations in the soil moduli. The properties used in the final analyses are presented in this paper. The soil profile used in the West Wall analysis was based on nearby soil explorations (i.e., borings, cone penetrometer tests, and test pits). Tables 1 through 3 summarize the static, seismic, and post-earthquake/residual strength soil properties used in this analysis based on the Mohr-Coulomb constitutive model. The soils layers used in the model are illustrated on Figure 3.

Table 1. Static Soil Properties

Soil Unit	Unit Weight (pcf)	Friction Angle (Degrees)	Cohesion (psf)	Dilation Angle (Degrees)	Young's Modulus (psf) [a]	Poisson's Ratio
1 - embankment fill	135	35	10	5	$3.1e4 * \sigma'_m{}^{½} \geq 8.9e5$	0.35
2 - reinforced fill	140	37	10	7	$3.1e4 * \sigma'_m{}^{½} \geq 8.9e5$	0.35
3 - roadway fill	140	37	10	7	$3.1e4 * \sigma'_m{}^{½} \geq 8.9e5$	0.35
4 - ground improvement	140	37	10	7	$3.1e4 * \sigma'_m{}^{½} \geq 8.9e5$	0.35
5 - loose to medium dense sand	125	32	10	2	$1.6e4 * \sigma'_m{}^{½} \geq 2.2e5$	0.35
6 - medium dense to dense sand	130	35	10	5	$2.1e4 * \sigma'_m{}^{½} \geq 5.2e5$	0.35
7 - dense to very dense sand	135	37	10	7	6.5e6	0.35
8 - till	140	40	250	10	6.5e6	0.35
9 - very stiff to hard silt	120	32	10	0	3.3e6	0.35
10 - silt and clay	115	32	10	0	$100*\sigma'_v \geq 1.5e5$	0.35
11 - peat	110	15	10	0	$56*\sigma'_v \geq 7.1e4$	0.4

[a] Where, σ'_v is the effective vertical stress and σ'_m is the mean effective.

Table 2. Seismic Soil Properties

Soil Unit[a]	Unit Weight (pcf)	Friction Angle (Degrees)	Cohesion (psf)	Dilation Angle (Degrees)	Young's Modulus (psf)	Poisson's Ratio
9 - very stiff to hard silt	120	0	4000	0	3.3e6	0.495
10 - silt and clay	115	0	$0.23\sigma'_v \geq 1000$	0	$100*\sigma'_v \geq 1.5e5$	0.495
11 - peat	110	0	$0.23\sigma'_v \geq 400$	0	$56*\sigma'_v \geq 7.1e4$	0.495

[a] Soil properties for units not shown are unchanged from their static values.

Table 3. Post-Earthquake and/or Liquefied Soil Properties

Soil Unit[a]	Unit Weight (pcf)	Friction Angle (Degrees)	Cohesion (psf)	Dilation Angle (Degrees)	Young's Modulus (psf)	Poisson's Ratio
5 - loose to medium dense sand (liquefaction)	125	0	700	2	3.5e4	0.495
9 - very stiff to hard silt	120	0	3200	0	3.3e6	0.495
10 - silt and clay	115	0	$0.184\sigma'_v \geq 800$	0	$100*\sigma'_v \geq 1.5e5$	0.495
10 - silt and clay (reduced strength)	115	0	$0.11\sigma'_v$	0	$33*\sigma'_v$	0.495
11 - peat	110	0	$0.184\sigma'_v \geq 320$	0	$56*\sigma'_v \geq 7.1e4$	0.495

[a] Soil properties for units not shown are unchanged from their static values.

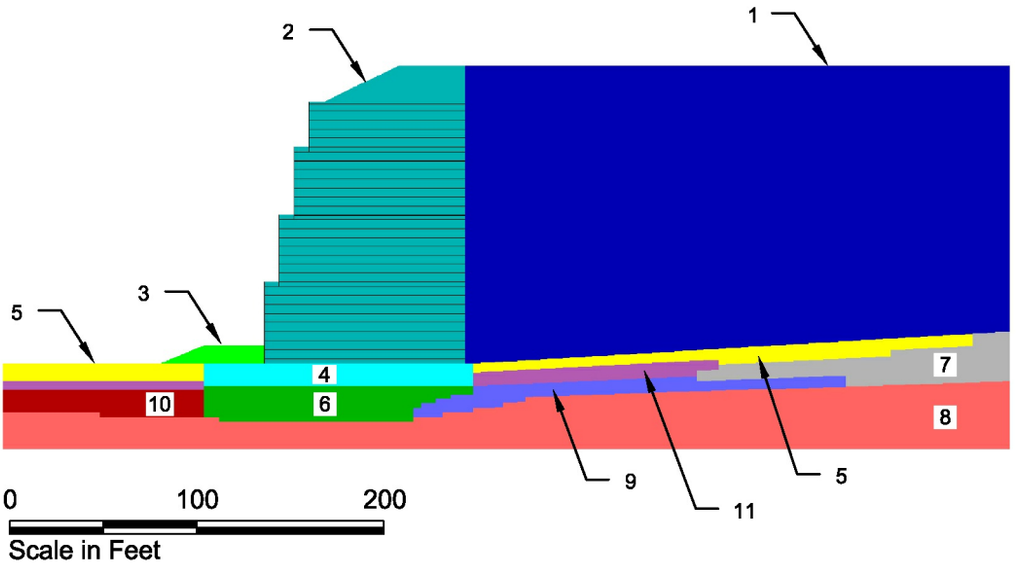


Figure 3. Soil Units in West Wall FLAC Model

Structural Properties. Components of the RECo wall design included in the FLAC analysis consist of the concrete facing panels and steel reinforcement strips extending from the concrete panels 110 feet into the soil mass (i.e., a length to wall height ratio of approximately 0.8). The concrete panels were 5 feet tall, 5 feet wide, and 7 inches thick. Reinforcement strips were approximately 2 inches wide by 1/4 inch thick with 3 to 25 strips per panel. The reinforcement strips were modeled as cable elements extending from the center of the facing panels into the soil mass as a single element per facing panel. Length, tensile, and pull-out capacity properties were assigned to each reinforcing layer to represent the actual length, cross section, and number of reinforcing strips of each panel. Also, dimensions of the steel reinforcement were reduced by 1/25 inch per side to account for corrosion during the 100-year design

life. This is a conservative assumption for the end of construction case, which will not yet have corrosion; however, it allows for direct comparison of stresses between the cases. Table 4 presents the steel reinforcement properties, and Table 5 presents the concrete facing properties used in the analyses.

Table 4. Steel Reinforcing Element Properties

Properties	Scaled FLAC Input per Strip[a]
Area	a = 0.00206 ft^2
Perimeter	p = 0.0693 ft/ft
Elastic Modulus	e = 8.49e8 psf
Yield Strength	yield = 3915 lb/ft
Compressive Strength	ycom = 3915 lb/ft
Soil/Reinforcement Adhesion	sbond = 0 psf
Soil/Reinforcement Friction	sfric = 37^o
Soil/Reinforcement Stiffness	kbond = 1e6 psf/ft

[a] These values are per 2 inch by 1/4 inch strip and are scaled by the panel width (5 feet), as necessary

Table 5. Concrete Facing Properties

Properties	FLAC Input
Area	A = 0.583 ft^2/ft
Elastic Modulus	e = 5.18e8 psf
Bending (plastic) Moment	Pmom = 996 lb-ft
Moment of Inertia	i = 0.01654 ft^4
Density	dens = 4.66 slugs/ft^3

Model Construction. The first step in the model construction consisted of inputting the pre-construction soil conditions and ground improvement zones. Following this initial set-up, the West Wall was "built" incrementally in lifts to provide a realistic estimate of stresses and deformations resulting from the weight of the fill as the wall was being construction.

Boundary Conditions. The static boundary conditions consisted of the left- and right-hand sides of the model being fixed in the horizontal direction and the base fixed in the horizontal and vertical conditions. During the seismic analysis, the sides were set to model a free field condition and the base was fixed in the vertical direction with a time history of acceleration applied in the horizontal direction.

Seismic Parameters. The time history of acceleration for the base of the model was obtained through the following multi-step process.

1. Rock outcrop response spectrum obtained from site-specific probabilistic seismic hazard analysis;

2. Recorded ground motion selected based on the earthquake mechanism, magnitude, source-site distance, and soil conditions;

3. Recorded ground motion scaled in the frequency domain to match the rock outcrop response spectrum; and

4. Ground motion sent through two-dimensional site response program (QUAD4) to obtain representative input ground motion for a location below the base of the wall for input at the base of the FLAC model.

The time at which liquefaction would be initiated was considered and preliminary analysis regarding the number of cycles to initiation was performed. Based on the uncertainty of this analysis, two scenarios were considered with regard to the timing of liquefaction to bracket the analysis.

- Liquefaction would occur at the beginning of shaking; and

- Liquefaction would follow the end of shaking.

Note: The current version of FLAC has built in constitutive models for treating liquefaction, which were not readily available at the time this work was performed.

A Rayleigh damping of 5 percent was applied to the seismic model with a central frequency of 20 Hertz.

Model Results

Displacements and stresses in the reinforcing were evaluated for the following cases:

1. At the end of staged construction;

2. During ground shaking without liquefaction (Table 6);

3. At the end of ground shaking without liquefaction (Figures 4 and 5);

4. After liquefaction occurred at the end of ground shaking;

5. During ground shaking, when liquefaction occurred at the beginning of shaking; and

6. At the end of shaking, when liquefaction occurred at the beginning of shaking.

The modeling predicted approximately 1 to 4 inches of lateral displacement and 0 to 3 inches of settlement near the face of the wall during construction (Case 1). Reinforcement stresses were predicted to be no more than 44 percent of yield (using a reduced steel section based on estimated corrosion for the 100-year design life). During Case 2 stresses in the reinforcement were recorded during shaking and the maximum calculated stress anywhere in the reinforcement was 57 percent of yield. The distribution of tensile stresses for Case 2 is shown in Table 6. The other cases had similar or slightly lower peak stresses.

Table 6. Maximum Reinforcement Stress (as a Percent of Yield) for Case 2

Strip Density / Panel	Depth Below Top of Wall in Feet	Segment Number 1	2	3	4	5	6	7	8	9	10	11	12	13	14	15	16	17	18	19	20	21	22	23	24	25	26	27
3	2.5							6	6	7	9	11	13	15	16	17	18	18	18	17	17	16	16	16	21	33	21	6
4	7.5							10	11	13	16	18	19	20	20	20	19	19	18	18	17	17	16	16	17	23	23	8
4	12.5						Tier 1	14	16	17	20	22	22	22	21	21	20	19	18	17	16	15	15	15	18	25	25	10
5	17.5							15	19	21	22	23	23	22	21	21	19	18	17	16	15	14	15	16	18	22	24	12
5	22.5							18	24	24	22	22	22	22	21	20	19	18	16	15	15	15	15	16	17	20	22	13
6	27.5							14	21	19	19	20	20	20	20	19	18	16	15	13	13	13	13	14	15	17	20	15
4	30					11	14	29	35	38	40	42	43	43	42	40	38	35	32	30	29	30	30	31	33	34	33	15
5	35					21	34	42	40	42	43	44	44	44	43	41	39	36	33	32	31	31	31	32	33	35	35	16
5	40					20	38	48	49	47	47	46	46	45	44	42	40	37	34	33	32	32	32	33	34	36	36	18
5	45				Tier 2	21	41	50	52	50	49	47	46	45	44	42	40	38	36	34	33	33	33	34	36	37	36	20
6	50					20	41	48	51	50	48	47	46	45	44	42	40	38	36	35	34	34	34	34	35	36	35	22
6	55					24	45	50	50	49	47	46	45	44	43	42	41	39	37	35	35	35	35	35	36	37	36	24
7	60					27	47	50	48	46	45	45	44	44	43	42	41	40	38	35	35	35	34	35	36	37	35	25
8	65					29	44	42	42	42	42	42	42	42	42	41	40	38	37	35	33	33	33	33	34	34	32	22
7	67.5			10	12	20	32	38	41	43	44	44	44	44	44	43	42	41	40	37	36	35	35	36	36	36	34	24
7	72.5			25	29	43	44	45	46	46	46	46	46	46	45	45	44	42	41	38	36	36	36	37	38	39	37	26
7	77.5			27	32	53	55	52	51	50	49	48	48	47	46	45	45	43	41	39	36	36	37	38	39	40	38	27
8	82.5		Tier 3	25	32	53	57	55	53	51	50	49	48	47	46	46	45	43	42	40	37	36	37	38	39	39	37	25
9	87.5			26	35	51	56	55	53	51	49	48	47	46	46	45	44	43	42	40	37	36	36	37	38	38	35	24
10	92.5			26	39	51	54	54	51	49	47	46	46	45	44	44	43	43	41	40	38	36	35	35	36	36	33	22
11	97.5			28	44	52	52	50	48	46	45	44	44	43	43	43	42	41	41	39	38	35	35	34	34	33	30	19
12	102.5			29	42	43	43	43	43	42	42	41	41	41	41	41	40	40	39	38	36	34	32	31	30	29	25	15
14	105	4	7	17	27	34	38	40	41	42	42	42	42	42	42	42	42	41	41	40	39	38	36	34	32	30	28	24	14
14	110	13	17	31	35	38	40	41	41	42	42	42	41	41	41	41	41	41	40	39	38	36	34	31	29	27	24	15
15	115	16	20	37	42	42	42	42	42	42	41	41	41	41	40	40	40	40	39	38	37	35	33	30	29	27	23	14
17	120	15	21	36	41	41	41	41	41	41	41	40	40	40	39	39	39	38	38	37	35	33	31	29	28	26	22	13
19	125	Tier 4 14	22	34	39	40	40	39	39	39	39	39	39	38	38	37	37	36	35	34	33	31	29	28	27	25	21	12
21	130	14	24	33	36	37	38	38	38	38	38	38	37	37	36	35	34	33	32	31	30	29	28	27	26	24	20	12
23	135	12	24	30	34	35	37	37	38	38	38	37	36	35	34	32	31	30	29	28	27	27	26	25	24	22	19	10
25	140	14	24	31	35	38	40	41	41	41	40	39	37	35	32	29	27	26	25	23	23	22	21	21	20	19	16	9
25	145	21	35	42	46	49	50	51	51	49	46	43	38	33	27	23	20	19	17	16	15	14	13	13	12	11	9	5

Notes: The lower 10 feet of the wall and reinforcing were embedded to achieve a 135-foot exposed height.
The maximum reinforcement stress is shown for each 4-foot-long cable element segment.
Shaded number indicated a reinforcement stress exceeding 55 percent of the yield stress.

Figures 4 and 5 illustrate contours of calculated horizontal and vertical displacements for the seismic model (Case 3). Figure 4 shows a bi-linear type of shear surface extending roughly horizontally through the reinforced zone and at a steeper angle in the soil mass behind (the surface generally follows the 0.1 foot contour). This is similar to what has been seen in other research using the seismic FLAC analyses (e.g., Lindquist, 1998) and the angle of the shear surface generally corresponds to slope angle predicted using the Mononobe-Okabe Method as enhanced by Zarrabi-Kashani (1979) and referenced by Kramer (1996). The vertical settlement is largest immediately behind the reinforced soil zone indicating the reinforced zone behaves as a semi-rigid block with a rotational movement mechanism. The largest vertical settlement was approximately 2 inches in this area. It is interesting to note that the 2H:1V slope to the left of the roadway at the base of the wall was calculated to have a similar amount of lateral movement as the entire wall. This is another indication that the wall is performing well during the ground shaking.

The FLAC models were constructed as large as practically possible to reduce "edge effects" on the wall and the part of the embankment adjacent to the wall. The deformations in the immediate vicinity of the model boundaries, however, should be discounted.

The displacements when liquefaction was added to the model (Cases 4 and 6) were larger than the model without liquefaction (Case 3). The peak horizontal movement at the top of the wall was 8 and 10 inches for Cases 4 and 6, respectively. The peak vertical movements were less than those of Case 3.

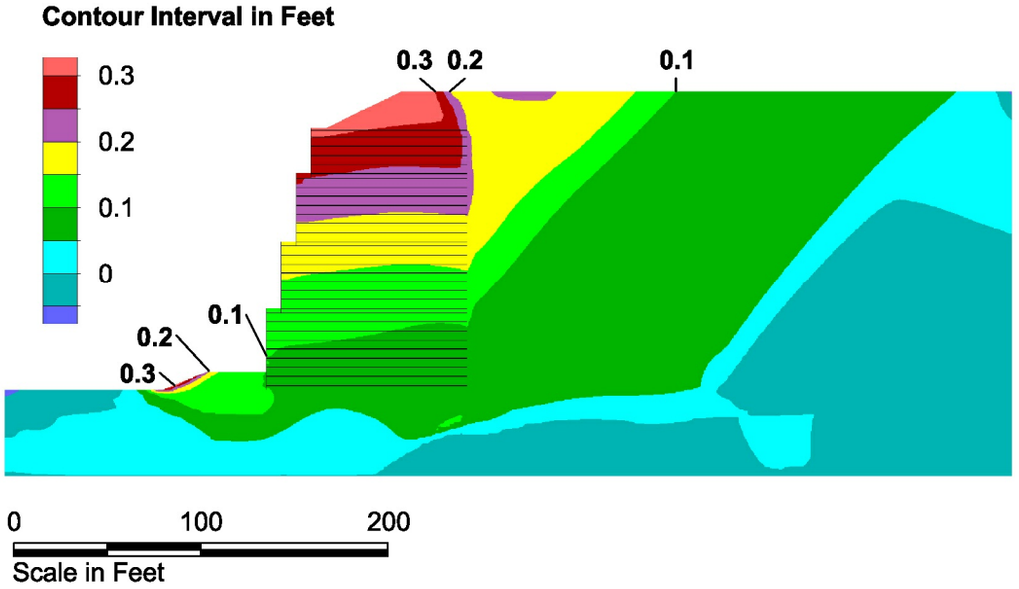


Figure 4. Permanent Horizontal Displacement for Case 3

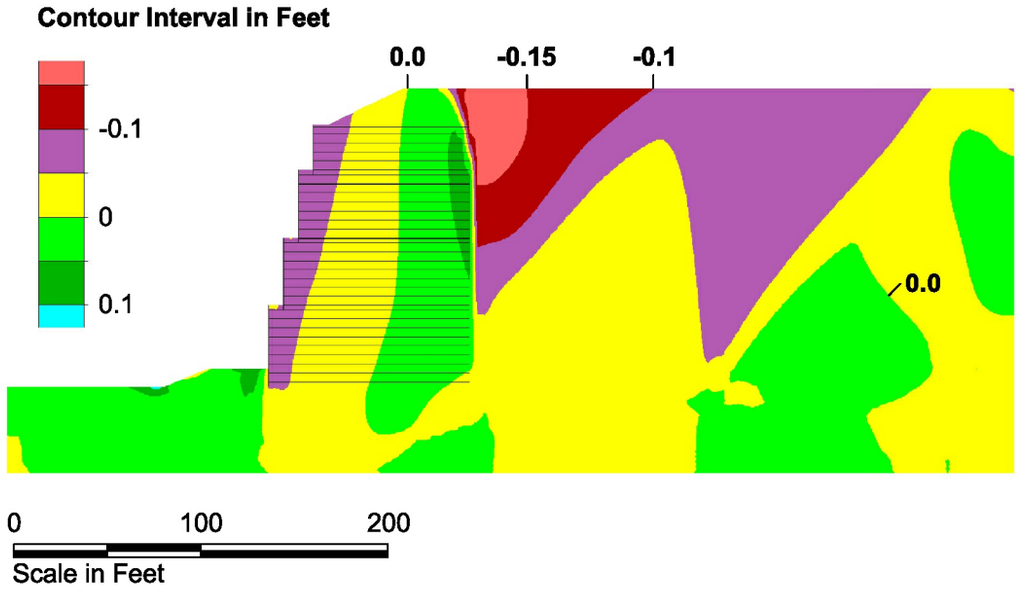


Figure 5. Permanent Vertical Displacement for Case 3

Conclusions

Use of displacement-based modeling by the design team provided an increased level of understanding regarding the MSE walls performance both during construction and in analysis of the design level seismic event. The FLAC analyses show that seismic response varies somewhat with stiffness of the modeled soil elements. This was of particular interest because soils at the site have: 1) varying resistance to liquefaction

and 2) potential variability in the timing of the onset of liquefaction relative to the start of shaking. The analyses indicated that softening of the foundation soil due to liquefaction reduced the magnitude of shear stress transferred into the embankment soils. Generally, the magnitude of wall displacement and stress in the MSE reinforcing was slightly reduced when liquefaction occurred at the beginning of shaking, compared to when liquefaction follows the end of shaking.

The wall sections analyzed show levels of seismic deformation generally less than 1 foot. Predicted stresses in the reinforcing elements did not exceed the yield strength of the reinforcement for any of the cases analyzed with FLAC. While in some cases the stress in portions of some of the reinforcing strips exceeds the limiting value (55 percent of yield) allowed by AASHTO, the magnitude and extent of this are so limited that they fall within the desired performance criteria. The FLAC results showed that traditional slope stability methods produced a design with tolerable seismic deformations and was used to provide increased understanding of the seismic performance of the tallest MSE structure in North America.

Units Conversion from Conventional US Units To SI Units

1 foot	=	0.3048 meter
1 inch	=	2.48 centimeters
1 cubic yard	=	0.765 cubic meter
1 pound	=	4.448 Newton
1 slug	=	0.0141 kilogram

References

AASHTO 1996-2000. *Standard Specifications for Highway Bridges*, 16th Edition, American Association of State Highway and Transportation Officials, 1996, with current interim addenda through 2000.

Chen, S. and Bailey, M. 2004. “Lessons Learned from a Stone Column Test Program in Glacial Deposits,” *GeoSupport 2004*, GSP No. 124, ASCE.

Itasca Consulting Group 2000. FLAC Version 4.0 User’s Guide.

Kramer, S. 1996. *Geotechnical Earthquake Engineering*, Prentice-Hall.

Lindquist, D. 1998. “Seismic Modeling of Geosynthetic-Reinforced Slopes,” Master of Science Thesis, University of Washington.

Stuedlein, A., Mikkelsen, P., and Bailey, B. 2007. “Instrumentation and Performance of the Third Runway North MSE Wall at Seattle-Tacoma International Airport,” *FMGM 2007: Seventh International Symposium on Field Measurements in Geomechanics*, ASCE.

Zarrabi-Kashani, K. 1979. “Sliding of gravity retaining wall during earthquakes considering vertical accelerations and changing inclination of failure surface,” Master of Science Thesis, Massachusetts Institute of Technology.

The Effect of Amplification on the Seismic Stability of Reinforced Soil Slopes Using Horizontal Slice Method

Hamid Reza Nouri [1], PhD Student and Ali Fakher[2], Professor

[1] PhD Student, Texas A&M University, Zachry Department of Civil Engineering, 3136 TAMU, College Station, TX 77843-3136, USA; Email: hrnouri@tamu.edu
[2] Professor, Geotechnical Group, School of Civil Engineering, University College of Engineering, University of Tehran, Enghelab St., Tehran, Iran; Email: afakher@ut.ac.ir

ABSTRACT: Horizontal Slice Method (HSM) is an approach employed to evaluate the seismic stability of soil slopes and walls in the framework of limit equilibrium method and pseudo-static analysis. HSM is also capable of applying variable accelerations at different levels within the horizontal slices of a slope or retaining structure, which is difficult when using other limit equilibrium procedures. In this paper the effect of amplification of seismic acceleration on the stability of slopes and soil structures has been evaluated. In combination with the HSM a pseudo-dynamic method is adopted in the present analysis, which also considers the effect of phase difference in the shear waves traveling through the backfill due to seismic excitation. The analysis is based on the observations of Nova-Roessig and Sitar (1999, 2006) relating to centrifuge tests performed on a number of scaled reinforced soil slopes. Two main sets of analyses are conducted. In the first one, seismic amplification is considered in the analysis by assigning amplified accelerations at different levels to the corresponding slices with different distributions. The second set of analyses is conducted for slopes having the same seismic acceleration for all the slices, which means there is no amplification. The main results of the analysis are presented in dimensionless form relating to the total force in the reinforcement layers to maintain the stability of the reinforced structure. This definition is equivalent to the coefficient of active lateral earth pressure. Therefore the effect of amplification on the active lateral earth pressure can be evaluated and compared with the case of no amplification. The failure surfaces for each set of analysis are also obtained and compared with the observed deformations in the physical model.

INTRODUCTION

In recent years the use of reinforced soil structures in seismic areas has increased due to their excellent performance during major earthquakes (Koseki *et al*., 2006). In addition, a number of analytical methods used to evaluate the seismic stability of such structures subjected to earthquake loads have been presented. An example is the

Horizontal Slices Method (HSM). Particularly suited to the analysis of reinforced soil slopes and walls (Lo and Xu, 1992), HSM is a limit equilibrium approach of slope stability analysis. The HSM concept has also been used to evaluate the stability of reinforced walls subjected to seismic loads (Shahgholi *et al*., 2001). The formulation of HSM was modified and verified by the Authors (Nouri *et al.*, 2006).

The main focus of this paper is to study the effects of amplification of pseudo-static acceleration on reinforced slopes and walls. The amplification of seismic acceleration and its effect on the stability of slopes and soil structures have been investigated by a number of authors. Steedman and Zeng (1990) have shown that amplification of seismic acceleration has an influence similar in character to the effect of increasing the acceleration coefficient in a uniform acceleration field. Segrestin and Bastick (1988), using a finite element analysis, and Nova-Roessig and Sitar (1999) with several centrifuge tests on scaled models, have demonstrated that the average acceleration recorded in the reinforced part of a slope is equal or greater than the maximum seismic horizontal acceleration of the base excitation.

Since HSM permits the designer to assign different pseudo-static seismic coefficients to individual slices of sliding wedge, it can be used to consider any desired distribution of amplified seismic acceleration in different slices.

HORIZONTAL SLICE METHOD (HSM)

In the HSM, the sliding mass is divided into several horizontal slices, Figure 1(a). The seismic inertia force is considered as pseudo-static force acting at the center of gravity of each slice. In the presented research, the backfill of the reinforced slope is assumed to be free draining and also the inertia force of the wall face is ignored; thus the results of the study are valid for relatively low mass facings and may not be applicable to some modular block wall systems. As the most frequently observed slip surface in physical models of reinforced slopes (Zornberg *et al.*, 1998), Log-spiral slip surface has been used as the dominant mode of failure in the analysis. Assuming a uniform distribution of the reinforcements, the failure surface is restricted to emerge at the toe. Moreover, the base of slope is assumed to be sufficiently hard/dense, so the failure surface does not penetrate the base, Figure 1(a).

The equations and unknowns of HSM formulation for N horizontal slices are detailed in Table 1. As shown in Table1, the HSM formulation uses the assumption of Morgenstern and Price (1965). In this assumption λ is an unknown constant and $f_i(y)$ is a function of the depth. Due to the small value of λ ($0< \lambda <1.0$) the influence of $f_i(y)$ on the results is negligible. Therefore, $f_i(y)$ is considered to be unity.

The normal (N_i) and shear (tangential) forces (S_i) (Figure 1) are assumed to act at the mid-point of base of each slice. As both λ and V_i in Morgenstern and Price assumption are unknowns, a trial and error procedure is adopted to solve the set of non-linear equations. The details have been presented by Nouri *et al.* (2006).

In order to account for the effects of time and body waves traveling through the reinforced soil wall during the excitation and resulted phase change, the finite shear wave velocity is also incorporated in the analysis.

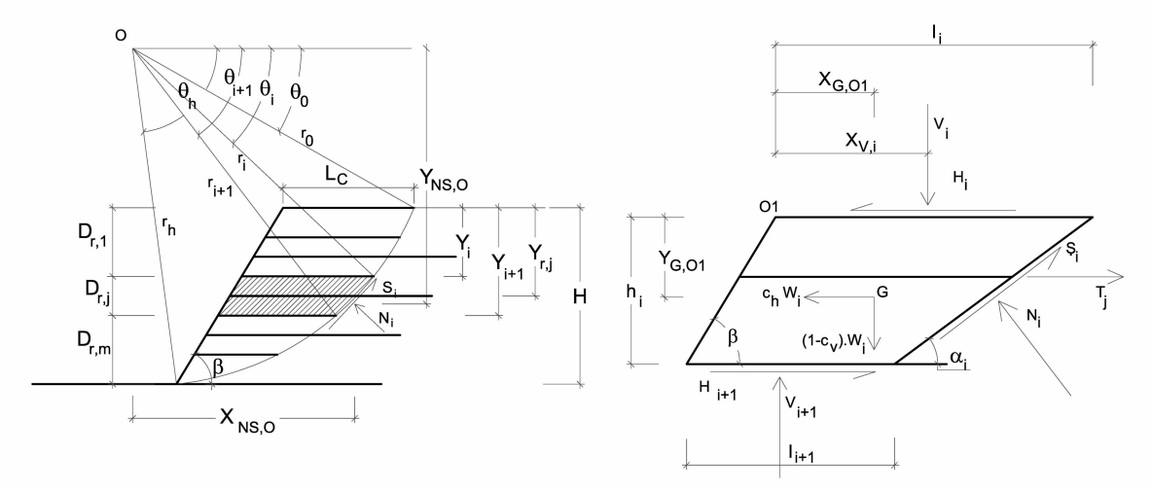


FIG. 1. (a) The Geometry of Log-spiral failure mechanism and horizontal slice method (b) the geometry and acting forces of each slice.

Table 1: List of unknowns and equations in the HSM formulation

Unknowns	Number	Equations	Number
Normal force upon each slice (N_i)	N	$\sum F_x = 0$ (Each slice)	N
Shear force upon each slice (S_i)	N	$\sum F_y = 0$ (Each slice)	N
Horizontal interslice force (H_i)	N-1	$\sum M_o = 0$ (Each slice)	N
Vertical interslice force (V_i)	N-1	$\tau_r = \frac{\tau_f}{F.S.}$ (Each slice)	N
Location of vertical interslice force ($x_{v,i}$)	N-1	$H_i = \lambda . f_i(y) . v_i$ Morgenstern & Price assumption	N-1
Morgenstern & Price factor (λ)	1		
Total required force in reinforcements to maintain stability ($\sum_{j=1}^{m} T_j$)	1		
Sum	5N-1	Sum	5N-1

The phase difference due to finite shear wave propagation can be considered using a pseudo-dynamic method proposed by Steedman and Zeng (1990). The method was also used for reinforced soil slopes thereafter by Nimbalkar *et al.* (2006).

In the present paper, the seismic accelerations acting on the reinforced-soil wall are considered as harmonic sinusoidal accelerations as originally proposed by Steedman and Zeng (1990). It is assumed that the shear modulus is constant with depth through the backfill, and the phase as well as the amplitude of the acceleration is varying during the excitation. For a sinusoidal base shaking, the seismic coefficient at depth Y and time t, $c_h(Y,t)$, is given by:

$$c_h(Y,t) = k_h.Sin\omega(t - \frac{H-Y}{V_s}) \quad (1)$$

Where H is the height of the reinforced soil wall, $\omega = 2\pi / T$ is the period of lateral shaking, $V_s = (G/\rho)^{0.5}$ is the shear wave velocity, and k_h is the horizontal seismic coefficient. In order to incorporate the effect of amplification or varying acceleration amplitudes, k_h can be substituted by any desired distribution of horizontal seismic accelerations from the base ($Y = H$) to the crest of slope ($Y = 0$) such that $k_h(Y=0) = f_a k_h(Y=H)$, where f_a is a constant. As a result, $c_h(Y,t)$ will be assigned as the pseudo-static horizontal seismic coefficient to each of the slices. For a constant value of shaking period (T) the most critical slip surface is determined by optimizing $\sum_{j=1}^{m} T_j$ (the required total force to maintain the stability of slope in m reinforcements) with respect to time and different Log-spiral slip surfaces. $\sum_{j=1}^{m} T_j$ can be normalized to obtain K, which is analogous to the earth pressure coefficient. The mobilized force in the j[th] reinforcement layer (T_j) can be substituted using an expression suggested by Ling *et al.* (1997), which represents a linear distribution of forces:

$$K = \frac{\sum_{j=1}^{m} T_j}{\frac{1}{2}\gamma H^2} \quad (2)$$

$$T_j = K.\gamma.Y_{r,j}.D_{r,j} \quad (3)$$

Where γ is the soil unit weight and $D_{r,j}$ represents the tributary distance of reinforcement layer j, Figure 1(a); for the first and the last reinforcements, $D_{r,1}$ and $D_{r,m}$ are shown in Figure 1. Based on the observations made by Allen *et al.* (2003) and Bathurst and Hatami (1998), the assumption of linear distribution of reinforcement loads is reasonable for wrapped face walls, which is the case of study in this paper.

THE EFFECT OF AMPLIFICATION OF SEISMIC ACCELERATION

As discussed before HSM permits the user to assign any desired pseudo-static seismic accelerations to slices. Furthermore, using the pseudo-dynamic method described earlier, the effect of phase difference between base and the surface can be

incorporated in the analysis as well as change in magnitude of acceleration, that is the amplification. However, HSM cannot calculate the varying magnitude of the acceleration at different levels so a distribution of acceleration magnitude should be assumed a priori when using the method.

The presented analysis is based on the observations of Nova-Roessig and Sitar (1999) relating to centrifuge tests performed on a number of scaled reinforced soil slopes. In this work the wrapped face reinforced slopes were inclined at an angle of 63.4° (2V: 1H) and had an assumed prototype height of 7.3m. The geotechnical and geometrical parameters of the backfill assumed in the analyses are shown in Table 2.

Table 2. Geometrical and geotechnical parameters of the backfill (After Nova-Roessig & Sitar, 1999)

	Backfill Dry Unit Weight $\gamma_{dry}(kN/m^3)$	**Soil Internal Friction Angle φ (°)**	**Shear Wave Velocity V_s (m/sec)**	**Slope Inclination Angle β (°)**	**Slope height of prototype H (m)**
$D_r = 55\%$	15.6	39.5	110	63.4	7.3
$D_r = 75\%$	16.2	42.5	180	63.4	7.3

The recorded acceleration at the top of the reinforced slope compared with the input base motion, showed that amplification occurs when the maximum acceleration of the input motion was less than (0.4 – 0.5)g. A reduction in seismic acceleration occurred when the input base motion was stronger than 0.5g. The peak accelerations measured at the foundation compared with those measured near the surface are shown in Figure 2. The observations show that amplification is greater in dense backfill.

Using the data presented in Figure 2, the response at the top of each slope for input accelerations of 0.1, 0.2 and 0.3g can be determined, Table 3.

In order to evaluate the effect of seismic amplification on the reinforced slope, the analyses of the centrifuge models were conducted using two assumptions. In the first, seismic amplification was considered by assigning amplified accelerations at different levels to the corresponding slices. The assigned amplified accelerations were determined using three different distributions between the base input acceleration ($k_{h,fdn} = k_h(Y = H)$) and the response output acceleration recorded at the crest ($k_{h,crst} = k_h(Y = 0) = f_a k_{h,fdn}$), Table 3. Three distributions of linear, parabolic - $y = ax^2$, and parabolic - $x = ay^2$ were applied such that $k_h(Y = 0) = f_a k_h(Y = H)$, where f_a is the ratio of the amplified and base accelerations. The second set of analyses was conducted for slopes having the same seismic acceleration for all the slices, (i.e. no amplification). This acceleration was considered equal to the input base acceleration and the pseudo-dynamic approach was also used to account for phase difference.

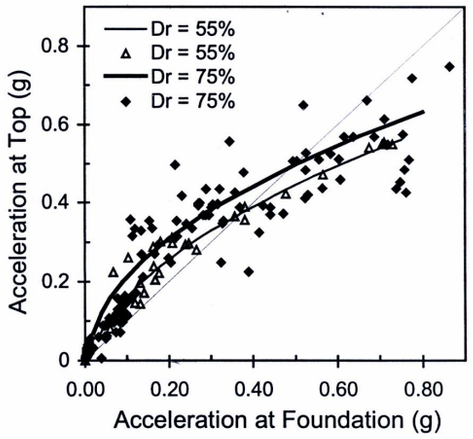


FIG. 2. Amplification of the input motion for the reinforced slope models (After Nova-Roessig & Sitar, 1999)

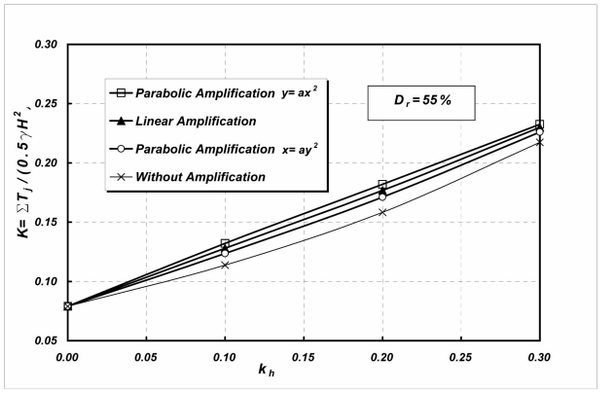
Table 3. Recorded amplified output acceleration at the crest of slope (After Nova-Roessig & Sitar, 1999)

Input Acceleration	0.1g	0.2g	0.3g
$D_r = 55\%$	0.160g	0.257g	0.330g
$D_r = 75\%$	0.207g	0.307g	0.378g

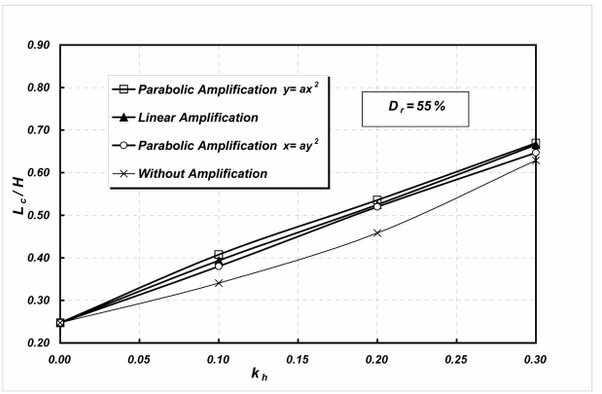
The period of lateral shaking used in the analysis was 0.4 sec. It should be noted that the values of shear wave velocity (V_s) presented in Table 2 are calculated based on the average value of the measured V_s during the shaking of the reinforced soil model (Nova-Roessig and Sitar, 2006). The results of the analyses relating to two slopes with different strength parameters and relative fill densities are shown in Figures 3 and 4.

The results show that amplification of the seismic acceleration results in a increase in the values of K and especially L_c / H for reinforced slopes. The average percentages increase in the values for K and L_c / H for slope of soil relative density D_r=55% are respectively 10% and 12% in comparison with analyses undertaken without amplification. The corresponding parameters for slope with more compacted material (D_r=75%) are respectively 23% and 20%.

Although, the slopes in the centrifuge models deformed without a distinct failure surface, in order to evaluate the results of the HSM in combination with pseudo-dynamic approach a comparison has been made between the HSM slip surface and the displacement vectors of the deformed slope models in Figure 5. The failure surface is for slope with soil of D_r=55% and $k_{h,fdn} = 0.3$ with linear distribution of amplified acceleration.

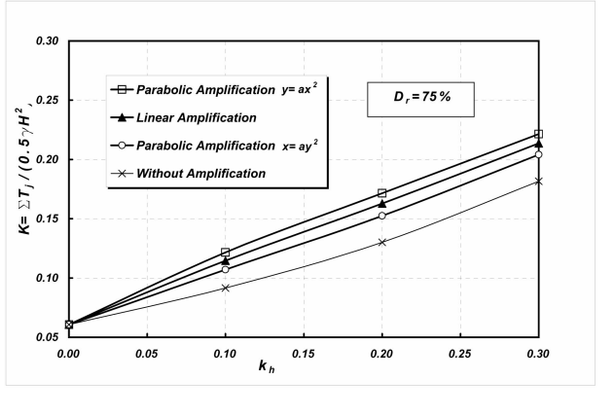


a

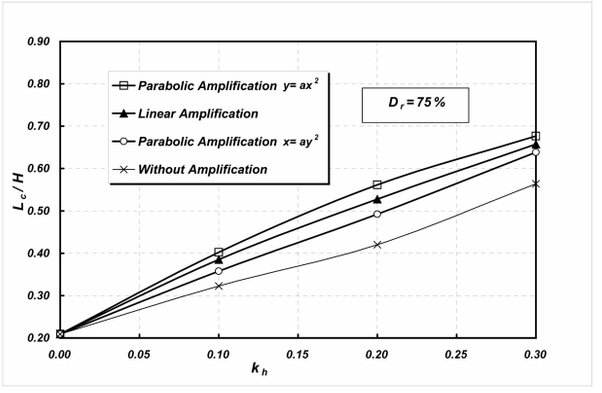


b

FIG. 3. Results of (a) *K* and (b) L_c/H parameter versus different seismic coefficients for the soil with density of D_r= 55% and slope of β= 63.40°



a



b

FIG. 4. Results of (a) *K* and (b) L_c/H parameter versus different seismic coefficients for the soil with density of D_r= 75% and slope of β= 63.40°

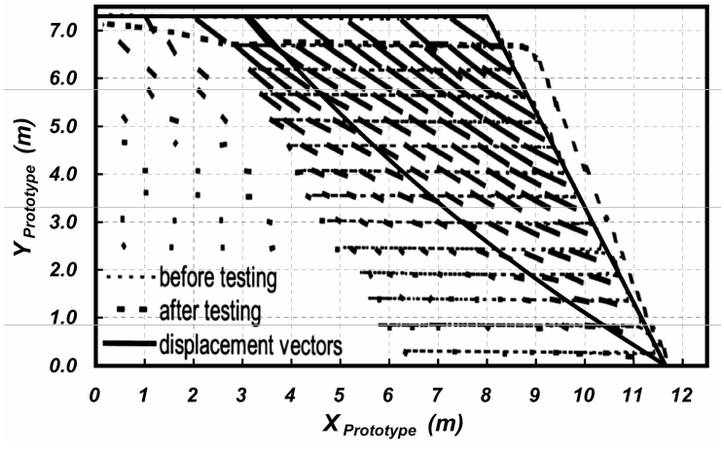


FIG. 5. Comparison between the HSM slip surface and displacement vectors (deformed slope from Nova-Roessig & Sitar (1999))

In the physical model, most of the shearing was found near the crest of slope. As in HSM failure surface is restricted to pass through the toe the HSM sliding wedge does not trace the deformation vectors exactly. In spite of this limitation, the volume of the sliding soil mass resulted from the model and HSM seems reasonably the same.

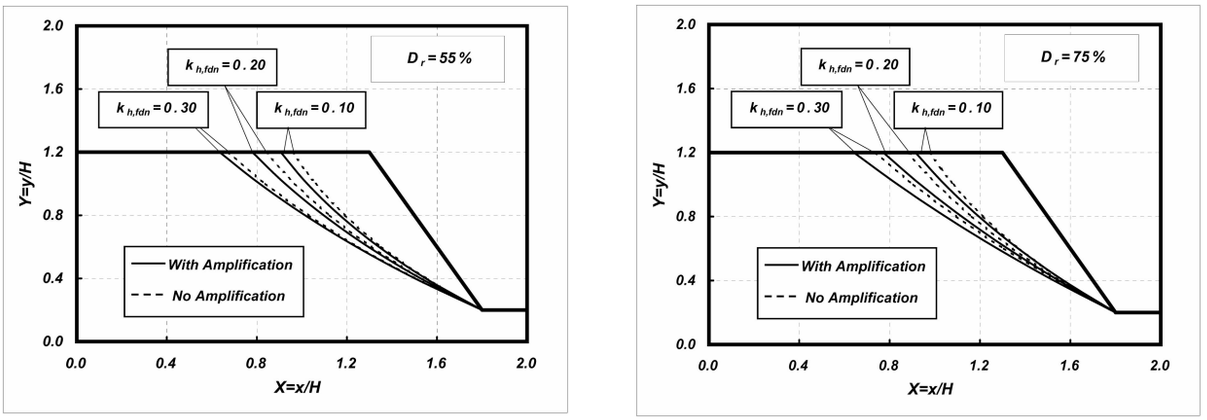
The obtained failure surfaces for slopes of two different soil relative densities are shown in Figure 6. These slip surfaces are generated for "With Amplification" and "No Amplification" conditions and three different base seismic coefficients ($k_{h,fdn} = k_h(Y = H) = 0.1,\ 0.2,$ and 0.3) for the case of linear distribution of the amplified seismic accelerations. The failure surfaces for the amplified and non-amplified cases show that the greater amplification that occurs in the slope of D_r= 75%, results in the larger sliding wedge in comparison with the slope of D_r= 55%.

Figure 7 shows the failure surfaces for different distributions of amplified acceleration for two base seismic accelerations of $k_{h,fdn} = 0.1$ and 0.3. The figure shows that there is no considerable difference in the shape and volume of the failure wedges of different distributions for the same base seismic acceleration.

Having calculated the weight of each slice, the weighed average or equivalent horizontal seismic coefficient ($c_{h,eqv}$) can be obtained for each slope:

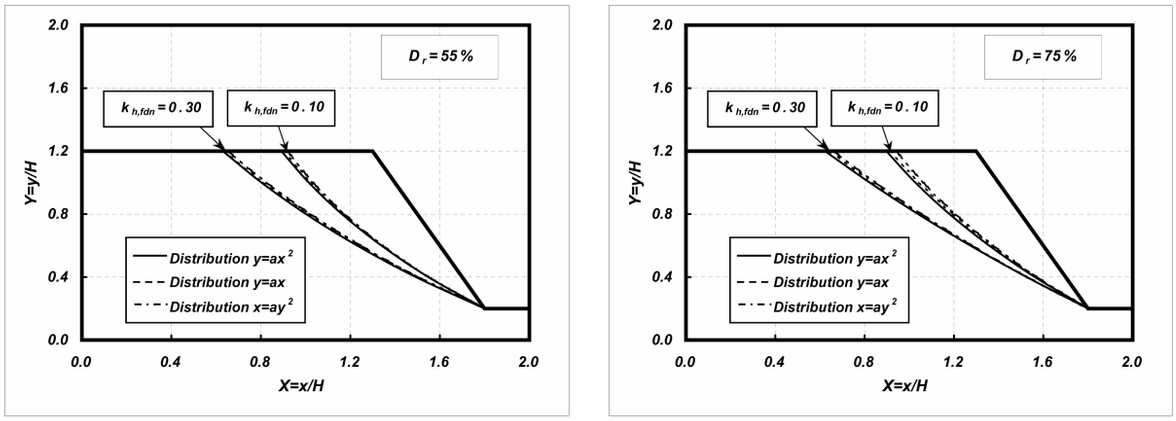
$$c_{h,eqv} = \sum_{i=1}^{n} (c_{h,i}.w_i) / \sum_{i=1}^{n} w_i \qquad (4)$$

Using $c_{h,eqv}$ in a pseudo-static analysis instead of amplified seismic coefficient can lead to an easier pseudo-static procedure. Figure 8 shows the results of $c_{h,eqv}$ versus seismic coefficient on the crest of slope ($k_{h,crest}$) which both are normalized with respect to $k_{h,fdn}$. The results of $c_{h,eqv}$ are only valid for slopes with the same geometric (β, H/TV_s), geotechnical (φ) and loading ($f_a = k_{h,Crst}/k_{h,fdn}$) characteristics. The complementary studies using HSM in combination with the pseudo-dynamic approach can be done to obtain $c_{h,eqv}$ and generate the same graphs for different conditions.



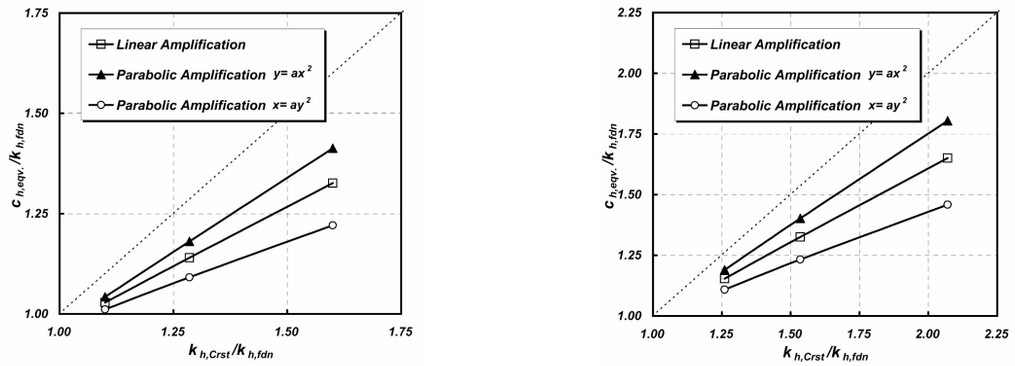
a **b**

FIG. 6. Failure surfaces for slopes with (a) D_r= 55% and (b) D_r= 75% in "With Amplification" and "No Amplification" conditions



a **b**

FIG. 7. Failure surfaces for slopes with (a) D_r= 55% and (b) D_r= 75% for different distributions of amplified acceleration



a **b**

FIG. 8. Results of $c_{h,eqv}/k_{h,fdn}$ versus $k_{h,crest}/k_{h,fdn}$ of (a) D_r= 55% and (b) D_r= 75% for different distributions of amplified acceleration

CONCLUSION

The main objective of the current study was to consider the effects of amplification on the seismic stability of reinforced slopes and walls using the Horizontal Slices Method (HSM) of analysis, in combination with a pseudo-dynamic approach. This approach considers the time and phase change effects as well as change in magnitude due to shear waves propagating vertically through reinforced backfill, along with other seismic input parameters. The study has shown that ignoring the effect of amplification of seismic acceleration could result in an underestimated design. In addition, the average percentage increase of the length and strength of the reinforcement layers is more for slopes with the higher values of amplification. The proposed HSM method can also generate the weighed average or equivalent horizontal seismic coefficient ($c_{h,eqv}$) for different slopes with various geometrical, geotechnical and amplification conditions.

REFERENCES

Allen, T.M., Bathurst, R.J., Lee, W.F., Holtz, R.D. and Walters, D.L. (2003). "A new working stress method for prediction of reinforcement loads in geosynthetic walls." *Canadian Geotechnical Journal,* Vol. 40 (5): 976–994.

Bathurst, R.J. and Hatami, K. (1998). "Seismic response analysis of a geosynthetic reinforced soil retaining wall." *Geosynthetics International,* Vol. 5(1&2): 127-166.

Ling, H.I., Leshchinsky, D. and Perry, E.B. (1997). "Seismic design and performance of geosynthetic-reinforced soil structures." *Geotechnique*, Vol. 47 (5): 933-952.

Lo, S-C and Xu, D-W. (1992). "A strain based design method for the collapse limit state of reinforced soil walls and slopes." *Canadian Geotechnical Journal*, Vol. 29 (8): 832-842.

Morgenstern, N.R. and Price V.R. (1965). "The analysis stability of general slip surfaces." *Geotechnique*, Vol. 15 (1): 79-93.

Nimbalkar, S.S., Choudhury, D. and Mandal, J.N. (2006). "Seismic stability of reinforced-soil wall by pseudo-dynamic method." *Geosynthetics International*, Vol. 13 (3):111-119.

Nouri, H.R., Fakher A. and Jones C.J.F.P. (2006). "Development of Horizontal Slice Method in stability analysis of reinforced slopes." *Geotextiles and Geomembranes*, Vol. 24 (3):175-187.

Nova-Roessig, L. and Sitar, N. (1999). "Centrifuge model studies of the seismic response of reinforced soil slopes." *Proceeding of the 2nd International Conference on Earthquake Geotechnical Engineering*, (Eds. Seco and Pinto): 679-684.

Nova-Roessig, L. and Sitar, N. (2006). "Centrifuge model studies of the seismic response of reinforced soil slopes." *ASCE Journal of Geotechnical and Geoenvironmental Engineering*, Vol. 132 (3): 388-400.

Segrestin, P. and Bastick, M. (1988). "Seismic design of reinforced earth retaining wall - The contribution of Finite Element Analysis." *Theory and Practice of Earth Reinforcement,* (Eds. Yamanouchi, Miura and Ochiai): 577-582.

Shahgholi, M., Fakher, A. and Jones, C.J.F.P. (2001). "Horizontal Slice Method of analysis." *Geotechnique,* Vol. 51 (10): 881-885.

Steedman, R.S. and Zeng, X. (1990). "The influence of phase on the calculation of pseudo-static earth pressure on a retaining wall." *Geotechnique*, Vol. 40 (1): 103-112.

Zornberg, J.G., Sitar, N. and Mitchel, J.K. (1998). "Performance of geosynthetic reinforced slopes at failure." *ASCE Journal of Geotechnical and Geoenvironmental Engineering*, Vol. 124 (8): 670-683.

Centrifuge modeling of pile pinning effects

R. J. Armstrong[1], R. W. Boulanger, Member ASCE, P.E.[2], U. Gulerce[3], B. L. Kutter, Member ASCE[4], D. W. Wilson, Member ASCE[5]

[1] Graduate student researcher, Department of Civil & Environmental Engineering, University of California, Davis, CA 95616; rjarms@ucdavis.edu

[2] Professor, Department of Civil & Environmental Engineering, University of California, Davis, CA 95616

[3] Graduate student researcher, Department of Civil & Environmental Engineering, University of California, Davis, CA 95616

[4] Professor, Department of Civil & Environmental Engineering, University of California, Davis, CA 95616

[5] Associate Project Science Manager, Center for Geotechnical Modeling, University of California, Davis, CA 95616

ABSTRACT: Earthquake-induced deformation of piled bridge abutments in approach embankments underlain by liquefied soils may be reduced by the restraining forces provided by the piles and bridge superstructure. Design methods accounting for these "pinning" effects have been applied in practice, but they lack significant comparison with actual physical data. Three dynamic centrifuge model tests were performed to investigate pile pinning effects, and the results are presented in this paper. The centrifuge models were composed of two identical embankments underlain by liquefiable soil, one with a pile group and another without. Data from the tests demonstrated that the embankment with a pile group had less lateral movement and settlement than the embankment without a pile group. The experimental results and back-calculated stress-strain responses are described, and the implications for design practice discussed.

INTRODUCTION

Deformation of bridge abutments in approach embankments caused by earthquake-induced liquefaction in the underlying soils can impose large loads or demands on pile groups embedded through the embankments. The restraining or "pinning" effects of the pile group and bridge superstructure can reduce the lateral spreading demands imposed on the piles by the embankment. Design methods which account for these pile pinning effects have been used in practice (Perez-Cobo and Abghari 1996, Law 2000, Zha 2004), have been incorporated in the NCHRP 472 specifications for seismic design of bridges (TRB 2002, Martin et al. 2002), and have had suggested modifications in recent years (Boulanger et al. 2006, Ledezma and Bray 2006, Boulanger et al. 2007).

Three dynamic centrifuge tests were conducted to investigate pile pinning effects. The models in the centrifuge tests consisted of two identical approach embankments of dry sand separated by a channel. One embankment had a pile group at the crest. The piles

extended through the dry embankment and the underlying saturated loose sand layer, into a saturated dense sand layer. Different pile group configurations and input motions were used. In this paper the mechanisms of loading and deformation for the embankments and piles are illustrated through examination of time histories, displacement patterns, bending moment distributions, and back-calculated stress-strain responses. Implications of these test results for design practice are briefly discussed.

CENTRIFUGE MODELS

The models in the centrifuge tests consisted of two identical approach embankments of dry sand separated by a river channel. One embankment had a pile group that extended through the underlying saturated loose sand layer and into saturated dense sand. All three centrifuge tests had essentially the same soil properties and soil geometry but had different pile group configurations or input motions (see Table 1 for a comparison of the three tests). A cross-section and plan view of Kobe_2X4 is presented in Fig. 1 showing instrument locations. The instruments that are labeled in Fig. 1 have time histories presented in a subsequent section. A photograph of the embankments for Kobe_2X4 during model construction is presented in Fig. 2 and photographs of each model during post-testing excavation are presented in Fig. 3. Note that for Fig. 3, the vertical blue and black lines show permanent deformation patterns in each soil layer and the horizontal green lines show permanent deformation patterns along the top of the loose sand layer. The white lines are thin silt layers placed at the bottom and top of the loose sand layer. All centrifuge tests were performed on the 9-m radius centrifuge at the University of California at Davis in a flexible shear beam container with centrifugal accelerations of 60 g. Results are presented in prototype units unless otherwise noted.

TABLE 1. Centrifuge test details.

Model code	Kobe_1X6	Kobe_2X4	Sine_2X4
Report name	DDC03	UGU01	UGU02
Date conducted	March 2005	December 2005	April 2006
Type of pile group	Row of 6 piles; outer diameter of pile 0.72 m	2x4 pile group; outer diameter of pile 1.22 m; pile-cap dimension 13.2 x 6.0 x 2.4 m	2x4 pile group; outer diameter of pile 1.22 m; pile-cap dimension 13.2 x 6.0 x 2.4 m
Input motion	Scaled Port Island motion	Scaled Port Island motion	Sine waves
Peak base acc.	0.8 g	0.7 g	0.5 g and 0.7 g

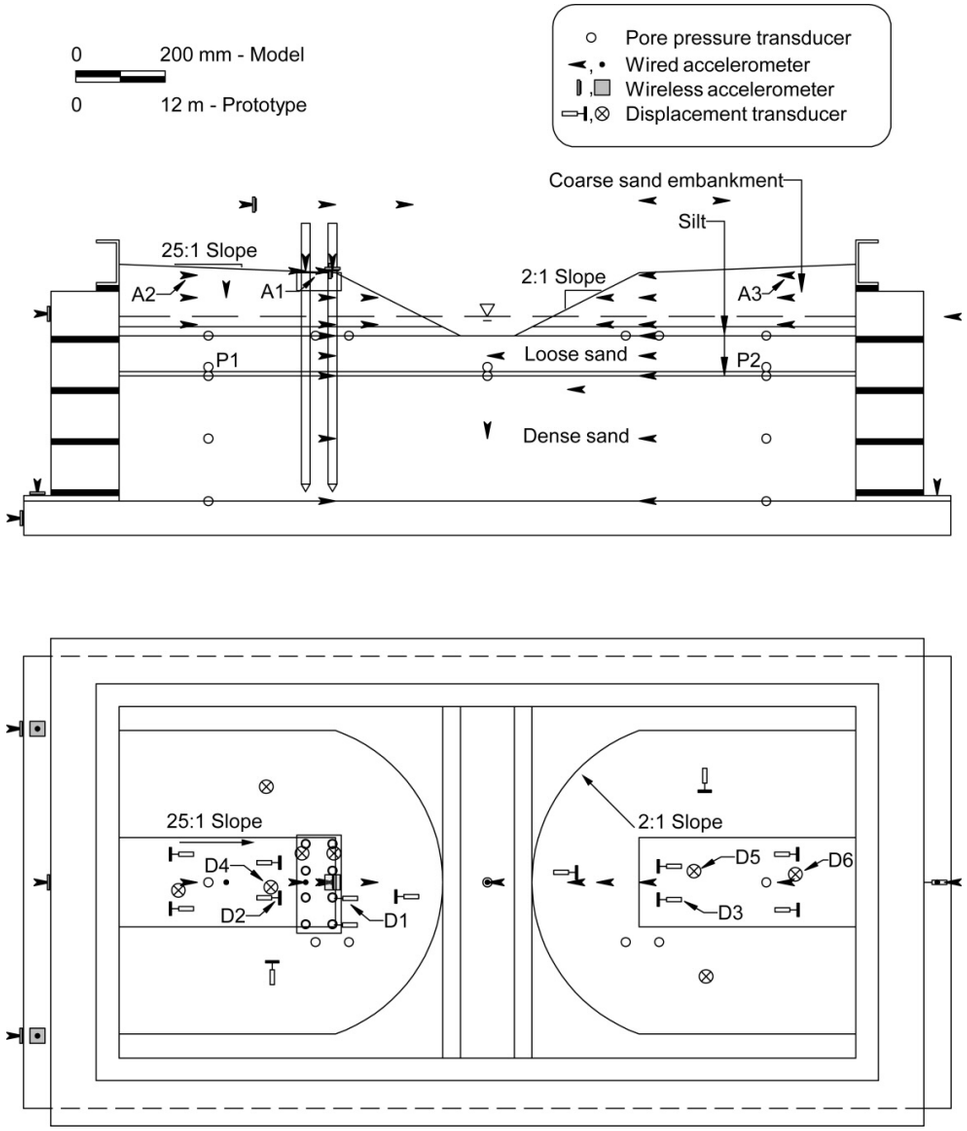
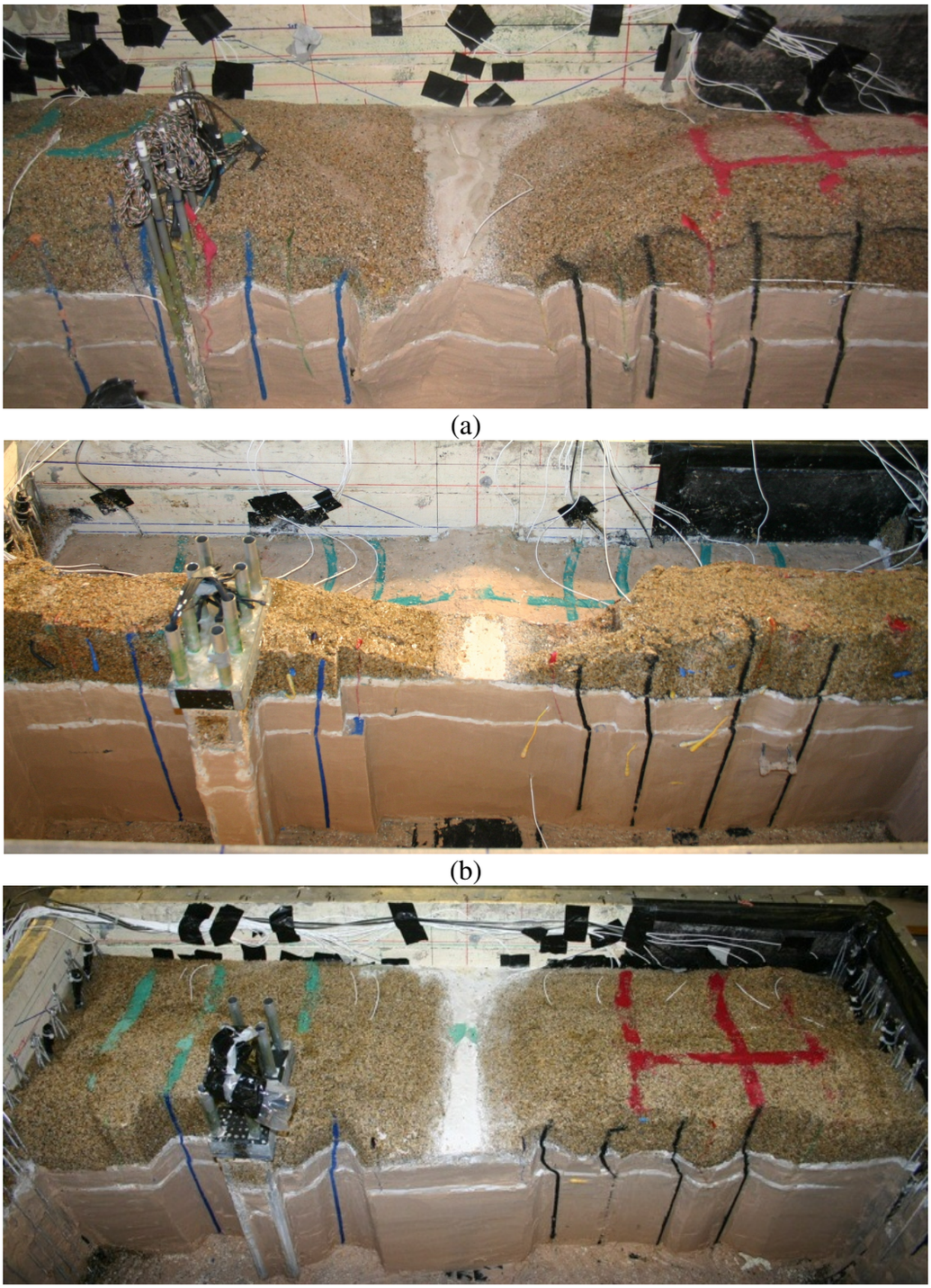


FIG 1. Model layout for Kobe_2X4. Only select transducers are labeled for clarity.



FIG 2. Photograph of Kobe_2X4 following construction of the pile group at 1 g.



(a) (b) (c)

FIG 3. Photograph of excavation for (a) Kobe_1X6, (b) Kobe_2X4, and (c) Sine_2X4. The discontinuities in picture are the result of the excavation plane not being flat.

The pile group used in model Kobe_1X6 was a row of 6 individual piles (left side of Fig. 3a). Piles were driven separately at 1 g after saturation was complete. The piles were made of 6061-T6 aluminum with an outer diameter of 9.53 mm (model scale) and a thickness of 0.71 mm (model scale). Moment gauges were affixed to three piles, and shear gauges were affixed to one pile. The pile tips were made of metal with a tip angle of 60^o. The piles were covered with plastic shrink-wrap and wax to prevent the gauges from becoming wet. The plastic shrink-wrap and the strain gauge wires increased the outer diameter of the piles so that the average outer diameter of piles with plastic shrink-wrap was approximately 12 mm (model scale), or 0.72 m prototype.

The pile group used in model Kobe_2X4 (Fig. 3b) and Sine_2X4 (Fig. 3c) was a 2x4 pile group. The piles were made of 6061-T6 aluminum with an outer diameter of 19.05 mm (model scale) and a wall thickness of 0.89 mm (model scale). Moment gauges were affixed to three piles, and shear gauges were affixed to one pile. Pile tips were made of metal with a tip angle of 60^o. The piles were also covered with plastic shrink-wrap and wax, producing average outer diameters of 20.3 mm, or 1.22 m prototype. Piles were driven at 1 g after saturation as two rows of four, then an aluminum-epoxy pile-cap (100 mm x 220 mm x 40 mm model scale) was constructed using an epoxy agent to interconnect the piles and a thin aluminum frame to mold the epoxy. The center-to-center spacing between the piles was three pile diameters.

The geometry and soil properties, which were essentially the same for all three centrifuge tests, are as follows. Embankments were 7.2 m high at the crest and 11.4 m high at the model container wall, had side slopes of about 2 to 1 (horizontal to vertical) in all directions, and were comprised of dry, coarse, medium-dense to dense Monterey sand. Below the embankment was a silt layer 1.2 m thick, a loose sand layer ($D_r \approx 30\%$) 5.4 m thick, a second silt layer 0.6 m thick and a dense sand layer ($D_r \approx 75\%$) 16.8 m thick. A channel 12 m wide was left between the two embankments in the middle of the container to avoid interactions between the two embankments. All soils were placed by dry pluviation. Silt layers were also statically compacted after pluviation. The model was saturated from the bottom of the container upwards until the channel between the two embankments was partially filled with fluid. The pore fluid was a methylcellulose solution with a viscosity about 20 times that of water.

Models Kobe_1X6 and Kobe_2X4 were subjected to a scaled version of the ground motion recorded at a depth of 83 meters at Port Island in the 1995 Great Hanshin Awaji Earthquake (later referenced as a “large Kobe” motion). Model Sine_2X4 was subjected to two shaking events: the first event contained sine wave cycles at 0.2g, 0.3g and 0.6g and the second event had 20 sine wave cycles at 0.3 g and 0.9g. Recorded accelerations at the base of the model differ slightly from the target input motion due to the system limitations.

EXPERIMENTAL OBSERVATIONS

Time histories

Time histories from the three centrifuge tests are plotted in Fig. 4, including the measured base accelerations, embankment accelerations, pore water pressure ratios in the bottom of the loose sand layer (defined as $r_u = \Delta u/\sigma_{vo}'$), bending moments at key locations, embankment settlements, lateral crest displacements, and pile or pile-cap displacements. These accelerations and lateral displacements are for the longitudinal direction, and the local coordinate system for each embankment assumes positive displacements and acceleration are towards the channel and positive settlements are downwards. The results for the second shake of Sine_2X4 are not presented. A summary of peak or final values for the aforementioned time histories is presented in Table 2 for the embankments without piles ("non-piled") and the embankments with piles ("piled").

TABLE 2. Peak responses and final displacements from three centrifuge tests.

	Kobe_1X6		Kobe_2X4		Sine_2X4	
	Non-piled	Piled	Non-piled	Piled	Non-piled	Piled
Final crest displacements	1.7 m	1.2 m	1.5 m	0.6 m	1.4 m	0.3 m
Final pile displacements	–	1.0 m	–	0.8 m	–	0.6 m
Final emb. settlements	1.3 m	0.9 m	1.4 m	0.5 m	1.2 m	0.5 m
Peak M_{peak}	–	1760 kN·m	–	6760 kN·m	–	5500 kN·m
Peak M_{cap}	–	–	–	1830 kN·m	–	2500 kN·m
Peak r_u	1.1	1.0	0.9	0.7	0.9	0.5
Peak a_{emb} (up-slope)	0.5g	0.2g	0.4g	0.5g	0.3g	0.5g
Peak a_{pile} (up-slope)	–	1.4g	–	1.0g	–	1.0g

All displacements are measured with respect to the base of the container. Lateral displacements were obtained either from displacement transducers or by combining the low frequency components of displacement transducer measurements with the high frequency components of displacements calculated by double integrating accelerometer measurements (Wilson et al. 1998). For the embankments without a pile group, lateral crest displacements are measured at the crest (location D3 in Fig. 1). For the embankments with piles, lateral crest displacements are measured up-slope of the piles (location D2). Pile displacements for the embankment with a row of 6 piles are measured on a pile, 5 m above the embankment. For the embankment with the 2x4 pile group the pile displacement is measure at the pile-cap (location D1). For all embankments, settlements are measured up-slope of the crest (locations D4, D5, and D6).

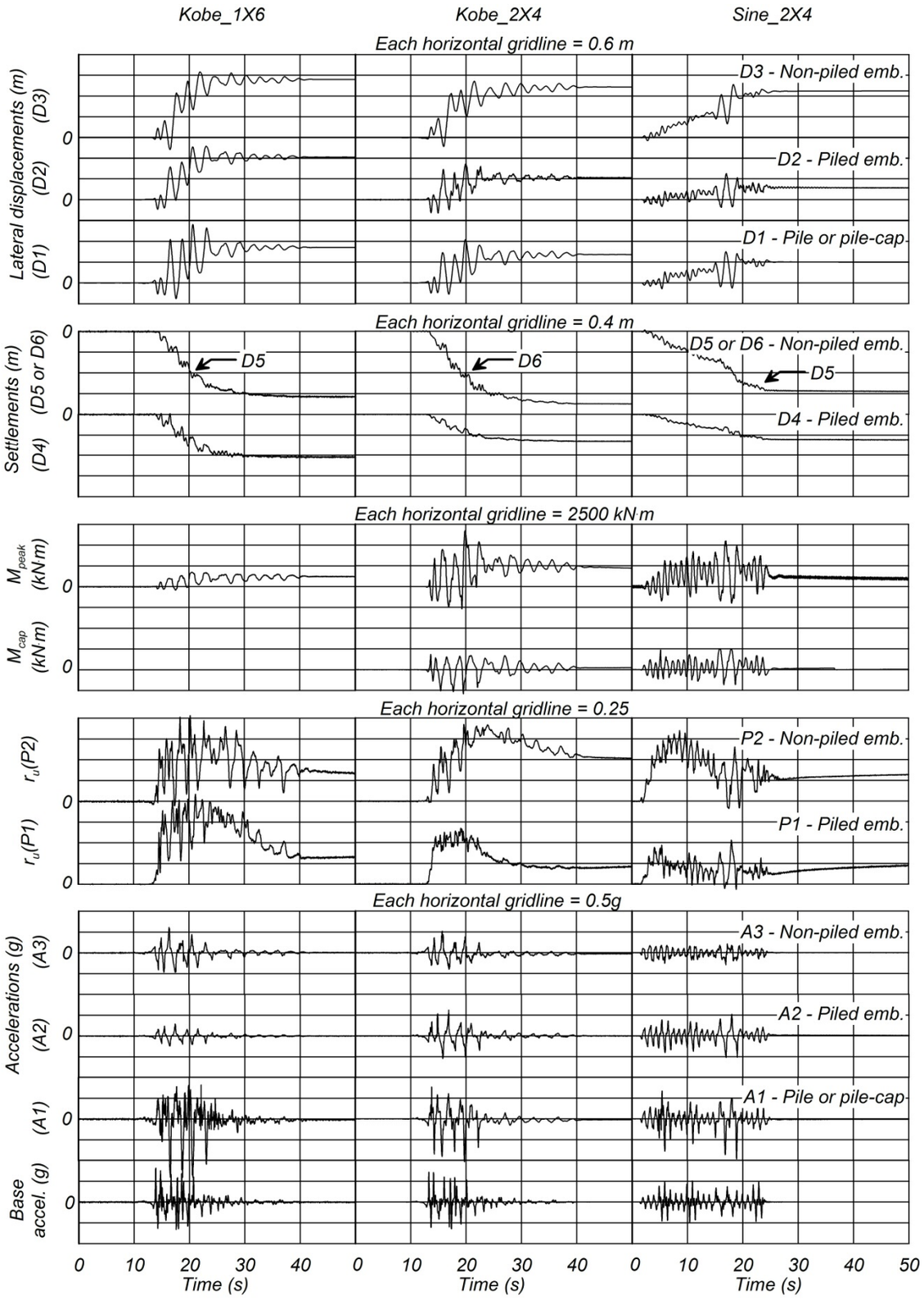


FIG 4. Time histories for the three centrifuge tests.

Measured base motion and embankment accelerations are plotted in Fig. 4. Also plotted are the accelerations on one of the six piles in Kobe_1X6 (5 m above the embankment) and on the pile-cap for Kobe_2X4 and Sine_2X4. The repeatability of the tests is demonstrated by observing that the base motions for Kobe_1X6 and Kobe_2X4 were almost the same and the responses of the embankments without a pile group were very similar. The embankment accelerations have smaller peaks and richer long-period components than the base accelerations, which is consistent with liquefaction causing a softening of the soil and an effective lengthening of the embankment's natural period.

The accelerations of the embankment with piles (A2) as compared to the embankment without piles (A3) decreased by 60% for Kobe_1X6 and increased by 25% and 67% for Kobe_2X4 and Sine_2X4, respectively (based on Fig. 4 or Table 2). The reason for an increase or decrease of embankment accelerations is attributed to how the different pile foundation stiffness and inertia affected the seismic response of the embankment-pile system. The far greater stiffness of the 2x4 pile groups in Kobe_2X4 and Sine_2X4 had a significant restraining effect on the embankment and enabled it to achieve greater up-slope accelerations than were possible with the more flexible piles in Kobe_1X6. It was also found that for the 2x4 pile groups, the peak inertia of the pile-cap was as much as 30% of the total inertia of the embankment mass behind the piles, based on their relative masses and measured accelerations.

The final lateral crest displacements for the embankment with piles (D2) was decreased by 30%, 60%, and 80% as compared to the embankment without piles (D3) for Kobe_1X6, Kobe_2X4, and Sine_2X4, respectively. This indicates that the lateral crest displacements were significantly decreased in all centrifuge tests by the pinning action of the piles, especially with the larger piles in the 2x4 pile group. The displacements of the piles and pile-caps (D1) were, however, consistently larger than the displacements of the embankment (D2) behind them, with an increase of 33% to 100% in the case of the 2x4 pile groups.

Crest settlement for the embankment with piles (D4) was decreased by 31%, 64%, and 58% as compared to the embankment without piles (D5 or D6) for Kobe_1X6, Kobe_2X4, and Sine_2X4, respectively. Both longitudinal and transverse deformations contributed to these settlements. These reductions in crest settlement are comparable in magnitude to the observed reductions in lateral crest displacements.

Bending moment time histories are plotted at two specific locations along a pile: at the gauge where the maximum positive bending moment (M_{max}) was recorded (top of the dense sand layer) and near the pile to pile-cap connection for Kobe_2X4 and Sine_2X4. Bending moment time histories at the same depths on different piles in the 1x6 and 2x4 pile groups were similar. For all three centrifuge tests the time of maximum moment occurred during shaking, after which time the moment decreased due to the "springing back" of the piles. This effect was greatest for the 2x4 pile group with the larger diameter piles. The maximum moments for the 2x4 pile groups (Kobe_2X4 and Sine_2X4) occurred near the top of the dense sand layer rather than at the pile heads. Bending moments at the pile heads were partly reduced by rotations that developed due to both flexibility in the pile-cap connection and axial movement of the piles.

Time histories of pore water pressure ratio, r_u are shown for the bottom of the loose sand layer underneath each embankment (P1 and P2). A r_u = 100% was reached in the loose sand beneath both embankments in Kobe_1X6. For Kobe_2X4, r_u reached 100% beneath the non-piled embankment but only 70% beneath the piled embankment. For Sine_2X4, r_u reached 90% beneath the non-piled embankment but only 50% beneath the piled embankment. The reduction in maximum r_u values beneath the embankments with the stiffer pile groups (Kobe_2X4 and Sine_2X4) coincides with those piles also causing greater reductions in both lateral crest displacement and embankment settlement.

Pile bending moments

The bending moment distribution at the time of peak measured compressive moment and after shaking for all three centrifuge tests for one specific pile are presented in Fig. 5. The peak moment occurred at a location corresponding to the top of the dense sand layer. The low moment at the pile-cap for Kobe_2X4 and Sine_2X4 is partly attributed to pile-cap rotation and soil deformation. The peak pile-cap rotation for Kobe_2X4 and Sine_2X4 was 0.03 radians and 0.04 radians, respectively, reducing the curvature demands near the pile-cap. The majority of pile-cap rotation was attributed to axial movement in the piles; flexibility in the pile-cap connection was measured as 1.3 X 10^6 kN·m/rad contributing 0.001 radians – at least an order of magnitude smaller than the measured pile-cap rotation. The curvature demands on the piles were also reduced by the significant shear strains in the embankment as compared to the loose sand layer. For example, the ratio of shear strain in the embankment to shear strain in the loose sand layer was 1.2 and 1.8 for Kobe_1X6 and Kobe_2X4, respectively (based on model dissection measurements).

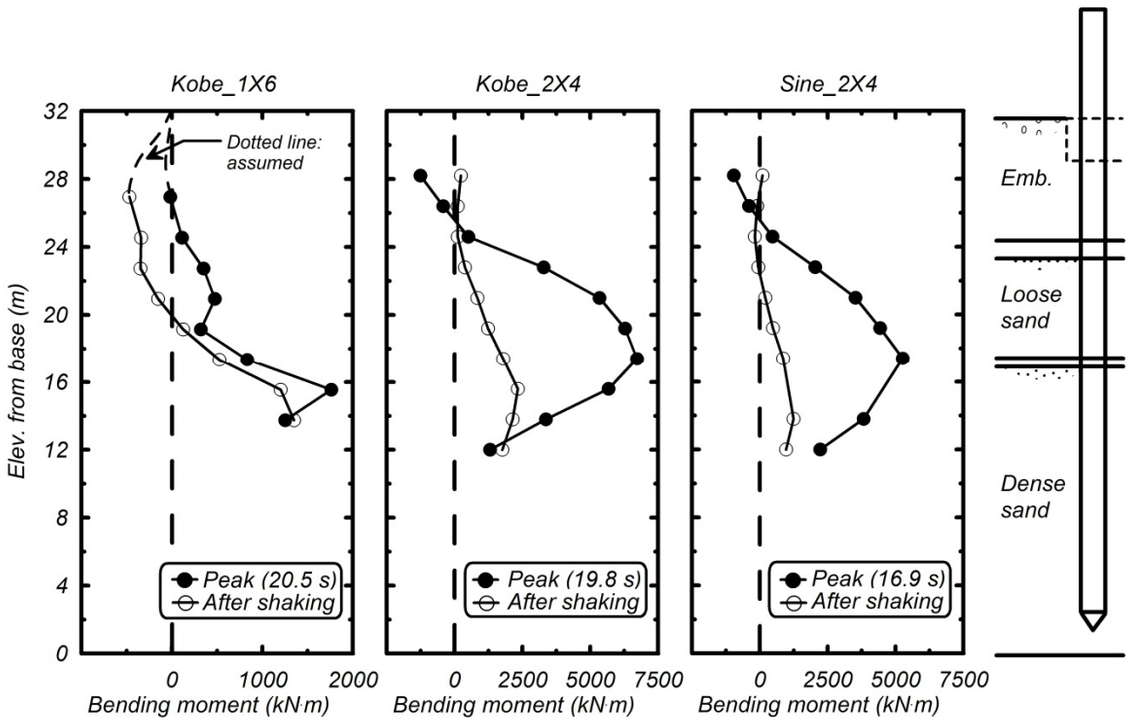


FIG 5. Bending moments versus depth for one of the piles in each centrifuge test at a time of peak positive moment and after shaking.

BACK-CALCULATED SHEAR STRESS AND SHEAR STRAIN

The stress-strain responses of the embankment materials and underlying sands were back-calculated for points in the non-piled embankments. Results from the non-piled embankment in Kobe_2X4 are shown in Fig. 6 in terms of normalized dynamic shear stress (τ_{dyn}/σ_{vo}') versus shear strain for: (1) a point in the embankment, 5 m below its surface, and (2) a point near the center of the loose sand layer beneath the embankment. For clarity, the computed responses are only shown for the first, third, and fourth cycles of strong shaking. This dynamic shear stress was computed by discritizing a vertical array of accelerometers into elements and multiplying the measured acceleration of each element by the mass of the element to obtain an inertia force. This dynamic shear stress excludes any initial static shear stress. The shear strain was computed using complementary filters to combine the high-frequency (transient) component from integration of accelerometer records with the low-frequency (including permanent) component from surface displacement transducers. The low-frequency component of strain was computed at each depth by assuming that the low-frequency components of shear strain at each depth were proportional to the low-frequency components of the surface displacement.

The embankment material exhibited similar stiffness during each of the three representative cycles, while progressively accumulating permanent strains of almost 3%. The loose sand exhibited substantial stiffness degradation from the first to fourth cycle as the effective stresses decreased and permanent strains of almost 8% accumulated. The stress-stain loops for the loose sand in the third and fourth cycles are qualitatively similar to the inverted s-shaped loops observed in cyclic laboratory element tests on saturated sands.

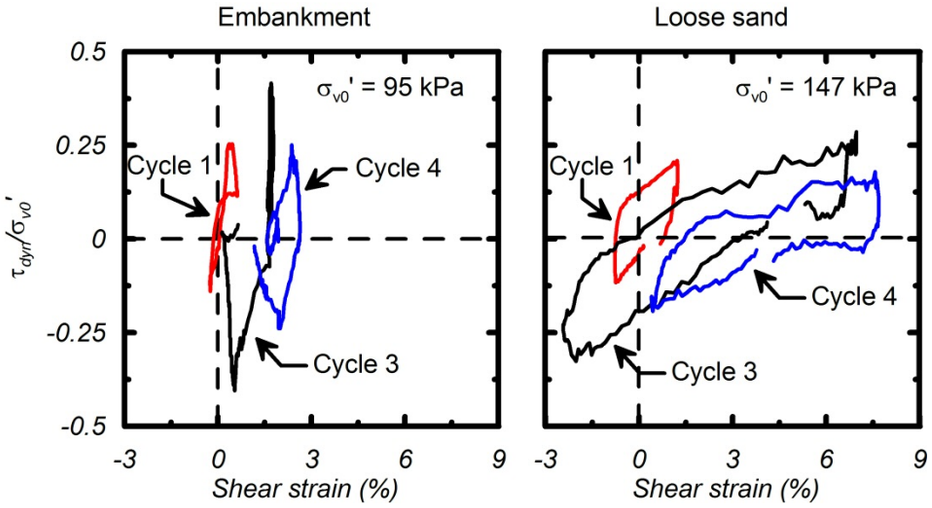


FIG 6. Plot of normalized dynamic shear stress and shear strain near the center of the loose sand layer for test Kobe_2X4.

IMPLICATIONS FOR DESIGN PRACTICE

Equivalent static pile pinning analysis procedures have been evaluated against these centrifuge tests, with results for the first two tests described in Boulanger et al. (2006, 2007). The following comments regarding pile pinning effects and equivalent static analyses are based on the results of these evaluations.

- The relative effect of pile pinning on embankment displacements was reasonably predicted provided that the residual strength was calibrated to make the Newmark displacements (Newmark 1965) match the observed displacements. The calibrated residual strengths were, however, significantly greater than would be obtained from case-history-based residual strength correlations.
- The accuracy of Newmark sliding block procedures for predicting the embankment displacements in these tests was poor for two reasons. First, the assumptions of rigid-plastic soil behavior and discrete sliding surfaces are crude approximations of the actual deformation processes (Figs. 3 and 6). Second, residual strengths are complicated by processes such as void redistribution and particle intermixing, which are difficult to quantitatively predict in practice (Idriss and Boulanger 2007). Common design relationships for residual strength that are based on case histories underestimate the residual strengths that were mobilized in these centrifuge tests, and therefore resulted in significant overestimations of embankment displacement.
- The shear strain profiles in the embankment had a significant effect on the computed pile responses. The common assumption that deformations occur solely in the liquefied layers while the embankment moves as a rigid body can significantly overestimate the restraining force provided by the piles.
- Predicting the magnitude and profile of liquefaction-induced soil displacements is often the dominant source of uncertainty in evaluating the performance of piles in bridge approach embankments.

SUMMARY

The results of three dynamic centrifuge tests demonstrated that the resisting forces from piles can reduce the embankment displacements that result from earthquake induced liquefaction in the underlying soils. Lateral displacements at the crests of the embankments without piles ranged from 1.4 to 1.7 m for the three model tests. The embankment with a row of six 0.72-m diameter piles experienced a 30% reduction in lateral crest displacements, whereas the embankments with two-by-four groups of 1.22-m diameter piles experienced 60% to 80% reductions in lateral crest displacements.

The mechanisms of loading and deformation for the embankments and piles are illustrated through examination of time histories, displacement patterns, bending moment profiles, and back-calculated stress-strain responses. Implications of these test results for design practice were briefly discussed.

ACKNOWLEDGEMENTS

Funding was provided by Pacific Earthquake Engineering Research (PEER) Center, through the Earthquake Engineering Research Centers Program of the National Science

Pile group, under contract 2312001, and the PEER Lifelines program, under contract 65A0058. The contents of this paper do not necessarily represent a policy of either agency or an endorsement by the state or federal government. Recent upgrades to the centrifuge were funded by NSF Award No. CMS-0086588 through the George E. Brown, Jr. Network for Earthquake Engineering Simulation (NEES). The first author acknowledges an NSERC scholarship from the government of Canada. The authors appreciate the contributions of Scott Brandenberg, Dongdong Chang, and the Center for Geotechnical Modeling staff in performing the centrifuge tests.

REFERENCES

Boulanger R.W., Chang D., Gulerce U., Brandenberg S.J., Kutter B.L. (2006). "Evaluating pile pinning effects on abutments over liquefied ground." *Seismic Performance and Simulation of Pile Foundations in Liquefied and Laterally Spreading Ground*, GSP 145, ASCE, pp 306–318.

Boulanger, R.W., Chang, D., Brandenberg, S.J., Armstrong, R.J., and Kutter, B.L. (2007). "Seismic design of pile foundations for liquefaction effects." *Earthquake Geotechnical Engineering, 4th Intl. Conf. on Earthquake Geotechnical Engineering – Invited Lectures*, K. D. Pitilakis, ed., Springer, The Netherlands, 277-302.

Idriss, I. M., and Boulanger, R.W. (2007). "SPT- and CPT- based relationships for the residual shear strength of liquefied soils." *Earthquake Geotechnical Engineering, 4th International Conference on Earthquake Geotechnical Engineering – Invited Lectures*, K. D. Pitilakis, ed., Springer, The Netherlands, 1-22.

Law, H. (2000). "Lateral spreading on a pile at the Oakland Mole SFOBB East Span Seismic Safety Project." *Memorandum 09-12-2000*, Earth Mechanics, Inc., CA.

Ledezma, C., and Bray, J. D. (2006). "A probabilistic design procedure that incorporates the pile-pinning effect in bridge foundations undergoing liquefaction-induced lateral spreading." 5th National Seismic Conf on Bridges and Highways, MCEER-06-SP09, Paper B22.

Martin, G.R., March, M.L., Anderson, D.G., Mayes, R.L., and Power, M.S. (2002). "Recommended design approach for liquefaction induced lateral spreads." *Proc. 3rd National Seismic Conf and Workshop on Bridges and Highways*, MCEER-02-SP04, Buffalo, NY.

Newmark, N.M. (1965). "Effects of earthquakes on dams and embankments." *Géotechnique*, 15(2): 139-160.

Perez-Cobo, A., and Abghari, A. (1996). "Lateral spreading and settlement potential for Salinas River Bridge (Bridge No. 44-0002)." *Memorandum 02-22-1996*, Caltrans, Office of Structural Pile groups, Sacramento, CA.

Transportation Research Board (2002). "Comprehensive Specification for the Seismic Design of Bridges." *National Cooperative Highway Research Program (NCHRP) Report 472*, National Research Council, 49 pp.

Wilson, D., Boulanger, R., and Kutter, B. (1998). "Signal Processing for and Analyses of Dynamic Soil-Pile Interaction Experiments." *Proc. Centrifuge 98*, Balkema, Rotterdam, Vol 1, 135-140.

Zha, Jin-xing (2004). "Lateral spreading forces on bridge abutment walls/piles." *Geotechnical Engineering for Transportation Projects, Geotechnical Special Pub.* 126, M. K. Yegian and E. Kavazanjian, eds, ASCE, Vol. 2, 1711-1720.

Closed-Form Force-Displacement Backbone Curves for Bridge Abutment-Backfill Systems

Anoosh Shamsabadi[1], M. ASCE, P.E. and Liping Yan[2], M. ASCE, P.E.

[1]Senior Bridge Engineer, California Department of Transportation, Office of Earthquake Engineering, 1801 30th Street, Sacramento, Sacramento, CA 95816; Anoosh_Shamsabadi@dot.ca.gov
[1]Principal Engineer, Earth Mechanics, Inc., 17660 Newhope Street, Suite E, Fountain Valley, CA 92708; L.Yan@earthmech.com

ABSTRACT: The abutment-soil-structure-interaction plays a significant role in the global response of bridge structures. This paper presents nonlinear closed-form formulas to describe force-displacement backbone curves of bridge abutments with typical backfill soils. The original closed-form formulas are modified Hyperbolic Force-Displacement ("HFD") equations developed to simulate the results of two field abutment tests for an abutment wall height of 5.5 feet. To extend the formulas to be applicable to abutment walls with other heights, a series of analyses are performed using the limit-equilibrium method that implements mobilized Logarithmic-Spiral failure surfaces coupled with a modified Hyperbolic soil stress-strain behavior ("LSH" model). The limit-equilibrium method with LSH model, which is a relatively simple approach, has been verified through analyses using a complex finite element model and also has been validated by abutment and pile cap field tests conducted on various typical structure backfills. Based on the results of the analyses, two height adjustment factors are derived for typical sandy and clayey backfill soils. The recommended closed-form formulas are the products of the original closed-form formulas and the height adjustment factors. The formulas are simple enough to be used by the practicing engineers and are capable of capturing the major characteristics of the force-displacement backbone curves.

INTRODUCTION

In recent years, Performance-Based Earthquake Engineering (PBEE) has been applied to bridge design, which involves the design of ductile bridge structures to resist earthquake loads in a predicable manner. New bridge designs with ductile columns may impose large displacements on abutments and cause more damage to the abutments than observed in past earthquakes. Proper evaluation and design of the bridge abutments reduce the column displacement demand during earthquake shaking, leading to a more efficient and economical design.

Measurements from instrumented bridges and results of large-scale field tests have demonstrated that the stiffness and strength of the abutment-backfill is a function of mobilized displacement and the level of shaking. The force-displacement relationship exhibits significant stiffness degradation at large abutment displacements. The abutment-backfill not only can provide significant lateral resistance but also is a good source of energy dissipation at large deformation due to nonlinear hysteretic behavior of the abutment-soil system. It is a major task for practicing engineers to realistically represent relationships between the resistance of the backfill (force) on the abutment wall and the wall movement (displacement) for dynamic analysis of bridge structures. The relationships are usually called force-displacement backbone curves.

Various approaches have been proposed to develop the force-displacement backbone curve for a give abutment-backfill system. One complex approach is to use the finite element method (FEM) whereby the abutment wall is represented by structural elements and the backfill soil is represented by solid elements with appropriate constitutive models (Shamsabadi 2007). Another approach, which is simpler than the FEM, is the limit-equilibrium method that implements mobilized Logarithmic-Spiral failure surfaces coupled with a modified Hyperbolic soil stress-strain behavior ("LSH" model) to estimate abutment nonlinear force-displacement capacity as a function of wall displacement and backfill soil properties (Shamsabadi et al. 2005). Both approaches are powerful and effective to generate force-displacement backbone curves of a bridge abutment. However, it is not economical to apply these approaches in routine analyses for seismic soil-structure interaction of bridges. The objective of this paper is to seek a simpler approach than the above two approaches to characterize force-displacement backbone curves.

For modern highway bridges, backfill soils behind bridge abutments usually satisfy certain specifications. Therefore, it is possible to find out the material properties for typical backfill soils. Because data are available from recent field abutment experimental tests on bridge abutments with typical backfill soils conducted at University of California, Davis and University of California, Los Angeles, interpretation and analysis of these data lead to our understanding of the characteristics of the force-displacement backbone curves, which motivated developing the closed-form formulas recommended in this paper.

FORMULATION OF MODIFIED HFD EQUATION

A typical abutment force-displacement backbone curve is shown in Figure 1, where F_{ult} is the maximum abutment force developed at the maximum displacement y_{max}, and y_{ave} is the displacement corresponding to half of the maximum abutment force ($1/2y_{max}$). We can define the average soil stiffness K as:

$$K = \frac{\frac{1}{2} F_{ult}}{y_{ave}} \tag{1}$$

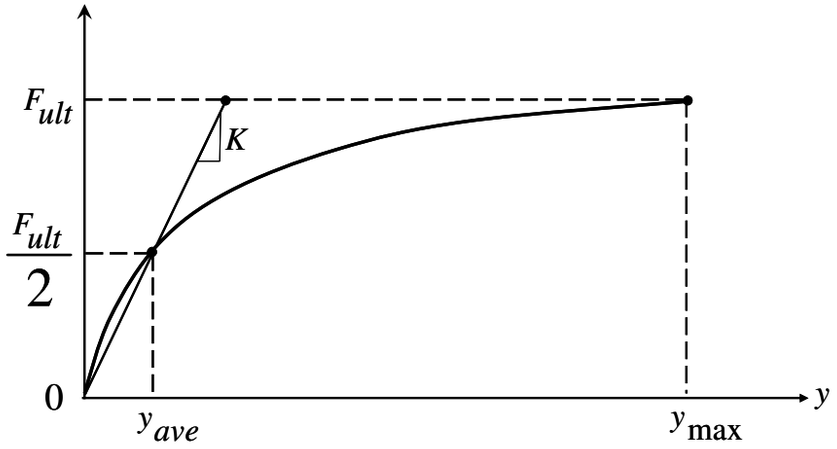


FIG. 1. A typical force-displacement relationship (i.e., backbone curve)

The force-displacement relationship in general hyperbolic form is defined as:

$$F(y) = \frac{Cy}{1 + D\,y} \tag{2}$$

The constants C and D are related to the key parameters (K, F_{ult}, y_{max}, y_{ave}) as:

$$C = \left(2K - \frac{F_{ult}}{y_{\max}}\right) \text{ and } D = 2\left(\frac{K}{F_{ult}} - \frac{1}{y_{\max}}\right) \tag{3}$$

Data from Field Abutment Experimental Tests

To develop closed form force-displacement backbone curves using Eq. (2), we made use of the available data from the full-scale abutment field experimental tests conducted at University of California, Los Angeles (UCLA) and University of California, Davis (UCD), which were part of the Caltrans seismic research program.

The UCLA cyclic load test was performed on a 15-foot by 3-foot seat-type abutment wall with a height of 5.5 feet having a silty sand backfill (Stewart et al. 2007). The backfill was placed in layers and compacted to over 95% relative compaction behind the wall and was extended about 3 times the backwall height in the longitudinal direction. The backwall was pushed horizontally in between the abutment wingwalls without any vertical movement. The abutment wingwalls were constructed using smooth plywood. Plastic sheeting was placed at the interior face of the plywood to minimize the friction along the wingwalls in order to simulate a plane strain condition.

The UCD test was conducted on a monolithic abutment by applying cyclic longitudinal loading to ultimate failure (Romstad et al. 1995). The abutment wall has a width of 10 feet and a height of 5.5 feet. The backfill consisted of Yolo Loam clay

that was compacted to a relative compaction of 90% or greater with an average value of 94%).

Table 1 summarizes the maximum capacity force and displacement, the capacity pressure and the average stiffness obtained from the UCLA and UCD abutment tests.

Table 1. Key Parameters from UCLA and UCD Abutment Tests

Test Site/Backfill	F_{ult} (kips)	Pressure (ksf)	y_{max} (in)	y_{max}/H	K (kips/in/ft)
UCLA/Silty Sand	455.0	5.515	3.3	0.05	54
UCD/Clay	312.0	5.673	6.6	0.10	25

Modified HFD Equations to Simulate Abutment Experimental Tests

The experimental data can be backfitted using the modified HFD relationship expressed as Eq. (2). Based on the data from the UCLA and UCD abutment tests, the following presumptive HFD parameters shown in Table 2 can be used to develop the nonlinear closed-form force-displacement curves for a typical highway bridge with typical backfills when no geotechnical data is available.

Table 2. Suggested HFD Parameters for Typical Abutment Backfills

Abutment Backfill Type	Pressure (ksf)	Ave. Soil Stiffness (kips/in/ft)	y_{max}/H
Granular	5.5	50	0.05
Cohesive	5.5	25	0.10
Note: The backfill should be compacted to at least 95% relative compaction per ASTM D-1557. Abutment wall height is 5.5 feet.			

The constants C and D in Eq. (3) can be found by substituting the values give in Table 2. Therefore, we obtain the modified HFD equations as follows.

For a granular backfill:

$$C = 90.84 \quad \text{and} \quad D = 2.70$$

$$F(y) = \frac{90.42\,y}{1 + 2.70\,y} \quad (y \text{ in inches, } F_{ult} \text{ in kips per ft of wall}) \tag{4}$$

For a cohesive backfill:

$$C = 45.42 \quad \text{and} \quad D = 1.35$$

$$F(y) = \frac{45.42\,y}{1 + 1.35\,y} \quad (y \text{ in inches, } F_{ult} \text{ in kips per ft of wall}) \tag{5}$$

Comparisons of the backbone curves calculated from the modified HFD equations with the UCLA and UCD experimental test data are shown in Fig. 2. The results agree reasonably well.

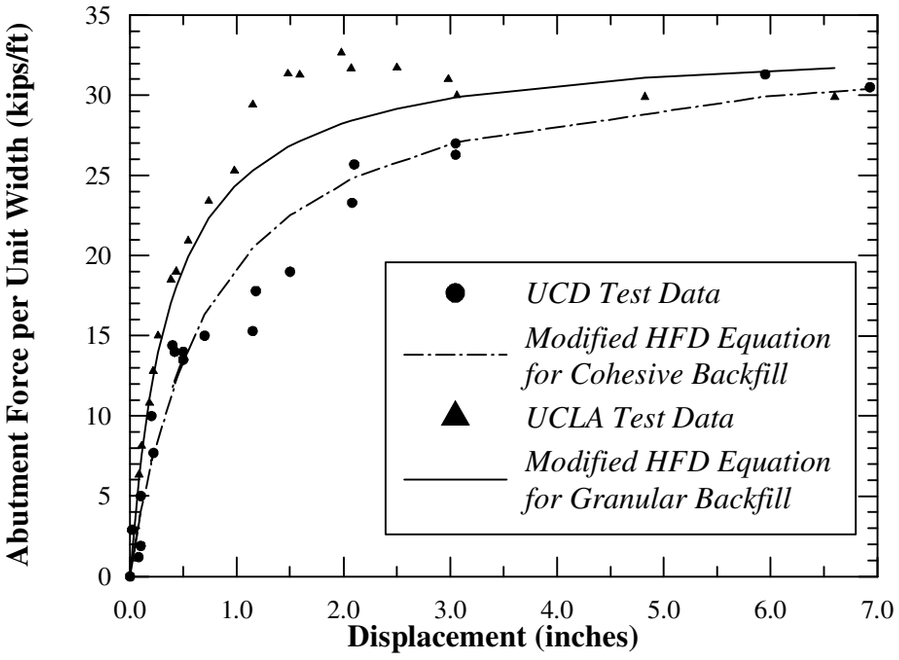


FIG. 2. Comparisons of modified HFD equations with test data

APPLICATION OF MODIFIED HFD EQUATIONS TO OTHER ABUTMENT WALL HEIGHTS

Eqs. (4) and (5) are applicable to calculation of nonlinear force-displacement relationships for a 5.5-foot high abutment wall with two types of backfills that have the conditions similar to the two abutment field tests. In order to develop nonlinear abutment force-displacement relationships for other wall heights, we have proposed that these two equations be multiplied by f_s and f_c, where f_s is the height adjustment factor for the granular backfill and f_c is the height adjustment factor for the cohesive backfill.

Derivation of the Height Adjustment Factors

To derive the height adjustment factors, we developed the following procedures:

- Computed nonlinear force-displacement relationships for various abutment heights using the LSH model (Shamsabadi et al. 2005), as shown in Figs. 3 and 4.
- Normalized the ultimate capacity of various wall heights to the ultimate capacity of the 5.5-foot wall (i.e., ultimate capacity ratio):

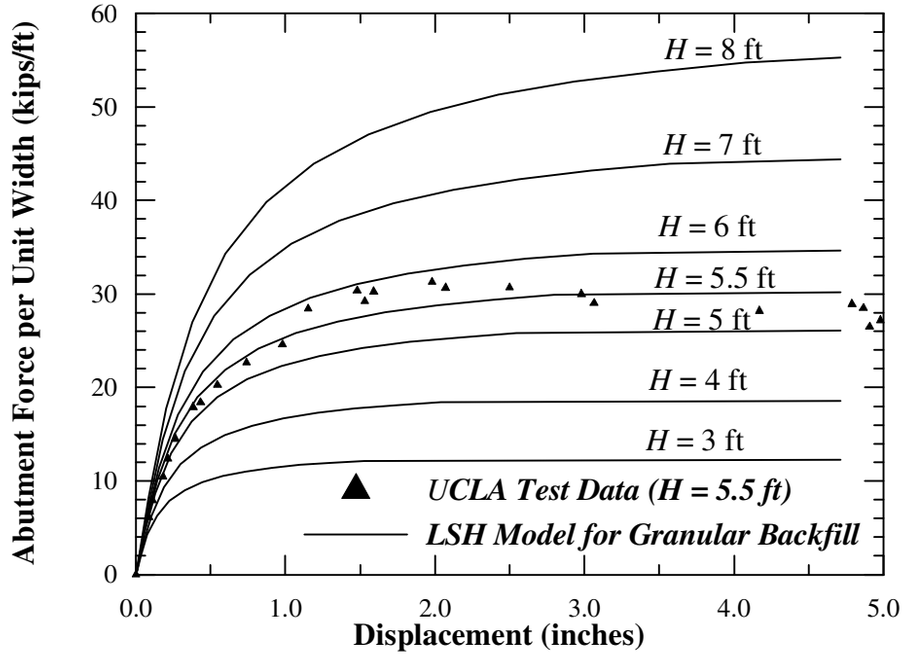


FIG. 3. Backbone curves for various abutment heights with typical granular backfill (silty sand)

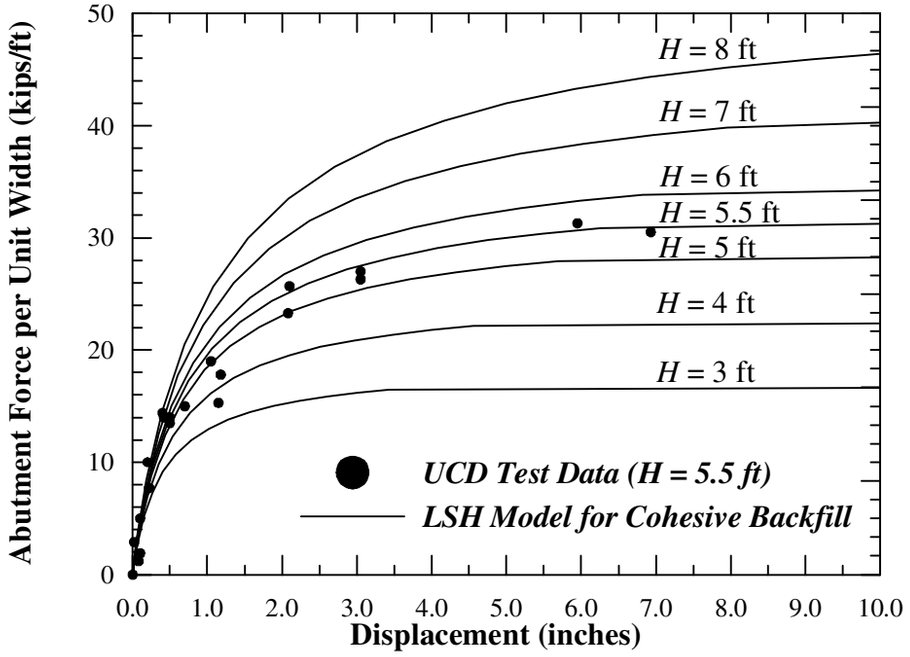


FIG. 4. Backbone curves for various abutment heights with typical cohesive backfill (clay)

$$f_r = \frac{F_{Hult}}{F_{5.5ult}} \tag{6}$$

where F_{Hult} is the ultimate capacity for a abutment wall height of H and $F_{5.5ult}$ is the ultimate capacity for a abutment wall height of 5.5 feet. If we assume the capacity ratios at other displacements are the same as the ultimate capacity ratio, f_r corresponds to the height adjustment factor, f_s or f_c.

The calculated values of f_r were obtained for abutment wall heights ranging from 3 to 8 feet and are listed in Table 3.

Table 3. Height Adjustment Factors

Height *H* (feet)	**3**	**4**	**5**	**5.5**	**6**	**7**	**8**
Granular Backfill							
f_r	0.41	0.61	0.86	1.0	1.15	1.47	1.83
f_s	0.40	0.62	0.87	1.0	1.14	1.44	1.75
Cohesive Backfill							
f_r	0.53	0.72	0.90	1.0	1.10	1.29	1.49
f_c	0.55	0.73	0.91	1.0	1.09	1.27	1.45

By trial-and-error, we obtained the following equations that can best fit the values of f_r:

$$f_s = \left(\frac{H}{5.5}\right)^{1.5} \tag{7}$$

$$f_c = \left(\frac{H}{5.5}\right) \tag{8}$$

The calculated values of f_s and f_c using Eqs. (7) and (8) are also listed in Table 3. It can be seen that their values are remarkably close to the respective values of f_r. Therefore, Eqs. (7) and (8) can be used to calculate the height adjustment factors for the granular and cohesive backfills, respectively.

Recommended Modified HFD Equations

Multiplying Eqs. (4) and (5) by Eqs. (7) and (8), respectively, leads to the following closed-form force-displacement equations:

For the typical granular backfill:

$$F(y) = \frac{7.042\,y}{1+2.70\,y} H^{1.5} \qquad (y \text{ in inches, } F \text{ in kips per ft of wall}) \tag{9}$$

For the typical cohesive backfill:

$$F(y) = \frac{8.26y}{1+1.35y}H \qquad (y \text{ in inches, } F \text{ in kips per ft of wall}) \qquad (10)$$

For all practical purposes, Eq.(9) and Eq.(10) can be approximated as follows.
For the typical granular backfill:

$$F(y) \approx \frac{8y}{1+3y}H^{1.5} \qquad (y \text{ in inches, } F \text{ in kips per ft of wall}) \qquad (11)$$

For the typical cohesive backfill:

$$F(y) \approx \frac{8y}{1+1.3y}H \qquad (y \text{ in inches, } F \text{ in kips per ft of wall}) \qquad (12)$$

Figs. 5 and 6 show comparisons of the nonlinear abutment force-displacement backbone curves calculated using the recommended modified HFD equations (11) and (12) with those predicted by the LSH model. They agree reasonably well.

Validation of Recommended Modified HFD Equation for Granular Backfill

Experimental results of the full-scale abutment test performed by Rollins and Cole (2006) at Brigham Young University (BYU) using a silty sand backfill was selected to examine the validity of Eq. (11). The Ovesen-Brinch Hansen 3-D correction factor (Ovesen, 1964) of 1.2 was applied to the pile cap width in Eq. (11) to account for the three-dimensional wedge effect similar to the LSH model.

Substituting the pile cap dimensions (*Height* = 3.67 ft, *Width* = 17 ft, *3D Factor* = 1.2) into Eq. (11), we obtain

$$F(y) = 17\left[\frac{8y}{1+3y}(3.67)^{1.5}\right]1.2 \qquad (y \text{ in inches, } F \text{ in kips}) \qquad (13)$$

The force-displacement relationship calculated using Eq. (13) is shown in Fig. 7. It can be seen that the HFD and LSH curves are very close to the experimental data.

CONCLUSIONS

Closed-form force-displacement backbone curves using the modified HFD equations were developed for abutments with typical backfills based on abutment test data and numerical analyses using the LSH model. These equations are simple but found to match the test data and the curves predicted using the LSH model.

In seismic analysis of bridge structures, capacity and stiffness of the abutment-backfill system are often required, such as the procedures specified in Caltrans seismic design criteria (Caltrans 2006). When no detailed geotechnical data is available, the recommended close-form equations in this paper are practical and versatile tools that can be used to generate force-displacement backbone curves as

long as the backfills are typical backfill materials satisfying the standard construction specifications for bridge abutment backfills.

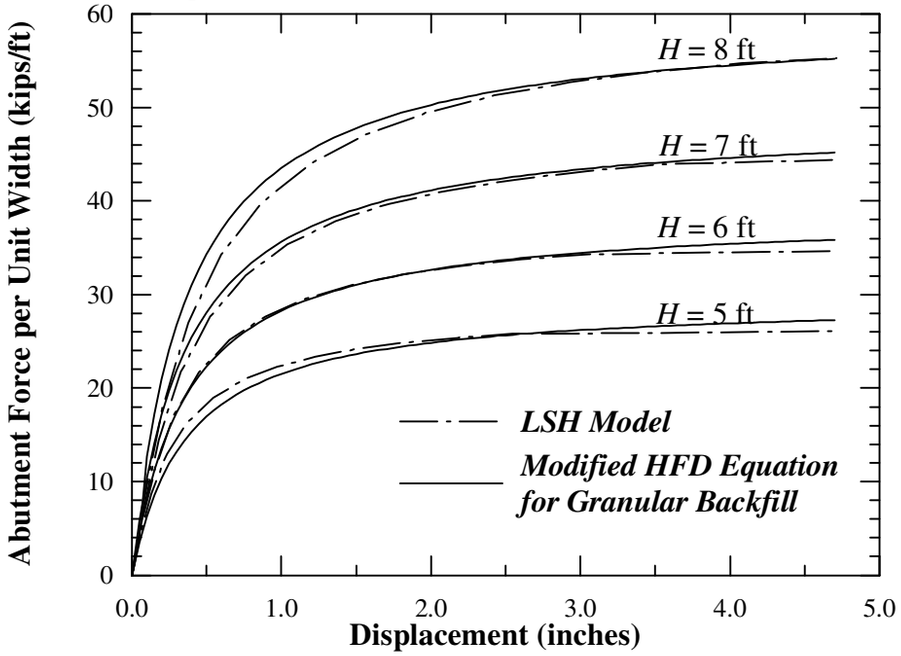


FIG. 5. Comparisons of the modified HFD equation with LSH model for typical granular backfill (silty sand)

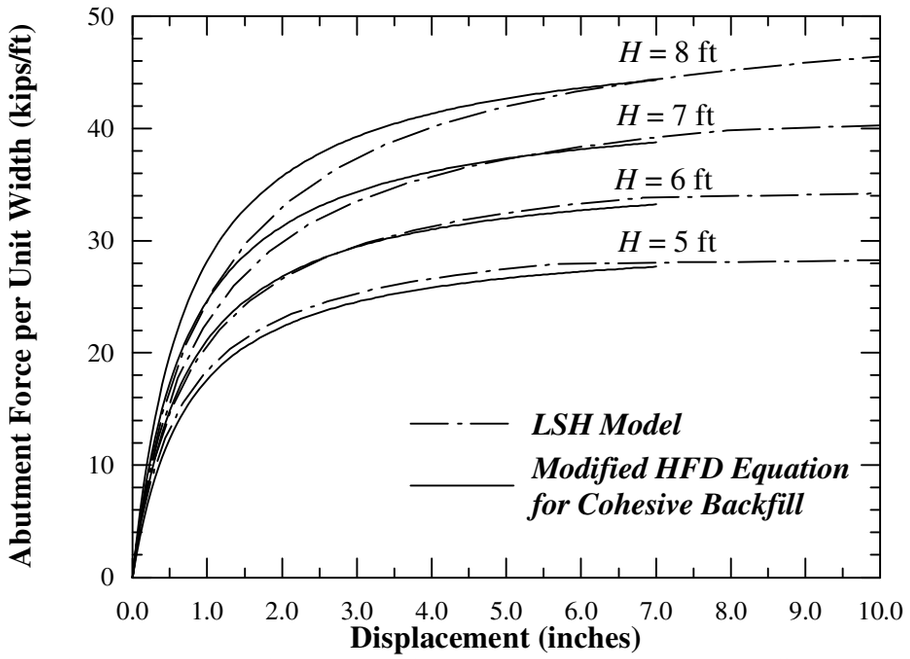


FIG. 6. Comparisons of the modified HFD equation with LSH model for typical cohesive backfill (clay)

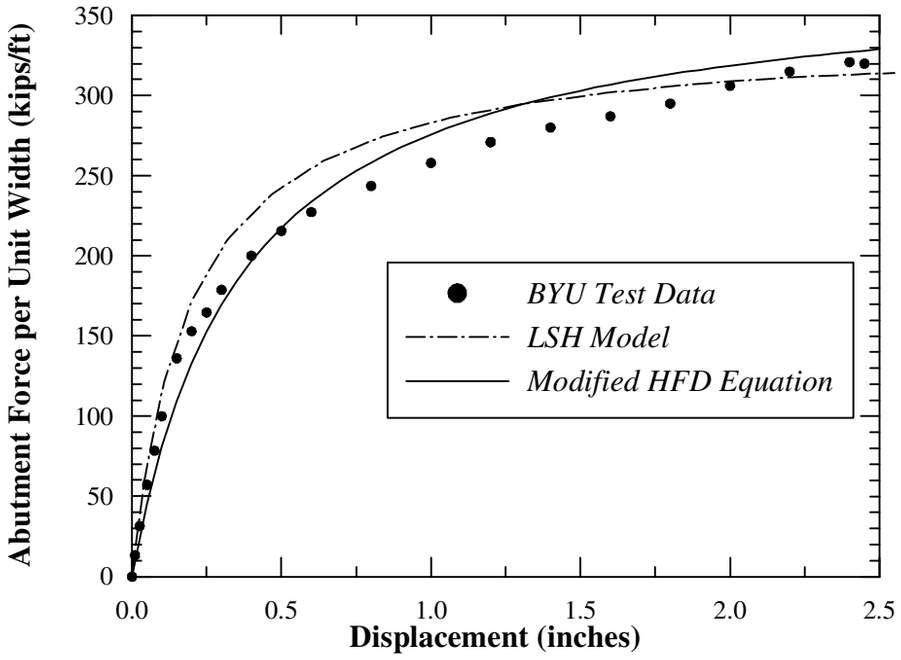


FIG. 7. Validation of the modified HFD equation using BYU test data

REFERENCES

California Department of Transportation (Caltrans, 2006). *Seismic design criteria, version 1.4*, Division of Engineering Services, Office of Structure Design, June.

Ovesen, N.K. (1964). "Anchor slabs, calculation methods, and model tests." *Danish Geotechnical Institute, Bulletin No. 16*, Copenhagen.

Rollins, K.M., and Cole, R.T. (2006). "Cyclic lateral load behavior of a pile cap and backfill." *J. Geotechnical and Geoenvironmental Engineering,* ASCE, 132 (9).

Romstad, K., Kutter, B., Maroney, B., Vanderbilt, E., Griggs, M., and Chai, Y.H. (1995). *Experimental measurements of bridge abutment behavior*. Dept. of Civil and Environmental Eng., University of California, Davis, Report No. UCD-STR-95-1, Sept.

Shamsabadi, A. (2007). *Three-dimensional nonlinear seismic soil-abutment-foundation structure interaction analysis of skewed bridges*, Ph.D. Dissertation, Department of Civil and Environmental Engineering, University of Southern California, Los Angeles, California.

Shamsabadi, A., Ashour, M., and Norris, G. (2005). "Bridge abutment nonlinear force-displacement-capacity prediction for seismic design." *J. Geotechnical and Geoenvironmental Engineering*, ASCE, 131 (2): 151-161.

Stewart, J. P. et al. (2007). "Full Scale Cyclic Testing of Foundation Support Systems for Highway Bridges. Part II: Abutment Backwalls." Structural & Geotechnical Engineering Laboratory, University of California, Los Angeles, Report No. UCLA-SGEL-2007/02, October.

Development of Innovative Foundation Systems to Optimize Seismic Behavior of Bridge Structures

Lijun Deng[1], Emrah Erduran[2], Jose Ugalde[1], Sivapalan Gajan[3], M. ASCE, Sashi Kunnath[4] , M. ASCE and Bruce Kutter[4], M. ASCE

[1]Graduate student researcher, Department of Civil and Environmental Engineering, University of California, Davis, CA 95616
[2]Post-doctoral researcher, Department of Civil and Environmental Engineering, University of California, Davis, CA 95616
[3]Assistant professor, Department of Civil Engineering, North Dakota State University, Fargo, ND 58105
[4]Professor, Department of Civil and Environmental Engineering, University of California, Davis, CA 95616

ABSTRACT: Preliminary results from a study to develop innovative bridge foundations to optimize bridge performance under earthquake events are presented. Numerical models of bridges with both flexible and stiff footings are compared to demonstrate the potential importance of soil-footing stiffness on the performance of a soil-footing-column-deck-abutment system. Detailed numerical models were developed to capture the inelastic behavior of soil-footing systems. This article summarizes two types of foundation models developed using the OpenSees computational platform. One model uses a contact interface model, soilFootingSection2D, to simulate the foundation and has been proven to be effective in analyzing the cyclic response and displacement of soil-foundation-bridge system. The other uses 2-D nonlinear Winkler foundation consisting of various constitutive springs. Although the former model is more detailed and fundamentally sound in modeling the footings, in its current state it is limited to 2-D use only. The latter model, once verified via comparison to experimental data, can be extended to 3-D. Future work will use the 3-D nonlinear footing models to more accurately simulate the 3-D response of a bridge system to 3-D ground motions.

INTRODUCTION

A research project aiming to develop a procedure for the design of innovative economical foundations funded by California Department of Transportation (Caltrans) is underway. The purpose of this research is to develop a procedure for optimizing the performance (moment capacity, stiffness, and energy dissipation) of a soil-foundation-bridge system under earthquake loading. The first phase of the study consists of an analytical part which aims to accurately model the soil-foundation-bridge system and

determine how the performance is affected by flexibility and yielding of the foundation. Innovative foundations will be designed that produce desired and reliable strength and stiffness while minimizing drift, maximizing energy dissipation in the foundations, and minimizing the acceleration demands on deck and ductility demands on the bridge column. Different foundation types will be investigated including shallow foundations, deep foundations with differing strength and stiffness. Included are shallow foundations in combination with ground improvement or different foundation shapes to optimize the system performance. Once the properties of the foundation systems that optimize the seismic behavior of the structural systems are determined, physical design of the foundations that will produce the desired properties will be verified in a series of centrifuge model tests.

So far, shallow foundations have been considered since they are considered to have potentially beneficial effects on bridge performance. They can be designed to have a well defined moment capacity, and there is a re-centering force associated with the uplift due to rocking behavior that has potential to minimize permanent drift of the bridge. As a baseline of the physical modeling track of the project, a centrifuge model, shown in Figure 1, has been designed to represent an actual prototype bridge. The model is a single bent foundation system, including deck, column, footing, and two seat-type abutments.

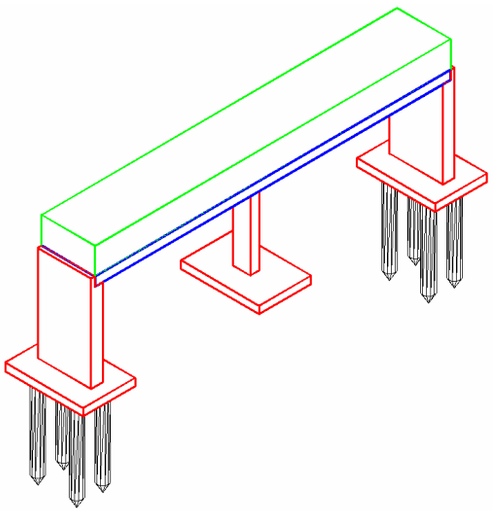


FIG. 1. Bridge model designed for centrifuge tests

This paper presents preliminary results to show that bridge performance is affected by foundation flexibility. This is done by comparing performance of a bridge with flexible and stiff foundation under a variety of input motions. Then the paper presents numerical simulation of bridge foundations as the second track of this project. The OpenSees finite element platform was used, adopting contact interface model and nonlinear Winkler foundation model in 2-D cases. Extension of the two numerical models to 3-D condition, which will then be used in 3-D nonlinear analyses of the soil-foundation-bridge systems, is expected in future studies.

PRELIMINARY ANALYSES

To be able to assess the effect of the foundation flexibility on the demands placed on the bridge columns, a series of nonlinear time history analyses were carried out on a typical highway overcrossing. It is a single bent bridge with span lengths of 30.95 m and 30.52 m. Two circular columns with a diameter of 1.78 m constitute the bent. The superstructure consists of a reinforced concrete box girder.

Diaphragm type abutments were used at both ends of the bridge. The end conditions both at the abutments and at the bottom of the columns were modeled using spring elements to simulate the flexibility of the soil-pile-foundation and abutments. The superstructure was modeled using several elastic elements. Potential plastic hinge regions of the columns were modeled using fiber elements with full axial force-moment interaction. Figure 2 presents the simulation model of the bridge.

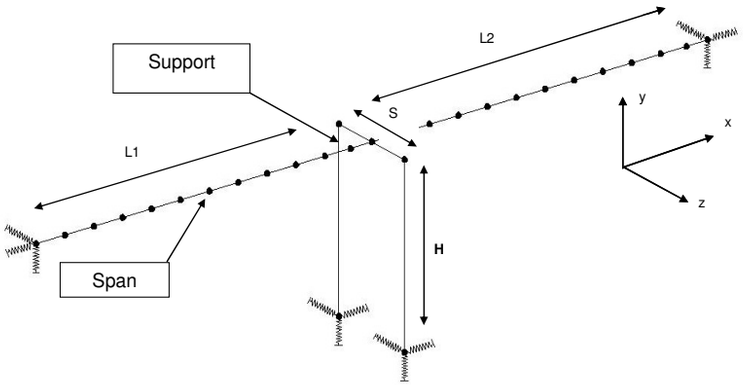


FIG. 2. Simulative model of a typical highway overcrossing in the present study

A total of 29 ground motions were scaled to match the acceleration response spectrum (ARS) curves used by Caltrans in the seismic design of bridges for a ground motion with a moment magnitude of 8.0 and PGA of 0.6g (Caltrans 2006). Two cases were considered in terms of the foundation flexibility in the nonlinear response history analyses of the prototype bridge: stiff and flexible. All the springs representing soil-foundation systems were modeled using elastic materials. Figure 3 depicts the maximum plastic rotation recorded at the bottom section of the column in the transverse direction under each ground motion for both stiff and flexible foundation systems.

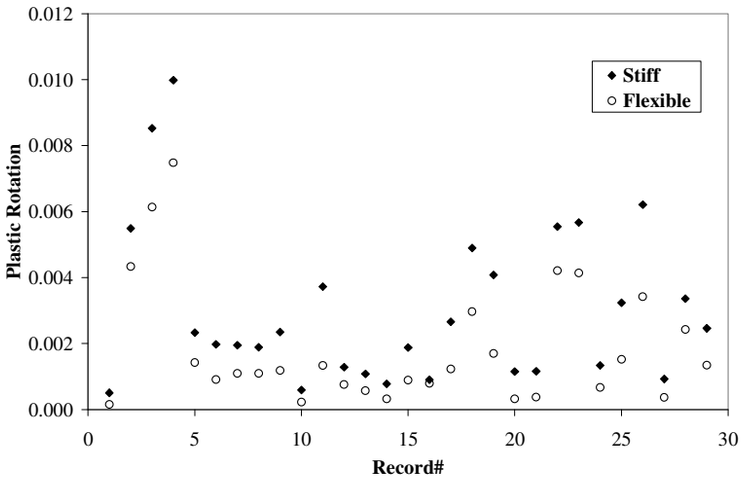


FIG. 3. Column plastic rotation obtained under each ground motion for stiff and flexible foundation systems

As Figure 3 shows, flexible foundations have a smaller demand on the plastic rotation of the column than stiff foundations. It is obvious that the plastic rotation demands will further decrease once the soil-foundation systems are allowed to undergo certain levels of plasticity.

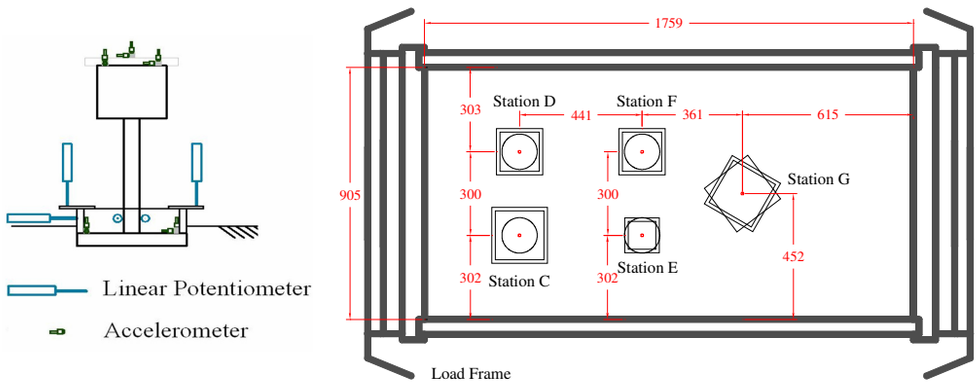
NUMERICAL APPROACHES

The next step of the analytical phase aims to develop a more detailed numerical model of the soil-footing systems that can effectively consider rocking and uplift of shallow foundations. These numerical models will then replace the elastic springs representing the footings in Figure 2 and the nonlinear response history analyses will be repeated for a larger suite of ground motions. Two approaches are being used to develop these nonlinear numerical models; the contact interface model and nonlinear "spring" model.

Contact interface model

This numerical approach is to model shallow foundations using the contact interface model developed by Gajan (2006). At present this simulation technique has been coded in OpenSees for rotation and uplift behavior of 2-D model and significant input parameters were listed in Gajan et al. (2005). Five structural nodes are used in the simplified numerical model of the simplified physical model used in the centrifuge tests. All structural elements are elastic beam-columns. A contact interface model, soilFootingSection2D section, is placed at the footing-soil interface, replacing the rigid foundation and surrounding soil in the zone of influence. The input parameters of the model are determined by footing geometry and soil properties according to guidelines of Federal Emergency Management Agency (FEMA-356, 2000). More details of this simulation can be reached via the report (Ugalde et al, 2007-a).

Physical data of a centrifuge model test on bridge shallow foundation of another project were used to validate the contact interface model. The bridge models are composed of a lumped mass deck, an aluminum column, and a shallow footing. Setup of the centrifuge model is depicted in Figure 4(a) and detailed descriptions of this experiment are in Ugalde et al (2007-b). Figure 4(b) shows the plan view of the tested structures in the model container. The input acceleration time history of event named JAU01_05_08 is shown in Figure 5.



(a) **(b)**

FIG. 4. (a) Side view of a typical structure setup and instrumentation (Ugalde et al, 2007-b); (b) Plan view of all tested structures

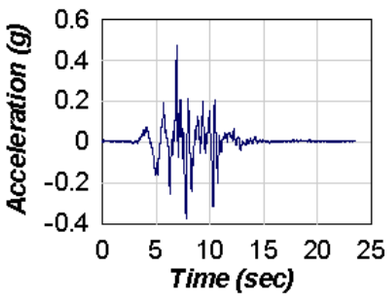


FIG. 5. Input acceleration time history of event JAU01_05_08

Figure 6 and 7 show the load-deformation response of the two stations (E and F) at the base center point of the footing along with the simulation results obtained using the contact interface model subject to an earthquake event named JAU01_05_08. The measured experimental results are then compared to the behaviors simulated using the contact interface model in OpenSees.

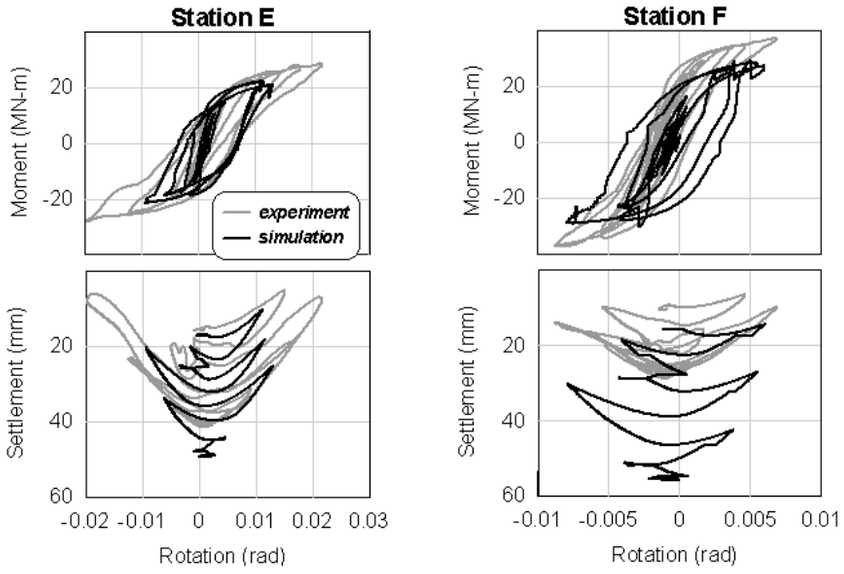


FIG. 6. Load deformation behavior of footing for (a) Station E and (b) Station F during JAU01_05_08

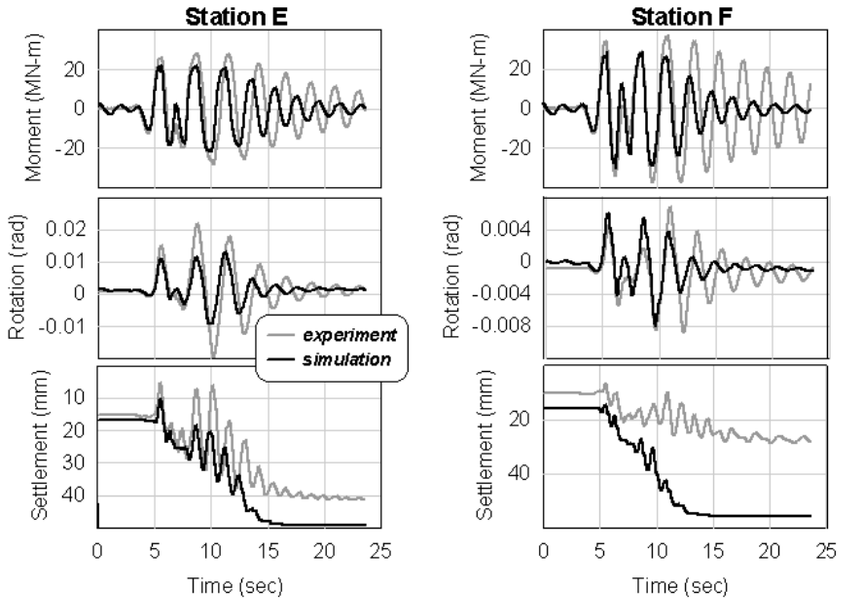


FIG. 7. Footing moment, rotation, and settlement time histories for (a) Station E and (b) Station F during JAU01_05_08

The contact interface model can capture the physical responses of footings of different dimensions. The moment capacity of the footing is underestimated by the contact interface model for both Station F and Station E in for this event, but the frequencies of curves are reasonably represented.

The energy dissipated by moment-rotation hysteresis is roughly captured by the contact interface model, although the Rayleigh damping introduced into the simulation inhibits the footing response after strong shaking is finished. The shape and thickness of moment-rotation curves are well represented by the numerical although the moment capacity of simulation is about 10% smaller than that observed in the experiments. The contact interface model does much better predicting the permanent settlement of Station E, the smaller footing although the magnitude of the cyclic uplift is under predicted and permanent rotations at zero moment is over predicted. The soilFootingSection2D model is based on physics observed in the centrifuge experiments and is considered to be theoretically robust; but the present implementation of this model is limited to two dimensions.

Nonlinear spring foundations

Although the behavior of the soil-footing systems can be effectively captured via the contact surface model, the limitation of this model to 2-D analysis resulted in efforts to develop a new model which can readily be extended to 3-D. To reach this goal we are making a logical extension of the approach of Raychowdhury and Hutchinson (2008) to model the 2-D soil-footing interaction using discrete nonlinear "q-z simple springs" that are available in the open source finite element platform, OpenSees. Following the recommendations of Harden et al. (2005), the representation of the Nonlinear Winkler foundation in 2-D application was developed based on the instruction of FEMA-356 (2000). Figure 8 shows an array of springs non-uniformly distributed along the footing base. There exist two different zones, end and mid zones, where the stiffness of each nonlinear spring is related to the stiffness per unit length recommended by FEMA-356 (2000).

Previous centrifuge test data are also used to validate the applicability of this "spring" foundation model. In the constitutive level, individual springs are independent with nonlinear inelastic behavior modeled using various material models such as elastic-perfectly plastic, elastic-no tension, elastic-perfectly plastic gap material implemented in OpenSees, to best capture the real behaviors of foundation.

Currently, the spring model is being refined. Once the model in 2-D is verified by comparing the numerical results with the experimental data, the model will be extended to 3-D shown in Figure 9, to allow rocking in two directions. Similarly, the footing will be divided into zones with different unit area stiffness.

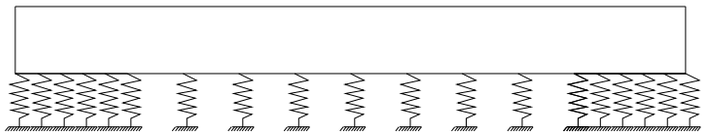


FIG. 8. Concept for distribution of springs for footing system in 2-D

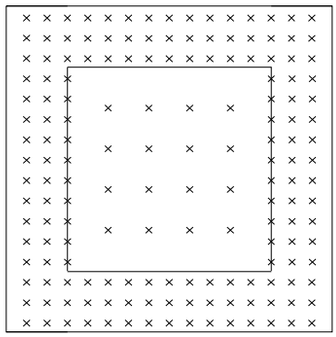


FIG. 9. Plan view of locations of nonlinear springs for footing system in 3-D

CONCLUSION AND FUTURE STUDIES

The performance of a soil-foundation-bridge system under seismic loading depends on the dynamic properties of the structure as well as the soil-foundation-structure interaction. The behavior of shallow foundation under seismic actions was investigated experimentally and numerically.

Preliminary analyses compared numerical results of shallow foundations with intentionally differing footing stiffness. It was shown that plastic rotation demands on columns decrease once the stiff foundation systems are replaced by more flexible systems.

Previous centrifuge model test data on bridge foundation were used to calibrate two numerical models: a contact interface model and nonlinear spring model. The former model, soilFootingSection2d, was proven to be able to roughly capture physical behaviors of footing in rotation, sliding and settlement even though there were slight discrepancies in between the observed and predicted moment capacities and ultimate settlements. This model is currently limited to 2-D conditions. A 2-D nonlinear inelastic spring model is being developed following guidelines described by Harden et al. (2005). Once it is calibrated by the physical data, it can be extended to 3-D which will be used in the nonlinear response history analyses of bridges under two horizontal components of ground motions. Various numerical models will be assigned to the springs representing the soil-footing systems. Physical model of the foundation system that will emulate the numerical model which optimizes the seismic behavior of the bridge will be developed and tested. A guideline to be used in the design process of innovative foundation systems will be developed.

ACKNOWLEDGMENTS

The authors would like to appreciate the financial support of Caltrans under Contract No. 59A0575 with the title: “Innovative Economical Foundations with Improved Performance that is Less Sensitive to Site Conditions”. Financial support of Caltrans under the project “STAP 13: Design Guidelines for Foundation Rocking of Bridge Piers” is also greatly appreciated.

REFERENCES

California Department of Transportation (Caltrans, 2006). "Seismic Design Criteria."

Federal Emergency Management Agency (FEMA-356, 2000). "Prestandard and Commentary for the Seismic Rehabilitation of Buildings."

Gajan, S. (2006). "Physical and numerical modeling of nonlinear cyclic load-deformation behavior of shallow foundations supporting rocking shear walls", Ph.D. Dissertation, College of Engineering, University of California, Davis.

Gajan, S., Kutter, B. L., and Thomas, J. (2005). "Physical and numerical modeling of cyclic moment-rotation behavior of shallow foundations." *Proc. 10th Intl. Conf. Soil Mechanics and Geotechnical Engineering*, Osaka, Japan.

Harden, C., Hutchinson, T., Martin, G. R., Kutter, B. L. (2005). "Numerical Modeling of the Nonlinear Cyclic Response of Shallow Foundations." *PEER Report 2005/04, Pacific Earthquake Engineering Research Center*.

Raychowdhury, P., and Hutchinson, T. (2008). "Nonlinear Material Models for Winkler-based Shallow Foundation Response Evaluation." GeoCongress 2008: The Challenge of Sustainability in the Geoenvironment, New Orleans, LA (accepted).

Ugalde, J. A., Kutter, B. L., Jeremic, B. (2007-a). "Soil-Foundation-Structure Interaction: Shallow Foundations". *Centrifuge Data Report for the JAU01 Test Series*. Center for Geotechnical Modeling Data Report UCD/CGMDR-03/06

Ugalde, J. A., Kutter, B. L., Jeremic, B., Gajan, S. (2007-b). "Centrifuge modeling of rocking behavior of bridges on shallow foundations". *Proc. 4th Intl. Conf. Earthquake Geotechnical Engineering*, Athens, Greece.

This page intentionally left blank

Factors that Affect the Performance of Bridge Foundations Undergoing Liquefaction-Induced Lateral Spreading

Christian Ledezma[1], Ph.D. and Jonathan D. Bray[2], F. ASCE, Ph.D., P.E.

[1] Assistant Professor, Dept. of Structural and Geotechnical Engineering, Pontificia Universidad Católica de Chile, Vicuña Mackenna 4860, Macul, Santiago, Chile. E-mail: ledezma@ing.puc.cl
[2] Professor, Dept. of Civil and Environ. Engineering, University of California, Berkeley, CA 94720-1710. E-mail: bray@ce.berkeley.edu

ABSTRACT: Liquefaction-induced lateral spreading has caused major damage to bridge structures in past earthquakes. Lateral spreading may cause large lateral deformations at the abutments, which may induce large forces in the foundation, superstructure, and connections, leading to severe damage or even the collapse of bridge structures. The post-earthquake condition of a bridge structure is strongly related to the level of residual lateral displacement of the pile caps and abutments in the longitudinal direction, and several factors may affect this level of residual deformation. In this paper, the relative importance of several key factors is evaluated through the use of a realistic design example. Results suggest that the most influential parameters in this problem are the characteristics of the ground motion in terms of its spectral acceleration at the degraded period of the potential sliding mass, followed by the post-liquefaction residual undrained shear strength of the potentially liquefiable material, and the error term in the estimation of the residual lateral displacements induced by lateral spreading.

INTRODUCTION

Past earthquakes have shown that pile foundations can be vulnerable to liquefaction-induced ground failures. In cases where the post-liquefaction static factor of safety is less than one, flow slides may occur and induce large lateral and vertical deformations causing extensive damage. The Showa Bridge, for example, failed catastrophically in part due to liquefaction-induced lateral spreading produced by the 1964 Niigata, Japan Earthquake, where spread during the earthquake caused displacements towards the Shinano River of as much as 10 m (Finn 2005). Compressional forces in the structure, additional shear forces in connections, and significant relative ground displacements across the supporting piles, which induce large bending moments, may all result due to lateral spreading. Each of these additional loads may lead to severe damage or collapse of structures. Even if flow slides do not occur, earthquake-induced seismic displacements of the ground may

progressively develop and damage piles and the overlying structure.

When liquefaction-induced displacements threaten the performance of an engineered structure, soil remediation techniques may be considered to minimize the expected damage. These techniques usually involve ground modification, ground improvement, or stabilizing measures that significantly reduce the liquefaction hazard or reduce the level of ground deformations to an acceptable level. However, mitigation may be difficult and costly at some sites, and it may not be necessary if the structure's foundation piles can be designed to withstand the displacement and forces induced by the lateral spreading. Moreover, if the foundation piles can be designed to "pin" the upper layer of soil, that would normally spread atop the liquefied layer below it, into the stronger soils below the liquefiable soil layer, then other ground remediation techniques may not be required to achieve satisfactory performance. This technique has been coined the "pile-pinning" effect, which is illustrated in Figure 1.

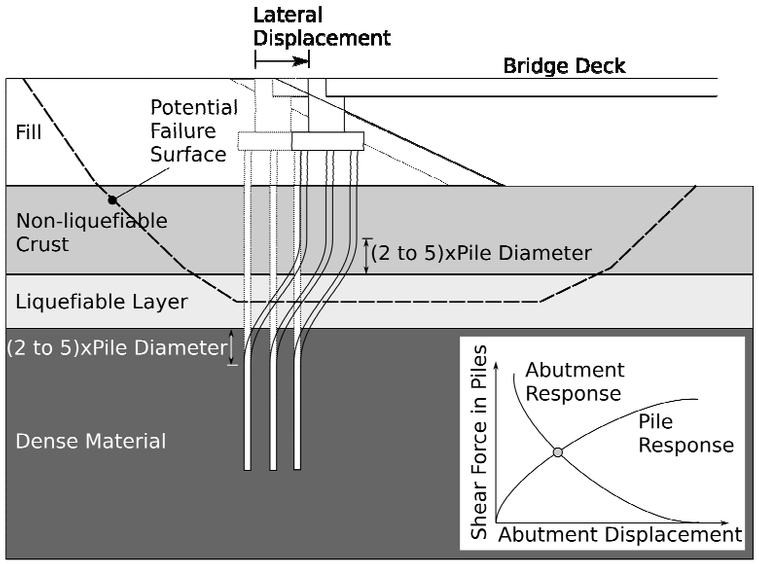


FIG. 1. "Pile-pinning" effect for the case of piles that are locked into to both the soil above and below the liquefiable soil layer

The pile pinning effect is now recognized as a legitimate remediation option when bridge or wharf structures built on pile foundations are located in areas susceptible to liquefaction-induced laterally spreading (e.g., Martin and Lam 2000, Martin et al. 2002). Work by Martin and others led to the development of a simplified design procedure for evaluating the effects of liquefaction-induced lateral spreads as proposed in the recommended seismic design document of bridges published by the Multidisciplinary Center for Earthquake Engineering Research (MCEER) and the Applied Technology Council (ATC) (ATC/MCEER Joint Venture, 2003).

Based on the MCEER/ATC methodology, Ledezma and Bray (2007) developed a simplified probabilistic procedure for evaluating the seismic performance of pile-supported bridges that are subjected to liquefaction-induced lateral spreading. This procedure formally incorporates the "pile-pinning" effect. Moreover, the uncertainty in parameters such as the SPT blow counts, the residual undrained shear strength of the critical liquefied soil layer, the distance between points of fixity of the piles, and

the probability of occurrence of liquefaction was also incorporated in their procedure so that the uncertainty involved in each of these important parameters could be incorporated in the overall seismic evaluation of the engineered system.

In this paper, a realistic example of a bridge structure that is founded on potentially liquefiable soil is used to illustrate the application of the Ledezma and Bray (2007) procedure to identify those factors that most affect the seismic performance of the bridge. A summary of the main results and characteristics of the bridge example is presented in the next section.

BRIDGE EXAMPLE

Figures 2 to 4 show some of the characteristics of the bridge. Figure 5 and Table 1 present the primary results of the application of the procedure proposed by Ledezma and Bray (2007), considering that the seismically induced permanent longitudinal lateral deformation of the piles is the governing engineering demand parameter and the proper index of the overall seismic performance of the bridge foundation. The vertical axis in Figure 5 indicates the probability of exceeding a lateral displacement threshold, $P(D > d)$, given an intensity of the ground motion (IM), and the occurrence (or not) of liquefaction. In Table 1, μ and σ denote the mean and standard deviation of the estimated repair cost ratios.

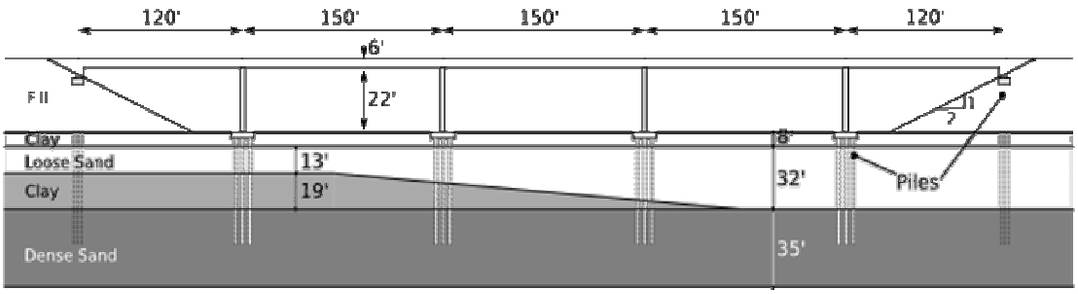
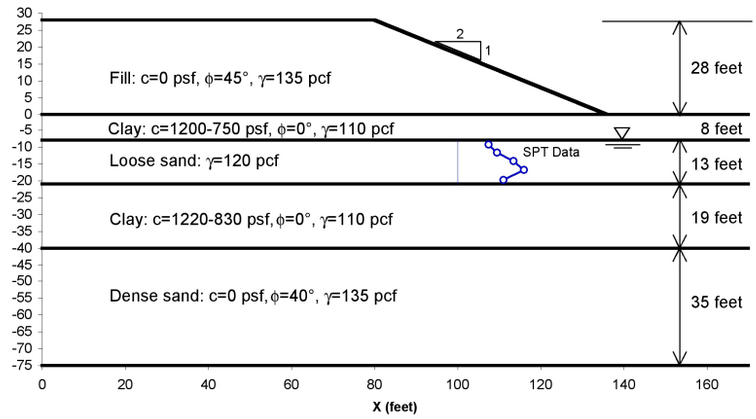


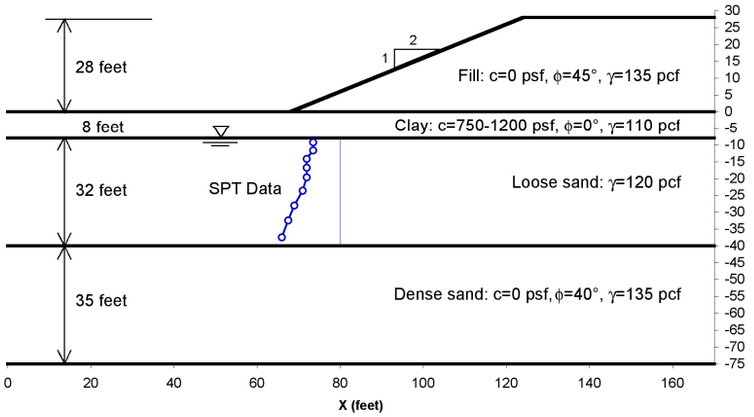
FIG. 2. Example bridge profile



SPT Data

Depth (feet)	N1,60-CS
9.3	15
11.7	19
14.2	27
16.8	32
19.7	22

FIG. 3. Left abutment – soil profile and dimensions (not to scale)



SPT Data

Depth (feet)	N1,60-CS
9.3	13
11.7	13
14.2	16
16.8	16
19.7	16
23.6	18
28.0	22
32.5	25
37.5	28

FIG. 4. Right abutment – soil profile and dimensions (not to scale)

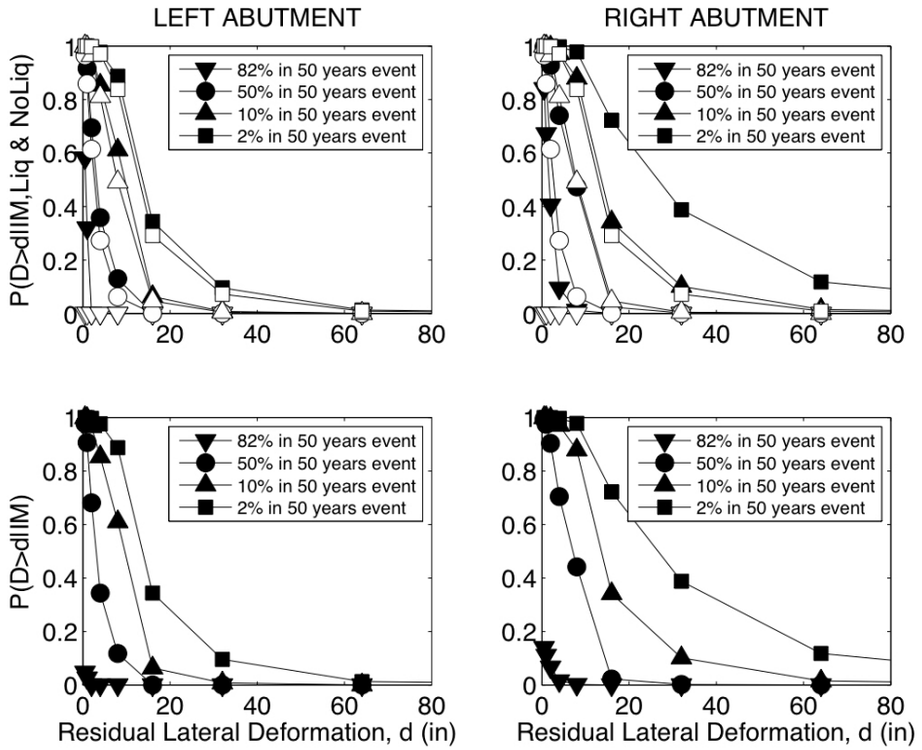


FIG. 5. Probability of exceeding an abutment (pile cap) lateral displacement threshold for different hazard levels

Table 1. Expected Repair Cost Ratios using First Order Reliability Method

	Left Abutment				Right Abutment			
	Probability of Exceedence in 50 years				Probability of Exceedence in 50 years			
	82%	50%	10%	2%	82%	50%	10%	2%
μ	0	0.03	0.11	0.21	0	0.08	0.21	0.37
σ	0	0.05	0.10	0.19	0.01	0.07	0.19	0.22

METHODOLOGY

The Pacific Earthquake Engineering Research (PEER) Center Performance-Based Earthquake Engineering (PBEE) approach can provide important insights through de-aggregation of the results to identify those components that impact the results most significantly. Additionally, sensitivity analyses may be performed that provide information about the relative importance of the random variables and the sensitivities of the first-order approximation of the failure probability with respect to parameters in the probability distributions. The First Order Reliability Method provides a useful set of importance and sensitivity measures. In this paper, seven random variables were considered in the estimation of the probability of exceeding a specified level of displacement for a given intensity measure. The random variables that were considered are: S_{ur}, the residual undrained shear strength of the liquefied material; α, the distance to the points of fixity of the piles expressed as number of pile diameters; ε, the error term in the estimation of the residual lateral displacement from the model by Bray and Travasarou (2007); T_s, the initial fundamental period of the potential sliding mass; Sa, the 5% damped spectral acceleration at $1.5T_s$, where spectral acceleration is defined as the maximum response (acceleration) of a damped, elastic, single-degree-of-freedom oscillator with a specific natural period of vibration to a given ground motion; H, thickness of the liquefiable material; and P_a, the passive reaction of the embankment against the backwall.

The probability density function of the S_{ur}/σ_{vc}' ratio given a corrected Standard Penetration Test blow-count ($N_{1,60-CS}$) is assumed to be lognormal. Its mean and coefficient of variation were estimated by combining five of the most commonly used procedures to estimate the residual undrained shear strength of the liquefiable layer, S_{ur}: Seed and Harder (1990), Olson and Stark (2002), and Kramer (2007), and the two correlations— S_{ur} with $N_{1,60-CS}$, and S_{ur}/σ_{vc}' with $N_{1,60-CS}$ —proposed by Idriss and Boulanger (2007). The resulting mean and standard deviation (μ and σ) are:

$$\mu_{S_{ur}/\sigma_{vc}'} \approx \exp\left(\frac{\mu_{N_{1,60-CS}}}{8} - 3.5\right) \times \left(1 + \frac{\left(0.3\mu_{N_{1,60-CS}}\right)^2}{128}\right) \qquad (1)$$

$$\sigma_{S_{ur}/\sigma_{vc}'} \approx 0.4\mu_{S_{ur}/\sigma_{vc}'}$$

From the model by Bray and Travasarou (2007), the variable ε is a normally-distributed random variable with zero mean and standard deviation $\sigma = 0.66$. This means that, using this model, the ratio of predicted to measured displacements is generally in the range of 0.5:1 to 2:1, similar to the results by e.g., Youd et al. (2002). The parameter α is assumed to have a uniform distribution between 2 and 5, i.e., that the distance to the points of fixity above and below the liquefiable layer is between 2 and 5 pile diameters.

The uncertainty in the parameter T_s was estimated recalling that $T_s = c \cdot H / V_s$ (where c is a constant), and considering that the uncertainty in H is small. In that case, the first-order approximations for the mean and standard deviation of T_s are

$$\mu_{Ts} \approx \frac{cH}{\mu_{Vs}}$$
$$\sigma_{Ts} \approx \sqrt{\left(\left.\frac{dT_s}{dV_s}\right|_{\mu_{Vs}}\right)^2 \sigma_{Vs}^{\,2}} = \sqrt{\left(-\frac{cH}{\mu_{Vs}^{\,2}}\right)^2 \sigma_{Vs}^{\,2}} = \frac{cH}{\mu_{Vs}^{\,2}}\sigma_{Vs} \tag{2}$$

Then, the coefficient of variation of T_s would be

$$c.o.v.[T_s] = \frac{\sigma_{Ts}}{\mu_{Ts}} = \frac{cH}{\mu_{Vs}^{\,2}}\sigma_{Vs} \cdot \frac{\mu_{Vs}}{cH} = \frac{\sigma_{Vs}}{\mu_{Vs}} = c.o.v.[V_s] \tag{3}$$

This means that the coefficient of variation of T_s and V_s should be similar. According to Jones et al. (2002), the Electric Power Research Institute undertook an investigation of appropriate methods for estimating earthquake ground motion in eastern North America. This work, which involved numerous investigators, included extensive, high-quality field and laboratory testing of soils at more than 200 different sites. The measured shear wave velocities were shown to be log-normally distributed with $\sigma_{\ln V} = 0.39$. Then, for the analysis that follows, it is assumed that the coefficient of variation of T_s is 0.4.

The uncertainty in the value of the spectral acceleration at $1.5T_s$ (Sa) was estimated by averaging the error terms in the attenuation relationships by Chiou and Youngs (2006) and Campbell and Bozorgnia (2007) for periods between 0 and 1 second. The result was a coefficient of variation of about 0.6. The coefficient of variation of the variables H and P_a was assumed to be 0.3.

Table 2 summarizes the estimated characteristics of the seven random variables used in this section.

RESULTS

The order of importance of the random variables is identified by their relative contribution to the variance of the linearized limit-state function. This contribution is reflected in the unit vector $\underline{\hat{\gamma}}$ (Der Kiureghian, 1999), which, in our case, changes from hazard level to hazard level, and it is also different for each threshold level of lateral displacement. Figure 6 shows the absolute value of the terms in $\underline{\hat{\gamma}} = [\hat{\gamma}_i]$ for each level of displacement and hazard level. The most important random variable was Sa, for all hazard and displacement levels, i.e., an important fraction of the uncertainty involved in this problem is due to the uncertainty in the estimation of the intensity measure, which in this case is the spectral acceleration at the fundamental degraded period of vibration of the potential sliding mass. The parameters ε and S_{ur}

Table 2. Characteristics of the Random Variables

Random Variable	Description	Probability Density Function	Coefficient of Variation
S_{ur}	Residual undrained shear strength of the liquefied material	Log-normal	0.40
α	Distance to the points of fixity of the piles	Uniform	0.87
ε	Error term in the estimation of the residual lateral displacement	Normal	0.66 (Standard Deviation)
T_s	Initial fundamental period of the potential sliding mass	Log-normal	0.40
Sa	Spectral acceleration at $1.5T_s$.	Log-normal	0.60
H	Thickness of liquefiable material	Log-normal	0.30
P_a	Passive reaction against the abutment's backwall	Log-normal	0.30

were also important, i.e., the overall uncertainty was also affected by the uncertainty in the estimation of the residual lateral displacement given an intensity measure, and the residual undrained shear strength of the liquefiable material. For small lateral displacements, S_{ur} is more important than ε, while for larger displacements the opposite is true. Lastly, Figure 6 shows that for all cases the importance of the parameters α, T_s, H, and P_a was rather small.

The sensitivity of the "failure" probability, i.e., the probability of exceeding a displacement threshold, $p_f = P(D > d)$, to variations in the distribution parameters of the random variables can be quantified through the vectors $\underline{\delta}$ and $\underline{\eta}$ (Der Kiureghian, 1999). Vectors $\underline{\delta}$ and $\underline{\eta}$ indicate the sensitivity of p_f to variations in the mean and the standard deviation of the random variables, respectively, i.e., the *i*-th term in the vector $\underline{\delta}$ is related to $\partial p_f / d\mu_i$, where μ_i is the mean of the *i*-th random variable, and the *i*-th term in the vector $\underline{\eta}$ is related to $\partial p_f / d\sigma_i$, where σ_i is the standard deviation of the *i*-th random variable.

To facilitate the comparison, the vectors $\underline{\delta}$ and $\underline{\eta}$ were normalized to have a unit length. Figures 7 and 8 show the absolute value of the terms in the normalized vectors $\underline{\hat{\delta}}$ and $\underline{\hat{\eta}}$, respectively, for each level of displacement and hazard level. The probability $p_f = P(D > d)$ is most sensitive to the parameters (mean or standard deviation) of the variables Sa, ε, and S_{ur}, and least sensitive to the parameters of the variables α, T_s, H, or P_a. For small to moderate displacements, $P(D > d)$ was more sensitive to variations in the mean of Sa than to the mean of the other parameters; but for large displacement, variations in the mean of ε and S_{ur} had an important effect on $P(D > d)$.

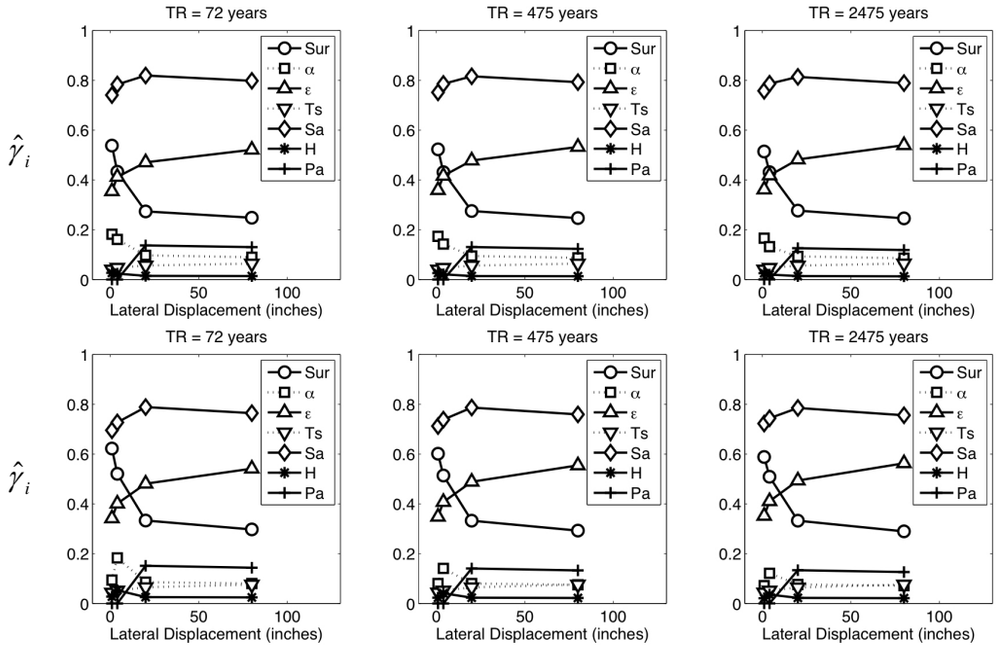


FIG. 6. Relative importance of the random variables for different hazard and displacement levels. Upper and lower figures correspond to the results for the left and right abutments, respectively.

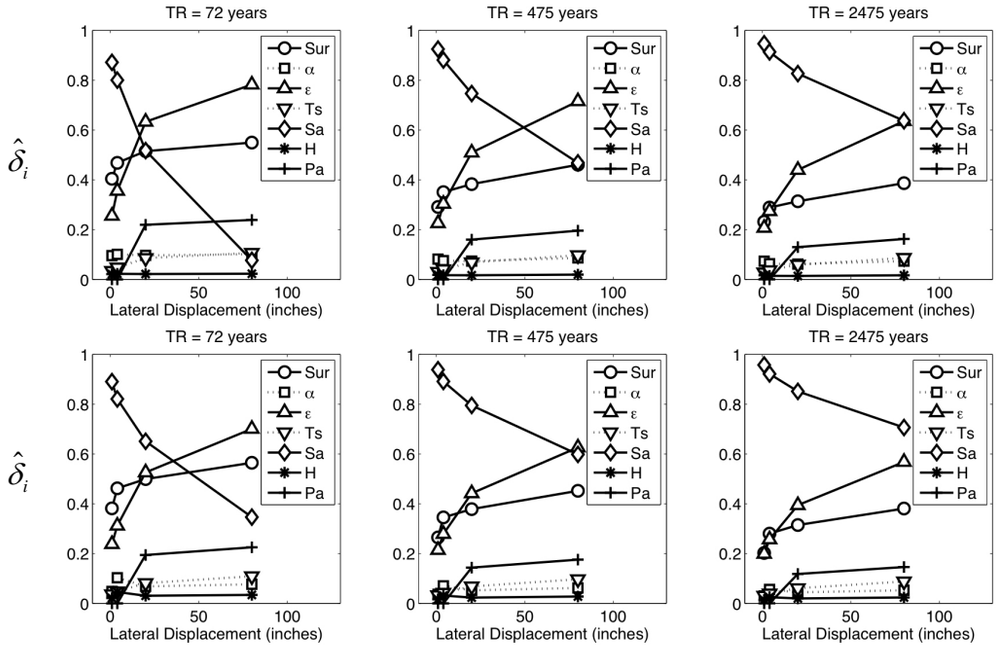


FIG. 7. Normalized relative sensitivity ($\hat{\underline{\delta}}$) of the probability $p_f = P(D > d)$ to variations in the mean of the random variables for different hazard and displacement levels. Upper and lower figures correspond to the results for the left and right abutments, respectively.

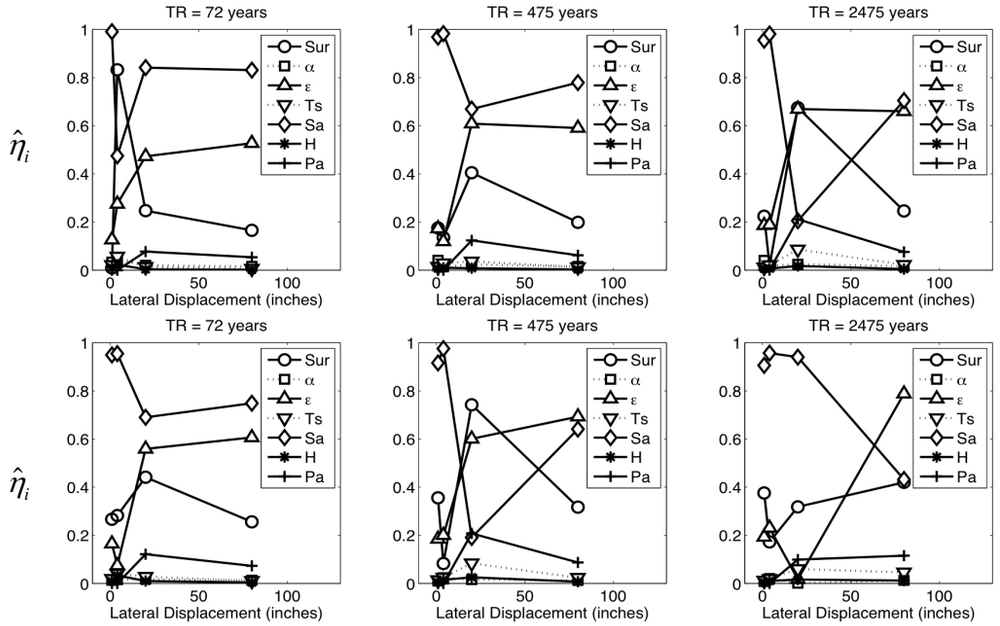


FIG. 8. Normalized relative sensitivity ($\hat{\eta}$) of the probability $p_f = P(D > d)$ to variations in the standard deviation of the random variables for different hazard and displacement levels. Upper and bottom figures correspond to the results for the left and right abutments, respectively.

The previous results show that the most relevant parameters in the estimation of the residual lateral displacement are Sa, ε, and S_{ur}. The effect of these random variables on the estimation of bridge repair cost ratios or downtimes was also assessed. Each variable was scaled up and down one standard deviation, and their effect on the mean estimates of these decision variables (DVs) was recorded. The result was that all three variables were almost equally important, i.e., each parameter had essentially the same effect on the estimated DVs, however, Sa and ε had a slightly larger influence on the estimated decision variables for higher hazard levels.

CONCLUSIONS

The post-earthquake condition of a bridge structure is strongly related to the level of residual lateral displacement of the pile caps and abutments in the longitudinal direction (a pile cap is a concrete block cast on the head of a pile, or a group of piles, to transmit the load from the structure to the pile or group of piles). Several factors affect the residual deformation, and the relative importance of these factors was evaluated through the use of a realistic design example.

The results of this study indicate that the most influential parameters in this problem are the intensity of the ground motion (Sa), followed by the error term in the estimation of the residual lateral displacements induced by lateral spreading (ε), and the residual undrained shear strength of the liquefiable material (S_{ur}). The contribution of the other four variables to the overall uncertainty, and their effect on the calculated probability, is relatively small for the problem studied.

ACKNOWLEDGMENTS

This work was supported by the Earthquake Engineering Research Centers Program of the National Science Foundation under Award EEC-9701568 through the Pacific Earthquake Engineering Research Center under sub-award Project ID: 2422006. Any opinions expressed in this material are those of the authors. Discussions with Professor Armen Der Kiureghian of the UC Berkeley were invaluable.

REFERENCES

ATC/MCEER Joint Venture (2003). "MCEER/ATC-49-1, Liquefaction Study Report, Recommended LRFD Guidelines for the Seismic Design of Highway Bridges." NCHRP Project 12-49, FY '98.

Bray, J.D. and Travasarou, T. (2007) "Simplified Procedure for Estimating Earthquake-Induced Deviatoric Slope Displacements," J. of Geotech. and Geoenviron. Engrg., ASCE, April 2007, Vol. 133, No. 4, pp. 381-392.

Campbell, K.W. and Bozorgnia, Y. (2007). "Campbell-Bozorgnia NGA Ground Motion Relations for the Geometric Mean Horizontal Component of Peak and Spectral Ground Motion Parameters." Report PEER 2007/2, Richmond, CA.

Chiou, B.S.-J. and Youngs, Y. (2006). "Chiou and Youngs PEER-NGA Empirical Ground Motion Model for the Average Horizontal Component of Peak Acceleration and Pseudo-Spectral Acceleration for Spectral Periods of 0.01 to 10 Seconds." Interim Report for USGS Review.

Der Kiureghian, A. (1999) "Introduction to Structural Reliability." Class notes for CE229-Structural Reliability, Dept. of CEE, U. C. Berkeley, Spring.

Finn, W.D.L. (2005) "A Study of Piles during Earthquakes: Issues of Design and Analysis." Bulletin of Earthquake Engineering (2005) 3:141-234.

Idriss, I. M. and Boulanger, R. W. (2007). "SPT- and CPT-based Relationships for the Residual Shear Strength of Liquefied Soils." Earthquake Geotechnical Engineering, K. D. Pitilakis, ed., Springer, The Netherlands, 1-22.

Jones, A.L., Kramer, S.L., and Arduino P. (2002). "Estimation of Uncertainty in Geotechnical Properties for Performance-Based Earthquake Engineering." Report PEER 2002/16, Pacific EQ Engineering Research (PEER), Center, Richmond, CA.

Kramer, S. L. (2007) Personal Communication.

Ledezma C. and Bray J.D. (2007) "Probabilistic Design Procedure that includes Pile-Pinning for Bridge Foundations undergoing Liquefaction-Induced Lateral Spreading." Proc. 13th PanAmerican Conf. on SMGE, Venezuela, pp 136-142.

Martin, G.R. and Lam, I.P. (2000). "Earthquake Resistant Design of Foundations: Retrofit of Existing Foundations." Proc. Int. Conf. on Geotech. and Geol. Engrg., Melbourne, Vol. 1, pp. 1025-1047.

Martin, G.R., March, M.L., Anderson, D.G., Mayes, R.L., and Power, M.S. (2002). "Recommended Design Approach for Liquefaction Induced Lateral Spreads." Proc. 3rd Nat. Seis. Conf. Bridges and Highways, MCEER-02-SP04, Buffalo, N.Y.

Olson, S. M. and Stark, T. D. (2002). "Liquefied Strength Ratio from Liquefaction Flow Failure Case Histories," Can. Geotech. J. 39: 629–647.

Seed, R.B. and Harder, L.F. (1990). "SPT-based Analysis of Cyclic Pore Pressure Generation and Undrained Residual Strength." H B Seed Mem Sym, V2, 351-376.

Youd, T.L., Hansen, C.M., and Bartlett, S.F. (2002). "Revised MLR Equations for Prediction of Lateral Spread Displacement," JGGE, ASCE, V 128(12), 1007-1017.

Proposed Changes to AASHTO LRFD Bridge Design Specifications for the Seismic Design of Retaining Walls

Donald G. Anderson[1], M. ASCE, P.E.; Geoffrey R. Martin[2], M. ASCE, P. Eng.; I. P. Lam[3], M. ASCE. P.E., J.N. Wang[4], M. ASCE, P.E.

[1]Principal Geotechnical Engineer, CH2M HILL, 1100 112th Ave. NE, Bellevue, WA 98004, Donald.Anderson@ch2m.com
[2]Professor, Department of Civil and Environmental Engineering, University of Southern California, Los Angeles, CA 90089, geomar@usc.edu
[3]Principal, Earth Mechanics, Inc., 17660 Newhope Street, Suite E, Fountain Valley, CA 92708, p.lam@earthmech.com
[4]Senior Engineering Manager, Parsons Brinckerhoff, One Penn Plaza, New York, NY 10119, WangJ@pbworld.com

ABSTRACT

An AASHTO-sponsored project, NCHRP 12-70, was conducted to address current limitations and deficiencies in the methods being used within the AASHTO *LRFD Bridge Design Specifications* for the seismic design of retaining walls. The existing AASHTO Specifications use the Mononobe-Okabe (M-O) equations. Under certain combinations of ground motions and wall geometry, unrealistically high seismic active earth pressures are estimated. NCHRP 12-70 Project was conducted to address this and other limitations of the M-O equations for estimating seismic earth pressures. The project also considered seismic design requirements for slopes and embankments, and for buried structures.

The products of the project include (1) recommendations on ground motions to use, (2) an updated method for estimating permanent ground movement, (3) charts for including the effects of soil cohesion in seismic earth pressure calculations, and (4) a generalized limit-equilibrium approach for evaluating seismic active earth pressures. This paper provides a summary of the NCHRP 12-70 work with a focus on seismic ground motions and earth pressure evaluations.

INTRODUCTION

One of the needs faced by Department of Transportation (DOT) staff is a simple, consistent, and reliable approach that can be used for the seismic design of retaining walls. Seismic design methods are provided within the current AASHTO (American

Society of State Highway and Transportation Officials) *LRFD Bridge Design Specifications* (AASHTO, 2007) for the seismic design of retaining walls; however, the methods use the Mononobe-Okabe (M-O) equations. This approach has limitations for seismic active and passive earth pressure determination where ground motions are high, slopes above the wall are steep, or mixed soil conditions occur.

In the absence of simple, consistent, and reliable approaches, geotechnical designers use various methods to address uncertainties in current methods and the lack of guidance. These methods range from simple pseudo-static approaches to relative complex numerical modeling. Due to the lack of guidance designers make various assumptions regarding seismic accelerations, soil properties, and performance expectations for design. These assumptions often result in excessive conservatism and unnecessary expenditure of limited DOT funds.

AASHTO through its Highway Subcommittee on Bridges and Structures (HSCOBS T-3) recognized these current limitations and initiated a project to address these issues. The project was handled through a National Cooperative Highway Research Program (NCHRP) project, referred to as the NCHRP 12-70 Project. The objective of the NCHRP 12-70 Project included development of seismic analysis and design methods for retaining walls that address current limitations and uncertainties.

QUESTIONS FACED BY DESIGNERS

A number of questions are faced during the seismic design of retaining walls. These occur in three broad categories:

- What ground motions should be used? Common practice is to use values that range from the peak ground acceleration (PGA) to one-third the peak. An important follow-up question is whether the seismic coefficient used for design should change for certain classes of retaining walls. For example, is the same seismic coefficient used for the design of gravity walls as for anchored walls?
- What soil strengths should be used? Current AASHTO Specifications focus on the long-term strength of the soil, because the structure will be in place for 75 years or more. In contrast seismic loading is a short-term event.
- What methods of analysis should be used for the seismic evaluation? Clearly, for retaining wall design, the M-O equations are very attractive because of their apparent simplicity, but as noted above they have limitations.

Several other fundamental issues had to be considered in the NCHRP 12-70 Project. First, it was recognized that the characteristics of ground motions differ between the Western United States (WUS) and Central and Eastern United States (CEUS). Generally, the frequency content of earthquakes in the CEUS is higher, and this change affects the approach to design. Another fundamental issue is the appropriate load and resistance factors to use for seismic design. While reliability methods have been used to define load and resistance factors for the design of foundations subject to gravity loading, the appropriate factors to use for extreme-event design have not been addressed. The desire is to avoid introducing too much

additional conservatism into the seismic design. As a final consideration, the desire is to avoid conducting unnecessary seismic analyses in areas with low seismicity.

PROJECT DEVELOPMENTS

The NCHRP 12-70 Project initially focused its efforts in two areas, methods for determining ground motions and methods of analysis.

Ground Motions

The starting point for the ground motion development was the new AASHTO seismic hazard maps that were recently adopted by AASHTO. These maps provide PGA and spectral acceleration at short (S_s) and 1-second (S_1) periods for soft rock/firm soil conditions based on a 7% probability of occurrence in 75 years. From this starting point two areas of development were undertaken. The first involved quantifying the average ground motions behind the retaining structure, and the second involved updating methods for estimating permanent ground displacements.

Wave Scattering Effects

Most simplified methods of seismic analysis assume that the soil behind the retaining wall behaves as a rigid mass with all ground motions moving in phase. Although this assumption makes sense for short retaining walls, it is not likely the case for higher retaining walls. Fig. 1 illustrates this concept.

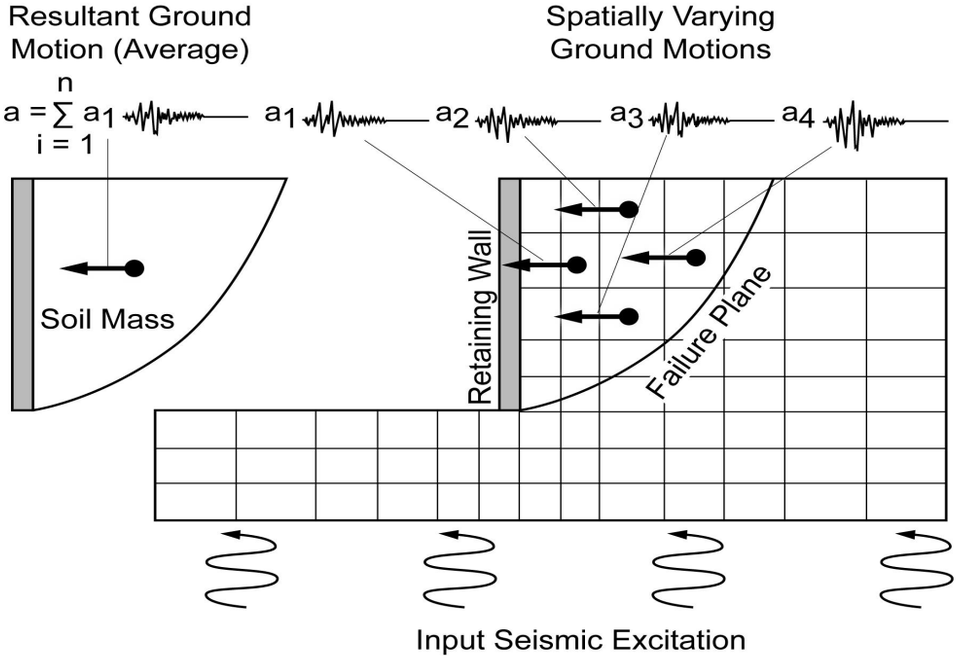


FIG. 1. Effects of Spatially Varying Ground Motions on Seismic Coefficient.

A series of numerical analyses were conducted for retaining wall configurations using the computer program QUAD 4M (UCD, 1994) to evaluate the wave coherency (or scattering) effect. The results of these analyses show that the average ground motion behind retaining walls is less than the peak ground motion, and this reduction changes with the characteristics of the ground motion and the height of the wall. Fig. 2 shows the form of this reduction. In this figure β, a parameter reflecting frequency characteristics of the ground motion, is defined as F_vS_1/PGA, where F_v is the Site Class factor for S_1.

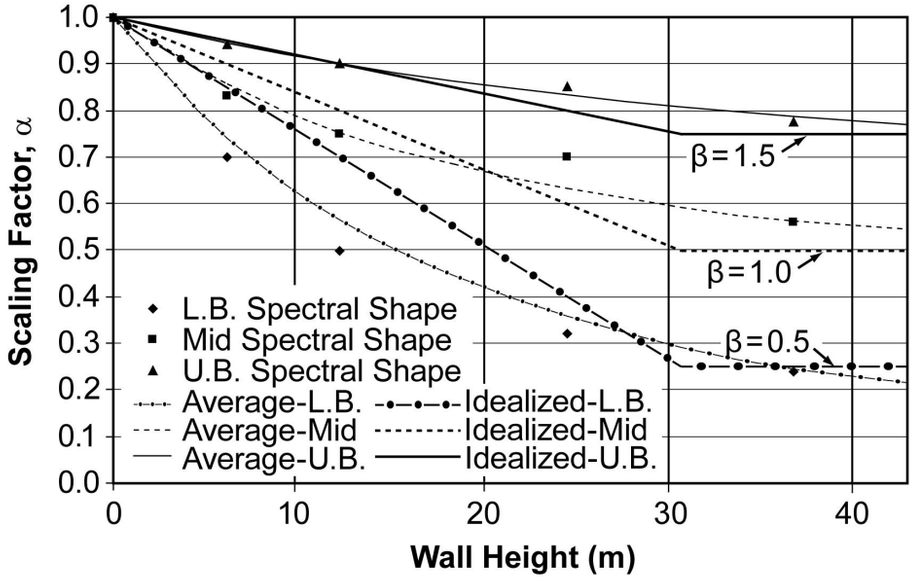


FIG. 2. Simplified Height-Dependent Scaling Factor (1 ft = 0.3 m).

For design purposes the curves shown in Fig. 2 can be defined by Eq. 1.

$$k_{av} = \alpha\, k_{max} \quad (1)$$

where k_{max} = PGA from the AASHTO maps (modified for Site Class) and α = height-dependent reduction factor. For AASHTO Site Classes C, D, and E foundation soils,

$$\alpha = 1 + 0.01H\,[(0.5\,\beta) - 1] \quad (2)$$

where H = fill height. For Site Class A and B foundation conditions (i.e., hard rock and soft rock), the α value is increased by 20 percent. For walls with a height of 6 m or less, an α value of 1.0 may be assumed; special studies are recommended for heights greater than 30 m.

Displacement Estimates

As part of the ground motion study, updated methods for estimating permanent displacements of retaining walls were developed following the Newmark sliding

block concept. This concept is the basis of the existing AASHTO Specifications that allow the peak seismic coefficient to be reduced by 50% if 10A inches of permanent movement are permissible, where A is the PGA adjusted for Site Class.

A database of over 1800 earthquake records was evaluated as part of the NCHRP 12-70 Project. Two equations were derived from this evaluation, one for soil sites in CEUS and WUS and another for CEUS rock sites. Fig. 3 shows the relationship between displacement (d) and the ratio of yield acceleration (k_y) to peak acceleration (k_{max}) for soil sites with PGV = 30 k_{max} (in/sec). This figure also shows the relationship found in the current AASHTO Specifications. The significant difference at $k_y/k_{max} < 0.1$ is attributed to the larger database used in NCHRP analyses. One of the conclusions from this analysis is that the common approach of using 50% of the PGA for design results in a permanent displacement estimate of less than 25 to 50 mm.

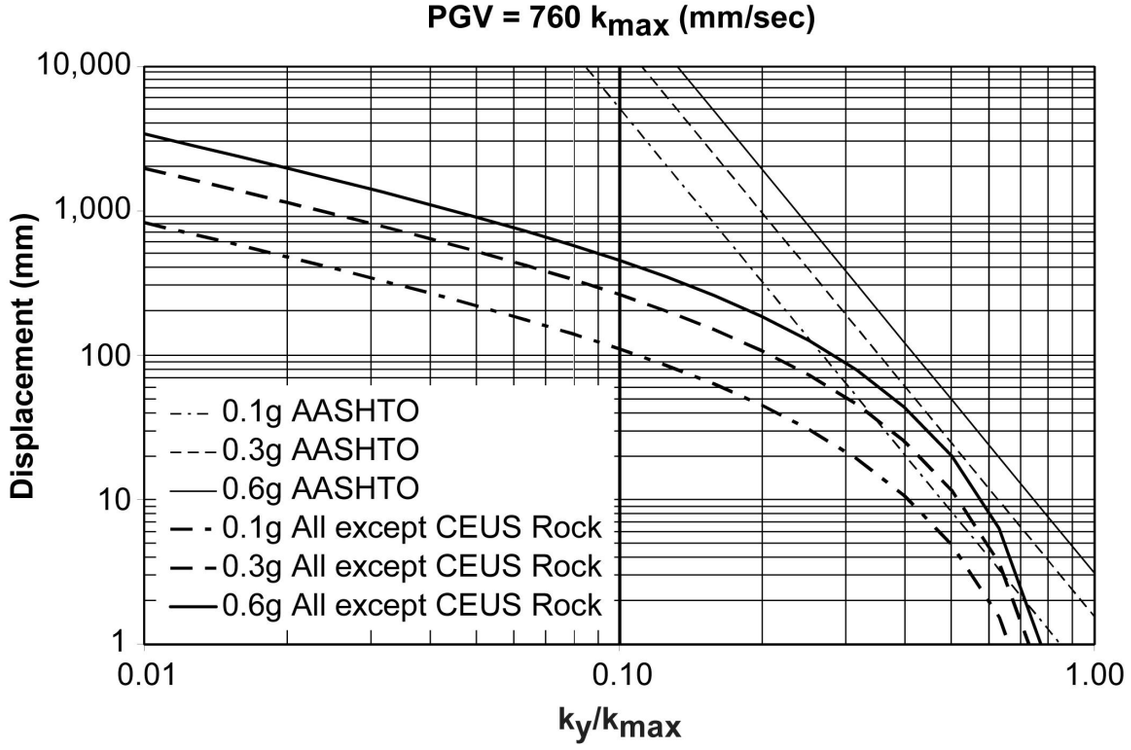


FIG. 3. Comparison between NCHRP 12-70 Results and Current AASHTO Correlations (1 inch = 25 mm).

Methods of Analysis for Retaining Walls

The second area of focus was on the computation of the seismic earth pressure to use for retaining wall design. Various wall types were considered in this evaluation, including rigid gravity and semi-gravity, nongravity cantilever, anchored, mechanically stabilized earth (MSE), prefabricated modular, and soil nail. The M-O equations formed the beginning point for the evaluation. This led to identification of more generalized approaches for seismic earth pressure determination.

M-O Equation for Active Earth Pressures

The M-O equation for active earth pressure assumes that a dry, homogeneous, cohesionless soil is located behind the wall. For these conditions the M-O equation provides a valid estimate of the seismic earth pressure. However, many retaining wall locations do not have these soil conditions. The other problem is that combinations of peak ground acceleration, soil friction angle, and backslope angle can result in an extremely high active earth pressure. In this case the failure angle of the Coulomb wedge becomes very flat, leading to very large inertial forces.

The assumption of cohesionless soil is a limitation in the M-O equation. If the soil behind the wall has a cohesive component, the seismic active earth pressure can be developed to include the cohesive component. Fig. 4 shows a chart that was developed to quantify this effect. The cohesive contribution in this chart has been normalized for the unit weight of the soil and the height of the wall (i.e., $c/\gamma H$). It can be observed that small amounts of cohesion result in a significant reduction in the seismic active earth pressure coefficient. Further background on this development is found in NCHRP (2008).

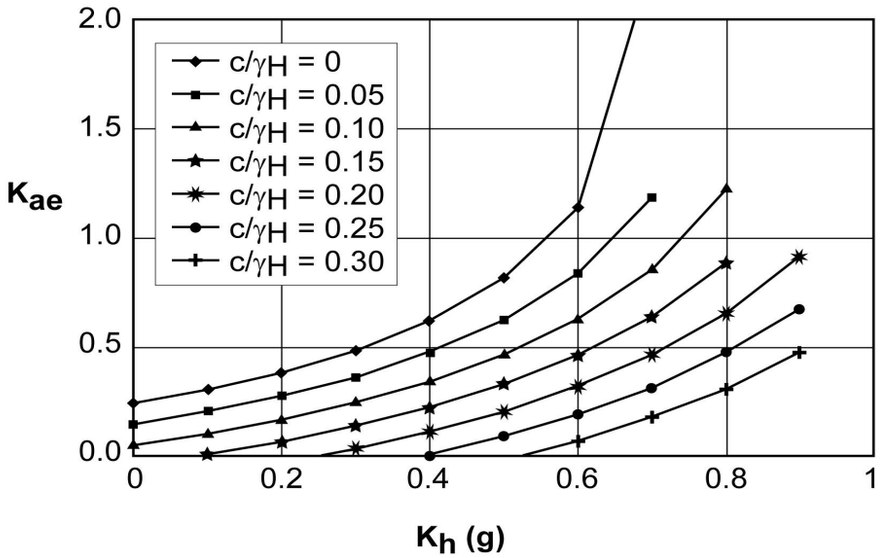


FIG. 4. Seismic Active Earth Pressure Coefficient Charts for c-ϕ Soils for ϕ = 35º.

Generalized Limit Equilibrium (GLE) Method

A more generalized approach can be taken for the evaluation of seismic active earth pressures. This approach involves use of a slope stability program to estimate the seismic earth pressure, as shown in Fig. 5. In this approach the seismic coefficient is input in the slope stability program, and failure surface for the maximum external resisting force P_{AE} determined. This maximum force defines the seismic active pressure for design. Both the location and the angle of P_{AE} can be varied when establishing the design pressure.

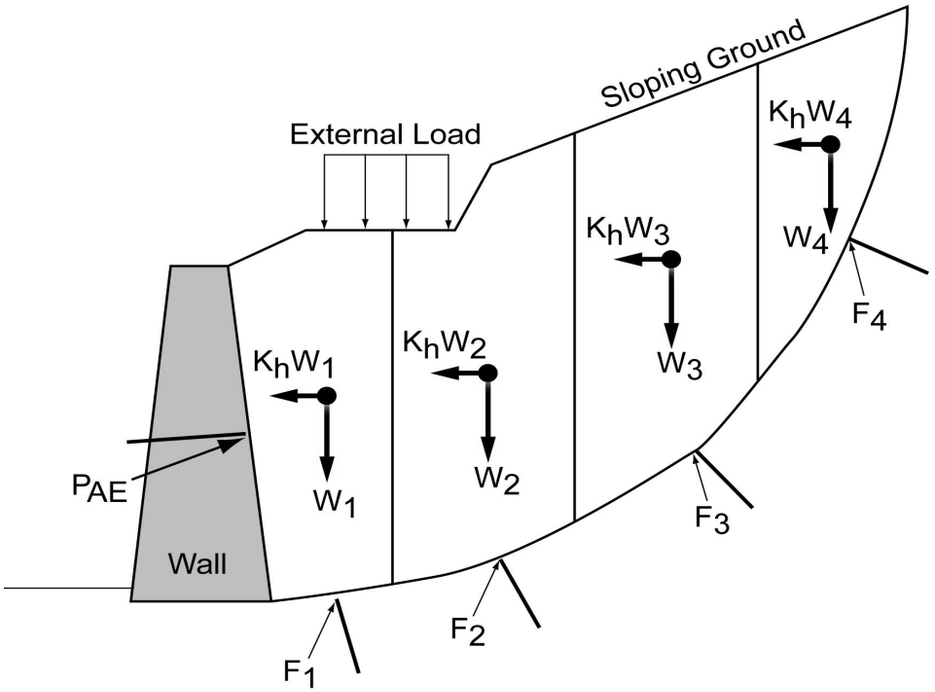


FIG. 5. Use of Slope Stability Program to Compute Seismic Earth Pressure.

This generalized method has several benefits. First, the layering and/or non-homogeneous soil behind the wall can be explicitly modeled. This ability is very important in cases where a steep cut slope in native soil or rock exists behind the wall with a granular drain material between the native material and wall. The seismic Coulomb failure surface for an active failure wedge in a homogeneous, cohesionless fill is often flatter than the slope used during construction for standard gravity, MSE, and prefabricated modular walls. This concept is shown in Fig. 6. Perhaps even more significant, cut slope walls constructed by top-down methods (e.g. nongravity cantilever, anchored, and soil nail walls) in soils that are layered and include cohesive and cohesionless materials can be modeled.

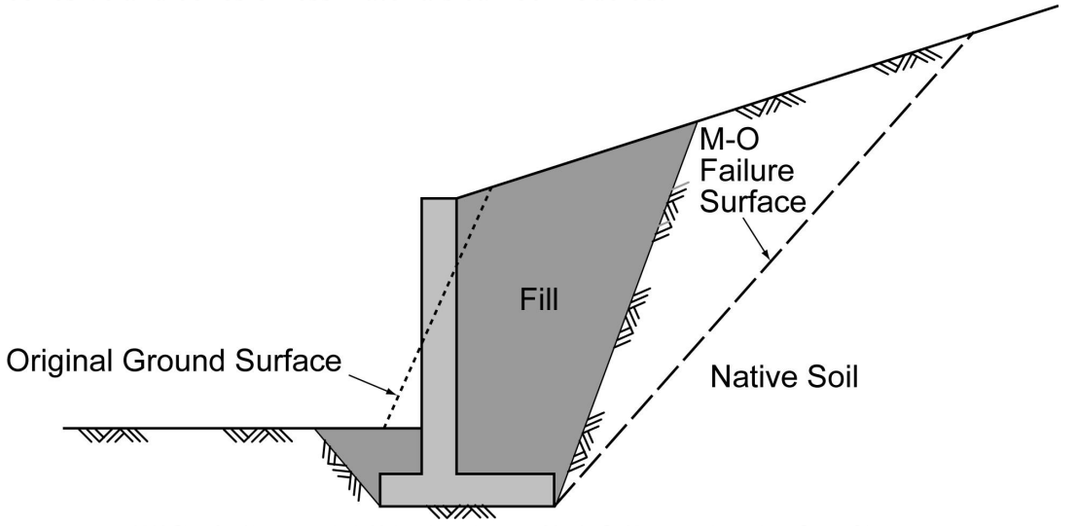


FIG. 6. Potential Limitation of M-O Equation in Cut Slopes.

Seismic Passive Earth Pressures

Seismic passive earth pressures also must be considered during the design of some semi-gravity cantilever walls, nongravity cantilever walls, and anchored walls. For these walls the passive earth pressure provides an important reaction to seismic demands. The most common procedure for estimating the seismic passive pressure involves the M-O equation for passive pressure, again because of its simplicity. However, since the M-O equation is based on a Coulomb failure wedge, this approach can overestimate the passive pressure.

The preferred approach for developing seismic passive earth pressures involves use of the log spiral method. For a more complete analysis, including inertial effects and soil cohesion, a procedure developed by Shamsabadi et al. (2007) is recommended. Fig. 7 illustrates one set of charts developed during the NCHRP 12-70 Project (NCHRP, 2007) using the Shamsabadi et al. method.

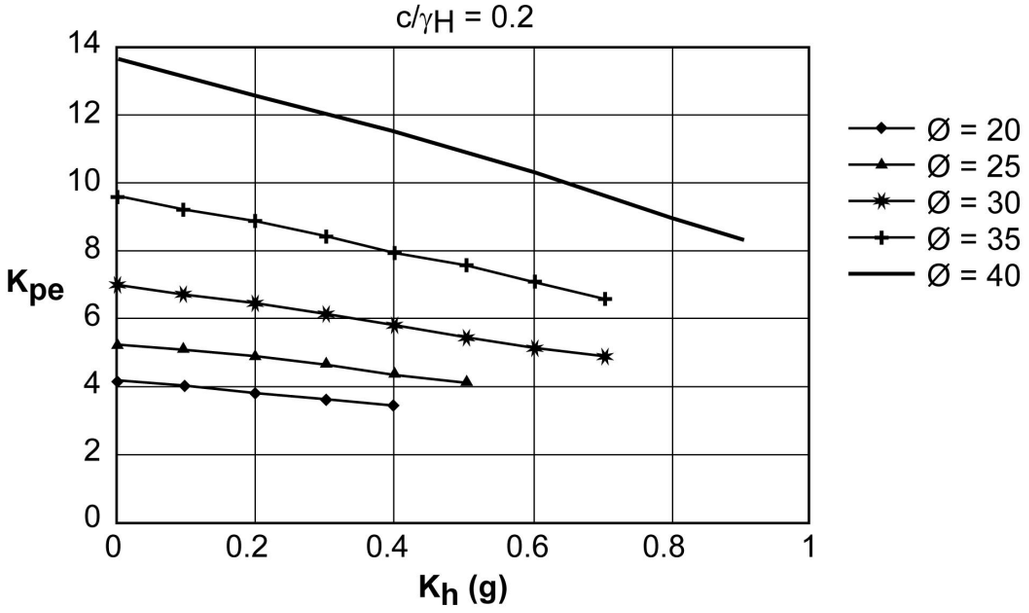


FIG. 7. Seismic Earth Pressure Coefficient based on Log Spiral Procedure (c = soil cohesion, γ = soil unit weight, and H = height).

DESIGN APPROACH

Procedures discussed above were developed into a design approach and documented in a set of proposed AASHTO Specifications. The proposed specifications are documented in the NCHRP 12-70 Project report (NCHRP, 2007). The proposed specifications use the current AASHTO Specifications as a starting point by requiring that the retaining wall be initially designed to meet non-seismic design requirements prior to checking seismic performance. The project report includes background for the specifications and example problems. The following discussions summarize two features of the proposed specifications.

Screening Methods

Screening methods were developed for deciding whether a seismic design check needs to be performed for an initial static loading design. The screening method for retaining walls is summarized in Table 1. If ground motions are below these levels, then there should be enough reserve capacity in the static design to handle seismic loads. The exception to the screening criteria shown in Table I is for sites where soils are liquefiable. For such locations the liquefaction potential should be established following procedures in the AASHTO Specifications.

Table 1. Screening Levels for Retaining Walls

Backslope Slope Angle Above Wall	PGA (g)
Flat	0.3
3:1	0.2
2:1	0.1

Load and Resistance Factors

The proposed specifications recommend that all load factors used for seismic design of retaining walls be set equal to 1.0. The use of a load factor of 1.0 recognizes that the demand from the seismic ground motion has a very low likelihood of occurrence – typically 0.001 annual events.

The resistance factor used for design will depend on whether force-based or displacement-based methods are used.

- Force-based design involves a conventional factor of safety approach, where the ratio of capacity to demand is evaluated. For this case a composite resistance factor combining individual resistance factors is used. For global stability the composite resistance factor is 1.0. For external stability of retaining walls (i.e., sliding, overturning, and bearing) the resistance factor will vary from 0.6 to 1.0, depending on wall type and mode of failure. Generally, for external stability sliding response is preferred to overturning and bearing failure in the case of gravity walls.
- Displacement-based design involves the estimation of displacements during the seismic event. If displacement-based methods are used, then the resistance factor should be set equal to 1.0. Uncertainties in the displacement analysis are accounted for by evaluating the effects of parametric variations.

CONCLUSIONS AND RECOMMENDATIONS

The work completed for the NCHRP 12-70 Project provides a systematic, rather simplified approach for evaluating the seismic response of retaining walls. This approach fits within the framework of the AASHTO Specifications, and it addresses problems with existing methods, particularly limitations of the M-O equations.

Overall the methodologies developed during the NCHRP 12-70 Project will need further testing for a wide range of design conditions as part of the implementation process.

A number of topics were identified during the NCHRP 12-70 Project that simply could not be adequately considered. Topics that require additional consideration include:

- Methods for determination of site amplification at sites characterized by shallow soil over rock and at sites that liquefy.
- Potential effects of shear banding on the development of seismic earth pressures.
- The soil mass to use for computing the internal stability of semi-gravity walls.
- The effective mass to use for evaluating reinforcement lengths in MSE walls.
- The potential for ground motion amplification for stiff nongravity cantilever or anchored walls.

Further research work involving both numerical studies and laboratory and field experimentation will be required to address the above issues. The final product of this research work needs to be design-oriented guidance suitable for use in AASHTO Specifications.

ACKNOWLEDGEMENTS

The opinions and conclusions expressed or implied in this paper are those of the authors. They are not necessarily those of the Transportation Research Board, the National Research Council, the Federal Highway Administration, the American Association of State Highway and Transportation Officials, or the individual states participating in the National Cooperative Highway Research Program.

REFERENCES

AASHTO (2007). *LRFD Bridge Design Specifications*, American Association of State Highway and Transportation Officials, 4th Edition.

ATC-MCEER (2003). "Recommended LRFD Guidelines for Seismic Design of Highway Bridges, Part 1 and 2," NCHRP 12-49, Multi-disciplinary Center for Earthquake Engineering Research/Applied Technology Council.

NCHRP (2008). "Seismic Analysis and Design of Retaining Walls, Slopes and Embankments, and Buried Structures," National Cooperative Highway Research Program, NCHRP 12-70, (in publication).

Shamsabadi. A., Rollins, K.M., and Kapuskar, M. (2007). "Nonlinear Soil-Abutment-Bridge Structure Interaction for Seismic Performance-Based Design," J. Geotechnical and Geoenvironmental Engrg. 133 (6): 707-720.

UCD (1994), "QUAD 4M: A Computer Program to Evaluate the Seismic Response of Soil Structures using Finite Element Procedures and Incorporating a Compliant Base," University of California, Davis.

Seismic Soil-Foundation Investigation of the Brooklyn Bridge

Yegian, M. K.[1], Arzoumanidis, S.[2], Kishore, K.[3], Patel, J.[3], Jain, S. K.[3], Strohman, B. P.[4], and Edwards, N.[2]

[1]Northeastern University, myegian@neu.edu, [2]Parsons Corp., [3]New York City Department of Transportation, [4]Simpson, Gumpertz, & Heger,

ABSTRACT: A comprehensive seismic investigation of the Brooklyn Bridge was completed to assess its potential retrofit needs. The Brooklyn Bridge, built in 1883, has become a national treasure and architectural and engineering marvel. To ensure that the seismic retrofit needs of the bridge were based on a rational framework, avoiding overconservatism that would potentially lead to unnecessary retrofit and impacting negatively on the architecture of the bridge, advanced engineering investigations of the condition of the bridge and its seismic response were made. Specifically, the seismic investigation of the main bridge was performed following two approaches, referred to as the **global** and **local analyses**. In the global analysis, the entire main bridge with its foundation caissons was modeled, and the effects of soil-foundation interaction were incorporate through the use of foundation impedances. In the local analysis, each bridge tower with its caisson and the surrounding soils was investigated with a model using solid finite difference and slip and gap interface elements. The local analyses of the towers were performed to confirm quality of the motions and foundation impedances used in the global analysis, and to ensure that the conclusions regarding the potential need for foundation retrofitting was realistic and essential. This paper presents the details of the two seismic evaluation approaches, and compares the bridge foundation responses from both analyses. It also demonstrates the benefits of local analysis in the seismic evaluation of long-span bridges.

INTRODUCTION

The Brooklyn Bridge is the oldest of the East River Bridges in New York City. When completed in 1883, it was the world's first steel suspension bridge and had a center span more than 40% longer than other bridges. A photograph of the bridge is shown in Figure 1. The Bridge has become one of world's most recognizable and nationally celebrated historic landmarks. A comprehensive seismic evaluation of the bridge was recently completed to assess the potential retrofit needs. The scope of the seismic investigations included the Manhattan and Brooklyn masonry and steel

approach structures, the ramps, and the main bridge. The main bridge is supported on massive cable anchorages and towers constructed of granite and limestone blocks.



Fig. 1 Photograph of the Brooklyn Bridge.

The main bridge has a center span of 1595.5 feet and side spans of 933 feet. The cable anchorages are founded on a 4 foot thick timber grillage constructed of 12 inch by 12 inch Southern Pine. The size of the grillage is 119.5 feet by 132 feet. Figure 2 shows elevations of the cable anchorages.

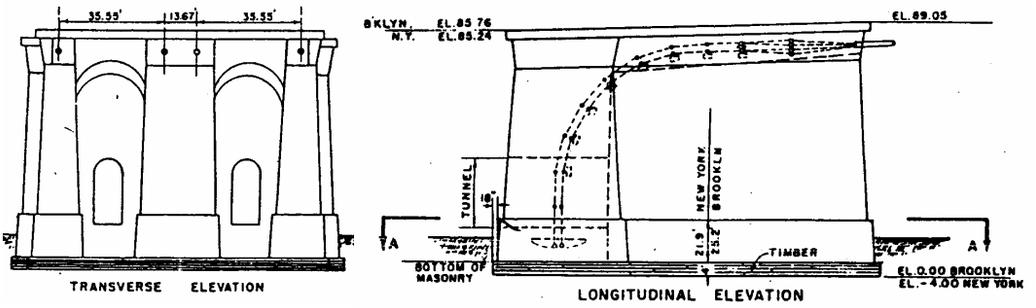


Fig. 2 Elevations of the Manhattan and Brooklyn Cable Anchorages.

The two towers of the Bridge are supported on caissons, which include a timber grillage 22 feet thick at the Manhattan Tower caisson, and 15 feet thick at the Brooklyn Tower caisson. Figure 3 shows elevations of the Manhattan and Brooklyn Towers. The Manhattan Tower caisson is entirely in the East River and is founded generally at elevation -78 feet on an approximately 7 foot thick layer of very dense gravel, cobbles, and boulders overlying bedrock. The Brooklyn Tower caisson is on land and there is a bulkhead that laterally holds 40 feet of fill adjacent to the tower foundation. The base of the caisson is at elevation -45 feet, in a sand and gravel layer, overlying a 30 foot thick till layer over bedrock. The bedrock at the tower locations is slightly weathered.

The Brooklyn Bridge is an unusual structure with foundations constructed of massive limestone blocks, unreinforced concrete, and timber grillage. Its seismic evaluation warranted the applications of the most advanced and rigorous engineering evaluations to ensure that the assessment of seismic retrofit is made on rational and realistic

scenarios, avoiding overconservatism that may lead to unnecessary retrofit and potential negative impact on the architecture of the bridge.

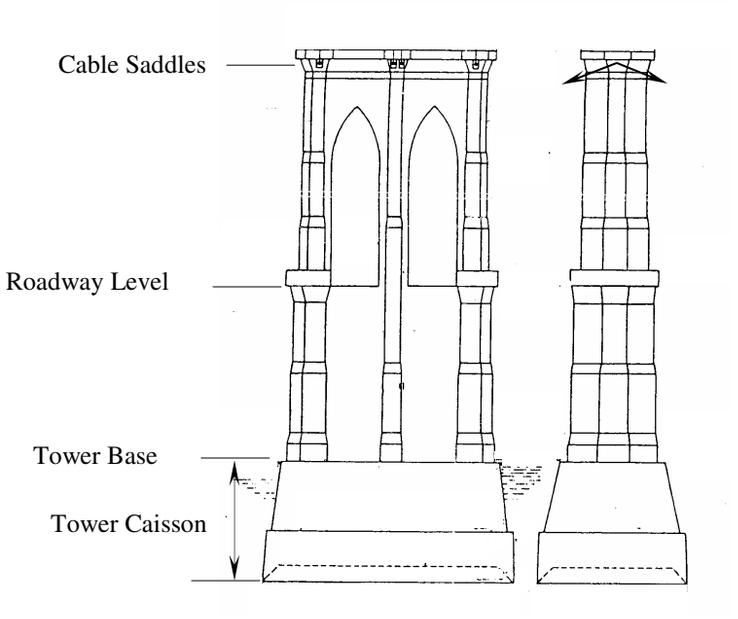


Fig. 3 Elevations of the Manhattan and Brooklyn Towers and their caissons.

This paper describes two advanced seismic analysis approaches that were utilized to assess the main bridge's retrofit needs. In the first approach, referred to as **global analysis**, the entire main bridge with its foundations was modeled in a single model in ADINA. Rigid elements were used to model the cable anchorages. The soil-caisson interaction was included through the use of foundation impedances. A spine model from beam elements and rigid links was used to represent the tower caissons. Non-linear springs with gap features along with dashpots represented the soil-structure interaction effects. Kinematic motions (motions influenced by the presence of the foundation caissons) were then applied to the foundation springs and dashpots. In the second approach, referred to as **local analysis**, each bridge tower, its caisson, and the surrounding soils were modeled in the computer program FLAC. In the analysis, the tower, caisson, and the soils were modeled using solid elements. The potential slip and gapping along the soil-caisson interfaces were modeled through the use of interface elements. The program uses the finite difference numerical technique to solve the static and dynamic response of the continuum consisting of the bridge tower, its caisson, and the surrounding soils. The purpose for using two soil-foundation-bridge interaction analysis approaches was to confirm the quality of the kinematic motions and foundation impedances, validate the analytical results from both models, and ensure that the final conclusions regarding the potential need for retrofitting, especially the bridge foundations are realistic and essential.

This paper presents descriptions of the global and local analysis approaches and demonstrates how these two analysis techniques complement each other in the seismic evaluation of the foundations of long span and critical bridges.

SOIL-FOUNDATION-BRIDGE ANALYSIS (GLOBAL ANALYSIS)

A global analysis of the bridge was performed using the computer program ADINA. The model of the bridge included the super- and sub-structures as well as foundation caisson elements. Figure 4 shows the global model of the bridge. The cable elements of the bridge were modeled with non-linear beam elements and the suspended structure and the towers with linear beam elements. Non-linear springs were included to account for cracking of the towers at specific locations. This cracking was identified using a detailed model from solid elements that was developed in the computer program ABACUS and the material properties of ANACAP-U material model 3 (2003). For the needs of the global analysis, the caissons were modeled in a manner that captured potential gapping and slipping along the caisson-soil interfaces.

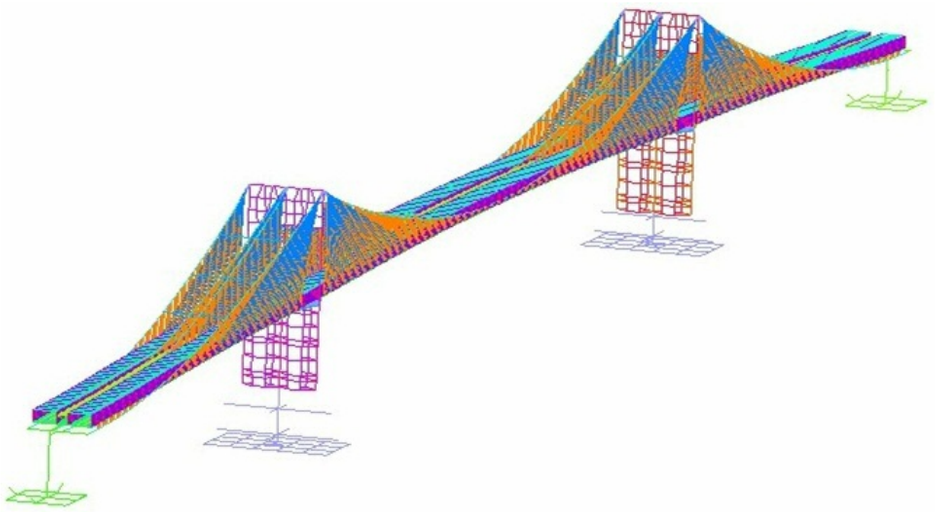


Fig. 4 Global analysis model of the Brooklyn Bridge.

The model consisted of three-dimensional elastic beam elements representing the spine of the caissons, rigid links, dashpots and truss elements with elasto-plastic hysteretic material properties and gapping features. In particular, the caisson base, which is a rigid surface 168 feet long by 102 feet wide, was modeled with rigid link elements and twenty-five non-linear truss elements in a configuration that facilitated the incorporation of the soil-caisson interaction at the base and calculation of peak soil stresses. This representation assumed rigid body motion of the base, which followed the deformations of the truss elements. The twenty-five elasto-plastic truss elements were connected at the other end to a rigid boundary surface, which was

excited by the ground motions. This model was supplemented by two traction elements, one for each horizontal direction, to simulate the friction behavior between the caisson base and the soil. The horizontal elements were similar to the twenty-five vertical elements except that they represented the behavior of the entire base.

The interaction between the caisson walls and surrounding soils was modeled in a similar fashion as the base of the caissons. Following the limits of the soil strata and caisson configuration, the vertical walls were divided into several zones. Outrigger rigid link elements were used from the centerline (spine) of the caissons to the walls and elasto-plastic truss elements with similar properties as those at the caissons' base. Traction elements with elasto-plastic multi-linear material properties were also used at each outrigger to represent friction in the tangential and vertical directions.

The geotechnical input to the global analysis consisted primarily of ground motions and foundation impedances. Extensive field geotechnical and geophysical testing programs were implemented to characterize the site conditions and obtain reliable estimates of the shear and compression wave velocities of the soils, bedrock, foundation timber grillage and limestone blocks.

Cable Anchorage Motions and Foundation Impedances

In the global model of the Bridge, the soil-foundation effects were incorporated through the use of distributed springs and dashpots. Figure 5 shows typical locations of the springs and dashpots for the Brooklyn Cable Anchorage. Similar springs and dashpots were used for the Manhattan Cable Anchorage.

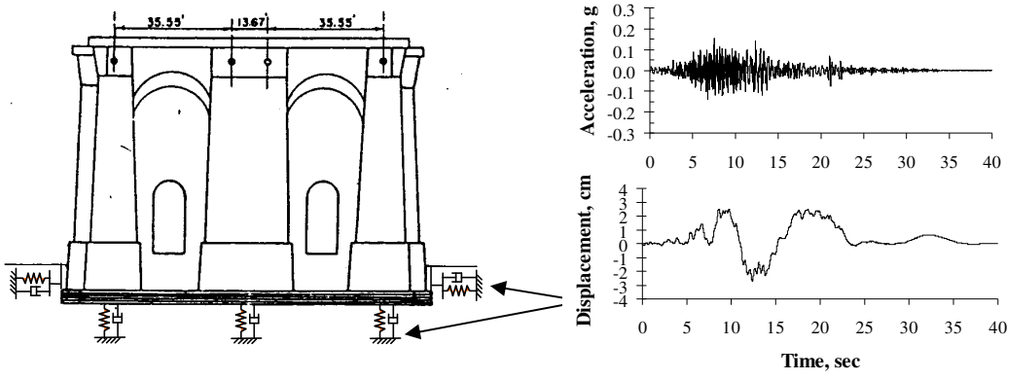


Fig. 5 Transverse elevation of the Brooklyn Cable Anchorage showing the locations of foundation springs and dashpots, and the kinematic displacement record used in the global analysis.

Springs and dashpots were placed at nine locations within the base and four locations along the sides of each anchorage. The kinematic motions of the anchorage that

needed to be applied at each of the spring and dashpot locations were computed using the computer program SASSI. Figure 6 shows the SASSI model of the Brooklyn Cable Anchorage.

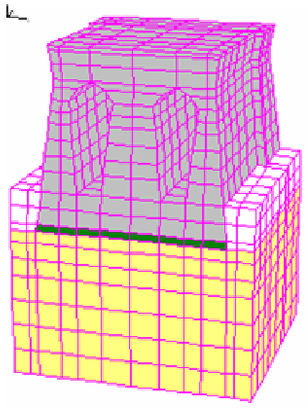


Fig. 6 SASSI model used in the kinematic motion and foundation impedance calculations for the Brooklyn Cable Anchorage.

Several rock motion time histories were selected from the set of records that the NYCDOT released in 2004 for analysis of its bridges. The appropriate records were selected and modified to represent the spatial variability of the motions and the rock condition at each of the bridge foundation locations. This paper presents motions corresponding to the 2500-year event.

The kinematic motions (motions ignoring the mass of the anchorage) at the base and along the sides of the cable anchorage were computed using the strain compatible shear moduli obtained from initial applications of one-dimensional site response analyses. To account for the effect of the spatial variability of the motions along the longitudinal axis of the bridge, the global analysis was performed using multi-support excitation, in which displacement time histories were specified at all foundation springs and dashpots, representing the interaction between foundations of the bridge and the soils. These displacement records for the cable anchorage caissons were obtained from the acceleration records calculated from SASSI after making the appropriate baseline corrections.

Figure 5 shows a typical displacement record that was specified in the global analysis at the base and sides of the Brooklyn Cable Anchorage. Similar records were computed for the Manhattan Cable Anchorage. Figure 7 shows a comparison of the response spectra of the motions at baserock, and at the bottom and sides of the Brooklyn Cable Anchorages.

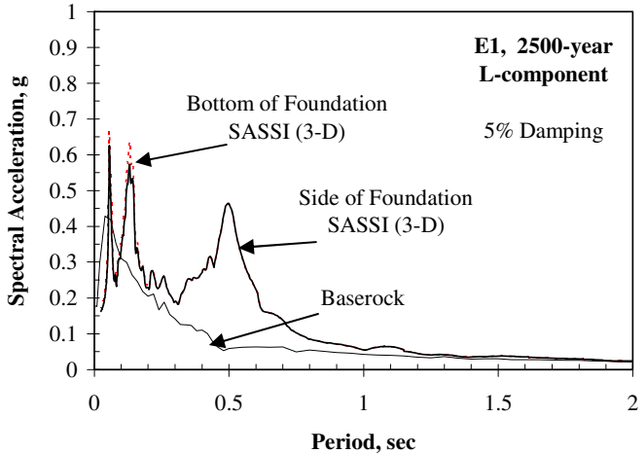


Fig. 7 Comparison of spectra of the bottom and sides of the Brooklyn Cable Anchorage foundation computed using three-dimensional SASSI analysis.

It is noted that the 37-ft thick stiff soil layer present below the caisson base has a large amplifying effect on the motion in the period range (0.47 seconds) of the stiff cable anchorage. Also, the motion along the side of the caisson is almost identical to that of the base, thus indicating that because of the large base dimensions of the caisson, it does not have a tendency to rock. Figure 8 shows comparisons of the spectra of the kinematic motions computed in the three-dimensional SASSI analysis with the spectra of the motions computed in the more conventional way of assuming a one–dimensional wave propagation (SHAKE analysis) without considering the presence of the caisson (free-field motion). As shown in Figure 8, clearly, the simplified one-dimensional analysis would have overestimated the intensity of the motion in the period range of the cable anchorage (0.47 seconds) by as much as 35%.

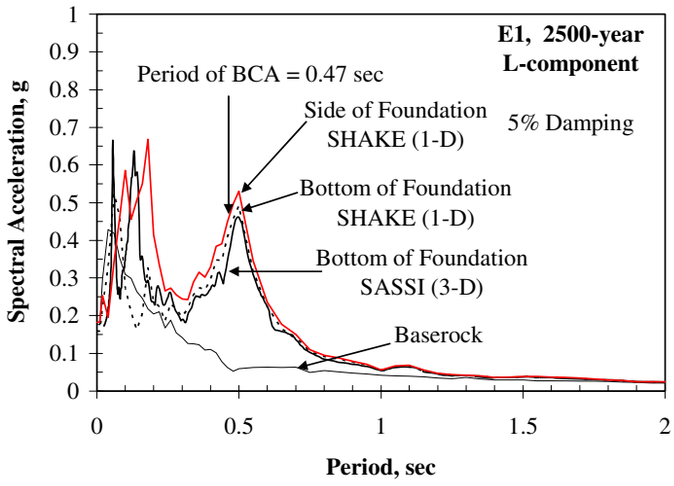


Fig. 8 Comparison of spectra from three-dimensional SASSI analysis with spectra obtained from one-dimensional SHAKE analysis.

The coefficients of the foundation springs and dashpots representing the soil-caisson interaction of the cable anchorages were computed using SASSI. The computed frequency-dependent stiffness coefficients in the longitudinal direction of the bridge for the Manhattan and Brooklyn Cable Anchorages are shown in Figure 9.

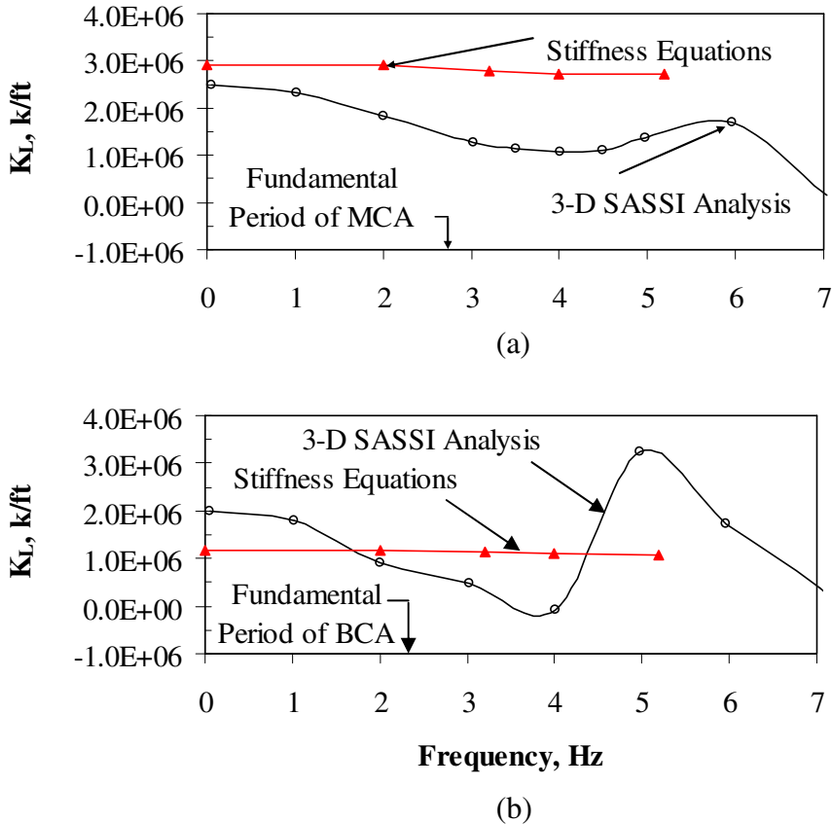


Fig. 9 Stiffness coefficients a) Manhattan Cable Anchorage, MCA, b) Brooklyn Cable Anchorage, BCA, obtained from SASSI, compared with stiffness coefficients obtained from stiffness equations for shallow foundations.

Included in Figure 9 are the stiffness coefficients computed based on simple stiffness equations for shallow foundations suggested by Gazetas (1991). Typically, within the frequency range of relevance to the anchorages (greater than 2 Hz), the simple equations overestimate the stiffness coefficients for the two cable anchorages. For example, the stiffness coefficient from the simple equations, for the Brooklyn Cable Anchorage with a fundamental period of 0.47 seconds (frequency of 2.2 Hz), is higher (by 60%) than the value computed from SASSI. This difference is not very large considering the approximations inherent in the formulations of the stiffness equations. However, because of the very stiff nature of the cable anchorage and the high frequency content of the earthquake motions, such overestimation of the stiffness would have resulted in the underestimation (by 40%) of the intensity of the

motion experienced in the global analysis at the Brooklyn Cable Anchorage location, as is shown in Figure 10.

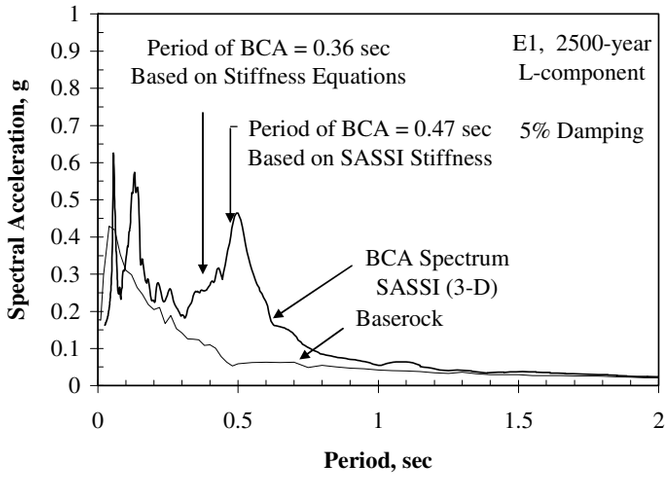


Fig. 10 Comparison of spectral accelerations for the Brooklyn Cable Anchorage computed based on stiffness coefficients from the three-dimensional SASSI analysis with stiffness coefficients from the equations for shallow foundations.

Through the comparisons made above, it is evident that simplified analysis procedures compared to more rigorous approaches may under- or over-estimate the dynamic responses of a structure depending on the characteristics of the soil and the foundation. Realistic estimates of seismic responses, especially for a critical structure such as the Brooklyn Bridge, warranted the application of advanced analytical procedures.

Table 1 presents a summary of the total stiffness and damping coefficients and damping ratios in the six modes of vibrations of the Brooklyn Cable Anchorage. These coefficients were then distributed to the nine springs and dashpots placed along the base and four along the sides of the caisson. The distribution of the total stiffness and damping coefficients to individual springs and dashpots was made by ensuring that the sum total horizontal and rocking stiffness and damping matched with the total values computed from SASSI. Note that because of large embedment of the Brooklyn Cable Anchorage caisson, the translational and torsional damping ratios are quite large due to radiational loss of energy away from the caisson. Similar calculations were made for the Manhattan Cable Anchorage caisson.

Table 1 Summary of SASSI soil-foundation dynamic impedances for the Brooklyn Cable Anchorage caisson.

Mode of Vibration	Approx. Natural Frequency, Hz.	Stiffness Coefficient K		Damping Coefficient C		Damping Ratio D
Longitudinal, L	2.3	K_L (k/ft)	8.0E+05	C_L (k-sec/ft)	4.2E+04	0.37
Transverse, T	2.3	K_T (k/ft)	8.0E+05	C_T (k-sec/ft)	4.2E+04	0.37
Vertical, V	3.8	K_V (k/ft)	2.2E+06	C_V (k-sec/ft)	4.6E+04	0.25
Rotation about L	3.3	K_{RL} (k-ft/rad)	6.0E+09	C_{RL} (k-ft-sec/rad)	4.8E+07	0.08
Rotation about T	3.4	K_{RT} (k-ft/rad)	7.0E+09	C_{RT} (k-ft-sec/rad)	7.0E+07	0.11
Rotation about V	4	K_{RV} (k-ft/rad)	5.0E+09	C_{RV} (k-ft-sec/rad)	2.6E+08	0.65

Tower Motions and Foundation Impedances

In the global analysis of the bridge, the soil-tower caisson interactions were considered through the use of springs and dashpots similar to those described for the Brooklyn Cable Anchorage. Figure 11 shows a longitudinal cross section of the Brooklyn Tower foundation depicting the locations of the springs and dashpots that were used in the global analysis model.

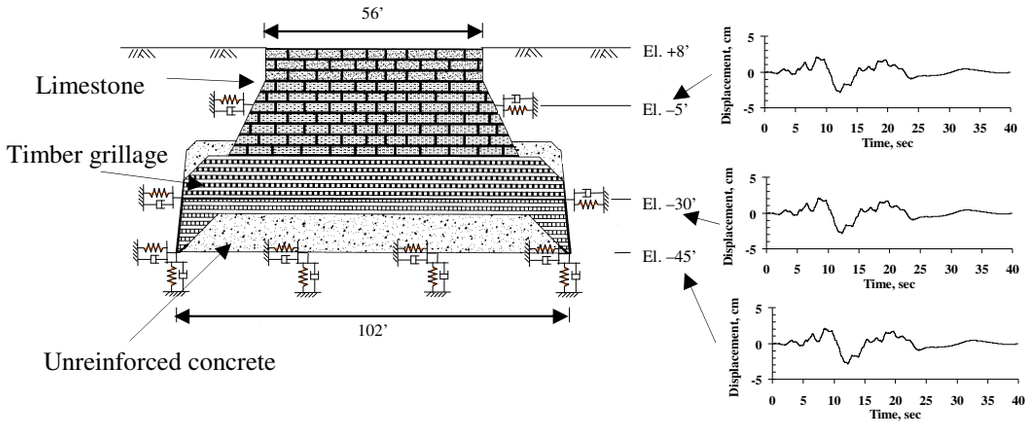


Fig. 11 Transverse elevation of the Brooklyn Tower foundation showing the locations of foundation springs and dashpots, and the kinematic displacement records used in the global analysis.

The kinematic motions applied at the locations of the springs were computed using the computer program FLAC. Figure 12 shows the FLAC model of the Brooklyn Tower foundation.

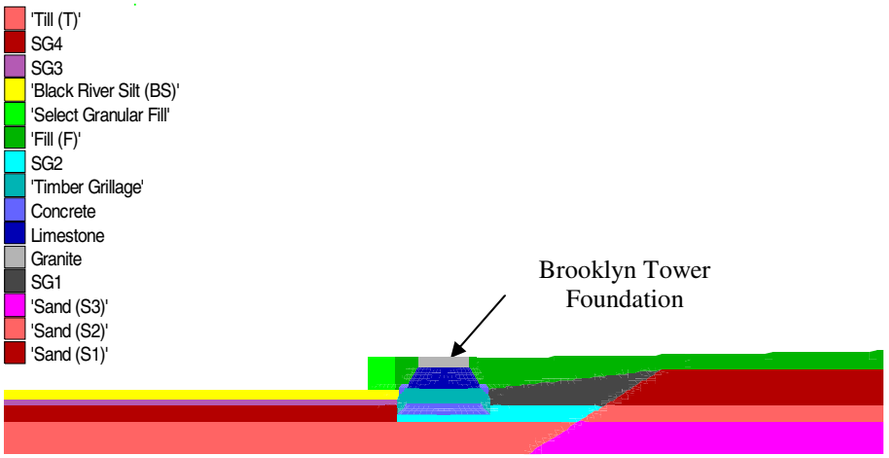


Fig. 12 FLAC model used to compute kinematic motions and impedances for the Brooklyn Tower foundation.

In the kinematic motion calculations, the foundation of the tower was given rigid properties and the mass of the structure was excluded. The baserock motion used in FLAC was computed using the rock outcrop motion appropriate for the Brooklyn Tower location and one-dimensional site response analysis. The dynamic soil-caisson interaction analysis performed by FLAC utilized a hysteretic soil model in which at every step of time integration, the soil moduli and damping ratios were adjusted according to appropriate normalized moduli reduction and damping ratio versus shear strain relationships.

As mentioned earlier, the global analysis of the bridge was performed using variable support excitation. In such an analysis, the input motions are specified at each foundation spring and dashpot as displacement time-histories. Typical computed displacement time histories along the base and sides of the Brooklyn Tower caisson are shown in Figure 11. Similar calculations were made for the Manhattan Tower caisson. The acceleration response spectra of the computed motions for the three elevations shown in Figure 11 are compared in Figure 13. It is evident that the Brooklyn Tower caisson, because of its large base and stiff foundation soils, has little tendency to rock, and hence, all the translational motions along the sides of the caissons are very similar to the motion at its base. These displacement records were subsequently used as input in the global analysis of the bridge.

The foundation impedances for the Brooklyn Tower caisson were initially computed, as a function of frequency and estimated loads on the caissons, using FLAC and the hysteretic soil constitutive model. Typical force-displacement and moment-rotation hysteresis loops at two levels along the side and at the base of the caissons were computed by applying sinusoidal forces and moments at the center of gravity of the caissons. The amplitudes of the forces and moments, as well as the frequency of excitation, were varied to capture the effect of soil non-linearity and frequency dependency of the caisson responses.

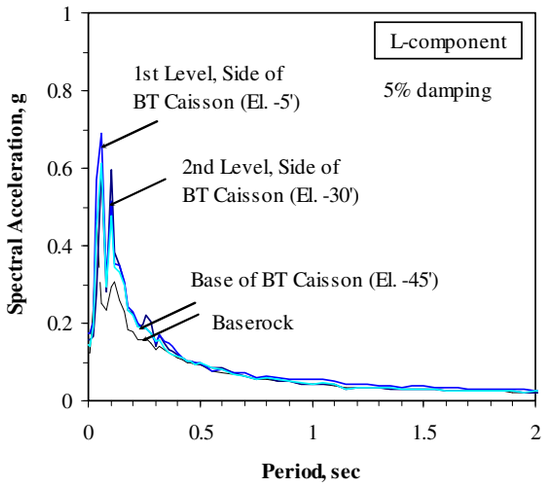


Fig. 13 Comparison of the spectra of the motions computed by FLAC for the sides and base of the Brooklyn Tower caisson.

Figure 14 shows typical results where an estimated seismic force of 88,000 kips was applied with a frequency of 10 Hz. The results show that the primary resistance to lateral inertial forces from the tower and caisson come from the base of the caisson (El. -45').

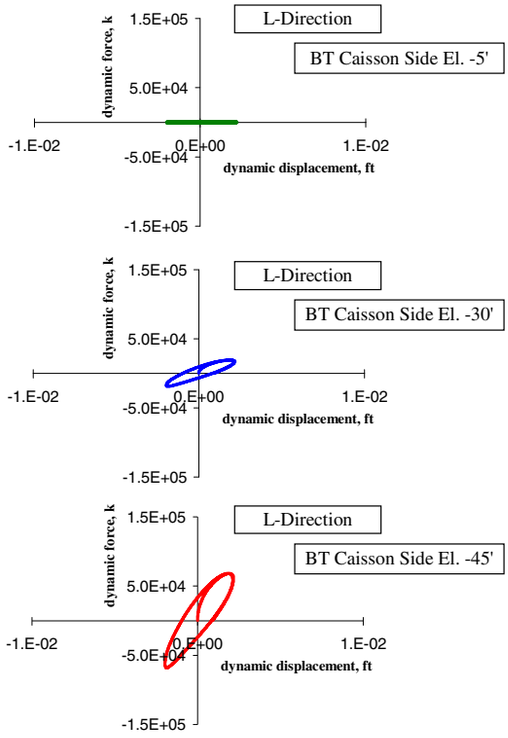


Fig. 14 Brooklyn Tower caisson force-displacement loops along the sides and base of the caisson for an estimated caisson longitudinal inertial force of 88,000 kips.

Figure 15 shows the total foundation impedances of the Brooklyn Tower caisson under two levels of lateral forces. The backbone curve of the hysteresis loop shows only slight effect of soil non-linearity up to an estimated upper bound shear force induced in the caisson of 175,000 kips.

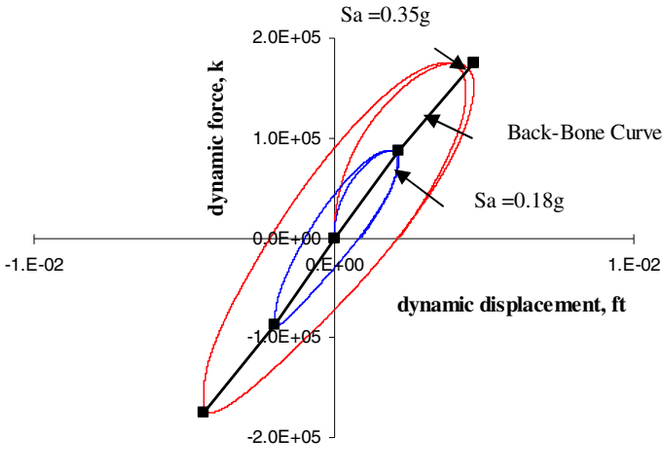


Fig. 15 Brooklyn Tower caisson total force-displacement loops for two levels of caisson inertial forces.

Using such hysteresis loops along the sides and base of the tower caisson, equivalent stiffness and damping coefficients were calculated. Table 2 summarizes the total stiffness and damping coefficients for the Brooklyn Tower caisson.

Table 2. Summary of soil-Brooklyn Tower caisson dynamic impedances, computed using SASSI.

Mode of Vibration	Applied Load on Caisson	Stiffness Coefficient K	Damping Coefficient C	Damping Ratio
Longitudinal, L	88,000 k			
Side of caisson El. -5'		K_L (k/ft) = 7.36E+05	C_L (k-sec/ft) = 5.96E+03	
Side of caisson El. -30'		K_L (k/ft) = 7.36E+06	C_L (k-sec/ft) = 5.96E+04	
Base of caisson El. -45'		K_L (k/ft) = 2.87E+07	C_L (k-sec/ft) = 2.32E+05	
Total		3.68E+07	2.98E+05	0.25
Transverse, T	88,000 k			
Side of caisson El. -5'		K_T (k/ft) = 1.53E+06	C_T (k-sec/ft) = 2.78E+03	
Side of caisson El. -30'		K_T (k/ft) = 7.31E+06	C_T (k-sec/ft) = 1.33E+04	
Base of caisson El. -45'		K_T (k/ft) = 2.52E+07	C_T (k-sec/ft) = 4.57E+04	
Total		3.40E+07	6.17E+04	0.06
Vertical, V	50,000 k			
Side of caisson El. -5'		K_V (k/ft) = 9.75E+05	C_V (k-sec/ft) = 1.00E+02	
Side of caisson El. -30'		K_V (k/ft) = 1.95E+06	C_V (k-sec/ft) = 2.00E+02	
Base of caisson El. -45'		K_V (k/ft) = 9.46E+07	C_V (k-sec/ft) = 9.70E+03	
Total		9.75E+07	1.00E+04	0.00
Rotation about L	2.60E+7 k-ft	K_{RL} (k-ft/rad) = 3.06E+11	C_{RL} (k-ft-sec/rad) = 2.05E+08	0.02
Rotation about T	2.60E+7 k-ft	K_{RT} (k-ft/rad) = 1.29E+11	C_{RT} (k-ft-sec/rad) = 5.08E+08	0.12

These total coefficients were subsequently distributed to 25 springs along the base of the caisson and 20 springs at each of two elevations along the sides of the caisson. The distribution was made ensuring the cumulative total stiffness and damping of the individual springs along the sides and base of a caisson matched the total stiffness and damping coefficients shown in Table 2. These foundation impedances were used in a preliminary seismic global analysis of the bridge to estimate the inertial loads on the caissons of the towers, and to make a preliminary assessment of the retrofit need of the tower caissons.

To account for the effect of potential sliding and tilting of the tower caissons on the non-linear soil-caisson response, the FLAC analyses were repeated using models that included the entire tower, and the tower caisson with its surrounding soils. In these models, slip and gap elements were included along the soil-caisson interfaces. The analysis involved first applying gravity to compute the initial stresses within the interface elements. Then, forces and moments were applied on the caissons, one direction at a time (pushover analysis) and the displacements and rotations of the caisson were computed.

Figure 16 shows the entire model of the Brooklyn Tower and its caisson in which slip and gap elements were included.

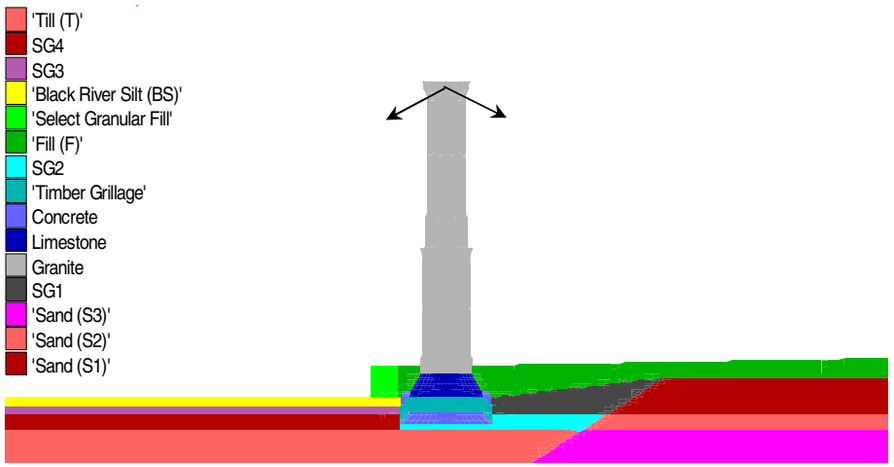


Fig. 16 Longitudinal model of the Brooklyn Tower and its foundation used in FLAC to compute non-linear force-displacement and moment-rotation relationships for the caisson, which included interface elements along its sides and base.

Also included in the model were static and equivalent dynamic cable forces and deck loads on the tower that were computed by the initial global analysis of the bridge. The properties of the interface elements included: the friction angle of the cohesionless soils, the undrained shear strength of the clay, and the normal and shear stiffness of the interface elements, which were based on the shear modulus of the soil and the dimensions of the soil elements adjacent to the interface elements.

The moduli of the timber grillage and the limestone of the tower foundation were measured in the field using the geophysical technique of shear and compression wave tomography. Figure 17 shows the results obtained using two boreholes drilled through the Brooklyn Tower foundation. On average, the shear and compression wave velocities of the timber grillage were 2700 fps and 5700 fps, respectively. The corresponding values for the limestone and granite blocks were 8700 fps and 13,600 fps, respectively.

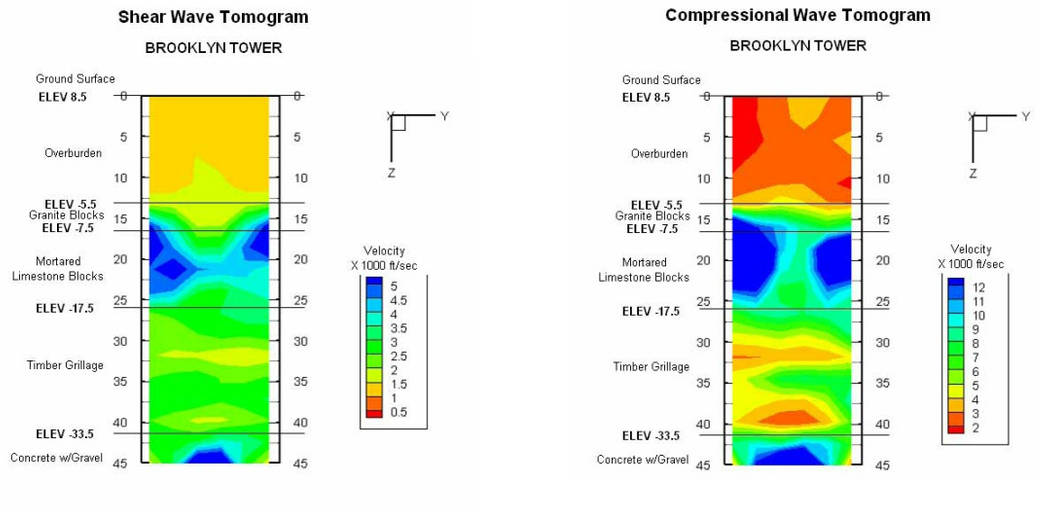


Fig. 17 Shear and compression wave tomography results of the timber grillage, and the limestone and granite blocks of the Brooklyn Tower foundations.

Figure 18 shows a typical force-displacement curve obtained for the Brooklyn Tower caisson, in the longitudinal direction. The solid curve represents the total stiffness of the caisson. The dashed curves show the relative contributions from the sides and base of the caisson.

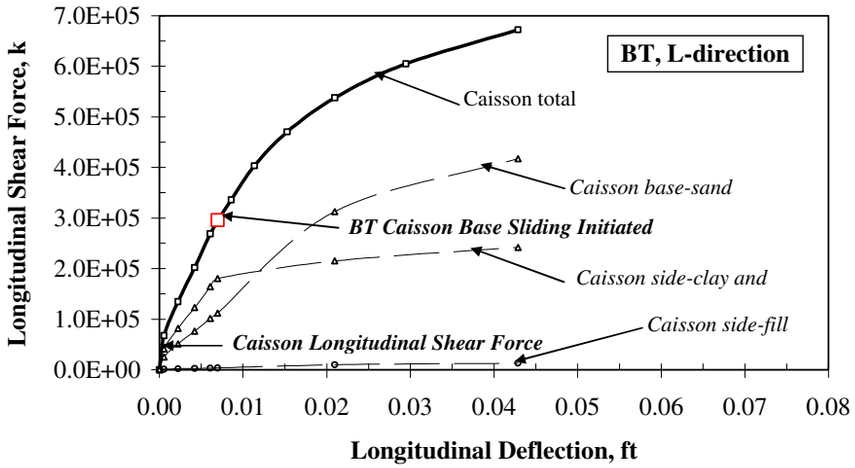


Fig. 18 Non-linear force-displacement relationship in the longitudinal direction for the Brooklyn Tower caisson, computed from the pushover analysis of the caisson, using FLAC with interface elements.

A number of observations are made from the results shown in Figure 18. Sliding of the caisson is initiated at a total shear force of about 300,000 kips acting at the center of gravity of the caisson. This is far larger in magnitude than what was computed (33,000 kips) from the initial global analysis using foundation impedances. Hence, sliding of the caisson under the design event is not likely to occur, a conclusion based on the non-linear force-displacement relationships and the results from the global analysis. This conclusion is later confirmed by the results from the local analysis. Also, at small levels of shear force, the total stiffness is linear and the primary resistance to the caisson inertial forces comes from its base, conclusions that are consistent with those arrived at from the frequency dependent impedance analysis of the caisson (Figures 14 and 15).

Figure 19 shows the transverse moment versus rotation curve of the Brooklyn Tower caisson. Again, the results show that gapping will be initiated along the base of the caisson only if the transverse moment exceeds 5.5×10^6 kip-feet, which is much greater than what was computed from the initial global analysis (3.5×10^6 kip-feet) using frequency dependent foundation impedances. Hence, the Brooklyn Tower caisson is not expected to separate from its base during the 2500-year event, a conclusion later confirmed using the local analysis of the tower and its foundation. Similar calculations using the Manhattan Tower caisson led to the same conclusions, that the caisson is safe against sliding and separation.

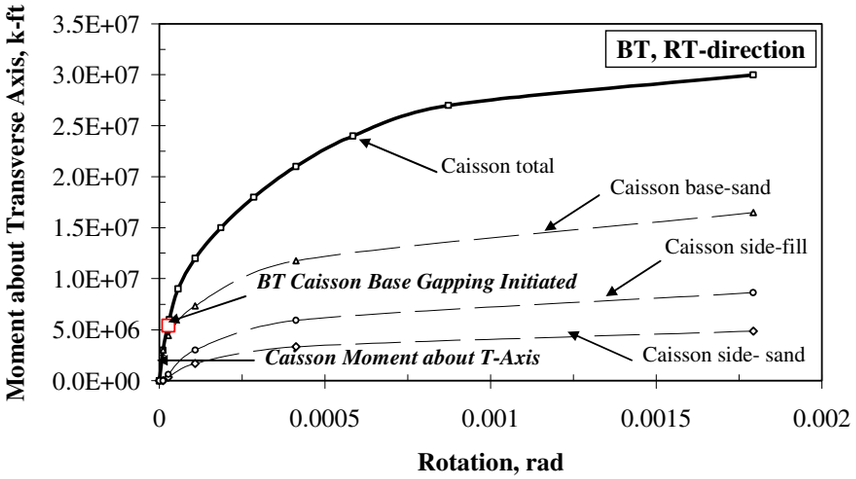


Fig. 19 Non-linear moment-rotation relationship about the transverse axis for the Brooklyn Tower caisson, computed from the pushover analysis of the caisson, using FLAC with interface elements.

A total of three translational force-displacement and three moment–rotation curves were generated for each tower caisson using FLAC and interface slip and gap elements. These total stiffness curves were then distributed to the base and side springs and the global analysis was repeated for the final results. In ADINA, these curves were used as initial loading backbone curves for base shear tractional and for

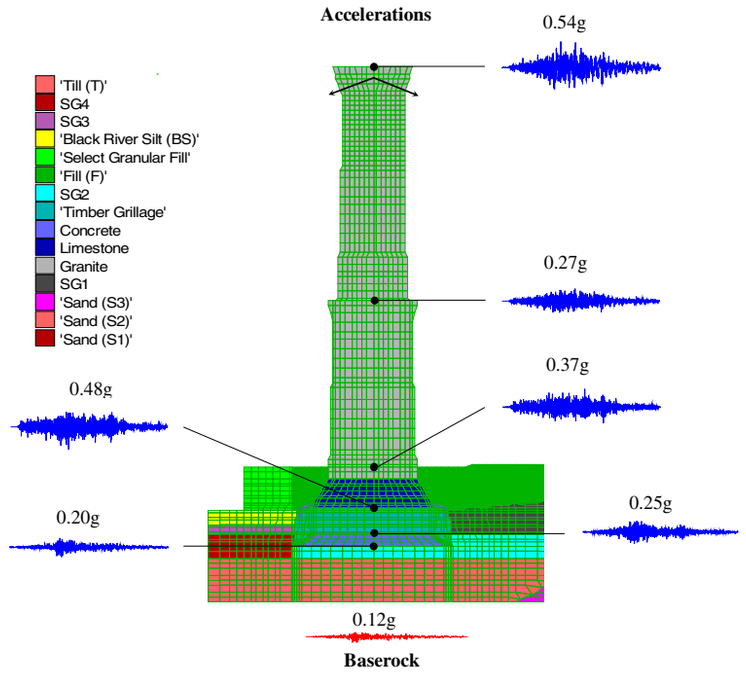
normal contact springs. Unloading of tractional springs was considered through the use of full Masing hysteresis, and of normal contact springs through the use of initial tangent stiffness. Later in this paper, selected results from the global analyses will be compared with corresponding results from the local analysis, which is described in the next section.

SOIL-FOUNDATION-TOWER ANALYSIS (LOCAL ANALYSIS)

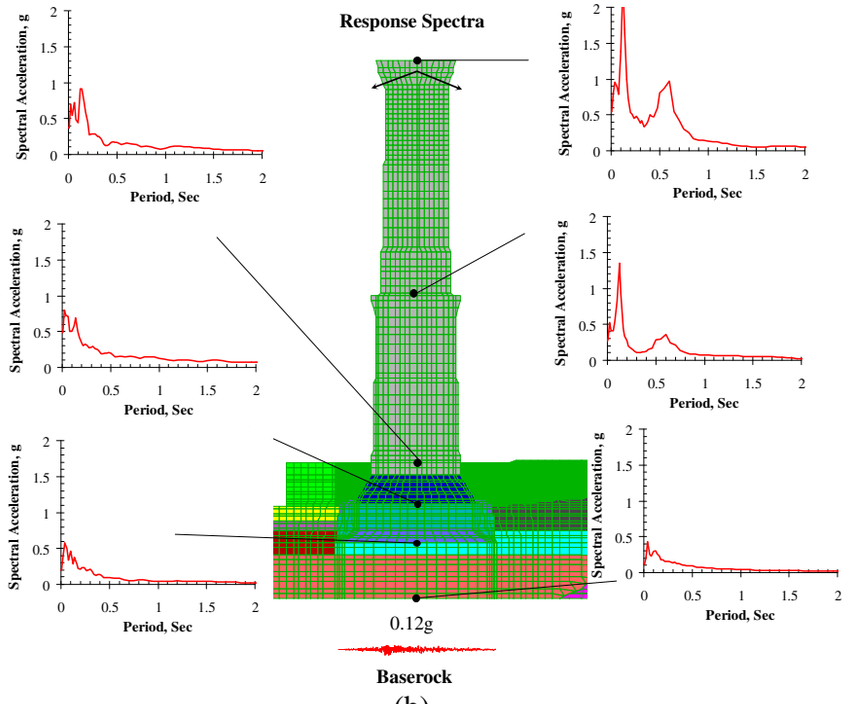
The Brooklyn Bridge towers are massive and rigid, while its superstructure is flexible in comparison with the towers. Furthermore, the design rock motions are rich in high frequencies and have little energy in the low frequency range. Therefore, it is quite reasonable to expect that the dynamic inertial loads from the deck and the dynamic component from the cables will make only a small contribution to the seismic response of a tower and its caisson. This expectation was clearly observed in the global analysis of the bridge. Hence, it was of interest to perform a local seismic analysis of each of the two towers with their caissons and surrounding soils using FLAC. Such an analysis avoided the various assumptions made in the calculations of the kinematic motions and foundation impedances and provided added benefits of including initial stresses, more accurate modeling of the soil non-linear behavior, and computing the stress distributions within the caisson as well as along its sides and base.

The Brooklyn Tower caisson model shown in Figure 16 was further used to investigate the vulnerability of the caisson. It also included static and equivalent dynamic cable forces, and hydrostatic effects. For the soils the hysteretic soil model was utilized in which the soil moduli and damping ratios were adjusted at every step of time integration based on parameters that approximated appropriate normalized moduli versus shear strain curves. The soil-caisson-tower model first was subjected to gravitational loads and all the initial total and effective normal stresses were calculated and saved within FLAC. The model was then subjected to the 2,500-year baserock horizontal and vertical motions used earlier in the calculations of the kinematic caisson motions. The time histories of acceleration, displacement, shear stress, and vertical normal stress were computed at various nodes of interest including at the top and bottom of the interface elements. The results were then processed to evaluate the response of the tower and its foundation.

Figures 20a and 20b present summary plots of the accelerations and response spectra at various nodes within the longitudinal model of the Brooklyn Tower and its foundation, under longitudinal earthquake excitation. Figures 21a and 21b present similar results within the transverse model.

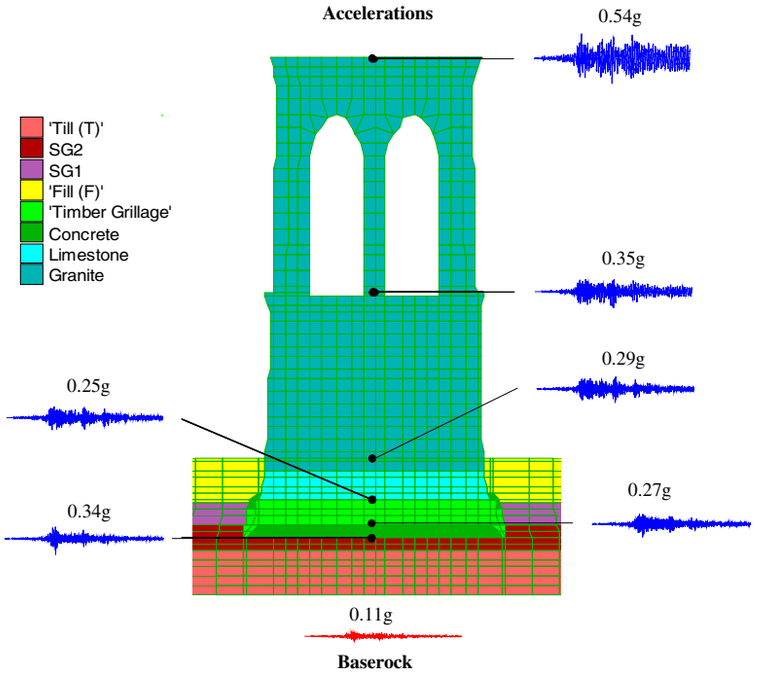


(a)

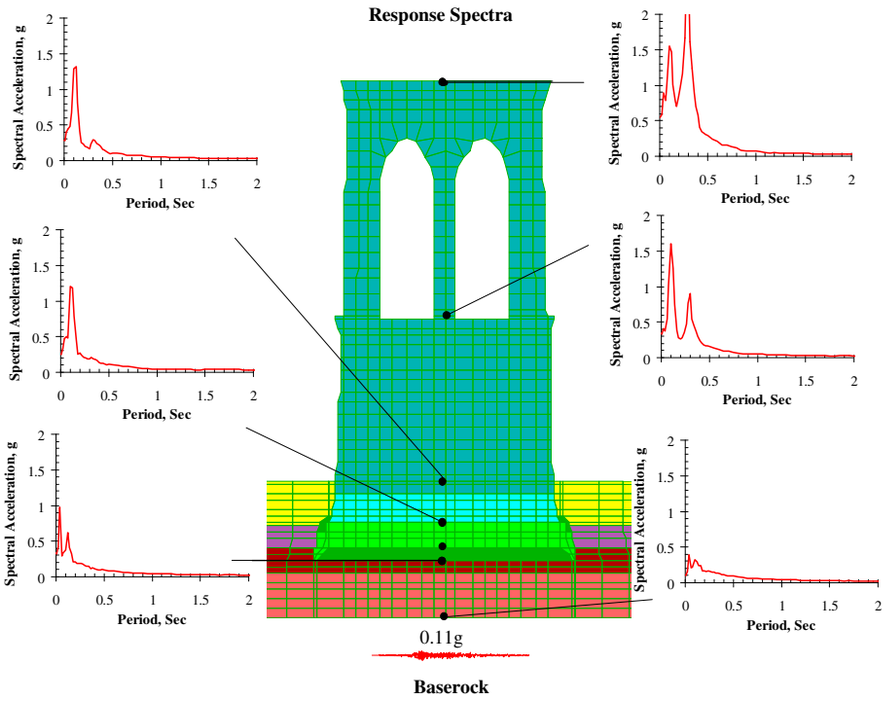


(b)

Fig. 20 Longitudinal responses of the Brooklyn Tower and its foundation, a) acceleration time histories, b) corresponding response spectra, under the 2,500-year event.



(a)



(b)

Fig. 21 Transverse responses of the Brooklyn Tower and its foundation, a) acceleration time histories, b) corresponding response spectra, under the 2,500-year event.

These results show that the baserock motion amplifies as it propagates through the structure. Figure 20b shows amplification at two particular periods, 0.15 seconds and 0.7 seconds. Figure 22 shows spectral acceleration ratios from the longitudinal model obtained by dividing the spectra at various elevations within the tower and its caisson with the spectrum at the base of the caisson.

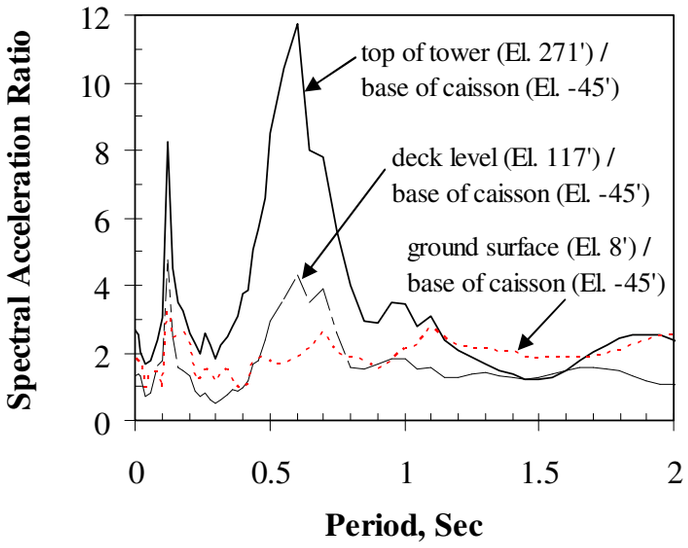
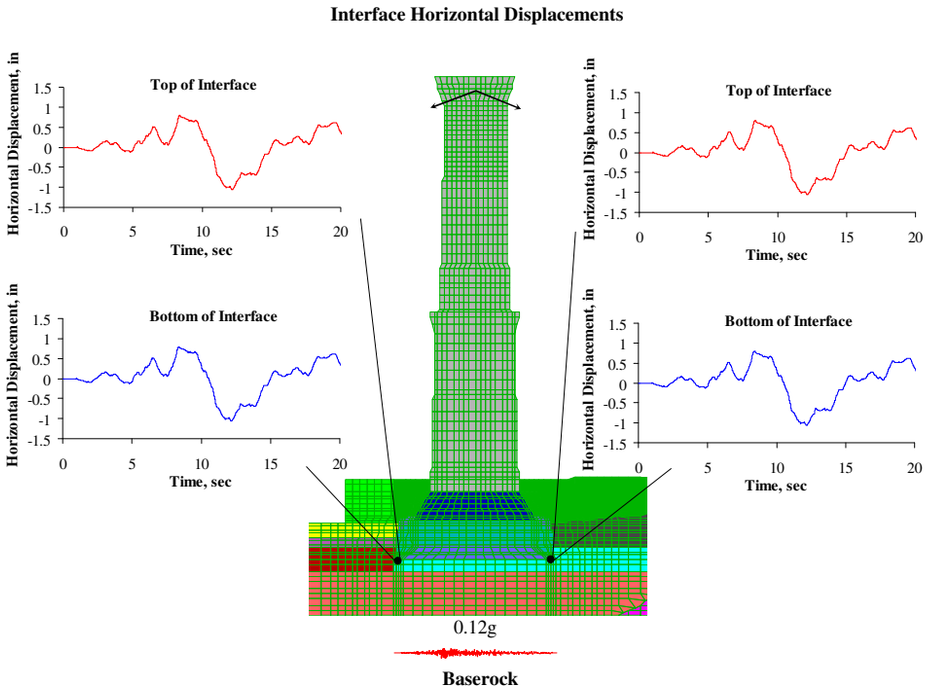


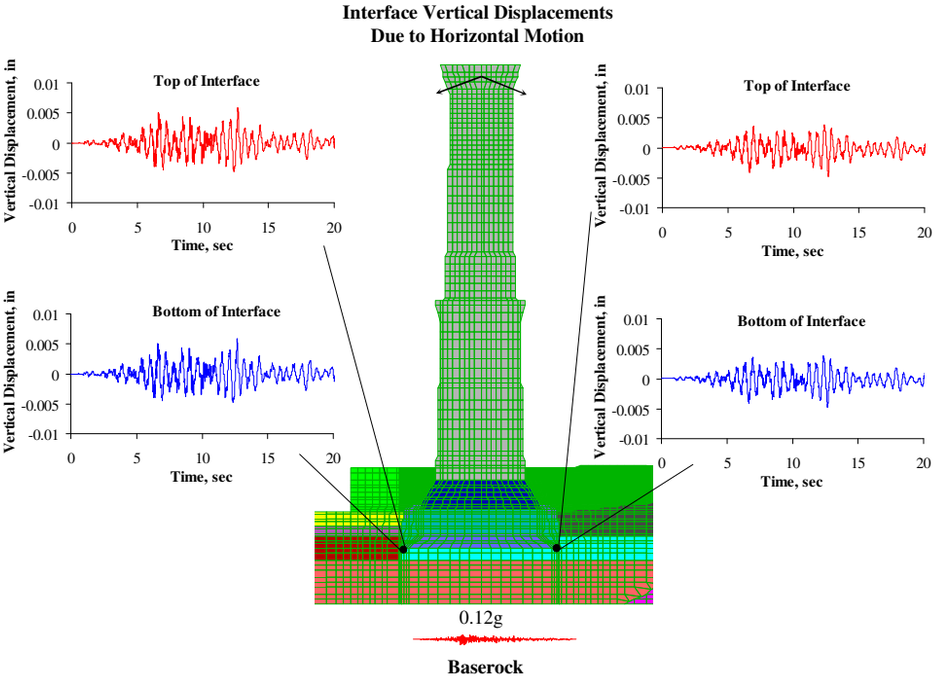
Fig. 22 Ratios of the longitudinal spectral accelerations, relative to the caisson base.

Two modal frequencies can be seen clearly to occur at about 0.12 seconds and 0.6 seconds. Simple calculations of the horizontal and rocking periods of the tower and its caisson confirmed that the first period corresponded to the longitudinal period of the tower and the second is most likely associated with the rocking period about the transverse axis of the bridge. These modal periods were also within the period ranges that were observed through ambient vibration measurements of the bridge.

Figures 23a and 23b show the horizontal and vertical displacement histories at the top and bottom of the interface elements at the base of the caisson, respectively under the longitudinal earthquake excitation of the 2500-year event. The top and bottom displacements are exactly identical, indicating that the interface elements do not exhibit slip or gapping along the base of the tower.



(a)



(b)

Fig. 23 Displacements at the top and bottom of the interface elements along the base of the Brooklyn Tower caisson, under the 2,500-year event, a) horizontal displacement, b) vertical displacement.

Figure 24 displays the vertical displacements at the top and bottom of the caisson base interface elements under the combined horizontal (longitudinal) and vertical motions. Even under this most severe condition, when the vertical motion can potentially reduce the base stresses, the vertical displacements at the top and bottom of the interfaces are exactly the same, indicating that there is no gapping (loss of contact) along the base of the caisson.

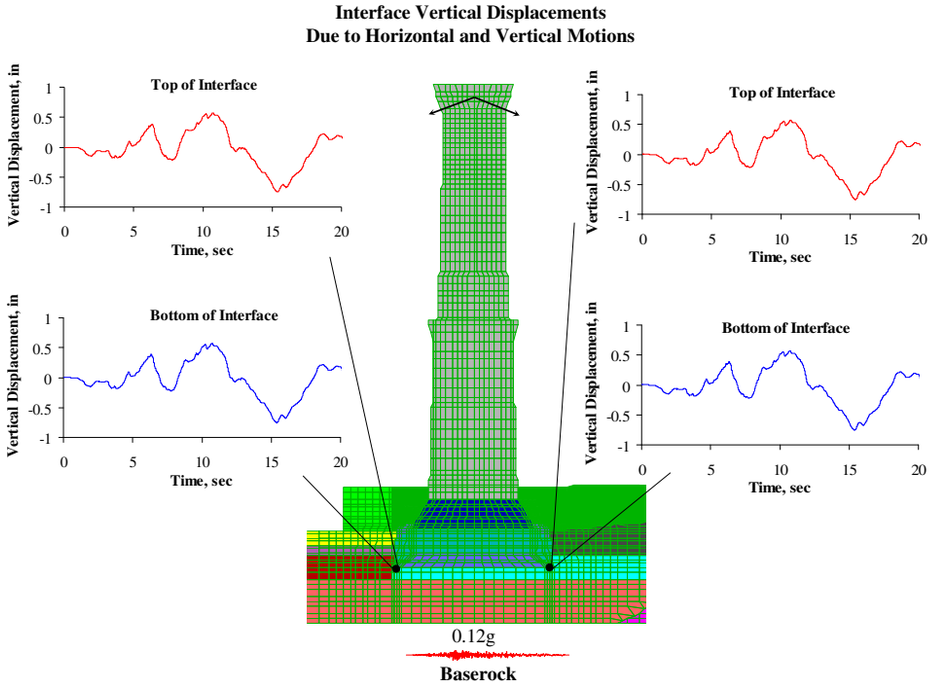


Fig. 24 Comparison of vertical displacements at the top and bottom of the interface elements along the base of the Brooklyn Tower caisson, induced by the combined longitudinal and vertical motions of the 2500-year event.

Figure 25 shows a summary of the initial static and dynamic shear stresses along selected cross sections within the Brooklyn Tower and its caisson. The maximum shear stress in the concrete of the caisson is about 45 psi (6.5 ksf) and in the timber grillage is about 50 psi (7.2 ksf). These values are significantly smaller than the shear capacities that were measured in the laboratory for the concrete and timber specimens.

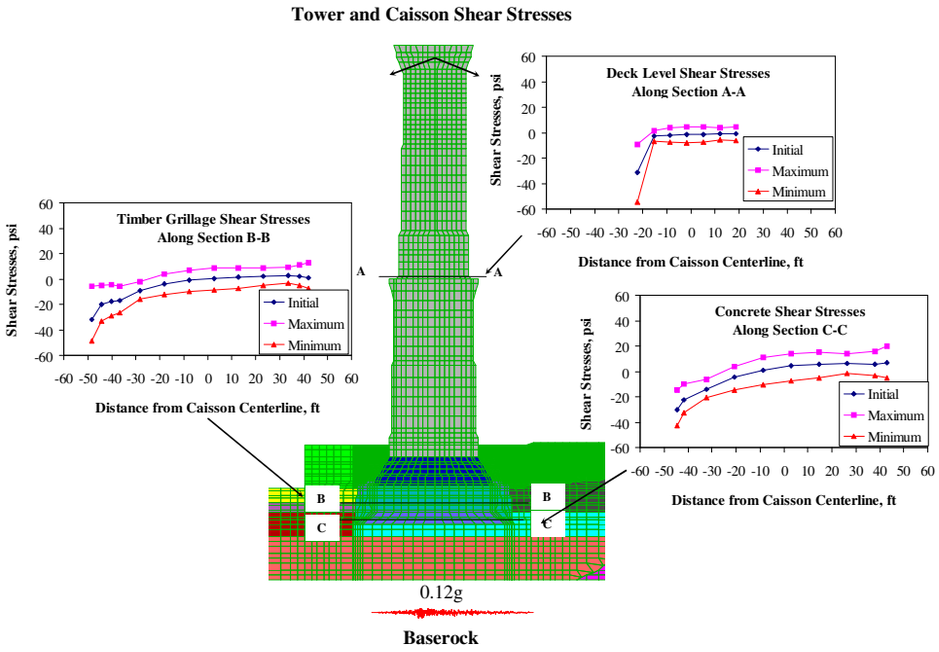


Fig. 25 Longitudinal shear stresses computed using the FLAC model of the Brooklyn Tower and its foundation, under the 2500-year event.

The total shear force time history along a cross section through the middle of the caisson (Section B-B) was computed by integrating the shear stress time histories along the cross section. The result is shown in Figure 26. This total shear force time history, obtained from the local analysis, is compared later in this paper with the results from the global analysis.

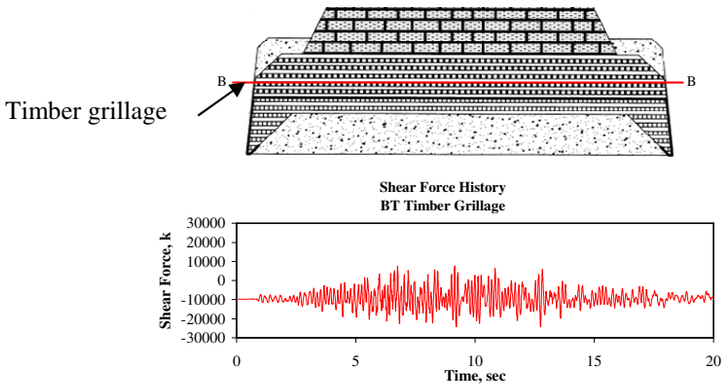


Fig. 26 Total longitudinal shear force history along cross section B-B in the middle of the timber grillage of the Brooklyn Tower caisson.

The maximum value of the total shear force within the caisson is about 20,000 kips as shown in Figure 26. Under such a magnitude of shear force, the caisson is not expected to slide or tilt as was demonstrated through the use of the force-displacement and moment-rotation curves described in the previous section of this paper.

Figure 27 shows the shear and effective normal stresses along the base of the caisson induced by gravity and the horizontal earthquake motion, without the vertical component of excitation.

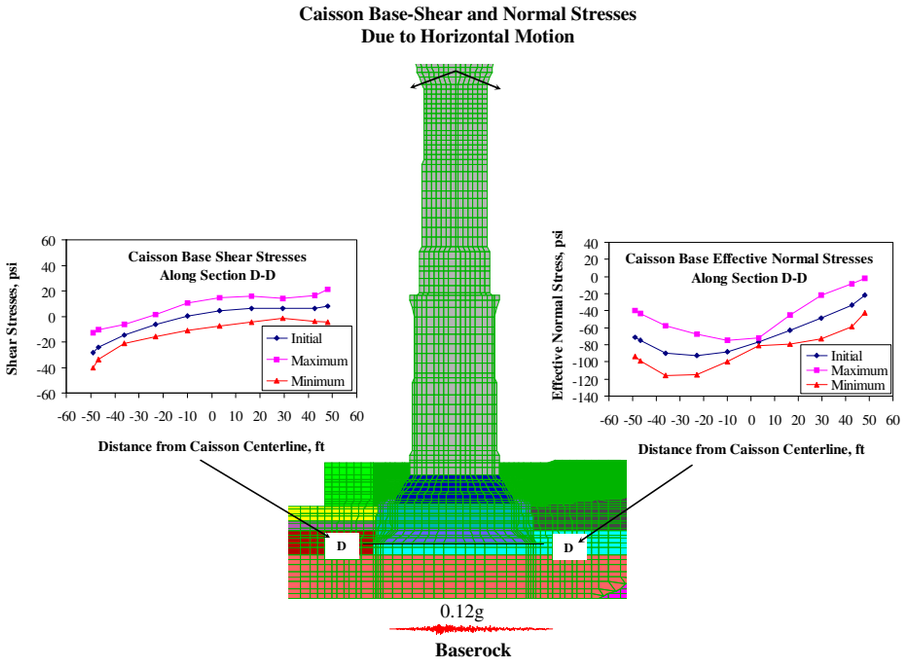


Fig. 27 Brooklyn Tower caisson base shear and effective normal stresses induced by the longitudinal motion of the 2500-year event.

Initially, under gravity, the effective normal stresses are negative (compression) with values larger to the right of the centerline of the tower due to the larger cable forces in the direction of the center span of the bridge (to the left when looking at Figure 27). Under the transverse moment induced by the longitudinal horizontal excitation, the maximum compression increases to about 120 psi (17 ksf) to the left of the tower centerline and decreases to about 0 psi to the right of the tower centerline.

Figure 28 shows the shear and effective vertical stresses under the combined horizontal and vertical excitations. Under this load combination, the maximum effective normal stress slightly increases to about 125 psi (18 ksf) and the minimum effective normal stress remains at about 0 psi.

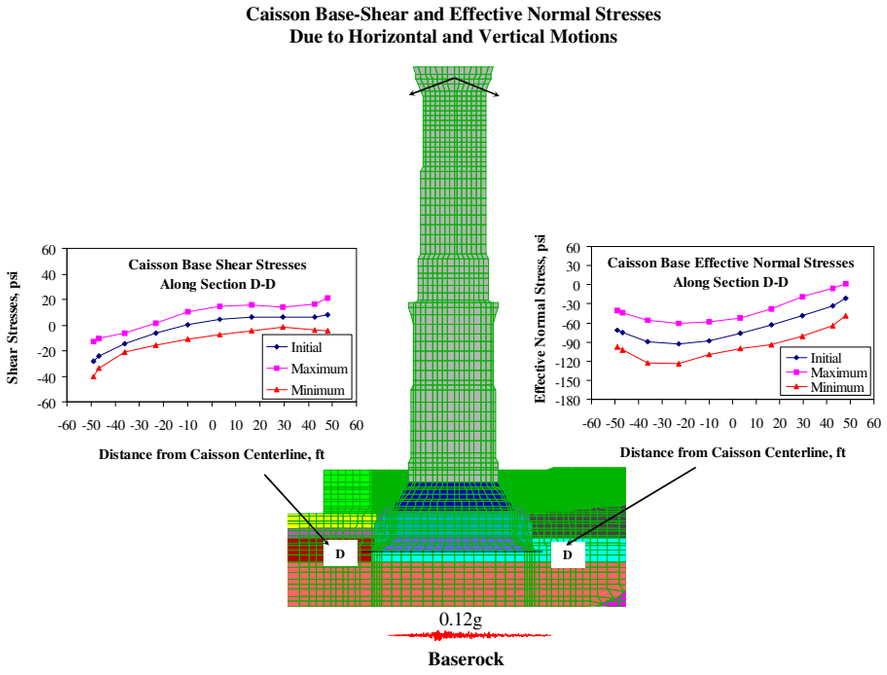


Fig. 28 Brooklyn Tower caisson base shear and effective normal stresses induced by the combined longitudinal and vertical motions of the 2500-year event.

In summary, seismic longitudinal and vertical analyses of the Brooklyn Tower caisson and the surrounding soils led to the conclusion that the effective normal stresses at the bottom of the caisson are small (18 ksf) relative to the ultimate capacity (>100 ksf). Additionally, the caisson is safe against sliding and will not lose contact with its base soils under the longitudinal and vertical components of the 2500-year earthquake.

Similar investigations of the Brooklyn Tower and its caisson were made considering seismic excitation in the transverse direction. The conclusions were identical to those inferred from the longitudinal analyses. A typical result is shown in Figure 29 which depicts the caisson base shear and effective normal stresses under the combined horizontal and vertical motions. Under this load combination, the maximum effective normal stress is about 110 psi (15.8 ksf) and the minimum effective stress is at about 10 psi (1.4 ksf) leading to the conclusion that the caisson is safe against sliding and bearing capacity type failure, and will not lose contact with its base soil under the transverse and vertical excitations induced by the 2500-year event.

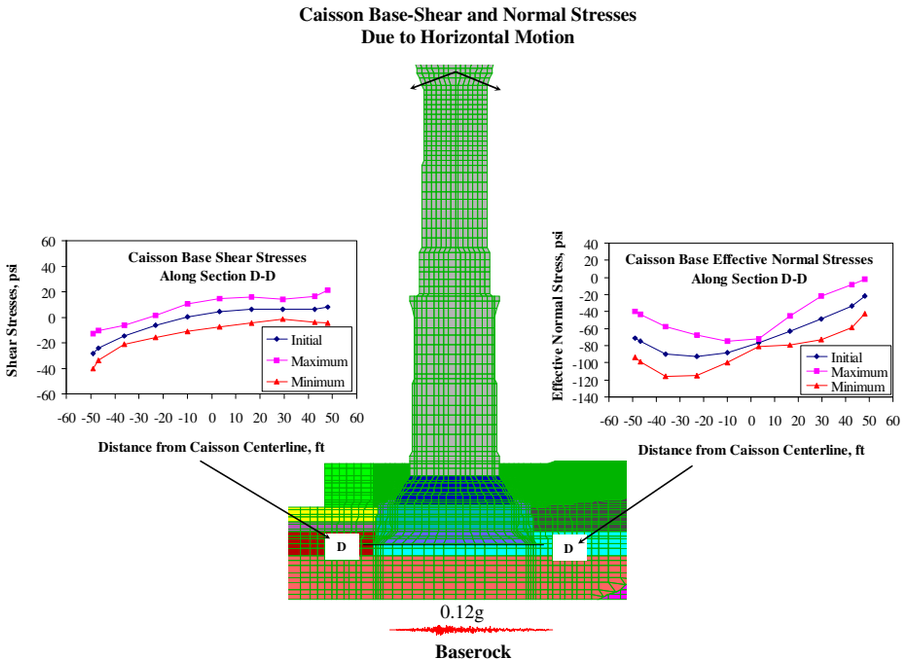


Fig. 29 Brooklyn Tower caisson base shear and effective normal stresses induced by the combined transverse and vertical motions of the 2500-year event.

COMPARISONS OF GLOBAL AND LOCAL ANALYSIS RESULTS

As described earlier, the global analysis of the Brooklyn Bridge incorporated the entire bridge including the towers, cables, suspended structure and foundations. Thus, it provided the means to consider the cable effects and the masonry tower potential for cracking. The caissons were modeled using beam elements, which permitted the calculation of stresses at only a few selected locations where the springs were placed.

The local analysis that involved the investigation of the seismic interaction of the bridge tower with its foundation and surrounding soils permitted more accurate considerations of the non-linear soil caisson interaction as well as the direct consideration of the potential slip and gapping around the caissons. The local analysis also provided a more detailed distribution of stresses that included initial effective vertical normal stresses, and the shear stresses within the tower and its foundations.

It is of interest to compare selected results from both the global and local analyses. Figure 30 shows a comparison of the total shear force time history in the longitudinal

direction along cross section B-B of the Brooklyn Tower caisson. The results from both analyses are quite comparable both in intensity and general frequency content.

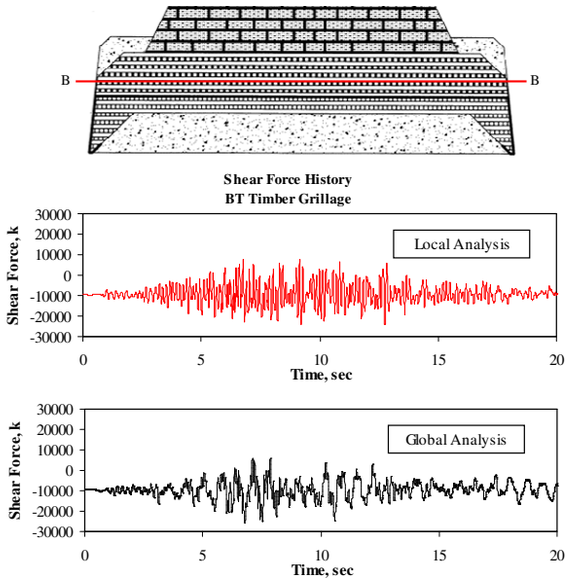


Fig. 30 Comparison of longitudinal total shear force time histories along cross section B-B of the BT caisson, from the local and global analyses.

In Figure 31, a comparison is made of the effective vertical normal stress along the base of the Brooklyn Tower caisson obtained from the global and local analyses. Again, the agreement is quite good considering the wide differences in the analysis approaches.

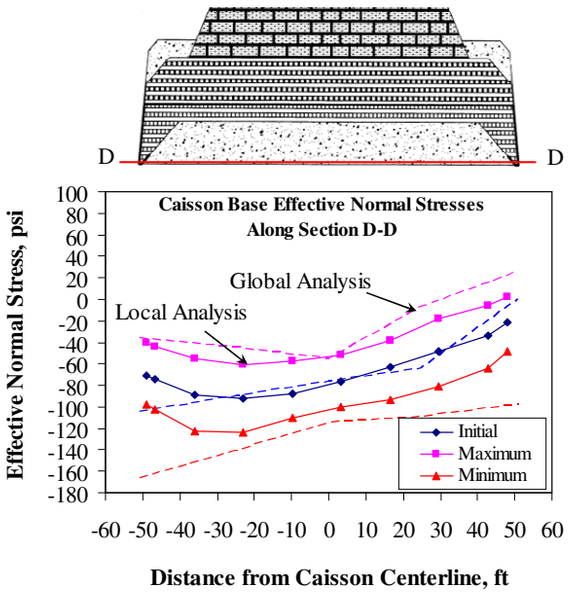


Fig. 31 Comparison of effective vertical normal stresses along the base of the Brooklyn Tower caisson obtained from the local and global analyses.

Finally, in Figure 32 a comparison is made of the drift of the Brooklyn Tower normalized with respect to the displacement at the base of the towercaisson.

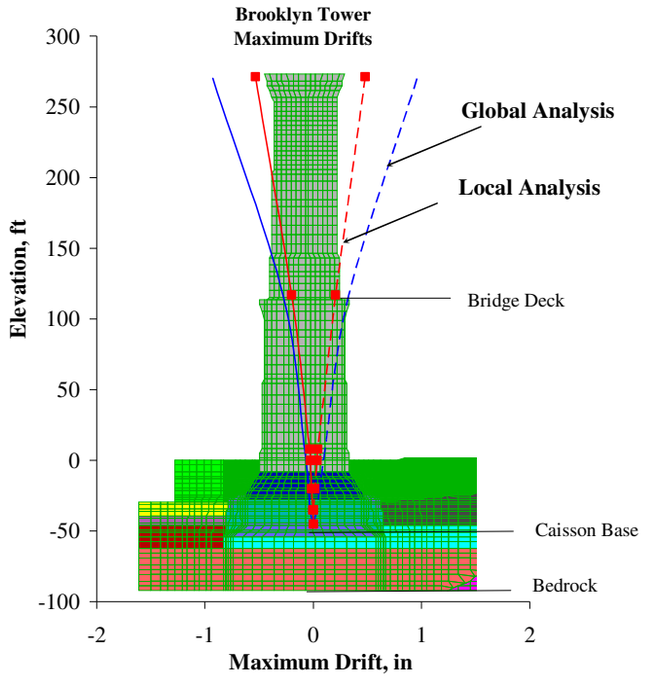


Fig. 32 Comparison of drifts along the Brooklyn Tower caisson and its foundation, normalized with respect to the drift at the base of the caisson, from local and global analyses.

It is noted that these drifts are maximum values and do not necessarily occur at the same time. The drift values from the local and global analyses are small and comparable with the global analysis results.

Comparisons of the results obtained from the analyses of the Manhattan Tower and its foundation led to the same conclusion, that the local and global analyses yield similar results and the main tower foundations are adequate to safely resist the 2500-year event without experiencing sliding or lift-off along its base, nor bearing capacity failure, and hence do not require retrofitting.

CONCLUSIONS

Seismic investigation of the historic Brooklyn Bridge was performed to assess its potential need for retrofitting. The bridge serves a critical transportation need in New York City, and very importantly is a national landmark and a world recognized architectural and engineering achievement. The seismic assessment of the bridge was completed using the most advanced engineering investigations to ensure that the evaluation of retrofit needs were based on a rational framework and avoided “pitfalls”

(as described by Peck, 1977) of overconservatism, including implementation of unnecessary retrofit schemes which may negatively impact the architecture of the bridge.

Two approaches were followed to determine the soil-foundation-bridge interaction, namely, **global** and **local analyses**. In the global analysis model, the soil-foundation interaction was introduced through the use of non-linear hysteretic springs with gapping features and dashpots. In the local analysis, each of the towers with their foundation caissons and the surrounding soils were investigated. The local analysis models included hysteretic soil behavior as well as interface slip and gap elements. Comparisons of various results obtained from the global and local analyses showed satisfactory agreement and led to the same conclusion, that the foundations of the Brooklyn Bridge under the 2500-year design event do not require retrofitting.

Based on extensive seismic evaluations of the Brooklyn Bridge, using global and local analytical approaches, the following observations and conclusions are drawn.

1. The Brooklyn Bridge is a long span bridge with massive cable anchorages and towers. The superstructure contributes very little to the tower dynamic responses. The global analysis has shown that, for the level of seismic loads in the New York City metropolitan area, very little cracking of the masonry towers is anticipated. Thus, the local analysis of the towers with their foundation caissons yielded dynamic responses of the towers and the caissons very similar to those obtained following the current state of practice of seismic analysis for critical bridges (global analysis).

2. The agreement in the results between the global and local analyses is a confirmation of the quality of the kinematic motions and the foundation impedances used in the global analysis of the bridge as well as a confirmation of the validity of the caisson modeling approach in the global analysis.

3. Quality kinematic motions and foundation impedances were computed following advanced soil-structure interaction analysis procedures. Such procedures, considered the three-dimensional kinematic effect of the foundations on the ground motions, and the non-linear force-displacement and moment-rotation stiffness relationships that included the effect of potential slip and gapping along the sides and bases of the caissons of the towers. These non-linear stiffness curves were obtained by performing pushover analyses of the foundation caissons. If ground motions and foundation impedances were computed using more simplified analytical procedures, the caisson and tower responses computed by the global analysis would not have been in agreement with those obtained from the local analysis.

4. The local analysis provided the advantage of considering the effect of the initial static tower and soil stresses, accounting for the non-linear soil response directly in the computations, modeling more accurately the potential

sliding and gapping of the tower caissons, and computing caisson static plus dynamic internal and external stresses as well as the stresses in the tower structure.

5. In suspension bridges, seismic response of bridge towers with large foundation caissons can be reliably evaluated following a local analysis in which the bridge support components with the soil continuum are considered together in a single model.

REFERENCES

ACS SASSI-C, "An Advanced Computational Software for Dynamic Soil-Structure Interaction Analysis on PCs," GP Technologies Inc. 6 South Main St., Pittsford, New York, (2004).

ADINA Software Program, ADINA R&D, Inc. Watertown, MA 02172, USA.

FLAC 5.0 (2005), "Fast Lagrangian Analysis of Continua," ITASCA Consulting Group, Inc., 111 Third Avenue South, Minneapolis, Minnesota.

Dunham, R.S. and Rashid, Y.R., (2003), "ANACAP Material Modeling of Reinforced Concrete," Anatech Corp.

Gazetas, G., (1991). "Foundation Vibrations." Foundation Engineering Handbook, Van Nostrand Reinhold.

New York City Department of Transportation, Ground Motion Time Histories, 2004.

Peck, R. (1977), "Pitfalls of Overconservatism in Geotechnical Engineering," ASCE Civil Engineering Magazine.

PROSHAKE, (1998), "Ground Response Analysis Program," EduPro Civil Systems, Inc. Redmond, Washington, Version 1.0.

Steinman Report (1945), "Brooklyn Bridge Technical Survey Final Report," Department of Public Works, City of New York.

ACKNOWLEDGMENTS

The authors acknowledge the contributions of Thomas Thomann of URS to the geotechnical field and laboratory investigations, and Paul Fisk of NDT to the geophysical field investigations. Also acknowledged are the following personnel from the New York City Department of Transportation: Henry Perahia, Deputy Commissioner, Division of Bridges, Seth Solomonow, Assistant Commissioner, Press Office, Walter Kulczycki, Project Manager, East River Bridges, Division of Bridges, and Jaktar Khinda, Project Seismic Engineer, Division of Bridges.

Seismic Response of a Typical Highway Bridge in Liquefiable Soil

HyungSuk Shin[1], A.M. ASCE, Pedro Arduino[2], M. ASCE, Steven L. Kramer[3], M. ASCE, and Kevin Mackie[4], M. ASCE

[1]Geotechnical Engineer, Kleinfelder Inc., 2405 140th Ave NE, Suite A101, Bellevue, WA 98005; hshin@kleinfelder.com
[2]Associate Professor, University of Washington, Seattle, WA 98195-2700; parduino@u.washington.edu
[3]Professor, University of Washington, Seattle, WA 98195-2700; kramer@u.washington.edu
[4]Assistant Professor, University of Central Florida, Orlando, FL 32816-2450; kmackie@mail.ucf.edu

ABSTRACT: For reliable estimation of bridge performance, especially when subjected to liquefaction and lateral spreading, appropriate modeling of soil-pile-structure interaction and understanding of the global bridge behavior are essential. In practice, soil and foundation systems are often approximated using very simple foundation springs or unrealistic lateral spreading mechanisms that may not represent all important aspects of the global system behavior. In this context, a detailed bridge model of a typical highway overpass bridge in liquefiable soils was developed with an emphasis on accurate characterization of the structural and soil behavior, including various soil-pile-structure (SPSI) modeling strategies for several components in the bridge system, such as piles, pile caps, and abutment structures. Using this model, the global behavior of the bridge system is more readily understood by capturing realistic force boundary conditions at the bridge pier bases and bridge deck ends. In addition, important bridge damage mechanisms are identified.

INTRODUCTION

The seismic response of a bridge depends on the force boundary conditions at the pier bases and bridge deck ends. The response can be complicated due to the interaction between the components of the bridge system - i.e., bridge structure, soil, foundation, and abutment structure, especially when bridge and pile structures are subjected to liquefaction and lateral spreading. However, soil and foundation systems are often approximated in practice using very simple foundation springs or unrealistic lateral spreading mechanisms that may not represent all important aspects of the global system behavior. Due to the interdependence and interaction between the bridge components, it is important to model the bridge as a complete system to better understand and quantify the global bridge response.

TARGET BRIDGE SYSTEM

This study considers a typical Caltrans highway bridge underlain by liquefiable soil susceptible to lateral spreading. The target bridge is shown in Figure 1. The bridge consists of a five-span reinforced concrete structure with a post-tensioned reinforced concrete box girder deck section. The three middle spans are 45.7 m (150 ft) long and the two end spans are 36.6 m (120 ft) long. The deck is 1.83 m (6 ft) deep and the four piers have a 6.71 m (22 ft) clear height. The pier columns are circular with a 1.2 m (4 ft)

diameter. Details on the bridge structure design are presented by Mackie and Stojadinovic (2007). The bridge columns are supported by 3x2 pile groups with center-to-center spacing of 1.83 m (6 ft). The individual piles are open-ended steel pipe piles with a diameter of 0.61 m (2 ft) and wall thickness of 0.0127 m (0.5 inch). The same pile type is used for the 6x1 abutment foundations with center-to-center spacing of 2.44 m (8 ft). The bridge piers and pile groups are labeled from the left abutment as Pier 1, Pier 2, Pier 3, Pier 4, and Pile 1, Pile 2, Pile 3, Pile 4, respectively. The pile groups in the left and right slope are labeled as Pile 0 and Pile 5. A seat-type abutment is considered in the analysis. The backwall is designed to shear off when subjected to large longitudinal bridge forces. The abutment piles are installed to the depth of the other bridge piles.

The soil below the left embankment consists of a medium stiff clay crust underlain by a thin, loose to medium dense sand, a layer of stiff clay, and a dense sand layer underlain by rock. The soil beneath the right embankment consists of the same clay crust underlain by a thicker layer of loose sand, followed by a dense sand layer underlain by rock. The lower clay layer below the left abutment becomes thinner toward the center of the bridge and does not exist below the right embankment. The embankments are 8.53 m (28 ft) in height and have 2:1 slopes. The groundwater table is located at the bottom of the surface clay layer. The properties of the loose and medium sand layers across the bridge are aimed to induce liquefaction under moderate ground shaking so that lateral spreading, especially on the right side, triggers broad bridge damage. The soil types and properties are shown in Table 1. Configuration of the bridge structure and abutment is shown in Figure 2.

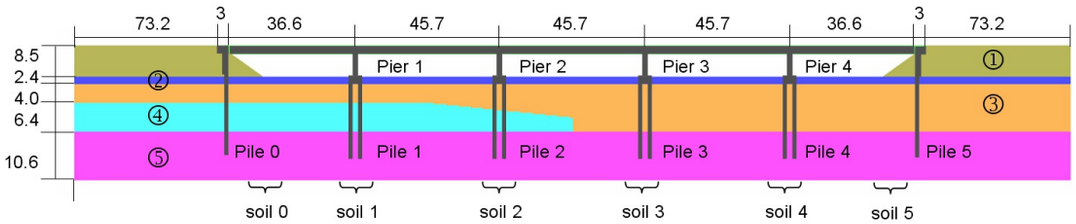


Figure 1 Target bridge system (dimensions in meter)

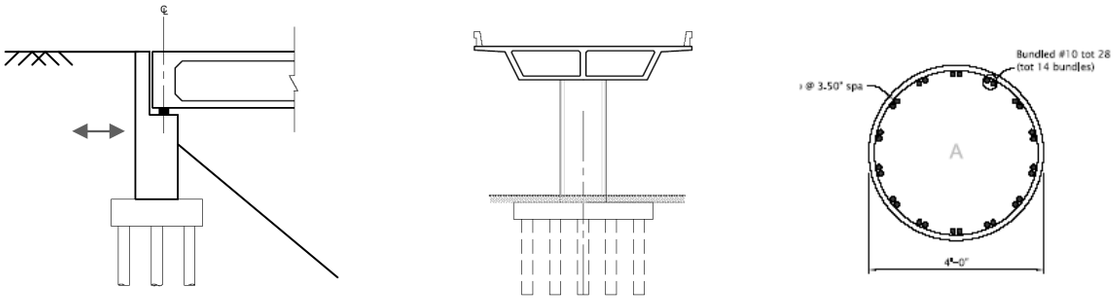
Table 1 Soil types and properties

Soil layer number	Soil type	Unit weight (kN/m^3)	Strength parameters
①	Dense sand	21.2	$\phi = 45^o$
②	Medium stiff clay	17.3	c = 36 ~ 58 kPa
③	Loose sand	18.0 ~ 20.2	$\phi = 33 \sim 36^o$
④	Medium stiff clay	17.3	c = 40 ~ 58 kPa
⑤	Dense sand	21.2	$\phi = 40^o$

NUMERICAL MODELING OF SOIL-FOUNDATION-STRUCTURE SYSTEM

Using the target soil profiles and foundation design, the soil-foundation system was modeled in OpenSees. The Pressure Dependent Multi-Yield (PDMY) elasto-plastic material model developed by Yang et al. (2003) was used to model sandy soils. To account for saturated conditions, the PDMY material was coupled with a Fluid Solid Porous Material (FSPM) model. This material imposes an incompressibility condition that allows the generation of pore pressures. For clays, the Pressure Independent Multi-

Yield (PIMY) material model was used. In the target soil profile, the clay below the left embankment had higher strength, due to consolidation, than the clay located in the center bridge area. The loose sand layer below the right abutment had increasing density (i.e., decreasing liquefaction potential) with depth. These variable soil conditions along the length of the bridge contributed to the generation of incoherent motions at each bridge pier. Fifty (50) sub-soil layers were used to capture these soil conditions. The soil parameters used in this study were based on recommendations (*http://cyclic.ucsd.edu/opensees*) for typical soil conditions. The embankment side soil was extended outward 73.2 m (240 ft) from the slope crest. The outer-most soil column elements were modified to generate a realistic free-field response by increasing their out-of-plane thickness and constraining the nodes at the same elevation to have the same horizontal movement.



(a) (b) (c)

Figure 2 Structural configurations (a) abutment structure (b) bridge structure, and (c) bridge column section

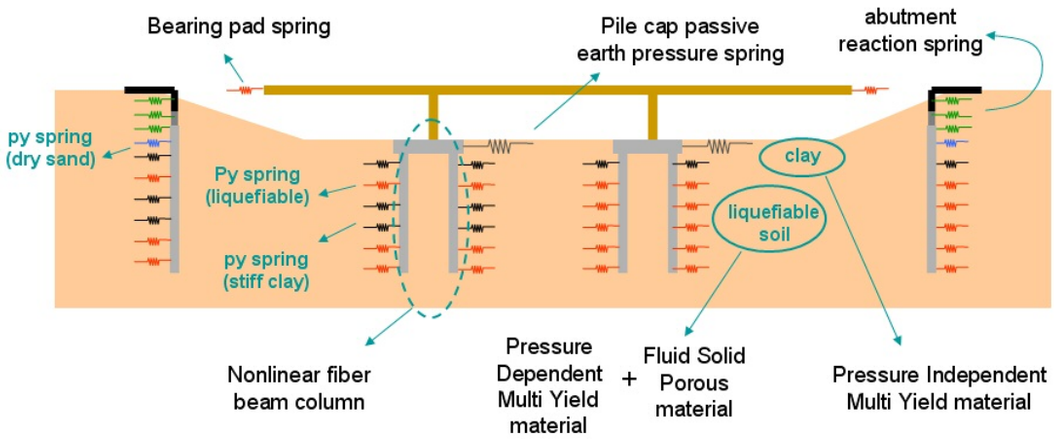


Figure 3 Modeling of soil-structure interaction in OpenSees

Several types of interface springs were used to model soil-structure interaction, as shown in Figure 3. The parameters of these interface elements reflect the existence of different soil types, ground water conditions, pile group effects, and passive earth pressures in the pile caps and abutments. The 3x2 pile groups that support the piers were simplified using equivalent two-dimensional 1x2 pile group models that combine the three piles in each out-of-plane row to produce an equivalent single pile. In OpenSees, the equivalent pile was generated by patching three individual pile sections without changing the diameter or pile wall thickness. The pile group spring parameters were

factored (using *p-multipliers*) to consider pile group effects. The *p-y* springs in the liquefiable soils were modeled using the *pyLiq1* model (Boulanger et al. 1999 and 2004) available in OpenSees. The *pyLiq1* material was coupled with adjacent soil elements that provide porewater pressure information. The spring resistance forces were based on API (1993) criteria and were factored by the porewater pressure ratio to approximate the liquefaction effect on soil-pile structure interaction. Residual strengths after liquefaction were calculated based on correlations to Standard Penetration Test (SPT) values. To capture the response of pile caps and abutment backwalls, passive earth pressure springs were used. The envelope of the pile cap passive earth pressure for clay followed the approach (ϕ=0 sliding wedge method) suggested by Mokwa (1999). For the abutment wall resistance, the resultant force-displacement envelope was based on Caltrans' Seismic Design Criteria (2004).

The height of the backwall (break-off wall) was 1.8 m (6ft) and its width was 13.7 m (45 ft). The interaction between the bridge deck and abutment was decomposed into two interaction components. A schematic of the bridge deck-abutment interaction and model is shown in Figure 4. The first component combined the bearing pad resistance and backwall resistance in a single spring model. This spring force was transferred to the stem wall and abutment pile foundation. The stem wall was connected to the soil without interface assuming its relative displacement was small. The second component included the expansion joint gap and backwall lateral soil resistance. In this case the force-displacement envelope was obtained using a series combination of a gap spring and a soil spring with parameters based on Caltrans' Seismic Design Criteria (2004). For the selected abutments, the initial stiffness and ultimate resistance used were 164,300 kN/m/m (20 kips/in/ft) and 6,258 kN (1290 kips), respectively.

The OpenSees nonliear bridge model was originally developed for a peformance-based earthquake engineering investigation by Mackie and Stojadinovic (2007). The original model used simple foundation springs at the bottom of the piers and abutment springs at the bridge deck-end to model soil compliance. To couple the bridge model with the soil model developed for this investigation, the simple foundation springs used by Mackie and Stojadinovic (2007) were removed and the pier columns were connected to pile groups. Details of the modeling of bridge system is described in Shin (2007).

INPUT MOTIONS

Four sets of input motions corresponding to return periods of 15, 72, 475, and 2475 years (97%, 50%, 10%, and 2% probability of exceedance in 50 years) at the site of an I-880 bridge study (Somerville 2002 [12]) were applied to the proposed model. These motions are near-fault motions that are distinguished by strong and long period pulses. To minimize dispersion in the input motion vs. response relationship, particularly for the case in which lateral spreading affects the bridge response, the 10 ground motions for each hazard level were scaled to a constant *PGA/MSF* value; where *MSF* is a magnitude scaling factor corresponding to the modal magnitude for each hazard level. Because the scaled motions were based on rock outcrop conditions, the motions were corrected to remove free surface effects prior to their uses as rigid base input motions in OpenSees. The ranges of *PGA* for each hazard level were 0.12 to 0.17g, 0.39 to 0.61g, 0.62 to 0.90g, and 1.1 to 1.4g, respectively. Additionally, a non-near-fault motion was considered.

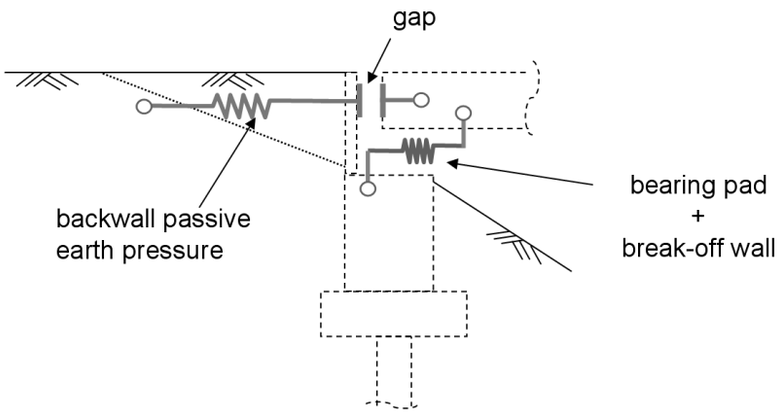


Figure 4 Abutment interaction springs

SEISMIC RESPONSE OF BRIDGE SYSTEM

Seismic responses of bridge system components such as soil, bridge structure, pile, *p-y* springs, and abutment were obtained from OpenSees simulations applying four hazard levels (40 motions). This section presents details of the local seismic bridge response characteristics for a moderate intensity motion (Northridge 1994 at Century city Lacc North, CMG Station 24389, a_{max} = 0.25g) and a strong motion with a 475-year return period (Erzincan, Turkey 1992, a_{max} = 0.70g).

Soil Response & Liquefaction

The loose sand layer across the bridge site was liquefied over its full or partial thickness depending on the input motion intensities. Liquefaction caused lateral spreading to occur in both abutment slopes. In Figure 5 (a), permanent displacement patterns of the bridge system for the Erzincan motions are presented. This figure shows that larger lateral deformation occurred near the right abutment, with permanent soil movement ranging from about 0.2 m to 1.3 m depending on the hazard level. Figure 5 (b) illustrates the pore pressure ratio in the soil. For stronger shaking, the entire loose sand layer across the bridge liquefied. Figure 6 shows the time variation of pore water pressure ratio with depth below the right abutment for the Northridge motion illustrating different degrees of pore water pressure generation with time.

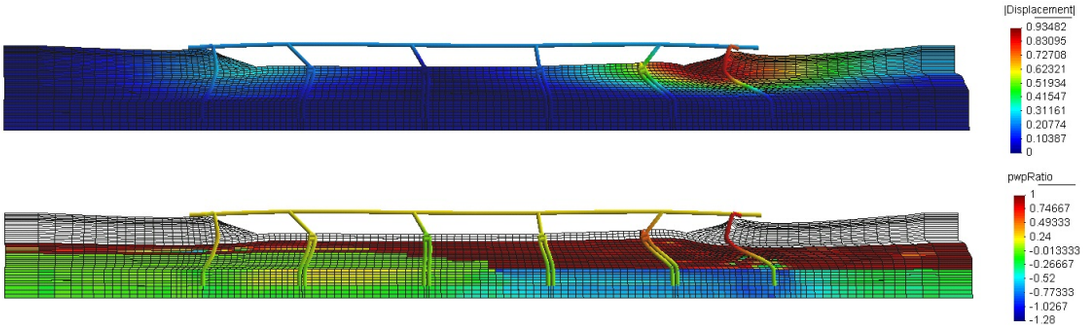


Figure 5 Displacement and pore water pressure ratio in soil (after shaking) - Erzincan, Turkey 1992, a_{max} = 0.70g: magnification factor = 20

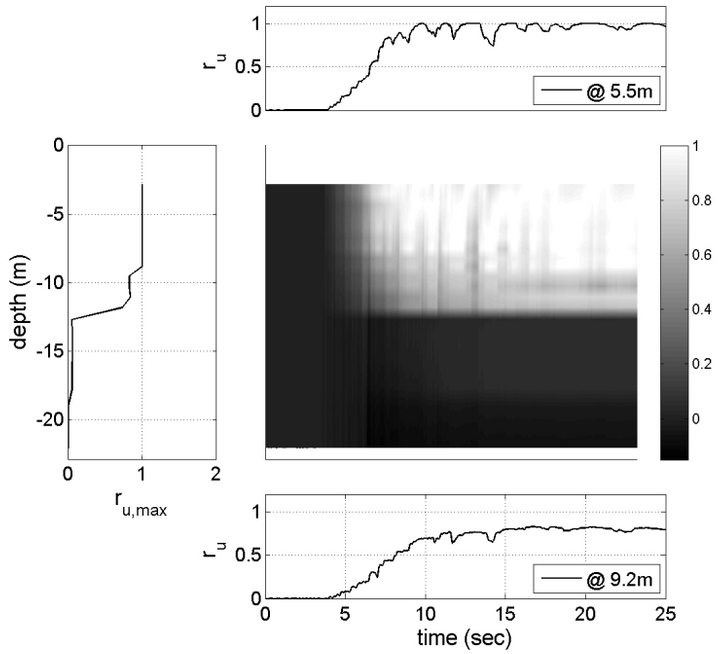


Figure 6 Spatial and temporal variation of pore pressure below right abutment in liquefiable soil – Northridge 1994, a_{max} = 0.25g

Bridge Pier Response

Actual input motions at the bottom of each bridge pier are presented in Figure 7 in terms of acceleration response spectra. Due to non-uniform soil conditions (i.e., different soil profile below the left and right abutments) and liquefaction induced lateral spreading, the bottom of each pier was subjected to different acceleration time histories and peak accelerations.

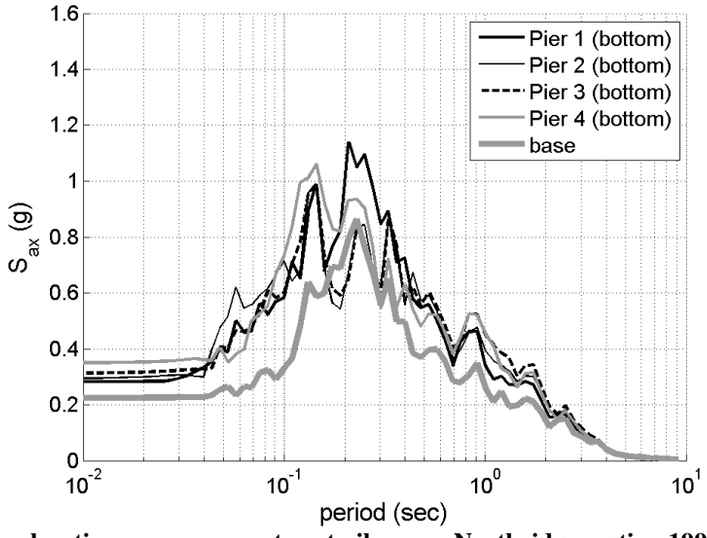


Figure 7 Acceleration response spectra at pile cap – Northridge motion 1994, a_{max} = 0.25g

Pile and *p-y* Spring Response

The horizontal slope movements significantly influenced the pile and pier bending moments. In particular, the bending moments in Pier 4 appeared to be closely correlated to horizontal slope movements. For small to moderate shaking events, the maximum bending moments at each bridge pier were greater than the residual bending moments after shaking, indicating that inertial forces controlled the maximum bending moments. For strong shaking events, however, the residual bending moment at each bridge pier or deck was greater than the transient maximum bending moment, indicating that the kinematic forces associated with lateral spreading controlled the maximum bending moment.

The pile force distribution and pile cap movement were significantly influenced by lateral spreading and the pattern of soil displacement with depth. This effect varied with ground motion intensity. Figure 8 shows maximum bending moments and their locations for motions corresponding to all four hazard levels in Piles 4 at the right abutment. In Pile 4, the maximum pile moment occurred, for small and moderate shaking, below the pile cap or at the interface between the surface clay and lower loose sand layers. However, for higher intensities, the maximum bending moment location moved down to the interface between the loose and dense sand layers (around 12 m depth).

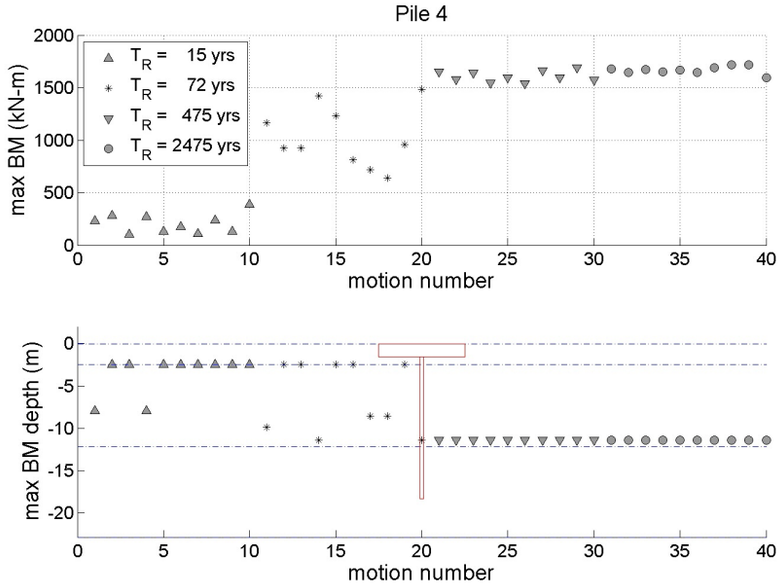


Figure 8 Maximum pile bending moments and their locations in Pile 4 near right abutment slope – four hazards (40 motions)

In Figure 9, the *p-y* spring response in Pile 4 at 5.5 m is plotted together with the corresponding pore pressure ratio (r_u) time history of an adjacent soil element. The API-based soil resistance time history mobilized by the same displacement is also presented in the figure. After 5 seconds, when the soil was liquefied, the lateral soil resistance reached an ultimate residual lateral resistance much smaller that what would have been obtained using conventional API-based values. The figure shows the clear effect of liquefaction on lateral soil resistance and the benefit of using p-y springs that can take into consideration the effect of pore water pressure generation on the ultimate strength.

Abutment Response

Figure 10 illustrates bridge deck and abutment interaction in terms of spring force-displacement response for a strong shaking motion. Figure 10 (a) shows the lateral resistance in the bearing pad and backwall. The initial 10 cm of displacement reflects only bearing pad resistance. After gap closure, large lateral resistance was mobilized in the break-off wall. The wall resistance contribution ends after backwall failure (shears off with respect to the stem wall). The bearing pad interaction force was delivered to the stem wall of the abutment. Figure 10 (b) shows that passive earth pressure resistance in the backfill soil was mobilized with the broken portion of the wall after closing the gap. Figure 10 (c) shows the total lateral resistance transmitted from the abutment system to the bridge deck.

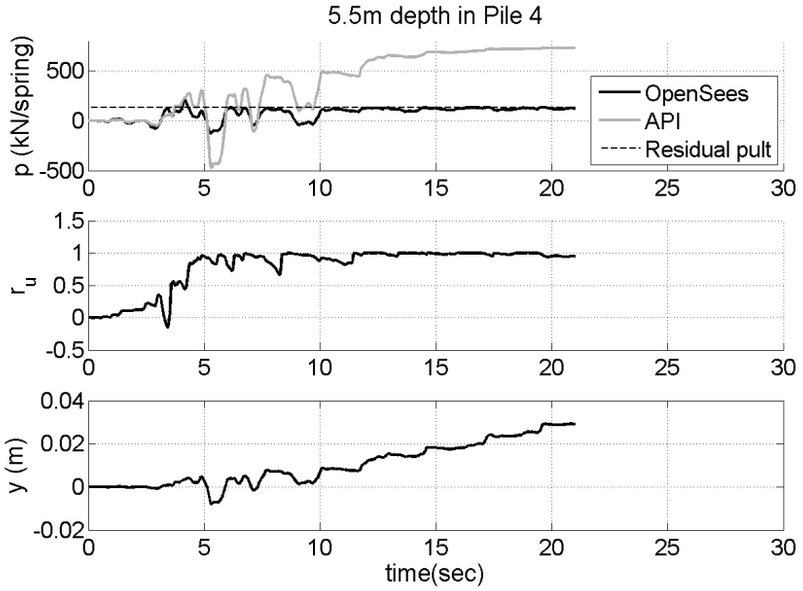


Figure 9 *p-y* time histories during earthquake excitation - Erzincan, Turkey 1992, a_{max} = 0.70g

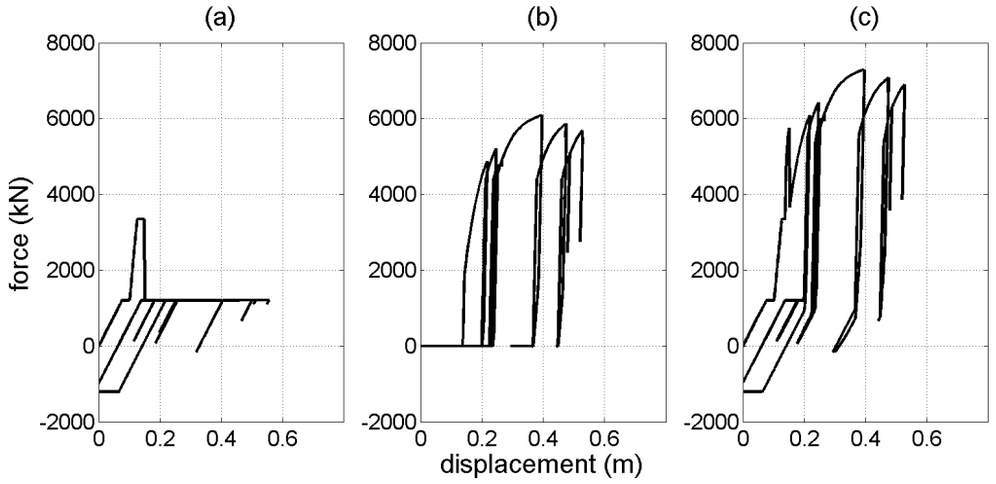


Figure 10 Response of abutment: (a) bearing pad spring response, (b) breakwall and soil spring response, and (c) total response - Erzincan, Turkey 1992, a_{max} = 0.70g

GLOBAL BRIDGE RESPONSE & ABUTMENT-BRIDGE INTERACTION

The expansion joints between the bridge deck and backwall closed when lateral spreading occurred. The entire bridge deck tended to move toward the left because the amount of lateral spreading in the right abutment was considerably larger than that in the left abutment. At the same time, lateral spreading also pushed the pile cap of Pier 4 to the left resulting in relatively small drift in that column. On the other hand, Pier 1 was subjected to very large column drifts because the bridge deck moved the upper end of the column to the left and lateral spreading moved the pile cap at the bottom of the column to the right. This global bridge behavior, which would likely not be anticipated by typical analyses that model only individual parts of the bridge, greatly affected the local response.

The bridge pier response was investigated using the displacements of the bridge deck and pile cap. Figure 11 shows drift ratios obtained by the column's displacement difference between the top and bottom at each pier. The bottoms of the four piers (pile caps) moved towards the center of the bridge and the amount of each pier base displacement varied due to different levels of lateral spreading. As shown in Figure 11, Pier 1 base residual lateral displacement was about 20 cm after shaking and Pier 4 base residual lateral displacement was about 60 cm. In the meantime, the top of all piers moved together to the left as the larger lateral spreading beneath the right abutment pushed the entire bridge deck to the left. This bridge deck movement increased Pier 1 drift and decreased Pier 4 drift. Due to this global response, similar drift ratios were observed in Pier 1 and Pier 4 for this particular motion even though the base residual lateral displacement of Pier 4 was greater than that of Pier 1. This demonstrates that lateral spreading in an abutment slope can affect the column drift in the other side of bridge.

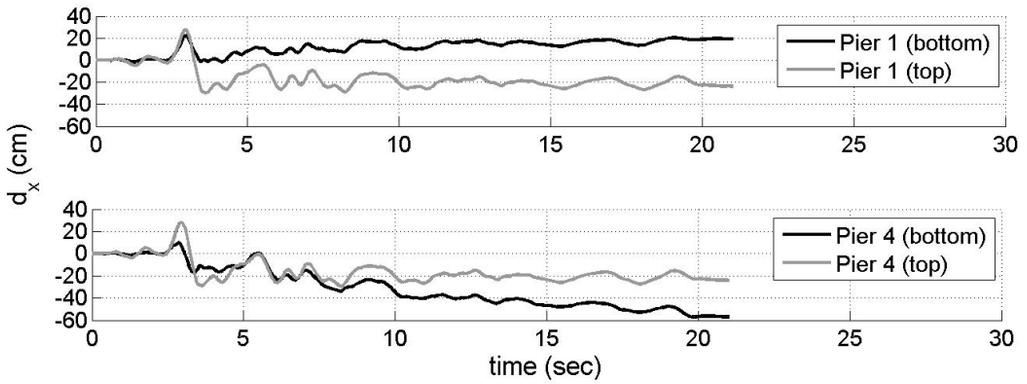


Figure 11 Displacement of Pier 1 and Pier 4 at top and bottom (column height = 6.7m) – Erzincan motion, Turkey 1992, a_{max} = 0.70g

CONCLUSIONS

A complete geotechnical bridge system model including pile foundations embedded in realistic soil conditions and abutment structures was developed and coupled to a bridge structure model (Mackie and Stojadinovic 2007). Appropriate modeling of soil-pile-structure interaction and soil-abutment-bridge interaction under lateral spreading soil conditions allowed the bridge structure to capture realistic force boundary conditions at

the pier base and bridge deck ends. Using this coupled model, the global behavior of the bridge system is better illustrated and important bridge performance variables can be identified. This study shows that the global response of a soil-foundation-bridge system was quite complex, particularly when soft and/or liquefiable soils are present. The use of OpenSees simulations provided improved understanding of the global response, and allowed identification of damage mechanisms that would not be captured by simplified analyses commonly used in contemporary practice.

One of the important components to the global bridge response was the abutment-to-abutment interaction caused by different level of lateral spreading and its effect on the bridge pier drift near slopes. Since the amount of lateral spreading at the right abutment in the simulation was considerably greater than that at the left abutment, the entire bridge deck moved toward to the left. At the same time, lateral spreading pushed the pile cap of the pier near the right slope to the left, so the column drift actually became smaller. On the other hand, the pier near the left slope was subjected to large column drift because the bridge deck moved to the left and the pile cap at the bottom of the column moved to the right due to lateral spreading of the left abutment. This type of response can only be obtained using advanced numerical models.

ACKNOWLEDGMENTS

This work was supported in part by the Earthquake Engineering Research Centers Program of the National Science Foundation under award number 2412005 through the Pacific Earthquake Engineering Research Center. Any opinions, findings, conclusions or recommendations expressed in this material are those of the author(s) and do not necessarily reflect those of the National Science Foundation. The project has benefited greatly from discussions with Jonathan Bray, Ross Boulanger, Christian Ledezma, Geoffrey Martin, and Scott Ashford. Their help is greatly acknowledged.

REFERENCES

API (1993). "Recommended practice for planning, designing and constructing offshore platforms, 1993" API Recommended Practice 2A (RP 2A) 20th Edition, Washington, D.C.

Boulanger, R., Curras C., Kutter B., Wilson D., and Abghari A. (1999). "Seismic soil-pile-structure interaction experiments and analysis", *Journal of Geotechnical and Geoenvironmental Engineering, ASCE,* 125 (No.9), 750-759.

Boulanger, R., D. Wilson, B. Kutter, S. Brandenberg, and D. Chang. (2004). "Nonlinear FE analysis of soil-pile-interaction liquefying sand", *Proceedings, Geotechnical Engineering for Transportation Projects, Geotechnical Special Publication,* No.126, 470-478.

Mackie, K., and Stojadinovic B, (2007). "Performance of Benchmark Bridge Structures," *ASCE Structures Congress*, Long Beach, CA. May 16-19 2007

Mokwa, R. (1999) "Investigation of the Resistance of Pile Caps to Lateral Loading", *Ph.D thesis, Virginia Polytechnic Institute*.

SDC (2004), Caltrans Seismic Design Criteria 2004.

Shin, H. (2007) "Numerical Modeling of a Bridge System & Its Application for Performance-Based Earthquake Engineering", *Ph.D thesis, University of Washington*.

Somerville, P.G. (2000). Characterizing near fault ground motion for the design and evaluation of bridges. Proceedings of the Third National Seismic Conference and Workshop on Bridges and Highways.

Yang, Z., Elgamal, A. and Parra E. (2003). "Computational model for cyclic mobility and associated shear deformation", *Journal of Geotechnical and Geoenvironmental Engineering, ASCE,* 129 (No.12), 1119-1127.

This page intentionally left blank

Sensitivity Study of an Older-Vintage Bridge Subjected to Lateral Spreading

Scott J. Brandenberg[1], A.M. ASCE, Pirooz Kashighandi[2], Jian Zhang[3], A.M. ASCE, Yili Huo[4], and Minxing Zhao[5]

[1] Assistant Professor, Department of Civil and Environmental Engineering, University of California, 5731 Boelter Hall, Los Angeles, CA 90095-1593, sjbrandenberg@ucla.edu
[2] Graduate Student, Department of Civil and Environmental Engineering, University of California, 5731 Boelter Hall, Los Angeles, CA 90095-1593, pirooz@ucla.edu
[3] Assistant Professor, Department of Civil and Environmental Engineering, University of California, 5731 Boelter Hall, Los Angeles, CA 90095-1593, zhangj@ucla.edu
[4] Graduate Student, Department of Civil and Environmental Engineering, University of California, 5731 Boelter Hall, Los Angeles, CA 90095-1593, huoyili@ucla.edu
[5] Graduate Student, Department of Civil and Environmental Engineering, University of California, 5731 Boelter Hall, Los Angeles, CA 90095-1593, zhaomx@ucla.edu

ABSTRACT: Static seismic analyses are used to characterize the vulnerability of an older-vintage bridge to liquefaction and lateral spreading. A sensitivity study is performed by varying key parameters and observing their influence on the predicted free-field lateral spreading displacement required to mobilize damage states ranging from minor damage to collapse. The thickness of the nonliquefiable crust layer was found to be the most influential parameter. Published fragility curves were reasonably consistent with the displacements required to cause major damage and collapse of the bridge.

INTRODUCTION

Past earthquakes have induced extensive damage to bridges due to soil liquefaction and lateral spreading. For example, the Showa Bridge collapsed during the 1964 Niigata earthquake (Yasuda and Berrill 2000) due to excessive movements of the piers on which the superstructure spans were simply supported, and a span of the Nishinomiya Bridge unseated during the 1995 Kobe earthquake (Wilson 2003) when two piers founded in laterally spreading ground moved toward each other. However, other bridges have performed reasonably well in lateral spreads. For example, the Landing Road Bridge suffered only moderate reparable damage despite as much as 2 meters of lateral spreading of the surrounding soils during the 1987 Edgecumbe earthquake (Berrill et al. 2001), and several bridges along the Sabaishi River remained in service despite moderate damage caused by lateral ground displacements of as much as a meter during the 2007 Niigata-Chuetsu Oki earthquake (Kayen et al. 2007). Recent advances in analytical methods (e.g., Boulanger and Tokimatsu 2006) show promise for capturing the full spectrum of bridge performance required for performance-based design and retrofit decisions.

The California Department of Transportation (Caltrans) owns approximately 13,000 bridges, most of which were constructed before 1971 at a time when liquefaction provisions had not yet been systematically implemented into design codes (Fig. 1). While many of the older bridges were evaluated and subsequently retrofitted for potential inadequate performance due to ground shaking, comprehensive evaluation of the bridges for damage due to liquefaction and lateral spreading has not been performed. This paper presents an analysis of the Mendocino Ave Overcrossing Bridge, designed in 1961 and constructed in 1964, for performance in liquefied, laterally spreading ground. Static beam on nonlinear Winkler foundation analyses were used in a sensitivity study to identify the parameters that most affect predicted performance.

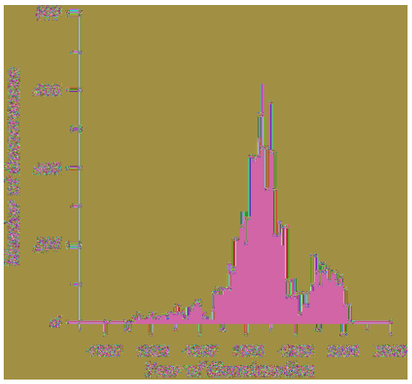


Figure 1: Histogram of year of construction of Caltrans bridges.

MENDOCINO AVE OVERCROSSING BRIDGE

The Mendocino Ave Overcrossing Bridge consists of a 4-span continuous concrete box girder superstructure attached to monolithic abutments and single column piers that was designed in 1961 and built in 1964 by Caltrans. The bridge has a straight geometry (i.e., no skew) and is supported on piles both at piers and at abutments. Each column is supported on a group of twenty 0.381 m diameter piles. The diaphragm walls at abutments are supported on a single row of six piles similar to the ones used for piers (Fig. 2).



Figure 2: Schematic of the Mendocino Ave Overcrossing Bridge

The 1.8 m diameter reinforced concrete piers consisted of 26 #11 longitudinal bars with spiral reinforcing consisting of #4 bars at 0.3 m (1 ft) pitch (Fig. 3). Moment curvature analysis of the section using RESPONSE 2000 (Bentz, 2001) identified that the ultimate bending moment of the pier section was 8000 kN·m (Fig. 4). A similar section analysis of the piles identified the ultimate moment capacity to be 230 kN-m.

The Mendocino Ave. Overcrossing Bridge is founded in sandy soil with some low SPT N-values, but the information provided in the as-built plans was insufficient to determine whether the site was liquefiable (e.g., position of groundwater table was not included). A synthetic liquefiable soil profile was assumed to exist at the bridge site for the purpose of assessing its vulnerability to liquefied soil loads. Modern design guidelines would result in different bridge components being considered in liquefiable soils compared with nonliquefiable soils, but the older bridges in the pre-1971 class were designed and constructed before systematic provisions for liquefaction were adopted in design codes.

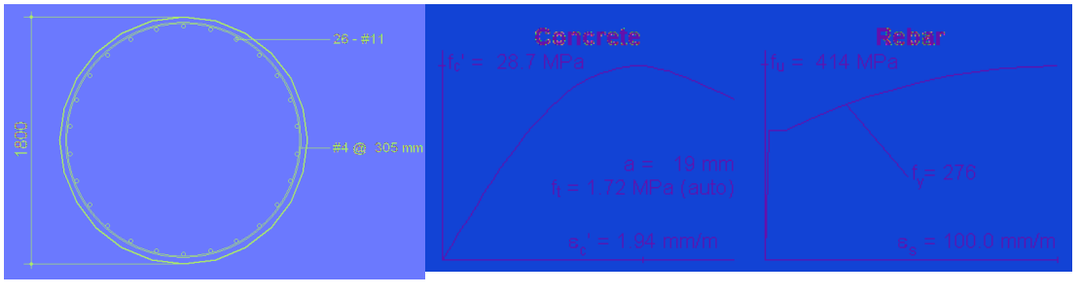


Figure 3: Section and material properties for reinforced concrete pier.

Therefore restricting selection of older-vintage bridges to liquefiable sites for this study was deemed unnecessary.

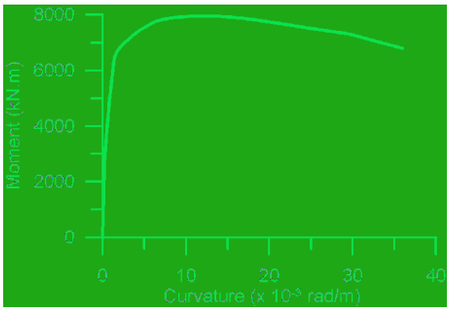


Figure 4: Moment-curvature response of pier.

The liquefiable soil profile fabricated for this study was based on cone penetrometer soundings included in a USGS database of the San Francisco east bay region including Alameda, Oakland, Berkeley and Emeryville (USGS, 2007). CPT soundings with potentially liquefiable soils were extracted from the database, and information such as the thickness of the liquefiable layer, the thickness and type of any nonliquefiable crust layer, and the tip resistance of any nonliquefiable crust layer used to estimate a reasonable average soil profile and variations in layer thicknesses and strengths for input to the sensitivity study (Table 1).

NUMERICAL SIMULATION APPROACH

The bridge was modeled in OpenSees, the finite element platform developed by the Pacific Earthquake Engineering Research Center (Mazzoni et al., 2006). The static seismic approach explained by Brandenberg et al. (2007b) was adopted for this study. Nonlinear beam columns were used to model the piles and piers and elastic beam columns were used for the superstructure, diaphragm walls and pile caps. Nonlinear beam column elements consisted of bilinear moment-curvature, linear shear-deformation, linear axial force-deformation, and linear torsion-deformation relationships based on the input parameters in Table 2. The nonlinear moment-curvature parameters were selected to best fit the section analysis in Fig. 4.

Table 1: Soil properties utilized in analyses.

Soil Layer		Depth to top of layer (m)	Unit Weight, γ (kN/m^3)	Friction Angle, ϕ (deg)	Cohesion, c (kPa)
Crust	Embankment	0	20	38	20
	Clay	6.1	20	0	70
Liquefied Sand		9.1	19	32	0
Dense Sand		11.3	20	38	0

Table 2: Modeling Parameters for the Nonlinear Beam Columns.

	Yield Moment M_y (kN.m)	Effective Bending Stiffness EI_{eff} (kN.m^2)	Post-yield Stiffness Ratio $EI_{post\text{-}yield}/EI_{eff}$	Axial Stiffness EA (kN)	Shear Stiffness GA (kN)
Piers	6635	9.53E+12	0.050	61,200,000	21,700,000
Piles	205	5.89E+10	0.016	3,400,000	940,000

Soil-structure interaction was modeled using p-y, t-z and q-z elements for lateral interaction, axial shaft friction, and pile tip end bearing resistances, respectively. Properties of the p-y elements were computed based on a nonliquefied soil profile and subsequently modified to account for the effects of liquefaction by (1) softening and weakening the p-y elements in the liquefied sand layer using a p-multiplier, and (2) softening (but not weakening) the p-y elements in the nonliquefiable crust layer to account for the influence of the underlying liquefied sand using models derived by Brandenberg et al. (2007a). Softening the p-y elements using this method accounts for the pinning effects of the bridge components on the spreading soils (TRB 2002, Boulanger et al. 2005) by coupling Newmark sliding block analyses with the load transfer behavior. Displacements were imposed on the free ends of the p-y elements to model lateral spreading demands. Two different load cases were considered: (1) equal but opposite lateral spreading at both bridge abutments and (2) lateral spreading in the same direction at one abutment and at the adjacent intermediate pier. The soil displacement profile consisted of some small strain in the nonliquefiable layers, and larger strains in the liquefiable layer, with a displacement discontinuity at the interface between the crust and underlying liquefied layer. Inertia forces can occur simultaneously with lateral spreading forces, and were imposed on the superstructure at connections with the piers and abutments, and also at the pile caps. Inertia forces were selected to be consistent with free-field ground displacements based on a Newmark sliding block method described by Brandenberg et al. (2007a).

RESULTS FOR BASELINE CASE

The deformed mesh for load case 1, with spreading at each abutment but no intermediate piers, is shown in Fig. 5a. The primary deformations in the bridge are in the piles that support the abutments, with little deformation evident in the piers or pile groups supporting the piers. This deformation mode is due largely to the nearly symmetrical loading imposed on the bridge, with the only sources of asymmetry being the geometry (elevation increases from left to right) and the inertia loads (imposed from left to right). Lateral spreading forces are transmitted as compression through the stiff superstructure, thereby shielding the piers from the influence of lateral spreading at the abutments. The entire bridge has shifted slightly from left to right, primarily due to the inertia forces.

The deformed shape for load case 2, with spreading at one abutment and the adjacent pier, is shown in Fig. 5b. Deformations are evident in piles supporting both abutments and at all three of the intermediate piers. The entire bridge has shifted from left to right under the combined action of the left-to-right lateral spreading and inertia forces. The

spreading soils loaded the leftmost pier, causing a translation of the pile cap that was nearly equal to the displacement of the superstructure, thereby causing little pier drift at this location but significant pile deformation. In contrast, the soil provided resisting forces to the other two pile groups and held the pile cap deformations to smaller values while the superstructure displacements caused significant pier drift.

The two load cases studied in this paper are not exhaustive of all of the possible loading combinations. They were presented simply as an illustration of how different load patterns can affect a bridge in different ways.

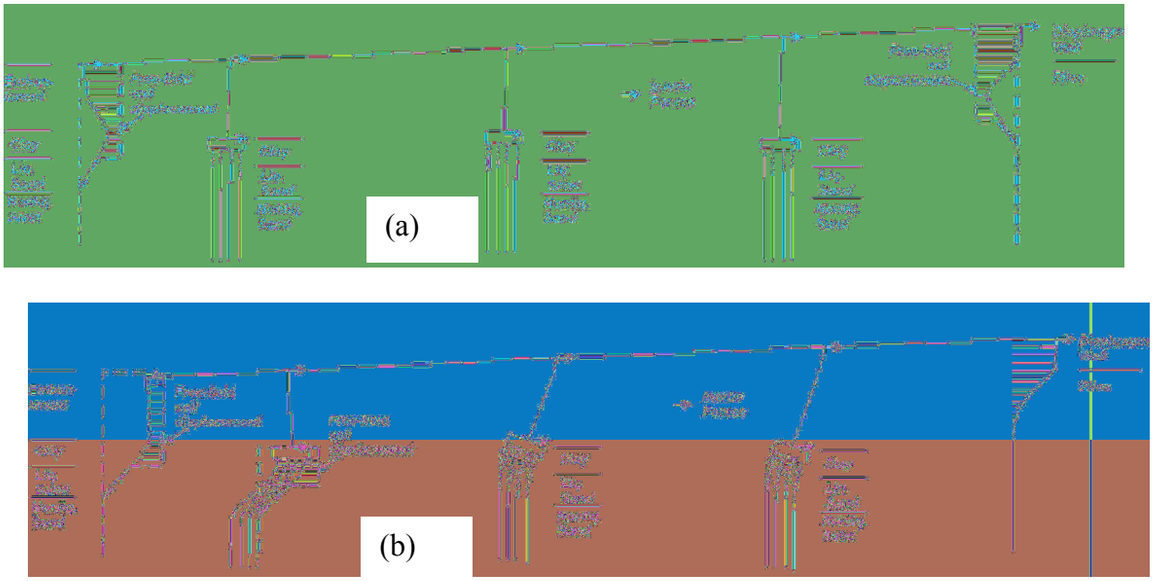


Figure 5: Deformed mesh for (a) Load Case 1 and (b) Load Case 2. Deformations amplified for clarity.

SENSITIVITY STUDY

A sensitivity study was performed to understand which of the input parameters most affected the prediction of damage caused by the two lateral spreading load cases. Table 3 summarizes the ranges that were assigned to each of the parameters considered in the study. These variations were selected, based on the authors' best judgment and available data where possible, to correspond roughly to one standard deviation above and below the mean values. This selection is admittedly subjective, but it is important when performing sensitivity studies that the range for each parameter corresponds to a common range of probabilities to obtain a proper assessment of the relative influence of each parameter. The sensitivity study proceeded by setting the value of one parameter to its high value while holding all of the other parameters at their mean values, then setting that parameter to its low value with all other parameters set to their mean values, and so on for all of the parameters for a total of 27 analyses (1 baseline analysis plus 26 with parameter variations).

Table 3: Parameter variations adopted in sensitivity study.

Parameter	Mean	Lowerbound	Upperbound
Crust Thickness	9.1 m Embankment 3 m Insitu Clay	5 m Embankment 1 m Insitu Clay	9.1 m Embankment 3 m Insitu Clay
Material Strength	c_{clay} = 70 kPa ϕ'_{sand} = 38° c'_{sand} = 20 kPa	c_{clay} = 40 kPa ϕ'_{sand} = 34° c'_{sand} = 20 kPa	c_{clay} = 120 kPa ϕ'_{sand} = 42° c'_{sand} = 20 kPa
$\Delta_{sand} / \Delta_{crust}$[2]	0.5	0.192	0.803
Liquefied Sand m_p	0.333	0.025	0.375
y_{50} for p-y springs in crust	$y_{50\,abutment}$ = 0.60 m $y_{50\,columns}$ = 0.03 m	Mean X 0.5	Mean X 1.5
Axial Capacity	Qtip = 1020 kN Side Friction based on Material Strength	Mean X 0.5	Mean X 1.5
Yield Strength, Pile	235 kN-m	Mean X 0.9	Mean X 1.1
Yield Strength, Pier	6535 kN-m	Mean X 0.9	Mean X 1.1
Pile Curvature Tolerance	0.2102 (1/m)	0.1575 (1/m)	0.2626 (1/m)
Inertia Load	Slope[3] = 0.775g/m	Mean Slope X 0.5	Mean Slope X 1.5
Strain in Dense Sand	0.53%	0.00%	1.06%
Strain in Crust	1.0%	0.0%	2.0%
Liquefied Sand Thickness	2 m	1 m	4 m

[1] number of standard deviations the variation in the parameter represents
[2] $\Delta_{sand} / \Delta_{crust}$ is the ratio between the displacement at the top of the loose sand to the displacement of the crust
[3] Inertia load was increased linearly with a slope of 0.775 g per every meter of ground displacement

Analyses proceeded by linearly increasing the ground displacements and inertia forces while tracking several engineering demand parameters that were used to define the bridge damage states (Table 4). Damage states were based on pier drift ratio using relations suggested by Basoz and Mander (1999), mobilized pile curvature ductility ($\phi_{mob}/\phi_{ultimate}$), and mobilized shear forces in the piers (V_{mob}/V_{cap}). The bridge was assumed to be in damage state 5 when pile curvature ductility exceeded the ultimate curvature because this was assumed to be the limiting value beyond which the piles would have significantly reduced axial load carrying capacity, thereby resulting in significant settlements and large damage to the bridge. Intermediate damage states (i.e. 2 through 5) were not assigned based on pile curvature ductility because it was assumed that any adverse effects of pile yielding would be manifested within the analysis as increased pier drift ratios, and intermediate damage levels in piles would otherwise not be detected. Damage state 5 was also assumed to have occurred when the shear force in the piers exceeded the shear capacity based on the assumption of a brittle type failure mechanism. As the analysis progressed the free-field ground displacement required to mobilize a damage state was recorded. The range of ground displacement required to mobilize a given damage state was computed for each parameter as the absolute value of the difference in ground displacements for the parameter set to its high and low values. The results were sorted based on the range, and plotted as a floating bar chart, or tornado diagram.

Table 4: Damage state definitions.

Damage State	Description	Pier Drift (%)	Pier Shear V_{mob}/V_{cap}	Pile Curvature $\Phi_{mob}/\Phi_{ultimate}$
1	No Damage	< 0.5		
2	Slight / Minor	0.5 - 1.0		
3	Moderate	1.0 - 2.0		
4	Extensive	2.0 - 5.0		
5	Collapse	> 5.0	> 1.0	> 1.0

The tornado diagram for load case 1 is shown in Fig. 6. The controlling mechanism for this tornado diagram was pile curvature because there was very little deformation in the piers. Hence, the bridge transitioned from damage state 1 to damage state 5 as soon as the pile curvature ductility reached the ultimate curvature. The only parameter that significantly influenced the results of the analysis was the thickness of the nonliquefiable crust layer. Increasing the crust thickness had little effect on the analysis, but decreasing the crust thickness had a significant effect, moving the ground displacement required to mobilize DS5 from about 0.3 m to about 0.9 m.

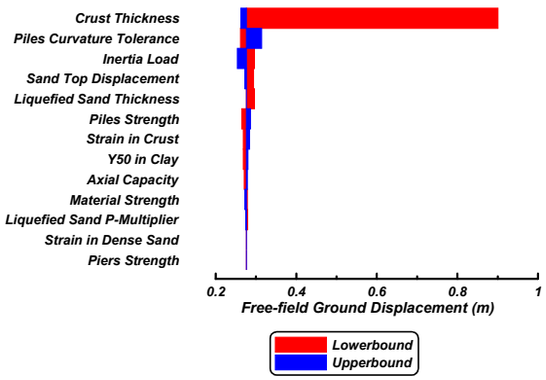


Figure 6: Tornado diagram for load case 1.

Tornado diagrams for load case 2 are shown in Fig. 7. In this case, intermediate damage states were mobilized by the pier drifts caused by asymmetrical loading of the bridge, but DS5 was caused by pile curvature ductility in all cases. The bridge is slightly more tolerant to ground displacement under load case 2, with DS5 being mobilized at about 0.4 m of displacement (compared with 0.3 m for load case 1). Again, crust thickness was an influential parameter, but inertia force and ultimate pile curvature were also important at DS5.

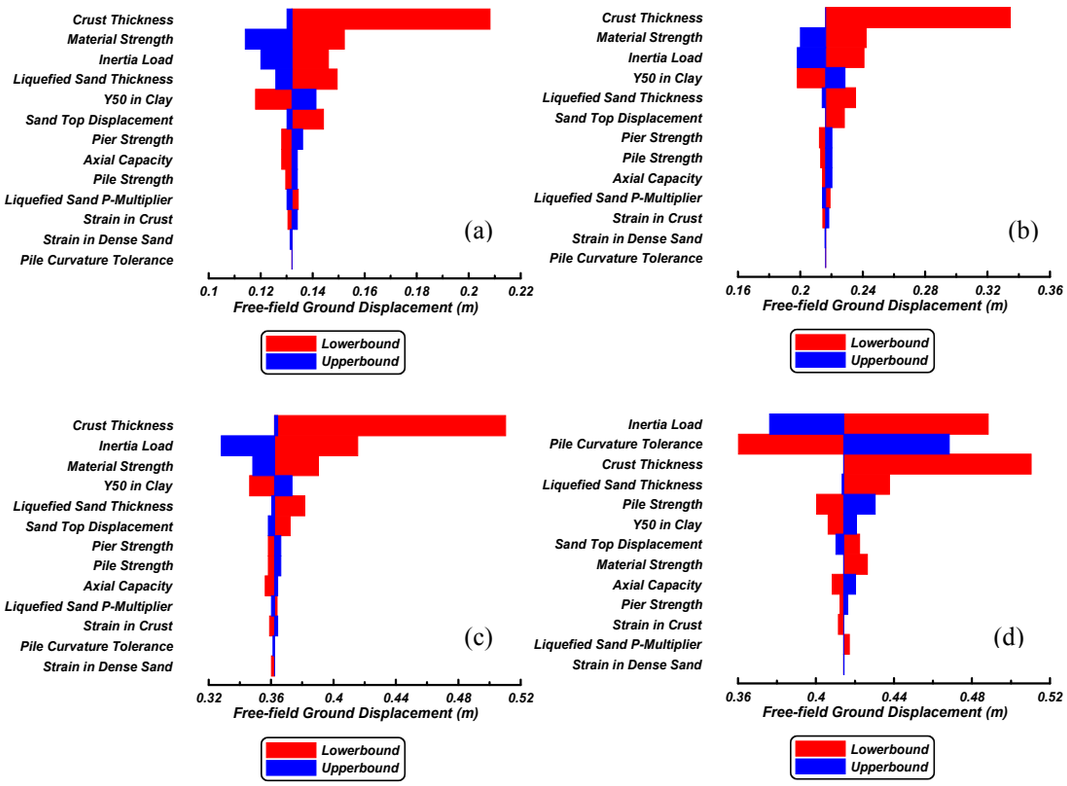


Figure 7: Tornado diagrams for load case 2 for (a) DS2, (b) DS3, (c) DS4, and (d) DS5.

The crust thickness was found to be the most influential parameter overall in the sensitivity study, so its influence warranted additional study. Increasing crust thickness had little effect; essentially the baseline case could be thought of as a thick crust case. However, decreasing crust thickness had a large effect, so another set of tornado diagrams was generated for the bridge by holding crust thickness constant at its lowerbound value while the other parameters were varied systematically to their upperbound and lowerbound values. The resulting tornado diagrams are plotted in Figs. 8 and 9. The ground displacement required to reach the various damage states increased about three-fold for load case 1, and by about 25% for load case 2. This observation is consistent with the expectation that bridge performance is better when the laterally spreading soils are thin (and associated crust loads are small).

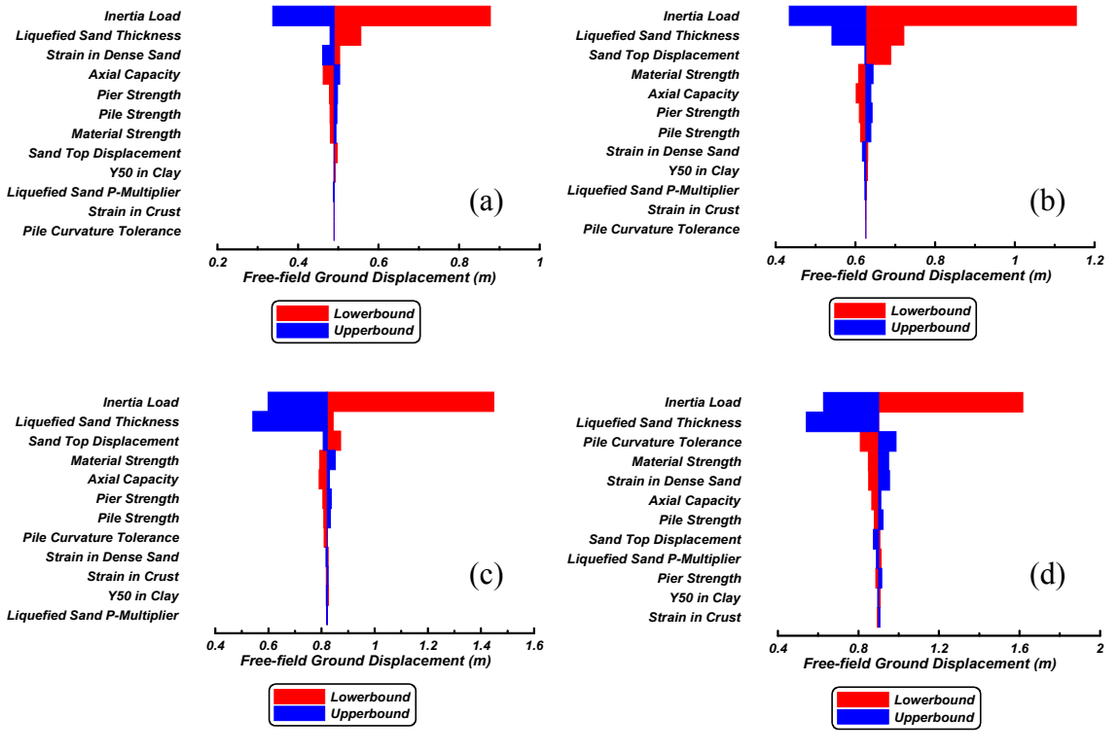


Figure 8: Tornado diagrams for load case 1, but with crust thickness held at its lowerbound value, for (a) DS2, (b) DS3, (c) DS4, and (d) DS5.

DISCUSSION

The Mendocino Ave Overcrossing Bridge was constructed in 1964, prior to the systematic introduction of liquefaction provisions in design codes. Therefore this bridge would be expected to perform poorly in liquefied and laterally spreading ground compared to more recent bridges designed with liquefaction considerations. The performance predicted in this study is reasonably consistent with fragility functions published in HAZUS (1999), which are the only known fragility functions for liquefaction and lateral spreading against bridges. The HAZUS provisions state that DS4 and DS5 are reached when lateral spreading displacements exceed 0.10 m and 0.35 m,

respectively, regardless of the class of bridge or soil conditions at the site. The HAZUS guidelines were identified as excessively conservative in transportation network analyses by Kiremidjian et al. (2006), which predicted unrealistically extensive collapse of bridges due to liquefaction for the 1989 Loma Prieta earthquake. More studies are needed to update the HAZUS guidelines for bridges of various vintages and structural configurations.

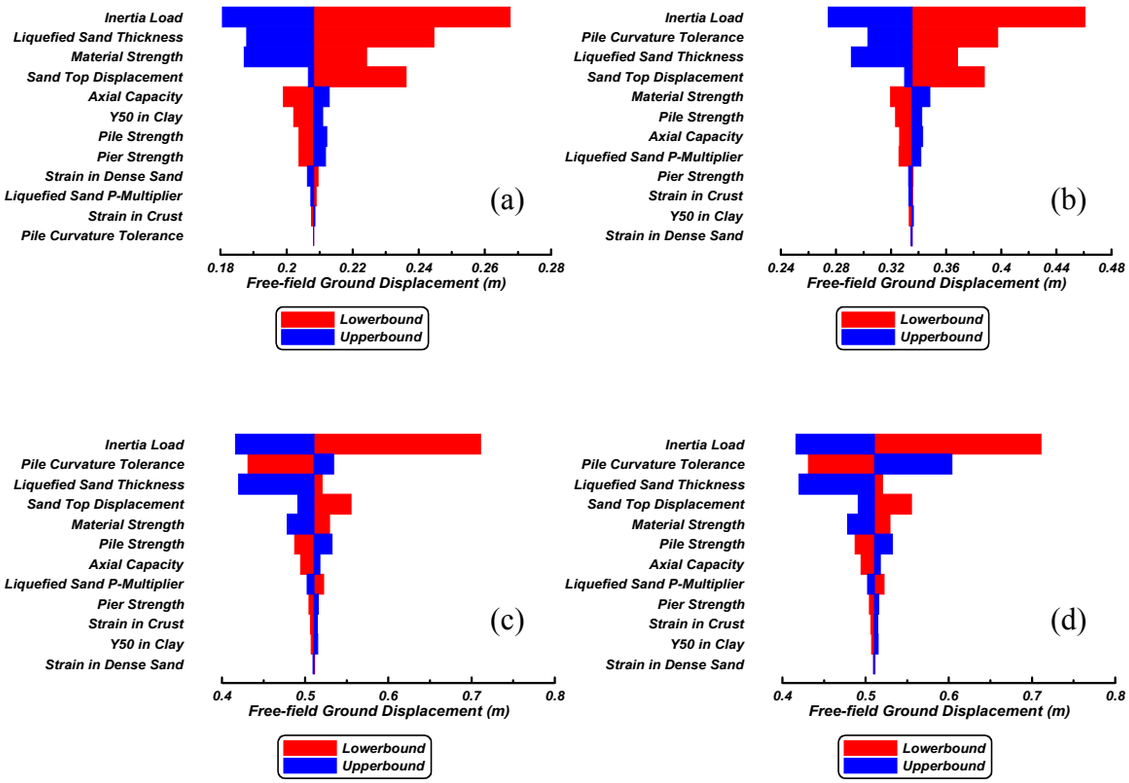


Figure 9: Tornado diagrams for load case 2, but with crust thickness held at its lowerbound value for (a) DS2, (b) DS3, (c) DS4, and (d) DS5.

ACKNOWLEDGMENTS

Tom Shantz and Mark Yashinsky of Caltrans provided valuable help in developing the bridge classification system and providing as built plans. Funding for this work is provided by the Pacific Earthquake Engineering Research Center under project no. 2572005, and by the Pacific Earthquake Engineering Research Center Lifelines program under project task No. 9C. The contents of this paper do not necessarily represent a policy of either agency or endorsement by the state or federal government.

REFERENCES

Basoz, N., and J. Mander (1999), *Enhancement of the Highway Transportation Module in HAZUS*, in *Report to National Institute of Building Sciences.* Washington, D.C.

Bentz, E. (2001). "Response-2000 User Manual". University of Toronto. 85 p.

Berrill, J.B., Christensen, S.A., Keenan, R.P., Okada, W., and Pettinga, J.R. (2001). "Case study of lateral spreading forces on a piled foundation." *Geotechnique*, 51(6). 501-517.

Boulanger, R.W., Chang, D., Gulerce, U., Brandenberg, S.J., and Kutter, B.L. (2005). "Evaluating pile pinning effects on abutments over liquefied ground." Simulation and Performance of Pile Foundations in Liquefied and Laterally Spreading Ground, Geotechnical Special Publication, ASCE, 306-318.

Boulanger RW, and Tokimatsu K (2006) Geotechnical Special Publication No 145: Seismic performance and simulation of pile foundations in liquefied and laterally spreading ground. ASCE Press, Reston, VA, 321 p

Brandenberg, S.J., Boulanger, R.W., Kutter, B.L., and Chang, D. (2007a). "Liquefaction-induced softening of load transfer between pile groups and laterally spreading crusts." *J. of Geotech. Geoenviron. Eng. 133(1). 91-103.*

Brandenberg, S.J., Boulanger, R.W., Kutter, B.L., and Chang, D. (2007b). "Static pushover analyses of pile groups in liquefied and laterally spreading ground in centrifuge tests." *J. of Geotech. Geoenviron. Eng. 133(9). 1055-1066.*

HAZUS (1999), Earthquake Loss Estimation, Technical Manual, National Institute of Building Sciences, Washington D.C.

Kayen, R. Pujol, S., Collins, B.D., Abrahamson, N., Ashford, S., Brandenberg, S.J., Dickenson, S., Johnson, L., Kabeyasawa, T., Kawamata, Y., Koumoto, H., Tanaka, Y., Marubashi, N., Tokimatsu, K., Tsai, B., Yanev, P., Yashinsky, M., and Yousok, K. (2007). "Niigata-Chuetsu Oki, Japan, Earthquake of July 16, 2007". EERI-GEER Web Report 2007-1 v. 6.

Kiremidjian, A., Moore, J., Fan, Y.Y., Basoz, N., Yazali, O., and Williams, M. (2006) "Pacific Earthquake Engineering Research Center highway demonstration project." *Pacific Earthquake Engineering Research Center*, Report No. PEER 2006/02.

Kulasingam, R., Malvick, E. J., Boulanger, R. W., and Kutter, B. L. (2004). "Strength loss and localization at silt interlayers in slopes of liquefied sand." *J. Geotech. Geoenviron. Eng.,* 130(11), 1192-1202.

Mazzoni, S., McKenna, F., Scott, M.H., and Fenves, G.L. (2006). "Open system for earthquake engineering simulation user command-language manual." *Pacific earthquake engineering research center*, University of California, Berkeley. 465 p.

Ovesen, N. K. (1964). *Anchor slabs, calculation methods and model tests*. Bulletin No. 16, The Danish Geotechnical Institute, Copenhagen.

Transportation Research Board (TRB). (2002). *Comprehensive specification for the seismic design of bridges.* National Cooperative Highway Research Program (NCHRP) Report 472, National Research Council, 47 pp.

United States Geological Survey (USGS) (2007). "CPT data Alameda County". Online database: http://earthquake.usgs.gov/regional/nca/cpt/data/?map=alameda.

Wilson, J.C. (2003). "Repair of new long-span bridges damaged by the 1995 Kobe earthquake." *J. Performance of Constructed Facilities.* 17(4), 196-205.

Yasuda, S., and Berrill, J.B. (2000). "Observations of the earthquake response of foundations in soil profiles containing saturated sands." *Proc. GeoEng 2000 Conf.,* Melbourne, Australia, CD Rom.

Soil-Structure Interaction Analysis of Bridge Columns Supported on CISS Piles

Pedro F. Silva [1], Majid T. Manzari [2]

[1]Associate Professor, Department of Civil and Environmental Engineering,
The George Washington University, silvap@gwu.edu
[2]Professor, Department of Civil and Environmental Engineering,
The George Washington University, manzari@gwu.edu

ABSTRACT: A pushover analysis on the inelastic response of bridge columns supported on pile groups consisting of full moment connection cast-in-place-steel-shell (CISS) piles is presented in this paper. An original component of the work presented in this paper is that the analytical models considered the nonlinear actions that develop in the column, supporting piles and soil. Analysis confirmed that variations in the horizontal and vertical soil stiffness affect the pile cap lateral deflection and rotation, respectively. Results from this analysis also indicate that for columns with aspect ratios lower than six the contribution of soil-structure interaction is significant; however, for columns with higher aspect ratios and for stiffer soils the effects of soil-structure interaction are negligible.

INTRODUCTION

The study presented herein considered the nonlinear actions that develop in the column, the supporting piles, and the soil surrounding the piles. The column was modeled under different sets of aspect ratios varying between 2 and 10. For the piles, the analytical models included the prying action that develops at the pile head when the steel shells are embedded into the pile cap. Analytical models previously developed for full moment connection CISS piles were used to evaluate the seismic performance of pile groups (Silva and Seible, 2001; Hose *et al.*, 2000).

Variables investigated in this study included: (a) nonlinear soil-structure horizontal stiffness interaction, and (b) nonlinear soil-structure vertical stiffness interaction. Numerical results indicate that for columns with aspect ratios lower than six the contribution of soil-structure interaction is significant; however, for columns with higher aspect ratios and for stiffer soils the effects of soil-structure interaction are almost negligible. This is a key finding from this study because it quantifies for what levels of column aspect ratio the soil-structure interaction can be of significance and for what levels should design engineers and researchers employ a more refined soil-structure interaction study. This paper presents a detailed discussion of these numerical results providing insightful information on the performance of CISS pile foundations and their influence on the nonlinear pushover analysis of bridges.

PILE GROUP ANALYTICAL MODELING

The finite element model shown in FIG. 1 was investigated in terms of: (1) nonlinear horizontal soil stiffness at the level of the pile cap and surrounding the piles, (2) nonlinear soil to pile vertical stiffness interaction, (3) variations in the column height or column aspect ratio, and (4) variations in the soil stiffness.

Influence of the column height on the lateral response of the pile group was considered for columns with aspect ratios (i.e. H_C / D_C) of 2, 3, 4, 5, 6, 7, 8, 9, and 10. The column diameter, D_C, was set at 1.83m, with an applied axial load of 9,000kN.

The piles were arranged in a 4x4 pile group with the centerline spacing between piles corresponding to nearly four pile diameters, $4D_p$; as such, no pile group effects were considered in the analysis. The pile cap was modeled as linear elastic with the stiffness computed based on a section with the dimensions 10.5m x 10.5m x 2.4m. The ground water table (G.W.T.) was assumed at the ground surface, as shown in FIG. 1.

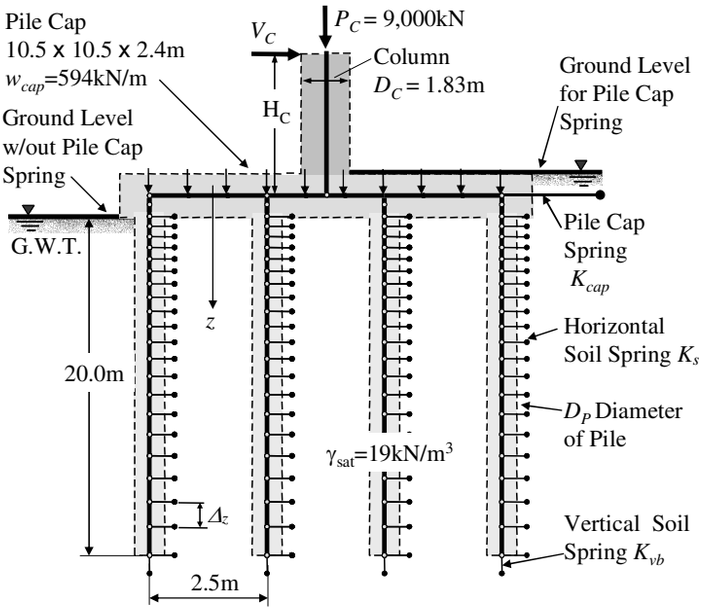


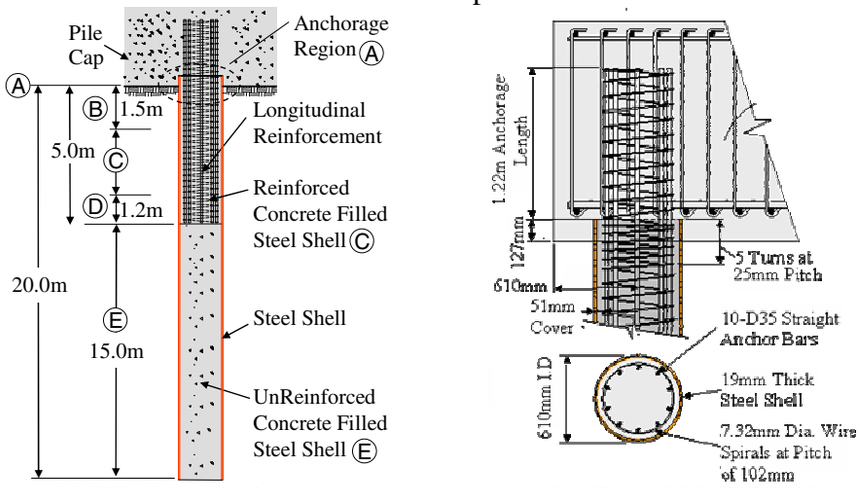
FIG. 1. Pile Group Finite Element Model

Full-moment connection CISS Piles Modeling

The CISS pile shown in FIG. 2 was used in this study. This pile is the standard full-moment connection Caltrans Class 200 pile (Caltrans, 1990). The pile consists of a steel shell that is embedded into the pile cap with an embedment length of 127mm, and the core is filled with concrete that is reinforced with straight anchor bars into the pile cap (Silva *et al.*, 1997). The anchorage reinforcement extends 5m below the pile cap and in this work the length of the piles was 20m. For this pile the allowable design axial loads are −1,780kN and +3,560kN (Caltrans, 1990), where the negative and positive values correspond to tensile and compressive axial loads, respectively.

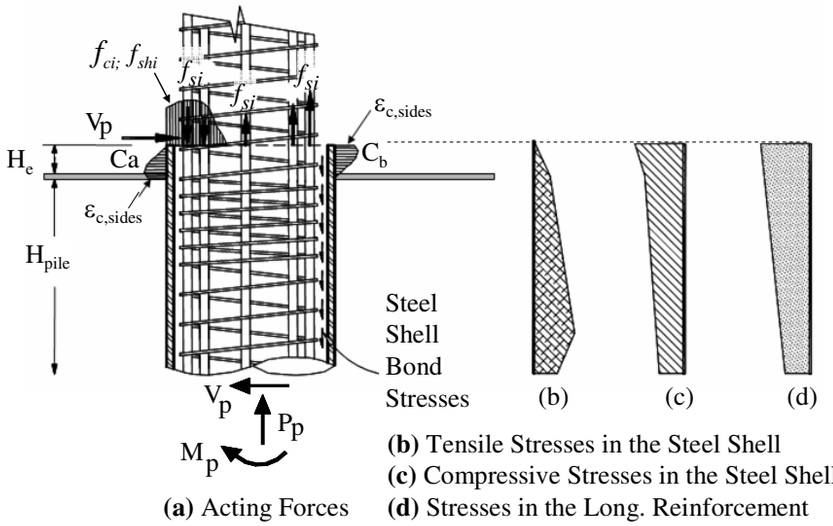
Moment-Curvature Relations and Interaction Diagrams: Reflecting the changes in the reinforcement layout shown in FIG. 2(a), the piles were investigated according to the five regions designated in this figure. For each of these five regions moment-curvature relations were evaluated were evaluated for the previously defined allowable design axial loads. Analytical models previously developed by Silva and Seible (2001)

were used to establish the stress profiles depicted in FIG. 3 and to obtain the pile section nonlinear moment curvature relationships.



(a) Pile Length Reinforcement **(b)** Class 200 CISS Pile

FIG. 2. CISS Pile Details



(a) Acting Forces

(b) Tensile Stresses in the Steel Shell
(c) Compressive Stresses in the Steel Shell
(d) Stresses in the Long. Reinforcement

FIG. 3. Anchorage Region Force Equilibrium Relations

These stress profiles were established by assuming the traditional linear variations of strains, the nonlinear material stress-strain relationships, and the axial loads imposed on a pile. As shown in FIG. 2(a), different section analysis along the length of the piles were required to account for the variations in the longitudinal reinforcement, and detailing of the steel shell at the connection to the pile cap. These analytical models were established for the anchorage region and at different sections along the length of the prototype CISS piles and were calibrated using experimental results for the prototype CISS pile depicted in FIG. 2 (Silva *et al.*, 1997).

Moment-curvature relations for the five regions shown in FIG. 2(a) were obtained and these analyses were used to model the nonlinear response of piles in a 4x4 pile group under lateral loads; however, for brevity only the results for the anchorage

region are presented in FIG. 4. The numerical values shown near each curve in FIG. 4 indicate the different axial load levels used in these analyses.

Column Modeling

Based on the reinforcement layout and section dimensions shown in FIG. 5, the axial load ratio on the column was ~9.8%, the column longitudinal reinforcement ratio was ~2.5%, and the transverse reinforcement volumetric ratio was ~1.1%. Results from the column section moment curvature analysis are presented in FIG. 5.

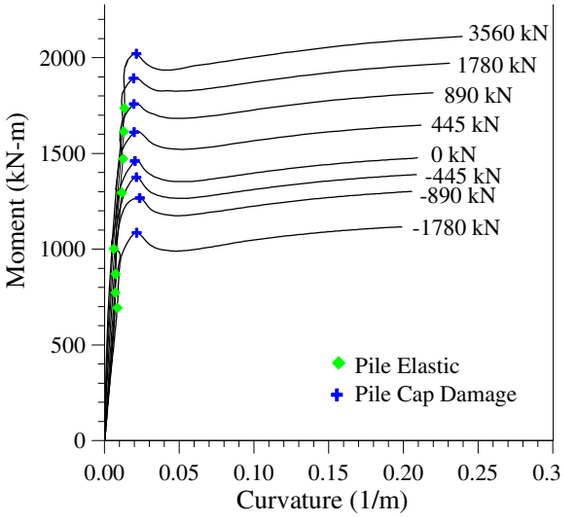


FIG. 4. Pile Section Analyses

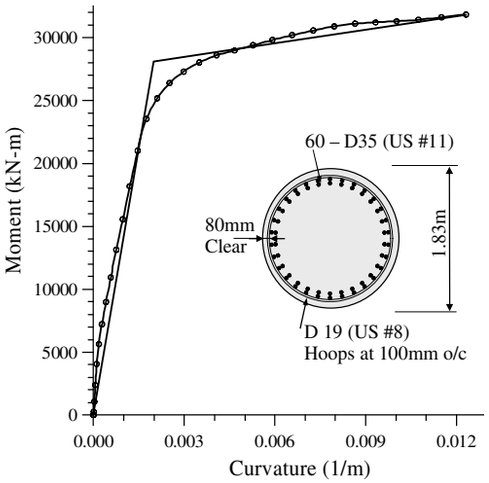


FIG. 5. Column Section Analysis

Single Pile Modeling

The anchorage zone or Region A in FIG. 2(a) was modeled by a single element positioned at the connection to the pile cap. The bending stiffness of this single element was obtained using the moment-curvature relations shown in FIG. 4. For the other regions a similar analysis was performed. As such, at each lateral load increment the pile's beam elements' bending stiffness properties were updated based on the moment curvature analyses, and the soil was modeled as an array of nonlinear uncoupled spring elements.

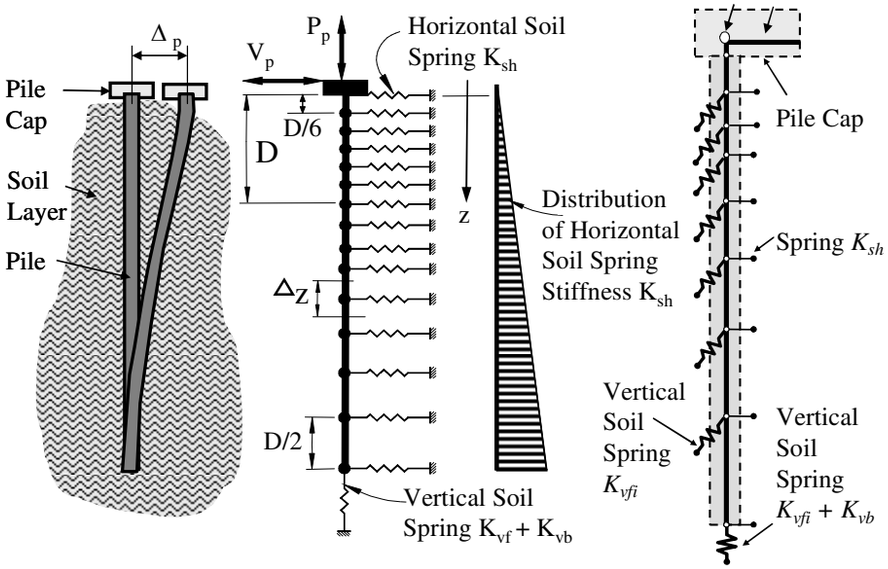
The analytical subgrade reaction model, typically known as the Winkler model, was used for the analysis of piles under lateral loading. Soil-structure interaction analysis was performed using beam elements for modeling of the piles, and the soil surrounding the piles was modeled by spring elements according to the discrete finite element model illustrated in Figs. 6(a) & 6(b).

Horizontal Soil Modeling

In this work, the soil was modeled with discrete nonlinear spring elements and properties representing cohesive soft and stiff soils with a modulus of elasticity of 5,000 kN/m^2 (soft clay) and 50,000 kN/m^2 (stiff clay).

Surrounding the Piles: Effects of the soil surrounding the piles in the horizontal direction were modeled in terms of elements with axial stiffness only. In this work, the soil surrounding the piles had an assumed shear strength varying between typical undrained shear strength of lightly overconsolidated clay (with an OCR of 2,

characteristic of soft soils) to that of highly overconsolidated clay (with an OCR of 10, characteristic of stiff soils). As shown in Table 1, the ratio of the undrained shear strength to the initial vertical effective stress was taken as 0.2 for the soft soils and 1.0 for the stiff soils. The ground water table (G.W.T.) was assumed at the ground surface, as shown in FIG. 1.



(a) Prototype **(b)** FEM Model **(c)** Vertical Springs

FIG. 6. Finite Element Model - Single Piles

Table 1. Shear Strength Used for Different Soil Types

Soil Type	Undrained shear strength/initial effective stress of the soil	Modulus of Elasticity, E_S, kN/m^2
Soft	$s_u/\sigma'_v = 0.2$	5,000
Stiff	$s_u/\sigma'_v = 1.0$	50,000

A bilinear relation between the horizontal soil pressure and lateral displacement was used to idealize the soil properties. Subsequently the modulus of subgrade reaction was obtained by using the following equation proposed by Vesic (1961):

$$k_h = 0.65 \sqrt[12]{\frac{E_s D_p^4}{E_p I_p}} \frac{E_s}{(1-\mu_s^2)} \qquad (1)$$

Given the pile's diameter D_p, elastic modulus E_p, and moment of inertia I_p, and the soil's elastic modulus of E_s with a Poisson μ_s ratio of 0.45, the values of k_h for the two cases of soft and stiff clays were computed based on the shear strengths values given in Table 1. The bilinear horizontal soil model expressed in terms of the soil pressure was given by (Poulos, 1971):

$$p_s = k_h \, \delta_h; \qquad p_s \le p_{ult} \qquad (2)$$

Where δ_h is the lateral displacement of the soil due to the pressure p_s. Note that p_s is the soil reaction force per unit length of the pile and p_{ult} is the ultimate soil reaction

force per unit length as given in the sequel by Eq. (4). The soil spring stiffness at any depth was computed based on:

$$K_{sh} = k_h \, \Delta_z \tag{3}$$

Where K_{sh} is the equivalent spring stiffness, k_h is the modulus of horizontal subgrade reaction modulus and Δ_z is the length contributed by the springs at a given depth z. Assuming the horizontal subgrade reaction modulus was normalized in terms of a nominal pile diameter of 1.80m (Pender, 1978), then k_h may be expressed in terms of the nominal pile diameter D^* and the pile section diameter D_p. Thus, the soil normalized spring stiffness was given by:

$$K_{sh} = k_h \, \Delta_z \left(\frac{D_p}{D^*} \right) \tag{4}$$

In Eq. (2) the limiting soil pressure, p_{ult}, was obtained according to the relation proposed by O'Neil and Gazioglu (1984):

$$p_{ult} = FN_p s_u D_p \tag{5}$$

Where F is a reduction factor depending on the failure strain of the soil in a triaxial undrained compression test and ranges from 0.5 for stiff clays to 1.0 for soft clays, s_u is the shear strength of the soil, and N_p is defined as:

$$N_p = 3 + 6\frac{z}{z_{cr}} \le 9; \quad z_{cr} = \frac{L_{cr}}{4} \tag{6}$$

Variable L_{cr} in Eq. (6) is the critical length of the pile and is usually chosen at $20D_p$. It is noted that normally a nonlinear curve precedes the limiting pressure. In this work, this nonlinear portion is approximated by *a linear secant modulus.*

Surrounding Pile Cap: The seismic response of the pile group was also characterized in terms of the passive pressure that develops in front of the pile cap. This was conducted by positioning a spring in front of the pile cap as illustrated in FIG. 1. The pile cap spring stiffness was computed according to the expression:

$$K_{cap} = [(k_h)_{avg.} / D_p] \, H_{cap} W_{cap} \tag{7}$$

Where $(k_h)_{avg.}$ is the average value of k_h over the height of the pile cap and H_{cap} and W_{cap} are the height and width of the pile cap, respectively. For this condition and as shown in FIG. 1 the soil was positioned at the upper level of the pile cap.

Vertical Soil Modeling

End Bearing Resistance: The vertical end bearing resistance was only considered for piles in compression with no resistance when the piles are in tension. The end bearing stiffness, K_{vb}, was calculated by using *q-w* relationship proposed by Aschenbrener and Olson (1984) for piles embedded in clays. Hence, the q-w relationship was assumed bilinear, and the initial slope of the q-w curve was obtained by:

$$K_q = \frac{9 s_u}{0.01 D_{tip}} \tag{8}$$

Where D_{tip} is the diameter of the pile tip and s_u is the average undrained shear strength of the soil from $3D_{tip}$ below to $3D_{tip}$ above the pile tip. Once the tip displacement reaches 1% of the pile diameter the soil pressure at the pile tip reaches

its maximum value, q_{max}, and remains constant with a limit given by (Aschenbrener and Olson, 1984):

$$q_{\max} = N_c.s_u \tag{9}$$

Where N_c ranges from 0.0 to 20.0 and is independent of the soil shear strength. In this work, N_c was set to 9. The vertical spring constant at the pile tip is then:

$$K_{vb} = K_q\ A_p \left(\frac{D_p}{D^*}\right) \tag{10}$$

Where A_p is the cross sectional area of the pile at the pile tip.

Vertical Skin Friction Resistance: The skin friction resistance was assumed equal for the piles in compression and tension. The distributed side friction was modeled by using the t-z relationships developed by Aschenbrener and Olson (1984), based on a large number of field load tests. Again a simple bilinear relationship was assumed between the side friction, τ, and the relative displacement of pile and soil, δ_v. The relationship is assumed linear up to a relative displacement of 0.4% of the pile diameter, where the maximum shear stress is mobilized in the soil-pile interface and is computed in terms of (Aschenbrener and Olson, 1984):

$$\tau = k_{tf}\delta_v; \quad \tau \le \tau_{\max} \tag{11}$$

The maximum mobilized shear stress is (Aschenbrener and Olson, 1984):

$$\tau_{\max} = \alpha s_u \tag{12}$$

Where s_u is the undrained shear strength of the soil, and α is a constant of proportionality computed as:

$$\alpha = \frac{P_{ou} - P_{tu}}{s_u A_s} \tag{13}$$

In this equation P_{ou} is the pile head load at failure, P_{tu} is the pile tip load at failure, and A_s is the area of soil-pile interface. The *t-z* relationship flattens as the shear stress reaches τ_{max}, and the initial stiffness of the vertical springs representing *t-z* is:

$$K_{vtf} = k_{tf}.(\pi D).\Delta z \tag{14}$$

PILE GROUP ANALYSIS RESULTS

System Performance

Three components of deformations influence the system response. The effects of these components on the global displacement of the structural system are illustrated in FIG. 7. Relevant to the study presented in this paper, it is important to emphasize that nonlinear deformations that develop in the piles are not possible to quantify in a separate component but they are represented within the response of the pile cap rotation and deflection. As such, the overall system displacement ductility with foundation flexibility, $\mu_{\Delta T}$, was computed based on:

$$\mu_{\Delta T} = \Delta_{UT} / \Delta_{yT} \tag{15}$$

Where Δ_{yT} and Δ_{UT} are the overall yield and ultimate displacements at the top of the column, respectively, and are given by:

$$\Delta_{yT} = H_C\theta_{cap,y} + \Delta_{cap,y} + \Delta_{col,y}; \tag{16}$$

$$\Delta_{UT} = H_C\theta_{cap,U} + \Delta_{cap,U} + \Delta_{col,U}$$

Where H_C is the column height, $\theta_{cap,y}$, $\theta_{cap,U}$, $\Delta_{cap,y}$ and $\Delta_{cap,U}$ are the pile cap rotations and lateral deflections evaluated at yield and ultimate conditions for the column, and $\Delta_{col,y}$ and $\Delta_{col,U}$, are the yield and ultimate deflections of the column. Based on these expressions the system displacement ductility's were evaluated and results from these analyses are presented in FIG. 8.

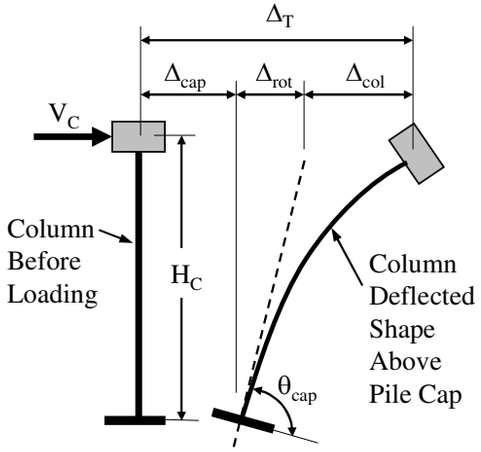


FIG. 7. System Deflection Components

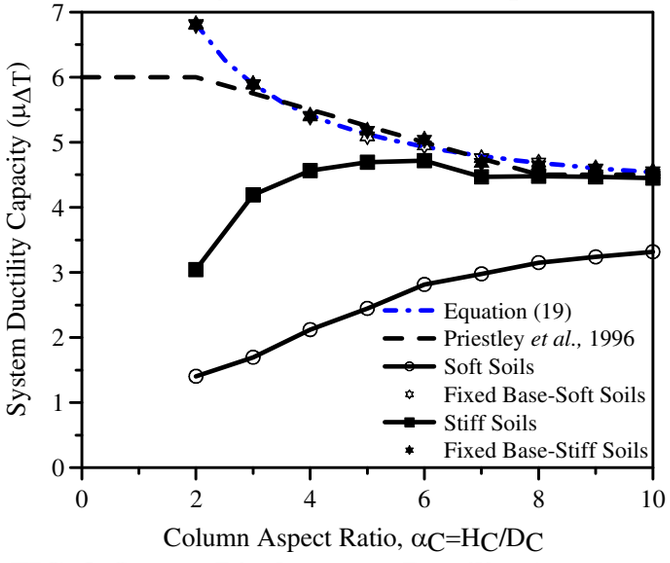


FIG. 8. System Displacement Ductility Assessment

In FIG. 8 the theoretical fixed base curve (shown as ▬ • ▬) was computed from the column analysis depicted in FIG. 5, and was computed by expanding the expression:

$$\mu_\Delta = 1 + 3\left(\frac{\phi_U - \phi_y}{\phi_y H_C^2}\right) L_p \left(H_C - \frac{L_p}{2}\right) \qquad (17)$$

Where ϕ_U and ϕ_y are the column ultimate and yield curvatures, and the plastic hinge length, L_p, was estimated by:

$$L_p = 0.08H_C + L_{sp}; \quad L_{sp} = 0.022 d_b f_y \tag{18}$$

Where L_{sp} is the strain penetration into the bent cap, and d_b and f_y are the column bar diameter and yield strength, respectively.

Substituting Eq. (17) with $H_C = \alpha_C D_C$ and $\mu_\phi = \phi_U / \phi_y$ one obtains the following fixed-base displacement ductility, μ_Δ, equation in terms of the column aspect ratio, α_C, the column diameter, D_c, and the column curvature ductility capacity, μ_ϕ:

$$\mu_\Delta = 1 + \frac{3(\mu_\phi - 1)}{{D_C}^2 {\alpha_C}^2} \left(0.0768 \times {D_C}^2 {\alpha_C}^2 + 0.92 \times D_C L_{sp} \alpha_C - \frac{{L_{sp}}^2}{2} \right) \tag{19}$$

Also shown in FIG. 8 by a dashed line is the limit proposed by Priestley *et al*. (1996) that has been used to estimate graphically the displacement ductility capacity of a single column as a function of the column aspect ratio. Comparing these two curves it is clear that the curve proposed by Priestley *et al*. (1996) represents a trilinear interpolation for the curve given by Eq. (19). In addition, the symbols ✡ and ✸ depict the computed column fixed-base displacement ductility. In this case, fixed-base refers to the column displacement contribution to the pile group analysis for stiff and soft soils and was computed based on:

$$\mu_{col,\Delta} = \frac{\Delta_{col,U}}{\Delta_{col,y}} \tag{20}$$

From these analyses, the remaining curves shown in FIG. 8 depict the system ductility $\mu_{\Delta T}$ for stiff soils (shown with solid circles) and soft soils (shown with open circles). These curves clearly show that for low aspect ratios there is a significant reduction in $\mu_{\Delta T}$ for both stiff and soft soils with a pronounced decrease under soft soils conditions. For higher aspect ratios the contribution of the soil-structure interaction is less pronounced and, for stiff soils with aspect ratios greater than 6 there is no appreciable difference in the analysis for a fixed base or pile group analysis.

Contribution of Pile Cap Rotation and Deflection on System Ductility

In this work the pile cap rotation, $\Delta_{cap,\theta}$, and deflection, $\Delta_{cap,\Delta}$, contribution to response of the system were also evaluated and were computed by:

$$\mu_{cap,\theta} = \frac{H_C \theta_{cap,U}}{\Delta_{yT}}; \qquad \mu_{cap,\Delta} = \frac{\Delta_{cap,U}}{\Delta_{yT}} \tag{21}$$

Results derived from these expressions were then normalized in terms of the system ductility expressed by Eq. (15) and results are presented in FIG. 9(a). In this figure it is shown that the pile cap deflection contributes significantly more to the system displacement ductility than the pile cap rotation within low aspect ratios. However, for high aspect ratio and soft soils the pile cap rotation dominates the response of the system, but a significant reduction in either the pile cap rotation or deflection contribution to the response of the system are observed for the stiff soils.

This is reasonable because, under low aspect ratios, the shear forces imposed on the system are considerably higher. Due to higher shear force demands on the soil foundation system nonlinearities develop in the soil leading to higher deformations of the pile cap. As such, in the presence of stiff soils, the pile cap lateral deflection is largely immobilized and the piles are well anchored by the skin friction resistance. In

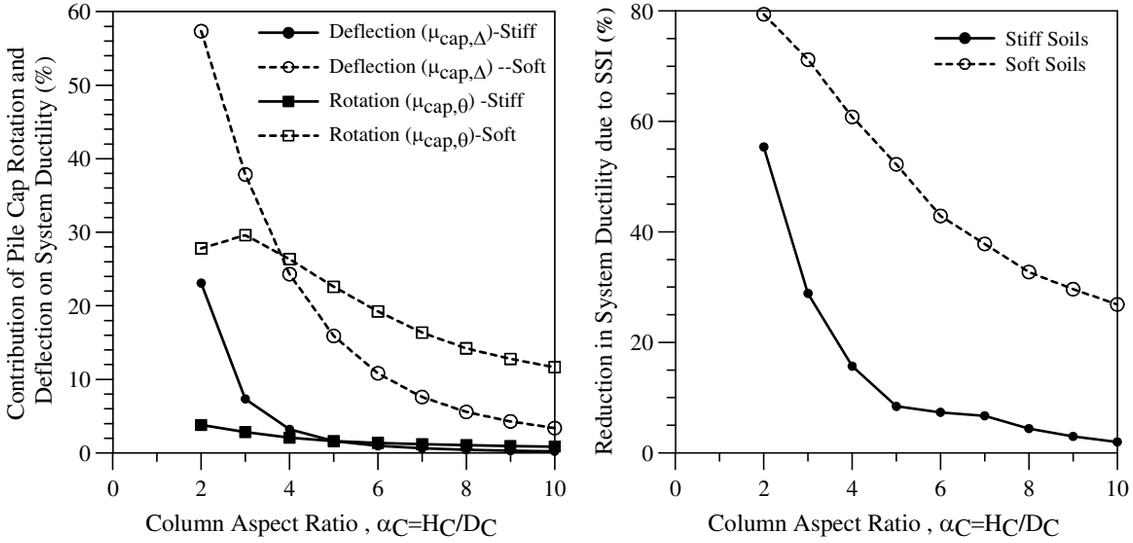
contrast, in the presence of soft soils, the pile cap lateral deflection is larger and the skin friction resistance is significantly smaller, leading to a higher contribution of the foundation system to the response of the overall bridge system.

Influence of Soil-Structure-Interaction on System Ductility

Once again, the nonlinear deformations that develop in the piles are not possible to quantify in a separate component but instead they are represented within the response of the pile cap rotation and deflection. In this work the influence of the soil-structure interaction, μ_{SSI}, on the system displacement ductility capacity was:

$$\mu_{\Delta,SSI} = \mu_{\Delta T} - \mu_{col,\Delta} \quad (22)$$

Where $\mu_{\Delta T}$ was previously defined in Eq. (15) and $\mu_{col,\Delta}$ in Eq. (20). In this case, results are normalized in terms of the column fixed-based ductility expressed by Eq. (20) and the normalized results are presented in FIG. 9(b). Results from this analysis indicate that under low aspect ratios and for soft and stiff soils, respectively, soil-structure interaction can reduce by almost 80% and 55% the system ductility capacity; however, under higher aspect ratios the influence of the soil-structure interaction is significantly reduced with almost negligible effects for stiff soils. Also for columns with aspect ratios larger than six the influence of the foundation system to the bridge overall response is negligible for stiff soil conditions.



(a) Pile Cap Rotation and Deflection **(b)** SSI Influence on System

FIG. 9 Influence of Soil-Structure-Interaction on System Ductility

CONCLUSIONS

This paper summarizes a study on the inelastic seismic response of bridge columns supported on a 4x4 pile group. Key findings from this work show that for columns with low aspect ratios there is a significant reduction in the system ductility displacement capacity for both stiff and soft soils with a pronounced decrease under soft soils conditions. For higher aspect ratios the contribution of the soil-structure interaction is less pronounced and, for stiff soils with aspect ratios greater than 6 there is no appreciable difference in the analysis for a fixed base or pile group analysis. This

is an important overall conclusion from this paper because it clearly quantifies for what levels of column aspect ratio the soil-structure interaction can be of significance and for what levels should design engineers and researchers employ a more refined soil-structure interaction study.

REFERENCES

Aschenbrenner, T. B., and Olson, R. E. (1984), "Prediction of settlement of single piles in clay." *Analysis and design of pile foundations*. American Society of Civil Engineers, J. R. Meyer, ed., 1984.

Caltrans, (1990) "Bridge Design Specifications - Seismic Design References," Sacramento, California, June 1990.

Hose, Yael D., Silva, P. F., and Seible, F. (2000), "Performance Evaluation of Concrete Bridge Components and Systems under Simulated Seismic Loads." *EERI Earthquake Spectra*, Vol. 16, No. 2, May 2000, pp. 413-442.

Pender, M. J. (1978), "Aeismic Pile Foundation Design Analysis." *Bulletin of the New Zealand National Society for Earthquake Engineering*, Vol. 11, No. 2, June 1978, pp 49 - 160.

O'Neil, M. W., and Gazioglu, S. M., "An evaluation of p-y relationships in clays." American Petroleum Institute, University of Houston, 1984.

Poulos, H. G. (1971), "Behavior of Laterally Loaded Piles: I - Single Piles." *Proceedings of the American Society of Civil Engineers*, Vol. 97, No. SM5, May 1971, pp. 711-731. - Elastic Continuum Concept

Priestley, M. J. N., Seible, F., and Calvi, M. (1996), *Seismic Design and Retrofit of Bridges,* John Wiley & Sons, Inc., New York, September 1996, 672 page.

Silva, P. F., and Seible, F. (2001), "Seismic Performance Evaluation of CISS Piles," *ACI Structural Journal*, Vol. 98, No. 1, January 2001, pp. 36-49.

Silva, P. F., Seible, F., and Priestley, M. J. N. (1997), Response of Standard Caltrans Pile-to-Pile Cap Connections Under Simulated Seismic Loads, Report SSRP 97/09, Department of Structural Engineering, University of California San Diego, La Jolla, CA, November 1997.

Vesic, A.S. (1961), "Bending of Beams Resting on Isotropic Solid." Journal of the Engineering Mechanics Division, American Society of Civil Engineers, Vol. 87, No. EM2, Feb. 1961, pp. 35-53.

Geoscience and Geotechnical Aspects of Recent Earthquakes

Robert C. Lo[1], P.Eng. and Yumei, Wang[2], P.E.

[1]Staff Consultant, Klohn Crippen Berger Ltd, 500-2955 Virtual Way, Vancouver, British Columbia, V5M 4X6; PH (604) 251-8455; FAX (604) 251-8510; email: rlo@klohn.com
[2]Geotechnical Engineer, Oregon Department of Geology and Mineral Industries, 800 NE Oregon St., #28, Portland OR 97232, email: yumei.wang@dogami.state.or.us

Abstract

The paper includes seven recent earthquakes investigated by the Earthquake Investigation Committee of ASCE Technical Council on Lifelines Earthquake Engineering: 1993 Hokkaido Nansei Oki, Japan, 1993 Guam, 1999 Kocaeli (Izmit), Turkey, 2001 El Salvador, 2001 Nisqually, Washington, 2003 Zemmouri, Algeria and 2004 Sumatra, Indonesia earthquakes. These events occurred over the past 15 years both inside the United States and overseas, and encompassed crustal, interplate and intraslab events. Following a brief outline of the characteristics and damages of these earthquakes, some of the geoscience and geotechnical aspects observed by the authors are discussed with lessons learned with respect to lifelines facilities outlined.

1. INTRODUCTION

The Earthquake Investigation Committee (EIC) of ASCE Technical Council on Lifelines Earthquake Engineering (TCLEE) conducts investigation after each significant earthquake. The committee either publishes a monograph for each investigation and/or participates in technical reports published by other organizations. These monographs and reports are referenced in the paper for detailed background information. As members of the committee, the authors have been involved in the investigation of the seven earthquakes covered in this paper, focusing on the geoscience and geotechnical aspects. Table 1 provides a thumb-nail sketch of these seismic events including: date and location, basic earthquake characteristics such as focal mechanism, magnitude (based on USGS and NOAA), peak ground motion, special features, fatalities, damage statistics and general references. Some of the geoscience and geotechnical aspects of these earthquakes are discussed in the paper with lessons learned with respect to lifelines facilities outlined.

2. GEOSCIENCE AND GEOTECHNICAL ASPECTS

2.1 Geoscience Aspect

- The Turkey Kocaeli earthquake of magnitude 7.6 was a major earthquake that occurred in a highly urbanized and industrialized area. The Indonesia Sumatra earthquake of magnitude 9.1 generated wide-spread tsunamis that swept

Table 1. Summary of Relevant Earthquake and Damage Data.

Date	Earthquake	Type	Focal Mechanism[1]	Strong Motion[2]	Special Features	Fatality	Damage		Ref. (ASCE TCLEE)
							General	Lifelines	
1993 Jul. 12	**Hokkaido Nansei Oki**	Interplate	M 7.8, depth 1 to 20 km 150 km by 30 km rupture	~0.4-0.5 g at Okushiri 0.2-0.5 g at Hokkaido	at Okushiri Island: >15 to 31.5-m tsunami arrival 2 to 5 min after eq. and fire; Lanslides, rockfalls, liquefaction	Low 231	Moderate US $ 1 billion Tsunami inundation and fire in Okushiri I.	Moderate Disruption to highways Damage to ports, river levees, water/sewer lines	EERI 1995
1993 Aug. 8	**Guam**	Interplate or Intraslab	M 7.8, depth 60 km	~0.15-0.25 g 0.5-2 hz 30-60 sec	Eq. Shaking Liquefaction, lateral spread, subsidence, rockfalls, Minor tsunami up to 0.6 m	Nil	Low Civil and military facilities Civil: US $ 112 million Building damages including hotels Impact on tourism	Low Damage to ports, power plants, water lines Cracks and upstream slope slump of Fena earth-rockfill dam	EERI 1995
1999 Aug. 17	**Kocaeli (Izmit)**	Crustal Right- lateral	M 7.6, depth 17 km Surf. fault rupture 126 km offset 3-4 m, max. 5.5 m vertical offset up to 2.4 m Tsunami up to 2.6 m	≤0.4 g 45-50 sec	Eq. shaking, site amplification Surface ruptures (a few meter wide single rupture to 200-m wide rupture zone), coastal subsidence, liquefaction, landslides, bearing pressure failure	High 17,118	Severe US $ 9 billion direct $16 billion (dir./indir.) Collpase and severe damage of buildings	Severe Significant damages to a variety of lifelines including a collaped overpass across TEM, a severed fibre optic cable	(Monograph No. 17) BSSA 2002 Erdik 2000
1999 Nov. 12	**Düzce**	Crustal Right- lateral	M 7.2 Surf. fault rupture 39 km offset 2.5-4.5 m, max. 5 m	≤0.8 g	Eq. shaking Surface ruptures, Further damage to structures weakened by Aug. 17 Kocaeli Eq.	Low 894	Moderate Collapse of and damage to buildings	Moderate Damage to highways, Bolu Viaducts and Tunnels	(Monograph No. 17) BSSA 2002
2001 Jan. 13	**El Salvador**	Intraslab	M 7.7, depth 39 km	≤0.6 g 1.13 g at an alluvial site	Landslides, ridge cracks, landslide lakes, liquefaction Heavy casualty due to landslides	Low 852	Moderate US $ 1.3 billion	Moderate US $ 475 million and 90% in transportation for both events Disrupted highways	(Monograph No. 24)
2001 Feb. 13	**El Salvador**	Crustal	M 6.6 F 13 km	≤0.4 g	Collapse of structures weakened by Jan. 13 Eq.	Low 315	US $ 350 million Limited to epicentral area		(Monograph No. 24)
2001 Feb. 28	**Nisqually**	Intraslab	M 6.8, depth 51 km Normal, Bi-lateral	≤0.31 g	Eq. shaking Limited landslides, liequefaction	Nil	Light < US 1 billion	Low to moderate	(Monograph No. 20)
2003 May 21	**Zemmouri Algeria**	Crustal	M 6.8, depth 10 km Zemmouri reverse fault, previously un-known, bi-lateral, asym.	≤0.58 g Soil sites ≤0.34 g Rock sites	Eq. shaking, site amplification Submarine landslides Uplift of shoreline ≤ 1 m 3-m tsunami at Balearic Islands	Medium 2,266	High US $5 billion	Light to Moderate 2 out of 5 submarine cables severed	(Monograph No. 27) Wang et al. 2004
2004 Dec. 26	**Sumatra**	Interplate	M 9.1, depth 30 km 1300 km rupture zone max. 20 m displacement Sea floor uplift 5 m, and move horizontally 11 m	No strong motion data available[3]	Heavy casualty in counries around Bay of Bengal and Indian Ocean due to no warning of incoming tsunami Earthquake damage in Aceh, North and West Sumatra	Very High 227,898	Severe US $ 13 billion Impact on tourism	Moderate Tsunami inundation - main cause of lifelines damage in affected areas	(Monograph No. 30) BSSA
2005 Mar. 28	**Nias**	Interplate	M 8.6, depth 30 km	No strong motion data available[4]	Eq. shaking, Ground tilted with up to 1 m uplift and subsidence Panic about tsunami, which was rather subdued, ranging from 1 to 3 m near epicenter and ≤ 0.4 m further away	Medium 1,313	Moderate Collapse of and damage to buildings	Moderate Damage to roads, bridges, pipelines and power facilities	(Monograph No. 30) BSSA 2007

Notes: 1. Earthquake magnitude, M, given in the table is based on USGS http://earthquake.usgs.gov/regional/world.php, except for Hokkaido-Nansei-Oki, which is based on NOAA http://nctr.pmel.noaa.gov/titov97.html.
2. ~ indicates estimated value.
3. Modified Mercalli Intensity ≤ X+
4. Modified Mercalli Intensity > VI in epicentral area, and smaller in adjacent regions.

the shores of the Bay of Bengal and Indian Ocean. Both events inflicted heavy loss of life and property. The former illustrates the high risk of structure inadequacy in populated and developed areas vulnerable to seismic hazard, while the latter the tragedy of un-warned people against the fast-advancing tsunami.

- Earthquakes usually occur according to a typical pattern, starting with a single main event followed by a series of smaller aftershocks that would diminish in magnitude and number with time. Exceptions to this pattern are not infrequent, and may be related to different focal mechanisms. As shown in Table 1, recent exceptions include:
  - Turkey Kocaeli (August) and Düzce (November) earthquakes in 1999 - triggered by rupture of adjacent segments of the North Anatolian transform fault;
  - El Salvador January and February earthquakes in 2001 - an offshore intraslab event followed by an inland crustal event; and
  - Indonesia Sumatra and Nias earthquakes in December 2004 and March 2005 - triggered by rupture of adjacent segments of the locked plate boundary offshore.

  Regardless of their triggering mechanisms, the fact that major events occur in adjacent areas within a short time interval has significant implications in earthquake restoration activity. First, there is a potential threat to the safety of personnel engaging in this activity. Second, any new or retrofitted structure may have to undergo severe seismic shaking shortly after its construction.

- Earthquake investigation tools and methods have continually evolved with significant recent advances, such as:
  - Global Positioning System (GPS) – GPS has been increasingly deployed along major faults to provide continuous deformation data over the tracked GPS stations;
  - Remote Sensing techniques – Interferometric Synthetic Aperture Radar (InSar), which is a satellite remote-sensing technique used to track areal ground deformation adjacent to faults, Light Detection and Ranging (LiDAR) and satellite imagery have been used in recent post-earthquake and tsunami studies;
  - Digital seismographs – Newly installed digital seismographs capture a wide spectrum of seismic ground motions accurately and efficiently and can be transmitted to regional centers for further data processing than their earlier analog counterparts;
  - Paleoseismic data – Coral has been successfully used by paleoseismic researchers to study co-seismic and inter-seismic ground movements caused by interplate subduction earthquakes, because coral acts as a natural record of relative sea-land movement (see Figures 1 and 2, Sieh 2006). Intertidal marsh plants, coastal trees that underwent co-seismic subsidence; lichen; and diatoms have also been used in paleoseismic studies;
  - Internet – The internet has been used by the U.S. Geological Survey for conducting surveys on earthquake intensities, and by the earthquake

investigators to coordinate international investigation efforts through dedicated websites, links and individual blogs; and

- Information technology - Modern equipment such as digital camera, GPS, laptop and satellite communication, GIS, and GoogleEarth all contribute to the efficiency of individual investigator.

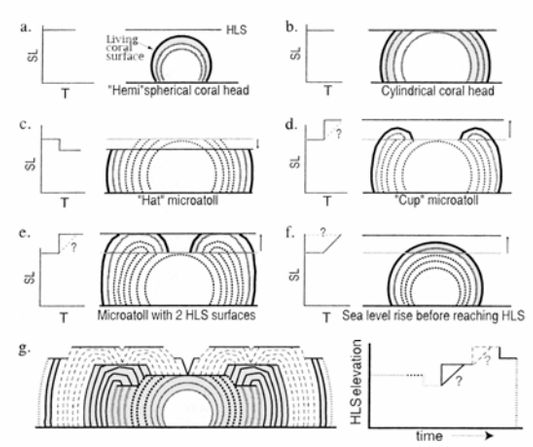


Figure 1. Idealized Diagrams of Coral Growth in Response to Sea-Level Changes (from Zachariasen et al. 2000).

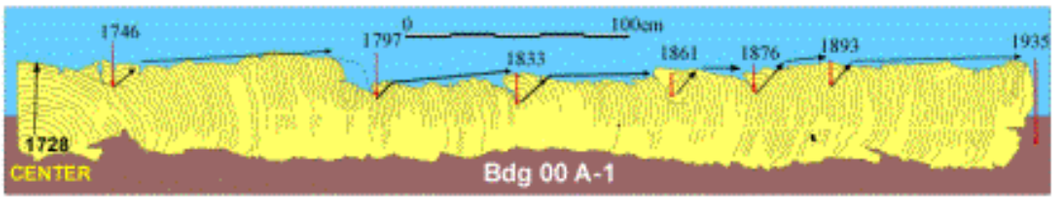


Figure 2. Sea Level Changes Inferred from Truncated Coral Growth Rings (from Caltech 2007).

2.2 Geotechnical Aspect

Geologically, earthquake secondary effects refer to non-tectonic surface processes that are related to earthquake shaking or tsunamis. They are often spectacular in expression and are main causes for loss of life and property. These effects include: site amplification, landslide, turbidite (dense, sediment-laden flows offshore), liquefaction and lateral spread, co-seismic subsidence, settlement and tsunamis. Their preserved geologic signatures sometimes serve as paleoseismic evidence for strong ground motion of prehistoric earthquakes (Yeats et al. 1997).

- Site amplification – Site amplification of ground motion through soft soil deposits has been well recognized and incorporated in the modern seismic design codes. Severe building damage suffered at soft sites at Adaparazi and Avcilar during Kocaeli earthquake illustrated the importance of this phenomenon. Avcilar, which is near Istanbul, is about 80 km west of the epicenter. The distance attenuation of ground motion was regained and increased by local site amplification (BSSA 2002). Similarly, topographic amplification of ground motion was also evident during the Hokkaido and El Salvador earthquakes (EERI 1995 and ASCE 2004).

- Ground displacement – Ground displacement includes tectonic movement or non-tectonic surface processes. When it occurs within the footprint of structures, it affects the structural stability and integrity. Where lifelines intersect fault traces, the impact of ground displacement related to fault rupture on structures was exemplified by the collapse of Arifiye overpass in the Kocaeli and significant damage to Bolu Viaducts in the Düzce earthquake. On the other hand, differential settlement of approach fill and pile supported bridge deck at bridge abutments is commonly observed in earthquakes.
- Foundation settlement – Subsurface soil volume decrease would lead to foundation settlement with no adjacent soil heave.
- Ground failure - Ground failure includes rockfalls, landslides, slope and embankment failures, lateral spreads, liquefaction and bearing capacity failures.
  - Landslides – Correlations between the number of landslides and earthquake magnitude have been established around the world. In regions with loose pyroclastic deposits, the number of landslides for a given magnitude far exceeds those in other regions. The areas threatened by a landslide include the sliding land mass as well as the area traversed by the fast-moving sliding debris. The higher degree of saturation of the soil involved, the greater probability of an earthquake-triggered slide. Whether an earthquake occurs in a wet or dry season makes a significant difference in the number of slides it would trigger. Heavy precipitation in an earthquake-stricken area could also trigger post-earthquake landslides, debris flows and/or lahars (mudflows of volcanic debris). The amount of water entrained within the sliding mass along its moving path increases its run-out distance and, hence, downslope impact (e.g., see Figure 3, ASCE 2002). The local topography along the debris travel path also dictates the area being buried by the slide debris. The formation of a landslide lake, caused by temporary blockage of river by unstable slide debris, poses a special flood hazard. Timely construction of a spillway to drain the lake was required to ameliorate the hazard after February 2001 El Salvador earthquake (see Figure 4).



Figure 3. Las Colinas Landslide after January 2001 El Salvador Earthquake (from E.L. Harp, USGS).



Figure 4. Spillway at abutment of Landslide Dam formed at Rio Jiboa (from Anthony J. Crone, USGS).

  - Slope failure – Failure in natural or man-made slope occurs where the available effective shear strength is exceeded by prevalent shear stress due to the earthquake-induced pore pressure increase and/or presence of inertia force

during earthquake shaking. Slope failure of highway and/or railway embankments could disrupt vital transportation corridor, disrupt community life and regional economy as evidenced in the Hokkaido, El Salvador and Turkey earthquakes. Cracks and upstream slope slump of the 26-m high Fena earth and rockfill dam after Guam earthquake required emergency repair by the U.S. Navy.

  - Lateral spreading and liquefaction – Lateral spreading and liquefaction occur in many gentle slopes or level ground where the soil deposits involve relatively loose cohesionless materials such as sand and silt and occasionally gravelly soils. Loss of shear strength and associated ground movements would affect structures located in areas with high groundwater table, such as low-lying areas, river banks and ports, and lead to slope failure and lateral spreading, foundation settlement and bearing pressure failure, and disruption of lifelines. Emergency repair of flood-control dikes damaged by liquefaction of subsurface soils was needed after the Hokkaido earthquake.
  - Bearing capacity failure – Foundation bearing failures also occur in cohesive soil due to the strain softening effect of earthquake shaking. The punch shear failure of footings is associated with adjacent soil heave. For tall and narrow buildings with an aspect ratio (height/width ratio) greater than 2, it could lead to severe tilting or overturning (see Figure 5). This type of foundation behavior was observed in Mexico City due to the presence of sensitive Mexico City clay during the 1985 Michoacan earthquake, and again in Adapazari City due to the presence of Holocene alluvium during the 1999 Kocaeli earthquake (EERI 2000).

- Surface expression of underground failure – Sinkholes may develop during earthquakes. The phenomenon may be puzzling until the cause is identified. Usually, a sinkhole occurs where underground voids already existed prior to the earthquake. These voids may be formed by solution of limestone, abandonment of mine workings or “piping” erosion of fine soils by groundwater flow. In other situations, earthquake-triggered failures of underground structures could also result in the formation of sinkholes. Former examples are sinkholes occurring along highway culverts in the El Salvador and Nisqually earthquakes where “piping” erosion of backfill around the culverts was present (see Figure 6). The latter example is the sinkholes formed over the collapsed sections of the Bolu Tunnels after the Düzce earthquake (Erdik 2000).
- Forces associated with tsunamis – In addition to the inundation effect of rapidly moving waves, tsunamis also exert additional physical forces to structures that include: hydrodynamic pressure (see Figure 7), debris impact and wave scour (see Figure 8). The overturning of a sea wall in Aonae, Okushiri Island after the Hokkaido earthquake (see Figure 9) could be caused by the combined effect of tsunami hydrodynamic pressure and scour. Both passive and active measures are used to mitigate tsunami damage. Passive measure involves the use of a buffer zone and/or natural barrier such as mangroves to avoid building structures in near shore areas. Where structures are required in tsunami-vulnerable zone, both the inundation effect and tsunami-related forces have to be considered in the overall design and operation of these structures.



Figure 5. Overturned Building of High Aspect Ratio in Adapazari City after Kocaeli Earthquake.



Figure 6. Sink-hole Formed by Collapse of Roadway in Nisqually Earthquake.



Figure 7. Wharf Deck Damaged by Tsunami Uplift in Sumatra Earthquake.



Figure 8. Foundation Scour by Tsunami Waves in Sumatra Earthquake.



Figure 9. Overturning of Sea Wall at Aoene, Okushiri Island in Hokkaido Earthquake.

3. LESSONS LEARNED FROM EARTHQUAKES

3.1 General

Earthquake damage in a given area tends to reflect its social-economic condition. Thus, in areas where earthquake-resistant design codes and engineering practices are updated with new knowledge, damage tends to be limited to older structures, or areas with special site conditions. Conversely, wide spread damage to structures and heavy loss of life seem to be repeated too frequently.

Outlined in the following are some of the lessons learned from the recent earthquakes covered in the paper:

- Tsunami warning – Timely warning of tsunami is a prerequisite for saving lives. The Sumatra earthquake-tsunami is an unprecedented tragedy to emphasize this point. Adequate warning requires the implementation of a system involving

instrumentation on land and on ocean floor, and international organization and communication protocol. The system has to be maintained vigilantly to be effective. While warning against tsunamis triggered by distant earthquakes is adequate in North America, further work is required for warning against tsunamis caused by nearfield earthquakes, such as for residents in the Pacific Northwest from Cascadia subduction zone earthquakes. Sumatra earthquake provided an impetus for the set up of a similar system for countries around the Indian Ocean. For inhabitants living along vulnerable shorelines, running to high ground in the event of shaking or unusual wave behavior including dramatically receding waters or advancing waves, remains to be practical means to escape tsunami inundation. Tragedy for Okushiri Island inhabitants who perished during the Hokkaido earthquake is a reminder that this is not always easy, even for earthquake-tsunami conscious Japanese people with an advanced tsunami warning system capable to issue warning within minutes of the earthquake occurrence. The need for reliable tsunami warning was further demonstrated by the case of the Nias earthquake. About three months after the Sumatra earthquake, the sensitized inhabitants were all too ready to run for their life after given the warning. Nevertheless, no significant tsunami was realized, because of a smaller body of sea water being displaced and wave focusing direction towards ocean. Thus, timely and reliable tsunami warning remains both a technical and societal challenge.

- Instrumentation for strong ground motion – Installation and maintenance of modern instrumentation for strong ground motion are important to characterize earthquake motion. Further instrumentation to measure the response of critical structures would improve the understanding and analysis of seismic behavior of the instrumented structures. However, lack of strong motion data in epicentral areas at Okushiri Island, Hokkaido, Guam, Sumatra and Nias, Indonesia serves to highlight the fact that it is not always possible to achieve this goal due to economic, political and/or technical constraints. Potential tsunami inundation should also be considered when selecting sites for strong motion instrumentation.
- Land use – Microzonation can be implemented by first identifying areas susceptible to tsunami run-up, strong earthquake shaking, or ground failure such as landslide, fault displacement, slope failure and liquefaction. Determination of appropriate land use should then be guided by the identified hazards to mitigate potential loss.
- Seismic design level – Upgrade of seismic design is to be achieved by implementation of up-to-date seismic design measures for new structures, and retrofit of existing structures whenever an opportunity suggests itself.
- Potential co-seismic impacts, due to damaging secondary effects of an earthquake such as liquefaction, landslide, debris flow, fire, dam breach, disruption of lifelines, are to be considered in order to devise realistic response strategy and to plan for orderly upgrade of existing facilities.
- Emergency response and public education – Emergency response drills need to be practiced regularly to enhance the capability of response agencies, and public awareness. Preservation of certain earthquake-stricken area as a memorial park would be an effective reminder for educating the public about the importance of earthquake preparedness.

3.2 Lifelines Facilities

Additional observations and lessons applicable to lifelines facilities include the following:

- Fault Displacement – Fault displacement caused: 1) the collapse of Arifiye overpass (see Figure 10) across the Trans-European Motorway (TEM) in the Kocaeli earthquake (with about 3 m to 3.5 m fault displacement) and 2) significant displacement and damage to the Bolu Viaducts (see Figure 11), which included the specially designed sliding elements at girder seats and energy dissipating devices, in the Düzce earthquake (with 1.5 m displacement of adjacent piers and 13^{o} rotation of pile caps across the fault). Besides large acceleration, potential fault displacement contributes to the design challenge for the sub- and super-structures crossing active faults. Two webinars: http://www.nees.org/ebrownbag/BrianSadden-LifelinesImplementation.pdf and http://www.nees.org/ebrownbag/TomORourke-LifelinesResearch.pdf illustrate recent efforts in meeting this challenge in engineering practice and research.



Figure 10. Collapsed Arifiye Overpass across Trans-European Motorway after Kocaeli Earthquake (from EERI 2000).



Figure 11. Damaged Bolu Viaducts after Dücze Earthquake (from Kandilli Observatory and Earthquake Research Institute 2007).

- Weak Soil Site - Structures constructed on weak subsurface soil often result in widespread damage from site amplification, liquefaction, lateral spreading, bearing capacity failures or excessive settlement. For a critical lifeline structure, it is important to consider appropriate soil improvement measures compatible with the site condition. In addition, flexible connections or other suitable measures should be used to mitigate seismic impact on the structure.
- Evaluation, Upgrade and Design Standard – The reliable service of a lifeline depends on proper functioning of all its important components at all times. It requires seismic risk evaluation and regular upgrade of these facilities in normal time as well as prompt repair of failed components after an earthquake. Although some seismic design standards are available for certain lifelines, such as bridges, many lifelines do not have widely adopted guidelines let alone design standards. We recommend seismic design standards be developed and adopted for new lifelines, and the performance standards be developed and applied to new and existing critical lifelines. More information on the state of practice of lifelines can be found at: http://www.americanlifelinesalliance.org/.

- Redundancy – Robustness of the lifelines relies on the built-in redundancy. As a certain line or node of a given lifeline is down, the availability of alternate lines or nodes is critical for maintaining the lifeline function during the critical period of emergency response and restoration. To illustrate this redundancy, two 380-kV transmission lines bypassed the Adapazari substation, which suffered circuit-breaker damage during the Kocaeli earthquake. These two lines were critical to power restoration after the earthquake. This type of redundancy requires careful planning and consideration of a variety of potential damage scenarios based on knowledge of potential earthquakes and physical conditions of the lifelines facilities.
- Tsunami Inundation – Low lying areas can be subject to widespread, extensive damage due to tsunami. Critical facilities built in areas at risk of tsunami, such as military base, port and nuclear power plant, should be evaluated for public safety concerns relating to potential seismic and tsunami impacts. One side effect of tsunami inundation during the Hokkaido and Sumatra earthquakes was pump failures due to salt water intrusion. This delayed the restoration of the water and waste water systems whose function relied on the pumps.

REFERENCES

American Lifelines Alliance, http://www.americanlifelinesalliance.org/

ASCE Monographs No. 17 (2000) Izmit (Kocaeli), No. 20 (2002) Nisqually, No. 24 (2002) El Salvador, No. 27 (2004) Zemmouri, No. 30 (2007 in press) Sumatra, Technical Council on Lifeline Earthquake Engineering.

BSSA (2002). Izmit, Turkey Earthquake of 17 August 1999, Bull. Seism. Soc. of Amer., Vol. 92, No. 1, Feb.

BSSA (2007). The 2004 Sumatra-Andaman Earthquake and the Indian Ocean Tsunami, Bull. Seism. Soc. of Amer. Vol. 97, No. 1A, Jan.

Caltech (2007). http://www.tectonics.caltech.edu/sumatra/public.html

EERI Earthquake Reconnaissance Reports. (1995) Hokkaido (Vol. 11, Supplement A) and Guam (Vol. 11, Supplement B), 2000 Kocaeli (Vol. 16, Supplement A), 2006 Sumatra and Nias (Vol. 22, Special Issue 3) Earthquake Spectra.

Erdik, M. (2000). Report on 1999 Kocaeli and Dücze (Turkey) Earthquakes, Dept. of Eq. Eng., Bogazici University.

Kandilli Observatory and Earthquake Research Institute (2007). http://www.boun.edu.tr

Sieh, K. (2006). Sumatran Megathrust Earthquakes: from Science to Saving Lives, Phil. Trans. R. Soc. A Vol. 364, pp. 1947- 1963.

Wang, Y., Edwards, C., Yashinsky, M., Kartoum, A., Hamdache, M. (2004). May 21, 2003 Zemmouri, Algeria Earthquake: Geosciences and Lifeline Damage, Proc. 11th Int'l. Conf. on Soil Dyn. & Eq. Eng., Berkeley, January, pp 278-285.

Yeats, R.S., Sieh, K. and Allen, C. R. (1997). The Geology of Earthquakes, Oxford Univ. Press.

Zachariasen, J., Sieh, K., Taylor, F.W. and Hantoro, W.S. (2000). Modern Vertical Deformation above the Sumatran Subduction Zone: Paleogeodetic Insights from Coral Microatolls, Bull. Seism. Soc. of Amer. Vol. 90, No. 4, pp. 897-913.

EFFECT OF BACKFILL SOIL TYPE ON STIFFNESS AND ULTIMATE CAPACITY OF BRIDGE ABUTMENTS

A. Bozorgzadeh[1], S. A. Ashford[2], and J. I. Restrepo[3]

[1] Structural Engineer, Moffatt & Nichol, Inc., Walnut Creek, CA; abozorgzadeh@moffattnichol.com
[2] Professor, Head of School of Civil and Construction Engineering, Oregon State University, OR; scott.ashford@oregonstate.edu
[3] Associate Professor, Dept. of Civil Engineering, University of California -San Diego, La Jolla CA; jrestrepo@ucsd.edu

ABSTRACT: Bridge abutments are earth-retaining structures which support the superstructure at the ends of a bridge and provide resistance to deformation and earthquake induced inertial forces from the bridge deck.

Current design practice in California makes use of bi-linear load-deformation curve and does not account for the structure backfill properties. An experimental and an analytical research program were conducted at UCSD to further investigate such structure backfill interaction characteristics. In order to meet the objectives of this research project, a field investigation was conducted to develop a proper characterization of the soil types used for abutment structure backfills. The experimental program included five large-scale tests to examine the effect of structure backfill soil type, backfill height, vertical movement of the wall, and pre-existing cut slope in backfilling on stiffness and capacity of the abutments in the longitudinal direction.

The study indicated that the response of bridge abutments in the longitudinal direction is nonlinear and a function of several influential factors which need to be considered. The passive resistance of the structure backfill is controlled by the soil shear strength and interface friction. It was shown that the vertical movement of the wall has a significant effect on the amount of maximum passive pressure.

Keywords: abutments, bridges, experimental testing, soil type, ultimate capacity, stiffness

INTRODUCTION

There are two types of bridge abutments generally used in state of California. Seat-type abutments support the bridge superstructure on a stemwall or "seat" as shown in Figure 1. Diaphragm abutments consist of an end diaphragm cast integrally with the superstructure and the abutment stemwall (see Figure 2). During an earthquake, the bridge superstructure moves longitudinally. Once the gap is closed, the superstructure collides with the backwall which induces deformation and inertial force to bridge

abutments. The current bridge design procedure (ATC 1996, SDC 2006) considers the backwall in seat-type abutments as a sacrificial element in order to protect abutment walls and piles from damage by limiting the inertial forces that can be transmitted into the abutment. Therefore, the force-resistance system of the bridge abutments in longitudinal direction during major seismic events is mainly provided by backwall-soil interaction, and the passive earth resistance behind the bridge abutments. Factors such as nonlinear soil behavior, soil properties, abutment dimensions, and soil-structure-interaction must be considered for a realistic characterization of abutment capacity and/or stiffness. However, for simplicity, in many existing models for abutment capacity and stiffness, the effects of soil nonlinearity and soil properties are not considered.

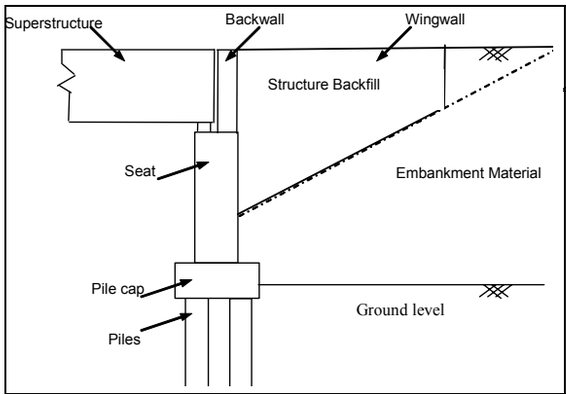


FIG. 1. Bridge seat-type abutment, side view

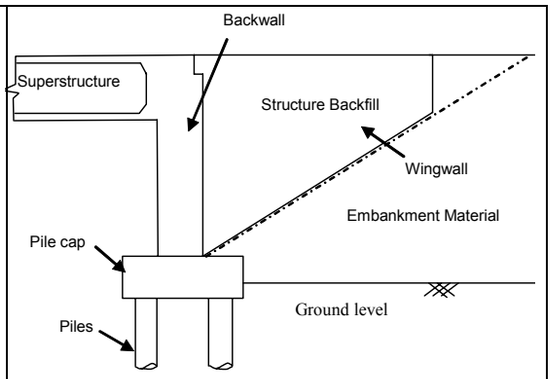


FIG. 2. Bridge diaphragm abutment, side view

Several researchers have studied the passive earth resistance on pile caps, and retaining/abutment walls both experimentally and analytically. Wilson (1988) proposed a theoretical model for determining abutment stiffness based on the abutment dimensions and soil properties. Maroney (1995) tested two large scale diaphragm bridge abutments to failure at University of California, Davis. A simplified model to evaluate nonlinear longitudinal bridge abutment stiffness has been developed by Siddharthan et al. (1995). Martin et al. (1997) conducted advanced theoretical studies using a two-dimensional explicit finite difference computer program (FLAC) to characterize the load-deformation behavior of bridge abutments under cyclic loading. Shamsabadi et al. (2005) proposed a method to predict the mobilized force-displacement for the seismic design of a bridge abutment-embankment system.

Extensive experimental work associated with passive earth pressure has been conducted by several researchers such as Rowe and Peaker (1965); Narain et al. (1969); James and Bransby (1970). Fang et al. (1994) conducted several experimental tests to investigate the variation of earth pressures induced by rotation about a point above the top, and rotation about a point below the wall base. There have been several large-scale tests conducted with interest in passive resistance recently (Romstad et al. (1995); Gadre (1997); Rollins and Sparks (2002). Duncan and Mokwa (2001) conducted several full-scale tests on pile caps and found that the passive resistance of the backfill soil contributes up to 50% of the total pile cap resistance. Rollins and Cole

(2006) performed a series of static cyclic lateral load tests on a full-scale on a pile cap.

The results of the literature review showed that only limited research has been done in the area of abutment capacity, and there is much uncertainty regarding appropriate modeling of bridge abutments. The experimental research program was conducted at the University of California, San Diego to investigate the effect of structure backfill properties, the area of structure backfill, the backfill height, and the vertical wall movement on abutment capacity and stiffness.

PASSIVE RESISTANCE FORCE-DISPLACEMENT BEHAVIOR

A wide variety of methods are available to determine the capacity provided by passive pressure against the retaining structures. These methods include the classical approaches such as Log Spiral (Terzaghi 1943, Terzaghi et al. 1996), Rankine, and Coulomb, which are ultimate capacity predictors and do not attempt to capture stiffness behavior. A good discussion and more details about these earth pressure theories are offered by Bowles (1988).

Several methods have been proposed to characterize the development of passive pressure with displacement; including the Caltrans method, and the hyperbolic model given by Duncan and Mokwa (2001). The Caltrans method is based on the results from large scale abutments testing at University of California Davis (Maroney 1995). Caltrans (Seismic Design Criteria, 2006) suggests the initial longitudinal abutment stiffness to be equal to $20\frac{kip/in}{ft}$. The initial stiffness must be adjusted proportional to the backwall height as:

$$k_{abut} = k_i(= 20.0\ \frac{\text{kip/in}}{\text{ft}}) \times b \times \left(\frac{h_{abut}}{5.5}\right) \tag{1}$$

where, b is the width of the backwall. The ultimate capacity of the abutment is given by Eq. (2). The maximum passive resistance of 5 ksf in Eq. (2) is based on the ultimate static force developed in large scale abutment testing at University of California, Davis. The height proportionality factor, $h_{abut}/5.5\,ft$, is based on the abutment test specimen height (5.5 ft) used at UC Davis (Maroney 1995). In Eq. (2), A_e is the effective abutment area. The passive pressure resisting the movement at the abutment increases linearly with the displacement, as shown in Figure 3.

$$P_{abut} = A_e \times 5.0\ \ ksf \times \frac{h_{abut}}{5.5} \tag{2}$$

Figure 4 shows the hyperbolic representation of passive resistance-displacement relationship developed by Duncan and Mokwa (2001). The hyperbolic p-y curve developed by Duncan and Chang (1970) is expressed as:

$$P = \frac{y}{\frac{1}{k_{\max}} + R_f \frac{y}{P_{\max}}} \tag{3}$$

where P is the load at any displacement y, P_{max} is the ultimate passive force (using Log Spiral method); k_{max} is the initial stiffness which corresponds to the initial slope of the

load deflection curve. This value can be approximated using elasticity theory. The failure ratio, R_f, is defined as the ratio between the actual failure force and the hyperbolic ultimate force. The Caltrans method, and the hyperbolic model given by Duncan and Mokwa (2001) were used to predict the force-displacement behavior of each test as discussed in Bozorgzadeh (2007).

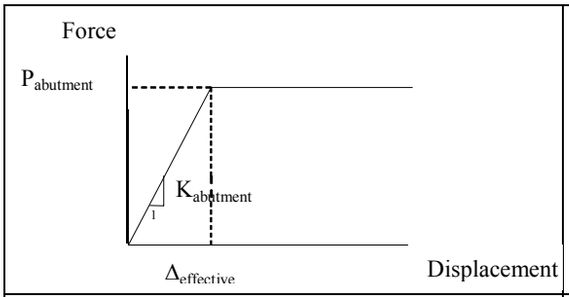


FIG. 3. Force-displacement behavior of bridge abutment (SDC 2006)

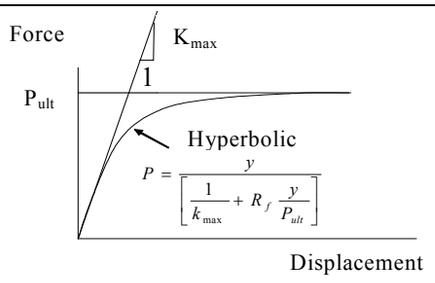


FIG. 4. Hyperbolic passive force versus displacement (Duncan et al. 2001)

FACTORS THAT CONTROL THE PASSIVE RESISTANCE

One of the factors that controls the magnitude of the passive earth pressure that resists the movement of the wall (Duncan and Mokwa 2001) is the direction in which the wall moves. If the wall moves horizontally slip will occur on the interface between the structure and soil, and the value of the interface friction, δ, will be controlled by the properties of the soil-structure interface (Figure 5a). This would be the case of diaphragm abutment that is restrained vertically by the pile foundation.

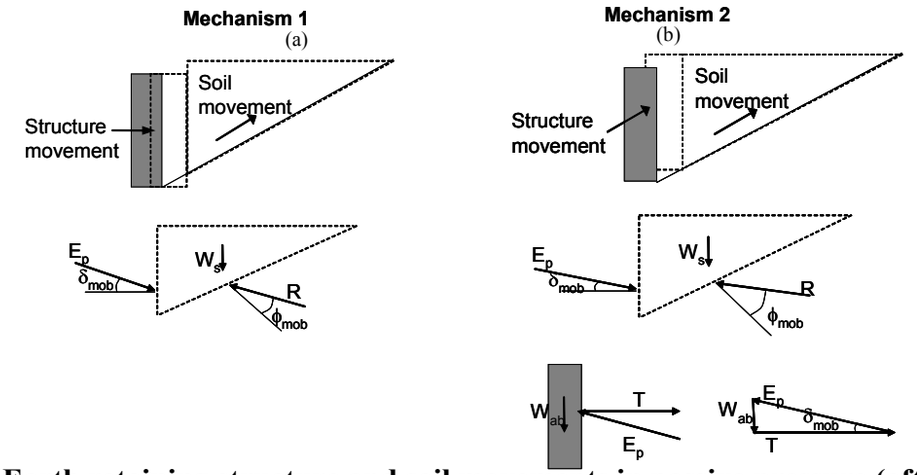


FIG 5. Earth retaining structure and soil movements in passive pressure (after Duncan et al. 2001)

If the vertical restraining force in the wall is smaller than the vertical component of the passive pressure force (the backwall is sheared off from the stemwall in seat-type abutment), smaller relative displacement across the interface will occur which results in only partial mobilization of the interface friction (Figure 5b). The value of δ_{mob} must satisfy the vertical equilibrium as following:

$$W_{ab} = E_p \sin(\delta_{mob}) \quad (5)$$

where δ_{mob} is the mobilized friction angle, W_{ab} is the weight of the structure, and E_p is the developed passive pressure.

FIELD AND EXPERIMENTAL PROGRAM

In order to meet the objectives of the research project, both a field and experimental program were carried out. The objective of the field program was to develop a proper characterization of the soil types used for abutment structure backfills and its potential variation in the field (EMI Report 2005, Bozorgzadeh A. 2007). Two different types of soil were imported to be used as structure backfill in this research project, clayey sand and silty sand. Table 2 describes the Index properties and unit weight for each soil type. Because of geographic, time, and budget limitation in selecting the structure backfill materials, it was decided to consider just materials which provide the lower bound capacity and stiffness.

The test units were modeled to reflect typical diaphragm and seat-type bridge abutments commonly used in practice. The specific aims of the experimental program were to examine the effect of

1) structure backfill soil type
2) backfill height
3) restraining the vertical movement of the wall
4) pre-existing weak planes (pre-existing cut slope)

on stiffness and capacity of abutments in longitudinal direction.

Table 2. Summary of Index Test Results of Structure Backfill Materials

Soil Type	USCS[a]	Grain Size Distribution (Percentage Passing, %)			Dry Unit Weight[c] (pcf)	SE[d]	PI[e] (%)
		75 mm	4.75 mm	74 μm[b]			
Clayey Sand	SC	100	93-100	35-40	126.0	16-22	10-13
Silty Sand	SM	100	82-85	25-30	127.0	20-22	<4

Notes :[a] ASTM D2487, [b] ASTM D1140, [c] ASTM D1557, [d] ASTM D2419, [e] ASTM D4318

Test Setup

The first phase of the experimental program was conducted on the performance of a component of a bridge abutment. An abutment wall (without a foundation) was built approximately at 50% scale of a prototype diaphragm abutment. The abutment wall was used for all four tests in Phase I. The wall was restrained from rotational movement about three directions. In Test 1, the wall was restrained vertically by means of proper configuration of actuators to simulate the diaphragm abutment wall with fixed connection to its foundation (see Figure 6). The actuators' setup in the rest of the tests in Phase I, allowed the vertical movement of the abutment wall to simulate the backwall sheared off from the stemwall in seat-type abutments. After completing Test 1, the structure backfill material (clayey sand) was excavated and replaced by

silty sand. The overall test setup for abutment Test 2 is depicted in Figure 6.
It was decided to extend the backfill area to deeper and larger area in Test 3 and 4 to prevent any potential weak plane of failure in the test setup. The setup of actuators in Test 3 was similar to that in Test 2 which allowed the upward movement of the abutment wall. Figure 6 shows the overall test setup of the Test 3. The height of the backfilling in Test 3 and 4 was 7.5 ft and 5.5 ft, respectively.

Table 3. Bridge Abutment Research Program Test Matrix, Phase I

Variables	Phase I				Phase II
	Test 1	Test 2	Test 3	Test 4	System Test
Soil Type	clayey sand	silty sand	silty sand	silty sand	silty sand
Structure Backfill Height	5.5 ft	5.5 ft	7.5 ft	5.5 ft	5.0 ft
Structure Backfill Area	small	small	Large	large	large
Vertical Movement of Wall	restrained	allowed	Allowed	allowed	allowed

Although the setup for Tests 2, 3, and 4 in Phase I replicated the seat-type abutment behavior, the backwall of the test specimen was built monolithically with its wingwalls as a diaphragm abutment. Therefore, the second phase of this research program was conducted on a seat-type abutment which had a backwall separated from the seat (stemwall) and wingwalls. The abutment test unit consisting of the seat (stemwall), shear keys, wingwalls, and backwall was built at a large-scale of a prototype abutment. The overall test setup and design of test units are discussed in Bozorgzadeh (2007).

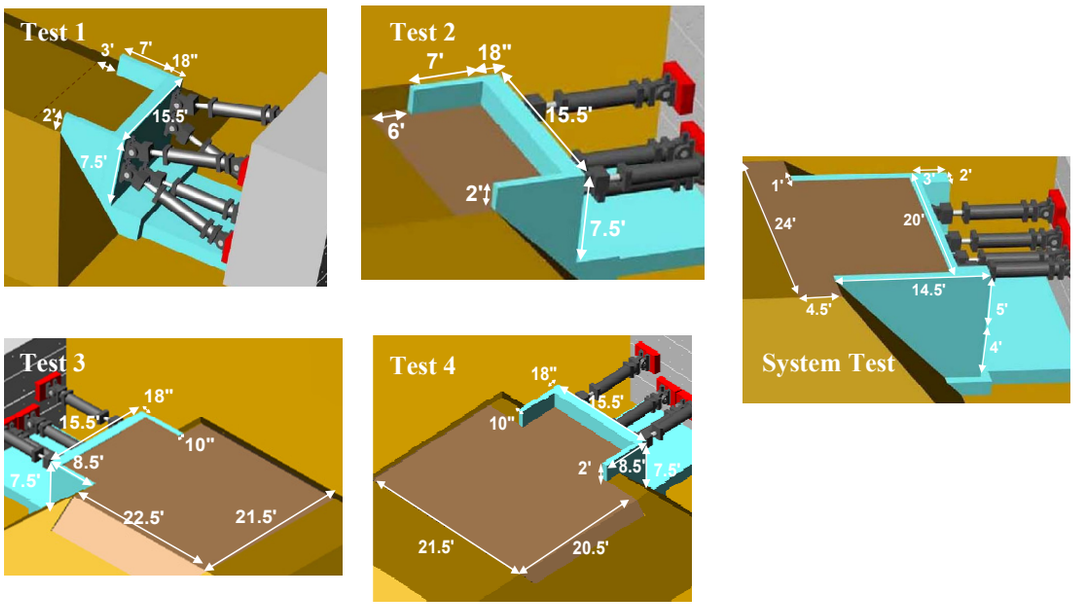


FIG. 6. Overall test setup of the UCSD field abutment tests.

FORCE-DISPLACEMENT CURVE

The measured horizontal force-displacement response of the abutment wall tests are shown in Figure 7. In Test 1, the abutment force-displacement behavior was nonlinear up to the peak point; and after the peak it became approximately a horizontal line. The test was stopped after four inch displacement due to reaching the maximum capacity of two actuators. Figure 7 shows that the abutment in Test 1 was degrading with each cycle by comparing the loads at cycles with equal displacement peak.

The measured horizontal force-displacement response of the abutment wall Test 2, 3, 4, and System Test are presented in Figure 7. The load test was under displacement control and performed monotonically. The abutment force-displacement behavior was nonlinear during the tests. After reaching the peak point, the load started degrading. The tests were stopped after developing distinct failure cracks at the top surface of the structure backfill.

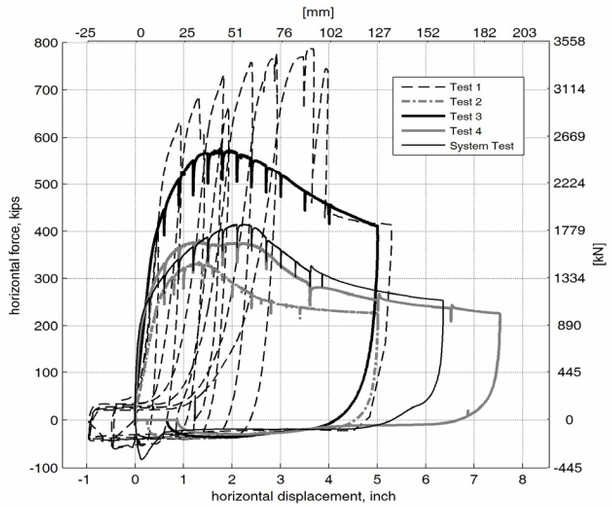


FIG. 7. Horizontal force-displacement response, Phase I and II

The force-displacement results indicate a substantial post-peak softening behavior in all the tests except in Test 1. The developed model to predict the force-displacement relationship of longitudinally loaded bridge abutments accurately is discussed in Bozorgzadeh, A. (2007). The following sections describe the effect of the influential factors on the results of longitudinally loaded bridge abutment test units.

Effect of Vertical Movement of the Wall: As discussed previously, one of the factors that controls the magnitude of the passive earth pressure is the direction of the wall movement. If the wall movement restrained vertically, slip will occur at the interface between the structure and soil, and the value of the interface friction, δ, will be controlled by the properties of the soil-structure interface (Figure 5(a)). In Test 1, the failure Mechanism 1 was developed and the value of the soil-wall interface friction angle, δ, was controlled by the properties of the interface (Figure 5(a)). The rest of the tests in Phase I and II were performed on the abutment wall which was free to move vertically. The failure Mechanism 2 was developed in these tests where the smaller relative displacement across the interface occurred resulting in only partial

mobilization of the interface friction (Figure 5(b)). It should be noted that the value of the δ has a considerable effect on the amount of maximum passive pressure. Therefore, in cases where the interface friction is partially mobilized, the developed passive pressure is much less than the cases with fully mobilized interface friction.

Effect of Excavated Area for Structure Backfill: Tests 2 and 4, in Phase I, were performed with two different structure backfill areas to evaluate the effect of structure backfill area on capacity of the abutment wall. All the variables, except the structure backfill area were kept the same in Test 2 and 4. In Test 2, excavated area was small, where in Test 4 the excavated zone was extended to a larger and deeper area. The maximum capacity of the abutment in Test 2 and 4 were not the same and was higher in Test 4 (Figure 7) which shows that the cut slope from the excavation in Test 2 introduced a weak plane of failure to the system and sliding occurred at that slope.

Effect of Backfill Height: The effect of backfill height can be studied by comparing the results of Test 3 and 4. Tests 3 and 4 were performed with two different backfill heights to evaluate the effect of backfill height on capacity of the abutment wall. All the other variables were the same. The ratio of the maximum passive pressure in Test 3 to the maximum passive pressure in Test 4 was compared with the ratio of the backfill height in Test 3 and Test 4. The ratio of maximum passive pressure of corresponding tests is:

$$\frac{p_{\max,Test3}}{p_{\max,Test4}} = \frac{4.96}{4.48} = 1.11 \quad (6)$$

and the ratio of the backfill height is equal to:

$$\frac{h_{Test3}}{h_{Test4}} = \frac{7.5}{5.5} = 1.36 \quad (7)$$

The comparison between the Eq. (6) and Eq. (7) shows that the maximum passive pressure ratio is not equal to backfill height ratio. It is indicated that the passive pressure ratio is not directly proportional to the backfill height ratio. It is believed that considering the constant value for the maximum passive pressure and the stiffness then, corrected by the height proportionality factor will be poorly capable of calculating the maximum capacity and the stiffness of the bridge abutments with the same structure backfill and different heights.

CONCLUSIONS

The experimental research program was conducted to investigate abutment capacity and stiffness from field tests. The key variables in the experimental study were structure backfill soil type, area of structure backfill, backfill height, and vertical movement of the wall.

The results from the field investigation showed a quite wide range of soil types have been used as structure backfill materials in bridge abutments in state of California.

A series of large-scale field tests were then performed at UCSD on bridge abutments to study the longitudinal stiffness and capacity of the abutment.

Results from testing program support the main theme of the research, that the

response of bridge abutments is nonlinear to longitudinal load. Furthermore, the capacity and stiffness of bridge abutments depend on many factors which were studied during this research program to evaluate their influence. These factors are:
(1) soil properties: the amount of passive resistance develops behind a bridge abutment depends on the soil shear strength; (2) vertical wall movement: abutment walls free to displace in the vertical direction develop less passive resistance; (3) height of the backfill: there is no direct proportionality between the maximum passive pressure and backfill height ratio; and (4) area of structure backfill: It is important to ensure that the structure backfill area is larger than the passive failure wedge.

ACKNOWLEDGMENTS

This study was made possible by funding from the California Department of Transportation under contract No. 59A0337 and the Pacific Earthquake Engineering Research Center, under NSF contract No. 9701568.

REFERENCES

Applied Technology Council (ATC). (1996). *Improved seismic design criteria for California bridges: Provisional recommendations.*

ASTM, D 1140, "Standard Test Method for Amount of Material in Soils Finer Than the No. 200 (75-μm) Sieve", American Society for Testing and Materials, West Conshohocken, Pennsylvania, USA.

ASTM, D 1557, "Standard Test Method for Laboratory Compaction Characteristics of Soil Using Modified Effort", American Society for Testing and Materials, West Conshohocken, Pennsylvania, USA.

ASTM, D 2419, "Standard Test Method for Soils for Sand Equivalent Value of Soils and Fine Aggregate", American Society for Testing and Materials, West Conshohocken, Pennsylvania, USA.

ASTM, D 2487, "Standard Classification of Soils for Engineering Purposes (Unified Soil Classification System", American Society for Testing and Materials, West Conshohocken, Pennsylvania, USA.

ASTM, D 4318, "Standard Test Method for Liquid Limit, Plastic Limit, and Plasticity Index of Soils", American Society for Testing and Materials, West Conshohocken, Pennsylvania, USA.

Bozorgzadeh, A., (2007). "*Effect of Structure Backfill on stiffness and Capacity of bridge Abutments.*" PhD thesis, Dept. of Structural Engineering, University of California San Diego, CA.

Bowls, J., (1988). Foundation Analysis and Design (4th edition), McGraw-Hill, Inc., New York.

Cole, R. T., Rollins, K. M. (2006). "Passive earth pressure mobilization during cyclic loading." *J. Geotech. and Geoenvir. Engrg.*, ASCE, 132(9), September, 1154-1164.

Duncan, J. M., and Chang, C. Y. (1970). "Nonlinear analysis of stress and strain in soils." *J. Soil Mech. And Found. Div*., ASCE, 96(5), 1629-1653.

Duncan, J. M., and Mokwa, R. L. (2001). "Passive earth pressure: theories and tests." *J. Geotech. and Geoenvir. Engrg.,* ASCE, 127(3), 248-257.

Earth Mechanics, Inc. (2005). *Field Investigation Report for Abutment Backfill Characterization,* January 2005.

Fang, Y-S., Chen, T-J., Wu, B-F. (1994). "Passive earth pressures with various wall movements." *J. Geotech. and Geoenvir. Engrg., ASCE*, 120(8), August, 1307-1323.

Fang, Y-S., Chen, J. M., Chen, C. Y., (1997). "Earth pressures with sloping backfill." *J. Geotech. and Geoenvir. Engrg.,* ASCE, 123(3), 250-259.

Gadre, A. D., Dobry, R. (1998). "Lateral cyclic loading centrifuge tests on square embedded footing." *J. Geotech. and Geoenvir. Engrg.*, ASCE, 124(11), November, 1128-1138.

James, R. G., Bransby, P. L. (1970). "Experimental and theoretical investigations of a passive pressure problem." *Geotechnique*, 20 (1), 17-37.

Narain, J., Saran, S., Nandakumaran, P. (1969). "Model study of passive pressure in sand." *J. of Soil Mech. and found. Engrg. Div.*, ASCE, 95(4), 969-983.

Maroney, B. H. (1995). "*Large scale bridge abutment tests to determine stiffness and ultimate strength under seismic loading*." PhD thesis, Dept. of Civil Engineering, University of California Davis, CA.

Martin, G. R., Yan, L.-P., and Lam, I. P. (1997). "Development and implementation of improved seismic design and retrofit procedures for bridge abutments." Final Report on a Research Project Funded by the California Dept. of Transportation.

Rollins, K. M., Sparks, A., E. (2002). "Lateral resistance of full-scale pile cap with gravel backfill." *J. Geotech. and Geoenvir. Engrg,* ASCE, 128(9), 711-723.

Romstad, K., Ketter, b., Maroney, B. H. (1995). "*Large scale bridge abutment tests to determine stiffness and ultimate strength under seismic loading*." PhD thesis, Dept. of Civil Engineering, University of California Davis, CA.

Rowe, P. W., Peaker, K., (1965). "Passive earth pressure measurements." *Geotechnique*, Londong, England, 15(1), 57-78.

SDC, Caltrans. (2006). *Seismic design of abutments for ordinary standard bridges.*

Shamsabadi, A., Ashur, M., and Norris, G. (2005). "Bridge abutment nonlinear force-displacement-capacity prediction of seismic design." *J. Geotech. and Geoenvir. Engrg.,* ASCE, 131(2), 151-161.

Siddaharthan, R., El-Gamal, M., and Maragakis, E. A. (1995). "Influence of free-field strains on nonlinear lateral abutment stiffness." *Proceedings of 7th Canadian Conference on Earthquake Engineering*, Montreal, Canada, 739-346.

Terzaghi, K. (1943). *Theoretical soil mechanics*, Wiley, New York.

Terzaghi, K., Peck, R. B., and Mezri, G., (1996). *Soil mechanics in Engineering Practice*, 3rd Ed., Wiley, New York.

Wilson, j. C. (1988). "Stiffness of non-skew monolithic bridge abutments for seismic analysis." *Earthquake Engineering and Structural Dynamics*, 14, 339-354.

Seismic Behavior of 2D Topographic Features Subjected to Vertically Propagating Incident SV at High Frequencies

Arash Razmkhah[1], Mohsen Kamalian[2], Hamid Alielahi[3]

[1]Assistant Professor, Islamic Azad University (IAU), Tehran South branch, Tehran, Iran, Email: ar.razm@iiees.ac.ir
[2] Assistant Professor, International Institute of Earthquake Engineering and Seismology (IIEES), Tehran, Iran, Email: Kamalian@iiees.ac.ir.
[3] PhD Student, Islamic Azad University (IAU), Science and Research branch, Tehran, Iran, Email: Elahi1979@yahoo.com

ABSTRACT: This paper focuses on the preliminary results of an extensive 2D parametric study of time domain site response analysis for high frequency input motion. Such study in which direct boundary element used as numerical tool evaluates the effects of such motion on seismic behavior characteristics of various homogenous shapes surface topographies (semi-elliptical, semi-sine and trapezoidal shapes). It is assumed that the medium behaves as a linear elastic material. Also, it is considered that Ricker-typed wavelet input motion is Incident SV in-plane wave. Obtained results are presented in the form of dimensionless parameters that is Shape Ratio (the ratio of height to half width of the topography) and dimensionless frequency (the ratio of half width of the topography to wave length). Hence presented results could be generalized and used for various geometric and input motion values. Parametric study results show that in all geometric cases. Various distributed plane wave interference cause to fully disturbed wave field within the topography as well as a scattering of in-plane waves, where in such condition wave separation is very troublesome. Finally, the responses of 2D analyses at the top of topography for different-typed topographies versus related shape ratios (SR) are calculated and then, compared and correlated with the results of response spectra of a free field Ricker-typed wavelet.

INTRODUCTION

Nowadays, site effects studies is one of most important issues in the earthquake engineering practice. Site characteristics of soil layering and topography could affect all parameters of strong ground motion such as time duration, amplitude, wavelength, etc. In the recent past there have been numerous cases of recorded motion and observed earthquake damage pointing toward topographic amplification as an important effect. Very high acceleration recorded at Pacoima Dam (1.25g) during the 1971 San Fernando earthquake (Trifunac and Hudson, 1971; Boore, 1973) and Tarzana hill (1.78g) during the 1994 Northridge earthquake (Spudich et al., 1996)

have been at least partly attributed to topographic effects. Observations from the 1983 Coalinga earthquake (Celebi, 1991), the 1985 Chile earthquake (Celebi, 1987), the 1987 Superstition Hills earthquake (Celebi, 1991) as well as observations from recent earthquakes in Greece (Athanasopoulos et al., 1999; Bouckovalas and Kouretzis, 2001) are only some examples of catastrophic events, during which severe structural damage has been reported on high elevated regions. Although nowadays it is well established that the seismic ground response of surface topographies could be different compared to those of the free field motion during earthquakes, but there are only few structural codes which have considered this issue (AFPS90; Eurocode8). This is due to complex nature of the seismic wave scattering by topographical structures which can only be solved accurately, economically and under realistic conditions, by advanced numerical methods. A recent compilation of works on the numerical modeling of seismic propagation has been presented by Beskos (1997) and Sanches-Sesma et al (2002). One reason for the scarcity of research on this subject is that topographic site effects are generally smaller than those due to subsurface irregularities and that, at the same time, there is the lack of good quality instrumental data.

The review of published studies on the effect of topographies on seismic motion shows that up to now, perfect parametric study which include the whole effects of geometrical and geomechanical properties (such as type and length of incident waves and shape, dimensions and geomechanical properties of hills) of this type of topographies hasn't been implemented. Most of the implemented studies of seismic behavior of 2D hills are concentrated on the evaluation of numerical method's capability rather than the seismic behavior analysis.

Bouchon (1973) was the first who attempted to evaluate the effect of semi-sine shaped hills on the surface motion. He used a frequency domain method which had been developed by Aki and Larner (1970) and studied incident SH, P and SV waves. However, as Bouchon (1973) mentioned, this method resulted in unreliable amplification factors for incident P and SV waves due to complicated calculations especially in high frequencies.

Later Geli et al. (1988) studied by use of the Aki and Larner method, the seismic behavior of 2D semi-sine shaped hills affected by nonhomogenity of the media and existence of adjacent similar hills. But their study too, was restricted to a specific shape ratio of 0.5 and to the special case of the incident SH wave.

Sanchez-Sesma and Campilo (1991) were the first group who evaluated the semi-elliptical hills effects on the ground surface seismic motion. While their studies was considered both P&SV body waves, but was limited to only one shape ratio and on Poisson's ratio. Pedersen et al. (1994) also was the next group who studied the seismic behavior of 2D semi elliptical hills subjected to different incident angles and azimuths, but their studies was restricted to only one shape ratio and Poisson's ratio, too. Sanchez-Sesma was the first who assessed the seismic behavior of sharp corner-type hills but he has considered only triangular hills, SH incident wave and one specified Poisson's ratio. Then, Moczo et al. (1997) was evaluated the seismic behavior of trapezoidal hills. Their studies were consisted of SV incident wave and only one shape ratio, crest angel and Poisson's ratio. Kamalian et al. (2006) were the first group who implemented and completed wide range parametric study on the seismic behavior of semi-sine (2006), semi-elliptical (2004) and trapezoidal hills (2004) subjected to vertical in plane P&SV incident waves. These parametric analyses

through boundary element method has been included the effects of shape ratio, the ratio between incident wave length and hill dimension (width), the crest angel (only for trapezoidal hills), wave type and Poisson's ratio, separately at low to medium range frequencies of input motion . In order to extend the results of above mentioned studies, in the present study the responses of 2D analyses at the top point of topography for different-typed topographies versus related shape ratios (SR) are calculated and then compared and correlated with the results of response spectra of a Ricker-typed wavelet in the free field. This paper present the selective comprehensive results and simple formula for estimating the top-topo/free-field PGA versus shape ratio of the different type of hills, which could be easily applied in site effect microzonation studies for topographic areas.

PARAMETRIC STUDY METHODOLOGY

The parametric studies comprise three distinct cases of trapezoidal, semi-sine and semi-elliptical shaped 2D hills. Geometry defining formulas and the parameters values range which used in parametric analysis are presented in table (1). Figures (1-a) to (1-c) schematically show the geometry of studied topography. Also, Figures (2-a) and (2-b) present the input motion for the Ricker–typed wavelet.

The parametric study was performed by solving the following well known transient boundary integral equation which is governing the dynamic equilibrium of isotropic elastic media:

$$c_{ij}(\xi).u_i(\xi,t) = \int_{\Gamma} (G_{ij} * t_i(x,t) - Fij * u_i(x,t)).d\Gamma \qquad (1)$$

In which u_i denotes the displacement vector and t_i represents the traction at the boundary. G_{ij} and F_{ij} are the transient displacement and traction kernels, respectively, and represent the displacements and tractions at a point x at time t due to a unit point force applied at ξ and at the preceding time τ. The terms $G_{ij}*t_i$ and $F_{ij}*u_i$ are the Riemann convolution integrals and c_{ij} denotes the well known discontinuity term resulting from the singularity of the F_{ij} kernel. The BE formulation of equation (1) was implemented in a general purpose two-dimensional nonlinear two-phase BEM/FEM code named as HYBRID (Kamalian, 2001). Several examples were solved in order to show the accuracy and efficiency of this implemented BE algorithm in carrying out site response analysis of topographic structures (Kamalian et. al, 2003; 2006). All results have been presented in dimensionless forms, using the dimensionless frequency Ω (or its inverse: the dimensionless period) definition. The dimensionless period means physically as the ratio of the incident's wave length to the width of the hill. The hills were subjected to vertically propagating incident SV waves of the Ricker- typed wavelet:

$$f(t) = \left[1 - 2\cdot(\pi\cdot f_p\cdot(t-t_0))^2\right] e^{-(\pi\cdot f_p\cdot(t-t_0))^2} \qquad (2)$$

In which, f_p and t_0 denote the predominant frequency and an appropriate time shift parameter, respectively. The incident Ricker-typed wavelet had in all cases a predominant dimensionless frequency of 1.5 and a dimensionless time shift parameter of 0.9.

Table 1. Formula and the range of parameters which used in parametric analysis

Parameters / Topographic shapes	Geometric Properties			Geomechanical Properties
	SR=h/b	**Inclination Slope (degree)**	**Equation**	**Poisson's ratio**
Semi-Elliptical	0.1-0.2-0.3-0.4-0.5-0.6-0.7-1.0	-	$\xi(x) = -\sqrt{h^2\left(\left(1 - x^2/b^2\right)\right)}$	0.33
Semi-Sine	0.1-0.2-0.3-0.4-0.5-0.6-0.7	-	$\zeta(x) = \frac{h}{2}(1 + Cos\frac{\pi x}{b})$	0.33
Trapezoidal	0.1-0.2-0.3-0.4-0.5-0.6-0.7	45	-	0.33

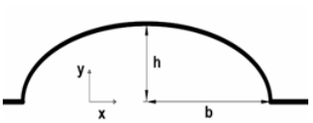


FIG.1-a. semi-elliptical topography

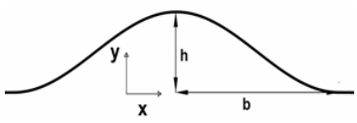


FIG. 1-b. semi-sine topography

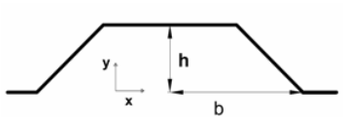


FIG. 1-c. trapezoidal topography

PARAMETRIC ANALYSIS RESULTS

Parametric analysis Results of different-typed topographies are presented in two groups. The first group includes the 3-D curves that are sketched beside each other for different point on the topography and its vicinities. These curves contain the time history of horizontal and vertical amplitude component for the whole and a part of chosen region. Some of them are presented in Figures (4) to (6). These Figures demonstrates clear perspectives of the amplification patterns of a 2D semi-sine, semi-elliptical and trapezoidal hills, with a shape ratio of 0.4 and a Poisson's ratio of 0.33, subjected to incident SV wave, at receiving points arranged within an interval of -4b to 4b from the origin.

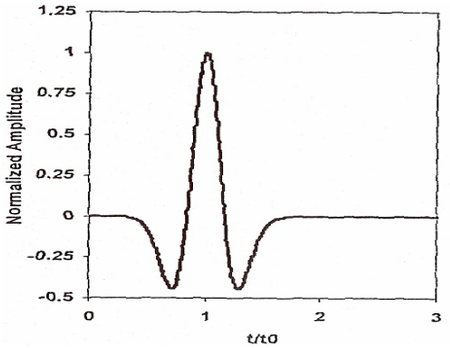


FIG. 2-a. Normalized input motion of the Ricker- typed wavelet in time domain

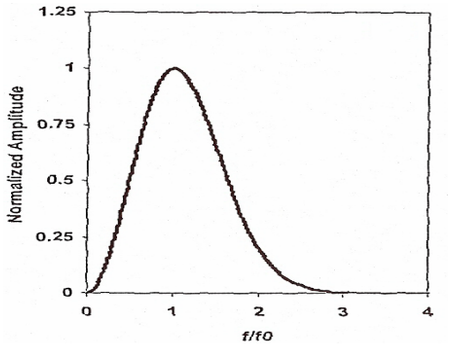


FIG. 2-b. Normalized input motion of the Ricker- typed wavelet in Frequency domain

Obtained results are composed of all ranges of frequency or period and demonstrate the total concept of topography's physical behavior. Therefore, it is only possible to discuss on these results qualitatively. In order to achieve applicable quantitative results, the number of variables involved in the problem should be lessened. Second group of results are smoothed and balanced form of the first group. In this group of results, for engineering interests, a dimensionless period interval of 0.125 to 4.0 was considered, which corresponds to incident waves with wave lengths of 0.125 to 4.0 times the hill's width. This broad period interval was divided into the following five subintervals: (0.125-0.25), (0.25-0.5), (0.5-1.0), (1.0-2.0), (2.0-4.0) and (0.125-4.0), corresponding to incident waves with very short, short, medium, large, very large wave lengths and all of periodic ranges, respectively. For the reason of simplicity and following the well known concept of average horizontal spectral amplification (AHSA) defined by Borcherdt et al. (1994) as spectral ratios representing averages over short, intermediate, mid and long period bands, five distinct amplification factors were computed for every point along the hills, by averaging the corresponding amplification curve over each of the above mentioned five period subintervals. Figures (7) to (9) show these results for these periodic ranges. Obtained results of the first group, at any point along the ground surface, the free field motion is amplified (or deamplified) and both components of motion exist. The amplification patterns, which consist of frequencies of amplifications and deamplification, are gradual and smooth, due to gentle variations of the slope along the hills. Each amplification pattern shows a characteristic frequency (or characteristic period), at which all points along the hills have amplification factors of greater than one and show in-phase motions. The amplification curve of the hills due to its characteristic frequency finds its maximum at the crest and decays toward the bases. If the incident wave has a frequency of smaller than the characteristic frequency of the hills, decreasing the wave's frequency reduces the hill's effect on the ground surface response. In other words, if the hill is impinged by incident waves with wave lengths of much greater than the hill's width, the ground surface response would be approximately the same as the well known free field motion. In the general form, based on two groups of results it can be understood that:

- Increasing the shape ratio of topography (SR) leads to intensification of the amplitude of scattering wave's magnification of the effect of topography on

seismic response. For low values of shape ratio (SR), seismic response of topography will approach to free field response.

- The Scattering waves coming up to the topography surface by the P wave velocity has the maximum amplitude near the topography and their amplitude will be reduced in proportion to distance from topography.
- The scattering waves with SV wave velocity received on the ground surface are mixed with Rayleigh surface waves due to the edges and have a low velocity which is relative to the distance from the topography.
- In high frequency (low periods) range, topography have a complicated behavior and there will be a lot of amplification / deamplification patterns on various points of topography.
- Increasing the shape ratio of topography leads to reduction of the range of amplification and deamplification.
- In second group of results, regarding the horizontal component, if the incident wave possesses a very long wave length, amplification factor of greater than one, which increases with the shape ratio. In this case, The maximum amplification factor occurs at the top of the hills and the amplification factor decays toward the bases. This trend is more complicated in the range of lower periods (very short, short, medium, large, wave lengths).
- In second group of results, regarding the vertical component, at any point across the hills, the vertical amplification factor increases with the shape ratio and decreases by increasing the wave length.

RESPONSE SPECTRUMS BASED ON PARAMETRIC ANALYSES

The output response spectra of the 2D analysis for different shape ratios and topographic shapes (Trapezoidal, Semi-Sine and Semi-Elliptical) at the top point of topography (x/b=0) for horizontal component of the acceleration are obtained. In addition, the response spectra for a Ricker-typed wavelet of a free field are calculated while 5% damping are used in all above mentioned calculations. The results are presented in Figures (10) to (13). Obtained results are termed as the ratio of the PGA (peak ground acceleration) values predicted at the topography top point to the PGA (peak ground acceleration) free field values for different-typed topographies, then the best line regressed among them with following equations:

The Semi-Elliptical topography:

$$\frac{PGA_{top-topo}}{PGA_{free-field}} = -21.126(SR)^4 + 37.816(SR)^3 - 17.124(SR)^2 + 1.7238(SR) + 1.9132 \qquad (R^2 = 0.9831)$$

The Semi-Sine topography:

$$\frac{PGA_{top-topo}}{PGA_{free-field}} = 65.807(SR)^4 - 134.87(SR)^3 + 77.931(SR)^2 - 10.19(SR) + 2.3236 \qquad (R^2 = 0.9992)$$

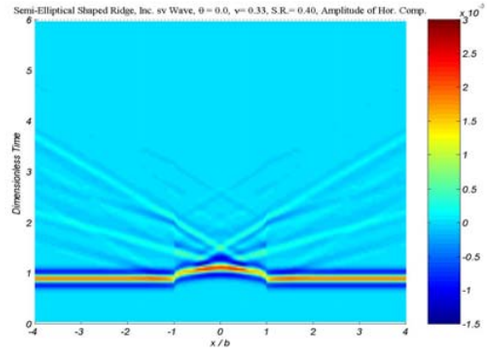


FIG. 4-a. Time history for horizontal component of semi-elliptical topography with the SR= 0.4

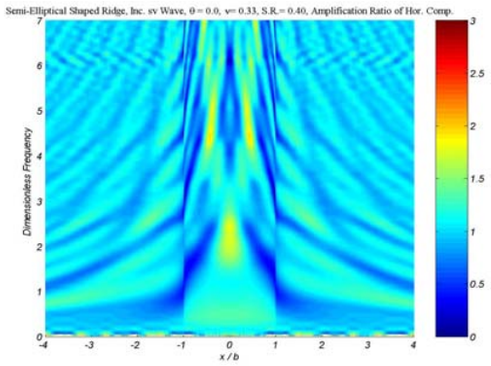


FIG. 4-b. Amplification factor at frequency-domain for horizontal component of semi-elliptical topography with the SR= 0.4

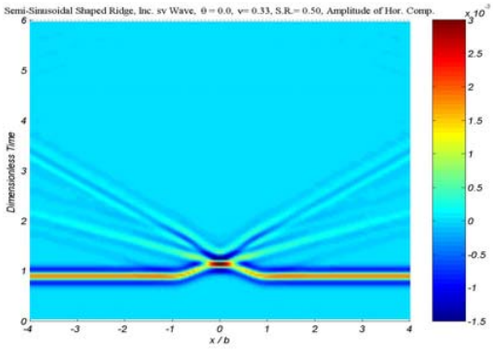


FIG. 5-a. Time history for horizontal component of semi-sine topography with the SR= 0.4

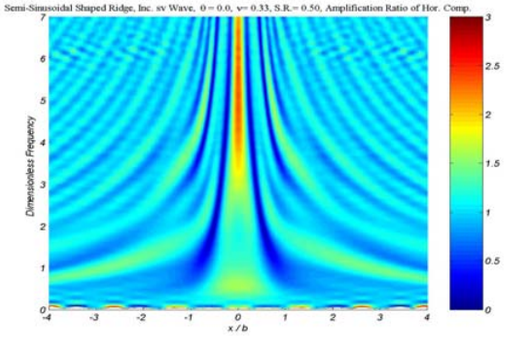


FIG. 5-b. Amplification factor at frequency-domain for horizontal component of semi-sine topography with the SR= 0.4

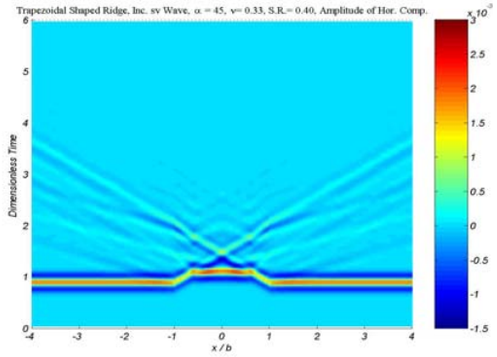


FIG. 6-a. Time history for horizontal component of trapezoidal topography with the SR= 0.4

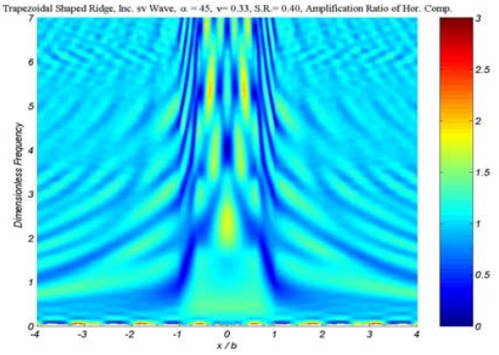


FIG. 6-b. amplification factor at frequency-domain for horizontal component of trapezoidal topography with the SR= 0.4

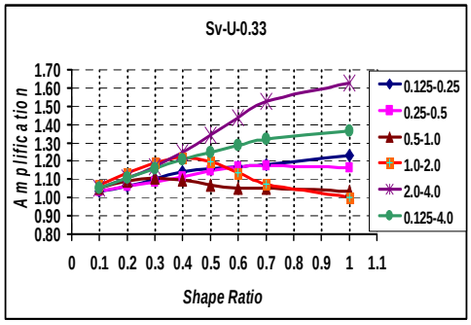


FIG. 7-a. Mean amplification factor for horizontal component of semi-elliptical topography for different shape ratio and periodic ranges

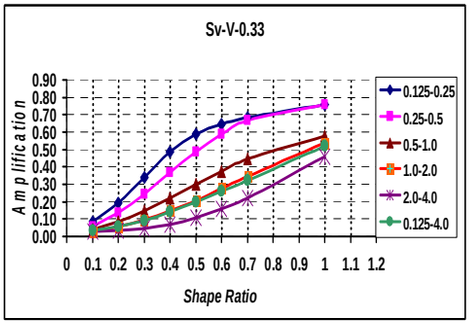


FIG. 7-b. Mean amplification fact or for vertical component of semi-elliptical topography for different shape ratio and periodic ranges

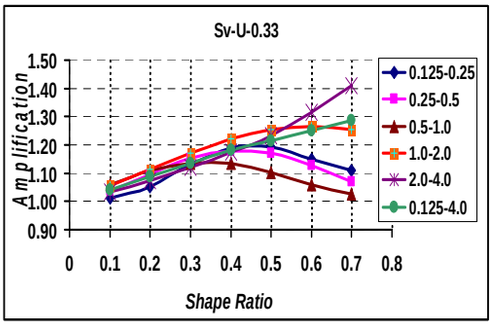


FIG. 8-a. Mean amplification factor for horizontal component of semi-sine topography for different shape ratio and periodic ranges

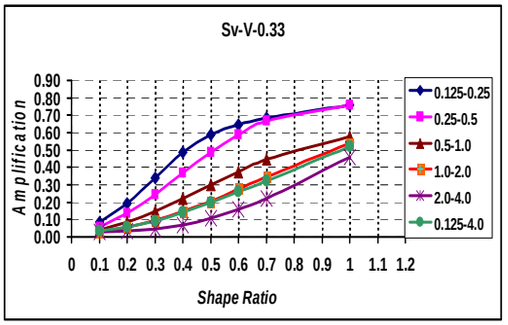


FIG. 8-b. Mean amplification factor for vertical component of semi-sine topography for different shape ratio and periodic ranges

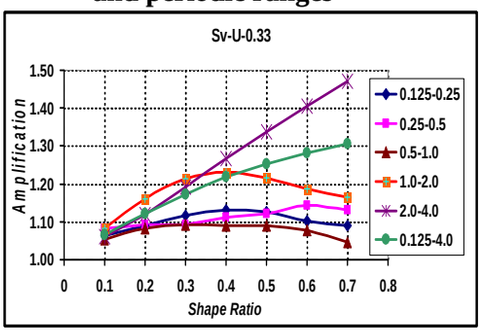


FIG. 9-a. Mean amplification factor for horizontal component of trapezoidal topography for different shape ratio and periodic ranges

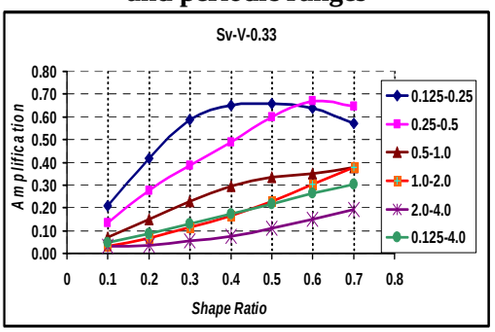


FIG. 9-b. Mean amplification factor for vertical component of trapezoidal topography for different shape ratio and periodic ranges

The Trapezoidal topography:

$$\frac{PGA_{top-topo}}{PGA_{free-field}} = -151.55(SR)^4 + 256.22(SR)^3 - 137.13(SR)^2 + 26.358(SR) + 0.4612 \qquad (R^2 = 0.993)$$

CONCLUSION

In this paper, comprehensive parametric analysis are performed for a wide range of surface-typed topographies in order to complete the previous studies of the topography effect on the seismic ground response under incident SV in-plane wave at high frequencies (low periods). For this purpose, a BEM based program which its results reliability is checked already, is applied to verification of three topographic models. Parametric study focus is on geometric properties variation and it is possible to use the results for other combinations of geometry in term of shape ratio and dimensionless frequency. The results are categorized into two groups. The first group of results is used to qualitative study of topographies physical behavior on the vicinities and investigating different phenomena of wave propagations. The second group of output results is applied for comparative evaluation of effective parameters on seismic response. It is shown that at:

- Increasing the shape ratio of hills (SR) leads to intensification of the amplitude of scattering waves magnification of the effect of topography on seismic response
- Increasing the shape ratio of topography leads to reduction of the range of amplification and deamplification.
- The amplification potential of the hills is strongly influenced by the length of the incident wave, by the shape ratio. Regarding the horizontal component, if the incident wave possesses a very long wave length, amplification factor of greater than one, this increases with the shape ratio. In this case, the maximum amplification factor occurs at the top of the hills and the amplification factor decays toward the bases. Regarding the vertical component, at any point across the hills, the vertical amplification factor increases with the shape ratio and decreases by increasing the wave length.

Finally, the responses of 2D analyses at the top of topography for different-typed topographies versus related shape ratios (SR) were calculated then compared and correlated with the results of response spectra of a Ricker-typed wavelet in the free field, which could be applied in site effect microzonation studies of topographic areas.

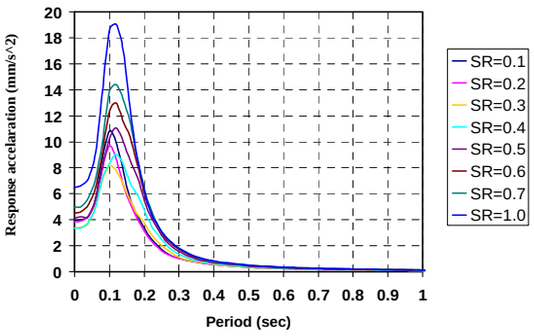


FIG. 10. 2D Response spectra of semi-elliptical topography for horizontal component of the acceleration vs. different shape ratios

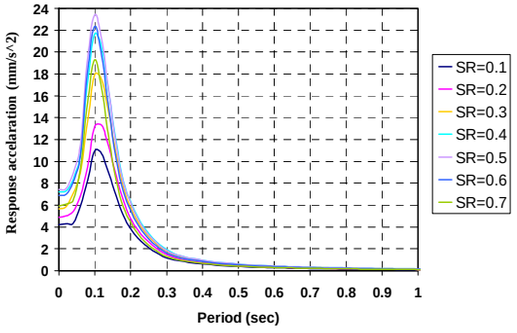


FIG. 11. 2D Response spectra of Semi- sine topography for horizontal component of the acceleration vs. different shape ratios

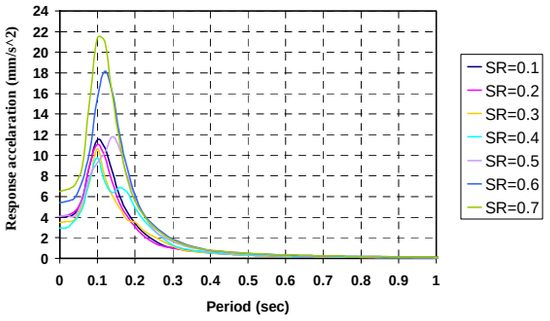


FIG. 12. 2D Response spectra of trapezoidal topography for horizontal component of the acceleration vs. different shape ratios

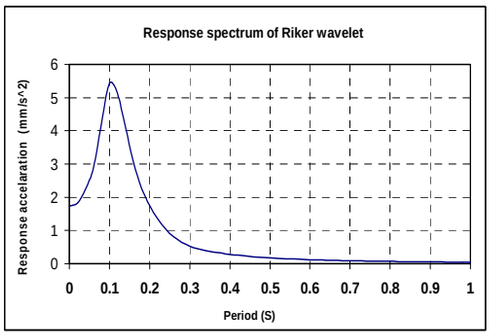


FIG. 13. Response spectra of Ricker-typed wavelet in the free field

REFERENCES

Aki, K., and K. Larner. (1970). "Surface motion of a layered medium having an irregular interface due to incident plane SH waves," J. Geophys. Res., 75, pp 933-954.

Association Française du Genie Parasismique (AFPS). (1990). "Recommandations de la AFPS". Paris: AFPS.183 pp.

Athanasopoulos GA, Pelekis PC and Leonidou EA. (1999). "Effects of Surface Topography on Seismic Ground Response in the Egion (Greece) 15-6-1995 Earthquake, " Soil Dynamics and Earthquake Engineering, 18, 135-149.

Boore DM. (1973). "The effect of simple topography on seismic waves: implications for the accelerations recorded at Pacoima Dam, San Fernando Valley, California," Bull Seismol Soc Am, 63, 1603- 1609.

Bouchon, M. (1973). "Effect of Topography on Surface Motion," Bull. Seism. Soc. Am., 63, pp. 615- 632.

Borcherdt RD. 1994. "Estimates of site-dependent response spectra for design (Methodology and Justification)," Earthquake Spectra, 10, 617-653.

Beskos, DE. "Boundary element methods in dynamic analysis:Pt.II (1986-1996)," Applied Mechanics Revision, 50, pp.97-149, 1997

Bouckovalas GD and Kouretzis G. (2001). "Review of Soil and Topography Effects in the September 7, 1999 Athens (Greece) Earthquake," Proceedings of the Fourth International Conference on Recent Advances in Geotechnical Earthquake Engineering and Soil Dynamics And Symposium in Honor of Professor WD Liam Finn, San Diego, California.

Celebi M. (1987). "Topographical and geological amplifications determined from strong-motion and aftershock records of the 3 March 1985 Chile earthquake," Bull Seismol Soc Am, 77, 1147-1167.

Celebi M. (1991). "Topographic and geological amplification: Case studies and engineering implications," Structural Safety, 10, 199-217.

Eurocode8 (EC8). (1998). "Design provisions for earthquake resistance of structures".

Geli, L., Bard, P. V., Julien, B. (1988). "The effect of topography on earthquake ground motion: a review and new results" Bull. Seism. Soc. Am., 78, pp. 42-63.

Sanchez–Sesma, F.J. & M. Campillo, (1991). "Diffraction of P, SV and Rayleigh waves by topographical features:a boundary integral formulation," Bull. Seism. Soc. Am., 81.

Sanchez-Sesma, F.J., V.J. Palencia and F. Luzon. (2002). "Estimation of local site effects during earthquakes: an overview", ISET journal of Earthquake Technology, Vol.39, No.3, pp.167-193.

Spudich. P, Hellweg. M and Lee. WHK. (1996). "Directional topographic site response at Tarzana observed in aftershocks of the 1994 Northridge, California, Earthquake: Implications for mainshock motions, " Bull Seismol Soc Am, 86, S139-S208.

Trifunac MD and Hudson DE. (1971). "Analysis of the Pacoima Dam accelerograms – San Fernando earthquake of 1971," Bull Seismol Soc Am, 61, 1393-1411.

Pedersen, H.A., F.J. Sanchez-Sesma and M. Campillo, (1994). "Three-Dimensional Scattering by Two-Dimensional Topographies," Bull. Seism. Soc. Am., Vol. 84, pp. 1169-1183.

Moczo, P., E. Bystricky, J. Kristek, J.M. Carcione and M .Bouchon. (1997). "Hybrid modeling of P-SV seismic motion at inhomogenous viscoelastic topographic structures," Bull. Seism. Soc. Am., Vol. 87, pp. 1305-1323.

Kamalian, M. (2001). "Time domain two-dimensional hybrid FEM/BEM dynamic analysis of non-linear saturated porous media," Ph.D. Dissertation, Tehran University, (In Persian).

Kamalian, M., Gatmiri, B., Sohrabi, A. (2003). "On Time-Domain Two-Dimensional Site Response Analysis of Topographic Structures by BEM," Journal of seismology and earthquake engineering, 5(2), pp. 35-45.

Kamalian, M., M.K. Jafari, A. Razmkhah and A. Sohrabi-Bidar. (2004). "Amplification Pattern of 2D Semi-Elliptical Shaped Hills Subjected To Vertically Propagating Incident Waves," AmirKabir Engineering Journal. (In Persian)

Kamalian, M., Jafari, MK., Sohrabi-bidar, A., Razmkhah, A., Gatmiri, B. (2006). "Time-domain two-dimensional site response analysis of non-homogeneous

topographic structures by a hybrid BE/FE method," Soil Dyn Earthquake Eng., 26:753-765.

Kamalian, M., M.K. Jafari, A. Sohrabi-Bidar and A. Razmkhah. (2006). "Amplification Pattern of 2D Semi-Sine Shaped Hills Subjected to Vertically Propagating Incident Waves", Earthquake Spectra Journal (in press).

Characterizing the Earthquake Ground Shaking Hazard in the Sacramento-San Joaquin Delta, California

Ivan Wong[1], R.G., Patricia Thomas[2], PhD, Jeffrey Unruh[3], PhD, P.G.,
Kathryn Hanson[4], and Robert Youngs[5], PhD

[1]Principal Seismologist/Vice President, Seismic Hazards Group, URS Corporation, 1333 Broadway, Suite 800, Oakland, CA 94612; ivan_wong@urscorp.com
[2]Project Earthquake Engineer, Seismic Hazards Group, URS Corporation, 1333 Broadway, Suite 800, Oakland, CA 94612; patricia_thomas@urscorp.com
[3]Vice President, William Lettis & Associates, 1777 Botelho Drive, Suite 262, Walnut Creek, CA 94596; unruh@lettis.com
[4]Principal Geologist, Geomatrix Consultants Inc., 2101 Webster Street, 12th Floor, Oakland, CA 94612; khanson@geomatrix.com
[5]Principal Engineer/Vice President, Geomatrix Consultants Inc., 2101 Webster Street, 12th Floor, Oakland, CA 94612; byoungs@geomatrix.com

ABSTRACT: The effects of earthquakes may be the most significant natural hazard that can impact the Delta levees, whose potential failure would be catastrophic to California's economy. A probabilistic seismic hazard analysis (PSHA) was performed to characterize the ground shaking hazard that could contribute to levee failure in the Delta. Based on a seismic source model that builds upon the characterizations of the major faults in the San Francisco Bay region from the Working Group on California Earthquake Probabilities (WGCEP, 2003) and several newly recognized faults, a PSHA was performed for key sites throughout the Delta and probabilistic hazard maps were developed. Of particular significance are several seismic sources within the Delta, which were characterized as part of this study including the northern and southern Midland fault and two areal zones of deformation, which we call the Montezuma Hills and Thornton Arch zones. These potential seismic sources have been the subject of very little research and thus there is greater uncertainty in their characterization compared to the better studied major faults in the Bay region. Ground motion attenuation relationships from the Next Generation Attenuation (NGA) Project were used in the PSHA. Quasi-time-dependent hazard in 2005, 2050, 2100, and 2200 was calculated. The time-dependent behavior of the major faults was adopted from the WGCEP (2003), which weighted both time-dependent and independent models in their forecasts. The hazard was calculated for a firm soil site condition (average shear-wave velocity in the top 30 m [V_S30] = 1100 ft/sec). For a return period of 500 years, the time-dependent probabilistic peak horizontal accelerations ranged from 0.2 to 0.4 g. Time-independent (Poissonian) hazard for the Delta differs little from the time-dependent hazard because the hazard is generally

being controlled by the local Delta faults. The hazard as expected is higher at sites closer to the major faults.

INTRODUCTION

As part of the Delta Risk Management Strategy (DRMS) Project (URS/JBA, 2007a) an evaluation of the ground shaking hazard of the Sacramento-San Joaquin Delta levees under present as well as foreseeable future conditions was performed. The Delta levees represent a critical element in California's water delivery infrastructure and damage to them in a large earthquake would be a major blow to the State's economy over a sustained period of time. In this paper, we summarize the approach, methodology, inputs, and the hazard results in terms of the probabilities of the levels and character of earthquake ground shaking events that will contribute to the risk of levee failure in the Delta. A detailed description of this study is contained in URS/JBA (2007b).

The approach of performing a probabilistic seismic hazard analysis (PSHA) is standard practice in the engineering seismology/earthquake engineering community. The PSHA methodology used in this study allows for the explicit consideration of epistemic uncertainties and inclusion of the range of possible interpretations of components in the seismic hazard model, including seismic source characterization and ground motion estimation. Epistemic uncertainties in models and parameters are incorporated into the hazard analysis through the use of logic trees.

A key assumption of the standard PSHA model is that earthquake occurrences can be modeled as a Poisson process. In this analysis, however, quasi-time-dependent hazard was calculated for the major Bay Area faults using the range of models that were considered by the U.S. Geological Survey's (USGS) Working Group on California Earthquake Probabilities (WGCEP, 2003). Based on the results of the WGCEP (2003), there is an increasing probability of a large ($\mathbf{M} \geq 6.7$) earthquake occurring in the San Francisco Bay region in the period 2002 to 2031. The estimated probability in 2002 was 62% and this value will increase with time. It should be noted that the models considered by WGCEP (2003) are not 100% time-dependent. For Bay area faults for which there is not sufficient information on the timing of the most recent earthquake, the hazard calculation approach used is time-independent. From hereon, what we refer to as "time-dependent hazard" in this study also contains a large "time-independent" component.

For the risk analysis (URS/JBA, 2007a), time-dependent probabilities of occurrence of all plausible earthquake events (defined by their locations, magnitudes, and ground motions) were needed. These have been used to develop estimates of risk (defined as the annual probability of seismically-induced levee failure) at selected times over the next 200 years (2005, 2050, 2100, and 2200) (URS/JBA, 2007a). We have also calculated the time-independent hazard in the Delta for the purposes of comparison.

Time-dependent probabilistic ground shaking hazard maps were also developed for 100- and 500-year return periods for the Delta area. The maps are for peak horizontal ground acceleration (PGA) and 1.0 sec horizontal spectral accelerations (SA), and a stiff soil site condition.

METHODOLOGY

The following steps were taken in the PSHA: 1) identify all seismic sources that can generate strong ground shaking at the site; 2) characterize each seismic source in terms of location, geometry, sense of slip, maximum magnitude, and earthquake occurrence rates for all magnitudes of significance to the site hazard (typically moment magnitude [**M**] ≥ 5); 3) select ground motion attenuation relationships appropriate for the seismic sources, seismotectonic setting, and site conditions; and 4) calculate the probabilistic hazard using a qualified computer program.

The traditional PSHA approach is based on the model developed principally by Cornell (1968). The calculations were made using the computer program HAZ38 developed by Norm Abrahamson. The program has been validated in a Pacific Earthquake Engineering Research (PEER) Center-sponsored "Validation of PSHA Software" Project (Wong et al., 2004).

The PSHA was performed consistent with the guidelines for a Level 2 analysis using the Technical Integrator (TI) approach as defined by the Senior Seismic Hazard Analysis Committee (1997). The Level 2 study was further enhanced by peer review by representatives of the USGS and the California Geological Survey (CGS). The TI consisted of: Ivan Wong, Patricia Thomas, Jeff Unruh, Kathryn Hanson, and Bob Youngs.

SEISMIC SOURCE MODEL

Seismic source characterization is concerned with three fundamental elements: (1) the identification, location, and geometry of significant sources of earthquakes; (2) the maximum size of the earthquakes associated with these sources; and (3) the rate at which they occur. In this study, the dates of past earthquakes on specific faults also are required in addition to the frequency of occurrence. The source parameters for the significant faults in the

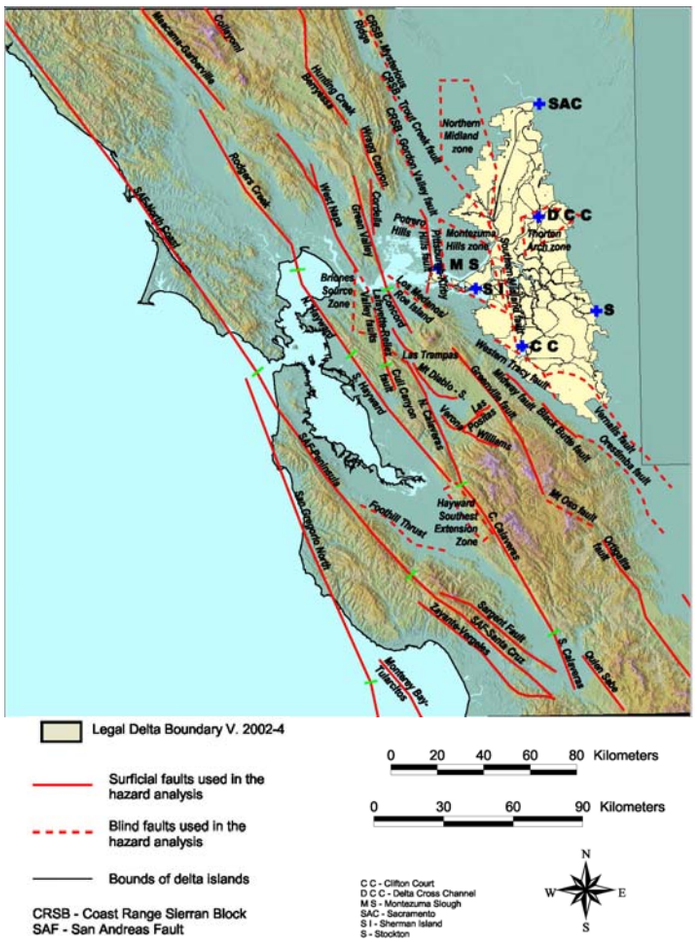


FIG. 1. Active Faults of the SFBR

site region (Fig. 1) are characterized for input into the PSHA. Areal source zones are used in the PSHA to account for the hazard from background earthquakes. Epistemic uncertainties in the seismic source parameters were incorporated into the PSHA using a logic tree approach.

The guiding philosophy for characterizing seismic sources in this study is the following. The fundamental seismic source characterization came from the work done by the USGS Working Group on Northern California Earthquake Potential (WGNCEP, 1996), the USGS WGCEP (2003), and the CGS's seismic source model used in the USGS National Hazard Maps (Cao et al., 2003). This characterization was updated and revised by the TI based on recent research. Also, more detailed characterizations of potential seismic sources in the Delta and the western margin of the Great Valley were performed by the TI in order to fully capture the range of assessments that might affect the Delta region.

Time-Independent Seismic Source Model

Based on reviews of published and unpublished data, a model of the active and potentially active seismogenic faults was developed for the greater San Francisco Bay region (Fig. 1). The major study completed by the WGCEP (2003) describes and summarizes the current under-standing of the major faults in the San Francisco Bay region. We have adopted their seismic source parameters for the San Andreas, Hayward/ Rodgers Creek, Calaveras, Concord/Green Valley, San Gregorio, Greenville, and Mt. Diablo thrust faults in our analysis. The characterization of the Calaveras fault was slightly modified by the TI. The characterizations of other faults such as the Sargent and Foothill thrust belt are based, to a large extent, on the CGS model (Cao et al., 2003) and other available studies.

Four Delta seismic sources were characterized and included in the PSHA that are not included in either the CGS (Cao et al., 2003) or WGNCEP (1996) model. They are the Northern Midland zone, Southern Midland fault, Thornton Arch Zone, and Montezuma Hills Zone (Fig. 2). As is the case for many "blind" faults, the characterization of the Delta seismic sources is highly uncertain because of the very limited amount of data. What is known about these sources has come from subsurface seismic data. A detailed discussion of the Delta faults is contained in URS/JBA (2007b).

Also, of significance to the study are the blind faults adjacent to the Delta: the Western Tracy and Vernalis faults, part of the Coast Ranges-Sierran Block boundary zone (Wong et al., 1988) (Fig. 2).

Magnitudes not adopted from WGCEP (2003) or Cao et al. (2003) were computed using the rupture area relationships of Wells and Coppersmith (1994) and Hanks and Bakun (2002) and the rupture length relationship of Wells and Coppersmith (1994). The relationships are equally weighted.

The choice of recurrence models used can significantly impact the resulting hazard. We considered the truncated exponential, maximum-magnitude, and characteristic recurrence models, with various weights depending on the source geometry and type of rupture model. For faults we have weighted the characteristic and maximum magnitude models 0.7 and 0.3, respectively.

To address the uncertainty in segmentation models, a "floating earthquake" was used in the PSHA for some seismic sources. The maximum magnitude of the floating earthquake is based on the observations of the rupture behavior of other faults.

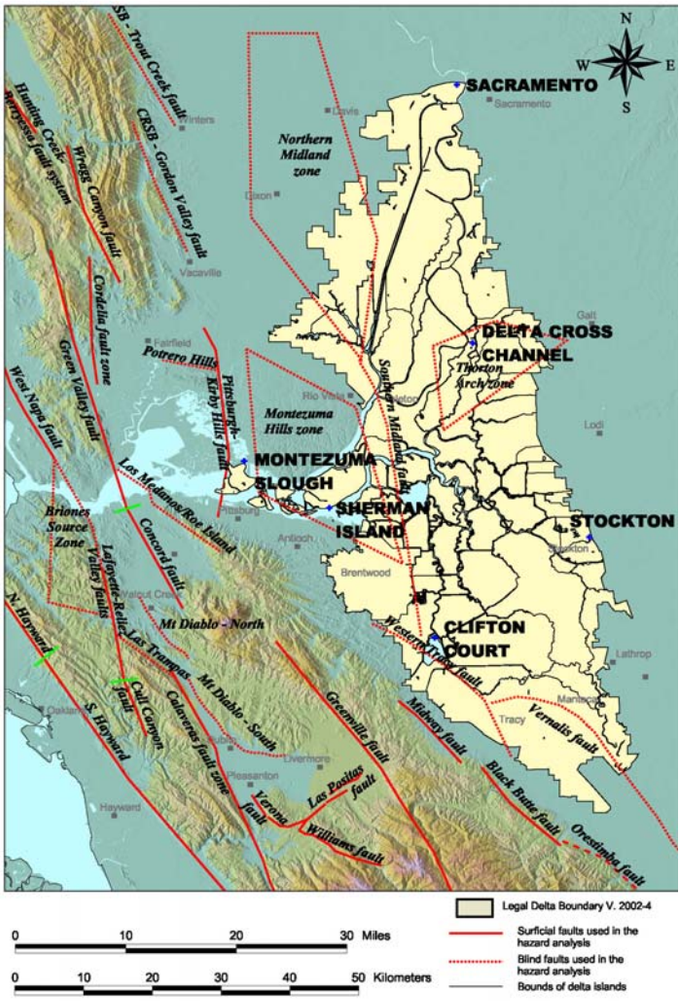


FIG. 2. Active Faults in the Site Region

WGCEP Time-Dependent Model

The WGCEP (2003) source characterization and earthquake probability models were used directly with computer codes obtained from the USGS to obtain rates of characteristic events for the seven major faults in the San Francisco Bay region. The five probability models account for various degrees of physics, date of last rupture, recent seismicity rates, and slip in the 1906 earthquake. The models include four time-dependent models, Empirical, Brownian Passage Time (BPT), BPT-step, and Time-Predictable, and the time-independent Poisson model (Table 1). WGCEP (2003) applied weights to these five models for each of the seven major faults it considered (Table 1). The five probability models and their weights along with the source characterization were used to compute the rates of characteristic events on each rupture source, which would then be used in the PSHA. Rupture probabilities were calculated for one-year exposure windows using starting dates of 2005, 2050, 2100, and 2200. The following modifications to the WGCEP (2003) inputs were made.

The program for computing the time-predictable probabilities for the San Andreas fault rupture scenarios was obtained from Dr. William Ellsworth, USGS. The inputs to this program were modified to change the exposure time to one year and to compute results for the four starting times. The Empirical Model of Reasenberg et al. (2003) was used to obtain the scale factors to modify the long-term rate. WGCEP (2003) used Reasenberg et al. (2003) models A through F and assigned weights of 0.1, 0.5, and 0.4 to the minimum, average, and maximum scale factor, respectively.

Using the values for models A through D listed in WGCEP (2003) and scaling the linear models E and F from WGCEP (2003), activity rates were calculated. The only modifications made for the Poisson, BPT and BPT-step model inputs were to change the exposure time to one year and to compute results for the four starting times.

TABLE 1. Mean Expert Weights for Probability Models Applied to the SFBR Fault Systems (Table 5.5, WGCEP, 2003)

Fault System	Poisson	Empirical	BPT	BPT-step	Time-Predictable
San Andreas	0.100	0.181	0.154	0.231	0.335
Hayward/Rodgers Creek	0.123	0.285	0.131	0.462	—
Calaveras	0.227	0.315	0.142	0.315	—
Concord/Green Valley	0.246	0.277	0.123	0.354	—
San Gregorio	0.196	0.292	0.115	0.396	—
Greenville	0.231	0.288	0.131	0.350	—
Mt. Diablo Thrust	0.308	0.396	0.092	0.204	—

The mean, 5th and 95th rates of characteristic events for each rupture source in the WGCEP (2003) model were used as input to the PSHA code, along with the source geometries, characteristic magnitudes and shape of the magnitude distributions. The PSHA code requires the activity rate of all events above the minimum magnitude and the rate of characteristic events. This activity rate is used along with the normalized magnitude probability density function (pdf) to describe the rate of all size magnitudes events on the rupture source. The activity rates were calculated by scaling up the normalized magnitude pdf such that the rate of characteristic events matched the rate provided by the WGCEP (2003) model. The characteristic event is defined by a normal distribution truncated at the upper and lower ends at two sigma, where sigma is 0.12 magnitude units. A portion of the moment rate of the fault is accounted for with an exponential tail of smaller events, defined by a b-value. WGCEP (2003) used a mean value of 6% of moment rate in the exponential tail, along with branches that used 4% and 8% with lower weights. For simplicity, a single value of 6% of the moment rate was applied to the exponential tail in the PSHA.

Background Seismicity

To account for the hazard from background (random) earthquakes in the PSHA that are not associated with known or mapped faults, two regional seismic source zones were used: the Coast Ranges and Central Valley. An example of a background earthquake is the 1986 **M** 5.7 Mt. Lewis earthquake that occurred east of San Jose. The recurrence parameters for the Coast Ranges source zone were adopted from Youngs et al. (1992). They calculated values based on the historical seismicity record after removing earthquakes within 10-km-wide corridors along each of the major faults. The recurrence values for the Central Valley zone were estimated by the TI. The maximum earthquake for both source zones is **M** 6.5 ± 0.3.

Cascadia Subduction Zone

Because of the large long-period ground motions that can be generated by very large (**M** > 8) earthquakes in the Cascadia subduction zone in northwestern

California, we have included it in the PSHA. The megathrust geometry was adopted from Wang et al. (2003). The maximum depth of the megathrust (defines the easternmost extent) was varied at 12 km, 20 km, and 25 km weighted 0.4, 0.5, and 0.1, respectively. The Wang et al. (2003) model shows the megathrust locked zone offshore of northernmost California and the transition zone extending to a depth of about 15 km. Rupture of the megathrust will initiate in the locked zone and may extend into the transition zone (Hyndmann and Wang, 1995). How far rupture will extend into the transition zone is highly uncertain. The maximum magnitudes assigned to the Cascadia subduction zone megathrust were **M** 9 ± ½ and the recurrence intervals were 450 ± 150 years.

ATTENUATION MODELS

To characterize the attenuation of ground motions in the PSHA, the recently developed PEER Next Generation Attenuation (NGA) empirical attenuation models were used. All relationships provide the attenuation of PGA and SA (5% damping). In this analysis, the hazard was defined for a stiff soil site condition characterized by an average V_S30 of 1,100 ft/sec. The fragility estimates for the levees are referenced to these ground motions. At the time when the PSHA was performed, only the models by Chiou and Youngs, Campbell and Bozorgnia, and Boore and Atkinson were available (see PEER NGA web site). The relationships were reviewed and weighted equally in the PSHA. Intra-event and inter-event aleatory uncertainties for each attenuation relationship were required for the risk analysis.

We have attempted to include 3D basin effects in the PSHA through the use of the NGA relationships. However, only one of the NGA models, Campbell and Bozorgnia, addresses basin effects through their use of the basin depth parameter $Z_{2.5}$, depth to a velocity of 2.5 km/sec. The basin depth beneath the Delta ($Z_{2.5}$) was assumed to be 5 km based on Brocher (2005). The response of the levees appears to be sensitive to ground motions out to a period of only 1 sec and so longer period motions (> 1 sec) where deep basin effects would be most pronounced, such as beneath the Delta, are probably not that significant to the Delta levees.

For the Cascadia subduction zone megathrust, the models by Youngs et al. (1997), Atkinson and Boore (2003), and Gregor et al. (2006) were used with equal weights.

TIME-DEPENDENT HAZARD RESULTS

The time-dependent hazard at the six locations in the Delta (Fig. 2) was calculated in terms of ground motion as a function of annual exceedance probability. This probability is the reciprocal of the average return period. The probabilistic PGA and 1.0 sec horizontal SA are listed in Table 2 for return periods of 100, 200, 500, and 2,500 years for the year 2005. At all return periods, the ground motions decrease from west to east due to increasing distance from the faults within the San Andreas system. At a 100-year return period, the PGA values range from 0.12 g in Sacramento, which is the most eastern site on the edge of the Delta to 0.27 g at Montezuma Slough (Fig. 2). The latter site is located adjacent to the Pittsburg-Kirby Hills fault.

Table 2. Ground Motions for Return Periods of 100 to 2,500 Years in 2005

Site	PGA (g's)			
	100 years	200 years	500 years	2,500 years
Clifton Court	0.22	0.29	0.40	0.66
Delta Cross Channel	0.15	0.19	0.25	0.37
Montezuma Slough	0.27	0.35	0.47	0.74
Sacramento	0.12	0.15	0.20	0.30
Sherman Island	0.24	0.31	0.41	0.64
Stockton	0.13	0.17	0.22	0.32

The seismic sources controlling the hazard varies from site to site but the Southern Midland fault and Northern Midland zone are major contributors to most of the sites within the Delta at return periods of 100 to 2,500 years (Table 3). At long-period ground motions, e.g., 1.0 sec SA, and a return period of 100 years, the faults of the San Andreas fault system are major contributors. At 2,500 years, the Southern Midland and the Cascadia subduction zone are contributing significantly to the hazard in 2005. An important assumption in the study is that a large earthquake in the SFBR does not occur in the 200-year time frame.

TABLE 3. Controlling Seismic Sources at a Return Period of 100 Years in 2005

Location	PGA	1.0 Sec SA
Clifton Court	Southern Midland Mt. Diablo	Mt. Diablo Hayward-Rodgers Creek
Delta Cross Channel	Southern Midland Northern Midland Zone	Mt. Diablo
Montezuma Slough	Concord-Green Valley	Concord-Green Valley
Sacramento	Northern Midland Zone	Mt. Diablo San Andreas
Sherman Island	Southern Midland	Southern Midland Hayward-Rodgers Creek San Andreas
Stockton	Southern Midland Hayward-Rodgers Creek Calaveras	Hayward-Rodgers Creek San Andreas

Note: Seismic sources are ordered by contribution.

Results indicate that the hazard is not sensitive to the time-dependent characterization of the major faults considered by the WGCEP (2003) because the hazard is controlled by the nearby Delta faults. Thus the hazard did not increase significantly when calculated for the year 2005 compared to the year 2200. An important assumption in the analysis is that a large earthquake on the major faults does not occur in the 200-year time frame.

We have produced ground shaking hazard maps for the Delta area for PGA and 1.0 sec SA for return periods of 100 and 500 years (e.g., Fig. 3). The same site condition of firm soil was assumed. The PSHA to develop the maps was updated to include: (1) the use of an unreleased NGA version of the Abrahamson and Silva attenuation model in addition to the three other NGA relationships; (2) an updated version of Boore and Atkinson (2007); (3) the weights for the subduction zone megathrust were

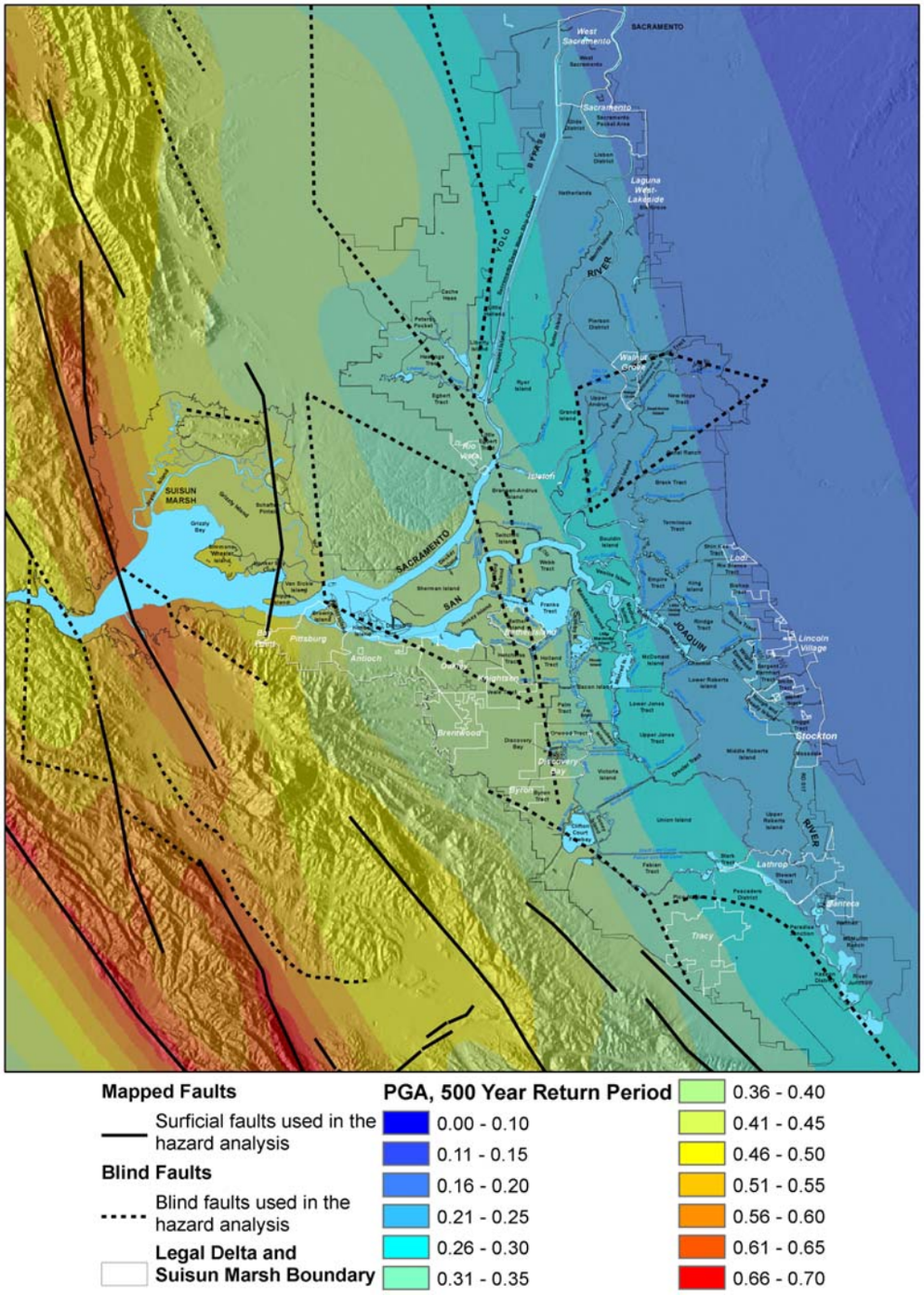


FIG. 3. PGA Hazard for a 500-Year Return Period

revised to: Youngs et al. (1997), 0.5; Atkinson and Boore (2003), 0.25; and Gregor et al. (2006), 0.25 based on consultation with Mark Peterson, USGS; and lastly (4) the basin factor in Campbell and Bozorgnia was not used because of the significantly different ground motions it provides relative to the other attenuation relationships. As

expected, the hazard decreases from west to east at these short return periods. An important point is that these maps are for a uniform site condition so site response effects are not apparent on these maps.

ACKNOWLEDGMENTS

This study was sponsored by the California Department of Water Resources as part of the DRMS Project. Our sincere thanks to Les Harder and Ralph Svetich for their support. The project was managed by Said Salah-Mars of URS and Marty McCann of JBA. Thanks to Melinda Lee, Doug Wright, and Fabia Terra for their assistance in the study. Review comments on the original study were provided by Tom Brocher, Russ Graymer, Tom Hanks, Tom Holzer, David Schwartz, and Jack Boatwright of the USGS and Tianqing Cao and Mike Reichle of the CGS. Our appreciation to them for their efforts. Our thanks to the two anonymous reviewers for their comments that helped improved the paper.

REFERENCES

Atkinson, G.M. and Boore, D.M. (2003). "Empirical ground-motion relations for subduction zone earthquakes and their applications to Cascadia and other regions." *Bull. Seism. Soc. Amer.* 93, 1703-1729.

Boore, D.M. and Atkinson, G.M. (2007). "NGA Ground motion relations for the geometric mean horizontal component of peak and spectra ground motion parameters." Pacific Earthquake Engineering Research Center Report 2007/01, 242 p.

Brocher, T.M. (2005). "A regional view of urban sedimentary basins in northern California based on oil industry compressional-wave velocity and density logs." *Bull. Seism. Soc. Amer.* 95, 2093-2114.

Cao, T., Bryant, W.A, Rowshandel, B., Branum, D., and Wills, C.J. (2003). "The revised 2002 California probabilistic seismic hazard maps, June 2003." California Geological Survey, http://www.consrv.ca.gov/CGS/rghm/psha/fault_parameters/pdf/2002_CA_Hazard_Maps.pdf.

Cornell, C.A. (1968). "Engineering seismic risk analysis." *Bull. Seism. Soc. Amer.* 58, 1583-1606.

Gregor, N., Silva, W., Wong, I., and Youngs, R. (2006). "Updated response spectral attenuation relationship for Cascadia subduction zone megathrust earthquakes." *Seis. Res. Let.* 77, 325.

Hanks, T.C. and Bakun, W.H. (2002). "A bilinear source-scaling model for M-log A observations of continental earthquakes." *Bull. Seism. Soc. Amer.* 92, 1841-1846.

Hyndman, R.D. and Wang, K. (1995). "The rupture zone of Cascadia great earthquakes from current deformation and the thermal regime." *J. Geoph. Res.* 100, 133-22.

Reasenberg, P.A., Hanks, T.C., and Bakun, W.H. (2003). "An empirical model for earthquake probabilities in the San Francisco Bay region, California, 2002-3031." *Bull. Seism. Soc. Amer.* 93, 1-13.

Senior Seismic Hazard Analysis Committee (SSHAC) (1997). "Recommendations for probabilistic seismic hazard analysis-guidance on uncertainty and use of experts." U.S. Nuclear Regulatory Commission NUREG/CR-6327, variously paginated.

URS/JBA (URS Corporation/Jack R. Benjamin & Associates, Inc.) (2007a). "Delta Risk Management Strategy, Phase 2: Evaluation of Delta Risk Management Strategy Report." Prepared for the Department of Water Resources.

URS/JBA (URS Corporation/Jack R. Benjamin & Associates, Inc.) (2007b). "Delta Risk Management Strategy, Phase 1: Seismology Technical Memorandum Draft 2." Prepared for the Department of Water Resources.

Wang, K., Wells, R., Mazzotti, S., Hyndman, R.D., and Sagiya, T. (2003). "A revised dislocation model of the Cascadia subduction zone." *J. Geoph. Res.* 108, ETG 9-1 – 9-13.

Wells, D.L. and Coppersmith, K.J. (1994). "New empirical relationships among magnitude, rupture length, rupture width, rupture area, and surface displacement." *Bull. Seism. Soc. Amer.* 84, 974-1002.

Wong, I.G., Ely, R.W., and Kollman, A.C. (1988). "Contemporary seismicity and tectonics of the northern and central Coast Ranges-Sierran block boundary zone, California." *J. Geoph. Res.* 93, 7813-7833.

Wong, I.G., Thomas, P.A., and Abrahamson, N. (2004). "The PEER-Lifelines validation of software used in probabilistic seismic hazard analysis," in M. Yegian and E. Kavazanjian (eds.) (2004). Geotechnical Engineering for Transportation Projects, Proceedings, American Society of Civil Engineers, Geotechnical Special Publication No. 126 (1), 807-815.

Working Group for California Earthquake Probabilities (WGCEP) (2003). "Earthquake probabilities in the San Francisco Bay area: 2002-2031." U.S. Geological Survey Open-File Report 03-214.

Working Group on Northern California Earthquake Potential (WGNCEP) (1996). "Database of potential sources for earthquakes larger than magnitude 6 in northern California." U.S. Geological Survey Open-File Report 96-705, 53 p.

Youngs, R.R., Chiou, S.-J, Silva, W.J., and Humphrey, J.R. (1997). "Strong ground motion attenuation relationships for subduction zone earthquakes." *Seis. Res. Let*. 68, 58-73.

Youngs, R.R, Coppersmith, K.J., Taylor, C.L., Power, M.S., Di Silvestro, L.A., Angell, M.L., Hall, N.T., Wesling, J.R., and Mualchin, L. (1992). "A comprehensive seismic hazard model for the San Francisco Bay Region," in Proceedings of the Second Conference on Earthquake Hazards in the Eastern San Francisco Bay Area, Borchardt, G., Hirschfeld, S.E., Lienkaemper, J.J., McClellan, P., Williams, P.L. and Wong, I.G. (eds.), *California Division of Mines and Geology Special Publication 113*, 431-441.

This page intentionally left blank

Damage Assessment and Seismic Modeling of Dams in Connection with the 2006 Hawaii Earthquakes

Horst G. Brandes[1], M. ASCE, P.E., Peter G. Nicholson[2], F. ASCE, P.E.
and Ian N. Robertson[3], M. ASCE, S.E.

[1]Associate Professor, Department of Civil and Environmental Engineering, University of Hawaii, Honolulu, HI 96822; horst@hawaii.edu

[2]Associate Professor, Department of Civil and Environmental Engineering, University of Hawaii, Honolulu, HI 96822; pnichol@eng.hawaii.edu

[3]Professor, Department of Civil and Environmental Engineering, University of Hawaii, Honolulu, HI 96822; ianrob@hawaii.edu

ABSTRACT: Two large earthquakes that rattled the Hawaiian chain in October of 2006 were strong enough to cause minor to moderate damage to four nearby dams, including longitudinal and transverse cracks in the embankment fills, incipient slope instability, and possibly delayed internal erosion and piping that triggered emergency water releases from two of the reservoirs. Recent seismic studies by the first author indicate that many dams in Hawaii are potentially susceptible to severe damage from earthquake shaking due to an active seismic environment in some parts of the State. Adding to a general level of uncertainty are outdated construction methods used for dams as old as 120 years, relatively unknown dynamic characteristics of local volcanic soils, and a lack of sufficient understanding of strong motion propagation throughout the Islands.

INTRODUCTION

On October 15, 2006, two strong earthquakes with magnitudes of 6.7 and 6.0 struck along the Northwest coast of the Island of Hawaii within 7 minutes of each other (Figure 1). Although the Mahukona earthquake occurred only 7 minutes after the Kiholo Bay one, each is considered a separate event because of significant differences in depth and location. Residents along the Kohala and North Kona coasts report that the second shaking felt equal to or larger than the first one, probably because the Mahukona earthquake was much shallower. A maximum Mercalli Intensity of VIII was reported close to the two epicenters. Both earthquakes were felt across all the major Hawaiian Islands, but damages, on the order of 140 million Dollars, were largely limited to the Big Island and the Eastern end of Maui. Such a relatively small amount is attributed to the rural character of the area (the similar

1994 6.7-magnitude Northridge earthquake in California caused 17.8 billion Dollars in losses).

In this article we describe the effect that these earthquakes had on reservoirs and dams within close proximity to the epicenters. Four sets of reservoirs were of particular concern because of their perceived hazard in relation to nearby development (Figure 1). We conducted post-earthquake inspections of the three closest reservoirs two days after the earthquakes as part of a larger post-earthquake reconnaissance of the Big Island sponsored by the Department of Civil and Environmental Engineering at the University of Hawaii (Robertson et al., 2006). Hawaii dam safety guidelines specify that for seismic events of magnitude 6.0 or greater post-earthquake inspections should be conducted at all reservoirs and dams within a 75-mile radius (Department of Land and Natural Resources, 2004). In this case that included reservoirs and dams on the islands of Hawaii and Maui. The State, with federal assistance, proceeded to conduct post-earthquake inspections throughout Maui and Hawaii counties a few days after our inspections.

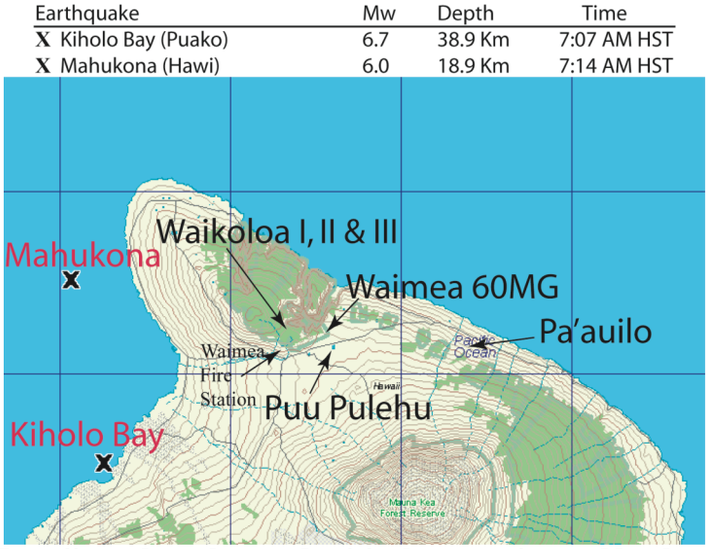


Fig. 1. 2006 Hawaii earthquakes and critical reservoirs on North end of Hawaii

SEISMICITY

The Kiholo Bay earthquake produced significant accelerations throughout much of the islands of Hawaii and Maui (Figure 2). Measured peak ground accelerations (*PGA*) were as high as 1.05g at the Waimea Fire Station (Figure 3). Spectral accelerations at this site easily surpassed the 2% and 5% probabilities of exceedance in 50 years as estimated by the USGS (2007). However, this particular recording station, as well as the one in Honokaa that measured a *PGA* of 0.65g, are likely located on a significant thickness of residual soil and may reflect the effects of ground amplification. Whether ground amplification is indeed a factor is not clear since the precise subsurface conditions at most USGS recording stations remains to be determined and the dynamic properties and behavior of Hawaiian volcanic soils are not yet well characterized. Work is now underway to accomplish these tasks.

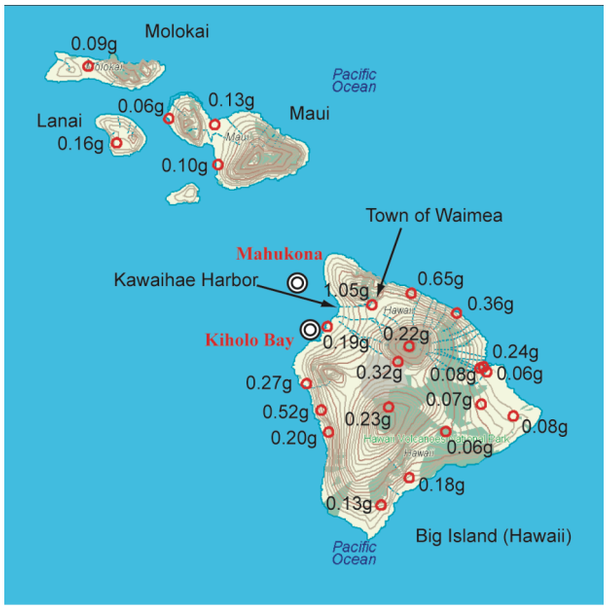


Fig. 2. Peak ground accelerations from Kiholo Bay earthquake (USGS).

There is also a need for reliable attenuation relationships specific to Hawaii. Munson and Thurber (1997) developed the most widely used expression for peak ground acceleration:

$$\log_{10} PGA = 0.518 + 0.387(M - 6) - \log_{10} r - 0.00256r + 0.335S \quad (1)$$

where PGA is measured in units of g, M refers to magnitude M_w, $r = (d^2 + 11.29^2)^{1/2}$, and S is 0 for lava rock sites and 1 for ash soil sites. Distance d (km) refers to the closest distance from the recording site to the surface projection of the earthquake source.

A quick check for a few of the stations in Figure 2 indicates that the predictions leave much to be desired (Table 1), although a linear trend would appear to result from comparing predicted versus measured PGA values. The lack of agreement can be traced to the limitations in the development of the Munson and Thurber relationship. The historic database includes only one event with a magnitude larger than the Kiholo Bay earthquake, while the vast majority of sources that were considered are clustered around the volcanically active South side of the Big Island and are associated with shallower depths and low-angle faults. The Kiholo Bay earthquake is unusual for its location and depth. Since only recording stations from the Big Island were included in the development, the Munson and Thurber relationship is not strictly applicable to neighbor islands. Predictions are consistently lower than the measured values, except for the nearby Waikoloa Hotel recording station. Since this station is located only 7 km from the source, it is possible that nearby effects may have influenced the PGA, although this is not certain.

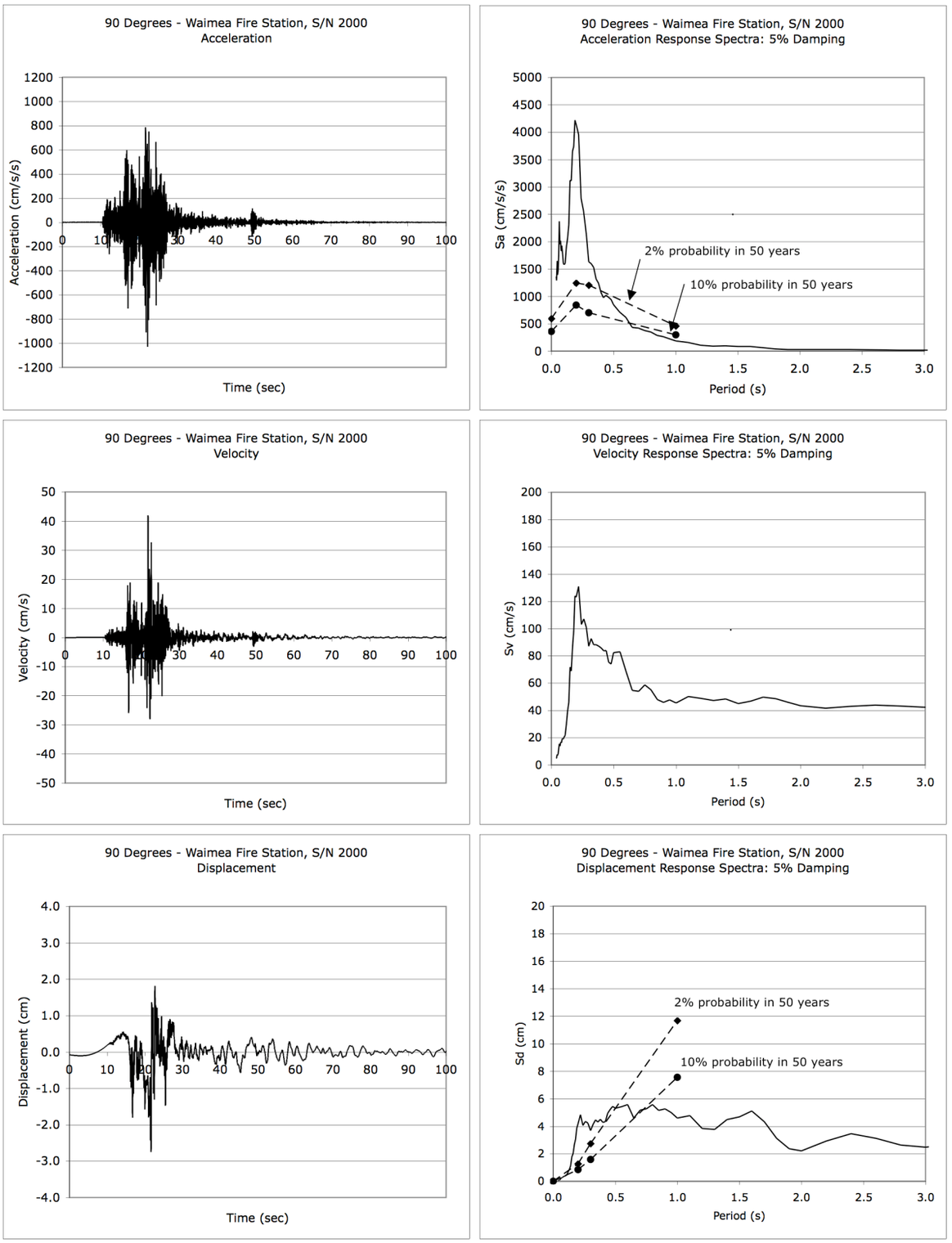


Fig. 3. Seismic motions from Kiholo Bay earthquake at Waimea Fire Station.

Table 1. Measured versus predicted *PGAs* for Kiholo Bay earthquake.

Station	No.	d (Km)	S	PGA Predicted (g)	PGA Measured (g)
Waikoloa Hotel	2847	7	0	0.43	0.19
Kailua-Kona Fire St.	2810	26	0	0.18	0.27
Waimea Fire St.	2825	33	1	0.31	1.05
Kealakekua Hospital	2849	40	0	0.12	0.52
Honokaa Police St.	2832	54	1	0.17	0.65
Laupahoehoe Post Of.	2833	74	1	0.11	0.36
Volcano Nat. Park HVO	2836	85	0	0.04	0.06
Hilo USDA Lab	2818	89	1	0.09	0.24
Pahala Ka'u Hospital	2812	90	1	0.09	0.18
Waiohinu Ka'u Baseyard	2822	96	0	0.04	0.13
Maui: Wailea Grand Hotel	2840	104	0	0.03	0.10
Lanai: Lanai City Fire St.	2841	147	0	0.02	0.16
Molokai: Kaunakakai Airp.	2806	186	0	0.01	0.08
Oahu: Honolulu Fire St.	2851	255	0	0.01	0.08
Oahu: Honolulu Int. Airport	2842	262	0	0.01	0.02

DAMAGE TO DAMS AND WATER CONVEYANCE STRUCTURES

Of greatest concern following the earthquakes were the series of three high-hazard Waikoloa water supply reservoirs that are perched on a mountainside some 500 to 1000 m above the town of Waimea-Kamuela (Figure 1). The three connected reservoirs consist of circular or elongated pool structures either fully or partially surrounded by earth fill embankments up to 40 feet in height and holding 50 MG of water each. The embankments are built of homogeneous clayey silt on a weathered basalt substrate. The inside of all the reservoirs are lined with concrete panels (Figure 4).

Our inspection two days after the earthquake revealed evidence of significant horizontal crest motions in the two topmost reservoirs (Waikoloa II – topmost, and Waikoloa I - second from top). It appears that the circular Waikoloa II earth embankment experienced large horizontal motions during shaking, as reflected by disturbance of fill on the crest adjacent to the top of the concrete panels. The ring of disturbed soil reflects relative movement between the concrete panels and the earthfill. Cracks 3 to 6 cm wide and up to 60 cm deep were noted adjacent to the upper lip of the concrete panels (Figure 4). Absolute horizontal crest displacements were likely significantly larger. The damage extended over a section spanning about 240 degrees around the embankment circumference and indicated a strong motion component in the East-West direction. The portion of the embankment located facing the downhill side of the mountain saw the least amount of damage. Despite the observed distress, no significant permanent lateral shifting of the overall embankment

was discerned. A similar damage pattern was observed on the embankment of Waikoloa I, although to a lesser degree.



Fig. 4. Disturbance of Waikoloa II embankment crest.

Two significant transverse cracks developed on the crest of the Waikoloa II embankment. These cracks were 1 m apart. Each was about 1.5 cm wide at the surface and of unknown depth. The area between these cracks was noticeably softer than adjacent portions of the crest. In addition, joints between some of the concrete panels opened up somewhat and spalling was noted along the upper lip of the concrete lining (Figure 5). We searched for evidence of unusual seepage flows but could not detect any two days after the earthquakes. Having carried out earlier assessments of these reservoirs, we were aware of a certain amount of toe seepage emanating from both Waikoloa I and II. However, there appeared to be no evidence of increased flows or piping following the earthquakes, and in the case of Waikoloa II such seepage was on the opposite side of where the transverse cracks were noted. On the other hand, a subsequent similar inspection seven days after the earthquakes by a different group of dam safety engineers reported substantial seepage at the same locations that we had focused on. As a precautionary measure, authorities decided to warn downhill residents and proceeded to empty the Waikoloa II reservoir and to lower the pool level in Waikoloa I until all seepage flows ceased. Since we did not participate in these later inspections, it is difficult to discern what may have transpired in between inspections and to what extent flows truly changed over a period of five

days. It is of course possible that the silty nature of the embankment fill may have resulted in non-visible internal cracks that slowly led to a piping condition. In this regard, a concrete liner represents somewhat of a problematic design feature since it makes inspection of the inside of the reservoirs much more difficult. Also, it makes sense to have all post-earthquake inspections conducted by teams that include at least one dam safety engineer that is familiar with the features and performance history of each particular reservoir.



Fig. 5. Transverse crack and concrete spalling on Waikoloa II embankment crest.

Two other earthfill dams in the area (Puu Pulehu and Paauilo) suffered some damage in the form of incipient slope instability on the downstream face. In the case of the Puu Pulehu dam, a line of head cracks developed along the edge of the embankment crest (Figure 6). The fill again consists of homogeneous clayey silt and the slope is on the order of 1H:1V to 1.5H:1V. The principal crack was about 135 feet long and resulted in vertical and horizontal offsets of at least 2 inches and depths of perhaps one to two feet or more. These conditions did not appear to represent an undue threat to property or life but will have to be rectified. Finally, the Waimea 60MG circular reservoir experienced minor raveling of rock rip-rap lining, along with small cracks in the fill beneath the rip-rap. The damage was not significant and required no emergency response.

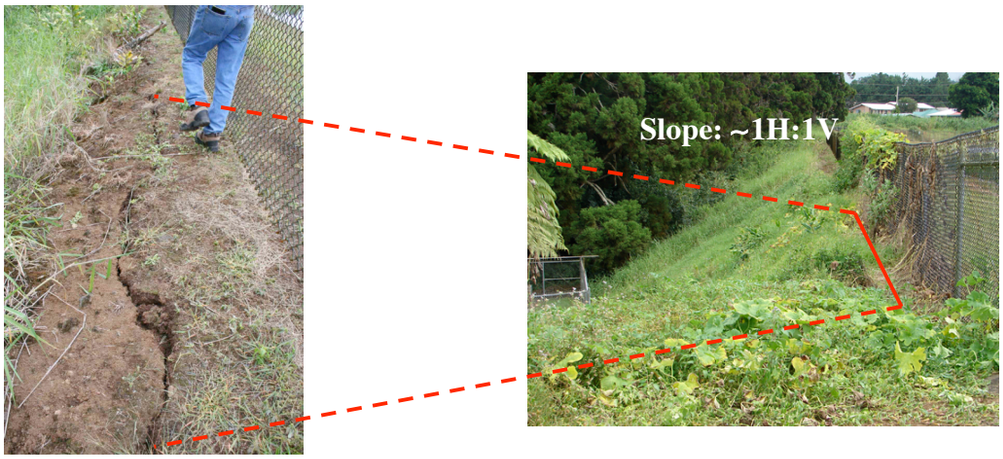


Fig. 6. Incipient sliding of Puu Pulehu dam.

In addition to damage to dams, the system of ditches that feeds some of these reservoirs was disrupted by numerous cave ins and obstructions that we could not inspect on short notice because of their remote location. These problems were serious enough to severely limit water flow into the reservoirs for a period of weeks after the earthquakes. They have since been repaired. Also, the water treatment plant downhill from the Waikoloa reservoirs saw minor to moderate damage to its holding tanks and water lines. Table 2 presents a summary of post-earthquake inspection findings of reservoirs on the Big Island closest to the epicenter of the two earthquakes.

SEISMIC MODELING AND SOIL CHARACTERIZATION EFORTS

A preliminary seismic investigation of the Waikoloa II reservoir conducted by the first author in 2002 indicated that while liquefaction was not a real concern because of the fine-grained and plastic nature of the embankment material, the location of the reservoir in an area of very high seismicity was problematic (Hirata and Associates, 2002). A potential for ground amplification of seismic waves has been associated with soils that have a high ash content (Munson and Thurber, 1997; Nielson et al., 1977). Dynamic computations in the 2002 study indicated large shaking at the crest of the embankment, very much as our post-earthquake inspections revealed.

A recently completed seismic investigation of a similar high hazard earth dam on Maui by the first author suggests that structures of this type are susceptible to large-scale damage from earthquakes with a return period on the order of 2,500 years. Dynamic computations were carried out using a range of specific time-history accelerations from the October 2006 earthquakes, suitably modified to reasonably match the probabilistic response spectrum parameters corresponding to the 2,500-year interval. The program Quake/W was used to determine the inertial forces during shaking, which were in turn used in the program Slope/W to conduct a Newmark-type analysis. The equivalent linear model was used to characterize the embankment fill,

residual soil and bedrock materials. Material parameters were determined from static, cyclic simple shear and bender element tests on representative specimens. Given the nature of the various soils, strength degradation and excess pore pressure changes were not considered important and were therefore neglected.

Table 2. Summary of damage to dams and other water structures.

Dam, Reservoir or Water Structure	Distance to Kiholo Bay Earthquake (Km)	Distance to Mahukona Earthquake (Km)	Principal Damage
Waikoloa II Dam	34	35	Longitudinal and transverse crest cracks Minor concrete liner damage Potential delayed piping
Waikoloa I Dam	34	35	Longitudinal crest cracks Potential delayed piping
Waikoloa III Dam	34	35	None visible
Puu Pulehu Dam	39	42	Incipient sliding cracks near crest
Waimea 60MG Dam	38	39	Minor sliding of rock rip-rap
Paauilo Dam	38.4	39.5	Incipient sliding cracks
Hamakua Ditch	~ 40-50	~ 40-50	Blocking from slides and debris
Waikoloa Treatment Plant	34	35	Minor concrete cracks and some damage to pipes

In this particular case, permanent deformations from the Newmark analysis were predicted to be as high as 8 feet or more. This would appear unacceptable for embankments made predominantly of clayey silt because of the danger of cracks that could lead to loss of reservoir water and potential piping and erosion (as some suspect may have occurred at Waikoloa II). Despite the sophisticated analysis in this case, the findings are still viewed with caution because of a general lack of soil characterization data for Hawaiian volcanic soils used in dam construction. For example, Figure 7 shows distinctly different stress-strain, degradation and damping characteristics for two specimens collected from the same bore hole at the Maui dam, despite the use of similar normal and shear stresses during cyclic simple shear testing. This indicates that one can expect a wide range of dynamic stress-strain characteristics for local volcanic soils depending on the particulars of each soil type.

Most of the older dams throughout Hawaii, some over 100 years old, were constructed using hydraulic fill methods. This technique can result in segregated fills that in some cases are poorly compacted. Such embankments can be problematic if

subjected to strong earthquake shaking. Clearly, much more work remains to be completed in order to better gauge the risk that earthquakes pose to reservoir and dam structures in Hawaii.

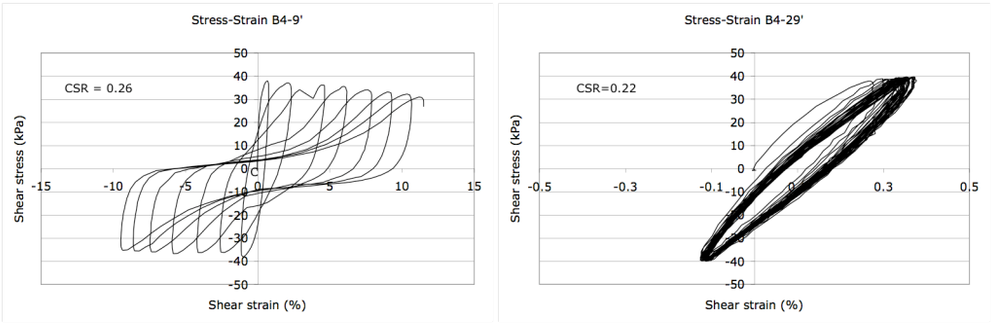


Fig. 7. Results of cyclic simple shear testing of two volcanic clayey silt specimens from Maui dam embankment.

REFERENCES

Department of Land and Natural Resources (2004). "Hawaii dam safety guidelines: seismic analysis & post-earthquake inspections." DLNR Circular C131, Prepared by H.G. Brandes.

Hirata & Associates, Inc. (2002). "Phase II dam safety inspection Waikoloa Reservoir No. 2 State I.D. No. HI122 County of Hawaii", *Engineering Report* to Department of Water Supply.

Munson, C.G. and Thurber, C.H. (1997). "Analysis of the attenuation of strong ground motion on the Island of Hawaii." *Bulletin of the Seismological Society of America,* 87 (4): 945-960.

Nielson, N.N., Furumoto, A.S., Lum, W.B., and Morrill, B.J. (1977). "The Honomu, Hawaii, earthquake: report of inspection." National Academy of Science, Washington, DC, 79 pp.

Robertson, I.N., Nicholson, P.G., and Brandes, H.G. (2006). "Reconnaissance following the October 15th, 2006 earthquakes on the Island of Hawai`i." University of Hawai`i Department of Civil & Environmental Engineering *Research Report UHM/CEE/06-07*, http://www.cee.hawaii.edu/reports/Kiholo_Bay_Report.pdf

USGS (2007). Earthquake Hazards Program, ground motion parameter calculator, http://earthquake.usgs.gov/research/hazmaps/design/.

Deformation Analysis for Seismic Retrofit of an Embankment Dam

Vlad Perlea[1], M. ASCE, P.E., David Serafini[2], M. ASCE, P.E., Ethan Dawson[3], M. ASCE, and Michael Beaty[4], M. ASCE, P.E.

[1]Civil engineer, PhD, US Army Corps of Engineers, Sacramento District, 1325 J Street, Sacramento, CA 95814; vlad.g.perlea@spk01.usace.army.mil
[2]Civil engineer, US Army Corps of Engineers, Sacramento District, 1325 J Street, Sacramento, CA 95814; david.c.serafini@spk01.usace.army.mil
[3]Civil engineer, PhD, URS Corporation, Oakland Office, 1333 Broadway, Suite 800, Oakland, CA 94612; Ethan_Dawson@URSCorp.com
[4]Civil engineer, PhD, private consultant, Beaverton, OR; m.h.beaty@comcast.net.

ABSTRACT: Success Dam located in Southern California is seismically deficient and remediation design is currently in progress. The proposed remediation includes partial excavation of the existing embankment dam and construction of a buttressing embankment immediately downstream. Liquefiable alluvium will remain under the existing dam and will continue to affect the seismic response of the combined structure. In accordance with Corps of Engineers guidance, the design must be validated using a seismic deformation analysis. The deformation analysis was performed in steps of increasing complexity, starting with simplified procedures and continuing with more complex, state-of-the-art methods: (1) liquefaction assessment using the simplified procedure and QUAD4M coupled with limit equilibrium analyses assuming post-liquefaction residual strength in potentially liquefiable zones; (2) FLAC computer analysis using the decoupled effective stress constitutive model used by URS, and (3) FLAC analysis with the coupled effective stress model UBCSAND developed at the University of British Columbia, Canada.

INTRODUCTION

Success Dam is located on the Tule River approximately five miles upstream of Porterville, California. Construction of the dam began in 1958 and was completed in 1961. Recent seismic stability evaluations found the dam deficient according to current requirements and methods of evaluation. As a consequence, remediation of the dam is required. The reservoir is currently operated under restriction, with the maximum pool about 10 m (32.5 feet) below the normal gross pool (spillway crest elevation), which reduces the available reservoir storage by 65%. The design team is currently developing and calibrating the methodology of seismic deformation analysis to be used in design of the remediation. This paper highlights these different analytical techniques and addresses some of the limitations of the analytical models.

CURRENT CONDITION OF THE DAM

Success Dam is a zoned earth-filled embankment, with a crest length of 1,064 m (3,490 feet) and the maximum height of 44.2 m (145 feet). The upstream slope of the dam transitions from 1:3.75 at the toe, 1:3 midway up the slope, and 1:2.5 at the crest. The downstream slope is 1:3 at the toe and steepens to 1:2.5 at the crest. The upper layer of foundation, consisting of recent alluvium, was found liquefiable, as well as some zones of the upstream shell. Beneath the recent alluvium are zones of older, non-liquefiable alluvium founded on weathered bedrock.

Gravels and cobbles in both the foundation alluvium and shell material was a major challenge in the selection of parameters for deformation analysis, in particular those related to the liquefaction potential and the residual strength. The investigation results and their interpretation are the objects of the companion paper titled "Geotechnical Investigation and Site Characterization of the Success Dam Seismic Remediation Project".

Deformation analysis of the existing dam found it susceptible to significant deformations and possible failure under the Maximum Credible Earthquake (MCE). Figure 1 is an example of the deformed shape at one of the analyzed sections. The computed displacement at the upstream toe at the end of the 50-second seismic event was of the order of 15 m (50 feet) and the loss of freeboard of the order of 1.5 m (5 feet). These displacements are not final estimates as movement was still in progress at the end of the analysis.

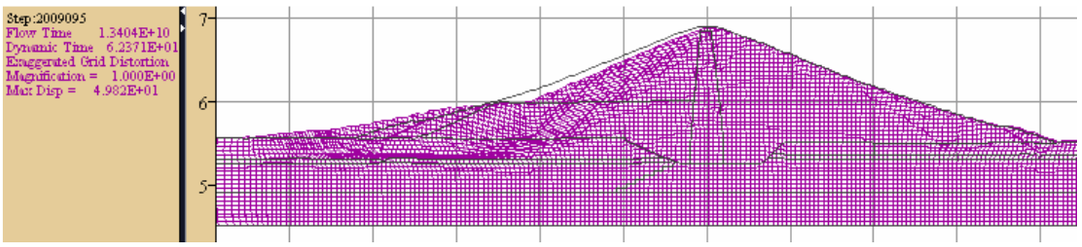


FIG. 1. Deformed mesh at the end of MCE. The original surface outline is shown for comparison. (Scales of all figures are in feet: 100 feet = 30.5 m.)

SEISMICITY ASSESSMENT

Seismic loading parameters were developed by the URS Corporation in 2004 and subsequently refined in 2006 and 2007. Table 1 summarizes the seismic design criteria in terms of Operating Basis Earthquake (OBE) and Maximum Credible Earthquake (MCE) and their corresponding moment magnitude (M), distance to site (D), and peak horizontal ground acceleration (PGA).

URS also provided time histories of acceleration, velocity, and displacements for the two categories of design earthquake. Five sets of three components (two horizontal and one vertical) were provided for both the OBE and MCE. Each selected record was scaled to the target response spectra in the period range of major response of the embankment.

Table 1. Recommended Seismic Design Criteria

Design Earthquake	M	D (km)	PGA (g)
OBE (probabilistic: 144-year average return period)	8.0	120	0.10
MCE (deterministic : median 84th percentile)	6.8	21	0.28

REMEDIATION CONCEPT

The option currently under evaluation includes the following main steps:

- Removing a portion of the downstream shell to expose as much recent alluvium as possible while still leaving the dam in a stable condition. The downstream slope during construction will be about 1:1.5. More severe reservoir restrictions will apply during construction, limiting the storage capacity to 10% of that originally designed.
- Complete removal of the liquefiable alluvium within the footprint of the new buttress.
- Construction of a buttress downstream of the existing dam that includes a new core and transition zones. The new core will address concerns related to seismically-induced fracture or deformation of the existing core.
- When the buttress elevation reaches a pre-determined height, the crest of the existing embankment will be lowered with the resulting material used to construct the top portion of the buttress.

SIMPLIFIED DEFORMATION EVALUATION ASSUMING POST-LIQUEFACTION PROGRESSIVE FAILURE

It was assumed that all recent alluvium under the existing embankment liquefies during the seismic loading. This assumption corresponds to the occurrence of the MCE event. The analysis was done at the end of major shaking, when seismic driving forces and the dissipation of excess pore water pressure were both assumed to be negligible. Correspondingly, the dam was analyzed in a static, steady state condition, assuming mobilization of the post-liquefaction residual strength in the alluvial deposit.

Liquefaction of the existing embankment shells was not considered in this preliminary analysis, but will be considered in later analyses.

Analyses Results

Conventional slope stability analyses were performed using the computer program UTEXAS4. Only the stability of the upstream slope of the remediated embankment was evaluated, as the downstream slope is not affected by potentially liquefiable materials. The residual strength of the liquefied recent alluvium was estimated using the correlation with SPT - $N_{1,60}$ recommended by Seed and Harder (1990). The critical pool level was found to be the relatively low conservation pool. The limit

equilibrium evaluations determined that local sliding should be expected at the upstream toe. For larger sliding surfaces, such as those through the existing core, the factor of safety was in excess of 1.25. However, once a failure occurs near the toe, the newly steepened slope of the embankment loses stability and successive failures are possible. This is illustrated in Fig. 2 which shows a series of conservatively formulated analyses.

These results were initially encouraging, suggesting the remediated dam should remain safe even if the entire recent alluvium layer were to completely liquefy. Parametric studies showed, however, that the results were highly dependent on the soil strength parameters (especially for the foundation saprolite).

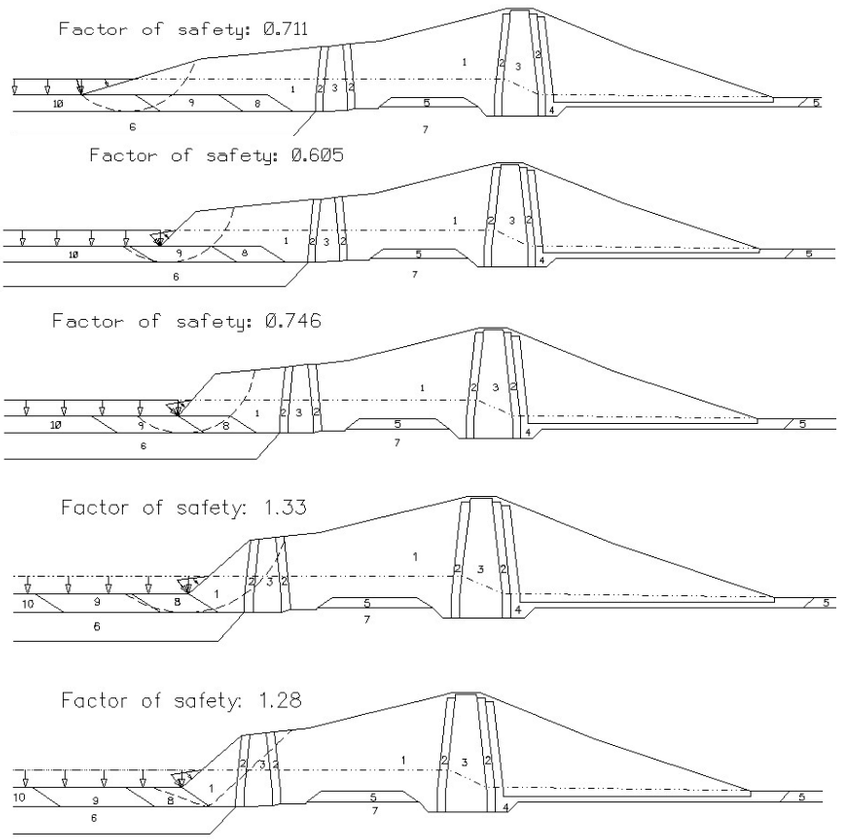


FIG. 2. Potential progressive failure. Materials: 1 - Random (pervious) shell; 2 - Transition; 3 - Impervious core; 4 - Drain; 5 - Recent alluvium (somewhat liquefiable); 6 - Saprolite (highly weathered rock); 7 - Bedrock (granite); 8, 9, and 10 - Recent alluvium (liquefiable) of decreasing residual strength. Broken lines: potential failure surfaces with factors of safety as noted.

QUAD4M EVALUATIONS

The QUAD4M analyses utilizing the Q4MESH software were used to estimate the peak acceleration at each node and the peak cyclic shear stress and shear strain in each element. The Q4MESH program has the ability to estimate cyclic stress ratios

(CSR) based on the peak shear stresses induced in the response. Using the calculation of the induced CSR, liquefaction triggering evaluations were performed.

The cyclic resistance ratio (CRR) was evaluated using the $N_{1,60}$ blowcount data as described by Idriss and Boulanger (2004). The factor of safety against liquefaction was defined by the ratio CRR / CSR corrected with the factors for magnitude (MSF) and for overburden stress (K_σ). To simplify the QUAD4M analysis, the static shear stress correction factor (K_α) was assumed equal to unity.

Excess pore water pressures were approximated from the liquefaction factor of safety. The selected relationship between excess pore water pressure and factor of safety was taken as the average gravel curve from data presented by Marcuson and Hynes (1990).

Figures 3 and 4 are the calculated CSR and CRR profiles, respectively. The CSR values were calculated from the peak shear stress, and the CRR values were calculated from $N_{1,60}$ values. Figures 5 and 6 are the results from the liquefaction triggering evaluation and resulting predicted excess pore water pressure response, response, under MCE loading. The evaluation shows that a portion of the 'sacrificial' upstream embankment, upstream recent alluvium, and downstream toe alluvium may have the potential of reaching a state of liquefaction. The recent alluvium between the two cores is only predicted to experience a 40-50% excess pore water pressure under MCE loading.

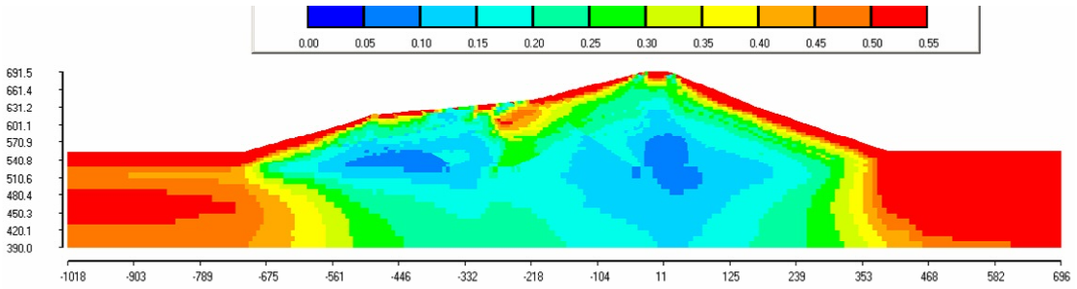


FIG. 3. CSR calculated from 65% of peak QUAD4M element shear stress.

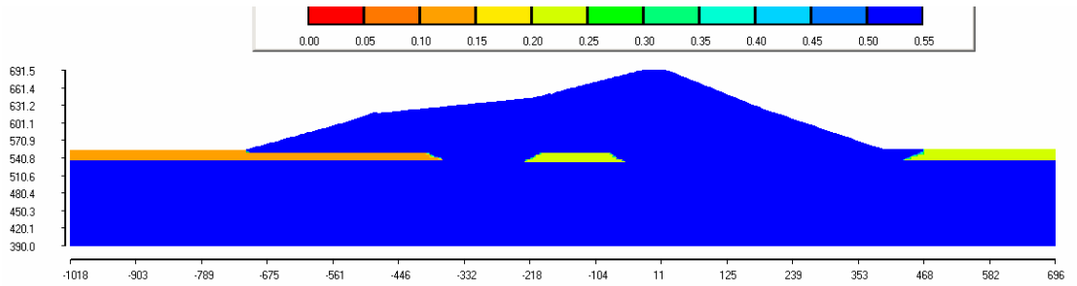


FIG. 4. Cyclic Resistance Ratio (CRR) calculated from input $N_{1,60}$ values.

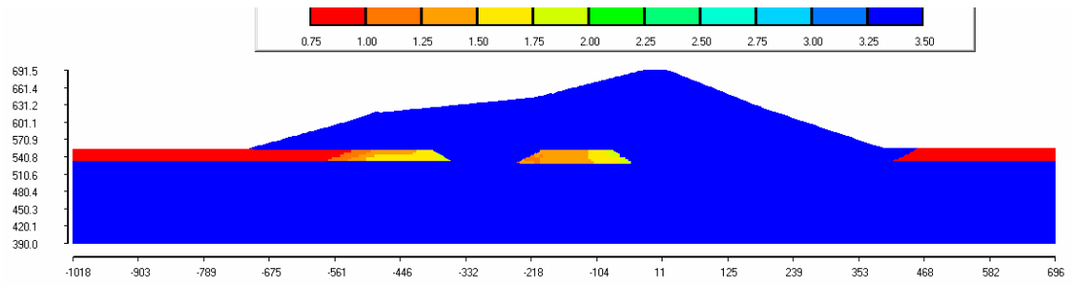


FIG. 5. Factor of safety against liquefaction (CSR-Quad4m, CRR-$N_{1,60}$)

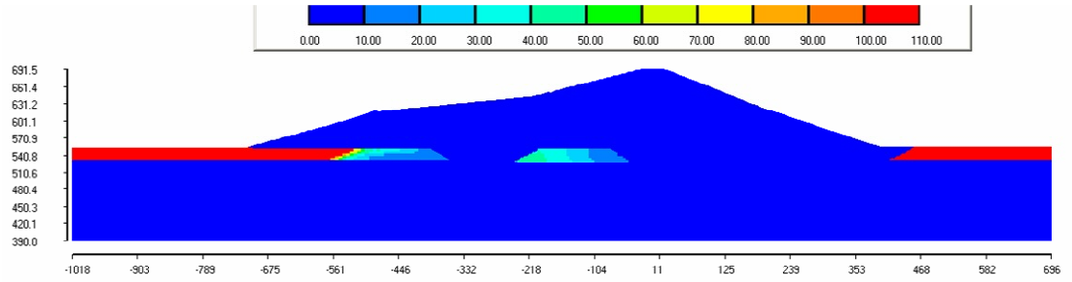


FIG. 6. Percent r_u estimated from CSR-QUAD4M / CRR-$N_{1,60}$)

FLAC SEISMIC DEFORMATION ANALYSIS

Among the programs capable of analyzing embankment deformations under seismic action is FLAC (Fast Lagrangian Analysis of Continua), commercially available from Itasca Consulting Group, Inc. (Itasca, 2005). The constitutive models that are provided with FLAC have limitations that can restrict their use in analyses involving liquefaction. The Corps of Engineers, Sacramento District, in cooperation with Ethan Dawson at URS Corporation and Michael Beaty, consultant, is using FLAC in conjunction with two supplemental constitutive models, named URS and UBCSAND in what follows.

Static Analysis

The initial in situ stress state prior to the earthquake is computed by simulating the proposed construction process and performing seepage analyses for the corresponding planned reservoir levels in various stages. Starting from a level-ground initial state, the modeling sequence included the steps illustrated in Fig. 7.

Dynamic and Post-Earthquake Analysis

The results of the dynamic analyses were significantly affected by the selected constitutive model for liquefaction simulation. Four models were considered:

- The URS model, a decoupled effective stress model (Dawson et al., 2001);
- The URS-modified model (URS 2007, by E. Dawson) to account for K_α;
- The UBCSAND model (Version 904a), a coupled effective stress model (Byrne et al., 2004) and
- The UBCSAND-modified (UBCSAND 904aR, by M. Beaty) to better address the effects of initial static shear stress during seismic loading.

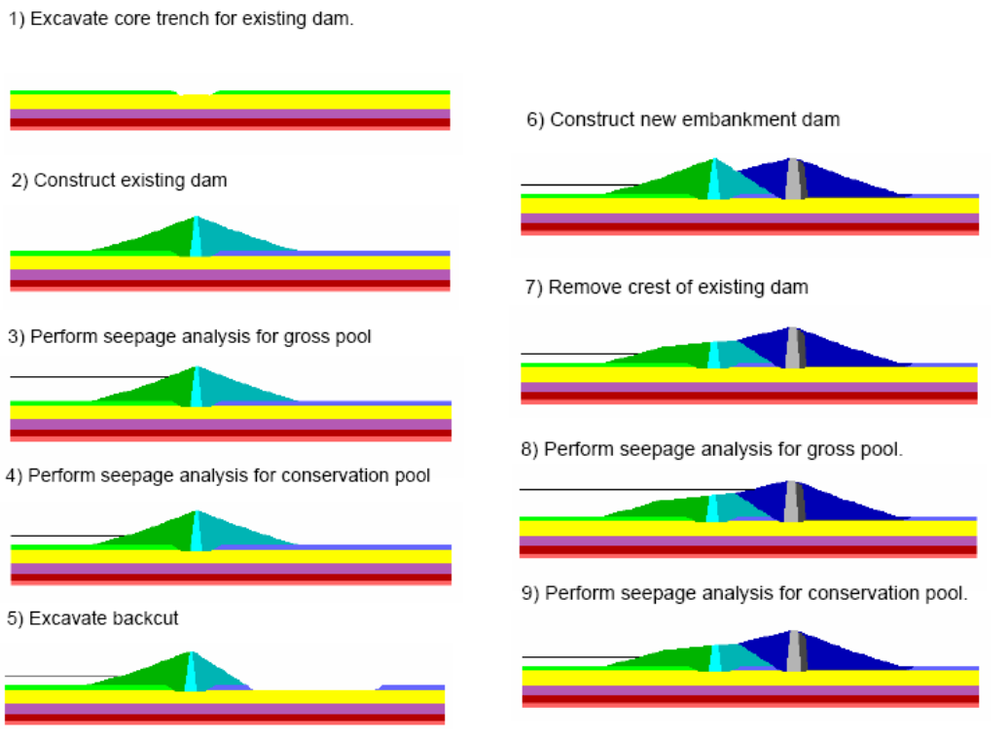


FIG. 7. Construction stages modeled in static analysis.

The constitutive models are briefly described below. As part of the evaluation of the models, each was used to analyze the Upper and Lower San Fernando dams and their response to the 1971 San Fernando earthquake.

URS Liquefaction Model

The URS model is a decoupled effective stress model. It uses FLAC's standard Mohr-Coulomb model coupled with an empirical pore pressure generation scheme. Pore pressure is generated in response to shear stress cycles, following the cyclic-stress approach developed by H. B. Seed and his co-workers. However, unlike common applications of the approach, where the effects of excess pore pressures are disregarded in the analysis of dynamic response, the excess pore-pressure generation is integrated with the dynamic analysis in the model.

Pore pressures are continuously updated for each element in response to shear stress cycles. As the effective stress decreases with increasing pore pressure, the strength of

the materials is reduced until it reaches the residual strength of the materials. As the available shear strength decreases, increments of permanent deformation are accumulated. In addition, the plastic strains generated as a result of reduced strengths result in significant hysteretic damping. The coupling of pore pressure generation with the stress analysis results in a more realistic dynamic response analysis than with total stress models. More detailed descriptions of the model and its applications are presented by Roth et al. (1991) and Dawson et al. (2001). For the Success Dam analyses, a few minor adjustments were made to the URS model, including an updated cyclic strength curve and updated K_α relationship.

UBCSAND Liquefaction Model

The UBCSAND model is a coupled effective stress model that simulates the compaction and dilation of granular soils subject to shearing. For saturated soil elements, the tendency for contraction of the soil skeleton increases pore pressures, while dilation decreases pore pressures. Changes in shear-induced pore pressures are estimated at each numerical time step. The formulation of the model is based on observations from monotonic and cyclic laboratory element tests. The model has also been calibrated to observed earthquake response of soil sites and geotechnical structures, as well as measured responses from centrifuge tests.

Key components of the model include the non-linear relationship between plastic shear strain and increases in stress ratio (defined as the maximum shear stress divided by the mean effective stress), the relationship between increments of plastic shear strain and plastic volumetric strain, and the importance of effective stress on the stiffness of each element. The model uses a hyperbolic relationship between stress ratio and plastic shear strain for virgin loading. Increments of unloading are modeled using a linear elastic approach.

The UBCSAND model is described in detail by Byrne et al. (2004). Several refinements were made to the 904a version for use in Success Dam. These refinements improve the ability of the modified model (version 904aR) to predict pore pressure changes in zones having a significant static shear stress bias. The overall structure and formulation of the model was not changed.

While the UBCSAND model is based primarily on observations from laboratory element tests, it is prudent practice to consider residual strengths in liquefied elements. This is accomplished by imposing a maximum strength equal to the residual strength in all liquefied elements after the earthquake shaking has stopped. The effect of residual strength on the permanent displacements is then directly estimated.

The UBCSAND model is expected to give a more detailed prediction of the dynamic response of the dam during shaking because increments of shear contraction and dilation are directly modeled and are rationally influenced by changes in effective stress. UBCSAND also incorporates the effects of groundwater flow on the element response. The model reproduces the ‘banana shaped’ stress strain loops after liquefaction, as observed in typical cyclic tests of saturated cohesionless material.

Examples of Preliminary Analyses Results

The analyses of the remediated dam are currently being performed. These analyses include the use of updated ground motions as well as newly developed soil parameters. However, some preliminary results have been developed during the process of refining the analysis procedure.

Figure 8 presents estimates of the deformed shape of the remediated dam after the MCE using the modified UBCSAND. Two variants are shown: (a) original remediation approach with degraded crest, and (b) modified remediation approach with no degradation of existing crest. The results presented in Figure 8 were somewhat surprising since a steeper, higher slope provided somewhat better protection to the new crest and core than the gentler degraded slope. This behavior was explained by the lesser extent of liquefaction predicted in the foundation when the confining stress was higher. Although significant deformation is predicted in both cases, the upstream portion of the existing embankment is considered sacrificial under an MCE occurrence. The primary goal of the remediation is to provide acceptable performance of the new core.

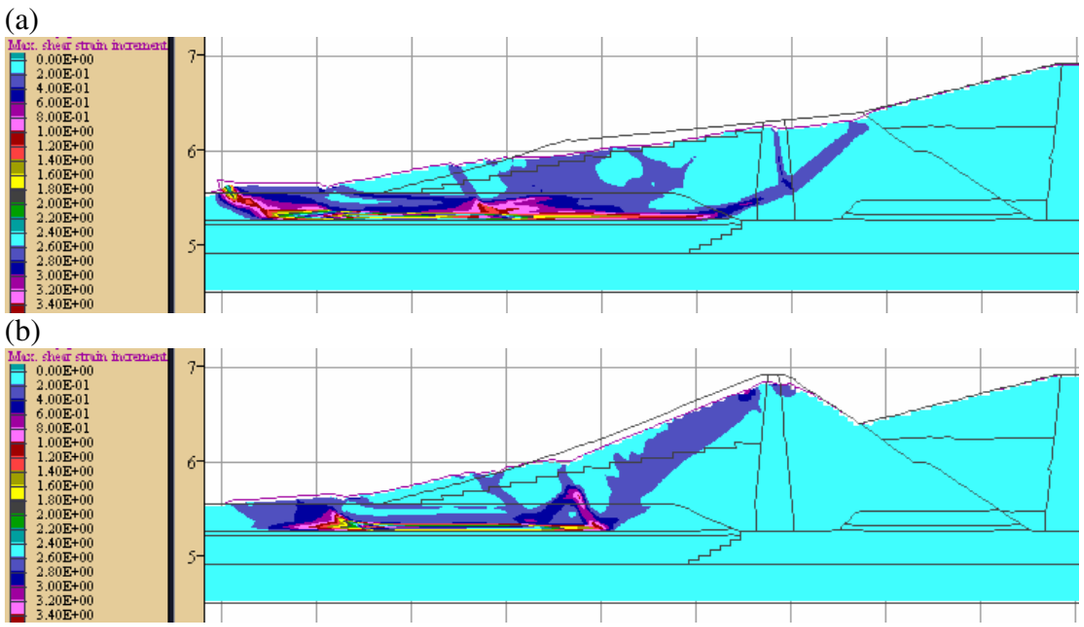


FIG. 8. Deformed shape and shear strain contours after MCE: (a) with degraded top of existing dam; (b) without degrading the existing dam.

CONCLUSIONS

A series of preliminary seismic deformation analyses have been performed for the proposed remediation of Success Dam. The analysis programs UTEXAS4, QUAD4M, and FLAC were used to estimate the post-earthquake condition of the dam. The QUAD4M and FLAC approaches were also used to estimate the dynamic response and the potential for liquefaction. The FLAC approach was used to directly

estimate resulting deformations. Two constitutive models were originally selected for the FLAC analyses. Both of these models were revised during the process of refining the analysis procedure.

The initial limit equilibrium approach detected both the vulnerability of the existing retaining structure and the possibility of seismic retrofit by constructing a strong buttress downstream. Although the coefficient of safety approach provided the justification for performing more sophisticated analyses, limit equilibrium was not able to correctly estimate the "failure" mode.

QUAD4M analyses have a long history and wide acceptance for predicting the extent of liquefaction triggering, but they do not directly provide estimates of deformations induced by the seismic action. The seismic deformation can be evaluated with specialized computer programs, such as the commercially-available program FLAC. For the final evaluation and design, QUAD4M will be used in conjunction with FLAC to verify the predicted extent of liquefaction, respectively the extent of zone where the residual strength is mobilized at the end of shaking.

The design team selected the revised UBCSAND 904aR model with FLAC for future analyses and design work, with the QUAD4M approach being used as a simplified check on the predictions. The UBCSAND model was considered to have a sound theoretical basis, provided results in reasonable agreement with laboratory element tests, and gave reasonable predictions of the observed response of the Lower and Upper San Fernando dams in the 1971 San Fernando earthquake.

REFERENCES

Byrne, P.M., Park, S.S., Beaty, M., Sharp, M.K., Gonzalez, L., and Abdoun, T. (2004). "Numerical modeling of liquefaction and comparison with centrifuge tests," Canadian Geotechnical Journal, Vol. 41(2):193-211.

Dawson, E.M., Roth, W.H., Nesarajan, S., Bureau, G., and Davis, C.A. (2001). "A practice-oriented pore pressure generation model." *Proceedings, 2nd FLAC Symposium on Numerical Modeling in Geomechanics*, Lyon, France.

Idriss, I. M., and Boulanger, R. W. (2004). "Semi-empirical procedures for evaluating liquefaction potential during earthquakes." *Proc., 11th International Conference on Soil Dynamics and Earthquake Engineering, and 3rd International Conference on Earthquake Geotechnical Engineering*, Vol. 1, 32-56.

Itasca Consulting Group (2005). *FLAC, Fast Lagrangian Analysis of Continua, Version 5.0*. Itasca Consulting Group, Minneapolis, Minnesota, USA.

Marcuson, W. F. III, Hynes, M. E., and Franklin, A. G. (1990). "Evaluation and Use of Residual Strength in Seismic Safety Analysis of Embankments," *Earthquake Spectra*, Vol 6, No. 3, 529-572.

Roth, W.H., Bureau, G., and Brodt, G. (1991). "Pleasant Valley Dam: An approach to quantifying the effect of foundation liquefaction." *17th International Congress on Large Dams*, Vienna, Austria.

Seed, R.B. and Harder, L.F. (1990). "SPT-based analysis of cyclic pore pressure generation and undrained residual strength." in J.M Duncan ed*., Proceedings, H. Bolton Seed Memorial Symposium*, University of California, Berkeley, Vol. 2, 351-376.

Dynamic behavior for lightweight spillway with geosynthetics on small earth dam

Toshinori Kawabata[1], Kazunori Uchida[2], Tomohiro Kitano[3], Koji Watanabe[4] and Yoshiyuki Mohri[5]

[1]M.ASCE, Ph.D., Associate Professor, Dept. of Agri. & Envir. Eng., Faculty of Agriculture, Kobe University, 1-1, Rokkodai, Nada, Kobe 657-8501, JAPAN; PH+81-78-803-5902; kawabata@kobe-u.ac.jp
[2]Ph.D., Professor, Dept. of Agri. & Envir. Eng., Faculty of Agriculture, Kobe University, 1-1, Rokkodai, Nada, Kobe 657-8501, JAPAN; PH+81-78-803-5902; uchidak@kobe-u.ac.jp
[3]Master Course Student, Dept. of Agri. & Envir. Eng., Graduate School of Agricultural Science, Kobe University, 1-1, Rokkodai, Nada, Kobe 657-8501, JAPAN, PH+81-78-803-5902, 069a402n@stu.kobe-u.ac.jp
[4]Master Course Student, Dept. of Agri. & Envir. Eng., Graduate School of Agricultural Science, Kobe University, 1-1, Rokkodai, Nada, Kobe 657-8501, JAPAN, PH+81-78-803-5902, 071a023a@stu.kobe-u.ac.jp
[5]M.ASCE, Ph.D., Research Manager, Geotechnical Laboratory, National Institute for Rural Engineering, 2-1-2, Kannondai, Tsukuba, Ibaraki 305-8609, JAPAN; PH+81-298-38-7574; mohri@affrc.go.jp

ABSTRACT: The spillway on the small earth dam is made by reinforced concrete. Therefore, the weight could be the weak point in earthquakes.

In this paper, shaking table tests were conducted to evaluate quake resistance of spillway focusing its attention to weight and stiffness of the spillway models, cross sectional shape of the models, and the effect of reinforced by geogrid. As the results, the proposed geogrid-reinforced spillway with lightweight material showed high earth protection.

1.INTRODUCTION

Japan has over 230,000 mid-small size reservoirs to hold enough water for the life. These pounds are used not only as the source of irrigation but also water supply or stormwater reservoir for flood control in emergency. The reservoirs have a facility called spillway fixed to the dam embankment. The spillways are maintained in order to flow floods safely.

In 1995, Hyogo-ken Nambu Earthquake, many reservoirs had been devastated. The damage of reservoirs accounted for 75% of total loss concerning agriculture by the earthquake. In the series of damage of reservoirs, the spillways were seriously damaged. The spillways detachment from the embankments or failure in the joint of the bottom

plate and the sidewalls was observed. The cause was discussed in the weight of the spillways made by reinforced concrete and their stiffness.

Photo 1 shows the damage by the detachment of the concrete type spillway from the embankment during Hyogoken-Nanbu earthquake in 1995.



Photo 1. The damage of small earth dam spillway

The spillway damage leads catastrophic damage to downstream sites, therefore the countermeasures to improve the earthquake protection of spillways are necessary. As a representative example for earthquake proofing construction, geosynthetics reinforced soils could be introduced. However, most research on the geogrid-reinforced techniques has discussed the single wall or plate with the reinforced soil, there is lacking in discussion that could be applied to spillways in terms of the rectangular cross-section.

In this paper, shaking table tests were conducted to investigate quake resistance of spillway focusing its attention to weight and stiffness of the spillway models, cross sectional shape of the models, and the effect of reinforced by geogrid.

2.EXPERIMENTAL PROGRAM

2.1 Equipment Setup

The shaking table for the tests had plane dimensions of 6.0 x 4.0m, with the maximum loading capacity of 50tf and the maximum displacement capacity of 150mm. The test pit (2400 x 1900 x 1000mm) was rigidly connected on the shaking table and the experimental embankment model was placed in the test pit. The embankment size was 2400 x 1900 x 800mm with 45degree slope and 300mm width of the crest as shown in Photo 2.

The spillway models were positioned in the center of the crests. Figure 1 shows schematic elevation view of the test models. The embankments and the spillway models were instrumented extensively with the followings: the accelerometers measuring horizontal acceleration response of the spillway models and the grounds, the

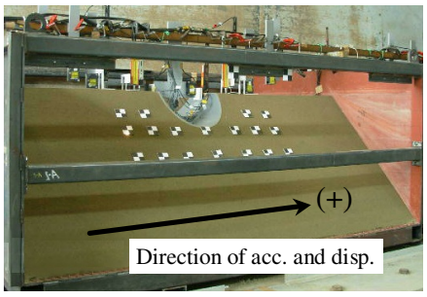


Photo 2 Embankment model in Case C

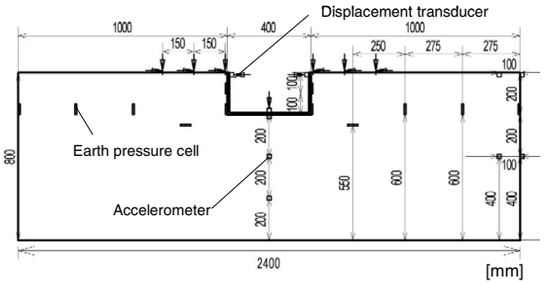
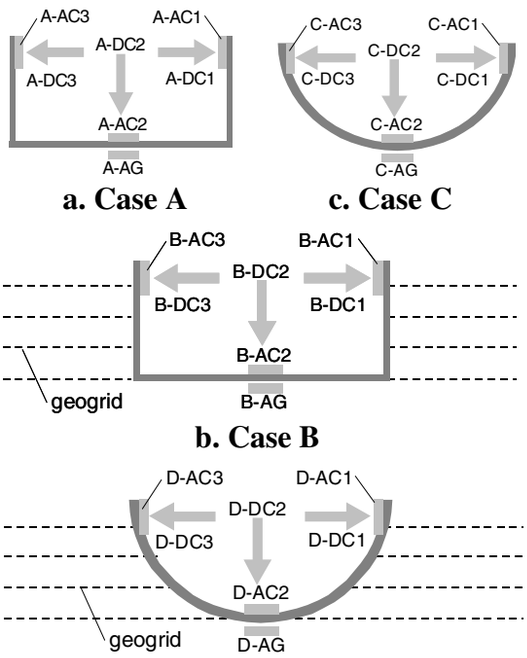


Figure 1. The test set in Case A

displacement transducers measuring displacement of the spillway models and the ground levels, and earth pressure cells measuring earth pressure around the soil of the models. As for the sign of the acceleration and the displacement, right on observer was positive in Figure 1. Note that the positions of the equipments were the same in every case. Figure 2. shows the measuring instruments around the spillway models. In this paper, these measured points were mainly discussed.

In the experiments, 5Hz horizontal sine wave was applied along the embankment axis. Figure 3 shows input wave. The shaking was applied at 200gal, 400gal, 600gal, and 800gal.



a. Case A **c. Case C**

b. Case B

d. Case D

Figure 2 Measure Instruments around the spillway models

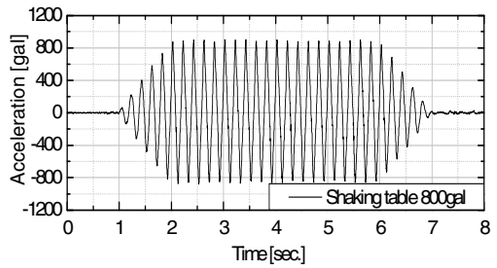
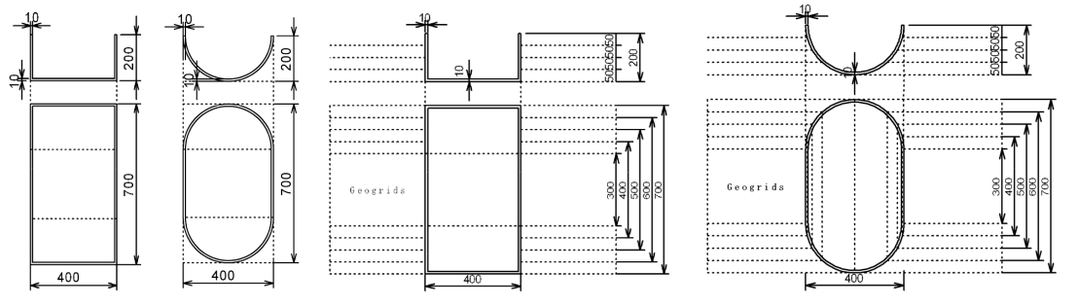


Figure 3. Input wave (800gal)

2.2 Soil Material and Test Models

The soil material for the embankment was Kasumigaura-sand with the mean particle diameter (D_{50}) of 0.40mm and the uniformity coefficient (U_C) of 3.16. The relative density (D_r) was about 65.5%. The geogrid used in the tests was high-density polyethylene and the tensile strength was 3.5 kN/m.

Figure 4 shows the spillway models. The model in Case A was made of rigid steel plate; other models were made of polyvinylchloride. The models in Case B



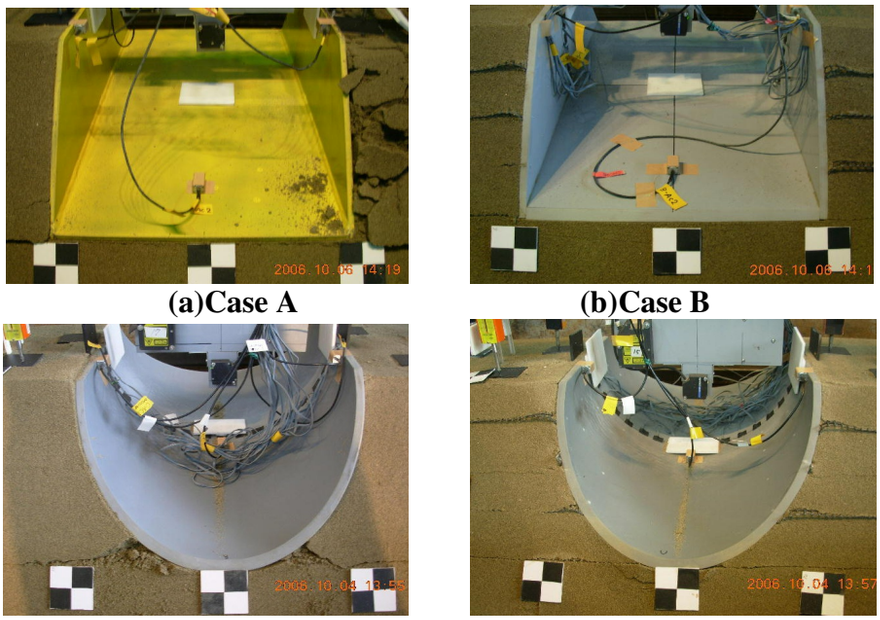
a.CaseA **b.Case B** **c.Case C** **d.Case D**

Figure 4. The spillway models

and D were reinforced by geogrids. In addition, strain gauges were attached on inner surface of the spillway models and both surfaces along centerline of geogrid at appropriate intervals.

3.RESULTS

3.1 Failures of Embankments



(a)Case A **(b)Case B**

(c)Case C **(d)Case D**

Figure 5. Spillway models after 800gal shaking

Figure 5 shows the failures of the embankments after 800gal shaking.

Figure 5(a) shows that the spillway model detached from the embankment in right side of observer and the shear surface developed from the bottom of the spillway model to backfill to both sides. Right part of the embankment was collapsed and the left part still remained intact. During the 800gal shaking, firstly, the model removed from the initial position, and the model slipped on the embankment. Then the heavy model compact the side backfills by the shaking along the longitudinal direction. As the result, the right embankment was collapsed. Figure 5(b) shows the spillway with geogrid didn't show any clear detachments in both backfills. From the fact, it is considered the model fixed to the embankment even in the shaking along longitudinal of the embankment, which act active earth pressure on the sidewalls. Moreover, it was confirmed the shear plane developed from the edge of bottom geogrid to the surrounding soils in both ends of the forth geogrids. It was considered this shear plane was the same as observed in reinforced soil structure shaking test and formed soil mass in reinforced area. Figure 5(c)

shows the shear plane developed not from the bottom of the model but from the point about 30-40 degrees away from the bottom of the model. This tendency of shear plane development is seen in pullout test of buried pipes. These failures were attributed to the fact that the compactions near the bottom of round shaped structure were less dense to support structure and that the round cross sectional shape lead specific passive earth pressure on the embankment as seen pipes. In addition, the model was rotated during shaking and the right edge moved about 2mm. Figure 5(d), Case D shows the crack in left bellow of the model. However, the shear planes from the spillway model surface were not developed as seen in Case C. In Case D, the geogrids hold the soil around the model. As for the surrounding soil of reinforced area, the shear planes developed along the bottommost geogrids in both sides. From these discussion about shear plane, the soil around the geogrid-reinforced model moved as soil mass.

3.2 Response Acceleration of Spillway models

Figure 6 shows the response acceleration of grounds beneath the spillway models (see Figure3, AG). The response acceleration was same in the magnitude and small difference in phase. This little phase difference was caused by the fact that the 4 case tests were conducted in 2 sets (Case A and B, Case C and D). Taking it into consideration, and from this figure, the grounds during 800gal shaking moved almost simultaneously.

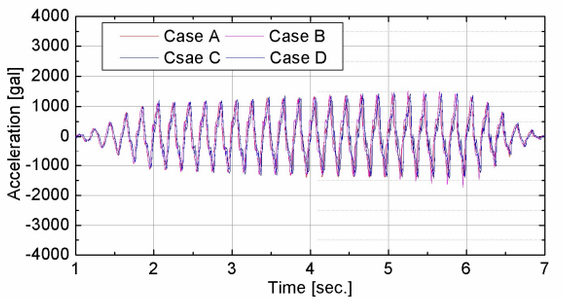


Figure 6. Ground Response Acceleration

Figure 7 shows the ratios of time integration of response acceleration of spillway (AC2) to that of the ground (AG) in each shakings. The time integration (I_E) was given by following equation,

$$I_E = \int_0^T a^2 dt \,, \qquad (1)$$

where, a is response acceleration, T is measurement time. The value of Case C in each shakings was larger than that of Case A. However, Figure 5(a) clearly shows that the embankment in Case A was failed largely than in Case C. In general, the failures were briefly given by the force that was affected by the material weight and the acceleration of the spillway models. From these results in the ratio about acceleration and Figure 5(a) and (c) concerning the failures, it was confirmed that the weight of

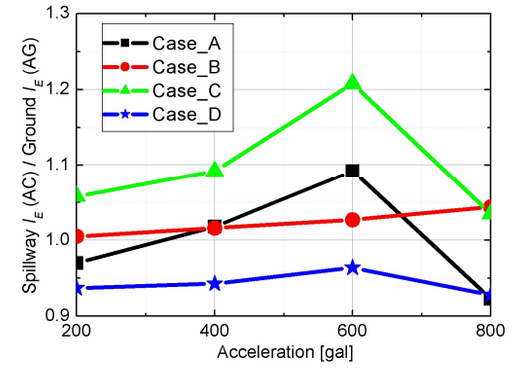


Figure 7. Ratio of Acceleration Power

spillway is quite essential to the spillway detachment from the embankment by shaking along longitudinal direction, which was pointed out in the damage in Hyogo-ken Nambu Earthquake spillway damage. Case B shows the values are near 1.0. Therefore, the spillway model in Case B was affected by almost the same level of acceleration on the ground beneath the model. Judging from the Figure 5(b), which doesn't show serious failure, the effect of reinforcement by geogrid could be developed to the ground beneath the model. On the other hand, the values of Case D show less than 1.0. This results showed larger acceleration acted on the ground than that acted on the spillway model. It would appear that the shaking of the spillway model was repressed by the aseismic affects of geogrid. Therefore, the response acceleration of the model was less than that of ground. However, further investigation about the affected area by the reinforcement was necessary. When it comes to 800gal shaking, the ratio of Case A was dropped sharply. That was because the spillway was slipped and moved independently during 800gal shaking, as the result, the value was small apparently. The same was applied to the sharp drop of the value in Case C.

3.3 Response Displacement of Spillway models

Figure 8 shows the horizontal response displacement during 800gal shaking. Right of the observer in Figure 1 was positive. The residual displacements are: Case A was about 10mm, Case B was 3.5mm, Case C was 8mm and Case D was 4mm. Every models had the time the displacement increase largely. The time was; Case A was

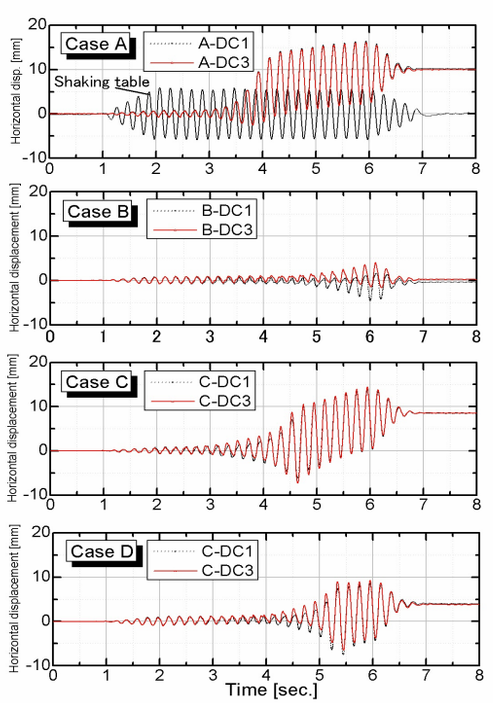


Figure 8. Horizontal Response Displacement in 800gal shaking

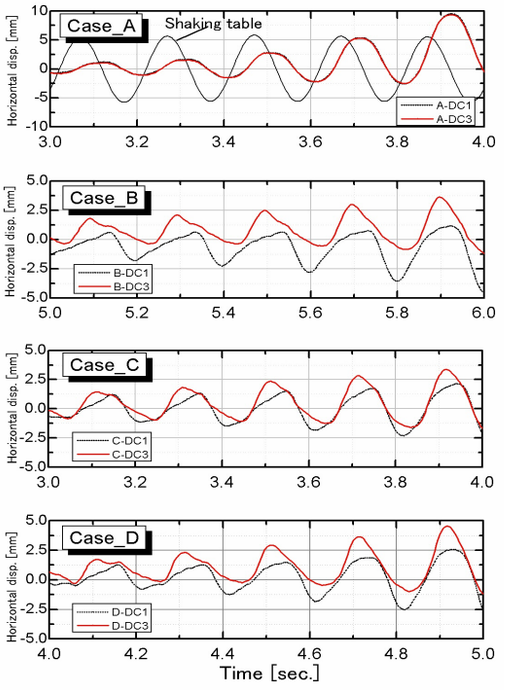


Figure 9. Extended Figure 8.

3.5sec., Case B was 5sec., Case C was 3.5sec. and Case D was 4.5sec. Therefore, the cases with geogrid showed durability in the response displacement of side walls. As for Case A, the response displacement of both walls showed simultaneous movement during the shaking, the model was moved as rigid body. As the result, the embankment in Case A was hit and failed by the rigid heavy spillway model from about 3.5sec.

Figure 9. shows the extended figure of Figure 8. These figures focus on the timing the displacement was largely increased. In Case B, it was observed that the width between both tops of the sidewalls become narrow because the right response displacement (DC1) was negative and the left (DC3) was positive. The both sidewalls were bended to inner side by the active earth pressure. Moreover, the side walls in the series of spillway models made by PVC (Case B, C, and D) showed that their falls by active earth pressure were faster than their recovery from the bend by inertia force. The behavior of recovery from bending resulted in reducing the spillway detachment from the embankment. The reactions in PVC cases were given by the material stiffness or reinforcement. However, more discussion is needed to identify the components causing the reaction.

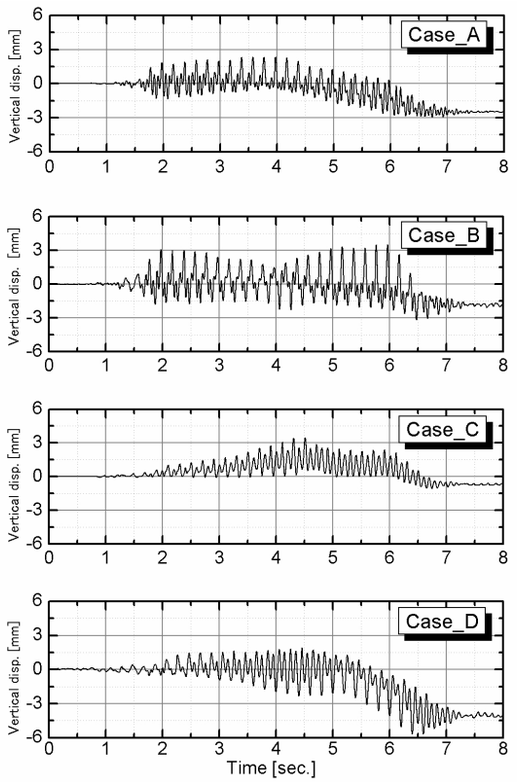


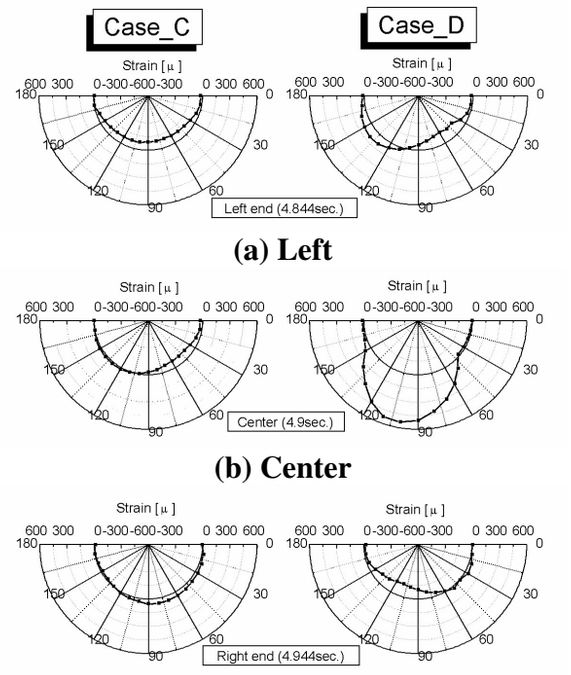
Figure 10. Vertical Response Displacement in 800gal shaking

Figure 10 shows the vertical response displacement in 800gal shaking. Although the shaking was applied to longitudinal direction of the embankment models, the spillway models showed settlements. The residual settlements were; Case A was 2.5mm, Case B was 1.8mm, Case C was 0.5mm and Case D was 4.0mm. In Case A, the time to start to settle was about 4.0sec. It was same as the time to start to displace horizontally largely. It was considered that the settlement in Case A was mainly given by the failure of the embankment. Case B showed response elevations from 2sec. to 6sec. when the response horizontal displacement increased largely in Figure 8. This behavior were given not only by the dilation of the soil but the bending of the bottom member of the rectangular spillway model by the moment from side walls affected by active earth pressure. If only the dilation was predomination component to raise the model, the peak of elevation must be 10times during 1.0sec. because the sine wave was applied by 5Hz. However, the peaks in Figure 9 showed 5times in 1.0sec and followed the timing that the shaking table

was positioned in right end. At that time, the inertia force which act on side walls were main factor to change the shape of the spillway model. Case C showed floating until 4.5sec. The backfill was settled to the beneath along the round surface of the spillway. Case D showed largest settlement although the spillway model was supported by geogrids and didn't show large failure in Figure 5(d). There was the possibility that the compaction under the model was not enough quality to support the model during 800gal.

3.4 Deformation of Semisylindrical Spillway Models

Figure 11 shows the transition of the deformation of the semicylindrical spillway models during one stroke of the skaking table in 800gal. The deformation of the spillway models followed the position of the shaking table. In Case C, the strain level was less than that of Case D. The model kept the shape during the stroke. This tendency was observed in other strokes of 800gal shaking. Judging from the discussion about durability by Figure 8 Case C, it was contemplated that the model removed the embankment and move independently keeping the shape during 800gal shaking. On the other hand, the model in Case D, large deformation was observed when the shaking table was positioned in the center. The behavior was given by the geogrids. This is because the geogrids affected by its pullout resistance were connected to the spillway. In other words, the spillway was deformed by the pullout resistance of the geogrids. In terms of failure, the geogrids were obviously effective. However, the geogrids was connected to the spillway model itself and the geogrids acted the pullout force on the spillway model. Therefore, in terms of the deformation of the spillway, it was necessary to consider the mutual effect of the geogrid and the stiffness of spillway models.



(a) Left

(b) Center

(c) Right

Figure 11. Transition of Spillway Deformation in one stroke

3.5 Strain Distribution of Geogrids

Figure 12 shows the transition of elongation strain of third and forth geogrids in Case B and D. The left-side forth geogrid in Case D had absence. The horizontal scale shows the position from the connection point with the spillway models. The graph titles show the

position of the shaking table during one stroke.

In Case B, the geogrids showed larger tension and compression strain than that in Case D. From this result, it was indicated that the rectangular cross section was more effective in the reinforcement than the semicylindrical cross section when the geogrids was equipped to the sidewalls. In general, the properties for earthquake protection by reinforced soil by geogrids were realized by mobilizing the tensile stress.

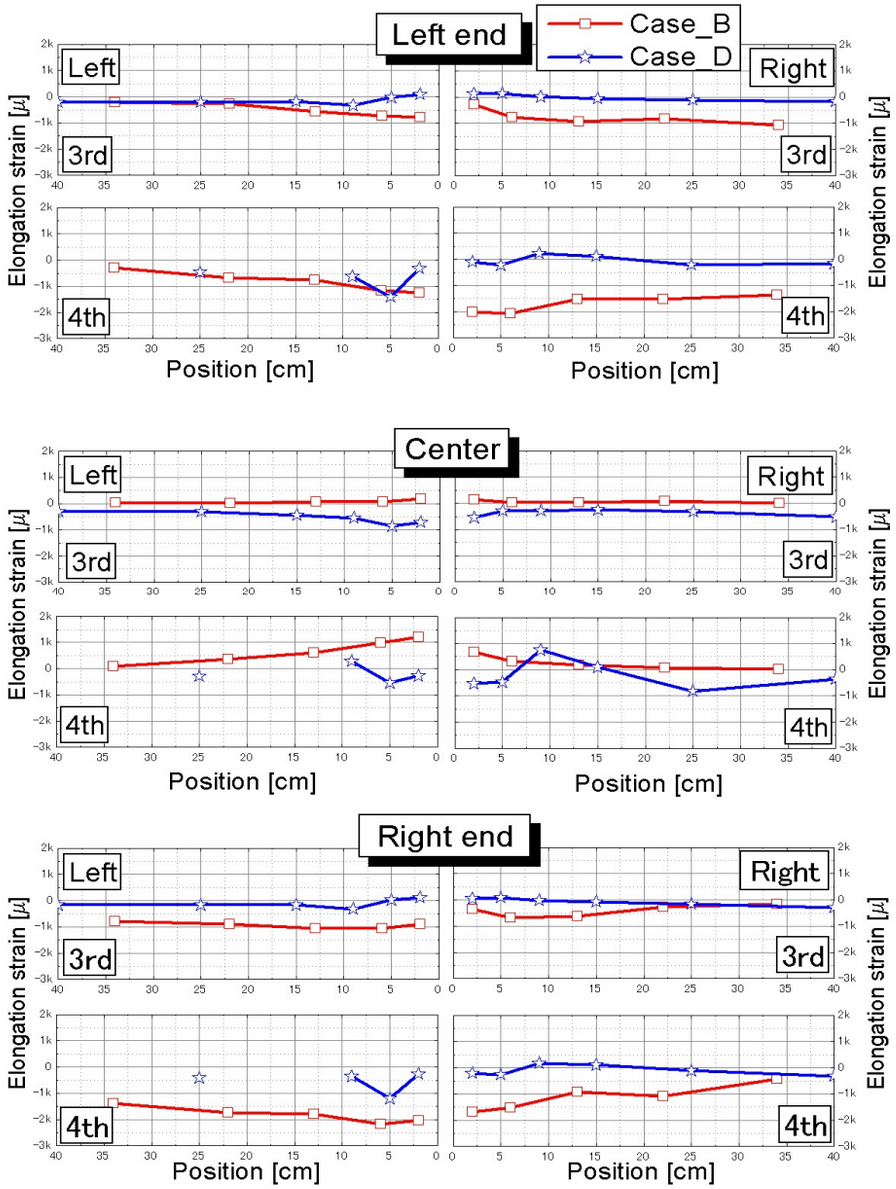


Figure 12. Elongation strain distribution of the geogrids

On the other hand, the geogrids in Case D showed compression during the stroke. This behavior indicated that the reinforced soil moved to the spillway model. This supposition was consistent with the deformation of Case D in Figure 11.

4.CONCLUSIONS

In this paper, shaking table tests were conducted on the traditional heavy spillway model and newly proposed spillway models. The studies on the weight, the stiffness, shape of the cross section and the geogrid effects were made. As the results, the followings were clarified.

a) The rectangular shaped heavy spillway model showed settlement and detachment from the embankment model.
b) The light weight rectangular spillway model with geogrids showed quake protection in detachment. However, the sidewalls were affected by active earth pressure by longitudinal shaking. As the result, the moment by the shaking was acted on the corner of the model.
c) The semicylindrical spillway model was rotated and detached from the embankment after shaking.
d) The semicylindrical spillway model with geogrid repress the detachment from the embankment. However, it was observed the model was larger settled in 800gal shaking than any other cases.

REFERENCES

Bathurst, R.J., El-emam, M.M., Mashhour, M.M. (2002) “Shaking table model study on the dynamic response of reinforced soil walls”, Geosynthetics-7thICG-, vol.1, pp.99-102.

Koseki, J., Watanabe, K., Tateyama, M., Kojima, K. (2002) “Comparison of model shaking test results on reinforcd-soil and gravity type retaining walls”, Geosynthetics-7thICG-, vol.1, pp.111-114.

Uchimura, T., Tatsuoka, F., Shinoda, M., Sugimura, Y., Kikuchi, T. (2002) “Roles of tie rods for seismic stability of preloaded and prestressed reinforced soil structures”, Geosynthetics-7thICG-, vol.1, pp.115-118.

Watanabe, K., Tateyama, M., Yonezawa, T., Aoki, H., Tatsuoka, F., Koseki, J. (2002) “Shaking table tsets on a new type bridge abutment with geogrid-reinforced cement treated backfill”, Geosynthetics-7thICG-, vol.1, pp.119-122.

Earthquake-Induced Deformations of Partially Saturated Embankments

Rolando P. Orense[1], M. ASCE, P.E., Masayuki Hyodo[2], Norimasa Yoshimoto[3], and Junya Ohashi[4]

[1]Senior Lecturer, Department of Civil and Environmental Engineering, University of Auckland, Private Bag 92019, Auckland, New Zealand r.orense@auckland.ac.nz
[2]Professor, Department of Civil and Environmental Engineering, Yamaguchi University, 2-16-1 Tokiwadai, Ube, Japan hyodo@yamaguchi-u.ac.jp
[3]Assistant Professor, Department of Civil and Environmental Engineering, Yamaguchi University, 2-16-1 Tokiwadai, Ube, Japan nyoshi@yamaguchi-u.ac.jp
[4]Graduate Student, Department of Civil and Environmental Engineering, Yamaguchi University, 2-16-1 Tokiwadai, Ube, Japan k006vf@yamaguchi-u.ac.jp

ABSTRACT: The amount of water in soil plays very important role in defining its shear strength. Thus, when considering partially saturated slopes subjected to earthquake-induced ground shaking, it is important to quantify how such slopes respond to the induced dynamic stresses. For this purpose, undrained cyclic triaxial tests were performed on decomposed granite soil in order to quantitatively investigate the effects of degree of saturation and initial static shear stress on its earthquake response characteristics. The experimental results obtained were then used in conjunction with pseudo-static slope stability analysis and modified Newmark sliding block model to estimate the deformation of embankments which were under different degrees of saturation. The example calculations clearly showed the effect of saturation on the magnitude of seismic-induced displacements of embankments.

1. INTRODUCTION

Recent large-scale earthquakes, such as the 2004 Niigata Chuetsu Earthquake in Japan, have highlighted the role of antecedent rainfall on the seismic instability of slopes. Days prior to the occurrence of the earthquake, the region was subjected to large amount of rainfall. The saturation of the ground and the increase in water table could have led to decrease in the strength of the soil. These may have contributed to the scale and number of earthquake-induced failure of slopes in the region. Typical examples of slope failure observed in the area during subsequent site visits are shown in Fig. 1.

Unfortunately, most studies concerning earthquake-induced slope failures have focused on extreme conditions: dry slopes (e.g., Newmark, 1965; Sarma, 1975; Makdisi and Seed, 1978) or completely saturated slopes (e.g., Baziar, 1992; Orense and Towhata,



FIG 1. Collapsed slopes during the 2004 Niigataken-Chuetsu Earthquake

1998). There has not been much quantitative investigation on the effect of degree of saturation on the cyclic shear response of sloping grounds. With the advent of performance-based design, it is believed that considering the effect of degree of saturation of the soil could lead to a more accurate evaluation of soil response during earthquakes.

In this paper, the results of undrained cyclic triaxial tests conducted on samples of decomposed granite soil under varying degrees of saturation (S_r) and initial static shear stresses (σ_s) are presented. Moreover, these experimental results are used in conjunction with pseudo-static stability analysis and a modified version of the Newmark sliding block model to estimate the magnitude of seismic-induced displacements of partially saturated embankment slopes under different earthquake loads.

2. MATERIAL USED AND TEST PROCEDURE

The samples employed in this study were decomposed granite soils, more popularly referred to as "Masado" in Japan, obtained in Iwakuni City, Yamaguchi Prefecture. The grain size distribution curve, as well as some physical properties, are shown in Fig. 2(a). Note that only particle sizes smaller than 2 mm were used because of the limitation of testing equipment. The material is silty sand with fines content, F_c=10%. The soil water characteristic curve obtained for this sample is illustrated in Fig. 2(b). Since the curve indicates abrupt change in suction from S_r=30%-60%, samples with S_r=30%, 60% and 100% were considered in the tests.

To prepare the unsaturated specimens (S_r=30%, 60%), a prescribed amount of water was added to air-dried Masado soils and mixed thoroughly to obtain the specified initial S_r. Then, the moist soil was placed in the mold in 10 layers, with each layer tamped by a rammer to obtain a specimen with initial relative density of D_r=70%. The procedure was repeated until the prescribed height of the sample was reached. The specimens were 5 cm in diameter and 10 cm high. For the fully saturated specimen (S_r=100%), CO_2 and de-aired water were infiltrated into the sample until a B-value > 0.95 was obtained.

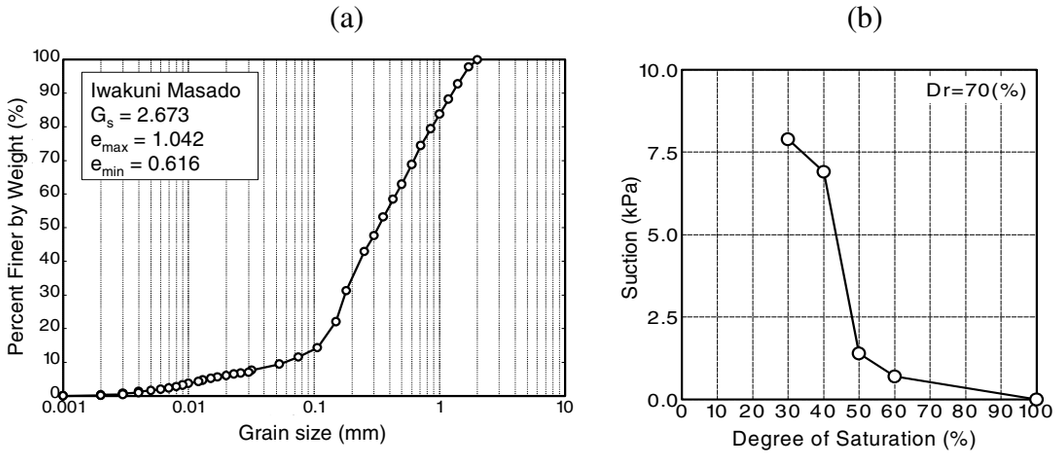


FIG 2. Properties of Iwakuni Masado soil: (a) grain size distribution and physical properties; and (b) soil water characteristic curve.

The specimens were first isotropically consolidated at effective confining stress of σ_c'=100 kPa, then anisotropically consolidated by subjecting them to various initial shear stress ratios, $\sigma_s/2\sigma_c$'=0.0, 0.2, 0.4, and 0.6. Cyclic triaxial tests were performed by applying cyclic deviator stresses, σ_d, under undrained condition with frequency of f=0.1 Hz until the specimen failed (i.e., large strain) or the prescribed number of load applications was reached. In the tests, ordinary porous stones were used and suction measurement during cyclic loading was not performed.

3. CYCLIC TEST RESULTS AND DISCUSSION

3.1 Undrained shear behavior

The effect of degree of saturation on the undrained cyclic shear behavior of isotropically consolidated samples ($\sigma_s/2\sigma_c$'=0.0) is shown in Fig. 3, which depicts typical stress-strain relations as well as the stress paths for specimens with S_r=100, 60 and 30%. Unlike the case of fully saturated specimen which showed large reduction in effective mean stress (p') because of development of excess pore water pressure, and consequently large axial strain (i.e., liquefaction), samples with low S_r showed stiffer response, even for comparatively higher cyclic shear stress ratio, $\sigma_d/2\sigma_c$', with less reduction in effective mean stress. Note that since suction was not monitored for these cases, the effective mean stress (p^*) was obtained by subtracting the total pore pressure (pore air + pore water) monitored by the pressure transducer at the bottom of the specimen from the initial mean confining stress. Moreover, the stress-strain relation showed that extension was more predominant. Similar trend was also observed for specimens subjected to initial shear stress ratios of $\sigma_s/2\sigma_c$'=0.2, 0.4, and 0.6. However, for these cases, the specimen failed either in compression or extension, depending on the magnitude of initial shear stress and applied cyclic deviator stress.

The relations between the shear stress (static plus cyclic) and the number of cycles required to attain peak residual axial strain ε_p=5% (or double amplitude strain, ε_{DA}=5%,

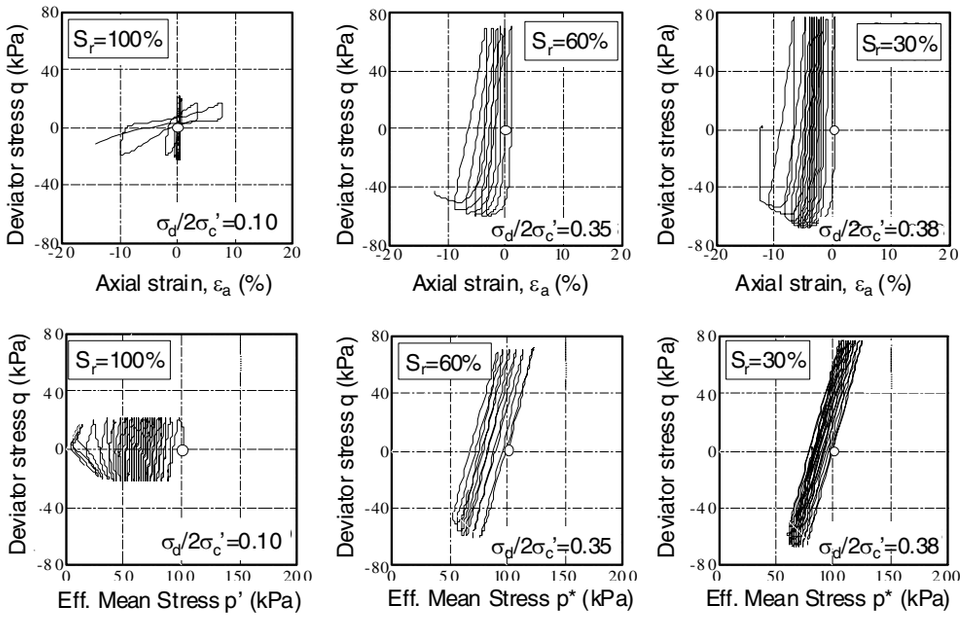


FIG 3. Typical stress-strain relations and stress paths for soil samples with different degrees of saturation, S_r

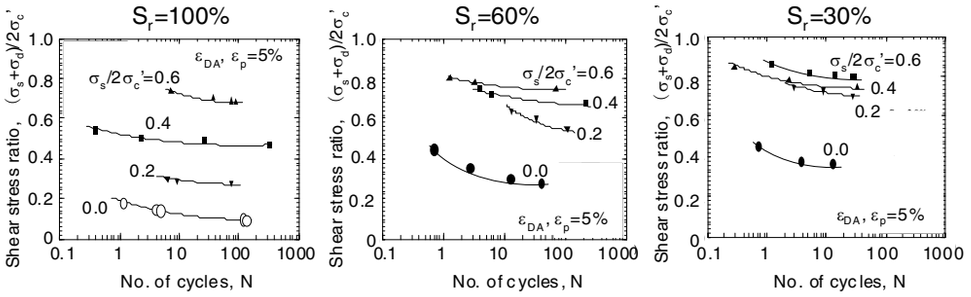


FIG 4. Relations between shear stress (cyclic + static) ratios and number of cycles for soil samples with different initial shear stress ratios, $\sigma_s/2\sigma_c$' and degrees of saturation, S_r

in case of $\sigma_s/2\sigma_c$'=0) for all cases are shown in Fig. 4. It can be seen that for any given S_r, the shear strength of specimen increases with increase in initial shear stress. This can be traced to the crushable nature of Masado soils (Kim et al., 2006). The shear stress applied on the specimen resulted in particle crushing (as evidenced by changes in particle size distribution) which increased the contact between particles, and thus, the higher strength. Similar results were obtained by Orense et al. (2006) using cyclic simple shear apparatus.

The cyclic shear strength ratios, $\sigma_d/2\sigma_c$', corresponding to N=20 cycles were read from the curves and plotted as a function of the initial shear stress ratio, $\sigma_s/2\sigma_c$', as shown in Fig. 5. At low $\sigma_s/2\sigma_c$', failure in the extension side was predominant; on the other hand, specimens subjected to high initial shear stress ratios failed in the compressive side.

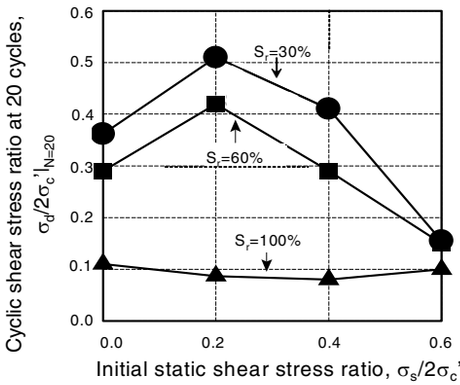


FIG 5. Relation between initial static shear stress and dynamic shear strength at *N*=20 cycles

Thus, the combination of initial shear stress and the applied cyclic deviator stress determines the failure mode of the specimen.

It is worthy to mention that although specimens with S_r=100% showed practically no change in cyclic shear strength as $\sigma_s/2\sigma_c$' increases, the opposite can be seen for both S_r=30% and 60%. For unsaturated specimens, the cyclic strength was largest when $\sigma_s/2\sigma_c$'=0.2, after which it decreases with the increase in $\sigma_s/2\sigma_c$' as the initial stress state plots near the failure line.

4. SEISMIC STABILITY OF SLOPES AND DISPLACEMENT PREDICTION

The stability of slopes is conventionally analyzed using limit equilibrium method. By using the results of the cyclic triaxial tests to represent the dynamic strength of the soil, it is possible to estimate the residual displacement of the slope using pseudo-static analysis and Newmark sliding block model.

4.1 Outline of proposed method

In performing slope stability analysis, two stages were considered: static analysis prior to the application of the seismic load, and dynamic analysis using pseudo-static approach. In the static analysis, the strength parameters (cohesion *c* and frictional angle ϕ) obtained from conventional tests were used. Since the calculated factor of safety, F_s, indicates the ratio of the shear strength, τ_{sf}, and shear stress, τ_s, along the slip surface (i.e., $F_s=\tau_{sf}/\tau_s$), it is possible to estimate the average static shear stress along the slip plane from the known values of F_s and τ_{sf}.

Knowing the average static shear stress along the slip plane, the corresponding cyclic shear strengths can be estimated based on relations such as those shown in Fig. 5. These cyclic shear strengths are added to the initial static shear stresses and then used as total strength in performing the pseudo-static analysis to compute the F_s for the specified earthquake load. Note that in this procedure, it is tacitly assumed that the earthquake

loading is applied for N=20 cycles. Based on the results of pseudo-static analysis, the yield acceleration, k_y, corresponding to the limit equilibrium condition, F_s =1.0, is calculated. For simplicity, the value of k_y is assumed to be constant throughout the duration of earthquake loading.

Next, the deformation of the embankment due to seismic loading is calculated using Newmark sliding block model. Instead of calculating displacement, the method is modified to calculate the rotation of the rigid block itself, as shown in Fig. 6. For this purpose, D'Alembert's principle is used to formulate the force equilibrium within the block, from which the angular rotation, $\ddot{\theta}$, at each time step, Δt, is computed. By integration, the angular velocity, $\dot{\theta}$, and angular displacement, θ, are calculated. Finally, the sliding displacement of the slope, δ, can be calculated from the known radius, R, of the sliding circle. The relevant equations are also summarized in the figure. Details of the modified method are discussed by Tateyama et al. (1998) based on the original formulation of Ling and Leshchinsky (1995).

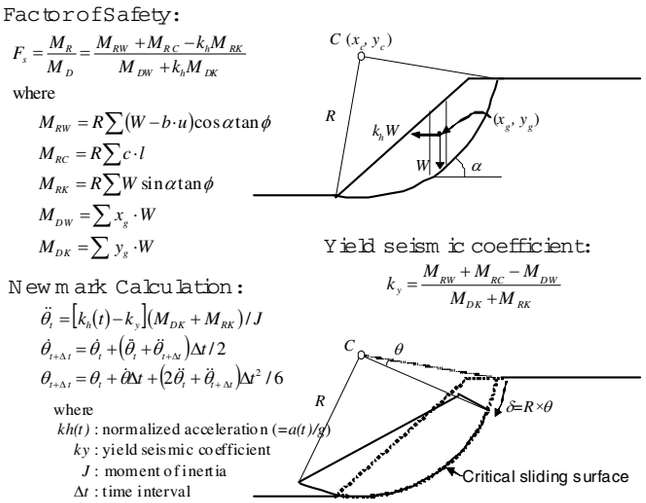


FIG 6. Outline of calculation based on modified Newmark model

4.2 Illustrative Examples

To illustrate the above method, six (6) types of soil embankments were considered, as shown in Fig. 7. The model ground consists of a foundation ground overlain by a 10 m high embankment with 1:1.7 slope. The embankment has horizontal Masado soil layers with varying degrees of saturation. Types 1, 2 and 3 correspond to the embankments having S_r=100%, 60% and 30%, respectively. Type 4 has an embankment with S_r=100% at the lower portion and S_r=60% in the upper portion, while Type 5 has S_r=30% in the upper portion. Type 6 has three layers consisting of S_r=100%, 60% and 30%, in that order from the bottom. The displacements of these model embankments were analyzed considering the earthquake record obtained in Nagaoka station during the 2004 Niigata Chuetsu Earthquake as input earthquake wave. The earthquake record, shown in the lower portion of Fig. 9, has a maximum acceleration of 369.01 cm^2/sec.

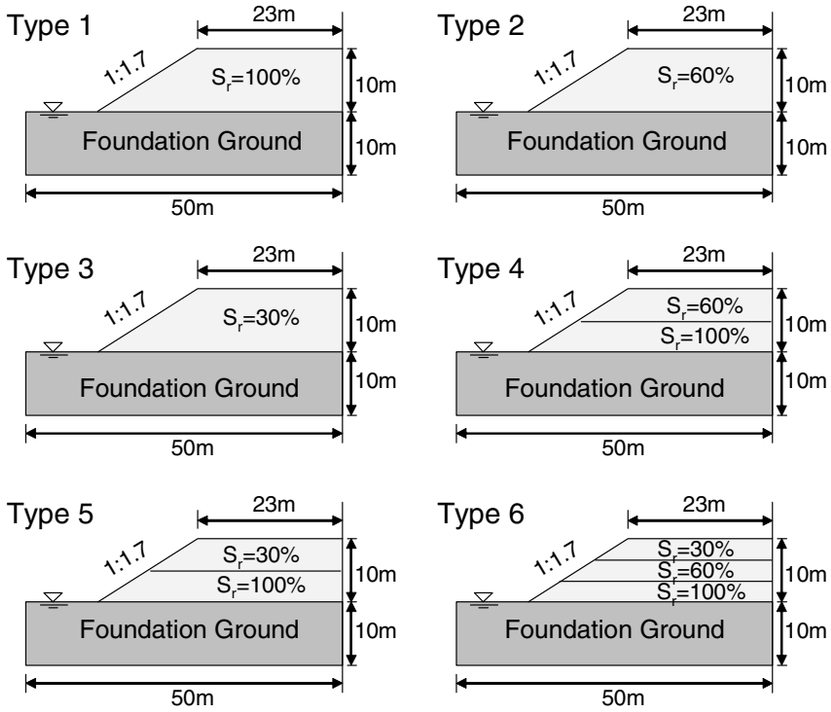


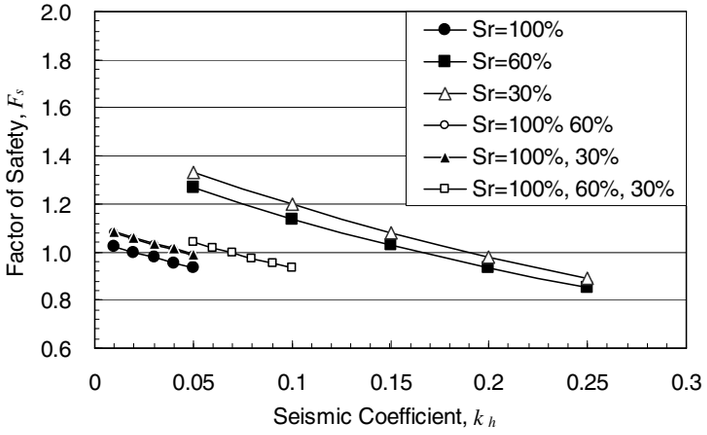
FIG 7. Embankment cases for example calculations

In the static analysis, the shear strength parameters (obtained from tests) for Masado soils are c=0 and ϕ=38°. For simplicity, similar parameters are assumed regardless of degree of saturation. Subsequent slip circle analysis indicates a factor of safety F_s=1.491, and this corresponds to an average initial static shear stress ratio τ_s/σ_c'=0.524.

For this given value of initial static shear stress ratio, the corresponding cyclic shear stress ratio for each layer with the prescribed S_r is read from Fig. 5. Instead of using conventional shear strength parameters in the subsequent pseudo-static analysis, the total (static + dynamic) shear strengths obtained are used for the corresponding layers in the model embankment. In the analysis, different seismic coefficients are considered to estimate the magnitude of the critical k_y.

The results of the pseudo-static analysis for different embankment types are expressed in terms of the relation between the applied seismic coefficient, k_h, and the calculated minimum factor of safety, F_s, as shown in Fig. 8. It can be observed that unsaturated embankments (S_r=30% and 60%) show the highest F_s for different k_h, while a saturated slope (S_r=100%) indicates the least F_s. Embankments consisting of several layers with different degrees of saturation (Types 4 - 6) show almost similar values of F_s for each k_h.

From the figure, the yield seismic coefficient, k_y, i.e., seismic coefficients corresponding to F_s=1.0 can be obtained for each embankment, and these are also indicated in the lower portion of the figure. As expected, k_y decreases as the degree of saturation increases, indicating that weaker soils will fail under smaller level of acceleration.



S_r (%)	100	60	30	100, 60	100, 30	100, 60, 30
k_y	0.019	0.165	0.189	0.043	0.047	0.068

FIG 8. Calculated relation between k_h and F_s and the values of k_y for each case

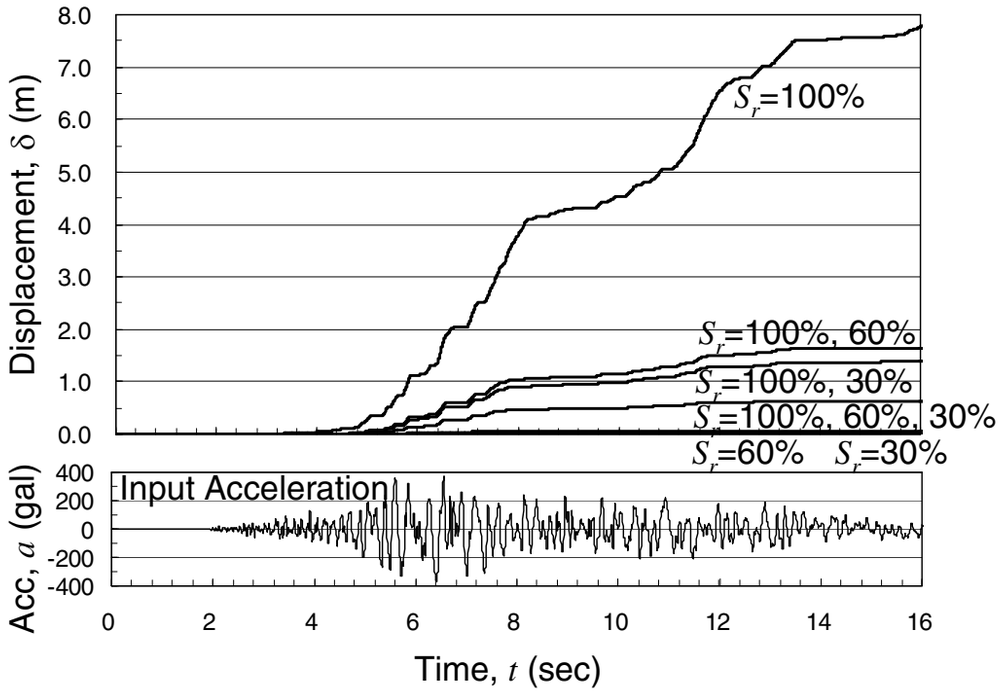


FIG 9. Time histories of displacement for each case and input acceleration

Knowing the value of k_y for each case, the time histories of angular displacements, θ, are calculated based on the procedure shown in Fig. 6, from which the sliding displacements, δ, of the rigid block are computed. The time histories for each case are shown in Fig. 9 with respect to the input acceleration. It can be seen that for a fully saturated embankment (S_r=100%), the displacement of the rigid block developed quite

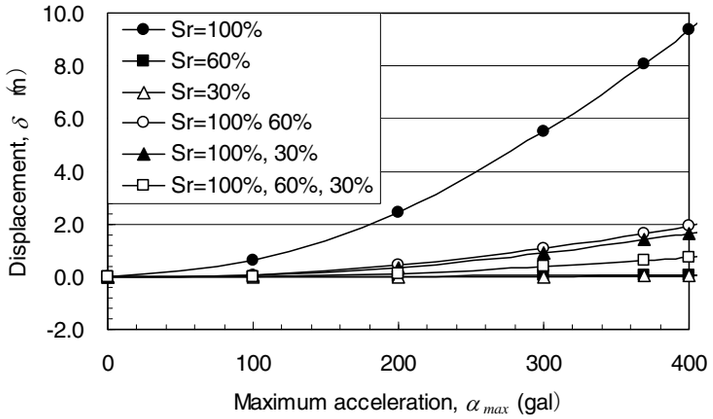


FIG 10. Relation between maximum acceleration and displacement

rapidly, owing to its low k_y. In contrast, unsaturated embankments (S_r =30% and 60%) underwent practically no displacement. For embankments with S_r=100% in the lower portion and different S_r in the upper portion, it can be seen that the progress of displacement is almost similar.

Finally, the variation of the maximum displacement of the sliding block with the amplitude of the peak ground acceleration is illustrated in Fig. 10. Except for the fully saturated embankment (Sr=100%) which shows large displacement from the start, other embankments which contain unsaturated layers show very small displacements when the maximum ground acceleration is less than 200 gals. However, at maximum acceleration greater than 300 gals, embankments with the lower layers fully saturated show increase in displacement. In contrast, unsaturated embankments showed negligible displacements throughout the investigated range of acceleration.

It can be observed from the example calculations that embankments with the lower portion saturated showed practically similar response, irrespective of the level of saturation in the upper portion. This indicates that the saturated layer behaved as the weak spot in the embankment and it more or less controls the dynamic strength in the sliding surface.

Although quite simplified in nature, the example calculations shown above clearly illustrate the effect of degree of saturation on the magnitude of seismic-induced displacement of embankments. It should be mentioned though that the above procedure has yet to be validated using well-documented case histories in the field.

5. CONCLUDING REMARKS

Undrained cyclic triaxial tests on Masado samples under different degrees of saturation and initial shear stresses were conducted. The results showed that for unsaturated specimens, large strength degradation typically observed in fully saturated specimens were not observed. Moreover, the combination of initial static shear stress and applied dynamic stress determines the mode of failure (extension or compression) of the

specimen.

The results of cyclic tests were then used in conjunction with pseudo-static slope stability analysis and Newmark sliding block model to estimate the deformation of embankments under different degrees of saturation. Although simplified in nature, the example calculations clearly showed the effect of degree of saturation on the magnitude of seismic-induced displacement of embankments. These illustrated the need in considering the effect of degree of saturation on the post-failure behavior of embankments and slopes.

ACKNOWLEDGMENTS

The study presented in this paper was part of the research work supported by Japan Society for Promotion of Science (JSPS, Grant-in Aid for Scientific Research (C) under grant number 18560487 (2006-2008). The authors would like to thank Messrs. K. Masaki, S. Takahashi and K. Yoshikuni, former students of Yamaguchi University, for the assistance in performing the experimental and computational works presented herein. The slope stability analysis was performed using the computer program COSTANA (developed by Fujitsu FIP Corp).

REFERENCES

Baziar, M.H. (1991). "Engineering evaluation of permanent ground deformations due to seismically induced liquefaction." *PhD Thesis*, Rensselaer Polytechnic Institute, Troy, New York.

Kim, W.T., Hyodo, M. and Kin, F.G. (2006). "Effect of compressibility and density on the undrained cyclic shear strength of decomposed granite soil Masado." *Proc. International Symposium on Geomechanics and Geotechnics of Particulate Media*, Ube, Japan, 109-112.

Ling, H.I. and Leshchinsky, D. (1995). "Seismic performance of simple slopes." *Soils and Foundations*, Vol. 35, No. 2, 85-94.

Makdisi, F.I. and Seed, H.B. (1978). "Simplified procedure for estimating dam and embankment earthquake-induced deformations." *Journal of Geotechnical Engineering Division, ASCE*, Vol. 104, GT7, 849-867.

Newmark, N. M. (1965). "Effects of earthquakes on dams and embankments." *Geotechnique*, Vol. 15, No. 2, 139-160.

Orense, R.P. and Towhata, I. (1998). "Three dimensional analysis on lateral displacement of liquefied soil." *Soils and Foundations*, Vol.38, No.4, 1-15.

Orense, R., Hyodo, M., Takahashi, S. and Yoshimoto, N. (2006) "Laboratory experiments on the cyclic shear behavior of partially saturated slopes." *Proc., Earthquake Geotechnical Workshop*, Canterbury, 231-240.

Sarma, S.K. (1975). "Seismic stability of dams and embankments." *Geotechnique*, Vol. 25, No. 4, 126-132.

Tateyama, M., Tatsuoka, F., Koseki, J. and Horii, K. (1998). "Studies on seismic design method of soil structures." *Railway Technical Research Institute Report*, Vol. 12, No. 4, 7-12 (in Japanese).

Effect of Heterogeneous Soil Strength on the Seismic Residual Displacement of Embankments

Yoshiya Hata[1], M. JSCE, Koji Ichii[2], M. JSCE, Takashi Tsuchida[3], M. JSCE, Seiji Kano[4], M. JSCE and Norihiko Yamashita[5], M. JSCE

[1]Researcher, R&D Center, Nippon Koei Co., Ltd.,
2304, Inarihara, Tsukuba, Ibaraki 300-1259 JAPAN; hata-ys@n-koei.jp
[2]Associate Professor, Graduate School of Engineering, Hiroshima University,
1-4-1, Kagamiyama, Higashihiroshima, Hiroshima 739-8527 JAPAN, ichiikoji@hiroshima-u.ac.jp
[3]Professor, Graduate School of Engineering, Hiroshima University,
1-4-1, Kagamiyama, Higashihiroshima, Hiroshima 739-8527 JAPAN, ttuchida@hiroshima-u.ac.jp
[4]Research Associate, Graduate School of Engineering, Hiroshima University,
1-4-1, Kagamiyama, Higashihiroshima, Hiroshima 739-8527 JAPAN, skano@hiroshima-u.ac.jp
[5]Associate Professor, Faculty of Civil Engineering, Kobe City College of Technology,
8-3, Gakuenhigashimachi, Nishi Ward, Kobe 651-2194 JAPAN, yamasita@kobe-kosen.ac.jp

ABSTRACT: The effect of heterogeneous soil strength on a performance design procedure, based on permanent displacement according to safety factors, is examined. Soils are heterogeneous in nature. However, at present, the seismic design of embankments has been implemented assuming homogeneous soil strength. In this study, a seismic reliability analysis using a Monte Carlo Simulation and heterogeneous soil strength was applied to the Newmark Method. Input data of the reliability analysis in this study were based on in-situ soil test results of an actual airport embankment. The numerical results in this study suggest that the estimated displacement will increase if the heterogeneity of material is considered. His study also shows that the setup of the numerical analysis model to include the heterogeneity of the soil strength is important.

INTRODUCTION

Embankments are important components of civil engineering structures. For example, highways, airports and railways usually have embankment structures. Both the FEM Method and the Newmark Method (Newmark 1965) can be useful tools. The Newmark Method is indicated as a method to compute the amount displacement for performance verification against Level 2 earthquake motions (beyond P.G.A. =600 gal with a small probability of occurrence) in the seismic design guidelines (JSCE 2000).

Soils are heterogeneous in nature. However, at present, the seismic design of embankments has been implemented assuming soil strength is homogeneous. When an embankment is under construction, it is almost impossible to keep the strength as a

constant. In previous studies, the heterogeneity of soil strength was evaluated using the theory of probability based on the general idea of the reliability design method. However, the characteristics of heterogeneity in the soil are not well known, and no reliability analyses based on actual in-situ soil data have been conducted in previous studies (e.g., Griffiths and Fenton 2004; Travasarou *et al*. 2004).

Based on the above background, in this study, a seismic reliability analysis using a Monte Carlo Simulation and the Newmark Method to consider the heterogeneity of soil strength was undertaken. The data for the analysis in this study is based on results of in-situ soil tests of an actual (but anonymous) airport embankment in Japan. The effects of the heterogeneity of soil strength to the residual displacement of the embankments will be investigated, and a rational and practical approach to determining design parameters will be presented.

MONTE CARLO SIMULATION

The analysis of an embankment was carried out following the flow shown in the FIG. 1. To begin, the model setup and the input ground motions are necessary. Next, the input parameters to consider the heterogeneity of the model are prepared. They are the variation coefficients, V, to prescribe the degree of heterogeneity and the correlation coefficient, ρ, to prescribe spatial correlation on the heterogeneity. The heterogeneous embankment model is made for each trial of a Monte Carlo Simulation. Then, the residual displacement is calculated by doing step -by- step calculations with that critical slip surface circle. Finally, the results are summarized to evaluate the effect of the heterogeneity of the soil strength on the slope stability. The trial number was decided as 1,000 times.

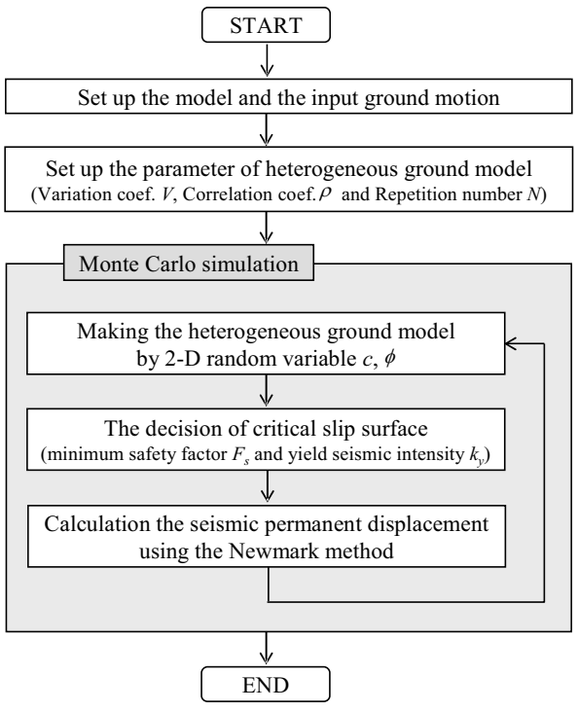
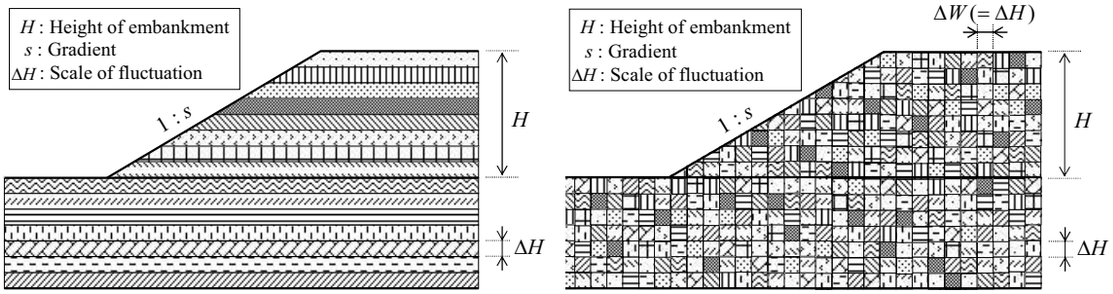


FIG. 1. The flow of analysis with Monte Carlo Simulation.

HETEROGENEOUS GROUND MODEL

In this study, two heterogeneous ground models were considered as follows. The first is a heterogeneous ground model which had a horizontal layer system shown in the FIG. 2. In this paper, this model is called the horizontal layer model (FIG. 2(a)). This model is base on the fact that the natural ground condition correlates highly in the horizontal direction due to the uniform sedimentation process; however, the correlation in the vertical direction is low (Matsuo 1984).However, considering the complex construction process of the artificial embankment, there is a possibility that the correlation in the horizontal direction is also low. So in this paper, another type of ground model, a lattice model, is considered (FIG. 2(b)). The soil strength is heterogeneous in the horizontal or vertical direction with the same interval of the scale of fluctuation, ΔH. The height of the foundation ground was set to be high enough compared with the embankment height, H. The slippage occurrence was assumed to be only in the embankment section.



(a) Horizontal layer model **(b) Lattice model**

FIG. 2. The heterogeneous ground model.

The strength parameters, cohesion, c, and internal friction angle, ϕ, were taken as parameters for both the embankment section and the foundation section. The distribution tendency of the strength parameters, c and ϕ, can be approximated with a normal distribution (Matsuo and Kuroda 1972). For each material, a two-dimensional normal distribution was adopted by supposing a correlation between c and ϕ. When the first variable, x, is calculated in the normal distribution $f_X(x)$, as shown in the Eq. (1), which is based on a two-dimensional normal distribution, the second variable can be calculated in the conditional normal distribution $f_{Y|X}(y|x)$, as shown in the Eq. (2). The conditional normal distribution above is prescribed by the standard deviation shown in Eq. (3), and the mean is shown in Eq. (4). Here, ρ is the correlation coefficient. A shown in Eq. (5), the degree of the heterogeneity of the soil strength was expressed by not the standard deviation, σ, but by the variation coefficient, V, (Duncan 2000).

$$f_X(x) = \frac{1}{\sqrt{2\pi}\sigma_X} \exp\left[-\frac{1}{2}\left(\frac{x-\sigma_X}{\sigma_X} \right)^2 \right] \tag{1}$$

$$f_{Y|X}(y \mid x) = \frac{1}{\sqrt{2\pi}\sigma_{Y|X}} \exp\left[-\frac{1}{2}\left(\frac{x-\sigma_{Y|X}}{\sigma_{Y|X}} \right)^2 \right] \tag{2}$$

$$\sigma_{Y|X} = \sigma_Y \sqrt{1-\rho^2} \tag{3}$$

$$\mu_{Y|X} = \mu_Y + \rho \frac{\sigma_Y}{\sigma_X}(x - \mu_X) \tag{4}$$

$$V_{(Y|X)} = \frac{\sigma_{(Y|X)}}{\mu_{(Y|X)}} \tag{5}$$

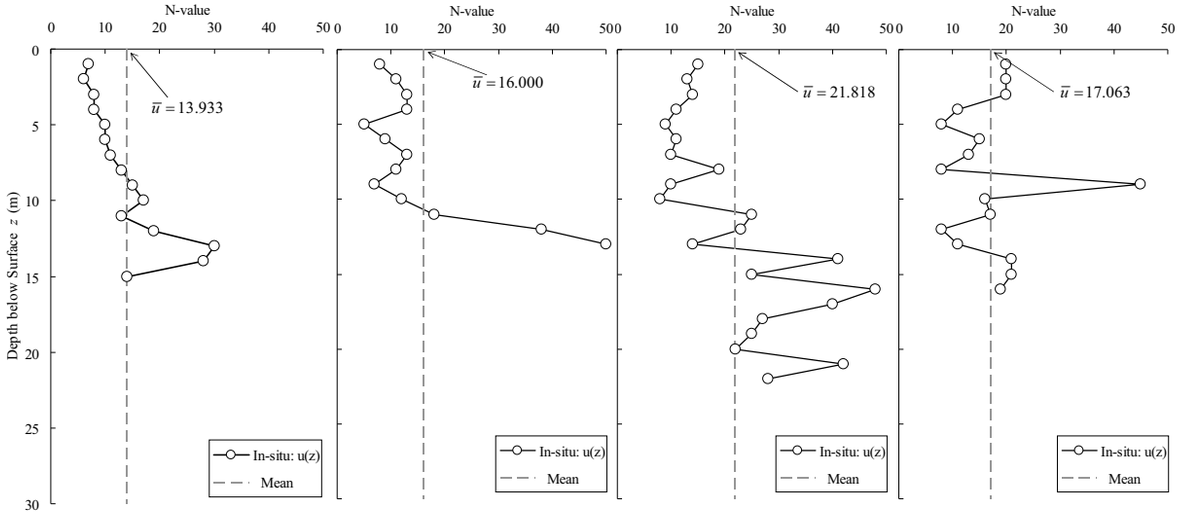
DETERMINATION OF THE SCALE OF FLUCTUATION

The scale of fluctuation (ΔH in FIG. 2) was determined by a consideration of the nugget effect presented by Vanmarcke (1977). The design guideline of the foundation structure in Japan (JGS 2004) and the final report of NCHRP to adopt the limit state design (Barcker *et al*. 1991) are already based on this method.

The distribution of the observed N-value in the airport embankment is shown in the FIG. 3. The first step is to evaluate the mean μ and the standard deviation σ. Adjacent observations on each pair of data are completed, and the standard deviation on spatial distance is computed. The latter quantity is an estimate of standard deviation $\sigma\Gamma_u(2)$. The ratio of standard deviations, $\Gamma_u(2)$, is plotted as the point corresponding to the abscissa value n=2 on the plot of $\Gamma_u(n)$ versus n. An example is the dotted line in FIG. 4. More generally, n denotes the spatial distance of $u(z)$ on average. For each value of n, the standard deviation of these spatial averages is computed and normalized with respect to σ, leading to a prediction of $\Gamma_u(n)$. These predicted values should approach the theoretical values (the solid line in FIG. 4) given by Eq. (6). The final step in the procedure is to fix n by the observation of $\Gamma(n)$, and to estimate $n*$ in which $n* = n\Gamma^2(n)$. Eq. (7) expresses ΔHas a multiple of the observation interval Δz=1.0, as shown in FIG. 3 and FIG. 4.

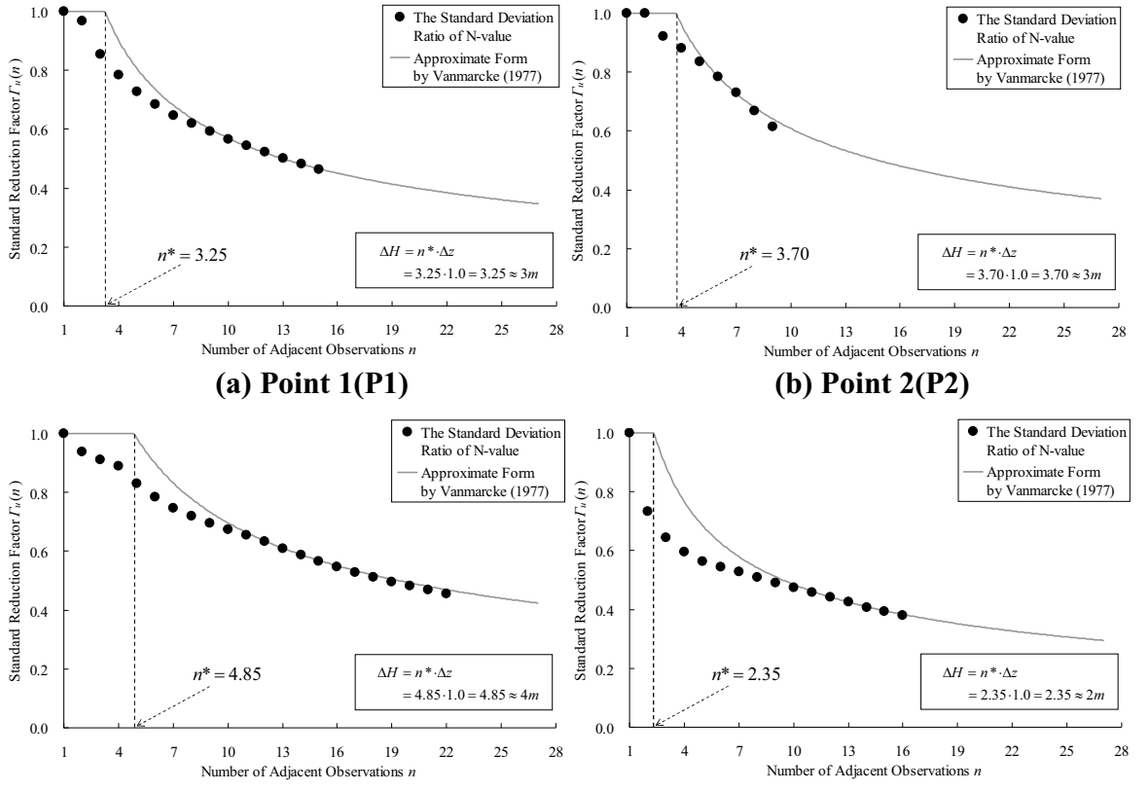
$$\Gamma(n) = \sqrt{\frac{\Delta H}{n \cdot \Delta z}} \tag{6}$$

$$\Delta H = n \cdot \Gamma^2(n) \cdot \Delta z = n* \cdot \Delta z \tag{7}$$



(a) Point 1(P1) (b) Point 2(P2) (c) Point 3(P3) (d) Point 4(P4)

FIG. 3. The distribution of N-value in an airport embankment.



(a) Point 1(P1) **(b) Point 2(P2)**

(c) Point 3(P3) **(d) Point 4(P4)**

FIG. 4. The computation of the scale of fluctuation.

According to FIG. 3, all distributions of the N value show a tendency to depend on depth. However, the depth distribution shape of the N value varies in each point. From FIG. 4., the scale of fluctuation, ΔH, is given as a fixed value; 2m, 3m and 4m in both the foundation ground section and the embankment section.

THE DETERMINATION OF INPUT PARAMETERS

In this study, the results of laboratory soil tests were adopted as the input data for the preparation of the heterogeneous ground model. The relation between the cohesion, c, and the internal friction angle, ϕ, in an airport embankment is shown in FIG. 5. The positive or negative correlation coefficient between c and ϕ has been debated in previous studies (e.g., Tanaka *et al*. 2005; Hata and Yamashita 2005). A negative correlation between c and ϕ was observed as shown in FIG. 5. Therefore, a negative value of the correlation coefficient, ρ, was input in equation (3) in this study. Table 1 shows the list of parameters determined by the results of the soil tests at the airport site. According to this table, the variation coefficient of the unit weight was very small, and the unit weight was supposed to be homogeneous in this study. The analytical cases are shown in the Table 2. A total six cases were made to consider the scale of fluctuation, ΔH, and the type of heterogeneous ground model as shown in the Table 2. The input ground motion was fixed as the NS (North-South) component of the Kobe JMA (Japan Meteorological Agency) in Hyogoken-nambu earthquake of 1995. FIG. 6 shows the

histogram of the residual displacement based on the above condition of the numerical analysis for analytical case 2, with the height of the embankment equal to 20m. The standard deviation (S.D.) is used as an index of the dispersion of residual displacement originated by the heterogeneity of the soil strength. For a general case, based on the importance of the target embankment and others, the practitioner chose the index of variation to be considered, such as 1 S.D., 2 S.D., or others.

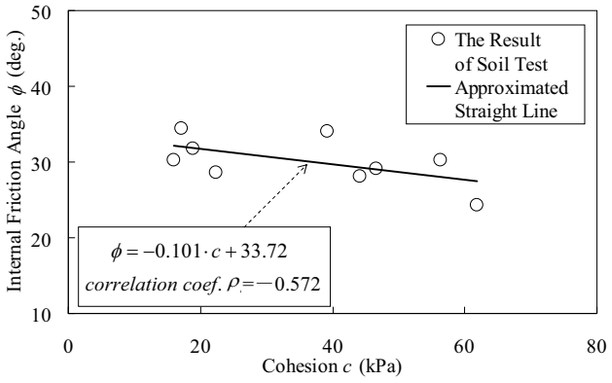


FIG. 5. Correlation between c and ϕ.

Table 1. Input data of the model.

Unit of weight γ_t (kN/m^3)	Sampling number	53
	Mean	21.03
	Variation coef.	0.008
Cohesion c (kPa)	Sampling number	10
	Mean	38.0
	Variation coef.	0.476
Internal friction angle ϕ (deg.)	Sampling number	10
	Mean	30.4
	Variation coef.	0.126
Correlation coef. (c vs ϕ)		-0.572
The scale of fluctuation ΔH (m)		3.0

Table 2. Analytical case.

Case No.	Heterogeneous ground model	Scale of fluctuation (m)	Grad.
Case 1	Horizontal layer model	2.0	1:1.5 (fixed)
Case 2	Horizontal layer model	3.0	1:1.5 (fixed)
Case 3	Horizontal layer model	4.0	1:1.5 (fixed)
Case 4	Lattice model	2.0	1:1.5 (fixed)
Case 5	Lattice model	3.0	1:1.5 (fixed)
Case 6	Lattice model	4.0	1:1.5 (fixed)

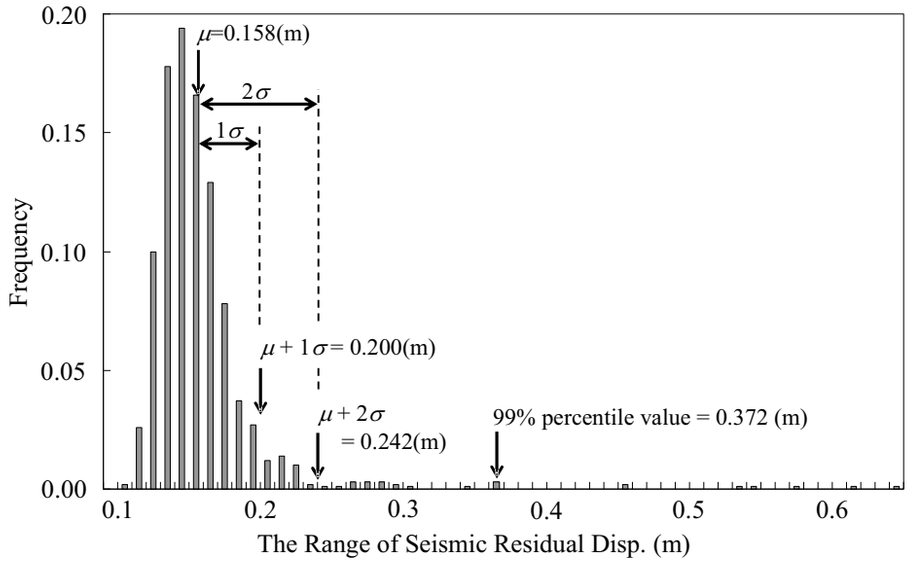


FIG. 6. Histogram of the residual displacement (Case 2, H=20(m)).

EFFECT OF HETEROGENEOUS SOIL STRENGTH

Relations between the ratio of the threshold acceleration, A_t, to peak acceleration, A_p, and the residual displacement are shown in the FIG. 7. Here, the height of embankment was varied from 10 m to 30 m in 1 m intervals. Note the peak acceleration A_p in this case is a fixed value of 818 gal in Kobe JMA. And, threshold acceleration A_t varies with the embankment height H. In other words, the ratio of the threshold acceleration to peak acceleration is a paraphrase of a seismic sliding safety factor. According to FIG. 7, mean + standard deviation (Mean + 1 S.D. or 2 S.D.) decreases as the ratio of the threshold acceleration to peak acceleration increases. When scale of fluctuation rises, the effect of the heterogeneity of soil strength is excessively evaluated. However, the differences in the horizontal layer model and lattice model hardly influence the results.

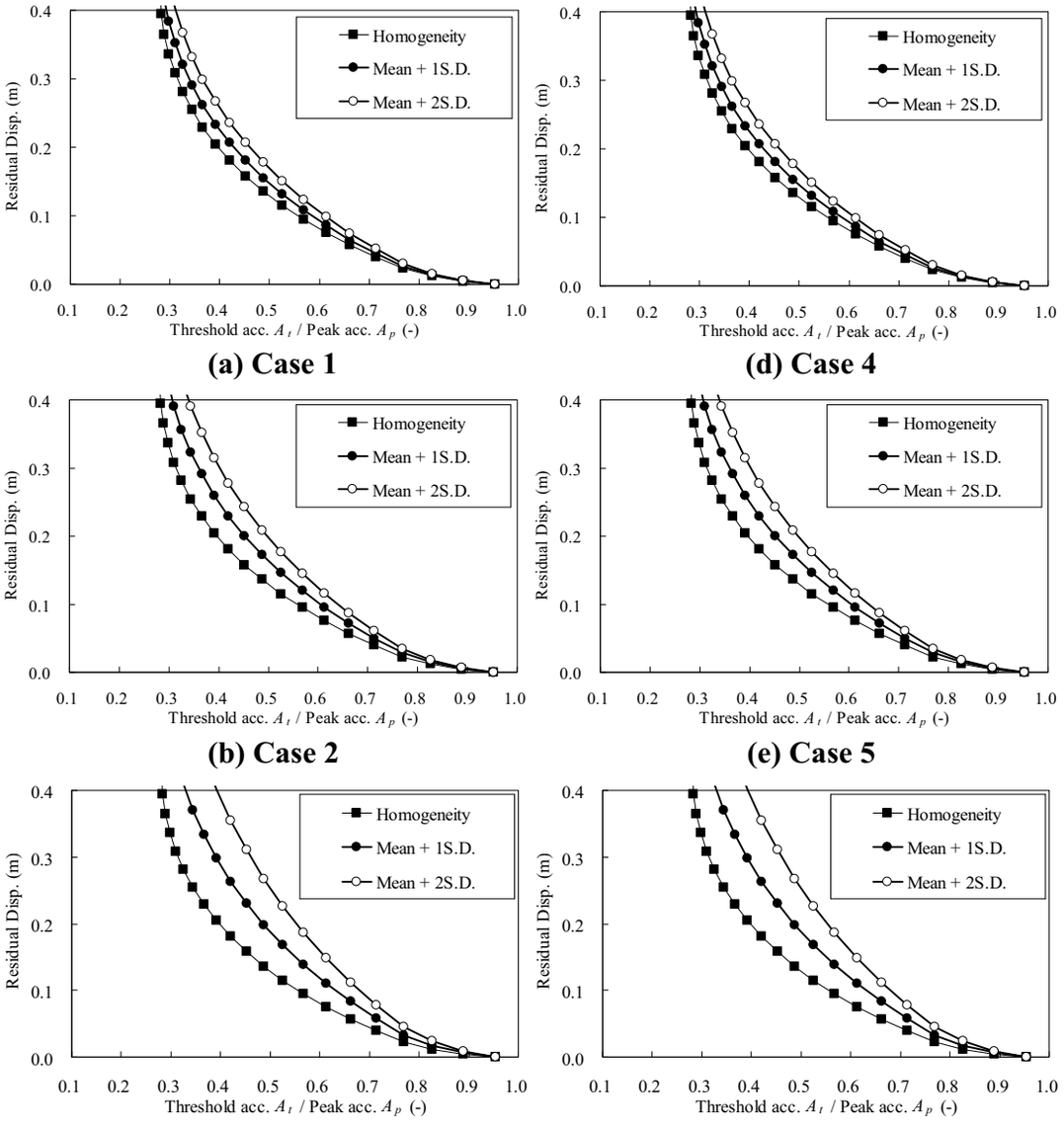


FIG. 7. The effect of heterogeneity of soil strength.

DISCUSSION

Based on the above-mentioned calculation results, the effect of the heterogeneity of soil strength can be discussed. Considering the conventional design scheme, the effect of the heterogeneity of soil strength can be evaluated with a reduction of soil strength (c, ϕ) which is equivalent to a reduction in threshold acceleration A_t, as shown in FIG. 8. In other words, without carrying out the complicated Monte Carlo Simulation every time, the reduction of parameters make it possible to calculate the displacement when heterogeneity of soil strength is taken into consideration.

FIG. 9 displays the calculation results of homogeneous ground condition with reduced input soil strength (c, ϕ). On average, the small effect of the heterogeneity of soil strength (1 S.D.) can be evaluated by about 6 kPa reduction in the initial cohesion, c, or about 2 deg. reduction in the initial internal friction angle, ϕ, as shown in the FIG.9. In addition, the large effect of the heterogeneity of soil strength (2 S.D.) can be evaluated by about 12 kPa reductions in the initial cohesion, c, or about 4 deg. reductions in the initial internal friction angle, ϕ, on average as shown in the FIG. 9. These values for reduction become large when the scale of fluctuations is large.

The discussion above did not mention reduction both of cohesion, c and the internal friction angle, ϕ. In the future, the reduction in the cohesion, Δc, and the reduction in the internal friction angle, $\Delta\phi$, should be computed. And, more parametric effort should be carried out for a various site conditions.

CONCLUSIONS

In this study, seismic analyses of embankments utilizing a Monte Carlo Simulation were conducted to consider the heterogeneity of soil strength using soil test results of actual airport embankments. The following conclusions were obtained.

1) According to the result of the triaxial tests of an actual airport embankment in Japan, the level of heterogeneity of cohesion c is larger than that of internal friction angle ϕ. Negative correlation between cohesion c and internal friction angle ϕ was observed.

2) The effect that heterogeneity of soil strength has on earthquake-induced residual displacement is small, when the seismic sliding safety factor is large.

3) The scale of fluctuation, ΔH, influences seismic residual displacement; however, using the horizontal layer model versus the lattice model has hardly any influence on the seismic residual displacement.

4) A practical Newmark Method to compute residual displacement of an embankment considering the effect of heterogeneity of soil strength is proposed. In this proposed method, the increase in the residual displacement due to the heterogeneity of soil can be computed practically by only using the usual input data.

More detailed examinations, such as the adoption of another input earthquake motion and another heterogeneous ground model, are expected in future study.

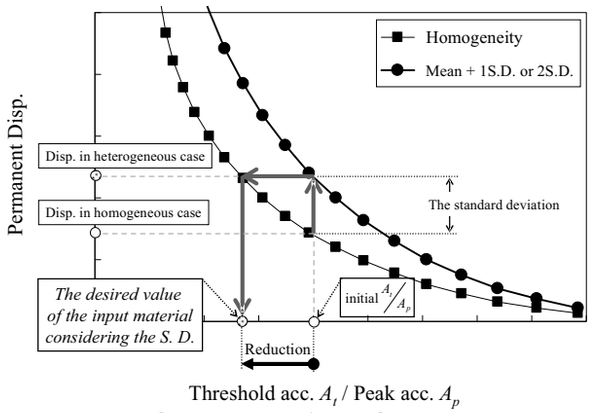
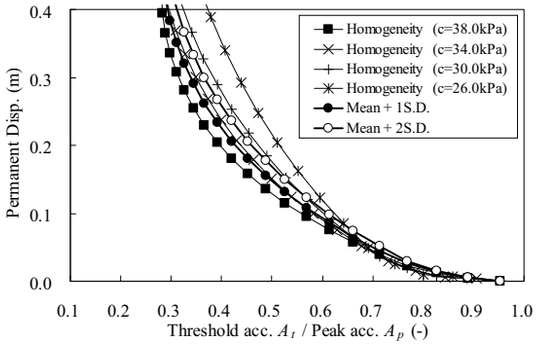
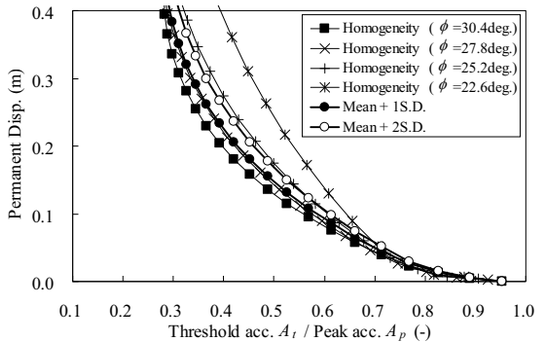


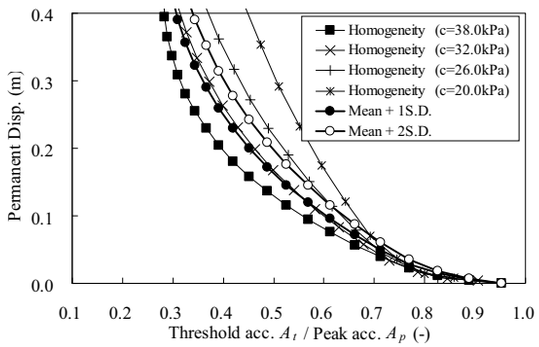
FIG. 8. The concept of the reduction of the threshold acceleration.



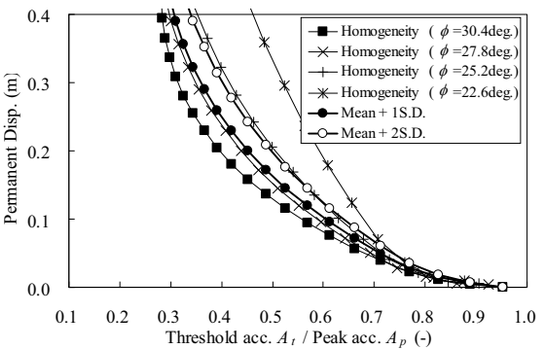
(a) Case 1&4, Only *c* is reduced.



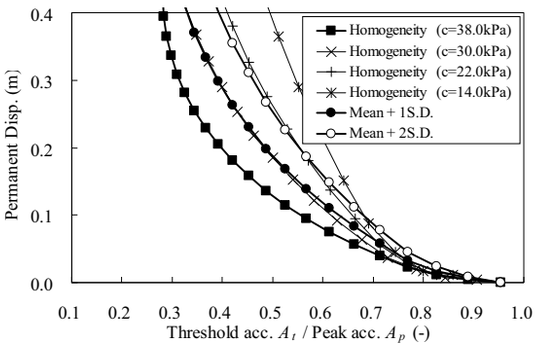
(d) Case 1&4, Only ϕ is reduced.



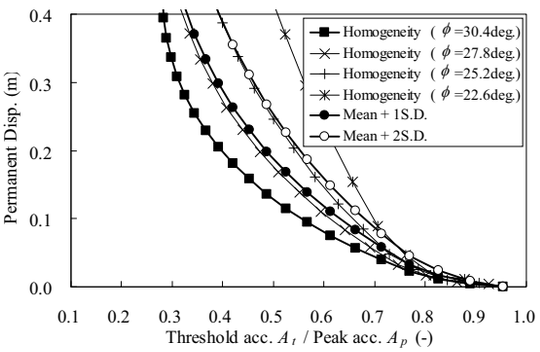
(b) Case 2&5, Only *c* is reduced.



(e) Case 2&5, Only ϕ is reduced.



(c) Case 3&6, Only *c* is reduced.



(f) Case 3&6, Only ϕ is reduced.

FIG. 9. The proposal of decrease technique of the input soil strength.

ACKNOWLEDGMENTS

For allowing us to use earthquake motion data, we thank the Japan Meteorological Agency (JMA). The anonymous airport construction offices also provided valuable geotechnical data.

REFERENCES

Barcker, R. M., Duncan, J. M., Rojiani, K. B., Ooi, P. S., Tan C. K. and Kim S. G. (1991). "Load factor design criteria for highway structure foundations." Final Report, NCHRP 24-4.

Duncan, J. M. (2000). "Factors of safety and reliability in geotechnical engineering." *Jour. of Geotechnical Engineering*, ASCE, Vol.125, No.4: 307-316.

Griffiths, D.V. and Fenton, G. A. (2004). "Probabilistic slope stability by finite elements." *Jour. of Geotechnical and Geoenvironmental Engineering*, ASCE, Vol.130, No.5: 507-518.

Hata, Y. and Yamashita N. (2005). "A study on the effect of input ground motion characteristics on the variation of seismic residual displacement of embankments which originates in the heterogeneity of the ground strength" (in Japanese with English abstract), *Jour. of Geotechnical Engineering Symposium*, JGS, Vol.50, No. 60: 421-428.

Matsuo, M. and Kuroda, K. (1972). "A study on the soil properties of the partial saturated ground and destruction probability." (in Japanese with English abstract) *Jour. of JSCE*, No. 208: 65-75.

Matsuo, M. and Kuroda, K. (1974). "Probability approach to design of embankments." *Soils and Foundations*, Vol. 14, No. 2: 1-17.

Newmark, N. M. (1965). "Effects of earthquakes on dams and embankments." *Geotechnique*, Vol. 15, No. 2: 139-159.

Railway Technical Research Institute (2000). "Design guidelines for railroad structures." (in Japanese) earth structure edition, Maruzen Co., Ltd., 336p.

Tanaka, H., Okimura, T. and Torii, N. (2005). "Effect of spatial heterogeneity of ground in evaluation of seismic response characteristics on embankments." (in Japanese with English abstract) *Jour. of JSCE Earthquake Eng*., Vol. 29, No. 5.

The Japan Geotechnical Society (2004). "A guideline about the foundation structure based on the performance design" (in Japanese) Appendix D: 24-39.

The Japan Society of Civil Engineers (2000). "The third suggestion and commentary about the civil structure" (in Japanese) Chapter 8 - Earth structures -: 29-34.

Travasarou, T., Bray J. and Kiureghian, A. D. (2004). "A probabilistic metrology for assessing seismic slope displacements." *Proc. of World Conference on Earthquake Engineering*, Paper No. 2,326.

Vanmarcke, E. H. (1977). "Probabilistic modeling of soil profiles." *Proc. of ASCE*, Vol.103, GT11: 1,227-1,246.

Geotechnical Investigations and Site Characterization of the Success Dam Seismic Remediation Project

David C. Serafini[1], M. ASCE, P.E., and Mathew G. Allen[2], M. ASCE, P.E.

[1]Civil engineer, US Army Corps of Engineers, Sacramento District, 1325 J Street, Sacramento, CA 95814; david.c.serafini@spk01.usace.army.mil
[2]Civil engineer, US Army Corps of Engineers, Sacramento District, 1325 J Street, Sacramento, CA 95814; mathew.allen@spk01.usace.army.mil

ABSTRACT: Success Dam is located on the Tule River, near the city of Porterville, California. The dam is a rolled earth-fill embankment approximately 44 meters (145 feet) high and 1036 meters (3,400 feet) long. The embankment is comprised of a central impervious core protected by upstream and downstream outer pervious zones. A majority of the dam is founded on a complex deposit of both Holocene and Pleistocene alluvium. Investigations and studies under the Corps of Engineers Dam Safety Assurance Program (DSAP) demonstrated that remediation is required to prevent dam failure from large earthquake shaking.

The Corps of Engineers is designing a seismic remediation of Success Dam that consists of a modified earth-fill embankment centered and aligned generally along the downstream toe of the existing dam. The modified embankment will shift the alignment of Success Dam about 95 meters (310 feet) downstream onto a prepared foundation and will increase the footprint of the dam by 40%. Similar to the DSAP studies that identified the need for remediation, the new foundation area has been investigated in numerous phases to characterize the material properties and distribution for remedial design analyses.

High-quality blowcount data ($(N_1)_{60}$) has been difficult to obtain at Success Dam. Conversely, a large volume of shear wave velocity data (Vs_1) has been collected. Liquefaction assessment has been conducted using both data sets and additional conservatism has been observed in the Vs_1-based procedure compared to the $(N_1)_{60}$-based procedures as reported in recent years by various researchers. A site-specific relationship between $(N_1)_{60}$ and Vs_1 is presented that reduces some of the additional conservatism.

This paper provides an overview of the investigations, the geotechnical site characterization, and the relationship between field exploratory data sets. Discussions include the in-situ testing methods, the challenges of characterizing potentially liquefiable materials containing significant quantities of large particles, and the development of a site-specific data correlation for liquefaction potential analyses and remediation design.

1. INTRODUCTION

The Corps of Engineers began seismic evaluation explorations of Success Dam in 1994 for its Dam Safety Assurance Program (DSAP). These explorations and seismic stability studies were conducted in multiple phases over the next 4-1/2 years leading to the conclusion that Success Dam would experience strength loss of some foundation and embankment materials leading to large deformation of the dam and probable release of the reservoir. More recent explorations conducted for remediation design revealed detrimental foundation characteristics that were more widespread and more complex than was previously known.

More specifically, the recent alluvium underlying both the upstream and downstream shells of the dam has the potential for liquefaction or severe strength loss during the Maximum Credible Earthquake (MCE) event. In addition, some regions of the upstream embankment shell also have the potential for liquefaction or strength loss during the MCE event. Given the potential for seismicity at the site, along with the characteristics of the materials, remediation is required to prevent loss of life, extensive downstream damage, functional loss of the project, and loss of all project benefits.

The initial preferred seismic remediation alternative was a new Roller Compacted Concrete (RCC) dam along the toe of the existing Success Dam embankment. However, initial foundation investigations determined that the RCC dam was not a feasible alternative because of a combination of deep bedrock, variability of the foundation and its parameters, and the potential for compressible soils in the foundation. As a result, design efforts switched to the next preferred alternative, a modification of the existing embankment dam.

1.1 Foundation Geology

Foundation soils include alluvial, residual, and slopewash. Alluvial soils include: recent alluvium, older alluvium, terrace deposits, and fan deposits. Residual soils were formed by weathering of the bedrock complex and the alluvial terrace deposits; while, slopewash material is present where movement of the residual soils by gravity has occurred.

Loose Holocene recent alluvium, underlies the upstream and downstream shells of the dam for approximately 50% of the dam's footprint. The recent alluvium deposit ranges in thickness from about 5 to 8 meters (15 to 25 feet) and consists of materials that are unconsolidated, frequently loose, totally uncemented, and unweathered. The recent alluvium is mainly an assortment of interbedded sands and sandy gravels with generally less than 10% non-plastic fines and occasional cobbles and boulders. A majority of the overlying pervious embankment shell material was constructed from the recent alluvium, and therefore, has a similar composition.

1.2 Existing Dam Design and Materials

Success Dam has a top elevation of 210.8 meters (691.5 feet), providing 11.9 meters (39 feet) of freeboard above the normally full (gross) pool, and 1.4 meters (4.7 feet) of freeboard above the maximum spillway design flood elevation. The embankment is comprised of a central impervious core supported by upstream and downstream transition and outer pervious zones (Figure 1). The impervious core is predominantly sandy clay and clayey sand. The transition zones are gravelly sands and the pervious zones were constructed with sand and rock sizes smaller than 305 mm (12 inches) obtained from recent alluvium deposits and from spillway excavation. These pervious shell materials generally classified as gravelly sand with a 305 mm (12 inch) maximum particle size and no more than 12% passing the No. 200 sieve. During construction the Contractor was granted a change to place previously wasted spillway excavation up to 487 mm (18 inches) in size in the pervious zones of the dam. These materials were placed within the closure section of the dam (Figure 2). Records indicate the pervious zones were placed in 0.6 meter (24-inch) loose lifts with a tracked dozer and compacted by 4 passes of a 445 kN (50-ton) pneumatic-tired roller. These larger size materials made drilling, sampling, and characterization of the embankment shells very difficult.

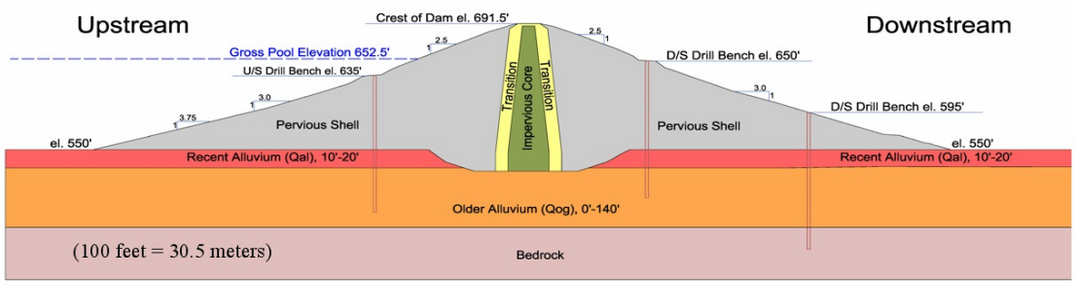


FIG. 1. Typical Valley Cross Section and Exploration Bench Locations



FIG. 2. Construction Photo of the Closure Section Prior to Closure

2. DSAP EXPLORATIONS AND STUDIES

DSAP field explorations were conducted in seven phases between April 1994 and November 2003. Explorations were preceded by the construction of access roads traversing the downstream toe, the downstream slope, and the upstream slope of the

dam as shown in Figure 1. The upstream road or drill bench was constructed at an elevation of 194 meters (635 feet), offset 46 meters (150 feet) from the centerline of the dam. The downstream road or drill bench was constructed at an elevation of 198 meters (650 feet), offset 34 meters (110 feet) from the centerline of the dam. The seven phases of DSAP explorations conducted a total of 22 open-bit Becker hammer holes, 32 closed-bit Becker Penetration Test (BPT) holes; 36 Standard Penetration Test (SPT) holes; and 19 Geophysical Triplets for cross-hole measurement of shear wave velocity.

2.1 BPT Testing

Becker hammer drilling consisted of alternating open-bit soundings and plugged-bit, 168 mm (6-5/8 inch) O.D. BPT's, generally 30 meters (100 feet) apart, across both benches and the downstream toe. Becker penetration tests were performed by two types of hammer rigs. The difference between the two rigs is in the complexity of the hydraulic systems and the manner in which the hammer is hung from the mast. Both the B-180 rig and the more complex AP-1000 rig were used at Success Dam.

Initial explorations showed that the BPT's had difficulty penetrating the embankment shells, resulting in numerous refusals, particularly on the downstream slope. Refusals of BPT's in the embankment were theorized to be caused by either segregated nests of larger particles, or perhaps, a significant number of undocumented over-sized rocks. Because the foundation was the target of the explorations, various procedures were adopted to penetrate through the shells in hopes of reaching the foundation.

The Becker hammer drill always penetrated better with an open bit and reverse-air circulation since the materials were retrieved and penetration resistance was relieved at the tip. When a BPT met refusal, the procedure was to withdraw the drill string, switch to an open bit, return the drill string down the hole, and continue the boring while retrieving cuttings. When the open bit blow count had decreased to values judged manageable with a plugged bit, the drill string was again retrieved and the bit changed back to a plugged end, and the sounding continued with the hope of obtaining meaningful BPT data. This technique was not always successful due to sloughing of the hole while the casing was removed. The sloughed material in the bottom of the hole would create a new obstruction for the closed bit BPT. Therefore, the withdrawal/bit-switching routine was sometimes repeated two or three times in a single boring. Despite these efforts in the first phase of BPT's, 25 out of 34 attempted through the upstream shell, and all the BPT's through the downstream shell eventually refused within the embankment and never reached foundation material.

In the next phase of DSAP explorations, additional BPT's targeting the foundation were again attempted from the downstream and upstream drilling benches. This time, no attempt was made to obtain BPT data from the embankment shell material. Open bits were used to penetrate the embankment to within about 3 meters (10 feet) above the foundation contact. At this point, the open bit drill string was removed and switched to a plugged end bit for conducting BPT's in the foundation. This technique was more successful and meaningful data was obtained within the recent alluvium. The field BPT data were converted to equivalent $(N_1)_{60}$ values for liquefaction

evaluation according to procedures proposed by Harder and Seed(1986); Stewart et al. (1990); and Sy and Campanella, (1993).

2.2 SPT Testing

In later DSAP exploration phases SPT's were conducted to develop a site-specific correlation with the BPT data. Seven SPT's were performed along the downstream toe and in the free field in close proximity to previous BPT's. Eight SPT's were performed from the upstream bench generally in close proximity to previous BPT's and geophysical sets. Based on lessons learned from the BPT's, the upstream SPT's were performed by first installing a steel casing through the embankment shell to about 3 meters (10 feet) above the foundation contact. An auger drill was advanced through the casing to perform the SPT's in the foundation. SPT's were performed at 0.76 m (2.5-foot) intervals of depth with an automatic trip hammer rated at 85 percent of theoretical energy and corrected to equivalent $(N_1)_{60}$ values as recommended by Youd et al. (2001).

2.3 Shear Wave Velocity Testing

The BPT and SPT data were obtained in less than ideal conditions due to the abundance of oversized particles. Therefore, early exploration phases also installed 102 mm (4-inch) diameter PVC casings for geophysical testing. The PVC casings were typically installed in sets of three with the casings spaced about 4.6 m (15 feet) apart. These "triplets" were used for conducting cross-hole measurements of shear wave velocities between the casings. Geophysical casings were installed during various exploration phases and by various methods including, an ODEX down-hole hammer system, an air-rotary casing hammer (ARCH), and even a Becker Hammer. In total, geophysical tests were conducted at 11 locations on the upstream bench, 6 locations on the downstream bench, and 4 locations along the downstream toe. For analysis, the shear wave velocity data was stress-corrected to a confining stress of 100 kPa (1 tsf) as recommended by Robertson et al. (1992).

2.4 Test Pits and Trenching

Test pits were excavated in the downstream free field, generally 30 to 60 meters (100 to 200 feet) from the toe of the dam, to provide a visual record of the materials to attempt to obtain field densities (sand cone and water-ring testing), and to collect bulk samples of the recent alluvium for laboratory cyclic triaxial testing.

3.0 EXPLORATIONS FOR REMEDIATION ALTERNATIVE DESIGN

Explorations for remediation design purposes were conducted starting in 2004 to evaluate the foundation for a proposed RCC replacement dam. Subsequent phases of design explorations were added to further evaluate the alluvium and foundation conditions under a proposed modified embankment alternative as shown in Figure 3.

The foundation posed too many challenges for the RCC alternative compared to the embankment alternative, which was chosen for continued remediation design studies.

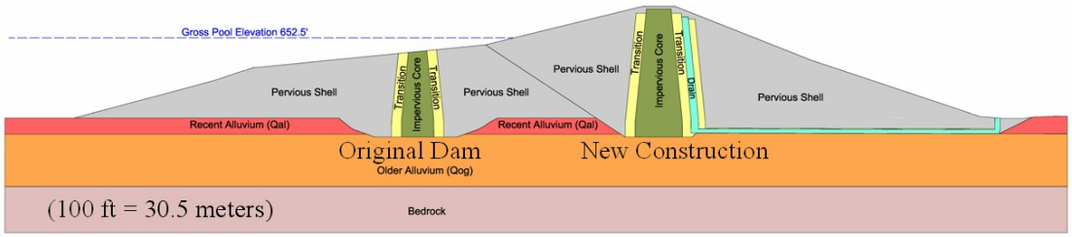


FIG. 3. Concept Design of the Modified Embankment Dam Alternative

3.1 Explorations and Testing

SPT's and large penetration tests (LPT's) were used as the primary testing and sampling tool in the alluvial and overburden materials. As in earlier explorations, casing was advanced through the embankment shells by ARCH or ODEX methods, and testing of the foundation was performed through the casing. The penetration tests were performed to estimate the relative density and character of the strata, and to obtain samples for field classification and laboratory testing. The penetration tests faced the same challenges as earlier programs, and most tests met refusal on oversized particles. Attempts were made to gather less disturbed samples using Pitcher barrels in zones of finer-grained, cohesive materials in the older alluvium. The Pitcher barrel samples were used for triaxial and consolidation laboratory testing. The upper bedrock profile and character were verified in most locations using HQ size rock core drilling.

The drilling programs indicated the underlying older alluvial layer was thicker, extending to greater depths than previously identified. Previous studies performed for the original dam construction and for the DSAP indicated that the older alluvium was no more than 21 meters (70 feet) in thickness. However, only a few of these explorations were deep enough to accurately identify the transition from older alluvium to bedrock. The current design explorations defined the top-of-rock profile and determined the older alluvium is as much as 73 meters (240 feet) thick.

Several of the design explorations made use of Sonic drilling techniques to rapidly obtain near continuous samples of materials that had been difficult to sample by other methods. The Sonic method retrieved representative 102 mm (4 inch) diameter samples of the recent alluvial and terrace deposits at a rate near 6 to 12 meters (20 to 40 feet) per hour. The method also obtained representative sample through the embankment shell material at nearly the same rate depending on the depth. In the older alluvium the Sonic sample was highly disturbed and most of the matrix structure was destroyed. Some of the larger materials broke into angular pieces during drilling, and additional fines were created at the boundary of the sample by the high-energy vibration. Cobbles and boulders were cored through with moderate difficulty and produced rock powder and fragments, along with solid sticks of core depending on the weathering of the material. Decomposed cobbles or boulders cored quickly and were sometimes recovered intact with a clay coating on the cut surface created from the vibratory drilling action.

4. SITE CHARACTERIZATION CHALLENGES

The characterization of the site has been an ongoing and challenging process. Despite numerous phases of penetration testing, the data-set of high-quality $(N_1)_{60}$ remains small due to the widespread presence of large particles throughout the dam and foundation. A more-comprehensive Vs_1 data-set was obtained at Success Dam and it was used in concert with $(N_1)_{60}$'s as the basis for a liquefaction potential characterization. Published studies of liquefaction assessment using $(N_1)_{60}$ or Vs_1 and comparative relationships were used to develop a correlation curve between $(N_1)_{60}$ and Vs_1 specifically for Success Dam.

One of the most important tasks facing remediation designers at Success Dam has been determining the liquefaction potential of the recent alluvium and pervious embankment shell materials. SPT, LPT, and BPT penetration testing were only sporadically reliable at Success Dam given the quantity of large particles at the site. Therefore, cross-hole shear wave velocity measurements were taken extensively throughout the site as a companion method. As described in Sections 2 and 3, field data was obtained mainly from three regions of the dam to determine material properties upstream and downstream of the core and at the downstream toe and free field area.

$(N_1)_{60}$ and Vs_1 data from the three regions were studied through statistical analyses and compared. Median values of $(N_1)_{60}$ and Vs_1 for selected groupings were plotted with other published correlations (Andrus and Stokoe 2000; Andrus et al. 2003) and are shown as square symbols in Figure 4. Regionally, some of the Success Dam data agrees closely with the published correlations. However, for the overall site, a close correlation between $(N_1)_{60}$ and Vs_1 was not observed.

Liquefaction triggering analyses of the most critical regions (*upstream alluvium and embankment shell materials*) was performed separately for $(N_1)_{60}$ data and procedures, and Vs_1 data and procedures. The $(N_1)_{60}$ analyses generally resulted in higher factors of safety against liquefaction (FSL) compared to the Vs_1 analyses. Other studies have shown this difference is not uncommon and may be typical (Rollins et al. 1998). Some of the disagreement could be attributed to the nature of penetration testing as a measurement of large strain effects compared to shear wave velocities measuring very small strain effects. More recent studies by others (Andrus and Stokoe, 2000; Liu and Mitchell, 2006) have identified greater conservatism in Vs_1-based liquefaction (CSR/CRR) curves compared to $(N_1)_{60}$-based curves.

A Vs_1-$(N_1)_{60}$ relationship was developed specifically for Success Dam (See Figure 4) by similar methods used in the recent studies; and considering the observations and conclusions of those studies; and incorporating Success Dam data. The Success Dam curve was derived by comparing the $(N_1)_{60}$-CRR relationship recommended by Idriss and Boulanger (2004) and the Andrus and Stokoe (2000) Vs_1-CRR relationship. For equal values of CRR, a Vs_1-$(N_1)_{60}$ relationship is implied that is also presented in Figure 4. The Idriss and Boulanger (2004) relationship was selected over the Youd et al. (2001) relationship for this project as it is believed to be a better curve fit to the lower range of field $(N_1)_{60}$-CRR data. The implied relationship demonstrates that the current Vs_1-based liquefaction analysis procedure may under-predict the liquefaction

resistance of a sand with FC<5%. Andrus and Stokoe (2000) also made this observation concluding the Vs_1-CRR procedure curve may yield an overall more conservative prediction of liquefaction resistance when compared to the SPT-CRR based procedure. The Success Dam relationship removes some of this additional conservatism in an effort to provide best estimates for remediation design analyses.

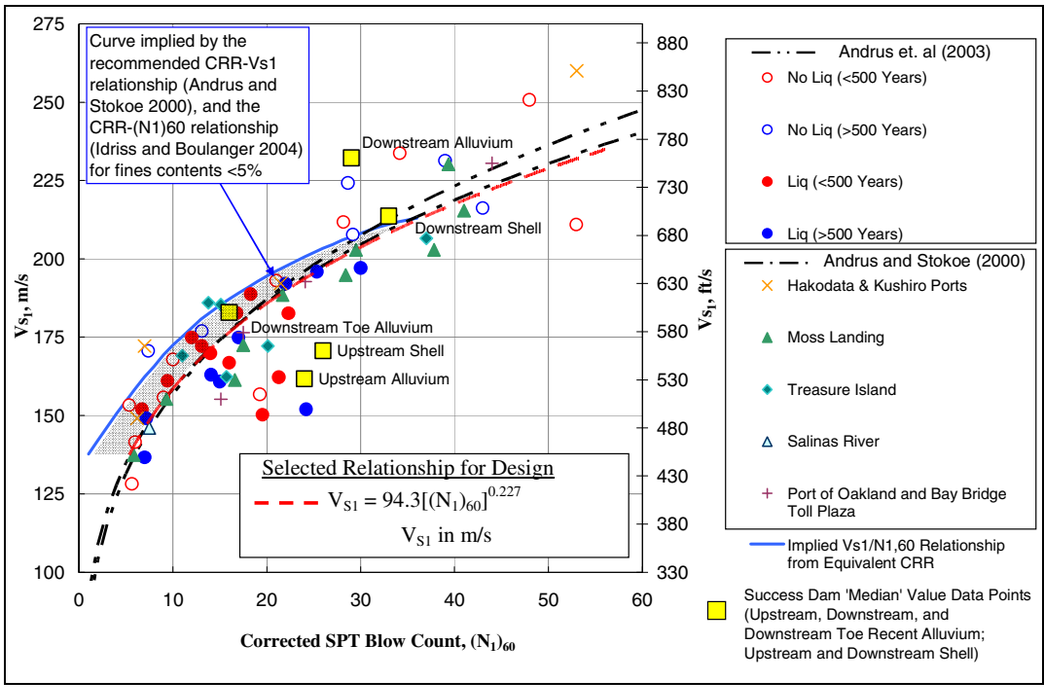


FIG. 4. Relationship of Vs_1 to $(N_1)_{60}$ and Implied CRR Relationship

Some of the added conservatism of the Vs_1-based procedure may be attributed to the presence of false positives identified by Liu and Mitchell (2006). Liu and Mitchell identified a few field performance data points in the Andrus and Stokoe (2000) Vs_1-CRR database that predicted liquefaction according to the procedure, but where no visual evidence of liquefaction was observed. When the Success Dam Vs_1-$(N_1)_{60}$ relationship is converted back to an implied Vs_1-CRR curve and compared to Andrus and Stokoe, as shown in Figure 5, four of the identified false positives within the critical lower range of data, are located slightly above the FSL=1.0 line.

Numerical deformation analyses for Success Dam have demonstrated sensitivity to the selection of material properties for the upstream recent alluvium and pervious embankment shell. Therefore, 'appropriately' conservative properties are critical so as not to over-design a costly project. The measured shear wave velocities in these two regions yield considerably lower CRR values when compared to the companion SPT and BPT $(N_1)_{60}$ values. The Success Dam Vs_1-$(N_1)_{60}$ relationship was selected for characterization and design analyses considering all the above relationships, to provide a best estimate, without unnecessary conservatism. The selected relationship is intended for uncemented sands with less than 10% non plastic fines. Using the selected relationship, implied CRR values can be determined for values of Vs_1 from the traditional $(N_1)_{60}$-CRR field performance database. The implied Vs_1-CRR curve

using the $(N_1)_{60}$-CRR curve by Idriss and Boulanger (2004) is also shown in Figure 5. The implied curve yields larger CRR values than what would be predicted by Andrus and Stokoe (2000) and plots slightly above several of the identified false positives, thus, putting them in the 'no liquefaction' category. The implied Vs_1-CRR curve plots above and below the best fit relationship for the bender element tests by Zhou and Chen (2007), but appears to adequately bound field performance Vs_1-CRR data.

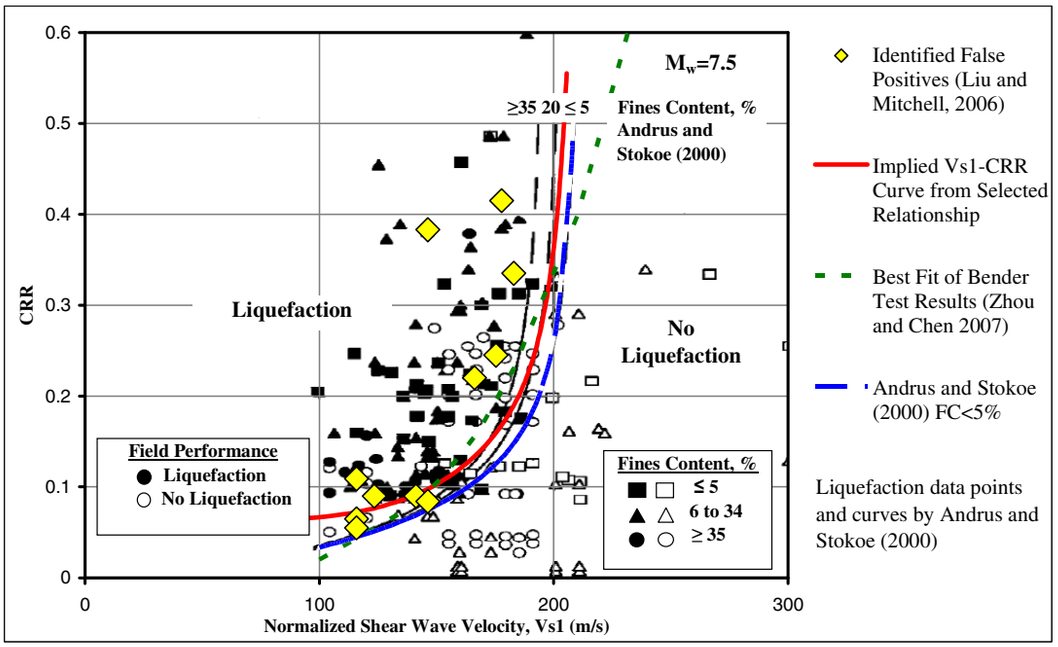


FIG. 5. Liquefaction CRR relationship for Vs_1 Data by Andrus and Stokoe, 2000

5. SUMMARY AND CONCLUSIONS

Extensive seismic evaluation explorations and foundation investigations have been conducted at Success Dam for the design of remediation. The air rotary casing hammer (ARCH), ODEX, and Sonic drilling methods have proved to be the most effective methods of boring through the embankment and alluvial foundation. Sonic drilling was found to be relatively fast and efficient through a variety of the materials that were difficult to penetrate with other techniques. Becker Penetration Tests (BPT) and Standard Penetration Tests (SPT), although challenging to conduct, were useful in collecting samples and in helping determine material density. Shear wave velocities determined by cross-hole geophysical techniques also were useful in defining material properties for seismic evaluation.

The procedures to evaluate liquefaction potential are still being developed and refined. Methods and techniques for the evaluation of sands are well established in comparison to sandy deposits containing significant amounts of large particles. These latter deposits are more difficult to characterize and evaluate for liquefaction potential. The large particles can impede the penetration of the SPT and even the BPT, leading to an over prediction of liquefaction resistance. Shear wave velocities are a promising alternative to evaluate these types of materials, but there appears to

be additional conservatism in the Vs_1-CRR procedure. The relationship between $(N_1)_{60}$ and Vs_1 and implied Vs_1-CRR were developed for this project to remove some of the added conservatism. Additional research in this area is needed.

6.0 REFERENCES

Andrus, R.D., and Stokoe, K.H., II (2000), "Liquefaction of Soils from Shear-Wave Velocity," J. Geotech. and Geoenvir. Engrg., Vol. 126(11), 1015-1025.

Andrus, R.D., Piratheepan, P., Ellis, B.S., Zhang, J., and Juang, C.H. (2003). "Comparing liquefaction evaluation methods using penetration-Vs relationships." U.S.-Taiwan Workshop on Soil Liquefaction, National Chiao Tung University, Hsin-Chu, Taiwan.

Harder, L.F., Jr., and Seed, H.B. (1986). "Determination of penetration resistance for coarse-grained soils using the Becker hammer drill." Earthquake Engineering Research Center, Report UCB/EERC-86/06, University of California, Berkeley.

Idriss, I. M., and Boulanger, R. W. (2004). "Semi-empirical procedures for evaluating liquefaction potential during earthquakes." Proc., 11th International Conference on Soil Dynamics and Earthquake Engineering, and 3rd International Conference on Earthquake Geotechnical Engineering, D. Doolin et al., eds., Stallion Press, Vol. 1, 32-56.

Liu, N., and Mitchell, J.K. (2006). "Influence of nonplastic fines on shear wave velocity-based assessment of liquefaction." J. Geotech. and Geoenvir. Engrg., Vol. 132(8), 1091-1097.

Robertson, P. K., Woeller, D. J., and Finn, W. D. (1992). ''Seismic cone penetration test for evaluating liquefaction potential under cyclic loading.'' Can. Geotech. J., Ottawa, 29, 686–695.

Rollins, K.M., Diehl, N.B., and Weaver, T.J. (1998). "Implications of VS - BPT (N,)60 Correlations for Liquefaction Assessment in Gravels," ASCE Geotechnical Special Publication No. 75, Volume l, p. 506-517.

Stewart, R.A., Kilpatrick, B.L., and Cattanach, J.D. (1990). "The Use of Becker Penetration Testing for Liquefaction Assessment of Coarse Granular Overburden." Proc., Prediction and Performance in Geotechnique, Canadian Geotecilnical Conference, Quebec, 275-283.

Sy, A. and Campanella, R.G. (1994). "Becker and Standard Penetration Tests (BPT¬SPT) Correlations with Consideration of Casing Friction," Can. Geotech. J., Vol. 31, No. 3, 343-356.

Youd, T. L. et al. (2001) "Liquefaction Resistance of Soils: Summary Report from the 1996 NCEER and 1998 NCEER/NSF Workshops on Evaluation of Liquefaction Resistance of Soils," J. Geotech. and Geoenvir. Engrg., Vol. 127(10), 817-833.

Zhou, Y.-G., and Chen, Y.M. (2007). "Laboratory investigation on assessing liquefaction resistance of sandy soils by shear wave velocity." J. Geotech. and Geoenvir. Engrg., Vol. 133(8), 959-972.

Motion Characteristics of Compacted Earth Dams Under Small Earthquake Excitations in Taiwan

Jin-Hung Hwang[1], Chia-Pin Wu[2] and Jui-Te Chou[3]

[1] Professor, Department of Civil Engineering, National Central University, No.300, Jhongda Rd., Jhongli City, Taoyuan County 32054, Taiwan, ROC; TEL: +886-3-4227151-34124; FAX: +886-3-4252960; E-mail: hwangjin@cc.ncu.edu.tw.

[2] Ph.D. student, Department of Civil Engineering, National Central University, Taiwan, ROC. E-mail: 92322030@cc.ncu.edu.tw.

[3] Master, Department of Civil Engineering, National Central University, Taiwan, ROC.

ABSTRACT: This paper summarizes the characteristics of small seismic motions of four major compacted earth dams in Taiwan. Seismic data of four major dams recorded in the past thirty years were collected and analyzed. In general, ground motion characteristics can be expressed by peak ground acceleration (PGA), velocity (PGV), displacement (PGD) and predominant frequency of each motion history. The different statistical correlations between the PGA, PGV and PGD have been derived. The correlations are very consistent for different dams. The PGA amplifications from dam base to dam crest were also derived and show that the larger the base PGA, the smaller the amplification ratio, a phenomenon called non-linear effect of geo-material. The fundamental frequency of each earth dam was identified by the ratio of Fourier and response spectra of the seismic records at the dam crest and base. It was found that the larger the base PGA, the lower the fundamental frequency of the earth dam. The fundamental frequencies of the earth dams in direction transverse to the dam axis range from 1.5Hz to 2.0 Hz. It is interesting to observe that the fundamental frequency does not correlate well with the dam height as expected in the 2D dynamic analysis of the earth dam. This may suggest a possibility that a 3D dynamic analysis is required to more reasonably capture the real seismic response of earth dam.

KEYWORDS: seismic record, compacted earth dam, fundamental frequency, system identification

1. INTRODUCTION

The seismic-resistant capacity of an earth dam is a very important issue in a seismic active country. How large the seismic capacity that an earth dam has was normally predicted by seismic response analysis of the earth dam under strong earthquake shaking. However, it is very difficult to verify or assure the analysis result being within reasonable accuracy owing to the rare records of seismic motions or field performances of earth dams during strong earthquakes. Hwang et al. (2007) have proved that motion records of earth dams under small earthquakes can be used to identify the vibration characteristics of a full scale dam, and based on the identified results, the derived small-strain dynamic properties can give a good

prediction of the dam responses recorded in larger earthquakes. Therefore, understanding the small motion characteristics is equally important to the large ones. This paper preliminary investigates the vibration characteristics of four well-instrumented compacted earth dams in Taiwan. The characteristics include the fundamental frequency, PGA amplification factor, relationships of peak ground acceleration, velocity and displacement. The followings summarize the background information of the selected earth dams and earthquake events, methods of identification and interpretation, analyzed results and discussions, and conclusions.

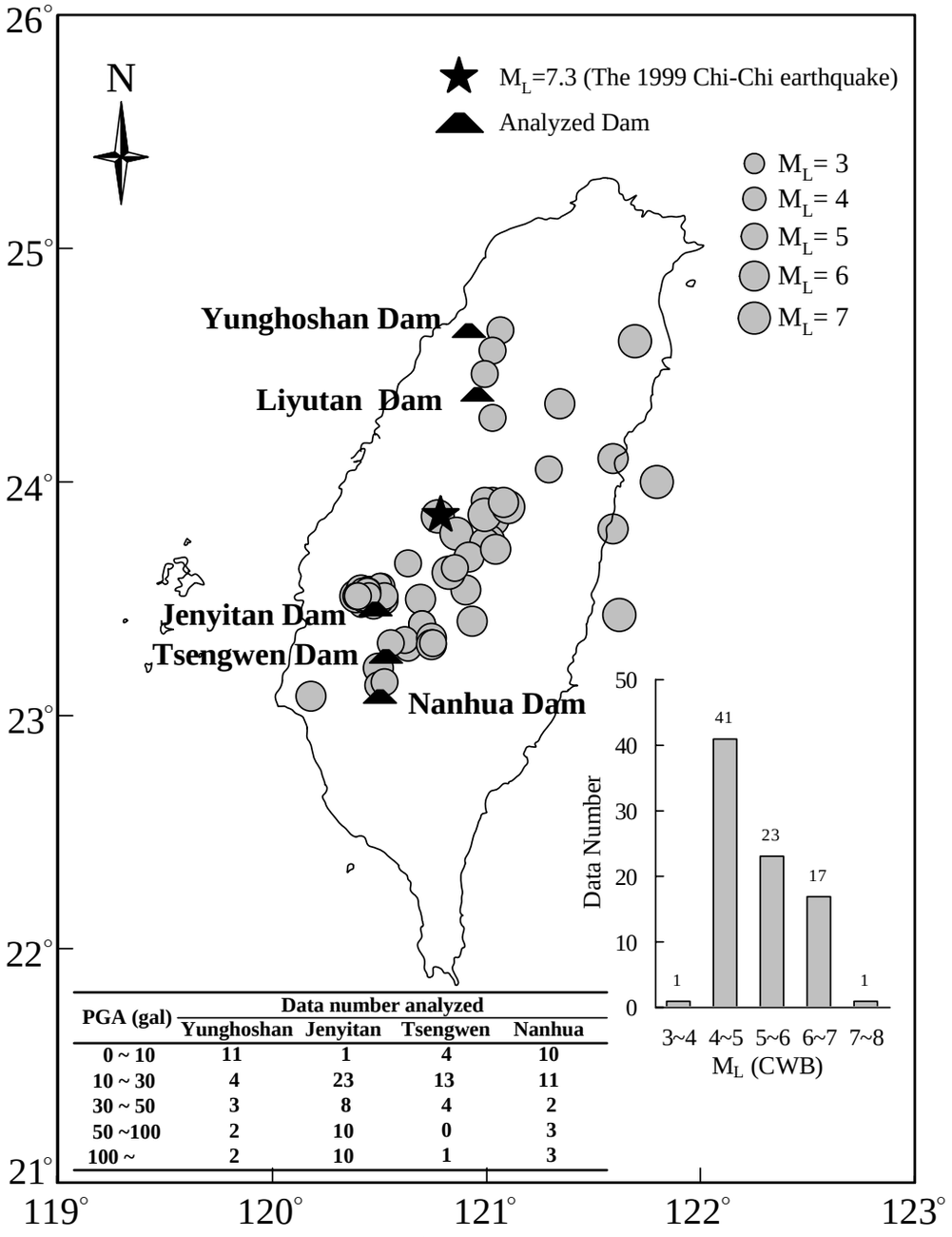
2. EARTH DAMS AND EARTHQUAKE EVENTS

Table 1 shows the basic data of the main earth dams in Taiwan. Most of them are zoned compacted fills with a central clay core as a cutoff wall. Among them, only four dams with enough earthquake records were chosen to be analyzed in the study. They are Tsengwen (height=133m, length=400m), Nanhua (height=87.5m, length=509m), Yonghoshan (height=62.5m, length=340m), Jenyitan (height=28m, length=1511m) reservoirs. The locations of these dams and earthquake events are displayed in Fig. 1 with a list of the statistics of earthquake events used in analysis. Fig. 2 shows the cross sections of these dams and the positions of the seismographic stations. A total five stations were installed on Nanhua dam, three on Tsengwen dam, and only two on Yonghoshan and Jenyitan dams. Forty earthquake events during 1984-2000 were used in analysis for Yonghoshan dam, thirty-nine events during 1987-2000 for Nanhua, thirty during 1976-2000 for Tsengwen and seventy-five during 1990-2000 for Jenyitan.

Table 1. Basic data of the main earth dams in Taiwan

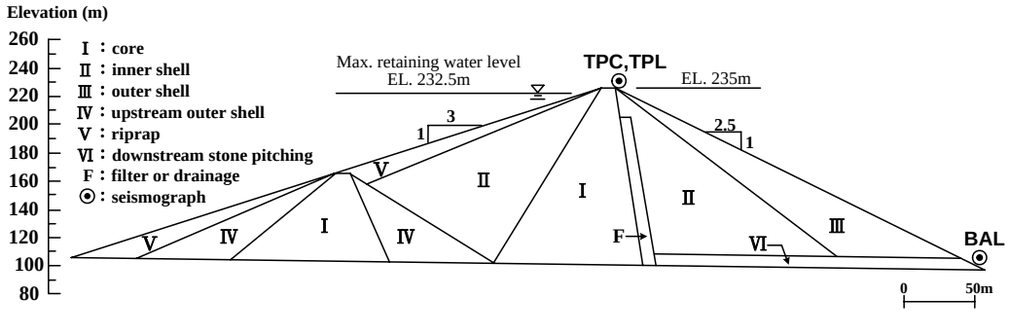
Dam name	River system	Construction year	Height (m)	Length (m)
Shihmen	Dahan River	1964	133.1	360
Tsengwen	**Zengwun River**	**1973**	**133.0**	**400**
Liyutan	Da-an River	1992	96.0	235
Nanhua	**Zengwun River**	**1993**	**87.5**	**509**
Yunghoshan	**Jhonggang River**	**1984**	**62.5**	**340**
Mutan	Sihchong River	1995	65.0	435
Wushantou[a]	Zengwun River	1920	56.0	1273
Hsinshan	Danshuei River	1980	51.0	231
Paiho	Jishuei River	1965	42.5	210
Fengshan	Donggang River	1984	39.5	325
Mingte	Houlong River	1970	35.5	187
Paoshan[b]	Toucian River	1985	34.5	260
Akungtien	Agongdian River	1952	31.0	2380
Jenyitan	**Bajhang River**	**1987**	**28.0**	**1511**

[a] Wushantou dam is a semi-hydraulic fill embankment.
[b] Paoshan dam used a concrete core wall as a cutoff.

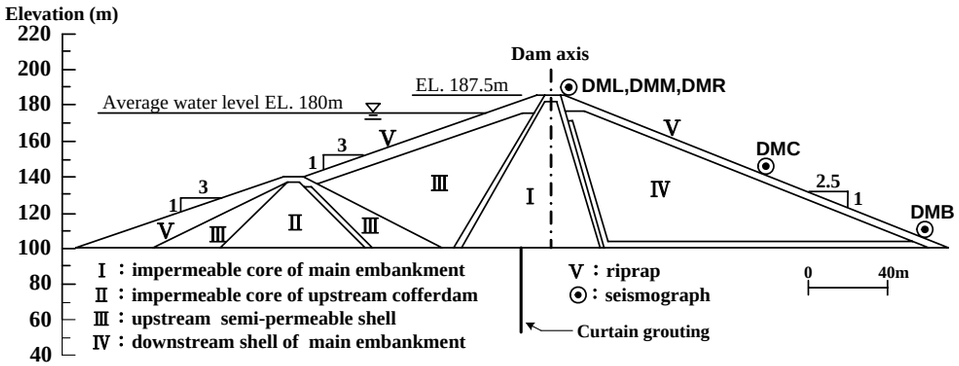


PGA (gal)	Data number analyzed			
	Yunghoshan	Jenyitan	Tsengwen	Nanhua
0 ~ 10	11	1	4	10
10 ~ 30	4	23	13	11
30 ~ 50	3	8	4	2
50 ~100	2	10	0	3
100 ~	2	10	1	3

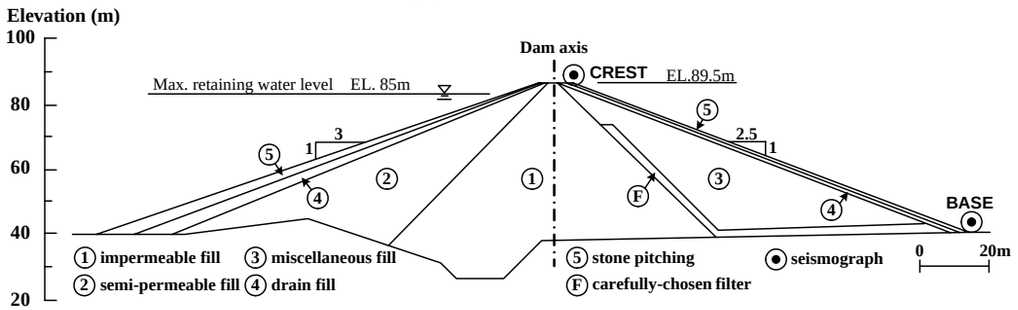
Fig. 1. The locations of dams and earthquake epicenters



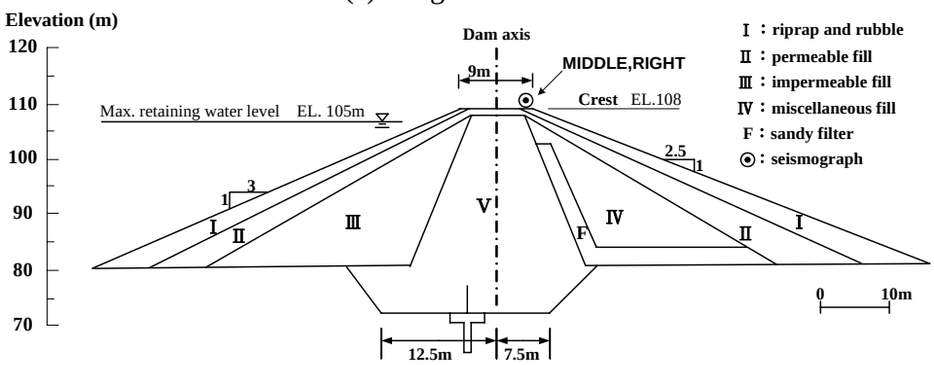
(a) Tsengwen Dam



(b) Nanhua Dam



(c) Yunghoshan Dam



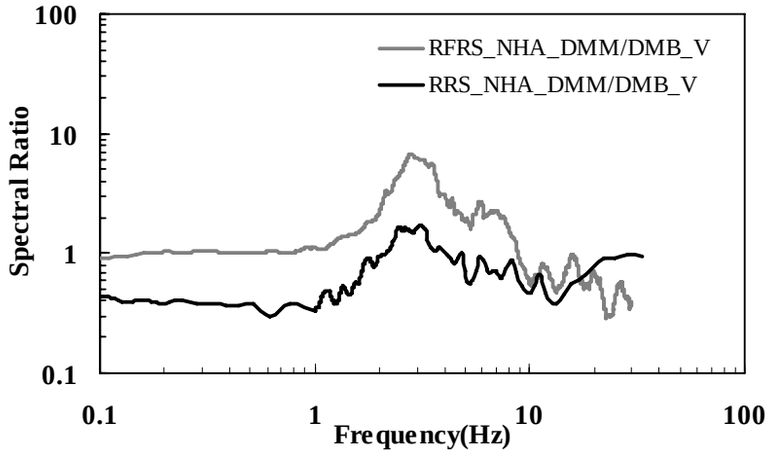
(d) Jenyitan Dam

Fig. 2. Analyzed dam embankment sections showing the construction materials and the positions of the seismographic stations

3. METHODS OF IDENTIFICATION AND INTERPRETATION

1. Fundamental vibration frequency

The seismic response of an earth dam is strongly influenced by its fundamental frequency (period). This frequency varies with the shaking intensity. It is a phenomenon due to the non-linear stress-strain behavior of geo-materials. In this work, we use seismic records to identify the fundamental frequencies of the above-mentioned earth dams. Two methods are used for this identification. One is the ratio of the Fourier amplitude response spectrum (RFRS) method. The Fourier amplitude response spectrum from the top station is divided by that of the bottom station to derive the transfer function of the dam body. The peak values of the transfer function are considered to occur at the resonant frequency of the dam, the smallest of the resonant frequencies is identified as the fundamental vibration frequency of the dam. The other method is the ratio of response spectrum (RRS) method which divides the response spectrum from the top station by that of the bottom station to derive the transfer function. Accordingly, the longest period, where the peak RRS value occurs, is identified as the fundamental vibration period of the dam, which is the inverse of fundamental frequency. Fig. 3 shows the RFRSs and RRSs of Nanhua dam in the vertical, transverse and longitudinal directions (relative to dam axis) for the 16 February 2000 earthquake. Note that the identified results of both two methods are nearly the same and the fundamental frequencies of the dam body are about 2.8, 2.1 and 2.0 Hz in the vertical, transverse and longitudinal directions respectively. Based on the same procedure, the fundamental frequency of the dam has been identified for the other earthquakes. The results are presented in the form of fundamental frequency versus peak ground acceleration, as shown in Fig. 4. In this case, the nonlinear effect is not obvious, i.e., the larger the excitation level, the lower the fundamental frequency, due to their excitation levels are small (less 40 gals). However, the trend is slight that can also be found if making a more careful observation. The diversity in vertical direction is larger than those in transverse and longitudinal directions. The fundamental frequencies of other dams have also been identified according to the same procedure.



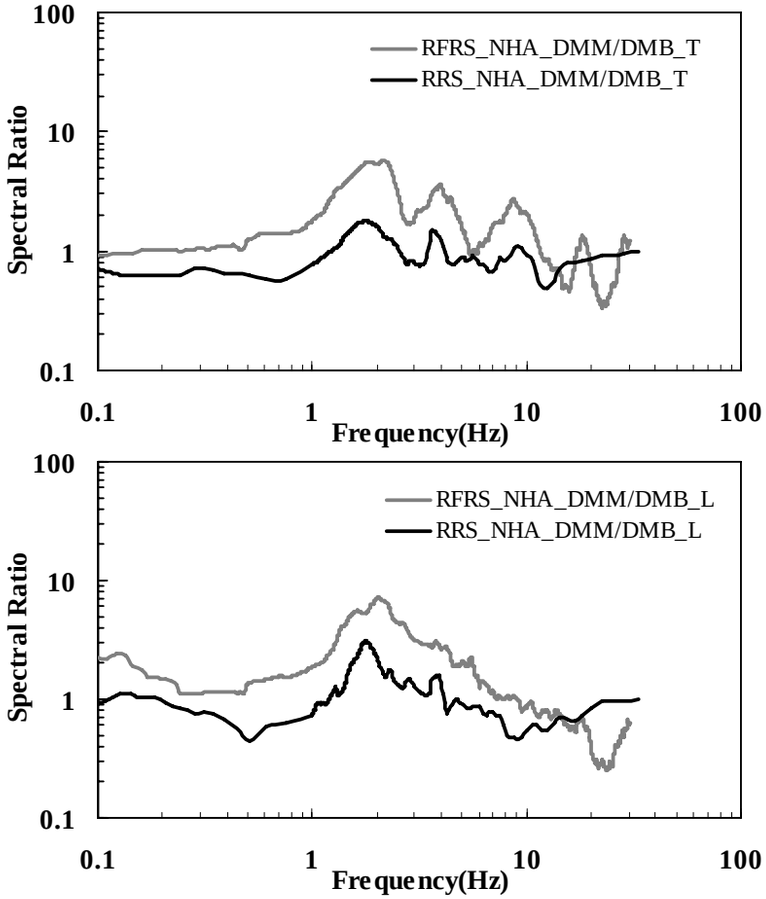
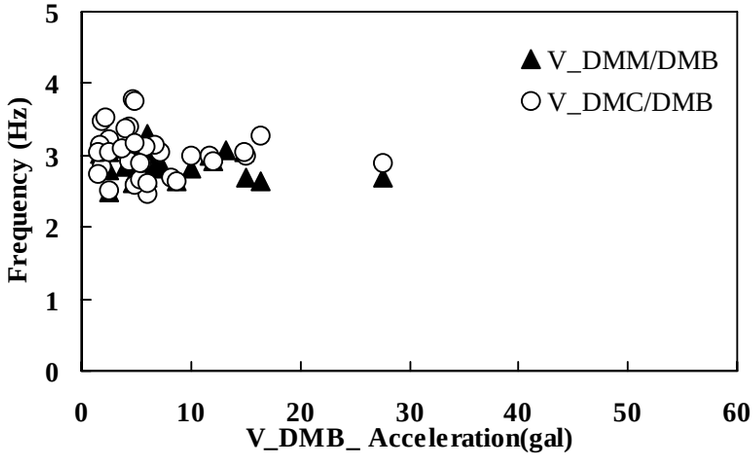


Fig. 3. Spectral Ratio of Nanhua dam during the 16 February 2000 earthquake



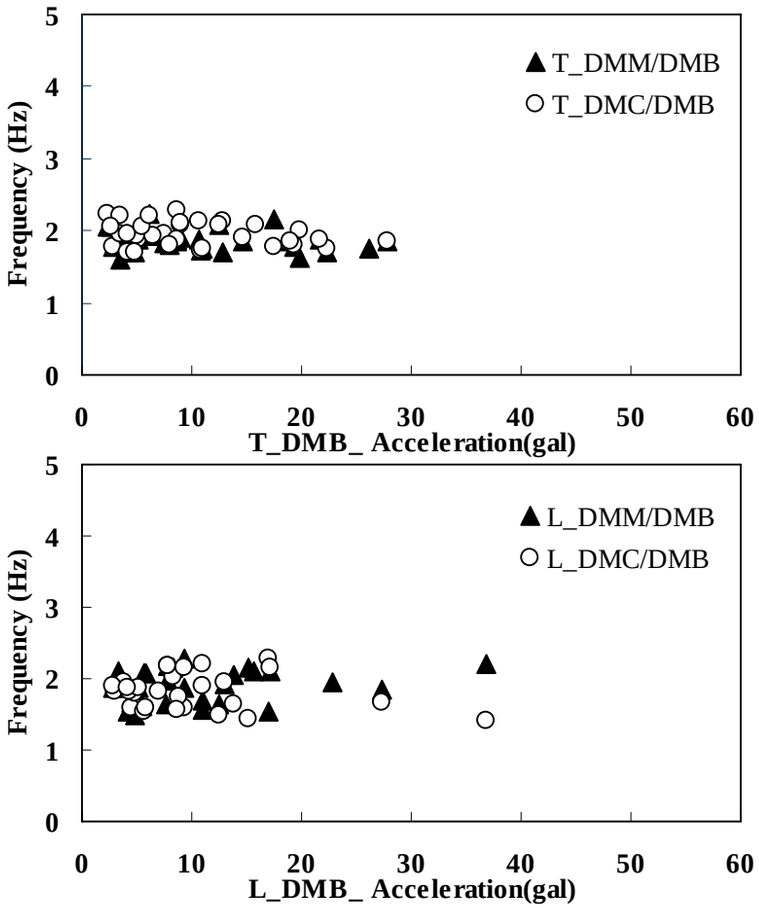


Fig. 4. Fundamental frequencies of Nanhua dam

2. PGA amplification factor

The PGA amplification factor α is defined as the peak ground acceleration (PGA) at the top of dam divided by that at the bottom of dam, i.e. $\alpha = PGA_{top} / PGA_{bottom}$. If the factor is greater than one, it means the PGA at the dam base is amplified when the seismic wave propagates through the dam body to the top of dam. On the contrary, if the factor is less than one, that means the PGA at the dam base is de-amplified. Fig. 5 shows the PGA amplification factors of Nanhua dam for different earthquakes in different directions. It can be seen that most of the factor larger than one, there seems a trend that the smaller the base PGA, the higher the α value. However, the variation range of the α value is also large due to varying earthquake source mechanisms and propagating paths. The same procedure was followed to derive the α values of the other dams.

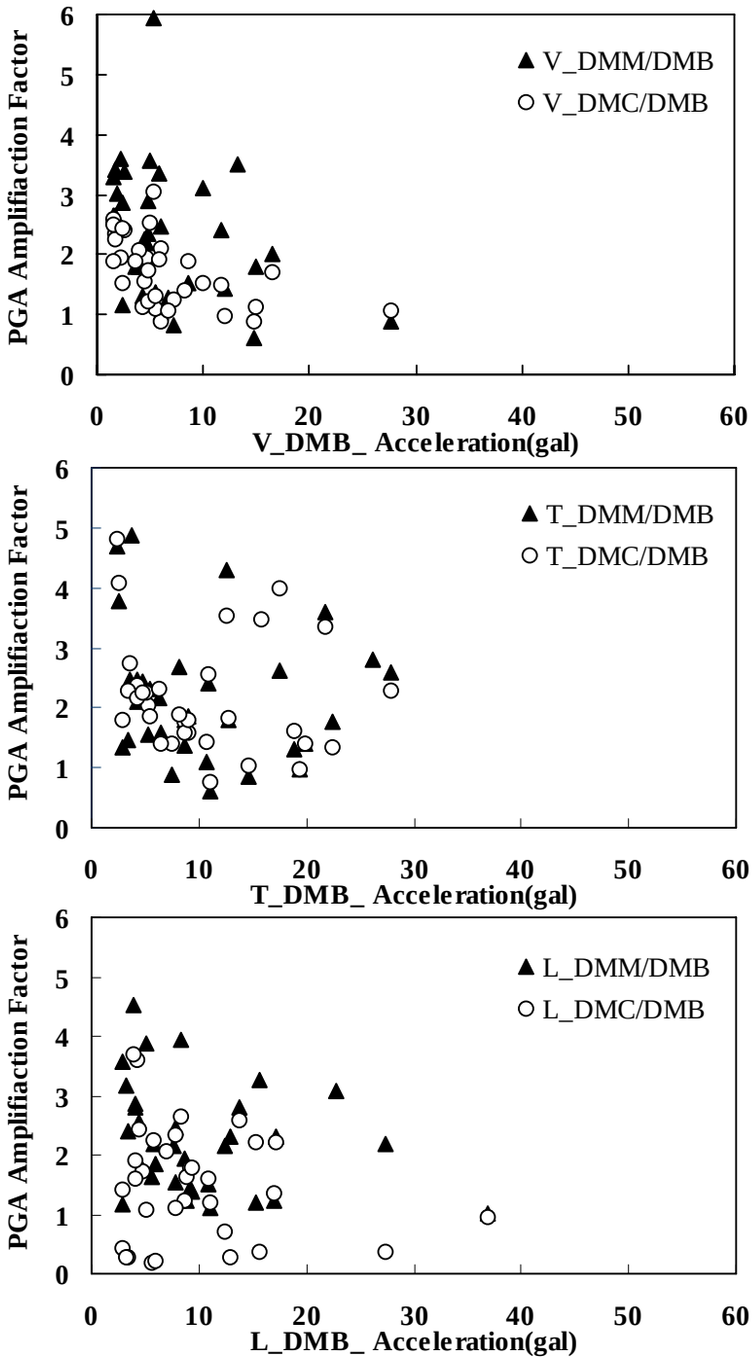


Fig. 5. PGA amplification factors of Nanhua dam

3. Relationships of PGA, PGV and PGD

This section investigates the mutual relationships of PGA, PGV and PGD of seismic motions of earth dams, where PGA is the peak acceleration, PGV is the peak

velocity, and PGD is the peak displacement of motion record. A dimensional factor $C = PGA \times PGD/PGV^2$ has been proposed by Newmark and Hall (1982) to feature the mutual relationships of PGA, PGV and PGD. Table 2 shows the derived C values for different dams. To observe the relation of PGA and PGV in the same direction, an empirical factor D is defined as D = PGV / PGA with a unit of cm/sec/g. The derived D values for these dams are also listed in Table 2. To observe the differences of PGA or PGV in different directions, the study uses the PGA or PGV in a direction transverse to the axis of the dam as the bases and defines the following factors to characterize the other two directional differences.

$$A_{V/T} = PGA_V / PGA_T \quad (1)$$

$$A_{L/T} = PGA_L / PGA_T \quad (2)$$

$$V_{V/T} = PGV_V / PGV_T \quad (3)$$

$$V_{L/T} = PGV_L / PGV_T \quad (4)$$

where PGA_V, PGA_L, PGA_T and PGV_V, PGV_L, PGV_T are PGA and PGV values in vertical, longitudinal and transverse directions of the same seismographic station, respectively. Table 2 also displays the derived $A_{V/T}$, $A_{L/T}$, $V_{V/T}$, $V_{L/T}$ for these dams.

Table 2. Statistical results from earthquake records of the four dams

Direction	Tsengwen		Nanhua		Yunghoshan		Jenyitan	
	Mean	SD	Mean	SD	Mean	SD	Mean	SD
	$C = PGA \times PGD / PGV^2$							
Vertical	2.19	1.18	2.10	0.805	2.64	1.01	3.55	2.17
Transverse	1.69	0.63	2.04	0.761	2.24	0.79	2.42	1.12
Longitudinal	1.68	0.72	1.96	0.664	2.13	0.66	2.23	1.01
	D = PGV/PGA (cm/sec/g)							
Vertical	42.14	24.94	72.42	49.23	64.00	37.37	25.94	16.55
Transverse	51.27	20.99	71.98	40.31	65.72	33.98	39.57	27.42
Longitudinal	49.02	25.85	74.51	43.43	65.08	30.62	34.22	25.12
	Relationship of PGA in different directions							
$A_{V/T}$	0.65	0.22	0.67	0.249	0.65	0.22	0.80	0.43
$A_{L/T}$	0.96	0.35	0.98	0.416	1.12	0.37	1.43	0.53
	Relationship of PGV in different directions							
$V_{V/T}$	0.64	0.28	0.53	0.248	0.63	0.27	0.54	0.30
$V_{L/T}$	0.99	0.38	1.02	0.496	1.15	0.47	1.24	0.51

4. ANALYZED RESULTS AND DISCUSSIONS

1. Fundamental frequency

Fig. 6 shows the fundamental frequency versus dam height for five dams which included the Liyutam earth dam (Height=96m, length=235m) that has been analyzed in detail by Hwang et al. (2007). It can be found that the fundamental frequency does not decrease with increasing height. This contrasts the result based on the conventional 2-D vibration theory of dam that indicates the fundamental frequency decreases as the height of dam increases. Among these dams, it is surprising that the

Jenyitan dam with the smallest height of 28m has the lowest fundamental frequency. This could be caused by many unknown factors. One of them, that the authors guessed, may be owing to its unusually longest length of 1151 m. It might also have a possibility that a 2-D vibration analysis may be not applicable to predicting the fundamental frequency of a real dam.

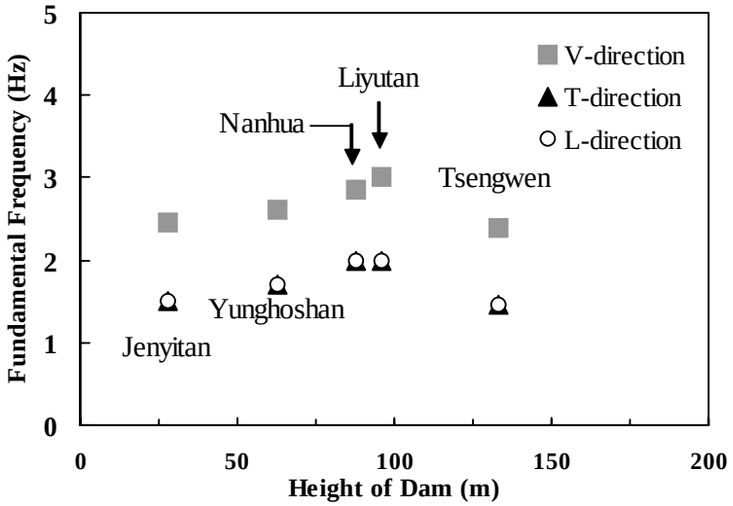


Fig. 6. Fundamental frequencies versus dam height for the five dams

2. PGA amplification factor

Fig. 7 shows the relationship of average amplification factor versus the height of dam in different directions for the above four dams. It can be seen that the factor obviously increases with the increasing dam height in longitudinal and transverse directions, except the Tsengwen dam in vertical direction. The results are consistent with the predictions of typical seismic response analyses for earth dams.

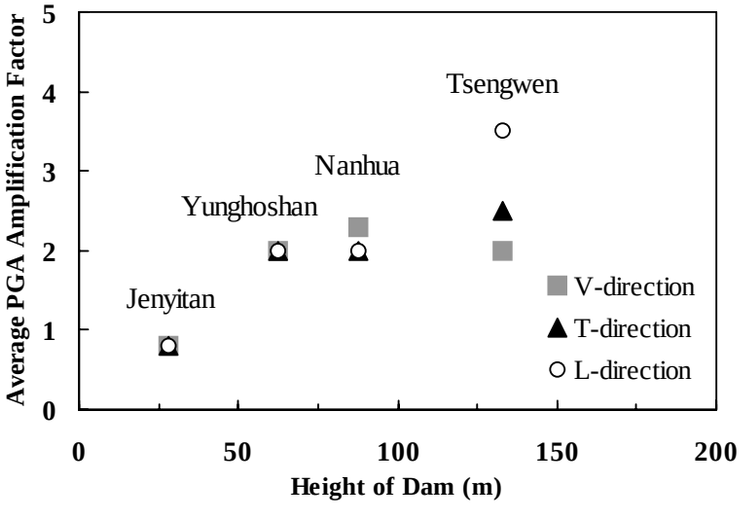


Fig. 7. Average amplification factors versus dam height for the four dams

3. Relationships of PGA, PGV and PGD

The relationships of PGA, PGV and PGD have been summarized in Table 2 for these dams and earthquake events. Table 3 is a comparison of C factor with some other researches (Chen and Cheng, 2000; Mohraz, 1976). It can be found that the C factor in the study is much less than those of other researches. This may be attributed to using only small motion records in this analysis and the vibration characteristics of earth dam. The D factors obtained in the study are also compared to those of other researches in Table 3. It was found that the D factors are less than those of the other researches, but the differences are not so large as the C factor. The directional factors $A_{V/T}$, $V_{V/T}$ are in the ranges of 0.6-0.8 and 0.5-0.6, respectively and the $A_{L/T}$, $V_{L/T}$ factors are in the ranges of 0.9-1.5 and 0.9-1.2, respectively. Especially, the Jenyitan dam has the highest values of these factors of $A_{L/T}$, $V_{L/T}$. The $A_{V/T}$ and $V_{V/T}$ of the other dams are close to 2/3(=0.66) and the $A_{L/T}$, $V_{L/T}$ are close to 1.0. The different behavior of the Jenyitan dam might be due to its smallest height (26m) as compared to its longest length (1151m).

Table 3. Comparisons of C and D factor with some other researches

Research references	C			D		
	V-dir.	T-dir.	L-dir.	V-dir.	T-dir.	L-dir.
Mohraz (1976)[c]	9.10	4.30	5.60	83.82	104.14	83.82
Cheng and Cheng (2000)[d]	7.73	4.80	—	77.74	80.69	—
Tsengwen Dam	2.19	1.69	1.68	42.14	51.27	49.02
Nanhua Dam	2.10	2.04	1.96	72.42	71.98	74.51
Yunghoshan Dam	2.64	2.24	2.13	64.00	65.72	65.08
Jenyitan Dam	3.55	2.42	2.23	25.94	39.57	34.22

[c] 30~200 ft of alluvium underlain by rock
[d] 51 horizontal earthquake records and 31 vertical earthquake records at soil sites in Taiwan

5. CONCLUSIONS

Based on the above results, the following conclusions are summarized here.

(1) The fundamental frequencies of four main compacted earth dams are identified from motion records under small earthquake excitations by the RFRS and RRS methods. The results of both methods are consistent, and indicate the fundamental frequency does not increase with the dam height as expected in the two dimensional vibration theory of dam. This discrepancy is worthy of performing further research to clarify it.

(2) In general, the PGA amplification factor increases with the dam height as expected in the one or two dimensional vibration theory of dam.

(3) The relationships of PGA, PGV and PGD for these earth dams are not quite similar to the statistical results of other researches based on the free-field motion records derived from small to large earthquakes. This might be attributed to the small motion records used in the study or the special vibration characteristics of earth dams.

(4) The identified and interpreted motion characteristics of earth dams in the study might be able to provide a data base to verify the numerical results of the

seismic response analyses for earth dams under small earthquake excitations. After that, the predicted dam response under large earthquake will be considered to be more reliable than that without performing verification under small excitation.

REFERENCES

Chen, S.S., and Cheng, D.S. (2000). "Site-Dependent Characteristics for Earthquakes in Taiwan Region." *Journal of the Chinese Institute of Civil and Hydraulic Engineering*, 12 (3): 445-453. (*in Chinese*)

Hwang, J.H., Wu, C.P., and Wang, S.C. (2007). "Seismic Records analysis of Liyutan Earth Dam." *Canadian Geotechnical Journal*. (Accepted)

Mohraz, B. (1976). "A study of earthquake response spectra for different geological conditions." Bulletin of Seismological Society of America, 66 (3): 915-935.

Newmark, N.M., and Hall, W.J. (1982). "Earthquake Spectra and Design." Earthquake Engineer Research Institute, Berkeley, California.

Nonlinear Dynamic SSI Analyses of a Concrete Water Reservoir

Wolfgang Roth[1], M.ASCE, G.E., Bei Su[1], Ethan Dawson[1], M.ASCE,
Allan Porush[1], M.ASCE, S.E., Meang Hassel[2], M.ASCE, P.E.,
Lynn Shutt[2], M.ASCE, S.E., Mohsen Beikae[2], M.ASCE, G.E.

[1]URS Corporation, 915 Wilshire Blvd. Suite 700, Los Angeles, CA 9001; wolfgang_roth@urscorp.com
[2] Metropolitan Water District of So Cal (MWD), 700 N Alameda St, Los Angeles, CA 90012; mhassel@mwdh2o.com

ABSTRACT: Seismic performance of the Finished Water Reservoir (FWR) at the Robert B. Diemer water treatment plant was evaluated by performing dynamic nonlinear soil-structure interaction analyses with FLAC. The reservoir sits on a terrace cut into siltstone near the top of a ridge. For the north wall, which retains high ground above the reservoir roof, the critical failure mode is governed by bending and shear. The partially buried south wall is supported by caissons where it straddles filled-in ravines. The critical failure mode is loss of vertical support from caissons damaged by down-slope sliding fill within the ravines. It was analyzed considering the deep, out-of-plane wall beam bridging over caissons which might be damaged during shaking. The study concluded that the reservoir would maintain its structural integrity during MCE-level shaking, such that uncontrolled release of water would be prevented.



FIG. 1. Robert B. Diemer water treatment plant (FWR in the foreground).

INTRODUCTION

The roughly 91x220x6 m (300'x720'x20') Finished Water Reservoir (Figures 1 and 2) at MWD's Robert B. Diemer water treatment plant in Yorba Linda, CA was constructed in 1963. Its concrete roof is supported by a 6x6 m (20x20-ft) grid of columns, and the floor slab sits on a terrace cut into Fernando Formation bedrock near the top of a ridge. Originally, the reservoir was fully buried, with about 1.2 m (4 ft) of fill placed on the roof. Following the damage experienced at MWD's Jensen plant in the 1971 San Fernando earthquake, the FWR structure at Diemer was modified in 1979. Two interior shear walls were constructed, the fill was removed from the roof, and lateral earth pressures were relieved along north and west walls by partially excavating the backfill and constructing external retaining walls. The original and current configurations of the north wall are shown in Figure 3.

The study described in this paper was performed as part of MWD's seismic reliability program. The criterion defining seismic stability was the prevention of uncontrolled release of water from the reservoir under Maximum Credible Earthquake (MCE) shaking represented by the three acceleration histories shown in Figure 4. A total of six wall sections were analyzed by nonlinear soil-structure interaction modeling with FLAC. The analyses of the two typical sections A-North and A-South, are discussed in this paper.

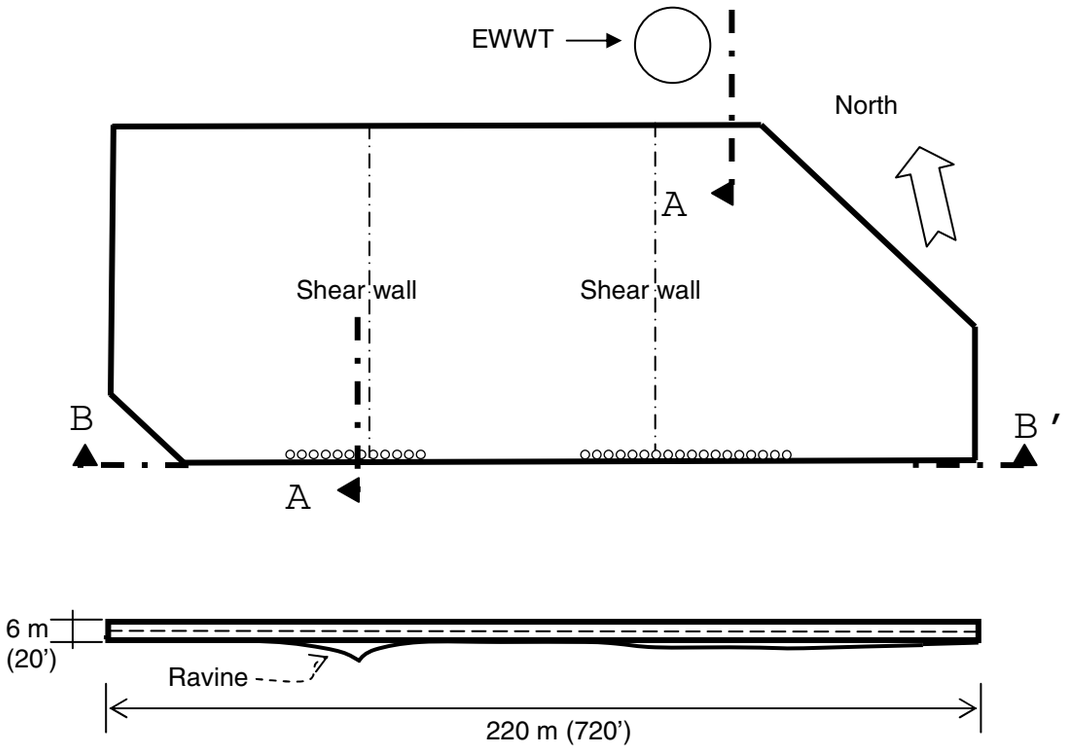


FIG 2. Finished Water Reservoir, plot plan and Section B-B'

METHOD OF ANALYSIS

Time domain, nonlinear seismic deformation analyses were performed with the computer code FLAC, Version 5.0 (Itasca, 2005), an explicit finite-difference program for solving static and dynamic problems in geomechanics and soil-structure interaction (SSI). FLAC and its predecessor codes have been widely utilized and verified in the last 30 years against closed-form solutions, physical models, and case histories in the field. Recent examples of seismic analyses with FLAC published by authors of this paper include Roth et al (2004), Roth and Dawson (2003), and Dawson et al (2001).

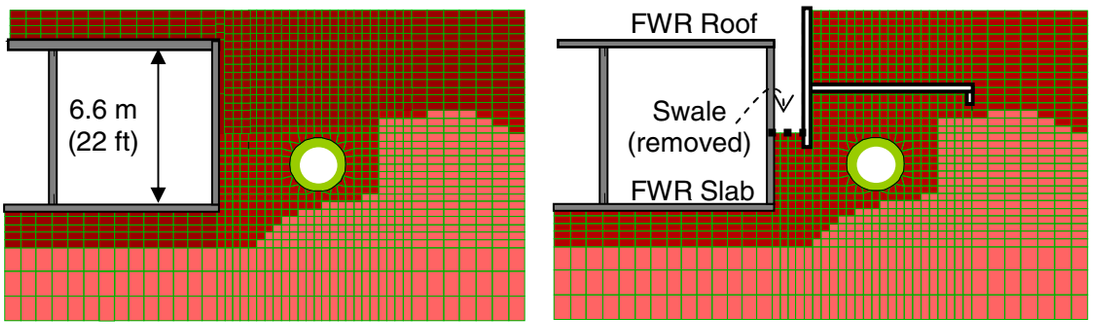


FIG. 3. Original and current FWR north wall configurations

Soils and bedrock were simulated using an elasto-plastic Mohr-Coulomb model with tension limits. Yielding at large strains automatically produced hysteretic damping, while for small strains in the elastic range nominal 0.5% Rayleigh damping was used for a center frequency of 3 Hertz. The reservoir, retaining wall, and bypass pipeline were modeled with elasto-plastic beam elements which developed plastic hinges at user-defined yield moments. Hydrostatic pressure was applied to both the wall and bottom slab; and the hydrodynamic effect of the reservoir water was modeled by adding mass to the nodes of the reservoir wall (Westergaard, 1933).

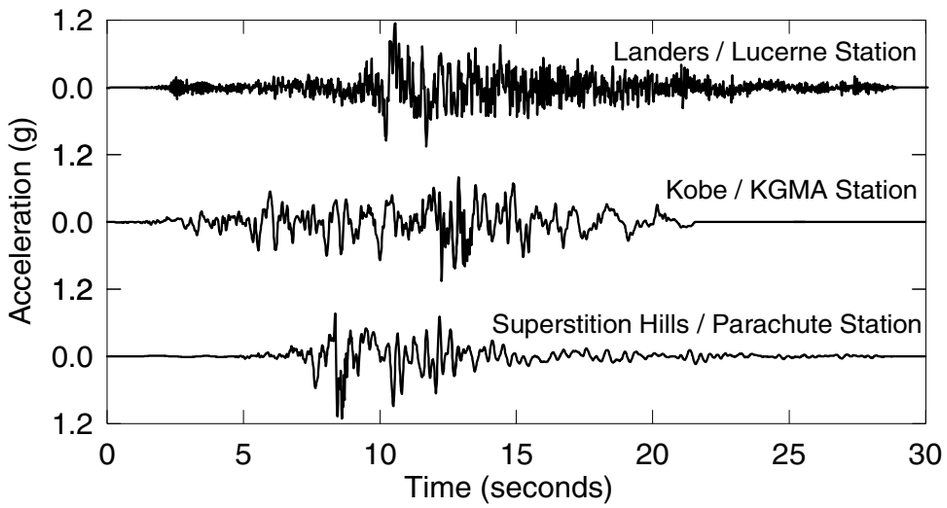


FIG. 4. MCE motion histories

MODEL SETUP

Figure 5 shows the basic model makeup for the north-south wall sections. Each model has compliant boundaries with viscous dashpots (Lysmer and Kuhlemeyer, 1969) which prevent outward traveling waves from being reflected back into the model. In addition, the lateral boundaries also receive real-time feedback from 1D "free-field" computations.

The stiffening effect of the two north-south shear walls (Figure 2) was simulated by rigidly linking horizontal displacements of the roof and floor slabs. The reservoir model was also simplified by including only the first 3 column bays, after initial trial runs indicated that the rotational constraint at the roof-to-wall and floor-to-wall corners were not affected by this cut off.

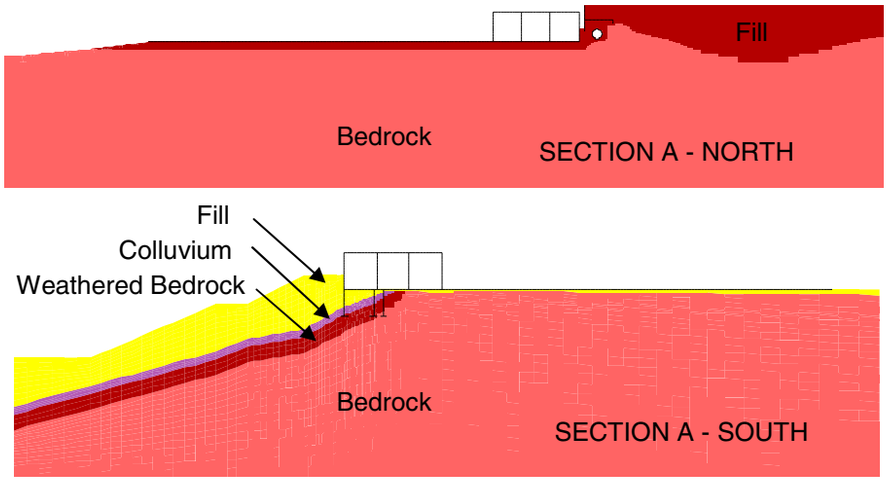


FIG. 5. Model setup

MATERIAL PROPERTIES

The soil and structural properties used for our analyses are summarized in Tables 1 and 2. Boundaries between soil and structure were modeled with elasto-plastic interface elements with 30 degr. friction angle, zero cohesion, and zero tension cutoff.

Soils. Soil properties were obtained from recent subsurface investigations around the FWR structure (URS, 2006a and 2006b). However, in deriving these properties the vast amount of geotechnical and geologic information from previous investigations at the Diemer site were also taken into account. Where soil parameters from previous investigations varied, values were selected which produced the most conservative results in terms of seismic performance of the FWR structure. Poisson's ratio was assumed to be 0.3 for all soil materials.

Table 1. Soil Properties

Material Type	Unit Weight [kg/m^3 (pcf)]	Friction Angle (Degr.)	Cohesion [kPa (psf)]	S-Wave Velocity * [m/s (ft/sec)]	Shear Modulus [MPa (ksf)]
Fill	2002 (125)	30	11 (240)	280 (920)	157 (3,280)
Colluvium	2002 (125)	17	0	229 (750)	115 (2,400)
Weathered Bedrock	2162 (135)	34	62 (1,300)	366 (1,200)	115 (2,400) **
Bedrock	2162 (135)	34	287 (6,000)	762 (2,500)	287 (6,000) **

*) Shear-wave velocity (V_s) derived from downhole geophysical surveys (URS, 2006a and 2006b)
**) Shear modulus adjusted for large shear strains

Structural Members. The moment capacity of structural beam elements was derived taking into account axial loads. For sections with rebar embedment lengths less than specified by ACI (2005), the capacity was scaled down by the ratio of actual embedment length over length needed to develop full moment capacity. The compressive strength of concrete (f'_c) was estimated at 31 MPa (4,500 psi), taking into account a 50% increase of the 28-day design strength due to aging (FEMA, 2000). Young's Modulus of concrete (E) was taken at 26,200 MPa (3,800 ksi), and tensile strength (f_l) was 3.4 MPa (500 psi) (ACI, 2005). The yield strength of steel reinforcement was estimated to be 517 MPa (75 ksi) by increasing the design strength for intermediate-grade steel by a factor of 1.25 (FEMA, 2000).

Table 2. Structural Properties – North Wall

Structural Element	Section Area [cm^2/m (ft^2/ft)]	Moment of Inertia * [cm^4/m (ft^4/ft)]	Yield Moment [kN.m/m (kip.ft/ft)]
FWR Roof Slab	2,530 (0.83)	68,200 (0.0241)	138 (31)
FWR Floor Slab	3,170 (1.04)	133,400 (0.0471)	151 (34)
FWR Columns **	670 (0.22)	53,500 (0.0189)	Elastic
FWR Wall - Top - Bottom	3,570 (1.17) 5,090 (1.67)	187,500 (0.0662) 546,200 (0.1929)	231 (52) 343 (77)
Retaining Wall (Horizontal Leg)	4,570 (1.50) 6,100 (2.00)	398,100 (0.1406) 943,800 (0.3333)	169 (38) 298 (67)
S-Wall Caissons	1,520 (0.5)	271,600 (0.0959)	74 (16.6)
S-Wall Beam ***	3.5 (m^2) [37.3 (ft^2)]	8.07 (m^4) [935 (ft^4)]	15,117 (kN.m) [11,150 (kip.ft)]

*) Cracked section (ACI, 2005)
**) Distributed over 3-m (10-ft) wide strip of assumed force trajectory for 6-m (20-ft) column spacing
***) Actual wall-beam properties (i.e. not distributed per ft)

ANALYSIS OF NORTH WALL

At the outset of this study, a series of initial analysis runs with Section A-North (Figure 3) were performed to accomplish the following:

- investigate the probable cause of horizontal cracking observed inside the reservoir at roughly mid-height of the north wall;
- explore the effect of pre-shaking earth pressure on the seismic performance of the wall;
- establish realistic pre-shaking gravity stresses, and calibrate the model, before subjecting it to MCE-level earthquake shaking; and
- select the most critical (governing) MCE motion (from Figure 4) to be used for analyzing the remaining wall sections.

Probable Cause of Cracking. The horizontal cracks could have been caused by the concrete swale shown in Figure 3 bracing the external retaining wall against the reservoir. While this condition has since been mitigated by saw-cutting the swale, the "strut" hypothesis was tested by subjecting the north-wall model, with the swale in place, to a series of low-level seismic events obtained by down-scaling the Landers-Lucerne MCE motion. Figure 6 presents a history plot of swale ("strut") forces acting on the reservoir wall during shaking with PGA=0.25g. This analysis run resulted in dynamic bending stresses exceeding the concrete's tensile strength, indicating cracking. Considering that the reservoir is sitting on a ridge, which tends to amplify earthquake motions, having experienced PGA values of 0.25g or greater in its lifetime is likely. Hence, the swale was concluded to have at least contributed to creating, or widening, the observed horizontal cracks. Candidate seismic events for causing cracking would include the M_w 5.9 Whittier Narrows earthquake of 1987.

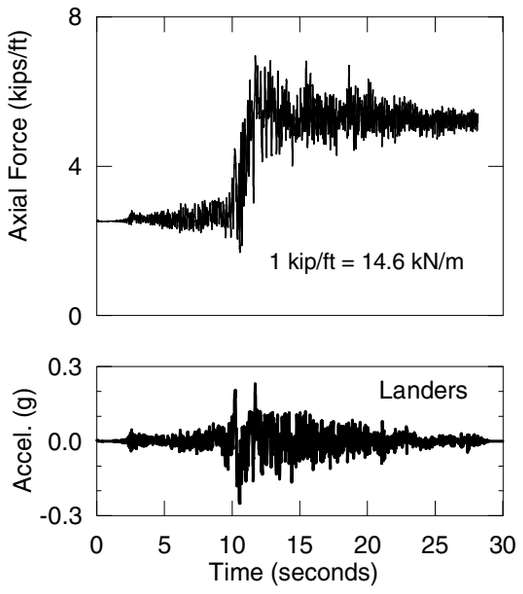


FIG. 6. Swale axial-force history, due to Landers EQ

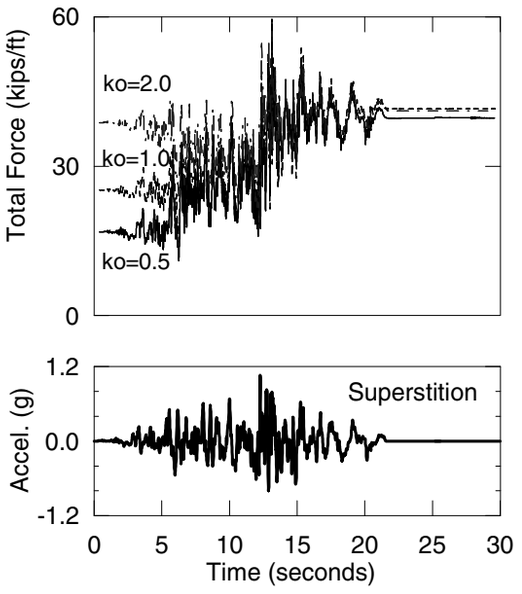


FIG. 7. Total-soil-force history, due to Superstition EQ

Effect of Pre-Shaking Earth Pressure. The effect of pre-shaking earth pressure on the seismic performance of the north wall was investigated by varying K_o. Figure 7 shows computed time histories of total soil forces acting on the reservoir wall for K_o=0.5, 1.0, and 2.0; and Figure 8 presents pre- and post-shaking earth-pressure distributions. Though starting out with significantly different K_o conditions, post-shaking earth pressures were found to be essentially the same for all 3 cases analyzed. This somewhat unexpected outcome suggested that the magnitude of pre-shaking earth pressure acting on the reservoir wall may have little effect on its seismic performance for severe, MCE-level shaking.

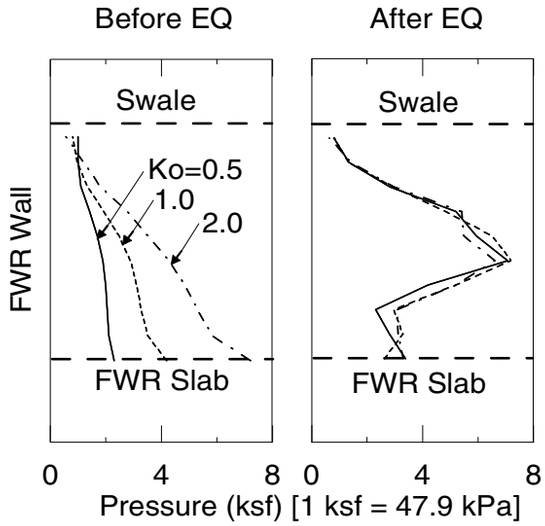


FIG. 8. Pressure distributions before and after EQ

Gravity Stresses and Model Calibration. Notwithstanding the finding above, an attempt was made to establish pre-shaking gravity stresses as realistically as possible by simulating the reservoir's construction history (Figure 3). This exercise also served to establish some degree of model verification, by comparing computed wall deflections for the empty reservoir with survey data from recent reservoir inspections. The pre-shaking analysis consisted of the following steps:

1. backfilling around the empty original reservoir with Ko=0.7 to account for compaction;
2. filling the original reservoir with water;
3. excavating the backfill and installing the external retaining wall; and
4. emptying the reservoir to simulate conditions during inspection when wall deflections were observed and surveyed.

For Steps 1 and 2, Young's Modulus (E) of fresh concrete was taken at 82% of its aged value; and Moments of Inertia (I) for structural members were assumed to be 22% of gross sections to account for creeping (ACI, 2005).

Earth pressure distributions before and after reservoir modification are shown in Figure 9. A maximum wall deflection of approximately ¾ inch was computed for the empty reservoir - within the range of typical deflections of ½ to 1 inch measured at the north wall during recent reservoir inspections (Beikae, 2006).

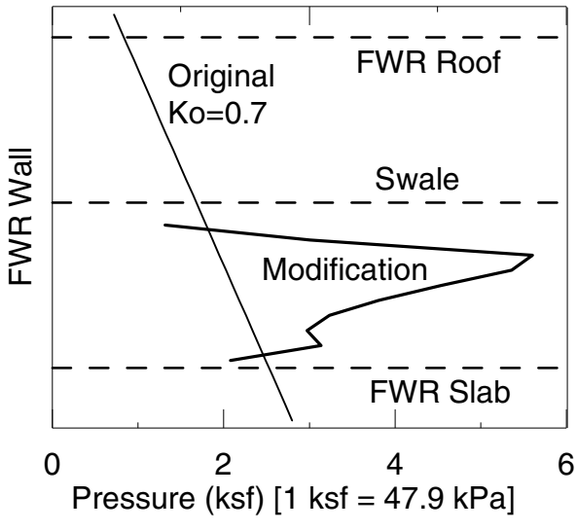


FIG. 9. Pre-shaking earth pressures

Governing MCE Motion. Initial analysis runs were performed for all three MCE motions shown in Figure 4, each applied with both normal and reverse polarity. These analyses identified two critical locations – the wall at mid-height, and the floor slab immediately adjacent to the wall – where plastic hinges developed during shaking. Based on the computed plastic rotations at these locations (Table 3), the Landers-Lucerne based MCE motion at normal polarity clearly governed the seismic performance of the reservoir structure.

Table 3. Initial Analysis Runs - Plastic Rotations

MCE Motion based on	Wall @ mid-height (Radians)	Floor Slab @ corner (Radians)
Landers (normal)	0.0076	0.0059
Landers (reversed)	0.0013	0.0010
Superstition Hills (normal)	0.0016	0.0011
Superstition Hills (reversed)	0.0040	0.0038
Kobe (normal)	0.0034	0.0059
Kobe (reversed)	0	0.05

Seismic Performance. Following Step 4 of the pre-shaking gravity computations, the reservoir was filled again and then subjected to the governing MCE motion. Figure 10 presents a plot of the deformed model after shaking; Figure 11 shows the time history of wall deflection at mid-height; and Figure 12 shows history plots of bending moments and plastic rotations at mid-height wall and the corner of the reservoir floor slab. With computed plastic rotations of less than 0.02 radians, the north wall was concluded to meet FEMA's (2000) "collapse prevention" level of seismic performance.

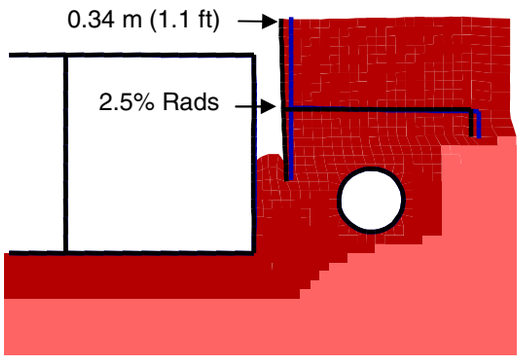


FIG. 10. Permanent deformations after Landers EQ

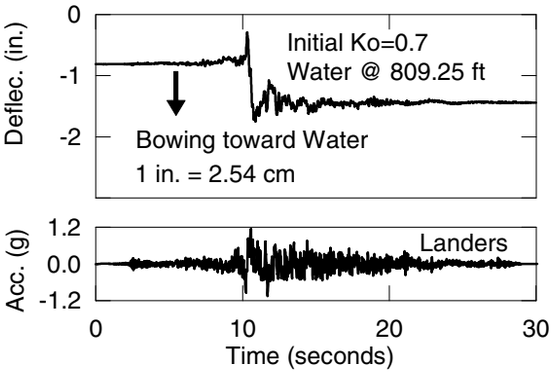


FIG. 11. Wall-deflection history

ANALYSIS OF SOUTH WALL

As shown in Figure 2, the FWR south wall straddles two filled-in ravines which extend about 6.1 (20) to 9.1 m (30 ft) into the reservoir's footprint. At these locations, the reservoir is supported by caissons to bedrock. Initial analyses with the 2D, plane-strain model of Section A-South (Figure 5) indicated that for MCE-level shaking, the outer caisson would fail in bending as it was dragged down-slope by fill sliding out from under the reservoir.

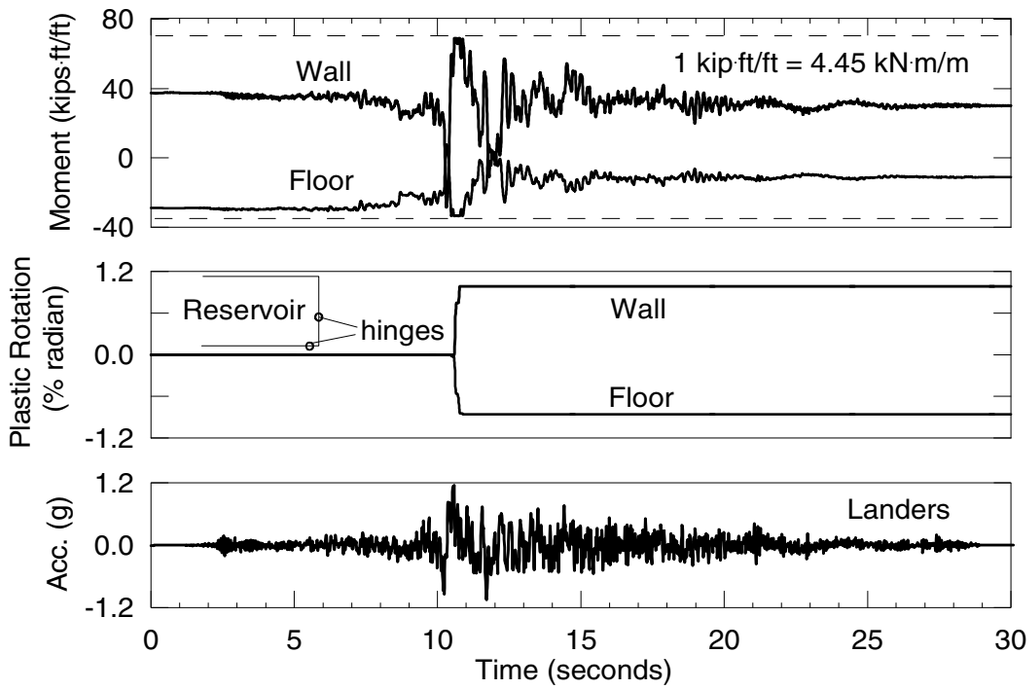


FIG. 12. Moment and plastic rotation histories at wall and floor

Without the possibility to account for out-of-plane bridging by the south wall acting as a deep stiff beam, losing the vertical support from the caisson in this 2D model caused the reservoir to sag and the roof and floor slabs to fail in bending.

The important contribution of the out-of-plane deep beam of the south wall was captured with a simplified 3D-analysis scheme after Mehrain and Naeim (2003). It involved linking, and simultaneously analyzing, two adjacent 2D models (A1 and A2 in Figure 13) with a third model representing the out-of-plane south-wall beam. In addition to being supported by the caissons of sub-models A1 and A2, the wall beam was also supported by 4 springs representing the other caissons along the south wall. Spring constants for the latter were derived from elastic half-space solutions (FEMA, 2000) based on weathered-bedrock properties. For the purpose of this linked analyses, Sections A1 and A2 were analyzed with soil and structural properties adjusted to represent 3 m (10 ft) thick plane-strain slices matching the out-of-plane caisson spacing. The south-wall beam was analyzed with actual (i.e. not distributed) properties; however, the Young's modulus of concrete was reduced by 50% to account for additional deep-beam shear deformations, since FLAC's beam elements only address flexural deformation due to moment bending.

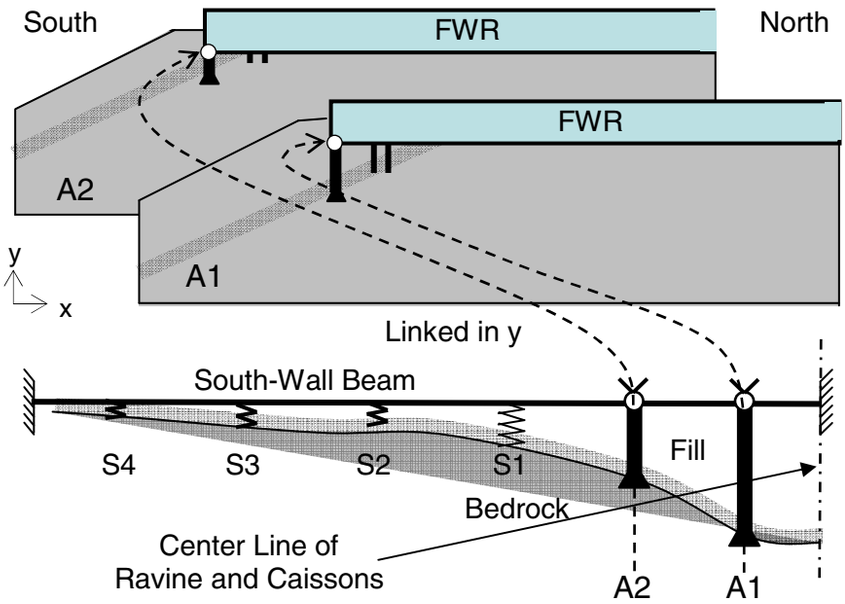


FIG. 13. Model setup for south wall

Figure 14 zooms in on areas of interest of the deformed A1 and A2 models after MCE-level shaking. As the fill outside of the reservoir was sliding down-slope, it separated from the south wall and toppled over into the gap created between it and the wall. The appearance of the fill "crashing through" the south wall is an artifact of the model's inability to "recognize" the presence of the wall once it separated from it. The outer caisson in Section A1 is visibly bent with plastic rotations in excess of 0.05 radians at mid-height and at the top where it connects with the reservoir floor. The axial-force histories in Figure 15 show that this caisson, not only lost its vertical-

support function, but even began pulling down on the reservoir structure as the fill in the ravine moved down-slope. In contrast, axial load of the adjacent shallower caisson in Section A2 was increased by picking up the vertical load shed by the failing A1 caisson.

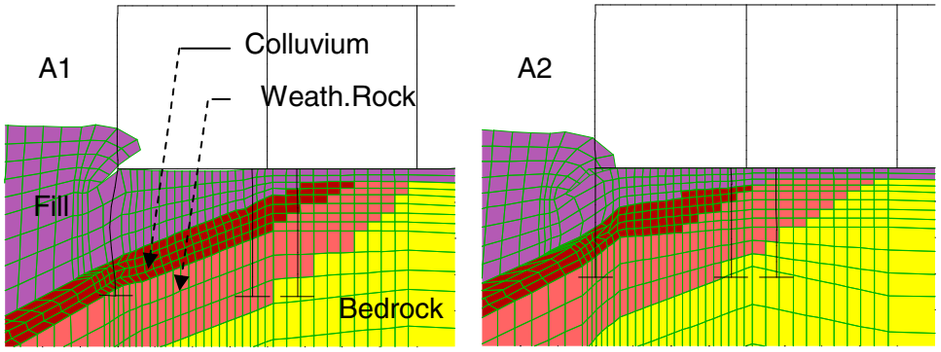


FIG. 14. Deformations for A1 and A2 after EQ

As shown in Figure 16, the deep south-wall beam remained in the elastic range throughout the duration of shaking. The maximum shaking-induced bending moment of the deep wall beam was 14,236 kN-m (10,500 kip-ft), less than its yield moment of 15,117 kN-m (11,150 kip-ft) (Table 2). The only structural member developing a plastic hinge was the reservoir roof (Figure 17). With a computed plastic rotation of less than 0.02 radians, the south wall was also concluded to meet FEMA's (2000) "collapse prevention" level of seismic performance.

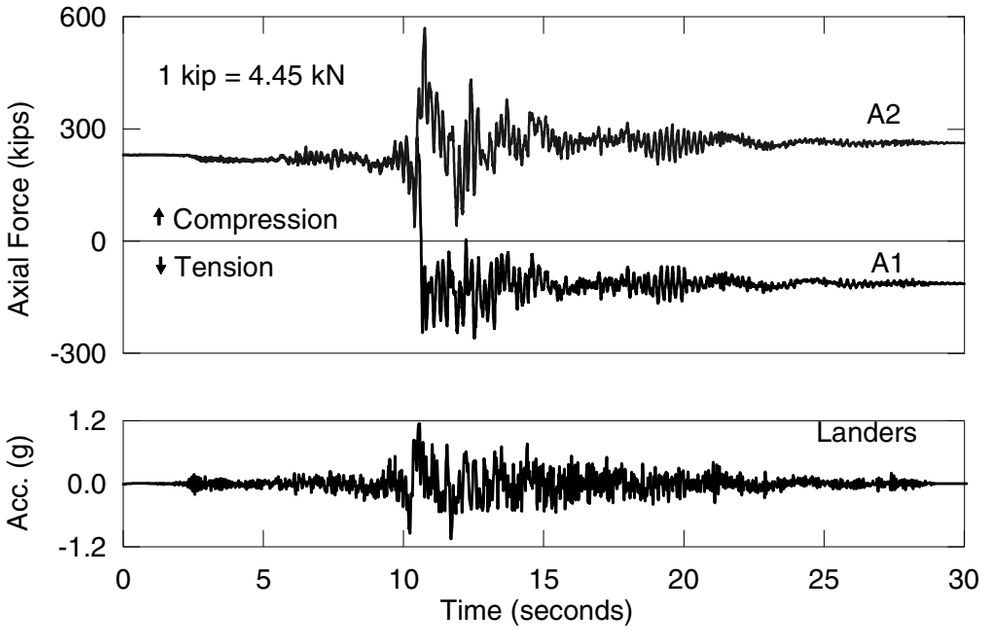


FIG. 15. Caisson axial force histories due to Landers EQ

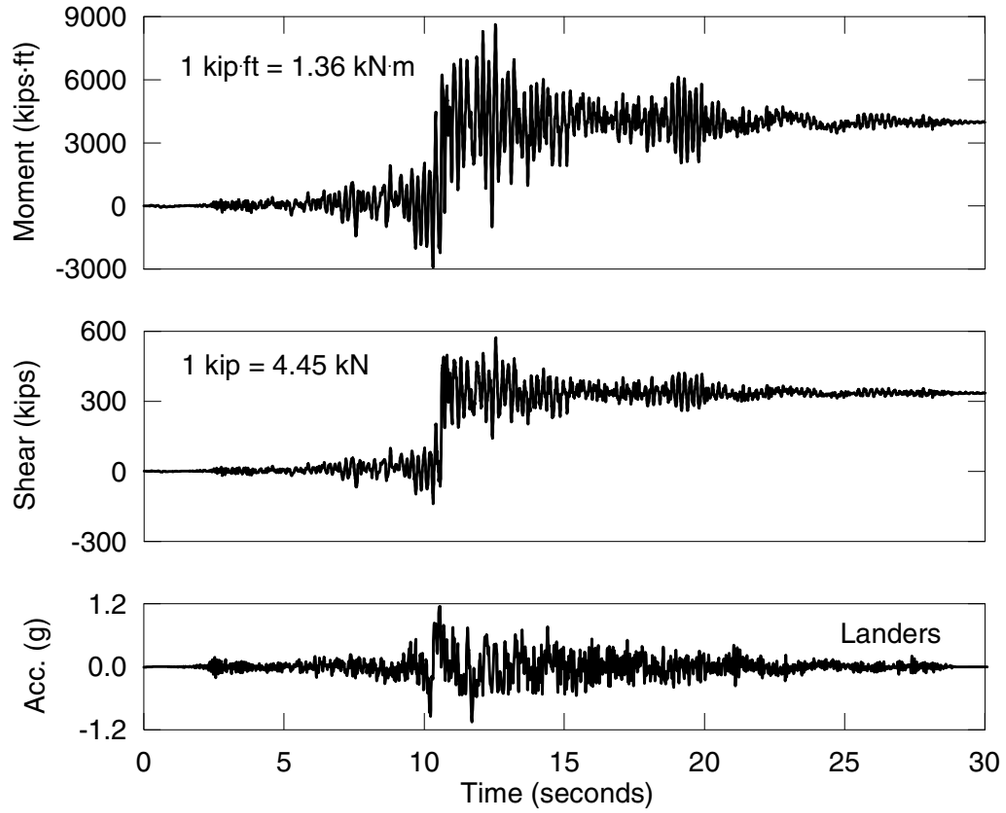


FIG. 16. Deep south-wall beam moment and shear force histories

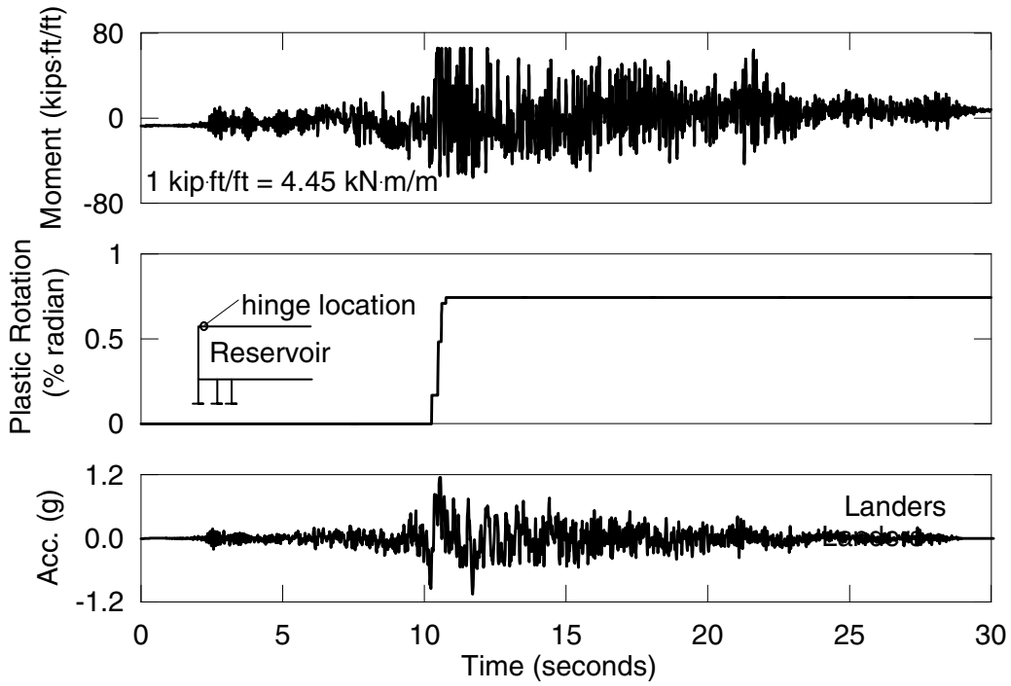


FIG. 17. Moment and plastic rotation histories at roof

STUDY CONCLUSIONS

The seismic performance of the partially buried Finished Water Reservoir (FWR) at MWD's Diemer facility was evaluated by performing dynamic nonlinear SSI analyses with FLAC. In the context of this study, the criterion defining seismic stability was prevention of structural collapse which would result in uncontrolled release of water from the reservoir. FEMA (2000) allows up to 0.02 radians of plastic rotation for "collapse prevention" level of performance of primary structural members. With computed plastic-hinge rotations of less than 0.02 radians for all sections analyzed, the FWR structure was concluded to be seismically stable, preventing uncontrolled release of water.

CLOSURE AND RETROSPECT

Seismic analysis of buried structures falls into the gray area between structural and geotechnical engineering; and to produce meaningful results, close cooperation between the two disciplines is required. This is easier said than done, however, because structural and geotechnical engineers traditionally use different analysis procedures and modeling tools, each focusing on their respective discipline. For analyzing structures, soils traditionally are treated as a mere external load or boundary condition to be applied. As such, the geotechnical engineer provides earth pressure, bearing capacity, or "even" 1D soil springs, and the structural engineer takes care of the rest. While this approach makes for a neat separation of tasks, analysis results can be grossly misleading in either direction - either giving a false sense of safety, or prompting implementation of costly retrofit measures which may be unnecessary.

The particular study discussed in this paper actually began with the traditional "neat separation" approach with geotechnical engineers initially providing dynamic earth pressures, which then would be applied by structural engineers to both the existing FWR north wall, as well as to a proposed retaining structure for confining the fill in the ravines under the FWR south wall. However, when initial trial runs with FLAC demonstrated the great dependency of computed earth pressures on the stiffness of structural members, it became obvious that a fully coupled soil-structure interaction analysis was required. While the structural elements in FLAC may not quite match the sophistication of some dedicated structural programs, this perceived shortcoming was more than compensated for by the intimate participation of structural engineers in interpreting the analysis results.

REFERENCES

ACI, (2005). "Building code requirements for structural concrete." American Concrete Institute, ACI 318-05.

Beikae, M., (2006). "R.B. Diemer Water Treatment Plant, Finished Water Reservoir – Results of inspections and historical report." Internal Report, MWD, Engineering Design Section – Design Unit, May 12.

Dawson, E.M., Roth W.H., Nesarajah S., Bureau G., and Davis C.A., (2001). "A

practice oriented pore-pressure generation model." Proceedings, 2nd Int. FLAC Symposium, Lyon France, October.
FEMA, (2000). "Prestandard and commentary for the seismic rehabilitation of buildings." Federal Emergency Management Agency, FEMA-356, November.
Itasca Consulting Group, (2005). "FLAC, Fast Lagrangian Analysis of Continua, Version 5.0." Minneapolis, Minnesota, USA.
Lysmer, J. and Kuhlemeyer R.L., (1969). "Finite Dynamic Model for Infinite Media." Proc. ASCE, Vol. 95, No.EM4, August.
Mehrain, M. and Naeim, F., (2003). "'Exact' three-dimensional linear and nonlinear seismic analysis of structures with two-dimensional models." Earthquake SPECTRA, Vol. 19, Nov. 2003
Roth, W.H., E.M. Dawson, P. Somerville, C. Davis, and C. Plumb, (2004). "Evaluating the seismic performance of Stone Canyon dam with 2-D and 3-D analyses." 13th World Conf. on Earthquake Eng., Vancouver, B.C., Canada
Roth, W.H. and Dawson, E.M. (2003). "Analyzing the seismic performance of wharves, Part 2: SSI analysis with non-linear, effective-stress soil models." 6th US Conf. and Workshop on Lifeline Earthquake Eng., Long Beach, Cal., August.
URS, (2006)a. "Geotechnical Investigation for Seismic Evaluation of East Wash Water Tank, Robert B. Diemer Water Treatment Plant, Yorba Linda, California." Report, November 22.
URS, (2006)b. "Geotechnical Investigation for Seismic Evaluation of Finished Water Reservoir, Robert B. Diemer Water Treatment Plant, Yorba Linda, California." Phase-1 Draft Report, December 8.
Westergaard, H.M., (1933). "Water Pressures on Dams during Earthquakes." Trans. ASCE, 98, 418-72.

Seismic Characterization and Its Limited Implication for San Pablo Dam

Yoshi Moriwaki[1] M.ASCE, P.E., Andrew Dinsick[2], John Barneich[3], M.ASCE, P.E., Guilaine Roussel[4], M.ASCE, P.E., Atta Yiadom[5], P.E., Fred Starr[6], P.E., and Phalkun Tan[7]M. ASCE, P.E.

[1]Principal, GeoPentech, 525 N. Cabrillo Park Dr. #280, Santa Ana, CA 92701;
yoshi_moriwaki@geopentech.com
[2]Staff Engineer, 525 N. Cabrillo Park Dr. #280, Santa Ana, CA 92701;
andrew_dinsick@geopentech.com
[3]Principal, GeoPentech, 525 N. Cabrillo Park Dr. #280, Santa Ana, CA 92701;
john_barneich@geopentech.com
[4]Principal, Terra Engineers, Inc., 350 Sansome Street, Suite 830, San Francisco, CA 94104;
GuilaineRoussel@terraengineers.com
[5]Associate Civil Engineer, East Bay Municipal Utility District, 375 11th Street, Oakland, CA 94607;
ayiadom@ebmud.com
[6]Senior Civil Engineer, East Bay Municipal Utility District, 375 11th Street, Oakland, CA 94607;
[7]Associate, GeoPentech, 525 N. Cabrillo Park Dr. #280, Santa Ana, CA 92701;
phalkun_tan@geopentech.com

ABSTRACT: This paper presents the results of the seismic characterization of San Pablo Dam in support of the design of seismic upgrades. The limited implication of characterization is also presented. Previous three seismic evaluations of the hydraulically constructed dam concluded that much of the shell portions of the embankment and the foundation soils were potentially liquefiable; these observations were considered appropriate given the perceived nature of the materials and the process of construction. However, a recent stratigraphic and property characterization conducted on the dam indicated a consistently very clayey, very "lumpy", and over-consolidated nature for almost all the hydraulic shell materials. The foundation soils were also found to be very clayey, but less so, and less over-consolidated. The undrained shear strengths of these materials were derived from the available results of laboratory tests. The recent characterization indicates that the shell materials are unlikely to liquefy while liquefaction of the some portions of foundation soils cannot be discounted. The limited implication of this new characterization is also presented.

INTRODUCTION

"San Pablo Dam, made of hydraulic fill (sand, silt and clay placed by pumping an earth-water slurry), was found to be susceptible in places to liquefaction under seismic shaking." So starts the 1985 Civil Engineering article on San Pablo Dam (Billings, 1985). The general perception of how San Pablo Dam might perform under major seismic events as typified by this statement persisted more or less until very recently. This paper presents the seismic characterization of San Pablo Dam located in El

Sobrante, Contra Costa County, California, to support the design of seismic upgrades of the dam. The characterization showed the nature of the embankment materials to be different from those presented or interpreted in previous studies; the paper also briefly addresses the implications of this new characterization on the potential seismic behavior of the dam.

SAN PABLO DAM

San Pablo Dam is a 145-foot-high hydraulic fill embankment dam, constructed between 1916 and 1920 in a canyon formed by San Pablo Creek, with a listed reservoir capacity of 38,600 acre-feet. Compacted downstream and upstream buttresses were added in 1967 and 1979, respectively, to improve the seismic performance of the embankment. The previous seismic evaluations of the dam postulated that much of the embankment shell materials and the foundation soils were potentially liquefiable; this was considered reasonable because the embankment consisted of hydraulic fill, and much of the foundation soils consisted of relatively recent alluvium, colluvium, and landslide materials.

Fig. 1 shows the composite maximum section of the dam, and Fig. 2 is a plan view of the general site area indicating the location of the section. Fig. 1 shows the various zones of the embankment and foundation: (1) upstream shell (hydraulic); (2) downstream shell (hydraulic); (3) ponded clay/silt; (4) core (hydraulic); (5) foundation soils; (6) upstream buttress (well-compacted); (7) downstream buttress (compacted); and (8) bedrock. It should be noted, as shown on Fig. 1, that the dam has a very wide crest of about 130 feet as result of the upstream buttress construction in 1979.

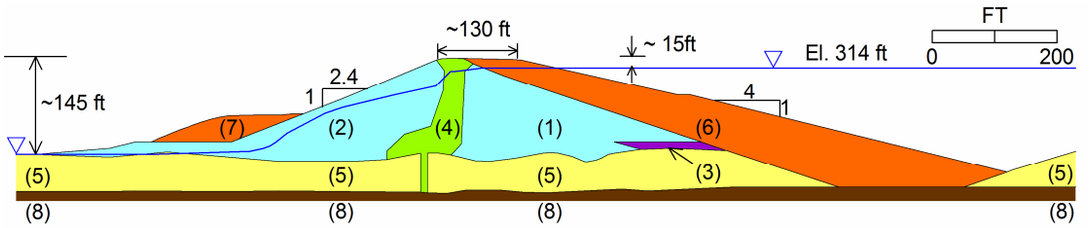


FIG. 1 – Idealized Maximum Composite Section of San Pablo Dam

CURRENT AND PREVIOUS INVESTIGATIONS

The 2006/2007 field investigation and the previous field investigations in the dam area by five organizations are summarized in Table 1; note that the 2006/2007 field investigation includes 24 cone penetration tests (CPT). The approximate locations of these investigations are shown on Fig. 2.

Table 1 – Summary of Current and Previous Field Investigations

Year	1962	1966	1973	1978	2004	*2006/2007*
No. of Borings	54	13	23	18	8	*20*
No. of CPTs	*0*	*0*	*0*	*0*	*0*	*24*

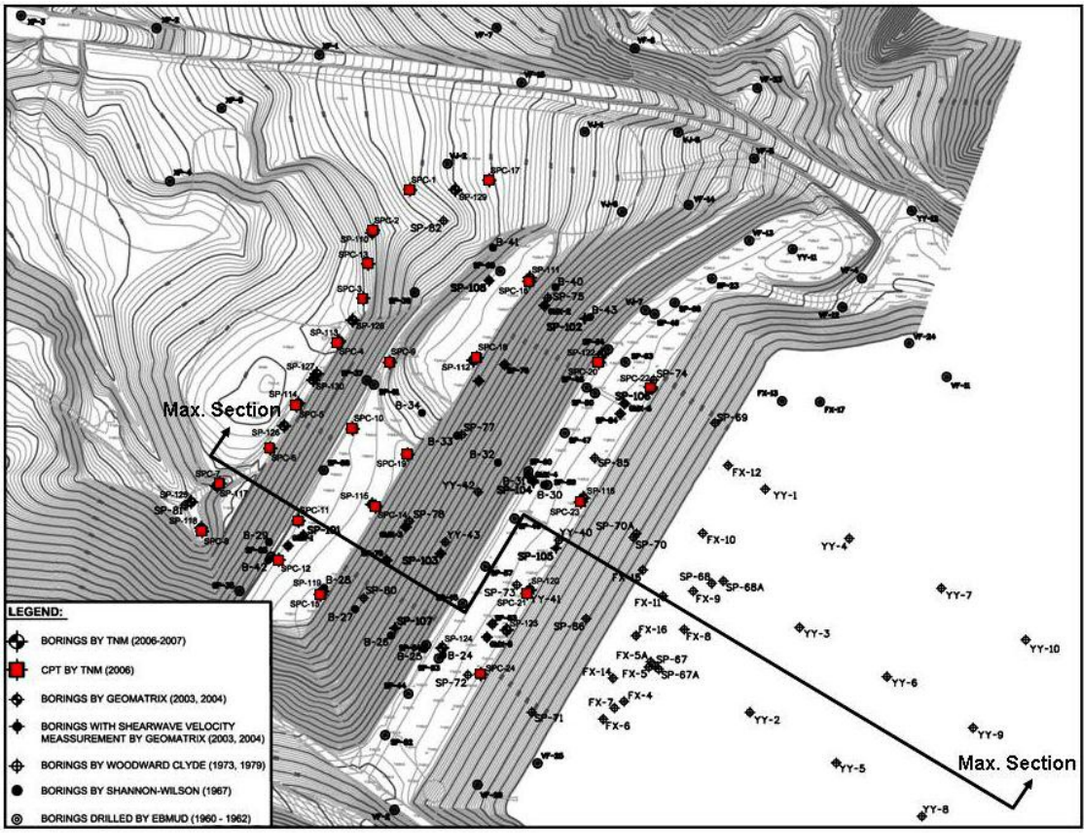


FIG. 2 – Current and Previous Field Investigation Locations

Table 2 summarizes the number of current and previous key laboratory test results on the site materials. The 2007 laboratory testing was in large part guided by the CPT data.

Table 2 – Summary of Laboratory Testing by Year

Year	MC[1]	DUW[2]	AL[3]	SA[4]	ICU'C[5]	CTC[6]	CONS[7]
1962	0	0	0	0	0	0	0
1966	15	15	11	8	17 (2A[8])	21	0
1973	172	90	173	166	0	45	4
1978	60	52	133	102	19	0	0
2004	118	82	117	132	11	0	0
2007	248	9	213	188	6	0	0

[1]Moisture Content; [2]Dry Unit Weight; [3]Atterberg Limits; [4]Sieve Analysis; [5]Isotrophically Consolidated Undrained Triaxial (ICU) Compression Tests; [6]Cyclic Triaxial Compression Tests; [7]Consolidation Tests; [8]Anisotrophically Consolidated Undrained (ACU) Triaxial Compression Tests.

MATERIAL CHARACTERIZATION

Fig. 3 shows typical CPT results in the shell materials and the foundation soils in

terms of tip resistance and friction ratio on the left and in terms of soil behavior index (I_c) and over-consolidation ratio (OCR) on the right. The OCR was estimated using a correlation (Robertson, 2006). The inferred OCR values shown on Fig. 3 correspond only to those with I_c greater than 2.6 (Robertson, 2006). These results were the first indication that the shell materials in particular may be significantly and consistently more clay-like and over-consolidated than stated in, or inferable from, previous studies.

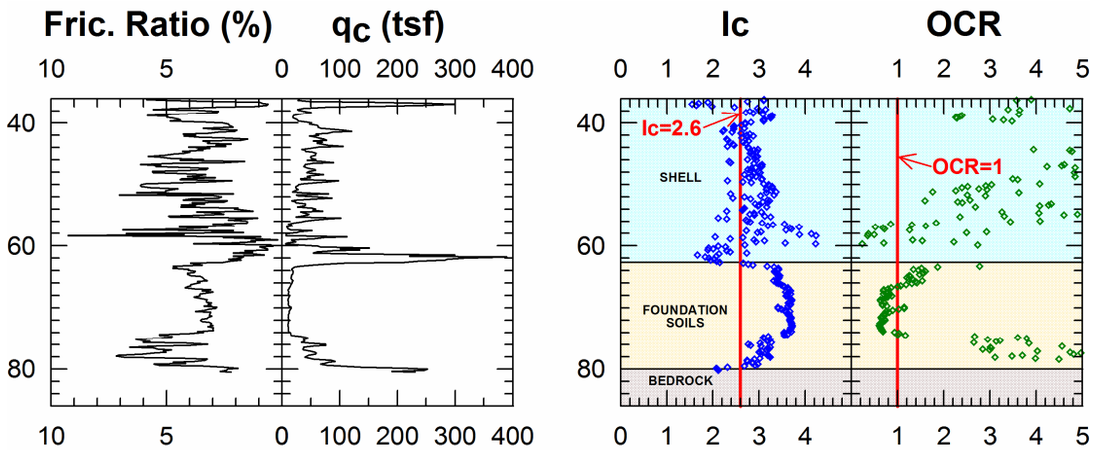
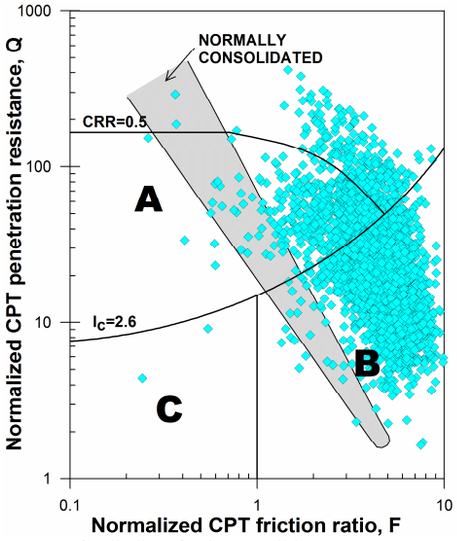


FIG. 3 – Typical CPT Results (I_c and OCR based on Robertson, 2006)

Shell Materials

The relatively large values of friction ratio combined with the moderate values of tip resistance in the shell materials shown on Fig. 3 suggest that the materials are clayey; both the friction ratio and the tip resistance values are also quite jagged. This pattern was seen almost consistently throughout all the CPT soundings in the shell materials. All available CPT results in the shell materials (4064 points) are presented, without "transition corrections," in a soil classification chart (Robertson, 2006) on Fig. 4. The potentially clayey and over-consolidated nature of the shell materials can be inferred from Fig. 4.

Although CPT results are excellent in, for example, evaluating the consistency of stratigraphy, one can only infer the nature of soils through correlations. Test results on actual soil samples are needed to confirm the CPT results. Fig. 5 shows a plasticity chart with all the results of the Atterberg limit tests on samples of shell materials. In total, 194 out of 211 (92%) samples of shell materials exhibited "clay-like" soil behavior with a Plasticity Index (PI) greater than 6. The 16 non-plastic data points shown on Fig. 5 were dominated by two previous studies that seemed to have focused the classification tests on non-plastic samples. Fig. 5 confirms the overwhelmingly clayey nature of the shell materials indicated by the CPT results.



Zone A: Cyclic liquefaction possible;
Zone B: Cyclic liquefaction unlikely;
Zone C: Flow/Cyclic liquefaction possible.

FIG. 4 – CPT Results on Shell

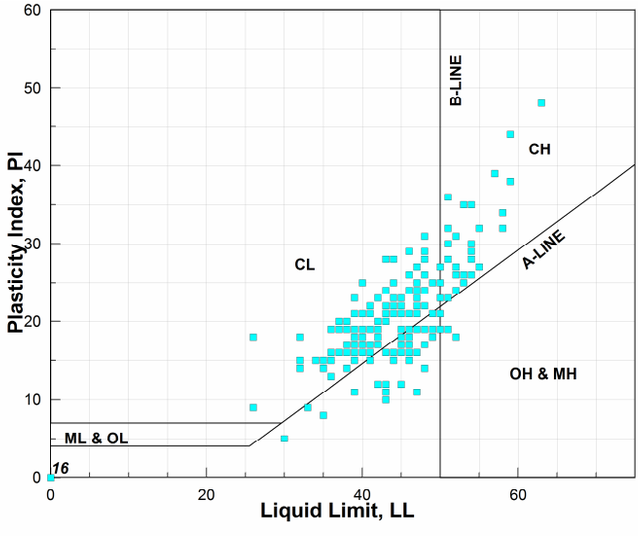


FIG. 5 Atterberg Limit Data on Shell

On Fig. 4 above, the central portion of the plot (shaded gray) is considered to be correlated with normally consolidated soils; the zone to the right of the gray area is correlated with over-consolidated soils while the zone to the left is correlated with sensitive soils (Robertson, 2006). Nearly all of the CPT data on the shell materials shown on Fig. 4 fall into the over-consolidated zone; this indicates that the over-consolidated nature of shell materials may persist throughout all the shell materials.

Observations based on CPT data should be confirmed by information obtained from actual soil samples. Fig. 6 shows a plot of Liquidity Index (LI) versus vertical effective stress using all the 152 samples collected from the shell materials. All but nine data points have a Liquidity Index (LI) below 0.5, strongly confirming the highly over-consolidated nature of the shell materials inferable from the CPT data.

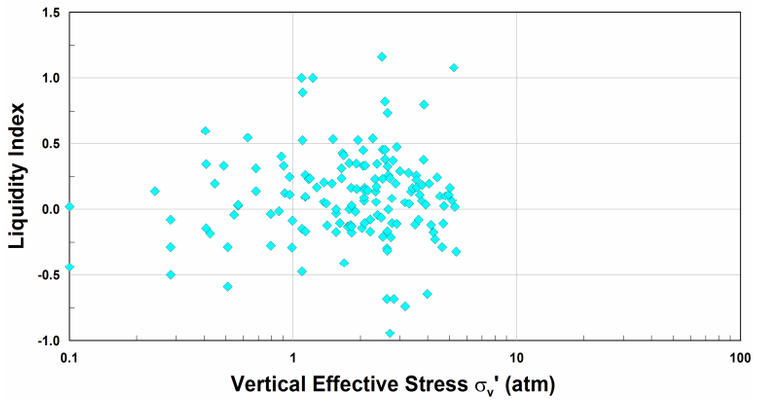


FIG. 6 – Liquidity Index Values of Shell

Although the LI data is based on soils finer than #40 sieve and the information on percent passing #40 was not obtained, the percent passing #200 averages about 40%. Therefore, the LI data are considered representative of the shell materials as a whole.

Tube samples from the site (22 on the shell materials and 36 on other materials) were split in half length-wise and the materials were directly inspected, visually classified, photographed, and sampled for classification testing. Fig. 7 shows typical results of this micro-stratigraphic documentation for the shell materials, visually confirming their clayey and lumpy nature; the CPT and the adjacent boring shown on Fig. 7 were about 10 feet of each other. The lumpy nature of the shell materials was first observed in the field and later confirmed in the micro-stratigraphic documentation. Of the 22 tube samples of shell materials selected for the micro-stratigraphic documentation, 17 subjectively were considered very lumpy and 5 were considered less lumpy. The "jaggedness" of the CPT tip resistance with depth in the shell materials as typified by the results shown on Fig. 3 is considered as reflecting the lumpy nature of the shell materials.

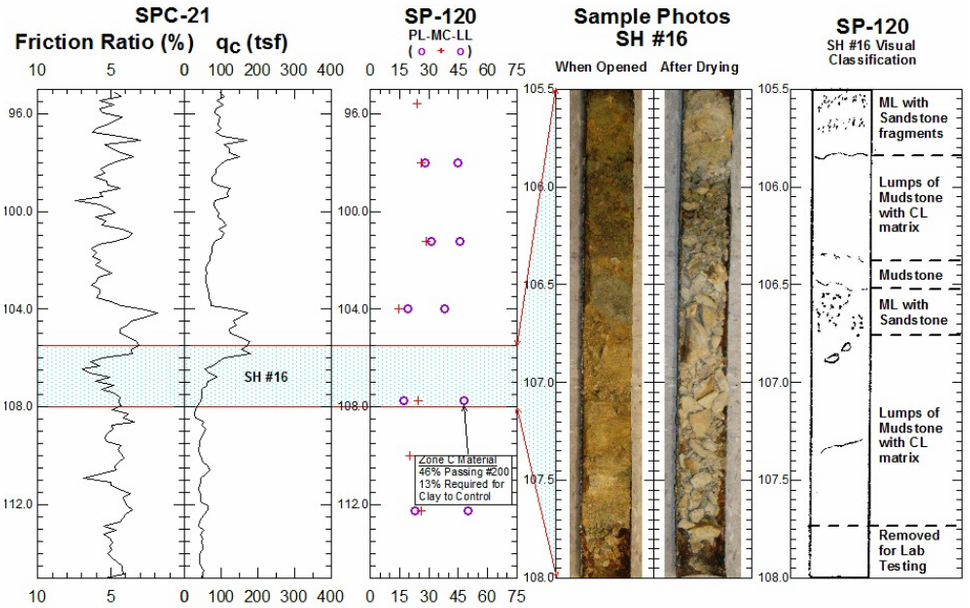


FIG. 7 – Typical Micro-Stratigraphic Results on Shell

Source Material and Construction Process

The shell of the dam was originally constructed from materials excavated from the left and right abutments consisting of siltstone, claystone, fine-grained sandstone, mudstone, and shale. The micro-stratigraphic documentation indicated that the shell materials generally consist of lumps reminiscent of these materials. Based on historical reports addressing the construction of San Pablo Dam (Hazen, 1920; DeCosta, 1934), the source material was excavated using powerful hydraulic jets (in some cases blasted) then hydraulically transported to the canyon using large open-air viaducts. This process preserved much of the source material as rock fragments of various sizes. Fig. 8 is a photograph from Hazen (1920) showing the shell materials as

they are deposited in the canyon. The title of Fig. 8 is the caption included with the original report indicating that rock fragments as large as 1 ft^3 were deposited. From Fig. 8 and other photographs showing the shell materials during construction, the shells of San Pablo Dam may be viewed as "rockfill" consisting of siltstone, claystone, fine-grained sandstone, mudstone, and shale.

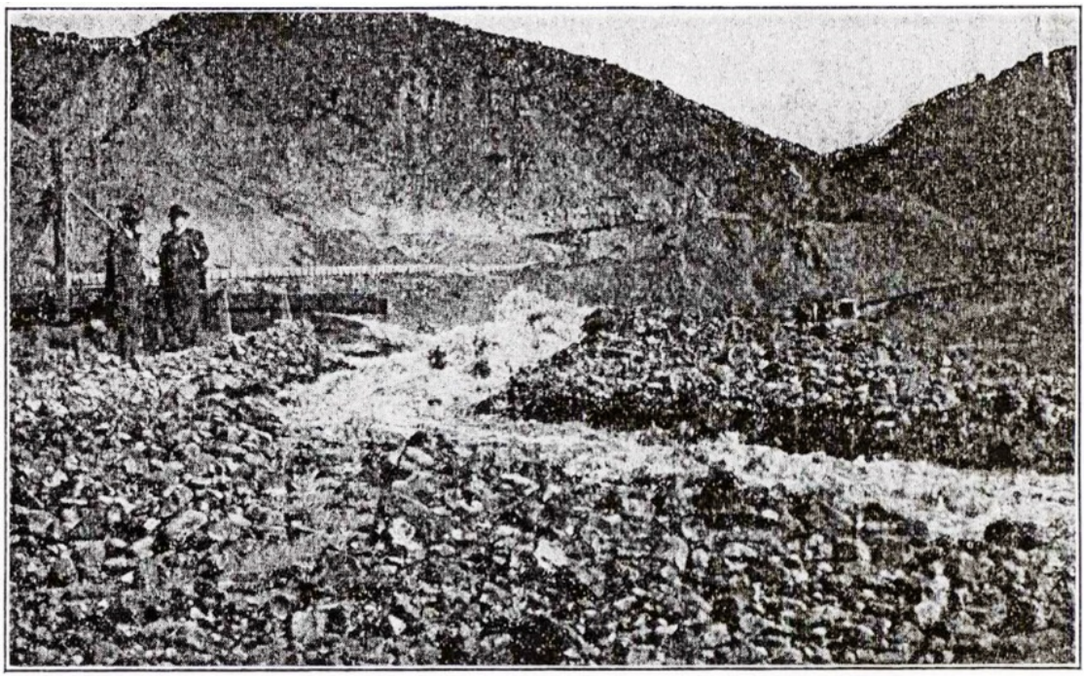


FIG. 8 – Placing Rock Hydraulically in San Pablo Dam, fragments up to 1 ft^3.

The rock fragments were deposited under mostly sub-aqueous environments, often dropped from significant heights. Finer rock particles and other degraded soil particles likely filled most of the void spaces. Unlike pure slurry materials used in typical hydraulic construction, these clayey rock fragments must have preserved their internal denseness. Through physical and chemical interactions with water, most of the clayey rock fragments softened from the surface to form more lumpy looking pieces. The continuing deposition of material along with gravity forced the lumps to be compacted into tighter arrangements. Later, as the reservoir was filled, more water became available to clayey rocks, and over the 90-year period between the deposition and today, the clayey lumps slowly continued to expand as units or to degrade into matrix soils to the extent allowed by surrounding space and pressures. Some lumps eventually became matrix soils although preserving their relative denseness.

The fact that the nature of source materials placed in large fragments often affects the nature of the resulting fill has been documented and discussed in the literature (e.g., Whitman, 1970; Karthikeyan et al., 2002).

Thus, occasional sandy zones such as those seen on Fig. 7 likely represent where sandstone fragments were lodged during construction. These sandy zones are generally tight and quite isolated. Given the very clayey, very lumpy, and over-consolidated nature of the shell materials with just occasional sandy zones, the

potential for liquefaction of significant portions of the shell materials is considered very low.

Foundation Soils

A similar approach was used for the stratigraphic characterization of the foundation soils consisting of alluvium, colluvium, and landslide materials. The foundation soils were also found to be clayey, but less so than the shell materials, and somewhat over-consolidated, but less so than the shell materials, and not lumpy as the shell materials. Out of 162 usable standard penetration tests (SPT), only six data points were considered non-plastic based on the liquefaction susceptibility criteria established by Boulanger and Idriss (2006). Therefore, the liquefaction potential for the foundation soils should not be high. It was conservatively concluded, however, that liquefaction of portions of foundation soils cannot be discounted. The six SPT data points indicate a median liquefied shear strength ratio of 0.16 per Idriss and Boulanger (2007).

Property Characterization

The values of undrained shear strength ratio S_u/σ_{vc}' estimated for the saturated shell materials and foundation soils for use in the seismic deformation analysis are shown on Fig. 9 as a function of effective vertical confining pressure σ_{vc}'. The values of S_u indicated on Fig. 9 were conservatively estimated from the available results of isotropically consolidated undrained triaxial compression (ICUC') tests with pore water pressure measurements. The shear resistance values on the potential failure plane at an axial strain ranging from about 3.4 to 5 percent were used to infer the S_u values from the tests. The estimates for the upstream shell materials were based on 7 tests, those for the downstream shell on 5 tests; and those for the foundation soils on 17 tests. The other properties and materials of less importance are not discussed herein.

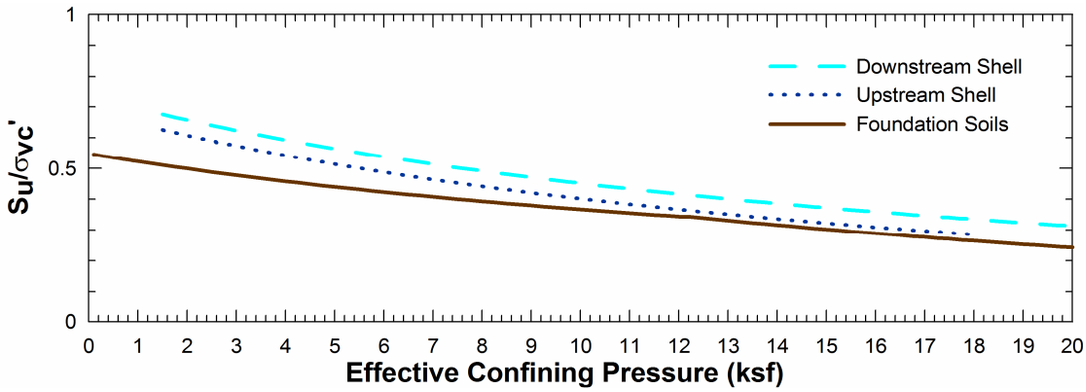


FIG. 9 – Undrained Shear Strength Estimate Comparison

SEISMIC PERFORMANCE EVALUATION

A recent seismic deformation analysis of the dam used an input motion

corresponding to an 84th percentile moment magnitude 7-1/4 earthquake on the Hayward-Rodgers Creek fault at about 3 km from the site. That analysis, which postulated liquefaction of all of foundation soils and all of the embankment materials excluding the core and buttresses, concluded that the crest of the dam may settle by as much as 35 feet accompanied by very large lateral downstream displacements of the embankment.

Fig. 10 shows the deformation contours of the section calculated using FLAC based on the new characterization of the shell materials, but very conservatively assuming that all of the foundation soils would liquefy to a strength ratio of 0.16. The input motion with a peak ground acceleration of 0.96g used in the analysis is similar to that used in the analysis results described above. The computed crest settlements vary from almost 4 feet to a slightly more than 6 feet.

Using the material characterization reflected on Fig. 10 as the extreme case to check the design, seismic upgrades of the dam that combine deep soil mixing through the foundation soils and a new downstream buttress are being designed at the time of writing.

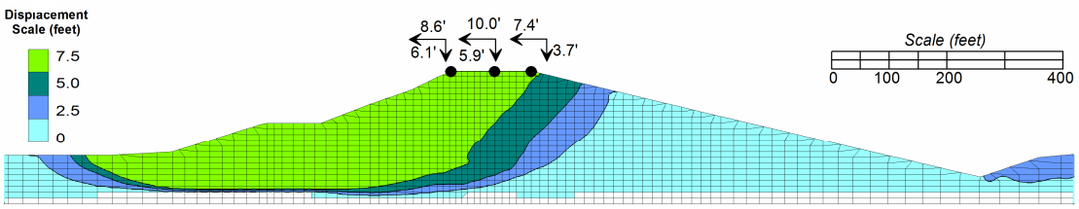


FIG. 10 – Contours of Calculated Total Seismic Displacements

CONCLUSIONS

Previous seismic evaluations of the hydraulically constructed San Pablo Dam concluded that much of the embankment materials and the foundation soils may be potentially liquefiable. However, the material characterization conducted recently that combined CPT, soil borings, and laboratory testing indicated a consistently very clayey, very “lumpy”, and over-consolidated nature for almost all the hydraulically placed embankment shell materials. The review of the source and the process of construction confirmed the reasonableness of these observations. The foundation soils were also found to be very clayey, but less so, and less over-consolidated. The undrained shear strengths of the embankment and foundation materials were derived from available laboratory test results. The results of the recent material characterization indicate that the shell materials are unlikely to liquefy while liquefaction of portions of the foundation soils cannot be discounted. The results of the seismic deformation analysis of the dam reflecting the new characterization emphasize the importance of the soil characterization in future seismic upgrade evaluations.

ACKNOWLEDGEMENT

J.K. Mitchell, R. Pyke, D. Babbitt, I.M. Idriss, R. Seed, R. Boulanger, P. Nicholson, and M. Tabatabaie reviewed many phases of the work presented herein as members of

two separate review boards.

REFERENCES

Boulanger, R.W. and Idriss, I.M. (2006). "Liquefaction Susceptibility Criteria for Silts and Clays," J. Geotech. and Geoenviron, Engineering, November.

Billings, H.J. (1985). "Hydraulic Fill Dam Made Earthquake Resistant," *Civil Engineering*, June: 56-59.

DeCosta J.D. (1934). "Feature Report #17 Investigation of the Embankment at San Pablo Dam," dated January 15.

East Bay Municipal Utility District, Foundation Design Section (1962). "San Pablo Dam Spillway, Soils and Foundation Investigation," dated February.

Geomatrix Consultants, 2004, Dynamic Stability Analysis of San Pablo Dam, Contra Costa County, California, Volumes 1 and 2: dated October 22.

Hazen A.M. (1920). "Hydraulic Fill Dams," *ASCE Papers and Discussions*, Vol. XLVI, No. 4, dated April.

Idriss, I. M., and Boulanger, R. W. (2007). "SPT- and CPT-based relationships for the residual shear strength of liquefied soils." Earthquake Geotechnical Engineering, 4th International Conference on Earthquake Geotechnical Engineering – Invited Lectures, K. D. Pitilakis, ed., Springer, The Netherlands, 1-22.

Itasca (2000). FLAC – Fast Lagrangian Analysis of Continua, User's Guide, Itasca Consulting Group Inc., Minneapolis, Minnesota.

Karthikeyan, M., Dasari, G. R., Tan, T.S. (2002). "In Situ Characterization of Land Reclaimed Using Big Clay Lumps," Canadian Geotechnical Journal, Vol. 41, 242-256.

Mitchell J. K. and Soga K. (2005). *Fundamentals of Soil Behavior*, Third Edition 2005, John Wiley & Sons, Inc.

Robertson P. K. and Wride C.E. (1998). "Cyclic Liquefaction and its Evaluation based on the CPT," *Canadian Geotechnical Journal*, Vol. 35, August.

Robertson P. K. (2006). *Guide to In-Situ Testing*, Gregg Drilling & Testing, Inc.: dated January.

Shannon and Wilson (1966a). "Review of Stability, San Pablo Dam" dated March 16.

Shannon and Wilson (1966b). "Addendum to Review of Stability, San Pablo Dam," dated August.

TNM (2007). "Design Services for San Pablo Dam Seismic Upgrades, Supplemental Field Exploration and Laboratory testing in Dam Area, Data Report," Prepared for East Bay Municipal Utility District: dated March.

Whitman, R. V. (1970). "Hydraulic Fills to Support Structural Loads," ASCE, Journal of Sol Mechanics and Foundation Divison, Vol. 98, No. SM1, January, 23-47.

Woodward-Lundgren & Associates (1973). "Evaluation of the Seismic Stability of San Pablo Dam, Contra Costa County, California," dated October 12.

Woodward-Clyde Consultants (1979). "San Pablo Dam Modifications Supplemental Exploration Program, Re-examination of Seismic Stability," dated October 5.

Seismic Deformation Analyses of the New Coquitlam Dam

Li Yan[1], M.ASCE, P.Eng., Alex, Sy[2], M.ASCE, P.Eng., and T. Thavaraj[3], P.Eng.

[1] Project Engineer Specialist, BC Hydro, A02 – 6911 Southpoint Drive, Burnaby, B.C., CANADA, V3N 4X8; Li.Yan@BCHydro.bc.ca
[2] Vice President, Engineering, Klohn Crippen Berger Ltd., Suite 500 – 2955 Virtual Way, Vancouver, B.C., CANADA, V5M 4X6; asy@klohn.com
[3] Geotechnical Engineer, Klohn Crippen Berger Ltd., Suite 500 – 2955 Virtual Way, Vancouver, B.C., CANADA, V5M 4X6; tthavaraj@klohn.com

ABSTRACT: Coquitlam Dam is a 30 m high embankment dam constructed in the early 1910s. The dam site is situated in a region of high seismic hazard in British Columbia, Canada. The existing dam's core and shells, and part of the dam foundation are deemed to be liquefiable under the design earthquake loading. Seismic upgrade to the Coquitlam Dam is currently being implemented by constructing a new compacted earth core rockfill dam at the downstream toe of the existing embankment. The new dam will be mostly founded on dense glacial deposits. Due to site and constructability constraints, a portion of the upstream slope of the new dam will sit on part of the downstream rockfill toe of the existing dam that is underlain by liquefiable sand and gravel alluvium along the original river channel. This paper describes the analyses carried out to conservatively assess the seismic performance of the new embankment dam. Deformation analyses using the 2-D plane strain finite difference program FLAC showed that displacements of up to about 1.1 m vertically and 0.4 m horizontally could occur at the dam crest under the design earthquake loading. Treatment of the liquefiable alluvium is thus deemed not necessary. The anticipated movements can be safely accommodated by the new dam that has been designed with sufficient freeboard, and suitably wide upstream and downstream filter and transition zones.

INTRODUCTION

Coquitlam Dam is located on the Coquitlam River, 15 km upstream of its confluence with the Fraser River, near the City of Port Coquitlam in British Columbia, Canada. The dam is owned and operated by BC Hydro that not only provides storage for power generation but also supplies fresh water to the Greater Vancouver Regional District. The existing earthfill dam has a crest length of 250 m, a crest width of 3.8 m, and a maximum height of 30 m. The dam was constructed between 1911 and 1913, and consists of upstream and downstream rockfill toes, and hydraulically placed earthfill core and shells. The core comprises silt and sandy silt with inter-layered fine sand and

silty sand, and the shell is inter-layered sand and gravel with local sandy silt and silty sand layers. Rockfill reinforcements were added to portions of the upstream and downstream slopes in the 1980s to improve the earthquake stability of the dam. The dam is generally founded on a unit of stiff silt which overlies a dense sand and gravel stratum, except along the original river channel where alluvium soils exist beneath the dam, and at the left abutment where a soft silt unit and bedrock form part of the dam foundation. The original river channel lies under the approximate centre of the dam.

The dam site is situated in a region of high seismic hazard. The design earthquake for the project is a moment magnitude of 7.5 with a firm-ground horizontal peak ground acceleration (PGA) of 0.66 g. Refer to Yan et al. (2007) for more details on the seismic hazard assessment and design criteria for this site.

As part of BC Hydro's dam safety program, the seismic stability and remediation options for Coquitlam Dam were assessed. The assessment showed that the existing dam's hydraulically placed core and shells, and part of its foundation comprising the alluvial soils within the original river channel are liquefiable under the design earthquake shaking. A seismic upgrade option, consisting of constructing a new embankment at the downstream toe of the existing dam, was selected. The new downstream embankment consists of an earth core rockfill embankment to be mostly founded on a sequence of glacial deposits, and a concrete transition to be founded on bedrock at the left abutment. Figures 1 and 2 show the plan and sectional views, respectively, of the existing and new dams.

Construction of the rockfill embankment for the new dam requires excavation of a small portion of the downstream slope of the existing dam and removal of a layer of potentially liquefiable alluvium deposit (Unit 6A – Sand and Gravel), which overlies the glacial deposits along the original river channel. The downstream excavation has to be limited within the existing downstream rockfill toe because of stability concern of the existing dam during construction. A portion of liquefiable alluvium deposit (Unit 6A) remains beneath the downstream rockfill toe of the existing dam, and forms part of the foundation for the upstream slope of the new embankment. The liquefiable alluvium left in place under the upstream slope of the new dam is highlighted in Figures 1 and 2. This zone is about 35 m by 40 m in plan and 3 m to 5 m thick. Jet grouting was initially considered to strengthen this liquefiable zone. However, because of the limited extent of this liquefiable material under the new dam, and the high costs and uncertainties associated with jet grouting of coarse sand and gravel (Unit 6A) deposits, the "no treatment" option, in which the liquefiable Unit 6A zone is left untreated and resulting potential dam deformations accommodated in the design of the new embankment, was chosen as the final solution.

This paper describes the analyses conducted to conservatively estimate the seismic deformation and to verify that the new dam will perform satisfactorily under the design earthquake shaking.

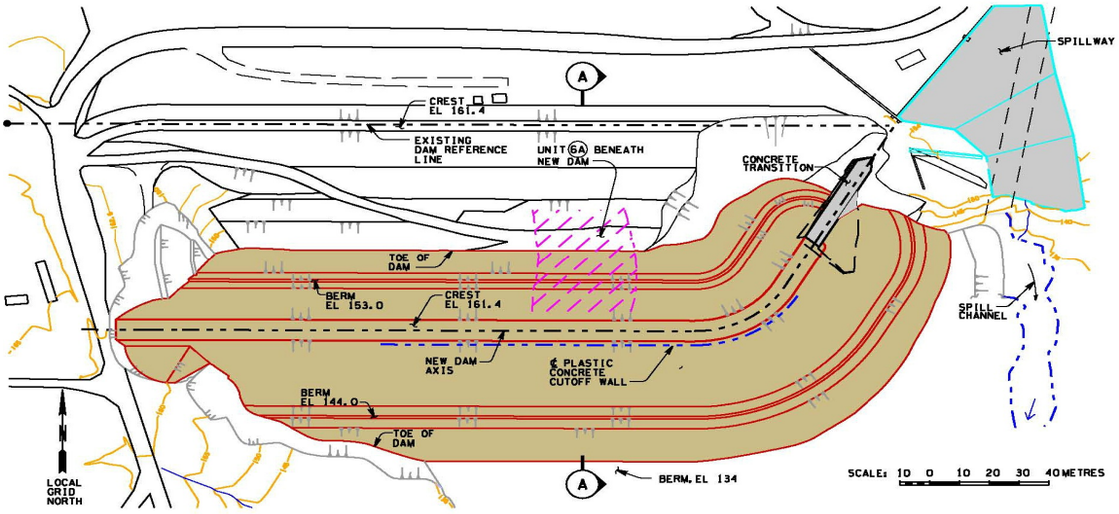


FIG. 1. Plan View of the Existing and New Coquitlam Dam

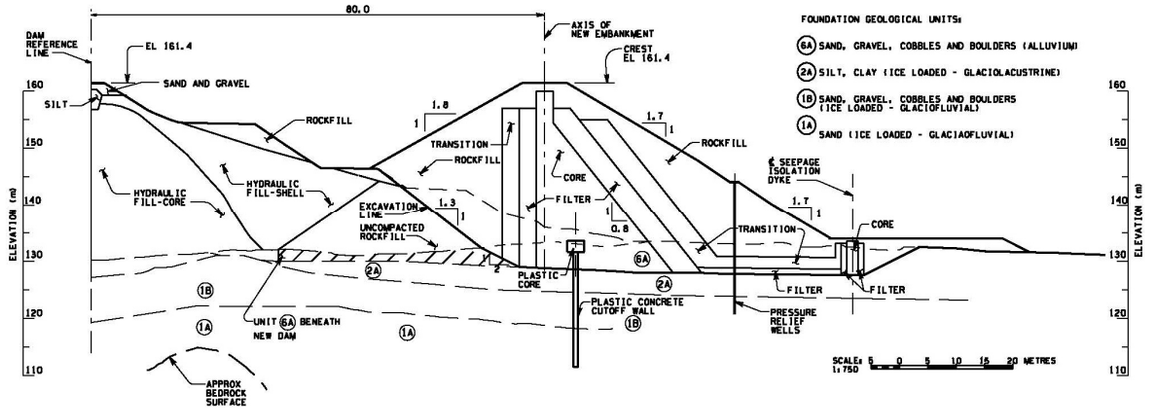


FIG. 2. Sectional View of the Existing and New Coquitlam Dam

FOUNDATION CONDITIONS

As shown in Figure 2, the downstream section of the existing embankment consists of a surficial rockfill slope layer (uncompacted, placed in 1980s) overlying the original hydraulic fill shell (sand, gravel and cobbles) and retained by the original rockfill toe (railcar-dumped gravel to boulder size). Unit 6A alluvium underlies the rockfill zone. Beneath Unit 6A lies the stiff to very stiff Unit 2A glacio-lacustrine silt, and the very dense Unit 1B glacio-fluvial sand and gravel. Refer to Yan et al. (2007) for more details of foundation conditions.

The Unit 6A alluvium is about 3 to 5 m thick in the former Coquitlam River channel. The deposit consists of gravel and sand, with up to 10% fines, and contains rounded cobbles and boulders. The gravel is typically sub-rounded to sub-angular. The equivalent $(N_1)_{60}$ values, evaluated from Becker Penetration Tests (BPT), typically range from 10 to 30, with an average of about 15, as shown in Figure 3. Figure 3 also

shows that the limited $(N_1)_{60}$ values measured directly from standard penetration tests were generally much higher than the equivalent $(N_1)_{60}$ values from BPTs, likely due to influence of large particles in the Unit 6A. Pump tests indicate that the deposit has horizontal permeability $k_h = 1x10^{-2}$ cm/s and vertical permeability k_v = 1/5 to 1/10 k_h. The water level in this section of the dam is near the top of the Unit 6A deposit.

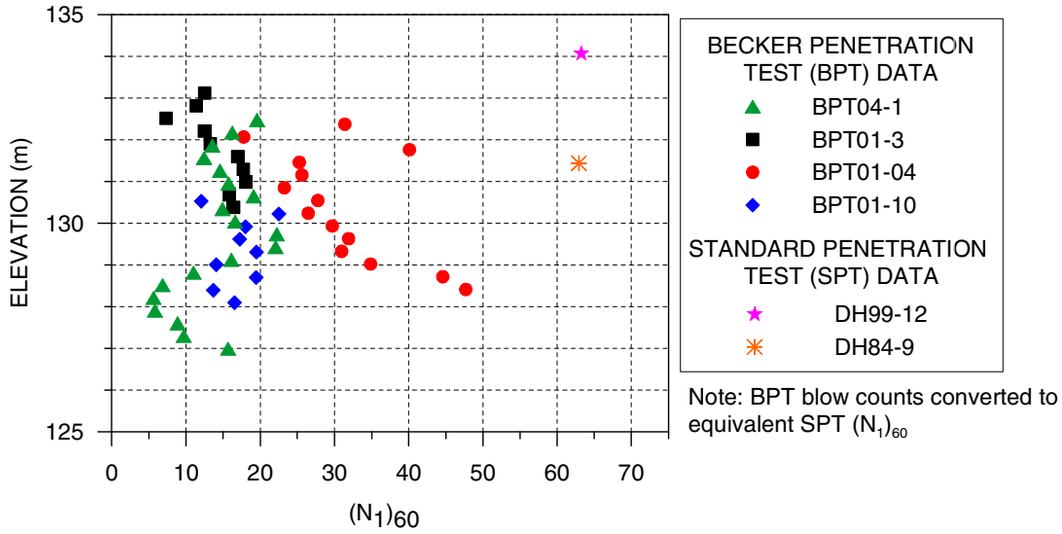


FIG. 3 Equivalent SPT $(N_1)_{60}$ Values of Unit 6A Alluvium

DAM MODEL USED IN ANALYSES

A simplified and conservative dam model was used in both the post-liquefaction static limit equilibrium analyses and seismic deformation dynamic analyses of the new dam. The existing dam was not modeled under its "as is" or pre-earthquake condition due to limitation of numerical modeling of large flow slides. The model assumes that the existing dam has already failed due to seismic liquefaction, and undergone a large upstream flow slide, resulting in a 10H:1V sloping berm resting on the upstream slope of the new dam, as shown on Figure 4. Post-liquefaction properties were assigned to this berm in the analyses. Therefore, the model is expected to give a conservative estimate of the seismic deformation and post earthquake stability of the new dam, as the existing dam is not likely to flow away during the period when the new dam is subjected to the design earthquake shaking. The actual upstream buttressing effect of the existing dam is expected to be more than assumed in the model. However, given the uncertainties in the post-earthquake performance of the existing hydraulic fill dam, the designers felt that it is prudent to use this conservative model in the assessment of the expected performance of the new dam that includes some liquefiable soils.

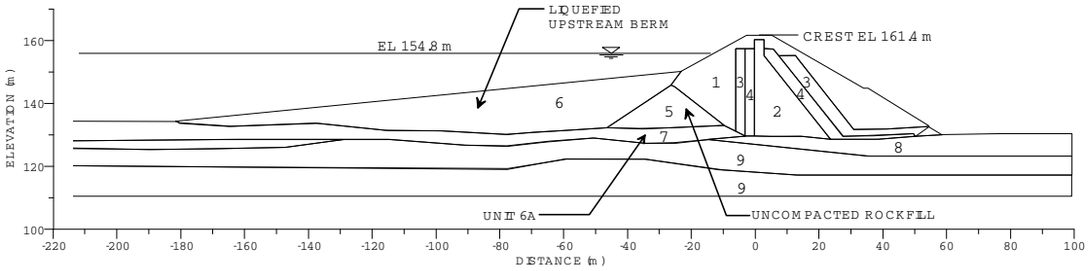


FIG. 4. Model of the New Dam Used in Seismic Stability Analyses

POST-LIQUEFACTION STATIC LIMIT EQUILIBRIUM ANALYSES

Post-liquefaction limit equilibrium analyses of the dam were first carried out using the computer program CLARA-W (Hungr, 2001) to assess any 3D effects of the limited extent of liquefiable Unit 6A beneath the upstream slope of the new dam. The Bishop's simplified method (Hungr, 1987) and Janbu's method were used to determine the 2D and 3D factors of safety (FOS). In the analyses, the Unit 6A was treated as liquefied, and post-liquefaction residual strength of 30 kPa was assigned to this unit, and the remnant of the failed existing dam represented by the upstream 10H:1V slope berm was assumed to have a residual strength of 10 kPa. These residual strengths were estimated from 33 percentile values from Seed and Harder (1990).

Nine transverse (perpendicular to the dam axis) sections were used to develop the 3D model of the dam. The width of the model measured along the dam axis was about 112 m, and it encompassed the entire Unit 6A existing beneath the upstream slope of the new dam. Table 1 shows the material properties used in the limit equilibrium analyses. Additional sensitivity analyses were carried out by varying the residual strength of the liquefied Unit 6A alluvium.

Table 1 Material Properties Used in Limit Equilibrium Analyses

Material Number/Type	Unit Weight (kN/m^3)	Cohesion (kPa)	Friction (Degrees)
New Dam			
1. Compacted Rockfill	21.6	0	45
2. Compacted Till Core	19.6	0	35
3. Compacted Transition Sand and Gravel	20.6	0	37
4. Compacted Filter Sand	20.6	0	35
Existing Dam and Foundation			
5. Uncompacted Downstream Rockfill Toe	21.6	0	40
6. Liquefied Downstream Hydraulic Fill Shell	20.0	10	0
7. Liquefied Unit 6A Alluvium	20.0	30	0
8. Unit 2A (Stiff to Very Stiff Silt)	19.6	0	37
9. Unit 1A and 1B (Dense Sand and Gravel)	21.2	0	40

A composite sliding surface consisting of a weak plane lying within Unit 6A and ellipsoid elsewhere was mainly considered in the CLARA-W 3D analysis. A systematic search was carried out to locate the critical sliding surface. The minimum 3D FOS is 2.2 by Bishop's method, and 2.1 by Janbu's uncorrected method. The corresponding 2D FOS is 1.4 by Bishop's method, and 1.3 by Janbu's method. These analyses indicate that the 3D post-liquefaction FOS is about 1.6 times higher than the corresponding 2D FOS. Therefore, a significant 3D effect is expected. The new dam will have sufficient FOS against post earthquake upstream movements, even with the liquefaction of the remaining Unit 6A alluvium underneath the upstream slope of the dam. Figure 5 shows a sectional view and an isometric of the 3D sliding surface.

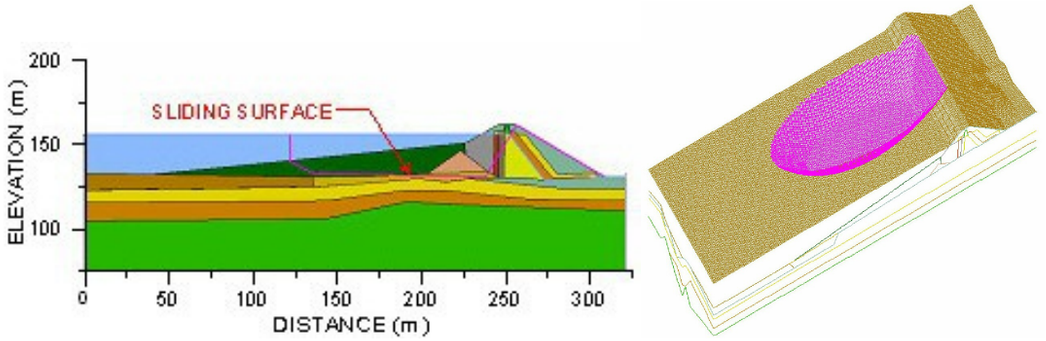


FIG. 5. Sectional and Isometric Views of the 3D Sliding Surface

SEISMIC DEFORMATION ANALYSES

Methodology

The seismic response of the remediated dam under the design earthquake was determined using the 2-D plane strain finite difference program FLAC Version 4 (Itasca, 2004). The input motion was applied at the base of the model, which was taken to be in Unit 1A, and the base at El. 110 m was treated as rigid. Unit 6A was treated as potentially liquefiable and allowed to trigger liquefaction during earthquake shaking. A linear elastic-perfectly plastic model with Mohr-Coulomb failure criterion was used for the dam and foundation materials in the static and dynamic FLAC analyses. The same model was also used to characterize the pre-liquefaction and post-liquefaction behavior of Unit 6A. The dam model (i.e. with failure of the existing dam) shown in Figure 4 was used in the FLAC analyses.

The seismic analysis was carried out essentially in three steps: (1) perform static analysis using static properties to establish the in-situ static stress state in the dam model; (2) perform dynamic analysis in time domain using dynamic properties starting from the insitu static stress state; and (3) trigger liquefaction in Unit 6A at a pre-selected time, reduce the strength and stiffness of Unit 6A to its post-liquefaction values, and continue the seismic analysis while maintaining dynamic equilibrium at every time step.

The dynamic phase of the analysis used the Mohr Coulomb model in combination with Rayleigh mass and stiffness proportional viscous damping. The elastic moduli for the dynamic analysis were obtained from the small strain shear moduli, G_{max}, along with an appropriate modulus reduction factor to account for the shear strain level effects on the modulus. A modulus reduction factor of 0.2 and equivalent viscous damping ratio of 10% were used for all materials. These parameters were estimated from FLUSH (Lysmer et al., 1975) and SHAKE (Idriss and Sun, 1992) analyses.

A total stress "instant triggering" approach similar to the one proposed by Beaty and Byrne (1999) was used to simulate the triggering of liquefaction of Unit 6A and take into account its effect on the overall seismic response of the dam. The time of liquefaction triggering was set to the time of the first major peak in the acceleration time history. Prior to triggering, pre-liquefaction properties were used for Unit 6A (friction angle of 35°), and the post-liquefaction properties, such as the post-liquefaction undrained residual strength and post-liquefaction modulus, were turned on at the time of the triggering and maintained until the end of earthquake shaking. The effects of excess pore pressure rise prior to liquefaction were not considered in this total stress approach.

The post-liquefaction undrained residual shear strength of Unit 6A was taken as 30 kPa, and the limiting shear strain to reach the residual strength was taken as 2.5%. The post-liquefaction undrained shear strength of the existing dam downstream shell material under the 10H:1V upstream berm was taken as 10 kPa. As a conservative approximation, this strength was used for the existing dam materials in the analysis, and no liquefaction triggering procedure was imposed for this material. The strength properties in Table 1 were used in the FLAC deformation analyses, except for the rockfill. For rockfill, the mean and lower bound correlations between friction angle and normal pressure proposed by Leps (1970) were used for the compacted and uncompacted rockfills, respectively, with maximum values limited to 50 and 45 degrees, respectively. For all dam fills and foundation Unit 6A, the low strain shear modulus, G_{max} was estimated using $G_{max}= 21.7\ K_{2max}\ P_a\ (\sigma'_m/P_a)^{0.5}$ where K_{2max} is the low strain shear modulus parameter, σ'_m is the in-situ mean normal stress, and P_a is the atmospheric pressure. K_{2max} values were estimated from Seed et al. (1986).

The earthquake time history used in the dynamic analysis was the TCU129 (E-W component) record from the M_w 7.6 Chi-Chi (Taiwan) earthquake of 1999. The recorded time history (PGA of 1.01 g) was scaled to a PGA of 0.66 g for use as the input motion. As shown in Figure 6, the response spectrum of the scaled Chi Chi earthquake reasonably matched the uniform hazard target spectrum for the site, around the fundamental period of 1.3 sec of the new dam. This time history was the most severe of the suite of time histories used in seismic stability analysis of the dam. The record was applied in both directions in FLAC analysis to determine the worse displacements.

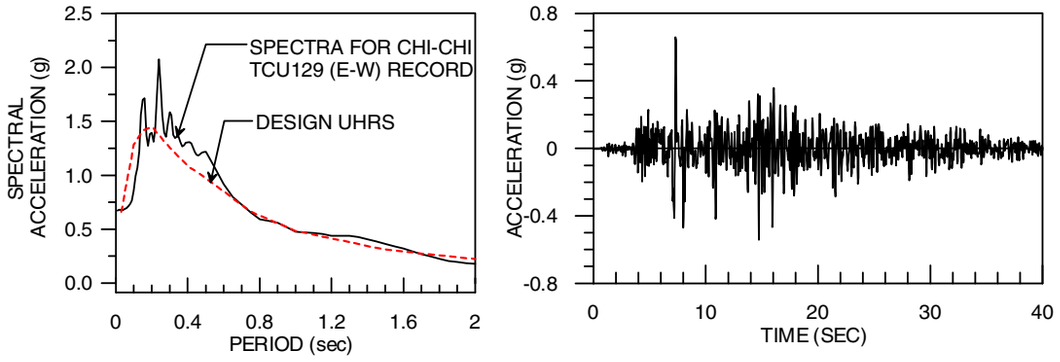


FIG. 6. Target vs. Response Spectra and Time History of Input Motion

Results of FLAC Analyses

Figure 7 shows part (area of interest) of the finite difference mesh used in the FLAC analysis. Figure 8 shows the deformed shape at the end of shaking, and Figure 9 shows the crest horizontal and vertical displacement time histories. The deformed shape in Fig. 8 shows that the dam is sliding mainly on the liquefied Unit 6A. The horizontal displacements at the top of Unit 6A were of the order of 1 m, and the crest horizontal and vertical displacements were 0.4 m and 1.1 m, respectively. These displacements were likely overestimated due to 3D effect as discussed below.

Using the Chi Chi input ground motion in the Newmark sliding block analysis (Jibson and Jibson, 2003) resulted in estimated upstream displacement of 1.0 m for 2D stability analysis and 0.3 m for 3D stability analysis, corresponding to yield accelerations of 0.03 g and 0.09 g, respectively. This indicates that the Newmark seismic displacement based on 3D sliding surface is much smaller than that from 2D sliding surface, due to significant 3D effect for the configuration analyzed at this site.

CONCLUSIONS

The 2D plane strain seismic deformation FLAC analyses performed for the new Coquitlam Dam showed that crest displacements of about 1.1 m vertically and 0.4 m horizontally could occur under the design earthquake loading. The actual displacements are expected to be smaller than predicted due to the 3D effects of the limited extent of the liquefiable Unit 6A. Therefore, it was decided that treatment of the remaining potential liquefiable Unit 6A beneath the dam was not necessary. The new dam, with 6.5 m freeboard and minimum 3 m wide filters and 3 m wide transitions at both upstream and downstream of the impervious core of the dam, can safely accommodate the predicted post-earthquake displacements.

ACKNOWLEDGMENTS

The authors wish to acknowledge the contributions of the other project team members, and the invaluable advice received from Technical Review Consultants (Drs. P.M.

Byrne, J.K. Mitchell, and V. Milligan), and Advisory Board (Dr. N. Morgenstern, A. Williams, and J. Ehaz). Permission to publish this paper from the Dam Safety Office of BC Hydro is gratefully acknowledged. The authors also thank the ASCE reviewers for their helpful comments.

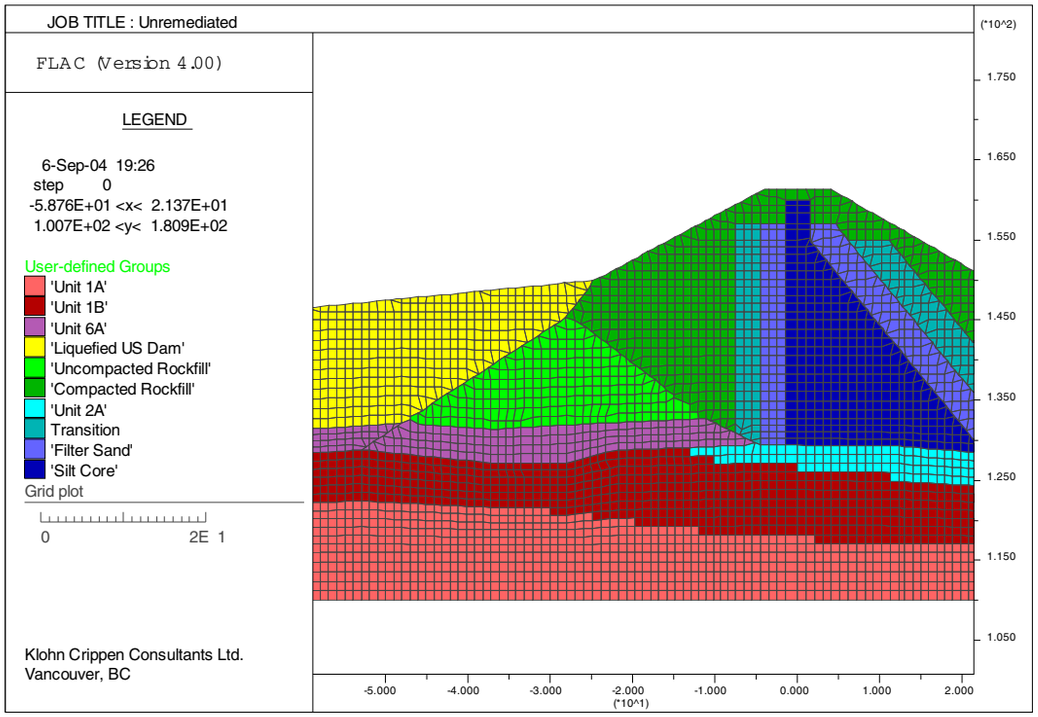


FIG. 7. Part of Finite Difference Mesh Used in FLAC Analysis

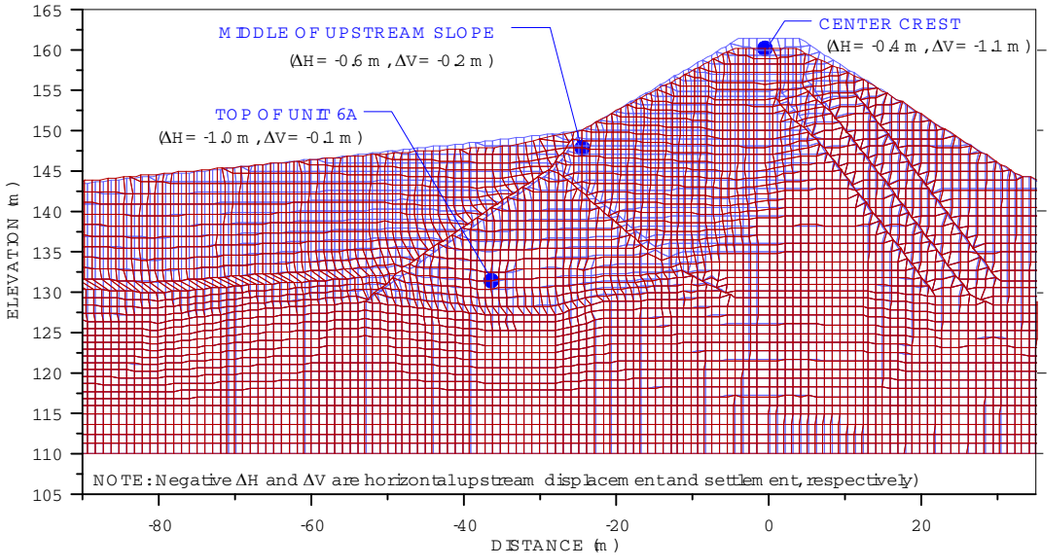


FIG. 8. Deformed Shape of the Dam from FLAC Analysis

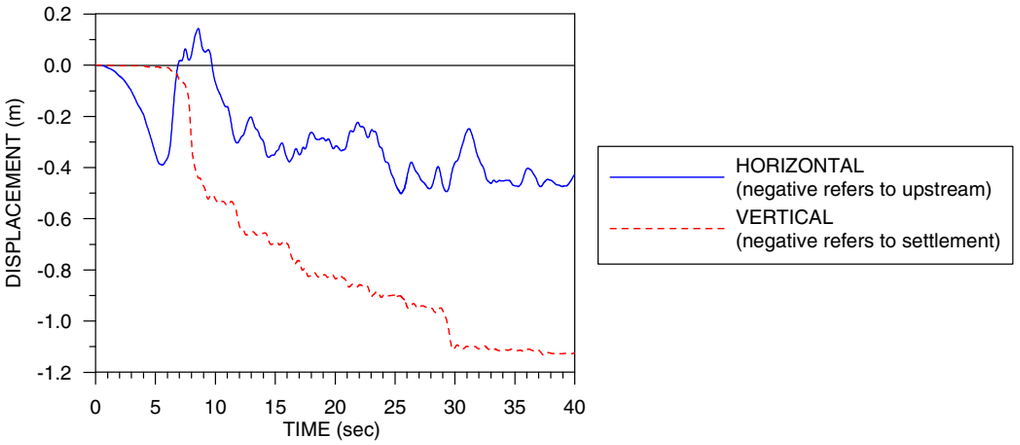


FIG. 9. Horizontal and Vertical Displacement Time Histories at the Center Crest

REFERENCES

Beaty, M.H. and Byrne, P.M. (1999). "A synthesized approach for modeling liquefaction and displacements." *FLAC and Numerical Modeling in Geomechanics, Proceedings of the International FLAC Symposium,* Minneapolis.

Hungr, O. (2001). "CLARA-W: slope stability analysis in two or three dimensions for microcomputers." *O. Hungr Geotechnical Research Inc.*, West Vancouver, BC., Canada.

Idriss, I.M. and Sun, J.I. (1992). "User's Manual for SHAKE91." *Center for Geotechnical Modeling*, Dept. of Civil and Environ. Eng., University of California, Davis, CA, USA.

Itasca (2004). "FLAC, version 4.0, fast Lagrangian analysis of continua." *Itasca Consulting Group, Inc.*, Minneapolis, Minnesota, USA.

Jibson, R. W. and Jibson, M. W. (2003). "Java programs for using Newmark's method and simplified analysis to model slope performance during earthquakes", USGS Open File Report 03-005.

Leps, T.M. (1970). "Review of shearing strength of rockfill." *Journal of the Soil Mechanics and Foundations Division*, SM4, July 1970, pp. 1159-1170.

Lysmer, J., Udaka, T., Tsai, C. F., Seed, H. B. (1975). "FLUSH: A computer program for approximate 3-D analysis of soil-structure interaction problems." *UCB/EERC-75/30*, Earthquake Engineering Research Center, University of California, Berkeley, Nov. 1975, 139 pages.

Seed, H.B., Wong, R.T. Idriss, I-M. and Tokimatsu, K. (1986). "Moduli and Damping Factors for Dynamic Analyses of Cohesionless Soils", *ASCE Journal of Geotechnical Engineering*, Vol. 112, No. 11, pp. 1016 – 1032.

Seed, R. B. and Harder, L.F. (1990). "SPT-based analysis of cyclic pore pressure generation and undrained residual strength", In Proceedings of the H. B. Seed Memorial Symposium, Bi-Tech Publishing Ltd., Vol. 2, pp. 351-376.

Yan, L., Lou, J. K., and Lum, K. Y. (2007). "Coquitlam dam seismic deficiency investigation and seismic upgrade design." Canadian Dam Association 2007 Annual Conference, St John's, NL. September 22-27, 2007.

Seismic Rehabilitations of Miyun Reservoir

Lei Fu, A.M. ASCE, P.E.

Senior Geotechnical Engineer, URS Corporation, Gaithersburg, MD 20878; lxf28@yahoo.com

ABSTRACT: During the 1976 Tangshan Earthquake, a liquefaction-induced slope failure occurred at the upstream slope of one main earth dams of the Miyun Reservoir in the suburb of Beijing, China. Later, the reservoir was dewatered and the dam repaired. Between 1998 and 2001, a major seismic rehabilitation project was carried out on several dams of the reservoir after potential seismic stability problems were found during a safety inspection. This paper reports the techniques and construction methods used in the two rehabilitations.

INTRODUCTION

The Miyun Reservoir, with a storage capacity of over 4 billion cubic meters, is located 100 kilometers northwest of Beijing, China. It was built between 1958 and 1960. The reservoir is mainly used for flood control and water supply for the City of Beijing. The main structures of the reservoir include seven earth dams, three flood spillways, two water outlet tunnels, and two diversion power plants. The plan view of the reservoir is shown in Figure 1. Of the seven dams, Baihe Dam and Chaohe Dam are the two main dams. Chaohe Dam was constructed on a 7- to 14-meter thick natural sandy gravel deposit, is 1,008 meters long at its crest, and 56 meters high at its maximum. The dam has an inclined clay core. Above the core is a sandy gravel protective layer about 2 meters thick, and under the clay core is the main body of the dam, which is constructed of compacted sandy gravel. Figure 2 is a typical cross-section of Chaohe Dam. Baihe Dam, which has a structure similar to Chaohe Dam, is 960 meters long with a maximum height of 66 meters. The sandy gravel foundation is 20 to 30 meters thick. Since the reservoir was built, two rehabilitations have been carried out. The first one was in 1976 after a slide developed at the upstream slope of Baihe Dam during the Tangshan Earthquake. The second one was between 1998 and 2001 after potential seismic stability problems were found during a safety inspection.

1976 MIYUN RESERVOIR REHABILITATION

During the 1976 Tangshan Earthquake (magnitude 7.8 at the epicenter, which was about 160 km away from Beijing), the corresponding intensity in the Miyun Reservoir

region was 6 on the Modified Mercalli Intensity Scale. A slope failure developed in the sandy gravel protective layer of Baihe Dam. The slide line started at the water level (Elevation 134.1 meters). The area of the slide was about 60,000 m^2 and the total volume of the sliding material was about 150,000 m^3. The reason for the slide was that the sandy gravel in the protective layer was liquefied and a flow slide developed due to the low residual strength of the sandy gravel (Finn, 1982). The grain size distribution of the soil is shown in Figure 3.

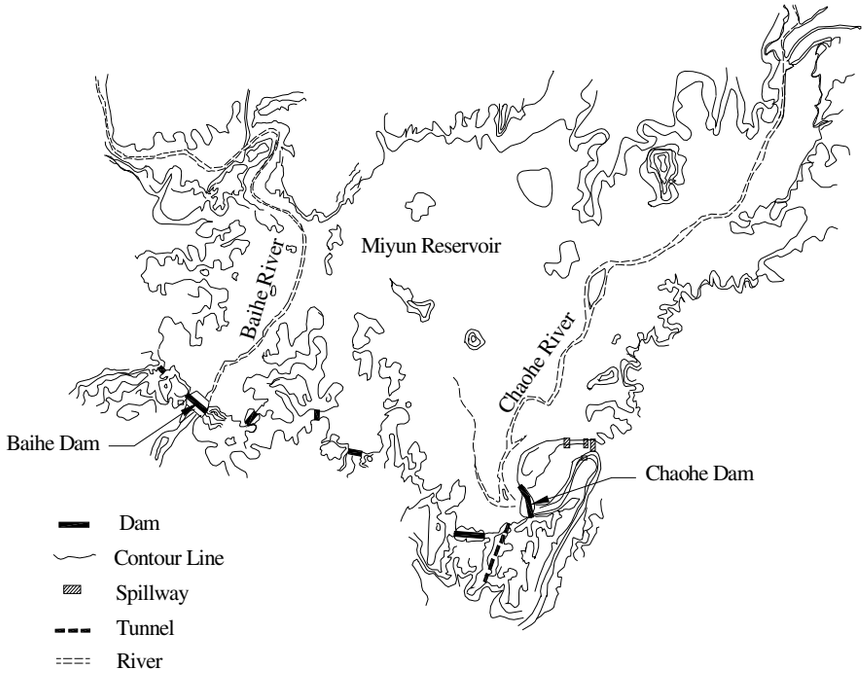


FIG. 1. Plan view of Miyun Reservoir

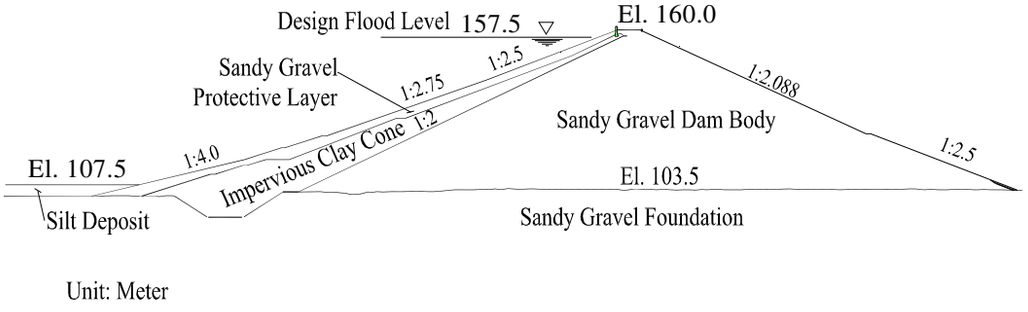


FIG. 2. Cross section of Chaohe Dam at the maximum height

Of the seven dams, Baihe Dam was the only dam that had problems during the earthquake. Baihe Dam and Chaohe Dam have the same dam structure and similar height, but Chaohe Dam held up well during the earthquake. One of the reasons for the different performances was that the foundation deposits for the two dams have different thicknesses. Numerical analyses conducted by the author showed that the thicker the foundation deposits, the larger the response of the dam due to amplification of ground vibrations (Fu, 1997).

After the earthquake, the reservoir was emptied and the damaged dam was repaired. The rehabilitation method was to replace all the liquefiable soil in the upstream protective layer of Baihe Dam with one kind of non-liquefiable material (quarry stones). The inclined clay core and the clay blanket of the dam were also thickened.

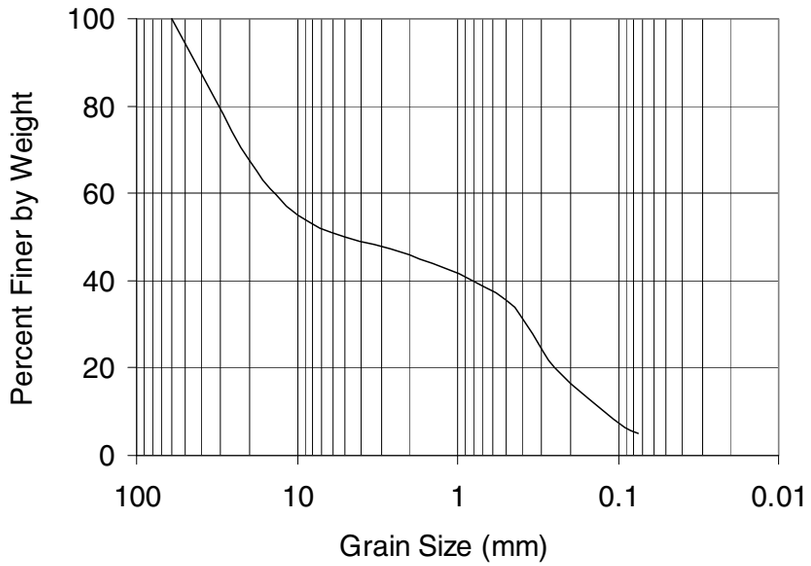


FIG. 3. Grain size distribution curve of Miyun sandy gravel

1994 MIYUN RESERVOIR SAFETY INSPECTION

After the first rehabilitation, there were no major problems for any of the Miyun Reservoir dams, but the seismic stabilities of the dams were still a concern. So, in 1994, all the components of the reservoir, including dams, tunnels, spillways, etc., were inspected for safety. The inspection approaches included visual inspections and numerical analyses. The results of two-dimensional dynamic finite element analyses indicated that the Chaohe Dam was in good condition under static loadings, but when it is subjected to a strong earthquake of magnitude larger than 7 on the Richter scale, liquefaction may occur in the protective layer of the dam and in the upstream of river deposits (Fu, 1997). Pseudo-static analyses indicated potential slides in the upstream slopes of six dams, including Chaohe Dam. Between 1998 and 2001, these dams were

rehabilitated to improve their seismic capacities. The following sections mainly focus on the methods and techniques used in the rehabilitation of Chaohe Dam.

METHOD OF REHABILITATION

Marcuson et al. (1996) reported several methods for the rehabilitation of seismically deficient earth dams, which include: adding upstream or downstream berms or buttresses, excavating and replacing problematic soils, in-situ densification, in-situ strengthening, increasing freeboard, and improving drainage systems.

The main function of the Miyun Reservoir is to supply water for Beijing, so it was required that the rehabilitation measures be implemented without dewatering. The depth of water in the reservoir was about 40 meters (from the bottom elevation of 110 meters to the water surface elevation of 150 meters) at the time of the rehabilitation. After careful evaluation of various rehabilitation methods, the combination of adding upstream berm and replacing problematic material was selected. Adding the upstream berm can improve the stress conditions and the liquefaction resistance of the soil underlying it. The following replacement method was used for the portion of the dam above the water surface: the sandy gravel in the protective layer above the water level was excavated and replaced by a kind of non-liquefiable rolled quarry stones with large particles excluded (see Figure 4). The dynamic friction angle of the quarry stones, determined by drained consolidated triaxial tests on samples with a diameter of 300 mm, was 40°. Below the water surface, the upstream berm was constructed by dumping full-grain quarry stones on the upstream slope of the dam (see Figure 4). The particle size distributions of the two kinds of quarry stones are shown in Figure 5. The maximum grain size of the full-grain quarry stones was 600 mm and the uniformity coefficient, C_u, is 10. The dynamic friction angle was 38°.

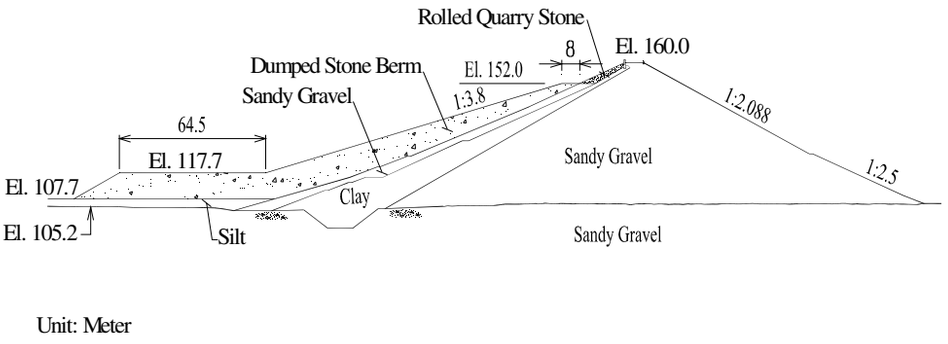


FIG. 4. Cross section of Chaohe Dam after rehabilitation

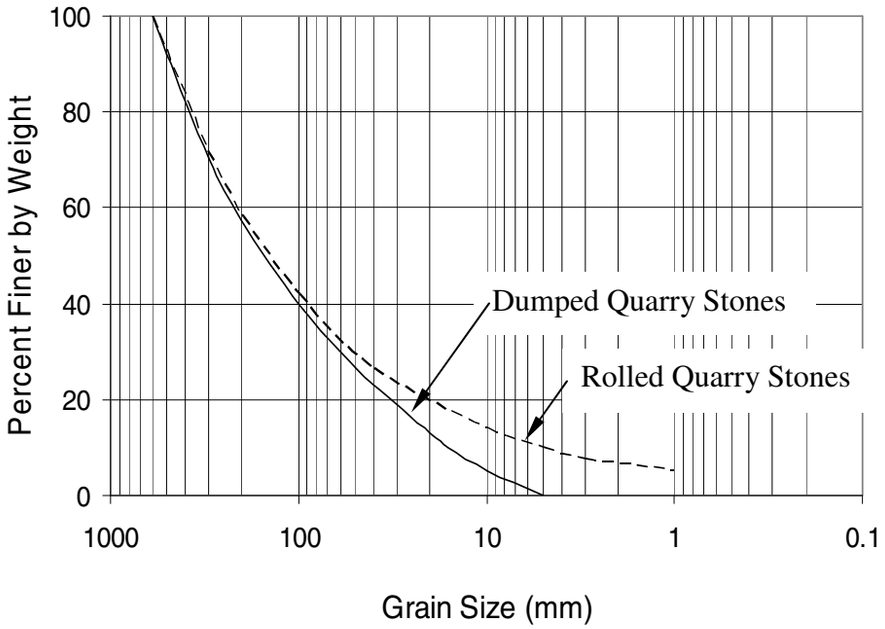


FIG. 5. Grain size distribution curves of quarry stones

The seismic stability of the dam after rehabilitation was evaluated using numerical methods. The design earthquake had local intensity of 8 on the Modified Mercalli Scale. The minimum safety factor from several pseudo-static analysis methods was 1.26 for the design earthquake loading, which satisfied the requirement of the corresponding Chinese design code. The dynamic response analysis results showed that after the seismic rehabilitation, the stress condition of the dam was improved and the liquefaction resistance of soil was enhanced. There were no liquefied zones in the dam or foundation under the design earthquake (Fu and Zeng, 2005).

CONSTRUCTION METHOD

The construction sequence was as follows: quarry stones were first loaded onto dumping barges near the bank of the reservoir. The barges were then hauled to the designed locations and the quarry stones were dumped into the water.

A special issue encountered in the project, which may also exist in many similar projects, was a very soft silt layer of reservoir deposits on the bottom of the reservoir from about 40 years' reservoir operations. The soft layer, with thickness ranging from 2 to 4 meters, was in a liquid-plastic state. It had a liquidity index of 1.04, shear strength (c') of 10 kPa, and friction angle of (ϕ') 13.7°. Under a consolidation pressure of 100 kPa, the coefficient of consolidation (C_v) was 1.25×10^{-7} m^2/s and the coefficient of

permeability (k) was 1.9×10^{-9} m/s. The upstream berm was designed to rest on the silt layer. During the construction period, the silt layer was in a state of consolidation. The shear strength of the silt was very low, so the silt layer could be a potential slip surface for the berm. It was necessary to treat this layer under water before construction. The treatment method was to pre-compress the layer to form a stable foundation for the berm. A layer of 2.5-meter thick quarry stones was first spread in the range of the foundation of the berm to pre-consolidate the silt. After consolidation, the friction angle of the silt was improved to 29° as determined by consolidated-undrained (CU) tests using the same consolidation pressure as expected in the field.

After pre-compression, more quarry stones were dumped into the water to build the upstream berm. After the berm was brought to the design height, the replacement operation was carried out above the water level. The liquefiable sandy gravel in the protective layer was excavated, backfilled with the quarry stones with large particles excluded, and rolled to high densities.

CONSTRUCTION MONITORING

A geophysical method, the Multichannel Analysis of Surface Waves (MASW) method, was used for construction monitoring. MASW uses the dispersive characteristics of surface waves (Rayleigh waves) for imaging and characterizing shallow subsurfaces (Park, et al., 1999). Data are acquired by measuring seismic surface waves generated by an impulsive source and received by an array of geophones. After the raw data are processed, a cross-sectional picture of subsurface strata can be obtained.

Before rehabilitation work started, the MASW method was used to obtain the subsurface images of the bottom of the reservoir. The thickness of the silt layer was measured from the images. The method had a high accuracy. Compared with the results of four drilled holes, the errors of the thickness of the silt layer were less than 5%. During the construction stage, the MASW method was used to obtain the profiles of the dumped quarry stones. At the Chaohe Dam site, 3 testing routes parallel to the dam axis and 16 routes perpendicular to the dam axis were set up to generate profiles of the upstream berm under water. The data were also used to estimate mechanical properties, such as seismic wave velocities and shear moduli, of the silt layer and quarry stones.

The MASW tests were conducted on the water surface (see Figure 6). The seismic waves were sent from a boat and receivers were mounted on another moving boat. Acoustic energy was generated using an 18-pound sledge hammer and a metal plate. The surface wave data were recorded using a 12-channel seismograph. MASW data sets were then transformed into 2-D shear-wave velocity profiles using a dispersion curve technique. Before applied to the project, tests were first conducted on the water, the silt layer, gravel, and quarry stones to determine their P-wave velocities. The velocities are shown in Table 1. During the construction stage, these velocities were used as references to produce profiles of the berm under water. Figure 6 shows a typical profile.

Table 1. Seismic velocities

Material	P-Wave Velocity (m/s)
Water	1,400 – 1,500
Silt	1,100 – 1,300
Sandy Gravel	>2000
Quarry Stones	>2000

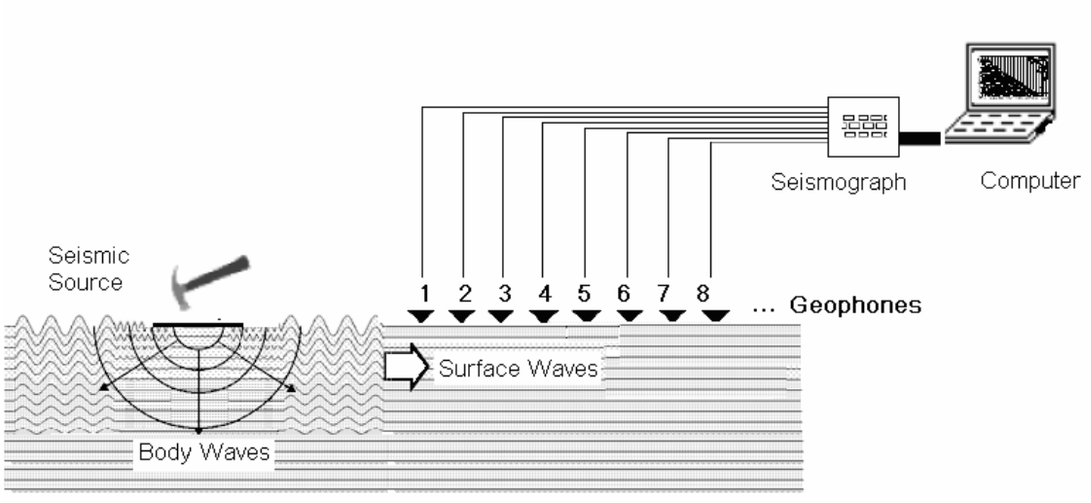


FIG. 6. A schematic of MASW test setup

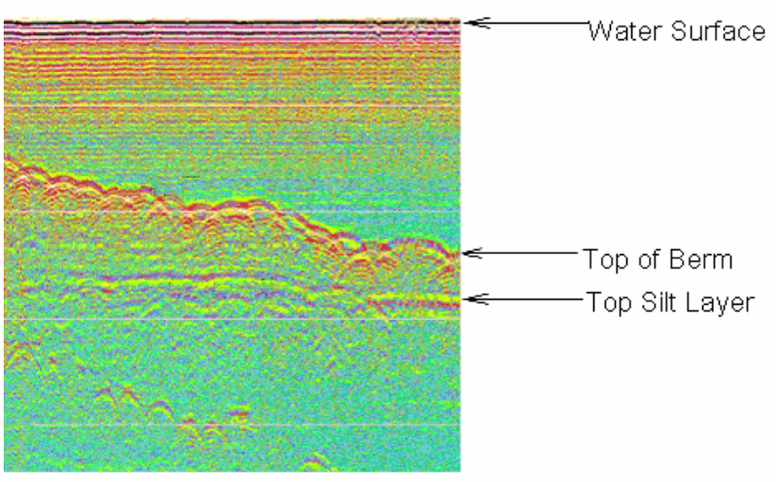


FIG. 7. A subsurface profile produced by the MASW method

CONCLUSIONS

The stability of earth dams during earthquakes has been a major concern for geotechnical engineers in seismically active regions. This paper reports the techniques and construction methods used in two seismic rehabilitations of dams of Miyun Reservoir. Based on project experience, these conclusions can be made:

(1) A berm can be added at the upstream slope of a dam by dumping non-liquefiable materials. The berm can improve the liquefaction resistance of the soil underlying it. The advantage of this method is that it has a minimal effect on the operations of the reservoir of the dam.
(2) The method of replacing problematic material is simple and reliable, but it can only be used above the water surface.
(3) The combination of excavation and replacement of liquefiable soil above the current water level and dumping quarry stones below the water surface seemed to work well for the seismic rehabilitation of Chaohe Dam with minimal interruption to the operation of the facilities.
(4) The existing reservoirs generally have deposits on their bottoms that are not consolidated and have very low strengths. Pre-treatment is required before these deposits can be used as foundations.
(5) The experience of the Miyun Reservoir rehabilitation shows the Multichannel Analysis of Surface Waves (MASW) technique is an effective method for imaging and characterizing subsurfaces under water.

REFERENCES

Finn, W.D.L. (1982). "Soil liquefaction studies in the people's republic of China." *Soil Mechanics – Transient and Cyclic Loads*, edited by G.N. Pande and O.C. Zienkiewicz, John Wiley and Sons Ltd., New York: 609-627.

Fu, L. (1997). Dynamic characteristic study of soil and dynamic stability analysis of rock-fill dams under complex stress state. *MS thesis*, Dept. of Hydraulic Engineering, Tsinghua University, Beijing, China.

Fu, L. and Zeng, X. (2005). "Seismic rehabilitation and analysis of Chaohe earth dam." *Journal of Earthquake Engineering and Engineering Vibration*, Vol. 4, No. 2: pp. 265-273.

Marcuson, W.F., Hadala, P.F. and Ledbetter, R.H. (1996). "Seismic rehabilitation of earth dam." *J. Geotech. Engrg. Div*., ASCE, 122(1):7-20.

Park, C.B., Miller, R. D. and Xia, J. (1999). "Multichannel analysis of surface waves." *Geophysics*, 64: 800–808.

Seismic Vulnerability of the Sacramento-San Joaquin Delta Levees

Said Salah-Mars[1], Arulnathan Rajendram[1], Ram Kulkarni[1], Martin W. McCann, Jr.[2], Segaran Logeswaran[1], Kanagalingam Thangalingam[1], Ralph Svetich[3], Sean Bagheban[3]

[1] URS Corporation, 1333 Broadway Ave, Suite 800, Oakland, CA 94612; said_salah-mars@urscorp.com
[2] President, Jack R. Benjamin & Associates, Inc., 530 Oak Grove Ave, Suite 202, Menlo Park, CA 94025 mccann@jbaslc.best.vwh.net
[3] California Department of Water Resources Delta-Suisun Marsh Office, Division of Flood Management, Sacramento, California.

ABSTRACT: As part of the Delta Risk Management Strategy (DRMS) project, the vulnerability of the Sacramento-San Joaquin Delta (the Delta) levees was assessed under various stressing events such as normal conditions, floods, and seismic events, and the effects of future climate change and subsidence. The seismic hazard of the project site was evaluated using a time-dependant probabilistic seismic hazard analysis to estimate the seismic hazard over the next 200 years. This paper discusses the methodology and results of a probabilistic seismic levee vulnerability analysis. The system of levees in the Delta was divided into a series of vulnerability classes using factors that differentiate the performance of the levees subjected to same earthquake ground shaking. The probabilistic evaluation of levee vulnerability (fragility) for a given vulnerability class is a function of random (aleatory) variables as well as epistemic uncertainties.

INTRODUCTION

The Sacramento-San Joaquin Delta (Delta) and Suisun Marsh are critically important to the state and the nation for a wide variety of environmental and economic services (benefits derived from the area). There are approximately 1,115 miles of levees in the Delta and 230 miles of levees in Suisun Marsh that define the configuration of the waterways and landforms of the area. The island floors in the central and western Delta are below sea level with some islands as much as 25 feet. The subsided land in the Delta is the result of farming-induced oxido-reduction of organic and peaty soils. Over the years, many state and federal agencies and stakeholders have voiced concern over the condition of the Delta and Suisun Marsh levees and the consequences of potential levee failures. The overall purpose of the DRMS is to assess the risk of failure of the Delta and Suisun Marsh levees including the potential impacts to the economy, the ecosystem, and the public health and safety from a regional and statewide perspectives. A subsequent phase (Phase 2) of the DRMS is to address the risk reduction options.

This paper focuses on the seismic vulnerability of Delta levees. Historically there have been 160 Delta flood-induced levee failures leading to island inundations since 1900. There is no evidence to indicate that seismic shaking has ever induced significant damage to Delta levees (CALFED, 2000). This lack of historic damage in the Delta due to seismic events is a result of the fact that no significant seismic events have occurred in proximity to the Delta which could potentially cause damage. At the same time, however, the historic records (the last 70 years) provide numerous examples of levee damage as a result of seismic shaking (Imperial Valley, 1940; Loma Prieta, 1989; Kobe, 1995) when shaking was significant.

VULNERABILITY CLASSES

The system of levees in the Delta was divided into a series of vulnerability classes using factors that differentiate the performance of the levees when subjected to the same seismic event. The definition of the vulnerability classes was based on available subsurface information, levee fill conditions and geometry, past performance, and maintenance history. More than 5000 soil borings were reviewed and analyzed as part of this study. This information was used to develop a geo-database which was integrated into the project GIS system for creating and displaying several maps to identify the spatial and temporal variation in the levee and foundation conditions.

In general, the upper portions of Delta levee embankments are comprised of dredged organic and inorganic sandy, silty, or clayey soils that have been placed on either natural peat or natural sand and silt. The foundation material consists generally of a consistent sequence of peat over loose organic silt and sands, over dense older sand and stiff clay deposits, in areas where peat is mapped which is predominantly in the central and western Delta. The non-peaty Delta foundation consists of dense sand overlaying stiff clay deposits.

The GIS-based maps such as the peat thickness (Figure 1), type of levee fill material and corrected blow counts for levee fill and foundation sand were used to define the vulnerability classes for the seismic vulnerability analysis. The vulnerability classes for the Delta were developed on the basis of factors that would differentiate the seismic behavior of levees such as: peat thickness, presence or absence of liquefiable foundation layers, and presence or absence of liquefiable of levee fill. Figure 2 shows spatial the distribution of the vulnerability classes for the study region.

METHODOLOGY

The development of the seismic fragility functions followed the method illustrated in Figure 3 for each vulnerability class. The first step involved the evaluation of levee response functions, which estimate the horizontal deformations as a function of the magnitude and peak ground acceleration for the reference site (see Figure 3-a). Seismic deformations were evaluated using generalized geotechnical models as discussed in the Analysis Methods Section.

The second step involved the development of the conditional probability of failure functions, which relate the conditional probability of a levee breach to the loss of freeboard (see Figure 3-b). This step relied solely on expert elicitation (epistemic uncertainties). The input from the expert elicitation process was used to define a mean curve and upper and lower confidence bounds around the mean values (see Figure 4). These curves quantify the epistemic uncertainties in the conditional probability of failure.

The third and last step involved the development of the levee fragility functions which relate the probability of failure to the ground motions and earthquake magnitudes for each vulnerability class (see Figure 3-c). This step combines the levee response functions with the conditional probability of failure functions, using Monte Carlo simulations, to generate the fragility functions.

The potential seismic modes of failure included: overtopping as a result of crest slumping and settlement, internal piping and erosion caused by earthquake-induced differential deformations, sliding blocks and lateral spreading resulting in transverse cracking, and exacerbation of existing seepage problems due to deformation and cracking.

EVALUATION OF LEVEE RESPONSE FUNCTIONS

The evaluation of levee response functions requires the estimation of seismic-induced levee and foundation deformations for each vulnerability class. The seismic-induced levee deformations can result from liquefaction-induced flow slides, inertia-induced seismic deformation in non-Liquefiable case, or a combination of the two. Two-dimensional effects were considered in the seismic deformation analysis to account for the interaction between the levee and foundation soil (upper foundation soil above the reference stiff half space). A review of the site geology indicates that the bedrock within Delta study area is at depth of 400 feet or greater below ground surface. Therefore, a stiff soil layer (100 feet deep with an average shear wave velocity of 1100 ft/sec) was used as a representative reference site for the ground motion calculations for the probabilistic seismic hazard analysis (PSHA).

Typical cross sections were developed to represent the various vulnerability classes. A typical cross section is shown for illustrative purpose in Figure 5. The geometry, the type of levee fill and the thickness of different foundation soil strata were developed based on the geo-database developed for this project.

Analysis Methods

The dynamic response and seismic deformations of the levees were evaluated using two approaches. The first approach consisted of estimating the dynamic response analysis using the two-dimensional equivalent-linear finite element method in the computer program QUAD4M (Hudson et al., 1994). The results of the dynamic response analysis were then used in a deformation analysis using the Newmark sliding block procedure. This approach was mainly used for the non-liquefaction susceptible cases. The yield acceleration (k_y) value associated with each potential sliding mass was computed using a limit-equilibrium slope stability analysis (UTEXAS3 [Wright, 1992]).

In the second approach, the earthquake-induced levee deformations were directly calculated using a time-domain nonlinear analyses with the computer program FLAC, Version 5.0 (Itasca, 2005) coupled with an empirical pore-pressure generation scheme (Wong, et al., 1998). The second approach was mainly used for liquefaction-susceptible cases (foundation and/or levee liquefaction).

When the deformations from the liquefiable foundation and levee were excessive, a simplified use of the FLAC model was applied to estimate the "post-liquefaction static slumping". In this simplified method, the levee fill was first modeled using the pre-liquefied shear strength values, then in a quasi-static analysis, these strength values were reduced in a single-step function to the post-liquefactions residual shear strength values. These analyses were conducted for the full range of distribution of the random variables considered in the analysis, as discussed in the sections below.

Ground Motions

The seismic hazard in the Delta was evaluated using a time-dependant PSHA. The PSHA methodology allows for the explicit consideration of aleatory and epistemic uncertainties. Uncertainties in source models and ground motion parameters are incorporated into the hazard analysis through the use of logic trees.

The time-dependent hazard was modeled for the major Bay Area faults using the range of models that were considered by the Working Group on California Earthquake Probabilities (WGCEP). The seismic hazard is calculated at selected times over the next 200 years. A product of the PSHA included hazard-consistent site-specific acceleration response spectra (ARS) at selected levee sites distributed throughout the Delta area. The ARS were generated for a reference site with an average 30-meter shear wave velocity profile (VS-30) of about 1100 feet/sec. These response spectra represent free-field motions for the reference stiff soil site outcrop along with their associated uncertainties.

Dynamic response and deformation analyses were performed using a suite of acceleration time histories with reference PGA ranging from 0.05g to 0.5g at the stiff soil site outcrop.

Liquefaction Triggering Analysis

As the first step in assessing the potential for triggering liquefaction, the project geo-database was reviewed to determine whether or not potentially liquefiable soils are present in the foundation/and or the levee, $N_{1,60} < 20$. Clean sandy soils, sandy soil with few fines (SM), and non-plastic silts were considered susceptible to liquefaction. The blow count data for these soils were compiled and corrected using standard procedures (e.g., NCEER, 1997).

The commonly used SPT-based liquefaction triggering analysis (NCEER, 1997) has no formal probabilistic basis and therefore provides no insight into uncertainty or probability of liquefaction. Since the overall, seismic vulnerability analysis is carried out in a probabilistic framework, the probabilistic-based liquefaction triggering analysis proposed by Seed et al. (2003) was used. In this approach, the probability of liquefaction was calculated as a function of equivalent normalized clean-sand blow count, cyclic shear stress ratio, earthquake magnitude, fines content and vertical-effective stress.

Levee and Foundation Soils

In general the upper portion of Delta levee embankments consists of a mixture of dredged organic and inorganic sandy, silty, or clayey soils that have been placed on either natural peat or natural sand and silt if peat is not present such as in the eastern Delta.

Several available transverse cross sections and their associated geology were reviewed to better understand the composition of Delta and Suisun Marsh levees and foundation materials. The levee materials consist of dredged loose to medium dense sand and silt. Beneath the levee is a thick layer of peat/organic material in the central and western Delta. This peat/organic layer is typically 5 to 45 feet thick. Under the levee, this layer has been consolidated under the weight of the levee. Underlying the peat/organic are layers of loose organic sand and silts, which are generally underlain by a dense sand and stiff clay strata.

Material Properties

Several geotechnical and environmental studies have been performed in the Delta to evaluate the properties of levee and levee foundation materials. These studies include several field investigations and laboratory tests dating back to 1950's (early data developed for the salinity control projects). The field investigations included exploratory borings, cone penetration tests, and down-hole geophysical surveys. Laboratory test results pertaining to seismic analysis were reviewed to develop both static and dynamic properties. In addition, reports containing levee cross sections with subsurface conditions (two to three borings across the levees) were reviewed to develop an understanding of the composition of the fills across the levees.

Soil properties exhibit spatial variability throughout the Delta. The Delta and Suisun Marsh were divided into zones of common ranges of peat thickness (no peat, 0-5 feet, 5-10 feet, 10-20 feet, etc.) and similarly zones with potentially liquefiable or non-liquefiable foundations. The soil properties considered as random variables included: cohesion C, friction angle ϕ, blowcount $N_{1,60\text{-}CS}$, residual shear strength S_{ru}, peat thickness, etc. Because the levee embankment may reach failure before the peat foundation has reached its ultimate shear strain ($\gamma \geq 15\%$), it was assumed the "apparent" shear strength of the peat/organic soils will develop at about 5% stain.

DWR has conducted shear (V_s) and body (V_p) wave velocity measurements of levee and foundation materials in six locations across the Delta and Suisun March, extending about 100 to 120 feet below the crest of the levees. Most of these velocity measurements were conducted during the installation of downhole arrays of accelerometers at Sherman Island, Clifton Court Forebay, Staten Island, and Montezuma Slough. The data suggest that the shear wave velocity (Vs) is less than 100 feet/sec for the free field peat, and over 200 feet/sec for peat confined under the levees. The shear wave velocity profiles tend to increase with depth, reaching values of about 1100 to 1200 feet/sec in the lower dense sand and stiff clay strata. Depending on the location of the near-surface soft deposits (peat and organic marsh deposits), relationships proposed by Wehling (2001) that relate maximum shear modulus, over consolidation ratio (OCR), and effective pressure for peat were used to account for the dependence of shear modulus (or shear wave velocity) on effective overburden.

The variation of shear modulus and damping with shear strain for the various soil profiles were represented by modulus reduction and damping relationships. Modulus reduction and damping curves proposed by Wehling et al., (2001) for the peat/organic soils were used. The shear modulus reduction curves (G/Gmax) and damping curves of Seed and Idriss (1970) and Vucetic and Dobry (1991) were applied for the sandy soils (embankment fill and alluvium) and clay, respectively.

Results

The results of the dynamic response and deformation analyses for each vulnerability class provide estimates of seismic deformations as a function of the reference site PGA and earthquake magnitude. For each vulnerability class, a regression analysis was performed to develop a relationship to estimate deformation as a function of soil properties, assumed levee profile, earthquake magnitude, and reference PGA. Separate regression equations were developed for the liquefaction and non-liquefaction outcomes.

The root mean square error (RMSE) of each best-fit regression equation was estimated and provided a measure of the aleatory uncertainty in the estimated deformations due to variations in ground motion time histories and soil properties. Typical mean levee response functions are presented in Figure 6.

CONDITIONAL PROBABILITY OF FAILURE FUNCTIONS

As part of the DRMS levee vulnerability analysis, a group of technical advisors worked with the project team. The advisors (a group of 7 geotechnical engineers with extensive experience in the Delta), assisted in the development of the seismic vulnerability methodology, the identification of vulnerability classes, etc. As part of the seismic analysis, this group was asked to assist in the development of relationships between the conditional probability of levee failure and the vertical deformation. The experts agreed the conditional probability of failure should be correlated to both the calculated vertical deformation and initial free board.

Each expert provided input for this correlation. Using the input from the experts, three curves corresponding to the probabilities of 16%, 50%, and 84% confidence levels were developed relating the conditional probability of failure to the relative loss of freeboard (i.e., ratio of vertical deformation/initial freeboard) assuming normal flood fight efforts during emergency response. Figure 3 shows the best estimate and confidence ranges. These curves represent the epistemic uncertainty associated the expected failure (levee breach) given earthquake-induced levee permanent vertical deformations. Excluding the post-deformation overtopping, these uncertainties consider the likelihood of post-deformation failure mechanisms such as cracks forming and leading to internal erosion and piping.

SEISMIC FRAGILITY FUNCTIONS

The response functions and the conditional probability of failure functions were combined using Monte Carlo simulation to develop levee fragility functions. The simulations involved the following steps: 1) Define the probability distributions of the random variables, 2) Estimate the deformation for the liquefaction and no-liquefaction cases, 3) Estimate the failure frequency for different combinations of earthquake magnitude, peak ground acceleration, and initial freeboard as discussed in the previous section, and 4) Develop fragility functions to estimate the failure frequency for each vulnerability class at different confidence levels as a function of the simulated values of the soil properties and specified values of the deterministic variables used in the deformation regression equations. Key aspects of these steps are described below.

Probability Distributions of Random Variables

For each vulnerability class, the levee response function was estimated for a range of seismic ground motions and random combinations of soil material properties. Several potential material properties were considered and the sensitivity of estimated deformations to the variations in each property was assessed. The material properties whose variations showed relatively little effect on levee response (deformation) were considered to be deterministic variables in the probabilistic analysis and best point estimates of these properties were used in the calculation of deformation for different

vulnerability classes. The material properties whose variations showed a significant effect on deformation were considered to be random variables and their probability distributions were defined based on a statistical analysis of available data. These probability distributions quantify the aleatory uncertainty in the materials properties. These probability distributions were used in Monte Carlo simulations to generate random values of material properties in the applicable range for each vulnerability class and to estimate the corresponding deformations for different combinations of magnitude and peak ground acceleration.

A lognormal distribution was assumed for each random input variable because it is a commonly accepted probability distribution of soil properties and the shape of this distribution provides a reasonable fit to the distribution of field data. A lognormal distribution is completely defined by two statistical parameters - the median and the logarithmic standard deviation. Shear strength of peat, residual strength of the liquefiable soil, corrected blow count of liquefiable soil, peat thickness were considered as random variables.

Estimation of Deformation

For a vulnerability class with liquefiable embankment or foundation, the probability of liquefaction was assessed as a function of the simulated soil properties and earthquake magnitude, and peak ground acceleration. In the case of liquefaction, the residual undrained shear strength was estimated as function of the simulated $N_{1\text{-}60\text{-}CS}$ and the deformation was estimated as a function of the residual undrained shear strength, earthquake magnitude, and peak ground acceleration. In case of no liquefaction, deformation was estimated as a function of the simulated values of the soil properties and assumed levee profile. For each Monte Carlo simulation trial, a value of deformation was simulated based on its (lognormal) probability distribution and the conditional failure probability was calculated at different confidence levels.

Development of Levee Fragility Functions

Using the results of Monte Carlo simulation, fragility functions were developed to estimate the frequency of failure at different confidence levels as a function of earthquake magnitude, peak ground acceleration, and initial freeboard. Typical seismic fragility functions are shown on Figure 7.

CONCLUSIONS

The results from the dynamic site response and deformation analyses for each vulnerability class were represented by a series of system *Response Functions* relating seismic deformations to PGA and earthquake magnitude considered in the analysis.

Except for the post-deformation overtopping failure, the uncertainties associated with the likelihood of post-deformation failure given levee deformation were represented by the *Conditional Probability Functions*, developed using expert elicitation.

Finally, *Fragility Functions* (relating frequency of failure to ground motions) were used in the risk model and combined with the frequency of occurrence of the various seismic events to produce the expected probability of failures of the Delta and Suisun Marsh levees.

AKNOWLEDGEMENT

The authors would like to extend their appreciation to Professor Ross Boulanger and Mr. Kishida Tadahiro for their contribution to this project by providing valuable data and independent site response analyses.

REFERENCES

CALFED. 2000. "Seismic Vulnerability of the Sacramento-San Joaquin Delta Levees", CALFED Bay-Delta Program, Seismic Vulnerability Sub-Team, April.

Hudson, M., I.M. Idriss, and M. Beikae. 1994. "User's Manual for QUAD4M", Center for Geotechnical Modeling, Department of Civil & Environmental Engineering, University of California, Davis, California, May.

Itasca. 2005. "FLAC, fast lagrangian analysis of continua, version 5.0, user's guide," Itasca Consulting Group, Inc., Thrasher Square East, 708 South Third Street, Suite 310, Minneapolis, Minnesota.

Kishida, T., R. Boulanger, T. Wehling, and M. Driller. 2006. "Variation of Small Strain Stiffness for Peat and Organic soil", Proceeding of 100th Anniversary earthquake conference, the 1906 San Francisco Earthquake, San Francisco, CA, April 18-22.

NCEER. 1997. "Proceedings of the NCEER Workshop on Evaluation of Liquefaction Resistance of Soils", Technical Report NCEER-97-0022, Edited by T.L Youd and I.M. Idriss, National Center for Earthquake Engineering Research, Buffalo, NY.

Newmark, N.M. 1965. "Effects Of Earthquakes On Dams And Embankments", Geotechnique, Vol. 15, No.2, June.

Seed, H.B., and Idriss, I.M, (1970). "Soil moduli and damping factors for dynamic response analyses," Report No. EERC 70-10, Earthquake Engineering Research Center, University of California, Berkeley.

Seed, R. B. and L. F. Harder. 1990. "SPT-Based Analysis of Cyclic Pore Pressure Generation and Undrained Residual Strength", Proceedings of the H. Bolton Seed Memorial Symposium, University of California, Berkeley, May 10-11, pp. 351-376.

Seed, R.B., K.O. Cetin, R.E.S. Moss, A.M. Kammerer, J. Wu., J.M. Pestana, and M.F. Reimer. 2003. "Recent Advances in Soil Liquefaction Engineering and Seismic Site Response Evaluation", Paper No. SPL-2, 26th Annual ASCE Los Angeles Geotechnical Spring Seminar, April 30.

Vucetic, M., and Dobry, R . 1991. "Effect of soils plasticity on cyclic response", Journal of Goetechnical Engineering, ASCE, 117 (1), pp. 898-907.

Wehling, T. M., Boulanger, R. W., Arulnathan, R., Harder, L. F., Jr., and Driller, M. W. (2003). "Nonlinear dynamic properties of a fibrous organic soil", Journal of Geotechnical and Geoenvironmental Engineering, ASCE, 129(10), pp. 929-939.

Wright, S.G. 1991. UTEXAS3, A Computer Program for Slope Stability Calculations, Austin, Texas, May, revised July.

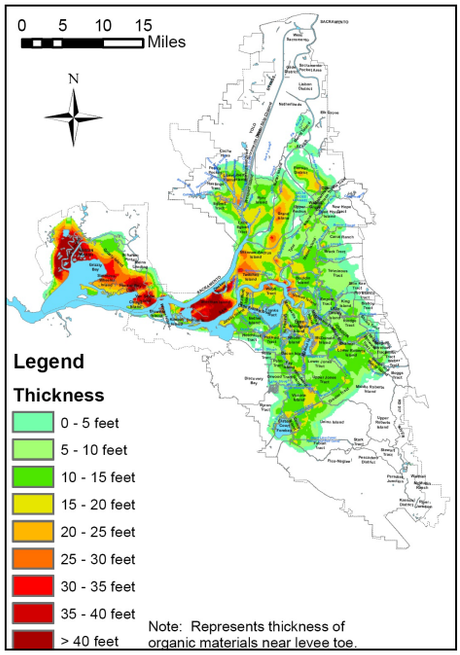


Figure 1 – Thickness of Organic Materials

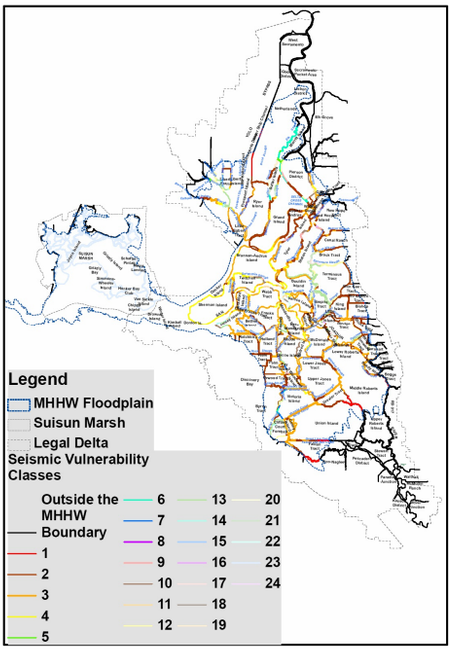


Figure 2 – Spatial distribution of vulnerability classes

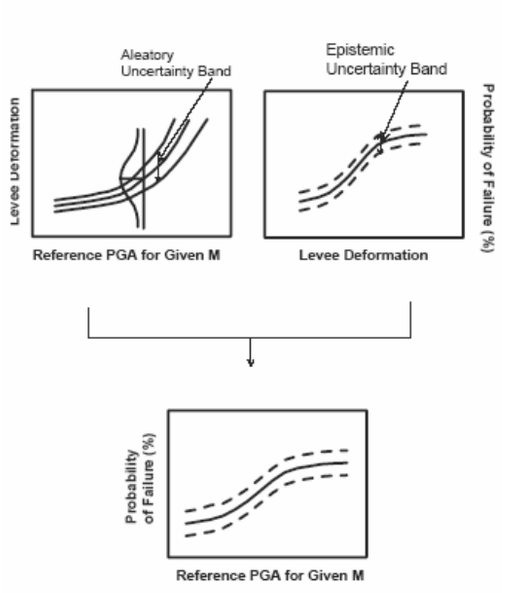


Figure 3 – Approach to Calculate Levee Fragility Functions

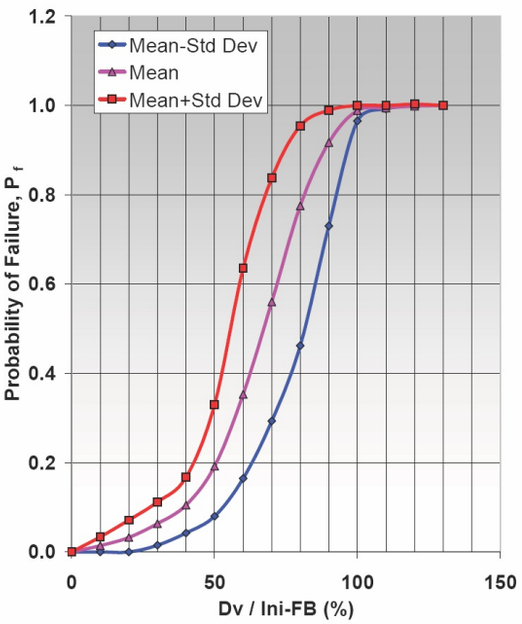


Figure 4 – Probability of Failure Versus Relative Free-Board

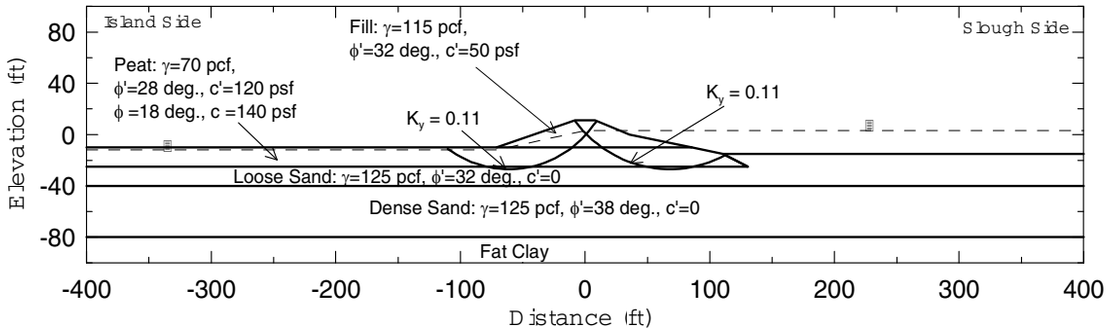


Figure 5 –Typical Cross Section

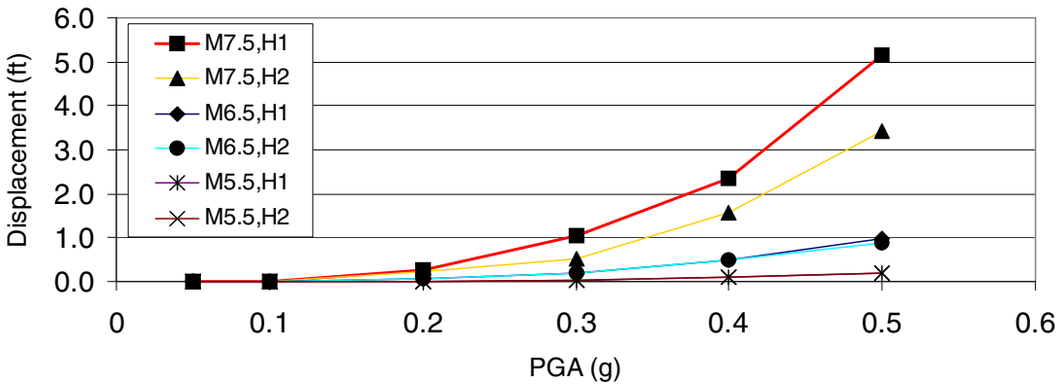


Figure 6 - Typical levee response relationships (15 ft PEAT, Non-liquefaction Case)

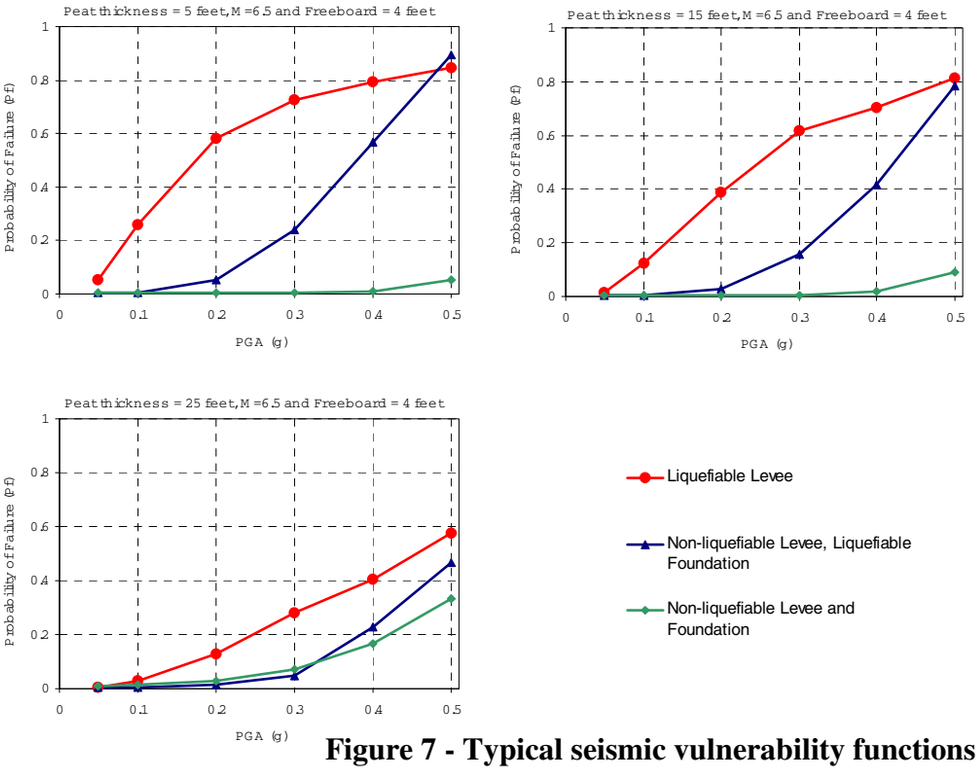


Figure 7 - Typical seismic vulnerability functions

Using ShakeMap and ShakeCast to Prioritize Post-Earthquake Dam Inspections

William A. Fraser[1], P.G., C.E.G., David J. Wald[2], and Kuo-Wan Lin[2]

[1]Chief, Geology Branch, California Division of Safety of Dams, P. O. Box 942836, Sacramento, CA 95826-0001, billf@water.ca.gov
[2]U. S. Geological Survey, Denver Federal Center, P.O. Box 25046, MS 966, Denver, Colorado, Lakewood, CO 80225

Abstract: The use of ShakeMap in conjunction with the U. S. Geological Survey (USGS) ShakeCast software provides an effective means to notify engineering and field inspection staff of the occurrence of a potentially damaging earthquake and its potential impact at all dam locations around the State of California. The ShakeCast software automatically downloads a ShakeMap immediately after it is generated, and evaluates whether selected sites have experienced ground motions exceeding predefined threshold levels. ShakeCast automatically sends a customizable notification to identified individuals via e-mail, PDA, or cell phone apprising them of the results. Instrumental Intensity, based on a combined regression of recorded peak acceleration and velocity amplitudes, is our chosen threshold parameter because it better indicates damage potential than PGA alone. In the absence of custom threshold values determined by engineering analysis, we have selected Instrumental Intensity 5 as the "damage possible" threshold and Instrumental Intensity 8 as the "damage likely" threshold. The latter was selected because a significant percentage of dams that experienced Instrumental Intensity 8 and greater in the Loma Prieta and Northridge earthquakes, were damaged.

Introduction

Dam inspections immediately after a potentially damaging earthquake are required to insure structural integrity. In the event a dam has suffered damage, quick decisions are needed to protect life and property. The Division of Safety of Dams (DSOD) staff notifies dam owners of the need for such inspections immediately after the occurrence of moderate and large earthquakes in California. In many cases, DSOD staff is immediately dispatched to personally inspect the dam and coordinate any emergency action that is required. With over 1,200 dams under our jurisdiction, a major earthquake in a metropolitan area can result in the need to inspect over 100 dams distributed over a wide area in the hours and days after the event.

Information about the location and severity of an earthquake event has improved significantly in recent years. For many years, the magnitude and epicenter was the only information available immediately after an earthquake. Although helpful, magnitude and epicenter do not provide reliable information on the distribution and intensity of strong ground motions. Moving beyond magnitude and epicenter is especially important for the larger magnitude events in which large fault dimensions can result in significant shaking over immense regions, particularly in areas of variable geology where site amplification can further complicate the pattern of strong shaking. With the advent of telemetric strong motion networks such as the California Integrated Seismic Network (CISN), details of the ground shaking can be obtained, transmitted and reported in near real time via ShakeMap (Wald et al., 1999).

This paper discusses the Division of Safety of Dams use of the USGS-developed ShakeCast software, a program that retrieves ShakeMap, evaluates the earthquake's likely effect on engineered structures, and notifies personnel immediately after the occurrence of the event on a 24 hour/7 day basis. We describe the technical aspects of the ShakeCast software and the current implementation of the software at the Division of Safety of Dams. We also discuss potential future modifications to the ShakeCast software, more detailed dam vulnerability function assessments, and additional seismic monitoring that could all further contribute to improve our ability to effectively prioritize post-earthquake dam inspections.

Technical Description of ShakeCast

ShakeCast, short for ShakeMap Broadcast, is a fully automated system for delivering specific ShakeMap products to critical users and triggering established post-earthquake response protocols. The computer application is built upon open source code. ShakeCast employs the Apache Web server and PHP for dynamic Web content, MySQL for facility and notification databases, and it is wrapped in PERL scripting. Exchange files are in Extensible Markup Language (XML) for standardized interfacing with Web, GIS, spreadsheets, databases and other applications (Wald et al., 2008).

ShakeCast was developed with the intent of providing the users the ability to run their own response operations in-house rather than providing notification as a centralized USGS service. The rational for this decision includes data security and quality assurance, as specific information on a given structure, such as fragility and contact information, can be proprietary, and can change often. In addition, users will need to make periodic changes to the facilities database and responders contact information. Needs of individual agencies vary, and the software is flexible enough to allow customization of the notification content and protocols.

Secure automated electronic delivery of information to distributed systems is a primary concern for operators of computer networks, and assuring connectivity via "push" technology has become a maintenance nightmare. By utilizing Really Simple Syndication (RSS) and interval polling, the users' computer initiates all

communication with the redundant USGS Web servers that host ShakeMaps, and retrieve selected products as a request rather than a data "push". This allows ShakeCast users to avoid most typical corporate and governmental agency concerns and firewall restrictions.

The Division of Safety of Dam uses the full version of the ShakeCast software, developed for critical users, which required the user to provide robust communications, power reliability, and round the clock computer support. It is further expected that critical users develop their own facility-specific vulnerability functions for more reliable assessments of potential damage. The new version of program (ShakeCast2) also provides two easier-to-use, limited function versions for non-critical users called ShakeCast "Lite" and ShakeCast "Remote" (see Wald et al., 2008, for more details).

Previous Post-Earthquake Response Procedures at DSOD

The Division of Safety of Dams historically has relied on the seismographic network operated by the Department of Water Resources (DWR) as part of the California State Water Project for notification of the occurrence of a major earthquake. The DWR network consists of instruments at the major facilities of the State Water Project as well as data feeds from additional instruments operated by the USGS and Caltech, to provide coverage throughout the state. When the network records an event, acquisition software automatically calculates the magnitude and epicenter, which would be confirmed by a seismologist within an hour of the occurrence.

Upon telephone notification, Division staff would input the magnitude and epicenter into a Fortran-based computer program that identified jurisdictional dams within a magnitude-dependant circular search area. The search area was selected based on a standard attenuation function to define the area believed to have experienced a PGA of 0.05g or greater. Division staff immediately contacted the dam owner and required that a post-earthquake inspection be performed of the facility. For events greater than magnitude M5.5, Division staff traveled to the region to personally inspect the dams.

Although a magnitude and epicenter certainly provides timely information on the occurrence, size, and general location of an earthquake, the approach had several limitations. The decision to inspect is based on assumed rather than observed parameters. For most earthquake events, the ground motion distribution is not circular about the epicenter; rather it is more elliptical along the rupture zone. Therefore, dams away from the rupture probably do not experience the threshold ground motion. During larger magnitude events with extended rupture dimensions and forward rupture directivity, high ground motions can occur at very large distances from the epicenter. Important geologic controls on the severity of ground motion, such as soil site amplification, were not considered. Finally, the magnitude and epicenter provided little insight into the actual character of the ground motion, such as

peak amplitude, frequency content, or durational aspects, which are the fundamental predictors of the performance of engineered structures.

With the development of Web-based ShakeMap reports in the late 1990's, the Division moved toward using "observed" rather than "predicted" ground motion data. This first consisted of physically overlying maps containing manually plotted areas, for example, overlying the 0.05g-observed area and 0.05g-predicted radius about the epicenter. During the planning of staff inspections in response to the 2000 M5.1 Napa Valley earthquake it was found that the observed area actually extended further south than the predicted area. This required that dams that fell within either area be inspected. In retrospect, a similar situation occurred during the 1989 M6.9 Loma Prieta earthquake because of soil amplification on the margins of San Francisco Bay; but the phenomena could not recognized immediately after the event because strong motion data was manually compiled and distributed and thus not available for rapid post-earthquake decision making.

When DSOD acquired GIS capability in 2002, we developed an application that directly compares observed ground motion from ShakeMap to a layer containing our jurisdictional dams (Figure 1). The ShakeMap shape file was manually downloaded from the Internet and the ground motion data were overlain on a composite base map containing shaded surface relief, fault traces, jurisdictional dams, major roads, and

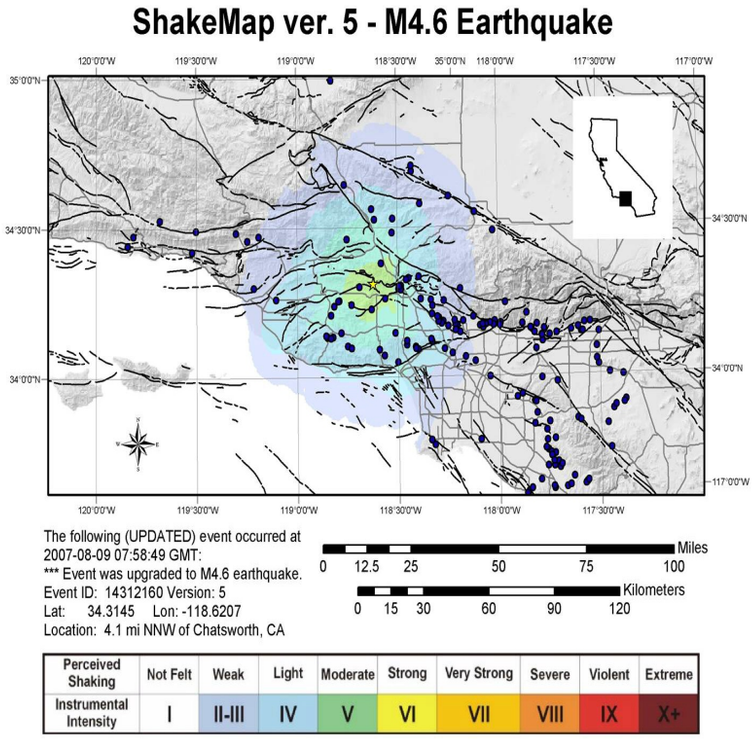


Fig. 1. GIS-developed overlay of ShakeMap and jurisdictional dams

populated areas compiled using ArcView 8.3 software. A table listing the interpolated ground motion at each jurisdictional dam accompanied the map. The GIS software is flexible enough to allow the operator to include any auxiliary information deemed necessary to coordinate post-earthquake dam inspections. Furthermore, the map and table could be readily converted to a file type such as Adobe Acrobat, allowing it to be conveniently e-mailed out of the office. However, while computer-savvy staff can create the map easily, the GIS software has a relatively steep learning curve and generating the map was time consuming for staff.

Current ShakeCast Capabilities at DSOD

The USGS approached the Division in 2004 and asked if we were interested in evaluating the beta version of the ShakeCast software. Since acquiring the software, a few moderate size earthquakes have occurred in California and we have been able to provide feedback regarding the functionality of the program.

Initially, the ShakeCast software ran on a computer located in our offices in Sacramento. However, because the building is subject to periodic power outages and there is no around-the-clock staffing, our system reliability was questionable. The solution involved entering into a cooperative agreement with the seismologic staff from the Department of Water Resources State Water Project, the same group that has historically provided DSOD with earthquake alerts. Two identically equipped Dell Power Edge 2850 computers were purchased to run the ShakeCast software. Each computer was equipped with three 36 GB hard drives to provide back up in case of a hard drive crash.

The primary system is housed in a secure computer area in DWR headquarters, a facility with around-the-clock computer maintenance staffing. The backup system is located at the State Water Project Operations Center located several miles to the east, also a facility with 24-hour staffing. Both installations are “hardened”, with the servers rack-mounted and bolted to the floor, running on conditioned power with uninterrupted power supply (UPS) backup power source. The State Water Project Operations Center has additional provisions for emergency power, as State Water Project and California Flood Operations are located there.

Setting up the software required an upfront effort by a computer technician to load the software, and a staff geologist to act as data administrator. Loading the operating system for the early version of ShakeCast proved difficult, and maintaining the installation was challenging. The installation and software stability have been greatly improved in ShakeCast Version 2. The program issues a daily heartbeat, indicating that is working properly, which the data administrator monitors.

ShakeCast set-up requires the data administrator to enter the location of each dam, its fragility information, and manage notification protocols and contact information that are used in the event that any of the facility’s shaking vulnerability thresholds are exceeded. The data on the 1,200 jurisdictional dams were entered in bulk from

existing databases, and edits to data records can be accomplished either individually or by bulk reloading of an edited database file. For reference, the data administrator charges approximately 150 hours per year (8 percent of his total chargeable hours) to the various ShakeCast software development, maintenance and reporting activities.

Specifying Fragilities

ShakeCast can use any of the ground motion parameters currently transmitted by ShakeMap for specify fragilities. These include peak acceleration (PGA), peak velocity (PGV), response spectral acceleration (SA) at 0.3 second, 1.0 second, and 3 seconds, and Instrumental Intensity (Wald et al., 1999).

Since PGA is commonly used in simplified engineering analyses and since formulas that predict it have been available for many years, it is not surprising a PGA-based fragility was traditionally used to predict damage. However, this approach ignores important frequency-dependent and durational aspects that are important for certain structures.

An interim solution is using the Instrumental Intensity parameter for expressing fragilities. Instrumental Intensity is based on a combined regression of peak acceleration and peak velocity vs. observed Modified Mercalli Intensity for eight significant California earthquakes (Wald et al., 1999). The relationship to the Modified Mercalli Intensity Scale is for user convenience as Modified Mercalli intensities have been a historically important parameter in damage assessments.

Shake Cast (version 1) allowed three levels of fragilities to be set; damage unlikely (green alert), damage possible (yellow alert), and damage likely (red alert). In the absence of custom fragility assignments, an assignment of general fragilities is necessary. Our philosophy was to set the “damage possible” fragility low enough to include moderate levels of ground motion that could conceivably damage the weakest of dams and would thus, conservatively, warrant inspection. We chose Instrumental Intensity 5, based on its correlation with the 0.05g PGA threshold historically used by the Division. In reality, well-built dams will not be affected by this moderate level of shaking.

For the “damage likely” threshold, we wanted a set the fragility high so there was a likelihood damage had occurred. Early recognition of dams shaken at the severe levels is important to effectively prioritize post-earthquake inspections. We chose Instrument Intensity 8 as the “damage likely” fragility based on our analyses that indicate 35% to 50% of the dams that experienced Instrument Intensity 8 during the Loma Prieta and Northridge earthquakes were actually damaged to some degree.

Selecting custom fragilities for each dam is the best use of the software. Ultimately, each structure’s fragility should be based on engineering analyses. This will be discussed in some detail below.

Custom Notifications

Earthquake notifications can be a text message to a cell phone, an alert to a pager, or e-mail message to a PDA or PC. Because the notifications occur on a 24 hour/7 day a week basis, we wanted the messages to be as clear and user-friendly as possible. ShakeCast offers users the flexibility to customize the style and content of messaging its triggers and this functionally is greatly expanded in Version 2. The cell phone and pager-based messages are somewhat abbreviated due to size limitations of cell phone messaging. However, e-mail transmission allows a clear detail message with considerable supporting information to be included. We transmit a table showing all dams that have been shaken above the fragility levels, along with hypertext links to web-based sources of addition information on the earthquake (Figure 2). Version 2 will take this further by allowing hypertext links to Web-based information on the affected infrastructure. It also automatically generates Web-based maps of shaking and facilities, which can be viewed in-house (Intranet) or linked via messages sent to users.

ShakeCast Event: Magnitude 4.6
ShakeMap (Unnamed Event) Version 5
Event Location: 3.1 mi NNW of Chatsworth, CA
Event Time: 2007-08-09 07:58:49
Generated at 2007-08-10 01:08:44
Reported by: Server ID = 2130, DNS = shakecast.water.ca.gov

Damage Summary
Number of Facilities Reported: 4
Max Value: MMI: 5.27; Acceleration: (not measured)
Number of Reports of Likely Damage: |NULL|
Number of Reports of Possible Damage: 4

Facility Damage Estimates from ShakeMap

Facility	Damage Level	Metric	Value	Exceedance Ratio
86-003 RUNKLE	Possible	MMI	5.27	0.090
775-000 PORTER ESTATE	Possible	MMI	5.16	0.053
6-004 CHATSWORTH	Possible	MMI	5.12	0.040
86-005 LAS LLAJAS	Possible	MMI	5.12	0.040

Note: the MMI values indicated are actually Instrumental Intensity rather than Modified Mercalli values.
Exceedance ratio is a ranking value which indicates the amount by which the threshold intensity is exceeded.
More information can be found regarding this event at
http://www.cisn.org/shakemap/nc/shake/ (Northern California) or
http://www.cisn.org/shakemap/sc/shake/ (Southern California)

Fig. 2. ShakeCast Damage Summary e-mailed to inspection staff

Future Improvements to DSOD Use of ShakeCast

ShakeCast currently provides a very functional means for recognizing the occurrence of an earthquake and provides an early assessment of structures that may have been damaged. The DSOD use of the existing technology is still in the growth stage, as we could do more with the existing technology. Providing custom fragility levels for individual engineered structures represents an area where immediate growth

can occur. Additionally, the ability to recognize when damage has actually occurred at a structure via ShakeCast, in conjunction with additional on-site monitoring, is an exiting idea that will be explored with the USGS as a future improvement to the system.

Custom Fragility Expressions

A custom fragility expression for ShakeCast involves two parts, selecting the appropriate ground motion parameter or parameters and then selecting values that are linked to the expected performance of the dam. When dealing with an inventory of over 1,200 dams this is a somewhat daunting task that will not be undertaken lightly. Several approaches are discussed in this section, as perhaps a phased approach is a more reasonable expectation for organizations with a large, complex facility inventories.

Certain types of dams such as hydraulic fill dams and multiple arch dams have historically poor performance during earthquakes. An initial step toward custom fragility could be to set values relating to a specific category of dam reflecting the current knowledge of their general earthquake resistance. In addition to design-based categories, age of dam, amount of freeboard, or consequence of failure, could also be used as criteria to assign dams to generalized fragility or risk categories.

Providing fragility values that are determined by detailed engineering analysis is the most defensible approach, but the most time consuming. Both the appropriate ground motion parameter and threshold value need to be selected based on analysis. For example, for a concrete dam whose stability has been confirmed by a peak stress analysis, the limiting spectral acceleration at the fundamental period of the structure may be the appropriate metric and fragility value to use. ShakeCast currently possesses the required functionality to deal with multiple peak ground motion parameters and assign unique vulnerability functions to individual structures. In addition, more than three levels of potential damage can be assigned, but this granularity warrants more detailed vulnerability functions than currently available for most dams.

However, many techniques used to analyze dams in California involve non-linear considerations and acceleration time histories are used to characterize the earthquake loading. This is especially true for earth dams in the higher seismic regions of the State. To calculate fragilities based on these analysis techniques, ShakeMap would need to transmit durational aspects of an acceleration time history, in addition to their peak parameters. A standard metric for this purpose is Arias Intensity (AI), defined as the integral of acceleration squared over the duration of the time history. AI is attractive as it combines both amplitude and durational aspects of an acceleration time history into a single parameter. The Division is considering augmenting its use of AI as a target parameter for the selection and modifications of time histories used in dam analyses (Howard et al, 2008). Use of the AI as a ground motion target has been made possible by the recent publication of two prediction equations that allow

estimation of AI as a function of magnitude, distance, site condition and style of faulting (Travasarou et al., 2003; Watson-Lamprey and Abrahamson, 2006). Based on these considerations, USGS ShakeMap developers are considering adding a duration-based parameter like AI to the list of ShakeMap parameters generated and delivered. However, any new parameters must be also computed by each seismic network contributing data to ShakeMap systems, so there are complications in adding new parameters.

On-Site Instrumentally Based Damage Detection

In as much as most dams do not have resident tenders and the time for even a well-staffed local agency to mobilize inspection teams after hours could be significant, direct instrumentally based identification of damage is an important long-term goal for dam safety. The USGS expects that future capacity can be made available on the ShakeCast system for multiple strong motion instrument arrays and other automated instrumentation data at a given site. The data transmittal and interpretation issues represent technical challenges that need to be addressed. However, to be a significant improvement over a well-constrained custom fragility assessment, the array needs to be designed so the occurrence of actual damage is confidently recognized and false alarms are minimized. There are several possible approaches for remotely recognizing indications of damage at a dam so that swift investigative or remedial action can be taken.

Conceivably, comparisons of the strong motion recordings from a suite of accelerometers at key locations around at a site might indicate the occurrence of damage. For example, lower than expected crest accelerations compared to adjacent abutment and toe records may indicate the inelastic response of an earth dam that resulted from sliding deformation. A more direct approach might be to instrument the crest of a dam with a series of GPS receivers at the survey monuments that could confidently record significant permanent crest settlement and horizontal deformations. The approach could involve other types of deformation measuring instrumentation such as continually reading inclinometers within the shells of an earth dam or extensometers mounted on the face of a concrete dam. Links to digital video camera images of the dam, a technology currently used routinely for traffic monitoring and security applications could provide confirmation of damage in conjunction with the methods listed above.

Conclusions

California Division of Safety of Dams is responsible for a large number of dams distributed over a wide, seismically active region. Under these conditions, DSOD recognizes the value of the USGS ShakeMap/ShakeCast systems as a means for automatically and more effectively coordinating post-earthquake response, in particular, initiating and prioritizing dam inspection activities. While DSOD has had a fully functional ShakeCast running under the prototype (Version 1), the updated Version 2 of ShakeCast provides additional functionality while simplifying use from

the users' perspective. To take full advantage of these developing tools for post-earthquake response, DSOD is further investigating methods for determining dam-specific vulnerability functions as well as exploring new approaches to on-site instrumentation that would allow for direct interpretation of damage at key facilities.

References

Howard, J.K., Fraser, W.A., and Schultz, M.G., (2008), "Using Probabilistic Arias Intensity in Geotechnical Engineering Analysis." *Proceedings GEESD IV Conference*, Sacramento, California

Travasarou, T., Bray, J. and Abrahamson, N. (2003). "Empirical attenuation relationship for Arias Intensity." *Earthquake Engineering and Structural Dynamics,* Vol. 23: 1133-1155.

Wald, D.J., Quitoriano, V., Heaton, T. H., Kanamori, H., Scrivner, C.W., and Worden, B.C., (1999). "TriNet ShakeMaps: Rapid generation of peak ground-motion and intensity maps for earthquakes in southern California", *Earthquake Spectra* 15**,** 537-556.

Wald, D.J., Lin, K.W., Porter, K., and Turner, L., (2008). "ShakeCast: Automating and Improving the Use of ShakeMap for Post Earthquake Decision–Making and Response." in review, *Earthquake Spectra*.

Watson-Lamprey, J., and Abrahamson, N. (2006). "Selection of ground motion time series and limits on scaling". *Soil Dynamics and Earthquake Engineering*, Vol. 26, 477-482.

Walnut Canyon Dam Seismic Performance Evaluation

John Barneich[1], M. ASCE, P.E., Yoojoong Choi[2], M. ASCE, P.E., David Shen[3], P.E., Yoshi Moriwaki[4], M. ASCE, P.E., and Phalkun Tan[5], M. ASCE, P.E.

[1]Principal, GeoPentech, 525 N. Cabrillo, #280 Santa Ana, CA 92701; john_barneich@geopentech.com
[2]Staff, GeoPentech, 525 N. Cabrillo, #280 Santa Ana, CA 92701; yoojoong_choi@geopentech.com
[3] CE-Water, City of Anaheim, 201 S. Anaheim Blvd, #601, Anaheim, CA 92805;DShen@anaheim.net
[4]Principal, GeoPentech, 525 N. Cabrillo #280 Santa Ana, CA92701;yoshi_moriwaki@geopentech.com
[5]Associate, GeoPentech, 525 N. Cabrillo #280 Santa Ana, CA 92701; phalkun_tan@geopentech.com

ABSTRACT

Seismic performance of an earthfill dam called the Walnut Canyon dam was evaluated in terms of seismic deformation and transverse cracking potential under postulated shaking conditions. A statistical review of construction data along with field investigation and laboratory testing played a vital role in characterizing materials comprising the dam for use in the nonlinear deformation analysis. As a result of this study, the continued use of the dam was approved by the California Division of Safety of Dams (DSOD) with provision for additional instrumentation.

INTRODUCTION

This paper presents the results of the seismic performance evaluation of Walnut Canyon dam (ID# CA 00175) located at the northwest end of the Santa Ana Mountains in Anaheim. The dam had been operating at a low reservoir level based in part on an inquiry by the DSOD regarding the seismic stability of the dam with specific emphasis on potential for seismically induced transverse cracking of the dam, potentially necessitating significant seismic upgrading of the dam. The seismic performance evaluation of the Walnut Canyon dam involved the following steps: (1) review of construction data, (2) field investigation and laboratory testing, (3) site characterization, (4) ground motion evaluation, (5) seismic deformation analysis, and (6) evaluation of transverse cracking potential.

WALNUT CANYON DAM

Walnut Canyon Dam, a 187-ft high earthfill dam with a crest length of 903 ft, was constructed in 1968 by the City of Anaheim and has been owned and operated by the City since that time. Fig. 1 shows the maximum section of the dam embankment. As

can be seen on Fig. 1, the upstream slope inclines at about 2-3/4:1 horizontal: vertical (H:V) with a single 8 foot wide bench at the elevation 800 ft. The area above the bench has been covered with rip rap extending up to elevation 841-ft. The upstream face of the dam has a drainage blanket overlain by a layer of compacted clayey sand. The downstream has (1) about 2H:1V slope from the crest at elevations of 847-ft to 849-ft to an about 15 foot wide upper bench at about elevation 797.5 ft, (2) about 2-1/2H:1V slope from the upper bench to an about 15 foot wide bench at about elevation 730 ft, and (3) about 3H:1V slope below about elevation 730 ft. A blanket sand drain underlies the downstream portion of the dam embankment. In addition, so-called 'waste fill' is placed on the down stream face of the dam below about elevation 770-ft as shown in section on Fig. 1.

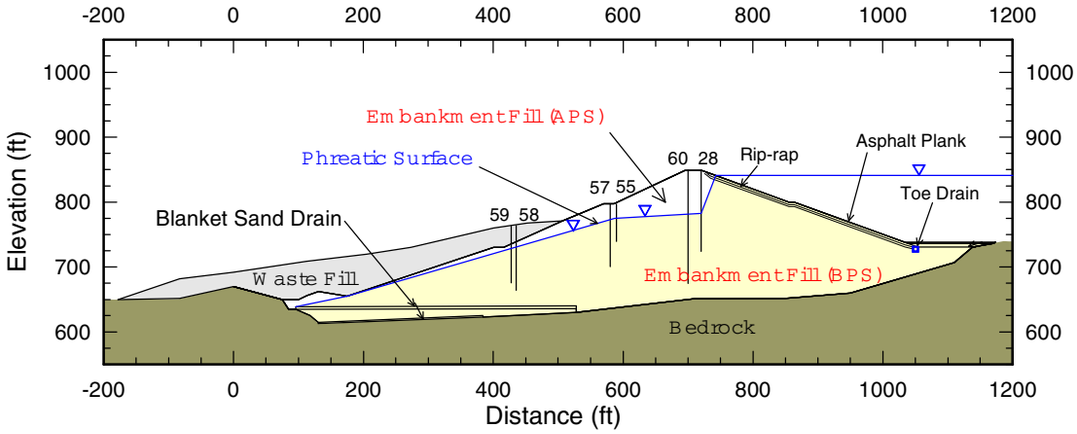


FIG. 1. Maximum Section

Review of Construction Data

The Walnut Canyon dam was constructed of clayey sand material from nearby sandstone sources by compaction. Based on 37 particle size analyses and 17 Atterberg limit tests, the clayey sand has fines content varying from 9 % to 37 % with an average of about 23 % and PI varying from 13 to 31 with an average of about 16. The compaction criteria used during construction of the dam embankment was 95 % relative compaction (RC) based on the Modified A.A.S.H.O. T180-57 (equivalent to ASTM test method D1557).

The review of 1497 field density tests performed on the embankment dam material during construction revealed that: (1) The median and average of RC were about 97 % and 98%, respectively. (2) About 80 % of field density tests were conducted on one borrow material, which implied that about 80 % of the dam embankment was likely made of one material type. The field density test results, which were undiscovered during a preliminary evaluation, significantly contributed to an improved and more appropriate characterization of the densely compacted embankment materials for the final evaluation presented herein; these test results also helped in the process of interpreting the analysis results. The summary of the field density tests during construction are provided in Table 1, and the cumulative density functions of RC and the field dry density are presented on Fig. 2.

Table 1. Summary of Field Density Tests Associated with Embankment

Max. Dry Density (pcf)	No. of Tests (All)	No. of Tests[a] (w/o "failed & retested")	% of Tests[b]	Avg. RC[b] (%)	Med. RC[b] (%)	Avg. Fill Dry Density[b] (pcf)	Med. Fill Dry Density[b] (pcf)
112.5	1	1	0.07	98.2	98.2	110.5	110.5
118.0	23	20	1.34	97.9	98.0	115.5	115.6
120.0	58	47	3.14	96.6	97.1	116.0	116.5
122.5	188	140	9.35	96.2	96.3	117.8	118.0
125.0	169	86	5.74	96.4	95.3	120.5	119.1
126.0	1287	1202	80.29	98.1	97.6	123.6	123.0
127.0	1	1	0.07	104.7	104.7	133.0	133.0
All ranges	1727	1497		97.8	97.2	122.5	122.2

Notes:
[a] no. of tests = no. of pass + no. of 'failed & no retest' = no. of tests (all) - no. of 'failed and retested'
[b] based on 'no. of Tests w/o "failed & retested"

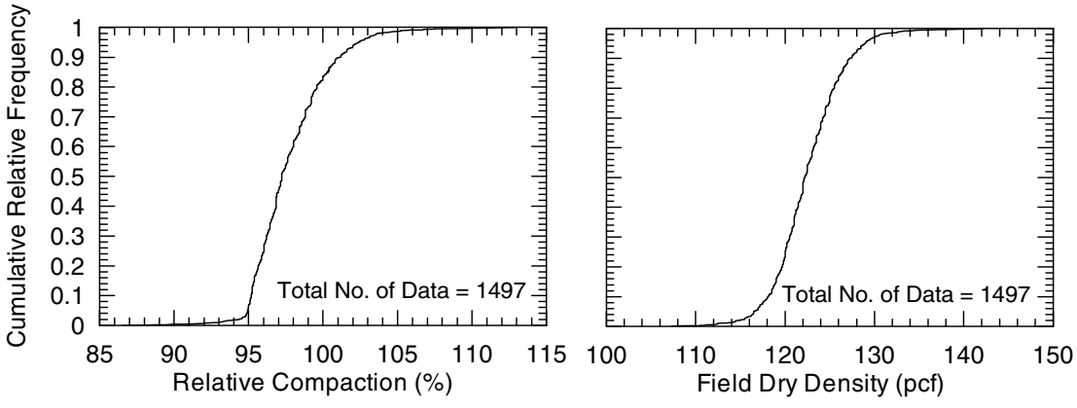


FIG. 2 Field Density Tests – Construction Records

SITE AND MATERIAL CHARACTERIZATION

Field Investigation

A field investigation, consisting of drilling a borehole and conducting geophysical measurements, was performed to supplement data from other previous borings/piezometers. A 177-ft deep borehole, chosen to be near the maximum cross section (No. 60 on Fig. 1) was drilled at the crest of the dam. During drilling, soil samples were obtained using a Standard Penetration Test (SPT) sampler and a Modified California (MC) sampler. In addition, Bulk samples were also obtained. The soil samples obtained were used for laboratory testing. An attempt to obtain a push-sample of embankment fill using a Shelby tube at a depth of 105 ft from the ground surface during the drilling resulted in the crushed Shelby tube due to the denseness of the embankment.

A geophysical testing program consisting of three downhole seismic measurements and one surface seismic refraction test along traverse was performed, and the downhole tests were located at the dam crest (No.60 on Fig. 1), mid-way up the dam

slope (No.57 on Fig. 1), and the waste fill area (No.58 on Fig. 1) for obtaining P-wave and S-wave velocities of the dam embankment materials and the waste fill as shown on Fig. 1. Seismic surface refraction measurements were performed adjacent to an outcrop of sandstone near the dam also for obtaining P-wave and S-wave velocities of bedrock.

Laboratory Testing

The laboratory tests were performed to examine the engineering properties of the Walnut Canyon dam embankment materials. The Standard Penetration Test (SPT) samples, the Modified California (MC) samples, and the Bulk samples obtained during the field investigation were used for the testing. The test program consisted of Atterberg limit tests, particle size analyses, compaction tests, isotropically consolidated undrained compression tests with pore pressure measurements (ICUC'), pinhole tests, and resonant column and torsional shear tests. In addition, for a qualitative evaluation of the ability of the embankment material to heal cracks, a Vaughan test (Vaughan, 1978) was performed on a re-compacted sample.

Characterization

The material properties of the Walnut Canyon Dam were evaluated based on (1) Review of the field density tests conducted during the dam construction, (2) Results of the filed investigation, (3) Results of the laboratory testing, and (4) Review of the original design by Dames and Moore (1964).

As can be seen on Fig. 1, the dam consists of mainly three materials: (1) the embankment fill; (2) the waste fill; and (3) the bedrock. The upstream and downstream drain zones were used in the seepage analysis but were not used in the dynamic analysis characterization. For each of three main materials in the dam, the (1) shear strength parameters, (2) total unit weight, (3) shear modulus, and (4) Poisson's ratio were evaluated. The characterized material properties for these materials are summarized in Table 2, with the drained and undrained strengths of the embankment, based on ICUC' tests, plotted as a function of confinement on Fig. 3a and 3b, respectively.

The embankment is very well compacted and uniform as evidenced by the statistical analysis results of the almost 1500 field density tests and also confirmed by SPT blow counts (larger than 30 to 40 blows/ft throughout the borehole 60), particle size analyses, and Atterberg tests. Further, the field S-wave velocity measurements of the embankment material are high and in the same range at the three locations in the dam and are in agreement with the results of the laboratory resonant column test on re-compacted samples of the same material as shown on Fig. 3c.

The phreatic surface was assigned as shown on Fig. 1 based on the historical maximum monitored during the life of the dam since 1968, supplemented by the results of seepage analysis.

Table 2. Material Properties used in Analysis

Material No.	Material Description	Unit Weight (pcf)	Shear Strength	Shear Modulus	Poisson's Ratio
	Embankment Fill				
1	Above Phreatic Surface (APS)	135	[a]	[c]	0.30
2	Below Phreatic Surface (BPS)	139	[b]	[c]	0.45
3	Waste Fill	120	c=0, ϕ'=16[d]	Vs=650 fps[e]	0.33
4	Bedrock	136	Elastic	Vs=1200 fps[e]	0.35

Notes:

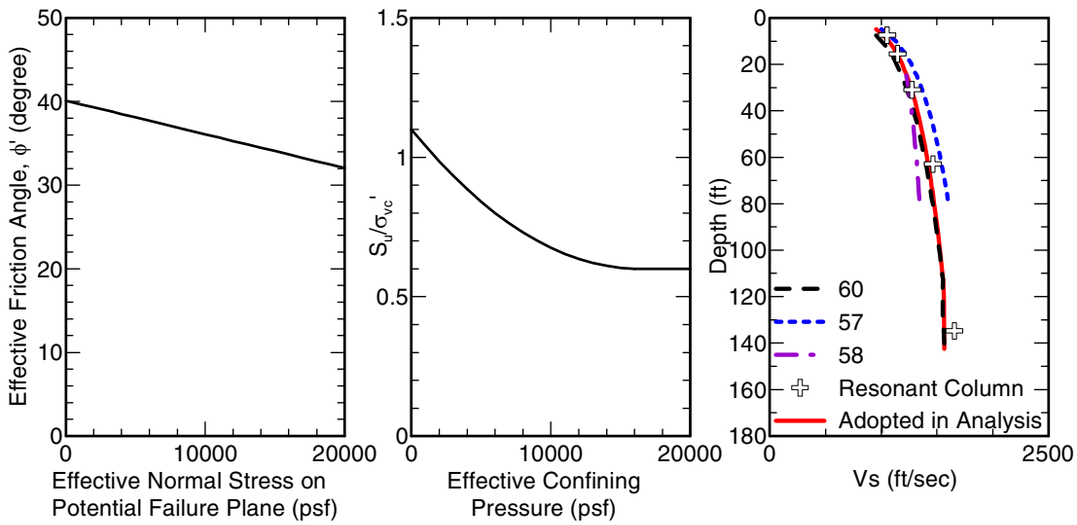
[a] see Fig. 3a

[b] if shear strength from Fig. 3a (effective friction angle) is lower than that from Fig. 3b (undrained shear strength) then, Fig. 3a is used; otherwise, Fig. 3b is used.

[c] equivalent linear shear modulus values used based on: $G_{max}=575500\ (\sigma_m')^{0.311}$ where, σ_m' is in psf

[d] an effective friction angle ϕ' of 16 degrees was conservatively assigned to this poorly documented material based on the relationship between ϕ' and plastic index (PI) for clay materials (Bowles, 1988)

[e] equivalent linear shear modulus based on the indicated shear wave velocity



(a) Effective Friction Angle (b) Undrained Shear Strength (c) Shear Wave Velocity Profile

FIG. 3 Shear Strength Parameters and Shear Wave Velocity profile

SEISMIC PERFORMANCE EVALUATION

Ground Motion

84th percentile deterministic spectral acceleration values for the project site were developed, following the guideline by Fraser and Howard (2002), using arithmetic

averages of the three attenuation relationships for soft rock by Sadigh et al. (1997), Abrahamson and Silva (1997), and Boore et al. (1997). The computed 5 percent damping response spectral values, corresponding to a moment magnitude of 6-1/2 event on the Peralta Hills fault at a distance of 3.7km from the site, are shown on Fig. 4.

Analysis acceleration time histories were developed by matching "seed" time histories to the response spectrum shown on Fig. 4. The three selected "seed" time histories were as follows: (1) Northridge earthquake (1994), station Jensen Filter Plant, component 032, (2) Northridge earthquake (1994), station Sylmar County Hospital, component 032, and (3) Kobe earthquake (1995) horizontal, station KJMA, component 000. The selected time histories were generally matched to the spectrum using RSPMATCH (Abrahamson, 1993). The adjusted acceleration time histories are also presented on Fig. 4.

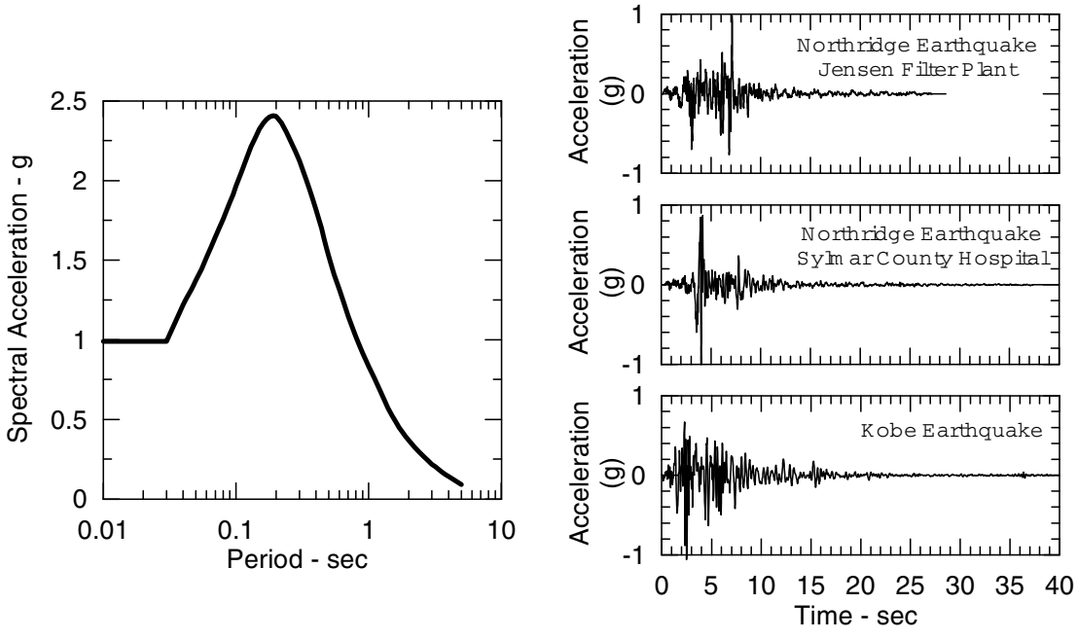


FIG. 4 84th Percentile Response Spectrum and Input Ground Motions

Seismic Deformation Analysis and Potential for Overtopping

A seismic deformation analysis was performed using computer program FLAC (Itasca, 2000) for the analysis section shown on Fig. 1 using six input motions (three different time histories, each with both positive and negative polarities). Two main stress-strain models were used in the analyses: linear elastic model for the bedrock and the Mohr-Coulomb model for the dam embankment and the waste fill. The material properties used in FLAC analysis are presented in Table 2. The values of shear modulus portion of the Mohr-Coulomb model used in FLAC were equivalent-linear values based on a series of one-dimensional SHAKE analysis.

Because (1) the overall patterns of computed seismic deformations are quite similar in all six cases, and (2) the Kobe input motion with positive polarity generally provides larger displacements than the other input motions, the FLAC analysis result presented herein is for the Kobe input motion with positive polarity. Fig. 5 shows the contours of the total seismic displacement at the end of shaking superposed on the discretized FLAC mesh. The large computed seismic displacements of the waste fill shown on Fig. 5 are the consequence of assigning an unrealistically low effective friction angle of 16 degrees to the poorly documented waste fill. The noticeable movements of the near surface embankment fill material in the upstream and downstream slopes are significantly caused by assigning shear strength based on effective friction angle (see Table 2 Notes (a) and (b)). In general, however, the computed seismic displacements within the embankment fill are less than 1/2 ft with a very significant part less than 1/4 ft. Even the total seismic displacements in the zones near the upper slope surfaces, where effective friction angles are assigned, are less than about 2 ft. The presence of rip-rap and other materials near the upstream slope should increase the shear strength of this zone to values significantly higher than those used in the analysis.

The computed shear-induced crest settlement values, ranging from ¼-ft to 1-ft, are also indicated on Fig. 5. On the basis of the results shown on Fig. 5, we can infer that the Walnut Canyon Dam under the postulated earthquake shaking conditions would unlikely deform in any significant way. With the expected free-board of about 6 ft, the potential for overtopping failure of the dam is considered minimal.

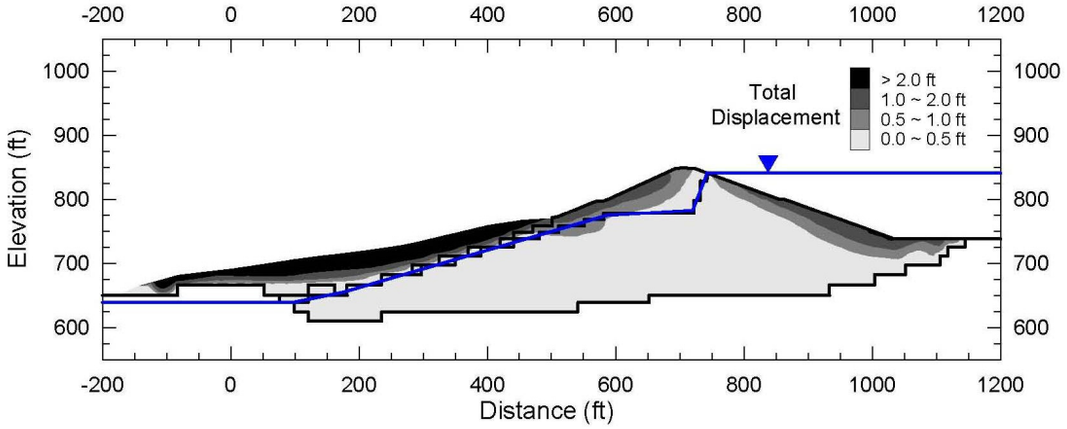


FIG. 5 Total Seismic Displacement

Transverse Cracking Potential

The potential for seismically induced transverse cracking is usually evaluated in terms of expected amount and variation of crest settlement along the longitudinal section of the embankment. The shear-induced crest settlements of the maximum section shown on Figure 5 are quite small. Further, seismically induced volumetric reduction is considered to be even smaller because of the clayey nature of the embankment. In addition, the embankment materials are rather uniform and very well

compacted. Therefore, a formal analysis of longitudinal cross section was considered unnecessary, and the potential for transverse cracking induced by crest settlements was considered very low.

There are some additional considerations that support this very low potential for transverse cracking. Fig. 6 shows the changes of the out-of-plane (i.e., longitudinal direction of the embankment) effective stresses due to the shaking normalized by the static out-of-plane effective stress prior to the shaking. As can be seen on Fig. 6, the out-of-plane effective stress changes in general increase during the postulated earthquake shaking although some small zones show the reduction of confining stresses. It should be noted that all zones showing stress reduction still remain in compression. The seismically induced increase in these horizontal effective stresses normal to the potential planes of transverse cracks throughout almost the entire embankment should help further reduce the already low potential for transverse cracks.

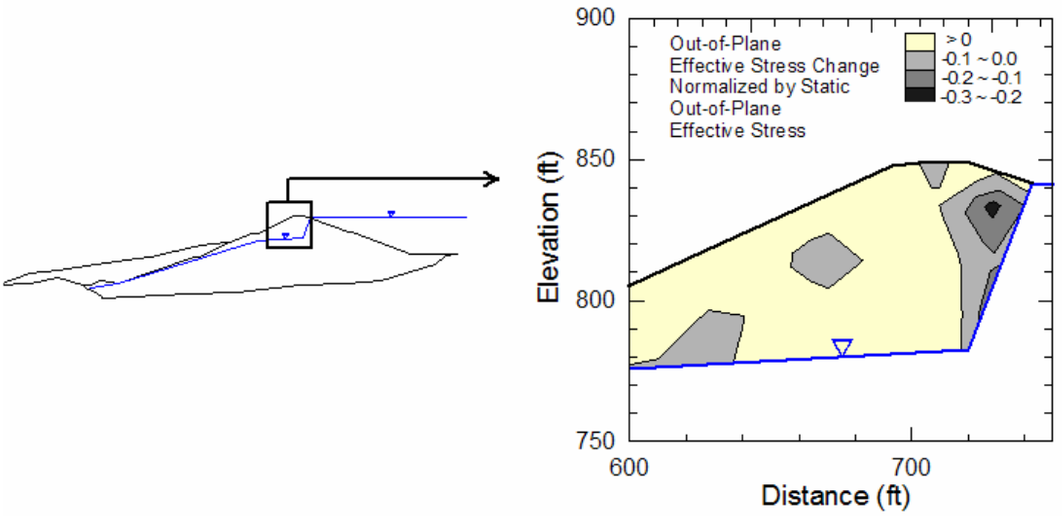


FIG. 6 Out of Plane Effective Stress Change

Jaworski and others (1981) indicated that the initiation of hydraulic fracture of compacted soils can be estimated using the following equation:

$$u_f = m\sigma_H + \sigma_{ta} \quad (1)$$

where u_f = water pressures required to cause hydraulic fracturing
m = constant varying from 1.5 to 1.8
σ_H = horizontal total stress
σ_{ta} = apparent tensile strength of soil

By using the lower value of 1.5 for "m" and ignoring apparent tensile strength, the pressure required for initiation of hydraulic fracture can be represented by 1.5 times total horizontal stress. Fig. 7 shows the contours of 1.5 times the total horizontal stress within the embankment. The contours extending into the reservoir area

represent the static water pressures corresponding to values equal in magnitude to those at 1.5 times the total horizontal stresses. The contours shown on Fig. 7 can be used to estimate the likelihood of hydraulic fracture advancing toward downstream direction assuming seismically induced cracks extend from upstream to various hypothetical locations within the embankment.

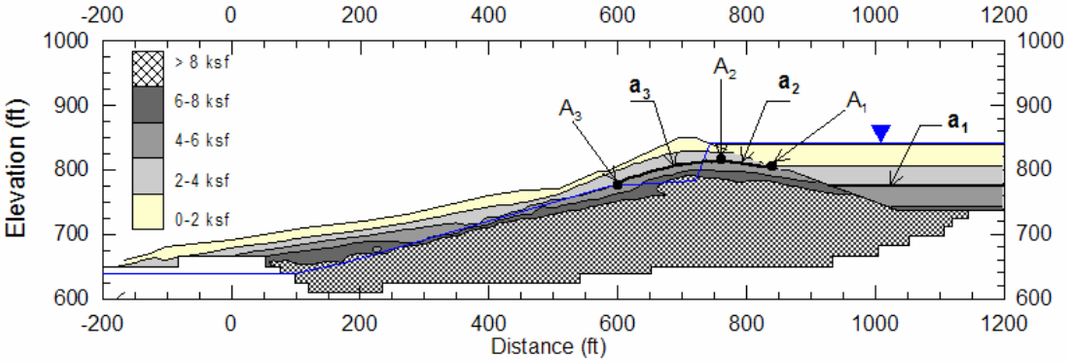


FIG. 7 Hydraulic Fracturing Evaluation

For example, on Fig. 7, one can trace the horizontal line a1 starting from the upstream reservoir area. Even if a transverse crack opens down to a_1 level and reaches downstream to point A_1 because point A_1 is considerably higher than the a_1 level, it is unlikely to continue downstream based on the equation above. Note that point A_2 is even higher than A_1. It is only under the very unrealistic assumption that the seismically induced transverse crack formed all the way to point A_3 that a further downstream extension of the crack due to water pressure may be possible. Although the above equation is for the initiation of cracks and not necessarily the extension of cracks, these results indicate that even in the very unlikely event of some upstream transverse crack formation, those transverse cracks are unlikely to lead to uncontrolled water release due to water pressures in the reservoir.

Finally, the results of the pin-hole tests showed that the embankment material to be non-dispersive and the results of the Vaughan test indicated that the remolded sample of embankment material progressively and quickly broke down when exposed to water, indicating that the material would not sustain a crack.

CONCLUSIONS

- The characterization of embankment material of the Walnut Canyon dam using the results of drilling, laboratory tests, downhole seismic data, and most importantly the statistical analysis of construction data proved to be vital in developing the appropriate engineering properties of materials comprising the dam for use in the nonlinear deformation analysis of the dam.
- The results of nonlinear seismic deformation analysis showed that the amount of seismic deformation as well as its pattern was such that the overtopping failure, or failure due to transverse cracking, is highly unlikely.

- The computed state of stress in the dam during and after shaking when evaluated with the computed seismic deformations was such that transverse cracking was not a significant issue and that the potential for hydraulic fracturing initiated by already unlikely seismically induced transverse cracks was not a concern. The result of Vaughan tests and pin-hole tests further supported this position.
- As a result of this study, where the seismic performance analysis of the dam was based only on nonlinear analysis, the DSOD approved the continued use of the dam with provision for additional instrumentation.

REFERENCES

Abrahamson, N.A. (1993). RSPMATCH computer program. Personal communication.

Abrahamson, N.A., and Silva, W.J. (1997). "Empirical response spectral attenuation relations for shallow crustal earthquakes," *Seismological Research Letters*, 68(1): 94-127.

Boore, D.M., Joyner, W.B., and Fumal, T.E. (1997). "Equations for estimating horizontal response spectra and peak acceleration from western north American earthquakes: A summary of recent work," *Seismological Research Letters*, 68(1): 128-153.

Bowles, J.E. (1988). *Foundation analysis and design*, 4th edition, McGraw-Hill.

Dames and Moore (1964). Comprehensive Design Studies - Proposed Walnut Canyon Dam and Reservoir Nohl Ranch, Orange County, California. Prepared for City of Anaheim, April 16.

Fraser, W.A., and Howard, J.K. (2002). "Guideline for use of the consequence-hazard matrix and selection of ground motion parameters," The resource Agency, Dept. of Water Resources, Div. of Safety of Dams, Oct.4.

Itasca (2000). FLAC – Fast Lagrangian Analysis of Continua, User's Guide, Itasca Consulting Group Inc., Minneapolis, Minnesota.

Jaworski, G.W., Duncan, J.M., and Seed, H.B. (1981). "Laboratory study of hydraulic fracturing field testing", *J. Geotechnical Engrg.* 107(GT6): 713-733.

Sadigh, K., Chang, C.Y., Egan, J., Makdisi, F., and Youngs, R. (1997). "Attentuation relationships for shallow crustal earthquakes based on California strong motion data," *Seismological Research Letters*, 68(1): 180-189.

Vaughan, P.R. (1978). "Design of filters for the protection of cracked dam cores against internal erosion," *ASCE Annual Convention and Exposition*, ASCE.

APPENDIX

Conversion Factors from English to SI Units

- 1 ft $\approx$ 0.3048 m
- 1 lb $\approx$ 4.448 N
- 1 lb/ft^2 $\approx$ 47.88 N/m^2
- 1 lb/ft^3 $\approx$ 157.2 N/m^3

Wavelet Signal Processing Technique in Analyzing Earthquake Records of Masjed Soleyman Embankment Dam

Davoodi[1], M. and Amel Sakhi[2], M.

Abstract

The amplitude and frequency content of non stationary earthquake records varies with time. For this reason, the classical signal processing techniques can't present the appropriate dynamic behavior of the dam under earthquake loadings and consequently, time–frequency distributions such as wavelet method is proposed. In this paper, the recorded earthquake signals will be processed by classical signal processing techniques, such as power spectral density, cross spectral density, coherency and phase difference of the signals. The wavelet method is used as one of the newest techniques of signal processing to extract the time dependent characteristics of earthquake records. Using the mentioned method, the benefits and accuracy of the new signal processing technique is described and its importance in evaluating dynamic characteristics of embankment dams is discussed.

1. Introduction

It is recommended to use the results of in-situ dynamic tests to check the numerical model of embankment dams and as basic input data to predict how the dam will behave in an earthquake. There is a worldwide interest in the proper seismic design of embankment dams in high seismic hazard zones. Seismic behavior study of embankment dams can be performed by different methods: observations made from dam response during earthquakes, experiments on prototype dams to determine dynamic properties such as blasting and ambient tests, experiments on reduced scale models such as shaking Tables or centrifuge testing and finally, analytical studies. It should be mentioned that, obtained results from earthquake records are more useful than other in situ tests such as forced, ambient and explosion tests, since these in situ tests are concerned with vibrations of much smaller amplitude than those normally encountered in earthquakes.

There are several engineering problems of relevance which can be modeled as the responses of linear multi-degree-of-freedom systems to non-stationary excitations and thus have been of interest to the civil engineers. In classical signal processing methods, the time representation is usually the first and the most natural description of a signal we consider, since almost all physical signals are obtained by receivers recording variations with time. The frequency representation, obtained by the Fourier transform, is also a very powerful way to describe a signal, mainly because the

[1] Assistant professor, Dept of Geotechnical Earthquake Engineering, International Institute of Earthquake Engineering and Seismology, Tehran, I.R .Iran, FAX (9821) 22289455; e-mail: m-davood@iiees.ac.ir

[2] PhD Student in Earthquake Engineering, IIEES, Tehran, Iran, FAX (9821) 22289455; e-mail: mamelsakhi@iiees.ac.ir

relevance of the concept of frequency is shared by many domains (physics, biology …) in which periodic events occur (Auger, 1996).

As has been argued (White, 1989), the assumption of stationary of a random process is, in general, inadequate for dealing with measuring the properties of physical systems. Thus methods based on this assumption are generally inappropriate for spectral analysis of signals derived from measurements mode on physical systems. As the earthquake is a non-stationary process, any frequency – energy spectrum would not be a good representation of the data. In recent years, a new and powerful mathematical tool, called wavelet transformation, has been developed.

The time-frequency character of wavelet transforms allows adaptation of both traditional time and frequency domain system identification approaches to examine nonlinear and non-stationary signals. The wavelet method transform provides a method for displaying and analyzing characteristics of signals that are dependent on time and scale. The wavelet transform produces a function of two variables: time and scale. Wavelet analysis originally was developed by mathematicians and seismologists working on seismic signal analysis. Seismologists' interest and contribution to wavelets stems from this fact that earthquake signals are non-stationary transient time series. Little research has been reported in the literature on the use of wavelet transform to analyze seismic signal from a geotechnical engineering point of view and to study the dynamic behavior of embankment dams under seismic loadings. Recently, Davoodi, Jafari and Amel Sakhi proposed blast signal processing using wavelet transform method (Davoodi et. al. 2007).

2. Review of the Wavelet Transform

The definition and basic properties of the time – frequency distributions (TFD) and wavelet transform will be reviewed in this part. TFD are appropriate tools for non-stationary signal analysis, synthesis, and processing. Different types of time-frequency distribution have been developed for that purpose. Two early forms of time-frequency analyses are: the Short-Time Fourier Transform (STFT), used to generate the spectrogram (SP) (Allen, and Rabiner, 1977), and the Wigner-Ville distribution (WVD). Studies of the well known linear TFD Short-Time Fourier Transform (STFT) have been published by Nawab and Quatieri, (Nawab, 1988), and (Allen 1977) among others.

The modern wavelet theory emerged as a coherent and full-grown theory in the early and mid 1980s from the work of French exploration geophysicists Grossman and Morlet and was motivated by the need for high resolution methods for analysis of seismic reflection signals. To implement wavelet transform, the signal $x(\tau)$ is first sampled at discrete points on the time axis and then the set of scaling parameters a is chosen to achieve an appropriate range of frequency resolution. The set of translation parameters b is usually taken at the same points where the original signal is sampled. After the parameters a and b are chosen, the basic wavelet, also called the mother wavelet, is dilated or compressed by the scaling factor a to produce a family of wavelets $\psi_{a,b}(t)$. The wavelets are multiplied by $x(\tau)$ at different scales a and different translations b. The wavelet transforms coefficients $W_{a,b}$ are then obtained by

summing the products, which indicate the correlation between the signal and the wavelet functions $\psi_{a,b}(t)$.

According to the modern wavelet theory, the wavelet transform is a transform, which decomposes a signal *x(t)* via basis functions that are simply dilations and translations of the parent wavelet $\psi_{a,b}(t)$.through the convolution of the signal and the scaled parent wavelet according to

$$W_{a,b}(t) = \frac{1}{\sqrt{a}} \int_{-\infty}^{+\infty} x(\tau)\psi^*(\frac{t-b}{a})d\tau, \qquad a\rangle 0,\ b \in R,\ t \in R \qquad (1)$$

Where * denotes complex conjugate, dilation by the scale, *a*, inversely proportional to frequency, represents the periodic or harmonic nature of the signal and b is called the translation parameter which localizes the wavelet basis function at time t=*b* and its vicinity. Both parameters, *a* and *b*, are dimensionless. The resulting wavelet coefficient, $W_{a,b}(t)$, represent a measure of the similitude between the dilated/shifted parent wavelet and the signal at time t and scale (frequency) a. the wavelet is dilated if $a>1$ and it is contracted for $a<1$, therefore, *a* is called the scaling parameter which captures the local frequency content. Totally, by proper selection of *a* and *b* parameters, a good time resolution is achieved at high frequencies, whereas a good frequency resolution is obtained at low frequency.

3. Description of the Masjed Soleyman Embankment Dam

The Masjed Soleyman Dam is a rockfill dam with a clay core located on the Karun River in Khuzestan province in southwest Iran, 25.5km to Masjed-E-Soleyman town (Figure 1). The dam has a maximum height of 177m, a dam body volume of nearly 13.4 million m^3 and a reservoir capacity of about 230 million m^3. The opening procession of the project body took place in 1380 and the first four units of the phase one are now in operation. The objective is to generate 2000MW of hydroelectric energy.



Figure 1. Masjed Soleyman embankment dam view

4. Analysis of Recorded Data

Since 2002, four SMACH accelerometers have been installed on the crest, dog-way and bottom gallery of the Masjed Soleyman dam, the highest embankment dam in

Iran. Totally there are 30 recorded signals on different stations in which, 3 events have been simultaneously recorded by 3 stations on the maximum dam cross section. GeoSIG sa 99 accelerometers were used in earthquake measurements. The sample per second (SPS) for each record is 200 and their locations on Masjed Soleyman dam body, are presented in Figure 2. As can be seen from this figure, accelerometers are installed on crest, dog-way and gallery of the Masjed Soleyman embankment dam. The earthquake signals were recorded in up stream – down stream, longitudinal and vertical directions. It should be mentioned that some events have not been recorded in gallery station. Before analyzing the earthquake records, in all the records, the base line has been corrected and the band pass filter has been used. For example one of the recorded events is summarized in Table 1. Since during this event, the response of the dam body has been completely recorded in three stations, this event and its related records have been selected for complete analysis. The acceleration time histories and related Fast Fourier Transforms (FFT) of these records are plotted in Figure 3 respectively.

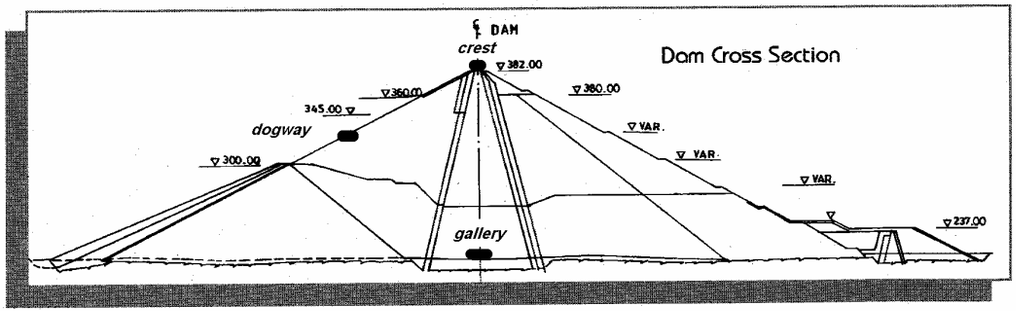
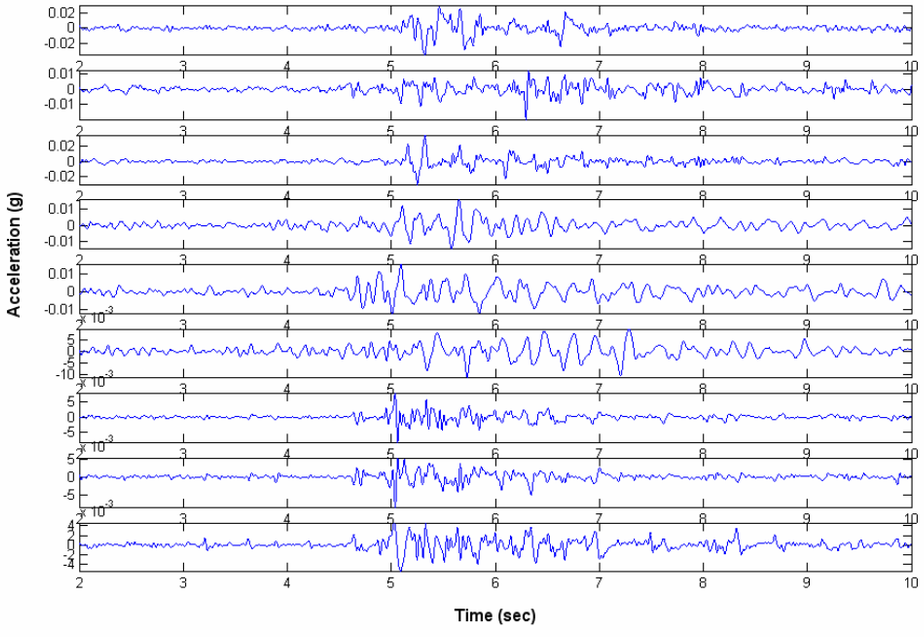


Figure 2. The location of the accelerometers on dam body

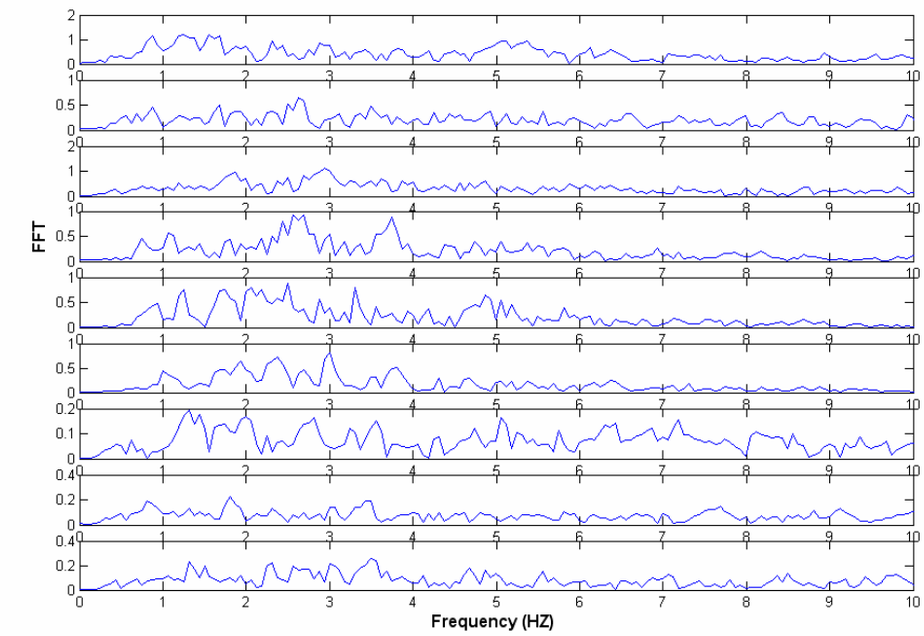
Table 1. General characteristics of recorded earthquakes on Masjed Soleyman dam dated 1/6/2004

File name	Position	Direction	PGA (mg)
Taj1610-003-x	crest	U-D	29.1
Taj1610-003-y		L	12.3
Taj1610-003-z		V	34.1
Dog-way16-10-82-03-x	dog - way	U-D	16.6
Dog-way16-10-82-03-y		L	15.3
Dog-way16-10-82-03-z		V	9.6
Gtb16-10-82-x	gallery	U-D	8
Gtb16-10-82-y		L	5.3
Gtb16-10-82-z		V	4.6

Note: U-D: Upstream-Downstream direction
L: Longitudinal
V: Vertical



(a)



(b)

Figure 3. a) Acceleration time histories and b) corresponding FFT values of the earthquake records of Masjed Soleyman embankment dam during earthquake according to table 1

Two important processing steps have been done on earthquake records. In the first step, the proposed natural frequencies of the dam are obtained based on classical signal processing methods called '4 spectra' (Jafari, 2006). The power spectral density

(PSD) function, cross power spectra (CPS) and also coherency spectra (CS) between two points of the dam, can be used to obtain dynamic properties of embankment dams. A PSD peak at any response point either represents a resonance frequency associated with one of the mode shapes of the dam body or corresponds to a peak in the excitation spectrum. To distinguish the spectral peaks representing the dam vibration modes from those corresponding to peaks in the input spectrum, the amplitude and phase of CPS may be used. That is, all points of the dam body in a lightly damped mode of vibration are in phase or 180° out-of-phase with each other, depending on the shape of the normal mode. The phase relationships between two response measurement points are obtained from the cross correlation phase spectrum (CCPS). Herein, a typical power spectral density, cross power spectra, coherency spectra and the cross correlation phase spectra of the crest station and the reference point (gallery station) is presented in Figure 4.

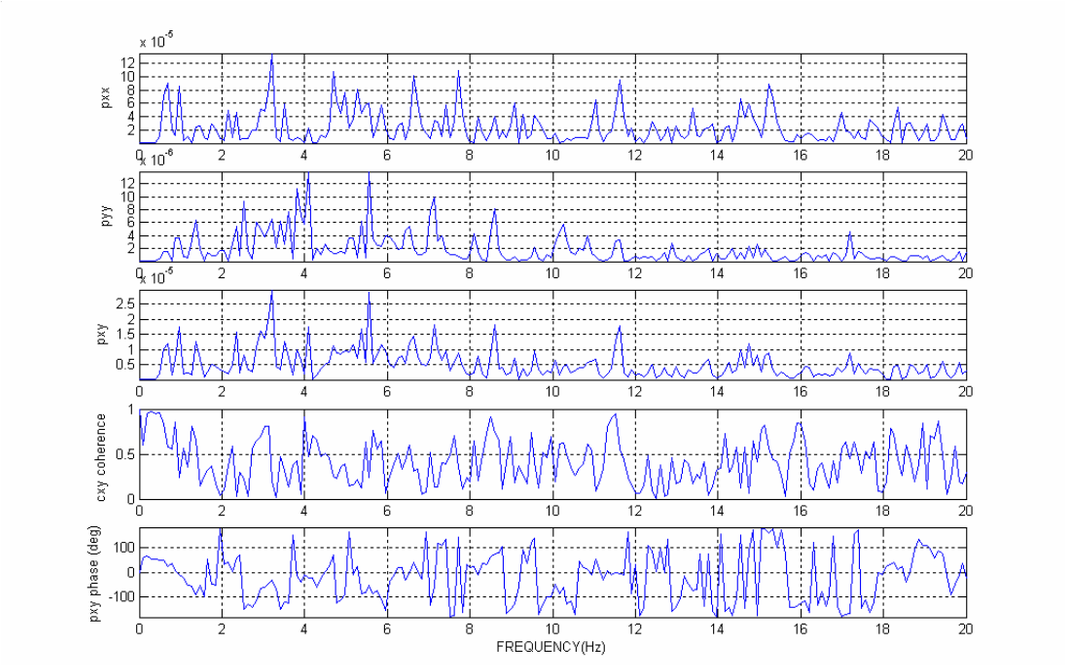


Figure 4. Example of processed earthquake records of Masjed Soleyman dam body in: U-D direction. From top to bottom: PSD of records of gallery and dog-way, CPS, CS, CCPS

To obtain results, all other plots for all the points and records are obtained by considering the gallery station as the reference point and the results are compared with each other. Because of limited points, it is impossible to draw the modal shapes to know which frequencies are modal frequencies exactly, but if we search the PSD, CPS, CS and CCPS of the event, we can understand that for example 1.3-1.35 (Hz) in U-D direction is clearly in phase, so it can be said this frequency is a dominant frequency of dam body in the mentioned direction. Also it should be mentioned that the other proposed dominant frequencies can be extracted based on comparing the results of all other points by the mentioned procedure and using the 4 spectra; PSD,

CPS, CS and CCPS. Based on the obtained results, proposed dominant frequencies of dam body in all three directions are presented in Table 2.

Table 2. Proposed modal frequencies (Hz) of the Masjed Soleyman dam body using classical signal processing technique on earthquake records

No.	U-D Direction	L Direction	V Direction
1	1.3-1.5	1.45-1.65	1.9-2.1
2	1.7-1.8	2.1-2.2	2.9-3.1
3	2.6-2.8	3.3-3.4	3.8-3.9
4	5.1-5.3		5.7-5.8
5	5.8-5.9		

In the next stage, the earthquake records are analyzed using the coefficients of the Morlet wavelet transform to describe the signal energy in time-frequency domain. For example, the corresponding wavelet transform for vertical direction in the crest record is presented in Figure 5. This figure clearly shows the variation of the signal content in time and scale domain. It should be mentioned that there is an inverse relationship between the wavelet scaling parameter *"a"* and the frequency of the signal, " f_a ":

$$f_a = \frac{f_s f_c}{a} \qquad (2)$$

The center frequency of the wavelet" f_c " is one of the characteristics of any given wavelet function. The center frequency for the Morlet wavelet is 0.8125. Also " f_s " is the sampling frequency of the original signal, which in this research is 200 Hz. Totally, the locations of peak values can be estimated from Figure 5, in which are probably belong to dominant frequencies. The inverse of the pseudofrequency is the pseudoperiod for any given scale.

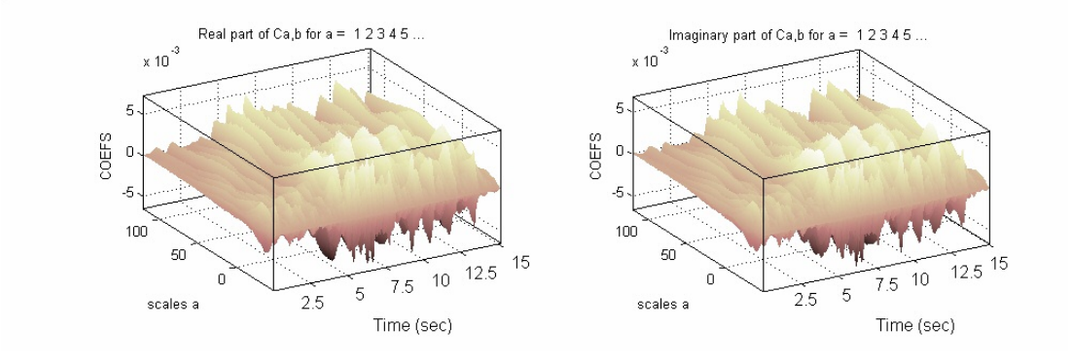


Figure 5. Three – dimensional surface plots of the wavelet coefficients for the dam's crest in vertical direction

Based on the complementary studies, all the earthquake records on the dam body were analyzed by above mentioned wavelet method. In Table 3 the proposed natural

frequencies of the dam is presented by the results of the wavelet method. It should be mentioned that because of limited stations, it is impossible to extract the mode shapes.

Table 3. Proposed modal frequencies (Hz) of the Masjed Soleyman dam body using wavelet signal processing technique on earthquake records

No.	U-D Direction	L Direction	V Direction
1	1.5	1.7-1.8	2.0-2.2
2	1.7-1.8	2.1-2.2	2.7-3.0
3	2.5-2.6	3.0-3.2	3.9-4.1
4	2.9-3.0	3.6-3.7	6-6.2

5. Comparison of the results

The signal processing results of recorded earthquake signals on Masjed Soleyman embankment dam show that the proposed dominant frequencies of the embankment dam can be detected, but due to limited stations, it is impossible to define exactly the modal frequencies of the dam. Comparing the 4 spectra and wavelet methods in analyzing the non stationary earthquake records (tables 2 and 3), show that some frequencies that can not be obtained in 4 spectra method are extracted by wavelet method. For example 2.5-2.6 Hz frequency in up stream-down stream direction and 3.6-3.7 Hz frequency in longitudinal direction are extracted by wavelet method.

In the other hand, by using time-frequency methods such as wavelet, it can be distinguished that which frequencies are more excited at any time during an earthquake excitation. The results show that as time passes and by decreasing the amplitude of the signal, low frequencies are more excited. This phenomenon is related to the non stationary property of the earthquake signal and this result can be explained by modern signal processing methods.

The obtained results show that 4 spectra method is a suitable method for stationary signals such as ambient records that the amplitude and frequency content of the signal doesn't vary with time, but modern signal processing methods are powerful tool for analyzing the non stationary earthquake and explosion records.

6. Conclusions

Earthquake records are known to be one of the non stationary signals in both intensity and frequency content. There are many published articles on signal processing techniques, which use classical transforms based on Fourier Spectra. Little research has been reported in the literature on the use of wavelet transform to analyze seismic signal from a geotechnical engineering point of view and to study the dynamic behavior of embankment dams under seismic loadings. Recently, it is proposed to process the non stationary blast signals by wavelet transform method (Davoodi et. al. 2007). The time – frequency character of wavelet transforms allow adoption of both traditional time and frequency domain system identification approaches to examine nonlinear and non – stationary data.

In this paper, two methods for analyzing the earthquake records on Masjed Soleyman embankment dam have been applied. In the first step, using classical methods (4 spectra method), the proposed dominant frequencies of dam body is obtained. As the

earthquake records are non stationary signals, the modern signal processing that analyze the signals in both time and frequency domains are necessary. So in the next step, for the first time, time–frequency signal analysis of earthquake records using wavelet decomposition was used to analyze the embankment dams. By using this method, dominant modal frequencies of dam body are extracted and the benefits of modern signal processing methods are compared with the obtained results based on classical methods

Totally, this study reveals that the wavelet – based scalograms are an efficient way of obtaining time – frequency insight not readily obtained in other signal processing approaches, since they provide a microscopic time – frequency image of non stationary signals such earthquake. Totally, it can be said that classical methods, such as 4 spectra method, are useful for stationary signals but in analyzing non stationary signals, it is necessary to use the modern signal processing methods to identify the dynamic characteristics of the systems such as embankment dams.

References

Allen, J. B. and Rabiner L. (1977). "A unified approach to short-time-Fourier analysis and synthesis", *Proc. IEEE*, 65, 11, pp1558-1564.

Allen, J. B. (1977). "Short-time spectral analysis, synthesis and modifications by discrete Fourier transform", *IEEE Trans. Acoust., Spech, Signal Processing*, pp. 235-238.

Auger, F. (1996). "Time – Frequency Toolbox For Use with MATLAB", Rice University, USA.

Davoodi, M., Jafari, M. K., and Amel Sakhi, M. (2007). "Using TFD Signal Processing to Evaluate Dynamic Characteristics of Masjed Soleyman Embankment Dam by Blasting Tests", 5th International Conference on Seismology and Earthquake Engineering, Iran.

Jafari, M. K., and Davoodi, M**.** (2006). "Dynamic Characteristics Evaluation of Masjed Soleyman Dam Using In-situ Dynamic Tests" *Canadian Geotechnical Journal,* 43 (10): 997-1014.

Nawab S. N. and Quatieri T. F. (1988). "Short time Fourier transform, Chapter in Advanced Topics in Signal Processing", J. S. Lim, and A. V. Oppenheim (eds), Englewood Cliffs, N. J. Prentice Hall.

White, L.B. (1989). Some aspects of the time – frequency analysis of random processes, Ph.D. Thesis, University of Queensland, Queensland, Australia.

This page intentionally left blank

Centrifuge Modeling of Earthquake-induced Failure Process of Soil Slopes

Ga Zhang[1], Jiyun Qian[2], and Jian-Min Zhang[3]

[1]Associate Professor, State Key Laboratory of Hydroscience and Engineering, Tsinghua University, Beijing, China 100084; zhangga@tsinghua.edu.cn
[2]Graduate student, State Key Laboratory of Hydroscience and Engineering, Tsinghua University, Beijing, China 100084; qianjiyun@gmail.com
[3]Professor, State Key Laboratory of Hydroscience and Engineering, Tsinghua University, Beijing, China 100084; zhangjm@tsinghua.edu.cn

ABSTRACT: To provide evidences for the aseismic evaluation of the soil mountain slopes of the Beijing Olympic Forest Park, the seismic response and failure process of mountain slopes during a strong earthquake were investigated using centrifuge shaking table model tests. The results showed that magnification factors and peak displacements of the slope increased with increasing altitude. The vertical displacement increased monotonically during shaking. The residue horizontal displacements pointed from the axis to both sides after the earthquake. The strain localization occurred mainly at the upper and middle of the slope and can lead to a final landslide. Water content has a significant effect on the strength and deformation modulus of the soil, and as a result significantly affects the aseismic stability level, magnification factors and deformations of the slopes.

INTRODUCTION

The earthquake-induced failure of slopes is one of the great concerns in geological disasters evaluation of engineering. As a mountainous country and with two active earthquake zones, China has lots of earthquake-induced geological problems. The mechanism study of the earthquake-induced failure of slopes takes a very important part in preventing the happening of the disasters.

A 50-meter-high soil mountain was completed in the Beijing Olympic Forest Park, China, in 2006. The mountain was constructed using millions cubic meters of soil within a short construction period, only 108 days. Such a soil mountain is evaluated with eight degree intensity earthquake of seismic possibility (China codes). Thus, the aseismic safety level of the mountain slope should be evaluated. Moreover, August when the Olympic Games 2008 will be held is a frequent rainfall

season. The rainfall may significantly change the water content of the slope; this can cause the reduction of the soil strength. Therefore, to evaluate the high soil mountain of the Beijing Olympic Forest Park, behavior of deformation and failure of the mountain slopes with different water contents should be concerned.

Dynamic centrifuge model tests have been used to evaluate the stability and discuss the failure and deformation mechanism of kinds of slopes (e.g., Taboada-Urtuzuastegui et al, 2002; Thusyanthan et al., 2005; Lili and Nicholas, 2006). However, the existing dynamic centrifuge tests mainly focus on the common slope; test results have been inadequate for the dynamic response of mountain slopes. In addition, the effect of water contents of soil needs a further study on the dynamic response of the slope.

To provide evidences for the aseismic evaluation of the soil mountain slopes of the Beijing Olympic Forest Park, this paper investigates the dynamic response and failure process of a soil slope using centrifuge model tests; the effect of water content of soil is also preliminarily discussed on the basis of test results.

DEVICES

The tests were conducted using the TH-50g-ton geotechnical centrifuge test machine and a specially manufactured shake table of Tsinghua University. This shake table can generate arbitrary earthquake wave with maximum acceleration of 20g using a complex hydraulic pressure servo system.

The model container for tests is 500mm long, 200mm wide and 350mm high. A transparent lucite window is installed on one side of the model container through which the deformation process can be observed and recorded.

An image-record and displacement measurement system was used to record the images of soils during centrifuge model tests. 48 frames of image can be captured per second. An image-correlation analysis algorithm was used to determine the displacement vectors of soil without disturbance of the soil itself (Zhang et al. 2006). The displacement history of an arbitrary point on the soils can be measured with sub-pixel accuracy. Only a colorful region with a random distribution is needed for this system; such a region can be obtained by embedding white particles in the lateral side of the soils. For the test conditions in this paper, the measurement accuracy can reach 0.02mm based on the model dimension.

A few acceleration transducers whose measurement accuracy can reach 0.3% were embedded in the soils to measure the acceleration response.

CONDITIONS

Soil and its dynamic behavior

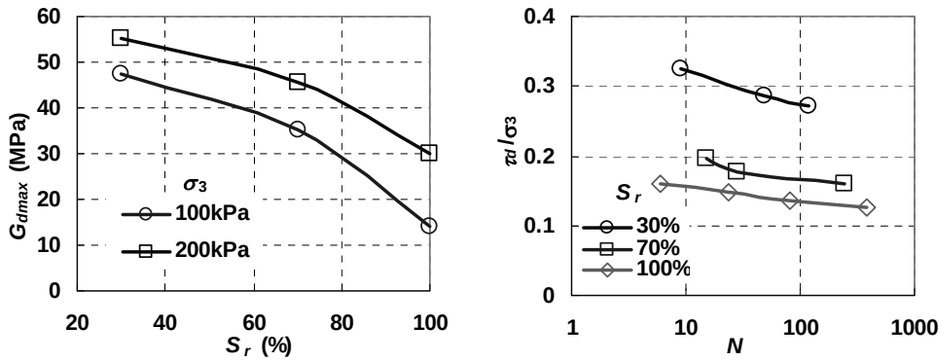
The soil used in the centrifuge tests was taken directly from the soil mountain of the Beijing Olympic Forest Park. The average grain size of the soil is 0.03mm. The plastic limit and liquid limit are 5% and 18%, respectively. Thus, the plastic index is 13. The dry density of the soil is 1.5 g/cm^3, as that of the prototype slope.

Dynamic triaxial tests were conducted to measure the dynamic modulus and strength of the soil with different water contents (Fig. 1).The dynamic strength is obtained if the axial strain reaches 5%. The test results showed that the maximum dynamic shear modulus and dynamic strength decreased with increasing saturation degree (i.e., water content); this demonstrate that the water content has a significant effect on the dynamic behavior of the soil.

Test Model

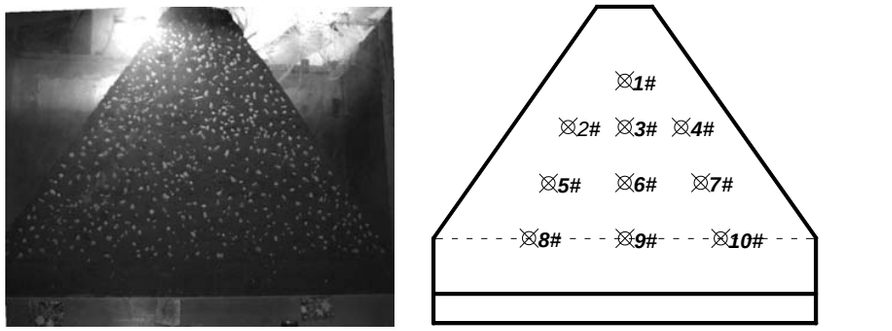
The soil was compacted into the container by six-cm-thickness layer with dry density of 1.5g/cm^3. The slope for test was obtained by cutting out the redundant soil. The both slopes of the mountain were maintained to obtain a similar response to the practical mountain (Fig. 2 (a)). To discuss the effect of water content, two centrifuge model tests were conducted on the slopes with water contents of 11% (saturation degree: 37%) and 16% (saturation degree: 54%), respectively. According to the container size, the slopes in the two tests were both 1.5:1 with 25cm in height. The white particles were embedded in the lateral side of the soils so that the image-based displacement measuring system can take effect (Fig. 2 (a)). In addition, a few patterns were pasted on the container to obtain its displacement during an earthquake. A total of ten acceleration transducers were buried in the soils to measure the dynamic response (Fig. 2 (b)). A six-cm-high horizontal soil layer under the slope was set to diminish the influence of the bottom container plate on the deformation of the slope. Moreover, the silicone oil was painted on both sides of the container to decrease the friction between slope and container sides.

The model slope was installed on the centrifuge machine and the centrifugal acceleration gradually increased to 50g, a centrifugal acceleration that was maintained during shaking tests. After the deformation became stable, an earthquake wave was input on the container bottom. The images of slope were recorded with a rate of 48 frames/second using the image-based measurement system with which the displacement field and its change can be furthermore obtained. The acceleration histories of the measuring points were also measured using the transducers.



(a) Maximum shear modulus **(b) Dynamic strength (σ_3=100kPa)**

FIG. 1. Dynamic triaxial test results. S_r, saturation degree; N, shear cycles; G_{dmax}, maximum shear modulus; τ_d, cyclic shear stress; σ_3, confining pressure.



(a) image **(b) acceleration transducer positions**

FIG. 2. slopes for centrifuge model tests.

Test Procedures

Earthquake Input

An artificial earthquake wave was used in the centrifuge model test (Fig. 3). It can be seen that the maximum acceleration is 0.2g, which corresponds to an earthquake of eight degree intensity (China codes). In the centrifuge model test, the acceleration is amplified to 50 times and the duration is reduced to one fiftieth according to the similarity law.

RESULTS

In this paper, the test results are based on the prototype dimension. In other words, the present responses of the slope have been transformed to the practical magnitudes according to the similar law of centrifuge tests.

Post-Earthquake behavior

A significant landslide occurred on the right side of the wetter slope with water content of 16% during the earthquake (Fig. 4 (a)). However, the drier slope with water content of 11% only exhibited significant residue deformation due to the earthquake; landslide did not occur (Fig. 4 (b)). This demonstrated that the water content has a significant effect on the failure of a slope. The measurement results showed that the residue settlements of the slopes increased with increasing altitude (Fig. 5 (a), Fig. 6 (a)). The horizontal residue displacements pointed from the axis to both sides (Fig. 5 (b), Fig. 6 (b)). The residue deformations of the slope with water content of 16% were significantly larger than those of the slope with water content of 11%. This is because the flexibility of the slope increased due to increasing water content; the landslide of the former slope may be another reason. Therefore, the comparison of post-earthquake behavior of the two slopes showed that increasing water content significantly decreases aseismic stability and increases the deformation of the slopes because the strength and deformation modulus of the soil were reduced by increasing water content (Fig. 1).

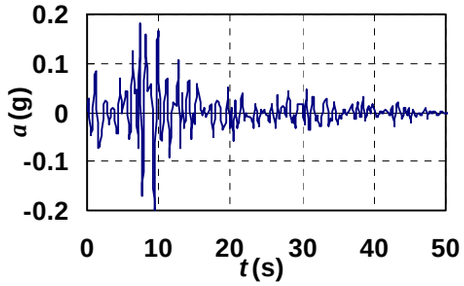
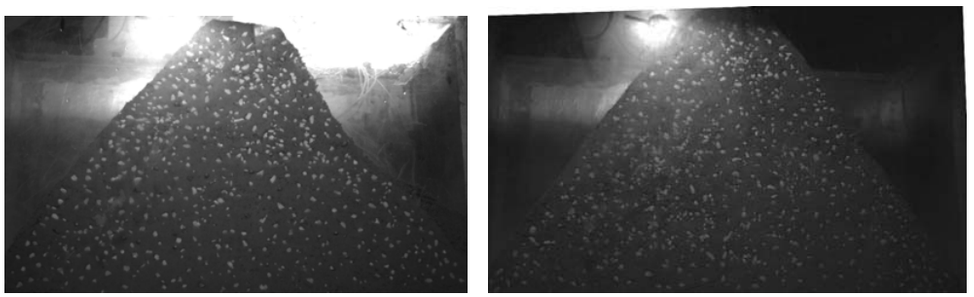
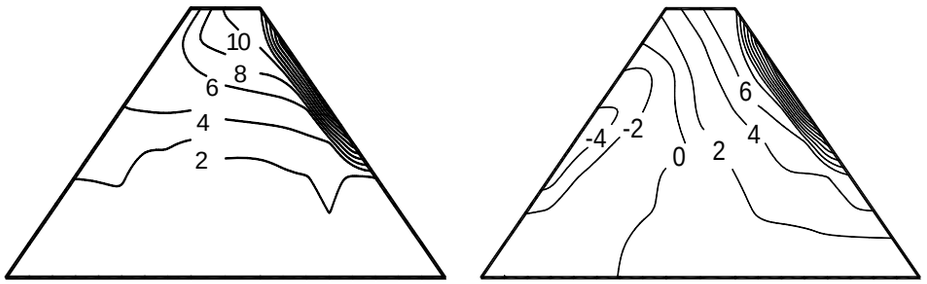


FIG. 3. Acceleration input for centrifuge model tests. *a*, acceleration; *t*, time.



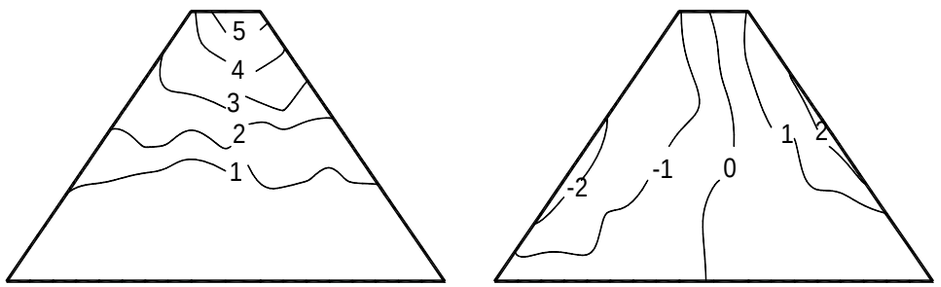
(a) water content: 16% **(b) water content: 11%**

FIG. 4. Images of the slope after earthquake.



(a) settlement **(b) horizontal displacement**

FIG. 5. Contour lines of residue deformation of the slope with water content of 16%. unit, cm.



(a) settlement **(b) horizontal displacement**

FIG. 6. Contour lines of residue deformation of the slope with water content of 11%. unit, cm.

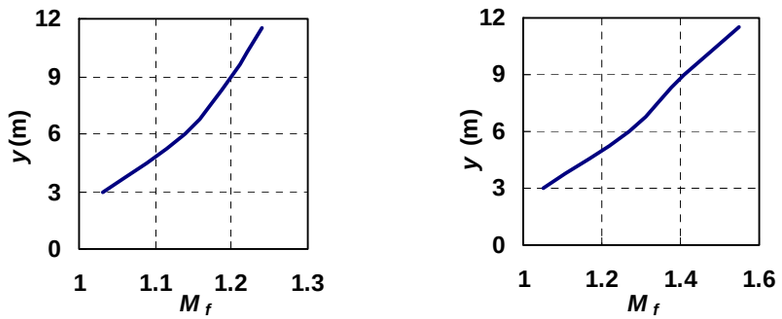
Acceleration and Displacement Response

The magnification factors gradually increased along the mountain axis with increasing altitude (Fig. 7). The drier slope, with water content of 11%, exhibited larger magnification factors than the wetter one; this may be because the soil of former slope is more stiffer due to influence of suction changed with the water content. The maximum magnification factors were 1.55 and 1.24 for the slopes with water contents of 11% and 16%, respectively. A similar exhibition can be found on the magnification factors near the surface of the slope.

Since the landslide occurred in the wetter slope with water content of 16%, we selected several points on the axis of the slope with water content of 11% to discuss the time history of dynamic response of the slope (Fig. 8).The displacements and accelerations have been transformed to practical magnitudes according to the similar law of a centrifuge model test. It should be noted that the high-frequency displacement waves have been filtered due to the frame rate limit of the capture images (48 frame/s in the model dimension) and measurement accuracy (0.1cm in prototype dimension); this resulted in that a few minor displacements, especially in the horizontal direction, cannot be captured. However, the fundamental rules of the displacement response can be analyzed based on the measurement results. It can be seen that the peak responses of acceleration and relative displacement increased with increasing altitude. The horizontal displacement fluctuated in magnitude during shaking. The vertical displacement increased monotonically during shaking; this demonstrated that significant irreversible volumetric deformation occurred due to shaking application. The increase rate of the vertical deformation was significantly dependent on the magnitude of the input shaking acceleration.

Deformation and Failure Process

We selected the wetter slope (water content: 16%, saturation degree: 54%) to discuss the deformation and failure process of a slope due to an earthquake. According to the images and corresponding displacement contour lines at four typical times (Fig. 9), the earthquake-induced deformation and failure process of a slope can be categorized into three stages: 1) small deformation stage, 2) strain localization stage, and 3) failure stage.



(a) water content: 16% **(b) water content: 11%**

FIG. 7. Magnification factors of slopes. *y*, height from the container bottom; M_f, magnification factor of acceleration.

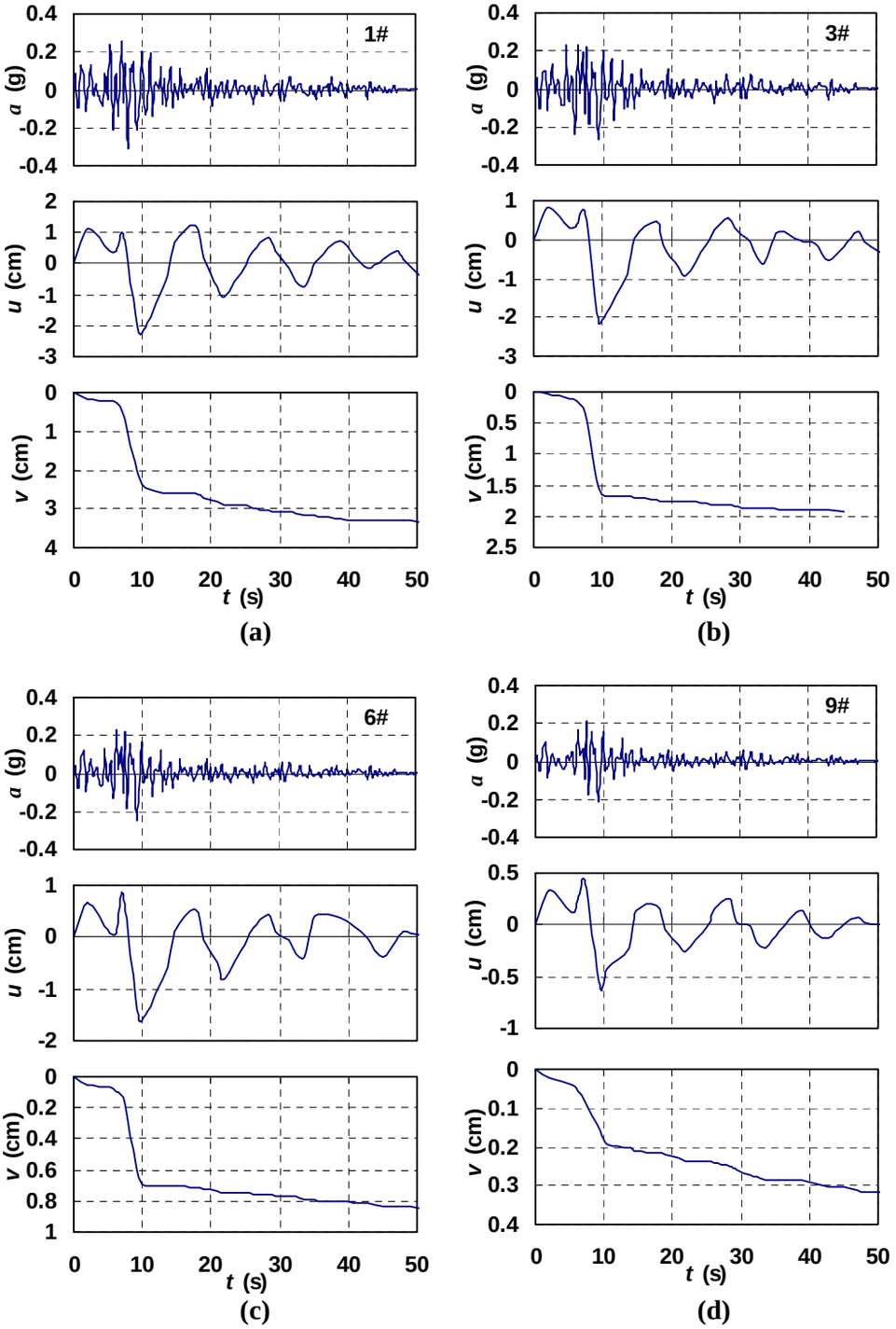


FIG. 8. Acceleration and displacement responses of typical points (Fig. 2 (b)) of the slope with water content of 11%. *a*, acceleration; *u*, horizontal displacement relative to the container; *v*, vertical displacement; *t*, time.

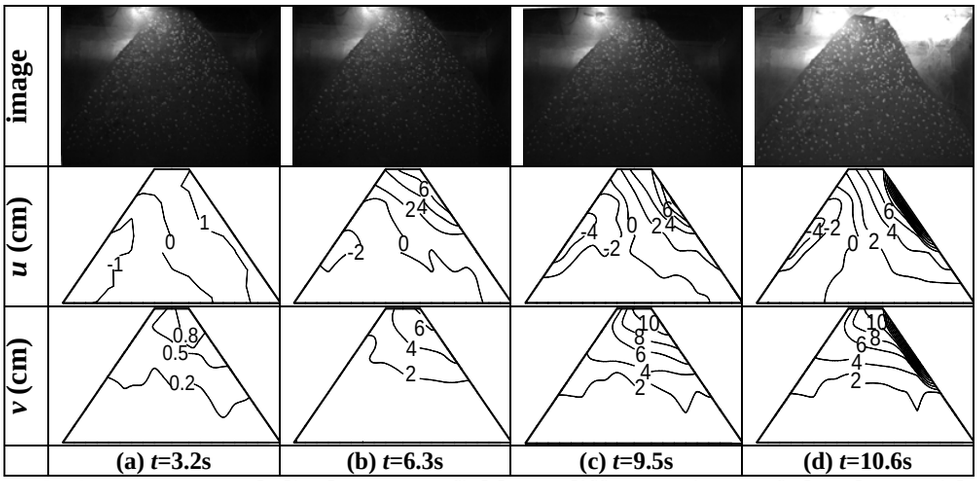


FIG. 9. Images and displacement fields at different times of the slope with water content of 16%. *u*, horizontal displacement relative to the container; *v*, vertical displacement.

1) Small deformation stage

In the early period of the shaking, the deformation of the slope occurred with small magnitude because the input acceleration was also small (Fig. 9 (a)). In this stage, there was insignificant strain localization in the slope; the slide body was difficult to distinguish from the base body.

2) Strain localization stage

The deformation of the slope increased during shaking (Fig. 9 (b) (c)). The contour lines implied that a significant deformation concentration, i.e., strain localization, occurred in the upper right region of the slope. This strain localization was reinforced with the application of shaking. Since final landslide occurred in the right slope (Fig. 4), the displacement histories of typical points, before the landslide of the slope (10.6s before), were given to illustrate the failure process (Fig. 10).

In the upper part of the slope, the displacements, both in the horizontal and vertical directions, exhibited significant changes during shaking (Fig. 10 (a)). It can be seen that the displacement responses of spots A and B were fairly close during the shaking; however, the displacement of spot C changed more significantly. For example, at 8.4s, the horizontal displacements of spots A, B, and C were 5.6cm, 0.3cm, and -0.8cm, respectively. Such a difference increased during shaking; this indicated that there were large shear strains between spots B and C.

In the middle part of the slope, the horizontal displacements of the three spots exhibited significant difference during shaking (Fig. 10 (b)). Whereas, the vertical displacement of the spot F, near the slope surface, was significantly different from those of other spots. This implied that significant strain localization occurred in the middle of the slope; the region near the surface was more significant.

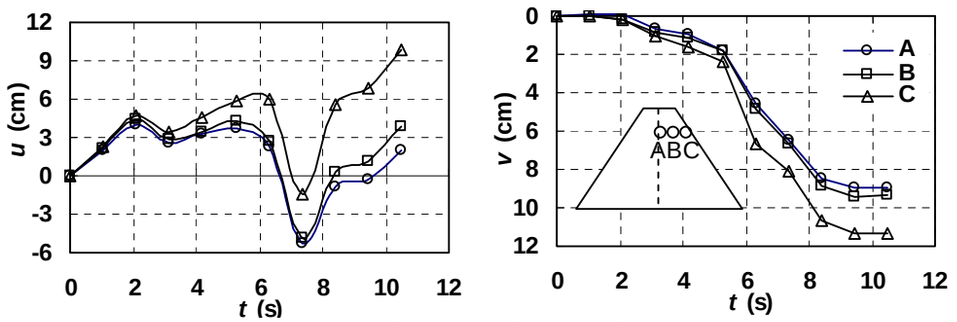
In the lower part of the slope, the displacements in the two directions exhibited similar changes during shaking (Fig. 10 (c)). The changes were fairly smaller than those of the upper slope. This indicated that the strain localization was insignificant; this can be confirmed by the contour lines of the deformation (Fig. 9 (c)).

In this stage, the slide body and base body may be nearly distinguished. The shear

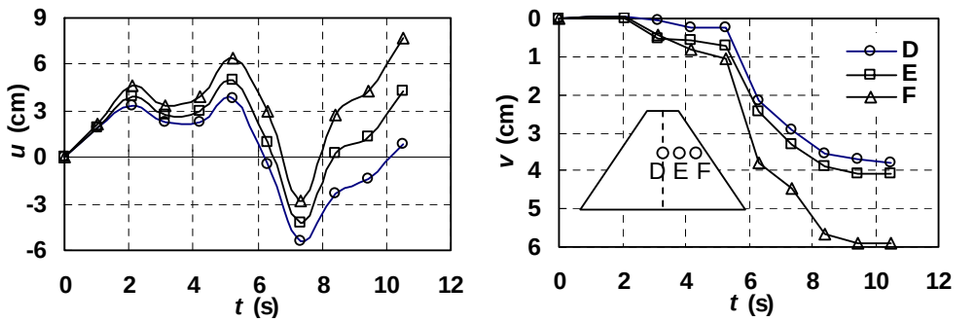
deformations concentrated in a narrow band; a significant strain localization occurred. Comparisons of the earthquake wave and displacement histories showed that the significant deformation of the slope, including strain localization, occurred when a larger acceleration was inputted (Figs. 3, 10). The strain localization occurred mainly in the upper and middle parts of the slope; this led to final landslide. Thus, the earthquake-induced failure process of a slope is significantly different from the one due to other loading styles (e.g., Mu, et al., 2006).

3) Failure stage

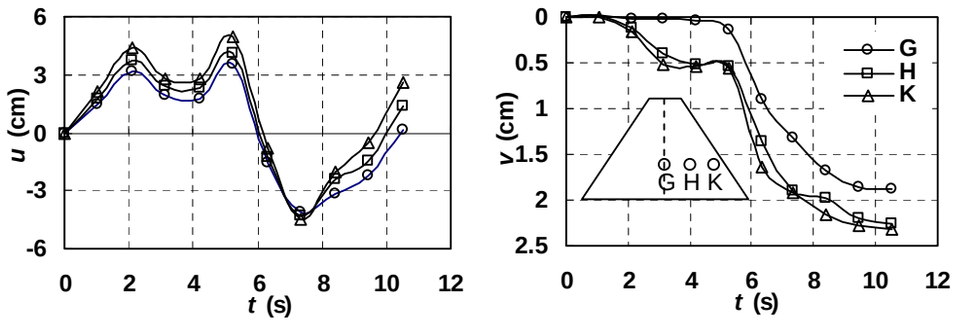
In this stage, the slide body slid along the final slip surface due to the development of strain localization (Fig. 9 (d)). This may be regarded as the movement between two rigid bodies.



(a) typical points of upper slope



(b) typical points of middle slope



(c) typical points of lower slope

FIG. 10. Displacement histories of typical points. *u*, horizontal displacement relative to the container; *v*, vertical displacement; *t*, time.

CONCLUSIONS

Centrifuge model tests were conducted to investigate the dynamic response and failure process of soil mountain slopes. The effect of water content of soil was also preliminarily discussed. based on the test results. The conclusions are summarized as follows:

1. The magnification factors and peak displacement of the slope increased with increasing altitude; the vertical displacement increased monotonically during shaking. After the earthquake, the residue settlements increased with increasing altitude; the residue horizontal displacements pointed from the axis to both sides.
2. Earthquake-induced deformation and failure process of a slope can be categorized into three stages: 1) small deformation stage, 2) strain localization stage, and 3) failure stage. Significant deformation, including strain localization, occurred when the larger acceleration was inputted. The strain localization occurred mainly in the upper and middle parts of the slope; this led to a final landslide. The earthquake-induced failure process of a slope is significantly different from the one due to other loading styles.
3. Water content significantly decreased the strength and deformation modulus of the soil. Therefore, increasing water content can significantly decrease aseismic stability and magnification factors; but increase the deformation of the slopes.

ACKNOWLEDGMENTS

The authors appreciate the support of the National Basic Research Program of China (973 Program) (No. 2007CB714108) and National Key Technology R&D Program of China (No. 2006BAK12B12).

REFERENCES

Taboada-Urtuzuastegui,V.M., Martinez-Ramirez, G., and Abdoun T. (2002). “Centrifuge modeling of seismic behavior of a slope in liquefiable soil.” *Soil Dynamics and Earthquake Engineering*, Vol. 22: 1043-1049.

Thusyanthan, N. I., Madabhushi, S. P. G., and Singh, S. (2005). “Seismic performance of geomembrane placed on a slope in a MSW landfill cell -A centrifuge study. “ *Geotechnical Special Publication*, n 130-142:: 2841-2852.

Lili N-R, and Nicholas S. (2006). “Centrifuge model studies of the seismic response of reinforced soil slopes” *Journal of Geotechnical and Geoenvironmental Engineering*, Vol. 132 (3): 388-400.

Zhang, G., Liang, D., and Zhang, J-M. (2006). "Image analysis measurement of soil particle movement during a soil–structure interface test." *Computers and Geotechnics*, Vol. 33 (4-5): 248-259.

Mu T, Zhang G, Zhang J-M. (2006). “Centrifuge modeling of progressive failure of soil slope.” *International Conference on Physical Modeling 2006*, Vol. 1: 373-377.

Constructing Hillside Ozone Facilities in a High Seismic Zone

M. Hassel, P.E., A. Woo, P.E., and M. Beikae, Ph.D., P.E., G.E.

Metropolitan Water District of Southern California

ABSTRACT

The Metropolitan Water District of Southern California (Metropolitan) has undertaken the addition of ozone disinfection facilities at all five of its water treatment plants as part of its Oxidation Retrofit Program (ORP). The ORP Site Preparation Project for the Robert B. Diemer Water Treatment Plant (Diemer Plant) is an integral part of this work. This project will prepare the plant site for construction of the ozonation facilities, i.e., ozone contactor, ozone generation building, and liquefied oxygen tank (LOX) farm.

The Diemer plant, with a rated treatment capacity of 520 million gallons per day (mgd), is one of Metropolitan's five treatment plants to be upgraded with ozonation facilities. The plant is located about 37 miles east of Los Angeles and provides treated water by gravity flow to Metropolitan's central pool area, which serves approximately 3.5 million people in the greater Orange and Los Angeles County areas. The plant was constructed during 1961 to 1963 in the Chino Hills 820 feet above sea level to allow for gravity flow to Metropolitan's service area without resorting to pumping. As such, the site was created by removing the top of a broad ridge and placing the excavated materials in adjacent ravines to provide a large level pad for construction of various treatment facilities. Since the completion of the initial construction work, the plant has experienced a major expansion, which includes the construction of many smaller facilities, and currently the addition of ozonation facilities. Design and construction of the new facilities are challenging due to stringent seismic criteria caused by the nearby Whittier fault located 0.5 kilometer north of the plant area and capable of generating an earthquake event with a moment magnitude of about 7. Based on site-specific deterministic seismic hazard analysis, the 84th percentile peak horizontal ground acceleration is approximately 1.15g.

Specifically, this paper describes the challenging issues and major design considerations that were associated with the preparation of construction documents for the Diemer Site Preparation Project. Major project elements that will be discussed in this paper include: the limited area of the Diemer site; the geology of the Diemer site and its nearby seismogenic sources; selection of site specific acceleration design criteria; alternative slope remediation methods investigated; selected slope remediation method and the design considerations; shoring and construction concerns during the design process; large excavation and backfill with roller compacted concrete; and current status of the construction project.

Keywords: Diemer; Ozone; site grading; contactor; seismic; compacted concrete; construction.

Introduction

The Metropolitan Water District of Southern California is a cooperative of 26 cities and water agencies serving 18 million people in six counties. Metropolitan imports water from the Colorado River and Northern California to supplement local supplies. Metropolitan also owns, operates, and maintains five conventional water treatment plants; five pumping plants; 16 power plants; 242 miles of aqueducts, pipelines, and tunnels; and 16 reservoirs and lakes.

In the past, Metropolitan's five water treatment plants used chlorine for primary disinfection. In order to comply with United States Environmental Protection Agency's Disinfectants/ Disinfection By-products (D/DBP) regulations, Metropolitan studied alternate replacement disinfectants. As a result, Metropolitan's Board elected to implement ozone, as its primary disinfectant for its five water treatment plants.

The Site Preparation Project stabilized the Diemer Plant's south-facing slope in preparation for construction of future ORP ozonation facilities. It also enhanced the reliability of the Diemer Plant by relocating a portion of the plant's 12-foot diameter inlet conduit out of seismically unstable fill slope material into competent bedrock. This inlet conduit brings untreated water into the plant. This paper outlines the challenges of designing and constructing a foundation to hold up the future ozonation facilities.

Proposed Ozonation Facilities Site Challenges

The Diemer Plant is located on the top of a hill in Orange County adjacent to Chino Hills State Park (Figures 1 and 2), with limited open areas suitable for new process facility construction. Due to hydraulic constraints and layout of existing pipelines, the ozone contactor/generation building must be located on the southwest portion of the site's main plant level, above a south-facing slope. For the new process facilities at the southwest portion of the main plant, the geotechnical analyses determined that the south-facing slope could potentially experience significant deformation in the event of a large earthquake and must be stabilized prior to construction of the ozonation facilities. As a result, relocation of the plant's existing maintenance and warehouse facility, various pipelines, electrical duct banks, and miscellaneous other facilities were required prior to remediation of the south slope area.

Geologic Setting and Original Site Grading

The east-west trending ridge on which the Diemer Plant is situated, is underlain by the Pleistocene-age Fernando formation, consisting of upper and lower members. The Fernando formation consists of marine sedimentary rock. The upper Fernando formation consists of predominantly sandstone and conglomerate with interbedded siltstone. The lower member of the Fernando formation consists predominantly of massive siltstone and clayey siltstone with sandstone. The Fernando formation overlies the Sycamore Canyon member of the Puente formation. These bedrock formations had been deformed by folding and faulting as the Puente Hills were uplifted. As a result of this deformation, Fernando formation bedding within the site dips towards the southwest or is locally overturned. In addition, a strike-slip Whittier fault capable of generating an earthquake event with a moment magnitude of about 7.0 is located at a distance of 0.5 kilometer north of the plant (Figure 2).



Figure 1 – Diemer Water Treatment Plant

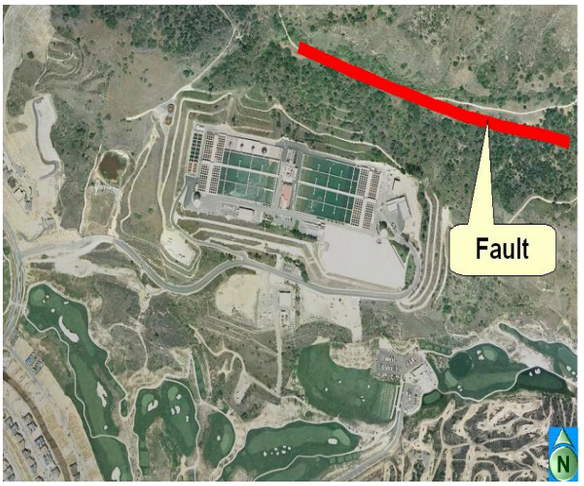


Figure 2 – Diemer Plant & Whittier Fault

The Diemer Plant was constructed in the early 1960's by cutting approximately 55 to 70 feet of native materials from the top of a broad ridge and placing the excavated materials in adjacent ravines to produce a large level pad at about Elevation 820 feet for construction of various water treatment facilities. The majority of the materials excavated were placed as fill on the south slope of the main ridge in the ravines south of the Diemer Plant. Based on geotechnical data, the majority of the fill placed at the Diemer Plant was generated from the siltstone of the lower member of the Fernando formation. Reportedly, the fill soils consist predominantly of clayey silt and silty clay. The perimeter cut and fill slopes created during the original site grading are inclined at a gradient of approximately 1.5H:1V. The approximate limits of the existing fills are mapped and compiled by Metropolitan as depicted in Figure 3.

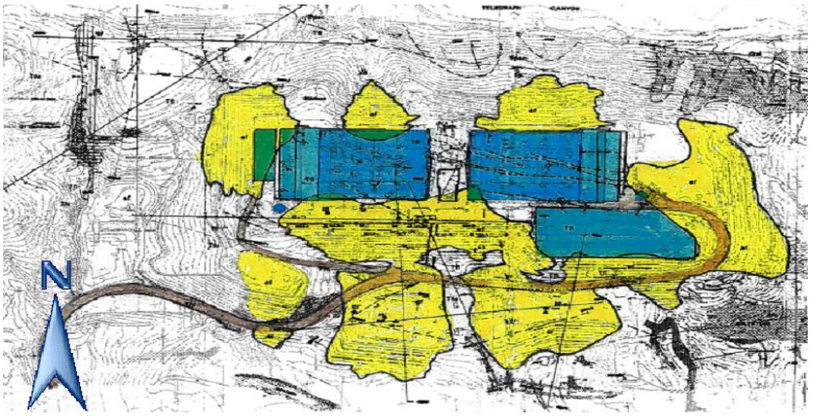


Figure 3 – Geological Map & Limits of Fill

Ground Motion, Performance, and Deformation Criteria

The ozone contactor (OC) will be placed above the south fill slope of the Diemer Plant. The contactor, consist of four basins with a total water volume of 28 acre-feet, will be a rigid structure 400 feet long, 110 feet wide and about 35 feet high. For the analyses of the south fill slope area beneath the contactor, allowable deformation criteria for total and differential settlements of 1 inch and ½ inch, respectively, were utilized. Due to the volume of water stored and height of the supporting fill, the contactor is considered a jurisdictional dam under the

California Water Code. Based on site-specific deterministic seismic hazard analysis (DSHA) results, the 84th percentile peak horizontal ground acceleration is approximately 1.15g corresponding to a moment-magnitude 7.0 event on the Whittier fault (GeoPentech, 2003). The south fill slope, which is only marginally stable under static conditions, was further evaluated under earthquake-shaking conditions for the postulated 84th percentile seismic event. The standards used in this analysis are comparable to those published by the California Division of Safety of Dams (DSOD). Once DSOD concurred with the performance and deformation criteria, a peak horizontal ground acceleration of 1.15g was selected and used for seismically induced displacement calculations for all alternatives.

Remediation Alternatives Challenges and Recommendation

Prior to the decision to use a roller-compacted-concrete (RCC) foundation, various remediation methods were studied and considered by the design team. The alternatives considered were 1) structural setback, 2) complete fill removal and replacement, 3) complete fill removal and replacement with structural geo-grid, 4) toe buttress with cast-in-drilled holes (CIDH) concrete piles, 5) tie-back system with CIDH concrete piles, 6) foundation shear walls, 7) *in-situ* soil-cement, 8) RCC buttress with CIDH concrete piles, and 9) RCC foundation. A general discussion of these alternatives is presented as follow:

Alternative 1 – Structural Setback

Alternative 1 considered establishing a setback zone at the top of the descending slope, within which no structures should be constructed and no additional loads should be added. Beyond the set back zone, the calculated static factor of safety was above the required 1.5. This alternative appeared to be inexpensive and not disruptive; however, sufficient setback was not available.

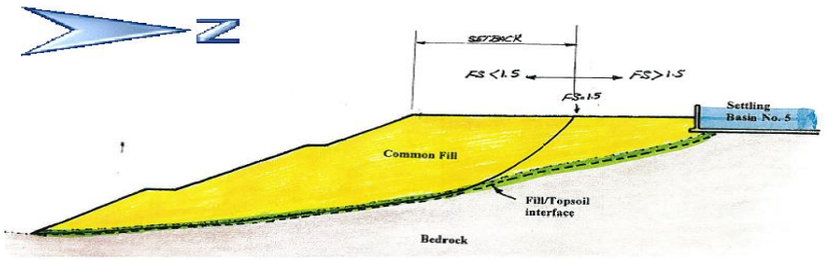


Figure 4 – Structural Setback

Based on studies, the setback zone was estimated to be about 60 feet north of the slope edge (Figure 4). The width of available area is insufficient for the proposed OC basin. As a result, the OC would be in the setback zone. Since the fill slope is susceptible to seismic deformation of a few feet for the postulated design ground motions, this alternative was not a viable option for the south slope remediation.

Alternative 2 – Complete Fill Removal and Replacement

Alternative 2 considered removal of the existing fill, the underlying topsoil/colluvium, and replacement with properly conditioned/compacted fill as a positive means of increasing the overall stability of the slope. The existing fill and topsoil/colluvium would be excavated to competent bedrock and replaced with compacted fill, properly keyed into the underlying bedrock

materials, to the final slope configuration (Figure 5). Since the slope is steep (1.5H:1V), the removal and replacement would not prevent seismic deformation of the fill slope during the postulated design earthquake. Based on seismic analysis results, the estimated seismically induced displacements would be in the range of 1.6 to 6.9 feet. Therefore, this alternative was not a viable option for the south slope remediation.

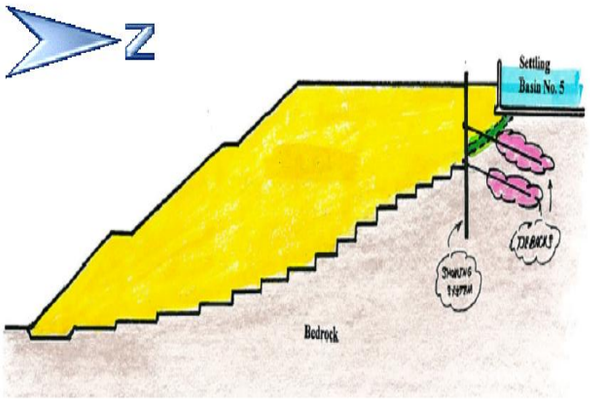


Figure 5 –Complete Fill Removal & Replacement

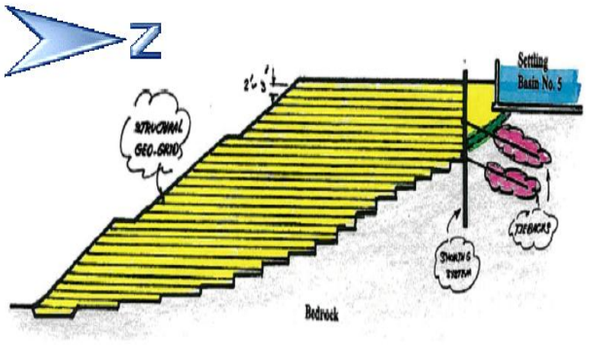


Figure 6 –Fill Removal & Replacement w/ Geo-grid

Alternative 3 – Complete Fill Removal and Replacement with Structural Geogrid
Alternative 3 considered removing existing fill and replacing it with properly conditioned and compacted fill; however, reinforced with structural geogrids (Figure 6).

Geogrid, a synthetic material that reduces lateral deformation of the soil, would be embedded in a sufficient distance from the slope face to develop their full allowable tensile resistance, or anchored in bedrock if the embedment length were not sufficient. The analysis results estimated that seismically induced displacements for geogrid at 3 and 2 feet vertical spacing were in the range of 0.7 to 3.8 feet and 0.5 to 2.5 feet, respectively. In addition, if the higher strength reinforcement with 2 feet vertical spacing were used, seismic displacements would still be in the range of 0.3 to 2.3 feet. Therefore, this alternative was not a viable option.

Alternative 4 – Toe Buttress with Cast-In-Drilled Holes (CIDH) Piles
Alternative 4 considered a shear key and earthen buttress constructed at the toe of the fill slope (see Figure 7).

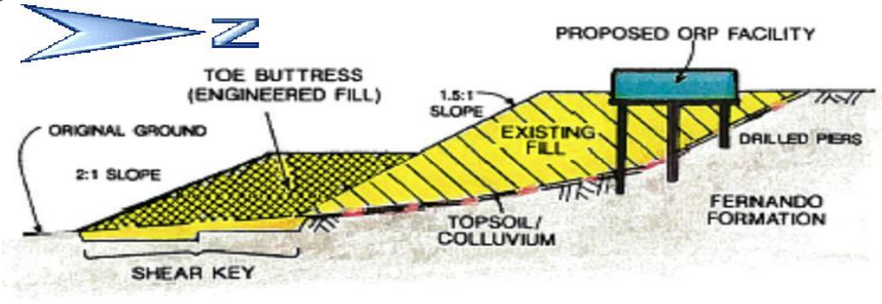


Figure 7 –Toe Buttress with CIDH Concrete Piles

The existing fill and the topsoil/colluvium underlying the fill would be left in place. To provide a stable foundation system, deep foundations such as CIDH piles would be required in conjunction with the toe buttress fill. The depth of fill in the area of the drilled piles to support the proposed OC structure would be in the range of 40 to 80 feet. The drilled piles would pass through the topsoil/colluvium and penetrate into competent bedrock, however, the existing fill would still be subject to potential downward slope movement due to the presence of the topsoil/colluvium. Although the piles would be stable under static condition, they would be subjected to horizontal seismic forces caused by the lateral movement of the fill and the horizontal inertial load due to the postulated earthquake shaking. As such, fill materials surrounding the piles not only could not provide lateral constraint against movement of the piles, they would also impose additional seismic earth pressures. Under the effects of the vertical and horizontal forces, the piles would act as cantilever beams/columns with 40 to 80 feet of unsupported length. Under these conditions, free-standing piles would have to be designed for the lateral seismic forces and bending under the simultaneous effects of gravity/earthquake motions. In addition, possibility of permanent lateral slope movements under the postulated earthquake could not be discounted. Therefore, this alternative was rejected due to the great design difficulty and high cost.

Alternative 5 – Tie-Back System with Cast-In-Drilled Holes (CIDH) Piles

Alternative 5 considered the installation of tie-backs anchored in competent bedrock and CIDH concrete piles supporting the OC (Figure 8). This would locally stabilize the slope immediately below the OC in order to increase the factor of safety. Thus, the slope below the stabilized zone would be of less concern so long as the performance of the lower slope did not adversely impact other plant facilities. CIDH piles would be used in conjunction with the tie-backs for support. Both the piles/anchors would pass through the topsoil/colluvium and penetrate into competent bedrock. In addition, construction of a continuous wall/concrete blocks at discrete locations on the slope would provide necessary reaction for the anchors/confinement of slope being stabilized. Unfortunately, the use of anchors for permanent installations has a few disadvantages, such as stress relaxation due to soil creep, corrosion of post-tensioning tendons, and permanent monitoring of the tie-back system. Due to these disadvantages, tie-back system was not acceptable as a permanent stabilization measure, it was not considered a viable option.

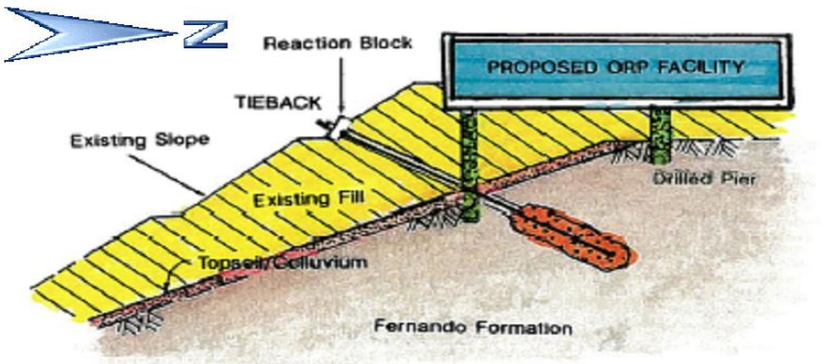


Figure 8 –Tie-back System with CIDH Concrete Piles

Alternative 6 – Foundation Shear Walls

Alternative 6 considered a structural slab or mat foundation founded on shear walls for the OC (see Figure 9). The walls would consist of 3-foot wide concrete-filled trenches extending into

competent bedrock, aligned perpendicular to the axis of the slope, and spaced in the east-west plant direction about every 15 to 20 feet. The existing fill over the topsoil/colluvium would be partitioned and confined by the walls. Any tendency for downslope movement of the partitioned fill would be reduced due to the arching effect of the fill soils between the walls.

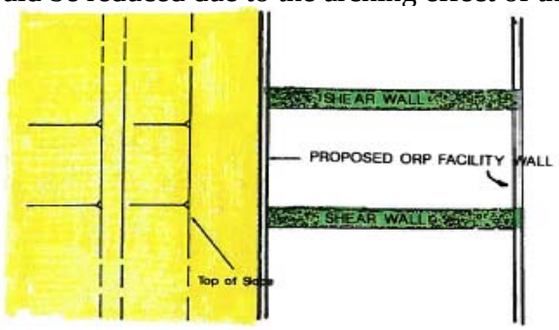


Figure 9-Foundation Shear Walls

During the analyses, it was noted that the geometrical configuration of shear walls would need to be designed to resist lateral loads in the north-south direction applied to them by the OC. In the east-west direction, the shear wall would need to be designed to resist both lateral loads and/or moments applied to them by the OC and seismically induced earth pressures. In addition, due to high horizontal design acceleration, wall depth was estimated to be 80 feet deep to transfer horizontal inertia and vertical gravity loads to competent bedrock. Due to construction difficulties of these deep shear walls, this alternative was not considered as a viable option.

Alternative 7 – *In-Situ* Soil-Cement

Alternative 7 considered *in-situ* soil-cement mixing to improve existing fill and topsoil/colluvium strength properties. Generally, mixing increasing amounts of cement with soil, the shear strength of the soil-cement mixture increases substantially. Review of case histories and laboratory test results indicated that mix designs used for slope stabilization generally consist of 1 to 10 percent cement by weight of the soil to produce cohesion in the range of 25 to about 125 psi. Implementation of soil-cement mixing would require treating all existing topsoil/colluvium and fill within the zone of influence and embedding the soil-cement mixture into the underlying competent bedrock. Unfortunately, the effectiveness of the soil mixing needs to be verified in place in critical location, and at interface of the fill/ bedrock. As such, it would be necessary to quantify fill strength and underlying topsoil before and after soil mixing operation and clearly demonstrate that the strengths of these materials had reached the design level required by static and seismic analyses results. Due to inherent difficulty and uncertainty of quantifying the shear strength of the soil-cement, this alternative was not a viable option.

Alternative 8 – Roller-Compacted-Concrete (RCC) with CIDH Concrete Piles

Alternative 8 considered an RCC buttress to provide higher strength material with conjunction of piles to support the OC (Figure 10). RCC is concrete, but it's hauled and placed by earth moving equipment (nontraditional methods for concrete) and uses a drier and stiffer consistency than conventional concrete. After the RCC has cured in place, it is concrete. The resulting strength properties of the placed RCC are considerably greater than compacted earth material, and in this case will exceed the strength of the underlying bedrock.

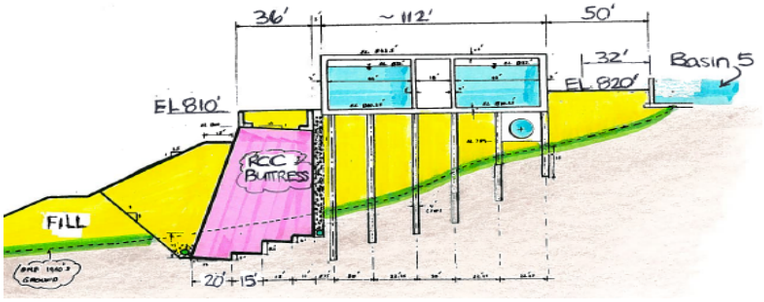


Figure 10 –RCC with CIDH Concrete Piles

The depth of fill for piles would range from 40 to 80 feet. The piles would pass through topsoil/colluvium and penetrate into competent bedrock, and existing fill would be supported by the RCC buttress. Although, the piles would be stable under static condition, they would be subjected to horizontal seismic forces caused by lateral movements and the horizontal inertial load due to design earthquake shakings. As such, the fill materials surrounding the piles would not provide lateral constraint against movement, it would also impose additional seismic earth pressures. Under simultaneous effects of vertical/horizontal forces, the piles would act as cantilever beams/columns with 40 to 80 feet of unsupported length. Under these conditions, free-standing CIDH piles would have to be designed for lateral seismic forces and bending under the simultaneous effects of gravity/earthquake motions. It was concluded that RCC Buttress would provide best solution for limiting seismically-induced deformations, nevertheless, residual displacement at the pile cap would induce large bending moment which could not be designed economically; therefore, it was not considered a viable option.

Alternative 9 – Roller-Compacted-Concrete (RCC) Foundation

Alternative 9 considered an RCC foundation to support the OC (Figure 11). In this approach, the existing fill and topsoil/colluvium would be excavated to competent bedrock and then replaced with an RCC foundation. The resulting strength properties of the placed RCC are considerably greater than compacted earth materials, and will exceed the strength of the underlying bedrock. After much consideration of construction cost and schedule, it was concluded that RCC foundation would provide the best overall solution for limiting seismically-induced deformations and support for OC. Nonlinear seismic deformation analyses were performed for critical sections of RCC foundation (GeopPentech, 2005). For a maximum section of the RCC foundation, Figures 12 and 13 show the deformed mesh and selected displacement histories at points A, B, and C due to Landers Earthquake, respectively. As the figures show, the residual displacements of OC are within the allowable deformation criteria. As a result, this alternative was selected for final design.

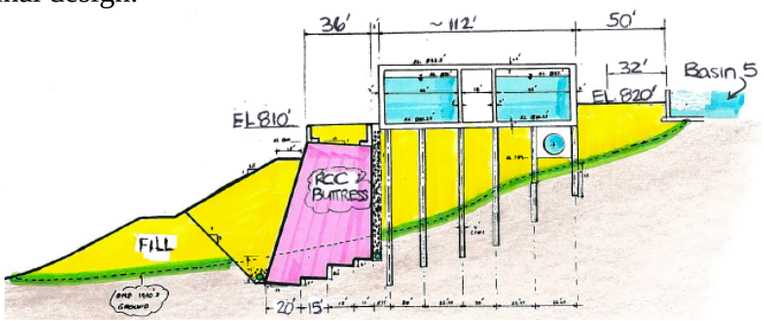


Figure 11 –RCC Foundation

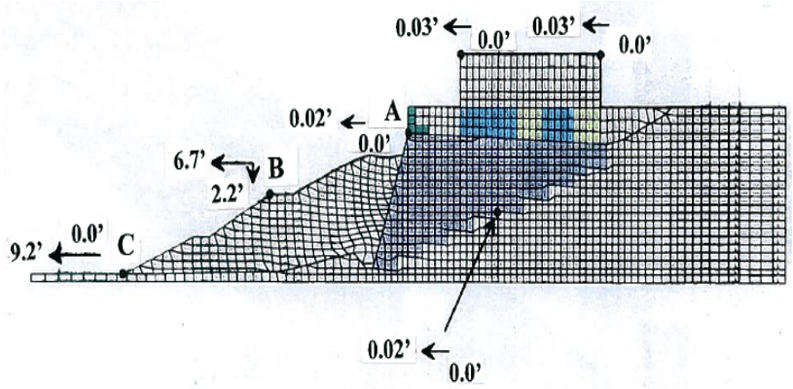


Figure 12 – Deformed Mesh Due to Landers Earthquake (Lucerne)

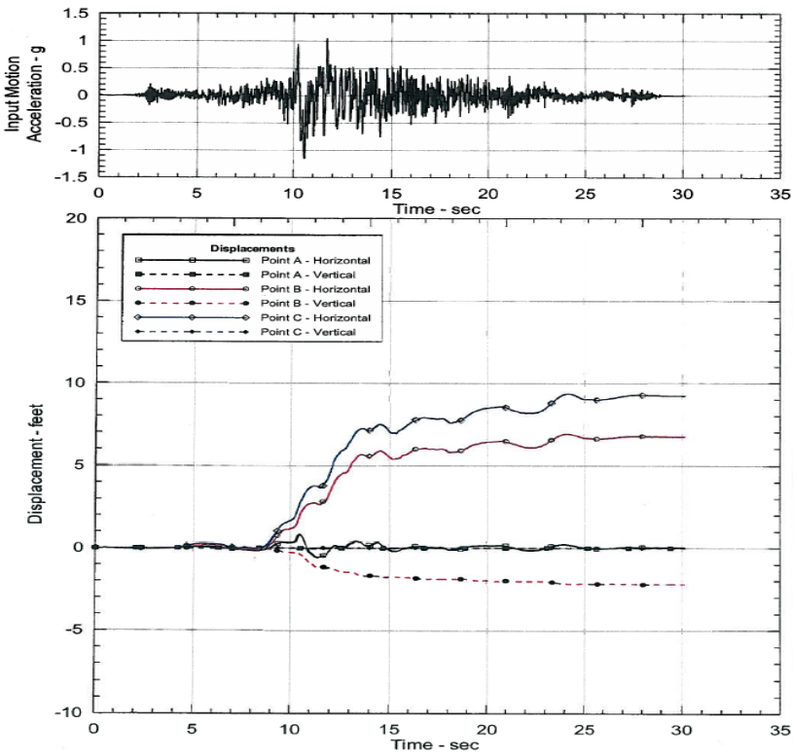


Figure 13 – Selected Displacement Time Histories Due to Landers Earthquake (Lucerne)

Design and Construction Challenges

Design of site preparation for OC needed to include relocation of existing facilities/pipelines that interfere with construction, keeping the water treatment plant operating and delivering water while preparing the ground for the RCC placement. Demolition and all relocations considered proper handling of materials, many of which are hazardous. New pipe reaches were relocated away from the RCC construction area and placing them in stable ground conditions. The relocation was to facilitate later ozone construction tie-in, provide the opportunity to install

larger diameter pipes, added valves to improve hydraulic performance, and provided plant staff operational flexibility.

The relocation included a segment of 144-inch steel pipe plant influent conduit into competent bedrock to clear the area for RCC construction. To ensure the existing operational influent conduit would not be damaged should a seismic event occur during construction, shoring requirement was designed to resist seismic forces. Since the Diemer plant supplies a major portion of water to Orange County, this extra measure was added to ensure the integrity, reliability, and continuity of the plant during construction. Further, the shoring system was monitored for movement by daily measurements from 4 inclinometers and a survey crew.

RCC Mix Design Program

Metropolitan designed and constructed numerous facilities/structures including treatment plants, pipelines, tunnels, reservoirs, and dams. This project, however, makes the first RCC construction of this magnitude in Metropolitan. The RCC placement for this project is similar to a dam, yet it won't contain water behind it, but rather will hold water above it within the OC. Due to limited RCC experience, Metropolitan retained the services of Montgomery Watson Harza Americas, Inc. for their expertise in RCC. Concurrent with the final design, Metropolitan and MWH implemented an RCC mix design, laboratory program, and prepared RCC construction specifications.

Similar to conventional concrete, RCC used less water and its hauling/placement used earthmoving equipment, making it lower in construction cost. RCC is drier, has stiffer consistency, and resulted in less shrinkage cracks. This project's RCC is made up of Class 2 crushed aggregate base, cement, fly ash and water. Since flyash is being used in a cementatious material, RCC attained its design strength over longer time interval than conventional concrete. The laboratory trial mixes prepared and tested at finding a mix design providing an unconfined compressive strength of 3,000 psi at one year; it developed a curve of design strengths to fine-tune the actual mix proportions used during RCC construction. Prior to construction, Metropolitan provided a recommended mix design of 150-150 pounds of Cement to Fly Ash.

Foundation Excavation and Protection of Existing Facilities

Excavation of the existing fill soils on the south slope at the proposed structures was required for construction of the RCC foundation. Existing fill, native soils, and unsuitable materials were removed to expose colluvium/bedrock interface. Further excavation was required since the RCC foundation must be deep enough to accomplish at least a 10-foot embedment below the colluvium/bedrock contact (Figure 14).



Figure 14 – RCC Foundation



Figure 15 – Shoring and Lagging System

For protection of existing structures where the proposed excavation was less than 15 feet deep, cantilevered soldier pile shoring with shotcrete lagging was used. For excavations deeper that 15 feet, tie-back soldier pile shoring with shotcrete lagging was utilized (Figure 15). Active, passive, and surcharge earth pressures were provided for design of the required shoring system and soldier piles.

The soldier piles installed are approximately 8 to10 feet on center with a maximum exposed height of 105 feet plus about 15 feet of embedment depth with a continuous minimum 6-inch thick reinforced shotcrete lagging between the soldier piles. To release the hydrostatic pressure, a continuous 24-inch wide geo-composite drainage strip was installed behind the lagging and 4-inch diameter weep holes 5-feet on center were installed in the shotcrete lagging between the soldier piles. The long soldier piles were anchored with a few rows of tiebacks.

To maintain the reliability, continuity, and integrity of the plant and to protect the existing structures above the shoring system, stringent displacement criteria were developed and specified for the 80,000 square feet of shoring system. Extensive coordination and communications with operational personnel were required to keep the plant operating while construction took place.

Site and Agencies Coordination Challenges and Project Status

The Diemer Water Treatment Plant operates 24/7 and cannot be interrupted by construction without approved advance notice. All shutdown work was coordinated with plant staff and Metropolitan's affected member agencies including local media. In addition, plant operation requires daily chemical deliveries; routine maintenance and water quality monitoring; employee vehicular traffic to and from work; and seven other concurrent construction contracts that share the access roads and facilities.

In summary, all construction milestones were met, RCC placement completed in November 2007, and construction contract completed in February 2008, as scheduled.

REFERENCE:

GeoPentech (2003). "Ground Motion Evaluation, Robert B. Diemer Filtration Plant, Yorba Linda, California." Letter Report to Metropolitan Water District of Southern California, Sep. 26.

GeoPentech (2005). "Geotechnical Evaluation – RCC Foundation for Ozone Contactor in South Slope Area, Robert B. Diemer Filtration Plant, Yorba Linda, California." Report to Metropolitan Water District of Southern California, May.

Hassel, M. K., Beikae, M., Woo, A. and Claisse, M. (2007). "Site Preparation Work for Constructing Hillside Ozone Facilities in a High Seismic Zone." 2007 World Congress on Ozone and Ultraviolet Technologies, Los Angeles, California.

This page intentionally left blank

Displacement – Based Seismic Stability Analyses of Reinforced and Unreinforced Slopes using Planar Failure Surfaces

Deepankar Choudhury[1], M. ASCE and Deepa Modi[2]

[1]Associate Professor, Department of Civil Engineering, Indian Institute of Technology (IIT) Bombay, Powai, Mumbai 400 076, India; dc@civil.iitb.ac.in
[2]Former PG Student, Department of Civil Engineering, Indian Institute of Technology (IIT) Bombay, Powai, Mumbai 400 076, India; deepa_modi@iitb.ac.in

ABSTRACT: In the present study, the most simplified planer failure surface is assumed for the seismic stability analysis of soil slopes and the behaviors of this simple failure surface over the existing complex surfaces are studied. A model reinforced soil slope is divided into a number of finite horizontal slices for the seismic analysis using a limit equilibrium method (LEM) with pseudo-static approach. The variations of factor of safety with respect to horizontal seismic acceleration coefficient under different soil and seismic conditions are shown. It is found that for the slope angle $\beta = 25^0$; angle of friction $\phi = 30^0$ and for the increase in the horizontal seismic acceleration coefficient k_h from 0.2 to 0.3, the respective decrease in the percentage of the factor of safety is about 21%. It is concluded that the stability of slope decreases with increase in both the horizontal and vertical seismic acceleration coefficients. The present results are compared with the available results in the literature. Also, the displacement of slope for different soil and seismic conditions and time of cycle of earthquake loading are evaluated. As expected, the displacement of the slope is found to increase significantly with increase in the seismic accelerations.

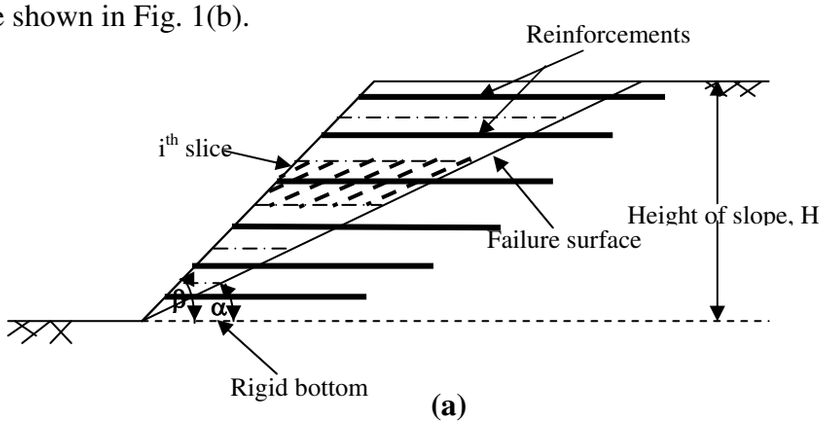
INTRODUCTION

Knowledge and safety of man made slopes under seismic conditions require special attention due to the devastating nature of the problem, which makes the topic extremely important to researchers and engineers. There are numerous methods like limit equilibrium method, limit analysis, finite element method, stress deformation analysis, etc. to analyze the stability of slopes under seismic conditions. Among all the available methods, limit equilibrium method (Saran 2006; Choudhury et al. 2007) is most commonly used. On this topic of earthquake-induced slope stability problems several researchers had given approximate solutions starting from Terzaghi (1950) using planar failure surface adopting limit equilibrium method, sliding block approach of Newmark (1965), which was modified by Sarma (1975) for the movement of rigid block on a slope, limit analysis by Loukidis et al. (2003), vertical slice method by

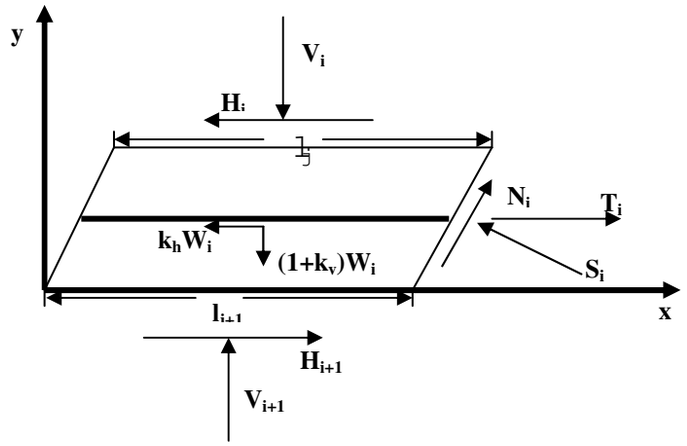
Choudhury et al. (2007). All these methods mostly used the conventional pseudo-static approach to consider the seismic forces for the analysis of unreinfocred soil slope. Also the recent horizontal slice method (HSM) given by Shahgholi et al. (2001) used the similar type of pseudo-static approach for the analysis of reinforced soil slope considering polylinear failure surface. However, the use of HSM is found to be better over vertical slice method as in the HSM both the reinforced and unreinforced soil slopes can be modeled without cutting the reinforcement which is not possible in vertical slice method and hence leading to more number of unknowns in the solution. Most of the researchers considered the complex failure surface for the static and seismic design of reinforced soil slopes as log spiral (Leshchinsky et al. 1995; Leshchinsky 1997) or polylinear (Shahgholi et al. 2001 by pseudo-static method; Nimbalkar et al. 2006 by pseudo-dynamic method). In the present study an attempt is made to use the simplest planar rupture surface for the analysis of seismic stability of both the reinforced and unreinforced soil slopes in a more comprehensive manner. By comparing the present results with the previous solutions using other types of complex failure surfaces in the analysis, an attempt is made to show the merits of the present study. As previous researchers work using force-based analysis (Kramer 1996) the displacement-based analysis did not get proper attention. However, a few research works for e.g. work reported by Kramer and Smith (1997) using the modified Newmark's method to estimate the seismic displacement of slopes and work by Rathje and Bray (1999) and some others had reported the simplified procedure to estimate the seismic displacement of earth structures. In the present paper, also the proper estimations of seismic displacement for soil slopes are reported using frequency, phase angle, time period of the earthquake and seismic horizontal acceleration coefficient with the use of appropriate boundary conditions.

METHOD OF ANALYSIS

In the present analysis, the method of horizontal slices proposed by Shahgholi et al. (2001) is used by considering the pseudo-static approach for seismic forces to obtain the stability of reinforced soil slope. Instead of using the complex polylinear failure surface as was used by Shahgholi et al. (2001), in the present study the simplest planar rupture surface is used for the seismic analysis of reinforced soil slope of height H, slope angle β and failure plane θ with respect to horizontal as shown in Fig. 1(a). The failure wedge is divided into a finite number of horizontal slices. The forces acting on each slice are shown in Fig. 1(b).



(a)



(b)

FIG. 1. (a) Model reinforced slope with planar failure surface and horizontal slices (b) Forces acting on i^{th} slice

The assumptions made in the present analysis are as follows:

- The vertical stress on each slice of the failure mass is equal to the overburden pressure acting on it.
- The factor of safety for each slice is assumed to be equal.
- The failure surface does not pass below the toe of the soil slope and the bottom is considered as rigid.

Using Fig. 1(b) one can write the following equilibrium equations:

$$\sum F_y = 0 \quad (\textit{for each slice})$$
$$\Rightarrow V_{i+1} - V_i - (1+k_v)W_i + S_i \sin\alpha_i + N_i \cos\alpha_i = 0 \tag{1}$$

$$\tau_r = \frac{\tau_f}{FOS} \qquad (\textit{for each slice})$$
$$\Rightarrow S_i = \frac{1}{FOS}\left(c\, b_i + N_i \tan\phi\right) \tag{1}$$

$$\sum F_x = 0 \qquad (\textit{for whole slice})$$
$$\Rightarrow \sum_{j=1}^{m} t_j + \sum_{i=1}^{N} S_i \cos\alpha_i - \sum_{i=1}^{N} N_i \sin\alpha_i - \sum_{i=1}^{N} W_i k_h = 0 \tag{2}$$

Solving equation (2) and equation (1), we get N_i as:

$$N_i = \frac{V_i - V_{i+1} + (1+k_v)W_i - \dfrac{c\, b_i}{FS}\sin\alpha_i}{\dfrac{\tan\phi}{FOS}\sin\alpha_i + \cos\alpha_i} \tag{3}$$

Substituting S_i from equation (2) and N_i from equation (4) in equation (3), the factor of safety (FOS) can be expressed as:

$$FOS = \frac{\sum_{i=1}^{N} N_i \tan\phi \cos\alpha_i}{\sum_{i=1}^{N} N_i \sin\alpha_i + \sum_{i=1}^{N} W_i k_h - \sum_{j=1}^{m} t_j} \quad (5)$$

Hence, it is seen that by applying the equilibrium equations on each slice and on the entire failure mass, the equation for factor of safety is determined [Eqn. 5]. Now by setting the factor of safety equal to 1.0, the required reinforcement strength of each reinforced layer is determined and compared with the reinforcement strength determined by horizontal slice method (HSM) of Shahgholi et al. (2001) using polylinear failure surface and by RESLOPE program of Leshchinsky (1997) with a log spiral failure surface as shown in Table 1. The variation of different soil and seismic parameters used in the present analysis are as follows:

Height of the slope, H: 5 m; Unit weight of the soil, γ: 18 kN/m^3; Cohesion of the soil, c: 0 kN/m^2; Friction angle of the soil, ϕ: Varies 20^0 – 45^0; Horizontal seismic acceleration coefficient, k_h: 0.0, 0.1, 0.2; Vertical seismic acceleration coefficient, k_v: 0.0, 0.5k_h, 1.0k_h.

Table 1. Comparison of present geosynthetic reinforcement strength results with those obtained by previous researchers

k_h	Required geosynthetic reinforcement strength, $\Sigma t_{j\,max}$(kN/m)							
	For $\phi=20^0$, k_v = 0.0				For $\phi=25^0$, k_v = 0.0			
	Case 1	Case 2	Case 3	Present study	Case 1	Case 2	Case 3	Present study
0.0	110	110	110	110	95	91	91	91
0.1	128	128	137	130	110	107	113	109
0.2	151	151	164	157	126	127	135	131
0.3	187	187	196	202	153	153	160	162

k_h	Required geosynthetic reinforcement strength, $\Sigma t_{j\,max}$(kN/m)						
	For $\phi=30^0$, k_v = 0.0				For $\phi=35^0$, k_v = 0.0		
	Case 1	Case 2	Case 3	Present study	Case 1	Case 2	Present study
0.0	74	75	75	75	63	61	61
0.1	90	89	93	91	74	74	75
0.2	106	106	109	110	90	89	92
0.3	128	128	130	135	106	108	113

[Note: Case 1: RESLOPE (1997), Case 2: HSM (2001), Case 3: Nimbalkar et al. (2006)]

Again, for the stability of unreinforced soil slope, the factor of safety varies with

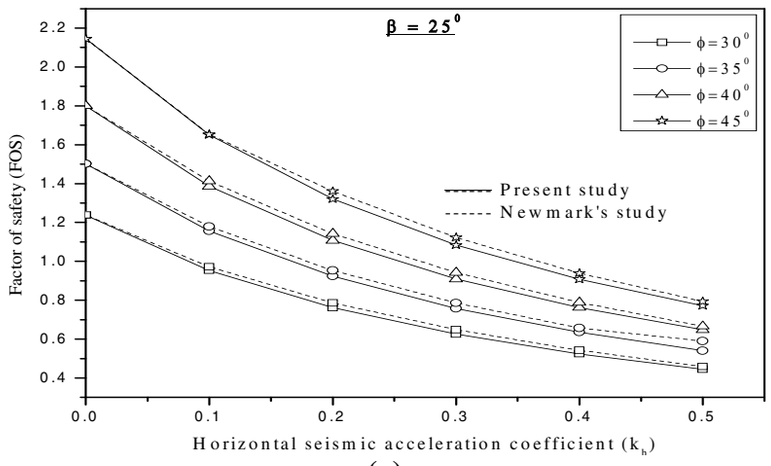
pseudo-static seismic acceleration as can be seen. If the inertial force acting on a potential failure mass become large enough that the total (static plus dynamic) driving forces exceed the available resisting forces, the factor of safety will drop below 1.0. Newmark (1965) considered the behavior of a slope under such conditions when the potential failure mass is no longer in equilibrium, consequently, accelerated by the unbalanced force. Newmark (1965) assumed the situation analogous to that of a block resting on an inclined plane. Thus, derived the factor of safety [FOS_d (t)] acting in the downward direction is to be given by Eq. (6).

$$FOS_d(t) = \frac{available\ resisting\ force}{pseudostatic\ driving\ force} = \frac{R_d(t)}{D_d(t)} = \frac{[\cos\beta - k_h(t)\sin\beta]\tan\phi}{\sin\beta + k_h(t)\cos\beta} \tag{6}$$

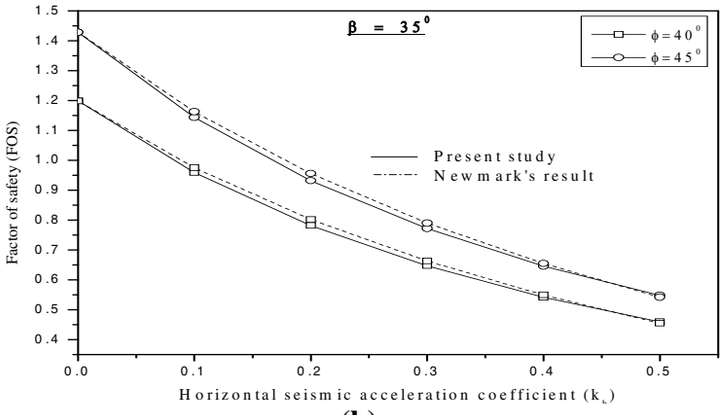
However, in the present study, the slope analysis has been done by horizontal slice method is based on the computation of the pseudo-static factor of safety by including the horizontal and vertical seismic forces. As the factor of safety for reinforced case is already derived in equation (5) above, hence the equation of factor of safety for unreinforced slope can obtained by putting t_j equal to zero in equation (5), is given as:

$$FOS = \frac{\sum_{i=1}^{N} N_i \tan\phi \cos\alpha_i}{\sum_{i=1}^{N} N_i \sin\alpha_i + \sum_{i=1}^{N} W_i k_h} \tag{7}$$

Using the equation (7), the factor of safety values are plotted with horizontal seismic acceleration coefficient, k_h and also those are compared with the results obtained by the Newmark's method as shown in Fig. 2. Some more results of factor of safety are shown for different values of soil friction angle (ϕ), slope angle (β) and horizontal seismic acceleration coefficient (k_h) and vertical seismic acceleration coefficient (k_v) as shown in Fig. 3.

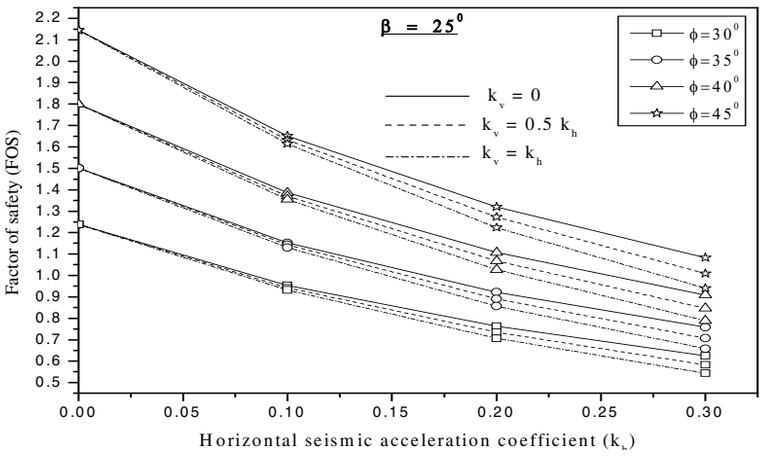


(a)

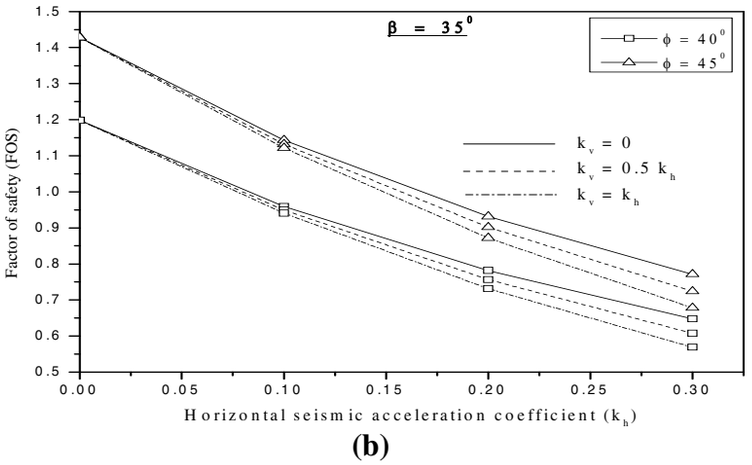


(b)

FIG. 2. Variation of FOS with k_h obtained by present study and compared with that obtained by Newmark's method (1965) for (a) $\beta = 25^0$ (b) $\beta = 35^0$



(a)



(b)

FIG. 3. Variation of FOS with k_h obtained by present study for different values of k_h , k_v and ϕ for slope angle, (a) $\beta = 25^0$ (b) $\beta = 35^0$.

Table 2. Displacement per cycle (cm/cycle) of the slope for $\beta = 25^0$ and $k_v = 0.0$ with different values of k_h, ϕ and time period (T) by pseudo-static method

T(sec.)	k_h	disp./cyc. for $\phi = 30^0$	disp./cyc. for $\phi = 35^0$	disp./cyc. for $\phi = 40^0$	disp./cyc. for $\phi = 45^0$
0.2	0.2	0.00352	-	-	-
	0.3	0.00737	0.00293	-	-
	0.4	0.01108	0.00729	0.00184	-
	0.5	0.01475	0.01138	0.00677	0.00012
0.3	0.2	0.00793	-	-	-
	0.3	0.01659	0.00659	-	-
	0.4	0.02494	0.01641	0.00414	-
	0.5	0.03318	0.02561	0.01522	0.00026
0.4	0.2	0.0141	-	-	-
	0.3	0.02949	0.01171	-	-
	0.4	0.04434	0.02918	0.00735	-
	0.5	0.05899	0.04552	0.02706	0.00047
0.5	0.2	0.02203	-	-	-
	0.3	0.04607	0.0183	-	-
	0.4	0.06928	0.04559	0.01149	-
	0.5	0.09217	0.07113	0.04229	0.00073

(Note: - shows that the values do not exist)

COMPUTATION OF SEISMIC DISPLACEMENTS OF SLOPES

Newmark (1965) defined the yield acceleration ($k_{hy}g$) as the acceleration which drops the dynamic factor of safety of the slope to unity. He concluded that there is no displacement in the slope when the magnitude of the applied acceleration ($k_{ha}g$) is less than that of the yield acceleration. While for applied acceleration to be more than that of the yield acceleration, the displacement is equal to the difference of the applied acceleration and the yield acceleration. i.e. (k_{ha} - k_{hy})g. Extending the Newmark's work (1965), Saran (2006) derived the following Eq. (8) for determining the displacement (x) of unreinforced soil slope using planar failure surface.

$$x = -\frac{1}{2} B k_{hy} t^2 - \frac{BP}{\omega^2} \sin\left(\omega t + \theta'\right) + \frac{BP}{\omega}\left[\frac{\sin\theta'}{\omega} + t\cos\theta'\right] \tag{8}$$

where,

$$k_{hy} = \tan\left(\phi_b - \beta\right)$$

$$B = g\left(\sin\beta\tan\phi_b + \cos\beta\right)$$

$$\theta' = \sin^{-1}\left(\frac{k_{hy}}{P}\right)$$

P = maximum value of acceleration coefficient; ω = angular frequency of earthquake; t = time for half cycle

In present study, the displacement of soil slope per cycle of earthquake loading with different soil and seismic conditions and time period (T) of earthquake excitation, obtained by using the equation (8) are shown in the tabular form in Tables 2 and 3. These results may be useful for the design of unreinforced soil slopes with the prediction of displacements under different seismic conditions.

Table 3. Displacement per cycle (cm/cycle) of the slope for $\beta = 30^0$ and 35^0 with $k_v = 0.0$ for different values of k_h, ϕ and time period (T) by pseudo-static method

T(sec.)	k_h	disp./cyc. $\beta = 30^0$ $\phi=35^0$	Disp./cyc. $\beta = 30^0$ $\phi=40^0$	disp./cyc. $\beta = 30^0$ $\phi=45^0$	disp./cyc. $\beta = 35^0$ $\phi=40^0$	disp./cyc. $\beta = 35^0$ $\phi=45^0$
0.2	0.2	0.00373	-	-	0.00398	-
	0.3	0.00779	0.00313	-	0.00833	0.00339
	0.4	0.01172	0.0078	0.00199	0.01253	0.00845
	0.5	0.01559	0.01217	0.00733	0.01667	0.01318
0.3	0.2	0.00838	-	-	0.00896	-
	0.3	0.01754	0.00704	-	0.01875	0.00763
	0.4	0.02637	0.01755	0.00448	0.02819	0.01901
	0.5	0.03508	0.02738	0.01649	0.03751	0.02966
0.4	0.2	0.0149	-	-	0.01594	-
	0.3	0.03117	0.01252	-	0.03334	0.01357
	0.4	0.04687	0.0312	0.00796	0.05012	0.0338
	0.5	0.06236	0.04868	0.02932	0.06669	0.05274
0.5	0.2	0.02329	-	-	0.0249	-
	0.3	0.04871	0.01957	-	0.05209	0.0212
	0.4	0.07324	0.04875	0.01244	0.07832	0.05282
	0.5	0.09744	0.07606	0.04581	0.1042	0.0824

(Note: - shows that the values do not exist)

COMPARISON OF RESULTS

The strength of the reinforcement required for the stability of the reinforced soil slope as per the present analysis using planer failure surface by pseudo-static method is slightly higher than the value obtained by the Shahgholi's HSM method (2001) using polylinear failure surface and Leshchinsky's RESLOPE program (1997) using log spiral failure surface as shown in Table 1 above. Specially, for the higher horizontal seismic acceleration coefficients, k_h the strength of the reinforcement determined by present analysis is found to be higher than those obtained by other methods. As shown in Figs. 2 and 3 above, the variation of the factor of safety with respect to the horizontal seismic acceleration coefficient obtained by the present analysis is compared with the Newmark's method (1965), shows that though the graph obtained by the present analysis follow almost the same pattern as that of Newmark's result. Hence the consideration of the simplest planar rupture surface is found to be useful for the analysis of seismic stability of both the reinforced and unreinforced soil slope for design purposes.

CONCLUSIONS

The seismic stability of soil slopes is analyzed by considering the planer failure surface and then dividing the failure zone into a finite number of horizontal slices using pseudo-static approach for the seismic forces. The strength of the reinforcements required for the reinforced soil slopes under different soil and seismic conditions are evaluated. Additionally, the variation of the factor of safety with respect to the horizontal seismic acceleration coefficient, k_h is plotted for different soil friction angle ϕ, slope angle β, and horizontal and vertical seismic acceleration coefficient (k_h and k_v). After comparing the results with the available results in the literature for different failure surfaces, it is concluded that the present results obtained by considering the simplest planer failure surface can also be used for design of both reinforced and unreinforced soil slopes under seismic conditions. The slope displacement per cycle of earthquake excitation for different soil and seismic conditions and time period of earthquake obtained shows that the displacement of slope increases with the increase in the time period of the earthquake, the horizontal seismic acceleration coefficient and the slope angle.

LIST OF NOTATIONS

The following symbols are used in this paper:

α_i = angle of the base of the i^{th} slice with horizontal
β = inclination of soil slope with horizontal
H = vertical height of the slope
γ = unit weight of the soil
c = cohesion of the soil
ϕ = friction angle of the soil
θ = inclination of planar failure surface with horizontal ($=\alpha_i$)
k_h, k_v = horizontal and vertical seismic acceleration coefficient
N = number of slices
b_i = length of side face of the i^{th} slice
H_i, V_i = horizontal and vertical interslice force
l_i = length of horizontal base of the i^{th} slice
m = number of reinforcements
S_i, N_i = shear and normal force on the side face of the i^{th} slice
W_i = weight of the i^{th} slice
τ_f = failure shear stress
τ_r = required shear stress
t_j = tensile force of reinforcement
ϕ_b = angle of friction between the block and the plane
$R_d(t)$ = available resisting force
$D_d(t)$ = pseudo-static driving force
$FOS_d(t)$ = factor of safety acting in the downward direction
FOS = factor of safety derived by present study

k_{hy} = yield acceleration coefficient
P = maximum value of acceleration coefficient
θ' = phase angle
ω = angular frequency of earthquake excitation
t = time for half cycle
x = displacement per cycle of earthquake excitation

REFERENCES

Choudhury D.**,** Basu S. and Bray J. D. (2007). Behaviour of slopes under static and seismic conditions by limit equilibrium method, In Embankments, Dams and Slopes: Lessons from the New Orleans Levee Failures and Other Current Issues, *Geotechnical Special Publication No. 161, ASCE,* USA, pp. 1-10.

Kramer, S. L. (1996). *Geotechnical earthquake engineering,* Prentice Hall Private Limited, New Jersey.

Kramer, S. L. and Smith, M. W. (1997). "Modified Newmark model for seismic displacements of compliant slopes", *Journal of Geotechnical and Geoenvironmental Engineering, ASCE,* 123(7), pp. 635–644.

Leshchinsky D. (1997). RESLOPE, *Geotechnical Fabrics Report* 15(1), pp. 40-46

Leshchinsky, D., Ling, H.I., and Hanks, G. (1995). Unified design approach to geosynthetic reinforced slopes and segmental walls. *Geosynthetic International,* 2(5), pp 845-881.

Loukidis, D., Bandini, P. and Salgado, R. (2003). "Stability of seismically loaded slopes using limit analysis." *Geotechnique*, 53(5), pp. 463-479.

Newmark, N. (1965). "Effects of earthquakes on the dams and embankments." *Getechnique,* 15(2), pp. 139-160.

Nimbalkar, S. S., Choudhury, D. and Mandal, J. N., (2006). "Seismic stability of reinforced-soil wall by pseudo-dynamic method." *Geosynthetic International,* 13(3), pp. 111-119.

Rathje, E. M., and Bray, J. D. (1999). "An examination of simplified earthquake-induced displacement procedures for earth structures." *Canadian Geotechnical Journal*, 36(1), pp. 72–87.

Saran, S. (2006). "Pseudo static seismic stability analysis of slopes", *Proceedings of Short Term Training Programme on Geotechnical Earthquake Engineering*, organized by Shantilal Shah Engineering College and Indian Geotechnical Society, Bhavnagar Chapter, 20 Nov. to 24 Nov. 2006.

Sarma, S. K. (1975). "Seismic stability of earth dam and embankments", *Getechnique,* 25(4), pp. 743-761.

Shahgholi, M., Fakher, A. and Jones, J. F. P. (2001). "Horizontal slice method of analysis." *Getechnique,* 51(10), pp. 881-885.

Terzaghi, K. (1950). *Mechanisms of Land Slides*. Engineering Geology (Berkeley) Volume, Geological Society of America.

Energy-Based Evaluation of Earthquake-Induced Slope Failure and Its Application

Takaji Kokusho[1], M. ASCE and Tomohiro Ishizawa[2]

[1]Professor, Civil Engineering Department, Faculty of Science and Engineering, Chuo University, 1-13-27 Kasuga, Bunkyo-ku, Tokyo, 112-8551, Japan; kokusho@civil.chuo-u.ac.jp
[2]Assistant Professor, ditto, ishizawa@civil.chuo-u.ac.jp

ABSTRACT: Slope failures during the 2004 Niigata-ken Chuetsu earthquake and their mechanisms are discussed herein. Slopes are composed of weak sedimented rock of alternating layers of strongly weathered sand stones and mud stones. Bedding planes had a strong effect on the failure mechanisms. An energy approach for run-out distance of failed soil mass in view of earthquake energy, together with potential energy, is applied to representative slope failures during the earthquake. It is found that the equivalent friction coefficient back-calculated by the energy approach is strongly dependent on the initial slope inclination. However, the absolute value of the former is smaller than the latter, indicating the failed soil mass initially accelerated.

CASE HISTORY DURING 2004 NIIGATAKEN CHUETSU EARTHQUAKE

The Niigata-ken Chuetsu earthquake (M_J=6.8) occurred on October 23, 2004. More than 4000 slope failures in the middle part of the main island of Japan occurred as a result of the main shock and several strong aftershocks. The damaged area (FIG. 1) is known as a landslide-prone area of green-tuff, with geological structures of active folding. Slopes are composed of weak sedimented rock of Neogene, alternating layers of strongly weathered mud stones and sand stones. Bedding planes had a strong effect on the slope failures. The slope failures due to this particular earthquake are classified into 3 types, as illustrated in FIG. 2:

Type-A: Deep slips parallel to sedimentation planes (dip slip), in gentle slopes of around 20 degrees. In many cases, displaced soil mass had originally been destabilized by river erosion or road construction, and glided as a rigid body along the slip plane. Displaced soil volume was very large and the translating soil block had little surface disturbance.



FIG. 1 Damaged area during 2004 Niigataken Chuetsu earthquake.

Type-B: Shallow slips of 1~2 m depth not parallel to sedimentation planes at steep slopes (>30 degrees). This type far out numbered Type-A failures, but the individual soil volume was not so large. Soils normally fell down as pieces, sometimes leaving trees with deep roots in their original locations.

Type-C: Deep slips in highly weathered colluvial soils in places where koi-ponds and terraced paddy fields were located. This type of failure seems unique to this earthquake and region because of the countless koi-ponds located in the damaged area. This failure type was obviously influenced by the ponds, which seem to have provided water for overflowing by seiche during shaking and also for piping causing delayed flow-type failure of the colluvial soils. Soil liquefaction or cyclic softening may have contributed to large ground deformation including cracks because sand boils were observed at some sites.

The most representative example of failure Type-A is Higashi-Takezawa, shown in FIG. 3, where highly weathered, thick sandstone (actually dense sandy soil) slid horizontally about 100 meter along an underlying mudstone slip plane of 20 degrees. The displaced soil mass dammed a river, making a natural reservoir. An emergency dewatering system and a spillway were constructed to prepare for flooding during the next spring. Another typical case of Type-A failure is shown in FIG. 4, where the upper rock mass laterally slid as a rigid body down the slip plane (inclined

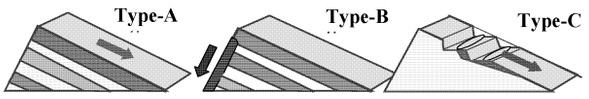


FIG. 2 3 types of slope failures, A, B, and C, occurred during 2004 Niigataken Chuetsu Earthquake.

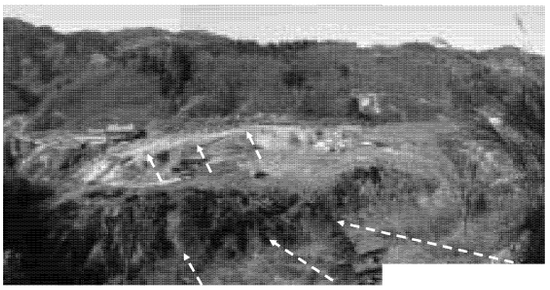


FIG. 3 Photograph of Higashi-Takezawa slide (Type-A) seen from top of scarp



FIG. 4 Photograph of Yokowatashi slide where mirror-like slip plane of mudstone appeared (Type-A)

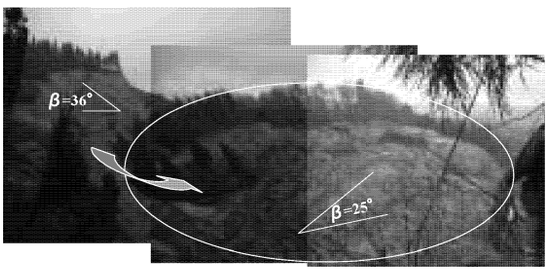


FIG. 5 Photograph of Dainichi-Yama slide where top portion of a huge slide belonging to Type-A rotated by 25 deg.

at an angle of 20-23 degrees) of a weathered silty sand seam sandwiched in mudstone. The Dainichi-Yama slide shown in FIG. 5 is the largest slope failure that occurred during the earthquake, and may be classified as a Type-A failure. A block of 500 m by 500 m in plan and more than 30 m thick slid as a block presumably along a dip plane of 16 degrees, exposing a scarp of 36 degrees, and the top portion of the block rotated by 25 degrees along a slip circle, leaving a very unusual landscape after the event.

In Type-B failures, the slip surfaces were generally shallow (one meter deep or so) leaving the trees with deep roots in place. Though the number of slope failures of Type-B was much greater than Type-A, the soil volume in individual failures was much less than Type-A. One of the largest Type-B failures is shown in FIG. 6 (Haguro Tunnel Entrance). Unlike Type-A failures, the failed soil mass was disintegrated into small pieces, but did not develop into a mudflow with a of long run-out distance despite the presumably high water content due to the heavy rainfall prior to the earthquake.



FIG. 6 Photograph of Haguro Tunnel Entrance; Large failure of Type-B.



FIG. 7 Photograph of Musikame failure involving koi-ponds (Type-C) (after http://www:ajiko.co.jp)

FIG. 7 shows a typical slope failure of Type-C located in Mushikame. Type-C failures were similar to Type-A, involving an underlying dip slip plane of mudstone. However, the displaced soil mass in the Type-C failures was highly weathered and the koi ponds and terraced paddies seem to have played an important role in triggering these failures. The ponds and paddies kept the soil water content high, making the slopes prone to seismic instability. Internal erosion by pond water eventually caused large-volume failures. Some of the failures probably occurred during or shortly after the earthquake shaking, while the others seem to have occurred a few days or weeks later. However, a lot still needs to be learned before the exact mechanism of Type-C failures is fully understood.

ENERGY APPROACH AND SIMPLE RUN-OUT DISTANCE EVALUATION

In order to evaluate run-out distance of failed slopes, an energy approach was developed by Kokusho et al. (2004). In this method, four energies are considered: change in potential energy $-\delta E_p$ (normally taken as negative); earthquake energy contributing to

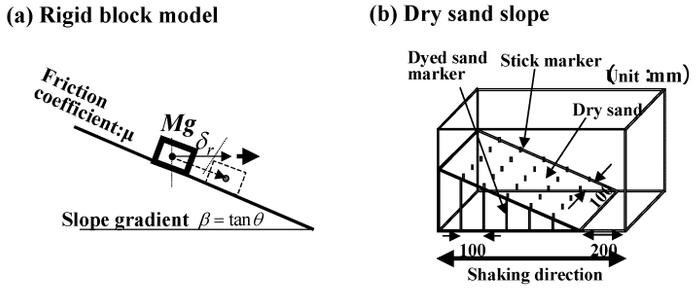


FIG. 8 Comparison of models of rigid block and dry sand slope.

the slope failure E_{EQ}; dissipated energy in the sliding soil mass E_{DP}; and kinetic energy E_k of the sliding soil mass:

$$-\delta E_p + E_{EQ} = E_{DP} + E_k \tag{1}$$

The basis of this method is illustrated using the rigid block resting on a slope shown in FIG. 8(a). The change in the potential energy $-\delta E_p$ and the dissipated energy due to the block slippage E_{DP} are related to the horizontal residual displacement δ_r as follows.

$$-\delta E_p = \beta Mg\delta_r \tag{2}$$

$$E_{DP} = \frac{\mu\left(1+\beta^2\right)}{1+\mu\beta} Mg\delta_r \tag{3}$$

where $\beta = \tan\theta$ (θ = slope angle) is the slope inclination, and $\mu = \tan\phi$ (ϕ= friction angle) is the friction coefficient. Then, starting from Eq.(1) and setting E_k = 0, if compared before and after slope failure, the earthquake energy is related to δ_r:

$$\delta_r = \frac{1+\mu\beta}{\mu-\beta}\frac{E_{EQ}}{Mg} \tag{4}$$

A series of shake table tests were carried out to investigate the energy balance in a model slope made from dry sand, as shown in FIG. 8(b) (Kokusho and Ishizawa 2007). The results were

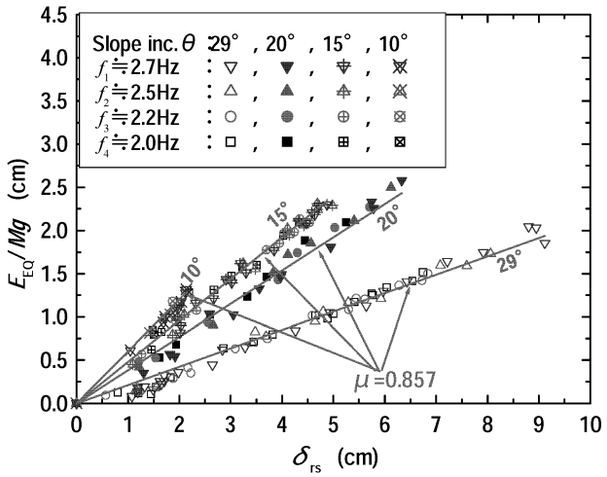


FIG. 9 Earthquake energy versus residual slope displacement for different slope angles by different input frequencies.

compared with the above energy balance. The surface displacement of the slope δ_{rs}, which is considered here to be equivalent to δ_r in the rigid block model, obtained by a number of tests for different input frequencies and different slope angles is plotted versus the normalized earthquake energy, E_{EQ}/Mg, in FIG. 9. The weight of the displaced soil mass, Mg, in the test was determined from Eq.(2) using the measured potential energy, $-\delta E_p$, and the measured displacement, δ_{rs}, to comply with the rigid block theory.

As may be observed from FIG. 9, for μ =0.86, Eq.(4) predicted the residual slope displacement almost perfectly for all slope angles and all input frequencies. This indicates that if an appropriate friction coefficient is known in advance, the simple rigid block model, which clearly involves a failure mechanism quite different from reality, can successfully predict the horizontal residual displacement in sand slopes.

For a saturated slip plane, Eq.(4) is replaced by Eq.(5), in which $\sigma_{n0} = Mg \Big/ \left[\left(1+\beta^2\right) A \right]$ is the total stress normal to the slip plane, σ'_{n0} is the corresponding effective stress and A is the horizontal area of the sliding soil mass (Kokusho and Ishizawa 2007).

$$\delta_r = \frac{1}{\left(\mu\sigma'_{n0} - \beta\sigma_{n0}\right)} \frac{E_{EQ}}{\left(1+\beta^2\right) A} \tag{5}$$

Based on the model test results and their analysis using the rigid block theory, an energy-based evaluation method for run-out distance of earthquake-induced slope failure is proposed. First, the sloping ground is idealized as an equivalent horizontal 2-layer system consisting of an upper layer, which includes the slope, and a base layer (Kokusho and Ishizawa 2007). The input energy, E_{IP}, transmitting upward through a unit horizontal area, A, can be formulated (Kokusho et al. 2007) as:

$$E_{IP}/A = \rho Vs \int \left(\dot{u}\right)^2 dt \tag{6}$$

where $\dot{u}$ is particle velocity of a wave propagating in one direction in a soil layer and ρV_S is the impedance of the layer (ρ= soil density and V_S = S-wave velocity). By subtracting the energy that is reflected downward, E_d, into the base layer due to the impedance contrast at the layer boundary from the input energy, E_{IP}, the earthquake energy, E_{EQ}, that is transmitted into the upper layer can be computed (i.e., $E_{EQ} = E_{IP} - E_d$). Assuming that all the energy transmitting into the upper layer is absorbed by the upper layer due to the slope failure, the energy ratio E_{EQ}/E_{IP} can be formulated as (Kokusho et al. 2007):

$$E_{EQ}/E_{IP} = 4\alpha/\left(1+\alpha\right)^2 \tag{7}$$

where α is the impedance ratio of the slope and the bedrock.

A portion of the energy that is transmitted into the upper layer (i.e., E_{EQ}) is dissipated by cyclic straining of soil or internal soil damping; this portion is designated as

E'_{EQ}. Accordingly, the energy causing the slope failure is (E_{EQ} - E'_{EQ}). Hence, if E'_{EQ} is not negligibly small, then E_{EQ} in Eq.(4) and (5) should be replaced by (E_{EQ} - E'_{EQ}).

The thickness or the mass of sliding soil necessary in Eq.(4) or (5) may be determined by conventional slip surface analyses, wherein the potential slip surface having the lowest factor of safety is found. However, in some cases, the potential slip surface may be reasonably assumed to coincide with a bedding plane or a weak seam observed in field survey.

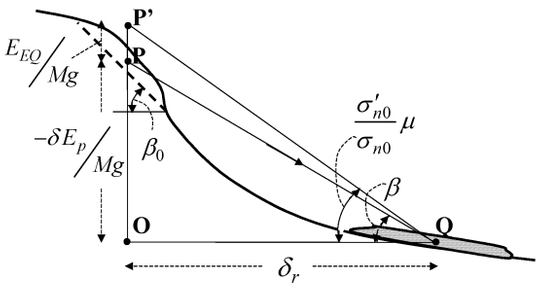


FIG. 10 Simplified evaluation method for run-out distance of seismically induced slope failure.

In the above analysis, the slope was idealized to be straight. However, for slopes that are not straight, Eqs.(1)-(5) can still be used if β is taken as the global inclination and μ as the averaged friction coefficient. This is illustrated using the slope shown in FIG. 10. As shown in this figure, the center of gravity of the sliding soil mass moves from P to Q during failure. The drop height PO can be expressed as $-\delta E_p/Mg$ and the horizontal displacement OQ is δ_r. The line PQ corresponds to the global inclination β, while the inclination of the local slope is β_0. For the case of saturated slip surface, the energy ratio can be expressed from Eqs.(2) and (5) as:

$$\frac{E_{EQ}}{-\delta E_p} = \frac{\mu\sigma'_{n0} - \beta\sigma_{n0}}{\beta\sigma_{n0}} = \frac{(\sigma'_{n0}/\sigma_{n0})\mu - \beta}{\beta} \tag{8}$$

Hence, due to the earthquake energy, the centroid increases by E_{EQ}/Mg, from P to P'. From Eq.(8), the inclination of the line P'Q can be obtained as $(\sigma'_{n0}/\sigma_{n0})\mu$, where μ is an averaged friction coefficient along the slip surface.

Consequently, the procedure for run-out distance evaluation is:

1) Determine the dimension of a potential sliding soil mass and its centroid P.
2) Evaluate the earthquake energy E_{EQ} from Eqs.(6) and (7).
3) Locate the point P', which is E_{EQ}/Mg higher than P or (E_{EQ} - E'_{EQ})/Mg higher if E'_{EQ} is not negligibly small.
4) Starting at point P', draw a line having an inclination of $(\sigma'_{n0}/\sigma_{n0})\mu$ until it intercepts the base of the slope (point Q). Then from geometry δ_r can be readily obtained.

This very simple procedure can be conveniently used to evaluate the run-out distance for seismically induced slope failure for developing slope failure hazard maps.

APPLICATION OF ENERGY APPROACH TO CHUETSU EARTHQUAKE.

In using the energy approach, it is very important that the equivalent friction co-

efficient be properly determined in advance. It may be possible in some cases to evaluate it directly from soil tests. However, due to complexity of actual slope failures in the field, a more robust method is to accumulate as many case studies as possible and back-calculate the friction coefficient. The resulting value will depend on various site conditions such as topography, geology, mechanical properties, water content, etc. The Niigata- ken Chuetsu earthquake in 2004 provides us with the rare opportunity to determine the equivalent friction coefficient using this latter approach.

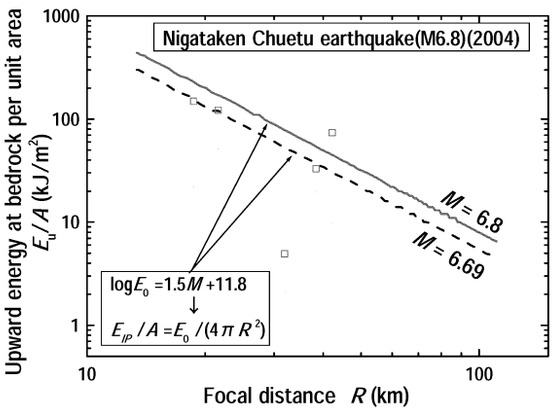


FIG. 11 Input energy at bedrock, E_{IP}, versus focal distance evaluated from KIK-net records during 2004 Niigataken Chuetsu EQ.

The input energy, E_{IP}, during the earthquake at the base layer of slopes was extrapolated from several KIK-net vertical array records around the area. In FIG. 11, the values of calculated input energy per unit area E_{IP}/A at several sites are plotted versus the corresponding hypocentral distance R on log-log scales. The solid line in the chart indicates the energy per unit area calculated by:

$$E_{IP}/A = E_0/\left(4\pi R^2\right) \tag{9}$$

where E_0 is the total wave energy released from a point source and is determined using the empirical equation by Gutenberg (1955):

$$\log E_0 = 1.5M + 11.8 \tag{10}$$

where E_0 has units of ergs (1 erg = 10^{-10} kJ), M is the earthquake magnitude using the Richter scale (Note: The Japanese Earthquake Magnitude, M_J, was used by the authors to compute E_0 because the Richter and Japanese magnitude scales are almost equivalent.). Data points for the calculated energy at bedrock may be approximated by the dashed line for M=6.69. Thus, input energies E_{IP} at bedrock during the earthquake may be readily computed by Eqs.(9) and (10), given earthquake magnitude and focal distances for the seismic slope hazard study.

The seven slope failures addressed earlier in the case history (3 for Type-A, 2 each for Types-B and C) are chosen here for the back-calculation. FIG. 12 depicts the run-out distances of those slopes, δ_{rn}, for centroids and δ_{rt} for tips of displaced soil masses, versus pre-failure slope inclinations evaluated from 3 dimensional Digital Elevation Model (3D DEM) data before and after the earthquake. As may be observed from this figure, there is a clear difference in the pre-failure slope inclinations, β_0, for the different failure types, with the most gentle being Type-A and the steepest being Type-B. Also, it may be readily observed from this figure that Type-C failures have

larger run-out distances than the other failure types, presumably due to the involvement of pond water.

FIG. 13 shows the rigid block models of the 7 slope failures (Note: The (a)-(g) labels on the data in FIG. 12 correspond to the models (a)-(g) in FIG. 13.). In each model, the displaced soil was idealized by a rectangular block of equivalent horizontal area and average thickness. In most of the slope failures, it was not difficult to estimate the depth of hidden slip surfaces from 3D DEM images before and after the failure. From these images, the dimension of the soil block before and after the failure, the horizontal and vertical displacements of the centroid and its gradient were quantified.

In order to back-calculate the equivalent friction coefficient, the global slope inclination β=tanθ in Eq.(5) was taken as the average slope inclination of a line connecting the pre- and

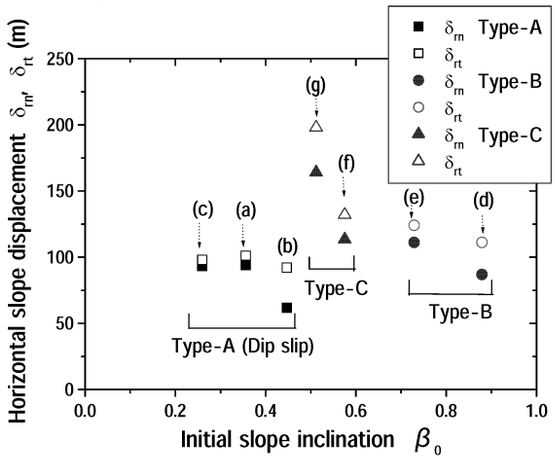


FIG. 12 Horizontal slope displacement (δ_{rn}; centroid, ; δ_{rt} tip) versus initial slope inclination for 3 failure types.

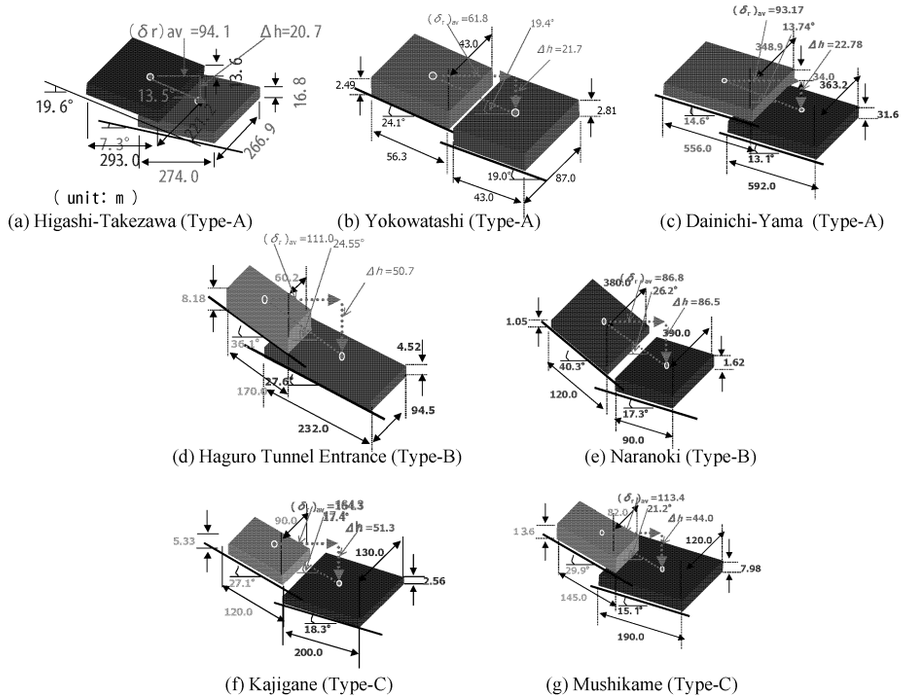


FIG. 13 Simplified rigid block models for 7 representative slope failures; (a)-(g), during the earthquake.

post-failure centroids. The input energy calculated from Eqs.(9) and (10) for this particular earthquake was E_{IP}/A = 244-301 kJ/m^2. The impedance ratio between the slopes and the bedrock was assumed to be α = 0.3 for all slopes. Finally, Eq.(7) gives E_{EQ}/E_{IP} = 0.71.

Slip planes were all assumed saturated at the time of earthquake. Water was running on most of the slip planes of impervious mudstone several days after the earthquake, while the upper portion was mostly unsaturated. Eq.(5) is used to back calculate the equivalent friction coefficient μ=tanϕ or equivalent friction angle ϕ from the block-model idealizations in FIG. 13. The internal dissipating energy E'_{EQ} by liquefaction or soil damping was assumed to be negligibly small compared to other energies and the total density of the soil, ρ_t, was assume to be 1.8 t/m^3.

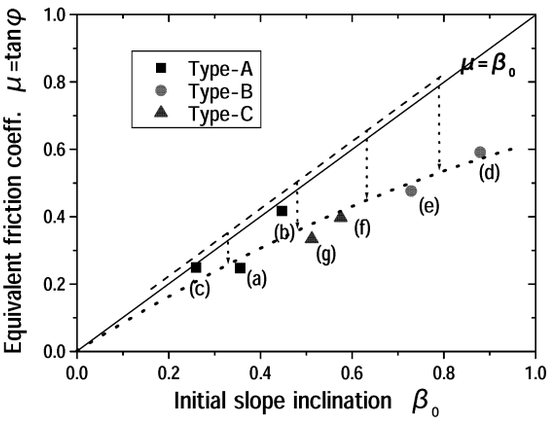


FIG. 14 Back-calculated equivalent friction coefficients μ versus initial slope inclinations β_0 for 7 slopes.

FIG. 14 shows a plot of back-calculated friction coefficients, μ versus slope inclinations, β_0, for the 7 slopes. Here, the β_0-values represent the initial (i.e., pre-failure) inclination of the each soil block, as shown in FIG. 13. The letters (a)–(g) in FIG. 14 correspond to the models (a)–(g) shown in FIG. 13. Note that all the back-calculated μ-values are smaller than β_0, indicating that friction coefficients μ, which were originally larger than β_0, decreased drastically due to the earthquake shaking. This implies that the failed soil mass accelerated first and then decelerated due to gentler or reverse slope angles in down-slope sections. In the Higashi-Takezawa failure, for example, the large difference between μ and β_0 allowed the failed soil mass to accelerate and start to go up the opposite side of the valley, as indicated in FIG. 3.

The exact mechanism how such low friction coefficients are realized is yet to be clarified. In some site conditions, seismically induced pore-pressure build-up or liquefaction may have been involved. The sandstone overlying the slip plane of cemented mudstone in the Higashi-Takezawa slide was highly weathered and almost equivalent to decomposed medium dense sand. In Type-C failures, weathered soils of high water content may have transitioned into high-speed mudflow due to pore-pressure build-up.

It is interesting to note that the μ versus β_0 relationship may be approximated by the dotted curve in FIG. 14, which appears to be uniquely dependent on pre-failure slope inclinations, irrespective of the failure type. This may suggest that the friction coefficient, which was larger than the initial slope inclination (represented by the dashed line in FIG. 14), drops to a value that is highly dependent on β_0. Thus, if the equivalent friction coefficient is determined from the initial slope inclination, the run-out distance of the sliding soil mass may be evaluated from the energy balance for slopes with variable down-slope inclinations.

It is, however, highly probable that various additional conditions may influence the equivalent friction coefficient. More case studies are certainly needed to make the

run-out distance evaluation more reliable.

CONCLUSIONS

Case histories of slope failures during the 2004 Niigata-ken Chuetsu earthquake were addressed and an energy approach developed for earthquake-induced slope run-out distance evaluation was applied. Major findings in this research are:

1) A great number of slope failures due to this particular earthquake are classified into 3 types, A, B and C considering significant role of bedding planes and strong weathering effect.
2) Energy-based evaluation and a simplified procedure for run-out distance, δ_r, of slope failures in realistic field conditions are explained.
3) In order to back-calculate the friction coefficient, μ, the energy-based method was applied to 7 representative failed slopes of different types. The computed equivalent friction coefficients were all lower than the initial slope inclinations, indicating that the failed soil mass first accelerated and then decelerated due to gentler or reverse slopes in down-slope sections.
4) The back-calculated friction coefficients, μ, were found to strongly depend on initial slope inclination, β_0, irrespective of failure type which have different involvement of pore-pressure. This suggests that the run-out distance during this particular earthquake may be evaluated almost uniquely from β_0.

ACKNOWLEDGEMENTS

Part of this research was supported by Special Coordination Funds for Promoting Science and Technology, "Earthquake damage in active-folding areas - Creation of a comprehensive data archive and suggestions for its application to remedial measures for civil-infrastructure systems -" of Japan Science & Technology Agency. KIK-net data was obtained from the website of NIED (National Research Institute for Earth Science and Disaster Prevention) in Tsukuba, Japan. Professor Russell Green, University of Michigan is gratefully acknowledged for his editing the final text.

REFERENCES

Gutenberg, B. (1955) "The energy of earthquakes." *Quarterly Journal of the Geological Society of London*, Vol.CXII, No.455, 1-14.

Kokusho, T., Ishizawa, T. and Harada, T. (2004): Energy approach for earthquake induced slope failure evaluation, *Proc. 11th International Conference on Soil Dynamics & Earthquake Engineering and 3rd International Conference on Earthquake Geotechnical Engineering*, Berkeley, California, Vol.2, 260-267.

Kokusho, T. and Ishizawa, T. (2007) "Energy approach to earthquake-induced slope failures and its implications." *Journal of Geotechnical and Geoenvironmental Engineering*, ASCE, Vol.133, No.7, 828-840.

Kokusho, T., Motoyama, R. and Motoyama, H. (2007) "Wave energy in surface layers for energy-based damage evaluation." *Soil Dynamics & Earthquake Engineering* 27, 354-366.

Failure mechanisms of landfills under dynamic loading

Varvara Zania[1], Yiannis Tsompanakis[2], Prodromos Psarropoulos[3] and Achilleas Papadimitriou[4], M.ASCE

[1]Doctoral Candidate, Division of Mechanics, Department of Applied Sciences, Technical University of Crete, Greece; zaniab@tee.gr
[2]Assistant Professor, Division of Mechanics, Department of Applied Sciences, Technical University of Crete, Greece; jt@science.tuc.gr
[3]Post-Doctoral Researcher, Division of Mechanics, Department of Applied Sciences, Technical University of Crete, Greece; prod@central.ntua.gr
[4]Lecturer, Department of Civil Engineering, University of Thessaly, Greece; apapad@civ.uth.gr

ABSTRACT: Seismic stability of above-ground landfills is an issue of extreme engineering interest, and the proper implementation of the corresponding analyses requires dealing with several uncertainties related mainly to the special features of such large-scale geostructures. This study aims at providing an insight into the role of these parameters on the development of the potential failure modes that may take place during a seismic event. Additionally, the different failure modes are compared with respect to their seismic instability potential. Furthermore, an insight is provided on phenomena related to the simultaneous generation of more than one failure surfaces within the landfill. This is examined by developing a simple model based on the Newmark's sliding-block approach. Results indicate that the circular surfaces may provide a more critical mode of failure than the base sliding.

INTRODUCTION

Seismic stability assessment of solid waste landfills is an issue that requires particular consideration. A potential failure during a seismic event may cause release of leachate and contamination of the surrounding soil, or even the development of overall instability of the waste impoundment. Hence, proper implementation of seismic design is mandatory, and accordingly it should take into account the role of the special characteristics of this type of geostructures. Certainly, the parameters of the landfill's geometry are important, since they affect the dynamic response of the structure, the mechanism of the seismic wave propagation and the inertial distress. Additionally, the mechanical properties of the waste material are related to numerous uncertainties, such as the compaction procedure and its composition. This was shown to result to a wide range of proposed parameters in the literature, and accordingly

their effects on the dynamic behavior is considerable (Zania et al. 2007). Finally, the existence of a base liner system ensures the isolation of the waste material from the environment, while on the other hand provides an interface characterized by low shear strength. Therefore, the impoundment is vulnerable to the development of relative displacements, especially during a seismic event. The seismic instability provided along the aforementioned interfaces has been investigated. Simplified procedures based on Newmark's sliding block (1965) have been proposed and utilized to determine the developed seismic displacements along either the cover liner (Ling and Leshchinsky, 1997) or the base liner (Bray and Rathje, 1998, Kramer and Smith, 1997 and Rathje and Bray, 2000).

Moreover, the most influential of the assumptions related to Newmark's sliding block (1965) method for earth structures is expected to be the rigidity of the sliding mass, since landfills are flexible structures characterized by relatively high eigenperiods. Initially, decoupled (Makdisi and Seed, 1978) procedures were proposed, taking separately into account the response of the structure and the slip displacement development. Furthermore coupled procedures, utilizing mainly lumped mass models, taking simultaneously into account the response of the structure and the displacement accumulation have been developed. Kramer and Smith (1997) found that the decoupled analyses of a linear lumped mass model may provide over-conservative estimates for low eigenperiod. Furthermore, Rathje and Bray (2000) concluded in similar results by examining a nonlinear lumped mass model. Additionally, the discrepancy of the two methods was suppressed for higher values of yield acceleration and lower than 0.5g peak ground acceleration.

The current study aims to investigate the seismic stability of landfills under the perspective of two different failure modes, which are providing instability along: (a) circular surfaces, and (b) base interface. For this purpose the procedure proposed by Makdisi and Seed (1978) is followed. The dynamic response is evaluated firstly by dynamic two-dimensional (2D) finite-element analyses, while the material nonlinearity is taken into account by an iterative equivalent-linear procedure. The Makdisi and Seed (1978) method is intentionally selected, in order to consider not only the 2D response characteristics but the circular geometry of the first failure mode as well in the calculation of the equivalent acceleration time history. The special characteristics of above-ground landfills are taken into account, and the role of the various involved parameters is highlighted. Additionally, the aforementioned Newmark method is utilized to investigate the interaction mechanism between the two examined failure modes within the landfill. The significant parameters affecting the phenomenon are determined, and their contribution to the mechanism of the accumulation of the permanent deformation along both failure surfaces is investigated.

COMPARISON OF THE POTENTIALLY DEVELOPED FAILURE MODES

In the first part of the current study the development of two different failure modes is examined, and the corresponding results are compared. As shown in Fig. 1 the configurations examined refer to above-ground landfills and the possible failure surfaces are characterized by either a circular shape on the waste slope of the

structure or a plane along the base liner related to an overall instability. The seismic stability assessment is performed following a decoupled procedure. The two-dimensional finite-element dynamic time-domain analyses were performed utilizing the code QUAD4M (Hudson et al. 1994) which follows an equivalent linear procedure to take into account the material nonlinearity. The horizontal equivalent acceleration (HEA) time history of each one of the specified failure surfaces is calculated according to the method proposed by Makdisi and Seed (1978). Two failure envelopes, consistent with the shear strength values for waste material proposed in the literature (Zekkos, 2005) were considered to provide good estimates of the instability of the waste mass. A characteristic value of the dynamic angle of friction of geosynthetics interfaces was selected among the range reported (De and Zimmie, 1998, and Yegian and Lahalf, 1992) to provide an adequate estimate of the overall instability (see Table 1). Limit equilibrium analyses were conducted to obtain the safety factor of the examined slip surfaces and the corresponding yield acceleration (a_y). Finally the accumulated seismic displacements were calculated according to the Newmark's sliding-block procedure (1965).

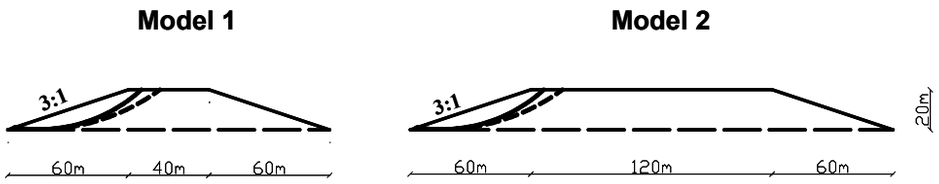


FIG. 1. The examined two typical above-ground landfills.

Table 1. Shear strength characteristics and corresponding yield accelerations

Interface	Failure surface	γ (kN/m^3)	c (kPa)	φ	a_y
waste	1st circular	10	18	34	0.65
			-	34	0.35
	2nd circular		18	34	0.63
			-	34	0.37
geosynthetics	base	-	-	16.5	0.29

The influence of the numerous uncertainties in the dynamic response, and furthermore the stability assessment were also investigated. Concerning the mechanical properties of waste material, values of shear-wave velocity were selected within the representative range of 130-400m/sec. Moreover, two curves of shear-modulus reduction and damping increase were selected to characterize the nonlinear behavior of the waste material, which are considered to cover the wide range of the curves proposed in the literature during the last 15 years. As shown in Fig. 2 sets of curves have been established by Singh and Murphy (1990) by using downhole shear wave velocity data measured at Richmond and Redwood landfills, and by Zekkos (2005) by conducting laboratory-testing. Additionally, the effect of the characteristics of the geometry and the waste material properties were indirectly

taken into account in stability assessment by the eigenperiod of the structure. The latter was estimated for both linear and nonlinear analyses (according to the modified properties) by conducting frequency analyses utilizing the finite-element code ABAQUS (2003). In order to cover a wide range of frequencies, three (3) excitations were used for the dynamic analyses (see Table 2). The excitations were scaled to three levels of peak ground acceleration (PGA): (a) 0.01g, (b) 0.10g, and (c) 0.36g, which correspond quantitatively to linear, moderately nonlinear, and nonlinear material behavior respectively.

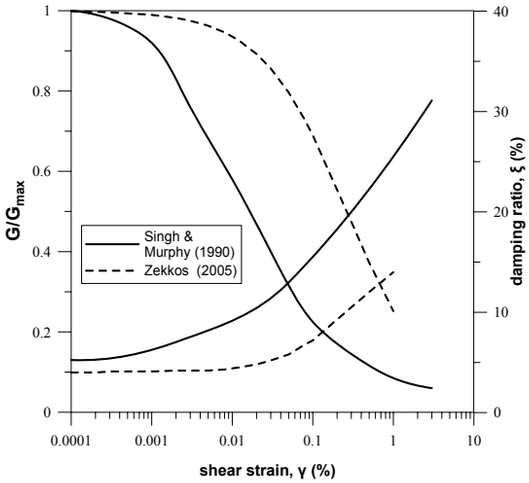


FIG. 2. Representative curves of shear modulus reduction (G/G_{max}) and damping (ξ) increase with shear strain (γ) determined for solid waste material.

The results of the analyses are initially presented in terms of maximum horizontal equivalent acceleration (MHEA). The two failure modes are compared by examining the ratio of the MHEA provided for base instability ($MHEA_{base}$) to the corresponding value for circular failure of the waste mass ($MHEA_{circ}$). In Fig. 3a the aforementioned ratio is shown as a function of the normalized eigenperiod of the structure (T_{str}/T_m) for linear material behavior (PGA=0.01g), where T_m is the mean period of the excitation. It is evident that the MHEA values for circular failure are consistently higher than those for base sliding. Assuming that the inertial force enforced by the excitation is represented by the MHEA, the safety factors related to circular failure are proven to be lower than those for base sliding. As the material behavior remains linear elastic, the results do not designate an instable state and therefore the safety factors remain always greater than unity.

Table 2. Frequency characteristics of the three excitations

Excitation	Predominant period (sec)	Mean period (sec)
Ricker pulse (f_0 =2Hz)	0.32	0.34
Aegion	0.50	0.47
Kobe	0.38	0.66

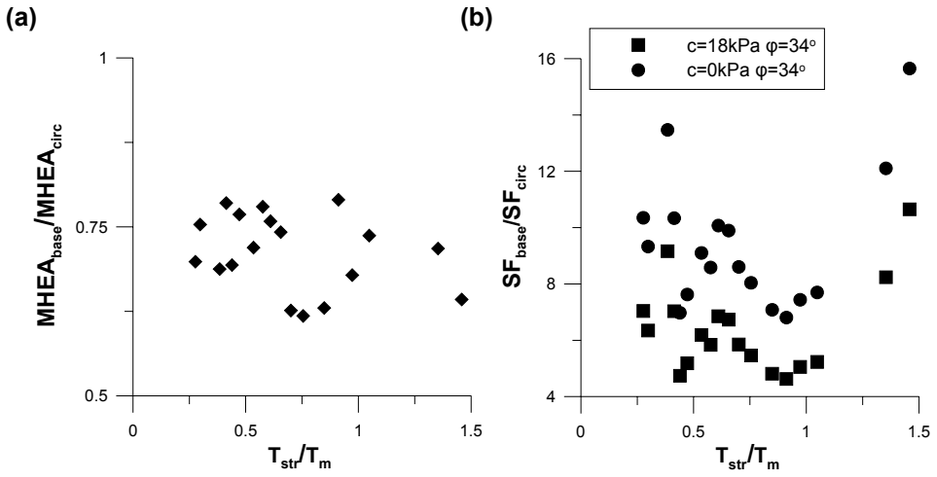


FIG. 3. (a) Ratio of MHEA and (b) the safety factor estimated for base failure to the corresponding value for circular failure vs. the normalized eigenperiod of the landfill for the linear case (PGA=0.01g).

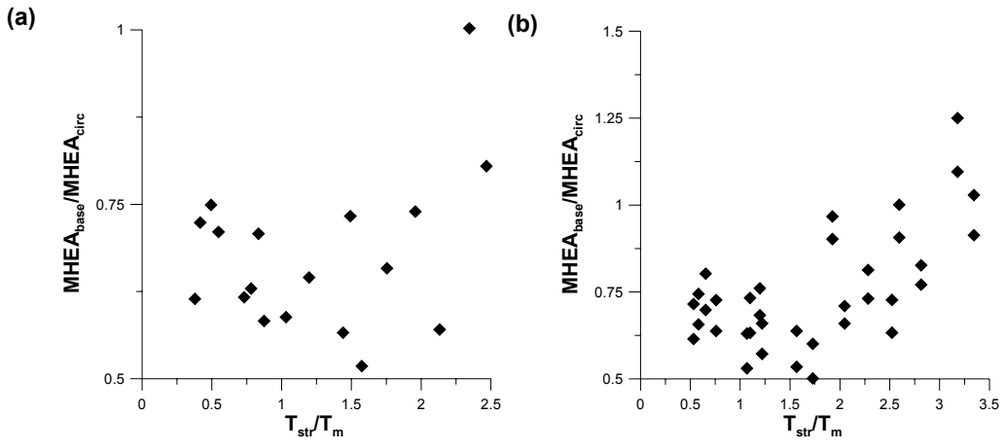


FIG. 4. Ratio of MHEA estimated for base failure to the corresponding value for circular failure vs. the normalized eigenperiod of the landfill for PGA: (a) 0.10g, and (b) 0.36g.

Fig. 4 presents the results of the nonlinear analyses, where the comparison of the two failure modes is shown in terms of the ratio of the MHEA values. The higher level of PGA in Fig. 4a, compared to the elastic analyses (Fig. 3), results to an increase of the scatter and an approximate decrease of the examined MHEA ratio values. This indicates that the circular failure becomes more critical when the material nonlinearity is considered. More specifically, the ratio was limited between 0.6 and 0.75 in the linear case (see Fig. 3), while the moderately nonlinear case (PGA=0.10g) ranges between 0.5 and 1 (see Fig. 4a). While approaching the value of normalized eigenperiod equal to 2.5, the critical failure mode is questionable since

the ratio $MHEA_{base}/MHEA_{circ}$ approaches and even exceeds unity. Observing the results corresponding to PGA equal to 0.36g this trend is more intense (see Fig. 4b). The ratio $MHEA_{base}/MHEA_{circ}$ takes values consistently lower than 0.75 for normalized eigenperiods lower than 2, while for higher values of the normalized eigenperiod the aforementioned ratio increases and takes values clearly higher than unity.

For the nonlinear cases analyzed, referring to PGA equal to 0.36g, the seismic displacements were also calculated. The seismic displacements are obtained by integrating the relative velocity time history. Fig. 5 summarizes the results of the displacement analyses. The permanent displacements developed during the circular failure, presented in Fig. 5a, are not regarded to be substantial. However, for the majority of the results, they are higher than the corresponding permanent displacements developed during a seismic event along the base of the examined configurations. This is evident in Fig. 5b where the ratio of the seismic displacements for the two examined failure modes is presented as a function of the normalized eigenperiod. Note that seismic displacements corresponding to higher a_y, are lower than 5cm for circular failure, and the corresponding base displacements are higher for T_{str}/T_m lower than unit.

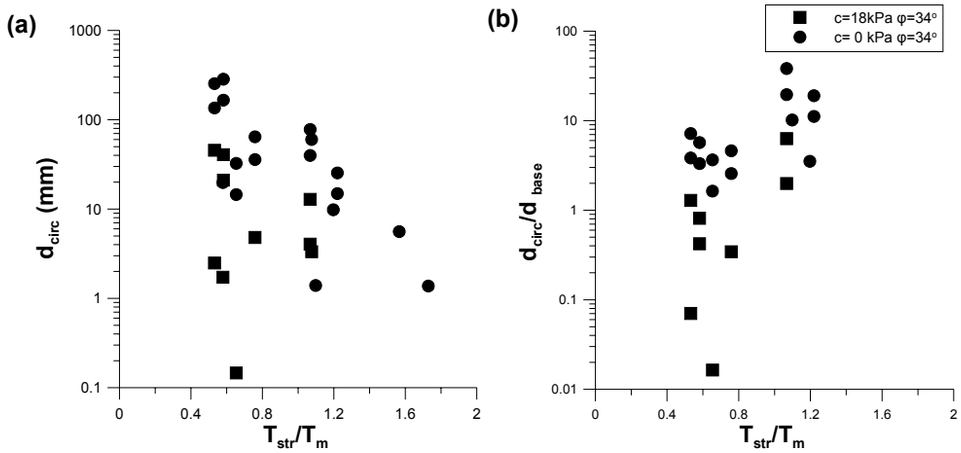


FIG. 5. Results of seismic stability analyses for the case of PGA=0.36g: (a) seismic displacements for the case of circular failure (d_{circ}), (b) ratio of displacements for circular failure (d_{circ}) versus those for base failure (d_{base}).

INTERACTION BETWEEN TWO FAILURE MECHANISMS

Seismic slope stability assessment may potentially result to a critical base failure mode. Nevertheless, significant dynamic shear stresses, resulting to an additional failure surface on the waste mass, may be developed, as the inertia forces developed within the waste may also be substantial. In this study, the potential development of two different failure surfaces, and the subsequent seismic displacements were considered along with the mechanism and the parameters influencing the aforementioned phenomena.

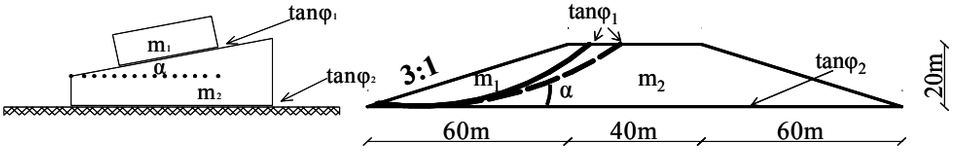


FIG. 6. Newmark-type model for the examination of the development of two failure modes and the equivalence with a typical above-ground landfill.

For this purpose a simple model based on the principles of the well-known Newmark's sliding block was developed. As shown in Fig. 6 the extended sliding block model consists of two rigid blocks, whose sliding interfaces are planes of finite shear strength characterized by rigid-plastic behavior. The lower plane is assumed to be horizontal, while the upper plane is inclined by an angle α, representing the angle of the plane characterizing the instable slope surface. The upper and lower interfaces are characterized by angles of friction φ_1 and φ_2, respectively. Upslope movement is taken into account in the formulation of the analytical expressions, though no indications of upslope movement were observed. Although the proposed model has the limitation that the flexibility of the structure is not taken into account, it can be still considered as a useful tool that provides adequate insight to this important issue.

The calculation of the developed displacements consists of two cases: (a) when sliding occurs only along the lower interface, and (b) when sliding occurs along the upper interface, and possibly along the lower as well. In the first case, the system responds like the single rigid block of Newmark's model. When the inertia forces may overcome the shear resistance of the upper block, the second case takes place, in which the displacements of the upper block result from double integration of the ratio of the difference between destabilizing forces and resistant forces to the mass of the block. During the estimation of the displacements of the lower block, the forces transmitted from the upper block (namely the contact pressure and the friction force) are also taken into account. In both cases displacements develop until the relative velocity becomes equal to zero.

The formulation of the model was followed by the examination of the significant parameters influencing the aforementioned failure mechanisms. All the examined parameters received values within a range, representative of the case of a typical above-ground landfill. An extended parametric study was performed, in which the displacement analyses were conducted for a Ricker pulse of central frequency equal to 2Hz, scaled to a PGA equal to 0.50g. The ratio of the two masses (m_1/ m_2), the angles of friction of the two interfaces, and the angle of the sliding plane were the selected parameters. The selection of the upper and lower interface properties was in accordance to the reported shear strength of waste material and the dynamic friction properties of geosynthetic interfaces, respectively. Therefore, the angle of friction of the lower interface (φ_2) was considered to range between 10 and 18 degrees. The angle of friction of the upper interface (φ_1) ranged between 20 and 34 degrees (17 intervals), resulting to a ratio of $\tan\varphi_1/\tan\varphi_2$ between 1 and 4. Since the inclination of the sliding plane cannot receive values higher than the slope inclination (characterized by low angles in the case of landfills) α was selected to obtain values between 10-20 degrees (3 cases).

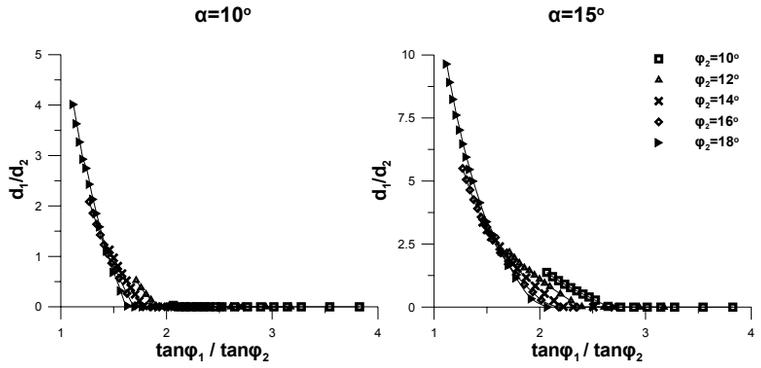


FIG. 7. Effect of failure surface slope inclination α, for mass ratio m_1/m_2 = 0.1, in terms of the ratio of the displacements of the upper (d_1) and the lower (d_2) block vs. the ratio of the tangent of the angles of the two planes ($\tan\varphi_1/\tan\varphi_2$).

The mass ratio m_1/m_2 was considered to range between 0.05 and 0.3 (5 cases), in order to take into account the effect of the size of the upper sliding mass. Due to space limitations, only some representative results will be presented.

The role of the angle of the sliding plane seems to be very important as it is related to the yield acceleration of the upper block, and thus to the initiation of sliding along both interfaces. In Fig. 7, the ratio of upper block's displacement to the corresponding of the lower block (d_1/ d_2) is shown, in variation with the ratio $\tan\varphi_1/\tan\varphi_2$. Only two characteristic cases of angle α of inclined plane equal to 10^o and 15^o are presented for mass ratio m_1/m_2 equal to 0.1. The sliding along both interfaces initiates for a lower value of $\tan\varphi_1/ \tan\varphi_2$ in the case of angle of plane equal to 10^o ($\tan\varphi_1/\tan\varphi_2 \approx 1.7$), while for 15^o inclination this value increases ($\tan\varphi_1/\tan\varphi_2 \approx 2$). Furthermore, the ratio of the developed displacements increases significantly as the angle α of the inclined plane increases, referring to the same values of angle of friction and mass ratio. This may be attributed to: (a) an increase of the displacement of the upper block due to significant decrease of its critical acceleration, and (b) to a decrease of the displacements of the lower block, which results from the increased upper block displacements. Furthermore, the slope instability appears more critical (ratio $d_1/d_2>1$) for a lower value of $\tan\varphi_1/ \tan\varphi_2$ in the case of angle of plane $\alpha = 10^o$ ($\tan\varphi_1/\tan\varphi_2 \approx 1.45$), while for $\alpha = 15^o$ this value is increasing and becomes obviously related to the angle of friction of the lower interface as well ($\tan\varphi_1/\tan\varphi_2 \approx 1.8$-$2.2$).

In Fig. 7 the influence of the friction angle of the interfaces is also evident. The ratio of the upper block's d_1 to lower block's displacement d_2 increases as the ratio $\tan\varphi_1/ \tan\varphi_2$ decreases; this may be attributed to the decrease of the difference between the shear strength of the two interfaces, and consequently of the frictional forces. In addition, observing the curves in Fig. 7 (each referring to a value of φ_2), the reduction of the angle of friction of the upper interface (φ_1) results to an increase of the displacement of the upper block, as it was expected. The increase of the angle of friction of the lower interface (φ_2) also results to an increase of the ratio of displacements d_1/d_2, and furthermore to a rise of the rate of increase as the ratio

$\tan\varphi_1/\tan\varphi_2$ decreases. Also, it can be seen that the shape of the curves changes, most probably due to the sliding of the lower block. The displacements of the upper block maintain a constant rate of increase for each value of φ_2, as φ_1 decreases. The same is not valid for the lower block, where the displacements decrease as the upper block starts to slide. This decrease of the lower block's displacement may be attributed to the increase of φ_1, as the shear strength transmitted from the upper block during sliding increases and so does the respective yield acceleration of the lower block.

In Fig. 8 the ratio d_1/d_2 is presented in variation with the ratio $\tan\varphi_1/\tan\varphi_2$ for the two extreme cases of the ratio of masses $m_1/m_2 = 0.05$ and 0.20 analyzed. The results presented here correspond to an angle of plane $\alpha = 20^o$. However, the results are qualitatively similar to the results for the other values of α examined. In all cases, the ratio d_1/d_2 increases as the mass ratio m_1/m_2 increases (note the different scales in Figs 8a and 8b). Also the shape of the curves is strongly influenced by the mass ratio m_1/m_2. The rate of decrease of the lower block displacement (occurring when the displacement of the upper block increases), appears to be more increased for greater mass ratios m_1/m_2. This may be attributed to the higher contact forces transmitted to the lower block during slip development of the upper block.

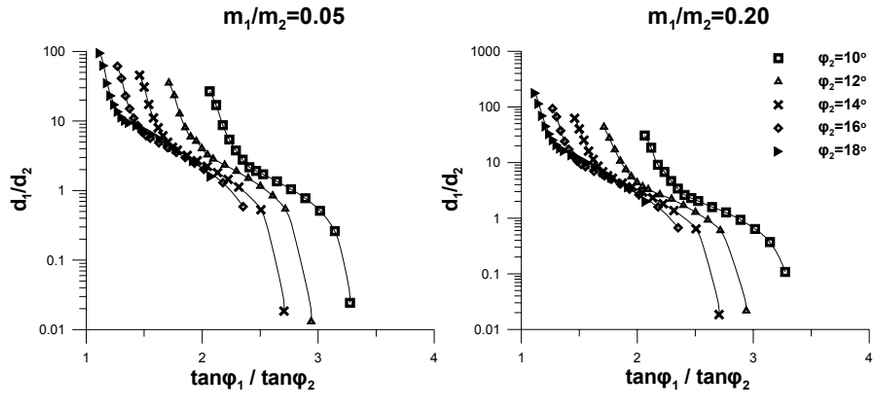


FIG. 8. Effect of mass ratio m_1/m_2 (for angle $\alpha = 20^o$); Results are presented as the ratio of the displacements of the upper (d_1) and the lower (d_2) block vs. the ratio of the tangent of the angles of the two planes ($\tan\varphi_1/\tan\varphi_2$).

CONCLUSIONS

The current study examined initially the seismic stability of two potential failure modes of above-ground landfills under the perspective of the uncertainties characterizing this type of structures. The results indicate that in most cases of above-ground configurations the circular failure surface instability is more critical than base sliding. Exception to this observation is the case of strongly nonlinear material behavior associated with high levels of induced acceleration and high normalized landfill eigenperiods. Additionally, it has been shown that for a representative range of shear strengths, the seismic displacements of a waste mass may be higher than the corresponding taking place at the same time along the base liner, especially for higher inclination and mass of the upper failure surface.

ACKNOWLEDGMENTS

This paper is part of the 03ED454 research project, implemented within the framework of the Reinforcement Programme of Human Research Manpower" (PENED) and co-financed by National and Community Funds (75% from E.U.-European Social Fund and 25% from the Greek Ministry of Development-General Secretariat of Research and Technology).

REFERENCES

ABAQUS (2003). "*Analysis User's Manual Version 6.4*." ABAQUS Inc., USA.

Bray, J.D. and Rathje, E.M. (1998). "Earthquake-induced displacements of solid-waste landfills." *J. Geotechnical & Geoenv. Engrg.,* Vol. 124(3): 242-253.

De, A. and Zimmie, T.F. (1998). "Estimation of dynamic interfacial properties of geosynthetics." *Geosynthetics International,* Vol. 5: 17-39.

Hudson, M. Idriss, IM. and Beikae, M. (1994). "*User's Manual for QUAD4M*." Center for Geotechnical Modeling, Civil and Environmental Engineering Dept, University of California, Davis, CA, USA.

Kramer, S.L. and Smith, M.W. (1997). "Modified Newmark model for seismic displacements of compliant slopes." *J. Geotechnical & Geoenv. Engrg.,* Vol. 123(7): 635-644.

Ling, H.I. and Leshchinsky, D. (1997). "Seismic stability and permanent displacement of landfill cover systems." *J. Geotechnical & Geoenv. Engrg.,* Vol. 123(2): 113-122.

Makdisi, F.I. and Seed, H.B. (1978). "Simplified procedure for estimating dam and embankment earthquake induced deformations." *J. of Geotechnical Engrg. Division,* Vol. 104: 849-867.

Newmark, N.M. (1965). "Effect of earthquakes on dams and embankments." *Geotechnique,* Vol. 15(2): 139-160.

Rathje, E.M. and Bray, J.D. (2000). "Nonlinear coupled seismic sliding analysis of earth structures." *J. Geotechnical & Geoenv. Engrg.* Vol. 126(11): 1002–1013.

Singh, S. and Murphy, B. (1990). "Evaluation of the Stability of Sanitary Landfills." In Landya, A. and Knowles, G.D. (eds.), *Geotechnics of Waste Fills – Theory and Practice*. American Society for Testing and Materials, pp. 240–258.

Yegian, M.K. and Lahlaf, A.M. (1992). "Dynamic interface shear strength properties of geomembranes and geotextiles." *J. of Geotechnical Engrg.* Vol. 118(5): 760-778.

Zania, V. Tsompanakis, Y. and Psarropoulos, P.N. (2007) "Slope stability of municipal solid waste landfills under seismic loading.", *Proc. 4th International Conference on Earthquake Geotechnical Engrg.* June 25-28, Thessaloniki, Greece, Paper No 1217.

Zekkos, D.P. (2005). "Evaluation of static and dynamic properties of municipal solid-waste." *PhD Dissertation*, Dept. of Civil and Environmental Engineering, University of California, Berkeley, CA, USA.

Validation of Generic Municipal Solid Waste Material Properties for Seismic Design of Landfills

Adda Athanasopoulos-Zekkos[1], S.M ASCE, Dimitrios Zekkos[2], M. ASCE and Neven Matasovic[3], M. ASCE

[1]Doctoral Candidate, University of California, Berkeley, USA; adda@berkeley.edu
[2]Engineer, Geosyntec Consultants, 475 14th Str., Suite. 400, Oakland, California-94612, USA; zekkos@geoengineer.org
[3]Associate, Geosyntec Consultants, Huntington Beach, California, USA; nmatasovic@geosyntec.com

ABSTRACT: In recent years, notable progress has been made with respect to the understanding of the mechanics of Municipal Solid Waste (MSW) response, and hence, generic MSW properties for static and seismic design of MSW landfills have been recommended. However, it is not clear if seismic design of MSW landfills based upon these generic material properties is conservative, and if it is, to what degree. An attempt is made to evaluate how adequate (i.e., conservative) seismic design of solid waste landfills based upon published generic material properties is. The basis for evaluation is one of very few well documented landfill case histories (the OII Landfill Case History) and selected generic material parameter sets. The results indicate that the use of generic material parameter sets at this site results in either reasonable prediction or slight over-prediction of recorded ground motions. The results of the parametric studies documented in this paper provide further insight on how to approach seismic design of MSW landfills.

INTRODUCTION

An engineer's ability to evaluate the seismic performance of an MSW landfill is partially dependent on the selection of representative material properties for the performance of site response analyses. Required MSW properties include: a) unit weight; b) small-strain shear modulus (G_{max}) or shear wave velocity (V_s); c) a strain-dependent normalized shear modulus reduction (G/G_{max}) relationship with its material damping ratio (λ) counterpart; and, for two-dimensional analyses, d) dynamic Poisson's ratio.

In recent years, significant progress has been made in our understanding of the mechanics of waste response and the development of generic MSW material properties that take into consideration the most important factors that affect the response of MSW fills. However, no landfills designed using these generic material properties were subjected to strong earthquake shaking (peak horizontal ground acceleration in bedrock in excess of 0.4 g) and only one case history of modern (i.e., lined/covered by a

composite liner) landfill response to moderate shaking has been reported (Matasovic and Kavazanjian, 2004).

This contribution presents a summary of the most recently developed generic MSW material properties followed by an evaluation of the response of a relatively well documented landfill case history as if it had been designed using these generic material properties. Conclusions have been derived based upon comparison of calculated and recorded response and upon a parametric study carried out on key MSW material properties.

OVERVIEW OF AVAILABLE GENERIC DYNAMIC PROPERTIES OF MSW

MSW unit weight

Historically, the total unit weight of MSW was assumed to be relatively low, with values ranging between 5 and 11 kN/m^3. Recent large-scale in situ unit weight measurements, including those reported by Matasovic and Kavazanjian (1998), indicate that the MSW unit weight is typically higher. Most recently, Zekkos et al. (2006) compiled large scale in situ unit weight test data from MSW landfills in Portugal, Southern and Northern California, New Jersey, Central Maine, Delaware, China, Canada, and Spain. The majority of data ranged from 8 kN/m^3 to 16 kN/m^3, with a trend of unit weight increase with depth (thickness of the waste pile). Based upon interpretation of this data, the authors presented a model for developing landfill-specific generic MSW unit weight profiles that consider both waste composition and compaction effort during placement. A plot of these generalized profiles is shown in Figure 1. The generalized unit weight profile for "low" compaction effort and volume of soil cover is significantly lower and varies significantly more with depth than the profile for "typical" compaction effort and volume of soil cover. The generalized unit weight profile for "high" compaction effort and volume of soil cover increases slightly with depth and has an average value of about 16 kN/m^3.

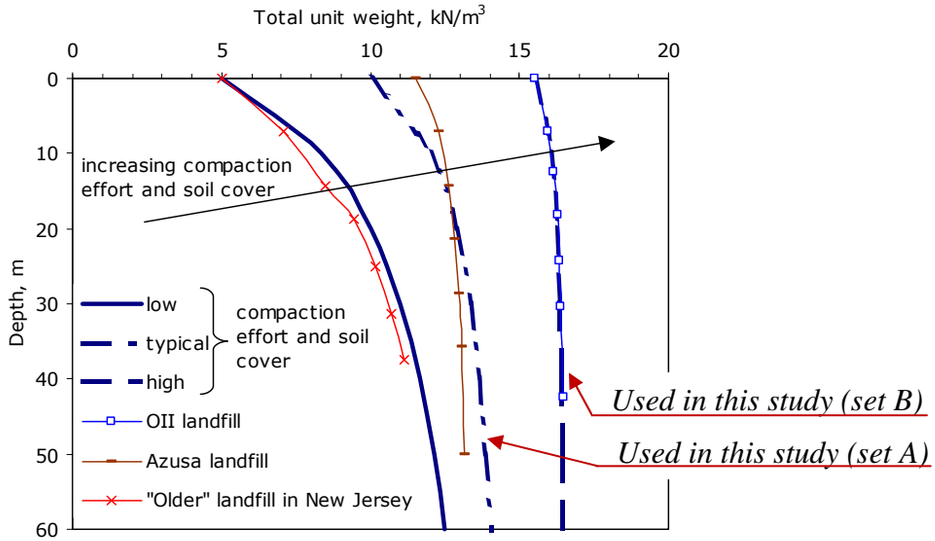


FIG. 1. Recommended unit weight profiles for seismic design of municipal solid waste landfills (after Zekkos et al., 2006).

Small-strain shear modulus and shear wave velocity

The small-strain shear modulus (G_{max}) is related to the shear wave velocity (V_s) and the mass density (ρ) of a material through the relationship:

$$G_{max} = \rho * V_s^2$$

Zekkos et al. (2007a) performed more than 90 large-scale cyclic triaxial (CTX) tests on 300-mm diameter specimens for three sample groups of solid waste with ages ranging from less than 2 years old to 15 years old collected from the Tri-Cities Landfill, located in Northern California. The study systematically examined the factors that affect the dynamic properties of MSW. The small-strain shear modulus G_{max} of MSW was found to be significantly affected by waste composition and confining stress. MSW unit weight, time under a sustained confining stress, and to a lesser degree, loading frequency, were also found to affect G_{max}.

The V_s of waste materials in a landfill can be measured in situ by various seismic methods, such as the Spectral Analysis of Surface Waves (SASW) method. When landfill-specific data are not available, Kavazanjian et al. (1996) recommended shear wave velocity profiles for Southern California MSW landfills. Based on a review of additional data presented in the literature, Kavazanjian (1999) stated that these recommended V_s profiles provide reasonable estimates of V_s for MSW landfills in temperate and arid climates. These profiles are shown in Figure 2.

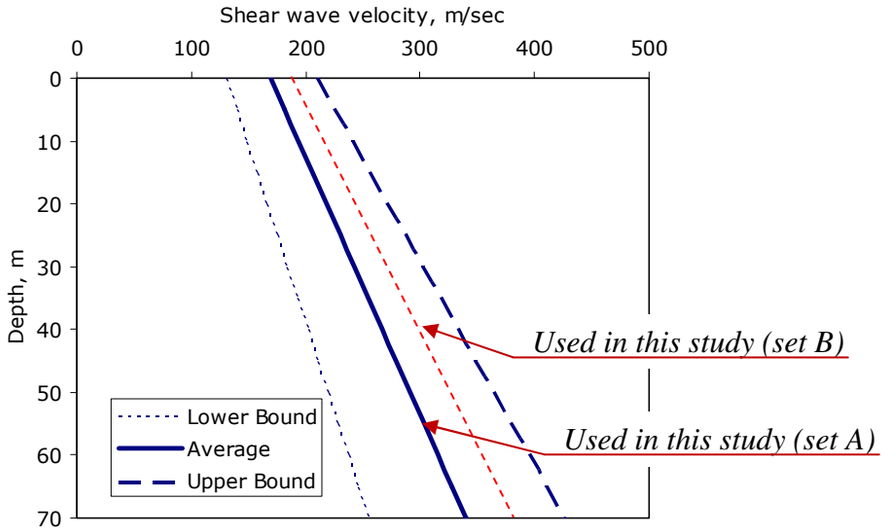


FIG. 2. V_s profiles for seismic design of MSW landfills (after Kavazanjian et al., 1996).

Strain-dependent normalized shear modulus reduction and material damping

Normalized shear modulus reduction (G/G_{max}) and material damping (λ) relationships for MSW have been developed by the following researchers (among others): Idriss et al. (1995), Matasovic and Kavazanjian (1998); Augello et al. (1998b); and Elgamal et al. (2004). The Matasovic and Kavazanjian (1998) and Augello et al. (1998) curves are reproduced from respective publications in Figure 3. With the exception of the Matasovic and Kavazanjian (1998) curves, these curves were developed based upon the back-analysis of the OII landfill strong motion data. The Matasovic and Kavazanjian (1998) curves were developed based upon two-dimensional (2-D) back analysis of OII

data (in the small-strain range, up to 0.1% shear strain) and large-diameter laboratory testing of OII Landfill MSW (in the large-strain range; 0.1 to 10% shear strain). It should be noted that the OII Landfill is located in the relatively dry climate of Southern California (average annual precipitation of approximately 33 cm) and may not be a typical representative of modern MSW landfills, as it was constructed in the early 1950s without waste separation and/or compaction, with, at several locations within the waste mass, co-disposal of MSW, liquid wastes, and impacted soil (Matasovic and Kavazanjian, 1998). It should be also noted that the Matasovic and Kavazanjian (1998) curves represent the upper-bound modulus and lower-bound damping as back calculated and measured by the authors, while the Augello et al. (1998) curves are an average of the authors back calculations.

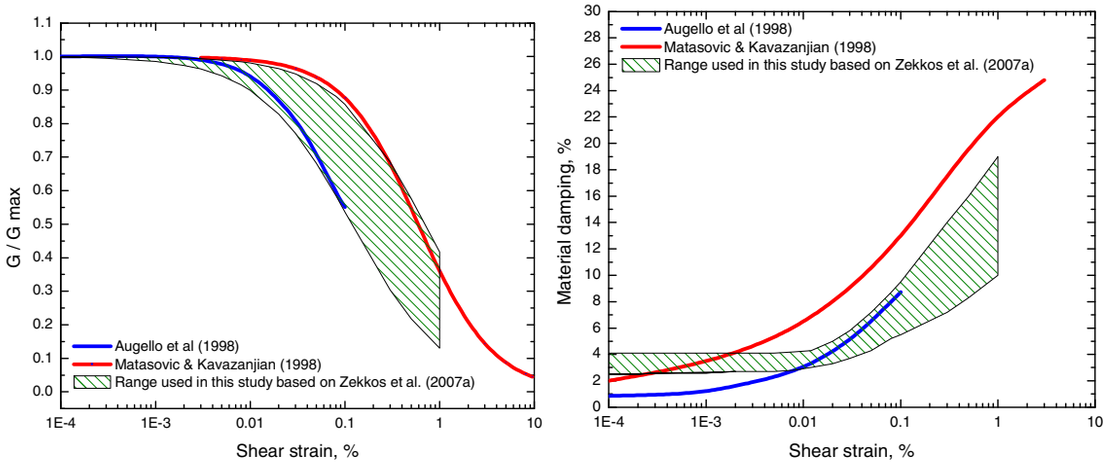


FIG. 3. MSW G/G_{max} and λ curves by Matasovic and Kavazanjian (1998), Augello et al. (1998), and range used in this study.

Recently, Zekkos et al. (2007a) developed a set of MSW G/G_{max} and λ relationships based upon laboratory testing of MSW recovered from the Tri Cities Landfill in the San Francisco Bay Area of Northern California. These curves, developed based upon laboratory testing of waste samples in the strain range of 2×10^{-4}% to 1% under normal stress of up to 800 kPa, have not been validated by back calculation of case histories so far. The Zekkos et al. (2007) curves are promising, however, as they allow for selection of strain-dependent G/G_{max} and material damping relationships of MSW based upon waste composition (100%, 62-76%, 8-25% by weight smaller than 20 mm material) and mean confining stress (<125kPa, 125-350 kPa, >350 kPa). The range of modulus reduction and damping data encompassed by the Zekkos et al. (2007a) study is also shown in Figure 3.

Poisson's ratio

Generic MSW Poisson's ratio, developed from the shear and compressional wave velocity measurements at the OII Landfill up to a depth of 100 m, can be found in Matasovic and Kavazanjian (1998). Poisson's ratio values measured as part of the cyclic triaxial program on MSW from the Tri-Cities Landfill is presented in Zekkos (2005)

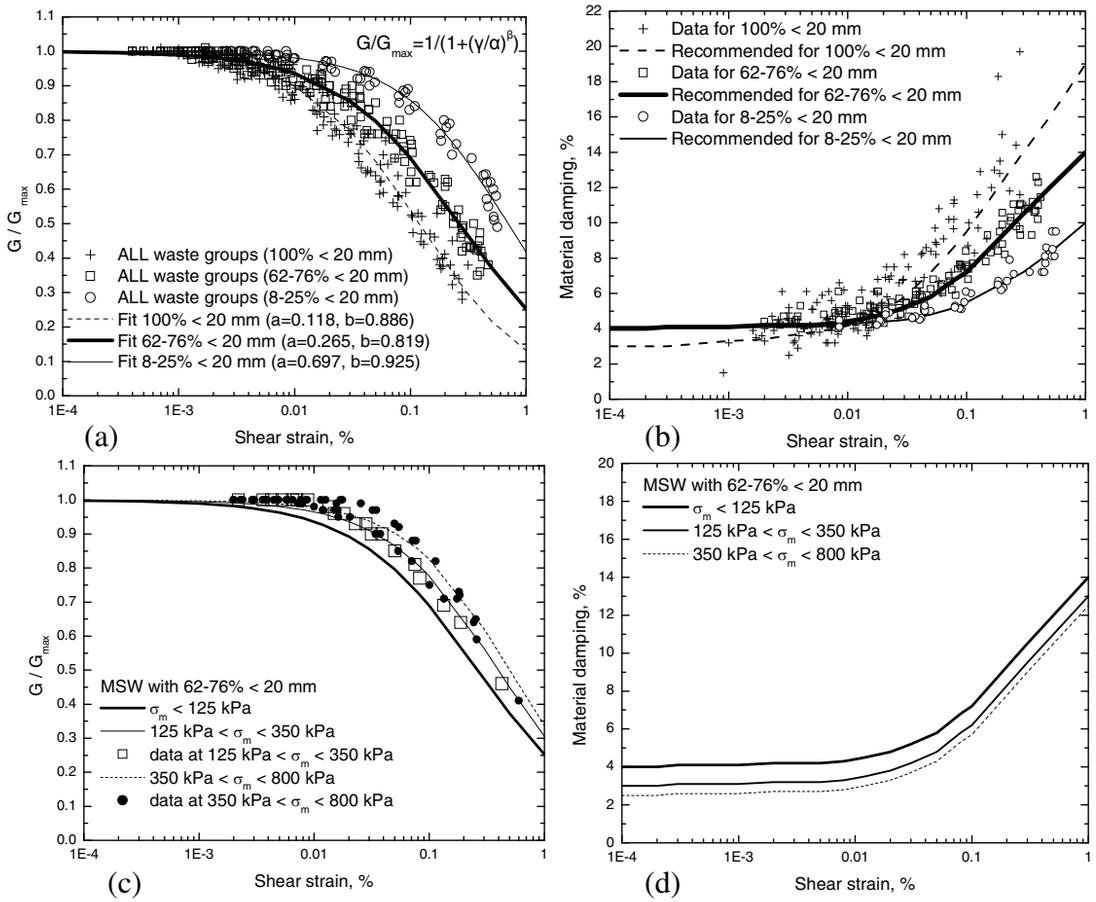


FIG. 4. Generalized G/G_{max} and λ curves as a function of composition for MSW based on results from all CTX tests at (a, b) confining stress <125 kPa. (c, d) higher confining stresses (Zekkos et al. 2007).

EVALUATION

General

In order to evaluate how good (i.e., accurate and/or conservative) the predicted seismic response of a MSW landfill using generic MSW properties can be, a one-dimensional (1-D) site response model was established. The basis for the model consisted of sets of generic MSW material properties described above and pairs of ground motion records recorded in several earthquakes at the base and top deck of the OII landfill. These ground motions are characterized in detail in PEA (1995), with information on soil conditions at the base station presented and interpreted in Matasovic et al. (1995), Idriss et al. (1995), Geosyntec (1996), and Matasovic and Kavazanjian (1998). The OII landfill may not be ideal for the evaluation of adequacy of generic MSW parameters for seismic design of landfills as recorded ground motion pairs are of relatively moderate intensity (up to approximately 0.1 g in bedrock underlying the site) and the landfill is not fully representative of modern landfills and of landfills in climates different than Southern California. Nevertheless, OII remains the best documented case history of landfill response to shaking, and hence a valuable basis for evaluation documented herein.

Approach

A total of eight strong motion pairs, each recorded on the top deck of the OII landfill and on an un-engineered fill near the toe of the landfill during different seismic events have been considered in these evaluations. For each event, the ground motion recorded on un-engineered fill was de-convoluted to a "weak rock" at the approximate elevation of the landfill pit base. Then, the de-convoluted ground motion was used as the input motion applied at the base of a 100-m thick waste column. In each evaluation, the column was characterized by one of the two complete sets of generalized MSW properties described below and shaken by deconvoluted motions from eight seismic events recorded at the site. The results of the evaluation were monitored at the landfill top deck where the calculated ground motion was compared to its recorded counterpart. Given the relatively low intensity of the ground motions considered, the analyses were conducted in frequency domain using SHAKE 2000 (Ordonez, 2000).

Input MSW properties

Site response analyses were performed using the following sets of generic MSW material properties:

- Set A includes the "average" (or "typical") generic MSW properties that an engineer would select in the absence of site-specific information: The generic unit weight profile for a "typical" landfill, as recommended by Zekkos et al. (2006) (dot-dash line starting at 10 kN/m^3 in Figure 1), the "average" shear wave velocity profile as recommended by Kavazanjian et al. (1996) (solid thick line in Figure 2), and the set of modulus and damping curves, as recommended by Zekkos et al. (2007) for typical (62-76%<20 mm) waste composition at various confining stresses (Figure 4c and 4d).
- Set B includes the generic MSW properties that would be selected for the OII Landfill if it was known that the waste material at the OII Landfill has significant amounts of soil materials: The generic unit weight profile for "high" volumes of soil material as recommended by Zekkos et al. (2006) (dashed line in Figure 1), a shear wave velocity (V_s) profile interpolated between the average and upper bound established by Kavazanjian et al. (1996) (Figure 2), and the same G/G_{max} and λ curves used in set A.

These sets purposely do not include the Augello et al. (1998) and Matasovic and Kavazanjian (1998) G/G_{max} and λ curves as they were developed based upon back-analyses of the OII case history and, as such, are biased with respect to the evaluations documented herein.

Results

The recorded ground motion at the top deck of the landfill is compared to the predicted response using Set A and Set B. The results of the analyses are shown in Figure 5. In some cases, (e.g. the Landers, the Joshua Tree and the Mojave Desert earthquakes), the predicted ground motion is similar to the recorded ground motion. In other cases (e.g., the Northridge and the Pasadena earthquakes) the recorded ground motion, particularly at periods below 0.4 sec, is overestimated or significantly overestimated.

In some cases, the use of Set B properties improves the prediction. However, in other cases, particularly the cases where the Set A properties provide a poor prediction, the use of set B properties may result in worse prediction. Again, however, when the prediction is not good, it is conservative, as the intensity of the ground motion is over-predicted.

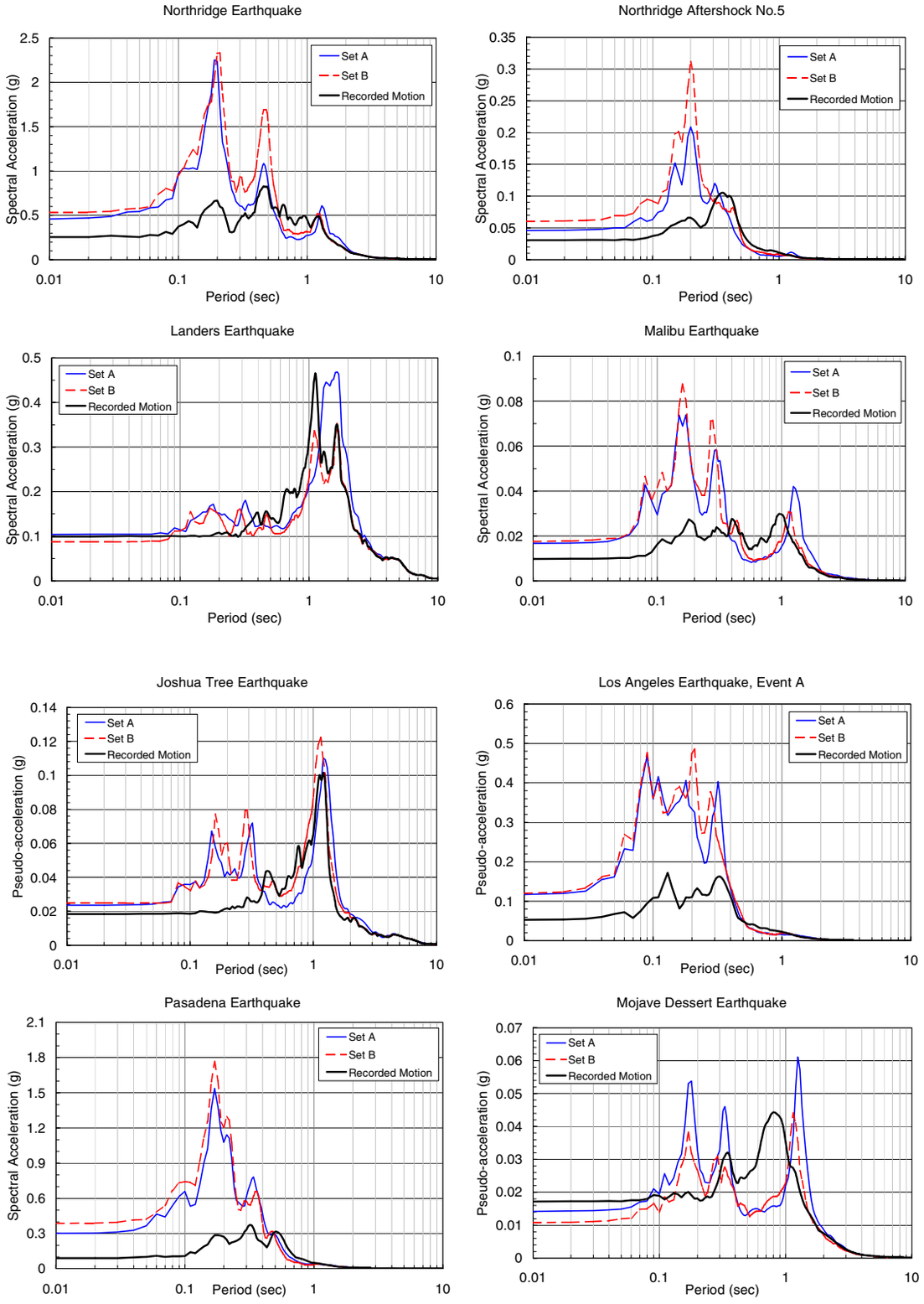


FIG. 5. Recorded vs. calculated acceleration response spectra (5% damped) using two sets of MSW material properties.

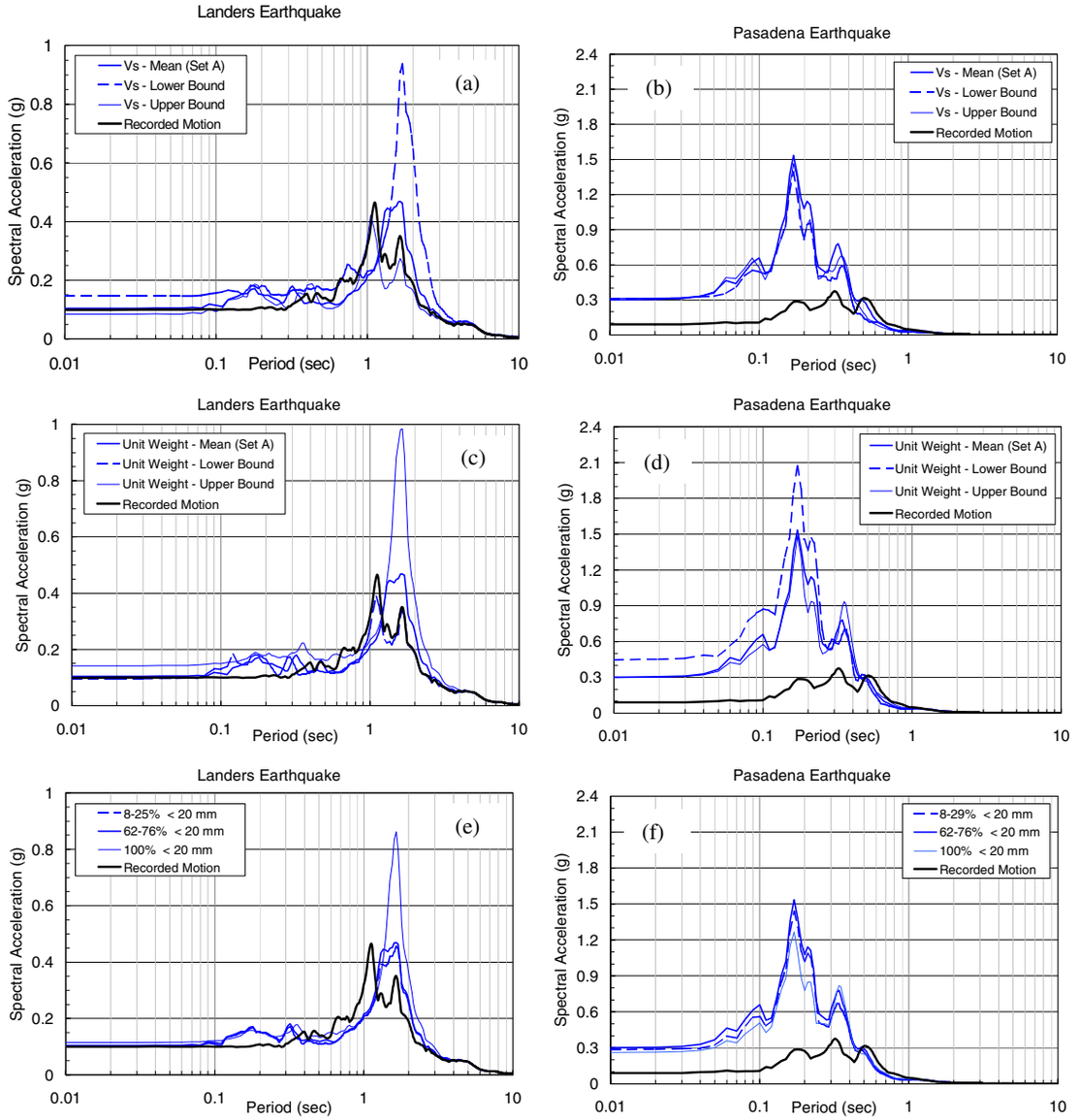


FIG. 6. Sensitivity analyses of the predicted ground motions at the landfill top deck for the Landers and Pasadena earthquakes.

Sensitivity Analyses

Additional analyses were performed to evaluate the sensitivity of the results to the assumed MSW shear wave velocity, unit weight, and G/G_{max} and λ curves. These input parameters were varied from the "average" or "typical" MSW properties (Set A). To evaluate the influence of these parameters, two ground motions were selected: the Landers earthquake, for which the predicted ground motion was in good agreement with the recorded ground motion, and the Pasadena earthquake, for which the prediction was poor.

The effect of the shear wave velocity is shown for the Landers and the Pasadena earthquakes in Figures 6a and 6b, respectively. For each earthquake, the shear wave velocity profile is varied from the average profile to the upper and lower bounds shown

in Figure 2. The use of the lower bound shear wave velocity results in an over-prediction of the intensity of the ground motion over almost the entire range of frequencies compared to the average properties for the Landers earthquake, but no significant difference is observed for the Pasadena earthquake.

The effect of the unit weight is also shown for the Landers and the Pasadena earthquakes in Figures 6c and 6d, respectively. For each earthquake, the unit weight profile is varied from the average profile, to the upper and lower bounds shown in Figure 1. The use of the upper bound unit weight results in an over-prediction of the intensity of the ground motion over almost the entire range of frequencies compared to the average properties for the Landers earthquake, but also, to some degree, for the Pasadena earthquake as well.

Finally, the effect of the G/G_{max} and material damping curves is shown for the Landers and the Pasadena earthquakes in Figures 6e and 6f, respectively. For each earthquake, the dynamic curves are varied from the average curves (62-76% < 20 mm) to the dynamic curves that would be estimated for a "soil-rich" (100% < 20 mm) and "waste-rich (8 - 25% < 20 mm) material, as shown in Figure 4. The use of "soil-rich" dynamic curves results in a significant over-prediction of the intensity of the ground motion at a period of 1.6 sec compared to the average properties for the Landers earthquake. No significant differences are observed for the Pasadena earthquake.

CONCLUSIONS

The mechanical properties of soils and soil-like materials like MSW are, even when placed in a controlled manner, difficult to assess without site-specific in situ and laboratory testing. That is especially true for materials like MSW that may, due to changes in the waste stream that occur over time, be affected by waste disposal and compaction techniques (e.g., the use of new compaction equipment; the use of an alternative daily cover in lieu of soil) or by extreme events such as earthquakes, floods, and hurricanes. Furthermore, while design engineering properties of soils are typically tested during construction (e.g., construction quality assurance of engineered fill), this is not true for MSW as testing of this material is difficult due to the large particle size, health and safety issues and, most importantly, as the waste changes over time due to decomposition, biodegradation, and compression. Therefore, use of generic material properties for seismic design of solid waste landfills is an attractive option.

The evaluations presented in this paper are based upon relatively simple one-dimensional (1-D) frequency domain site response analysis and monitoring the results at the top deck of a landfill in terms of spectral response. The input motions considered are of relatively low intensity, but encompass a variety of seismic events with respect to style of faulting and site-to-source distance. The results of evaluations documented in this paper demonstrate that, for cited seismic loading conditions, the use of generic MSW properties for seismic design of solid waste landfills results in reasonable and, in some cases, lead to a conservative seismic design. The results of parametric studies indicate that a less conservative assessment of the site response may be achieved if generic material properties are modified based upon site-specific conditions established by site exploration.

REFERENCES

Augello, A.J., Bray, J.D., Abrahamson, N.A. and Seed, R.B. (1998), "Dynamic Properties of Solid Waste Based on Back-Analysis of OII Landfill," ASCE Journal of Geotechnical and Geoenvironmental Engineering, Vol. 124, No. 3, pp. 211-222.

Elgamal A, Lai, T, Gunturi R. and Zeghal M. (2004), "System Identification of Landfill Seismic Response," Journal of Earthquake Engineering, 8 (4): 545-566, Imperial College Press.

GeoSyntec (1996), "Summary Report of Findings, Seismicity, Settlement, and Slope Stability Work plan, Operating Industries, Inc. Landfill, Monterey Park, California," Technical Report No. SWP-9, GeoSyntec Consultants, Huntington Beach, California, November.

Idriss I.M., Fiegel G., Hudson M.B., Mundy P.K. and Herzig R. (1995), "Seismic Response of the Operating Industries landfill. In Earthquake design and performance of solid waste landfills", ASCE GSP No.54, editors M.Y. Yegian, W.D. Liam Finn, pp.83-118.

Kavazanjian E., Matasovic N., Stokoe K.H. and Bray J.D. (1996), "In Situ Shear Wave Velocity of Solid Waste from Surface Wave Measurements," Proc. Environmental Geotechnics, Kamon, (editor), Balkema, Vol. 1, pp. 97-102.

Kavazanjian E. (1999), "Seismic Design of Solid Waste Containment Facilities," Proc. 8th Canadian Conference on Earthquake Engineering, Vancouver, BC, pp. 51-89.

Matasovic, N., Kavazanjian, E., Jr. and Abourjeily, F. (1995), "Dynamic Properties of Solid Waste from Field Observations," Proc. 1st International Conference on Earthquake Geotechnical Engineering, Tokyo, Japan, Vol. 1, pp. 549-554.

Matasovic N and Kavazanjian E. (1998), "Cyclic Characterization of OII Landfill Solid Waste," Journal of Geotechnical and Geoenvironmental Engineering, March, 124 (3), pp. 197-210.

Matasovic, N., Williamson, T.A. and Bachus, R.C. (1998), "Cyclic Direct Simple Shear Testing of OII Landfill Solid Waste," Proc. 11th European Conference on Soil Mechanics and Foundation Engineering, Porec, Croatia, Vol. 1, pp. 441-448.

Matasovic, N. and Kavazanjian, E., Jr. (2006), "Seismic Response of a Composite Landfill Cover," ASCE Journal of Geotechnical and Geoenvironmental Engineering, Vol. 132, No. 4, pp. 448-455.

Pacific Engineering and Analyses (1995), "Processing and Spectral Analysis of Eighteen Earthquakes Recorded at the Operating Industries, Inc. Landfill in Monterey Park, California," Prepared for US Environmental Protection Agency, final report, March 17, 1995.

Ordonez, G. A. (2000), SHAKE2000: A Computer Program for the 1-D Analysis of Geotechnical Earthquake Engineering Problems, http://www.shake2000.com.

Zekkos, D. P. (2005), "Evaluation of Static and Dynamic Properties of Municipal Solid-Waste," Dissertation submitted in partial fulfillment of the requirements for the degree of Doctor of Philosophy, Department of Civil and Environmental Engineering, University of California, Berkeley, Fall 2005 (Also available at http://waste.geoengineer.org).

Zekkos D., Bray J.D., Riemer M., Kavazanjian E., Matasovic N., Rathje E. and Stokoe K.H. (2006), "Unit Weight of Municipal Solid-Waste," ASCE Journal of Geotechnical and Geoenvironmental Engineering, 132 (10), pp.1250 -1261.

Zekkos, D., Bray, J. D., Riemer, M. F. (2007a), "Shear Modulus and Material Damping of Municipal Solid-Waste based on Large-Scale Cyclic Triaxial Testing," Canadian Geotechnical Journal, Vol. 44, Issue 12 (in press).

Zekkos, D., Bray J. D., Athanasopoulos, G.A., Riemer, M. F., Kavazanjian, E., Founta, X., Grizi, A. (2007b), "Compositional and Loading Rate Effects on the Shear Strength of Municipal Solid Waste," Proc. 4th International Conference on Earthquake Geotechnical Engineering, Thessaloniki, Greece, Paper no. 1525 (Also available at http://waste.geoengineer.org).

Assessing Geotechnical Hazards for Water Pipes with Uniform Confidence Level

Craig A. Davis Ph.D., PE, GE, Member ASCE

Waterworks Engineer, Geotechnical Engineering Group, Los Angeles Department of Water and Power, 111 N. Hope Street, Room 1368, Los Angles, CA, 90051, craig.davis@ladwp.com.

ABSTRACT: A uniform confidence hazard evaluation provides a methodology to assess earthquake hazards so all pipes in a water system are designed consistent with their intended function and with a uniform confidence that design forces are greater than or equal to actual forces a pipe may experience during an earthquake. The method also provides design uniformity between different water systems. This paper summarizes: (1) how to define a pipe function in relation to its importance in aiding a community in post-earthquake recovery, and (2) how to identify transient, fault, landslide, and liquefaction induced lateral spreading ground movements with uniform confidence for pipeline design. The uniform confidence methodology is also useful for building and other infrastructure and lifeline systems designs.

INTRODUCTION

The seismic design of water pipe lifeline systems must consider effects of the different geotechnical earthquake hazards (i.e., transient and permanent ground movements) in a uniform manner. A uniform approach is needed for the design of network components subjected to different seismic sources having very different recurrence intervals. In practice, the uncertainties associated with the different ground movements are not applied consistently resulting in non-uniform designs within a water system and throughout an urban environment. Thus, if a single pipe is designed for different hazards, it is likely that some of the hazards would be developed on a less conservative basis than others. Additionally, pipes serving a more important function need to have stricter seismic criteria in order to ensure that the design value is greater than the actual seismic force. The analysis methodology presented herein identifies how geotechnical parameters can be developed for pipelines of different importance in a uniform and consistent manner.

The purpose of this report is to present the initial development of a method for evaluating ground movement earthquake hazards that provides: (1) for the design of water pipelines consistent with their intended function, (2) a uniform confidence that the actual forces a pipe may experience during an earthquake are less than or equal to the design forces, and (3) a process engineers can easily incorporate into standard practice. Application of the uniform hazard approach improves a water system's capability to operate during and following earthquakes. Davis (2005) presented an initial version of the uniform confidence methodology that is used by the American Lifelines Alliance (ALA, 2005). This paper presents some improvements to ALA and can be easily modified for buildings and other infrastructure and lifeline systems (e.g., Liu, 2007).

PURPOSE FOR UNIFORM CONFIDENCE HAZARD EVALUATION

The purpose of a uniform confidence hazard evaluation is to provide a methodology to assess earthquake hazards so that all pipes in a water system are designed for life safety and economy, consistent with their intended function, and with a uniform confidence (reliability) that the actual forces a pipe may experience during an earthquake are less than or equal to the design forces. The method also provides design uniformity between different water systems.

Pipelines are linear facilities that makeup a portion of a water supply and distribution system. Single pipelines may be exposed to several earthquake hazards and different pipelines in a system of different importance may be exposed to the same or different earthquake hazards. A water system provides service to a greater community and the importance of each pipe must consider the community as a whole. For example, pipes providing fire suppression for large communities or a supply to an emergency facility (e.g., hospital) are inherently more important than that supplying irrigation water to recreational parks. As a result, the importance of each pipeline should be determined based on its needed performance following an earthquake. All pipelines of similar importance should be designed with a consistent set of parameters to establish a uniform confidence that each pipe will survive an earthquake. The acceptable pipeline risk exposure may be assessed using analogous community risk acceptance for similar important building facilities, which are documented in existing building codes. Each hazard for which a pipe may be exposed can then be evaluated, accounting for uncertainty in earthquake parameters, and related to acceptable risk.

GEOTECHNICAL EARTHQUAKE HAZARDS

The primary geotechnical earthquake hazards of concern for water pipes are transient and permanent ground movements. Transient ground movement describes the shaking hazard by waves propagating from the energy source and the amplifications due to surface and near surface ground conditions and topography. Permanent ground movement describes the ground failures resulting from surface fault rupture, slope movements and landslides, shear deformations, liquefaction induced lateral spreading and flow failure, and differential settlement. Tsunami, bearing failure, settlement, floatation and other seismic hazards pose threats to pipelines, but will not be evaluated further in this report.

Figure 1 presents an example water transmission pipe subjected to several different geotechnical hazards. Transient motions will change along the pipe alignment due to conditions differing from firm to soft sandy soils, weak clay soils, and rock. Also, if the earthquake source were Fault 1 or Fault 2, portions of the pipe would be subjected to large near-source pulses. The transmission pipe is also subjected to several different permanent ground deformation hazards including: fault rupture, lateral spreading, landslide, differential settlement, and shear deformations in clay. In most practical situations, for a given fault movement, there will be different probabilities of occurrence on Fault 1 and Fault 2. Similarly, Landslides 1 and 2 have different strengths and different probability of movement.

Seismic hazard analyses are generally performed using deterministic or probabilistic seismic hazard analyses (PSHA) methods. Consider Fault 1 and Fault 2 capable of generating the same size earthquake, but on different return periods (e.g., Fault 1 generating the earthquake on an average of 1,000 years and Fault 2 on an average of 10,000 years). The use of deterministic scenario earthquakes, which is common in analysis of water systems, would specify similar ground motion levels for similar ground conditions at similar fault distances, but has difficulty accounting for uncertainties in the evaluation and the risks associated with the accumulation of all seismic sources potentially affecting the pipe; Whereas PSHA ground motion

evaluations simultaneously consider the effects from multiple earthquake source hazards on a pipe and the probabilities of a likely range of magnitudes over the length of each seismogenic source. A ground motion PSHA accounts for uncertainties in the evaluation and the risks associated with the accumulation of all seismic sources potentially affecting the pipe. As a result, the PSHA is recommended for use to evaluate ground motions in a uniform confidence hazard analyses, or alternatively scenario earthquakes should be derived consistent with a regional ground motion PSHA (Lee, et al., 2005). Similarly, it is best to perform full probabilistic analysis for permanent ground movement hazards such as fault displacement, landslides, liquefaction and lateral spreading. Unfortunately, permanent ground movement PSHA results are not readily available to the same level as transient ground motions (e.g., Leyendecker et al., 2000; McGuire, 2004) and developing them on a project specific basis is very difficult and costly, and many times cannot be practically utilized for evaluation of water conveying pipes. Additionally, ground motion PSHA do not include some aspects important for evaluating certain earthquake settings (e.g., near source effects). As a result, an alternate approach to a full multi-PSHA that uniformly accounts for the variation in uncertainty of the different hazards, while attempting to ensure design level forces will not be exceeded by actual seismic forces, is presented herein for a more practical employment by practicing engineers and geologists. This approach includes readily available ground motion PSHA and is recommended to incorporate other more advanced PSHA when available.

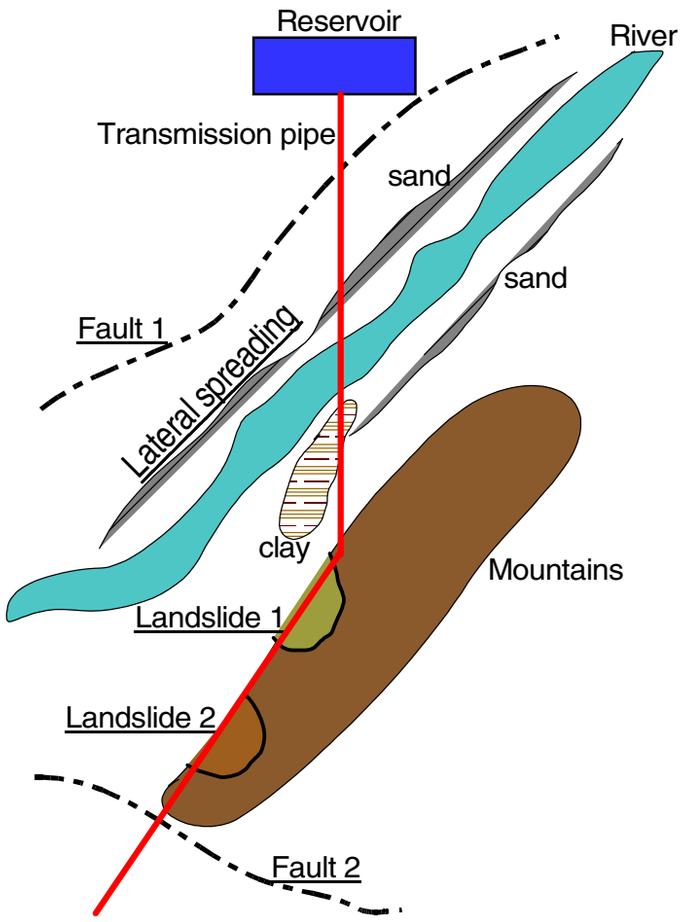


FIG. 1. Example water transmission pipe subjected to several different faulting, landslide, lateral spreading, and ground motion geotechnical hazards.

PIPE FUNCTION

Different types of pipelines in water supply and distribution networks serve different functions. Aqueducts, trunk lines, mains, and service connections identify the pipe type. The pipe function is related to its importance in providing water supply to the community and individual facilities and may not have a direct correlation to the pipe type. Table 1 classifies pipes into four functions related to their importance in aiding a community in post-earthquake response and recovery. The ALA Commentary (ALA, 2005) provides additional guidance on how to classify pipes as Function I, II, III, or IV based on how critical they are and consequences of failure, with consideration of: the facilities they serve; importance to the community for fire fighting, health, and post-earthquake emergency response and recovery; potential for secondary disasters resulting from pipe damage or failure; difficulty in making repairs; effects on community socio-economics; and a pipes location and size considering disruption of emergency response or evacuation. Davis (2007) presents example water distribution system pipe classifications.

Pipelines are essential for providing domestic water supplies to the community. As a result, pipelines are critical for helping communities recover from an earthquake and to help prevent secondary disasters, such as fire and disease, following an earthquake. It is also important to develop consistent seismic design criteria for the community as a whole; that is, on a conceptual level a pipeline need not be designed with greater seismic criteria than the facility(ies) in which is serves or for its intended post-earthquake use, nor should it be design to a lesser standard than what the community expects. The pipeline function classification in Table 1 are consistent and analogous with building code definitions (BSSC, 1998; ICC, 2003; ICBO, 1997), which establish higher level seismic design criteria for facilities that are more important to the community. For example, pipelines servicing facilities defined as essential in the building code are similarly defined as essential in the methodology proposed herein.

Table No. 1. Pipe Function Classifications.

Function	Seismic Importance	Description
I	Very low to None	Pipelines that represent very low hazard to human life in the event of failure. Not needed for post earthquake system performance, response, or recovery.
II	Ordinary, normal	Normal and ordinary pipeline use, common pipelines in most water systems. All pipes not identified as Function I, III, or IV.
III	Critical	Critical pipelines and appurtenances serving large numbers of customers and present a substantial hazard to human life and property in the event of failure.
IV	Essential	Essential pipelines required for post-earthquake response and recovery and intended to remain functional and operational during and following a design earthquake.

Other function and confidence considerations can be incorporated into the analysis (Davis, 2005; ALA, 2005) such as multiple use pipes, continuity, redundancy, branch lines, isolation capabilities, maintenance, and emergency response capabilities, but will not be reviewed here due to space limitations.

CONFIDENCE LEVEL

For operational purposes, a pipeline has a minimum performance reliability following an earthquake. The need for operational reliability in any given pipe increases with increasing functional importance. Table 2 identifies the recommended design basis for each pipe function. The reliability of a pipe being operational

following an earthquake is expressed in terms of a confidence level C defining the confidence that the pipe design parameters will not be exceeded. C is an indicator for the probability of not having pipe damage and is related to the probability P that a design parameter may be exceeded when the design earthquake occurs: $C = 1 - P$. C increases and P decreases with increasing pipe functional importance. P is defined in relation to a time period t, where t identifies the time basis for facility design. A 50-year design basis is used for this evaluation procedure to be consistent with standard engineering practice, and P is related to the t = *50*-year timeframe. T identifies the average time between seismic hazard occurrences and is related to P and C through: $T = -t / \ln(1 - P) = -t / \ln C$, $0 \le C \le 1$.

Table No. 2. Recommended design basis for each pipe function.

Function	Probability of Exceedance P in 50 years	Confidence Level C	Return Period T (years)
I	Undefined	Undefined	Undefined
II	10%	90%	475
III	5%	95%	975
IV	2%	98%	2,475

The design basis for Function II pipes is determined consistent with common codes (BSSC, 1998; ICC, 2003) for building structures performing similar functions. The design basis for Function IV pipes is determined from a geologic earthquake recurrence interval of 2,475 years, which is considered a rare but possible event and one that must be considered for design of essential facilities (Leyendecker et al., 2000). The design basis defined for Function III pipes is considered a reasonable intermediate value between Function II and IV pipes. The seismic design basis for Function I pipes is undefined because even pipes that are not specifically designed for earthquake effects hold an undefined level of seismic resistance.

ASSESSING GEOTECHNICAL EARTHQUAKE HAZARDS

Nearly all of the earthquake parameters needed for analyzing seismic hazards threatening a pipeline can be obtained from a ground motion PSHA and deaggreation of the PSHA (McGuire, 2004; Bazzurro and Cornell, 1999). The PSHA results provide a consistent set of seismic design parameters having a uniform confidence that each parameter will not be exceeded. Ground motion PSHA can be performed with computer programs (e.g., Blake, 1995) or through the United States Geological Survey (USGS) interactive deaggregation web page http://eqint.cr.usgs.gov/deaggint/2002/index.php.

A PSHA can be performed for 2, 5, and 10% probability of exceedance in 50 years at selected locations, consistent with known hazards and critical pipe locations, along Function II, III, and IV pipes to evaluate peak ground acceleration (pga) and spectral accelerations at various frequencies. The peak ground velocity (pgv) may not be standard output for common PSHA results, but can be estimated by factoring the 5% damped acceleration at 1 Hz (SA_1) from (Newmark and Hall, 1982):

$$pgv(cm/s) = SA_1 / (1.65 * 2\pi) \quad (1)$$

As shown in Figure 2, ground motion PSHA deaggregation will provide results for mean and modal fault distance R, magnitude M, and ε representing the ground motion distribution in relation to M and R.

PSHA estimates for M are generally dominated by the characteristic magnitude; as a result, M is usually similar for all ground motion confidence levels. M is an important parameter for estimating permanent ground movements and the effects

of characteristic magnitude are accounted for in the different permanent ground movement evaluations presented below. The PSHA does not necessarily account for all active or potentially active faults that pipelines may cross. When crossings are encountered that need evaluation, but the active fault is not included as part of the PSHA, an engineering geologist is recommended to evaluate the characteristic earthquake magnitude consistent with methods used for the PSHA.

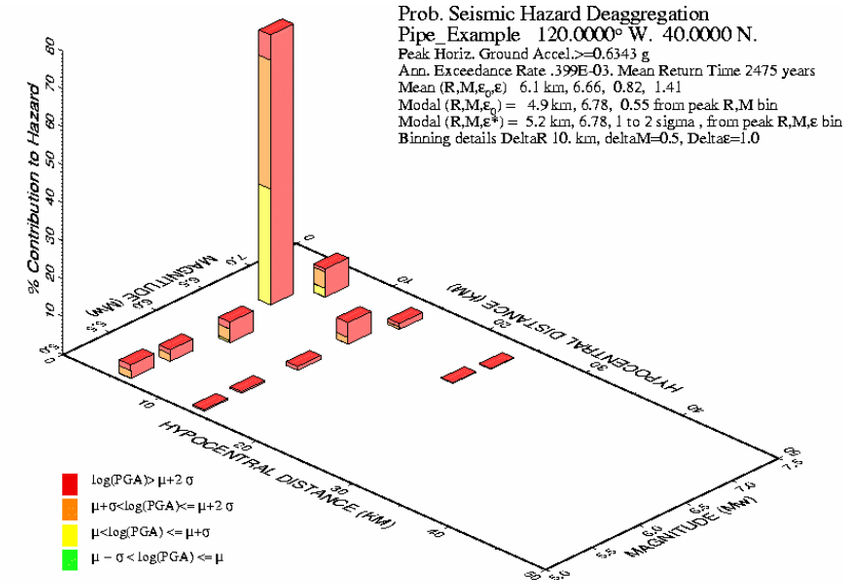


FIG. 2. Probabilistic Seismic Hazard Deaggregation for site "Pipe Example" presented for pga with a 2% chance of exceedance in 50 years.

Alignment Specific Transient Ground Movement Design Parameters

Ground motion evaluations along pipelines should consider the transient ground movement effects for all conditions along the alignment. In some PSHA analyses attenuation relationships may specify the existing subsurface conditions (Blake, 1995). In other cases the PSHA results will be given for a standard site condition (e.g., USGS results for NEHRP site class B). In the latter case site specific ground motion parameters, F_{ag} for short period (e.g., pga) and F_{vg} for long period (e.g., pgv) motions, may be obtained by using the NEHRP site coefficients (BSSC, 1998), which are not repeated herein due to space limitations.

Pipelines located relatively close to the seismic source may be subjected to near-source seismic shaking, resulting in significantly larger ground motion parameters and ground strain than pipes located further away from the source. Near source factors N_a and N_v from Table 3 are applied to Function III and IV pipes when $R < 15$ km and $M > 6.5$. Amplifications for topographic, basin edge, and ground oscillation effects require specific alignment evaluations.

Table No. 3. Near-source factors N_a and N_v (modified from ICBO, 1997)

Factor	R ≤ 2 km	5 km	10 km	R ≥ 15 km
N_a [1]	1.5	1.2	1.0	1.0
N_v [1]	2.0	1.6	1.3	1.0
[1]Near source factors may be linearly interpolated.				

The design peak transient movements, PGA_D and PGV_D, are determined from:

$$PGA_D = F_{ag} * N_a * pga \quad (2)$$

$$PGV_D = F_{vg} * N_v * pgv \quad (3)$$

Alignment Specific Permanent Ground Movement Design Parameters

The following subsections present recommended pipeline design parameters for fault, slope, and liquefaction induced lateral spreading permanent ground deformations. The design movements are conditional upon the triggering of fault rupture, slope movement, or liquefaction. The design coefficients account for the conditional probability and the largest coefficients were determined by using mean deformations for Function II pipes. Movements for Function III and IV pipes were proportioned to Function II by assuming a maximum of 20% probability of the movement condition occurring, which allows the largest Function III and IV coefficients to be approximated by a half and one standard deviation, respectively. As a result, the coefficients are related to the analysis method and will therefore change with different methods used for evaluating fault, slope, and lateral spread movements from those presented herein. The coefficients provide a uniform confidence between each hazard and the different pipe Functions.

Fault Movement

A fault is considered active if it has moved within the past 11,000 years and potentially active if it has moved within the past 190,000 years. All fault crossings are recommended to be considered along the pipeline, regardless of whether the fault was included in the ground shaking hazard evaluation, by designing pipes for active fault movements as shown in Tables 4 and 5 and considering for sympathetic movements on potentially active faults. An Engineering Geologist should be consulted for all fault activity determinations. M can be estimated from the ground motion PSHA, as described above, or from site specific evaluations.

The surface fault rupture hazard evaluation procedure needs to consider all fault crossings, determine movement orientation of each and if the faults are active or potentially active, estimate the expected surface displacement, and estimate the width in which movement is expected to occur. Most fault rupture occurs over a zone and not along a single line. Pipe designs need to account for the total fault rupture zone and distribution of fault rupture throughout the zone.

The average surface fault displacements PGD_F in meters can be estimated from (Wells and Coppersmith, 1994):

$$Log(PGD_F) = -4.80 + 0.69M \qquad [\, Log(\sigma_F) = 0.36 \,] \quad (4)$$

where σ_F is the standard deviation of average displacement regression. Equation 4 was developed from data regressions using a combination of strike-slip, normal, and reverse faulting. Displacements represent the vector sum of horizontal and vertical movements along fault strike.

The characteristic, or alternatively the maximum, magnitude M is recommended for use in Equation 4, which is consistent with most ground motion PSHA results. Equation 4 does not consider the uncertainty in the recurrence of an earthquake of magnitude M. The probability of an earthquake occurring on a fault is considered by estimating the recurrence interval R_I for M and the elapsed time T_e since the last earthquake. The effective fault activity is estimated from $\Delta T = R_I - T_e$. If there is insufficient information for estimating T_e, an assumption $T_e = 0.15R_I$ is reasonable to account for some time lapse since the last earthquake. Table 4 defines the effective activity from very high to low in terms of ΔT.

Table 5 presents the recommended design movements as a function of effective activity level. The design fault movements reduce for lower effective fault

activity to correlate with their lower probability of fault movement. Coefficients in Table 5 for Function III and IV pipes do not change for the "High" activity level because the recurrence interval is within the level of intended performance for those functions as identified for the design basis in Table 2.

Table No. 4. Effective fault activity.

	Very High	High	Moderate	Low
ΔT (years)	*0-500*	*501-2,500*	*2,501-5,000*	*>5,000*

Table No. 5. Fault movement design recommendations.

	Design Movement for Effective Fault Activity			
Pipe Function	Very High	High	Moderate	Low
II	PGD_F	$0.66*PGD_F$	$0.44*PGD_F$	$0.29*PGD_F$
III	$1.5*PGD_F$	$1.5*PGD_F$	PGD_F	$0.66*PGD_F$
IV	$2.3*PGD_F$	$2.3*PGD_F$	$1.5*PGD_F$	PGD_F

Slope Movement

The assessment of slope movement resulting from earthquake shaking first requires an assessment of the static slope stability factor of safety *FS*. The slope, soil or rock resisting shear strength, groundwater conditions, bedding, jointing, fracturing, and other pertinent factors depending on the slope conditions need to be considered. The critical acceleration at which slope movements initiate is determined from $a_c = (FS - 1)\sin\alpha$, where α is the thrust angle. The average coherent landslide induced permanent down-slope ground displacement PGD_s can be estimated from (Jibson, 1994):

$$Log(PGD_S) = 1.546 + 1.460 * Log(I_A) - 6.642 * a_c \quad [\, Log(\sigma_S) = 0.409 \,] \qquad (5)$$

σ_S is the standard deviation of mean displacement regression and I_A is the Arias intensity in m/sec, which is estimated from $I_A = -4.1 + M - 2 * Log(R)$, R has units of km. PGD_s is in cm. I_A is not modified for magnitude R_I, because M and R in the preceding equation are parameters representing intensity consistent with the ground motion PSHA. Table 6 presents recommended design slope movements.

Table No. 6. Slope movement design recommendations.

Pipe Function	Design Movement
II	PGD_S
III	$1.6*PGD_S$
IV	$2.6*PGD_S$

Lateral Spreading

Lateral spreading is the liquefaction induced down slope movement occurring when cyclic inertial loads exceed the reduced effective soil strength and is generally associated with shallow surface ground slopes (as low as a fraction of a percent slope). An assessment of the liquefaction potential must first be made followed by an evaluation for the possibility of a lateral spread along the pipe alignment. Preliminary regional assessment of soil susceptibility to liquefaction can be made based on geological characteristics, age, and deposition mode (Youd and Perkins, 1978) and grouped as having a very high, high, moderate, low, or very low chance of liquefaction. Table 7 presents the recommended design movements as a function of liquefaction susceptibility.

The average ground displacement PGD_L in meters can be estimated from (Bardet et al., 2002):

$$Log(PGD_L + 0.01) = -7.280 + 1.017 * M - 0.278 * Log(R) - 0.026 * R + 0.497 * Log(W) + 0.454 * Log(S) + 0.558 * Log(T_{15}) \quad (6)$$

W is the free-face ratio (%), S is the ground slope (%), T_{15} it the total thickness of all liquefiable layers in meters having SPT blow counts of $N < 15$ blows per foot, and R has units of km. Parameter descriptions and allowable range of data is provided in (Bardet et al., 2002). Geotechnical engineers and engineering geologists are recommended to be consulted for evaluation of potential liquefaction hazards. Use of Equation 6 indicates a certain amount of field investigations are necessary for proper liquefaction evaluations. Investigations may be difficult for some pipes, but proper mapping and initial reconnaissance can reduce the amount of field work needed. Proper investigations, with due consideration of the pipes importance, are necessary for an adequate hazard assessment. An improper assessment of groundwater, soil type, T_{15}, etc. may greatly overestimate or underestimate the hazard. As an alternative to Equation 6 and Table 7, liquefaction and lateral ground movements may be evaluated with more advanced methods.

Table No. 7. Liquefaction induced permanent ground movement recommendations.

	Design Movement for Liquefaction Susceptibility			
Pipe Function	Very High	High	Moderate	Low
II	PGD_L	0	0	0
III	$1.35*PGD_L$	PGD_L	PGD_L near-source zone only[1]	0
IV	$1.5*PGD_L$	$1.35*PGD_L$	PGD_L	PGD_L near-source zone only[1]

[1]Design pipes for PGD_L if $N_a > 1.0$ or $N_v \geq 1.3$. Otherwise recommend using $PGD_L = 0$.

Table 7 shows the design lateral spread movements reduce to a 0 lower bound value to account for lower strain potential with decreasing liquefaction susceptibility. PGD_L is not modified for magnitude R_I, because M and R in Equation 6 are parameters representing intensity consistent with the ground motion PSHA.

CONCLUSIONS

An approach for evaluating earthquake hazards to pipelines with uniform confidence has been presented. The procedure ensures consistency for assessing permanent and transient ground movements. The goal is to have a uniform confidence level for the design of a single pipe crossing many hazards and for all similar pipes subjected to similar hazards throughout a water system. Pipes serving similar functions will be designed similarly, with more stringent design requirements applied to the more important pipes in uniform manner. Different earthquake hazards are evaluated for pipeline design with a uniform confidence that the design forces will not be exceeded in future earthquakes. The information presented herein represents an initial work in developing a uniform confidence hazard approach. Additional research is needed to refine the hazards considered and to add additional hazards to the approach.

ACKNOWLEDGMENTS

The support from the ALA under NIBS contract G&E-1-2004 and input from the ALA (2005) team members in developing the initial evaluation procedure is acknowledged. J. Hu is acknowledged for lateral spread ground deformation analysis.

REFERENCES

American Lifelines Alliance (ALA), 2005 "Design Guidelines for Seismic Resistant Water Pipeline Installations," *FEMA and National Institute of Building Sciences*. www.americanlifelinesalliance.org

Bardet, J. P., T. Tobita, J. Hu, and N. Mace, 2002, "Large Scale Modeling of Liquefaction-Induced Ground Deformation, *Earthquake Spectra*, EERI, Vol. 18.

Bazzurro, P., and C. Cornell, 1999, Disaggregation of Seismic Hazard," *Bull. Seism, Soc. Am.*, 89, pp. 501-520.

Blake, T. F., 1995, "FRISKSP A Computer Program for the Probabilistic Estimation of Peak Acceleration and Uniform hazard Spectra using 3-D Faults as Earthquake Sources," *Computer Services and Software*, Newbury Park, CA.

Building Seismic Safety Council (BSSC), 1998, "1997 NEHRP Recommended Provisions for Seismic Regulations for New Buildings and Other Structures," Part 1 (Provisions) and Part II (Commentary), *FEMA 302/303*, Washington D.C.

Davis, 2005, "Uniform Confidence Hazard Approach for the Seismic Design of Pipelines," 4th Japan-US Workshop on Seismic Measures for Water Supply, *JWWA and AWWARF*, Kobe, Japan.

Davis, C.A., 2007, "Evaluating Earthquake Hazards to Water Pipelines with Uniform Confidence," 5th China-Japan-US Trilateral Symposium Lifeline Earthquake Engineering, Haikao, China, Nov. 26-30, *Beijing Univ. of Tech.*, http://gees.usc.edu/China2007, pp. 149-157.

International Code Council (ICC), 2003, "International Building Code" *Building Officials and Code Administrators International, Inc., International Conference of Building Officials, and Southern Building Code Congress Internationals Inc.*, Birmingham, Al.

International Conference of Building Officials (ICBO), 1997, "Uniform Building Code," Whittier, CA.

Jibson, R., 1994, "Predicting Earthquake-Induced Landslide displacement using Newmark's Sliding Block Analysis," TRR 1411, *Transp. Res. Board*, National Academy Press, Washington, D.C., 9-17.

Leyendecker, E. V., R. J., Hunt, A. D., Frankel, and K. S. Rukstales, 2000, "Development of Maximum Considered Earthquake Ground Motion Maps," Earthquake Spectra, EERI, Vol. 16, No. 1, pp. 21-40.

Lee, J., Graf, W., Somerville, P., O'Rourke, T. D., and Shinozuka, M., 2005, "Development of Earthquake Scenarios for Use in Earthquake Risk Analysis for Lifeline System," *Report for the Los Angeles Department of Water and Power*, 34p.

Liu, A., 2007, "The New Seismic Code for Oil & Gas Transmission Pipelines of China," 5th China-Japan-US Trilateral Symposium Lifeline Earthquake Engineering, Haikao, China, Nov. 26-30, *Beijing Univ. of Tech.*, http://gees.usc.edu/China2007, pp. 53-62.

McGuire, R., 2004, "Seismic Hazard Analysis," MNO-10, *Earthquake Engineering Research Institute*, Oakland, CA.

Newmark, N. and W. Hall, 1982, "Earthquake Spectra and Design," MNO-3, *Earthquake Engineering Research Institute*, Oakland, CA.

Wells, D., K. Coppersmith, 1994, "New Emperical Relationships among Magnitude, Rupture Length, Rupture Width, Rupture Area, and Surface Displacement, *Bull. Seism, Soc. Am.*, 84, No.4, 974-1002.

Youd, T. L., and D. M. Perkins, 1978, "Mapping Liquefiable Ground Failure Potential," *Journal of the Geotechnical Engineering Division*, ASCE, 104, 4, 433-445.

Characteristics of Uplifting Velocity of a Buried Pipe in Liquefied Ground

Koji ICHII[1], M. JSCE, Nobuyasu SETO[2] , M. JSCE and Hiroshi KIDERA[3], M. JSCE

[1]Associate Professor, Graduate School of Engineerng, Hiroshima University,
1-1-1 Kagamiyama, Higashi-Hiroshima, Hiroshima, 739-8527, Japan; ichiikoji@hiroshima-u.ac.jp
[2]Reseach Student, Department of Engineerng, Hiroshima University,
1-1-1 Kagamiyama, Higashi-Hiroshima, Hiroshima, 739-8527, Japan
[3]Engineer, Kunisaki Construction Office, Oita Prefecture, 786-1 Ankokuji, Kunisaki-cho,
Higashi-Kunisaki, Oita, 873-0504, Japan

ABSTRACT: Uplift behavior of a buried pipe is a typical damage to structures in liquefied ground. Since uplift of pipes could causes the functional loss of emergency supply of fire extinguish water, and the ground surface deformation due to these uplift of pipe could be a barrier for rescue transportation, an evaluation scheme of uplift deformation level in various ground conditions should be proposed. A series of shaking table tests was conducted to investigate the uplifting velocity of a pipe during shaking. Test results revealed the uplift velocities in various soils were dependent on the soil characteristics; especially the effect of fines contents. In comparison with the case with viscous waters, these effects might be not based on the effect of permeability. However, hollow-cylindrical cyclic shear tests indicated that the difference should be based on the difference of stress-strain relationships. Thus, the importance of laboratory test to evaluate the behavior of soil during liquefaction is clarified.

INTRODUCTION

It is reported that underground structures such as buried pipes in liquefied ground uplift toward ground surface. Although these phenomena do not directly cause a severe disaster in usual cases, it becomes barriers for emergency transportation. And leakage of water and/or gas in the pipe also could occur due to this phenomenon.

Some experimental investigation and analytical trial for the evaluation of these uplift behaviors has been reported. Yasuda et al. (1995) experimentally studied the mechanism of uplift behavior of a buried pipe. Mohri et al. reported model test results of uplift resistance on buried pipe. Sugano et al. (2002) reported the real-scale test in liquefaction induced by blasting works. JGS (A committee in Japanese Geotechnical Society) (2003) reported a blind test trial for numerical simulation of uplift behavior.

The test results used for the blind test in JGS report is shown in FIG. 1. Except for the results of manhole type structure, it indicates that the uplift behavior only occur in the duration of shakings, and uplift behavior stops when shakings were terminated.

Furthermore, the uplift velocity is almost constant for each case. Thus, the final uplift magnitude can be easily estimated by the product of shaking duration and uplift velocity.

Estimation of shaking duration is not an easy task, but recent development of engineering seismology enables a rough estimation of future ground motions. FIG.2 shows an example of the estimation of future earthquake in southern Kanto area, Japan, and an observed motion in Kobe Earthquake, 1995 (Sugano, 2005). Note, the time scales of both figures are equalized to compare the duration. The duration of shakings is very different in these motions due to the difference of source mechanism; however, the former type of motions with long durations is anticipated in many places in Japan, and in some regions, these ground motions for design are proposed by engineering seismologist.

Thus, the uplift velocity can be a key factor to estimate the magnitude of uplift. Following this idea, some shake table tests in various soils were conducted in this research to investigate the velocity characteristics of buried pipes in liquefied ground.

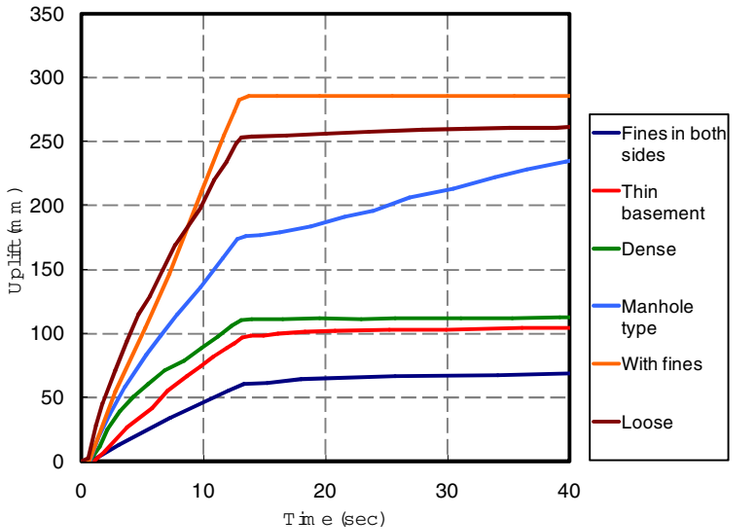


FIG. 1. Experimental results of uplift behavior in shake tests (JGS, 2003)

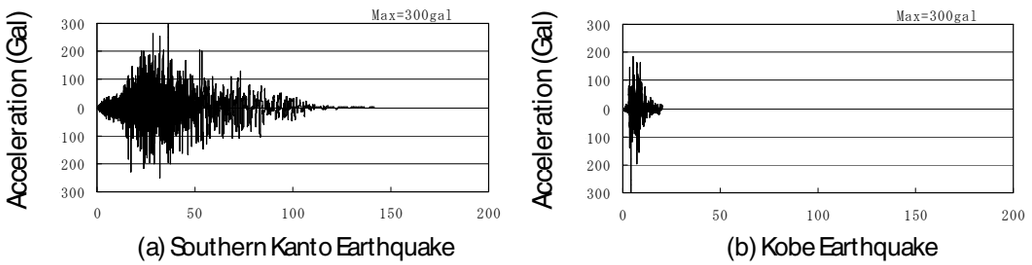


FIG. 2. Example of ground motions in different sources (Sugano, 2005) (PGA were adjusted as 300 Gals)

OUTLINE OF THE MODEL TEST

Small size shaking apparatus had been used for a series of shake tests. FIG.3 shows the outline of the tests. A pipe with 60 mm in diameter was buried in a sand layer with 200 mm in depth. A target marker was connected at the top of the buried pipe. Only a sinusoidal horizontal shaking perpendicular to the pipe direction was applied.

Vertical displacement of the target, pore water pressure (PWP) of soils, and displacement of the shake table were measured as shown in FIG.4. The vertical displacement of the target was measured by a high-speed CCD camera, and the displacement of the shake table was measured by a laser displacement transducer. The locations of PWP measurement were selected not to be affected by the existence of the pipe and walls as shown in FIG.5.

Silica sand with D50 of 0.3 mm was used in the tests. In order to investigate the effect of fine contents, crushed-stone powder was added on the sand layer in some cases. The grain size distribution curves in these cases are shown in FIG.6. Since the existence of fine contents affects not only the stress-strain relationships of soils but also permeability of soil layer, the cases only the permeability of soils were changed by using methylcellulose admixture as the water. The test cases and permeability in these cases are summarized in Table.1. Note, the fines used in this study are non-cohesive stone powder with silt size, and the behavior will be different if cohesive clayey particle were used as fines.

Sand layers were constructed by the method of placing sands in underwater condition. Especially in the case of much fine contents, sand with fines was carefully placed to avoid separation of fines. In this preparation, a specialized small sized spoon was utilized and the sand mass in each placement was less than 100 cm^3. After the placing sands, the sand layer was compacted by hand to the targeted relative density in each case. Note, the compaction is so gentle that the authors believe there are no significant impacts to cause the separation of FC. However, it is better to conduct a detailed study on similarity of FC distribution in real site and models site in future.

Sinusoidal shaking inputs of 10Hz, 50 waves (5 sec.) were applied. The targeted peak acceleration level was 300 gals in each case; however, the actual peak acceleration was fluctuated up to 400 gals due to the difficulties of control. Note, the control of the input level is manual pre-adjustment of the volume by the operator and there are no measures to prevent the occurrence of reflecting waves. These might be the reasons of the difficulties in control.

A typical test results is shown in FIG.7 (Dr = 50% without fines and cellulose). Displacement of the table were almost constant (1.0 mm in maximum) during the duration, but it implies that the maximum acceleration were about 400 gals exceeding the target level of 300 gals. Uplift of the pipe occurred slightly after the beginning of shaking, and it is correspondent to the timing of pore water pressure increase. After 5 seconds, shakings and uplift behavior stopped simultaneously. Since the uplift velocity is difficult to be calculated as a unique value due to fluctuation of measurement, two type of velocity defined by the difference of displacement in 2 sampling points (average of 0.2 sec.) and 5 sampling points (average of 0.5 sec.) are shown in the figure. It indicates that the uplift velocity had been almost constant during shaking. The measured PWP was normalized as the ratio of excess pore water pressure to the initial vertical

stress in this figure. At the deepest point of 19 cm in depth shows relatively small PWP increase. This is maybe because of the effect of overburden pressure and rigid box wall used in the test. At all points of measurement, PWP ratios fluctuate extensively due to the effect of dynamic water pressure.

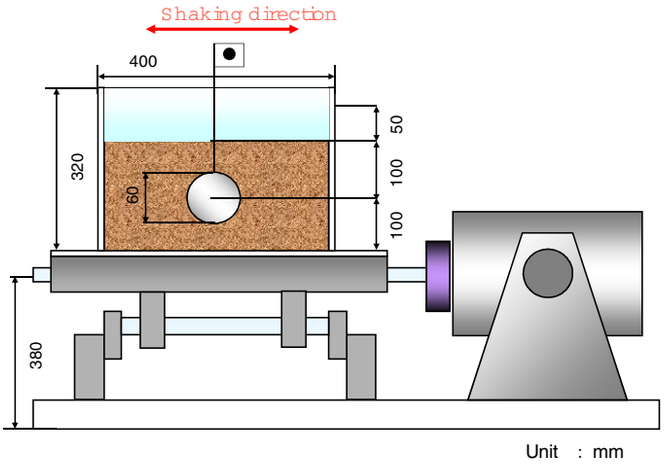


FIG. 3. Model set up for shake tests

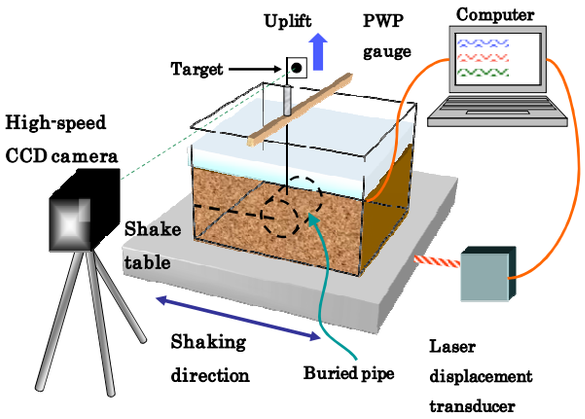


FIG. 4. Measurement set up

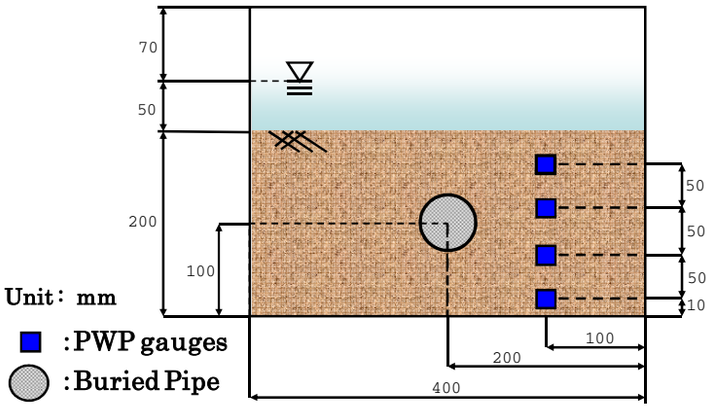


FIG. 5. Location of PWP gauges

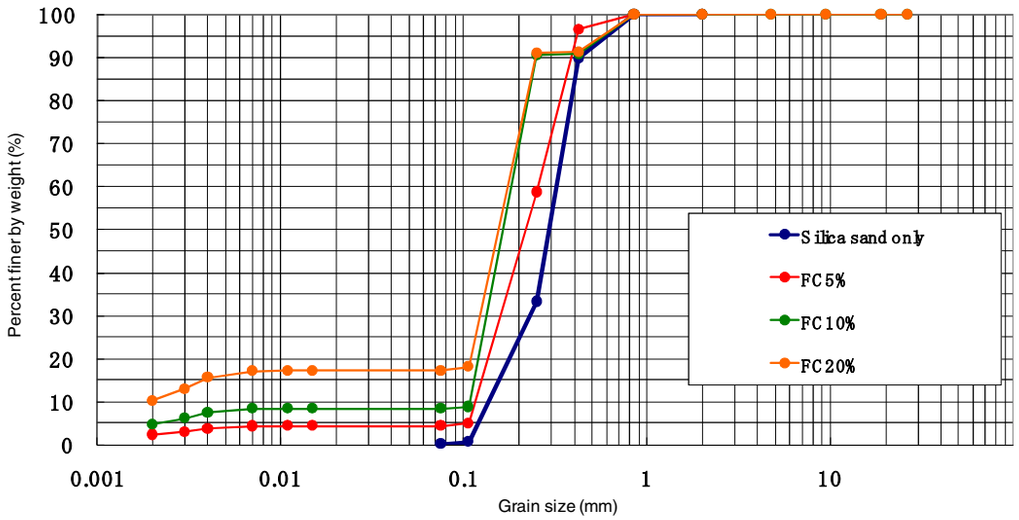


FIG. 6. Grain size distribution of the test materials

Table 1. Test cases and corresponding permeability of soils

Cases	Dr(%)	Fc(%)	Methylcellulose (%)	Permeability (cm/s)
Case1	50	0	0	2.3×10^{-2}
Case2-A	30	0	0	N/A
Case2-B	40	0	0	N/A
Case2-C	60	0	0	N/A
Case3-A	50	5	0	1.5×10^{-3}
Case3-B	50	10	0	1.0×10^{-3}
Case3-C	50	20	0	4.6×10^{-4}
Case4-A	50	0	0.1	8.8×10^{-3}
Case4-B	50	0	0.5	3.1×10^{-3}
Case4-C	50	0	1	8.8×10^{-4}

TEST RESULTS

The test results with different relative densities were shown in FIG.8. Only the most different cases of Dr = 30% and Dr = 60 % were shown in the figure. First of all, input shaking level and increased PWP were not so much different except for the PWP in deep points (-19 cm and -14 cm). However, the uplift behaviors are far different. In the case of Dr = 30%, the pipe uplift very rapidly. The calculated uplift velocity showed an interesting phenomenon that it increased rapidly in the beginning, but decreased later, and increased again at the end of the shaking. Thus, the uplift velocity was not constant in this case. In the case of Dr = 60%, this tendency is observed slightly, but it is not significant.

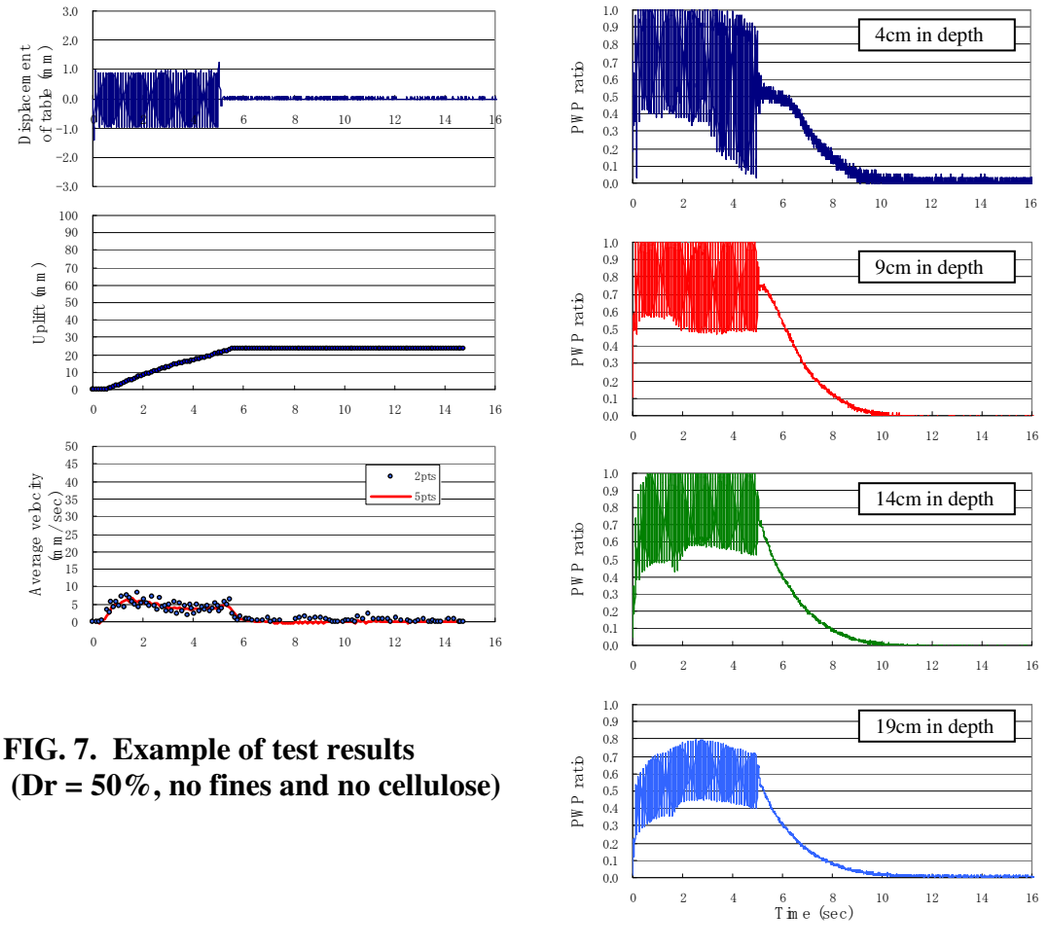


FIG. 7. Example of test results (Dr = 50%, no fines and no cellulose)

The time histories of uplift in all various Dr cases are summarized in FIG.9. It shows that the small relative density increase the speed of uplift. And in this case, if the relative densities were higher than 50%, no significant difference on the uplift velocity can be observed.

The time histories of uplift in the cases with fines contents are summarized in FIG.10. Although the shaking duration is only 5 seconds, the uplift behavior did not stop at the end of shakings in the cases with much fine contents. Especially, in the cases with 20 % FC, the uplift behavior continues more than one minute until the pipe reached at the ground surface.

The details of uplift behavior in shaking duration are summarized in FIG.11. For the cases with FC = 0% to 10%, the uplift velocity increases when FC increases. However, the case with FC = 20% shows far different tendency as uplift velocity suddenly decreased at the time of 1 to 2 seconds. It implies that the increase of FC basically accelerates the uplift behavior, but some complicated phenomenon will be occurred when FC exceeds a certain amounts. Note, time histories of observed PWP have no much difference in these cases and they are not shown in this paper.

The effects of methylcellulose admixture on uplift behavior are summarized in FIG.12. The uplift of methylcellulose cases starts earlier than that of usual water cases.

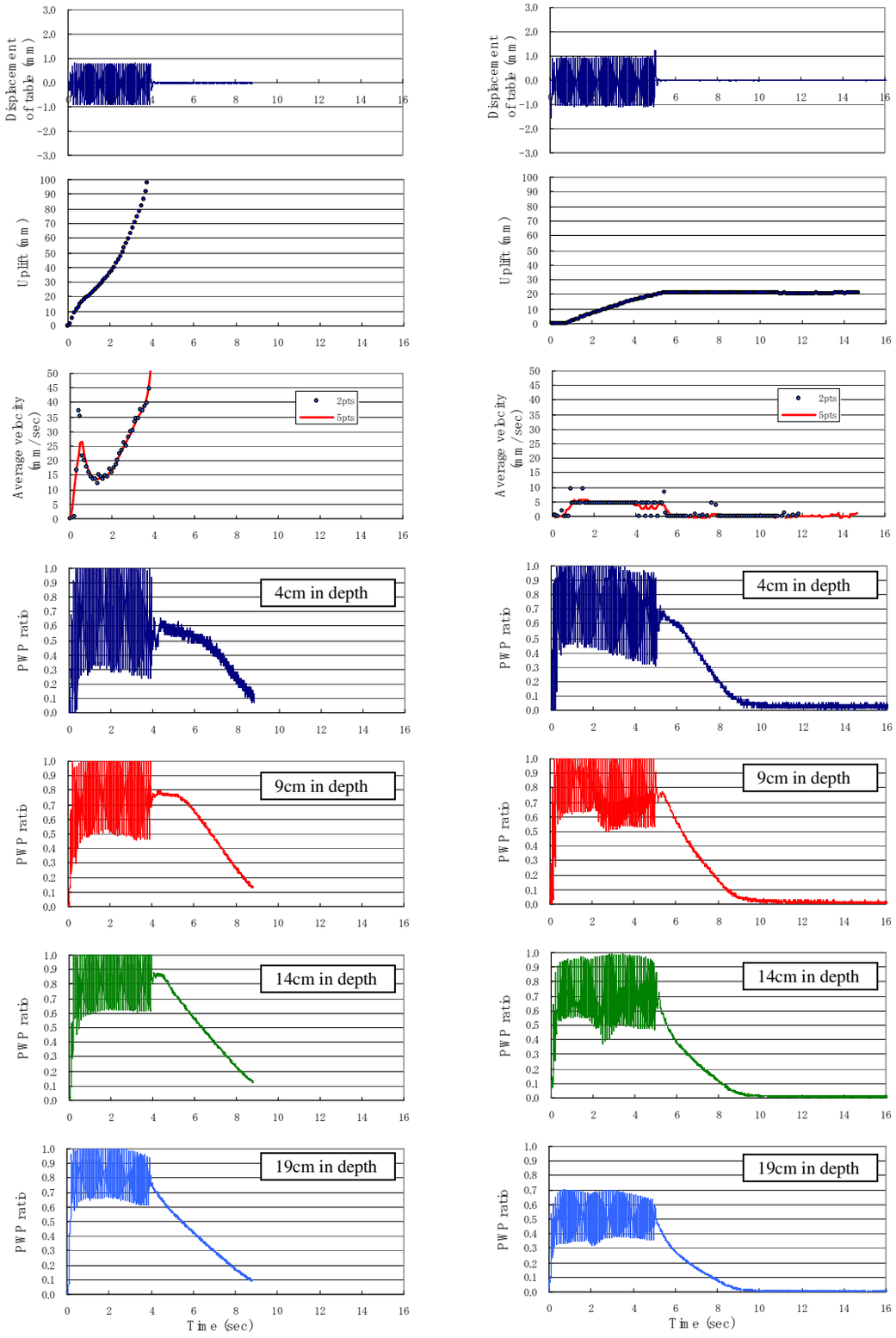


FIG. 8. Example of test results
(Dr = 30%, no fines and no cellulose) (Dr = 60%, no fines and no cellulose)

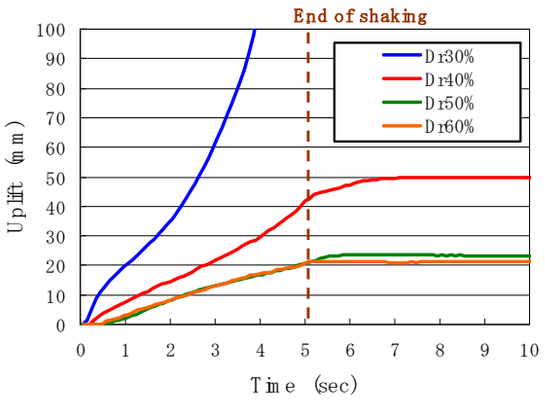


FIG. 9. Time histories of uplift (Dr cases)

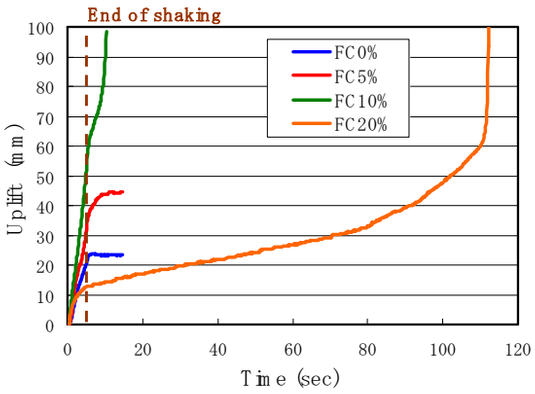


FIG. 10. Time histories of uplift (FC cases)

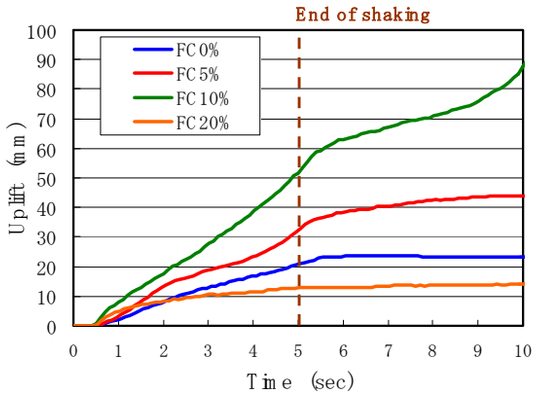


FIG. 11. Time histories of uplift (FC cases)(During shakings)

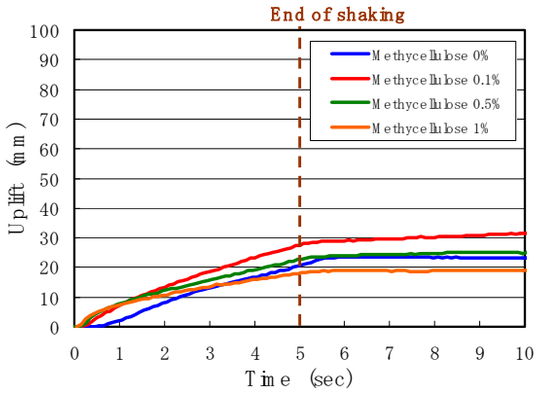


FIG. 12. Time histories of uplift (Methycellulose cases)

The reason of this phenomenon could be the reduction of permeability. It implies that the complete undrained condition might be not maintained in usual water cases due to the smallness of model. In the beginning of uplift behavior, no difference was observed in these three different concentration cases. After 1.5 seconds, the velocities gradually decreased. This tendency is dependent on the degree of concentration. Thus, the uplift velocities were not constant in methylcellulose cases. It indicates that the effect of viscosities of methylcellulose admixture is observed not only on the permeability of soil but also on the uplift resistances of soil. Note the differences of permeability in these methylcellulose cases were as large as that of FC cases, however, no significant difference of uplift velocity was observed. Thus, the effect of permeability difference is less significant than that of the stress-strain relationships of soils.

DISCUSSION

The stress-strain relationships of the sand with FC can be investigated by laboratory tests. However, shear strength in liquefied states are almost zero and no difference could be observed in cases with different FC. The authors assume the difference of uplift velocity is mainly dependent on the strength recovery characteristics due to dilatancy, and a series of torsional hollow cylinder shearing test for the liquefied state were conducted.

In the shearing test, liquefied states were arranged by strain controlled cyclic shear at first. Then, a monotonic strain controlled shearing were applied till a large shear strain. During this monotonic shear, effective stresses were recovered due to dilatancy, and shear strength increases. It takes some amount of shear strain to initiate this shear strength recovery.

The shear strains necessary to initiate strength recovery could be dependent on various factors such as the particle size distribution, initial relative density of sand, etc. Example of the test results considering the relative density and FC are shown in FIG.13 and FIG.14, respectively.

Based on the assumption that the shear strength linearly recovers until some amount of strain, the stiffness of the ground can be calculated. For example, defining the shear strain to recover 5kPa of shear stress as the strain with small shearing resistance γ_{5kPa}, the stiffness of the ground can be defined as $G_{small} = 5/\gamma_{kPa}$ (kPa).

The uplift velocities at the end of the shakings are compared with the stiffness of the ground defined above as shown in FIG.15. Except for the case with FC = 20%, a certain relationships can be observed. Thus, the possibility that the uplift velocity can be assessed by laboratory test was indicated.

Note, the uplift velocities of the pipe are not exactly constant during shakings. This is due to the effects of viscosity of pore water, permeability of soils, deformation of ground surface induced by the uplifted pipe, etc. And the fact that the strength recovery characteristics are dependent on various factors of soils also implies that the velocity of uplift is dependent on soil profile. Thus, the real phenomena are very complicated and more studies including larger size experiments are necessary.

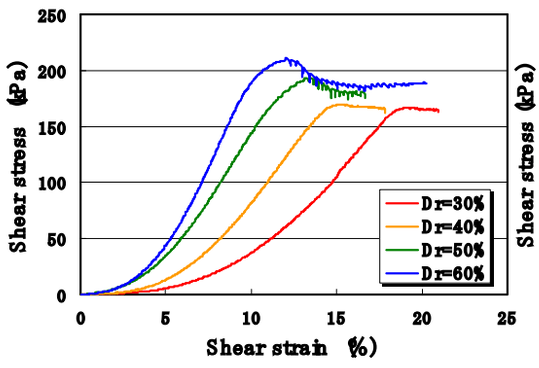


FIG. 13. Stress recovery process (Dr cases)

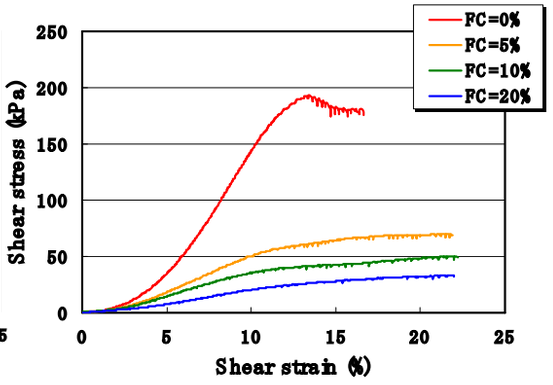
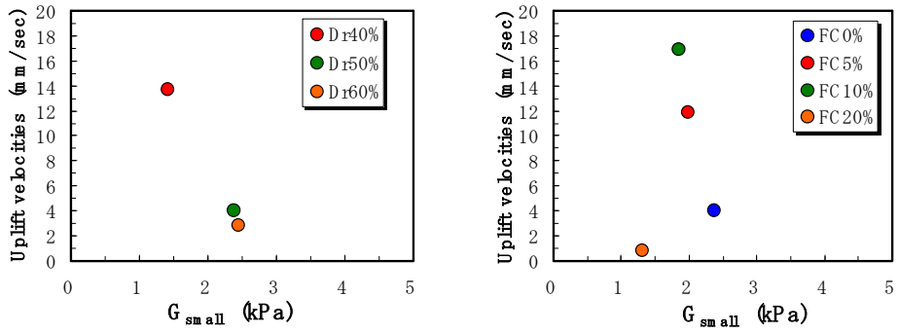


FIG. 14. Stress recovery process (FC cases)



(Dr cases) **(FC cases)**

FIG. 15. Uplift velocities and G_{small}

CONCLUSIONS

An experimental study focusing on uplift velocity of a buried pipe in liquefied ground had been conducted. Followings are main conclusions obtained in this study.

(1) For the case of small relative density, the uplift velocity increased rapidly in the beginning, but decreased later, and increased again at the end of shaking. This tendency also can be observed slightly in higher relative density cases.

(2) Uplift velocity of the case with non-cohesive fines is larger than that of the case with cohesive fines. When fines contents exceed a certain amount, the uplift behavior drastically changed as the velocity at the initial phase is very small but uplift will not stop for a long time even after the shaking halted.

(3) Based on the test results of permeability differences by methylcellulose, the effect of permeability on uplift velocity can be regarded as insignificant.

(4) Based on the results of shake test and laboratory test, the strength recovery behavior of sand due to dilatancy is a key factor to estimate the uplift velocity.

REFERENCES

JGS (2003). "Report of the research committee for damage induced by the uplift behavior of underground structure in liquefied ground", Japanese Geotechnical Society. (in Japanese)

Mohri, Y., Kawabata, T., Ling, H. I. and Sun, L. (2000). "Model Tests of Uplift Resistance on Buried Pipe", *Trans. of JSIDRE*, No. 205, pp. 25-33. (in Japanese)

Sugano, T., Kohama, E., Mitou, M. and Shiozaki, Y. (2002). "Seismic Performance of Urban, Reclaimed and Port Areas - Full Scale Experiment at Tokachi Port by Controlled Blasting Technique", *Proceedings of 11th Japan Earthquake Symposium*, Vol.11, 901-906.

Sugano, T. (2005). "New design method for gravity-type quay walls based on in-situ observation and model tests." *Report of lectures associated with the in-situ observation project on real- scale gravity quay walls*, Hokkaido development Agency, 66-72. (in Japanese)

Yasuda, S., Nagase, H., Itafuji, S., Sawada, H. and Mise, K. (1995). "A study on the mechanism of the floatation of buried pipes due to liquefaction", *Soil dynamics and Earthquake Engineering*, VII, 125-135.

Shake-Table Testing and FLAC Modeling of Liquefaction-Induced Slope Failure and Damage to Buried Pipelines

Lei Qiao[1], Chang Yuan[2], Masakatsu Miyajima[3] and Endi Zhai[4]

[1]Assistant Engineer, Geo-Engineering Investigation Institute of Jiangsu Province, China.
[2]President, Geo-Engineering Investigation Institute of Jiangsu Province, China.
[3]Professor, Dept. of Civil Engineering, Kanazawa University, Japan; miyajima@t.kanazawa-u.ac.jp
[4]Principal Engineer, Kleinfelder West, Inc., USA; ezhai@kleinfelder.com

ABSTRACT: This paper presents Shake-Table testing and FLAC numerical modeling of liquefaction-induced large ground lateral movement and settlement, and pipeline behavior induced by soil movement. A series of laboratory Shake-Table experiments were performed using a model slope ground and model pipe buried under the crest of the slope in a box 1,800 mm long by 600 mm wide by 800 mm high. A typical 2H:1V slope was prepared with its crest at the center of the box. The model pipe had an outside diameter of 25 mm and was buried crossing the full box width and 100 mm below the crest. The above model ground was repeated for different amplitudes of input sine waves varying from 0.1g to 0.25g. Observed and recorded ground failures included lateral spreading and settlement, sand boiling, time histories of excess pore water pressure buildup, input acceleration and model pipe responded acceleration. The above experimental cases were modeled using a nonlinear effective-stress modeling approach with computer code FLAC coupled with a practical-oriented pore pressure model based on cyclic stress method by Seed and co-workers (Seed, 1979). Pore water pressure buildup and dissipation were modeled using alternative stepping of fluid flow-mechanical interaction. The computed ground failures reasonably agree with the observations in the Shake-Table test. The FLAC modeling further revealed the soil liquefaction mechanism and induced ground deformation and pipe deflection.

INTRODUCTION

Soil Liquefaction during earthquakes has been a subject of continuing research over the past four decades. Liquefaction-induced ground deformation has caused severe damage to buried pipeline systems during past earthquakes. These permanent lateral displacements ranged from few centimeters to 10 meters or more (Bardet et al., 1999). Examples of documented pipeline damages due to liquefaction-induced ground deformations in terms of lateral spreading and settlement can be found in the reconnaissance reports of major earthquakes.

The goal of this research was to better understand the mechanism of liquefaction underneath a slope and induced ground deformation and pipe deflection. A series of laboratory Shake-Table experiments were performed using model slope ground and model pipe buried under the crest of a typical 2H:1V slope. The above model ground was repeated for different amplitudes of input sine waves varying from 0.1g to 0.25g. Observed and recorded ground failures included lateral spreading and settlement, sand boiling, time histories of excess pore water pressure buildup, input acceleration and model pipe responded acceleration.

The above experimental case was modeled using a nonlinear effective-stress modeling approach with computer code FLAC coupled with a practical-oriented pore pressure model (Dawson et al., 2001) based on cyclic stress method by Seed and co-workers (Seed, 1979). Pore water pressure buildup and dissipation were modeled using alternative stepping of fluid flow-mechanical interaction. The computed ground failures were compared with the observed failures in the Shake-Table test. The excess pore water pressures under the top and toe areas of the slope were also compared and the extent of liquefaction under the slope area was further discussed.

LABORATORY SHAKING TABLE EXPERIMENTS

Test Materials and Test Setup

The Shake-Table experiments used a model slope ground and a model pipe buried under the crest of the slope in a box 1,800 mm long by 600 mm wide by 800 mm high. The model ground consisted of 400 mm thick fully-saturated liquefiable No.5 silicon sand made by water-pouring method, overlaid by free-falling 200 mm thick dry No.5 silicon sand in a 2H:1V slope with its crest at the center of the box. Figure 1 presents a cross section of the model ground, locations of pore water pressure gauges, location of the model pipe and accelerometer locations. The model pipe had an outside diameter

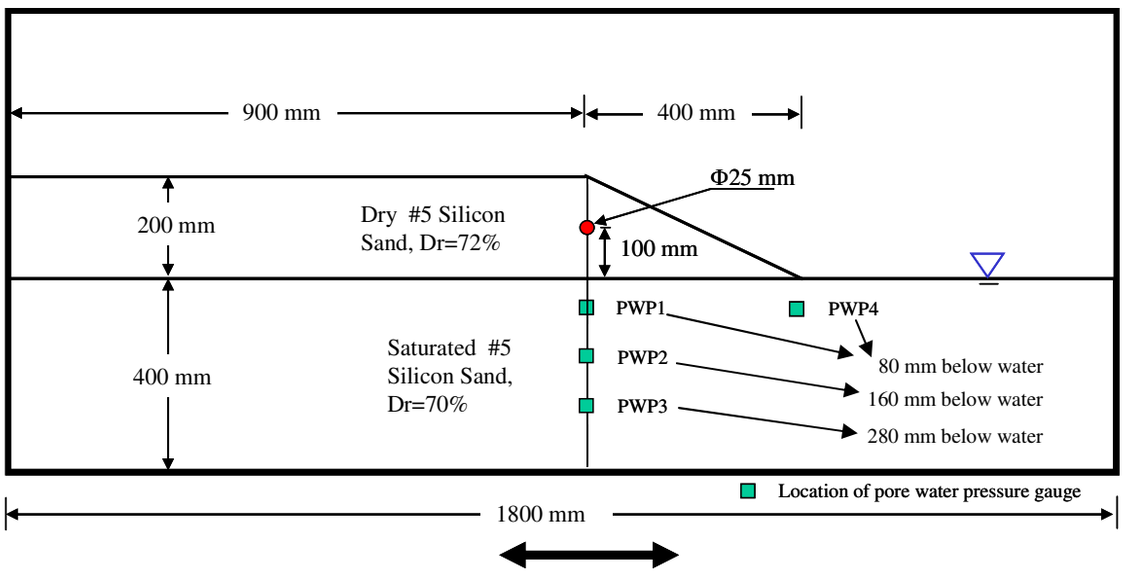


Figure 1 Shake table experimental equipment for the model slope ground and model pipe

of 25 mm and was buried crossing the full box width and 100 mm below the crest. The above model ground was repeated for different amplitudes of horizontal input sine waves varying from 100 gal (0.1g) to 250 gal (0.25g) with a frequency of 5 Hz. The shaking time during each case was 20 seconds. Observed and recorded ground failures included lateral spreading and settlement, sand boiling during liquefaction, time histories of excess pore water pressure buildup, input acceleration and model pipe responded acceleration.

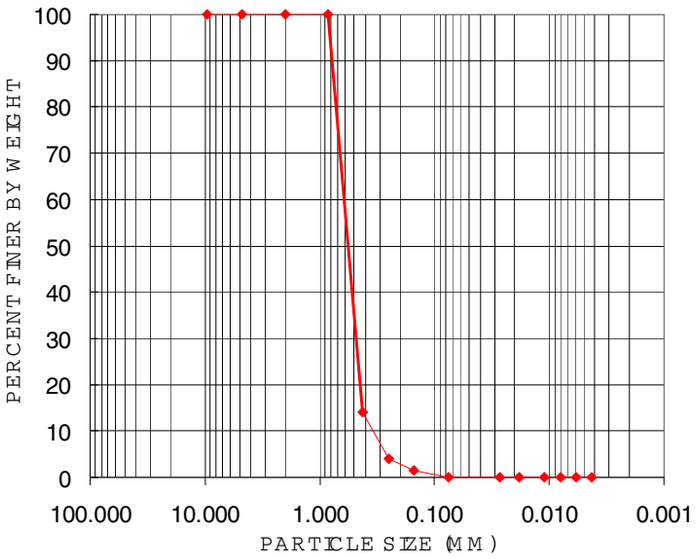


Figure 2 Grain size distribution of No. 5 silicon sand

Laboratory testing based on the samples of similarly prepared saturated and dry No. 5 silicon sands indicated a relative density of approximate 70% for the saturated sand and 72% for the dry sand. The No. 5 silicon sands are poorly-graded granular materials. The distribution of the grain size is shown in Figure 2. The coefficient of uniformity $C_u=D_{60}/D_{10}=0.62/0.33=1.9$, where D_{60} and D_{10} are the particle sizes corresponding to 60% and 10% finer passing by weight, respectively. The coefficient of curvature $C_c=(D_{30})^2/(D_{10} \times D_{60}) = 0.49^2 / (0.33 \times 0.62) = 1.2$, where C_{30} is the particle sizes corresponding to 30% finer passing by weight. The coefficient of uniformity and coefficient of curvature will be used to estimate permeability in the numerical modeling.

In order to facilitate the observations of lateral spreading uniform grids were marked on the side walls of the sand box, as can be seen from Figure 3. Each grid size is 10 cm by 10 cm. Figure 4 shows a close look for the slope portion.

Due to sidewall friction of the sand box and columns used to fix the instruments in the sand box, soil lateral movements are anticipated to be non-uniform during testing. Therefore, in addition to the meshes marked on the sidewalls, we installed 5 rows by 5 columns of small stakes near the crest and toe of the slope. The stake lines looking from one side-wall to the other is defined as rows, and from one end-wall to the other defined as columns. 3 rows were arranged at the crest area and the remaining 2 rows were on the toe area, as shown in Figures 5 and 6, respectively. Each row of stakes was spaced 10 cm apart, and each stake in a row was 10 cm apart. Row-1 (see Table 1) was 10 cm from the crest on top of the embankment (dry sand), Row-3 was 10 cm from the crest on the slope. Row-2 was just at the crest line. Row-4 was just at the toe line. Row-5 was 10 cm away from the toe line and on top of the saturated sand. Column-1 and Column-5 were near the sidewalls. Column-3 was in the middle. Column-2 was between Column-1 and Column 3. Column-4 was between Column-3 and Column-5. Model pipe was a 2.5 cm diameter PVC pipe with two ends fixed to

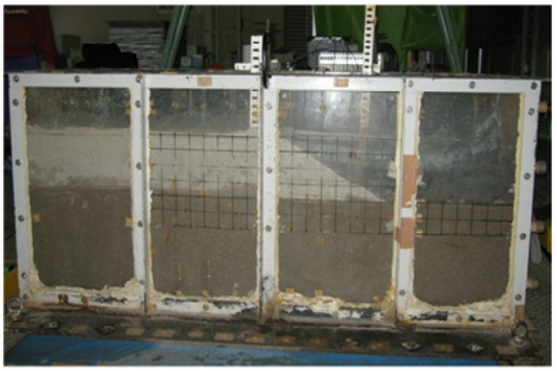


Figure 3 Test model before shaking



Figure 4 A close look of Figure 3



Figure 5 Stakes at top of the slope (used to measure top deformation)



Figure 6 Stakes at toe of the slope (used to measure toe deformation)



Figure 7 Configuration of Model Pipe

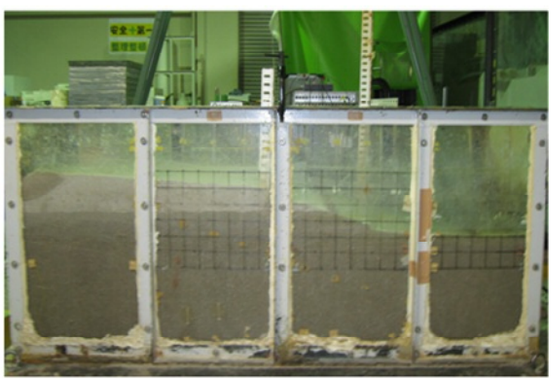


Figure 8 A side view of 2000 gal post-shaking ground deformation

have a simple-support beam boundary condition. A horizontal accelerometer was fastened on the pipe at the central location, as shown in Figure 7. Also shown in Figure 7 was the saturated portion of the model ground right before dry sand was placed.

Test Results and Observations

The initial planned input motions were 5 Hz 100 gal sine waves for 20 seconds and 5 Hz 150 gal sine waves for 20 seconds. These two shaking levels did not result in significant ground deformation that can be seen by visual observation. The test setup was repeated for the following two level input motions:

- 5 Hz 200 gal sine wave for 20 seconds
- 5 Hz 250 gal sine wave for 20 seconds

The overall model ground performance after shaking was observed at the end of each level of input shaking. Figure 8 shows a side view of 200 gal level post shaking ground deformations, which compares with the before-shaking side view as shown in Figure 3. It needs to be noted that the photos shown in Figures 3 and 8 were not taken from the same angle. In addition to these photographs, each stake horizontal and vertical locations before and post shaking were measured using a flexible ruler hanged on a plate that can move on top of the sand box.

Table 1 Observed Ground Deformations after the 200 gal Shaking

	Column-1		Column-2		Column-3		Column-4		Column-5	
	Lateral Spread (cm)	Settlement (cm)	Lateral Spread (cm)	Settlement (cm)	Lateral Spread (cm)	Settlement (cm)	Lateral Spread (cm)	Settlement (cm)	Lateral Spread (cm)	Settlement (cm)
Row-1	0.9	2.0	1.0	2.0	1.8	2.0	1.6	2.0	1.7	2.0
Row-2	1.4	2.0	1.7	2.0	1.7	2.0	2.1	2.0	2.1	2.0
Row-3	4.5	5.0	4.7	5.0	6.0	4.8	4.8	5.0	5.0	5.0
Row-4	4.5	1.0	3.5	1.0	3.8	1.0	4.5	1.0	4.0	1.0
Row-5	3.8	N/A	4.3	N/A	4.5	N/A	4.1	N/A	2.4	N/A

The measured post-shaking lateral spreads and settlements for the 200 gal shaking levels are presented in Tables 1. The definition of rows and columns are provided in the previous section. The lateral spreads listed in Table 1 are plotted in Figure 9. As anticipated, each row of stakes was not displaced uniformly, due to frictions provided by the sidewalls, obstacles of the steel columns used to fasten the instruments and localized failures due to sand boils during liquefaction. The movements of stakes in the central column (Column-3) are believed to be the best representatives of the ground deformations.

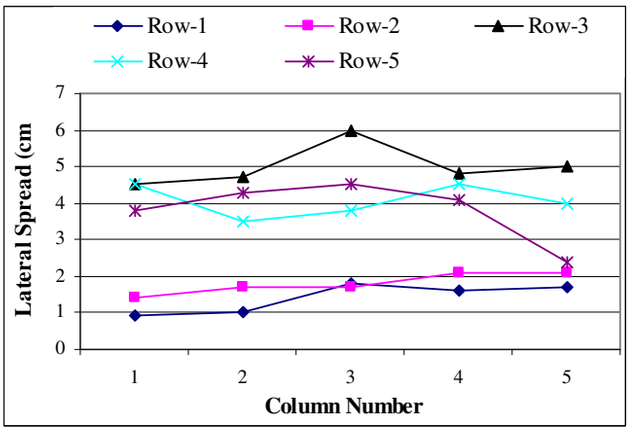


Figure 9 Plot of lateral spreads after 250 gal shaking

Liquefaction phenomena, such as sand boiling, were observed during shaking.

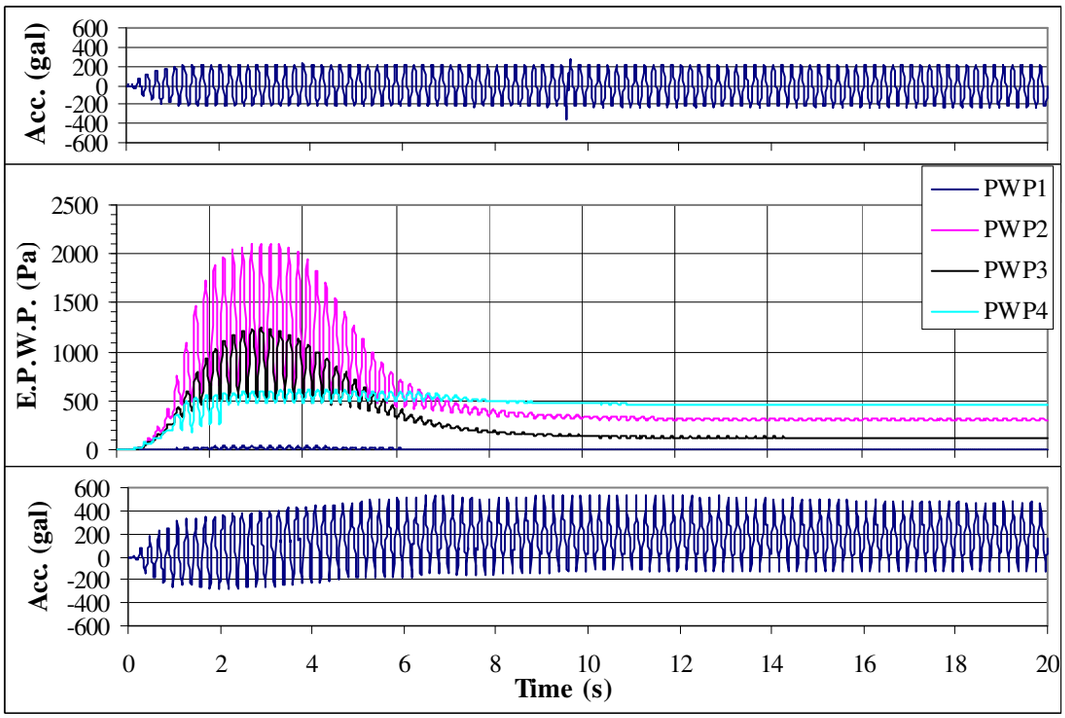


Figure 10 Time histories of input motion (200 gal), recorded excess pore water pressures and accelerations of model pipe

Significant amount of water occurred above the toe of the slope right after the shaking. The input motions (upper), recorded excess pore water pressures (middle) and responded accelerations of model pipe (lower) are presented in Figure 10. Hydrostatic pressures were zeroed out before shaking. The locations of PWP1 through PWP4 were plotted in Figure 1. Sand boiling at the toe areas was observed. Hence, the excess pore pressure during sand boiling after about 2 to 4 seconds of shaking reached the effective overburden pressure, i.e., the excess pore pressure ratio reached unity, indicating the occurrence of complete liquefaction. Under the slope and embankment areas, no sand boiling occurred. Some portion of the dry sand close to the original water level became wet. This rise of moisture might be due to dissipation of pore water pressure upward and capillary phenomena.

FLAC NUMERICAL MODELING AND ANALYSES

Analysis Approach and Model Makeup for FLAC Analyses

FLAC (Itasca, 2006) was used to model the shaking table configuration and liquefaction-induced ground deformation and pipe's response. Since FLAC is a two-dimensional program, effect of frictions between the model ground and the sidewalls of the sand box will not be modeled. It is believed that soil deformation along the central line of the sand box is a good approximation of a plain-strain deformation problem. The Mohr-Coulomb soil constitutive relationship was used for the model ground. Model pipe was modeled using structural element interacted with soil by non-

linear springs. The pore pressure generation model is a practice-oriented constitutive model (Dawson et al., 2001) for performing nonlinear effective-stress analysis of liquefaction of sands due to earthquake shaking. Pore pressure is generated in response to shear stress cycles, following the cyclic-stress approach of H.B. Seed (Seed, 1979). However, unlike the standard cyclic-stress approach, pore pressure is generated incrementally during shaking. Thus, pore-pressure generation is fully integrated with the dynamic effective-stress analysis. The model requires input as a cyclic-strength curve, a plot of the cyclic stress ratio (CSR) versus the number of cycles which would cause liquefaction at that stress ratio. The cyclic strength can be adjusted to account for an initial static "driving" shear stress acting on horizontal planes using the correction factor K_α as described by Seed and Harder (1990). What is actually input into the constitutive model is the slope of the K_α versus static-shear-stress-ratio. The cyclic strength can be adjusted for initial vertical effective stress greater than 1 atmosphere pressure, with the variable K_σ as described by Seed and Harder (1990). Again, what is input into the model is the slope of the K_σ versus effective overburden stress curve.

This static shear stress is typically called initial static "driving" shear stress or "non-zero" static shear stress. The presence of initial static stresses will influence liquefaction resistance (Zhai et al., 2004). For the problem to be concerned in this study, "non-zero" static shear stresses exist under the slope area.

Table 2 Input Soil and Structural Properties

Soil Layer	Soil Type	Total Density (kg/m^3)	Friction Angle (deg)	Shear Modulus (Pa)	Poisson's Ratio	Coefficient of Permeability (m/s)	Cyclic Strength Parameters		
							CSR_3	CSR_{25}	CSR_{limit}
1	Dry #5 Silicon Sand	1730	34	1.50E+07	0.3	-	-	-	-
2	Saturated #5 Silicon Sand	2090	33	2.40E+07	0.3	1.3E-04	0.5	0.15	0.15
Pipe Physical Parameters: Elastic Modulus = 2.9E9 Pa; Poisson's ratio = 0.38; Density = 1,039 (kg/m^3)									

In the initial static analysis to compute gravity stresses, the base boundary was fixed both horizontally and vertically and the side boundaries were only fixed horizontally. In the dynamic analysis, the horizontal input acceleration was applied at the base boundary. The horizontal restraints of the side boundaries were released and replaced by attaching the two sides to force a rigid side boundary condition at both sides. The hysteretic damping option in FLAC was selected and damping parameters were obtained by curve-fitting the modulus reduction curve for sand (Seed and Idriss, 1970). Input soil and structural parameters are summarized in Table 2.

Analysis Results

Contours of the end-of-shaking excess pore pressure ratios are presented in Figure 11. The excess pore pressure ratio is the ratio between excess pore water pressure and the effective overburden pressure. If it reaches unity, complete liquefaction would occur. This often results in sand boiling if it occurs at a shallow depth. It can be observed from Figure 11 that the degree of liquefaction was not

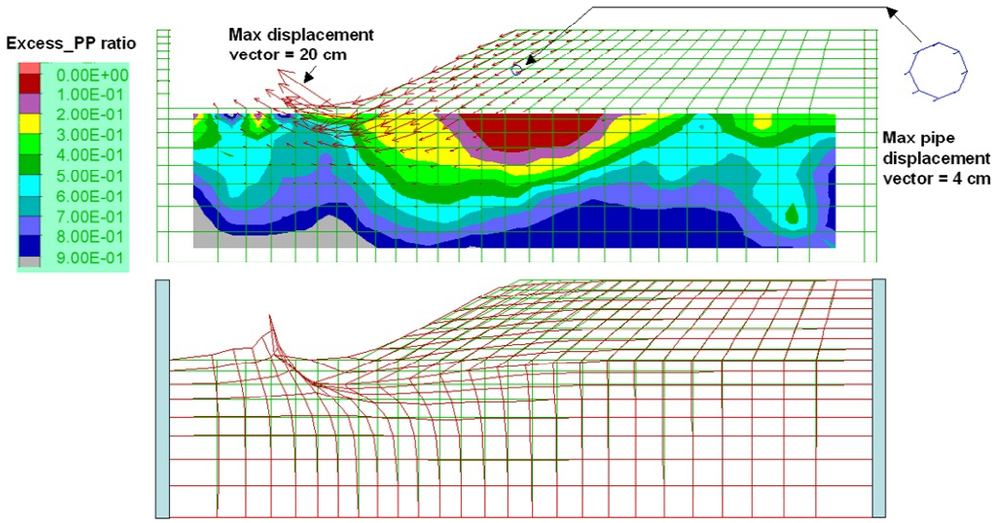


Figure 11 Contour of excess pore water pressure ratios and soil/pipe displacements after 200 gal shaking

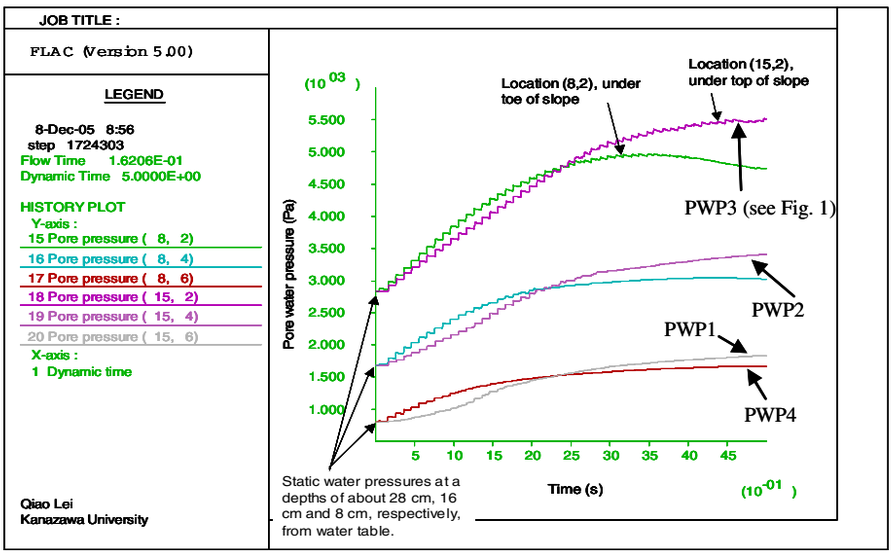


Figure 12 Time histories of excess pore water pressures during the first 5 seconds of 200 gal shaking

uniform within the soil profile. While close-to-complete liquefaction occurred at the toe areas, there was a portion under the crest close to the interface between the saturated sand and the dry sand to have excess pore pressure ratios close to zero, indicating little liquefaction had occurred. The deformed shape after shaking is presented also in Figure 11. The steep displacement between the left wall and the toe may be due to limitation of the sand-box wall. In the laboratory shaking table tests, such steep displacement may not be observable because the upward dissipated pore water will erode the sand before it reaches the maximum displacement. Time histories of pore water pressures at depths of 8 cm, 16 cm and 28 cm from the water table under both the top (izone number=15 in FLAC mesh) and the toe (izone number=8) were saved and plotted in Figure 12.

The majority of soil horizontal displacements range from approximately 3 cm to 8 cm in the slope area. These values are on the same orders compared with the observed horizontal displacements during the laboratory shaking table test as presented in Table 1. The upper slope and embankment settled 2 to 3 cm. The down slope and the area between the toe and the left wall moved upward. The computed amount of upward movement (heave) ranged from about 4 to 7 cm. The observed toe area heave in the centerline of the sand box was not available. The maximum displacement vector of 20 cm (containing both horizontal and vertical movements) is larger than the observed maximum value. It is believed that actual difference between the computed and the observed would be less because extensive sand boiling occurred during shaking that might erode upward displaced sand.

Both the laboratory testing and the numerical modeling indicated that the area under the crest and near the interface of the saturated and the dry sands appeared to have little buildup of excess pore pressure. The maximum measured value at PWP1 (See Figure 1) was close to zero and the maximum calculated value is about 1.0 kPa (equal to about 0.2 excess pore pressure ratio, indicating little liquefaction). The maximum measured value at PWP2 was about 1.5 kPa, compared reasonably well with the calculated value of about 1.7 kPa. The maximum measured value at PWP3 was about 1 kPa; however, the maximum calculated value was about 2.5 kPa. The maximum measured value at PWP4 was about 0.6 kPa, compared with the calculated value of about 0.8 kPa (the calculated excess pore pressure ratio is about 0.7.) Overall, both the measured and calculated pore water pressure values showed lower excess pore water pressure ratios at PWP1 location and higher ratios at PWP3 and PWP4, which agreed with what was observed based on soil boiling during shaking.

As shown in Figure 11, the maximum calculated pipe deflection is about 4.0 cm, caused by permanent ground deformation. Since the numerical model was only a 2-D plain-strain model, it could not simulate the fixed end conditions used in the shake-table test. Therefore, a direct comparison is not available.

CONCLUDING REMARKS

Laboratory shake-table testing and numerical modeling were performed to reveal the mechanism of liquefaction-induced large ground deformation and failures, and damage to buried pipelines. The computed results reasonably agreed with the shake-table testing results, suggesting that the FLAC nonlinear effective-stress model

coupled with the cyclic-stress-based pore pressure model can fairly predict liquefaction-induced lateral spreading and damage to buried structures. The observed and computed excess pore water pressures suggested that the extent of liquefaction under the slope was not uniform and little liquefaction had occurred under the top-of-slope close to the toe elevation while nearly complete liquefaction occurred at the toe area at a shallower depth. It appears that a retrofit using a non-liquefiable key at the toe area could greatly increase the factor of safety against sliding and lateral spreading resulted from liquefaction.

It is desired that the same test be repeated in a centrifuge testing facility to simulate greater overburden stress condition and with a laminated sand box to minimize effects from the rigid sand box.

ACKNOWLEDGMENTS

Dr. Hong Sun of Kanazawa University is highly appreciated for her help in setting up the test plan and equipment during the shake-table tests.

REFERENCES

Bardet, J.P., N. Mace and T. Tobita, (1999). "Liquefaction-induced ground deformation and failure," *A Report to PEER/PG&E*, Task 4A – Phase 1, May.

Dawson, E. M., W. H. Roth, S. Nesarajah, G. Bureau and C. A. Davis, 2001. A practice oriented pore-pressure generation model, *Proceedings of the 2nd International FLAC Conference*, Lyon, France, 47-54.

Itasca Consulting Group, Inc., (2006). "FLAC – Fast Lagrangian analysis of continua, user's manual."

Seed, H.B., (1979). "Soil liquefaction and cyclic mobility evaluation for level ground during earthquakes." *Journal of the Geotechnical Engineering Division*, ASCE, 105(GT2), 201-255.

Seed, R.B. and L.F. Harder, (1990). "SPT-based analysis of cyclic pore-pressure generation and undrained residual strength." *Proceedings, H.B. Seed Memorial Symposium*, UC Berkeley, Vol. 2, 351-376.

Seed, H.B. and I.M. Idriss, (1970). "Soil moduli and damping factors for dynamic response analysis." Report No. EERC 70-10, University of California, Berkeley, December.

Zhai,E., K. Bhushan and M. Miyajima, (2004). "Tiggering of liquefaction under non-zero static driving shear stress." *Proceedings of the 11th International Conference on Soil Dynamics & Earthquake Engineering/the 3rd International Conference on Earthquake Geotechnical Engineering*, pp. 589-596. January.

Soil-Pipeline Interaction Behavior under Strike-Slip Faulting

Da Ha[1]; Tarek H. Abdoun[2]; Michael J. O'Rourke[3]

[1]Postdoc Research Associate, Dept. of Civil and Environmental Engineering, Rensselaer Polytechnic Institute, Troy, NY 12180-3590. E-mail: had@rpi.edu
[2]Associate Professor, Dept. of Civil and Environmental Engineering, Rensselaer Polytechnic Institute, Troy, NY 12180-3590. E-mail: abdout@rpi.edu
[3]Professor, Dept. of Civil and Environmental Engineering, Rensselaer Polytechnic Institute, Troy, NY 12180-3590. E-mail: orourm@rpi.edu

ABSTRACT: Permanent ground deformation (PGD) is one of the most damaging hazards for continuous buried lifelines. This hazard is especially severe when the PGD results in net compression in the pipe. In that case, buckling of pipe material can occur. In this paper, centrifuge tests of buried pipelines subject to abrupt ground failure in the form of surface faulting are presented. The fault movement results mainly in compression in the pipe. The test results are compared with a case history of pipe failure in the 1999 Izmit, Turkey earthquake and also with the results from the centrifuge tests which result in net tension in the pipe. The experimental setup, procedures, and instrumentation are described in detail. Suggestions for design practice are offered based on the analysis of results from both the 1999 Izmit case history and the centrifuge modeling.

INTRODUCTION

Permanent ground deformation (PGD) is a significant hazard for many man-made structures including buildings, highways, tunnels, bridges, as well as water, gas, oil and electric conduits (pipelines). Whether the differential ground movement results in a buried pipe primarily in tension or compression depends on the relative orientation of the fault and the pipe as well as the direction of faulting (for example, right lateral or left lateral strike-slip faulting).

In this paper, centrifuge tests simulating strike-slip faulting during an earthquake are presented in comparison with a well documented field case history. The centrifuge tests were specially designed for pipes made of high density polyethylene (HDPE).

CASE HISTORY

The 1999 Izmit (Turkey) earthquake subjected a number of welded steel pipelines to fault offset. Eidinger, et al. (2002) examined the performance of a 2.2 m diameter (18 mm wall thickness, D/t = 122, operating pressure = 1000 kPa) welded steel pipeline

operated by Thames Water Utilities Ltd., which was subjected to about 3 m of right-lateral offset of the North Anatolian Fault with a pipe-fault intersection angle of $\alpha = 55.5^{o}$ (longitudinal offset = 1.70 m and transverse offset = 2.47 m). The offset resulted in two major pipeline wrinkles, one just to the south of the fault, one to the north of the fault, and a minor wrinkle further to the north.

Numerical analysis was carried out to simulate the performance of the pipeline at the fault crossing (Eidinger, et al., 2002). The calculated pipe strain is shown in Figure 1.

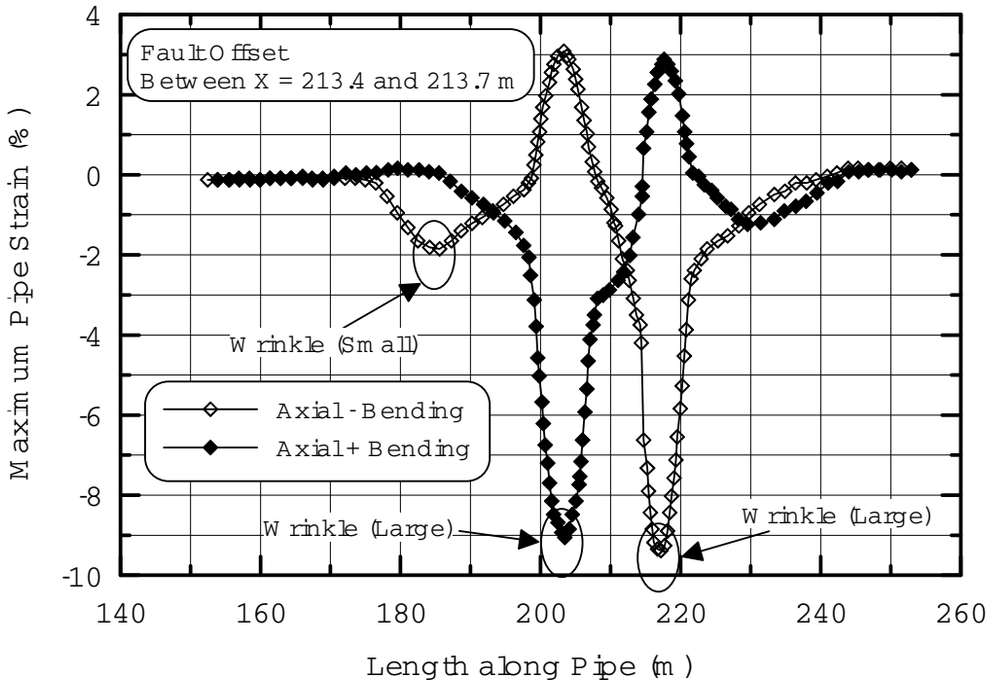


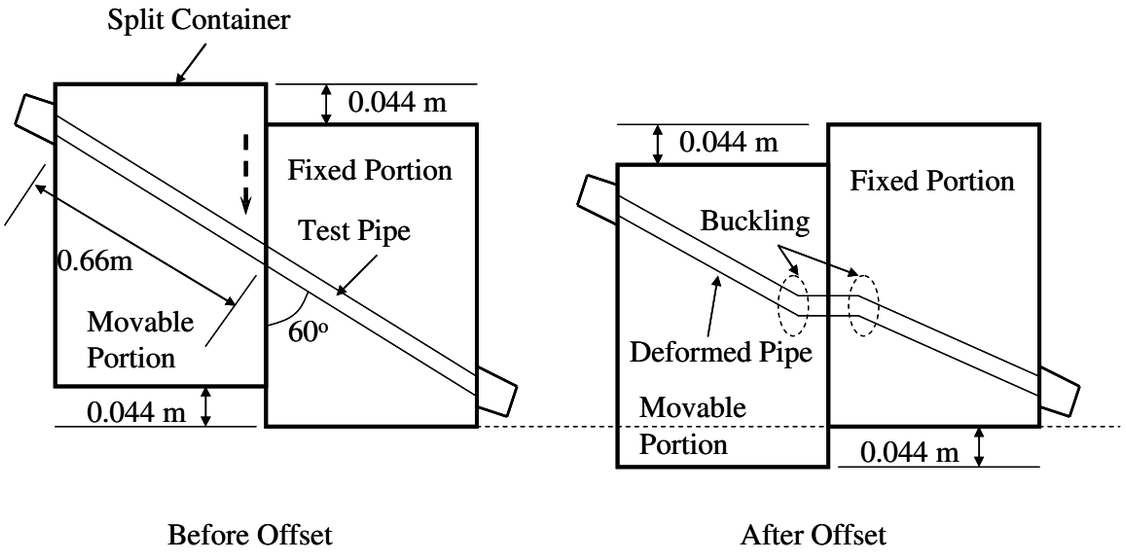
Figure 1. Variation of strain along the pipeline near the fault. (reproduced from Eidinger, et al., 2002).

CENTRIFUGE MODELING OF HDPE PIPE RESPONSE TO PGD

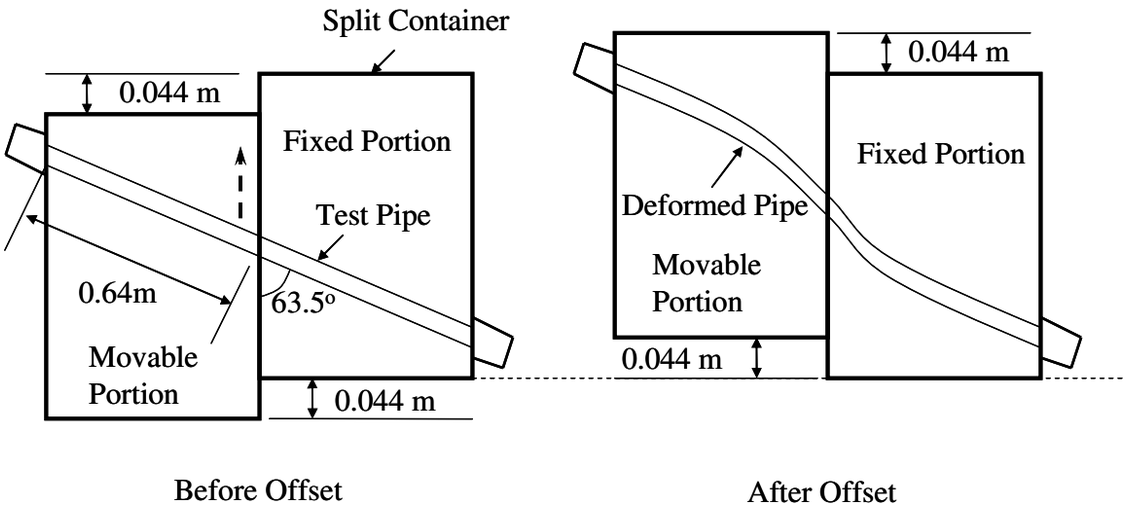
Test setup

In the centrifuge tests reported herein, the abrupt ground displacement was simulated using an advanced split-box container, which is driven by a hydraulic actuator and controlled by a servo-controller. Detailed technical information about the split container is presented in a separate paper (Ha, et al., 2006).

Figure 2 shows the configuration of the RPI split container and the HDPE pipe before and after fault offset. The initial pipe-fault intersection angle is about 60^{o}. As one might expect, the non-perpendicular initial orientation results in significant axial as well as flexural strain for both sets of test. In tests 1 and 2 (Figure 2a) the split container movement simulates a left-lateral offset that induces mostly compression in the pipe. However, in tests 3 and 4 (Figure 2b) the split container movement simulates a right-lateral offset that induces net tension.



a) Plan View of Test Setup for 60° Model (tests 1 and 2)



b) Plan View of Test Setup for -63.5° Model (tests 3 and 4)

Figure 2. Configuration of the centrifuge model before and after offset (dimensions in model scale).

To monitor pipeline performance during fault displacement, two sets of instrumentation were utilized. In tests 1 and 3, the HDPE pipe was instrumented with strain gages, which were attached along the pipe springline and hence measured the total (axial plus bending) strain distribution on both the active and passive sides of the pipe. Bending strains were calculated as one-half the difference between the total strains at opposite springlines. The axial strain (strain component due to direct tension or compression) is the average of the total strain at the springlines. In tests 2 and 4, the pipe was instrumented with a tactile pressure sensor sheet. The sensor sheet was wrapped around the test pipe for a longitudinal distance of 0.25 m in model scale (3.0 m in prototype) on either side of the fault. The tactile sensor sheet measures the pressure

(normal traction) at the soil-pipe interface.

The tests were conducted on a HDPE pipe which satisfies AWWA standard C901 (AWWA, 2003) for water service. The pipe has an OD = 33.4 mm and a wall thickness t = 1.96 mm (SDR = 17). All the centrifuge tests were carried out at a centrifuge g level of 12.2, and thus the pipe geometry simulate a prototype pipe with OD = 407.5 mm and t = 24.0 mm.

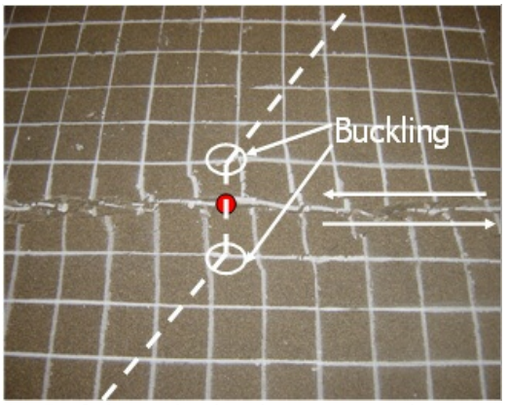
The soil used in the Rensselaer centrifuge tests was prepared from a glacio-fluvial, well graded sand. The original sand was sieved to produce a grain size distribution suitable for centrifuge testing. Soil passing the #40 sieve (0.42 mm), but retained on the #200 sieve (0.075 mm) was used. The sieving process resulted in a very uniform subangular to subrounded sand with an average grain size diameter of D_{50} = 0.29 mm. The sieved sand was placed at a water content of about 4-4.5%. The post-test water content of the sand at the pipe burial depth was in the same range as at pre-test.

The pipe was pinned to the split container end wall. As such, the centrifuge tests simulate the case where a thrust or anchor block is located at each split container end wall. The soil was compacted in layers to a dry unit weight of 14.7 kN/m^3. This unit weight corresponds to a peak friction angle $\phi = 40^o$, as determined by direct shear tests.

The duration of fault offset in the centrifuge tests is 200 second, which corresponds to an fault offset rate of 0.32 m/min in the prototype scale. This offset rate for the centrifuge tests was chosen so that comparisons could be made with full-scale test measurements at Cornell University on the same HDPE pipe material in similar, partially saturated sand. However, an upper bound for the expected prototype (actual earthquake) offset rate is around 1 m/sec (60 m/min). Additional centrifuge tests were conducted at higher offset rate to investigate the fault offset rate effect on buried HDPE pipe behaviors (Abdoun, et al. 2008). The test results showed that the influence of fault offset rate is very limited.

Post-Offset Observations

In the centrifuge tests, observations were made of both the ground surface and HDPE pipeline after excavation of the backfill soil. Very different ground surface deformation patterns (see Figure 3) were observed depending upon the direction of offset (i.e., right or left lateral). For the right lateral tests, there were large cracks nominally parallel to the pipe on the passive side. That is, in Figure 3b there is a ground crack far to the left of the pipe in the top portion of the photo and another crack far to the right of the pipe in the lower portion of the photo (cracks indicted by thinner dashed lines). The cracks appear to be the surface expressions of passive soil wedges. Additional cracks also appear between the outermost surface expression of the passive soil block and the trace of pipeline, likely due to soil heaving during the soil wedge formation process. The absence of soil wedge failure evidence in Figure 3a (left lateral offset, pipe in compression) is likely due to the manner in which the “compressed” pipe accommodated the offset. In contrast, Figure 3b shows the “tension” pipe flexing over a relatively large distance from the fault. Large lateral pressures at the soil-pipe interface eventually overcome the soil capacity, resulting in the formation of a failure wedge. Note the shape of the deformed pipe is indicated in Figure 3 as thicker dashed lines. This was made possible by using the surface grid to locate the center and the two ends of the test pipe.



(a) Left lateral, pipe in compression



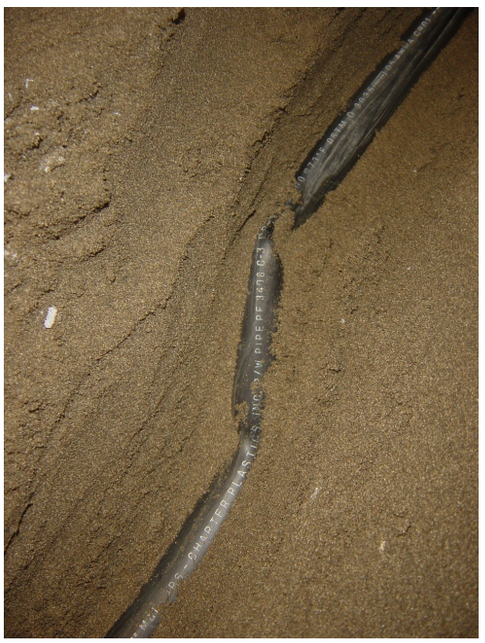
(b) Right lateral, pipe in tension

Figure 3. Post-test surface observations of the two test types.

Figure 4 shows two photographs taken after excavation of the deformed pipe from test 1 (pipe in compression). It was observed that the pipe buckled at two locations fairly close to the fault during fault offset and the buckle locations were symmetric with respect to the fault. At each buckling location severe concentrated angular distortion in the pipe accommodated the fault offset. Large wrinkles at the pipe buckle location reduced the pipe cross section by at least 50%. No buckling of the pipe was observed for test 3 (pipe in tension).



(a) Deformed pipe after excavation



(b) Close-up View of buckled section

Figure 4. Deformed pipe after left lateral offset (model 1)

Pipe Strains

The measured strains on one side of the pipe spring-line in test 1 are shown in Figure 5. Note that the shape of measured strain distribution from test 1 (pipe in compression) is very similar to the numerical results from the Thames pipeline shown in Figure 1. That is, at a large offset there is moderate tensile strain on one side of the fault and large compressive strain on the other. The peak compression (negative) strain is initially located about 1.2 m from the fault. However, as pipe buckling occurs, the location of the peak negative strain shifts to about 0.6 m from the fault. The final peak negative strain is -13.1% and the final tension (positive) strain at the same location on the other side of the pipe is about 2%. In contrast, for "tension" test 3 all measured strains are positive and the peak strain is located about 1.2 m from the fault and remains at this same location throughout the offset (Figure 5).

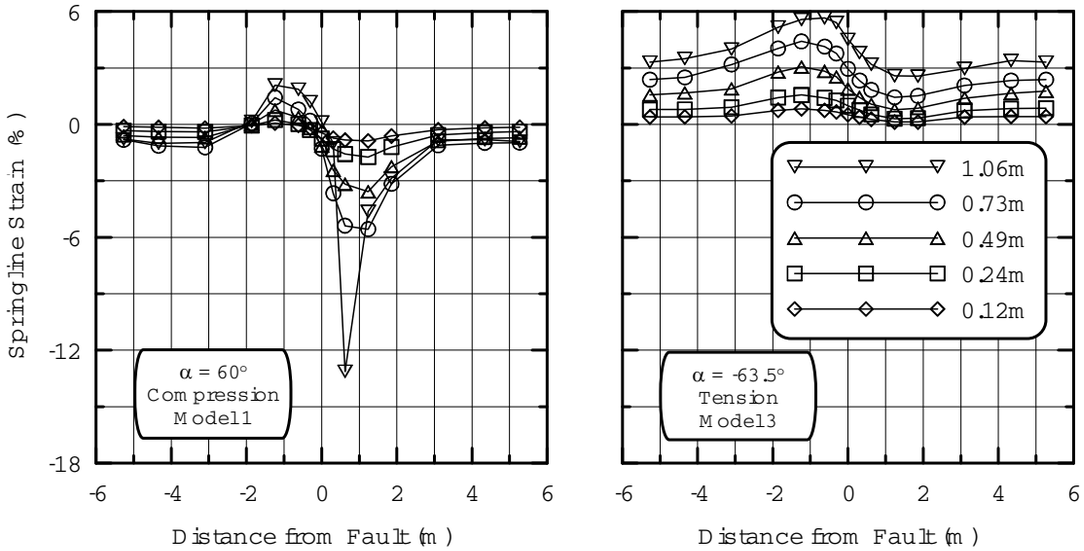


Figure 5. Strain distribution along the pipe springline in models 1 and 3.

Figure 6 shows the axial and bending strains from tests 1 and 3. In both tests, at least initially, the strains at a given location on the pipe increase more or less in proportional to the offset. The axial strains, in the tension test are largest at or near the fault. In both tests, the bending strains correspond to double curvature bending, being zero at the point of contraflexure at the fault, positive on one side and negative on the other. However, after about 0.8 m offset the axial strain in the compression test started to concentrate at the two buckling locations. Note that at the middle of the pipe (crossing the fault) the axial strains started to drop when buckling occurred and finally dropped to about zero. This suggests that each buckling point is working as a flexible joint. The central portion of the pipe can freely rotate, and the axial stress is low. As with the axial strains, initially the bending strains have peak values at a distance of about 1.2 m from the fault. When buckling occurs, the location of peak flexure strain shifts to about 0.6 m from the fault.

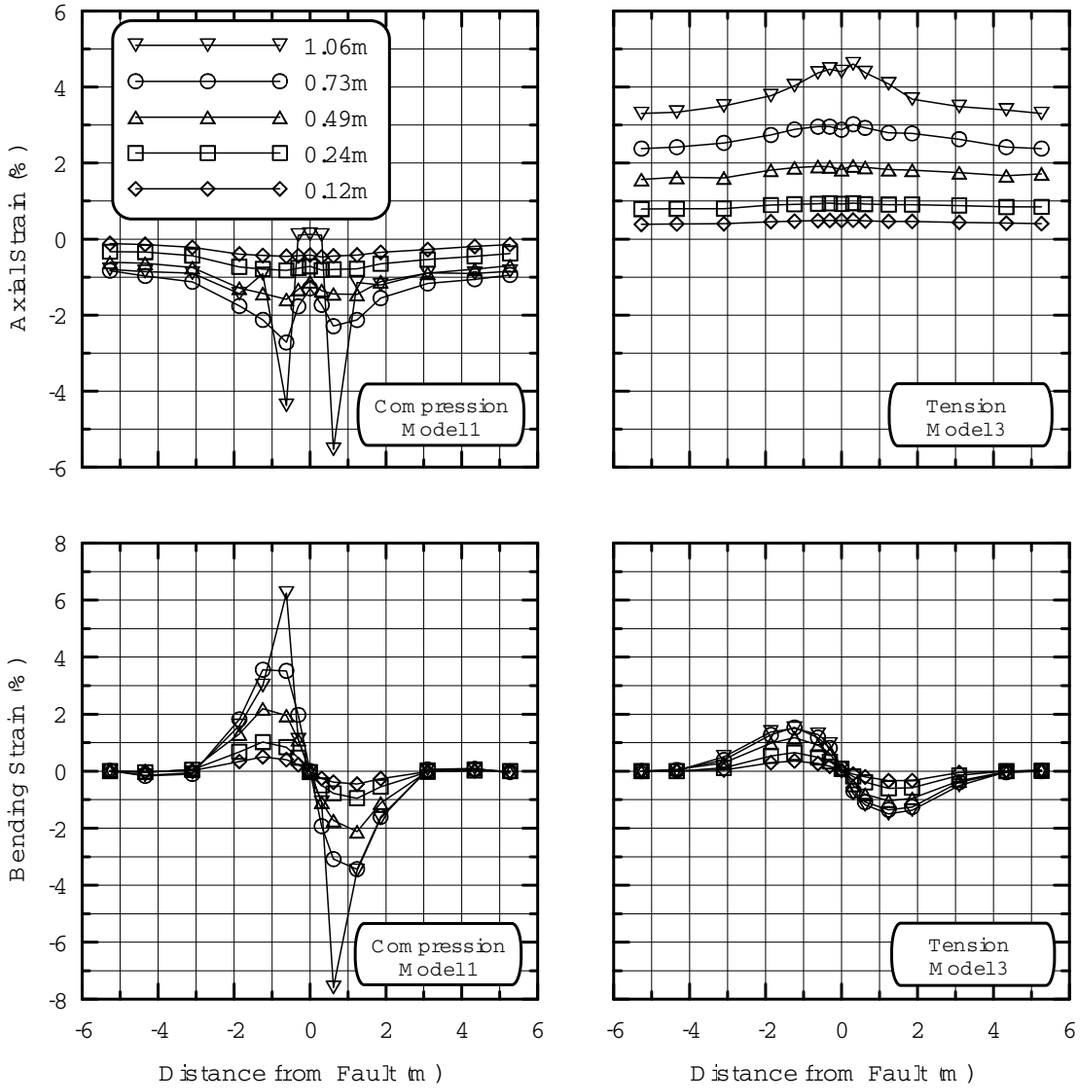


Figure 6. Axial and bending strain of test pipe in models 1 and 3.

Soil-Pipe Interaction

Due to space limitations, the detailed data interpretation technique for the tactile pressure sensor is presented in a separated paper (Ha, et al. 2007). Figure 7 shows the resulting lateral force profile along the pipe for both types of test. Note the peak lateral force for the "compression" test is about 70% of that for the tension test. In addition, the lateral force along the pipe in the compression tests begins to approach zero at about 1.5 m from the fault. The significant difference in the soil-structure interface forces is likely due to the pipe buckling behavior in the compression tests. That is, when the imposed offset is accommodated by buckling or wrinkling of the pipe, the soil–pipe interface forces are comparatively small. On the other hand, when the imposed offset is accommodated by significant stretching and flexing of the pipe in tension, comparatively large soil-pipe interface forces are developed.

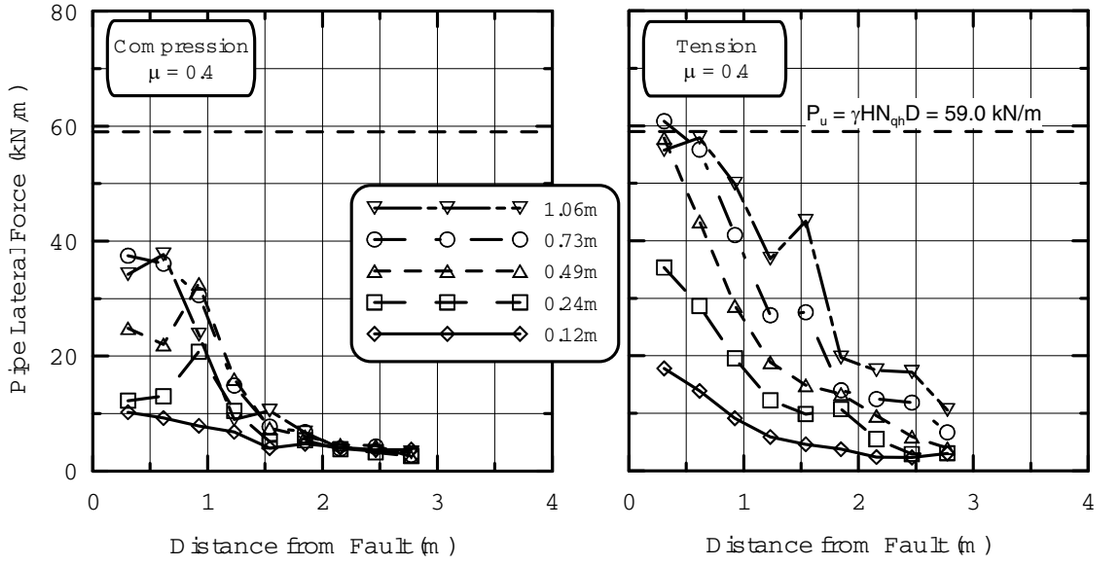


Figure 7. Lateral force along the pipe - considering pipe-soil friction (μ = 0.4)

The ASCE Guidelines (1984) suggests the following equation for the calculation of maximum lateral force on pipeline buried in sand:

$$P_u = \gamma H N_{qh} D \tag{1}$$

where, γ = effective unit weight of soil backfill; H = depth to center-line of the pipeline; N_{qh} = is the horizontal bearing capacity factor for sand; D = pipe outer diameter.

In the centrifuge testing case reported herein, γ = 14.7*(1+4%) = 15.3 kN/m, N_{qh} = 8.5 for $\phi = 40^o$ and H/D= 2.8, H= 1.12 m, and D = 0.41 m.

Hence,

$$P_u = \gamma H N_{qh} D = 15.3 * 1.12 * 8.5 * 0.41 = 59.0 kN/m \tag{2}$$

This value is plotted in Figure 7 together with the measured lateral force on the pipe. The observed peak value of the lateral force per unit length (near fault at the maximum offset) for the tension test is reasonably close to the ASCE (1984) value. In the compression test, pipe buckling at an offset of roughly 0.8 m precluded development of a peak lateral force comparable to that in the tension case.

Table 1 summarizes the information from the Thames Water pipeline case history as well as information from centrifuge tests conducted as part of this work. A detailed description of the centrifuge tests and interpretation of results is presented in the following sections.

Implications for Design

Based on the earthquake case history and centrifuge modeling, the following suggestions for engineering practice can be concluded.

1) Whenever possible a situation with a buried pipeline under net compression should be avoided. A careful review of the historical record of the movement of the fault is necessary.

2) Due to its excellent ductility, HDPE is a good choice for pipe subject to the fault crossing hazard. Although local bucking was observed in the centrifuge testing in the compression case, there is no sign of any tearing of the pipe wall or loss of the pressure boundary in the HDPE pipe. The test pipe almost bounced back to its original shape after removal of the backfill soil.
3) The ASCE Guidelines (1984) provides a method of estimating the maximum lateral force at the soil-pipe interface. For the range of parameters considered the centrifuge test results confirmed that the Guidelines provide reasonably values for design purposes.

Table 1 Comparison between case history and centrifuge tests

	1999 Izmit Case History	**Centrifuge Tests (Compression)**	**Centrifuge Tests (Tension)**
Pipe Material	Steel	HDPE	HDPE
OD (m)	2.20	0.408	0.408
Pipe SDR	125	17	17
Depth to Springline, H_c (m)	3.05	1.12	1.12
Soil	Variable: Medium stiff , dark brown clay and silty clay	Uniform: Moist sand (WC = 4~4.5%)	Uniform: Moist sand (WC = 4~4.5%)
Pipe-Fault Angle, α	55.5^o	60^o	-63.5^o
Fault Offset (m)	≈3.0	1.06	1.06
Transverse Offset (m)	2.47	0.92	0.95
Longitudinal Offset (m)	1.70	0.53	0.47
Surface Cracking	N/A	No	Yes
Buckling	Yes	Yes	No
Cross-section Opening Reduction (%)	58.2	≥50	Little or no reduction
Peak Strain (%)	-9.6 (Numerical)	-13.1	5.7

CONCLUSIONS

A case history was reviewed in which a pipeline was damaged due to earthquake induced PGD. Centrifuge tests were conducted to compare with the case history. Buckling observed in the prototype case history compared favorably with buckling observed in the centrifuge at model scale.

For the HDPE pipelines subjected to net tension, significant ground rupture was observed, with a passive soil wedge developing near the zones of maximum bending strain. This passive wedge formed where the maximum lateral pressures developed against the pipe.

The compression centrifuge tests resulted in pipe buckling at two locations along the pipe, one on each side of the fault. The fault offset at onset of buckling was roughly 0.8 m. At the fault crossing, the axial strains began to drop after the onset of buckling. The buckling region of the pipe appeared to act as flexible joints, allowing the portion of the pipe near the fault crossing to rotate freely.

These experiments and comparisons with field observations unveiled the failure mechanism of the buried pipeline under compression. Design implications and suggestions are given based on the observations from both the case history and centrifuge tests.

ACKNOWLEDGMENTS

This work is part of a collaborative project involving full-scale buried pipe tests at Cornell University and companion centrifuge tests at Rensselaer Polytechnic Institute. This work was supported primarily by the George E. Brown, Jr. Network for Earthquake Engineering Simulation (NEES) Program of the National Science Foundation under Grant Nos. CMS-0421142, CMS-0086555, and CMS-0217366. Any opinions, findings and conclusions or recommendations expressed in this material are those of the authors and do not necessarily reflect the views of the National Science Foundation.

REFERENCES

Abdoun, T., Ha, D., O'Rourke, M., Symans, M., O'Rourke, T., Palmer, M. & Stewart, H. "Factors Influencing the Behavior of Buried Pipelines Subject to Ground Faulting", *Soils and Foundations* (under review).

American Society of Civil Engineers. (1984). "Guidelines for the seismic design of oil and gas pipeline systems. Committee on Gas and Liquid Fuel Lifelines." Technical Council on Lifeline Earthquake Engineering, ASCE, New York.

American Water Works Association. (2003). "AWWA Standard for Polyethylene (PE) Pressure Pipe and Tubing, 1/2 in. (13 mm) Through 3 in. (76 mm), for Water Service." ANSI/AWWA C901-02, January 2003.

Eidinger, J., O'Rourke, M. and Bachhuber, J. 2002. "Performance of pipelines at fault crossings." 7th U.S. National Conference of Earthquake Engineering, Earthquake Engineering Research Institute (EERI), July 21-25, Boston, MA.

Ha, D., Abdoun, T., O'Rourke, M., Symans, M., O'Rourke, T., Palmer, M. and Stewart, H. (2007). "Centrifuge Modeling of Permanent Ground Deformation Effect on Buried HDPE Pipelines", *ASCE Journal of Geotechnical and Geoenvironmental Engineering* (Accepted).

Ha, D., Abdoun, T., O'Rourke, M., Van Laak, P., O'Rourke, T. and Stewart, H. (2006). "Split-containers for centrifuge modeling of permanent ground deformation effects on buried pipeline systems." The Sixth International Conference on Physical Modeling in Geotechnics, August 4-6, 2006, Hong Kong, China. 729-734.

Seismic Performance and Design of Port Structures

Susumu Iai[1], Tetsuo Tobita[2], M. ASCE, and Yukio Tamari[3]

[1]Professor, Disaster Prevention Research Institute, Kyoto University, Gokasho, Uji, Kyoto 611-0011 Japan; iai@geotech.dpri.kyoto-u.ac.jp
[2]Assistant Professor, ditto; tobita@geotech.dpri.kyoto-u.ac.jp
[3]Senior Research Engineer, Tokyo Electric Power Services, 3-3-3 higashi-Ueno, Taito-ku, Tokyo 110-0015 Japan, etamari@tepsco.co.jp

ABSTRACT: This paper describes an emerging methodology for seismic evaluation and design of port structures. The methodology is based on minimum life-cycle cost principle through probabilistic evaluation of performance. While conventional seismic design of port structures are based on a particular return period specified for design, the methodology based on life-cycle cost allows for consideration of ground motions with all (or varying) return periods and uncertainty in geotechnical conditions. The methodology based on life-cycle cost also allows the probability of failure being evaluated rather than prescribed by an authority. Since ordinary port structures are for commercial use, the method based on the life-cycle cost has potential advantages over conventional design. An example is presented. In particular, the simplified design charts that are based on a series of parametric studies of effective stress analyses have great benefit for implementing the proposed methodology in practice. Apart from the ordinary port structures, higher priority should be assigned for safety as a performance objective. This issue is especially relevant if port structures are essential parts of post-earthquake emergency strategies for recovery and restoration of urban areas. The paper also discusses the importance of this issue and the future direction of study.

INTRODUCTION

Seismic performance of port structures, such as caisson quay walls, sheet pile quay walls, and pile-supported wharves, are significantly affected by ground displacements and soil-structure interaction phenomena, and pose complicated engineering problems. In particular, seismic performance of these structures in the past earthquakes indicate that deformations in ground and foundation soils and the corresponding structural deformation and stress states are key design parameters and, unlike the conventional limit equilibrium-based methods, some residual deformation may be acceptable in design. Since 1995 Hyogo-ken Nambu, Japan, earthquake (Fig. 1), significant advances



Fig. 1 Kobe port paralyzed at 1995 Hyogo-ken Nambu earthquake, Japan

have been made in the effective stress analyses for evaluating the degree of damage to port structures due to seismic shaking and ground displacement, including soil liquefaction (Iai, 1998; Iai *et al.*, 1998). Confidence has been gradually born among the port engineers on the applicability of these analytical methods as a new option of engineering design tools. In addition, there is a growing awareness that uncertainty in ground motions and geotechnical conditions should be adequately evaluated in geotechnical engineering practice (e.g. Iai, 2005; Kramer *et al.*, 2006).

This paper presents an emerging methodology for seismic evaluation and design of port structures incorporating these recent advances discussed above. The principles in the methodology and their implications in geotechnical earthquake engineering are discussed through an example.

PERFORMANCE OBJECTIVES

The principles in the performance-based approach applied for port structures may be summarized as follows by following the guidelines presented in International Standard (ISO23469) (Iai, 2005). In this approach, the objectives and functions of port structures are defined in accordance with broad categories of use such as commercial, public and emergency use. While the objectives and functions of port structures managed by most of the US port authorities are commercial use, there is a certain category of port structures designated as an essential part of emergency bases in Japan with objectives and functions being emergency use.

Depending on the functions required during and after an earthquake, performance objectives for seismic design of port structures are specified on the following basis:

-serviceability during and after an earthquake: minor impact to social and industrial activities, the port structures may experience acceptable residual displacement, with function unimpaired and operations maintained or economically recoverable after temporary disruption:

-safety during and after an earthquake: human casualties and damage to property are minimized, critical service facilities, including those vital to civil protection, are maintained, and the port structures do not collapse.

The performance objectives also reflect the possible consequences of failure.

For each performance objective, a reference earthquake motion is specified as follows:

-for serviceability during or after an earthquake: earthquake ground motions that have a reasonable probability of occurrence during the design working life;

-for safety during or after an earthquake: earthquake ground motions associated with rare events that may involve very strong ground shaking at the site.

Although these descriptions are very general, they constitute the essential principles of emerging methodologies for performance-based evaluation and design of port structures as described in the next section.

EVALUATION OF SERVICEABILITY THROUGH LIFE-CYCLE COST

While safety should be one of primary performance objectives for ordinary buildings, serviceability and economy become higher priority issues for ordinary port structures. For these port structures, a methodology based on the principle of minimum life-cycle cost may be ideal (eg. Sawada, 2003). This methodology is emerging and will be eventually adopted as the state-of-practice in the coming decade.

Life-cycle cost is a summation of initial construction cost and expected loss due to earthquake induced damage. Probability of occurrence of earthquake ground motion (i.e. earthquake ground motions with all (or varying) return periods) is considered for evaluating the expected loss due to earthquake induced damage. The life-cycle cost also includes intended maintenance cost and cost for demolishing or decommissioning when the working life of the structure ends.

When evaluating serviceability through life-cycle cost, failure of a port structure is defined by the state that does not satisfy the prescribed limit states typically defined by an acceptable displacement, deformation, or stress. If a peak ground motion input to the bottom boundary of soil structure systems is used as a primary index of earthquake ground motions, probability of failure $F_{\mathrm{F}}(a)$ at peak ground motion a is computed considering uncertainty in geotechnical and structural conditions. A curve described by a function $F_{\mathrm{F}}(a)$ is called a fragility curve (Fig. 2(a)). Probability of occurrence of earthquake ground motions is typically defined by a slope (or differentiation) of a function $F_{\mathrm{H}}(a)$ that gives annual probability of exceedance of a peak ground acceleration a. A curve described by a function $F_{\mathrm{H}}(a)$ is called a seismic hazard curve (Fig. 2(b)).

Given the fragility and seismic hazard curves for a port structure, annual probability of failure of the port structure P_1 is computed as follows:

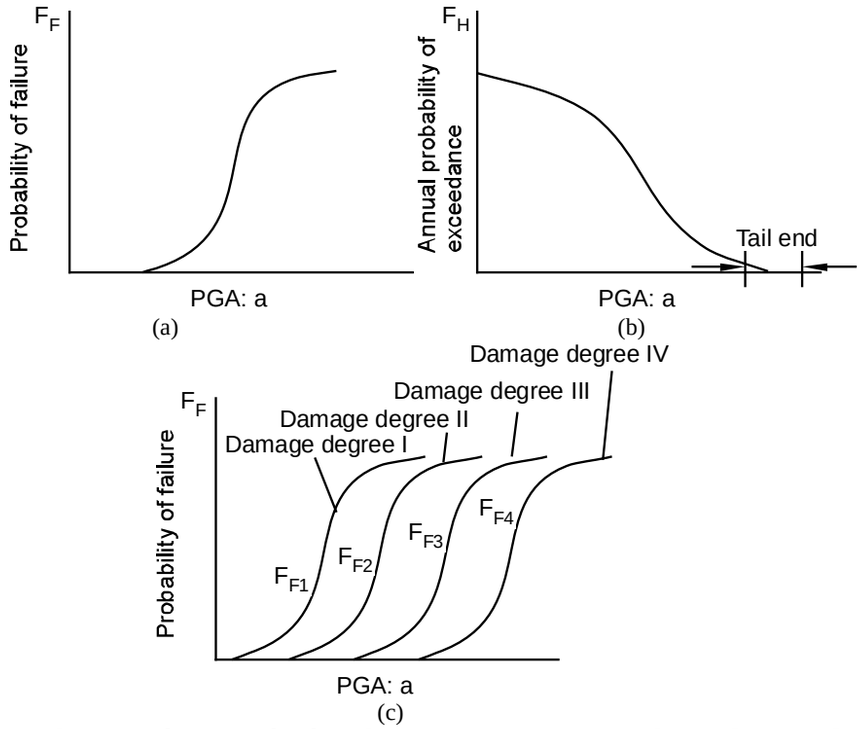


Fig. 2 Schematic figures of a fragility curve (a), a seismic hazard curve (b), and a group of fragility curves for multiple limit states (c)

$$P_1 = \int_0^\infty \left(-\frac{dF_{\mathrm{H}}(a)}{da} \right) F_{\mathrm{F}}(a) da \tag{1}$$

If a design working life is T years, probability of failure of the port structure over the design working life is given by

$$P_T = 1 - \left(1 - P_1\right)^T \tag{2}$$

If loss due to earthquake induced damage associated with the prescribed limit state is designated by c_{D}, expected loss over the design working life of a port structures C_{D} is given by

$$C_{\mathrm{D}} = P_T c_{\mathrm{D}} \tag{3}$$

Thus, the life-cycle cost C_{LC} is given by adding initial construction cost C_{I}, maintenance cost C_{M} and demolishing cost C_{END} as

$$C_{\mathrm{LC}} = C_{\mathrm{I}} + C_{\mathrm{D}} + C_{\mathrm{M}} + C_{\mathrm{END}} \tag{4}$$

This is generalized further by introducing more than one serviceability limit state. Given the fragility curve defined for the i^{th} limit state as $F_{\text{F}i}(a)$ (Fig. 2(c)), Eqs.(1) through (4) are generalized as follows:

$$P_{1i} = \int_0^\infty \left(-\frac{dF_{\text{H}}(a)}{da} \right) F_{\text{F}i}(a) da \tag{5}$$

$$P_{Ti} = 1 - \left(1 - P_{1i}\right)^T \tag{6}$$

$$C_{\text{D}i} = P_{Ti} c_{\text{D}i} \tag{7}$$

$$C_{\text{LC}} = C_{\text{I}} + \sum_i C_{\text{D}i} + C_{\text{M}} + C_{\text{END}} \tag{8}$$

As demonstrated for liquefaction hazard evaluation by Kramer *et al.* (2006), the probability evaluated by Eqs.(1) and (2) is a consistent index of hazard and the conventional approach based on the return period prescribed in design provisions and codes can be either too conservative or unconservative depending on the site. Expected loss evaluated by Eq.(3) is an index that reflects the consequence of failure. Life-cycle cost evaluated by Eq.(4) is an index that properly reflects the trade-off between initial cost and expected loss. The design option that gives the minimum life-cycle cost is the optimum in terms of overall economy. Thus, the optimum design has a certain probability of failure given by Eq.(2). This probability is not prescribed by an authority (such as 10% over 50 years) but rather determined as a result of the minimum life-cycle cost procedure. The probability of failure can be large if a consequence of failure in meeting the performance criteria, as measured by seismic loss c_{D}, is minor. The probability can be small, however, if a consequence of failure, as measured by c_{D}, is significant. Thus, the minimum life-cycle cost procedure reflects the possible consequences of failure and, thereby, satisfies the principles in performance objectives in the ISO guidelines described in the previous section.

AN EXAMPLE

A caisson quay wall with a water depth of 15m is considered for a design example. The quay wall is constructed on loosely deposited sand for replacing alluvial clay layer beneath the rubble foundation as shown in Fig. 3. The design options considered in this example include sand compaction piles (SCP) for foundation only (Case A), cementation of foundation only (Case B), SCP both for foundation and backfill with a spacing of 1.8m (Case C), the same as Case C but with a spacing of 1.6m (Case D), and SCP for foundation only and structural modification by expanding the width of caisson by 3m (Case E).

More than one limit states are typically defined for port structures as shown in Table 1. Limit states as specified by the acceptable normalized horizontal displacement of a caisson is shown together with the associated repair cost (or direct loss) in Fig. 4. Ideally, all of these limit states should be used for life cycle cost evaluation (Ichii, 2002). For simplicity, however, only one limit state was assigned for the example in this paper: the

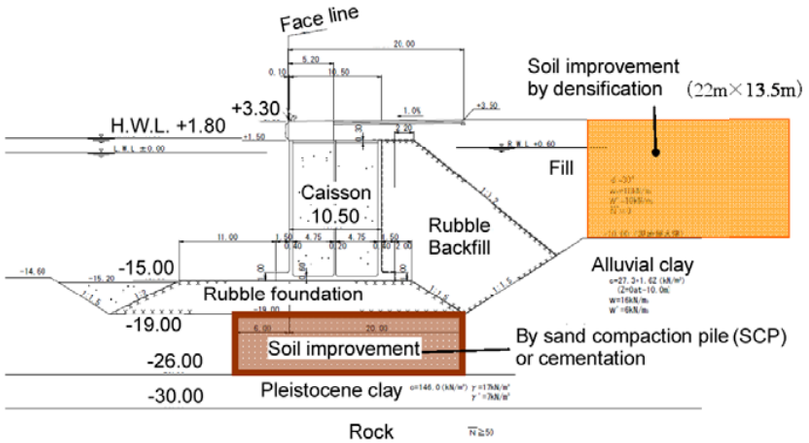


Fig. 3 Cross section of a caisson quay wall considered for a design example

Table 1 Acceptable level of damage in performance-based design*

Acceptable level of damage	Structural	Operational
Degree I : Serviceable	Minor or no damage	Little or no loss of serviceability
Degree II: Repairable	Controlled damage**	Short-term loss of serviceability***
Degree III: Near collapse	Extensive damage in near collapse	Long-term or complete loss of serviceability
Degree IV: Collapse****	Complete loss of structure	Complete loss of serviceability

* Considerations: Protection of human life and property, functions as an emergency base for transportation, and protection from spilling hazardous materials, if applicable, should be considered in defining the damage criteria in addition to those shown in this table.
** With limited inelastic response and/or residual deformation
*** Structure out of service for short to moderate time for repairs
**** Without significant effects on surroundings

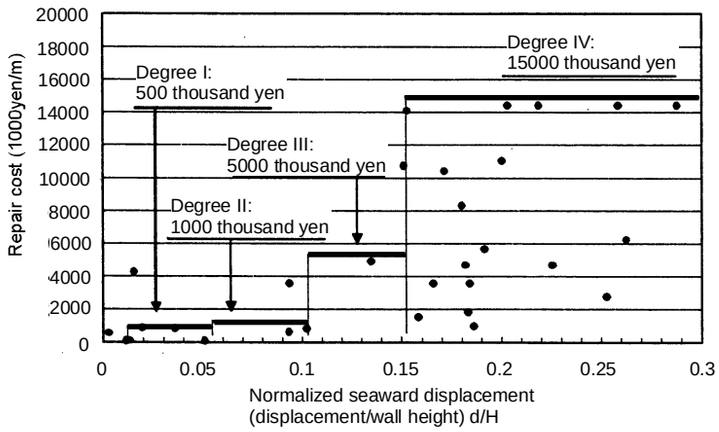


Fig. 4 Repair cost (or direct loss) for a gravity quay wall (Ichii, 2002)

acceptable horizontal displacement of caisson wall is assumed to be 10% of wall height that corresponds to the displacement of 1.5m. Design working life was assigned as 50 years.

Fragility curves $F_F(a)$ were computed through Monte Carlo simulation by considering the uncertainty in SPT N-values with 1000 trials for each peak ground acceleration a input at the base rock. Coefficient of variance in SPT N-values was assigned as 0.1 based on the number specified in the technical standard of Japanese ports (2006).

In the performance-based design, displacement of wall should be evaluated for each trial SPT N-value. In theory, this is achieved by running an effective stress analysis of soil-structure systems for each trial SPT N-values. An example of the results of effective stress analysis specifically run for the caisson quay wall for a particular earthquake motion is shown in Fig. 5.

In practice, this is not feasible. In order to overcome this difficulty in practice, a set of simplified performance evaluation charts were developed through a parametric study (Iai *et al.*, 1999; Ichii *et al.*, 2002; Higashijima *et al.*, 2006).

The cross sections and primary dimensions used as input parameters are shown in Fig. 6. Typical examples of the results of the parametric study are shown in Fig. 7. These results were compiled as a comprehensive set of data for the simplified performance evaluation charts. These charts are incorporated in a spread sheet format. Input data required are (1) basic parameters defining the cross section of structures, (2) geotechnical conditions as represented by SPT N-values, and (3) earthquake data, as represented by wave form, peak ground acceleration, or distance and magnitude from the seismic source. These charts can be also conveniently used for efficiently assessing the vulnerability of coastal geotechnical structures that extends a long distance, such as tens of kilometers, over a variable geotechnical and structural conditions.

The fragility curves computed by using these simplified performance evaluation charts are shown in Fig. 8(a). Together with a hazard curve at a port in Japan considered for the example exercise shown in Fig. 8(b), probability of failure (i.e. probability that does not meet the prescribed limit state) was computed through Eqs.(1) and (2). For example, probability of failure over 50 years was 0.96 and 0.32 for Cases A and B, respectively.

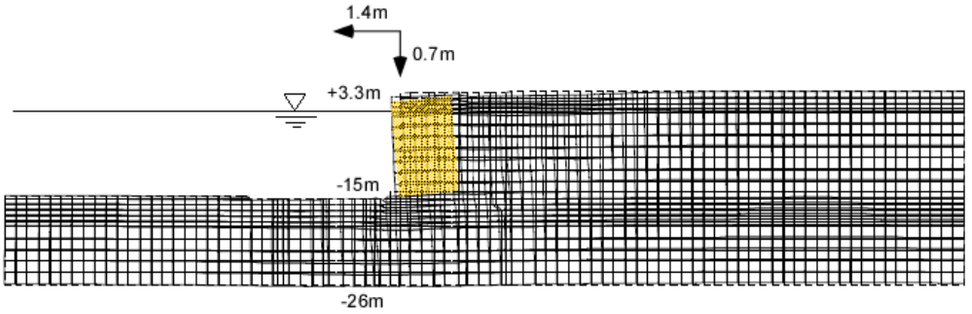
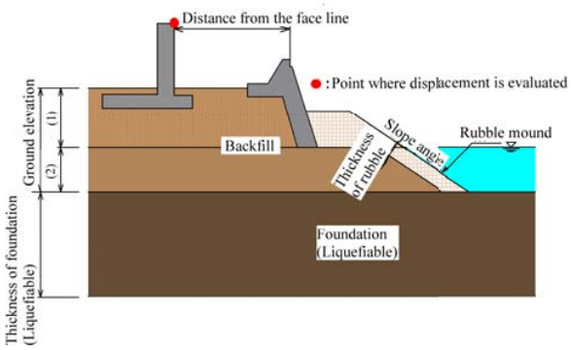
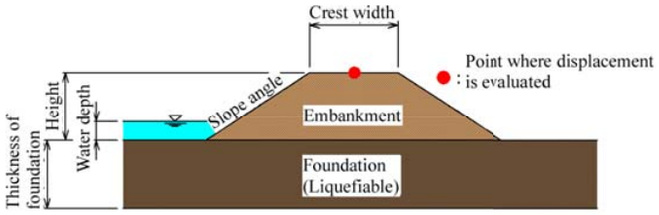


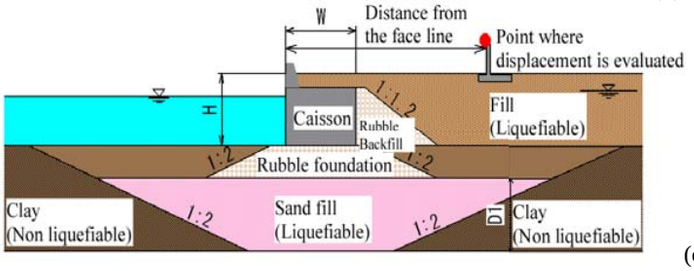
Fig. 5 Residual displacement of a caisson wall through effective stress analysis



(a) Leaning bulkhead

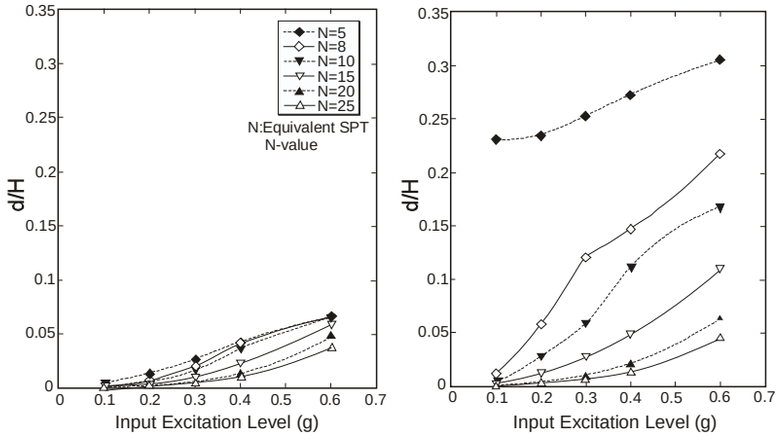


(b) Embankment type



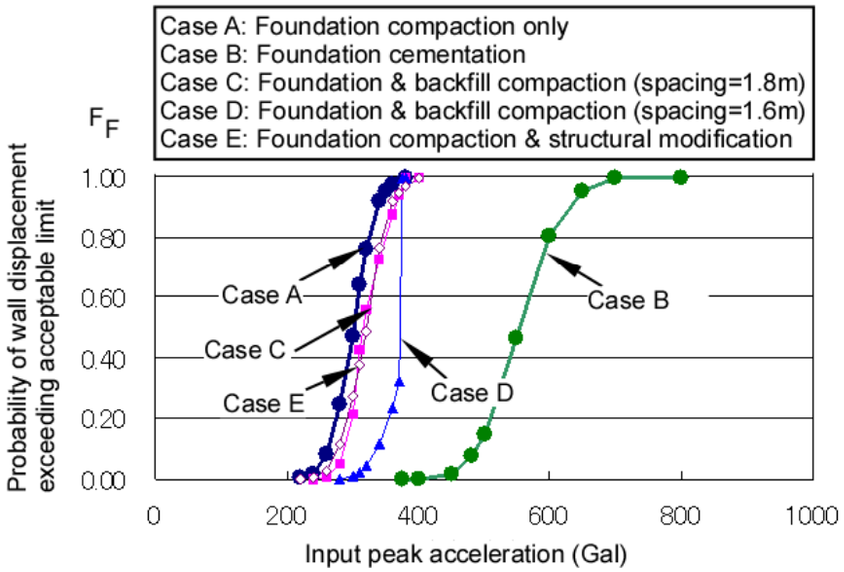
(c) Gravity type

Fig. 6 Cross sections and primary parameters used for the simplified design charts (Higashijima *et al.*, 2006)

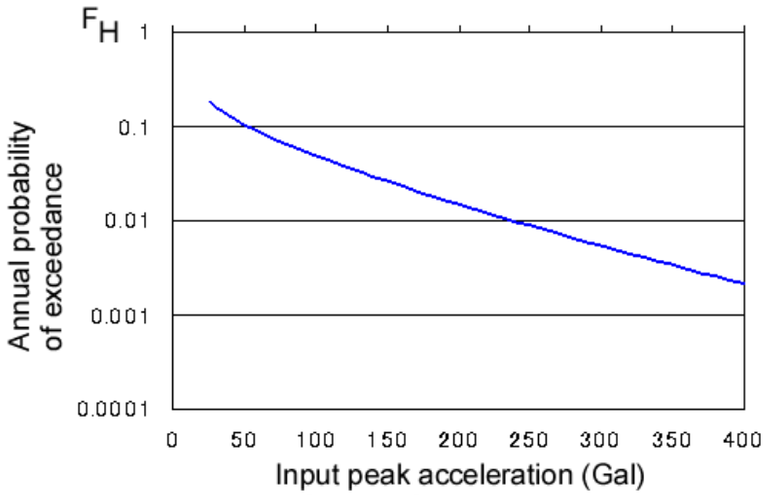


(a) D1/H=0.0 (b) D1/H=1.0

Fig. 7 Parameter study of normalized horizontal residual displacements of a gravity caisson wall over varying maximum accelerations (Iai et al., 1999)



(a) Fragility curves



(b) Hazard curve

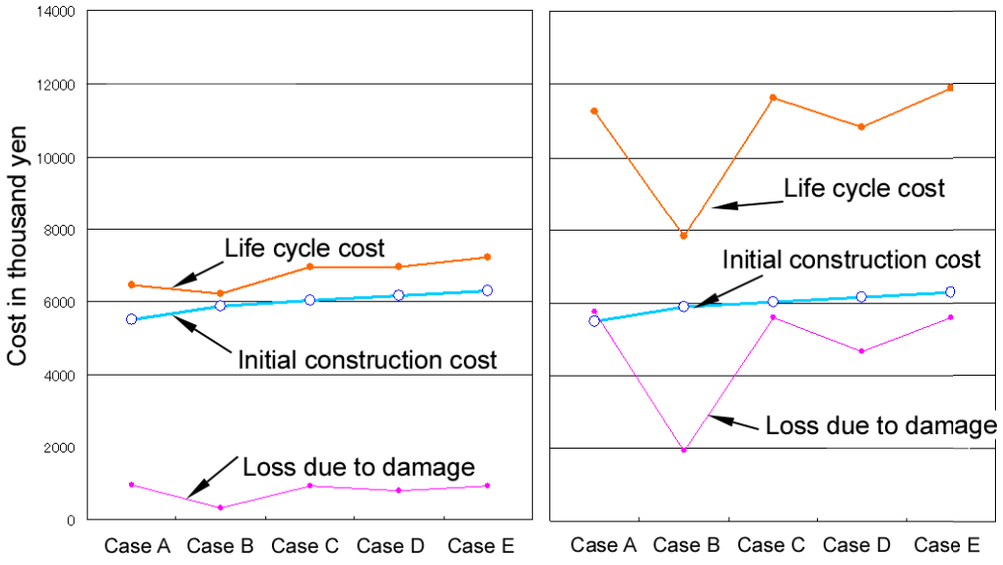
Fig. 8 Fragility curves and a hazard curve

The loss due to earthquake induced damage is typically defined on the basis of the acceptable level of structural and operational damage given in Table 1. The structural damage category in this table is directly related to the amount of work needed to restore the full functional capacity of the structure and is often referred to as direct loss due to earthquakes. The operational damage category is related to the amount of work needed to restore full or partial serviceability. Economic losses associated with the loss of

serviceability are often referred to as indirect losses. In addition to the fundamental functions of servicing sea transport, the functions of port structures may include protection of human life and property, functioning as an emergency base for transportation, and as protection from spilling hazardous materials. If applicable, the effects on these issues should be considered in defining the acceptable level of damage in addition to those shown in Table 1.

In the example exercise, the direct loss that is needed for restoring the damage caisson wall was assigned as one million yen/m following the results shown in Fig. 4 (Ichii, 2002). Together with the initial construction cost, including the cost for soil improvement or structural modification, the life-cycle costs considering only the direct loss were computed as shown in Fig. 9(a). Design option Case B base on cementation of foundation showed the minimum life-cycle cost whereas design option Case E based on structural modification showed the most expensive life-cycle cost.

Indirect loss due to earthquake induced damage to port structures needs careful evaluation in economic loss of industries associated with service of port. In this example, for simplicity, indirect loss was assumed as five times as the direct loss. The results shown in Fig. 9(b) indicate that inclusion of indirect loss reflects the difference in design options and resulting seismic performance much more clearly than when only direct loss is considered. Serviceability during and after the earthquake is obviously closely related to the operational aspect of port structures.



(a) Considering direct loss only (b) Considering both direct and indirect losses

Fig. 9 Life-cycle cost of a caisson quay wall (per meter)

EVALUATION OF SAFETY

As previously mentioned, evaluation of safety becomes the primary issue for a certain category of port structures designated as an essential part of emergency bases with objectives and functions being emergency use. The emergency base is used for emergency cargo and human transport through sea when the inland transports are seriously damaged (Figs. 10 and 11). The emergency base is also used as a heliport to allow emergency air transport.

For evaluation of safety, scenario type approach of urban infrastructure systems becomes important. In particular, modal shifts in transportation at emergency may be one of the important aspects of operation of ports for emergency. As shown in Figs. 12 and 13, air transport is the fastest to respond to emergency transport of humans whereas sea transport can be an intermediate means of emergency transport when the recovery of land transport is slow and difficult as in Kobe during 1995 earthquake.

Once the safety is guaranteed, then the design options will be evaluated based on the life-cycle cost following the procedure described in the previous section. In this way, the optimal design is achieved for the type of port structures that are essential part of emergency base.

In seismic hazard analysis for evaluating earthquake ground motions, earthquake ground motions for safety evaluation may be determined by either probabilistic or deterministic analysis. This earthquake ground motion can be determined by a deterministic analysis when an active seismic fault is located nearby. A deterministic analysis evaluates earthquake ground motion by selecting individual earthquake scenarios, including earthquake magnitude, fault location, fault dimension, and source mechanism. Deterministic analysis does not explicitly consider the probability of occurrence of earthquakes but it does consider uncertainties involved in the evaluation of ground motion from a scenario earthquake. The deterministic analysis is widely adopted in Japan and western coast of U.S.A.(Leyendecker *et al.*, 2000)

The methods for seismic hazard analysis include empirical, semi-empirical, and theoretical methods, and a combination of these methods, and are chosen, consistent with the degree of refinement required for analysis of the geotechnical works, based on

- the importance of a structure, and
- the available information on seismic faults and deep basin structures in the vicinity of a site.

In the past, either the largest earthquake motion recorded was adopted as design ground motion, or magnitude of a scenario earthquake and distance to the site were used to scale the given time history for specifying design ground motions. Those simplified methodologies were once called the deterministic approach. Probabilistic approach was introduced in seismic hazard analysis based on the frequency-magnitude relation by Gutenberg & Richter (1942).

Extensive studies on the earthquake ground motions near a seismic fault have revealed that, if a focus is directed to the near seismic fault regions, regularities of earthquake occurrence (i.e. maximum magnitude or characteristic earthquakes, relations between the energy accumulation and release periods of fault activities) can be recognized in contrast to the random occurrence model as represented by the Gutenberg-Richter relation. In addition, new methodologies for characterizing the



Fig. 10 Emergency operation of cargo supply through Japanese navy at Kashiwazaki, Niigata, port at 2007 Niigata-ken chuetsu-oki earthquake, Japan



Fig. 11 Collapse of a highway in Kobe city during 1995 Hyogo-ken Nambu earthquake, Japan

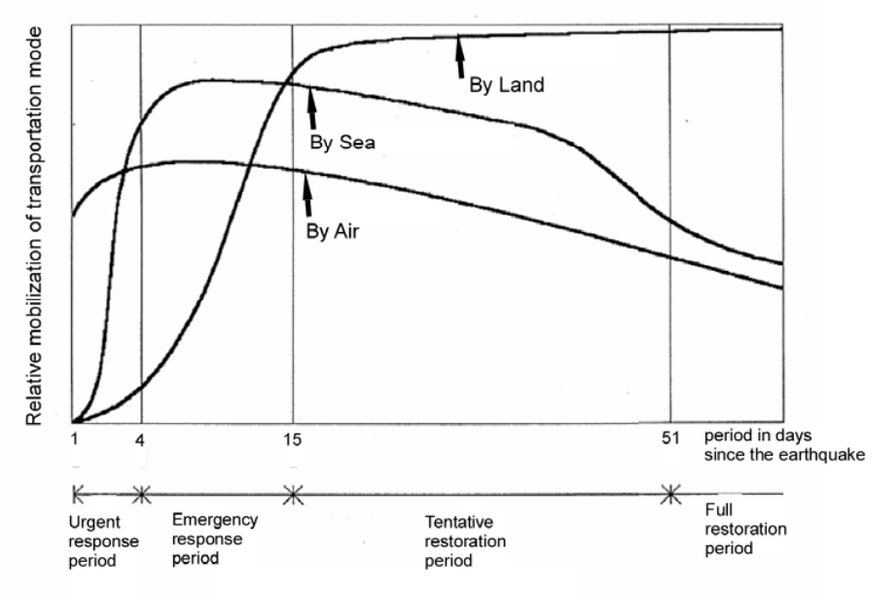


Fig. 12 Modal shifts for human transport in Kobe after 1995 Hyogo-ken Nambu earthquake (Takahashi *et al.*, 1997)

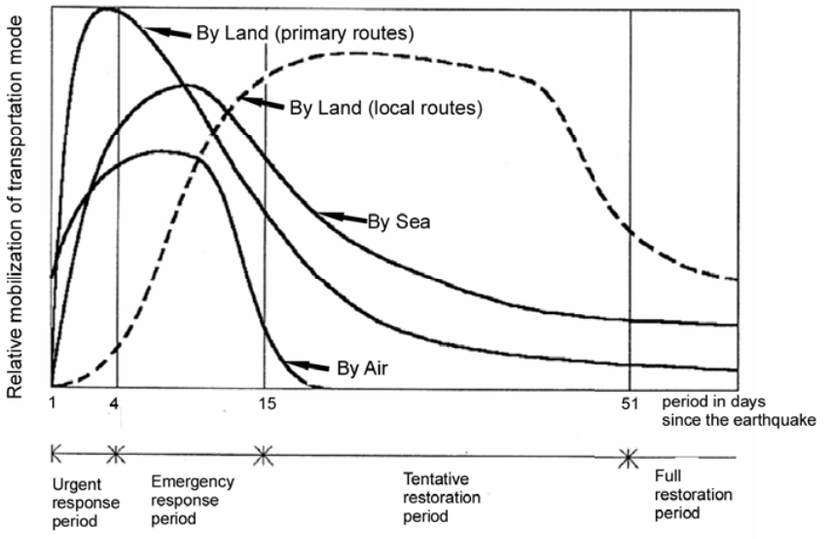


Fig. 13 Modal shifts for cargo transport in Kobe after 1995 Hyogo-ken Nambu earthquake (Takahashi *et al.*, 1997)

strong earthquake motions have been developed by taking into account realistic source mechanisms including the effects of asperities and source-to-site path through appropriate numerical methods such as empirical Green's function method. The discussions on the probabilistic and deterministic approaches made with respect to ISO23469 reflect these recent developments in seismic hazard analysis and strong earthquake ground motions.

Primary discussions provided for introducing the deterministic approach as an alternative to probability approach may be summarized as follows (Iai, 2005):

(1) The new methodologies for characterizing the strong earthquake motions such as empirical Green's function method are easily incorporated in the deterministic approach. Incorporation of these methodologies into the probabilistic approach has not yet been established for use in practice.

(2) Probabilistic approach explicitly specifies the probability in dealing with the uncertainty whereas deterministic approach deals with the uncertainty through a series of engineering and scientific judgments. There seems a misleading impression that the probabilistic approach does not involve the engineering judgments. In particular, epistemic uncertainty is considered to be due to a lack of scientific knowledge and is evaluated by processing opinions from a number of experts. A logic tree is often used to process the differing experts' opinions in the march to a final hazard estimate. The weights assigned for differing opinions are also based on the engineering judgments. The probability explicitly specified in the probabilistic approach reflects those engineering judgments.

(3) The deterministic approach is applicable and adequate for determining earthquake ground motions for design especially when uncertainty is small in evaluating the parameters of the scenario earthquake. In this case, the deterministic approach can be an adequate method for evaluating a low probability event as an alternative to the probability approach that typically involves a large uncertainty in the tail end of the probability function (Fig. 2(b)).

(4) Probability of occurrence of earthquakes at nearby active seismic faults is often less than a few percent over 30 years. For example, 1995 Hyogoken-Nambu (Kobe) earthquake had the probability ranging from 0.4 to 8% over 30 years when the earthquake occurred in 1995 (Shimazaki, 2001). Depending on the probability specified for seismic hazard analysis, the effects of seismic hazard due to nearby seismic faults might be obscured or ignored, resulting in an unconservative seismic hazard evaluation.

As listed above, there are many issues that should be studied before applying the probabilistic approach in seismic hazard analysis for evaluating safety requirements. Depending on the seismic activities around the site and the available research and investigation results, an appropriate approach, including the deterministic approach based on the scenario earthquake, should be used when active seismic fault is located nearby. It would be advisable to avoid the mechanical use of the probabilistic approach for seismic hazard analysis.

SUMMARY AND CONCLUSIONS

An overview is given on an emerging methodology for seismic evaluation and design of port structures based on life-cycle cost.

For ordinary port structures where primary objectives and functions are for commercial use, serviceability and economy become high priority issues and the methodology based on life-cycle cost has potential advantages over the conventional seismic design. In this methodology, failure is defined as the state where a structure does not meet the limit state or acceptable damage level. Probability of failure over design working life is computed based on fragility curve(s) and a seismic hazard curve. The fragility curve(s) reflect uncertainty in geotechnical and structural conditions. The seismic hazard curve allow consideration of ground motions with all (or varying) return periods. The performance is evaluated in terms of expected loss due to earthquake induced damage that reflects the consequence of failure. Life-cycle cost properly represents the trade-off between the initial construction cost and the expected loss. The design option that gives the minimum life-cycle cost is the optimum in terms of overall economy.

An example presented in this paper demonstrates that the simplified performance evaluation charts that are based on a series of parametric studies of effective stress analyses have great benefit for implementing the methodology based on life-cycle cost in practice.

Apart from the ordinary port structures, higher priority should be assigned for safety if port structures are essential parts of post-earthquake emergency strategies for recovery and restoration of urban areas as planned by local, regional, or federal governments. The methodology based on the life-cycle cost still plays an important role for arriving at the optimum design from the design options that have been already confirmed to meet the performance objectives of emergency facilities or safety requirements. There are certain controversial issues that need careful study for specifying the earthquake ground motions used for safety evaluation.

ACKNOWLEDGMENTS

The authors acknowledge the financial support by NEDO for this study.

REFERENCES

Gutenberg, B. and Richter, C. F. (1942). "Earthquake magnitude, intensity, energy, and acceleration." *Bulletin of the Seismological Society of America*, 32: 163-191.

Higashijima, M., Fujita, I., Ichii, K., Iai, S., Sugano, T. and Kitamura, M. (2006). "Development of a simple seismic performance evaluation technic for coastal structures." *2006 Ocean Development Symposium*.

Iai, S., Ichii, K., Liu, H. and Morita, T. (1998). "Effective stress analyses of port structures." *Soils and Foundations, Special Issue on Geotechnical Aspects of the January 17 1995 Hyogoken-Nambu Earthquake*, 2: 97-114.

Iai, S. (1998). "Seismic analysis and performance of retaining structures." *Geotechnical*

Earthquake Engineering and Soil Dynamics III Geotechnical Special Publication No.75, ASCE. 1020-1044

Iai, S., Ichii, K., Sato, Y. and Liu, H. (1999). "Residual displacement of gravity quaywalls - parameter study through effective stress analysis." *7th U.S.-Japan Workshop on Earthquake Resistant Design of Lifeline Facilities and Countermeasures against Soil Liquefaction*, Seattle, Vol. NCEER-99-0019, 549-563.

Iai, S. (2005). "International standard (ISO) on seismic actions for designing geotechnical works - An overview." *Soil Dynamics and Earthquake Engineering*, 25: 605-615.

Ichii, K., Iai, S., Sato, Y. and Liu, H. (2002). "Seismic performance evaluation charts for gravity type quay walls." *Journal of Structural Mechanics and Earthquake Engineering, JSCE,* 19 (1): 21-31.

Ichii, K. (2002). "A seismic risk assessment procedure for gravity type quay walls." *Journal of Structural Mechanics and Earthquake Engineering, JSCE,* 19 (2): 131-140.

Kramer, S. L., Mayfield, R. T. and Anderson, D. G. (2006). "Performance-based liquefaction hazard evaluation: implications for codes and standards." *8th U.S. National Conference on Earthquake Engineering*, San Francisco, Paper No.888.

Leyendecker, E. V., Hunt, R. J., Frankel, A. D. and Rukstales, K. (2000). "Development of maximum considered earthquake ground motion maps." *Earthquake Spectra*, 16 (1): 21-40.

Sawada, S. (2003). *A new look at Level 1 earthquake motions for performance-based design of civil engineering structures*: Japan Society of Civil Engineers. http://www.jsce.or.jp/committee/eec2/taishin/index.html.

Shimazaki, K. (2001). "Recent progress in long-term earthquake forecasts in Japan." *Journal of Geography*, 110 (6): 816-827.

Takahashi, H., Nakamoto, T. and Yoshimura, F. (1997). *Analysis of performance of sea transport mode immediately after 1995 Hyogo-ken Nambu earthquake* Port and Harbour Research Institute. Technical Note, No.861

Comparison of Panama Wharf Performance Using Numerical Analysis and Limit Equilibrium Methods

King H. Chin[1], A.M. ASCE, P.E., Daniel W. Mageau[2], M. ASCE, P.E., and Scott T. Peterson[3], Ph.D., P.E, M.ASCE

[1]Senior Engineer, GeoEngineers, Inc., 600 Stewart Street, Suite 1700, Seattle, WA 98101; kchin@geoengineers.com
[2]Principal Engineer, GeoEngineers, Inc., 600 Stewart Street, Suite 1700, Seattle, WA 98101; dmageau@geoengineers.com
[3]Project Engineer, Berger/ABAM Engineers, Inc., 33301 Ninth Ave S., Suite 300, Federal Way, WA, 98003. scott.peterson@abam.com

ABSTRACT: Evaluation of the performance of pile supported wharf structures under seismic conditions has evolved in recent years through the use of numerical analysis programs (for example, PLAXIS and FLAC). Before the use of numerical analysis programs, the performance of a pile supported wharf structure was evaluated using a decoupled approach, where the stability and movement of the embankment is first evaluated using the limit equilibrium and Newmark's method, and the deformation and pile forces and moments are then estimated using structural analysis. However, unlike numerical analysis programs, this decoupled analysis method does not allow precise evaluation of the interaction between the soil mass and the embedded structure.

This paper presents the results of seismic analyses of a pile-supported wharf on a fill embankment in Panama. Both the limit equilibrium/Newmark and numerical analysis methods were used to evaluate the response of the new wharf under two levels of earthquakes: an operating level earthquake (OLE) and a contingency level earthquake (CLE). The stability of three different embankment sections (compacted fill soil with a slender zone of rock, intermediate zone of rock and thick zone of rock) was first analyzed for slope stability (limit equilibrium method) and embankment deformation (Newmark's method) for each of the two design earthquake levels. These same embankment sections were then evaluated for deformation using PLAXIS V8.5 with the inclusion of the pile-supported wharf structure using earthquake time histories representative of the design earthquake levels as input. The factor of safety of embankment stability from limit equilibrium analysis and deformations of the embankment from Newmark's method were compared to the wharf performance (deformation, pile shear and moment) calculated by PLAXIS. The results of these

comparisons indicate that the conventional decoupled method of analysis can provide a general evaluation of wharf performance but may underestimate the performance of a wharf that has irregular structure geometry or eccentric loading, or if the structure is sensitive to small movements under larger earthquake events. Recommendations for selection of appropriate pseudostatic coefficients for limit equilibrium analyses that compare well with expected slope/wharf deformation and pile shear and bending moments are provided.

INTRODUCTION

The Panama Ports Company (PPC) is expanding the container terminal areas at the Port of Balboa, located near the western entrance to the Panama Canal in Panama. As part of this expansion, PPC is reclaiming approximately 35 hectares of land area and extending the existing berth by 450 meters. The existing structures at the main berthing area were designed as pier structures and are unable to carry the lateral load required of a retaining structure. A rock dike retaining structure located to the land side of the existing pier structures was determined to be the most economical solution to retain the sand fill to be placed during reclamation in this case. A pile supported wharf-type link structure was designed to span over the rock dike to connect the future container yard area with the existing berth structures.

While shipping containers are typically not stored on the deck of a structure, the new link structure is required carry container stacking loads due to the location of the structure within the new container yard. The future layout of the Port Balboa site is shown in Figure 1. The Port of Balboa is located in a moderate seismic zone, which made necessary a thorough seismic analysis of the rock dike, link structure, and the soil-structure interaction between them. The native soils consist of about 6 to 9 meters of soft sediment termed “Pacific Muck” over native bedrock. The overlying fill soils within the existing container yard area generally consist of dredged fill. The reclamation areas for the future expansion will be dredged to hard material and filled with sand which will be vibro-compacted to 85% optimum density. In areas where the native soils will not be dredged, a wick drain and surcharge program will be used to minimize future settlement of the container yard in these areas.

A two level seismic design was performed for both the rock dike and link structure to properly account for the damage which may occur during an Operating Level Earthquake (OLE) while maintaining life safety and prevention of collapse during a Contingency Level Earthquake (CLE). This paper presents the analysis procedures used to design the new link structure at the Port of Balboa.

The designers adopted a design philosophy regarding earthquake risk similar to that used by many of the ports along the west coast of the United States. They expect the new wharf structures to experience little to no damage during an OLE (10% probability of exceedance in 50 years) and limited damage for a CLE event (50% probability of exceedance in 50 years) such that operations are disrupted only for a few days, and some structural damage that is repairable.

Three embankment sections were considered for this project, all consisting of rock fill over densified dredged fill consisting of fine to medium sand. Embankment Section 1 consists of densified sand with a 1-meter-thick armor rock along the slope

face (Figure 2a). Embankment Section 2 has a thicker zone of rock fill consisting of a series of smaller rock dikes constructed on top of each other (Figure 2b). Embankment Section 3 consists of a rock dike that is about 25 meters high with a base width of about 45 meters (Figure 2c). The embankments are supported directly on the underlying bedrock after the soft sediment within the footprint of the embankment is dredged. Embankment 3 was selected for construction at the Port of Balboa.

The primary geotechnical issue for the wharf structures is the impact of the embankment movement on the pile-supported wharf structures during OLE and CLE events. Of particular interest are the forces exerted on piles that support the wharf deck and the resulting bending moments in the piles caused by laterally moving ground.

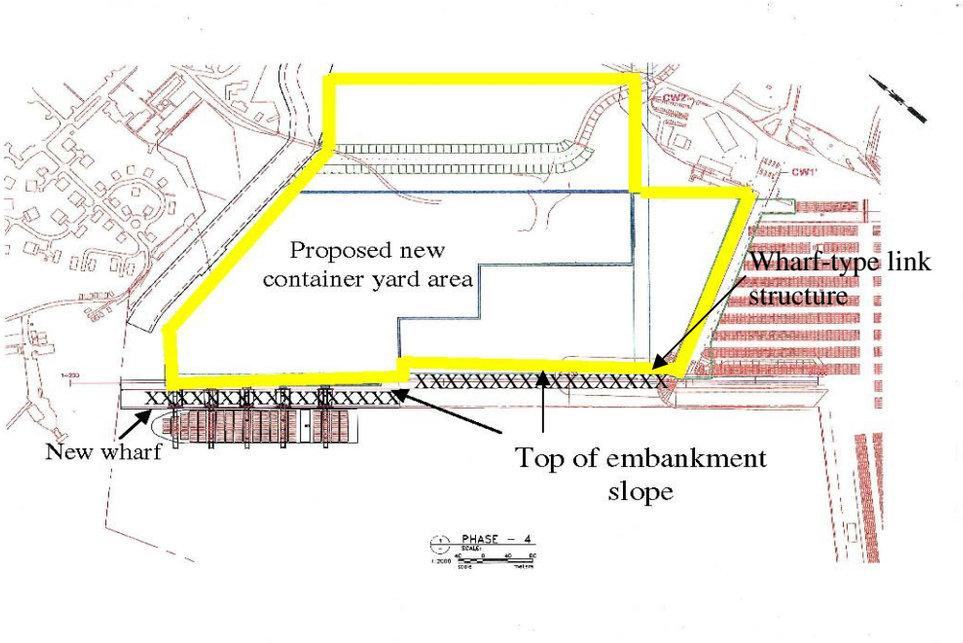


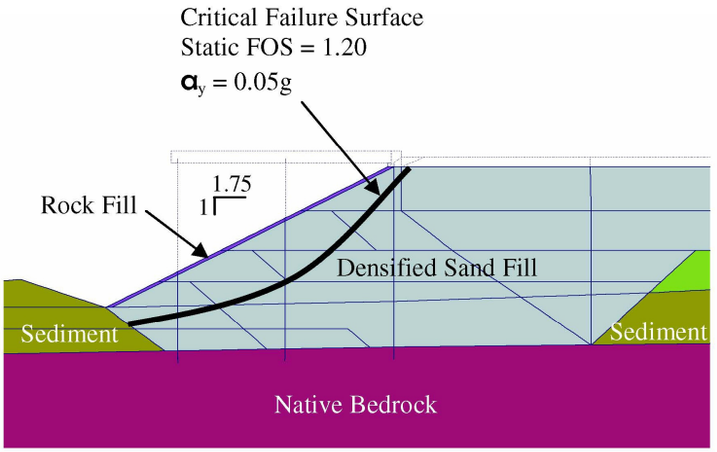
FIG 1. Site Plan – Port Balboa Expansion

SLOPE STABILITY

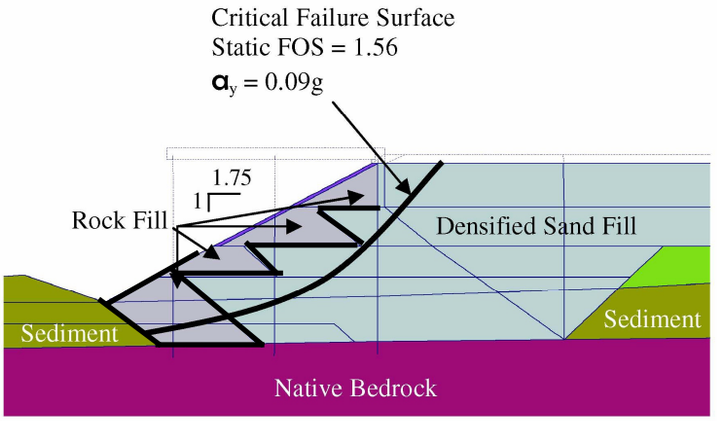
The stability of the three fill embankment sections shown in Figure 2 was evaluated using a limit equilibrium approach under the design earthquake levels. The embankments are about 25 meters high with a 1.75H:1V (horizontal to vertical) slope. The properties for each of the soil/rock units shown in Figure 2 are presented in Table 1 below. Mohr Coulomb soil model was used in both the limit equilibrium and finite element analysis.

Table 1. Soil/Rock Properties

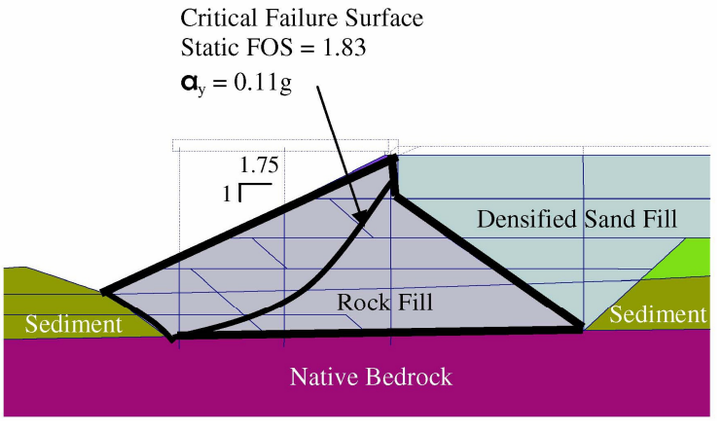
Soil Unit	γ (kN/m^3)	ϕ (degree)	c (kN/m^2)	E (kN/m^2)
Bedrock (Shale)	22.8	0	4310	3.4×10^6
Angular Rock Fill	20.4	45	5	2.8×10^5
Densified Fill	20.4	38	0	1.4×10^5
Sediment	14.5	0	15.4	1.0×10^4



a) Embankment Section 1



b) Embankment Section 2



c) Embankment Section 3

FIG. 2. Embankment Sections Considered and Evaluated.

The slope stability of each embankment section was evaluated using the strength reduction method available in PLAXIS. Figure 2 shows the critical failure surface determined for each embankment section and its associated factor of safety under static conditions. The yield acceleration (a_y), which results in a factor of safety of 1.0, was calculated using the pseudo-static method for each critical failure surface shown in Figure 2. No piles were included in the slope stability and yield acceleration analysis.

EMBANKMENT DEFORMATION

The deformation of the critical failure surface identified for each of the three embankment sections is estimated using both Newmark's method and PLAXIS under seismic loading input developed as follows. Three earthquake time histories representative of OLE and CLE events were selected for the deformation analyses based on seismic hazard maps developed by Tanner and Shedlock (2004). According to Tanner and Shedlock, the most common and damaging earthquakes in Central and South America generally consist of shallow earthquakes that have magnitudes between 5.0 and 6.5. For this project, thirty earthquake time histories that consist of shallow crustal events with magnitudes between 5 and 7.0 were downloaded from the PEER website. Out of the 30 earthquake time histories, three with magnitudes between 5.3 and 6.1 were selected to simulate OLE event and another three with magnitudes between 6.1 and 7.0 were selected to simulate CLE event. The six earthquake time histories were selected because they best match the rock outcrop target spectrum developed for the OLE and CLE events per Tanner and Shedlock. The characteristics of the selected earthquake time histories for use in the analysis are presented in Table 2 below.

Table 2. Selected Earthquake Characteristics

Design EQ Level	Earthquake	Recorded Station	Mag.	Recorded PGA
OLE (50% in 50 Years)	1. 1986 N. Palm Springs	Desert Hot Springs	6.1	0.33g
	2. 1987 Whittier Narrow	Mill Creek, Angeles Nat. For.	6.0	0.08g
	3. 1994 Northridge	Sunland – Mt Gleason Ave.	5.3	0.06g
CLE (10% in 50 Years)	4. 1989 Loma Prieta	Gilroy Array #6	6.9	0.16g
	5. 1994 Northridge	Pacoima Kagel Canyon	6.7	0.30g
	6. 1994 Northridge	Burbank – Howard Rd.	6.7	0.12g

Prior to completing Newmark's and PLAXIS analyses, the selected earthquake time histories were first scaled to a peak ground acceleration (PGA) of 0.08g and 0.15g for the OLE and CLE respectively, with the associated scaled response spectrum

generally match the spectral shape of the rock outcrop target spectrum for OLE and CLE. These accelerations are the target rock outcrop PGA (PGA_r) for the project site obtained from the seismic hazard map developed by Tanner and Shedlock (2004).

The computer program developed by Jibson and Jibson of the United States Geological Survey (USGS) (2003) was used to complete Newmark's analysis. The rigorous rigid-block analysis was used to calculate the maximum horizontal deformation of each embankment section under each of the six earthquake time histories. The maximum horizontal deformation of each embankment section under each of the six earthquake time histories were also calculated using PLAXIS. Table 3 below summarizes the calculated maximum horizontal deformation for each embankment section under the six earthquake time histories using both Newmark's method and PLAXIS. Also shown in Table 3 is the ratio of yield acceleration calculated to the design rock outcrop PGA (a_y/PGA_r).

Table 3. Calculated Embankment Deformation

	Static Factor of Safety	**OLE**		
		Newmark Δ (mm)	**PLAXIS Δ (mm)**	**a_y/PGA_r**
Embankment Section 1	1.20	1 to 2	10 to 14	0.63
Embankment Section 2	1.56	0	4 to 6	1.12
Embankment Section 3	1.83	0	1 to 2	1.38
	Static Factor of Safety	**CLE**		
		Newmark Δ (mm)	**PLAXIS Δ (mm)**	**a_y/PGA_r**
Embankment Section 1	1.20	30 to 77	33 to 83	0.33
Embankment Section 2	1.56	2 to 15	10 to 39	0.60
Embankment Section 3	1.83	1 to 4	4 to 15	0.73

As shown in Table 3 above, both Newmark's method and PLAXIS indicate a relatively small amount of embankment deformation under the OLE. Bray and Rathje (1998) and Stewart, et al. (2003) demonstrated that slope deformations are generally low when the a_y/PGA_r ratio is higher than about 0.6. The results shown here are consistent with this conclusion. For the CLE, both Newmark's method and PLAXIS predict a similar deformation for Embankment Section 1 where the a_y/PGA_r ratio is less than 0.6. For Embankment Sections 2 and 3, where the a_y/PGA_r ratio is 0.6 or higher, Newmark's method calculated significantly lower deformation compared to PLAXIS. This is likely caused by the limitation of Newmark's method in modeling the slope as a rigid body. In reality, the slope response like continua medium with discrete elements where higher modes of vibration can be engaged during an earthquake, which is accounted for by PLAXIS.

WHARF STRUCTURE RESPONSE

The response of the wharf structure embedded in the fill embankment was evaluated in terms of deformation and stress using PLAXIS V8.5. Ground motions for this modeling are simulated by inputting an earthquake time history at the base of the

mesh. Six earthquake time histories listed in Table 2 were developed as input to these deformation analyses.

The new wharf structure will consist of a concrete deck supported by three rows (rows H, J and K) of 700-mm diameter prestressed concrete octagonal piles. The spacing between pile row H and J is 11.5 meters, and the spacing between pile row J and K is 11.75 meters. The typical pile bent spacing is 6.4 meters for rows H and K and is 3.2 meters for row J. A typical section of the wharf structure constructed in Embankment Section 3 is presented in Figure 3. Also shown in Figure 3 are the uniform live loads that will be applied to the concrete deck through truck traffic loading on the span between rows H and J, and container storage loading on the span between rows J and K.

In PLAXIS, the piles are modeled as vertical plates with strength and stiffness properties of the pile divided by the pile spacing. The pile is modeled using elastic-plastic behavior with specified limiting in-ground and above-ground plastic moments as determined through nonlinear analysis by the project structural engineer. The soil-pile interface is modeled using an interface coefficient of 0.67.

Table 4 below presents the properties of the structural elements modeled in PLAXIS.

Table 4. Structure Properties

Structural Element	γ (kN/m^3)	E_c (kN/m^2)	M_{pa} (kN-m)	M_{pi} (kN-m)
Concrete Deck	23.6	2.5×10^7	N/A	N/A
Row H Piles	23.6	2.5×10^7	1420	1150
Row J Piles	23.6	2.5×10^7	1560	1240
Row K Piles	23.6	2.5×10^7	1030	1270

Note: M_{pa} = above-ground pile plastic moment; M_{pi} = in-ground pile plastic moment

A series of computer runs using PLAXIS was completed to evaluate the response of the wharf structure under seismic ground motions and to determine the maximum bending moments of the piles under these motions for both the OLE and CLE events. Table 5 below presents the range in wharf deck deformations calculated at the end of the earthquake time histories. The range is the result of different responses from the three earthquake time histories. The maximum bending moment of the pile that occurs during the earthquake is calculated by PLAXIS. The locations where the plastic moment is reached are identified as hinge points, as shown in Figure 4.

Table 5. Calculated Wharf Deck Deformation

	OLE Deck Δ (mm)	CLE Deck Δ (mm)
Embankment Section 1	18 to 24	59 to 131
Embankment Section 2	10 to 14	27 to 74
Embankment Section 3	4 to 5	5 to 40

As shown in Table 5, a relatively small amount of deck deformation is calculated under the OLE, and all the piles supporting the wharf structure stay elastic throughout the design earthquake time histories. Under the CLE, the magnitude of the wharf

deformation is much higher, as expected. Note that the horizontal deformation of the wharf is significantly greater than the free-field slope deformation shown in Table 3. This is the result of inertia forces acting on the wharf structure in combination with slope movements. Wharf deformation and the number of pile hinge points formed in the piles are inversely proportional to the factor of safety and yield acceleration of the embankment section. The tables in Figure 4 summarize the cumulative total length of piles that reach the plastic moment during the CLE event. While this is not perfectly meaningful from a structural standpoint, these quantities were used to compare the change in apparent structural performance for the different embankment sections investigated using the PLAXIS analyses discussed earlier. For row K piles that are fully embedded in soil/rock, the length of pile that reach the plastic moment is 41%, 10% and 5% of the total pile length with corresponding static factor of safety of 1.20, 1.56 and 1.83.

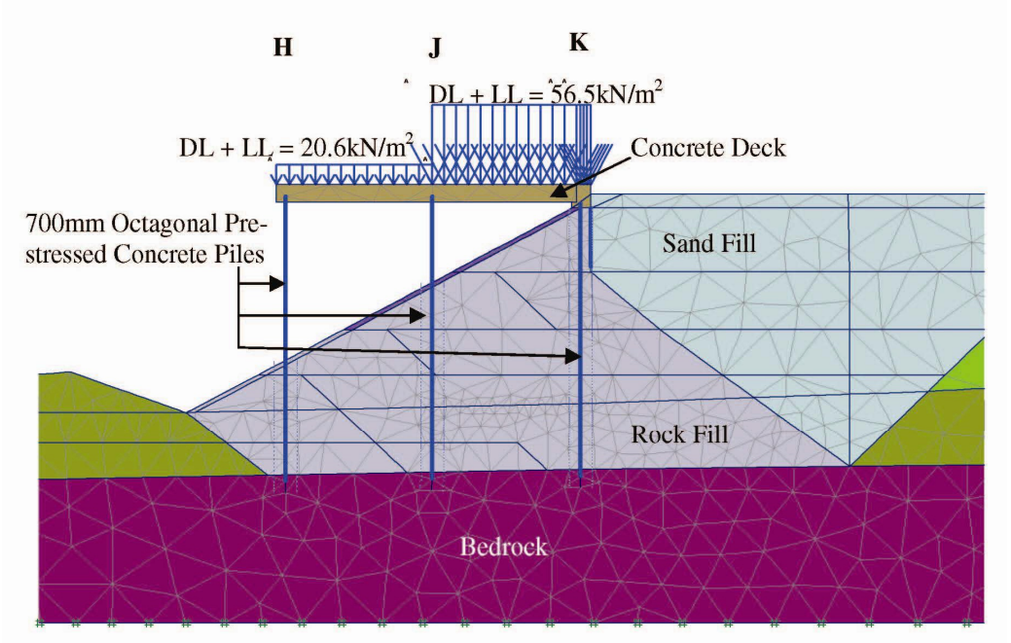


FIG. 3. Typical Section of Pile-Supported Wharf Structure in Embankment.

CONCLUSIONS

Both the limit equilibrium and numerical methods were used to complete the design of the pile-supported wharf structure in fill embankment for the Port Balboa project in Panama. The results of the analysis suggest that the conventional decoupled methods of analysis are appropriate to evaluate embankment stability/wharf performance for a typical wharf structure, it may underestimate wharf deformation and the level of damage to the supporting piles under uneven loading conditions and larger earthquake events. This demonstrates that numerical methods using a finite element or finite difference programs are better tools for evaluating the complex conditions of pile-supported structures embedded in soil embankments under seismic loading conditions.

Based on the results of our analysis, we also conclude that if a static factor of safety is

at least 1.5 with an a_y/PGA_r ratio of higher than 0.6, then a pile-supported structure embedded in such slope should perform adequately under seismic conditions. However, if there is additional complexity such as irregular structure geometry or eccentric loading, or if the structure is sensitive to small movements, then a numerical analysis is recommended.

ACKNOWLEDGMENTS

The authors appreciate the guidance provided by Gary Henderson of GeoEngineers and collaborative engineering efforts by George Sheng, Manfred Zinserling, V.K. Kumar, Carlos Ospina, and Kaiyuan Liu of Berger/ABAM Engineers, Inc. We would also like to thank Briana Wakefield and Stephen Lynch of our office for helping in figures preparation and editing of this paper.

REFERENCES

Bray, J.D. and Rathje, E.M., 1998. "Earthquake-induced Displacements of Solid-waste landfills," *J. of Geotech. and GeoEnviron. Eng*., 124, pp. 242-253.

Blake, T.F., Hollingsworth, R.A., and Stewart, J.P., editors, 2002. "Recommended Procedures for Implementation of DMG Special Publication 117 Guidelines for Analyzing and Mitigating Landslide Hazards in California," Southern California Earthquake Center.

Jibson, R.W. and Jibson, M.W., 2003. "Java Program for Using Newmark's Method and Simplified Decoupled Analysis to Model Slope Performance during Earthquakes," United States Geological Survey Open-File Report 03-005.

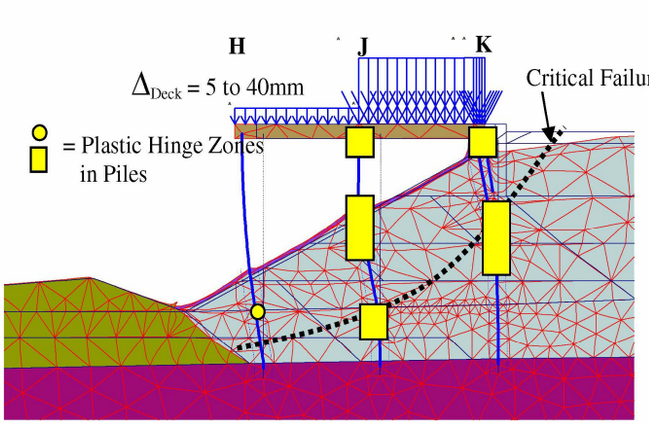
PLAXIS V8 (2002). Finite Element Code for Soil and Rock Analysis, PLAXIS b.v., Netherlands.

Kramer, S.L., 1996. Geotechnical Earthquake Engineering, Prentice-Hall, New Jersey, USA, 653 pp.

Stewart, J.P., Blake, T.F., and Hollingsworth, R.A., 2003, "A Screen Analysis Procedure for Seismic Slope Stability," *Earthquake Spectra*, Vol. 19, No.13, pp 697-712.

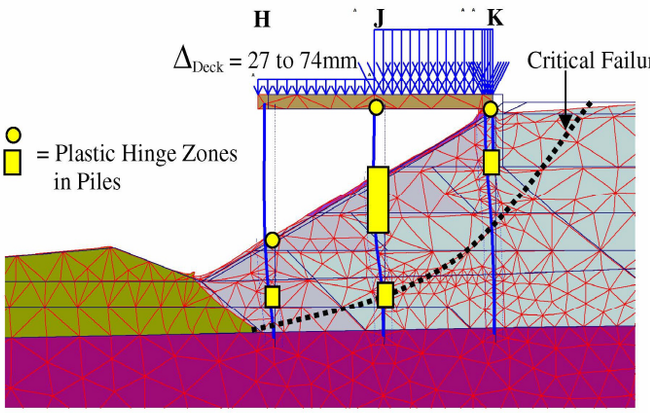
Werner, S., editor, 1998. "Seismic Guidelines for Ports," American Society of Civil Engineers Monograph No. 12.

Tanner, J.G. and Shedlock, K.M., 2004. "Seismic Hazard Maps of Mexico, the Caribbean, and Central and South America," Tectonophysics, 390, pp 159-175.



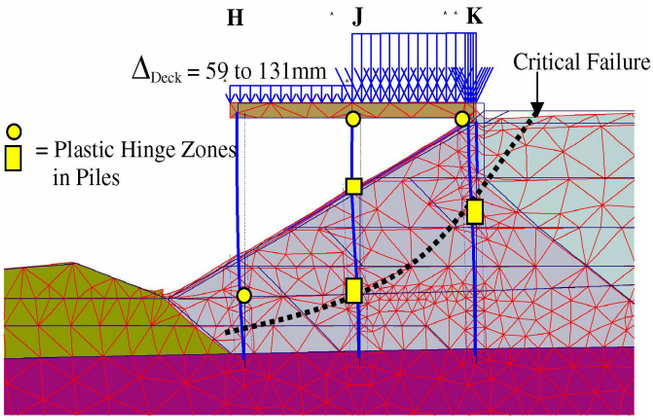
Pile Row	% Pile Length Reached Plastic Moment
H	5%
J	46%
K	41%

a) Embankment Section 1



Pile Row	% Pile Length Reached Plastic Moment
H	5%
J	43%
K	10%

b) Embankment Section 2



Pile Row	% Pile Length Reached Plastic Moment
H	3%
J	19%
K	5%

c) Embankment Section 3

FIG. 4. Plastic Hinges Formed in the Piles.

Full-Scale Lateral Pile Load Test in Rock Fill

Yohsuke Kawamata[1], Scott A. Ashford[2], and Nontapat Nimityongskul[3]

[1] PhD Student, School of Civil and Construction Engineering, Oregon State University, 337 Owen Hall, Corvallis, OR 97331-3212; email: kawamaty@onid.orst.edu
[2] Professor and Head, School of Civil and Construction Engineering, Oregon State University, 220 Owen Hall, Corvallis, OR 97331; email: scott.ashford@oregonstate.edu
[3] PhD Student, School of Civil and Construction Engineering, Oregon State University, 337 Owen Hall, Corvallis, OR 97331-3212; email: nimityon@onid.orst.edu

Abstract

The recently approved seismic code for the Port of Los Angeles (POLA) requires performance evaluation for two levels of earthquakes: the Operating Level Earthquake (OLE) which has 50% probability of exceedance in 50 years and the Contingency Level Earthquake (CLE) having 10% probability of exceedance in 50 years. For the OLE event, structures should remain operational with insignificant structural damage, while for the CLE event structures should undergo controlled inelastic structural behavior and limited permanent deformations which can be repaired within an acceptable period of time.

For the case of pile-supported wharves, the expected level of performance is based on the estimation of the displacement capacity of the structure. Therefore, soil-pile-interaction has to be evaluated with a higher degree of accuracy. One of the most important factors is to properly define key soil parameters, such as soil stiffness, commonly characterized by *p-y* curves. Unfortunately,, little information is available in the literature on the behavior of laterally loaded piles embedded in the large-diameter quarry-run material typically used in port dikes.

In light of this, a series of full-scale load tests on piles in quarry-run material were carried out at University of California, San Diego's Englekirk Center from April through August, 2007, in order to obtain better understandings of the behavior of the wharf-foundation-dike system during lateral loading. This paper presents test setup, instrumentation, and the results of a full-scale test for a single pile.

Previous Research

The current POLA seismic code specifies reaction-displacement curves (*p-y* curves) for large grain size quarry-run material used for wharf dikes at POLA. These *p-y* curves have been based on previous research.

Diaz *et al.* (1984) carried out some tests on instrumented octagonal piles placed directly at a port construction site. A monotonic force was operated to test piles, and a displacement relationship could be obtained as well as *p-y* curves. However, because this set of tests was conducted with sparse instrumentation, the available information for model validation is quite limited. In addition, the test piles were located close to dike crest and pushed only in the downslope direction, thus no information was available for the response on level ground.

Extensive research was carried out by McCullough *et al*. (2001) using the centrifuge in order to understand the dynamic behavior of pile supported wharves. However, the lack of large- and full-scale test results make the centrifuge result difficult to properly scale up for practice.

With the limited amount of information available in the literature, it is clear that additional full-scale testing is necessary to obtain supplemental data in order to better understanding the interaction between wharf piles and quarry-run material.

Test Specimens and Setup

A total of five prestressed concrete octagonal piles were constructed and instrumented. The piles have the same properties as piles currently used in POLA wharves and the pile-load stub connection is also the same as pile-deck connection of real wharves at the Port of Los Angeles. More details about the test piles and the connection are available elsewhere (Juirnarongrit *et al*. 2007).

The piles were arranged in three test sets with different boundary conditions and geometries as outlined in Table 1 and shown in Figure 1. The pile for the single pile test was located at the level part of the quarry-run (P1 in Figure 1) as shown in Figure 2, and fixity condition at the pile top is free. The results from single pile test can be used for the calibration of analytical parameters.

In the construction practice, the embankment and dike are constructed first and then the pile is installed to the design depth by vibration. However, it is quite difficult for

experimental work to follow the same procedure because of the potential for damage to the instrumentation in the piles. Therefore, the piles were placed inside a soil pit excavated previously and the rock then vibrated using a vibratory roller to simulate pile driving, at least to some extent. Since the final pile locations were critical to proper actuator placement for testing, a concrete footing was built at the bottom of the pile to fix the locations during backfilling.

Due to the large transportation cost that would be involved in backfilling with the same material used at the POLA, it was decided to use material from a local quarry in San Diego area. Gravel was used to fill the bottom 7 ft of the pit as a working platform, and then the quarry-run was placed on top of this layer. The gradation of used quarry-run is shown in Figure 3 along with typical POLA specifications. According to this figure, the quarry-run material, No.2 backing aggregate, was poorer-graded than the typically used at the port.

Instrumentation

Because of non-linear behavior of prestressed concrete pile and effect of cyclic loading,

Table 1 List of the test sets

Test name	Test piles	Boundary condition at the pile top	Clear space between the bottom of cap and dike crest (H)
Single pile test	P1	Free	3.5 ft (1.07 m)
System test 1	P3&P5	Fixed	3.5 ft (1.07 m)
System test 2	P2&P4	Fixed	5.5 ft (1.68 m)

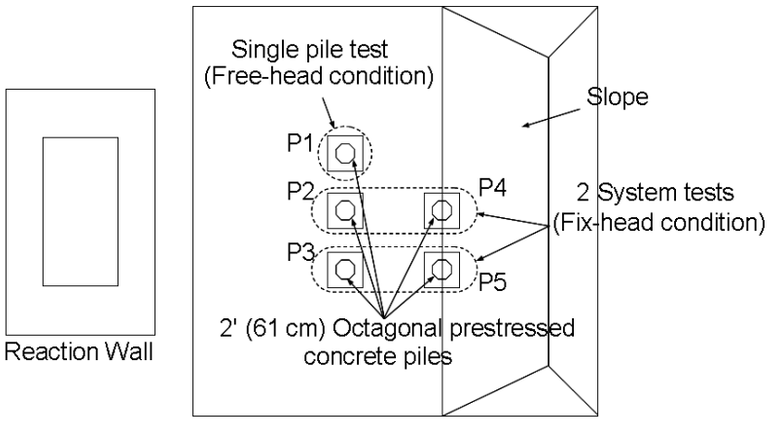


Figure 1 Plan view of pile setup

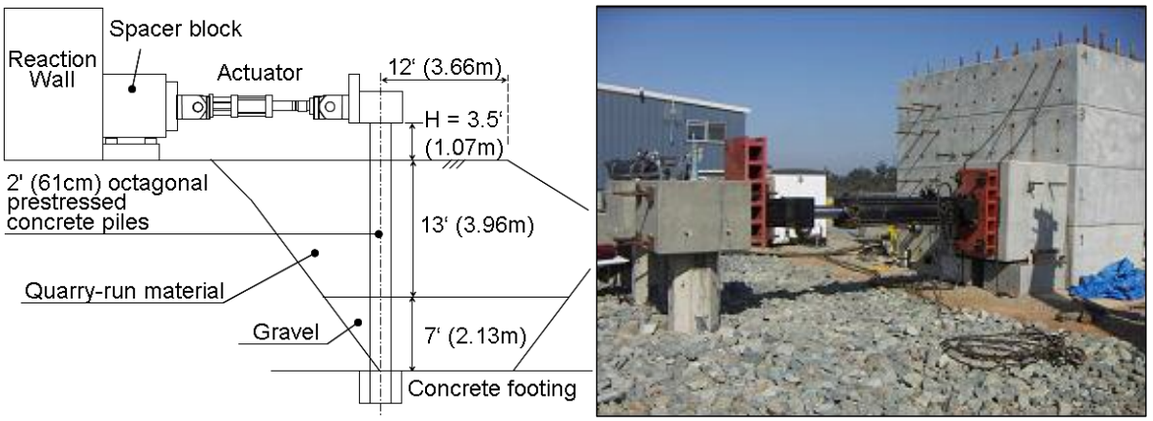


Figure 2 Transverse view of free head single pile

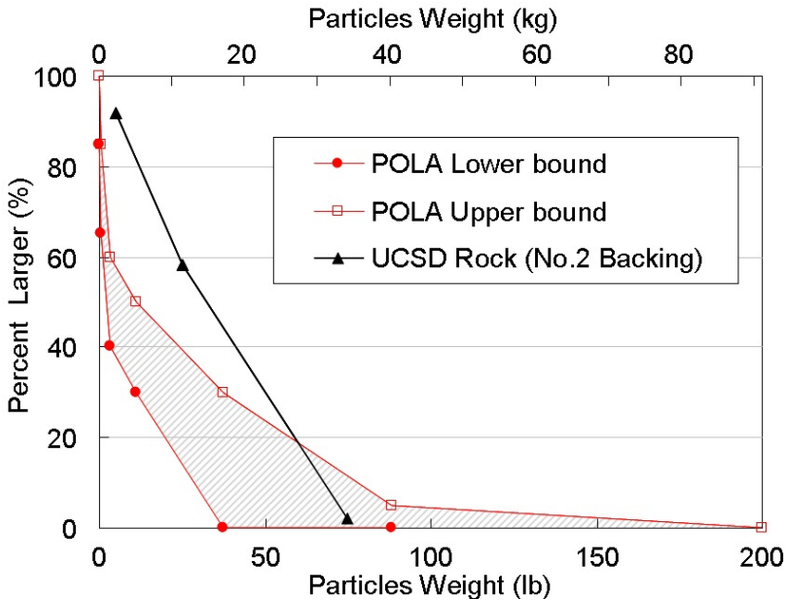


Figure 3 Gradation of used quarry-run material

it is not easy to define bending stiffness of test piles and derive moment from the curvature profile along the pile. Therefore, *p-y* curves for quarry-run material should be derived by back analysis. Load-displacement curves at the pile top, profiles of rotation, deflection, and curvature and maximum moment location can be useful information for this back analysis.

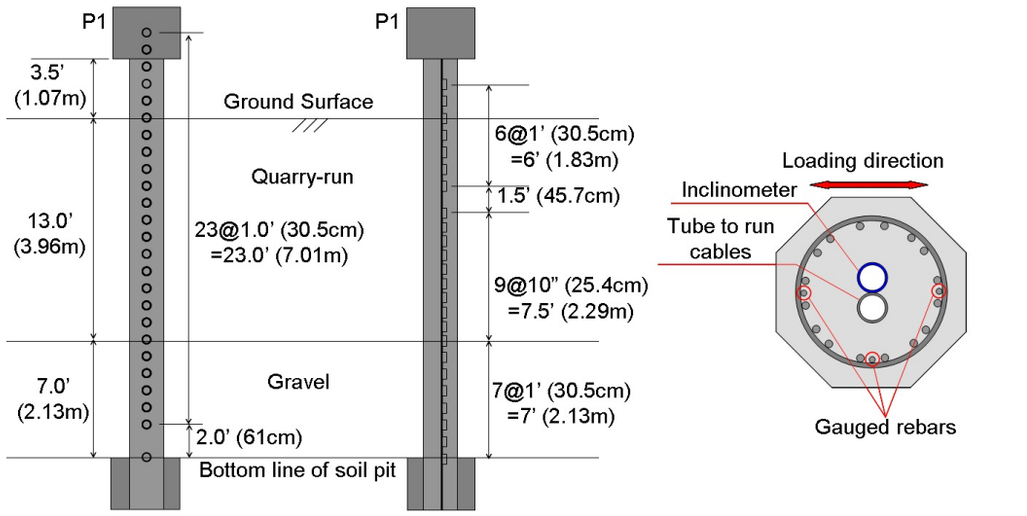
Load and displacement at the pile top were recorded by sensors on the hydraulic actuator, and the load-displacement relationship can be plotted from these records. Tiltmeters are one of the most useful sensors to find profile of rotation along test pile. Data from a series of tiltmeters along the pile can be used to determine pile displacements and curvatures. The pile displacement profile can be calculated from the integration of

measured pile rotation along the length. Average curvature can be obtained by dividing the measured rotation by the distance of each sensor.

Tiltmeters, however, can not detect local effects, such as cracking and spalling of surface concrete. To make up this disadvantage of tiltmeters, strain gages were also embedded during pile fabrication. Three independent gages were placed at various elevations as shown in Figure 4(c), and curvature was derived from these gages. Tiltmeters and strain gages were placed approximately every one foot along the pile axis, and more strain gages were installed at the area where the plastic hinge formation was expected. Elevations of sensors for single pile test are shown in Figure 4. More details on the instrumentation plan can be found in Juirnarongrit *et al*. (2007).

Test results

The single pile test specimen was loaded cyclically as shown in Figure 5. There were two stages of loading; the initial stage was load controlled until test piles reached yielding, and after that the load protocol was switched to displacement control. Because bending stiffness of a concrete pile is much higher at smaller displacements and the increment of displacement is quite sensitive to its behavior, load controlled loading is more reasonable at the first stage. At the second stage, displacement controlled loading is better option for the opposite reason.



(a) Tiltmeters (b) Strain gages (c) Section of test pile

Figure 4 Locations of sensors for single pile test

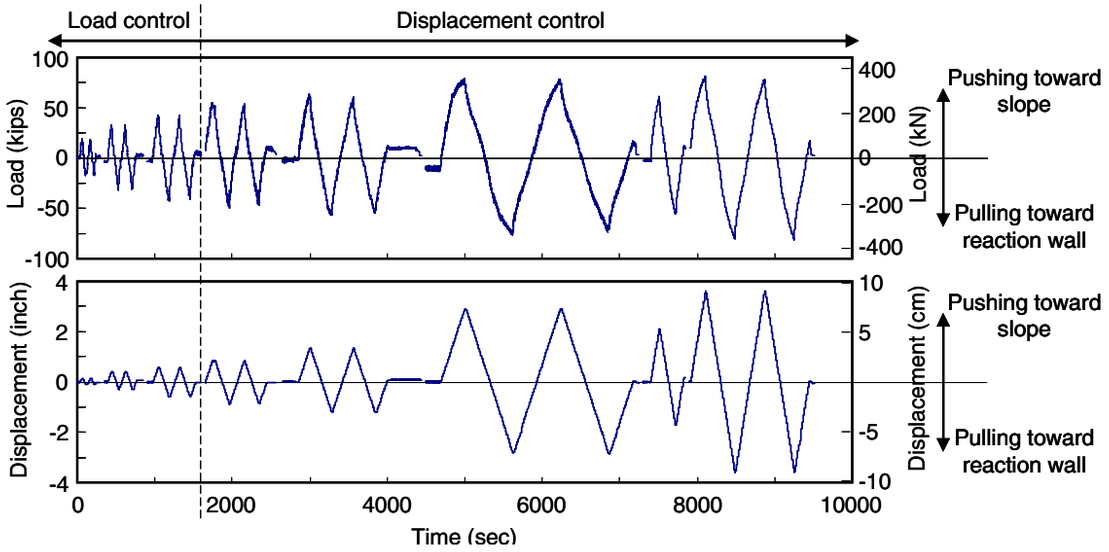


Figure 5 Applied load/displacement at the pile top (positive: pushing)

Load-displacement curves from a series of tests at pile top are shown in Figure 6, with load-displacement curves derived from current design practice plotted as well. There is no significant difference on load-displacement curves in pushing and pulling directions. It is because the pile was located 6 times of pile diameter far from the dike crest. One of curves for current design was calculated using *p-y* curves for level ground provided by the Port of Los Angeles, and the other was derived using *p-y* curves for upper bound (twice the stiffness and *p* as the one for level ground). From this figure, the test pile had higher lateral resistance than what current design practice would have expected.

Examples of profiles of curvature, rotation, and deflection are shown in Figure 7. There is a big jump of curvature on profile derived from strain gage records at 17 ft in depth (Figure 7(a)). When the excavation for in-ground inspection was carried out, tension cracks were found at the corresponding depth. Displacement at the pile top derived from a series of tiltmeters was in reasonable agreement with recorded displacements on the actuator, though the derived displacement from rotation at pile top is little smaller than recorded at actuator (Figure 7(c)). This small difference may come from localized rotation which could not be measured well by tiltmeters.

Inspection and excavation around pile were carried out during and after loading in order to find possible reasons inducing the difference between test results and current design. Figure 8(a) shows settlement of rock fill around pile. The settlement was about 20 inches (51cm) in maximum. Though only the portion of the pile above ground was painted before

testing, the unpainted portion became exposed during loading because of settlement generated from densification of rock fill. Figure 8(b) shows the gap between pile and quarry-run material. The gap will result in less reaction at small displacements than without a gap. Figure 8(c) shows crushed rocks under ground, one of the most important observations. If the quarry-run is a pure frictional material, these rocks should be only redistributed without crushing. These crushed rocks can be evidence of existence of interlocking between rocks. Figure 8(d) shows "craters" on pile surface. These craters represented the locations of strong point contacts between rock and pile, and they indicated contacts are uneven.

Summary of Single Pile Test

A comparison of the test results to the current design practice shows the actual resistance tends to be somewhat greater and stiffer than would be predicted, though that does not necessarily mean current design is always conservative. It does demonstrate the need for further study.

The observations mentioned above should be reasonably considered in order to modify *p-y* curves for large rock fill material like the quarry-run used in these experiments. One option to increase the stiffer at shallow depths is to include a "pseudo-cohesion" representing structural interlocking of rock particles. In fact, Diaz *et al.* mentioned the rock fill near the surface is stiffer than sand and it may imply the rock fill generates stress independent reaction from structural interlocking.

The testing phase of the project was completed in August 2007, and back analyses are being carried out to obtain better understanding about interaction between pile and rock fill. However, the amount of experimental data is still short for formal revising of design code because only couple tests were carried out in this project. Also, influence of gradation of rock fill and existence of water should be clarified in future researches.

Acknowledgements

The authors would like to express their sincere gratitude to the project sponsors: the Port of Los Angeles, the Port of Long Beach, and the Pacific Earthquake Engineering Research Center. Professor Nigel Priestly (Rose School, Italy), Professor Jose Restrepo (University of California, San Diego), and Carlos Blandon (Rose School, Italy) gave much

advice and help on this project. Their support is gratefully acknowledged.

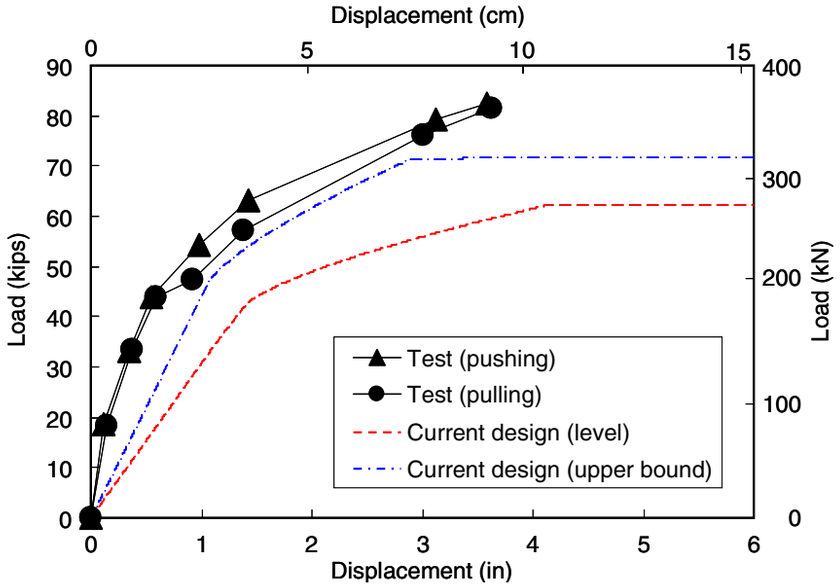


Figure 6 Load-displacement curves at the pile top

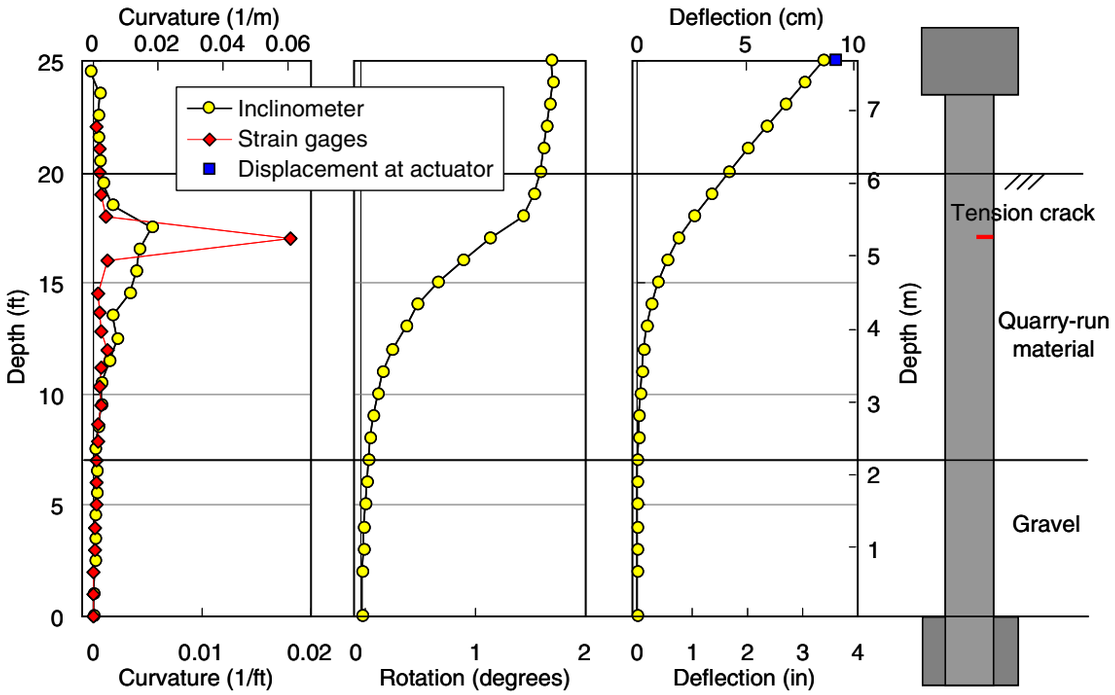


Figure 7 Profiles of curvature, rotation and deflection (3.6 in displacement at pile top)



(a) Settled ground around pile (b) Gap between pile and rock fill

(c) Crushed rocks (d) "Craters" on pile surface

Figure 8 Observations around test pile

References

Diaz, G. M., Patton, B. W., Armstrong, G. L., and Joolazadeh, M. (1984) "Lateral Load Tests of Piles in Sloping Rock Fill" Proceedings of the Analysis and Design of Pile Foundations Conference. J.R. Meyer editor. Held at the ASCE National Convention, San Francisco, California, Oct 1-5. pp 214-231.

Juirnarongrit, T. *et al*. (2007) "Full-Scale Testing of Piles in Wharf-Foundation-Dike System", ASCE Ports 2007, March 25-28, San Diego, CA.

Nason, J., McCullough, N., Dickenson, S., and Schlechter, S. (2001) "The Seismic Performance of Piles in Waterfront Applications" ASCE Ports 2001, April 29-May 2, Norfolk, VA.

This page intentionally left blank

Geotechnical Considerations and Soil-Structure Interaction: Proposed ASCE Standards for Seismic Design of Piers and Wharves

Arul K.Arulmoli[1], Ph. D., G.E., F.ASCE, Gayle S. Johnson[2], P.E., M. ASCE, Peter Yin[3], P.E., S.E., M. ASCE, Omar A. Jaradat[4], Ph.D., P.E., M. ASCE, and Timothy W. Mays[5], Ph.D., P.E., M. ASCE

[1]Earth Mechanics Inc., 17660 Newhope Street, Suite E, Fountain Valley, CA 92708, arulmoli@earthmech.com, [2]Halcrow HPA, 1939 Harrison Street, Suite 730, Oakland, CA 94612, gjohnson@halcrow.com, [3]The Port of Los Angeles, 425 South Palos Verdes Street, San Pedro, CA 90731, pyin@portla.org, [4]PBS&J, 625 The City Drive South, Suite 200, Orange, CA 92868, ojaradat@pbsj.com, [5]The Citadel, 171 Moultrie Street, Charleston, SC 29409, timothy.mays@citadel.edu

ABSTRACT

ASCE 7-05 sets the minimum life-safety standards for designing buildings and other structures. However, it does not directly address all of the issues designers typically face in the seismic design of piers and wharves, especially with respect to dealing with kinematic loading from permanent ground deformation. In 2005, ASCE's Codes and Standards Committee and Coastal, Oceans, Ports, and Rivers Institute formed a formal Standards Committee to develop a national consensus standard for seismic design of pile supported piers and wharves. Within this Standards Committee, several Task Committees were formed to address various aspects of seismic design of piers and wharves. Task Committee 7 was charged with developing standards for the geotechnical and soil-structure interaction aspects pertaining to piers and wharves. In addition to recommending different levels of ground motions for different performance levels and importance categories of the structure, the ground motions per ASCE 7-05 are being adopted to maintain consistency with the minimum standards of this document. This paper discusses the efforts to develop the standards and commentaries for the ground motion, geotechnical, and soil-structure interaction aspects of the proposed standard, especially those that are unique to piers and wharves.

Introduction

The U.S. port system is a mature, major industry, with annual expenditures for construction and development in the billions of dollars. It is clear that large scale damage to port facilities due to natural hazards such as an earthquake would have major regional and likely national impacts. Life-safety has not been a historical problem at piers and wharves, because of relatively low occupancy and few working personnel on these structures, and because most of these structures consist primarily of open area with no enclosed building structures which can collapse onto personnel.

ASCE 7-05, which sets the minimum life-safety standards for designing buildings and other structures, does not directly address all of the issues designers typically face in the seismic design of piers and wharves, especially with respect to dealing with kinematic loading from permanent ground deformation. Some major West Coast ports have developed their own seismic design criteria and methodologies (for

example, Port of Los Angeles, 2004; Port of Long Beach, 2007). Many of the ports are not subject to the jurisdiction of local building officials and the port-developed seismic criteria and methodologies do not necessarily follow conventional building codes. Often, because of the economic importance and capital costs associated with port facilities, the criteria developed by ports are in reality more stringent than those set by building codes. The current practice at these California ports follows a "performance-based" seismic design to achieve a specific level of performance using a displacement approach based on at least two levels of earthquake motions.

In 2005, ASCE's Codes and Standards Committee (CSC) and Coastal, Oceans, Ports, and Rivers Institute (COPRI) formed a formal Standards Committee that consists of structural engineers, geotechnical engineers, academics, and owners with interest in seismic design of piers and wharves to develop a national consensus standard for seismic design of piers and wharves. Several Task Committees were formed within this Standards Committee to address various aspects of seismic design of piers and wharves. Task Committee 7 (TC7) was charged with developing standards for the geotechnical and soil-structure interaction aspects pertaining to piers and wharves.

Another committee, Task Committee 2 (TC2), was responsible for developing seismic performance requirements for piers and wharves according to their importance categories. Working closely with TC7, this task committee also developed seismic performance requirements and seismic hazard levels for different importance categories.

Following sections describe the performance levels and importance categories developed by TC2 and address the geotechnical and soil-structure interaction issues associated with the design of pile-supported piers and wharves.

Performance Levels

The following three performance levels are defined:

Life-Safety Protection. A structure is classified as providing "life-safety protection" when (a) it maintains sufficient residual strength following an earthquake such that it does not constitute a public hazard; and (b) there is no loss of containment of any toxic materials that may be handled at the structure.

Controlled and Repairable Damage. A structure is classified as providing "controlled and repairable damage" when: (a) the structure experiences controlled, inelastic, and ductile response and residual deformations which are limited in order to keep the structure repairable; (b) the required repairs result in a loss of serviceability that can range from a few weeks to up to several months; and (c) there is no loss of containment of any toxic materials that may be handled at the structure.

Minimal Damage. A structure is classified as providing "minimal damage" when: (a) it corresponds to near-elastic structural response with minor or no residual

deformation; (b) there is no loss of serviceability of the structure; and (c) there is no loss of containment of any toxic materials that may be handled at the structure.

Importance Categories

Three importance categories are defined as follows:

High Importance. A structure is classified as having a "high" level of importance if it is essential to the region's economic/social recovery and/or to the owner's business interests. This implies that the loss of operation following an earthquake must be minimized to a desired duration.

Moderate Importance. A structure is classified as a "moderate" level of importance if it: (a) is important but not essential to the region's economic/social recovery and to the owner's business interests (i.e., a less stringent serviceability requirement is imposed for post-event operations); or (b) otherwise requires a level of seismic performance beyond collapse protection.

Low Importance. A structure is classified as having a "low" level of importance if its loss of operations has only a minor impact on the region's economic/social recovery and the owner's business interests.

Seismic Hazard Levels and Ground Motion Parameters

Three seismic hazard levels are defined as follows:

Operating Level Earthquake. Operating Level Earthquake (OLE) is defined as a ground motion whose probability of exceedance is 50% in 50 years with a return period of 72 years.

Contingency Level Earthquake. Contingency Level Earthquake (CLE) is defined as a ground motion whose probability of exceedance is 10% in 50 years (return period of 475 years) and 20% in 50 years (return period of 224 years) for high-importance and moderate-importance structures, respectively.

Design Earthquake. Design Earthquake (DE) is defined in accordance with ASCE 7 (ASCE, 2005).

The ground motion parameters for the above seismic hazard levels should consider near fault directivity effects and amplification associated with local site conditions. As a minimum, ground motion parameters should include peak ground acceleration and corresponding most probable magnitude of the earthquake, and acceleration response spectrum.

Ground motion parameters for 5 percent damping may be evaluated using the U. S. Geological Survey website (http://eqint.cr.usgs.gov/deaggint/2002/index.php), adjusted for local site conditions using the factors provided in Chapter 11 of ASCE 7 (ASCE, 2005). Appropriate de-aggregation of the seismic hazard may be necessary in regions of seismicity from multiple types of earthquake sources. Ground motion

parameters for probabilities of exceedance that are not available from the USGS website and for damping values other than 5 percent may be obtained using the procedure outlined in FEMA 356 (FEMA, 2000). Alternatively, site-specific evaluations, including site response analysis, may be performed to obtain the ground motion parameters. Some major West Coast ports have already commissioned studies to perform site-specific ground motion evaluations (Vahdani et al., 2004; Arulmoli et al., 2007).

If non-linear time history analyses are deemed necessary, appropriate orthogonal sets of design time histories should be developed. As a minimum, three sets of time histories should be developed. If three sets of time histories are used in the evaluations, the response parameter should be the envelope of the response parameter for each time history; when seven or more sets of time histories are used, the average value of each response parameter may be used (CBC, 2008).

The development of design spectra for vertical ground accelerations is typically not needed. Vertical ground shaking is typically confined to very short period motions (i.e. periods less than 0.2 second). Principal wharf and pier deck vibration modes are typically expected to have a predominant response period outside this very short period range. Capturing the short-period vibration modes can present undue complexities to designers, especially within the context of a response spectrum analysis design approach, as opposed to a time history analysis method. In view of the above, less complex engineering design measures may be considered acceptable to accommodate potential effects of vertical ground motions, such as those favored by Caltrans design criteria (Caltrans, 2006b).

Seismic Performance Requirements

The minimum seismic performance requirements for structures designed according to this proposed standard depend on the importance category assigned to the structure. For each importance category, these requirements consist of the performance level that must be met when the structure is subjected to each of the hazard levels defined above. These performance requirements are defined in Table 1.

Geotechnical and Soil-Structure Interaction Considerations

Geotechnical and soil-structure interaction issues associated with seismic evaluation of piers and wharves were addressed by TC7 and appropriate text was developed for the standards. This text was intended for the use of geotechnical engineers having a good understanding of geotechnical earthquake engineering and with adequate experience in performing seismic evaluations of geotechnical structures and soil-structure interaction.

Liquefaction Potential. Liquefaction potential of the soils in the immediate vicinity of the structure and associated embankment or rock dike, including soils in front of, beneath, and behind the pier or wharf, should be evaluated. If liquefaction is likely, the effects of liquefaction should be addressed during the seismic design of the structure.

Table 1. Minimum Seismic Performance Requirements

Importance Category	Seismic Hazard Level and Performance Level					
	OLE		CLE		DE	
	Ground Motion Probability of Exceedance	Performance Level	Ground Motion Probability of Exceedance	Performance Level	Seismic Hazard Level	Performance Level
High	50% in 50 years	Minimal Damage	10% in 50 years	Controlled and Repairable Damage	as per ASCE-7	Life Safety Protection
Moderate	n/a	n/a	20% in 50 years	Controlled and Repairable Damage	as per ASCE-7	Life Safety Protection
Low	n/a	n/a	n/a	n/a	as per ASCE-7	Life Safety Protection

Liquefaction potential evaluation should follow the procedures outlined in "Liquefaction Resistance of Soils: Summary Report from the 1996 NCEER and 1998 NCEER/NSF Workshops on Evaluation of Liquefaction Resistance of Soils" (Youd et al., 2001), "Recommended Procedures for Implementation of DMG Special Publication 117, Guidelines for Analyzing and Mitigating Liquefaction Hazards in California" Martin et al., 1999), "Chapter 31F, Supplement to the 2001 California Building Code" (CBC, 2008), "Recent Advances in Soil Liquefaction Engineering: A Unified and Consistent Framework" (Seed et al., 2003), or other appropriate documents. The cyclic resistance of fine-grained soils should be evaluated using current method of analysis (Andrews and Martin, 2000; Seed et al., 2003; Bray and Sancio, 2006; Boulanger and Idriss, 2006). In light of recent advances in the characterization of the seismic performance of fine-grained soils, sole reliance on dated procedures (pre-2000) is not recommended.

If liquefaction is shown to be initiated in the above evaluations, the specific liquefiable strata and their thickness (including zones of liquefaction induced in the backland area) should be clearly shown on site profiles. Potential effects or hazards associated with potential liquefaction should be evaluated including:

1. Flow slides or large translational or rotational failures mobilized by the static driving stresses associated with the dike/embankment system.
2. Limited lateral spreading of the dike/embankment system on the order of a few feet or less triggered and sustained by the earthquake ground shaking.
3. Post-liquefaction settlement of the dike/embankment system and underlying foundation soils.

Slope Stability and Lateral Ground Deformation. The static factor of safety of the slope or embankment for slope stability should not be less than 1.5. Pseudo-static

slope stability analysis should be performed using a horizontal seismic coefficient of 0.15g or one-third of horizontal peak ground acceleration (PGA), whichever is greater. If the PGA is less than 0.15g, then the PGA value should be used in the analysis. If the estimated factor of safety is greater than 1.1, then no further evaluation for deformations or kinematic analysis as outlined below is necessary (Caltrans, 2006a). Under these conditions, it should be recognized that some limited deformations are expected to occur; however, the seismic performance of the slope and structure under these deformations are considered satisfactory.

The static factor of safety immediately following a design earthquake should not be less than 1.1. Shear strength values compatible with the appropriate residual strength of liquefied soils and sensitive clays should be used in both pseudo-static and post-earthquake analyses.

"Free Field" Lateral Ground Deformations. The "free field" lateral deformations of the slope or embankment and associated foundation soils should be evaluated without considering the presence of the foundation system. Initial estimates of "free field" seismic dike deformations may be determined using the simplified Newmark sliding block method. Strength values compatible with the post earthquake residual strength of liquefied soils (Seed and Harder, 1990; Olson and Stark, 2002; Seed et al., 2003) and/or sensitive clays (Skempton, 1964; Duncan and Wright, 2005; Hsai-Fang and Daniels, 2006) should be used in the evaluation. If the "free field" lateral deformations do not compromise the structural performance of the foundation, further kinematic analysis as outlined below is not required.

Soil-Structure Interaction. Two loading conditions for the foundation should be considered: (1) Inertial loading under seismic conditions, and (2) Kinematic loading from lateral ground deformations. Inertial loading is associated with earthquake-induced lateral loading on the structure, while kinematic loading refers to the loading on foundation piles from earthquake-induced lateral deformations of the slope/embankment/dike system. The inertial loading condition in some situations tends to induce maximum moments in upper part of the piles while kinematic loading tends to impose maximum moments in the deep lower regions of the piles. In addition, the two loading conditions tend to induce maximum moments at different times during the earthquake shaking and therefore, can be considered independently. If both of these conditions exist for a pier or wharf, inertial and kinematic loading conditions can be uncoupled (separated) from each other during design. This assumption, however, should be checked on a project-specific basis. A coupled analysis may be needed if these two loading conditions cannot be separated.

Loading associated with the inertial response of the seismic mass, should be considered in the analysis using appropriate lateral soil springs or other appropriate methods. The evaluation of inertial loading can be performed by ignoring the slope/embankment/dike system deformations (i.e., one end of the lateral soil spring at a given depth is attached to the corresponding pile node and the other end is assumed fixed). For simplicity, it is justifiable to analyze piles for the inertial response of the

effective mass of deck, based on the assumption that free-field deformation of the ground in the vicinity of the piles may be ignored.

The evaluation of kinematic loading from permanent lateral ground deformation of the foundation material may include the beneficial effects of piles on lateral ground deformations. Piles should be designed such that the lateral deformations do not compromise the structural performance of the foundation. As mentioned earlier, initial estimates of "free field" seismic dike deformations may be determined using the simplified Newmark sliding block method. If deformations are considered acceptable, no further analyses will be required. Exceptions may be cases where subsurface conditions indicate the presence of thin, liquefiable and/or thin, soft soils beneath the dike/embankment that could result in concentrated deformations within these layers. The resulting double curvature imposed on the piles could lead to potentially unacceptable pile performance. In such cases, more detailed evaluations may be necessary.

Further analysis of kinematic loading may not be necessary if it can be shown that a previously conducted dynamic soil-structure interaction analysis of a similar structure in the vicinity of the considered project with similar soil conditions representing a conservative upper bound solution results in higher pile curvature demands than the structure under consideration, and still satisfies the performance limits for the pile.

In cases where dike deformations estimated using the simplified Newmark sliding block method are unacceptable, site-response evaluations may be necessary to revise the free-field dike deformation estimates based on revised ground motions. One-dimensional site response analyses may need to be performed to incorporate local site effects and develop site-specific acceleration-time histories at the base of the sliding block for Newmark analyses. Sensitivity analyses should be performed on factors affecting the results. The site-specific time histories representing the ground motions at the depth of interest may be used in the simplified Newmark sliding block method to revise the dike deformation estimates.

If the above method does not result in displacements that are considered acceptable, additional evaluations can be made by incorporating the effects of "pile pinning". If it can be shown by structural analysis that the displacement demands estimated by simplified Newmark evaluations while incorporating the "pile pinning" effects are structurally acceptable, no further kinematic evaluations are necessary. This process is described in the following paragraph. It should be reminded that it is an iterative process and requires close coordination between the geotechnical engineer and structural engineer.

The geotechnical engineer should provide the structural engineer with level ground lateral soil springs (p-y springs) for the weak soil layer and soil layers above and below the weak layer for performing pushover analysis to estimate the displacement capacities and corresponding pile shear within the weak soil zone. For the pushover analysis, the estimated displacement profile may be assumed to be linear within the

thickness of the weak soil layer (i.e., zero at and below the bottom of the layer to the maximum value at and above the top of the weak layer). At some distance above and below the weak soil layer (10 pile diameters or more), the pile should be modeled as fixed against rotation, and also against translation relative to the soil displacement. Between these two points (+/- 10 times the pile diameter from the soil layer), lateral soil springs are provided, which allow deformation of the pile relative to the deformed soil profile. The geotechnical engineer should perform pseudo-static slope stability analysis with the "pinning" effects of piles incorporated and estimate the displacement demands using simplified Newmark analysis. If the estimated displacement demands are less than the displacement capacities, no further analysis for kinematic loading will be necessary. As mentioned before, in cases where subsurface conditions indicate the presence of continuous, thin, liquefiable and/or soft soils beneath the dike that could result in concentrated deformations within these layers, more detailed soil-dynamic structure interaction (SSI) analyses may be necessary.

If more detailed numerical analyses are deemed necessary to provide input to the structural engineers, two-dimensional dynamic soil-structure interaction analysis of the deck-pile-dike-soil system using numerical finite element or finite difference analyses should be performed. Sensitivity analyses should also be performed on factors affecting the results. As a minimum, deformation profiles along the length of the various pile rows should be provided to the structural engineer to estimate strains and stresses in the piles for the purpose of checking performance criteria.

Soil Behavior under Lateral Loading. For design of piles under loading associated with the inertial response of the superstructure, level-ground inelastic lateral soil springs (p-y springs) should be developed and used in the analysis. In order to account for the uncertainties associated with the development of p-y springs, including uncertainties arising from soil and rock properties, sloping ground condition, and the simplified spring stiffness used, both upper-bound and lower-bound spring values should be developed for use in the superstructure inertial response analyses.

Seismically Induced Settlement. Seismically induced settlement resulting from liquefaction of saturated soils and settlement of dry and unsaturated soils should be evaluated for use in the design.

Axial Pile Performance. Geotechnical pile capacity evaluation under axial loading should include the effects of pile capacity reduction due to downdrag forces induced by seismically induced settlement. Due to the short-term nature of the seismically induced downdrag forces, the factor of safety may be less than that used in the static pile capacity evaluation. The unit skin friction used to compute downdrag forces should account for the effects of cyclic loading, dissipation of excess pore pressures and reconsolidation of liquefiable layers, and the elevation of pore pressures in adjacent layers. The minimum factor of safety should not be less than 1.0 when

seismically induced downdrag loads are combined with the seismic structural loads on the pile.

Axial Pile Springs. Axial pile performance evaluations should include axial soil springs (t-z or q-w springs) for use in the analyses. The springs (linear or non-linear, as requested by the structural engineer) may be developed either at the top of the pile or along the piles. The appropriate locations where the springs are to be used should be clearly stated. In order to account for the uncertainties associated with the development of springs, such as the axial soil capacity and load distribution along the pile and the simplified spring stiffness used, both upper-bound and lower-bound spring values should be provided to the structural engineer.

Earth Pressures. The effect of earth pressures on wharf structures resulting from seismic loading of backfill soils should be considered in addition to static pressures. The earth pressures should include the effect of liquefaction and porewater pressure build-up in the backfill.

Summary

The proposed ASCE Standards for Seismic Design of Piers and Wharves are expected to address issues designers typically face in the seismic design of piers and wharves and provide consistent minimum standards for design of piers and wharves across different parts of U.S.A. Working closely with the entire Standards Committee that is in the process of developing the standards and other Task Committees, TC7 developed the standards for performing geotechnical and soil-structure interaction evaluations for piers and wharves. The full version of the proposed Seismic Standards is expected to be available for balloting by the end of 2008.

Acknowledgement

The authors would like to acknowledge contributions of all members of the ASCE Standards Committee for Seismic Design of Piers and Wharves, particularly the members of TC7, including Scott Ashford, Billy Camp, Domenic D'Argenzio, Steve Dickenson, Kerop Janoyan, Po Lam, Nason McCullough, Kevin O'Malley, Rick Pearce, Ray Sandiford, Patrick Smith, Shah Vahdani, Saroj Weeraratne, and Zia Zafir. Efforts of Task Committee 2 and its Chair, Stu Werner, in developing seismic performance requirements for piers and wharves are also acknowledged. Valuable comments and suggestions provided by the ASCE reviewers are greatly appreciated.

References

Andrews, D. C. A. and Martin, G. R., 2000, "Criteria for Liquefaction of Silty Soils," Proceedings of the 12th World Conference on Earthquake Engineering, Auckland, New Zealand.

American Society of Civil Engineers (ASCE), 2005. ASCE 7-05, Minimum Design Loads for Buildings and Other Structures, ASCE, Reston, VA.

Arulmoli, K., Lam, I. P., Schell, B. A., Abrahamson, N. A., Santa Ana, J., and Yin, P., 2007, "Ports of Los Angeles and Long Beach Port-Wide Ground Motion Study," Proceedings of the Ports 2007 Conference, La Costa, California, March.

Boulanger, R.W. and Idriss, I. M., 2006, "Liquefaction Susceptibility Criteria for Silts and Clays," Journal of Geotechnical and Geoenvironmental Engineering, ASCE, Vol. 132, No. 11, November.

Bray, J. D. and Sancio, R. B., 2006, "Assessment of the Liquefaction Susceptibility of Fine-Grained Soils," Journal of Geotechnical and Geoenvironmental Engineering, ASCE, Vol. 132, No. 9, September.

California Building Code (CBC), 2008, "Chapter 31F, 2007 California Building Code" January 1.

Caltrans, 2006a, Guidelines for Structures Foundation Report, Version 2.0, March.

Caltrans, 2006b, "Seismic Design Criteria," Version 1.4, June.

Duncan, J.M. and Wright, S.G., 2005, Soil Strength and Slope Stability, John Wiley.

Federal Emergency Management Agency (FEMA), 2000. FEMA-356, Prestandard and Commentary for the Seismic Rehabilitation of Buildings, Washington, DC.

Hsai-Fang and Daniels, J., 2006, Introductory Engineering, An Environmental Perspective, Taylor and Francis, New York and London, pp 306-313.

Martin, G.R., and Lew, M. (eds.), 1999, "Recommended Procedures for Implementation of DMG Special Publication 117, Guidelines for Analyzing and Mitigating Liquefaction Hazards in California," Southern California Earthquake Center, University of Southern California, March.

Olson, S. M. and Stark, T. D., 2002, "Liquefaction Strength ratio from Liquefaction Flow Failure Case Histories," Canadian Geotechnical Journal, Vol. 39, May.

Port of Long Beach, 2007, "Wharf Design Criteria," Draft Version 1.1, March.

Port of Los Angeles, 2004, "Code for Seismic Design, Upgrade, and Repair of Container Wharves," May.

Seed, R.B. and Harder, L. F. Jr., 1990, "SPT-Based Analysis of Cyclic Pore pressure Generation and Undrained Residual Shear Strength," Proceedings, H. Bolton Seed Memorial Symposium, BiTech Publishers, Ltd., May.

Seed, R. B. et al., 2003, "Recent Advances in Soil Liquefaction Engineering: A Unified and Consistent Framework," 26th Annual ASCE Los Angeles Section, Spring Seminar, Long Beach, California, April.

Skemton, A. W., 1964, Long Term Stability of Clay Slopes, Geotechnique, V. 14 No. 2, pp 71-102.

Vahdani, S., Egan, J., Pyke, R., Balakrishnan, A., Chen, C., Ogunfunmi, K., and Labasco, T., 2004, "Seismic Microzonation Study at the Port of Oakland," Proceedings of the Ports 2004 Conference, Houston, Texas, May 23-26.

Youd, T.L. et al., 2001, "Liquefaction Resistance of Soils: Summary Report from the 1996 NCEER and 1998 NCEER/NSF Workshops on Evaluation of Liquefaction Resistance of Soils," ASCE, Journal of Geotechnical and Geoenvironmental Engineering, Vol. 127, No. 10, October.

Integrating Soil-Structure Interaction Analyses of Pile-Supported Wharfs in Seismic Risk Management of Port Systems

Varun[1], S.M. ASCE and Dominic Assimaki[2], M. ASCE

[1]Graduate Research Assistant, Georgia Institute of Technology, School of Civil and Environmental Engineering, 790 Atlantic Drive, NW, Atlanta GA30332-0355; varun.varun@gatech.edu
[2]Assistant Professor, Georgia Institute of Technology, School of Civil and Environmental Engineering, 790 Atlantic Drive, NW, Atlanta GA30332-0355; dominic.assimaki@ce.gatech.edu

ABSTRACT: This paper presents the general framework for the development and calibration of simplified nonlinear Winkler-type mechanical models via finite element simulations for the analysis of seismic response of pile foundations in soil conditions remediated against liquefaction. These models are currently being developed for implementation in Monte Carlo simulations for risk assessment analyses of waterfront structures, to allow computationally efficient seismic response predictions of 3D pile-supported wharves for alternative scenarios of ground motion intensity and remediation configurations. The macro-elements are formulated to account for the multitude of soil resistance mechanisms mobilized at the foundation of pile-supported structures by considering both material and soil-pile interface (geometric) nonlinearities during dynamic loading of single piles, thus retaining the physical soundness of the mechanical configuration. This paper describes work under progress, and focuses on the alternative formulations investigated to identify the optimal macroscopic model that will allow credible yet efficient simulations of the seismic performance of pile-supported structures required for the quantification of damage states in liquefiable and treated-against sites.

INTRODUCTION

Ports require pier and wharf structures that provide a work surface for port operations. The most common type of wharf structure at large U.S. ports is a pile-supported marginal wharf (Figure 1). These structures consist of long, narrow pile-supported deck segments on sloping subsurface materials ranging from rock dikes to hydraulic fills. The seismic response of pile-supported wharves is inherently a complex soil-structure interaction problem that involves large ground displacements, pore pressure generation potentially leading to liquefaction of the backfill, and coupled transverse, longitudinal, and torsional response of the wharf. For a comprehensive assessment of the soil-structure system performance during seismic loading, detailed 3D finite element coupled solid-fluid simulations should be ideally

conducted, where the soil and structural components would be represented by means of appropriate non-linear constitutive models. Inasmuch such analyses are feasible, however, they are associated with increased cost resulting from the input parameter acquisition for the constitutive models, and the engineering expertise necessary for the numerical modeling and the target result interpretation. Furthermore, the substantial computational effort involved in the realization of these analyses prohibits their use in statistically sound risk assessment studies that are based on a large number of alternative hazard analyses.

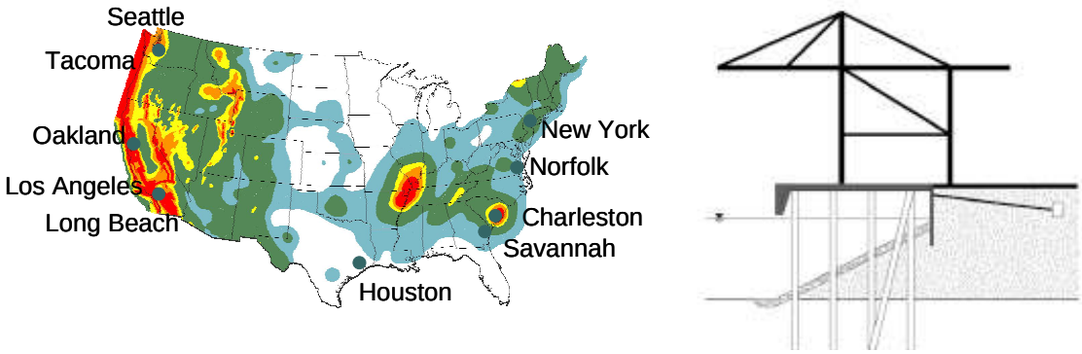


FIG. 1. (left) Large US-ports and seismic hazard by USGS (PGA with 2% PE in 50 years); (right) Soil-foundation-structure system (not to scale)

Results presented in this paper are part of a multi-disciplinary project (**www.neesgc.gatech.edu**) funded by NEES, the George E. Brown, Jr. Network for Earthquake Engineering Simulation Program of the National Science Foundation (**www.nees.org**). The project focuses on the seismic risk mitigation of port structures by assessing the relative effectiveness of alternative remediation and retrofitting techniques for both geotechnical and structural components, and within the context of this effort, the overarching goal of the research described here is the development of macroscopic mechanical models, to simulate the soil response for different types of remediated site conditions for soil-structure interaction analyses, and evaluate their effectiveness for alternative earthquake scenarios. The ensemble of these analyses, integrated within the context of a risk management assessment study for port systems, are anticipated to lead to reliable and cost-effective design methodologies that will optimally improve the seismic resistance of waterfront structures. While the macro-elements developed in this study are calibrated to approximate the response of soil formations treated via two remediation techniques, (a) installation of prefabricated vertical drains and (b) colloidal silica grout, the general framework can be used in conjunction with the suitably idealized constitutive law for any type of soil conditions.

MACROELEMENT FORMULATION

In contrast to the constitutive modeling of soil-structure interaction problems, macroelements are derived by integrating the material behavior over the locally affected volume of soil in contact with the foundation elements, and evaluating the global stress-strain response at representative locations of the soil-structure interface based on the externally applied loading. Bounded by limit equilibrium conditions, macroelements can simulate the coupled effects of soil plasticity and interface

nonlinearities, anticipated to be substantially different for dynamic loading than those predicted for pushover or cyclic loading in simplified design procedures. Successively, decomposition of the far-field and near-field domain allows efficient frequency-domain methods to be employed in the far field, since analysis of the superstructure supported by macroelements incorporates nonlinear soil-structure interaction effects. Figure 2 shows the various resistance mechanisms as identified by Gerolymos and Gazetas (2006a) and Varun et al (2007). Varun et al (2007) showed that for length to diameter ratios greater than 8, the contribution of rotational resistance mechanisms, i.e., the distributed rotational resistance due to shear stresses parallel to pile axis and the base concentrated rotational resistance due to normal stresses to the global stiffness of the foundation becomes negligible. Thus, only lateral resistance mechanisms will be accounted for in the model, which is formulated as a displacement driven rather than a load driven one, more suited to capture kinematic interaction effects which play a key role in response of piles to seismic excitation.

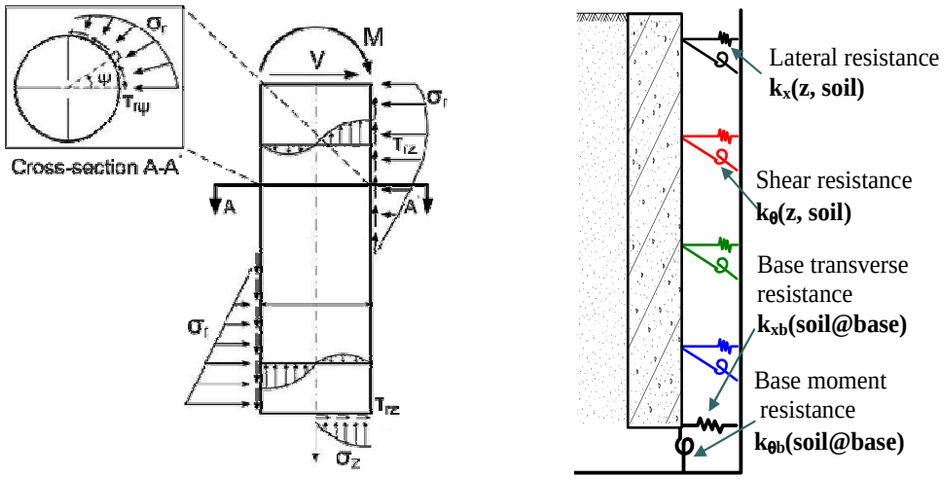


FIG. 2. Various soil resistance mechanisms at soil pile interface.

The challenge of this project lies on the development of simplified mechanical models, capable of representing the material and geometric nonlinearities at the soil-foundation interface via combinations of stiffness, damping and Coulomb friction elements, and account for the soil strength degradation due to pore pressure built-up - critical for the simulation of liquefiable site conditions- via physically sound, pressure-dependent stiffness elements.

Two types of macroelement formulations are being currently investigated, and selection of the most suitable for the purpose of this work will be based on the efficient integration potential of pore pressure effects on the macroscopic behavior of the model, as well as the benchmarking of its effectiveness via comparison with 3D finite elements and small-scale (centrifuge) experimental data.

The first type of models is based on direct mechanical representation of the critical physical resistance and energy propagation mechanisms manifesting during the transient response of foundation elements. Conceptually-similar models have been implemented in the past for simplified analyses for quasi-static (Taciroglu et al, 2006) and dynamic (Boulanger et al, 2003) lateral pile loading conditions. In particular, the first type of macroelement consists of a front-face and rear-face resistance elements

and a drag component, each one of which comprises combinations of spring, dashpot, gap and friction elements. Figure 3 shows the various components of macroelement and a brief description of each component is given below.

1. **Front and rear-face component**: These components represent the soil resistance on the front and the rear side of the pile, respectively. They comprise the following elements:

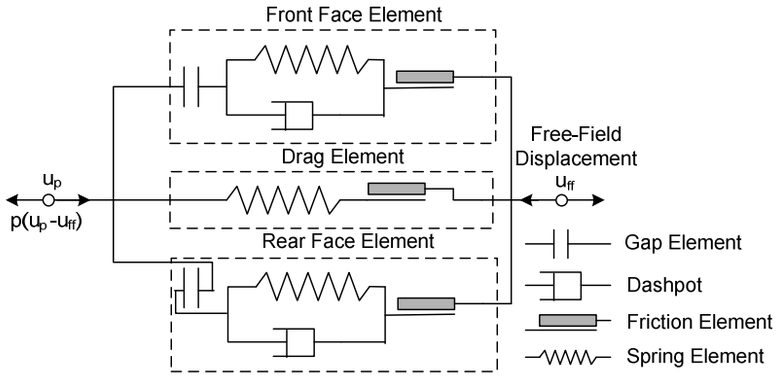


FIG. 3. Schematic of the mechanical components comprising a multi-component macroelement. The relative effectiveness of this configuration vs. the so-called Bouc-Wen type elements (Fig. 4) that comprise fewer mechanical components, each one described by complex mathematical formulations for soil-structure interaction analyses of pile-supported wharves is being currently investigated.

   a. A *gap element*, which relates the force transmitted from the soil to the pile p(σ) to the force existing in soil σ. For a 'perfect' gap, p(σ) = σ when the force is compressive and the gap is closed (perfect contact), while p(σ) = 0 when the force is tensile and greater than the interface cohesion, causing the gap to open (no contact).
   b. A *damping element*, which represents the frequency-dependent mechanism of radiation damping due to waves emanating away from the pile surface. For weak oscillations of the system, during which the soil and pile respond in the elastic range, Makris and Gazetas (1992) developed an approximate expression assuming that the wavefield can be divided into four quadrants, two of which are dominated by P-waves and the other two by S-waves. The expression is given below

$$F_D = \left(\rho_s v_s a_o^{-0.25} 2 \left[1 + \frac{3.4}{\pi(1-\nu_s)} \right]^{1.25} \left(\frac{\pi}{4} \right)^{0.75} \right) B\dot{u} \qquad (1)$$

   where B is the diameter of pile, ρ, V_s and ν are the density, low strain shear wave velocity and Poisson ratio of the soil respectively. a_o is the dimensionless frequency given as $a_o = \omega B / V_s$ where ω is the frequency of excitation. For the case of nonlinear soil-structure interaction problems, however, Badoni and Makris (1996) showed that the soil yielding in the vicinity of the interface prevents the energy from being carried as far, and the expression developed for the elastic case may give unrealistically high values for the associated force.

To avoid this phenomenon, the damper is put in series with the friction element so that the maximum force exerted is always less than the yield strength of the soil. The force exerted by the damper in the non-linear strain range will be calibrated for the alternative treated conditions as the difference in soil reactions between a hyperbolic (including mass and time derivative terms) and an elliptical (quasi-static) solver.

c. A *spring element*, which represents the low strain stiffness of soil. This element is linear elastic and all the displacements in this element are completely recoverable. This element also controls the unloading part of the macroelement. It is a function of shape of the pile (circular vs square for same soil stiffness) and effective stress as described by equation (2):

$$E = E_o \left(\frac{p}{p_o} \right)^n \tag{2}$$

where E_o is the reference spring modulus at a reference effective stress p_o and n is the exponent controlling the shape of the dependence curve.

d. Finally, a *friction element*, which accounts for the plastic (irrecoverable) deformation of the material. The yield surface of the friction element is formulated as a function of both yield force σ_Y and displacement softening/hardening parameter α. Furthermore, Karthigeyan et al (2007), among others, reported coupling between the vertical pile load and the lateral capacity of the soil. The observations show a small increase in lateral capacity for small vertical loads due to confinement effect in sands and then as the vertical load increases and soil in vicinity starts yielding, the lateral capacity goes down. The lateral yield capacity will also be expressed as a function of existing vertical in form of a failure envelope. The flow rule which determines the evolution of yield force and hardening/softening parameter is determined by the constitutive model used for the soil.

2. **Drag Component**: The drag component represents the drag force exerted due to the flow of soil around the pile. As can be readily seen, this phenomenon does not produce any waves traveling away from pile as it is associated with plastic flow, and as a result, there is no damping element coupled to this component. It has a bilinear behavior characterized by a stiffness of the spring and the yield force associated with the friction element which is controlled by the residual friction angle of soil.

The second type of models was originally proposed by Bouc (1971) and Wen (1977) and extended for pile foundations by Gerolymos and Gazetas (2006a, 2006b). It uses a system of constitutive equations in differential form to model the global behavior. Though such a model is derived by means of stepwise curve fitting, the parameters can be linked to measurable physical properties such as engineering properties of soil and geometry of foundation. The advantage of this model over the previous one is that they are controlled by fewer equations and are able to capture much more complex shapes. This macroelement consist of a spring and a dashpot connected in parallel as shown in Figure 4. The governing equations are given as:

$$p_s = \alpha k u + (1-\alpha) p_y \zeta \tag{3}$$

in which: p_s is the resultant in the direction of loading of the normal and shear tractions along the perimeter of the pile of a unit thickness, u is the horizontal displacement of the pile at the location of the spring; k is the initial stiffness of the translational spring; α is a parameter that controls the post-yield stiffness; p_y is the ultimate soil reaction; and ζ is a hysteretic dimensionless quantity controlling the nonlinear behavior of the lateral soil reaction. The latter is governed by

$$d\zeta = \frac{\lambda h}{u_y}\left\{1-(1+r)\left|\zeta\right|^n\left[b+gsign(du\zeta)\right]\right\}du \text{ where } h(\zeta)=1-\zeta_o\exp\left[-\left(\frac{u_y\zeta}{\delta\Delta}\right)^2\right] \quad (4)$$

is the 'pinching factor', for modeling the effect of the gap formation/displacement hardening. In the above equations $u_y = p_y/k$ is the value of lateral displacement at initiation of yielding in the soil at the specific depth, Δ is the maximum attained displacement or gap width and b, g, n, λ, r, ζ, δ are dimensionless quantities. The parameter n controls the smoothness of transition from elastic to plastic zone. For n > 10, the transfer is almost elastic-perfectly plastic behavior. b and g control the width of hysteretic loop, b = g = 0.5 reproduce the Masing unloading-reloading criteria whereas b = 1 and g = 0 produce no hysteretic damping at all. The parameter λ controls the stiffness whereas r controls the strength of the macroelement. The parameter ζ_0 controls the sharpness of separation and δ controls the gap growth. The lateral reaction resulting from the viscoplastic dashpot is given by:

$$p_d = c\frac{\partial u}{\partial t}\left[a+(1-a)\frac{\partial \zeta}{\partial u}\right]^{c_d} \quad (5)$$

where 'c' is the dashpot coefficient at small amplitude motions, and 'c_d' is a viscoplastic parameter which controls the coupling of soil and soil-pile interface nonlinearity with radiation damping.

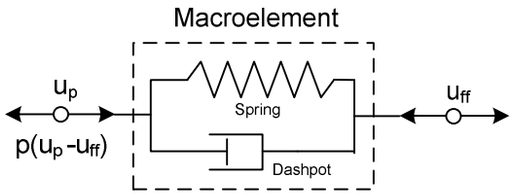


FIG. 4. Schematic of the Bouc-Wen macroelement investigated in this project

NUMERICAL SIMULATIONS AND PRELIMINARY RESULTS

Within the general framework of a macroelement development, which is based on the effective identification of the most critical resistance mechanisms and their corresponding "translation" into mechanical components, numerical simulations are next conducted for their calibration in absence of a sufficient number of experimental results for that purpose. Therefore, the formulation of macro-elements is primarily based on simulations, which -while validated by means of the typically limited number of laboratory and small-scale (centrifuge) experimental results- play a critical role in the development process and need to have ensured accuracy and stability.

For the purpose of this study, sensitivity analyses were initially performed for the lateral far-field distance and optimum element size as a function of material properties for typical ground motion frequency content (1-15Hz). In order to ensure accuracy of the numerical simulations in the far-field representation, a boundary energy-absorbing layer of progressively increasing viscous damping and no impedance contrast with the far-field material is used to simulate the infinite domain energy radiation damping while effective forcing functions are applied at the boundaries to match the expected motion.

The development of macroelements is based on the computed response of single piles subjected to dynamic loading and vertically propagating seismic waves via finite element analyses using DYNAFLOW, for constitutive models developed for treated soils by means of laboratory test results on the remediated material. Two-dimensional (2D) and three-dimensional (3D) parametric analyses are currently being conducted for this purpose, while pile-group interaction factors and coupling effect factors between the in-plane, out-of-plane shear and compressional behavior of the elements will be developed in the future on the basis of the FE simulations.

As an example of preliminary results, simulations were first conducted for plane strain conditions for a pressure-dependent material, where the overburden pressure was applied by means of initial stress in the model. Figure 5 shows a typical series of these analyses, namely the gap growth when a sinusoidal load is applied to a pile embedded in plastic soil (Drucker-Prager material). Note that the gap size reaches a steady state width after certain number of cycles depending on magnitude of load. Successively, Figure 6a shows the effect of friction at soil pile interface by means of two extreme cases, namely zero and perfect friction. While for zero friction the transfer zone from one side to other has a flat slope, the perfect friction case shows a variable slope which is governed by the shear strength of soil itself. Figure 6b shows the effect of stiffness of soil on p-y curves. Based on sequels of parametric investigations as the one described above, for fixed constitutive behavior idealization of the soil material, the development of a macroelement involves the formulation of pressure-dependent functions that describe the behavior of the various mechanical components as a function of the critical parameters dictated by the constitutive law of the soil, the interface properties, and the type and characteristics of the applied load.

Once the macroelements are formulated to account for the material and geometric nonlinearities in dry soil conditions, the development framework implemented here involves the representation of the effect of pore pressure generation due to transient strong ground motion on the lateral capacity of pile. The following two alternatives are currently being investigated:

1. Computation of the excess pore water pressure time-histories as part of the site response estimation, namely in absence of the structure, and use of the computed values in addition to the far-field response as input into the macroelement strength functions. The total strength of the macroelement will be accordingly scaled down by a degradation factor as a function of pore pressure ratio, in the form of $r_u = p/\sigma_v$. Approximate expressions for the degradation factor as a function of pore pressure ratio have been developed by Dobry et al (1995) based on centrifuge studies on lateral resistance of liquefied sand. A similar approach has been implemented by Boulanger et al (2003) for dynamic analyses conducted by means

of macroelements.

2. The integration of a semi-empirical method to compute the excess pore pressure within the macroelement while conducting total stress analyses for the free-field conditions. This approach is based on the observation by Towhata and Ishihara (1985) that the pore pressure generation is proportional to total amount of shear work done and thus no information about the loading history is required as long as the total shear work done is known. Iai (1991) generalized it to a concept of liquefaction front in normalized stress space and developed a multi-shear mechanism model in strain space to determine the evolution of pore-pressure history with time. In this approach, an integrated version of Iai's model will be used in a feedback mode to generate the pore pressure time histories within the macroelement.

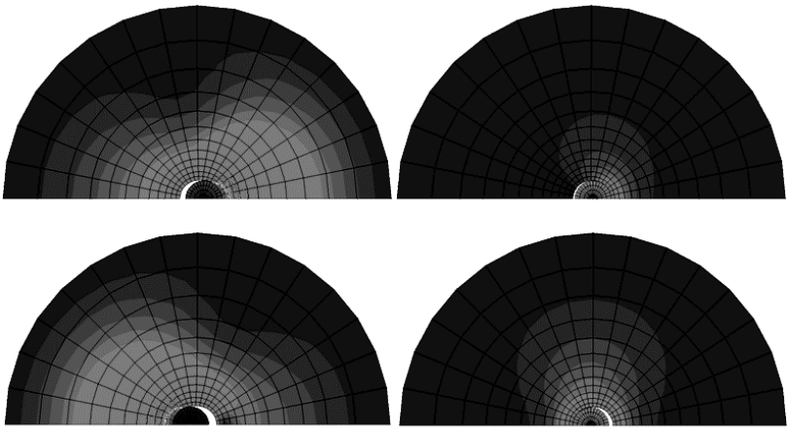


FIG. 5. Gap growth in a plastic soil with repetitive loading.

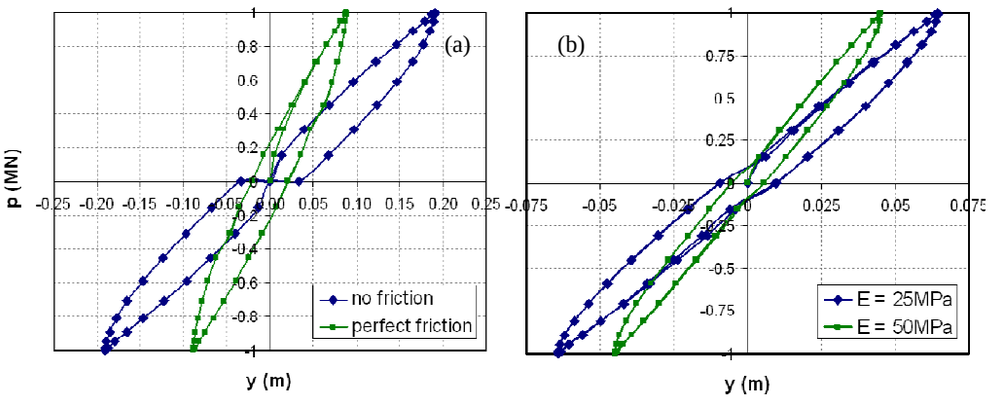


FIG. 6. (a) Effect of interface friction (b) Effect of soil stiffness

The input displacement time histories required for this type of analysis are planned to be calculated by means of 2D plane strain free-field simulations. The evaluation of 2D site response analyses is considered here necessary to account for the topographic amplification that originates from diffraction and scattering of seismic waves at the crest of the embankment that cannot be captured by means of 1D soil-column oriented site response analyses. While both alternative macro-elements considered are strain-driven namely require displacement input at the free-field nodes of the formulations,

the first pore pressure function approach requires effective stress and the second total stress analyses, a fact that renders the latter more efficient yet less accurate than the former. Selection the most suitable combination for the purpose of this work is conditioned on the relative efficiency of the empirical versus the increased accuracy of the numerical pore pressure effect representation, validated via numerical simulations and small-scale experimental data produced within the context of this project (Marinucci et al., 2007).

VALIDATION OF RESPONSE EVALUATION VIA MACROELEMENTS

Centrifuge tests conducted at UC Davis along with dynamic shear and resonant column tests conducted at Georgia Tech and MIT are currently being used to validate and benchmark the constitutive models for remediated soil conditions. Once developed and calibrated, the pressure-dependent constitutive models will be next used for the development of dynamic soil-structure macroelements. Validation of these dynamic mechanical models will be carried out by means of comparison of the simplified analyses with fully coupled, 3D FEM simulations and the limited number of experimental results. In order to investigate the relative effectiveness of the alternative remediation methodologies, soil-structure interaction simulations for multiple alternative ground motion scenarios will be also conducted for the corresponding untreated sites at a series of typical base wharf configuration, which will also be validated by means of centrifuge data available for the dynamic response of wharf structures from previous studies (McCullough et al, 2007).

CONCLUSIONS – WORK UNDER PROGRESS

The substantial computational effort involved in the realization of fully coupled dynamic non-linear FEM analyses prohibits their use in statistically sound risk assessment studies that are based on a large number of alternative hazard analyses. To allow the investigation of alternative remediation techniques for port facilities, a dynamic macroelement is currently developed that will allow simplified dynamic analyses at acceptable accuracy and substantially reduced computational effort. Soil structure interaction simulations will be then conducted for different earthquake scenarios to investigate the relative effectiveness of two alternative remediation techniques as a function of the site conditions and structural configuration investigated. The latter includes the evaluation of acceptable deformation limits and associated damage states of the waterfront structure, and the development of fragility curves for the soil-pile-deck-superstructure system under investigation.

ACKNOWLEDGMENTS

This material is based upon the work supported by the National Science Foundation under Grant Nos. CMS-0530478 and CMS-0402490. Any opinions expressed in this material are those of the author(s) and do not necessarily reflect the views of NSF.

REFERENCES

Badoni, D. and Makris, N. (1996) "Nonlinear response of single pile under lateral inertial and seismic loads." Soil Dynamics and Earthquake Engineering, 15, 29–43.

Bouc R. (1971) Modele mathematique d' hysteresis. Acustica;21:16–25 [in French].

Boulanger, R. W., Kutter, B. L., Brandenberg, S. J., Singh, P., and Chang, D. (2003). Pile Foundations in Liquefied and Laterally Spreading Ground During Earthquakes: Centrifuge Experiments and Analyses. Report UCD/CGM-03/01, Center for Geotechnical Modeling, University of California, Davis, CA, 205 pp.

Dobry, R., Taboada, V., and Liu, L. (1995). "Centrifuge modeling of liquefaction effects during earthquakes." Proc., 1st Int. Conf. on Earthquake Geotechnical Engineering, K. Ishihara, ed., Vol. 3, Balkema/Rotterdam, Tokyo, 1291–1324.

Gerolymos N, Gazetas G. (2006a) Development of Winkler model for static and dynamic response of caisson foundations with soil and interface nonlinearities. Soil Dyn. Earthquake Eng. 26:363-376.

Gerolymos N, Gazetas G. (2006b) Static and dynamic response of massive caisson foundations with soil and interface nonlinearities—validation and results. Soil Dyn. Earthquake Eng. 26:377–394.

Iai, S. (1991). ''A strain space multiple mechanism model for cyclic behavior of sand and its application.'' Earthquake Engineering Research Note No. 43, Port and Harbor Research Institute, Ministry of Transport, Japan.

Karthigeyan, S., Ramakrishna, V.V. and Rajagopal, K. (2007) "Numerical Investigation of the effect of Vertical Load on the Lateral Response of Piles." Journal of Geotechnical and Geoenvironmental Engrg., ASCE, 133(5), 512-521.

Marinucci, A., Rathje, E., Boulanger, R., Rix, G., Kano, S., Conlee, C. and Kamai, R. (2007) "Evaluation of Effectiveness of Prefabricated Vertical Drains for Liquefaction Remediation", Centrifuge Data Report SSK01, UCDavis, Davis.

McCullough, N.J., Dickenson, S.E., Schlechter, S.M. and Boland, J.C. (2007) "Centrifuge Seismic Modeling of Pil-Supported wharves." Geotechnical Testing Journal, 30(5), 1-11.

Makris, N. and Gazetas, G. (1992) "Dynamic pile–soil–pile interaction. Part II: lateral and seismic response." Earthquake Engrg. and Structural Dynamics, 21,145–162.

Taciroglu, E., Rha, C.S. and Wallace, J.W. (2006). "A Robust Macroelement Model for Soil-Pile Interaction under Cyclic Loads." Journal of Geotechnical and Geoenvironmental Engineering, ASCE, 132(10), 1304-1314.

Towhata, I., and K. Ishihara (1985). Modeling soil behavior under principal axes rotation, paper presented at the Fifth International Conference on Numerical Methods in Geomechanics, Nagoya, Japan 523–530.

Varun, Assimaki D., & Gazetas G. (2007). "Linear transient response of deep rigid foundations", Proc. 2nd Greece-Japan Workshop on Seismic Design, Observation and Retrofit of Foundations, Tokyo, Japan, 3-4 April 2007.

Wen YK. (1976) Method for random vibration of hysteretic systems. J Eng Mech ASCE ;102:249–63.

Seismic Retrofit and Improvement of Alpha-Bravo Wharves in Guam

(Raj) S.Varatharaj[1], P.E., M.ASCE, Arul K.Arulmoli[2], G.E., F.ASCE,
Dick Chan[3], Ph.D., P.E., Kijun Ahn[4], Ph. D., P.E., and Ukrit Siriprusanan[5], P.E.

[1]Project Engineer, Earth Mechanics Inc., 17660 Newhope Street, Suite E, Fountain Valley, CA 92708, e-mail: Raj@Earthmech.com, [2]Principal, Earth Mechanics Inc., 17660 Newhope Street, Suite E, Fountain Valley, CA 92708, e-mail: Arulmoli@Earthmech.com, [3]Vice President, Moffatt & Nichole Engineers, 3780 Kilroy Airport Way, Suite 750, Long Beach, CA 90806, e-mail: DChan@MoffattNichol.com, [4]Project Manager, Moffatt & Nichole Engineers, 3780 Kilroy Airport Way, Suite 750, Long Beach, CA 90806, e-mail KAhn@MoffattNichol.com, [5]President, Geo-Engineering & Testing, Inc., P O Box 8170, Tamuning, GU 96931, e-mail: Ukrit@GeoGuam.com

ABSTRACT

Guam has experienced several large earthquakes in the past several decades. The 1993 earthquake with a moment magnitude of 7.7 caused significant damage throughout the island. Liquefaction and lateral spreading caused damages to commercial and naval port facilities at Apra Harbor. The Alpha-Bravo wharf, built in 1947 without proper seismic considerations, suffered some damage during the 1993 earthquake, including backland liquefaction. The U.S Navy commissioned a seismic improvement program that included upgrade of the Alpha-bravo wharf. The improvements to the wharf included increasing the water depth from approximately 10.7 m to 12.8 m, and retrofitting the existing wharf to meet current seismic and future operational requirements. A two-level seismic performance criterion was used: under the Level 1 earthquake associated with a 72-year return period, wharf elements sustain only minor or no structural damages with no interruption to operations; under the Lever 2 earthquake events with 475-year return period, the wharf elements undergo controlled inelastic structural behavior with repairable damage. Sheet piles and tie-back system were designed to accomplish the seismic retrofit and improvement of the wharf. In order to withstand high tie-back forces, the anchor blocks in the backlands were supported on battered, steel H piles. During construction, the test piles driven at anchor blocks showed softer driving, and dynamic pile analyses results indicated lower axial capacities than the design capacities. Adjustments were made by adding lugs to piles and increasing pile lengths to incorporate the findings from test piles. Partnering meetings and proactive participation of all interested parties including the owner, designers, and contractor throughout the construction of the project helped minimize project delays and cost overruns.

Introduction

The Alpha-Bravo wharf is a US Naval facility located within Apra Harbor (Figure 1) in Guam, a US territorial island located directly south of Tokyo and east of Manila, near 13° N latitude and 145° E longitude. Guam's east coast faces the Pacific Ocean and west coast faces the Philippine Sea. Guam is the largest island located near the

southern end of the chain of islands known as Mariana Islands Archipelago, a curvilinear, arcuate alignment of active and inactive volcanoes that extends in a general north-south direction for about 1200 km in the western Pacific Ocean.

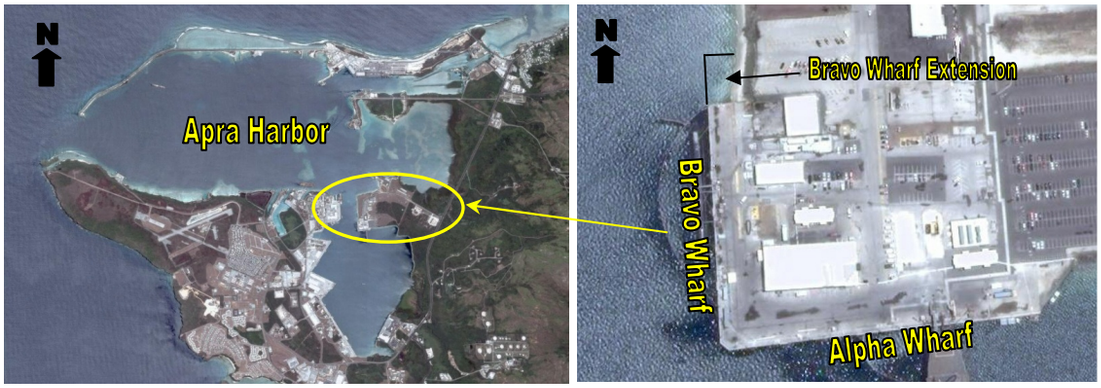


Figure 1. Site Location

The existing Alpha-Bravo wharves were built in 1947. The Alpha wharf is approximately 204m long with the deck at approximate El. +3.1m and a mudline at approximate El. -10.7m (Figure 2a). The approximately 135m western side of the wharf consists of relieving platform at approximate El. +0.3m supported by timber piles. Sheet piles supported by tie-back anchor system retains fill placed behind the wharf.

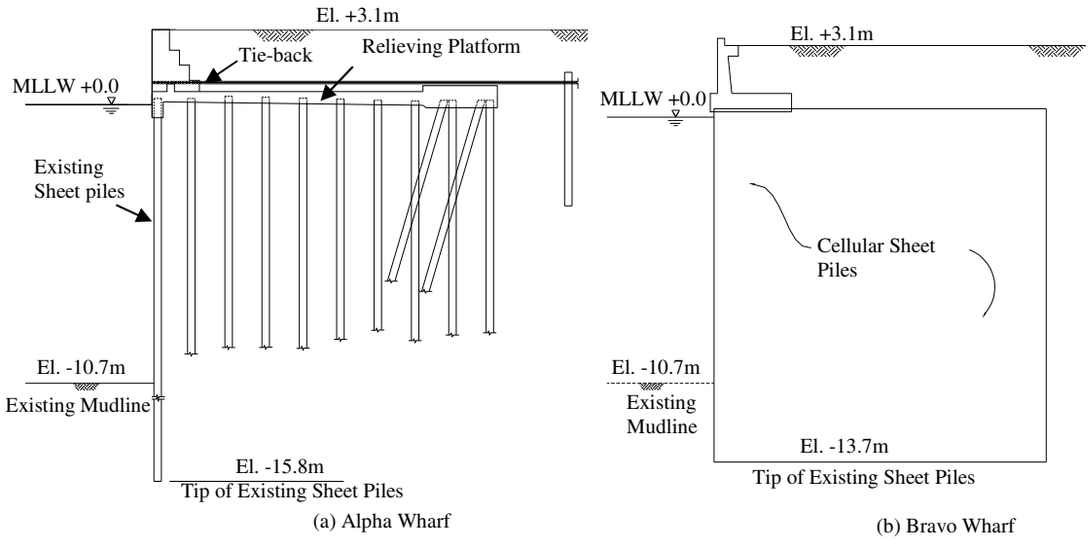


Figure 2. Existing Wharf Cross-Sections

The existing Bravo wharf was constructed as a cellular sheet pile structure with fill (Figure 2b). The Bravo wharf is approximately 151m long with the deck at

approximate El. +3.1m and a mudline at approximate El.-10.7m. The top and bottom elevation of cellular sheet piles are at approximately El. +0.3 m and El. -13.7m.

In 1993 a major earthquake with a moment magnitude of 7.7 struck Guam and caused substantial damages to several commercial wharves located within the Apra Harbor and moderate damages to Alpha-Bravo wharves. In early 2000, US Navy commissioned a retrofit program to improve the Alpha-Bravo wharves to meet the current seismic criteria and to increase the water depth to El. -12.8m to accommodate larger vessels. In addition, an approximately 52m long Bravo wharf extension was proposed to increase the length of existing Bravo wharf (Figure 1). King piles with a tie-back anchor system as shown in Figure 3 was selected as a suitable option by the designers to meet current seismic and increased water depth requirements for both Alpha and Bravo wharves. Due to high lateral demand, the anchor blocks were designed to be supported by battered piles.

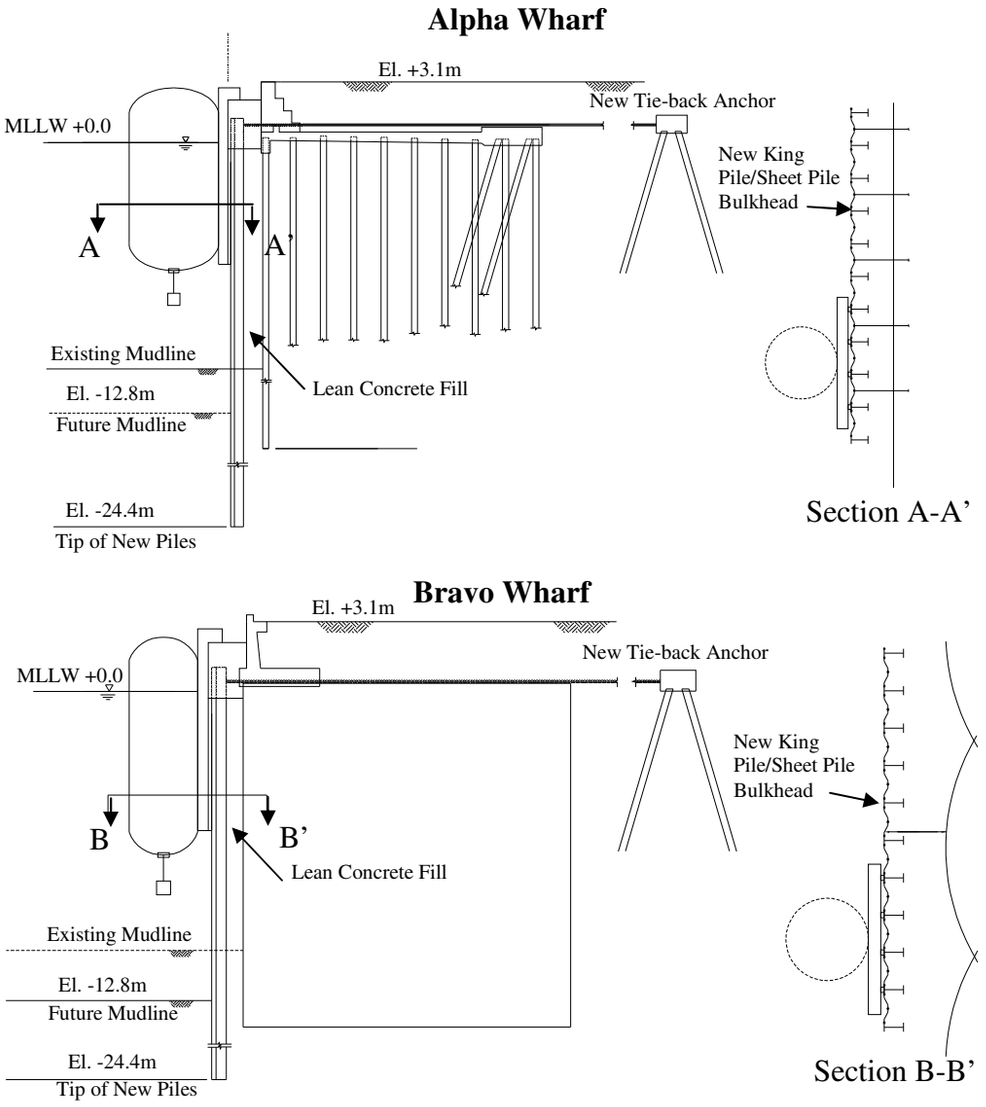


Figure 3. Proposed Improvements

Site Geotechnical Conditions

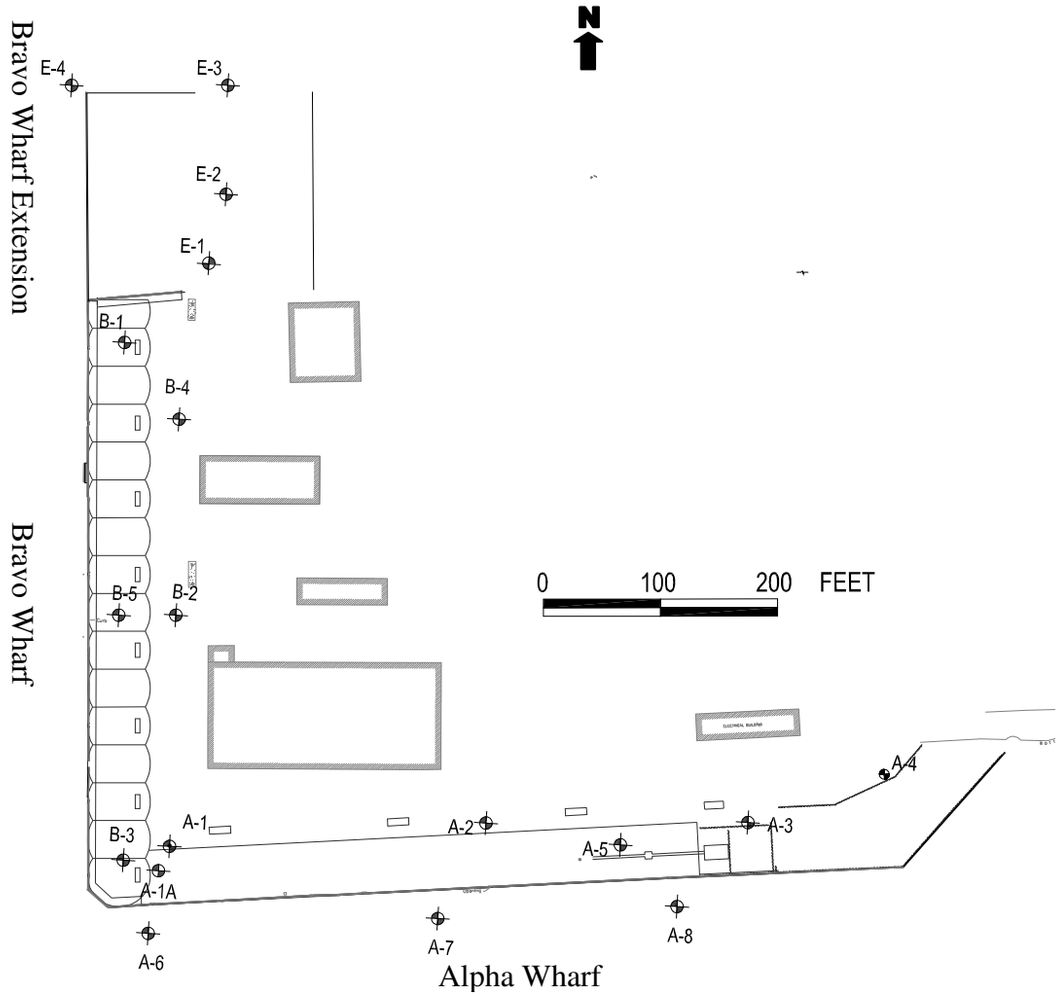


Figure 4. Boring Locations

Geotechnical investigations consisting of 4 overwater borings and 14 land borings were performed at various times to evaluate the subsurface conditions of the project site. The locations of soil borings are shown in Figure 4. Based on the boring information, the subsurface materials generally consisted of loose to medium dense liquefiable coralline sandy materials with blowcounts ranging from 2 to 15 with isolated high blowcounts down to El. -12.2m. The presence of fines, primarily consisted of non plastic silts, ranged from 5 to 30 percent in the liquefiable material. Hard to very hard argillaceous coralline limestone materials were encountered in boring below El. -21.3m with pockets of erratic low blowcounts. The material between El. -12.2m and El. -21.3m generally consisted of medium dense to dense gravelly coralline sand with silt to silty gravel that have a very low potential to liquefaction.

Liquefaction evaluations of coralline subsurface materials were performed following guidelines provided in Youd et al. (2001) and Martin et al. (1999). Following the 1993 earthquake, Mejia and Yeung (1995) concluded based on their observations that liquefaction evaluation of coralline sands can be performed using simplified procedures presented by Seed et al. (1985) that are commonly used for siliceous soils.

Regional Geology and Seismicity

The island archipelago, or island arc of which Guam is the southern island, and the associated Mariana Trench are a result of movements and interactions of the earth's crust within the framework of a geological theory called plate tectonics. Plate tectonic elements in the Guam region include 1) the Mariana Trench, the deepest oceanic depth in the world at 11,950 meters-(39,198 feet), which is the locus of subduction of the Pacific Plate beneath the Philippine Plate, 2) the Mariana island arc which consists of the islands and volcanoes west of the subduction zone, 3) the Mariana Trough which is the zone of rifting (ocean-floor spreading) where new oceanic crust is formed, and 4) the Mariana Ridge to the west of the Trough which is probably a former, now inactive, island arc or rift zone. The vast majority of earthquakes in the region are thrust events that occur along the subduction zone, but significant shallow earthquake activity occurs throughout the island arc and within the subducted Pacific plate.

Active crustal faults include Adelup, Talofofo, Santa Rosa, Tamuning-Yigo, Cabras and Cocos are present. These faults appear to deform late-Quaternary terraces on the island and control the tilt of structural blocks, and in some cases offset the late-Holocene deposits.

In order to determine the seismic hazards of the site, probabilistic seismic hazard analyses (PSHA) were performed to define ground motion parameters as a function of earthquake return period. The PSHA analyses were performed using the computer program SEISRISK III (Bender and Perkins, 1987). A project-specific seismic risk probability model was developed for the computer program. The seismic hazard model generates the probabilistic ground motion levels based on the input of 1) source zone geometry, 2) recurrence intervals, and 3) attenuation relationships. The source zone model for the seismic hazard analysis included subduction zone faults (Mariana Trench-slip rate 55mm/year, Mariana Trough-slip rate 20mm/year, Transform Fault-slip rate 5.0mm/year) and a generalized local shallow source zone (slip rate 0.1mm/year). For Mariana Trench, the attenuation by Crouse (1991) was considered. The Abrahamson & Silva attenuation (1997a&b) relationship was selected for the local source zone.

Seismic Design Levels

Design parameters were determined from the PSHA for two levels according current standards (Ferritto, 1997a).

- Level 1 earthquake - defined as the ground motion that has a 50% probability of being exceeded in 50 years (72-year return period)
- Level 2 earthquake - defined as the ground motion that has a 10% probability of being exceeded in 50 years (475-year return period).

Based on the hazard analyses, Peak Ground Accelerations (PGA) for the project site were determined to be 0.21g with magnitude of 6.0 and 0.38 g with magnitude 6.5 for the Level 1 and Level 2 events, respectively.

Performance Criteria

In order to meet current seismic design standards (Ferritto, 1997b), performance criteria for the project under the two levels of earthquakes were established as follows:

1. Under Level 1 event - no/minimal damages that will not interrupt the operations of the wharves.
2. Under Level 2 event - repairable damages with a short period of interruption to wharf operations.

Minimum factors of safety for geotechnical analyses were established as 1.5 under static conditions and 1.2 and 1.0 under Level 1 and Level 2 seismic conditions respectively.

Geotechnical Design Recommendations

Geotechnical design work for the proposed improvements to the wharves included characterization of subsurface conditions and, evaluation of potential seismic hazards such as liquefactions, seismically induced settlements, and lateral spreading. Geotechnical evaluations were also conducted to develop earth pressure recommendations during static and seismic conditions and to evaluate overall stability of the proposed improvements, lateral and axial capacities of anchor blocks piles and recommendations for pile driving and king pile/sheet pile installation.

As discussed before, liquefaction potential evaluation indicates that potentially liquefiable materials are present above approximate El. -12.2m. Seismically induced settlements of up to 225mm under Level 1 and 325mm under Level 2 were estimated using procedures outlined by Tokimatsu and Seed (1987). Since the tie-back anchor blocks are supported on piles, these settlements are not considered to cause significant damages to wharf structural elements.

Standard static earth pressures were recommended based on the subsurface characterization. Moderately hard to hard limestone encountered in the borings generally below El. -21.3m was assumed to provide very high equivalent lateral passive pressure (Kp on the order of 9 to 10). Seismic earth pressures were recommended based on Mononobe-Okabe equation using modified horizontal seismic coefficient. As the original Mononobe-Okabe equation was derived for dry yielding backfill retained by a rigid wall, when the backfill is saturated with water, the common practice is to assume that the pore water moves with the soil grains. Considering a fully saturated Coulomb wedge, the horizontal inertia force is proportional to the saturated total unit weight and vertical gravity force is proportional to the buoyant unit weight. Therefore, the modified seismic coefficient is determined as the ratio of total soil weight to buoyant weight times the seismic coefficient. The effective points of rotation to determine the active failure surfaces were estimated using Gazetas et al. (1990). In addition to the earth pressures,

hydrodynamic pressures exerted by free water in front of the structure during seismic event (Westergaad, 1933) were also included in the evaluation.

Based on the analyses, king pile/sheet pile systems with section moduli of 7957 cm^3/m for Alpha wharf with relieving platform, 10591 cm^3/m for Alpha wharf without relieving platform and 6667 cm^3/m for Bravo wharf were recommended by the designers. The tip elevation for king piles was estimated to be El. -24.4m as shown in Figure 3. Tip elevation for sheet piles was recommended to be El. -21.8m.

The design of anchor blocks was controlled by Level 2 seismic conditions. Lateral demand of anchor blocks under Level 2 seismic conditions was significantly higher than the demand under static conditions. Anchor blocks were supported by "A-frame" piles with 5H:12V front (compression piles) and back (tension piles) batter to provide adequate lateral capacity to meet the seismic demands. At some anchor blocks, compression pile batters were steeper than 5:12 due to presence of existing utility lines and other site constraints. Piles with steeper batters were designed for higher axial capacities to balance out the tie-back force demand.

Based on the discussion with designers, HP 14x89 steel piles were chosen. Steel piles with 5:12 batter were required to provide 1330 kN compression and 890 kN tension (ultimate) capacities under Level 2 seismic conditions. Compression piles with batter steeper than 5:12 were required provide ultimate capacity of 1510 kN. Based on subsurface conditions, the tip elevation for all the piles was recommended to be El. -27 m.

Indicator Pile Driving Results

The total number of piles to support the anchor blocks was 442 for the entire project, of which 256 were compression piles and 186 were tension piles. Due to large number of piles being used, an indicator pile program with pile driving analyzer (PDA) measurements was conducted. A total of 5 indicator piles for Alpha wharf and 4 indicator piles for Bravo wharf were driven. The objectives of the testing were to evaluate stresses, hammer performance, and soil resistance at the time of testing and to develop pile acceptance criteria. PDA data were obtained during driving and restriking. Piles were driven using Delmag D22 diesel hammer which has a ram weight of 21.8 kN and a maximum rated energy of 55 kN-m. PDA measurements were made during driving and some piles were restruck after allowing to set-up.

Ultimate capacity of indicator piles determined from PDA measurements at the end of driving (EOD) and beginning of restrike (BOR) are shown in Figure 5 together with capacity curve developed using ENR pile driving formula for average delivered energy of 38 kN-m.

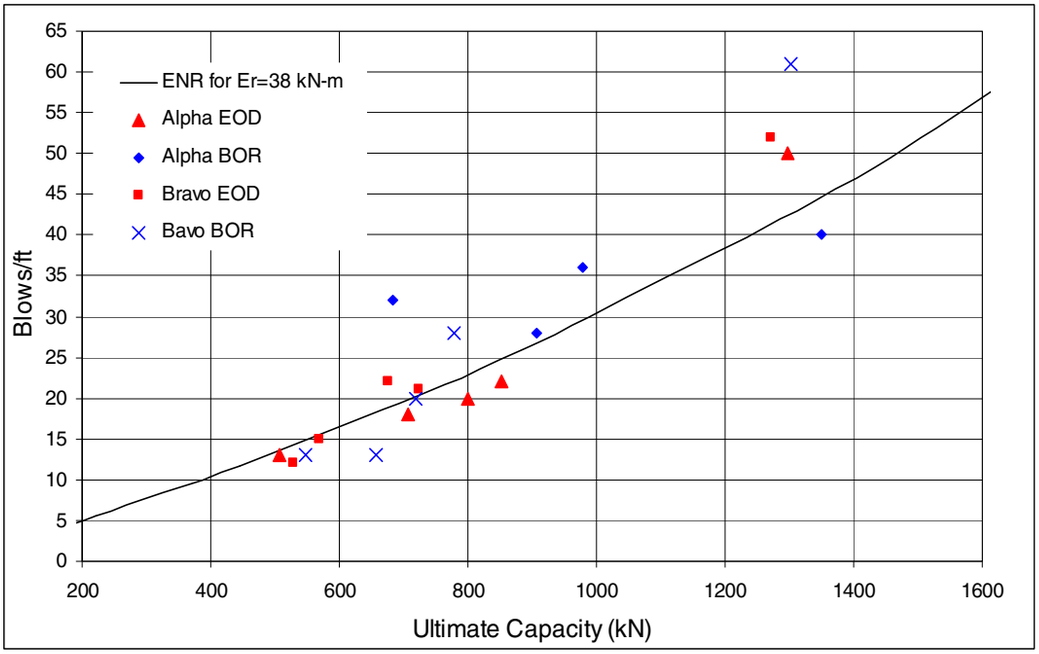


Figure 5. PDA Results

The PDA measurements showed lower capacity of piles than anticipated. As a result, corrective measures were required for the production piles. Skin friction resistance of coralline material especially during pile driving tends to be lower than siliceous material. In addition, H-piles (and open-ended pipe piles) may behave differently under dynamic and static loading conditions. Under dynamic loads (during driving) the soil between the flanges of the pile may slip and produce internal friction while under static loads the plug may move with the pile. It was observed that pile capacities increased up to 40 % during restrike on the following day due to soil set-up effects.

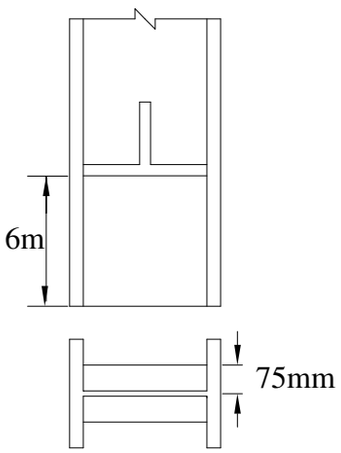


Figure 6. Pile Lug Detail

Contractor purchased production piles in 10.3m, 12.1m, and 18.3m segments during the indicator pile testing. Only a limited number of extra piles were purchased per contract requirement. Since additional pile procurement might delay the project and increase project cost, it was decided to reduce the compression pile lengths by installing lugs (Figure 6) to the piles as the corrective measure. Due to a presence of dense to very dense layer of coralline material approximately 6m above the pile tip elevation, lugs were installed on the piles at a location 6m above the tip to gain resistance from this layer. The tension pile lengths were increased using the saved compression pile lengths and extra piles. Indicator pile results and set-up effects were carefully studied

to determine the required tip elevations of production piles. Permutations on different combination of pile segments were performed so that only single splicing was needed at each location.

During production pile driving, it was found that lugs were effective meeting the acceptance blowcounts or refusal criteria and tension piles were driven to new tip elevations providing adequate capacities. Corrective measures worked well to solve the lower pile capacity problem evaluated during the indicator pile program.

Partnering meetings and proactive participation of all interested parties including the owner, designers, and contractor throughout the construction of the project helped minimize project delays and cost overruns.

Conclusion

The design to retrofit and improve Alpha-Bravo to meet current seismic standards was completed and at the time of this was written construction is in progress. A reasonable number indicator pile tests with PDA measurements helped to evaluate field pile capacities and take appropriate corrective measures without delay and cost overruns. Close interaction among the owner, designers and contractor during construction helped move the project smoothly without interruptions and delays.

References

Bender, B. and Perkins, D.M. (1987), "SEISRISK III; A Computer Program for Seismic Hazards Estimation," US Geological Survey Bulletin 1772.

Crouse, C.B. (1991a), "Ground Motion Attenuation Equaions for Earthquakes on the Cascdia Subduction Zone". Earthquake Spectra, Vol. 7, No. 3.

Crouse, C.B. (1991b), "Errata Ground Motion Attenuation Equaions for Earthquakes on the Cascdia Subduction Zone". Earthquake Spectra, Vol. 7, No. 3.

Ferritto, J.M. (1997a), "Criteria for Seismic Ground Motion for Essential Structures", Technical Report TR-2076-SHR, Naval Facilities Engineering Service Center, Port Hueneme, CA.

Ferritto, J.M. (1997b), "Design Criteria for Earthquake Hazard Mitigation of Navy Piers and Wharves", Technical Report TR-2069-SHR, Naval Facilities Engineering Service Center, Port Hueneme, CA

Gazetas, G., Dakoulas, P. and Dennehy, K. (1990), "Empirical Seismic Design Method for Waterfront Anchored Sheetpile Walls", Proc. ASCE Specialty Conference on Design and Performance of Earth Retaining Structures, Geotechnical Special Publication No. 25, ASCE.

Mejia, Lelio H. and Yeung, M. Ronald (1995), "Liquefaction of Coralline Soils During the 1993 Guam Earthquake", Geotechnical Special Publication No. 55, ASCE.

Martin, G. R. et al. (1999), "Recommended Procedures for Implementation of DMG Special Publication 117, Guidelines for Analyzing and Mitigating Liquefaction in California", Southern California Earthquake Center, University of Southern California.

Seed, H. B., Idriss, I. M., and Arango, I. (1983),"Evaluation of Liquefaction Potential Using Field Performance Data", Journal of Geotechnical Engineering, ASCE, Vol. 109, No. 3.

Tokimatsu, K., and Seed, H. B. (1987), "Evaluation of Settlements in Sands Due to Earthquake Shaking", Journal of Geotechnical Engineering, ASCE, Vol. 113, No. 8.

Youd, T. L. et al. (2001), "Liquefaction Resistance of Soils: Summary Report from the 1996 NCEER and 1998 NCEER/NSF Workshops on Evaluation of Liquefaction Resistance of Soils," Journal of Geotechnical and Geoenvironmental Engineering, ASCE, Vol. 127, No. 10.

Westergaad, H.M. (1933), "Water Pressure on Dams during Earthquakes", Transactions of ASCE 98.

Centrifuge Testing of the Seismic Performance of a Submerged Cut-and-Cover Tunnel in Liquefiable Soil

Bruce L. Kutter, M. ASCE, Jui-Ching Chou, S.M. ASCE and
Thaleia Travasarou, A.M. ASCE

[1]Professor, Civil and Env. Engrg., University of California, Davis, 95616, blkutter@ucdavis.edu
[2]PhD Candidate, Civil and Env. Engrg., University of California, Davis, 95616, jccchou@ucdavis.edu
[3]Project Engineer, Fugro West, Inc., Oakland, CA, 94607, ttravasarou@fugro.com

ABSTRACT: Centrifuge model tests were performed to verify numerical methods being used to assess the stability of a cut-and-cover subway tunnel in a highly seismic area. Since the tunnel is less dense than the backfill soils and the backfill soils are liquefiable, there is concern that the tunnel could suffer large deformations due to buoyancy forces in the event that liquefaction does occur. Numerical analyses indicated that tunnel deformations would be limited due to the dilatancy of the backfill soils, the geometry of the problem, and dissipation of excess pore pressures. The design, testing, results of the centrifuge tests are presented in this paper. The experiments provided added confidence to the design and review team that the analysis is capturing the dominant deformation mechanism. The centrifuge model tests clarified the mechanisms of deformation and are playing an important role in evaluating if a very expensive retrofit project is necessary.

INTRODUCTION

Overview

Centrifuge model tests were conducted to investigate the seismic performance of a cut and cover tunnel. The goal of these tests was to help with understanding the uplift mechanism and provide a set of data to calibrate and validate the numerical tools used in assessing the vulnerability of the actual structure. Much of the backfill around the tunnel was placed under water and it has a relative density less than 50%, so liquefaction of the backfill material is likely in a major earthquake. The unit weight of the tunnel structure is about 11.2 kN/m^3, hence there is some concern that the tunnel will be subject to uplift because it is less dense than the potentially liquefied soil. The centrifuge experiment presented in this paper is being used to evaluate the need for a retrofit of the liquefiable soil surrounding the tunnel.

The Bay Area Rapid Transit (BART) District's Transbay Tube tunnel is about 6 km long and hence the depth of overburden soil above the tunnel and the geological conditions vary along the length. A 1 km long section of the tunnel, with a representative cross-section sketched in Fig. 1, was chosen as the prototype of the centrifuge model test. This section was chosen for the model test because: (1) numerical analyses indicated that expensive retrofit may not be necessary in this section, and (2) due to shipping activity and other access constraints, external retrofits would be relatively difficult. The primary goals of the model test were to model this cross section as accurately as possible and confirm that the numerical analysis was capable of modeling the dominant mechanisms that control the magnitude of the tunnel uplift in the liquefiable soil.

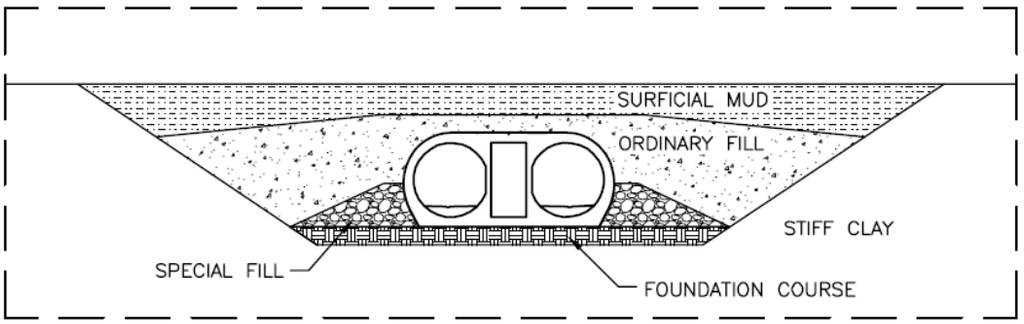


FIG.1. Configuration of the tunnel and backfill materials.

Referring to Fig. 1, an approximately 10 meter deep trench with approximately 1.5:1 side slopes was cut by dredging into the native soil. In the area being modeled the native soils are primarily very stiff, Pleistocene-age, silty clay materials of the Merritt-Posey-San Antonio Formations. The "Foundation Course" (gravelly sand with little fines) was placed by tremie and screeded to form about a 1.2 m thick layer along the base of the trench. Next, precast segments of the tunnel were lowered through the water on to the foundation course. After connecting the segments of the tunnel, the "Special Fill" (similar material to the Foundation Course) was placed by tremie to form the wedges of soil along the lower sides of the tunnel. The tunnel was then covered by the "Ordinary Fill" (medium poorly graded sand with some fines). Finally natural deposits collected above the ordinary fill to form a soft low permeability, normally consolidated "Surficial Mud" cover. Table 1. summarizes some basic properties of the "Foundation Course", "Special Fill", and "Ordinary Fill".

The permeabilities of the granular fill materials were found to be key parameters affecting the magnitude of tunnel deformations. Permeability estimates were obtained from in situ measurements and also by correlation to grain size distributions using the Fair and Hatch (1933) relationship. The range of predicted permeability estimates are indicated in Table 1, and the best estimates of the permeability for design purposes are indicated by the number in parentheses.

Major design considerations include:

(1) Significant movements of the tunnel could restrict rail traffic through the tunnel.

(2) A breach of tunnel structural integrity could result in an inrush of water that could endanger rail passengers.
(3) The difficulty of performing retrofit offshore and constraints associated with shipping traffic make retrofit expensive.
(4) Uniform movements of the tunnel are much less of a concern than differential movements of the tunnel.
(5) The allowable movements of the tunnel are dependent on structural details of the tunnel, on the non-uniformity of the movements as well as discontinuities in movement associated with variation in geological conditions.
(6) Analyses have shown that differential movements of the soil surrounding the tunnel cause larger distress to the tunnel structure if the structure is surrounded by stiff soil.

Fig. 2 shows finite difference meshes, used in FLAC2D, to model the prototype and to perform pre-test predictions of the centrifuge test results. The UBCsand constitutive model (Beatty and Byrne 1998) was used to model the granular backfill materials. The numerical analyses indicated that tunnel movements would be limited, and hence expensive retrofit (estimated to be on the order of $15 million per kilometer) may not be necessary.

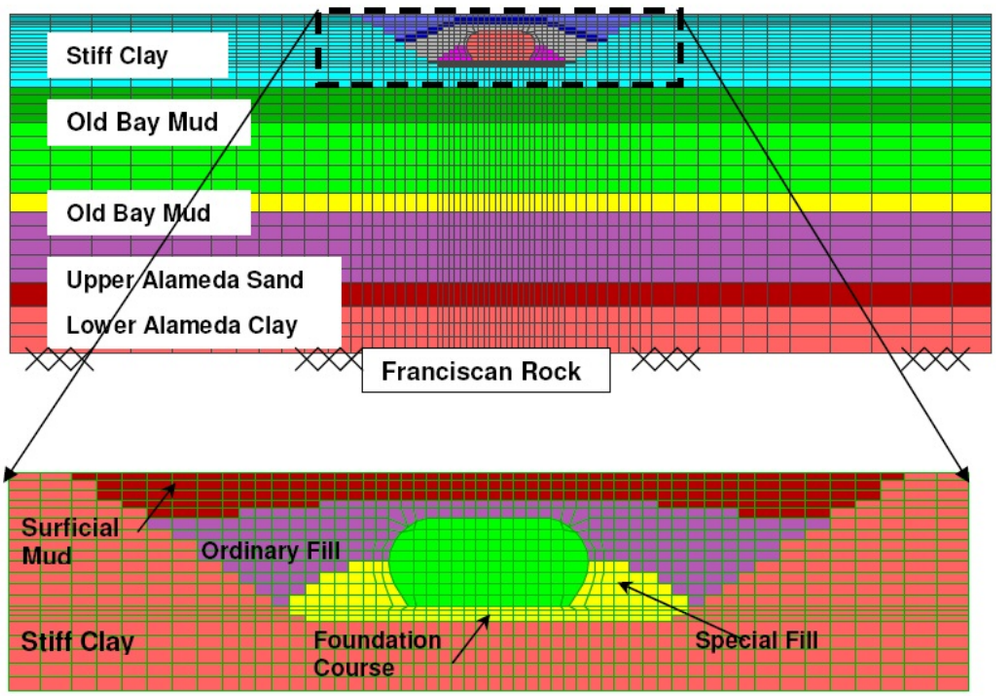


FIG.2. Soil profiles showing the finite difference mesh used to analyze the prototype (top) and the centrifuge model (bottom).

On the recommendation of the geotechnical consultant (Fugro West Inc.), BART and their program managers (Bechtel Infrastructure Corporation) agreed to the performance of two centrifuge model tests to verify the findings from the numerical analyses, and to explore the possibility that there might be some important deformation mechanism that is not appropriately captured by the numerical model. The centrifuge tests were conducted at facilities operated by the University of California, Davis.

Related Research

Koseki et al. (1997a) conducted a variety of 1 g model tests on uplift of structures in liquefiable soil. They found that uplift was caused by two mechanisms: a nearly instantaneous deformation of surrounding soil, and by gradual movement of pore fluid. They observed that flow of pore water under the structure could actually result in a water-filled cavity beneath the structure. Koseki et al. also observed that reconsolidation after liquefaction resulted in settlement and indicated that the triggering of uplift could be evaluated using a factor of safety defined as (weight of the structure + frictional resistance along side boundaries)/(buoyant force due to hydrostatic water pressure + uplift force due to liquefaction-induced excess pore pressure + upward seepage forces due to soils beneath the structure). While the triggering of uplift could be predicted using the factor of safety proposed by Koseki et al (1997a), the magnitude of deformations was not well correlated to the factor of safety.

Yang et al. (2004) reported a numerical and centrifuge study of the seismic stability of the Massey Tunnel built in Vancouver, Canada. There are many similarities between the study of Yang et al. (2004) and the present study. Both tunnels were built by the cut and cover method, both studies involve validation of FLAC analyses (Itasca 2006) using the constitutive model UBCSAND (Puebla et al. 1997; Beaty and Byrne 1998), and both studies included centrifuge model testing of tunnels in liquefiable soils. There are a few notable differences. The Massey Tunnel is underlain by deep natural liquefiable sediments, while the present study involves a tunnel placed in a trench cut in natural “impermeable” clayey deposits with liquefiable backfill materials. For the present study, there is a relatively thin permeable liquefiable layer (the foundation course) under the tunnel. The relatively thin foundation course makes a restricted channel for flow of water under the tunnel. This could potentially limit the uplift of the tunnel by restricting flow of water, an important contributor to deformations observed by Koseki et al. (1997a). The centrifuge testing for the Massey Tunnel was performed for relatively short durations of shaking with a peak acceleration of about 0.13 g whereas the tunnel for the present study was to be designed to withstand longer duration and stronger (0.5 g) shaking, corresponding to approximately a 1000-year event in the Bay Area.

DESIGN, CONSTRUCTION, AND TEST PROCEDURE

Initial discussions between the BART, Bechtel, Fugro West, Inc., and UC Davis addressed the desired complexity and number of experiments that should be

conducted. Due to the scheduling constraints, it was important to decide if several simple models compared to only one or two detailed models should be tested. It was concluded that the most detailed and realistic model possible would provide the most convincing and realistic information in the shortest practical time. The centrifuge at Davis accommodates the largest specimens of the available centrifuges and hence it was decided that it would enable testing of the most accurate and realistic models. Fig. 3 is a photograph of the first centrifuge model installed in the rigid walled container.

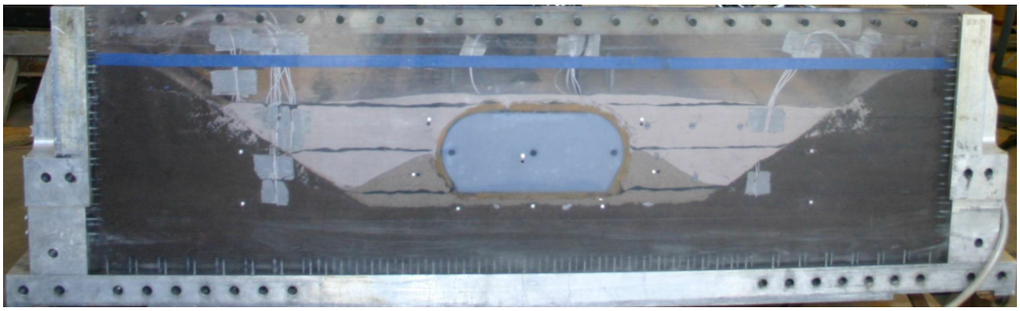


FIG. 3. Centrifuge model including ordinary fill, model tunnel, special fill, and stiff clay trench in the rigid model container prior to saturation and placement of the surficial mud.

Geometry, Model Container and Scale Factor

A scale factor of 1:40 was selected for the model tests. This was determined by making the model dimensions as large as possible subject to the considerations that (1) it must fit in the container, and (2) severe boundary affects should be precluded. One reason for making the model as large as possible is that preliminary analyses showed that the thickness of the foundation course has a large effect on the predicted tunnel deformations. It would be more difficult to accurately model the thickness of the foundation course at small scale. Fig. 1 presents a cross section of the constructed 1:40 scale model. At this scale, the foundation course in the model is 31 mm thick, which was considered to be sufficiently thick to permit accurate construction and to enable inclusion of a limited number of sensors to monitor pore water pressure and acceleration in this layer. In order to achieve 1:1 scaling of stress while linear dimensions are scaled by 1:40, the 1 g gravitational acceleration in the prototype was modeled by 40 g centrifugal acceleration in the model.

To explore the potential for boundary effects on the dynamic response of the model, preliminary numerical analyses were performed with FLAC2D before the centrifuge experiment was conducted. Analyses were performed using three possible geometries around the trench: (1) full geometry extending vertically to the Franciscan bedrock and horizontally to a sufficiently large distance, (2) reduced mesh, modeling the extent of soil around the trench that would fit in the rigid box container for a centrifuge acceleration of 40g and the appropriate boundary conditions, and (3) reduced mesh, modeling the extent of soil around the trench that would fit in the shear

beam box container for a centrifuge acceleration of 40g and the appropriate boundary conditions. Fig. 4 shows the estimated vertical tunnel and trench displacement for each of the three cases. The analyses indicate that the numerical model of the rigid container captures appropriately the mechanism of tunnel uplift, both qualitatively and quantitatively. Contrary to the shear beam container, the rigid box container at UC Davis has transparent side windows that allow visual monitoring of a cross-section during shaking, hence the rigid container was chosen for this study. The dimensions of this container are: 1758 x 911 x 537 mm (length x width x height).

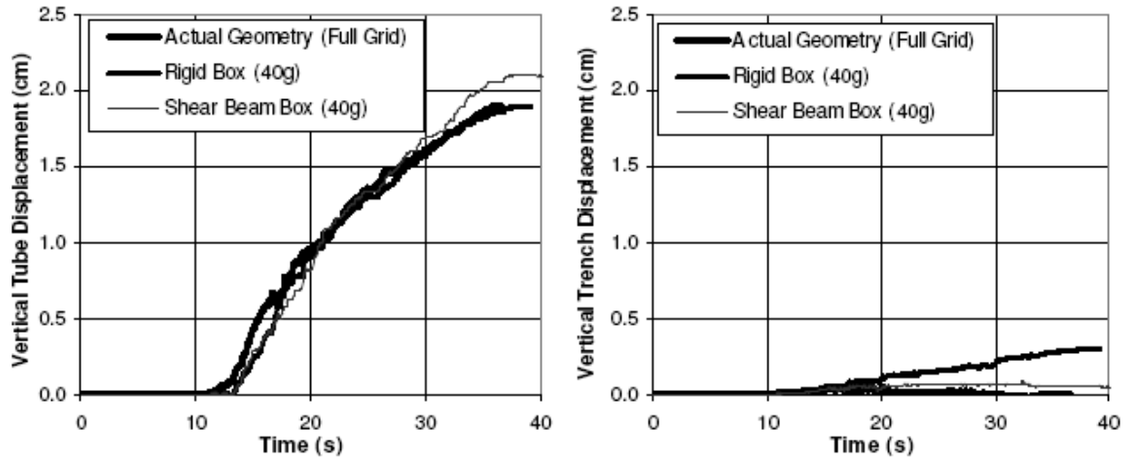


FIG.4. Preliminary analysis of the effect of different model containers on the deformations of the tunnel and trench.

Soil Properties

Trench Soils

The key properties of the *in situ* trench materials are: permeability, relative density (inferred from cone tip resistance measurements), and unit weight. Table 1. shows typical ranges of these properties from field measurements. The values in parenthesis indicate the target values selected for the centrifuge model. According to the original tunnel design specifications the foundation course and the special fill were similar; hence the same properties were targeted for the centrifuge test.

Monterey 0/30 Sand and Nevada Sand were used to model the special fill and the ordinary fill, respectively in the centrifuge experiment. Both sands have been used in laboratory experiments in the past Arulmoli (1992), Kammerer et al (2000, 2004). Hence, key properties and elements of cyclic behavior have been characterized. The densities achieved by pluviating the Monterey and Nevada sand in air are also indicated in Table 2. Values of the minimum and maximum void ratio for the Monterey and Nevada sand, respectively, are provided in Table 3. The void ratio at the target relative density is also shown.

Table 1. Typical Values of Key Properties of In situ Trench Materials

Property	Ordinary Fill Range (Target)	Special Fill Range (Target)	Foundation Course Range (Target)
USCS Soil Classification	SP-SM	GP-SP	GP-SP
Permeability (cm/s)	0.01 – 0.1 (0.05)	0.8 – 5.0 (1.0)	0.8 – 5.0 (1.0)
Median Grain Size (mm)	0.8	12	12
% finer than 0.075 mm	2 to 10%	1 to 2	1 to 2
Cone Tip Resistance (MPa)	5.8 – 6.7 (6.2)	2.8 – 3.8 (3.4)	2.8 – 3.8 (3.4)
Relative Density (%)[1]	(45 +/- 5)	(35 +/- 5)	(35 +/- 5)
Unit Weight (kN/m^3)	(20.4)	(18.9)	(18.9)

[1] Cone tip resistance was converted to relative density using the relationships proposed by Kulhawy and Mayne and Jamiolkowski et al. published in Kulhawy and Mayne (1990)

Table 2. Key Properties of Trench Materials in Centrifuge Model

Property	Ordinary Fill	Special Fill	Foundation Course
Name	Nevada Sand	Monterey 0/30	Monterey 0/30
USCS Soil Classification	SP	SP	SP
Conventional Permeability (water as pore fluid) (cm/s)	0.014	0.22	0.22
Model Viscosity Scale Factor	10	10	10
Prototype Permeability (cm/s)[1]	0.057	0.88	0.88
Median Grain Size (mm)[2]	0.15	0.35	0.35
% finer than 0.075 (mm)[2]	1 to 2	< 1	< 1
Cone Tip Resistance, q_{c1} (MPa)	2.9	6.9	4.5
Relative Density Target (%)	40	35	35
Relative Density from cpt (%)[3]	32	50	40
Unit Weight (kN/m^3)	19.5	19.0	19.0

[1] Prototype permeability is obtained from conventional permeability times model scale factor (40) divided by viscosity scale factor.
[2] Balakrishnan (2000) and Wu (2003)
[3] Cone tip resistance was converted to relative density using the relationships proposed by Kulhawy and Mayne and Jamiolkowski et al. published in Kulhawy and Mayne (1990).

Table 3. Maximum and Minimum Void Ratios for Model Materials

Property	Monterey Sand 0/30	Nevada Sand
e_{min}	0.56	0.51
e_{max}	0.88	0.79
e at target Dr	0.76	0.68

The Monterey sand Foundation Course was placed using dry pluviation techniques, using a pluviator consisting of a sand reservoir from which sand was dropped through a 4-inch flexible hose with a wire screen at the outlet. This pluviator was calibrated by pluviating the sand into a known volume from a given drop height to determine the delivered relative density. A trial and error procedure of varying the drop height and adjusting the aperture of the screened openings on the bottom of the flexible hose was used to estimate the required drop height for the desired relative density of 35%. Once this drop height was known the sand was pluviated into the model container, while maintaining this drop height by means of an overhead crane. The sand was over-pluviated into the container and then excess sand was removed using a vacuum hose moving over the sand surface at a fixed height to achieve the desired geometry.

Fig. 5 shows the process of placing one segment of the model tunnel on the Foundation Course. Fig. 6 shows all three tunnel segments on the foundation course, with a black layer of sand placed on top of the foundation course. Also shown in Fig. 6 are vertical tubes that were positioned in the sand for installation of colored sand marker columns.

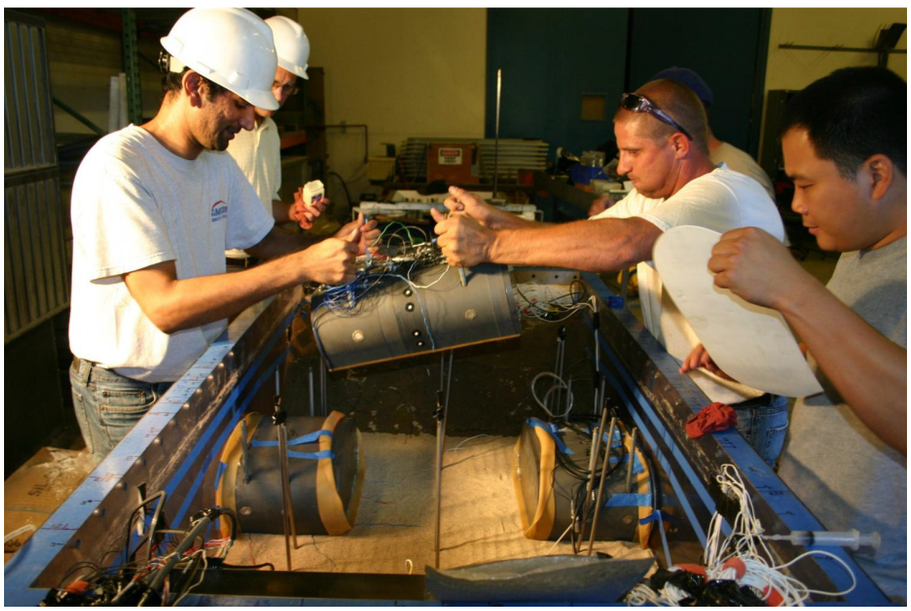


FIG.5. Lowering the central segment of the tube onto the base course into the rigid walled model container.

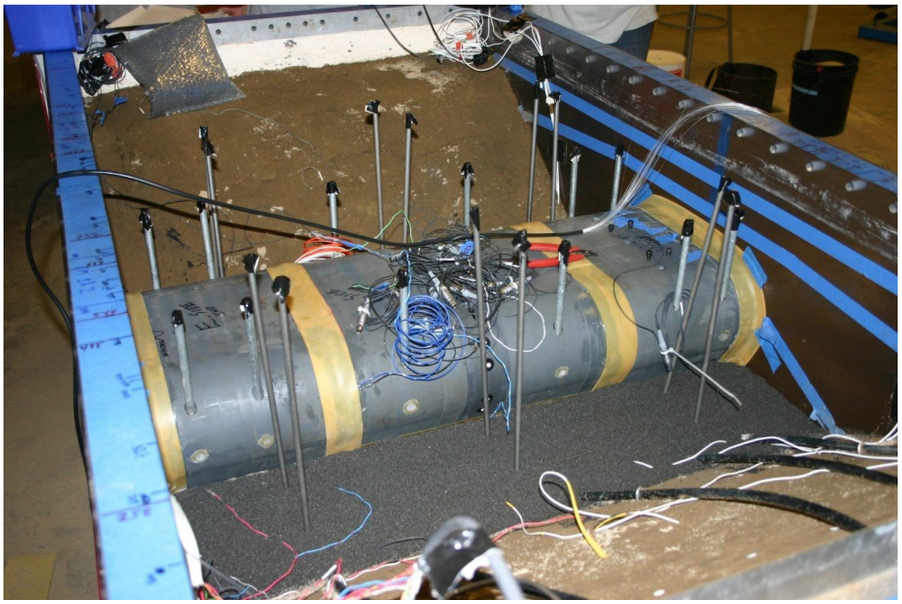


FIG.6. Tube segments separated by teflon sheets with joint sealed by latex bands. vertical tubes are for placement of vertical columns of colored sand.

Fig. 7 presents the results of falling head permeability tests in the laboratory on samples of Monterey Sand 0/30 and Nevada Sand prepared at a variety of void ratios. Some permeability tests used water and the others used a dilute solution of hydroxylpropyl methylcellulose and water that produced a fluid with a viscosity ten times greater than that of pure water. As expected, the permeability was observed to be approximately inversely proportional to the fluid viscosity.

Preliminary numerical analyses showed tunnel uplift maybe sensitive to the ratio of the permeabilities of the ordinary fill and the special fill. Hence it was important to model this ratio in the centrifuge experiment. The target design ratio of 20 (i.e., 1/0.05 from Table 1.) is in good agreement with the permeability ratio of 15 (i.e., 0.88/0.057 from Table 2.) of the model soils.

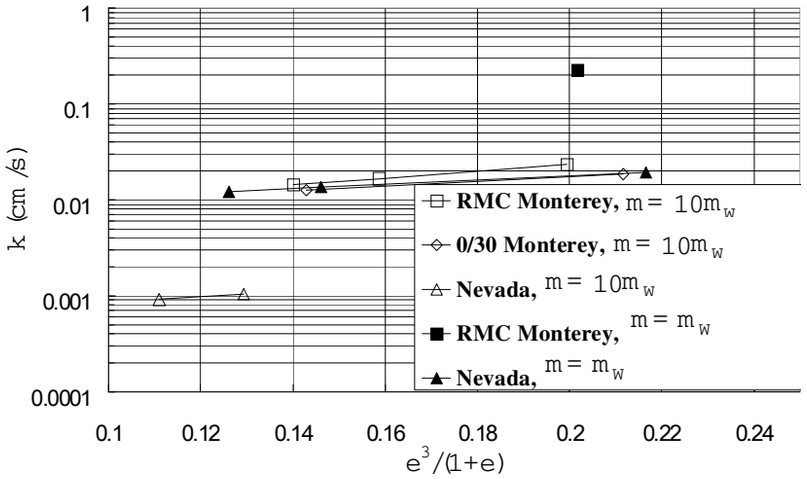


FIG.7. Falling head permeability test results for Nevada Sand and Monterey 0/30 Sand with water and a viscous water solution.

Native Soils

As seen in Fig. 1, the trench is surrounded by stiff clay of the Merritt-Posey-San Antonio Formations (MPSA-Clay). In addition, soils in the trench are overlain by soft clay, as a result of sedimentation after the trench excavation and placement of the tunnel and trench fill materials. Numerical analyses suggest that the magnitude of the uplift is impacted by the strength of the MPSA-Clay, which underlies the trench.To minimize heave of the clay underlying the trench a value of Su > 100 kPa was targeted. Results from numerical analyses suggest that clay heave is reduced to negligible values when the strength exceeds this value.

Compacted Yolo Loam, a locally available low plasticity silty clay was used to represent the MPSA-Clay. The moisture content and compactive effort were varied to enable achievement of a state with the required strength (Su > 100 kPa) and low swell potential. Results from these tests indicated that a target water content of 16% produced sufficient strength when compacted until it was very near the zero-air-voids condition, well on the wet side of optimum. This moist material was placed in the model container in approximate 10 cm lifts, compacted into place using a pneumatic compactor. Readings that were taken routinely throughout construction with a pocket penetrometer indicated the achievement of strengths greater than the target strength. As the compaction of successive lifts proceeded, the clay slopes and bottom were shaped to the desired geometry using various hand tools.

The effect of the surficial mud is that it provides some confining stress and is an impermeable layer restricting escape of some of the excess pore pressures from the ordinary fill. The layer representing the surficial mud was also constructed using the locally available Yolo Loam. Yolo Loam was mixed in a slurry/paste and placed on the special fill. The soil was brought to a nearly normally consolidated during spinning of the centrifuge before the strong seismic shaking. Complete consolidation was not considered critical because the shear strength of the surficial mud was not considered to be a critical design parameter.

Tunnel Design

The tunnel was machined from solid cylinders of Polyvinyl Chloride (PVC) and made from three independent segments (Fig. 5 and 6). The density of the PVC is about 1.4 Mg/m^3, which is larger than that of the tunnel. Holes were cut into the PVC to achieve a density similar to that of the tunnel, or about 1.15 Mg/m^3.

To minimize potential restraint on tunnel deformations by friction against the windows, the tunnel was modeled by three different segments of unequal length: two edge segments (i.e., east and west) and one middle segment as shown in Fig. 5 and 6. Each of the tunnel segments was separated from each other and the windows and by teflon sheet to isolate them and allow for independent response during shaking. A small clearance gap of about 0.5 mm was allowed at each connection, and grease was used to fill the gap. Filling the gap with grease was considered important to minimize friction and also to prevent water pressures from draining through the gaps. Large latex rubber bands were wrapped around the tunnel joints to prevent sand from migrating into the sealed gap. Using three independent tunnel segments would enable comparison of the response of the middle and edge segments. The deformations of all

the tunnel segments was approximately the same indicating negligible boundary effects. Instrumentation ports were drilled at the centerline of the middle segment to mount pore pressure transducers; some of these are visible as white dots in the central segment in Fig. 5.

Instrumentation

Data from a total of 40 pore pressure sensors, 44 accelerometers, 27 displacement sensors, and 3 digital and 2 analog cameras were successfully recorded during the experiment. The instrumentation plan was designed to capture the following key elements of the model response:
(1) Permanent displacement of each tunnel segment were measured by means of either Linear Variable Differential Transformers (LVDTs) or string potentiometers, connected to the tunnel. The central segment was instrumented with redundant sensors to ensure that all six degrees of freedom of displacement could be deduced. The displacement of the east and west segments of the tunnel were monitored at a sufficient number of points to compare their movement with that of the central segment.
(2) The deformation patterns of the soil around the tunnel and underneath the trench were monitored by video cameras viewing through the container windows; in addition, layers and vertical columns of colored sand were installed in the trench to reveal internal deformation patterns through post-test excavation.
(3) The vertical displacement of the mudline was monitored using Linear Variable Differential Transformers LVDTs;
(4) Pore pressures in the liquefiable layers and underneath the tunnel were measured using Druck PDCR 81 pore pressure transducers. Ports were made in the central segment of the tunnel to enable accurate determination of the distribution of excess pore pressures on the tunnel surface.
(5) Horizontal and vertical accelerations of the container base were measured.
(6) A few accelerometers were placed in the compacted soil to monitor its dynamic response.
(7) Dynamic response of soil within the trench was monitored using a vertical array of horizontal accelerometers and two independent vertical accelerometers recorded potential sloshing of the liquefiable soils in the trench.
(8) Transient response of the tunnel: vertical and horizontal accelerometers were mounted on each of the tunnel segments. A sufficient number of accelerometers determined all six degrees of freedom of the central tunnel segment, which was assumed to behave as a rigid body.

Centrifuge Spin Schedule and Input Ground Motion Sequence

Spinning Sequence
A total of three centrifuge spins were performed during the centrifuge test. In the first, the centrifuge was spun up to 40 g, for 1 hour, until the specimen was in equilibrium. A cone penetrometer was then pushed into the model. The results of the

penetrometer data are given in Fig. 8. The centrifuge was then stopped and the penetrometer apparatus was removed.

During the second spin, the model was spun up to 40 g, again allowed to come to pore pressure equilibrium, and the ground motion sequence (see Table 4.) was initiated. After the final shake, the centrifuge was stopped, the penetrometer re-attached to the container and the centrifuge brought back up to speed (third spin) and a second penetrometer sounding was obtained. After stopping the centrifuge (after the third spin), sampling tubes were pushed into the specimen and then the container was removed from the centrifuge and excavation/dissection commenced.

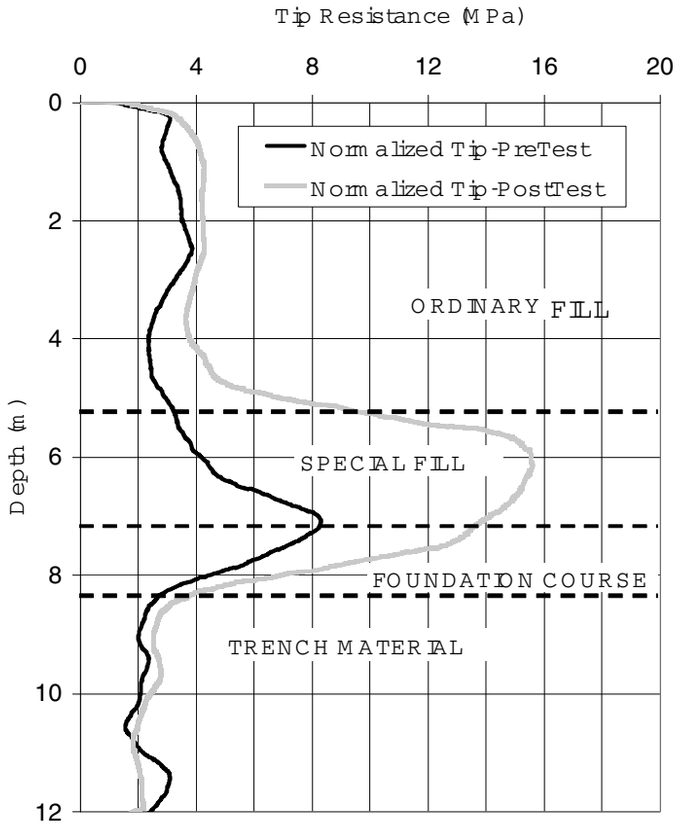


FIG. 8. Cone penetration data from the centrifuge model; dotted lines indicate boundaries between ordinary fill, special fill, foundation course, and stiff clay beneath the trench.

Ground Motion Sequence

The centrifuge model was shaken by a series of events as presented in Table 4. The small amplitude step shake was designed to help identify problems with instrumentation, if any. Prior to shaking with the TCU078 motion, the model was shaken by a modified version of the Yerba Buena Island (YBI) record from the M 6.9 1989 Loma Prieta earthquake. The tunnel was actually subjected to this earthquake; no damage was reported and the tunnel displayed satisfactory performance. Small amplitude shakes were performed prior to the full amplitude shakes (events 3 and 6) for the YBI and TCU078 motions. These shakes were used to help calibrate the shaker controllers and modify the command motions to better simulate the waveform of full design ground motions.

The primary input motion for the centrifuge experiment was a modified version of the TCU078 record (from the M 7.6 1999 Chi-Chi Earthquake in Taiwan), which is one of the seven design motions for this project. This motion was considered to be an

appropriately conservative selection because of its long duration and the fact that it is the design motion that typically generates the largest uplift in the FLAC2D numerical analyses. The input motion at the base of the model container approximately corresponds to an elevation of about -30 m , near the interface between the stiff MPSA-Clay and the underlying Old Bay Clay in the prototype (Fig. 2). To calculate appropriate input motions to be applied at the base of the container in the model test, 1D site response analyses were conducted for the full soil column using the equivalent linear program SHAKE91 (Idriss and Sun 1992) with "bedrock", and "within" motions extracted at El –30 m.

Table 4. Sequence of Shaking Events and Obtained Amplitude of Input Motions

Event	Ground motion description	PGA (g)
1	Step wave	< 0.01
2	Loma Prieta – YBI Record, filtered & scaled	0.013
3	Loma Prieta – YBI Record, filtered & scaled	0.17
4	1999 Chi-Chi Taiwan, TCU078 record, filtered & scaled	0.06
5	1999 Chi-Chi Taiwan, TCU078 record, filtered & scaled	0.17
6	1999 Chi-Chi Taiwan, TCU078 record, filtered & scaled	0.75

Note: PGA values are based on sensor AB1

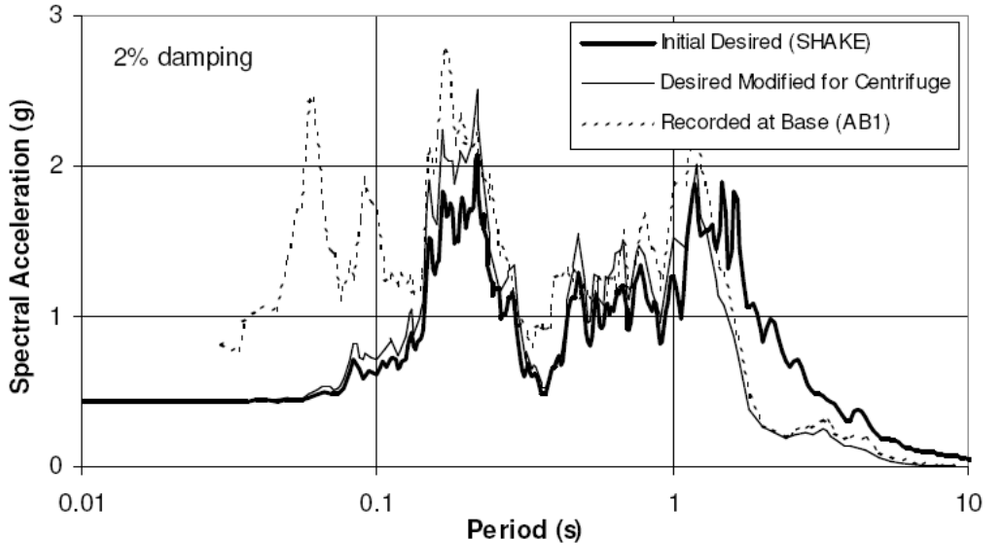


FIG. 9. 2% damped acceleration response spectra comparing desired motions to the achieved (recorded) motions in the centrifuge.

Fig. 9 presents the acceleration response spectra for the design ground motion, for the centrifuge target motion and the achieved input motion applied to the model container. The initial desired motion is the motion calculated at an elevation of El -30 m using SHAKE when the design ground motions are applied at depth. The desired motion included significant frequency content at the 1st and 2nd bending resonant frequencies of the centrifuge arm (i.e., 20 Hz and 5 Hz, which correspond to 2 s and 8 s period in prototype scale shown in Fig. 9). To minimize excitation of the centrifuge arm at its resonant frequencies, input motions at these frequencies were filtered to a significant extent. The ground motions were altered in the frequency domain using a combination of one low pass and two high pass filters, and the result is labeled "Desired Modified for Centrifuge" in Fig. 9. Preliminary FLAC2D analyses indicated that the modification of the input motion only reduces the estimated uplift displacement by about 5%. Fig. 9 also shows the achieved motion in the centrifuge.

To closely match a desired motion on a real shake table, when the actuators are driven to their capacity and above their resonant frequency, and when the nonlinear payload mass is a significant fraction of the system mass is a challenge. Based upon previous experience and a trial spin and shake on a similar dummy specimen, we obtained a linear transfer function that approximated the nonlinear system. The "Desired Modified for Centrifuge" motion was preprocessed by applying the inverse of this transfer function to obtain a command motion for the shake table on the centrifuge. The obtained motion, recorded at the base of the container is also shown in Fig. 9. As can be seen, the spectrum of the obtained motion is approximately 10% larger than the desired modified motion for periods larger than about 0.14 s at prototype scale. At model scale, 0.14 s corresponds to shaking periods of 0.0035 s (frequency = 285 Hz). At frequencies greater than 285 Hz, the shaker actually achieved substantially larger excitation than the desired motion, and as a result, the achieved peak ground acceleration (PGA) in the centrifuge was substantially greater than the desired PGA. FLAC2D analyses performed after the experiment indicate that the discrepancy between the desired and achieved input motions had a relatively small effect on the predicted permanent deformations of the system.

Fig. 10 illustrates the sequence of shaking events listed in Table 4. Data from a sensor monitoring vertical displacement of the tunnel (DTV1) and a pore pressure sensor (P5) located in the base course near the centerline of the tunnel are presented over the 5 hour duration of the main spin. At this time scale, pore pressures are observed to increase as the centrifuge speed increases (i.e. spin-up), some decrease in pore pressure due to dissipation of pore pressures is apparent. Spikes in pore pressure are observed during each shaking event. The permanent deformations of the tunnel are very small during all of the shaking events except the large TCU event. During the large TCU event, there was a substantially larger uplift (about 200 mm in prototype scale) and some post-shaking settlement. Finally, the pore pressures decreased during the spin-down of the centrifuge.

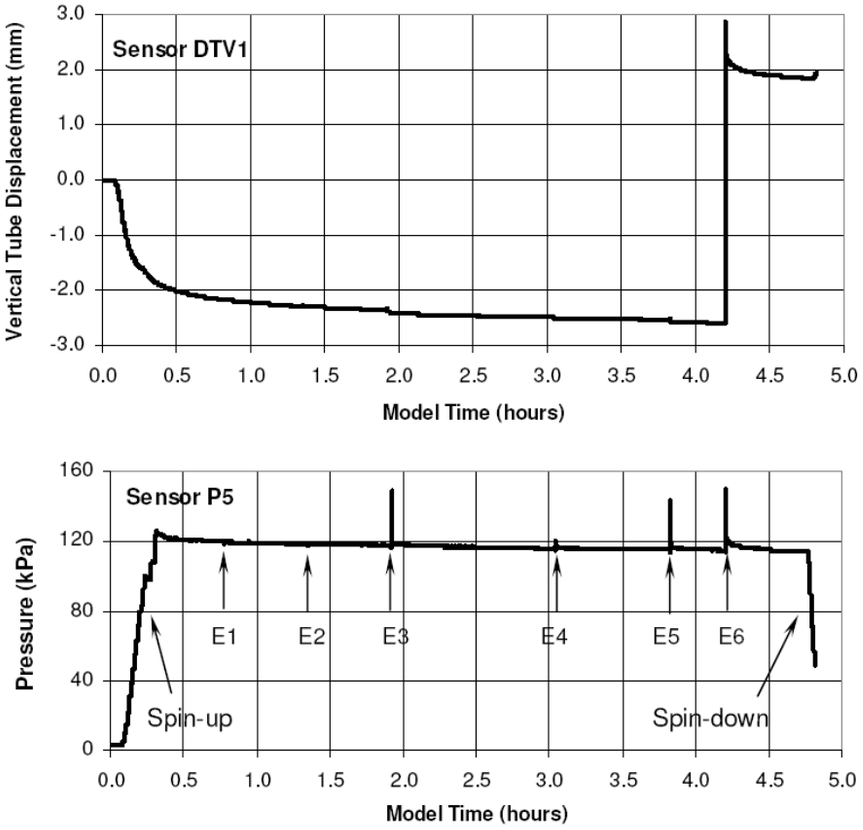


FIG.10. Results from selected sensors to illustrate the entire test sequence.

PHOTOGRAPHS, SURVEY, AND MOVIE DATA

Images through the Window

Fig. 11 shows photographs taken through the west side window of the container before loading and after removing the model from the centrifuge. The small (6 mm diameter) black and white dots were pieces of paper taped to the window, used as fiducial marks for displacement reference points. Three counter-bored black screw-heads (approximately 10 mm in diameter) used to attach the white Teflon sheet to the model tunnel are good references for monitoring of the tunnel displacement. The layers of black sand and interfaces between the different soil types are excellent references for monitoring of the deformed shape of the sand next to the window. Outlining the tunnel, a latex rubber seal obscures the sand adjacent to the tunnel. From these images, it is apparent that the tunnel raised, the black sand was uplifted above the tunnel and sand settled along the left side of the tunnel. On the right side, some water leaked upward between the sand and the window producing the upside down "w" shape in the colored sand next to the tunnel. The interface between the special fill (Monterey Sand) and the ordinary fill (Nevada Sand) clearly settled significantly.

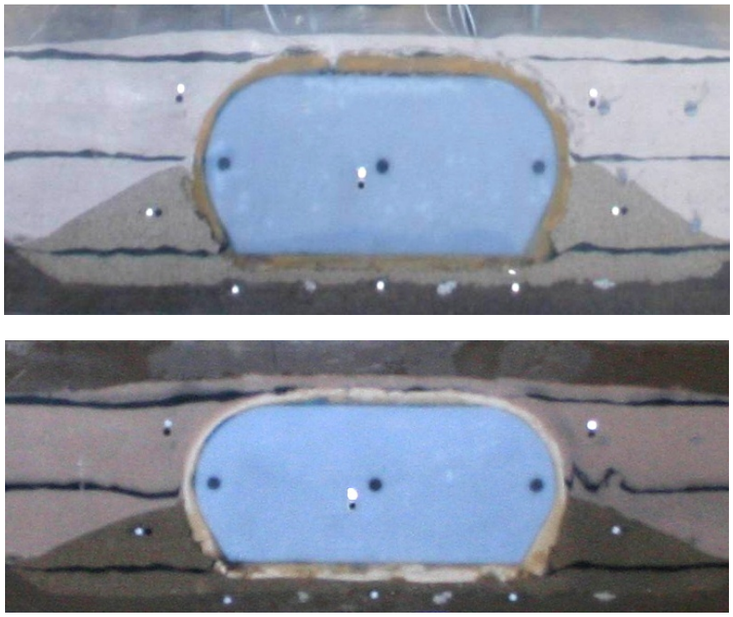
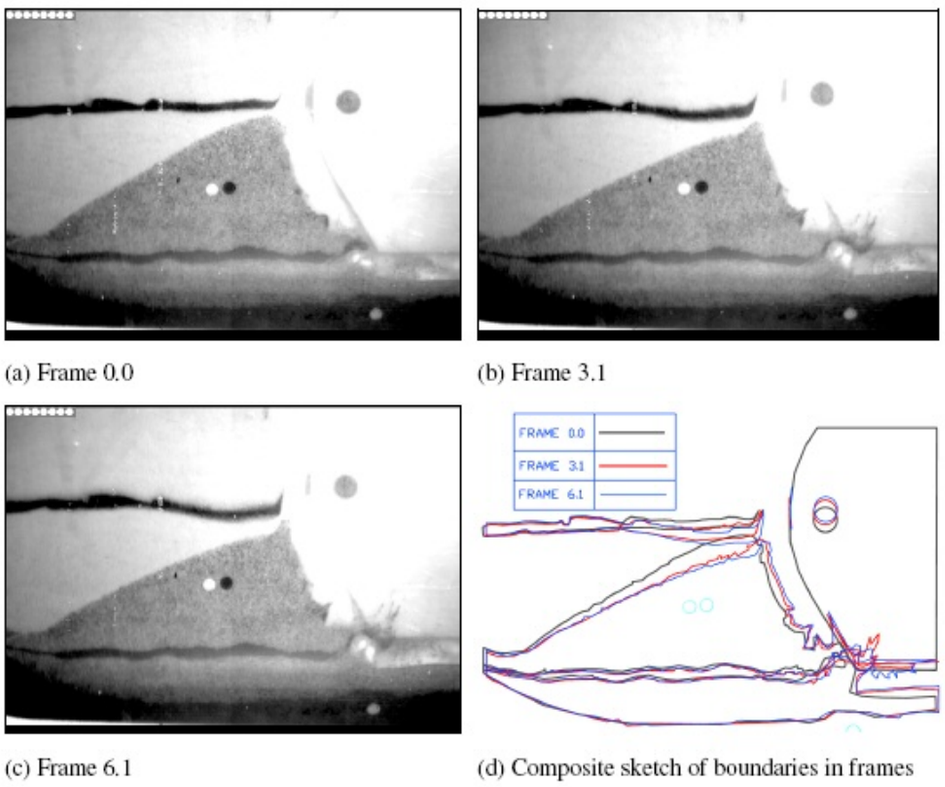


FIG.11. Views of west side of model through the window before and after the centrifuge test.



(a) Frame 0.0 (b) Frame 3.1

(c) Frame 6.1 (d) Composite sketch of boundaries in frames

FIG.12. Three images from high speed video frames and tracings of movements of tube, soil interfaces, and colored sand layers.

Consistent observations from a high-speed video camera focusing on the special fill on the west side of the tunnel are shown in Fig. 12. The first image is taken immediately prior to the large TCU event, the second after strong shaking, and the last after detectable movement ceased. Again note that the black and white dots near the center of the image, and the white dot near the bottom right corner are taped to the window, so they may be used as reference points on the model container. These images were imported into a drafting program, and the outlines of the interfaces between sand types, the latex seal, and the tunnel outline for the three frames are superimposed in Fig. 12.

Images from Excavation

After the centrifuge test the free water was drained from the model and the container was moved to the sample preparation laboratory and systematically dissected. A photograph of one set of blue colored sand columns, originally installed in vertical tubes is shown in Fig. 13. Also apparent are the horizontal black sand layers. From this image the migration of the special fill and ordinary fill toward the base of the tunnel is apparent. In order to estimate the volume of sand flowing under the tunnel, the area of sand between the original position of the lines (estimated by the thin vertical black line on the photograph, and the centerline of the distorted sand column was calculated by importing the picture in a drafting program and calculating areas. The displaced sand volume from Fig. 13 was estimated to be approximately 750 to 950 mm^3 per mm of tunnel length in the model scale. Dividing the displaced volume of sand by the width of the tunnel provides an estimate of the uplift due to flow of soil. This estimate was calculated to be 4 to 5 mm in model scale, which corresponds to

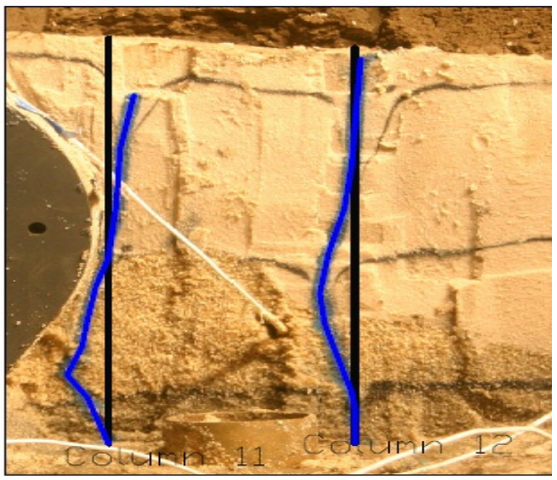


FIG.13. Colored sand columns indicate lateral flow of sand toward the foundation course beneath the tunnel.



FIG.14. Black sand exposed beneath the tunnel after the test. Prior to testing, the black sand was placed along the side of the tube as indicated in Fig. 15.

about 200 mm in prototype scale, close to the total observed uplift. Thus it appears that most of the uplift may be explained by mass flow of sand under the tunnel.

Fig. 14 shows a view of the foundation course after removing the central segment of the tunnel. This shows that black sand from the horizontal sand layer next to the base of the tunnel had migrated under the tunnel. During construction, the edge of this black sand layer was at the bottom corner of the tunnel, as indicated in Fig. 15. The presence of the black sand under the tunnel may only be explained by substantial lateral flow of sand in the foundation course.

During excavation, the surface elevation of the compacted clay that represented the MPSA-Clay was surveyed and this indicated a small heave beneath the tunnel of approximately 1 or 2 mm in model scale. Along with the lateral flow of sand toward the base of the tunnel, this is the third component contributing to the observed uplift. There is one other mechanism of tunnel uplift, and that is uplift due to the flow of water under the tunnel, which will be presented later.

SENSOR DATA

Fig. 15 shows a sketch of the model configuration with locations of selected instruments and the colored sand columns and layers.

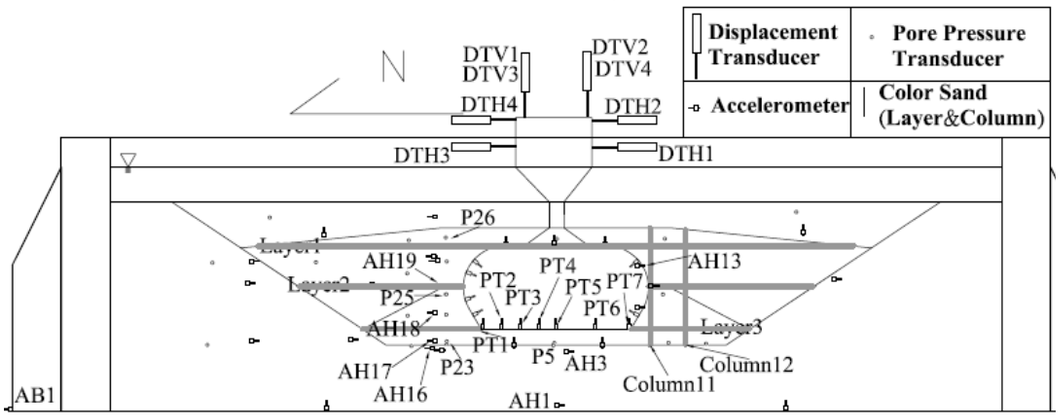


FIG.15. Sketch of model showing location of selected instrumentation. Locations of colored sand columns and layers are indicated by thickened lines.

Acceleration

Fig. 16 compares the base motions from two selected events (3, and 6 in Table 4.) in the ground motion sequence. Data from a vertical array of accelerometers measured in the large TCU event is given in Fig. 17(a). The figure shows a base motion of approximately 0.75 g, which was significantly greater than our target motion. As seen in Fig. 9, the achieved motion contained a significant short period content that resulted in large peak accelerations. Later numerical analyses indicated that the short period input motions had little effect on the predicted movement of the tunnel. In the intermediate period range (period between about 0.15 s and 1.4 s, as seen in Fig. 9) the input motion was about 20% greater than the target. In the long period range (greater than about 1.4 s), the achieved motion was very close to the target ground

motion. The time series data show that the character of the motion in the MPSA-clay and at the bottom of the trench was very similar to that at the base, but some amplification is observed with elevation. The motion near mid-depth in the special fill shows large spikes of acceleration that have been observed for soils that generate large pore pressures during unloading of shear stress and then stiffen up as pore pressures decrease due to dilatancy. Chou and Kutter (2008) and others discuss the phenomenon of spiky acceleration records in liquefiable soil. Near the interface between the special fill and the lower permeability ordinary fill, water may accumulate (void redistribution) due to vertical hydraulic gradients results in loosening at this location, and dilatancy spikes are not seen. Where the dilatancy of the soil is not mobilized, the liquefaction tends to isolate the soil from the input base motion.

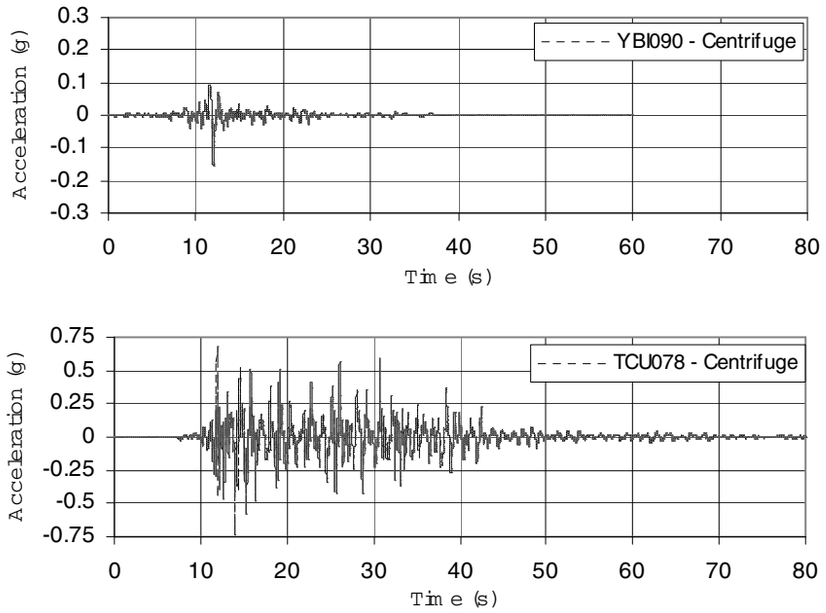


FIG.16 A plot comparing the base accelerations for the Loma Prieta Event and the large TCU078 event (sensor AB1).

Pore Water Pressures

Data from a vertical array of pore pressure sensors and one sensor beneath the tunnel is shown in Fig. 17 (b). The pore pressure in the ordinary fill (P26) indicates liquefaction of this layer, and a very slow dissipation rate. The pore pressure near the top of the special fill (P25) indicates liquefaction, but pore pressures begin to dissipate at the end of strong shaking. The pore pressures in the base course (P23) nearly reached the overburden pressure, but the pore pressures tended to reduce during shaking. It is known to be difficult to liquefy the bottom portion of a permeable material near an impermeable base because the pore pressure gradients tend to cause upward flow of water away from the base.

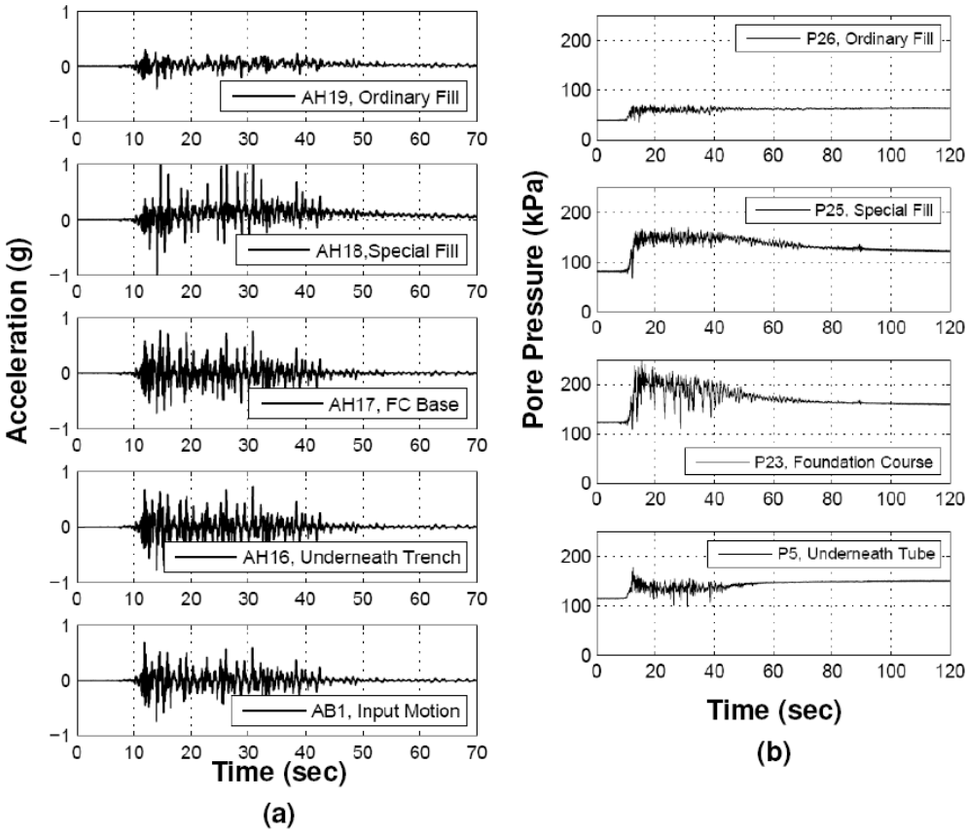


FIG.17. Pore pressure and acceleration data from selected sensors during the large TCU event; sensor locations are given if Fig. 15.

In the case of sensor P23, it is also quite close to the tunnel. The sensors beneath the tunnel (e.g., P5) displayed much smaller pore water pressures, consistent with the lower overburden associated with the presence of the low density tunnel. The lower pore pressures under the tunnel will result in some flux of water toward the base of the tunnel. Thus the pore pressures adjacent to the base of the tunnel are reduced due to flow toward the base of the tunnel.

The flow of water beneath the tunnel can be visualized by looking at results of seven sensors (i.e., PT1 to PT7) that were imbedded in the tunnel, with their porous stones flush with the tunnel surface. Fig. 18 shows larger pore pressures near the edges of the tunnel and smaller pore pressures near the centerline during the large TCU event. This is consistent with the fact that overburden pressures are larger in the fill beside the tunnel than the overburden pressures directly beneath the tunnel. The horizontal position of the pore pressure traces in Figs. 18(b) and (c) are shifted so that their initial value lines up with the sensor location in Fig. 18(a).

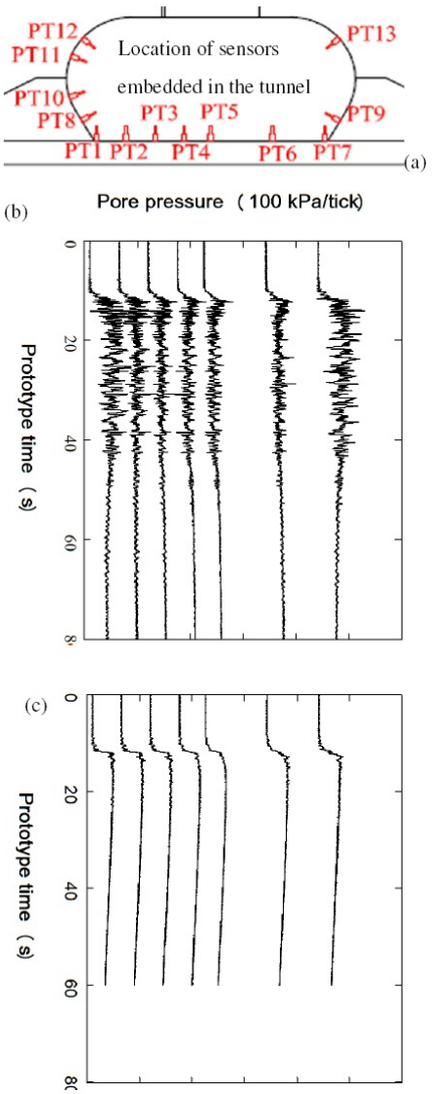


FIG.18. Pore pressure data from sensors PT1 – PT7 embedded on the base of the tunnel (a) embedded location of sensors (b) large TCU event; (c) Loma Prieta event.

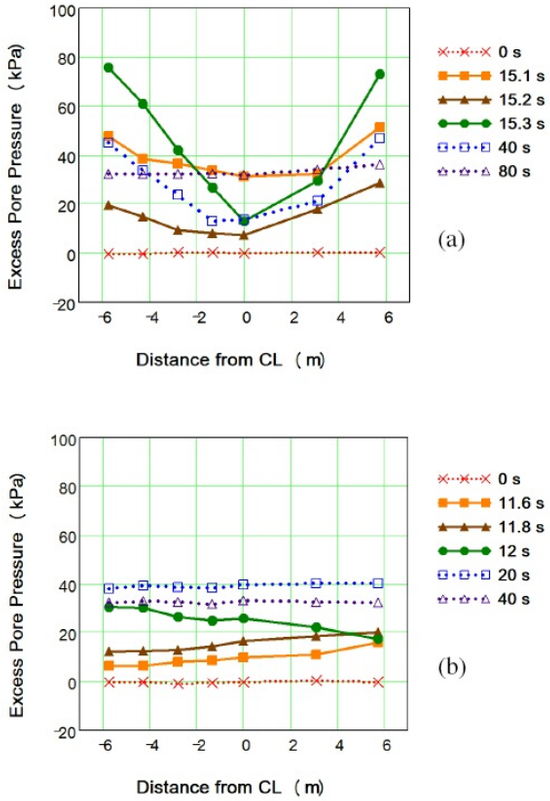


FIG.19. Snapshots of pore pressure distribution from sensors PT1-PT7 in (a) large TCU event, and (b) Loma Prieta event.

Fig. 19(a) shows six snapshots of the excess pore pressure distribution under the tunnel during the large TCU shaking event. The initial effective stress beneath the tube obtained using a 1-D calculation of vertical stress from the surficial mud, ordinary fill and the tunnel, is about 36 kPa. The excess pore pressure distribution tends to be U-shaped, with smaller pore pressures in the middle of the tunnel than near the edges, indicating flow of water toward the centerline. The average excess pore pressure at the base of the tunnel during shaking is approximately equal to the initial effective stress, which suggests that the effective stress on the base of the tunnel is near zero. The fact that the pore pressure is greater near the edges of the tunnel suggests that the total stress

distribution is not uniform; the soil is squeezing in from edges so the vertical total stress may be expected to be greater near the edges. Also the stresses near the edge of the tunnel are affected by the heavier soil adjacent to the tunnel. The three snapshots drawn in solid lines are only 0.1 s apart, indicating the rapid fluctuation of the pore pressures during shaking.

Fig. 19(b) shows a similar graph of the pore pressure distribution during the Loma Prieta event. Three snapshots in solid lines are taken during shaking, when the average pore pressure is rapidly increasing (see the step in pore pressure in Fig 18(c). As the lateral loads on the tunnel may generate moments about the base of the tunnel, the pore pressures are greater on one side of the tunnel or the other. Just after shaking (about 20 s), the pore pressure is very uniform across the base of the tunnel, and it seems to be noticeably greater than the initial effective stress of about 36 kPa; this is possible if there are significant downward shear stresses on the sides of the tunnel. In other words, the base pore pressure required to push the tunnel upward is greater than the overburden stress above the centerline of the tunnel. There was very little upward movement of the tunnel during the Loma Prieta event.

Although the Loma Prieta event caused very small permanent movement of the tunnel, and the large TCU caused significant movements, it is interesting to see that the pore water pressure after shaking for the Loma Prieta event (Fig. 19(b)) is slightly larger than the pore pressures after shaking for the TCU event (Fig. 19(a)). From this it appears that the upward movement of the tunnel is not driven by pore pressures alone; during the many cycles of lateral movement due to strong shaking, soil seems to funnel down toward the base of the tunnel and squeeze into the space under the tunnel. This results in non-uniform total stresses and hence non-uniform pore pressures. Thus the U-shaped pore pressure distribution is a result of soil squeezing under the edges of the tunnel.

The pore pressure data may be processed to obtain an estimate of the vertical movement of the tunnel due to flow of water under the tunnel as follows:

$$q_{jk} = -\frac{kh}{\gamma_w}\frac{u_j - u_k}{x_j - x_k} = \frac{d(s_{jk})}{dt}\frac{(x_j + x_k)}{2} \tag{1}$$

$$s_{jk} = \int \frac{d(s_{jk})}{dt}\,dt \tag{2}$$

q_{jk} is the horizontal volume of flow through the base course per unit time at the midpoint between two sensors located at points indicated by the subscripts j and k. u_j is the excess pore pressure recorded by the sensor at point j, and x_j is the distance from point j to the centerline of the tunnel. The permeability of the foundation course is indicated k, h is the thickness of the foundation course, and s_{jk} is the settlement of the tunnel deduced from pore pressure sensors at points j and k.

The first expression for q is basically an expression of Darcy's Law. The expression in Eq. (1) that includes s assumes that the tunnel does not tilt and that the horizontal hydraulic gradient at the centerline is zero, so that the rate of vertical movement with time multiplied by the distance between the midpoint between the sensors and the centerline of the tunnel must equal the volumetric flow rate of water. The vertical

movement is then obtained by time integration of the rate of vertical movement (Eq. 2). This calculation was performed using experimentally measured pore water pressures to estimate the vertical movement of the tunnel for the sensors labeled PT1 and PT2, PT2 and PT3, and PT6 and PT7 in Fig. 18. The results are presented in Fig. 20(b), which suggests that the uplift due to flow of water is about 0.07 m.

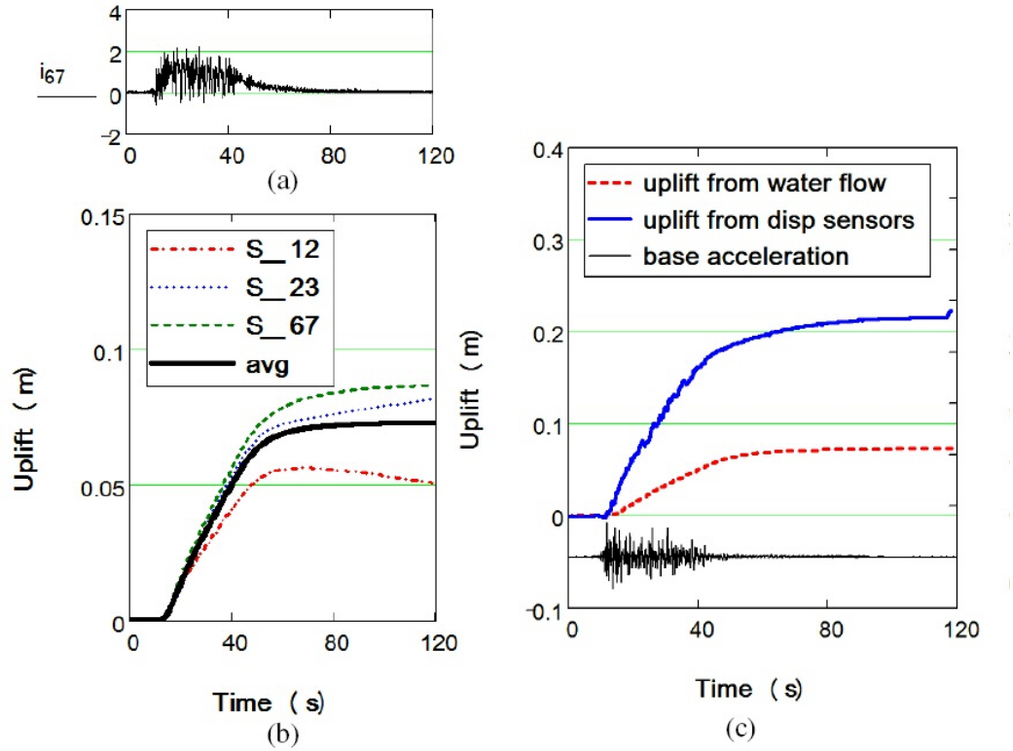


FIG.20. Uplift of tube. (a) Hydraulic gradient beneath the tube for sensors PT6 and PT7. (b) Uplift of tube computed from Darcy's Law and hydraulic gradients. (c) Comparison of uplift due to flow and uplift directly measured from vertical displacement sensors.

Displacements

Multiple displacement sensors were used to record the horizontal and vertical displacement of the tunnel. Assuming that the tunnel segments behaved as rigid bodies, the vertical displacement of the centerline of the tunnel segments was obtained by interpolation between two vertical displacement sensors on the central segment, and this result is presented in Fig. 20(c). Also indicated in Fig. 20(c) is the vertical movement due to the flow of water, from Fig. 20(b). The shapes of the displacement traces for the two methods of calculating uplift are very similar, but it is clear that only about one third of the uplift may be explained by flow of water under the tunnel. The other two thirds of the uplift must have been caused by the movement

of soil particles under the tunnel. The time history of base acceleration is also included in the Fig. 20(c). From this it is apparent that most of the vertical movement occurs during strong shaking; only about 20% of the movement was observed to occur after t = 41 s (the end of strong shaking).

The trajectory of the movement of the center of the tunnel relative to the model container is presented in Fig. 21. The vertical axis indicates the vertical movement from the vertical displacement sensors (the data previously presented in Fig. 19(c)). The horizontal axis indicates the horizontal movement determined by combining data from (1) horizontal potentiometers measuring the horizontal movement of a flag that extended from the tunnel up above the ground surface with (2) horizontal movement obtained by integration of the horizontal relative acceleration between the tunnel and the container. The relative horizontal acceleration was obtained by averaging the data from two accelerometers on the side of the tunnel and subtracting the base acceleration. This relative acceleration was then integrated to obtain relative displacement. The horizontal displacement sensors are not able to provide accurate information at high frequency due to the flexibility of the flag attached to the tunnel and the flexibility of the support beam that held the body of the displacement sensor, but they do provide accurate low frequency measurements. Displacement data obtained by integration of accelerometer data, on the other hand, is known to provide accurate information at high frequencies but inaccurate data at low frequencies. Therefore a low pass, zero phase shift filter ($G_L(f)$) was applied in the frequency domain to the displacement data, and a complementary filter ($G_H(f) = 1 - G_L(f)$) was applied to the accelerometer data. After conversion back to the time domain, the filtered displacement from the displacement sensors was simply added to the filtered displacement from the accelerometers.

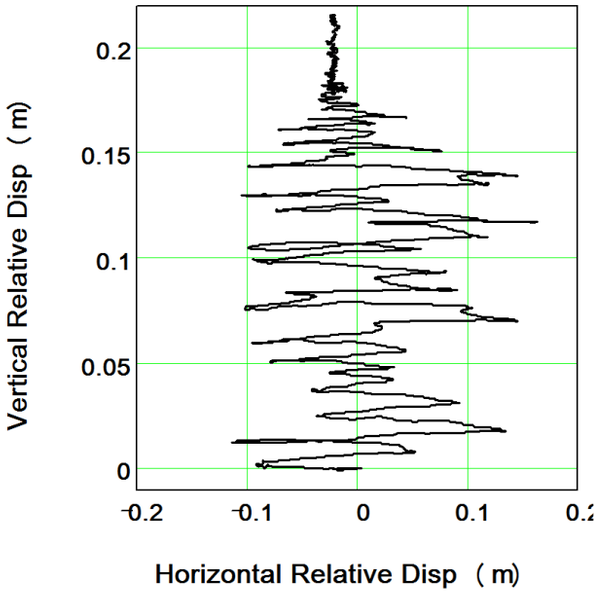


FIG.21. Trajectory of movement of the center of the tunnel.

From Fig. 21, it appears that there are significant large cycles of lateral displacement occurring while vertical movement is almost monotonically increasing. The ratio of vertical to horizontal velocity may be largest immediately following a reversal of the horizontal displacement.

DISCUSSION OF NUMERICAL ANALYSIS AND MECHANISMS

Fig. 22 compares predicted and measured vertical displacement of the tunnel, and pore pressure beneath the tunnel centerline. The numerical analysis was carried out using FLAC2D with the UBCSAND constitutive model. The constitutive model includes the pore pressure generation due to cyclic loading, dilatancy associated with shearing, and flow of pore water. The parameter selection, boundary conditions, and ground motion selection protocols are described in detail by Fugro (2007a, 2007b, 2007c). A detailed analysis of the quality of numerical analysis predictions is outside the scope of this paper. However, it may be stated that the analysis is in reasonable agreement with the experimental results.

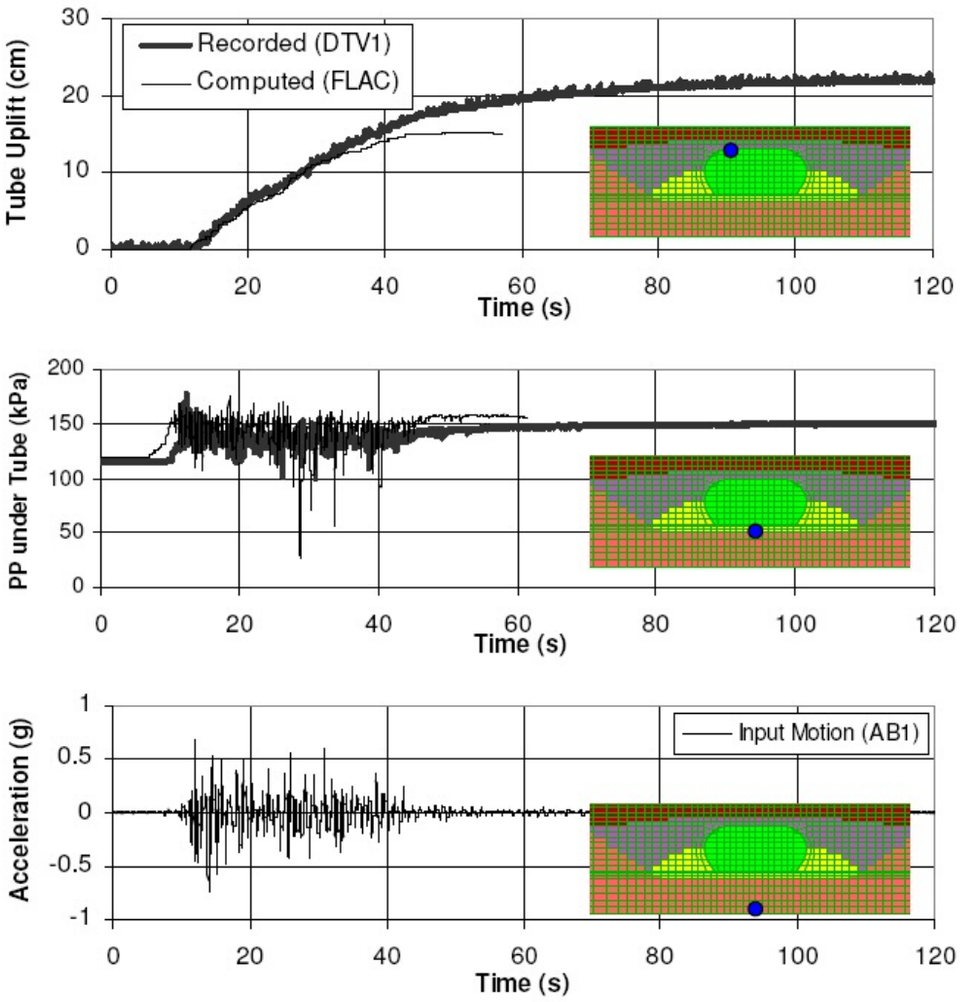


FIG.22. Selected comparisons between experimental data and numerical model predictions.

Preliminary analyses were conducted prior to the centrifuge test using the design target input motion with the goal to provide "Class A" estimates of the tunnel response. Those analyses predicted total uplift of the tunnel of about 100 mm. The analyses were repeated after the experiment, using the ground motion recorded during the test as an input. In addition, small modifications were made in the calibration of the numerical model to address differences in the as-built compared to the design soil parameters. Finally, an interface was introduced between the tunnel and the underlying soil. The analyses after the experiment predicted about 150 mm of uplift, as shown in Fig. 22. This compares to about 180 mm of movement that was observed during shaking in the centrifuge test. Hence, the numerical analyses appear to capture the mechanism and magnitude of tunnel uplift reasonably well. Discrepancies between the recorded response and the numerical predictions may be attributed to a number of reasons associated with this complicated problem involving dynamics, liquefaction, pore pressure migration, and large strains in the base course soil. For example, some of this discrepancy may be explained by potential heaving of the clay beneath the tunnel at the base of the trench. Although the heave was not directly recorded during the experiment, pre and post shake survey data suggest the stiff clay underlying the trench may have heaved by about 20 mm.

Additional tunnel uplift followed by settlement was observed after the end of shaking. In the centrifuge model tests we observed approximately 30 mm of uplift to occur after strong shaking. However, the analysis only predicted approximately about 5 mm of post-shaking uplift. This discrepancy points to a limitation of the constitutive model, which does not have a plastic volumetric stiffness. Hence the large volumetric changes that occur during consolidation are not well captured.

Although the ordinary fill and the special fill around the tunnel were placed in a loose condition with relative densities of 30 to 45%, this material is dilative under monotonic shearing conditions. Therefore in the absence of shaking (which generates positive pore pressures), the dilatancy absorbs excess pore water, reducing pore pressures and displacement ceases shortly after shaking.

The contrast between the permeability of the special fill and that of the ordinary fill along with the volume change due to densification of the special fill is also considered to have a significant potential effect on the uplift of the tunnel. The relatively low permeability of ordinary fill limits the rate that water can escape vertically in the special fill. Conversely, the relatively large permeability of the special fill allows for the pore water pressures to be redistributed during the earthquake and move upwards away from the tunnel. Still, there is potential for a pocket of pressurized water, produced by densification of the special fill, to collect near the top of the special fill. The magnitude of pore pressure in this water pocket would be limited by the total stress in the ordinary fill above the top of the special fill. For the geometry of the tunnel under consideration, the magnitude of the excess pore pressure is approximately equal to the initial average effective stress under the tunnel, so it is then possible for this water to flow under the tunnel and cause uplift. Fortunately, the *volume* of the special fill and hence the *volume change* of the special fill is limited, so the amount of uplift will be limited.

Based on the FLAC analysis and the centrifuge test, the primary mechanism of uplift is the funneling of soil under the tunnel in a ratcheting mechanism driven by the

cyclic horizontal displacements of the tunnel. For example, when the relative movement of the tunnel is toward the South, some soil drops down to fill the void on the North side of the tunnel. As the displacement cycles back to the North some of the soil works its way under the tunnel through the gap (the thickness of the base course) between the base of the tunnel and the base of the trench.

The thickness of the base course was found to be a key parameter controlling the amount of uplift. The amount of soil that squeezes into this space was found to increase as the thickness of the base course increases. The rate of uplift due to seepage of water under the tunnel is also expected to be nearly proportional to the thickness of the base course because this increases the cross sectional area across which water may flow.

The number of shaking cycles that occur after the soil is softened by pore pressure build up seems to be an important factor in determining the amount of movement. For the Loma Prieta shaking event, the uplift predicted by the analysis and the uplift observed in the centrifuge tests was quite small (about 3 mm at prototype scale). The actual tunnel did experience the 1989 Loma Prieta earthquake and it performed well with no significant deformations. This event only produced a couple of significant cycles of ground motion. The Loma Prieta event did cause pore pressures indicative of liquefaction, but did not result in significant movement because the amplitudes of motion were smaller and there was very little cyclic lateral movement after the pore pressures were generated. For the large TCU event on the other hand, the duration of strong ground motion was on the order of 30 seconds, so there were many cycles of ground oscillation after the pore pressures build up, and significant uplift was observed.

CONCLUSIONS

The most important concern about the stability of the tunnel was the possibility that a tunnel might even pop out of the liquefied ground with unlimited deformation. This would breach the tunnel allowing water to flood the tunnel. Ground improvement was considered but this is complicated by the large volume of soil, working offshore, and interference with shipping traffic to a large port facility. Preliminary numerical analyses suggested that the mechanism of uplift is displacement-limited, with relatively small vertical displacements. Hence, retrofit may not improve the overall performance of the system, especially in zones where the trench is dug into stiff MPSA-clay. A centrifuge model test was therefore conducted to provide validation of the numerical methods.

The first of two centrifuge model tests is described in this paper. The model test confirmed that the uplift of the tunnel occurs during shaking and is predominantly caused by soil moving underneath the tunnel. Based on the centrifuge tests and numerical analyses, the magnitude of the uplift of the tunnel may not be large enough to warrant retrofit via ground improvement, although this issue is still being considered.

Based on the results of the centrifuge test and numerical analyses, the overall magnitude of movements of the tunnel appears to be relatively low. Differential movements remain an important consideration in the final decision on how and if the

tunnel should be retrofitted. Differential movements may be caused by differential ground motions, varying geological conditions along the length of the tunnel, and lateral deformation of the ground due to slope instability through which the tunnel may run.

The centrifuge model test was used to help make a decision for a real design problem. It provided insight into the mechanism of uplift, provided reference data to calibrate the numerical tools and highlighted the strengths and potential limitations of the numerical analyses. As a result of this work, there is a potential for savings of tens of millions of dollars in retrofit expenditures.

ACKNOWLEDGEMENTS

This project was funded by a subcontract from Fugro West Inc., who was in turn a subcontractor of the Bechtel Infrastructure Corporation, with funds originating from the San Francisco Bay Area Rapid Transit District (BART). The project would not have occurred without the leadership of the project leader at Fugro West, Jacob Chacko; he led the group that performed the analysis and pushed for the funding of the centrifuge model test, and participated in the detailed design and the construction and testing of the centrifuge model. Stephen Coulter, Fugro West Inc. participated in every phase of the model construction and testing. Yan Lucille, Fugro West Inc. participated in early phase of the model construction and testing.

Anthony Hitchings, Tom Horton, and Kathy Mayo of BART and Mark Salmon and Ken Mark from the Bechtel Team must be given credit for authorizing advanced tools such as the large scale centrifuge model tests and advanced numerical modeling to be used in this project. These advanced tools are expensive and non-standard in design. Having the courage and vision to go beyond conventional engineering procedures to use the most advanced tools available to address this difficult problem to the long-term benefit of this high-profile project must be acknowledged.

Dan Wilson of UC Davis participated in the design and testing. Lijun Deng and M. Ilankatharan, UC Davis graduate students, assisted with instrumentation, sample preparation, testing and data processing. Lars Pedersen, Chad Justice, Ray Gerhard, Mark Hannum, Peter Rojas, Nick Sinikas, and Joel Mireles, staff of the UCD Center for Geotechnical Modeling provided necessary assistance and valuable expertise.

Peter Byrne assisted with the FLAC analyses. BART's Peer Review Panel (PRP) and Design Review Board (DRB) have provided valuable guidance and oversight to the project. In particular, Jonathan Bray, Raymond Seed, and I.M. Idriss provided important input to the centrifuge model tests as part of this study.

REFERENCES

Arulmoli, K., K. K. Muraleetharan, M. M. Hosain, and L. S. Fruth, (1992). "VELACS Laboratory Testing Program, Soil Data Report," *The Earth Technology Corporation*, Irvine, California, Report to the National Science Foundation.

Balakrishnan, Ariyaputhirar. (2000). "Liquefaction remediation at a bridge site." *Ph.D. diss.*, University of California at Davis, Davis, CA, United States (USA).

Beaty, M. and Byrne, P.M. (1998). "An effective stress model for predicting liquefactioin behaviour of sand" *Geotechnical Earthquake Engineering and Soil*

Dynamics, (Dakoulas, Yegian, Holtz, Eds.) ASCE Geotechnical Special Pub. , 75 (1), pp. 766-777.

Chou, J.-C., and Kutter, B.L (2008). "Nonlinear Shear Wave Propagation in Strain Stiffening and Strain Softening Soil" accepted by *GEESD IV 2008.*

Fair G.M. and Hatch L.P. (1933). "Fundamental factors governing the streamline flow of water through sand," *Journal of the American Waterworks Association*, 25 (II): pp. 1551-1565.

Fugro, (2007a). "Detailed Design of the First Centrifuge Experiment for the BART Transbay Tube," August, 2007, submittal number FUGR-BEC 118.

Fugro (2007b). "Preliminary Report No-Densification Assessment," prepared for Bechtel Infrastructure Corporation Bart Earthquake Safety Program, September 2007.

Fugro (2007c). "Results from the first centrifuge experiment for the BART Offshore Transbay Tube," Project Memorandum to Bechtel, November, 2007.

Itasca Consulting Group Inc. (2006). "Fast Langrangian Analysis of Continua (FLAC2D)," version 5.0.

Idriss, I.M. and Sun, J.I. (1992) "SHAKE91 - A computer program for conducting equivalent linear seismic response analysis of horizontally layered soil deposits. User's Guide", Center for Geotechnical Modeling, Civil Engineering Department, U.C. Davis.

Kammerer, A., Wu, J., Riemer, M., Pestana, J, and Seed, R. (2004). "Shear Strain Development in Liquefiable Soil under Bidirectional Loading Condition," *13WCEE, paper No. 2081.*

Kammerer, A., Wu, J., Pestana, J, Riemer, M., and Seed, R. (2000). "Cyclic Simple Shear Testing of Nevada Sand for PEER Center Project 2051999," *Geotechnical Engineering Research Report*, UBC/GT/00-01, University of California, Berkeley, January 2000.

Koseki, J., Matsuo, O., Ninomiya, Y., and Yoshida, T. (1997b). "Uplift of sewer manholes during the 1993 Kushiro-Oki Earthquake" *Soils and Foundations*, 37 (1), pp. 109-121.

Koseki, J., Matsuo, O., Koga, Y. (1997a). "Uplift behavior of underground structures caused by liquefaction of surrounding soil during earthquake" *Soils and Foundations*, 37 (1), pp. 97-108.

Kulhawy, F.H. and Mayne, P.W. (1990). "Manual on estimating soil properties for foundation design" Report EL-6800, Electric Power Research Inst., Palo Alto, California, 306 p.

Puebla, H. Byrne, P.M., Phillips, R. (1997). "Analysis of CANLEX liquefaction embankments: prototype and centrifuge models," *Canadian Geotech. J.* 34: pp. 641-657.

Wu, J., Seed, R.B., and Pestana, J.M. (2003). "Liquefaction Triggering and Post Liquefaction Deformations of Monterey 0/30 Sand under Uni-Directional Cyclic Simple Shear Loading," *Geotechnical Engineering Research REPORT*, No. UCB/GE-2003/01, University of California, Berkeley.

Yang, D., Naesgaard, E., Byrne, P.M., Adalier, K., Abdoun, T. (2004). "Numerical model verification and calibration of George Massey Tunnel using centrifuge models", *Canadian Geotech. J.* 41: pp. 921-942.

This page intentionally left blank

THEME PAPER: EARTHQUAKE ENGINEERING FOR TUNNELS AND UNDERGROUND STRUCTURES. A CASE HISTORY

Ignacio Arango[1], L.M., ASCE, P.E.

Geotechnical Manager, SVRT Project, 35% engineering phase.
Geotechnical Consultant, Bechtel Corporation; iarango@bechtel.com

ABSTRACT

Tunnel and large cut-and-cover structure response to earthquakes is dominated by the surrounding ground, and, contrary to shallow-founded structures, does not depend on the inertial properties of the structures themselves. The focus of the underground design is on the free-field deformation of the ground and its interaction with the structure, i.e., a soil-structure interaction phenomenon. This paper summarizes the performance in recent past seismic events of deep, large underground structures, and then elaborates on their design approach: geotechnical, seismic criteria and structural factors. Analytical models are examined and conclusions drawn about their advantages and limitations. A general approach to the design of deep underground structures is illustrated through the on-going design of a particular project.

INTRODUCTION

This Conference Session focus is on the earthquake engineering response, analysis and design of large concrete-lined tunnels and deep cut-and-cover excavations hereby globally called underground structures (US); and, in particular, TU for tunnels and C/C for cut-and-cover structures, respectively.

The invited theme presentation consists of two parts: 1) a review of the observed behavior of underground structures in previous seismic events, and a summary overview of the principal elements entering into the analysis and design of US; and 2) an introduction to a case history illustrating the application of the methodology to the Silicon Valley Rapid Transit Project currently in the 65% stage of design. The material presented in the second part of this paper is expanded in the following contributions to the Specialty Session of the Conference:

1 Silicon Valley Rapid Transit Project– John Hawley, James Chai, and Andrew Liu
2 Seismic Design Criteria and Ground Motions– Joe Litehiser and Jim Marrone
3 Site Response to Develop Design Ground Motions for the Silicon Valley Rapid Transit Project– Daniel Pradel and Peter Chiu
4 Kramer et al. (2007) described the seismic design of the tunnel and tunnel liner.
5 Cut-and-Cover Structures: Seismic Response and Design—Ching Wu, Farhang Ostadan, and Wen Tseng

PERFORMANCE OF UNDERGROUND STRUCTURES (US) SUBJECTED TO EARTHQUAKE LOADING

Underground structures are affected by seismic events in two ways: a) ground response (liquefaction, fault displacements, and slope instability); and b) vibratory ground motions characterized by the amplitudes of acceleration, velocity, displacement and duration of shaking. The specialty session deals with vibratory ground motions and their impact on US.

Earthquake waves impose on US different types of deformations: a) axial compression and extension (seismic waves producing motions parallel to the tunnel axis); longitudinal bending (components of seismic waves producing particle motions perpendicular to the tunnel axis); ovaling of circular section tunnels; and racking of rectangular cross-section tunnels and C/C excavations induced primarily by vertically propagating shear waves.

Damage to Tunnels (TU)

Numerous investigators have presented reports dealing with damage to TU due to shaking. Power et al. (1998) reviewed the seismic performance of 204 tunnels, 27 of them having RC liners. Damage was rated on a scale varying from 1 (none), 2 (slight), 3 (moderate), and 4 (severe). Figure 1 is a graphic presentation of the data from the reference. Numbers in parentheses indicate cases corresponding to RC-lined tunnels. It can be observed that peak ground acceleration levels as low as 20% may inflict slight damage to un-reinforced liner tunnels; while, except for one case, peak ground acceleration levels beyond 40% will inflict a minimum moderate damage to RC-lined tunnels. Note that the above cases pertain exclusively to the performance of tunnels resulting from seismic shaking excluding damage caused by other causes. Based on the analysis of the performance of the 204 case histories compiled by Power et al. (1998) the authors concluded:

- *Compared with the performance of shallow structures, tunnels show appreciably less damage from earthquake events. As is to be expected, damage severity is a function of their shape, depth, structural features, geotechnical properties of the surrounding soils, and the intensity of the ground motions. The methodology to analyze and design deep underground structures must address these separate factors.*
- *Tunnels having a stronger lining system perform better, especially those tunnels having reinforced concrete and/or steel lining.*
- *Damage to tunnels is greatly influenced by the amplitude of the ground acceleration. In general, for peak ground accelerations below 20%, ground shaking caused very limited damage to tunnels. Damage was slight to heavy for acceleration amplitudes between 20% and 50%.*
- *Acceleration levels above 40% are required in order to cause slight damage to RC-lined tunnels.*

0	2	1	1	Heavy Damage
0	0	6 (1)	11	Moderate Damage
2	2	15 (1) 1*	8 (2)	Slight Damage
48 (10)	29 (6) 2*	68 (3) 1*	11 (4) 1	No Damage

0 20 40 60 80

Peak Ground Acceleration, g's%

Notes: 1 Data and damage ratings taken from Powell, et.al (1998)
2 Numbers in parentheses represent RC-lined tunnels
3 Numbers with asterisks represent tunnels with Precast Concrete Liner (PCTL)

FIG. 1. Seismic Performance of Tunnels

An exhaustive literature search was conducted by the Silicon Valley Rapid Transit Project (SVRT, 2006a) to search for reports on the performance and damage to tunnels with pre-stressed concrete liner segments (PCTL) in seismic events. Between 1960 and 1990, the use of PCTL replaced steel or cast iron segments as the most widely used lining for tunnels in soft ground. These tunnels perform particularly well in earthquakes because of their circular, largely symmetrical shape, and because they are jointed and have ample flexibility.

The study compiled an extensive list of applications of PCTL in seismically active areas and collected historical earthquake records and seismic hazard maps at the locations of this type of liner system. PCTL tunnels have been extensively used in seismically active locations in Japan, Venezuela, Puerto Rico, Iran, Taiwan, Mexico, Turkey, Spain, Italy, Greece, the United States and elsewhere. The research indicated that hundreds of tunnels with this type of liner have been constructed in areas that are prone to earthquake shaking. No reports of significant damage to tunnels in seismic events were found during the literature search. In general, there is limited

information on PCTL performance in technical literature and earthquake reconnaissance reports. This likely is a result of the fact that earthquake reconnaissance reports typically do not report good performance; they focus on problems instead. After a significant earthquake, thorough reconnaissance studies are always performed to evaluate structural performance. On this basis, the study concluded that no significant damage occurred if performance problems were not mentioned or documented in reconnaissance reports and other literature.

The occurrence of strong seismic events in California, Greece, Taiwan and Japan in the last decade provided additional data on observed damage in tunnels. Locations and acceleration levels to which four (PCTL) tunnels subjected to the indicated peak ground acceleration levels are: Northridge (40% of gravity), Athens (25% gravity), Hualien (20% gravity), and Kobe (50% gravity). No damage was observed in the first three tunnels while minor spalling at segment joints was observed at the fourth tunnel. The performance of these four cases is also shown in Figure 2 with an asterisk.

Damage to C/C Structures

Information about the performance of C/C structures is not readily available in the technical literature. For this paper, the author reviewed earthquake damage reports resulting from two seismic events: the Michoacan in Mexico (1985) and the Chibu in Japan (1995).

The Metro system in Mexico City was built following a cut-and-cover construction procedure. Inspection of the tunnels and stations after the earthquake revealed only minor cracks at junctions between stations and tunnels and at sites with drastic changes in stiffness, for example, near ventilation shafts (NCEER, 1989). The Metro was subjected to peak ground acceleration levels varying between 9% and 17% induced by a Magnitude 8 earthquake centered 300 km away.

The Kobe underground stations were also built following a cut-and-cover construction procedure. Extensive damage was observed at two stations of the Kobe Rapid Transit Railway and at three stations of the Kobe Municipal Subway (Metro). Of particular significance is the failure of the Daikai Station (KRTR) *"… because it is the first instance of catastrophic earthquake damage to a modern tunnel for reasons other than fault displacement and instability near the portal,"* (NIST, 1996). Acceleration levels in the general area were above 50% of gravity. The station failed along a 100m long section. It was a reinforced concrete box structure, 7.2m high and 17m wide at a depth of 4.8 m from street surface to the top of the box. The central reinforced columns of the station failed apparently by a combination of shear and vertical loading, (NIST, 1996).

Based on the limited number of case histories, it appears that damage to C/C structures may be associated to large increases in the lateral earth pressures acting on the walls resulting in structural racking, damage to walls and construction joints, formations of cracking and development of plastic hinges.

DESIGN APPROACH

The analysis of US, be they tunnels or cut-and-cover, requires a good understanding of the geotechnical and seismologic environments where the project is to be located, definition of the seismic project design criteria, and an evaluation of ground response to the prescribed ground motions. Analytical and design work proceed after this information has been compiled. This process is schematically presented in Figure 2. Details about each of the elements entering into the design are discussed below.

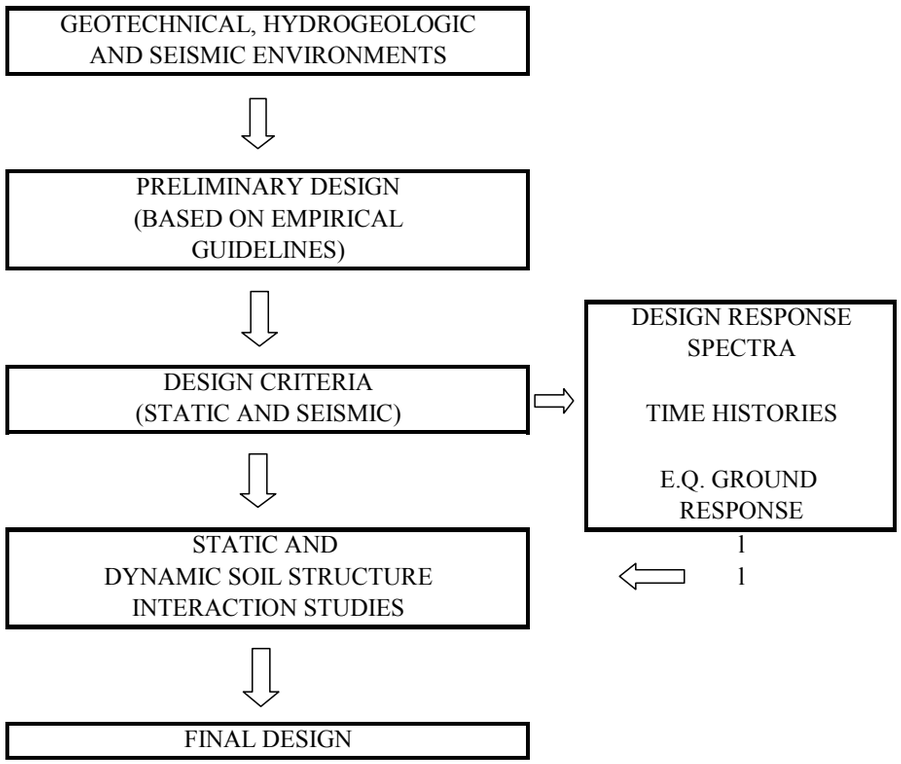


FIG. 2. Earthquake engineering design of underground structures

Geotechnical

The purpose of field and laboratory geotechnical investigations is to obtain a clear understanding of site stratigraphy and of geotechnical parameters to be used in the static and seismic design.

Field and laboratory investigations include engineering properties of the materials involved (strength, compressibility, stress-strain characteristics, hydraulic properties, dynamic properties including small-strain modulus and its degradation with strain amplitude). Table 1 lists field and laboratory tests routinely carried out for US.

Table 1. Field and Laboratory Investigations

Activity	Tests
Field	Borings
	SPTs
	Vane Shear
	CPTs
	Pressure meter
	Down-hole geophysical
	Piezometers, wells
Laboratory	Standard Classification:
	(Moisture content, unit weight,
	specific gravity, Atterberg
	Limits, strength)
	Resonant column
	Cyclic triaxial
	Cyclic simple shear

For tunneling design purposes whether static or dynamic, the behavior and characterization of soils are usually based on the classification originally proposed by Terzaghi (1977). Table 2 shows a simplified classification prepared based on his. For tunnel design, the geotechnical characterization of the environment should also cover an assessment of geologic-related features such as likelihood of encountering boulders in the formations, site aerial subsidence, ground movements, seismic liquefaction evaluation, and proximity to geologic faults.

Table 2. Simplified Tunnel Classification System*

Classi-fication	Behavior	Typical Soil Type
Firm	Heading can be advanced without initial support. Final lining can be constructed before ground starts to move.	Hard clays; cemented sand and gravel; till deposits.
Raveling	Chunks or flakes of material begin to drop out of the arch or walls after exposure.	Residual soil or clean sands below water table (fast raveling), or slow raveling above. Stiff fissured clays and tills ravel slowly or fast depending upon cover and fracturing.
Squeezing	Ground extrudes plastically into tunnel without visible fracturing.	Very soft to medium consistency clays at shallow depth; stiff to hard clays under high cover.
Running	Materials exposed at steeper slope than the angle of repose; run like granular sugar or dune sand.	Clean granular, weakly-cemented materials.
Flowing	A mixture of water and soil flows into tunnel as a viscous fluid.	Silts and clean sands and gravels below water table; sensitive clays.
Swelling	Ground absorbs water, increases in volume and expands slowly into tunnel.	Highly preconsolidated clay with plasticity index above 30%.

*Prepared Based on Terzaghi's "Earth Tunneling with Steel Supports," Chapter 4, 1977.

Hydrogeology

Studies are carried out to define the site conceptual hydro-geologic model including the distribution of aquifer and aquitard zones within the profile; hydraulic properties of the soil formations, historic and future trends of ground water elevations, artesian conditions if present, occurrence of gases, requirements for deep pressure relief systems for C/C excavations and seepage rates. Several tests are available to obtain the in-situ hydraulic properties of the formations at the site. These include in order of importance: pumping, slug and cone dissipation tests. Networks of piezometers and

observation wells installed early in the design process help define the subsurface ground water regime. Table 3 compiles the hydro-geologic resources available to characterize a site and the expected information to be obtained from the investigations.

Table 3. Site Hydrogeologic Characterization

TOOLS	Previous site studies and data
	Pumping tests
	Site monitoring with piezometers and observation wells
	Slug and CPT dissipation tests
RESULTS	Hydro-geologic profile showing aquifers and aquitard zones
	Hydraulic properties
	Ground water elevation trends
	Occurrence of gas
	Artesian condition
	Pumping requirements

Seismic Environment and Definition of Earthquake Ground Motions

The seismic source model must include characterization of all seismogenic sources that could cause strong ground shaking to any part of the project. The source model includes characterization of known faults and possibly unknown faults. It also includes the possibility of earthquakes occurring on un-mapped faults. Each seismogenic source must be characterized by geometry, maximum credible magnitude distribution, and rate of earthquake occurrence. Characterization of seismic sources for seismic hazard analysis of faults entails describing a number of fault parameters and the uncertainty associated with each. These parameters include the probability of activity, rate of slip, three-dimensional geometry, rupture segmentation, maximum earthquake magnitude, fault slip rate, and ground motion attenuation with distance. Table 4 compiles the information that describes the seismic environment of a site.

Table 4. Seismic Environment Characterization

TOOLS	Previous studies and data Site stratigraphic profiles Geophysical surveys
RESULTS	Characterization of Seismogenic Sources: Geometry Maximum magnitude distribution Rate of earthquakes Probability of activity Sense of slip Rupture segmentation Maximum earthquake magnitude Fault slip rate Ground motion attenuation

Most ground motion attenuation relationships are based on empirical data that average out the theoretical effects of fault direction, i.e., toward or away from the Project site location; and also the horizontal orientation of site ground motion relative to the causative fault, i.e., fault normal or fault parallel. The combined effects of rupture directivity and fault-relative horizontal ground motion orientation are generally referred to as the "directivity effect." The amplification or de-amplification effects of rupture directivity and fault-relative orientation should be taken into account in the derivation of the design response spectra and earthquake time histories, which may need the inclusion of large velocity pulses and displacements.

Design seismic motions are specified by horizontal and vertical equal hazard response spectra at 5% critical damping properly accounting for directivity effects.

Two approaches are used to define earthquake design ground motions: Probabilistic and Deterministic.

Probabilistic Seismic Hazard Analysis (PSHA)

An important aspect of the PSHA methodology is its explicit incorporation of uncertainty in seismic source and attenuation using the logic tree approach. Current procedures for these analyses are described in several publications: Coppersmith and Youngs (1986 and 2000); Coppersmith (1991); Cornell (1968 and 1971). The approach consists of four steps: 1) identification of earthquake sources, 2) evaluation

of source recurrence rates, 3) determination of ground motion attenuation parameters, and 4) formal definition of seismic hazard.

Probabilistically, the Maximum Design Earthquake (MDE) is the ground motion at the site corresponding to a certain probability of occurrence in a prescribed number of years (100 to 2500 years). The Operating Design Earthquake (ODE) is usually selected as being the motion that can reasonably be expected to occur at least once during the life of structure.

Deterministic (DSHA)

Unlike the PSHA, the DSHA defines ground motions for specific controlling earthquake(s) rather than considering all uncertainties associated with the seismogenic sources. For each source, the parameters entering into the characterization of the motions are earthquake magnitude, distance from the fault, and corresponding ground motion attenuation relationship. Controlling earthquake(s) are those that generate the maximum ground motion at the site. The approach consists of three steps: 1) identification of earthquake sources, 2) specification of motion parameters, and 3) formal definition of seismic hazard.
In a deterministic analysis, the MDE is defined as the median or the median plus/minus a fraction of the standard deviation of the controlling earthquake(s).

Preliminary Design

Preliminary design of US is performed based on well-established practices. To begin, the geotechnical, hydro geologic and seismologic characterizations of the site, based on the scope and detail discussed in the previous paragraphs, provide the tools to identify conditions that may impact the project and that would require special attention: presence of geologic faults, obstructions, exposure to contaminated soils and ground water, seismic liquefaction, and ground instability.

At this stage decisions are made regarding the number of bores and size of the openings needed to accommodate the expected design traffic. This is followed by the study and selection of alternative alignments, depths of burial, earth pressures and dynamic ground strains, grades, tunneling and equipment techniques, supports, liners, grades, ventilation structures, number and location of cross-passages, need of ground treatment and dewatering, spoil disposal, and construction approaches.

Shallow-tunnel construction may modify the ground water regime and the conditions of the soil cover above the crown. The results of these impacts are settlement due to ground water depression and settlement due to loss of ground. Settlement caused by effective vertical stress increase can be estimated based on the well-known soil mechanic theories of soil compressibility and consolidation. Empirical procedures are available to estimate loss of ground assuming a Gaussian curve-shaped through, centered above the tunnel alignment as shown in Figure 3. A width parameter “i” determines the width of the Gaussian curve. The parameter “i” is

usually taken as i = KZ, where "i" is the horizontal distance to a point of inflection, Z is the depth of the tunnel spring line, and K is a constant based on soil type above the tunnel spring line. The maximum value of the surface settlement is theoretically equal to the volume of the surface settlement divided by 2.5i. Structural damage resulting from ground settlement varies with the angular distortion and lateral strain as Figure 4 shows, (Moorak, S. and Cording, E.J., 2005).

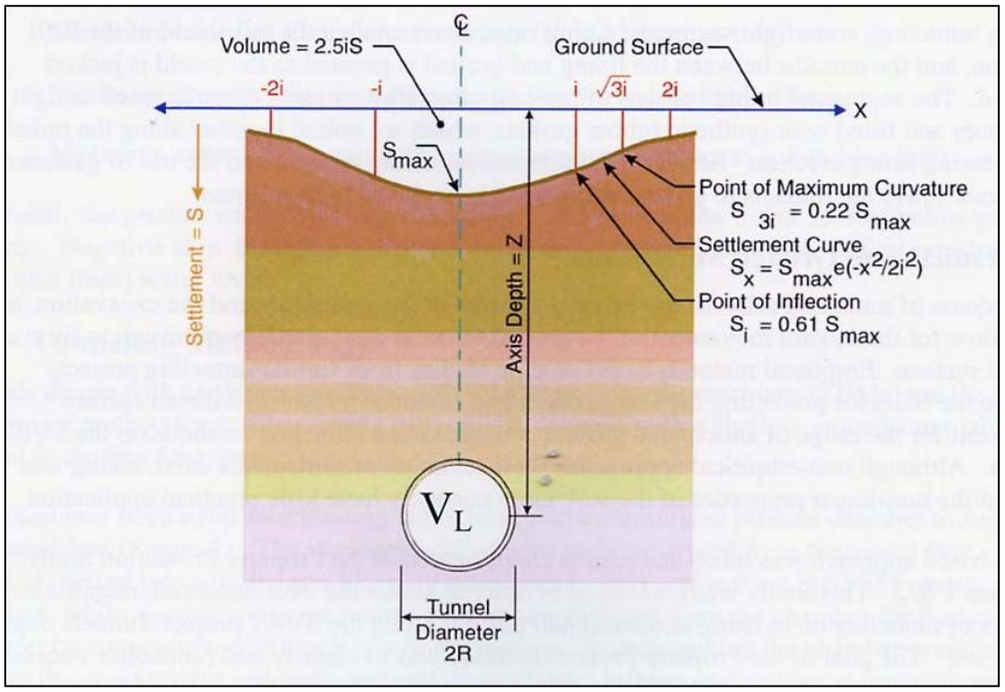


FIG. 3. Gaussian curve for predicting ground settlement (SVRT 2003)

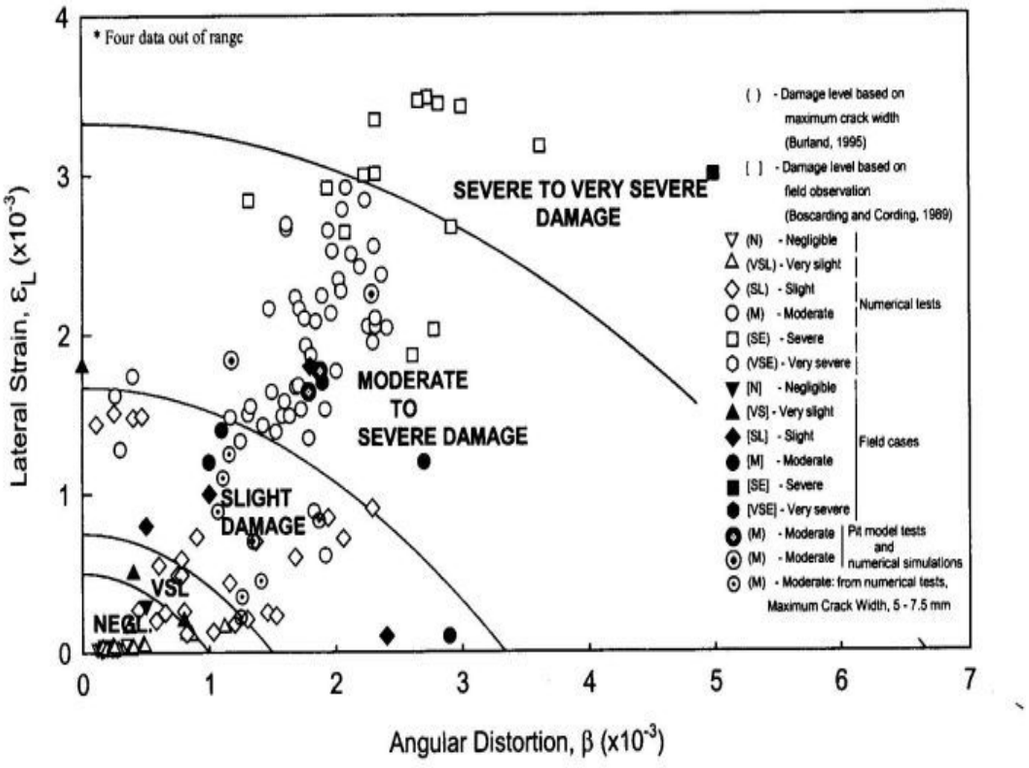


FIG. 4. Comparison between damage estimation criterion and damage level resulting from field observations (after Moorak and Cording, 2005)

Construction of cut-and-cover excavations may also modify the ground water regime. In addition, deflection of excavation supports causes lateral deformations and settlements of the soils behind the walls. These deflections can be estimated, for preliminary design purposes, knowing the wall stiffness, factor of safety against basal heave, and the geometry of the excavation (Figures 5 and 6, Clough et al. 1989). Other studies addressed during preliminary design, include excavation support alternatives, lateral earth pressures, distribution of loading among wales and struts, and factors of safety against base shear failure and heave.

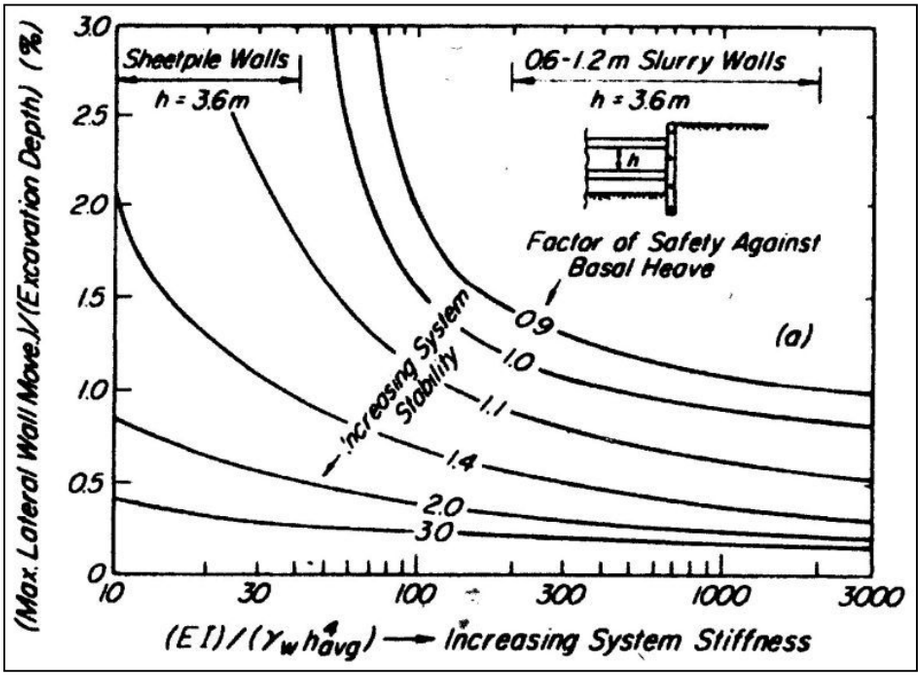


FIG. 5. Relationship between maximum lateral wall movement, system stiffness, and factor of safety against basal heave for cuts in plastic clay (after Clough et al. 1989)

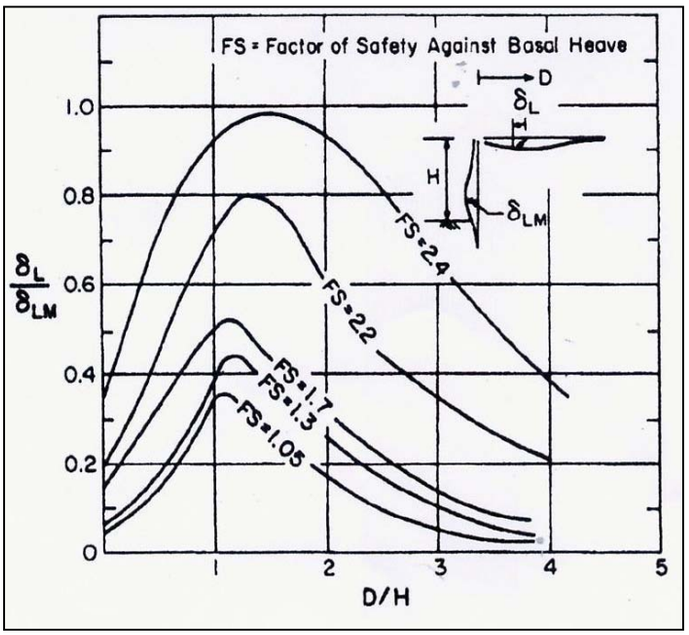


FIG. 6. Settlement envelope behind support walls in clays (after Clough et al. 1989)

Seismic Design Criteria

In general, the goal of the criteria is to ensure safety to personnel and patrons, and to provide post-earthquake performance consistent with the function and importance of the facility or equipment.

Ground Response Analysis

The response of US is dominated by the surrounding ground deformation or strain and not by their inertial response properties. Therefore, the focus of the design is on the free-field deformation of the ground depth and its interaction with the structure, i.e., a soil-structure interaction phenomenon (SSI). The emphasis on displacement (deformation) is in obvious contrast to the design of surface structures, which focuses on the inertial effects of the structures themselves.

SSI studies require that free field ground strains and ground motion parameters be known. Ground strain formulations require that the motion parameters be specified at tunnel depth. For this purpose, 1- wave propagation theory, 2- empirical correlations, 3- acceleration time histories compatible with design spectra, and 4- numerical methods can be used, Figure 7.

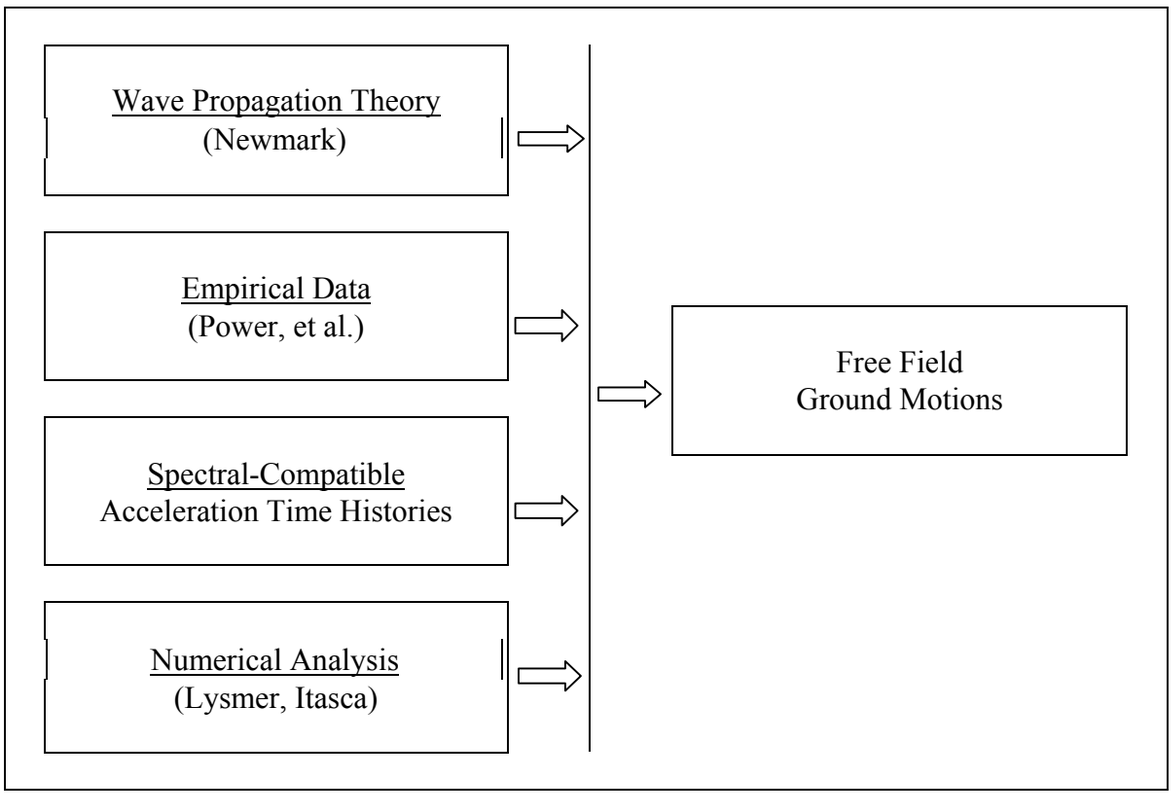


FIG. 7. Approaches to evaluate earthquake ground motions

Approach based on wave propagation

The simplified method proposed by Newmark in 1968 considers a harmonic wave at a given angle of incidence relative to the tunnel axis, propagating through a homogeneous, isotropic, elastic medium. Strain formulations by this method are expressed in function of peak particle acceleration and peak particle velocity, apparent velocities associated with P, S and Raleigh waves, and the angle of incidence of the wave front with respect to the longitudinal axis of the tunnel. Expressions for the free-field strains derived by this approach can be found elsewhere: (Power et al. 1998), (Hashash et al. 2001).

Approach based on empirical data

Correlations between surface ground acceleration, velocity and displacement are available for sites with different geologic conditions at a prescribed distance from the controlling seismic source. Table 5 presents the relationship between ground acceleration and ground velocity for stiff soils proposed by Power et al. (2004).

Table 5. Relationship between Ground Acceleration and Ground Velocity: Stiff Soils*

Moment Magnitude, Mw	Ratio of Peak Ground Velocity (cm/sec) to Peak Ground Acceleration (g) Source-to-Site Distance (km)		
	0-20	20-50	50-100
Stiff Soil*			
6.5	92	98	104
7.5	130	135	140
8.5	150	155	161

*Shear Wave Velocity Range: 200m/s--750 m/s (After Power et al. 2004)

Approach based on spectrum-compatible acceleration time histories

Design criteria for US are usually specified by a ground surface response spectrum. Time histories compatible with the spectra can be prepared from which ground surface accelerations, velocities, and displacements can be calculated by simple integration. Time histories at locations below the ground surface can be obtained by analytical methods.

Approach based on results of numerical analysis

Free-field ground strains and ground motion parameters can be carried out with several analytical tools. Computer codes such as SHAKE, (Schnabel et al.1972) considers equivalent linear soil properties and one-dimensional vertical propagation of seismic shear waves. Analysis can also be done considering two or three-dimensional space with for example computer codes FLUSH, (Lysmer et al. 1975), SASSI, (Lysmer et al. 1991). Codes that are based on non-linear soil properties include FLAC, DESRA, SUMDES and others.

Ground strain formulations require that the motion parameters be specified at tunnel depth. Approaches 1 through 3 provide motion parameters at the ground surface. Since ground motions generally decrease with depth below surface, a reduction factor needs to be applied to the surface motions. Power et al. (2004) recommended ground peak acceleration reduction factors on which Table 6 was based.

Table 6. Influence of Depth on Surface of Ground Motions*

Tunnel Depth (m)	Ratio of Ground Motion at Tunnel Depth to Motion at Ground Surface
≤ 6	1
6 to 15	0.9
15 to 30	0.8
> 30	0.7
*After Power et al. 2004	

The numerical approach provides free-field soil strains and ground motion parameter values at any depth below the surface. Input acceleration time histories may be specified at depth or at ground surface.

Soil-Structure Interaction Studies

Earthquake waves impose on tunnels different types of deformations as was discussed above: axial stresses and bending moments, ovaling, and racking. Described below are different methodologies to study SSI. Solutions are based either on free-field models that do not account for the presence of the structure or on models that do account for it.

Axial Stresses and Bending Moments in Tunnels: Table 7

Free-field Elastic Plane-Wave Formulation in Combination with the Beam on Elastic Theory Methodology

Free-field strains can be estimated by the plane wave formulation upon knowing the following parameters obtained from empirical data: a) ground surface peak particle accelerations and velocities corresponding to P, S and R waves modified to tunnel depth; b) apparent velocities of P, S and R waves; and c) peak particle displacement associated with shear waves. Ground response analysis SHAKE, (Schnabel et al, 1972) associated with the beam on elastic foundation theory also provides free-field axial stresses and bending moments.

Numerical Analysis (Pseudo-static)

Since the inertia of the tunnel is small compared to that of the surrounding ground-mass, axial and curvature deformations can be estimated with a pseudo-static analysis by applying displacement time histories to soil springs connected to the liner. Computer codes ADINA (1996), ABACUS (Hibbit et al. 1998) and SADSAP (Wilson 1998) can be used for this purpose.

Table 7. Simpified Analysis of Tunnels, Axial Stresses and Bending Moments

Approach	Methodology	Input	Results
Free Field	Elastic wave propagation	a_i, v_i, C_i*	Axial and curvature deformations
	As above, and beam on elastic foundation	As above, plus peak particle displacement of "S" waves	As above, plus: plus maximum axial and shear forces. Bending moments
Numerical	Quasi-static	Soil Springs; displacement time histories	Axial and curvature deformations
	*a_i, v_i, C_i:	Peak values of particle acceleration, velocity and apparent velocity of P, S, and R waves, respectively.	

Soil Structure Interaction Studies: Tunnel Ovaling (Table 8)

Simplified Static Analysis

Cheng et al. (1979) proposed a free-field estimation of tunnel ovaling. The calculation is based on the results of one-dimensional response analysis (SHAKE) and the P-wave and S-wave particle velocities. Chen's formulation gives an estimation of lined and un-lined tunnel hoop stresses.

Closed-form Solutions

Wang (1993) proposed a numerical solution accounting for soil-structure effects considering the relative stiffness of the tunnel and the soil (Flexibility Ratio). Maximum shear strain at tunnel depth is calculated, for example, by the one-dimensional site response analysis (SHAKE), or estimated by the ratio between the peak particle velocity associated with shear waves and the effective shear wave velocity of the medium. Outputs of the method are tunnel diametric change, tangential thrust and bending moments.

Penzien et al (1998)

Numerical Solution accounts for soil-structure effects by requiring displacement compatibility between tunnel liner and soil cavity (no slippage condition) or by full slippage without normal separation, resulting in no tangential shear force. Ovaling of the tunnel accounts for soil-structure effects considering the relative stiffness of the tunnel and the soil (Flexibility Ratio). Free-field shear strain at tunnel depth is obtained, for example, by the one-dimensional site response analysis (SHAKE)

Table 8. Soil-Structure Interaction Studies

Approach	Ovaling	Racking
Simplified/ closed-form solutions	Penzien and Wu (1998) Wang (1993) Cheng et al. (1979)	Penzien, et.al (2000) Wang (1993) Penzien et al. (1992)
Notes:	Earthquake loading represented by free-field shear strains Slippage and non-slippage solutions Methods account for soil-structure interaction	
Numerical	Finite elements; finite differences, methods Springs and dashpots	

Soil Structure Interaction Studies: Racking of Rectangular Cross-sections

Closed-form Solutions

Wang (1993) developed a simplified procedure relating numerical and free-field racking based on the results of a series of finite element analyses. The analyses included a range of soil dynamic properties, tunnel geometries and stiffness. Wang (1993), Ostadan and Penzien (2001) and others have shown that, depending on the relative flexibility (stiffness) of the soil and of the C/C structure, the assumption of free-field deformation for design that ignores the presence of the structure may be unduly conservative or may severely underestimate ovaling or racking displacements. The former author defined the racking coefficient R_r as the racking distortion of the structure embedded in the soil Δ_r to that of the free-field Δ_{ff} over the height of the structure, and the flexibility ratio Fr as that of the free-field soil shear stiffness to that of the structure:

$$Fr = G_m W/SH$$

where

S = force required to cause a unit racking of the structure,

W, H = width and height of the structure,

G_m = shear modulus of the medium

The results of their analysis presented in Figure 8 show that the deformation of the box accounting for the presence of the structure and the deformation calculated based on the free-field strains are equal only for the case when the flexibility ratio is equal to one. Deformation is overestimated when the flexibility ratio is less than one, and underestimated otherwise.

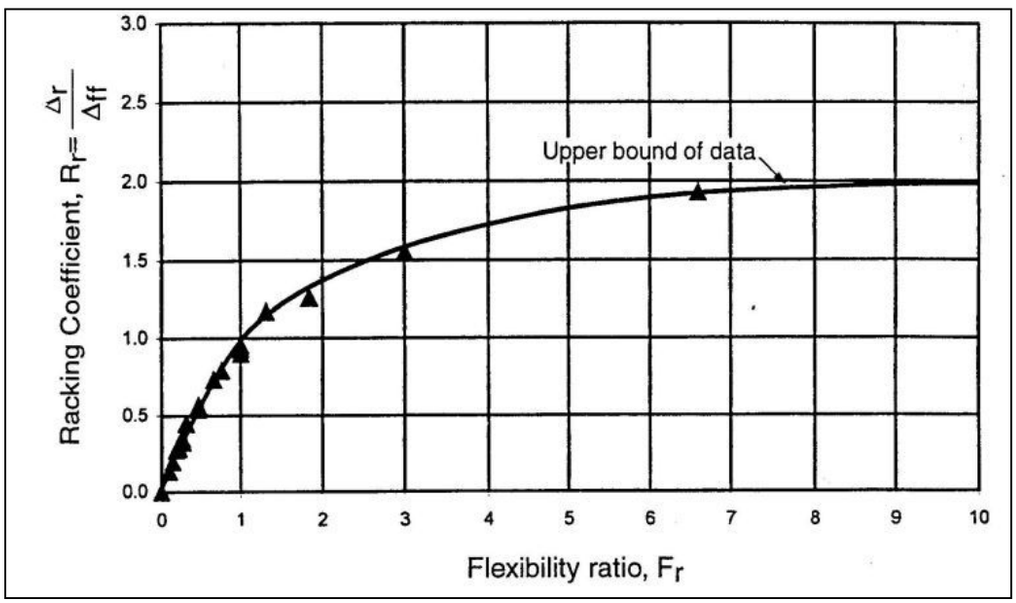


FIG. 8. Racking coefficients for rectangular tunnels (modified from Wang, 1993)

Penzien et al. (1992) developed a closed-form soil-structure interaction analysis based on two considerations: 1) the dimensions of a typical lining cross-section are small compared with the wave lengths in the dominant ground motions producing the racking, and therefore the lining cross-section can be assumed to be interacting with soil having a uniform strain field; and 2) inertia effects in both the lining and its surrounding soil as produced by soil-structure interaction are relatively small, and therefore the seismically induced racking deformations in a lining take place in a quasi-static fashion. The author prepared graphs depicting a relationship of the racking between free field and the soil-structure system as a function of the relative stiffness of the structure and the soil medium.

Numerical Analysis

Numerical analysis accounting for soil-structure interaction effects could also be carried out adopting Lump-Mass, Finite Element or Finite Differences codes such as SASSI (Lysmer et al. 1975), (Lysmer et al. 1991); FLAC (ITASCA 1995), (Hibbitt et al. 1989).

Final Design

Preliminary design, usually at a 35% level of development is expanded and updated in each of its activities up to the final level of development in this phase of the project. In particular, the design based on empirical data is confirmed or modified as necessary with the results of analytical work.

Additional activities completed during final design are the preparation of construction drawings and specifications, instrumentation plan, and the preparation of the Geotechnical Base Line Report.

CASE HISTORY

The Tunnel Segment of the Silicon Valley Rapid Transit Project currently under design by the Hatch Mott MacDonald and Bechtel Joint Venture (HMM/B) is used as an illustrative case history.

Project Description

Over the past 25 years, a series of transportation improvement studies have identified, analyzed, and evaluated highway and transit solutions for the Silicon Valley Rapid Transit Corridor. This 20-mile corridor extends from Fremont in southern Alameda County to Silicon Valley and downtown San Jose in Santa Clara County, and is one of the most severely congested and rapidly growing travel corridors in the San Francisco Bay Area region. These studies have led to decisions to implement major capacity improvements to the corridor's highway and transit systems to provide needed additional capacity to address an anticipated 52% growth in corridor travel over the next 25 years.

In November of 2001, the Valley Transportation Authority (VTA) Board unanimously selected extending the Bay Area Rapid Transit (BART) as the Preferred Investment Strategy for the Silicon Valley Rapid Transit Corridor. The Silicon Valley Rapid Transit Project will connect the BART system from BART's planned Warm Springs Station in Fremont in southern Alameda County to the cities of Milpitas, San Jose and Santa Clara in Silicon Valley (Figure 9). It will link to the existing BART system, which is a 95-mile, automated heavy rapid transit system serving over three million people in Alameda, Contra Costa, and San Francisco counties, as well as northern San Mateo County.

BART and VTA executed a "Comprehensive Agreement" in November 2001 that establishes a framework for Project implementation and operation. Within the terms of the "Comprehensive Agreement", VTA will design and construct the BART extension and in addition pay BART an annual subsidy to operate it. The Project will be built to BART criteria and standards.

A 10% Conceptual Engineering effort started in May 2002 and was completed in 2003. A 35% preliminary engineering phase started in February 2004 and was completed in December 2006. At the same time, a 65% engineering phase commenced, with the aim of completing 65% design in 2008. A final design is planned to commence in 2009 in order to meet the overall project milestone dates leading up to Revenue Service by end of 2016.



FIG. 9. SVRT Project location within the San Francisco Bay Area (Source: BART)

The alignment is comprised of three major segments: a Line Segment which will be approximately 18 km of at-grade, elevated and cut-and-cover track extending from Warm Springs to San Jose; approximately an 8 km long Tunnel Segment, consisting of twin-bored tunnels and cut-and-cover structures through downtown San Jose; and a Yard & Shops Segment with a surface station that will serve to connect to the San Jose International Airport and to the CALTRANS station.

The Tunnel Segment follows Santa Clara Street between 24th Street and Downtown San Jose, Figure 10. It includes at-grade and open-cut track at the two portals; approximately 8 km of twin circular tunnels with mined cross passages for emergency egress and two ventilation towers; three cut-and-cover stations (Alum Rock, Downtown San Jose, and Diridon/Arena) and a cut-and-cover track crossover structure adjacent to the Downtown San Jose Station.

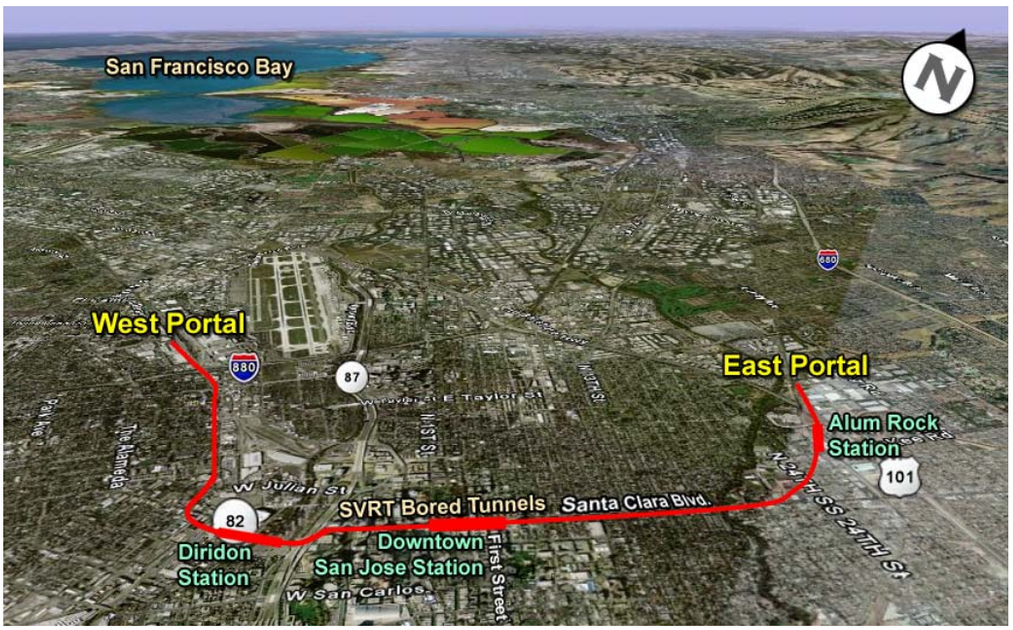


Fig. 10. Alignment through downtown San Jose (SVRT 2005c)

Regional Geology and Hydrogeology

The Tunnel Segment is located in the Santa Clara Valley, which is bounded by San Francisco Bay to the north, the Diablo Range to the northeast and the Santa Cruz Mountains to the southwest. Figure 11 depicts the surface geology of the region where the project is located. Tertiary, Upper Cretaceous marine sedimentary rocks, and Cretaceous-age Franciscan Complex bedrock underlie alluvial deposits at depths greater than 300 m.

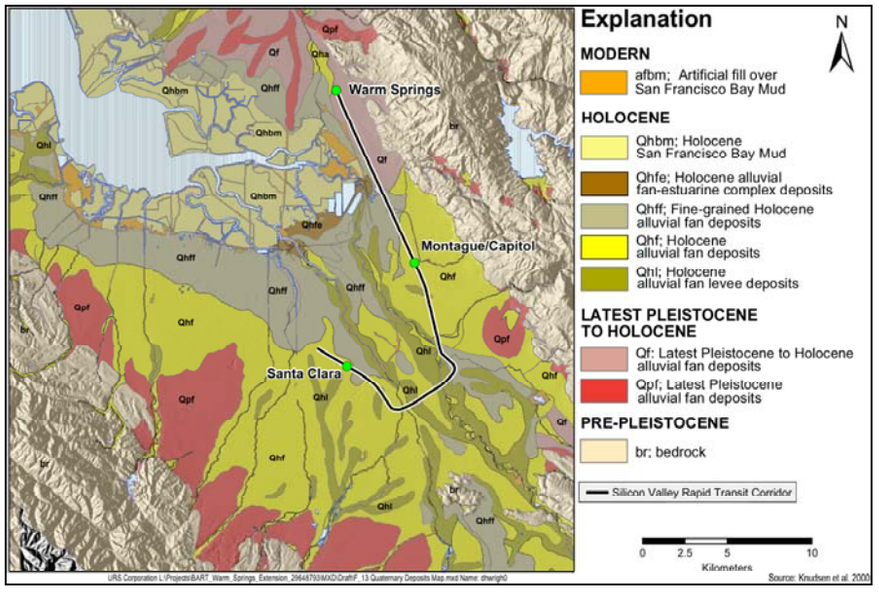


FIG. 11. Surficial Geologic Map (SVRT 2003) From URS (2003)

The alluvial deposits within the depth of the station excavations are variable across the alignment but generally consist of slightly over-consolidated stiff silty clay with thin sand layers. The clay is underlain by a highly permeable upper granular dense silty sand and gravel Upper Aquifer. Below it is a highly variable sequence of clay, sand and gravel, where the cutoff wall toe of the C/C excavations will terminate. The clay layers within the inter-layered strata serve as the major Aquitard to the Lower Aquifer, which is well below the bottom of the excavations cutoff wall, Figure 12.

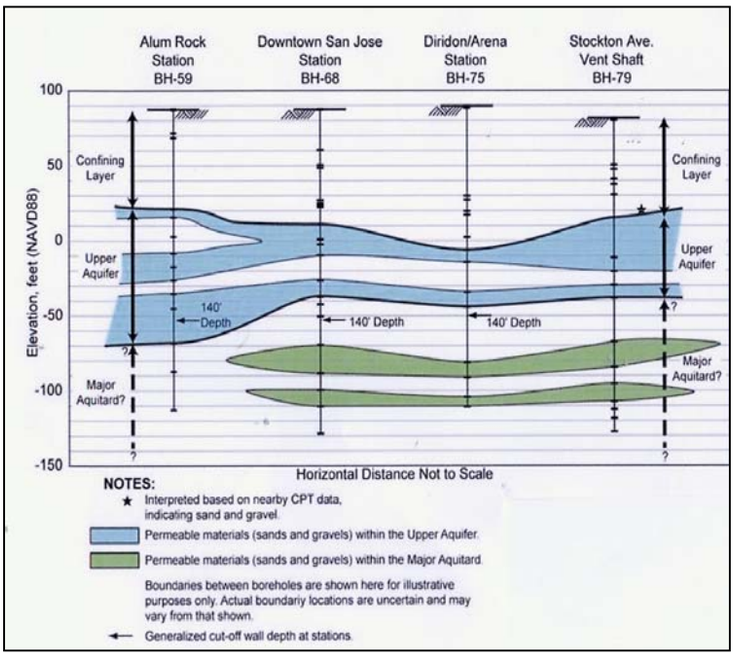


FIG. 12. Hydrogeologic profile (SVRT 2005d)

Ground water table elevations along the majority of the alignment are predicted to be within 3 m to 5 m below ground surface during construction. However, piezometric readings taken at several locations during the wet season (January through May) of the 35% Preliminary Design Phase encountered water at the ground surface, possibly under artesian conditions. For design purposes, the Project adopted two ground water levels: 1) for temporary design, and 2) for final design.

GEOTECHNICAL EVALUATIONS

Extensive programs of field and laboratory investigations defined the site lithology and the geotechnical engineering properties of the alluvial soils.

Field investigations included:

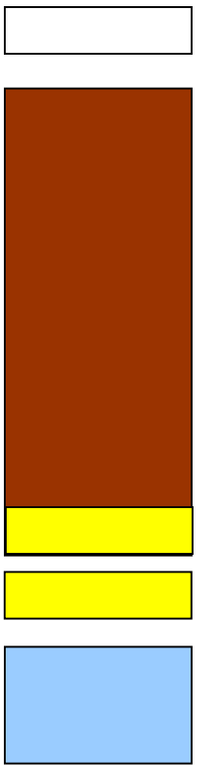
Borings
CPTs (piezo and seismic cones)
Vane shear, pressure meter, hydro-punch, and water pressure dissipation tests
Ground water observation wells
Down-hole geophysical logging

Laboratory investigations included:

Visual material classifications
Moisture content, unit weight and specific gravity
Sieve and hydrometer analysis
1-D constant rate consolidation,
Unconfined compression,
Consolidated drained triaxial
Ko-consolidated undrained triaxial (compression, extension and Bishop-type)
Static direct shear and resonant column tests

The results of the laboratory test program defined shear strength, compressibility and hydraulic conductivity, stress-strain behavior and dynamic properties of relevant alluvial soils at the site. Figure 13 presents a highly simplified sketch of the distribution of the main soil strata and corresponding geotechnical properties of the subsurface materials. Figure 14 shows a detailed subsurface cross-section at the location of the San Jose Downtown Station and Crossover. Strata in these figures are identified as follows:

Soil Type "A": man-made fill and desiccated crust: lean clays (CL) with some silty sands(SM).
Soil Type "B", lean clays (CL)
Soil Type "C": silty sands (SM, SW)
Soil Type "D": dense sands and gravel (SW, SM, GW, GM)
Soil Type "E": inter-layered stiff to hard clays (CL) and dense sands and gravel (SW, SM, GW, GM), (Soil types B, C, and D)



Material Type

A Fill
W = 27 γ_D = 15 (above 10m)
W = 20 γ_D = 16(below 10m)

L.L ≈ 24-65 PI = 5-34

Su = 96 above 10m linearly increasing to 310 at 50m

B

OCR = 3-4 above 6m; OCR = 2-3 below

φ^{I} = 32; c^{I} = 0

G = 43 x 10^3

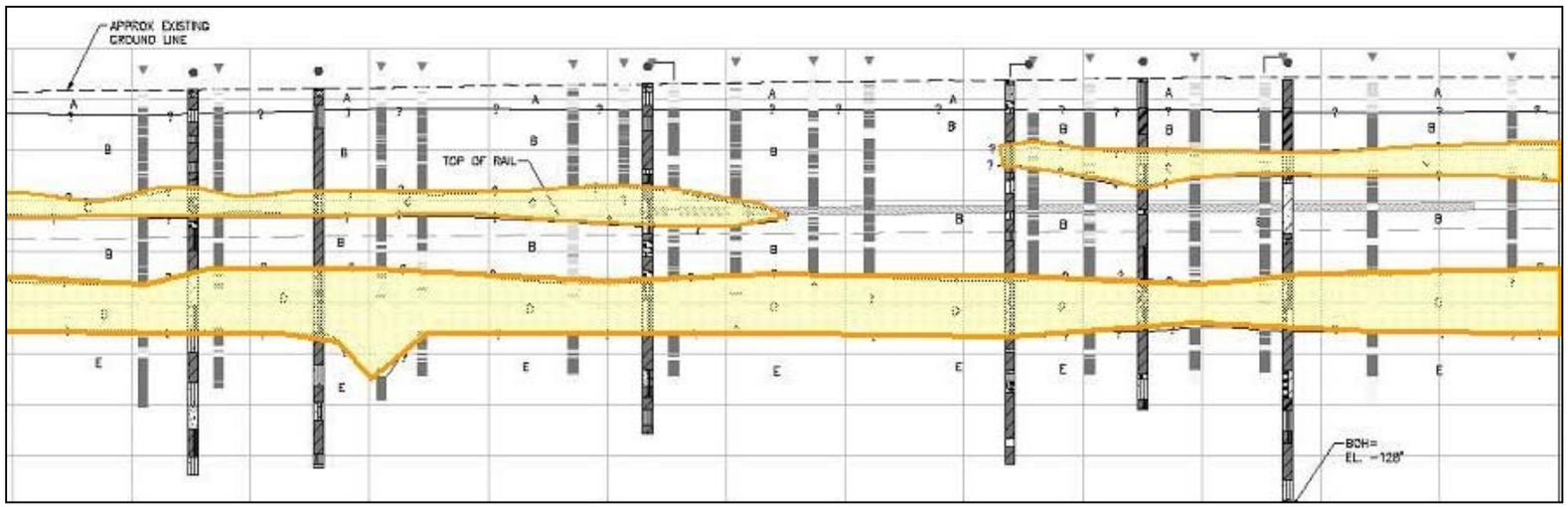
C N = 73 ± 28; (107 tests) ; φ^{I} = 33; G = 76.3 x 10^3

D N = 87 ± 22; (60 tests); φ^{I} = 37; G = 76.3 x 10^3

E (B, C, D Mixed)

Notes:
W = Water content % γ_D = Dry unit weight kN/m^3
L = Liquid limit % PI = Plasticity Index %
Su = Undrained shear strength (compression) kPa
OCR = Overconsolidation ratio
φ^{I} = Effective friction angle, degrees
c^{I} = Effective cohesion
N = Uncorrected SPT blow-count
G = Secant shear modules at 0.01% strain, kPa

FIG. 13. Simplified soil column and summary of soil properties. (SVRT 2005c)



Material Descriptions (see Text)

Above and below upper sand: Soil Type B
Upper granular: Soil Type C
Lower granular: Soil Type D
Below lower granular; Soil Type E

FIG. 14. Partial subsurface profile at the location of the downtown/crossover structures. (SVRT 2005c)

DESIGN CRITERIA AND DESIGN GROUND MOTIONS

The Project is located within an area subjected to high seismicity. As Figure 15 shows, the site is surrounded by well-recognized active faults including the San Andreas Fault to the west and the Hayward Fault to the east, both of these being capable of generating high magnitude earthquakes.

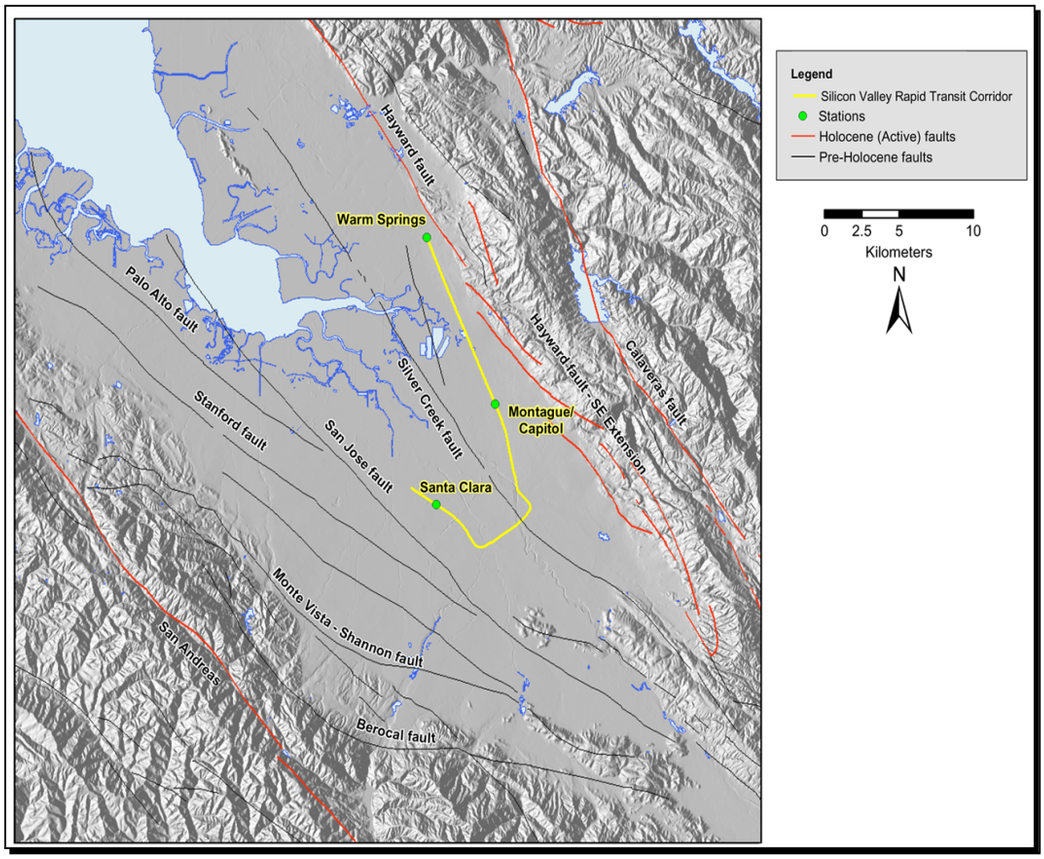


FIG. 15. Geologic faults in the vicinity (SVRT 2005a)

The agreement between the Valley Transportation Agency (VTA) and the Bay Area Rapid Transit Authority (BART) required all design development to be performed in accordance with the BART Facilities Standards– except as specifically modified or supplemented for the SVRT – and to meet federal, state and local requirements.

The intent of BART Facilities Standards is to limit strains, deflections and damage under design ground motions such that structures and facilities whose integrity is essential to the operation of the BART system (revenue structures) are capable of being returned to operation within 72 hours without repair or shoring. Structures and facilities whose functions are less critical to the operation of the BART system are designed for life safety in lieu of these functionality limits.

Revenue structures are those whose structural integrity is necessary for continued operation of trains. For the Tunnel Segment of the SVRT project, the revenue structures include the bored tunnels, tunnel portals, crossover structure, and ventilation towers. Temporary excavation support structures of the SVRT Tunnel Segment are those erected for the construction of permanent structures.

As directed by the seismic design criteria, there are two levels of the seismic design ground motions. The greater of the 500-year probabilistic and deterministic (median) response spectra define the design response spectra for permanent structures. The 100-year probabilistic response spectra define the design response spectra for temporary structures.

Horizontal design ground motion response spectra were developed for the two design levels accounting for average rupture directivity, and fault-parallel and fault-normal directivities. Vertical response spectra were developed through analysis and application of vertical-to-horizontal spectral scaling factors. Figure 16 shows horizontal design response spectra for both permanent and temporary structures along the entire alignment.

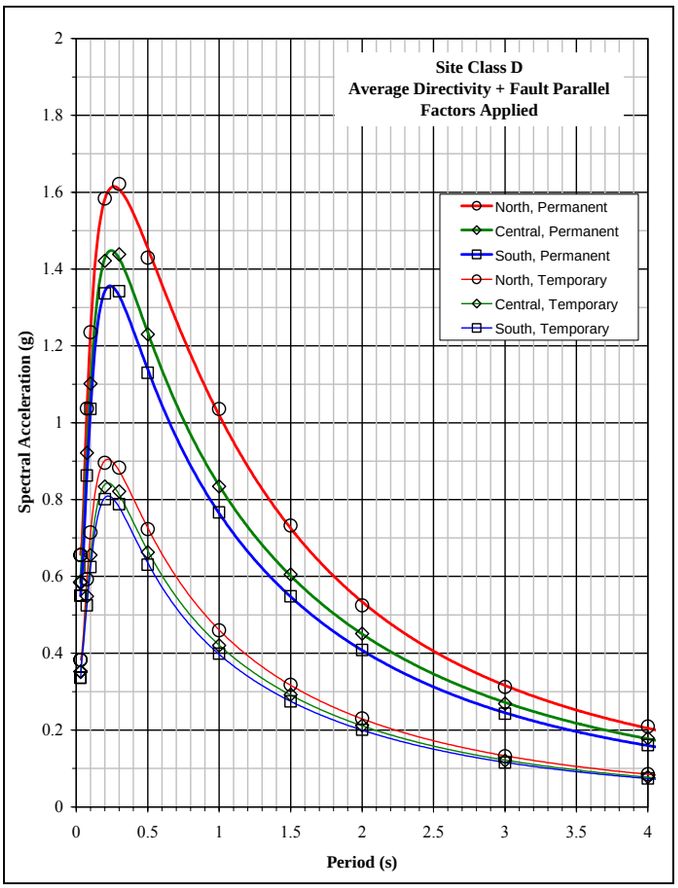


FIG. 16. Horizontal design spectra, "D" site classification (SVRT 2005a)

TUNNEL SEGMENT STRUCTURES

Approximately 8 km of the alignment will be twin circular tunnels constructed by a two-closed face earth pressure balance tunnel-boring machine (TBM) to interconnect the stations and portals. The TBMs will be used to install a 5.5 m internal diameter, single pass lining system consisting of pre-cast concrete segmental rings. Typical ground cover above the tunnel crown will be 12 m but may increase to as much as 27 m.

The twin bores will be connected by mined cross-passages at intervals spaced between 150 and 200 m apart. The primary purpose of the cross-passages is to enable evacuation of patrons from one running to the other in the event of an emergency. In addition, mechanical and electrical equipment may be located in cross-passages where permitted. Each cross-passage is designed to have a minimum clear, unobstructed width of 1 m and a minimum height of 2 m. Figure 17 shows a typical cross-section of the two bores.

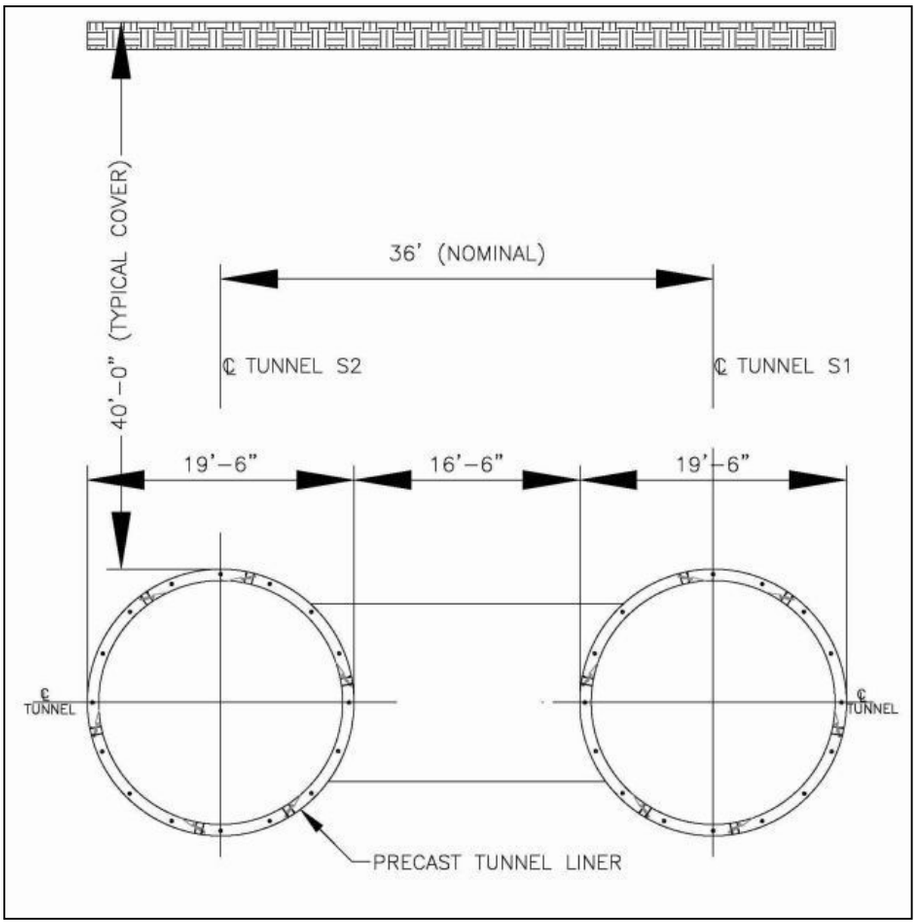


FIG. 17. Tunnel and cross-passage section (SVRT 2005b)

Ground treatment such as jet grouting or soil mixing will be used prior to mining in the zones where the tunnel will break in and break out. Ground treatment or improvement will also be required prior to mining the cross passages between the twin-bored tunnels for emergency egress.

There will be two mid-tunnel vent structures: one located between Alum Rock Station and the Downtown San Jose Station, approximately 35 m deep, and one located between the Diridon Arena Station and the West Portal, approximately 24 m deep. The vent shaft structures extend from the tunnel/track level to grade. The shafts connect to a plenum that opens to grade.

The Portal Structures consist of a concrete U-wall section and a cut-and cover concrete box section. The U-walls, each about 30 m long, consist of approximately 1.2 m thick slab supporting retaining walls at each side of the cut. The height of the walls varies between 3.6 m and 8.5 m. The length of the cut-and-cover boxes is 49 m (east Portal) and 61 m (west Portal), with inside dimensions 4.9 m (wide) and the height varies between 4 m and 8 m.

The three underground stations along the Tunnel Segment are Alum Rock, Downtown San Jose/Crossover, and the Diridon/Arena Stations. Excavation for the three stations is approximately 18 m wide and deep. The combined Downtown San Jose/Crossover excavation is approximately 500 m long. Alum Rock and Diridon/Arena station are about 265 m long each.

Multiple construction methodologies were considered for supporting the excavation of the stations and for constructing the cutoff walls. For ground water control during construction, Deep Soil Mix (DSM) cutoff walls will be constructed down to approximately 36.5 m bgs prior to excavation. To support the lateral soil pressures and minimize surrounding ground deformation, two of the three stations (Downtown San Jose and Diridon/Arena) will utilize an internal steel bracing system and will have soldier piles inserted within the DSM walls, Figure 18. The current design considers four levels of struts that will need to support the open excavation for a period of up to two years before construction of the permanent structure begins. The third station (Alum Rock) will utilize soil tiebacks to support lateral soil pressures and control deformation.

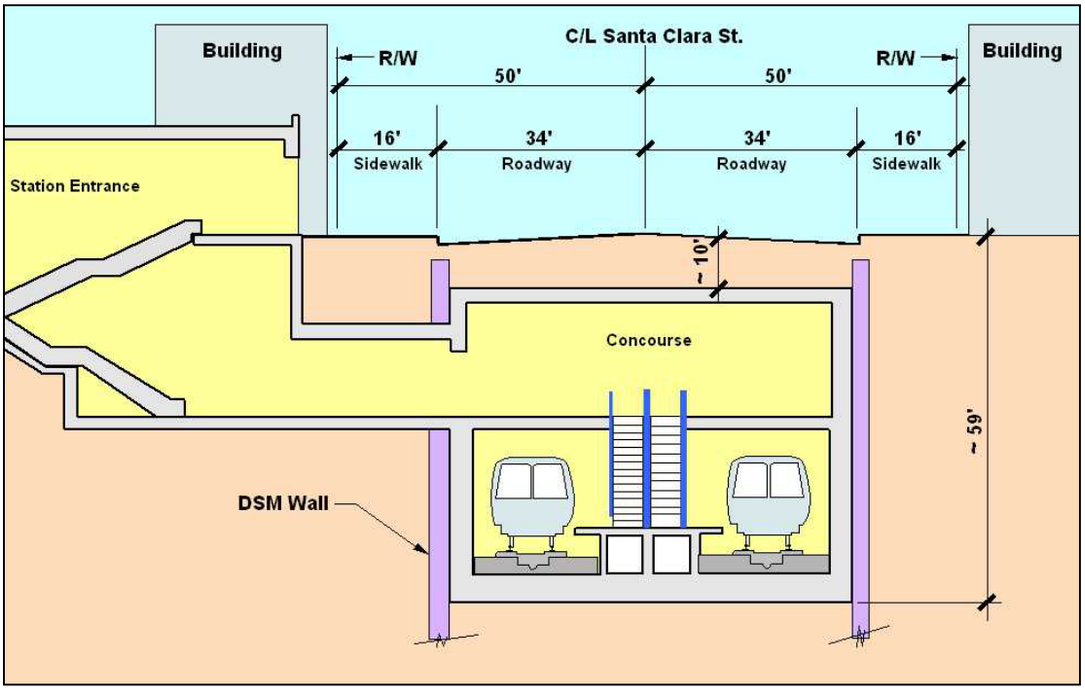


FIG. 18. Downtown San Jose Station—structure cross-section (SVRT 2006b)

CONCLUSIONS

Observations of underground structures subjected to earthquake ground motions show that they perform better than surface structures subjected to the same seismic activity. Based on these empirical observations several investigators have proposed design guides that may be used for preliminary design of tunnels and cut-and cover structures. Closed form analytical solutions and computer codes are available to verify the adequacy, or need to modify, preliminary designs. The Silicon Valley Rapid Transit Project described in the paper supplemented by the information included in several companion papers exemplifies the use of design guides and the application of computer codes towards the final design.

ACKNOWLEDGEMENTS

The author wishes to thank VTA for reviewing and allowing the publication of the paper. He also wishes to thank Gary Kramer, Andrew Liu, and Joe Litehiser for reviewing and providing comments to the draft document.

REFERENCES

ADINA R & D, Inc. (1996). *ADINA Software program system.* Watertown, MS.

Chen, P. C., Deng, D. Z. F., Birkmyer, A. J. (1979). "Considerations of dynamics stress concentrations in the seismic analysis of buried structures." *Proc., 2nd*

U. S. National Conference on Earthquake Engineering, Stanford, California, August: 22-24.

Clough, G. W., Smith, E. M., Sweeney, B. P. (1989). "Movement control of excavation support systems by iterative design," *Proc., Foundation Engineering: Current Principles and Practices,* ASCE, Vol. 2: 869-884.

Coppersmith, K. J. (1991). "Seismic source characterization for engineering seismic hazard analysis." *Proc. Fourth International Seismic Zonation Conference,* V. 1: 1-60.

Coppersmith, K. J. and Youngs, R. R. (1986). "Capturing uncertainty in probabilistic seismic hazard assessments within intraplate environments." *Proc. Third National Conference on Earthquake Engineering,* Charleston, South Carolina, August 24-28, Vol. I: 301-312.

Coppersmith, K. J. and Youngs, R. R. (2000). "Data needs for probabilistic fault displacement hazard analysis," *J. Geodynamics*, 29: 329-343.

Cornell, C. A. (1968). "Engineering seismic risk analysis." *Bulletin of the Seismological Society of America*, Vol. 58: 1583-1606.

Cornell, C. A. (1971). "Probabilistic analysis of damage to structures under seismic loads," in Howells, D. A., Haigh, I. P., and Taylor, C. (eds.), *Dynamic Waves in Civil Engineering*: John Wiley, London.

Hashash, Y. M. A., Hook, J. J., Schmidt, B, Yao, J. I-C. (2001). "Seismic design and analysis of underground structures." *Proc. Tunneling and Underground Space Technology 16:* 247-293.

Hibbitt, Karlson and Sorensen (West), Inc., (1989). *ABAQUS, Users Manual,* Version 5.8, Newark, California.

Itasca Consulting Group, Inc. (1995). *FLAC,* version 3.3, Fast Lagrangian analysis of continua, Minneapolis, Minnesota.

Kramer, G.J., Seradat, H., Kozak, A, Liu, A., Chai, J. (2007). "Seismic Response of Precast Tunnel Lining". Proceedings of the Rapid Excavation and Tunneling Conference1225-1242

Lysmer, J., Ostadan, F., Tabatabaie, M., Tajirian, F., and Vahdani, S. (1991). *SASSI, A system for analysis of soil-structure interaction, User's Manual*." Geotechnical Engineering Division, Civil Engineering Department, University of California, Berkeley, and Bechtel Corporation, San Francisco, California.

Lysmer, J., Udaka, T., Tsai, C. F., Seed, H. B. (1975). *"FLUSH, A computer program for approximate 3-D analysis of soil-structure interaction problems."* Earthquake Engineering Research Center, Report No. EERC 75-30, Berkeley, California.

Moorak, S. and Cording, E. J. (2005). "Estimation of building damage due to excavation-induced ground movements." *J. Geotechnical and Geoenvironmental Engineering*, ASCE, Vol. 131, (2): 162-177.

National Center for Earthquake Engineering Research (1989). *"Effects of the 1985 Michoacan earthquake on water systems and other buried lifelines in Mexico."* Technical Report NCEER-8990-0009, Buffalo, New York.

National Institute of Standards and Technology (NIST) (1996). *"The January 17, 1995 Hyogoken-Nanbu (Kobe) Earthquake. Performance of structures,*

lifelines, and fire protection systems," Special Publication 901, Gaithersberg, Maryland.

Newmark, N. M. (1968). "Problems in wave propagation in soil and rock." *Proc., International Symposium on Wave Propagation and Dynamic properties of Earth Materials*, University of New Mexico Press, Albuquerque, New Mexico, August: 23-25.

Ostadan, F. and Penzien, J. (2001). "Seismic design of cut-and-cover sections of the Bay Area Rapid Transit extension to San Francisco Airport." *Proc. 2nd US-Japan SSI Workshop*, Tsukuba, Japan.

Penzien, J. and Wu, C. L. (1998). "Stresses in linings of bored tunnels." *J. Earthquake Engineering and Structural Dynamics,* Vol. 27: 283-300.

Penzien, J. and Chen, C. H., Lee, Y. J., Jean, W. Y. (1992). "Seismic analysis of rectangular tunnels in soft ground." *Earthquake Engineering, Tenth World Conference*, Rotterdam, Netherlands: 1619-1624.

Penzien, J. (2000). "Seismically induced racking of tunnel lining." *J. Earthquake Engineering and Structural Dynamics*, Vol. 2: 683-691.

Power, M. S., Rosidi, D., Kaneshiro, J., Gilstrap, S. D., and Chiou, S-J. (1998). Draft Report, *"Summary and evaluation of procedures for the seismic design of tunnels."* Report NCEER-98, FHWA Contract No. DTFH61-92-C-00112, Task 112-D-5.3c. National Center for Earthquake Engineering Research, Buffalo, New York.

Power, M.S., Fishman, K., Richards, R., Makdisi, F., Musser, S., and Youd, T. L. (2004). *"Seismic retrofit manual for highway structures: Part 2, retaining structures, slopes, tunnels, culverts, and roadways."* Publication No. FWHA-HRT-05-067. Federal Highway Administration, McLean, Virginia.

Schnabel, P. B., Lysmer, J, and Seed, H. B. (1972). *"SHAKE--A computer program for earthquake response analysis of horizontally layered sites*." Report No. EERC 72-12, Earthquake Engineering Research Center, University of California, Berkeley, California.

Silicon Valley Rapid Transit Project (2003). *"Geotechnical exploration findings and recommendations report. Santa Clara Valley Transportation Authority (VTA). BART extension to Milpitas, San Jose, and Santa Clara, 10% Conceptual Engineering, Vol. II: tunnel and underground segment."* Report prepared by URS to Earth Tech, Inc., San Jose, California.

Silicon Valley Rapid Transit Project (2005a*). "Report on seismic ground motions."* SVRT Report P0503-D300-RPT-DE-012, San Jose, California.

Silicon Valley Rapid Transit Project (2005b). *"Tunnel segment, tunnel methodology report Part 1: Bored and mined tunnels."* SVRT Report P0503-D300-RPT-DE-009, San Jose, California.

Silicon Valley Rapid Transit Project (2005c). *"Tunnel segment geotechnical data report."* SVRT Report P0503-D300-RPT-GEO-002, San Jose, California.

Silicon Valley Rapid Transit Project (2005d). *"Tunnel segment: Hydrogeology."* SVRT Report P0503-D300-RPT-DE-020, San Jose, California.

Silicon Valley Rapid Transit Project (2006a). *"Tunnel segment, pre-cast concrete tunnel lining (PCTL) seismic performance study."* SVRT Report P0503-D300-STY-DE-008, San Jose, California.

Silicon Valley Rapid Transit Project (2006b). *"Tunnel segment, tunnel methodology report. Part 2: Station shells, cut-and-cover structures, and portals."* SVRT Report P0503-D300-RPT-DE-007, San Jose, California.

Terzaghi, R. (1977). "Mechanics of squeezing and swelling," Chapter 4,*"Earth tunneling with steel support."* Commercial Bearing, Inc., Youngstown, Ohio: 37-46.

Wang, J. N. (1993). "*Seismic design of tunnels—a simple state-of-the-art design approach*." Parsons Brinckerhoff, Monograph 7, Figure 15a (modified from Wang) in "Summary and evaluation of procedures for the seismic design of tunnels." Report NCEER-98, FHWA Contract No. DTFH61-92-C-00112, Task 112-D-5.3c, National Center for Earthquake Engineering Research, Buffalo, New York.

Wilson, E. L. (1998*). SADSAP 4.1, Static and dynamic structural analysis program*. Structural Analysis Programs, Inc., El Cerrito, California.

Cut-and-Cover Structures: Seismic Response and Design

Ching L. Wu[1], M. ASCE, P.E., Farhang Ostadan[2], M. ASCE, P.E.,
Wen S. Tseng[3], M. ASCE, P.E. and James Chai[4], P.E.

[1]Senior Project Manager, Bechtel Civil Company, 3103 North First Street, San Jose, CA 95134; clwu@bechtel.com
[2] Bechtel Fellow and Chief Geotechnical Engineer, Bechtel National, Inc, 50 Beale Street, San Francisco, CA 94119; fostadan@bechtel.com
[3]Principal, International Civil Engineering Consultants, a Division of Paul C. Rizzo Associates, Inc., 1995 University Avenue, Suite 119, Berkeley, California 94704; wentseng@icec.com
[4]Transportation Engineering Manager, Santa Clara Valley Transportation Authority, 3103 North First Street, San Jose, CA 95134; james.chai@vta.org

ABSTRACT: The Hatch Mott MacDonald / Bechtel Joint Venture (HMM/Bechtel) team is designer and construction manager for the 5.25-mile Central Area Guideway (Tunnel Segment) of the overall 16.1-mile Silicon Valley Rapid Transit (SVRT) Project. This proposed project extends the existing Bay Area Rapid Transit (BART) system southward from Fremont to San Jose. The Tunnel Segment includes twin bored tunnels, mined cross passages, deep excavations for three underground stations, two portals, and two ventilation structures, situated in an area with highly variable subsurface ground soils, high seismicity, shallow ground water table, and within a dense urban setting with high-rise buildings adjacent to the largest excavation. This paper discusses the seismic analysis and design of the cut-and-cover structures of the SVRT project.

INTRODUCTION

The proposed 5.25-mile long Tunnel Segment of the SVRT Project includes twin-bored tunnels, mined cross passages and cut-and-cover structures. The cut-and-cover structures include excavations for three underground stations (Alum Rock Station, Downtown San Jose Station, and Diridon Station), two underground ventilation structures (East and West Ventilation Structures) and two portals (East and West Portals), as shown in Figure 1.



FIG 1. SVRT Project Tunnel Segment Site Map

The largest cut-and-cover excavation is the proposed Downtown San Jose Station and the adjoining Crossover Structure (shown in Figure 2), having dimensions of approximately 60 ft deep by 60 feet wide and 1,500 ft long. The excavation will be centered on Santa Clara Avenue in Downtown San Jose and extend to within 15 ft of existing buildings on either side of the street. Due to the tunnel mining operation, the excavation has to remain open for more than two years. There are two other planned cut-and-cover stations with a shorter length but similar width and depth, and two ventilation structures of approximately 80 ft deep and 30 ft wide by 70 ft long. The proposed temporary excavation support system consists of soil-cement-mix walls reinforced with soldier piles and a waler/strut bracing system. In addition, the use of slurry walls and/or tiebacks is also being considered for some specific excavations.

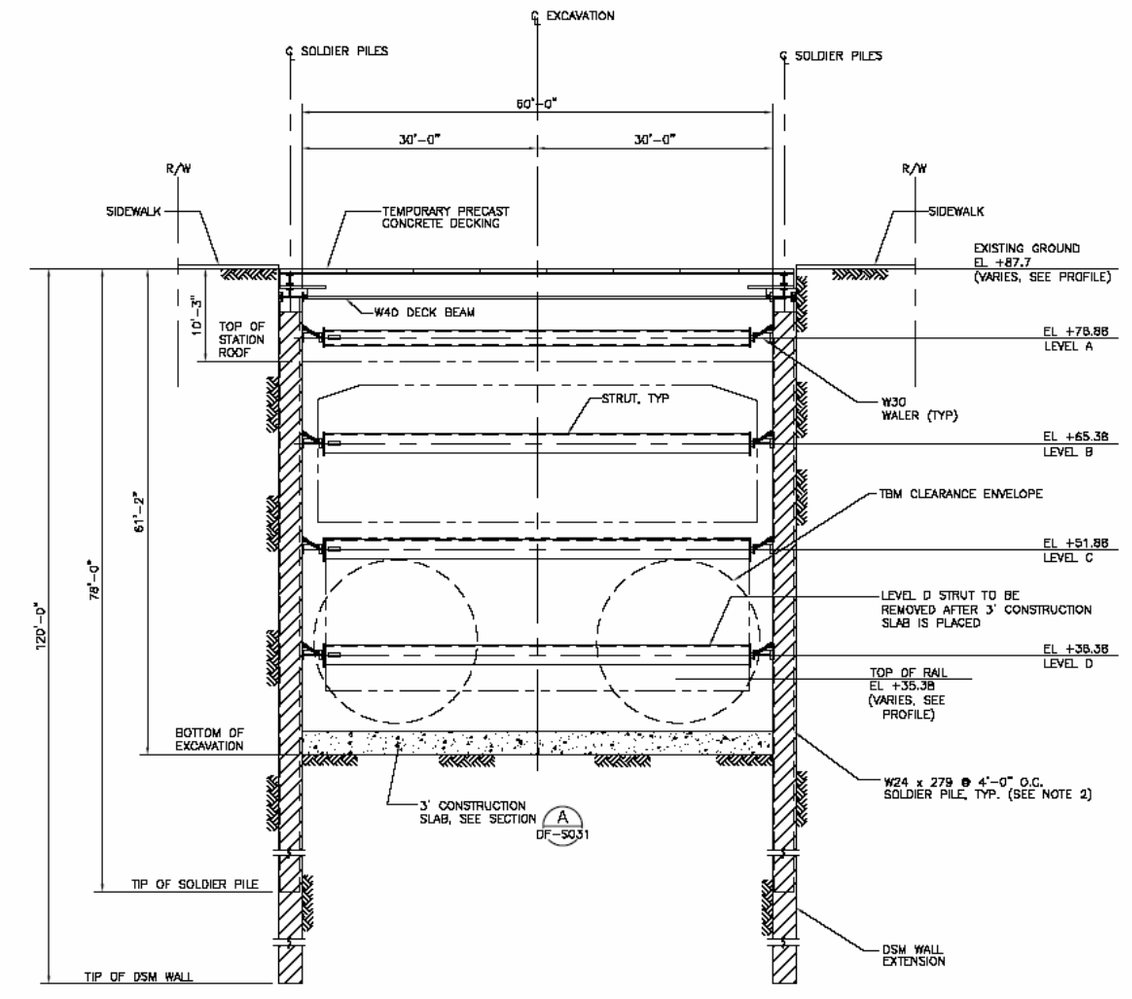


FIG 2. Cut-and-Cover Excavation for San Jose Downtown Station

Seismic Design Ground Motions and Performance Criteria

The SVRT Project developed two sets of design ground motions and corresponding performance acceptance criteria separately for the temporary structures and permanent structures due to their different lengths of service life and relative importance. The temporary structures referred to herein are mainly the temporary excavation support structures that are erected as the excavation proceeds to shore the excavation pits for construction of the permanent portal, ventilation, and station structures.

Seismic Design Ground Motions for Permanent Structures

Although the SVRT facilities are being funded and constructed by Santa Clara Valley Transportation Authority (VTA), these facilities once completed will be

handed over to BART, and BART will operate and maintain the facilities. The agreement between VTA and BART requires that the permanent facilities be designed and constructed to meet the requirements of BART Facilities Standard (BFSR1.2, August 18, 2004). Accordingly, the design earthquake ground motions are the larger of the ground motions obtained from a site specific 10% in 50-year probabilistic seismic hazard analysis and the median ground motions obtained from a deterministic analysis considering maximum magnitude events of the most significant faults existing near the SVRT facilities. The most significant faults in the region are the San Andreas, Hayward, and Calaveras faults. The maximum magnitude events considered are as follows:

San Andreas	-	Magnitude 8.0
Hayward	-	Magnitude 7.25
Calaveras	-	Magnitude 7.0

The 10% probability of exceedance in 50 years corresponds to a mean return period of 475 years, or roughly, 500 years. Two horizontal (fault normal and fault parallel) and one vertical response spectra were developed.

Assuming NEHRP (National Earthquake Hazards Reduction Program) soil type D based on regional subsurface conditions for the SVRT project-wide use, baseline probabilistic and deterministic ground motion estimates were developed for free-field ground surface. The NEHRP Soil Class D ground surface seismic design ground motion response spectra represent generic response spectra developed using empirical ground motion data from recordings made at sites with a range of soil properties (soil columns whose average shear-wave velocity over the upper 30 m ranges from 180 m/s to 360 m/s). To account for differences between ground surface motions and motions at depth of subsurface facilities, design ground motion estimates for NEHRP soil type C condition were also developed for use in design of subsurface facilities. In checking the seismic performance of the underground facilities, the soil type C ground motions so developed are to be applied as outcrop (surface) motions at soil depth below the underground facilities where the site soil condition corresponds to the NEHRP soil type C condition. The NEHRP site class C is defined to represent the soil columns with the average shear wave velocity of 360 to 760 m/sec in the upper 30 m. For both site class D and C, a set of empirical attenuation relationships have been used to develop the design motion.

Seismic Design Ground Motions for Temporary Structures

For the design of the temporary excavation support structures, a reduced level for the design earthquake ground motions is judged appropriate. This reduced ground motion level uses a probabilistic ground motion estimate based on 10% probability of exceedance in 10 year with the peak horizontal ground acceleration not less than 0.2g.

The ground motion level specified above is based on the guidelines provided by California Department of Transportation (Caltrans' Bridge Memo to Designers 20-12,February 2003). This Memo prescribes a 10% exceedance probability in (1)

twice the number of years that the temporary structures are expected to exist, or (2) 10 years, whichever is longer, and (3) the lateral seismic load so determined to be not less that 0.1g. The 10% probability of exceedance in 10 years corresponds to a mean return period of 95 years, or roughly, 100 years.

According to the current construction schedule, the longest estimated duration of the construction of the excavation support structures for the three underground stations, two ventilation structures, and two portals within the Tunnel Segment is approximately 50 months. Therefore, a 10-year duration, which is only slightly longer than the estimated 8.3-year (twice the longest 50-month) construction duration, is selected and used in the site-specific probabilistic seismic hazard analysis with a 10% probability of exceedance. The 0.1g minimum lateral seismic load covers generally the entire State of California. For the San Francisco Bay Area, including the SVRT project site, the peak horizontal design ground acceleration so defined should not be less than 0.2g.

Design Ground Motion Response Spectra

The two horizontal and one vertical, 5%-dapmped design ground motion response spectra developed for soil types C and D for use in design of the permanent and temporary SVRT structures are shown in Figure 3. Only the fault normal and vertical components of the spectra are shown in this figure. The fault parallel component is similar to the fault normal component with reduced spectra values at long periods.

Design Ground Motion Time-Histories

Time-history analysis will be performed for the underground facilities using a minimum of three sets of three-component acceleration time-histories developed to match the 5%-damped design earthquake response spectra. When three sets of time-histories are used for design analysis, the maximum response obtained from the three sets of time-histories of response shall be used in design.

Each set of the time-histories consists of three components, namely, horizontal fault-normal and fault-parallel, and vertical time-histories. The fault-normal and fault-parallel time-histories need be transformed into time-history components corresponding to the principal longitudinal and transverse axes of the structures under design. The transformation of the time histories avoids over or under prediction of response forces and displacements depending on the orientation of the structure.

As an example, the three-component response-spectrum-compatible time-histories developed from the time-histories recorded during the 1989 Loma Prieta earthquake at the abutment of Coyote Lake Dam located nearby the project site region that are compatible with the design ground motion response spectra for the permanent structures are shown in Figure 4.

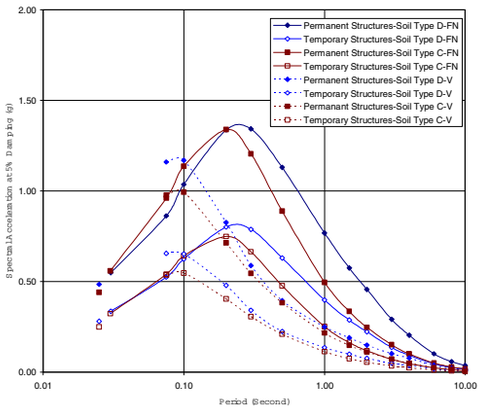


FIG 3. Design Response Spectra for Fault Normal and Parallel Directions

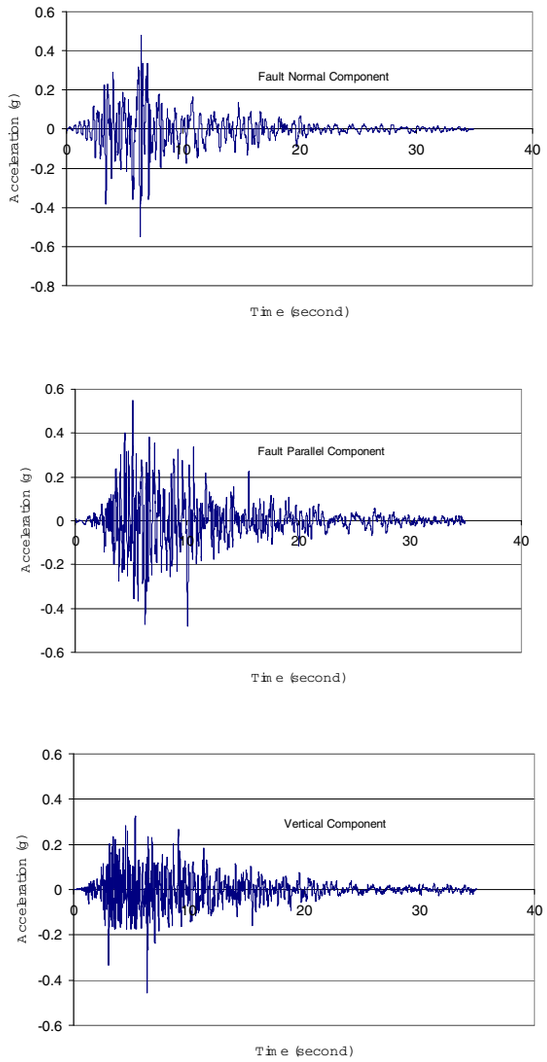


FIG 4. Three-Component Response-Spectrum-Compatible Time-Histories.

Seismic Performance Criteria for Permanent Structures

According to BFS and the SVRT Project design criteria, the transit system revenue structures shall be designed to return to revenue operation within 72 hours after a major earthquake. Thus, only minor damage, such as small cracks and spalling of concrete, that can be repaired during off revenue hours is allowed.

For design of underground permanent structures, the structures are proportioned and sized based on the site geologic, geotechnical, and underground hydraulics considerations and to resist the basic static gravity load cases satisfying the normal design margins of safety specified in the project design criteria. Then, the structures are checked for their seismic performance. In the seismic performance evaluation, the seismic loads are combined with the dead, service, hydrostatic, and other loads, all with a load factor of 1.0 using the strength design method. The maximum earthquake loads from separate time-history analyses, each with a single directions of ground motion input, are combined using the (1.0, 0.4, 0.4) component-factor rule, which considers positive and negative signs of the earthquake loads. Alternatively, when time history analyses are performed, the maximum earthquake loads can be obtained from direct combinations of the co-directional response time-histories resulting from individual directions of ground motion input.

If non-ductile structural components are used, they are not allowed to undergo inelastic deformation, and are designed to meet the strength capacity requirements. Design of permanent structure components, for which the design load combination, including seismic, is controlled by load-induced soil deformations. The structure components are designed to be capable of undergoing ductile inelastic deformation modes such as flexural bending deformation, and a displacement ductility ratio up to 1.5 is acceptable as operability performance criteria. However, to avoid brittle shear failure and ensure ductile behavior of concrete structure components, the shear capacities of these components are designed to be greater than the shear forces required for developing plastic hinging in the components multiplied by an over-strength factor of 1.25. The walls of underground box structures are also checked for soil pressure generated by the localized, liquefied soil condition.

Seismic Performance Criteria for Temporary Structures

The main focus for design of the temporary excavation support structures is life safety of the construction workers and the nearby occupants, and to limit foundation movement of adjacent structures to an acceptable limit. Excavation shoring struts shall be analyzed as simply supported continuous beams subject to earthquake excitation to calculate their bending and end-shear stresses. Under the specified design seismic condition, temporary steel and concrete structural members may be designed by using either the strength design method or the allowable stress design method. For steel members designed using the allowable stress method, allowable stresses per AISC code can be increased by 33%. For concrete structures designed using the strength design method, their shear capacities shall be designed to be greater than the shear forces corresponding to the controlling plastic-hinging-moment capacities with an over-strength factor of 1.25. Special attention shall be paid to checking axial buckling potentials of the shoring struts and the connections of all the structural members. Positive connections shall be designed and detailed by engineers.

Seismic Analysis and Design

Seismic effect on underground structures is more critical in the transverse direction of the structures. A realistic design should consider the effects of soil-structure interaction for evaluation of structural deformation during design earthquake. Consequently, these structures must be designed and detailed to withstand the imposed deformations without losing capability to carry applied loads and meet their performance goals, which are continued safe operation following the design level earthquake and prevention of excessive damage that will lead to unacceptable levels of water infiltration. For concrete structures, shear capacity degradation and compressive strains shall be evaluated and designed to accommodate transverse racking displacements without losing their vertical load carrying capability. If necessary, additional confinement reinforcement shall be added to increase ductility and shear capacity. Interior columns and longitudinal interior walls shall be designed and detailed to accommodate transverse racking displacements. Interior columns and transverse walls shall also be designed to resist dynamic forces in the longitudinal axis of the structures. The effect soil overburden and its inertia load will be considered in design of the roof slabs and supporting columns and walls.

Seismic loads for the Central Area Guideway structures include using demands determined from empirical formulas for preliminary design and in the early stage of the final design. In this design process, the underground permanent box structures need to be designed to resist soil pressures (static and seismic), live and surcharge loads, floatation from the long-term high ground water table and also the artesian water pressures that exists in certain areas in the Santa Clara Valley. Additionally, the temporary excavation support structures have to be designed to maintain the stability of the excavation against basal heave and hydraulic uplift. This effort provides the initial sizing of the structural elements and configurations of the permanent and temporary structures. The preliminary design concept forms the basis

for further seismic analyses, including numerical analyses. The numerical analyses include site response analysis and soil-structure interaction analyses using equivalent linear technique to model the soil behavior. The results of the numerical analyses are used to check and verify the initial design based on empirical formulas. Design adjustments and revisions are carried out in the process to complete the final design.

Empirical Formula for Seismic Soil Pressure

During the preliminary design phase and the early stage of final design, dynamic loads on the earth retaining structures were determined by empirical formulas, such as the Mononobe-Okabe method. This method estimates the seismic horizontal earth pressure assuming that the earth retaining structure is relatively flexible and an inverse triangular soil wedge can be mobilized by the ground motions to exert a horizontal dynamic pressure increment on the structure at 60% of the wall height.

For yielding walls like the temporary excavation support structure at the portal and the braced temporary excavation steel structure for the stations and ventilation structures, the horizontal seismic soil pressure load was calculated assuming horizontal ground acceleration equal to one half of the peak ground acceleration. On the other hand, for non-yielding walls, such as the permanent portal walls, and walls for the ventilation structures, the horizontal seismic load is increased by 50% according to the provisions of BFS.

Free-Field Site Response Analyses

During the preliminary design phase, seismic site response analyses were performed to assess the free-field deformation of the site soil using the SHAKE computer program based on preliminary soil properties obtained during the conceptual design phase and the early soil exploration program during the preliminary design phase. Site soils at key facility locations were modeled as soil columns. Within each soil column, plane-strain soil-layer models were established according to the soil density, classification, and shear wave and compression wave velocities measured for each layer in the soil profile. The analysis is performed iteratively in frequency domain. Since the bedrock is very deep at the SVRT project region, seismic input ground motions used in the site response analyses are specified at the surface of a firm soil layer equivalent to the NEHRP soil type C condition, which is approximately 300-600 ft below the ground surface. Parametric studies were performed to conclude that the depth of input motion in the range of 300-600 ft has small effects on the soil column response motions at the locations of the structure. Time-history analyses were performed separately for the horizontal and vertical directions. The analyses utilize an iterative equivalent linear analysis procedure and calculate the seismic response of the soil column assuming plane seismic shear and compression waves propagating vertically upward from the NEHRP type-C firm soil layer to the ground surface. For a horizontal site response analysis, equivalent linear soil properties simulating the non-linear soil hysteresis behavior are characterized by the soils' degradation of shear moduli and increase of hysteresis damping values as function of seismic shear strain. The equivalent linear soil properties are updated for each

iterative analysis according the modulus degradation and damping increase curves well established from laboratory test data that correspond to each soil classification. For the temporary structures, the vertical site response motions for SSI analyses will be obtained by applying the V/H ratios, developed as part of the development of design ground motions, to the horizontal motion at the elevation of the structures in the free-field soil column. For the permanent structures, vertical site response analyses will be performed by using the low-strain Young's moduli of soils below the ground water table and shear-strain-compatible soil damping values (but limited to no more than 10%) without strain-compatibility iterations. For soils above the ground water table, a reduction of the low-strain Young's modulus values is made using the empirical relationship recommended by the Caltrans Seismic Advisory Board, Ad Hoc Committee on Soil-Foundation-Structure Interaction (1999).

The site response analyses provide free-field soil shear-strain and deformation profiles for preliminary structural design. They also produce the degraded, free-field-strain-compatible equivalent-linear soil properties and corresponding acceleration time-histories at various soil layers for use in soil-structure interaction analyses. The soil shear-strain and displacement profiles so obtained for the Downtown San Jose Station during the preliminary design phase are shown in Figures 5, and6, respectively.

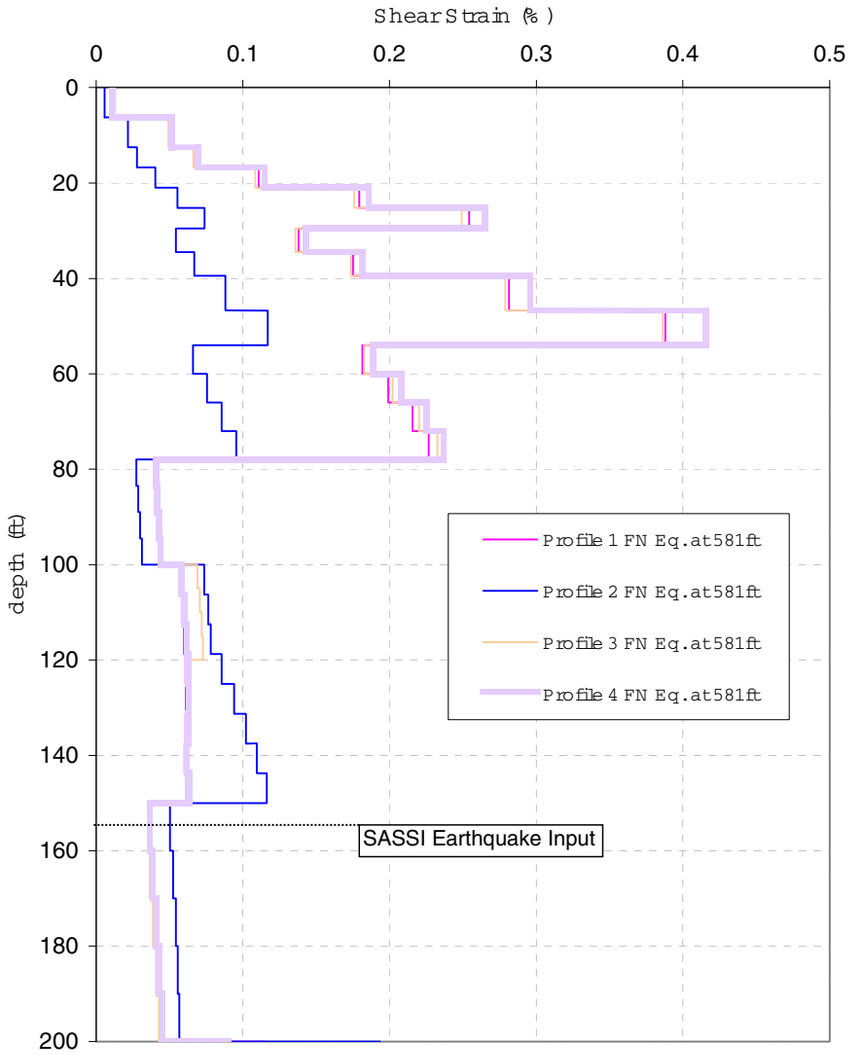


FIG 5. Strain Profile, Downtown San Jose Station Temporary Structures, Using Four Soil Profiles from Preliminary Investigation

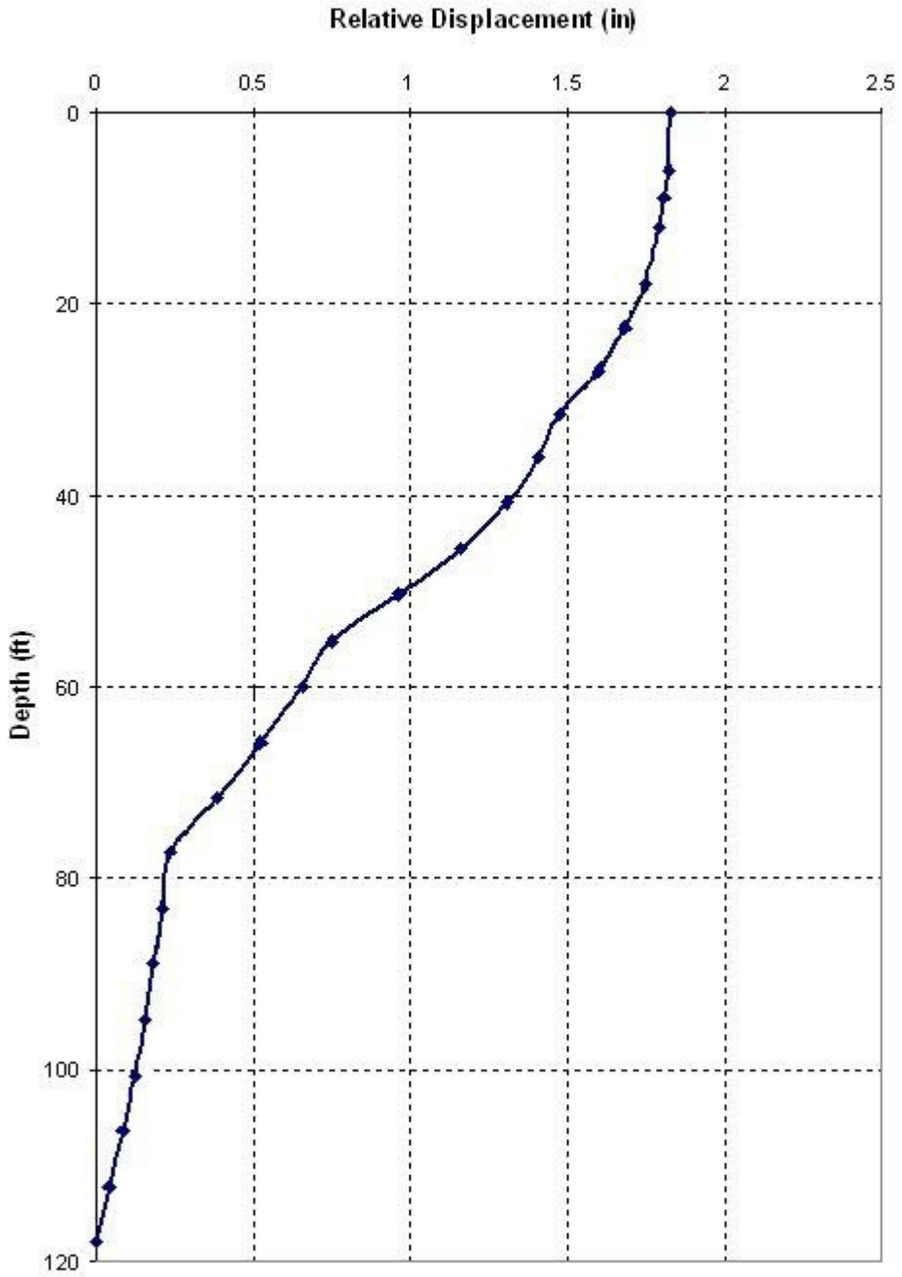


FIG 6. Displacement Profile, Downtown San Jose Station Temporary Structure, Free-Field Relative Displacement

When the 65% design phase began in January 2007, an additional geotechnical exploration program also started. Additional seismic site response analyses using SHAKE are being carried out. The new analyses incorporate not only the existing soil data obtained during the preliminary-design phase exploration program, but also

the additional data from explorations during the 65%-design phase. The results of the site response analyses using SHAKE will be used in the subsequent soil-structure interaction analyses.

Soil-Structure Interaction (SSI) Analyses

When the shear waves propagate vertically passing the embedded shoring and permanent cut-and-cover structures, the structure deforms with the surrounding soil medium but the amount of deformation depends upon the extent of interaction between the surrounding soil medium and the structure, i.e., soil-structure interaction (SSI) effect. The SSI effect may cause an increase or decrease in shear deformation, or racking, of the structure depending on the difference in stiffness, damping, and inertia properties between the embedded structure and the corresponding properties of the soil mass it replaces (replaced soil). In general, if the structure is more flexible than the replaced soil, the SSI effect tends to amplify the free-field soil racking deformation. For embedded structures in uniform soil media, such an amplification factor, which is a function of soil's Poisson's ratio and stiffness ratio (ratio of stiffness of replaced soil-volume over stiffness of cut-and cover underground structure), can range from 1.0 to a maximum theoretical value of about 3.0. It approaches asymptotically to the amplification factor of racking of cavity with the same outside dimensions of the structure. During the preliminary design stage, the stiffness of the structure and the stiffness of the replaced soil were calculated and the racking amplification factor was estimated based on the stiffness ratio to determine the seismic racking strain of the structure and subsequently used in preliminary design of the structure. For this project, the stiffness ratio of the cut-and-cover underground structures is expected to be in the range of 3 to 7.

For the final design, SSI analyses using the computer program SASSI will be performed, incorporating the results from free-field site response analyses. SASSI is a three-dimensional finite-element equivalent-linear analysis computer program, which performs the analysis in frequency domain. In the SASSI analysis, degraded soil shear modulus and damping ratios that are compatible with the free-field shear strains will be utilized. The analyses will be performed separately using the horizontal and vertical seismic soil response motions obtained from the free-field site response analyses.

The SSI analyses will determine the seismic response demands resulting from both the free-field site response and dynamic SSI effects. The seismic demands will be determined in terms of the racking shear strain/deformation of the embedded structures and the forces and moments induced in their structural components. Structural analyses and detail design will follow to ensure that the structural strength and ductility capacities meet the performance requirements.

Structural Analysis and Design

The proposed temporary excavation-support structures typically consist of steel waler and strut systems, which are relatively flexible. They are subjected to a lower-level design earthquake with lower seismic demand. The performance requirements

for these structures are life-safety protection or non-collapse during a design-level earthquake, and limiting ground movement adjacent to existing structures. These structures are designed to remain within the yield point of structural steel, using either the strength design method or the allowable stress design method. The forces and shear strains obtained from soil-structure interaction analyses can be used directly in the structural design.

The proposed permanent structures are typically concrete box structures, with thick walls and slabs. They are heavily reinforced concrete structures that are relatively rigid and are subject to a higher-level design earthquake. In addition, the performance requirements for these structures are limited only to minor and repairable damages due to the design earthquake such that the system's operation can resume within 72 hours. For these structures, the seismically induced racking strains are significant and, thus, ductile reinforced concrete design and post-elastic ductility capacity consideration are usually required. To design the reinforced concrete in the inelastic deformation range, non-linear structural analyses using a nonlinear analysis computer program, such as ADINA, in conjunction with a nonlinear member cross-section capacity analysis computer program, such as *X*SECTION, are anticipated in the final design process. These analyses are performed to ensure that the structural strength and/or deformation capacities of the structures meet the performance requirements of the project. The analysis and design procedure outlined above was used for a limited number of structures during the preliminary design.

CONCLUSIONS

Engineering analyses of the cut-and-cover underground structures along the Central Area Guideway of the Silicon Valley Rapid Transit Project utilize the latest analysis and design methodology in earthquake engineering to develop the design ground motions and evaluate seismic demand using both empirical formulas and more rigorous numerical analyses to demonstrate that the designs meet the performance criteria of the project. Nonlinear capacity evaluations are also planned in further design phases. The seismic design methodology and performance criteria developed recognize the critical role of the SVRT system for the region following a major earthquake and the complex geology and high seismicity at the project site. Since most of the more rigorous design analyses are being performed as the project is progressing in the current 65%-design phase, it is anticipated that results will be ready for presentation during the conference in the summer of 2008.

ACKNOWLEDGEMENTS

The authors would like to thank our client, Santa Clara Valley Transportation Authority, for allowing us to present the information contained herein. We would also like to acknowledge the HMM/Bechtel Design Team, our peer reviewers and our board of consultants for their contributions along the way.

REFERENCES

Seed, H.B. and R.V. Whitman. (1970). "Design of Earth Retaining Structures for Dynamic Loads." *Lateral Stresses in the Ground and Design of Earth-Retaining Structures*, ASCE, Reston/VA: 103-147.

Schnabel, P. B., Lysmer, J., and Seed, H. B. (1972). "SHAKE – A Computer Program for Earthquake Response Analysis of Horizontally Layered Sites." *Report No. EERC/72-12*, Earthquake Engineering Research Center, University of California, Berkeley.

Lysmer, J., Tabatabaie-Raissai, M., Tajirian, F., Vahdani, S., and Ostadan, F. (1981). "SASSI – A System for Analysis of Soil-Structure Interaction." *Report No. UCB/GT/81-02*, Department of Civil Engineering, University of California, Berkeley.

Sayed-Mahan, M. (1998). "xSECTION – Cross Section Analysis Program." *User's Manual*, California Department of Transportation (Caltrans), Sacramento, California.

ADINA R & D, Inc. (2007). "ADINA – Automatic Dynamic Incremental Nonlinear Analysis." *User's Manual*, Version 8.4.1.

The Caltrans Seismic Advisory Board, Ad Hoc Committee on Soil-Foundation-Structure Interaction (1999), "*Seismic Soil-Foundation-Structure Interaction*" Final Report submitted to Caltrans, February 26, 1999.

This page intentionally left blank

Damage of New Sanyi Railway Tunnel During the 1999 Chi-Chi Earthquake

Chih-Chieh Lu[1] and Jin-Hung Hwang[2]

[1] Ph.D. student, Department of Civil Engineering, National Central University, No.300, Jhongda Rd., Jhongli City, Taoyuan County 32001, Taiwan(R.O.C.), Tel.: 886-3-4227151#34163, E-mail: 92322031@cc.ncu.edu.tw

[2] Professor, Department of Civil Engineering, National Central University, No.300, Jhongda Rd., Jhongli City, Taoyuan County 32001, Taiwan(R.O.C.), Tel.: 886-3-4227151#34163, E-mail: hwangjin@cc.ncu.edu.tw

ABSTRACT: Historically, the damaged cases of tunnels during earthquake are rare due to their good earthquake-resistant performances. However, the tunnel may still be damaged owing to the violent squeeze of surrounding ground when subjected to an extreme strong shaking. On 21 September 1999, the new Sanyi railway tunnel in central Taiwan was seriously damaged by the Chi-Chi earthquake. At that time, the tunnel has been in operation for about one year. The damaged conditions of the tunnel were carefully investigated and well-documented. This paper summarizes the background information related to the geology, strong ground motions, design and construction of the tunnel and presents the damage patterns of the tunnel. Based on the compiled data, the possible reasons why the damages only occurred at some special locations have been proposed. Numerical analyses have been conducted to analyze one of the typical damaged cross-sections in order to explore the damage mechanism of the tunnel. The analyzed damage pattern agrees very well with field condition. The numerical results show that the bad shape of tunnel, the imperfect backfill grouting, and the secondary lining without any steel reinforcement were main factors that caused the tunnel seriously damaged during the earthquake.

Keywords: new Sanyi railway tunnel, Chi-Chi earthquake, numerical analysis, damage investigation

1. INTRODUCTION

Most modern tunnels in the world were constructed by NATM (New Australian Tunneling Method). The NATM is a design concept using flexible primary support, such as rock bolt, shotcrete, wire-mesh and light steel rib to take part of rock pressure from geostatic stress during tunnel excavation, and let the rock surrounding the tunnel also take the other part of rock pressure during its deforming process. By doing that, the design of tunnel support is more economic than traditional American Steel Support Method (ASSM) which assumes the rock pressure is fully taken by support. Thus, when the interaction of rock and tunnel support reaches a stabilized state of equilibrium, the secondary lining installed after that state will not bear any rock load theoretically in NATM concept. In general, constructing second lining is only for esthetic demand. However, when a large earthquake occurs, surrounding ground will shake and squeeze the tunnel, an extra load will apply on the second

lining. If this extra load is not considered at the beginning of second lining design, the non-reinforced lining will be damaged and even collapse during strong earthquake. For instance, in the 1999 Chi-Chi earthquake, a total of fifty tunnels were reported to have been damaged. Among them, twenty-six were slightly damaged, eleven were moderately damaged, and thirteen were severely damaged (Wang et al., 2000). After the earthquake, seismic capacity of the second lining became an important topic to tunnel engineers in Taiwan, a seismically active area.

New Sanyi railway tunnel is the most seriously damaged tunnel in the 1999 Chi-Chi earthquake. It is located in the western foothills of central Taiwan, which passes through Sanyi fault and Shihliufen fault zones, and other weak ground. The tunnel was completed and opened to vehicle traffic in 1998 for replacing old Sanyi railway tunnel built in 1908. This 7261m long mountain tunnel was designed and excavated with NATM, Its overburden ranges from 20m to 150m. Unfortunately, after operating just about one year, the tunnel was shaken by the 1999 Chi-Chi earthquake and severely damaged. The railway traffic was interrupted several months after this catastrophic earthquake. There are eight main damaged sections and various types of damage conditions were observed. Some damaged conditions are shown in Photo. 1-4. Based on the field investigation, a number of damaging factors were identified, which include excessive earthquake shaking, bad geometry of tunnel, imperfect backfilling, non-reinforced second lining, and geological weak zone. Since well-documented literatures of damaged tunnels are rare in the past, this paper summarizes and arranged the background data of new Sanyi railway tunnel, identifies its failure mechanism to provide a valuable data base for tunnel engineering profession. Moreover, this paper uses the modified cross section racking deformation (MCSRD) method proposed by the authors (Hwang and Lu, 2007) to analyze the failure mechanism of the damaged zone at Sta. 161K+300, which was the most seriously damaged place. The simulation agrees well with the field damage pattern observed in 1999 Chi-Chi earthquake. Thus, the MCSRD might provide a simple and effective numerical tool for analyzing seismic capacity of tunnel second lining to tunnel engineers.



Photo. 1 Spalling of lining extended to the opening of side wall (161K+300) (Wang et al., 2001).



Photo. 2 Spalling of crown (164K+740) (Hsu and Weng, 2000).

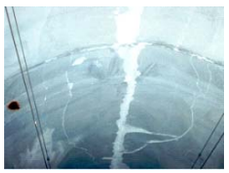


Photo. 3 Longitudinal cracks of crown (164K+775) (Hsu and Weng, 2000).



Photo. 4 Inclined cracks of side wall (161K+380) (Hsu and Weng, 2000).

2. SEISMIC GROUND MOTIONS

On 21 September 1999, a strong quake with a magnitude of 7.3 on the Richter scale occurred near the town of Chi-Chi. A large earthquake like this had never been experienced in Taiwan for the past 100 years. The maximum ground accelerations measured by the strong motion seismographic stations in the Nantou-Wufeng area

were as high as 0.7-1.0g. It caused significant damage in the nearby area in central Taiwan. Due to sufficient seismographic stations in that area, the acceleration history records of the earthquake were available. The ground acceleration values can refer to the nearby seismographic stations. The closest seismographic station with a distance of 5km to the tunnel is Jian-Jhong elementary school and was used in this analysis. Since the axis of tunnel is about South-North direction, the critical motion is in the East-West direction due to the racking action on the tunnel section. Therefore, Fig. 1 shows the acceleration, velocity and displacement histories in EW direction at that station. Note that although the maximum ground acceleration is only 0.14g, the maximum velocity is 26.5cm/sec, which is a more important motion index than acceleration in using MCSRD method to assess the seismic capacity of the tunnel.

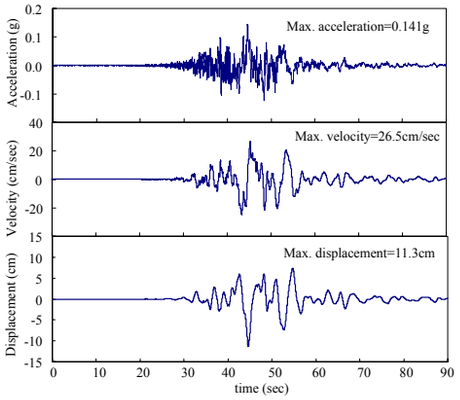


Fig. 1 Seismic motion histories in East-West direction near the tunnel (after the Central Weather Bureau).

3. THE NEW SANYI RAILWAY TUNNEL

3.1 Geology and construction condition

The new Sanyi railway tunnel passes through a series of small mountain ridges and terraces neighboring a small valley, as shown in the Digital Terrain Model (DTM) of Fig. 2. Its overburden depths range from 20m to 150m. The ground formations that the tunnel passes through are the Miocene Kuantaoshan Sandstone, the Shihliufeng Shale, the Toukeshan Gravel, and the river gravel terrace. The tunnel crosses over two fault zones, Sanyi fault and Shihliufen fault. Based on engineering characteristics, the rock mass along the tunnel can be classified into 6 grades, as shown in Table 1, and the geological profile accompanying with construction conditions during tunneling are shown in Fig. 3. In addition, the geological investigation, conducted by United Geotech (1989), indicated that the ground formations can be roughly divided into eight kinds of formations. The physical and mechanical properties of these formations are summarized in Table 2.

The tunnel cross section was designed for electric double-track railway system. To satisfy the demand of operation and maintenance, the refuge spaces were excavated on the side wall in 20m spacing for the small refuge and 300m spacing for the large one. The three types of cross-section, including the standard one, of tunnel are shown in Fig. 4. For ordinary sections, the tunneling adopted Drill and Blasting (D&B) method with bench excavation. In case of encountering some difficult ground condition, ground treatment or special excavation method were adopted. From the monitored records during the construction, the horizontal converge deformation ranged from 15-555mm, and the settlement of crown ranged from 2-155mm in most typical sections. The problems encountered during excavation included (1) roof spalling due to fractured rock, (2) rock mass sliding along the planes of cleavage and

join, and (3) rock softening owing to ground water leakage, The problematic locations are also indicated in Fig. 3.

Table 1 Rock mass classification of the new Sanyi railway tunnel (after Hsu and Weng, 2000).

Classification	Rating	Description
Stable	I	Sandstone or alternations of sandstone and silty sand. Some local zones have the conditions of leakage or seepage but would not affect the strength of rock mass.
Slight fracture	II	Alternations of sandstone and shale, which intercalate thin shale. Degree of fracture is slight with some local severe fracture. If there is not suitable support, wedge failure would occur.
Moderate fracture or swelling	III	Alternations of sandstone and silty sand, which intercalate thin shale. Degree of fracture increases obviously and usually coincides with fault zones. Unfavorable orientations of discontinuity are existent.
High fracture or swelling	IV_a	Thin alternations of sandstone and shale. Strength of rock mass obviously decreases due to high fractured zones and faults. Quantity of water leakage is not serious.
	IV_b	The geological characteristic is similar to IV_a, but the excavated surface would be unstable due to a great quantity of water leakage and wide fault zone.
Weak and non-cohesive	V_a	Lateritic gravel. It is a different type overburden, a great part of which contains large pebble and gravel intercalated sandy and silty soil.
	V_b	The geological characteristic is similar to V_a, but the excavated surface would be unstable due to a great quantity of water leakage and wide fault zone.

Table 2 The geological parameters of the formations (after United Geotech, 1989).

Formation type	Unit weight (t/m^3)	G (GPa)	B (GPa)	Vp (m/sec)	Vs (m/sec)	φ^o	c (kPa)	Description
A	2.50	9.3	30	3968	1933	45	85	Sandstone
B	2.40	4.5	6	2190	1364	44	80	Sandstone intercalated siltstone or shale
C	2.45	5.4	10	2803	1484	32.5	60	Siltstone or Shale intercalated fine sandstone
D	2.37	3.1	8	2300	1150	32	50	Siltstone or Shale
E	2.20	4.4	7	2387	1419	31	4.7	Fault gouge and mudstone
F	1.97	0.8	3	1423	638	30	50	Weak bonding sandstone
TK	-[a]	-	-	2000	1000	-	-	river gravel terrace or lateritic gravel
FK	-	-	-	1900	950	-	-	Toukeshan gravel

[a] Lack of experimental data

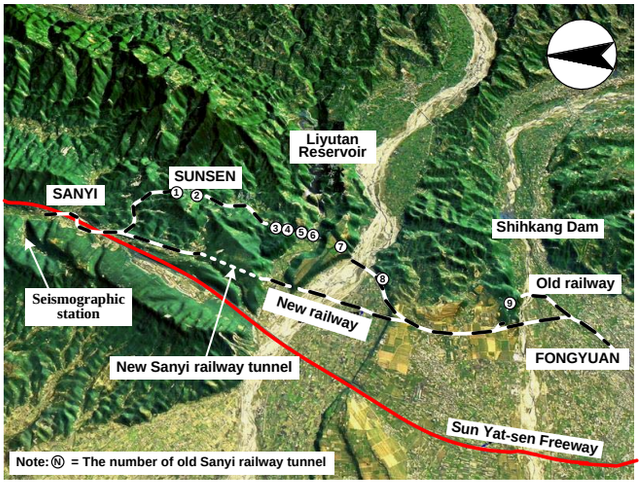


Fig. 2 The geographical location of the tunnel and the surrounding topography (after Hwang and Lu, 2007)

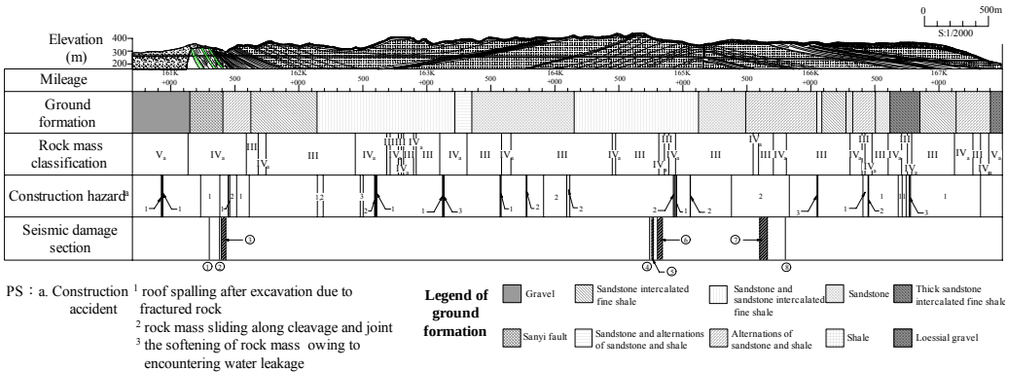


Fig. 3 Geological profile and construction conditions along the new Sanyi railway tunnel (after United Geotech, 1989).

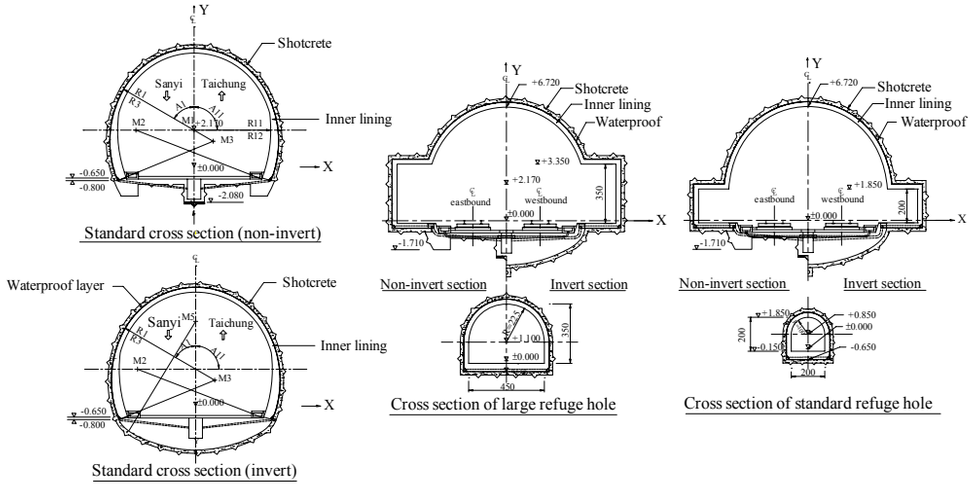


Fig. 4 The cross sections of the main tunnels and the tunnels with refuge spaces (after Hsu and Weng, 2000).

Table 3 The basic information of eight damaged sections along the new Sanyi railway tunnel after the 1999 Chi-Chi earthquake (after Wang et al., 2001).

Sec.	Location	Damage types[a]	Overburden (m)	Geological condition	Rock mass classification	Construction hazard	Opening	Concrete condition
①	Approx. 161k+300	2,4	55-65	Sanyi Fault	IV_a	-	Large refuge	Local void existing
②	Approx. 161k+360	2,4	35-45	Sanyi Fault	IV_a	Cave-in and collapse	Small refuge	Good
③	161k+375-410	1,3,4	25-35	Sanyi Fault	IV_a	-	Small refuge	Void existing
④	Approx. 164k+740	1,4	120		III	-	Small refuge	Local void existing
⑤	164k+758-810	1,3	125		III	-	-	Good
⑥	164k+842-880	1	130-150		IV_a	-	-	Void existing
⑦	165k+600-660	1,2,3	105-110		III	Squeezing and support damage	-	Void existing
⑧	Approx. 165k+800	1,4	125	Fractured zone	IV_a	-	Small refuge	Void existing

[a] Damage types: (1) longitudinal cracks; (2) transverse cracks; (3) inclined cracks; (4) cracks nearby the opening.

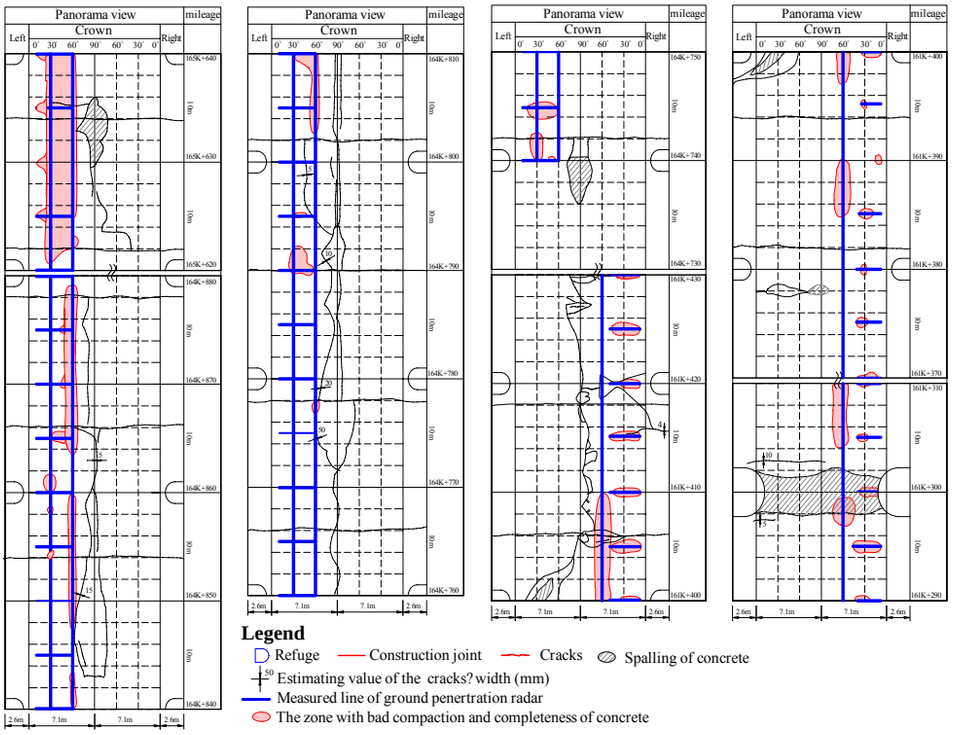


Fig. 5 The mapping results of GPR at the vault of the crown (after Hsu and Weng, 2000).

3.2 Field investigation of the tunnel after the Chi-Chi earthquake

In order to understand the damaged conditions of second linings caused by the earthquake, a non-destructive inspection technique, ground penetration radar (GPR), was used in combination with visual inspection to map the 3-D failure conditions. The mapping results of which are shown in Fig. 5. It was observed that there are eight main damaged sections, and the relevant information of these sections is summarized in Table 3. Based on the field investigation, the following damaging factors were identified (Hsu and Weng, 2000), which include **(1) excessive earthquake loading**: the design of second lining did not consider such a large earthquake loading ; **(2) bad geometry of tunnel cross section**: the small and large refuges was symmetrically installed on side walls of the tunnel every 20m and 300m, respectively. It was found that the cross sections with refuges were most easily damaged due to the irregular geometry which will cause stress concentration at the corner or intersection when subjected to ground shaking; **(3) imperfect backfill**: since the new Sanyi railway tunnel was constructed for electric double-track railway system, the electric leakage should be avoided. Therefore, the complete circumferential waterproof membrane was installed after constructing the primary support to prevent the leakage of ground water. This causes an interface between the first and second linings and might generate some voids during concreting the second lining. If the voids are not perfectly backfilled, the second lining will not tightly bond with the surrounding ground which will cause the spalling of concrete of crown and sidewall during strong shaking; **(4) non-reinforced second lining**: the

tunnel was designed using NATM concept, so the second lining was not reinforced with steel rebar. Therefore, it is weak in resisting shear force and bending moment. When a strong earthquake happens, large shear force and bending moment will be induced in the second lining due to dynamic squeezing of the surrounding ground. Thus, the lining will be easily damaged, even collapse; **(5) geological weak zones**: most of the eight damaged sections are at geological weak zones. For Sta. 161K+300-400, it is located at Sanyi fault and its overburden is about 23-65m. There were cave in and collapse of supporting system during construction and the deformation of crown was about 8-44cm. For Sta. 164K+740-880, the ground formation is sandstone intercalated with fine-grained shale. Its mass classification is III. The deformation of crown was about 3.5-25cm and there was a collapse of support system happened nearby. For Sta. 165K+620-800, the ground formation is alternations of sandstone and shale, and its rock mass classification is III-IV. The deformation of crown was about 40cm. There were lots of emergent ground treatments at 165K+757-785 and 165K+805-818.

4. NUMERICAL ANALYSIS

Among all damaged sections, the most seriously damaged one is located at the Sta. 161K+300 (Section ①). It would therefore be selected to be analyzed in detail by the modified cross section racking deformation (MCSRD) method, to understand the failure mechanism of the lining when subjected to ground squeezing. This method imposes a prescribed seismic shear strain on the boundaries of a ground domain with a tunnel built in. Then, observe the mechanical interaction of the tunnel and surrounding ground through numerical steps. The MCSRD method had been used to assess the seismic capacity of old Sanyi railway tunnel, and gave a good prediction of seismic performance of the tunnel by comparison with its field performances in the 1935 Hsinchu-Taichung and 1999 Chi-Chi earthquakes (Hwang and Lu, 2007). The procedures of the MCSRD method can be summarized as below and Fig. 6.

1. Set up a numerical model with a suitable mesh domain, and initialize in-situ geostatic stresses, and construct a tunnel in the domain.
2. Apply a small seismic shear strain with a slow shear strain rate on the boundaries of the analyzed domain.
3. Check whether or not the internal forces, such as the moment, shear and axial forces on the lining, exceed the nominal lining member's strength curves of P_u-M_u and P_u-V_u. If some segments of lining reach the limit state, that means the lining will begin cracking and lose its strength. It is very difficult to trace the after cracking behavior of the non-reinforced concrete with temperature steel bar. However, in order to conduct pushover analysis, it is necessary to set up the capacity curves of each lining segment first. Thus, this research assumes the segment's strength will reduce to 10% of the original strength to simulate the behavior of non-reinforced concrete after cracking. If more experimental data are added, the assumption can be modified accordingly.
4. Repeat step 2 to 3 until the applied seismic shear strain reaches to the design value, which is calculated by the following equation:

$$\gamma_{des} = \frac{v}{V_s} \quad (1)$$

Where: γ_{des} is the design seismic shear strain, which is the maximum shear strain of the site induced by earthquake; v is the peak ground velocity (PGV) of the site during the earthquake; V_s is the average shear wave velocity of the ground.

5. Keep the analyzed records on each loading stage and observe the failure mechanism of the lining.

4.1 Numerical modeling

The geological parameters and the grid mesh of the analyzed model are shown in Fig. 7. The boundaries were located at 25m distant from the center line of the tunnel. The shear strain was imposed on the whole boundaries with a sufficient slow rate to make the shear strain distribution uniform in the whole analyzed domain. In the numerical model, the ground formations were modeled by solid elements with Mohr-Coulomb failure criteria. Based on the in-situ drilling data, the geological parameters are of the formation type C shown in table 2. The second lining was modeled by piece-wise beam elements with three different interface conditions between lining and surrounding ground. The parameters of second lining and three interface conditions, which simulate three different qualities of backfill, are shown in Table 4. Based on the measured PGV in E-W direction, the total imposed shear strain on the boundaries was 0.0179% according to equation (1), and the applied shear strain rate was as slow as about 5.12×10^{-5}m/sec.

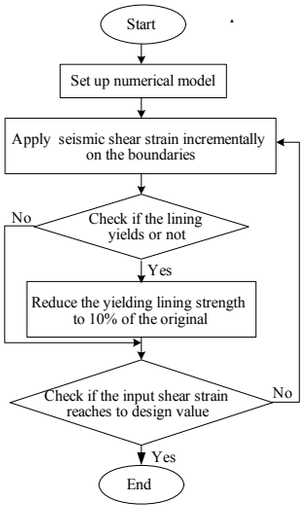


Fig. 6 Flow chart of the MCSRD analysis procedure.

Table 4 The parameters of lining and interfaces

Case	Thickness(m)	f_c'(kg/cm^2)	E(GPa)	Moment inertia(10^{-4}m^4)	Tensional bond of interface(kPa)
1	0.3	235	23	22.5	-[a]
2					62
3					3070

[a] No interface between lining and surrounding ground (No slip)

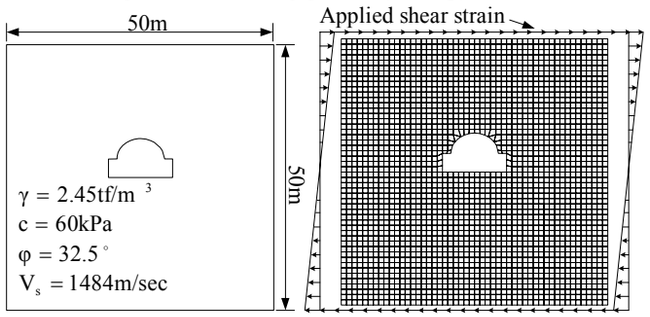


Fig. 7 The geological parameters and grid mesh of the model.

4.2 Results and Discussion

The internal forces of the tunnel lining in different cases are shows in Fig. 8. The result of case 2 is not shown owing to the final collapse of the tunnel lining. It can be seen that the internal forces of lining are quite small at the beginning (before earthquake shaking). That is compatible with the concept of NATM, which assume the second lining does not take any forces from geostatic stresses. However, when seismic shear strain was applied to the boundaries of model, forcing the ground motion to squeeze the tunnel, the internal forces of lining largely increase, especially at the corners of refuge space. The computed results seem to be similar whether the interface between lining and surrounding ground was considered or not.

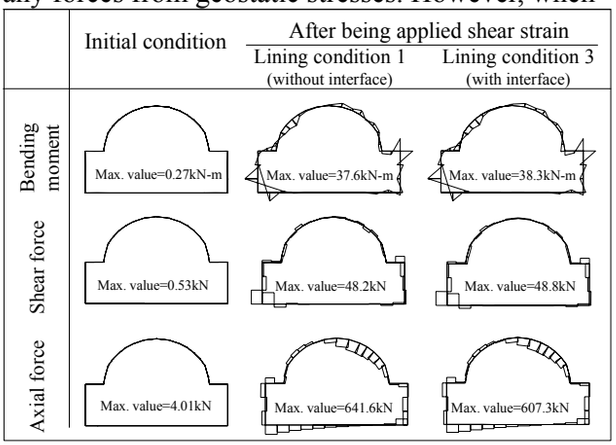


Fig. 8 The internal forces of lining before and after ground squeezing due to earthquake.

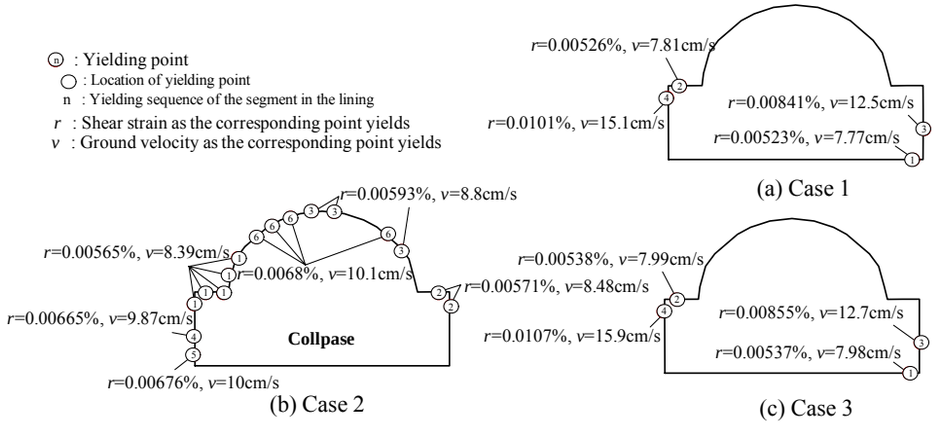


Fig. 9 The yielding damage mechanism of the lining.

Through observation in the process of numerical simulation, the yielding mechanism of second lining is that one of the lining segments yields first due to suffering too much internal forces and then loses its load-carrying capacity, and then the extra forces have to be shared by the other non-yielding lining elements, which will reach the state of yielding in turn, and finally the lining system will collapse. Fig. 9 shows the development of yielding mechanism along the tunnel lining in three different cases. For Case 1 and 3, both yielding states occur at the left-upper and right-lower corners of the refuge owing to the rightward seismic shear strain. Nonetheless, the development of yielding states of Case 1 is faster than Case 3, which demonstrates the allowance of relative slip between the tunnel lining and

surrounding ground slows down the development of yielding state in the same loading conditions. In this case, when the upper corners of refuge yield, the crown of tunnel can only sustain its weight by its small tensional bond with the upper ground. Since the bonding force is weak, the crown finally collapses as shown in Fig. 10. This indicates imperfect backfilling between the lining and the surrounding ground is harmful.

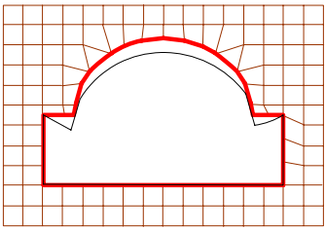


Fig. 10 The collapse of the tunnel lining in Case 2.

5. CONCLUSION AND SUGGESTION

1. This paper summarizes and documents the background information and the damage pattern of the new Sanyi railway tunnel, which is the most valuable case of the seriously damaged tunnels during the 1999 Chi-Chi earthquake in Taiwan.
2. The major damaging factors to the tunnel are strong ground shaking, bad geometry of tunnel section, imperfect backfilling, non-reinforced second lining, and weak geological conditions.
3. The proposed MCSRD method can simulate the harmful effects of all the above major damaging factors, and the numerical analysis of the section at Sta. 161K+300 can identify its failure mechanism and agree well with its performance during the Chi-Chi earthquake.
4. The second lining is suggested to be reinforced with steel bars to resist earthquake loading, especially in seismic area.

6. REFERENCES

Central Weather Bureau: http://www.cwb.gov.tw/index.htm.

Hsu, L.P. and Weng, S.L. (2000). “The geological treatment for railway tunnel after seismic damage – a case study of Sanyi no.1 railway tunnel.” *Treatment Technology of Engineering Geology on Tunnel*. 125-153. (in Chinese)

Hwang, J.H. and Lu, C.C. (2007). “Seismic capacity assessment of old Sanyi railway tunnels.” *Tunnelling and Underground Space Technology*. 22(4): 433-449.

United Geotech (1989). “Drilling and testing report of route changing section of Sanyi no. 1 runnel – route changing and double track project.” *Technical Report*, United Geotech, Taipei. (in Chinese)

Wang, W.L., Wang, T.T., Su, J.J., Lin, C.H., and Huang, T.H. (2000). “The seismic hazard and the rehabilitation of the tunnels in central Taiwan after Chi-Chi.” *Sino-Geotechnics*. 81: 85-96. (in Chinese)

Wang, W.L., Wang, T.T., Su, J.J., Lin, C.H., and Huang, T.H. (2001). “Assessment of damage in mountain tunnels due to the Taiwan Chi-Chi earthquake.” *Tunneling and Underground Space Technology*. 16: 133-150.

Seismic Analyses For The Fourth Bore of Caldecott Tunnel

By Chien-Tai Yang[1], Hubert Law [2], Anoosh Shamsabadi[3]

ABSTRACT

This paper presents a brief summary of seismic analyses for Caldecott Tunnel Improvement Project. It includes seismic hazard analysis, wave scattering analyses to evaluate soil structure interaction (SSI) for the proposed 4th bore, and development of seismic coefficient for slope stability design. Probabilistic Seismic Hazard Analysis (PSHA) was used to establish the rock motion criteria; 1,500-year and 300-year return periods were adopted for the Safety Evaluation Earthquake (SEE) and Functional Evaluation Earthquake (FEE), respectively. The wave scattering analyses were performed using the spectrum-compatible time histories to account for localized geologic features including site specific topography and soil properties specific to the current project. The analyses enable evaluation of the degree of ground distortion that contributes to racking and ovaling of the tunnel liner. Seismic coefficients for several critical slopes near portals were also derived considering the concept of wave propagation within the slope mass.

Keywords: seismic design, wave scattering analyses, seismic coefficients

INTRODUCTION

The Caldecott Tunnel connects Alameda and Contra Costa Counties via California State Route 24 (SR-24). The existing tunnel consists of two bores constructed in 1937 and a third bore, north of the original two, built in 1964. The tunnels pass through Berkeley Hills which is composed of a sequence of sedimentary rocks. The bedding of the rocks is high angled; the average dip of the bedding is about 60^{o} to the southeast and the strike is nearly normal to the tunnel axis. The basal rocks are located near the west portal which are locally known as Sobrante and Claremont Formations. At the east portal, Orinda Formation is encountered.

The Caldecott Improvement Project is intended to alleviate traffic congestion along SR-24 by constructing a fourth bore of the Caldecott Tunnel. The Caldecott Tunnel is located in San Francisco Bay region, one of the more seismically active regions in the U.S. In addition, SR-24 is considered as a lifeline route by California Department of Transportation (Caltrans) in this region which includes other important facilities such as the Benicia-Martinez bridge and San Francisco-Oakland Bay bridge (SFOBB). Therefore, the site-specific seismic design criteria for the proposed 4th bore of

[1] Earth Mechanics, Inc; 17660 Newhope St., Suite E, Fountain Valley, CA 92708; email: c.yang@earthmech.com
[2] Earth Mechanics, Inc; 17660 Newhope St., Suite E, Fountain Valley, CA 92708; email: h.law@earthmech.com
[3] California Department of Transportation; email: anoosh_shamsabadi@dot.ca.gov

Calecott Tunnel must be consistent with the risk levels adopted for other important facilities.

The elements of seismic analyses include development of seismic ground motion criteria, use of wave scattering analyses to evaluate soil structure interaction (SSI) for the proposed 4th bore, and development of seismic coefficient for slope stability design. The paper will discuss seismic ground motion criteria including seismic hazard analyses for development of target design rock spectra, and development of spectrum-compatible rock motion time histories. Example results from one tunnel cross section are provided to discuss the wave scattering analysis to evaluate degree of ground distortion that contributes to racking and ovaling of the liner. For development of seismic coefficients for slope stability evaluation, wave propagation analysis results are provided to illustrate reduction of effective ground shaking from the reference input motion.

SEISMIC HAZARD ANALYSIS

Seismicity

Figure 1 presents a fault map of the Northern California region with the Caldecott Tunnel site shown on the map. Table 1 presents the magnitude of some major faults and their distances to the tunnel portals. The Hayward fault is considered the controlling fault for design to this project due to its high activity rate and close proximity (only 1.2 mile to the west portal). The Hayward fault is considered capable of producing an earthquake with a moment magnitude of up to 7.5 and there is an approximately 27 percent probability of an earthquake of moment magnitude 6.7 or larger on the Hayward fault within the next 30 years (Working Group on California Earthquake Probabilities, 2003). All other faults shown on the map were also considered in the following hazard analysis.

Probabilistic Seismic Hazard Analysis (PSHA)

The PSHA considers uncertainties in the size, location, and rate of recurrence of earthquakes, in contrast to the deterministic seismic hazard analysis that considers a seismic scenario consisting of the postulated occurrence of an earthquake of a specified size occurring at a particular location. Main parameters for PSHA include seismic source model, magnitude density function, recurrence relationships, rupture dimension relations, attenuation relationships and directivity effects (Earth Mechanics, 2007).

Two new developments in PSHA are used in this project. First, the source model used in this project is based on a model produced by the USGS Working Group (WG03) on Earthquake Probabilities in Northern California and on the 1999 California State hazard map (Petersen et al., 1999).

Second, the rock motion attenuation relationships adopted for the analyses considered the Next Generation Attenuation (NGA) model. The NGA research program

sponsored by Pacific Earthquake Engineering Research (PEER) is intended to predict strong-ground motions for earthquakes in the western using empirical data and guided by findings from recent large earthquakes in Taiwan and Turkey.

Target Rock Spectra

Uniform risk hazard spectra of the fault normal component from the probabilistic analyses at four return periods (1,500, 500, 300 and 100 years) are presented in Figure 2. The above target rock spectra were defined at the bedrock depth with an average shear velocity of approximately 610 m/s (2,000 fps).

For consistency with the other Caltrans structures along the lifeline route, the 1,500- and 300 year return period uniform hazard spectra are used for the tunnel structures under the Safety Evaluation Earthquake (SEE) and Functional Evaluation Earthquake (FEE), respectively. The SEE is associated with life safety to the public and some repairable damage is allowed. The FEE is related to serviceability and frequency of repairs (economic trade off).

Spectrum-Compatible Time Histories

To perform the seismic analysis for the tunnel structures and slope stability evaluation, spectrum-compatible time histories were developed. Start-up motions were selected for spectrum matching based on corresponding range of magnitude, distance, and directivity requirements associated with specific return period earthquakes. The start-up motions were modified through an iterative process using the program RSPM22B developed by Abrahamson (1993) so that the response spectrum of the modified time history was compatible with the target rock spectrum. Three sets of time histories were developed for both SEE and FEE events, each set consists of three components.

WAVE SCATTERING FOR TUNNEL DESIGN

The target rock spectra and their corresponding spectrum-compatible ground motion time histories represent the first benchmark rock ground motion criteria as a reference. The above spectrum-compatible time histories do not explicitly consider topographic features such as hills and valleys, or the tunnel cavities. Therefore, the wave scattering analyses are required to account for localized geologic features, including site-specific topography and soil properties specific to the project.

Unlike above-ground structures, seismic design of a tunnel cannot be accomplished with a response spectrum approach. Due to lack of distinct fundamental mode of vibration, the force-based design approach (response spectrum method) is inadequate. One must employ the deformation approach in order to examine the racking behavior. Time history analysis involving wave propagation (scattering) is suitable for seismic design of underground structures. The wave scattering phenomenon alters the ground motion as the seismic waves travel through the rock. Also, the irregular boundaries of hills and valleys, in conjunction with the presence of the tunnel cavities, cause

complex wave propagations that lead to differential ground deformation around the tunnel cross sections.

The wave scattering analyses were conducted using the two-dimensional finite element computer program, QUAD4M (Hudson et al., 1994). The finite element models included a transmitting boundary, capable of minimizing seismic wave reflection at the finite element boundary, which is used to model a semi-infinite space outside the finite element domain (Hudson et al., 1994; Lysmer and Kuhlemeyer, 1969).

Several transverse cross sections were developed to evaluate the degree of ground distortion that contributes to racking and ovaling of the tunnel liner under different soil stiffness, heights of soil covers, and tunnel types (cut-and-cover or bored). One finite element mesh was shown in Figure 3. A modulus reduction and increase in damping at large shear strains were considered in the seismic analysis (i.e., the shear modulus and damping ratio vary with the shear strain level). Ground motions were computed at the perimeter of the tunnel which are proved to be non-synchronized among the nodes. This non-synchronized behavior led to differential deformations between nodes.

Figure 4 shows the differential displacements computed between the invert and crown nodes at the fourth bore in horizontal and vertical directions. Figure 5 shows a comparison of the intensity of the ground motions at the perimeter of at the 4th Bore tunnel opening represented by their acceleration response spectra. The reference rock motion is also included in the plot. The spreading of the response spectra is another indicator of non-coherent wave propagation resulting in differential motion around the tunnel cavity. Figure 6 show a snapshot deformation patterns for the fourth bore tunnel opening. It clearly shows the racking and ovaling of the tunnel opening.

SEISMIC COEFFICIENT ANALYSES FOR RETAINING WALLS AND SLOPES

Wave propagation of ground motion within slopes offers an alternative method to estimate seismic coefficients which are used in a pseudo-static slope stability analysis approach. The traditional practice in selecting the seismic coefficient assumes rigid body-soil response where seismic coefficients are associated with the peak bedrock acceleration. The wave propagation analysis for slopes allows assessment of effective inertia force of the slope which varies with time. The effective inertia force can be further examined to establish a proper seismic coefficient in a rational manner. This approach was adopted for seismic designs of various walls and slopes for the Caldecott Tunnel Project.

To illustrate the methodology, Figure 7 shows a slope near west portal of the Caldecott Tunnel with several potential failure surfaces. The wave propagation analyses were performed using the reference rock motion time history for the SEE event. From the wave propagation analyses, summation of element shear forces along

each failure plan was computed. The sum of shear forces was then normalized with the total weight of the soil mass bounded by the failure surface. The resultant normalized shear force, which is a time function, represents the average horizontal acceleration of the soil mass (it has the same unit as the acceleration in terms of a fraction of normal gravity).

Figure 8 presents time histories of average horizontal acceleration for Blocks 1, 3, and 5 bounded by the respective failure surfaces. These average horizontal acceleration time histories are compared with the input reference rock motion time history on the figure. In summation of element shear force time histories, high frequency components are non-coherent and thus tend to cancel out. As a result, the average horizontal acceleration is smaller than the input rock motion. For larger blocks, the cancellation effect is more pronounced, and substantial reduction in the peak value of the average horizontal acceleration from the peak rock motion is observed. For the slope stability analysis, this quantity of average horizontal acceleration is more relevant because it relates to effective inertia force exerting on the soil mass.

However, use of the peak value from the average horizontal acceleration for seismic slope stability analyses in the context of a limit equilibrium approach is conservative because the seismic coefficient is traditionally applied as a constant force on a potential sliding mass. In order to determine appropriate values for constant seismic coefficients, we conducted Newmark deformation analyses using the complete time histories of the average horizontal acceleration.

Figure 9 depicts the computed maximum permanent displacements using a series of yield accelerations (k_h) for Block 1 from the site response analyses. The average horizontal acceleration histories derived from the three sets of ground motions were used in these analyses, including reversing the polarity. The computed maximum permanent displacements decrease with increase of k_h. We considered a computed Newmark displacement of less than 4 inches (10 cm) to be considered stable (DM117 criteria). If a seismic coefficient (k_h) is greater than the yield acceleration value at 4 inches of Newmark displacement, some permanent deformation is expected. Based on the results shown on Figure 9 and 4-inch criteria, a seismic coefficient of 0.3 is used for pseudo-static analyses, which is about 1/4 of the peak input rock motion. Similar analyses were conducted for other slopes and walls with different heights.

CONCLUSIONS

The methodologies and some examples are presented in this paper to demostrate the current industry practice for the seismic analyses. Target rock spectra were developed based on PSHA incorporating new developments of source model and NGA model. Spectrum-compatible time histories were generated for seismic evaluation. Wave scattering analyses considering the specific soil condition, topography, site response and tunnel opening provided estimate the tunnel liner distortions. Seismic coefficient analyses incorporating wave scattering and Newmark sliding analyses enabled more logic and reasonable estimate on the seismic coefficient for pseudo-static analyses.

REFERENCES

California Department of Conservation, "Guidelines for Evaluating and Mitigating Seismic Hazards in California," SP 117, 1997.

Earth Mechanics, Inc. (2007), "Technical Memorandum No. 14, Seismic Hazard Report and Ground Motions," Report to CCTA, Caltrans and Jacobs Associates.

Hudson, M., Idriss, I. M. and Beikae, M. (1994), User's Manual for QUAD4M, A Computer program to Evaluate the Seismic Response of Soil Structures Using Finite Element Procedure and Incorporating a Compliant Base, Department of Civil & Environmental Engineering, University of California, Davis.

Lysmer, J. M. and Kuhlemeyer, R. L (1969), "Finite Dynamic Model for Infinite Media," J. of the Engineering Mechanics Division, ASCE, Vol 95, No. EM4, August, pp 859-877.

Mualchin, Lalliana (1996), California Seismic Hazard Map, Based on Maximum Credible Earthquakes.

Petersen, M.D. and Branum, D. (1999), Seismic shaking hazard maps of California, Department of Conservation, California. Division of Mines and Geology.

U.S. Geologic Survey (USGS) (2003), Working Group on Northern California Earthquake Potential, Earthquake Probabilities in the San Francisco Bay Region: U.S. Geologic Survey Open-File Report 03-214.

Table 1: Magnitude and Distance to Portals for Nearby Major Faults

Fault	Fault Type	Moment Magnitude, M_w (1)	Distance from West Portal	Distance from East Portal
San Andreas	Right Lateral	8.0	31.1	32.5
Hayward	Right Lateral	7.5	1.2	2.5
Calaveras	Right Lateral	7.5	19.0	19.3
Greenville	Right Lateral	7.25	28.1	29.3
Rodger Creek	Right Lateral	7.0	37.2	37.7
Concord	Right Lateral	6.5	20.1	21.3
Franklin	Right Lateral	6.5	12.8	14.1
(1) From Mualchin, 1996				

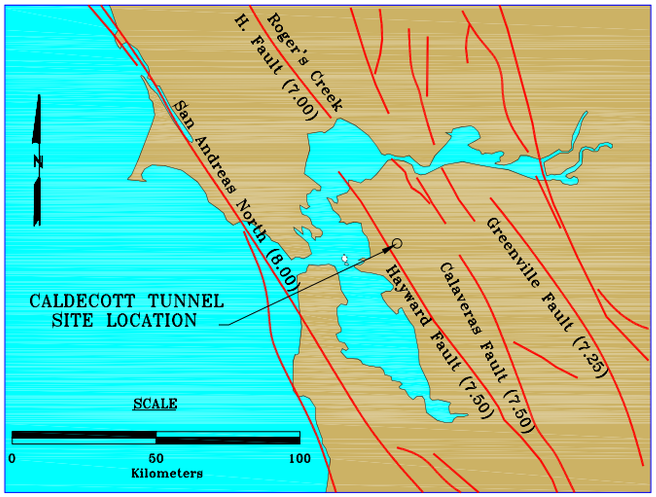


Figure 1. Fault Map of San Francisco Bay Region

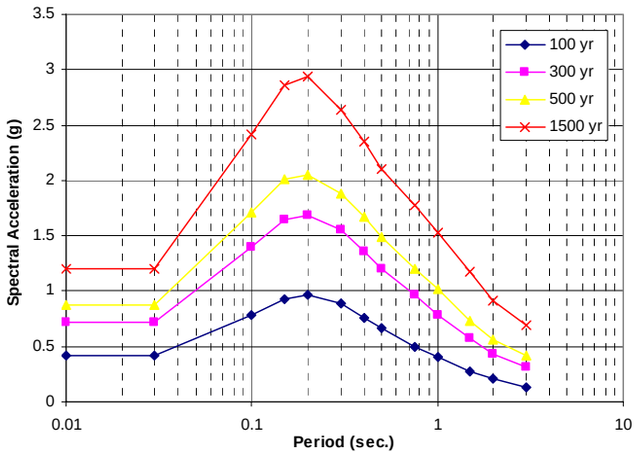


Figure 2. Uniform Risk Equal Hazard Spectra

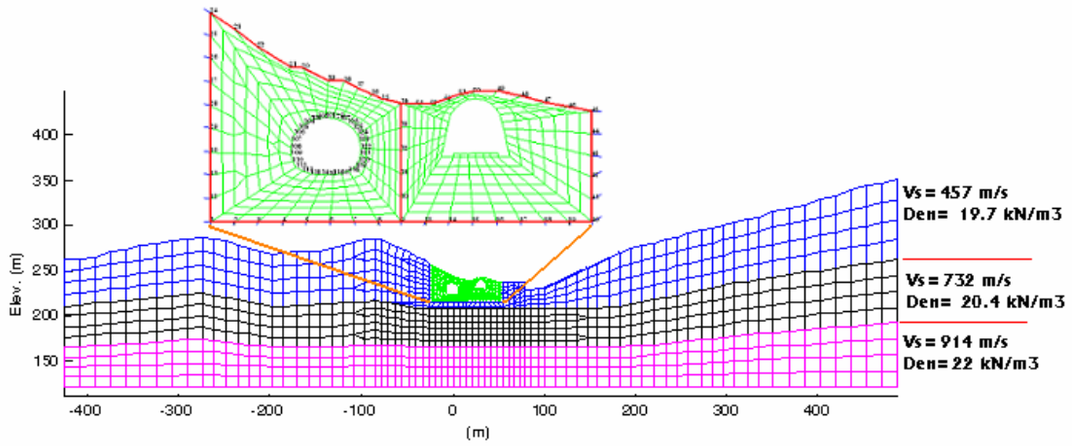


Figure 3. Finite Element Mesh for Transverse Cross Section at Station 107+60

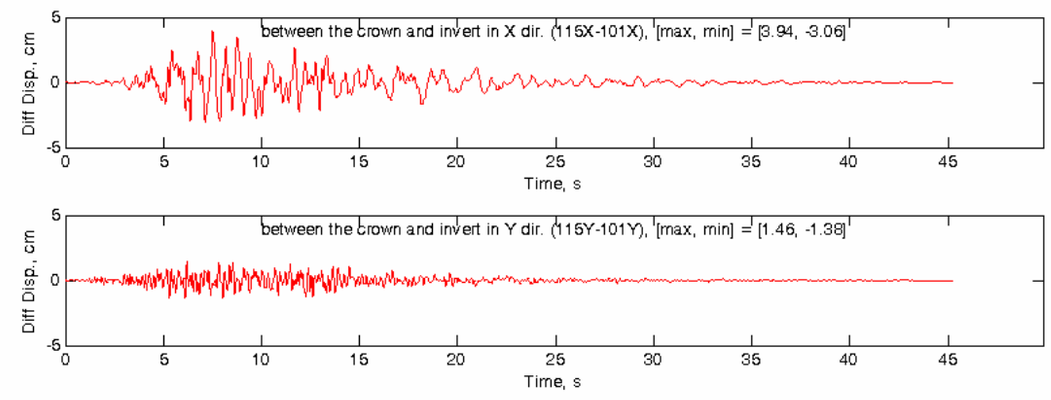


Figure 4. Differential Displacements between the Crown and Invert Nodes

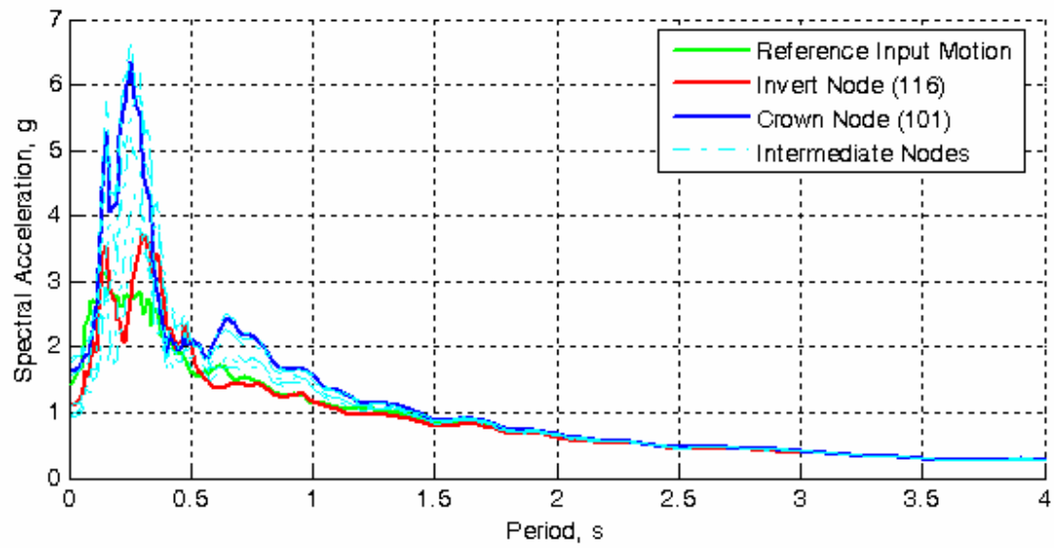


Figure 5. Acceleration Response Spectra at 4th Bore Perimeter

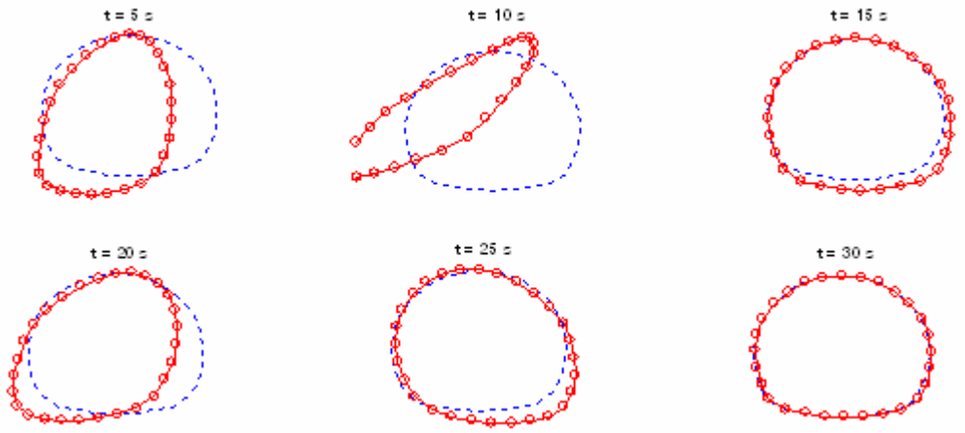


Figure 6. Snapshot Deformation of 4th Bore (x500 times)

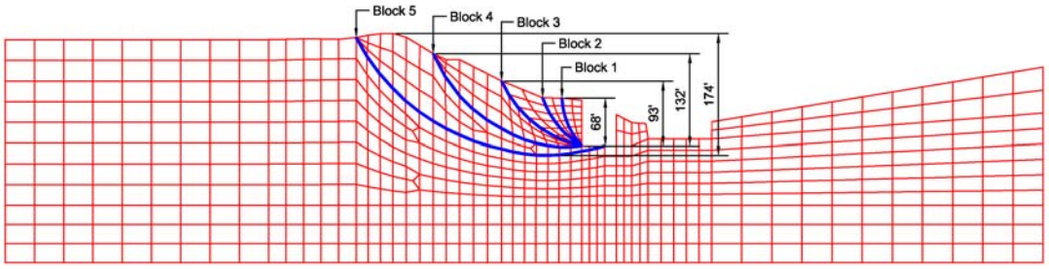


Figure 7. Geometries and Finite Element Models for a Slope at Station 107+18

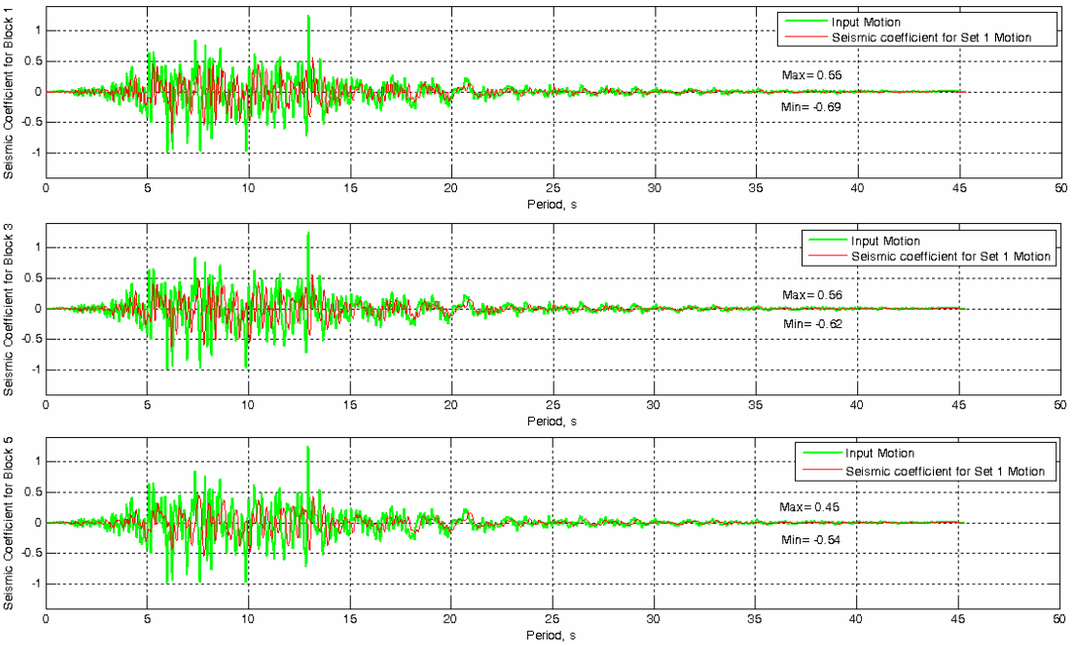


Figure 8. Seismic Coefficient Time Histories for Three Blocks under SEE 1 Motion

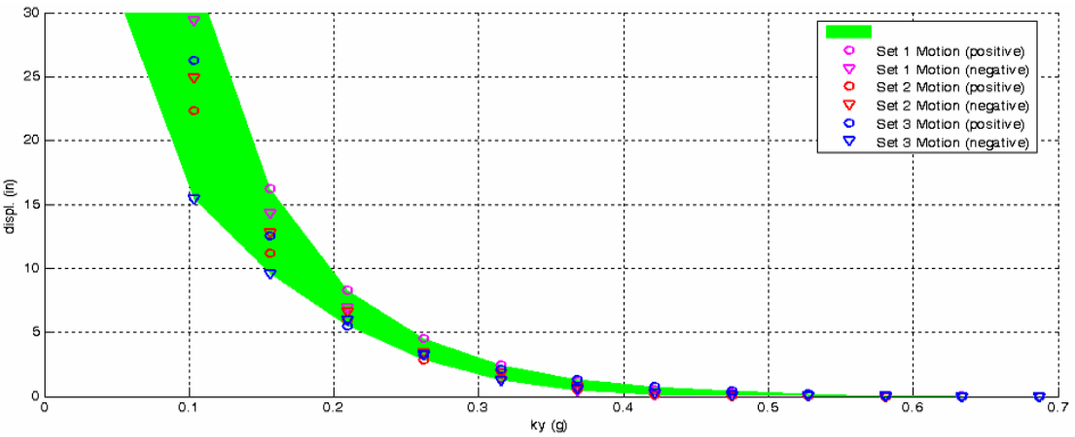


Figure 9. Newmark Sliding Block Analyses for Block 1 under SEE Motions

Seismic Analyses of the Bay Tunnel

Yiming Sun[1], Steve Klein[1], John Caulfield[1], Victor Romero[1], and Johanna Wong[2]

[1]Jacobs Associates, 465 California Street, Suite 1000, San Francisco, CA 94104
[2]San Francisco Public Utilities Commission, 1145 Market Street, San Francisco, CA 94103

ABSTRACT: The Bay Tunnel is a major water supply facility to be constructed between the San Andreas Fault and the Hayward Fault in the San Francisco Bay Area. The design earthquake for the Bay Tunnel has a return period of 1,000 years and a horizontal peak ground acceleration of approximately 0.6g. A full dynamic analysis of the Bay Tunnel, considering the soil-structure interactions, was performed to evaluate the performance of the tunnel final lining system during the design earthquake. This paper discusses the methods employed to perform the dynamic analysis and the results obtained. A brief comparison of the results from the dynamic analysis with those from the closed-form solutions and numerical racking analysis is also presented.

INTRODUCTION

The San Francisco Public Utilities Commission (SFPUC) is in the process of a major upgrade of their water conveyance system. One key element of this program is the Bay Division Pipeline Reliability Upgrade Project, which consists of constructing a new 21-mile Bay Division Pipeline No. 5. This pipeline extends from the Irvington Tunnel Portal in Fremont, California to the Pulgas Tunnel Portal near Redwood City, California. It includes a tunnel under the San Francisco Bay (the Bay Tunnel) and adjacent marshlands. The Bay Tunnel is approximately 5 miles long and crosses under the Bay in soil conditions (i.e., soft ground). Excavation and construction of the Bay Tunnel will be staged from two shafts constructed at either end of the tunnel: the Ravenswood Shaft at the west end, and the Newark Shaft at the east end.

The Bay Tunnel will have a two-pass lining system with a watertight precast concrete segmental lining as the initial lining. The precast concrete segmental lining thickness will be about 10 inches with an inside diameter of approximately 12 feet. The final lining for the tunnel will be a Grade 40 steel pipe with an inside diameter of 9 feet and a wall thickness of 9/16 inch. The annular space between the steel pipe and the segmental lining will be backfilled with low-density cellular concrete.

The Bay Tunnel is located between two of the most seismically active faults in the Bay Area, the San Andreas Fault to the west and the Hayward Fault to the east. An essential aspect of the Bay Tunnel design was evaluation of the response of the tunnel

facilities to the seismic activities of these faults. To support the design of the shafts, connecting tunnel, and pipelines, and to ensure that the seismic performance objectives defined by the SFPUC can be met (SFPUC, 2006), detailed seismic analyses were completed for the Bay Tunnel. This paper discusses the methods employed to perform a dynamic analysis and the results obtained. A brief comparison of the results from the dynamic analyses with those from the closed-form solutions and numerical racking analysis is also presented.

TUNNEL PROFILE AND GEOLOGICAL CONDITIONS

The proposed Bay Tunnel vertical alignment is shown in Figure 1, along with the anticipated geologic conditions along the alignment. The tunnel has a slope of about 0.13%. The high point of the tunnel is at the east end (at the Newark Shaft), where the tunnel invert is at at Elevation -71 feet. The low point is at the west end (at the Ravenswood Shaft), where the tunnel invert is at Elevation -104 feet. The ground cover above the tunnel varies along the alignment. The lowest cover (measured from the ground surface to the tunnel springline) is about 50 feet at the deepest point under the Bay. The greatest cover is about 110 feet at the low point of the tunnel alignment.

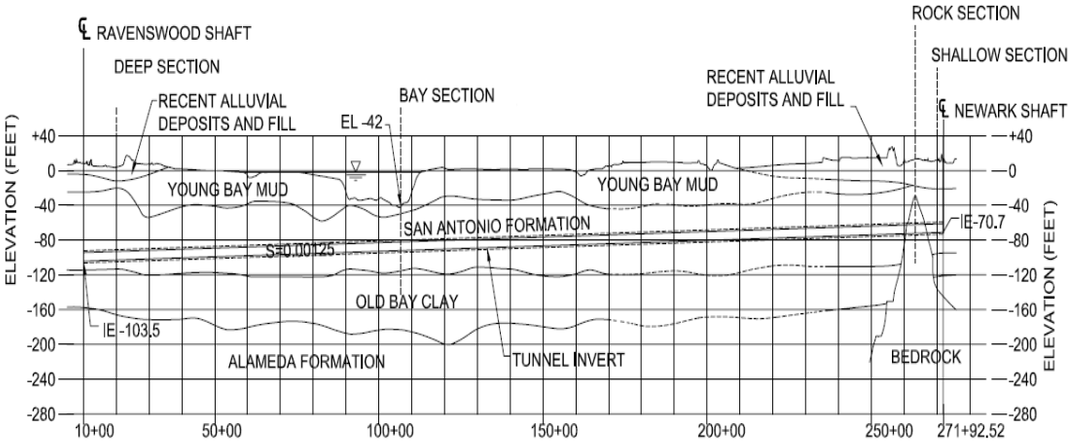


Figure 1. Geologic Profile and Vertical Alignment of the Bay Tunnel

Soil deposits present along the tunnel alignment can be grouped into six principal strata: artificial fill, Young Bay Mud (YBM), San Antonio (SA) Formation, Old Bay Clay (OBC), Alameda Formation, and Franciscan Complex bedrock. The entire Bay Tunnel will be constructed within the SA Formation, except at a reach between Station 260+00 and Station 270+00, where the tunnel will be excavated within the Franciscan Complex rock.

Four tunnel sections were selected for two-dimensional seismic analyses. They are called the Shallow, Bay, Deep, and Rock Sections. The locations of these sections are shown in Figure 1. These sections were selected to represent the range of overburden depths and anticipated ground conditions. Evaluation of the seismic performance of the tunnel at these sections is considered to encompass the range of seismic responses expected along the alignment. A typical cross-section of the tunnel is shown in Figure 2.

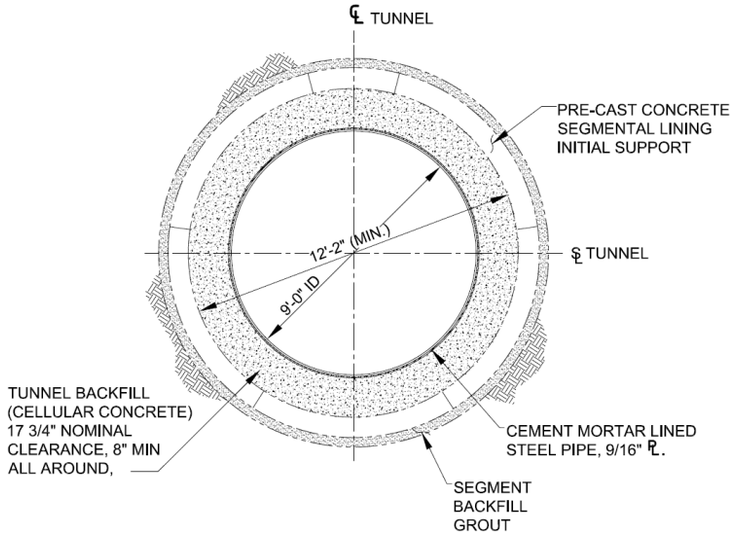


Figure 2. Typical Cross-section of the Bay Tunnel for Seismic Analyses

The key parameters associated with the four tunnel sections and used for seismic analyses are summarized in Table 1. The peak ground velocities were calculated based on the probabilistic seismic hazard analysis (PSHA) (Jacobs Associates, 2007a). The average material property values of various soil and rock formations are presented in Table 2. Soil formation properties were estimated based on laboratory tests and field downhole suspension loggings. Franciscan rock properties were assumed based on relevant data collected for other tunnel projects in the Bay Area. The maximum dynamic shear moduli were calculated from the shear wave velocities and unit weights with a 30% reduction for cyclic degradation at the expected seismic strain levels.

Table 1. Parameters Associated with Tunnel Sections for Seismic Analysis

Parameter	Shallow Section	Bay Section	Deep Section	Rock Section
Overburden Depth to Tunnel Springline (ft.)	76	50	110	81
Groundwater Head (ft.)	76	95	110	81
Head of Internal Water Pressure (ft.)	473	494	505	475
Peak Ground Velocity (PGV) at Tunnel Invert (ft./s)	2.37	2.99	3.42	2.37

Table 2. Material Properties of Soil and Rock Formations

Material Constant	Fill	YBM	SA Formation	OBC	Alameda Formation	Franciscan Rock
Unit Weight (pcf)	125	125 (90[a])	130	115	130	140
Poisson's Ratio	0.35	0.35	0.35	0.35	0.35	0.3
Static Shear Modulus (ksf)	50	130	280	230	850	6,700
Static Undrained Shear Strength (psf)	280	100-900	1,500	1,500	2,500	6,000
Maximum Dynamic Shear Modulus (ksf)	287	679	2,052	1,580	3,235	17,280
Dynamic Undrained Shear Strength (psf)	560	1,000	2,000	2,900	3,000	7,000
Shear Wave Velocity (ft./s)	325	500	850	800	1,330	2,000

Note: [a] Unit weight for YBM under the San Francisco Bay (for Bay Section).

GROUND MOTIONS OF DESIGN EARTHQUAKE

The design earthquake for the Bay Tunnel was developed using a probabilistic seismic hazard analysis with two major controlling earthquakes: a M 7.9 earthquake on the San Andreas Fault and a M 7.1 earthquake on the Hayward Fault (Jacobs Associates, 2007a). The San Andreas and Hayward Faults are as close as 8 and 5 miles, respectively, to the Bay Tunnel. The design earthquake has a 5% probability of exceedance in 50 years (a return period of 1,000 years) and a horizontal peak ground acceleration (PGA) of approximately 0.6g. The ground motion time histories of the design earthquake were generated for a hard rock site condition with V_{s30} (shear wave velocity in the top 30 m) equal to 5,000 ft./sec based on the following three seed earthquake records:

- 1999 M 7.4 Kocaeli, Turkey – Arcelik station
- 1992 M 7.5 Landers, California – Joshua Tree station
- 1999 M 7.6 ChiChi, Taiwan – TCU089 station

With these three seed earthquake records, a total of nine sets of spectrally matched site-specific ground motion time histories were calculated for three locations along the tunnel alignment: the Ravenswood Shaft, the Bay Tunnel, and the Newark Shaft (Jacobs Associates, 2007a). Each set of time histories contains two horizontal (fault-normal and fault-parallel) components and one vertical component. A typical time history of accelerations for the horizontal component 2 (ChiChi H2) (fault-parallel) at the Ravenswood Shaft (for the Deep Section) is shown in Figure 3.

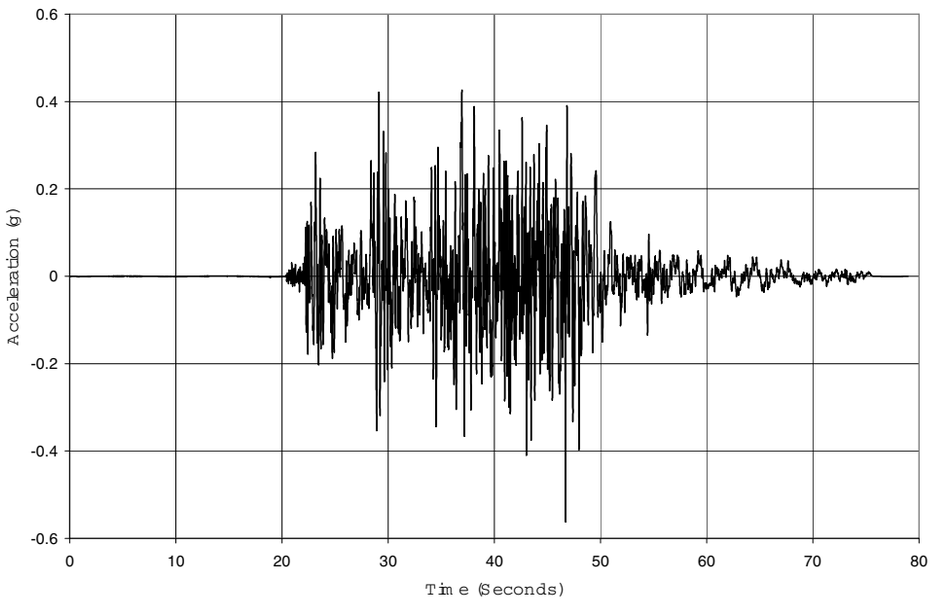


Figure 3. Typical Time History of Accelerations for the Bay Tunnel (Deep Section)

SHEAR-MODULUS DEGRADATION AND DAMPING

The amplitudes of seismic waves attenuate with distance when traveling through soil and rock. Factors affecting this attenuation include energy dissipation, volume changes, and stiffness degradation of soil and rock subjected to seismically-induced cyclic ground motions. Stiffness (shear-modulus) degradation and resulting damping of soil and rock increase with the increase of cyclic shear strains. This nonlinear, hysteretic characteristic of soil formations present along the Bay Tunnel was investigated using cyclic triaxial tests. Results of these cyclic tests using the soil samples taken from the SA Formation indicate that the shear-modulus reduction and damping curves for this soil formation can be represented by the empirical curves proposed by Vucetic and Dobry for stiff clay with a plasticity index (PI) of 50, as shown in Figure 4 (Vucetic and Dobry, 1991). For the Franciscan rock, the site-specific data are not available, and assumed shear-modulus reduction and damping curves, also shown in Figure 4, were used. These curves were selected from the seismic analyses for another Bay Area tunnel project: the Caldecott Fourth Bore Tunnel Project (Earth Mechanics, Inc., 2007).

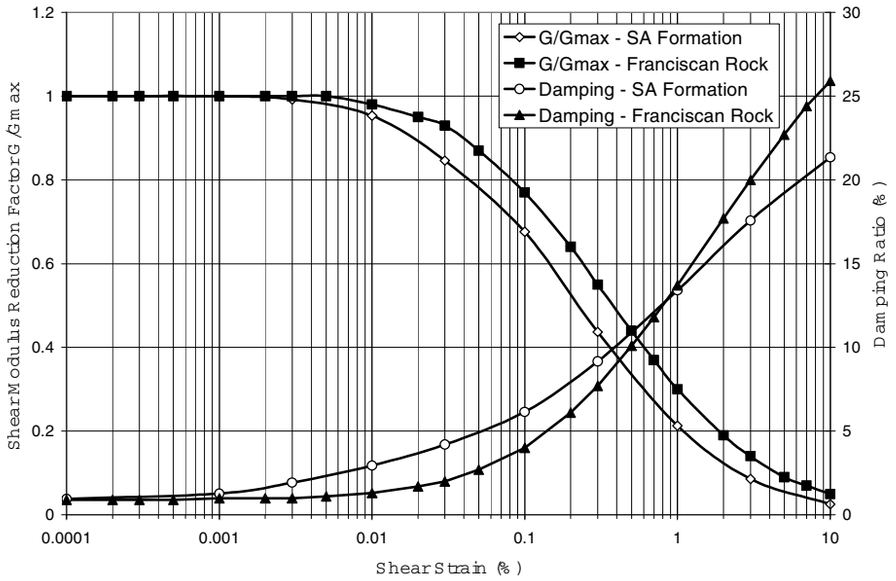


Figure 4. Shear-Modulus Reduction and Damping Curves for San Antonio Formation and Franciscan Rock

METHODS OF ANALYSIS

Seismic analyses for the Bay Tunnel were performed using three methods (Jacobs Associats, 2007b): closed-form solutions based on Hashash et al. (2001), numerical racking analysis based on an equivalent linear elastic approach, and full nonlinear dynamic analysis using a hysteretic damping model. Closed-form solutions are simplified methods based on theory of elasticity. In these solutions, the free-field deformation and ground-lining interaction approaches are used to examine the longitudinal and transverse effects caused by seismic waves. Racking analysis is used to quantify the racking deformations (shear distortions) and their effects on the tunnel final

lining due to seismically-induced free-field shear strains in the ground. The racking and dynamic analyses were performed using the FLAC computer program (Itasca, 2005). This paper focuses on the methods employed for the dynamic analyses and the results obtained. Some of the results from the other two methods will be presented for comparison.

A dynamic analysis is usually considered more realistic than closed-form solutions or racking analyses for projects with complex features, such as tunnels, because dynamic analysis can account for more complex soil-structure interactions and can more realistically simulate the motions of a tunnel when subjected to earthquake shaking. Ground motion time histories and a wide range of frequency spectra can be directly input into a dynamic analysis. The behavior and effect of more complex tunnel deformations than only racking can be evaluated. Shear-modulus reduction and damping of soil and rock during earthquake shaking can be incorporated into the dynamic analysis in a realistic manner.

Other key aspects of this approach are that the static effects of in situ ground stresses, groundwater pressures, and tunnel internal water pressure can also be taken into account. These effects are assessed by simulating the tunnel excavation, initial lining installation, and final lining installation prior to applying the dynamic loads to the FLAC model.

The static effect was modeled using the static properties of soil or rock and a Mohr-Coulomb failure criterion to govern the behavior of the soil or rock during excavation and normal operational conditions. Under earthquake shaking, the response of the ground and tunnel were simulated using the dynamic properties of soil or rock. In addition, the ground was assumed to follow a hysteretic damping model during earthquake shaking, based on the results of laboratory cyclic tests (as noted above).

Boundary Conditions

In a FLAC dynamic analysis, two boundary conditions are usually used (Itasca, 2005). One is the quiet boundary, and the other is the free-field boundary. A quiet boundary involves dashpots attached independently to the boundary in the normal and shear directions, which provide viscous normal and shear tractions. The quiet boundary prevents the reflection of outward-propagating waves back into the model and allows the necessary energy radiation. A free-field boundary enforces free-field motion at the lateral boundaries of the model such that these boundaries retain their non-reflecting properties (i.e., outward waves are properly absorbed). In FLAC, the free-field boundaries are coupled with viscous dashpots to simulate a quiet boundary.

In a dynamic analysis, seismic ground motions (accelerations or velocities) as a function of time are applied to the model base. For a model with a quiet boundary on the base, the acceleration or velocity boundary condition cannot be applied directly because it is not compatible with the quiet boundary in FLAC. Instead, a shear or normal stress time history is applied. The shear or normal stress time history is converted from the shear or normal component of seismic velocities using the following relations (Itasca, 2005):

$$\sigma_s(t) = 2\rho C_s v_s(t) \quad (1)$$

$$\sigma_n(t) = 2\rho C_p v_n(t) \quad (2)$$

Where σ_s is applied shear stress as a function of time; σ_n is applied normal stress as a function of time; ρ is mass density; C_s is speed of s-wave propagation through ground; C_p is speed of p-wave propagation through ground; v_s is input horizontal component of velocity as a function of time; v_n is input vertical component of velocity as a function of time.

In this study, only the ground motions associated with the shear waves were considered; those associated with the compressional waves were neglected because their effects on the tunnel performance are not very significant compared to those caused by the shear waves. In the Tunnel Analyses, the ground motion time histories determined for the three locations (Ravenswood Shaft, tunnel segment under the Bay, and Newark Shaft) were applied to the Deep, Bay, and Shallow Sections, respectively. The time histories applied to the Rock Section were the same as those for the Shallow Section. The dynamic properties presented in Table 2 were used in the dynamic analyses. Figure 5 shows a typical FLAC model with its dimensions (140 feet × 140 feet) and boundary conditions.

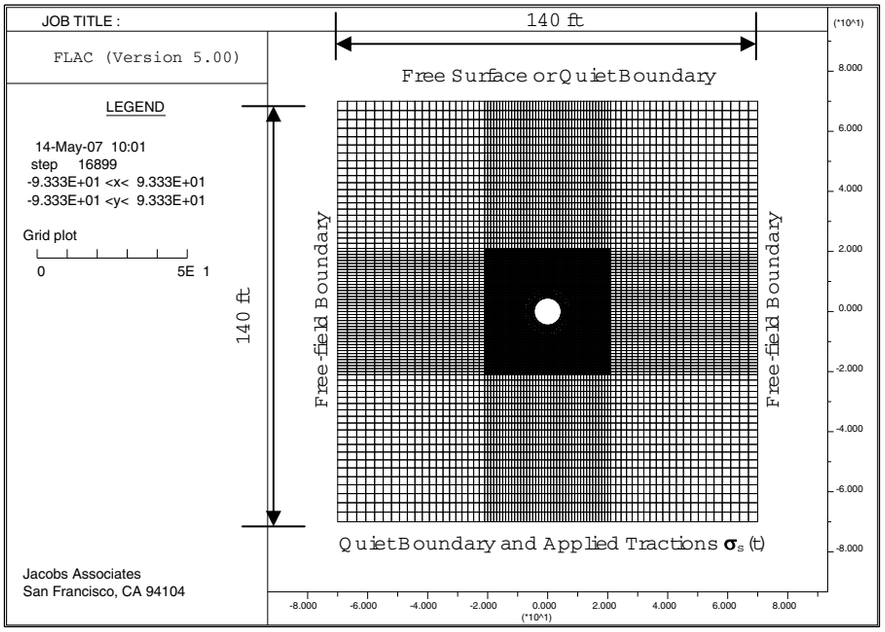


Figure 5. Model Configurations and Boundary Conditions for Dynamic Analysis

Calibration of Shear-Modulus Reduction Curves

Hysteretic damping models used in the dynamic analysis impose the shear-modulus reduction and damping ratios as a function of cyclic shear strains. A built-in three-parameter hysteretic damping model in FLAC was selected for the dynamic analysis. This three-parameter hysteretic damping model is defined in Eq. 3 (Itasca, 2005), and its parameters were calibrated by best-fitting to match the shear-modulus reduction curves proposed for the SA Formation and Franciscan Complex rock (shown in Figure 4). The resulting model parameters are: a=1.01, b=-0.55, and x_o=-0.25 for SA Formation; and a=1.01, b=-0.525, and x_o=-0.0005 for Franciscan rock.

$$M_s = \frac{a}{1+\exp\left[-\left(L-x_o\right)/b\right]} \quad (3)$$

Where M_s is normalized shear modulus; L is logarithmic shear strain.

To verify that the shear-modulus reduction and damping curves used were appropriate for the analyses, a series of numerical simple shear tests with a single-zone FLAC model were carried out. In these tests, damping ratio curves corresponding to the shear-modulus functions were developed over a range of shear strains of interest. Both the shear-modulus reduction and damping ratios as a function of shear strains were recorded during these test runs, and the three parameters were adjusted if necessary to produce a reasonable fit. Figure 6 shows a comparison of the calibrated curves with the proposed functions for the SA Formation. A similar comparison was made with Franciscan rock. It appears that the calibrated shear-modulus reduction and damping curves are in good agreement with the proposed curves over the range of shear strains considered suggesting that the hysteretic damping model in FLAC is reasonable for use in the dynamic analysis of the Bay Tunnel.

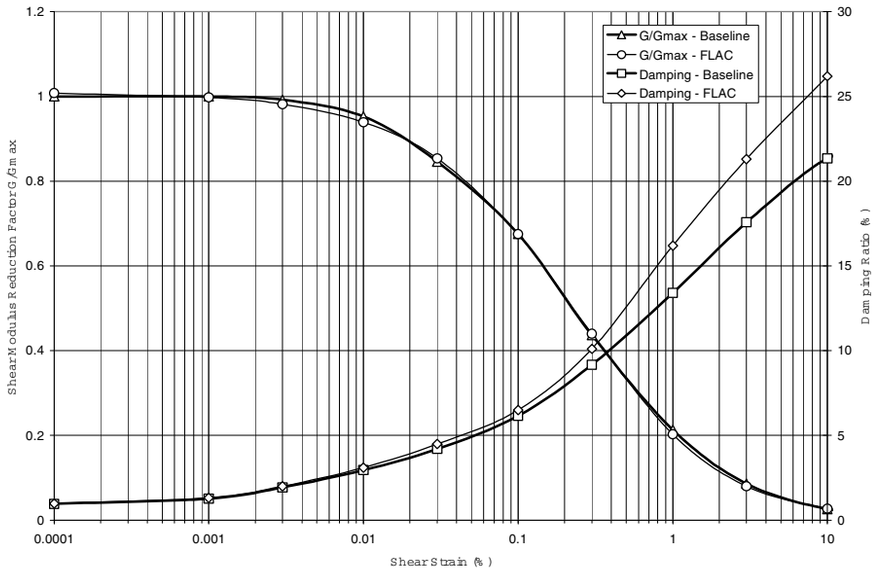


Figure 6. Comparison of Shear-Modulus Reduction and Damping Curves for San Antonio Formation

PREDICTED SEISMIC RESPONSE OF BAY TUNNEL

The applied ground motions used in the seismic analyses were shear waves propagated vertically from the bedrock to the ground surface. The critical ground deformations caused by the shear waves were the shear distortions. Shear distortions induce additional shear strains in the ground and the tunnel final lining. Since the dynamic analyses are two-dimensional, evaluation of the tunnel response is limited to the transverse effects. Variations of the tunnel shear distortions and stresses in the final lining along the tunnel alignment can be assessed by comparing the results for different sections, which represent the tunnel at various critical locations.

Seismically-induced Tunnel Shear Distortions

The shear distortions defined here are the relative horizontal displacements between the tunnel crown and invert. Time histories of the calculated shear distortions at the four tunnel sections are presented in Figure 7. It is apparent that the shear distortions are transient, following similar cycles of ground displacements. The magnitude of shear distortions is highly dependent on the amplitude of shear waves and ground conditions. The peak shear distortion occurs when the amplitude of shear waves reaches its peak over the duration of shaking.

It is noted that the input ground motion time histories vary along the tunnel alignment. These variations can be seen from the PGV values presented in Table 1. Among the four tunnel sections analyzed, the highest PGV is associated with the Deep Section, and the lowest with the Shallow and Rock Sections. This is why the calculated shear distortion at the Deep Section is larger than that at the Shallow Section, even though there is greater ground cover at the Deep Section.

For the Shallow and Rock Sections, the same time histories of shear wave velocities were used as input to the analyses. But due to the difference in ground stiffness, the calculated shear distortions are different at these two sections. The higher ground stiffness associated with the Rock Section reduces the shear distortion by about 0.2% over that of the Shallow Section. These results suggest increasing the stiffness of the backfill materials between the initial segmental lining and final lining may be a viable approach to limit shear distortions, if required.

Near the soil and rock transition zone, a differential shear stain of about 0.2% was estimated. This differential shear strain is expected to occur over a distance of more than 50 feet, so the transition between rock and soil will be gradual. In addition, the presence of concrete segments and backfill grout will serve as a cushion to make the transition less abrupt. Therefore, this differential shear strain is not expected to have a significant impact on the tunnel final lining performance.

Seismically-induced Stresses in Final Lining

Time histories of the calculated hoop stresses that developed in the final lining are shown in Figure 8 for the four tunnel sections. Along the entire tunnel alignment, the final lining is in tension. Like shear distortions, hoop stresses are dependent on the amplitude of shear waves and ground conditions. The maximum tensile hoop stress is predicted to be about 29 ksi, occurring at the Deep Section. This stress is below the allowable design stress of 30 ksi for the Grade 40 steel specified for the final lining (Jacobs Associates, 2007b). As indicated in Figure 8, stresses are transient, and the maximum stress occurs only once during the design earthquake. Stresses in the second-highest load cycle are approximately 25 ksi, and average dynamic stresses are even lower at only about 18 ksi, which is about 40% lower than the highest stress of 29 ksi and only about 45% of the yield stress of 40 ksi.

Comparison of Results from Different Methods

Table 3 compares the seismically-induced maximum hoop stresses in the final lining as calculated from closed-form solutions, numerical racking analysis, and dynamic analysis. The estimated stress levels calculated using the three different methods are generally consistent, within 2 to 4 ksi of each other. The largest difference is associated

with the Deep Section. The stresses from the dynamic analysis are higher than those from the other two methods. One possible reason is that in the dynamic analysis, the ground degradation represented by the shear-modulus reduction curve is accounted for, while in the closed-form solutions and racking analysis, the ground degradation is ignored. This may result in a larger shear distortion, and therefore a higher hoop stress in the final lining.

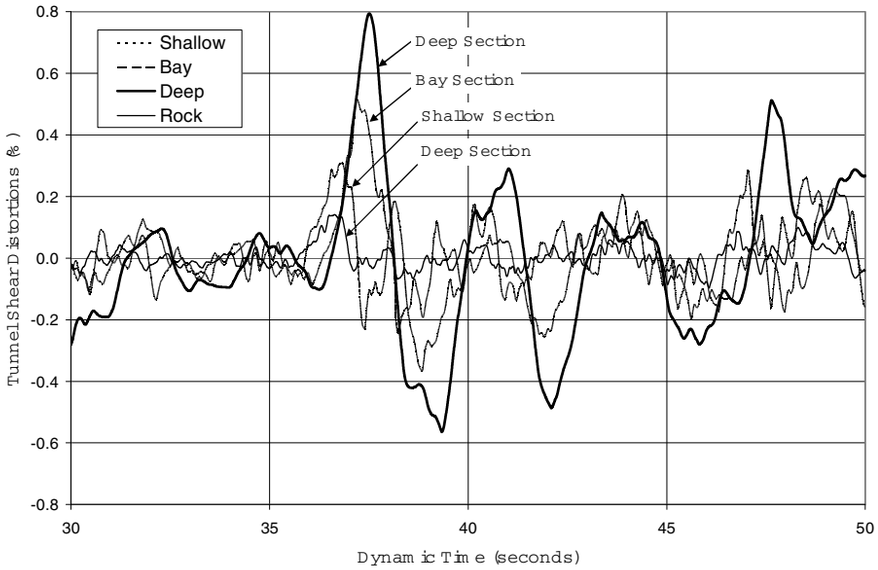


Figure 7. Time Histories of Final Lining Shear Distortions at Various Sections

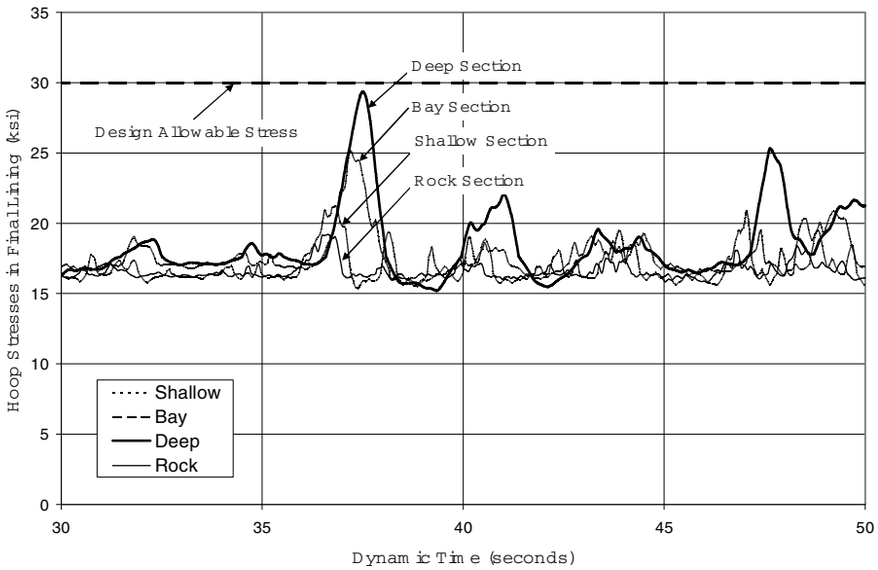


Figure 8. Time Histories of Hoop Stresses in Final Lining at Various Sections

Table 3. Maximum Hoop Stresses in Final Lining Due to Seismic Effects

Tunnel Section	Closed-form Solutions (ksi)	Racking Analysis (ksi)	Dynamic Analysis (ksi)
Shallow	±5.1	±5.1	±5.0
Bay	±6.4	±6.4	±4.8
Deep	±7.4	±7.4	±12.4
Rock	±1.6	±3.3	±3.0

Note: Maximum stresses can be tension (+) or compression (-).

CONCLUSIONS

The following conclusions may be drawn from the seismic analyses completed for the Bay Tunnel:

- Use of a hysteretic damping model to represent the ground degradation during seismic ground motions is reasonable for the dynamic analysis of the Bay Tunnel.
- Dynamic analysis can produce more realistic results since it can account for various load combinations considered in the tunnel design.
- The predicted response of the proposed Bay Tunnel final lining during the design earthquake meets the SFPUC's seismic performance objectives.
- Closed-form solutions, numerical racking analysis and dynamic analysis appear to produce generally consistent results.

REFERENCES

Earth Mechanics, Inc. (2007). *Technical Memorandum No. 3: Wave Scattering Analysis at West Portal*. Caldecott Improvement Project, 60% Design.

Hashash, Y.M.A., Hook, J.J., Schmidt, B. and Yao, J.I. (2001). "Seismic design and analysis of underground structures." *Tunnelling and Underground Space Technology*, 16, 247-293.

Itasca Consulting Group (2005). *Fast Lagrangian Analysis of Continua* (FLAC), Version 5.0, Itasca Consulting Group, Minneapolis, Minnesota.

Jacobs Associates (2007a). *Technical Memorandum No. 6: Seismicity.* Bay Division Pipelines Reliability Upgrade Bay Tunnel Project.

Jacobs Associates (2007b). *Technical Memorandum No. 7: Seismic Analysis.* Bay Division Pipelines Reliability Upgrade Bay Tunnel Project.

SFPUC (2006). *General Seismic Requirements for Design of New Facilities and Upgrade of Existing Facilities*. San Francisco Public Utilities Commission.

Vucetic, M. and Dobry, R. (1991). "Effect of soils plasticity on cyclic response," *Journal of Geotechnical Engineering*, ASCE, 117 (1), 898-907.

This page intentionally left blank

Seismic Response Analyses for the Silicon Valley Rapid Transit Project

Peter Chiu[1], Daniel E. Pradel[2], Annie On-Lei Kwok[3], and Jonathan P. Stewart[4]

[1]Senior Engineer, Praad Geotechnical, Inc., 5465 S. Centinela Avenue, Los Angeles, CA 90066; peter_chiu@praad.com
[2]Chief Engineer, Praad Geotechnical, Inc., 5465 S. Centinela Avenue, Los Angeles, CA 90066; daniel_pradel@praad.com
[3]Project Engineer, Praad Geotechnical, Inc., 5465 S. Centinela Avenue, Los Angeles, CA 90066; annie@praad.com
[4] Professor and Vice Chair, Dept. of Civil & Environmental Engr., Univ. of Calif., Los Angeles, 5731 Boelter Hall, Los Angeles, CA 90095; jstewart@seas.ucla.edu

ABSTRACT:

This study presents results from one-dimensional seismic ground response analyses performed for the Silicon Valley Rapid Transit (SVRT) project. Due to the large amplitude of the design input motion, large levels of shear strain are calculated in the soil column that are highly sensitive to modeling details. Critical issues affecting the results include: (1) the use of an innovative stress-strain (backbone) curve that captures expected behavior at small strains from empirical modulus reduction models along with expected large strain behavior as represented by material-specific rate-adjusted shear strengths; (2) assessment of velocity variability and randomness from variable stratigraphy (conditional on depth and soil type) on the computed response; (3) comparison of results computed from equivalent-linear and nonlinear codes; and (4) use of empirical amplification factors to help identify potential limitations of the results obtained from ground response analysis. Consideration of these issues indicates that our results are generally reasonable to use as input to subsequent soil-structure interaction analyses.

INTRODUCTION

The Silicon Valley Rapid Transit (SVRT) project will connect San Jose to the Bay Area Rapid Transit (BART) system. The tunnel segment portion of the alignment is approximately 8.2 km long and includes two portals, twin bored tunnels, three stations, one crossover structure, and two ventilation structures. The response of the structures to earthquakes is a major design consideration as the project is located near major active faults, including the San Andreas, Hayward, and Calaveras faults. This response is evaluated in a two-phase process, the first of which involves the analysis of free-field

ground response (i.e., the response of the soil column away from the structures). The second phase involves analysis of the structural response to the free-field motions. The subject of this paper is the first phase analysis of free-field ground response.

The specific purpose of the ground response analyses was to develop horizontal and vertical ground motions at selected depths and to define strain degraded dynamic soil properties for use as input in subsequent dynamic soil-structure interaction analyses. The ground motions developed are conditional on a 475-year return period uniform hazard spectrum for a reference NEHRP Site Class C condition.

SHAKE2000, an updated Windows-based version of the original SHAKE program (Schnabel et al. 1972, Idriss and Sun 1992), was selected for the one-dimensional equivalent-linear analyses. SHAKE is widely used in practice due to its relative ease of obtaining the dynamic soil properties required as input as well as its fast runtime. SHAKE utilizes a frequency-domain analysis procedure with time-invariant shear modulus and damping that are iterated upon until the equivalent-linear dynamic properties utilized in an iteration are consistent with the calculated shear strains. The computer code, DEEPSOIL (Hashash and Park, 2001, 2002; Park and Hashash 2004; http://cee-zzvy.cee.uiuc.edu/Website/Deepsoil/) was selected to perform nonlinear analyses of the soil profile for comparison. The nonlinear code operates in the time-domain, utilizing time-varying soil properties evaluated using a nonlinear backbone curve, unload-reload rules to capture hysteretic damping, and cyclic degradation effects.

In this paper, we discuss the site conditions and input motions, difficulties encountered during the analyses, comparisons between equivalent-linear and nonlinear analysis results, and the steps taken to evaluate and interpret the results.

DESIGN GROUND MOTIONS

Input ground motions for ground response analyses consisted of recorded acceleration histories modified through time-domain response spectral matching to be compatible with 5%-damped uniform hazard spectra for a 475 year return period. We were provided with design ground motions of this type for a NEHRP Site Class C "rock" condition (V_{s30} = 620 m/s). The motions were used as the input ground motion for ground response analyses. The recordings modified for use in these analyses were as follows:

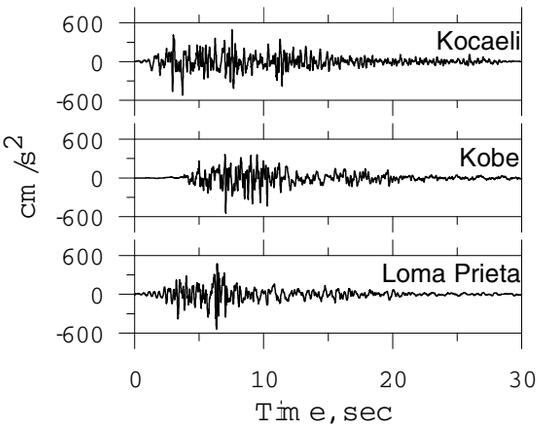


FIG. 1. Modified horizontal input motions in the fault normal direction.

- 1989 Loma Prieta Earthquake – Coyote Lake Dam Southwest Abutment station
- 1995 Kobe Japan Earthquake – Nishi-Akashi station
- 1999 Kocaeli, Turkey Earthquake – Izmit station

The peak ground accelerations (pga) for the horizontal and vertical components of the Site Class C design motion were specified as approximately 0.56 g and 0.47 g, respectively. Figure 1 shows the modified acceleration time histories of the Kocaeli,

Kobe, and Loma Prieta motion in the fault normal direction.

DYNAMIC SOIL PROPERTIES

Seismic Wave Velocity

Subsurface conditions along the tunnel segment generally consist of interbedded fine- and coarse-grained soils. The subsurface exploration program conducted to define the stratigraphy included shear wave velocity measurements at numerous locations using seismic cone penetration test (SCPT) and PS-suspension logging techniques. In the upper 60 m, data was measured from 3 suspension logs and 17 SCPTs. Deep seismic wave velocity data up to 410 m were available from two USGS suspension logs (Wentworth, pers. comm. 2004). Initial low-strain shear wave velocity profiles for use in the analyses were developed from the measured seismic velocity data.

As shown in Figure 2, the shear wave velocity data were separated into fine- and coarse-grained soils at depths up to approximately 60 m. Over this depth range, coarse-grained sediments have systematically higher seismic velocities than fine-grained sediments. Depth-dependant lognormal means and standard deviations were determined for the shear wave velocity data to develop best estimate, and reduced and increased profile fits. Below 60 m, the stratigraphy is largely unknown and therefore statistical moments of depth-dependent velocity were developed irrespective of material grain size (Figure 2).

Input motions were applied at a depth of 250 m, which is within the sedimentary basin above the base rock. Input motions were applied at that depth because the seismic velocities are consistent with a NEHRP C site condition (620 m/s). The depth to basement rock at the project site is estimated to be over 1000 m.

Figure 3 shows the upper 60 m of a typical site profile used for ground response analysis. The velocities labeled as “best estimate,” “reduced,” and “increased” correspond to mean (μ) and $\mu \pm \sqrt{3}\sigma$ values, which provide a convenient basis for estimating the probability density function representing the variability of ground response due to variability in shear wave velocity according to the first-order second moment method (Baker and Cornell 2003, Melchers 1999). In Figure 3, the jumps in velocity at material interfaces reflects the different mean distributions for fine- and coarse-grained materials (Figure 2). At larger depths, the soil shear wave velocity profile blends into an average of the fine and coarse-grained soils.

Shear Strength

The undrained static shear strength, S_u, of the fine-grained soil at the site was estimated using the SHANSEP method (Ladd 1991). The normalized shear strengths used in SHANSEP were derived from consolidated-undrained laboratory simple shear tests (Figure 3). The relationship between the measured static shear strength and the shear wave velocity at the project site is consistent with observations from literature (Weiler 1988). For the dynamic shear strength, previous studies have observed that the static shear strength can be increased by approximately 10 to 40% (Ishihara 1981; Sheahan et al., 1996). For our analyses, an increase of the static shear strength by 15% was considered.

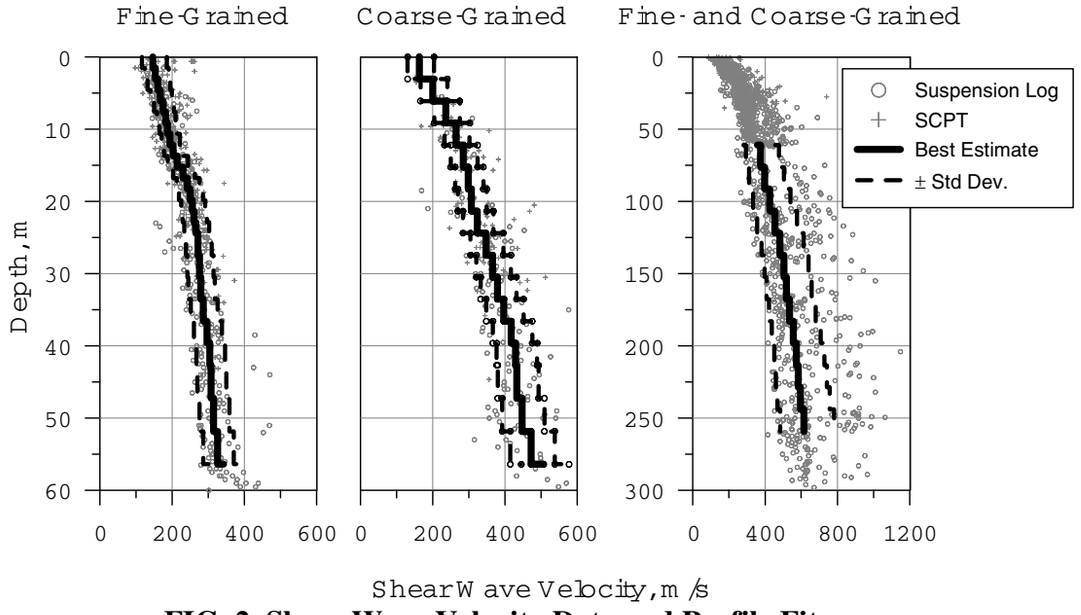


FIG. 2. Shear Wave Velocity Data and Profile Fits.

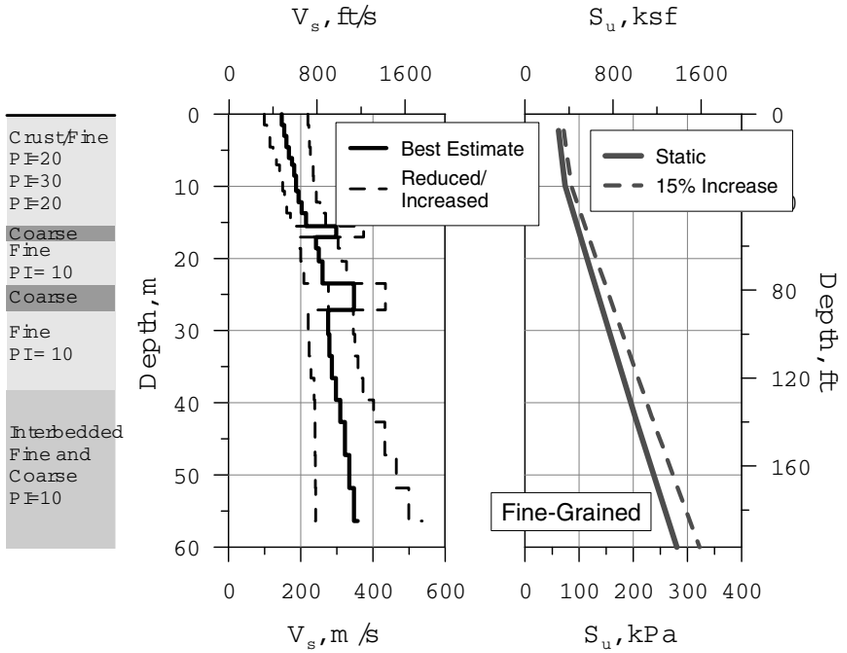


FIG. 3. Typical shear wave velocity profile and undrained shear strength.

Reduction and Damping Curves

Curves predicted by the empirical model of Darendeli (2001) were primarily used for the analyses. The Darendeli model is based on a database of laboratory data. The model predicts modulus reduction and damping curves as a function of plasticity index, effective confining pressure, overconsolidation ratio, and other parameters. Figure 4 shows typical reduction and damping curves predicted by Darendeli. Also shown in the figure are the data points considered in the Darendeli model. Limited site-specific

modulus reduction and damping curves were developed using simple shear testing of Shelby tube samples of the onsite soils to check certain aspects of the nonlinear curves, as discussed further below. This testing was performed in the UCLA geotechnical lab.

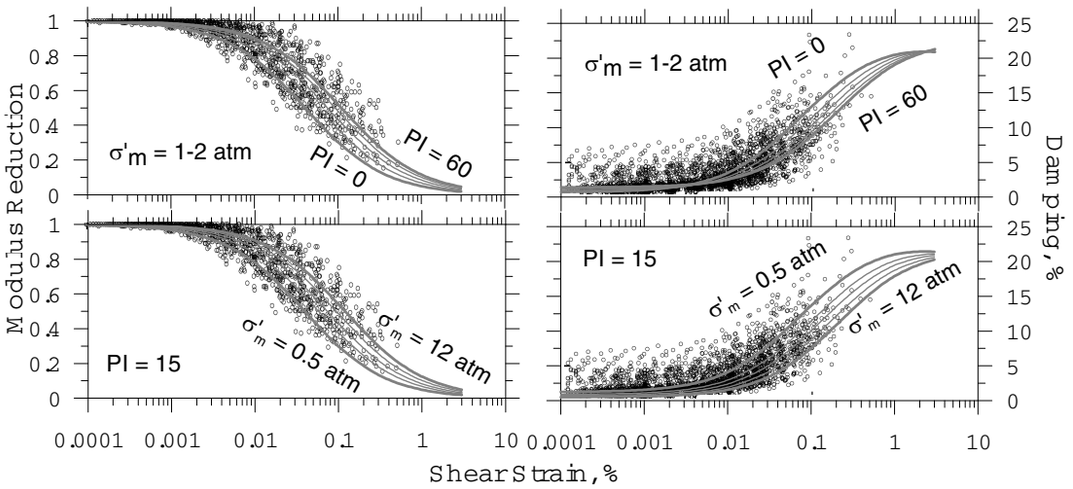


FIG. 4. Typical Darendeli (2001) Modulus Reduction and Damping Data.

KEY ISSUES IN GROUND RESPONSE ANALYSES

Assessment of Modulus Reduction Curves

Because of the large amplitude of the design input motions, large shear strains are expected. Based on empirical methods relating shear strain to peak ground velocity, strains for the design level of shaking were expected to be on the order of approximately 0.4 to 0.5% (Bommer and Alarcon, 2006). At strains of this magnitude, the shape of the backbone curve is affected not only by the relatively small strain ordinates of empirical modulus reduction curves, but also by the shear strength (Stewart et al. 2008). There is extensive data available for shear strains up to approximately 0.1% considered in the Darendeli model whereas the data is relatively limited beyond approximately 0.3%. If the Darendeli model were used without modification, the shape of the backbone curve at large shear strains would be based principally on extrapolation. This extrapolation tends to underestimate shear strength at shallow

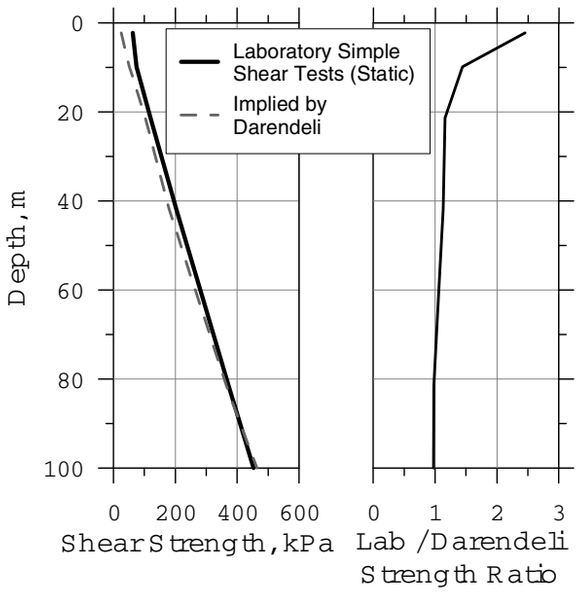


FIG. 5. Measured undrained shear strength vs. implied shear strength.

depths, as shown in Figure 5. The profile comparison is in agreement with previous observations, with the bias minimizing at large overburden pressure (larger depths). Hence, backbone curves were evaluated using the Darendeli curves at small strains (<0.1%) and then extrapolated to the rate-adjusted shear strength based on a procedure described in more detail by Stewart et al. (2008).

Figure 6 shows an example of backbone curves derived directly from the Darendeli model and with the strength-based extrapolation procedure. The example applies for a soil at a particular layer (plasticity index of 20 and effective confining pressure of 0.5 to 1 atm). As shown in Figure 6, results of site-specific simple shear testing of soil specimens up to large shear strains (approaching 1%) support the general slope of the strength-compatible modulus reduction curve at high shear strains. For coarse-grained soils, the shear strength at high shear strains was estimated by $S_u = \sigma'_v \tan(\phi)$ without adjustment for dynamic rate effects. For SHAKE, damping was estimated using the mean Darendeli curve and limited to 20% to reduce the potential for overdamping.

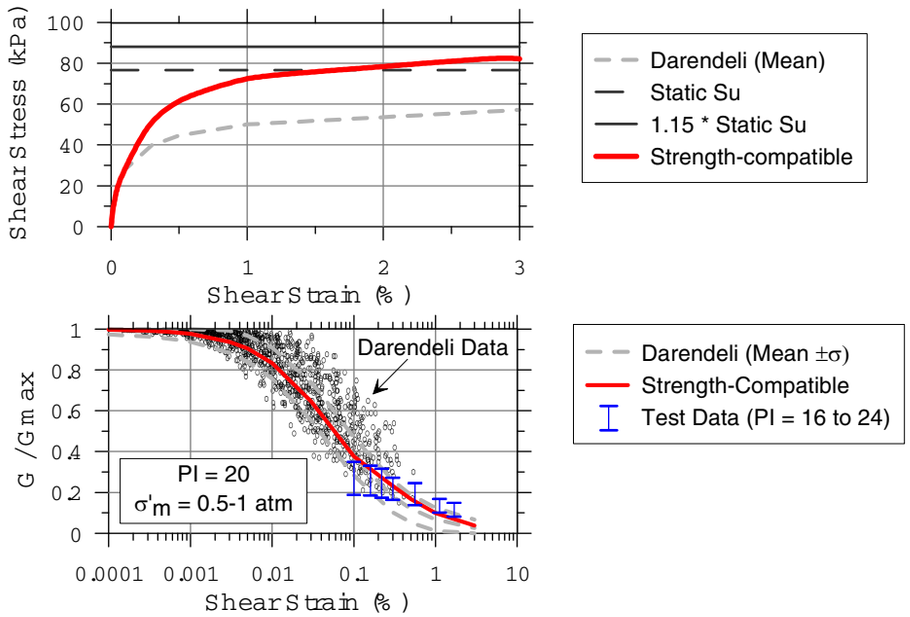


FIG. 6. Example of adjusted modulus reduction curve for strength-compatibility.

Figure 7 shows surface response spectra and shear strains (to depths of approximately 60 m depth) computed from the equivalent-linear (SHAKE) analyses using modulus reduction and damping curves compatible with the Darendeli model and the adjusted, strength-compatible model. The case shown is for the best estimate soil profile under the Kocaeli motion in the fault normal direction. The shear strains computed using the strength-compatible model are lower in critical layers between 10 and 40 m because of larger secant moduli. Shear strains approaching 1% were computed from the Darendeli model alone, which are judged to be unrealistic.

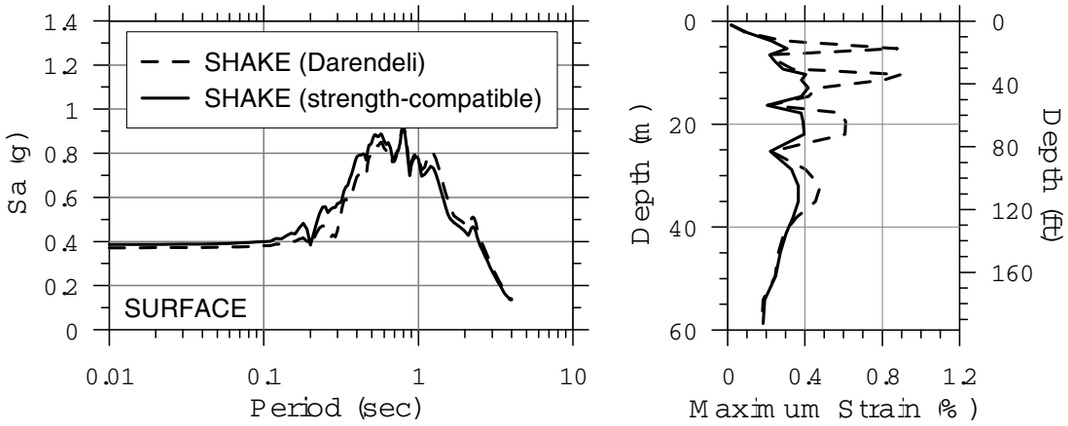


FIG. 7. Comparison of ground response results using Darendeli and strength-compatible reduction and damping curves.

Effect of Shear Wave Velocity Profile and Input Motion Variability

Figure 8 shows surface response and shear strains computed from the equivalent-linear (SHAKE) analyses using strength-compatible reduction and damping curves for all the shear wave velocity profiles (best estimate, reduced and increased) and input motions (Kobe, Kocaeli, and Loma Prieta) in the fault normal direction. Also shown is the weighted average and ± standard deviation curves through the results. As the figure indicates, the variability in the response is largely due to the variation in velocity which is conditional on depth and soil type. There is less variability observed in the response from the input motions used. This is to be expected since the motions were matched to the same design ground motion.

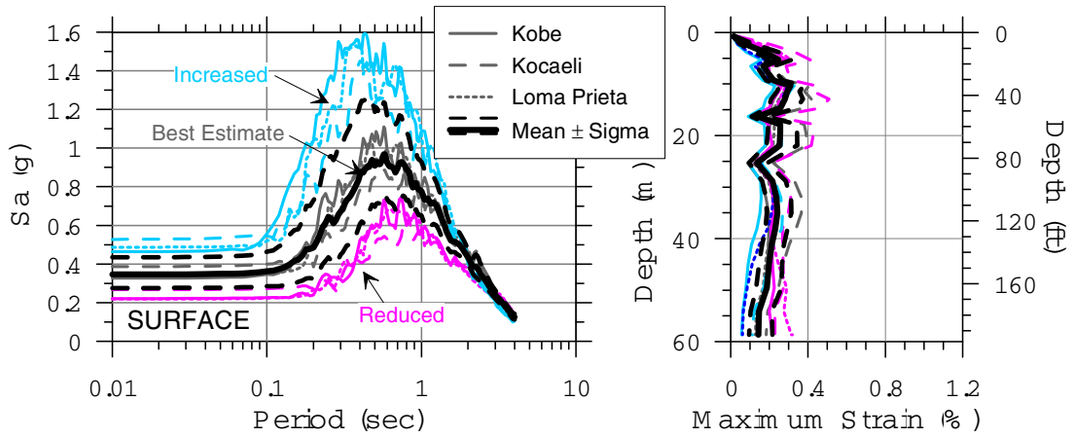


FIG. 8. Typical ground response using strength-compatible reduction and damping curves for all Vs profiles under 3 input motions in fault normal direction.

Equivalent-linear and Nonlinear Analyses Comparison

Though equivalent-linear analyses are the most commonly used procedure in practice (Kramer and Paulsen, 2004), there are known issues with their application at high strain levels. Nonlinear codes have the potential to yield more realistic results at large strain conditions due to more realistic simulation of nonlinear soil behavior. In order to check the results obtained from SHAKE, a comparison to the results computed from a nonlinear code (DEEPSOIL) was made (Figure 9). The case shown is for the best estimate soil profile under the Kocaeli motion in the fault normal direction.

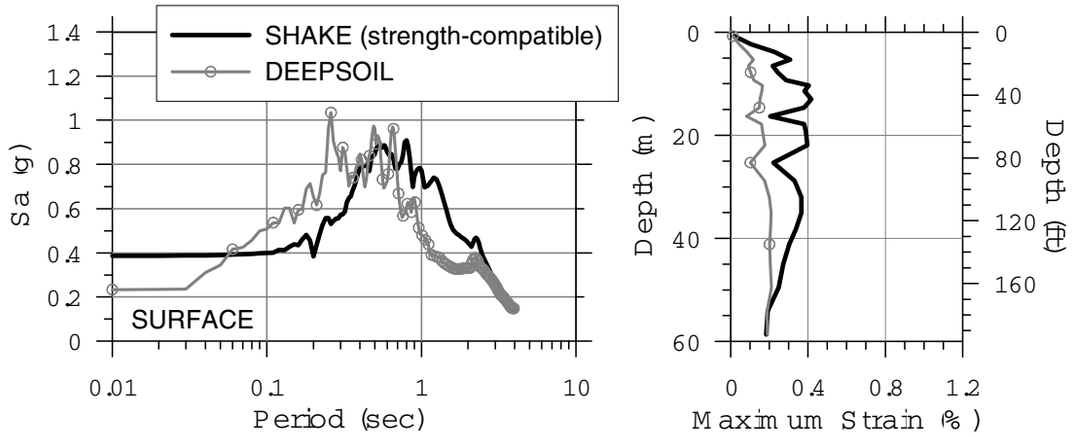


FIG. 9. Comparison of ground response results from SHAKE and DEEPSOIL.

In the SHAKE analyses, the estimated response spectrum appears to be low and "flat" for periods between approximately 0.03 and 0.4 seconds. This is a common problem with equivalent-linear modeling of strong shaking (Stewart et al. 2008). The spectra calculated from the nonlinear codes appear to estimate a more realistic response spectral shape at this period range. The lower peak ground acceleration computed in DEEPSOIL may be a result of viscous damping implemented in the model. Figure 9 also indicates that the equivalent-linear analysis computed higher shear strains than the nonlinear analysis.

Amplification factors were computed for both equivalent-linear and nonlinear analyses to facilitate comparisons to empirical amplification factors in the literature (Figure 10). The case shown is for the best estimate soil profile under the Kocaeli motion in the fault normal direction. The trough of the computed amplification factors from equivalent-linear analyses at periods between 0.03 and 0.4 seconds is not a feature shared by empirical estimates nor the nonlinear analysis results. The comparison between equivalent-linear

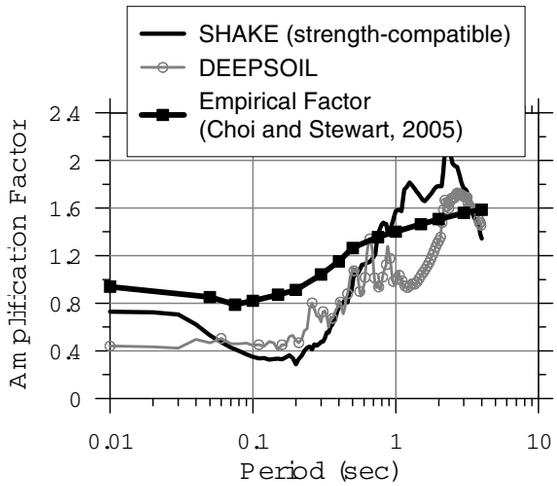


FIG. 10. Comparison of empirical and theoretical amplification factors.

and empirical amplification factors shows generally good agreement for the peak ground accelerations and at periods greater than 0.4 seconds. For the period range of interest for the structures considered in the soil-structure interaction analyses for the project (approximately 0.5 to 2 seconds), the computed response spectra demonstrate reasonable agreement with the empirical model, which establishes some degree of confidence in the results.

CONCLUSIONS

This paper outlines the site response analysis procedure and example results for the SVRT project. We describe key issues including the representation of velocity variability in consideration of variable stratigraphy and the randomness of velocity conditional on depth and soil type, the selection of appropriate modulus reduction and damping curves, and the use of equivalent-linear versus nonlinear methods of analysis. The following conclusions were made:

1. In the absence of site specific modulus reduction and damping curves, predictions using the curves predicted by Darendeli (2001) appear appropriate for shear strains less than approximately 0.1%-0.3%.
2. The curves predicted by Darendeli underestimate the shear strength of the onsite materials at shallow depths, which in turn leads to unrealistically large shear strains computed by the equivalent-linear method.
3. A limit to the backbone curve based on shear strength data provides more realistic modeling of large strain behavior. Darendeli-based stress-strain curves can be modified with a hyperbolic interpolation function to predict large strain response.
4. When strength-compatible nonlinear curves are used, the predicted shear strains computed by equivalent-linear analyses are consistent with expected values.
5. The estimated response spectra from SHAKE appear to be low for periods between approximately 0.03 and 0.4 seconds. This is a common problem with equivalent-linear modeling of strong shaking.
6. The peak ground accelerations and spectral accelerations for periods greater than 0.4 sec computed by our equivalent-linear analyses are relatively consistent with those predicted by empirical relationships, which established a degree of confidence in the results.

REFERENCES

Baker, J.W. and Cornell, C.A. (2003). "Uncertainty specification and propagation for loss estimation using FOSM methods," *Proceedings, 9th Int. Conf. on Applications of Statistics and Probability in Civil Engineering (ICASP9)*, San Francisco, California: Millpress. 8 p.

Bommer, J.J. and Alarcon, J.E. (2006). "The Prediction and Use of Peak Ground Velocity," *Journal of Earthquake Engineering*, 10(1), 1-31.

Choi, Y. and Stewart, J.P. (2005). "Nonlinear site amplification as function of 30 m shear wave velocity," *Earthquake Spectra*, 21 (1), 1-30.

Darendeli (2001). "Development of a new family of normalized modulus reduction and material damping curves," *Ph.D. Dissertation*, Dept. of Civil Engineering, Univ. of Texas, Austin, TX.

Hashash, Y.M.A. and Park, D. (2001). "Non-linear one-dimensional seismic ground motion propagation in the Mississippi embayment." *Engrg. Geology*, 62(1-3), 185-206.

Hashash, Y.M.A. and Park, D. (2002). "Viscous damping formulation and high frequency motion propagation in nonlinear site response analysis." *Soil Dynamics and Earthquake Engrg.*, 22(7), 611-624.

Park, D. and Hashash, Y. M. A. (2004). "Soil damping formulation in nonlinear time domain site response analysis." *J. of Earthquake Engrg.,* 8(2), 249-274.

Idriss, I.M. and Sun J.I. (1992). SHAKE91: A computer program for conduction equivalent-linear seismic response analyses of horizontally layered soil deposits, Center for Geotechnical Modeling, Univ. of California, Davis.

Ishihara, K. (1981). "Strength of Cohesive Soils Under Transient and Cyclic Loading Conditions," *State-of-the-Art in Earthquake Engineering*, 154-169.

Kramer, S.L. and S.B. Paulsen (2004). "Practical use of geotechnical site response models," *Proc. Int. Workshop on Uncertainties in Nonlinear Soil Properties and their Impact on Modeling Dynamic Soil Response*, PEER Center Headquarters, Richmond, CA.

Ladd, C.C. (1991). "Stability evaluation during staged construction: 22nd Terzaghi Lecture." *Journal of Geotechnical Engineering*, ASCE, 117(4), 537-615.

Masing, G. (1926). "Eigenspannungen and verfertigung beim messing," *Proc. 2nd Int. Congress on Applied Mechanics*, Zurich.

ShakeEdit Software (2007), SHAKE2000, Version 3.0.0. Lacey, WA.

Sheahan, T.C., Ladd, C.C. and Germaine, J.T. (1996). "Rate-dependent undrained shear behavior of saturated clay." *Journal of Geotechnical Engineering*, ASCE, 122(2), 99-108.

Stewart. J.P. Kwok, A.O.L. (2008). "Nonlinear Seismic Ground Response Analysis: Code Usage Protocols and Verification against Vertical Array Data," *Proc. 4th Decennial Geotechnical Earthquake Engineering and Soil Dynamics Conference*, ASCE, Sacramento, CA.

Hsu, C. and Vucetic, M. (2002). "Dynamic and Cyclic Behavior of Soils over the Wide Range of Shear Strains in NGI-type Simple Shear Testing Devices," *Research Report*, Dept. of Civil Engineer, University of California, Los Angeles, ENG-02-228.

Weiler, W.A. (1988). "Small strain shear modulus of clay," *Proceedings, ASCE Conference on Earthquake Engineering and Soil Dynamics II: Recent Advances in Ground Motion Evaluation*, Geotechnical Special Publication 20, ASCE, New York, 331-335.

Development and Verification of A Pseudo-Static Solution for Evaluation of Seismic-Induced Deformations of Rectangular Tunnels

Hongbin Huo, Ph.D., P.E.
Earth Systems Southwest, Indio, CA.

ABSTRACT

An iterative procedure is proposed to estimate seismic-induced distortions in cut and cover rectangular structures. The procedure is based on an existing analytical solution for deep rectangular structures. The existing solution assumes elastic behavior of soil and structure, tied contact at soil-structure interface, and static loading. The new procedure builds on the analytical solution and approximates dynamic response with a pseudo-static analysis, and soil-stiffness degradation through an iterative procedure where the soil's shear modulus is changed in each iteration based on the shear strain of the soil obtained in the previous iteration. Predictions obtained from the analytical solution have been verified by a series of numerical tests which include the response of the Daikai station during the 1995 Kobe earthquake. The relative errors in terms of deformation between analytical and numerical results are less than 15%.

1. INTRODUCTION

As an integral part of the infrastructure of modern society, tunnels are used for a wide range of applications, including storage, sewage, water transport, and in transportation systems such as subways and railways. The support of tunnels in seismic zones must be designed for static overburden loads as well as for additional deformations imposed by earthquakes. Seismic-induced deformations can be produced by ground failure or by ground shaking. Ground failure includes several types of ground instability such as direct shearing displacements of active faults intersecting the structure, landslides, liquefaction of the surrounding ground, and tectonic uplift and subsidence. Ground shaking refers to the vibration of the ground produced by seismic waves propagating through the ground. The waves most damaging to underground structures are shear waves which produce racking or ovalization of the structure (Hashash et al., 2001). There are two basic approaches in present seismic design of underground structures. One approach is to carry out dynamic, non-linear soil-structure interaction analysis using finite element methods. The input motions in these analyses are time histories emulating design response spectra, and the input motions are applied to the boundaries of a "soil island" to represent vertically propagating shear waves. The second approach assumes that the seismic ground motions induce a pseudo-static loading on the structure. This approach allows for the development of analytical relationships to evaluate the magnitude of seismic-induced strains in underground structures.

A closed-form solution for rectangular tunnels has been developed by Huo et al. (2006). The development of the solution is based on complex variable theory and conformal mapping techniques, and relies on the following assumptions: (1) deep rectangular structure inside an infinite medium; (2) plane strain conditions in any

transverse section perpendicular to the longitudinal axis of the structure; (3) homogeneous and isotropic ground; (4) elastic response of structure and surrounding ground; (5) pseudo-static analysis. The solution gives the normalized deformation of a rectangular structure in an infinite elastic medium subjected to a far field shear stress (Figure 1).

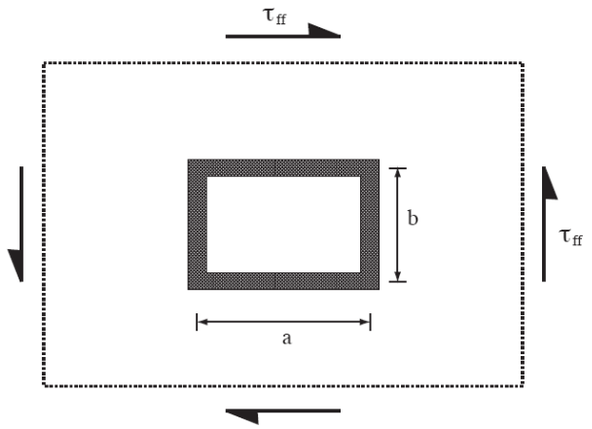


Figure 1. Rectangular Structure in an Infinite Medium

The structure deformations are given by:

$$\frac{\Delta_{stru.}}{\Delta_{ff}} = (1-\nu_s^2)\left\{N\,\Delta_{p_2^i} + \left[M\,\Delta_{p_2^i} + \Delta_{\tau^i}\right]L\right\}\frac{G}{b} \tag{1}$$

where $\frac{\Delta_{stru.}}{\Delta_{ff}}$ is the structure's racking deformation normalized by the free field ground deformation; ν_s is the Poisson's ratio of the structure; G is the shear modulus of the ground and b is the height of the structure. Because of the symmetry of the problem, the stress distribution around the structure is as depicted in Figure 2a. The shear stress τ^i is constant along the perimeter of the structure and the normal stress has a linear distribution along the four sides of the rectangle with a maximum magnitude p_1^i along the side of length "a" and p_2^i along the height "b". Because of moment equilibrium, $p_1^i a^2 = p_2^i b^2$. A positive sign of the normal stress denotes compression whereas a negative sign denotes tension (decompression given the initial static loading due to the overburden). Δ_{τ^i} is the deformation of the structure due to a unit shear stress τ^i, and $\Delta_{p_2^i}$ is the deformation of the structure due the linear normal stress distribution (Figure 2a) with $p_2^i = 1$ and $p_1^i = (b/a)^2$. The values of Δ_{τ^i} and $\Delta_{p_2^i}$ can be obtained analytically or numerically from structural analysis.

The structure's deformation Δ_{stru} is the difference between the displacements of the top and bottom of the structure (see Figure 2b), and is equal to:

$$\Delta_{stru} = (1-\nu_s^2)\left(\tau^i\,\Delta_{\tau^i} + p_2^i\,\Delta_{p_2^i}\right) \tag{2}$$

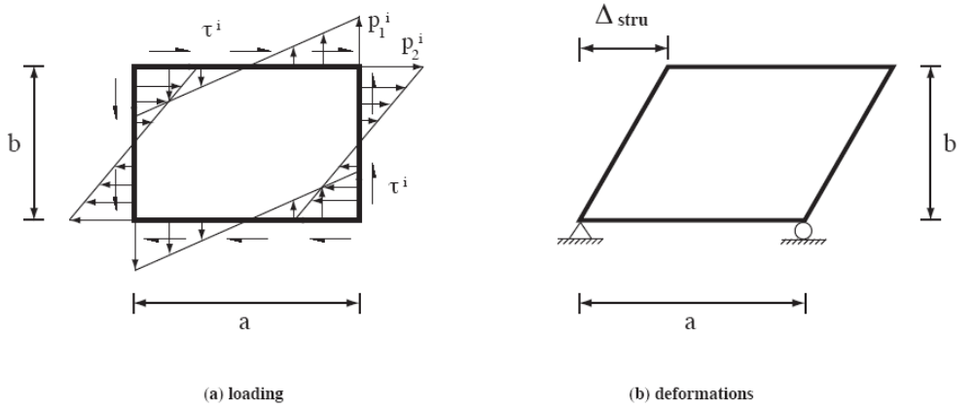


Figure 2. Structure Loading and Deformations

The parameters M and N in equation (1), which are quite complex in mathematical expressions and depend on the Poisson's ratio of the ground ν and on the aspect ratio λ = a/b of the structure (Bobet et al., 2008), are given in Figure 3.

The parameter L is defined as:

$$L = -\frac{(1-\nu_s^2)\, N\, \Delta_{p_2^i} - \frac{a}{G} F_1}{(1-\nu_s^2)\left(M\, \Delta_{p_2^i} + \Delta_{\tau^i}\right) - \frac{a}{G} F_2} \tag{3}$$

where F_1 and F_2 can be found from Figure 4. F_1 and F_2 are also a function of ν and λ.

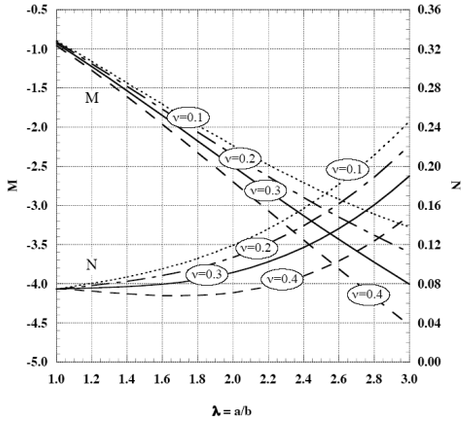


Figure 3. Parameters M and N

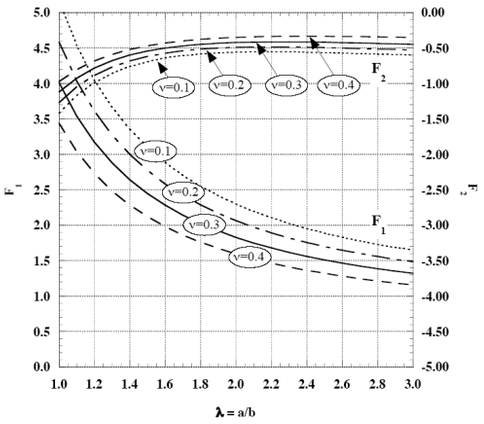


Figure 4. Parameters F_1 and F_2

Huo (2005) provided extensive comparisons between predictions obtained with the analytical solution and results from numerical simulations using Finite Element Methods.

The comparisons show that the analytical solution provides accurate results with errors typically within a 2-8% range. The author also showed that the normalized structure displacement is independent of the absolute size of the structure; in other words the normalized displacement depends on $\lambda = a/b$, the ratio of length to height of the structure, which is a measure of the shape of structure. It was shown that the normalized displacement depends on the relative stiffness between the structure and the surrounding ground, and not on the absolute stiffness of the structure or the ground. A practical method is proposed where the analytical solution is combined with an iterative scheme to account for the ground shear modulus degradation with cyclic loading. The equivalent linear approximation of soil properties is taken to express nonlinearity of the shear modulus and damping. The values of these moduli are assumed to be the function of shear strain amplitude and determined by iterations to be consistent with a level of strain, which is called the effective strain. The proposed method does incorporate this procedure through iteration. The new method is validated with comparisons with numerical simulations of the seismic responses of the Daikai station in Kobe, Japan.

2. DESCRIPTION OF THE METHOD

The first step in the method is to obtain the earthquake induced free field ground deformations at the locations where the top and bottom of the structure are. The free field ground deformations are: $\Delta_{ff} = \gamma_{ff}\, b = \tau_{ff}\, b/G$, where G is the ground shear modulus, b is the height of the structure, and τ_{ff} and γ_{ff} are the far field ground shear stress and shear strain, respectively. The shear modulus, shear stress and strain are those computed at the center of the structure. The far field shear strain can be obtained from ground response analyses. The computer program SHAKE (Schnabel et al., 1972) is widely employed to estimate the free field soil deformations for various types of ground and for any given ground motion. The normalized structure deformation can thus be obtained from equation (1), given the structure's shear and normal compliances Δ_{τ^i} and $\Delta_{p_2^i}$ and the aspect ratio λ, and the ground's shear modulus G and Poisson's ratio ν.

The analytical formulation is based on the assumption that both the ground and the structure behave elastically. This may be acceptable for a well designed structure since one may expect little damage during the earthquake and thus a small reduction of the stiffness of the structure. It has to be noted that if the structure moves into its non-linear regime the degradation of the structure's stiffness may be significant and thus the assumption may introduce large errors (a similar methodology to that proposed for the soil could also be used). The change of soil's stiffness with structure deformations can be introduced in the formulation by an iterative process. The stain-compatible shear modulus of the soil, which is adjusted depending on the ground deformations obtained in the previous iteration, is then input into the equations. The process ends when the shear modulus used in the last iteration corresponds to the ground deformations.

Figure 5 shows the flowchart for the iterative procedure. It is summarized in the following steps:

1. Obtain the free field ground deformation Δ_{ff} at the location of the center of the structure. The free field ground deformation can be obtained from ground response analyses; e.g. SHAKE.
2. Compute the structure compliances Δ_{τ^i} and $\Delta_{p_2^i}$ and the aspect ratio λ. This can be done from structural analysis, or through equations (Huo et al. 2006).
3. Compute parameters M, N, and L as described earlier. The value of the ground's shear modulus is that obtained from step 6 in the previous iteration. An initial guess is needed to start the iteration process.
4. Find the structure deformation $\Delta_{stru.}$ from equation (2), given Δ_{ff} from step 1.
5. Determine the shear strain of the ground close to the structure. The volume of ground that determines the structure response is the ground "attached" to the structure, which moves with the structure (Huo et al., 2005); thus $\gamma = \Delta_{stru.}/b$.
6. Update the ground shear modulus. The shear modulus is obtained from the G-γ curve of the soil (e.g. Seed et al., 1986), given the magnitude of the shear strain found in step 5.
7. Evaluate the difference between strains computed in the current and previous iterations. If the differences are small (e.g. error, $\varepsilon < 1\%$), convergence has been reached and the iteration process is completed. The structure deformation is that obtained in step 4. If the differences are larger than the maximum error allowed, a new iteration is attempted with the updated shear modulus of the soil. In the cases presented in the paper convergence has been always found stable.

3. VERIFICATION OF THE METHOD WITH DAIKAI SUBWAY STATION

The Daikai station, a cut and cover rectangular structure with central columns in the subway system in Kobe, collapsed during the Hyogoken-Nambu (Kobe) earthquake of January 17, 1995 in Japan. Three different sections can be distinguished in the station (Figure 6): Section 1, which is the section that collapsed during the earthquake; Section 2, the running tunnels between stations; and Section 3, the two-story access structure.

Section 1 (Figure 6a) was a rectangular reinforced concrete box structure, 7.17 m high and 17.0 m wide, with a soil cover of 4.8 m above the top of the structure (Shawky and Maekawa, 1996). The central columns had rectangular cross section of 0.4 m by 1.0 m with axial spacing of 3.5 m in the longitudinal direction. The thickness of the lateral wall was 0.7 m, and of the top and bottom slabs 0.8 m and 0.85 m, respectively. The running tunnel (Figure 6b) was also a rectangular reinforced concrete box structure 6.36 m high, 9.0 m wide, with a 5.2 m of soil cover. The central columns of the running tunnel had cross sections of 0.4 m by 0.6 m with axial spacing of 2.5 m in the longitudinal direction. The thickness of the lateral walls and the top slabs was 0.4 m and of the bottom slab 0.44 m. The access station, Section 3, had 2 levels (Figure 6c). The section was 10.12 m high, 26.0 m wide with an average of 1.9 m of soil cover. The central columns were identical to those of Section 1. The thickness of the lateral walls was 0.5 m, of the

top slab 0.75 m, and of the bottom slab 0.85 m at the center and 0.55 m at the sides. The thickness of the middle slab was 0.35 m.

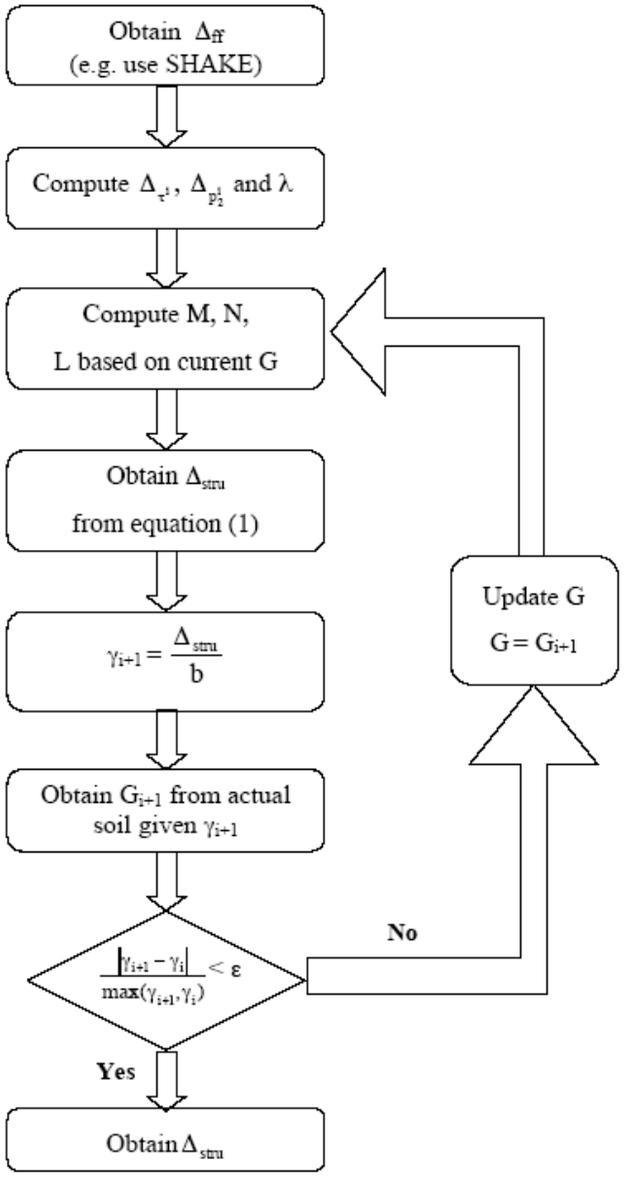
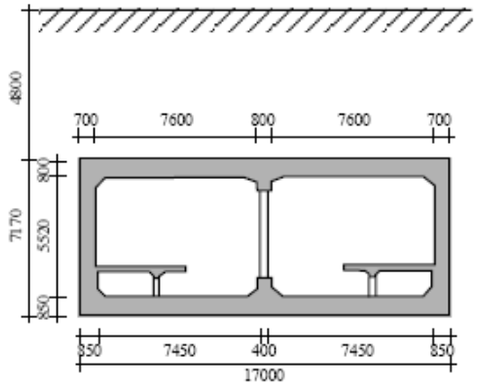
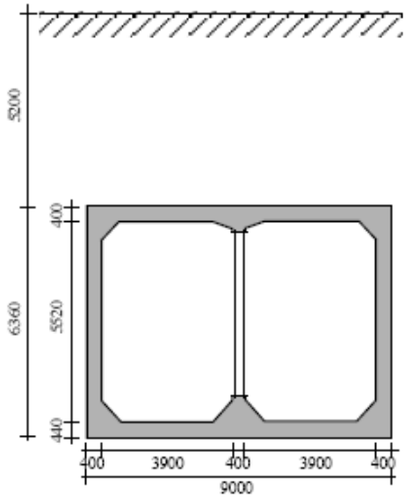


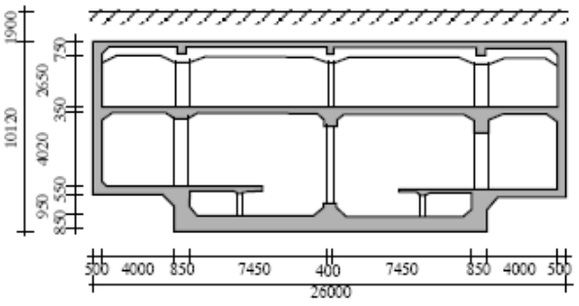
Figure 5. Iterative procedure for computing structure deformations



(a) Section 1 (collapsed station)



(b) Section 2 (tunnel)



(c) Section 3 (access)

Figure 6. Cross Sections of the Daikai Station
Dimensions in mm

For the analytical solution, the dimensions of the structure used are those of Figure 6. The aspect ratios of each section, $\lambda = \frac{a}{b}$, are: for Section 1, λ = 2.82; for Section 2, λ = 1.48; and for Section 3, λ = 2.93. The dimensions "a" and "b" are measured from wall to wall which are the interior dimensions of the structure. The elastic propoerties of the structure elements are the same as those used for the numerical analyis, with the Young's modulus of the central colum in each section reduced accordingly to approximate a 3D response. The deformations of the structure with a unit shear and a unit normal, Δ_{τ^i} and $\Delta_{p_2^i}$, are obtained from structural analysis numerically, and are for Section 1: Δ_{τ^i} = 0.6 and $\Delta_{p_2^i}$ = 0.092; for Section 2: Δ_{τ^i} = 0.76 and $\Delta_{p_2^i}$ = 0.23; and for Section 3: Δ_{τ^i} = 0.62 and $\Delta_{p_2^i}$ = 0.08. The small-strain shear modulus of the ground is obtained at the center of each structure, and it is G_{max} = 97 MPa for Sections 1 and 2, and 94 MPa for Section 3. The freefield soil deformations due to the Kobe earthquake are obtained from the ground response analyses using the program SHAKE 91 (Idriss and Sun, 1992), given actual soil properties and input accelerations. Effective free field soil strains calculated with SHAKE were used. The free field ground deformations obtained at the center of each section are 14 cm, 12 cm, and 19 cm for Sections 1, 2 and 3, respectively. The structure deformations for each section are obtained following the proposed iterative method (Figure 5). The final horizontal structure (column) deformations of Sections 1, 2 and 3 are 3.8 cm, 3.5 cm and 2.1 cm, respectively.

The structure deformations for each section are obtained following the proposed iterative method (Figure 5). The procedure followed to obtain the solution for Section 1 is included in Appendix I as an example; the same process is repeated for sections 2 and 3. The proposed method iterates not only to satisfy equation (1), but also to incorporate the equivalent linear method to capture nonlinear cyclic response of soil. SHAKE result is only used in the initial iteration as a starting point for initial condition. The shear modulus reduction of the soil with shear strain is taken from Figure 7, which also shows the increase of damping with shear strain (data from Seed et al., 1986; and Vucetic and Dobry, 1991). Note that the comparison between the model and numerical experiments is good. The final horizontal structure (column) deformations of Sections 1, 2 and 3 are 3.8 cm, 3.5 cm and 2.1 cm, respectively.

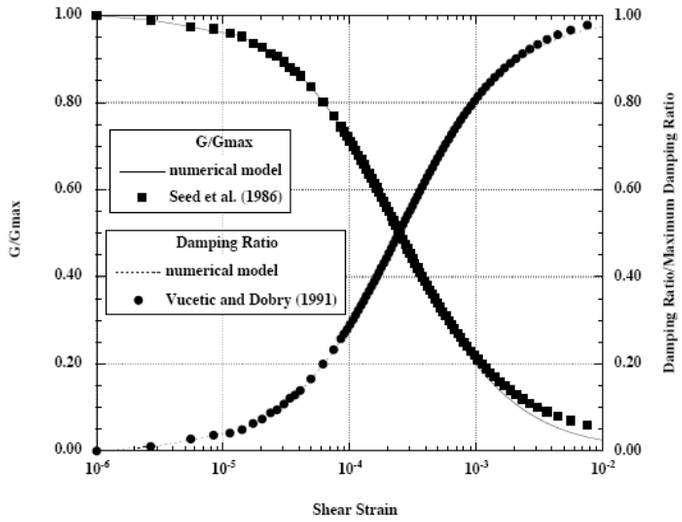


Figure 7. Shear Modulus Reduction and Damping Increase with Strain

Extensive numerical modeling of each of the sections and the surrounding soil was carried out by Huo (2005) employing finite element program ABAQUS (2002) to investigate the load transfer mechanisms between the structures and the soil and to identify the causes for the observed different behavior of the sections during the earthquake. In essence each of the three sections of the Daikai station was placed inside a large discretization of the soil medium with the lateral boundaries far enough from the structure to minimize their influence on the structure. Dynamic transient analyses were carried out in ABAQUS. The actual acceleration recorded at Kobe earthquake was input at the bottom of the discretization. The soil properties used for the model were obtained from shear wave velocity and SPT measurements at the site. Elastoplastic, hysteretic user defined nonlinear soil model was utilized in the numerical analyses (Huo, 2005). Analogous simulations were conducted for Sections 2 and 3. Table 1 shows the maximum central column distortion for each section. The analytical results compare well with the numerical results by ABAQUS, which are 4.0 cm, 3.1 cm and 2.2 cm respectively (Table 1). The differences between the analytical and numerical results are 5%, 12.9% and 4.5%, well within the degree of accuracy expected given the uncertainties involved in this analysis.

Table 1. Predicted Column Distortions. Comparison between Numerical and Analytical Models. Values in cm.

Station	Numerical	Analytical	Error (%)
Daikai, Section 1	4.0	3.8	5.0
Daikai, Section 2	3.1	3.5	12.9
Daikai, Section 3	2.2	2.3	4.5

It is important to point out that the $\Delta_{stru}/\Delta_{ff}$ ratios obtained (e.g. 3.8/14 = 0.27 for Section 1, 0.29 and 0.11 for Sections 2 and 3, respectively) result in structural deformations significantly lower than the free-field. Thus the proposed method is a considerable improvement of current analytical methods which suggest that underground structures behave as flexible members that follow free field deformations.

4. SUMMARY AND CONCLUSIONS

An iterative scheme is presented in this paper to estimate deformations of cut and cover rectangular structures during earthquakes. The method is based on an existing analytical solution for deep rectangular structures in an elastic medium (Huo et al., 2006), and on previous work on the failure of the Daikai station in Japan during the 1995 Kobe earthquake (Huo et al., 2005). The previous research found that the relative stiffness between the soil and the structure was the parameter that controlled structure deformations during an earthquake, and that the presence of a structure stiffer than the surrounding soil significantly constrained the deformations of the soil adjacent to the structure. The existing analytical solution has been modified by including an iterative procedure where the ground shear modulus is reduced based on the deformations of the structure (e.g. equivalent linear method). The iteration scheme is completed when the ground stiffness used as input in the analytical solution matches the stiffness that the ground should have with the deformations predicted by the solution. In the scheme the deformations of the ground are taken as those of the structure since the ground-structure interface is assumed tied, and the ground adjacent to the structure controls the deformations of the structure.

Three cases are used for verification of the proposed solution: the three sections of the Daikai station (Sections 1, 2, and 3). The three cases are analyzed with a dynamic numerical method with an elasto-plastic hysteretic soil model, using actual ground motions recorded during the Kobe earthquake of 1995 for the Daikai station. The same three cases are also analyzed using the analytical solution with the iterative scheme, with free field ground deformations obtained at mid depth of the structure, given the actual ground motions and ground properties at each of the sites. Comparisons between the numerical and the analytical results show that the deformations are well predicted by the analytical method, with differences within 5-15%.

Given the level of accuracy provided by the analytical solution and the number of cases investigated for its verification, it can be concluded that the solution proposed is a good approximation for a preliminary seismic design of underground structures, in particular where deformations need to be estimated. The solution, taking into consideration the level of uncertainty that still exists for predicting the response of ground and structure during cycles of loading, should be viewed as a first approximation and not as a replacement of detailed dynamic numerical models. Additional verifications should be made with other structures and earthquake input motions with a sufficiently large and diverse number of cases.

APPENDIX I

Calculations of deformations of Section 1 of the Daikai station during the Kobe earthquake are included as an example. Calculation steps follow the procedure depicted in Figure 5.

1. Free field ground deformations are computed from the effective shear strain at the mid-depth of the structure using the computer code SHAKE 91. Δ_{ff} = 14 cm.
2. Structure compliances are obtained from numerical analysis of the cross section of the structure by imposing unit shear and normal loads. Thus, Δ_{τ^i} = 0.6 and $\Delta_{p_2^i} = 0.092$. λ = 15.6 m/5.52 m = 2.82.
3. Soil and structure Poisson's ratios: $\nu = 0.35$, $\nu_s = 0.15$.
   From Figure 3, M = -3.941, N= 0.145
   From Figure 4 and equation (3), L = 0.65. It is assumed in the first iteration that $G = G_{max}$ = 97 MPa. Note that L depends on G and changes with iterations.
4. From equation (1), $\frac{\Delta_{stru.}}{\Delta_{ff}} = 2.881$. Thus $\Delta_{stru.}$ = 40.34 cm.
5. $\gamma_1 = \frac{\Delta_{stru.}}{b} = 0.073$.
6. A shear modulus G_1 = 0.16 MPa is obtained from the G-γ curve (Figure 7), given the magnitude of the shear strain γ_1.
7. A new iteration is attempted with $G = G_1$ = 0.16 MPa. New iterations are performed with updated shear modulus until the error is small. All iterations are included in Table A.1. The final structure deformation is 3.8 cm.

The number of iterations could be significantly reduced with a better estimate of the final shear modulus in the first iteration. In the example $G = G_{max}$ was taken as the starting value. For strong ground motions it is unlikely that the soil deformations are going to be that small. In general smaller number of iterations may be attained with the initial guess $G = 0.5\ G_{max}$.

Table A. 1. Iterations for Section 1 of the Daikai station

Iteration	γ_i	G_i (MPa)	$\frac{\Delta_{stru}}{\Delta_{freefield}}$	Δ_{stru} (cm)	γ_{i+1}	G_{i+1} (MPa)	$\frac{\lvert\gamma_{i+1}-\gamma_i\rvert}{\max(\gamma_{i+1},\gamma_i)}$
1st	N/A	97.00	2.8811	40.34	7.31E-02	0.16	100%
2nd	7.31E-02	0.16	0.0222	0.31	5.64E-04	30.00	99%
3rd	5.64E-04	30.00	1.9636	27.49	4.98E-02	0.30	99%
4th	4.98E-02	0.30	0.0413	0.58	1.05E-03	4.60	98%
5th	1.05E-03	4.60	0.5720	8.01	1.45E-02	0.85	93%
6th	1.45E-02	0.85	0.1164	1.63	2.95E-03	2.90	80%
7th	2.95E-03	2.90	0.3642	5.10	9.24E-03	1.08	68%

8th	9.24E-03	1.08	0.1456	2.04	3.69E-03	2.70	60%
9th	3.69E-03	2.70	0.3584	5.02	9.09E-03	1.17	59%
10th	9.09E-03	1.17	0.1568	2.20	3.98E-03	2.50	56%
11th	3.98E-03	2.50	0.3350	4.69	8.50E-03	1.40	53%
12th	8.15E-03	1.40	0.1876	2.63	4.76E-03	2.30	42%
13th	4.76E-03	2.30	0.3053	4.27	7.74E-03	1.80	39%
14th	7.74E-03	1.80	0.2390	3.35	6.06E-03	2.15	22%
15th	6.06E-03	2.15	0.2854	4.00	7.24E-03	1.90	16%
16th	7.24E-03	1.90	0.2522	3.53	6.40E-03	2.10	12%
17th	6.40E-03	2.10	0.2788	3.90	7.07E-03	2.00	10%
18th	7.07E-03	2.00	0.2655	3.72	6.73E-03	2.05	5%
19th	6.73E-03	2.05	0.2721	3.81	6.90E-03	2.03	2%
20th	6.90E-03	2.03	0.2695	3.77	6.83E-03	2.04	1%
21st	6.83E-03	2.04	0.2708	3.79	6.87E-03	2.04	0%

REFERENCES:

ABAQUS (2002). *Explicit User's Manual*, Hibbit, Karlsson and Sorensen, Inc.

Bobet, A., Fernández, G., Huo, H., and Ramírez, J. (2008), A Practical Iterative Procedure to Estimate Seismic-Induced Deformations of Shallow Rectangular Structures, *Canadian Geotechnical Journal*, In press.

Hashash, Y.M.A., Hook, J.J., Schmidt, B., Yao, J.I. (2001). Seismic Design and Analysis of Underground Structures. *Tunneling and Underground Space Technology*, Vol. 16, pp. 247–293.

Huo, H. (2005). *Seismic Design and Analysis of Rectangular Underground Structures*. Ph. D. Thesis, Purdue University, West Lafayette, IN.

Huo, H., Bobet, A., Fernández, G. and Ramírez, J. (2005), Load Transfer Mechanisms between Underground Structure and Surrounding Ground: Evaluation of the Failure of the Daikai Station, *Journal of Geotechnical and Geoenvironmental Engineering*, ASCE, Vol. 131, No. 12, pp. 1522-1533.

Huo, H., Bobet, A., Fernández, G. and Ramírez, J. (2006), Analytical Solution for Deep Rectangular Underground Structures Subjected to Far-Field Shear Stresses. *Tunneling and Underground Space Technology*. Volume 21, Issue 6, November 2006, Pages 613-625.

Idriss, I.M. and Sun, J.I. (1992). SHAKE 91: A Computer program for Conducting Equivalent Linear Seismic Response Analyses of Horizontally Layered Soil Deposits. *User's Guide*, University of California, Davis, 13 pp.

Schnabel, P.B., Lysmer, J. and Seed, H.B.. (1972). *SHAKE: A Computer Program for Earthquake Response Analysis of Horizontally Layered Sites*. Report No. UCB/EERC-72/12, Earthquake Engineering Research Center, University of California, Berkeley, 102 pp.

Seed, H.B., Wong. R.T., Idriss, I.M., and Tokimatsu, K. (1986). Moduli and Damping factors for Dynamic Analyses of Cohesionless Soils. *Journal of the Geotechnical Engineering Division*, ASCE. Vol. 112, No. 11, pp. 1016-1032.

Shawky, A. and Maekawa, K. (1996). Collapse Mechanism of Underground RC Structures during Hanshin Great Earthquake. *Proceedings of the First International Conference on Concrete Structures,* Cairo, Egypt, pp. 1-17.

Vucetic, M. and Dobry, R. (1991). Effect of Soil Plasticity on Cyclic Response. *Journal of the Geotechnical Engineering Division*, ASCE. Vol. 117, No. 1, pp. 89-107.

This page intentionally left blank

Performance-Based Earthquake Engineering: Opportunities and Implications for Geotechnical Engineering Practice

Steven L. Kramer[1], M. ASCE

[1]Professor, Department of Civil and Environmental Engineering, University of Washington, Seattle, WA 98195-2700; kramer@u.washington.edu

ABSTRACT: Great advances have been made over the 40-some years in which geotechnical engineers have actively been involved in the practice of earthquake engineering. Most recently, advances have come through the development of performance-based earthquake engineering, which seeks to predict the seismic performance of structures and facilities in ways that are useful to a wide variety of stakeholders. Performance-based earthquake engineering requires the integrated, collaborative efforts of several groups of earthquake professionals, including geotechnical engineers; as such, it will affect the practice of geotechnical engineering in seismically active areas. This paper reviews the evolution of performance-based earthquake engineering, discusses the notion of performance and its description, and describes a recently developed framework for performance evaluation. The nature and effects of the many uncertainties that apply to the prediction and description of ground motions, system response, physical damage, and loss are described. The paper gives examples of different manners in which performance-based earthquake engineering can be implemented into practice. Finally, a series of challenges and opportunities presented by performance-based earthquake engineering for geotechnical engineering practitioners are identified and discussed.

INTRODUCTION

Geotechnical engineers have always based evaluation and design on their perception of performance, so the concept of performance-based engineering is, in a broad sense, nothing new. The manner in which performance is characterized, however, has become more refined over the years. In early geotechnical practice, the notion of performance was essentially binary – poor, or unacceptable, performance constituted "failure" and the lack of failure was taken as evidence of satisfactory performance. The evaluation or prediction of performance was generally based on comparison of the shear stresses required to maintain static equilibrium with the available shear strength of the soil, and expressed in terms of a factor of safety.

Design-level factors of safety were selected with consideration of uncertainty and the consequences of failure, but were also based on experience, precedent, engineering judgment, and, to varying degrees, expedience. These design-level factors of safety were generally high enough that the average induced shear stresses were limited to a small enough fraction of the average shear strength that large strains, and consequently large deformations, were avoided. While geotechnical engineers recognized that serviceability was more directly related to deformations than to stresses, the unavoidable fact that stresses could be predicted much more accurately than deformations helped support the continuing use of stress-based prediction of geotechnical performance.

As the profession has developed, however, it has become possible to define, characterize, and predict performance in ways that were not previously possible. In more recent years, the ready availability of powerful computers and development of improved numerical tools has led to greatly improved capabilities for prediction of deformations under static conditions. Commercial software packages, such as FLAC and PLAXIS, with convenient graphical interfaces are being used with increasing frequency in professional practice. The design of many important geotechnical systems, such as braced excavations, dams, foundations, and tunnels, is increasingly performed with explicit consideration of limiting static (short- and long-term) deformations.

Consideration of deformations is particularly important for earthquake-related problems. Performance-based earthquake engineering (PBEE) is a relatively new paradigm that is gaining widespread acceptance in the broad field of earthquake hazard mitigation. PBEE implies that structures and facilities can be designed and evaluated in such a way that their performance under anticipated seismic loading can be predicted. The purpose of this paper is to review the basic concepts of seismic performance, to describe a framework for the implementation of PBEE, and to describe the opportunities and implications of PBEE for geotechnical engineering practice.

PERFORMANCE IN EARTHQUAKES

The development and implementation of PBEE requires that earthquake professionals be able to define performance in terms that are understandable and useful to the wide range of technical and non-technical professionals who make decisions on the basis of performance predictions. The term “performance” can mean different things to different people. To a seismologist, spectral acceleration may be a good descriptor of the potential performance of a building subjected to earthquake shaking. To an engineer, maximum interstory drift would likely be a better descriptor of performance. To an estimator preparing a bid for repairs, crack width and spacing could be more useful measures of performance. Finally, to an owner, the economic loss associated with earthquake damage could be the best measure of performance.

These different notions of performance lead to an intuitive way of viewing the earthquake process. As illustrated in Figure 1, an earthquake produces ground motion, which leads to dynamic response of a structure. That response can lead to physical damage, and that damage leads to losses. The prediction of losses, therefore,

requires that we also be able to predict ground motion intensity, system response, and physical damage. If losses are the ultimate measure of performance (and the fact that they are usually of greatest importance to those who make the final decisions on seismic design, repair, and retrofitting efforts suggest that they should be), PBEE should focus on predicting losses as accurately, consistently, and reliably as possible. Working from the end to the beginning, the following sections describe losses and the progression of events that produce them.

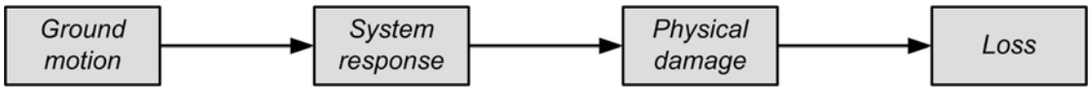


Fig. 1. Schematic illustration of the progression that leads to earthquake losses.

Losses

Loss can have many components, but they are usually divided into three categories often described informally as the "three D's" – deaths, dollars, and downtime.

Death and serious injury are certainly the worst kinds of losses, and their prevention has been the fundamental basis of seismic design since the concept of designing for earthquakes was first contemplated. While the goal of preserving life safety during earthquakes has largely been achieved in many urban areas of well-developed countries, millions of people remain at risk in the many areas around the world where, for economic, political, or other reasons, earthquake-resistant design and construction are not practiced.

The economic losses associated with earthquake damage are many, but are often divided into two categories – direct and indirect losses. Direct losses are those associated with the repair and/or replacement of structures and facilities damaged by earthquake shaking. Direct losses also include those associated with the contents of structures, which in some cases (e.g., museums, data centers, medical research laboratories, etc.) can be far more valuable than the structures that house them. Indirect losses include those associated with delayed or lost business, environmental damage, compromised infrastructure, etc.

Downtime, which refers to the period of time in which structures or facilities are unavailable for their intended use, is among the most important of indirect economic losses and can produce, for critical systems, losses that far exceed direct losses. The loss of a major bridge or water supply line in a non-redundant system, for example, can lead to inefficiencies in moving goods, services, and people or to health problems that have very real, and very high, economic consequences.

While desirable, efforts at expressing all three dimensions of loss in common terms have been understandably difficult. The most obvious metrics of loss are economic – quantities such as present value, expected annual loss, and probable maximum loss can and have been used to express performance in economic terms. Such quantities lend themselves very well to the description of direct losses. Putting

indirect losses in economic terms can be more difficult, particularly given the wide spatial and temporal scales on which earthquake damage and recovery occur, but the problem at least seems tractable. The expression of deaths and serious injuries in economic terms has long been studied, and approaches considering factors such as age and future earnings potential have been developed to address the purely economic part of the problem; the emotional and social components of such losses, however, remain unquantifiable.

Physical Damage

The various forms of loss described in the previous section result from physical damage to structures and facilities. Consider a building, for example, subjected to earthquake shaking of various intensities. At low levels of shaking, some unrestrained objects within the structure may shift or fall – this could be as innocuous as books falling from a shelf or as serious as bottles of acid falling in a laboratory; in either case, losses can occur. At stronger levels of shaking, sheetrock and interior partitions can crack, plumbing pipes can break, cover concrete can spall, and windows or cladding can break and fall, all leading to further losses. At even stronger levels of shaking, beams can crack, joints can fail, foundations can rock and settle, diagonal braces can buckle – this is structural damage, which results in even greater losses. At very strong levels of shaking, ground movement can occur, foundations can fail, welded connections can fracture, columns can lose capacity and collapse can occur – such severe physical damage can lead to extremely high losses. In order to predict the losses associated with these and other forms of physical damage, it is necessary to identify the specific form(s) of physical damage that contribute most strongly to the losses of interest, and to be able to predict the physical damage associated with the response of the system of interest.

System Response

The types of physical damage described in the preceding section occur when the response of a structure and its components, which can be expressed in terms of force/stress or displacement/strain, exceed their capacities. Structures, whether comprised of steel, concrete, or soil, are compliant and therefore respond more strongly at some frequencies than others. They exhibit generally linear behavior at very low levels of loading but can become highly nonlinear and inelastic at higher levels of shaking. Their stiffnesses can change dramatically from the beginning of an earthquake to the end and even as in the cases of liquefiable soils and damage to reinforced concrete buildings, within a given cycle of loading. Response to earthquake loading will depend on the mass, geometry, stiffness, and damping characteristics of the structure and its foundation and on the amplitude, frequency content, and duration of the ground motion. In order to predict the damage associated with structural response, it is necessary to identify the measures of response that are most closely related to damage, and to be able to predict the response caused by earthquake ground motion.

Ground Motion

The response of a compliant system can vary dramatically from one earthquake to another, and from one location to another in the same earthquake, because of differences in the intensity of the ground motion. Earthquake engineers characterize the intensity of ground motions using parameters such as peak acceleration, spectral acceleration, duration, etc. The most useful ground motion parameters are those to which the response of the system of interest is most closely related. The optimum parameters for predicting response should be recognized as being different for different types of systems.

EVOLUTION OF PERFORMANCE-BASED EARTHQUAKE ENGINEERING

The concept of PBEE is a natural extension of the basic concepts that have underlain seismic design and evaluation for many years. Even the first edition of the Structural Engineers Association of California Blue Book (SEAOC, 1959) described the intention of its lateral force requirements as ensuring that a structure would be able to resist:

- a minor level of shaking without damage (non-structural or structural),
- a moderate level of shaking without structural damage (but possibly with some non-structural damage), and
- a strong level of shaking without collapse (but possibly with both non-structural and structural damage).

In this early document, basic performance goals are specified (albeit in terms of somewhat vaguely defined levels of "damage") and different performance goals are specified for different levels of ground motion.

Early efforts at seismic design were scenario-based, i.e., based on the identification of one or more "design earthquakes" (e.g., maximum credible and maximum probable earthquakes) typically specified by source (fault), magnitude, and location. The ground motions associated with the design earthquakes were estimated deterministically, initially by heuristic specification of peak ground acceleration, but later using median values from early attenuation relationships.

A major step forward in seismic design came in the late 1970s with the publication of the ATC-3-06 (1978) report. ATC-3-06 built on the probabilistic seismic hazard analysis concepts of Cornell (1968) and the mapping work of Algermissen and Perkins (1976) to express design seismic loading in a probabilistic manner. Recognizing the dramatic differences in seismic activity across the United States, ATC-3-06 presented contour maps of effective peak acceleration (*EPA*) and effective peak velocity (*EPV*) which, together with soil profile coefficients, could be used to develop design response spectra for structures. The use of these two measures of ground motion intensity accounted for differences in the high- and low-frequency characteristics of ground motions, and the soil profile coefficient controlled spectral shape. ATC-3-06 recommended that design be based on a single level of ground shaking – that with a 10 percent probability of exceedance in a 50-yr period, i.e., a 475-yr return period. On the structural side, ATC-3-06 provided guidance for the allowance of inelastic behavior of components through the provision of ductility,

and based performance on the relationship between estimated and allowable interstory drifts. The allowable story drifts were presented for four seismic performance categories in three seismic use groups. Thus, the use of deformation-based response and capacity measures was introduced.

Subsequent U.S. building codes have maintained the basic approach of ATC-3-06 but have refined many of the details. Instead of basing design spectra on *EPA* and *EPV*, they are now based on short-period (0.2 sec) and long-period (1.0 sec) spectral accelerations. Soil effects are accounted for by more refined soil classification systems with site class coefficients that account for basic effects of nonlinear response. Design response spectra within UBC are based on 2/3 of the values of 2,475 yr (2% probability of exceedance in 50 yrs) spectral accelerations rather than 475-yr values, a change of somewhat convoluted logic that increases design requirements in areas subjected to relatively infrequent occurrence of large earthquakes (e.g., central and eastern United States) without substantially increasing them in more active areas (e.g., California).

The first document widely recognized as establishing procedures for performance-based design of new structures was the Vision 2000 report (SEAOC, 1995). Vision 2000 described procedures intended to produce structures "of predictable performance" with respect to a series of discrete hazard levels. Figure 2 shows how Vision 2000 coupled four discrete performance levels (fully operational, operational, life safe, and near collapse) with four ground motion hazard levels (frequent, occasional, rare, and very rare) for structures with performance objectives for three categories of structures (basic, essential/hazardous, and safety critical). The Vision 2000 report describes the general levels of damage to various building components and provides allowable inter-story drift limits associated with the four performance levels. These limits are expressed deterministically but are intended to be conservative; the degree of conservatism, however, is not known. Thus, Vision 2000 provides for design based on multiple levels of performance at multiple hazard levels, with performance related to deformation-related quantities (e.g., inter-story drift) that are closely related to damage.

Subsequent efforts, such as the investigations summarized in FEMA 273 (Applied Technology Council, 1996a), FEMA 274 (Applied Technology Council, 1996b), FEMA 356 (American Society of Civil Engineers, 2000), and ATC-40 (Applied Technology Council, 1996), used performance-based frameworks similar to that of Vision 2000, but differ in the manner in which performance and hazard levels are defined and in their recommended procedures for estimating force- and displacement-related demands.

In Europe, Eurocode 8 (EC 8, 2004) provides two design levels of ground motion: a damage limitation level (95-yr return period) and a no-collapse level (475-yr return period), along with importance factors for special structures (1.2 for high-occupancy structures; 1.4 for essential structures). Individual countries, however, are given a degree of flexibility in how they choose to implement certain aspects of the code. The Building Standard Law of Japan was revised in 1998 and enacted in 2000 (Kuramoto, 2006) with performance-based concepts. Two limit states are considered: a life safety limit state in which collapse of the entire structure or any floor of the structure does not occur, and a damage limitation limit state in which structural

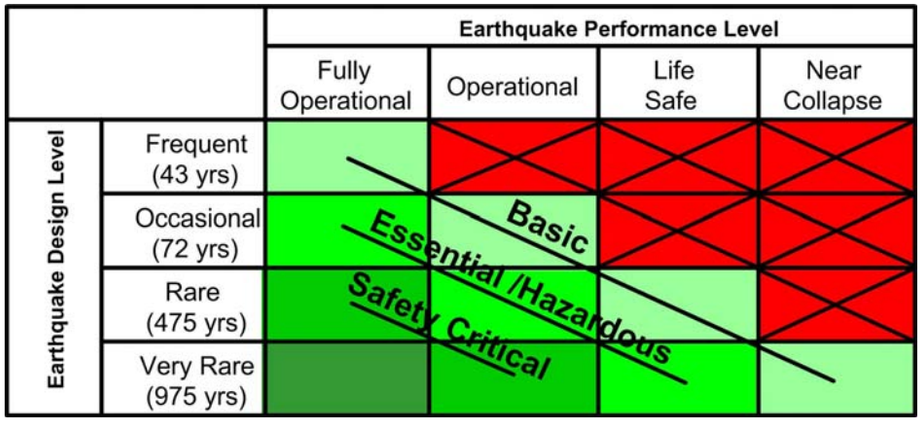


Fig. 2. Combinations of earthquake hazard and performance levels proposed by Vision 2000.

damage sufficient to cause future exceedance of the life safety limit state criterion does not occur. The life safety limit state must be satisfied for an "extremely rare" ground motion expected to occur once in approximately 500 yrs and the damage limitation limit state for a motion one-fifth as strong.

Thus, the current state of PBEE practice can be characterized by design for specific, discrete performance goals at up to about four ground motion hazard levels. The performance goals are generally expressed in terms of limiting values of response parameters (e.g., interstory drift) or, for structures, in terms of limit states (e.g., collapse). In geotechnical engineering, the ground motions associated with the design hazard levels are determined probabilistically but the response predictions and performance goals are generally deterministic. The implicit assumption is that limiting system response to certain levels will limit physical damage and losses to acceptable levels, but the actual amounts of expected damage and loss are not explicitly considered.

PERFORMANCE PREDICTION

Although the previously described PBEE frameworks are based on small integer numbers of discrete performance levels, there is no fundamental reason why performance cannot be considered on a continuous scale. Evaluations of the performance of existing structures or assessment of the performance of new structural designs require an ability to predict the anticipated performance of a structure subjected to seismic loading. As suggested by the discussion in the preceding section, performance depends on physical damage, physical damage depends on system response, and system response depends on ground motion intensity.

Terminology

In order to describe these quantities and the relationships between them, the notation developed by the Pacific Earthquake Engineering Research (PEER) Center will be adopted. The level of ground motion produced by earthquake shaking can be

characterized by one or more *Intensity Measures*, *IM*s, which could be any of a number of ground motion parameters (e.g., a_{max}, S_a, Arias intensity, etc.). The response of the system of interest (e.g., excess pore pressure, interstory drift, etc.) to the ground motion can be described by *Engineering Demand Parameters*, or *EDP*s. The physical damage associated with the response (e.g., slab cracking, wall tilt, etc.) is expressed in terms of *Damage Measures*, or *DM*s. Finally, the losses associated with the physical damage (e.g., casualties, repair cost, downtime, etc.) are expressed in a form that is useful to decision-makers by means of *Decision Variables*, *DV*.

With this basic terminology in place, the performance prediction process can be viewed as moving from ground motion (*IM*) to response (*EDP*) to damage (*DM*) and, finally, to loss (*DV*). As illustrated in Figure 3, this progression takes place through the use of three predictive models: a response model, a damage model, and a loss model. A *response model* predicts the response of a structural system due to imposed ground motion, i.e., it predicts *EDP* from *IM*. Due to the various uncertainties in ground motions, response model parameters, and the response model itself, the response prediction process must be viewed as uncertain. A *damage model* predicts the physical damage associated with a given level of response (*DM* from *EDP*). The level of damage caused by a given level of response depends on the capacity of the system and capacity is, for a number of reasons, uncertain. As a result, uncertainty is associated with the damage model. Finally, a *loss model* predicts losses from physical damage, i.e., *DV* from *DM*. Due to uncertainties in quantities and unit costs, which can be affected by uncertain factors such as future material and labor costs, interest rates, repair times, etc., considerable uncertainty also exists in loss modeling.

Estimator Characteristics

Statistical inference states that good estimators should be unbiased, consistent, robust, efficient, and sufficient. The first three of these requirements are well-known and relatively intuitive, but the latter two are important enough to consider in some detail. A variable, *A*, is an *efficient* estimator of *B* if the uncertainty in $B|A$ (e.g., $\sigma_{B|A}$) is small. For example, peak acceleration (as an *IM*) is a relatively efficient estimator of slope displacement (as an *EDP*), but duration (by itself) is not. The variable, *A*, would be a *sufficient* estimator of *B* if the uncertainty in *B* is not reduced by additional information (i.e., $\sigma_{B|A,\boldsymbol{X}} = \sigma_{B|A}$ where $\boldsymbol{X}$ is a vector of additional variables). Peak acceleration, for example, is an insufficient predictor of liquefaction potential, as evidenced by the need for a duration proxy (i.e., magnitude, in the form of the magnitude scaling factor) to enable accurate predictions of liquefaction potential. A perfectly efficient and sufficient estimator would be one to which the estimated variable is uniquely related. Such estimators do not exist in the process of moving from *IM* to *EDP* to *DM* to *DV*, but some estimators are considerably more efficient and sufficient than others. As will be shown, the benefits of working with efficient and sufficient estimators in PBEE are great enough to make their identification and use worthwhile.

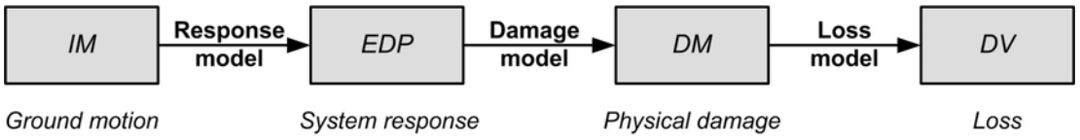


Fig. 3. Schematic illustration of performance prediction process.

THE PEER FRAMEWORK

The Pacific Earthquake Engineering Research Center (PEER) has proposed a framework for PBEE that is encapsulated in a "framing equation" formally presented in its most general form as

$$\lambda(\boldsymbol{DV}) = \iiint G(\boldsymbol{DV} \mid \boldsymbol{DM}) \left| dG(\boldsymbol{DM} \mid \boldsymbol{EDP}) \right| \left| dG(\boldsymbol{EDP} \mid \boldsymbol{IM}) \right| \left| d\lambda(\boldsymbol{IM}) \right| \tag{1}$$

In Equation (1), $G(a|b)$ denotes a complementary cumulative distribution function (CCDF) for a conditioned upon b (the absolute value of the derivative of which is the probability density function for a continuous random variable) and the bold type denotes vector quantities. From left to right, the three CCDFs result from the loss, damage, and response models; the final term, $d\lambda(\boldsymbol{IM})$ is from the seismic hazard curve. The framing equation implicitly assumes that the quantities used to describe ***IM***, ***EDP***, and ***DM*** are sufficient predictors of ***EDP***, ***DM***, and ***DV***, respectively. This triple integral can be solved directly only for an idealized set of conditions, so it is solved numerically for most practical problems; the numerical integration can be accomplished (assuming scalar parameters for simplicity) as

$$\lambda_{DV}(dv) = \sum_{k=1}^{N_{DM}} \sum_{j=1}^{N_{EDP}} \sum_{i=1}^{N_{IM}} P[DV > dv \mid DM = dm_k] P[DM > dm_k \mid EDP = edp_j] P[EDP > edp_j \mid IM = im_i] \Delta\lambda_{IM}(im_i) \tag{2}$$

where P[$a|b$] describes the probability of a given b, and where N_{DM}, N_{EDP}, and N_{IM} are the number of increments of *DM*, *EDP*, and *IM*, respectively; accuracy increases with increasing number of increments.

The PEER framework has the important benefit of being modular. The discretized framing equation (Equation 2) can be broken down into a series of components, e.g.,

$$\lambda_{EDP}(edp) = \sum_{i=1}^{N_{IM}} P[EDP > edp \mid IM = im_i] \Delta\lambda_{IM}(im_i) \tag{3a}$$

$$\lambda_{DM}(dm) = \sum_{j=1}^{N_{EDP}} P[DM > dm \mid EDP = edp_j] \Delta\lambda_{EDP}(edp_j) \tag{3b}$$

$$\lambda_{DV}(dv) = \sum_{k=1}^{N_{DM}} P[DV > dv \mid DM = dm_k] \Delta\lambda_{DM}(dm_k) \tag{3c}$$

which means that hazard curves can be computed for *EDP*, *DM*, and *DV* and interpreted in the same manner as the more familiar seismic hazard curve (for *IM*) produced by a PSHA.

The conditional probability terms in Equations (3) can be expressed graphically in the form of fragility curves (Figure 4). Using Equation (3a) as an example, the fragility curves can express the variation of mean (or median) *EDP* with *IM* and the uncertainty in *EDP*|*IM* (represented by the response dispersion, β_R). The spacing of the fragility curves (for equal increments of *EDP*) reflects the linearity of the *EDP*-*IM* relationship and the steepness of the curves indicates the uncertainty in that relationship; a perfectly vertical fragility curve would correspond to no uncertainty in *EDP*|*IM*.

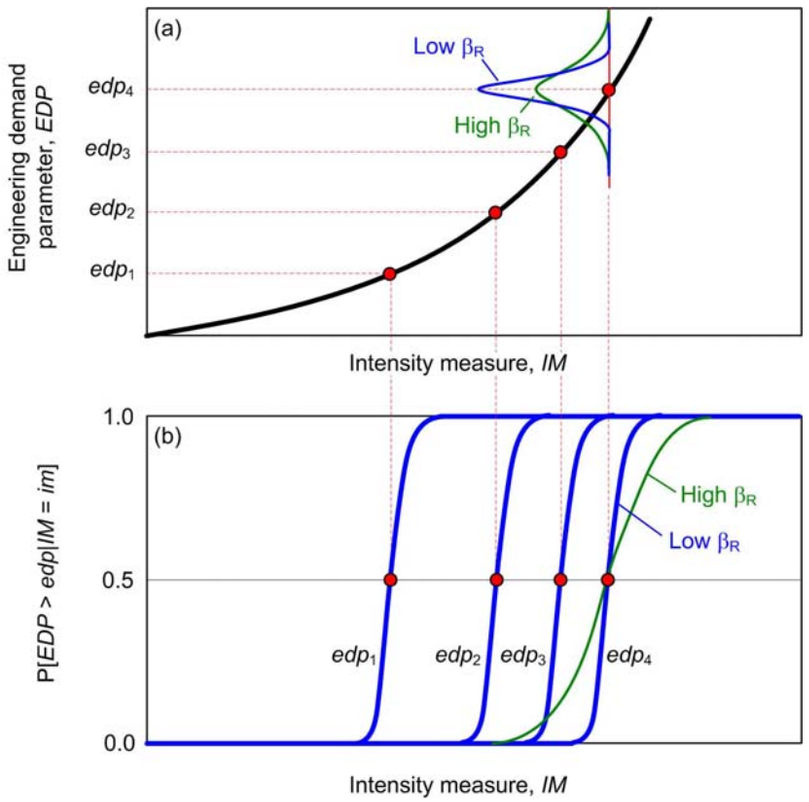


Fig. 4. Schematic illustration of relationship between (a) response relationship and (b) fragility curves. The effects of uncertainty on fragility curve shape is shown for *EDP* = edp_4.

The problem of performance evaluation can therefore be broken into four basic components – evaluation of ground motion hazard, evaluation of system response to the ground motions, evaluation of physical damage caused by the system response, and evaluation of losses associated with the physical damage. Using probabilistic response, damage, and loss models, the PEER framework allows this to be accomplished with proper consideration of uncertainty.

Randomness and Uncertainty

The PEER PBEE framework is inherently probabilistic, as evidenced by the chain of CCDFs that make up much of Equation (1). The need for probabilistic treatment is evident from previous discussion of the accuracy with which ground motions, response, damage, and losses can be predicted. The term "uncertainty" is usually used in discussions of statistical parameters and probabilistic models, but it can be helpful to distinguish between randomness and uncertainty when developing, implementing, and interpreting PBEE models.

Randomness, which is frequently described by the term "aleatory uncertainty," refers to the inherent or intrinsic variability of some quantity or phenomenon; as a result, it cannot be reduced by additional data or more thorough investigation. Randomness can manifest itself, for example, in the variability of response produced by different ground motions, even when scaled to the same *IM*. This record-to-record variability, which results from the apparently random, unpredictable nature of earthquakes, is a very significant component of the overall uncertainty in a typical PBEE investigation. Uncertainty due to lack of data or knowledge concerning the quantity or phenomenon is frequently referred to as "epistemic uncertainty." Epistemic uncertainty differs from aleatory uncertainty in that it can be reduced by the acquisition of new information, e.g., by additional data, more extensive investigation, or by new research.

The distinction between aleatory and epistemic uncertainties can be difficult, ambiguous, and confusing. In practice, the distinction often depends as much on pragmatic as theoretical concerns. While arguments can be made that all uncertainty is epistemic, practical considerations require that some be treated as aleatory; one could, for example, gain knowledge of the inherent variability of a natural soil deposit by drilling and sampling the entire site with boreholes on a six-inch spacing – an action so obviously impractical (and destructive) that it illustrates why such variability is treated as aleatory. The assignment of aleatory vs. epistemic uncertainty can also be situation-dependent. For example, uncertainty in the shear wave velocity of an existing earth dam would be characterized as epistemic if it is possible to measure it using various geophysical techniques; the shear wave velocity of a future earth dam, however, would be characterized as aleatory if the source of the fill material from which it is to be constructed is not known.

The nature of the models used to predict performance will also affect the aleatory-epistemic distinction. All predictive models should be recognized as mathematical idealizations of reality – they are not perfect. Model uncertainty, i.e., errors in model predictions, have two primary components: (a) the effect of missing predictive variables, and (b) the effects of inaccurate model form. Missing variables may be those not recognized as being influential or those that cannot be measured or otherwise characterized. Inaccurate model form may result from practical consideration of computational complexity/effort or lack of understanding of the basic physics of the problem. Both components of model uncertainty can potentially be reduced, by including additional predictive variables and/or the use of improved mathematical expressions, but there will usually be a limit to the number of variables that can be identified and/or measured or to the understanding of the physics of the

problem of interest that will limit the degree to which uncertainty can be reduced. Therefore, model uncertainty will generally have both aleatory and epistemic components. The fact that different models are frequently of different form and use different predictive variables means that they will predict different output values. The variability of mean (or median) predictions from different plausible models, therefore, represents another component of epistemic uncertainty. This situation is familiar in the context of PSHA where different attenuation relationships, for example, are used with their weighted contributions accounted for through a logic tree. To properly account for epistemic uncertainty in response, damage, and loss predictions, multiple predictive models, where available, should also be used.

The need for distinguishing between aleatory and epistemic uncertainty depends on the manner in which the results of the PBEE analysis will be used. The final result of the PEER PBEE framework is a mean annual rate of exceedance (or corresponding return period) of some loss level; the mean value is invariant with respect to the characterization of uncertainty as aleatory or epistemic. As such, that characterization doesn't matter in the end – the numerical value of the loss hazard will be the same regardless of whether some component of uncertainty is treated as aleatory or epistemic – what matters is properly capturing the total uncertainty. It should be noted that the aleatory/epistemic distinction can become important if design or evaluation is to be based on some percentile (rather than mean) loss value. In such cases, the value of interest can be sensitive to the manner in which uncertainty is divided into aleatory and epistemic components, and care must be taken to ensure that this division can be justified as fair and objective (i.e., not influenced by economic or competitive factors).

Even when the mean hazard is used, however, it is still useful to consider which components of uncertainty can and cannot be reduced and the costs and benefits of doing so. As will be illustrated shortly, increasing uncertainty tends to drive the ground motions, response, damage, and losses for a given return period higher in a performance-based evaluation. The ability to show the benefits of increased investment, for example, in additional subsurface investigation or more sophisticated response modeling, represents a tremendous opportunity for geotechnical earthquake engineering practitioners.

Idealized Performance Model

With the aid of some simplifying, but not unrealistic, assumptions, the PEER PBEE framing equation (Equation 1) can be solved in closed form (Jalayer, 2003) providing expressions that are very useful for understanding the effects of the relationships between ground motion, response, damage, and loss, and particularly of the uncertainties in those quantities on performance.

Many seismic hazard curves are nearly linear on a log-log plot, at least over significant ranges of ground motion intensity (Department of Energy, 1994; Luco and Cornell, 1998), which implies a power law relationship between mean annual rate of exceedance and *IM*, i.e.,

$$\lambda_{IM}(im) = k_0 (IM)^{-k} \tag{4}$$

In this expression, k_0 is the value of $\lambda_{IM}(im = 1)$ and k is the slope of the seismic hazard curve (in log-log space, in which Equation (4) plots as a straight line); it should be noted that the slope of the hazard curve describes the relative frequencies of low and high *IM* values, which vary from one location to another. If the response model is also assumed to be of power law form,

$$EDP = a(IM)^b \tag{5}$$

with lognormal dispersion ($\sigma_{\ln EDP|IM} = \beta_R$) that has statistically independent aleatory and epistemic components, $\beta_{R,A}$ and $\beta_{R,E}$, such that $\beta_R^2 = \beta_{R,A}^2 + \beta_{R,E}^2$, the resulting *EDP* hazard curve can be expressed as

$$\lambda_{EDP}(edp) = k_0 \left[\left(\frac{edp}{a} \right)^{1/b} \right]^{-k} \exp\left[\frac{k^2}{2b^2} \left(\beta_{R,A}^2 + \beta_{R,E}^2 \right) \right] \tag{6}$$

This equation describes the mean annual rate of exceeding some level of response, *EDP = edp*, given the seismic hazard curve, which is the result of a probabilistic seismic hazard analysis, and a probabilistic response model. It therefore considers *all* possible values of *IM* rather than only those corresponding to the small integer number of return periods considered by codes and even PBEE approaches such as that described in Vision 2000. Equation (6) is composed of two parts, the first of which is a function of *edp* and the constants (k_0, k, a, b) that describe the mean hazard curve and the median *EDP-IM* relationship (i.e., the response model). The second part depends on the slopes of the hazard curve and median response model relationship and, most significantly, on the uncertainty in the response model. The second term can be viewed as an "uncertainty multiplier" since its value is 1.0 when there is no uncertainty and becomes progressively greater than 1.0 as the response model uncertainty increases. This result shows that the mean annual rate of exceedance of a particular *EDP* value increases with increasing uncertainty. Put another way, the *EDP* value corresponding to a given mean annual rate of exceedance (or return period) increases with increasing response model uncertainty.

As an example, Figure 5(a) shows *PGA* hazard curves for downtown San Francisco at the six return periods available through the USGS National Seismic Hazard Map website (2002 maps) and an approximation of the form of Equation (4) (k_0 = 0.00015, k = -3.374) that is exact at return periods of 225 and 975 years. Figure 5(b) shows the permanent displacement of a rigid slope with yield coefficient, k_y = 0.05, in a M_w = 7 earthquake predicted by the empirical model of Bray and Travasarou (2007), and an approximation to that response in the form of Equation (5) (a = 277.1, b = 2.162). Using the closed form solution of Equation (6), slope displacement hazard curves can be computed for various levels of uncertainty in displacement given *PGA* as shown in Figure 5(c)). The displacements at each return period exceed the zero-uncertainty (β_R = 0) displacements by factors of 1.08, 1.36, 1.98, and 3.38 for β_R values of 0.25, 0.50, 0.75, and 1.00, respectively. Bray and

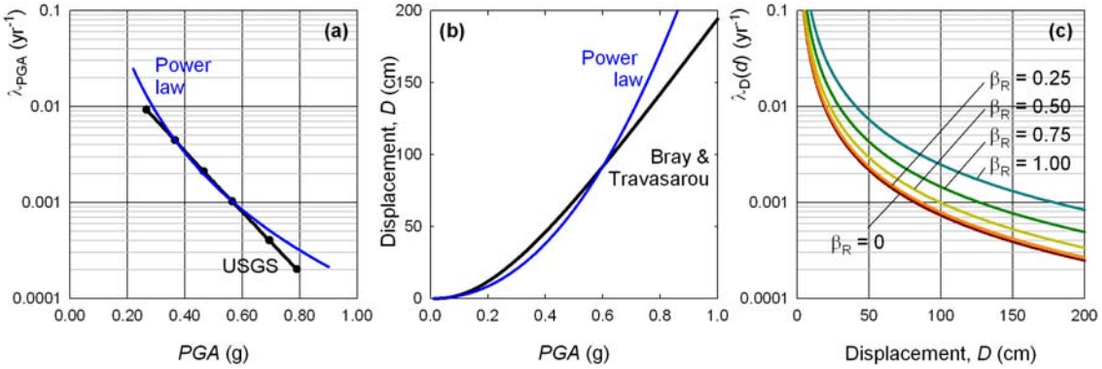


Fig. 5. Use of idealized power law models for (a) *IM* hazard curve and (b) *EDP-IM* response model to predict (c) *EDP* hazard curves for different response model uncertainties.

Travasarou (2007) indicate that β_R = 0.66 for the data on which their model was calibrated. Although a more accurate displacement hazard curve could have been obtained by numerically integrating Equation 3(a) over the USGS hazard curve using the Bray and Travasarou (2007) model, the simple idealized model shows clearly that the effect of uncertainty on response hazard is significant. While the Bray and Travasarou (2007) model is likely the most advanced empirical model available at this time, it is not the only plausible empirical model available; analysis of this problem with other empirical models would produce similar, but nevertheless different, mean (or median) response curves (Figure 5(b)) that would add additional epistemic uncertainty.

Assuming damage and loss models to also be of power law form, i.e., $DM = c(EDP)^d$ and $DV = e(DM)^f$ with lognormally distributed residuals, $\sigma_{\ln DM|EDP} = \beta_D$ and $\sigma_{\ln DV|DM} = \beta_L$, respectively, the *DV* hazard curve can be expressed in closed form as

$$\lambda_{DV}(dv) = k_0 \left[\frac{1}{a} \left\{ \frac{1}{c} \left(\frac{dv}{e} \right)^{1/f} \right\}^{1/d} \right]^{-k/b} \exp\left[\frac{k^2}{2b^2 d^2 f^2} \left(d^2 f^2 \beta_R^2 + f^2 \beta_D^2 + \beta_L^2 \right) \right] \qquad (7)$$

Again, it is apparent that the loss curve consists of a term that depends on the mean *IM* hazard curve and the median response, damage, and loss model relationships, and a second term that depends on the various uncertainties in the prediction of response, damage, and loss (and the slopes of the *IM* hazard curve and median response, damage, and loss model relationships). Increased uncertainty in any of these models will increase the mean annual rate of *DV* exceedance.

Mackie and Stojadinovich (2006) produced a Matlab program called Fourway that performs the PBEE calculations described in the previous section. The program allows users to change hazard, response, damage, and loss model characteristics (median relationships and/or uncertainties) and see the corresponding effects on response damage, and loss hazard curves in a convenient graphical format.

Numerical Solution

While the assumptions underlying the development of the closed-form solution described in the preceding section are not grossly unreasonable, they do not capture all of the details of ground motion hazard, response, damage, and loss for specific structures located at specific sites. In such cases, the PEER framing equation must be solved numerically. Given the modular nature of the framing equation, the numerical integration process can be applied three times – first, to go from *IM* to *EDP*, then from *EDP* to *DM*, and finally from *DM* to *DV*. Considering the first step, the integration can be performed as

$$\lambda_{EDP}(edp) = \sum_{i=1}^{N_{IM}} P[EDP > edp \mid IM = im_i]\Delta\lambda_{IM}(im_i) \tag{8}$$

The integration process involves two terms. The $\Delta\lambda_{IM}(im_i)$ term is a function of the seismic hazard curve, which comes from a PSHA. The PSHA can be site-specific or from the results of regional PSHAs such as those available from the USGS National Hazard Mapping Program (http://earthquake.usgs.gov/research/hazmaps/). The conditional probability term is a function of the response of the system which comes from a probabilistic response model and can be expressed in terms of fragility curves.

The procedure involves dividing the hazard curve into N_{IM} hazard intervals, determining the *IM* values at the center of each interval, and then using the response model to compute the probability of exceeding the *EDP* value of interest for each *IM* value. Summing the products of those exceedance probabilities and the hazard rate increments produces a single point on the *EDP* hazard curve at *EDP = edp*. The accuracy of the numerical integration process depends on the number of hazard rate increments – if 100 hazard rate increments were used to define 50 points on an *EDP* hazard curve, a total of 5,000 response model calculations would be required. Depending on the complexity of the response model, which could range from the algebraic equation of an empirical response model to a dynamic nonlinear finite element model, these calculations could be quite time-consuming.

Rather than run response models repeatedly for each hazard rate increment, it is more common to run a series of response analyses to define the relationship between *IM* and *EDP* and to then characterize that relationship with relatively simple functions. Two such functions are required – one to establish the relationship between median *EDP* and *IM*, and one to describe the uncertainty in *EDP*|*IM*. Two basic procedures can be followed:

1. A suite of ground motions can be scaled to a common *IM* value and applied to the response model to predict *EDP*s. The fact that the computed *EDP* values are not all the same is an indication of the record-to-record variability that is inherent in earthquake ground motions. By repeating this process for a number of *IM* values (with due consideration of dominant source characteristics in selection of the motions corresponding to each *IM* value), a plot with a series of "stripes" of response data (Figure 6(a)) can be generated.

Median values of *EDP* for each stripe can be used to establish a median *EDP-IM* relationship, and the distributions of residuals at each *IM* level can be used to characterize uncertainty in *EDP*|*IM*; it is common for *EDP*|*IM* values to be characterized as lognormally distributed.

2. A series of ground motions spanning a wide range of *IM* values (again selected with consideration of source characteristics) can be identified and used as input to a series of response analyses. The resulting *EDP* values form a "cloud" of data points on a plot of *EDP* vs. *IM* (Figure 6(b)). Regression techniques can be used to establish a median *EDP-IM* relationship and the residuals of the regression can be analyzed to characterize the distribution of *EDP*|*IM*.

Both approaches allow estimation of parameters describing the conditional distribution of *EDP* given *IM*, i.e., the development of fragility curves. The stripes approach is generally more efficient when considering a single *IM* level, and the cloud approach when multiple *IM* levels are considered (Mackie and Stojadinovich, 2006); the use of multiple stripes, however, allows improved characterization of *IM*-dependent dispersion, which can be significant over the wide range of *IM*s considered in a PBEE analysis (Baker, 2007).

Implementation of PBEE

The basic concepts of PBEE described in this paper can be implemented into engineering practice in a number of different ways. The modular nature of the PEER framing equation lends itself to different levels of implementation. In the simplest approach, PBEE could be implemented at the response level, i.e., by specifying performance in terms of *EDP* values at different response hazard levels (or response return periods); this approach would involve the application of Equation 3(a). An intermediate approach would be to specify performance in terms of damage limit states, which involves the comparison of demand (response) and capacity; this approach would involve prediction of *DM*s with the use of Equations 3(a) and 3(b). The most complete level of implementation would be to involve the definition of performance in terms of losses (*DV*s), which would involve Equations 3(a) – 3(c), i.e., the entire PEER framing equation (Equation 2). These levels of implementation are described in the following sections.

Response-Level Implementation

A response-level implementation of PBEE would allow evaluation of the mean annual rate of exceedance (or return period) of various levels of response. By combining the results of a PSHA with a probabilistic response model, this approach would provide a more consistent and objective evaluation of seismic response hazards than current procedures (which consider a single level of ground motion at a time).

Performance-based procedures for liquefaction hazard evaluation have been developed (Marrone et al., 2003; Kramer and Mayfield, 2005; 2007) and permanent slope displacements (Travasarou et al., 2004). Kramer and Mayfield (2007)

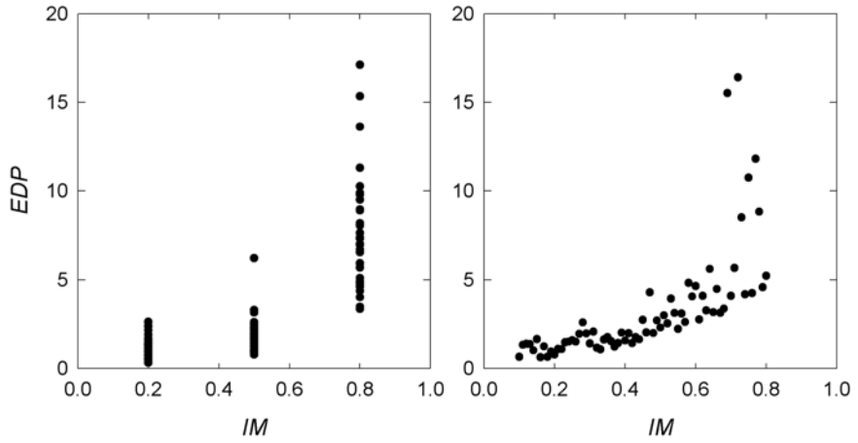


Fig. 6. Schematic illustration of (a) "stripes" approach, and (b) "cloud" approach to *EDP*|*IM* characterization.

described a performance-based procedure for evaluating liquefaction potential that resulted in factor of safety hazard curves (Figure 7) that account for all *PGA* levels and all magnitudes that contribute to those *PGA* levels, thereby rendering the question of which magnitude (mean or mode) to base magnitude scaling factor calculations on moot. Comparison of these hazard curves with factors of safety computed using conventional procedures (i.e., using one *PGA* level and one corresponding magnitude value) showed that typical designs (in this case, assuming FS_L = 1.2 for 475-yr *PGA* and mean magnitude) using conventional procedures produced highly variable actual likelihoods of liquefaction (i.e., return periods of liquefaction itself ranging from about 350 to 600 yrs) in different seismic environments. Basing design on a particular return period for liquefaction (Kramer et al., 2006) would provide more uniform performance than the current process of basing it on a deterministic factor of safety computed for a single ground motion hazard level.

Damage-Level Implementation

Once the response model has been used to compute the *EDP* resulting from a given *IM*, i.e $EDP = \mathcal{R}(IM)$, a probabilistic damage model can be used to estimate the *DM* resulting from a given *EDP*, i.e., $DM = \mathcal{D}(EDP)$. The damage model must be probabilistic so that it can predict the distribution of damage for a given level of response, i.e., the distribution of *DM*|*EDP*. The maximum allowable damage has frequently been referred to as a damage limit state in the structural engineering literature, where attempts at their explicit prediction are more advanced at this time than in geotechnical engineering.

Fragility Curve Approach

A probabilistic damage model can be used to develop damage fragility curves in much the same manner as probabilistic response models are used to develop response fragility curves. Characterization of damage using continuous *DM* scales has proven

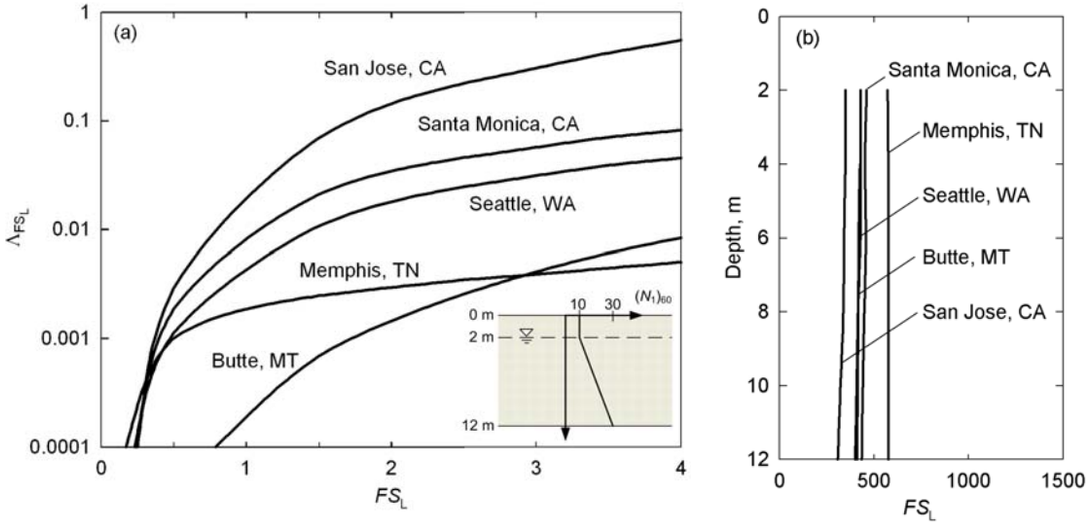


Fig. 7. (a) Mean annual rate of non-exceedance of factor of safety (factor of safety hazard curves) for an element of soil at 6 m depth in the standard soil profile (inset) defined by Kramer and Mayfield (2007), and (b) profiles of return periods of liquefaction (after Kramer and Mayfield, 2007).

to be somewhat problematic. In some cases, pertinent damage limit states (e.g., collapse of a structure or initiation of a flow slide) are essentially binary – they either occur and produce catastrophic damage or they don't. In other cases, loss estimators indicate that they do not use continuous scales, rather they consider small integer numbers of damage levels when estimating, for example, repair costs.

When discrete damage states are used, the process for estimating *DM* values remains straightforward. The continuous range of *EDP* levels must be discretized into an integer number of *EDP* intervals. For each damage state (e.g., negligible, slight, moderate, severe, and catastrophic), discrete distributions of *DM*|*EDP* can be defined by means of a matrix, perhaps $\boldsymbol{X}$, for which $X_{ij} = P[DM = dm_j \mid EDP = edp_i]$ and the sum of each row and column is unity. The matrix can be illustrated in tabular form as shown in Table 1.

Table 1. Damage state matrix for definition of *DM*|*EDP* relationship.

Damage State, *DM*	Description	*EDP* interval				
		edp_1	edp_2	edp_3	edp_4	edp_5
dm_1	Negligible	X_{11}	X_{12}	X_{13}	X_{14}	X_{15}
dm_2	Slight	X_{21}	X_{22}	X_{23}	X_{24}	X_{25}
dm_3	Moderate	X_{31}	X_{32}	X_{33}	X_{34}	X_{35}
dm_4	Severe	X_{41}	X_{42}	X_{43}	X_{44}	X_{45}
dm_5	Catastrophic	X_{51}	X_{52}	X_{53}	X_{54}	X_{55}

The total probability theorem can then be used to compute the probability of being in a given damage state using the conditional distribution of *DM*|*EDP* and the distribution of *EDP* ranges as

$$P[DM = dm_j] = \sum_{i=1}^{N_{EDP}} P[DM = dm_j \mid EDP = edp_i] P[EDP = edp_i] \quad (9)$$

Demand and Capacity Factor Approach

A damage-level implementation can also be stated in an LRFD-like format of demand and capacity factors (Jalayer, 2003). Such a format, which underlies recent steel design codes (Federal Emergence Management Agency, 2000a-c; Cornell et al., 2002), can also be applied to geotechnical damage. The format can be conveniently described using the closed form approximations described previously.

Loss-Level Implementation

The most complete performance evaluation can be accomplished by specifying performance in terms of losses. Such evaluations represent the ultimate expression of PBEE, and are likely to be justified primarily for particularly large and/or important projects in the near future. Nevertheless, they provide a useful and instructive look into the future of earthquake engineering practice.

Conte and Zhang (2007) describe a complete, detailed evaluation of the performance of the Humboldt Bay Middle Channel (HBMC) bridge (Figure 8) near Eureka in northern California. The 330-m-long, nine-span bridge, which was designed in 1968 and constructed in 1971, is supported on groups of precast, prestressed piles that extend through Tertiary and Quaternary alluvial soils. A 1.5 to 3-m-thick layer of soft to very soft organic silt blankets the entire site and is underlain by medium dense to dense silty sand (SP/SM) under the left abutment area, dense silty sand and sand (SP) in the central area, and soft sandy silt to loose silty sand (OL/SM) under the right abutment. These soils are underlain by dense and stiff soils. The river channel slopes toward the center of the channel at an average inclination of about 7 percent. The central piers (Piers 3-7, counting from the left) are supported on groups of 1.37-m-diameter, 1800 kN piles and the abutments and outer piers (Piers 1, 2, and 8) on groups of 356-mm-square, 400 and 625 kN piles. Expansion joints at the abutments and the tops of Piers 3 and 6 effectively divide the bridge structure into three frames. The fundamental period of the bridge-soil system was determined to be 0.71 sec.

The first-mode spectral acceleration, i.e., $S_a(T=0.71)$, was taken as the *IM* for this study. The results of USGS seismic hazard analyses were used to approximate the *IM* hazard curve for the site. A total of 51 ground motions were assembled (and scaled to appropriate $S_a(T=0.71)$ values) to represent the *IM* hazard at return periods of 72, 475, and 2,475 yrs (50-yr exceedance probabilities of 50%, 10%, and 2%, respectively).

A two-dimensional finite element model (Figure 9) using OpenSees (Mazzoni et al., 2006) was developed to estimate the response of the soil-foundation-structure system. The OpenSees model represented the nonlinear, inelastic behavior of cohesive and granular soils using pressure-independent and pressure-dependent multi-yield models (Yang et al., 2003), respectively. Piles in out-of-plane rows were



Fig. 8. Aerial view of Humboldt Bay Middle Crossing (Conte and Zhang, 2007).

lumped into composite piles and modeled as nonlinear beam-columns using a fiber model (although local interaction through *p-y* and *t-z* springs was not included). The superstructure was modeled using high-level nonlinear structural models that included expansion joints, bearings, and shear keys.

Examples of the computed response are presented in Figure 10, which shows the displacements of the tops and bases of all eight bridge piers in response to a single motion scaled to match the 2,475-yr *IM*. The response of the bridge is relatively coherent until the shear key at the Pier 6 expansion joint breaks (at t = 16.52 sec) after which the right frame responds differently (Figure 10(a)) than the other two frames which remain connected. The response at the bases of all piers (Figure 10(b)) is relatively coherent until about 28 sec at which time liquefaction occurs and lateral spreading causes the bases of the piers to move laterally toward the center of the river channel.

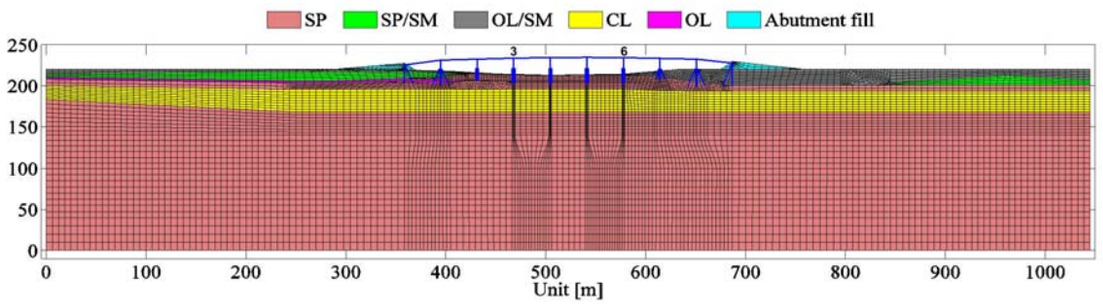


Fig. 9. Two-dimensional finite element model of Humboldt Bay Middle Crossing bridge site (Piers 3 and 6 are labeled); dimensions are in meters (after Conte and Zhang, 2007).

The results of even this single analysis illustrate some of the benefits of detailed soil-foundation-structure interaction analyses. While model development and calibration can be time-consuming, such analyses can explicitly model the response (and failure) of critical components like the Pier 6 shear key and account for whatever effects the soil and foundations might have on their response. They can also explicitly account for the generation of excess pore pressure in liquefiable soils, and for its effects on cyclic and permanent deformations of the soil and structure.

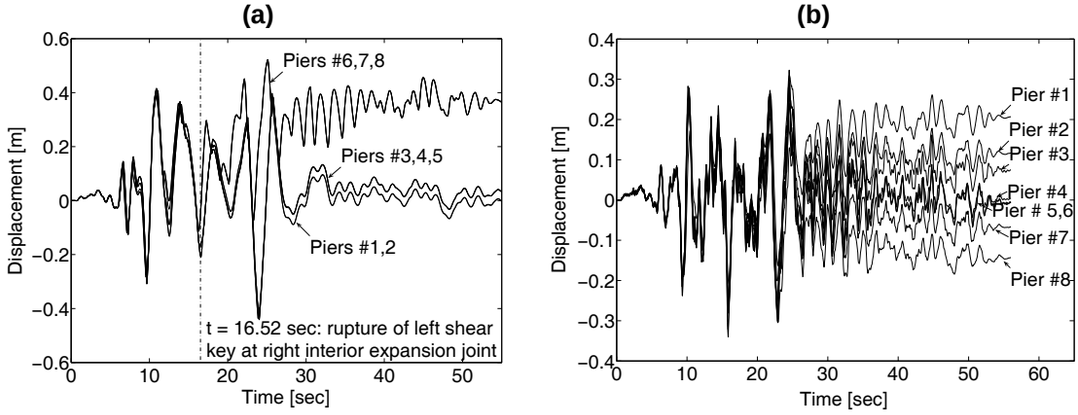


Fig. 10. Computed time histories of displacement: (a) tops of piers, and (b) bases of piers (Conte and Zhang, 2007).

Preliminary analyses had revealed that flexural failure in the regions of lap-splices at the bases of the piers, failure of unconfined shear keys, and unseating at the abutments and interior expansion joints were the most critical failure mechanisms for the HBMC bridge. *EDP*s considered to efficiently represent the response leading to those damage mechanisms were peak lateral bridge pier drift, peak shear key deformation, and peak unseating displacement at the expansion joints. The maxima of those *EDP*s over all components (i.e., all piers, shear keys, and expansions joints) were used to predict damage and loss.

The damage analyses were based on discrete damage states described by fragility curves developed from analytical and experimental investigations of pier flexure and shear key failure. Median displacements for unseating failure were taken as the width of the abutment seat or half the pier width at the interior expansion joints but, due to lack of experimental or field data on unseating, uncertainties in that damage mechanism had to be estimated. The *DM* fragility curves were combined with the *EDP* hazard curves to compute mean annual rates of exceedance for the various damage states. The results of these analyses, summarized in Table 2, showed that shear key failure was quite likely to occur (Damage State IV reached, for example, at a return period of 14.5 yrs), flexural failure of piers was also likely (Damage States III-IV-V reached at 47.6-yr return period), and collapse due to unseating was much less likely (return periods over 800 yrs).

Conte and Zhang (2007) used total repair cost as their decision variable. This cost was taken to be the construction cost of a new bridge (estimated at $24M) for global failure (i.e., collapse) damage states and the sum of the repair costs of all damaged components for non-collapse cases; indirect losses associated with downtime were not considered. Estimation of repair costs required identification of repair schemes for each damage state, and estimation of required repair quantities and unit costs for each repair scheme. These estimates were based on experience with retrofits on bridges in California, compiled unit cost data (California Department of Transportation, 2003), and consultation with experienced practitioners. Conte and

Table 2. Computed mean annual rates of exceedance and return period for various damage limit states.

Damage Mechanism	Limit State	λ_{DM} (yr^{-1})	Return Period (yrs)
Flexural failure of piers	II: Yielding of reinforcement	0.034	29.4
	III-IV-V: Initiation of failure mechanism; full formation of failure mechanism; strength loss	0.021	47.6
Shear key failure	I-II-III: Onset of cracking; reinforcement yielding; large open cracks and onset of spalling	0.080[a] 0.046[b] 0.064[c]	12.5[a] 21.7[b] 15.6[c]
	IV: Cracks and spalling over full region of key	0.069[a] 0.039[b] 0.058[c]	14.5[a] 25.6[b] 17.2[c]
	V: Loss of load-carrying capacity; fracture of reinforcement	0.010[a] 0.00008[b] 0.0058[c]	100[a] 12,500[b] 172[c]
Unseating	V: Collapse	0.0011[a] 0.0012[c]	909[a] 833[c]

[a]abutments; [b]continuous joints; [c]interior expansion joints

Zhang used a multi-layered Monte Carlo procedure to perform the integrations required to compute losses, producing the loss curve shown in Figure 11. The loss curve indicates that repair costs of $2M or more are relatively likely (return period on the order of 67 yrs), but costs exceeding $3.6M are quite unlikely (return period of about 1,000 yrs) since the loss curve drops quickly as repair costs exceed about $3M. A performance-based analysis also allows deaggregation of *EDP*, *DM*, and *DV* values just as *IM*s are deaggregated in PSHAs. Figure 12 shows the relative contributions of pier failure, shear key failure, and collapse as a function of *IM*. At *IM* levels less than about 0.2 g, losses are dominated by repair of shear key failures. At intermediate *IM* levels (0.2 g to 1.5 g), losses are associated with shear key and pier flexural failures. At *IM*s greater than about 2 g, collapse becomes more likely and increasingly dominates the expected losses. The unseating mechanism makes essentially no contribution to loss due to its relatively long return period (Table 2) and low repair cost. It should be noted that the repair costs in Figures 11 and 12 become asymptotic (at long return period/high *IM*) to the replacement cost of the bridge.

IMPLICATIONS AND OPPORTUNITIES FOR PRACTICE

The preceding sections have described a framework for PBEE and the basic mechanics of its use. The framework is clearly formulated to allow consideration of the many uncertain aspects of ground motion, response, damage, and loss estimation, and it has been shown that each of those quantities increase, for a given return period, with increasing levels of uncertainty. Performance-based concepts are making their

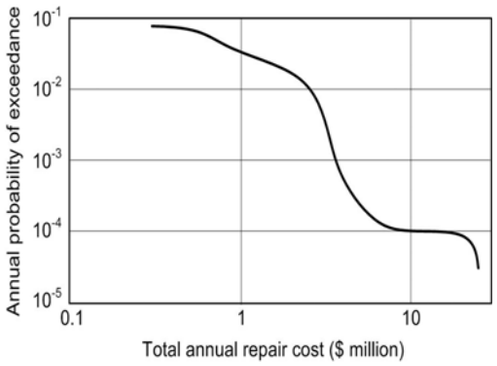


Fig. 11. Loss curve for Humboldt Bay Middle Crossing bridge (after Conte and Zhang, 2007).

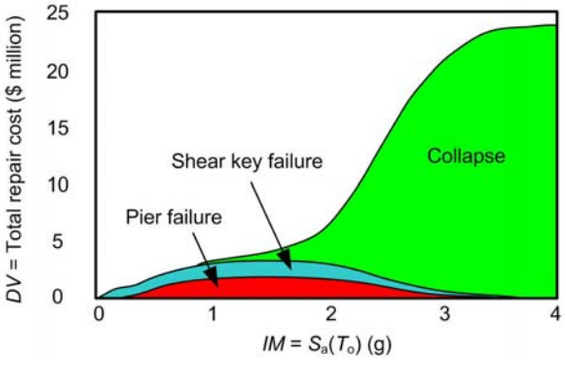


Fig. 12. Deaggregation of repair cost as function of ground motion intensity (after Conte and Zhang, 2007).

way into practice and into the codes and standards that strongly influence practice. The successful implementation of performance-based concepts into practice provides both challenges and opportunities for geotechnical engineering practice.

Challenges

In order to participate equally with other earthquake professionals in the future development, implementation, and practice of PBEE, geotechnical engineers will need to develop new awareness, knowledge, and tools; these can be thought of as challenges for the geotechnical earthquake engineering profession that will require its practitioners to:

1. *Understand the "big picture" and geotechnical engineering's place in it.* A variety of professionals are involved in the full process of estimating earthquake losses. Seismologists predict ground motion hazards for a reference site condition. Geotechnical engineers evaluate the effects of actual site condition on ground motion hazards and predict ground failure potential. Structural engineers evaluate structural response to the ground motions and predict the physical damage that occurs when response exceeds capacity. Loss analysts use physical damage estimates to predict direct and indirect economic and other losses. Finally, a decision-maker, typically the owner, will decide how to address earthquake risk – to accept (or ignore) it or to take steps to reduce it through planning, retrofitting, or insurance. Each of these professions play a key role in the big picture and each depends on the others for accurate and unbiased information. Each also deals with uncertainty, from the uncertainty in fault slip distribution that affects ground motions to the uncertainty in future interest rates that affects repair costs, and all of these uncertainties combine to affect estimated performance.

2. *Think probabilistically*. While it is not necessary for geotechnical practitioners to understand all of the daunting calculus of probability, it is necessary to develop a conceptual understanding of its basic tenets, and of the critical effects of uncertainty in performance estimation. Geotechnical engineers must recognize, and work to characterize, all sources of aleatory and epistemic uncertainty in their portion of the performance evaluation process. It is important that such characterizations be done accurately, i.e., without bias – the place for conservatism is not in the estimation of mean (or median) response. Uncertainties should be characterized realistically with proper recognition of the uncertainty associated with what is not known in addition to the uncertainty in what is known; the natural tendency for people to optimistically underestimate uncertainties in their estimates of things they are familiar with has been well documented by social scientists, and must be guarded against in engineering practice.

3. *Identify improved parameters*. Geotechnical engineers must strive to identify and validate the ground motion parameters (*IM*s) that correlate best to response, the response parameters (*EDP*s) that correlate best to physical damage, and the physical damage metrics (*DM*s) that correlate best to the losses of interest. These parameters should be efficient and sufficient, and the *IM*s must also be predictable (i.e., the uncertainty in their prediction by an attenuation relationship should be low – an *IM* that efficiently predicts *EDP* is not effective if its own value cannot be predicted accurately). For complex structures and facilities, more than one *IM* may be required to produce the least dispersed estimates of response. The use of vector *IM*s will require the development of ground motion "hazard surfaces" (the multi-dimensional equivalent of hazard curves) using vector-based PSHA, the basics of which have been laid out by Bazzuro and Cornell (2002) and Baker (2007). In such cases, the geotechnical engineer will have the added responsibility of estimating statistical correlation between the various parameters.

   For geotechnical-related response, optimal *IM*s will likely correlate well to deformations, which are related to strains. Basic wave propagation concepts show that strain amplitudes in a linear material are proportional to particle velocity, which suggests that optimal geotechnical *IM*s would likely lie in a frequency range closer to those associated with peak velocities than peak accelerations. Bray and Travasarou (2007) suggest the use of spectral acceleration at 1.5 times the fundamental period of a potentially unstable slope as an optimal *IM* for slope deformation predictions. Kayen and Mitchell (1997) suggested the use of Arias intensity as an *IM* for liquefaction analyses; Kramer and Mitchell (2003) identified another parameter, *CAV5*, as an optimal *IM* for liquefaction problems. Each of these parameters are associated with frequencies closer to those associated with peak ground velocity than to peak ground acceleration, and the use of each offers the potential to reduce the level of record-to-record variability that contributes strongly to uncertainty in *PGA*-based response models.

   Because geotechnical aspects of damage are generally related to deformations, optimal geotechnical *EDP*s are likely to consist of

deformations, whether the permanent deformation (horizontal and/or vertical) of a sloping bridge approach or the peak curvature of a pile foundation. While traditional force-based (e.g., factor of safety) measures of response can be used in the PBEE framework described in this paper, the much higher uncertainty in damage given factor of safety (relative to damage given deformation) results in a substantial "penalty" in performance when they are used.

For a given type of structure or facility, identification of optimal *DM*s will likely require the input of loss analysts or construction estimators who would be asked questions such as "what type(s) of physical damage would most strongly control your estimated repair costs and repair times?" Continuous, measurable quantities such as crack width or wall tilt could be identified by respondents, but early investigations of such questions indicate that many professionals involved in estimating losses tend to use a small integer number (perhaps 3-4) of perceived damage states that are loosely defined functions of multiple damage observations. The use of discrete, rather than continuous, *DM*s presents no particular difficulty in the PEER framework, but the heuristic means by which damage is described can come with a substantial level of uncertainty.

4. *Develop improved response models*. For both site response and ground failure, improved response models that use optimal *IM*s as input and produce optimal *EDP*s as output are required. These models must be capable of predicting response over a wide range of ground motions – the PEER framework, for example, integrates all ground motion levels (ranging from the very weak motions associated with short return periods to the potentially very strong motions associated with long return periods) to estimate response. They must also be probabilistic, i.e., capable of producing the distribution of *EDP*|*IM*.

   Analytical models for estimating the response of soil and soil-structure systems have developed dramatically over the past 10-20 years. Early geotechnical models represented both ground motions and the physical systems of interest in crude, grossly simplified ways. Pseudo-static analyses, for example, replaced transient earthquake ground motions with constant, uni-directional accelerations, modeled physical systems as rigid and infinitely strong), and expressed response in terms of factors of safety. Subsequent geotechnical models allowed the use of actual ground motion time histories and accounted for at least some of the most basic characteristics of the physical system; Newmark-type sliding block analyses, for example, use an entire ground motion time history as input and model a slope using a rigid block bounded by a pre-determined failure surface with rigid-perfectly plastic (with shearing resistance equal to the average shear strength) force-displacement behavior. This type of analysis is more time-consuming than a pseudo-static analysis in that it requires identification of suitable input ground motions and a critical failure surface, and performance of the sliding block analysis itself, but it produces output in the form of an estimated slope displacement, a much more efficient *EDP* for damage prediction than pseudo-

static factor of safety. In 2008, we have at our disposal advanced stress-deformation (finite element and finite difference) analyses that allow ground motions and the physical systems of interest to be represented with great rigor. Soil-foundation-structure interaction (SFSI) analyses can be performed without prior constraint of deformation mechanisms and with as complete a characterization of nonlinear, inelastic soil behavior as our constitutive models allow. The performance of such analyses is far more time-consuming than sliding block analyses, but can provide direct estimates of a wide range of geotechnical and structural *EDP*s without the constraints of *a priori* assumptions required by the simpler models.

Response models should be capable of predicting threshold levels of shaking below which response may not occur (for example, weak shaking may produce strains below the threshold shear strain and thereby produce no excess pore pressure in potentially liquefiable soils). They should also address upper limits to response (for example, when reasonable levels of uncertainty are applied to existing post-liquefaction settlement models, many of which include "estimated" volumetric strain contours that extend well beyond the levels observed in available laboratory tests, unrealistically high volumetric strains of 30-40% are produced with sufficiently high probability to significantly affect estimated settlements). Improvements are needed in both empirical and numerical response models. Empirical models need more case history data and better characterization of that data. Numerical models need user-friendly interfaces and sufficient computational efficiency to allow sensitivity and simulation (e.g., Monte Carlo) analyses to be performed and interpreted.

Characterization of response model uncertainty, from relatively simple empirical models to complex numerical models, is urgently needed. This will require application of the various models to case histories and, where appropriate, physical models. In such studies, uncertainties in the inputs must be characterized and accounted for to separate parametric uncertainty from model uncertainty. For years, the general public has asked why ground shaking hazards have continuously increased despite the acquisition of more and more data from recent earthquakes and expanded seismographic networks. A primary reason (Bommer and Abrahamson, 2006) is that uncertainties in previous hazard analyses were ignored or underestimated. Today, clients are frequently reluctant to allow engineers to perform the types of detailed response analyses they should perform because they fear a more conservative (hence, expensive) result. This situation may well exist because the uncertainties in simplified and/or empirical response analyses are being ignored or underestimated. A number of response models are based on limited and/or highly scattered data and should be recognized as such with high model uncertainties.

5. *Develop improved damage models*. A great deal more emphasis has been placed, particularly in research, on response prediction than on prediction of the physical damage (both structural and non-structural) resulting from that response. Geotechnical engineers must work with structural engineers and

loss analysts to identify the damage measures that most closely correlate to losses and to characterize the levels of response that produce physical damage for different structures. This procedure essentially requires the characterization of capacity, specifically the probabilistic characterization of capacity. Capacities have historically been thought of in force-related terms such as bearing capacity, shearing force, and bending moment, but can also be expressed in deformation-related terms. Since geotechnical aspects of damage are most closely related to deformations, particularly permanent deformations, capacities will need to be expressed in terms of permanent deformations for PBEE. Geotechnical engineers must be deeply involved in determining, for example, the distributions of slope displacements that cause various levels of damage to a bridge abutment or the amounts of settlement that cause various levels of damage to different building types. The classical studies of "tolerable" movements completed some 30-50 yrs ago (e.g. Skempton and MacDonald, 1956; Burland and Wroth, 1974) need to be updated with additional case history data, supplemented by modern soil-structure interaction analyses, and adapted to seismic conditions. Until such research becomes available, capacity characterization may take the form of elicitation of multiple expert opinions on issues such as the amount of displacement required for 50% probability of severe damage and 90% probability of severe damage under various scenarios. Opinion-based estimates of this type will necessarily be accompanied by relatively high uncertainties.

6. *Develop tools*. The performance-based procedures described in this paper require multiple calculations in the definition of median response, damage, and loss relationships and in the integration across distributions of *IM*, *EDP*, and *DM*. The calculations are not necessarily more complicated than those performed in current practice, but they need to be repeated many times. Furthermore, to properly account for epistemic uncertainty, multiple models should be used with user-determined weights and the variance in their results added to the variances from other sources of uncertainty.

7. *Consider the role and application of engineering judgment*. Geotechnical engineering has a long history of the beneficial application of experience in the form of engineering judgment. Because gravity never rests, the profession has developed a substantial history of performance under static loading conditions. The field of geotechnical earthquake engineering, however, is considerably younger than geotechnical engineering itself, and the relative infrequency of strong earthquakes provides fewer data on which to base engineering judgment. Furthermore, the loading induced by earthquakes is much more complicated than gravitational loading, and the relatively simple concepts on which conservatism can be induced in static evaluations (e.g., assuming a reduced strength) do not work the same way for dynamic problems. Engineering judgment can play an important role in geotechnical earthquake engineering as long as there is a strong basis for that judgment. The judgment that comes from carefully examined, evaluated experience can be used to reduce uncertainties in estimated response, damage, and loss. Peer

review may prove to play an important role in the validation of such judgment.

8. *Engage in professional practice issues*. The manner in which performance-based concepts are implemented will have a direct effect on the professional practice of geotechnical engineering in seismically active areas. Performance-based concepts have been making their way into codes in recent years and that trend is likely to continue in the future. Many of the seismic problems that geotechnical engineers deal with are significantly different than those faced by structural engineers, so it is important that geotechnical engineers be involved in the development of future codes and standards.

Opportunities

The development and implementation of PBEE also offers important and exciting opportunities for geotechnical practice. The fact that losses are so strongly affected by uncertainty and that geotechnical engineers frequently deal with high levels of uncertainty means that geotechnical engineering has great potential for reducing design and construction costs for new structures and for reducing earthquake losses in existing structures. The opportunities are for geotechnical engineers to:

1. *Produce improved products*. The application of PBEE principles, whether interpreted at the response, damage, or loss levels, will result in more consistent and uniform designs and evaluations. The levels of risk/safety can be made much more consistent from one geographic region (i.e., seismic environment) to another.
2. *Balance risk*. The application of PBEE principles, along with the use of improved analytical tools, can lead to more balanced designs by explicitly considering the effects of both geotechnical (e.g., foundation) and structural (e.g., superstructure) aspects of a particular facility in a consistent manner.
3. *Extend professional development*. The basic concepts of PBEE, and the skills required to implement it, will improve the technical skills of geotechnical engineers and will require them to work closely and communicate with earth scientists, structural engineers, and other earthquake professionals. These concepts, skills, and interactions are also transferable to other natural hazards and other aspects of geotechnical practice. The development and use of these skills can provide engineers with new and useful insights into the sources and effects of various uncertainties in many areas of geotechnical practice.
4. *Demonstrate value*. Current geotechnical earthquake engineering practice centers on the prediction of response, which is typically performed deterministically and presented with an informally determined level of conservatism. That conservatism frequently fails to adequately reflect the potential benefits (i.e., reduction of uncertainty) of factors such as additional

subsurface investigation, additional insitu testing, additional laboratory testing, and more detailed/sophisticated analyses. Each of these factors has the potential to reduce uncertainty, which has been shown in this paper to reduce losses at a particular return period. The PBEE framework provides an opportunity to demonstrate the value (or, to be fair, lack of value) that may be associated with different levels of geotechnical services.

5. *Engage in professional practice issues*. As stated previously, performance-based concepts will likely be implemented into future codes for buildings, bridges, etc., which presents geotechnical engineers with the opportunity to influence how that is done. Over the years, some codes have evolved from safety nets that ensured a minimum level of safety (and protected the public from the lowest levels of design/construction practice) to *de facto* design standards, as evidenced by the difficulty in gaining approval of a design, no matter how well-documented, that involves lower levels of loading or greater levels of resistance than specified by the code. Implementation of performance-based concepts such as those described in this paper into codes would allow the geotechnical engineer's ability to reduce uncertainty through comprehensive site investigation, detailed analysis, and application of relevant experience to benefit his/her client.

CONCLUDING REMARKS

This paper has reviewed the development of PBEE and shown how a modular PBEE framework can provide more objective, consistent, and accurate estimates of seismic performance. Different levels of implementation have been introduced, and a number of important challenges and opportunities that PBEE brings to the geotechnical engineering profession have been identified.

PBEE provides a framework in which the improved field, laboratory, and analytical tools now available to geotechnical engineers can be used to the advantage of the engineer and client. Its further development and implementation raises a number of important challenges that must be addressed in coming years, but it also provides important opportunities for geotechnical engineers to improve their products and demonstrate the value of the services they provide.

ACKNOWLEDGMENTS

The performance-based concepts described in the paper have been developed by a group of PEER researchers with whom the author has been fortunate to work, and his understanding of the subject has benefited particularly from discussions with Prof. C. Allin Cornell. Much of the author's own work in this area germinated while he was on sabbatical leave at the International Centre for Geohazards at the Norwegian Geotechnical Institute in Oslo. The author would also like to acknowledge support from the Washington State Department of Transportation to develop and implement performance-based procedures for liquefaction hazard evaluation. The author is also grateful to Dr. Don Anderson and Dr. Roy Mayfield for their insightful comments on a draft of this paper. Finally, the author has benefited greatly from the work of

several students on performance-based topics, particularly Dr. Roy Mayfield, Yi-Min Huang, and Kevin Franke.

REFERENCES

Algermissen, S. T. and Perkins, D. M., (1976). "A probabilistic estimate of maximum acceleration in rock in the contiguous United States," *U.S. Geological Survey Open- File Report 76-416*, 45 pp.

American Society of Civil Engineers (2000). "Prestandard and commentary for the seismic rehabilitation of buildings," *FEMA Publication 356*, ASCE, Reston, Virginia.

Applied Technology Council (1978) "Tentative Provisions for the Development of Seismic Regulations for Buildings," *ATC 3-06*, NSF 78-8, Applied Technology Council, Redwood City,

Applied Technology Council (1996). "Seismic evaluation and retrofit of concrete buildings," *ATC-40*, Applied Technology Council, Redwood City, California.

Applied Technology Council (1997a). "NEHRP Guidelines for the Seismic Rehabilitation of Buildings," *FEMA Publication 273*, Applied Technology Council, Redwood City, California.

Applied Technology Council (1997b). "NEHRP commentary on the guidelines for the seismic rehabilitation of buildings," *FEMA Publication 274*, Applied Technology Council, Redwood City, California.

EC 8 (2004). *Eurocode 8: Design of structures for earthquake resistance, Part 1: general rules, seismic actions and rules for buildings*, European Norm. European Committee for Standardisation, European Committee for Standardisation Central Secretariat, rue de Stassart 36, B-1050 Brussels.

Applied Technology Council (1997). "Seismic Evaluation and Retrofit of concrete Buildings," *ATC-40*, NSF 78-8, Applied Technology Council, Redwood City, California.

Baker, J.W. (2007). "Probabilistic structural response assessment using vector-valued intensity measures," *Earthquake Eng. and Struct.l Dyn.*, 36, 1861-1883.

Bazzurro, P. and Cornell, C.A. (2002). "Vector-valued probabilistic seismic hazard analysis," *Proceedings*, Seventh U.S. National Conf. on Earthquake Engineering, Boston, Massachusetts.

Bommer, J.J., and Abrahamson, N.A. (2006). "Why do modern probabilistic seismic-hazardanalyses often lead to increased hazard estimates?" *Bull. Seismol.l Soc. of America*, **96**, 1,976–1,977.

Bray, J.D. And Travasarou, T. (2007) "Simplified Procedure For Estimating Earthquake-Induced Deviatoric Slope Displacements," *J. of Geotech. Geoenv. Eng.*, ASCE, Vol. 133, No. 4, 381-392.

Burland, J.B. and Wroth, C.P. (1974). "Settlement of buildings and associated damage," *Settlement of structures*, British Geotech. Soc., Pentech Press, London.

California Department of Transportation (2003). "Contract cost data, a summary of cost by items for highway construction projects," *Business, Transportation, and Housing Agency*, Dept. of Transportation, State of California.

Conte, J.P. and Zhang, Y. (2007). "Performance Based Earthquake Engineering: Application to an Actual Bridge-Foundation-Ground System,"*L'Ingineria Sismica in Italia*, (CD-ROM), XII Convegno ANIDIS Associazione Nazionale Italiano di Ingineria Sismica.

Cornell, C.A. (1968). "Engineering seismic risk analysis," *Bull. Seismol.l Soc. of America*, 58, 1583-1606.

Cornell, C.A., Jalayer, F., Hamburger, R.O., and Foutch, D.A. (2002). "Probabilistic basis for 2000 SAC Federal Emergency Management Agency steel moment frame guidelines," *J. Struct. Eng.*, ASCE, 128(4), 526-533.

Department of Energy (1994). "Natural phenomena hazards design and evaluation criteria for Department of Energy Facilities", *DOE-STD-1020-94*, U. S. Dept. of Energy, Washington, D. C.

Federal Emergency Management Agency (2000a). "Recommended seismic design criteria for new steel moment-frame buildings." *Report No. FEMA-350*, SAC Joint Venture, Federal Emergency Management Agency, Washington, DC.

Federal Emergency Management Agency (2000b). "Recommended seismic evaluation and upgrade criteria for Existing Welded Steel Moment-Frame Buildings." *Report No. FEMA-351*, SAC Joint Venture, Federal Emergency Management Agency, Washington, DC.

Federal Emergency Management Agency (2000c). "Recommended post-earthquake evaluation and repair criteria for welded steel moment-frame buildings." Report No. FEMA-352, SAC Joint Venture, Federal Emergency Management Agency, Washington, DC.

Jalayer, F. (2003). "Direct probabilistic seismic analysis: Implementing non-linear dynamic assessments," *Ph.D. dissertation*, Stanford University, Stanford, California, 244 pp.

Kayen, R. E., and Mitchell, J. K., (1997). "Assessment of liquefaction potential during earthquakes by Arias intensity," *J. Geotech. Geoenv. Eng.*, 123(12), 1162–1174.

Kramer, S.L. and Mitchell, R.A. (2003). "Ground motion intensity measures for liquefaction hazard evaluation," *Earthquake Spectra*, 22(2), 413-438.

Kramer, S.L. and Mayfield, R.T. (2005). "Performance-based liquefaction hazard evaluation," *Proceedings*, GeoFrontiers 2005, ASCE, Austin, Texas, 18 pp.

Kramer, S.L., Mayfield, R.T., and Anderson, D.G. (2006). "Performance-based liquefaction hazard evaluation: Implications for codes and standards," *Proceedings*, Eighth U.S. National Conf. on Earthquake Eng., San Francisco, Paper No. 888.

Kramer, S.L. and Mayfield, R.T. (2007). "The return period of liquefaction," *J. Geotech. Geoenv. Eng.*, ASCE, Vol. 133, No. 7, pp. 1-12.

Kuramoto, H. (2006). "Seismic design codes for buildings in Japan," *J.Disaster Res.*, 1(3), 341-356.

Luco, N. and Cornell, C. A. (1998). “Seismic drift demands for two SMRF structures with brittle connections”, *Structural Engineering World Wide 1998*, Elsevier Science Ltd., Oxford, England, 1998, Paper T158-3.

Mackie, K.R. and Stojadinovich, B. (2006). “Fourway: Graphical tool for performance-based earthquake engineering,” *J. Struct. Eng.*, ASCE, 132(8), 1274-1283,

Marrone, J., Ostadan, F., Youngs, R., and Litehiser, J. (2003). “Probabilistic liquefaction hazard evaluation: Method and application.” *Proc., 17th Int. Conf. Struct. Mech. in Reactor Tech. (SMiRT 17)*, Prague, Czech Republic, Paper No. M02-1.

Mazzoni, S, McKenna, F., Scott, M. H., and Fenves, G. L. (2006). “Open system for earthquake engineering simulation: User command language manual”, Berkeley, California (http://opensees.berkeley.edu/OpenSees/manuals/usermanual/index.html)

SEAOC (1959). *Recommended Lateral Force Requirements and Commentary (SEAOC Blue Book)*, Structural Engineers Association of California, Sacramento, California.

SEAOC (1995). “Vision 2000: Performance-Based Seismic Engineering of Buildings,” Structural Engineers Association of California, Sacramento, California.

Skempton, A.W. and MacDonald (1956). “Allowable settlement of buildings,” *Proc. Inst. Civ. Engrs*., Pt. III, 5, 727-768.

Taghavi, S. and Miranda, E. (2003). “Probabilistic study of peak floor acceleration demands in linear structures,” *Proceedings*, Appl. of Stat. and Prob. in Civil Engineering, ICASP9, Der Kiureghian, Madanat, and Pestana (eds.), Millpress, Rotterdam.

Travasarou, T., Bray, J.D., and Der Kiureghian, A.D. (2004). “A Probabilistic Methodology for Assessing Seismic Slope Displacements,” *Proceedings*, 13th World Conf. on Earthquake Eng., Vancouver, Canada, Paper No. 2326, Aug 1-6.

Yang, Z., Elgamal, A. and Parra E. (2003). "Computational model for cyclic mobility and associated shear deformation", *J. Geotech. Geoenv. Eng., ASCE,* 129 (12), 1119-1127.

Full-Scale Laboratory Tests using a Shape-Acceleration Array System

T. Abdoun[1], V. Bennett[2], R. Dobry[3], S. Thevanayagam[4] and L. Danisch[5]

[1]Associate Professor, Department of Civil and Environmental Engineering, Rensselaer Polytechnic Institute, 110 8th Street, Troy, NY 12180; PH: (518) 276-6544; FAX: (518) 276-4833; email: abdout@rpi.edu
[2]PhD Student, Department of Civil and Environmental Engineering, Rensselaer Polytechnic Institute, 110 8th Street, Troy, NY 12180; PH: (518) 276-6365; FAX: (518) 276-4833; email: bennev@rpi.edu
[3]Professor, Department of Civil and Environmental Engineering, Rensselaer Polytechnic Institute, 110 8th Street, Troy, NY 12180; PH: (518) 276-6934; FAX: (518) 276-4833; email: dobryr@rpi.edu
[4]Associate Professor, Department of Civil and Environmental Engineering, University at Buffalo, 133 Ketter Hall, Buffalo, NY 14260; PH: (716) 645-2114 x2430; FAX: (716) 645-3733; email: theva@eng.buffalo.edu
[5]President, Measurand Inc., 2111 Hanwell Road, Fredericton, New Brunswick, Canada E3C1M7; PH: (506) 462-9119; FAX: (506) 462-9095; email: lee@measurand.com

ABSTRACT: Geotechnical instrumentation using Micro-Electro-Mechanical Systems (MEMS) are relative newcomers to this field and, as such, require extensive validation testing. This paper presents the use of a Shape-Acceleration Array (SAA) to instrument full-scale laminar container tests at the University of Buffalo. The SAA is a sensor array based on MEMS accelerometer measurements of angles relative to gravity. The sensors are contained in 30 cm long rigid segments which are connected by composite joints that prevent torsion but allow flexibility in two degrees of freedom. These rigid segments and flexible joints are combined to form a sensor array which is capable of measuring three-dimensional (3D) ground deformations at 30 cm intervals and 3D accelerations at 2.4 m intervals to a depth of 100 m. Two of these MEMS-based sensor arrays were utilized in a series of tests as part of a liquefaction and lateral spreading study. Extensive instrumentation was possible in this laboratory setting, thus the acceleration and deformation measurements from the SAAs can be compared to the traditional instrumentation, such as accelerometers and potentiometers. The goal of validating and calibrating the measured accelerations and displacements of the SAA system was achieved through these full-scale tests.

INTRODUCTION

Ground failure, landslides and damage to geotechnical systems due to earthquake excitations impact all seismically active areas around the world. The associated mechanisms of ground response are being documented through a worldwide network of sites instrumented with vertical downhole accelerometer arrays, often supplemented at liquefiable sites with pore pressure piezometers and in some cases with slope inclinometer arrays. In the United States, early vertical array data sets were recorded at the San Francisco Bay area (Joyner et al 1976, Johnson and Silva 1981) and at Union Bay in Seattle (Seed and Idriss 1970, Dobry et al 1971). During the 1980s, data from seismic arrays that include pore-pressure piezometers became available such as data from the Wildlife Refuge site in California, (Holzer et al 1989). To monitor lateral spreading and possible slope failures of active grounds, state Departments of Transportation and other agencies also use in-place slope inclinometer arrays. These arrays can provide real-time monitoring with good angular resolution capability; however, they are expensive and inflexible. This high cost makes it impractical to install multiple arrays on a single slope, thus severely limiting the ability of conducting comprehensive real-time monitoring.

Soil-structure systems and natural soil deposits exhibit a broad range of complex response patterns when subjected to dynamic loading conditions (NRC 1982, Arulanandan and Scott 1993). Some of these patterns reflect local mechanisms associated with the particulate nature of soils, and others are related to abrupt changes in properties. Our understanding of the mechanisms of soil dynamic response, large deformation and failure due to earthquakes has improved considerably over the last two decades. However, significant challenges remain in modeling soils response when subjected to large deformations and ground failure. This state of affairs stems partly from limitations of existing monitoring tools and system identification techniques. Thus, computational soil models generally have somewhat restricted predictive capabilities for severe loading conditions, as these models remain to be validated using adequate case history data. For instance, the lack of accurate measurements of permanent deformation is one of the factors that hinders the development of soil models capable of reliably predicting site lateral spreading induced by seismic excitations. Furthermore, natural and man-made soil systems are generally massive and have distributed parameters and state. Some deposits are in fact semi-infinite and have no well-defined boundaries. A thorough monitoring of the whole response of such systems may not be technically possible, and would generally be prohibitively expensive. However, a sparse monitoring of a massive soil system generally does not provide enough information to uniquely and accurately identify the associated response mechanisms based on boundary value problem analyses.

This paper presents: (1) the evolved design of a Shape-Acceleration Array (SAA) to monitor the acceleration and permanent deformation of soil and soil-structure systems and (2) data comparisons between SAAs and traditional instrumentation utilized in full-scale tests at the University of Buffalo's 6 m high laminar container.

SHAPE-ACCELERATION ARRAY

This MEMS-based system has been developed in an effort to combine recent advances in the miniaturization of sensors and electronics with an established

wireless infrastructure to enhance geotechnical monitoring. The concept is based on MEMS accelerometer measurements of angles relative to gravity. These same MEMS accelerometers also provide signals proportional to vibration during earthquakes or construction activities. The sensors are contained in 30 cm long rigid segments which are connected by composite joints that prevent torsion but allow flexibility in two degrees of freedom. These rigid segments and flexible joints are combined to form a sensor array called a Shape-Acceleration Array, or SAA, which is capable of measuring three-dimensional (3D) ground deformations at 30 cm intervals to a depth of 100 m. These sensor arrays are manufactured by Measurand, Inc.

Microprocessors, within every eight segments of the arrays, collect data from groups of sensors and transmit this digital data to the ground surface using just two communication wires. Because of this limited wiring field the array diameter is less than 25 mm and the sensor is flexible enough to be rolled up on a reel for shipping and storage. The SAAs are factory-calibrated and completely sealed, requiring no field assembly or calibration (Danisch et al 2004).

The following section presents some design characteristics of the research versions of this sensor array followed by comparative results from full-scale laminar container tests at the University of Buffalo aimed at validating the accelerations and displacements measured using two of the developed SAAs, see also Abdoun et al, 2007 for further details.

Sensor Characteristics

The research version of the SAA consists of many MEMS sensors installed in a flexible water-tight casing and is currently capable of measuring three-dimensional (3D) deformation and 3D lateral acceleration at 0.30 m intervals up to a length of 7 m. The MEMS accelerometers are applied to a flexible substrate at 0.30 m intervals, a distance chosen to include at least two sensors within any expected monotonic curve and to allow for easy shipping and handling.

The employed MEMS devices enable gravity-based shape calculation along a sensorized substrate. The MEMS also offer the possibility of measuring the differential tilt at a low sampling rate and the accelerations at a higher rate. From a networking point of view, MEMS offer the possibility of multiplexing a significant number of devices using conventional CANbus or similar high-speed multiplexing technology, such that electrical interference can be minimized by converting to digital signals locally along an array (Danisch 1998). Multiarray software enables data acquisition from up to eight arrays in one computer, in addition to remote recording and synchronization input capabilities. Table 1 provides a summary of some of the research SAA specifications.

Table 1. Summary of Research SAA Specifications.

Specification	Value
Standard length of segments	305 mm
Maximum number of segments	24
Maximum tilt	$\pm$ 45^{o} from vertical

Range of lateral acceleration	± 2 g
Operating and storage temperature	0 to 70 °C
Absolute accuracy of tilt within 20° of vertical	0.2 deg (3.4 mm/m)
Resolution of tilt within 20° of vertical	0.01 deg (0.17 mm/m)
3 dB bandwidth for slope and vibration measurements	20 Hz
Sampling rate	70 Hz or better

Large-Scale Laminar Container Tests

Researchers at the University at Buffalo (UB) and Rensselaer Polytechnic Institute (RPI) studying earthquake-induced soil-liquefaction and its effects on foundations that support waterfront infrastructure developed a large-scale earthquake simulator to model the response of saturated sand to earthquake forces. The earthquake simulator is part of the NEES@Buffalo equipment and research site, a National Science Foundation (NSF) facility. The laminar container at the University at Buffalo is 5 m long, 2.75 m wide and 6 m high and is capable of containing 150 tons of sand, see Figure 1.

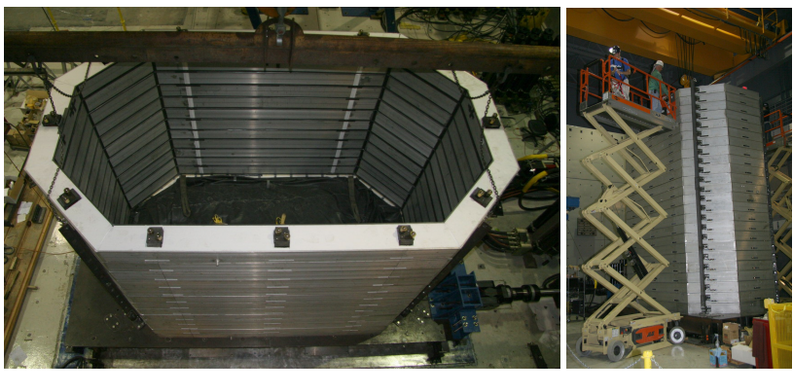


FIG. 1. Assembly of laminar container at the University at Buffalo.

Specially designed ball bearings are used between each of the 0.254 m thick laminar rings to achieve nearly frictionless sliding. After filling the container with loose sand and water, two 100-ton hydraulic actuators are used to input pre-determined motion to the base of the box. The resultant soil liquefaction and lateral spreading is monitored using accelerometers within the deposit and on the laminates, LVDTs on the laminates, pore-pressure transducers and two SAAs within the soil deposit, see Figure 2. The results from two 7m long SAAs installed in a sloping ground test, where the base of the box was inclined 2°, will be presented herein. Each of these sensor arrays contained 24 3D sensing elements. One of these sensor arrays was placed in the center of the laminar container and a second array was 1m east of the center, along the centerline of the container, see Figure 3. Traditional instrumentation included variable capacitance accelerometers within the soil and on the rings and potentiometers (displacement sensors) on the rings. Since the sensor arrays were 1 m longer than the height of the laminar container, the excess length was fastened to a

frame above the box with elastic connections. Complementary experimental and numerical simulations conducted prior to this sloping ground test predicted 50 cm of permanent lateral displacement. Thus, the top of the SAAs were fixed approximately 25 cm downslope, in an effort to lessen any restrictive effects from the top of the array on the rest of the sensor array within the soil. Arrays were fixed at the bottom of the container with a two-point clamp to provide a reference end and were installed prior to the soil placement.

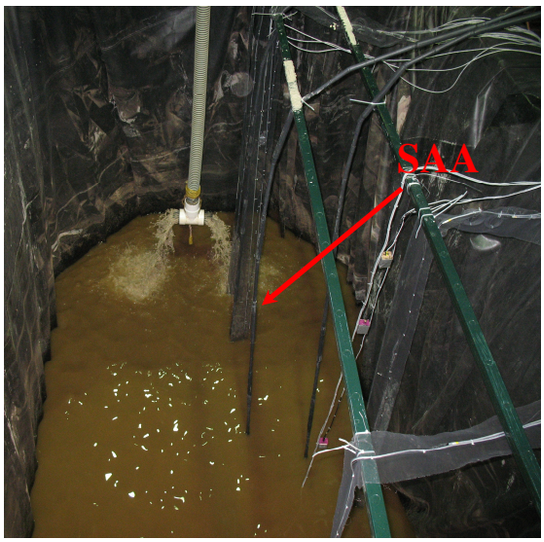


FIG. 2. Hydraulic placement of sand.

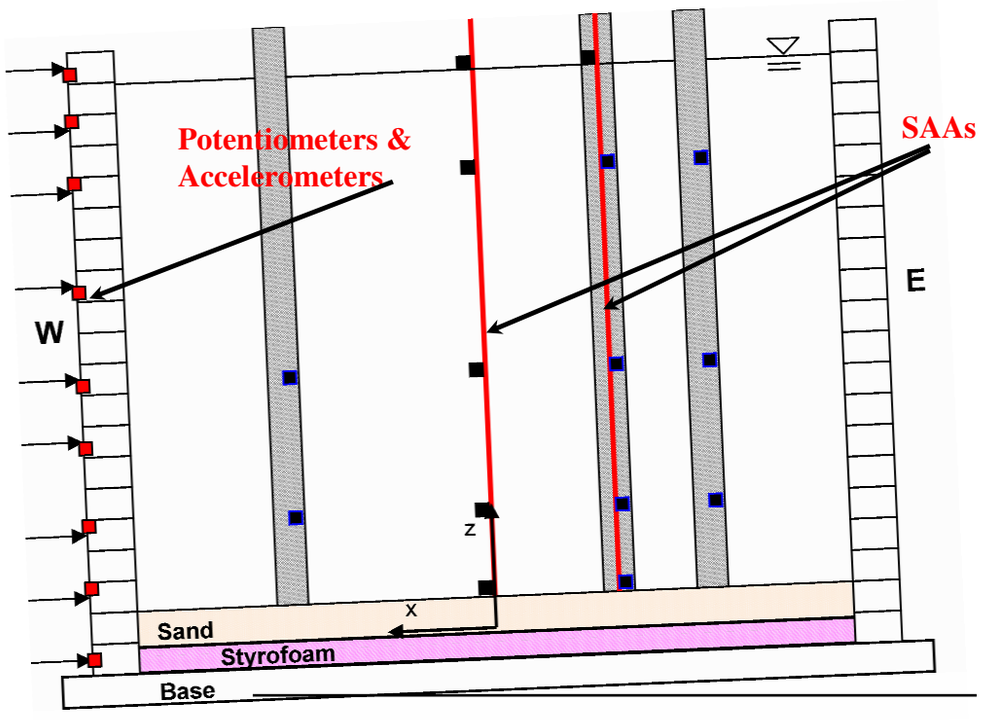


FIG. 3. Layout of instrumentation within container and on laminar rings.

The 5 m soil model was subjected to input motion that induced 30 cm of permanent lateral displacement at ground surface after 8.5 s of shaking. A representative sample of test results is included below. Figure 4 presents a comparison between acceleration time histories recorded using the center SAA and the traditional accelerometers located on the rings.

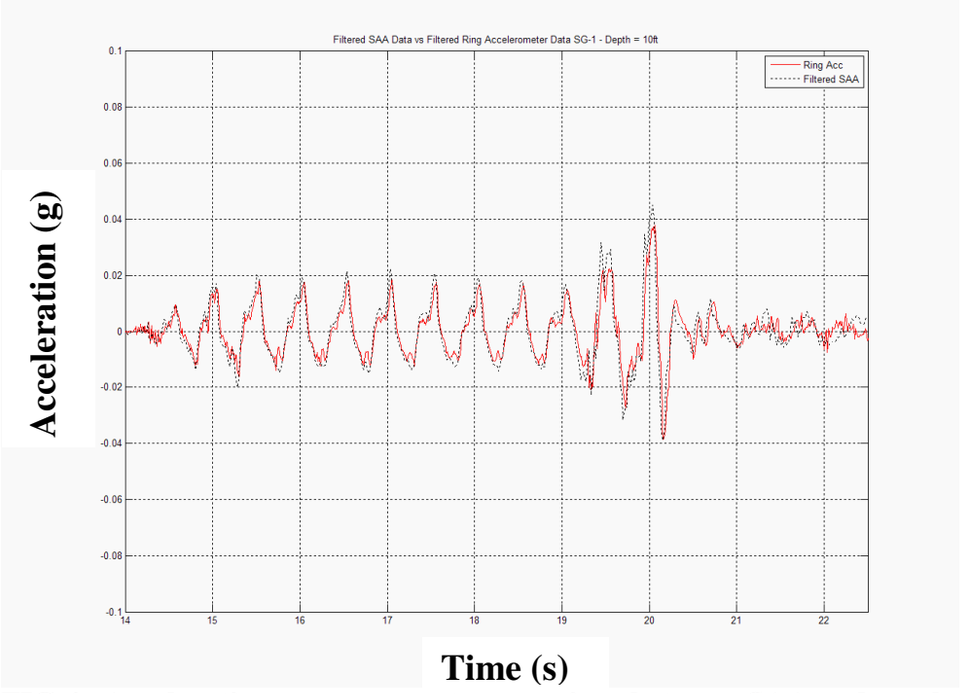


FIG 4. Acceleration measurement comparison between SAA and accelerometer on the laminar ring at mid-height of the laminar container.

Displacement readings from potentiometers were only available for the outside of the laminar box as these displacement gauges were fixed to the laminar rings. It is expected that the soil movement will match that of the laminar rings at the soil surface, thus a displacement comparison is included of that location. Figure 5 presents a comparison between lateral deformation time histories measured using the center SAA and the potentiometer on the uppermost laminar ring.

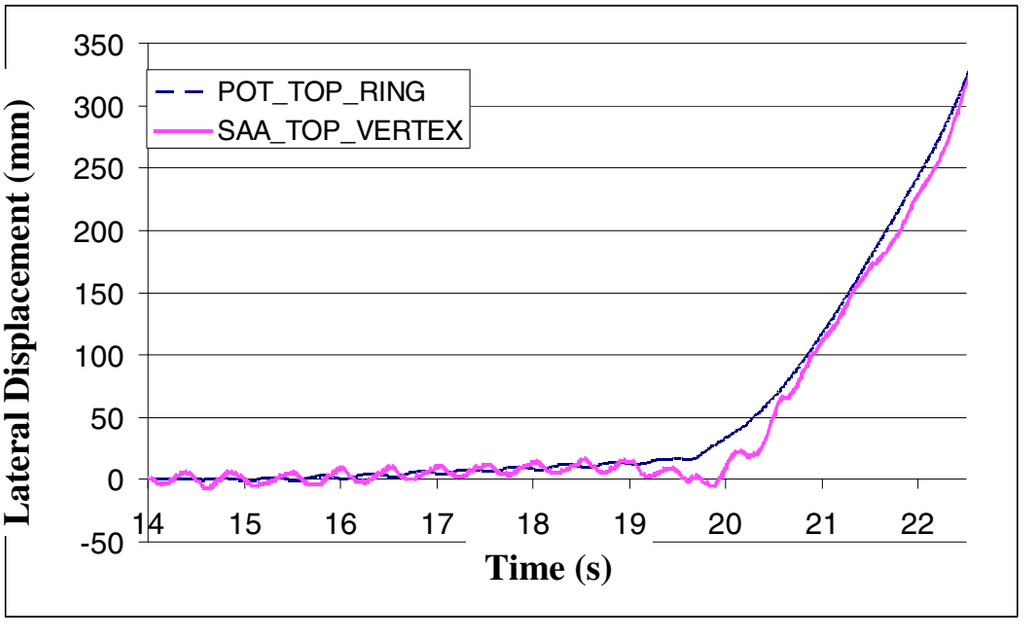


FIG 5. Lateral displacement comparison between SAA and potentiometer on the ring at the soil surface.

Figures 4 and 5 show a very good comparison between the acceleration and lateral displacement measured by the traditional sensors and the SAA. Similar results were obtained with the east sensor array. The SAA was also used to obtain a lateral displacement profile during the lateral spreading event. This profile is seen in Figure 6.

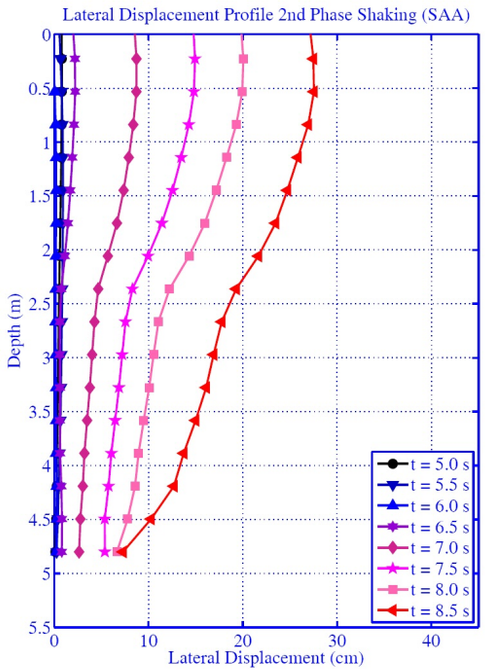


FIG. 6. Lateral displacement profile obtained with SAA during lateral spreading event.

CONCLUSIONS

The work presented in this paper constitutes a major step toward autonomous monitoring technology for soil systems susceptible to earthquakes and lateral spreading. The wireless Shape-Acceleration Array (SAA) is currently being further developed for in situ and research applications, taking advantage of the continuous advances in Micro-Electro-Mechanical Systems (MEMS) and wireless networking technologies. These preliminary full scale test results demonstrate that the SAA system is capable of simultaneously and accurately measuring acceleration and permanent ground deformation in situ. Based on the excellent agreement between SAA and traditional sensor data, the SAA data is currently being utilized in system identification techniques and for further investigation of the lateral spreading mechanism.

REFERENCES

Abdoun, T., A. Abe, V. Bennett, L. Danisch, M. Sato, K. Tokimatsu and J. Ubilla. (2007). "Wireless Real Time Monitoring of Soil and Soil-Structure Systems." Geotechnical Special Publication 161 – Embankments, Dams and Slopes: Lessons from the New Orleans Levee Failures and Other Issues. *Proceedings of GeoDenver 2007: New Peaks in Geotechnics*, Feb 18-21.

Arulanandan, K. and R. F. Scott, eds. (1993). *Verification of Numerical Procedures for the Analysis of Soil Liquefaction Problems*, Vol. 1, Balkema, Davis, CA.

Danisch, L.A. (1998). *Fiber optic bending and positioning sensor*. PCT 0702780, International PCT patent.

Danisch, L. A., M. S. Lowery-Simpson and T. Abdoun. (2004). *Shape-Acceleration Measurement Device and Method.* Patent Application.

Dobry, R., R. V. Whitman and J. M. Roesset. (1971). "Soil Properties and the One-Dimensional Theory of Earthquake Amplification." *Research Report R71-18*, School of Engineering, Massachusetts Institute of Technology.

Holzer, T. L., T. L. Youd and T. C. Hanks. (1989). "Dynamics of Liquefaction During the 1987 Superstition Hills, California Earthquake." *Science*, Vol. 244: 56-59.

Johnson, L. R. and W. Silva. (1981). "The Effects of Unconsolidated Sediments Upon the Ground Motion During Local Earthquakes." *Bulletin of the Seismological Society of America*, Vol. 71 (1): 127-142.

Joyner, W. B., R. E. Warrick, and A. A. Oliver. (1976). Analysis of Seismograms from a Downhole Array in Sediments Near San Francisco Bay. *Bulletin of the Seismological Society of America*, Vol. 66: 937-958.

NRC. (1982). Earthquake Engineering Research – 1982, Overview and Recommendations. *Report by the Committee on Earthquake Engineering, National Research Council, National Academy Press*. Washington, D.C.

Seed, H. B. and I. M. Idriss. (1970). Analyses of Ground Motion at Union Bay, Seattle During Earthquakes and Distant Nuclear Blasts. *Bulletin of the Seismological Society of America*, Vol. 60 (1): 125-136.

This page intentionally left blank

Recent Improvements in MOC for Earthquake Response

Richard P. Ray, M. ASCE, Ph.D., P.E.[1]

[1]Associate Professor, Department of Civil and Environmental Engineering, University of South Carolina, 300 Main St., Columbia, SC, 29208; ray@engr.sc.edu

ABSTRACT: The Method of Characteristics was introduced by Streeter, Wylie, and Richart (1974) over thirty years ago. The method demonstrated the ability to faithfully reproduce 1-dimensional, horizontally polarized, vertically propagating shear waves through soil. Since then, many adjustments and improvements have been introduced. This paper summarizes some of those improvements and presents further refinements to the approach. Such features as independent energy balance evaluation, interpolation along time (as opposed to space) lines, stress-reversal checking, and non-linear stress-strain table look-up are also included. These improvements have eliminated past problems with numerical damping and accuracy of stress-strain hysteresis. The newer version, WinMOC, employs a more user-friendly interface with a multitude of soil stress-strain models, full graphing capabilities, response spectra generation, and evaluation of many ground motion parameters.

The Method of Characteristics is compared to an equivalent linear frequency domain method. Results generally show more accurate representation of strong motion with the same ease of use. This is especially demonstrated at sites with deep (> 150 ft) soil layers. A computational example is presented so that reader may judge the efficacy of the method.

INTRODUCTION

One dimensional seismic response analysis has been a mainstay in earthquake engineering for over 30 years. Most analyses use either a time domain solution (Hashash and Park, 2001) or a frequency domain solution (Kramer, 1996). While solutions in frequency domain are computationally more convenient, they suffer from inherent inaccuracies. Most of the inaccuracy occurs due to the way frequency domain solutions treat non-linear soil behavior. Modulus reductions due to higher strains are applied over the entire duration of the event. This is necessary because there is no sense of time-history in a frequency domain solution. Modulus and damping values are the same throughout the entire event. Given the present state of computational sophistication, this is no longer necessary. Time domain solutions are computationally fast enough to perform the same tasks as their frequency domain counterparts, but without the inherent problems associated with equivalent linear approaches.

The method of characteristics is a very efficient method of computing true nonlinear response of soils to earthquake excitation. The problem of a vertically propagating, horizontally polarized shear waves traveling through any number and depth of soil layers is solved in seconds. Numerical damping due to interpolations is reduced to negligible amounts by interpolation in time, as opposed to space, and energy budgets can be tracked and evaluated. Furthermore, stress-strain behavior is

evaluated independently from the constitutive model, allowing the operator to verify if the response analysis makes sense.

METHOD OF CHARACTERISTICS

Most earthquake analysis programs presume a depth of analysis to approximately 100 ft. This assumption is valid for many earthquake-prone areas. However, in and around Charleston, South Carolina, as well as the Central U.S. this assumption is incorrect. Soil deposits in these areas can be detected to depths over 700 ft (Bybell et al, 1998, Hashash and Park, 2001, Andrus et al, 2006). Such conditions require a robust analysis tool for evaluating earthquake wave propagation to the surface. This paper presents one such method. The method of characteristics has been applied to one-dimensional shear wave propagation through layered soil with non-linear stress-strain properties (Streeter et al. 1974). It has been further modified by others and is presented here as yet another refinement.

The major advantage of the method is its ability to faithfully model the non-linear, hysteretic, stress-strain behavior of soil when subjected to high levels of acceleration. In the next sections, a brief discussion of governing equations is first presented, followed by methods of numerical interpolation, energy accounting, and finally, application to a deep soil deposit

Governing Equations

An excellent presentation of the derivation of the method has been presented, and often cited, in the literature (Streeter et al. 1974). For brevity, the resulting equations are presented directly. A one-dimensional, horizontally-polarized, vertically-propagating shear wave (Fig. 1) can be represented by the following equations:

Along the C^+ characteristic

$$\frac{d\tau}{dt} - \rho v_s \frac{dV}{dt} = 0 \quad and \quad \frac{dz}{dt} = v_s \tag{1a}$$

Along the C^- characteristic:

$$\frac{d\tau}{dt} + \rho v_s \frac{dV}{dt} = 0 \quad and \quad \frac{dz}{dt} = -v_s \tag{1b}$$

Where τ = shearing stress;
t = time;
ρ = mass density;
v_S = phase (shear wave) velocity;
V = particle velocity.

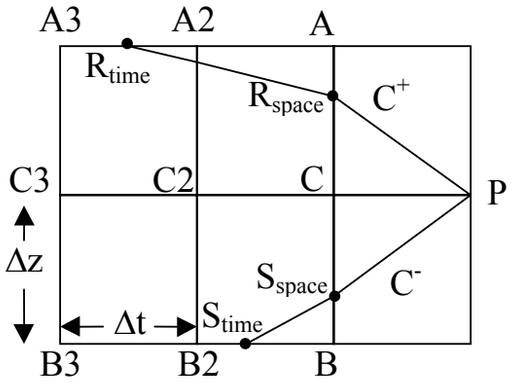


Figure 1. Computational Grid

The C^+, C^- lines are interpreted physically as the phase velocity of the shear waves moving up and down the soil column. One may also view them as packets of shear stress/particle velocity information moving at the prescribed velocities. Equations 1a,b are total derivatives and easily translated into finite difference form.

$$\tau_P - \tau_A - \rho_{AP} v_{AP} (V_P - V_A) = 0 \quad (2a)$$

$$\tau_P - \tau_B + \rho_{BP} v_{BP} (V_P - V_B) = 0 \quad (2b)$$

Phase velocities and mass densities may be different for the reach from A to P and B to P, depending on soil properties within the respective reaches. If the stress and velocity are known at the previous time step (A, B) then stress and velocity are computed directly at the present time step (P). Additional terms for viscous damping (e.g. Hashash and Park, 2002; Park and Hashash, 2004) may be added to the formulation; however viscous damping (as opposed to non-linear stress-strain hysteresis) is not considered in this paper.

Earthquake wave input occurs in the form of a velocity vs. time history at the base of the column. Since velocity is prescribed at the base in the form of an earthquake time series, the equations reduce to only the C^+ condition. At the surface, one may assume a free-stress (τ=0) condition, requiring only the C^- characteristic equation, or more commonly, assume a block of material with weight w, (to represent a building or foundation) at the surface, whereby additional equations of motion are imposed.

$$V_P = \frac{\tau_B}{\rho v} + V_B \quad \text{if } \tau_P = 0 \text{, or with a surface mass,} \quad (3a)$$

$$F = \frac{\tau_C + \tau_P}{2} = ma = m\frac{dV}{dt} = m\frac{V_P - V_C}{\Delta t} = \frac{w}{g}\frac{(V_P - V_C)}{\Delta t} \text{ then} \quad (3b)$$

$$V_P = \frac{\tau_B + \tau_C + \frac{2wV_C}{g\,\Delta t} + V_B\ \rho v_B}{\rho v_B + \frac{2w}{g\,\Delta t}} \quad (3c)$$

Either way, the surface node requires only the C^- characteristic from the soil below.

Nonlinear Behavior and Interpolations

Nonlinear stress-strain behavior complicates the numerical estimates in that the phase velocities slow down, requiring more time to reach the point of computation (point P). In order to satisfy the requirements for numerical stability, (i.e. the packets of information must arrive on time; the Cauchy criterion) some scheme of interpolation must be invoked. Interpolating in space between the previous points A, B, and C is easily accomplished at the cost of reduced accuracy manifested as "numerical damping". Values with subscripts $R_{space,}$ S_{space} will replace A and B respectively, in the equations. The precise location of interpolation is not known since one cannot compute reduced phase velocity until stress is known at the destination point. However, a simple Newton's method can readily solve the problem. Better results are achieved by interpolating in time, rather than space, where $R_{time,}$ S_{time} now replace A and B. An average phase velocity can then be computed by the same Newton's method and applied to the equations at point P.

Work-Energy Balance

In order to evaluate the degree of numerical damping that may take place, the computational sequence tracks work input at the base due to the earthquake, and energy stored and dissipated throughout the soil column. Work input is simply calculated as force times displacement at the base of the soil column. In finite difference form; average base stress for a time step times displacement for the same step.

$$dW = \int_{t}^{t+\Delta t} F\delta dt = \frac{\Delta t}{4}\left(V_{base\ t+\Delta t} + V_{base\ t}\right)\left(\tau_{base\ t+\Delta t} + \tau_{base\ t}\right) \tag{4}$$

Energy through the column can take the form of stored elastic and dissipated hysteretic energy, and instantaneous kinetic energy. The stored and hysteretic energy is computed by

$$dSH = \int_{\overline{V}} \int_{\gamma}^{\gamma+\Delta\gamma} \tau d\gamma d\overline{V} \tag{5}$$

This is simply the area under the stress-strain curve over the volume of soil in question. In terms of computed stress and displacements, as well as discreet reaches, this works out to:

$$SH = \sum_{j=1}^{m} \frac{\Delta z_j}{4}(\tau_j + \tau_{j+1} + \tau_{jold} + \tau_{j+1old})\left[(\delta_{j+1} - \delta_j) - (\delta_{j+1old} - \delta_{jold})\right] \tag{6}$$

For nonlinear behavior, the unloading curve is below its loading counterpart and the hysteretic component is never recovered (but still accounted for). Kinetic energy is computed as the instantaneous value over the soil column at the end of the time step. For a single reach,

$$dKE = \frac{1}{2}\rho\Delta z\left(\frac{V_j + V_{j+1}}{2}\right)^2 \tag{7}$$

Energy and work can be compared as a ratio of stored and kinetic energy divided by work input. An energy/work ratio can be tracked during computation to determine the effect, if any, of numerical damping. An energy ratio value of 1.0 indicates no numerical damping while less than 1.0 indicates some damping has taken place.

Stress Reversals and Forecasting

The numerical method is readily modified to deal with stress reversals using the extended Masing criteria. While the criteria are easily written, the algorithm to apply the criteria is less obvious. One outcome of the algorithm and the use of values from previous time steps is the "loss" of information immediately after the turnaround points (τ_i, γ_i) resulting in stress-strain curves that do not turn around correctly (Ray, 2002). The phase velocity is not properly updated since the existence of a turnaround is not known until all computations are complete for that time step. The only way to update the analysis properly is to go back in time one step and use the new (anticipated) phase velocity to re-compute values of velocity (hence displacement and strain) and stress. This procedure works well in the analysis, even without a reversal, since it more accurately represents conditions in the soil over the last time step. Consequently the entire solution algorithm steps forward to estimate the phase velocity and then applies the new phase velocity to the same calculation step again (Fig 2).

Stress-Strain Model

The Ramberg-Osgood model is a convenient numerical representation of shearing stress vs. shearing strain. It is readily made dimensionless and can be scaled to field generated values of shear modulus. The stress strain equation is normally written

$$\gamma = \frac{\tau}{G_o}\left(1+\alpha\left|\frac{\tau}{C_1\tau_m}\right|^{R-1}\right) \tag{8}$$

Where γ=shearing strain; τ=shearing stress; G_o=maximum (low strain amplitude) shear modulus; α, C_1, R=curve-fitting constants. Stress reversals are computed by the same equation with the substitutions

$$\frac{\gamma-\gamma_i}{2} \text{ and } \frac{\tau-\tau_i}{2} \quad \text{for} \quad \gamma \text{ and } \tau \tag{9}$$

Where γ_i, τ_i are values at a reversal point

For computing phase velocity, a value of tangent modulus is required. This is computed by the following equations.

$$v_s = \sqrt{\frac{G_{\tan}}{\rho}} \qquad G_{\tan} = \frac{G_o}{\left(1+\alpha R\left|\frac{\tau}{C_1\tau_{\max}}\right|^{R-1}\right)} \tag{10}$$

Note that the equations, as cast, render direct calculation of v_s as a function of strain impossible. In order to circumvent this problem, and make the code more generally applicable, a table look-up method is used instead of direct calculation.

Prior to running the time sequence, values of γ and G_{tan} are computed for common values of τ/τ_{max} and are stored in an array. In this study, 128 values were computed.

During the time sequence, values of strain are known, and G_{tan} is determined by binary search. Each lookup requires 7 comparisons and a final linear interpolation. Such a method can be applied to any soil model with any degree of precision (e.g. 256, 512 values). Nonlinear stress-strain models can be represented by any relationship the user wishes (e.g. Assimaki et al, 2000; EPRI, 1993). Actual values of modulus reduction versus strain are stored as tabular data (128 data pairs) for each soil type. A binary look-up scheme finds the correct range and then a simple linear interpolation is performed. Users can extend the tables to 256, 512, etc., values if necessary.

Computation of Stress, Strain

Solutions to equations 1a and 1b lead to values of shearing stress, τ, and particle velocity V, at every reach point. Values for displacement are computed by integration of velocity over time at every reach point. For a specific soil interval between two reach points, shearing strain is computed as the difference in displacements above and below, divided by the interval length. Shearing stress in the interval is computed as the average stress at points above and below.

The only computational tie between stress and strain is through calculation of phase velocity (via non-linear models such as Ramberg-Osgood) and its application into equation 1a and 1b. Therefore, if stress strain curves generated from the above calculations along each layer accurately represent nonlinear behavior of the soil, the model is a good one. This is *very different* from applying a stress-strain model to an already-computed stress-time history and observing strain behavior.

COMPARISON WITH EQUIVALENT LINEAR ANALYSIS

In order to show comparison to a familiar profile, WinMOC was used to analyze the profile first given by Schnabel et al (1972) with an acceleration history from the EduShake (EduPro Civil Systems, 1999) program: Treasure Island, Loma Prieta. The soil models required special handling since the WinMOC program uses a non-dimensional approach to non-linear stress-strain models. However, the parameters chosen matched the Seed and Idriss (1970) sand curves as well as the Sun et al (1988) clay curves. The WinMOC analysis used 50 computational reaches to discretize the profile. The earthquake record was identical to the record used in EduShake. Plots of surface velocity vs. time are shown in figure 2. Note that the response is given for the time interval from 10 to 20 seconds in order to increase visibility. The responses are typical for the types of approaches used: the time-stepping approach can carry along high frequencies even at high strains while the equivalent linear approach cannot. The high frequencies can be better imagined when one looks at the impact of turnarounds in the stress-strain behavior during high-amplitude loading. Figure 3 shows the stress-strain history for the same profile and event at depths of 132 and 145 ft. The stress reversals show a sharp response and stiff behavior which is carried through the rest of the profile. Notice also the Masing behavior (Ray and Woods, 1987) throughout the event. Since these are response stresses and strains, the fidelity of the model is excellent with respect to Masing behavior.

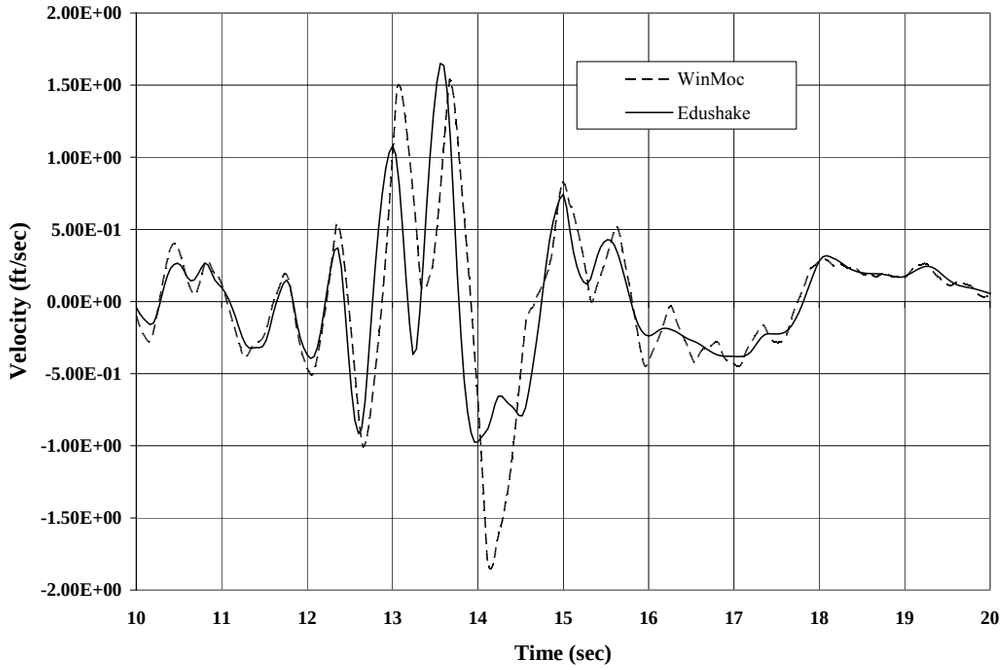


Figure 2. Surface Velocity For WinMOC and EduShake

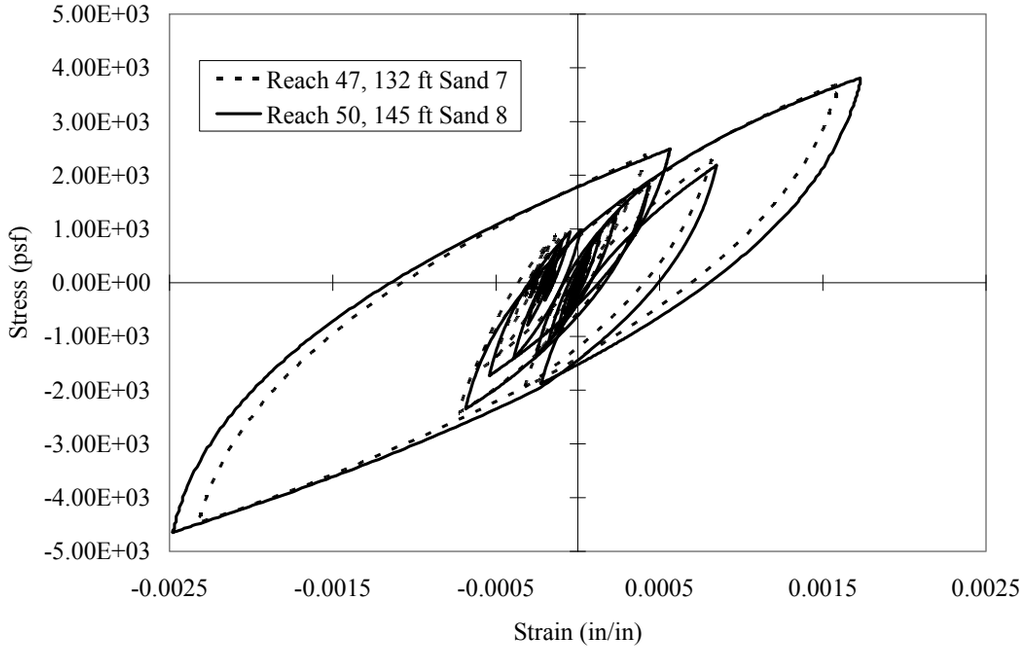


Figure 3. Stress-Strain Response in Deep Sands

Energy Results

The ability to track energy is shown in figure 4 where work at the base, elastic and hysteretic energy, and kinetic energy are tracked during the entire event. Energy ratio is plotted on the secondary axis and shows a value between 1.00 and 0.992 for the duration of shaking. Virtually no numerical damping is present.

Implications for Liquefaction Evaluation

Since the stress-strain behavior of all individual reaches are tracked for the entire event, approaches to liquefaction evaluation using damage parameters or pore-pressure generation (Bonilla et al, 2005) by exceeding threshold strain levels becomes simply a matter of a subroutine within the analysis. Tracking maximum stresses, maximum strains, number of major cycles of loading are also easily implemented. This program has been used to develop profiles of maximum shear stress, and maximum shear strain in order to compare to liquefaction resistance profiles.

CONCLUSIONS

The method of characteristics is indeed a robust method that computes one-dimensional response in a matter of seconds. The method is capable of faithfully reproducing nonlinear earthquake behavior with a high degree of accuracy over a wide range of conditions. Interpolation in time with forecasting showed to be very accurate while computationally frugal. High frequency components of shaking are not lost in the analysis and provide valuable information for critical structures sensitive to such shaking. Time histories of velocity, acceleration, displacement, shear stress, shear strain, hysteretic dissipation, are all computed as a matter of course in the model. The Masing criterion is well modeled as seen from the stress-strain curves presented here. Further program information can be obtained from the author.

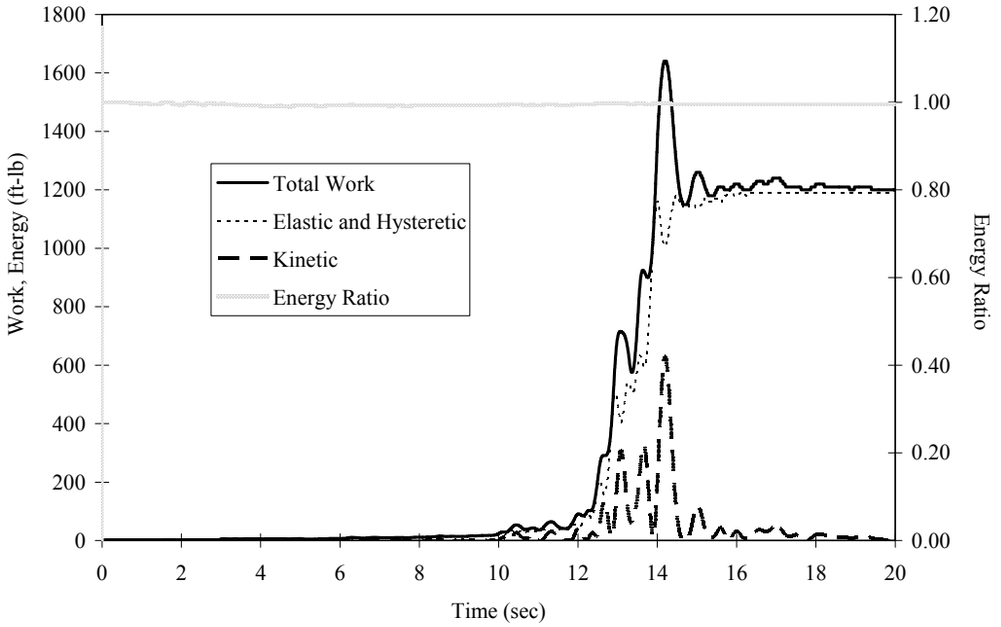


Figure 4. Work, Energy, Energy Ratio vs. Time

REFERENCES

Andrus, R.D., Fairbanks, C.D., Zhang, J., Camp., W.M., Casey, T.J., Cleary, T.J., and Wright, W.B., (2006) "Shear-Wave Velocity and Seismic Response of Near-Surface Sediments in Charleston, South Carolina," *Bulletin of the Seismological Society of America*, Vol. 96, No. 5, pp. 1897-1914.

Assimaki, D., Kausel, E., and Whittle, A (2000) "Model for Dynamic Shear Modulus and Damping for Granular Soils," *Journal of the Geotechnical and Geoenvironmental Engineering*, ASCE, (126)10: 859-869.

Bonilla, L.F., Archuleta, R.J, and Lavalle, D. (2005) "Hysteretic and Dilatant Behavior of Cohesionless Soils and Their Effects on Nonlinear Site Response: Field Data Observations and Modeling," *Bulletin Seismological Society of America*, Vol. 95, No. 6, pp. 2373-2395

Bybell, L.M., Conlon, K.J., Edwards, L.E., Frederiksen, N.O., Gohn, G.S., & Self-Trail, J.M. (1998) "Biostratigraphy and physical stratigraphy of the USGS-Cannon Park core (CHN-800), Charleston County, South Carolina," *U.S. Geological Survey Open-file Report 98-246*. Reston, Virginia

EPRI. (1993) "Guidelines for determining design basis ground motions," EPRI TR-102293, Palo Alto, CA,

EduPro Civil Systems (1999) EduShake Version 1.10, June.

Hashash, Y. M. A., and Park, D. (2001). "Non-linear one-dimensional seismic ground motion propagation in the Mississippi embayment," *Engineering Geology*, 62(1-3), 185-206.

Hashash, Y. M. A., and Park, D. (2002). "Viscous damping formulation and high frequency motion propagation in nonlinear site response analysis," *Soil Dynamics and Earthquake Engineering*, 22(7), pp. 611-624.

Kramer, S. L. (1996). *Geotechnical Earthquake Engineering*, Prentice Hall, Upper Saddle River, N.J.

Park, D., and Hashash, Y. M. A. (2004). "Soil damping formulation in nonlinear time domain site response analysis," *Journal of Earthquake Engineering*, 8(2), 249-274.

Ray, R.P. (2002) "Modeling Earthquake Response in Deep Soil Deposits," *Numerical Models in Geomechanics* (*NUMOG VIII*), edited by Pande & Pietruszczak, Swets & Zeitlinger, The Netherlands, pages 667-71, ISBN 90 5809 359X.

Ray, R.P. and Woods R.D., (1987) "Modulus & Damping Due To Uniform and Variable Cyclic Loading," *Journal of the Geotechnical Engineering Division*, ASCE, Vol 114, No, 8, August, pp. 861-876.

Schnabel, P.B., Lysmer, J., and Seed, H.B. (1972). "SHAKE: A computer program for earthquake response analysis of horizontally layered sites," Report No. EERC 72-12, Earthquake Engineering Research Center, University of California, Berkeley, California.

Streeter, V.L., Wylie, E.B., & Richart, F.E. (1974) "Soil motion computations by characteristics method," *Journal of the Geotechnical Engineering Division, ASCE* 100,(GT3): 247-263.

Seed, H.B. and Idriss, I.M. (1970). "Soil moduli and damping factors for dynamic response analyses," Report No. EERC 70-10, Earthquake Engineering Research Center, University of California, Berkeley.

Sun, J.I., Golesorkhi, R., and Seed, H.B. (1988). "Dynamic moduli and damping ratios for cohesive soils," Report No. EERC-88/15, Earthquake Engineering Research Center, University of California, Berkeley.

Some Characteristics of Ground Vibration as Induced by High-Speed Trains

Yit-Jin Chen[1], Yi-Jiun Shen[2], Kuo-Yen Chen[3] and Shih-Ming Chang[4]

[1,3,4] Department of Civil Engineering, Chung Yuan Christian University, Chung-Li 32023, Taiwan; PH 886-3-2654227; FAX 886-3-2654299; email:yjc@cycu.edu.tw; g9572039@cycu.edu.tw; g9572040@cycu.edu.tw

[2] CECI Engineering Consultants, Inc., Taiwan, 7F, 280, Chung-Hsiao E. Rd, Sec. 4, Taipei, Taiwan; PH 886-2-27814151; FAX 886-2-27780023; email: yjs@ceci.com.tw

Abstract

This paper examines some characteristics of ground vibration as induced by high-speed trains using a wide variety of field-measured data. The measurements for analysis consist of different geological conditions, train speeds, foundation types, and superstructures. Based on these analyses, geological condition is found to be a very important factor which obviously influences initial mobilized vibration level and vibration attenuation. For the train speed factor, the vibration level increases with increasing train speed, but the incremental rate is more obvious on soft ground. The foundation type has an influence on the initial mobilized vibration level and its attenuation rate with distance. In addition, the trains on an embankment and a bridge with shallow foundation present relatively consistent vibration characteristics. Finally, some recommendations for further studies are proposed.

INTRODUCTION

In recent decades, more and more high-speed rail lines have been constructed to connect major cities in Europe, Asia and the United States. This is because travel by high-speed rail has become more competitive especially in areas of higher population density. Meanwhile, the high-speed rail systems in use today have a much lower energy consumption than air or road travel. Therefore, the high speed-rail has an advantage over other transport systems. However, the ground vibration induced by the train system can reach levels that cause human annoyance and interruption of sensitive instrumentation in some areas. Thus, the ground vibrations induced by high-speed trains have drawn researchers' interest in recent years.

Researchers have studied vibration characteristics in order to develop a scheme for vibration mitigation. In the United States, the US Department of Transportation developed manuals (FTA 1995; FRA 1998) to assess the vibration impact for rapid transit and high-speed railways. In these manuals, the factors affecting vibration source, vibration path, and vibration receiver are clearly specified and easily used. Geological condition is also known to have a significant effect on the vibration level, but there is lack of clarified methodologies to assess the effect of geological condition in these manuals.

In Japan, studies on train-induced vibration are mainly for the Shinkansen system, the high-speed rail in Japan. For instance, Yoshioka (2000) reviewed the acceleration spectrum of many measurement sites and interpreted the peak vibrations of these measurement results as the periodicity of axle arrangement and speed of train. The periodic effects of axle arrangement on different train speeds decide the peak frequency of the train-induced vibration spectrum. For the effects of elevated structures, Ejima (1980) conducted a large-scale measurement for the issue of bridge structure sections, and the results indicated that the vibration value becomes smaller when the bending rigidity of the superstructure and the concrete volume in the substructure of the bridge increase. As examined in Ejima's data, Yoshioka (2000) also concluded that a bridge foundation built in soft ground can easily agitate the ground vibration than in hard ground.

The vibration measurements of Eurotrain were carried out during the test-run of the high-speed railway line, Hanover-Wurzburg, in Germany (Tseng 1999). The Eurotrain consisted of two ICE-2 power-cars and eight TGV-duplex coaches. It was the first time that this combination of German and French rolling stock was tested on a regular high-speed line. The measurements were conducted in two situations: (1) an at-grade situation, and (2) a viaduct situation (Kassemuhle Valley Bridge). The maximum peak velocity for the at-grade situation is 4.5 mm/sec at a distance 8 m from the rail. The vibrations of the z-component (vertical direction) and y-component (at the right angle of the railway) are higher than that of the x-component (parallel to the railway line). The maximum peak velocity for the viaduct situation is 5 mm/sec at the base of the pier and 1 mm/sec at a distance 16 m from the rail. In addition to the peak value, frequency analyses were conducted with the max-hold-spectra. The main excitation frequency for Eurotrain is around 16~31.5 Hz for the case of 16 m from the railway bridge.

On the other hand, the Taiwan high-speed rail has been completed, and it started on its commercial operation in January 2007. In this study, a broad base of the ground vibration induced by the Taiwan high-speed rail on different geological conditions, train speeds, and structures was measured. The characteristics affecting ground vibration are correspondingly discussed in this paper.

MEASUREMENT METHOD

To perform the train-induced ground vibration measurements, a reliable measurement scheme is needed. The trainset, measuring equipment, measuring procedure, and presentation of the measurement results are briefly described below. Some details are presented elsewhere (Chen et al. 2006)

Trainset

The Japanese Shinkansen 700-series system is used for the Taiwan high-speed rail. The trainset of the Taiwan high-speed rail consists of 12 train-cars with 10 cars for passengers and 2 cars for motivation. The length of the passenger car (PC) and motive car (MC) is 25 m and 27 m, respectively, and thus the total length of the trainset is 304 m. The sketch of the trainset configuration and related dimensions of the Taiwan high-speed rail is shown in Fig. 1.

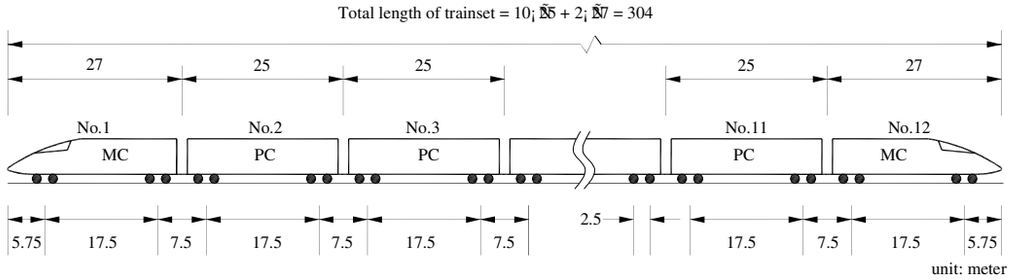
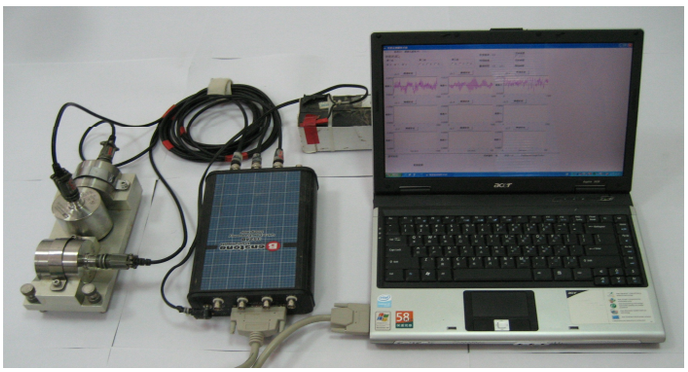


Figure 1 Configuration of trainset for the Taiwan high-speed rail

Measuring Equipment

A goal of train-induced ground vibration measurement is to accurately record the combination effects of vibration source and the propagation path at a particular location within the range of amplitudes (10~100 dB ref. 1 micro-inch/sec) and frequencies (1~100Hz) needed for various assessments and research applications. The measuring equipment for this study includes accelerometers, integrator, and a data acquisition system. A set of the measuring instruments and equipment used in this study is shown in Fig. 2. The seismic accelerometers, including the x, y, and z directions, incorporate an isolated piezoelectric sensing element which minimizes the effects of transverse motion, base strain, and thermal transients. The accelerometer also contains a proprietary solid state charge amplifier with an extremely low noise floor. This enables the sensor to measure an acceleration range of ± 0.5 g and feature a sensitivity of 10 V/g.



(a) (b) (c)

Figure 2 Measuring equipment: (a) three accelerometers in the x, y, and z directions; (b) integrator; and (c) data acquisition system

Since the velocity vibration level is normally used to evaluate the vibration magnitude, the integrator was used to transfer the acceleration signal to the velocity signal, and transform the physical vibration value into voltage. The data acquisition system consists of a data acquisition card, a computer program, and a notebook. The data acquisition card can digitize input voltages. Through the control of a computer program, including Microsoft Visual C++ and Visual Basic, the measured vibration data can be stored in a notebook.

In order to evaluate the frequency effect of ground vibration, the frequency domain of a one-third octave band is adopted to describe the vibration velocity as decibel (dB). The advantage of this method is that the frequency effect can be presented as according to the international standard of the semiconductor industry and some environmental vibration criteria. The frequency range of interest is from 1 to 100 Hz, and a scale of one-third octave band has been developed. The sampling frequency used for time domain measurement is 512 Hz. Through an appropriate Fast Fourier Transform (FFT), the frequency response of the measurement is presented using a one-third octave band for the central frequency range of 1 to 100 Hz.

Measuring Procedure

The following procedure is used to measure the ground vibration for each location:

1. Place firmly the three-dimensional accelerometers on the ground at the requested distances.
2. Set the accelerometer direction: the x-direction is in the train moving direction; the y-direction is perpendicular to the train moving direction; and the z-direction is for the direction of gravity.
3. Configure the measuring system and set the measuring parameters.
4. Trigger the measuring system as the high-speed trains pass.

Fig. 3 shows the typical result of vibration velocity, which is integrated from the acceleration measurement, in the x-direction. The train consists of 12 cars with a 300 km/h train speed, and the measuring equipment is located at a 25 m perpendicular distance from the bridge pier. For this case, it can easily be found that a group of peaks is marked distinctly in the figure when the train passes the measurement location. The speed of the train can be determined from the passing time with the given length of the trainset. From Fig. 3, it can also be clearly found that there are basic inherent background ground vibrations before and after the train passes the measured location.

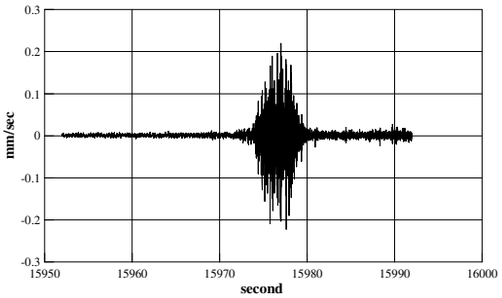


Figure 3 Time domain data of vibration velocity measured in the x-direction

Presentation of the Measurement Results

As described previously, one-third octave band velocity spectra were used to present the time domain data. All the measurements are carried out using the one-third octave band analyzer with a central frequency ranging from 1 Hz to 100 Hz. The ground vibration level is expressed in terms of its root-mean-square (RMS) velocity using the decibel scale (dB). The RMS velocity level in decibels is defined as follows:

$$VL = 20 \log_{10} (v_m/v_{ref}) \quad (1)$$

in which v_m = the measured velocity and v_{ref} = the referred velocity (where $v_{ref} = 10^{-6}$ in/sec = 2.54×10^{-6} cm/sec in this study).

The overall vibration level (VL_{OA}) is sometimes used to evaluate the total vibration energy (e.g., FTA 1995). The overall vibration level can be transferred from the RMS velocity of each 1/3 octave band vibration level, as calculated below:

$$VL_{OA} = 10 \log_{10} \sum_{k=1}^{n} 10^{VL(fk)/10} = 10 \log_{10}(10^{0.1\ VL(f1)} + 10^{0.1\ VL(f2)} + \ . \ . \ + 10^{0.1\ VL(fn)}) \qquad (2)$$

in which VL_{OA} is the overall vibration level in decibels, fk is each 1/3 octave band's central frequency (1 ..100 Hz for the frequency of f1 ..fn), and VL(fk) is the vibration level for each frequency of the 1/3 octave band.

DATABASE

A series of measurements is performed for this study in order to observe the characteristics of ground vibration as induced by high-speed trains. These measurements consisted of bridge and embankment superstructure types with different foundation types, train speeds, and geological conditions. Table 1 lists the basic information of these measurements. It can be seen that a wide variety of structures and train speeds is included, and the soil conditions range from soft ground to hard ground. The database is considered as enough for the purpose of this analysis.

Table 1 Basic information of the high-speed train vibration measurements

Super-Structure	Sub-structure	Soil condition	Train speed[a] (km/h)	Measurement distance from source (m)
Bridge	spread footing	gravel	2-280, 2-300	0, 25, 50, 100, 200
Bridge	pile	sandstone	5-210	0, 50, 100, 180
		gravel	2-120, 130, 2-150, 230, 250, 2-300	0, 25, 50, 100, 200
		sand, clay, silt	12-200, 2-220, 4-230, 6-240, 2-250, 5-270, 2-280, 3-290, 4-300	0, 12.5, 100, 200, 300, 400
embankment	—	gravel	2-280, 290, 300	30, 60, 100, 140, 200

a: 2-280 express two measurements with train speed 280 km/h.

CHARACTERISTICS OF GROUND VIBRATION AS INDUCED BY HIGH-SPEED TRAINS

As can be seen in Table 1, the same measurements were performed several times. The following analyses and presentations in subsequent figures are all taken as an average from these measurements.

Geological Factor

Figs. 4 and 5 show the comparisons of vibration response at different ground conditions for near and far distances, respectively, from the vibration source (pier of the

bridge). The structural layout of the high-speed rail for these measurements is a bridge with pile foundation. One location is on the interlayer of sand, clay, and silt with an SPT-N (N value of standard penetration test) between 10 and 20 which is denoted as soft ground, while the other location is on sandstone which is denoted as hard ground. The train speed is 200 km/h, and the measuring equipment is located at 0 m (for near distance) and 100 m (for far distance) from the high-speed rail.

From Figs. 4 and 5, it is evident that the peak ground vibrations at soft ground are much higher than those at hard ground. On the average, the difference in initial mobilized vibration level (at near distance) for most frequencies is about 10-15 dB for the x, y, and z directions, and the difference is at 5-10 dB even if the distance reaches 100 m. When checking the further distance (180-200 m), the obvious difference still exists. Therefore, with the higher initial mobilized vibration levels, a much longer distance is needed at a soft ground to attenuate the vibration to a relatively small value.

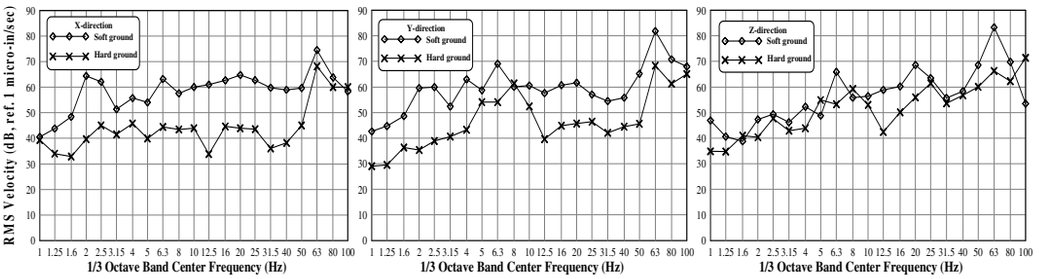


Figure 4 Comparison of initial mobilized vibration for different ground conditions at near distance (0 m)

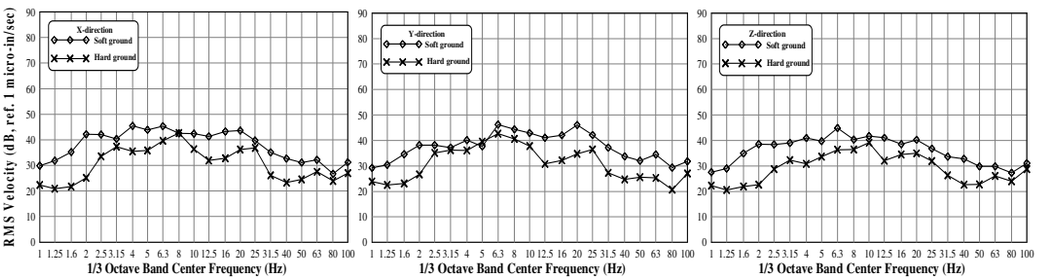


Figure 5 Comparison of vibration for different ground conditions at far distance (100 m)

Speed Factor

The comparisons of vibration for train speed at soft and hard grounds are shown in Figs. 6 and 7, respectively. All structural layouts of the high-speed rail for these measurements are a bridge with pile foundation, and the measurement distance for comparison is 12.5-25.0 m from the high-speed rail. The soft ground is on the interlayer of sand, clay, and silt, while the hard ground is on the gravel layer with an SPT-N value greater than 100, which is also denoted as hard ground. There is a wide range of train speeds from 150 to 300 km/h for these measurements.

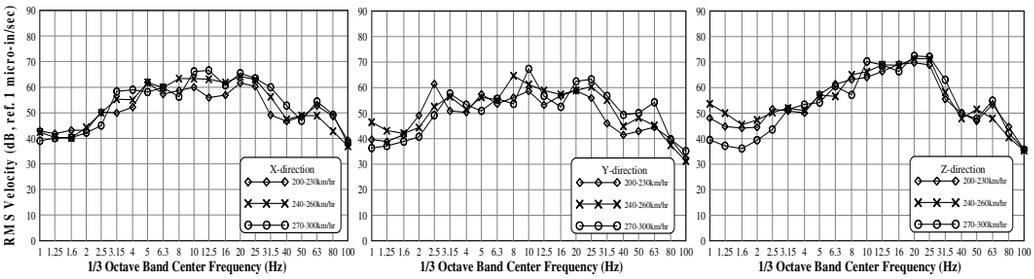


Figure 6 Comparison of vibration for different train speeds on soft ground

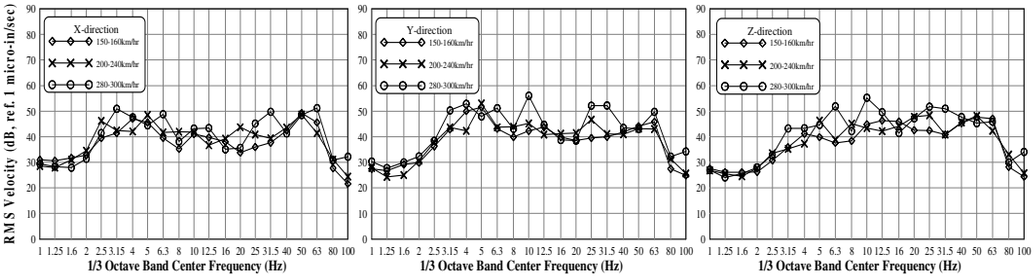


Figure 7 Comparison of vibration for different train speeds on hard ground

From Figs. 6 and 7, it can be seen that the peak vibration level increases with increasing train speed for both soft and hard grounds. However, the increment of vibration level due to the train speed factor for each frequency is relatively slight. Fig. 8 shows the regression relationship, denoted as a solid line, of overall vibration level versus train speed. For convenient comparison, Eqs. (3) and (4) present the results of regression analyses for soft and hard ground, respectively, at x-direction.

$$\text{adjustment } VL_{oa} = 27.4 \log_{10} [V(\text{speed})/V(\text{speed}_{ref})] \quad \text{(for soft ground)} \quad (3)$$

$$\text{adjustment } VL_{oa} = 7.9 \log_{10} [V(\text{speed})/V(\text{speed}_{ref})] \quad \text{(for hard ground)} \quad (4)$$

where adjustment VL_{oa} = the adjustment of the overall vibration level of the train with the speed of $V(\text{speed})$, and $V(\text{speed}_{ref})$ = the train speed of the known vibration source. The slope is steeper at soft ground than that at hard ground. Therefore, this means that the incremental rate of vibration level due to train speed factor is more obvious on soft ground than on hard ground.

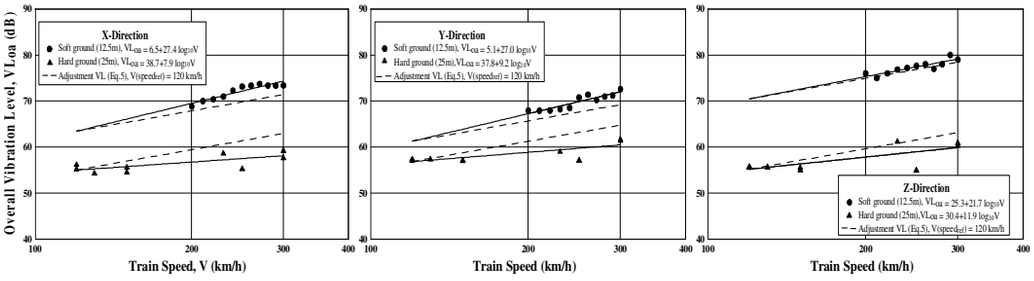


Figure 8 Comparison of vibration for different train speeds

The general equation between the increase of vibration level and train speed (FTA 1995) is given below:

$$\text{adjustment VL} = 20 \log_{10} [V(\text{speed})/V(\text{speed}_{\text{ref}})] \quad (5)$$

Comparing these results with the general equation, Fig. 8 also shows the variation of vibration level with train speed based on Eq. 5, denoted as a dashed line, for the x, y, and z directions. In general, the general equation is somehow more consistent with the measured results for soft ground. However, the general equation presents an over-estimation in the x, y, and z directions for hard ground.

Substructure Factor

Fig. 9 shows the comparison of measured vibration level and attenuation with distance at different foundation types. All regression equations are also shown in Fig. 9. The shallow foundation was constructed by spread footing, while the deep foundation has group piles below the pile cap. Both measurements were located at gravel layer with the same train speed of 300 km/h. Therefore, except for the foundation type, all other conditions are relatively as comparable as possible.

From Fig. 9, it can be seen that the shallow foundation shows a higher overall vibration level at near distance. On the average, the differences in vibration level are 6-9 dB at near distance for the x, y, and z directions. This may be attributed to the main vibration energy which takes place at the shallow soil layer for the shallow foundation, while some vibration energy is transmitted to the deep soil layer for the deep foundation. However, the shallow foundation presents a much more quick attenuation with distance than the deep foundation. Since some vibration energy of deep foundation is transmitted from the deep soil layer and then to the surface area, the attenuation becomes much slower on a deep foundation.

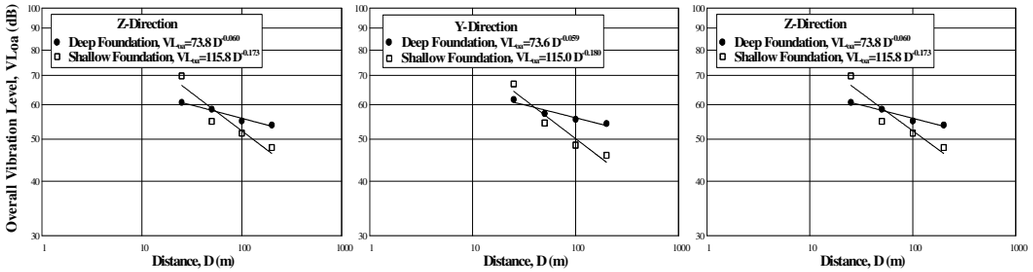


Figure 9 Comparison of vibration response for different foundation types

Superstructure Factor

A comparison of vibration response as induced by a bridge with a shallow foundation, deep foundation, and embankment structures is shown in Figs. 10 and 11 for near and far distances, respectively. The measurement distance is 25-30 m and 100 m from the high-speed rail. The geological conditions for these measurements are a gravel layer location and a train speed of 280-300 km/h.

As can be seen, there are several observations from these results. For near distance, the vibration level for all structures is essentially comparable at a low frequency, but the

difference is obvious between a bridge with deep foundation and an embankment or shallow foundation for high frequency. The difference in vibration level at a high frequency can reach 10-20 dB. For the measurements of far distance, both bridge and embankment show relatively consistent results.

Comparing these results, the vibration behavior of an embankment seems more like that of a bridge with shallow foundation. The embankment and shallow foundation present a higher vibration level than a deep foundation at near distance, and the vibrations of the embankment and the shallow foundation can be quickly attenuated. 0From a geotechnical viewpoint, this is reasonable because the vibration propagation behavior for an embankment is more similar to that of a shallow foundation than a deep foundation.

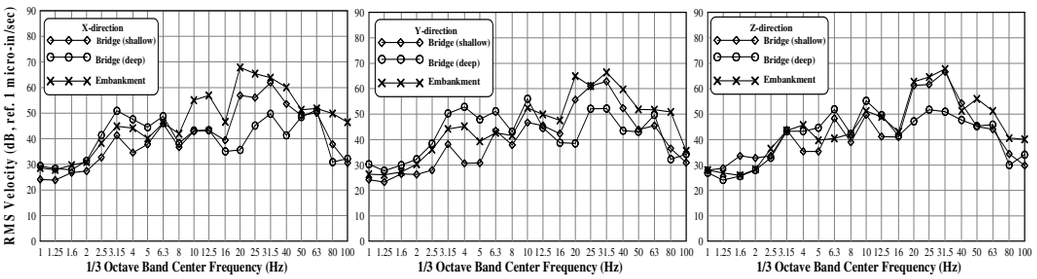


Figure 10 Comparison of vibration for bridge and embankment at near distance (25-30 m)

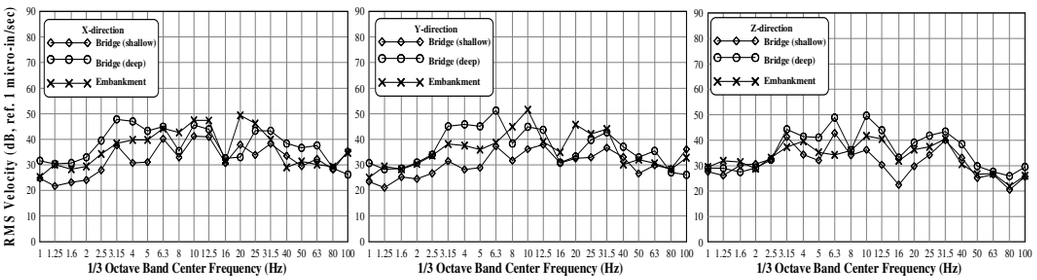


Figure 11 Comparison of vibration for bridge and embankment at far distance (100 m)

CONCLUSIONS AND RECOMMENDATIONS

A wide variety of field-measured data was used to examine some characteristics of ground vibration as induced by high-speed trains. This database included different geological conditions, train speeds, foundation types, and superstructure structures. Four main characteristics were evaluated from these available data. Based on these analyses, the following preliminary results emerged.

1. Geological condition is an important factor for high-speed train-induced ground vibration. The geological factor affects the initial mobilized vibration and vibration attenuation with distance. Soft ground is easier to agitate in terms of vibration level and is more difficult to attenuate than hard ground.
2. The change in peak vibration due to the train speed factor for each frequency is relatively slight either on soft ground or hard ground. In general, the general

equation (FTA 1995) is somehow more consistent with measured results for soft ground. However, the general equation presents over-estimated results in the x, y, and z directions for hard ground.

3. The bridge with a shallow foundation presents a higher initial mobilized vibration level than deep foundation at near high-speed rail alignment, but it is more quickly attenuated with an increasing distance than deep foundation.
4. High-speed trains on embankment and a bridge with shallow foundation present more consistent vibration characteristics. However, the measurement results show relatively comparable vibration characteristics for these high-speed rail structures at a far distance.

Based on this study, for hard ground, the vibration at near distance is the main issue for high-speed trains on an embankment and a bridge with shallow foundation. For soft ground and a bridge with deep foundation, both near and far distances are both critical issues. However, these vibration characteristics need to be supported by more measurement data and precise analysis.

ACKNOWLEDGEMENTS

This study was supported by the National Science Council, Taiwan, under contract number: NSC 96-2221-E-033-034.

REFERENCES

Chen, Y.-J, Ni, S.-H., and Shen, Y.-J (2006) "Evaluation of ground vibration induced by an urban train system", *The 10th IAEG International Congress*, Paper No. 773.

Chen, Y.-J., Shen, Y.-J., and Chen, K.-Y. (2006) "The characteristics and measurement scheme for ground vibration induced by passing train in bridge structures", *Inter-Noise 2006*.

Chen, Y.-J., Ju, S.-H., Ni, S.-H., and Shen, Y.-J. (2007) "Prediction methodology for ground vibration induced by passing trains on bridge structures", *Journal of Sound and Vibration*, 302, 806-820.

Ejima, A. (1980) "Basic research for countermeasures against ground vibration from concrete girder type elevated of Shinkansen", *Ph.D. Thesis*, University of Tokyo.

Tseng, W.S. (1999) "Vibration impact evaluation and mitigation measures development work for Tainan Science-Based Industrial Park, First Phase Work," *Reported by CTCI Corporation and International Civil Engineering Consultants, Inc.*, Taiwan High Speed Rail Corporation, 38-60.

U.S. Department of Transportation Federal Railroad Administration (FRA) (1998). *Manual for high-speed ground transportation noise and vibration impact assessment*, 6-1-18.

U.S. Department of Transportation Federal Transit Administration (FTA) (1995) *Manual for transit noise and vibration impact assessment*.

Yoshioka, O. (2000) "High-speed trains on soft ground: track-embankment-soil response and vibration generation", *Proceedings of the International Workshop Wave 2000*, Bochum Germany, 219-237.